15 APRIL 1996
PART 2A
VOLUME 79 NUMBER 8

JOURNAL OF APPLIED PHYSICS

Proceedings of the 40th Annual Conference on Magnetism and Magnetic Materials

AMERICAN INSTITUTE OF PHYSICS

DISTRIBUTION STATEMENT A
Approved for public release;
Distribution Unlimited

JOURNAL OF APPLIED PHYSICS

CODEN: JAPIAU
ISSN: 0021-8979

Editor
Steven J. Rothman
Argonne National Laboratory
Argonne, IL

Associate Editors at Argonne National Laboratory
Roy Benedek
Robert C. Birtcher
Gian P. Felcher
John N. Mundy
Simon R. Phillpot

Editorial Board

Term ending 31 December 1996
Gene F. Dresselhaus (MIT, Cambridge, MA)
Allen M. Goldman (Univ. Minnesota, Minneapolis)
Klaus H. Ploog (Paul Drude Inst., Berlin, Germany)
Robert Sinclair (Stanford Univ., Stanford, CA)

Term ending 31 December 1997
Federico Capasso (AT&T Bell Labs, Murray Hill, NJ)
Esther M. Conwell (Xerox Corp., Rochester, NY)
C. Y. Fong (University of California, Davis, CA)

Term ending 31 December 1998
Dieter M. Gruen (Argonne Nat'l Lab., Argonne, IL)
James S. Williams (The Australian Nat'l Univ., Canberra, Australia)
Patricia M. Mooney (IBM Corp., Yorktown Heights, NY)

Editorial Office
Diane M. Kurtz, *Editorial Supervisor*

Editorial Staff: Catherine M. Dial, *Assistant to the Editor;* Jennifer A. Smeets, *Secretary*

AIP Production
Deborah McHone, *Editorial Supervisor*
Margaret Reilly, *Journal Coordinator*
Janet Panarelli, *Chief Production Editor*
Cindy Klingensmith, *Senior Production Editor*
Daniela Boscia, *Production Editor*

Submit manuscripts (3 copies) to Editor, *Journal of Applied Physics,* Argonne National Laboratory, Bldg. 203, Room R-127, 9700 South Cass Avenue, P.O. Box 8296, Argonne, IL 60439-8296.

Physics Auxiliary Publication Service (PAPS) and/or Electronic PAPS (E-PAPS): For a nominal fee, authors may submit material that is part of and supplemental to a paper, but is too long to be included in the journal. PAPS deposits may be on paper or in electronic media, and can include text, data in graphic or numeric form, computer programs, etc. Retrieval instructions are footnoted in the related published paper. Direct requests to the editor.

The *Journal of Applied Physics* (ISSN: 0021-8979) is published semimonthly by the American Institute of Physics, 500 Sunnyside Blvd., Woodbury, NY 11797-2999. Second-class postage paid at Woodbury, NY, and additional mailing offices. POSTMASTER: Send address changes to *Journal of Applied Physics,* AIP, 500 Sunnyside Blvd.,

The *Journal of Applied Physics* is the American Institute of Physics' (AIP) archival journal for significant new results in applied physics. The journal publishes articles that emphasize understanding of the physics underlying modern technology. There are two issues per month. The subject coverage includes, but is not limited to, experimental or theoretical physics applied to all aspects of materials: for example, charge and mass transport, superconductivity, magnetism; surfaces, interfaces, thin films, crystal lattice defects; electrical, optical, magnetic, and structural properties; processing; ion implantation. Materials covered include semiconductors, superconductors, metals and alloys, amorphous materials, and oxides. Other important topics are: electrical, optical, and magnetic devices; optics and lasers; nonlinear optics; electrical discharges; acoustics. The Proceedings of the Annual Conference on Magnetism and Magnetic Materials is a regular feature. *Applied Physics Reviews* is a series of occasional review articles on similar subjects.

Publication Charge: To support the cost of wide dissemination of research results through publication of journal pages and production of a database of articles, the author's institution is requested to pay a page charge of $55 per page (with a one-page minimum) and an *article charge* of $20 per article. For any regular, published article that exceeds 10 journal pages, a mandatory $150 page charge will be added for each page in excess of 10 pages. For Errata the minimum page charge is $10, with no article charge.

Subscription Prices* (1996)	U.S.A. & Poss.	Can., Mex., Central & S. Amer. & Caribbean	Foreign Surface Mail	Air Freight (Europe, Asia, Africa & Oceania)	Optional Air Freight (Europe, Asia, Africa & Oceania)
Members†	$210	$295	$295	—	$480
Nonmembers	$2045	$2130	—	$2315‡	—

*The journal is available on microfiche at $210 per year to members and $2045 per year at the nonmember rate.
†AIP Member and Affiliated Societies. ‡Includes air freight service.

Back-Number Prices: 1996 single copies: $95. Prior to 1996 single copies: $26 for members; $95 for nonmembers. Prices for conference supplements available on request.

Subscription, renewals, and address changes should be addressed to *AIP Circulation and Fulfillment Division (CFD), 500 Sunnyside Blvd., Woodbury, NY 11797-2999.* Allow at least six weeks advance notice. For address changes please send both old and new addresses and, if possible, include a mailing label from a recent issue.

Claims, Single Copy Replacement and Back Volumes: Missing issue requests will be honored only if received within six months of publication date (nine months for Australia and Asia). Single copies of a journal may be ordered and back volumes are available in print or microform. Members—contact AIP Member Services at (516) 576-2288; (800) 344-6901. Nonmember subscribers—contact AIP Subscriber Services at (516) 576-2270; (800) 344-6902; Internet: subs@aip.org.

Page Charge and Reprint Billing: Contact: AIP Publication Page Charge and Reprints—CFD, 500 Sunnyside Blvd., Woodbury, NY 11797-2999; (516) 576-2234; (800) 344-6909.

Copying: Single copies of individual articles may be made for private use or research. Authorization is given (as indicated by the Item Fee Code for this publication) to copy articles beyond the use permitted by Sections 107 and 108 of the U. S. Copyright Law, provided the copying fee of $10 per copy per article is paid to the Copyright Clearance Center, 222 Rosewood Drive, Danvers, MA 01923, USA. Persons desiring to photocopy materials for classroom use should contact the CCC Academic Permissions Service. The Item Fee Code for this publication is 0021-8979/96 $10.00.
Authorization does not extend to systematic or multiple reproduction, to copying for promotional purposes, to electronic storage or distribution, or to republication in any form. In all such cases, specific written permission from AIP must be obtained.

Permission for Other Use: Permission is granted to quote from the journal with the customary acknowledgment of the source. To reprint a figure, table, or other excerpt requires the consent of one of the authors and notification to AIP.

Requests for Permission: Address requests to AIP Office of Rights and Permissions, 500 Sunnyside Boulevard, Woodbury, NY 11797-2999; Fax: 516-576-2327; Telephone: 516-576-2268; Internet: rights@aip.org.

Publisher Item Identifier: A Publisher Item Identifier (PII) has been adopted by AIP and other publishers to provide unique and concise identification of individual published documents. The PII appears at the end of the abstract of each article. The PII should be included in all document requests for copies of the article.

Document Delivery: Copies of articles can be ordered for $15 per copy from the AIP/Member Society document delivery service, "Articles in Physics," 1722 Gilbreth Road, Burlingame, CA 94010-1305; Fax: 415-259-6044; Telephone: 800-480-PHYS (in U.S. and Canada), or 415-259-6002; Internet: articles@aip.org.

Reprints: Reprints can be ordered with or without covers only in multiples of 50 (with a minimum of 100 in each category) from AIP, Circulation & Fulfillment/Reprints, 500 Sunnyside Boulevard, Woodbury, NY 11797-2999; Fax 516-349-9704; Telephone: 800-344-6909 (in U.S. and Canada), or 516-576-2234.

Microform: *Journal of Applied Physics* is available on microfiche issued at the same frequency as the printed journal and annually on microfilm. A microform catalog is available from AIP, Circulation & Fulfillment/Single Copy Sales, 500 Sunnyside Boulevard, Woodbury, NY 11797-2999; Fax: 516-349-9704; Telephone: 800-344-6908 (in U.S. and Canada), or 516-576-2277.

Online Availability: Abstracts of journal articles published by AIP and Member Societies (and several other physics publishers) are available in the SPIN database via the AIP online

PROCEEDINGS OF THE FORTIETH ANNUAL CONFERENCE ON MAGNETISM AND MAGNETIC MATERIALS

PART A

November 6–9, 1995
Philadelphia, Pennsylvania

Edited by E. Dan Dahlberg, W.-Y. Ching,
J. K. Howard, Y. Idzerda, M. Lederman, and J.-G. Zhu

DISTRIBUTION STATEMENT A
Approved for public release;
Distribution Unlimited

19960424 112

DTIC QUALITY INSPECTED 1

Journal of Applied Physics
Volume 79, Number 8, Part 2, 1996

International Standard Serial Number: 1087-3848
International Standard Book Number: 1-56396-613-1
CONF-951101—Vol. 1
Copyright © 1996 by the American Institute of Physics
Published by the American Institute of Physics
500 Sunnyside Blvd., Woodbury, New York 11797-2999
Printed in the United States of America

All papers in this volume, and in previous Proceedings of the Conference on Magnetism and Magnetic Materials published in this series, have been reviewed for technical content. The selection of referees, review guidelines, and all other editorial procedures are in accordance with standards prescribed by the American Institute of Physics.



FORTIETH ANNUAL CONFERENCE ON MAGNETISM AND MAGNETIC MATERIALS November 6–9, 1996 Philadelphia, Pennsylvania

Sponsored by

The American Institute of Physics
The Magnetics Society
of the
Institute of Electrical and Electronics Engineers

In Cooperation with

The Minerals, Metals, and Materials Society
The American Society for Testing and Materials
The Office of Naval Research
The American Ceramic Society

The Conference is especially grateful to

THE OFFICE OF NAVAL RESEARCH
for its support of the expenses of foreign and interdisciplinary speakers

CONTRIBUTORS TO THE 40TH ANNUAL CONFERENCE ON MAGNETISM AND MAGNETIC MATERIALS

The 40th Annual Conference on Magnetism and Magnetic Materials wishes to express appreciation to the following Corporations for their generous support.

BASF Magnetics GmbH
Crucible Magnetics
Eastman Kodak Company
F. G. Jones Associates, Ltd.
Fujitsu, Ltd.
General Electric Company
Hitachi, Ltd.
IBM Corporation
Innovative Instrumentation, Inc.
KJS Associates Inc.—Magnetics Engineering
Lake Shore Crytronics, Inc.
Magnequench
Mitsubishi Chemical Corporation
NEC Corporation
The Permanent Magnet Co., Inc.
Quantum Corporation
SONY Corporation
TDK Corporation
3M
Toda Kogyo Corporation

Conference Organization
40th Conference on Magnetism and Magnetic Materials

General Conference Chairman

K. B. Hathaway

Program Committee

C.-L. Chien and T. Suzuki, *Co-Chairmen*

S. Bader
J. Bass
F. Cadieu
W.-Y. Ching
C. Contreras
E. Dan Dahlberg
W. Doyle
J. Fidler
R. Gambino
G. Haejipanayis
K. Howard
Y. Idzerda
I. S. Jacobs
D. Lambeth
M. Mansuripur
R. O'Handley
M. Pardavi-Horvath
F. Pinkerton
D. Pierce
G. Prinz
R. Proksch
M. Rubenstein
P. Schroeder
Y. Sugita
R. Victora
C. Vittoria
D. Weller
P. Wigen
G. Xiao
W. Yelon
J.-G. Zhu

Publications Chairmen

W.-Y. Ching
E. Dan Dahlberg
K. Howard
Y. Idzerda
M. Lederman
J.-G. Zhu

Secretary

D. Lambeth

Treasurer

W. Yelon

Publicity

J. Nyenhuis

Industrial Support

M. P. Sharrock

Local Chairman

B. Lorenz

Chairman Elect

R. Fontana

Magnetism Conference Advisory Committee

S. H. Charap, *Chairman*
D. Lambeth, *Secretary*

Term Expires 1995

R. J. Cellota
W. D. Doyle
G. E. Fish
K. B. Hathaway
R. R. Katti
H. Jensen
D. R. Krahn
J. W. Shula

Term Expires 1996

W. Cain
S. H. Charap
C.-L. Chien
R. E. Fontana
F. Hellman
D. L. Huber
T. M. Jagielinski
D. Lambeth
R. Victora
R. M. White

Term Expires 1997

E. Della Torre
G. Felcher
P. M. Levy
J. E. Opfer
C. Perlov
D. Sellmyer
D. D. Stancil
T. Suzuki
S. von Molnar
W. Yelon

Sponsoring Society Representatives

American Institute of Physics

J. T. Scott

IEEE Magnetics Society

C. D. Graham

Cooperating Society Representatives

The Minerals, Metals, and Materials Society

M. Hong

ASTM Comm. A-6

K. H. Moyer

Office of Naval Research

L. Kabacoff

American Ceramic Society

B. B. Ghate

PREFACE

The Conference on Magnetism and Magnetic Materials held its 40th anniversary meeting, November 6–9, 1995 in Philadelphia, Pennsylvania. The history of the Conference was highlighted in a special session of remembrances by three members of the original 1955 MMM organizing committee, W. (Bill) Meiklejohn, John Osborn, and J. E. (Jack) Goldman, followed by a champagne reception. Over 60 magneticians who had attended the early meetings participated in these activities. Another session with historical significance was the Commemorative Symposium on Neutron Scattering which featured talks by the 1994 Physics Nobel Laureates, Clifford G. Shull and Bertram Brockhouse. The scientific program of the meeting ranged broadly from fundamental to applied topics. Symposia were organized on High Performance Permanent Magnets, 10 Gbit/in.^{2} Magnetic Recording, Giant and ''Colossal'' Magnetoresistance, Magnetic Nanostructures, Spin Tunneling and Injection, and unusual Fe magnetism as seen in $Fe_{16}N_2$ and fcc-Fe. A total of 958 papers were presented; selected from 1192 submitted abstracts.

Before thanking all of the people who contributed to the success of the Conference, I would like to take the opportunity to describe briefly how the Conference is organized. The MMM Conference was founded 40 years ago to bring together for mutual discussions those pursuing basic research and applications in magnetism. A volunteer advisory committee of 30 members, half appointed by the IEEE Magnetics Society and half by the American Institute of Physics (the sponsoring societies) has responsibility for all financial, administrative, and technical aspects of the conference. Individual jobs are filled by volunteers from the magnetism community, with the able assistance of the professional conference managers at Courtesy Associates and the publications staff at AIP. New volunteers are always sought, and the aim is to make the Conference management as democratic and as broadly representative of the community as possible. The community served by MMM is truly international as reflected by the 1002 attendees at the 1995 conference of which 278 registrants and 74 students were from outside the US, and includes many students and posdoctoral researchers.

My role as General Chairman gave me the unique pleasure of leading a group of talented and creative individuals, each of whom independently did an outstanding job. Their names are listed in these proceedings and I offer each my heartfelt thanks. I would also like to thank Israel Jacobs for organizing the historical activities to remind us how far we have come in 40 years, and let us marvel at the continuing vitality and fascination of the field of magnetism.

Kristl Hathaway
General Chairman
MMM '95

Symposium on 10 GB/in.$_2$ Magnetic Recording

4485 Approaches to 10 Gbit/in.^{2} recording (invited) — M. H. Kryder, W. Messner, L. R. Carley

4491 Impact of new magnetoresistive materials on magnetic recording heads (invited) — J. A. Brug, L. Tran, M. Bhattacharyya, A. Jander, J. H. Nickel, T. C. Anthony

4496 Media for 10 Gb/in.^{2} hard disk storage: Issues and status (invited) — D. N. Lambeth, E. M. T. Velu, G. H. Bellesis, L. L. Lee, D. E. Laughlin

4502 Signal processing for 10 GB/in.^{2} magnetic disk recording and beyond (invited) — Kevin D. Fisher, Cory S. Modlin

4508 Head/disk tribology: Toward 10 Gb/in.^{2} (invited) (abstract) — B. Marchon

Interlayer Coupling

4509 Quantum oscillations of properties in magnetic multilayers (invited) — G. Bayreuther, F. Bensch, V. Kottler

4515 Calculated spacer-layer Friedel oscillations in Co/Cu(001) — Lars Nordström, David J. Singh

4518 Interface alloying at Fe/Cr interfaces and its role in exchange coupling, angular resolved Auger electron, magneto-optic Kerr effect, and Brillouin light scattering studies (invited) — B. Heinrich, J. F. Cochran, D. Venus, K. Totland, D. Atlan, S. Govorkov, K. Myrtle

4524 Suppression of biquadratic coupling at the Cr Néel temperature in Fe/Cr(001) superlattices (invited) (abstract) — Eric E. Fullerton, S. Adenwalla, G. Felcher, C. H. Sowers, S. D. Bader, J. L. Robertson, A. Berger

4525 Interlayer thickness Dependence of the strong 90° coupling in epitaxial CoFe/Mn/CoFe trilayers — J. J. Krebs, G. A. Prinz, M. E. Filipkowski, C. J. Gutierrez

4528 Dependence of the interlayer exchange coupling on the constitution of the magnetic layers — K. Ounadjela, Li Zhou, R. Stamps, P. Wigen, M. Hehn, J. Gregg

4531 Domain structure and anisotropy of exchange coupled Co/Cr/Fe multilayers (abstract) — Th. Kleinefeld, M. Figge, K. Theis-Bröhl, R. Scheidt, Th. Zeidler, Ch. Mathieu, B. Hillebrands

4532 Magnetic coupling in Co/face-centered-cubic Fe/Co sandwiches — R. K. Kawakami, Ernesto J. Escorcia-Aparicio, Z. Q. Qiu

Colossal Magnetoresistance in Perovskite Oxides I

4535 Transport and magnetism correlations in thin-film ferromagnetic oxides — M. F. Hundley, J. J. Neumeier, R. H. Heffner, Q. X. Jia, X. D. Wu, J. D. Thompson

4538 Colossal magnetoresistance in the antiferromagnetic $La_{0.5}Ca_{0.5}MnO_3$ system — G. Q. Gong, C. L. Canedy, Gang Xiao, J. Z. Sun, A. Gupta, W. J. Gallagher

4541 Lattice effects on the magnetoresistance in doped manganese perovskites (abstract) — H. Y. Hwang, S-W. Cheong, P. G. Radaelli, M. Marezio, T. T. M. Palstra, B. Batlogg

4542 Electrical conductivity in ferromagnetic perovskite structures — Shufeng Zhang

4545 Response to an electric field of $Nd_{0.7}Sr_{0.3}MnO_3$ films in a MOSFET configuration (abstract) — S. B. Ogale, V. Talyansky, G. C. Xiong, R. P. Sharma, R. Ramesh, R. L. Greene, T. Venkatesan

4546 Magnetotransport and hysteretic behavior in epitaxial $La_{0.67}Ca_{0.33}MnO_{3-\delta}$ films — C. L. Canedy, K. B. Ibsen, Gang Xiao, J. Z. Sun, A. Gupta, W. J. Gallagher

4549 Magnetoresistance and magnetic properties of $La_{1-x}\square_xMnO_{3-\delta}$ thin films — T. R. McGuire, A. Gupta, P. R. Duncombe, M. Rupp, J. Z. Sun, R. B. Laibowitz, W. J. Gallagher, Gang Xiao

(Continued)

4552 Superparamagnetic behavior and giant magnetoresistance in oxygen deficient $R_{0.67}Sr_{0.33}MnO_z$ (R=Nd, Pr) epitaxial films (abstract) — H. L. Ju, Qi Li, G. C. Xiong, T. Venkatesan, R. L. Greene

4552 Role of lattice distortions in the transport property of $R_{0.7}Me_{0.3}MnO_3$ (R=Pr,Nd,La and Me=Ba,Sr,Ca) (abstract) — R. P. Sharma, G. C. Xiong, S. B. Ogale, R. L. Greene, T. Venkatesan

4553 The effect of disorder and fluctuations on the magnetotransport of a double-exchange ferromagnet (abstract) — Jeff M. Byers

4553 Ozone assisted, block-by-block, molecular beam epitaxy of La–M–Mn–O (M=Ca,Ba,Sr) thin films and La–M–Mn–O/Dy–Ba–Cu–O multilayers (abstract) — V. A. Vas'ko, P. A. Kraus, V. S. Achutharaman, C. A. Nordman, A. M. Goldman

4554 Transport properties and magnetic behavior of $La_{1-x}Sr_xMnO_3$ single crystals (abstract) — A. Anane, C. Dupas, K. Le Dang, J. P. Renard, P. Veillet, A. M. de Leon Guevarra, F. Millot, L. Pinsard, A. Revcolevschi

4555 Density-functional studies of the electronic structure of the perovskite oxides: $La_{1-x}Ca_xMnO_3$ — S. Satpathy, Zoran S. Popović, Filip R. Vukajlović

4558 Electron spectroscopic studies of colossal magnetoresistance material $La_{1-x}Ca_xMnO_3$ — J.-H. Park, C. T. Chen, S.-W. Cheong, W. Bao, G. Meigs, V. Chakarian, Y. U. Idzerda

Soft Ferrites and Alloys I

4561 Cation distribution in NiZn-ferrite films determined using x-ray absorption fine structure — V. G. Harris, N. C. Koon, C. M. Williams, Q. Zhang, M. Abe

4564 Possible nearly loss-free ferrimagnetic resonance in small samples — J. B. Sokoloff

4567 Anomalous low dimensional system: Study of magnetism and electrical conductivity in $Na_2Ru_4O_{9-\delta}$ — G. Cao, S. McCall, F. Freibert, M. Shepard, P. Henning, J. E. Crow

4570 Growth of epitaxial films of iron oxide, nickel oxide, cobalt oxide, strontium hexagonal ferrite, and yttrium iron garnet by laser ablation (abstract) — Robin J. Kennedy

4570 Resolution of conflicts concerning $Fe_{16}N_2$ (abstract) — A. S. Arrott

4571 Influence of the plastic anisotropy on the magnetic properties of a nonoriented 3% silicon iron — E. Hug, O. Hubert, M. Clavel

4574 Magnetic properties of 3%Si-Fe thin sheets annealed in Ar atmosphere (abstract) — Y. Yamashiro, A. Yonesu, S. Hashi, K. Ishiyama, K. I. Arai

4575 Power losses in thick steel laminations with hysteresis — C. Appino, G. Bertotti, O. Bottauscio, F. Fiorillo, P. Tiberto, D. Binesti, J. P. Ducreux, M. Chiampi, M. Repetto

4578 High temperature magnetic properties of 49%Co–2%V–Fe alloy — Lin Li

4581 Effect of nucleating layers on the soft magnetic properties of multilayer permalloy films — Craig A. Grimes

Hard Magnet Nitrides, Carbides, and Hydrides

4584 A spin reorientation in $Pr_2Fe_{17}D_3$ as revealed by Mössbauer spectroscopy — F. Grandjean, Dimitri Hautot, Gary J. Long, O. Isnard, S. Miraglia, D. Fruchart

4587 Neutron diffraction and Mössbauer spectral study of the $Nd_2Fe_{16}TiC_x$ solid solutions — G. K. Marasinghe, Peter C. Ezekwenna, W. J. James, Gary J. Long, O. A. Pringle, Z. Hu, W. B. Yelon, F. Grandjean

4590 Mössbauer study of permanent-magnet $R_2Fe_{17-x}M_xC_y$ compounds — I. A. Al-Omari, E. W. Singleton, Y. Zheng, G. C. Hadjipanayis, D. J. Sellmyer

4593 Crystal field induced anisotropy in rare earth intermetallics as studied by ^{155}Gd Mössbauer spectroscopy — D. P. Middleton, F. M. Mulder, D. A. van de Straat, R. C. Thiel, K. H. J. Buschow

4596 Study of the nitrogen diffusion mechanism in R_2Fe_{17} — Y. D. Zhang, J. I. Budnick, W. A. Hines, D. P. Yang

(Continued)

4599 Nuclear magnetic resonance study of expanded lattice permanent magnet nitrides and carbides at high pressure — Cz. Kapusta, J. S. Lord, G. J. Tomka, P. C. Riedi, K. H. J. Buschow

4602 Band theoretical investigation of the Curie temperatures of modified R_2Fe_{17}-based intermetallic compounds — W. Y. Ching, Ming-Zhu Huang

4605 Metastable RFe_7 compounds (R=rare earths) and their nitrides with $TbCu_7$ structure — O. Mao, J. Yang, Z. Altounian, J. O. Ström-Olsen

4608 High field magnetization isotherms of the $Pr_2Fe_{17}D_5$ system — O. Isnard, M. Guillot, S. Miraglia, D. Fruchart

4611 Structural and magnetic properties of rapidly quenched $(R,Zr)(Fe,Co)_{10}N_x$ (R=Nd,Sm) — S. Sakurada, A. Tsutai, T. Hirai, Y. Yanagida, M. Sahashi, S. Abe, T. Kaneko

4614 Aligned high magnetization $Nd(Fe,Co,Mo)_{12}$ films nitrided by N ion implantation — X. R. Qian, H. Hegde, F. J. Cadieu

4616 Magnetic and phase transformation studies in $Nd_{15}DyFe_{75}(C,B)_9$ cast alloys — A. S. Murthy, I. Panagiotopoulos, G. C. Hadjipanayis

4619 Characteristics of $Sm_2Fe_{17}C_x$ compounds prepared from ball-milled blends of Sm_2Fe_{17} and graphite — O. Mao, J. O. Ström-Olsen, Z. Altounian, J. Yang

4622 Exchange and crystal-field interactions in $R_3(Fe,Ti)_{29}$ and $R_3(Fe,Ti)_{29}N_y$ (R=Nd,Sm) — Hong-Shuo Li, D. Courtois, J. M. Cadogan

Critical Phenomena I

4625 Magnetic ordering in clustered Fe-based materials synthesized from laser plasma (abstract) — Yuri Blyakhman, N. I. Polushkin, A. D. Akhsakhalyan, S. A. Gusev, N. N. Salashchenko, V. G. Semenov

4626 Magnetization processes of free- and fixed-single-crystal antiferromagnets — Z. G. Zhao, P. F. de Châtel, F. R. de Boer, K. H. J. Buschow

4629 Dynamics of quantum spin systems in dimer and valence-bond-solid ground states stabilized by competing interactions — Yongmin Yu, Gerhard Müller

4632 Spin correlation functions in random-exchange $s=1/2$ XXZ chains — Heinrich Röder, Joachim Stolze, Richard N. Silver, Gerhard Müller

4635 Rotational hysteresis and self-organized criticality in magnetic recording media — T. L. Templeton, A. S. Arrott

4638 Quantum correction to the BKT transition for 2D easy-plane antiferromagnets — Cristiano Biagini, Alessandro Cuccoli, Valerio Tognetti, Ruggero Vaia, Paola Verrucchi

4641 Homogeneous magnetization dynamics below T_c of EuO: Effects of spin waves and anisotropy — A. Flosdorff, D. Görlitz, J. Kötzler

4644 Concentration-dependent critical behavior in dilute ferromagnetic $Fe_{1-x}As_x[S_2CN(C_2H_5)_2]_2Cl$ — G. C. DeFotis, G. A. Coffey, G. S. Coker, J. L. Marmorino, K. L. Beers, S. Chandarlapaty, W. W. Brubaker, V. J. Pugh, S. A. Carling, P. Day

Magnetoelastic Effects

4647 Magnetovolume effects of $MnAs_{1-x}Sb_x$ — O. Nashima, T. Suzuki, H. Ido, K. Kamishima, T. Goto

4650 Transmission electron microscopy of Terfenol-D crystals — A. P. Holden, D. G. Lord, P. J. Grundy

4653 Propagation and reflection properties of magnetoelastic wave in FeSiB amorphous wire — Y. Takemura, S. Masuda, T. Yamada, K. Kakuno

4656 Anomalous compressibility and magnetovolume effects in $Ce_3(FeTi)_{29}$ — J. Kamarád, Z. Arnold, L. Morellon, P. A. Algarabel, M. R. Ibarra, C. D. Fuerst

4659 Magnetostriction and thermal expansion measurements on $FeRh_{1-x}Pt_x$ alloys — P. A. Algarabel, M. R. Ibarra, C. Marquina, S. Yuasa, H. Miyajima, Y. Otani

(Continued)

4662 Magnetostriction of a superconductor: Results from the critical-state model — Z. Koziol, R. A. Dunlap

4665 Magnetostriction and anisotropy of twin-free single-crystals $Tb_{0.5}Dy_{0.5}(Fe_{0.9}Mn_{0.1})_2$ — Jinghua Wang, Guangheng Wu, Xuegen Zhao, Kechang Jia, Wenshan Zhan

4668 Magnetic properties and magnetostriction of twin-free single-crystal $Tb_{0.27}Dy_{0.73}(Fe_{1-x}Al_x)_2$ — Jinghua Wang, Guangheng Wu, Xuegen Zhao, Kechang Jia, Wenshan Zhan

Numerical Methods and Design Techniques

4671 Perfect conductivity approximation: Modification for polyphase systems — K. V. Namjoshi, J. D. Lavers, P. P. Biringer

4674 Dual-complementary variational methods in eddy currents (abstract) — P. Lois, D. Baldomir, J. Rivas

4675 Solution of induction heating problems involving media with hysteresis — A. A. Adly

4678 Solution of magnetic field and eddy current problem induced by rotating magnetic poles (abstract) — Z. J. Liu, T. S. Low

4679 Nonlinear flux diffusion and ac susceptibility of superconductors: Exact numerical results — Z. Kozioł, R. A. Dunlap

4682 New method of evaluating the explicit magnetic-state-dependent energy of iron in semiempirical calculations — Genrich L. Krasko

4685 Three-dimensional modeling techniques applied to regions with small susceptibility variations (abstract) — R. J. Hill-Cottingham, J. F. Eastham, I. R. Young, J. V. Hajnal

4685 An efficient three-dimensional demagnetizing field calculation scheme (abstract) — A. S. Kazmi, R. C. Giles

4686 Computational calculations of magnetic relaxation and viscosity in small magnetic grains — J. M. Hernàndez, X. X. Zhang, J. Tejada

4689 Loss simulations in magnetostrictive actuators — G. Engdahl, A. Bergqvist

4692 Analysis and optimization of synchronous magnetic couplings — E. P. Furlani

4695 Irregular grain structure in micromagnetic simulation — D. G. Porter, E. Glavinas, P. Dhagat, J. A. O'Sullivan, R. S. Indeck, M. W. Muller

Biochemical Magnetism

4698 Low temperature magnetic properties of a molecular compound (abstract) — J. L. Tholence, M. Novak, D. Luneau, P. Rey, E. Belorisky

4699 An application of the wavelets to the magnetic field source searching — T. Doi, S. Yoshida, Y. Nakaya, S. Hayano, Y. Saito

4702 Functionalization and applications of nanosized γ-Fe_2O_3 particles — Qingxia Liu, Zhenghe Xu

4705 Catalytic activity of catalase under strong magnetic fields of up to 8 T — S. Ueno, M. Iwasaka

4708 Measurement of clottability of fibrin polymers using magnetic orientation — M. Iwasaka, S. Ueno, H. Tsuda

4711 Analysis of extremely low frequency brain magnetic fields associated with short-term memory and recognition processes (abstract) — Hideki Yoshida, Shoogo Ueno, Douglas Cheyne, Harold Weinberg

4712 Artifacts in magnetic resonance imaging from metals — L. H. Bennett, P. S. Wang, M. J. Donahue

4715 Magnetic phase transitions in perovskite-type anilinium-based tetrachlorocuprates — D. J. Nelson, K. Chan, F. Cervantes-Lee, L. W. ter Haar

4718 $NiBr_2 \cdot 3H_2O$, a lower dimensional antiferromagnet — G. C. DeFotis, J. R. Goodey, A. A. Narducci, M. H. Welch

4721 Magnetic field effect on interface profile between immiscible nonmagnetic liquids—Enhanced Moses effect — Hiroharu Sugawara, Noriyuki Hirota, Takuro Homma, Masayuki Ohta, Koichi Kitazawa, Hiroyuki Yokoi, Yozo Kakudate, Shuzo Fujiwara, Mitsutaka Kawamura, Shoogo Ueno, Masakazu Iwasaka

(Continued)

Symposium on Spin Tunneling and Injection Phenomena

4724	Ferromagnetic–insulator–ferromagnetic tunneling: Spin-dependent tunneling and large magnetoresistance in trilayer junctions (invited)	Jagadeesh S. Moodera, Lisa R. Kinder
4730	Theory of spin-dependent tunneling and transport in magnetic nanostructures (invited)	S. Maekawa, J. Inoue, H. Itoh
4733	Spin-dependent tunneling effect and GMR in metal–nonmetal granular systems (invited) (abstract)	H. Fujimori, S. Mitani, S. Ohnuma
4734	Spin-dependent transmission of free electrons through ultrathin cobalt layers (invited)	H.-J. Drouhin, A. J. van der Sluijs, Y. Lassailly, G. Lampel

Instrumentation and Measurement Techniques

4740	The vibrating sample magnetometer: Experiences of a volunteer (invited)	S. Foner
4746	Measurement of texture in magnetic recording media using a biaxial vibrating sample magnetometer	F. Schmidlin, P. R. Bissell, J. A. Gotaas
4749	Application of Barkhausen effect measurements for detection of near surface stress (abstract)	D. A. Kaminski, D. C. Jiles
4750	Nondestructive inspection of a fractured nickel bar by Barkhausen and magnetoacoustic emissions	C. C. Yu, C-D. Qin, D. H. L. Ng
4753	A two-dimensional single sheet tester incorporating controlled magnetization direction	J. J. Dalton, J. Liu, A. J. Moses, D. H. Horrocks, A. Basak
4756	A magnetoelastic torque transducer utilizing a ring divided into two oppositely polarized circumferential regions	I. J. Garshelis, C. R. Conto
4759	Hall-effect characterization in semiconductor heterostructure junctions using polarized laser signal	Hoton How, Ta-Ming Fang, Feng Lu, Brian Ahern

Giant Magnetoresistance and Anisotropy in Multilayers

4762	Nature of the interlayer coupling in annealed $Ni_{80}Fe_{20}$/Ag multilayers	J. A. Borchers, P. M. Gehring, R. W. Erwin, C. F. Majkrzak, J. F. Ankner, T. L. Hylton, K. R. Coffey, M. A. Parker, J. K. Howard
4765	Magnetization, magnetoresistance, and x-ray diffraction measurements of discontinuous [$Ni_{80}Fe_{20}$/Ag] multilayers (abstract)	T. Lorenz, M. Moske, A. Käufler, H. Geisler, K. Samwer
4766	Exchange coupling in sputtered giant magnetoresistance NiFe/Cu/CoFe/Cu multilayers	M. T. Kief, J. Bresowar, Q. Leng
4769	Spin polarized neutron scattering study of NiCo/Cu multilayers	Ming Mao, S. H. Nguyen, B. D. Gaulin, Z. Tun, X. Bian, Z. Altounian, J. O. Ström-Olsen
4772	Magnetic properties of epitaxial and polycrystalline Fe/Si multilayers	A. Chaiken, R. P. Michel, C. T. Wang
4775	Anomalous temperature dependence of interlayer coupling in Fe/Si multilayers (abstract)	R. P. Michel, A. Chaiken, M. A. Wall, J. W. Dykes, J. F. Ankner, H. Kaiser
4776	Antiferromagnetic coupling in magnetic multilayers with a narrow gap semiconductor spacer	Zhu-Pei Shi, Barry M. Klein
4779	Magnetic properties of $(1\bar{1}02)$ Dy/Y superlattices	K. Theis-Bröhl, K. A. Ritley, C. P. Flynn, K. Hamacher, H. Kaiser, J. J. Rhyne
4782	Structural, field, and temperature dependence of noncollinear magnetic coupling in Fe/Cr(001) superlattices (abstract)	J. F. Ankner, H. Kaiser, K. Hamacher, A. Schreyer, Th. Zeidler, H. Zabel, C. F. Majkrzak, M. Schäfer, P. Grünberg
4783	Structural and magnetic properties of fcc Pt/Fe(111) multilayers	Ruqian Wu, Lujun Chen, Nicholas Kioussis
4786	Magnetic properties and magnetization reversal in Co/Au multilayers (abstract)	Z. S. Shan, J. X. Shen, R. D. Kirby, D. J. Sellmyer
4787	Coordinated RHEED, XRD, and FMR investigations of MBE grown Co–Cu (100) superlattices	R. A. Lukaszew, R. Naik, K. R. Mountfield, J. O. Artman

(Continued)

4790 Studies of the magnetic anisotropies of Co($1\bar{1}00$)/Cr(211) and Co($11\bar{2}0$)/Cr(100) multilayers — J. C. A. Huang, F. C. Tang, W. W. Fang, R. L. Liu, Y. M. Hu, C. K. Lo, Y. Liou, Y. D. Yao, W. T. Yang, C. P. Chang, S. Y. Liao

4793 Reorientational transition of the magnetic anisotropy and antiferromagnetic coupling of Co/Cr(001) superlattices — Th. Zeidler, F. Schreiber, H. Zabel

Itinerant Magnetism

4796 Spin-resolved density of states of 3*d* magnets — A. K. See, L. E. Klebanoff

4799 Electronic structure and exchange interactions in fcc Fe — M. van Schilfgaarde, V. P. Antropov, B. N. Harmon

4802 Critical dynamics at the spin-density-wave transition of chromium — B. J. Sternlieb, J. P. Hill, T. Inami, G. Shirane, W.-T. Lee, S. A. Werner, Eric Fawcett

4805 Theory of non-Heisenberg exchange: Results for localized and itinerant magnets — O. N. Mryasov, A. J. Freeman, A. I. Liechtenstein

4808 Local density approximation of magnetocrystalline anisotropy: An approach for narrowband materials — R. P. Erickson

4811 Magnetic properties of melt-quenched Ni-rich amorphous and bcc Zr–Ni alloys (abstract) — László F. Kiss, Lajos K. Varga, Imre Bakonyi

4812 Specific heat and magnetization of $Co_{2-x}Sc_{1+x}Sn$ — Z. W. Chen, C. L. Lin, T. Mihalisin, J. T. Wang, X. Q. Wang

4815 On the conduction band polarization in metallic systems with a periodic array of localized magnetic moments — A. Hernando, J. M. Rojo, J. C. Gómez Sal, J. M. Novo

4818 Electronic and magnetic properties of the 4*d* itinerant ferromagnet $SrRuO_3$ — David J. Singh

4821 Magnetic and transport properties of Na doped $SrRuO_3$ and $CaRuO_3$ — M. Shepard, G. Cao, S. McCall, F. Freibert, J. E. Crow

4824 Goldstone modes of incommensurate chromium alloys — R. S. Fishman, S. H. Liu

Hard Magnets, Borides, and Exchange Coupling

4827 Magnetic hardening of melt-spun nanocomposite $Nd_2Fe_{14}B$/Fe magnets — I. Panagiotopoulos, L. Withanawasam, A. S. Murthy, G. C. Hadjipanayis, E. W. Singleton, D. J. Sellmyer

4830 Microstructural control of NdFeB cast ingots for achieving 50 MGOe sintered magnets — D. W. Scott, B. M. Ma, Y. L. Liang, C. O. Bounds

4833 Formation of $Nd(Fe_{1-y}Co_y)_2$ in rapidly quenched $Nd_{13.75}(Fe_{1-x}Co_x)_{80.25}B_6$ (x=0–0.5) alloys — Er. Girt, M. Koknaeva, Z. Altounian

4836 Hard and soft magnetic properties of nanocrystalline Fe–Nd–Zr–B alloys containing intergranular amorphous phase (abstract) — A. Inoue, A. Kojima, A. Takeuchi, T. Masumoto, A. Makino

4837 Melt-spun $Pr_2Co_{14}B$/Co nanocomposite magnets — L. Withanawasam, I. Panagiotopoulos, G. C. Hadjipanayis

4840 Hydrogen induced corrosion mechanism in NdFeB magnets — A. S. Kim, F. E. Camp, T. Lizzi

4843 Magnetic properties and transmission electron microscopy microstructures of exchange coupled $Nd_{12-x}Fe_{82+x}B_6$ melt spun ribbons — W. C. Chang, D. M. Hsing

4846 Microstructure of flash and conventionally annealed melt spun NdFeB (abstract) — M. V. P. Altoé, M. Chandramouli, G. Thomas

4847 A metallurgical approach toward alloying in rare earth permanent magnet systems (abstract) — D. J. Branagan, K. W. Dennis, M. J. Kramer, R. W. McCallum

4848 Microstructure and composition in rapidly quenched NdFeB-based hard magnet alloys — Tai D. Nguyen, Kannan M. Krishnan, Laura Henderson Lewis, Yimei Zhu, David O. Welch

4851 Explosive compaction of Magnequench Nd–Fe–B magnetic powders — S. Guruswamy, M. K. McCarter, J. E. Shield, V. Panchanathan

4854 The protective coatings of NdFeB magnets by Al and Al(Fe) — C-D. Qin, A. S. K. Li, D. H. L. Ng

(Continued)

Magnetic Recording Media I

4857	Twin screw extrusion of a metal particle dispersion	H. Göktürk, K. Maki
4860	Preparation of acicular iron nanoparticles by the reduction of ferrous salt in the presence of tubular lecithin assemblies	Jason L. Cain, David E. Nikles
4863	Iron particle surface chemistry and corrosion protection by amine-quinone polyurethanes	Antony P. Chacko, David E. Nikles
4866	Synthesis and magnetic properties of electrodeposited metal particles on anodic alumite film	Xiaohua Bao, Feiyue Li, Robert M. Metzger
4869	Lanthanide and boron oxide-coated α-Fe particles	Feiyue Li, Xiaohua Bao, Robert M. Metzger, Massimo Carbucicchio
4872	Time effects in exchange anisotropy-affected metal-evaporated tapes	G. Bottoni, D. Candolfo, A. Cecchetti
4875	The archival stability of metal evaporated tape for consumer digital VCRs	Seiichi Onodera, Tsutomu Takeda, Takahiro Kawana
4878	Effects of Cr_2O_3 or Y_2O_3 doping in barium ferrite thin-film medium for high-density recording	Y. J. Chen, M. H. Kryder
4881	Sputtered hexagonal Ba-ferrite films for high-density magnetic recording media	Akimitsu Morisako, Mitsunori Matsumoto, Masahiko Naoe
4884	Recording characteristics of Co-γFe_2O_3 perpendicular magnetic recording media	S. Yamamoto, T. Andou, H. Kurisu, M. Matsuura, T. Doi, K. Tamari
4887	Preparation and the magnetic properties of Co-γ-Fe_2O_3 perpendicular magnetic films on NiO underlayer	T. Doi, K. Tamari
4890	Determination of local order in the amorphous precursor to Ba-hexaferrite thin-film recording media	J. E. Snyder, V. G. Harris, B. N. Das, N. C. Koon, X. Sui, M. H. Kryder
4893	Fabrication and magnetic properties of metal/cobalt ferrite composite thin films	J. G. Na

Magnetic Recording Media II

4896	Co–Cr films prepared by sputtering using electron cyclotron resonance microwave plasma	S. Yamamoto, K. Sato, H. Kurisu, M. Matsuura
4899	Magnetic viscosity and switching volumes of annealed Fe/Pt multilayers	C. P. Luo, Z. S. Shan, D. J. Sellmyer
4902	Seed layer induced (002) crystallographic texture in NiAl underlayers	Li-Lien Lee, David E. Laughlin, David N. Lambeth
4905	Plastic substrate preembossed 100 kbpi, 3.4 μm track width magnetic disk (abstract)	O. Ishizaki, T. Ohnuki, K. Adachi, K. Akagi, H. Momiji, O. Komoda, N. Ohta
4906	Nonlinear partial erasure and its correlation with transition noise in longitudinal thin-film media	Jian-Gang Zhu, Terence Lam, Yansheng Luo, Xiao-Guang Ye
4909	Magnetic force microscopy study of submicron track width recording in thin-film media	Yansheng Luo, Terence T. Lam, Jian-Gang Zhu, Hua-Ching Tong, Robert Rottmayer
4912	Magnetic force microscopy images of ultrahigh-density bit patterns recorded on high-coercivity longitudinal and perpendicular thin-film media	Xing Song, John Sivertsen, Jack Judy
4915	The effect of physical structure on δI curves of longitudinal thin film (abstract)	N. S. Walmsley, A. Hart, D. A. Parker, C. Dean, R. W. Chantrell
4916	Micromagnetic studies of inhomogeneous CoPtCr bicrystal thin-film media	Qingzhi Peng, H. Neal Bertram, Mary Doerner
4919	Multilevel master equation for bicrystal clusters	I. Klik, Y. D. Yao, C. R. Chang
4922	Coercivity mechanism in CoPt alloy films with perpendicular magnetic anisotropy (abstract)	Th. Kleinefeld, J. Heimel, D. Weller
4923	Grain morphology and magnetic properties of CoCrPt/Cr(Si,Ti) films sputtered at room temperature	G. Choe

(Continued)

Thin Films, Interfaces, and Anisotropy

4926	Ultrahigh vacuum SQUID magnetometry study of the magnetic properties of Co/Co-oxide thin films	S. Spagna, M. B. Maple, R. E. Sager
4929	Ferromagnetic resonance of sputtered Co/Mn multilayers	D. Spoddig, F. Schreiber, J. Pflaum, J. Pelzl, Q. Wang, H. Zabel
4932	Structural and magnetocrystalline anisotropy contributions to the blocking temperatures of $Ni_xCo_{(1-x)}O$ exchange couples (abstract)	Kentaro Takano, Ami E. Berkowitz, Wei Cao, Gareth Thomas
4933	Rotatable anisotropy in radio frequency diode sputtered iron thin films	W. Win, E. J. Yun, R. M. Walser
4936	Coupling effects in Fe/CoNbZr and Fe/Ag/CoNbZr sandwiches studied by magneto-optical techniques	M. C. Contreras, J. F.-Calleja, M. O. Gutiérrez, M. Rivas, R. Krishnan
4939	Low-energy ion beam-assisted deposition of giant magnetoresistive thin films	S. J. Guilfoyle, R. J. Pollard, P. J. Grundy
4942	Dynamic hysteresis of two-dimensional magnetic islands with uniaxial anisotropy	C. N. Luse, A. Zangwill
4945	Uniaxial magnetic anisotropy of iron thin films deposited by oblique incidence of deposition particles	Y. Hoshi, E. Suzuki, M. Naoe
4948	Complex anisotropies in sputtered $Co_{90}Fe_{10}$ alloy thin films (abstract)	E. J. Yun, W. Win, R. M. Walser
4949	Ferromagnetic resonance studies of noble metals based sandwiches	Y. D. Wang, L. Y. Chen, Y. X. Sui, S. M. Zhou, Y. Wang, Y. X. Zheng, Y. H. Qian, Q. Y. Jin
4951	Finite temperature magnetization reversal in ultrathin magnetic films	S. T. Chui
4954	The growth of magnetic Fe overlayers on sulphur passivated GaAs(100)	G. W. Anderson, M. C. Hanf, P. R. Norton, M. Kowalewski, K. Myrtle, B. Heinrich
4957	Epitaxial ferromagnetic MnAs thin films grown on Si (001): The effect of substrate annealing	K. Akeura, M. Tanaka, T. Nishinaga, J. De Boeck
4960	Thickness dependence of effective magnetic anisotropy	Ching-Ray Chang
4963	Uniaxial and planar magnetic anisotropy of thin transition-metal films (abstract)	R. Lorenz, J. Hafner
4964	Structural and magnetic properties of face-centered-cubic Fe films grown on Co(100)	Ernesto J. Escorcia-Aparicio, R. K. Kawakami, Z. Q. Qiu
4967	Galvanomagnetic properties and magnetic domain structure of epitaxial MnAs films on GaAs(001)	M. C. Park, Y. Park, T. Shin, G. M. Rothberg, M. Tanaka, J. P. Harbison
4970	GMR properties of spin valves using multilayered $Co_{90}Fe_{10}$ for free magnetic layer	Koichi Nishioka, Takayuki Iseki, Hideo Fujiwara, Martin R. Parker
4973	Micromagnetics of uneven ultrathin film trilayers	A. S. Arrott
4976	Magnetization of two-dimensional *XY* magnets with symmetry breaking fields: Relevance to ultrathin magnetic films (abstract)	J. Rothman, P. C. W. Holdsworth, S. T. Bramwell
4976	Characterization of iron-oxide films grown on Cu(001) and Ag(001) (abstract)	L. Scipioni, B. Sinkovic
4977	Thickness dependence of magneto-optical properties in face-centered-cubic Co/Cu(001) ultrathin films	K. Nakajima, T. Miyazaki
4980	Investigation of magnetic coupling in sputtered epitaxial Fe/Cr and Co/Cu wedged structures	X. Bian, H. T. Hardner, S. S. P. Parkin
4983	Enhancement of orbital magnetism at surfaces: Co on Cu(100) (abstract)	M. Tischer, F. May, K. Baberschke, O. Hjortstam, D. Arvanitis, J. Hunter Dunn, J. Trygg, B. Johansson, O. Eriksson, J. M. Wills
4984	Critical phenomena in the two-dimensional *XY* magnet Fe(100) on W(100)	H. J. Elmers, J. Hauschild, G. H. Liu, U. Gradmann
4987	*In situ* Brillouin light scattering from ultrathin epitaxial Fe/Ag(100) films with Cr and Ag overlayers	R. J. Hicken, A. Ercole, S. J. Gray, C. Daboo, J. A. C. Bland

(Continued)

4990	Magneto-optical investigation of the fcc–bcc phase transition of Fe wedges sandwiched between CuNi alloys (abstract)	H. Theuss, D. Weller, A. Carl
4991	Dependence of structural and magnetic properties on deposition angle in electron-beam evaporated Co/Pt multilayer thin films	Ki-Seok Moon, Sung-Chul Shin
4994	Simulations of inhomogeneous magnetization processes in ultrathin films with growth-induced roughness (abstract)	A. Moschel, A. Zangwill, M. D. Stiles

Recording Heads and Materials

4995	Measurement of the crystalline anisotropy in sputtered single-crystal FeTaN thin films	L. Varga, W. D. Doyle
4998	Magnetic properties and crystal structure of FeTaAlN soft magnetic materials for MIG head (abstract)	Yiqun Li, Bingchu Cai, Xianglin Zeng, Dong Xu
4999	Magnetic domain control of thick Fe-M(Zr,Ta)-N films for digital VCR metal in gap heads	M. Uchizawa, J. Fujita, H. Kobayashi, S. Tanabe
5002	Contact magnetoresistive head for perpendicular magnetic recording	Ken-ichi Takano, Hiroaki Muraoka, Yoshihisa Nakamura
5005	Magnetostriction and thin-film stress in high magnetization magnetically soft FeTaN thin films	M. K. Minor, B. Viala, J. A. Barnard
5008	Exchange coupling between NiO and NiFe thin films	J. X. Shen, M. T. Kief
5011	Search for high moment soft magnetic materials: FeZrN (abstract)	A. Chakraborty, G. H. Bellesis, K. R. Mountfield, D. N. Lambeth, M. H. Kryder
5011	Magnetic properties of CoFeB sputtered films for high Bsat applications (abstract)	Durga Ravipati, Hua-Ching Tong, Lena Miloslavsky
5012	Exchange coupling of sputter deposited NiCo–O/NiFe thin films	Minshen Tan, Hua-Ching Tong, Swie-In Tan, Robert Rottmayer
5015	Preparation of soft magnetic Fe/Ta and Fe:N/Ta:N multilayered films with large magnetization for inductive recording head	Masahiko Naoe, Shigeki Nakagawa
5018	Cr\(CoPtCr,$CoPt_x$) layered film studies for hard bias applications	A. Tsoukatos, S. Gupta, D. Marx

Commemorative Symposium on Neutron Scattering

5021	Early development of neutron scattering by magnetic materials (invited) (abstract)	C. G. Shull
5022	Magnetic scattering of neutrons (invited) (abstract)	R. M. Moon
5022	Neutron scattering as a probe of unconventional superconductivity in $YBa_2Cu_3O_7$ (invited) (abstract)	B. Keimer
5023	Strong magnetic fluctuations in transition metal oxides (invited)	C. Broholm, G. Aeppli, S.-H. Lee, W. Bao, J. F. DiTusa

Symposium on High Performance Permanent Magnets and Coercivity

5029	Overview of Nd–Fe–B magnets and coercivity (invited)	J. Fidler, T. Schrefl
5035	High performance NdFeB magnets (invited)	A. S. Kim, F. E. Camp
5040	Anisotropic Nd–Fe–B bonded magnets made from HDDR powders (invited)	T. Takeshita, K. Morimoto
5045	Sm_2Fe_{17} interstitial magnets (invited)	K.-H. Müller, Lei Cao, N. M. Dempsey, P. A. P. Wendhausen
5051	Disorder and noncollinear magnetism in permanent-magnet materials (invited)	R. Lorenz, J. Hafner

Small Particles/Lithography

5056	Long range order in 2-D arrays of nanometer-sized Fe islands on CaF_2/Si(111) (invited) (abstract)	M. R. Scheinfein, K. E. Schmidt, K. R. Heim, G. G. Hembree
5057	Fabricating nanoscale magnetic mounds using a scanning probe microscope	K. Bessho, Y. Iwasaki, S. Hashimoto
5060	Magnetic properties of nanometer-size CoPt particles	S. H. Liou, Y. Liu, S. S. Malhotra, M. Yu, D. J. Sellmyer

(Continued)

5063	Oxidation states and magnetism of Fe nanoparticles prepared by a laser evaporation technique	B. J. Jönsson, T. Turkki, V. Ström, M. S. El-Shall, K. V. Rao
5066	65 Gbits/in.^{2} quantum magnetic disk (abstract)	Stephen Y. Chou, Peter R. Krauss
5066	Quantized writing processes in quantum magnetic disks (abstract)	Usman Suriono, Stephen Y. Chou
5067	Nonmonotonic length dependence of switching field of nanolithographically defined single-domain nickel and cobalt bars (abstract)	Linshu Kong, Stephen Y. Chou
5067	Ultramicro fabrications on Fe-Ni alloy films using electron-beam writing and reactive-ion etching (abstract)	I. Nakatani
5068	Structural and magnetic study of submicronic single crystal cobalt box arrays	M. Hehn, K. Ounadjela, S. Padovani, J. P. Bucher, J. Arabski, N. Bardou, B. Bartenlian, C. Chappert, F. Rousseaux, D. Decanini, F. Carcenac, E. Cambril, M. F. Ravet
5071	High field irreversibility in $NiFe_2O_4$ nanoparticles (abstract)	R. H. Kodama, A. E. Berkowitz, E. J. McNiff, Jr., S. Foner
5072	Sputter deposited Co/CoO composite materials	J. Y. Yi, C. L. Platt, M. L. Rudee, A. E. Berkowitz, T. L. Cheeks
5075	High-resolution observation of magnetization processes in 2 μm $\times$ 2 μm $\times$ 0.04 μm permalloy particles	K. Runge, Y. Nozaki, Y. Otani, H. Miyajima, B. Pannetier, T. Matsuda, A. Tonomura
	Critical Phenomena II	
5078	Neutron diffraction determination of the nuclear spin ordering in Cu and Ag at nano- and subnano-K temperatures (invited)	M. Steiner, A. Metz, K. Siemensmeyer, O. V. Lounasmaa, J. T. Tuoriniemi, K. K. Nummila, R. T. Vuorinen, K. N. Clausen, K. Lefmann, F. B. Rasmussen
5081	Critical properties of the spin Peierls transition in $CuGeO_3$	M. D. Lumsden, B. D. Gaulin, H. Dabkowska
5084	Evidence for crossover effects in the spin dynamics of the two-dimensional antiferromagnet $Sr_2CuO_2Cl_2$ from ^{35}Cl nuclear magnetic resonance	B. J. Suh, F. Borsa, L. L. Miller, D. C. Johnston, D. R. Torgeson, M. Corti
5087	Magnetic and nonmagnetic glass transitions in the Blume–Emery–Griffiths model with competing biquadratic interactions (abstract)	Daniel P. Snowman, Susan R. McKay
5087	The three-dimensional RFIM: Existence of a tricritical point? (abstract)	Laura Hernandez, H. T. Diep
5088	m=3 Ashkin–Teller-like cubic model on an FCC lattice	Ron ald Fisch
5091	Phase transitions in disordered systems: Exactly solvable model	D. Nicolaides, A. A. Lisyansky
5094	Effect of exchange anisotropy on susceptibility of one-dimensional spin 1/2 ferromagnets	Ying Liu, John E. Drumheller
5096	Effects of randomness in gapped antiferromagnetic quantum spin chains	Kun Yang, R. A. Hyman, R. N. Bhatt, S. M. Girvin
5099	Competition between spin-Peierls phase and three-dimensional antiferromagnetic order in $CuGe_{1-x}Si_xO_3$	J. P. Renard, K. Le Dang, P. Veillet, L. P. Regnault, G. Dhalenne, A. Revcolevschi
	Exchange Bias and Interface Roughness	
5102	Domain structure in NiO biasing layers (abstract)	R. W. Erwin, J. A. Borchers, D. M. Lind, E. Lochner, K. A. Shaw, B. Singer, P. Stoyonov, R. C. DiBari, S. D. Berry
5103	Exchange biasing in MBE grown Fe_3O_4/CoO bilayers: The antiferromagnetic layer thickness dependence	P. J. van der Zaag, A. R. Ball, L. F. Feiner, R. M. Wolf, P. A. A. van der Heijden
5106	Magnetic properties of exchange-coupled Fe/FeO bilayers	D. V. Dimitrov, A. S. Murthy, G. C. Hadjipanayis, C. P. Swann

(Continued)

5109	Effects of cooling field strength on exchange anisotropy at permalloy/CoO interfaces	Timothy J. Moran, Ivan K. Schuller
5112	The role of interface crystalline and magnetic structure in exchange anisotropy (abstract)	J. Nogués, D. Lederman, Ivan K. Schuller, K. V. Rao
5113	Topological coupling in magnetic multilayer films	J. Zhang, R. M. White
5116	Surface roughness in Cu(100)/$[Co/Cu]_n$ systems grown by ion-beam sputtering	Timothy J. Minvielle, Robert L. White, Robert J. Wilson
5119	^{59}Co nuclear magnetic resonance studies of the effect of annealing molecular beam epitaxy grown Co/Cu(111) multilayers	T. Thomson, P. C. Riedi, B. J. Hickey
5122	Field dependent resonance frequency of hysteresis loops in a few monolayer thick Co/Cu(001) films	Q. Jiang, H.-N. Yang, G.-C. Wang
5125	Fe adsorption and film growth on GaAs(001) (2×4)-As (abstract)	E. Kneedler, P. M. Thibado, B. T. Jonker, B. R. Bennett, L. J. Whitman, B. V. Shanabrook, J. J. Krebs
5126	Magnetic properties and Pd–H miscibility gap in Ni/Pd composite fine particles	Takashi Manago, Yoshichika Otani, Hideki Miyajima, Etsuo Akiba
5129	Magnetic impurities and clusters on Ag, Pd, and Pt surfaces (abstract)	V. S. Stepanyuk, K. Wildberger, P. Lang, R. Zeller, P. H. Dederichs

Soft Amorphous and Nanocrystalline Materials I

5130	High-frequency magnetic properties in metal–nonmetal granular films (invited)	S. Ohnuma, H. Fujimori, S. Mitani, T. Masumoto
5136	Giant magnetoimpedance effect in soft and ultrasoft magnetic fibers	P. Ciureanu, P. Rudkowski, G. Rudkowska, D. Menard, M. Britel, J. F. Currie, J. O. Ström-Olsen, A. Yelon
5139	Giant magneto-impedance effects in Metglas 2705M	R. L. Sommer, C. L. Chien
5142	Barkhausen noise in FeCoB amorphous alloys (abstract)	G. Durin, G. Bertotti
5143	Magnetism and microstructure of nanocrystalline nickel	H. Kisker, H. Kronmüller, H.-E. Schaefer, T. Suzuki
5146	Small-angle neutron scattering behavior of $Fe_{91}Zr_9$ glass under magnetic field	L. Fernández Barquín, J. C. Gómez Sal, S. N. Kaul, J. M. Barandiarán, P. Gorría, J. S. Pedersen, R. Heenan
5149	Time-temperature-transformation study of a nanocrystalline $Fe_{91}Zr_7B_2$ soft magnetic alloy	K. Suzuki, J. M. Cadogan, V. Sahajwalla, A. Inoue, T. Masumoto
5152	Soft magnetic properties of Fe–Zr–B thin films (abstract)	N. B. Shevchenko, J. A. Christodoulides, X. Meng-Burany, A. S. Murthy, G. C. Hadjipanayis
5153	The change of magnetic properties in nanocrystalline $Fe_{88}Zr_7B_4Cu_1$ alloy by cooling rate	K. S. Kim, V. Ström, J. Wittborn, K. V. Rao, K. Y. Kim, T. H. Noh, S. C. Yu
5156	Improvement of soft magnetism of $Fe_{90}Co_{10}$ sputtered films by addition of N and Ta	Shigeki Nakagawa, Satoshi Tanaka, Katsumi Suemitsu, Masahiko Naoe
5159	Effect of nitrogen interstitial in α-Fe crystalline on the magnetic soft properties of FeTaN thin films	W. C. Chang, D. C. Wu, J. C. Lin, C. J. Chen

Colossal Magnetoresistance in Perovskite Oxides II

5162	Giant magnetoresistance induced by spin-correlation scattering in magnetic thin films and other compounds	Liang-Jian Zou, X. G. Gong, Qing-Qi Zheng, C. Y. Pan
5165	Giant magnetoresistive memory effect in $Nd_{0.7}Sr_{0.3}MnO_z$ (abstract)	G. C. Xiong, Q. Li, H. L. Ju, R. L. Greene, T. Venkatesan, M. Dominguez, S. E. Lofland, S. M. Bhagat

(Continued)

5166 Ferromagnetic resonance and intrinsic properties of $La_{0.67}Ba_{0.33}MnO_z$ — S. E. Lofland, S. M. Bhagat, H. L. Ju, G. C. Xiong, T. Venkatesan, R. L. Greene, S. Tyagi

5169 Role of epitaxy and polycrystallinity in the magnetoresistance and magnetization of $La_{0.8}Sr_{0.2}MnO_3$ thin films — Kannan M. Krishnan, A. R. Modak, C. A. Lucas, R. Michel, H. B. Cherry

5172 Magnetic exchange and charge transfer in mixed-valence manganites and cuprates — Gerald F. Dionne

5175 Correlation between magnetovolume and giant magnetoresistance effects in doped $La_{2/3}Ca_{1/3}MnO_3$ perovskites — J. M. De Teresa, J. Blasco, M. R. Ibarra, J. García, C. Marquina, P. Algarabel, A. del Moral

5178 Pressure effect on the resistivity in GMR $La_{0.60}Y_{0.07}Ca_{0.33}MnO_3$ compound (abstract) — Z. Arnold, K. Kamenev, M. R. Ibarra, P. A. Algarabel, C. Marquina, J. Blasco, J. García

5179 Hall effect and giant magnetoresistance in lanthanum manganite thin films — J. E. Núñez-Regueiro, D. Gupta, A. M. Kadin

5182 Magnetic properties of colossal magnetoresistive manganese oxides — J. Fontcuberta, B. Martínez, A. Seffar, S. Piñol, A. Roig, E. Molins, X. Obradors, J. Alonso, J. M. González-Calbet

5185 Magnetic and magnetoresistance studies on radio frequency sputtered La–Pb–Mn–O films — G. Srinivasan, T. E. Brusca, A. S. Fisher, V. Suresh Babu, M. S. Seehra

5188 Composition dependence of giant magnetoresistance in $(La_{1-x}Y_x)_{2/3}Ca_{1/3}MnO_\delta$ $(0 \leq x \leq 1)$ — Zisen Li, X. T. Zeng, H. K. Wong

Magnetic Semiconductors

5191 Effects of high-temperature annealing on the optical absorption of Ca:YIG films — R. E. Bornfreund, P. E. Wigen

5193 Determination of Mn composition in $Zn_{1-x}Mn_xSe$ from Faraday rotation analysis — Yu-Xiang Zheng, Liang-Yao Chen, Shi-Ming Zhou, Ya-Dong Wang, Yu Wang, You-Hua Qian, Jie Wang, Cai-Xia Jin, Xun Wang

5195 Microstructural properties of (ZnSe/FeSe) and (ZnSe/MnSe) diluted magnetic semiconductor superlattices (abstract) — K. Park, L. Salamanca-Riba, B. T. Jonker

5196 Polaron-polaron interactions in diluted magnetic semiconductors — P. A. Wolff, R. N. Bhatt, A. C. Durst

Instrumentation and Measurement Techniques II

5199 Hybrid pole pieces for permanent magnets — M. G. Abele, J. H. Jensen

5202 Method based on the saturation approach law for monitoring the quality of texture in 3% Si–Fe — M. Birsan, J. A. Szpunar

5205 Construction of novel magnets for generating astatic fields in x-ray topography — Tetsuo Nakajima, Masami Yoshizawa

5208 Automized magnetic hysteresis measurement system — Rolf Disselnkötter

5211 Alternating current-excited magnetoresistive sensor — P. Ripka

5214 Magnetic field distribution caused by a notebook computer and its source searching — T. Doi, S. Hayano, Y. Saito

5217 Highly sensitive magneto-optic transverse Kerr effect measurement system for the detection of perpendicular anisotropy and magnetic phases in thin films — J. A. Corrales, M. Rivas, J. F.-Calleja, I. Iglesias, M. C. Contreras

Itinerant Magnetism and Other Fundamental Properties

5220 First-order magnetic phase transition in (Er, Tb)M_2(M=Co, Ni) (abstract) — A. Y. Takeuchi, F. Garcia, S. F. da Cunha

5221 Magnetism in URhSi — K. Prokeš, E. Brück, K. H. J. Buschow, F. R. de Boer, V. Sechovský, P. Svoboda, X. Hu, H. Maletta, T. J. Gortenmulder

(Continued)

5224 Magnetic and crystallographic properties of $CrAs_{1-x}S_x(0 \leq x < 1)$ — Takanobu Suzuki, Hideaki Ido

5227 Impact of criticality and phase separation on the spin dynamics of the one-dimensional $t-J$ model — Shu Zhang, Gerhard Müller, Joachim Stolze

5230 Rapid loss of magnetic order in Ni on alloying with Cr, Mo, Re, and Si — V. Suresh Babu, A. S. Pavlovic, Mohindar S. Seehra

5233 Magnetic properties of the $SmMn_2(Ge_{1-x}Si_x)_2$ system — Shibaji Saha, Naushad Ali

5236 Remanent magnetization in the linear chain antiferromagnet $(CH_3NH_3)Mn_{1-x}M_xCl_3 \cdot 2H_2O$, M=Cd or Cu — A. Paduan-Filho, C. C. Becerra, F. Palacio

5238 Magnetic properties of Ni_2In type $(Co_{1-x}Mn_x)_{65}Ge_{35}$ compounds — Hiroshi Shiraishi, Tomiei Hori, Yasuo Iguchi, Yasuo Yamaguchi, Masayoshi Ohashi, Kazuo Kanematsu

5241 Magnetism of the solid solution $GdGa_{1-x}Ge_x$ (abstract) — A. Leithe-Jasper, K. Hiebl

5242 Neutron scattering and magnetization clouds in dilute Pd based alloys — R. E. Parra, A. C. González

5245 Polarization analysis of the electron spin resonance lines in the $S=1$ one-dimensional antiferromagnet $Ni(C_3H_{10}N_2)_2NO_2ClO_4$ — M. Hagiwara, K. Katsumata

New Materials

5247 Highly crystallized $(La,Sr)MnO_3$ films deposited by facing targets sputtering apparatus — N. Matsushita, K. Noma, S. Nakagawa, M. Naoe

5250 α''-$Fe_{16}N_2$ phase epitaxially grown by sputter beam method — Satoshi Okamoto, Osamu Kitakami, Yutaka Shimada

5253 The formation of stable Co/Co_2MnSn two phase magnets — T. W. Kim, R. J. Gambino

5256 Magnetic phase transitions in $RENi_2B_2C$ (RE=Ho,Dy,Tb) studied by ^{57}Fe Mössbauer spectroscopy (abstract) — D. Sánchez, H. Micklitz, M. B. Fontes, S. L. Bud'ko, E. Baggio-Saitovitch

5257 Morin-like spin reorientation in BiPb-2201 ferrates with iron in octahedral oxygen coordination — M. Rosenberg, Th. Sinnemann, G. Filoti, S. Kemmler-Sack

5260 Magnetization behavior of $(NBu_4)_2Mn_2[Cu(opba)]_3$ and related solvated ferromagnets — S. A. Chavan, R. Ganguly, V. K. Jain, J. V. Yakhmi

5263 Magnetic properties and grain growth stability of nanocomposite $Fe-ZrO_2$ granular solids prepared by mechanical milling — S. C. Axtell, R. Schalek

5266 The macroscopic ferri-ferromagnetic transition in amorphous Y–Co/Gd–Co bilayers — T. Yonamine, Y. Souche, A. D. Santos

5269 Weak ferromagnetic resonance of Gd_2CuO_4 small particles (abstract) — J. Mira, J. Rivas, A. Butera, M. Tovar, C. Vázquez-Vázquez, J. Mahía, M. A. López-Quintela, S. B. Oseroff

Symposium on Giant and Colossal Magnetoresistance

5270 Inverse giant magnetoresistance (invited) — J.-P. Renard, P. Bruno, R. Mégy, B. Bartenlian, P. Beauvillain, C. Chappert, C. Dupas, E. Kolb, M. Mulloy, J. Prieur, P. Veillet, E. Vélu

5276 *Ab initio* calculations of spin-dependent transport properties (invited) (abstract) — I. Mertig

5277 Optimizing the giant magnetoresistance of symmetric and bottom spin valves (invited) — W. F. Egelhoff, Jr., P. J. Chen, C. J. Powell, M. D. Stiles, R. D. McMichael, C.-L. Lin, J. M. Sivertsen, J. H. Judy, K. Takano, A. E. Berkowitz, T. C. Anthony, J. A. Brug

5282 First principles calculations of electrical conductivity and giant magnetoresistance of periodic multilayers and spin valves (invited) — W. H. Butler, X.-G. Zhang, D. M. C. Nicholson, T. C. Schulthess, J. M. MacLaren

5288 Origins of colossal magnetoresistance in perovskite-type manganese oxides (invited) — Y. Tokura, Y. Tomioka, H. Kuwahara, A. Asamitsu, Y. Moritomo, M. Kasai

(Continued)

5292	Colossal magnetoresistivity in manganese-based perovskites (invited) (abstract)	R. Ramesh, T. Venkatesan, S. B. Ogale, R. L. Greene, S. M. Bhagat

Small Particles/Nanocrystals

5293	Magnetic properties of monodomain Nd-Fe-B-C nanoparticles	E. M. Brunsman, J. H. Scott, S. A. Majetich, M. E. McHenry, M.-Q. Huang
5296	Magnetic properties and imaging of Mn-implanted GaAs semiconductors	Jing Shi, J. M. Kikkawa, D. D. Awschalom, G. Medeiros-Ribeiro, P. M. Petroff, K. Babcock
5299	Finite size effects in nanoscale Tb particles	D. Johnson, P. Perera, M. J. O'Shea
5302	Effect of preparation technique on the structural and magnetic properties of granular Fe-SiO_2 (abstract)	J. A. Christodoulides, N. B. Shevchenko, A. S. Murthy, G. C. Hadjipanayis
5303	Preparation and quantitative magnetic studies of single-domain nickel cylinders	R. O'Barr, M. Lederman, S. Schultz, Weihua Xu, A. Scherer, R. J. Tonucci
5306	Magnetic domain percolation in granular Co-Ag	A. Gavrin, M. H. Kelley, J. Q. Xiao, C. L. Chien
5309	Observation of perpendicular anisotropy in granular magnetic solids	John Q. Xiao, C. L. Chien, A. Gavrin
5312	Self-stabilized magnetic colloids: Ultrafine Co particles in polymers	Diandra L. Leslie-Pelecky, X. Q. Zhang, Reuben D. Rieke
5315	Complementary imaging of granular Co-Ag films with magneto-optical indicator film technique and magnetic force microscopy	M. J. Donahue, L. H. Bennett, R. D. McMichael, L. J. Swartzendruber, A. J. Shapiro, V. I. Nikitenko, V. S. Gornakov, L. M. Dedukh, A. F. Khapikov, V. N. Matveev, V. I. Levashov
5318	Perpendicular spin valve behavior in a microstructured Co/Cu-Cu oxide/Co trilayer	K. Matsuyama, H. Asada, I. Matsuguma, T. Saeki, K. Taniguchi
5321	Epitaxial $Fe_{16}N_2$ films grown on Si(001) by reactive sputtering	M. A. Brewer, Kannan M. Krishnan, C. Ortiz
5324	Classical and quantum magnetism in synthetic ferritin proteins	S. Gider, D. D. Awschalom, T. Douglas, K. Wong, S. Mann, G. Cain

Magnetic Recording Media III

5327	Magnetic recording measurements of high coercivity longitudinal media using magnetic force microscopy (MFM)	P. Giljer, J. M. Sivertsen, J. H. Judy, C. S. Bhatia, M. F. Doerner, T. Suzuki
5330	Grain growth and ordering kinetics in CoPt thin films	K. Barmak, R. A. Ristau, K. R. Coffey, M. A. Parker, J. K. Howard
5333	Co-Sm $(\bar{1}100)[0001]$//Cr $(\bar{1}2\bar{1})[\bar{1}01]$ epitaxy and its effects on magnetic properties of Co-Sm//Cr films	Y. Liu, D. J. Sellmyer, B. W. Robertson
5336	Magnetic and recording properties of monolayer and multilayer thin-film media by using composite targets	Brij B. Lal, A. Bourez, Michael A. Russak
5339	Dependence of media noise on grain size and intergranular coupling in thin-film media	Akira Kikuchi, Shinya Kawakita, Junichi Nakai, Takehito Shimatsu, Migaku Takahashi
5342	The role of stress-induced anisotropy in longitudinal thin film magnetic recording media	C. A. Ross, M. E. Schabes, R. Ranjan, G. Bertero, T. Chen
5345	The role of Ta and Pt in segregation within Co-Cr-Ta and Co-Cr-Pt thin film magnetic recording media	K. M. Kemner, V. G. Harris, V. Chakarian, Y. U. Idzerda, W. T. Elam, C.-C. Kao, Y. C. Feng, D. E. Laughlin, J. C. Woicik

(Continued)

5348 Microstructure and magnetic properties of CoCrPt/Cr films on ultrasmooth NiP/AlMg substrates — Li Tang, David E. Laughlin, David N. Lambeth, Mary F. Doerner

5351 Reduction of Co–Cr–Pt media noise by addition of Ti to Cr underlayer — Y. Matsuda, Y. Yahisa, J. Inagaki, E. Fujita, A. Ishikawa, Y. Hosoe

5354 Magnetic and crystallographic properties of CoCrPt thin films formed on Cr–Ti single crystalline underlayers — N. Inaba, A. Nakamura, T. Yamamoto, Y. Hosoe, M. Futamoto

5357 Magnetic and microstructural properties of CoCrTa/Cr/Al thin films (abstract) — H. S. Chang, T. D. Lee, J. K. Park, K. H. Shin, K. Park

5358 Influence of sputter gas and sputter pressure on the structure and magnetic properties of Co–Pt–Cr thin films (abstract) — A. Roshko, L. L. Dulcie, T. Nguyen, T. Yogi

5359 Improvement of $Co_{71}Cr_{19}Pt_{10}/Ti_{90}Cr_{10}$ perpendicular recording media by independent optimization of film nucleation and growth processes — T. P. Nolan, Y. Hirayama, M. Futamoto

5362 High recording performance of Co–Cr medium sputter-deposited at high Ar pressure and high substrate temperature — Naoki Honda, Satoshi Yanase, Kazuhiro Ouchi, Shun-ichi Iwasaki

Magnetic Excitations I

5365 Microwave solitons in magnetic films (invited) (abstract) — A. D. Boardman, K. Xie, H. Mehta, S. A. Nikitov

5366 Thresholds of spin wave envelope soliton formation in magnetic films with dissipation (abstract) — A. N. Slavin

5367 Phase properties of microwave magnetic envelope dark solitons in yttrium iron garnet thin films (abstract) — J. M. Nash, P. Kabos, C. E. Patton, R. Staudinger

5368 Two-dimensional solitons in the classical Heisenberg antiferromagnet with nonmagnetic impurities — Kala Subbaraman, Craig E. Zaspel, John E. Drumheller

5371 Interaction of light with a nonlinear spin wave in a normally magnetized ferromagnetic film — A. A. Stashkevich, M. G. Cottam, A. N. Slavin

5374 Variations in auto-oscillation frequency at the main resonance in rectangular yttrium–iron–garnet films — A. Prabhakar, D. D. Stancil

5377 Driven spin-wave dynamics in yttrium–iron–garnet films (abstract) — D. J. Mar, T. L. Carroll, L. M. Pecora, J. F. Heagy, F. J. Rachford

5378 Synchronization of chaos in circular yttrium iron garnet films — D. W. Peterman, M. Ye, P. E. Wigen

5381 Experimental observation of the longitudinal resonance mode in ferromagnets with random anisotropy — G. Suran, E. Boumaiz, J. Ben Youssef

5384 Investigation of the spin-Peierls phase diagram of $CuGeO_3$: Far-infrared electron spin resonance in high field — W. Palme, G. Ambert, J. P. Boucher, G. Dhalenne, A. Revcolevschi

5387 Magnetic anisotropies in thick body centered cubic Co — X. Liu, R. L. Stamps, R. Sooryakumar, G. A. Prinz

5390 Two magnon ferromagnetic resonance linewidths in uniaxial and planar single crystal hexagonal ferrites (abstract) — D. R. Franklin, M. J. Hurben, C. E. Patton

One-Dimensional Magnetism and Other Cooperative Phenomena

5391 Finite temperature effects in the $S=1/2$ Heisenberg chain $Cu(C_6D_5COO)_2 \cdot 3D_2O$ (abstract) — D. Dender, D. H. Reich, C. Broholm, K. Lefmann, G. Aeppli

5392 Cu_2(1,4-diazacycloheptane)$_2Cl_4$: A quasi-one-dimensional $S=1/2$ spin liquid system — Philip R. Hammar, Daniel H. Reich

5395 Magnetic fluctuation spectrum of $CuGeO_3$: Raman scattering — P. H. M. van Loosdrecht, J. P. Boucher, G. Martinez, G. Dhalenne, A. Revcolevschi

5398 Neutron diffraction study of the magnetic structures of $CeMn_2Ge_2$ and $CeMn_2Si_2$ — J. A. Fernandez-Baca, Peggy Hill, B. C. Chakoumakos, Naushad Ali

5401 Magnetic studies of the metal–insulator transition in $CuIr_2S_{4-x}Se_x$ ($x=0$, 0.1, and 4) — P. Somasundaram, J. M. Honig, T. M. Pekarek, B. C. Crooker

5403 Magnetization and specific heat studies of Gd_2In — Chan-Soo Jee, C. L. Lin, T. Mihalisin, Xue-Qin Wang

(Continued)

5406 Magnetic viscosity far and close to equilibrium in the superparamagnetic alloy — A. Maraner, X. Zhang, A. Cavalleri, J. Tejada, S. Vitale

5409 Simultaneous molecular and spin dynamics: Quasiclassical approximation and quantum effects — V. P. Antropov, B. N. Harmon

5412 Magnetic exchange coupling mediated by bound states — C. A. R. Sá de Melo

5415 Phenomenological description of the magnetization relaxation (abstract) — V. L. Sobolev, Huei Li Huang

5416 Atomic magnetic moments and spin notion — Xavier Oudet

5419 Aharonov–Bohm oscillations at finite temperature — P. Schlottmann, A. A. Zvyagin

Soft Ferrites and Alloys II

5422 Study of the frequency dependence of the ferromagnetic resonance linewidths of nickel ferrites from 8–60 GHz — L. Torres, M. Zazo, A. G. Flores, V. Raposo, J. Iñiguez

5425 Variable texture $NiOFe_2O_3$ ferrite films prepared by pulsed laser deposition — P. Samarasekara, R. Rani, F. J. Cadieu, S. A. Shaheen

5428 Atomic migration in Ni–Co ferrite — Chul Sung Kim, Seung Wha Lee, Seung Iel Park, Jae Yun Park, Young Jei Oh

5431 EXAFS and magnetic characterization of inverted ball milled zinc ferrite powders (abstract) — S. A. Oliver, V. G. Harris, H. H. Hamdeh, J. C. Ho

5432 High-power-use Mn–Zn ferrites with monodomain structure prepared by low-temperature sintering — C. S. Liu, J. M. Wu, I. Nan Lin, C. J. Chen

5435 Magnetic properties of Zn–Mg ferrite fine powders (abstract) — H. H. Hamdeh, J. C. Ho, S. A. Oliver, R. J. Willey, M. J. O'Shea

5436 Comparison between disaccommodation and ferromagnetic resonance measurements in polycrystalline yttrium–iron–garnet samples — L. Torres, M. Zazo, J. Iñiguez, C. de Francisco, J. M. Muñoz, P. Hernandez

5439 Magnetic properties of $BaFe_{12-(x+y)}Sn_xCo_yO_{19}$ single crystals (abstract) — R. Solé, X. X. Zhang, X. Ruiz, M. Aguiló, F. Díaz, J. Tejada

5440 Epitaxial single crystal $Fe_{16}N_2$ films grown by facing targets sputtering — D. C. Sun, E. Y. Jiang, M. B. Tian, C. Lin, X. X. Zhang

5443 (100)-textured 3% silicon steel sheets by manganese removal and decarburization — Toshiro Tomida

5446 Deposition condition and thickness dependence on magnetic properties of sputtered NiFeCo thin films — A. Tsoukatos, S. Gupta, Y. K. Kim

5449 Ferromagnetism of $Y_2(Fe_{1-y}Co_y)_{17-x}Al_x$ — N. Ohkubo, K. Kanematsu

5452 Ferromagnetism of deuterides YFe_2D_x (abstract) — K. Kanematsu, N. Ohkubo, K. Itoh, S. Ban, T. Miyajima, Y. Yamaguchi

5453 Hydrogen charging in nickel and iron and its effect on their magnetic properties — A. Ramesh, M. R. Govindaraju, D. C. Jiles, S. B. Biner, J. M. Roderick

Soft, Amorphous, and Nanocrystalline Materials II

5456 Magnetic viscosity investigations of nanograin iron powder — U. Atzmony, Z. Livne, R. D. McMichael, L. H. Bennett

5459 Magnetic properties and the crystallization of amorphous $Fe_{83}B_9Nb_7Cu_1$ — Chul Sung Kim, Sung Baek Kim, J. S. Lee, T. H. Noh

5462 Resonant microwave cavity response of amorphous ribbons — A. N. Medina, M. Knobel, S. Salem-Sugui, F. G. Gandra

5465 Coercivity and remanence of amorphous and nanocrystalline Fe–(Cu,Ta)–SiB ribbons — N. Murillo, J. González, J. M. Blanco, J. M. González

5468 NMR study of the local inhomogeneities in the soft magnetic alloy $Co_{74.26}Fe_{4.74}Si_{2.1}B_{18.9}$ (abstract) — L. Iannarella, C. Kim, R. C. O'Handley, A. P. Guimarães

5469 Evolution from soft to hard magnetic behavior in Co-based devitrified glassy alloy — G. Bottoni, D. Candolfo, A. Cecchetti

5472 Nanocrystalline Fe-M-B-Cu (M=Zr, Nb) alloys with improved soft magnetic properties (abstract) — A. Makino, T. Bitoh, A. Inoue, T. Masumoto

(Continued)

5472 Comparison of experimental and theoretical initial permeability taking into account anistropy dispersion in CoNbZr thin films (abstract) — M. C. Contreras, M. Rivas, J. F. Calleja, I. Iglesias, M. Guyot, V. Cagan, R. Krishnan

5473 Crystallization behavior of a mechanically alloyed amorphous $Fe_{80}Zr_8B_{11}Cu_1$ alloy — Jianqiang Zhang, Bingyao Wu, Xiaohua Wu, Guiqin Wang, Jiwan Zhao

5476 Microstructure and magnetic properties of $Cu_{0.8}(Fe_{1-x}Co_x)_{0.2}$ alloy powders manufactured by a mechanical alloying process — Yong Goo Yoo, Seong Cho Yu, Won Tae Kim

5479 Mechanically ground $Fe_{73.5}Cu_1Nb_3Si_{13.5}B_9$: A soft magnetic material in powdered form — Anit K. Giri, P. García Tello, J. González, J. M. González

5482 Correlation of magnetic and mechanical properties of hydrogenated, compositionally modulated, amorphous $Fe_{80}Zr_{20}$ films (abstract) — S. Rengarajan, E. J. Yun, B. H. Lee, B. I. Cho, R. M. Walser

Soft Materials—Applications and Other Properties

5483 Application of Co-based amorphous ribbon to a noise filter and a shielded cable — Osamu Ishii, Masakatsu Senda, Koji Takei, Yasuhiro Koshimoto, Toshinori Mori

5486 A gigahertz-range electromagnetic wave absorber with wide bandwidth made of hexagonal ferrite — Morihiko Matsumoto, Yoshimori Miyata

5489 Rapidly solidified Fe–6.5%Si alloy powders for high frequency use (abstract) — Seung Duk Choi, Choong Jin Yang

5490 Large shielding factor obtained by a multiple-shell magnetic shield having separate magnetic shaking — I. Sasada, T. Yamamoto, T. Yamauchi

5493 The magnetomechanical effect in electrolytic iron — M. K. Devine, D. C. Jiles

5496 Effect of cutting techniques on local magnetic characteristics of SIFE (abstract) — D. A. Philips, L. R. Dupre, K. Eloot, J. A. Melkebeek

5497 The soft magnetic properties of stripes fabricated using laser ablation of multilayer thin films — Craig A. Grimes, Janet K. Lumpp

5500 Magnetic garnet film epitaxy on nonsingular faces (abstract) — S. S. Gorelik, L. M. Letyuk, A. T. Morchenko

Hard Magnets, 2-14-1, Interstitials

5501 The effects of average grain size on the magnetic properties and corrosion resistance of NdFeB sintered magnets — D. W. Scott, B. M. Ma, Y. L. Liang, C. O. Bounds

5504 Unusual magnetic behavior in Nd–Fe–B alloy powder compacts — H. Wan, F. T. Parker, F. F. Putris, A. E. Berkowitz

5507 Magnetocrystalline anisotropy and spin reorientation in $Gd_{1-x}Dy_xCo_4B$ — T. Ito, H. Asano, H. Ido, M. Yamada

5510 Dependence of energy dissipation on annealing temperature of melt–spun NdFeB permanent magnet materials — Z. Gao, D. C. Jiles, D. J. Branagan, R. W. McCallum

5513 Quantitative characterization of additional ferromagnetic phase in melt-quenched and sintered Nd–Fe–B-based magnets — L. H. Lewis, D. O. Welch, F. Pourarian

5516 Crystallographic and magnetic properties of $NdFe_{10.7}TiM_{0.3}$(M=B, Ti) — Chul Sung Kim, Young Jong Lee, Seung Wha Lee, Y. B. Kim, C. S. Kim

5519 Structure and magnetic properties of mechanically alloyed $Nd(Fe,V)_{12}N_x$ compounds — Jun Yang, Ou Mao, Z. Altounian

5522 Neutron diffraction and magnetic studies of $RFe_{12-x}T_xC_y$ (R=Y,Er; T=V,Ti,Mo) alloys — Z. Hu, W. B. Yelon, X. Zhang, W. J. James

5525 Structure and magnetic properties of mechanical alloyed Nd–Fe–Ti compounds and their nitrides — Zhi-qiang Jin, X. K. Sun, W. Liu, X. G. Zhao, Q. F. Xiao, Y. C. Sui, Z. D. Zhang, Zhi-gang Wang

5528 High coercivity of melt–spun $Sm_2Fe_{15}Al_2C_{1.5}$ compound — Jun-Xian Zhang, Zhao-Hua Cheng, Bao-Gen Shen

5530 Nuclear magnetic resonance study of R_2Fe_{17} (R=Y, Sm, and Gd) hydrides — N. X. Shen, Y. D. Zhang, J. I. Budnick, W. A. Hines, U. Binninger

5533 Structural and magnetic studies of $Er_2Fe_{17-x}M_xC_y$ (M=Ga and Al) compounds — W. C. Chang, S. L. Lu, S. K. Chen, Y. D. Yao

(Continued)

5536 Thermal stability of nanostructured $Sm_2Fe_{17}C_x$ compounds prepared by ball milling — O. Mao, Z. Altounian, J. Yang, J. O. Ström-Olsen

5539 Synthesis and magnetic properties of rare earth–iron–chromium phases and their nitrides — O. Kalogirou, V. Psycharis, M. Gjoka, D. Niarchos, C. D. Fuerst

5542 High field magnetization measurements of $SmFe_{11}Ti$ and $SmFe_{11}TiH_{1-\delta}$ — O. Isnard, M. Guillot, S. Miraglia, D. Fruchart

5545 First-principles calculation of the electronic and magnetic properties of $Nd_2Fe_{17-x}M_x$ (M=Si, Ga) solid solutions — Ming-Zhu Huang, W. Y. Ching

Applications of Hard Materials

5548 A novel integrated electric motor/pump for underwater applications — C. Peter Cho, Barry K. Fussell, John Y. Hung

5551 Imposition of periodic magnetization patterns on high-energy-product magnetic plates — H. A. Leupold, A. S. Tilak, E. Potenziani II

5554 Effects of slot closure by soft magnetic powder wedge material in axial-field permanent magnet brushless machines — S. Gair, J. F. Eastham, A. Canova

5557 An efficient design to reduce the flux leakage of a spindle motor — T. F. Ying, C. M. Chen, C. P. Liao, M. D. Wu, D. R. Huang

5560 Magnetic profiles of bonded magnets affected by the magnetizing fixtures — Donyau Chiang, Shyh-Jier Wang, Der-Ray Huang

5563 Magnetic multipole cylinders from mould-injection $Nd_2Fe_{14}B$ plastic bonded magnets (abstract) — G. K. Nicolaides, D. Niarchos, D. Tsamakis, I. Koubouros, A. Mitsis

Symposium on Magnetism of Fe–N and fcc Fe

5564 Structure and magnetic moment of α''-$Fe_{16}N_2$ compound films: Effect of Co and H on phase formation (invited) — Migaku Takahashi, H. Takahashi, H. Nashi, H. Shoji, T. Wakiyama, M. Kuwabara

5570 Electronic and magnetic structure of iron nitride, $Fe_{16}N_2$ (invited) — Akimasa Sakuma

5576 Magnetic and electrical properties of single-phase, single-crystal $Fe_{16}N_2$ films epitaxially grown by molecular beam epitaxy (invited) — Yutaka Sugita, Hiromasa Takahashi, Matahiro Komuro, Masukazu Igarashi, Ryo Imura, Takashi Kambe

5582 Mössbauer-effect study of face-centered-cubic-like Fe on Cu(001) (invited) (abstract) — W. Keune, A. Schatz, R. D. Ellerbrock, A. Fuest, K. Wilmers, R. A. Brand

5583 Magnetic properties of fcc-Fe multilayer (invited) (abstract) — M. Matsui, M. Doi, A. Kida, Y. Yamada

Giant Magnetoresistance–Granular Systems

5584 Giant magnetoresistance and high sensitivity in annealed NiFeCo/Ag multilayers — J. W. Dykes, Y. K. Kim, A. Tsoukatos, S. Gupta, S. C. Sanders

5587 Finite-size effect and its temperature dependence of giant magnetoresistance in magnetic granular materials — Jian-Qing Wang, Gang Xiao

5590 Thickness dependence of giant magnetoresistance of AgNiFe heterogeneous alloys films — J. Wiggins, M. L. Watson, P. A. Gago-Sandoval, K. O'Grady

5593 Jitterbug spin channel mixing in heterogeneous giant magnetoresistive material — J. F. Gregg, W. Allen, S. M. Thompson, M. L. Watson, G. A. Gehring

5596 Modeling effects of temperature annealing on giant magnetoresistive response in discontinuous multilayer NiFe/Ag films — J. O. Oti, Y. K. Kim

5599 Giant magnetoresistance in melt-spun $Cu_{80}Ni_{10}Fe_{10}$ ribbons — L. H. Chen, S. Jin, T. H. Tiefel, S. Y. Liao, Y. D. Yao

5602 Giant magnetoresistance properties in multilayered Co-Ag/Cu granular alloys — Makoto Iijima, Yutaka Shimizu, Naomi Kojima, Atsushi Tanaka, Kazuo Kobayashi

(Continued)

5605	Modeling giant magnetoresistance and magnetization of $Ag_{1-x}Ni_{x-y}Fe_y$ heterogeneous alloy films (abstract)	J. Wiggins, M. L. Watson, P. A. Gago-Sandoval, X. Batlle, F. Badia, A. Labarta
5606	Structural evolution in sputtered $Co_{90}Fe_{10}$/Ag giant magnetoresistance multilayers	J. D. Jarratt, J. A. Barnard

Ultra-Thin Films

5609	Magnetic domain structure in ultrathin Cu/Ni/Cu/Si(001) films (invited)	Hans J. Hug, B. Stiefel, A. Moser, I. Parashikov, A. Klicznik, D. Lipp, H.-J. Güntherodt, Gabriel Bochi, D. I. Paul, R. C. O'Handley
5615	Magnetization and finite-size effects in Gd/W multilayers	J. Samuel Jiang, C. L. Chien
5618	Magnetism and structure of ultrathin fcc Fe_xCo_{1-x} films on Cu(001) (abstract)	A. Dittschar, M. Zharnikov, W. Kuch, C. M. Schneider, J. Kirschner
5619	Magnetization reversal properties near the reorientation phase transition of ultrathin Fe/Ag(100) films	A. Berger, H. Hopster
5622	Structure and magnetism in fcc magnetic transition metals on (001) diamond (abstract)	J. A. Wolf, J. J. Krebs, Y. U. Idzerda, G. A. Prinz, K. M. Kemner
5623	Anomalous perpendicular magnetism in Ni/Cu(001) films and the effects of capping layers	W. L. O'Brien, B. P. Tonner
5626	Magnetic x-ray linear dichroism in the photoelectron spectroscopy of ultrathin magnetic alloy films	J. G. Tobin, K. W. Goodman, G. J. Mankey, R. F. Willis, J. D. Denlinger, E. Rotenberg, A. Warwick
5629	New magnetic phases of Fe on fcc Co(001) and Ni(001)	W. L. O'Brien, B. P. Tonner
5632	Nonlinear magneto-optical Kerr effect study of quantum-well states in a Au overlayer on a Co(0001) thin film	M. Groot Koerkamp, A. Kirilyuk, W. de Jong, Th. Rasing, J. Ferré, J. P. Jamet, P. Meyer, R. Mégy
5635	Growth and magnetic properties of Fe_xNi_{1-x} ultrathin films on Cu(100)	F. O. Schumann, S. Z. Wu, G. J. Mankey, R. F. Willis
5638	Quantum well states and interlayer coupling: Co/Cu(100)	L. Nordström, P. Lang, R. Zeller, P. H. Dederichs
5641	The growth of Fe on sulphur passivated Ge(100): A technique for avoiding intermixing	G. W. Anderson, P. Ma, P. R. Norton

Recording Phenomena and Modeling

5644	Data storage based on proximal probe techniques (invited) (abstract)	H. J. Mamin, B. D. Terris, D. Rugar
5645	Recording performance of submicron track width thin film heads	T. T. Lam, Y. Luo, J.-G. Zhu, H.-C. Tong, R. Rottmayer
5648	Effects of write current switching time on recording characteristics (abstract)	F. Tomiyama, H. Takano, Y. Shiroishi, M. Suzuki, Y. Sugita
5649	Bit-shift performance investigations at different skew angles and for different media orientations	S. B. Hu, B. Liu, C. S. Lee
5652	Track-width dependence of transition jitter	P. Dhagat, E. Glavinas, A. Jander, D. G. Porter, R. S. Indeck, M. W. Muller
5655	Trilayer media for high track density longitudinal recording	J. Akiyama, Y. Ohinata, T. Hikosaka, T. Taguchi, Y. Tanaka
5658	Experimental analysis of the effects of tape thickness on magnetic recording	A. Friedmann, D. Wei, H. N. Bertram, J. K. Wolf, R. Swanson, F. Jeffers
5661	Signals and nonlinearities in thin metal-particle tape	Dan Wei, H. Neal Bertram, A. Friedmann
5664	Computer simulation of ultrahigh-density perpendicular magnetic recording	K. Yoshida, M. Hara, Y. Hirayama, Y. Sugita
5667	Barkhausen jumps during domain wall motion in thin magneto-optical films	S. Gadetsky, M. Mansuripur
5670	Simulation of magneto-optic readout signal spectrum using digitized mark and beam patterns (abstract)	S. Jo, J. W. Sohn, S. K. Lee, S. G. Kim

(Continued)

5671	Prediction of the limitations placed on magnetoresistive head servo systems by track edge writing for various pole tip geometries	R. Davidson, R. Simmons, S. Charap
5674	Autotuning of a servowriter head positioning system with minimum positioning error	Y. H. Huang, S. Weerasooriya, T. S. Low

Magneto-Optic Recording Media III

5677	The effect of additives on MSR performance of GdFeCoM/TbFeCo (M=Ta, Pt) double layer	Isao Moritani, Koyata Takahashi, Akio Kondo, Takao Suzuki
5680	Exchange coupling in rare-earth/transition-metal multilayers for magnetic super-resolution	A. M. Ayres, E. E. Marinero
5683	Transition from in-plane to perpendicular magnetization in MSR magneto-optical disks	Naoki Nishimura, Tomoyuki Hiroki, Takeshi Okada, Shigeru Tsunashima
5686	Magnetic parameter control for high-density quadrivalued MO recording (invited) (abstract)	N. Ohta, K. Shimazaki, M. Yoshihiro, N. Nagai, S. Ohnuki
5687	Magneto-optical recording on patterned substrates (invited)	S. Gadetsky, J. K. Erwin, M. Mansuripur, T. Suzuki
5693	Comparison of the magneto-optical figure of merit of NdFeCo and TbFeCo alloys	W. A. Challener
5696	Effect of sputtering condition on dynamic characteristics and microstructures of magneto-optical 5.25 in. SiN/TbFeCo/SiN/Al disks for 532 nm recording media	M. D. Ro, B. I. Cho, M. J. Kim, S. S. Kim, Y. M. Ahn, K. G. Lee, B. L. Gill
5699	A study on the Kerr angle enhancement by the magnetic image effect (abstract)	S. P. Chang, Y. P. Lee, D. R. Huang
5700	A dynamic study of domain formation mechanism during thermomagnetic recording based on micro-Hall effect measurements	Yung-Chieh Hsieh, S. N. Gadetsky, M. Mansuripur, M. Takahashi
5703	The rate of domain growth in magneto-optic recording media (abstract)	J. Earl, A. Lyberatos, R. W. Chantrell
5704	Sensitivity enhancement of Co/Pt superlattices through underlayer composition modification	T. K. Hatwar, C. F. Brucker

Magnetic Excitations II

5707	Magnetic circular x-ray dichroism in Fe_7S_8 and Fe_7Se_8 (abstract)	T. Koide, H. Miyauchi, T. Shidara, N. Nakajima, H. Kawabe, H. Fukutani, K. Shimada, A. Fujimori, K. Iio, T. Kamimura
5708	Magnetic circular x-ray dichroism in Co/Pt multilayers (abstract)	T. Koide, N. Nakajima, T. Shidara, H. Miyauchi, H. Kawabe, H. Fukutani, A. Fujimori, K. Iio, T. Katayama, Y. Suzuki
5709	Mössbauer and x-ray diffraction studies of the phase composition of crystallized $Nd_xFe_{81.5-x}B_{18.5}$ alloys with $7 \leq x \leq 16$ (abstract)	Zhao-hua Cheng, Bao-gen Shen, Jun-xian Zhang, Ming-xi Mao, Ji-jun Sun, Fa-shen Li, Yi-de Zhang
5710	Superexchange interactions in $Ni_{0.5}Co_{0.5}Fe_2O_4$	Choong Sub Lee, Chan Young Lee
5713	A ^{57}Fe Mössbauer study of $Gd_2Fe_{17-x}Ga_xC_2$ ($x=0-6$)	Bo-Ping Hu, Hong-Shuo Li, Bao-Gen Shen, Suharyana, Fang-Wei Wang, J. M. Cadogan, Wen-Shan Zhan
5716	The low-temperature rate of electron capture beta decay in magnetic materials	L. M. Folan, V. I. Tsifrinovich, V. A. Sheverev
5718	Bragg diffraction of laser light by magnetostatic forward volume waves in a layered yttrium–iron–garnet film geometry	Liang-Ping Peng, J. P. Parekh, H. S. Tuan
5721	Modulation of magnetostatic surface wave in garnet film by optical pulses	Y. K. Fetisov, A. V. Makovkin
5724	Dipole-exchange spin wave spectra of exchange-coupled magnetic multilayers calculated by transfer matrix formalism	I. V. Rojdestvenski, M. G. Cottam, A. N. Slavin
5727	Nonlinear magneto-acoustic waves in ferromagnets	G. T. Adamashvili, A. A. Maradudin

(Continued)

5730 Parametrical interaction of magnetostatic volume waves in a space-time periodic magnetic field — Y. K. Fetisov, N. V. Ostrovskaya, A. F. Popkov

5733 Characteristic analysis of coupled microstrip patch resonators on ferrimagnetic substrates — Kunquan Sun, Yinchao Chen, Walter Barry, John Corlett

5736 Characteristics of microstrip directional coupler on magnetized ferrites — E. L. Albuquerque, M. R. M. L. Albuquerque, A. G. d'Assunção

5739 Magnetic losses in stripline/microstrip circulators — H. How, T. M. Fang, C. Vittoria, R. Schmidt

5742 Experimental determination of an effective demagnetization factor for nonellipsoidal geometries — Guobao Zheng, M. Pardavi-Horvath, Xiaohua Huang, B. Keszei, J. Vandlik

5745 Quantum fluctuations in antiferromagnets of the BX_2 family (abstract) — E. Rastelli, A. Tassi

5745 Spin configurations in VBr_2 supported by uniaxal anistropy and quantum fluctuations (abstract) — E. Rastelli, A. Tassi

Micromagnetics and Hysteresis

5746 Henkel plots and the Preisach model of hysteresis — C. J. Buehler, I. D. Mayergoyz

5749 Kinetic Ising systems as models of magnetization switching in submicron ferromagnets — Howard L. Richards, Scott W. Sides, Mark A. Novotny, Per Arne Rikvold

5752 Simple function for a complex domain configuration — A. S. Arrott, J.-G. Lee

5755 Dynamical micromagnetics of a ferromagnetic particle: Numerical studies — Bo Yang, Donald R. Fredkin

5758 Anomalous time-induced curvature in Henkel plots based on the Preisach model — P. D. Mitchler, E. Dan Dahlberg, E. Wesseling, R. M. Roshko

5761 Magnetization reversal and small lancettes calculated by statistic domain behavior (abstract) — Paul L. Fulmek, Hans Hauser

5762 Surface anisotropy of a fine γ-Fe_2O_3 particle — Kezhao Zhang, Donald R. Fredkin

5764 Random free energy model for the description of hysteresis — G. Bertotti, V. Basso, G. Durin

5767 Micromagnetics of polycrystalline two-dimensional platelets — K. M. Tako, M. A. Wongsam, R. W. Chantrell

5770 Three-dimensional analysis of the magnetization process of thin-film media — E. Miyashita, Y. Yoneda, J. Numazawa

5773 Characterization of minor loops using Preisach-based models — Ferenc Vajda, Edward Della Torre

Head–Media Interface and Tribology

5776 Radio frequency ion beam deposition of diamond-like carbon for sliders and heads — Lien-Chang Wang, Gary Halada, Richard J. Gambino, Alan Hayes, Sal DiStefano

5779 Nanoindentation study of the mechanical properties of metal evaporated magnetic tapes — Hong Deng, John A. Barnard

5782 Comparison of tribological performance of pure carbon and carbon-nitrogen coated thin film head sliders — Geng Wang, John M. Silversten, Jack H. Judy, Ga-Lane Chen

5785 Transient response of ultralow flying sliders over contaminated and textured surfaces — Paul R. Peck, Ki-Ook Park, Myung S. Jhon, Soo-Choon Kang, Tom I.-P. Shih

5788 Surface diffusion of thin perfluoropolyalkylether films — Teresa M. O'Connor, Young R. Back, Myung S. Jhon, Byung G. Min, Do Y. Yoon, Thomas E. Karis

5791 Wear studies of contact recording interface with a microfabricated head — Bharat Bhushan, Youlin Li

5794 Non-Gaussian surface roughness distribution of magnetic media for minimum friction/stiction — Bharat Bhushan, Sameera Chilamakuri

5797 A micro-remote centered compliance suspension for contact recording head (abstract) — M. Nakao, S. Sugiyama, Y. Hatamura, T. Hamaguchi, K. Watanabe

5798 Micro/nanoscale studies of boundary layers of liquid lubricants for magnetic disks (abstract) — Vilas N. Koinkar, Bharat Bhushan

(Continued)

5799	Rough surface contact analysis and its relation to plastic deformation at the head–disk interface	Chin Y. Poon, Bharat Bhushan
5802	Environmental effects on the pause mode performance of metal-evaporated and metal-particle tapes	Steven T. Patton, Bharat Bhushan
	Giant Magnetoresistance and Magnetic Multilayers	
5805	Spin-dependent interface transmission and reflection in magnetic multilayers (invited)	M. D. Stiles
5811	How predictable is the current perpendicular to plane magnetoresistance? (invited)	W. P. Pratt, Jr., Q. Yang, L. L. Henry, P. Holody, W.-C. Chiang, P. A. Schroeder, J. Bass
5816	The role of impurity scattering in Co/Cu (111) M.B.E. multilayers (abstract)	K. P. Wellock, B. J. Hickey
5817	Giant magnetoresistance multilayers of high thermal stability with thicker magnetic layers	S. A. Hossain, B. H. Pirkle, J. Yang, M. R. Parker
5820	Relaxation in NiFe/Ag giant magnetoresistive devices	R. W. Cross, A. B. Kos
5823	New methods to measure the current perpendicular to the plane magnetoresistance of multilayers	P. Dauguet, P. Gandit, J. Chaussy
5826	Engineering coercivities by dual ion beam sputtering for synthesizing soft permalloy-based spin-valve multilayers (abstract)	C. J. Gutierrez, R. Dail, R. Selestino, L. Tristan, M. Khater, Steve Michel
	Electronic Structure and Anisotropy	
5827	First principles determination of magnetocrystalline anisotropy for surfaces and interfaces using a torque method (abstract)	Xindog Wang, A. J. Freeman, R. Wu, D. S. Wang
5828	Theoretical predictions of magnetic interface anisotropy in (Pd/Co/Pd)/X superlattices	J. M. MacLaren
5831	Orientation and structure dependence of interface magnetocrystalline anisotropy of Co/Cu overlayers and superlattices	Lieping Zhong, Miyoung Kim, Xindong Wang, Dingsheng Wang, A. J. Freeman
5834	Onset of C(2×2) ferrimagnetic order in Cr islands deposited on Fe(001) as a function of island size	L. Pizzagalli, D. Stoeffler, A. Vega, S. Bouarab, C. Demangeat, H. Dreyssé, F. Gautier
5837	On the γ-like surface of α-Ce: Theory (abstract)	O. Hjortstam, J. Trygg, B. Johansson, O. Eriksson, J. M. Wills
5838	Spin polarization of the conduction bands and secondary electrons of Gd(0001)	Dongqi Li, J. Pearson, S. D. Bader, D. N. McIlroy, C. Waldfried, P. A. Dowben
5841	Spin-resolved electron spectroscopies of epitaxial magnetite (001) (abstract)	Kimberly A. Shaw, Eric Lochner, David M. Lind, Rebecca C. DiBari, Plamen Stoyanov, Brian Singer
5841	Origins of giant biquadratic coupling in CoFe/Mn/CoFe sandwich structures (abstract)	Norman C. Koon
5842	New estimation of surface anisotropy	Xiao Hu, Yoshiyuki Kawazoe
5845	Perpendicular magnetization and surface magnetoelastic anisotropy in epitaxial Cu/Ni/Cu (001)	Gabriel Bochi, C. A. Ballentine, H. E. Inglefield, C. V. Thompson, R. C. O'Handley
5848	Magnetization reversal in patterned Co(0001) ultrathin films with perpendicular magnetic anisotropy	N. Bardou, B. Bartenlian, C. Chappert, R. Mégy, P. Veillet, J. P. Renard, F. Rousseaux, M. F. Ravet, J. P. Jamet, P. Meyer
5851	Magnetic force microscopy of single-domain single-crystal iron particles with uniaxial surface anisotropy	R. M. H. New, R. F. W. Pease, R. L. White, R. M. Osgood, K. Babcock
5854	Surface-induced miscibility gap in vapor deposited $Co_{1-x}Pt_x$ (abstract)	M. Q. Tran, A. L. Shapiro, P. W. Rooney, F. Hellman
5855	Effects of magnetostatic interaction between two single-domain cobalt bars on crystal anisotropy and switching field (abstract)	Stephen Y. Chou, Linshu Kong

(Continued)

Superconductivity

5856	Synthesis and physical properties of RNi_2B_2C and related materials (invited) (abstract)	R. J. Cava
5857	Neutron scattering studies of the magnetic order in RNi_2B_2C	J. W. Lynn, Q. Huang, S. K. Sinha, Z. Hossain, L. C. Gupta, R. Nagarajan, C. Godart
5860	Superconducting metastable phase in rapid quenched Y–Pd–B–C borocarbides	Valter Ström, K. S. Kim, A. M. Grishin, K. V. Rao
5863	Field dependence of magnetic transitions for magnetic superconductors RNi_2B_2C (R=Dy, Ho)	H. C. Ku, M. S. Lin, Y. Y. Hsu, J. H. Shieh, Y. B. You
5866	Systematic variation of T_N(Pr) for the two-CuO_2-layer cuprate $m212$ ($m=1, 2, 3$) systems	H. C. Ku, C. L. Yang, C. H. Chou, Y. Y. Hsu, Y. B. You, J. H. Shieh
5869	Magnetic structure and ordering of Nd ions in Ga substituted $NdBa_2Cu_3O_7$ (abstract)	A. M. Niraimathi, E. Gmelin, P. Allenspach, C. Ritter
5869	Influence of the crystalline electric field on the magnetic properties of Ga-doped $NdBa_2Cu_3O_x$ (abstract)	P. Allenspach, A. M. Niraimathi, E. Gmelin
5870	Synthesis and superconductivity of intermetallic compounds $Y_2Ni_xB_{8-x}C_2$, $YNi_xCu_{2-x}B_2C$, and $YNi_xCu_{2-x}Si_2C$	Wei Zhao, Jinke Tang, Young-sook Lee, Charles J. O'Connor
5873	Oxygen dependence of the Josephson weak link effect, specific heat, and the transition temperature of $YBa_2Cu_3O_x$	S. Glenis, G. Choi, C. L. Lin, T. Mihalisin, X. Q. Wang
5876	Effects of Pr, Tb, and Zn doping into $YBa_2Cu_3O_7$ on magnetoresistivity and magnetic phase boundaries	F. Freibert, G. Cao, S. McCall, M. Shepard, J. E. Crow
5879	Rotational magnetic measurements of vortex pinning in polycrystalline superconductors (abstract)	M. K. Hasan, S. J. Park, J. S. Kouvel

Recording Heads and Materials

5880	4 Gbit/in.^{2} inductive write heads using high moment FeAlN poles	W. P. Jayasekara, S. Wang, M. H. Kryder
5883	Experimental studies of nonlinearities in MR heads	Xinzhi Xing, H. Neal Bertram
5886	Micromagnetics of dual spin-valve GMR heads	Jian-Gang Zhu, Xiao-Guang Ye, Samuel W. Yuan, Hua-Ching Tong, Robert Rottmayer
5889	Experimental and analytical properties of 0.2-μm-wide, end-on, multilayer, giant magnetoresistance, read head sensors	A. V. Pohm, R. S. Beech, J. M. Daughton, E. Y. Chen, M. Durlam, K. Nordquist, T. Zhu, S. Tehrani
5892	Magnetization reversal processes of NiFe elements exchange coupled by NiO antiferromagnetic films	Juren Ding, Jian-Gang Zhu
5895	Domain structures at the cross sections of thin film inductive recording heads	Francis H. Liu, Hua-Ching Tong, Lena Miłosvlasky
5898	Picosecond time-resolved magnetization dynamics of thin-film heads	M. R. Freeman, J. F. Smyth
5901	Stress and magnetic properties in high moment FeN thin films	Kyusik Sin, Shan X. Wang
5904	Effect of base layers on the soft magnetic properties of FeTaN films	V. R. Inturi, J. A. Barnard
5907	Soft magnetic properties of nanocrystalline FeRuGaSi-Hf alloy films and head characteristics for the embedded thin film tape head	H. Ohmori, M. Shoji, T. Kobayashi, T. Yamamoto, Y. Sugiyama, K. Hayashi, K. Hono
5910	Theory, fabrication and testing of dual track complimentary type of thin-film recording heads for perpendicular magnetic recording system	T. Ichihara, S. Nakagawa, N. Matsushita, M. Naoe
5913	Permeability of microstrip thin films of various materials	Kiyoshi Yamakawa, Kazuyuki Ise, Naoki Honda, Kazuhiro Ouchi, Shun-ichi Iwasaki
5916	Pole tip recession studies of hard carbon-coated thin-film tape heads	Bharat Bhushan, Steven T. Patton, Ramesh Sundaram, Subrata Dey

(Continued)

Exchange Coupling in Oxides and Composites

5919 Heat capacity measurements of NiO/CoO superlattices (invited) (abstract) — E. N. Abarra, K. Takano, F. Hellman, A. E. Berkowitz

5920 Finite-size scaling in thin antiferromagnetic CoO layers — T. Ambrose, C. L. Chien

5923 Magnetic properties of epitaxial ferrite multilayer films — Y. Suzuki, R. B. van Dover, E. M. Gyorgy, Julia M. Phillips, V. Korenivski, D. J. Werder, C. H. Chen, R. J. Felder, R. J. Cava, J. J. Krajewski, W. F. Peck, Jr.

5926 Interlayer exchange coupling in amorphous/crystalline $NiFe_2O_4$ thin-film bilayers — V. Korenivski, R. B. van Dover, Y. Suzuki, E. M. Gyorgy, J. M. Phillips, R. J. Felder

5929 Magneto-optic properties and exchange interaction of the macroscopic ferrimagnet $Co_{1-x-y}Tb_x(EuS)_y$ — P. Fumagalli, A. Schirmeisen, R. J. Gambino

5932 Bi–DyIG films: Enhancement of the Dy contribution to the Faraday rotation — M. Guillot, H. Le Gall, J. Gouzerh, J. M. Desvignes, M. Artinian

5935 Microstructural characterization of ferrimagnetic substituted iron garnet heterostructures for magneto-optical applications (abstract) — B. M. Simion, R. Ramesh, G. Thomas

5936 A study of the magneto-optical Kerr spectra of bulk and ultrathin Fe_3O_4 — P. J. van der Zaag, W. F. J. Fontijn, P. Gaspard, R. M. Wolf, V. A. M. Brabers, R. J. M. van de Veerdonk, P. A. A. van der Heijden

Other Hard Magnetic Materials I

5939 Site affinity of substituents in $Nd_2Fe_{17-x}T_x$ (T=Cu,Zr,Nb,Ti,V) alloys — W. B. Yelon, Z. Hu, W. J. James, G. K. Marasinghe

5942 Electronic structure and magnetism in $Sm_2Fe_{17-x}A_x$ (A=Al,Ga,Si) — R. F. Sabirianov, S. S. Jaswal

5945 of the $Ce_2Fe_{17-x}Al_x$ solid solutions (abstract) — Sanjay R. Mishra, Gary J. Long, O. A. Pringle, Z. Hu, W. B. Yelon, D. P. Middleton, K. H. J. Buschow, F. Grandjean

5946 Magnetization and coercivity of $Mn_{3-\delta}Ga$ alloys with a $D0_{22}$-type structure — Hiroshi Niida, Tomiei Hori, Hideya Onodera, Yasuo Yamaguchi, Yasuaki Nakagawa

5949 Magnetic characteristics of $RCo_{13-x}Si_x$ alloys (R=La, Pr, Nd, Gd, and Dy) — M. Q. Huang, W. E. Wallace, R. T. Obermyer, S. Simizu, M. McHenry, S. G. Sankar

5952 First-principles calculation of the 3*d* magnetocrystalline anisotropy energy of YCo_5 — M. Yamaguchi, S. Asano

5955 Magnetic viscosity and microstructure: Particle size dependence of the activation volume — J. M. González, C. de Julián, Anit K. Giri, S. Castro, M. Gayoso, J. Rivas

5958 High coercivity rare earth–cobalt films — S. S. Malhotra, Y. Liu, Z. S. Shan, S. H. Liou, D. C. Stafford, D. J. Sellmyer

5961 High-temperature magnetic properties of $TbCu_7$-type SmCo-based films — H. Hegde, X. R. Qian, Jong-Guk Ahn, F. J. Cadieu

5964 Nanocomposite Sm_2Co_{17}/Co permanent magnets by mechanical alloying — S. K. Chen, J. L. Tsai, T. S. Chin

5967 Control of the axis of chemical ordering and magnetic anisotropy in epitaxial FePt films — R. F. C. Farrow, D. Weller, R. F. Marks, M. F. Toney, A. Cebollada, G. R. Harp

5970 Ba ferrite films with large saturation magnetization and high coercivity prepared by low-temperature sputter deposition — K. Noma, N. Matsushita, S. Nakagawa, M. Naoe

5973 Characterization of $Fe_{17}R_2$ phases (R=Pr and Sm) oxidized at 200 °C — S. Gama, C. A. Ribeiro, F. A. O. Cabral, C. C. Colucci, E. de Morais, N. L. Sanjurjo, C. Campos, J. D. Ardisson, A. I. C. Persiano

(Continued)

Magneto-Optical Materials

5976	Magneto-optical properties of (BiGdY) iron garnets for optical magnetic field sensors	O. Kamada
5979	An investigation on the magneto-optical enhancement in Ni-substituted barium ferrites	Xijuan Zhang, You Xu, Mingqian Duan, Maurice Guillot
5982	Second harmonic investigation of ac magnetized in-plane anisotropic garnet film	Sergey V. Lebedev
5985	Magneto-optical properties of Sc-substituted holmium iron garnet single crystals	J. Ostoréro, M. Guillot
5988	Effect of structural irregularity on propagation properties of optical waves in discontinuous magneto-optical media with one-dimensional quasirandom array structures	Mitsuteru Inoue, Takeshi Yamamoto, Keiji Isamoto, Toshitaka Fujii
5991	Magneto-optic and microwave properties of epitaxial garnet thin film heterostructures and superlattices (abstract)	R. Ramesh, T. Venkatesan, S. Lofland, M. Dominguez, S. M. Bhagat, B. M. Simion, G. Thomas

New Magnetic Materials

5992	Mössbauer effect and electronic transport studies of icosahedral $Al_{50}Pd_{10}Mn_{25-x}Fe_xB_{15}$ alloys	M. Yewondwossen, J. E. Jagger, Z. Koziol, R. A. Dunlap
5995	Magnetic and electronic properties of the magnetically ordered quasicrystalline alloys $Al_{70-x}Pd_{15}Mn_{15}B_x$	M. Yewondwossen, Z. Koziol, D. Bahadur, Z. J. Yang, M. Foldeaki, R. A. Dunlap
5998	Structural, magnetic, and magnetocaloric properties of $(Hf_{0.83}Ta_{0.17})Fe_{2+x}$ materials	J. F. Herbst, C. D. Fuerst, R. D. McMichael
6001	Magnetic properties of a high T_c superconductivity related system $Y_{1-x}Pr_xBa_2Fe_3O_8$	T. Yuen, M. Seyedahmadian, R. E. Salomon, G. H. Myer, G. Cao
6004	Observation of independent iron and rare-earth ordering in RFe_6Ge_6 (R= *Y*, Gd–Lu) compounds	D. H. Ryan, J. M. Cadogan

Small Particles/Ferrofluids

6007	Cobalt-doped carbon nanotubes: Preparation, texture, and magnetic properties	K. Lafdi, A. Chin, N. Ali, J. F. Despres
6010	Magnetic properties of nanosized wires	J. Meier, B. Doudin, J.-Ph. Ansermet
6013	Negative remanence in magnetic nanostructures	X. Yan, Y. Xu
6016	Preparation of Co–Fe–P amorphous fine needles with anodization technique and measurement of demagnetizing factor	A. Tayaoka, E. Tayaoka, J. Yamasaki
6019	Nonhomogeneous magnetization reversal in 2D Ising clusters	D. García-Pablos, P. García-Mochales, N. García, P. A. Serena
6022	Alternating current (ac) susceptibility studies in Ni-SiO_2 granular film	B. Zhao, Jeff Y. Chow, X. Yan
6025	High coercivity single-domain particles in glass matrix	C. Tsang, H. D. Gafney, D. Sunil, M. Rafailovich, J. Sokolov, R. J. Gambino
6028	Identification of a high-temperature magnetic phase transition in ball-milled and compacted nanocrystalline Fe-Cu alloys	R. D. Shull, J. P. Cline, I. Baker, F. Liu
6031	Steps in the hysteresis loops of a high-spin molecule	Jonathan R. Friedman, M. P. Sarachik, J. Tejada, J. Maciejewski, R. Ziolo
6034	Computer simulation of microstructure and interaction effects in fine particle systems (abstract)	G. N. Coverdale, R. W. Chantrell, M. El-Hilo, K. O'Grady
6034	Periodic breathing oscillations and instabilities in ferrofluids (abstract)	Weili Luo, Tengda Du
6035	Effects of Zn ion on magnetic properties of Fe_3O_4 magnetic colloids (abstract)	C. H. Lin, P. C. Kuo, J. L. Pan, D. R. Huang

(Continued)

Domains and Magnetization Processes

6036	Measurements of local magnetization by Kerr effect on Si-Fe nonoriented sheets	S. Defoug, R. Kaczmarek, W. Rave
6039	The energy loss per cycle in bar domain Si–Fe	Bryen E. Lorenz
6042	Correlation between the Barkhausen noise power and the total power losses in 3% Si–Fe	M. Birsan, J. A. Szpunar, T. W. Krause, D. L. Atherton
6045	Effects of surface condition on Barkhausen emissions from steel	A. P. Parakka, D. C. Jiles, H. Gupta, S. Jalics
6047	Simultaneous Barkhausen discontinuities of multiple die-drawn Fe-Si-B amorphous wires connected with amorphous ribbons (abstract)	M. Soeda, J. Yamasaki
6048	The influence of domain activities on MR head performance	Weichun Ye, Jinyue Yu, Bingchu Cai
6051	Iron whisker domain patterns imaged by garnet films	J.-G. Lee, S. A. Govorkov, A. S. Arrott
6054	Temperature and field dependence of domain wall dynamics up to the Curie point of EuO	A. Flosdorff, D. Görlitz, J. Kötzler
6057	The dependence of magnetoacoustic emission on magnetizing frequency in nickel and mild steel	D. H. L. Ng, C. C. Yu, C-D. Qin, C. C. H. Lo, J. P. Jakubovics
6060	180° domain wall with the coordinate dependent azimuthal angle of magnetization	V. L. Sobolev, C. T. Teh, H. L. Huang

Imaging and Applied Magnetics

6063	Modeling MFM images of periodic magnetization patterns (abstract)	R. Madabhushi, R. D. Gomez, E. R. Burke, I. D. Mayergoyz
6064	Magnetic force microscope study of domain wall structures in magnetite	Taras G. Pokhil, Bruce M. Moskowitz
6067	A scanning microscope using a magnetoresistive head as the sensing element	R. O'Barr, M. Lederman, S. Schultz
6070	Surface deformations and domains in Terfenol-D by scanning probe microscopy	A. P. Holden, D. G. Lord, P. J. Grundy
6073	Magneto-optical indicator film (MOIF) microscopy of granular and layer structures (abstract)	V. I. Nikitenko, V. S. Gornakov, L. M. Dedukh, A. F. Khapikov, L. H. Bennett, R. D. McMichael, L. J. Swartzendruber, A. J. Shapiro, M. J. Donahue, V. N. Matveev, V. I. Levashov
6074	High density recorded patterns observed by high-resolution Bitter scanning electron microscope method	O. Kitakami, T. Sakurai, Y. Shimada
6077	A new magnetic bar code system based on a magnetic anisotropy detection (abstract)	I. Sasada, N. Watanabe

Symposium on Magnetic Nanostructures

6078	Giant magnetoresistance as a probe of interfacial electronic character (invited) (abstract)	S. S. P. Parkin
6079	Nanostructure fabrication via laser-focused atomic deposition (invited)	R. J. Celotta, R. Gupta, R. E. Scholten, J. J. McClelland
6084	Perpendicular transport and magnetic properties in patterned multilayer magnetic microstructures (invited)	J. J. Krebs, W. Vavra, G. A. Prinz, S. F. Cheng, Anita Fink
6090	Arrays of multilayered nanowires (invited)	B. Doudin, A. Blondel, J.-Ph. Ansermet
6095	Femtosecond near-field spin microscopy in digital magnetic heterostructures (invited)	J. Levy, V. Nikitin, J. M. Kikkawa, D. D. Awschalom, N. Samarth
6101	The energy loss per cycle in bar domain Si–Fe	Bryen E. Lorenz

Macroscopic Quantum Tunneling and Transport Properties

6107	Chiral quantum spin solitons	Hans-Benjamin Braun, Daniel Loss

(Continued)

6110 Quantum dynamical calculations in clusters of spin 1/2 particles: Resonant coherent quantum tunneling on the magnetization reversal — D. García-Pablos, N. García, P. A. Serena, H. De Raedt

6113 Frequency mixing phenomena in a bistable system — A. N. Grigorenko, P. I. Nikitin, G. V. Roschepkin

6116 Low temperature magnetic relaxation and quantum tunneling in nanocrystalline particles (abstract) — X. X. Zhang, J. M. Hernandez, E. C. Kroll, R. Ziolo, J. Tejada

6117 Annealing and geometric effects in the magneto-impedance of amorphous $Co_{70.4}Fe_{4.6}Si_{15}B_{10}$ alloys — R. L. Sommer, C. L. Chien, R. Hasegawa

6120 Size dependence of the magnetoresistance in submicron FeNi wires — A. O. Adeyeye, J. A. C. Bland, C. Daboo, Jaeyong Lee, U. Ebels, H. Ahmed

6123 Effect of interstrip gap on the sensitivity of high sensitivity magnetoresistive transducers — Bharat B. Pant

6126 Large magnetic Hall effect in ferromagnetic Fe_xPt_{100-x} thin films — C. L. Canedy, G. Q. Gong, J. Q. Wang, Gang Xiao

6129 Resistivities of sputtered Ag(3.3 nm)/Cu(t_{Cu}), Ag(3.3 nm)/Au(t_{Au}), and Ni(4.2 nm)/Co(t_{Co}) multilayers at 4–5 and 295 K — L. L. Henry, M. Oonk, R. Loloee, Q. Yang, W.-C. Chiang, W. P. Pratt, Jr., J. Bass

6132 Resonant near-sound reorientation of the domain wall plane in yttrium orthoferrite — M. V. Chetkin, Yu. N. Kurbatova, A. I. Akhutkina

6134 Approach to the anhysteretic surface — M. J. Sablik, R. A. Langman

6137 Studies of remanence in granular Ni–SiO_2 films — Y. Xu, B. Zhao, X. Yan

6140 Observation of giant Hall effect in granular magnetic films — A. B. Pakhomov, X. Yan, Y. Xu

Spin Glasses and Frustrated Ferromagnets

6143 Freezing of the extended state in the random local field theory of Ising spin glasses with long range interactions — B. E. Vugmeister, D. Nowakowski, D. L. Huber

6146 Criticality of the fully frustrated *XY* model: A study using Monte Carlo hard-spin mean-field theory (abstract) — James E. Tesiero, Susan R. McKay

6147 Magnetization and dynamics of reentrant ferrimagnetic spin-glass $[MnTPP]^{\cdot+}[TCNE]^{\cdot-}\cdot 2PhMe$ — W. B. Brinckerhoff, B. G. Morin, E. J. Brandon, Joel S. Miller, A. J. Epstein

6150 The anhydrous alums: A versatile new series of model triangular lattice magnets (abstract) — S. T. Bramwell, L. Nixon, I. P. Parkin, B. M. Kariuki, K. D. M. Harris, S. G. Carling, C. J. Harding

6151 Finite size effects in thin NiMn spin glass layers — L. Hoines, J. A. Cowen, J. Bass

6154 A new type of spin glass in spin-density-wave CrMn alloys (abstract) — V. Yu. Galkin, P. C. de Camargo, Naushad Ali, J. Schaf, E. Fawcett

6155 Magnetic phase diagram of the $Fe_xMn_{0.6-x}Al_{0.40}$ alloys series — G. A. Pérez Alcázar, Ligia E. Zamora, A. Bohórquez, E. González, J. M. González

6158 Ferromagnetic critical correlations and dynamics in AuFe reentrant ferromagnets — C. Pappas, M. Alba, A. Brulet, V. Viel, F. Mezei

6161 Neutron depolarization study of magnetic order in a-Fe_xZr_{100-x} (x=90–93), a-$Fe_{90}Sc_{10}$ and their hydrides — D. H. Ryan, J. M. Cadogan, S. J. Kennedy

6164 Spin glass behavior of $Zn_{1-x}Mn_xTe$ — P. M. Shand, A. D. Christianson, L. S. Martinson, J. W. Schweitzer, T. M. Pekarek, I. Miotkowski, B. C. Crooker

6167 Observation of spin-glass freezing in the S=1 linear-chain Heisenberg antiferromagnet NENP — M. Hagiwara, K. Katsumata, S. Sasaki, N. Narita, I. Yamada, T. Yosida

6170 Nonlinear susceptibility measurements at the spin-glass transition of the pyrochlore antiferromagnet $Y_2Mo_2O_7$ — M. J. P. Gingras, C. V. Stager, B. D. Gaulin, N. P. Raju, J. E. Greedan

(Continued)

6173 Magnetic ordering in pyrochlore $Ho_2Mn_2O_7$ — N. P. Raju, J. E. Greedan, J. S. Pedersen, Ch. Simon, A. Maignan, A. M. Niraimathi, E. Gmelin, M. A. Subramanian

6176 λ-MnO_2, a new frustrated antiferromagnet with the defect spinel structure (abstract) — J. E. Greedan, Guo Liu, N. P. Raju, J. N. Reimers, Zin Tun

Magneto-Optic Kerr Effect: Theory and Experiment

6177 Theory of nonlinear magneto-optics (invited) — U. Pustogowa, T. A. Luce, W. Hübner, K. H. Bennemann

6181 Giant nonlinear magneto-optical Kerr effects from Fe interfaces (invited) — Th. Rasing, M. Groot Koerkamp, B. Koopmans, H. v.d. Berg

6186 Symmetry of the magneto-optic response of the Sagnac interferometer — J. S. Dodge, L. Klein, M. M. Fejer, A. Kapitulnik

6189 Second-order magneto-optic effects in anisotropic thin films (abstract) — R. M. Osgood III, B. M. Clemens, R. L. White

6190 Spectroscopic Kerr investigations of CoNi/Pt multilayers — W. P. Van Drent, T. Suzuki, Q. Meng, J. C. Lodder, Th. J. A. Popma

6193 *In situ* and *ex situ* optical characterization of electro deposited magneto-optic materials — James N. Hilfiker, Darin W. Glenn, Scott Heckens, John A. Woollam, Kurt W. Wierman

6196 Theoretical predictions of the polar Kerr effect in Fe and Co — J. M. MacLaren, W. Huang

6199 First principles calculations of the Kerr effect in MnBi, MnSb, and Mn_2BiSb (abstract) — W. Huang, J. M. MacLaren, R. H. Victora

6200 Dielectric tensor characterization of $Mn_{0.53}Bi_{0.47}$ and $Mn_{0.52}Bi_{0.44}Sb_{0.04}$ films — Z. Celinski, Zheng Yan

6203 Influence of Al capping layers on growth, topography, and magnetic properties on MnBi thin films — U. Rüdiger, P. Fumagalli, P. Dworak, A. Schirmeisen, G. Güntherodt

6206 Magnetic and magneto-optical properties of $Mn_xPt_{1-x-y}Zn_y$ — Kurt W. Wierman, Roger D. Kirby

Magnetostriction

6209 First principles determinations of magnetostriction in transition metals (invited) — Ruqian Wu, A. J. Freeman

6213 Zero field damping capacity in $(Tb_xDy_{1-x})Fe_y$ — J. P. Teter, K. B. Hathaway, A. E. Clark

6216 Anomolous ΔE effects in TbDyZn alloys — J. R. Cullen, M. Wun-Fogle, J. B. Restorff, J. P. Teter, A. E. Clark

6219 Enhancement of piezomagnetic response of highly magnetostrictive rare earth-iron alloys at kHz frequencies — P. P. Pulvirenti, D. C. Jiles, R. D. Greenough, I. M. Reed

6222 Texture in magnetic annealed Terfenol-D films — M. Loveless, S. Guruswamy

6225 Stress dependence of magnetostrictions and strains in ⟨111⟩-oriented single crystals of Terfenol-D — Xuegen Zhao, Guangheng Wu, Jinghua Wang, Kechang Jia, Wenshan Zhan

Giant Magnetoresistance in Multilayers and Granular Systems

6228 Effects of surface topology and texture on exchange anisotropy in NiFe/Cu/NiFe/FeMn spin valves — C.-M. Park, K.-I. Min, K. H. Shin

6231 High sensitivity in magnetoresistance of epitaxial NiFe/Cu/Co (/Cu) (100) superlattices — Y. Kawawake, H. Sakakima, Y. Irie, M. Satomi

6234 Factors affecting performance of NiO biased giant magnetoresistance structures — S. F. Cheng, J. P. Teter, P. Lubitz, M. M. Miller, L. Hoines, J. J. Krebs, D. M. Schaefer, G. A. Prinz

6237 Giant magnetoresistance effect and electric conduction in amorphous-CoFeB/Cu/Co sandwiches — M. Jimbo, K. Komiyama, S. Tsunashima

(Continued)

6240	Size effects and giant magnetoresistance in unannealed NiFe/Ag multilayer stripes	S. C. Sanders, R. W. Cross, S. E. Russek, A. Roshko, J. O. Oti
6243	Effect of sputter gas on the physical and magnetic microstructure of Co/Cu multilayers	D. M. Donnet, K. Tsutsumi, P. de Haan, J. C. Lodder
6246	Giant thermopower in 3D-magnetic multilayers. Structural and electron band effects (abstract)	M. M. P. de Azevedo, B. G. Almeida, V. S. Amaral, M. E. Braga, J. B. Sousa, P. P. Freitas, R. Krishnan
6247	Structural characterization of epitaxial Co–Ag	A. Azizi, L. El Chahal, K. Ounadjela, J. P. Deville, S. M. Thompson, J. F. Gregg
6250	Spin-dependent scattering in the nonmagnetic layers of annealed Co/Cu multilayers	H. Laidler, B. J. Hickey
6253	Interfacial roughness of Fe–Cr GMR superlattices (abstract)	W. Dmowski, T. Egami, D. Kelly, I. Schuller
6254	Giant magnetoresistance in evaporated NiFe/Cu and NiFeCo/Cu multilayers (abstract)	A. M. Zeltser, Neil Smith
6255	Giant magnetoresistance in magnetic granular systems	L. Sheng, R. Y. Gu, D. Y. Xing, Z. D. Wang, Jian-Xin Zhu
6258	Giant magnetoresistance in granular Fe–MgF_2 films	T. Furubayashi, I. Nakatani
6261	The influence of Ni on the microstructure and GMR of the Co–Cu alloy granular films (abstract)	S. Y. Zhang, Q. Q. Cao
6261	Real-space analysis of inhomogeneous scattering versus superlattice-potential effects for magnetotransport (abstract)	Horacio E. Camblong
6262	Magnetic tunneling effect in Fe/Al_2O_3/$Ni_{1-x}Fe_x$ junctions	N. Tezuka, T. Miyazaki
6265	Spin polarized tunneling in half-metallic ferromagnets (abstract)	C. T. Tanaka, J. S. Moodera
Anisotropy, Magnetoresistance, and Interface Coupling		
6266	Ferromagnetic resonance of sputtered Co/Mn multilayers (abstract)	D. Spoddig, F. Schreiber, J. Pflaum, Q. Wang, H. Zabel, J. Pelzl
6266	Thermal effects in magnetization, anisotropy, and interface width in Fe/Cu multilayers (abstract)	Michael J. Pechan, Eric E. Fullerton, Ivan K. Schuller
6267	Study of magnetic reorientation phenomenon and magnetic properties of Pd/(Pt/Co/Pt) multilayers	Ying Xiao, Jun-Hao Xu, K. V. Rao
6270	Structural anisotropy of Tb/Fe multilayers	Y. Fujiwara, X. Y. Yu, S. Tsunashima, S. Iwata, M. Sakurai, K. Suzuki
6273	Occurrence of large perpendicular magnetic anisotropy in bilayered films with nanometer-thick TbFeCo and Al layers	H. Ito, K. Song, M. Naoe
6276	Studies of anisotropic and giant magnetoresistance in Co/Cu(111) epitaxial multilayers	J. C. A. Huang, Y. H. Lee, Y. M. Hu, T. C. Chang
6279	Effects of discharge pressure on the properties of Ag/Ni superlattices prepared by facing-target sputtering	X. T. Zeng, H. K. Wong
6282	Influence of the crystal structure on the magnetic property of Co/Cr superlattices	Y. Liou, J. C. A. Huang, Y. D. Yao, W. T. Yang, S. Y. Liao, C. P. Chang
6285	Magnetoresistance in NiFe/Au multilayers and spin-valve structures (abstract)	K. T. Wu, R. J. Gambino
6286	Temperature dependence of the pinning field and coercivity of NiFe layers coupled with an antiferromagnetic FeMn layer	H. Fujiwara, K. Nishioka, C. Hou, M. R. Parker, S. Gangopadhyay, R. Metzger
6289	Magnetic and magnetotransport properties of Ni/Fe multilayers	M. Cai, T. Veres, R. Morel, R. W. Cochrane
6292	Studies of Fe/Cr multilayer and trilayer films	E. M. Ho, A. C. Daykin, A. K. Petford-Long

(Continued)

6295 Spin orientation in an exchange coupled Fe/Cr/Fe trilayer determined by polarized neutron reflection — J. A. C. Bland, H. T. Leung, S. J. Blundell, V. S. Speriosu, S. Metin, B. A. Gurney, J. Penfold

6298 Superconductivity and magnetic properties of Fe/Nb multilayers (abstract) — Th. Mühge, I. Zoller, K. Westerholt, H. Zabel, Yu. V. Goryunov, N. N. Garif'yanov, G. G. Khaliullin, I. A. Garifullin, L. R. Tagirov

6299 A comparison of structure and magnetoresistance in Fe/(Ag–Cu) films (abstract) — S. J. Kwon, S. J. Choi

6300 ^{59}Co and ^{55}Mn NMR of CoMn alloys and multilayers — T. Thomson, P. C. Riedi, Q. Wang, H. Zabe

6303 Study of interface structure of Fe/Al multilayers — Ataur R. Chowdhury, Andrea E. Freitag

6306 Effect of ion beam mixing on microstructure and magnetic properties of Gd-Co multilayer films — G. Choe, R. M. Walser

6309 Nonlinear dynamics in microwave driven coupled magnetic multilayer systems — S. M. Rezende, F. M. de Aguiar

Other Hard Magnetic Materials II

6312 Magnetic interactions in nanocrystalline SmFeCo — D. R. Cornejo, F. P. Missell, J. M. González

6315 Neutron diffraction studies of $Nd_nFe_{m-x-y}V_xAl_y$ [$(n,m)=(1,12)$, (2,17), (3,29)] — Z. Hu, W. B. Yelon, W. J. James

6318 Neutron diffraction structural study of $Ce_2Fe_{17-x}Ga_x$ — H. Luo, Z. Hu, W. B. Yelon, S. R. Mishra, G. J. Long, O. A. Pringle, D. P. Middleton, K. H. J. Buschow

6321 Magnetic properties of $DyCo_{10-x}Ni_xSi_2$ compounds — Z. G. Zhao, N. Tang, E. Brück, K. H. J. Buschow, F. R. de Boer

6324 Magnetic properties of $R(Fe,Mn)_{11}Ti$ compounds — T. Zhao, X. C. Kou, Z. D. Zhang, X. K. Sun, Y. C. Chuang, F. R. de Boer

6327 Temperature and field-induced spin reorientations in $NdFe_{10-x}Co_xMo_2$ single crystals — W. A. Mendoza, S. A. Shaheen

6330 Magnetic anisotropy and spin reorientation transition in a $TbFe_{11}Ti$ single crystal (abstract) — C. Abadía, P. A. Algarabel, M. R. Ibarra, C. Marquina, N. V. Kudrevatykh, P. E. Markin

6331 Magnetic and structural characteristics of $LaCo_{9+\delta}Si_4$ and $LaCo_{8.5+\delta}Si_{4.5}$ alloys (δ=0–4) — M. Q. Huang, Jason Wolf, W. E. Wallace

6334 Magnetic and crystallographic properties of $R_2Fe_{14}Si_2$ (R=Y, Gd, Dy, Er, and Tm) compounds (abstract) — K. Konno, H. Ido, F. Pourarian, R. T. Obermyer, S. G. Sanker

6335 Effect of Fe and/or Cu contents on the intrinsic coercivity of Sm_2Co_{17}-type coercive powders for the bonded magnet application — W. L. Liu, Y. L. Liang, D. W. Scott, B. M. Ma, C. O. Bounds

6338 $CoFe_2O_4$ thin films grown on (100) MgO substrates using pulsed laser deposition — P. C. Dorsey, P. Lubitz, D. B. Chrisey, J. S. Horwitz

6341 Optical and magnetic studies of SmCo and SmFe films (abstract) — K. T. Wu, Y. D. Yao, T. C. Chen

6341 Aspects of sintering barium hexaferrite with SiO_2, Al_2O_3, $CaCO_3$, and $Y_6Fe_{10}O_{24}$ additions for microwave applications (abstract) — J. G. Fagan, R. L. Snyder, C. Hach, L. Jones, J. B. Ings, J. May, J. J. Simmins

6342 Finite element modeling of powder aligning and multipole magnetizing systems for anisotropic bonded permanent magnets — C. D. Riley, G. W. Jewell, D. Howe

Kondo, Mixed Valence, and Heavy Fermions I

6345 Metal-insulator transition in the presence of excitonic correlation — Mucio A. Continentino, Gloria M. Japiassú, Amós Troper

6347 Resistivity and L_{III}-edge absorption studies in valence fluctuation system $Ce_2Ni_3Si_5$ — Chandan Mazumdar, R. Nagarajan, C. Godart, L. C. Gupta, B. D. Padalia, R. Vijayaraghavan

(Continued)

6349 Transport, magnetic, and ^{119}Sn Mössbauer studies on magnetically ordered valence fluctuating compound $SmRuSn_3$ — Chandan Mazumdar, Z. Hossain, R. Nagarajan, C. Godart, S. K. Dhar, L. C. Gupta, B. D. Padalia, R. Vijayaraghavan

6352 Kondo behavior in $CeNi_{0.4}Cu_{0.6}$ — J. I. Espeso, J. García Soldevilla, J. C. Gómez Sal, M. Reiffers, J. A. Blanco

6355 Temperature dependence of the electrical resistivity and thermopower of U_2Ni_2In and Nd_2Ni_2Sn — R. P. Pinto, M. M. Amado, M. E. Braga, J. B. Sousa, B. Chevalier, D. Laffargue, J. Etourneau

6358 Thermal expansion of single-crystalline UNiAl — K. Prokeš, A. de Visser, A. A. Menovsky, E. Brück, F. R. de Boer, V. Sechovský, T. J. Gortenmulder

6361 Electronic properties of U_2Pt_2Sn — K. Prokeš, F. R. de Boer, H. Nakotte, L. Havela, V. Sechovský, P. Svoboda, J. M. Winand, J. Rebizant, J. C. Spirlet, X. Hu, T. J. Gortenmulder

6364 The spin-glass state of $Y_{1-x}U_xPd_3$ — M. A. Lopez de la Torre, J. Rodriguez Fernandez, K. A. McEwen

6367 Search for hybridization gap in the electronic density of states in CeNiSb — Latika Menon, S. K. Dhar, S. K. Malik, W. B. Yelon

Giant Magnetoresistance of Magnetic Multilayers II

6370 Anisotropy and angular variation of the giant magnetoresistance in magnetic multilayers (invited) — B. Dieny, C. Cowache, A. Nossov, P. Dauguet, J. Chaussy, P. Gandit

6376 Theory of the temperature dependence of giant magnetoresistance (invited) — Hideo Hasegawa

6382 Currents at angle to the planes of the layers (abstract) — P. M. Levy, S. Zhang, T. Ono, T. Shinjo

6383 Oblique electron transport in the presence of collinear and noncollinear magnetizations — Horacio E. Camblong

6386 Simulating device size effects on magnetization pinning mechanisms in spin valves — J. O. Oti, R. W. Cross, S. E. Russek, Y. K. Kim

6389 Exploration of magnetization reversal and coercivity of epitaxial NiO {111}/NiFe films — Chih-Huang Lai, Hideo Matsuyama, Robert L. White, Thomas C. Anthony, Gary G. Bush

6392 Change of magnetoresistance characteristic and crystal structure by ion bombardment to interfaces in $[Ni_{81}Fe_{19}/Cu]$ multilayers (abstract) — Y. Miyamoto, T. Yoshitani, S. Nakagawa, M. Naoe

6393 Structural comparisons of ion beam and dc magnetron sputtered spin valves by high-resolution transmission electron microscopy — William E. Bailey, Nan-Chang Zhu, Robert Sinclair, Shan X. Wang

6396 Giant magnetoresistance and magnetic phase diagram of UNiGa — K. Prokeš, E. Brück, F. R. de Boer, M. Mihálik, A. Menovsky, P. Burlet, J. M. Mignot, L. Havela, V. Sechovský

6399 Giant magnetoresistance and soft magnetic properties of $Co_{90}Fe_{10}/Cu$ spin-valve structures — Y. Kamiguchi, K. Saito, H. Iwasaki, M. Sahashi, M. Ouse, S. Nakamura

6402 Giant magnetoresistance effect in multilayered wire arrays — Minoru Kume, Atsushi Maeda, Toshio Tanuma, Kazuhiko Kuroki

Kondo, Mixed Valence, and Fermions II

6405 Superconductivity and structural transformation in HfV_2 and Nb-doped HfV_2 — F. Chu, Z. W. Chen, C. J. Fuller, C. L. Lin, T. Mihalisin

6408 Electronic properties of UCuSn — H. Nakotte, A. Purwanto, R. A. Robinson, K. Prokeš, F. R. de Boer, L. Havela, V. Sechovský, I. P. Swainson

(Continued)

6411 Crystallographic and magnetic structure of $UCu_{1.5}Sn_2$ — A. Purwanto, R. A. Robinson, H. Nakotte, I. P. Swainson, M. S. Torikachvili

6414 Metal-insulator transition in dirty Kondo insulators — P. Schlottmann, C. S. Hellberg

6417 Tb impurities in Th: A Kondo system with undercompensated magnetic moment? — J. G. Sereni, P. Schlottmann

6420 Hybridization-induced magnetism in correlated cerium systems — Nicholas Kioussis, J. Thevenot, Bernard R. Cooper, Q. G. Sheng

6423 Theoretical interpretation of optical conductivity of $YbCu_4Ag,Au$ — A. Continenza, P. Monachesi, M. Galli, F. Marabelli, E. Bauer

6426 Magnetic dichroism study of the relativistic electronic structure of perpendicularly magnetized Ni/Cu(001) — W. Kuch, M. Zharnikov, A. Dittschar, K. Meinel, C. M. Schneider, J. Kirschner, J. Henk, R. Feder

6429 Density functional study of fcc iron and iron particles in copper — Diana Guenzburger, D. E. Ellis

6432 The magnetic response at the metal–insulator transition in $La_{1-x}Sr_xTiO_3$ (abstract) — R. Osborn, M. C. Aronson, E. A. Goremychkin, J. E. Greedan

6433 On perturbation theory for the three-band model of cuprates — T. A. Kaplan, S. D. Mahanti, Yen-Sheng Su, K. Kubo

6436 Magnetic measurements on $Cd_{1-x}Cr_xTe$ and $Zn_{1-x}Cr_xTe$ — T. M. Pekarek, I. Miotkowski, B. C. Crooker

6439 Specific heat of R_3Co (R: La,Pr, and Nd) (abstract) — I. Umehara, K. Nakano, Q. F. Lu, K. Sato

Magnetic Microscopy and Imaging

6440 Submicron characterization of recording media using magnetic force microscopy (invited) (abstract) — K. Babcock, S. Manalis, V. Elings, M. Dugas, W. Challener

6441 Magnetic imaging in the presence of external fields: Technique and applications (invited) — Romel D. Gomez, Edward R. Burke, Isaak D. Mayergoyz

6447 Domain structure of iron single crystals grown on Si(111) investigated by magnetic force microscopy (abstract) — S. Foss, R. Proksch, K. Moloni, E. D. Dahlberg, Y. Cheng

6447 Force gradient mapping of domain wall structures in magnetite (abstract) — Roger Proksch, Tilman E. Schäffer, Sheryl Foss

6448 Superparamagnetic magnetic force microscopy tips — P. F. Hopkins, John Moreland, S. S. Malhotra, S. H. Liou

6451 Sensitive detection of magnetic field distribution using scanning interference electron microscope (abstract) — Y. Yajima, Y. Takahashi, K. Kuroda, Y. Sugita

6452 Magnetization reversal process in TbCo-biased spin valves — J. N. Chapman, M. F. Gillies, P. P. Freitas

6455 Direct observation of domain walls in NiFe films using high-resolution Lorentz microscopy — Bunsen Y. Wong, David. E. Laughlin

Computational Magnetics

6458 Numerical micromagnetics in hard magnetic and multilayer systems (invited) — T. Schrefl, J. Fidler

6464 Simulation of three-dimensional nonperiodic structures of π-vertical Bloch line and 2π-vertical Bloch line in magnetic garnet — M. Redjdal, F. B. Humphrey

6467 Simulations of highly anisotropic Co–Cr–Ta thin films — C. Dean, R. W. Chantrell, H. Suzuki, N. Kodama, P. R. Bissell

6470 Modeling of permanent magnets: Interpretation of parameters obtained from the Jiles–Atherton hysteresis model — L. H. Lewis, J. Gao, D. C. Jiles, D. O. Welch

6473 Superconducting hysteresis and the Preisach model — I. D. Mayergoyz

6476 A model for magnetomechanical hysteresis and losses in magnetostrictive materials — A. Bergqvist, G. Engdahl

6479 On the relaxation of simple magnetic systems — J. M. González, R. Ramírez, R. Smirnov-Rueda, J. González

(Continued)

6482	Response of a kinetic Ising system to oscillating external fields: Amplitude and frequency dependence	S. W. Sides, R. A. Ramos, P. A. Rikvold, M. A. Novotny
6485	Study of residual magnetization of hard steel samples	M. Saadi, F. Jellali, A. Delmas, G. Quichaud

Magnetic Circular Dichroism and Hyperfine Fields

6488	Magnetic reversal in perpendicularly oriented thin films subjected to picosecond magnetic fields (abstract)	Juergen Heidmann, Dieter Weller, Hans C. Siegmann, E. L. Garwin
6489	A theoretical description of magnetic switching experiments in picosecond field pulses	L. He, W. D. Doyle
6492	Structural and magnetic studies of heteromagnetic multilayers by reflectivity of circularly polarized soft x rays (abstract)	Y. U. Idzerda, V. Chakarian, C. J. Gutierrez, G. A. Prinz, C.-C. Kao, J.-H. Park, G. Meigs, C. T. Chen
6493	Giant magnetic effects in the *L*-edge extended x-ray absorption fine structure of 3*d* transition metals	V. Chakarian, Y. U. Idzerda, K. M. Kemner, J.-H. Park, G. Meigs, C. T. Chen
6496	Magnetic circular dichroism in EELS (abstract)	G. R. Harp, R. F. C. Farrow, R. F. Marks
6497	Temperature and field-induced magnetization flips in amorphous Er–Fe alloys evidenced by x-ray magnetic circular dichroism	L. M. Garcia, S. Pizzini, J. P. Rueff, J. Vogel, R. M. Galéra, A. Fontaine, J. P. Kappler, G. Krill, J. Goedkoop
6500	Magnetic circular dichroism at the *K* and *L* edges of Co and Cu in Co/Cu(001)	Ruqian Wu, A. J. Freeman
6503	Determination of the energy dependence of the off-diagonal terms of the dielectric tensor by means of $M_{2,3}$ reflection MCD measurements (abstract)	Hartmut Höchst, Dai Zhao, David Huber
6504	Magnetic dichroism in angle-resolved UV photoemission from valence bands, using linearly polarized light	D. Venus, W. Kuch, A. Dittschar, M. Zharnikov, C. M. Schneider, J. Kirschner
6507	Spin polarized photoemission studies of the 3*s* core level in ferromagnetic systems (abstract)	Y. Liu, J. Xu, D-J. Huang, P. D. Johnson
6508	Magnetic dichroism in the soft x-ray regime for magnetic domain imaging by total yield microscopy (abstract)	F. U. Hillebrecht, T. Kinoshita, Ch. Roth, H. B. Rose, D. Spanke, J. Dresselhaus, E. Kisker
6509	Spin resolved resonant Raman scattering	W. A. Caliebe, C.-C. Kao, L. E. Berman, J. B. Hastings, M. H. Krisch, F. Sette, K. Hämäläinen
6512	Raman heterodyne detection of magnetic resonance in a phosphate glass	G. K. Liu, C.-K. Loong, James V. Beitz, Ruoxin Cao, Y. H. Chen, K. Suzuya
6515	Magnetic and Mössbauer studies of hot-pressed MnZnNi ferrites (abstract)	V. K. Babbar, R. K. Puri

Transport—Mostly Magnetoresistance

6516	Quantum vortex motion in high-T_c superconductors	A. García, X. X. Zhang, J. Tejada
6519	An ultrasonic study of spin-density-wave effects in a Cr+0.2 at. % Ir alloy single crystal	J. Martynova, H. L. Alberts, P. Smit
6522	Hall-effect measurements on Cr films deposited on Ge substrates	Chien-Sheng Hsieh, Klaus Schröder
6525	Modeling the stress dependence of Barkhausen phenomena for stress axis linear and noncollinear with applied magnetic field (abstract)	M. J. Sablik, B. Augustyniak, M. Chmielewski
6526	Magnetovolume and magnetoelastic effects in ternary Cr–Ru–Mo alloys	J. T. Mochele, P. Smit, H. L. Alberts
6529	Magnetoelastic energy in domains separated by 90° walls	A. S. Arrott
6532	High frequency (1–1200 MHz) magnetoimpedance in CoFeSiB amorphous wires (abstract)	V. P. Paramonov, A. S. Antonov, A. N. Lagarikov, L. V. Panina, K. Mohri
6533	Enhancement of magnetoresistance in Co($1\bar{1}00$)/Cr(211) bilayered films on MgO(110)	Y. D. Yao, Y. Liou, J. C. A. Huang, S. Y. Liao, I. Klik, W. T. Yang, C. P. Chang, C. K. Lo

(Continued)

6536 Magnetic and electrical properties of CoFeSiB:O thin films near the percolation threshold — R. Banerjee, A. P. Valanju, G. Choe, R. M. Walser

6539 Circumferential magnetization processes in CoFeBSi wires — L. Domínguez, J. M. Blanco, P. Aragoneses, J. González, R. Valenzuela, M. Vázquez, A. Hernando

6542 Measurements of magnetization dynamics and magnetoimpedance in FeCoSiB and FeSiB amorphous wires — S. Masuda, K. Komatsu, Y. Takemura, T. Yamada, K. Kakuno

6545 Transport properties of amorphous CoZrNd thin films with very low Nd content (abstract) — C. de Francisco, J. M. Muñoz, J. F. Calleja, M. Rivas, M. C. Contreras

6546 Domains and giant magneto-impedance in amorphous ribbons by magneto-optical Kerr effect — A. D. Santos, L. G. C. Melo, C. S. Martins, F. P. Missell, Y. Souche, F. L. A. Machado, S. M. Rezende

6549 A position sensor based on magnetoimpedance — R. Valenzuela, M. Vazquez, A. Hernando

6552 The field-annealing effect on magnetoimpedance of a zero magnetostrictive metallic glass — S. U. Jen, Y. D. Chao

6555 Giant transversal magnetoimpedance and Hall-effect measurements in $Co_{70.4}Fe_{4.6}Si_{15}B_{10}$ — K. C. Mendes, F. L. A. Machado, L. G. Pereira, S. M. Rezende, F. C. Montenegro, M. V. P. Altoé, F. P. Missell

6558 A theoretical model for the giant magnetoimpedance in ribbons of amorphous soft-ferromagnetic alloys — F. L. A. Machado, S. M. Rezende

Superconductivity and Applied Superconductivity

6561 Superconducting properties of Fe-doped YNi_2B_2C — X. Z. Zhou, H. P. Kunkel, P. A. Stampe, Gwyn Williams

6564 Magnetic properties of polycrystalline $Sm_{2-x}Ce_xCuO_{4-y}$ at high magnetic fields — R. F. Jardim, C. H. Westphal, C. H. Cohenca, L. Ben-Dor, M. B. Maple

6567 Thermal conductivity of $Bi_2Sr_2Ca_nCu_{n+1}O_x$ bulk superconductors in high magnetic fields (abstract) — S. C. Nakamae, J. Schwartz

6568 Cu spin reorientation in $Tl(BaSr)PrCu_2O_7$ — W.-H. Li, Y. F. Lin, S. Y. Wu, W. T. Hsieh, K. C. Lee, J. W. Lynn, C. C. Lai, H. C. Ku

6571 Alternating current susceptibility studies of Tb ordering in $Pb_2Sr_2TbCu_3O_8$ — S. Y. Wu, W.-H. Li, K. C. Lee, T. H. Meen, H. D. Yang

6574 Field dependence of magnetic relaxation in BiPbSrCaCuO superconductors — V. Raposo, A. G. Flores, M. Zazo, L. Torres, J. Iñiguez

6577 Gd concentration dependence of the spin reorientation critical field in $Eu_{2-x}Gd_xCuO_4$ — A. Butera, A. Fainstein, M. Tovar, Z. Fisk, S. B. Oseroff

6580 Magnetization of $HgBa_2CuO_{4+\delta}$ with $0.03 \leqslant \delta \leqslant 0.4$ — Q. Xiong, S. Afonso, Y. Q. Tang, F. T. Chan, G. Salamo, Y. Y. Xue, C. W. Chu

6583 Superconducting properties of Hg-1223 prepared by using fluorides — B. J. Jönsson, T. Turkki, V. Ström, Z. Iqbal, K. V. Rao

6586 Vortex pinning in layered organic superconductors: κ-$(BEDT\text{-}TTF)_2Cu[N(CN)_2]Br$ — S. Khizroev, F. Zuo, G. C. Alexandrakis, J. A. Schlueter, U. Geiser, J. M. Williams

6589 Experimental evidence of a crossover in the vortex dimensionality in high-T_c superconductors — A. García, X. X. Zhang, J. Tejada

6592 Vortex gliding between Cu–O planes in an anisotropic high temperature superconductor (abstract) — C. A. Durán, P. L. Gammel, D. J. Bishop

6593 Magnetic field and temperature dependence of critical current densities in multilayer $YBa_2Cu_3O_{7-\delta}$ films — S. Afonso, F. T. Chan, K. Y. Chen, G. J. Salamo, Y. Q. Tang, R. C. Wang, X. L. Xu, Q. Xiong, G. Florence, S. Scott, S. Ang, W. D. Brown, L. W. Schaper

(Continued)

6596 Flux trapping and levitation forces in directionally solidified superconducting $YBa_2Cu_3O_7$ ingots — J. Mora, M. Carrera, X. Granados, J. Fontcuberta, S. Piñol, X. Obradors

6599 Magnetostatic effect on magnetic flux penetration in superconducting Nb film covered with a micron–size magnetic particle array — Yukio Nozaki, Yoshichika Otani, Katharina Runge, Hideki Miyajima, Bernard Pannetier, Jean Pierre Nozières

6602 "Standing" diffusion of electromagnetic fields in superconductors with gradual resistive transitions — I. D. Mayergoyz, M. Neely

6605 Low-temperature specific heat of the degenerate supersymmetric *t-J* model in one dimension — Kong-Ju-Bock Lee, P. Schlottmann

Spin Glasses and Frustrated Magnets

6608 Magnetic and thermodynamic properties of $Sr_2LaFe_3O_9$ — J. T. Wang, C. L. Lin, T. Mihalisin

6611 Low-temperature Mössbauer study of the mechanically alloyed $Fe_xMn_{0.7-x}Al_{0.3}$ ($0.4 \leq x \leq 0.5$) series — J. M. González, Anit K. Giri, G. A. Pérez Alcázar, Ligia E. Zamora

6614 Magnetic and crystal phase transitions in $KNiCl_3$ — O. A. Petrenko, M. F. Collins, C. V. Stager, B. F. Collier, Z. Tun

6617 New spin glass $Fe_{0.67}Cr_{1.33}Sn_{0.67}S_4$ with magnetic ions in tetrahedral and octahedral sublattices (abstract) — L. I. Koroleva, L. N. Lukina, A. G. Odintsov, T. V. Virovets

6618 Scaling of the thermoremanent relaxation in FeNiCr — D. Li, R. M. Roshko

6621 ^{7}Li nuclear magnetic resonance spectra and relaxation in $Ni_{1-x}Li_xO$ — M. Corti, S. Marini, A. Rigamonti, V. Massarotti, D. Capsoni

6624 Susceptibility and ^{89}Y nuclear magnetic resonance in $Y_{1-x}Ca_xVO_3$ — F. Cintolesi, M. Corti, A. Rigamonti, G. Rossetti, P. Ghigna, A. Lascialfari

6627 Spin glass behavior of amorphous $Fe_5(InTe_4)_3$ — Jian H. Zhang, Damon Williams, Cuihong Tao, Charles J. O'Connor

6630 Order-parameter fluctuations in the frustrated Heisenberg model on the square lattice — Shu Zhang, Gerhard Müller

6633 Mictomagnetism of ϵ-MnZn alloys — T. Hori, H. Shiraishi, Y. Nakagawa

6636 Low temperature spin dynamics of geometrically frustrated antiferromagnets $Y_2Mo_2O_7$ and $Y_2Mo_{1.6}Ti_{0.4}O_7$ studied by muon spin relaxation — S. R. Dunsiger, R. F. Kiefl, K. H. Chow, B. D. Gaulin, M. J. P. Gingras, J. E. Greedan, A. Keren, K. Kojima, G. M. Luke, W. A. MacFarlane, N. P. Raju, J. E. Sonier, Y. J. Uemura, W. D. Wu

Alternative Memories, Concepts, and Bubbles

6639 Quarternary giant magnetoresistance random access memory — Zhigang Wang, Yoshihisa Nakamura

6642 Important factors included in nondestructive readout of GMR MRAM (abstract) — Y. Nakamura, Z. Wang

6642 Domain collapse in grooved magnetic garnet material (abstract) — J. C. Peredo, G. N. Patterson, Y. N. Fedyunin

6643 Fundamental studies of stripe-domain chopping in the presence of magnetic fields — K. J. Fogarty, K. Matsuyama, H. Asada, W. W. Clegg

6646 Micromagnetic study on write operation in submicron magnetic random access memory cell — H. Asada, K. Matsuyama, K. Taniguchi

6649 Analytical model in a weakly coupled sandwich for memory purposes — Zhigang Wang, Yoshihisa Nakamura

AUTHOR INDEX

A publication of the American Institute of Physics, 500 Sunnyside Blvd., Woodbury, NY 11797-2999

Approaches to 10 Gbit/in.^{2} recording (invited)

M. H. Kryder, W. Messner, and L. R. Carley
Data Storage Systems Center, Carnegie Mellon University, Pittsburgh, Pennsylvania 15213-3890

The areal density of manufactured magnetic disk drives is currently advancing at a rate of about 60% per year. Assuming this continues, an areal density of 10 Gbit/in.^{2} will be reached sometime shortly after year 2000. In this paper, the characteristics of a disk drive with 10 Gbit/in.^{2} density and the requirements that such an areal density places upon the component technologies necessary to make such a drive possible are discussed. It is projected that smooth, high coercivity and fine grain media, high moment thin film write heads, spin-valve read heads, advanced signal processing techniques, and improved servo systems will make it possible to achieve this goal using flying heads and longitudinal recording. © *1996 American Institute of Physics.* [S0021-8979(96)28508-8]

I. INTRODUCTION

Magnetic recording has advanced approximately 500 000 times in areal density since its introduction into magnetic disk drives by IBM in 1957, and is approaching 1 Gbit/in.^{2} in manufactured products. Now, at the 1995 Magnetism and Magnetic Materials Conference, a group of us have been asked to describe how 10 Gbit/in.^{2} recording density is going to be achieved. The purpose of this paper is give an overview of what technologies need to be developed to enable it to occur. There are several other papers in this session, which go into considerably more detail about the individual component technologies, and it would be surprising if this overview and the other papers agreed in all areas. It is probably best that they do not, because there are still many unanswered questions, and if we all agreed, the chances are we would be missing some of the best solutions.

II. 10 Gbit/in.^{2} DRIVE CHARACTERISTICS

Before considering the enabling technologies, let us consider what sort of a drive a recording density of 10 Gbit/in.^{2} would make possible. An approximately linear extrapolation of both bit and track density from today's drives suggests that the track density will be about 1000 tracks/mm (25 000 tpi) and that the linear density will be about 16 000 bits/mm (400 000 bpi). At the present time, this linear extrapolation is about what is expected, but the actual tradeoff between track and bit density will be decided by factors such as the servo accuracy which is achieved and the media signal-to-noise ratio.

Using zone recording on the disk, a density of 10 Gbit/in.^{2} would enable one to pack about 2.5 Gbytes on a single 1.3 in. (3.3 cm) disk. If the disk were spun at 10 800 rpm, the linear bit density of 16 000 bits/mm would enable a data rate of 18.4 Mbytes/s off the inner track and nearly twice that off the outer track. Although the 1.3 in. H. P. Kittyhawk may have been ahead of its time, we can expect such small drives in the future, because such data rates will be a challenge for the channel electronics, and the data rate off a 3.5 in. disk will be proportionately higher.

Of course, the small disk size will reduce the access time. Smaller disks may be spun at higher velocities, because vibrations are less. This shortens the latency. At 10 800 rpm the average latency time (half way around the disk) is only 2.8 ms. In addition, the smaller disk diameter shortens the stroke of the actuator during a seek. Assuming an actuator with a force of 100 times the force of gravity the average (1/3 of full stroke) seek time would be 3.3 ms on a 3.3 cm disk. Although the data rate is climbing sufficiently rapidly that the channel electronics has a hard time keeping up, even *smaller disk size and faster spindle speeds don't help the access time nearly as much as computer engineers would like*. The above calculation suggests this situation is not likely to change.

III. SPACING LOSS AND TRANSITION PARAMETER

Before discussing the types of media and heads which might be used in a 10 Gbit/in.^{2} disk drive, let us consider what requirements such densities place upon the head-medium spacing and the width of the recorded transition.

Taking into account the effect that a finite transition width and a finite media thickness has upon playback, the effective spacing loss, during readback for magnetic recording may be written as

$$\frac{d+a+\delta/2}{b}\times 27.3 \quad \text{dB}, \tag{1}$$

where d is the head to medium spacing, a is the Williams–Comstock transition parameter,[1] δ is the medium thickness, and b is the spacing between transitions.

In scaling from 1 Gbit/in.^{2}, which drives are approaching today, to 10 Gbit/in.^{2}, the linear density is expected to increase by about a factor of three. Thus, to maintain signal level, it is desirable that the quantities in $(d+a+\delta/2)$ be scaled down by about a factor of three. This linear scaling suggests that $(d+\delta/2)$ should be reduced to about 25 nm from the 80 nm used in the IBM 1 Gbit/in.^{2} demonstration[2] and that the Williams–Comstock transition parameter,

$$a=[M_r\delta(d+\delta/2)/\pi H_c]^{1/2}, \tag{2}$$

 0021-8979/96/79(8)/4485/6/$10.00 © 1996 American Institute of Physics

should be reduced from a typical 38 nm for the 1 Gbit/in.^{2} density to about 13 nm for 10 Gbit/in.^{2}

Achieving 25 nm head-to-medium spacing will require that the media be extremely smooth and have very thin overcoats. Texturizing the disk surface to prevent stiction is unlikely to be used, except possibly in a restricted landing zone on the disk surface.[3] It is believed that flying heads will be able to achieve such small head-medium spacings on smooth disks; however, an alternative approach is to use a lightly loaded contact recording head of the type proposed by Censtor.[4]

IV. MAGNETIC MEDIA

To achieve such a narrow transition parameter, not only must the head-media spacing be low, but low $M_r\delta$ media with high H_c must be used. Utilizing Eq. (2) and solving for H_c with $a=13$ nm, $(d+\delta/2)=25$ nm, and $M_r\delta=5\times10^{-3}$ A (0.5 memu/cm^2) which is believed to be appropriate for a spin-valve head, one obtains $H_c=235$ kA/M (3000 Oe).

In addition to being thin and having high coercivity, it is also necessary that the media have low noise. Mallinson showed a number of years ago that the media signal-to-noise power ratio was roughly equal to the number of independent magnetic particles being sensed at any one time by the recording head.[5] For a thin film medium in which the grains extend through the medium thickness, this is approximately

$$\mathrm{SNR}=10\log_{10}\frac{b\times W}{d^2} \tag{3}$$

where SNR is the signal-to-noise ratio, b is the minimum spacing between transitions, W is the trackwidth, and d is the grain size.

As is discussed below in the section on signal processing, it is not yet certain what type of coding will be used for these densities, and therefore it is not yet known what the minimum linear transition spacing, b, will be. For a 2/3 (1,7) run length limited (RLL) code, there are 1.33 bits per linear transition spacing, whereas, for a $d=0$, 8/9 rate code, there are 0.89 bits per linear transition spacing. For a linear density of 6000 bits/mm, assuming the 2/3 rate (1,7) code is used, $b=84$ nm (12 000 fr/mm), whereas, for the $d=0$, 8/9 rate code, $b=56$ nm (18 000 fr/mm). Assuming a SNR of 30 dB is required and using $W=1$ μm, one calculates that the maximum grain size should be about 9 nm for the 2/3 rate (1,7) encoded data and 7.5 nm for the $d=0$, 8/9 rate encoded data. More accurate calculations of the expected SNR, based upon micromagnetic calculations,[6] confirm these approximate grain size requirements.

Such small grain sizes raise the concern that thermal effects may destabilize the magnetization in the recorded transitions. Lu and Charap[7,8] have pointed out that the demagnetizing fields in a recorded transition act in a manner to destabilize the grains and broaden the transitions. When they took the demagnetizing fields into account, they nevertheless were able to identify a region of magnetization and anisotropy in which media with a grain size of about 10 nm would be stable. For media with a thickness of 10 nm, they found that it was necessary to have an anisotropy in excess of about 3.5×10^6 ergs/cm^3 to have adequate stability.

In an accompanying paper in this session, an extensive discussion of the progress toward making media with sufficiently small grain size for adequate SNR, sufficiently high anisotropy for thermal stability and sufficiently high coercivity to achieve 10 Gbit/in.^{2} recording density is described.[9]

V. WRITE HEADS

The requirements for high track density and high linear density place stringent requirements upon the magnetic recording heads which are used for 10 Gbit/in.^{2} recording. The write head pole width has to be narrower than the trackpitch to allow for a narrow erase band between tracks and for track misregistration. Prior numerical modelling indicated that a write head with trackwidth of 0.6 μm, trimmed poles and a gapwidth of 0.18 μm would write a trackwidth which was about 0.8 μm wide and which would have a 0.05 μm wide erase band at both edges.[10] This would allow about 0.1 μm for track misregistration. Imperfect pole edge trimming, or more track misregistration tolerance would require either a slightly narrower gap or narrower pole.

The needs for a narrow transition parameter and for thermal stability of the magnetization require the coercivity of the media to be large. This in turn makes it necessary for the record head to be able to produce large fields. With the extremely short throat heights expected to be required for 10 Gbit/in.^{2} recording, pole tip saturation, rather than saturation at the back gap or in the sloping region near the throat is expected to be the limiting factor for thin film write heads.

To achieve good overwrite, it is generally required that the head produce a record field at the back of the medium, which is 2.5 times the coercivity.[11] The field H_x produced by the record head may be estimated by calculating the Karlqvist head field[12] at the gap center and at a distance $d+\delta$ from the pole tips,

$$H_x=\frac{2H_g}{\pi}\tan^{-1}\left[\frac{g}{2(d+\delta)}\right], \tag{4}$$

where H_g is the deep gap field of the head and g is the gap length of the head. By setting $H_x=2.5$ H_c and rearranging the equation, one can calculate the deep gap field H_g required to write on a given coercivity medium:

$$H_g=1.25\pi H_c/\tan^{-1}\left[\frac{g}{2(d+\delta)}\right]. \tag{5}$$

As described above, it is expected that, for 10 Gbit/in.^{2}, it will be required that $H_c=3000$ Oe, $d=20$ nm, $\delta=10$ nm, and $g=0.18$ μm. Substituting these values into Eq. (5), one finds that the deep gap field of the head must exceed 9400 Oe to achieve good overwrite. Saturation effects generally become significant when the deep gap field is 50% to 80% of the saturation flux density.[13] Hence, Permalloy, with a saturation flux density of 10 000 G, is not adequate for writing on such high coercivity media, even at such low flying heights.

To write at such densities on 3000 Oe media will require write head materials with larger saturation flux densities than

Permalloy. A very promising class of materials for this application is FeXN. These materials have saturation flux densities approaching 20 kG.[14,15] Using the criterion given in Eq. (5) and that the deep gap field be no larger than 50% to 80% of the saturation flux density, these materials are expected to be able to saturate media with coercivities up to 3200–5100 Oe.

In addition to having a high saturation magnetization, these materials exhibit hardness of 19 GP (twice that of Permalloy) and resistivities of the order of 100 $\mu\Omega$ cm (about four times that of Permalloy). The higher resistivity of these materials makes them operate well to high frequencies. Single layer films exhibit a roll off in permeability at about 60 MHz, and lamination with SiO_2 or Al_2O_3 has been shown to push the roll-off frequency up to beyond 200 MHz.[14]

These materials have also been shown to operate well in thin film head structures. Measurements of core inductance show no roll off in the 0 to 50 MHz range,[16] and in an accompanying paper in this conference, a FeAlN head with 1 μm trackwidth and a gap length of 0.2 μm is described.[17] This head was shown to saturate media with 2950 Oe coercivity and to provide more than 40 dB overwrite at a head to medium-midplane spacing of 80 nm. With a reduced flying height, it is likely such heads could be used to achieve the linear recording densities of 12 000 to 18 000 fr/mm required for recording at 10 Gbit/in.^{2}

VI. READ HEADS

It is expected that, to achieve an adequate signal at 10 Gbit/in.^{2}, giant magnetoresistive (GMR) read heads will be necessary. This is because the sensitivity of standard magnetoresistive (MR) heads is too low to enable media noise limited performance with the trackwidths required.

To allow for track misregistration during readout, the read trackwidth is usually made somewhat narrower than the write trackwidth. Thus, a read trackwidth on the order of 0.5 μm might be used for 1 μm trackpitch. Conventional MR heads have been shown to produce an output sensitivity on the order of 0.3 mV/μm of trackwidth^2 and would provide only about 150 μV of signal, which is likely to be too low to be media noise limited. On the other hand, spin-valve read heads have been demonstrated to have outputs of 1 mV/μm of trackwidth[18] and could produce as much as 500 μV of output, which is expected to be adequate to enable media noise limited performance.

A challenge in fabricating 10 Gbit/in.^{2} recording heads will be to achieve the linear resolution necessary. To obtain sufficient resolution during readout, the spin valve must be placed between two shields, the spacing between which will determine the readback resolution. To achieve the 18 000 fr/mm density (b=56 nm) for the d=0, 8/9 rate code, the shield-to-shield spacing ($2g$ for a MR or spin-valve head) would have to be of the order of 0.1 μm to stay well below the first gap null of the recording head which occurs approximately when $2b=g$.

A more extensive discussion of spin-valve heads for 10 Gbit/in.^{2} recording is given in an accompanying paper in this session.[19]

VII. SERVOS AND ACTUATORS

Control systems consist of four fundamental parts—a dynamic system to be controlled, sensors, actuators, and a means of computation. The goal of achieving 10 Gbit/in.^{2} with the corresponding track density of 1000 tracks/mm provides challenges in each of these areas. The problem is not only one of maintaining a sufficiently small position error during tracking (less than 10% of the track width or 0.1 μm); it is also one of achieving sufficiently high seek performance to make random access data retrieval practical.

A. HDA dynamics

The spindle bearing contributes both repeatable and nonrepeatable runout during tracking. Current methods of compensating for repeatable runout are very effective up to several harmonics of the spindle frequency, but uncompensated runout above the bandwidth of the actuator must be reduced to 0.02 μm for a typical track misregistration budget with a 1 μm trackpitch.

Ironically, fluid bearing spindles have been developed as components with virtually unmeasurable runout, but when used in operating prototype disk drives, nonrepeatable runout in the position error signal has not been significantly reduced. This is no doubt due to disturbance induced from aerodynamic forces from turbulent flow around the swing arm, suspension, and slider and from friction dynamics from contact or near contact of the slider with the disk surface. As disk components decrease in size, the relative importance of these forces will increase, since they scale with area. It is likely that the flow and friction dynamics will determine the required bandwidth of the servo system.

Ball bearings exhibit complex behavior for very small motions (approximately 0.001° for a single track seek at 1000 tp mm) associated with use in disk drives.[20] Dynamics of the rotary actuator pivot bearing affect the performance of the servo system. The hysteresis in the bias torque of the bearing can cause "hunting" or limit cycling in the seek servo, for instance. The performance of the seek servo can be dramatically improved by using an accurate prediction of the bias force to set the initial condition of the integrator of the track follow controller.[21] Compensation for the nonlinear dynamics of the pivot bearing during tracking may also give significant performance improvements.

B. Position sensing

Determining the position of the read/write head relative to the center of the data track is an enormous challenge. An accurate position error signal (PES), which is available at a sufficiently high bandwidth and which is robust to noise, is essential for high performance servo control. State of the art PES generation using spin valve head sensors and sector servo is the most likely candidate for achieving 0.1 μm tracking accuracy. The difficulty is providing a PES at a sufficiently high sample rate while maintaining a servo overhead less than 10% of the disk area. (A servo bandwidth of 2 kHz on a drive rotating at 6000 rpm, from a practical standpoint, would require a PES of at least 6 kHz corresponding to 60 servo sectors on a platter.) Experimental and theoretical

investigations of amplitude (split burst), phase, and null servo methods, indicate that the null servo pattern is the most robust to media and electronics noise.[22]

There are several impediments to simply scaling existing servo patterns. Making reading and writing patterns difficult are the differing positive and negative pulse responses of spin valve heads and how the side-writing properties of thin film inductive heads change with size.[22] Simply writing the servo patterns will take much longer because there will be more tracks. If external sensing of position is used during servo write, then the nonrepeatable runout must be very low to avoid pinch and squeeze in the data tracks. Self-servo writing may be the way to avoid these last two problems, and improvements in heads and media may alleviate the first two.

C. Actuators

The central problem of current disk drive servos is that the actuator and the sensor are not colocated. Resonances in the actuator structure between the voice coil motor (VCM) and the read/write head limit the bandwidth of the servo system. The bandwidth of the servo can be no greater than approximately 1/5 of the frequency of the lowest resonance of the actuator. Assuming that disk and spindle inertias remain constant, the amplitude of the response disturbances generally decrease with the square of the frequency of the disturbances. The 1 μm trackwidth specification is approximately a factor of 4 beyond the state of the art, so the actuator bandwidth will need to increase by a factor of 2.

While much progress has been made in improving actuators, it is unclear if the frequencies of the mechanical resonances of a single stage actuator can be increased sufficiently without reducing size dramatically. A possible solution is to dampen the first resonance so that the bandwidth of the servo can be closer to the first resonance frequency.

The problem of noncolocated actuator and sensing has led to many proposals for dual stage actuation in which a high bandwidth secondary actuator is located between the primary VCM actuator and the read/write head. While the certainty in the technical community about the need for dual stage actuation to reach the 1000 tracks/mm target has lessened, there remains a tremendous amount of interest in the idea. The two central issues in dual stage actuation are where to put the secondary actuator and what type of electromechanical energy conversion to use. Attempted solutions include putting a piezoelectric actuator on the swing arm of a rotary actuator,[23] putting an electrostatic actuator between the gimbal and slider[24] and putting an electromagnetic actuator between the suspension and slider.[25] These designs have failed to gain wide acceptance for a variety of reasons including (in selected cases) large actuator voltage requirements and lack of robustness against the shock encountered in the head-gimbal assembly.

An important issue for the use of microactuators is again servo writing. The closer the secondary actuator is located to the write head, the more difficult it is to use a laser interferometer based servo writer. The actuators would need to be locked, a self-servo-writing scheme must be used, or something akin to the Sony PERM media[26] which has tracks that are separated by grooves, would be necessary.

In spite of their current problems, microactuators are expected to be used in future disk drives, if not at 10 Gbit/in.^{2}, then later.

D. Computation needs

The computation needs of the algorithms for compensating for repeatable runout, time varying plant parameters, bearing dynamics, etc., place increasing demands on the digital signal processor of the disk drive. Nonlinear control is especially difficult because it may require the use of transcendental functions which must be computed on line or referenced from a lookup table. Friction models, for instance, often use exponentials, and compensation methods may use logarithms. Nor is there relief from the lower sample rates imposed by sector servo PES generation. The low sample rates for actual data mean that multirate control must be used. Beyond just the update of the control signal at 2–4 times the PES sample rate, multirate control requires open loop estimation of the plant states. Accurate plant parameters estimates needed for the state observer may necessitate the use of sophisticated adaptive identification schemes as well.

VIII. CHANNEL ELECTRONICS

There exist a wide range of tradeoffs in the design of a magnetic recording channel for 10 Gbit/in.^{2} recording. This makes it possible to develop channel designs with widely different characteristics. The easiest way to illustrate this is to consider three extremely different cases. In the first case, heads, media, and suspension (fly height) have all achieved their goals. In this case, channel electronics will be operating at familiar linear densities—around 2.5 user bits/PW_{50} (PW_{50} is the width of the response to an isolated transition at half of its peak amplitude. It is a standard measure of the time resolution of the channel.)—but at lower SNRs than in today's products. Error correction codes (ECC), detection and equalization algorithms would be extensions of those used today but designed for operation at lower SNRs.

In the second case, the PW_{50} achieved is significantly larger than that needed to achieve 10 Gbit/in.^{2} at only 2.5 bits/PW_{50}. In this case, 10 Gbit/in.^{2} may still be achievable by using more sophisticated signal processing algorithms designed to operate at 3.0 user bits/PW_{50} or even higher linear densities. However, the SNR required to achieve an acceptable overall error rate before ECC is applied (on the order of 10^{-4} or 10^{-5} raw bit error rate) will be higher at higher user bit densities. In this case, the constraints on media noise and electronics noise (head noise+preamp noise) will be tighter, but the constraint on PW_{50} will be relaxed. It is this tradeoff between the performance requirements on the head, media, and fly height that can be facilitated by changing the channel electronics.

In the third case, the PW_{50} of an isolated pulse is acceptable, but when transitions are written at the spacing necessary to support a density of 10 Gbit/in.^{2}, a supra-linear decrease in the SNR occurs. Typically, this is a result of the zig–zag domain walls of one transition approaching or even merging with those of an adjacent transition.[27] A density of 10 Gbit/in.^{2} could still be achieved by using a run-length-

limited (RLL) code in which adjacent transitions are prohibited [e.g., the 2/3(1,7) RLL code frequently used with peak detection channels]. For the 2/3(1,7) code, we must read and write "symbols" at 1.5 times the desired bit rate, but flux reversals will never occur in adjacent symbol cells. Therefore, flux reversals are 1.33 times further apart than they would be on an uncoded channel at the same density. Note, for reasons of clock recovery alone all channels use some form of RLL code; hence, they suffer some rate loss. Currently, $d=0$ codes with a rate of 8/9 are common and ones with a rate of 15/16 are being used in research. Again, the use of an RLL code with $d>0$ results in a loss in SNR if the channel itself was purely linear. However, when the channel exhibits a supra-linear decrease in SNR with increasing flux reversal density a $d>0$ coded channel may offer improved performance. Note, one serious implementation penalty which must be addressed in this scenario is that the channel clock must operate roughly 33% faster than that of a $d=0$ rate 8/9 channel.

Advanced channels for 10 Gbit/in.^{2} density are expected to utilize "sampling" detectors which make their decisions based on a sequence of samples of the equalized readback signal taken at the symbol rate. They fall into two broad approaches. The first approach employs nonideal equalization (i.e., equalization that decreases the detection SNR of the signal) followed by an ideal detector. The pulse response (two opposite going transitions at adjacent symbol times) of the channel plus equalizer is adjusted to match that of a simple partial response (PR) polynomial; e.g., PR4 is $(1,0,-1)$ and EPR4 is $(1,1,-1,-1)$.[28] The better the spectrum of the selected PR polynomial matches that of the original channel, the less the SNR is degraded. Detection is performed by the optimal (provably so in the presence of only additive Gaussian white noise, assumed so in all other cases) detector,[29] a maximum likelihood (ML) detector implemented recursively using the Viterbi Algorithm.[30]

The second approach employs equalization of the channel as well, but in this case the equalizer does not degrade the SNR of the channel. Its job is only to "sharpen" the leading edge of the pulse response so that "precursor" intersymbol interference (ISI) is suppressed. Note, in a magnetic recording channel, the read head senses the magnetic field from a transition even before it arrives over the transition. Because the trailing edge of the equalized pulse response is relatively unconstrained (we do try to limit the total energy in the trailing ISI) it is always possible to shape the frequency response of the equalizing filter so that the SNR is not degraded. Typically the number of nonzero symbols (i.e., the "extent") of the pulse response of this type of equalizer is significantly longer than the extent of the above PR responses. Therefore, it is impractical to use the Viterbi algorithm as a detector in this case. (Its complexity grows exponentially with the pulse response extent.) However, the general class of feedback detectors can be used. The simplest feedback detector is the Decision Feedback Equalizer (DFE).[31] In this case the detector's own decisions are used to subtract the trailing ISI. Assuming these decisions are correct and an accurate model of the channel pulse response is used, trailing ISI can be completely removed. The nonideality of this approach is that there is energy which could help in making the decisions in the trailing ISI and the DFE subtracts off that energy. This can be mitigated by taking several terms of the pulse response into account in a fixed-delay tree search (FDTS) detector in place of the DFE slicer resulting in an FDTS/DF detector.[32]

The relative SNR of several of these signal processing algorithms as a function of user bits/PW_{50} for RLL codes with $d=0$, $d=1$, and $d=2$ are compared in Ref. 32. Based on the comparisons, sequence detectors in general perform much better than traditional peak detectors, especially at high density. In addition, the most common sequence detector, PR4-ML, is seen to be somewhat poorer in performance relative to other sequence detection algorithms as user densities approach 3 bits/PW_{50}. And, when $d>0$, FDTS/DF detectors outperform nearly all other sequence detectors as density approaches 3 user bits/PW_{50}.

An issue which cannot be neglected when selecting a channel equalization and detection algorithm is the implementation complexity of the overall design. This problem has grown acute in recent years because more sophisticated signal processing algorithms are being implemented at increasingly fast clock rates. Clock rates have increased dramatically because (1) disk rotation speeds continue to increase (10 000 rpm will be common by the year 2000), (2) the recent rapid increase in linear density of magnetic recording channels based on the use of magneto-resistive heads, and (3) a relatively slow decrease in disk diameters.[33] For example, the user bit rate at the outer diameter of a 3.5″ disk, assuming a linear density of 400 Kbpi and a rotation rate of 10 000 rpm, is 733 Mb/s. The IC designer is further challenged by power consumption limitations set by battery life issues in portable applications and by power dissipation limits of inexpensive plastic packages in desktop applications. Die area must be kept to a minimum in order to decrease cost. These constraints demand new innovative approaches to channel design. For example, one alternative is to implement signal processing using high speed analog electronics circuits for equalization and detection.[34]

IX. CONCLUSIONS

It is expected that, shortly after year 2000, commercial disk drives will achieve a storage density of 10 Gbit/in.^{2} It is believed this level of performance will be achieved with flying heads on longitudinal, high coercivity, fine grain, magnetic media. The heads will likely use high magnetization (>13 kG) materials for recording and spin valves for readout. Although some form of micro-actuator technology is eventually expected, it may not be necessary in order to achieve 10 Gbit/in.^{2} recording if a robust sector servo pattern such as the null pattern is used for the PES. If the channel is approximately linear, $d=0$ codes and some form of partial response detector are expected to be used; however, if the channel exhibits a supra-linear noise increase at the PW_{50} required to support 10 Gbit/in.^{2} density, a $d>0$ coded channel with a FDTS/DF detector may be preferred.

ACKNOWLEDGMENT

This work was supported by the National Science Foundation under Grant No. ECD-8907068 and by the National Storage Industry Consortium.

[1] M. L. Williams and R. L. Comstock, AIP Conf. Proc. **5**, 738 (1971).
[2] C. Tsang, M. Chen, T. Yogi, and K. Ju, IEEE Trans. Magn. **26**, 1689 (1990).
[3] R. Ranjan, D. N. Lambeth, M. Tromel, P. Goglia, and Y. Li, J. Appl. Phys. **69**, 5745 (1991).
[4] H. Hamilton, R. Anderson, and K. Goodson, IEEE Trans. Magn. **27**, 4921 (1991).
[5] John C. Mallinson, IEEE Trans. Magn. **5**, 182 (1969).
[6] Jian-Gang Zhu, IEEE Trans. Magn. **29**, 195 (1993).
[7] P. L. Lu and S. H. Charap, IEEE Trans. Magn. **30**, 4230 (1994).
[8] P. Lu and S. Charap, IEEE Trans. Magn. **31**, 2767 (1995).
[9] D. N. Lambeth, E. M. T. Velu, G. Bellesis, L. L. Lee, and D. E. Laughlin, Media Issues and Status of 10 Gbit/in.^{2} Hard Disk Storage, MMM Conference, Philadelphia, 1995.
[10] M. H. Kryder and W.-Y. Lai, IEEE Trans. Magn. **30**, 3873 (1994).
[11] A. S. Hoagland and J. E. Monson, *Digital Magnetic Recording*, 2nd ed. (Wiley, New York, 1991).
[12] O. Karlqvist, Trans. Roy. Inst. Technol. Stockholm **86**, 3 (1954).
[13] F. Jeffers, Proc. IEEE **74**, 1540 (1986).
[14] M. H. Kryder, S. Wang, and K. Rook, J. Appl. Phys. **73**, 6212 (1993).
[15] G. Qui, E. Haftek, J. C. Cates, C. Alexander, Jr., and J. A. Barnard, Mater. Res. Soc. Symp. Proc. **313**, 339 (1993).
[16] S. Wang, F. Liu, K. D. Maranowski, and M. H. Kryder, IEEE Trans. Magn. **30**, 281 (1994).
[17] W. P. Jayasekara, S. Wang, G. Spratt, and M. H. Kryder, 4 Gbit/in.^{2} Inductive Write Heads using High Moment FeAlN Poles, MMM Conference, Philadelphia, 1995.
[18] C. Tsang, R. E. Fontana, T. Liu, D. E. Heim, V. S. Speriosu, B. A. Gurney, and M. L. Williams, IEEE Trans. Magn. **30**, 3801 (1994).
[19] J. Brug, L. Tran, M. Bhattacharyya, A. Jander, J. Nickel, and T. Anthony, Impact of New Magnetoresistive Materials on Magnetic Recording Heads, MMM Conference, Philadelphia, 1995.
[20] K. Eddy and W. Messner, Effects of Bearing Dynamics on Tracking Bias in Hard Disk Drive Actuators, Proc. Am. Controls Conf., 1055, Seattle, 1995.
[21] K. Eddy and W. Messner, A State Space Model for Prediction of Actuator Tracking Bias in Hard Disk Drives, presented at ASME Int. Mech. Eng. Congress and Exposition, San Francisco, 1995.
[22] A. Sacks, Ph.D. thesis, Carnegie Mellon University, 1995.
[23] K. Akagi, T. Nakao, Y. Myamura, T. Munemoto and K. Mori, IEEE Trans. Magn. **27**, 5301 (1991).
[24] L.-S. Fan, H. H. Ottesen, T. C. Reiley, and R. W. Wood, IEEE Trans. Ind. Elect. **42**, 234 (1995).
[25] D. Miu and Y-C Tai, IEEE Control Systems Magazine **14**, 52 (1994).
[26] K. Watanabe T. Takeda, K. Okada, and H. Takino, IEEE Trans. Magn. **29**, 4030 (1993).
[27] J. G. Zhu and H. N. Bertram, IEEE Trans. Magn. **24**, 2706 (1988).
[28] H. Thapar and A. Patel, IEEE Trans. Magn. **23**, 3666 (1987).
[29] E. A. Lee and D. G. Messerschmitt, *Digital Communications* (Kluwer, Boston, 1994).
[30] G. D. Forney, Jr., Proc. IEEE **61**, 268 (1973).
[31] K. Fisher, J. Cioffi, and C. Melas, Proc. IEEE Int. Conf. Comm., Boston, 1989.
[32] J. J. Moon and L. R. Carley, IEEE Trans. Magn. **26**, 6 (1990).
[33] Peripheral Research Corp., Rigid Disk Head/Media Technology Newsletter, Vol. IX, No. 1, July, 1995
[34] R. G. Yamasaki, T. Pan, M. Palmer, and D. Browning, A 72 Mb/s PRML Disk Drive Channel Chip with an Analog Sampled-Data Signal Processor, Digest of Technical Papers, Int. Solid-State Circuits Conf., 1994.

Impact of new magnetoresistive materials on magnetic recording heads (invited)

J. A. Brug, L. Tran, and M. Bhattacharyya
Hewlett-Packard Laboratories, Palo Alto, California 94304

J. H. Nickel and T. C. Anthony
Hewlett-Packard Laboratories, Palo Alto, California 94304

A. Jander
Washington University, St. Louis, Missouri 63130

Advances in magnetoresistive materials have recently enabled magnetic recording heads to achieve higher levels of performance. This article describes why higher signal outputs are necessary for improvements to be made in areal density. The requirements for recording at an areal density of 16 Mb/mm^2 (10 Gb/in.^{2}) are discussed with regards to both the channel and the head design. Increased output from new multilayer magnetoresistive materials is required to counteract the decrease in output due to the reduction in the size of the head geometry. An areal density of 16 Mb/mm^2 is shown to be feasible with spin valve recording heads using materials with magnetoresistance ratios of 10%. Fabrication issues relating to the manufacturing of these materials are shown to be more stringent than previously required. © *1996 American Institute of Physics.*
[S0021-8979(96)14008-5]

I. INTRODUCTION

Magnetoresistive recording heads have only recently been introduced into the magnetic recording industry but they have heralded a new interest in the basic properties of magnetic materials. What is driving this interest is the direct link between the magnitude of the magnetoresistance of the sensor material and the final storage capacity of the disk drive. With the storage requirements for applications increasing rapidly it is not surprising that there has been a keen interest in pushing materials to larger magnetoresistance. New multilayer films, for example the giant magnetoresistive materials,[1] are being developed with a variety of properties that can be tailored to meet the needs of the new technology. Other novel sensors have been proposed, for instance tunneling devices which depend on the tunneling of electrons from one magnetic layer to another,[2] and colossal magnetoresistive materials[3] which have a structure similar to high Tc superconductors. With the phenomenon of electron transport at small length scales becoming better understood it is well within possibility that a "magnetic switch" is only just around the corner.

This article will describe the reasons why higher magnetoresistance is needed in order to achieve areal densities of 16 Mb/mm^2 (10 Gb/in.^{2}). Section II will show how the drive electronics set the requirements for the signal-to-noise ratio (SNR), and that the SNR is dependent on both the head and the media. Geometrical constraints conspire to reduce the output of the head and some of the design principles will be discussed. Multilayer giant magnetoresistive (GMR) recording heads are one direction that industry is pursuing to take advantage of higher magnetoresistance effects, and some of the fabrication issues will be described in Sec. III. Finally, we will indicate some future directions for magnetic materials that appear promising in the pursuit of even higher areal densities.

II. OUTPUT REQUIREMENTS FOR 16 Mb/mm^2

An example of a typical magnetoresistive (MR) head geometry that could be used to achieve 16 Mb/mm^2 is shown in Fig. 1. Sandwiched between shields is a magnetoresistive element with two conductors that make contact with the MR element. A sense current is used to measure the change in resistance of the element as a recorded bit in the media passes underneath the head. The bits are written by fringing fields that jump the gap between the write pole and the shield when current is applied to the write coils.

The read width ℓ in this particular head geometry is defined by the region of the element that is sensed by the two contacts. The distance between the shields, called the gap length g, controls the resolution of the sensor along the track. The distance from the bottom of the sensor to the top of the magnetic layer in the media is defined as the magnetic spacing, d.

There is a trade-off between the read width and the gap length in order to reach the areal density goal of 16 Mb/mm^2. A number of different cases have been considered by Murdock, Simmons, and Davidson[4] in an article outlining the trends in media for achieving 16 Mb/mm^2. As an example that is equally aggressive in both dimensions, we will use a

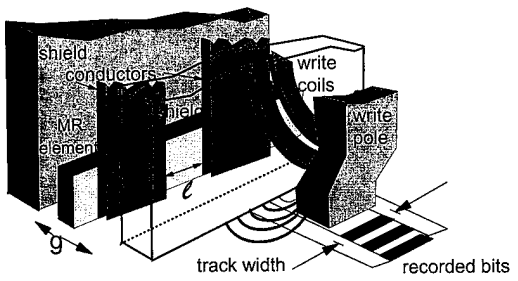


FIG. 1. Geometry of a dual gap MR recording head. The top shield of the read element also serves as the bottom pole of the write element.

 0021-8979/96/79(8)/4491/5/$10.00 © 1996 American Institute of Physics

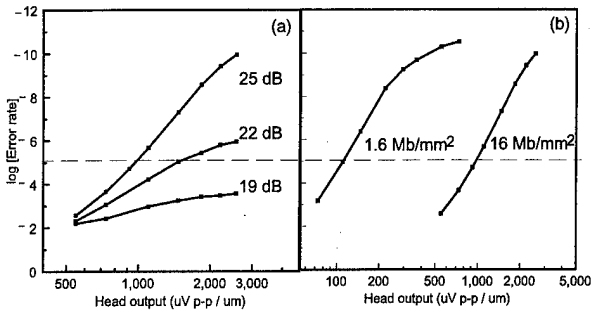


FIG. 2. (a) The error rate of a recording channel at 16 Mb/mm^2 as a function of head output. The media noise is indicated as a SNR where all electronics noise is subtracted and only the media noise contributes to the dB figure (channel density=2.5 bits/Pw50). (b) The error rate as a function of head output for an areal density corresponding to current products (1.6 b/mm^2: 6.8 kb/mm, 275 b/mm) and at 16 Mb/mm (16 kb/mm, 1000 tr/mm).

design point of 1000 recorded tracks/mm and 16 000 bits/mm along the track for a total of 16 Mb/mm^2 [case three in Ref. 4]. This results in the width of the track being 1 μm and the length of each bit being 63 nm.

A. Head SNR

An increase in the linear density from the present day 5000 bits/mm to 16 000 bits/mm requires that the head produce more signal in order to maintain an adequate signal-to-noise ratio. To understand the demands that this places on the head output we will use a model of a recording channel to show how an increase in signal leads to an increase in the ability to achieve higher areal densities.

The usual starting point is from the error rate. Although error correction codes are continually being improved, in the time frame for products at 16 Mb/mm^2 the error rate should probably not exceed one error in 10^5. This error rate will determine the output signal that will be required from the recording head. A standard PR4 partial response channel with Viterbi detection was used.[5] The input to the model was an isolated pulse that was measured for a MR head with present day recording heads and media. This pulse was scaled to higher outputs and narrower pulse widths to simulate recording at the higher density. The data rate determines the overall bandwidth of the system and this was set at an aggressive 325 Mbits/s (e.g., reading 16 000 bits/mm at the outer diameter of a 1.3 in. hard disk spinning at 12 000 rpm).

An important parameter for any channel is the amount of noise. Three sources of noise were assumed: the noise from the media, the Johnson noise of the magnetoresistive sensor, and the preamp noise. Media noise is the most important and was determined by linearly extrapolating the measured noise of currently available media. The amount of noise was scaled to simulate better media yet to be developed, and was also extrapolated to narrower tracks by assuming that the noise will vary as the square root of the track width (track edge noise was not included). Johnson noise was for a head with 25 Ω of resistance and the preamp noise was 0.5 nV/$\sqrt{\text{Hz}}$. The final bit error rate for the PR4 channel as a function of head output is shown in Fig. 2.

Figure 2(a) shows that the final error rate is determined both by the head output and by the media noise properties. So long as the system is not media noise dominated an increase in output will give a better SNR and hence a better error rate. If media noise is dominant, the head senses the media noise in the same manner as it does the recorded transitions and an increase in signal does not improve the SNR.

Examples of typical head outputs are obtained from Fig. 2(a). For example, if the media has very low noise, 25 dB, the required output of the head is only 1 mV/μm. More realistically, given the difficulties of developing low noise media, a media with 22 dB of noise will require a head output of 1.5 mV/μm. As a spur to media development, Fig. 2(a) also indicates that with present day media at 19 dB we will never reach 16 Mb/mm^2 regardless of the output of the head.

The model was used to determine the output at 1.6 Mb/mm^2 using parameters representative of today's products (1.8 bits/Pw50, 190 Mb/s). This is compared with data for 16 Mb/mm^2 in Fig. 2(b). The SNR for the media at the lower density was also 25 dB (it should be noted 25 dB media at 1.6 Mb/mm^2 and 25 dB media at 16 Mb/mm^2 are not the same media since the SNR is measured at each density). The SNR requirement of the channel drives the need for more signal from the head. Whereas today's products only need 100 uV/μm from the recording head, products at 16 Mb/mm^2 will need a factor of 10 greater output to compensate for the lower signal from the narrower track and the higher bandwidth.

B. Head geometry

The reduced read width at higher track densities will, in general, result in less output. Providing other parameters are kept constant, the signal will decrease proportionally with the read width. It might be argued that the output can be kept the same merely by going to narrower MR heights in order to keep the resistance constant. Unfortunately, power dissipation also needs to be taken into consideration. With a smaller MR height the current needs to be decreased to keep the power dissipated per unit area the same and, as a result, the output signal will be reduced. This is somewhat mitigated by the ability of smaller geometries to dissipate heat more efficiently[6] but, in general, to maintain a constant SNR the magnetoresistance of the device will need to be increased to compensate for the decreased read width.

An additional effect that reduces the output is due to the decrease in response at the edge of the defined read area. A number of factors may contribute to this effect, for instance the current distribution at the edge of the track may not be sufficiently sharp or the magnetic material in the active region may interact with the magnetic material outside the region.[7] Since the track edge effects become a proportionally larger part of the total signal as the track width decreases, these effects will also make it necessary to increase the head output.[8]

The output of the recording head will, in general, depend strongly on the gap length. With a shorter gap length there is effectively a smaller aperture exposed to the flux from the media and, in addition, the flux will decay into the shield

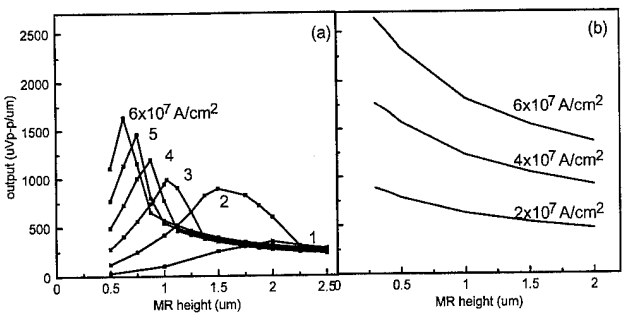


FIG. 3. (a) Variation in output for a dual-stripe head as a function of the MR height (track width=0.5 μm, gap=0.13 μm, $dR/R=2.5\%$, $Mr\delta=0.5$ m emu/cm^2, flying height=25 nm). (b) Output of a spin valve head as a function of element height for different current densities (parameters same as for (a) except gap=0.15 and $dR/R=10\%$). The media was included in the models using a Green's function method (Ref. 9).

more quickly, resulting in a lower head efficiency. This loss of efficiency can be countered by either designing the head to fly closer to the media to minimize the effect of a smaller aperture, or by reducing the MR height to reduce the loss to the shields. While in both cases signal can be regained, there may be practical limitations on the ability to either fly lower or fabricate narrower MR heights, leading to the need for greater magnetoresistance to regain signal.

Reducing the MR element height to regain efficiency makes a conventional MR head more difficult to bias. This purely magnetic effect arises from the demagnetizing fields present in the MR element which become stronger as the element is reduced in height. In principle, these fields could be reduced by going to thinner MR films. However, in a conventional MR head a certain current density is required in order to bias the head into a region where the output is linear. An example is shown in Fig. 3(a) where the output of a dual-stripe head was calculated at 16 Mb/mm^2 using a model similar to Smith's 2D micromagnetic model.[9] For a given current density there is an optimum MR height where the maximum output is obtained. Below this optimum the output will drop drastically. Higher currents permit narrower heights to be used, but this increases the resistance and the power dissipation becomes prohibitive.

C. Parameter trade-offs

The need for higher signal level is also driven by the fact that other parameters are becoming ever harder to improve. For instance, the pulse width is a function of both the flying height and the gap length. This is described by the equation[10]

$$\mathrm{Pw50} \cong \sqrt{[g^2/2+4(a+d)^2]}, \tag{1}$$

where g and d are defined above and a is the transition length in the media. Assuming 16 kb/mm and 2.5 bits/Pw50 gives the pulse width Pw50=0.16 μm. Assuming improvements in tribology will lead to magnetic spacings of roughly 30 nm leads to the required gap length for 16 Mb/mm^2 being 0.16 μm. As was seen above, if the output of the head is sufficiently large to be able to use a narrower gap and still achieve the same SNR, then a higher flying height would still give the same Pw50. Improvements in the magnetoresistance would lead to a relaxation of the magnetic spacing requirement allowing perhaps a thicker wear layer and better robustness of the disk drive.

A similar trade-off was illustrated above in Fig. 2(a), where a higher signal would allow media with poorer noise properties to be used to achieve the same areal density. Basically, a certain level of performance is required from the head; however, if additional signal were possible this would allow other tolerances to be relaxed.

III. GIANT MAGNETORESISTIVE HEADS

A. Head design

Giant magnetoresistive materials have recently been developed[11] and the most promising candidates for a read head with the output necessary to achieve 16 Mb/mm^2 are spin valve devices[12] (alternate designs for GMR heads have recently been proposed by Rottmayer *et al.*[13] and Smith *et al.*[14] but they will not be described here).

Conventional magnetoresistance materials (permalloy) have magnetoresistance ratios of 2.5%; single spin valves, 10%; and dual spin valves up to 23%.[15] Films at the higher percent ranges tend to have more coercivity than desirable for devices,[16] so typical spin valve recording heads have magnetoresistive ratios of ~10%, a factor of 4 greater than that of permalloy.

A spin valve head utilizes a magnetoresistive element that is composed of two magnetic layers separated by a conducting but nonmagnetic spacer. One film serves as the sense film with the magnetization along the length of the element. Separated from it by a thin metallic layer, usually Cu, is another magnetic layer with a magnetization that is oriented transverse to the length of the element. The magnetization of this film is typically pinned by an antiferromagnet. The field from the media rotates the magnetization in the sense layer, and changes the relative angle of the magnetizations in the two magnetic layers. The resistance of the device scales as the cosine of this angle.[12] The design of the structure requires a careful balancing of magnetic fields present in the device: the demagnetizing fields of individual magnetic layers, the fields from the sense current, internal anisotropy fields, and fields that arise from coupling between the layers. This latter field is of special importance as it depends strongly on the thickness of the Cu layer.[17] Micromagnetic models have recently been published outlining this optimization.[18]

A major feature of the spin valve device that makes it useful for 16 Mb/mm^2 recording is that it remains biased even as the MR element height is reduced. This is because the magnetization of the sense film remains along the element length resulting in the output of the device being linear about zero field. An AMR head requires that the magnetization be oriented at an angle relative to the sense current and this becomes harder to achieve for smaller geometries where demagnetizing fields become important. To illustrate the effect of bias a spin valve head was modeled at 16 Mb/mm^2 using 2D micromagnetics, shown in Fig. 3(b), and it is seen that the head output monotonically increases as the MR height is reduced. In contrast, the dual-stripe head output shown in Fig. 3(a) decreases below a certain MR height be-

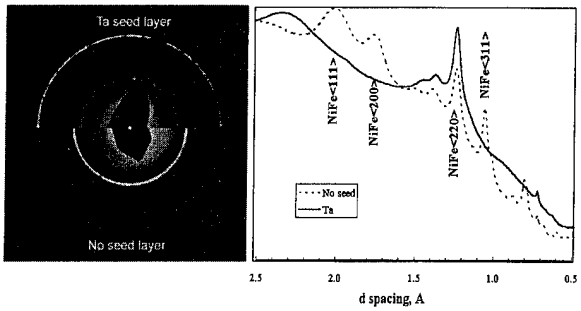


FIG. 4. Illustration of the effect of a Ta and a Cr underlayer on the crystallographic texture of 10 nm thick NiFe.

cause of the increasing difficulty in maintaining the proper orientation of the magnetization. With a magnetoresistance ratio of 10% the output of the spin valve head can easily achieve 1–2 mV p-p/μm, a value that was shown above to be adequate for 16 Mb/mm^2 recording. Outputs in this range have recently been demonstrated by IBM and Hitachi for spin valve heads.[19]

B. Fabrication challenges

The giant magnetoresistance effect requires that the films be very thin. For instance, the total thickness of the conducting layers must be within the mean free path of the electron, about 10 nm, otherwise the effect is reduced. This is an advantage because the gap length decreases at higher recording densities and a thin sensor allows a thicker dielectric to be used as the insulator in the gap. In addition, the trend for media at higher density is to become thinner[4] and to remain matched to the media the sense layer must also be reduced in thickness. A typical spin valve will have a 5–10 nm thick magnetic sense layer, a 2–3 nm spacer layer of copper, and a 2–5 nm pinned magnetic layer. The pinning is achieved by using an antiferromagnetic film such as FeMn or NiO. The magnetic layers will typically be of NiFe and Co; the Co is used to increase the GMR effect and improve the stability of the interface and the NiFe is used to increase the sensitivity of the sense layer.

Fabricating multilayers with individual films in this thickness range for a commercial product will be a challenge not only from the standpoint of thickness control, but also because of the need to control the film structure. For instance, the crystallographic structure of giant magnetoresistive films is very important in determining the magnetic and the transport properties of the materials. Grain boundaries cause the electrons to be scattered and this results in a decrease in the magnetoresistance. Additionally, it has been shown that the orientation of the films is important in determining the coupling strength between the ferromagnetic film and the antiferromagnetic film that is used to pin the magnetization.[20]

The crystallographic texture of the film can be controlled by using underlayers. This is illustrated in Fig. 4, where a plan-view TEM diffraction pattern is used to determine the orientation of NiFe deposited with and without an underlayer. Without any underlayer diffraction was from (111), (200), (220), and (311) planes, suggesting a randomly oriented polycrystalline film. In contrast, a Ta layer produces a NiFe film that is strongly (111) textured, as evidenced by the presence of only the (220) diffraction ring.

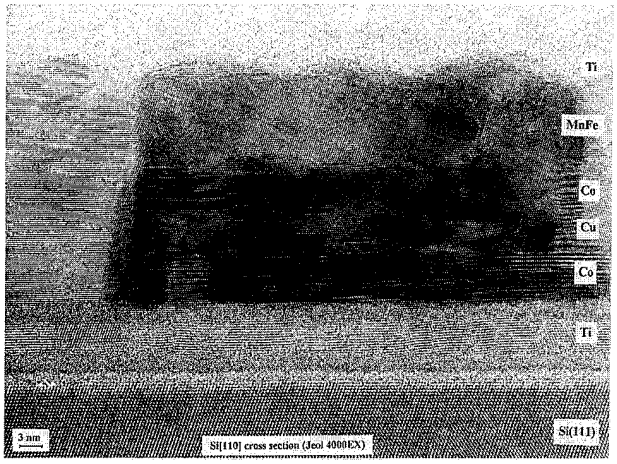


FIG. 5. Cross-sectional TEM micrograph of a sputtered Ti/Co/Cu/Co/FeMn spin valve structure.

The ability of one layer to control the orientation of subsequently deposited layers has serious consequences for structures that are composed of many different layers. Fortunately, cross-sectional TEM opens up a window on the microstructure of the thin films used in giant magnetoresistive heads. In Fig. 5 is shown a TEM cross section of a GMR spin valve that uses Ti as an underlayer to control the orientation.

The structure shows good epitaxy between layers. This translates into superior transport properties over films that show poor epitaxy. Relating the structure of the films and their interfaces to transport properties is presently one of the main challenges that are being faced by groups working on the optimization of GMR structures. Theoretical models for transport properties are becoming more refined and serve to guide experimentalists in the design of the multilayer materials.[21]

IV. FUTURE DIRECTIONS

Even more exciting is the potential for materials that behave like magnetic switches. Figure 6 shows the change in resistance of the perovskite $La_{0.67}Ca_{0.33}MnO_3$ grown by metal-organic chemical-vapor deposition (MOCVD). At room temperature the change in resistance is 94% (defined as $\Delta R/R_{max}$). However, the field required is 5 T, much too high for application as a sensor, but these materials are only beginning to be understood and many research groups have taken on the task of reducing the saturation field. As above, the epitaxial growth of the materials is important but, in addition, the stoichiometry and postprocessing of these films has also been found to be important for achieving high magnetoresistance.

The drive electronics for a material of this type would probably not be of the same type as for a conventional head. The sensor would switch from a relatively low resistance, perhaps 10 Ω to a very large resistance on the order of kΩ or

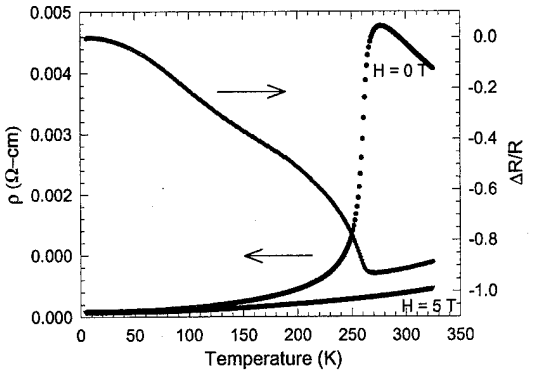


FIG. 6. Resistivity and magnetoresistive signal of the perovskite $La_{0.67}Ca_{0.33}MnO_3$.

even MΩ. The resistive noise would be determined not by the head, but rather by other resistances in the input circuitry. For cases where the magnetoresistance change approaches 100% the SNR of the head could be extremely large, leading the way to areal densities much higher than 16 Mb/mm^2.

Tunnel junctions composed of two magnetic materials separated by a dielectric have also shown promise recently. Miyazaki and Tezuka[2] have demonstrated magnetoresistive effects of 18% at room temperature in low fields. The entire subject of magnetotransport in heterostructures is only in its infancy.[22] However, the careful tuning of material properties to achieve the required electrical and magnetic properties is proving to have a large impact on the recording industry.

V. SUMMARY

Future increases in areal density and data rate require that the output of the read head become larger. This has been shown to arise from the need to maintain a constant SNR while contributions from noise sources increase. The decrease in gap length, element height, and read width all conspire to reduce the head output, necessitating a gain in the signal by improving the magnetoresistive ratio of the material. New spin valve devices promise to provide a factor of 10 improvement in magnetoresistance over conventional materials and on the horizon are even newer materials that promise even greater magnetoresistance. However, careful control over structural properties will be required because the films are so thin and because they rely on subtle effects in magnetotransport. The theoretical understanding of new types of magnetoresistive materials is making rapid progress and it would not be surprising if a low-field "magnetic switch" were soon to be developed.

ACKNOWLEDGMENTS

The authors would like to thank the members of the National Storage Industry Consortium's project on Ultrahigh Density Recording Heads for many stimulating discussions regarding high-density recording. They also would like to thank Dick Baugh for use of his channel model, Pascale Bayle and Amanda Petford-Long of Oxford for the cross-sectional TEM pictures, Jeff Rosner at HPL for the plan-view TEM picture and analysis, and Ron Hiskes of HPL and Michael Hundley of Los Alamos for the CMR data.

[1] R. L. White, IEEE. Trans. Magn. **28**, 2482 (1992); R. E. Camley and R. L. Stamps, J. Phys.: Cond. Mater. **5**, 3727 (1993); Gary A. Prinz, Phys. Today **48**, 58 (1995).
[2] Miyazaki and Tezuka, J. Magn. Magn. Mater. **139**, L231 (1994); J. S. Moodera, T. M. Wong, L. R. Kinder, and R. Meservey, Phys. Rev. Lett. **74**, 3273 (1995).
[3] S. Jin, T. H. Tiefel, M. McCormack, R. A. Fastnacht, R. Ramesh, and L. H. Chen, Science **264**, 413 (1994).
[4] Edward S. Murdock, Ralph F. Simmons, and Robert Davidson, IEEE Trans. Magn. **28**, 3078 (1992).
[5] J. J. Moon and L. Richard Carley, IEEE Trans. Magn. **26**, 2172 (1990).
[6] N. Ishiwata, H. Matsutera, and K. Yamada (to be published).
[7] J.-G. Zhu and D. O. O'Connor (to be published).
[8] Samuel Yuan, Neal Bertram, and Manoj Bhattacharyya, IEEE Trans. Magn. **30**, 381 (1994).
[9] Neil Smith, IEEE Trans. Magn. **23**, 259 (1987).
[10] H. Neal Bertram, *Theory of Magnetic Recording* (Cambridge University Press, Cambridge, England 1994).
[11] M. Baibich, J. Broto, A. Fert, F. Nguyen Van Dau, and F. Petroff, Phys. Rev. Lett. **61**, 2472 (1988).
[12] B. Dieny, V. S. Speriosu, S. Metin, S. S. P. Parkin, B. A. Gurney, P. Baumgart, and D. R. Wilhoit, J. Appl. Phys. **69**, 4774 (1991).
[13] Robert Rottmayer and Jian-Gang Zhu (to be published).
[14] N. Smith, A. M. Zeltser, and M. R. Parker (to be published).
[15] Thomas C. Anthony, James A. Brug, and Shufeng Zhang, IEEE Trans. Magn. **30**, 3819 (1994); W. F. Egelhoff, Jr., T. Ha, R. D. K. Misra, Y. Kadmon, J. Nir, C. J. Powell, M. D. Stiles, R. D. McMichael, C.-L. Lin, J. M. Sivertsen, J. H. Judy, K. Takano, A. E. Berkowitz, T. C. Anthony, and J. A. Brug, J. Appl. Phys. **78**, 273 (1995).
[16] V. S. Speriosu, B. A. Gurney, R. E. Fontana, T. Lin, M. M. Dovck, C. Tsang, D. E. Heim, and M. L. Williams (to be published).
[17] J. C. S. Kools, Th. G. S. M. Rijks, and R. Coehoorn (to be published).
[18] D. Heim, R. Fontana, C. Tsang, V. Speriosu, B. Gurney, and M. Williams, IEEE Trans. Magn. **30**, 316 (1994); Samuel W. Yuan and H. Neal Bertram, J. Appl. Phys. **75**, 6385 (1994); Danzhu Lu and Jian-Gang Zhu (to be published).
[19] Ching Tsang, Robert E. Fontana, Tsann Lin, D. E. Heim, Virgil Speriosu, Bruce Gurney, and Mason L. Williams, IEEE Trans. Magn. **30**, 3801 (1994); T. Kawabe, H. Hoshiya, Y. Hamakawa, Y. Suzuki, K. Nakamoto, M. Fuyama, and Y. Sugita (to be published).
[20] Ryoichi Nakatani, Katsumi Hoshino, Shin Noguchi, and Yutaka Sugita, Jpn. J. Appl. Phys. **33**, 133 (1994).
[21] H. E. Camblong, P. M. Levy, and S. Zhang, Phys. Rev. B **51**, 16052 (1995); D. M. C. Nicholson, W. H. Butler, X.-G. Zhang, J. M. Maclaren, B. A. Gurney, and V. S. Speriosu, J. Appl. Phys. **76**, 6805 (1994).
[22] Henri J. F. Jansen, Phys. Today **48**, 50 (1995).

Media for 10 Gb/in.^{2} hard disk storage: Issues and status (invited)

D. N. Lambeth, E. M. T. Velu, G. H. Bellesis, L. L. Lee, and D. E. Laughlin
Data Storage Systems Center, Carnegie Mellon University, Pittsburgh, Pennsylvania 15213

Future 10 Gb/in.^{2} recording densities represent submicron trackwidths and sub-100 nm bit lengths. This requires extremely small magnetic switching units and very high coercivities of the media to satisfy the signal-to-noise ratio requirements. At the same time the question of magnetic thermal stability and the lack of transducers capable of performing at these densities makes it difficult to evaluate media. An uncoupled, highly uniform magnetic grain size of about 10 nm is a compromise toward maintaining an adequately low media noise and yet maintaining magnetic stability. Here we discuss current media construction, the detrimental role of substrate roughness, the role of new media structures and alloys on microstructure and magnetic properties as well as techniques for evaluating media performance prior to the availability of the required playback heads. © *1996 American Institute of Physics.* [S0021-8979(96)39908-9]

I. INTRODUCTION

The introduction of sputtered thin-film media, onto electrolessly plated NiP on an Al substrate, has lead to a substantially smoother surface enabling record and playback heads to become closer to the medium—the single most important characteristic in magnetic recording. These advances have recently lead to an approximate 60% compound annual growth rate for areal densities[1] plus three demonstrations of areal densities in the Gb/in.^{2} range.[2–4] The technology which is commercially available today incorporates 0.4–0.8 Gb/in.^{2} areal densities and is on the 60% growth curve.

In 1992, Murdock *et al.*[5] described several possible recording formats and outlined the required mechanical, magnetic, and recording performance requirements to achieve 10 Gb/in.^{2} areal densities. The selection and matching of the head and media components as well as the tracking and signal processing techniques is currently a complex iteration process and the evaluation of each of these individual components is hampered by the lack of the other. Here, we review and describe some of the hard disk media issues and a philosophy for developing future media when advanced recording and playback heads are not available. By example, we will try to put into perspective where media technology is today and what limits its performance.

II. RECORDING FORMAT AND MAGNETIC REQUIREMENTS

Over a period of several years disk drives have maintained a fairly constant recording trackwidth to linear bit density ratio. Hence, scaling the current areal density to a 10 Gb/in.^{2} system yields a format entirely consistent with Murdock *et al.*'s projections. One format would call for 25 400 tpi (0.5 μm read head width) and a linear density of 400 000 bpi. A 4/3's rate code would then dictate a 300 Kfci linear density.

It is assumed that high moment inductive heads will be available for recording while spin valve head[6] technology will be available for playback. The playback head dynamic range and head-medium spacing, then determines the desired moment of the medium. Scaling arguments[5] indicate that for a 30–40 nm head to the center of medium spacing, a $M_r\delta = 0.4$ to 0.6 memu/sq cm is needed to optimize head response while preventing head saturation nonlinearities during playback. From a medium noise view point, it turns out to be especially advantageous to lower the recording head to medium spacing. Fortunately, the low $M_r\delta$, that spin valve head technology requires, minimizes the transition demagnetization effects to allow higher linear bit densities. As a rule of thumb the flux reversal spacing is limited to approximately πa_x.[7] Hence, to achieve 300 Kfci density, one requires that $a_x < 27$ nm. The coercivity of the medium should approach 3000 Oe while δ should be less than 15 nm.

As usual it is anticipated[6] that the medium noise will slightly dominate the head noise and so an isolated signal pulse to broad band media noise of 27–30 dB is required for 10 Gb/in.^{2} (Ref. 5). Fortunately, we have the experience of particulate recording media as a guide in understanding the media noise issues. Baugh *et al.* and Belk *et al.*[8,9] showed that media noise, measured in the frequency domain, is the smallest when the magnetic regions are composed of small, well-isolated, magnetic particles. For particulate media they found that the noise power was nearly a constant, as a function of transition density, and the smallest at high recording densities. For thin-film media, the noise power increases linearly with increasing transition density and then increases supra linearly.

The magnetic playback head samples a finite volume of the medium determined by the head field distribution. Hence, when a particulate medium is dc erased, the particles are magnetized, largely, all in one direction and fluctuations in the magnetization sensed by the head are due to either nonuniformities in the density of particles or in the random orientation of their magnetic axes. These statistically independent fluctuations yield a Gaussian probability distribution. This gives a noise power proportional to the number of particles, while the signal power is proportional to the square of the number. Hence, the lowest particulate medium noise results when the particles are small so that the number of particles sensed by the head field is maximized and when the size and orientation distribution of the particles is uniform. For the Baugh type of plot, the lowest noise is observed when the medium is in the ac-erased state as the magnetization of individual particles orient to a flux closure condition which minimizes the external fields that the head senses.

Thin film media are usually composed of closely packed, randomly oriented grains which are either magnetically

 0021-8979/96/79(8)/4496/6/$10.00 © 1996 American Institute of Physics

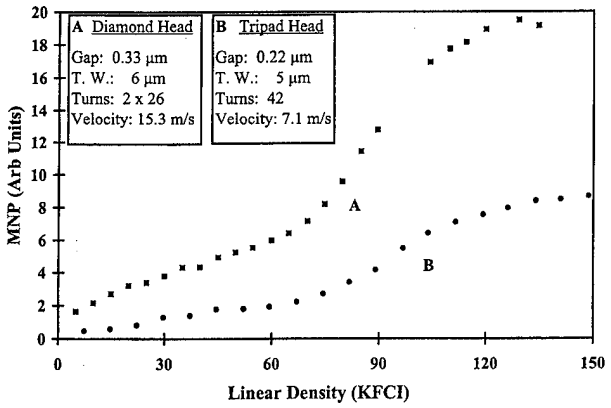


FIG. 1. Effect of record head field gradient on medium noise power for a commercially available CoCrTa hard disk.

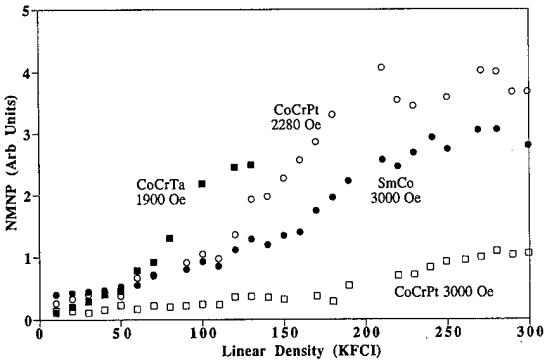


FIG. 2. Medium noise power vs linear density for CoCrTa, CoCrPt, SmCo, and CoCrPt hard disks. The data was normalized by the power in the isolated pulse signal.

exchange-coupled at the grain boundary, grouped as exchange-coupled clusters of grains, or, at best, grains which are somewhat isolated by nonmagnetic material. The latter behaves as particulate media, while the former behaves as large regions of continuous magnetization. For the former, the dc-erased state is the lowest noise situation as the media can be viewed as one large domain with no flux leakage from the media surface. However, at a flux reversal, the fluctuation amplitude manifests as large medium noise. Hence, a medium in which the grains are exchange-coupled exhibits a noise power that is associated with the transition and the noise power increases linearly with the transition density until the transitions are so closely spaced that they begin to interact[10] and the noise power increases supra-linearly. Practically, for a medium noise limited system, the flux spacing, πa_x is usually set to be at or slightly beyond the onset of this supra-linear regime. Therefore the following three simultaneous conditions are desired in a Baugh plot: (1) Small isolated magnetic units to give a low slope in the linear regime. (2) Small, uniform, uncoupled grains to give a low dc noise. (3) A recording transition density chosen to occur prior to the onset of the supra-linear regime.

It should be pointed out that the transition fluctuation amplitude is largely determined by the dispersion in the media characteristics (uniformly of grain size, orientation, exchange coupling, stress, etc.) and these fluctuations are exacerbated by a poor record head field gradient. That is, if the head field gradient is poor, then both a_x (Ref. 7) and the fluctuation (noise) of the transition location will be large.[10,11] Figure 1 shows two non-normalized recording results, on the same medium, where the record head field gradient has been varied. The lower-noise curve B was obtained using a 5-μm-wide Read Rite Tripad head with a 0.22 μm gap and flying at approximately 25 nm (at 7.1 m/s velocity) while the higher-noise curve A was generated using a 6-μm-wide Quantum Diamond head with a 0.33 μm gap and flying at approximately 100 nm. Note that, not only does the supra-linear noise regime begin earlier, but the slope of the linear noise regime is larger for the recordings with the poor record field gradient. Obviously it is difficult to evaluate medium noise without the ideal head and fly height, since medium noise dependents upon the head field gradient. The practical approach, then, is to use a head with the smallest available gap and to fly it as low as possible. The measured medium noise will then be an upper bound. Since the noise power is mostly contained in the low-frequency spectrum,[9,11,12] the playback system does not need to perform to the same linear densities as the recording test system. In brief, we see that the medium grains must be small, magnetically isolated, and of uniform size to minimize the noise, the film moment must be chosen to maximize the spin valve response without overdriving it, the coercivity must be high enough to prevent demagnetization, and the medium structure must be extremely smooth to allow low fly heights both to write low noise transitions and to resolve the playback pulses.

For single-domain Stoner–Wohlfarth particles, the coercivity is determined by both orientation and crystalline anisotropy energy. Also, as the grain size is reduced and the thermal energy fluctuations threaten the stability of the recorded bit it is important to maximize the magnetic crystalline anisotropy. Charap and Lu's[13] modeling indicated that for 400 Kfci recording and cobalt parameters ($K_u=4\times10^6$ erg/cc, $M_s=900$ emu/cc), a grain size below 8 nm would tend to be thermally unstable. A 10 Gb/in.^{2} medium should then have magnetic units in the 10–12 nm diameter range. The quest then is to achieve isolated grains of this size while maximizing the anisotropy. An approach to achieving high anisotropy is to build grains of such crystalline perfection that the magnetocrystalline anisotropy is maximized. The alignment of the anisotropy axis along the record track direction will also help to maximize the coercivity. However, there is modeling evidence that this type of orientation may increase medium noise.[14]

III. STATUS OF CURRENT MEDIA DEVELOPMENT

Figure 2 provides a comparison of the normalized medium noise power for a number of media designed for various recording densities. Table I lists the magnetic properties of each of these media. An all ones pattern was recorded on each of these media using a Read Rite Tripad head with the head to medium velocity (7.1 m/s) adjusted such that the head was flying just beyond contact of the disk. The medium

TABLE I. Magnetic properties and surface roughness details of high coercivity hard disks.

Media		Magnetic properties		Substrate			Overlayer thickness (nm)
Type	material	H_c (Oe)	$M_r t$ (memu/cm^2)	Material	State	Roughness R_{rms} (nm)	
A	CoCrTa	1900	2.1	NiP/Al	Textured	8.7	15(C)
B	CoCrTa	2200	1.0	NiP/Al	Textured	5.0	15(C)
C	CoSm	3000	0.6	Glass	Smooth	1.3	7(Cr) 10(C)
D	CoCrPt	3000	0.55	NiP/Al	Super Smooth	0.4	5(C)

noise power was obtained using the technique described earlier.[8,9,12] Medium A (CoCrTa) was removed from a modern commercial drive operating at 0.4 Gb/in.^{2} density. In Fig. 2, one can observe the supra-linear noise regime beginning at approximately 50 Kfci. Medium B (CoCrPt) is a commercially emerging medium designed for approximately 1–1.2 Gb/in.^{2} density. We observe a lower slope and the supra-linear behavior at 125–150 Kfci indicating a superior medium. Sample C is a SmCo medium[12,15] with a grain size of about 20 nm, while sample D is a CoCrPt medium with a grain size of approximately 15–20 nm. Using this close flying head neither of these latter two media appear to possess a supra-linear noise regime when recorded up to 300 Kfci. However, the linear regime's nonzero slope indicates that these media are still transition noise limited and have exchange coupling. Eventually, at higher densities the supra-linear noise behavior should be observed. A gap null occurs at 230 Kfci. A significantly sharper head field gradient should decrease the transition noise for these media provided the inherent transition noise is limited by the head field gradient and not by the media microstructure.

While a signal-to-noise ratio could be obtained by extrapolating out to 300 Kfci, MFM images can provide more accurate information plus insight into the microstructural properties. Figures 3–5 show MFM images of transition patterns at different densities for three of the four media of Fig. 2. Clearly, just as was shown in the noise power curve, the onset of the exchange coupled transition-transition interaction has occurred for the CoCrTa medium well prior to the 150 Kfci density, Figs. 3(a)–3(c). An atomic force microscope (AFM) image, Fig. 3(d), shows the film's roughness and grain clustering due to the mechanical texturing of the substrate. Close examination of the large magnetic switching units observed in the dc-erased areas of the MFM images correlate to the AFM observed grain clusters. To avoid this noise source, future media should be prepared using smooth substrates having a smooth data zone surface.[16]

Experimental media C and D were prepared on a smooth glass substrate and a supersmooth NiP-Al substrate, respectively. The MFM images of these disks [Figs. 4(a)–4(c) and Figs. 5(a)–5(c), respectively] show well-resolved transitions into the 200 and the 250 Kfci regimes, respectively. The smaller magnetic unit size correlates to the substrate quality shown in Figs. 4(d) and 5(d). Other MFM features worth noting are the quiet dc-erased backgrounds, as well as, the small substrate scratch in the center of the 250 Kfci track in medium D. Even though the magnetic switching unit size of this latter medium is largely determined by the underlayer microstructure, the roughness of the scratch dominates the

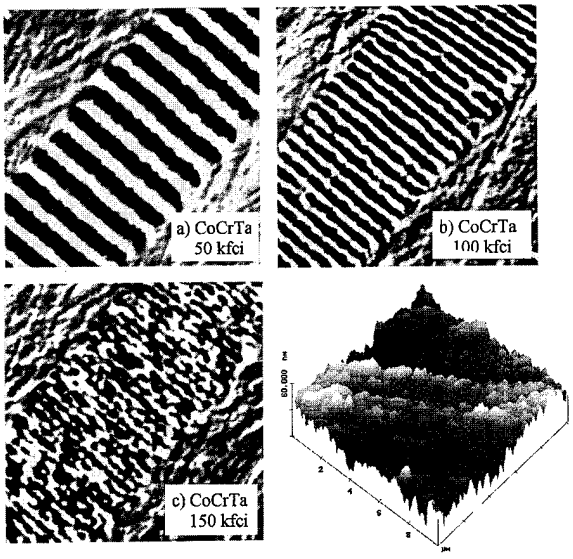


FIG. 3. (a)–(c) MFM images of magnetic transitions and (d) AFM image of the surface in a CoCrTa hard disk. The substrate was mechanically textured.

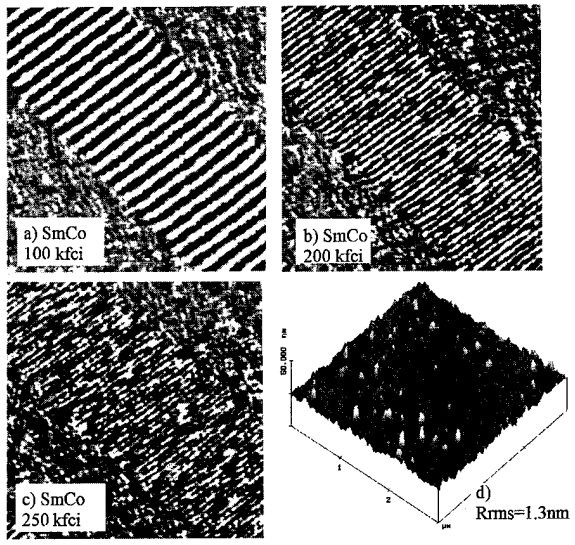


FIG. 4. (a)–(c) MFM images of magnetic transitions in a SmCo hard disk and (d) AFM image of the smooth blank glass disk substrate.

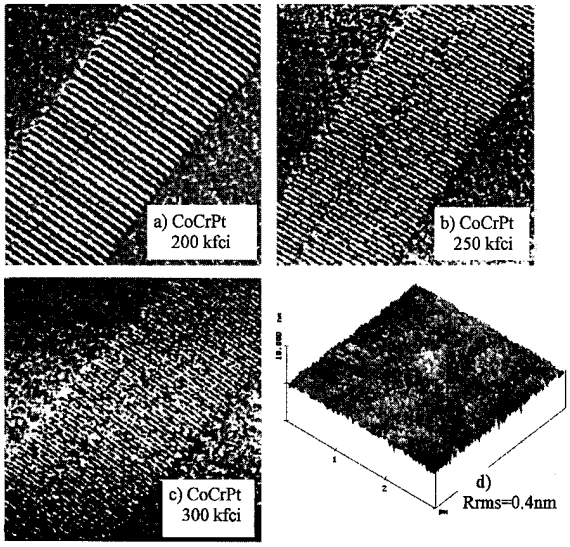


FIG. 5. (a)–(c) MFM images of magnetic transitions in a CoCrPt (medium D) hard disk and (d) AFM image of the supersmooth NiP/Al disk substrate.

transition location. Transitions at 300 Kfci were clearly visible for medium D, but Fig. 5(c) indicates that the medium SNR is unacceptable for a 0.5 μm trackwidth.[6,17]

IV. CURRENT MEDIA STRUCTURE APPROACH

Modern commercial media are prepared by sputter deposition and consist of a structure of a lubricant, a carbon overcoat, a magnetic layer, and a Cr underlayer, on a substrate. The carbon overcoat and the lubricant are used to provide mechanical and chemical protection to the underlying metals. Daval and Randet[18] showed that an underlayer of Cr could significantly improve the magnetic properties of a Co alloy thin film. Since then, much work has been published on how the Cr underlayer influences the Co alloy microstructure and magnetic properties. The medium's coercivity and noise performance are largely determined by the Co alloy composition, grain size, and crystal orientation, perfection, and isolation. The underlayer largely effects the latter of these via promoting epitaxial growth onto the Cr crystallites. Likewise, the substrate surface strongly influences the Cr growth via both surface bonding energy[19] and roughness.

In brief, depending upon the growth conditions[19–21] the bcc Cr tends to develop with a variety of crystallographic textures. The closest packed planes are {110} and so at low substrate temperatures, or when prepared with a substrate bias, the low-energy state (110) texture is obtained which promotes an epitaxial (10.1) cobalt texture. Since the atomic sizes of Cr and Co are similar, the atomic spacing of the atoms at these two surfaces approximately match and so, on a small grain size scale, an epitaxial growth results. This places the magnetic easy axis (c axis) of the HCP Co tilted approximately 28° from the film plane. Since the Cr axes are random in-plane, the in-plane magnetization components of the Co crystallites are random in-plane. On the other hand, under higher-temperature deposition conditions, it is possible to obtain (002) Cr texture from which epitaxial growth yields a (11.0) textured Co film. Since this texture calls for the HCP

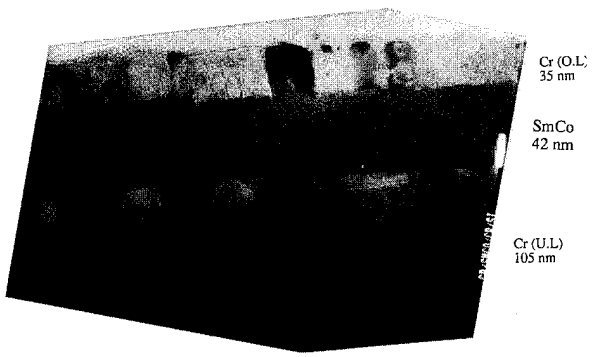


FIG. 6. Cross-sectional TEM image of the SmCo/Cr interface.

c axis to lie totally in the film plane higher coercivities usually result. Less often reported, but still commonly observed, is a (10.0) Co texture which is now believed to be due to a (112) underlayer texture.[23] Peng *et al.*[22] recently showed that epitaxial growth alone is not sufficient to achieve high coercivity. If the grain size of the Cr underlayer is large enough and the processing conditions are such to promote cobalt alloy bi- and quadcrystal structures,[24] then the effective magnetocrystalline anisotropy is compromised and, hence, the coercivity is degraded.

Due to the Cr surface roughness and grain boundaries the Co grains tends to replicate the Cr grain size. Hence, provided the Co grains do not grow together, and enable the Co to connect at the interfaces, the magnetic switching unit size is largely determined by the underlayer grain size. To decouple the grains and to keep the magnetic switching unit small various Co alloys have been studied to provide a nonmagnetic grain boundary phase. For example, in CoCrTa and in CoCrPt, it has been argued that preparation of the films at elevated temperatures causes Cr segregation to the grain boundaries. However, compared to the influence of the underlayer, it is hard to conceive how this mechanism could set the basic grain size.

Clearly, it can be argued that when the lateral scale of the substrate roughness is similar to the desired magnetic unit scale media noise can be decreased.[25,26] Likewise, a very smooth substrate could tend to promote large grain features were it not for the underlayer microstructure taking over and controlling the resulting magnetic unit size. As an example of the controlling effect of the underlayer a fairly uniform roughness results when 28 nm of SmCo is deposited upon a 100 nm (110) textured Cr layer prepared at room temperature on a smooth substrate.[25] Without the controlling Cr underlayer identically prepared SmCo films result in nonuniform, enlarged grains and a noisy media. The uniform roughness provided by the Cr underlayer leads to, a uniform SmCo unit size, a delineation between magnetic units, and consequently a lower-noise medium. Further evidence of this delineation is shown in the transmission electron microscope (TEM) cross section, Fig. 6. This structure is composed of a Cr underlayer, a SmCo magnetic layer, and a Cr overlayer. The underlayer grain structure clearly propagates not only into and through the SmCo layer, but continues into the Cr overlayer. A high-resolution TEM image of this film is shown in Fig. 7.



FIG. 7. High-resolution TEM cross-sectional image at the SmCo/Cr interface.

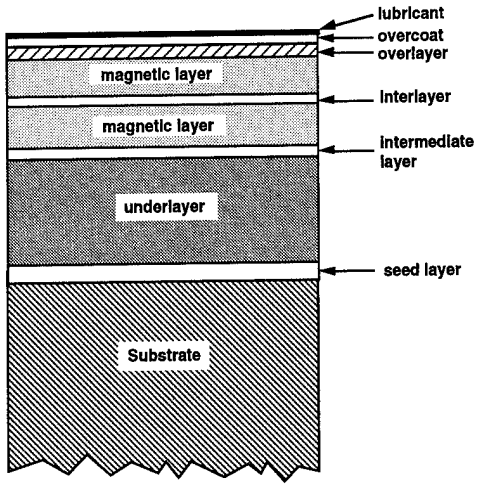


FIG. 8. Thin-film layer structure in novel high coercivity media with multiple magnetic and nonmagnetic layers.

Here, the Cr grain structure is clearly evident and close examination shows the shadowing of the SmCo units at the Cr grain boundaries continuing through the film thickness. At first glance, it appears that the SmCo layer is amorphous, which is consistent with the reported high temperatures (>600 °C) needed to crystallize the films.[27] However, close examination shows that a large number of SmCo nanocrystallites (2–5 nm size) grow even at room temperature when prepared on the Cr underlayer. Epitaxial growth between the Cr and the SmCo interface is also weakly visible. Bright-field, plane-view TEM microstructural images of this film shows a clear separation between the grains while the selected area electron diffraction pattern shows evidence that a lattice matched crystallinity exists in the SmCo. The underlayer has strongly influenced the magnetic switching unit size and has also induced at least partial crystallinity into the, otherwise, amorphous, SmCo film. This results in the low-noise performance indicated in Fig. 2.

V. NEW MEDIA STRUCTURE APPROACH

In order to further minimize medium noise, even smaller magnetic switching unit sizes need to be achieved while more perfect crystals are needed to maintain coercivity. One approach is to use sputtered multiple epitaxial layers. Figure 8 depicts such a structure. If the substrate is assumed to be perfectly smooth, then the first sputtered layers will dominate the magnetic film's microstructure. Each of the layers can have multiple purposes, but the following gives a simplified picture of their roles: The seed layer is to provide an initial texture, while still providing a smooth surface to the underlayer. This way the underlayer texture is formed early during film growth. The underlayer is to control the fundamental grain size and, also, to transfer a high quality texture via epitaxial growth to the latter layers. The intermediate layer can provide both chemical effects and a buffer interface to promote a better Co layer texture as we shift from a BCC lattice to the HCP. The magnetic layers provide the storage mechanism while the interlayer has been used in the past to double the number of magnetic particles.[28,29] The overlayer, overcoat, and lubricant are to provide their normal protective functions.

We now discuss two media structures which follow this format. The first consists of an alternative underlayer with $B2$-type crystal structure.[23] The $B2$ is a derivative structure of the bcc Cr and for NiAl the atomic spacing is almost identical to that of Cr thus providing a potential epitaxial match for HCP Co.[23] Because the sputtered NiAl grain size is more uniform and about half that of Cr,[23] there is the potential for smaller Co grains and lower media noise. When CoCrPt (or CoCrTa) is deposited onto NiAl or Cr underlayers, using identical processing conditions, very similar coercivities are obtained provided the NiAl is thicker. However, if even a very thin, 2.5 nm, intermediate layer of Cr is used on the NiAl then the coercivity is even greater than for the medium with a Cr underlayer. The dramatic effect of the intermediate layer is believed to be due to a smoother atomic interface resulting in a more perfect Co crystallite. Preliminary measured values of noise have shown a significant improvement.[30] Other evidence of the benefit of an intermediate layer is the use of a thin layer of CoCrTa between a Cr underlayer and a Pt-rich $Co_{72}Cr_{10}Pt_{18}$ alloy.[31] By using 5-nm-thick CoCrTa as an intermediate layer on Cr, a HCP template was provided for the epitaxial growth of the larger lattice constant $Co_{72}Cr_{10}Pt_{18}$ and the coercivity increased by over 30% (>4000 Oe).

The second approach is to use a seed layer to initialize the underlayer crystal texture which may in turn enhance crystal perfection by minimizing internal lattice defects. Nakamura and Futamoto[32] demonstrated that Cr could be epitaxially grown on single-crystal [001] MgO. For this $B1$-type crystal the {001} planes have the lowest surface energy.[33] Hence, we have found that even very thin layers of sputtered MgO are (001) textured. This surface matches well with the bcc Cr[34] to induce a strong (002) Cr texture, Fig. 9, even when the films are prepared without preheating the substrate. Coercivities greater than 4000 Oe have been achieved for CoCrPt magnetic layers grown on this structure.[34] A similarly impressive effect on coercivity is found when NiAl is used as the underlayer on the MgO seed layer.[35]

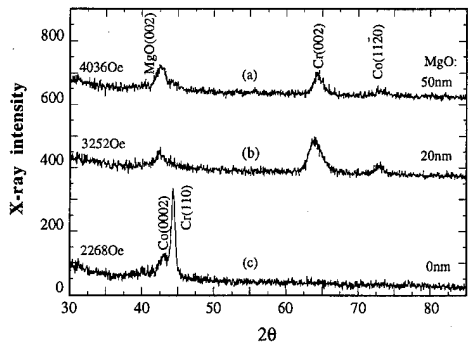


FIG. 9. X-ray diffraction patterns of CoCrPt films grown on 100-nm-thick Cr underlayers sputtered onto MgO seed layers of (a) 50 nm, (b) 20 nm, and (c) zero thicknesses.

VI. BEYOND 10 Gb/in^2

Here we have compared current hard disk media to experimental media approaching 10 Gbit/in.^{2} densities. We have shown that apparent media noise is tied to the recording head field gradient as well as to the substrate and underlayer smoothness. In addition, we have outlined epitaxial procedures for developing media with both higher coercivities and smaller magnetic switching units.

It may very well be possible to continue on the current technology path to recording densities even beyond 10 Gbit/in.^{2} However, it is hard to see how recording densities can increase another order of magnitude without a considerably different approach.[36] If a medium with uniformly placed magnetic units is conjectured, many of today's technical limitations are eliminated. If a bit is defined as either a single, or a fixed number of magnetic switching units, then the noise issues change from asking how many particles are in a bit to whether or not manufacturing inaccuracies spatially misplaced the magnetic units. The system noise may then be dominated by tracking and transducer sensitivity limits. Hence, a uniform array of magnetic particles, each just larger than the superparamagnetic size limit, would represent the ultimate recording medium. For uniaxial cobalt alloys, 8-nm-diameter particles centered on a 10 nm array spacing should provide stable data bits. This corresponds to a recording density of over 6000 Gbit/in.^{2} Clearly producing this array of sublithographic particles will require novel patterning or self assembly techniques and depending upon the transducers it may be important to have a single magnetic orientation. This raises entirely new challenges for those who will develop the tracking and signal processing technologies. Nevertheless, these technologies are within the realm of imagination and lend support to a continuity of the 60% areal density growth curve.

ACKNOWLEDGMENTS

The authors would like to acknowledge and thank D. Baral of Western Digital, S. Bhatia, and M. Doerner of IBM, R. Ranjan of Komag, E. Williams of Read-Rite Corp., Q. Ng and S. Charap for many helpful discussions and for components during the course of this work. The authors also wish to thank the many friends and members of the DSSC who have lent their support. Portions of this material are based upon work supported by DOE Grant No. DE-FG02-90ER45423 or by the Data Storage Systems Center via NSF Grant No. ECD-8907068, ARPA Contract No. MDA972-93-1-0009, and by the DSSC industrial sponsors. The government has certain rights in this material.

[1] J. L. Simonds, Phys. Today **48**, 26 (1995).
[2] T. Yogi, C. Tsang, T. A. Nguyen, K. Ju, G. L. Gorman, and G. Castillo, IEEE Trans. Magn. **MAG-26**, 2271 (1990).
[3] M. Futamoto, F. Kugiya, M. Suzuki, H. Takano, Y. Matsuda, N. Inaba, Y. Miyamura, K. Akagi, T. Nakao, H. Sawaguchi, H. Fukuoka, T. Munemoto, and T. Takagaki, IEEE Trans. Magn. **27**, 5280 (1991).
[4] C. Tang, D. McCown, H. A. Santini, J. Lo, and R. E. Lee, IEEE Trans. Magn. (to be published).
[5] E. S. Murdock, R. F. Simmons, and R. Davidson, IEEE Trans. Magn. **8**, 3078 (1992).
[6] J. A. Brug, T. A. Anthony, and J. H. Nickel, Paper AA02, this conference.
[7] M. L. Williams and R. L. Comstock, AIP Conf. Proc. **5**, 738 (1972).
[8] R. A. Baugh, E. S. Murdock, and B. R. Natarajan, IEEE Trans. Magn. **MAG-19**, 1722 (1983).
[9] N. R. Belk, P. K. George, and G. S. Mowry, IEEE Trans. Magn. **MAG-21**, 1350 (1985).
[10] M. J. Freiser, IBM J. Res. Dev. **23**, 330 (1979).
[11] K. E. Johnson, E. Y. Wu, D. C. Palmer, and J. G. Zhu, IEEE Trans. Magn. **28**, 2713 (1992).
[12] E. M. T. Velu and D. N. Lambeth, IEEE Trans. Magn. **28**, 3249 (1992).
[13] P.-L. Lu and S. H. Charap, IEEE Trans. Magn. **30**, 4230 (1994).
[14] J.-G. Zhu, X.-G. Ye, and T. C. Arnoldussen, IEEE Trans. Magn. **29**, 324 (1993).
[15] Y. Liu, D. J. Sellmyer, B. W. Robertson, S. S. Shan, and S. H. Liou, IEEE Trans. Magn. **31**, 2740 (1995).
[16] R. Ranjan, D. N. Lambeth, M. Tromel, P. Goglia, and Y. Li, J. Appl. Phys. **69**, 5745 (1991); U. S. Patent Nos. 5 062 021 and 5 108 781.
[17] P. Glijer, J. M. Sivertsen, J. H. Judy, C. S. Bhatia, M. F. Doerner, and T. Suzuki, Paper DC-01, this conference.
[18] J. Daval and D. Randet, IEEE Trans. Magn. **MAG-6**, 768 (1970).
[19] Y. C. Feng, D. E. Laughlin, and D. N. Lambeth, J. Appl. Phys. **76**, 7311 (1994).
[20] D. E. Laughlin and B. Y. Wong, IEEE Trans. Magn. **27**, 4713 (1991).
[21] T. Lin, R. Alani, and D. N. Lambeth, J. Magn. Magn. Mater. **78**, 213 (1989).
[22] Q. Peng, H. N. Bertram, N. Fussing, M. F. Doerner, M. Mirzamaani, D. Margulies, R. Sinclair, and S. Lambert, IEEE Trans. Magn. **31**, 2821 (1995).
[23] L.-L. Lee, D. E. Laughlin, and D. N. Lambeth, IEEE Trans. Magn. **30**, 3951 (1994).
[24] B. Y. Wong, D. E. Laughlin, and D. N. Lambeth, IEEE Trans. Magn. **27**, 4733 (1991).
[25] E. M. T. Velu, D. N. Lambeth, J. T. Thornton, and P. E. Russell, J. Appl. Phys. **75**, 6132 (1995).
[26] M. Mirzamaani, "Alternate Substrates Magnetic and Tribology Issues," Presented at DISCON, San Jose, CA, September 1995.
[27] F. J. Cadieu, T. D. Cheung, L. Wickramasekara, N. Kamprath, H. Hegde, and N. C. Liu, J. Appl. Phys. **62**, 3866 (1987).
[28] E. S. Murdock, B. R. Natarajan, and R. G. Walmsley, IEEE Trans. Magn. **MAG-26**, 2700 (1990).
[29] S. E. Lambert, J. K. Howard, and I. L. Sanders, IEEE Trans. Magn. **MAG-26**, 2706 (1990).
[30] M. Doerner (private communication).
[31] L. Fang and D. N. Lambeth, Appl. Phys. Lett. **65**, 3137 (1994).
[32] A. Nakmura and M. Futamoto, Jpn. J. Appl. Phys. **32**, Pt. 2, 10A, L1410 (1993).
[33] P. W. Tasker, Adv. Ceram. **10**, 176 (1984).
[34] L.-L. Lee, B. K. Cheong, D. E. Laughlin, and D. N. Lambeth, Appl. Phys. Lett. (to be published).
[35] L. L. Lee, D. E. Laughlin, and D. N. Lambeth, IEEE Trans. Magn. **31**, 2728 (1995).
[36] R. M. H. New, R. F. W. Pease, and R. L. White, J. Vac. Sci. Techol. B **12**, 3196 (1994).

Signal processing for 10 GB/in.^{2} magnetic disk recording and beyond (invited)

Kevin D. Fisher[a)]
Quantum Corporation, 500 McCarthy Boulevard, Milpitas, California 95035

Cory S. Modlin
Information Systems Laboratory, Stanford University, Stanford, California 94305

After providing an overview of the read channel function in a magnetic disk recording system, we describe a range of possible partial-response maximum-likelihood (PRML) detection schemes. Improvements upon the current industry-standard PRML system can potentially provide substantial increases in areal density, as is shown by means of computer simulation of channel and detector.
© *1996 American Institute of Physics.* [S0021-8979(96)06308-4]

I. INTRODUCTION

The past several years have seen an explosion in the use of signal processing for the magnetic recording channel. The traditional analog peak detecting read channel is rapidly being displaced by the mixed-signal (analog and digital) partial-response maximum-likelihood (PRML) read channel[1] as a means of supplementing areal density increases which are due to improved head and media components.

Implementation for PRML technology in high-end disk drives was first described in Refs. 2 and 3. Thanks to new high density integrated circuit processes and streamlining of the signal processing algorithms, PRML technology is now rapidly finding its way into mainstream low cost disk drive products which are intended for desktop and notebook personal computers.[4]

While the main portion of the areal density increase in magnetic recording will likely always come from improved heads and media, signal processing and coding can provide a significant benefit that should be exploited. A case in point is the PRML demonstration described in Ref. 5 where a 1.08 GB conventional (1,7) run-length limited (RLL) peak detection disk drive was converted into a 1.4 GB PRML disk drive. This 30% density increase was achieved using the same generation of head and disk technology as the peak detection drive.

Signal processing and coding are also providing more subtle benefits by compensating for nonidealities in the magnetic recording channel, such as thin film head undershoots,[6] nonlinear transition shift,[7] media defects and magnetoresistance head thermal asperities.[8] When the signal processing is made adaptive, it can also help to compensate for manufacturing tolerances of the magnetic components such as the variation of readback pulse widths. By becoming more tolerant to component variation, adaptive signal processing can increase the number of heads and disks that can be built into one head/disk assembly with high yield. This effectively increases the capacity of a drive that can be attained at a fixed yield.

We begin in Sec. II with some background material regarding the functions of a read channel, and a brief description of how analog peak detection works. Section III is an overview of PRML systems, including extended and generalized partial-response. Generalized partial-response holds the promise of providing optimum performance over an uncoded channel. (By "uncoded" we mean that no additional noise immunity is obtained directly from the code. A run-length code is still assumed.) In Sec. IV, we show typical areal density gains that can be anticipated as systems evolve from peak detection to more complex detectors. Section V concludes with a discussion of some options for adding a channel code as a means of increasing immunity to noise. While coding gain in the high density magnetic recording channel is difficult to attain, such codes can potentially improve upon generalized PRML when sufficient complexity is permitted.

II. BACKGROUND

A. The read channel

The function of the read channel (data receiver) is to convert the preamplifier analog output signal into the original user data. All of the proposed data receivers share some common features (Figure 1).

They consist of automatic gain control (AGC), equalization, timing recovery, bit detection, and modulation decoding. The AGC system gain normalizes the preamplifier output to the predetermined range which is expected by the bit detector. The equalizer first filters the signal to eliminate out-of-band noise and also to shape the in-band spectrum (possibly adaptively) to improve the bit detection quality. The timing recovery system locks the detector to the phase and frequency of the incoming data stream. The bit detector may consist of a simple peak detection circuit or a more complicated Viterbi detector. In either case, the bit detector recovers the encoded data that was originally written to the disk. The

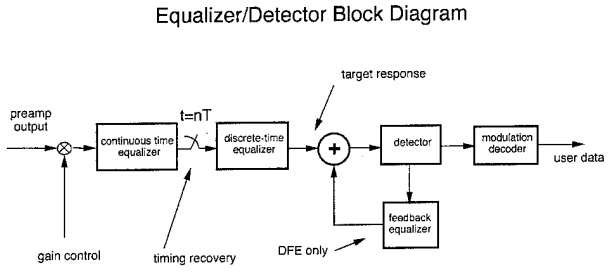


FIG. 1. Read channel block diagram.

[a)]Electronic mail: kfisher@qntm.com, fax 408-894-3207.

 0021-8979/96/79(8)/4502/6/$10.00 © 1996 American Institute of Physics

modulation code usually consists of a RLL code whose "d" and "k" constraints control the minimum transition spacing on the disk and the maximum spacing between transitions. The "d" constraint impacts the head and disk design, as the magnetic components must support this minimum transition spacing. The "k" constraint is intended to ensure a minimum number of transitions on the disk, and thus enable the timing and gain loops to accurately track the signal. The timing loop and gain recovery, while important, are not central to the subsequent material and will not be discussed further.

B. Peak detection

Peak detection is typically accomplished by means of a differentiator and threshold detector. If during a timing window the undifferentiated peak is above a threshold at the same time that the differentiated wave form is at zero, then a peak (noted as a binary "1") is declared. Otherwise no peak (or "0") is indicated. Peak detect systems work best when adjacent pulses do not interfere. The interference of adjacent pulses (equivalently "peaks") is called intersymbol interference (ISI).[9]

The main function of the equalization and coding in this case is to eliminate interference between peaks. This aim is generally accomplished by means of a rate 2/3 (1,7) RLL code and a "pulse slimming" equalizer. The (1,7) code effectively increases the spacing in time (or on disk) between peaks by 33%, at the expense of the code rate.

In spite of the RLL code, it is inevitable that the unequalized peaks will begin to interfere as densities increase. To improve detection performance, the equalizer is used to boost the high frequencies and thus decrease the width of the pulses. In this case, the high frequencies are boosted until a tradeoff between residual ISI and noise enhancement is attained.

III. PRML SYSTEMS

Partial-response systems differ from peak detect systems in that the amount of required high frequency boost can be dramatically reduced and the stringent d=1 RLL requirement is eliminated, provided that an appropriate PR target is used.[10] By permitting d=0, much higher code rates, such as 8/9 or 16/17, are possible. The higher code rate reduces the effective $pw50/T$ at the detector, where $pw50$ is the pulse width at 50% amplitude and "T" is bit time on the disk. Unless otherwise stated, we assume all PRML systems use a (0,k) code.

Partial-response provides a means for improving areal densities, as the amount of noise in the detector is reduced. The ISI need not be eliminated but is instead controlled. A maximum-likelihood (ML) detector is then used to extract the original recorded data from the PR wave form. The ML detector considers a span of channel outputs during the decoding process, and thus uses the ISI to its advantage.

A. Partial-response class IV

Partial-response class IV (or PR4), the *de-facto* industry standard, was a natural first step when departing from peak detect systems.[1,11,12] PR4 is characterized by its dibit response (response to two adjacent transitions), which is $1-D^2=(1+D)(1-D)$, where D is a unit delay relative to the write clock (Figure 2). PR4 provides a reasonable match to the magnetic channel at moderate user densities in the range of $pw50/T=2.0$.

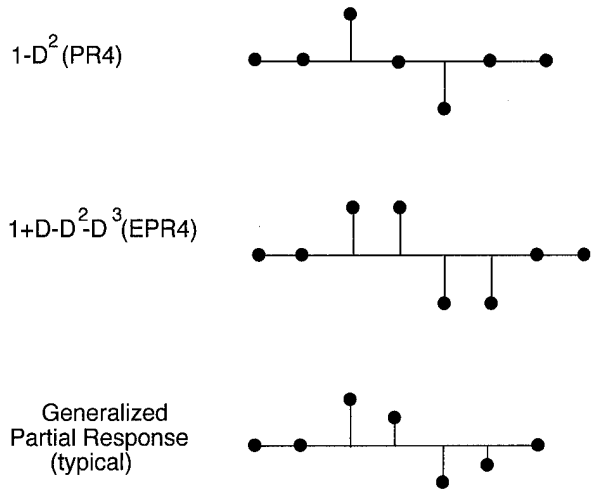


FIG. 2. Dibit response for PR4, EPR4 and generalized partial-response.

Viewed from the frequency domain, the PR4 response has spectral nulls at both zero and the Nyquist frequency which matches the magnetic channel's failure to pass low frequencies and the inherent high frequency losses at high densities (Figure 3). The required amount of high frequency noise boost is thus minimized.

PR4 was a natural first step for implementation reasons as well. The $1-D^2$ partial-response can be decomposed into two interleaved $1-D$ channels operating at half-rate. It is thus possible to have two (simpler) detectors running at half-rate as opposed to one high rate detector. This is a distinct advantage in high data-rate magnetic recording systems. One negative aspect of maximum-likelihood detection is that there is often significant decoding delay, as it is necessary to look at a span of the disk samples to make optimal decisions

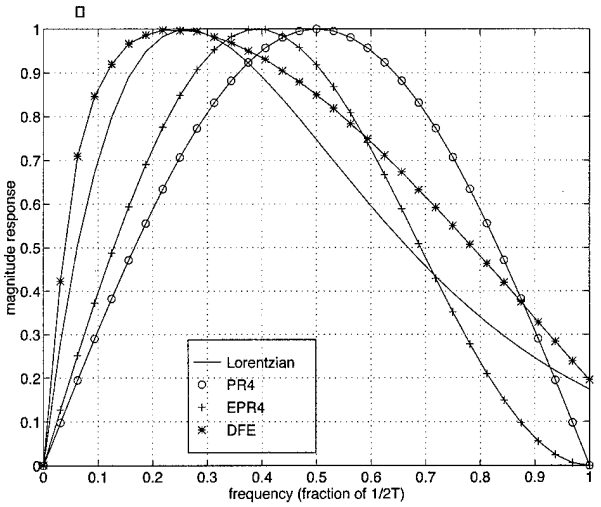


FIG. 3. Frequency response for some partial-response polynomials and the magnetic channel at density $pw50/T=2.3$.

TABLE I. PR4 channel output sample levels.

PR4 output	Channel inputs	
	b_k	b_{k-2}
0	−1	−1
−2	−1	+1
+2	+1	−1
0	+1	+1

(decoded disk data). This is not acceptable for decision directed timing recovery and gain control, which need low latency feedback loops to function properly. In PR systems, it is thus necessary to make preliminary decisions on the equalized wave form before the maximum-likelihood detector. In this regard, PR4 has another distinct advantage. As shown in Table I, the PR4 signal has only three levels. A simple threshold detector can easily resolve these three levels, thus resulting in adequate quality decisions for gain and timing.

B. Extended PRML

To achieve higher user densities, new PR targets that better match the inherent magnetic channel are needed. In an attempt to better match the high frequency losses that are present at very high densities, a class of extended partial-responses, $(1-D)(1+D)^N$, has been proposed,[10] for integers $N>0$. Two notable choices from this class are $(1-D)\times(1+D)^2=1+D-D^2-D^3$, which is called EPR4, and $(1-D)(1+D)^3$, which is called EEPR4. Higher orders than $N=3$ are at this point deemed impractical.

EPR4 is a straightforward extension of PR4. The second-order spectral null at the Nyquist frequency results in a reasonable match to the channel at densities of $pw50/T=2.5$. The primary drawbacks to EPR4 are the increased complexity ML detector (more than twice the complexity and twice the required speed compared with the PR4 detector), and the difficulty in maintaining good timing recovery and gain control from the preliminary five-level EPR4 decisions. As discussed earlier, preliminary decisions are necessary because of the decoding delay in the ML detector. In order to overcome these difficulties, a number of suboptimal "postprocessor" approaches to EPR4 decoding have been proposed.[13,14] In general, the postprocessor assumes a PR4 ML detector as a preprocessor. By using knowledge about the magnetic channel and the types of error events that are common in the PR4 ML detector, the postprocessor can correct those errors that would not have occurred in the EPR4 ML detector. Performance of a suboptimal detector is tightly coupled to the specific implementation and magnetic channel assumptions. In subsequent figures, we assume true EPR4 ML detection.

EEPR4 has been proposed in combination with a rate 2/3 (1,7) code.[6] Assuming that a (1,7) code is required by head and media constraints, EEPR4 provides a good match to the channel at the higher $pw50/T$ values that are required by the low rate code. While a ML detector for EEPR4 is twice as complex as the EPR4 detector, some simplifications result when taking the (1,7) code constraints into account. Coincidentally, these code constraints also improve the ML detector performance. Probably the biggest drawback to EEPR4 is the high clock rates which will result from the low code rate.

C. Generalized PRML

Until this point, only integer coefficient partial-response polynomials have been mentioned. By permitting the PR target, first, to be nonintegers and, second, to vary with the channel response, a better match to the channel is possible (see the DFE case of Fig. 3), which can result in additional performance gains. This possibility has been proposed for magnetic recording in many different forms, including fixed-delay tree search (FTDS)[15] and nonlinear reduced-state sequence estimation (RAM-RSE).[16]

It is not obvious which choices of polynomials will result in superior performance. The mean-square noise-whitening matched filter (MS-WMF) is known from communication theory to be an optimum equalizing filter. Quite fortunately, a minimum mean square error decision feedback equalizer (MMSE-DFE) turns out to naturally include this filter as its forward equalizer.[17] In this case, the forward equalizer output will have a dibit response of the form $1+w_1D+w_2D^2+w_3D^3+\ \ldots$ for real-valued w_i. A DFE in its simplest form will use past decisions to cancel the tail $w_1D+w_2D^2\ \ldots$ and use a simple threshold at zero to resolve to two possible decisions, +1 and −1. This tail cancellation is the source of the term "decision feedback." As greater performance is required, the threshold detector is replaced by a ML detector which uses part or all of the ISI in the tail to resolve the most likely recorded data. The remaining portion of the tail that is not used in the ML detector will continue to be cancelled by decision feedback. In the case of a varying channel, the DFE may be made adaptive.

With sufficient complexity (i.e. number of polynomial terms used), the DFE with a ML detector provides the best attainable performance for a (0,k) coded system that does not have any "coding gain."

IV. POTENTIAL AREAL DENSITY GAINS

We project the areal density gains that are possible using currently proposed signal processing techniques. We start with a basic peak detect system. From the published demonstrations described earlier (Sec. I), a 30% areal density improvement is shown to be achievable in the transition to PR4 ML detection. Since demonstrations like this are not available for more advanced systems, we must rely on computer simulations for further projections.

These simulations were done using a linear superposition model. We used an experimental magnetoresistive head response normalized so that its peak amplitude is one and we included a small amount of nonlinear transition shift. Media noise is assumed to be accurately described by a microtrack model[18] with a magnetization pattern, $m(x)=\tanh(2x/(a\pi))$, and electronics noise is assumed to be additive Gaussian noise. The system parameters are summarized in Table II.

In order to compare the detection schemes at different track and linear densities, SNR_e, and SNR_m, the signal to noise ratio of the electronics and media noise, respectively,

TABLE II. Simulation parameters.

System parameter	Value
User data rate	150 Mbits/s
$pw50$ (seconds)	16.7 ns
$pw50$ (inches)	5.7 μin.
Reference SNR_e	30.5 and 29 dB
Model	microtrack
Magnetization pattern	$m(x)=\tanh(2x/(a\pi))$
Number of microtracks	20,35,**50**,65,80
Values of a	0.35 μin., 0.60 μin.
Nonlinear transition shift	0.228 μin.
Write asymmetry	0.095 μin.
Anti-aliasing filter	7th order Butterworth
Code	(0,4) RLL ideal (rate 0.96)
Length of feedforward filter	20 taps symbol spaced
Span of feedback for RAM-RSE	10T
Detectors	PR4 ML, EPR4 ML, RAM-RSE3 (8 state)

were scaled appropriately.[19] The SNR_e was measured as the peak of an isolated step response squared divided by the power of the Gaussian noise in a 0−50 MHz band. We can write SNR_e in terms of a reference, $SNR_{e,0}$ as

$$SNR_e = SNR_{e,0}\left(\frac{w}{w_0}\right)^2,$$

where w is the track width. Because of the way we defined SNR_e, its value does not decrease as linear density grows, though in simulation results presented here, the average signal power (rms) does fall and the average electronics noise power does grow linearly as linear density rises. Similarly we write SNR_m in terms of a reference, $SNR_{m,0}$ as

$$SNR_m = SNR_{m,0}\left(\frac{w}{w_0}\right)\left(\frac{\eta_0}{\eta}\right),$$

where $\eta = pw50/T$ is the linear density. We neglect any micromagnetic nonlinear effects as transitions get closer and neglect any inter-track interference that may result from a higher track density.

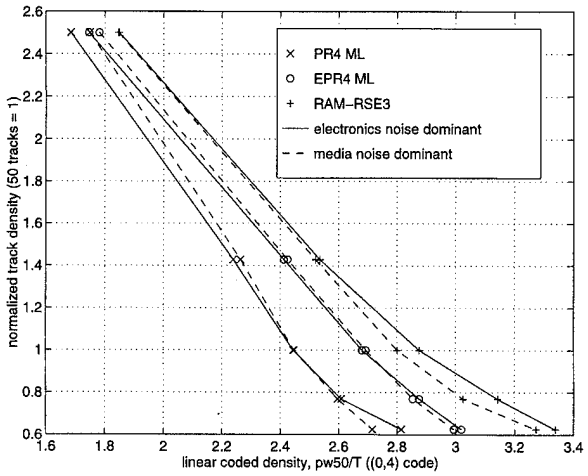


FIG. 4. Track width vs linear density for a disk dominated by electronics noise (solid) and media noise (dashed).

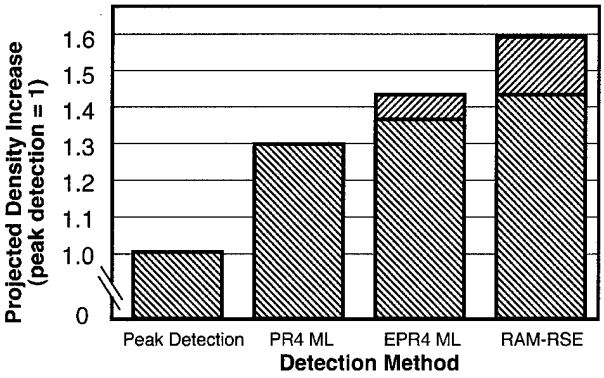


FIG. 5. Areal gains.

The scaling of media noise power (or of SNR_m) with linear and track density is a natural property of the microtrack model. Varying track width is accomplished with the microtrack model by changing the number of microtracks. For the results presented here, 50 microtracks corresponded to a normalized track width of one. For example, a track 50% narrower (twice the track density) would have only 25 microtracks.

For density gain projections, we chose to compare PR4 ML with EPR4 ML and the RAM-RSE with eight states. The RAM-RSE is a nonlinear DFE with an ML detector. We know of no currently proposed detectors that outperform the RAM-RSE (without coding gain).

Simulation results are depicted in Fig. 4 under the assumptions listed in Table II. A normalized track width of one is the point of reference. There are two sets of results, one for which electronics noise dominates (solid lines) and one where the media noise is stronger (dashed lines). The total amount of noise is the same for both cases. At the reference track density, the ratio of electronics to media noise per transition was 3:1 and 1.5:2 for the two results respectively. The curves represent a trade-off between linear density and track width holding the bit error rate constant at 10^{-5}.

For both sets of three curves, with the scaling described previously, we assume the same head and disk: only the track width and linear density are varied. In this way, the projected gains are the result of signal processing only and do not include any other technology improvements.

We see that it is advantageous to make the track width as narrow as possible. Even a substantial drop in SNR caused by narrower tracks has only a relatively minor affect on the achievable linear density. We assume, therefore, that the track width is fixed, limited by the accuracy of servo tracking, erase bands, and other physical factors, and summarize achievable density increases in Fig. 5. A range of linear density improvement is seen as we change the reference track density. The most advanced uncoded detection schemes can improve upon peak detection by between 45% and 60% and upon PR4 ML by about 30%.

V. CODING GAIN

Coding gain is achieved by increasing the minimum distance between all pairs of channel output sequences thus

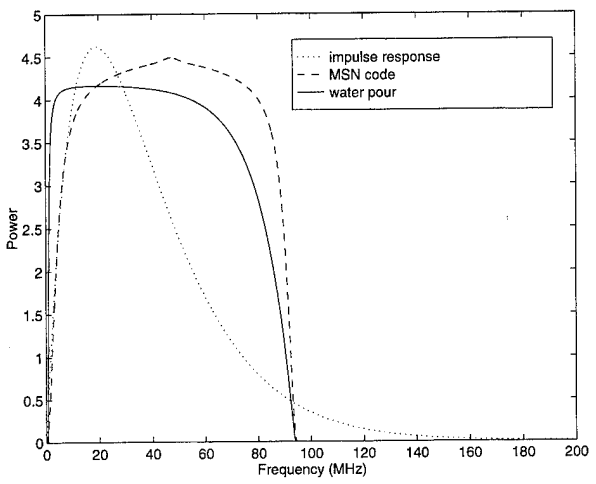


FIG. 6. "Water pour" spectrum assuming a Lorentzian impulse with $pw50$ as in Table II and $SNR_e=21$ dB, power spectral density of an MSN code at a coded density of $pw50=3.5T$, and the spectrum of the Lorentzian impulse response.

making it easier to distinguish between them. In recording, this is typically done by selectively removing input strings from usage in the channel and taking this into account in the ML detector.

Achieving coding gain is especially difficult in the magnetic recording channel for several reasons. First, excluding some strings from usage in the encoder results in code rate loss, which increases the effective $pw50/T$ at the detector. In order for a code to be effective, the coding gain needs to be significantly greater than the loss due to increasing the density. This suggests high-rate codes, which are usually quite complicated to implement. Second, the channel itself acts as a code by introducing memory into the channel at the equalizer output. The performance evaluation of a code must explicitly take into account the combined impact of the channel and code. Trellis codes for the PR4 channel have been proposed,[20,21] but the relatively low code rate has as yet limited their use. A RLL (1,7) code may also be viewed as distance enhancing but its low code rate far outweighs its coding advantage. While higher rates are possible, complexity has thus far been an impediment.

Although we have not yet found a coding scheme that offers significant benefits over the best uncoded detection, communication theory indicates room for improvement.[22] Viewing the disk drive channel as a linear ISI communication channel with white Gaussian noise and continuous, Gaussian inputs, the maximum achievable data rate is obtained when the power spectral density of the input sequence roughly matches that of the impulse response of the channel. This is the "water pour" spectrum whose power spectral density, $P(f)$, at frequency, f, normalized to $1/T$ maximizes

$$C=\frac{1}{2}\int_{-1/2}^{1/2}\log_2[1+\mathrm{SNR}(f)P(f))]df,$$

where C is the capacity of the discrete-time channel in bits/sample over the Nyquist frequency band and $P(f)$ is subject to some overall power constraint.[23]

It is not possible to store a continuous input sequence on a disk drive, however, it is possible to shape the spectrum of the binary input sequence.[24] For example, in Fig. 6, we compare the spectrum of a matched spectral null (MSN) trellis code[21] with the capacity achieving water pour spectrum having made the previous assumptions. Intuitively, it makes sense to store a sequence whose spectral content is high where the channel has the most power. Unfortunately simply writing an input pattern whose spectrum matches the water pour spectrum is not enough to achieve capacity. The MSN code's 3 dB coding gain is nearly completely forfeited to the rate loss at high linear densities.

As long as the power spectrum of the input sequence matches that of the water pour distribution, it is theoretically possible to design a capacity achieving system even with a binary input constraint if the number of transitions per symbol is allowed to grow.[25] For example, a pattern written with transitions spaced at $T/4$ but with only one symbol per T can nearly achieve capacity. From another perspective, as the input resolution increases, there is more freedom to shape the spectrum and to add coding. This suggests creating lower rate matched-spectral codes with higher input resolution.

As we move transitions closer together, or simply increase the resolution but maintain a minimum transition spacing, nonlinear properties of the head and media will undermine any coding gains. Future codes that are both able to use the best parts of the channel's spectrum without violating the properties of the magnetic media and that offer more gain will provide the only long-term solution for improving upon generalized partial-response.

ACKNOWLEDGMENTS

Thanks to Jim Fitzpatrick and Bill Abbott for helpful discussions. This work was partially supported by the ARPA funded National Storage Industry Consortium UHDR project.

[1] R. Cideciyan, F. Dolivo, R. Hermann, W. Hirt, and W. Schott, "A PRML system for digital magnetic recording," IEEE J. Sel. Areas Comm., Jan. (1992).
[2] J. Coker, R. Galbraith, G. Kerwin, J. Rae, and P. Ziperovich, "Integrating a PRML data channel into the IBM 0681 disk drive," 24th Asilomar Conference Proceedings, Monterey, CA, Feb. (1991).
[3] W. Abbott *et al.*, "A digital chip with adaptive equalizer for PRML detection in hard disk drives," ISSCC (1994).
[4] J. L. Sonntag *et al.*, "A high speed, low power PRML read channel device," IEEE Trans. Magn., March (1995).
[5] T. Howell, W. Abbott, and K. Fisher, IEEE Trans. Magn. Nov. (1994).
[6] D. Welland *et al.*, "Implementation of a digital read/write channel with EEPR4 detection," IEEE Trans. Magn. March (1995).
[7] K. Fisher, J. Cioffi, W. Abbott, P. Bednarz, and C.M. Melas, "An adaptive RAM-DFE for storage channels," IEEE Trans. Commun., Nov. (1991).
[8] S. Jove, K. Klaassen, and J. van Peppen, "Method and circuitry to suppress additive disturbances in data channels containing MR sensors," *United States Patent*, issued Apr. 1990.
[9] P. Siegel, "Applications of a peak detection channel model," IEEE Trans. Magn. Nov. (1982).
[10] H. Thapar and A. Patel, "A class of partial-response systems for increasing storage density in magnetic recording," IEEE Trans. Magn. Sept. (1987).
[11] H. Kobayashi, "Application of probabilistic decoding to magnetic recording systems," IBM J. Res. Dev., Jan. (1971).
[12] R. Wood and D. Peterson, "Viterbi detection of class IV partial-response

on a magnetic recording channel," IEEE Trans. Commun., May (1986), Nov. (1991); IEEE Trans. Magn. March (1995).
[13] R. Wood, "Turbo-PRML: a compromise EPRML detector," IEEE Trans. Magn. Nov. (1993).
[14] H. Yamakawa and T. Nishiya, "SPERD: simplified partial error response detection," 1995 IEEE Int. Conf. Mag., San Antonio, TX.
[15] J. Moon and L. R. Carley, "Performance comparison of detection methods in magnetic recording," IEEE Trans. Magn. Nov. (1990).
[16] C. Modlin, K. Fisher, and J. Cioffi, "An analysis of the RAM-RSE read channel," 1995 IEEE Int. Conf. Magn. San Antonio, TX.
[17] J. W. M. Bergmans, "Density improvements in digital magnetic recording by decision feedback equalization," IEEE Trans. Magn. May (1986).
[18] J. Fitzpatrick and X. Che, "An Evaluation of Partial Response Polynomials for Magnetic Recording Systems," IEEE Trans. Magn. March (1995).
[19] J. Caroselli and J. K. Wolf, "A New Model for Media Noise in Thin Film Magnetic Recording Media," presented at the Photonics East Symposium on Voice, Video, and Data Communications, October 22–26, 1995.
[20] J. Wolf and G. Ungerboeck, "Trellis coding for partial-response channels," IEEE Trans. Commun., Aug. (1986).
[21] P. Siegel and J. Wolf, "Modulation and coding for information storage," IEEE Commun. Magn. Dec. (1991).
[22] P. A. Voois and J. M. Cioffi, "Achievable radial information densities in magnetic recording systems," GLOBECOM '92, 1067 (Dec. 1992).
[23] E. A. Lee and D. G. Messerschmitt, *Digital Communication* (Kluwer, Dordrecht, The Netherlands, 1994).
[24] K. A. S. Immink, *Coding techniques for digital recorders* (Prentice Hall, Englewood Cliffs, NJ, 1990).
[25] G. Ungerboeck, "Channel coding with multilevel/phase signals," IEEE Trans. Info. Theory, Jan. (1982).

Head/disk tribology: Toward 10 Gb/in.^{2} (invited) (abstract)

B. Marchon
Seagate Technology, Fremont, California 94538

As the race to ever increasing areal densities and lower flying heights becomes more ferocious year after year, the need for an improved understanding of the various physical and chemical processes taking place at a sliding head/disk interface becomes more urgent. This talk will review the various aspects of thin film media technology that will become essential components of a 10 Gb/in.^{2} interface. Modeling of surface topography and its relationship with glide and stiction properties will be addressed. Recent advances in overcoat and lubrication technology will be assessed, and attempts to decrease magnetic spacing and increase durability and flyability will be discussed. Finally, the concepts of near- and/or full-contact recording and their feasibility will be reviewed. © *1996 American Institute of Physics.* [S0021-8979(96)45208-0]

 0021-8979/96/79(8)/4508/1/$10.00 © 1996 American Institute of Physics

Quantum oscillations of properties in magnetic multilayers (invited)

G. Bayreuther, F. Bensch, and V. Kottler
Institut für Angewandte Physik, Universität Regensburg, 93040 Regensburg, Germany

An oscillatory interlayer exchange coupling observed in many sandwich and multilayer films can be understood as an interference effect of electron waves partially reflected at each interface with spin dependent reflection coefficients. Consequently, we might expect all magnetic properties in some way related to the density of states to oscillate as a function of the magnetic and nonmagnetic layer thickness. In order to experimentally test this concept we have measured different magnetic properties of Ni/Au multilayer films prepared by magnetron sputtering on glass substrates. The Ni thickness was kept constant at $t_{Ni}=(7.3\pm0.5)$ Å while the Au layer thickness was varied between 4 Å and 80 Å. The films had a coherent fcc structure with (111) texture. The saturation field and the remanence oscillate as a function of t_{Au} with a period which agrees well with a theoretical value calculated from the bulk Fermi surface of Au and proves that indeed an oscillatory exchange coupling is present. The Curie temperature shows oscillations with t_{Au} clearly correlated with the exchange coupling constant, J: T_C oscillates like the absolute value of J. This behavior is indeed expected from mean field theory. Similar oscillations are found for the spin wave parameter and the ground state magnetic moments. The variation of the exchange coupling with temperature and the role of inhomogeneities for the interpretation of the experimental data are discussed. © *1996 American Institute of Physics.* [S0021-8979(96)48208-4]

I. INTRODUCTION

Total or partial confinement of itinerant electrons in a solid in one or more dimensions leads to quantized states. These in turn produce a variety of phenomena not observed in bulk material with macroscopic extension. The most widely studied class of material in this respect have been semiconductors: structures fabricated in the form of two-dimensional quantum wells, of quantum wires or quantum dots show a wealth of novel effects in their electronic, optical or transport properties. A simple picture to describe these consequences of electron confinement is the following: at each interface between different materials the moving electron experiences an abrupt change of potential. This is equivalent to a change of the index of refraction for the electron wave causing its partial reflection and partial transmission through the interface. In a layered structure, all the reflected and transmitted electron waves will interfere. Under certain conditions for electron wavelength, layer thickness, and phase shift upon reflection the interference will be constructive or destructive giving rise to oscillations of the density of states as a function of, e.g., layer thickness and in many cases to oscillations of related properties.

The same scenario can be applied to metallic multilayers consisting of ferromagnetic layers separated by nonmagnetic interlayers. An important extension of this simple picture now is brought in by the fact that the (complex) reflection coefficient is different for the two possible spin orientations of the moving electron if the material at one side of the boundary (or both) is magnetically ordered.

In a natural way this general concept leads to a number of phenomena which are to be expected in magnetic layer systems: (i) quantum well states in multilayers and even in nonmagnetic overlayers should be spin polarized; (ii) the total electron spin polarization, i.e., the projected magnetic moment per atom in the (itinerant) ferromagnetic layer should be affected by the layer structure and, in particular, should be an oscillatory function of the nonmagnetic interlayer thickness; (iii) a similar oscillatory behavior is expected for all magnetic properties which are related to the spin dependent density of states in a direct or indirect way like magnetic anisotropy and magneto-optic effects which are both a consequence of spin-orbit coupling; (iv) the total energy of a multilayer system will depend on the relative magnetization directions in adjacent ferromagnetic layers for a given combination of layer thickness, or in other words, the difference of the total energy between parallel and antiparallel alignment will oscillate as a function of layer thickness. This is the well known oscillatory indirect interlayer exchange coupling; (v) other magnetic phenomena which are related to the interlayer exchange coupling directly, e.g., spin wave excitations, or indirectly like the giant magnetoresistance effect (GMR) are also expected to show oscillations with increasing layer thickness.

Historically, the starting point for the study of such quantum oscillations in magnetic multilayers was the discovery first of an antiferromagnetic[1] and later of an oscillatory interlayer exchange coupling[2] in Fe/Cr layered structures. The interlayer exchange and the related GMR effect, which are certainly the most spectacular findings in magnetism during the last decade, have also been the most widely studied subjects in magnetic materials recently. A comprehensive theoretical description of interlayer exchange coupling based on the interference of electron waves has recently been given by Bruno.[3] It is pointed out there that this general concept indeed comprises the different model descriptions proposed in the literature as special cases. A generalization of the concept even allows to explain the exchange coupling across

nonmetallic interlayers. In addition to the well established correlation between the oscillation periods and the Fermi surface of the interlayer material[4] also an oscillatory dependence of the coupling strength on the thickness of the *ferromagnetic* layer is expected in this framework; this indeed was found subsequently in several experiments.[5,6]

In the literature a large number of experimental and theoretical studies can be found on topics (iv) and (v) mentioned above; most of them are focused on the influence of layer thickness and structure, interface sharpness, chemical composition, etc. on interlayer coupling and magnetoresistance. However, relatively few results have been reported concerning the other predictions stated above. The existence of quantum well states with spin dependent density of states in Cu overlayers on Co and Ag on Fe has been demonstrated by photoemission and inverse photoemission experiments.[7–9] An indication of an oscillating magnetic anisotropy of Co ultrathin films successively covered with a nonmagnetic metal (Au, Cu, Pd, etc.) of increasing thickness has been seen in several experiments.[10–12] Recently, oscillations of the Kerr rotation angle from an ultrathin Co film as a function of the thickness of a Au overlayer have been observed and related to spin polarized quantum well states in the Au.[13] On the other hand, oscillations of ground state magnetic moments and the Curie temperature have not been reported until now.

Within the category of magnetic properties directly related to interlayer exchange coupling, the shape of the magnetization curve is by far the most widely used criterion for the presence of this indirect coupling: low remanence is often interpreted as an indication of antiferromagnetic coupling and the saturation field can directly provide the coupling strength in the antiferromagnetic case. Brillouin light scattering and FMR are also affected by interlayer coupling and can be used to evaluate the coupling strength.

Thermal spin wave excitations are closely connected with exchange coupling between spins. Within the Heisenberg model of exchange interaction between nearest neighbors the spin wave stiffness constant is proportional to the (average) exchange integral and, therefore, should be modified by the presence of an interlayer exchange coupling. Such an effect has indeed been observed in Fe/Ag multilayer films[14] where an oscillation of the spin wave parameter, B, with Ag layer thickness was found.

In an analogous way, the Curie temperature, T_C, of a ferromagnet is proportional to the average exchange energy per atom within mean field theory (MFT). Consequently, we might expect the Curie temperature of a periodic stack of ferromagnetic and nonmagnetic layers to oscillate as a function of nonmagnetic layer thickness. This can be seen if we assume the component of the total exchange energy density due to interlayer coupling, E_{ex}^{interl}, to be given by

$$E_{ex}^{interl} \propto -J_1 \cdot \vec{M}_a \cdot \vec{M}_b \tag{1}$$

with an interlayer coupling constant J_1 oscillating between positive and negative values depending on the nonmagnetic layer thickness t_i.

A change in sign of J_1 will reverse the relative alignment of the magnetizations $\vec{M}_a, \vec{M}_b$ of the ferromagnetic layers from parallel to antiparallel or vice versa in the equilibrium state. So, E_{ex}^{interl} is always negative and depends only on the absolute value of J_1. If we now assume the Curie temperature to be proportional to the total exchange energy per atom which is the sum of interlayer and intralayer coupling energy, then we expect T_C to oscillate as a function of the interlayer thickness with a period of oscillation half of the period of J_1. However, no experimental verification of this effect has been reported in the literature previously.

In order to check the general validity of the concept outlined above we have investigated several magnetic properties of a series of Ni/Au multilayer films. Ni was chosen because of its relatively low Curie temperature; by sufficiently reducing the Ni layer thickness the Curie temperature can be reduced below room temperature. This allows to eliminate the risk of irreversible structural changes when measuring around the critical point. For the nonmagnetic layer Au was used because it can easily be grown with a strong (111) texture on glass substrates even by sputtering. The magnetization curves showed oscillations of the remanence and the saturation field with the period of the Au layer thickness theoretically predicted for the interlayer exchange coupling through Au(111), J_1. The Curie temperature showed pronounced oscillations with a period like $|J_1|$ in accordance with the mean field argument given above.[15] Oscillations of the spin wave parameter were observed which are clearly correlated with the oscillations of T_C. A similar behavior was found for the ground state magnetic moments.

II. EXPERIMENT

For sample preparation dc magnetron sputtering sources were used in an UHV based sputtering system. The argon pressure during deposition was $6 \cdot 10^{-3}$ mbar, the sputtering rate was 0.27 nm/s for Au and 0.13 nm/s for Ni.

To study the interlayer coupling a series of Au(30 nm)/[Ni(t_{Ni})/Au(t_{Au})]$_{10}$/Au(30 nm) multilayers (t_{Ni}=0.73 ±0.05 nm, t_{Au}=0.4–8.0 nm) was deposited on glass substrates at room temperature. A second series of samples was prepared with t_{Ni}=0.4–1.4 nm and t_{Au}=8.0 nm ("*uncoupled films*") in order to determine the dependence of T_C on the thickness of the Ni layers alone. The Au layer is expected to be thick enough to exclude any interlayer exchange coupling. The data of this series were used to correct for the effect of the variation of t_{Ni} (±0.05 nm) on T_C within the first series (see below).

The total amount of Ni and Au of each sample was determined by x-ray fluorescence analysis (XFA) and converted into a nominal layer thickness assuming the bulk densities. The statistical error is ±0.006 nm for Ni and ±0.016 nm for Au. The variation of the Ni thickness within the first series of ±0.05 nm was due to the finite precision of the shutter operation.

Small angle x-ray diffraction and high resolution electron microscopy (HREM) were used to study the structure of the films. The layer thickness or multilayer period determined in this way agreed with the XFA data with an error below 1%. The layer structure turned out to be quite uniform. The films are polycrystalline with a pronounced (111) texture. For $t_{Au} \leq 2$ nm a coherent fcc structure is observed

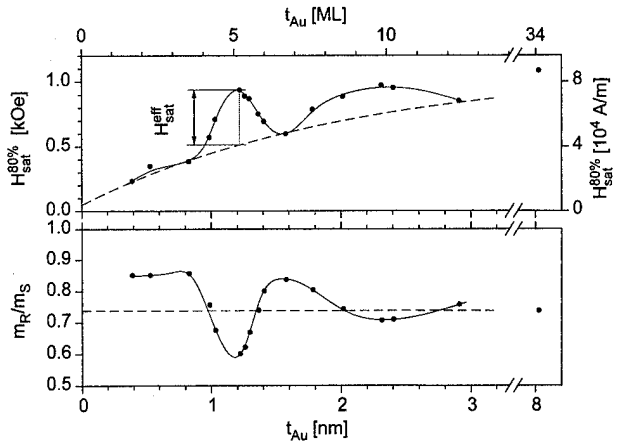


FIG. 1. Saturation field, $H_{sat}^{80\%}$, and magnetic remanence, m_R/m_S, versus Au layer thickness, t_{Au}, at 10 K. Dashed lines mark the behavior expected without interlayer coupling. Solid lines represent a spline fit and serve as a guide for the eye.

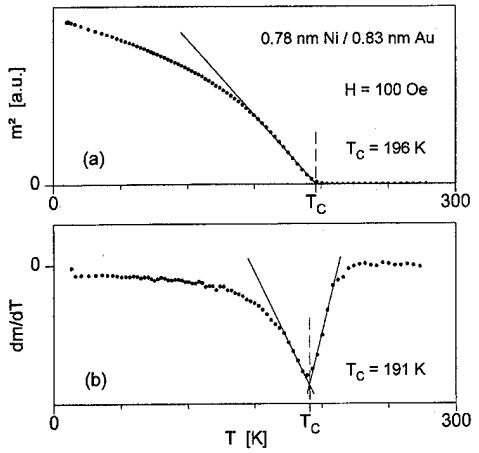


FIG. 2. Determination of the Curie temperature, T_C, by two different methods: (a) linear extrapolation of $m^2(T)$ to $m=0$; (b) minimum of dm/dT.

throughout the whole multilayer although the lattice parameters of Ni and Au differ by about 14%. This means that there is significant lattice strain in the film plane which is tensile for Ni and compressive for Au. So one might expect the Au lattice to be expanded and the Ni lattice to be compressed perpendicular to the plane; however, this is not observed. A more detailed discussion of thickness dependent strain in Ni/Au multilayers and its influence on magnetic properties is given by Nakayama *et al.*[16] and Childress *et al.*[17]

Magnetic measurements were carried out using a SQUID magnetometer at temperatures between 10 K and 400 K in magnetic fields up to 50 kOe.

III. EXCHANGE COUPLING

Like in previous studies magnetization curves of the films were used to detect the presence of an interlayer exchange coupling. The magnetic field was always applied parallel to the film plane since all samples exhibit a magnetic easy plane anisotropy. The spontaneous magnetic moment, m_S, was determined by linear extrapolation of the saturated part of the magnetization loop between 2 and 10 kOe back to zero field. The remanent moment, m_R, is the magnetic moment in zero field after saturation at 50 kOe. $H_{sat}^{80\%}$ is taken as the external magnetic field for which the sample moment reaches 0.8 m_S. 80% saturation has been chosen for convenience because this value can be determined with much better precision than the real saturation field H_{sat}. The latter is approximately twice the value of $H_{sat}^{80\%}$ for all samples.

The plot of the saturation field, $H_{sat}^{80\%}$, and the magnetic remanence, m_R/m_S, at 10 K as a function of Au layers thickness, t_{Au}, (Fig. 1) clearly shows an oscillatory interlayer coupling. The observed oscillation period, $\Lambda_{exp}=(1.15\pm0.1)$ nm, is in good agreement with the value $\Lambda_{theor}=1.135$ nm theoretically predicted on the basis of experimental data on the Fermi surface of bulk gold.[4] The additional continuous increase of the saturation field with increasing Au layer thickness is probably due to local magnetic anisotropies caused by the increasing strain in the Ni layers. It is also observed that m_R/m_S does not reach zero at its minima which correspond to the strongest antiferromagnetic coupling. This can be explained by a certain uncorrelated interface roughness which creates local thickness fluctuations. The presence of such a roughness can also be concluded from x-ray diffraction and HREM data. As a consequence, interface regions with ferromagnetic coupling will coexist with antiferromagnetically coupled ones giving rise to a finite remanence.

From the interlayer coupling contribution to the saturation field, H_{sat}^{eff} (Fig. 1), we can estimate the interlayer coupling energy per unit area, I_1: if we assume that for $H=H_{sat}=2H_{sat}^{eff}$ the interlayer exchange energy is balanced by the magnetostatic energy of the Ni layers in the applied field we get $I_1\approx0.004$ erg cm^{-2} for the first antiferromagnetic maximum at $t_{Au}=1.2$ nm.

IV. CURIE TEMPERATURE

The Curie temperature was determined from the magnetic moment vs temperature $m(T)$ measured with the SQUID magnetometer. The data were taken at decreasing temperature in the presence of a constant magnetic field of 100 Oe parallel to the film plane. This approach will also work in the case of antiferromagnetic coupling provided that the moments do not completely cancel; this does not happen in practice. From $m(T)$ curves T_C is evaluated by two different methods as shown in Fig. 2: either by linear extrapolation of $m^2(T)$ to $m=0$ as suggested by molecular field theory [Fig. 2(a)] (fitting with $m\propto[(T_C-T)/T_C]^{\beta}$ with T_C and β as free parameters yields similar results but with less precision) or by the minimum of dm/dT [Fig. 2(b)]. The first value is expected to be closer to the true transition temperature than the second one which, however, can be determined with higher accuracy. Both values are shifted by a constant amount of (5 ± 0.5) K relative to each other for all films. Therefore, the difference is irrelevant for the question of a possible variation of T_C with the Au layer thickness. T_C values discussed below were determined according to Fig. 2(b).

The dependence of the Curie temperature on the thickness of the Ni layers, t_{Ni}, has been determined using the *uncoupled films* mentioned above. The results are shown in Fig. 3. In order to interpolate between the experimental data points, the following power law is used:

$$T_C(t_{Ni})=T_C(\infty)\cdot[1-(t_{Ni}/t_0)^{-\lambda}], \quad (2)$$

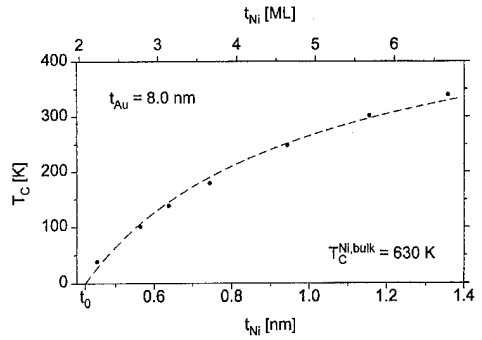


FIG. 3. Curie temperature, T_c, of Ni/Au multilayers with t_{Au}=8 nm (uncoupled films) as a function of Ni layer thickness, t_{Ni}. The uncertainty of T_C is ±3 K. The dashed line represents a fit according to Eq. (2).

suggested by scaling theory.[17] A numerical fit to the experimental data yields $\lambda=0.63\pm0.02$ and $t_0=(0.422\pm0.009)$ nm while $T_C(\infty)=630$ K was held constant. These values are in excellent agreement with those found by Childress *et al.*[18] As already mentioned above, within the first series of films with a nominal Ni thickness of 0.73 nm a certain variation of the Ni layer thickness could not be avoided (±0.05 nm). In order to eliminate the effect of the Ni layer thickness on T_C the data of Fig. 3 were used. It was assumed that the variation of T_C with t_{Ni}, dT_C/dt_{Ni}, is the same for all multilayers. This would not be exactly true for films with thin Au layers if T_C is indeed affected by interlayer exchange. However, for all films the *intra*layer exchange energy is still much larger than the *inter*layer exchange energy and, therefore, the procedure used will be approximately correct. This point will be discussed further at the end of this section.

The corrected Curie temperatures, $T_C(t_{Au})$, of all samples from the first series are plotted in Fig. 4(a) in comparison with the magnetic remanence, $m_R/m_S(t_{Au})$ [Fig. 4(b)], as a function of Au layer thickness. It is apparent that T_C does not increase monotonically with decreasing thickness of the Au interlayer but rather shows pronounced oscillations. There is an unambiguous correlation between the Curie temperature, T_C, and the remanence, m_R/m_S: maxima of T_C are observed for those values of t_{Au} where m_R/m_S has a maximum or a minimum; minima of T_C occur wherever the interlayer exchange coupling is zero, i.e., when m_R/m_S equals the value observed for very thick Au interlayers. It means that the Curie temperature of the Ni layers is enhanced both by a ferromagnetic and an antiferromagnetic interlayer coupling. This is exactly what is expected from the argument given above that the interlayer exchange energy has always the same sign both for ferro- and antiferromagnetic interlayer coupling. Furthermore, this type of oscillation with a shorter period compared to the oscillation of J_1 supports the conclusion that the observed T_C oscillation is not an artefact produced by the method used to determine T_C because otherwise we might expect the same oscillation period for m_R (i.e., J_1) and T_C.

We can also rule out a possible interpretation of the oscillatory Curie temperature as a consequence of some structural changes with increasing Au layer thickness by the following arguments: (1) if a structural change affects T_C it is hard to understand how this could cause an *oscillation* of T_C; (2) the close correlation between the oscillations of T_C and of the remanence and saturation field is a strong indication of a

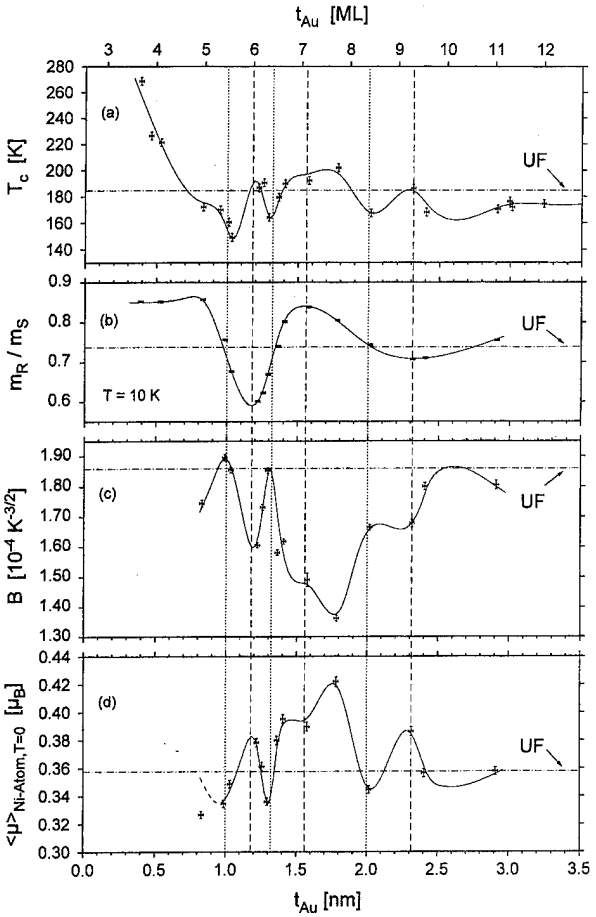


FIG. 4. Magnetic properties of exchange coupled Ni/Au multilayer films as a function of Au interlayer thickness, t_{Au}. The thickness of the Ni layers is kept constant with t_{Ni}=0.73 nm. Small variations of the Ni layer thickness have been corrected as described in the text. (a) Curie temperature, T_C, (b) remanence, m_R/m_S; (c) effective spin wave parameter, B; (d) average ground state magnetic moment per Ni atom, $\langle\mu\rangle$. Horizontal dashed-dotted lines represent the respective values for uncoupled films, i.e., for t_{Au}=8 nm. The dashed (dotted) vertical lines indicate interlayer thicknesses where the absolute value of the interlayer coupling strength is expected to have a maximum (zero) amount. Solid lines are a guide to the eye.

common origin of both phenomena; (3) the observed oscillation period agrees well with the value which was theoretically predicted on the basis of the Au Fermi surface;[4] (4) oscillations of the spin wave parameter, B, and the magnetic ground-state moments of Ni have been found from magnetization measurements at temperatures far below T_c which are strongly correlated with the T_C oscillations. These will be discussed in the next section.

Mean field theory predicts the critical temperature of a ferromagnet to be related to the exchange energy per magnetic atom, ε_{ex}, according to $k_B \cdot T_C \approx \varepsilon_{ex}$ for an fcc lattice with $S=1$. This allows us to estimate the interlayer coupling energy per atom from the variation of the Curie temperature, $\Delta T_C \approx 40$ K, between $t_{Au}=1.2$ nm and $t_{Au}=1.3$ nm resulting in $\varepsilon_{ex}^{interlayer}=k_B \cdot \Delta T_C=3.4$ meV.

For the calculation of the coupling energy per unit area, I_1, we need the areal density of those Ni atoms which are responsible for the enhancement of T_C due to interlayer exchange coupling. The simplest assumption is that all Ni atoms are equally affected by interlayer coupling; however, it might be more realistic to assume that only a certain part of

the Ni atoms experience the maximum coupling strength which determines T_C. Using the first assumption we obtain a [coupling energy density of I_1=36 erg/cm^2. This value seems unrealistically large, i.e., several orders of magnitude larger than the coupling strength derived from the saturation field (0.004 erg/cm^2) and also much larger than theoretical values[4] (e.g., 0.4 erg/cm^2).

On the other hand, we know from the measurement of the remanence discussed above that there is no homogeneous antiferromagnetic coupling in our multilayer films. In this case local values of ε_{ex} will have a broad distribution and the Curie temperature will be determined rather by the maximum of ε_{ex} than by its average value. Therefore, I_1 will be drastically smaller than the first estimate. A more elaborate theory of phase transitions in exchange coupled multilayer films should also consider the crossover from a 2-dimensional to a 3-dimensional phase transition when the interlayer coupling is switched on.

A final remark must be made to the procedure applied above to correct for the variation of the Ni layer thickness within the series of coupled multilayers. After it has been shown that T_C is indeed affected by interlayer exchange it is also clear that Eq. (2) cannot hold in general for exchange coupled multilayers because the coupling strength is known to depend also on the ferromagnetic layer thickness.[3,5,6] Once this dependence is measured for Ni/Au multilayers a complete discussion of the Curie temperature as a function of t_{Ni} and t_{Au} will be possible for the coupled films.

V. SPIN WAVES AND GROUND STATE MAGNETIC MOMENTS

The spontaneous magnetic moment of the coupled multilayer films, m_S, was determined from the magnetization loops by extrapolation to H=0 as described above. The temperature dependence $m_S(T)$ was fitted by two different expressions which have been proposed in the literature for spin wave excitations in thin films, i.e.,

$$m_S(T)=m_S(0)\cdot(1-B\cdot T^{3/2})$$

and

$$m_S(T)=m_S(0)\cdot[1-A_0\cdot T\cdot\ln(A_1\cdot T)].$$

The validity of spin wave theory being limited to sufficiently low temperature, the discussion was restricted to $T<T_C/2$.

Within the experimental uncertainty the $T^{3/2}$ law valid in bulk ferromagnets gave an equally good fit to the data as a $T\ln T$ law which was suggested in the literature[19,20] for monolayer films. The approximate validity of an "effective $T^{3/2}$ law" for surfaces and ultrathin films has been pointed out before.[21] Therefore, both the parameter B from the $T^{3/2}$ fit and the interlayer coupling constant, J_1, derived from a $T\ln T$ fit according to Qiu *et al.*[20] have been calculated. It turned out that a $T\ln T$ fit yields a very large uncertainty of J_1; therefore no meaningful values of J_1 could be obtained and no clear correlation with the exchange coupling strength calculated from the saturation field (Sec. III) was found. Hence, we exclusively consider the effective $T^{3/2}$ law in the following. From the corresponding fit to the data we obtain the spin wave parameter B and the average ground state magnetic moment $\langle\mu\rangle$.

It is well known[21] that the spin wave parameter B increases with decreasing thickness of a ferromagnetic film. This can be understood in the following way: From spin wave theory on the basis of the Heisenberg model we know that B is proportional to $D_0^{-3/2}$ and the spinwave stiffness constant, D_0, is proportional to the exchange energy per atom. In an inhomogeneous system we assume D_0 to scale with the *average* exchange energy per magnetic atom; hence, in an ultrathin film due to the reduced coordination at the interfaces D_0 will be reduced and B enhanced. This argument would therefore predict an enhancement of D_0 by an interlayer exchange coupling of any sign, i.e., a decrease of the spin wave parameter.

In order to study the influence of the interlayer coupling on the parameter B we have to eliminate the influence of thickness variations of the Ni layer within the series of "coupled films" like it was done for the Curie temperature in Sec. IV. We follow the same principle by first measuring $B(t_{Ni})$ for the uncoupled films and use a numerical interpolation to calculate $B(t_{Au}, t_{Ni}$=0.73 nm) for the coupled films. With the same reasoning as before we assume that the variation of B with t_{Ni}, dB/dt_{Ni}, is the same for both series of samples.

The corrected values of the spin wave parameter are plotted versus Au layer thickness in Fig. 4(c) in comparison to the remanence as a measure of the interlayer coupling [Fig. 4(b)] and to the Curie temperature [Fig. 4(a)]. Qualitatively, the correlation of B to m_R is the same as for T_C: minima of the spin wave parameter, i.e., maxima of spin wave stiffness coincide with strongest ferro- (=maximum of m_R) or antiferromagnetic (=minimum of m_R) coupling, maxima of B occur for zero interlayer exchange (e.g., for $t_{Au}\approx$1 nm and 1.3 nm). This means that both ferromagnetic and antiferromagnetic interlayer coupling stabilize the magnetic order in the multilayer stack against thermal fluctuations.

The same qualitative result was obtained by Keavney *et al.*[14] for Fe/Ag multilayer films. They determined the B parameter (or more precisely, a prefactor, k, which accounts for the interlayer coupling) from the interface hyperfine field in relatively thick Fe layers (>20 ML). Using their numerical analysis[14] we are able to estimate the interlayer coupling constant, J_1, from the variation amplitude of B and get values around 0.5 erg/cm^2 for the largest coupling energy density. This result agrees with the value given by theoretical estimates.[4]

Finally we discuss the ground state magnetic moments obtained from the fits to $m_S(T)$ with a $T^{3/2}$ law: by dividing the total saturation moment of the sample for $T\rightarrow$0 by the total number of Ni atoms which are directly obtained by XFA we determine the average ground state atomic moment $\langle\mu\rangle$. The result is shown in Fig. 4(d) in comparison to the other quantities discussed above. Clear variations are seen and the dependence of $\langle\mu\rangle$ on t_{Au} qualitatively follows the Curie temperature. It is worth mentioning that both quantities have been determined by completely independent measurements in different temperature regimes. Apparently, a ferromagnetic or antiferromagnetic interlayer coupling not only stabilizes the magnetic order at finite temperatures but also enhances

the ground state moments in the itinerant ferromagnet compared to the uncoupled ultrathin layer. The effect of interlayer coupling on ground state moments has been studied theoretically using a tight binding scheme for the Fe/Cr system[22] and indeed a correlation between the coupling and the magnetic moments was found. For Ni/Au, however, no calculations of the moments are known and, in particular, first principles calculations are lacking.

The average Ni moment is considerably reduced compared to bulk Ni ($\mu=0.6\mu_B$). This may be a consequence of hybridization of Ni states at the interfaces. A more detailed discussion of this effect in connection with band calculations will be presented elsewhere.

VI. DISCUSSION AND CONCLUSIONS

It has been shown for Ni(111)/Au(111) multilayered films that all the magnetic properties investigated here—remanence, saturation field, Curie temperature, spin wave stiffness and ground state magnetic moments—show pronounced oscillations as a function of the Au interlayer thickness between 3 and 12 ML. These observations confirm the basic idea that in a metallic multilayer film consisting of ferromagnetic layers separated by nonmagnetic interlayers all magnetic properties should reflect the interference of electron waves which are produced by multiple spin-dependent reflections at the interfaces.

The oscillations observed for the different quantities agree in their wavelength and their phase within the uncertainty of the present experiments. The coupling strength determined from the different properties, however, differ substantially. Several circumstances might account for this fact:

(i) The respective properties are measured at quite different temperatures ranging from $T\rightarrow 0$ up to T_C. The interlayer coupling constant itself is known to vary with temperature; this has been found experimentally[23,24] and studied theoretically from the standpoint of the Fermi–Dirac statistics of the electrons[4,25] as well as in relation to spin wave interactions;[26] however, no data are available in the literature which refer to the Ni/Au system.

In particular, our data show that the interlayer exchange coupling does not vanish when the critical temperature of the interlayer ferromagnetic order is approached. This is not *a priori* evident and merits further theoretical work.

If J_1 varies with temperature then the spin wave parameter, B, of a coupled multilayer will also depend on temperature. This is not compatible with the established methods of measuring B because they assume B to be constant in a finite temperature range. For a quantitative comparison with more elaborate theories a different fitting scheme will have to be employed.

(ii) In a strongly simplified model we have assumed that all the oscillatory quantities are uniform within each layer in our films. This is not realistic; instead, it is certain that neither the ground state moments nor the spin deviation by spin waves and the interlayer exchange coupling are homogeneous in the perpendicular direction within the individual Ni layers. We indeed measure average values by our magnetometric technique as pointed out earlier. In addition, we have to expect lateral inhomogeneities like different grain orientations, layer thickness fluctuations and roughness. All these deviations from uniformity will affect the different magnetic properties in a different way, the individual components having different weight in the respective physical averaging process. This is probably the main reason for the extremely large values of the exchange coupling energy determined from variations of T_C compared to the oscillations of the saturation field: a cancellation of ferro- and antiferromagnetically coupled regions does not take place with respect to the Curie temperature, but for the remanence and (partially) for the saturation field. Apparently, the influence of local maxima of $|J_1|$ on T_C is very strong but weaker on B and very small on the saturation field.

It would be helpful to measure depth profiles of the magnetic moments and spin wave parameter by using Mössbauer spectroscopy with probe layers. However, this method is practically restricted to Fe and not applicable to Ni; T_C of Fe, on the other hand, is so high that its variation with interlayer coupling could only be studied on superlattices with 1 monolayer Fe films between Au layers.

As a consequence of the arguments given above similar experiments will be carried out on epitaxially grown films with controlled flatness and better structural uniformity. It is expected that this will allow a more quantitative study of the phenomena discussed in this communication, in particular the oscillations of the Curie temperature observed for the first time. Complementary efforts will be made to use a more comprehensive theory of thermal spin waves and phase transitions as well as band calculations for the ground state magnetic moments in exchange coupled multilayer films.

ACKNOWLEDGMENT

A part of this work has been supported by the European Union within the HCM programme.

[1] P. Grünberg, R. Schreiber, Y. Pang, M. B. Brodsky, and H. Sower, Phys. Rev. Lett. **57**, 2442 (1986).
[2] S. S. P. Parkin, N. Moore, and K. P. Roche, Phys. Rev. Lett. **64**, 2304 (1990).
[3] P. Bruno, Phys. Rev. B **52**, 411 (1995).
[4] P. Bruno and C. Chappert, Phys. Rev. Lett. **67**, 1602 (1991); P. Bruno and C. Chappert, Phys. Rev. B **46**, 261 (1992).
[5] P. J. H. Bloemen, M. T. Johnson, M. T. H. van de Vorst, R. Coehoorn, J. J. de Vries, R. Jungblut, J. aan de Stegge, A. Reinders, and W. J. M. de Jonge, Phys. Rev. Lett. **72**, 764 (1994).
[6] S. N. Okuno and K. Inomata, Phys. Rev. Lett. **72**, 1553 (1995).
[7] J. E. Ortega and F. J. Himpsel, Phys. Rev. Lett. **69**, 844 (1992).
[8] K. Garrison, Y. Chang, and P. D. Johnson, Phys. Rev. Lett. **71**, 2801 (1993).
[9] C. Carbone, E. Vescovo, O. Rader, W. Gudat, and W. Eberhardt, Phys. Rev. Lett. **71**, 2805 (1993).
[10] B. N. Engel, M. H. Wiedmann, R. A. Van Leeuwen, and C. M. Falco, J. Appl. Phys. **73**, 6192 (1993); Phys. Rev. B **48**, 9894 (1993).
[11] P. Beauvillain, A. Bounouh, C. Chappert, R. Mégy, S. Ould-Mahfoud, J. P. Renard, P. Veillet, D. Weller, and J. Corno, J. Appl. Phys. **76**, 6078 (1994).
[12] J. Kohlhepp and U. Gradmann, J. Magn. Magn. Mater. **139**, 347 (1995).
[13] R. Mégy, A. Bounouh, Y. Suzuki, P. Beauvillain, P. Bruno, C. Chappert, B. Lecuyer, and P. Veillet, Phys. Rev. B **51**, 5586 (1995).
[14] D. J. Keavney, D. F. Storm, J. W. Freeland, M. D.Wieczorek, J. C. Walker, M. G. Pini, P. Politi, and A. Rettori, Phys. Rev. Lett. **71**, 927 (1993).
[15] V. Kottler, F. Bensch and G. Bayreuther (unpublished).
[16] N. Nakayama, L. Wu, H. Dohnomae, T. Shinjo, J. Kim, and C. M. Falco, J. Magn. Magn. Mater. **126**, 71 (1993).
[17] J. R. Childress, C. L. Chien, and A. F. Jankowski, Phys. Rev. B **45**, 2855 (1992).
[18] G. A. Allan, Phys. Rev. B **1**, 352 (1970).
[19] P. Bruno, Phys. Rev. B **43**, 6015 (1991).
[20] Z. Q. Qiu, J. E. Mattson, C. H. Sowers, U. Welp, and S. D. Bader, Phys. Rev. B **45**, 2252 (1992).
[21] G. Lugert and G. Bayreuther, Phys. Rev. B **38**, 11 068 (1988). G. Bayreuther, Hyperfine Interactions **47**, 1145 (1989).
[22] A. Vega, L. C. Balbas, A. Chouairi, C. Demangeat, and H. Dreyssé, Phys. Rev. B **49**, 12 797 (1994).
[23] S. Demokritov, J. A. Wolf, and P. Grünberg, Europhys. Lett. **15**, 881 (1991).
[24] Z. Zhang, L. Zhou, P. E. Wigen, and K. Ounadjela, Phys. Rev. Lett. **73**, 336 (1994).
[25] D. M. Edwards, J. Mathon, R. B. Muniz, and M. S. Phan, Phys. Rev. Lett. **67**, 493 (1991).
[26] N. S. Almeida, D. L. Mills, and M. Teitelman, Phys. Rev. Lett. **75**, 733 (1995).

Calculated spacer-layer Friedel oscillations in Co/Cu(001)

Lars Nordström
Institute for Computational Sciences and Informatics, George Mason University, Fairfax, Virginia 22030-4444, and Complex Systems Theory Branch, Naval Research Laboratory, Washington, D.C. 20375-5345

David J. Singh
Complex Systems Theory Branch, Naval Research Laboratory, Washington, D.C. 20375-5345

The induced complete position-dependent magnetization density of the copper spacer layer is calculated for Co/Cu(001), as modeled by a $Co/Cu_9/Co$ slab. This density is then analyzed in terms of Friedel oscillations. It is found that the variation of the density is well described by two periods, 1.2 and 1.6 monolayers, which are the nonaliased versions of the RKKY periods found in the interlayer coupling. The induced Cu magnetization is not well described in terms of local Cu moments, arising from local exchange interactions, but rather has significant free electron character, in the way that it is mainly induced by magnetic interface scattering. © *1996 American Institute of Physics.* [S0021-8979(96)48308-2]

I. INTRODUCTION

The magnetic interlayer coupling through nonmagnetic spacer layers has attracted a huge interest in recent years mainly because of potential applications of the related giant magnetoresistivity (GMR). Until now, the induced magnetization in the spacer layer has been largely neglected, in part because its direct contribution to the coupling may be very small. There have, however, been some recent experimental attempts to measure the magnetization distribution within a copper spacer layer.[1–3] Since the induced local magnetic moments are so much smaller than those of the magnetically ordered layers, these attempts have only achieved partial success. Also first principles calculations have obtained local magnetic moments of the atoms within the spacer layer.[4] These small magnetic moments typically vary both in magnitude and sign as a function of the distance from the magnetic layer. Due to restrictions on spacer-layer thickness imposed by present-day computers, there are usually not enough independent calculated magnetic moments to get full information on the functional form of these oscillations. In this paper we present density functional based calculations of the full magnetization density for Co/Cu(001) systems. The calculated density, as opposed to the local magnetic moments, is then analyzed in terms of Friedel oscillations.[5]

II. METHOD

The calculations have been performed with the linearized augmented plane wave (LAPW) method within the local spin density approximation. The calculations were self-consistent and no shape approximations to the densities or potentials were made. The systems studied were based on a fcc crystal with the copper lattice constant and consisted of $Co/Cu_9/Co$ units separated by an empty gap of three atomic layers. This structure permits both a ferromagnetic (F) and antiferromagnetic (AF) alignment of the magnetic moments of the two cobalt layers within one unit. The Brillouin zone integrations were performed with a dense two-dimensional mesh of special **k** points, 528 points in the irreducible part.

III. RESULTS

In Fig. 1 the induced density $m(\mathbf{r})$ for the F case is shown for a slice in the (100) plane which goes through atoms of all the different atomic layers of the spacer layer [$m(\mathbf{r})/|m(\mathbf{r})|^{1/2}$ is plotted in order to bring out the small features]. Due to the inversion symmetry present when the magnetic layers are F aligned, there are only five independent spacer-layer atoms, and the plot is therefore only over half the spacer layer. The atoms are situated at those places where the density has most structure. The local magnetic moments deduced from this magnetization density are in good agreement with other studies, with a relatively large moment (here 0.006 μ_B) at the first Cu layer parallel aligned to the Co moments and smaller ones of varying sign at larger distances. From this figure one can deduce that the magnetization is oscillatory and decaying when going away from the magnetic layer.

The oscillatory behavior may be viewed as arising from the spin-dependent interference of spacer-layer Bloch waves with the waves reflected at the interface with the magnetic layer. This behavior is generally known as Friedel oscillations.[5] It can be shown that in a generalization to realistic cases this induced magnetization satisfy,[6]

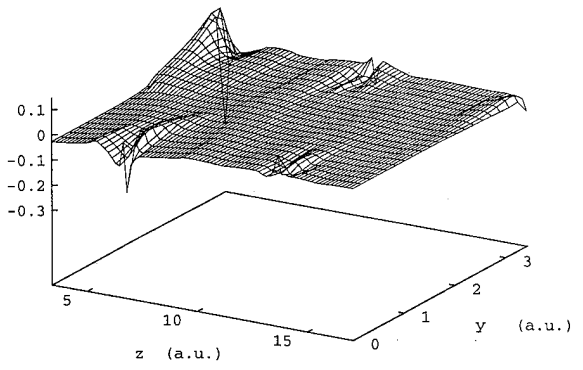


FIG. 1. The magnetization density within the spacer layer is plotted in the form $m/|m|^{1/2}$ for a slice in the (100) plane. The slice is chosen so it goes through atoms of each atomic layer within one half of the spacer layer.

 0021-8979/96/79(8)/4515/3/$10.00 © 1996 American Institute of Physics

$$m(\mathbf{r})=\sum_i \frac{A_i}{z^2}\,|\psi(\mathbf{k}_i,\mathbf{r})|^2\,\cos(\Delta k_i z+\phi_i), \tag{1}$$

for an asymptotically large distance from the magnetic layer. Here z is the distance to the interface, the sum is over the stationary Fermi surface calipers Δk_i, well-known from RKKY theory,[7] A_i and ϕ_i are, respectively, the amplitude and phase of the ith oscillation, and ψ is the Block wave function corresponding to an end-point $\mathbf{k}_i$ of the ith caliper. The space dependent weighting factors $|\psi|^2$ are the cause of the structures in the magnetization density centered at the spacer-layer atoms in Fig. 1. These make the interpretation of the magnetization density nontrivial.

In order to make an analysis of the magnetization density possible in terms of the expression in Eq. (1) without assuming any prior knowledge of Fermi surface calipers or the corresponding amplitude, an approximation that $\psi(\mathbf{k},\mathbf{r})$ is independent of the specific Fermi surface wave vector has to be made. Further, this Fermi-surface-averaged $|\psi|^2$ is assumed to be proportional to the magnetization density $m_0(\mathbf{r})$ of pure fcc Cu obtained in a calculation with a small external magnetic field. This assumption should be valid for a small enough field strength, here we have used a field giving rise to a magnetic moment of $10^{-4}\ \mu_B$. With the above assumptions, the dimensionless quantity $\mu=(z/a)^2 m/m_0$, where a is the lattice constant, should be a superposition of pure oscillations as a function of z for large distances from the interface

$$\mu(\mathbf{r})=\sum_i B_i\,\cos(2\pi z/\lambda_i+\phi_i), \tag{2}$$

where $\lambda_i=2\pi/\Delta k_i$ is the RKKY wavelength and B_i is the new amplitude. Although the normalization with m_0 takes away a large part of the atomic-like structure in Fig. 1, some unwanted features remain due to the approximations involved in this procedure. In order to get rid of this remaining noise, and at the same time to get down to only one variable $\mu(\mathbf{r})$ is also integrated over the plane perpendicular to z,

$$\tilde{\mu}(z)=\int dx\,dy\;\mu(x,y,z). \tag{3}$$

In our systems there is more than one interface and each causes Friedel oscillations. By adding the two different magnetization densities calculated with F and AF ordering, the contribution from the second interface may be largely canceled. In Fig. 2 the resulting renormalized magnetization density $(\tilde{\mu}_F+\tilde{\mu}_{AF})/2$ has been plotted. There are clearly smooth oscillations throughout the spacer with an effective period just above one monolayer (ML). However, these oscillations are not centered around zero; they are below zero for distances shorter than 5 ML and above for larger distances.

As is well known from RKKY theory for the case of fcc Cu(001) there are two Fermi surface calipers contributing to the oscillations of Eq. (2). A fit to two independent oscillation periods finds 1.58 and 1.28 ML with the amplitude of the latter three times larger than that of the former. The resulting curve is also plotted in Fig. 2. While the fit becomes better the further away the fitting interval is taken from the

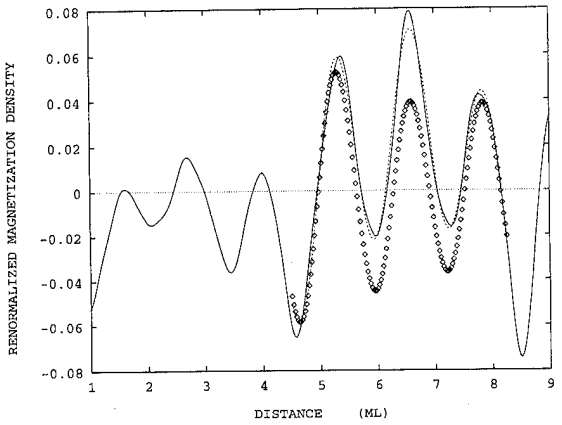


FIG. 2. The sum of the ferromagnetic and antiferromagnetic induced magnetization density in the form given by Eq. (3), is plotted for the spacer layer (full curve). The distance is with respect to the closest Co atom in units of monolayers (ML). Fits of this curve to the form in Eq. (2) when using two (diamonds) and three (dashed curve) independent oscillations are also shown.

magnetic layer, a fair asymptotic limit is already reached at 3.5 ML. The fast oscillations are well reproduced with this fit, but it fails to mimic the apparent long wavelength feature of the negative and positive offsets. This is probably because the latter is not of oscillatory nature but is caused by the finite size of the spacer layer used in the calculation. The magnetization density in our calculation has not only to fulfill the boundary condition at the interface as the "true" Friedel oscillation, but is in addition forced to be symmetric (F) or antisymmetric (AF) around the central fifth atom in the spacer layer. In the present case, the AF solution has taken a somewhat peculiar form in order to fulfill this latter condition. This results in the steplike feature at 5 ML. A better fit to the curve is obtained when allowing for three oscillations, the result of which is also shown in Fig. 2. The third period becomes just above 5 ML in order to reproduce the step.

The two physical periods are very close to what is expected from the two calipers of the "dog-bone" of the Cu Fermi surface, 1.2 and 1.6 ML. These periods correspond to 5.9 and 2.6 ML, respectively, when they are sampled on the discrete lattice as when studying atomic moments or interlayer coupling,[8] i.e., with the "aliasing effect."

IV. CONCLUSIONS

As is clear from Eqs. (1) and (2) there is a connection between the Friedel oscillations and the RKKY oscillations of the interlayer coupling. The periods, apart from the aliasing, are identical, and since both phenomena arise from spin-dependent interface reflections the relative strengths of the different oscillations should be related. So in principle, with a calculation for one interlayer distance, which, among all possible RKKY oscillation periods are most important, can be determined. As true Friedel oscillations only exist for asymptotic distances from the interface, a relatively thick spacer layer has to be used in the calculation. But as has been shown, one way to double the effective thickness is to do

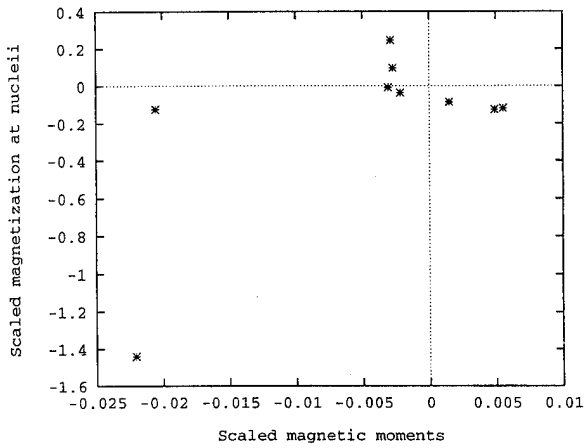


FIG. 3. The local magnetic moments within a muffin-tin sphere of radius 2.25 a.u. are plotted against the magnetization density at the corresponding atomic nucleus for all independent atoms of the spacer layer. Both quantities have been multiplied with the squared distance from the interface and the units are arbitrary.

both a F and an AF calculation. In the analysis, besides the pure Friedel oscillations, care is needed to avoid extrinsic features due to the finite interlayer distance.

Another thing to observe is that the rather rapid oscillations found make the concept of local atomic moment in the spacer layer more ambiguous than usual. The magnitude of a local magnetic moment depends on which part of space is ascribed to each atom. Fortunately, reasonable choices of atomic or muffin-tin spheres usually give magnetic moments in fair agreement with each other. However, when there is an oscillation with an effective period of almost atomic dimensions, a change of sphere radii may not only change the magnitude but also the sign of the magnetic moment. In order to illustrate this we chose two quantities related to the atomic part of the magnetization density, the local magnetic moment within a muffin-tin sphere with radius 2.25 a.u., and the magnetization density at the atomic nucleus, and plotted these, both multiplied with the square of the distance from the interface, against each other for all independent atoms of the F and AF systems (Fig. 3). These two quantities are usually proportional, as in, e.g., a ferromagnet, but here they are all scattered around and not even the sign is consistent. One way to view this is that instead of having local magnetic moments arising from a local exchange mechanism the Cu spacer layer has a more "free electron-like" induced magnetization, in accordance with the fact that it is well described as Friedel oscillations. This also affects interpretations of experimental results as, e.g.,[1–3] where the magnetization density is probed close to the nucleus implicitly assuming a sort of local magnetic moment.

In summary, a way to analyze the induced magnetization density within a spacer layer has been presented. When applied to Cu(001) a very good agreement with the expected Friedel oscillations is obtained. The method presented here is quite general and can be applied straight-forwardly to other types of spacer layers as well.

ACKNOWLEDGMENTS

Work at the Naval Research Laboratory is supported by the Office of Naval Research. The computations were performed at the CEWES and NAVO computer centers of Department of Defense.

[1] M. G. Samant, *et al.*, Phys. Rev. Lett. **72**, 1112 (1994).
[2] S. Pizzini, *et al.*, Phys. Rev. Lett. **74**, 1470 (1995).
[3] Q. Y. Jin, *et al.*, Phys. Rev. Lett. **72**, 768 (1994).
[4] See, e.g., A. M. N. Niklasson, *et al.*, J. Magn. Magn. Mater. **148**, 209 (1995).
[5] J. Friedel, Philos. Mag. **43**, 153 (1952).
[6] L. Nordström and P. H. Dederichs (unpublished). The form of Eq. (1) actually assumes that the interface is parallel to a mirror plane of the unperturbed crystal. This is the case for fcc (001).
[7] P. Bruno and C. Chappert, Phys. Rev. Lett. **67**, 1602 (1991).
[8] P. Lang, L. Nordström, R. Zeller, and P. H. Dederichs, Phys. Rev. Lett. **71**, 1927 (1993).

Interface alloying at Fe/Cr interfaces and its role in exchange coupling, angular resolved Auger electron, magneto-optic Kerr effect, and Brillouin light scattering studies (invited)

B. Heinrich, J. F. Cochran, D. Venus,[a] K. Totland, D. Atlan, S. Govorkov, and K. Myrtle
Simon Fraser University, Physics Department, Burnaby, British Columbia, V5A 1S6, Canada

Angular resolved Auger electron studies were carried out for Fe whisker/Cr(001) interfaces which were prepared at 100, 180, 246, and 296 °C. The Cr atoms penetrate progressively into the second (counting from the surface) atomic layer at 100, 180, and 246 °C. At 296 °C the Cr atoms enter the third atomic layer. No noticeable fraction of the Cr atoms was found in the fourth atomic layer. The exchange coupling was studied in Fe whisker/Cr/Fe(001) films which were grown in a nearly perfect layer by layer mode. Magneto-optic Kerr effect and Brillouin light scattering measurements showed that the measured change in the phase of the short wavelength oscillations, the presence of a slowly varying exchange coupling bias, and the small measured values of exchange coupling are caused by the same mechanism: interface alloying. The exchange coupling in Fe whisker/Cr/nFe specimens, for $n=10$, 20, 30, and 40 ML, showed no obvious dependence on the Fe layer thickness. © *1996 American Institute of Physics.* [S0021-8979(96)48408-9]

I. INTRODUCTION

Fe whisker/Cr/Fe(001) systems have played a crucial role in the study of exchange coupling between two ferromagnets separated by a nonferromagnetic spacer. The scanning electron microscopy with polarization analysis (SEMPA) studies by the NIST group[1] and the magneto-optic Kerr effect (MOKE) measurements by the Philips group[2] using Fe whisker/Cr/Fe(001) samples showed that the exchange coupling oscillates with a short wavelength period of ~2 ML. The SEMPA measurements very clearly revealed short wavelength and long wavelength oscillations in the thickness range of 5–80 ML of Cr. The period of the short wavelength oscillations was found to be slightly incommensurate with the Cr lattice spacing, $\lambda=2.11$ ML, the period of the long wavelength oscillations was found to be 12 ML. Short and long wavelength oscillations have been observed also for samples grown on a GaAs(001) substrate covered with a thick buffer layer of Ag(001).[3] The SFU group has carried out quantitative studies using Fe whisker/Cr/Fe(001) samples.[4,5] The objective of the SFU group was to grow samples having the best available interfaces, to measure quantitatively the strength of the exchange coupling, and to compare it with *ab initio* calculations which included explicitly the presence of spin-density waves in Cr.[6,7] The requirement of smooth interfaces limited the study to samples which were grown on Fe whisker templates with the Cr spacers terminated at an integral number of Cr atomic layers. It was found that the strength of the exchange coupling through the Cr(001) spacer is extremely sensitive to small variations in growth conditions. The measured exchange coupling was found to be reproducible only in those samples that exhibited layer by layer growth. The existence of unattenuated reflection high-energy electron diffraction (RHEED) intensity oscillations of the specular spot during the growth of the Cr spacer did not guarantee reproducible results. The width of the RHEED specular spot profiles had to be monitored and one had to establish conditions such that the atom island formation followed a prescribed pattern of nucleation and growth. The best results were obtained for the case when the spot profiles oscillated repeatedly between narrow peaks (filled atomic layers) and split intensity peaks (half-filled layers). This was possible to achieve by maintaining the substrate temperature in a narrow range of temperatures, 280 °C$<T_{s,\mathrm{opt}}<$320 °C. The presence of the specular spot splitting for half-filled atomic layers indicated that new atomic layers were formed from nucleation centers which were separated by a well defined mean distance. The mean separation between atomic islands was found to be ~800–900 Å at $T_{s,\mathrm{opt}}$.[4,5] This interpretation is in agreement with the recent scanning tunneling microscopy (STM) studies by Stroscio.[8] Samples grown in that way showed unattenuated RHEED intensity oscillations with well defined cusps at the RHEED intensity maxima. The first monolayer of Cr exhibits a unique behavior; the first RHEED intensity oscillation shows a strong peak with a very sharp cusp even at substrate temperatures as low as 150 °C indicating that the first atomic layer grows very smoothly. The situation changes when Cr is deposited on a Cr template. In that case the growth of Cr proceeds layer by layer only if the substrate temperature is adjusted to an optimum growth temperature, $T_{s,\mathrm{opt}}$.

Quantitative Brillouin light scattering (BLS) studies have clearly exhibited short wavelength oscillations in the exchange coupling.[4,5] These studies showed also for the first time that the exchange coupling through Cr(001) contains both oscillatory bilinear, J_1, and positive biquadratic, J_2, exchange coupling terms. The exchange energy is given by

$$E=-J_1\cos(\theta)+J_2\cos^2(\theta),$$

where θ is the angle between magnetic moments of the ferromagnetic layers. The thickness dependence of J_1 in Cr exhibits several interesting features. Firstly, for a Cr spacer which is thinner than 8 ML the strength of the short wavelength oscillations is quite weak, $|J_1|\sim 0.1$ ergs/cm^2. The exchange coupling in this range is antiferromagnetic only due to the presence of an antiferromagnetic (AF) long-wavelength bias. The coupling crosses over to ferromagnetic (FM) coupling for thicknesses less than 3 ML. The AF bias is peaked around 4 ML and dies out gradually as the thickness

[a]Permanent address: Dept. of Physics and Astronomy, McMaster Univ., Hamilton, Ontario, Canada.

 0021-8979/96/79(8)/4518/6/$10.00 © 1996 American Institute of Physics

approaches 9 ML. It is interesting to note that the strength of the AF bias is very nearly the same as that observed in Fe/Cr/Fe(001) epitaxial multilayers prepared by sputtering where the interface roughness has annihilated the presence of the short wavelength oscillations.[9] For a Cr spacer thicker than 8 ML, $d_{Cr}>8$ ML, the exchange coupling is dominated by the short-wavelength oscillations. In this thickness range the samples are strongly antiferromagneticaly coupled, $J_{tot}=|J_1-2J_2|\sim 1.0-1.5$ ergs/cm^2, for an odd number of Cr atomic layers and weakly ferromagnetically (FM) coupled for an even number of Cr atomic layers, $J_{tot}\sim 0.01-0.1$ ergs/cm^2. The thin film peak position in the BLS spectra for FM coupled samples is right at the threshold of the bulk Fe (whisker) spin manifold. This asymmetric behavior in J_{tot} can be explained by the presence of the biquadratic exchange coupling, J_2. The total exchange coupling through the Cr spacer for the parallel orientation of the magnetic moments is given by $J_{tot}=J_1-2J_2$, and therefore the biquadratic exchange, $J_2>0$, increases the strength of AF coupling, and decreases the strength of FM coupling. The observed weak FM coupling implies that $J_1\sim 2J_2$. The biquadratic coupling J_2 was found to be approximately 0.25 ergs/cm^2 and this leads to a bilinear exchange coupling strength of $J_1=0.5$ ergs/cm^2 for FM coupled samples. This strength of J_1 is close to that found for AF coupled samples; and therefore an apparent weak FM coupling in Cr is more the consequence of a strong J_2, than the result of a weak intrinsic FM bilinear coupling J_1.

The coupling between the Fe and Cr atoms at the Fe/Cr interface is expected to be strongly antiferromagnetic[10,11] and in consequence the spin density wave in Cr is locked to the orientation of the Fe magnetic moments. Since the period of the short wavelength oscillations is close to 2 ML one expects AF coupling for an even number of Cr atomic layers and FM coupling for an odd number of Cr atomic layers. For the period of $\lambda=2.11$ ML the first phase slip in the short wavelength coupling is predicted to occur at 24 ML. Surprisingly, the SEMPA[12] and BLS[13] measurements showed that the phase of the short-wavelength oscillations is exactly opposite to that expected. It is also important to note that the strength of the exchange coupling $|J_{max}|\sim 1.0$ ergs/cm^2, was found to be much less than that obtained from the first principal calculations, $|J_1|=30$ ergs/cm^2.[6] This represents a significant disagreement between experiment and theory. Since Fe whisker/Cr/Fe(001) samples can be prepared in a nearly perfect layer by layer growth, the above disagreement between the measured exchange coupling and the theoretical calculations cannot be *a priori* blamed on poor sample quality. The possibility that the theoretical calculations provide too great a strength for the exchange coupling is not entirely out of the question, but the reversed phase of the short wavelength exchange coupling is rather hard to accept in the light of two facts: (a) Cr metal is known to possess an intrinsic short wavelength spin density wave, and (b) the coupling between Fe and Cr atoms is known to be strongly antiferromagnetic. Therefore, one should entertain the possibility that the above discrepancies between theory and experiment are caused by sample structural features.

Our recent studies showed that the strength of the bilinear exchange coupling J_1 is very sensitive to the initial growth conditions. The bilinear exchange coupling can be changed by as much as a factor of 5 by varying the substrate temperature during the growth of the first Cr atomic layer. On the contrary, the strength of the biquadratic exchange coupling was found to be quite insensitive to the initial growth conditions. This is a surprising result considering that the first RHEED intensity oscillation, corresponding to the first Cr atomic layer, usually shows a large oscillatory amplitude with a sharp cuspy maximum even at relatively low substrate temperatures, $T\sim 150$ °C, and therefore it was expected that a perfect formation (no pile-up of Cr atoms) of the first Cr atomic layer would not negatively affect the subsequent growth. The sensitivity of J_1 to the initial growth conditions has led us to believe that the atomic formation of the Cr layer is more complex then has been so far acknowledged. In the following we will demonstrate by using angular resolved Auger electron spectroscopy (ARAES) that atomic interface alloying at the Fe whisker/Cr interface due to an atom interface exchange mechanism plays a very significant role and strongly affects the exchange coupling through the Cr spacer.

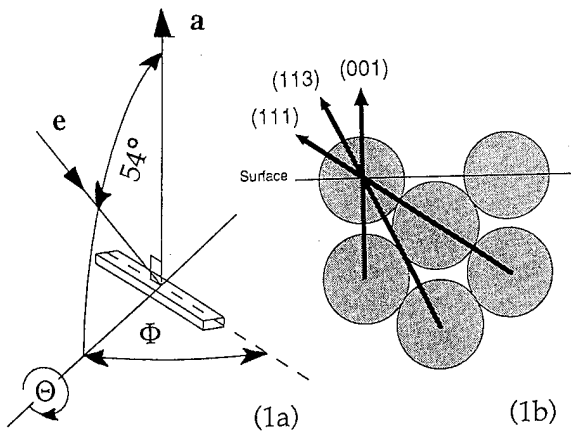


FIG. 1. (a) Experimental configuration for angular resolved Auger electron spectroscopy (ARAES) measurements. **a** is the line of acceptance of Auger electrons, and the incident electron beam (2.0 keV) is directed along the line **e**. The angle between **a** and **e** is 54°, and **n** is the sample surface normal. The drawing shows the configuration for $\Theta=0°$, **n** parallel to **a**. Angular resolved studies were carried out varying the polar angle Θ (measured from **n**). The azimuthal angle Φ was used to select an appropriate lattice plane for the ARAES measurements. (b): An illustration of rows of atoms in the bcc (011) crystallographic plane ($\Phi=45°$) which dominantly contribute to forward scattering of Auger electrons, see details in the text.

II. GROWTH AND ARAES STUDIES

The angular distribution of the Cr KVV Auger electrons (529 eV) was used to investigate interface alloying in the Fe whisker/Cr(001) interface. Auger electrons having an energy of several hundred eV energy are strongly forward scattered in the directions interconnecting the emitter with its nearest and next nearest neighbors. This forward scattering is strongest when the effect is limited to single scattering events;[14–16] i.e., when the ARAES measurements are limited to a few MLs. The experimental configuration in our ARAES studies is shown in Fig. 1. The ARAES studies were carried

out using an uncommon whisker blade, $100\times500\times10^4$ μm, with the [001] axis along its long edge and with the large facets oriented in {001} planes. The Fe whisker was mounted on an ultrahigh vacuum (UHV) goniometer equipped with polar, Θ, and azimuthal, Φ, rotational degrees of freedom. The line of acceptance of Auger electrons, **a**, to an OMNI lens of the hemispherical analyzer, PHI-10−360 (2° angle of acceptance with the focal area of ϕ=500 μm in diameter), and the normal to the sample, **n**, are perpendicular to the polar axis, Θ, of our UHV goniometer. In our ARAES studies the Fe whisker was initially oriented with its (011) crystallographic plane perpendicular to Θ corresponding to the azimuthal angle Φ=45°. The incident electron beam (2 keV), **e**, lies in the plane formed by the polar axis Θ and **a**. The angular dependence of the LVV Cr and Fe Auger peaks was measured by rotating the sample, using the polar angle Θ of our UHV goniometer, thus all atomic rows lying in the (011) plane were available to the input of the Auger analyzer. In this configuration the Auger electrons originating from the top surface layer have a flat angular dependence. The atoms in the second, third, and fourth atomic layers have their Auger peaks enhanced for the polar angle Θ=54.7° (along the body diagonal [111]), the third and fourth atomic layers have their Auger peaks also enhanced along Θ=0° (along the cube edge [001]), and the fourth layer is also enhanced for 25.2° (along the [1,1,3] direction, see Fig. 1). Thus the Cr occupation of the individual atomic layers near the surface can be determined by measuring the polar angular dependence of the Cr LVV (529 eV) Auger peak. The orientation of the incident electron beam, **e**, in our system leads to a more complex behavior when the Auger signal is measured along the [001] axis. For Θ=0° the impinging electron beam is nearly parallel to the body diagonal. In this case the flux of impinging electrons is significantly enhanced for those atoms that are located in the first and second atomic layer below the surface. The effect is caused by the forward focusing due to the row of atoms along the body diagonal. In that case, the maximum around Θ=0° could be incorrectly interpreted as evidence for the presence of Cr atoms in the third layer. This spurious effect was eliminated by rotating the azimuth Φ of the sample away from 45° to 34.5°. The 45° azimuth was perfectly suitable for measurements made off the sample normal, θ>10°, where the forward focusing effect is absent.

The goal of our ARAES measurements was to identify the level of interface Fe–Cr alloying. For this purpose we deposited 0.5 ML of Cr at various substrate temperatures, and carried out appropriate ARAES using the Cr LVV Auger peak. The results of our studies are shown in Fig. 2, where the ARAES data are shown for substrate temperatures, T_{sub}=180, 246, and 296 °C. Further details of this work can be found in Ref. 17. Figures 2(b) and 2(d) show no maximum around θ=0°, but a clear maximum is visible for θ=54° in Figs. 2(a) and 2(c). Figures 2(e) and 2(f) show maxima for both angles. The presence of these maxima clearly indicates that interface mixing is present during the growth of Cr on Fe whisker substrates. At 180 °C the Cr atoms only penetrate into the second atomic layer. At 296 °C the Cr atoms even enter the third atomic layer. No peak is evident along 25° indicating that for this range of substrate

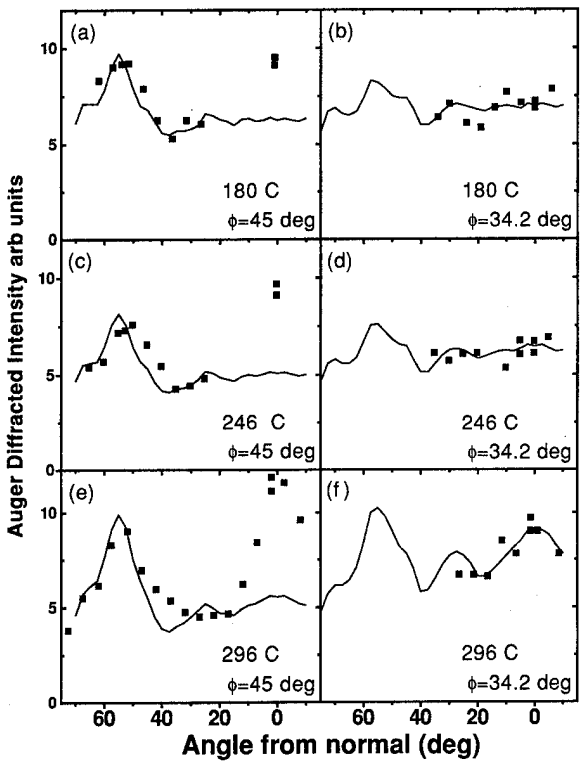


FIG. 2. Polar angular dependence of the LVV Cr Auger electron peak from a 0.5 ML thick Cr layer deposited on an Fe(001) whisker blade. The deposition of Cr was carried out at the substrate temperatures of 180°, 246° and 296 °C, respectively. The peaks around Θ=0° for the azimuth Φ=45° are caused by forward focusing effect of the incident electron beam, see the text. The solid lines are fits using the computer program SSC,[16] see the text.

temperatures the Cr ad atoms do not penetrate into the fourth atomic layer. The measured ARAES data were analyzed using the computer program SSC developed by Fadley and his co-workers.[16] The scattering is treated using scattering phase shifts from the computer program FEFF-3 developed by Rehr and his co-workers.[18] The single scattering approach is fully justifiable for Cr atoms distributed in the first two atomic layers. For atoms in the third atomic layer the single scattering approach is not fully adequate for θ=54°. In that case the Auger electrons propagate along two atoms in the body diagonal where the effect of multiple scattering is not negligible. Calculations along the close packed directions show that the effect of multiple scattering is equivalent to the reduction of the intensity of the Auger electrons to 60% of its value calculated using the single scattering approach.[16] The results of our analyses are summarized in Table I. Table I shows that interface alloying plays a role even at low substrate temperatures and becomes very significant at substrate temperatures for which a thick Cr spacer can be grown in the layer by layer mode.

One should point out that interface alloying is an asymmetric effect; it happens only at one interface.[19] Interface alloying is driven by the difference in binding energies between the substrate and ad atoms. The binding energy is proportional to the melting point of the appropriate solids. Interface alloying has been observed in systems for which the substrates have lower melting points than those of the ad

TABLE I. Fractions of the Cr atoms in the first (surface layer), second and third atomic layers obtained from SSC fits (Ref. 16). A half ML of Cr was grown on an Fe(001) whisker template at 100, 180, 246, and 296 °C. The use of a third layer in SSC calculations for samples prepared at 100, 180, and 246 °C provide better overall fits around $\Theta=0°$, but the measured angular variations around $\Theta=0°$ are on the border line of our experimental accuracy, and therefore the fractions determined in the fourth column might well be incorporated into the second layer (shown in brackets in the third column).

Temp [°C]	First	Second	Third
100	0.82	0.13(0.18)	0.05
180	0.74	0.21(0.26)	0.05
246	0.67	0.30(0.33)	0.03
296	0.51	0.30	0.19

atom solids.[19,20] The melting point of Fe (1808 K) is lower than the melting point of Cr (2130 K), and thus the condition for interface alloying is satisfied.

Cr and Fe form miscible alloys. At this point it is fair to ask whether the substrate Fe atoms are involved in surface segregation at the top of the Cr spacer. To investigate this point an 11 ML Cr film was grown and then the Fe LVV peak intensity was compared to that with no Cr coverage. It was found that the Fe Auger signal decreased by 8.8-fold. Since the Auger signal was collected perpendicular to the surface this decrease is caused by two factors: (a) The removal of the forward scattering enhancement due to the presence of the 11 ML thick Cr layer. (b) The attenuation of the Fe Auger signal due to the propagation through the 11 ML thick Cr. The first factor decreases the signal by 2.5 times, the second factor can be estimated using the formula for the electron inelastic mean free path 1. For the Fe LVV Auger electrons(729 eV) in Cr. $1=12$ Å,[21] and results in an attenuation of 3.7 times. The total expected attenuation is 9.3 times, this is very close to the observed attenuation of 8.8 times. Therefore there is no evidence that the interface alloy mixing goes beyond the first Fe/Cr interface. The ARAES measurements were always carried out for both the Fe whisker template and the Cr overlayers. By integrating the Cr and Fe Auger intensities between $\Theta=0°$ to 60° one can obtain a good estimate for an effective Cr coverage as seen by the Auger analyzer. The reference point used in this calculation was the total Fe AES signal. Using a simple formula which includes the appropriate Auger atomic sensitivities[22] and the Fe Auger electron mean free path in the bulk Fe results in an effective Cr coverage of 0.8 ML. This is somewhat bigger than that predicted by the RHEED intensity oscillations, 0.5 ML. Considering that the Fe Auger signal involves at least 10 atomic layers, where the contribution of electron multiple scattering is non-negligible, the above estimate of an effective Cr coverage is very reasonable. The Cr atoms were confined to the vicinity of the Fe whisker surface.

III. MAGNETIC STUDIES AND DISCUSSION OF RESULTS

The exchange coupling through Cr is most likely affected by interface alloying. This point was verified by using two Fe whisker/11Cr/20Fe(001) samples. In the first sample the Fe/Cr interface was formed at $T_s=180$ °C and then the rest of the Cr spacer was grown with T_s at 250 °C and 300 °C to maintain a good layer by layer growth at higher Cr coverages. The second sample was grown starting at a substrate temperature $T_s=244$ °C. and then the last 4 ML were grown at $T_s=294$ °C. The MOKE and BLS measurements exhibited two critical fields. For fields $H>H_2$ the magnetic moments in the Fe whisker and in the ultrathin film were clearly parallel to the applied external field, the sample was fully saturated, and no gradual approach to saturation was observed. For $H<H_2$ the magnetic moments were noncollinear, the magnetic moments deviated from the external field direction. The anticollinear configuration was reached for fields $H<H_1$, where H_1 is the lower critical field. The existence of a fully saturated state for fields $H>H_2$ is consistent with the assumption that the angular variation of the exchange coupling is expressed in terms of bilinear and biquadratic exchange coupling. The positions of critical fields H_1 and H_2 were used to calculate J_1 and J_2 using a micromagnetic calculation for an Fe whisker/Cr/20Fe sample.[23] The results of these calculations showed that the exchange coupling depended very strongly on interface alloying. The sample with the Fe/Cr interface prepared at a lower substrate temperature, $T_s=180$ °C, exhibited a much larger bilinear exchange coupling, $J_1=-1.23$ ergs/cm^2, than the specimen having an Fe/Cr interface prepared at a higher substrate temperature, $T_s=244$ °C (-0.4 ergs/cm^2). For $T_s=180$ °C two samples were grown; in the second sample the Cr spacer was 10 ML thick. This sample was strongly coupled ferromagnetically so that the thin film peak was sufficiently shifted in frequency that it disappeared into the spin-wave manifold of the Fe whisker. This result is a consequence of a large positive J_1. Since J_2 is weakly dependent on the substrate temperature the effective total FM coupling, J_1-2J_2, increased substantially.

Stoeffler and Gautier have shown that the presence of Fe in Cr atomic layers around the interfaces affects the magnetic behavior. The Cr atoms at the interface are subjected to conflicting exchange coupling requirements due to the particular geometrical configuration of their neighbors. The orientation of the Cr atomic moments is magnetically frustrated by the lack of a sharply defined chemical environment. Stoeffler and Gautier showed[24] that an interface composed of two ordered {Fe(75%)–Cr(25%), Cr(75%)–Fe(25%)} atomic layers already shows a sufficient level of magnetic frustrations to change the phase of the coupling and to substantially decrease J_1. The magnetic moment of the mixed Cr layer (75%Cr–25%Fe) was found to be parallel to the adjacent Fe magnetic layer. It is the second Cr atomic layer which has its magnetic moment oriented antiparallel to the Fe layer. The magnetic moments in the subsequent Cr atomic layers oscillate between parallel and antiparallel configurations. Since this effect is only confined to one interface the phase of the exchange coupling through Cr(001) is reversed from that expected for an ideal interface. Magnetically speaking the Cr spacer lost one atomic layer. The parity is changed, an odd number of Cr atomic layers becomes an even number and vice versa. The calculated strength of the short wavelength coupling in the sample with intermixed interfaces was found to be close to that obtained in our measurements. It is also

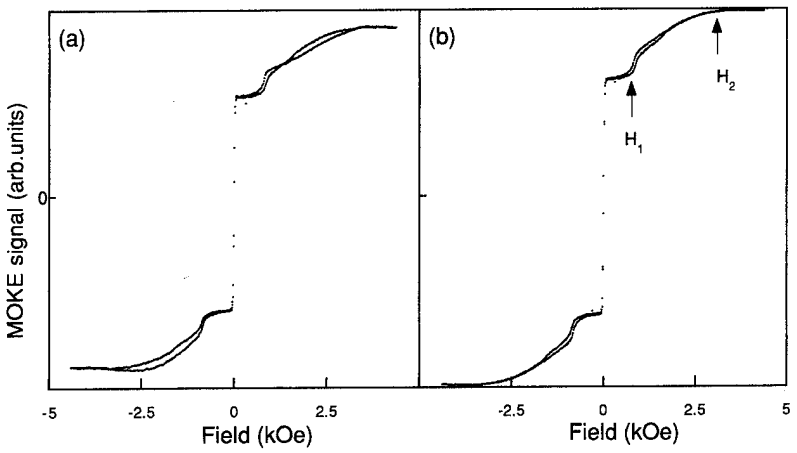


FIG. 3. (a) MOKE signal for the Fe whisker/11Cr/30Fe/20Au(001), thicknesses are measured in ML. The curve has asymmetric features which are most likely associated with the magnetization component transversal to the external field H.[25] (b) A symmetrized hysteresis loop. The contribution of the transversal component has been removed by subtracting the measured MOKE data for positive and negative fields; $M(H)=[M(H)-M(-H)]/2$. The upper and lower curves correspond to decreasing and increasing fields, respectively.

interesting to point out that the magnetic frustrations in their calculations led to AF coupling for $d_{Cr}<4$ ML and resulted in a FM bias between 4 and 10 ML of Cr. Our measurements showed FM coupling up to 3 ML and a slowly varying AF background between 4 and 9 ML of Cr. The slowly varying background in the measured exchange coupling has the same thickness variations as the above calculations, but the phase is reversed. The calculations were carried out for the symmetric case. In our samples the magnetic frustrations occur at one interface only. The Cr moment distribution at the alloyed interface[24] suggests that for the thicknesses between 1 and 4 ML of Cr the coupling changes to FM and that results again in the reversal of the phase. The level of interface alloying in our samples is comparable to that used in the Stoeffler, Gautier calculations, and therefore we believe that the following statement can be accepted with a reasonable degree of credibility: The measured change in the phase of the short wavelength oscillations, the presence of a slowly varying exchange coupling bias and the small measured values of exchange coupling are caused by the same mechanism, namely interface alloying.

Ab initio tight binding calculations predict that the coupling through Cr should be only weakly dependent on the thickness of Fe layers when the thickness of the Fe layers is more than several ML. This result is a direct consequence of the presence of spin density waves in Cr and the Heisenberg like nature of the exchange interactions in Fe/Cr.[6] We prepared four samples with thicknesses of 10, 20, 30, and 40 ML of Fe to investigate this point. The samples were grown on the same Fe whisker using a shutter during the growth of the Fe layer. The same Cr thickness of 11 ML was used for all samples. The first four atomic layers of Cr were grown at $T_s=180$ °C to decrease the interface alloying. Quantitative measurements were carried out using MOKE (longitudinal Kerr effect) and BLS. A typical hysteresis loop is shown in Fig. 3(a): It clearly shows a well defined saturation field H_2 and a jump in the total magnetic moment when the Fe film magnetic moment becomes oriented antiparallel to the Fe whisker magnetic moment. The measured magnetization loops show a certain degree of hysteresis and also an asymmetric behavior for positive and negative fields. The asymmetry could be caused by the component of the magnetic moment transverse to the field for $H_1<H<H_2$, as described recently by Osgood *et al.*[25] In order to eliminate the role of the transversal magnetic component in our measurements the data for negative and positive fields were subtracted. The subtraction was carried out for decreasing fields [lower curve in Fig. 3(b)] and for increasing fields [upper curve in Fig. 3(b)]. This procedure resulted in a symmetric curve as expected, Fig. 3(b). The measured magnetization curves were fit using a full micromagnetic calculation. The results of the analysis, shown in Table II, clearly indicate that the coupling through Cr is independent of the Fe thickness. Only a small decrease (10%) was found in the total exchange coupling, $|J_1-2J_2|$, for the 10 ML thick sample. However in this case the upper field H_2 as measured by MOKE (~7 kOe) was almost at the upper limit of our magnet, and therefore the difference in the strength of the coupling could have been due to underestimating H_2.

BLS measurements were carried out on the same sample. The AF coupling led to a well defined thin film peak. The BLS spectrum for the 30 ML thick sample is shown in Fig. 4. The data are characterized by two well defined fields

TABLE II. The bilinear, J_1 and biquadratic, J_2, exchange couplings as determined from the BLS and MOKE measurements. The coupling is in ergs/cm^2 and the Fe thickness, d, is in ML. The MOKE results were obtained using the critical fields H_1, H_2, see Fig. 3. The BLS results were obtained by fitting the measured field dependence of the Fe film resonance peak, see Fig. 4.

	BLS		MOKE	
d	$-J_1$	J_2	$-J_1$	J_2
10	0.74	0.23	1.0	0.25
20	1.02	0.23	1.1	0.33
30	0.96	0.23	1.15	0.31
40	0.95	0.23	1.08	0.34

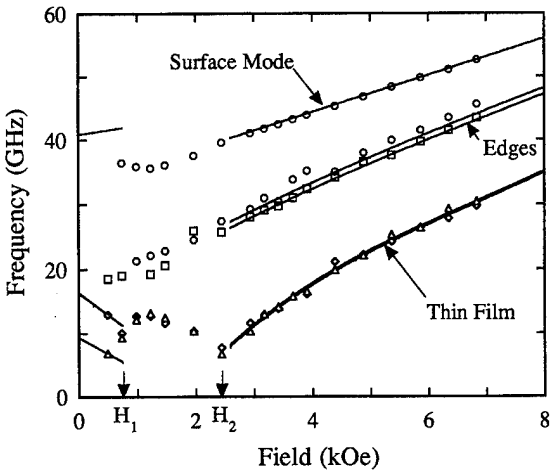


FIG. 4. Frequency vs applied magnetic field for the whisker/11Cr/30Fe/20Au specimen (thicknesses are in ML). Frequencies were measured using BLS in the backscattering configuration and 0.5145 μm laser light incident at 45°. The solid lines were calculated using $4\pi M_s = 21.44$ kOe. $K_1 = 4.76\times10^5$ ergs/cm^3, and $g = 2.09$ for both bulk iron and the 30 ML thin film. We used uniaxial surface energy parameter $K_{\mu A} = 1.0$ ergs/cm^2 (0.5 ergs/cm^2 at each surface)[26] which is in agreement with our recent measurements of the surface anisotropy on Ag/Cr/Fe/Au(001) samples. The exchange stiffness $A = 2.03\times10^{-6}$ ergs/cm. The exchange coupling parameters were $J_1 = -0.96$ ergs/cm^2 and $J_2 = 0.23$ ergs/cm^2. Micromagnetic calculations using these values gave lower and upper critical fields $H_1 = 0.77$ kOe and $H_2 = 2.49$ kOe. Note the large frequency splitting between up-shifted frequencies Δ and down shifted frequencies $\diamond$ for fields lower than H_1 where the magnetic moments are antiparallel

H_1 and H_2 (the lower field H_1 is defined by the sudden change in the frequency splitting between up and down shifted thin film frequencies). The fields H_1 and H_2 were used to determine J_1 and J_2. The results of these analyses are shown in Table II. The MOKE and BLS results for J_1 and J_2 are similar, but the BLS results are consistently smaller than the MOKE results. By comparing Figs. 3 and 4 it is clear that the saturation fields H_2 are not in agreement. In fact, the saturation fields, H_2, measured using MOKE are greater by ~0.8–0.9 kOe compared with those using BLS. The fields H_1 measured using both techniques are in agreement. The values of J_1 and J_2, determined from the BLS analysis, together with the known magnetic anisotropies of the Fe whisker and the Fe film were used to fit the field dependence of the Fe film resonance frequency. Figure 4 shows that this fit is nearly perfect. This indicates very clearly that the position of the upper cusp in the BLS measurements correctly determines the saturation field H_2 for the Fe film. The discrepancy with the saturation field H_2 measured using MOKE indicates that the BLS and MOKE techniques do not follow exactly the same features of the magnetization loops. No difference between MOKE and BLS measurements was found for samples with simple metallic spacers such as Cu and Ag.[5] It is therefore very likely that the above discrepancy is related to the Fe whisker/Cr system.

IV. CONCLUSIONS

The above ARAES studies showed unambiguously that interface atom alloying is present in the growth of Cr on Fe(001). It has been shown that the relatively small measured values for the bilinear coupling, the reversed phase of the short wavelength oscillations compared to those predicted by *ab initio* calculations, and the presence of a slowly varying exchange coupling bias are most likely caused by interface alloying. The dependence of the strength of the exchange coupling on the Fe film thickness was found to be negligible as predicted by *ab initio* calculations.

ACKNOWLEDGMENTS

We would like to thank the Natural Sciences and Engineering Research Council of Canada for funding our work. K. Totland gratefully acknowledges support from the Swiss National Science Foundation. D. Atlan would like to express his gratitude for a Lavoisier fellowship granted by the French Ministry of Foreign Affairs.

[1] J. Unguris, R. J. Celotta, and D. T. Pierce, Phys. Rev. Lett. **67**, 140 (1991); **69**, 1125 (1992).
[2] S. T. Purcell, W. Folkerts, M. T. Johnson, N. W. McGee, K. Jager, J. aan de Stegge, W. B. Zeper, W. Hoving, and P. Grunberg, Phys. Rev. Lett. **67**, 903 (1991).
[3] J. A. Wolf, Q. Leng, R. Schreiber, P. A. Grunberg, and W. Zinn, J. Magn. Magn. Mater. **121**, 253 (1993).
[4] B. Heinrich, M. From, J. F. Cochran, L. X. Liao, Z. Celinski, C. M. Schneider, and K. Myrtle, Proc. MRS Spring Meet., San Francisco **313**, 119 (1993).
[5] B. Heinrich and J. F. Cochran, Adv. Phys. **42**, 523 (1993).
[6] D. Stoeffler and F. Gautier, *Proceedings of NATO Advanced Study Institute*, edited by R. F. C. Farrow, B. Dieny, M. Donath, A. Fert, and B. D. Hermsmeir, Series B, **309**, 411 (1993).
[7] M. van Schilfgaarde and F. Herman, Phys. Rev. Lett. **71**, 1923 (1993).
[8] J. A. Stroscio, D. T. Pierce, J. Unguris, and R. J. Celotta, J. Vac. Sci. Techol. B **12(3)**, 1789, 1994.
[9] E. E. Fullerton, M. J. Conover, J. E. Mattson, C. H. Sovers, and S. D. Bader, Phys. Rev. B **48**, 15755 (1993).
[10] C. Carbone and S. F. Alvarado, Phys. Rev. B **36**, 2433 (1987).
[11] T. G. Walker, A. Pang, H. Hopster, and S. F. Avarado, Phys. Rev. Lett. **69**, 1121 (1992).
[12] J. Unguris, D. T. Pierce, R. J. Celotta, and J. A. Stroscia, *Proceedings of NATO Advanced Study Institute*, edited by R. F. C. Farrow, B. Dieny, M. Donath, A. Fert, and B. D. Hermsmeir, Series B **309**, 101 (1993).
[13] B. Heinrich, Z. Celinski, J. F. Cochran, and M. From, *Proceedings of NATO Advanced Study Institute*, edited by R. F. C. Farrow, B. Dieny, M. Donath, and A. Fert, NATO ASI Series B **309**, 175 (1992).
[14] W. F. Egelhoff, Jr., in *Ultrathin Magnetic Structures I,* edited by J. A. C. Bland and B. Heinrich (Springer, Berlin, 1994), Vol. 5.2, p. 220.
[15] S. Chambers, Adv. Phys. **40**, 357 (1991).
[16] P. Kaduwalla, D. J. Friedman, and C. S. Fadley, J. Electron. Spectrosc. **51**, 689 (1990).
[17] D. Venus and B. Heinrich, Phys. Rev. B **53**, R1733 (1996).
[18] J. J. Rehr and R. C. Albers, Phys. Rev. B **41**, 8139 (1990).
[19] P. J. Schurer, Z. Celinski, and B. Heinrich, Phys. Rev. B **51**, 2506 (1995).
[20] D. D. Chamblis, R. J. Wilson, and S. Chiang, J. Vac. Sci. Technol. A **10**, 1993 (1992).
[21] *Practical Surface Analysis*, 2nd ed., edited by D. Briggs and M. P. Seah (Wiley, New York), p. 209.
[22] *Handbook of Auger Electron Spectroscopy*, edited by L. E. Davis *et al.* (Physical Electronics, Eden, Prairie, MN, 1978).
[23] J. F. Cochran, J. Magn. Magn. Mater. **147**, 101 (1995).
[24] D. Stoeffler and F. Gautier, Phys. Rev. B **44**, 10 389 (1991).
[25] R. M. Osgood, B. M. Clemens, and R. L. White, *Symposium on Magnetic Ultrathin Films, Multilayers, and Surfaces*, Mater. Res. Soc. Symp. Proc. **384**, 491 (1995)].
[26] J. F. Cochran, K. Totland, B. Heinrich, D. Venus, and S. Govorkov, *Symposium on Magnetic Ultrathin Films, Multilayers, and Surfaces*, Mater. Res. Soc. Symp. Proc. **384**, 131 (1995)].

Suppression of biquadratic coupling at the Cr Néel temperature in Fe/Cr(001) superlattices (invited) (abstract)

Eric E. Fullerton, S. Adenwalla, G. Felcher, C. H. Sowers, and S. D. Bader
Materials Science Division, Argonne National Laboratory, Argonne, Illinois 60439

J. L. Robertson
Solid State Division, Oak Ridge National Laboratory, Oak Ridge, Tennesee 37831-6393

A. Berger
Department of Physics, University of California at Irvine, Irvine, California 92717

We present the effects of antiferromagnetic (AF) order of the Cr spacers in Fe/Cr(001) superlattices on the interlayer coupling of the Fe layers. AF order of the Cr spacers is suppressed for layer thicknesses less than 42 Å. For >42 Å of Cr, the Néel temperature (T_N) increases rapidly and asymptotically approaches the bulk value for thick Cr spacers as characterized by a transition-temperature shift exponent $\lambda = 1.4 \pm 0.3$. Neutron diffraction confirms both the AF order of the Cr layers in superlattices with 62, 100, and 200 Å thick Cr layers, and the existence of the incommensurate, transverse spin-density-wave magnetic structure whose nesting wave vector is equal to that of bulk Cr. The AF ordering of the Cr results in anomalies in a variety of magnetic properties, including the interlayer coupling, remanent magnetization, coercivity, and magnetoresistance. Most strikingly, the 90° or "biquadratic" coupling of the Fe layers observed for $T > T_N$ is suppressed below T_N as confirmed by polarized neutron reflectivity. This behavior can be understood in terms of the combination of finite-size and spin frustration effects at rough Fe/Cr interfaces. © *1996 American Institute of Physics.* [S0021-8979(96)58608-9]

Work at ANL supported by the U.S. Department of Energy, Basic Energy Sciences-Materials Sciences, under Contract No. W-31-109-ENG-38. Work at ORNL supported by the U.S. Department of Energy, the Division of Materials Sciences, under Contract No. DE-AC05-84OR21400.

 0021-8979/96/79(8)/4524/1/$10.00 © 1996 American Institute of Physics

Interlayer thickness Dependence of the strong 90° coupling in epitaxial CoFe/Mn/CoFe trilayers

J. J. Krebs and G. A. Prinz
Naval Research Laboratory, Washington, DC 20375

M. E. Filipkowski
Department of Physics, University of Arkansas, Fayetteville, Arkansas 72701

C. J. Gutierrez
Department of Physics, Southwest Texas State University, San Marcos, Texas 78666

Trilayers of CoFe/Mn/CoFe(001) have been prepared by molecular beam epitaxy and their magnetic properties measured by magnetometry and ferromagnetic resonance. Very strong near-90° coupling between the CoFe layers, with no evidence for 180° coupling, was found in all but the thickest Mn-layer samples. The coupling energy has the form suggested recently for the case when the interlayer itself is antiferromagnetic. An analysis of the ferromagnetic resonance data indicates that the magnitude of the coupling oscillates with the Mn thickness. © *1996 American Institute of Physics.* [S0021-8979(96)48508-5]

In this paper, we present experimental results on single crystal epitaxial sandwich samples of CoFe/Mn/CoFe. These samples exhibit the largest near-90° type magnetic layer coupling ever observed and are without any detectable bilinear coupling.[1] The actual form of the coupling is consistent with a recent theoretical model based upon the intervening layer being antiferromagnetic.[2] In this work, using in-plane ferromagnetic resonance (FMR) data on the acoustic mode of the coupled trilayer, we show that the coupling constant has an oscillatory dependence on the Mn thickness t(Mn).

The trilayer samples were prepared by molecular beam epitaxy on GaAs substrates. The $Co_{75}Fe_{25}$ (001) alloy layers are all about 100 Å thick and were grown using methods described earlier.[3] They are bcc and exhibit reflection high energy electron diffraction (RHEED) patterns indicating excellent crystalline quality. The Mn interlayer thicknesses range from 6 to 30 Å as determined by x-ray fluorescence. They are single crystal as shown by RHEED, while extended x-ray-absorption fine structure (EXAFS) measurements show a tetragonally distorted bct structure.[4] Vibrating sample magnetometer (VSM) and superconducting quantum interference device (SQUID) magnetometry, as well as 35 GHz FMR angular dependence, were carried out in plane near 300 K on all samples to measure their magnetic properties. All trilayers with t(Mn)<29 Å exhibit evidence of coupling between the ferromagnetic (FM) layers.

The low-field VSM magnetization data for a strongly coupled sample are shown in Fig. 1. Note that the data seem to imply easy ⟨100⟩ and hard ⟨110⟩ behavior in the (001) plane, exactly the reverse of the behavior of isolated CoFe films with the above composition.[3] However, if the Mn thickness is increased to 30 Å, the usual isolated film behavior is observed in both VSM and FMR. Thus, in this no-coupling limit, the two CoFe layers each have anisotropy parameters equal to those of an isolated film.

The above results can be understood easily if the magnetizations $\mathbf{M}_1$ and $\mathbf{M}_2$ of the CoFe layers of the coupled samples lie nearly perpendicular to one another in zero field, and along the expected in-plane ⟨110⟩ easy directions, so that the net magnetization $\mathbf{M}=\mathbf{M}_1+\mathbf{M}_2$ is along ⟨100⟩ (see inset in Fig. 1). For strong nearly 90° coupling, as found here, $\mathbf{M}_1$ and $\mathbf{M}_2$ initially rotate as a rigid unit in an attempt to align $\mathbf{M}$ with $\mathbf{H}$ when a field $\mathbf{H}$ is applied along ⟨110⟩, and they come together very slowly for $\mathbf{H}$ applied parallel to $\mathbf{M}$ along ⟨100⟩. This type of behavior will be found as long as the coupling is large compared to both the in-plane anisotropy and $-\mathbf{M}\cdot\mathbf{H}$ energy density terms, as explicit calculations show. The SQUID magnetization data for $\mathbf{H}\|\langle 110\rangle$ are shown for the same sample over a much more extended range in Fig. 2. Note that after the magnetization break near 1 kOe (when the above rotation is complete), M continues to increase and approaches saturation slowly above 20 kOe.

In order to determine the magnitude and form of the coupling, one must make a quantitative fit to the above data (and the corresponding $\mathbf{H}\|\langle 100\rangle$ data) by writing down the free energy per unit area,

$$F=F_c+F_a-\mathbf{H}\cdot(\mathbf{M}_1+\mathbf{M}_2)t(\mathrm{CoFe}), \tag{1}$$

where F_c is the coupling energy/area, F_a is the correspond-

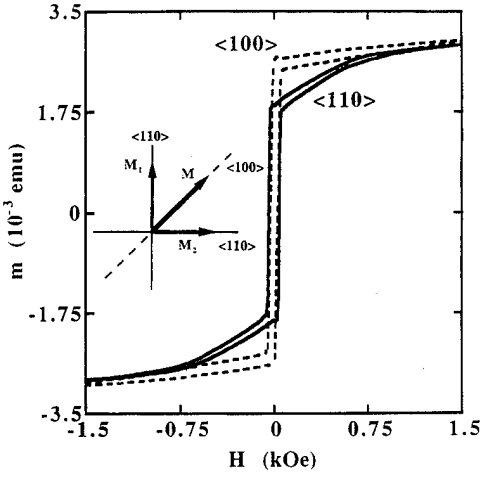


FIG. 1. Magnetic moment vs magnetic field data for a CoFe/Mn/CoFe trilayer sample with t(Mn)=11.2 Å. The in-plane magnetic field is along the directions indicated. Inset: Moment directions in zero field.

 0021-8979/96/79(8)/4525/3/$10.00 © 1996 American Institute of Physics

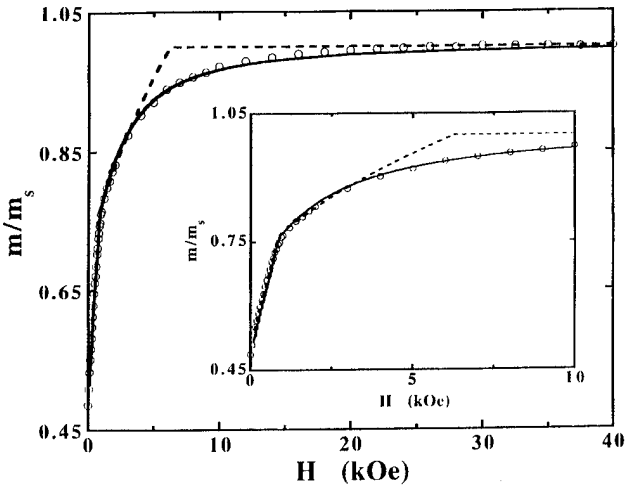


FIG. 2. Field dependence of the magnetization of the sample of Fig. 1 over an extended field range with $\mathbf{H}\|\langle 110\rangle$. Inset: Details of the low field region. The data are indicated by the open circles and the fits shown by the dashed and solid curves are discussed in the text.

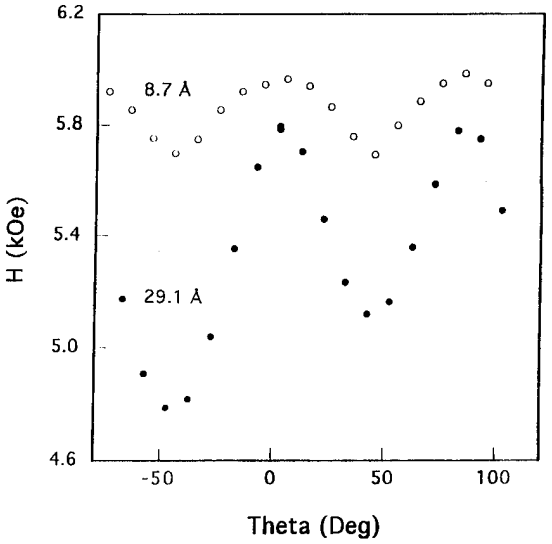


FIG. 3. Dependence of the resonance field of the acoustic (in-phase) FMR mode on the in-plane field angle for two samples with t(Mn) equal to 8.7 and 29.1 Å.

ing anisotropy term, and t(CoFe) is the thickness of a FeCo layer. Based on our previous FMR measurements on isolated CoFe films, we expect F_a to contain cubic and in-plane uniaxial anisotropies with K_1/M and $|K_u/M|$ about -0.25 and 0.05 kOe, respectively.[3] Further details can be found in Ref. 1.

The usual coupling which has been found experimentally in the many types of magnetic trilayer and superlattice samples studied to date has the form

$$F_c = -2A_{12}\hat{\mathbf{M}}_1\cdot\hat{\mathbf{M}}_2 - 2B_{12}(\hat{\mathbf{M}}_1\cdot\hat{\mathbf{M}}_2)^2, \tag{2}$$

where A_{12} and B_{12} are the so-called bilinear and biquadratic coupling contants, respectively, and $\hat{\mathbf{M}}_\mathbf{i}$ is a unit vector in the direction of $\mathbf{M}_\mathbf{i}$. The values of A_{12} and B_{12} observed in other systems generally oscillate and decrease in magnitude as the interlayer thickness increases.[5] If $|B_{12}| \gg |A_{12}|$ and $B_{12}<0$, the configuration $\mathbf{M}_1 \perp \mathbf{M}_2$ is favored. Both Fe/Cr/Fe and Fe/Al/Fe trilayers have this 90° configuration for some interlayer thicknesses[6–9] but this is not the usual behavior for coupled magnetic films.

Slonczewski[2] proposed a new form of coupling in which strong deviations from bilinear coupling are attributed to quasiantiferromagnetic exchange coupling within the interlayer itself. Due to competition between areas of differing interlayer thickness which favor either alignment or antialignment of the FM layers, the mean coupling has the following anticipated form:

$$F_c = C_+(\phi_1-\phi_2)^2 + C_-(\phi_1-\phi_2-\pi)^2, \tag{3}$$

where C_+ and C_- are the FM and AFM coupling constants and ϕ_i is the in-plane orientation angle of $\mathbf{M}_\mathbf{i}$. For $C_+ \approx C_-$, it is easy to show from Eq. (3) that the favored configuration[2] has $\mathbf{M}_1$ and $\mathbf{M}_2$ nearly 90° apart.

The dashed and solid lines in Fig. 2 are least-squares fits to the data based on free-energy expressions using the coupling forms of Eq. (2) (dashed) or Eq. (3) (solid). At each field, F is minimized, yielding the orientations of $\mathbf{M}_1$ and $\mathbf{M}_2$ as well as the moment along the field. Note that the Eq. (2) best fit, for which $2A_{12}=0$ and $2B_{12}=-3.0$ ergs/cm^2, is rather poor above the break in the curve and shows an abrupt rather than a slow approach to saturation. Previously, the largest value of $2B_{12}$ found is -0.3 ergs/cm^2 for Fe/Al/Fe.[9]

Conversely, Eq. (3) type coupling gives a much better fit over the entire range of fields with the following parameters: $C_+=0.95$ ergs/cm^2 and $C_-=1.07$ ergs/cm^2, with $K_1/M = -0.34$ kOe and $K_u/M=0.03$ kOe. Note that $C_+ \approx C_-$, as expected for the zero field 90° orientation found. The fit for the $\mathbf{H}\|\langle 100\rangle$ data using the same parameters (not shown) is similarly improved by using the Slonczewski coupling model of Eq. (3).

The above data thus offer strong evidence that Eq. (3) is the proper coupling for CoFe/Mn/CoFe and, furthermore, imply that the Mn interlayer is antiferromagnetically ordered, at least for small t(Mn). Recent soft x–m-ray magnetic circular dichroism and polarized neutron diffraction measurements on multilayers of CoFe/Mn, with t(Mn) chosen for very strong coupling, support the existence of Mn moments[11] as well as the near-90° orientation of adjacent CoFe layer moments.[10]

We now consider the FMR behavior of the trilayer samples and show how it can be used to obtain the t(Mn) dependence of the coupling constant C_+. In the following, only the in-phase or acoustic FMR mode of the coupled layers is considered and, based on the preceding discussion, the coupling is assumed to have the Eq. (3) form. The free-energy expression of Eq. (1) must be expanded by including the demagnetizing term $-2\pi(M_{1z}^2 + M_{2z}^2)t$(CoFe) and an extra coupling term $C_z(\theta_1-\theta_2)^2$ to deal properly with the out-of-plane motion of the moments. Once this is done, one can use the coupled mode technique discussed earlier for Fe/Cr/Fe[12] to calculate the angular dependence of the acoustic FMR mode in terms of the coupling and anisotropy parameters.

The experimental angular dependences of the resonance field H_r are shown in Fig. 3 for two trilayers as the magnetic

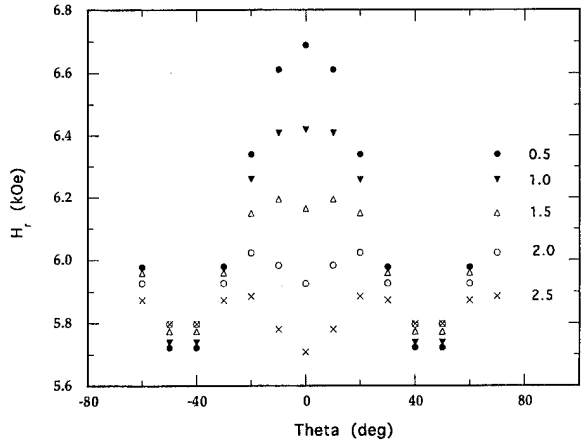


FIG. 4. Calculated angular dependence of the acoustic mode FMR field for the $2C_+$ values indicated (in ergs/cm^2). This calculation assumes $C_- = C_+ = 1.5C_z$ as found in Ref. 1.

field is rotated in the plane of the sample. As mentioned earlier, for t(Mn)$\geqslant$29 Å the FMR mode behaves essentially like that of an isolated CoFe film. For samples which show strong coupling, such as the 8.7 Å Mn sample, the apparent fourfold anisotropy is greatly reduced in amplitude and it can even be reversed in sign for yet stronger coupling. Since all the CoFe films have about the same thickness, it seems very unlikely that the true anisotropy behaves in this way. Using the above mode calculation technique, the expected angular dependence was calculated for a number of fixed values of C_+ with all other parameters including K_1 fixed. The results are given in Fig. 4 and clearly show a reduced angular variation as the coupling is increased. The physical reason for this is that, for strong coupling, $\mathbf{M}_1$ and $\mathbf{M}_2$ are not aligned along the resonance field $\mathbf{H}$ but are symmetrically displaced about it. As a result, the local curvatures of the free-energy surface seen by $\mathbf{M}_1$ and $\mathbf{M}_2$ as they precess are reduced in magnitude from the uncoupled case.

By comparing the observed variation in fourfold anisotropy with t(Mn) with that calculated for different coupling values C_+ in Fig. 4, one can deduce the dependence of C_+ on Mn thickness. The results of this comparison are shown in Fig. 5 and indicate that the coupling amplitude oscillates with an ill-defined period of about 7 or 8 Å as t(Mn) increases. It will be interesting to see if future theoretical coupling models can reproduce this behavior.

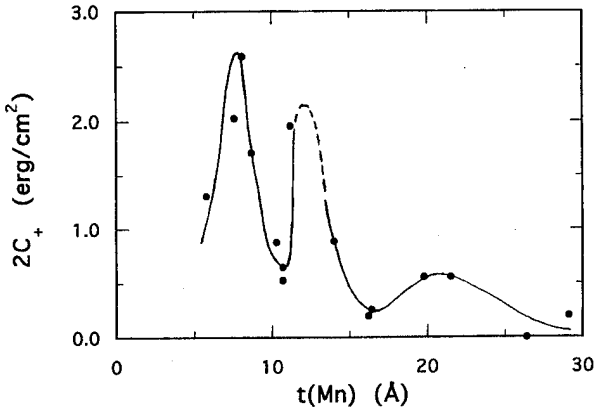


FIG. 5. Deduced dependence of the coupling coefficient $2C_+$ on the Mn interlayer thickness t(Mn).

We believe that this system, which employs metastable bct Mn to couple the CoFe ferromagnetic layers, represents a new departure for studies of coupled layers, and the strong near-90° coupling at room temperature may prove useful for technological applications.

This work was supported by the Office of Naval Research. We wish to thank J. C. Slonczewski, Y. U. Idzerda, and J. A. Borchers for providing us with relevant research results prior to publication.

[1] M. E. Filipkowski, J. J. Krebs, G. A. Prinz, and C. J. Gutierrez, Phys. Rev. Lett. **75**, 1847 (1995).
[2] J. C. Slonczewski, J. Magn. Magn. Mater. **150**, 13 (1995); J. Appl. Phys. **75**, 6474 (1994) (summary abstract).
[3] C. J. Gutierrez, J. J. Krebs, and G. A. Prinz, Appl. Phys. Lett. **61**, 2476 (1992). Note that the K_1 values listed need to be multiplied by a factor of 10^5.
[4] Y. U. Idzerda, private communication.
[5] B. Heinrich and J. F. Cochran, Adv. Phys. **42**, 523 (1992); J. C. Slonczewski, Phys. Rev. Lett. **67**, 3172 (1991).
[6] M. Ruhrig, R. Schafer, A. Hubert, R. Mosler, J. A. Wolf, S. Demokritov, and P. Grünberg, Phys. Status Solidi A **125**, 635 (1991).
[7] J. Unguris, R. J. Celotta, and D. T. Pierce, Phys. Rev. Lett. **67**, 140 (1991).
[8] A. Fuss, S. Demokritov, P. Grünberg, and W. Zinn, J. Magn. Magn. Mater. **103**, L221 (1992).
[9] C. J. Gutierrez, J. J. Krebs, M. E. Filipkowski, and G. A. Prinz, J. Magn. Magn. Mater. **116**, L305 (1992).
[10] V. Chakarian, Y. U. Idzerda, H. J. Lin, C. J. Gutierrez, G. A. Prinz, G. Meigs, and C. T. Chen, Phys. Rev. B (to be published).
[11] J. A. Borchers, private communication.
[12] J. J. Krebs, P. Lubitz, A. Chaiken, and G. A. Prinz, J. Appl. Phys. **67**, 5920 (1990); Phys. Rev. Lett. **63**, 1643 (1989).

Dependence of the interlayer exchange coupling on the constitution of the magnetic layers

K. Ounadjela
IPCMS, CNRS, UMR46, 23, rue du Loess, F-67037 Strasbourg, France

Li Zhou, R. Stamps, and P. Wigen
Department of Physics, Ohio State University, Columbus, Ohio 43210

M. Hehn
IPCMS, CNRS, UMR46, 23 rue du Loess, F-67037 Strasbourg, France

J. Gregg
Clarendon Laboratory, University of Oxford, Parks Road, Oxford OX1 3PU, England

We describe the consequences on the interlayer exchange coupling by the addition of a small amount of Ag impurities within the Co layers of high crystalline quality Co/Cu/Co(Ag) and Cu/Ru/Co(Ag) trilayers, while maintaining the integrity of the spacer layers. We discuss the consequent changes in the amplitude, period, and phase of the coupling in terms of the modification of interfacial spin-dependent potentials. © *1996 American Institute of Physics.*
[S0021-8979(96)48608-0]

Since the first observations of exchange coupling in magnetic multilayers,[1,2] much effort has been expended in attempting to elucidate the microscopic details of the coupling mechanism. Various models with varying degrees of complementarity have been advanced to explain the interlayer interaction[3–6] and its oscillation when the thickness of any of the films is changed. The exchange coupling can be thought of either as a form of RKKY interaction, a consequence of size quantization for electrons confined within the layers, or in terms of spin-dependent transmission and reflection across the ferromagnetic/nonmagnetic metal interface. In turn, these have suggested experimental refinements designed to discriminate between the predictions of the various competing theoretical treatments.

Along this idea, we have studied the effect on the interlayer exchange coupling with the variation of the spin-dependent potentials at the interfaces while causing *minimal* perturbation of the interlayer band structure. To this end, we have doped the *magnetic* layers with varying percentages of nonmagnetic impurities while leaving the constitution of the nonmagnetic spacer layer unaltered. This doping causes various changes which will be discussed in detail in this paper.

We chose to investigate two experimental trilayer systems. In each the magnetic metal chosen was Co and the impurity metal with which it was doped was Ag. The spacer materials were, respectively, Cu and Ru. This selection was prompted by the contrast in electronic "*d*" band structure between these two metals. In Cu, the *d* band is completely below the Fermi level, while in Ru the Fermi level lies within the *d* band and the *d* electrons may be expected to play a significant role in mediating the magnetic coupling.

The samples were prepared by molecular-beam epitaxy on a smooth and clean single crystalline hcp (0001) 100-Å-thick Ru buffer layer deposited on a mica substrate at a pressure less than 2×10^{-10} mbar. First the pure Co film is deposited, then the interlayer (Ru or Cu) followed by the Ag-doped Co. The film growth is monitored by reflection high energy electron diffraction (RHEED). As Co and Ag are immiscible metals, the substrate temperature is held at 240 K to discourage clustering of the Ag impurities within the impure Co layer and hence maximize charge transfer within the metastable alloy. Cross-sectional transmission electron microscopy indicates that phase separation has been very effectively suppressed since the size of the Ag aggregates present is less than the resolution of the instrument, which is 15 Å diameter or less.

Overall, the RHEED patterns obtained during the sample growth (Fig. 1) reveal well-defined structures which suggest good crystalline quality throughout the deposition. The quality of the Ru buffer layer in particular is evident from the

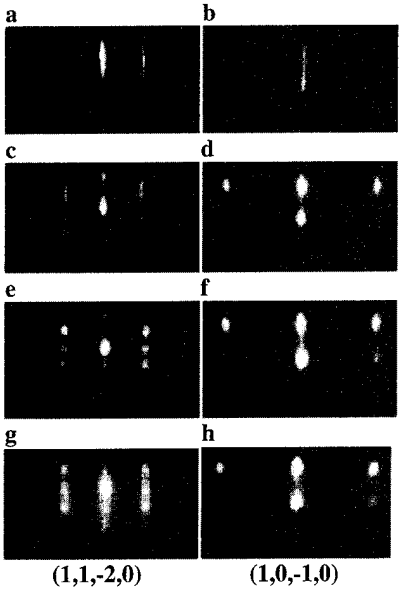


FIG. 1. Pairs of RHEED patterns observed during growth along two azimuths $(11\bar{2}0)$ and $(10\bar{1}0)$ for the Ru buffer layer and subsequent growth: (a), (b) after deposition of 100-Å-thick Ru buffer layer; (c),(d) after deposition of the pure 32-Å-thick Co layer; (e),(f) after deposition of 30-Å-thick Ru interlayer; (g),(h) for deposition of the impure $Co_{92}Ag_8$ layer with the same amount of Co as the previous Co layer (32 Å).

 0021-8979/96/79(8)/4528/3/$10.00 © 1996 American Institute of Physics

narrowness of the streaks and the presence of a 2×2 reconstruction [Figs. 1(a) and 1(b)]. The pure Co [Figs. 1(c) and 1(d)] grows epitaxially on the Ru buffer with the hexagonal basal plane parallel to the surface as may be seen from the patterns for the two azimuthal directions. Using three-dimensional (3D) RHEED diffraction analysis on the pure Co layers, it is observed that there is a high content of fcc (111) character in the growth [Figs. 1(c) and 1(d)].

For the Co/Cu/Co trilayers, the RHEED patterns observed along the $(11\bar{2}0)$ and $(10\bar{1}0)$ directions at the end of the Cu layer correspond to epitaxial pseudomorphic growth on top of the pure Co layer. As the Cu growth proceeds, the streaks become more intense and thinner with marked decrease of spot intensity. This indicates that the Cu tends to adopt a two-dimensional (2D) growth mode which is almost certainly favored by the small lattice mismatch between Co and Cu. Moreover, the RHEED information from the impure Co layer grown on top of the Cu retains the same features.

The RHEED patterns for the Ru spacer layer in the Co/Ru/Co systems are shown in Figs. 1(e) and 1(f). The deliberately enhanced 3D nature of the diffraction allows us to confirm that the structure is predominantly hcp. However, the most surprising feature of the RHEED data is seen in Figs. 1(g) and 1(h) where it is apparent that the *impure* Co grown on the Ru layer follows the hcp morphology of the latter. This is in contrast to the behavior of the pure Co growth, which, as discussed by Zhou *et al.*,[7] possesses a high concentration of stacking faults and looks like a mixture of hcp and fcc.

As already discussed, the RHEED and x-ray data show that, at least for the Co/Ru/CoAg systems, the epitaxy of the Co is maintained in the presence of the Ag impurities, and that the overall structural quality has improved with reduced stacking fault density and better-defined growth morphology. This in turn suggests that the Co band structure may not be seriously modified, particularly at these relatively low impurity concentrations. Moreover, since the Ag clusters are very small, a high degree of charge transfer may be expected with consequent adjustment in the doped Co Fermi energy.

The ferromagnetic resonance (FMR) measurements of the Co/Ru/Co, Co/Ru/$Co_{97}Ag_3$, and Co/Ru/$Co_{92}Ag_8$ systems show two resonance modes, a strong acoustic mode and a weak optic mode for most of the samples when the external field was rotated from the parallel to the perpendicular direction to the film plane. In the symmetric Co/Ru/Co structure, the magnetization vectors of the two Co layers are antiparallel coupled when the Ru thickness t_{Ru} is in the range of $t_{Ru}<13$ Å and 18 Å$<t_{Ru}<25$ Å, but parallel coupled for the 16-Å-Ru thick sample. While a similar coupling behavior is observed for the Co/Ru/$Co_{92}Ag_8$ structure except at low Ru thicknesses, the coupling behavior differs significantly in the Co/Ru/$Co_{97}Ag_3$, showing an antiparallel coupling for the 16-Å-Ru thick sample and parallel coupling for 18 Å$<t_{Ru}<25$ Å. For the 12-Å-thick Ru sample, the optic mode cannot be observed suggesting that the coupling is very small. In the analysis of the FMR data, only the effective anisotropy field, and the bilinear exchange field $H_{ex} = 2A_{12}/t_{Co}M_s$ ($A_{12}>0$ for antiparallel coupling of the magnetic layers) are included.[8] The analysis of the FMR data concerning the Co/Cu systems

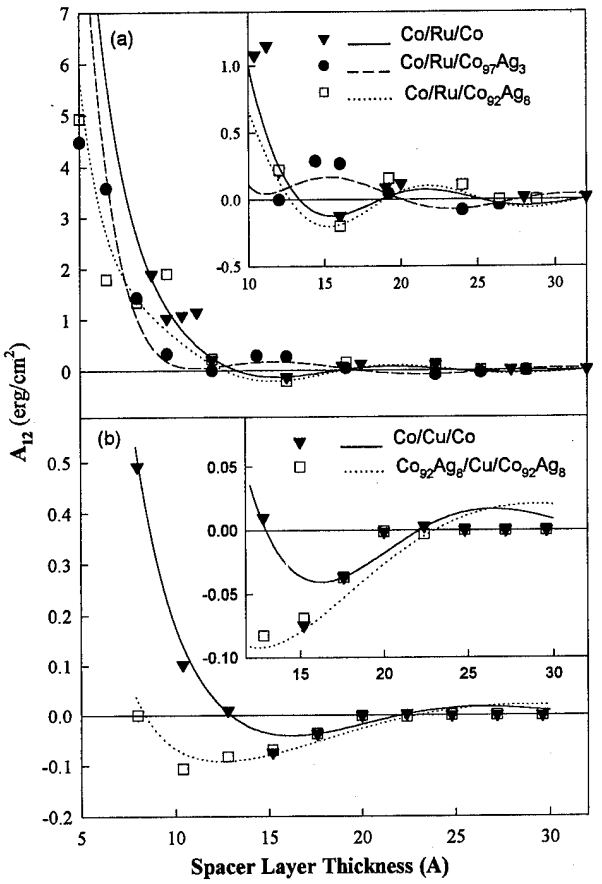


FIG. 2. Variation of the exchange coupling constant as a function of the spacer-layer thickness (a) for the three series of samples with Ru spacer layer (b) for the two series of samples with Cu spacer layer. The best fit for the data using Eq. (1) is shown.

has already been described by Zhou *et al.*[9] The results are shown in Figs. 2(a) and 2(b). Concentrating initially on the data for the trilayers with pure Co films, two features are immediately apparent.

First, the difference in coupling strengths for the Cu and Ru spacer-layer systems is striking. The coupling in the Ru systems is about an order of magnitude stronger. This observation was anticipated in our initial choice of two complementary spacer-layer materials, it being expected that the broad partially filled *d* bands of the Ru would afford more significant interlayer interaction.

Second, in the coupling data of the Co/Ru/Co trilayers there is clearly a strong antiferromagnetic bias at low spacer-layer thicknesses. As shown in Fig. 2(a), the best fit for the exchange coupling is obtained using an additive exponential decay to the sinusoidal term of the following form with the fit parameters given in Table I:

$$A_{12}=a\times\exp(-t_{Ru}/d)+b\times\sin(q\times t_{Ru}+\varphi)/t_{Ru}^2. \quad (1)$$

This is exactly what has been predicted by Shi *et al.*[3] for Ru metal spacers. This prediction is based on an analysis of the effect of superexchange between the magnetic layers which concludes that the oppositely signed biases of RKKY and superexchange coupling mechanisms no longer cancel in

TABLE I. The fitting parameters for the exchange coupling obtained using Eq. (1) for both Ru and Cu spacer trilayers. The calculated curves are shown in Fig. 2.

Samples	a (erg/cm^2)	d (Å)	b (10^{-16} erg)	q (1/Å)	ϕ (π)
Co/Ru/Co	240	1.7	35.8	0.49	1.07
Co/Ru/$CoAg_3$	240	1.6	39.8	0.42	0.32
Co/Ru/$CoAg_8$	243	1.4	49.7	0.49	−0.95
Co/Cu/Co	28	1.8	12	0.31	−0.18
$CoAg_8$/Cu/$CoAg_8$	20	1.2	18	0.21	0.46

the presence of a large density of states just above the Fermi surface. This prediction in turn is highly significant in interpreting the observed change in coupling as impurity is introduced into one of the magnetic layers.

Turning now to the exchange coupling for the impure magnetic layers, we consider first the Ru spacer systems Co/Ru/Co(Ag). For large thicknesses, the coupling may be fitted satisfactorily using the same procedure as for the symmetric trilayer systems and it is apparent that the change in spin-dependent potentials produces a shift in the phase while the period and amplitude are not significantly altered. For small spacer thicknesses, the AF bias is weaker than for the pure system, perhaps owing to a relative shift of the Fermi level and the singularity in Ru density of states.

The behavior of the impure Co/Cu/Co trilayers is rather different. As seen in Fig. 2(b), 8% Ag impurity is enough to change the sign of the coupling for spacer thicknesses between 10 and 12 Å. In contrast with the previous case, the exchange coupling can be fitted very satisfactorily using either an additive [Fig. 2(b)] or a functional exponential decay to the sinusoidal term. Using both functions, these data could be interpreted as a significant increase in the period of the exchange coupling together with a reduction in amplitude. In turn this may be attributed to alteration of the interfacial scattering potentials perhaps owing partially to moderation of the "*s-d*" mixing.

This work was supported by the European Capital and Mobility, the Alliance Programme, and the North Atlantic Treaty Organization.

[1] P. Grunberg, R. Schreiber, Y. Pang, M. B. Brodsky, and H. Sowers, Phys. Rev. Lett. **57**, 2442 (1986).
[2] S. S. P. Parkin, Phys. Rev. Lett. **67**, 3598 (1991).
[3] Z-P. Shi, P. M. Levy, and J. L. Fry, Phys. Rev. B **49**, 15159 (1994), and references therein.
[4] D. M. Edwards *et al.*, J. Phys.: Condens. Matter **3**, 4941 (1991).
[5] P. Bruno and C. Chappert, Phys. Rev. Lett. **67**, 1602 (1991); Phys. Rev. B **46**, 261 (1991).
[6] M. van Schilfgaarde and F. Herman, Phys. Rev. Lett. **71**, 1923 (1993).
[7] K. Ounadjela *et al.*, Phys. Rev. Lett. (submitted).
[8] Z. Zhang, L. Zhou, P. Wigen, and K. Ounadjela, Phys. Rev. B **50**, 6094 (1994).
[9] L. Zhou, Z. Zhang, P. Wigen, R. Stamps, K. Ounadjela, M. Hehn, and J. F. Gregg, IEEE Trans Magn. **31**, 3924 (1995).

Domain structure and anisotropy of exchange coupled Co/Cr/Fe multilayers (abstract)

Th. Kleinefeld and M. Figge
Universität Duisburg, FB10/Angewandte Physik, D-47048 Duisburg, Germany

K. Theis-Bröhl, R. Scheidt, and Th. Zeidler
Ruhr-Universität Bochum, D-44780 Bochum, Germany

Ch. Mathieu and B. Hillebrands
Universität Karlsruhe, D-76128 Karlsruhe, Germany

We have studied the magnetic properties of Co/Cr/Fe multilayers by means of magneto-optic methods. These multilayers are of special interest because they combine different anisotropies and exchange coupling through the nonmagnetic Cr-spacer layer which was found to oscillate from ferromagnetic to antiferromagnetic coupling. The samples were grown by MBE methods on MgO(100) substrates at temperatures of about 300 °C. The fourfold crystalline symmetry is also obtained in the magnetic easy axis structure of Fe and Co. From the results of magneto-optic Kerr hysteresis loops we were able to distinguish between crystalline anisotropy and exchange coupling contributions. Additional monitoring of the domain structure by applying longitudinal Kerr microscopy was necessary to identify the regime were magnetization reversal occurs via domain wall motion or coherent rotation of the magnetization of the entire layer, respectively. From these results we were able to perform numerical simulations of the micromagnetic properties of trilayer samples. We discuss the results in terms of bilinear and biquadratic coupling. © *1996 American Institute of Physics.* [S0021-8979(96)58708-8]

Magnetic coupling in Co/face-centered-cubic Fe/Co sandwiches

R. K. Kawakami, Ernesto J. Escorcia-Aparicio, and Z. Q. Qiu
Department of Physics, University of California at Berkeley, Berkeley, California 94720, and Materials Science Division, Lawrence Berkeley National Laboratory, Berkeley, California 94720

Ferromagnetic (FC) and antiferromagnetic coupling (AFC) of Co layers across a metastable fcc Fe spacer layer has been observed. Room-temperature-grown Fe on Co/Cu(100) was chosen as a spacer layer because it exhibits three distinct structural and magnetic phases depending on the thickness range: fct and ferromagnetic (region I), fcc and nonferromagnetic (region II), bcc and ferromagnetic (region III) (listed in order of increasing thickness). Co/Fe/Co sandwiches were grown on Cu(100) by molecular beam epitaxy with a base pressure of $\sim 2\times 10^{-10}$ Torr, and characterized by low-energy electron diffraction and reflection high-energy electron diffraction. The magnetic properties were studied *in situ* using surface magneto-optic Kerr effect. Using a wedged Fe spacer layer, we investigated the magnetic coupling between Co films across many thicknesses of Fe. We found FC in region I, strong AFC at the boundary between regions I and II, and weak AFC in region II. We also studied the effect of just the Co overlayer on the metastable fcc Fe. We find that Co/Fe/Cu(100) differs qualitatively from Fe/Co/Cu(100). Finally, we find an oscillation in the AFC with a periodicity of ~ 12 Å by artificially increasing the thickness range of region II. © *1996 American Institute of Physics.* [S0021-8979(96)48708-8]

It is well known that Fe has bcc structure at low temperatures and fcc structure at high temperatures ($T > 910$ °C). The lattice matching between fcc Fe and fcc Cu led to the idea of stabilizing the metastable phase of fcc Fe at room temperature either as particles in a Cu matrix or as thin films on top of a Cu substrate. Both ferromagnetic and antiferromagnetic states have been found in this metastable phase of fcc Fe, which depends sensitively on the preparation conditions. In particular, the room temperature growth Fe films on Cu(100) were shown to exhibit three distinct phases.[1,2] For thickness less than 5 monolayers (ML), the films have a fct structure (a distorted fcc structure, see Ref. 3 for details) and are in the ferromagnetic state. Between 5 to 11 ML, the films have a fcc structure and are antiferromagnetic with a surface magnetic live layer. Above 11 ML, the films revert to the natural bcc state. These magnetic phases are believed to be correlated with the structural changes in the films. Recent structural analysis[4] indicates that within the above three different phases, there are different crystal reconstructions at both the surface and the sublayers of the films. These complicated structural phases made it very difficult to analyze the structural effect on the magnetic phases of the films.

In an attempt to separate the structural and the electronic effects of the substrate on the magnetic properties of the fcc Fe overlayer, we investigated the Fe films grown on fcc Co(100) substrate. Since fcc Co can be stabilized on Cu(100) with exactly the same in-plane lattice spacing, we expect a similar structure for Fe films on Co(100) as on Cu(100). On the other hand, Co is ferromagnetic and Cu is not. Therefore, any different magnetic behavior in the Fe/Co(100) system as compared to the Fe/Cu(100) system should be caused by the Co–Fe magnetic interaction. Detailed results on the Fe/Co(100) system are reported in another paper[5] of this proceedings. Basically, we got three distinct phases for different thicknesses of the Fe film. Different from the Fe/Cu(100) system which shows a perpendicular magnetization and a surface magnetic live layer between 5–11 ML, the Fe/Co(100) system shows an in-plane magnetization and an interface magnetic live layer between 5–11 ML. Figure 1 summarizes our results: region I ($d_{Fe}<5$ ML) is fct ferromagnetic, region II (5 ML$<d_{Fe}<$11 ML) is fcc nonferromagnetic with an interfacial magnetic live layer, and region III ($d_{Fe}>11$ ML) is bcc ferromagnetic.

To further explore the magnetic nature of the fcc Fe films, we applied the fcc Fe as a spacer layer to investigate the magnetic coupling between two Co films. Antiferromagnetic coupling (AFC) between two ferromagnetic layers across a nonferromagnetic spacer layer was first found in an Fe/Cr/Fe sandwich.[6] Many other systems were also found to exhibit a similar behavior. The materials for the spacer layer include antiferromagnets (e.g., Cr and Mn),[7–9] nonmagnetic metals,[10] and other nonmetallic elements (e.g., Si and silicides).[11,12] The oscillations in the magnetic coupling are related to the spanning vector of the Fermi surface of the spacer layer. Since region II of the fcc Fe exhibits nonferro-

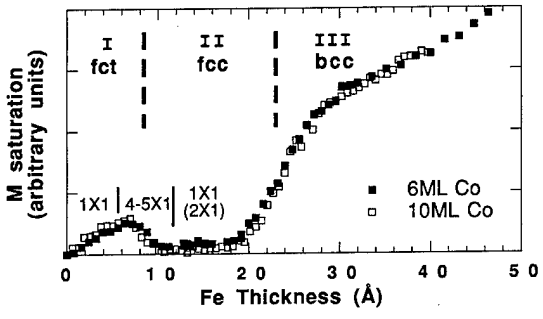


FIG. 1. M_{sat} from longitudinal surface magneto-optic Kerr effect vs Fe thickness for molecular beam epitaxy-grown Fe/Co(6 ML)/Cu(100) and Fe/Co(10 ML)/Cu(100), with the uniform Co signal subtracted out. Room-temperature growth and measurement shows three regions, all with in-plane magnetization: (I) fct and ferromagnetic, (II) fcc and nonferromagnetic with a magnetic live layer, (III) bcc and ferromagnetic. The reconstructions observed by low energy electron diffraction are also presented above. From Ref. 5.

 0021-8979/96/79(8)/4532/3/$10.00 © 1996 American Institute of Physics

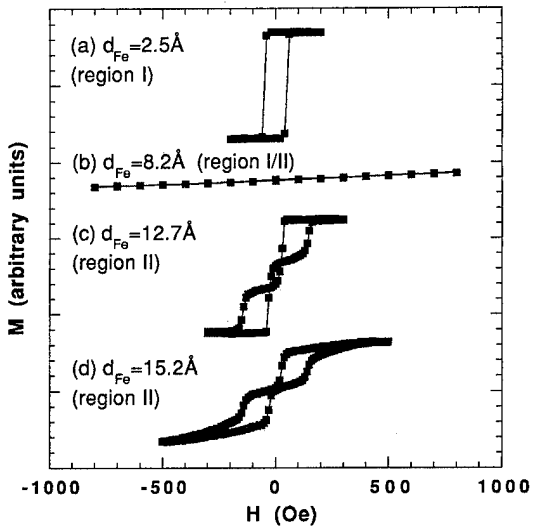


FIG. 2. Longitudinal SMOKE hysteresis loops for Co(15 ML)/Fe/Co(15 ML). Many Fe thicknesses (d_{Fe}) were studied by using a wedged Fe layer. Four representative loops are shown: (a) d_{Fe}=2.5 Å. Ferromagnetic coupling was found for d_{Fe} in region I (see Fig. 1), (b) d_{Fe}=8.2 Å. Strong AFC was found at the boundary between regions I and II. We were not able to saturate the magnetization with our electromagnets ($H<1.9$ kOe) (Note: H greater than 600 Oe caused our sample manipulator to move. We subtracted out the background signal due to this motion.) (c) d_{Fe}=12.7 Å. Weak AFC was observed for d_{Fe} in region II. (d) d_{Fe}=15.2 Å. The weak AFC is beginning to get "stretched out," signifying either the beginning of the fcc–bcc transition or a strong AFC oscillation. Loops (a) and (b) were easily reproducible, while (c) and (d) were not.

magnetic character, an investigation on the AFC across fcc Fe may help in understanding the magnetic phase of the fcc Fe in that thickness range.

A series of ultrathin film Co/Fe/Co and Co/Fe samples were grown by molecular beam epitaxy (MBE) on Cu(100) in an ultrahigh vacuum (UHV) chamber with a base pressure of $\sim 2\times 10^{-10}$ Torr. The deposition rates were 0.5–4.8 Å/min for Co, and 0.6–1.7 Å/min for Fe. Structural characterizations were performed with reflection high energy electron diffraction (RHEED) and low energy electron diffraction (LEED). Magnetic properties were studied using an *in situ* surface magneto-optic Kerr effect (SMOKE) setup. Two pairs of electromagnets provided longitudinal [along the (011) direction] and polar magnetic fields up to 1.9 kOe.

The single crystal Cu(100) substrate was mechanically polished down to 0.25 μm diamond paste and finished with vibratory polishing using 0.05 μm Al_2O_3 powder. The substrate was cleaned *in situ* with cycles of Ar^+ sputtering at 2–5 keV and annealing at 650 °C.

"Symmetric" Co/Fe/Co sandwiches with Co thicknesses of 13, 15, 20, and 40 ML were fabricated at room temperature. The Co layers were of uniform thickness and the Fe layer was a wedge (0–30 Å).

Figure 2 shows a representative longitudinal SMOKE hysteresis loops observed in a Co(15 ML)/Fe/Co(15 ML) sample at room temperature. Figure 2(a) shows FC of the Co layers for Fe thicknesses (d_{Fe}) corresponding to region I of Fig. 1. Figure 2(b) shows strong AFC at the boundary between regions I and II. We call the AFC "strong" when we cannot saturate the magnetization with a 1.9 kOe magnetic

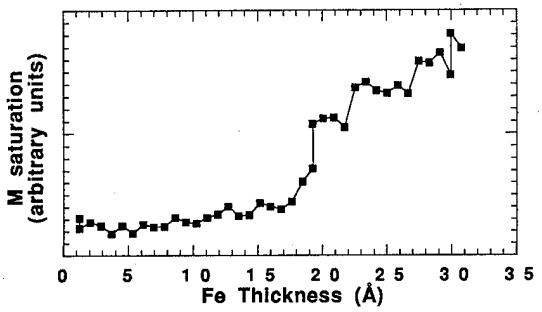


FIG. 3. M_{sat} from longitudinal SMOKE vs. Fe thickness for Co(15 ML)/Fe/Cu(100). Comparing with Fe/Co (Fig. 1) shows qualitative differences. For Fe/Co, M_{sat} increases linearly with the Fe thickness in region I. For corresponding Fe thicknesses in Co(15 ML)/Fe, M_{sat} is approximately constant.

field. Otherwise it will be called "weak." Figure 2(c) shows weak AFC for d_{Fe} in region II. It was found that the splitting of the loops changed very little as d_{Fe} varied from ~10 to ~15 Å. Figure 2(d) shows a "stretched out" AFC loop, for d_{Fe} in the thicker part of region II. This loop will be discussed later.

Loops 2(a) and 2(b) were easily reproducible, but loop 2(c) was not easily reproducible. Typically the loop was not well split. We hypothesized that structural instabilities of the fcc Fe might allow restructuring of the Fe as the Co overlayer is deposited. We based this on several observations.

First, we believed that a structural instability would not arise from the Co underlayer. The studies of fcc Fe/Co/Cu(100)[5] performed in our lab showed that the structural and magnetic properties of Fig. 1 were easily reproducible. In fact, for each of our sandwiches we performed quick SMOKE measurements before putting on the Co overlayer. We found that for all samples the qualitative features of Fig. 1 persisted–linear increase in region I, and a drop to a roughly constant signal in region II. In addition, the LEED patterns of the Fe/Co/Cu(100) systems were sharp. During the growth of the Co overlayer, however, we were never able to obtain RHEED oscillations. This is in contrast to the Co underlayer growth where we were able to get ~30 oscillations with very little amplitude drop. Also, after growth the LEED patterns became diffuse.

To further support our idea, we investigated the properties of Co on fcc Fe without the Co underlayer. This allowed us to remove any effect that the Co underlayer may have had, thus isolating the effect of the Co overlayer. We first made an Fe wedge on Cu(100) and then grew a uniform Co layer on top of it. Figure 3 shows the result of a longitudinal SMOKE measurement for 15 ML Co. The middle region is flat, like region II of Fe/Co/Cu(100) (Fig. 1). The thicker region has increasing signal, like the fcc–bcc transition in Fig. 1. However, the thinner region does not have a linearly increasing signal like region I of Fig. 1. This result is consistent with the idea that the Co overlayer somehow changes the structural properties of the underlying fcc Fe. However, more studies are needed to determine the effect of overlayers on fcc Fe.

Returning to the Co(15 ML)/Fe/Co(15 ML) sample, Fig. 4 shows the magnetization (Kerr signal) at $H=200$ Oe vs. Fe thickness, taken from SMOKE hysteresis loops. This pro-

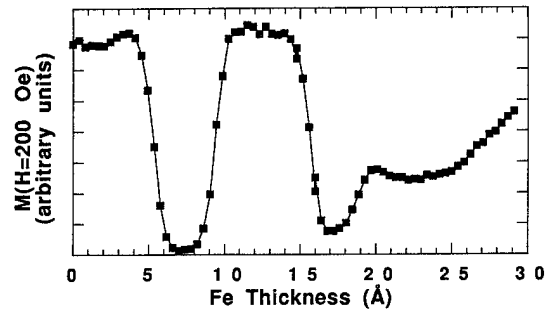


FIG. 4. Longitudinal SMOKE measurement of $M(H=200$ Oe) vs. Fe thickness for the Co(15 ML)/Fe/Co(15 ML) sample. 200 Oe is sufficient to saturate the magnetization for the weak AFC and the ferromagnetic coupling across fcc Fe. However, it does not saturate the magnetization for the strong AFC or in the fcc–bcc transition region. Hence dips in $M(H=200$ Oe) signify the onset of the strong AFC or the fcc–bcc transition. The first dip at ~7 Å is strong AFC. The second dip at ~17 Å is due to either strong AFC or the onset of the fcc–bcc transition.

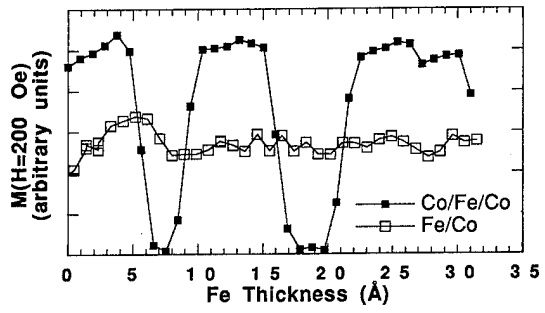


FIG. 5. Longitudinal SMOKE measurements of $M(H=200$ Oe) vs. Fe thickness for Fe/Co(6 ML) and Co(6 ML)/Fe/Co(6 ML), on a dirty Cu(100) substrate. The dirty substrate allows the fcc structure to persist to a higher Fe thickness, allowing a second strong AFC peak to fully develop. The Fe/Co measurement verifies that region II is longer than usual; it normally ends at d_{Fe}~20 Å. The Co/Fe/Co measurement shows a second dip at d_{Fe}~19 Å signifying a strong AFC peak.

vides an efficient way of representing our data: 200 Oe is sufficient to saturate the magnetization for the weak AFC in region II but not enough to saturate the magnetization for a strong AFC. Hence dips in $M(H=200$ Oe) signify a strong AFC peak. The first dip at d_{Fe}~7 Å is a strong AFC peak. The second dip is ambiguous because of the onset of the fcc–bcc transition.

Thus loop 2(d), which lies at the beginning of the second dip, poses an interesting question. Does the stretching out of the loop signify the beginning of the fcc–bcc transition, or does it signify the development of a strong AFC peak? Perhaps there would be another strong AFC peak if the fcc–bcc structural transition did not occur. Unfortunately, the fcc–bcc transition begins and the structure of the Fe changes drastically before a strong AFC peak can fully develop.

To examine this issue, we made a compromise. We know from Li *et al.*[13] and our own experience, that if the Cu(100) substrate is "dirty" (has a few percent of carbon and oxygen impurities), the fcc phase of Fe can persist to a higher thickness. Of course the fcc Fe on a dirty substrate will be different from the fcc Fe on a clean substrate, but we assume the difference is negligible with regard to the *existence* of a second strong AFC peak. We made a Co(6 ML)/Fe/Co(6 ML) sample on a dirty substrate which contains of a few percent of carbon and oxygen impurities. The signature of a dirty film in practice is that region II in Fig. 1 gets bigger and that the surface reconstruction is 2×2 instead of 2×1.[14] Figure 5 shows the Kerr signal before and after the Co overlayer was grown. The Fe/Co signal shows that the fcc region is indeed longer. To study the oscillations of the magnetic coupling in the Co/Fe/Co sandwich, we measured the magnetization (Kerr signal) at a field of 200 Oe, as before. Two dips were observed, each signifying a strong AFC peak. We conclude that we have found an oscillation in the AFC with a periodicity of ~12 Å. It is interesting to note that the first AFC occurs at the transition point between regions I and II. We do not know if this is a coincidence or if this is somewhat associated with the fct–fcc structural transition.

We have observed FC, strong AFC, and weak AFC in the Co/fcc Fe/Co sandwiches grown on Cu(100). We have shown that Co/Fe/Cu(100) is different from Fe/Co/Cu(100). This could be due to an instability in the structure of epitaxial fcc Fe. How this instability affects the coupling is not yet understood and requires further investigation. We have also observed an oscillation in the coupling. A strong AFC peak exists at d_{Fe} corresponding to the boundary between regions I and II of Fe/Co/Cu(100). By using a dirty sample to artificially lengthen the flat region, we also find strong AFC at d_{Fe} ~19 Å.

This work was supported in part by the DOE under Contract No. DE-AC03-76SF00098.

[1] J. Thomassen, F. May, B. Feldman, M. Wuttig, and H. Ibach, Phys. Rev. Lett. **69**, 3831 (1992).
[2] D. Li, M. Freitag, J. Pearson, Z. Q. Qiu, and S. D. Bader, Phys. Rev. Lett. **72**, 3112 (1994).
[3] H. Magnan, D. Chandesris, B. Villette, O. Heckman, and J. Lecante, Phys. Rec. Lett. **67**, 859 (1991).
[4] S.Müller *et al.*, Phys. Rev. Lett. **74**, 765 (1995).
[5] Ernesto J. Escorcia-Aparicio, R. K. Kawakami, and Z. Q. Qiu, these proceedings.
[6] P. Grünberg, R. Schreiber, Y. Pang, M. B. Brodsky, and H. Sowers, Phys. Rev. Lett. **57**, 2442 (1986).
[7] J. Unguris, R. J. Celotta, and D. T. Pierce, Phys. Rev. Lett. **67**, 140 (1991).
[8] S. T. Purcell *et al.*, Phys. Rev. Lett. **67**, 903 (1991).
[9] S. T. Purcell, M. T. Johnson, N. W. E. McGee, R. Coehoorn, and W. Hoving, Phys. Rev. B **45**, 13064 (1992).
[10] S. S. P. Parkin, Phys. Rev. Lett. **67**, 3598 (1991).
[11] S. Toscano, B. Briner, H. Hopster, and M. Landolt, J. Magn. Magn. Mater. **114**, L6 (1992).
[12] E. E. Fullerton, J. E. Mattson, S. R. Lee, C. H. Sowers, Y. Y. Huang, G. Felcher, S. D. Bader, and F. T. Parker, J. Magn. Magn. Mater. **117**, L301 (1992).
[13] D. Li, M. Freitag, J. Pearson, Z. Q. Qiu, and S. D. Bader, J. Appl. Phys. **76**, 6425 (1994).
[14] P. Xhonneux and E. Courtens, Phys. Rev. B **46**, 556 (1992).

Transport and magnetism correlations in thin-film ferromagnetic oxides

M. F. Hundley, J. J. Neumeier, R. H. Heffner, Q. X. Jia, X. D. Wu, and J. D. Thompson
Materials Science and Technology Division, Los Alamos National Laboratory, Los Alamos, New Mexico 87545

To determine the T_c dependence of the colossal magnetoresistance (CMR) exhibited by the ferromagnetic $La_{0.7}A_{0.3}MnO_{3+\delta}$ (A=Ba, Ca, Sr) system, we examine the magnetic-field and temperature-dependent resistivity and magnetization of a series of thin films that were grown via pulsed-laser deposition. The films had magnetic ordering temperatures (T_c) ranging from 150 to 350 K. All samples display a large negative MR that is largest near T_c, and samples with a low T_c display significantly larger MR values than do samples with large T_c's. The quantity $\rho(T_c)/\rho(4\text{ K})$, the amount by which the resistivity is reduced by full ferromagnetic order, varies as $\exp(E_a/T_c)$ with an activation energy $E_a=0.1$ eV. These results indicate that the magnitude of the CMR effect in a given specimen is controlled not by $\rho(T_c)$, but by T_c via the ratio $\rho(T_c)/\rho(4\text{ K})$. Phenomenological scaling relationships are also reported that link $\rho(H,T)$ to both H and $M(H,T)$. © *1996 American Institute of Physics.* [S0021-8979(96)48808-4]

The recent observations[1–3] of a colossal negative magnetoresistance (MR) near T_c in the ferromagnetic (FM) doped lanthanum manganites ($La_{1-x}A_xMnO_{3+\delta}$, A=Ba, Ca, Sr) has sparked renewed interest in this system. The divalent substitution for La^{3+} leads to a mixed $Mn^{3+/4+}$ valence, a ferromagnetic ground state driven by double-exchange,[4] a metal-insulator transition at $T_{MI}=T_c$, and the colossal magnetoresistance (CMR) effect. The unusual temperature- and magnetic (H)-field-dependent resistivity exhibited by these compounds reflects a novel interplay between magnetism and electronic transport that does not occur in conventional metals, ferromagnets, or semiconductors. Recent publications have focused on the magnitude of the MR effect,[3] the interplay between magnetic order and electronic transport,[5–7] and the effects of oxygen stoichiometry[8] on the transport and magnetic properties.

To determine the dependence of the CMR effect on T_c, we examine the temperature- and H-field dependent resistivity $\rho(H,T)$ of a series of $La_{0.7}A_{0.3}MnO_{3+\delta}$ thin-films (A=Ba, Ca, and Sr) with T_c's ranging from 150 to 350 K. Both the zero-field resistivity and the magnetoresistance are strongly dependent upon a given film's ordering temperature; low-T_c films exhibit a substantial negative MR, while films with T_c's above 300 K exhibit a more modest MR ratio. We also find that a direct correlation exists between $\rho(H,T)$ and $M(H,T)$ near and below T_c. In addition, the MR at T_c follows a simple phenomenological expression that contains a single scaling parameter which is a monotonic function of T_c. The form of this scaling expression as well as the expression that links $\rho(H,T)$ and $M(H,T)$ provide important clues as to the nature of the underlying mechanisms responsible for the CMR effect.

Transport and magnetism measurements were performed on a series of six $La_{0.7}A_{0.3}MnO_{3+\delta}$ thin films grown via pulsed-laser deposition (PLD). The highly oriented, 1000-Å-thick films were deposited on (100) $LaAlO_3$ substrates in a 200 mTorr oxygen atmosphere. The films were post-annealed in flowing oxygen at 950 °C for ten hours. Sample T_c was controlled both by varying the dopant element A,[9] and by varying the substrate temperature T_s used during the deposition process. Growth parameters for each film, along with their respective magnetic ordering temperatures (determined from magnetization Arrott plots), are presented in Table I. The Ca-doped films (films 1–4) have T_c's ranging from 150 to 290 K, while the Ba- and Sr-doped films (films 5 and 6) have T_c's that are above room temperature. Both the FM transition width and the low-temperature saturation magnetization are T_s-independent. Details of the underlying sample-to-sample differences (stoichiometry, microstructure, etc.) that are responsible for the variation in T_c in the Ca-doped samples will be considered in a future publication;[10] the variation is most likely due to an oxygen deficiency ($\delta<0$) that rises with increasing T_s.[8] Four-probe ρ measurements were made with dc currents ranging from 1 nA to 10 μA. The magnetoresistance is defined here as $\Delta\rho/\rho_0=[\rho(H)-\rho_0]/\rho_0$, with $\rho_0=\rho(H=0)$. Magnetization (M) measurements were performed with a Quantum Design SQUID magnetometer.

The $H=0$ resistivities of the films with $T_c<300$ K are depicted in Fig. 1(a). Sample 1 ($T_c=152$ K) exhibits a sharp

TABLE I. Stoichiometry, substrate temperature T_s, and magnetic ordering temperature T_c for the six $La_{1-x}A_xMnO_{3+\delta}$ thin-film specimens examined in this work. All films were post-annealed.

Sample number	A	x	T_s (°C)	T_c (K)
1	Ca	0.3	900	152
2	Ca	0.3	750	224
3	Ca	0.3	600	255
4	Ca	0.3	500	292
5	Ba	0.3	600	325
6	Sr	0.3	600	350

 0021-8979/96/79(8)/4535/3/$10.00 © 1996 American Institute of Physics

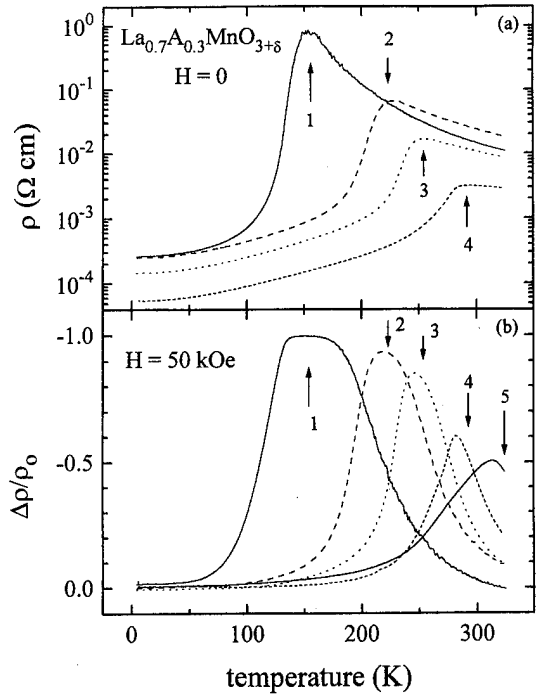


FIG. 1. (a) Resistivity vs temperature, and (b) 50 kOe magnetoresistance vs. temperature. The arrows indicate T_c for each sample while the integers indicate the sample number that corresponds to each data set.

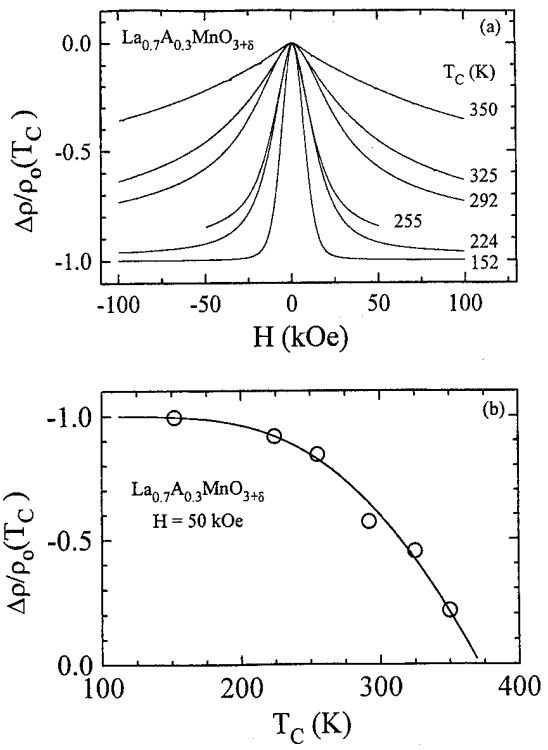


FIG. 2. (a) Magnetoresistance vs. applied magnetic field measured at T_c for six samples (T_c for each curve is indicated on the right). (b) 50 kOe magnetoresistance measured at T_c for samples 1–6 plotted against sample T_c; the solid line is a fit to the data (see text).

drop in ρ below T_c [$\rho(4\text{ K})/\rho(T_c)=5\times10^{-4}$] and activated behavior (activation energy $E_a\approx0.1$ eV) above T_c. Samples 2 and 3 also exhibit activated behavior above T_c with simiar E_a values. For the other samples, $\rho(T_c)$ progressively decreases with increasing T_c. Well below T_c, ρ saturates to a value near 100 $\mu\Omega$ cm for all samples. When normalized by their respective low-T resistivities, $\rho(T>T_c)$ roughly fall on a common curve for all samples.

The T-dependent magnetoresistance MR(T) in 50 kOe is shown in Fig. 1(b). Sample 1 displays a wide, flat-topped peak centered at T_c with a maximum MR of $\Delta\rho/\rho_0=-0.996$. With increasing T_c the MR data indicate the following trends: (a) the width of the MR peak decreases, (b) the MR peak temperature T_{max} shifts somewhat below T_c, (c) the magnitude of the MR peak decreases, and (d) $\Delta\rho/\rho_0$ is very small at $T\ll T_c$ for all six films. MR(T) data measured in $H<50$ kOe indicate that T_{max} approaches T_c as H is increased. The H-dependent magnetoresistance MR(H) for samples 1–6 at their respective ordering temperatures are shown in Fig. 2(a) in fields to 100 kOe. Sample 1's MR saturates at a value near $\Delta\rho/\rho_0=-1$ in 25 kOe; sample 2's MR also saturates, but in a larger H field and at a smaller value of $\Delta\rho/\rho_0$. The magnetoresistance of samples 3–6 does not saturate even in the largest fields applied. Extrapolations of the MR data to $H>100$ kOe for these higher-T_c films suggest that the saturation values of $\Delta\rho/\rho_0$ decreases with increasing T_c.

The key finding from the MR(T,H) data presented in Figs. 1 and 2 is that the size of the CMR effect decreases with increasing film T_c. This result is summarized in Fig. 2(b) where $\Delta\rho/\rho_0$(50 kOe) at T_c is plotted against sample T_c for films 1–6. The 50 kOe field essentially saturates the MR of sample 1 ($T_c=152$ K), reduces ρ by 50% for the film with a T_c near room temperature, and only reduces ρ by roughly 20% for the high-T_c Sr-doped film (film 6). This CMR T_c dependence is simply a reflection of the fact that the order-induced drop in ρ that occurs below T_c is far larger in low-T_c samples than in high-T_c samples. This is made clear in Fig. 3, where $\rho(T_c)$ in both zero field and 50 kOe is plotted versus $1000/T_c$ for the six films; the resistivity is normalized by the low-temperature (4 K) saturation resistivity. The quantity $\rho(T_c)/\rho(4\text{ K})$ is a measure of the reduction in ρ brought on by complete FM order. In zero field $\rho(T_c)/\rho(4\text{ K})$ varies as

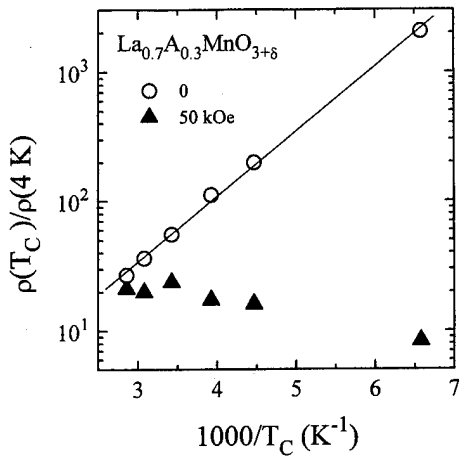


FIG. 3. Normalized resistivity plotted against $1000/T_c$ for samples 1–6 at their respective ordering temperatures in both zero field and 50 kOe.

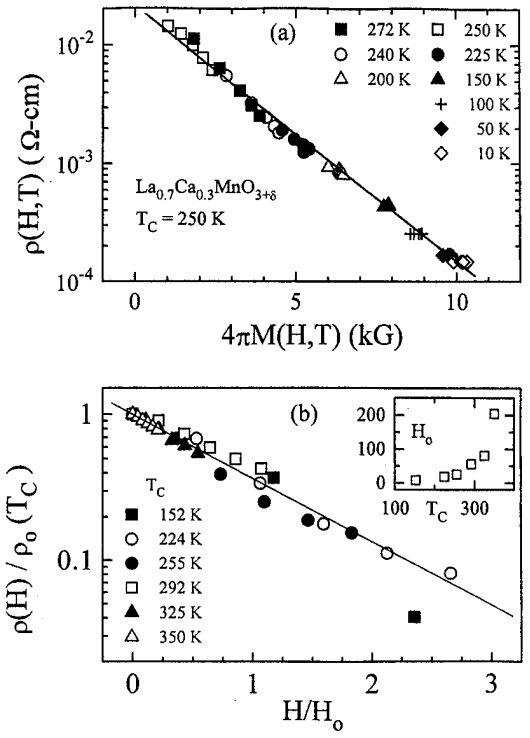


FIG. 4. (a) $\rho(H,T)$ vs. $M(H,T)$ for sample 3. At each T, points are included at $H=10$, 20, 30, 40, and 50 kOe. The solid line is a least-squares fit to the data. (b) Normalized magnetoresistance at T_c plotted vs. H/H_0 for samples 1–6; the scaling parameter H_0 (in kOe) is plotted against sample T_c in the inset.

$\exp(E_a/T_c)$ with an activation energy $E_a=0.1$ eV. This is the same activation energy evident in $\rho(T>T_c)$ in films 1–3. The normalized resistivity in 50 kOe is essentially T_c independent. The zero-field and 50 kOe results in Fig. 3 lead directly to the fit $\Delta\rho/\rho_0(T_c)=\alpha\exp(-E_a/T_c)-1$ that is displayed in Fig. 2(b) ($\alpha=20$). The data in Figs. 2(b) and 3 indicate that the key quantity that controls the MR in a given film is the normalized resistivity $\rho(T_c)/\rho(4\text{ K})$ (which is set by T_c), and not just $\rho(T_c)$. Hence, attempts to increase $\rho(T_c)$ by growth nonoptimization should also increase $\rho(4\text{ K})$, and would presumably have little affect on the magnitude of the CMR effect.

To determine how the enhancement in M and the huge drop in resistivity that occur below T_c are linked, measurements of $\rho(H,T)$ and $M(H,T)$ were made on sample 3 ($T_c=255$ K). The results are presented in Fig. 4(a), where $\rho(H,T)$ is plotted against $M(H,T)$ rather than as a function of H or T. The data were measured at nine temperatures from 272 to 10 K in fields from 10 to 50 kOe (where M reflects the local magnetization).[5] The data exhibit a correlation encompassing a two order-of-magnitude variation in ρ that can be parametrized as $\rho(H,T)\propto\exp[-M(H,T)/M_0]$, with $4\pi M_0=2.0$ kG. The data follow this phenomenological expression both close to and below T_c; the expression does not describe the data above 280 K where FM fluctuations are no longer present. The data in Fig. 4(a) clearly indicate that the magnetization and resistively are inextricably linked in the FM state. A similar relationship exists for the MR(H) data plotted in Fig. 2(a). The field-dependent data at T_c for all six films can be scaled via the expression $\rho(H)/\rho_0(T_c)\propto\exp(-H/H_0)$, where the scaling parameter H_0 is T_c dependent. The scaled data appear in Fig. 4(b), with $H_0(T_c)$ plotted in the inset. With the exception of sample 1 in fields sufficient to saturate that film's magnetoresistance, the data are qualitatively well-described by this phenomenological expression. The scaling parameter H_0 is a simple, monotonically increasing function of T_c. The relationship that links ρ and H follows directly from that between ρ and M because the magnetization varies quasilinearly in H for fields much less than the saturation field at T_c.

The phenomenological relationships between ρ, M, and H may provide insight into the form of the transport mechanism in the CMR films. In the double exchange (DE) model, which is thought to explain the magnetism in the CRM compounds,[4] the bandwidth W is proportional to the magnetization. Polaron hopping transport leads to a resistivity of the form $\rho\propto\exp(-W)$.[11] With $W\propto M$, polaron hopping and double exchange combine to give $\rho\propto\exp(-M)$, precisely that which is observed in Fig. 4(a). A somewhat surprising feature of the data is the fact that this exponential relationship persists down to temperatures well below T_c where it is reasonable to expect, given the drastic drop in ρ, that the polarons will be delocalized and transport would proceed via a conventional metallic process. The data in Fig. 4(a) may indicate that the quasiparticles evolve into large polarons at temperatures well below T_c. Additional theoretical and experimental work is needed to clarify this point.

In conclusion, field-dependent resistivity measurements on a series of six PLD-grown CMR films indicate that the magnitude of the CMR effect is determined by a given film's magnetic ordering temperature. Films with a low T_c exhibit both a large drop in the resistivity in the FM state and a large, negative magnetoresistance, while both effects are significantly smaller in films with a high ordering temperature.

This research was performed under the auspices of the U.S. Department of Energy.

[1] K. Chahara, T. Ohno, M. Kasai, and Y. Kozono, Appl. Phys. Lett. **63**, 1990 (1993).
[2] R. von Helmolt, J. Wecker, B. Holzapfel, L. Schultz, and K. Samwer, Phys. Rev. Lett. **71**, 2331 (1993).
[3] S. Jin, T. H. Tiefel, M. McCormack, R. A. Fastnacht, R. Ramesh, and L. H. Chen, Science **264**, 413 (1994); S. Jin, M. McCormack, T. H. Tiefel, and R. Ramesh, J. Appl. Phys. **76**, 6929 (1994).
[4] C. Zener, Phys. Rev. **82**, 403 (1951); P. W. Anderson and H. Hasegawa, Phys. Rev. **100**, 675 (1955); P. G. deGennes, Phys. Rev. **118**, 141 (1960).
[5] M. F. Hundley, M. Hawley, R. Heffner, Q. X. Jia, J. J. Neumeier, J. Tesmer, J. D. Thompson, and X. D. Wu, Appl. Phys. Lett. **67**, 860 (1995).
[6] J. Z. Sun, L. Krusin-Elbaum, S. S. P. Parkin, and Gang Xiao Appl. Phys. Lett. **67**, 2726 (1995).
[7] M. Rubinstein, J. M. Byers, R Treece, P. Dorsey, J. S. Horwitz, and D. B. Chrisey (unpublished).
[8] H. L. Ju, J. Gopalakrishnan, J. L. Peng, Qi Li, G. C. Xiong, T. Venkatesan, and R. L. Greene, Phys. Rev. B **51**, 6143 (1995).
[9] G. H. Jonker and J. H. van Santen, Physica **16**, 337 (1950).
[10] R. H. Heffner, C. Adams, M. Hawley, M. F. Hundley, Q. X. Jia, J. J. Neumeier, J. Tesmer, J. D. Thompson, and X. D. Wu (unpublished).
[11] I. G. Austin and M. F. Mott, Adv. Phys. **18**, 41 (1969).

Colossal magnetoresistance in the antiferromagnetic $La_{0.5}Ca_{0.5}MnO_3$ system

G. Q. Gong, C. L. Canedy, and Gang Xiao[a)]
Physics Department, Brown University, Providence, Rhode Island 02912

J. Z. Sun, A. Gupta, and W. J. Gallagher
IBM Research Division, Yorktown Heights, New York 10598

We have explored the colossal magnetoresistance (CMR) effect in the antiferromagnetic $La_{0.5}Ca_{0.5}MnO_3$ compound. In the absence of a magnetic field (H), the solid is a canted antiferromagnetic (AFM) insulator. An applied H in the Tesla scale induces a first order AFM to FM phase transition, and correspondingly, an insulator to metal transition. The observed CMR is attributed to the H-induced charge localization-delocalization behavior associated with the AFM–FM transition. At low temperatures ($T<100$ K), the solid remains in the AFM phase, where we have observed a phenomenal one millionfold change in resistivity between 0 and 8 Tesla. The origin of CMR in low T-region is a thermal activation energy gap which is strongly dependent on H.
© *1996 American Institute of Physics.* [S0021-8979(96)58808-7]

The magnetotransport and magnetic properties of the perovskite $La_{1-x}A_xMnO_{3+\delta}$ ($0 \leq x \leq 1$) system have received a great amount of attention recently after the discovery of the so-called colossal magnetoresistance (CMR) effect in the ferromagnetic phase (FM) of this system.[1–6] Essential to the CMR is the existence of the mixed valence state of Mn, evolving from Mn^{3+} (spin $S=2$) in the parent phase ($x=0$) to Mn^{4+} (spin $S=3/2$) in the end compound such as $CaMnO_3$ (i.e., $A=Ca$). The low energy t_{2g}^3 triplet contributes a local spin of $S=3/2$ to both Mn^{3+} and Mn^{4+}. In addition, Mn^{3+} has an additional electron in the e_g^1 state with its spin parallel to the local spin, whereas the e_g^1 state is empty in Mn^{4+}. Whether the e_g^1 electron is localized or mobile depends on the local spin orientation. If the local spins are aligned as in a FM, the e_g^1 electron will be mobile so as to lower its kinetic energy. However in the AFM configuration, the intra-atomic exchange between the e_g^1 electron and the local spin would forbid the electron transfer, hence, resulting in a charge localization. Because of these reasons, the electron transport in $La_{1-x}A_xMnO_3$ is sensitive to an underlying magnetic structure and its dynamics.[7] It is believed that the origin of CMR is directly related to this sensitivity.

To date, research on CMR has focused on the FM phase, in particular, on $La_{0.67}Ca_{0.33}MnO_3$ and other similar compounds.[1–4] CMR as large as ten-thousandfold has been obtained in polycrystals,[3] single crystals,[8] and epitaxial thin films.[1,2] A maximum MR is generally associated with the FM phase transition. We have studied the CMR effect using a different approach, and have searched for the maximum MR with an emphasis on the AFM phase. As a consequence we have achieved record CMR values of 830 000% at $T=125$ K and 10^8% at $T=57$ K in a well-prepared $La_{0.5}Ca_{0.5}MnO_3$ compound. Coupled with such a dramatic CMR is a field induced AFM–FM first order phase transition. At low T, we have also observed a strongly field dependent activation energy gap in the AFM phase.

The bulk $La_{0.5}Ca_{0.5}MnO_3$ compound was prepared using a solid-state reaction method. Appropriate proportions of La_2O_3, $CaCO_3$, and MnO_2 precursors were thoroughly mixed and then pressed into pellets. The sintering process lasted over a long period of 150 h in an oxygen atmosphere. Two intermediate grindings and mixings were carried out for homogenization. The annealing temperature was 1200 °C for the first two sinterings and was 1300 °C for the last. The sample was cooled to room temperature in more than 8 h. Four-probe magnetoresistance was measured in a cryostat equipped with an 8 T magnet. The magnetization of the sample was measured using the Quantum Design SQUID magnetometer. X-ray diffraction analysis indicated that the sample has a single phase with a cubic perovskite structure. The lattice constant is 7.66 Å.

Figure 1 shows the temperature (T) dependence of resis-

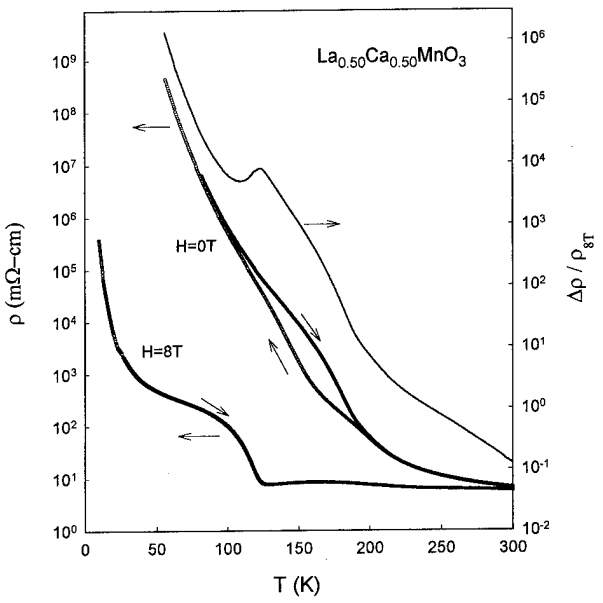


FIG. 1. The temperature (T) dependence of the resistivity, $\rho(T)$, (in log scale) measured in zero and 8 T field for $La_{0.5}Ca_{0.5}MnO_3$. The magnetoresistance ratio defined as $[\rho_0(T)-\rho_{8T}(T)]/\rho_{8T}(T)$ is also shown. The arrows indicate directions of measurement.

a)Electronic mail: gxiao@watson.ibm.edu

 0021-8979/96/79(8)/4538/3/$10.00 © 1996 American Institute of Physics

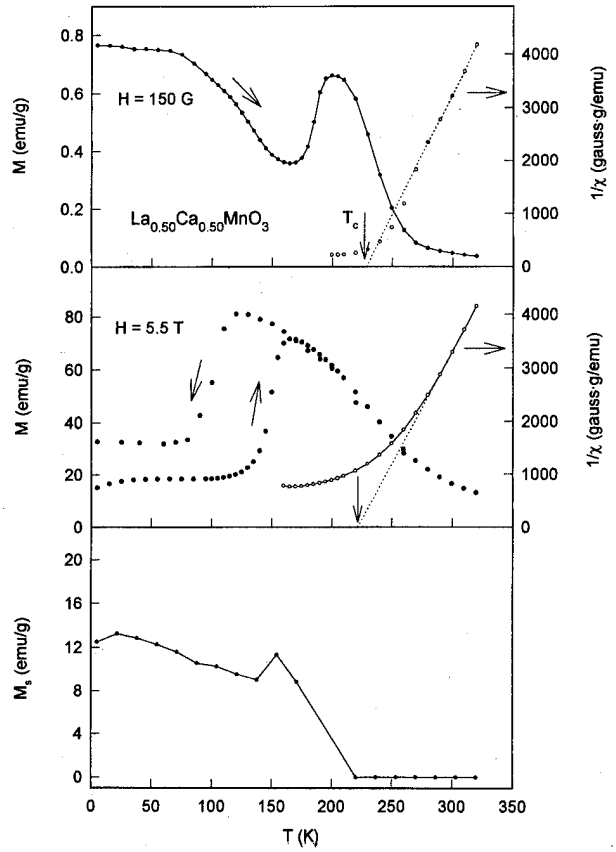


FIG. 2. The T-dependence of magnetization $M(T)$ and inverse susceptibility $\chi^{-1}(T)$ measured at H=150 G and 5.5 T. By extrapolating $M(H)$ in the high-H region to H=0, we have obtained a small ferromagnetic spontaneous magnetization $M_s(T)$ which is shown in the lower panel.

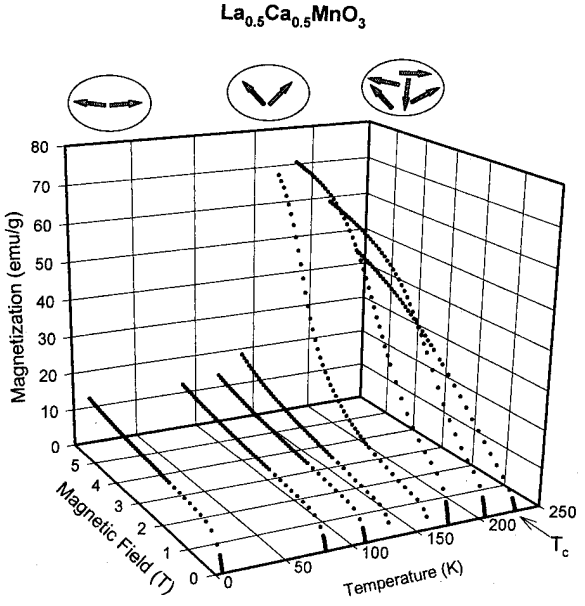


FIG. 3. Magnetization curves $M(H)$ measured at various temperatures. Three magnetic states are shown schematically in various temperature regions: a canted antiferromagnet, a canted ferromagnet, and a paramagnet.

tivity, $\rho(T)$, (in log scale) measured in 0 and 8 T field. The zero field $\rho_0(T)$ reveals a thermal hysteresis between 110 and 190 K in the cooling and warming-up mode. The $\rho_{8T}(T)$ at 8 T was measured only during warming-up. Over the T-range studied, $\rho_0(T)$ experiences a change spanning over eight orders of magnitude. Its T-dependence is semiconductorlike with an activation energy $\Delta(0)\approx 67$ meV. On the other hand, $\rho_{8T}(T)$ is substantially smaller than $\rho_0(T)$ at any given T. Above 120 K, $\rho_{8T}(T)$ is weakly dependent on T, having a value (a few mΩ-cm) typical of a poor metal. Below 120 K, $\rho_{8T}(T)$ experiences a sudden increase and evolves into an activation region with a gap $\Delta(8T)\approx 7.5$ meV, which is about one order of magnitude smaller than $\Delta(0)$. Also shown in Fig. 1 is MR ratio defined as $[\rho_0(T)-\rho_{8T}(T)]/\rho_{8T}(T)$. At $T\approx 60$ K ρ changes over six orders of magnitude between 0 and 8 T, and at $T\approx 125$ K over four orders of magnitude. To our knowledge the CMR effect shown here is the largest reported in $La_{1-x}A_xMnO_3$ and similar systems. It is noted that the maximum CMR in the FM $La_{0.67}Ca_{0.33}MnO_3$ occurs near T_c and vanishes as T approaches zero. However, in $La_{0.5}Ca_{0.5}MnO_3$, CMR seems to increase exponentially with reducing T.

To understand the anomalous magnetotransport, we have measured the magnetic properties of $La_{0.5}Ca_{0.5}MnO_3$. Figure 2 shows the T-dependence of magnetization $M(T)$ and invese susceptibility $\chi^{-1}(T)$ measured in a low field (150 G) and a high field (5.5 T). We have also measured a series of $M(H)$ curves from 0 to 5.5 T and in the T-range between 5 and 230 K. Some representative $M(H)$ curves are shown in Fig. 3. By extrapolating $M(H)$ in the high-H region to H=0, we have obtained a small FM spontaneous magnetization $M_s(T)$, which is shown in the lower panel of Fig. 2. Based on Figs. 2 and 3, we describe some of the important features of the magnetic properties.

(1) There exist two magnetic transitions in the T-range studied. The high-T $\chi^{-1}(T)$ provides an extrapolated Curie–Weiss $T_c\approx 225$ K as shown in Fig. 2, indicating a FM transition from a paramagnetic state. Another magnetic transition occurs at a T_d lower than T_c. The transition temperature, T_d, depends on H and on thermal history (zero-field-cooled or field-cooled). The substantial drop of M below T_d is indicative of an FM–AFM transition. The thermal hysteresis in M vs T (see the middle panel of Fig. 2) reveals a first order phase transition.

(2) At a fixed T, the FM–AFM transition can also be induced by an applied H_d (see Fig. 3). At a low T (<100 K), the solid is an AFM up to the maximum 5.5 T of our instrument. At a high T, for example, 150 K, the AFM–FM transition starts at about 4 T. As T approaches T_c, the AFM–FM transition shifts to a lower H, and becomes much smeared. In the zero H field, the solid is probably never a FM even at T near T_c. For example, at T=205 K, the $M(H)$ curve is hardly of any FM nature.

(3) Under a high H (e.g., 5.5 T), M approaches ~90 emu/g as $T\rightarrow 0$ K. Comparing with the theoretical limit of M_0=102 emu/g, one concludes that the canting angle θ_{FM} is about 56° at H=5.5 T in the FM phase [note that $\cos(\theta/2)=M_s^{\mathrm{exp}}/M_0$.] On the other hand, in the AFM phase, the spin orientations are canted too as evidenced from a small FM $M_s(T)$ component shown in the lower panel of Fig. 2. We

estimated that $\theta_{AFM} \approx 165°$. In other words, the AFM–FM transition, that can be either induced by H or by varying T, corresponds to a transition in θ from 165° to 56°.

With the above magnetic properties in mind, we can proceed to explain the magnetotransport data presented in Fig. 1. In zero field, θ remains large between 5 K and T_c. As a consequence, a charge transfer between neighboring sites is difficult, according to the prediction of the double exchange model[9–11] that charge transfer integral t is proportional to $\cos(\theta/2)$. At low T, charges are almost fully localized, which leads a thermally activated $\rho_0(T)$. Neutron diffraction studies[12] on $Pr_{0.5}Sr_{0.5}MnO_3$ have shown that Mn^{3+} and Mn^{2+} sites are spatially ordered at a low T similar to a Wigner lattice.

At a high H (e.g., 8 T), the system is FM above $T \approx 125$ K. In the FM phase, because of a much smaller canting angle, the charge transfer is enhanced substantially, allowing the formation of extended electronic states. The solid then behaves like a metal, albeit a poor one, with a resistivity of a few mΩ-cm. At about 125 K, a FM–AFM transition occurs, causing a charge localization and a thermally activated transport. However, as mentioned earlier, the energy gap at 8 T is much smaller than that at zero field. This is due to the fact that the canting angle in the AFM phase is reduced in the high H region because of the Zeeman energy. A smaller canting angle makes the charge transfer easier. In short, the dramatic CMR effect in the low-T region observed in Fig. 1 is caused by the strongly H dependent energy gap $\Delta(H)$ in the AFM phase. This differs from the CMR mechanism in the FM $La_{0.67}Ca_{0.33}MnO_3$, where the effect of H is to suppress the randomness in spin orientation. The dynamics of the two phenomena, though related, is very different.

Recently Tomioka *et al.*,[5] have studied a single crystal of $Pr_{0.5}Sr_{0.5}MnO_3$ which shows similar magnetic and transport properties to those presented here. The CMR effect they reported, however, is much smaller. Application of a field of 7 T changes ρ by about two orders of magnitude at $T \approx 0$ K. Comparing with the $La_{0.5}Ca_{0.5}MnO_3$ system that has a MR of one-millionfold, the latter seems to develop a much more rigid charge-ordered lattice, yielding a larger energy gap in the AFM phase. The metallic phases of the two systems, on the other hand, do share a similar resistivity (a few mΩ-cm).

In summary, we have obtained record values of CMR in the AFM phase of $La_{0.5}Ca_{0.5}MnO_3$. At $T=125$ K, the CMR is about one million percent. It increases exponentially to 100 million percent at 57 K. The CMR effect at intermediate T's (e.g., 125 K) is associated with a field induced first order FM–AFM phase transition. In the low-T region (<100 K), the AFM phase leads to a charge localization and, possibly, spatially charge ordering. The energy gap in the insulating AFM phase is dependent on H, with a higher H corresponding to a smaller gap. It is this particular nature of the energy gap in the AFM phase that brings about the phenomenal CMR effect.

This work was supported in part at Brown University by NSF under the Materials Research Group Grant No. DMR-9121747, and partially by DMR-9414160.

[1] R. von Helmolt, J. Wecker, B. Holzapfel, L. Schultz, and K. Samwer, Phys. Rev. Lett. **71**, 2331 (1993).
[2] S. Jin, T. H. Tiefel, M. McCormack, R. A. Fastnacht, R. Ramesh, and L. H. Chen, Science **264**, 413 (1994).
[3] S. Jin, H. M. O'Bryan, T. H. Tiefel, M. McCormack, and W. W. Phodes, Appl. Phys. Lett. **66**, 382 (1995).
[4] M. F. Hundley, M. Hawley, R. H. Heffner, Q. X. Jia, J. J. Neumeier, J. Tesmer, J. D. Thompson, and X. D. Wu, Appl. Phys. Lett. **67**, 860 (1995).
[5] Y. Tomioka, A. Asamitsu, Y. Moritomo, H. Kuwahara, and Y. Tokura, Phys. Rev. Lett. **74**, 5108 (1995).
[6] G. Q. Gong, C. L. Canedy, Gang Xiao, J. Z. Sun, A. Gupta, and W. J. Gallagher, Appl. Phys. Lett. (in press).
[7] J. Inoue and S. Maekawa, Phys. Rev. Lett. **74**, 3407 (1995).
[8] A. Urushibara, Y. Moritomo, T. Arima, A. Asamitsu, G. Kido, and Y. Tokura, Phys. Rev. B **51**, 14 103 (1995).
[9] P.-G. de Gennes, Phys. Rev. **118**, 141 (1960).
[10] C. Zener, Phys. Rev. **82**, 403 (1951).
[11] P. W. Anderson and H. Hasegawa, Phys. Rev. **100**, 675 (1955).
[12] K. Knížek, Z. Jirák, E. Pollert, F. Zounová, and S. Vratislav, J. Solid State Chem. **100**, 292 (1992).

Lattice effects on the magnetoresistance in doped manganese perovskites (abstract)

H. Y. Hwang,[a] S-W. Cheong, P. G. Radaelli,[b] M. Marezio,[c] T. T. M. Palstra, and B. Batlogg
AT&T Bell Laboratories, Murray Hill, New Jersey 07974

A detailed study of doped $LaMnO_3$ with fixed carrier concentration has revealed a direct relationship between the Curie temperature T_c and the average ionic radius of the La site $\langle r_A \rangle$, which is varied by substituting rare earths of different ionic radii for La. With decreasing $\langle r_A \rangle$ magnetic order and significant magnetoresistance occur at lower temperatures with increasing temperature hysteresis, and the magnitude of the magnetoresistance increases dramatically. The predominant structural effect of decreasing $\langle r_A \rangle$ is to decrease the Mn–O–Mn bond angle, which is accompanied by slight variations in the Mn–O bond distance. These results demonstrate that the notion of "double exchange" must be generalized to include changes in the Mn–Mn electronic hopping element as a result of microstructural changes induced by composition, temperature and pressure variations. © *1996 American Institute of Physics.* [S0021-8979(96)58908-6]

[a]Also Joseph Henry Laboratories of Physics, Princeton University, Princeton, New Jersey 08544.
[b]Institut Laue-Langevin, BP 156, 38042 Grenoble Cedex 9, France.
[c]Also Laboratoire de Cristallographie, CNRS-UJF, BP 166, 38042 Grenoble Cedex 9, France.

 0021-8979/96/79(8)/4541/1/$10.00 © 1996 American Institute of Physics

Electrical conductivity in ferromagnetic perovskite structures

Shufeng Zhang
Department of Physics, New York University, New York, New York 10003

A spin-polaron Hamiltonian is proposed to study the electrical conductivity in perovskite structures. A crossover from the metallic conduction at low temperatures to the hopping-type conduction at high temperature is calculated within the proposed model Hamiltonian. It is found that most of the experimental observations on resistivity and colossal magnetoresistance can be well explained with the assumption of the existence of spin clusters. © *1996 American Institute of Physics.* [S0021-8979(96)48908-0]

The subject of magnetotransport properites of perovskite lanthanum manganite, i.e., $La_{1-x}A_xMnO_3$ (A=Ca, Ba, Sr, etc.), has received much attention recently[1–4] in spite of the fact that these materials have been known for quite a long time.[5,6] There are two primary reasons for justifying the necessity for revisiting this "old" topic. First, new observations of the giant magnetoresistive effect at room temperature may lead to potential applications. Second, anomalous magnetic and transport properties in these materials have never been satisfactorily explained, in particular, no quantitative theory exists for understanding magnetotransport properties in these structures.

Since there are many competing interactions in perovskites, e.g., double exchange[7,8] which favors ferromagnetic coupling and superexchange which favors antiferromagnetic coupling, the problem of magnetic structures becomes extremely difficult. One would expect quite complex and rich magnetic phases. Several possible magnetic phases have been suggested: canted moments,[9] spiral structures,[10] ferromagnetism,[11] disordered magnetization,[9] magnetic clusters or giant spins,[12] and Jahn-Teller distorted lattices.[13] The actual affair of magnetic phases in these structures is far from clear at present. In this paper, we do not focus our attention to details of magnetic phases, rather we discuss essential features of electrical conduction in these structures. In particular, we aim at understanding of the colossal magnetoresistance observed recently.[1–4]

Let us first construct the following spin-polaron Hamiltonian

$$H=\sum_{\langle ij\rangle,\sigma} t_{ij}c_{i\sigma}^{+}c_{j\sigma}+H_L+H_{\rm int}, \tag{1}$$

where the first term describes the ordinary tight binding band of mobile (itinerant) carriers, the second term represents various magnetic interactions between localized spins, and the last term is the exchange interaction between mobile carriers and localized spins. To proceed we must made some plausible simplifications: (1) The double exchange is strong enough such that the ground state is assumed to be at least locally ferromagnetic (ferromagnetic spin clusters); this is applicable for optimally doped compounds, e.g., $La_{2/3}Ca_{1/3}MnO_3$. (2) The excitations of H_L can be written as a simple magnon spectrum $H_L=\Sigma_{\mathbf{q}}\omega_{\mathbf{q}}a_{\mathbf{q}}^{+}a_{\mathbf{q}}$, where the $a_{\mathbf{q}}$ is the annihilation operator for a magnon with wave vector $\mathbf{q}$. While we do not include complicated underlying ground states for our system they determine the magnon spectrum $\omega_{\mathbf{q}}$; this in turn determines the *temperature dependence* of the resistivity and magnetoresistance. However, it is understood that the magnon spectrum may be quite different from that of ordinary ferromagnetic metals due to the existence of several competing antiferromagnetic couplings in the structure (notice that the undoped material is antiferromagnetic). Therefore, the quasiparticle $a_{\mathbf{q}}^{+}$ should not be interpreted as a ferromagnetic magnon. (3) This observation leads us to write the interaction between mobile carriers and localized spins as

$$H_{\rm int}=\sum_{i,\mathbf{q}} K_{\mathbf{q}}e^{i\mathbf{q}\cdot\mathbf{R}_i}(c_{i\uparrow}^{+}c_{i\downarrow}+c_{i\downarrow}^{+}c_{i\uparrow})(a_{\mathbf{q}}+a_{-\mathbf{q}}^{+}), \tag{2}$$

where we have neglected the ordinary non-spin flip interaction $S^z\cdot(n_{i\uparrow}-n_{i\downarrow})$ because the effect of this interaction is to shift the on-site energy for spin up and down mobile carriers. However, one immediately notices that Eq. (2) is different from the usual form of the electron–magnon interaction in a normal ferromagnetic metal which takes the form of $c_{i\uparrow}^{+}c_{i\downarrow}a_{\mathbf{q}}^{+}+c_{i\downarrow}^{+}c_{i\uparrow}a_{-\mathbf{q}}$ as required by spin conservation. For our system, the magnon is understood as an excitation from all competing magnetic interactions as mentioned above. $a_{\mathbf{q}}^{+}$ is not simply a spin raising operator, rather it contains both creation and annihilation of a spin, similar to an antiferromagnetic magnon or a magnon for a magnetically disordered state. This interpretation is further supported by the experimental fact that the magnetization is smaller than that of fully aligned Mn ions.[1–4]

With these simplifications, we rewrite our model Hamiltonian as

$$H=H_0+V, \tag{3}$$

where

$$H_0=\sum_{\mathbf{q}} \omega_{\mathbf{q}}a_{\mathbf{q}}^{+}a_{\mathbf{q}}+\sum_{i,\mathbf{q}} K_{\mathbf{q}}e^{i\mathbf{q}\cdot\mathbf{R}_i}(c_{i\uparrow}^{+}c_{i\downarrow}+c_{i\downarrow}^{+}c_{i\uparrow})(a_{\mathbf{q}}+a_{-\mathbf{q}}^{+}) \tag{4}$$

and

$$V=\sum_{\langle ij\rangle,\sigma} t_{ij}c_{i\sigma}^{+}c_{j\sigma}. \tag{5}$$

Next, we make a canonical transformation to decouple the magnon and electron parts of the Hamiltonian H_0, and treat V in Eq. (3) as a perturbation. We choose an S operator

 0021-8979/96/79(8)/4542/3/$10.00 © 1996 American Institute of Physics

so that the new transformed Hamiltonian $H_0^s=\exp(S)H_0\times\exp(-S)$ can be written as a sum of magnon and electron Hamiltonian. Such an S is found to be

$$S=\sum_{i\mathbf{q}}(K_{\mathbf{q}}/\omega_{\mathbf{q}})e^{i\mathbf{q}\cdot\mathbf{R}_i}(c_{i\uparrow}^{+}c_{i\downarrow}+c_{i\downarrow}^{+}c_{i\uparrow})(a_{\mathbf{q}}^{+}-a_{-\mathbf{q}}). \quad (6)$$

After some straightforward algebra, we find

$$H_0^s=\sum_{\mathbf{q}}\omega_{\mathbf{q}}a_{\mathbf{q}}^{+}a_{\mathbf{q}}-\sum_{\mathbf{q},i}(K_{\mathbf{q}}^2/\omega_{\mathbf{q}})(n_{i\uparrow}+n_{i\downarrow}-2n_{i\uparrow}n_{i\downarrow}) \quad (7)$$

and

$$V^s=\sum_{ij}t_{ij}[\cosh(x_i-x_j)(c_{i\uparrow}^{+}c_{j\uparrow}+c_{i\downarrow}^{+}c_{j\downarrow})+\sinh(x_i-x_j)\times(c_{i\uparrow}^{+}c_{j\downarrow}+c_{i\downarrow}^{+}c_{j\uparrow})], \quad (8)$$

where $x_i=\Sigma_{\mathbf{q}}e^{i\mathbf{q}\cdot\mathbf{R}_i}(K_{\mathbf{q}}/\omega_{\mathbf{q}})(a_{\mathbf{q}}-a_{-\mathbf{q}}^{+})$. The new Hamiltonian $H^s=H_0^s+V^s$ describes the same physical system as the original Hamiltonian, However, H^s has made the perturbation to V^s possible. The magnon part is unchanged by the transformation, while the electron part becomes a Hubbard-like Hamiltonian as evidenced by the $n_{i\uparrow}n_{i\downarrow}$ term in H_0^s. It is this Coulomb term which makes the spin-polaron different from the ordinary polaron Hamiltonian; it becomes a many-body Hamiltonian and cannot be solved exactly. Here we will not further address the effect of the electron–electron interaction, rather we concentrate on the perturbation, Eq. (8).

To obtain the electrical conductivity, one requires a proper treatment of the dynamics of $\cosh(x_i-x_j)$ and $\sinh(x_i-x_j)$. There are two independent processes for the conduction: *elastic* and *inelastic*. For the elastic process the electron transport is described by an effective band with a background of magnons. The effect of this background can be included by calculating the thermal average of $\cosh(x_i-x_j)$ and $\sinh(x_i-x_j)$ in Eq. (8). The inelastic process is that of an electron hopping into its neighbors while absorbing and emitting magnons, i.e., the transport is by incoherent hopping. These two conduction processes have very different temperature dependence. The former is a band description in which the effective mass (inversely proportional to the bandwidth) increases as the temperature increases. This is because the thermal fluctuations of magnons makes the electron hard to move. Thus, the resistivity increases when temperature increases. For the inelastic process, the hopping is assisted by magnons, therefore, this conduction process is favored at high temperatures. We now explicitly write down these two contributions to the conductivity.

For the elastic process, we calcualte the thermodynamic averages, $\langle\cosh(x_i-x_j)\rangle$ and $\langle\sinh(x_i-x_j)\rangle$. Since all magnons are assumed to be independent,[14] the thermal average can be done for each magnon frequency. In analog with the conventional polaron problem,[15] we find

$$\langle\cosh(x_i-x_j)\rangle=\exp\left[-\sum_{\mathbf{q}}\left(\frac{K_{\mathbf{q}}}{\omega_{\mathbf{q}}}\right)^2|1-e^{i\mathbf{q}\cdot\delta}|^2(N_{\mathbf{q}}+1/2)\right] \quad (9)$$

and $\langle\sinh(x_i-x_j)\rangle=0$, where $\delta=\mathbf{R}_i-\mathbf{R}_j$ is the distance between two nearest Mn sites, and $N_{\mathbf{q}}=[\exp(\beta\omega_{\mathbf{q}})-1]^{-1}$ is the number of magnons.

The effective bandwidth of mobile carriers for the elastic process, $\langle t_{ij}\cosh(x_i-x_j)\rangle$, see Eq. (8), depends on temperature through $N_{\mathbf{q}}$; it decreases as the temperature increases. Correspondingly, the effective mass, which is inversely proportional to the bandwidth, increases. The interaction between local spins and mobile electrons leads to an enhancement of the effective mass. Near the transition temperature, the effective mass becomes exponentially large and resistivity can be several orders of magnitude larger than that at low temperatures. If one simply assumes that the metallic conduction is inversely proportional to the effective mass, the conductivity at finite temperature is

$$\sigma(T)=\sigma(0)\exp\left[-\sum_{\mathbf{q}}\left(\frac{K_{\mathbf{q}}}{\omega_{\mathbf{q}}}\right)^2|1-e^{i\mathbf{q}\cdot\delta}|^2N_{\mathbf{q}}\right], \quad (10)$$

where $\sigma(0)$ is the zero temperature conductivity and the factor 1/2 in Eq. (9) has been absorbed in $\sigma(0)$ since it comes from the zero-point motion of magnon.

For *inelastic process*, the conduction will be provided by *incoherent* magnon-assisted hopping, as mentioned before. The conductivity is giving by the Einstein relation

$$\sigma_{in}=ne^2\delta^2w/k_BT, \quad (11)$$

where n is the density of mobile carriers, and w is the transition probability which can be obtained by Fermi golden rule, $w=(t^2/\hbar\epsilon)\exp(-\epsilon/k_BT)$, where the activation energy $\epsilon=(1/2)\Sigma_{\mathbf{q}}(K_{\mathbf{q}}^2/\omega_{\mathbf{q}})|1-e^{i\mathbf{q}\cdot\delta}|^2$.

The metallic conduction, Eq. (10), and hopping conduction, Eq. (11), are independent conducting processes. At low temperatures, band conduction dominates while at high temperatures hopping dominates. Here, let us take a simple example where there is only one magnon frequency, $\omega_{\mathbf{q}}=\omega_0$. The conductivity from Eqs. (10) and (11) is

$$\sigma(T)/\sigma(0)=\exp[-\alpha N(\omega_0)]+(b^2/\epsilon k_BT)\exp(-\epsilon/k_BT), \quad (12)$$

where $\alpha=\Sigma_{\mathbf{q}}K_{\mathbf{q}}^2|1-e^{i\mathbf{q}\cdot\delta}|^2/\psi_0^2$, $b=e\delta t\sqrt{n/\hbar\sigma(0)}\omega_0^2$, and $N(\omega_0)=(e^{\omega_0/k_BT}-1)^{-1}$. In Fig. 1 we show the resistivity as function of temperature for several plausible values of the parameters. We point out that the peak of the resistivity is not necessary at the Curie temperature as evidenced by the different peak tempeatures for different parameters when we hold the magnon frequency constant.

We now briefly comment on colossal magnetoresistance. In our Hamiltonian, the external magnetic field is implicitly included in the magnon frequency $\omega_{\mathbf{q}}$. The variation of the magnon spectrum with the magnetic field is not known at present. If one uses a relation similar to that used in ordinary ferromagnetic metal, i.e., by replacing $\omega_{\mathbf{q}}$ by $\omega_{\mathbf{q}}+g\mu_BH$, we find the magnetoresistance is too small to explain colossal magnetoresistance; this is because $g\mu_BH$ is small compared to intrinsic magnon frequency $\omega_{\mathbf{q}}$ for several Tesla of magnetic field. However, as mentioned in the introduction, the inhomogeneity and various competing magnetic interactions make it plausible for the formation of spin clusters as reported experimentally.[16] In fact, the possibility of spin-

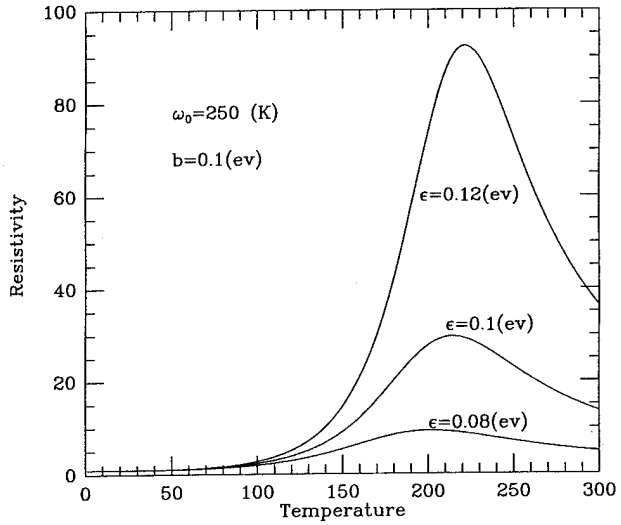


FIG. 1. Resistivity (normalized to $T=0$) as a function of temperature in the absence of magnetic field for three different activation energies ϵ=0.12 eV (upper curve), ϵ=0.1 eV (middle curve), and ϵ=0.8 eV (bottom curve). The parameters are $b=0.1$ eV and ω_0=240 K.

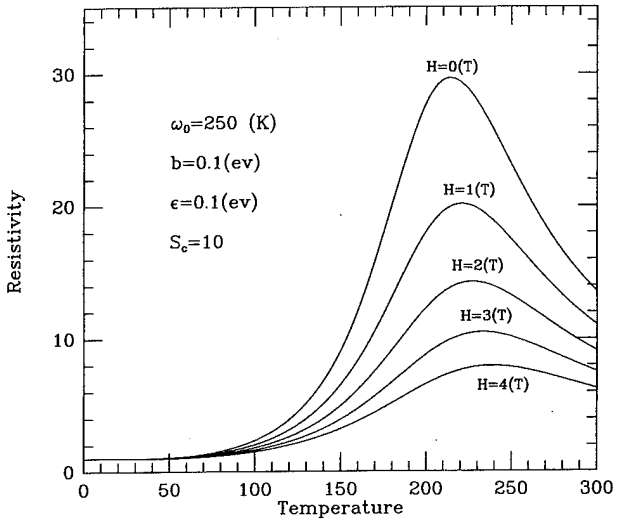


FIG. 2. Resistivity (normalized to $T=0$) as a function of temperature for several values of magnetic fields. We have chosen the cluster size to be ten spins. The parameters are $b=0.1$ eV, ω_0=240 K, and ϵ=0.1 eV.

cluster or giant spins had been modelled by Kasuya.[12] Therefore, one should replace $\omega_{\mathbf{q}}$ by $\omega_{\mathbf{q}}+g\mu_B S_c H$, where S_c is the nmber of spins in spin clusters. In Fig. 2, we show the resistivity as function of temperature for several values of magnetic fields. We notice that the effects of the magnetic field are to suppress the resistivity peak and to push it to higher temperatures. If one assumes the average cluster size to be order of ten spins, one can achieve the colossal magnetoresistance in a few Tesla.

In summary, a spin-polaron Hamiltonian is introduced to study the magnetotransport of doped perovskite compounds. At low temperature, the interaction of mobile carriers with local spins leads to an enhancement of the effective mass of carriers; at higher temperature, the same interaction assists the carrier hopping to nearest neighbor via *inelastic* magnon absorption and emission. Therefore, the metal–insulator transition in the conductivity is a natural result of our Hamiltonian. When we apply our theory to calculate magnetoresistance, we find that most of the experimental features can be explained *as long as* we rely on the existence of spin clusters. Details of the effects of the spin cluster on magnetization and domain boundaries scattering will be published elsewhere.

The author wishes to thank the hospitality of the Thin Film Department of Hewlett-Packard Laboratories where part of the work was done during his visit there. Special thanks to Peter M. Levy, Andy Millis, and Kuising Wang for their very helpful suggestions and discussions. This work is supported by the Office of Naval Research under Grant No. N9100014-91-J-1695 and by Hewlett-Packard Laboratories.

[1] R. von Helmolt, J. Wecker, B. Holzapfel, L. Schultz, and K. Samwer, Phys. Rev. Lett. **71**, 2331 (1993).
[2] K. Chahara, T. Ohno, M. Kasai, and Y. Kozono, Appl. Phys. Lett. **63**, 1990 (1993).
[3] S. Jin, T. H. Tiefel, M. McCormack, R. A. Fastnacht, R. Ramesh, and L. H. Chen, Science **264**, 413 (1994).
[4] H. L. Ju, C. Kwon, Q. Li, R. L. Greene, and T. Venkatesen, Appl. Phys. Lett. **65**, 108 (1994).
[5] E. O. Wollan and W. C. Koehler, Phys. Rev. B **100**, 545 (1955).
[6] B. C. Tofield and W. R. Scott, J. Solid State Chem. **10**, 183 (1974).
[7] C. Zener, Phys. Rev. **82**, 403 (1951).
[8] P. W. Anderson and H. Hasegawa, Phys. Rev. **100**, 675 (1955).
[9] P. -G. de Gennes, Phys. Rev. **118**, 141 (1960).
[10] J. Inoue and S. Maekawa, Phys. Rev. Lett. **74**, 3407 (1995).
[11] J. B. Goodenough, Phys. Rev. B **100**, 564 (1955).
[12] T. Kasuya and A. Yanase, Rev. Mod. Phys. **40**, 684 (1968).
[13] A. J. Millis, P. B. Littlewood, and B. I. Shraiman, Phys. Rev. Lett. **74**, 5144 (1995).
[14] Magnon–magnon interaction may be large near the transition temperature. However, one can include the effect by introducing renormalized magnons, see for example, M. Bloch, Phys. Rev. Lett. **9**, 286 (1962).
[15] G. D. Mahan, in *Many-Particle Physics* (Plenum, New York, 1990).
[16] S. Oseroff, (private communication).

Response to an electric field of $Nd_{0.7}Sr_{0.3}MnO_3$ films in a MOSFET configuration (abstract)

S. B. Ogale, V. Talyansky, G. C. Xiong, R. P. Sharma, R. Ramesh, R. L. Greene, and T. Venkatesan

The effect of an electric field on GMR oxide films was studied in a MOSFET configuration where the gate dielectric was a layer of $SrTiO_3$ epitaxially grown on an underlying layer of the manganate which served as the source/drain. The response of the manganate channel was studied for different gate voltages. The following significant features were observed. The peak resistance temperature shifted to lower temperature for both polarities of the field. The resistance change varied quadratically with the field indicating the dominance of strain or polarization effects. In dynamical studies of the system using the gate voltage as an excitation the system showed anomalous slowing down near the peak of the resistivity. These results are understood on the basis of a stress effect on the film due to electro-elastic effects in the $SrTiO_3$ layer, which introduces a tensile stress in the manganate layer upon the application of a gate voltage. The anomalous slowing down of the system near the ferromagnetic phase transition suggests a strong coupling between the spins, transport and structural distortions in the system. © *1996 American Institute of Physics.*
[S0021-8979(96)59008-9]

Magnetotransport and hysteretic behavior in epitaxial $La_{0.67}Ca_{0.33}MnO_{3-\delta}$ films

C. L. Canedy, K. B. Ibsen, and Gang Xiao[a)]
Department of Physics, Brown University, Providence, Rhode Island 02912

J. Z. Sun, A. Gupta, and W. J. Gallagher
IBM Research Division, Yorktown Heights, New York 10598

We have fabricated epitaxial $La_{0.67}Ca_{0.33}MnO_{3-\delta}$ thin films using pulsed laser deposition and performed subsequent thermal treatments. Magnetoresistance values as large as 14 000% ($\Delta\rho/\rho_H$) were obtained. Above magnetic ordering temperatures, we observed a thermally activated conductivity that also has a quadratic magnetic field dependence. At low temperatures, we found a large hysteresis in the magnetoresistance that correlates with an unusual magnetic hysteresis curve. We interpret the hysteretic behavior as the result of a "frozen-in" canted spin structure. Our results suggest that the electron conduction in this material is most sensitive to the canting angle of the neighboring Mn spins. © *1996 American Institute of Physics.* [S0021-8979(96)49008-5]

Sparked by the recent discovery of "colossal" magnetoresistance (CMR)[1,2] the perovskite (La-A)MnO_3 system (A =Ca, Ba, Sr, or Pb) has witnessed a resurgence of the work started back in the 1950's.[3,4] It is fascinating that the magnetoresistance can be as large as 100-fold in polycrystalline bulk materials[5] and 1000-fold in epitaxial thin films.[2] Recently, phenomenal values of MR, in excess of one-millionfold, were observed in the antiferromagnetic $La_{0.5}Ca_{0.5}MnO_3$ compound.[6] The underlying mechanism for CMR remains unsettled, but it is clear that it is of a different origin than that of the giant magnetoresistance (GMR) effect observed in many metallic layered[7,8] or granular structures.[9] With the freedom of varying doping level (x) and oxygen content (δ), the $La_{1-x}A_xMnO_{3+\delta}$ system can develop diverse types of magnetic orderings, ranging from the layered antiferromagnetic (AFM) parent phase, to a canted spin structure, a ferromagnetic phase, and finally to the alternating AFM state.[3] Associated with these magnetic structures is the rich magnetotransport behavior, of which the CMR is one of the most interesting.[1,2,5,6] The extreme sensitivity of the electron transport to the underlying magnetically static and dynamic states can be traced to the intimate coupling between the charge carriers and the local spin structure. In this perovskite system, not only do the doped carriers participate in the electrical conductivity, but they are also responsible for the magnetic ordering, a mechanism commonly dubbed as double exchange.[10–13]

The effect of CMR is most pronounced at temperatures near the ferromagnetic ordering temperature (T_c).[1,2,5,6] For low T, the value of resistivity decreases rapidly with decreasing T. At high T, resistivity decreases with increasing T. A study focused on the high-T region above T_c provides useful information about the electron transport in a disordered magnetic state. On the other hand, the low-T region (e.g., 4.2 K) provides an ordered magnetic state free of thermal excitations (magnons, phonons, etc.), allowing one to probe the correlation between the electron transport and the static magnetic structure. In this work, we present results obtained from the $La_{0.67}Ca_{0.33}MnO_{3+\delta}$ thin films both in the high- and low-T regions. We have observed different field-dependent characteristics of resistivity in these two regions. The thermally activated resistivity persists to a high T of about 500 K. In the low-T region, an unusual type of magnetic hysteresis loop leads to a corresponding MR with a large hysteresis. We attribute the origin of the hysteresis to a glassy canted-spin structure. Our results point to a strong coupling between the electron motion and the local spin orientations.

Thin films were grown from a sintered ceramic target of $La_{0.67}Ca_{0.33}MnO_3$ using pulsed laser deposition. The oxygen pressure during ablation was 300 mTorr. The substrates, single crystal (100) $SrTiO_3$, were kept at a temperature of 700 °C. The deposition rate was about 0.5 Å pulse, and the laser power density around 3 J/cm^2. The film thickness is about 1000 Å. X-ray diffraction patterns of these films showed intense and sharp ($00n$) peaks, indicating (001) oriented growth. Magnetization measurements were performed in a Quantum Design SQUID magnetometer. For magnetotransport measurements, the samples were patterned into Hall bars using the standard photolithography and ion-beam etching. Platinum was deposited onto contact pads on which wires were attached with the help of a wedge bonder. Four-probe transport measurements were then carried out in a cryostat equipped with an 8 T magnet.

We focus on the results of two $La_{0.67}Ca_{0.33}MnO_{3+\delta}$ films (L011 and L012), that were subjected to a postdeposition thermal treatments at 850 °C for 0.5 h in either an oxygen (L011) or argon atmosphere (L012). The oxygen content in the films was not determined. However, it is expected to be different for the two samples. Shown in Fig. 1 is the T dependence of resistivity $\rho_0(T)$ and $\rho_{8\ T}(T)$ measured in zero and an applied 8 T magnetic field (H), respectively. The peak of $\rho_0(T)$ occurs near T_c which is determined from the initial susceptibility $\chi(T)$ vs T curve. The T_c values of the two samples (L011 and L012) are about 140 and 204 K, respectively. Above T_c, $\rho_0(T)$ exhibits a thermal activation behavior with an activation energy of 0.12 eV for L011 and 0.10 eV for L012. This behavior persists up to at least 500 K. Between 500 K and our maximum measurement T of 600 K, $\rho_0(T)$ starts to increase slightly with T for sample L012,

a)Electronic mail: gxiao@watson.ibm.com

 0021-8979/96/79(8)/4546/3/$10.00 © 1996 American Institute of Physics

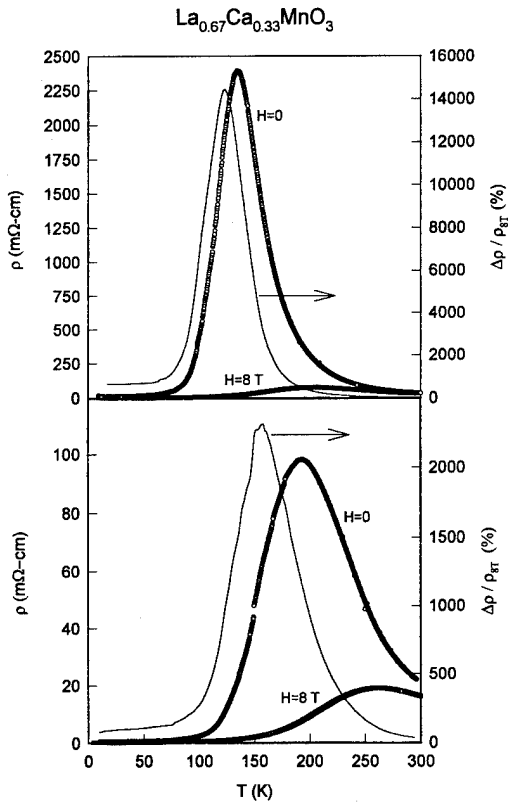


FIG. 1. The temperature dependence of resistivity, $\rho_0(T)$ and $\rho_{8\ T}(T)$, measured in zero magnetic field and an applied field of 8 T for two $La_{0.67}Ca_{0.33}MnO_{3-\delta}$ thin films, L011 (top) and L012 (bottom) annealed under different conditions. Also shown is the corresponding magnetoresistance ratio $[\rho_0(T)-\rho_{8\ T}(T)]/\rho_{8\ T}(T)$ vs T.

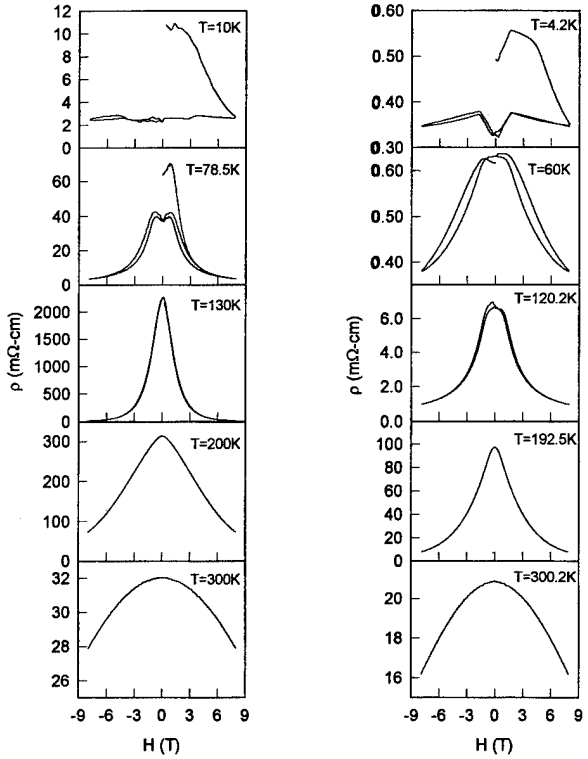


FIG. 2. The field dependence of resistivity $\rho(H)$ measured at various temperatures for the L011 (left) and L012 (right) thin films. Note the large hysteresis (up to 8 T) at a low T between the initial and the magnetized state.

which could be an indication that the electron–phonon interaction starts to dominate the transport. Figure 1 also shows the MR ratio, defined as $[\rho_0(T)-\rho_{8\ T}(T)]/\rho_{8\ T}(T)$, as a function of T. The sample L011 with a lower T_c has a maximum MR of about 14 000%, whereas L012 has a maximum MR of about 2300%. This is consistent with the general observation that samples with a lower T_c tend to have a larger MR.

We have also measured resistivity $\rho(H)$ as a function of H at various T's between 4.2 and 300 K. The results are shown in Fig. 2. When $T>T_c$, the conductivity $\sigma(H)$ shows a quadratic dependence on H, i.e., $\sigma(H)=\sigma_0+\sigma_1 H^2$. As T approaches and then is lowered below T_c, a different H dependence of $\rho(H)$ emerges. Most interestingly, at a sufficient low T, $\rho(H)$ develops an anomalous hysteretic behavior between the unmagnetized and the magnetized states. When a sample is initially magnetized, a large and primarily negative MR appears up to our maximum field of 8 T. Then as H is reduced, a large deviation in $\rho(H)$ sets in and the $\rho(H)$ curve becomes much flatter. Further H cycling between ± 8 T yields a much smaller MR with only a tiny hysteresis. It is surprising that the large hysteresis between the initial and the subsequent magnetizing processes could persist up to a field as large as 8 T. This hysteresis is most pronounced at low-T.

Since the magnetotransport of this system is strongly correlated with the magnetization,[14] we have subsequently measured the magnetic hysteresis loop as shown in Fig. 3 for sample L011. Indeed an intimate correspondence between $M(H)$ and $\rho(H)$ is revealed. Starting from the unmagnetized state (i.e., the virgin state) the $M(H)$ curve shows a rapid

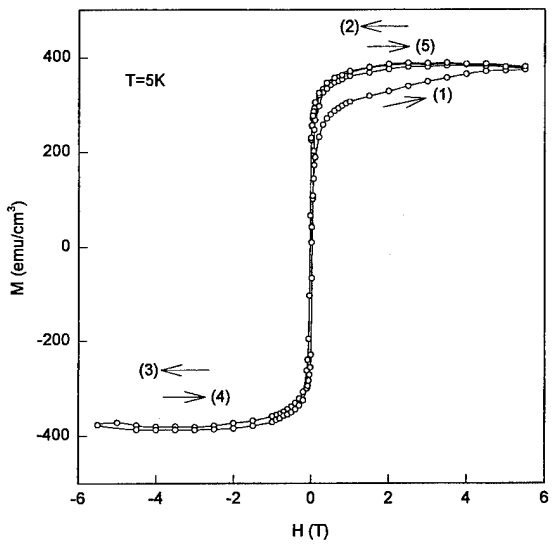


FIG. 3. The anomalous magnetic hysteresis curve for the L001 thin film measured at 5 K. The arrows indicate the magnetizing sequence. Arrow 1: starting from the unmagnetized state; Arrows 1-2-3-4, cycling field from +5.5 to −5.5 T and back to +5.5 T. Note the correspondence between the hysteresis in $M(H)$ shown here and that in $\rho(H)$ at a low T shown in Fig. 2 for the L001 sample.

increase in M within a couple of kG, and then a more gradual increase in M with H (see arrow 1) up to 5.5 T. The subsequent H cycling (arrows 2-3-4-5) leads to a loop where $M(H)$ is always larger than the initial $M(H)$, and where $\rho(H)$ much less than the initial $\rho(H)$. Without the initial curve (arrow 1), the loop is of the type of a soft ferromagnet with small hysteresis. It is the large hysteresis persisting to a very high field that makes the magnetizing process highly unconventional. Comparing the low-T data in Figs. 2 and 3, one observes that $\rho(H)$ and $M(H)$ share a similar hysteretic behavior.

A study of the correlation between $\rho(H)$ and $M(H)$ and their hysteresis at low T may shed light into the transport process. Because of the negligible thermal disturbances at low T, the magnetotransport is mostly dependent on the static magnetic structure. Based on the observations from Figs. 1 and 2, a couple of qualitative comments can be made.

(1) The unmagnetized state has a canted ferromagnetic structure as indicated by the high-H susceptibility in the first $M(H)$ curve. This is consistent with the double exchange model that predicts a stable canted spin arrangement under the influence of doped carriers.[11–13] However, the high-H susceptibility should not be hysteretic if the carriers are truly delocalized. Moreover, the canting angle should depend on H in a unique and reversible fashion (following states with minimized free energies).[12] However, experimentally the canting angle seems to have a memory of its value at high H even after H is released. This is reminiscent of a glassy magnetic state, having many H-dependent local free energy minima that can trap the local spin distortions. For this glassy state to exist, the carriers cannot be completely delocalized. Otherwise one would expect the "frozen" spin state to relax to the global energy minimum rapidly. If the above scenario is indeed valid, it would be more appropriate to treat the doped carriers as not being completely free. In fact even at $T=4.2$ K, these materials are rather poor metals having resistivities in the range of a few mΩ cm, over three to four orders of magnitude larger than that of a typical metal.

(2) The correlation between $\rho(H)$ and $M(H)$ is again consistent with the double exchange mechanism.[10–13] A parallel spin arrangement facilitates transfer of carriers from one site to the other, whereas an antiparallel configuration would block the carrier motion. The application of a field on the unmagnetized state tends to align the spins, hence, improving the electrical conductivity. When the field is reduced, the spin system retains memory of its high-H configuration, therefore, the conductivity becomes less dependent on H as seen in the low-T data in Fig. 2.

In summary, we have observed an anomalous low-T hysteretic behavior in $\rho(H)$ and $M(H)$ in the ferromagnetic $La_{0.67}Ca_{0.33}MnO_{3+\delta}$ system. This large hysteresis which persists to a very high H (8 T in our setup) may be caused by a glassy type of local spin structure. It is likely that the carriers are somewhat localized in the unmagnetized state. An application of H allows the carriers to diffuse with increasing ease. In the high-T region, we found that thermally activated transport persists to about 500 K, and that the conductivity exhibits a quadratic H dependence.

This work was supported in part by NSF through the Materials Research Program at Brown University, Grant No. DMR-9121747, and partially by NSF Grant No. DMR-9258306.

[1] R. von Helmolt, J. Wecker, B. Holzapfel, L. Schultz, and K. Samwer, Phys. Rev. Lett. **71**, 2331 (1993).
[2] S. Jin, T. H. Tiefel, M. McCormack, R. A. Fastnacht, R. Ramesh, and L. H. Chen, Science **264**, 413 (1994).
[3] E. O. Wollan and W. C. Koehler, Phys. Rev. **100**, 545 (1955).
[4] G. H. Jonker and J. H. van Santen, Physica **16**, 337 (1950); G. H. Jonker, Physica **22**, 707 (1956).
[5] S. Jin, H. M. O'Bryan, T. H. Tiefel, M. McCormack, and W. W. Phodes, Appl. Phys. Lett. **66**, 382 (1995).
[6] G. Q. Gong, C. L. Canedy, G. Xiao, J. Z. Sun, A. Gupta, and W. J. Gallagher, Appl. Phys. Lett. (in press).
[7] M. N. Baibich *et al.*, Phys. Rev. Lett. **61**, 2472 (1988).
[8] S. S. P. Parkin, R. Bhadra, and K. P. Roche, Phys. Rev. Lett. **66**, 2152 (1991).
[9] J. Q. Wang and Gang Xiao, Phys. Rev. B **49**, 3982 (1994).
[10] C. Zener, Phys. Rev. **82**, 403 (1951).
[11] P. W. Anderson and H. Hasegawa, Phys. Rev. **100**, 675 (1955).
[12] P.-G. de Gennes, Phys. Rev. **118**, 141 (1960).
[13] J. Inoue and S. Maekawa, Phys. Rev. Lett. **74**, 3407 (1995).
[14] M. F. Hundley, M. Hawley, R. H. Heffner, Q. X. Jia, J. J. Neumeier, J. Tesmer, J. D. Thompson, and X. D. Wu, Appl. Phys. Lett. **67**, 860 (1995).

Magnetoresistance and magnetic properties of $La_{1-x}\square_xMnO_{3-\delta}$ thin films

T. R. McGuire, A. Gupta, P. R. Duncombe, M. Rupp, J. Z. Sun, R. B. Laibowitz, and W. J. Gallagher
IBM Research Division, Thomas J. Watson Research Center, Yorktown Heights, New York 10598

Gang Xiao
Department of Physics, Brown University, Providence, Rhode Island 02912

Epitaxial thin films of $La_{1-x}\square_xMnO_{3-\delta}(0\leqslant x\leqslant 0.33)$ where $\square$ is a vacancy have been grown on (100) $SrTiO_3$ substrates by pulsed laser deposition. The lanthanum deficiency results in self doping of the system without the need for divalent ion substitution. Both the films and the bulk targets used for deposition were ferromagnetic and showed giant magnetoresistance (GMR). The films increased in saturation magnetization M_s and Curie temperature T_c with increasing x. The T_c, however, was about the same as found in Ca_x substitutions. Bulk samples showed little change in M_s and T_c with vacancy concentration. M_s in bulk samples is about half the value found in the films which have theoretical saturations for $x>0.2$. GMR in the films is a few hundred percent but the bulk values are 25% at $H=1.8$ T. © *1996 American Institute of Physics.* [S0021-8979(96)49108-1]

I. INTRODUCTION

Oxide films of manganese with the formula $La_{1-x}A_xMnO_3$, where A is a divalent ion, are ferromagnetic over a wide compositional range and have been shown to exhibit a giant magnetoresistance (GMR). Films in particular have large GMR. Jin *et al.*,[1,2] find that films of La-Ca-Mn-O can have GMR of over 100 000%. Bulk polycrystalline samples have smaller GMR but recently Tokura *et al.*[3] report on bulk single crystals of La-Sr-Mn-O which have a GMR of several hundred percent.

$LaMnO_3$ has the perovskite structure and it is an antiferromagnetic insulator. The divalent substitution for La maintains the perovskite structure but causes the normally Mn^{3+} to change to Mn^{4+}. This results in conductivity as well as ferromagnetic exchange interactions between the Mn^{3+} and Mn^{4+} which was suggested to be Zener double exchange.[1] In our study we form $La_{1-x}\square_xMnO_{3-\delta}$ where $\square_x$ represents x atomic fraction vacancies having zero valence and thus is self doping. The doping should vary linearly with x, having all Mn^{3+} at $x=0$ and all Mn^{4+} at $x=0.33$, if the oxygen stoichiometry is held constant ($\delta=0$). No direct measurement of oxygen content was made.

Thin films of $La_{1-x}\square_xMnO_{3-\delta}$ were made by pulsed laser ablation[4] from bulk target samples. Targets of $La_{1-x}MnO_{3-\delta}$, with varying ratios of La/Mn, were prepared from powders obtained by reaction of the high purity component oxides La_2O_3 and MnO at 1050 °C. High density (>95%) targets were obtained by isostatic pressing of the prepared powders and subsequent sintering for 0.1–0.5 h at 1550 °C in air. Powder x-ray diffraction indicated that the targets have single-phase orthorhombically distorted perovskite structures which index to $LaMnO_{3.00}$.

Films ~1000-Å thick were deposited on $SrTiO_3$ substrates held at 700 °C. After deposition the films were cooled to room temperature in 700 Torr oxygen. X-ray diffraction measurements of the films showed a small but systematic decrease in lattice parameter with increasing x consistent with the formation of mixed valence Mn^{3+}/Mn^{4+}.[5]

The electrical resistance and MR were measured as a function of magnetic field using a four probe technique. Magnetization studies were made using a Quantum Design SQUID magnetometer over a temperature range of 5–360 K. We have investigated both the film and the bulk target samples of this vacancy doped system.

II. RESULTS AND DISCUSSION

Figures 1 and 2 show the magnetic data of the films and target samples, respectively. Because of the wide range of resistivity ρ and MR, these data are listed in Table I. Films are 1 cm×0.5 cm rectangles and both magnetic moments M and ρ are measured on the same rectangular sample. The bulk samples are cut in two sizes for convenience on M and ρ measurements.

Saturation magnetic moments for the film are plotted in volume units and roughly increase from 340 to 480

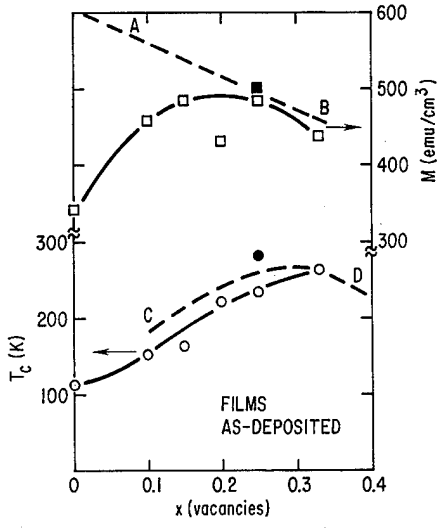


FIG. 1. Saturation magnetic moment M in fields of 4 T and Curie temperature T_c for $La_{1-x}\square_xMnO_{3-\delta}$ films. The value of T_c are within ±10 K. The filled data points for $x=0.25$ are for an annealed sample. Dashed line AB is calculated M for all Mn moments aligned parallel. Dashed curve CD are T_c for $La_{1-x}Ca_xMnO_{3-\delta}$ from Ref. 6.

 0021-8979/96/79(8)/4549/3/$10.00 © 1996 American Institute of Physics

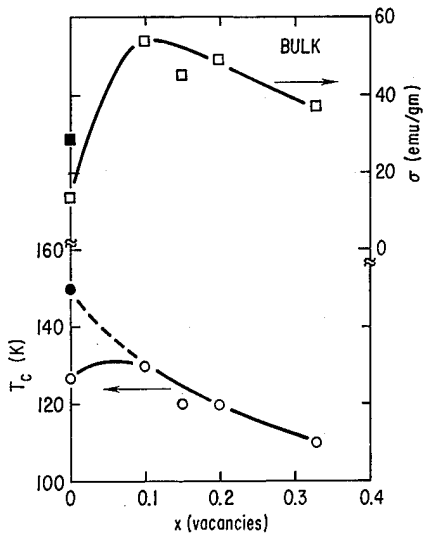


FIG. 2. Saturation magnetic moment σ at 4 T for the bulk target samples of $La_{1-x}\square_xMnO_{3-\delta}$. Curie temperatures are within ±10 K. The filled data points at $x=0$ are for an annealed sample.

(emu/cm^3) with increasing vacancy concentration as shown in Fig. 1. The dashed line marked (AB) on Fig. 1 is a calculated M based on all Mn^{3+}/Mn^{4+} magnetic moments aligned parallel and using densities of 6.6 gms/cc at $x=0$ reduced to 5.3 gms/cc at $x=0.33$ due to the vacancy concentration. Comparing the data points with the calculated values M increases with x and has parallel alignment of Mn^{3+}/Mn^{4+} for $x>0.2$. There is a corresponding increase in Curie temperature T_c with x. As seen in Table I, resistivity for films decrease with x, an effect also observed by Ju *et al.*,[6] for the $La_{1-x}Sr_xMnO_z$ system. Our magnetic measurements for $La_{1-x}\square_xMnO_{3-\delta}$ are compatible with an increase in the number of Mn^{4+} ions but it is not clear that we have reached all Mn^{4+} at $x=0.33$ which is expected to be an insulator. The maximum MR for the films as listed in Table I decreases with increasing x which means that MR is smaller in films with high T_c. The last column of Table I lists the temperature at which approximately maximum GMR is found and this is in the region of the Curie temperature for the various compositions.

As shown in Fig. 1, the film for $x=0$ which might be expected to be antiferromagnetic has a ferromagnetic component possibly due to a canted arrangement of Mn moments. Any canted atomic moments of the Mn disappears for $x>0.2$. The two filled data points for $x=0.25$ represent a sample annealed in oxygen at 850 °C for 30 min. There is a small increase in T_c and M for the annealed sample. The dashed line CD follow T_c values given for $La_{1-x}Ca_xMnO_3$.[6] Note that we use x regardless of the valency represented but there is little difference in T_c between Ca_x and $\square_x$.

TABLE I. Films $La_{1-x}\square_xMnO_{3-\delta}$.

x	$\rho(0)$ (Ω cm)	$\rho(1.8)$ (Ω cm)	GMR (%)	T(GMR) (K)
0	2.6	2.0	30	130
0.10	8.6	2.3	274	130
0.15	0.20	0.075	167	150
0.20	0.12	0.04	200	225
0.25	0.016	0.006	168	240
0.25[a]	0.008	0.004	100	290
0.33	0.22	0.11	100	250

[a]Annealed.
Resistivity $\rho(0)$ is at $H=0$ and $\rho(1.8)$ is for $H=1.8$ T. GMR=$[\rho(0)-\rho(1.8)]/\rho(1.8)$. T(GMR) is temperature for listed GMR estimated to be at maximum value of GMR for $H=1.8$ T.

TABLE II. Bulk.

x	(Ω cm×10^3)		%	K
0[a]	3.1	2.4	29	150
0.20	107	96	12	100
0.33	440	350	26	115

[a]Annealed.
Resistivity $\rho(0)$ is at $H=0$ and $\rho(1.8)$ is for $H=1.8$ T. GMR=$[\rho(0)-\rho(1.8)]/\rho(1.8)$. T(GMR) is temperature for listed GMR estimated to be at maximum value of GMR for $H=1.8$ T.

The bulk data shown in Fig. 2 also indicate that the $x=0$ sample has ferromagnetic character but similar to the film values the M and T_c are depressed. After annealing in oxygen at 850 °C for several hours both M and T_c increase as shown by the filled data points at $x=0$. Figure 2 illustrates that M and T_c decrease slightly with increasing x which is opposite in behavior to the films. From Table II we note that there is a sharp increase in ρ with x and that MR at ~25% is much smaller than found in the films. It would appear that the almost constant value of M and T_c with high ρ mean that not much Mn^{4+} is present in the bulk samples or at least the concentration of Mn^{4+} remains constant with x.

The values of M (bulk) range from 40 to 50 emu/gm close to one-half that of the films if the theoretical densities mentioned previously are used to calculate film moments in emu/gm. The low values of M and T_c, also the high ρ for the bulk samples, are further evidence of weak double exchange because of low Mn^{+4} concentration. We have determined the intrinsic value of the Mn moment in the bulk sample from measurements of the paramagnetic susceptibility χ above T_c by fitting the data to a Curie–Weiss law $\chi_M=C_M/(T-\theta)$ where χ_M and C_M are molar values. We find for $x=0$ (as deposited $C_M\approx3.38, \theta\approx70$ K; $x=0$ (anneal) $C_M\approx3.06$, $\theta\approx133$ K; $x=0.2$, $C_M\approx3.06$, $\theta=115$ K and $x=0.33$, $C_M\approx2.74$, $\theta\approx122$ K. Experimental values of C_M reported for Mn^{3+} range from 2.89 to 3.01 ($\mu_{eff}\approx4.9$) while Mn^{4+} has $C_M\approx1.82$ ($\mu_{eff}\approx3.9$).[7] It therefore appears that Mn^{3+} is dominant in the bulk samples for all values of x with possibly only 5% Mn^{4+}. Stoichiometry of the oxygen must compensate for the vacancy concentration. The paramagnetic measurements have two interesting features. First, there is a Curie–Weiss law behavior with C_M values representative of Mn^{3+} with some Mn^{4+}, and second, there is good agreement of the θ intercept with T_c. This means the exchange interactions stay constant with temperature in the bulk samples and that they are homogeneous magnetic materials. The low concentration of Mn^{4+} believed to exist in these target samples place a limit on extending the above interpretation to high conductivity film samples which have a larger Mn^{4+} concentration.

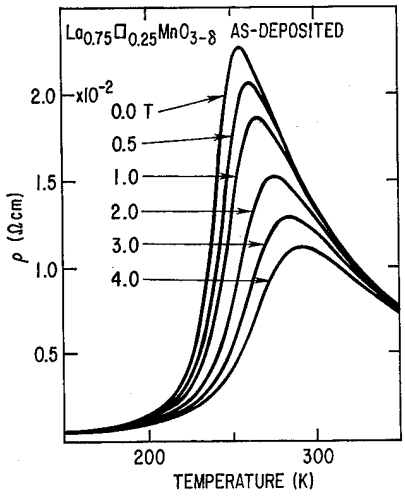


FIG. 3. Resistivity for film $x=0.25$ as a function of temperature at applied fields 0–4 T. The MR in the temperature range, 240–250 K is over 400% for $\Delta H=4$T.

The resistivity values obtained in fields of 1.8 T are shown in Tables I and II. In Fig. 3 are shown results for the $x=0.25$ film made in a superconducting magnet system with fields from 0 to 4 T and temperatures from 5 to 350 K. It shows clearly the effect of the magnetic field on the resistivity with maximum ρ moving to high temperature for increased H. In Fig. 4 we plot ρ vs H and M for a constant temperature of 240 K in the region of maximum MR for the $x=0.25$ sample of Fig. 3. Approximately ρ is linear over this limited range of M indicating that scattering of the conduction carriers by the Mn moments is the dominant feature. How ρ changes with M and H as a function of temperature has been discussed by Tokura *et al.*[3] for La-Sr-Mn-O and Hundley *et al.*[8] for La-Ca-Mn-O.

Based on the scattering behavior and the paramagnetic Curie–Weiss susceptibility our description of the MR in

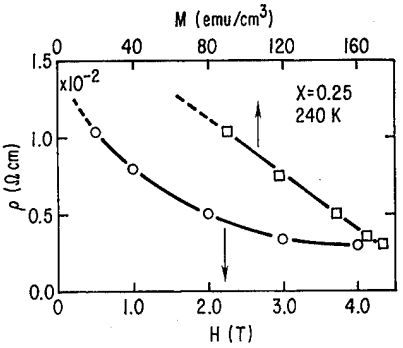


FIG. 4. Resistivity ρ as a function of H and M for film sample shown in Fig. 3 at a fixed temperature of 240 K.

these materials would agree with that given by Tokura *et al.*[3] Namely, that spin polarized conduction carriers become prominent in the region of T_c as the spontaneous magnetic order increases but there remains large scattering from still disordered Mn moments. As the Mn disorder is reduced by either lowering the temperature or applying a magnetic field the resistivity decreases as illustrated in Fig. 3.

The work at Brown University was supported by the National Science Foundation under the Materials Research Group Grant No. DMR-9121747, and partially supported by DMR-9258306.

[1] S. Jin, T. H. Tiefel, M. McCormack, R. A. Fastnacht, R. Ramesh, and L. H. Chen, Science **264**, 413 (1994).
[2] S. Jin, M. McCormack, T. H. Tiefel, and R. Ramesh, J. Appl. Phys. **76**, 6929 (1994).
[3] Y. Tokura, A. Urushifara, Y. Moritomo, T. Arima, A. Asamitsu, G. Kido, and N. Furukawa, J. Phys. Soc. Jpn. **63**, 3931 (1994).
[4] A. Gupta, T. R. McGuire, P. R. Duncombe, M. Rupp, J. Z. Sun, W. J. Gallagher, and G. Xiao, Appl. Phys. Lett. **67**, 3494 (1995).
[5] E. O. Wollan and W. C. Koehler, Phys. Rev. **100**, 545 (1955).
[6] H. L. Ju, C. Kwon, Q. Li, R. L. Greene, and T. Venkatesan, Appl. Phys. Lett. **65**, 2108 (1994).
[7] L. F. Bates, *Modern Magnetism*, 2nd ed. (Cambridge University Press, Cambridge, 1947), Chap. 3, p. 130.
[8] M. F. Hundley, M. Hawley, R. H. Heffner, Q. X. Jia, J. J. Neumeier, J. Tesmer, J. D. Thompson, and X. D. Wu, Appl. Phys. Lett. **67**, 860 (1995).

Superparamagnetic behavior and giant magnetoresistance in oxygen deficient $R_{0.67}Sr_{0.33}MnO_z$ (R=Nd, Pr) epitaxial films (abstract)

H. L. Ju, Qi Li, G. C. Xiong, T. Venkatesan, and R. L. Greene
Center for Superconductivity Research, Department of Physics, University of Maryland, College Park, Maryland 20742

We have studied the magnetic and magnetotransport properties of oxygen deficient $R_{0.67}Sr_{0.33}MnO_z$ (R=Nd, Pr) films and have observed superparamagnetic behavior in these films. The superparamagnetism is indicated by (i) the increasing spread between zero field cooled (ZFC) and field cooled (FC) magnetization curves as temperature decreases, (ii) a sharp drop of the ZFC magnetization at low temperature, (iii) enhanced Curie–Weiss constant above the ferromagnetic temperature, and (iv) at low temperature a sharp drop of coercivity (H_c) with increasing temperature. These findings strongly suggest that all oxygen deficient manganites are magnetically inhomogeneous; i.e., ferromagnetic clusters exist. We estimate the spin cluster diameter to be 7–10 nm at low temperature ($T<30$ K). We discuss a possible origin of the giant magnetoresistance effect based on the existence of spin clusters. © *1996 American Institute of Physics.* [S0021-8979(96)59108-5]

Role of lattice distortions in the transport property of $R_{0.7}Me_{0.3}MnO_3$ (R=Pr,Nd,La and Me=Ba,Sr,Ca) (abstract)

R. P. Sharma, G. C. Xiong, S. B. Ogale, R. L. Greene, and T. Venkatesan
University of Maryland, Center for Superconductivity Research, College Park, Maryland 20742

There are different models which to try to explain the transport properties of the manganese oxides in terms of magnetic polarons, Zener double exchange and Jahn-Teller distortions of the lattice which is temperature dependent. Using Rutherford backscattering techniques (2–3 MeV He ions) we are measuring the presence of lattice distortions by studying the angular scans in the channeling mode. The angular widths (FWHM) can be used to extract both dynamic and static displacements of the atoms from their equilibrium sites. The technique is extremely powerful in the sense that *local uncorrected* displacements as small as 0.01 Å from the equilibrium position can be detected. The extraction of the physics from the data is relatively straight forward compared to other techniques such as XRD or neturon scattering. Using a variable temperature backscattering system at our center (one of three or four systems around the world) the angular width (FWHM) is found to exhibit a dramatic change with temperature increasing with decreasing temperature showing a possible correlation with both the transport and magnetic properties. The results suggest a decrease in the lattice disorder with reduced temperature far in excess of what one would predict on the basis of a simple Debye behavior. The reduction in the lattice disorder correlates very well with the resistance vs temperature dependence. A variety of manganese oxide epitaxial thin films grown by pulsed laser deposition have been studied and the data suggests a role for structural distortions in any mechanism to explain the transport properties of these materials. © *1996 American Institute of Physics.* [S0021-8979(96)59208-1]

 0021-8979/96/79(8)/4552/1/$10.00 © 1996 American Institute of Physics

The effect of disorder and fluctuations on the magnetotransport of a double-exchange ferromagnet (abstract)

Jeff M. Byers
Naval Research Laboratory, Washington, D. C. 20375

The discovery of colossal magnetoresistance (CMR) in the doped perovskite manganites has reawakened interest in the double-exchange mechanism proposed to Zener. To account for the close relation between ferromagnetism and metallic transport in lanthanum manganites doped with divalent cation (Ca, Sr, Ba) Zener claimed that an electron could delocalize on lattice of spins and still conform to Hund's Rule if a ferromagnetic coupling between spins were mediated by that same electron. Thus, the onset of metallic behavior (delocalization) is intimately linked to ferromagnetic ordering of the spin lattice. Clearly, the double-exchange mechanism provides some necessary physics but is not sufficient in explaining the key mystery of the CMR materials: What causes the large peak in the resistivity vs. temperature and why is it removed by an applied magnetic field. The effect of disorder and fluctuations on the double-exchange mechanism may provide the answers. Several sources of disorder in these materials act to form a mobility edge via Anderson localization: intrinsic divalent/trivalent cation disorder, off-diagonal disorder caused by the spin lattice and oxygen vacancy disorder. A mean-field calculation reveals that below the Curie temperature those carriers aligned opposite to the magnetization experience a narrowing band as the temperature is reduced. Fermi glass behavior is induced in this minority carrier band by the Fermi level falling below the mobility edge. However, the mean-field result does not contain a peak in resistivity since the majority carrier band does not behave as a Fermi glass and effectively "shorts out" the more resistive minority conduction channel. The formation of the resistivity peak requires the inclusion of ferromagnetic fluctuations above the Curie temperature that tend to "mix" the two conduction channels. The application of a magnetic field unmixes the conduction channels once again allowing the carriers aligned with the magnetization to carry current solely in the low-resistance channel (causing the dramatic negative magnetoresistance). This work supported by a National Research Council postdoctoral fellowship. © *1996 American Institute of Physics.* [S0021-8979(96)59308-8]

Ozone assisted, block-by-block, molecular beam epitaxy of La–M–Mn–O (M=Ca,Ba,Sr) thin films and La–M–Mn–O/Dy–Ba–Cu–O multilayers (abstract)

V. A. Vas'ko, P. A. Kraus, V. S. Achutharaman, C. A. Nordman, and A. M. Goldman
Center for the Science and Application of Superconductivity and School of Physics and Astronomy, University of Minnesota, Minneapolis, Minnesota 55455

We report the growth of thin (<100 nm) La–M–Mn–O(M=Ca,Ba,Sr) films by ozone assisted, block-by-block, molecular beam epitaxy on single crystal $SrTiO_3$, and $LaAlO_3$, substrates. The films were characterized by RHEED, high resolution x-ray diffraction, x-ray reflectively, RBS, Ion channeling, SEM, and STM. These films show a very high degree of crystalline perfection as evidenced by very low rocking curve widths (<0.06 deg), extremely low surface roughness (of the order of one unit cell) and the observation of thickness fringes using x-ray diffraction. Careful magnetic, transport and magnetotransport measurements of these films will be presented. Multilayer structures of La–M–Mn–O and Dy–Ba–Cu–O/La–Sr–Cu–O superconductors have also been fabricated. The effect of interfacial chemistry on the transport properties of such layers and the compatibility issues for the growth of manganate/cuprate superconductor multilayers will be discussed. © *1996 American Institute of Physics.* [S0021-8979(96)59408-4]

Supported in part by the Air Force Office of Scientific Research under the Grant No. F-49620-93-1-0076.

Transport properties and magnetic behavior of $La_{1-x}Sr_xMnO_3$ single crystals (abstract)

A. Anane, C. Dupas, K. Le Dang, J. P. Renard, and P. Veillet
Institut d'Electronique Fondamentale, CNRS URA 022, Bâtiment 220, Université Paris-Sud, 91405 Orsay Cedex, France

A. M. de Leon Guevarra, F. Millot, L. Pinsard, and A. Revcolevschi
Laboratoire de Chimie du Solide, CNRS URA 446, Université Paris-Sud, 91405 Orsay Cedex, France

Single crystals of $La_{1-x}Sr_xMnO_3$ with x ranging from 0.06 to 0.42 have been investigated by various techniques: resistivity and magnetoresistance, superconducting quantum interference device magnetometry, and ^{55}Mn nuclear magnetic resonance. In addition, for two Sr concentrations, $x=0.13$ and 0.25, the $I(V)$ characteristic of the oxide-metal junction has been measured versus temperature. Semiconductor-metal transition occurring just below the Curie temperature T_c was observed for $x\geqslant 0.175$ whereas, for $x\leqslant 0.15$, the crystals exhibits only semiconducting behavior, in agreement in the previous studies.[1] These transport properties are closely connected with the electron transfer mediated by the double exchange interaction between Mn^{3+} and Mn^{4+}, as revealed by ^{55}Mn spin-echo experiments. A cusp in the magnetoresistance (MR) was observed near T_c for the crystals with $x\geqslant 0.13$ with typical maximum resistivity ratio $R(0)/R(10\ \mathrm{T})\approx 10$; for the sample with $x=0.1$, the huge MR persists well below $T_c\approx 140$ K, which is probably due to a noncollinear spin configuration. The $I(V)$ characteristic of the oxide-aluminum junction is strongly dependent on temperature and applied magnetic field. In the semiconducting phase, a nonlinear behavior reminiscent to that of a strongly doped dirty semiconductor is observed. © *1996 American Institute of Physics.* [S0021-8979(96)81408-0]

[1] Y. Tokura *et al.*, J. Phys. Soc. Jpn. **63**, 3931 (1994).

 0021-8979/96/79(8)/4554/1/$10.00 © 1996 American Institute of Physics

Density-functional studies of the electronic structure of the perovskite oxides: $La_{1-x}Ca_xMnO_3$

S. Satpathy
Department of Physics and Astronomy, University of Missouri, Columbia, Missouri 65211

Zoran S. Popović and Filip R. Vukajlović
Laboratory for Theoretical Physics, Institute of Nuclear Sciences- "Vinča", 11001 Belgrade, Yugoslavia

Using density-functional methods, we study the electronic structures of the lanthanum-based "double-exchange" perovskite magnets. Antiferromagnetic insulating solutions are obtained for both the end members, $LaMnO_3$ and $CaMnO_3$, within the local density approximation (LDA), with the Jahn-Teller (JT) distortion of the oxygen octrahedron taken into account. The JT distortion splits off the Mn($3d$)e_g bands producing an energy gap within the LDA, with the bands derived from the (z^2-1) orbital, pointed along the long basal-plane Mn—O bond, occupied and the (x^2-y^2) bands empty. The on-site Coulomb repulsion and the intra-site exchange terms are found to be, respectively, $U\simeq 8-10$ eV and $J\simeq 0.9$ eV, from the "constrained" density-functional theory. The large value of U as compared to the bandwidth indicates that the manganese perovskite oxides are strongly correlated systems. © *1996 American Institute of Physics.* [S0021-8979(96)49208-8]

The hole-doped manganese perovskite oxides, such as $La_{1-x}Ca_xMnO_3$, are prime examples of solids with a ferromagnetic conducting state caused by the "double exchange" mechanism, where the magnetic coupling between localized spins on neighboring atoms is mediated via conduction electrons.[1–4] Both the end-members, $LaMnO_3$ and $CaMnO_3$, are antiferromagnetic (AF) insulators with, respectively, Mn^{3+} $(t_{2g}^3e_g^1)$ and Mn^{4+} $(t_{2g}^3e_g^0)$ configurations of the Mn ions. The localized spins of the t_{2g} electrons are coupled ferromagnetically by the doped holes in the partially filled e_g band introduced by the Ca atoms. Thus, the partially filled e_g band is responsible simultaneously for ferromagnetism and conduction in the solid. This is precisely what is experimentally observed, viz., that the mixed valence compound $La_{1-x}Ca_xMnO_3$ shows the highest electrical conductivity for $0.2\leqslant x\leqslant 0.4$, exactly in the concentration range where the material is ferromagnetic.[5] New interest on these systems has been revived by the recent discovery of colossal magnetoresistance (CMR) in the La-Ca-Mn-O films.[6,7]

In this paper, we examine the electronic structure of the two end members, $LaMnO_3$ and $CaMnO_3$, from density-functional band calculations using the local spin-density approximation (LDA), as well as the "constrained" density-functional and the "LDA+U" theories.[8]

Both $LaMnO_3$ and $CaMnO_3$ form in the orthorhombic crystal structure[9] which is a distorted form of the cubic perovskite structure. While in the Ca compound, the distortion of the O octahedra surrounding the manganese atoms is largely absent, in the La compound, the octahedra are distorted significantly with three distinct Mn—O bond lengths. The Jahn-Teller (JT) distortion of the O octahedron is understandable in view of the $t_{2g}^3e_g^1$ configuration of the Mn ion. In addition to the JT distortion, there is a slight rotation of the octahedra, which is neglected in the calculations reported here. All our calculations reported here were performed using the linear muffin-tin orbitals (LMTO-ASA) method[10] and the ideal tetragonal crystal structure for the two perovskites with inclusion of the JT distortions. Thus, the magnetic unit cell in our calculation has four formula units for $LaMnO_3$ and two for $CaMnO_3$.

The antiferromagnetic band structures of $LaMnO_3$ and $CaMnO_3$ are shown in Fig. 1. The observed AF order, type A for the former and type G for the later compound,[11] is reproduced from the local-density calculations. The key features of the AF band structures agree with the independent LAPW calculations of Pickett and Singh.[12] As seen from Fig. 1, the key orbitals near E_f are the O($2p$) and Mn($3d$) orbitals with the energy gap occurring in the middle of the Mn($3d$) bands. The outer electrons from the La, Ca, and Mn atoms are transferred to complete the $2p$ shell of the oxygen atoms, resulting in the nominal chemical formulas of $La^{3+}Mn^{3+}O_3^{2-}$ and $Ca^{2+}Mn^{4+}O_3^{2-}$, respectively.

We have studied the effect of the Jahn-Teller distortion of the cubic octahedra on the band structure by performing a series of calculations for $LaMnO_3$ with various amounts of the distortion. There are three types of distortions[13] affecting the Mn—O bond lengths: (i) The breathing mode (Q_1), (ii) the basal-plane distortion mode (Q_2) with one diagonally opposite O pair displaced outwards and the other pair displaced inwards, and (iii) the octahedral stretching mode (Q_3) where the four in-plane O atoms are displaced inwards and the two apical O atoms are displaced outwards. The amplitudes of these three modes in $LaMnO_3$ are, respectively, 0.08, 0.20, and 0.11 Å, resulting in the three distinct Mn—O bond lengths: 1.91, 2.19, and 1.96 Å. We find that the basal-plane distortion mode Q_2 is the most effective in splitting up the e_g bands in $LaMnO_3$ thereby producing an energy gap, and that the Q_1 or the Q_3 distortions are relatively ineffective in opening up the gap. We find that a JT distortion of the Q_2 type, with the oxygen atoms displaced by at least the amount $\approx$0.1 Å from their ideal positions, is necessary to produce a band gap in $LaMnO_3$. In the crystal, the measured value of this distortion is about 0.15 Å, which is therefore enough for the insulating solution. The t_{2g} bands in contrast remain more-or-less unaffected by the distortions.

The splitting of the Mn($3d$) bands in $LaMnO_3$ due to the

 0021-8979/96/79(8)/4555/3/$10.00 © 1996 American Institute of Physics

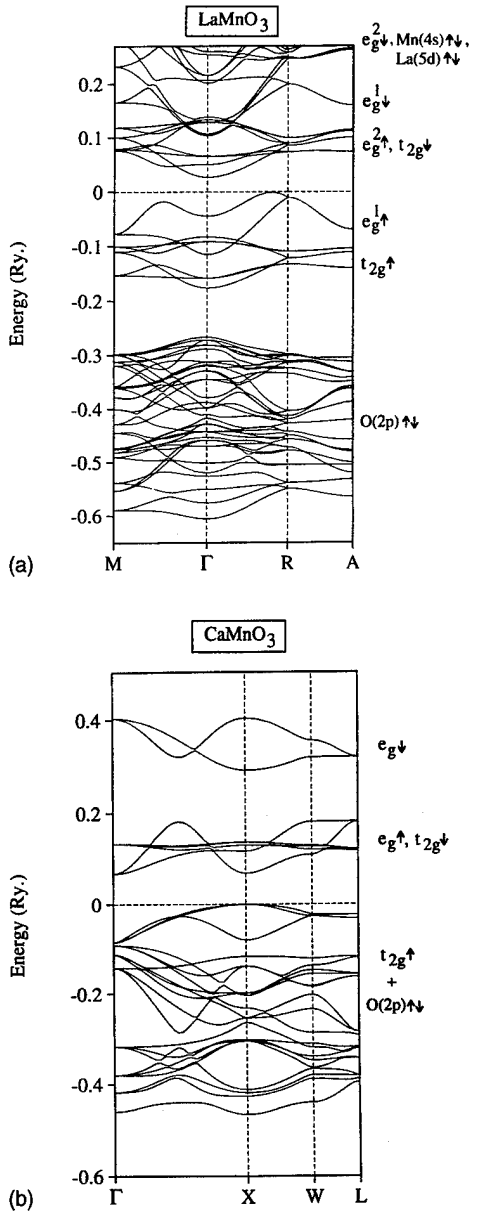


FIG. 1. Electronic band structures of antiferromagnetic $LaMnO_3$ and $CaMnO_3$ in the ideal tetragonal structure with, respectively, type A and type G magnetic configurations. The Jahn-Teller distortion of the oxygen octahedra was included for $LaMnO_3$. The symmetry components e_g and t_{2g} correspond to the Mn($3d$) orbital, and spin components ($\uparrow$ or $\downarrow$) are local to individual atoms. Energies are with respect to E_f.

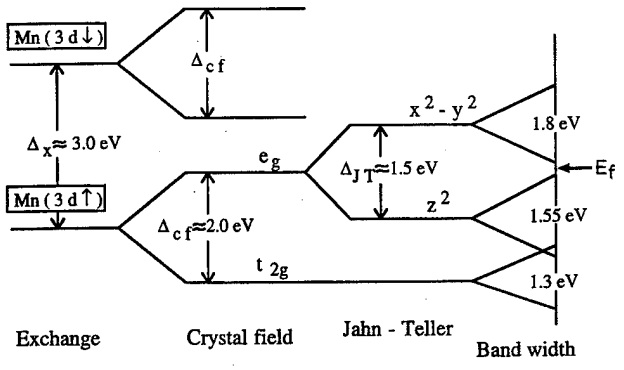


FIG. 2. Multiplet splitting of the Mn($3d$) orbital for $LaMnO_3$ as obtained from the density-functional calculation.

combined effects of the cubic crystal field, exchange, and the Jahn-Teller distortion as obtained from our calculations has been shown in Fig. 2. The exchange splitting is about 3.0 eV which removes the minority-spin bands up above E_f. The cubic crystal-field splitting between the t_{2g} and the e_g orbitals is about $\Delta_{cf} \simeq 2.0$ eV, while the Q_2 distortion of the oxygen octahedron splits the e_g bands by $\Delta_{JT} \simeq 1.5$ eV. The total band width of the occupied Mn($3d$) bands is about 2.4 eV. Of this, the t_{2g} bands are 1.3 eV wide, while the Jahn-Teller split e_g^1 band just below E_f has a width of about 1.6 eV.

We find that the occupied Mn(e_g) band is derived from the z^2-1 orbital, while the unoccupied band is derived from the x^2-y^2 orbital, in a Mn-atom-based *local* coordinate system with the z axis along the long, basal-plane Mn—O bond. This is illustrated in Fig. 3, where we have shown the dominant orbital contribution[14] to the band structure. Occupation of the z^2-1 band gives rise to the $t_{2g}^3 e_g^1$ configuration of the Mn atom for $LaMnO_3$. In the mixed compound, the e_g^1 band is progressively depleted with Ca concentration x, with complete depletion for the end-member $CaMnO_3$ ($x=1$).

Electron bands[12,16] for $LaMnO_3$ in the experimentally observed crystal structure are not very different from the band structure shown in Fig. 1(a). Two differences may be noticed: (i) the O($2p$) bands are separated from the Mn($3d$) bands here, a feature that disappears for the experimental structure, and (ii) the e_g^1 and the t_{2g} bands just below the E_f overlap, while for the experimental crystal structure, additional interaction results in a small separation between the e_g^1 and the t_{2g} bands. In spite of this separation, however, the

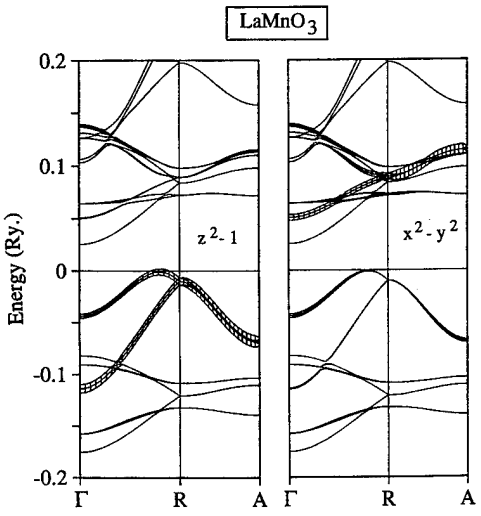


FIG. 3. Contribution of the Mn($3d$)z^2-1 and x^2-y^2 orbitals, to the band structure. The orbitals are with respect to a Mn-atom-based *local* coordinate system with the z axis pointing towards a long Mn—O bond on the basal plane. The width of each band in the figure shown by cross hatching, is proportional to the contribution of the $3d$ orbital (z^2-1 or x^2-y^2) on a specific Mn atom.

TABLE I. Energy $\bar{\epsilon}_d$ of the central site Mn($3d$) level (in Rydberg) for two different values of the "constrained" occupancy n_d for the case of $LaMnO_3$. The occupancies of the s and p electrons on the Mn site and the total valence charges on the neighboring in-plane (n_{O1}) and out-of-plane (n_{O2}) oxygen atoms are also shown.

n_d	$\bar{\epsilon}_d$	n_s	n_p	n_{O1}	n_{O2}
4.5	−0.44	0.39	0.51	6.05	6.16
5.5	0.33	0.26	0.38	5.96	6.17

excursion of the z^2-1 character into the t_{2g} group of bands, as seen from the left panel of Fig. 3 near the Γ point, is nevertheless retained in the electron bands for thef experimental crystal structure [see inset of Fig. 2(a) in Ref. 16].

To assess the importance of the correlation effects, we have estimated the magnitudes for the on-site Coulomb (U) and the intra-atomic exchange (J) parameters for the Mn atom from constrained density-functional calculations.[15] The Coulomb parameter U was calculated from the dependence of the on-site energy $\bar{\epsilon}_d$ of the Mn(d) orbital on the number occupancy n_d of a central Mn site,

$$\bar{\epsilon}_d = \epsilon_d + U \times (n_d - 1), \tag{1}$$

with the interaction of the central Mn(d) orbitals with the rest of the system switched off. This procedure is somewhat different from the one we reported earlier,[16] where we employed a Slater's transition rule for the calculation of U, but we get very similar results in both cases. By constraining all d electrons on a central Mn site in a 4-atom supercell calculation, we obtain a value of about 10.4 eV for U.[17]

In Table I, we show the screening charges on the central Mn atom and the neighboring O atoms, for two different constrained values of n_d. The change in the number of $3d$ electrons is screened by only about 13% each by the Mn s and p electrons. The four in-plane oxygen atoms together contribute about 36% while the two out-of-plane oxygen atoms contribute a negligible 2% to the screening charge. The rest of the screening charge resides on more distant neighbors. Such relatively poor screening results in the high value for the Coulomb parameter U.

However, since the screening charges reside on the sphere centers in the LMTO calculation, while in reality such charges on neighboring atoms are displaced towards the central atom, the Coulomb interaction may be somewhat overestimated.[18] A lower bound for U is obtained by supposing that the screened charges on the neighboring oxygen atoms are located at the surface of the central Mn sphere, which then yields the maximum value for the error to be about 2.1 eV, with the resultant lower bound of $U \simeq 8.3$ eV. Thus, our calculations indicate a value of $U \simeq 8$—10 eV, which is consistent with the estimate of $U \simeq 7.5$ eV from an analysis of the photoemission data.[19] Such large values for U indicate significant electronic correlation. The calculated magnitude of the on-site parameter is $J \simeq 0.86$ eV, which is typical of binary transition-metal oxides, where it varies between 0.78 to 0.98 eV.[8]

With the calculated Coulomb and exchange parameters, we have minimized the LDA+U functional,[8] which takes into account the effects of the large Hubbard U term in a meanfield sense. The results discussed in detail elsewhere[16] show that there is a significant spectral redistribution. In particular, while in the LDA calculations, the Mn($3d$) bands occur above O($2p$) bands, in the LDA+U calculations in the Mn($3d$) bands have shifted down in energy with respect to the O($2p$) states and occur in the lower part of a joint band of about 7-eV wide, which is consistent with the valence-band photoemission data.[22] Even though the relative positions of the Mn($3d$) and the O($2p$) bands are reversed in the LDA+U results as compared to the LDA results, both results are consistent with the 7-eV-wide joint Mn($3d$)—O($2p$) double-peak structure seen in the valence-band photoemission.[20–22] A clearer experimental evidence for a large Coulomb U is indicated by the Mn($2p$) core-level photoemission spectra, where a satellite peak is seen at the binding energy of ≈ 10 eV.[19,20,23]

This work was supported in part by the Office of Naval Research under Contract No. ONR N00014-95-1-0439 and by the Serbian Scientific Foundation under the project, "Physics of Condensed Matter and New Materials," Grant No. 3.

[1] C. Zener, Phys. Rev. **82**, 403 (1951).
[2] P. W. Anderson and H. Hasegawa, Phys. Rev. **100**, 675 (1955).
[3] P.-G. De Gennes, Phys. Rev. **118**, 141 (1960).
[4] J. B. Goodenough, Phys. Rev. **100**, 564 (1955).
[5] G. H. Jonker and J. H. Van Santen, Physica **16**, 337 (1950); J. H Van Santen and G. H. Jonker, Physica **16**, 599 (1950).
[6] R. von Helmolt, J. Wecker, B. Holzapfel, L. Schultz, and K. Samwer, Phys. Rev. Lett. **71**, 2331 (1993).
[7] S. Jin, T. H. Tiefel, M. McCormack, R. A. Fastnacht, R. Ramesh, and L. H. Chen, Science **264**. 413 (1994).
[8] V. Anisimov, J. Zaanen, and O. K. Andersen, Phys. Rev. B **44**, 943 (1991).
[9] J. B. A. A. Elemans, B. van Laar, K. R. van der Veen, and B. O. Loopstra, J. Solid State Chem. **3**, 238 (1971).
[10] O. K. Andersen, Phys. Rev. B **12**, 3060 (1975).
[11] E. O. Wollan and W. C. Koehler, Phys. Rev. **100**, 545 (1955).
[12] W. E. Pickett and D. J. Singh, Phys. Rev. B **53**, 1146 (1996).
[13] M. D. Sturge, *Solid State Physics*, edited by F. Seitz, D. Turnbull, and H. Ehrenreich (Academic, New York, 1967), Vol. 20.
[14] O. Jepsen and O. K. Andersen, Z. Phys. B **97**, 35 (1995).
[15] P. H. Dederichs, S. Blügel, R. Zeller, and H. Akai, Phys. Rev. Lett. **53**, 2512 (1984); A. K. McMahan, R. M. Martin, and S. Satpathy, Phys. Rev. B **38**, 6650 (1988).
[16] S. Satpathy, Z. S. Popović, and F. R. Vukajlović, Phys. Rev. Lett. **76**, 960 (1996).
[17] Instead, if we constrain only the number of e_g electrons on the central Mn atom, allowing the rest of the electrons including the central site t_{2g} electrons to screen the interaction, we get the value of $U \simeq 8.5$ eV.
[18] V. Drchal, O. Gunnarsson, and O. Jepsen, Phys. Rev. B **44**, 3518 (1991).
[19] A. E. Bocquet, T. Mizokawa, T. Saitoh, H. Namatame, and A. Fujimori, Phys. Rev. **46**. 3771 (1992).
[20] A. Chainani, M. Mathew, and D. D. Sharma, Phys. Rev. B **47**, 15 397 (1993).
[21] J. Zhang, D. N. McIlroy, P. A. Dowben, S. H. Liou, R. F. Sabrianov, and S. S. Jaswal, Solid State Commun. **97**, 39 (1996).
[22] R. P. Vasquez (unpublished).
[23] M. Abbate *et al.*, Phys. Rev. B **46**, 4511 (1992).

Electron spectroscopic studies of colossal magnetoresistance material $La_{1-x}Ca_xMnO_3$

J.-H. Park, C. T. Chen, S.-W. Cheong, W. Bao,[a] and G. Meigs
AT&T Bell Laboratories, Murray Hill, New Jersey 07974

V. Chakarian and Y. U. Idzerda
Naval Research Laboratory, Code 6345, Washington, DC 20375

High resolution photoemission measurements have been performed for the ferromagnetic transition of $La_{0.67}Ca_{0.33}MnO_3$ and for the order–disorder transition of $La_{0.4}Ca_{0.6}MnO_3$. The band gap collapsed below the Curie temperature and the density of states at the Fermi level increases with cooling. Upon cooling through the order–disorder transition temperatures, T_{CO}, the band gap increases by ~50 meV. This change in the gap is consistent with the change in the activation energy above and below T_{CO} estimated from conductivity data. We have also performed soft x-ray magnetic circular dichroism measurements at Mn $L_{2,3}$ edges for ferromagnetic $La_{0.67}Ca_{0.33}MnO_3$ and $La_{0.8}Ca_{0.2}MnO_3$. © *1996 American Institute of Physics.* [S0021-8979(96)49308-4]

I. INTRODUCTION

With a discovery of "colossal" magnetoresistance (CMR), mixed-valent manganese perovskites, such as $La_{1-x}Ca_xMnO_3$ and $La_{1-x}Sr_xMnO_3$, have attracted renewed attention, particularly due to their potential technical application.[1–5] These manganese perovskites exhibit a variety of electrical and magnetic phases depending on the doping concentration, x, and the temperature, T.[6] Especially, for a doping range of $\sim 0.2 < x < \sim 0.5$ in which CMR has been observed near the Curie temperature, T_c, the system undergoes a ferromagnetic transition. This magnetic transition is accompanied by a large change in resistance, and further upon heating, the resistivity increases below T_c but decreases above T_c.[5–8] Hence, the transition has often been referred to as a paramagnetic insulator to ferromagnetic metal (PI–FM) transition. However, these intriguing resistivity behaviors have been attributed to a spin-dependent scattering mechanism instead of the electronical transition such as the gap closing observed in most metal–insulator transitions.[7,9]

$LaMnO_3$ contains Mn^{3+} ($t_{2g}^3 e_g^1; S=2$). Substitution of La sites with alkaline earth elements induces Mn^{4+} ($t_{2g}^3; S=3/2$), and the system becomes mixed valent. The ferromagnetic transition in hole doped $LaMnO_3$ has been traditionally explained in the framework of the "double-exchange" model, which engenders the spin-dependent scattering mechanism.[7,10–12] Theoretical calculations based on the model shows that the calculated results qualitatively agree with the observed transport data,[7] but also reveal significant contrasts such as the insulating behavior above T_c.

Besides the ferromagnetic transition, a real space charge-ordering of Mn^{3+} and Mn^{4+} has recently been reported in a similar family member, $Pr_{0.5}Sr_{0.5}MnO_3$.[13] Further, in $La_{1-x}Ca_xMnO_3$, this charge ordering has been observed in a wide range of doping concentrations, $0.5 < x \leq 0.75$,[14] in which the system has an antiferromagnetic ground state. Upon cooling through the charge-ordering temperature, T_{CO}, ~500 K (40 meV) increase has observed in the resistivity slope, $d[\ln(R)]/d(T^{-1})$, which correspond to the activation energy in a semiconductor model.[14]

As a powerful experimental tool to study magnetic structure of ferromagnetic systems and magnetic multilayers, soft x-ray Magnetic Circular Dichroism (MCD) has been introduced.[15–18] Since the manganese perovskites undergo ferromagnetic transition accompanied by the colossal magnetoresistance, MCD measurements on these systems are quite useful to study the magnetic properties.

Here, we present temperature dependent high resolution photoemission data through the ferromagnetic transition temperature, T_c, of $La_{0.67}Ca_{0.33}MnO_3$ and through the charge-ordering temperature, T_{CO}, of $La_{0.4}Ca_{0.6}MnO_3$. We also present MCD results on ferromagnetic $La_{0.67}Ca_{0.33}MnO_3$ and $La_{0.8}Ca_{0.2}MnO_3$ at Mn $L_{2,3}$ edges. The organization of the paper is the following. The experimental details are described in Sec. II, and the results and discussions and the conclusions are followed in Secs. III and IV, respectively.

II. SAMPLES AND EXPERIMENTS

The photoemission spectroscopy (PES) and MCD measurements were performed at the AT&T Bell Laboratories Dragon beamline at the National Synchrotron Light Source (NSLS).[19] Polycrystalline $La_{0.67}Ca_{0.33}MnO_3$ and $La_{0.4}Ca_{0.6}MnO_3$ samples were prepared by standard solid-state reaction method. All the samples were oxygen-stoichiometric and x-ray powder diffraction measurements showed single phase patterns. The samples were cleaved in a vacuum better than 1.5×10^{-10} Torr, and during the measurements the temperature was controlled within 1 K. The cleaned surfaces were found to last about 4 hr, as confirmed by absence of 9 eV binding energy peak which is known to appear with surface contamination. All the measurements were repeated at least twice to ensure reproducibility of data and each set of data was obtained from a newly cleaved fresh surface. The high resolution PES spectra were measured at 110 eV photon energy with a 60 meV overall experimental resolution, including the photon and electron kinetic energy

[a]Permanent address: Department of Physics, Johns Hopkins University, Baltimore, MD 21218.

 0021-8979/96/79(8)/4558/3/$10.00 © 1996 American Institute of Physics

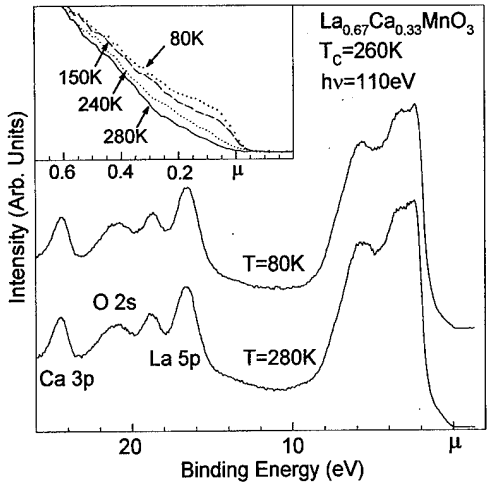


FIG. 1. High resolution photoemission spectra of $La_{0.67}Ca_{0.33}MnO_3$ ($T_c \approx 260$ K) taken at different temperatures.

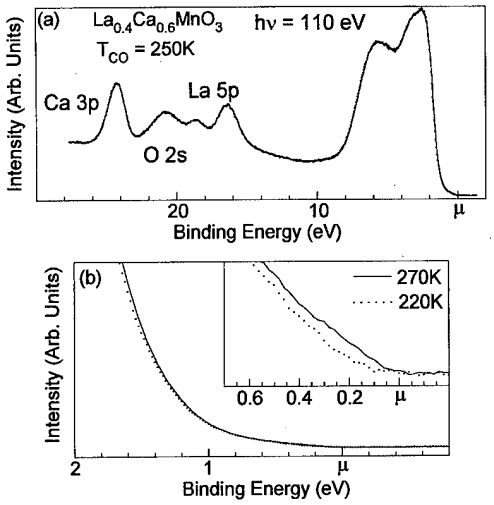


FIG. 2. High resolution photoemission spectra of $La_{0.4}Ca_{0.6}MnO_3$ taken at 270 K, above the charge ordering temperature, $T_{CO} \approx 250$ K, and at 220 K, below T_{CO}. (a) wide range spectra and (b) spectra near the chemical potential.

resolution. The binding energies were referred to the chemical potential of a clean Pt in electrical and thermal contact with the samples.

For MCD measurements, the photoabsorption spectra were obtained at normal incidence on $La_{0.67}Ca_{0.33}MnO_3$ and $La_{0.8}Ca_{0.2}MnO_3$ by monitoring the sample photocurrent. The samples were scraped in a vacuum better than 1×10^{-9} Torr. A 0.4 Tesla permanent magnet was used for magnetization of samples. Since the Curie temperatures of $La_{0.67}Ca_{0.33}MnO_3$ and $La_{0.8}Ca_{0.2}MnO_3$ are 260 and 200 K,[6] respectively, the spectra were recorded at liquid-nitrogen temperature (~80 K). The degree of circular polarization was set ~85%, and the photon energy resolution was set 300 meV.

III. RESULTS AND DISCUSSIONS

Figure 1 shows the high resolution PES spectra of $La_{0.67}Ca_{0.33}MnO_3$ which has $T_c \approx 260$ K. The wide-scan spectra, which include the valence band and the Ca $3p$, O $2s$, and La $5p$ shallow core levels as well, exhibit nearly no difference between $T=80$ K and $T=280$ K, excepting for a minor chemical shift of ~70 meV and an intensity variation very near E_F. The magnified near E_F spectra taken at four different temperatures, 80, 150, 240, and 280 K, are shown in the inset. In the 280-K spectrum, no density of states at E_F, $n(E_F)$, is observed indicating the insulating phase. Upon cooling below T_c, $n(E_F)$ gradually increases, and the 80-K spectrum clearly reveals the metallic Fermi edge. These results provide a microscopic evidence for an insulator–metal transition, and the large change in the resistivity as well as the sign change around T_c in the temperature dependence of the resistivity, $d[R(T)]/dT$, can be understood by the insulator–metal transition.

What causes the insulating nature above T_c? Our photoemission data show negligible $n(E_F)$ above T_c and very tiny $n(E_F)$ even well below T_c, while within the double exchange model, a considerable amount of density of states are expected at E_F both below and above T_c. These contrasts prove that some additional effects to the double exchange model are required to suppress $n(E_F)$ substantially. Recently, the additional effects were also pointed out from a theoretical analysis of the transport data, and a Jahn-Teller polaron effect has been suggested for the candidate.[20] However, the Jahn-Teller effect is expected to be at most a few hundred meV, which is an order of magnitude smaller than the conducting e_g bandwidth obtained in the band calculation. Hence, addition to the Jahn-Teller effect, the polaron formation due to a large difference in the ionic size between Mn^{3+} and Mn^{4+} can be an alternative to explain the insulating behavior above T_c as well as the low metallic conductivity below T_c in $La_{1-x}Ca_xMnO_3$.

Figure 2 shows the high resolution PES spectra of $La_{0.4}Ca_{0.6}MnO_3$ which has been found to exhibit a real-space charge-ordering below $T_{CO} \approx 250$ K,[14] taken at $T=270$ K, above T_{CO}, and at $T=220$ K, below T_{CO}. Except in the region very near E_F, both spectra are exactly identical to each other. The near E_F spectra above and below T_V are compared in Fig. 2(b) and the very near E_F spectra are presented in the inset. Both spectra exhibit no density of states at E_F indicating the insulating phase. Upon cooling through the charge-ordering temperature, T_{CO}, we found that the threshold energy is shifted by ~50 meV to higher binding energy. This small increase in the gap is consistent with the observed ~40 meV (500 K) increase in the resistivity slope, $d[\ln(R)]/d(T^{-1})$, which corresponds to an activation energy in a semiconductor model. These results show that the breaking of charge ordering is accompanied by ~50 meV reduction of the band gap.

Now we present the first MCD spectra of the manganese perovskite system. Mn $L_{2,3}$ edge photoabsorption spectra of $La_{0.67}Ca_{0.33}MnO_3$ and $La_{0.8}Ca_{0.2}MnO_3$ by using the magnetic circular dichroism are shown in Fig. 3. I_+ and I_- denote the absorption spectra with the photon helicity direction parallel and antiparallel to the magnetization direction, respectively. The overall shape of the MCD spectrum, $I_+ - I_-$, is quite similar for two different Ca concentrations, while the peak height MCD ratio $(I_+ - I_-)/(I_+ + I_-)$, is found to be slightly

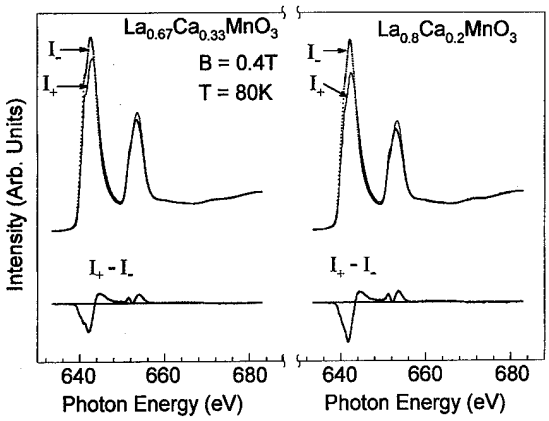


FIG. 3. X-ray Magnetic Circular Dichroism spectra at Mn $L_{2,3}$ photoabsorption edges of ferromagnetic $La_{0.67}Ca_{0.33}MnO_3$ and $La_{0.8}Ca_{0.3}MnO_3$.

larger for the low Ca concentration sample. Taking into account the circular polarizability of 85%, we estimate the L_3 edge MCD ratios' 11% and 13% for $La_{0.67}Ca_{0.33}MnO_3$ and $La_{0.8}Ca_{0.2}MnO_3$, respectively. This result indicates that $La_{0.67}Ca_{0.33}MnO_3$ has slightly smaller magnetization than $La_{0.8}Ca_{0.2}MnO_3$. Ca doping replaces Mn^{3+} (d^4) with Mn^{4+} (d^3), and the magnetic moment is expected to be reduced with Ca doping. Hence, the smaller MCD effect in the low Ca doped system seems to be consistent with the expected lower magnetic moment. However, it should be noticed that the saturating magnetic field (>4 Tesla) is one order of magnitude larger than the magnetic field used here.[6] Below the saturating magnetic field, the magnetization strongly depends on temperature and the applied magnetic field. Hence, quantitative analysis should be preceded by detailed studies of the magnetization versus applied magnetic field.

IV. CONCLUSIONS

We have investigated the ferromagnetic transition of $La_{0.67}Ca_{0.33}MnO_3$ and the order–disorder transition of $La_{0.4}Ca_{0.6}MnO_3$ using high resolution photoemission spectroscopy. The data show that the insulator–metal transition (the band-gap closing) occurs near the Curie temperature, T_c, and that the band gap increases by ~50 meV upon cooling through the charge-ordering temperature T_{CO}. We also present Magnetic Circular Dichroism spectra of ferromagnetic $La_{0.67}Ca_{0.33}MnO_3$ and $La_{0.8}Ca_{0.8}MnO_3$ at Mn $L_{2,3}$ photoabsorption edges.

ACKNOWLEDGMENTS

The National Synchrotron Light Source is supported by Department of Energy under Contract No. DE-AC02-76CH00016.

[1] C. W. Searle and S. T. Wang, Can. J. Phys. **47**, 2703 (1969).
[2] K. Chabara *et al.*, Appl. Phys. Lett. **63**, 1990 (1993).
[3] S. Jin *et al.*, Science **264**, 413 (1994).
[4] R. von Helmolt *et al.*, Phys. Rev. Lett. **71**, 2331 (1993).
[5] N. Furukawa, J. Phys. Soc. Jpn. **63**, 3214 (1994).
[6] P. Schiffer *et al.*, Phys. Rev. Lett. (in press).
[7] Y. Tokura *et al.*, J. Phys. Soc. Jpn. **63**, 3931 (1994).
[8] J. Z. Liu *et al.*, Appl. Phys. Lett. **66**, 3218 (1995).
[9] Y. Okimoto *et al.*, Phys. Rev. Lett. **75**, 109 (1995).
[10] C. Zener, Phys. Rev. **82**, 403 (1951).
[11] P. W. Anderson and H. Hasegawa, Phys. Rev. **100**, 675 (1955).
[12] P. -G. de Gennes, Phys. Rev. **118**, 141 (1960).
[13] Y. Tomioka *et al.*, Phys. Rev. Lett. **74**, 5108 (1995).
[14] A. P. Ramirez *et al.* (unpublished).
[15] G. Schütz *et al.*, Phys. Rev. Lett. **58** 737 (1987).
[16] C. T. Chen, N. V. Smith, and F. Sette, Phys. Rev. B **43**, 6785 (1991).
[17] B. T. Thole *et al.*, Phys. Rev. Lett. **68**, 1943 (1992).
[18] Y. U. Idzerda *et al.*, J. Magn. Magn. Mater. **127**, 109 (1993).
[19] C. T. Chen, Rev. Sci. Instrum. **63**, 1229 (1992).
[20] A. J. Millis, P. B. Littlewood, and B. I. Shraiman, Phys. Rev. Lett. **74**, 5144 (1995).

Cation distribution in NiZn-ferrite films determined using x-ray absorption fine structure

V. G. Harris and N. C. Koon
Naval Research Laboratory, Washington, DC 20375-5000

C. M. Williams
Morgan State University, Baltimore, Maryland 21339

Q. Zhang and M. Abe
Tokyo Institute of Technology, Okayama, Meguro-Ku, Tokyo 152, Japan

We have applied extended x-ray absorption fine structure (EXAFS) spectroscopy to study the cation distribution in a series of spin-sprayed NiZn-ferrite films, $Ni_{0.15}Zn_yFe_{2.85-y}O_4$ (y=0.16, 0.23, 0.40, 0.60). The Ni, Zn, and Fe EXAFS were collected from each sample and analyzed to Fourier transforms. Samples of Ni-ferrite, Zn-ferrite, and magnetite were similarly studied as empirical standards. These standards, together with EXAFS data generated from the theoretical EXAFS FEFF codes, allowed the correlation of features in the Fourier transforms with specific lattice sites in the spinel unit cell. We find that the Ni ions reside mostly on the octahedral (B) sites whereas the Zn ions are predominantly on the tetrahedral (A) sites. The Fe ions reside on both A and B sites in a ratio determined by the ratio of Zn/Fe. The addition of Zn displaces a larger fraction of Fe cations onto the B sites serving to increase the net magnetization. The fraction of A site Ni ions is measured to increase peaking at ≈25% for y=0.6. At higher Zn concentrations ($y \geq 0.5$) the lattice experiences local distortions around the Zn sites causing a decrease in the superexchange resulting in a decrease in the net magnetization. © *1996 American Institute of Physics.* [S0021-8979(96)35808-4]

In spinel oxides, as well as other complex metal-oxide systems, the site and valence distribution of the metallic cations dictate the sample's magnetic and electronic properties. As a result, the need for this type of information has been the subject of much experimental and theoretical research. Traditionally, researchers have empirically studied the effects of substitutional metals on the magnetic and electronic properties of spinel ferrites owing to the difficulties involved with directly measuring the site distribution in these materials. The use of x-ray,[1] neutron diffraction,[2] and Mössbauer effects (ME)[3] have all been used with varying degrees of success. The first two techniques are strongly influenced by the elements' cross section to x rays or neutrons and both are sensitive to the sample mass. ME is an excellent tool for the study of the local environment of Fe ions, being able to extract both structural and magnetic information, but is less effective when dilute or nonmagnetic additives are the focus. In recent years, with the increasing demand for planar ferrite devices the interest in ferrites has shifted to thin films supported by rigid substrates. This has created still more challenges associated with their local structural characterization. In this article we describe the use of extended x-ray absorption fine structure (EXAFS) as a tool to study the site distribution of metal cations in ferrite films. Because this technique offers both element specificity and local structure sensitivity it is ideally suited for such a study. Further, this technique is readily applied to thin films on thick supporting substrates without significant loss of signal-to-noise. Samples studied here are spin-sprayed NiZn-ferrite films [$Ni_{0.15}Zn_yFe_{2.85-y}O_4$ (y=0.16, 0.23, 0.40, 0.60)] where the Ni concentration is fixed and the Zn concentration is varied at the expense of the Fe.

Samples consist of films prepared using a spin-spray, ferrite plating process developed by Abe and Tamaura.[4] The films were deposited onto glass substrates with compositions: $Ni_{0.15}Zn_yFe_{2.85-y}O_4$ (y=0.16, 0.23, 0.40, 0.60). These films were chosen for this particular study because of the three transititon metals: one is fixed and the other two are systematically varied, thus simplifying the trends between cation distribution and sample composition. Magnetic measurements were performed using a vibrating sample magnetometer (VSM) and the results were correlated with the structural results obtained from the EXAFS measurements.

Data collection entailed measuring the x-ray absorption coefficient encompassing the K edges of Fe (7111 eV), Ni (8333 eV), and Zn (9659 eV) for each sample. Data were collected via a total electron yield (TEY) detection scheme[6] on beam line X23B[7] at the National Synchrotron Light Source. Following standard EXAFS analysis procedures[8] these data were analyzed to obtain Fourier transforms of the EXAFS data. In this form the data directly reflect the average local environment around the absorbing atoms where the peaks in the transform typically represent shells of atoms around the absorber.[9] Data collected from standards of Fe_2O_3, Fe_3O_4, $ZnFe_2O_4$, and $NiFe_2O_4$ were similarly analyzed and compared to theoretical partial radial distribution functions (PRDFs) to assist in identifying the main features of the Fourier transformed EXAFS data. Additionally, theoretical EXAFS data, generated using the multiple-scattering (MS) codes (FEFF 6) of Rehr and co-workers,[10] were used to assist in the identification of Fourier features that arise from multiple scattering events. Together, an interpretation of the data collected from the NiZn-ferrite films was possible.

 0021-8979/96/79(8)/4561/3/$10.00 © 1996 American Institute of Physics

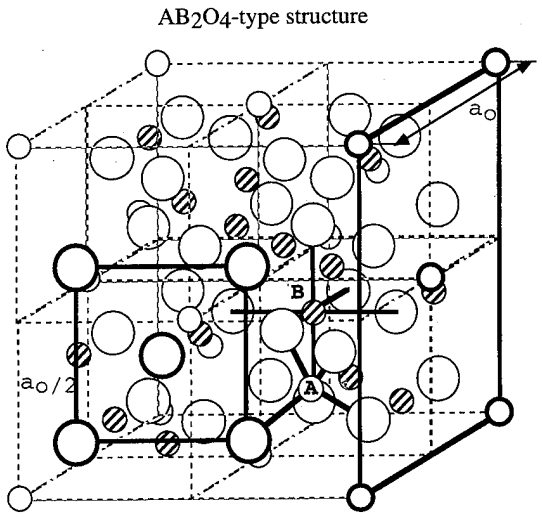


FIG. 1. The AB_2O_4 unit cell. Heavy lines are used to make clear the fcc packing of oxygen ions ($a_0/2$) and A-site cations (a_0). The B-site cations are distributed on the vertices of four interpenetrating fcc lattices (a_0) whose periodicity is not clearly visible.

The spinel ferrite unit cell has the $fd3m$ space group and is based on a close-packed oxygen lattice where metal cations reside on 8 of the 64 tetrahedral sites (A sites) and 16 of the 32 octahedral sites (B sites). The O ions reside on a face-centered-cubic lattice of $a_0/2$, while the A-site ions reside on the interstices of two interpenetrating fcc lattices of a_0, and the B-site ions reside on the interstices of four interpenetrating fcc lattices of a_0. Figure 1 depicts a schematic of a single unit cell illustrating the A- and B-site locations relative to each other and to the O lattice. The close-packed nature of the individual lattices are made clear by the heavy-lined spheres. The A-site cations have 4 O neighbors at a distance of $\approx$1.9 Å, while the B-site cations have 6 O neighbors at a distance of $\approx$2.1 Å.[11]

Hastings and Corliss[5] found $ZnFe_2O_4$ to be a *normal* spinel, meaning that the 8 divalent ions occupy the 8 A sites and the 16 trivalent ions occupy the 16 B sites, and $NiFe_2O_4$ to be an *inverse* spinel, meaning that the 8 divalent ions occupy 8 of the 16 B sites and the 16 trivalent ions randomly occupy the remaining sites. In studies of bulk powders it was found that when Zn is added to the $NiFe_2O_4$ at the expense of Ni the Zn^{+2} ions preferentially occupy the A sites displacing some of the Fe ions to the B sites.[12] We postulate that when Zn^{+2} is added at the expense of the Fe ions that a similar redistribution takes place: Zn^{+2} preferentially occupy the A sites and displace the Fe ions to the B sites.

Fourier transformed Ni EXAFS data, collected from the $Ni_{0.15}Zn_yFe_{2.85-y}O_4$ samples, are presented in Fig. 2. These data, and those of Figs. 3 and 4, have been analyzed using identical procedures and parameters and are plotted on the same x and y axes to allow direct comparison with one another. The Fourier peaks seen in Fig. 2 have been identified to correspond with atom pair correlations unique to B sites in the ferrite unit cell.[13] The chief features which act to fingerprint the B-site are the shell of 6 O^{-2} ions near 2.1 Å (appearing at 1.6 Å due to an electron phase shift) and the shell of 6 B-site cations centered near 2.96 Å. The peak centered near 3.2 Å arises predominantly from the 6 A-site cations

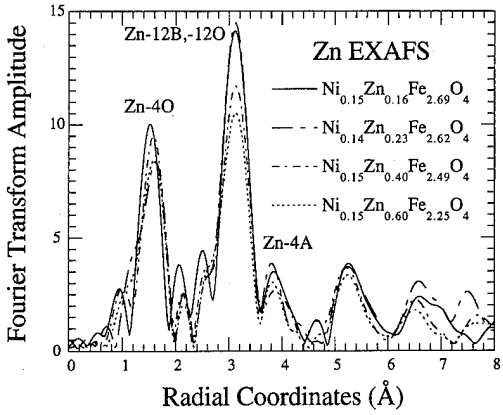


FIG. 3. Fourier transformed Zn EXAFS data acquired from the $Ni_{0.15}Zn_yFe_{2.85-y}O_4$ (y=0.16, 0.23, 0.40, 0.60) film samples. All transforms were obtained using k^3 weighting and a k range of 2.6–11.7 Å^{-1}.

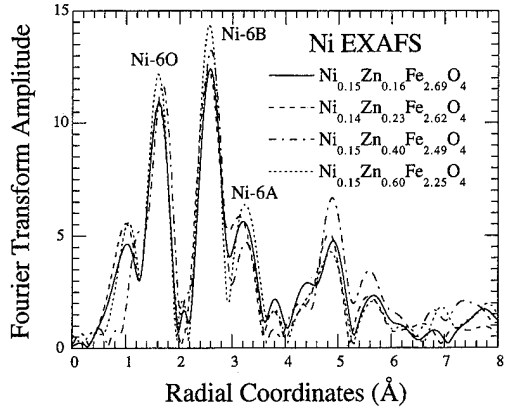


FIG. 2. Fourier transformed Ni EXAFS data acquired from the $Ni_{0.15}Zn_yFe_{2.85-y}O_4$ (y=0.16, 0.23, 0.40, 0.60) film samples. All transforms were obtained using k^3 weighting and a k range of 2.6–11.7 Å^{-1}.

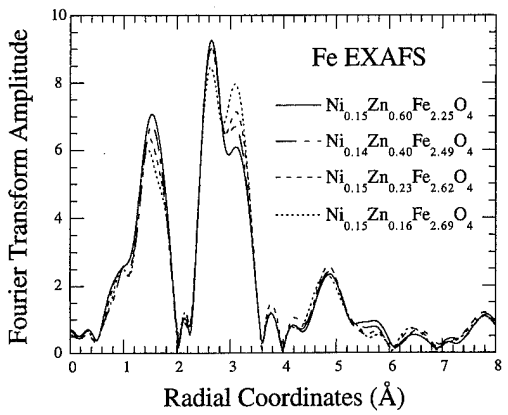


FIG. 4. Fourier transformed Fe EXAFS data acquired from the $Ni_{0.15}Zn_yFe_{2.85-y}O_4$ (y=0.16, 0.23, 0.40, 0.60) film samples. All transforms were obtained using k^3 weighting and a k range of 2.6–11.7 Å^{-1}.

around to the B sites, however, this peak is not unique to the B-site environment as it also appears with even a larger relative amplitude in the A-site environment. The amount of Ni in these samples is fixed at a stoichiometry of 0.15 which corresponds to the filling of 1.2 B sites. With decreasing Zn/Fe concentration the Fourier profile remains largely unchanged except for the amplitude of these features. Because the total number of cations remains the same for these samples the change in amplitude cannot arise from a change of coordination. Hence, the changes can only be accounted for by a change in the atomic order (i.e., the Debye–Waller coefficient) of the specific correlations contributing to the Fourier peaks. Fitting of this region of the plot using data generated from the MS FEFF (v6.01) codes indicates that these changes are indeed due to this effect. The trend is one of increasing local order on the B site with increasing Zn/Fe concentration.

Figure 3 is a plot of the Fourier transformed Zn EXAFS for the $Ni_{0.15}Zn_yFe_{2.85-y}O_4$ samples. The Fourier peaks seen in Fig. 3 have been identified to correspond with atom pair correlations unique to A sites in the ferrite unit cell. The chief features which act to fingerprint the A-site environment are the shell of 4 O^{-2} ions at 1.9 Å (appearing near 1.5 Å due to a $\approx$0.4 Å electron phase shift) and the shell of 12 B-site cations at 3.5 Å (appearing near 3.1 Å due to $a\approx$0.4 Å electron phase shift). The peak centered near 3.1 Å also corresponds with 12 O anions which is also unique to the A-site environment. Although the profile of the data changes very little with changes in composition the amplitudes of the Fourier peaks change significantly and in a systematic fashion. The trend is one of increasing amplitude with decreasing Zn/Fe concentration. For the reasons cited above these changes in amplitude are caused by variations in atomic order specific to the A-site environment. Hence, the A–B correlations experience greater disorder for higher Zn/Fe concentration and more order for decreased Zn/Fe concentration. Another noteworthy observation from Fig. 3 is that the Zn–O bond expands with increased Zn concentration. This indicates that for dilute Zn additives the local lattice accommodates these cations without local distortion. However, with increased Zn/Fe concentration the bonds dilate to accommodate the increased Zn content.

Figure 4 is a plot of the Fourier transformed Fe EXAFS collected from the four $Ni_{0.15}Zn_yFe_{2.85-y}O_4$ samples. The Fe EXAFS data illustrate features characteristic of both A- and B-site environments. It is clear, however, that the amplitudes of these Fourier features vary in a systematic manner with sample composition. Upon close inspection, one sees that the variations are largest in the first three peaks of the Fourier transform. The large asymmetric peak centered near 1.5 Å corresponds with the two Fe–O bond distances of the A- and B-site Fe cations. This peak decreases in amplitude with decreasing Zn/Fe concentration. The large split peak centered near 2.9 Å corresponds with both A- and B-site environments. The low-r split-peak corresponds with the Fe_B–M_B correlation, where as the high-r split-peak consists of three correlations, specifically, the Fe_B–M_A, Fe_A–M_B, and the Fe_A–O: This peak may also contain amplitude from the Fe_A–M_A, and two Fe_B–O correlations. The low-r split-peak decreases in amplitude with decreasing Zn/Fe concentration while the high-r split-peak increases in amplitude for the same compositions. All of these trends can be explained by the site distribution of the Fe cations. From Fig. 3 we know that Zn preferentially occupies the A sites for all compositions. This forces a larger fraction of Fe ions to occupy the B sites for increased Zn/Fe. Hence, the Fe_B/Fe_A increases with the Zn/Fe causing an increase in the amplitude of the low-r peak at 2.6 Å and a decrease in amplitude of the high-r peak at 3.1 Å. The oxygen peak, centered near 1.5 Å, varies in amplitude and shape due to the change in occupancy between the six-fold coordination B site and the four-fold coordination A site. The trends in the Debye-Waller coefficient mentioned in the Ni- and Zn-EXAFS discussion are found from a least squares fitting of the data, using the FEFF generated data, to be small compared to the change in amplitude brought on by the changes in site occupancy.

It was mentioned earlier that Ni-ferrite has an inverted cation distribution and, consequently, its magnetization arises solely from the Ni^{+2} ions. The introduction of Zn^{+2} ions, which prefer the A sites, upsets the ferric balance by displacing the Fe cations from the A to B sites. The effect of a small amount of Zn is to increase the saturation magnetization. This occurs as a result of the Zn^{+2} ions displacing the trivalent Fe ions from the A to the B sites so that there is no longer a complete cancellation of the Fe moments. The now unbalanced Fe ion moments add to those of the Ni^{+2} ions. We measure magnetization values to increase near linearly with increased Zn concentration for $0\leqslant y\leqslant 0.4$ and then decrease for $y=0.6$. The decrease in magnetization is due to the deterioration of the superexchange between the A–B sites brought on by the lattice distortions caused by the increased number of Zn ion on the A sites. This local distortion was clearly seen in the Zn EXAFS.

This work was performed at the National Synchrotron Light Source at Brookhaven National Laboratory which is sponsored by the U. S. Department of Energy.

[1] A. Claasen, Proc. Phys. Soc. **38**, 482 (1925–1926).
[2] C. G. Shull, E. O. Wollan, and W. C. Koehler, Phys. Rev. **84**, 912 (1951).
[3] G. K. Wertheim, J. Appl. Phys. **32**, 110S (1961).
[4] M. Abe and Y. Tamaura, J. Appl. Phys. **55**, 2614 (1984).
[5] J. M. Hastings and L. M. Corliss, Rev. Mod. Phys. **25**, 114 (1953).
[6] W. T. Elam, J. P. Kirkland, R. A. Neiser, and P. D. Wolf, Phys. Rev. B **38**, 26 (1988).
[7] R. A. Neiser, J. P. Kirkland, W. T. Elam, and S. Sampath, Nucl. Instrum. Methods A **266**, 220 (1988).
[8] D. E. Sayers and B. A. Bunker, in *X-ray Absorption: Basic Principles of EXAFS, SEXAFS, and XANES*, edited by D. C. Koningsberger and R. Prins (Wiley, New York, 1988).
[9] Because electron phase shift corrections have not been included at this stage in the analysis the peak positions of the Fourier transformed EXAFS data do not correlate directly with bond distances but are instead shifted to lower radial distances by an amount equal to the unique electron phase shift of the pair correlations contributing to the Fourier peak.
[10] J. J. Rehr, J. Mustre de Leon, S. I. Zabinsky, and R. C. Albers, J. Am. Chem. Soc. **113**, 5135 (1991).
[11] Radial distances were calculated assuming a lattice constant of 8.39 Å with $u=0.379\pm0.001$ Å. These parameters correspond with the Fe_3O_4 compound after: A. Claasen, Proc. Phys. Soc. **38**, 482 (1925–1926); C. G. Shull, E. O. Wollan, and W. C. Koehler, Phys. Rev. **84**, 912 (1951).
[12] *Handbook of Microwave Ferrite Materials*, edited by W. E. von Aulock (Academic, New York, 1965), pp. 379–393.
[13] V. G. Harris *et al.*, IEEE Trans. Magn. **31**, 3473 (1995).

Possible nearly loss-free ferrimagnetic resonance in small samples

J. B. Sokoloff
Northeastern University, Boston, Massachusetts 02115

Relaxation occurs in ferrimagnetic resonance by processes which transfer energy from the uniform precession magnon mode, which is excited in the resonance process, to other magnons and to phonons. The relaxation due to these processes is usually calculated using Fermi Golden Rule time dependent perturbation theory, whose application depends on the modes involved in the relaxation processes forming a continuum. Since for a finite isolated solid this is not generally true, the possibility exists that such relaxation processes might not occur for sufficiently small samples. Because it is reasonable to consider the phonons as belonging to both the sample and sample holder, it is reasonable to assume that they form a continuum. The intrinsic linewidth (i.e., inverse lifetime for a defect-free single crystal), which is due to phonons excited by the Kasuya–Le Craw mechanism, is already comparable to the magnon mode spacing for samples of linear dimensions of the order of 10 μm, indicating that finite sample effects could potentially become important for samples of fairly large size. Previous work by the present author on the one-dimensional Heisenberg model has shown that nonlinearity in the magnons can lead to a transition from lossy to loss-free behavior as the sample size decreases, if the temperature is sufficiently low. Here, model calculations of this effect in a two-dimensional Heisenberg model magnet are presented in order to show that loss-free behavior can occur for sufficiently low temperature and sufficiently small sample size. These results open up the interesting possibility of producing high anisotropy magnetic materials as a collection of very small crystals with extremely small linewidths. © *1996 American Institute of Physics.* [S0021-8979(96)35908-1]

INTRODUCTION

In a ferrimagnetic resonance (FMR) experiment, an electromagnetic field couples to a magnon mode (usually the zero wave vector or uniform magnon mode). The energy absorbed by this mode from the field is then transferred to other magnon and to phonon modes via various mechanisms,[1,2] which results in the uniform magnon being given a nonzero linewidth. The mechanism for this can be understood using Fermi's Golden Rule perturbation theory, in which the uniform magnon is scattered into a continuum of other magnons of nearly the same frequency.[2] When one considers a finite size solid, however, the magnon and phonon modes do not form a continuum, and hence Fermi's Golden Rule will not lead to a nonzero linewidth because, in general, the uniform mode will not be in resonance with any of the excitations of the solid. In previous work, it was suggested that nonlinearity can lead to dissipation in finite solids,[3] in the same way that it leads to relaxation to a state of equilibrium in a finite solid, but this only occurs if the mode spacing is smaller than the the width of the modes which results from the nonlinearity (because a nonlinear oscillator's resonant frequency depends on the amplitude of the vibrations), because in this case, the system exhibits chaos.[4,5] There have been other studies that indicate that chaos may be responsible for dissipation and friction in a finite solid which is isolated from its environment.[5,6] Although it is nearly impossible in most experimental situations to completely isolate a sample from its surroundings, it is possible to make the mode spacing much larger than the width of the nonlinear modes (the spin waves in the present case). Although the phonon modes of the sample alone are discrete, contact between the sample and infinite solid (e.g., the sample holder) will broaden these phonons into a continuum.[7] In the case of FMR, however, the energy is first imparted to the uniform magnon mode. Dissipation in this case consists primarily of the transfer of energy from this mode to many of the other magnon modes. Energy can also be transferred directly from the uniform magnon mode to the phonons through the Kasuya–Le Craw (KL) one magnon one phonon mechanism.[1] This mechanism by itself would give a linewidth of less than 1 Oe (about 10^6 Hz) for yttrium iron garnet (YIG).[2] The magnon mode spacing is already of this order for samples of linear dimensions of the order of 10 μm. Although the accepted value among experimentalists for the intrinsic (presumably due to the Kasuya–Le Craw mechanism) FMR linewidth for barium ferrite is 30 Oe,[8] estimates of the contribution due to the KL mechanism give a value closer to that of YIG.[9] The remainder of the contribution to the linewidth for macroscopic samples (which is generally much larger than that of the KL mechanism) is due to the transfer of energy to the other magnon modes. From the arguments given above, we conclude that the possibility exists that the contribution to the FMR linewidth from such mechanisms might be eliminated if the sample is sufficiently small (and hence the mode spacing is sufficiently large). The appearance of finite mode width effects on the Suhl instabilities was considered by Schlomann.[10] This work clearly deals with a regime in which the mode spacing is small compared to the width of the nonlinear resonance. In the present case, in contrast, we are interested in much smaller samples for which the mode spacing is much larger than the width caused by the nonlinearity. In support of my claim that small magnetic crystal can exhibit FMR with very small linewidths, I have performed some calculations of the magnetic energy of a small anisotropic classical Heisenberg model magnetic crystal in both a dc and an ac magnetic field. In previous

 0021-8979/96/79(8)/4564/3/$10.00 © 1996 American Institute of Physics

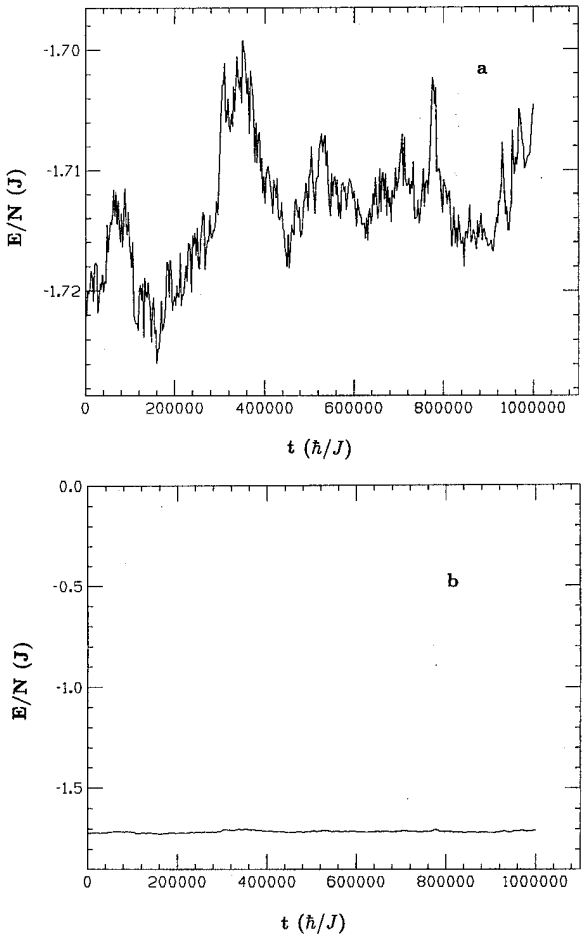


FIG. 1. (a) The energy (in units of J, the exchange interaction) is shown as a function of the time (in units of $\hbar/J$) for a 4×4 atom square lattice. (The anisotropy $A=0.3$ J, H multiplied by the Bohr magneton is 0.1 J, h_0 times the Bohr magneton is 0.01 J, and $\omega=1.0J/\hbar$.) (Before the dynamics are studied, the system is equilibrated to a temperature of 0.5 J using a Monte Carlo calculation.) (b) The results presented in a over a larger energy range. (Zero energy occurs in the infinite temperature limit.)

calculations which I reported on such a model, I considered only a one-dimensional model. I showed that there is a well defined transition as a function of system size from a regime in which the system absorbs energy from the ac field (as evidenced by the fact that the energy of the magnet increases as a function of time) to one in which the energy oscillates but does not increase on the average as a function of time.[3] The one-dimensional system studied has nondegenerate magnon modes, whereas higher dimensional systems have degeneracy and the minimum mode spacing for samples with the same linear dimensions is much smaller.[7] It is well known that degeneracy can lead to a situation in which the system becomes chaotic, even for vanishingly small nonlinearity.[5] This fact opens the question of whether the dissipationless behavior found for the one-dimensional magnet will still occur in higher dimensions. Therefore, in this article, I present calculations on a two-dimensional anisotropic Heisenberg model, which support the occurrence of dissipation in higher than one dimension.

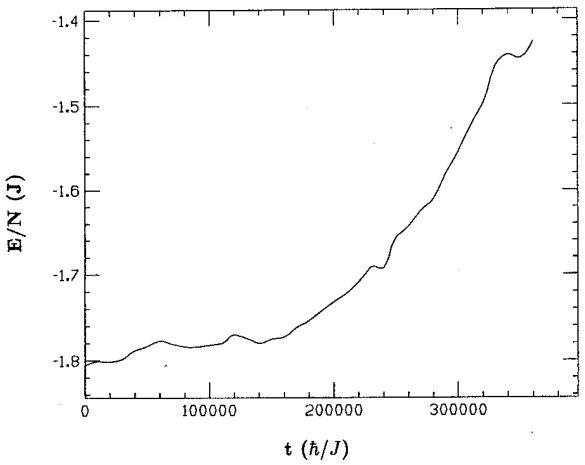


FIG. 2. The energy (in units of J, the exchange interaction) is shown as a function of the time (in units of $\hbar/J$) for a 10×10 atom square lattice for the same parameters as in Fig. 1.

RESULTS

There are some well established results for the chaotic behavior of classical spins in an ac magnetic field. Frahm and Mikeska[11] have found that a single spin with single ion anisotropy in a circularly polarized ac magnetic field, which is in the plane favored by the anisotropy, is a completely integrable problem (i.e., a nonchaotic system), whereas when the field is linearly polarized in the same plane, the system is nonintegrable, exhibiting chaos for sufficiently strong field. Magyari *et al.*[12] have shown that the completely isotropic Heisenberg model with infinite range exchange interaction is integrable. It is also easy to show by simply writing down the equations of motion that for the finite range isotropic Heisenberg model in a uniform ac field, the total spin of the system (i.e., the sum of the spins of all of the lattice sites) satisfies the same equations of motion as for a single spin without anisotropy in a uniform ac field.

The model studied is the classical Heisenberg model with single ion anisotropy, which satisfies the equations of motion

$$\dot{\mathbf{S}}_l=\mathbf{H}_{\text{eff}}\times\mathbf{S}_l, \tag{1}$$

where $\mathbf{H}^{\alpha}_{\text{eff}}=-\partial H/\partial S^{\alpha}_l+h(t)\delta_{\alpha,x}$, where $H=-\Sigma_{j,l}J_{j,l}\mathbf{S}_j\cdot\mathbf{S}_l-A\Sigma_j(S^z_j)^2-H_0\Sigma_j S^z_j$, $h(t)=h_0\cos(\omega t)$ is the applied ac field, H_0 is the dc field, and A is the anisotropy. These equations were solved using a Runge–Kutta integration routine, and the total energy of the system was calculated as a function of time. Energy was conserved in these calculations to at least fourth place accuracy. Results for a two-dimensional lattice with free end boundary conditions with a side length of four atomic distances is shown in Fig. 1. Results for a side length of ten atoms, with the same parameters as in Fig. 1, are shown in Fig. 2. As can be seen, there is clearly a transition from nonidissipative to dissipative behavior as a function of system length, in the sense that for the smaller size system there is clearly no absorption of energy, whereas for the larger system, the energy clearly increases as a function of time. Thus, mode degeneracy, which certainly occurs in

higher than one dimension, does not appear to prevent the occurrence of a transition from a dissipationless state.

QUANTUM MECHANICAL EFFECT

In this article, it has been assumed that classical dynamics was a good description of the magnetic system. Since classical mechanics is only an approximation to the correct quantum mechanical treatment, which is based on the Schrödinger equation, which is linear, it is important to question whether the present mechanism for dissipation will work in a quantum mechanical treatment. This question has been considered for other models, which can be solved both classically and quantum mechanically, and which exhibit chaos in the classical limit.[13] It was determined in these studies that the system initially behaves classically (and hence is able to exhibit chaos) for a time of the order of $\lambda^{-1} \ln(I/\hbar)$, where λ is a typical Lyapunov exponent and I is a typical action for the problem. For longer times, quantum mechanics takes over and classical chaos is no longer possible. For this problem, we expect I to be of the order of J times a typical time in the problem such as the inverse of a typical magnon frequency, which is of the order of $\hbar/J$, and hence, the critical time for classical dynamics to no longer be valid is of the order of the inverse Lyapunov exponent. Thus, unless the inverse Lyapunov exponent is ridiculously long, in which case effects dependent on the occurrence of classical chaos would be almost undetectable, long time steady state dissipation cannot occur in an isolated system. The fact that interaction with the environment generally seems to suppress the occurrence of quantum phenomena[14] could justify the use of the classical Heisenberg model to treat the problem of dissipation in a magnetic system. This is still a controversial point,[15] however. The question of the existence of dissipation in a small isolated magnetic system, raised in this article, could possibly provide a good testing ground for answering these questions experimentally.

ACKNOWLEDGMENT

The author wishes to thank the Office of Naval Research (Contract No. N00014-91-1049) for their financial support.

[1] T. Kasuya and R. C. Le Craw, Phys. Rev. Lett. **6**, 223 (1961).
[2] M. Sparks, *Ferromagnetic Relaxation Theory* (McGraw-Hill, New York, 1964), pp. 147–157.
[3] J. B. Sokoloff, J. Appl. Phys. **75**, 6075 (1994).
[4] F. M. Israelev and B. V. Chirikov, Dokl. Akad. Nauk. USSR **166**, 57 (1966) [Sov. Phys. Dokl. **11**, 30 (1966)]; B. V. Chirikov, Phys. Rep. **52**, 263 (1979).
[5] J. Ford, Phys. Rep. **213**, 271 (1992); J. Ford and G. H. Lunsford, Phys. Rev. A **1**, 59 (1970); S. D. Stoddard and J. Ford, *ibid.* **8**, 1504 (1973); G. H. Walker and J. Ford, Phys. Rev. **188**, 416 (1969).
[6] E. Fermi, J. Pasta, and S. Ulam, in *Collected Papers of Enrico Fermi 2* (Chicago University Press, Chicago, 1955), p. 978.
[7] J. B. Sokoloff, Wear **167**, 59 (1993).
[8] M. Lemke, W. Hope, W. Tolksdorf, and F. Welz, Microwaves Opt. Acoust. **3**, 253 (1979); R. Karim, K. D. McKinstry, J. R. Truedsun, and C. E. Patton, IEEE Trans. Magn. **28**, 3225 (1992).
[9] S. P. Marshall, J. B. Sokoloff, and C. Vittoria, IEEE Trans. Magn. **25**, 3491 (1989).
[10] E. Schlomann and J. J. Green, Phys. Rev. Lett. **3**, 129 (1959); E. Schloemann, Phys. Rev. **116**, 828 (1959).
[11] H. Frahm and H. J. Mikeska, Z. Phys. Condensed Matter **60**, 117 (1985).
[12] E. Magyari, H. Thomas, R. Weber, C. Kaufman, and G. Muller, Z. Phys. Condensed Matter **65**, 363 (1987).
[13] G. Casati, J. Ford, I. Guarneri, and F. Vivaldi, Phys. Rev. A **34**, 1413 (1986).
[14] W. H. Zurek and J. P. Paz, Phys. Rev. Lett. **72**, 2508 (1994); A. Caldeira and A. J. Leggett, Physica (Amsterdam) A **121**, 587 (1983).
[15] G. Casati and B. V. Chirikov, Phys. Rev. Lett. **75**, 350(C) (1995); W. H. Zurek and J. P. Paz, *ibid.* **75**, 351(C) (1995).

Anomalous low dimensional system: Study of magnetism and electrical conductivity in $Na_2Ru_4O_{9-\delta}$

G. Cao, S. McCall, F. Freibert, M. Shepard, P. Henning, and J. E. Crow
National High Magnetic Field Laboratory, Florida State University, Tallahassee, Florida 32306-4005

The magnetic susceptibility $\chi_{\|}(H\|b)$, $\chi_{\perp}(H\perp b)$ ($2\leqslant T\leqslant 700$ K) and electrical resistivity $\rho(T)$ ($2\leqslant T\leqslant 300$ K) of single crystal $Na_2Ru_4O_{9-\delta}$ ($\delta\geqslant 0$) with various oxygen content were measured. The crystal structure of this compound is monoclinic with single, double, and triple chains along the b axis. The most striking feature of this compound is the drastically large anisotropy reflected in the resistivity which exhibits metallic behavior along chains and semiconducting behavior perpendicular to the chains. The resistivity ratio for these two directions ($\rho_{\perp}/\rho_{\|}$) is larger than 10^5. This ratio is exceptionally large, indicating that the anisotropy of the bandwidth is substantial. It is remarkable that, after reduction of oxygen content in the system, the magnetic susceptibility undergoes a drastic change, whereas the electrical resistivity along the conducting chains is altered only slightly. It is argued that the different sensitivity to oxygen content reflected in magnetic and transport properties may be attributed to the complexity of the crystal structure. The striking observations presented here may suggest a one-dimensional system that possesses unique physical properties. © *1996 American Institute of Physics.* [S0021-8979(96)36008-6]

INTRODUCTION

The discovery of superconductivity in the cuprates has led to a resurgence of interest in the $3d$ transition-metal oxides. However, physical properties of the $4d$ and $5d$ metal oxides, though recently drawing moderate attention, remain largely unexplored. One class of these oxides is the ruthenium oxides which exhibit a rich variety of unusual magnetic behavior while also possessing rather high electrical conductivity. While exploring magnetic and electrical properties, looking, in part, for superconductivity in the oxides, we have found that $Na_2Ru_4O_9$ displays an anomalously large anisotropy in conductivity with metallic behavior in one direction and semiconducting behavior in others. In addition, the magnetic susceptibility parallel to the chains $\chi_{\|}$ has a maximum in the vicinity of 70 K with significant anisotropy in $\chi_{\|}$ and $\chi_{\perp}$ below the maximum. It is remarkable that, after reduction of oxygen content in the system, the maximum completely disappears, and $\chi(T)$ is radically changed, whereas the electrical resistivity along the b axis is altered only slightly.

EXPERIMENTAL

The crystal structure of $Na_2Ru_4O_9$ shown in Fig. 1[1] is monoclinic with $a=23.180$, $b=2.832$, $c=10.990$ A, $\beta=104.50°$, and space group $C2/m$.[1,2] The Ru_4O_9 network is formed by single, double, and triple chains of RuO_6 octahedra sharing edges. These chains share oxygen on the corner of the RuO_6 octahedra and run parallel to the shortest axis (b axis). The sodium ions are inserted in three different sites in the tunnels.[1] This compound is very stable in air. Additionally, the results of x-ray powder diffraction indicate that $Na_2Ru_4O_9$ can accommodate a relatively large oxygen deficiency without a breakdown of its crystal structure, however, the monoclinic structure appears to be unstable with small oxygen overdoping.

The starting materials were Na_2CO_3 and RuO_2 with purity of 99.9%. The single crystals of $Na_2Ru_4O_9$ were then grown out of a Na-rich flux, yielding needle-shaped crystals with the largest dimension along the b axis. The size of the average crystals is of $1.0\times10\times0.5$ mm^3. Deoxygenated $Na_2Ru_4O_{9-\delta}$ ($\delta>0$) crystals were obtained by sealing as-grown crystals in evacuated quartz tubes which were then heated at 400–550 °C for 100 h. The crystal structure and lattice parameters obtained from powder x-ray diffraction patterns of both as-grown and deoxygenated single crystals were in excellent agreement with published data.[2] Scanning electron microscopy (SEM) and energy dispersive x-ray (EDX) were also performed on the single crystals, confirming that the crystals were of high quality. The electrical resistivity was measured using four standard probe techniques, and the magnetic susceptibility was measured using a superconducting quantum interference device (SQUID) magnetometer.

RESULTS AND DISCUSSION

Shown in Fig. 2 is the magnetic susceptibility $\chi_{\|}(H\|b)$ and $\chi_{\perp}(H\perp b)$ vs temperature for an as-grown crystal $Na_2Ru_4O_9$. A broad maximum occurs at 70 K. The orientation dependence of χ below the maximum seems to be attributed to the anisotropy of sublattice magnetization and would suggest an antiferromagnet. However, no anomaly in the vicinity of 70 K in specific heat is seen, implying that the maximum observed may not be associated with long range order. The low temperature Curie tail is somehow sample dependent, and probably an extrinsic effect. The magnetic susceptibility $\chi(T)$ well above the peak (100 K$<T<$300 K) indicates an extremely narrow electronic band and can be described by a modified Curie–Weiss law, i.e., $\chi=\chi_0+C/(T+\theta)$, where χ_0 is a temperature independent contribution to $\chi(T)$, C is the Curie constant, and θ is the Curie–Weiss temperature. Fitting $\chi(T)$ for $100\leqslant T\leqslant 300$ K to the Curie–Weiss law leads to the values of $\chi_0=7.92\times10^{-4}$ and 1.06×10^{-3} emu/mol for $\chi_{\|}$ and $\chi_{\perp}$, respectively. These values are unusually large when compared to those typically reported for ordinary metals (10^{-5} emu/mol). Such large values of χ_0, when taken as a measure of

 0021-8979/96/79(8)/4567/3/$10.00 © 1996 American Institute of Physics

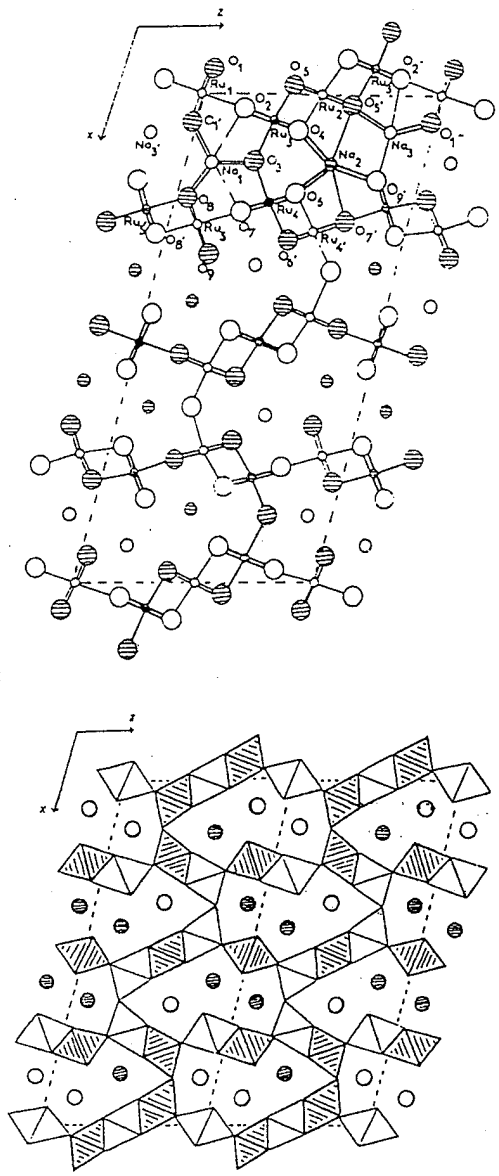


FIG. 1. Crystal structure of $Na_2Ru_4O_9$ (Ref. 1). Note: The b axis, i.e., the multichain direction, is perpendicular to the paper.

the density of states at the Fermi level, represent either a highly correlated spin state or strong electron–electron correlation.

The valence state of Ru for $Na_2Ru_4O_9$ is Ru^{4+} $(4d^4)$ which is in the low-spin state with $S=1$. Were the charges localized, the material would be an insulator. $Na_2Ru_4O_9$ is a metallic conductor along the b axis which will be described later, and remains metallic below the maximum. The effective magnetic moment obtained from χ is 1.67 μ_B for both $\chi_{\|}$ and $\chi_{\perp}$, which is only 58% of the Hund's rule value (2.83 μ_B), assuming quenching of orbital contribution.

The resistivity $\rho_{\|}(T)$ for the as-grown $Na_2Ru_4O_9$ single crystal measured with electrical current running along the b axis is shown in Fig. 3. While showing metallic behavior, $\rho_{\|}(T)$ decreases with a slightly negative curvature from 0.54 to 0.24 mΩ cm as temperature decreases from 300 to 40 K. No unusual structure is apparent in $\rho_{\|}(T)$ in the vicinity of

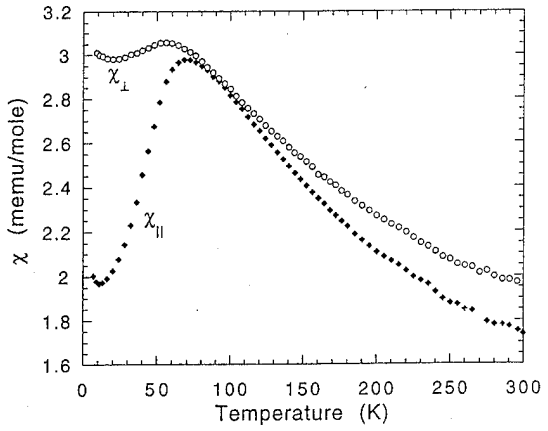


FIG. 2. The magnetic susceptibility $\chi(T)$ vs temperature for the as-grown single crystal $Na_2Ru_4O_9$.

the maximum observed in $\chi(T)$. Near 40 K, however, a slightly sharper drop is developed. For $T<30$ K, $\rho(T)$ is well described by $\rho(T)=A+BT^2$. The resistivity characterized by the T^2 dependence is reflective of spin fluctuations which apparently dominate the scattering process in this temperature region.

The most striking feature of the conductivity in this compound, however, is the drastically large anisotropy reflected in the resistivity. Also shown in Fig. 3 is the resistivity perpendicular to the b axis, i.e., the chain direction. Yet, like $\rho_{\|}(T)$, in the vicinity of 40 K, $\rho_{\perp}(T)$ displays a slight but well defined slope change which, again, may be associated with the reduction of spin scattering. The most noteworthy feature is the extremely large anisotropy, i.e., the ratio of $\rho_{\perp}(T)/\rho_{\|}(T)$ at $T=280$ and 2 K is about 2×10^5 and 7×10^5, respectively. Evidently, the resistivity with such a severe anisotropy suggests that the nature of electron scattering processes governing the conductivity in these two directions must be completely different. Although the anisotropy in conductivity is commonly seen in many compounds and alloys such as high T_c materials, the ratio of the resistivity for the conducting direction and the less conducting direc-

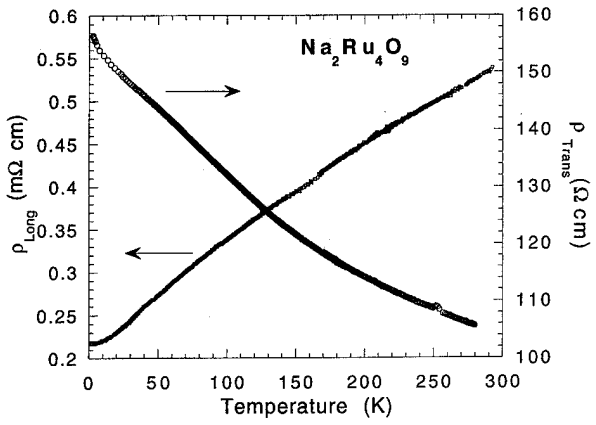


FIG. 3. $\rho_{\|}(T)$ and $\rho_{\perp}(T)$ vs T for the as-grown single crystal $Na_2Ru_4O_9$.

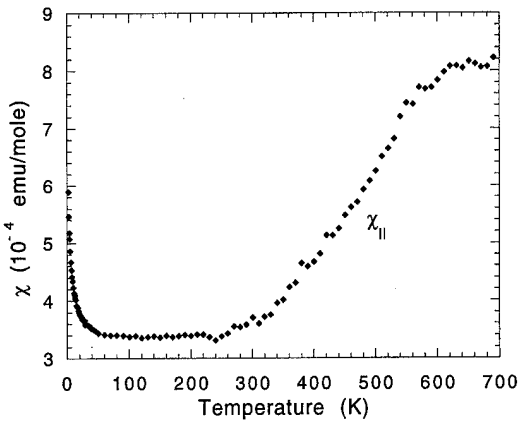


FIG. 4. The magnetic susceptibility $\chi(T)$ vs temperature for the deoxygenated single crystal $Na_2Ru_4O_{9-\delta}$ ($\delta>0$).

tion is typically much smaller, e.g., $\rho_c/\rho_{ab}=20-100$ for $YBa_2Cu_3O_7$.

The unusual behavior of $Na_2Ru_4O_{9-\delta}$ becomes even more interesting after comparing magnetic and transport properties observed in crystals which were deoxygenated. Shown in Fig. 4 is magnetic susceptibility $\chi_\parallel$ for $Na_2Ru_4O_{9-\delta}$ with $\delta>0$ vs temperature for $2\leqslant T\leqslant 700$ K. The great fascination of this data is that the system undergoes a drastic change in magnetic spin interactions due to reduction of oxygen content. The low temperature up-turn in $\chi_\parallel$ may reflect a small impurity phase. However, the unusual temperature dependence at higher temperatures is quite interesting. For $60\leqslant T\leqslant 270$ K, $\chi(T)$ is essentially independent of temperature, and then develops a rapid up-turn near 270 K which is followed by a saturation occurring in the vicinity of $T=600$ K. The origin of such behavior is not yet clear. However, it cannot be ruled out that oxygen deficient $Na_2Ru_4O_{9-\delta}$ ($\delta>0$) may be involved in one-dimensional spin interactions which leads to an energy gap opening below 270 K. In fact, the behavior displayed by $\chi(T)$ mimics those of known low dimensional systems, such as Y_2BaNiO_5,[3] $CuGeO_3$,[4] $SrCu_2O_3$,[5] etc.

On the other hand, the electrical resistivity $\rho(T)$ for the deoxygenated sample changes only slightly with an increase in linearity down to 40 K and a mild decrease in magnitude. Yet, above 40 K, $\rho(T)$ shows, to the first order approximation, the linear-T behavior with the slope $d\rho/dT=1.16\times10^{-6}$ (Ω cm K^{-1}). Interestingly, this linear-T behavior, though with the faster slope (10^{-7} Ω cm K^{-1} for $YBa_2Cu_3O_7$, for instance), is reminiscent to that observed in optimally doped high T_c superconductors when $T>T_c$. The linear-T dependence in $\rho(T)$ is thought to be non-Fermi liquid behavior. Below 30 K, the temperature dependence of $\rho(T)$ evolves the T^2 behavior, which is also seen in the as-grown sample. Fitting $\rho(T)$ to $A+BT^2$ for $0<T<30$ K yields $A=2.2\times10^{-4}$, 2.0×10^{-4} (Ω cm) and $B=3.2\times10^{-8}$, 2.0×10^{-8} (Ω cm K^{-2}) for the as-grown and deoxygenated samples, respectively. While A, which is due to the impurity scattering, remains essentially unchanged, B for the deoxygenated sample is almost 40% smaller than that for the as-grown sample. However, the change in the conductivity is by no means significant when compared to that in magnetism.

Nevertheless, it becomes clear that $Na_2Ru_4O_{9-\delta}$ ($\delta\geqslant0$) is indeed unique in that it shows a wide range of unusual properties that may be attributed to one-dimensional behavior. The most striking feature of this compound is the drastically large anisotropy reflected in resistivity which exhibits metallic behavior along one direction and semiconducting behavior along others. The resistivity ratio for these two directions $\rho_\perp/\rho_\parallel$ is larger than 10^5. This result doubtlessly suggests that the bandwidth in this material is highly anisotropic. Consistently, the magnetic susceptibility also suggests occurrence of low dimensional behavior with a maximum in the vicinity of 70 K. It is remarkable that, after reduction of oxygen content in the system, the magnetic susceptibility undergoes a drastic change in spin interactions, whereas the electrical resistivity along the b axis alters only slightly with an increase in linearity. The striking observations reported here require more careful study including measurements of the oxygen deficiency in the deoxygenated samples. These and other studies are being pursued.

ACKNOWLEDGMENTS

We are very grateful to Dr. Elbio Dagotto, Dr. James Brooks, Dr. Alfred Kleinhammes, and Dr. Lou Testardi for their enlightening comments. We also thank Tom Fellers for SEM and EDX measurements on the single crystals studied.

[1] J. Darrier, Acta Crystallogr. Sect. B **30**, 1459 (1974).
[2] I. S. Shaplygin and V. B. Lazarev, Russ. J. Inorg. Chem. (Engl. Transl.) **25**, 1837 (1980).
[3] For example, J. Darriet and L. P. Regnault, Solid State Commun. **86**, 409 (1993); B. Batlogg, S.-W. Cheong, and L. W. Rupp, Jr., Physica B **194–196**, 173 (1994).
[4] For example, M. Hase, I. Terasaki, and K. Uchinokura, Phys. Rev. Lett. **70**, 3651 (1993).
[5] M. Azuma, Z. Hiroi, and M. Takano, Phys. Rev. Lett. **73**, 3463 (1994).

Growth of epitaxial films of iron oxide, nickel oxide, cobalt oxide, strontium hexagonal ferrite, and yttrium iron garnet by laser ablation (abstract)

Robin J. Kennedy
Physics Department, Florida A&M University, Tallahassee, Florida 32307

Thin films of iron oxide, nickel oxide, cobalt oxide, strontium hexagonal ferrite, and yttrium iron garnet have been grown by laser ablation. With the exception of Co_3O_4 deposited on $LaAlO_3$, the first three materials deposited on [100] $LaAlO_3$, $SrTiO_3$, and MgO result in high quality c axis [100] growth. Co_3O_4 deposited on $LaAlO_3$ produces highly oriented but random in-plane growth. Similar highly oriented but random in-plane growth occurs for all three materials deposited on glass. The same three materials deposited on cubic zirconia grow [111] oriented and twinned. Strontium hexagonal ferrite and yttrium iron garnet have been deposited on [111] large lattice constant garnet. Epitaxial [0001] films are obtained for the former while the latter gives [111]-oriented films. For yttrium iron garnet the closeness of lattice match to the substrate necessitates that the mosaicity (rocking curves) obtained from area maps be compared to the growth temperatures and pressures to determine the optimum growth conditions for epitaxiality. © *1996 American Institute of Physics.* [S0021-8979(96)81508-7]

Resolution of conflicts concerning $Fe_{16}N_2$ (abstract)

A. S. Arrott
Simon Fraser University, Burnaby, British Columbia, V5A 1S6, Canada

The 1994 3M-Intermag meeting featured an invited session on $Fe_{16}N_2$ in which many of the research workers in this exciting field put forth apparently conflicting views on the nature and possibilities for the use of, perhaps, the most promising transition metal based alloy for magnetic applications. The debate centers on the promise of $3\mu_B$ per atom at transition metal densities if pure $Fe_{16}N_2$ could be made. A particularly compelling resolution of the conflicts was not mentioned at the meeting, even though it has been in the past. The conflict arises primarily from the original classification of $Fe_{16}N_2$ as a phase denoted by α'' to distinguish it from Fe_8N classified as a phase denoted by α' and the substitutional alloy α-Fe(N). The conflicts arise because data are interpreted as a mixture of two phases α' and α''. For any measured property, it is then sufficient to know the ratio of the two component phases for two different compositions to deduce the apparent properties of the individual phases. But this is not the case. The distinction between α'' and α' is not that of two separate phases but, rather, the end points of a continuum characterized by the degree of order. This makes it necessary to produce the fully ordered state in order to determine its properties, unless it is possible to have enough data about those properties for various degrees of order to justify extrapolation to the fully ordered state. The most ordered $Fe_{16}N_2$ is produced using molecular beam epitaxy. It also shows the highest magnetic moments. The high magnetic moments are supported by Mössbauer measurements of large hyperfine fields in bulk materials (not the molecular beam epitaxy material) and by some of the theoretical calculations for the ordered state. One of the criticisms of the molecular beam epitaxy work is that those thin films do not decompose into Fe_4N and Fe(N) on heating as do bulk alloys of the same composition. (The implication is that the thin films contain something else.) But this criticism is not valid, simply because one cannot predict the stability of a highly ordered state from observations of a weakly ordered state. This is particularly the case where the ordering is accompanied by large lattice distortions. The existing literature is analyzed to extract the dependence of magnetic moment on the degree of order. These considerations lend support to those who are pursuing $Fe_{16}N_2$ for its potential for producing a magnetic material with $3\mu_B$ per atom at transition metal densities. How to increase the degree of order in bulk materials becomes a central concern. © *1996 American Institute of Physics.* [S0021-8979(96)81608-3]

 0021-8979/96/79(8)/4570/1/$10.00 © 1996 American Institute of Physics

Influence of the plastic anisotropy on the magnetic properties of a nonoriented 3% silicon iron

E. Hug, O. Hubert, and M. Clavel
LG2mS, URA CNRS 1505, Université de Technologie de Compiègne, BP649, 60206 Compiegne, France

Modifications of the magnetic properties of a nonoriented 3% SiFe alloy with plastic strains are reported. The samples have been tested along rolling and transverse directions lying in the sheet plane by means of a suitable experimental system of measurements using a 50 Hz sinusoidal magnetic field. The magnetic properties markedly deteriorate when measurements are carried out in the direction of the applied stress. This phenomenon is less important perpendicular to the applied stress. Quasistatic experiments ($f=0.1$ Hz) have been accomplished to separate the total losses into hysteresis and dynamic components. Hysteresis losses strongly increase and dynamic losses sensitively decrease with the plastic deformation whatever the direction in sheet plane. Compression-tension fatigue tests carried out have shown that the material displays a strong kinematic strengthening behavior representative of internal and long range stresses in the strained sample. The degradation of the magnetic properties of nonoriented 3% SiFe alloys with plastic strains is the result of two effects: one due to dislocations and another due to internal stresses. The latter display along the direction of magnetic measurements the same effects as an outside elastic stress. © *1996 American Institute of Physics.* [S0021-8979(96)36108-2]

I. INTRODUCTION

Plastic strains are induced in a rotating electrical machine lamination during its manufacture and can damage its magnetic properties. These deformations result in the generation of dislocations which cause the magnetic properties of electrical steel sheets to deteriorate,[1] especially in the range of low strains level, say, 0%–5%, and for low and medium magnetic field amplitudes (0–5000 A/m).[2,3] These experimental results have been obtained for mechanical stresses and magnetic measurements in the same direction. Nonoriented (N.O.) alloys are generally considered to be magnetically isotropic. The question arises whether the magnetic properties remain isotropic after cold drawing.

In the present article we are dealing with the magnetic properties of a N.O. 3% SiFe along the rolling (RD) and the transverse (TD) directions. The influence of a constant plastic strain imposed along one of these two directions is studied. In addition, tension-compression fatigue tests have been performed with a view to identify the internal stresses in the sample after strengthening. The influence of these stresses on the magnetic properties of N.O. SiFe alloys is discussed.

II. PROCEDURE

Magnetic measurements have been performed on N.O. 3% SiFe alloys (0.5 mm thick). Samples (20×20 mm) have been cut from the unstrained laminations and from the middle of the tensile test specimens previously strained at plastic deformation level $\epsilon_p=4.5\%$ [$\epsilon_p=(L-L_0)/L_0$ where L_0 is the initial length and L is the final length of the specimens]. Tensile tests have been carried out at room temperature and constant strain rate.

Magnetic characteristics have been investigated along RD and TD by means of a suitable experimental system of measurements described elsewhere.[2,4] A quasistatic excitation ($f=0.1$ Hz) and a 50 Hz sinusoidal magnetic field have been used. A number of numerical calculations and calibrations were made to confirm the accuracy of this experimental apparatus.

Tension-compression fatigue tests ($\Delta\epsilon_p/2=0.25\%-1\%$) have been carried out on thicker hot rolled 3% SiFe specimens (3 mm). Appropriate heat treatment ensures the same properties (magnetic, mechanical, and metallurgical) between these samples and the final manufactured product.

III. EXPERIMENTAL RESULTS

A. Magnetization characteristics and core losses

The initial magnetization curves (maximum magnetic flux density B_m vs maximum magnetic field H_m) measured along RD and TD are plotted in Figs. 1 and 2 for $f=50$ Hz. A weak anisotropy of the initial magnetic properties (unstrained specimens) is observed. In order to study the plastic anisotropy of the magnetic properties of the material, 4.5% of plastic strain is applied along RD or TD. The magnetic measurements are then implemented along either the tensile or cross directions. The evolution of the magnetization curves is shown in Figs. 1 and 2. The outcome of the experiments shows that the magnetic properties markedly deteriorate when measurements are carried out in the direction of the applied stress. Crossing experiments, i.e., tensile test in RD or TD and magnetic test at 90°, indicate an attenuated effect of the plastic strain on the magnetic properties. Clearly, the decay of the magnetic properties along RD is more important with an applied stress lying along RD than along TD. The magnetic properties along TD behaves similarly: the decay is more sensitive with the applied stress parallel to TD than parallel to RD. This effect is slightly less for magnetic measurements along the transverse direction.

Quasistatic experiments ($f=0.1$ Hz) carried out on both undeformed and deformed samples allow us to determine the various hysteresis parameters, namely, hysteresis losses W_h [J/(kg cycle)] and coercive field strength H_c. Using the hy-

 0021-8979/96/79(8)/4571/3/$10.00 © 1996 American Institute of Physics

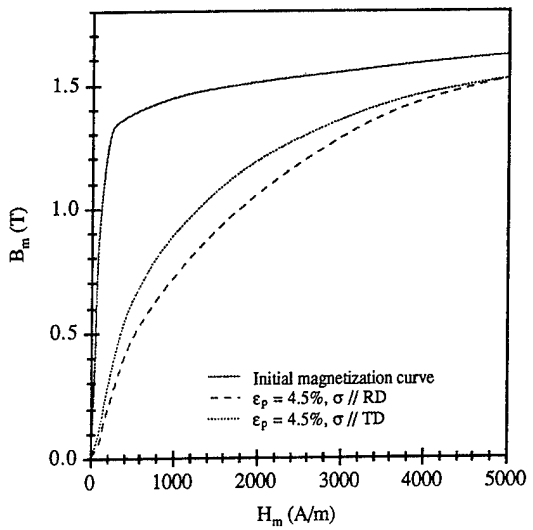


FIG. 1. Magnetization curves of a N.O. 3% SiFe alloy measured along the rolling direction, $f=50$ Hz. Influence of a plastic strain applied along either the rolling or the transverse directions.

pothesis of the separation of losses,[5] the dynamic losses W_d for $f=50$ Hz are extracted from $W_d=W_t-W_h$, with W_t the total losses per cycle. In Table I the different values of W_t, W_h, and W_d are tabulated for the plastic strain along the rolling direction. As is made clear by this table, W_h strongly increases and W_d decreases with the plastic strain. On the whole, there results an increase of the total energy losses. Coercive field strength measurements give for the unstrained samples $H_c=43$ A/m along RD and $H_c=79$ A/m along TD. H_c reaches 162 A/m along RD and 152 A/m along TD after straining along RD. Energy losses and coercive field strength behave similarly when the plastic deformation is applied along the transverse direction.

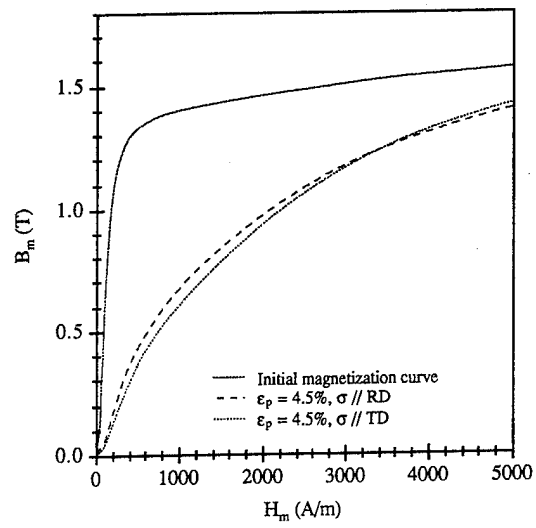


FIG. 2. Magnetization curves of a N.O. 3% SiFe alloy measured along the transverse direction, $f=50$ Hz. Influence of a plastic strain applied along either the rolling or the transverse directions.

TABLE I. Separation of the total energy losses: $W_t=W_h+W_d$ calculated for $f=50$ Hz. The plastic strain has been applied along RD. (W_t: total losses; W_h: hysteresis losses; W_d: dynamic losses; RD: rolling direction; TD: transverse direction; $W_{0.8}$, $W_{1.4}$: energy losses for $B_m=0.8$ and 1.4 T).

$W=P/f$ (J/kg cycle)	RD, $\epsilon_p=0\%$	RD, $\epsilon_p=4.5\%$	TD, $\epsilon_p=0\%$	TD, $\epsilon_p=4.5\%$
$W_{h0.8}$	0.0099	0.0495	0.0158	0.0495
$W_{d0.8}$	0.0043	0.0035	0.0052	0.0025
$W_{t0.8}$	0.0142	0.0530	0.0210	0.0520
$W_{h1.4}$	0.0342	0.1090	0.0560	0.1300
$W_{d1.4}$	0.0552	0.0050	0.0440	0.0200
$W_{t1.4}$	0.0894	0.1140	0.1000	0.1500

B. Mechanical behavior of the alloy and internal stresses

The study of internal stresses which may exist inside the sample after strengthening requires plastic fatigue experiments. The total applied stress σ may be conveniently expressed as follows (Fig. 3): $\sigma=\sigma_e+R+X$. σ_e is the initial yield stress, R the isotropic, and X the kinematic components of the strengthening.[6] R and X are obtained from fatigue test results and applied to a monotonous tensile test (Fig. 4). The results highlight a strong kinematic strengthening behavior of the material representative of strong internal and long range stresses in the deformed sample.

IV. DISCUSSION

The degradation of the magnetic properties of N.O. 3% SiFe alloys with plastic strains seems clearly to result from two effects: a first one representative of the metallurgical defects created by strengthening and a second one due to the internal stresses present in the sample after straining.

It has been shown in a previous article[3] that small dislocation tangles are created during cold drawing in the range 0%–5% of plastic strain. These defects act as pinning centers for the magnetic domain walls.[7] As a result, H_c and W_h rise dramatically with small increases in plastic strains. Indeed, these two parameters are representative of the irreversible changes of magnetization due to pinning/unpinning of the magnetic domain walls against dislocation tangles. In view of our results, the growth of H_c and W_h can be considered to

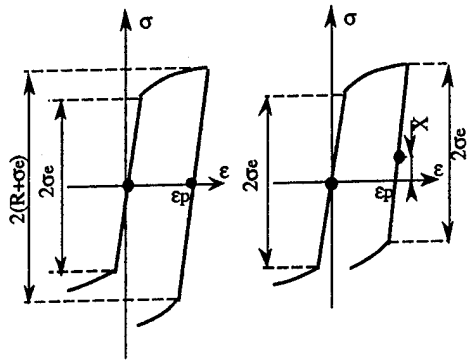


FIG. 3. Determination of the isotropic (R) and the kinematic (X) components of the strengthening from plastic test experiments.

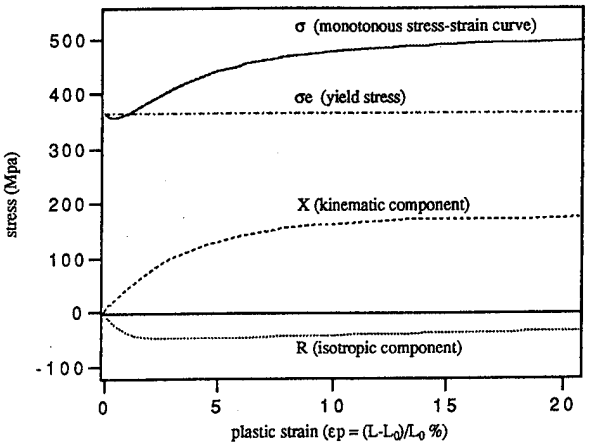


FIG. 4. Variation of the isotropic (R) and the kinematic (X) components of the strengthening with the monotonous plastic strain (tensile test experiments).

be independent of the direction of straining. The initial magnetic anisotropy of the alloy is roughly maintained. The dynamic losses, on the other hand, are representative of the eddy current losses due to changes in magnetic flux in the metallic samples. The dislocation tangles result in many more pinned magnetic walls. The motion of each wall is then reduced. Consequently, the changes in magnetic flux produce less eddy current losses in the deformed specimens because dislocation tangles lead to more walls moving smaller distances.

Beside the isotropic effect of dislocation tangles, it is necessary to take into account the internal stresses in the samples. The latter give rise to a plastic anisotropy. After a tensile test, there is zero exterior applied stress. Considering an area perpendicular to the tensile direction, the sum of stresses on this area is on average zero. Nevertheless, the plastic anisotropy (seen as the strong kinematic behavior in Fig. 4) can be explained by the existence of compressed areas alternating with tensile ones. Moreover, the dislocation network presents many inhomogeneities (tangles, grain boundaries,...). Following Mughrabi,[8] this configuration implies that strong tension areas (volume V_t) are enclosed in the dislocation tangles and grain boundaries. The latter are counterbalanced by much larger areas of weakly compression stresses (volume V_c). V_c is then larger than V_t in the tensile direction and the magnetic properties along this direction are on average dominated by compression effects. Consequently, an internal tension stress effect does exist perpendicular to the tension test direction (Poisson's effect).

This could explain the increase of the degradation of the magnetic properties when magnetic tests are carried out along the tensile test direction. Conversely, degradation of the magnetic properties with the plastic deformation are less sensitive when magnetic tests are carried out perpendicular to the tensile test direction. The residual stresses which exist in direction of the measurements display the same effect as an outside elastic stress.[9] This phenomenon is less sensitive for magnetic measurements along TD. This could be related to the small initial anisotropy of the mechanical properties of the material.

V. CONCLUSION

The investigation of the magnetic properties of a N.O. 3% SiFe with plastic strain, frequency, and orientation lying into the sheet plane allows the following conclusions.

(1) The strong degradation of the magnetic properties of a 4.5% plastic strained alloy (increase of W_h and H_c) is the consequence of the strong pinning effect of the dislocation tangles on magnetic domain walls.

(2) The dynamic losses decrease with plastic strains. The changes in magnetic flux produce less eddy current losses in the strained samples because dislocation tangles lead to more magnetic domain walls moving smaller distances.

(3) The strengthening of the material gives rise to an important plastic anisotropy because of the presence of strong internal stresses after the tensile test. This tends to increase the magnetic degradation when magnetic tests are carried out along the tensile test direction and conversely to reduce this degradation when magnetic tests are made perpendicular to it.

[1] L. J. Dijkstra and C. Wert, Phys. Rev. **29**, 979 (1950).
[2] O. Hubert and E. Hug, Mater. Sci. Technol. **11**, 482 (1995).
[3] E. Hug, M. Kant, and M. Clavel, J. Phys. III (France) **4**, 1267 (1994).
[4] O. Hubert, E. Hug, and M. Clavel (unpublished).
[5] E. T. Stephenson, J. Appl. Phys. **57**, 4226 (1985).
[6] J. Lemaitre and J. L. Chaboche, *Mécanique des Matériaux Solides* (Dunod, Bordas, 1988), pp. 196–239.
[7] D. C. Jiles, *Introduction to Magnetism and Magnetic Materials* (Chapman and Hall, London, 1991), pp. 156–172,
[8] H. Mughrabi, Acta Metall. **31**, 1367 (1983).
[9] K. C. Pitman, IEEE Trans. Magn. **26**, 1978 (1990).

Magnetic properties of 3%Si-Fe thin sheets annealed in Ar atmosphere (abstract)

Y. Yamashiro and A. Yonesu
Electrical Engineering Department, Ryukyu University, Okinawa, 903-01, Japan

S. Hashi, K. Ishiyama, and K. I. Arai
Institute of Electrical Information, Tohoku University, Sendai, 980-77, Japan

It has been actually required in recent years to decrease iron losses in transformer cores, as increment of electric energy consumption in all industries and homes. Answering to such requirements, Arai *et al.* developed a new type magnetic core material; it was tertiary recrystallized Si steel with 50 μm thickness, and it was of as low iron loss as an amorphous materials one.[1] The Si steel was made by an annealing in a vacuum of 1×10^{-3} Pa and at a temperature of 1200 °C. In this study, we prepared samples for measurements from (110)[001] grain-oriented 3%Si steel with 300 μm thickness. We coldrolled them to about 50 μm using a four-high rolling mill, and then annealed in an atmosphere of highly pure Ar gas, from a point of view of saving energy. We investigated effects of annealing time, heating rate and gas flow rate on magnetic properties. The annealing temperature was fixed at 1000 °C. Hysteresis loops were drawn with single-sheet tester. Grain structure and its direction were decided by etch pit method. Coercive force H_c and induction B_8 which is the induction at 800 A/m applied field were obtained from the hysteresis loops. The magnetic properties were somewhat changed according to the annealing condition. The coercive force varied from 5 to 30 A/m, and the induction varied from 1.45 to 1.85 T. The best properties, H_c was 5 A/m and B_8 was 1.85 T, were obtained under the annealing condition; annealing time was 60 min, heating rate was 3 °C/s, and gas flow rate was 2 *l*/min. The surfaces of the samples were not covered with tertiary recrystalline, but wholly with secondary recrystalline. About 90% grains were (110) plane, the rest was (100) plane. And about 90% [001] axes oriented to the rolling direction within five degree misorientation. © *1996 American Institute of Physics.*
[S0021-8979(96)81708-X]

[1] K. I. Arai and K. Ishiyama, J. Appl. Phys. **64**, 5352 (1988).

 0021-8979/96/79(8)/4574/1/$10.00 © 1996 American Institute of Physics

Power losses in thick steel laminations with hysteresis

C. Appino, G. Bertotti, O. Bottauscio, F. Fiorillo, and P. Tiberto
Istituto Elettrotecnico Nazionale Galileo Ferraris, C. so M. d'Azeglio 42, 10125 Torino, Italy

D. Binesti and J. P. Ducreux
Electricité de France, DER, Les Renardières BP 1, 77250 Moret-sur-Loing, France

M. Chiampi and M. Repetto
Politecnico di Torino, C. so Duca degli Abruzzo 44, 10129 Torino, Italy

Magnetic power losses have been experimentally investigated and theoretically predicted over a range of frequencies (direct current—1.5 kHz) and peak inductions (0.5–1.5 T) in 1-mm-thick FeSi 2 wt. % laminations. The direct current hysteresis properties of the system are described by the Preisach model, with the Preisach distribution function reconstructed from the measurement of the recoil magnetization curve (B_p=1.7 T). On this basis, the time behavior of the magnetic induction vs frequency at different lamination depths is calculated by a finite element method numerical solution of Maxwell equations, which takes explicitly into account the Preisach model hysteretic $B(H)$ relationship. The computed loop shapes are, in general, in good agreement with the measured ones. The power loss dependence on frequency is predicted and experimentally found to change from a $\sim f^{3/2}$ to a $\sim f^2$ law with increasing peak induction. © *1996 American Institute of Physics.* [S0021-8979(96)36208-9]

I. INTRODUCTION

Power loss phenomena in soft magnetic laminations can be understood and assessed to a good extent through the statistical description of domain wall dynamics and the related development of new concepts in the Preisach modeling of hysteresis.[1] Several interesting problems arise when this interpretative framework is applied to bulk materials and the related skin effects.[2] In fact, one has to properly characterize the hysteretic magnetic behavior of the sheet, solve Maxwell equations in the presence of hysteresis, and carry out convenient dynamic hysteresis measurements in order to appropriately test the model predictions.

In this article, we study the dynamic behavior of 1-mm-thick FeSi sheets, for frequencies from direct current (dc) to 1.5 kHz and peak inductions in the interval from 0.5 to 1.5 T. The material hysteresis properties are described by the Preisach model (PM), and Maxwell equations are solved by the finite element method (FEM), and by using the fixed point (FP) technique to treat the nonlinear hysteretic behavior of the material. This requires the use of PM in a reversed fashion, in order to obtain, at each iteration step, the time behavior of the local field **H** from the known local induction wave form.[3] From the knowledge of the magnetic flux density distribution, the dynamic hysteresis loops and the local losses at different frequencies can be calculated.

We have found that the calculated loop shapes are in general in good agreement with the measured ones. At low peak inductions B_p, the skin effect prevents the complete flux penetration in the sheet and the power loss dependence on frequency is close to a $f^{3/2}$ law. With increasing B_p, however, the skin effect is no longer able to hinder the flux penetration and a complicated phase shift pattern in the flux densities at different lamination depths sets in. In this case the power loss vs frequency law moves to a f^2 law.

The present approach does not take into account magnetic domain effects responsible for excess losses. This aspect could be dealt with by using the dynamic Preisach model instead of the conventional one.[1,4]

II. THEORETICAL MODELING

Calculations were based on the standard FEM solution of Maxwell equations expressed in term of the vector potential **A**. The starting point is the equation

$$\nabla\times[H(\nabla\times\mathbf{A})]=-\sigma\frac{\partial\mathbf{A}}{\partial t}+\frac{\sigma}{S}\int_\Omega\frac{\partial\mathbf{A}}{\partial t}\,dS', \tag{1}$$

together with nonhomogeneous Dirichlet conditions, which impose the stated flux wave form. In Eq. (1), σ is the electric conductivity and Ω is the cross section of the lamination with area S. We assumed the local **H** and **B** vectors to always be collinear, and a scalar treatment of the **H(B)** relation was considered. Following the fixed point (FP) technique, the relation between **H** and **B** is expressed as $\mathbf{H(B)}=\nu_T\mathbf{B}+\mathbf{R}$. The coefficient ν_T is related to the slope of the initial magnetization curve and is held constant throughout the calculation. The residual term **R** is iteratively evaluated, starting from a trial value.

Under periodic conditions, the problem is formulated in the frequency domain, introducing a set of complex vector potential harmonics $\mathbf{A}^{(n)}$, where n is the harmonic order corresponding to the angular frequency $n\omega$. The application of the iterative FP scheme to Eq. (1) leads to a sequence of linear problems, having the form

$$\nabla\times(\nu_T\nabla\times\mathbf{A}_k^{(n)})=-i\omega n\sigma\mathbf{A}_k^{(n)}+i\omega n\frac{\sigma}{S}\int_\Omega\mathbf{A}_k^{(n)}\,dS'-\nabla\times\mathbf{R}_{k-1}^{(n)}, \tag{2}$$

where k is the iteration index. The problem is unidimensional, since any quantity depends only on the depth x across the lamination thickness. Following FEM, the lamination is subdivided into a conveniently high number (~100) of lay-

 0021-8979/96/79(8)/4575/3/$10.00 © 1996 American Institute of Physics

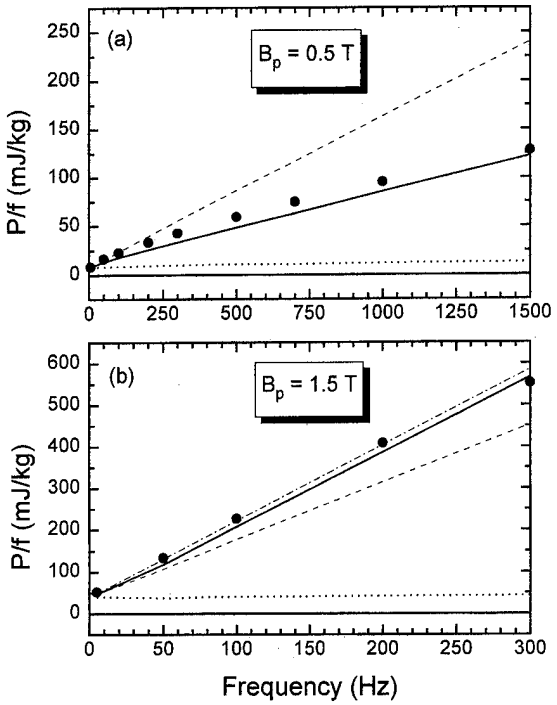


FIG. 1. (a) Energy loss vs frequency at B_p=0.5 T. Points: experiments; dotted line: computed hysteresis loss; continuous line: computed total loss; dashed line: total loss obtained by adding to the hysteresis loss the standard classical expression holding in the absence of skin effect. (b) Same for B_p=1.5 T. Dash–dotted line: analytical prediction obtained by assuming $B=+B_p$ when $H>0$, $B=-B_p$ when $H<0$.

ers and on each layer the solution is interpolated by means of first order shape functions. It is worth noting that the FP iterations change only the right-hand side of Eq. (2), without requiring any modification of the stiffness matrix.

At each iteration step, all the harmonic components of the vector potential **A** are calculated, providing the corresponding components of the magnetic induction $\mathbf{B}=\nabla\times\mathbf{A}$. The time behavior of **B** is obtained by an inverse fast Fourier transform of the harmonic components. The **H(B)** dependence is described through PM, used in a reversed fashion,[3] in order to compute the local field wave form **H(t)** that generates the known local **B** wave form. Once the **B** and **H** wave forms are known, the time evolution of the residue $\mathbf{R_k}$ is computed over each element, the harmonic decomposition is performed again and the right-hand side of Eq. (2) is upgraded. The computation scheme is iterated until convergence.

For any given solution, the total loss was calculated by taking the time integral of the field at the lamination surface times the mean induction rate, i.e., averaged over all mesh elements. The hysteresis loss was instead calculated by taking the time integral of **H dB** in each mesh element and integrating the result over the whole lamination volume. Classical losses can be also evaluated by integrating the quantity J^2/σ in space and time, where the current density **J** is evaluated from the vector potential **A**. The comparison between the total loss and the sum of the hysteresis and classical losses provided an additional check of the computation accuracy.

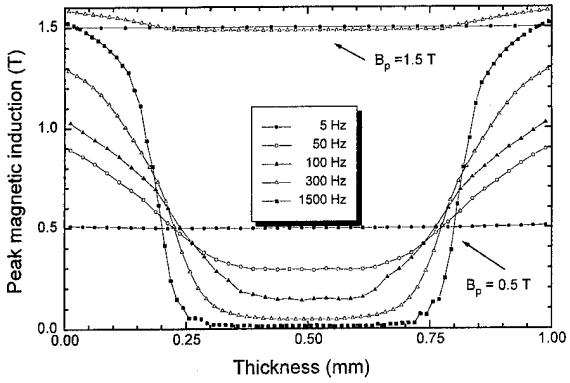


FIG. 2. Computed profiles of the peak induction vs lamination depth at different exciting frequencies for macroscopic peak induction B_p=0.5 and 1.5 T.

The switching field Preisach distribution used to characterize the material was assumed to have the factorized form $p(\alpha,\beta)=f(\alpha)f(-\beta)$, which is the natural factorization expected in soft magnetic laminations.[5] $p(\alpha,\beta)$ was reconstructed, as suggested in Ref. 6, from the recoil curve of the loop measured at peak induction B_p=1.7 T. The obtained distribution function $p(\alpha,\beta)$ was found to be sharply peaked at low (α, β) values, as expected from the shape of the experimentally determined static hysteresis loops. In order to efficiently handle the numerical problem, the Preisach plane was covered with a mesh having increased density in the region where the peak of $p(\alpha,\beta)$ was located.

III. EXPERIMENTAL RESULTS AND DISCUSSION

Dynamic hysteresis loops and power losses were measured by a digital feedback wattmeter which allows one to carry out measurements under controlled induction wave form in a wide frequency range (0.5 Hz–100 kHz).[7] Static hysteresis loops and the normal magnetization curve were determined by means of a precision ballistic setup. Experiments were performed on 2 wt % Si–Fe alloys. Laminations 1 mm thick were tested as 30×300 mm strips, inserted in an Epstein frame with a reduced number of turns.

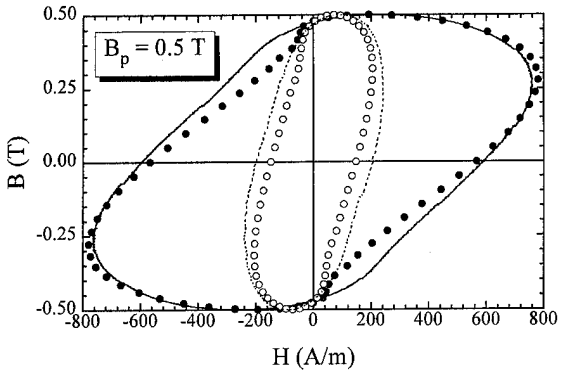


FIG. 3. Experimental and computed hysteresis loops for B_p=0.5 T. Lines: measurements (dashed: f=300 Hz, continuous; f=1.5 kHz). Symbols: theoretical prediction.

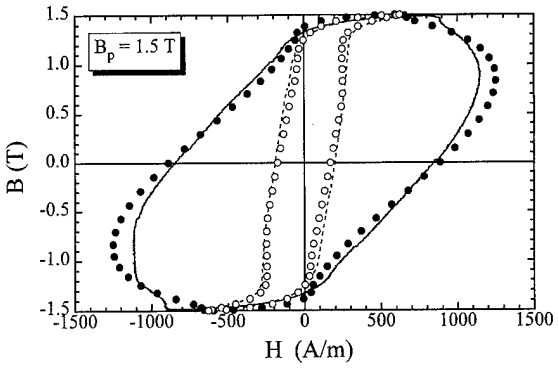


FIG. 4. Instantaneous profiles of the induction $B(x)$ at different times t along the period T, at $f=300$ Hz and macroscopic peak induction $B_p=1.5$ T. A: $t=0$; B: $t=T/8$; C: $t=T/4$; D: $t=3T/8$; E: $t=T/2$.

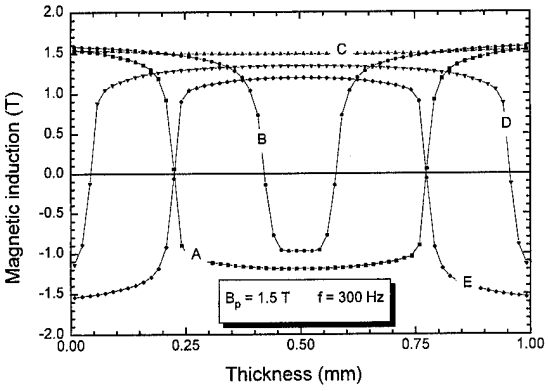


FIG. 5. Experimental and computed hysteresis loops for $B_p=1.5$ T. Lines: measurements (dashed: $f=50$ Hz, continuous; $f=300$ kHz). Symbols: theoretical prediction.

The loss per cycle vs frequency at 0.5 T is shown in Fig. 1(a). The continuous line represents the FEM calculated total loss, while the dotted line is the hysteresis loss, obtained from the integral of local **H dB** over time and over the mesh elements. The calculations show that the hysteresis loss, which would be independent of f in the absence of any skin effect, increases with frequency, because of the nonconstant peak induction profile vs lamination depth. The dashed line represents the sum of the hysteresis loss and the standard classical loss $P_c/f=(\pi^2/6)\sigma d^2 B_p^2 f/\delta$ (d is the lamination thickness and δ is the mass density). As expected, this law gives a grossly overestimated total loss figure in the frequency range where the skin effect becomes important. This is well illustrated by Fig. 2, which shows the FEM calculated frequency dependence of the peak induction profiles vs lamination depth. Above a few hundred Hz, about half of the lamination becomes flux depleted, an effect compensated by the strong increase of $B_p(x)$ near the surface. The measured and calculated hysteresis loops at 300 Hz and 1.5 kHz are shown in Fig. 3. At low f, some disagreement between the predicted and measured loop shapes was found. This is likely due to limitations in the identification of the Preisach distribution, which was based on data at 1.7 T only.

The loss behavior at 1.5 T shows that, with the increase of the macroscopic peak induction, the slope of the experimental P/f vs f curve suffers a progressive increase, which is correctly predicted by the model [see Fig. 1(b), and Fig. 4 for the loop shapes]. The loss values obtained by both measurements and FEM calculations are larger than the ones calculated through the standard classical loss expression given above, just the opposite of what was observed at 0.5 T. This difference is the consequence of the qualitatively different flux penetration pattern in the lamination. As shown in Fig. 2, the peak induction attains quite a uniform profile over the lamination cross section. But such a peak value is reached at different times for different depths (see Fig. 5) and it is this phase difference that causes additional inhomogeneities in the magnetization rate spatial distribution and ensuing higher losses. Some useful information on this behavior can be obtained analytically, without resorting to FEM calculations. In fact, when B_p is comparable with the saturation magnetization and the dynamic fields involved in the problem are much larger than the material coercivity, the **B(H)** relation can be approximated by a step function of the form $B=+B_p$ when $H>0$, $B=-B_p$ when $H<0$. In this case, the flux and field distribution inside the lamination can be calculated analytically, and the loss turns out to be equal to $(4/3)P_c$, where P_c is the standard expression given above.

IV. CONCLUSIONS

The present calculations predict hysteresis and classical losses, but not excess losses due to magnetic domain effects. From the quantitative point of view, this is not expected to lead to important errors in the steel here considered, where the excess loss plays a minor role due to the fine grain size, but it might become relevant for those laminations where the grain size exceeds values of the order of 100 μm. In cases of interest, one can include domain effects into the treatment by considering the so-called dynamic Preisach model, as recently proposed by some authors.[4] This model is equivalent to introducing a local **B(H)** relationship which depends not only on the **H** history, but also on the field rate $d\mathbf{H}/dt$. The use of the dynamic Preisach model would not require any substantial change in the design of the FEM algorithm presented here. The main difference is likely to be the drastic increase of the computation time, as a consequence of the complex internal structure of the dynamic Preisach model.

[1] G. Bertotti and M. Pasquale, IEEE Trans. Magn. **28**, 2787 (1992).
[2] R. M. Del Vecchio, J. Appl. Phys. **53**, 8281 (1982).
[3] O. Bottauscio, M. Chiampi, D. Chiarabaglio, and M. Repetto, IEEE Trans. Magn. **31**, 3548 (1995).
[4] D. A. Philips, L. R. Dupre, and J. A. A. Melkebeek, IEEE Trans. Magn. **30**, 4377 (1994).
[5] V. Basso, M. Lo Bue, and G. Bertotti, J. Appl. Phys. **75**, 5677 (1994).
[6] G. Kadar, J. Appl. Phys. **61**, 4013 (1987).
[7] G. Bertotti, E. Ferrara, F. Fiorillo, and M. Pasquale, J. Appl. Phys. **73**, 5375 (1993).

High temperature magnetic properties of 49%Co–2%V–Fe alloy

Lin Li
Research and Development Center, Carpenter Technology Corporation, Reading, Pennsylvania 19612-4662

Direct current hysteresis loops of 49%Co–2%V–Fe alloy have been measured at temperatures up to 800 °C. Two phase structure is evident in the $B-H$ loops between 580 and 730 °C. This alloy cannot be reliably operated above 580 °C. The second magnetic phase is believed to result from the nucleation and growth of disordered α phase in the ordered α' phase matrix. Magnetic properties (measured as B at $H=2.5$ and 10 Oe) degrade with time during aging at 450 °C, but approach stable values after about 1000 h, which provides the possibility for long-term high temperature (e.g., 450 °C) operation if the degraded properties are still acceptable for the application. The coercive field remains unchanged while the permeability decreases irreversibly during aging. The irreversible magnetic property changes that occur during aging at 450 °C are most likely caused by an increase in the long range order parameter. © *1996 American Institute of Physics.* [S0021-8979(96)36308-5]

I. INTRODUCTION

Hiperco® Alloy 50 with the composition of 49%Co–2%V–Fe has high saturation induction, high Curie temperature, and low coercive field. Some possible applications for Hiperco Alloy 50 are at temperatures up to 600–800 °C. However, no magnetic property data are available at such high temperatures. Furthermore, these potential applications also raise the question of the stability of this alloy at high temperatures.

Pandey *et al.*[1] have studied the aging behavior of 49%Co–2%V–Fe up to 450 °C. However, the data, for instance, the testing point of permeability μ and the magnetic field strength corresponding to B_m, are not well defined and therefore are difficult to apply in practical design.

In this study, we measured the change in magnetic properties (at various fields) of Hiperco Alloy 50 from 25 to 800 °C, and during long term aging at 450 °C.

II. EXPERIMENT

The specimens used were stamped rings (i.d.=1.25 in., o.d.=1.5 in.) made from a 0.014 in.-thick strip. The rings were heat treated in dry hydrogen at 760 °C for 2 h and cooled at 180 °C/h.

In order to determine magnetic properties at elevated temperatures (500–800 °C), technical difficulties such as insulation of the windings and shielding (used Hiperco Alloy 27 strip in this experiment) against interference from the heating coils had to be overcome.

A stack of about 50 rings was placed in a quartz core box. Nickel wire (24 gauge) coated with ceramic was used for the windings. The magnetization of the Ni wires appears to have no effect on the magnetic measurements. A type-N thermocouple was attached to the ring pack to monitor the specimen temperature. The rings were heated under high purity argon with neither magnetic field nor mechanical stress being applied. The magnetic measurements were made using a Yogokawa dc magnetic hysteresis loop tracer (type 3257). Two separate test fields were used in the aging study, 2.5 and 10 Oe.

III. RESULTS AND DISCUSSIONS

After several initial tests, we realized that two kinds of magnetic property changes occur at high temperature: reversible changes that occur as a function of temperature, and irreversible changes caused by prolonged heating (aging) at a relatively high temperature. The irreversible changes mean that the properties at a given test point and temperature in a heating–cooling cycle will be different from the properties in the previous cycle, even if the cycles are identical. These effects have not been clearly distinguished in prior studies[1,2] on high temperature magnetic properties. Although it is impossible to separate these two changes completely, the measured changes are fairly reversible at temperatures lower than 450 °C and for short heating times, i.e., less than 15 min, as shown in Table I. However, we observed a large irreversible change in B at temperatures above 450 °C even with short heating times.

Figure 1 shows the $B-H$ loops of specimen B in Table I held at elevated temperatures for short times. As the temperature is increased to 580 °C, the $B-H$ loop becomes more square and starts to show small irregularities, as indicated by arrows. These irregularities become larger at 650–700 °C but disappear above 730 °C. Hiperco Alloy 50 has an order–disorder transition at about 730 °C.[3] It is reasonable to assume that these irregularities result from the nucleation and growth of the disordered α phase in the matrix of ordered α' phase. This was confirmed by observation of a smooth $B-H$ loop at temperatures above 730 °C when the $\alpha' \rightarrow \alpha$ transition is complete and only the single phase α exists.

Long-term operation of the alloy above 580 °C is not recommended due to the irregularities in the $B-H$ loops. However, high temperature (e.g., 450 °C) operation may still be possible provided the limited magnetic property deterioration can be tolerated. Figure 2 shows the change in magnetic induction B versus aging time. The reversible change in B is shown at the initial point, i.e., at aging time=0, compare $B_{25\,°C}$ to $B_{450\,°C}$. The induction B then continues to decrease (irreversible change portion) as aging proceeds. This irreversible change is the greatest in the first 200 h, and B stabilizes after about 1000 h. Actual applications have complicated heating cycles but the peak temperature can be

 0021-8979/96/79(8)/4578/3/$10.00 © 1996 American Institute of Physics

TABLE I. Magnetic property changes of Hiperco Alloy 50 during the first rapid heating–cooling cycle. Each temperature was held for 15 min and each $B-H$ loop measurement took 30 s.

Test temp.	Specimen A $H=2.5$ Oe B_m (kG)	B_r (kG)	H_c (Oe)	Specimen A $H_m=10$ Oe B_m (kG)	B_r (kG)	H_c (Oe)
25 °C	19.2	16.2	1.1	22.0	17.2	1.1
180 °C	18.4	15.8	1.0	21.6	16.0	1.0
380 °C	18.0	15.2	1.0		No data	
240 °C	18.4	15.4	1.0	21.4	16.8	1.0
25 °C	18.7	15.5	1.0	21.8	17.0	1.1
Test temp.	Specimen B $H_m=5$ Oe B_m (kG)	B_r (kG)	H_c (Oe)			
25 °C	20.8	17.6	1.7			
500 °C	18.8	15.3	1.4	The coercive fields of		
580 °C	18.7	16.8	1.1	specimens A and B before the		
650 °C	17.8	15.8	1.3	cycles differ slightly due		
700 °C	16.6	15.1	1.5	to different heat		
800 °C	15.0	13.6	0.9	treatments.		
25 °C	strongly cooling rate dependent					

determined. The curves in Fig. 2 define the minimum values for B at 2.5 and 10 Oe after the material has been exposed at peak temperatures up to 450 °C. The value of H_c remains unchanged (1.4 Oe) during the entire aging process at 450 °C.

After aging at 450 °C for 1150 h, the specimen was cooled to 25 °C and the $B-H$ curve determined again. Notice that in Fig. 2 the differences between $B_{25\,°C}$ and $B_{450\,°C}$ at the beginning and the end of the aging cycle are fairly similar. That is to say, the reversible B change remains rela-

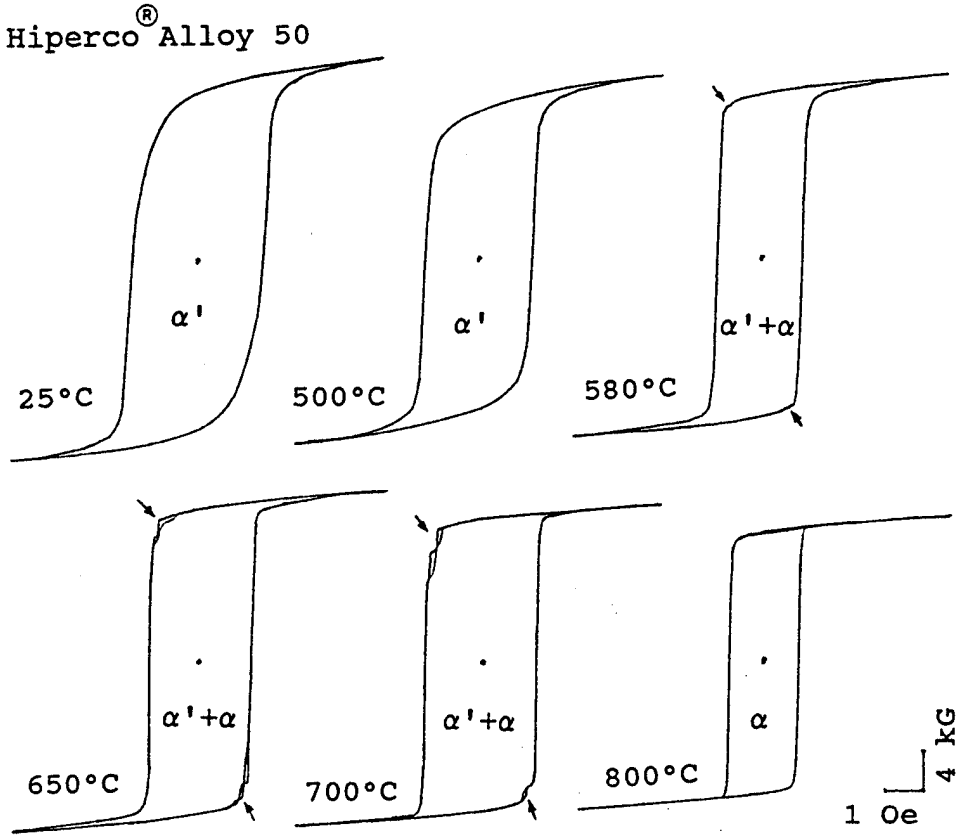


FIG. 1. $B-H$ loops of Hiperco Alloy 50 at elevated temperatures ($H_m=5$ Oe). Arrows indicate the irregularities caused by nucleation and growth of disordered α phase in the ordered α' phase.

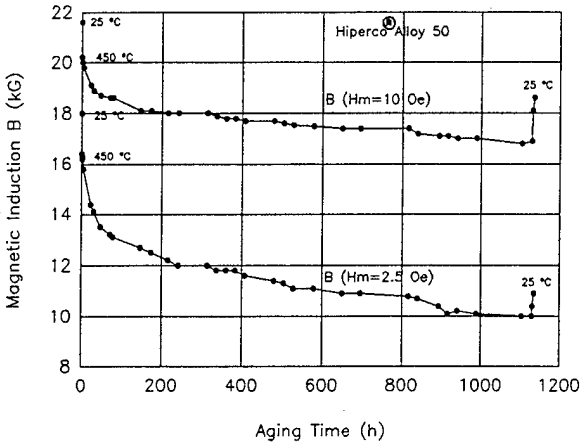


FIG. 2. Induction B change during aging of Hiperco Alloy 50 at 450 °C.

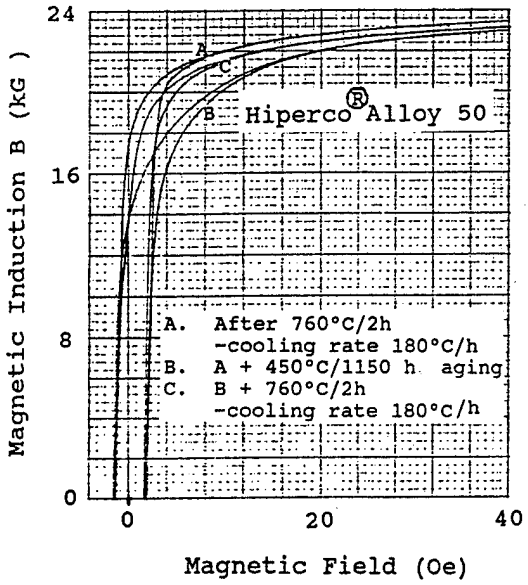


FIG. 3. Room temperature $B-H$ loops of Hiperco Alloy 50 before and after aging at 450 °C, and after reannealing.

tively constant during the aging cycle.

In Fig. 3, loops A and B show the decrease in permeability after aging at 450 °C. The decrease in B is less severe at higher magnetic fields. This permeability decrease can be recovered to a great extent by a normal heat treatment, as loop C shows.

X-ray diffraction and transmission electron microscopy results did not show any major metallurgical structure changes in the specimens after aging. Therefore, we believe that the irreversible property change during aging is mainly caused by the change in the long range ordering parameter.

ACKNOWLEDGMENTS

The author would like to thank Dr. M. Scott Masteller and Donald K. Schlosser for their very stimulating discussions and extended review of the manuscript. Bradford A. Dulmaine and David A. Englehart also provided helpful technical advice and assistance.

[1] R. K. Pandey, M. H. Weichold, and D. W. Palmer, IEEE Trans. Magn. **16**, 749 (1980).
[2] P. E. Kueser, D. M. Pavlovic, D. H. Lane, J. J. Clark, and M. Spewock, NASA Special Publication No. NASA SP-3043 (1967), pp. 135–160.
[3] T. Nishizawa and K. Ishida, Metal Progr. **1986**, 57 (February).

Effect of nucleating layers on the soft magnetic properties of multilayer permalloy films

Craig A. Grimes
Department of Electrical Engineering, The University of Kentucky, Lexington, Kentucky 40506

The effects of different undercoats and silicon nitride nucleating layers on the coercive force, anisotropy field, and 5 to 100 MHz complex permeability spectra of magnetically soft, $Ni_{81}Fe_{19}$ multilayer thin films sputtered onto flexible, 52-μm-thick polyethylene terephthalate substrate for use as identification markers or electromagnetic interference shields is reported. In comparison to films deposited directly onto the substrate, nonmagnetic undercoat layers, including aluminum, copper, silicon, and silicon nitride, are found to increase the soft magnetic properties of subsequently deposited films. Nucleating layer effects are dependent upon the undercoat/nucleating layer combination. © *1996 American Institute of Physics.* [S0021-8979(96)36408-1]

I. INTRODUCTION

Sputter deposition of thin films onto flexible, thin, polymeric-type substrates is currently an area of considerable interest[1–3] for fabrication of sensors, identification markers, and films for the control of electromagnetic interference (EMI). This work focuses on the deposition of magnetically soft, multilayer thin films onto 52-μm-thick polyethylene terephthalate (PET) substrates that can be used as identification markers or for the control of EMI. The commercial significance of these products to the magnetics community is significant. For example, the European retail market has a current annual consumption of approximately 320 million magnetically soft thin film antitheft markers, each approximately 1 μm thick and 3 cm^2 in size, made by sputter deposition onto flexible webs of PET approximately 50 μm thick using roll to roll winding. Films used for identification markers require a low coercive force, and a complex permeability spectra, $\mu=\mu'-j\mu''$, where μ' is large and μ'' small. So that the film does not saturate, films used for control of EMI must have a coercive force larger than the field strength of the incident magnetic field, and a large permeability magnitude over the frequency range of interest.

Although sputtering allows for fabrication of a magnetically soft film, sputtering a film onto a thin polymeric-type sheet is difficult due to the topology of the substrate–film interface; the incident sputtered atom melts the substrate on a microscale dimension, resulting in an initial nucleation layer containing hydrocarbons that affect film performance. Polyimide substrates, such as kapton, are durable, smooth, offer good film adhesion, and have been used in earlier work,[1,2] but are too expensive for use in large volume manufacture of identification markers. PET substrates are inexpensive, durable, and offer good film adhesion. In an earlier work,[4] it was shown that the uniformity of magnetic films sputtered onto untreated PET was quite poor, but could be greatly enhanced by briefly sputter etching the substrate in oxygen prior to film deposition; the incident oxygen ions act to clean the surface and remove asperites or surface irregularities.[5] It was also found that the soft magnetic properties of a film stack could be enhanced by deposition of an aluminum metal undercoat or barrier layer atop the plastic substrate prior to deposition of the magnetic film.[4] To clarify the terminology used in this article, an undercoat layer is a homogeneous film thick enough to totally cover the substrate, generally 100 nm or more, so that the magnetic stack does not come into contact with the hydrocarbons of the substrate. In contrast to the relatively thick undercoat layers, nucleating or seed layers are quite thin, generally less than 15 nm thick, and are therefore nonhomogeneous layers. This article reports on further investigations into the use of different undercoat layers, with and without the use of silicon nitride nucleating layers to enhance the soft magnetic properties of sputter deposited multilayer permalloy films. In earlier work,[4] it was found that the simplest multilayer stack, deposited onto a flexible PET substrate, for which optimal soft magnetic properties were obtained, i.e., low coercive force and high permeability, consisted of six magnetic layers; therefore a fixed stack geometry of six magnetic layers is used while investigating the effect of undercoat and nucleating layers. The in-plane coercive force H_c, anisotropy field H_k, quasistatic (5 MHz) permeability magnitude $|\mu|$, and the 5 to 100 MHz complex permeability spectra of dc planar magnetron sputtered $Ni_{81}Fe_{19}$ multilayer films are measured as a function of undercoat and silicon nitride nucleating layer. The hard-axis permeability spectra are measured using a permeameter;[6] in-plane H_c and H_k values are measured at 10 Hz using a BH looper.

II. EXPERIMENT

Our choice of substrate is determined by the nature of the end product. EMI shields need to be flexible in order to be incorporated into building supplies, packages, electronic containers, etc. For widespread application identification markers need to be very inexpensive; large scale production requires them to be cut from a large volume, wide web substrate that is as thin as possible. Untreated PET is inexpensive, offers good film adhesion, can be handled easily, and is suitable for deposition of high performance soft magnetic films. Scanning electron microscope (SEM) examination of the untreated PET surface shows a large number of asperities, surface defects, and nonuniformities that result in localized variation of the magnetic properties of subsequently deposited films. It was found that the asperites and defects could be greatly reduced, and the uniformity of subsequently deposited films enhanced, by sputter etching the substrate web in oxygen[5] at a power level of 3 W/cm^2 for 6 s. Lower

 0021-8979/96/79(8)/4581/3/$10.00 © 1996 American Institute of Physics

TABLE I. Effect of different 150-nm-thick undercoats. Six 80 nm $Ni_{81}Fe_{19}$ layers, five 10 nm, Si_3N_4 spacers.

Undercoat	H_c (Oe)	H_k (Oe)	$\|\mu\|$
No undercoat	0.19	4.6	2600
Silicon nitride	0.10	1.4	3800
Silicon	0.12	3.1	3550
Copper	0.16	3.6	3200
Aluminum	0.12	3.3	3500
$Co_{79}Cr_{21}$	>100	>100	5500

power levels resulted in greater levels of nonuniformity, while larger power levels tended to overheat the web which resulted in creases. Therefore, throughout this study the 52-μm-thick PET substrate web was cleaned by sputter etching at the above power level prior to film deposition. Background pressure in the sputtering chamber was 1.8 mTorr, the sputtering gas was argon, and the silicon nitride layers were deposited by sputtering from a silicon target in a nitrogen rich environment.

A. Undercoat layers

It was found earlier[4] that multilayer magnetic films with silicon nitride spacer layers result in substantially higher permeabilities than spacer layers of either aluminum oxide or silicon. It was also found[4] that the soft magnetic properties of a film could be enhanced by depositing the films onto an aluminum undercoat that covered the PET substrate. Focusing on Si_3N_4 as the spacer material of interest, the magnetic properties of a multilayer stack were examined as a function of different undercoats. Table I lists the quasistatic magnetic properties of multilayer films consisting of six 80 nm $Ni_{81}Fe_{19}$ layers and five 10 nm Si_3N_4 spacer layers, deposited onto different types of undercoats 150 nm thick; the first magnetic layer is deposited directly onto the undercoat. We see that of the undercoats examined, the Al, Cu, Si, and Si_3N_4 undercoats greatly improved the soft magnetic properties of the subsequently deposited films. The largest permeability value measured was with the 150 nm hcp oriented thick $Co_{79}Cr_{21}$ undercoat; the measured permeability spectra is shown in Fig. 1. Although the permeability of the films deposited onto the CoCr undercoat are quite high, indicative of a small anisotropy field value, there are no signs of a resonance usually associated with high permeability/low anisotropy films.

It was reported by Nakagawa *et al.*[7] that a very thin, approximately 10 nm, undercoat of $Co_{79}Cr_{21}$ sputter deposited onto polyethylene naphthalate (PEN) tape, greatly improved the crystalline structure of a subsequently deposited $Ni_{81}Fe_{19}$ layer, which has been shown by Ohji *et al.*[8] to play a significant role in the fabrication of a high permeability film. It was not possible to measure either H_c or H_k of the film deposited atop the CoCr undercoat since the BH loop measurements appeared to be dominated by the magnetically hard undercoat, the values of which were beyond the 100 Oe limit of the BH looper. The origin of such high permeability values in connection with large H_c and H_k values imposed by the CoCr undercoat is not yet understood, and the subject

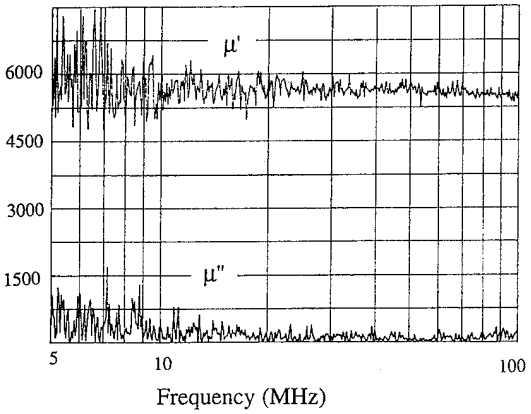


FIG. 1. Complex permeability spectra of six 80 nm $Ni_{81}Fe_{19}$ layers and five 10 nm Si_3N_4 spacer layers, on top of a 150 nm $Co_{21}Cr_{79}$ undercoat.

of ongoing research; one possibility is that the stray fields of the CoCr undercoat act to align the magnetization vector of the subsequently deposited soft magnetic layers. The CoCr undercoats in this work are much thicker than those used by Nakagawa *et al.*;[7] although Nakagawa did not make any magnetic measurements, studying only the crystalline structure, as the undercoat layer decreases in thickness the stray field will become weaker, and hence the measured H_c and H_k values of the subsequently deposited films more permalloy like. It is possible that, like the films of Ohji *et al.*,[8] the CoCr acts to orient the permalloy into a high permeability crystalline structure; we will address this point further in the discussion of nucleating layers.

Since high permeability values were obtained using a CoCr undercoat, the combined use of CoCr as an undercoat and spacer layer material was examined. Table II summarizes the 5 MHz permeability magnitude $|\mu|$ data for multilayer films consisting of six 80 nm permalloy layers, with CoCr spacers 10 or 30 nm thick, deposited on top of CoCr undercoats 150 or 300 nm thick. The combined use of a CoCr undercoat and spacer layer results in a lower permeability film than use of a CoCr undercoat alone.

B. Nucleating layers

Exclusive of the affects of undercoat layers, which are thick enough to be homogeneous, very thin nonhomogeneous layers of material, denoted as "seed" or "nucleation" layers, can be used to alter the properties of subsequently deposited magnetic films; see, e.g., Refs. 7 and 9. Since undercoat layers were shown to enhance the soft magnetic properties of subsequently deposited films we combined undercoat layers with nucleation layers to see how soft mag-

TABLE II. $Co_{79}Cr_{21}$ undercoat and spacer layers. Six 80 nm $Ni_{81}Fe_{19}$ layers, five $Co_{79}Cr_{21}$ spacer layers.

Undercoat (nm)	Spacer layer (nm)	$\|\mu\|$
150	10	1200
150	30	750
300	10	1150

TABLE III. Combined undercoat and 10 nm Si_3N_4 nucleating layer. Undercoat at 150 nm; six 80 nm $Ni_{81}Fe_{19}$ layers with 10 nm Si_3N_4 spacer layers.

	With nucleating layer			Without nucleating layer		
Undercoat	H_c (Oe)	H_k (Oe)	$\|\mu\|$	H_c (Oe)	H_k (Oe)	$\|\mu\|$
None	0.16	3.4	2950	0.19	4.6	2600
Silicon nitride	0.10	1.4	3800	0.10	1.4	3800
Silicon	0.10	2.5	3600	0.12	3.1	3550
Copper	0.13	2.8	3300	0.16	3.6	3000
Aluminum	0.11	2.7	3400	0.13	3.3	3200
$Co_{21}Cr_{79}$	>100	>100	2600	>100	>100	5500

netic properties could be further enhanced or controlled. Table III summarizes the effect of a 10 nm silicon nitride nucleating layer, in combination with the different undercoats previously examined, on the quasistatic magnetic properties of multilayer films consisting of six 80 nm $Ni_{81}Fe_{19}$ layers and five 10 nm silicon nitride spacer layers. The silicon nitride nucleating layer has made no apparent affect on the films deposited upon the silicon nitride undercoat. The nucleating layer has made the films deposited upon the copper, aluminum, and silicon undercoats magnetically softer, decreasing the coercive force and anisotropy field, and increasing the low frequency permeability. The nucleating layer has also increased the soft magnetic properties of films deposited without benefit of an undercoat. The nucleating layer has caused a dramatic drop in the permeability of the multilayer film on top of the CoCr undercoat layer. Since the thickness of the nucleating layer is too thin to affect coupling of the CoCr stray field with the subsequently deposited permalloy layers, it appears that the decrease in permeability due to the silicon nitride nucleating layer has its origin in the growth induced microstructure of the permalloy film;[8] this issue will be addressed in future work.

III. CONCLUSIONS

The coercive force, anisotropy field, and the 5 MHz permeability magnitude of multilayer films deposited onto 52-μm-thick PET webs, for use as identification markers or EMI shields, are examined as a function of undercoat and silicon nitride nucleating layer. It is found that nonmagnetic undercoats including aluminum, copper, silicon, and silicon nitride improve the soft magnetic properties of subsequently deposited films; the films deposited on top of the silicon nitride undercoat demonstrated the lowest coercive force and anisotropy field values. Silicon nitride undercoats had a tendency to flake. Silicon undercoats were much more durable than the silicon nitride undercoats, but did demonstrate a small amount of flaking. Aluminum and copper undercoats were deposited to thicknesses of 2 μm without ductility or adhesion problems. A $Co_{79}Cr_{21}$ undercoat resulted in the highest permeability values; although the permeameter measurement was able to determine the permeability, the coercive force and anisotropy field could not be measured as those values were beyond the field strength of the *BH* looper. The high permeability of the films deposited on top of the $Co_{79}Cr_{21}$ undercoat is indicative of a magnetically soft film. However the high coercive force and anisotropy field values, greater than the 100 Oe limit of the *BH* looper, stand in contradiction to the apparent magnetic softness indicated by the high permeability. The combination of high permeability and large anisotropy field is not to be expected, and will be the subject of further examination.

When used with a silicon, aluminum, or copper undercoat silicon nitride nucleating layers are found to enhance soft magnetic properties. When the CoCr undercoat was used with a 10 nm silicon nitride nucleating layer the film permeabilities were rather low, falling to approximately half that obtained with just the CoCr undercoat. This result, in agreement with earlier work,[8] indicates that the hcp CoCr acts to orient the permalloy into a high permeability regime which the very thin silicon nitride layer is able to disrupt.

ACKNOWLEDGMENT

This work was sponsored by the NASA-EPSCOR Office under Contract No. NCCW-60.

[1] T. A. Lafford, M. R. J. Gibbs, and C. Shearwood, J. Magn. Magn. Mater. **132**, 89 (1994).
[2] E. Lindner *et al.*, J. Chem. Soc. Faraday Trans. **89**, 361 (1993).
[3] C. Piotrowski, C. L. Bruzzone, and J. W. McAllister, U. S. Patent No. 5,083,112.
[4] C. A. Grimes, IEEE Trans. Magn. **MAG-31**, 4109 (1995).
[5] O. Auciello and R. Kelly, Radiat. Effects **66**, 195 (1982).
[6] C. A. Grimes, P. L. Trouilloud, and R. M. Walser, IEEE Trans. Magn. **MAG-24**, 603 (1988).
[7] S. Nakagawa, S. Akiyama, M. Sumide, and M. Naoe, IEEE Trans. Magn. **MAG-26**, 1608 (1990).
[8] H. Ohji, S. Tanabe, M. Kataoka, and T. Ozeki, J. Magn. Magn. Mater. **134**, 292 (1994).
[9] N. Mahvan, E. Ziera, and A. Eltoukhy, IEEE Trans. Magn. **MAG-29**, 3691 (1993).

A spin reorientation in $Pr_2Fe_{17}D_3$ as revealed by Mössbauer spectroscopy

F. Grandjean
Institute of Physics, B5, University of Liège, B-4000 Sart-Tilman, Belgium

Dimitri Hautot and Gary J. Long
Department of Chemistry, University of Missouri-Rolla, Rolla, Missouri 65409-0010

O. Isnard,[a] S. Miraglia, and D. Fruchart
Laboratoire de Cristallographie du CNRS, Associé à l'Université J. Fourier, F-38042 Grenoble Cedex 09, France

The Mössbauer effect spectra of $Pr_2Fe_{17}D_3$, which have been measured between 85 and 295 K, indicate the presence of a spin reorientation of the iron magnetic moments at 105±5 K. At this magnetic transition a large increase of ~50 kOe in the 6*c* iron magnetic hyperfine field and abrupt changes in all of the remaining hyperfine fields are observed. A study of the changes in the quadrupole shifts at the transition indicates that this spin reorientation takes place within the basal plane of this rhombohedral compound. As expected, the temperature dependence of the isomer shifts does not show any anomaly at the transition. The origin of this spin reorientation is attributed to competing effects between lattice expansion upon deuteration and lattice contraction upon cooling.
© *1996 American Institute of Physics.* [S0021-8979(96)36508-8]

I. INTRODUCTION

As Coey and Sun[1] first showed in 1990, insertion of nitrogen into R_2Fe_{17}, where R is a rare earth, improves their magnetic properties and dramatically increases their Curie temperatures. We have previously studied[2,3] the Mössbauer spectra of Pr_2Fe_{17} and $Pr_2Fe_{17}N_{2.6}$ and the hydrides of Nd_2Fe_{17}. Hence, it is useful to study the deuterides of Pr_2Fe_{17} and to compare their Mössbauer spectral properties with those of the nitride, $Pr_2Fe_{17}N_{2.6}$, and the related hydrides. In this article, we will report the interesting and unexpected behavior of $Pr_2Fe_{17}D_3$. $Pr_2Fe_{17}D_5$ will be discussed in a future article[4] along with various other deuterides and hydrides of R_2Fe_{17}.

II. EXPERIMENT

$Pr_2Fe_{17}D_3$ was prepared as described[5] earlier and its deuterium content is known to an accuracy of ~3.0±0.1. Mössbauer absorbers of 36 mg/cm^2 thickness were prepared from powdered samples which had been sieved to a 0.045 mm or smaller diameter particle size. Mössbauer spectra were obtained between 85 and 295 K on a constant-acceleration spectrometer which utilized a rhodium matrix cobalt-57 source and was calibrated at room temperature with α-iron foil. The resulting spectra have been fitted as discussed below and the estimated errors are at most ±1 kOe for the hyperfine fields, ±0.005 mm/s for the isomer shifts, and ±0.01 mm/s for the quadrupole shifts.

III. MÖSSBAUER SPECTRAL RESULTS

The Mössbauer spectra of $Pr_2Fe_{17}D_3$, obtained between 85 and 295 K, are shown in Fig. 1. It is immediately apparent that dramatic changes occur in the spectra between 95 and 120 K. A closer examination of the spectra indicates that between 120 and 295 K they are similar but different from those obtained below 95 K. Additional spectra obtained between 95 and 120 K show a superposition of the high and low temperature spectra.

Because in both Pr_2Fe_{17} and $Pr_2Fe_{17}D_5$, the magnetic moments are oriented[5] ferromagnetically in the basal plane of the Th_2Zn_{17} rhombohedral unit cell, we assume that the magnetic moments in $Pr_2Fe_{17}D_3$ have the same orientation. Because of this basal orientation of the moments and because of the point symmetry of the four iron crystallographic sites in the Th_2Zn_{17} structure, the spectra were fitted[2] with seven sextets, with relative areas of 6:6:3:12:6:12:6, for the seven magnetically inequivalent, $6c$, $9d_6$, $9d_3$, $18f_{12}$, $18f_6$, $18h_{12}$, and $18h_6$ sites. The constraints applied to the hyperfine parameters have been described in detail elsewhere.[2] The most important constraint is that the isomer shifts of crystallographically equivalent, but magnetically inequivalent, sites be equal. Furthermore, all lines in a spectrum have been fit with a single linewidth, of between 0.28 and 0.30 mm/s. Finally, a sextet corresponding to α-iron with a relative area of ~5% was required to fit the observed spectra.

Figure 2 shows the temperature dependence of the four site averaged hyperfine fields. Clearly between 120 and 95 K there is a large increase of ~50 kOe in the 6*c* magnetic hyperfine field and there are abrupt changes in all of the remaining hyperfine fields. These changes indicate the presence of a magnetic transition in $Pr_2Fe_{17}D_3$ at 105±5 K. The nature of this transition, which does not show any obvious hysteresis, may be elucidated through the study of the quadrupole shifts, as discussed below.

The weighted average hyperfine fields are larger than those found in Pr_2Fe_{17} but smaller than those found in $Pr_2Fe_{17}N_{2.6}$ at the corresponding temperatures.[2] This trend parallels the evolution of the magnetic moment[2,5] upon hy-

[a]Also at: Institut Laue Langevin.

 0021-8979/96/79(8)/4584/3/$10.00 © 1996 American Institute of Physics

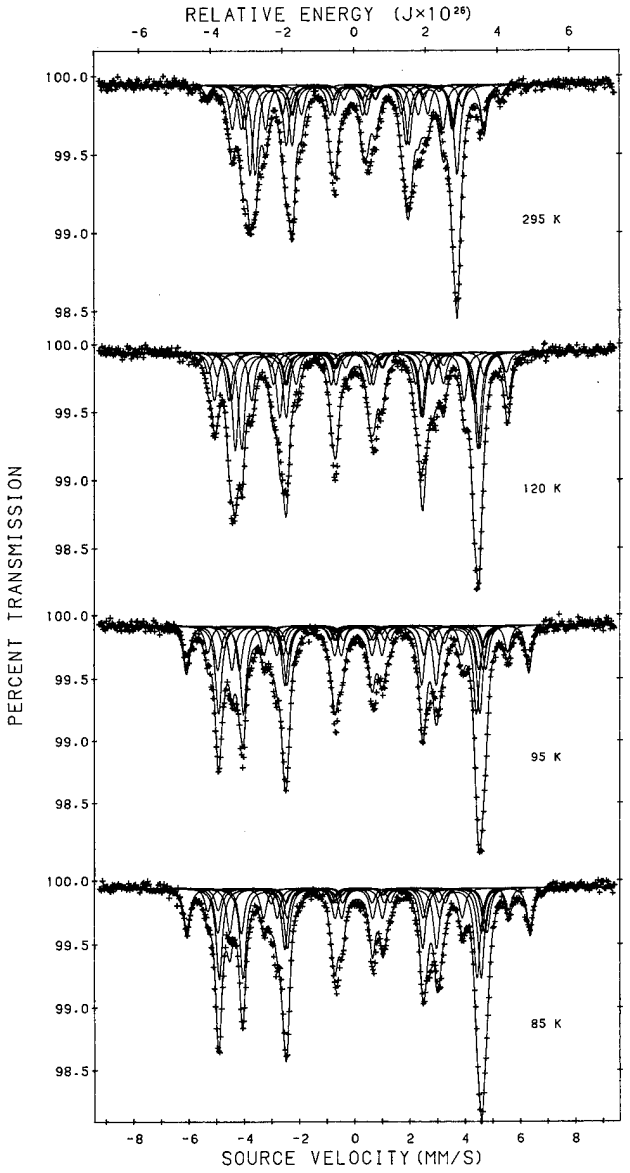


FIG. 1. The Mössbauer spectra of $Pr_2Fe_{17}D_3$ obtained at the indicated temperatures.

drogenation and nitrogenation. The hyperfine fields at the four crystallographic iron sites decrease in the order $6c > 9d > 18f > 18h$, an order previously observed[2,6–8] in the R_2Fe_{17} compounds, where R is Pr, Nd, Sm, Ho, and Th, and an order which agrees with the decreasing number of iron near neighbors for each site.

The spectra of $Pr_2Fe_{17}D_3$ in both magnetic states are different from those of $Nd_2Fe_{17}H_3$. This difference indicates that the orientation of the magnetic moments within the basal plane is different in the two compounds, a difference already noted[2] for Pr_2Fe_{17} and Nd_2Fe_{17}. The weighted average hyperfine fields in $Pr_2Fe_{17}D_3$ at 155, 225, and 295 K are ~5 kOe smaller than those observed[3] at the same temperature in $Nd_2Fe_{17}H_3$. In contrast, the weighted average hyperfine field at 85 K is 15 kOe larger. Hence, the magnetic transition which occurs in $Pr_2Fe_{17}D_3$ at ~105 K increases the low temperature average magnetic moment above the value in $Nd_2Fe_{17}H_3$.

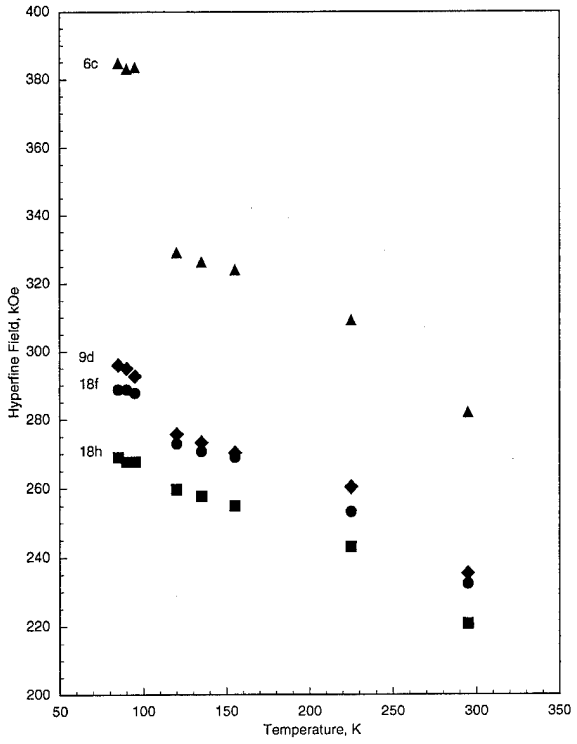


FIG. 2. The temperature dependence of the hyperfine fields in $Pr_2Fe_{17}D_3$.

Figure 3 shows the temperature dependence of the isomer shifts of the four crystallographically distinct iron sites and their weighted average. It is clear that none of the isomer shifts, nor their weighted average, show any anomaly in their

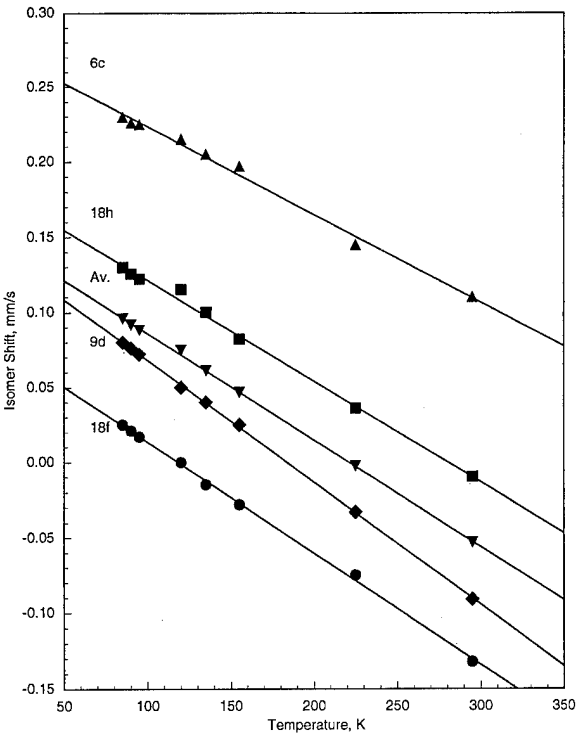


FIG. 3. The temperature dependence of the four isomer shifts in $Pr_2Fe_{17}D_3$ and their weighted average.

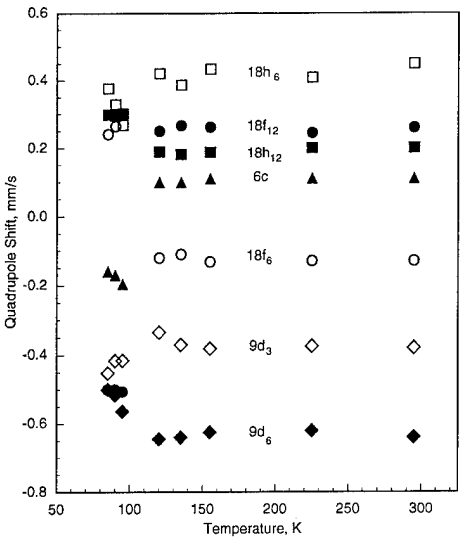


FIG. 4. The temperature dependence of the seven quadrupole shifts in $Pr_2Fe_{17}D_3$.

temperature dependence around 105 K. Of course, no anomaly in the isomer shift would be expected at a magnetic transition. This behavior supports our fitting model both above and below the magnetic transition. The slopes of the straight lines in Fig. 3 range between -5.85×10^{-4} and -8.30×10^{-4} mm/(s K) and are similar to those measured[2] in Pr_2Fe_{17}.

The weighted average isomer shift of $Pr_2Fe_{17}D_3$ is larger than that of Pr_2Fe_{17} at the same temperature in agreement with the unit cell expansion upon deuteration. A similar increase of ~0.05 mm/s was observed[3] upon hydrogenation of Nd_2Fe_{17}. The correlation between the Wigner–Seitz cell volume and the isomer shift for each iron site in going from Pr_2Fe_{17} to $Pr_2Fe_{17}D_3$ shows a behavior similar to that observed for Nd_2Fe_{17} and $Nd_2Fe_{17}H_3$ and will be discussed in detail elsewhere.[4]

Figure 4 shows the temperature dependence of the seven quadrupole shifts in $Pr_2Fe_{17}D_3$. It is immediately apparent that at the magnetic transition at 105 K the quadrupole shifts of the $6c$ and $18f$ sites change sign and that those of the $9d$ and $18h$ sites change their values. These abrupt changes cannot result from a sudden change in the electric field gradient value, because no change in crystallographic structure is observed[9] at low temperature. Hence, they can only result from a change in the angle between the hyperfine field and the principal axis of the electric field gradient tensor, or, in other words, a change in the direction of the magnetic moments at 105±5 K. In Pr_2Fe_{17}, the magnetic moments are believed[10,11] to lie along the b axis or $[1, -1, 0]$ in the basal plane of the unit cell. Because the signs of the quadrupole shifts of the $6c$, $18f$, and $18h$ sites are the same in Pr_2Fe_{17} and $Pr_2Fe_{17}D_3$ above 105 K, we conclude that the moments lie along the b axis in $Pr_2Fe_{17}D_3$ in the high temperature magnetic phase. Because the spectra below 105 K are still well fit with seven sextets, the magnetic moments still lie in the basal plane but the changes in quadrupole shifts at the magnetic transition indicate that the moments have rotated within the basal plane. Unfortunately, it is not possible to deduce the direction of the moments from the values of the quadrupole shifts. The measurement of a Mössbauer spectrum above the Curie temperature of $Pr_2Fe_{17}D_3$ may help to solve this question, if the compound does not lose deuterium upon heating and if the spectrum shows enough resolution to permit a reliable fit with four doublets.

The magnetic anisotropy in the R_2Fe_{17} compounds is determined[12] by the rare-earth single ion anisotropy through the interaction between the aspherical crystal field potential at the rare-earth sites and the aspherical charge density of the rare-earth $4f$ shell, described by the Stevens coefficients of the second, fourth, and sixth order, α_J, β_J, and γ_J. The Stevens coefficients are characteristic of the rare-earth atom and do not vary with temperature. Hence, the spin reorientation in $Pr_2Fe_{17}D_3$ at 105 K can only result from changes in the crystal field potential, changes probably resulting from the competing effects of lattice expansion, atomic rearrangement upon deuteration, and lattice contraction upon cooling. No similar spin reorientation was observed[3] in $Nd_2Fe_{17}H_3$, between 85 and 295 K, but, of course, it could occur below 85 K and Mössbauer measurements between 4.2 and 85 K will be carried out in the near future to check this possibility. However, it is known[6,10,11] that the magnetic moments in Nd_2Fe_{17} and Pr_2Fe_{17} lie in different directions in the basal plane, probably because the sixth order Stevens coefficients γ_J have different signs. Because the three deuterium atoms are located in the basal plane, they may change dramatically the high order crystal field terms and, in particular, the sixth order term γ_J. Mössbauer spectroscopy is a unique technique to observe this spin reorientation because of its sensitivity to the quadrupole shift. Such a spin reorientation within the basal plane cannot be observed by powder neutron diffraction.

ACKNOWLEDGMENTS

The authors acknowledge, with thanks, NATO for Cooperative Scientific Research Grant No. 92-1160, the Division of Materials Research of the U.S. National Science Foundation, for Grant No. DMR-92142711, and the "Ministère de la Communauté Française," Belgium, for Grant No. A.R.C. 94/99-175.

[1] J. M. D. Coey and H. Sun, J. Magn. Magn. Mater. **87**, L251 (1990).
[2] G. J. Long, O. A. Pringle, F. Grandjean, W. B. Yelon, and K. H. J. Buschow, J. Appl. Phys. **74**, 504 (1993).
[3] F. Grandjean, G. J. Long, S. Mishra, O. A. Pringle, O. Isnard, S. Miraglia, and D. Fruchart, Hyperfine Interactions **95**, 277 (1995).
[4] D. Hautot, G. J. Long, F. Grandjean, O. Isnard, S. Miraglia, and D. Fruchart (unpublished).
[5] O. Isnard, S. Miraglia, J. L. Soubeyroux, and D. Fruchart, Solid State Commun. **81**, 13 (1992).
[6] G. J. Long, O. A. Pringle, F. Grandjean, and K. H. J. Buschow, J. Appl. Phys. **72**, 4845 (1992).
[7] G. J. Long, S. Mishra, O. A. Pringle, F. Grandjean, and K. H. J. Buschow, J. Appl. Phys. **75**, 5994 (1994).
[8] G. J. Long, O. A. Pringle, F. Grandjean, T. H. Jacobs, and K. H. J. Buschow, J. Appl. Phys. **75**, 2598 (1994).
[9] O. Isnard (unpublished).
[10] P. C. M. Gubbens, Ph.D. thesis, Delft University of Technology, Delft, The Netherlands, 1977.
[11] P. C. M. Gubbens, J. J. Van Loef, and K. H. J. Buschow, J. Phys. (Paris) Colloq. **35**, C6-617 (1974).
[12] R. Coehoorn, in *Supermagnets, Hard Magnetic Materials*, edited by G. J. Long and F. Grandjean (Kluwer, Dordrecht, 1991), p. 133.

Neutron diffraction and Mössbauer spectral study of the $Nd_2Fe_{16}TiC_x$ solid solutions

G. K. Marasinghe, Peter C. Ezekwenna, W. J. James, Gary J. Long, and O. A. Pringle
Departments of Physics and Chemistry and the Graduate Center for Materials Research, University of Missouri-Rolla, Rolla, Missouri 65401-0249

Z. Hu and W. B. Yelon
University of Missouri Research Reactor, University of Missouri-Columbia, Columbia, Missouri 65211

F. Grandjean
Institut de Physique, Université de Liège, B-4000 Sart-Tilman, Belgium

Three samples of $Nd_2Fe_{16}TiC_x$, with x equal to 0.0, 0.3, and 2.8, with the Th_2Zn_{17}-type rhombohedral structure, have been studied by powder x-ray and neutron diffraction, magnetic measurements, and Mössbauer spectroscopy. $Nd_2Fe_{16}Ti$ and $Nd_2Fe_{16}TiC_{0.3}$ were synthesized by induction melting stoichiometric amounts of the constituent elements, whereas $Nd_2Fe_{16}TiC_{2.8}$ was synthesized by methane-derived gas phase insertion of carbon into finely ground $Nd_2Fe_{16}Ti$ at 600 K. The neutron diffraction determined titanium site occupancies are similar in both $Nd_2Fe_{16}Ti$ and $Nd_2Fe_{16}TiC_{2.8}$ in which titanium preferentially occupies the $6c$ transition metal site. In contrast, the titanium occupancies in $Nd_2Fe_{16}TiC_{0.3}$ are markedly different in that titanium avoids the $6c$ transition metal site and randomly occupies the other three transition metal sites. This difference in occupancies most likely occurs because the titanium diffusion rate during the quenching of $Nd_2Fe_{16}TiC_{0.3}$ is affected by the presence of carbon in the melt. Even though the unit cell volume of $Nd_2Fe_{16}TiC_{2.8}$ is larger than that of $Nd_2Fe_{17}N_3$, the 615 K Curie temperature of $Nd_2Fe_{16}TiC_{2.8}$ is much lower than the 746 K Curie temperature of $Nd_2Fe_{17}N_3$. This is an indication that the volume expansion, which occurs upon nitrogenation of R_2Fe_{17}, is not the only factor which contributes to the increase in the Curie temperature. The Mössbauer spectra of $Nd_2Fe_{16}Ti$ confirm the high preferential titanium occupancy of the $6c$ site. At 85 K the weighted average hyperfine field of $Nd_2Fe_{16}Ti$ is approximately 263 kOe, a value which is 33 kOe smaller than that in Nd_2Fe_{17}. The 85 K Mössbauer spectrum of $Nd_2Fe_{16}TiC_{0.3}$ is virtually identical to that of Nd_2Fe_{17} and indicates an approximately random titanium occupancy of the four transition metal sites. © *1996 American Institute of Physics.* [S0021-8979(96)36608-4]

I. INTRODUCTION

The discovery[1] that the addition of interstitial nitrogen dramatically increases the Curie temperature of R_2Fe_{17} and changes the magnetocrystalline anisotropy from basal in Sm_2Fe_{17} to axial in $Sm_2Fe_{17}N_3$ has led to a renewed interest in the R_2Fe_{17} compounds. Even though the Curie temperatures[1] of the resulting $R_2Fe_{17}N_x$ compounds are significantly higher than those of the $R_2Fe_{14}B$ compounds, they are lower than those of the previous generation of permanent magnets based on $SmCo_5$. However, the interstitially modified $Sm_2Fe_{17}C_x$ and $Sm_2Fe_{17}N_x$ compounds have high energy products,[2] approximately 80 kJ/m^3, at room temperature and Curie temperatures high enough to make them useful in a wide variety of magnetic applications. Unfortunately, interstitial $R_2Fe_{17}N_x$ and $R_2Fe_{17}C_x$, prepared by gas–solid reactions, are thermally unstable, decomposing at temperatures slightly above their Curie temperatures.[3] In contrast, recent studies[4,5] have shown that certain $R_2(Fe,M)_{17}C_x$ solid solutions, where M is Ga, Al, or Si, which were synthesized by a solid–solid reaction, exhibit high thermal stability. In this article we report the results of a crystallographic and magnetic study of three $Nd_2Fe_{16}TiC_x$ samples, with x equal to 0.0, 0.3, and 2.8.

II. EXPERIMENTAL METHODS

$Nd_2Fe_{16}Ti$ and $Nd_2Fe_{16}TiC_{0.3}$ were prepared from 99.9% pure elements by induction melting followed by annealing at 950 °C for 120 h. $Nd_2Fe_{16}TiC_{2.8}$ was synthesized by methane-derived gas phase insertion of carbon into finely ground $Nd_2Fe_{16}Ti$ at 600 K. The phase purity of the samples was checked by x-ray diffraction with Cu K_α radiation on a Philips PW 1800/10 x-ray diffractometer equipped with a single crystal graphite monochromator. The Curie temperatures of the samples were measured by a SQUID magnetometer. The powder neutron diffraction patterns were measured in thin walled vanadium containers in approximately 24 h each at 295 K with 1.4766 Å neutrons, and were refined by the Rietveld method on the basis of the Nd_2Fe_{17} structure.[6] The titanium and carbon site occupancies refined to an accuracy of approximately ±2%.

The Mössbauer spectra were measured at 85 and 295 K on a constant acceleration spectrometer which utilized a room temperature rhodium matrix cobalt-57 source and was calibrated at room temperature with α-iron foil. The typical linewidth of the outer lines of α-iron was 0.26 mm/s. Mössbauer absorbers, with a typical thickness of 30 mg/cm^2, were prepared from powders which had been sieved to a 0.038 mm or smaller particle diameter. The spectra were fitted with

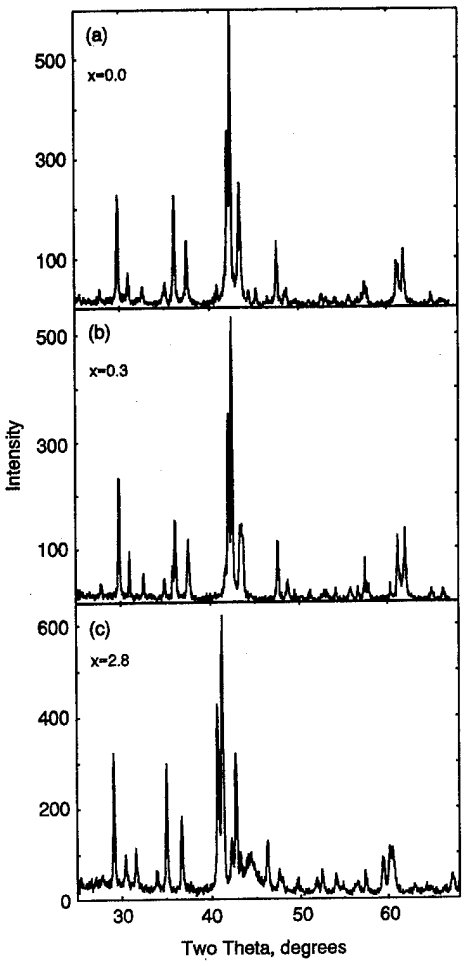


FIG. 1. X-ray diffraction patterns of (a) $Nd_2Fe_{16}Ti$, (b) $Nd_2Fe_{16}TiC_{0.3}$, and (c) $Nd_2Fe_{16}TiC_{2.8}$.

seven magnetic sextets corresponding to the seven magnetically inequivalent iron sites expected[7] for a basal orientation of the magnetization. Details of this fitting procedure have been published elsewhere.[8,9] The magnetic structures of these $Nd_2Fe_{16}TiC_x$ samples have been determined by neutron diffraction studies[10] to be basal, consistent with the magnetic structures of other Nd_2Fe_{17} based interstitial compounds.[8]

III. RESULTS AND DISCUSSION

The Curie temperatures are 380, 440, and 615 K for $Nd_2Fe_{16}TiC_x$ with x equal to 0.0, 0.3, and 2.8, respectively.

X-ray diffraction patterns, see Fig. 1, indicate that the three samples crystallize in the rhombohedral Th_2Zn_{17}-type structure. However, a small amount of α-iron is observed in $Nd_2Fe_{16}TiC_{2.8}$. The lattice parameters, atomic positional parameters, and site occupancies, obtained from the neutron diffraction data, are given in Table I. As can be seen in this table, the replacement of one iron by titanium in Nd_2Fe_{17} increases slightly the unit cell volume. A similar small increase has been observed in the $R_2Fe_{14-x}Ti_xB$ solid solutions.[11] However, in contrast, the 857 Å^3 unit cell volume of $Nd_2Fe_{16}TiC_{2.8}$ is much larger than the 802 Å^3 volume of $Nd_2Fe_{16}Ti$ and even larger than the 844 Å^3 volume[12] of $Nd_2Fe_{16}N_{2.7}$, whereas the 615 K Curie temperature of $Nd_2Fe_{16}TiC_{2.8}$ is much lower than the 746 K value[13] of $Nd_2Fe_{17}N_3$. This indicates that the volume expansion which occurs upon nitrogenation or carbonation of R_2Fe_{17} is not the only factor responsible for the accompanying increase in the Curie temperature.

As seen in Table I, the titanium site occupancies in $Nd_2Fe_{16}Ti$ and $Nd_2Fe_{16}C_{2.8}$ are similar and titanium preferentially occupies the 6c transition metal site. In contrast, the titanium site occupancies in $Nd_2Fe_{16}TiC_{0.3}$ are markedly different in that titanium appears to avoid the 6c site and almost randomly occupies the other three transition metal sites. The

TABLE I. Room temperature powder neutron diffraction results for Nd_2Fe_{17} and $Nd_2Fe_{16}TiC_x$.

Parameter		Nd_2Fe_{17}[a]	$Nd_2Fe_{16}Ti$	$Nd_2Fe_{16}TiC_{0.3}$	$Nd_2Fe_{16}TiC_{2.8}$
Lattice parameters	a (Å)	8.6002(1)	8.6042(3)	8.6452(5)	8.8385(6)
	c (Å)	12.4835(2)	12.5133(5)	12.4875(9)	12.6662(11)
	V (Å^3)	799.62(3)	802.28(9)	808.27(15)	856.9(2)
Positional parameters	Nd, 6c, z	0.3426(3)	0.3429(6)	0.3451(7)	0.3417(6)
	Fe/Ti, 6c, z	0.0957(2)	0.0973(7)	0.0956(5)	0.0967(12)
	Fe/Ti, 18f, x	0.2882(1)	0.2934(3)	0.2886(4)	0.2847(4)
	Fe/Ti, 18h, x	0.1682(1)	0.1680(2)	0.1691(3)	0.1736(3)
	Fe/Ti, 18h, z	0.4893(1)	0.4907(2)	0.4891(4)	0.4865(4)
	C, 18g, x	...	...	0.880[b]	...
Percent occupancy	Ti, 6c	...	38	1	37
	Ti, 9d	...	0	5	3
	Ti, 18f	...	3	6	0
	Ti, 18h	...	2	8	6
	C, 9e	...	...	6	99
	C, 18g	...	...	2	0
Fit parameters	R_p (%)	...	6.6	5.3	4.6
	χ^2	...	4.3	5.2	2.7

[a]Data taken from Ref. 9.
[b]Parameter determined by manual iteration refinement.

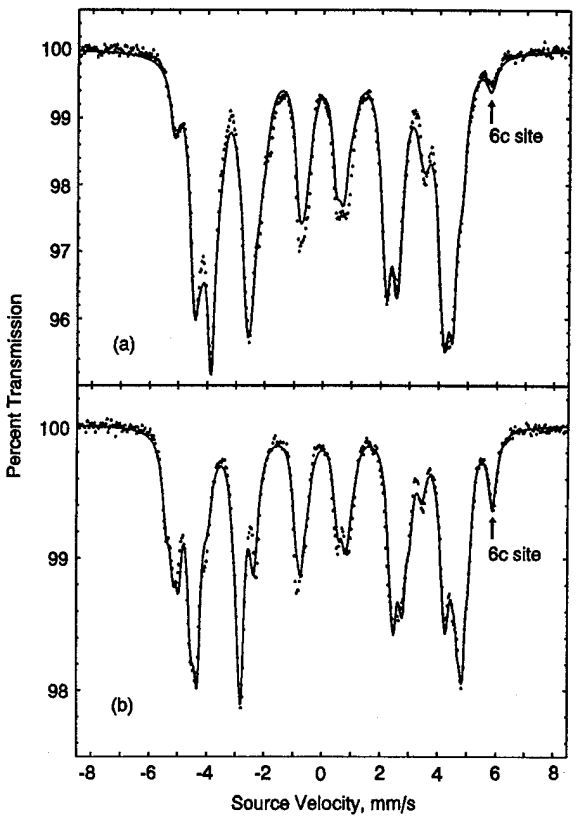


FIG. 2. The Mössbauer spectra of (a) $Nd_2Fe_{16}Ti$, and (b) $Nd_2Fe_{16}TiC_{0.3}$ obtained at 85 K.

difference in titanium occupancies in the two carbided samples can be attributed to the difference in their preparation. The similar titanium occupancies in $Nd_2Fe_{16}Ti$ and $Nd_2Fe_{16}TiC_{2.8}$ are expected because $Nd_2Fe_{16}TiC_{2.8}$ was synthesized by methane-derived gas phase insertion of carbon at 600 K into fine powders of the induction melted $Nd_2Fe_{16}Ti$. Iron and titanium have 12 coordinate metallic radii of 1.26 and 1.47 Å, respectively, and, as a consequence of its larger radius, titanium preferentially occupies the $6c$ iron site in Nd_2Fe_{17}, the iron site with the largest Wigner–Seitz cell volume.[8] None of the metal atoms are appreciably mobile at 600 K and thus the metal occupancies in $Nd_2Fe_{16}Ti$ and $Nd_2Fe_{16}TiC_{2.8}$ are expected and found to be similar. In contrast to the preparation of $Nd_2Fe_{16}TiC_{2.8}$, carbon was present in the melt during the induction melting preparation of $Nd_2Fe_{16}TiC_{0.3}$. Carbon has a very high affinity for titanium and this affinity influences the mobility of the carbon and titanium atoms in the melt.[14] Because of this affinity one expects, as is observed, to find that the titanium prefers the $18f$ and $18h$ sites, the sites which have carbon near-neighbors. Consequently, one would expect the titanium occupancies after quenching of $Nd_2Fe_{16}TiC_{0.3}$ to be different from those in $Nd_2Fe_{16}Ti$ and $Nd_2Fe_{16}TiC_{2.8}$.

The 85 K Mössbauer spectra of $Nd_2Fe_{16}Ti$ and $Nd_2Fe_{16}TiC_{0.3}$, see Fig. 2, confirm the difference in titanium occupancies of the $6c$ transition metal site. In these Mössbauer spectra the highest velocity absorption line is the sixth line of the $6c$ sextet. As may be seen in Fig. 2, the absorption area of the $6c$ sextet of the $Nd_2Fe_{16}Ti$ spectrum is smaller than in $Nd_2Fe_{16}TiC_{0.3}$ and confirms that the titanium $6c$ occupancy in $Nd_2Fe_{16}Ti$ is higher than in $Nd_2Fe_{16}TiC_{0.3}$. The weighted averaged hyperfine fields at 85 K are 263, 292, and 254 kOe for the samples with x equal to 0.0, 0.3, and 2.8, respectively. At 295 K, the weighted average hyperfine fields are 189, 191, and 227 kOe, respectively. The dependence of the weighted averaged hyperfine field at 295 K on the carbon content follows that of the Curie temperature. However, $Nd_2Fe_{16}TiC_{0.3}$, whose Curie temperature is much lower than that of $Nd_2Fe_{16}TiC_{2.8}$, has the highest hyperfine field at 85 K.

ACKNOWLEDGMENTS

The authors acknowledge, with thanks, the Division of Material Research of the U.S. National Science Foundation for Grant Nos. DMR-9214271 and DMR-9305782. The authors also thank Dr. M. Shumsky and Mr. S. Mishra for experimental assistance and valuable discussions.

[1] J. M. D. Coey and H. Sun, J. Magn. Magn. Mater. **87**, L251 (1990).
[2] R. Skomski and N. M. Dempsey, in *Interstitial Intermetallic Alloys*, edited by F. Grandjean, G. J. Long, and K. H. J. Buschow (Kluwer Academic, Dordrecht, 1995), p. 665.
[3] B. G. Shen, F. W. Wang, H. Y. Gong, Z. H. Cheng, B. Liang, J. X. Zang, and S. Y. Zang, J. Phys. Condensed Matter **7**, 883 (1995).
[4] B. G. Shen, L. S. Kong, F. W. Wang, and L. Cao, Appl. Phys. Lett. **75**, 6253 (1994).
[5] Z. H. Cheng, B. G. Shen, F. W. Wang, J. X. Zang, H. Y. Gong, and J. G. Zhao, J. Phys. Condensed Matter **6**, L185 (1995).
[6] J. F. Herbst, J. J. Croat, and R. W. Lee, J. Appl. Phys. **53**, 250 (1982).
[7] G. J. Long, O. A. Pringle, F. Grandjean, W. B. Yelon, and K. H. J. Buschow, J. Appl. Phys. **74**, 504 (1993).
[8] F. Grandjean and G. J. Long, in *Interstitial Intermetallic Alloys*, edited by F. Grandjean, G. J. Long, and K. H. J. Buschow (Kluwer Academic Dordrecht, 1995), p. 463.
[9] G. J. Long, G. K. Marasinghe, S. Mishra, O. A. Pringle, Z. Hu, W. B. Yelon, D. P. Middleton, K. H. J. Buschow, and F. Grandjean, J. Appl. Phys. **76**, 5383 (1994).
[10] G. K. Marasinghe, Z. Hu, W. J. James, W. B. Yelon, G. J. Long, and O. A. Pringle (to be published).
[11] C. Lin, J. Lan, and X. F. Xu, J. Appl. Phys. **61**, 3457 (1987).
[12] O. Isnard, S. Miraglia, C. Kolbeck, E. Tomey, J. L. Soubeyroux, and D. Fruchart, J. Alloys Comp. **178**, 15 (1992).
[13] O. Isnard, S. Miraglia, D. Fruchart, J. Deportes, and P. L'Heritier, J. Magn. Magn. Mater. **131**, 76 (1994).
[14] *Corrosion and Corrosion Control*, 3rd ed., edited by H. H. Uhlig and R. W. Revie (Wiley, New York, 1992), p. 309.

Mössbauer study of permanent-magnet $R_2Fe_{17-x}M_xC_y$ compounds

I. A. Al-Omari and E. W. Singleton
Behlen Laboratory of Physics and Center for Materials Research and Analysis, University of Nebraska, Lincoln, Nebraska 68588-0111

Y. Zheng and G. C. Hadjipanayis
Department of Physics and Astronomy, University of Delaware, Newark, Delaware 19716

D. J. Sellmyer
Behlen Laboratory of Physics and Center for Materials Research and Analysis, University of Nebraska, Lincoln, Nebraska 68588-0111

We report Fe^{57} Mössbauer spectroscopy studies of the effect of carbon doping on the magnetic properties of the Fe sites of $R_2Fe_{17-x}M_xC_y$, and of the presence of multiple phases in these systems. In this study two systems, $Sm_2Fe_{14}Al_3C_y$, where $y=0$, 1.0, 2.0, and 3.0, and $Nd_2Fe_{14.54}Si_{2.46}C_y$, where $y=0$, 0.432, and 2.544, were measured at room temperature and analyzed. The ternary compounds $R_2Fe_{17-x}M_xC_y$ studied here have the rhombohedral Th_2Zn_{17} structure with c-axis anisotropy. The Al and Si site occupation used in the fitting were taken from previous results. Analysis of the Mössbauer spectra showed that the hyperfine fields for the different sites decreased in the order $6c$, $9d$, $18f$, and $18h$. The average hyperfine field for $Sm_2Fe_{14}Al_3C_y$ was found to increase with increasing carbon concentration, which is in qualitative agreement with magnetic measurements. For $Nd_2Fe_{14.54}Si_{2.46}C_y$ the average hyperfine field was found to increase for low C concentration and decrease for high C concentration; this behavior is in agreement with our magnetization measurements. The measured average isomer shift relative to α-iron was found to increase with y. In these compounds alloying with C and/or M can improve the magnetic properties such as Curie temperature and magnetization which make them potential candidates for permanent magnet development. © *1996 American Institute of Physics.* [S0021-8979(96)36708-0]

I. INTRODUCTION

A large improvement of the hard-magnet properties of Fe-rich intermetallic compounds can be considerably achieved upon introducing nitrogen,[1–3] carbon,[4–8] or substitutional impurities in the compounds of the type $R_2Fe_{17-x}M_x$ (R=Ho, Y, Sm, Ce, Pr, and Nd; M=Al, Ga, Si, V, Co, and Ni).[9–15] In all these studies the magnetic ordering temperatures were found to increase by substituting other elements for iron or by nitrogenation or carbonation. Wang and Dunlap[16] found that the Curie temperature (T_c) changed from 391 K for Sm_2Fe_{17} to 471 K for $Sm_2Fe_{14}Al_3$. A further increase in T_c can be achieved by adding C or N to these compounds. Shen *et al.*[17,18] have discovered recently that $Sm_2Fe_{17-x}Ga_xC_y$ can be formed by arc-melting. It is claimed that these materials are more stable at high temperature than those prepared by the gas reaction method. Zheng *et al.*[19] found that T_c goes to 563 K for $Sm_2Fe_{14}Al_3C_3$ which is close to T_c (585 K) for $Nd_2Fe_{14}B$.[20,21] They found also that the compounds $Sm_2Fe_{14}Al_3C_y$, $0\leqslant y\leqslant 3$, have c-axis anisotropy and the anisotropy field increases from 15 kOe for $y=0$ to more than 100 kOe for $y\geqslant 2$. Additionally, they found that the magnetization of these compounds increases by a small amount, 96 emu/g for $y=0$ to 100 emu/g for $y=2$, with increasing C concentration.

A neutron diffraction study of $Nd_2Fe_{14.54}Si_{2.46}C_y$, y between 0 and 2.544, by Yelon and Hu[22] showed that there are two carbon phases in the sample with $y=2$; one of these phases has low C concentration, $y=0.432$, and the other has high carbon concentration, $y=2.544$; C was found to occupy the $18g$ site for $y=0.432$ and $9e$ site for $y=2.544$. They also found that the fraction of occupancy of Si are 6%, 8%, and 30% for the sites $9d$, $18f$, and $18h$, respectively.

In this article we report on Mössbauer experiments for $Sm_2Fe_{14}Al_3C_y$ and $Nd_2Fe_{14.54}Si_{2.46}C_y$ to study the effect of C on the magnetic properties of these compounds. We also use Mössbauer spectroscopy to determine the amount of α-Fe and the presence of multiple phases in these systems.

II. EXPERIMENTAL PROCEDURE

Bulk samples of $Sm_2Fe_{14}Al_3C_y$ with $y=0$, 1, 2, and 3, were prepared by arc-melting the constituent elements with an Fe–C alloy in a water-cooled copper boat in a flowing argon-gas atmosphere. All the starting elements used were at least of 99.9% purity. The alloys were melted several times to ensure homogeneity. The $Sm_2Fe_{14}Al_3C_y$ samples were wrapped separately in tantalum foil and heat treated in a vacuum at 1100 °C for about 17 h,[19] and subsequently quenched in water.

Samples of nominal composition $Nd_2Fe_{15}Si_2$ were prepared by arc-melting with constituent elements of at least 99.9% purity under an argon atmosphere. For homogeneity, samples were remelted several times. The resulting ingots were vacuum annealed in quartz crucibles at 1000 to 1100 °C for 4 days. Carbide samples were prepared by heating ground powders, <45 μm diameter, of the original alloy in methane (CH_4) gas. The system was flushed several times with methane gas to ensure minimum oxygen contamination. The carbide samples were prepared by heating at a rate of 10 °C/min to 500 °C and held for 2 h to allow carbon diffusion into the samples. After carbonation the system was evacuated and held at a temperature above 100 °C to ensure that hydrogen was removed from the system.

 0021-8979/96/79(8)/4590/3/$10.00 © 1996 American Institute of Physics

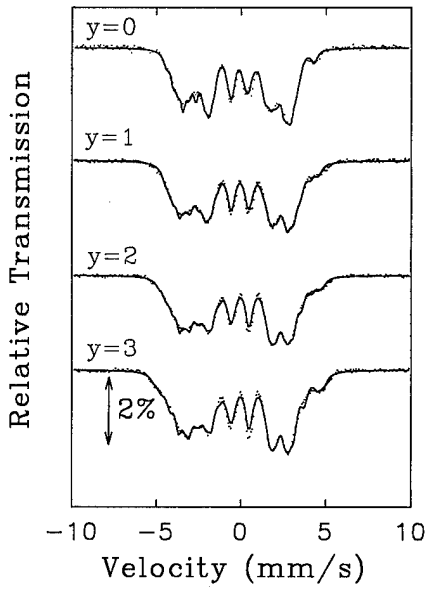


FIG. 1. Room temperature Mössbauer spectra of $Sm_2Fe_{14}Al_3C_y$ compounds. The solid curves represent the fitting.

Room temperature x-ray diffraction measurements on powder samples using a Phillips PWD1710 diffractometer with Cu K_α radiation showed only the rhombohedral Th_2Zn_{17} structure with a small amount of α-Fe.

The samples for Mössbauer spectroscopy were prepared by sprinkling a homogeneous thin layer of the powder of the $R_2Fe_{17-x}M_xC_y$ compounds on a piece of tape. The samples were studied with a Ranger Mössbauer spectrometer, model MS1200. The velocity drive of this spectrometer operates in the constant acceleration mode. A 35 mCi Co^{57} in Rh γ-ray source was used in this experiment. All the isomer shifts were measured relative to α-iron at room temperature and α-iron, with outer lines width of 0.30 mm/s, was also used for calibration. Some of the samples were found to have a small amount of α-iron, less than 5% in $Sm_2Fe_{14}Al_3C_y$, 12% in $Nd_2Fe_{14.54}Si_{2.46}$, and 20% in $Nd_2Fe_{14.54}Si_{2.46}C_2$; this component was subtracted from the raw data before the final fitting.

III. RESULTS AND DISCUSSION

Figures 1 and 2 show the room temperature Mössbauer spectra and the fitting (the solid curves) for $Sm_2Fe_{14}Al_3C_y$ with $y=0$, 1, 2, and 3 and $Nd_2Fe_{14.54}Si_{2.46}C_y$ with $y=0$ and 2. The spectra show that the samples are magnetically ordered for all values of y and all of them have different subspectra with different magnetic hyperfine fields. The spectra were fitted with a set of four subspectra, with linewidth of about 0.40 mm/s, because of the c-axis anisotropy, as mentioned by Long *et al.*,[23] which is similar to the models used by Hu *et al.*,[24] Long *et al.*,[25] and Yelon *et al.*[26] for 2:17 compounds. For the rhombohedral Th_2Zn_{17} structure there are four different iron sites, $6c$, $9d$, $18f$, and $18h$, with different environments. Previous Mössbauer measurements by Al-Omari *et al.*[14,15] for $Sm_2Fe_{17-x}Ga_xC_y$ and $Sm_2Fe_{17-x}Al_x$, Long *et al.*[23,25,26] for Nd_2Fe_{17} and $Nd_2Fe_{17}N_{2.6}$, Mössbauer and neutron diffraction by Yelon *et al.*[27] for $Nd_2Fe_{17-x}Al_x$,

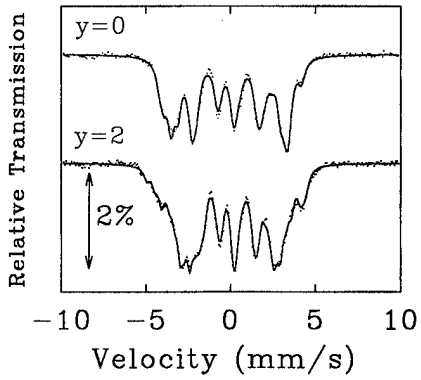


FIG. 2. Room temperature Mössbauer spectra of $Nd_2Fe_{14.54}Si_{2.46}C_y$ compounds. The solid curves represent the fitting.

and Mössbauer measurements by Hu *et al.*[24] for $R_2Fe_{17}N_{3-\delta}$ showed that the hyperfine fields decrease in the order $6c$, $9d$, $18f$, and $18h$. In our fitting and analysis of the data we used the same order.

The relative intensity of various subspectra for different C concentration were the same as of those of $Sm_2Fe_{14}Al_3$ found by Al-Omari *et al.*[15] For $Sm_2Fe_{14}Al_3C_y$ the hyperfine fields for different sites were found to increase with increasing concentration of C as seen in Fig. 3. The average hyperfine field was found to increase from 198 kOe for $y=0$ to 214 kOe for $y=3$ which is in qualitative agreement with the magnetization measurements by Zheng *et al.*[19] The Curie temperature for these compounds increases with y from 483 K for $y=0$ to 563 K for $y=3$.[19] The increase in the average hyperfine field and in the magnetization must be due to the increase in Curie temperature which is due to the increase in the interatomic exchange interactions upon volume expansion.

For $Nd_2Fe_{14.54}Si_{2.46}C_2$ the spectrum was fitted with three phases. The first was $Nd_2Fe_{14.54}Si_{2.46}C_{0.432}$, the second was $Nd_2Fe_{14.54}Si_{2.46}C_{2.544}$, and the third was FeSi. The first two phases were ferromagnetic with four subspectra, with different isomer shifts, quadrupole shifts, and hyperfine fields, and the third phase was paramagnetic with 5% relative intensity.

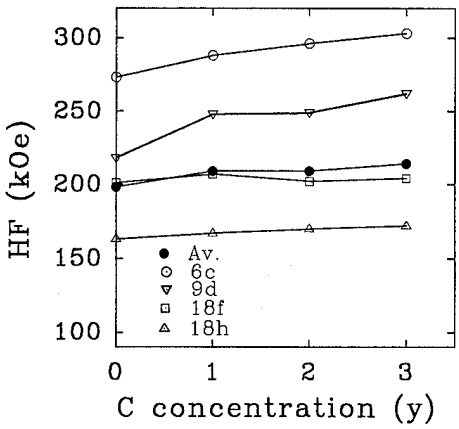


FIG. 3. Dependence of the hyperfine field for the different Fe sites of $Sm_2Fe_{14}Al_3C_y$ on the C concentration y, at $T=295$ K.

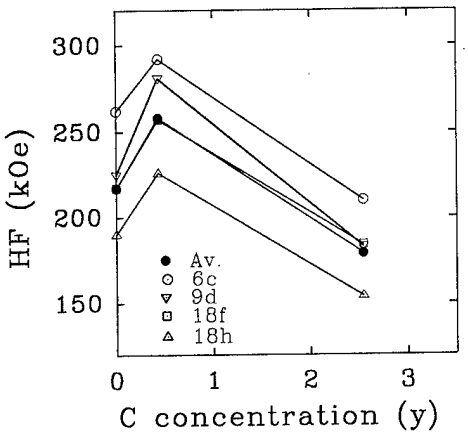


FIG. 4. Dependence of the hyperfine field for the different Fe sites of $Nd_2Fe_{14.54}Si_{2.46}C_y$ on the C concentration y, at $T=295$ K.

Guided by the results of Yelon and Hu,[22] the intensity of the second phase, high C concentration, was twice the intensity of the first phase, low C concentration. The relative intensities of various subspectra for different C concentrations were the same as of those of $Nd_2Fe_{14.54}Si_{2.46}$ found by Yelon and Hu,[22] since we used the same samples. The hyperfine fields for different Fe sites were found to increase for $y=0.432$ and decrease for $y=2.544$ as shown in Fig. 4. The increase of H_{hf} at lower carbon concentration is due to the enhancement of the Curie temperature which shifts the thermomagnetization curve to higher temperature which is similar to previous observations by Shen *et al.*[5] for $Tm_2Fe_{17}C_x$. The magnetizations for $Nd_2Fe_{14.54}Si_{2.46}C_y$ were measured with our magnetometer and found to decrease from 123.2 emu/g for $y=0$ to 118.4 emu/g for $y=2$; this behavior is in agreement with our Mössbauer measurements for the weighted average hyperfine field which decreases from 217 kOe for $y=0$ to 205 kOe for $y=2$.

The average isomer shift ($\overline{IS}$) relative to α-iron was found to increase by increasing the carbon concentration for both systems: the increase was from -0.04 mm/s for $y=0$ to -0.01 mm/s for $y=3$ in $Sm_2Fe_{14}Al_3C_y$ and from -0.04 mm/s for $y=0$ to -0.03 mm/s for $y=2.544$ in $Nd_2Fe_{14.54}Si_{2.46}C_y$. This increase implies a decrease in the s-electron density at the nucleus which can be attributed to the expansion of the cell volume which is similar to the effect of adding nitrogen to the 2:17 compounds as seen by Hu *et al.*[24] IS for FeSi was found to be 0.24 mm/s which is in agreement with other values by Shinjo *et al.*[28]

IV. CONCLUSIONS

Samples of $R_2Fe_{17-x}M_xC_y$ magnetic compounds have been fabricated and studied by Mössbauer spectroscopy. These compounds have the rhombohedral Th_2Zn_{17} structure with a small amount of α-Fe impurity. All the samples studied are ferromagnetic and the average hyperfine fields and hence the magnetic moments are found to depend on C concentration in each system. There is a qualitative agreement between the measured hyperfine fields and the magnetization values. Samples prepared by arc-melting were found to have a single carbon phase, in contrast to those prepared by the gas reaction method, which we and others have found to possess multiple C phases probably due to the different particle sizes. The change in isomer shift with increasing C concentration corresponds to the decreasing s-electron density at the nucleus caused by the volume expansion. The high Curie temperature and uniaxial anisotropy for these compounds with $0<y<3$ are promising properties for hard magnets.

ACKNOWLEDGMENTS

The authors are grateful to Professor S. S. Jaswal for helpful discussion, and to Professor Bill Yelon for communicating his results prior to publication. The authors thank the United States Department of Energy for the support under Grant No. DE-FG2-86ER45262.

[1] X. P. Zhong, R. J. Radwanski, F. R. De Boer, T. H. Jacobs, and K. H. J. Buschow, J. Magn. Magn. Mater. **86**, 333 (1990).
[2] J. M. D. Coey and H. Sun, J. Magn. Magn. Mater. **87**, L251 (1990).
[3] B. P. Hu and J. M. D. Coey, J. Less-Common Metals **142**, 295 (1988).
[4] B.-G. Shen, L. Kong, and L. Cao, Solid State Commun. **83**, 753 (1992).
[5] B.-G. Shen, L. Kong, L. Cao, H. Gong, F. Wang, Z. Cheng, and J. Zhao, J. Appl. Phys. **76**, 6714 (1994).
[6] L. Kong, L. Cao, and B. Shen, J. Magn. Magn. Mater. **115**, L137 (1990).
[7] L. Cao, L. Kong, and B. Shen, J. Phys. Condens. Matter **4**, L515 (1992).
[8] H. Gong, B. Shen, L. Kong, L. Cao, W. Zhan, Z. Cheng, and F. Wang, J. Appl. Phys. **76**, 6711 (1994).
[9] M. Valeanu, N. Plugaru, and E. Burzo, Solid State Commun. **89**, 519 (1994).
[10] B.-G. Shen, F. Wang, L. Kong, and L. Cao, J. Phys. Condens. Matter **5**, L685 (1993).
[11] T. H. Jacobs, K. H. J. Buschow, G. F. Zhou, X. Li, and F. R. de Boer, J. Magn. Magn. Mater. **116**, 220 (1992).
[12] F. Wertzer, K. Hiebl, and P. Rogl, J. Appl. Phys. **65**, 12 (1989).
[13] Z. W. Li, X. Z. Zhou, and A. H. Morrish, Phys. Rev. B **51**, 2891 (1995).
[14] I. A. Al-Omari, S. S. Jaswal, E. W. Singleton, D. J. Sellmyer, Y. Zheng, and G. C. Hadjipanayis, J. Magn. Magn. Mater. **151**, 145 (1995).
[15] I. A. Al-Omari, S. S. Jaswal, A. S. Fernando, and D. J. Sellmyer, J. Appl. Phys. **76**, 6159 (1994).
[16] Z. Wang and R. A. Dunlap, J. Phys. Condens. Matter **5**, 2407 (1993).
[17] B.-G. Shen, F. Wang, L. Kong, L. Cao, and H. Cuo, J. Magn. Magn. Mater. **127**, L267 (1993).
[18] B.-G. Shen, F. Wang, H. Gong, Z. Cheng, B. Liang, J. Zhang, and Z. Zhang, J. Phys. Condens. Matter **7**, 883 (1995).
[19] Y. H. Zheng, A. S. Murthy, and G. C. Hadjipanayis, IEEE Trans. Magn. (to be published).
[20] J. J. Croat, J. F. Herbst, R. W. Lee, and F. E. Pinkerton, Appl. Phys. Lett. **44**, 148 (1984).
[21] M. Sagawa, S. Fujimura, M. Tagawa, H. Yamamoto, and Y. Matsuura, J. Appl. Phys. **55**, 2083 (1984).
[22] W. B. Yelon and Z. Hu, J. Magn. Magn. Mater. (to be published).
[23] G. J. Long *et al.*, Solid State Commun. **88**, 761 (1993).
[24] B.-P. Hu, H.-S. Li, H. Sun, and J. M. D. Coey, J. Phys. Condens. Matter **3**, 3983 (1991).
[25] G. J. Long, S. Mishra, O. A. Pringle, F. Grandjean, and K. H. J. Buschow, J. Appl. Phys. **75**, 5994 (1994).
[26] G. J. Long, O. A. Pringle, F. Grandjean, and K. H. J. Buschow, J. Appl. Phys. **72**, 4845 (1992).
[27] W. B. Yelon, H. Xie, G. J. Long, O. A. Pringle, F. Grandjean, and K. H. J. Buschow, J. Appl. Phys. **73**, 6029 (1993).
[28] T. Shinjo, Y. Nakamura, and N. Shikazono, J. Phys. Soc. Jpn. **18**, 797 (1963).

Crystal field induced anisotropy in rare earth intermetallics as studied by ^{155}Gd Mössbauer spectroscopy

D. P. Middleton,[a] F. M. Mulder, D. A. van de Straat, and R. C. Thiel
Kamerlingh Onnes Laboratory, Leiden University, Nieuwsteeg 18, NL-2300 RA Leiden, The Netherlands

K. H. J. Buschow
Van der Waals–Zeeman Laboratory, University of Amsterdam, Valckenierstraat 65, NL-1018 XE Amsterdam, The Netherlands

We have investigated the effect of substitution and nitrogenation on the hyperfine parameters in $Gd_2Fe_{17-x}(Ga,Al)_x$ ($x=1-10$) and $Gd(Fe,Co)_{12-x}Mo_x(N_y)$ ($x=1.5-3.0$ and $y\approx1$) by means of ^{155}Gd Mössbauer spectroscopy. We have observed marked changes in the values of the electric field gradient V_{zz}, the effective Gd-hyperfine field, and isomer shift. Al substitution in Gd_2Fe_{17} leads to a sign reversal of the electric field gradient. No sign reversal of V_{zz} has been observed in the $Gd_2Fe_{17-x}Ga_x$ compounds. The effective hyperfine fields of the $Gd_2Fe_{17-x}(Ga,Al)_x$ compounds are decreasing with increasing x, due to the reduction of the $6s$ electron polarization resulting from the decreasing Fe moments. The ultimate value of the isomer shift based on a simple model on chemical effects that would be reached for $x=17$ is 0.52 mm s^{-1} for Al and 0.64 mm s^{-1} for Ga substitution in Gd_2Fe_{17}, respectively. The electric field gradient of the $GdFe_{12-x}Mo_x$ compounds were obtained for $x=1.5$ and $x=3.0$. Nitrogenation is shown to lead to a sign reversal of the $4f$ and Fe sublattice anisotropy. Mo substitution in $GdCo_{12-x}Mo_x$ shows a decreasing negative value of V_{zz} with increasing Mo concentration x. The values $|H_{\text{eff}}|$ in $GdCo_{12-x}Mo_x$ increase with increasing Mo concentration. This can be attributed to a different near neighbor Gd and $3d$-metal contribution to the effective hyperfine field compared to those of $GdFe_{12-x}Mo_x$. © *1996 American Institute of Physics.* [S0021-8979(96)36808-7]

Magnetocrystalline anisotropy is of large importance for permanent magnet materials. Depending on the crystal structure and on the other elements in the compound, there may result a nonsymmetric valence electron distribution. At the site of the rare-earth $4f$ electrons, this charge distribution causes an electric field gradient (EFG). The electrostatic interaction of the spherical $4f$ charge cloud with the EFG gives rise to the crystal field interaction. The $4f$ charge cloud, and its magnetic moment, can be oriented in a preferential direction by the crystal field, and this is the main factor determining the crystalline magnetic anisotropy of the rare-earth sublattice.

By varying the elements which form an isostructural series of intermetallic compounds with gadolinium, the variation of the EFG at the rare-earth nuclear site can be studied in a systematic way using ^{155}Gd Mössbauer spectroscopy. The second-order crystal field parameter A_2^0 is strongly influenced by the variation of the concentration of the substitutional elements, because of hybridization of the rare-earth $5d$ and $6p$ valence electrons with the valence electrons of its neighboring atoms. Gadolinium has a half-filled, spherical $4f$ shell. The $4f$ shell itself thus gives no contribution to the EFG measured at the nucleus, so that this EFG has the same origin as the EFG experienced by the $4f$ electron cloud. Since the $4f$ shell is not involved in the chemical bonding, the EFG at the nuclear site does not depend on the type of rare-earth atoms. Therefore the results of the ^{155}Gd Mössbauer measurements can be used for related rare-earth compounds. In this article we present the results obtained for the $CaCu_5$ related compounds, the rhombohedral Th_2Zn_{17}, and the tetragonal $ThMn_{12}$ compounds, as studied by ^{155}Gd Mössbauer spectroscopy.

The samples were prepared from 99.9% pure elements by arc melting in an argon atmosphere. After arc melting, the samples were wrapped in tantalum foil and vacuum annealed in quartz tubes at 900–1050 °C for several weeks and quenched into water. The samples were investigated by powder x-ray diffraction with Cu K_α radiation on a Philips PW 1800/10 x-ray diffractometer equipped with a single crystal monochromator.

^{155}Gd Mössbauer spectra were measured on a spectrometer described in detail elsewhere,[1] using the 86.5 keV resonance of the ^{155}Gd. The source was neutron-irradiated $SmPd_3$, for which we employed samarium enriched to 98% in ^{154}Sm. The measurements were carried out at 4.2 K. The spectra have been analyzed by means of a least square fitting procedure that involved diagonalization of the full nuclear Hamiltonian and use of a transmission integral. The independently refined variables considered in the fitting procedure are the isomer shift (IS), the effective hyperfine field H_{eff}, and the quadrupole splitting (QS). From the latter quantity we obtained the electric field gradient tensor element V_{zz}, via the relation $QS=\frac{1}{4}eQV_{zz}(\cos^2\theta-1)$ using the value $Q=1.30\times10^{-28}$ m^2 given by Tanaka *et al.*[2] The angle θ between H_{eff} and the c axis was kept at 0° or 90°. The linewidth of the absorber and source were constrained for the transmission integral to 0.25 and 0.36 mm s^{-1}, respectively. In some cases where there is some degree of disorder in the compounds due to substitution, the absorber linewidth was kept as an adjustable parameter.

[a]Also at Philips Research Laboratories, prof Holstlaan 4, NL-5656 AA Eindhoven, The Netherlands.

 0021-8979/96/79(8)/4593/3/$10.00 © 1996 American Institute of Physics

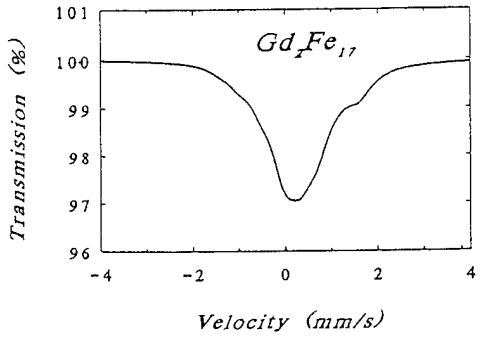


FIG. 1. ^{155}Gd Mössbauer spectrum of the Gd_2Fe_{17} compound at 4.2 K. The solid line represents a fit.

Substitution of s and p elements with large atomic radii, such as Al and Ga, for iron in R_2Fe_{17} compounds, has been shown to lead to changes in the crystallographic and magnetic properties. Substantial changes in the magnitude and sign of the Gd valence electron asphericity are expected when Al or Ga preferentially substitutes into specific crystallographic sites.[3]

The ^{155}Gd Mössbauer spectrum of Gd_2Fe_{17} is shown in Fig. 1 and of $Gd_2Fe_{17-x}Ga_x$ are shown in Fig. 2. From the

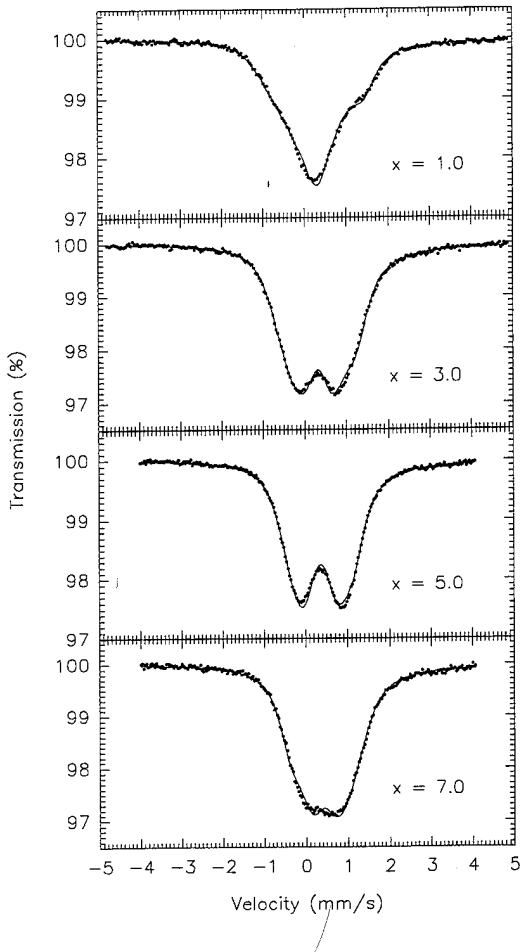


FIG. 2. ^{155}Gd Mössbauer spectra of the $Gd_2Fe_{17-x}Ga_x$ compounds at 4.2 K for several Ga concentrations x. The solid curve through the data points represents a fit.

TABLE I. Hyperfine parameters derived from fitting the ^{155}Gd Mössbauer spectra at 4.2 K for various $Gd_2Fe_{17-x}Al_x$ and $Gd_2Fe_{17-x}Ga_x$ compounds.

Compound	V_{zz} (10^{21} V m^{-2})	$\mu_0\lvert H_{\text{eff}}\rvert$ (T)	IS (mm s^{-1})	θ (deg)
Gd_2Fe_{17}[a]	+4.4	21	0.27	90
$Gd_2Fe_{14}Al_3$	−4.9	7.3	0.31	90
$Gd_2Fe_{13}Al_4$	−5.0	5.8	0.31	90
$Gd_2Fe_{11}Al_6$	−4.3	6.1	0.37	90
$Gd_2Fe_9Al_8$	−3.8	7.6	0.40	90
$Gd_2Fe_8Al_9$	±4.6	10.1	0.41	90
$Gd_2Fe_7Al_{10}$	±4.8	10.9	0.42	90
$Gd_2Fe_{16}Ga_1$	5.4	14.2	0.25	90
$Gd_2Fe_{15}Ga_2$	5.7	11.7	0.29	90
$Gd_2Fe_{14}Ga_3$	5.5	8.5	0.32	90
$Gd_2Fe_{13}Ga_4$	5.5	6.9	0.35	90
$Gd_2Fe_{12}Ga_5$	5.2	6.2	0.37	90
$Gd_2Fe_{11}Ga_6$	4.9	7.2	0.39	90
$Gd_2Fe_{10}Ga_7$	4.8	8.1	0.42	90
$Gd_2Fe_9Ga_8$	4.5	9.1	0.43	90

[a]According to Ref. 4.

concentration dependence of hyperfine parameters listed in Table I, it follows that the electric field gradient at the nuclear Gd site changes its sign when Al substitution into Gd_2Fe_{17} takes place. Therefore, we would expect a similar change in sign for the second-order crystal field parameter A_2^0 in these compounds. Furthermore, using the relationship

$$K_1 = -\tfrac{3}{2}N\alpha_J\langle r_{4f}^2\rangle\langle 3J_z^2 - J(J+1)\rangle A_2^0 \qquad (1)$$

one would expect that the rare-earth sublattice anisotropy also changes its sign. If $R_2Fe_{17-x}Al_x$ compounds with rare earths having $\alpha_j<0$ are employed, one would expect a preferred magnetization direction perpendicular to the c axis for small x values, but a direction parallel to the c axis is expected for larger x values. No sign reversal of V_{zz} has been observed in the $Gd_2Fe_{17-x}Ga_x$ compounds (Table I), this is in contrast with previous neutron diffraction studies on $Tb_2Fe_{17-x}Ga_x$ where the easy direction of magnetization changes from planar to uniaxial.[10] This indicates that the rare-earth anisotropy can be large enough to overcome the basal plane oriented iron sublattice anisotropy.

The concentration dependence of hyperfine parameters of the Al and Ga substituted compounds is listed in Table I. In a previous analysis of the hyperfine field in Gd_2Fe_{17}, it was shown that the total hyperfine field can be decomposed into various contributions[4] of different sign and magnitude. The contribution of the Fe moments predominates and band structure calculations (see Ref. 12 and references cited therein) confirm an important role of the 6s conduction electrons in determining the hyperfine field in Gd_2Fe_{17} and other intermetallic compounds. The 6s electron polarization resulting from the Fe moments will gradually disappear, which is apparent in the decrease in effective hyperfine field.

The concentration dependence of the isomer shift has been compared with a simple model based on the charge transfer and intra-atomic $s-d$ electron redistribution and volume effects.[11] On the basis of this model, one expects that the ultimate value of the isomer shift that would be reached for $x=17$ is 0.52 and 0.64 mm^{-1} for Al and Ga substituted Gd_2Fe_{17} compounds, respectively.[4,6]

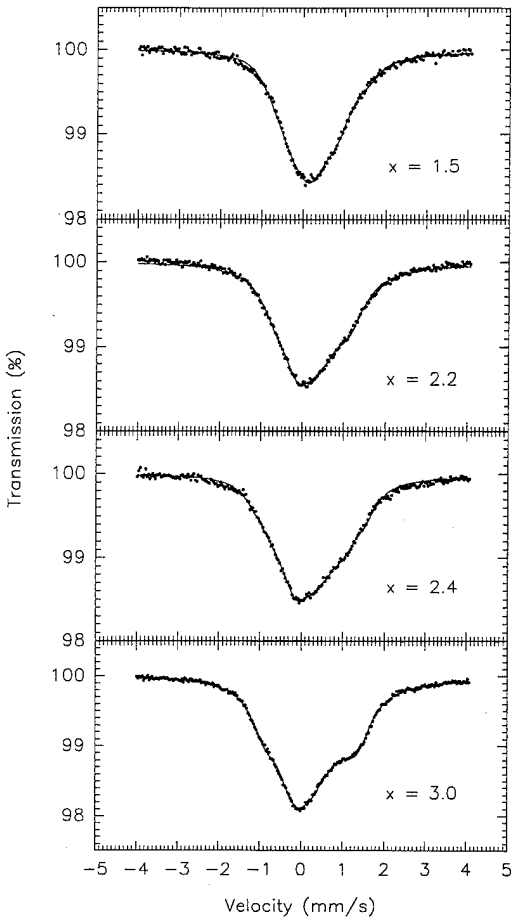


FIG. 3. ^{155}Gd Mössbauer spectra of the $GdCo_{12-x}Mo_x$ compounds at 4.2 K for several Mo concentrations x. The solid curve through the data points represents a fit.

Ternary compounds with Gd, Fe, or Co having the $ThMn_{12}$ type of structure can be stabilized by substitution of Mo for part of the Fe (Co). Nitrogenation has shown to lead to improved magnetic properties of the $GdFe_{12-x}Mo_x$ compounds.[5] The nitrogen atoms will occupy the interstitial $2b$ site, which is located near the Gd atoms. The ^{155}Gd Mössbauer spectra of $GdCo_{12-x}Mo_x$ are shown in Fig. 3. The concentration dependence of the hyperfine parameters of $GdFe12-_xMo_x(N_y)$ and $GdCo_{12-x}Mo_x$ are listed in Table II. Nitrogenation is seen to lead to a sign reversal of V_{zz} and the value of V_{zz} exceeds in magnitude the large electric field gradient measured in $R_2(Fe,Co)_{17}N_y$ compounds.[7] The angle θ between the effective hyperfine field and the V_{zz} shows a change from 0° to 90°. The latter feature indicates that there is a nitrogen-induced change in the easy magnetization direction of the Fe sublattice. A decreasing negative value of the electric field gradient V_{zz} can be observed in the $GdCo_{12-x}Mo_x$ compounds. The Co sublattice remains uniaxial with increasing Mo concentration. Using Eq. (1) and bearing in mind that A_2^0 has a sign opposite to V_{zz}, one can expect an easy axis type of anisotropy in the

TABLE II. Hyperfine parameters derived from fitting the ^{155}Gd Mössbauer spectra at 4.2 K for various $GdFe_{12-x}Mo_x(N_y)$ and $GdCo_{12-x}Mo_x$ compounds.

Compound	V_{zz} (10^{21} V m^{-2})	$\mu_0\lvert H_{\text{eff}}\rvert$ (T)	IS (mm s^{-1})	θ (deg)
$GdFe_{10.5}Mo_{1.5}$	1.6	9.2	0.21	0
$GdFe_9Mo_3$	1.9	4.3	0.18	0
$GdFe_{10.5}Mo_{1.5}N_y$	−21.3	7.2	0.35	90
$GdFe_9Mo_3N_y$	−19.9	6.9	0.35	90
$GdCo_{10.5}Mo_{1.5}$	−2.1	18.5	0.21	0
$GdCo_{9.8}Mo_{2.2}$	−3.1	21.5	0.21	0
$GdCo_{9.6}Mo_{2.4}$	−3.2	22.9	0.21	0
$GdCo_9Mo_3$	−4.5	24.4	0.20	0

$GdFe_{12-x}Mo_xN_y$ and $GdCo_{12-x}Mo_x$ compounds when rare earths with $\alpha_j<0$ are employed.[8,9]

It can be inferred from the data listed in Table II that the hyperfine fields of the Fe compounds are small and decrease with Mo concentration whereas the hyperfine fields of the Co compounds are comparatively large and increase with Mo concentration. This somewhat surprising behavior can tentatively be explained by strongly different transferred contribution of the Fe and Co moments, bearing in mind that the Fe as well as the Co moments decrease markedly with Mo concentration.

Apparently, the Fe transferred field is positive and dominates the negative core polarization contribution of Gd, leading to a decreasing overall contribution when the former decreases with Mo concentration. The Co contribution, when also positive, is not dominant, when it decreases with increasing Mo concentration the absolute value of the overall hyperfine field increases.

The authors would like to acknowledge the stimulating support of L. J. de Jongh. This work is part of the research program of the "Stichting voor Fundamenteel Onderzoek der Materie" (FOM), which is financially supported by the "Nederlandse Organisatie voor Wetenschappelijk Onderzoek" (NWO).

[1] H. de Graaf, thesis, University of Leiden, 1982.
[2] Y. Tanaka, O. B. Laubacher, R. M. Stoffen, E. B. Shera, H. D. Wohlfarth, and M. V. Hoehn, Phys. Lett. **108**, 8 (1982).
[3] W. B. Yelon, H. Xie, G. J. Long, O. A. Pringle, F. Grandjean, and K. H. J. Buschow, J. Appl. Phys. **73**, 6029 (1993).
[4] F. M. Mulder, R. C. Thiel, T. H. Jacobs, and K. H. J. Buschow, J. Alloys Comp. **197**, 25 (1993).
[5] D. P. Middleton, F. M. Mulder, R. C. Thiel, and K. H. J. Buschow, J. Magn. Magn. Mater. **146**, 123 (1995).
[6] D. P. Middleton, D. A. van de Straat, R. C. Thiel, and K. H. J. Buschow, J. Alloys Comp. (to be published).
[7] F. M. Mulder, R. C. Thiel, R. Coehoorn, T. H. Jacobs, and K. H. J. Buschow, J. Magn. Magn. Mater. **117**, 413 (1992).
[8] T. Zhao, Z. G. Zhao, F. R. de Boer, and K. H. J. Buschow, J. Alloys Comp. (to be published).
[9] O. Kalogirou, V. Psycharis, L. Saettas, and D. Niarchos, J. Appl. Phys. (to be published).
[10] Z. Hu, W. B. Yelon, S. Mishra, G. J. Long, O. A. Pringle, D. P. Middleton, K. H. J. Buschow, and F. Grandjean, J. Appl. Phys. **76**, 443 (1994).
[11] J. W. C. de Vries, R. C. Thiel, and K. H. J. Buschow, J. Phys. F **15**, 1413 (1985).
[12] F. M. Mulder, Ph.D. thesis, Leiden University, 1994.

Study of the nitrogen diffusion mechanism in R_2Fe_{17}

Y. D. Zhang, J. I. Budnick, and W. A. Hines
Department of Physics and Institute of Materials Science, University of Connecticut, Storrs, Connecticut 06269

D. P. Yang
Department of Physics, College of the Holy Cross, Worcester, Massachusetts 01610

Previously, nuclear magnetic resonance experiments and diffusion calculations have indicated that the distribution of nitrogen atoms in a $Y_2Fe_{17}N_x$ particle with intermediate N content is characterized by a nitrided region and an unnitrided region. In order to *directly* detect this two-region configuration, x-ray diffraction experiments have been carried out on systematically ground nitrogenated samples. Furthermore, x-ray diffraction and ^{89}Y nuclear magnetic resonance on vacuum-annealed samples show that the two-region configuration is stable, and that the nitrogen atoms do not diffuse further into the particle. Thermal conductivity detection measurements indicate that only 5% of the inserted N atoms can be released by vacuum annealing at the nitrogenation temperature. © *1996 American Institute of Physics.* [S0021-8979(96)36908-3]

I. INTRODUCTION

It is now well known that nitrogen insertion into rare-earth+Fe intermetallics, such as R_2Fe_{17}, produces materials with significantly improved magnetic properties, namely, the Curie temperature, magnetocrystalline anisotropy, and Fe magnetic moment.[1,2] A thorough understanding of the nitrogen diffusion process in the host lattice is important for determining the optimal nitrogenation conditions that will result in homogeneous and stable magnetic properties.

Recently, it has been shown that the distribution of nitrogen in a $Y_2Fe_{17}N_x$ particle with intermediate N content is characterized by a nitrided/unnitrided configuration.[3,4] In a simple case, this can be a shell/core structure. In the nitrided outer shell, all of the *accessible* interstitial sites are occupied by N atoms, and in the inner core, the host lattice is almost devoid of N atoms. These two regions share a thin interface, and the nitrogen atoms in a spherical $Y_2Fe_{17}N_x$ particle have an overall steplike radial distribution. The experimental evidence for this configuration came from ^{89}Y nuclear magnetic resonance (NMR) spectra, which showed that, across the entire range of nitrogen content ($0.6 \leqslant x \leqslant 2.8$), there are predominantly two types of Y–N coordination, namely, yttrium with two nitrogen atoms as nearest neighbors (Y+2N), and yttrium with no nitrogen atom as a nearest neighbor (Y+0N).[3] This implies that in the nitrided region, two of the three octahedral sites are occupied, and in the unnitrided region, the octahedral sites are empty. The process of nitrogenation results in the growth of the nitrided outer shell at the expense of the unnitrided inner core, with the nitrided region maintaining a Y+2N coordination. The Y+2N coordination for the nitrided region in $Y_2Fe_{17}N_x$ has also been determined from neutron diffraction.[5] The nitrided/unnitrided configuration was observed in $Nd_2Fe_{17}N_x$ using neutron diffraction,[6] and in $Pr_2Fe_{17}N_x$ using Mössbauer spectroscopy.[7] This steplike distribution was studied in several systems, such as $Nd_2Fe_{17}N_{2.3}$, where a sharp interface with thickness of only 1 μm was detected using electron microprobe analysis.[8]

In this article, additional experimental evidence supporting the above nitrided/unnitrided configuration is presented. In order to detect the two regions *directly*, x-ray diffraction patterns have been obtained from $Y_2Fe_{17}N_x$ samples after successive stages of grinding, and they confirm that the nitrogen distribution is not continuous and the inner core is not nitrided. The stability of the two-region configuration is studied by both x-ray diffraction and ^{89}Y NMR which show essentially no change for a nitrogenated sample upon vacuum annealing. Finally, the number of mobile N atoms is measured directly using thermal conductivity detection (TCD) in an outgassing process, and found to be approximately 5% of the total N content.

II. EXPERIMENTAL APPARATUS AND PROCEDURE

The parent Y_2Fe_{17} ingot, made by arc melting, was homogenized, powdered, and sieved to give particle diameters from 32 to 37 μm. The powder was annealed at 900 °C in an Ar atmosphere for 5 days before nitrogenation, which was performed at 480 °C under an ultrahigh purity (99.999%) N_2 flow. $Y_2Fe_{17}N_x$ samples with different N content ($0.3 \leqslant x \leqslant 2.8$) were obtained by varying the nitrogenation time from 0.5 to 18 h. Further vacuum annealing of the $Y_2Fe_{17}N_{1.7}$ sample was performed at 480 °C for 12 h using the same apparatus.

X-ray diffraction patterns were obtained on a Norelco diffractometer using Cu $K\alpha$ radiation. Nitrogen outgassing experiments were carried out on a temperature-programmed desorption apparatus.[9] A tube containing the $Y_2Fe_{17}N_{2.8}$ sample was subject to a flow of helium gas at a fixed rate. The desorbed nitrogen effluent was detected with a thermal conductivity detector. Spin-echo NMR measurements were made at 4.2 K, in zero external field, using a 120°–120° pulse sequence. The pulsed NMR apparatus, signal coil arrangement, calibration, and data taking procedure have been described in detail elsewhere.[10]

III. RESULTS AND ANALYSIS

Figure 1 compares the x-ray diffraction patterns of three powder samples: (a) the parent sample Y_2Fe_{17}; (b) the "completely" nitrided sample $Y_2Fe_{17}N_{2.8}$; and (c) the intermediate N content sample $Y_2Fe_{17}N_{1.7}$. In Fig. 1(a), a single hexagonal

 0021-8979/96/79(8)/4596/3/$10.00 © 1996 American Institute of Physics

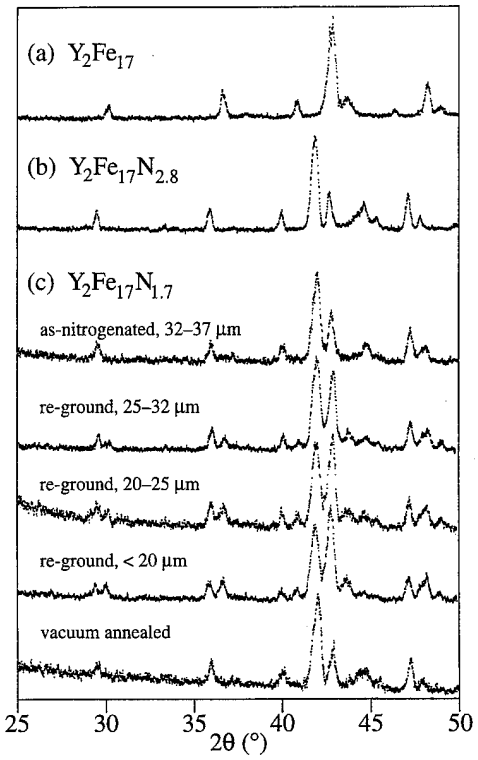


FIG. 1. X-ray diffraction patterns from (a) the parent sample Y_2Fe_{17}, (b) the "completely" nitrided sample $Y_2Fe_{17}N_{2.8}$, and (c) an intermediate N content sample $Y_2Fe_{17}N_{1.7}$. Two sets of Bragg peaks are visible in the reground $Y_2Fe_{17}N_{1.7}$ samples, showing the nitrided outer shell and the unnitrided inner core. Also, there is no significant structural differences between the as-nitrogenated and vacuum-annealed samples of $Y_2Fe_{17}N_{1.7}$.

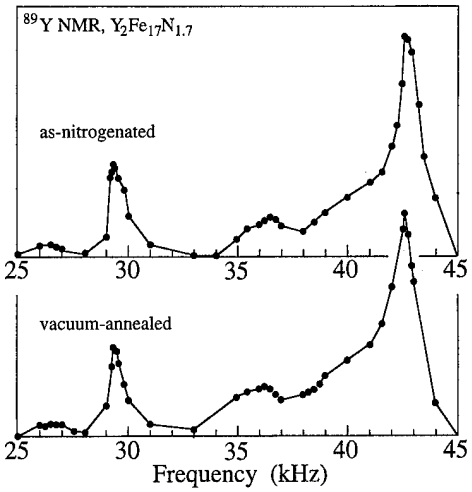


FIG. 2. ^{89}Y NMR spectra from as-nitrogenated and vacuum-annealed samples of $Y_2Fe_{17}N_{1.7}$, showing no significant structural changes after vacuum annealing at the nitrogenation temperature.

Y_2Fe_{17} phase with no bcc α-Fe is identified for the parent sample. For the $Y_2Fe_{17}N_{2.8}$ sample [Fig. 1(b)], the same structure as the parent sample is identified except that all of the Bragg peaks are shifted to lower angles due to volume expansion. Also, a small amount of α-Fe precipitation is present. In Fig. 1(c), the Bragg peaks from the as-nitrogenated $Y_2Fe_{17}N_{1.7}$ sample are *not* located, commeasurate with its intermediate N content, between the diffraction peaks in Figs. 1(a) and 1(b). Rather, they are located essentially at the same angles as those in Fig. 1(b), indicating a near complete nitrogenation of the surface region of the particle since the penetration depth for x rays in $Y_2Fe_{17}N_x$ is less than 5 μm. In order to expose the interior of the particles to the x rays, the $Y_2Fe_{17}N_{1.7}$ sample was ground in stages to obtain three samples with particle diameters of 25–32, 20–25, and <20 μm. As shown in Fig. 1(c), the three ground $Y_2Fe_{17}N_{1.7}$ samples have an extra set of Bragg peaks that correspond to the unnitrided parent sample Y_2Fe_{17} shown in Fig. 1(a). Furthermore, the smaller the particle size, the larger the peaks in the second set, showing directly more of the unnitrided inner core. A careful inspection of the x-ray patterns shows that the 2θ value of a peak in the unnitrided phase for a sample with intermediate N content is a little smaller than that for the parent Y_2Fe_{17} sample, and the 2θ value of a peak in the nitrided phase for a sample with intermediate N content is a little larger than that for the completely nitrided sample. The result can be explained by lattice strain since the two phases coexist in the sample particle. Lattice strain will result in the phase with smaller lattice constants being stretched, and the phase with large lattice constants being compressed.

As discussed below, the reason for the formation of such a two-region distribution is a strong chemical bond between a nitrogen atom in an interstitial octahedral site and the surrounding environment in the lattice. If there is such a trapping of the N atoms at the nitrogenation temperature (480 °C), then the distribution should be stable at the same temperature. The nitrogenated samples have been vacuum annealed, and x-ray diffraction and ^{89}Y NMR have been used to detect any changes in the N distribution. Both the x-ray diffraction pattern [Fig. 1(c)] and the NMR spectrum (Fig. 2) of the vacuum-annealed $Y_2Fe_{17}N_{1.7}$ sample remain unchanged from the as-nitrogenated sample. These experiments verify the stability of the two-region distribution, and therefore, the strong N-lattice bonding.

Finally, the number of mobile N atoms in the $Y_2Fe_{17}N_{2.8}$ sample was analyzed quantitatively in an outgassing experiment using thermal conductivity detection (TCD). The TCD signal voltage which was recorded as the temperature of the sample increased showed three peaks, each corresponding to an effluence of N atoms from the sample. A first peak near 120 °C was attributed to those N atoms adsorbed on the surface, which accounted for about 1% of the total N content. A second peak near 380 °C was attributed to the outgassing of the mobile N atoms inside the sample. Finally, a third peak, or sudden increase in the TCD signal, above 600 °C was attributed to nitrogen release during the phase decomposition into YN and α-Fe. In order to obtain a reasonable estimate for the amount of nitrogen release associated with the second peak, the TCD experiment was repeated with the temperature scan programmed to stop rising at 460 °C (above the second peak but below the temperature of phase decomposition). During a 15 min period at a constant temperature of 460 °C, the mobile N atoms were completely evacuated from the

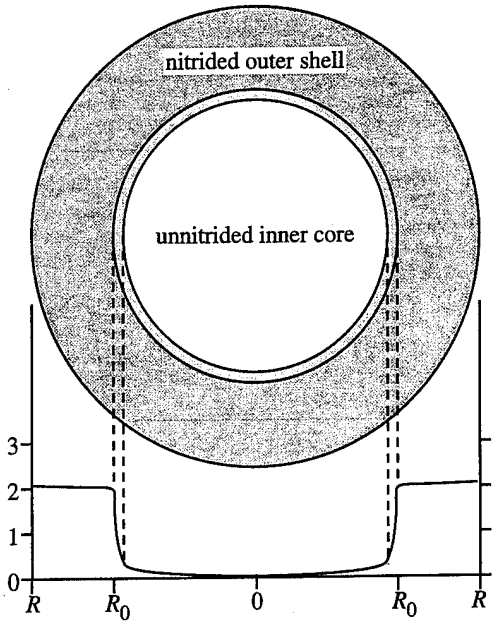


FIG. 3. Schematic diagram showing the nitrogen distribution in a spherical particle. The horizontal scale represents the radial direction across the particle, and the vertical scale represents the N concentration in nitrogen atoms per unit cell in $Y_2Fe_{17}N_x$.

sample. Integration of the second peak and comparison with a standard calibration curve showed that about 5% of the total N content can be released. If none of N atoms were trapped in the interstitial sites, then during the vacuum-annealing process the N atoms would either diffuse further towards the interior of the particle or leave the particle through its surface. The first possibility would have caused changes in the x-ray diffraction pattern and NMR spectrum, whereas the second possibility would have been detected in the outgassing experiment. The experiments rule out both of these scenarios for the majority of N atoms in the $Y_2Fe_{17}N_x$ system.

IV. DISCUSSION AND CONCLUSIONS

To date, two different models have been proposed for describing the nitrogen distribution in $R_2Fe_{17}N_x$. One is based on a simple diffusion mechanism that results in a continuous solid solution distribution (CSSD) with a smooth concentration gradient.[11,12] The second model considers a chemical reaction diffusion process with two types of N atoms that leads to a steplike radial distribution with a nitrided shell and an unnitrided core (see Fig. 3).[4] One type of nitrogen atom is characterized by its immobility once the atom enters an accessible octahedral site (trapped type, or t-type), and the other has a relatively large diffusion constant (free-type, or f-type). It is reasonable to believe that the f-type atoms are located in the tetrahedral interstitial sites as reported in a previous ^{14}N NMR study on both hexagonal and rhombohedral $Y_2Fe_{17}N_x$.[13] The t-type atoms are immobilized because of a strong chemical bond with the lattice. The f-type atoms can diffuse easily only in the region where all the "traps" are filled, otherwise an f-type atom would fall into an octahedral site and convert itself into a t-type atom. In the outer shell, therefore, all accessible interstitial octahedral sites are occupied by t-type N atoms, and a relatively small number of f-type atoms "ride" on the nitrided region and diffuse towards the interface where octahedral interstitial sites are available. Once an f-type atom reaches the interface, it is immediately trapped and converts to a t-type atom, leaving a sharp boundary between the nitrided outer region and an unnitrided inner one. Through this process, the interface advances towards the center of the particle, and the nitrogen content in the sample increases with nitrogenation time. If the nitrogenation is terminated, either by removing the nitrogen gas source or by reducing the temperature, then the interface ceases to move and the steplike distribution is preserved. In the case that the trapping has a relatively deep potential well, this two-region configuration is stable. The chemical reaction diffusion process with two types of N atoms described above has been treated theoretically in a previous work which calculates the radial dependence of the nitrogen distribution (see Fig. 3).[4] In addition, this model explains the abnormally small (apparent) diffusion frequency factor which characterizes these newly developed R_2Fe_{17} nitrides.[4]

Finally, the "nominal" nitrogen content is usually obtained by weighing the sample before and after nitrogenation; consequently, there are errors as not all the N atoms absorbed into the entire sample are coordinated with the Y atoms in the 2:17 phase. Also some of the weight gain of the sample may be due to factors other than N absorption. This may offer an explanation as to why different studies have reported different N content values, while the corresponding lattice expansion and magnetic properties were not so different. A detailed analysis of the difference between the N content measured gravimetrically and the Y–N coordination measured by NMR has been published previously.[14]

ACKNOWLEDGMENT

This work was supported by NSF Grant No. DMR9319367.

[1] J. M. D. Coey and H. Sun, J. Magn. Magn. Mater. **87**, L251 (1990).
[2] K. H. J. Buschow, J. Alloys Comp. **193**, 223 (1993).
[3] Y. D. Zhang, J. I. Budnick, D. P. Yang, G. W. Fernando, W. A. Hines, T. D. Xiao, and T. Manzur, Phys. Rev. B **51**, 12091 (1995).
[4] Y. D. Zhang, J. I. Budnick, W. A. Hines, and D. P. Yang, Appl. Phys. Lett. **67**, 208 (1995).
[5] S. S. Jaswal, W. B. Yelon, G. C. Hadjipanayis, Y. Z. Wang, and D. J. Sellmyer, Phys. Rev. Lett. **67**, 644 (1991).
[6] O. Isnard, J. L. Soubeyroux, S. Miraglia, D. Fruchart, L. M. Garcia, and J. Bartolomé, Physica B **180–181**, 624 (1992).
[7] A. I. C. Persiano, J. D. Ardisson, F. A. Batista, C. C. Colucci, and S. Gama, J. Magn. Magn. Mater. **136**, 149 (1994).
[8] C. C. Colucci, S. Gama, C. A. Ribeiro, and L. P. Cardoso, J. Appl. Phys. **75**, 6003 (1994).
[9] W. Q. Xu, S. L. Suib, and C. L. O'Young, J. Catal. **144**, 285 (1993).
[10] Y. D. Zhang, W. A. Hines, J. I. Budnick, M. Choi, F. H. Sanchez, and R. Hasegawa, J. Magn. Magn. Mater. **61**, 162 (1986).
[11] J. M. D. Coey, R. A. Skomski, and S. Wirth, IEEE Trans. Magn. **28**, 2332 (1992).
[12] R. Skomski and J. M. D. Coey, J. Appl. Phys. **73**, 7602 (1993).
[13] Y. D. Zhang, J. I. Budnick, W. A. Hines, N. X. Shen, T. D. Xiao, and T. Manzur, J. Magn. Magn. Mater. **145**, L11 (1995).
[14] Y. D. Zhang *et al.*, Scr. Metall. Mater. **33**, 1817 (1995).

Nuclear magnetic resonance study of expanded lattice permanent magnet nitrides and carbides at high pressure

Cz. Kapusta
Department of Solid State Physics, Faculty of Physics and Nuclear Techniques, University of Mining and Metallurgy, 30-059 Cracow, Poland and J. F. Allen Laboratories, Department of Physics and Astronomy, University of St. Andrews, St. Andrews KY16 9SS, Scotland

J. S. Lord, G. J. Tomka, and P. C. Riedi
J. F. Allen Laboratories, Department of Physics and Astronomy, University of St. Andrews, St. Andrews, KY16 9SS, Scotland

K. H. J. Buschow
Van der Waals–Zeeman Laboratorium, University of Amsterdam, 1018 XE Amsterdam, The Netherlands

The nuclear magnetic resonance spin-echo spectra of ^{89}Y and ^{147}Sm for Y_2Fe_{17}, $Y_2Fe_{17}C_{0.4}$, $Y_2Fe_{17}C_{1.5}$, $Y_2Fe_{17}N_{2.5}$, $Y_2Fe_{17}CN_{1.5}$, $Y_2Fe_{17}H_{1.6}$, and Sm_2Fe_{17} have been measured at pressures up to 10 kbar at 4.2 K. A reduction of the magnitude of the valence electron polarization contribution to the effective field B_e at Y and Sm sites with pressure is observed. The effect is strongly related to the nearest neighbor environment of the site. A significant reduction of $\partial B/\partial p$ is observed for the sites with nitrogen neighbors. Carbon increases (decreases) $\partial B/\partial p$ in the rhombohedral (hexagonal) structure of the compound. A decrease of the lattice electric field gradient at the Sm site in Sm_2Fe_{17} with pressure is observed. A corresponding decrease of the crystal electric field coefficient A_2^0 at the Sm site with pressure of 0.7% per kbar is derived, indicating an anisotropic compressibility of the material. © *1996 American Institute of Physics.* [S0021-8979(96)37008-8]

I. INTRODUCTION

The compounds $RE_2Fe_{17}A_x$ where RE is a rare earth or yttrium and A is a light interstitial element belong to the family of the recently discovered interstitially modified materials for permanent magnet applications.[1,2] An uptake of carbon or nitrogen by these materials dramatically raises their magnetic ordering temperatures and induces a strong uniaxial anisotropy in the Sm_2Fe_{17} nitride and carbide making them eligible for applications. In our recent nuclear magnetic resonance (NMR) study of these materials, information on the site distribution of interstitial atoms and their influence on the effective (hyperfine) magnetic fields B_e and electric field gradients (EFG) measured at nuclei was obtained.[3,4] In the present study we report high pressure NMR measurements of the individual site yttrium and samarium hyperfine fields as well as the Sm electric field gradient in these materials. The pressure dependence of these quantities reflects the individual site contributions to the magnetoelastic properties of the materials. In order to compare the influence of different interstitial atoms, samples of Y_2Fe_{17}, $Y_2Fe_{17}C_{0.4}$, $Y_2Fe_{17}C_{1.5}$, $Y_2Fe_{17}N_{2.5}$, $Y_2Fe_{17}CN_{1.5}$, $Y_2Fe_{17}H_{1.6}$, and Sm_2Fe_{17} were measured.

The host compounds crystallize in the hexagonal structure for Y and in the rhombohedral structure for Sm. The carbide $Y_2Fe_{17}C_{0.4}$ and the nitride are hexagonal, whereas $Y_2Fe_{17}C_{1.5}$ and the carbonitride $Y_2Fe_{17}CN_{1.5}$ and Sm_2Fe_{17} are rhombohedral. RE elements occupy a single site ($6c$) in the rhombohedral and two sites ($2b$,$2d$) in the hexagonal structure. The $2b$ site has 18 Fe and 2 RE atoms as the nearest neighbors (NN), the $2d$ has 20 Fe and 0 RE neighbors and for the $6c$ the numbers of neighbors are 19 Fe and 1 RE, respectively. Neutron diffraction experiments have shown that the C atoms randomly occupy the interstitial positions $6h$ ($9e$).[5] Hydrogen atoms for hydrogen content $x<3$ per formula unit mostly locate at $6h$ ($9e$) sites.[6] Nitrogen locates almost entirely at $6h$ ($9e$) interstitial positions,[7] but recently a discussion about its possible location at the $18g$ ($12i$) sites has aroused considerable interest.[8] The number of $9e$ ($6h$) NN sites to a RE site is 3.

Pressure measurements were carried out using a Be–Cu pressure cell with an untuned rf coil as the NMR probe head. The cell, filled with petroleum spirit, was pressurized to about 12 kbar and locked at room temperature and then cooled down to 4.2 K. The maximum pressure obtained at 4.2 K was about 10 kbar which was measured by a semiconductor pressure transducer. The ^{89}Y and ^{147}Sm NMR spin-echo spectra were taken at 4.2 K, using an automated, computer controlled spin-echo spectrometer.[9] A sequence of two constant amplitude radio frequency pulses of 0.2 and 0.4 μs, spaced at 15 μs was applied. Powder samples, the same as those used in Refs. 3 and 4 were measured. The spectra taken at ambient pressure are shown in Figs. 1 and 2.

II. RESULTS AND DISCUSSION

A. $Y_2Fe_{17}A_x$

The NMR spectra obtained at ambient pressure, Fig. 2, are very similar to those reported in Ref. 3. The spectrum for Y_2Fe_{17} consists of a single, asymmetric ^{89}Y line ($I=1/2$—no quadrupole splitting) with a shoulder at its high frequency side, reflecting the presence of the two Y sites in the compound. For the carbides $Y_2Fe_{17}C_{0.4}$, $Y_2Fe_{17}C_{1.5}$, and the nitride three additional lines appear indicating a strong effect of C and N neighbors on the Y valence electron polarization. Following Ref. 3 they are assigned to the Y sites with one, two, and three C (N) atoms, respectively. A single ^{89}Y line is observed for the hydride indicating the lack of a local influ-

 0021-8979/96/79(8)/4599/3/$10.00 © 1996 American Institute of Physics

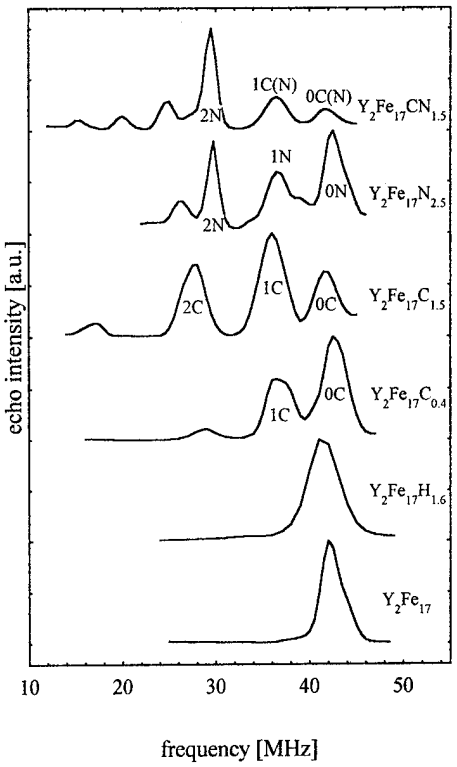


FIG. 1. The ^{89}Y NMR spin-echo spectra of the $Y_2Fe_{17}A_x$ (A=N,C,H) compounds at 4.2 K and ambient pressure.

ence of hydrogen on Y electronic structure. The line has a slightly larger width and is shifted to a lower frequency with respect to that of Y_2Fe_{17}.

The ^{89}Y spectra obtained at high pressure show shifts of the resonance lines towards lower frequencies, which corresponds to a decrease in magnitude of B_e at Y nuclei with pressure. The values of B_e corresponding to the frequencies of the Y resonance lines were obtained using the conversion factor of -0.5647 T/MHz. The values of $\partial B_e/\partial p$ and $(1/B_e)\partial B_e/\partial p$ corresponding to the Y sites with zero, one, and two C (N) neighboring atoms are listed in Table I. The data for three C (N) lines bear large errors and they are not shown here. Since the changes of B_e up to maximum pressure of 10 kbar were found to be small (<0.5%), we assume that B_e is a linear function of pressure over this range.

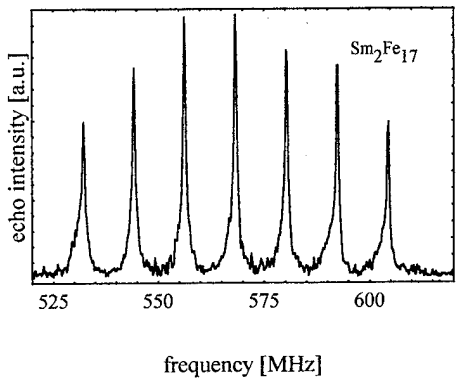


FIG. 2. The ^{147}Sm NMR spin-echo spectrum of Sm_2Fe_{17} at 4.2 K and ambient pressure.

TABLE I. The magnetic field induction B_e at Y sites at ambient pressure, the pressure derivatives $\partial B_e/\partial p$ and $(1/B_e)\partial B_e/\partial p$ for the individual Y sites in the carbides, in the nitride and in the carbonitride of Y_2Fe_{17} at 4.2 K.

Sample	Site	B_e (T)	$\partial B_e/\partial p$ (10^{-3}T/kbar)	$(1/B_e)\partial B_e/\partial p$ (10^{-4}/kbar)
Y_2Fe_{17}[b]		−20.4	49	−24
$Y_2Fe_{17}H_{1.6}$[b]		−19.9	58	−29
$Y_2Fe_{17}C_{0.4}$[b]	0C	−20.3	50	−25
	1C	−17.6	30	−17
$Y_2Fe_{17}C_{1.5}$[a]	0C	−20.1	28	−14
	1C	−17.3	36	−21
	2C	−13.2	34	−26
$Y_2Fe_{17}N_{2.5}$[b]	0C	−20.3	51	−25
	1C	−17.4	14	−8
	2C	−14.2	8	−5
$Y_2Fe_{17}CN_{1.5}$[a]	0C(N)	−20.1	30	−15
	1C(N)	−17.5	29	−17
	2N	−14.1	4	−3
Sm_2Fe_{17}[a]		331.2	44	

[a]Rhombohedral structure.
[b]Hexagonal structure.

The value of $(1/B_e)\partial B_e/\partial p$ obtained for Y_2Fe_{17} amounts to -24×10^{-4}/kbar, close to that of -29×10^{-4}/kbar derived from theoretical calculations.[10] The present value is 30% larger in magnitude than was reported previously.[11] The discrepancy can be attributed to the fact that Y_2Fe_{17} samples which show hexagonal structure, also contain stacking faults corresponding to the rhombohedral 6*c* sites. The derived value of $(1/B_e)\partial B_e/\partial p$ therefore corresponds to an average over the three environments which vary their relative population in a way sensitively dependent on sample preparation conditions.

Comparing the values of $(1/B_e)\partial B_e/\partial p$ of the same sites [e.g., hexagonal zero C (N)] in the carbides, the nitride and the carbonitride we see the same pressure sensitivity irrespective of the material in which they appear, i.e., their local environment predominantly determines their pressure behavior. The rhombohedral zero C (N) sites have a pressure sensitivity 40% lower than the hexagonal ones. Hexagonal sites with carbon neighbors slightly decrease their pressure sensitivity with increasing number of C neighbors, whereas an opposite effect is observed for the rhombohedral sites. Nitrogen neighbors reduce considerably pressure effects in both structures. For the hydride a slightly larger pressure derivative from that in the host compound is found. It corresponds to an average over the Y sites with zero, one, two, and three H neighbors which are not resolved in the spectrum.

The effective field induction B_e at Y nuclei originates mainly from the polarization of Y 5*s*-like electrons by neighboring magnetic Fe atoms, contributing to B_e via direct contact interaction. A smaller contribution originates from the 4*d* electrons bearing a small magnetic moment and contributing to B_e via core electron polarization. These contributions are of opposite sign. The contribution from the valence *s*-electron polarization is often called the transferred hyperfine field (THFF) and is antiparallel to the direction of neighboring Fe moments. From theoretical calculations for Y_2Fe_{17}

using the experimental lattice constants and for the expanded lattice[12] one can see that both contributions decrease in magnitude with applied pressure, reflecting a decrease of Fe magnetic moments. The THFF contribution changes more rapidly under pressure and thus determines the sign of the total change. The total B_e and the relative ratio of both contributions, however, change with nitriding or carbiding. The ratio of THFF to the $4d$ contribution for $Y_2Fe_{17}C_3$ is smaller than for Y_2Fe_{17} whereas for $Y_2Fe_{17}N_3$ it is larger. Assuming a similar pressure behavior of both contributions at the sites with C (N) neighbors to that in Y_2Fe_{17} one would expect a larger pressure sensitivity for the nitride. Surprisingly, nitrogen neighbors cause a dramatic reduction of $(1/B_e)\partial B_e/\partial p$ which is especially large for the two N sites. Thus, a different mechanism of the effect has to be considered and we attribute it to different compressibilities of the local environments of the sites with C or N neighbors.

B. Sm_2Fe_{17}

The ^{147}Sm spectrum obtained at ambient and high pressure was found to be similar to that reported in Ref. 13. It consisted of a single quadrupole septet corresponding to the single Sm crystallographic site $6c$. The change of B_e with pressure was derived from the central line frequency shift using the conversion factor of 0.5689 T/MHz. The value of quadrupole splitting derived from the line separations at ambient pressure ν_q is 12.017 MHz, and it decreases with pressure by 0.004 MHz/kbar. The corresponding change of the electric field gradient (EFG) component along the hyperfine field V_{ii} was derived using the conversion factor of -21.85×10^{20} V/m^2 MHz. The change of V_{ii} at pressure amounts to 0.084×10^{20} V/m^2 kbar. Since the change at the maximum pressure of 7.5 kbar is found to be small (<0.3%), we assume that V_{ii} is a linear function of pressure over this range.

The effective field on Sm nuclei is dominated by a huge contribution from the orbital current of $4f$ electrons. As the coupling between the Sm and Fe spins is antiparallel and the Sm spin and orbital moments are also coupled in aniparallel, the contribution is positive with respect to the local magnetization direction determined by Fe moments. A much smaller contribution to B_e arising from polarization of Sm valence electrons by the Fe magnetic moments is of opposite sign. A similar pressure derivative $\partial B_e/\partial p$ of Y and Sm HFF in Y_2Fe_{17} and Sm_2Fe_{17} indicates that the effect of pressure is related to the behavior of valence electrons. In view of the above analysis an increase of B_e with pressure corresponds to a decrease of valence electron contribution and is consistent with the effect observed for Y_2Fe_{17}.

The NMR signal for Sm_2Fe_{17} corresponds to the local magnetization direction in the basal c plane.[13] Thus, B_e has its direction in the c plane and the EFG value obtained from quadrupole splitting corresponds to this plane. The EFG is a sum of the contributions from $4f$ electrons $V_{zz}(4f)$ and from the nonspherical distribution of the $5d$ and $6p$ electrons of the parent atom. This nonspherical distribution originates from interaction with neighboring ions in the lattice.[14] The $4f$ contribution lies in the Sm moment direction,[4] whereas the latter contribution, called the lattice EFG, is coupled to the crystal lattice. The lattice EFG tensor for the $6c$ site is axially symmetric along the c axis.

We attribute the decrease of magnitude of the EFG under pressure to a change of magnitude of the lattice EFG. The possibility of a change of $4f$ contribution is rather unlikely, since it would be accompanied by a corresponding decrease of the orbital contribution to B_e and thus a decrease of B_e, which is not the case. Another possibility is that the change of V_{ii} could be caused by a change of B_e direction possibly related to a tilting of Sm moments towards the c axis. This is also unlikely, as it would also imply a decrease of B_e.[4] The change of V_{ii} related to the lattice EFG component in the basal c plane, $[1/V_{ii}(\text{latt})]\partial V_{ii}(\text{latt})/\partial p$, amounts to 7×10^{-3}/kbar from a V_{ii} value of -13×10^{20} V m^{-2}. This change corresponds to a decrease in magnitude as compared to the value at ambient pressure. A simple point charge model, assuming isotropic compressibility, predicts an increase of magnitude of $[1/V_{ii}(\text{latt})]\partial V_{ii}(\text{latt})/\partial p$.

The lattice EFG measured at RE nuclei in these materials is roughly proportional to the EFG exerted by the $4f$ electron shell quadrupole moment.[14] Thus, assuming a proportionality between lattice EFG and the crystal electric field (CEF) coefficient A_2^0 we arrive at a relative change of A_2^0 with pressure of -0.7%/kbar. The negative sign corresponds to a decrease of A_2^0 with increasing pressure. For isotropic compressibility one would expect an increase of A_2^0. Thus, the result indicates a large anisotropy in the compressibility of the material.

ACKNOWLEDGMENTS

The financial support for Cz. K. from the Leverhulme Trust during his stay at the University of St. Andrews is gratefully acknowledged. Work partly supported by the Engineering and Physical Sciences Research Council, UK and the State Committee for Scientific Research, Poland, Grant No. 2P03B11909.

[1] D. B. de Mooij and K. H. J. Buschow, J. Less-Common Met. **142**, 349 (1988).
[2] Hong Sun, J. M. D. Coey, Y. Otani, and D. P. F. Hurley, J. Phys. Condensed Matter **2**, 6465 (1990).
[3] Cz. Kapusta, M. Rosenberg, J. Zukrowski, H. Figiel, T. H. Jacobs, and K. H. J. Buschow, J. Less-Common Met. **171**, 101 (1991).
[4] Cz. Kapusta, M. Rosenberg, P. C. Riedi, M. Katter, and L. Schultz, J. Magn. Magn. Mater. **134**, 106 (1994).
[5] R. B. Helmholdt and K. H. J. Buschow, J. Less-Common Met. **155**, 15 (1989).
[6] O. Isnard, S. Miraglia, J. L. Soubeyroux, and D. Fruchart, Solid State Commun. **81**, 13 (1992).
[7] O. Isnard, S. Miraglia, J. L. Soubeyroux, and D. Fruchart, J. Alloys Comp. **190**, 129 (1992).
[8] Q. W. Yan, P. L. Zhang, Y. N. Wei, K. Sun, B. P. Hu, Y. Z. Wang, G. C. Liu, C. Gau, and Y. F. Cheng, Phys. Rev. B **48**, 2878 (1993).
[9] J. S. Lord and P. C. Riedi, Meas. Sci. Technol. **6**, 149 (1995).
[10] T. Beuerle and M. Fähnle, J. Magn. Magn. Mater. **110**, L29 (1992).
[11] J. G. M. Armitage, T. Dumelow, P. C. Riedi, and J. S. Abell, J. Phys. Condensed Matter **1**, 3987 (1989).
[12] T. Beuerle and M. Fähnle, Phys. Status Solidi B **174**, 257 (1992).
[13] Cz. Kapusta, R. J. Zhou, M. Rosenberg, P. C. Riedi, and K. H. J. Buschow, J. Alloys Comp. **178**, 139 (1992).
[14] R. Coehoorn and K. H. J. Buschow, J. Appl. Phys. **69**, 5590 (1991).

Band theoretical investigation of the Curie temperatures of modified R_2Fe_{17}-based intermetallic compounds

W. Y. Ching and Ming-Zhu Huang
Department of Physics, University of Missouri–Kansas City, Kansas City, Missouri 64110

The Curie temperatures of several Nd_2Fe_{17}-based intermetallic compounds are calculated based on the spin-fluctuation model of Mohn and Wohlfarth and the band structure results calculated using the self-consistent orthogonalized linear combinations of the atomic orbitals method in the local spin density approximation. It is shown that the calculated T_c can qualitatively account for the observed T_c enhancement in this class of modified compounds by interstitial doping of N or C, or by elemental substitution of Fe by Si, Al or Ga. A simple explanation of T_c enhancement based purely on the magnetovolume effect is not justified. It is also shown that neither the Stoner–Curie temperature nor the characteristic spin-fluctuation temperature is adequate to explain the experimentally observed T_c enhancement in these compounds. © *1996 American Institute of Physics.* [S0021-8979(96)49408-8]

In recent years, research on hard magnets has shifted from $R_2Fe_{14}B$ (2-14-1) phase to the R_2Fe_{17} (2-17) phase (R =rare earth) of intermetallic compounds. This is because the latter has a greater Fe content and the possibility of increasing Curie temperature T_c by interstitial doping of N or C,[1–5] or by elemental substitution of Fe by other metal or metalloid elements such as Al, Si, and Ga.[6–12] The rational is that T_c can be increased by expanding the lattice thereby increasing the Fe–Fe separation. The change in the Fe–Fe exchange interaction coupled with local moment increase result in the enhancement of T_c. However, it was soon realized that in the case of Si substitution in Nd_2Fe_{17}, T_c increases even when the lattice contracts.[9] Thus magnetovolume effects can account at most only a part of the observed T_c enhancement. It is highly desirable if theoretical calculations can shed some light on the underlying mechanism for T_c enhancement in these promising hard magnets. Quantitative prediction of transition temperatures in magnetic materials is an outstanding problem in the theory of magnetism.[13] Ferromagnetic phase transition involves complicated many particle and spin interactions, and even for the pure $3d$ transition metal crystals, quantitative prediction of T_c has not been fully successful. The simplest approach using the spin-polarized band results appears to be the theory of Gunnarsson[14] based on the Stoner model for itinerant electron magnetism[15] in which T_c^s, the Stoner–Curie temperature is identified as the solution of the equation:

$$I\int_{-\infty}^{+\infty}\frac{\partial f(E,T)}{\partial E}N(E)dE+1=0, \tag{1}$$

where I is the Stoner parameter generally given by $I = \Delta E/M_0$, $N(E)$ is the density of states (DOS) per atom per spin and $f(E,T)$ is the Fermi function. ΔE is the exchange splitting energy and M_0 is the equilibrium magnetic moment at $T=0$. Gunnarsson estimated the T_c for Fe, Co, and Ni using expression (1) and found the T_c to be a factor of 3 to 5 larger than the measured T_c.[14] It was soon realized that a correct theory should include the effect of spin fluctuation.[16] Mohn and Wohlfarth (MW)[17] have derived an expression for the characteristic temperature T_{sf} describing the effect of spin fluctuation in the long wavelength limit given by $T_{sf}=[M_0]^2/10k_B\chi_0$, where k_B is the Boltzmann's constant and χ_0 is the exchange-enhanced susceptibility at equilibrium:

$$\chi_0^{-1}=\frac{1}{4\mu_B^2}\left(\frac{1}{N^{\uparrow}(E_F)}+\frac{1}{N^{\downarrow}(E_F)}\right)-\frac{I}{2\mu_B^2}, \tag{2}$$

where $N^{\uparrow}(E_F)$ and $N^{\downarrow}(E_F)$ are the DOS of the majority (spin-up) and the minority (spin-down) spin bands at the Fermi level (E_F), respectively. The Curie temperature T_c is obtained from the quadratic equation involving both T_{sf} and T_c^s

$$\frac{T_c^2}{(T_c^s)^2}+\frac{T_c}{T_{sf}}=1. \tag{3}$$

In the limit of pure spin fluctuation, $T_c=T_{sf}$ and on the opposite limit of pure Stoner model with no spin fluctuation, $T_c = T_c^s$. Mohn and Wohlfarth obtained T_c for Fe, Co, and Ni in good agreement with the experimental data.[17] In addition, the T_c obtained for several Y-based intermetallic Fe and Co compounds using the band structures calculated by others were also in reasonable agreement with experimental data.

We have recently calculated the spin-polarized band structures of Nd_2Fe_{17} and Y_2Fe_{17} crystals using the first-principles orthogonalized linear combinations of the atomic orbitals (OLCAO) method,[18,19] and also their modified forms with interstitial doping of C or N[19] or by replacing Fe on selected sites by Al, Si, or Ga.[20,21] It is therefore instructive to see if the variation of T_c in these compounds can be accounted for by the spin-fluctuation model of MW. Such calculations for T_c can be considered first-principles since the only experimental information used is the crystal structure of the compound. However, before we present the results, it should be pointed out that such investigation may not be very quantitative for the following reasons. First, calculations for the modified Nd_2Fe_{17} compounds have a much greater degree of uncertainty than in pure transition metals. The calculations were carried out on the rhombohedral unit cell ($R3m$, 19 atoms/unit cell). Ideally, a supercell approach with statistical distribution for the modified sites should be used. Second, the effect of the presence of Nd is treated in the context of localized moment theory and thus plays no role in the present theory for T_c which is based on itinerant magnetism. However, the presence of Nd does change the

 0021-8979/96/79(8)/4602/3/$10.00 © 1996 American Institute of Physics

TABLE I. Calculated magnetic properties of some Nd_2Fe_{17}-based compounds. ΔV is the % change of the cell volume relative to Nd_2Fe_{17}. T_c(expt.) and T_c(cal.) are the experimental and the calculated Curie temperature in K. T_{sf} and T_s^c are the spin-fluctuation and the Stoner–Curie temperatures respectively in K. $N^{\uparrow}(E_F)$ and $N^{\downarrow}(E_F)$ are the density of states at the Fermi level for spin-up and spin-down bands, respectively, in the unit of states/spin-formula unit of Fe sublattice. ΔE is the calculated exchange splitting in eV. $M(\mu_B)$ is the calculated total moment for the Fe sublattice. I is the Stoner parameter.

System	ΔV (%)	T_c (expt.)	T_c (cal.)		$T_{sf}T_c^s$	$N^{\uparrow}(E_F)$	$N^{\downarrow}(E_F)$	ΔE	$M(\mu_B)$	I
Nd_2Fe_{17}	–	329[a]	337	984	416	13.29	9.45	1.85	31.67	1.00
$Nd_2Fe_{16}Si_1$	−0.6	425[b]	599	760	1304	11.88	10.39	1.92	30.20	1.02
$Nd_2Fe_{15}Si_2$	−1.0	480[c]	747	1495	1056	6.75	10.50	1.99	28.86	1.04
$Nd_2Fe_{14}Si_3$	−1.2	500[b]	773	1584	1080	6.65	8.38	2.00	27.05	1.04
$Nd_2Fe_{15}Ga_2$	+1.2	520[d]	1382	2316	2148	5.61	10.78	2.00	27.91	1.08
$Nd_2Fe_{15}Al_2$	+1.6	440[e]	665	1277	960	8.74	9.41	1.96	29.56	1.00
$Nd_2Fe_{17}N_3$	+5.5	740[f]	649	995	1100	9.30	9.82	1.92	28.97	1.13
$Nd_2Fe_{17}C_3$	+5.5	658[g]	1043	1154	3352	9.63	10.34	1.92	31.03	1.05

[a]References 2, 5, 6, 9.
[b]Reference 9.
[c]References 6, 9.
[d]Reference 12.
[e]References 6, 12.
[f]References 2, 4.
[g]Reference 5.

electronic structure, and hence the calculated T_c due to the slight hybridization of the Nd $4f$ orbitals with the conduction electrons. Third, the presence of the nonmagnetic elements in system is not anticipated in the original theory for T_c^s and T_{sf}. In the present calculations, only the moments and the DOS of the Fe sublattice are used. It is not clear if this is the most valid choice. Electronic structure results show the nonmagnetic atoms are slightly polarized and order antiferromagnetically with the Fe lattice.[20,21] Fourth, the experimental values for T_c and also the crystal parameters used in the calculations are uncertain to a large extent. Most of these materials are susceptible to partial disorder and nonstochiometry. In the case of elemental substitutions, the actual site occupation of the substituted sample may involve several Fe sites with different probability of occupation. Also, the calculations do not consider any lattice relaxation effects which

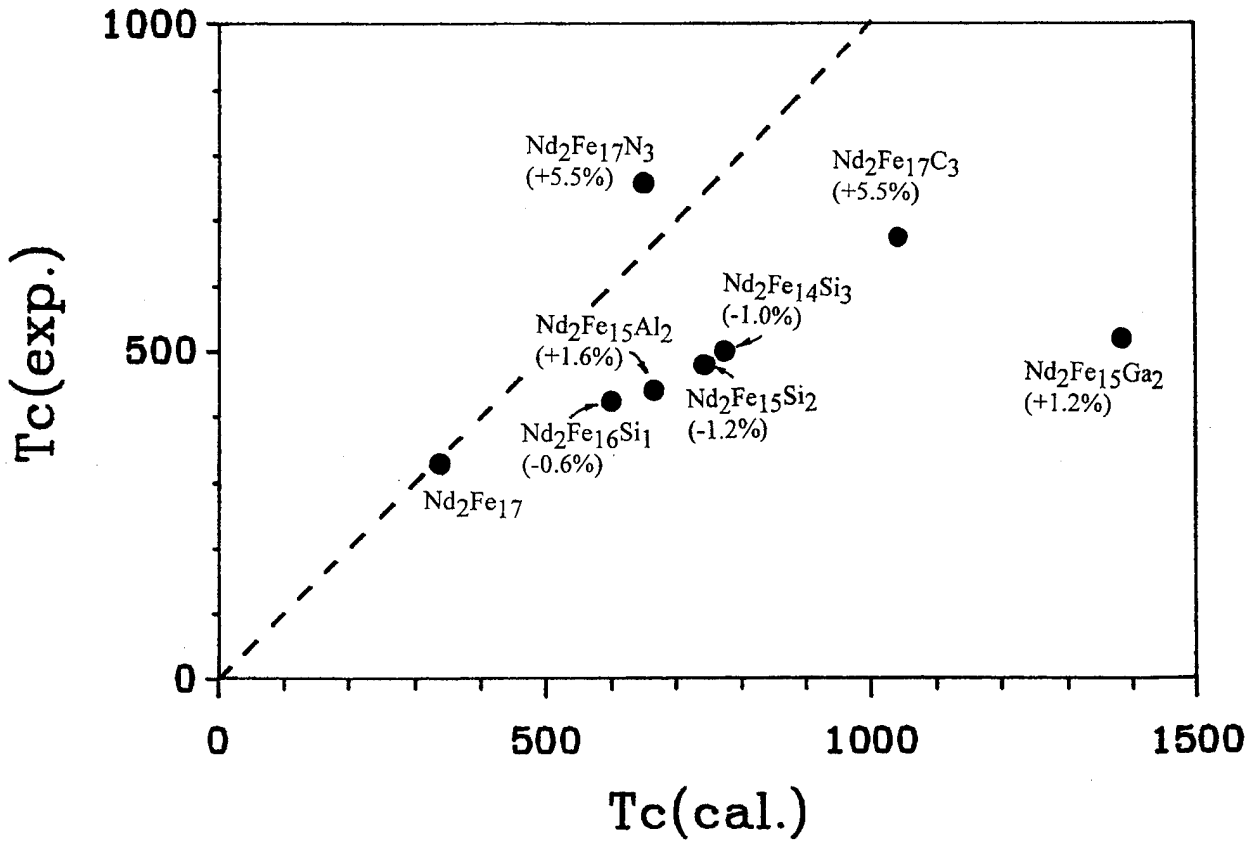


FIG. 1. Calculated and measured T_c for some Nd_2Fe_{17} based compounds. There are uncertainties in the experimental T_c values. See the text for explanation. % numbers in the parentheses indicate the change in the crystal volume.

may occur. In spite of all these uncertainties, we believe a systematic calculation on as many systems as possible and a careful interpretation of the calculated results can provide some understanding on the nature of T_c enhancement in the Nd_2Fe_{17}-based hard magnets.

We chose eight systems where the experimentally measured T_c are either available or can be reasonably extrapolated. They are: (a) Nd_2Fe_{17}, (b) $Nd_2Fe_{16}Si_1$, (c) $Nd_2Fe_{15}Si_2$, (d) $Nd_2Fe_{15}Si_3$, (e) $Nd_2Fe_{15}Ga_2$, (f) $Nd_2Fe_{15}Al_2$, (g) $Nd_2Fe_{17}N_3$, and (h) $Nd_2Fe_{17}C_3$. We used the Nd_2Fe_{17} systems as the reference[22] and investigate the relative changes in T_c under various substitutions. Only the average Fe moments are used and the slight negative polarizations of the other atoms are ignored. The exchange splitting energy is defined as the separation between the center of gravities of the projected spin-up and spin-down Fe partial DOS.

Our calculated results for the eight crystals are summarized in Table I. It can be seen that the calculated T_c are generally higher than the experimental values. The largest deviation is in the case of $Nd_2Fe_{15}Ga_2$. This is more clearly shown in Fig. 1. The experimental data for $Nd_2Fe_{17}N_3$ and $Nd_2Fe_{17}C_3$ are actually taken from the measurements on $Nd_2Fe_{17}N_x$ ($x=2.3-2.7$),[2–4] and $Nd_2Fe_{17}C_2$,[5] so the more appropriate values for experimental T_c corresponding to the crystals in the calculation should be somewhat higher. Also shown in Fig. 1 are the percentage increase (decrease) in the crystal volume compared to the reference crystal Nd_2Fe_{17}. The volumes are calculated according to the structural measurements for each compound, and are the same ones that enter into the calculation. As can be seen, $Nd_2Fe_{16}Si_1$, $Nd_2Fe_{15}Si_2$, and $Nd_2Fe_{15}Si_3$ actually have slight reduction in volume of about 0.6%, 1.0%, and 1.2%, respectively. All three crystals show relative increase in T_c over Nd_2Fe_{17}. Thus the qualitative estimates for T_c obtained from the present calculation is in fair agreement with experiments and do not support the notion that magnetovolume effect alone can explain the T_c enhancement in the R_2Fe_{17}-based hard magnets. From Table I, it is also observed that the Stoner parameters for seven of the eight crystals are all very close, being in the range of 1.0–1.08. For $Nd_2Fe_{17}N_3$, it is a bit higher at 1.13 because of a smaller value of the average Fe moment. This is probably due to the stronger negative polarization of the N atoms which reduces the moments of the nearby Fe atoms.

One interesting observation of the results from Table I is that both T_c^s and T_{sf} are larger than T_c. This is not surprising since this was also the case with the transition metals and Y-based Fe compounds.[10] However, our calculations show that T_{sf} can be larger or smaller than T_c^s and there is really no obvious trend in correlation with the volume expansion or contraction. This is due to the fact that the DOS at the Fermi level are very much system dependent. For Nd_2Fe_{17}, $N(E_F)$ for the majority spin band is greater than the $N(E_F)$ for the minority spin band. The order is reversed in six of the seven doped or substituted systems with the largest shift found in $Nd_2Fe_{15}Si_3$ and $Nd_2Fe_{15}Ga_2$. This is mainly due to a large reduction in the majority spin bands DOS by a factor of more than two, while the change in the minority spin band is much smaller. This sensitive dependence of the $N(E_F)$ can be traced to the changes in the electronic structure due to crystal modifications at various Fe sites,[20,21] and obviously significantly affects χ_0, and hence the final T_c. Since the calculated T_c and T_{sf} do not exhibit the same relative change, the use of spin-fluctuation temperature T_{sf} as an estimation for T_c may not be totally justified.[23]

In conclusion, we have estimated the Curie temperatures of several Nd_2Fe_{17}-based hard magnets using the electronic structure results calculated according to the local spin-density approximation and the spin-fluctuation model of Mohn and Wohlfarth. Our results indicate that the MW model can provide a qualitative account for the T_c variation and the simple argument based on magnetovolume effect is inadequate. However, accurate determination of T_c from first principles for these complicated intermetallic compounds is quite difficult because T_c is related not only to the total Fe moments, the Stoner parameter and the density of states at the Fermi level, but also to the subtle interplay among these physical parameters. Additional theoretical work and more precise calculations are clearly needed to further advance the understanding of the magnetic properties of the rare-earth Fe-based permanent magnets.

This work was supported by the U.S. Department of Energy under Grant No. DE-FG02-84ER45170.

[1] R. B. Helmholdt and K. H. J. Buschow, J. Less Comm. Metals. **155**, 15 (1989).
[2] H. Sun, J. M. D. Coey, Y. Otani, and D. P. F. Hurley, J. Phys. Condens. Matter **2**, 6465 (1990); J. M. D. Coey and H. Sun, J. Magn. Magn. Mater. **87**, L251 (1990).
[3] K. H. J. Buschow, D. B. de Mooij, K. Waard, and T. H. Jacobs, J. Magn. Magn. Mater. **92**, L35 (1992).
[4] J. F. Liu and H. L. Luo, J. Magn. Magn. Mater. **94**, 43 (1991).
[5] Z. Altonian, X. Chen, L. X. Liao, D. H. Ryan, and J. D. Ström-Olsen, J. Appl. Phys. **73**, 6017 (1993).
[6] B.P. Hu and J. M. D. Coey, J. Less-Common Met. **142**, 295 (1988).
[7] T. H. Jacobs, K. H. J. Buschow, G. F. Zhou, X. Li, and F. R. de Boer, J. Magn. Magn. Mater. **116**, 220 (1992).
[8] G. J. Long *et al.*, J. Appl. Phys. **76**, 5383 (1994); W. B. Yelon, H. Xie, G. J. Long, O. A. Pringle, F. Grandjean, and K. H. J. Buschow, J. Appl. Phys. **73**, 6029 (1993).
[9] G. J. Long *et al.*, Solid State Commun. **88**, 761 (1993).
[10] Z. Hu and W. B. Yelon, J. Appl. Phys. **76**, 6162 (1994).
[11] Z. Hu, W. B. Yelon, S. Misha, G. J. Long, O. A. Pringle, D. P. Middleton, K. H. J. Buschow, and F. Grandjean, J. Appl. Phys. **76**, 443 (1994).
[12] F. Weitzer, K. Hiebl, and P. Rogl, J. Appl. Phys. **65**, 4963 (1989).
[13] See, for example, *Metallic Magnetism*, edited by H. Capellmann (Springer, New York, 1987).
[14] O. Gunnarsson, J. Phys. F: Met. Phys. **6**, 687 (1976).
[15] E. C. Stoner, Proc. R. Soc. A **154**, 656 (1936); *ibid.* **169**, 339 (1939).
[16] T. Moriya, *Spin-Fluctuations in Itinerant Electron Magnetism* (Springer, Berlin, 1985).
[17] P. Mohn and E. P. Wohlfarth, J. Phys. F: Met. Phys. **17**, 2421 (1987).
[18] Z.-Q. Gu, X.-F. Zhong, and W. Y. Ching, Phys. Rev. B **46**, 13874 (1992); Z.-Q. Gu, W. Lai, X.-F. Zhong, and W. Y. Ching, J. Appl. Phys. **73**, 6928 (1993).
[19] W. Y. Ching, M.-Z. Huang, and X.-F. Zhong, J. Appl. Phys. **76**, 6047 (1994).
[20] M.-Z. Huang and W. Y. Ching, J. Appl. Phys. **76**, 7046 (1994).
[21] M.-Z. Huang and W. Y. Ching, paper DS-20, 40th Annual MMM Conference, 1995 (submitted).
[22] We found that a factor of 1.12 to the first term in Eq. (1) is necessary in order to obtain a solution for T_c^s that will yield T_c in close agreement with experiment. The same factor is then applied to all the other Nd_2Fe_{17}-based crystals for consistency.
[23] S. S. Jaswal, W. B. Yelon, G. C. Hadjipanayis, Y. Z. Wang, and D. J. Sellmyer, Phys. Rev. Lett. **67**, 644 (1991).

Metastable RFe_7 compounds (R=rare earths) and their nitrides with $TbCu_7$ structure

O. Mao, J. Yang, Z. Altounian, and J. O. Ström-Olsen
Center for the Physics of Materials, Department of Physics, McGill University, Montréal, Québec H3A 2T8, Canada

RFe_7 compounds with the $TbCu_7$ structure have been synthesized by annealing of mechanically alloyed powders. The lattice constants a and c decrease with increasing atomic number of the rare earths except for Ce which has a different valence state. Introduction of nitrogen interstitial atoms into the structure results in a ~6.0% volume expansion. In addition, nitriding gives rise to a dramatic enhancement of the magnetic properties of the compounds. Curie temperatures are increased by ~300 °C upon nitriding. RFe_7 nitrides with R=Sm, Tb, Dy, and Ho have high coercivities. A substantial enhancement in the magnetic remanence for the RFe_7 nitrides with R=Tb, Dy, and Ho is attributed to the magnetic exchange coupling between grains of nanocrystalline structure in the powders. © *1996 American Institute of Physics.* [S0021-8979(96)37108-4]

I. INTRODUCTION

In the preparation of Sm_2Fe_{17}-type compounds, a metastable Sm–Fe phase with $TbCu_7$ structure commonly appears in samples prepared by nonequilibrium processes, such as rapid solidification,[1] mechanical alloying (MA),[2] and film growth. Similar to other R–T compounds (T=transition metals), the $TbCu_7$ structure can be derived from RT_5 ($CaCu_5$ structure), by replacing an appropriate amount of R atoms with pairs of T dumbbells. In the $TbCu_7$ structure this substitution takes place randomly. Therefore, the $TbCu_7$ structure can also be considered as a derivative of the 2:17 structure without long range ordering and this structure is sometimes described as a disordered 2:17 structure or even as 2:17 by some authors. To clarify the confusion between the RFe_7- and the R_2Fe_{17}-type structures, we report the synthesis of the RFe_7-type compounds and their nitrides by MA with subsequent annealing, and a systematic study of the structural and magnetic properties of these compounds.

II. EXPERIMENTAL TECHNIQUES

The RFe_7 alloy ingots were prepared by melting the appropriate amounts of Fe (purity better than 99.99 wt. %) and rare earth (99.9 wt. %) in a cold crucible induction furnace. The as-made ingot was crushed to small pieces of size less than 1 mm and, together with two hardened steel balls of diameter 12.7 mm, loaded to a hardened steel vial and sealed. Mechanical alloying (MA) was carried out in a high energy SPEX-8000 Mixer/Mill for 20 h. Ball-to-material ratio was 10:1. The crushing, weighing, loading, sealing, as well as subsequent handling procedures were performed in a specially designed glove box with oxygen and humidity levels of less than 1 ppm. For annealing treatments, the samples were sealed in a quartz tube under Ar. Annealing time was kept at 30 min. Nitriding was carried out by holding the powders at 450 °C for 10 h under 1 atm of nitrogen pressure. X-ray diffraction (XRD) was performed in an automated Nicolet–Stöe powder diffractometer with graphite monochromated Cu $K\alpha$ radiation. Curie temperatures, T_c's, were measured by thermomagnetometry using a Perkin–Elmer thermogravimetric analyzer (TGA-7) in a small magnetic field gradient (TGAM). Vibrating sample magnetometry (VSM) with 1.6 T maximum field were used to measure the hysteresis loops and the saturation magnetizations at room temperature.

III. RESULTS AND DISCUSSION

A. Formation and the structure of the RFe_7 compounds

After MA, the as-milled powder contained a mixture of metastable phases including a large amount of nanocrystalline α-Fe of grain size ~10 nm estimated through the width of the related Bragg peaks. For RFe_7 with R=Ce and Pr a high pressure phase (fcc γ phase) of the rare earth is also present similar to melt-spun samples,[3] while for the other rare earths, an amorphous phase is formed in addition to α-Fe. Upon annealing of the as-milled powders, RFe_7-type compounds were formed. XRD patterns of the compounds show no superlattice diffraction peaks related to R_2Fe_{17}-type compounds, which should be at 2θ~37.5° (40.8°) for R_2Fe_{17} with rhombohedral (hexagonal) Th_2Zn_{17} structure. The XRD patterns are indexed with the $TbCu_7$ structure of the hexagonal unit cell as shown in Fig. 1(A) for R=Sm. The lattice constants a and c of the compounds were obtained by fitting the XRD patterns. The 1:7 structure is derived by randomly substituting an appropriate amount of the R atoms by pairs of Fe dumbbells. As the dumbbell is introduced along the c axis, the substitution of the Fe dumbbell for R should result in an expansion in the c direction increasing the c/a ratio with increasing Fe concentration. The ratio increases from 0.84 to 0.85 for Gd and Ho when the composition changes from RFe_7 to $RFe_{8.5}$. This result also suggests that the compounds have a range of solubility. The lattice constants and v for the various rare earths are described in Fig. 2 (filled circles). All of the RFe_7-type compounds can absorb a large amount of nitrogen atoms resulting in a remarkable lattice expansion, $\Delta v/v$, of the structure. The corresponding XRD pattern shifts to low angle as illustrated in Fig. 1(A). a, c, and v for various RFe_7 nitrides are shown in Fig. 2 (open circles). As can be seen in Fig. 2, a, c, and v of the hexago-

 0021-8979/96/79(8)/4605/3/$10.00 © 1996 American Institute of Physics

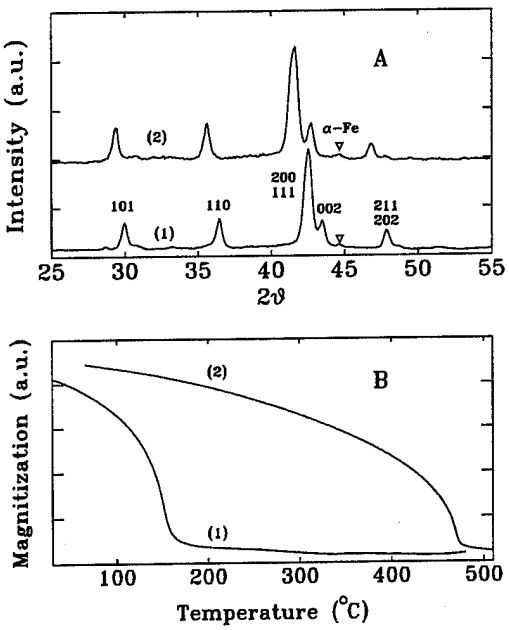


FIG. 1. X-ray diffraction and thermomagnetic scans of $SmFe_7$ powder annealed at 700 °C for 30 min (1) and its nitride (2).

nal unit cell decrease with increasing atomic number of the rare earths except for Ce which has a different valence state.

B. Magnetic properties

The Curie temperatures, T_c's, for various RFe_7-type compounds and their nitrides were obtained from TGAM scans, an example of which is shown in Fig. 1(B) for R=Sm. The data for all R are shown in Fig. 3. As can be seen from Fig. 3, T_c for the nitride is, on average, ~300 °C higher than its corresponding parent RFe_7 compound and the differences in T_c's among the various nitrides are less remarkable than that among the corresponding RFe_7 parent compounds.

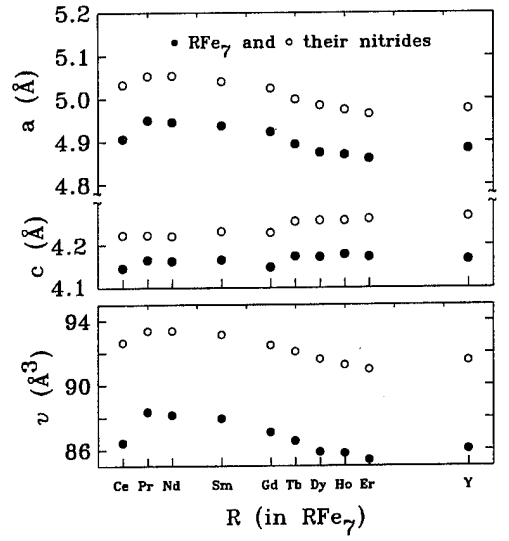


FIG. 2. a, c, and v of RFe_7-type compounds and their nitrides for various R's.

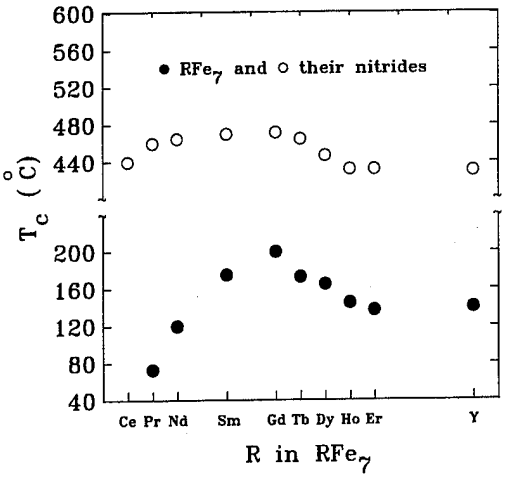


FIG. 3. Curie temperatures of RFe_7-type compounds and their nitrides for various R's.

Room temperature saturation magnetizations (M_s's) and coercivities (H_c's) for the RFe_7 compounds and their nitrides are listed in Table I. M_s's for the early rare earths are generally much higher than that for the late rare earths suggesting that the magnetic exchange coupling between the iron sublattice and the R sublattice is ferromagnetic for the early rare earths and antiferromagnetic for the late rare earths, similar to what has been reported for the related structures of R_2Fe_{17}- and $R(Fe,M)_{12}$-type compounds (M=structure-stabilizing element).[4] The coercivity for the $SmFe_7$ nitride in Table I was obtained by a pulsed-field magnet with 20 T maximum field and is in good agreement with published values.[5] Besides the $SmFe_7$ nitride, the nitrides of $TbFe_7$, $DyFe_7$, and $HoFe_7$ have high coercivities, as can be seen from Table I. A typical hysteresis loop for the above three types of nitrides is shown in Fig. 4. This is the first time that the high coercivities are observed in RFe_7 compounds other

TABLE I. Saturation magnetizations σ_s in emu/g, and coercivities H_c in Oe, of various RFe_7-type compounds and their nitrides. The atomic moments per formula unit, M_s in μ_B, is derived from σ_s.

Compounds	σ_s	M_s	H_c
$CeFe_7N_x$	128	12.6	180
$PrFe_7$	104	9.9	70
$PrFe_7N_x$	133	13.3	420
$NdFe_7$	111	10.6	120
$NdFe_7N_x$	144	14.3	520
$SmFe_7$	100	9.8	470
$SmFe_7N_x$	~120	~12	~33 000
$GdFe_7$	60	5.9	380
$GdFe_7N_x$	96	9.8	380
$TbFe_7$	60	5.9	510
$TbFe_7N_x$	83	8.5	3 500
$DyFe_7$	83	8.2	305
$DyFe_7N_x$	86	8.8	3 700
$HoFe_7$	58	5.8	390
$HoFe_7N_x$	75	7.7	2 100
$ErFe_7$	68	6.8	300
YFe_7	100	8.6	200
YFe_7N_x	148	13.3	280

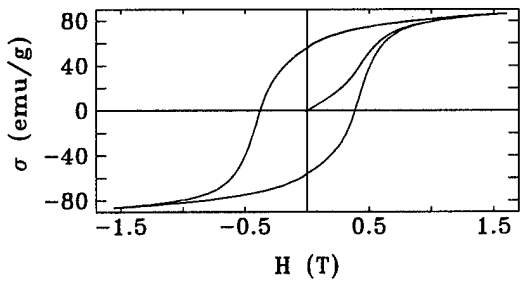


FIG. 4. A typical hysteresis loop of $DyFe_7$ nitride.

than for R=Sm. The hard magnetic behavior of the RFe_7 nitrides are distinct from their R_2Fe_{17} and $R(Fe,M)_{12}$ counterparts: for R_2Fe_{17} nitrides they are magnetically soft for R=Tb, Dy, and Ho but hard for R=Sm, while for $R(Fe,M)_{12}$ nitrides hard magnets are obtained for R=Tb, Dy, and Ho but soft for R=Sm. Although the origin of the hard magnetic behavior needs further investigation, our results suggest a new family of R–Fe metastable compounds which are different in both the structure and magnetic properties. Moreover, one can see from Fig. 4 that although the powder is isotropic, the remanence σ_r is substantially higher than $\sigma_s/2$ (σ_s, saturation magnetization). The remarkable enhancement in the remanence ($\sigma_r/\sigma_s=0.64$ for the $DyFe_7$ nitride) is most likely caused through the magnetic coupling between neighboring grains with a nanocrystalline structure produced by the MA technique.

IV. CONCLUSIONS

RFe_7 compounds of the $TbCu_7$ structure type through most of the rare earth series have been synthesized by annealing of MA powders. The lattice constants and the volume of unit cell for both RFe_7 compounds and their nitrides decrease with increasing atomic number of the rare earths except for Ce which has a different valence state. This 1:7 structure has a range of solubility with the c/a ratio increasing with Fe content. Nitriding results in a dramatic enhancement of the magnetic properties of the compounds. T_c's are increased by ~300 °C upon nitriding. RFe_7 nitrides with R=Sm, Tb, Dy, and Ho have high coercivities. The substantial enhancement in the remanence for RFe_7 nitrides with R=Tb, Dy, and Ho is attributed to the possible magnetic exchange coupling between nanocrystalline grains in the MA powders.

ACKNOWLEDGMENTS

This work was supported by grants from the Natural Sciences and Engineering Research Council of Canada (NSERC) and le Fonds pour la Formation de Chercheurs et l'Aide à la Recherche de la Province du Québec.

[1] M. Katter, J. Wecher, and L. Schultz, J. Appl. Phys. Mater. **70**, 3188 (1991).
[2] L. Wei, W. Qun, X. K. Sun, Z. Xin-Guo, Z. Tong, Z. Zhi-dong, and Y. C. Chuang, J. Magn. Magn. Mater. **131**, 413 (1994).
[3] L. X. Liao, Z. Altounian, and D. H. Ryan, J. Appl. Phys. **67**, 4821 (1990)
[4] For a review see: K. H. J. Buschow, Rep. Progr. Phys. **54**, 1123 (1991).
[5] J. Ding, P. G. McCormick, and R. Street, J. Alloys Compounds **189**, 83 (1992).

High field magnetization isotherms of the $Pr_2Fe_{17}D_5$ system

O. Isnard
Laboratoire de Cristallographie, associé à l'Université J. Fourier, CNRS, 38042 Grenoble, France

M. Guillot
Laboratoire des Champs Magnétiques Intenses, CNRS/MPI 38042 Grenoble, France

S. Miraglia and D. Fruchart
Laboratoire de Cristallographie, associé à l'Université J. Fourier, CNRS, 38042 Grenoble, France

We have investigated the magnetic properties of the ferromagnetic compounds Pr_2Fe_{17} and $Pr_2Fe_{17}D_x$. First, the sample preparation is described and the location of interstitial deuterium atoms is reviewed according to previous neutron diffraction analysis. In this article, we report high field magnetization measurements performed up to 200 kOe in continuous fields, and isothermal magnetization curves measured between 2 and 300 K on oriented powder samples. Below 250 K, an anomaly in the magnetization curves of $Pr_2Fe_{17}D_5$ has been detected. We discuss the influence of hydrogen on this field-induced anomaly, which is strongly temperature dependent and possible origins such as crystal field effects or first order magnetization process. A comparison is made with $Pr_2Fe_{17}N_x$ in which no anomaly was observed. © *1996 American Institute of Physics.* [S0021-8979(96)80108-4]

INTRODUCTION

R_2Fe_{17} compounds (R=rare earth metal) are known to crystallize with the rhombohedral Th_2Zn_{17} structure type or hexagonal Th_2Ni_{17} structure type depending on the rare earth size. Most of these compounds are ferromagnetic with rather moderate Curie temperatures (slightly above room temperature). Insertion of light elements such as H, C, or N in the R_2Fe_{17} series has been found to modify the magnetic properties of these compounds, which thus become prospective candidates for metal-bonded permanent magnets. The most spectacular changes are increases of the Curie temperature, T_C, and of the magnetization, M_s, upon interstitial insertion.[1–3] Hydrogenated compounds are suitable materials for fundamental studies because a solid solution behavior of hydrogen insertion is observed.[4,5] This allows modulation of stoichiometry upon reaction and a consequent controlled variation of the magnetic properties.

In the $R_2Fe_{17}D_x$ series, we focus here on the Pr compound investigated by high field magnetic measurements performed up to 200 kOe in a continuous field.

EXPERIMENT

Samples of Pr_2Fe_{17} were prepared by induction melting in cold crucible under argon atmosphere and then annealed at 950 °C for 10 days. Standard x-ray diffractometry revealed that the samples are single phase. The diffractograms of the rhombohedral compounds were indexed using the hexagonal multiple cell. Deuteridation was then performed in a dedicated stainless steel autoclave under a deuterium pressure of about 5 MPa leading to a stable hydride. A short thermal activation was needed to initiate the reaction. The deuterium uptake was determined by gravimetric methods, and the accuracy of the interstitial concentration can be estimated to about 2%. The Curie temperature was determined using a homemade Faraday-type torque balance, the powder was sealed in a small silica tube in order to avoid outgassing or oxidation while heating. Magnetic measurements from 4.2 to 300 K were performed using an automatic device equipped with a cryostat and a calorimeter described in detail elsewhere.[6] The extraction technique was used to measure the magnetization in continuous magnetic fields up to 200 kOe produced by a water-cooled Bitter magnet. No single crystals are available due to the decrepitation process which is known to occur when deuterium is inserted in R_2Fe_{17} compounds. All the samples were sieved down to a mean particle size of 25 μm, the larger grains being of 40 μm. Then the powder was mixed with epoxy resin and subsequently aligned at room temperature using an orientation field of typically 10 kOe.

RESULTS AND DISCUSSION

Details about the structure can be found in Ref. 7; insertion of deuterium induces a drastic increase of the Curie temperature from T_C=293 to 531 K for Pr_2Fe_{17} and $Pr_2Fe_{17}D_5$, respectively. The 4.2 K magnetization isotherms of the starting alloy Pr_2Fe_{17} and of its corresponding deuteride $Pr_2Fe_{17}D_5$ are shown in Figs. 1 and 2 in the directions parallel and perpendicular to the alignment direction. The anisotropy field is the field that is required to align the moments in the easy magnetization direction from a direction perpendicular to it. It can be seen that at 4.2 K this field is lowered from 140 kOe (Fig. 1) to 110 kOe (Fig. 2) upon deuteridation. Since Pr_2Fe_{17} and $Pr_2Fe_{17}D_5$ both exhibit planar anisotropy, the decrease of the anisotropy field reflects a decrease of the planar character of magnetic anisotropy. We also note that the magnetization process along the parallel direction is slightly different in the alloy and the deuterated material. At 4.2 K the deuterated compound saturates for a smaller field and its saturation magnetization is larger by 1.5 μ_B per formula unit. Another noticeable feature is the moment carried by the Pr atoms. A rough estimation of its magnitude can be made from the values of the extrapolated saturation magnetization and assuming a value of 2 μ_B for the iron moments (within the standard deviation of Ref. 7)

 0021-8979/96/79(8)/4608/3/$10.00 © 1996 American Institute of Physics

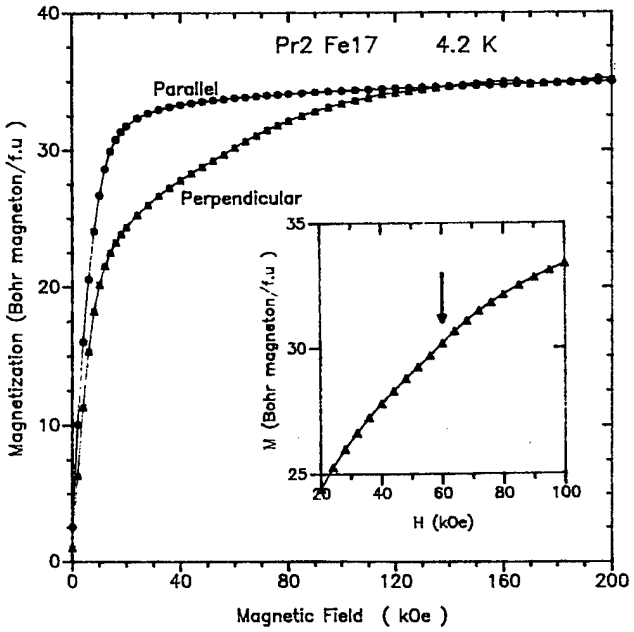


FIG. 1. Magnetization isotherms of oriented Pr_2Fe_{17} at 4.2 K. The inset is a zoom of the magnetization in the direction perpendicular to the applied field, the arrow points to the anomaly.

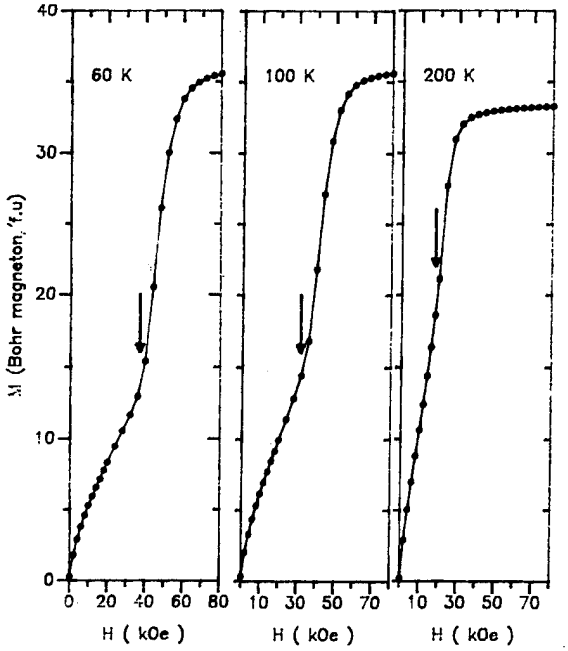


FIG. 3. Details of the magnetization isotherms of $Pr_2Fe_{17}D_5$ in the direction perpendicular to the applied field. The anomaly is defined at the inflection point and is indicated by arrows.

equivalent to 34 μ_B for the iron sublattice. Since the saturation magnetization observed is 35.2 and 36.7 μ_B for the alloy and the deuterated compound, respectively, one can deduce a value of 0.6 μ_B/Pr atom in the alloy, which is well below the free-atom value. The discrepancy with the values published in Ref. 7 may originate from the fact that this estimation assumes a collinear structure, and that the polarization effects are not taken into account. Furthermore, neutron powder diffraction is known to give mainly access to localized magnetic moment ($4f$ contribution in the case of Pr) rather than valence electron magnetism. Unlike neutron powder diffraction, magnetic measurements are leading to an overall magnetization including the valence electrons polarization (i.e., $5d$ electrons of rare earth) that is known to be opposite to that of the $3d$ of iron[8] and also opposite to that of the $4f$ states in the light rare earth. An underestimation of the $4f$ magnetism is thus expected when using the saturation magnetization without taking into account the valence electron contribution. This contributes to the observed discrepancy in the Pr magnetic moment determined from magnetic measurements and that deduced from neutron diffraction.

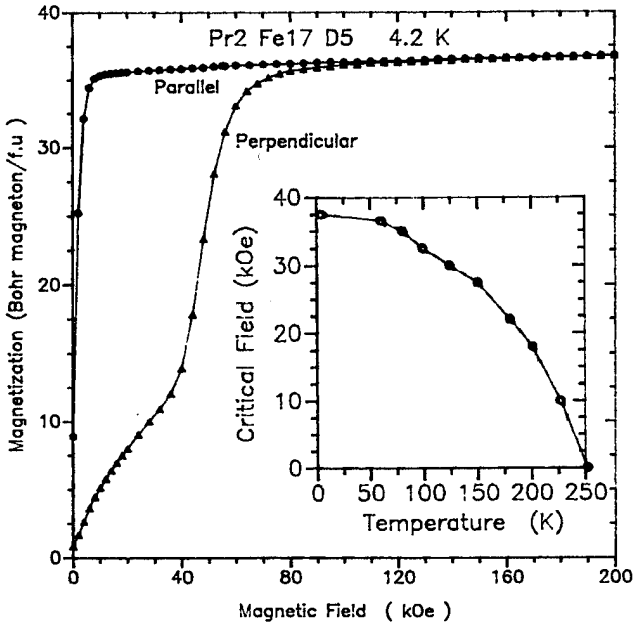


FIG. 2. Magnetization isotherms of oriented $Pr_2Fe_{17}D_5$ at 4.2 K. The variation of the critical field as a function of temperature is displayed in the inset.

The most remarkable feature is the anomaly which occurs in the magnetization curves in the direction perpendicular to the alignment. This anomaly is merely distinguishable in the magnetization curve of the alloy (see inset of Fig. 1) but it is clearly seen in the curves of the deuteride (Figs. 2 and 3).

This anomaly is field induced and disappears near 250 K. The critical field has been defined at the inflection point (arrows on Fig. 3) and its variation as a function of temperature is shown in the inset of Fig. 2.

We now discuss the origin of this anomaly. In this compound, the magnetic anisotropy arises from both the rare earth sublattice and the iron sublattice. A previous study on the $Gd_2Fe_{17}H_x$ system[9] has shown that hydrogen insertion dramatically decreases the crystal electric field gradient at the rare earth site. We have shown in particular that hydrogen acts on terms such as the second-order parameter A_2^0 and even higher order terms. One can thus expect a significant reduction of the first-order contribution to the rare earth anisotropy. This is consistent with the experimental observation of a decrease of the total anisotropy due to the decrease of the Pr contribution ($\alpha_J<0$). Since Pr and Nd have both negative α_J (first-order Stevens coefficients), high order

terms in the anisotropy energy have to be taken into account to explain the difference of easy magnetization within the basal plane. By Mössbauer spectroscopy, Gubbens[10] has shown that Pr_2Fe_{17} exhibits a particular anisotropy within the basal plane. Unlike Nd_2Fe_{17}, for which magnetization lies along the [100] direction, Pr_2Fe_{17} is found to have its easy magnetization axis along the [1−10] crystallographic direction (referred to as *b* axis by Gubbens). In particular, Pr has a positive γ_J (higher order Stevens coefficient) whereas that of Nd is negative. All this shows the important role played by the higher order anisotropy terms. Going from Pr_2Fe_{17} to the corresponding deuteride a relative increasing contribution of the higher order anisotropy terms is expected since the first-order term vanishes upon insertion of deuterium. This could be at the origin of the strong discontinuous change observed on $Pr_2Fe_{17}D_5$ magnetization curves.

For the deuteride, the huge steplike behavior of the magnetization along the hard axis observed in Figs. 2 and 3 could be interpreted at a microscopic scale as a first-order magnetization process (FOMP). A FOMP manifests itself as a discontinuous change of the magnetization direction in presence of the field applied parallel to a specific crystallographic direction, it is characterized by its critical temperature T_{FOMP} below which the FOMP occurs and by its critical field B_{cr}. The physical origin of the FOMP is that two relative minima appear in the macroscopic free energy (as a function of the angle between a crystalline direction and the magnetization direction) giving way to a jump between very close equilibrium configurations. One or the other minimum may be favored depending on the temperature and the strength of the applied magnetic field. In the Pr_2Fe_{17} deuteride, after the step observed on the field dependence of the magnetization, the saturation magnetization is almost reached; this is specific of a so-called type I FOMP as proposed by Asti and Bolzoni.[11] The observed critical field at 4.2 K is about 50 kOe. We have already mentioned that there is a slight indication of the same anomaly on the alloy (see Fig. 1). The fact that it is much less visible can be attributed to changes of anisotropy related to changes in the crystal field. It may also be due to the temperature at which the sample was oriented, temperature which in the case of the alloy lies very close to the Curie temperature and hence makes the orientation less effective. Let us note that no anomaly of that kind has been observed on the nitride $Pr_2Fe_{17}N_3$;[6] this may be due to the fact that nitrogen, contrarily to deuterium, induces an increase of the crystal electric field gradient acting on the rare earth site, and thus of the rare earth contribution to anisotropy. Finally, we mention that original features of the magnetization of Pr_2Fe_{17} deuterides have also been observed in the course of a Mössbauer study as discussed elsewhere in these proceedings.[12]

CONCLUSION

We have shown that a field-induced and temperature-dependent anomaly exists in the magnetization process of the $Pr_2Fe_{17}D_x$ system. It is suggested that it can be interpreted as a first order magnetization process. An interesting comparison can be made with the corresponding nitrogenated system and it suggests that the occurrence of the phenomenon is related to the nature of the interstitial itself.

[1] O. Isnard, S. Miraglia, and J. Deportes, J. Magn. Magn. Mater. **103**, 157 (1991).
[2] X. P. Zhong, R. J. Radwanski, F. R. de Boer, R. Verhoef, T. H. Jacobs, and K. H. J. Buschow, J. Magn. Magn. Mater. **83**, 143 (1990).
[3] J. M. D. Coey and H. Sun, J. Magn. Magn. Mater. **87**, L251 (1990).
[4] O. Isnard, J. L. Soubeyroux, S. Miraglia, D. Fruchart, L. M. Garcia, and J. Bartolomé, Physica B **180**, 629 (1992).
[5] O. Isnard, S. Miraglia, D. Fruchart, C. Giorgetti, S. Pizzini, E. Dartyge, G. Krill, and J. P. Kappler, Phys. Rev. B **49**, 15 692 (1994).
[6] O. Isnard, S. Miraglia, M. Guillot, and D. Fruchart, J. Appl. Phys. **75**, 5988 (1994).
[7] O. Isnard, S. Miraglia, J. L. Soubeyroux, and D. Fruchart, Solid State Commun. **81**, 13 (1992).
[8] I. A. Campbell, J. Phys. F.: Metal Phys. **2**, 647 (1972).
[9] O. Isnard, P. Vulliet, A. Sanchez, S. Miraglia, and D. Fruchart, J. Magn. Magn. Mater. **131**, 83 (1994).
[10] P. C. M. Gubbens, Ph.D. thesis, University of Delft, The Netherlands, 1977.
[11] G. Asti and F. Bolzoni, J. Magn. Magn. Mater. **20**, 29 (1981).
[12] F. Grandjean, D. Hautot, G. J. Long, O. Isnard, S. Miraglia, and D. Fruchart, these proceedings.

Structural and magnetic properties of rapidly quenched $(R,Zr)(Fe,Co)_{10}N_x$ (R=Nd,Sm)

S. Sakurada, A. Tsutai, T. Hirai, Y. Yanagida, and M. Sahashi
Materials and Devices Research Labs., Toshiba R&D Center, Kawasaki, Japan

S. Abe and T. Kaneko
Institute for Materials Research, Tohoku University, Sendai, Japan

The structural and magnetic properties of $(R,Zr)(Fe,Co)_{10}$(R=Nd,Sm) prepared by the rapid-quenching method have been investigated. The presence of zirconium makes it possible to realize a $TbCu_7$-type crystal structure with a high c/a ratio of more than 0.87, while the same crystal structure has a c/a ratio of just 0.84–0.85 in the zirconium-free case. The saturation magnetization of crystals having such a high c/a ratio as 0.87 exceeds 1.7 T at room temperature. These materials can be nitrogenated, and remarkable enhancement of magnetocrystalline anisotropy by nitrogenation can be seen in the case of Sm. The magnetic hardening of these nitrogenated materials can be achieved by annealing before nitrogenation. The highest value of $(BH)_{max}$ obtained so far for the nitrogenated materials is 144 kJ/m^3 (18.0 MGOe). The $_iH_c$ and B_r values for this sample are 503 kA/m (6.3 kOe) and 1.08 T, respectively. © *1996 American Institute of Physics.* [S0021-8979(96)37208-0]

I. INTRODUCTION

Search for new permanent magnet materials has been concentrated on iron-rich rare-earth intermetallic compounds since the discovery of Nd–Fe–B magnets.[1,2] In binary rare-earth-iron systems, the R_2Fe_{17} alloys have been known as iron-rich compounds and have attracted much attention since Coey and Sun reported on the improvement of their intrinsic magnetic properties by introducing interstitial nitrogen.[3]

Simultaneously, much effort has been devoted to search for new iron-rich rare-earth compounds in ternary systems. In the course of this search, $R(Fe,M)_{12}$ with $ThMn_{12}$-type tetragonal structure (M=Al, Si, Ga, Ti, V, Cr, Mn, Mo, W, and Re)[4–9] and in recent years, $R_3(Fe,M)_{29}$ (M=Ti, V, Cr, and Mn)[10] with monoclinic structure have been found. In these compounds there exists a greater number of iron sites than that of R_2Fe_{17}. However, the elements M, which play an important role in stabilizing these structures, occupy the iron sites and significantly reduce the magnetization which hypothetical compounds RFe_{12} and R_3Fe_{29} might possess.

On the other hand, we have studied the formation of the $ThMn_{12}$ structure in the $R(Fe,Si)_{12}$ system and found that most of the zirconium occupies the rare-earth site and facilitates the formation of this structure.[11] This result seems to suggest that the zirconium in the rare-earth site, like the above-mentioned M elements in the iron site, might also stabilize the iron-rich phases.

The objective of this research is to find new permanent magnet materials with high iron concentration and therefore with high saturation magnetization. In this respect, we have focused our attention on the iron-rich composition in the R–Zr–Fe ternary system and have investigated the structural and magnetic properties of $(R,Zr)Fe_{10}$ and $(R,Zr)(Fe,Co)_{10}$ alloys (R=Nd,Sm) prepared by the rapid-quenching method. We have also extended our research to their nitrogenated alloys.

II. EXPERIMENT

Ingots of the $(R,Zr)(Fe,Co)_{10}$ (R=Nd,Sm) were prepared by arc-melting in an argon gas atmosphere. Rapidly quenched ribbons were obtained from these ingots by conventional melt spinning with a copper roll in an argon gas atmosphere. The roll velocity was 40 m/s. Some of these ribbons were annealed in vacuum at 670–750 °C for 15 min. Part of the prepared ribbons was pulverized to a diameter smaller than 22 μm and nitrogenated in a 1 atm N_2 atmosphere at 420–460 °C for 8–140 h. The crystal structure of these ribbons and powders were determined by x-ray diffraction (XRD) analysis using Cu $K\alpha$ radiation. Magnetic measurements were performed using VSM at room temperature. In particular, the magnetization curves were measured with applied fields up to 12 MA/m (150 kOe) at the High Field Laboratory of Tohoku University.

III. RESULTS AND DISCUSSION

Figures 1(a) and (b) show (XRD) patterns for rapidly quenched $NdFe_{10}$ and $Nd_{0.5}Zr_{0.5}Fe_{10}$ alloy ribbons, respectively. These patterns indicate that both of them consist mainly of the $TbCu_7$-type crystal structure with a certain amount of α-Fe. Lattice parameters of the $TbCu_7$ structure are a=0.493 nm, c=0.416 nm, c/a=0.845 for $NdFe_{10}$ and a=0.484 nm, c=0.423 nm, c/a=0.873 for $Nd_{0.5}Zr_{0.5}Fe_{10}$. This result shows that zirconium substitution stabilizes the $TbCu_7$ structure with an extremely high c/a ratio.

It is known that the Th_2Zn_{17} and $ThMn_{12}$ structure can be transformed to the $TbCu_7$ structure. According to Katter *et al.*,[12] the c/a ratio of the $TbCu_7$ structure transformed from the Th_2Zn_{17} structure is 0.840 and that from the $ThMn_{12}$ structure is 0.894. The c/a ratio of the $TbCu_7$ structure appeared in rapidly quenched $NdFe_{10}$ and $Nd_{0.5}Zr_{0.5}Fe_{10}$ alloy ribbons takes intermediate values between that of the Th_2Zn_{17} and that of the $ThMn_{12}$ structure. Therefore, the iron concentration in the $TbCu_7$ structure appeared in these alloys

 0021-8979/96/79(8)/4611/3/$10.00 © 1996 American Institute of Physics

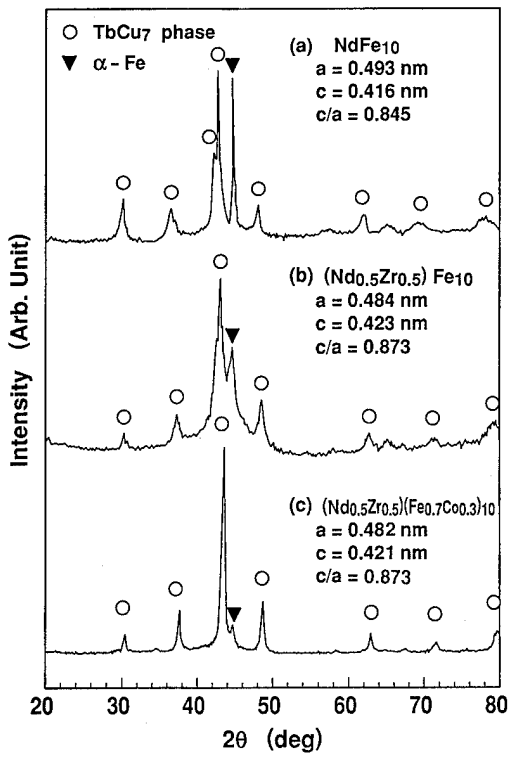


FIG. 1. X-ray diffraction patterns for rapidly quenched alloy ribbons: (a) $NdFe_{10}$; (b) $(Nd_{0.5}Zr_{0.5})Fe_{10}$; and (c) $(Nd_{0.5}Zr_{0.5})(Fe_{0.7}Co_{0.3})_{10}$.

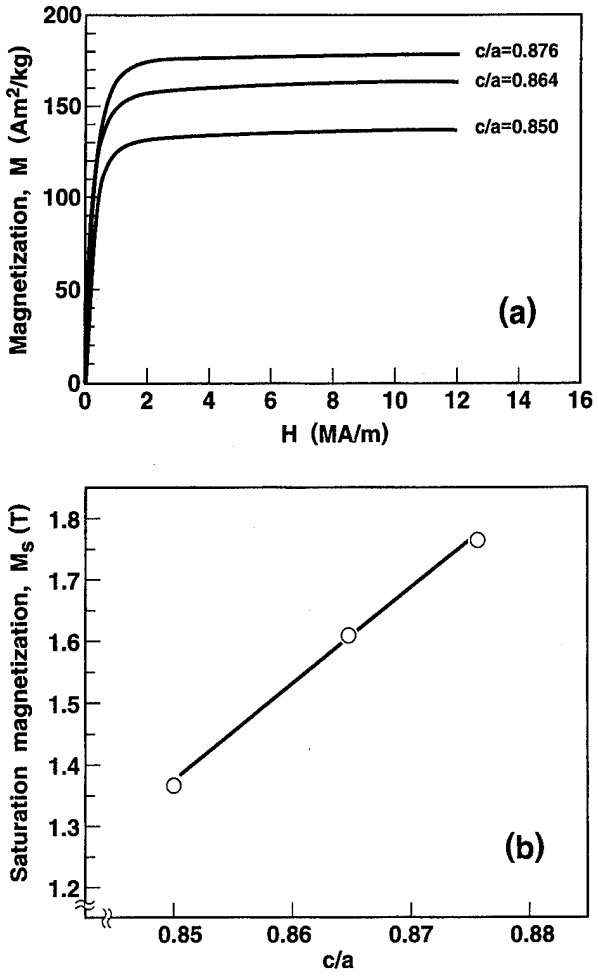


FIG. 2. (a) Magnetization curves for the rapidly quenched $(Nd_{0.5}Zr_{0.5})(Fe_{0.7}Co_{0.3})_z$ alloys having $TbCu_7$ structure with various c/a and (b) the saturation magnetization as a function of c/a.

should also take the intermediate values between them and the obtained high c/a crystal by zirconium substitution should have a greater number of the dumbbell arrangements of iron atoms. The $TbCu_7$ structure with high c/a of more than 0.87 was also obtained in the case of Sm and the amount of α-Fe could be decreased by a partial replacement of iron by cobalt in both cases of Nd and Sm.

Figure 1(c) shows the x-ray diffraction pattern for rapidly quenched $(Nd_{0.5}Zr_{0.5})(Fe_{0.7}Co_{0.3})_{10}$. As shown in this figure, the intensity of the α-Fe peak is relatively low. Considering this result and composition of this cobalt substituted alloy, we conclude that most of zirconium occupies the rare-earth site in the $TbCu_7$ structure. These materials can be nitrogeneted, resulting in a lattice expansion without a change in the crystal structure. Their c/a ratio is almost the same as that before nitrogenation.

Magnetization measurement was made for the rapidly quenched $(Nd_{0.5}Zr_{0.5})(Fe_{0.7}Co_{0.3})_z$ alloy ribbons having the $TbCu_7$ structure with various c/a values in order to make clear the relation between the saturation magnetization (M_s) and the c/a ratio. To change the c/a ratio, a series of compounds having different z values were prepared. Figure 2 shows the magnetization curves at room temperature for these alloys and M_s as a function of the c/a ratio. It can be seen from Fig. 2(b) that M_s increases linearly with increasing c/a and exceeds 1.7 T for high c/a crystals. As shown in Fig. 2(a), the magnetocrystalline anisotropy of these alloys seems to be relatively low. Therefore, we nitrogenated these alloys in order to enhance the magnetocrystalline anisotropy. Figure 3 shows the magnetization curves of rapidly quenched $(R_{0.75}Zr_{0.25})(Fe_{0.7}Co_{0.3})_{10}$ alloy ribbons (R=Nd,Sm) and their nitrogenated powders. Remarkable enhancement of the magnetocrystalline anisotropy by nitrogenation can be seen only in the case of Sm. The values of M_s and anisotropy field (H_A) were estimated by means of the M vs H^{-2} plots, using the high field part of the magnetization curves. The values obtained were M_s=1.76 T, H_A=3.2 MA/m (40 kOe) for $(Nd_{0.75}Zr_{0.25})(Fe_{0.7}Co_{0.3})_{10}N_x$ and M_s=1.70 T, H_A=6.2 MA/m (77 kOe) for $(Sm_{0.75}Zr_{0.25})(Fe_{0.7}Co_{0.3})_{10}N_x$. It is concluded that nitrogenated alloy in the case of Sm with the $TbCu_7$ structure having c/a as high as 0.87 seems to be promising for high performance permanent magnet materials because of their excellent intrinsic magnetic properties.

Next, attention was paid to the hard magnetic properties of the Sm-containing materials which consist mainly of $TbCu_7$-type compounds with a high c/a ratio. These rapidly quenched and subsequently nitrogenated materials typically have rather low coercivity of about 240 kA/m (3 kOe). Therefore, we investigated the annealing effect on rapidly quenched ribbons before nitrogenation in order to improve the hard magnetic properties.

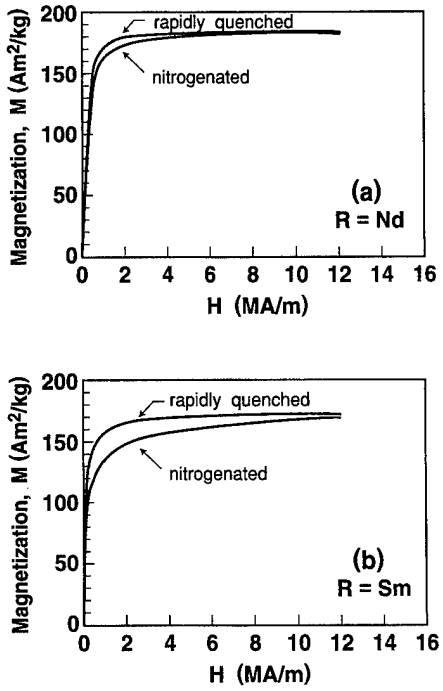


FIG. 3. Magnetization curves for the rapidly quenched $(R_{0.75}Zr_{0.25})(Fe_{0.7}Co_{0.3})_{10}$ alloy ribbons and their nitrogenated powders: (a) R=Nd and (b) R=Sm.

Figure 4 shows the energy product $(BH)_{max}$, the remanence B_r, and the coercivity ${}_iH_c$ for rapidly quenched, annealed, and then nitrogenated $(Sm_{0.75}Zr_{0.25})(Fe_{0.7}Co_{0.3})_{9.3}$ which has the $TbCu_7$ structure with the c/a of 0.867 as a function of the annealing temperature T_a. As seen in Fig. 4, the value of ${}_iH_c$ monotonously increases with increasing T_a in the range 670–750 °C. On the other hand, the values of B_r and $(BH)_{max}$ first increase with increasing T_a and reach the maximum at T_a=700 °C. By further increasing T_a above 700 °C, both B_r and $(BH)_{max}$ decrease. From the result of the x-ray diffraction study, it was confirmed that the initial crystal structure was maintained after annealing although α-Fe appeared above 700 °C remarkably. Decreases in B_r and $(BH)_{max}$ above 700 °C may be caused by the appearance of α-Fe due to partial decomposition of the main phase during annealing. The maximum $(BH)_{max}$ of 144 KJ m^3. (18.0 MGOe) was obtained for a sample which was annealed at 700 °C and subsequently nitrogenated. The ${}_iH_c$ and B_r values for this sample are 503 kA/m (6.3 kOe) and 1.08 T, respectively.

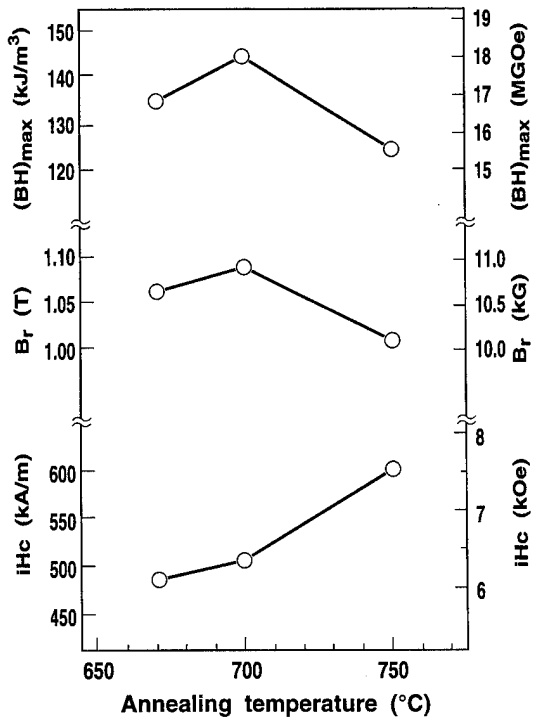


FIG. 4. Energy product $(BH)_{max}$, remanence B_r, and coercivity ${}_iH_c$ for rapidly quenched, annealed, and nitrogenated $(Sm_{0.75}Zr_{0.25})(Fe_{0.7}Co_{0.3})_{9.3}$ as a function of the annealing temperature.

It should be noted here that B_r for this sample is greater than $M_s/2$ although the sample is magnetically isotropic. This result presumably reflects that the grain of the $TbCu_7$ phase are magnetically coupled with each other or with some α-Fe grains and thus B_r is enhanced above $M_s/2$.

IV. CONCLUSIONS

(1) In preparing rapidly quenched rare-earth-iron alloys, zirconium substitution for the rare-earth ions stabilizes the $TbCu_7$ structure with extremely high c/a ratio.

(2) The saturation magnetization of $TbCu_7$-type compounds increases with increasing c/a ratio and exceeds 1.7 T in a crystal having such high c/a as 0.87.

(3) Remarkable enhancement of the magnetocrystalline anisotropy by nitrogenation can be seen in the case of Sm-containing samples. The intrinsic magnetic properties of $(Sm_{0.75}Zr_{0.25})(Fe_{0.7}Co_{0.3})_{10}N_x$ at room temperature are M_s=1.70 T and H_A=6.2 MA/m (77 kOe).

(4) In the case of Sm, the magnetic hardening of materials based on $TbCu_7$-type compounds with high c/a ratio can be achieved by rapid quenching and subsequent nitrogenation, involving an optional annealing before nitrogenation. The highest value of $(BH)_{max}$ obtained so far for such material is 144 kJ/m^3 (18.0 MGOe). The ${}_iH_c$ and B_r value for this sample are 503 kA/m (6.3 kOe) and 1.08 T, respectively.

[1] M. Sagawa, S. Fujimura, N. Togawa, H. Yamamoto, and Y. Matsuura, J. Appl. Phys. **55**, 2083 (1984).
[2] J. J. Croat, J. F. Herbst, R. W. Lee, and F. E. Pinkerton, J. Appl. Phys. **55**, 2078 (1984).
[3] J. M. D. Coey and H. Sun, J. Magn. Magn. Mater. **87**, L251 (1990).
[4] K. H. J. Buschow, J. Appl. Phys. **63**, 3130 (1988).
[5] Y. C. Yang, B. Kebe, W. J. James, J. Deportes, and W. Yelon, J. Appl. Phys. **52**, 2077 (1981).
[6] I. A. Griniv, O. I. Golovanets, R. V. Labunova, Yu. N. Grin, and Ya. P. Yarmolyuk, Dopov. Akad. Nauk Ukr. RSR Ser. A **1**, 74 (1983).
[7] M. Jurczyk, J. Less-Common Met. **166**, 335 (1990).
[8] X.-Z. Wang, B. Chevalier, T. Berlureau, J. Etourneau, J. M. D. Coey, and J. M. Cadgan, J. Less-Common Met. **138**, 235 (1988).
[9] K. Ohashi, T. Yokoyama, R. Osugi, and Y. Tawara, IEEE Trans. Magn. **MAG-23**, 3101 (1987).
[10] J. M. Cadgan, H.-S. Li, A. Margarian, J. B. Dunlop, D. H. Ryan, S. J. Collocott, and R. L. Davis, J. Appl. Phys. **76**, 6138 (1994).
[11] S. Sakurada, A. Tsutai, and M. Sahashi, J. Alloys Comp. **187**, 67 (1992).
[12] M. Katter, J. Wecker, and L. Schultz, J. Appl. Phys. **70**, 3188 (1991).

Aligned high magnetization $Nd(Fe,Co,Mo)_{12}$ films nitrided by N ion implantation

X. R. Qian, H. Hegde, and F. J. Cadieu
Department of Physics, Queens College of CUNY, Flushing, New York 11367

Ion implantation has been used to nitride highly aligned $ThMn_{12}$-type structure $Nd(Fe,Co,Mo)_{12}$ film samples. The initial 1–12-type films were made by sputtering with the crystallite c axes aligned perpendicular to the film plane. The films were then nitrided to produce fully nitrided 1–12 films, but only for a limited range of N ion doses. Much of the 1–12 phase was made amorphous before full nitriding was observed. It was not possible to thermally anneal the N implanted samples to lower the α-Fe concentration resulting from the N ion bombardment. This is only consistent with the $Nd(Fe,Co,Mo)_{12}N$ phase being metastable. Low temperature heat treatments of the N implanted films at temperatures less than 270 °C produced evidence for $Fe_{16}N_2$ formation, but little restoration of the 1–12 phase. For heat treatments at temperatures of 270 °C and above no evidence of $Fe_{16}N_2$ was detected. These results indicate that it is not possible to produce nitrided $ThMn_{12}$ films with $Fe_{16}N_2$ inclusions by ion implantation. © *1996 American Institute of Physics.* [S0021-8979(96)37308-7]

INTRODUCTION

We have reported the synthesis of $Nd(Fe,Co,Mo)_{12}N$ films made by sputtering with the magnetization aligned perpendicular to the film plane. Such films were made with room temperature energy products up to 46.3 MGOe and a low temperature value of 59.6 MGOe at 10 K.[1] Those films were thermally nitrided by heating the films in ≈500 Torr N_2 gas at temperatures of 550 °C for 1 to 2 h.[2] The highest energy product films were completely free of any α-Fe contamination. To further increase the available moment of rare earth transition metal compounds, recent studies have studied the use of α-Fe mixed on a nanoscale basis to obtain enhanced saturation and remanent flux density values.[3–5] Generally in such studies isotropic magnetic material has been studied. We have used an alternative procedure which starts with highly crystallographically aligned $Nd(Fe,Co,Mo)_{12}$ film samples. The possibility of nitriding such samples by N ion implantation was studied. It has been shown that $Fe_{16}N_2$ films can be made by a two-step process by the N ion implantation of Fe films with a subsequent low temperature heat treatment.[6] Since thermal nitriding $ThMn_{12}$ phases often results in some α-Fe increase, an alternative approach to making remanent enhanced magnetic materials could be to use N ion implantation for nitriding and have the α-Fe phase present or created converted to high magnetization $Fe_{16}N_2$. In this article we have synthesized $ThMn_{12}$-type structure $Nd(Fe,Co,Mo)_{12}$ films with the crystallite c axes aligned perpendicular to the film plane. Nitriding of these films has then been done by using N ion implantation. Low temperature anneals have then been used to see if α-Fe inclusions could be converted to high magnetization $Fe_{16}N_2$. The results indicate that it is inherently not possible to use N ion implantation to produce $Nd(Fe,Co,Mo)_{12}$ N films with $Fe_{16}N_2$ inclusions due to the metastable nature of the $ThMn_{12}$ nitrided phases.

EXPERIMENT

Sputtering has been used to synthesize $Nd(Fe,Co,Mo)_{12}$ $ThMn_{12}$-type structure films such that the crystallographic c axes are oriented perpendicular to the film plane. This growth method has been previously reported. In contrast to our previous reporting where the films have been thermally nitrided, N ion implantation has been investigated as a possible nitriding method. The N ion implantation has been done by Implant Sciences using 200 KeV N^+ ions. The samples were nitrided about 7° away from the film normal to minimize any channeling effects either along the crystallite c axes or along any columnar growth pattern of the films. The films investigated were 3000 to 5000 Å thick. X-ray diffraction data were obtained using Cu $K\alpha$ radiation.

RESULTS AND DISCUSSION

Figure 1 shows x-ray diffraction traces for a 3500-Å-thick (002) textured $Nd(Fe,Co,Mo)_{12}$ film that was subjected to 200 keV N ion flux doses of 0, 5.0 e16, 10 e16, 20 e16, and 40 e16 N/cm^2. The initial film exhibited only the (002) $Nd(Fe,Co,Mo)_{12}$ line and the two Al_2O_3, 35.15° (104), and 37.78 (110) from the polycrystalline substrate in this angular range. The low dose of 5 e16 N/cm^2 reduced the 1–12 phase

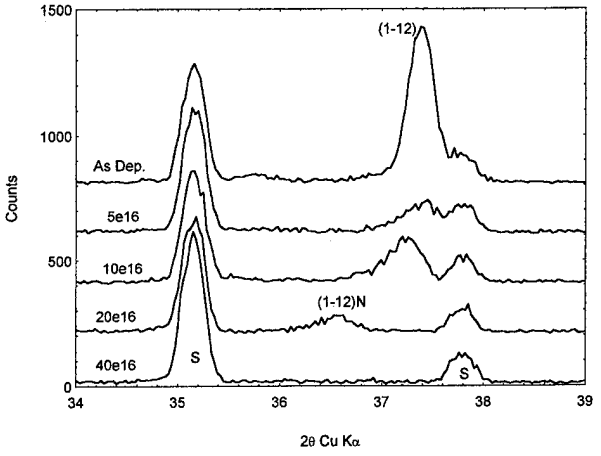


FIG. 1. The effects of successively higher N ion flux doses in N/cm^2 is shown for a 3500-Å-thick $Nd(Fe,Co,Mo)_{12}$ film. The y axis zero for the successive traces has been shifted by 200 counts to separate the traces. The substrate lines from the polycrystalline Al_2O_3 substrate are denoted by the letter S.

 0021-8979/96/79(8)/4614/2/$10.00 © 1996 American Institute of Physics

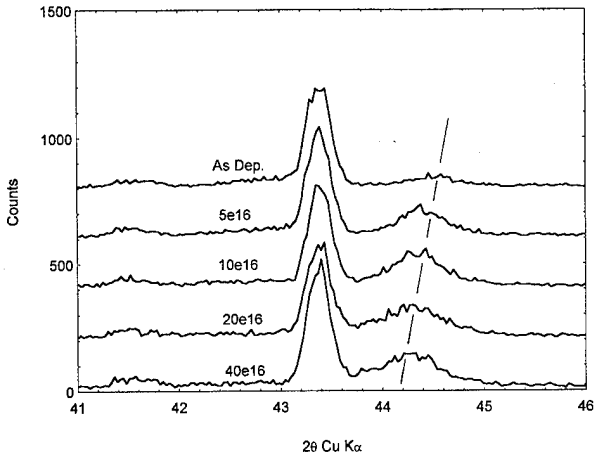


FIG. 2. For the same sample of Fig. 1 the x-ray trace in the region of the α-Fe (110) line is illustrated. The y axis for each successive trace has been shifted by 200 counts to separate the traces. The slanted line shows the lattice expansion of the α-Fe phase with the successively increased N doses. The prominent Al_2O_3 (113) line at 43.36° remains unshifted and acts as a reference line.

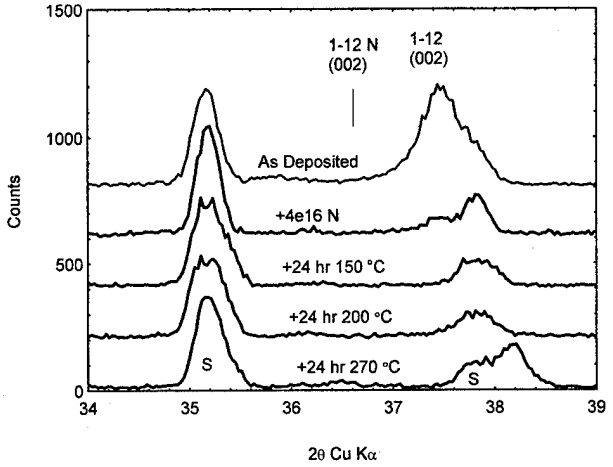


FIG. 3. The effects of a 4 e16 N/cm^2 N ion flux dose and then subsequent low temperature heat are shown for a 3000-Å-thick $Nd(Fe,Co,Mo)_{12}$ film. The y axis zero for the successive traces has been shifted by 200 counts to separate the traces. The substrate lines from the polycrystalline Al_2O_3 substrate are denoted by the letter S.

(002) intensity. For a N dose of 10 e16 N/cm^2 a clear shift of the 1–12 (002) line to lower angles, which corresponds to a lattice cell expansion is evident. For a dose of 20 e16 N/cm^2 the 1–12 (002) line has shifted to 36.6°. The 1–12 c axis has then shifted from 4.817 Å for the film as deposited to 4.906 Å for the nitrided films. This corresponds to a c lattice parameter shift of +1.8% which is typical for thermally nitrided 1–12 phase films. It should be noted that the volume expansion observed for 1–12 films is normally somewhat larger because of substrate film strain, than that observed in bulk samples. The further dose of 40 e16 N/cm^2 has acted to completely amorphisize the 1–12 phase.

Figure 2 shows the shifting of the α-Fe (110) line, as indicated by the slanted line, with successively increased N dosage. This shows that the α-Fe lattice expanded with increased N incorporation.

Figure 3 shows x-ray diffraction traces for a 3000-Å-thick $Nd(Fe,Co,Mo)_{12}$ film that exhibited a somewhat broader 1–12 (002) line, before and after N ion implantation at a dose of 4 e16 N/cm^2. Sections of the N implanted film were then heat treated at temperatures of 150, 200, and 270 °C for 24 h. No evidence for the nitrided 1–12 phase recovery was observed following low temperature heat treatments. The $Fe_{16}N_2$ phase has been shown to be unstable above about 250 °C.[6] For any thermal recovery of the amorphized 1–12 phase following ion bombardment to be consistent with $Fe_{16}N_2$ inclusions must occur below 250 °C. The $ThMn_{12}$ phase was not recovered by such low temperature anneals which would also be consistent with the formation of $Fe_{16}N_2$. Some intensity developed for the 200 °C heat treatment at 36.1° which would correspond to the (112) $Fe_{16}N_2$ phase. Annealing at 270 °C destroyed the 36.1° peak with a new peak forming at 38.2°. No peak developed at 28.35 which would correspond to the $Fe_{16}N_2$ (002) reflection. That peak would be strong in these textured films only if the $Fe_{16}N_2$ was textured with the c axes perpendicular to the film plane.

The results of Fig. 1 indicate that the 1–12 phase can be nitrided by N implantation. The nitriding is sensitive to the N implant dose with much of the 1–12 phase made amorphous before substantial nitriding was observed. In our experience and that of others it has never been possible to reduce the amount α-Fe present in nitrided $Nd(Fe,Co,Mo)_{12}$ samples by any thermal heat treatment. This is evidence that the nitrided $ThMn_{12}$ compounds are inherently metastable only. In contrast to this metastable behavior with nitrogen, hydrogen can be reversibly introduced and removed from the samples through thermal cycling without $ThMn_{12}$ phase deterioration. High coercive forces and the highest energy products have only been observed in samples which were completely free of α-Fe. Evidence of $Fe_{16}N_2$ formation was observed following implantation and then heat treatments at temperatures of less than 270°. No detectable $Fe_{16}N_2$ remained after the 270 °C heat treatment. In addition the fraction of the 1–12 phase could not be recovered at the low temperature anneals required to stabilize the $Fe_{16}N_2$ phase. Since it has not been possible to nitride the $Nd(Fe,Co,Mo)_{12}$ samples without appreciable phase disproportionation, it is inherently not possible to anneal the samples and recrystallize the samples into a composite richer in $ThMn_{12}$ phase than the disproportion level reached during the ion bombardment. Consequently it has not been possible to use N ion implantation to simultaneously obtain well defined nitrided $Nd(Fe,Co,Mo)_{12}$ phase samples and to simultaneously convert the α-Fe inclusions to high moment $Fe_{16}N_2$.

[1] A. Navarathna, H. Hegde, R. Rani, K. Chen, and F. J. Cadieu, IEEE Trans. Magn. **29**, 2812 (1993).
[2] A. Navarathna, H. Hegde, R. Rani, S. U. Jen, and F. J. Cadieu, IEEE Trans. Magn. **28**, 2838 (1993).
[3] T. Schrefl, R. Fischer, J. Fidler, and H. Kronmuller, IEEE Trans. Magn. **30**, 7053 (1994).
[4] L. Withanawasam, A. S. Murphy, G. C. Hadjipanayis, and R. F. Krause, IEEE Trans. Magn. **30**, 7065 (1994).
[5] K. O'Donnell, C. Kuhrt, and J. M. D. Coey, IEEE Trans. Magn. **30**, 7068 (1994).
[6] K. Kakajima and S. Okamoto, Appl. Phys. Lett. **56**, 92 (1990).

Magnetic and phase transformation studies in $Nd_{15}DyFe_{75}(C,B)_9$ cast alloys

A. S. Murthy,[a] I. Panagiotopoulos, and G. C. Hadjipanayis
Department of Physics and Astronomy, University of Delaware, Newark, Delaware 19716

Previous studies have shown that high coercivities can be achieved in cast Nd–Fe–C alloys through an annealing heat treatment at 900 °C, which causes a peritectoidal transformation from $Nd_2Fe_{17}C_x$ to $Nd_2Fe_{14}C_x$. We have studied the characteristics of this transformation in cast $Nd_{15}DyFe_{75}(C,B)_9$ alloys. Optimum coercivities were obtained by annealing for 6 h at 900 °C. A highly faulted carbide phase was identified in samples annealed for 5 min at 900 °C. From electron diffraction investigations, this phase was identified to be hexagonal with lattice parameters, $a=0.48$ nm and $c=0.81$ nm. The development of coercivity in the various stages of transformation is related to the crystal structure and microstructure developed in the transformation. The presence of α-Fe in samples with increased Fe content leads to reduced coercivities. © *1996 American Institute of Physics.* [S0021-8979(96)37408-3]

INTRODUCTION

Cast alloyed materials based on the $R_2Fe_{14}C$ phase have attracted considerable attention in recent years as candidates for permanent magnets.[1–8] In these materials, the $R_2Fe_{14}C$ phase responsible for high coercivities is obtained upon annealing of the $R_2Fe_{17}C$ phase through a complex peritectoidal transformation. In the Nd–Fe–C system, the $Nd_2Fe_{14}C$ phase is not stable above 900 °C, and transforms peritectically to the equilibrium $R_2Fe_{17}C$ phase at higher temperatures. The solid peritectoidal transformation involving $Nd_2Fe_{17}C$, the ternary χ phase[8] and Fe to $R_2Fe_{14}C$ is sluggish, and requires very long annealing times for the completion. Addition of boron in small amounts is reported to have the beneficial effects of enhancing the kinetics of the Nd_2Fe_{17} to $Nd_2Fe_{14}C$ transformation as well as strengthening the phase stability of the $Nd_2Fe_{14}C$ phase by increasing the peritectic transformation temperature.

The phase transformation characteristics and the magnetic properties observed at different stages of annealing are of considerable interest. In this study, we have undertaken such an effort by investigating the phases with transmission electron microscopy (TEM) and x-ray diffraction (XRD), and correlating them with the corresponding magnetic properties in $Nd_{15}DyFe_{75}(C,B)_9$ samples. The effects of composition and annealing times and temperatures were evaluated to obtain optimal coercivities in samples with increased iron content.

EXPERIMENT

Nd–Dy–Fe–C–B alloys with various compositions were prepared by arc-melting the constituent elements in an Ar atmosphere. The samples were annealed in evacuated quartz tubes at temperatures from 800 to 950 °C for time intervals ranging from 2 min to 3 days.

The hysteresis loops were measured in a vibrating sample magnetometer (VSM) with a maximum field of 20 kOe. Magnetization measurements in higher fields were done in a superconducting quantum interference device (SQUID) magnetometer with a maximum field of 55 kOe. X-ray diffraction (XRD) spectra were measured with Cu $K\alpha$ radiation in a Philips APD3520 diffractometer. The microstructural investigations were carried out using a Jeol JEM 2000FX transmission electron microscope.

RESULTS AND DISCUSSION

The as-cast samples consist of a mixture of the 2:17 phase and α-Fe as indicated by x-ray (Fig. 1) and electron diffraction results and have coercivities of a few Oe. The grain size in these samples was estimated by TEM studies to be in the range of 1–5 μm. For our present studies on the transformation behavior of a sample with composition $Nd_{15}DyFe_{75}(C_{0.95}B_{0.05})_9$, an annealing temperature of 900 °C was chosen, and the annealing time was varied from 2 min to 1 h (Fig. 2). Coercivities of 8.5 kOe were developed after annealing at 900 °C for 6 h (Fig. 3). There was no significant change in the magnitude of the coercivity in the samples annealed for extended periods of time up to several days.

The crystal structure of the phase in these high coercivity samples was identified to be the $Nd_2Fe_{14}C$ phase (Fig. 4). The precipitation of the 2:14:1 phase occurs very fast as

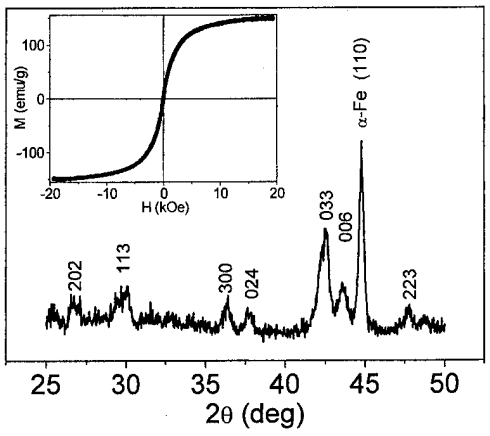


FIG. 1. X-ray diffraction pattern of an as-cast $Nd_{15}DyFe_{75}(C_{0.95},B_{0.05})_9$ sample indicating the existence of a mixture of the 2:17 phase and α-Fe. The hysteresis loop of the same sample is shown in the inset.

[a]Present address: Intel Corporation, D1-73, Hillsboro, OR 97124-6497.

 0021-8979/96/79(8)/4616/3/$10.00 © 1996 American Institute of Physics

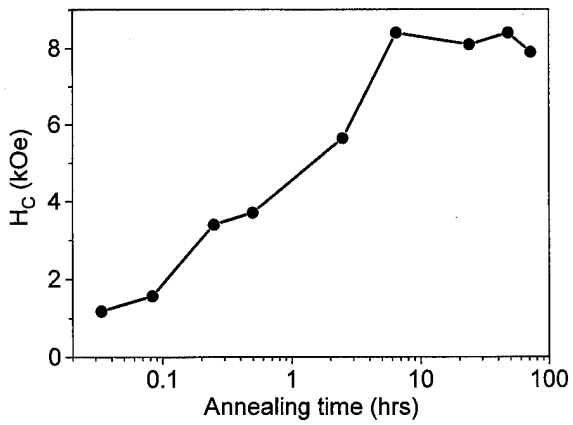


FIG. 2. Coercivity as a function of annealing time for $Nd_{15}DyFe_{75}(C_{0.95},B_{0.05})_9$ samples annealed at 900 °C.

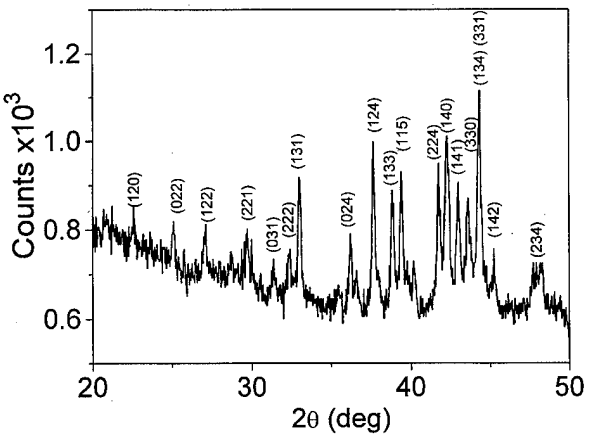


FIG. 4. X-ray diffraction pattern of an $Nd_{15}DyFe_{75}(C_{0.95},B_{0.05})_9$ sample annealed at 900 °C for one day indicating the existence of tetragonal 2:14:1 phase.

indicated by the rapid increase of H_C. After 30 min of annealing the sample has half the maximum coercivity attainable in these samples.

The microstructure in these samples consisted of large grains of $Nd_2Fe_{14}C$ phase with occasional and often smaller grains of a highly faulted phase, a feature similar to that observed by Zhang *et al.* in a different system containing a high amount of Dy.[4] The phase is observed at grain boundaries and triple grain junctions. Figure 5 shows a bright field image of a $Nd_2Fe_{14}C$ grain adjacent to a grain consisting of high density planar faults. It was observed that in samples annealed for shorter periods of time, the volume fraction of the faulted phase increased significantly. A corresponding decrease in the value of the coercivity may be noticed from Fig. 2.

The crystal structure of the faulted phase is of considerable interest. This was determined by employing a procedure similar to that described in Ref. 4. First, three electron diffraction patterns sharing a common crystal axis were obtained. The patterns are shown in Fig. 6. These diffraction patterns are of respective zone axes, [010], [110], and [210] all sharing a common axis with reciprocal lattice vector along (001). Following an analysis carried out very similarly to that described in Ref. 4, the structure of this faulted phase is analyzed to be also hexagonal. The lattice parameters a and c were obtained by making use of the lattice parameter a from a pattern for which the camera length was determined from a known 2:14:1 diffraction pattern. The final result indicates that $a=0.48$ nm and $c=0.81$ nm which gives a ratio $c/a\sim1.7$ compared to the value of 1.45 of the 2:17 phase.

The hexagonal carbide phase observed in our samples is a metastable phase, which readily forms from the 2:17 phase upon annealing at 900 °C for short periods of time. Its volume fraction decreases with increasing annealing times, concomitant with an increase in the volume fraction of the tetragonal $Nd_2Fe_{14}C$ phase. Presence of any other carbide phase could not be ascertained in these studies.

Attempts were made to increase the saturation magnetization of the alloys by increasing the Fe content. Figure 7 shows H_C as a function of at. % Fe for samples annealed at 900 °C for one day. XRD data reveal the presence of α-Fe peaks in samples with increased Fe content leading to this drastic reduction of H_C. The inset in Fig. 6 shows the de-

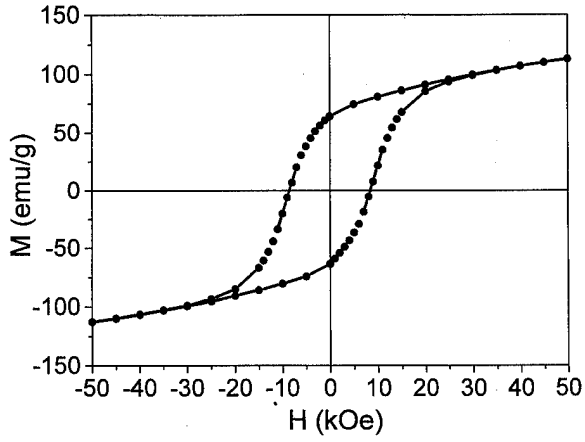


FIG. 3. Hysteresis loop of a $Nd_{15}DyFe_{75}(C_{0.95},B_{0.05})_9$ sample annealed at 900 °C for 6 h.

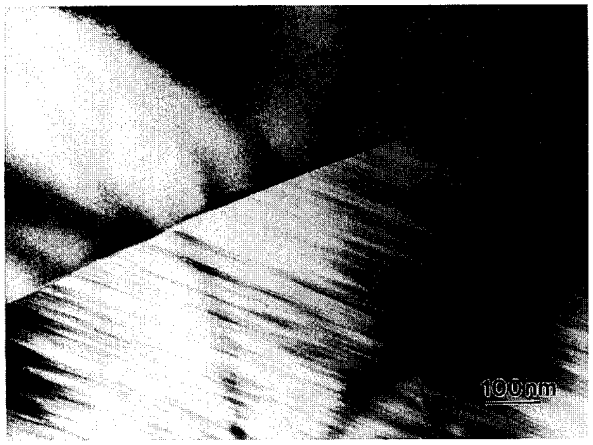


FIG. 5. Bright field image of a $Nd_{15}DyFe_{75}(C_{0.95},B_{0.05})_9$ sample annealed at 900 °C for 30 min.

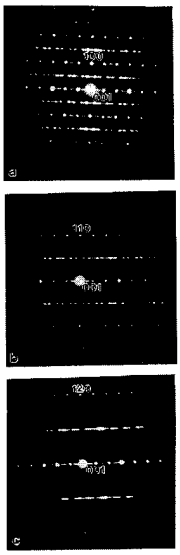


FIG. 6. Electron diffraction patterns sharing a common crystal axis were obtained. The respective zone axes are (a) [010], (b) [110], and (c) [210].

pendence of H_C on the annealing time for a $Nd_{12.6}Dy_{0.8}Fe_{79}(C_{0.95},B_{0.05})_{7.6}$ sample. The maximum attainable coercivity is significantly reduced (2.5 kOe) and corresponds to an annealing time of only 10 min.

CONCLUSIONS

As-cast $Nd_{15}DyFe_{75}(C_{0.95},B_{0.05})_9$ samples consist of a mixture of the 2:17 phase and α-Fe and upon annealing at temperatures around 900 °C a peritectoidal transformation from 2:17 to 2:14:1 occurs. A highly faulted carbide metastable phase was identified in the early stages of this transformation. From electron diffraction investigations, this phase was identified to be hexagonal with lattice parameters, $a=0.48$ nm and $c=0.81$ nm. After 6 h of annealing these samples showed coercivities of 8.5 kOe. In samples with

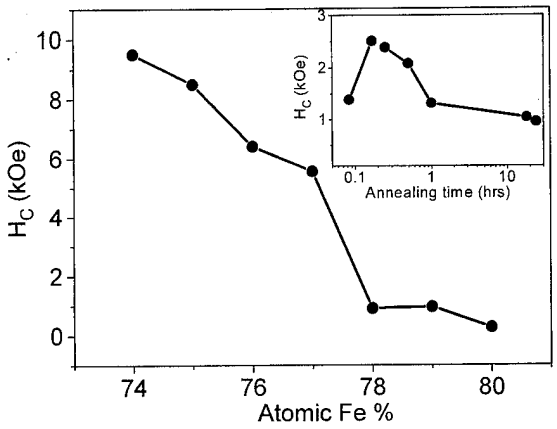


FIG. 7. H_C as a function of at. % Fe for samples annealed at 900 °C for one day. The inset shows the dependence of H_C on the annealing time for a $Nd_{12.6}Dy_{0.8}Fe_{79}(C_{0.95},B_{0.05})_{7.6}$ sample.

higher at. % Fe the magnetization is increased but attainable coercivity is significantly reduced due to the existence of larger grains of α-Fe.

ACKNOWLEDGMENT

This work was supported by the U.S. Army Research Office.

[1] J. Eisses, D. B. de Mooij, K. H. J. Buschow, and G. Martinek, J. Less-Common Met. **171**, 17 (1991).
[2] N. C. Liu, H. Stadelmaier, and G. Schneider, J. Appl. Phys. **61**, 3574 (1987).
[3] F. R. de Boer, Y.-K. Huang, Z.-D. Zhang, D. B. de Mooij, and K. H. J. Buschow, J. Magn. Magn. Mater. **72**, 167 (1988).
[4] A. T. Pedziwiatr, W. E. Wallace, and E. Burzo, J. Magn. Magn. Mater. **59**, L179 (1986).
[5] Y. J. Zhang, A. S. Murthy, Y. Z. Wang, and G. C. Hadjipanayis, J. Alloys Compounds **223**, 18 (1995).
[6] Coehoorn, J. P. W. B. Duchateau, and C. J. M. Denissen, J. Appl. Phys. **65**, 704 (1989).
[7] X. C. Kou, X. K. Sun, Y. C. Chuang, R. Grossinger, and H. R. Kirchmayr, J. Magn. Magn. Mater. **80**, 31 (1989).
[8] B. Grieb, K. Fritz, and E.-Th. Henig, J. Appl. Phys. **70**, 6447 (1991).

Characteristics of $Sm_2Fe_{17}C_x$ compounds prepared from ball-milled blends of Sm_2Fe_{17} and graphite

O. Mao, J. O. Ström-Olsen, Z. Altounian, and J. Yang
Department of Physics, Centre for the Physics of Materials, McGill University, Montréal, Québec H3A 2T8, Canada

A series of $Sm_2Fe_{17}C_x$ ($x=0-6$, nominal) interstitial compounds were synthesized by blending Sm_2Fe_{17} and graphite in a ball mill followed by annealing of the sample powders at 450 °C for 10 h. X-ray structural analyses show that the lattice constants and the unit cell volume, v, of the carbides increases with x almost linearly up to $x=2.5$ and become constant above $x=3.0$. The Curie temperature, T_c, linearly increases with x up to $x=1.7$ and saturates for $x>2.0$. The saturation values of lattice expansion, $\Delta v/v$, and T_c are 6.1% and 403 °C, respectively. $Sm_2Fe_{17}C_x$ powders synthesized with this technique are highly anisotropic. Coercivities for powders with $x>2.2$ are 0.8 T at room temperature. A coercivity of 1.6 T has been achieved in such powders after nitriding.
© *1996 American Institute of Physics.* [S0021-8979(96)37508-X]

I. INTRODUCTION

Introduction of interstitial nitrogen and/or carbon atoms into Sm_2Fe_{17} intermetallic compound of the Th_2Zn_{17} structure type results in a dramatic enhancement of the magnetic properties of this compound and turns it into a promising starting material for permanent magnet application.[1] There have been several preparation techniques for the interstitial compounds of the $Sm_2Fe_{17}C_x$-type: (i) direct alloying (DA) with carbon above the melting temperature followed by either 1000–1200 °C annealing[2] or melt-spinning,[3] (ii) absorbing carbon through the gas-solid reaction (GSR) of the Sm_2Fe_{17} compound with a hydrocarbon gas,[4] or (iii) through the solid–solid reaction (SSR) with carbon from the pure solid state.[5] Among the three techniques, the first two (DA and GSR techniques) are widely used in the research for interstitial modification of the rare earth–iron intermetallic compounds. The DA technique produces carbides with carbon content <1.5 atoms per formula unit due to the metastable nature of the $Sm_2Fe_{17}C_x$ with high carbon concentration, whereas the GSR technique leads to an almost fully carbided compound corresponding to a carbon content of 2–2.5 per formula unit. Few results has been reported for the SSR technique. To prepare the carbide by the SSR technique, Sm_2Fe_{17} powders are usually blended with an excess amount of solid carbon and heated to 500–600 °C to start the SSR.[5,6] This technique also produced fully carbided Sm_2Fe_{17} powders similar to the GSR technique. The intermediate carbon concentrations x between 1.5 and 2 has not been reported previously. In addition, an abrupt change of lattice constants, both a and c axes, occurs in the concentration range of $1.5<x<2.0$.[7,8] On the other hand, recent studies[9] for the intermediate nitrogen concentrations ($0<y<3.0$) in $Sm_2Fe_{17}N_y$ compounds report no abrupt change of the lattice constants. It is interesting, therefore, to study $Sm_2Fe_{17}C_x$ compounds in the whole carbon concentration range with self-consistent samples. In this contribution we report the synthesis, structure, and magnetic properties of $Sm_2Fe_{17}C_x$ interstitial compound with the SSR technique.

II. EXPERIMENTAL TECHNIQUES

The Sm_2Fe_{17} compound was prepared by melting the constituents in a cold crucible induction furnace. Purity of Fe and Sm were 99.99 wt % and 99.9 wt %, respectively. An excess of 15% Sm (corresponding to a starting composition of $Sm_{2.3}Fe_{17}$) was added to compensate for Sm loss during melting. For homogeneity the ingots were melted four times. The as-prepared alloy were annealed at 1150 °C for 5 h under an Ar atmosphere to produce an almost single phase Sm_2Fe_{17} alloy. The resulting Sm_2Fe_{17} ingot and a pure graphite were crushed to coarse powder of size <0.5 mm and loaded to a hardened steel vial and sealed. The blend of Sm_2Fe_{17} and graphite were prepared by ball milling (BM) appropriate amounts of the constituents. The crushing, weighing, mixing, loading, and sealing procedures were performed in a specially designed glove box with oxygen and humidity levels of <1 ppm. The ball milling was carried out in a high energy SPEX-8000 Mixer/Mill. The hardened steel balls used for BM were 4 mm in diameter. Ball-to-material ratio was kept at 1:1 as higher ratios led to decomposition of the compound. Carbiding of the powders was carried out by annealing the sample in a quartz tube sealed in the glove box. For structural analysis, x-ray diffraction (XRD) was performed in an automated Nicolet–Stöe powder diffractometer with graphite monochromated Cu K_α radiation. The Bragg peaks of the diffraction pattern were fitted with the Cauchy distribution function

$$I=\frac{I_0}{\{1+[2(x-x_0)/B]^2\}}, \tag{1}$$

where, I_0 is the intensity, B the full width at half-maximum and x_0 the peak position. Fitting all the Bragg peaks in the range of $2\theta=20°-55°$ gave high accuracy in determining a and c of the hexagonal unit cell that describes the rhombohedral Th_2Zn_{17} structure. The width of the Bragg peak gives the average grain sizes of the powder by using the Scherrer equation

$$B(2\theta)=\frac{0.94\lambda}{L\cos\theta}. \tag{2}$$

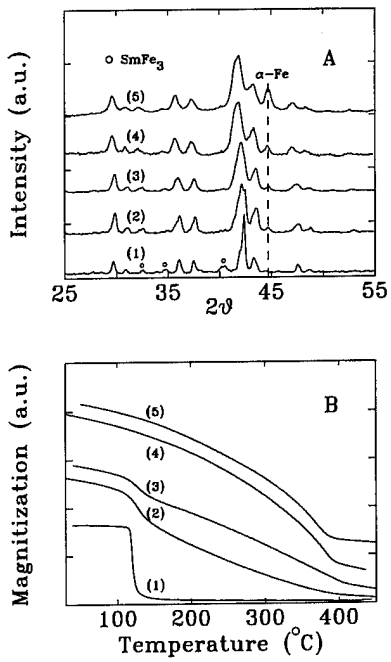


FIG. 1. X-ray diffraction (A) and thermomagnetic (B) scans: (1) Sm_2Fe_{17} ingot; (2)–(5) powders ball milled for 20 (2), 50 min (3), 2 h (4) and 5.5 h (5) followed by annealing at 450 °C for 10 h.

The Curie temperature, T_c, was measured by thermomagnetometry using a Perkin–Elmer thermogravimetric analyzer (TGA-7) in a small magnetic field gradient (TMA).

III. RESULTS AND DISCUSSION

The starting Sm_2Fe_{17} ingot prepared by 1150 °C annealing is almost single phase except for the presence of very small amount of α-Fe and $SmFe_3$ phases, as shown by the XRD [curve 1 in Fig. 1(A)]. XRD measurements on ball milled Sm_2Fe_{17}/graphite powders show no noticeable change in the lattice constants except a broadening of the Bragg peaks due to a finer grain size and severe lattice strain generated by BM. The carbiding reaction starts in the blend at temperatures above 300 °C. The metastable Sm_2Fe_{17} carbide tends to decompose when it is heated to above 500 °C. The heat treatment condition usually used to form the carbides is 450 °C for 10 h. We have tried to anneal blends prepared with various milling times. Annealing of short-time-milled blends gives rise to partial carbiding of the sample. Curves 2 and 3 in Fig. 1(A) and 1(B) indicate a distribution of lattice constants and T_c caused by the nonuniform carbon distribution in the sample. Full carbiding occurs in powders milled longer than 2 h. Full carbiding of the sample with milling times longer than 2 h is further confirmed by comparing to the sample with the same carbon content prepared by the DA technique: TMA curves 2 and 3 in Fig. 2 are essentially identical. From the widths of the Bragg peaks (subtracting out the broadening due to the intrinsic resolution of the diffractometer and the strain in the lattice), the grain sizes are estimated to be 80 nm and 40 nm for powders milled 2 h and 5.5 h, respectively. The faster carbiding process in powders with longer milling time may be due to the formation of nanocrystallites resulting in an enhancement of carbon diffu-

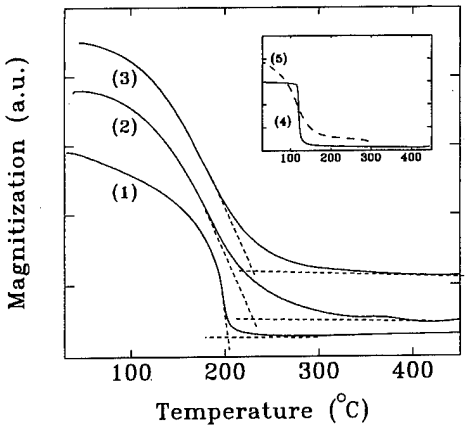


FIG. 2. Thermomagnetic scans: (1) $Sm_2Fe_{17}C_{0.5}$ ingot (prepared by DA technique), (2) $Sm_2Fe_{17}C_{0.5}$ ingot ball milled for 3 h and (3) $Sm_2Fe_{17}C_{0.5}$ prepared by SSR technique. Inset shows (4) Sm_2Fe_{17} ingot and (5) Sm_2Fe_{17} ingot ball milled for 3 h. The dashed lines are guidelines showing how to determine T_c's from the thermomagnetic measurements.

sion through grain boundaries. It is noticed that TMA measurements show a wider transition region and a higher T_c (20–30 °C higher) in the BM sample than in the ingot for both Sm_2Fe_{17} carbides and pure binary alloy (inset in Fig. 2). This effect is caused by the defects generated by BM. Longer milling time results in higher α-Fe content due to the tendency of decomposition of the compound. The dependence of lattice constants and the unit cell volume, v, on the nominal carbon concentration is plotted in Fig. 3(A)–3(C). v increases almost linearly with x up to three, while the increase of T_c saturates at 2.0 as shown in Fig. 3(D). The saturation values of lattice expansion, $\Delta v/v$, and T_c are 6.1% and 403 °C, respectively, shown in Fig. 3(C) and 3(D). As carbon or nitrogen interstitials occupy the $9(e)$ sites in the R_2Fe_{17} structures of the Th_2Zn_{17} type, the maximum carbon or nitrogen content is three atoms per formula unit. It has been

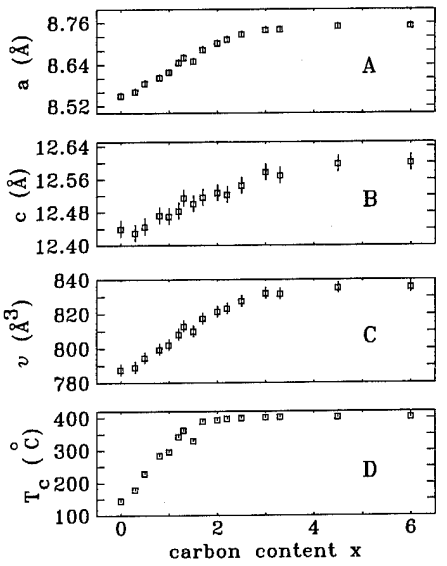


FIG. 3. Dependences on the nominal carbon concentration x of (A) a, (B) c, (C) v, and (D) T_c.

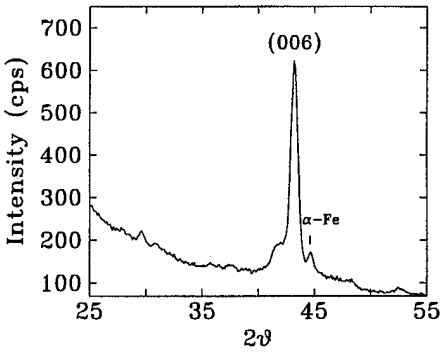


FIG. 4. XRD patterns of magnetically aligned $Sm_2Fe_{17}C_x$ powder.

reported that GSR produces $Sm_2Fe_{17}C_x$ with $x=2$–2.5. Since a carbon layer may exit on the particle surfaces, and does not contribute to the interstitial modification, this makes it difficult to determine the actual carbon content in Sm_2Fe_{17} carbide, even in the samples prepared with GSR. The actual carbon concentration in our carbide sample needs further investigation.

Finally, this technique was explored as a processing routine to prepare anisotropic Sm_2Fe_{17} powders. XRD measurements on magnetically aligned Sm_2Fe_{17} carbide powders show the highly anisotropic nature of the powder as shown in Fig. 4. The presence of graphite during BM separates the Sm_2Fe_{17} particles effectively because graphite forms coating layers on the particle surfaces due to its particular layered-structure. BM favors the formation of a fine microstructure giving rise to high coercivity. $Sm_2Fe_{17}C_x$ ($x>2.2$) powders show coercivities >0.8 T at room temperature. A coercivity of 1.6 T has been achieved in such powders after nitriding.

IV. CONCLUSIONS

Annealing of blends of Sm_2Fe_{17} and graphite prepared by BM at 450 °C for 10 h results in carbiding of the Sm_2Fe_{17} compounds. Structural measurements show that the lattice constants and the unit cell volume, v, increase with carbon concentration x almost linearly up to $x=2.5$ and become constant above $x=3$. Magnetic measurements indicate that T_c increases linearly with x up to $x=1.7$ and saturates for $x>2.0$. The saturation values of $\Delta v/v$ and T_c are 6.1% and 403 °C, respectively. $Sm_2Fe_{17}C_x$ powders prepared with the present technique are highly anisotropic. Samples with high coercivities has been synthesized.

ACKNOWLEDGMENTS

This work was supported by grants from the Natural Sciences and Engineering Research Council of Canada and le Fonds pour la Formation de Chercheurs et l'Aide à la Recherche de la Province du Québec.

[1] J. M. D. Coey and Hong Sun, J. Magn. Magn. Mater. **87**, L251 (1990).
[2] D. B. de Mooij and K. H. J. Buschow, J. Less-Common Met. **142**, 349 (1988).
[3] Bao-gen Shen, Lei Cao, Lin-shu Kong, Tai-shan Ning, and Ming Hu, J. Appl. Phys. **75**, 6256 (1994).
[4] L. X. Liao, X. Chen, Z. Altounian, and D. H. Ryan, Appl. Phys. Lett. **60**, 129 (1992).
[5] R. Skomski, C. Murray, S. Brennan, and J. M. D. Coey, J. Appl. Phys. **73**, 6940 (1993).
[6] R. V. Skolozdra, E. Tomey, D. Gignoux, D. Fruchart, and J. L. Soubeyroux, J. Magn. Magn. Mater. **139**, 65 (1995).
[7] K. Kobayashi, IEEE Trans. J. Magn. **8**, 842 (1993).
[8] K. Kobayashi, *Proceedings of 13th International Workshop on RE Magnets and their Applications,* edited by C. A. F. Manwaring, D. G. Jones, A. J. Williams, and I. R. Harris (The University of Birmingham, Birmingham, AL, 1992), p. 717.
[9] M. Katter, J. Wecker, C. Kuhrt, and L. Schultz, J. Magn. Magn. Mater. **117**, 419 (1992).

Exchange and crystal-field interactions in $R_3(Fe,Ti)_{29}$ and $R_3(Fe,Ti)_{29}N_y$ (R=Nd,Sm)

Hong-Shuo Li, D. Courtois, and J. M. Cadogan
School of Physics, The University of New South Wales, Sydney 2052, Australia

A quantitative analysis of the available magnetization data on the $R_3(Fe,Ti)_{29}$ and $R_3(Fe,Ti)_{29}N_y$ (R=Nd,Sm) compounds have been carried out. The two R sites of $R_3(Fe,Ti)_{29}$ compounds have opposite signs of their leading crystal-field coefficient A_{20}; namely, $A_{20}<0$ for the $4e$ site (2:17 like) and $A_{20}>0$ for the $2a$ site (1:12 like) (site notation is that of the space group $P2_1/c$). A R–Fe exchange coefficient of $285\pm5\mu_0$ and crystal field coefficients $A_{20}(2a)=+16$ Ka_0^{-2} and $A_{20}(4e)=-25$ Ka_0^{-2} were obtained. The type-II first-order magnetization processes observed in both $Nd_3(Fe_{1-x}Ti_x)_{29}$ and $Sm_3(Fe_{1-x}Ti_x)_{29}$ have been well reproduced: $\mu_0H_{cr}=2.4$ T for R=Nd at 5 K (observed ~2 T), and $\mu_0H_{cr}=3.0$ T for R=Sm at 4.2 K (~3.2 T). Based on the bonding charge model, we estimate that the values of $A_{20}(4e)$ and $A_{20}(2a)$ for the fully nitrided 3:29 compounds are $A_{20}(4e)=-187$ Ka_0^{-2} and $A_{20}(2a)=-184$ Ka_0^{-2}. Our calculations show that $R_3(Fe_{1-x}Ti_x)_{29}N_y$ nitrides become uniaxially anitsotropic for $y\geqslant2$ and a maximum room temperature uniaxial anisotropy field of 11.4 T for fully nitrided $Sm_3(Fe_{1-x}Ti_x)_{29}N_4$ is predicted which compares well with the experimental values which lie in the range 10.7–13 T. © *1996 American Institute of Physics.* [S0021-8979(96)37608-6]

I. INTRODUCTION

The ternary $R_3(Fe,Ti_x)_{29}$ (3:29) phase has a monoclinic $Nd_3(Fe,Ti_x)_{29}$ structure with the space group $P2_1/c$ (Ref. 1 and 2) (its site notation is used throughout this article); recently it was proposed that the structure can be described more accurately with the space group $A2/m$.[3] This structure is an intermediate structure between the well known rhombohedral Th_2Zn_{17} (2:17R) and tetragonal $ThMn_{12}$ (1:12) structures, and consists of a combination of the 2:17R and 1:12 segments in a ratio of 1:1.[1] There are two distinct crystallographic R sites, namely $2a$ and $4e$ ($2a$ and $4i$ in the notation of $A2/m$), and fifteen Fe(Ti) sites in the structure. The $4e$ and $2a$ R sites have a local environments corresponding to those found in 2:17R and 1:12 structures, respectively.

The new $R_3(Fe_{1-x}M_x)_{29}$ (R=Ce–Dy; M=Ti,V,Cr,Mn, Mo) compounds are magnetically ordered with Curie temperatures in the range 322 K (Ce)–524 K (Gd).[4–12] It has been shown that after introduction of interstitial N or C atoms, the Curie temperature is enhanced to ~700 K in $R_3(Fe_{1-x}Ti_x)_{29}X_y$ (X=N,C) (Ref. 3, 4, 6, and 11–15) which is comparable to that of $R_2Fe_{17}N_y$, 740 K.[16] The room temperature saturation magnetization, μ_0M_s~1.5 T, is also close to that of $Nd_2Fe_{17}N_y$, $\mu_0M_s=1.45$ T. In fact, significant coercivity, has been developed, reaching 0.7–0.85 T in $Sm_3(Fe_{1-x}M_x)_{29}N_y$ (Ref. 13 and 14) and 0.3 T in $Sm_3(Fe_{1-x}Ti_x)_{29}C_y$.[15] These promising magnetic properties suggest that the new $R_3(Fe_{1-x}Ti_x)_{29}N_y$ compounds might be alternative hard nitride magnets to $Sm_2Fe_{17}N_{3-\delta}$ (Ref. 16) and $NdFe_{11}TiN_{1-\delta}$.[16]

In order to understand the magnetocrystalline anisotropy of rare earth sublattices in the $R_3(Fe_{1-x}Ti_x)_{29}$ series, we previously estimated the leading crystal-field coefficients A_{20} by the simple point charge model.[17] We showed that two R sites have opposite signs of A_{20}; namely, $A_{20}<0$ for the $4e$ site (2:17 like) and $A_{20}>0$ for the $2a$ site (1:12 like). Thus, it is likely that the competition of the two R sublattices may result to unusual magnetization behavior. In fact, the magnetization measurements show the existence of the type-II first-order magnetization processes FOMPs in both $Nd_3(Fe_{1-x}Ti_x)_{29}$ (Ref. 5) and $Sm_3(Fe_{1-x}Ti_x)_{29}$ (Ref. 7) systems. The magnetization shows an upturn at a critical applied magnetic field of: μ_0H_{cr}~2 T for R=Nd at 5 K,[7] and μ_0H_{cr}~2 T for R=Sm at 4.2 K and ~2.2 T at 77 K.

Here, we present a detailed crystal field (CF) analysis of the $R_3(Fe, Ti)_{29}$ and $R_3(Fe,Ti)_{29}N_y$ (R=Nd,Sm) compounds based on available magnetization data.

II. RESULTS AND DISCUSSION

We have developed a first-principles theoretical model,[18,19] incorporating exchange and crystal-field interactions, which has been highly successful in explaining the complex magnetic behavior of a large number of rare-earth, iron series including $R_2Fe_{14}B$, $RFe_{11}Ti$, $R_2Fe_{17}(N,C)_x$, and $RFe_{11}TiN_x$. The model is based on two coupled equations that describe the Fe and R sublattices. The Fe sublattice is treated classically whereas the R sublattice is treated from first-principles. The single-ion rare-earth Hamiltonian can be expressed as

$$H_R=H_{SO}+H_{ex}+H_{cf}+H_{Zeeman}, \tag{1}$$

where $H_{SO}=\lambda\mathbf{L}\cdot\mathbf{S}$ is the spin-orbit coupling. H_{ex} is the exchange term and can be expressed as $H_{ex}=2\mathbf{B}_{ex}\cdot\mathbf{S}\mu_B$, where the exchange field acting on the rare-earth spin S is given by $\mathbf{B}_{ex}=-n_{RFe}\langle M_{Fe}\rangle H_{cf}$ is the R^{3+} crystal-field Hamiltonian whose form depends on the local symmetry of the R crystallographic site. In general, H_{cf} can be expressed in terms of the Racah tensor operators $\mathbf{U}_q^k$ as follows:

$$H_{cf}=\sum_{n=0}^{6}{}_{\text{even}}\sum_{q=-k}^{k}N_k^qA_k^q\langle r^k\rangle U_q^k, \tag{2}$$

where $\{A_k^q\}$ are the CF coefficients which reflect the strength and symmetry of the CF interactions. If $J-J$ mixing is neg-

 0021-8979/96/79(8)/4622/3/$10.00 © 1996 American Institute of Physics

TABLE I. Crystal field coefficients of R_2Fe_{17} and $R(Fe,Ti)_{12}$ (Refs. 20–23) and those used in the calculations of $R_3(Fe,Ti)_{29}$.

A_{nm} ($K\,a_0^{-n}$)	R_2Fe_{17}	$R_3(Fe,Ti)_{29}$		$R(Fe,Ti)_{12}$
	6c	4e	2a	2a
A_{20}	~−20	−25.0	+16.5	−32.3
A_{22}^c	···	···	−48.5	···
A_{40}	−10	−3.0	+10.1	−12.4
A_{42}^c	···	···	+90.0	···
A_{44}^c	···	···	−39.5	+118.0
A_{60}	~−3.0	−3.5	−0.84	+2.56
A_{62}^c	···	···	+8.5	···
A_{64}^c	···	···	−9.6	+0.64
A_{66}^c	~−2.0	−2.2	+18.7	···

ligible, H_{cf} reduces to the familiar tesseral form in which H_{cf} is developed in Stevens operator equivalents O_{nm}^{α} and $\{A_{nm}{}^{\alpha}\}$.[16,18,19] For the sake of consistency, in this article we use only $\{A_{nm}^{\alpha}\}$ (the relations between $\{A_{nm}^{\alpha}\}$ and $\{A_k^q\}$ are given in Ref. 16). The final term in Eq. (1) accounts for the interaction of the R magnetic moment with an applied magnetic field; $H_{Zeeman}=-\mu_B(\mathbf{L}+2\mathbf{S})\cdot\mu_0\mathbf{H}_{ext}$.

Having chosen a set of CF and exchange parameters, the R^{3+} Hamiltonian can be diagonalized for selected H_{ext} and temperature values to yield the free energy of the R^{3+} ion, $F_R(T)$. Finally, the total energy of the system is

$$E_{Total}=K_1^{Fe}\sin^2\theta-\langle M_{Fe}\rangle\mu_0 H_{ext}+F_R(T). \quad (3)$$

The magnetic structure of the intermetallic compound may be found by minimizing E_{Total}. Further details of this procedure may be found in Refs. 16, 18, and 19.

The crystal field analysis for 3:29 compounds is complicated by the low symmetry of the monoclinic $Nd_3(Fe,Ti_x)_{29}$ structure. The local point symmetry of the rare earth sites are $2/m$ for $2a$ site and m for $4e$ site, respectively. Hence, there are nine nonvanishing crystal-field parameters for each rare earth site, i.e., eighteen CF parameters in total. The lack of a comprehensive set of magnetization data (e.g., single crystal magnetization measurements) makes the crystal field analysis unmanageable for 3:29 system. However, there is a simple approach to estimate the CF parameters in 3:29, based on a consideration of the structural relationship between the 3:29 structure and the 2:17R and 1:12 structures. In fact, as we have previously shown in our previous article,[17] the local environment of the R ions in the $4e$ site of 3:29 corresponds to that of the $6c$ site in 2:17R, while the $2a$ site in 3:29 corresponds to the $2a$ site in 1:12. Therefore, as a first approximation, we use the crystal field parameters deduced for the R ions in 2:17R (Ref. 20–22) and 1:12 (Ref. 23) as starting parameters for the $4e$and $2a$ sites in the 3:29 phase. The values of the CF parameters for 2:17R and 1:12 phases are listed in Table I;[20–23] it should be mentioned that the reported CF parameter values of the 2:17 phase are largely scattered.

In order to consider the three crystallographic structures 3:29, 217R, and 1:12, we have chosen the $CaCu_5$-type (1:5) structure as a reference coordinate system throughout this article since all three of the above structures are ultimately derived from the 1:5 parent structure.[1] It is well known that the c-axis of 2:17R is perpendicular to that of 1:12.[1] Therefore, in our calculations we need to transform the CF parameters from 1:12 system to that of 1:5. Using the transformation relationships given by Rudowicz,[24] the CF parameters used for our analysis of 3:29 are listed in Table I.

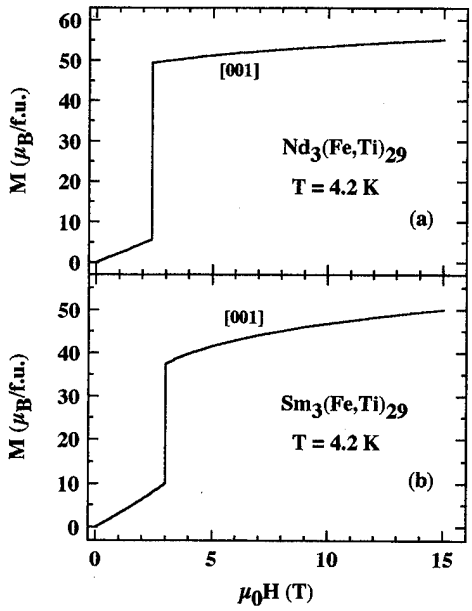


FIG. 1. Theoretical magnetization curves for applied field along the c-axis of 1:5 system for (a) $Nd_3(Fe,Ti)_{29}$ and (b) $Sm_3(Fe,Ti)_{29}$. Crystal field coefficients used are listed in Table I and the exchange coefficient used is $n_{RFe}=285\pm5\mu_0$.

The temperature dependence of the Fe sublattice magnetization and anisotropy of 3:29 phase were determined in our previous magnetization study of $Y_3(Fe,Ti)_{29}$.[25] The exchange coefficient n_{RFe} was taken to be $288\pm5\mu_0$. The results of our crystal field calculations are shown in Fig. 1 where the theoretical magnetization curves for R=Nd and Sm are plotted, for an applied field along the c-axis (referring to the underlying 1:5 structure). It can be seen from Fig. 1 that there is a type-II FOMP for both compounds; the calculated critical field values are $\mu_0H_{cr}=2.4$ T for R=Nd at 5 K compared to the experimental value of ~2 T,[7] and $\mu_0H_{cr}=3.0$ T for R=Sm at 4.2 K compared to ~3.2 T found experimentally.[5] The agreement between the theoretical and experimental values is very good, especially considering the fact that the set of CF coefficients used are virtually identical to those of the corresponding R sites in the 2:17 and 1:12 structures. Our analysis suggests that this magnetic field induced magnetization process is due to the competition between two opposing R-sublattices anisotropies. At the critical field, the magnetization jumps from $\theta=85°$ to a canted angle of 35° for R=Nd and from 79° to 44° for R=Sm, respectively.

Having the CF parameters of the parent 3:29 compounds, it is interesting to investigate the crystal field interactions of their nitrides and carbides. We have previously shown, based on the so-called bonding charge model (BCM), that the shift in A_{20} due to one neighboring N atoms is $\Delta A_{20}=-54\ K\,a_0^{-2}$ for $R_2Fe_{17}N_{3-\delta}$ (Ref. 26) and $-100\ K\,a_0^{-2}$ for $RFe_{11}TiN_{1-\delta}$.[27] The number of neighboring inter-

stitial atoms for the fully nitrided compounds is 3 for 2:17 and 2 for 1:12 structures, respectively. Therefore, we have

$$A_{20}(4e) = -25 + (3/4)y(-54)\ \text{K}\ a_0^{-2},$$
$$A_{20}(2a) = +16 + (1/2)y(-100)\ \text{K}\ a_0^{-2} \quad (4)$$

for the $R_3(Fe_{1-x}Ti_x)_{29}N_y$ compounds. The values of $A_{20}(4e)$ and $A_{20}(2a)$ deduced from Eq. (4) for the fully nitrided are $A_{20}(4e) = -187\ \text{K}\ a_0^{-2}$ and $A_{20}(2a) = -184\ \text{K}\ a_0^{-2}$. Using these leading crystal field coefficients, our calculations show that $R_3(Fe_{1-x}Ti_x)_{29}N_y$ nitrides become uniaxial anisotropic for $y \geq 2$. We predict a room temperature uniaxial anisotropy field of 11.4 T for the fully nitrided $Sm_3(Fe_{1-x}Ti_x)_{29}N_4$ compound which compares well with the experimental values of 10.7 (Ref. 28) to 13 T (Ref. 13). For the 3:29 carbides, the changes in A_{20} are slightly smaller than those of corresponding nitrides.[19] Therefore, the expected anisotropy should be slightly smaller than the value of 11.4 T.

III. CONCLUSION

A quantitative analysis of the available magnetization data on the $R_3(Fe,M)_{29}$ and $R_3(Fe,M)_{29}N_y$ (R=Nd,Sm) compounds have been carried out. The type-II FOMPs observed in both $Nd_3(Fe_{1-x}Ti_x)_{29}$ and $Sm_3(Fe_{1-x}Ti_x)_{29}$ are well reproduced with a unique set of crystal-field coefficients. The agreement between the theoretical and experimental critical field values is very good, given that the set of CF coefficients used is virtually identical to those of the corresponding R sites in the 2:17 and 1:12 structures.

Based on the bonding charge model, our calculations show that $R_3(Fe_{1-x}Ti_x)_{29}N_y$ nitrides become uniaxial anisotropic for $y \geq 2$ and a maximum room temperature uniaxial anisotropy field of 11.4 T for the fully nitrided $Sm_3(Fe_{1-x}Ti_x)_{29}N_4$ compound was predicted, which compares well with the experimental value of 10.7–13 T.

ACKNOWLEDGMENT

This work was mainly supported by Research grants from the Australian Research Council.

[1] H.-S. Li, J. M. Cadogan, R. L. Davis, A. Margarian, and J. B. Dunlop, Solid State Commun. **90**, 487 (1994).
[2] Z. Hu and W. B. Yelon, Solid State Commun. **91**, 223 (1994).
[3] O. Kalogirou, V. Psycharis, L. Saettas, and D. Niarchos, J. Magn. Magn. Mater. **146**, 335 (1995).
[4] S. J. Collocott, R. K. Day, J. B. Dunlop, and R. L. Davis, Proceedings of the 7th International Symposium on Magnetiz Anisotropy and Coercivity in R–T Alloys, Canberra, July, 1992, (unpublished), p. 437.
[5] F.-M. Yang, B. Nasunjilegal, H.-Y. Pan, J.-L. Wang, R.-W. Zhao, B.-P. Hu, Y.-Z. Wang, H.-S. Li, and J. M. Cadogan, J. Magn. Magn. Mater. **135**, 298 (1994).
[6] Ye. V. Shcherbakova, G. V. Ivanova, A. S. Yermolenko, Ye. V. Belozerov, and V. S. Gaviko, J. Alloys Compounds **182**, 199 (1992).
[7] C. D. Fuerst, F. E. Pinkerton, and J. F. Herbst, J. Magn. Magn. Mater. **129**, L115 (1994).
[8] J. M. Cadogan, H.-S. Li, R. L. Davis, A. Margarian, J. B. Dunlop, and P. B. Gwan, J. Appl. Phys. **75**, 7114 (1994).
[9] M. R. Ibarra, L. Morellon, J. Blasco, L. Pareti, P. A. Algarabel, J. García, F. Albertini, A. Paoluzi, and G. Turilli, J. Phys.: Condens. Matter **6**, L717 (1994).
[10] H.-S. Li, D. Courtois, J. M. Cadogan, J.-M. Xu, and S. X. Dou, J. Phys.: Condens. Matter **6**, L771 (1994).
[11] O. Kalogirou, V. Psycharis, M. Gjoka, and D. Niachos, J. Magn. Magn. Mater. **147**, L7 (1995).
[12] D. Courtois, H.-S. Li, and J. M. Cadogan, Intermag'95, IEEE Trans. Mag. **31**, 3677 (1995).
[13] B.-P. Hu, G.-C. Liu, Y.-Z. Wang, B. Nasunjilegal, R.-W. Zhao, F.-M. Yang, H.-S. Li, and J. M. Cadogan, J. Phys.: Condens. Matter **6**, L197 (1994).
[14] S. Suzuki, S. Suzuki, and M. Kawasaki, Intermag'95, IEEE Trans. Mag. **31**, 3695 (1995).
[15] B.-P. Hu, G.-C. Liu, Y.-Z. Wang, B. Nasunjilegal, N. Tang, F.-M. Yang, H.-S. Li, and J. M. Cadogan, J. Phys.: Condens. Matter **6**, L595 (1994).
[16] H.-S. Li and J. M. D. Coey, *Handbook of Magnetic Materials*, edited by K. H. J. Buschow (Elsevier, Amsterdam, 1991), Vol. 6, Chap. I, p. 1.
[17] H.-S. Li, J. M. Cadogan, B.-P. Hu, F.-M. Yang, B. Nasunjilegal, A. Margarian, and J. B. Dunlop, J. Magn. Magn. Mater. **140–144**, 1037 (1995).
[18] J. M. Cadogan, J. P. Gavigan, D. Givord, and H. S. Li, J. Phys. F: Met. Phys. **18**, 779 (1988).
[19] H.-S. Li, and J. M. Cadogan, J. Magn. Magn. Mater. **116**, 361 (1992).
[20] K. Clausen and B. Lebech, J. Phys. C: Solid State Phys. **15**, 5095 (1982).
[21] H.-S. Li and J. M. Cadogan, Solid State Commun. **82**, 121 (1992).
[22] X.-F. Han, H.-M. Jin, Y. Yan, C. C. Sun, and B. F. Li, Phys. Status Solidi B **171**, K35 (1992).
[23] B.-P. Hu, H.-S. Li, J. M. D. Coey, and J. P. Gavigan, Phys. Rev. B **41**, 2221 (1990).
[24] C. Rudowicz, J. Phys. C: Solid State Phys. **15**, 1415 (1985).
[25] H.-S. Li, D. Courtois, J. M. Cadogan, B.-P. Hu, and W.-S. Zhan, Intermag'95, IEEE Trans. Mag. **31**, 3680 (1995).
[26] H.-S. Li and J. M. Cadogan, Solid State Commun. **80**, 905 (1991).
[27] H.-S. Li and J. M. Cadogan, J. Magn. Magn. Mater. **109**, L153 (1994).
[28] A. Margarian, J. B. Dunlop, S. J. Collocott, H.-S. Li, J. M. Cadogan, and R. L. Davis, 13th International workshop on RE Magnets and their Applications, Birmingham, UK, 1994.

Magnetic ordering in clustered Fe-based materials synthesized from laser plasma (abstract)

Yuri Blyakhman
New York University, Department of Physics, New York, New York 10003

N. I. Polushkin, A. D. Akhsakhalyan, S. A. Gusev, and N. N. Salashchenko
Institute for Physics of Microstructures, Russian Academy of Sciences, 603600 Nizhny Novgorod, Russia

V. G. Semenov
Chemical Institute, St.-Petersburg State University, 198904 St.-Petersburg, Russia

Using Mössbauer spectroscopy and the magneto-optical Kerr effect, we investigate how magnetic order arises and develops in Fe/C and Fe/Cr layered mixtures prepared by pulsed laser deposition. Two different magnetic transformations are found to occur in these systems under their thermal annealing. The first is the paramagnetic–ferromagnetic crossover that takes place at annealing temperatures of 420–570 K in dependence on the average iron content. Varying the latter quantity, we also observed the same crossover to the ferromagnetic state. The second transformation is magnetic hardening at 700–800 K. The specific feature of both transformations is that they occur within narrow ranges of annealing temperature (<10 K). The first transformation is supposed to result from an additional iron enrichment of Fe-rich clusters and is associated with magnetic phase transition near the Curie temperature. The cluster enrichment was directly observed with transmission electron microscopy and was also shown in small angle x-ray scattering patterns of the compositionally modulated structures. The observed sharpening of the magnetic behavior near the Curie temperature is presumably a manifestation of the clustered structure. The second transformation is found to be induced by the onset of crystallization and the formation of particles of the new Fe-rich phase. © *1996 American Institute of Physics.* [S0021-8979(96)62808-0]

Magnetization processes of free- and fixed-single-crystal antiferromagnets

Z. G. Zhao, P. F. de Châtel, F. R. de Boer,[a] and K. H. J. Buschow
Van der Waals-Zeeman Institute, University of Amsterdam, Valckenierstraat, 65, 1018 XE Amsterdam, The Netherlands

A simple two-sublattice model is used to analyze the magnetization process of anisotropic antiferromagnets at $T=0$. The magnetization is calculated for samples free to be oriented by the applied field (free single crystals or powders consisting of single-grain particles). We find that the anisotropy does not necessarily lead to a nonlinear $M(B)$ relation, but that the magnetic isotherms are broken into two linear sections separated by a discontinuity. The difference between the slopes in the two regions enables a determination of the anisotropy constant K_1. The results will be discussed in relation to our findings for the ferrimagnetic case and to the behavior of oriented antiferromagnetic crystals. © *1996 American Institute of Physics.* [S0021-8979(96)00108-0]

The study of magnetization processes in two-sublattice systems is mostly conducted with reference to rare-earth—transition-metal compounds. Such compounds are composed of two very dissimilar sublattices. The ferrimagnetic case, with antiferromagnetic intersublattice coupling, is relevant to the compounds formed with heavy-rear-earth elements. These compounds have been studied extensively in recent years because of their relationship to materials used for several technological applications, including permanent magnets, magneto-optical recording, and magnetoelastic transducer devices.

Model calculations of the magnetization processes in two-sublattice ferrimagnets have been based on a phenomenological free-energy expression consisting of the anisotropy energies of both sublattices, the energy of the interaction between the sublattices and the Zeeman energy.[1] Such analyses implicitly include the case of antiferromagnetism, where the anisotropy parameters and the magnetization of the two sublattices are identical. Such parameter values being far removed from those occurring in ferrimagnets of practical interest, this case has received little attention so far. The purpose of the present paper is to reconsider the results on ferrimagnets with this special case in mind and to point out that the magnetization of field-oriented (or free-powder) samples of antiferromagnets with uniaxial sublattice anisotropy show some general features not commonly observed in ferrimagnets. Many of such antiferromagnetic rare-earth compounds have been reported in Ref. 2.

The interest in magnetization curves of field-oriented single- crystalline samples or powders consisting of single-crystal particles arose from the realization that such curves may turn out to be very simple, consisting of three straight sections. The first one of these, stretching to a first critical field B_{cr1}, is horizontal at the value of the spontaneous magnetization $|M_1-M_2|$. This is followed by a section where the magnetization is proportional to the field, $M=n_{12}^{-1}B$, the slope being equal to the inverse of the intersublattice coupling constant. When the magnetization reaches its saturation value M_1+M_2 at a second critical field B_{cr2}, it becomes again independent of the field. This simple behavior has been shown to prevail in two cases: (1) if at least one of the sublattices is isotropic and (2) if both sublattices have planar (easy-plane) anisotropies, with no anisotropy in the plane. Clearly, case (1) is irrelevant to anisotropic antiferromagnets and case (2) implies that easy-plane antiferromagnets show the simple magnetization curves known from the ferrimagnet case. Since $M_1-M_2=0$ for antiferromagnets, the first one of the three straight sections described above is absent; the bending of the two sublattice magnetizations towards each other begins at $B_{cr1}=0$, the linear increase of the magnetization with a slope n_{12}^{-1} stretching to $M=M_1+M_2$, which is reached at $B_{cr2}=n_{12}(M_1+M_2)$. This being a very straightforward application of the results known for ferrimagnets, we shall concentrate on antiferromagnets with easy-axis anisotropy in what follows, which will be shown to have some interesting features.

The simplest anisotropic two-sublattice magnets, when they are free to be oriented by the field, can be described by the free energy

$$E=K_1^{(1)}\sin^2\vartheta_1+K_1^{(2)}\sin^2\vartheta_2+n_{12}M_1M_2\cos\alpha-BM, \tag{1}$$

where the first two terms stand for the anisotropy energy, with ϑ_i the angle between the magnetization vector $\mathbf{M}_i$ and the c axis, α is the angle between the magnetization vectors, and M is the magnitude of the total magnetization vector $\mathbf{M}=\mathbf{M}_1+\mathbf{M}_2$, which is supposed to point into the direction of the applied field $\mathbf{B}$ throughout the magnetization process. It has been shown[1] that the bending of the two magnetization vectors towards each other always takes place within a plane containing the c axis and therefore two angular variables suffice to characterize any state occurring in the process. It turns out that the symmetry properties of an antiferromagnet, $M_1=M_2=M_0$ and $K_1^{(1)}=K_1^{(2)}=K_1$, can be best exploited if the free energy is written in terms of $\vartheta=(\vartheta_1+\vartheta_2)/2$, the angle between the total magnetization vector and the c axis, and $\alpha=\vartheta_2-\vartheta_1$, the angle between the sublattice magnetizations:

$$E(\vartheta,\alpha)=2K_1\left(\sin^2\vartheta\cos^2\frac{\alpha}{2}+\cos^2\vartheta\sin^2\frac{\alpha}{2}\right)+n_{12}M_0^2\cos\alpha-2BM_0\cos\frac{\alpha}{2}. \tag{2}$$

[a]Electronic mail: FRB@Phys.UvA.NL

 0021-8979/96/79(8)/4626/3/$10.00 © 1996 American Institute of Physics

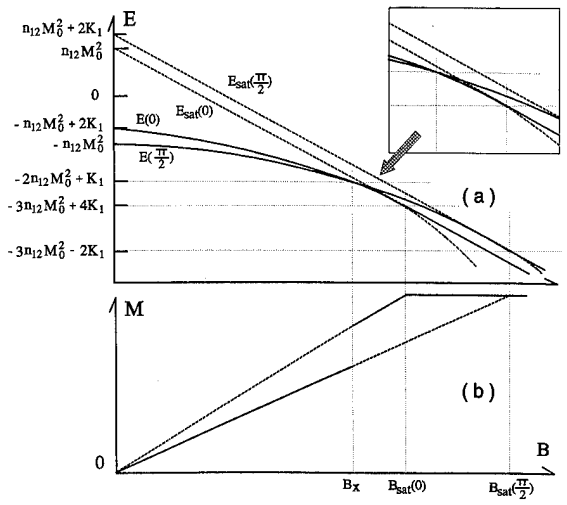


FIG. 1. (a) Field dependence of the free energy for a free-single-crystal antiferromagnet with easy-axis anisotropy. (b) Field dependence of magnetization. $T=0$ K, $B_{sat}(0)>B_x$.

To find the minima of the function (2), we first differentiate with respect to ϑ to find

$$\frac{\partial E}{\partial \vartheta}=2K_1 \sin 2\vartheta \cos \alpha; \quad \frac{\partial^2 E}{\partial \vartheta^2}=4K_1 \cos 2\vartheta \cos \alpha. \tag{3}$$

The condition $\partial E/\partial\vartheta=0$ is satisfied at $\alpha=\pi/2$, but this is not a minimum since in this case $\partial^2 E/\partial\vartheta^2$ (as well as all further derivatives) vanishes. The other condition for a vanishing first derivative is $\sin 2\vartheta=0$. There are two cases of interest, $\vartheta=0$ and $\vartheta=\pi/2$, where the necessary condition of a minimum, $\partial^2 E/\partial\vartheta^2>0$, will be satisfied for $\alpha<\pi/2$ and $\alpha>\pi/2$, respectively. These findings accord with the intuitive notion of uniaxial antiferromagnets: at low fields, where the magnetization vectors are still close to the antiparallel configuration, the $\mathbf{B}\perp c(\vartheta=\pi/2)$ configuration is favorable, whereas close to the forced ferromagnetic alignment $\mathbf{B}\|c(\vartheta=0)$ gives the lowest anisotropy energy.

Though it is clear that the two conditions found above correspond to two distinct regions, it is instructive to derive the free energy as a function of the magnetic field for both. From Eq. (2) we find for $\vartheta=\pi/2$,

$$E\left(\frac{\pi}{2},\alpha\right)=2K_1 \cos^2\frac{\alpha}{2}+n_{12}M_0^2 \cos\alpha-2BM_0 \cos\frac{a}{2} \tag{4}$$

and for $\vartheta=0$,

$$E(0,\alpha)=2K_1 \sin^2\frac{\alpha}{2}+n_{12}M_0^2 \cos\alpha-2BM_0 \cos\frac{\alpha}{2}. \tag{5}$$

The conditions for energy minima, $dE/d\alpha=0$, give in both cases an explicit expression for $\cos\alpha/2(\sin\alpha/2\neq 0)$ which, substituted back into Eqs. (4) and (5) give the desired functions of the applied field: for $\vartheta=\pi/2$,

$$E\left(\frac{\pi}{2},B\right)=-n_{12}M_0^2-\frac{B^2}{2(n_{12}+K_1/M_0^2)} \tag{6}$$

and for $\vartheta=0$,

$$E(0,B)=2K_1-n_{12}M_0^2-\frac{B^2}{2(n_{12}-K_1/M_0^2)}. \tag{7}$$

Through the relation $M=\partial E/\partial B$ both of these equations imply linearly increasing magnetizations, but this of course cannot prevail beyond saturation where, with $\alpha=0$, Eqs. (4) and (5) give

$$E_{sat}\left(\frac{\pi}{2},B\right)=2K_1+n_{12}M_0^2-2BM_0, \tag{8}$$

$$E_{sat}(0,B)=n_{12}M_0^2-2BM_0. \tag{9}$$

Equating the respective energies given by Eqs. (6), (7) and by Eqs. (8) and (9) gives the field values where saturation sets in. In both cases we find only one such value,

$$B_{sat}\left(\vartheta=\frac{\pi}{2}\right)=2M_0\left(n_{12}+\frac{K_1}{M_0^2}\right), \tag{10}$$

$$B_{sat}(\vartheta=0)=2M_0\left(n_{12}-\frac{K_1}{M_0^2}\right) \tag{11}$$

indicating that the straight lines given by Eqs. (8) and (9) are tangent to the parabolae (6) and (7), as illustrated by Fig. 1(a).

Having constructed the free-energy curves, it is now easy to identify the lowest-energy track, which will be followed in the magnetization process. Clearly, up to $B=B_x$, where the two parabolae cross, $\vartheta=\pi/2$ and beyond this field $\vartheta=0$. Setting the energies given by Eqs. (6) and (7) equal, we find

$$B_x^2=2M_0^2\left[n_{12}^2-\left(\frac{K_1}{M_0^2}\right)^2\right]; \quad (3K_1\leq M_0^2 n_{12}). \tag{12}$$

The condition satisfied by this equation will be discussed below. The slopes of the two curves being different at B_x, there must be a discontinuity in the magnetization,

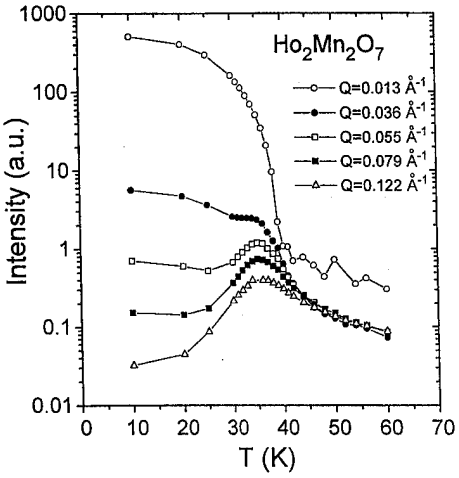


FIG. 2. (a) Field dependence of the free energy for a free-single-crystal antiferromagnet with easy-axis anisotropy. (b) Field dependence of magnetization. $T=0$ K, $B_{sat}(0)<B_x$.

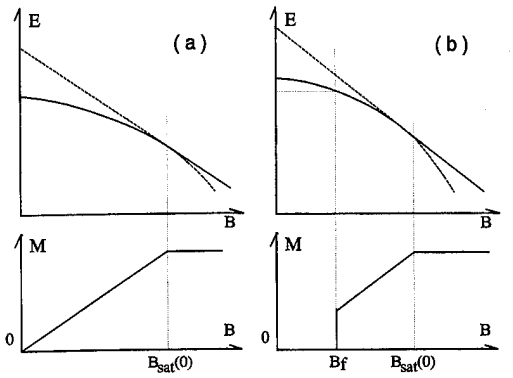


FIG. 3. Field dependence of the free energy and magnetization for a fixed-single-crystal antiferromagnet with easy-axis anisotropy. (a) The applied field is along the hard-magnetization direction. (b) The applied field is along the easy-magnetization irection.

$$\Delta M = 2\sqrt{2} M_0 \sqrt{(K_1/M_0^2)^2/[n_{12}^2 - (K_1/M_0^2)^2]}. \quad (13)$$

Figure 1(b) shows the magnetization curve derived from the solid free-energy curve in Fig. 1(a). The magnetization will jump directly to its saturation value whenever $B_{sat}(\vartheta=0) < B_x$. Using Eqs. (11) and (12), we find that this will be the case when $3K_1 > n_{12}M_0^2$. Under this condition, Eq. (12) has to be replaced by the expression found after equating the energies given by Eqs. (6) and (9)

$$B_x = 2M_0(n_{12} + K_1 M_0^2)(1 - \sqrt{K_1/[n_{12}M_0^2 + K_1]}),$$

$$3K_1 \geqslant n_{12}M_0^2. \quad (14)$$

Figure 2 shows the free-energy and magnetization curves for such a case.

The linear behavior of the magnetization seen in Figs. 1 and 2 is a consequence of the simple form of the anisotropy energy assumed in Eq. (1). However, the occurrence of a jump in the magnetization is a general feature of easy-axis antiferromagnets, as can be seen from the following argument.

Replacing the lowest-order expression $K_1 \sin^2 \vartheta$ by a more general form $E_{an}(\vartheta)$ of the sublattice anisotropy energy will not prevent the crossing of the $E(\pi/2,B)$ and $E(0,B)$ curves. Since $E_{an}(0) < E_{an}(\pi/2)$ must hold to ensure easy-axis anisotropy, it follows that $E(\pi/2,0) - E(\vartheta,0) = 2[E_{an}(0) - E_{an}(\pi/2)] < 0$, whereas at saturation (in the forced ferromagnetic state) $E_{sat}(\pi/2,B) - E_{sat}(0,B) = 2[E_{an}(\pi/2) - E_{an}(0)] > 0$. The form of the function $E_{an}(\vartheta)$ is thus seen to influence the shape of the curved parts of the free-energy functions, but the order of the energy values at zero field and high fields ($B > B_{sat}$) will remain inverted, making an intercept with different slopes and hence a jump in the magnetization inevitable.

The discontinuity in the magnetization is reminiscent of first-order phase transitions, but it should be born in mind that this transition is related to the additional degrees of freedom introduced by the free rotation of the crystals. Indeed, switching from the $\vartheta = \pi/2$ curve to the $\vartheta = 0$ one in Figs. 1 and 2 signifies a rotation of the sample by 90°. The discontinuous changes (spin-flop transitions) known to occur in oriented antiferromagnets are of a different nature. Preliminary experimental results have been reported in Ref. 3.

The free-energy functions (6)–(9) are relevant to the magnetization process in samples fixed at $\mathbf{B} \perp c$ and $\mathbf{B} \| c$ orientations. If $\mathbf{B} \perp c$, the bending process traces the $E(\pi/2,B)$ curve to $B_{sat}(\vartheta = \pi/2)$ and the $E_{sat}(\pi/2,B)$ line thereafter. The magnetization increases continuously up to saturation [Fig. 3(a)]. If $\mathbf{B} \| c$, bending does not begin at $B=0$, because in weak fields the Zeeman energy cannot overcome the anisotropy. The sublattice magnetizations remain in the c direction, fully compensated ($M=0$), until the point is reached (at B_f), where the $E(0,B)$ curve falls below $E(\pi/2,0)$ [Fig. 3(b)]. The transition taking place at this point is not necessarily to a state with $\alpha < \pi/2$, which is one of the features distinguishing it from what takes place in freely rotating samples. Another related feature is the distinct value of B_f, which follows from the condition $E(\pi/2,0) = E(0,B_f)$: $B_f^2 = 4K_1(n_{12} - K_1/M_0^2)$, provided $2K_1 \leqslant n_{12}M_0^2$. The limitation of K_1 to low values comes from the requirement that B_f be less than B_{sat} ($\vartheta = 0$). If that is not the case, the spin-flop will be total, leading to saturation, and B_f is to be determined from the condition $E(\pi/2,0) = E_{sat}(0,B_f)$, which gives $B_f = n_{12}M_0$, provided $2K_1 \geqslant n_{12}M_0^2$. Comparing these results with Eqs. (12) and (14) it clear that B_x and B_f mark the occurrence of transitions of different nature.

[1] Z. G. Zhao, X. Li, J. H. V. J. Brabers, P. F. de Châtel, F. R. de Boer, and K. H. J. Buschow, J. Magn. Magn. Mater. **123**, 74 (1993).
[2] K. H. J. Buschow, Rep. Prog. Phys. **42**, 1373 (1979).
[3] L. D. Tung, K. H. J. Buschow, J. J. M. Franse, and N. P. Thuy, these proceedings.

Dynamics of quantum spin systems in dimer and valence-bond-solid ground states stabilized by competing interactions

Yongmin Yu and Gerhard Müller
Department of Physics, The University of Rhode Island, Kingston, Rhode Island 02881-0817

For special coupling ratios, the one-dimensional (1D) $s=1/2$ Heisenberg model with antiferromagnetic nearest and next-nearest neighbor interactions has a pure dimer ground state, and the 1D $s=1$ Heisenberg model with antiferromagnetic bilinear and biquadratic interactions has an exact valence-bond-solid ground state. The recursion method is used to calculate the $T=0$ spin dynamic structure factor for both models and, for the $s=1/2$ model, also the dimer dynamic structure factor. New results for line shapes and dynamically relevant dispersions are obtained.
© *1996 American Institute of Physics.* [S0021-8979(96)00208-7]

Correlated quantum fluctuations in the ground state are a generic feature of quantum many-body systems. They make it hard to take finite-size effects into account in computational studies of zero-temperature dynamical properties. Interestingly, there are several known cases, where a relatively simple-structured ground state is stabilized by competing terms in the microscopic Hamiltonian. This ground state may or may not be long-range ordered. The essential attribute is that its fluctuations are not correlated or only over a short distance on the lattice. This phenomenon typically occurs with no accompanying simplification in the excitation spectrum or any dynamical quantity. Nevertheless, any such situation provides an unsuspected window for dynamical studies which promise to be much less plagued with finite-size effects than is typically the case. The recursion method[1] in combination with recently developed techniques of continued-fraction analysis[2] is an ideal calculational tool for that purpose, the key property being that it extracts the dynamical information from the ground-state wave function.

In a previous paper we have reported the study of one such case, namely the one-dimensional (1D) spin-s XYZ model.[3] In a magnetic field of particular strength, this model has a product ground state with spontaneous ferro- or antiferromagnetic long-range order perpendicular to the field. Here we present new results for two different models with simple-structured ground states.

The first model is the 1D $s=1/2$ Heisenberg antiferromagnet with competing nearest and next-nearest neighbor interactions,

$$H=\sum_{l=1}^{N}\{J_1\mathbf{S}_l\cdot\mathbf{S}_{l+1}+J_2\mathbf{S}_l\cdot\mathbf{S}_{l+2}\}, \tag{1}$$

with an even number of spins and periodic boundary conditions. This system undergoes a $T=0$ phase transition at $J_2/J_1\simeq 0.25$ from a spin-fluid phase to a phase with spontaneous dimer long-range order.[4] In the (critical) spin-fluid phase, the correlations of the quantum fluctuations are particularly strong. In the dimer phase, their continued presence, albeit much attenuated, manifests itself, for example, in the finite-size splitting of the ground-state doublet. The exception is the special coupling ratio $J_2/J_1=0.5$, where the pure dimer ground-state is realized.[5,6] Here the ground-state energy per site is size-independent: $E_0/N=-\frac{3}{8}J_1$.

The two (translationally invariant) dimer ground-state wave functions can be expressed in terms of products of singlets formed by pairs of nearest neighbor spins:

$$|\Phi_\pm\rangle=[2\pm(-1/2)^{(N-4)/2}]^{-1/2}\{|\Phi_1\rangle\pm|\Phi_2\rangle\}, \tag{2}$$

where $|\Phi_1\rangle=[1,2][3,4]\cdots[N-1,N]$, $|\Phi_2\rangle=[2,3][4,5]\cdots[N,1]$, $\times[l,l+1]=\{|\uparrow\downarrow\rangle-|\downarrow\uparrow\rangle\}/\sqrt{2}$.

The dimer order parameter, $D=N^{-1}\Sigma_l(-1)^l D_l$, $D_l=S_l^+S_{l+1}^- + S_l^-S_{l+1}^+$, has a nonzero expectation value, $\langle D\rangle=\pm 1/2$ in the (non-orthogonal) symmetry-breaking states $|\Phi_1\rangle$ and $|\Phi_2\rangle$. The order-parameter correlation function in this case is not a two-spin correlation function, ($\langle S_l^zS_{l+n}^z\rangle=0$ for $|n|>1$), but a four-spin correlation function: $\langle D_lD_{l+n}\rangle-\langle D_l\rangle\langle D_{l+n}\rangle=(-1)^n/4$ for $n\neq 0$. Hence it will be instructive to compare the spin dynamic structure factor $S_{zz}(q,\omega)$ and the dimer dynamic structure factor $S_{DD}(q,\omega)$, i.e. the function

$$S_{AA}(q,\omega)=\int_{-\infty}^{+\infty}dt\; e^{i\omega t}\langle A_q(t)A_{-q}\rangle, \tag{3}$$

where A_q stands for the spin fluctuation operator, $S_q^z=N^{-1/2}\Sigma_l e^{iql}S_l^z$ or the dimer fluctuation operator, $D_q=N^{-1/2}\Sigma_l e^{iql}[D_l-\langle D_l\rangle]$.

By means of the recursion method[1] in combination with a strong-coupling continued-fraction analysis,[2,7] we calculate the dynamically relevant excitation spectra and the spectral-weight distributions of these two functions. The recursion algorithm in the present context is based on an orthogonal expansion of the wave function $|\Psi_q^A(t)\rangle=A_q(-t)|\Phi\rangle$. It produces (after some intermediate steps) a sequence of continued-fraction coefficients $\Delta_1^A(q),\Delta_2^A(q),\ldots$ for the relaxation function,

$$c_0^{AA}(q,z)=\cfrac{1}{z+\cfrac{\Delta_1^A(q)}{z+\cfrac{\Delta_2^A(q)}{z+\ldots}}}, \tag{4}$$

which is the Laplace transform of the symmetrized correlation function $\Re\langle A_q(t)A_{-q}\rangle/\langle A_qA_{-q}\rangle$. The $T=0$ dynamic structure factor (3) is then obtained from (4) via

$$S_{AA}(q,\omega)=4\langle A_qA_{-q}\rangle\Theta(\omega)\lim_{\varepsilon\to 0}\Re[c_0^{AA}(q,\varepsilon-i\omega)]. \tag{5}$$

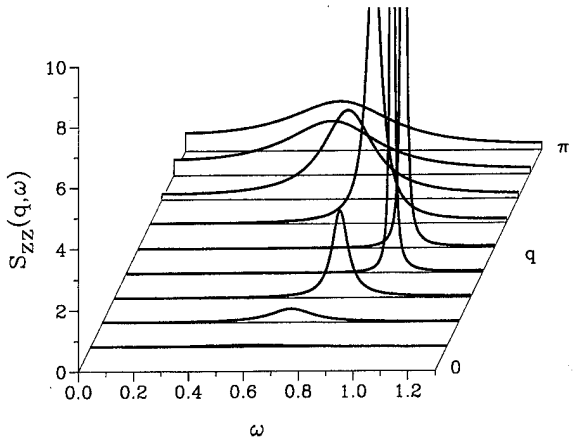


FIG. 1. Dynamic structure factor $S_{zz}(q,\omega)$ vs ω for $q=2\pi l/N$, $l=0,1,\ldots,N/2$ in the dimer ground state $|\Phi_+\rangle$ of the Hamiltonian (1) at $J_2=0.5$ and $J_1=1$ with $N=18$, obtained via strong-coupling continued-fraction reconstruction based on the coefficients $\Delta_1,\ldots,\Delta_9$ and a Gaussian terminator as explained in Refs. 2 and 7.

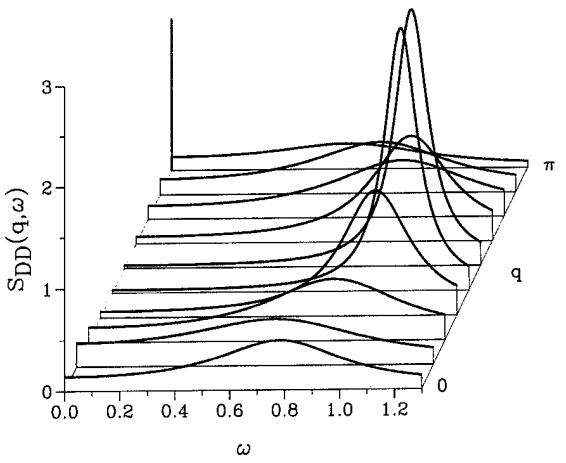


FIG. 2. Dynamic structure factor $S_{DD}(q,\omega)$ vs ω for $q=2\pi l/N$, $l=0,1,\ldots,N/2$ in the dimer ground state $|\Phi_+\rangle$ of the Hamiltonian (1) at $J_2=0.5$ and $J_1=1$ with $N=18$, obtained via strong-coupling continued-fraction reconstruction based on the coefficients $\Delta_1,\ldots,\Delta_9$ and a Gaussian terminator.

The simple N-dependence of the dimer ground-state wave functions (2) offers the advantage that we can compute a significant number of N-independent coefficients $\Delta_k^A(q)$. These data are the input to the well-tested strong-coupling continued-fraction reconstruction.[2,7]

The results for the frequency-dependence of the dynamic structure factor $S_{zz}(q,\omega)$ at the wave numbers realized for $N=18$ are displayed in Fig. 1. The set of curves is perfectly compatible with a function $S_{zz}(q,\omega)$ that varies smoothly in q as well as in ω. For every q-value we observe a single peak in the frequency range of interest. This peak is very broad at q near zero or π. The width shrinks as q approaches $\pi/2$ from either side.

At $q=\pi/2$ (not realized for $N=18$) the dynamically relevant excitation spectrum reduces to a single mode. The states $S^z_{\pi/2}|\Phi_\pm\rangle$ are, in fact, known to be exact eigenstates of the system.[8,9] The dynamically relevant dispersion of $S_{zz}(q,\omega)$ is symmetric about $q=\pi/2$, where it has a smooth maximum at frequency $\omega/J_1=1.0$. For $q=0$ and $q=\pi$ it has smooth minima at $\omega/J_1\simeq 0.5$.

On the basis of a variational calculation for the pure dimer state, Shastry and Sutherland[6] obtained an excitation spectrum for this model which consists of a continuum of two-defect scattering states with a lower boundary $\epsilon(q)=J_1(\frac{5}{4}-|\cos q|)$ and, for the restricted range $0.36\pi<q<0.64\pi$ of wave numbers, a branch of defect bound states, which emerges from the lower continuum boundary and has a smooth maximum reaching up to $\omega/J_1=1$ at $q=\pi/2$.

In this context, our results suggest that for q near zero or π, the spectral weight of $S_{zz}(q,\omega)$ is distributed over a broad frequency range of two-defect scattering states. As q approaches $\pi/2$ from either side, the spectral weight is shifted gradually to the two-defect bound state.

Our result for the dynamic structure factor $S_{DD}(q,\omega)$ is plotted in Fig. 2 for the same set of wave numbers. The line shapes and peak positions resemble those shown in Fig. 1 for $S_{zz}(q,\omega)$, but there are some notable differences: The spectral weight in $S_{DD}(q,\omega)$ is concentrated at somewhat higher energies. The intensity at $q=0$ is nonzero. The shape of the dimer dispersion is different. $S_{DD}(\pi/2,\omega)$ does not reduce to a single line. In $S_{DD}(\pi,\omega)$ the spectral weight is shared between a continuum and a δ-peak at $\omega=0$. The latter contribution reflects the presence of dimer long-range order in the ground state.

The Hamiltonian of the 1D $s=1$ model with isotropic bilinear and biquadratic exchange, our second example, is most conveniently expressed in the form

$$H_\gamma=J\sum_{l=1}^{N}\{\cos\gamma\mathbf{S}_l\cdot\mathbf{S}_{l+1}+\sin\gamma(\mathbf{S}_l\cdot\mathbf{S}_{l+1})^2\} \tag{6}$$

with a single parameter $-\pi<\gamma\leq\pi$. More than a decade of research on this model has established a $T=0$ phase diagram consisting of the short-range ordered Haldane phase and three phases with dimer, trimer, and ferromagnetic long-range order.[10] In the Haldane phase, which includes the Heisenberg antiferromagnet ($\gamma=0$), the ground state is a non-degenerate singlet state ($S_T=0$) separated by a gap from the threshold of the excitation spectrum.

At the parameter value $\gamma=\arctan(1/3)\simeq 18.4°$ within this phase, the ground-state wave function is exactly known.[11] It is a realization of the so-called valence-bond-solid (VBS) wave function, which can be assembled from the same parts as the dimer state (2). The spin 1 at each lattice site is expressed as a spin-1/2 pair in a triplet state. The singlet-pair forming valence bond involves one fictitious spin 1/2 from each of two neighboring lattice sites. The VBS state can then be regarded as a chain of valence bonds linking successive symmetrized spin-1/2 pairs, which are given by the $S^z_T=0$ vector of the triplet on each lattice site.

The static spin correlation function in the VBS state,[11] $\langle S^z_l S^z_{l+n}\rangle=\frac{4}{3}(-1)^n 3^{-|n|}$, $(n\neq 0)$, reflects magnetic short-range order with a very short correlation length:

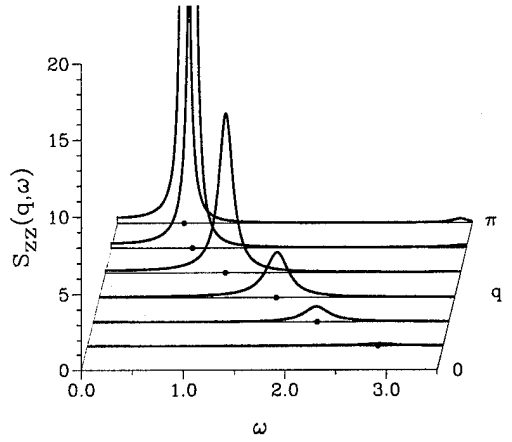


FIG. 3. Dynamic structure factor $S_{zz}(q,\omega)$ vs ω for $q=2\pi l/N$, $l=0,1,\ldots,N/2$ in the VBS ground state of the model system (6) at $J=1$ and $\gamma=\arctan(1/3)$ with $N=12$, obtained via a strong-coupling continued-fraction analysis based on the coefficients $\Delta_1,\ldots,\Delta_6$ and a Gaussian terminator.

$\xi=1/\ln 3\simeq 0.91$. The static structure factor is then a non-singular function with a smooth minimum at $q=0$ and a smooth maximum at $q=\pi$:

$$S^{zz}(q)=2(1-\cos q)/(5+3\cos q). \tag{7}$$

The simple structure of the VBS state makes this quantity free of finite-size effects for $q=2\pi l/N$, $l=0,\ldots,N-1$. Again, this simplification does not extend to the excitation spectrum and the dynamical properties.

In Fig. 3 we have plotted $S_{zz}(q,\omega)$ as obtained from a strong-coupling continued-fraction analysis with coefficients extracted from the $N=12$ VBS wave function. At each value of q the spectral weight of $S_{zz}(q,\omega)$ is found to be concentrated in a single peak with symmetric line shape. The peak frequency decreases monotonically with q. The suggested gap value at $q=\pi$ is $\Delta E/J\simeq 0.66$, in good agreement with the result $\Delta E/J\simeq 0.70$ of the single-mode approximation.[12] The linewidth tends to be very small at q near π, where the peak frequency is lowest and the intensity highest. It gains considerably in breadth at q near 0, where the peak frequency is higher and the intensity much lower.

The monotonic q-dependence of the dynamically relevant dispersion for $S_{zz}(q,\omega)$ in the VBS state ($\gamma\simeq 18.4°$) is markedly different from the corresponding quantity in the Heisenberg antiferromagnet ($\gamma=0$), which belongs to the same phase. In the Heisenberg case, the dispersion has a smooth maximum at $q\simeq\pi/2$ and smooth minima of unequal height at $q=0$ and $q=\pi$.[13]

This work was supported by NSF Grant DMR-93-12252 and by the NCSA at Urbana-Champaign.

[1] R. Haydock, Solid State Phys. **35**, 215 (1980); M. H. Lee, Phys. Rev. B **26**, 2547 (1982); E. R. Gagliano and C. A. Balseiro, *ibid.* **38**, 11766 (1988).
[2] V. S. Viswanath and G. Müller, *The Recursion Method. Application to Many-body Dynamics*, Lecture Notes in Physics Vol. 23 (Springer, New York, 1994).
[3] V. S. Viswanath, J. Stolze, and G. Müller, J. Appl. Phys. **75**, 6057 (1994).
[4] F. D. M. Haldane, Phys. Rev. B **25**, 4925 (1982); T. Tonegawa and I. Harada, J. Phys. Soc. Jpn. **56**, 2153 (1987).
[5] C. K. Majumdar and D. K. Ghosh, J. Math. Phys. **10**, 1388 (1969); P. M. Van den Broek, Phys. Lett. A **77**, 261 (1980).
[6] B. S. Shastry and B. Sutherland, Phys. Rev. Lett. **47**, 964 (1981).
[7] V. S. Viswanath, S. Zhang, J. Stolze, and G. Müller, Phys. Rev. B **49**, 9702 (1994).
[8] W. J. Caspers and W. Magnus, Phys. Lett. A **88**, 103 (1982).
[9] The single-mode spectrum of $S_{zz}(\pi/2,\omega)$ causes the recursion algorithm to terminate spontaneously during the first iteration.
[10] A concise recent review was compiled by U. Schollwöck, Th. Jolicoeur, and T. Gorel, Phys. Rev. B (to be published).
[11] I. Affleck, T. Kennedy, E. H. Lieb, and H. Tasaki, Phys. Rev. Lett. **59**, 799 (1987).
[12] D. P. Arovas, A. Auerbach, and F. D. M. Haldane, Phys. Rev. Lett. **60**, 531 (1988).
[13] O. Golinelli, Th. Jolicoeur, and R. Lacaze, J. Phys. C: Cond. Matter **5**, 1399 (1993); S. Haas, J. Riera, and E. Dagotto, Phys. Rev. B **48**, 3281 (1993).

Spin correlation functions in random-exchange $s=1/2$ XXZ chains

Heinrich Röder[a] and Joachim Stolze[b]
Physikalisches Institut, Universität Bayreuth, 95440 Bayreuth, Germany

Richard N. Silver
Theoretical Division, LANL, Los Alamos, New Mexico 87545

Gerhard Müller
Department of Physics, The University of Rhode Island, Kingston, Rhode Island 02881-0817

The decay of (disorder-averaged) static spin correlation functions at $T=0$ for the one-dimensional spin-1/2 XXZ antiferromagnet with uniform longitudinal coupling $J\Delta$ and random transverse coupling $J\lambda_i$ is investigated by numerical calculations for ensembles of finite chains. At $\Delta=0$ (XX model) the calculation is based on the Jordan-Wigner mapping to free lattice fermions for chains with up to $N=100$ sites. At $\Delta \neq 0$ Lanczos diagonalizations are carried out for chains with up to $N=22$ sites. The longitudinal correlation function $\langle S_0^z S_r^z\rangle$ is found to exhibit a power-law decay with an exponent that varies with Δ and, for nonzero Δ, also with the width of the λ_i-distribution. The results for the transverse correlation function $\langle S_0^x S_r^x\rangle$ show a crossover from power-law decay to exponential decay as the exchange disorder is turned on. © *1996 American Institute of Physics.* [S0021-8979(96)00308-3]

The combination of randomness and quantum fluctuations is well known to be a fertile ground for interesting physical phenomena including Anderson localization. In one-dimensional (1D) tight-binding systems the rule is that disorder always leads to localization. However, if the randomness is purely off-diagonal, the localization length diverges at the band center,[1] which is bound to affect the decay law of correlation functions. One particular off-diagonally disordered fermion model, the 1D half-filled tight-binding model with random hopping, is equivalent to the special XX case ($\Delta=0$) of the 1D $s=1/2$ XXZ model with random transverse exchange coupling, described by the Hamiltonian

$$H=J\sum_i [\lambda_i(S_i^x S_{i+1}^x+S_i^y S_{i+1}^y)+\Delta S_i^z S_{i+1}^z]. \tag{1}$$

The uniform longitudinal spin coupling corresponds to a fermion interaction. Here we consider the range $0\leqslant\Delta\leqslant 1$, use periodic boundary conditions, and take the random transverse coupling $J\lambda_i$ to be described by a Gaussian distribution with $\overline{\lambda_i}=1$, $\overline{\lambda_i\lambda_j}=1+\sigma^2\delta_{ij}$. The spin correlations at $T=0$ of this model were recently investigated by means of a real-space renormalization group (RSRG) method[2,3] based in part on ideas from earlier work,[4] and by means of a finite-chain study.[5]

One interesting proposition made in the context of the RSRG study is the existence of a *random-singlet phase* with algebraically decaying spin pair correlations:[2,3]

$$\langle S_0^\alpha S_r^\alpha\rangle\sim(-1)^r r^{-\eta_\alpha},\quad \alpha=x,z. \tag{2}$$

The singlet nature of that phase would imply that the characteristic exponent η_α assumes the same value in the longitudinal (z) and transverse (x) correlation functions, in marked contrast to the case with no exchange disorder ($\sigma=0$), for which we know the exact result[6]

$$\eta_x=1/\eta_z=1-(1/\pi)\arccos\Delta. \tag{3}$$

The RSRG study further predicts that this exponent value is $\eta_x=\eta_z=2$, independent of the longitudinal coupling Δ and the disorder strength σ, provided the latter is not too small. It is indeed quite unusual that the anisotropic randomization of an anisotropic exchange interaction should effectively remove the effects of anisotropy in the spin correlations.

Here we report results of a finite-chain study which goes significantly beyond that of Ref. 5 in statistics and system sizes. For the XX model ($\Delta=0$), we carry out the computation in the (free-) fermion representation, which enables us to handle chains with up to $N=100$ spins and beyond. For $\Delta \neq 0$ we must resort to Lanczos diagonalizations. Here the largest system for which we can perform the computation with reasonable statistics has $N=22$ sites. For graphical purposes we shall consider, henceforth, the absolute value, $|\langle S_0^\alpha S_r^\alpha\rangle|$, of the spin pair correlations.

We first consider the case $\Delta=0$ (XX model). If the longitudinal correlation function does exhibit power-law decay, $|\langle S_0^z S_r^z\rangle| \sim r^{-\eta_z}$, as predicted, then the exponent η_z also governs the N-dependence of the function $|\langle S_0^z S_{N/2}^z\rangle|$ in a cyclic chain of N sites.[5] We have evaluated this quantity for systems with $N\leqslant 100$ sites and for disorder strengths $\sigma\leqslant 2$, all with ensemble averages over up to 10^5 configurations.

The data analysis yields $\eta_z=2$ independent of σ. This is consistent with the RSRG prediction[2,3] but in contradiction to the earlier finite-size study,[5] where a significant σ-dependence of η_z was observed.[7] Our data also confirm that the disorder-averaged logarithm of $|\langle S_0^z S_r^z\rangle|$ exhibits the decay law $\sim -r^{1/2}$ as predicted in Ref. 3.

The decay of the transverse correlation function $\langle S_0^x S_r^x\rangle$ is much more sensitive to the presence of exchange disorder, as is demonstrated by the data shown in Figs. 1 and 2. In the main diagram of Fig. 1 we show the function $|\langle S_0^x S_r^x\rangle|$ versus r in a logarithmic plot for ensembles with different disorder strengths. Turning on the exchange disorder with gradually

[a]Theoretical Division, LANL, Los Alamos, New Mexico 87545 (permanent address).
[b]Institut für Physik, Universität Dortmund, Germany (permanent address).

 0021-8979/96/79(8)/4632/3/$10.00 © 1996 American Institute of Physics

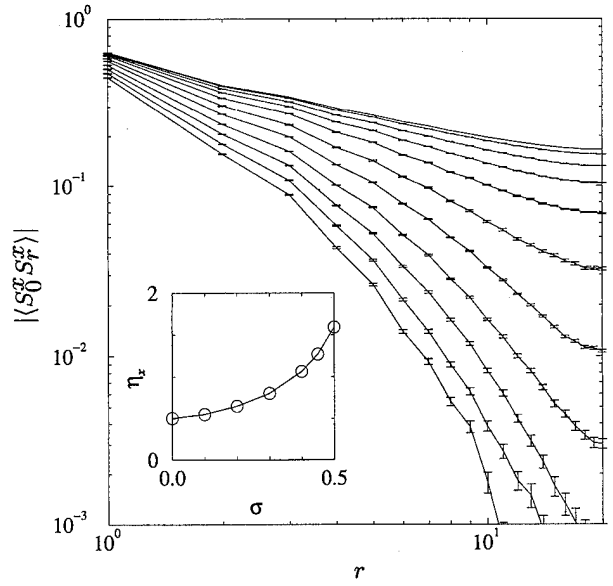


FIG. 1. Log-log plot of $|\langle S_0^x S_r^x \rangle|$ at $T=0$ in the random-exchange XX chain ($\Delta=0$) with $N=40$ spins at disorder strengths $\sigma=0,0.1,\ldots,1$ (top to bottom). For $0<\sigma\leq 0.5$ the expectation value of $\langle S_0^x S_r^x \rangle$ has been averaged over 10^4 configurations, and for $\sigma>0.5$, over 10^5 configurations. The inset shows the (effective) decay exponent η_x as a function of the disorder strength σ.

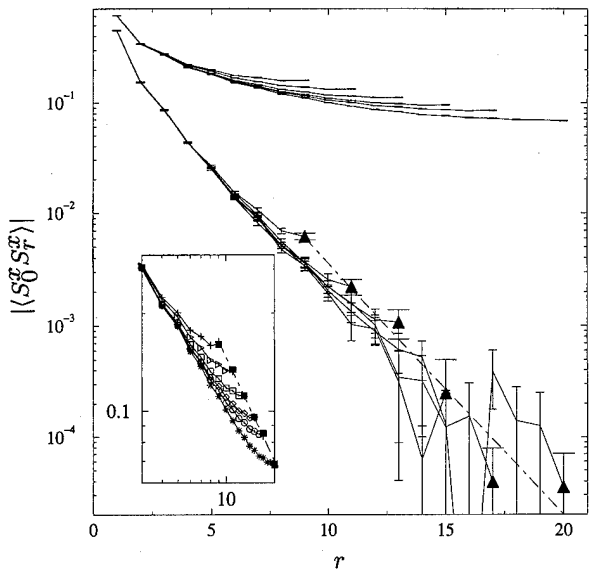


FIG. 2. Semi-logarithmic plot of $|\langle S_0^x S_r^x \rangle|$ with $r\leq N/2$ at $T=0$ in the random-exchange XX chain ($\Delta=0$) with $N=18, 22, 26, 30, 34, 40$, for $\sigma=0.4$ (upper set of curves, averaged over 10^4 configurations) and $\sigma=1$ (lower set of curves, averaged over 10^5 configurations). The data points for $\sigma=1$ at maximum distance ($r=N/2$) are marked by full triangles. The straight line which best fits these data points is shown dot-dashed and determines the correlation length ξ. The inset shows the data for $\sigma=0.4$ in a log-log plot. The data points at maximum distance ($r=N/2$) are marked by full squares. The straight line which best fits these data points is shown dot-dashed and determines the correlation exponent η_x.

increasing σ causes the transverse correlations to decay more and more rapidly as one might expect.[8]

For $0\leq\sigma\lesssim 0.5$ the data describe a power-law behavior. This is also evident in the bundle of curves near the top of Fig. 2, which shows the r-dependence of the function $|\langle S_0^x S_r^x \rangle|$ semi-logarithmically at $\sigma=0.4$ for various system sizes. The values $|\langle S_0^x S_{N/2}^x \rangle|$ at the endpoints of these curves plotted vs $N/2$ in a log-log graph fall onto a straight line, and the slope of that line determines the exponent η_x. This is illustrated by the full squares in the inset to Fig. 2.

The σ-dependence of η_x as obtained from this procedure is shown in the inset to Fig. 1. For the system without exchange disorder we reproduce the exactly known value $\eta_x=1/2$,[9] which is a special case of (3). As σ increases from zero, η_x grows gradually and monotonically, at first slowly, then more and more rapidly.

For $\sigma\gtrsim 0.5$ the curves in Fig. 1 suggest the occurrence of a crossover from algebraic decay to exponential decay, $|\langle S_0^x S_r^x \rangle| \sim \exp(-r/\xi)$, in the range of r for which we have data. The exponential character of the decay is more strikingly manifest in the lower bundle of data shown in the main plot of Fig. 2, representing the function $|\langle S_0^x S_r^x \rangle|$ at $\sigma=1$ for various system sizes.[8] The smallest expectation values are known only with considerable (relative) uncertainty despite the augmented statistics.

The triangles, which represent the values $|\langle S_0^x S_{N/2}^x \rangle|$ vs $N/2$ in this semi-logarithmic plot, are consistent with a straight line. Its slope determines the disorder-induced correlation length ξ. Over the range of disorder strengths, where our data suggest exponential decay of $|\langle S_0^x S_r^x \rangle|$, ξ thus determined decreases monotonically with increasing σ.

Our data for the exchange disordered XX model are consistent with two alternative scenarios, which are equally interesting:

(i) There exists a transition at some nonzero value of the disorder strength, $\sigma_c\simeq 0.5$, from algebraically to exponentially decaying transverse spin correlations.

(ii) A transition of the same nature occurs at $\sigma_c=0$ instead, which produces very similar crossover effects in the finite-chain data.

A more extensive study for longer chains and with better statistics will be necessary to discriminate with confidence between the two scenarios.[10] The data are definitely incompatible with a persistent power-law decay as predicted by RSRG.

Now we turn to one case, $\Delta=0.75$, with fermion interaction (XXZ model). Since the computations are much more involved, the available data are limited by comparison with the case $\Delta=0$. At $\Delta\neq 0$ neither our data for the longitudinal correlations nor those for the transverse correlations are compatible with the RSRG predictions.

The function $|\langle S_0^z S_r^z \rangle|$ for various system sizes and $\sigma=1.5$ is shown logarithmically in Fig. 3. The endpoint data ($r=N/2$), which fall neatly onto a straight line, describe a power-law decay with $\eta_z=1.26$. The exponent values obtained for two smaller disorder strengths are $\eta_z=1.17$ ($\sigma=0.5$) and $\eta_z=1.31$ ($\sigma=0.25$). The exact result (3) for $\sigma=0$ assumes the value $\eta_z=1.298\ldots$

All combined, the data suggest that the function $|\langle S_0^z S_r^z \rangle|$ is governed by a power-law which persists in the presence of randomness. The σ-dependence of the exponent

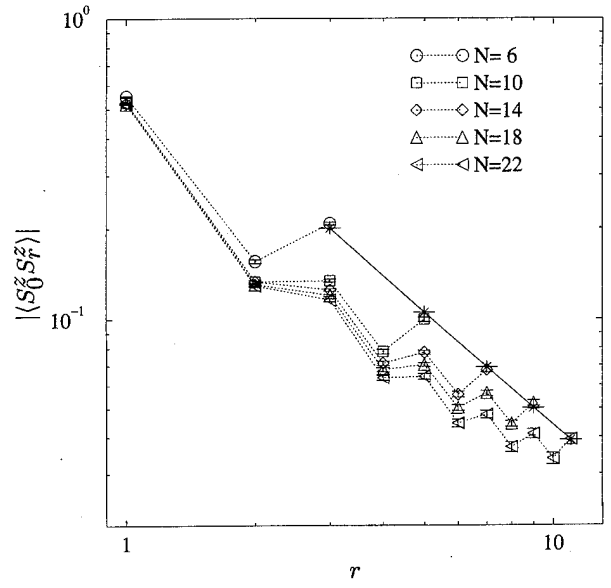


FIG. 3. Log-log plot of $|\langle S_0^z S_r^z\rangle|$ for the XXZ model with uniform longitudinal exchange ($\Delta=0.75$) and random transverse exchange ($\sigma=1.5$) on chains of various lengths. The data points represent averages over 1000 configurations for $N=6,\ldots,18$, and 450 configurations for $N=22$.

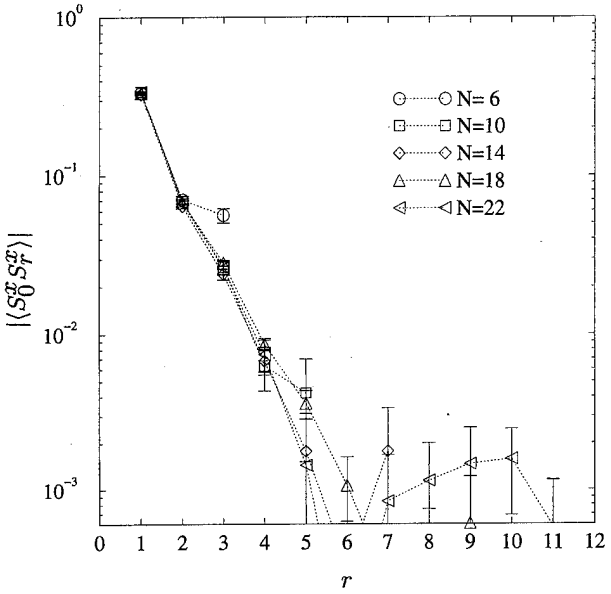


FIG. 4. Semi-logarithmic plot of $|\langle S_0^x S_r^x\rangle|$ for the XXZ model with uniform longitudinal exchange ($\Delta=0.75$) and random transverse exchange ($\sigma=1.5$) on chains of various lengths. The data points represent averages over 1000 configurations for $N=6,\ldots,18$, and 450 configurations for $N=22$.

η_z appears to go through a minimum of considerable depth at $\sigma \neq 0$,[11] which implies the curious phenomenon that the longitudinal correlations are enhanced by a small amount of transverse exchange disorder relative to the correlations in the uniform-exchange system.

The data for the transverse correlations $|\langle S_0^x S_r^x\rangle|$ at $\Delta=0.75$ exhibit properties very similar to what we have observed and described for the free-fermion case ($\Delta=0$). For not too large disorder strengths ($\sigma\lesssim 0.5$), we see a power-law behavior with an exponent that increases monotonically from the exactly known value $\eta_x=0.769\ldots$ at $\sigma=0$, as given by expression (3), to $\eta_x=1.00$ at $\sigma=0.25$ and $\eta_x=1.49$ at $\sigma=0.5$, at which point a crossover to exponential behavior makes itself felt. The exponential decay law at $\sigma=1.5$ is quite evident in the semi-logarithmic plot of Fig. 4.

The discrepancies between our results and the RSRG predictions of Refs. 2,3 call for an explanation in future studies. Possibly, the strongly *anisotropic* nature of the exchange in the model system (1) – even for $\Delta=1$ – is not adequately taken into account by the RSRG procedure, which derives from a method originally developed for a model with *isotropic* exchange.[4]

In order to gain further insight into the properties of the XXZ chain with random exchange, we plan to investigate the nature of low-lying excitations and the properties of dynamic correlation functions. At $\Delta=0$ the Jordan-Wigner mapping to free fermions will make it possible to carry out these calculations for large systems. At $\Delta \neq 0$ the KPM method developed recently[12] promises to be an adequate calculational instrument.

The work at URI was supported by NSF Grant DMR-93-12252 and by the NCSA at Urbana-Champaign.

[1] T. P. Eggarter and R. Riedinger, Phys. Rev. B **18**, 569 (1978).
[2] C. A. Doty and D. S. Fisher, Phys. Rev. B **45**, 2167 (1992).
[3] D. S. Fisher, Phys. Rev. B **50**, 3799 (1994).
[4] C. Dasgupta and S.-K. Ma, Phys. Rev. B **22**, 1305 (1980).
[5] S. Haas, J. Riera, and E. Dagotto, Phys. Rev. B **48**, 13174 (1993).
[6] A. Luther and I. Peschel, Phys. Rev. B **12**, 3908 (1975).
[7] See Fig. 2 of Ref. 5.
[8] The upward curvature in the vicinity of $r=N/2$ is an obvious finite-size effect attributable to periodic boundary conditions.
[9] B. M. McCoy, Phys. Rev. **173**, 531 (1968).
[10] Preliminary results for chains with up to $N=200$ sites indicate that scenario (ii) is more likely.
[11] The same effect had previously been observed in Ref. 5, also for the case $\Delta=0$, where it is absent in our data.
[12] R. N. Silver and H. Röder, Int. J. Mod. Phys C **5**, 735 (1994).

Rotational hysteresis and self-organized criticality in magnetic recording media

T. L. Templeton and A. S. Arrott
Physics Department, Simon Fraser University, Burnaby, British Columbia, V5A 1S6, Canada

Collective magnetic dipoles are written into sections of commercial magnetic recording tapes by application of high fields at angles θ_{set} with respect to the tape axis. The media is rotated 2000 times about the tape normal in a lower magnetic field H_m in the plane of the tape. The magnetization along the direction of H_m is measured in steps of $\Delta\theta=\pi/5$. Harmonic analysis of the angular dependence of the magnetization is used to discover how the dipole term depends on cycle number n, H_m, the direction of rotation, and θ_{set}. The data are analyzed using $\mu_d(n)=\mu_d(\infty)+[\mu_d(1)-\mu_d(\infty)]n^{-\gamma}$. This dipole disappears on rotation for an infinite number of cycles in fields $H_m>H_{crit}$. For $H_m<H_{crit}$, $\mu_d(\infty)$ depends on H_m much as $M_s(T)$ depends on temperature. For H_m close to H_{crit}, γ becomes as small as 0.1 for which 10^{10} cycles would be required to produce 90% of the change.
© *1996 American Institute of Physics.* [S0021-8979(96)04108-8]

The purpose of this paper is to call the attention of theorists interested in self-organized criticality[1] to a system that is more amenable to both numerical simulations and experimental realization than several previously studied phenomena.[2–5] The object of our studies is a previously magnetized piece of magnetic recording tape in which, during rotation by 360° in a field H_m of the order of the coercivity, some of the particles switch the direction of magnetization and some of them do not. Which particles switch depends on the field and on past history. For rotation through many cycles, an equilibrium should be approached in which a fraction $f_{+\infty}$ remains magnetized in the original direction, another fraction $f_{-\infty}$ remains magnetized in the opposite direction, and the rest $f_{S\infty}=1-f_{+\infty}-f_{-\infty}$ switch twice on each cycle or some small set of cycles. We can not measure directly these fractions because there are angular distributions of the magnetic moments. These come from the spatial dispersion of the axes of the particles, the effect of the applied field on the direction of the moment, and the effects of dipole-dipole interactions. We measure the magnetic moment along the field direction at 10 angles during a rotation through 360° for up to 2000 cycles. We analyze the response in each cycle into its harmonic components. From the component that goes as

$$\mu_d(\theta,n)=\mu_d'(n)\cos(\theta)+\mu_d''(n)\sin(\theta), \tag{1}$$

we extract the net dipole in the nth cycle,

$$\mu_d(n)=\sqrt{[\mu_d'(n)]^2+[\mu_d''(n)]^2}, \tag{2}$$

and its angle

$$\beta_d(n)=\arctan[\mu_d''(n)/\mu_d'(n)]. \tag{3}$$

We normalize these moments to the moment μ_s measured at saturation, $\mu_0 H_s=1.2$ T. (Because the dipole changes more in the first half than the second half of a cycle there is some ambiguity about the meaning of n; we use $n=p+1/2$ for the pth cycle.) This is repeated for up to 20 different fields and for both clockwise, cw, and counter clockwise, ccw, rotations.

In the limit of an infinite number of cycles, $\mu_d(\infty)$ should be finite below some critical field H_{crit} and zero above. We fit the dependence of $\mu_d(n)$ on the cycle number using the three parameter expression

$$\mu_d(n)=\mu_d(\infty)+[\mu_d(1)-\mu_d(\infty)]n^{-\gamma}, \tag{4}$$

where $\mu_d(\infty)$ and $\mu_d(1)$ are parameters rather than direct measurements and therefore depend on the choice of the power γ. The data for the first two cycles are not used. From our measurements we determine the dependence of the three parameters $\mu_d(\infty)$, $\mu_d(1)$, and γ on the measuring field for fields from zero to saturation. This is done for various directions of the initial dipole with respect to the tape axis; that is, the initial saturating field is applied at an angle θ_{set}. The cycles are started from the direction of θ_{set}. The range of θ_{set} from 0 to 90° should be sufficient, but we carry out measurements for θ_{set} from 0 to 144° to be sure. The angles of most interest are $\theta_{set}=0$, 81°, and 90°. The analysis here differs from that given previously in that the order of extrapolation and harmonic analysis are reversed.[6] It is reassuring that the order does not matter.

The experiments have been carried out using four basic types of magnetic recording tapes. The data reported here are for a "FUJI FR metal" tape. There are time effects that cannot be ignored for CrO_2 tapes and which are troublesome for γ-Fe_2O_3 based tapes, whereas for the metallic tapes they are barely detectable. The study of time effects will be reported separately.

Equation (4) is empirical, based on the ubiquitous presence of power laws throughout the physical world. Three parameters is the minimum number required by the data shown on the left in Fig. 1 for $\theta_{set}=0$, 81°, and 90° and for measuring fields $\mu_0 H_m=0.073$, 0.081, 0.094, 0.104, and 0.119 T. Here we plot $\Delta\mu_d\equiv[(\mu_d(n)-\mu_d(\infty)]/[\mu_d(1)-\mu_d(\infty)]=n^{-\gamma}$. The solid line curve fits are generated from Eq. (4) which requires that $\Delta\mu_d=1$ at $n=1$ and $\Delta\mu_d=0$ at $n=\infty$. It should be noted that the decay is slowest for H_m just below the coercivity H_c, as discussed previously.[6] For $\gamma=0.1$, the extrapolation from $n=2000$ spans one half of the change. The normalization to $\mu_d(1)-\mu_d(\infty)$ accentuates the error bars for the results at the higher and lower fields where

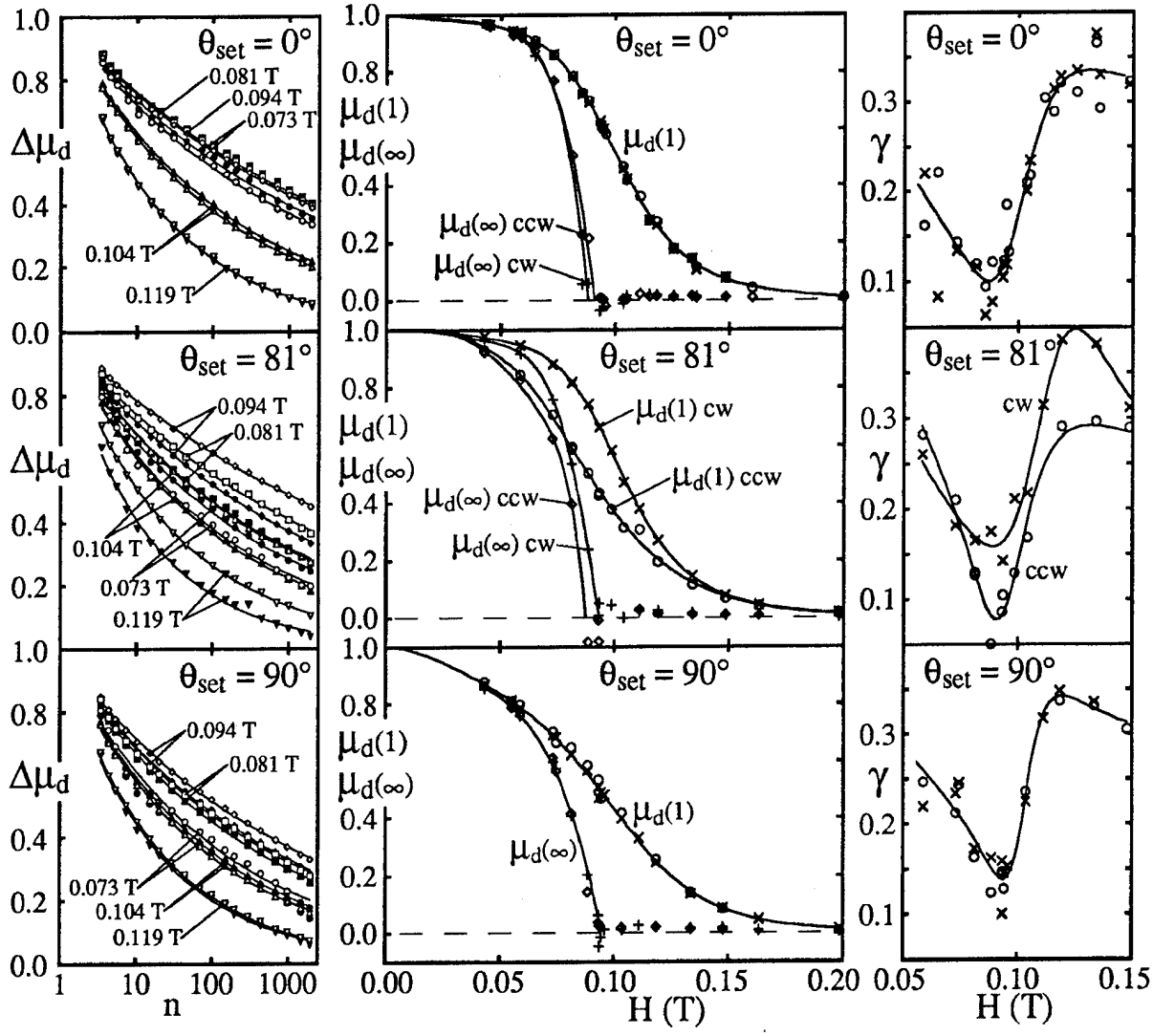


FIG. 1. Analysis of the angular dependence of the magnetization of a "FUJI FR metal" recording tape, first magnetized in the direction θ_{set} at $\mu_0 H_s = 1.2$ T and then measured in a field H_m. The dipolar component of the magnetization along H_m is extracted using Eqs. (1) and (2) and plotted in the three panels on the left as $\Delta\mu_d = n^{-\gamma}$, defined in Eq. (4), for H_m as noted, for up to 2000 cycles. The filled points are for cw and the open points are for ccw rotations. The dependence of the parameters $\mu_d(1)$ and $\mu_d(\infty)$ in Eq. (4) on H_m is shown in the three middle panels for cw and ccw directions. The values of the power γ in Eq. (4) used to fit the data on the left are shown in the panels on the right with cw data designated by x's and ccw data by o's.

the changes become small. The field dependence of $\mu_d(1) - \mu_d(\infty)$ can be extracted from the middle panels of Fig. 1 where we show $\mu_d(1)$ and $\mu_d(\infty)$.

The data in the middle panels of Fig. 1 are normalized to the magnitude of the remanence μ_r at $\theta_{set}=0$, measured by rotation in zero field after saturation. The dependence of μ_r on θ_{set} has been reported and analyzed previously;[7] $\mu_r(\theta_{set})$ is shown in the top panel of Fig. 2, also normalized to μ_r at $\theta_{set}=0$. The values of γ used in each fitting are shown in the right-hand panels of Fig. 1. The curves in these panels are empirical fits to guide the eye.

There are no significant differences between the cw and ccw measurements for $\theta_{set}=0$ or 90°. This is expected if the distribution of particle axes is symmetric with respect to the tape direction. There is a significant difference between cw and ccw rotations for $\theta_{set}\neq 0$ or 90°. This effect is largest for $\theta_{set}\sim 81°$ which is a ccw rotation from the tape axis. When the dipole is written at 81°, ccw rotation drags the net moment toward 90°, enhancing the flipping, while cw rotation from drags it back toward 0° enhancing stability. Thus one anticipates bigger changes in the initial cycles for the ccw rotations. This is shown in the central panel of Fig. 1 where $\mu_d(1)$ is definitely smaller for ccw than for cw rotations.

Note that the curves in the mid panels of Fig. 1 bear some resemblance to the temperature dependence of the magnetization for a typical ferromagnetic material; the field dependence for $\mu_d(1)$ corresponds to the temperature dependence of the magnetization in a large applied field, while the field dependence for $\mu_d(\infty)$ corresponds to $M_s(T)$. The power laws observed here are related to a form of critical behavior, popularized recently as self-organized criticality, one example being the cascades occurring when adding grains of sand to a sand pile.[1]

Note that the extrapolation to $n=\infty$ produces positive dipole moments for $H<H_{crit}$ and no moment for H sufficiently larger than H_{crit}. H_{crit} is just below the smallest of the

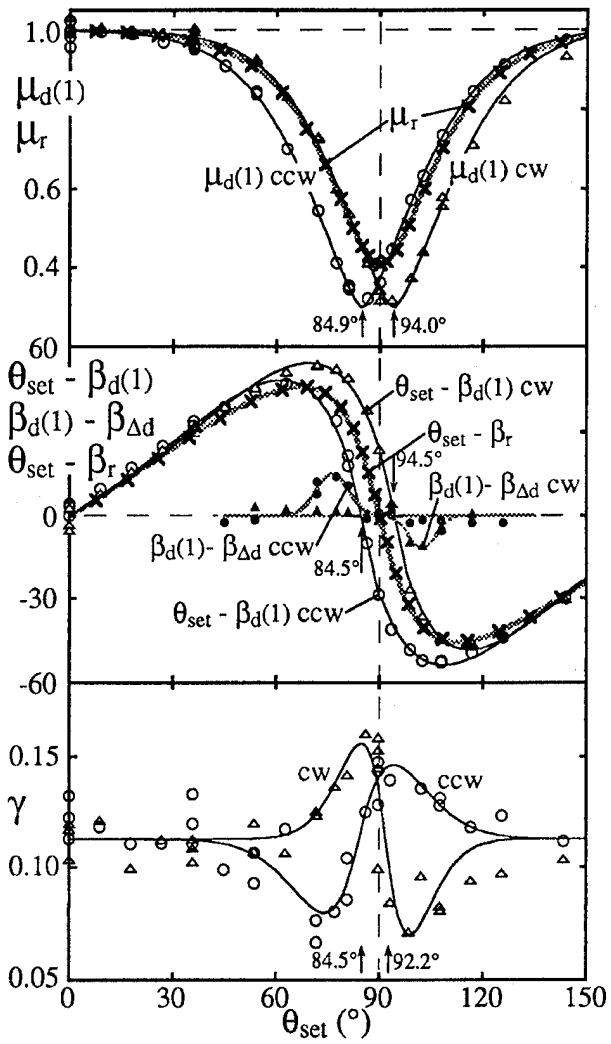


FIG. 2. The dependence on θ_{set} of the parameters in Eq. (4) for $\mu_0 H_m = 0.094$ T. In the top panel, the dependence on θ_{set} of $\mu_d(1)$ for cw and ccw rotations are compared with that for the remanent moment μ_r. The dependence on θ_{set} of γ for cw and ccw rotations are shown in the bottom panel. The angles $\beta_d(1)$ of the dipolar components $\mu_d(1)$ are shown as a function of θ_{set} in the middle panel by plotting the difference between the angles and θ_{set} for cw and ccw rotations. The angle between the remanent moments β_r and θ_{set} are plotted in the same way for comparison. The differences between $\beta_d(1)$ and $\beta_{\Delta d}$, defined in the text, are also shown in the middle panel. The solid lines in all cases are empirical fits to guide the eye and extract angles that measure the offsets of symmetry points from 90 for cw and ccw rotations.

coercive fields $H_c(\theta_{set})$ measured by reversing fields at each θ_{set}.[6] Very close to H_{crit} the extrapolated moments go slightly negative. Most likely this is a comment on the difficulty of extrapolation of real data when γ is as low as 0.1, but it might also raise questions about the adequacy of the simple power law. (The data for $H_m \approx H_{crit}$ do not justify an expression with more than three parameters.) That the smallest values of γ occur for H_m close to H_{crit} can be taken as another indication of the critical nature of the phenomena. The behavior for $H_m \approx H_{crit}$ is shown in more detail in Fig. 2 where the dependence of the various parameters on θ_{set} is analyzed.

The dependence on θ_{set} of the parameters $\mu_d(1)$ for cw and ccw rotations is shown in the top panel of Fig. 2 for $\mu_0 H_m = 0.094$ T. Recall that these are extrapolated quantities, not measured, but after normalization they bear a striking relation to the remanent moments, also shown here. The normalization is to the value for $\theta_{set}=0$ at this field. The curves for cw and ccw are mirror images, offset from 90° by about 5°. The sections for cw for $\theta_{set}<90°$ and for ccw for $\theta_{set}>90°$ coincide with the curve for $\mu_r(\theta_{set})$ normalized to μ_r at $\theta_{set}=0$.

The dependence of the power law exponent γ on both θ_{set} and the direction of rotation are shown in the bottom panel of Fig. 2 for $\mu_0 H_m = 0.094$ T. Though the data are rather scattered, due to the small values of γ and the limit of 2000 cycles, there is clear evidence for a variation of γ both with direction of rotation and with θ_{set} near 90°.

The angle of the moment, $\beta_d(n)$ in Eq. (3), is zero for $\theta_{set}=0$ and close to 90° for $\theta_{set}=90°$. For intermediate θ_{set}, the angle of the moment deviates from θ_{set} with the maximum effect coming near $\theta_{set}=60°$ or 75° depending on direction of rotation. This is similar to the dependence of the angle β_r of the remanence on θ_{set} as previously discussed[7] and shown as the heavy line in the central panel of Fig. 2, where we plot $\theta_{set}-\beta_r(\theta_{set})$. We introduce two parameters to describe the change of the angles of the moment with cycle number, $\beta_d(1)$ and $\beta_{\Delta d}$, which are found by fitting $\mu_d'(n)$ and $\mu_d''(n)$ with Eq. (4) to obtain $\mu_d'(1)$, $\mu_d''(1)$, $\mu_d'(\infty)$, and $\mu_d''(\infty)$. $\beta_d(1)$ is calculated using Eq. (3) with $\mu_d'(1)$ and $\mu_d''(1)$ and $\beta_d(\infty)$ is calculated using Eq. (3) with $\mu_d'(\infty)$ and $\mu_d''(\infty)$. $\beta_{\Delta d}$ is found from the angle of the vector difference between the extrapolated moments at $n=1$ and $n=\infty$,

$\beta_{\Delta d} = \arctan\{[\mu_d''(1) - \mu_d''(\infty)]/[\mu_d'(1) - \mu_d'(\infty)]\}$. If the moments extrapolated to ∞ were zero, there should be no difference between $\beta_d(1)$ and $\beta_{\Delta d}$, but there seems to be a small systematic difference near 90° that correlates with whether the rotation is cw or ccw.

We have made detailed theoretical analyses of the response of noninteracting Stoner–Wohlfarth particles with uniaxial anisotropy for which there are distributions of axes and strengths of the anisotropy in order to separate the single-particle behavior from that of interacting particles. We have carried out computer simulations that show the presence of cascades of interacting particles in the reversal process. Also, we have developed a cleaner experimental approach in which we determine the remanent magnetic dipole at each angle in each cycle for each field. This done by rotating the sample in field H_m by a given angle then lowering the field from H_m to zero before measuring the remanence while rotating through 360°. These topics will be presented elsewhere.

[1] P. Bak and K. Chen, Sci. Am. (1991).
[2] J. S. Urbach, R. C. Madison, and J. T. Markert, Phys. Rev. Lett. **75**, 276 (1995).
[3] B. Alessandro, C. Beatrice, G. Bertotti, and G. Montoise, J. Appl. Phys. **68**, 2901, 2909 (1990).
[4] P. Bak and H. Flyvbjerg, Phys. Rev. A **45**, 2192 (1992).
[5] J. P. Sethna, K. Dahmen, S. Kartha, J. A. Krumhansl, B. W. Roberts, and J. D. Shore, Phys. Rev. Lett. **70**, 3347 (1993).
[6] A. S. Arrott, T. L. Templeton, and Y. Yoshida, IEEE Trans. Magn. **MAG-31**, 3790 (1995).
[7] T. L. Templeton, A. S. Arrott, and Y. Yoshida, IEEE Trans. Magn. **MAG-30**, 4263 (1994).

Quantum correction to the BKT transition for 2D easy-plane antiferromagnets

Cristiano Biagini, Alessandro Cuccoli, and Valerio Tognetti
Dipartimento di Fisica dell'Università di Firenze, largo E. Fermi 2, I-50125 Firenze, Italy

Ruggero Vaia
Istituto di Elettronica Quantistica del Consiglio Nazionale delle Ricerche, via Panciatichi 56/30, I-50127 Firenze, Italy

Paola Verrucchi
ISIS Science Theory Division, Rutherford Appleton Laboratory, Chilton, Didcot, Oxfordshire OX11 0QX, United Kingdom

We consider the quantum antiferromagnet with easy-plane exchange anisotropy, namely, the antiferromagnetic XXZ model, on the square lattice. Its classical counterpart, compared to the planar model shows a reduction of the critical temperature T_{BKT} of the Berezinskii–Kosterlitz–Thouless phase transition, that is a consequence of the thermal out-of-plane fluctuations. For the quantum system we use the pure-quantum self-consistent harmonic approximation to calculate how much the effective exchange interaction is weakened as an effect of the pure-quantum part of the fluctuations. One can then predict the further reduction of T_{BKT} with respect to the corresponding classical system. The theory works well in a wide range of values of the easy-plane anisotropy. In the extreme case of the spin-$\frac{1}{2}$ model, the result is compatible with the estimate of T_{BKT} obtained by previous quantum Monte Carlo simulations. When the anisotropy is weak the theory leads to an unphysical "isotropization" due to the use of the Villain spin-boson transformation. © *1996 American Institute of Physics.* [S0021-8979(96)01208-9]

The two-dimensional antiferromagnetic XXZ model is described by the general Hamiltonian

$$\hat{\mathscr{H}}=\frac{1}{2}J\sum_{\mathbf{i},\mathbf{d}}(\hat{S}_{\mathbf{i}}^{x}\hat{S}_{\mathbf{i}+\mathbf{d}}^{x}+\hat{S}_{\mathbf{i}}^{y}\hat{S}_{\mathbf{i}+\mathbf{d}}^{y}+\lambda\hat{S}_{\mathbf{i}}^{z}\hat{S}_{\mathbf{i}+\mathbf{d}}^{z}), \tag{1}$$

where the index $\mathbf{i}\equiv(i_1,i_2)$ runs over the sites of a two-dimensional lattice, and $\mathbf{d}\equiv(d_1,d_2)$ represents the displacements of the z nearest neighbors of each site.

The sum describes an exchange interaction $J>0$ between nearest-neighbor spins, with an easy-plane anisotropy $\lambda\in[0,1)$.

The lattice is such that it can be considered as two interpenetrating identical sublattices (the "positive" sublattice and the "negative" one), in such a way that the nearest neighbors of any site in a sublattice belong to the other one; in other words, we do not consider lattices with frustrated bonds.

For $\lambda=0$ the above Hamiltonian describes the $XX0$ model, often (improperly) called "quantum XY model"; it is to be noticed that the $XX0$ model is equivalent to its ferromagnetic counterpart. Indeed, the canonical transformation

$$(\hat{S}_{\mathbf{i}}^{x},\hat{S}_{\mathbf{i}}^{y},\hat{S}_{\mathbf{i}}^{z})\rightarrow[(-)^{\mathbf{i}}\hat{S}_{\mathbf{i}}^{x},(-)^{\mathbf{i}}\hat{S}_{\mathbf{i}}^{y},\hat{S}_{\mathbf{i}}^{z}],$$

where $(-)^{\mathbf{i}}=\pm1$ is the sign of the sublattice containing the site $\mathbf{i}$, transforms the antiferromagnetic $XX0$ model into the ferromagnetic $XX0$ model. More generally, for the XXZ model this canonical transformation is equivalent to put $J\rightarrow-J$ and $\lambda\rightarrow-\lambda$.

The classical counterpart of the Hamiltonian (1) is obtained by associating to each spin operator $\hat{\mathbf{S}}_{\mathbf{i}}$ a classical vector $\mathbf{S}_{\mathbf{i}}$ of given length $\tilde{S}$. In terms of unit vectors $\mathbf{s}_{\mathbf{i}}=\mathbf{S}_{\mathbf{i}}/\tilde{S}$,

$$\mathscr{H}=\frac{1}{2}\epsilon\sum_{\mathbf{i},\mathbf{d}}(s_{\mathbf{i}}^{x}s_{\mathbf{i}+\mathbf{d}}^{x}+s_{\mathbf{i}}^{y}s_{\mathbf{i}+\mathbf{d}}^{y}+\lambda s_{\mathbf{i}}^{z}s_{\mathbf{i}+\mathbf{d}}^{z}), \tag{2}$$

with the exchange energy $\epsilon=J\tilde{S}^2$; in the following we will only use the dimensionless temperature $t=T/\epsilon$. The choice of $\tilde{S}$ is ambiguous, since values as S or $\sqrt{S(S+1)}$ are both reasonable: a different answer, $\tilde{S}=S+\frac{1}{2}$, is suggested by the pure-quantum self-consistent harmonic approximation (PQSCHA) to the quantum Hamiltonian (1), as we will show below. The minimum-energy configuration of the classical Hamiltonian corresponds to the Neél state: the two sublattices are ordered ferromagnetically in the xy plane, but in opposite directions.

In contrast to the quantum case, in the classical case the ferromagnetic and the antiferromagnetic cases are fully equivalent (i.e., $J\rightarrow-J$), as far as the static properties are concerned.

In the approximation of dominating easy-plane anisotropy the z components of the spins are neglected and the so-called *planar* model (frequently "classical XY model") is obtained. Since the spins are reduced to two-component vectors in the xy plane, $\mathbf{s}_i=(\cos\varphi_{\mathbf{i}},\sin\varphi_{\mathbf{i}})$, its Hamiltonian can be written in terms of the azimuthal angles, $\mathscr{H}=\frac{1}{2}\epsilon\Sigma_{\mathbf{i},\mathbf{d}}\cos(\varphi_{\mathbf{i}}-\varphi_{\mathbf{i}+\mathbf{d}})$. This is the prototype system that undergoes the Berezinskii–Kosterlitz–Thouless (BKT) phase transition[1–3] occurring at the temperature $t_{\mathrm{BKT}}=T_{\mathrm{BKT}}/\epsilon\simeq0.89$, that has been calculated by Monte Carlo simulations.[4,5] The antiferromagnetic order parameter $\langle(-)^{\mathbf{i}}\mathbf{s}_{\mathbf{i}}\rangle$, vanishes at any nonzero temperature, and the mechanism underlying the transition is the unbinding of vortex pairs.[2,6] For $t<t_{\mathrm{BKT}}$ the correlation function $\langle(-)^{\mathbf{i}-\mathbf{j}}\cos(\varphi_{\mathbf{i}}-\varphi_{\mathbf{j}})\rangle$ displays a power law decay, $\sim|\mathbf{i}-\mathbf{j}|^{-\eta(t)}$, whereas for $t>t_{\mathrm{BKT}}$ the behavior is exponen-

 0021-8979/96/79(8)/4638/3/$10.00 © 1996 American Institute of Physics

tial; moreover, the susceptibility has an exponential divergence for $t \to t_{\mathrm{BKT}}^{+}$.

With the inclusion of the out-of-plane components $s_{\mathbf{i}}^{z}$ of the spins still a BKT transition is expected at a finite temperature $T_{\mathrm{BKT}}(\lambda)$, which vanishes logarithmically[7,8] in the isotropic limit $\lambda \to 1$. Monte Carlo simulations for the classical XXZ model that provide useful data have been published in Ref. 9.

The quantum system (1) preserves the rotational symmetry around the z axis; therefore, from universality arguments, it displays the qualitative features of a BKT system as its classical analogue, with quantitative modifications of the critical parameters arising from quantum fluctuations.

Due to the absence of demagnetizing fields, an experimental observation of BKT behavior should be easier in antiferromagnetic XXZ systems (a $S=5/2$ compound with magnetic Mn ions is under study[10]). The aim of this work is to apply a recent theoretical approach, the PQSCHA,[11] to the quantum antiferromagnetic XXZ model (1). The ferromagnetic system has been already treated by PQSCHA.[12] In Ref. 13 one also finds—for the ferromagnetic case—an outline of the derivation of the effective Hamiltonian $\mathscr{H}_{\mathrm{eff}}$ in terms of classical spins, a procedure that involves the Villain transformation from quantum spin to bosonic variables,[14] and the identification of the classical counterpart of the transformed Hamiltonian by the prescription of Weyl ordering.[15] It is just the Weyl ordered form of the Villain transformed spin operators that leads to the identification $\tilde{S}=S+\frac{1}{2}$.[16]

Eventually, the PQSCHA recipe gives the following effective Hamiltonian for the antiferromagnetic XXZ model:[17]

$$\mathscr{H}_{\mathrm{eff}}=\frac{\epsilon}{2} j_{\mathrm{eff}} \sum_{\mathbf{i},\mathbf{d}} (s_{\mathbf{i}}^{x} s_{\mathbf{i}+\mathbf{d}}^{x}+s_{\mathbf{i}}^{y} s_{\mathbf{i}+\mathbf{d}}^{y}+\lambda_{\mathrm{eff}} s_{\mathbf{i}}^{z} s_{\mathbf{i}+\mathbf{d}}^{z})+N\epsilon G(t). \quad (3)$$

As in Eq. (2), $\{\mathbf{s}_{\mathbf{i}}\}$ are classical normalized spin variables. Within the PQSCHA,[11] the contribution of quantum fluctuations (treated up to the harmonic level) is embodied in the following dimensionless interaction parameters:

$$j_{\mathrm{eff}}(S,\lambda,t)=(1-\tfrac{1}{2}D_{\perp})^{2} e^{-1/2\mathscr{D}_{\parallel}}, \quad (4)$$

$$\lambda_{\mathrm{eff}}(S,\lambda,t)=\lambda(1-\tfrac{1}{2}D_{\perp})^{-1} e^{1/2\mathscr{D}_{\parallel}}, \quad (5)$$

while $G(t)$ is an additive renormalization quantity that does not enter the calculation of operator averages. The self-consistent renormalization parameters

$$D_{\perp}=\frac{1}{2\tilde{S}} \frac{1}{N} \sum_{\mathbf{k}} \frac{b_{\mathbf{k}}}{a_{\mathbf{k}}} (\coth f_{\mathbf{k}}-f_{\mathbf{k}}^{-1}), \quad (6)$$

$$\mathscr{D}_{\parallel}=\frac{1}{2\tilde{S}} \frac{1}{N} \sum_{\mathbf{k}} (1-\gamma_{\mathbf{k}}) \frac{a_{\mathbf{k}}}{b_{\mathbf{k}}} (\coth f_{\mathbf{k}}-f_{\mathbf{k}}^{-1}) \quad (7)$$

represent, within the PQSCHA, the pure-quantum part of the square fluctuations[11,16] of the z-components of the spins and of the relative azimuthal angle of nearest-neighbor spins, respectively, and are decreasing functions of t and S, vanishing both for $t \to \infty$ or $S \to \infty$. They depend on t, S, and λ through the quantities

$$a_{\mathbf{k}}^{2}=z e^{-1/2\mathscr{D}_{\parallel}} (1+\lambda_{\mathrm{eff}}\gamma_{\mathbf{k}}), \quad (8)$$

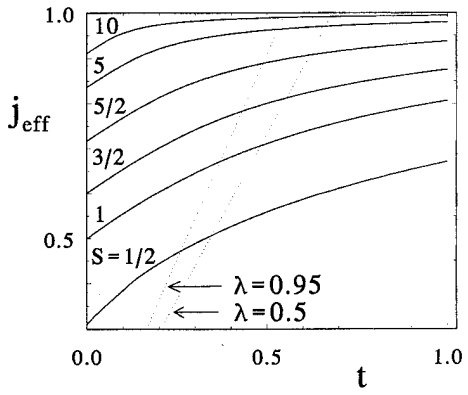


FIG. 1. The effective exchange coupling $j_{\mathrm{eff}}(S,\lambda=0.5,t)$ for the $XX0$ antiferromagnetic model vs temperature $t=T/\epsilon$ and for different values of the spin S (solid lines). The energy scale is $\epsilon=J\tilde{S}^{2}=J(S+\frac{1}{2})^{2}$. The dotted lines are the curves $t/t_{\mathrm{BKT}}^{(\mathrm{cl})}(\lambda)$ for $\lambda=0.5$ and 0.95. See the text for the discussion about the use of such curves for graphically solving Eq. (10).

$$b_{\mathbf{k}}^{2}=z(1-\tfrac{1}{2}D_{\perp})^{2} e^{-1/2\mathscr{D}_{\parallel}} (1-\gamma_{\mathbf{k}}), \quad (9)$$

$f_{\mathbf{k}}=a_{\mathbf{k}}b_{\mathbf{k}}/(2\tilde{S}t)$, $\gamma_{\mathbf{k}}=z^{-1}\Sigma_{\mathbf{d}} \cos(\mathbf{k}\cdot\mathbf{d})$, and $\mathbf{k}$ is a wave vector varying in the first Brillouin zone. Therefore, the exchange energy is renormalized by the factor j_{eff}, and the easy-plane anisotropy is weakened ($\lambda_{\mathrm{eff}} \geqslant \lambda$), due to the cooperative effect of in-plane and out-of-plane pure-quantum fluctuations. Their typical temperature behavior in the case of the square lattice is reported in Figs. 1, and 2, respectively. For $S \to \infty$, i.e., in the classical limit, $j_{\mathrm{eff}} \to 1$ and $\lambda_{\mathrm{eff}} \to \lambda$. We notice that the integrals of the pure-quantum fluctuation parameters, Eqs. (6) and (7), get the main contribution from the high-frequency part of the effective magnon spectrum $\omega_{\mathbf{k}}=(J\tilde{S}/\hbar)a_{\mathbf{k}}b_{\mathbf{k}}$, just because the pure-quantum part of the square fluctuations is obtained by subtracting from the full (harmonically approximated) expression the corresponding classical part (i.e., the leading behavior for $f_{\mathbf{k}} \to 0$); on the other hand, those effects due to the presence of nonlinear excitations (vortices) would mainly affect the low-frequency part; i.e., they are essentially "classical" and therefore they cannot sensitively change $D_{\perp}$ and $\mathscr{D}_{\parallel}$.

Using the PQSCHA formalism[11] one can calculate averages and correlations by means of classical expressions in-

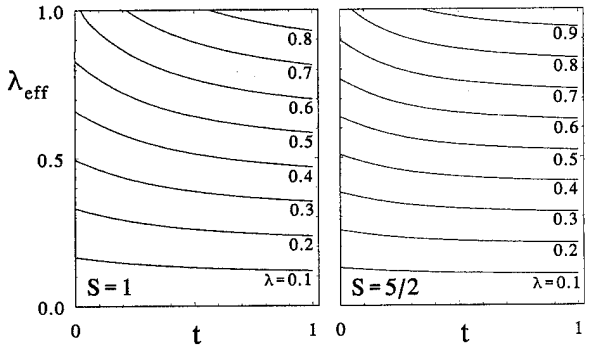


FIG. 2. The effective anisotropy parameter λ_{eff} for the $XX0$ antiferromagnetic model vs temperature and for spin $S=1$ and $S=5/2$, at different values of λ. For high values of λ the curves reach the isotropic value $\lambda_{\mathrm{eff}}=1$.

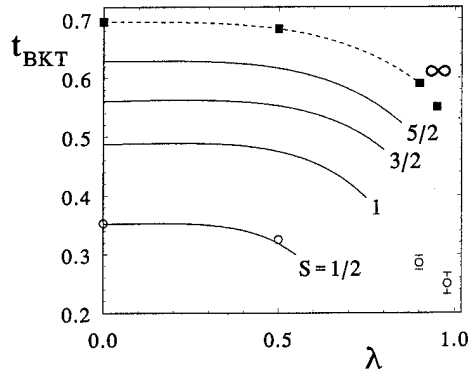


FIG. 3. The critical temperature t_{BKT} of the XXZ antiferromagnetic model vs the value of the anisotropy λ and for different values of the spin S. The classical values (squares) from Ref. 9 are 0.695 ± 0.005, 0.683 ± 0.005, 0.59 ± 0.01, 0.55 ± 0.01, for $\lambda=0$, 0.5, 0.9, and 0.95, respectively. The circles report QMC results from Refs. 21 and 22. Note that $t_{BKT}(S,\lambda)$ decreases when λ is increased, and the theory would lead to the disappearance of the transition by a mechanism of "isotropization."

volving the Boltzmann factor corresponding to the effective Hamiltonian. In the present case the classical average with the effective Hamiltonian is defined as

$$\langle\cdots\rangle_{\rm eff}=\mathscr{Z}^{-1}\left(\prod_{\mathbf{i}}\int d\mathbf{s}_{\mathbf{i}}\right)(\cdots)e^{-\beta\mathscr{H}_{\rm eff}}.$$

In order to obtain the PQSCHA thermal average of a quantum observable, the dots are to be replaced by a phase-space function that is obtained by Gaussian smearing, on the scale of the pure-quantum fluctuations, of the Weyl symbol associated with the same observable.[11,16] In this way we find expressions for the in-plane correlations

$$\langle\hat{S}^x_{\mathbf{i}}\hat{S}^x_{\mathbf{j}}\rangle=\tilde{S}^2(1-\tfrac{1}{2}D_\perp)^2e^{-1/2\mathscr{C}_{\mathbf{ii}}}e^{D^{\parallel}_{\mathbf{ij}}}\langle s^x_{\mathbf{i}}s^x_{\mathbf{j}}\rangle_{\rm eff},$$

where the renormalization parameters $D^{\parallel}_{\mathbf{ij}}$ (Ref. 17) for the relative azimuthal fluctuations between sites $\mathbf{i}$ and $\mathbf{j}$ are such that $D^{\parallel}_{\mathbf{ij}}\to0$ for $|\mathbf{i}-\mathbf{j}|\to\infty$. Therefore, the asymptotic behavior and the correlation length are just those obtained for the effective classical model. The quantum transition temperature $t_{BKT}(S,\lambda)$ can then be estimated from the knowledge of the corresponding classical one $t^{(cl)}_{BKT}(\lambda)$, with a self-consistency arising from the dependence on t and λ of the renormalized interaction parameters, Eqs. (4) and (5):

$$\frac{t_{BKT}(S,\lambda)}{j_{\rm eff}(S,\lambda,t_{BKT})}=t^{(cl)}_{BKT}[\lambda_{\rm eff}(S,\lambda,t_{BKT})]. \tag{10}$$

It is rather easy to solve this equation for the $XX0$ model,[12] since $\lambda_{\rm eff}=0$ for $\lambda=0$. In order to solve it for $\lambda\neq0$ we have made a rough fit of $t^{(cl)}_{BKT}(\lambda)$ using the available values[9] reported as squares in Fig. 3. The fit, as shown in the figure, is considered only for $\lambda<0.8$, in such a way that we do not run into the zone where $t^{(cl)}_{BKT}\sim[-\ln(1-\lambda)]^{-1}$ vanishes logarithmically.[7] Then Eq. (10), rewritten as $j_{\rm eff}=t_{BKT}/t^{(cl)}_{BKT}$, can be solved graphically in Fig. 1 in a recursive way: one estimates the transition temperature using $t^{(cl)}_{BKT}(\lambda)$ and then the value of $\lambda_{\rm eff}$ at this temperature is taken for redoing the procedure, and so on. The results obtained in this way are also reported for different values of S in Fig. 3.

For the $XX0$ model there is a possible comparison with other data in the extreme case of $S=\frac{1}{2}$. Our result is $t_{BKT}=0.36$ and compares very well with the values found by high-temperature expansions[18] (0.39), by real-space renormalization group techniques[19] (0.40), and by recent quantum Monte Carlo (QMC) simulations[20,21] (0.353 ± 0.003). For $\lambda=0.5$, we have $t_{BKT}=0.30$, to be compared with the QMC value[22] 0.325 ± 0.007.

When λ is large enough, we see from Fig. 2 that it may happen that $\lambda_{\rm eff}(S,\lambda,t)\geq1$. When $\lambda_{\rm eff}=1$ is reached the effective Hamiltonian becomes isotropic, and the theory therefore predicts the disappearance of the BKT transition at sufficiently high values of $\lambda\geq\lambda_c(S)$ (some values are $\lambda_c=0.58$, 0.75, 0.85, 0.90, 0.92, for $S=\frac{1}{2}$, 1, $\frac{3}{2}$, 2, $\frac{5}{2}$, respectively). However, this situation has to be considered with care, because the derivation of the effective Hamiltonian relies on the validity of the Villain transformation,[14] which is meaningful only for easy-plane systems. Indeed, for high λ the out-of-plane fluctuations become so strong that the assumed dominant easy-plane character becomes meaningless. The breakdown does not occur for $\lambda\ll\lambda_c$, of course, and therefore does not affect the results reported in Fig. 3.

The suppression of the BKT transition by "effective isotropization" is therefore unlikely to be physical, as confirmed also by quantum Monte Carlo simulations of the $S=\frac{1}{2}$ XXZ antiferromagnet:[22] at $\lambda=0.90$ and 0.98 the BKT behavior is still observed, with substantially high transition temperatures, $t_{BKT}=0.285$ and 0.25, respectively.

[1] V. L. Berezinskii, Zh. Eksp. Teor. Fiz. **59**, 907 (1970).
[2] J. M. Kosterlitz and D. J. Thouless, J. Phys. C **6**, 1181 (1973).
[3] J. M. Kosterlitz, J. Phys. C **7**, 1046 (1974).
[4] J. Tobochnik and G. V. Chester, Phys. Rev. B **20**, 3761 (1979).
[5] R. Gupta and C. F. Baillie, Phys. Rev. B **45**, 2883 (1992).
[6] J. Villain, J. Phys. (Paris) **36**, 581 (1975).
[7] S. B. Khokhlachev, Zh. Exp. Teor. Fiz. **70**, 265 (1976).
[8] S. Hikami and T. Tsuneto, Prog. Theor. Phys. **63**, 387 (1980).
[9] A. Cuccoli, V. Tognetti, and R. Vaia, Phys. Rev. B **52**, 10221 (1995).
[10] M. Steiner (private communication).
[11] A. Cuccoli, V. Tognetti, P. Verrucchi, and R. Vaia, Phys. Rev. A **45**, 8418 (1992).
[12] A. Cuccoli, V. Tognetti, P. Verrucchi, and R. Vaia, Phys. Rev. B **51**, 12840 (1995).
[13] A. Cuccoli, V. Tognetti, P. Verrucchi, and R. Vaia, J. Appl. Phys. **75**, 5814 (1994).
[14] J. Villain, J. Phys. (Paris) **35**, 27 (1974).
[15] F. A. Berezin, Sov. Phys. Usp. **23**, 763 (1980).
[16] A. Cuccoli, V. Tognetti, P. Verrucchi, and R. Vaia, Phys. Rev. B **46**, 11601 (1992).
[17] C. L. Biagini, *Tesi di Laurea* (Universitá di Firenze, Firenze, 1995).
[18] J. Rogiers, E. W. Grundke, and D. D. Betts, Can. J. Phys. **57**, 1719 (1979).
[19] A. Drzewiński and J. Sznajd, Phys. Lett. **138**, 143 (1989).
[20] H.-Q. Ding and M. S. Makivić, Phys. Rev. B **45**, 491 (1992).
[21] H.-Q. Ding, Phys. Rev. B **45**, 230 (1992).
[22] H.-Q. Ding, Phys. Rev. Lett. **68**, 1927 (1992).

Homogeneous magnetization dynamics below T_c of EuO: Effects of spin waves and anisotropy

A. Flosdorff, D. Görlitz, and J. Kötzler
Institut für Angewandte Physik, Universität Hamburg, Jungiusstr. 11, D-20355 Hamburg, Germany

Using a broadband reflectometer, the dynamic susceptibility $\chi(\omega)$ of a EuO sphere has been measured from 0.3 to 20 GHz at temperatures ranging between 4.2 K and T_c=69.5 K. For fields applied parallel to the hard [100] direction one heavily damped Lorentzian is observed which for internal fields H larger and smaller than the anisotropy field arises from the dynamics of the homogeneous and the wall magnetization, respectively. For fields near H_A applied along one of the easy [111] axes, both processes contribute to $\chi(\omega)$ but with increased and decreased values of the resonances and damping frequencies of the homogeneous and wall processes, respectively. The homogeneous process is identified by the static susceptibility $\chi_z(0)$ which obeys the $H^{-1/2}$ divergence due to spin waves. Its line shape is explained by a frequency variation of the kinetic coefficient of the relaxation damping, $L_z(\omega)=L_z(0)/[1+(i\omega/\omega_c)]$. The characteristic frequency, $\omega_c/2\pi$=18 GHz, turns out to be independent of temperature and magnetic field, and is related to the relaxation rate of the long-wavelength longitudinal magnetization fluctuations. The field and temperature variation of the kinetic coefficient of the relaxation can be described by the same scaling function, $L_z(\chi_z(T,H))$, as previously observed above T_c. Based on results of numerical mode-coupling work, this behavior is associated with the dipolar anisotropy of the magnetic fluctuations. © *1996 American Institute of Physics.* [S0021-8979(96)04208-4]

Extensive investigations of the homogeneous magnetization dynamics on the cubic chalcogenides EuS and EuO[1–4] revealed an almost perfect agreement with predictions of mode-coupling work for dipolar Heisenberg ferromagnets valid for the unmagnetized state above T_c.[5] The kinetic coefficient L_z of the magnetic relaxation rate, $\Gamma_z=L_z/\chi_z$, displayed a crossover from a critical speeding-up, $L_z\sim\chi_z^{7/4}$, arising from isotropic exchange dominated fluctuations ($\chi_z<1$), to L_z=const for $\chi_z>1$, where the dipolar anisotropy becomes effective. This dynamic crossover is described by a universal scaling function, $L_z(\chi_z)$, which for H=0 has been verified for numerous Heisenberg-like ferromagnets above T_c, including EuO.[1] More recently it was found for EuS that the same scaling function could also explain the variation of L_z with field[2] and with temperature below T_c,[3,4] i.e., $L_z(T,H)=L_z(\chi_z(T,H))$.

Here we communicate first results of a corresponding investigation below the Curie temperature of EuO, T_c=69.5 K. The work is intended to explore possible effects on the dynamics of the homogeneous magnetization by the stronger exchange and by the cubic magnetic anisotropy, where the latter is one order of magnitude larger in EuO than in EuS.[6] It is also the hope that the results reported here will motivate further theoretical activity towards a more detailed understanding of the dynamics in the ordered regime of real ferromagnets, similar to that gained above T_c.

By means of a broadband microwave reflectometer described elsewhere,[4,7] we measured the linear complex susceptibility $\chi(\omega)$ parallel to the applied field H_z at fixed temperatures. In order to examine the effect of the cubic anisotropy, the field was aligned parallel to one easy [111] and also to one hard [100] direction of a single crystalline sphere (∅=3 mm). For example, Fig. 1 shows the frequency variation of $\chi(\omega)$ recorded at T=0.43 T_c. There the anisotropy field attains the value H_A=110 Oe,[6] which has been bracketed by the two chosen internal fields, $H=H_z-N_zM$. The magnetizations required for the demagnetization correction have been determined on the same sphere by a superconducting quantum interference device (SQUID) magnetometer (see inset to Fig. 2).[8] Not unexpectedly, the dynamic susceptibility becomes independent of orientation for H=700 Oe$\gg H_A$, whereas a pronounced anisotropy emerges for H=50 Oe$<H_A$.

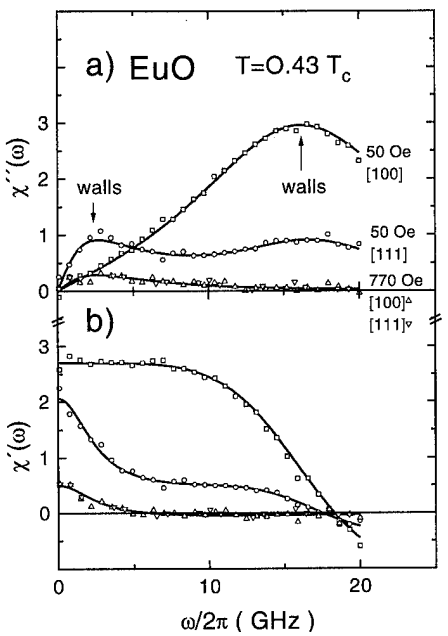


FIG. 1. Absorption (a) and dispersion (b) of the dynamic susceptibility measured parallel to the applied field on a EuO sphere in fields smaller and larger than the anisotropy field $H_A(0.43T_c)\approx$110 Oe along two sample orientations. Full lines represent fits to single and double damped harmonic oscillator, Eqs. (1) and (2).

 0021-8979/96/79(8)/4641/3/$10.00 © 1996 American Institute of Physics

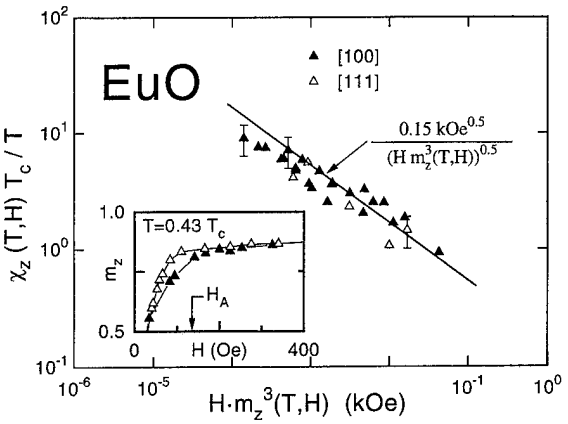


FIG. 2. Fitted internal static susceptibility normalized to relative temperature T/T_c vs scaled internal magnetic field for two sample orientations at temperatures $T \geqslant 0.43T_c$ for internal fields $H>H_A$ [100], [111] and at $T=0.43T_c$ for fields $H_A<H$ [111]. Inset: magnetization data along [100] and [111] showing anisotropy below internal fields $H \leqslant H_A$.

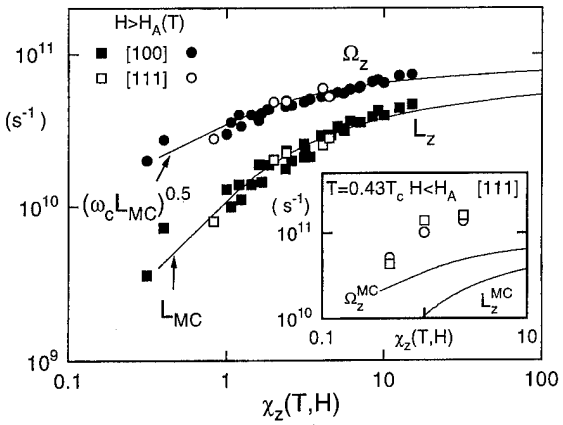


FIG. 3. Scaling behavior of the kinetic coefficient L_z and the resonance frequency Ω_z in terms of the internal susceptibility along two crystal orientations for $T \geqslant 0.43T_c$ and $H>H_A(T)$. Full lines correspond to solutions of the mode-coupling equations strictly valid above T_c and for $H=0$. Inset: L_z and Ω_z for fixed temperature $T=0.43T_c$ at internal fields $H<H_A$.

Like the corresponding results on EuS,[3,4] the data can be well fitted either by one or by a sum of two heavily damped Lorentzians (solid lines in Fig. 1)

$$\chi(\omega)=([\chi_z(\omega)+\chi_w(\omega)]^{-1}+N_z)^{-1}, \tag{1}$$

where the "internal" dynamic susceptibilities are given by

$$\chi_\alpha^{-1}(\omega)=\chi_\alpha^{-1}+\frac{i\omega}{L_\alpha}-\frac{\omega^2}{\Omega_\alpha^2}, \quad \alpha=z,w. \tag{2}$$

Again, the situation is simpler for $H \gg H_A$. Here only one process is effective, which obviously has to be associated with the dynamics of the homogeneous magnetization, $\chi_z(\omega)$. For $\mathbf{H}\|[111]$ and $H \leqslant H_A$, on the other hand, two processes occur around 3 and 17 GHz. If the same internal field is applied parallel to the hard [100] direction, again there is only one Lorentzian at high frequencies. This high-frequency dispersion as well as the low-frequency one for $\mathbf{H}\|[111]$ have been traced down to $H_z=0$ and were identified with domain wall motion.[9]

The designation of the other process as the homogeneous dynamics can be further substantiated by the field and temperature variation of the static susceptibility χ_z. In Fig. 2 the values fitted from data for $T \geqslant 0.43T_c$ and scaled by the reduced temperature T/T_c are plotted versus the internal field multiplied by $m_z^3(T,H)=(\mathrm{M(T,H)/M_0})^3$, where $M_0=24.8$ kOe is the saturation magnetization. This representation allows for a direct comparison to a prediction based on spin-wave fluctuations,[10] which in this form was successfully tested for EuS.[11] The data, except those for the lowest fields, display the characteristic divergence, $\chi_z=A_0(T/T_c)(Hm_z^3)^{-1/2}$, with $A_0=0.15(5)$ kOe$^{1/2}$. In the dipolar anisotropic regime, $\chi_z>1$, this amplitude is given by $A_0=(k_BT_c/16\pi\mu_0M_0^{3/2})q_d^{3/2}$,[10] which implies for the so-called dipolar wave number $q_d=0.19(3)$ Å^{-1}. This value is in reasonable accord with $q_d=0.15$ Å^{-1} (see Ref. 12) inferred from the $H=0$ paramagnetic susceptibility and correlation length of EuO. It is interesting to note that—similar as in the case of EuS[11]—even susceptibilities at rather high temperatures, $T=0.99T_c$, obey the $H^{-1/2}$ divergence. This indicates that the spin-wave induced singularity is rather robust against longitudinal critical fluctuations. Even more surprising is the fact that $\chi_z(T=0.43T_c, H<H_A)$ for $\mathbf{H}\|[111]$ also obeys the $H^{-1/2}$-scaling (open triangles in Fig. 2). Hence this singularity of χ_z also seems to be unaffected by the cubic anisotropy if the field is applied along the easy direction.

We now discuss the behavior of the kinetic coefficient of the damping, $L_z(T,H)$, and the intrinsic resonance frequency, $\Omega_z(T,H)$, of the homogeneous process, obtained from the fits to Eqs. (1) and (2). Based on the validity of the scaling behavior detected for L_z in the magnetized state of EuS,[3–5] we depict our results for $L_z(T,H)$ and $\Omega_z(T,H)$ in Fig. 3 versus the static susceptibility, $\chi_z(T,H)$. Indeed we find that for $H>H_A$ and $T \geqslant 0.43T_c$ each of both quantities collapses on a single curve. This means that the temperature and field variations are determined entirely by the static susceptibility. The inset to Fig. 3 illustrates for $T=0.43T_c$ that this scaling property of Ω_z and L_z, however, is violated for internal fields smaller than the anisotropy field H_A if $\mathbf{H}$ is parallel to [111]. Since, in this case, Ω_z and L_z are significantly enhanced over the L_z scaling function obtained for $H>H_A$, while the static susceptibility follows the spin-wave law, $\chi_z \sim H^{-1/2}$, the dynamics appear to be more sensitive against the anisotropy than the static properties.

Theoretical considerations of the dynamics in the magnetized state of dipolar Heisenberg ferromagnets, which include fluctuations, exist only for $\mathbf{q}>0$ (see Ref. 13) so that our discussion rests only on purely phenomenological arguments. First of all, we emphasize that, according to Fig. 3 the experimental kinetic coefficients agree almost perfectly with the scaling function, $L_z^{MC}(\chi_z(T,H))=L_z^{MC}(\infty)[1+\chi_z^{-1}(T,H)]^{-7/4}$ predicted by the mode coupling (MC) work[5] for $T \geqslant T_c$ and $H=0$ (solid curve in Fig. 2). This implies that below T_c, at least above the dipolar crossover, i.e., for $\chi_z \geqslant 1$, the effect of the dipolar anisotropy, which also determines the nonsingular value of L_z at T_c, $L_z(\infty)=(g\mu_B/\hbar^2)\sqrt{k_bT_c}q_d^{5/2}$,[1,5] diminishes in the same manner as above T_c. The question of whether below T_c the dipolar

anisotropy governs the dynamics of the $q \rightarrow 0$ fluctuations in a similar manner as above T_c (see Ref. 14) is currently investigated by inelastic neutron scattering.[15]

The Lorentzian shape of $\chi_z(\omega)$ and the scaling behavior of the resonance frequency Ω_z can be explained by a pure relaxational dynamics, $\chi_z(\omega)=[\chi_z^{-1}+i\omega/\hat{L}_z(\omega)]^{-1}$, containing a frequency-dependent kinetic coefficient, $\hat{L}_z(\omega)=L_z/(1+i\omega/\omega_c)$. This implies $\Omega_z = \sqrt{\omega_c L_z}$ (see Ref. 3) and in fact, assuming a constant value, $\omega_c/2\pi=18(2)$ GHz, the scaling behavior of $\Omega_z(T,H)$ is well described by that of $L_z(T,H)$ [see Fig. 3]. This value for ω_c is rather close to the relaxation rate of the $q \rightarrow 0$ longitudinal fluctuations,[2] $\Gamma_\ell/2\pi = Aq_d^{5/2}/2\pi=18(3)$ GHz calculated from the measured value for $A=\Gamma_t(q)/q^{5/2}$ (Ref. 16) and $q_d=0.15(2)$ Å^{-1}.[12] Such correspondence has been predicted by extending the MC approach[5] for the damping of the homogeneous magnetization to finite frequencies.[3,4] Because Γ_ℓ is much larger than the maximum frequency associated with the anisotropy, $\Gamma_A/2\pi=\gamma H_A(0)=0.67$ GHz, it is plausible that the latter has no influence on $L_z(T,H)$.

There are, however, clear effects of the anisotropy if the internal field is reduced toward H_A. For $\mathbf{H}\|[100]$, where all easy directions enclose the same angle with $\mathbf{H}$, only one dynamic process appears (see Fig. 1). From the static susceptibility $\chi(0)$ we infer that this process arises from the homogeneous magnetization for internal fields larger than the anisotropy field and from the wall motion[9] for $H<H_A$. In contrast, if $\mathbf{H}$ is aligned parallel to one of the easy [111] axes, we observe two processes for fields near H_A which arise from both the homogeneous and the wall process. It emerges as main feature that in the transition region around H_A the kinetic coefficient and resonance of the homogeneous dynamics are enhanced while those of the wall motion are reduced.[9] This signalizes a novel dynamical interference between both processes for the asymmetric configuration, which will be the subject of more detailed future work.[17]

[1] J. Kötzler, Phys. Rev. B **38**, 12027 (1988) and references therein.
[2] J. Kötzler, E. Kaldis, G. Kamleiter, and G. Weber, Phys. Rev. B **43**, 11280 (1991).
[3] R. Dombrowski, D. Görlitz, J. Kötzler, and Chr. Marx, J. Appl. Phys. **75**, 6054 (1994).
[4] J. Kötzler, D. Görlitz, M. Hartl, and Chr. Marx, IEEE Trans. Magn. **30**, 828 (1994).
[5] E. Frey and F. Schwabl, Z. Phys. B **71**, 355 (1988); Adv. Phys. (to be published).
[6] See, e.g., A. Kasuya and M. Tachiki, Phys. Rev. B **8**, 5298 (1973).
[7] D. Görlitz, J. Kapoor, and J. Kötzler, J. Phys. E **22**, 884 (1989).
[8] M. Baumann (private communication).
[9] A. Flosdorff, D. Görlitz, and J. Kötzler, these proceedings.
[10] T. Holstein and H. Primakoff, Phys. Rev. **58**, 1098 (1940); V. L. Prokrovsky, Adv. Phys. **28**, 595 (1979); M. E. Fisher and V. Privman, Phys. Rev. B **32**, 447 (1985); S. W. Lovesey and K. Trohidou, J. Phys.: Condens. Matter **3**, 1827 (1991).
[11] J. Kötzler, D. Görlitz, R. Dombrowski, and M. Pieper, Z. Phys. B **94**, 9 (1994).
[12] J. Kötzler, J. Magn. Magn. Mater. **54-57**, 649 (1986).
[13] H. Schinz and F. Schwabl, J. Magn. Magn. Mater. **140-144**, 1527 (1995).
[14] P. Böni, D. Görlitz, J. Kötzler, and J. L. Martinez, Phys. Rev. B **43**, 8755 (1991).
[15] P. Böni *et al.* (unpublished).
[16] F. Mezei, J. Magn. Magn. Mater. **45**, 67 (1984).
[17] D. Görlitz and J. Kötzler (unpublished).

Concentration-dependent critical behavior in dilute ferromagnetic $Fe_{1-x}As_x[S_2CN(C_2H_5)_2]_2Cl$

G. C. DeFotis, G. A. Coffey, G. S. Coker, J. L. Marmorino, K. L. Beers, S. Chandarlapaty, W. W. Brubaker, and V. J. Pugh
Chemistry Department, College of William and Mary, Williamsburg, Virginia 23187-8795

S. A. Carling and P. Day
The Royal Institution of Great Britain, London W1X 4BS, United Kingdom

The dilute insulating ferromagnet $Fe_{1-x}As_x[S_2CN(C_2H_5)_2]_2Cl$ is examined in single crystal form for several compositions spanning the range $x=0.014$ to $x=0.040$. For $x=0.014_3$ and $x=0.016_2$ crystals, the inverse molar susceptibility along the [101] ferromagnetic easy axis is quite linear in temperature for T greater than a few times T_c. In the case of $x=0.031_3$ and $x=0.040_2$ crystals, in contrast, significant curvature appears in χ^{-1}vs T throughout the 20–80 K temperature range. The initial (low-field) susceptibility along [101] for each crystal is measured in the critical region and analyzed via a standard power law form $\chi_0=\Gamma t^{-\gamma}$, where $t=(T-T_c)/T_c$. T_c decreases with increasing x, but somewhat slowly. The critical exponent γ increases with increasing x, from 1.19 ± 0.01 near $x=0.014$ to 1.22 ± 0.01 near $x=0.040$. The prefactor Γ is significantly smaller for the two higher As crystals, probably due to increased disorder. The variation in γ is not entirely unexpected, since the pure material, which is a candidate Z_2xS_1 system, has an unusual set of critical exponents, including a large positive α. Thus new critical behavior on dilution can occur by the Harris criterion. © *1996 American Institute of Physics.* [S0021-8979(96)01308-5]

I. INTRODUCTION

Previous examination[1–4] of the novel pentacoordinate Fe^{3+} compound $Fe[S_2CN(C_2H_5)_2]_2Cl$ with $S=3/2$, Fig. 1, revealed unusual critical behavior at the 2.457 K ferromagnetic transition. Independent values of the exponents for the initial susceptibility, $\gamma=1.165\pm0.03$, and for the sublattice magnetization (from NMR data), $\beta=0.245\pm0.02$, were determined. Scaling analysis of magnetization isotherms yielded an independent pair of exponents $\beta=0.24\pm0.01$ and $\delta=5.65\pm0.15$, the latter exponent controlling behavior at the critical isotherm. The values of γ, β, and δ are consistent with the scaling relation $(\delta-1)\beta=\gamma$ within the experimental uncertainties. Only some sparse heat capacity data are available,[5] but from these the provisional estimate $\alpha=0.38\pm 0.06$ was inferred,[3] a large value but consistent with the above in light of the scaling relation $\alpha=2-2\beta-\gamma$.

The above exponents differ substantially from theoretical values for any conventional universality class, e.g., 3D-Ising, to which structural considerations and the strongly anisotropic magnetic susceptibility and magnetization point. Ising model behavior can be rationalized based on the $^4A_2$ crystal field ground term and its large zero-field splitting.[1] Kawamura has studied the critical behavior of magnets where the ground state has Z_2xS_1 symmetry, i.e., an Ising-like chiral symmetry combined with an XY-like rotational symmetry.[6] The latest values of the critical exponents for the 3D version of the Z_2xS_1 model are $\alpha=0.34\pm0.06$, $\beta=0.253\pm0.01$, $\gamma=1.13\pm0.05$ and, for the correlation length, $\nu=0.54\pm0.02$.[7] From the scaling relation given earlier one also obtains $\delta=5.47\pm0.35$. These values agree remarkably well with those determined for $Fe[S_2CN(C_2H_5)_2]_2Cl$. Moreover, Z_2xS_1 symmetry may characterize a canted ferromagnet with Ising anisotropy, as our system is thought to be. Neutron investigations are underway on deuterated material.[8]

If $Fe[S_2CN(C_2H_5)_2]_2Cl$ is indeed an example of the Z_2xS_1 universality class study of the variation, if any, of its critical behavior with dilution is important. No theoretical predictions for the dilute Z_2xS_1 model are available, but from the Harris criterion[9] the positive α value means that a change in critical behavior with dilution (disorder) is expected. In an earlier report[10] an extremely dilute single crystal with $x=0.0039$ was examined. Relative to the pure system T_c was lower by only 0.011 K. A slight decrease in γ of ~0.015 was also observed, though this shift was not very much beyond experimental uncertainty. In the present work several crystals somewhat more concentrated in diamagnetic diluent are examined.

II. EXPERIMENT

Diamagnetic $As[S_2CN(C_2H_5)_2]_2Cl$ was prepared as reported previously,[10] as was $Fe[S_2CN(C_2H_5)_2]_2Cl$.[1] The substances were dissolved in methylene chloride to form solutions of nominal molar composition 10%/90%, 20%/80%, 30%/70%, and 40%/60% arsenic/iron complexes. Single crystals obtained on evaporating the solutions to dryness displayed a trend towards smaller size, and somewhat less regular shape, with increasing arsenic concentration. Crystals of

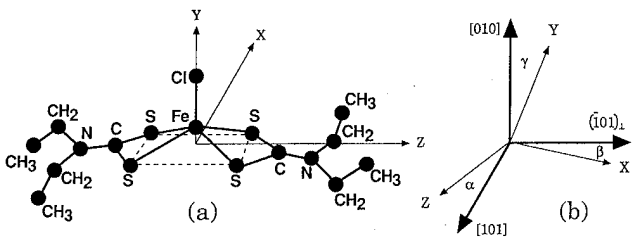


FIG. 1. (a) Molecular structure of $Fe[S_2CN(C_2H_5)_2]_2Cl$, (b) relation of molecular principal axes to principal axes of crystal susceptibility.

 0021-8979/96/79(8)/4644/3/$10.00 © 1996 American Institute of Physics

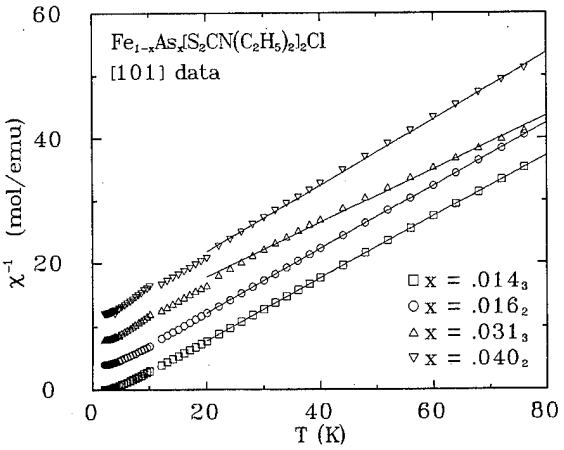


FIG. 2. Inverse molar susceptibility vs temperature along the [101] ferromagnetic easy axis for different composition single crystals of $Fe_{1-x}As_x[S_2CN(C_2H_5)_2]_2Cl$. For clarity the data are shifted up 4, 8, and 12 mol/emu for $x=0.016_2$, 0.031_3, and 0.040_2, respectively.

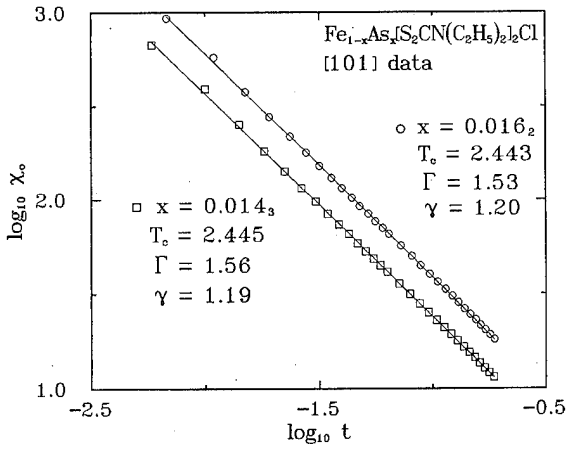


FIG. 3. Critical law fits to initial susceptibility along [101] for $x=0.014_3$ and 0.016_2 single crystals of $Fe_{1-x}As_x[S_2CN(C_2H_5)_2]_2Cl$. For clarity the $x=0.016_2$ log χ_0 are shifted up 0.2. T_c is in K and Γ in emu/mol.

adequate size for magnetic measurements and of similar morphology to those of the pure iron compound were selected from each nominal composition batch. They were cleaved to expose the $(\bar{1}01)$ cleavage plane within which lie the monoclinic b axis and the [101] ferromagnetic easy axis. The masses of the crystals used in the measurements were 2.89, 3.16, 0.4561, and 0.6518 mg (the latter two weighed with a microbalance) for the 10%, 20%, 30%, and 40% As preparations, respectively. Chemical elemental analysis by atomic absorption spectrometry gave the following actual molar compositions: $x_{As}=0.016_2$, 0.014_3, 0.031_3, and 0.040_2 for the nominal 10%, 20%, 30%, and 40% crystal, respectively. Absolute uncertainties in mole fractions are estimated to be ±5% for the first two values and ±10% for the latter two. As previously,[10] only a small fraction of the As complex in solution goes into the Fe-complex crystal lattice, probably because of molecular size considerations.

The magnetization of each single crystal was measured along the [101] axis using a Quantum Design MPMS7 SQUID magnetometer. The applied field was 15.0, 75.0, and 975.0 G for the 2–10, 10–20, and 20–80 K temperature ranges, respectively. The accuracy of the set field was checked by measuring M vs H between 50 and −50 G at 5 K for each crystal, observing linearity, and confirming that $M=0$ at $H=0$ to within ~0.5 G uncertainty. Susceptibilities, calculated as M/H, have been corrected for diamagnetism (−0.000 212 emu/mol) and demagnetization. For each crystal the demagnetization factor N_{eff}, in $H(\text{internal})=H(\text{applied})-N_{\text{eff}}M_v$, where M_v is the volume magnetization, was calculated as the reciprocal of the levelled volume susceptibility below T_c. Only an effective demagnetization factor is obtained because the crystals, of hexagonal prismatic shape, cannot be worked into ellipsoids of revolution. The N_{eff} are 5.68, 4.00, 5.60, and 6.71 for the 10%, 20%, 30%, and 40% As-complex crystals, respectively. Temperatures were measured with a calibrated Ge-resistance thermometer below 38 K and a calibrated Pt-resistance thermometer above 38 K; absolute accuracies are ±0.5%.

III. MEASUREMENTS AND ANALYSIS

In Fig. 2 appear the inverse molar susceptibilities for each of the crystals. For $x=0.014_3$ and 0.016_2, χ^{-1} is quite linear above 20 K, and deviations from linearity do not become marked until well below 10 K. Such behavior had also been seen for the pure material. For the $x=0.031_3$ and 0.040_2 samples, however, and more strongly for the former, there is significant curvature in the 20–80 K range. Also present in these two data sets are anomalies where the field changes at 20 and 10 K occurred.

The applied field of 15.0 G for the lower-temperature data is similar to fields employed in previous measurements of the initial susceptibility of $Fe[S_2CN(C_2H_5)_2]_2Cl$. For each crystal the susceptibility increased rapidly with decreasing T and then levelled off, characteristic behavior of a ferromagnet below T_c due to demagnetization effects. The corrected initial susceptibility χ_0 was analyzed using the critical law

$$\chi_0=\Gamma t^{-\gamma}, \tag{1}$$

where $t=(T-T_c)/T_c$. As for earlier analyses of critical behavior in $Fe[S_2CN(C_2H_5)_2]_2Cl$, a maximum fitted temperature of 2.90 K was employed. The minimum temperature fitted was 2.459 K in each case. The results appear in Figs. 3 and 4, with parameters indicated. The fits are quite good, with rms deviations 0.91%, 0.97%, 0.95%, and 0.82% for $x=0.014_3$, 0.016_2, 0.031_3, and 0.040_2, respectively. Data below 2.459 K exhibit transition rounding effects, and including them leads to serious deterioration in the fit. The precision of the fitted parameters is at the level or better of the last significant figures shown. Taking into account potential sources of absolute error, we estimate that the Γ are ±0.03 emu/mol, the γ are ±0.01 and the T_c are ±0.003 K.

IV. DISCUSSION

In Fig. 5 is shown the ferromagnetic ordering temperature versus composition, earlier results for the pure material and the very weakly dilute crystal of Ref. 10 being included. In constructing this plot corrections to the T_c values in Figs.

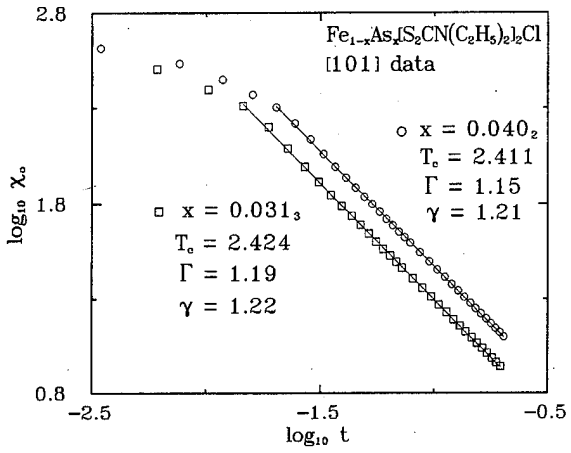


FIG. 4. Critical law fits to initial susceptibility along [101] for $x=0.031_3$ and 0.040_2 single crystals of $Fe_{1-x}As_x[S_2CN(C_2H_5)_2]_2Cl$. For clarity the $x=0.040_2$ log χ_0 are shifted up 0.2. T_c is in K and Γ in emu/mol.

3 and 4 have been made. Independent critical region measurements, and analysis via Eq. (1), on the $x=0.014_3$ and 0.016_2 crystals were made using the same vibrating sample magnetometer (VSM) system employed in previous work (only these two crystals are large enough to measure in a small field on the VSM). The results implied that temperatures from the SQUID device were 0.017±0.003 K higher, in the vicinity of 2.4 K, than those read by the carbon-glass resistance thermometer of the VSM system. The same VSM system yielded[10] a $T_c=2.453$ K for the pure material. This is 0.004 K lower than the accepted value of 2.457 K which was obtained independently from three different instruments previously. Hence the T_c in Figs. 3 and 4 have been reduced by 0.013 K, and Ref. 10 results have been increased by 0.004 K.

The variation of T_c with x is regular but, following an initial drop, rather weak. If the interval $x=0$–0.0039 can be taken as sufficiently small to approximate infinite dilution, then the characteristic quantity at this limit, $-(dT_c/dx)/T_c$, is 1.15±0.11, as noted previously.[10] This is similar in size to the predictions 1.33 and 1.06 for the 2D square planar Ising and 3D simple cubic Ising models, respectively.[9] No corresponding prediction for the dilute Z_2xS_1 model is available.

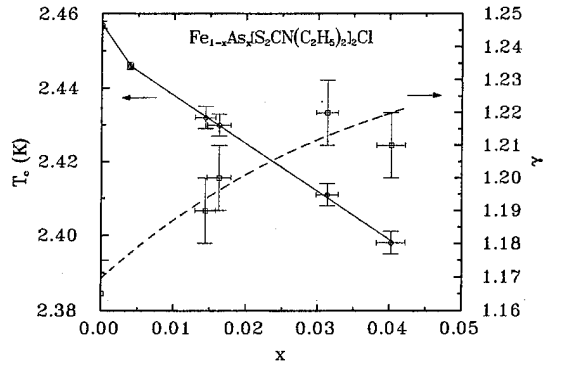


FIG. 5. Ferromagnetic ordering temperature and critical exponent γ vs composition in $Fe_{1-x}As_x[S_2CN(C_2H_5)_2]_2Cl$. Lines are guides to the eye only.

The weak dependence of T_c on x throughout most of the concentration range examined cannot be accounted for by correlated dilution,[11,12] in which the coupling between nearest-neighbor magnetic ions depends on the state (magnetic versus nonmagnetic occupancy) of associated nearest-neighbor sites. Such effects have been shown to lead to "upward curvature" in T_c vs x plots. But this curvature appears at rather larger x(diluent) values than those spanned in this work. Moreover, the initial slope $-(dT_c/dx)/T_c$ is significantly enhanced, e.g., to 2.48 for the 2D square planar Ising model with strong correlation.[11]

Although the variation of γ with x is not perfectly regular, it seems clear that a gradual increase occurs with increasing dilution. A change in critical behavior is predicted by the Harris criterion if $\alpha>0$. Whether or not a continuous variation of critical exponents with dilution will occur may depend on the strength of the disorder.[13] The increase in γ reported here is in the same sense as in simulations of the dilute 3D-Ising model.[13] In the only studies we know of involving dilution of a definite Z_2xS_1 system, $CsMn_xMg_{1-x}Br_3$,[14,15] it was found that α decreased more or less continuously from 0.4 at $x=1$ to 0.2 at $x=0.95$,[15] and β increased from 0.22 to 0.31 over the same range.[14] From the scaling relation $\gamma=2-2\beta-\alpha$, such variations would lead to an increase in γ of about 0.02. We may be seeing an analogous effect two or three times larger. The substantially smaller Γ for the two higher As crystals probably reflects increased disorder, as the $\chi^{-1}(T)$ behavior presumably does. Consequently less moment can be induced per unit field.

ACKNOWLEDGMENTS

This work was supported by National Science Foundation-Solid State Chemistry, Grant No. DMR-9213198. Acknowledgement is also made to the donors of the Petroleum Research Fund, administered by the ACS, for partial support of this research. Professor Gary Rice is thanked for chemical analysis, as is the College of William and Mary for support.

[1] G. C. DeFotis, F. Palacio, and R. L. Carlin, Physica B **95**, 380 (1978); Phys. Rev. B **20**, 2945 (1979).
[2] G. C. DeFotis and J. A. Cowen, J. Chem. Phys. **73**, 2120 (1980).
[3] G. C. DeFotis and S. A. Pugh, Phys. Rev. **73**, 6497 (1981).
[4] G. C. DeFotis and J. R. Laughlin, J. Magn. Magn. Mater. **54–57**, 713 (1986); J. Chem. Phys. **84**, 3346 (1986).
[5] N. Arai, M. Sorai, H. Suga, and S. Seki, J. Phys. Chem. Solids **38**, 1341 (1977).
[6] H. Kawamura, J. Phys. Soc. Jpn. **35**, 2095 (1986); J. Appl. Phys. **61**, 3590 (1987).
[7] H. Kawamura, J. Phys. Soc. Jpn. **61**, 1299 (1992).
[8] G. C. DeFotis, W. W. Brubaker, S. Chandarlapaty, K. L. Beers, and G. A. Coffey, J. Appl. Phys. **75**, 5940 (1994).
[9] A. B. Harris, J. Phys. C **7**, 1671 (1974).
[10] E. W. Harlan, W. R. A. Jarvis, R. V. Chamberlain, and G. C. DeFotis, J. Magn. Magn. Mater. **104–107**, 189 (1992).
[11] A. A. P. daSilva and F. G. Brady Moreira, Phys. Rev. B **40**, 10986 (1989).
[12] N. S. Branco, S. L. A. deQueiroz, and R. R. dosSantos, Phys. Rev. B **42**, 458 (1990).
[13] H.-O. Heuer, Europhys. Lett. **12**, 551 (1990).
[14] D. Visser, A. Harrison, and G. J. McIntyre, J. de Physique **49**, Colloque C-8, 1255 (1988).
[15] R. Deutschmann, H. v. Lőhneysen, J. Wosnitza, R. K. Kremer, and D. Visser, Europhys. Lett. **17**, 637 (1992).

Magnetovolume effects of $MnAs_{1-x}Sb_x$

O. Nashima, T. Suzuki, and H. Ido
Department of Applied Physics, Tohoku Gakuin University, Tagajo, 985, Japan

K. Kamishima and T. Goto
Institute for Solid State Physics, University of Tokyo, Roppongi, Minato-ku, Tokyo, 106, Japan

Thermal expansion, high-field magnetization, and susceptibility measurements have been made for $MnAs_{0.7}Sb_{0.3}$. The thermal expansion measurements show that the spontaneous magnetostriction is large and anisotropic below T_c. The spontaneous magnetostriction at 0 K is estimated to be 1.2×10^{-2} for a axis, -0.8×10^{-2} for c axis, and 1.6×10^{-2} for the volume. The spontaneous magnetization decreases sharply in the narrow temperature region below $T_c=230$ K. All the spontaneous magnetostrictions are found to be proportional to the square of spontaneous magnetization. The magnetization curves measured in a high field up to 40 T show the metamagnetic-like transitions at temperatures above T_c, and they are almost perfectly reproduced by an equation $H=A_1\sigma+A_2\sigma^3+A_3\sigma^5$, where H is the applied field and σ is the relative magnetization. © *1996 American Institute of Physics.* [S0021-8979(96)65708-X]

I. INTRODUCTION

It has been known that the mixed compound $MnAs_{1-x}Sb_x$ with $x\geqslant0.1$ is a ferromagnet of hexagonal NiAs-type structure and has the large and anisotropic exchange magnetostriction.[1–3] The spontaneous magnetization decreases sharply in the narrow temperature region below the Curie temperature like a first-order transition. Magnetization curves at the temperatures above T_c show the field-induced magnetic transitions.[1,2] These unusual characteristics were explained on the basis of the localized electron model.[4,5] However, it is of no doubt that magnetic properties of this kind of intermetallic compounds have to be explained on the itinerant electron model.[6] In the present work, we have carefully examined the magnetization process under a pulsed high magnetic field up to 40 T and the lattice parameters a and c by the x-ray diffraction technique on $MnAs_{0.7}Sb_{0.3}$. We have also measured the susceptibility of the compound at the temperatures in a wide temperature range up to 1100 K. We discuss the results on the basis of the itinerant electron model.

II. SAMPLE PREPARATION

A mixture of powdered Mn, As, and Sb with more than 99.99% purity was heated at 800 °C in vacuum for 100 h to prepare the compound $MnAs_{0.7}Sb_{0.3}$. The crystal structure of the sample was confirmed by x-ray diffraction to be of the hexagonal NiAs type as shown in Fig. 1.

III. EXPERIMENTAL RESULTS

The temperature dependences of the lattice parameters a and c shown in Fig. 2 have been measured by the x-ray diffraction technique at the temperatures between 77 and 290 K. The normal thermal expansion of the c axis depicted by the dashed line is obtained by moving in parallel the thermal expansion of the c axis of MnSb, which shows no anomaly at the Curie temperature.[7] The lattice parameters a and c show sharp increase and decrease, respectively, due to the ex-

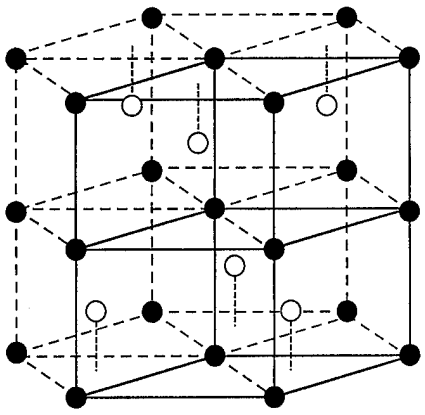


FIG. 1. Crystal structure of the hexagonal NiAs type.

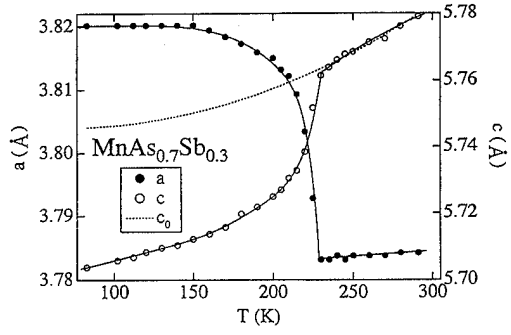


FIG. 2. Temperature dependences of lattice parameters of $MnAs_{0.7}Sb_{0.3}$.

 0021-8979/96/79(8)/4647/3/$10.00 © 1996 American Institute of Physics

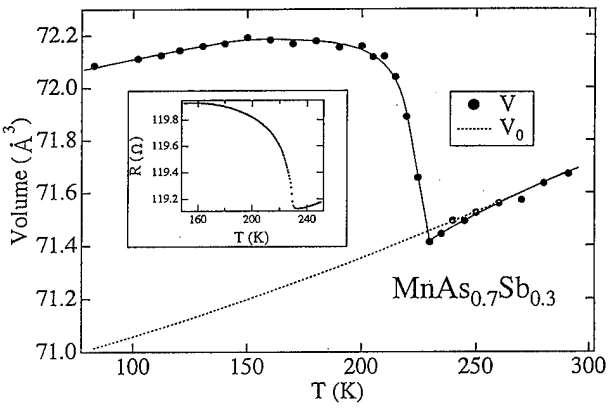


FIG. 3. Temperature dependence of the unit cell volume of $MnAs_{0.7}Sb_{0.3}$. The inset shows the temperature dependence of the electric resistivity of strain gauge pasted on disk-shaped $MnAs_{0.7}Sb_{0.3}$.

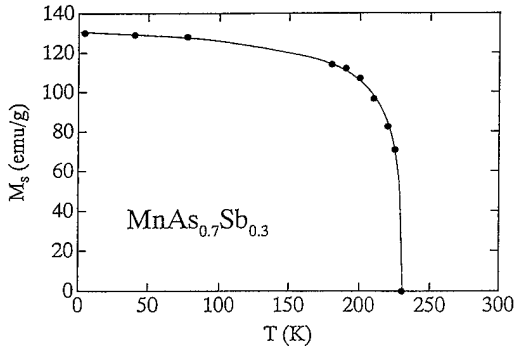


FIG. 5. Temperature dependence of spontaneous magnetization of $MnAs_{0.7}Sb_{0.3}$.

change striction, with decreasing temperature at the Curie temperature. In Fig. 3, the unit cell volume V is plotted against the temperature. The normal thermal expansion shown by the dashed line is deduced by applying the Grüneisen relation[8] to the temperature variation of the specific heat of MnAs. Temperature dependence of the electric resistance R of the strain gauge pasted on a disk-shaped polycrystal specimen is shown in the inset of Fig. 3. Since R has a linear relation with the thermal expansion of the specimen, the Curie temperature T_c is clearly determined to be 230 K, and the positive exchange striction shown in the inset agrees qualitatively well with the data by the x-ray diffraction. Temperature dependences of the spontaneous magnetostrictions $\omega_c=(c-c_0)/c_0$ and $\omega_V=(V-V_0)/V_0$ are obtained from the difference of the observed thermal expansion curves $c(T)$ and $V(T)$ and the normal thermal expansions $c_0(T)$ and $V_0(T)$ shown in Fig. 2 and Fig. 3, respectively. Temperature dependence of $\omega_V(T)$ and $\omega_c(T)$ are similar to each other except for their signs. Since $\omega_V=2\omega_a+\omega_c$, $\omega_a(T)$ must be similar to $\omega_V(T)$ and to $\omega_c(T)$. by linear extrapolation to $T=0$ K of $\omega_V(T)$ etc., we obtain the spontaneous magnetostrictions at $T=0$ K $\omega_a=1.2\times10^{-2}$, $\omega_c=-0.8\times10^{-2}$, and $\omega_V=1.6\times10^{-2}$.

As shown in Fig. 4, magnetization curves for $MnAs_{0.7}Sb_{0.3}$ have been measured in a pulsed magnetic field up to 40 T at various temperatures between 4.2 and 270 K. Field-induced magnetic transitions of the second order occur in the paramagnetic temperature region. The critical fields H_c which is defined as the inflection points of the magnetization curves are also shown in the inset. The saturation magnetic moment per Mn has been obtained to be $3.35\mu_B$ at 4.2 K, which is almost equal to the Mn moments of 3.4 and $3.57\mu_B$ in MnAs[9] and MnSb,[10] respectively. The spontaneous magnetizations M_s at temperatures between 180 and 230 K have been determined by applying the Arrott plot for the observed magnetization curves. In the range of $T\leqslant200$ K, the linearity of M^2-H/M curves is good except for the range of $H/M<0.05$ where the effects of magnetic domains may exist. However, in the temperature range of 200 K$<T<T_c$, M^2-H/M curves are not linear, hence M_s is estimated by the low-field part of the Arrott plot. The spontaneous magnetizations thus obtained are plotted against temperature in Fig. 5. It is noteworthy that the M_s decreases drastically in the temperature range just below $T_c=230$ K. The temperature de-

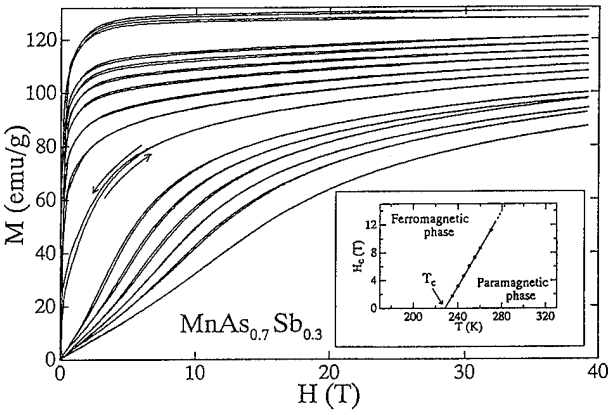


FIG. 4. Magnetization curves of $MnAs_{0.7}Sb_{0.3}$ at the temperature of 4.2, 77, 180, 190, 200, 210, 220, 225, 230, 240, 250, 255, 260, and 270 K from top to bottom, respectively. The inset shows the temperature dependence of critical field.

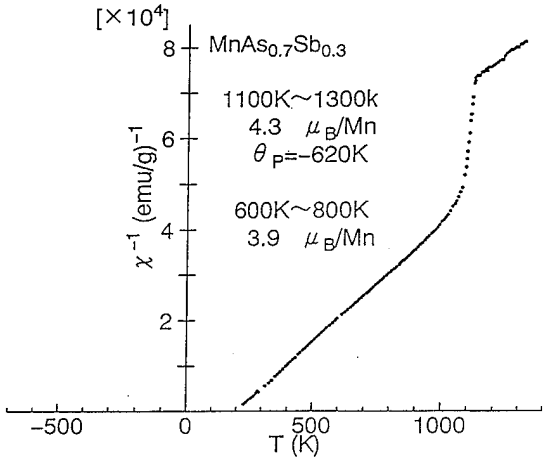


FIG. 6. Temperature dependence of inverse susceptibility of $MnAs_{0.7}Sb_{0.3}$.

pendence of inverse susceptibility χ^{-1} is shown in Fig. 6. The melting temperature of the compound is about 1100 K. The χ^{-1}-T curve is out of straight line, and slightly convex upward, which implies a spin fluctuation effect,[6] so magnetic moment $2S_{\mathrm{Mn}}\mu_B$(S_{Mn}: spin per Mn atom) has been estimated to be $3.9\mu_B$ by fitting the Curie Weiss low to the χ^{-1}-T curve between 600 and 800 K where the highest temperature region is below the melting point. In the liquid state ($T \geqslant 1100$ K), $4.3\mu_B$ is obtained. The paramagnetic Curie temperature is about -600 K for the liquid state.

IV. DISCUSSION

The large and anisotropic spontaneous magnetostrictions are shown in Fig. 2. In the Stoner model, the requirement of $I\rho(\epsilon_F)>1$ is needed to stabilize ferromagnetism, where I is exchange interaction and $\rho(\epsilon_F)$ is the density of state at the Fermi energy. In general, I and $\rho(\epsilon_F)$ become large as the volume increases. So, positive ω_a and ω_V are reasonable, however, the negative large value of ω_c cannot be explained from the above point of view. Detailed calculation of the energy band structures is expected to explain the large and anisotropic ω_a and ω_c.

It is found that $\omega_V(T)$ and $\omega_c(T)$ and consequently $\omega_a(T)$ are proportional to the square of the spontaneous magnetization (M_s^2). When the coefficients α, β and γ are defined as $\omega_\alpha=\alpha M_s^2$, $\omega_c=\beta M_s^2$, and $\omega_V=\gamma M_s^2$, we have obtained $\alpha=7.1\times10^{-7}$, $\beta=-4.7\times10^{-7}$, and $\gamma=9.5\times10^{-7}$ (emu/g)$^{-2}$. The temperature independent constant α, β, and γ are explained by the Bean and Rodbell model,[4] if the interatomic exchange interaction depend on a and c axis separately. However, the Bean and Rodbell theory is not appropriate to this kind of compound which has characteristics of itinerant electrons such as that of MnAs etc. which were explained by Motizuki and Kato.[6] So, the relation between ω_a etc. and M_s^2 mentioned above have to be explained on the basis of itinerant electron model.

We have analyzed the magnetization processes with the field-induced magnetic transitions at the temperatures above T_c by fitting the following equation to the experimental curves:

$$H=A_1(T)\sigma+A_2(T)\sigma^3+A_3(T)\sigma^5, \tag{1}$$

where A_1, A_2, and A_3 are coefficients, H the applied magnetic field in units of Oe, and σ the relative magnetizations defined as $\sigma=M/M_s(0)$. According to the theory of metamagnetism by Yamada,[11] the parameters A_1, A_2, and A_3 in Eq. (1) are expressed by the following equations:

$$A_1(T)=\chi_p(T)^{-1}=a_1+(5/3)a_2\xi_p(T)^2+(35/9)a_3\xi_p(T)^4, \tag{2}$$

$$A_2(T)=a_2+(14/3)a_3\xi_p(T)^2, \tag{3}$$

$$A_3(T)=a_3, \tag{4}$$

where a_1, a_2, and a_3 are constants and $\xi_p(T)^2$ is mean square of the spin fluctuation. The magnetization curves at the temperatures above T_c are perfectly reproduced by Eq. (1), and then $A_1(T)$, $A_2(T)$, and $A_3(T)$ have been obtained and plotted against temperature in Fig. 7. As shown in Fig. 7, A_1 varies almost linearly to the temperature, which is consistent with the temperature variation of inverse susceptibility. On the other hand, A_2 and A_3 are almost temperature independent. The result of A_3 is consistent with Eq. (4), however the temperature independent A_2 is difficult to explain. According to the Bean and Rodbell theory, A_1 increases linearly to the temperature and A_3 is temperature independent, however A_2 increases linearly to the temperature, so the temperature independent A_2 in Fig. 7 cannot be explained. The requirement for metamagnetic transition to occur is $3/16<A_1A_3/A_2^2<9/20$, therefore if the linearity of A_1 keeps to 230 K, the requirement will be satisfied at 230 K. However, the magnetization curve at 230 K is not metamagnetic, probably because of the effects of short-range magnetic order. Metamagnetic transition will be realized if the Curie temperature is shifted to the lower temperature[1] by high pressure.

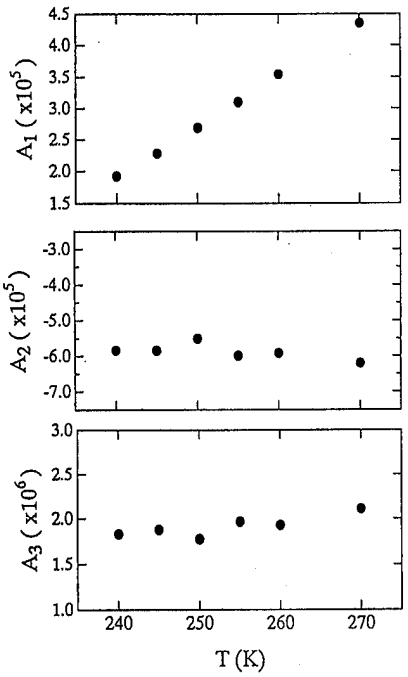


FIG. 7. A_1, A_2, and A_3 vs T at the paramagnetic temperatures.

[1] H. Ido, S. Yasuda, M. Kido, G. Kido, and T. Miyakawa, J. Phys. (Paris) Colloq. **49**, C8-167 (1988).
[2] H. Ido, S. Yasuda, and G. Kido, J. Appl. Phys. **69**, 4621 (1991).
[3] K. Bärner, Phys. Status. Solidi A **5**, 405 (1971).
[4] C. P. Bean and D. S. Rodbell, Phys. Rev. **126**, 104 (1962).
[5] R. W. DeBlois and D. S. Rodbell, Phys. Rev. **130**, 1347 (1963).
[6] K. Motizuki and K. Kato, J. Phys. Soc. Jpn. **53**, 735 (1984).
[7] H. Krokoszinski, C. Santandrea, E. Gmelin, and K. Bärner, Phys. Status Solidi **113**, 185 (1982).
[8] C. Kittel, *Introduction to Solid State Physics,* 2nd ed. (Wiley, New York, 1956).
[9] C. Guillaud, J. Phys. Radium **12**, 223 (1951).
[10] T. Okita and Y. Makino, J. Phys. Soc. Jpn. **25**, 120 (1968).
[11] H. Yamada, Phys. Rev. B **47**, 11 211 (1993).

Transmission electron microscopy of Terfenol-D crystals

A. P. Holden, D. G. Lord, and P. J. Grundy
Physics Department, Joule Laboratory, University of Salford, M5 4WT, United Kingdom

Magnetic domain and microstructure observations are presented from samples of pseudo-single-crystal Terfenol-D examined by transmission electron microscopy (TEM). This ternary alloy is of significant technological interest since it exhibits the highest known magnetostriction to anisotropy ratio near room temperature. Specimens for TEM studies in (110), (111), and (112) orientations have also shown regions of unusual diffraction contrast in bright field which appears to be very sensitive to specimen tilt. Lorentz mode TEM has subsequently shown such regions to correspond exactly with magnetic domains. This contrast is attributed to the high magnetostrictive strain causing a local distortion of the lattice and thus a local deviation from the Bragg condition. This conclusion has been investigated and supported by TEM observations with the samples cooled below the spin reorientation temperature. When this transition is reached the diffraction contrast in bright field is considerably decreased and cannot be made to vary by tilting the specimen. The latter experiments also indicate that the change from ⟨111⟩ to ⟨100⟩ easy axis is not a well-defined one but, rather, that the spin reorientation is a sluggish change. High-resolution lattice images show the coherency of the twin boundaries. © *1996 American Institute of Physics.*
[S0021-8979(96)65808-6]

I. INTRODUCTION

This paper presents the results of magnetic domain and microstructure observations in samples of pseudo-single-crystal Terfenol-D ($Tb_{0.3}Dy_{0.7}Fe_2$) examined by transmission electron microscopy (TEM). This cubic Laves phase compound, which exhibits a giant positive coefficient of magnetostrictive strain (~2000 ppm along ⟨111⟩) coupled with a relatively low magnetocrystalline anisotropy ($K_1 \sim 10^5$ J m^{-3} at room temperature), is of current interest for device applications which utilize these properties. The work forms part of a general program which, using high-resolution TEM, optical microscopy, and scanning probe microscopy, is concerned with the investigation of the magnetization processes and magnetic domain/defect structure interactions in this unique material.

II. EXPERIMENT

Start material (obtained from Etrema Products in the form of 8-mm-diam rods) is produced using a free-standing-zone (FSZ) method. Such a preparation route has been previously shown[1] to have a dendritic growth front along the rod axis, ⟨112⟩, and to produce material with a high concentration of twin boundaries with the {111} twinning plane orthogonal to the growth front. Thin disc samples with $(1\bar{1}0)$ and $(11\bar{2})$ orientations have been prepared for TEM observations, by spark erosion, mechanical dimpling and ion beam milling. Lorentz mode TEM observations were carried out using a JEOL 200CX TEMSCAN electron microscope equipped with a "field-free" objective lens. High-resolution lattice fringes have been obtained using a JEOL 3010 HRTEM.

III. RESULTS AND DISCUSSION

Figure 1(a) shows a near-focus bright-field micrograph obtained from a $(1\bar{1}0)$ orientation sample. Figure 1(b) shows a Foucault mode micrograph of the same area. Figure 1(c) shows the same area near focus in bright field with the sample tilted slightly (<2°). In obtaining these micrographs the same objective aperture, positioned concentrically about the optical axis in the case of Fig. 1(a) and Fig. 1(c), was used and was of such a size that only the straight through beam was used to compose the image. In obtaining the micrograph shown in Fig. 1(c) the tilt position selected was that one where the obvious bright-field diffraction contrast could first be seen to such an extent. One can immediately see from a comparison of the three figures that the magnetic domains which are revealed in the Foucault mode can be easily discerned in the near-focus bright-field image [Fig. 1(c)] and that the contrast produced in bright field is comparable to that produced in the Foucault mode. Such effects have also been observed in (111) and $(11\bar{2})$ samples. Previous studies[2] of the domain structure in Terfenol-D by Lorentz TEM have also mentioned similar effects. The mechanism by which this contrast arises can be considered to be due to a local change in the reflecting conditions within the magnetic domains. Such a change can be brought about by giant magnetostrictive effects causing a change in the crystal lattice spacing thus altering the Bragg condition locally. Such changes can be quantified,[3] in the light of the dynamical theory of image contrast, by calculating changes in the deviation parameter s. Such a change in s can be approximated by

$$\Delta s = \lambda_s \theta_B g,$$

where θ_B is the Bragg angle, λ_s is the magnetostrictive strain, and g is the reciprocal lattice vector for the operating reflection. Estimating the extinction distance ξ_g for Terfenol-D to be ~50 nm and λ_s to be 2000 ppm, one obtains an estimate for the product $\xi_g \Delta s$ of 5×10^{-3}. It can be shown[3] that changes in $\xi_g \Delta s$ of this order of magnitude in alternate domains can lead to changes in intensity of ~5%. It is therefore feasible that in materials which possess giant magnetostriction this property can lead to noticeable contrast effects in TEM (as it also has been shown to do in x-ray

 0021-8979/96/79(8)/4650/3/$10.00 © 1996 American Institute of Physics

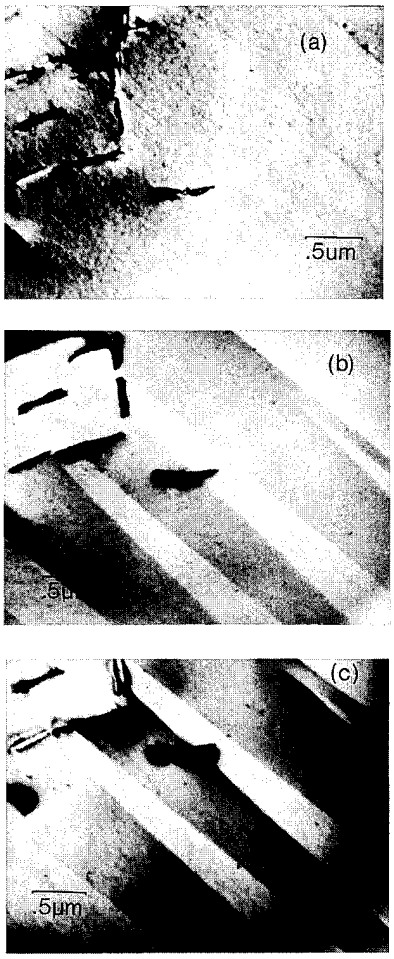


FIG. 1. TEM micrographs revealing magnetic domains and bright-field diffraction contrast in a $(1\bar{1}0)$ orientation FSZ specimen showing (a) near-focus image, (b) Foucault contrast, and (c) near-focus image tilted to show bright-field diffraction contrast.



FIG. 2. Fresnel out-of-focus micrographs from $(1\bar{1}0)$ specimen obtained at (a) 273 K, (b) 230 K,and (c) 220 K.

topography). We also note that for the changes in contrast commonly observed in this work (~10%) $\xi_g \Delta s$ would be approximately twice as large as that value calculated above. It might therefore be reasonable to assume that the magnetostrictive strain on the microscopic level is somewhat higher than that measured at the macroscopic level. In addition it should also be noted that Δs will increase (via increases in both g and ξ_g) for higher-order reflections.

When samples showing the diffraction contrast in bright field were cooled to 100 K, thus making ⟨100⟩ the easy direction, similar contrast effects to those shown in Fig. 1 were not observed. Since $\lambda_{111} \gg \lambda_{100}$ (Ref. 4) we might assume that the bright-field diffraction contrast, such as that shown in Fig. 1(c), is due to magnetostrictive distortion of the lattice.

Utilizing the change in features of Mössbauer spectra, previous workers[5] have reported that ⟨111⟩ is easy down to approximately 273 K and that ⟨100⟩ is easy below ~175 K. In between these temperatures the easy direction was quoted as being intermediate. A later study[6] based on the changes in characteristic x-ray diffraction data reported that the spin reorientation temperature lies in the range 263–273 K with ⟨100⟩ easy below this temperature range and ⟨111⟩ easy above it. Figure 2 shows a series of Fresnel out-of-focus micrographs obtained from a (110) sample. The micrograph shown in Fig. 2(a) was obtained at 273 K and the domain structure shown is identical to that which was observed at room temperature. Figure 2(b) shows a micrograph obtained from the same region with the sample temperature at 230 K. Figure 2(c) shows the same area as that shown in Fig. 2(b) at a temperature of 220 K. We note from these micrographs that the room-temperature domain structure is only just starting to change at 230 K and is almost completely gone at 220 K. We therefore report the occurrence of typical ⟨111⟩ easy axes patterns as low as 230 K and that the onset of the transition to ⟨100⟩ easy axes appears to occur at around 220 K. We also note that domain wall motion is still observed as low as 170 K. The transition thus appears to take place at a temperature lower than that most recently reported.[6] Our studies also show that the transition from ⟨111⟩ to ⟨100⟩ easy axes shows some variability from sample to sample and even in different areas of the same sample. This suggests that magnetoelastic interactions and pinning effects are influential in determining the domain structure.

We have also made observations which focus on domain configurations in the vicinity of twin boundaries. This is mainly influenced by the results of previous[2] TEM investigations of Terfenol-D. In general the walls one observes in the vicinity of twin boundaries, in $(1\bar{1}0)$, are of 109° and 71°

character and arise due to out-of-plane components of magnetization. This is despite the existence of an in-plane easy direction, orthogonal to the twin boundaries, which is common to both parent and twin regions and would lead to 180° walls. The observed configurations require the twin boundary itself to be a domain wall which, if previous suppositions[7] are correct, should be "frozen in." We have observed areas in which there are twin boundaries which show domain wall contrast at 293 K and then cooled the samples to ~100 K to see whether the twin boundary walls are mobile. A close examination and comparison of such domain patterns obtained at 293 and 100 K show that when the ⟨100⟩ easy axis pattern is adopted this is done in such a way that the twin boundary remains as a wall and therefore the associated domains must have walls consistent with such a scheme. Such domain configurations must arise from magnetization lying in the plane creating walls with 180° and 71° character. That such patterns are adopted in the vicinity of the twin boundary is indicative of the pinning action there. The latter observation is also supported from high-resolution TEM studies. When operating the JEOL 3010 HRTEM in high magnification mode the vertical field in which the sample sits is of the order of 2 T. Such a field easily suffices to saturate the samples and therefore magnetic domain wall contrast should not be seen. A comparison of areas observed using the JEOL 200CX and the JEOL 3010 HRTEM shows this to be the case except for those walls which lie along the twin boundaries. A HRTEM micrograph of a twin boundary is shown in Fig. 3 where lattice fringes can easily be seen. We also note from this micrograph the presence of some bands of contrast running in to the twin boundary in the [110] direction as indicated on the figure. This is as yet unexplained and remains a feature of some interest given the direction and marked linearity of the features. If the twin boundary domain walls are frozen then it is evident that such high-resolution images have the potential to reveal much information regarding the magnetic coherence of the twin boundaries. This latter work forms part of an on-going programme concerned with the magnetoelastic properties of Terfenol.

IV. CONCLUSION

It has been shown that in materials exhibiting giant magnetostriction magnetic domains can be revealed by means other than Lorentz microscopy. This has been supported by quantitative considerations and by examining the material in a state where it no longer shows such giant magnetostriction. The spin reorientation process has been studied for the first time by means of TEM and the temperature at which this takes place has been shown to be slightly lower than that previously suggested. The domain wall pinning action at twin boundaries which also happen to be domain walls has been shown. High-resolution lattice fringes from twin boundary regions have been shown for the first time and show, as yet, unexplained contrast effects.

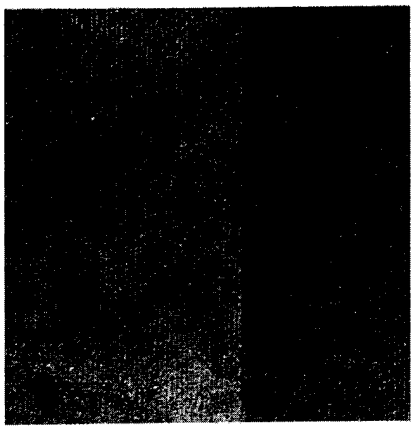


FIG. 3. HRTEM micrograph of twin boundary (TB) in $(1\bar{1}0)$ specimen showing lattice fringes and further bright-field contrast effects.

ACKNOWLEDGMENTS

The authors wish to thank the UK EPSRC for support of this work (under Grant No. GR\H65320 and GR\J31186) and Brian Ashworth for his assistance in TEM sample fabrication.

[1] J. P. Teter, K. Mahoney, M. Al-Jiboory, D. G. Lord, and O. D. McMasters, J. Appl. Phys. **69**, 5768 (1991).

[2] M. Al-Jiboory, D. G. Lord, Y. J. Bi, J. S. Abell, A. M. H. Hwang, and J. P. Teter, J. Appl. Phys. **73**, 6168 (1993).

[3] P. B. Hirsch, A. Howie, R. B. Nicholson, D. W. Pashley, and M. J. Whelan, *Electron Microscopy of Thin Crystals* (Butterworths, London, 1972).

[4] A. E. Clark, in *Ferromagnetic Materials, Vol. 1,* edited by E. P. Wohlfarth (North Holland, Amsterdam, 1980), p. 531.

[5] U. Atzmony, M. Dariel, E. Bauminger, D. Lebenbaum, I. Nowik, and S. Offer, Phys. Rev. B **7**, 4220, (1973).

[6] M. Al-Jiboory and D. G. Lord, IEEE Trans. Magn. **MAG-26**, 2583, (1990).

[7] G. S. Kandaurova, L. G. Onoprienko, and N. I. Sokolovskaya, Phys. Status Solidi A **73**, 351 (1982).

Propagation and reflection properties of magnetoelastic wave in FeSiB amorphous wire

Y. Takemura, S. Masuda,[a] T. Yamada, and K. Kakuno
Division of Electrical & Computer Engineering, Yokohama National University, 156 Tokiwadai, Hodogaya-ku, Yokohama 240, Japan

Propagation and reflection properties of magnetoelastic waves in $Fe_{77.5}Si_{7.5}B_{15}$ amorphous wires are studied. The attenuation constant increases with increasing the driving frequency of the wave. As the attenuation constant of the wave driving at 500 kHz is quite small (0.18 m^{-1}), the wave is expected to be observed after the propagation of 20 or 30 m. As for the reflection, the magnetoelastic wave is reflected with the efficiency as much as 0.9 at the driving frequency below 2 MHz using a clamp as reflector. © *1996 American Institute of Physics.* [S0021-8979(96)65908-2]

I. INTRODUCTION

Amorphous magnetic wires, such as FeSiB and FeCoSiB wires, provide attractive features including the magnetoelastic wave[1] and the magnetoimpedance effect.[2] Among them, it has been found that the magnetoelastic wave in FeSiB amorphous wire is well controllable and that it is suitable for sensors and the other applications. A large magnetostriction ($\lambda_s = 35 \times 10^{-6}$) in FeSiB realizes a large magnetoelastic coupling, and an efficient driving and pickup of the magnetoelastic wave. Due to the high electrical resistivity of amorphous FeSiB, an eddy current loss of the propagated magnetoelastic wave is low. Only a longitudinal mode of the magnetoelastic wave is propagated in the one-dimensional shape of the wires. Because of these characteristics, the attenuation constant of the magnetoelastic wave is low (0.18 m^{-1} at 500 kHz) and it is propagated through the long distance, which is applicable for the wide-range distance sensor.[3] It detects a distance from 0 to 5 m with an accuracy less than 1 mm. In the sensor, sensitivity and resolution depend much on an attenuation constant and a reflection efficiency of the wave at the reflector. The experimental study of the propagation and reflection properties of magnetoelastic waves in FeSiB wire are reported.

II. EXPERIMENTS

Amorphous $Fe_{77.5}Si_{7.5}B_{15}$ wires supplied from Unitika Co., Japan are used in this study. They are produced by the in-rotating-liquid spinning method.[4] As-quenched wires of 125 μm in diameter are cold drawn to 90 μm. The as-drawn wires are magnetically hard. They have the following features: (1) a low efficiency to drive or to pick up the magnetoelastic wave, (2) a low attenuation of the magnetoelastic wave, (3) few interaction between the magnetoelastic wave and external magnetic and electric fields.

In order to realize the efficiency driving and pickup of the wave, small regions of the as-drawn wire are annealed by the partial annealing technique.[1] The annealing is performed by blowing a hot air from a nozzle connected with a ceramic heater (400 °C for 15 min without applying magnetic field). The annealed parts are magnetically soft and they are settled at the positions of driving and pick-up coils as shown in Fig. 1. Bias coils surrounding the driving and pick-up coils are equipped in order to enhance an efficiency in driving and pickup of the wave. By applying a high-frequency current through the driving coil, the magnetoelastic wave is excited in the wire. The magnetoelastic wave excited by the high-frequency current of a tone-burst waveform is used for measurements of amplitudes of the wave. Details on driving and pickup of the wave have been reported.[1] The velocity of the wave is 4.7 km/s and its wavelength is about 1 mm at the driving frequency of 5 MHz.

III. RESULTS AND DISCUSSION

A. Propagation property

For the measurements of propagation property of the wave, the system shown in Fig. 1 is used. The amplitude of the wave propagated directly from the driving position and the amplitude of the wave propagated after reflecting at the reflector are measured by the pick-up coil, which are indicated as A_0 and A_1 in the figure, respectively. The ratio of A_1/A_0 is an attenuation ratio of the wave propagated for a length of x, where $x/2$ is a distance between the pick-up coil and the reflector. The reflection of the wave is performed by clamping the wire by a brass tool. The reflection efficiency as much as 0.8 is obtained by this method, which is discussed in the next section. Although the ratio of A_1/A_0 also includes an loss of the wave at the reflector, the measurement system shown in Fig. 1 is useful for the experiments of the propagation of the wave for a long distance. It is because the

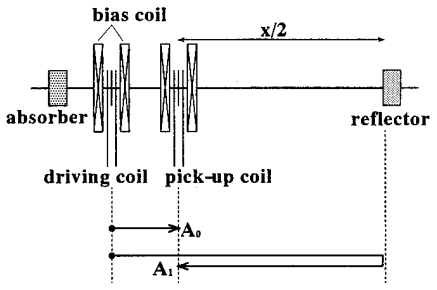


FIG. 1. System for driving and pickup of the magnetoelastic waves and for measuring propagation and reflection properties of the waves.

[a]Research & Development Dept., Jeco Co. Ltd., 1-4-1 Fujimicho, Gyoda-shi, Saitama 361, Japan.

 0021-8979/96/79(8)/4653/3/$10.00 © 1996 American Institute of Physics

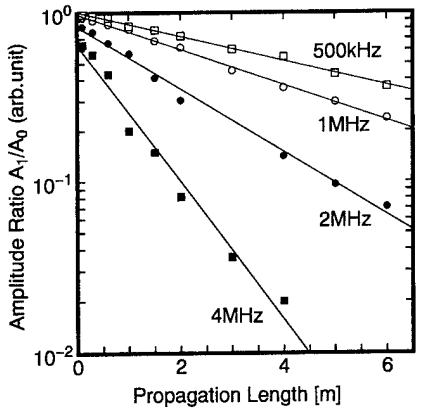


FIG. 2. Measured amplitude ratio A_1/A_0 as a function of the propagation length of the magnetoelastic wave. The driving frequency of the wave is varied from 500 kHz to 4 MHz.

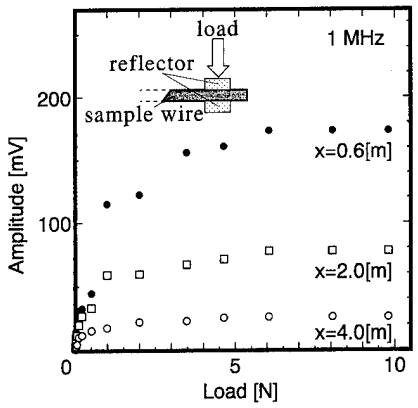


FIG. 3. Measured amplitudes of the reflected magnetoelastic wave as a function of the load on the clamp reflector. The driving frequency of the wave is 1 MHz.The insertion shows the reflector clamping the sample wire.

propagation length can be easily varied by changing the position of the clamp reflector without changing the position of the driving and pick-up coils. This technique is applied for the distance sensor.[3]

Figure 2 shows the measured amplitude ratio (A_1/A_0) indicated as a function of the propagation length up to 6 m. The driving frequency was varied from 500 kHz to 4 MHz. In the figure, the attenuation constant of the wave is obtained as a slope of the amplitude ratio against the propagation length. The intercept of the amplitude ratio where the propagation length equals to zero indicates a reflection efficiency of the wave at the reflector. With increasing driving frequency, the attenuation of the wave increases for the measured frequency range. It is because eddy current loss increases for a propagation of the high-frequency magnetoelastic wave. The wave driven at 500 kHz is propagated with a low attenuation constant of 0.18 m^{-1}, which corresponds to 8.6 dB for 10 m. It is expected to be observed with a sufficient-signal intensity after the propagation of 20 or 30 m.

B. Reflection property

The distance sensor using the magnetoelastic wave measures a distance between the driving/pick-up coil and the reflector by counting the propagation time of the wave. In order to obtain a sufficient signal intensity of the wave propagated through a long distance, an efficient reflection of the wave is required. Figure 3 shows the measured amplitudes of the wave propagated after the reflection (A_1 in Fig. 1) in the cases of $x=0.6$, 2.0, and 4.0 m, where x is the propagation length indicated in Fig. 1. The driving frequency of the wave is 1 MHz. As shown in the insertion in Fig. 3, the sample wire is clamped between pieces of brass material. It is found that the load of 5 N is required to obtain a sufficient reflection of the wave by the reflector used in this experiment. The frequency dependence of the reflection efficiency is also studied. As for materials of the clamp reflector, acrylic resin, stainless steel, and brass are studied. The load on the clamp is enough to obtain a maximum reflection in the measurement. As shown in Fig. 4, it is found that the reflection efficiency decreases with increasing the driving frequency of the magnetoelastic wave and that it is as much as 0.9 for the driving frequency below 2 MHz. The reflector of stainless steel has a high reflection efficiency in the high-frequency region above 2 MHz compared with that of brass, which is attributed to the large elastic constant of stainless steel. The figure also indicates the reflection efficiency for the acrylic resin reflector. The reflection of the wave is not observed for the driving frequency above 2 MHz. It is also found that when a soft urethane rubber is utilized as wave absorber shown in Fig. 1 the reflection efficiency is quite low.

Because the attenuation constant of the wave is small and the reflection efficiency is large for the wave driven at lower frequency, the frequency around 500 kHz is advantageous for applications such as the distance sensor. Although an accuracy of the distance sensor is high for the high driving frequency, the resolution as small as 1 mm, which is practically sufficient, is obtained at 500 kHz in the distance sensor having a detect range of 0–5 m.

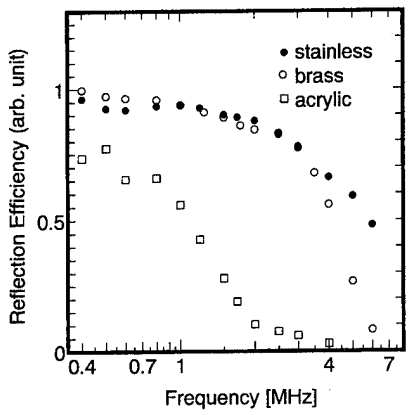


FIG. 4. Reflection efficiency of the magnetoelastic waves as a function of the driving frequency. (●), (○), and (□) indicate the results for stainless steel, brass, and acrylic resin used as materials of the clamp, respectively.

IV. CONCLUSIONS

Propagation and reflection properties of the magnetoelastic waves in $Fe_{77.5}Si_{7.5}B_{15}$ amorphous wires are studied. Due to a large magnetostriction of $Fe_{77.5}Si_{7.5}B_{15}$, efficient driving and pickup are obtained. The attenuation constant of the wave is measured at various driving frequency. With increasing frequency, the attenuation constant increases, which is due to an enhancement of eddy current loss. As the attenuation constant is quite small ($0.18\ m^{-1}$) at 500 kHz, the wave is expected to be observed with a sufficient-signal intensity after the propagation of a long distance. The reflection efficiency is also investigated. Using a clamp as reflector, the magnetoelastic wave is reflected with the efficiency as much as 0.9 for the wave driven below 2 MHz. These fundamental properties of the magnetoelastic wave are utilized to examine the device performance for devices such as the distance sensor.

[1] S. Masuda and K. Kakuno, IEEE Trans. Magn. **MAG-26**, 1801 (1990).
[2] L. V. Panina, M. Noda, and K. Mohri, J. Appl. Phys. **76**, 6198 (1994).
[3] Y. Takemura, S. Masuda, T. Yamada, and K. Kakuno, IEEE Trans. Magn. **MAG-31**, 3155 (1995).
[4] M. Hagiwara, A. Inoue, and T. Masumoto, Metall. Trans. **13A**, 373 (1982).

Anomalous compressibility and magnetovolume effects in $Ce_3(FeTi)_{29}$

J. Kamarád and Z. Arnold
Institute of Physics, AS CR, Cukrovarnická 10, 162 00 Praha 6, Czech Republic

L. Morellon, P. A. Algarabel, and M. R. Ibarra
Departamento de Física de la Materia Condensada-ICMA, Facultad de Ciencias, Universidad de Zaragoza-CSIC, 50009 Zaragoza, Spain

C. D. Fuerst
Physics Department, General Motors NAO Research and Development Center, 30500 Mount Road, Warren, Michigan 48090-9055

In this contribution we present the results of direct measurements of the compressibility, in a wide temperature range, and studies of the linear thermal expansion under hydrostatic pressure using a modified strain gauge method in $Ce_3(FeTi)_{29}$. A large magnetic contribution (κ_m=0.13 $Mbar^{-1}$) to the isothermal compressibility was observed in the ferromagnetic state in comparison with the compressibility in the paramagnetic state induced by pressure at room temperature. The pronounced lambda-shaped anomalies in the thermal expansion coefficient (negative values of α) and in the compressibility of the $Ce_3(FeTi)_{29}$ compound were simultaneously observed in the vicinity of T_C.
© *1996 American Institute of Physics.* [S0021-8979(96)66008-7]

I. INTRODUCTION

The $R_3(FeTi)_{29}$ compounds belong to a family of iron-rich intermetallics (such as $R_2Fe_{14}B$ or $RFe_{12-x}M_x$) with outstanding properties for permanent magnet applications. These compounds crystallize in a monoclinical structure. X-ray and neutron diffractions were analyzed considering the space group $P2_1/c$ (Refs. 1–3) and A_2/m.[4] The Curie temperatures T_C of the compounds are rather low, from 319 (R=Ce) to 520 K (R=Gd). However, the existence of a large magnetovolume coupling offers the possibility of increasing T_C by introducing interstitial atoms. Actually, this has stimulated an intensive study of both magnetic properties and magnetovolume effects in these compounds.

High-pressure experiments have revealed a significant influence of the volume changes on the magnetic interactions.[5,6] A large spontaneous magnetostriction ω_S (Ref. 7) and an anomalous Invar-like behavior in the thermal expansion coefficient has been observed in the vicinity of T_C in the $R_3(FeTi)_{29}$ compounds[8,9] (R=Nd, Pr, Tb, and Gd). The discovery of the Invar phenomena in the $R_3(FeTi)_{29}$ compounds[7] enlarges the family of Invar materials. The large variation of T_C under pressure is considered as an important Invar characteristic that has been described within the band model of very weak itinerant ferromagnets by the well-known Wohlfarth's relation:[10] $dT_C/dp \approx -A/T_C$, where A is constant within a wide temperature range in some Invar alloys (A=2200 K/kbar for FeNi). The results obtained in $R_3(FeTi)_{29}$ showed that the parameter A is constant and A=1200 K/kbar, along the series.[11] This is additional evidence of the existence of the Invar effects also in nearly strong itinerant systems.

Recently, we have measured the pressure dependence of the Curie temperature T_C on $Ce_3(FeM)_{29}$ (M=Ti, Cr). A large decrease of T_C was observed under hydrostatic pressure up to 12 kbar for both compounds [dT_C/dp=−3.75 K/kbar for $Ce_3(FeTi)_{29}$ and dT_C/dp=−3.6 K/kbar for $Ce_3(FeCr)_{29}$].[6] To correlate these pressure data with the spontaneous magnetostriction and other magnetovolume effects, we have performed compressibility measurements using a modified strain gauge method. In this contribution we present the results of direct measurements of the compressibility in a wide temperature range and studies of the linear thermal expansion under hydrostatic pressure.

II. EXPERIMENT

The polycrystalline sample was prepared by induction melting high-purity elemental constituents in a boron nitride crucible. The sample was annealed in vacuum for ten days at a temperature of 900 °C. X-ray diffraction and electron beam microprobe energy dispersed analytical x-ray (EDAX) analyses were carried out to monitor phase occurrences. The sample was found to be single-phase $Ce_3Fe_{27.4}Ti_{1.6}$. Crystallographic and magnetic information on this compound can be found in Ref. 12. The compressibility and the thermal expansion of the $Ce_3(FeTi)_{29}$ compound was measured under pressure up to 8 kbar using strain gauges (Micro-Measurements Inc., SK-350) in the temperature range 100–550 K. The strain gauges were calibrated using as reference data the compressibility and thermal expansion of silica, Cu, and Fe. The pressure apparatus (made of a maraging steel) consists of two parts, a pressure generator and a pressure cell, both connected by a capillary. The pressure generator (with a manganic pressure sensor inside) was kept at room temperature. The temperature of the sample was measured using Thermocoax thermocouples inside the pressure cell.

III. RESULTS AND DISCUSSION

First studies of the changes of relative volume under pressure were made at room temperature. A decrease of the value of compressibility was observed for high pressures as well as a peak-like anomaly around 5 kbar. This can be related to the transition from the ferromagnetic to the paramagnetic state induced by pressure at room temperature. Figure 1 illustrates how the pressure range where the anomalous behavior of compressibility is observed at room temperature

 0021-8979/96/79(8)/4656/3/$10.00 © 1996 American Institute of Physics

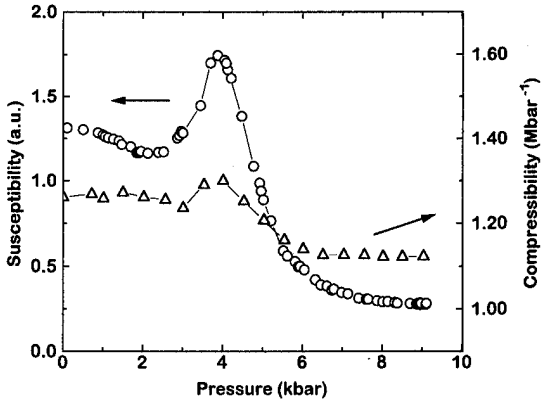


FIG. 1. Pressure dependence of the ac initial magnetic susceptibility (○) and compressibility (△) of $Ce_3(FeTi)_{29}$ at room temperature.

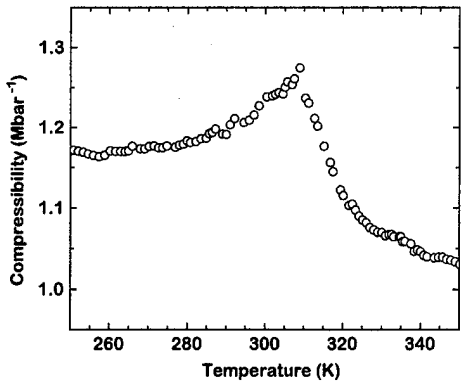


FIG. 3. Compressibility of the $Ce_3(FeTi)_{29}$ compound in the vicinity of T_C at 2 kbar.

coincides with the transition of the sample from the ferromagnetic to the paramagnetic state as determined by susceptibility measurements. A similar behavior of the compressibility through a pressure-induced transition from ferromagnetic to paramagnetic state has recently been observed in $Er_2Fe_{14}B$.[13]

Figure 2 presents the linear thermal expansion and linear thermal expansion coefficient α for $Ce_3(FeTi)_{29}$ at normal pressure and under a pressure of 5 kbar in the temperature range 240–400 K. The thermal expansion results are in relation to ambient conditions (0 kbar, 295 K). A well-defined anomaly is observed at the magnetic ordering temperature T_C. The decrease of temperature of this anomaly corresponds to the decrease of T_C under pressure observed by Arnold *et al.*[6]

Figure 3 shows the temperature dependence of the compressibility $\kappa(T)$ of the $Ce_3(FeTi)_{29}$ compound. It is worth noting that the compressibility has a maximum followed by a steep decrease near T_C. This behavior of the compressibility reflects some softening of the crystal lattice within the ferromagnetic state and during the transition from the ferromagnetic to the paramagnetic state. If we compare the compressibility values at temperatures well above and below T_C (± 50 K), we can estimate that the magnetic contribution to the compressibility is $\kappa_m = 0.13$ Mbar^{-1}.

Figure 4 presents the temperature dependencies of the bulk modulus $B = 1/\kappa$ determined at 2 kbar and the linear thermal expansion coefficient α for the $Ce_3(FeTi)_{29}$ compound. Both quantities exhibit pronounced lambda-shaped anomalies in the vicinity of T_C. Such behavior is not typical for Invar alloys. The studies of the anomaly of the bulk modulus of Invar Fe-Ni alloys and disordered Fe_3Pt alloys

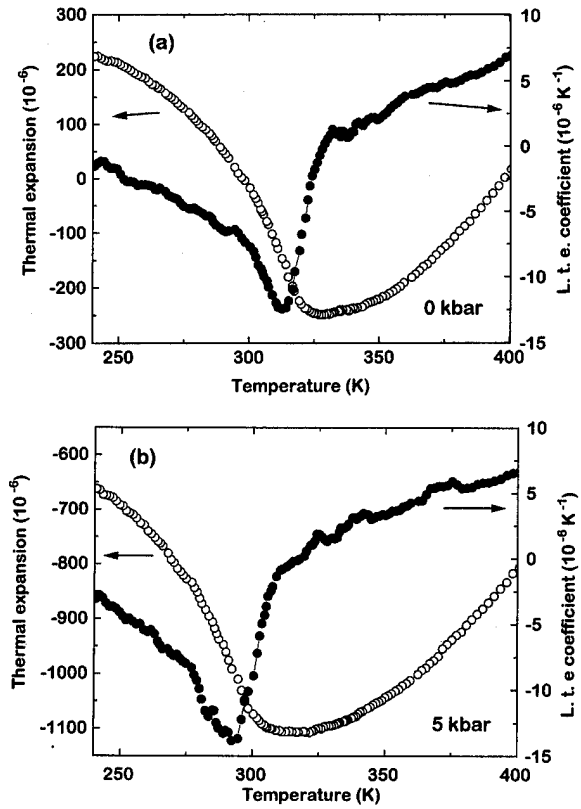


FIG. 2. Thermal dependence of the linear thermal expansion and the linear thermal expansion coefficient of $Ce_3(FeTi)_{29}$ under (a) normal pressure and (b) under 5 kbar.

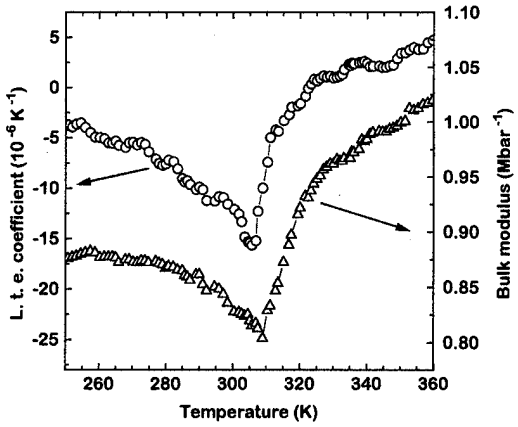


FIG. 4. Thermal dependence of the linear thermal expansion coefficient and bulk modulus in the vicinity of T_C for $Ce_3(FeTi)_{29}$.

showed that the anomalies of elastic constants around T_C on Invar Fe-Ni alloys are very smooth and spread through several hundred degrees.[14,15]

The relatively high value of the compressibility for $Ce(FeTi)_{29}$ in the ferromagnetic state, κ=1.22 $Mbar^{-1}$, has another consequence. The volume derivative $dT_C/d \ln V$ has a value of 3100 K, which is the same as was observed for the $Nd_3(FeTi)_{29}$ compound[5] within the experimental error. From this result one can conclude that the volume dependence of the exchange interaction is identical for both $Ce_3(FeTi)_{29}$ and $Nd_3(FeTi)_{29}$ compounds, although their T_C differs by 100 K (25%). Similar behavior of volume derivatives $dT_C/d \ln V$ was revealed for several Fe-rich Nd-based intermetallics.[16]

Recently, the nitrides $Ce_3(FeTi)_{29}N_x$ were prepared and both the increase of interatomic distances and increase of T_C caused by nitration were found to be the highest in the whole family of the $R_3(FeTi)_{29}$ compounds.[17] Using the value of $dT_C/d \ln V$, we can estimate that an increase in volume of 1% will produce an increase of 31 K in T_C in $Ce_3(FeTi)_{29}$. As the nitration causes an increase in volume of 6.96% in this compound we can expect an increase in T_C of about 220 K because of an increase in volume. However, in the nitrogenated compound an increase of 340 K in T_C has been found (T_C=670 K). This comparison clearly shows, as was observed in Mössbauer experiments,[18] that not only the lattice expansion but also the electron transfer to the N atoms is relevant in the magnetic behavior in interstitial $R_3(FeTi)_{29}$ compounds. A similar behavior was observed in pressure experiments in R_2Fe_{17} compounds.[19]

We can conclude that a large magnetic contribution (κ_m=0.13 $Mbar^{-1}$) to the isothermal compressibility was observed in the ferromagnetic state in comparison with the compressibility in the paramagnetic state of the $Ce_3(FeTi)_{29}$ compound. Pronounced lambda-shaped anomalies in the thermal expansion coefficient and in the compressibility of $Ce_3(FeTi)_{29}$ were simultaneously observed in the vicinity of T_C. The volume dependence of the exchange interaction of the $Ce_3(FeTi)_{29}$ compound is the same as in Fe-rich Nd-based intermetallics.[16]

ACKNOWLEDGMENTS

We acknowledge financial support from Projects: No. 202/93/0184 (GA CR), No. 110 117 (GA AS CR), and No. PB 92-95 (CICYT).

[1] H. S. Li, J. M. Cadogan, R. L. Davis, A. Margarian, and J. B. Dunlop, Solid State Commun. **90**, 487 (1994).

[2] C. D. Fuerst, F. E. Pinkerton, and J. F. Herbst, J. Magn. Magn. Mater. **129**, L115 (1994).

[3] Y. Hu and W. B. Yelon, Solid State Commun. **91**, 223 (1994).

[4] O. Kalogirou, V. Psycharis, L. Saettas, and D. Niarchos, J. Magn. Magn. Mater. **146**, 335 (1995).

[5] Z. Arnold, J. Kamarád, L. Morellon, P. A. Algarabel, and M. R. Ibarra, Solid State Commun. **92**, 807 (1994).

[6] Z. Arnold, J. Kamarád, L. Morellon, P. A. Algarabel, M.R. Ibarra, and C. D. Fuerst, J. Appl. Phys. (in press).

[7] L. Morellon, P. A. Algarabel, B. Garcia-Landa, M. R. Ibarra, F. Albertini, A. Paoluzi, and L. Pareti, Proceedings of the 8th International Symposium on Magnetic Anisotropy and Coercivity in RE-TM Alloys, Birmingham, 1994, p. 361.

[8] L. Morellon, L. Pareti, P. A. Algarabel, F. Albertini, and M. R. Ibarra, J. Phys.: Condens. Matter. **6**, L379 (1994).

[9] M. R. Ibarra, L. Morellon, J. Blasco, L. Pareti, P. A. Algarabel, J. Garcia, F. Albertini, A. Paoluzzi, and G. Turilli, J. Phys.: Condens. Matter. **6**, L717 (1994).

[10] E. P. Wohlfarth, IEEE Trans. Magn. **MAG-11**, 1638 (1975).

[11] J. Kamarád, M. R. Ibarra, L. Morellon, P. A. Algarabel, and Z. Arnold, J. Magn. Magn. Mater. (in press).

[12] C. D. Fuerst, F. E. Pinkerton, and J. F. Herbst, J. Appl. Phys. **76**, 6144 (1994).

[13] V. A. Sidorov and L. G. Khvostantsev, J. Magn. Magn. Mater. **129**, 356 (1994).

[14] G. Ooomi and N. Môri, J. Phys. Soc. Jpn. **50**, 2917 (1981).

[15] E. Török and G. Hausch, Phys. Status Solidi A **53**, K147 (1979).

[16] Z. Arnold, M. R. Ibarra, L. Morellon, P. A. Algarabel, and J. Kamarád, J. Magn. Magn. Mater. (submitted).

[17] O. Kalogirou, V. Psycharis, M. Gjoka, and D. Niarchos, J. Magn. Magn. Mater. **147**, L7 (1995).

[18] J. M. Cadogan, R. K. Day, J. B. Dunlop, and A. Margarian, J. Alloys and Compounds **201**, L1 (1993).

[19] Z. Arnold, J. Kamarád, P. A. Algarabel, B. Garcia-Landa, and M. R. Ibarra, IEEE Trans. Magn. **30**, 619 (1994).

Magnetostriction and thermal expansion measurements on $FeRh_{1-x}Pt_x$ alloys

P. A. Algarabel, M. R. Ibarra, and C. Marquina
Departamento de Física de la Materia Condensada & ICMA, Facultad de Ciencias, Universidad de Zaragoza-CSIC, 50009 Zaragoza, Spain

S. Yuasa and H. Miyajima
Department of Physics, Faculty of Science and Technology, Keio University, Hiyoshi 3-14-1, Kohoku, Yokohama 223, Japan

Y. Otani
Department of Material Science, Faculty of Engineering, Tohoku University, Senday 980-77, Japan

We report high-field magnetostriction and thermal expansion measurements in $FeRh_{1-x}Pt_x$ ($x=0.75$, 0.765, and 0.7) compounds. From the thermal expansion measurements we have observed the para-ferromagnetic and ferro-antiferromagnetic transitions for $x=0.75$ and 0.765, and the para-antiferromagnetic transition in the 0.7 compound. The volume expansion associated with the first-order transitions has been determined. The results of the magnetostriction measurements are complex and are explained here on the basis of an induced transition from an antiferromagnetic to a ferromagnetic state, induced by the applied magnetic field. © *1996 American Institute of Physics.* [S0021-8979(96)66108-0]

I. INTRODUCTION

In some recent works[1,2] we have reported a huge positive volume magnetostriction and a giant magnetoresistance[3] at and above room temperature in cubic bcc FeRh and Fe-Rh-Pd alloys. Such effects are related to the ferro-antiferromagnetic (F-AF) phase transition observed in these alloys, which is accompanied by a large magnetovolume effect and a change in the magnetic moment of the Rh from $\approx 1\,\mu_B$ in the F phase to $0\,\mu_B$ in the AF phase.[4]

The substitution of Rh by Pt in the FeRh system is effective in stabilizing the tetragonal bct phase in a wide range of Pt concentrations.[5] Bct $FeRh_{1-x}Pt_x$ alloys are therefore suitable for investigating the influence of the crystalline structure on the magnetic properties of the FeRh-based alloys. The most interesting property of the bct alloys is the first-order phase transition from the low-temperature AF state to the high-temperature paramagnetic (PM) or F state.[5,6]

Bct $FeRh_{1-x}Pt_x$ with $0.81 \leqslant x \leqslant 1$ is a simple ferromagnet, while bct alloys with $0.72 \leqslant x \leqslant 0.81$ are antiferromagnetic at low temperatures and undergo a first-order AF-F transition with increasing temperature. This transition is accompanied by a reduction in the lattice parameter a and an increase along c. In the case of $x=0.8$ the changes in the lattice parameters a and c were -0.3% and $+0.75\%$, respectively, giving a volume expansion of $+0.15\%$ and an increase in the axial ratio c/a of 1.05%. In the composition range $0.3 \leqslant x \leqslant 0.72$ a direct transition from a low-temperature AF state to a high-temperature PM state is observed in the $FeRh_{1-x}Pt_x$ alloys. This transition is also a first-order transition with a volume expansion of $+0.15\%$ and an increase in the axial ratio c/a of $+0.36\%$ in the case of $x=0.7$ (see the phase diagram of this series of alloys in Ref. 5).

In this work the spontaneous and field-induced magnetovolume effects on the $FeRh_{1-x}Pt_x$ alloys were studied by performing linear thermal expansion (LTE) and magnetostriction measurements.

II. EXPERIMENT

The samples were prepared by a plasma jet melting from pure Fe ($4N$), Rh ($3N$), and Pt ($4N$) in an argon atmosphere. Details of sample preparation can be found in Ref. 5. Magnetization measurements were performed in order to characterize the magnetic transitions, using a pendulum-type magnetometer with an applied magnetic field of 6 kOe. Thermal expansion measurements were obtained using a "push-rod" based dilatometer in the temperature range 150–500 K. The magnetostriction experiments were carried out using the strain-gauge technique, under high-pulsed magnetic field up to 15 T with a pulse width of 50 ms.

III. RESULTS AND DISCUSSION

A. Thermal expansion

The results of linear thermal expansion experiments for the different compounds are shown in Fig. 1. For the compounds with $x=0.75$ and 0.765 three magnetic regions are observed in the studied temperature region (Figs. 1(a) and 1(b)]. The first one is $T>450$ K and corresponds to the paramagnetic state. The temperature region $350>T>450$ K (for $x=0.75$) and $300>T>450$ K for ($x=0.765$) corresponds to the ferromagnetic phase. For lower temperatures an AF ordering appears. The temperatures at which the different magnetic phase transitions take place are indicated by the anomalies observed in the LTE coefficient, α (see Fig. 1). The longitudinal spin fluctuations (Stoner excitation, proportional to the square of the local magnetic moment) and transverse spin fluctuations (spin-wave excitations) are responsible for the extra contribution to the LTE (also called the Invar effect).[7] Due to the low value of this extra contribution in the PM to F phase transition, the transverse spin fluctuations of magnetic moments could be the origin of such a change.

 0021-8979/96/79(8)/4659/3/$10.00 © 1996 American Institute of Physics

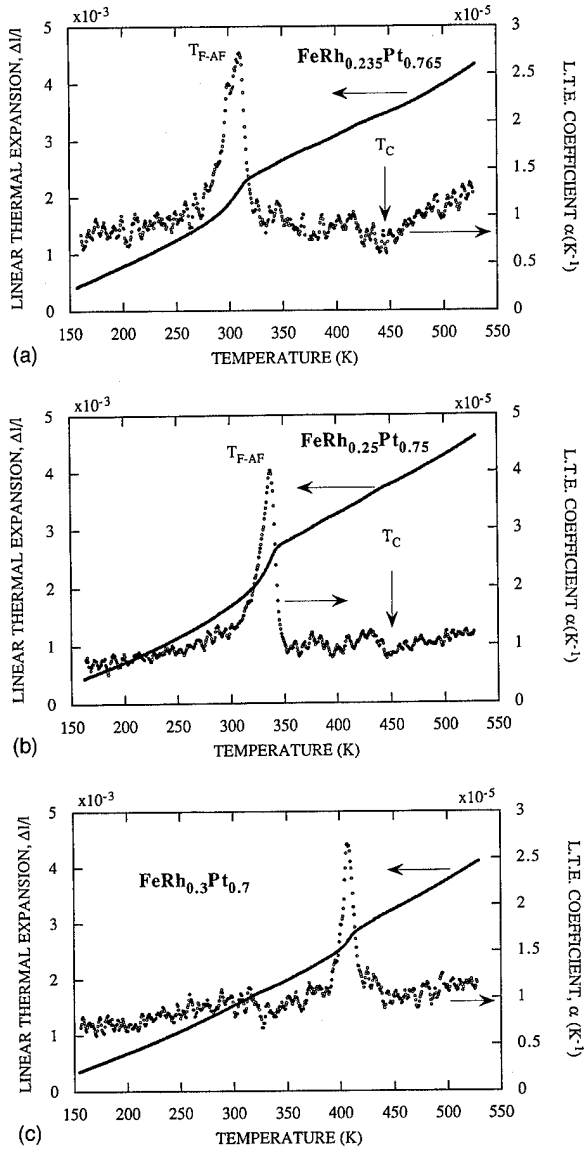


FIG. 1. Linear thermal expansion (LTE) and LTE coefficient α for the $FeRh_{1-x}Pt_x$ alloys, (a) $x=0.75$, (b) $x=0.765$, and (c) $x=0.7$.

The F-AF phase transition (at $T_{F\text{-}AF}$) is accompanied by a very large and sharp drop in the LTE and a volume change ($\omega=\Delta V/V=3\Delta l/l$) of 0.15% for both compounds [see Figs. 1(a) and 1(b)]. In this transition transverse spin fluctuations do not play any role because the transition starts in the F phase and therefore, the large spontaneous extra contribution to the LTE could be ascribed to the longitudinal spin fluctuations. Although an experimental determination of the magnetic moment in the different phases does not exist, a theoretical band calculation performed in the isostructural $FeRh_{1-x}Pd_x$ alloys obtained a local magnetic moment of $\mu_{Fe}=3.1\mu_B$, $\mu_{Rh}=0.69\mu_B$, and $\mu_{Pd}=0.32\mu_B$ in the F state, and $\mu_{Fe}=3.15\mu_B$ and $\mu_{Rh}=\mu_{Pd}=0\mu_B$ in the AF state, with a larger volume in the F state.[8] Therefore, such spontaneous magnetostriction can be ascribed to the collapse of the Rh and Pt local magnetic moment within the AF phase, and this behavior can be accounted for within the framework of the Invar effect, as in the case of the FeRh and FeRhPd alloys.

It is worth remarking that in the case of the cubic alloys the spontaneous magnetostriction associated with the F-AF transition is isotropic (only volume changes) but in the case of the bct alloys the spontaneous magnetostriction has an anisotropic character with a change in the c/a ratio in the F-AF transition as has been mentioned before.

From our LTE measurements performed on polycrystalline samples only the spontaneous volume magnetostriction can be obtained. The volume change, determined from our experiments, associated with the F-AF transition is $\approx$0.15% for both samples. This is in good agreement with the results from x-ray experiments.[5]

For the $FeRh_{0.3}Pt_{0.7}$ alloy [see Fig. 1(c)] only one transition from PM to AF state is observed at $T_{PM\text{-}AF}\approx405$ K. The large extra contribution to the LTE associated with this phase transition ($\omega\approx0.15\%$) suggests that both contributions,

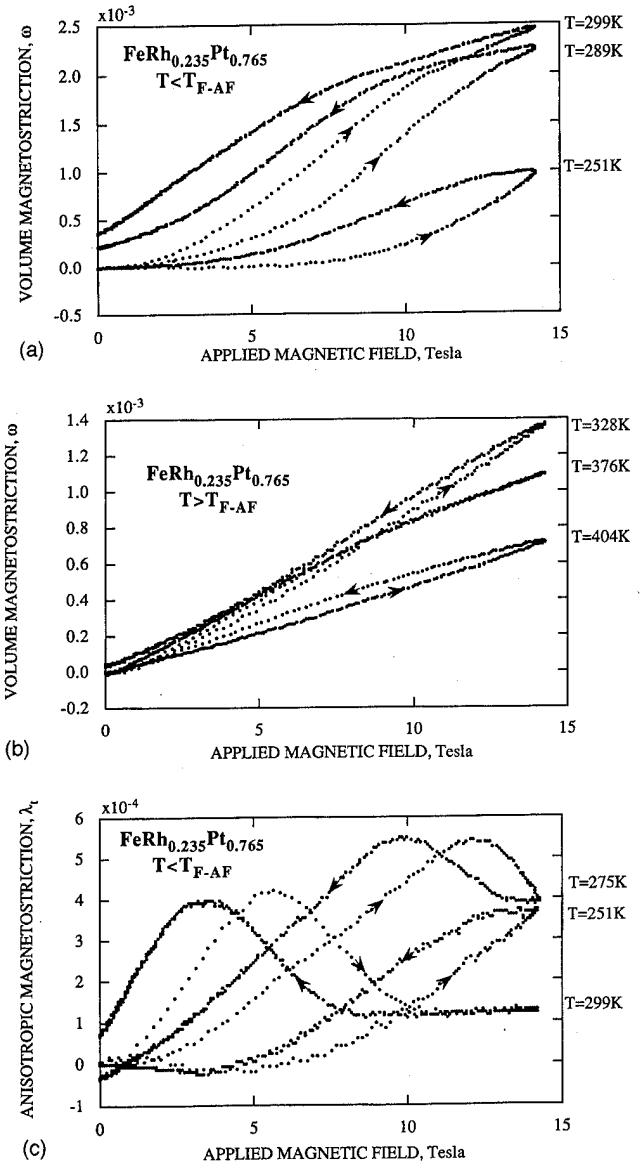


FIG. 2. Isotherms of the volume (ω) and anisotropic (λ_t) magnetostriction vs applied magnetic field of the $FeRh_{0.235}Pt_{0.765}$ compound, (a) ω in the AF state, (b) ω in the F state, (c) λ_t in the AF state.

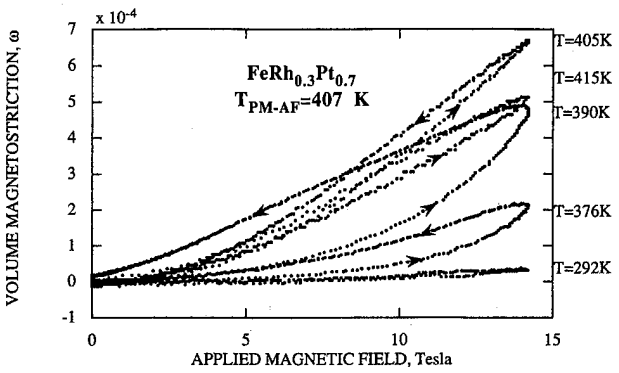


FIG. 3. Isotherms of the volume magnetostriction vs applied magnetic field of the $FeRh_{0.3}Pt_{0.7}$ alloy.

longitudinal and transverse spin fluctuations, are relevant in the PM-AF phase transition.

B. Magnetostriction

Parallel ($\lambda_{\parallel}$) and perpendicular ($\lambda_{\perp}$) magnetostrictions, to the applied magnetic field, were measured using high-pulsed magnetic fields. From these experimental measurements the anisotropic ($\lambda_t = \lambda_{\parallel} - \lambda_{\perp}$) and volume ($\omega = \lambda_{\parallel} + 2\lambda_{\perp}$) magnetostriction were obtained.

In Fig. 2 we present the results obtained for the $FeRh_{0.235}Pt_{0.765}$ alloy, as representative of the compounds with F and AF states. The volume magnetostriction isotherms in the AF state are shown in Fig. 2(a). For the lowest measured temperature ($T = 251$ K), ω is almost zero for low magnetic fields and starts to increase at $H \approx 10$ T. At higher temperatures (near the F-AF transition temperature) the isotherms present a similar behavior, but the increase of magnetostriction takes place at lower magnetic fields. At high magnetic fields the slope changes, becoming constant (see for instance the isotherm at $T = 299$ K). Such behavior can be explained considering that the applied magnetic field is able to induce the AF-F transition, which starts when the magnetostriction increases, and that the F state is reached at the change of the slope. A large hysteresis of about 3 T is observed in the field induced transition. The change of slope at high magnetic fields corresponds to the linear magnetostriction observed in the F state [see Fig. 2(b)]. Such behavior is completely different to that observed in the cubic compounds, in which the volume magnetostriction observed in the F state was nearly zero. Such difference can be ascribed to the different crystallographic structure of both compounds.

In the anisotropic magnetostriction results in the AF state we observed a complex behavior, with the appearance of a maximum at a determined magnetic field, which corresponds to the magnetic field needed to induce the F state [see Fig. 2(c)]. In the F state a negligible anisotropic magnetostriction is observed.

The situation in the $x = 0.7$ compound is different. In this alloy only one transition corresponding to a first-order P to Af phase transition at $T_{PM\text{-}AF} \approx 407$ K takes place [see Fig. 1(c)]. The experimental results obtained for the volume magnetostriction are presented in Fig. 3. The behavior of the isotherms is similar to the lower-temperature isotherms for the $x = 0.765$ compound in the AF state. In this state zero magnetostriction is obtained at low magnetic field and starts to increase at some particular value of the applied magnetic field. This value of the magnetic field decreases as the temperature increases, approaching the critical temperature of the PM-AF phase transition. Such behavior suggests a possible transition from the AF to a F metastable state, which is not thermally reached, but could be obtained by an applied magnetic field higher than our maximum available field. As in the case of the $x = 0.765$ alloy the anisotropic magnetostriction is negligible.

ACKNOWLEDGMENTS

The Spanish authors acknowledge financial support of the Spanish CICYT under Grant No. PB92-0095, and from the European Commission under Contract No. CHRX-CT93-0352.

[1] M. R. Ibarra and P. A. Algarabel, Phys. Rev. B **50**, 4196 (1994).
[2] M. R. Ibarra, P. A. Algarabel, C. Marquina, Y. Otani, S. Yuasa, and H. Miyajima, J. Magn. Magn. Mater. **140-144**, 231 (1995).
[3] P. A. Algarabel, M. R. Ibarra, C. Marquina, A. del Moral, J. Galibert, M. Iqbal, and S. Askenazy, Appl. Phys. Lett. **66**, 3062 (1995).
[4] G. Shirane, C. W. Chen, P. A. Flinn, and R. Nathans, J. Appl. Phys. Suppl. **33**, 1044 (1963).
[5] S. Yuasa, H. Miyajima, and Y. Otani, J. Phys. Soc. Jpn. **63**, 3129 (1994).
[6] S. Yuasa, T. Akiyama, H. Miyajima, and Y. Otani, J. Phys. Soc. Jpn. **64**, 3978 (1995).
[7] For a review of the Invar effect, see E. F. Wasserman, *Handbook of Magnetic Materials*, edited by K. H. J. Buschow and E. P. Wohlfarth (Elsevier, New York, 1990), Vol. 5, p. 238.
[8] S. Yuasa, H. Miyajima, Y. Otani, and A. Sakuma, J. Magn. Magn. Mater. **140-144**, 79 (1995).

Magnetostriction of a superconductor: Results from the critical-state model

Z. Koziol[a] and R. A. Dunlap
Department of Physics, Dalhousie University, Halifax, Nova Scotia B3H 3J5, Canada

In many cases, the critical-state theory can be treated as a sufficiently accurate approximation for the modeling of the magnetic properties of superconductors. In the present work, the magnetostrictive hysteresis is computed for a quite general case of the modified Kim–Anderson model. The results obtained reproduce many features of the giant magnetostriction (butterfly-shaped curves) reported in the literature for measurements made on single-crystal samples of the high-temperature superconductor $Bi_2Sr_2CaCu_2O_8$. It is shown that the addition of a contribution to the magnetostriction in the superconducting state which is of similar origin as in the normal state, offers a broader phenomenological interpretation of the complex magnetostriction hysteresis found in such heavy-fermion compounds as UPt_3, URu_2Si_2, or UBe_{13}. © *1996 American Institute of Physics.* [S0021-8979(96)66208-X]

I. INTRODUCTION

Measurement of the magnetization has been the most commonly used experimental technique for the study of flux pinning. Recently, however, magnetostriction studies have been shown informative. For example, Ikuta *et al.*[1] observed a giant magnetostriction in $Bi_2Sr_2CaCu_2O_8$ single crystals in the superconducting state and showed that the largest contribution to this effect comes from the interaction between the critical currents induced by changing the external field and the applied field, i.e., the Lorentz force. Much attention has also been directed to dilatometry studies of heavy-fermion superconductors. In UPt_3,[2] the irreversible contribution to the magnetostriction is small but in UBe_{13},[3] UPd_2Al_3,[4] and URu_2Si_2,[5] large sample size changes are observed.

In large fields, when the magnetic induction B changes negligibly across the sample (e.g., in URu_2Si_2, for $H \geqslant 10^3$ Oe,[6] the idealized situation for a slab of thickness 2D may be written as $B(x) \approx H-(4\pi/c)j_c(D-x)$, with $x=0$ at the center of the slab. Here, H is the external magnetic field and j_c is the critical current density, $(4\pi/c)j_c=-dB/dx$. The local Lorentz force exerted on the current carriers, $f=(1/c)j_cB(x)$, is directed towards the center of the sample and leads to its compression, for increasing external field. This force must be compensated by the internal local stress, $\sigma(x)$; $\partial\sigma/\partial x=(1/c)j_cB(x)$. Hence, with $j_c=-(c/4\pi)dB/dx$, we find that $\sigma(x)=-[H^2-B^2(x)]/8\pi$, for the boundary condition $\sigma(D)=0$. For a material characterized by the elastic constant c_{11}, the relative change of the sample size, $\Delta D/D$, is given by

$$\frac{\Delta D}{D}=\frac{1}{D}\int_0^D \frac{\sigma(x)}{c_{11}}\,dx, \tag{1}$$

which is equal to $-1/(8\pi c_{11}D)\int_0^D[H^2-B^2(x)]dx$. For the present case, with $(c/4\pi)j_c \ll B/D$, we have: $\Delta D/D \approx -f_p/(2c_{11})D$. Hence, $\Delta D/D$ is directly related to the flux-pinning force density, $f_p=(1/c)Bj_c$.

[a]Electronic mail: zkoziol@is.dal.ca; http://is.dal.ca/~zkoziol/zkoziol.html

II. MAGNETOSTRICTION IN THE MODIFIED KIM–ANDERSON MODEL

For qualitative calculations, we shall consider the simplest possible geometry: a slab of thickness 2D, with the external magnetic field H applied along its surface. We use a modified Kim–Anderson formula for defining the critical current density, $j_c(B)$, corresponding to a local gradient of the magnetic induction:

$$j_c=\alpha/(B+h)^n=-(c/4\pi)dB/dx. \tag{2}$$

This dependence unifies many forms of the critical state models. The calculating the magnetization for this geometry and for $j_c(B)$ given by Eq. (2) can be found in Ref. 7. This previous work[7] contains an analysis of other effects observed in superconductors which can be explained using the model of a critical state. The present work provides additional explanation of these phenomena and may be considered as a continuation of our work on this subject.

The calculation of the magnetostriction consists of: (i) finding the magnetic field distribution during the magnetization process, (ii) integrating the equation $\partial\sigma/\partial x=(1/c)j_cB(x)$ with the boundary condition that $\sigma(D)=0$, and (iii) using Eq. (1) for calculation of the magnetostriction. The solution of Eq. (2) determines the flux distribution and has the form: $B(x)=[\pm(4\pi/c)\alpha(n+1)x+\beta]^{1/(n+1)}-h$, where the integration constant β is determined from the boundary condition $B(\pm D)=H$, with the sign of $dB(x)/dx$ dependent on the most recent field change direction occurring at point x. For the virgin magnetization curve, β is given by: $\beta=(H+h)^{n+1}-H_m$, where $H_m=(H^*+h)^{n+1}-h^{n+1}$, and H^* is the field of the first full flux penetration into the center of the slab, $H^*=[\alpha(n+1)D+h^{n+1}]^{1/(n+1)}$. Some examples of the flux distribution for different situations are drawn schematically in Fig. 1. In this figure, B_0 is the magnetic induction in the sample center and is given in Table I for various stages of the magnetization process. The magnetostriction during the virgin magnetization process, for $H<H^*$, is found to be

$$\frac{8\pi c_{11}\Delta D(H)}{D}=H^2-\frac{1}{H_m}\left\{h^2[(H+h)^{n+1}-h^{n+1}]\right.$$

 0021-8979/96/79(8)/4662/3/$10.00 © 1996 American Institute of Physics

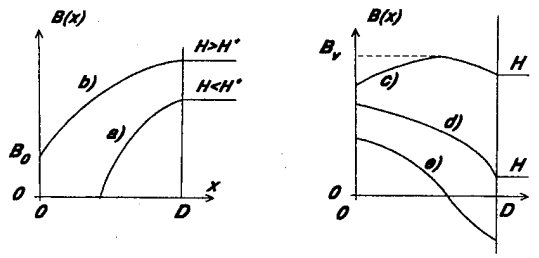


FIG. 1. The magnetic induction distribution in a sample volume when (a) field increases from 0 to $H<H^*$, (b) field increases to $H>H^*$, (c) and (d) when field decreases from $H_{\max}$ to H, and (e) when field decreases below 0. B_0 is the field at the slab center. B_v is the field at the kink of the flux distribution at x_v, occurring for a certain range of H values after the sweep direction of H is changed. x_v is equal to $1-[(H_{\max}+h)^{n+1}-(H+h)^{n+1}]/(2H_m)$. B_v and B_0 are defined in Table I.

$$+(n+1)\left[\frac{(H+h)^{n+3}-h^{n+3}}{n+3}-2h\,\frac{(H+h)^{n+2}-h^{n+2}}{n+2}\right]\Bigg\}. \tag{3}$$

In order to provide the results for the entire magnetization loop in a transparent form, we define the following quantities:

$$F_{i,1}(H_{i,-},H_{i,+})=h^2[(H_{i,+}+h)^{n+1}-(H_{i,-}+h)^{n+1}]/H_m,$$

$$F_{i,2}(H_{i,-},H_{i,+})=-(n+1)/(n+2)2h[(H_{i,+}+h)^{n+2}-(H_{i,-}+h)^{n+2}]/H_m,$$

$$F_{i,3}(H_{i,-},H_{i,+})=(n+1)/(n+3)[(H_{i,+}+h)^{n+3}-(H_{i,-}+h)^{n+3}]/H_m,$$

with $H_{i,-}$ and $H_{i,+}$ defined in Table I, for situations corresponding to those in Fig. 1. The index i enumerates different branches of the magnetic induction curves of continuous $j_c(x)$ dependence. Using the above equations, the magnetostriction can be written as

$$8\pi c_{11}\Delta D(H)/D=H^2-\sum_{i=1,2} f(H_{i,-},H_{i,+}), \tag{4}$$

where

$$f(H_{i,-},H_{i,+})=S(H_{i,-},H_{i,+})[F_1(H_{i,-},H_{i,+})+F_2(H_{i,-},H_{i,+})+F_3(H_{i,-},H_{i,+})]. \tag{5}$$

TABLE I. Characteristic fields corresponding to the curves (a) to (e) in Fig. 1. B_v is equal to $\{0.5[(H_{\max}+h)^{n+1}+(H+h)^{n+1}]\}^{1/(n+1)}-h$.

Case	$H_{0,-}$	$H_{0,+}$	$H_{1,-}$	$H_{1,+}$
a	0	H	0	0
b	$B_0=[(H+h)^{n+1}-H_m]^{1/(n+1)}-h$	H	0	0
c	$B_0=[(H_{\max}+h)^{n+1}-H_m]^{1/(n+1)}-h$	B_v	B_v	H
d	$B_0=[(H+h)^{n+1}+H_m]^{1/(n+1)}-h$	H	0	0
e	$B_0=[-(\lvert H\rvert+h)^{n+1}+(H^*+h)^{n+1}+h^{n+1}]^{1/(n+1)}$	0	0	H

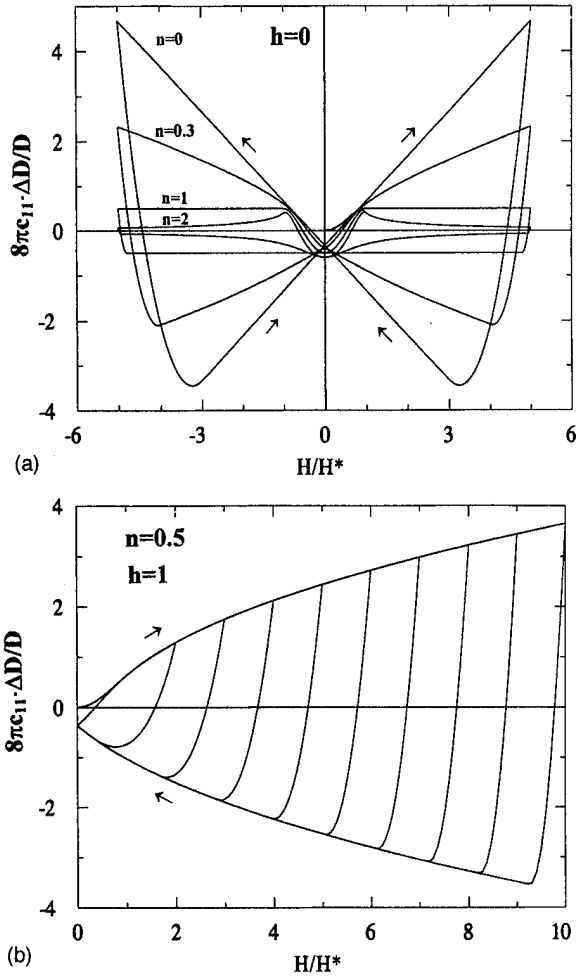


FIG. 2. The calculated magnetostriction curves, the virgin one and the entire hysteresis loop; (a) $h=0$, while n changes from 0 (the Bean model) to $n=2$, (b) when $n=0.5$, $h=1$ while $H_{\max}$ ranges between 2 and 10. The arrows indicate the direction of field change.

The function $S(H_{i,-},H_{i,+})$ in Eq. (5) is equal to $+1$ when $H_{i,-}\leqslant H_{i,+}$ and to -1, otherwise. The remaining part of the magnetostriction hysteresis curve, not covered in the Table I, may be computed using symmetry: $\Delta D(-H)=\Delta D(H)$.

Some examples of the calculated magnetostriction hysteresis curves are shown in Fig. 2. A large variety of $\Delta D(H)$ dependences is found: from $\Delta D(H)$ proportional to H at $H>H^*$, when $n=0$ (Bean model), to $\Delta D(H)$ strongly suppressed by field when $n>1$. For $n>0$, an abrupt passing through $\Delta D(H)=0$ is found, when the field sweep direction changes. The field width of this transition region decreases strongly with an increase of the maximum field applied [Fig. 2(b)]. This is due to a low value of the critical current density at large fields and a decrease in the field change required to reverse the direction of current flow in the sample volume. A significant remanent magnetostriction due to a frozen-in magnetic field is observed. The features discussed above are commonly observed for high-T_c and heavy-fermion superconductors.

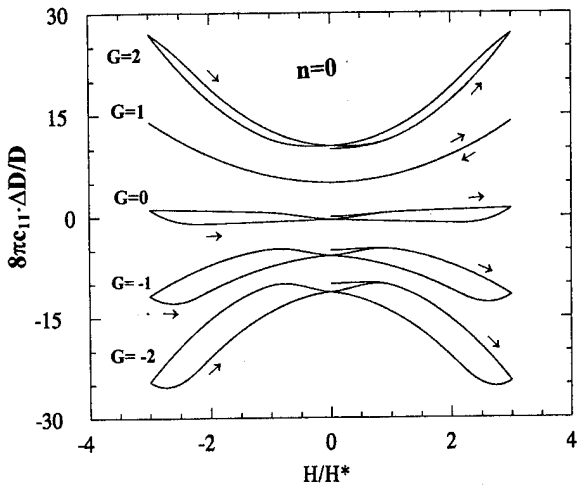


FIG. 3. The calculated magnetostriction curves for $n=0$ (the Bean model) for several values of the parameter G, determining the normal-state contribution to the magnetostriction: $G=2,1,0,-1$, and -2, for curves from top to bottom, respectively. One must note that the values of G depend on the units of the magnetic field assumed, which are here equal to H^*. The vertical scale has been shifted for some curves, for better clarity. The arrows indicate the direction of field change.

An unusual effect has been observed recently[5] for single crystal of URu_2Si_2. For fields near the upper critical field, $H_{c2}(T)$, the irreversible contribution to the magnetostriction changes sign compared to the sign observed at lower fields. Moreover, it was observed[5] that the sign of the irreversible contribution to the magnetostriction for some experimental configurations disagreed with the prediction of the critical-state model. On the other hand, a large background contribution to the magnetostriction, $\Delta D/D=bB^2$, with the parameter b of the order of $10^{-16}/G^2$, has been reported for heavy-fermion materials,[2,3,5] which is apparently of the same origin as the normal-state magnetostriction. The role of this contribution on the overall shape of the magnetostriction may be considered. We note that the critical-state magnetostriction component results from the calculation of an integral over the $B^2(x)$ dependence. The total magnetostriction in the superconducting state is then assumed to be the sum of the critical state and the normal-state-like components. The sign of both contributions must be considered carefully. The critical-state magnetostriction depends on the sign of the magnetic field and current while the normal-state contribution depends on the sign of the coefficient b. Using these arguments, we may write

$$8\pi c_{11}\Delta D(H)/D=H^2-\sum_{i=1,2}\,[f(H_{i,-},H_{i,+}) - G|f(H_{i,-},H_{i,+})|], \qquad (6)$$

with $f(H_{i,-},H_{i,+})$ given by Eq. (5) and $G=8\pi c_{11}b$. Magnetostriction calculated from Eq. (6) for a few values of the parameter G is shown in Fig. 3. An important feature of these results is that both signs of the magnetostriction and both signs of the irreversible contribution to the magnetostriction hysteresis are possible, while the shape of the curves might only be weakly affected by the presence of a normal-state contribution (except for the presence of a large background proportional to H^2). The hysteresis of the normal-state-like contribution to the magnetostriction in the superconducting state is due to inhomogeneity of the magnetic induction across the sample volume, which is caused by the presence of critical current. It is easy to show that at large fields, in particular, near the upper critical field, both contributions to the irreversible magnetostriction are proportional to the critical current density. Hence, the most intriguing property of the magnetostriction in some heavy-fermion superconductors, i.e., the change of sign of the irreversible part of the magnetostriction as a function of the applied field, cannot be explained by this model, if it is assumed that the parameter G in Eq. (6) is independent of the magnetic field value.

Using Eq. (5), magnetic measurements[6] in conjunction with the value of the elastic constant c_{11} allow for a determination of $\Delta D/D$. In URu_2Si_2, $c_{11}=2.4\times10^{12}$ erg/cm^3,[8] yields $2\Delta D/D=3.6\times10^{-8}$ and $2\Delta D/D=6\times10^{-8}$, for $H//c$ and $H//a$, respectively, in reasonable agreement with measured properties.[5] On the other hand, for UPt_3, the elastic constant is larger, about 6×10^{12} erg/cm^3,[9] and the critical current density is much lower,[7] resulting in an irreversible contribution to the magnetostriction which is hardly observable experimentally.

Gloos *et al.*[4] reported significant difference between the thermal-expansion curves measured during cooling in a magnetic field through the superconducting transition and those measured during heating with the same magnetic field applied at low temperature, for the heavy-fermion superconductor UPd_2Al_3. Any hysteresis of this kind finds its phenomenological explanation within the critical state model and is of the same nature as the magnetization hysteresis in $M_{FC}(T)$ and in $M_{ZFC}(T)$ measurements, as described by us in detail in Ref. 7.

ACKNOWLEDGMENTS

This work has been made possible by a Killam Postdoctoral Fellowship awarded to Z. K. and by a grant from the NSERC. The initial studies of the subject have been carried out by Z. K. at the University of Amsterdam. These have been inspired by the experimental results (some not published yet) of N. van Dijk, A. de Visser, V. Duijn, and have been discussed with them as well with J. J. M. Franse and P. F. de Châtel.

[1] H. Ikuta *et al.*, Phys. Rev. Lett. **70**, 2166 (1993).
[2] N. H. van Dijk *et al.*, Physica B **186-188**, 267 (1993).
[3] A. de Visser *et al.*, Phys. Rev. B **45**, 2962 (1992).
[4] K. Gloos *et al.*, Phys. Rev. Lett. **70**, 501 (1993).
[5] N. H. van Dijk *et al.*, Phys. Rev. B **51**, 12 665 (1995).
[6] Z. Koziol *et al.*, J. Magn. Magn. Mater. **140-144**, 2065 (1994).
[7] Z. Koziol *et al.*, Phys. Rev. B **50**, 15 978 (1994).
[8] P. Thalmeier *et al.*, Physica C **175**, 61 (1991).
[9] A. de Visser, thesis, University of Amsterdam, 1986.

Magnetostriction and anisotropy of twin-free single-crystals $Tb_{0.5}Dy_{0.5}(Fe_{0.9}Mn_{0.1})_2$

Jinghua Wang, Guangheng Wu, Xuegen Zhao, Kechang Jia, and Wenshan Zhan
State Key Laboratory for Magnetism, Institute of Physics, CAS, P.O. Box 603, Beijing 100080, People's Republic of China

A study of the effects of substituting a small amount of Mn for Fe in the Terfenol-D system is presented. The twin-free and ⟨111⟩-oriented single-crystal rods of $Tb_{0.5}Dy_{0.5}(Fe_{0.9}Mn_{0.1})_2$ were prepared by Czochralski method. The magnetization, lattice constant, Curie temperature, and magnetostriction were examined. From the experimental results, it is possible to determine the effect of Mn substitution on magnetic anisotropy and magnetostriction. Because of Mn substituting for Fe, magnetic moment values of $Tb_{0.5}Dy_{0.5}(Fe_{0.9}Mn_{0.1})_2$ show two inflections and the easy magnetization directions also show changes from 1.5 to 300 K at an applied field of 1000 Oe. It strongly suggests that Mn substitution remarkably influences magnetocrystalline anisotropy of $Tb_{0.5}Dy_{0.5}(Fe_{0.9}Mn_{0.1})_2$. Its saturation magnetostrictions are 1.48×10^{-3} and 1.67×10^{-3}, maximum d_{33} values are 1 and 1.5 under compressive stress of 0 and 12 MPa, respectively. These magnetostrictive properties are clearly better than those measured from the ⟨112⟩-oriented twinned samples. This is the first time that the experimental data measured from the single-crystalline samples on the magnetic properties of $Tb_{0.5}Dy_{0.5}(Fe_{0.9}Mn_{0.1})_2$ are reported. © *1996 American Institute of Physics.* [S0021-8979(96)66308-9]

I. INTRODUCTION

$Tb_xDy_{1-x}Fe_2$, commercially known as Terfenol-D, possesses the largest magnetostriction from −150 to 350 °C. However, the large magnetostriction is often associated with a large magnetocrystalline anisotropy. In 1989, Sahashi *et al.*[1] showed that the substitution of Mn in the polycrystalline $Tb_{0.5}Dy_{0.5}(Fe_{0.9}Mn_{0.1})_2$ appeared to increase the magnetostriction at lower magnetic field strengths (~2 kOe). In 1990, Teter *et al.*[2] established that twinned single crystals of $Tb_{0.5}Dy_{0.5}(Fe_{1-x}Mn_x)_2$ along the [112] growth direction showed similar results. This suggests the possibility of obtaining lowered anisotropy and reduced hysteresis materials. Since the materials require low anisotropy and large magnetostriction in application, the lower magnetocrystalline anisotropy of $Tb_{0.5}Dy_{0.5}(Fe_{0.9}Mn_{0.1})_2$ may make it become a useful magnetostrictive material. Because the samples investigated in previous works are polycrystalline or twinned, and the magnetostriction and d_{33} of the measured samples must be strongly affected by the random orientations of polycrystalline grains and the pinning by the grain and twin boundaries, it is necessary to investigate the single crystals in detail in order to reveal the intrinsic influences of Mn substituting for Fe to the magnetocrystalline anisotropy of this material.

II. EXPERIMENTS AND DISCUSSION

Starting materials of composition $Tb_{0.5}Dy_{0.5}(Fe_{0.9}Mn_{0.1})_2$, with $y=1.80-1.95$, were prepared from Tb, Dy, Fe of the purity of 99.95%, and Mn of the purity of 99.9%. [111]-oriented single-crystal bars approximately $2\times2\times10$ mm^3 were used as seeds. Crystals were grown by the MCGS-3 CZ instrument.[3] The single crystals of $Tb_{0.5}Dy_{0.5}(Fe_{0.9}Mn_{0.1})_2$ with the [111] axial orientation were obtained with diameters of 6 mm and a maximum length of 50 mm. Chemical analysis was carried out for assuring that the composition of the single crystals were stoichiometric and Mn had been doped at the expected value. The twin-free single-crystalline quality of the crystals were determined by the characterizations with x-ray Laue method and metallographic observation. The characteristic diffraction peaks of (111), (222), and (333) obtained by the x-ray diffraction on the transverse sections of the crystals, as shown in Fig. 1, indicates their high perfection.

The x-ray powder diffraction proved that the sample was pure cubic Laves phase. The lattice constant is calculated by diffraction peak datum of crystal surface (422) because diffraction peak data of all crystal surfaces except the (422) surface change with spontaneous magnetization.[4,5] Its lattice constant of 7.350 A is larger than that of $Tb_{0.5}Dy_{0.5}Fe_2$ of 7.325 A. The σ-T curves of all samples were measured by vibrating sample magnetometer under 300–700 K. Then the Curie temperature of 260 °C is calculated, which is smaller than that of $Tb_{0.3}Dy_{0.7}Fe_2$, 380 °C. It is believed that the Curie temperature decreased with the dopant of Mn is due to

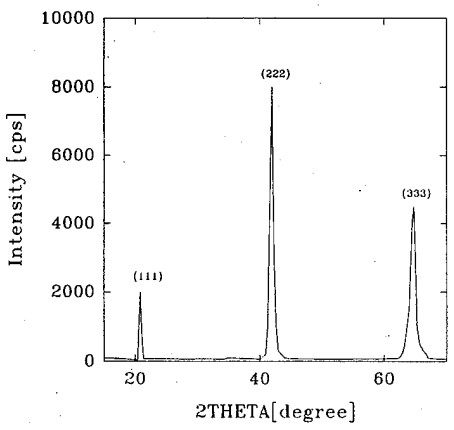


FIG. 1. The x-ray diffraction peak of transverse section of single-crystal $Tb_{0.5}Dy_{0.5}(Fe_{0.9}Mn_{0.1})_2$.

 0021-8979/96/79(8)/4665/3/$10.00 © 1996 American Institute of Physics

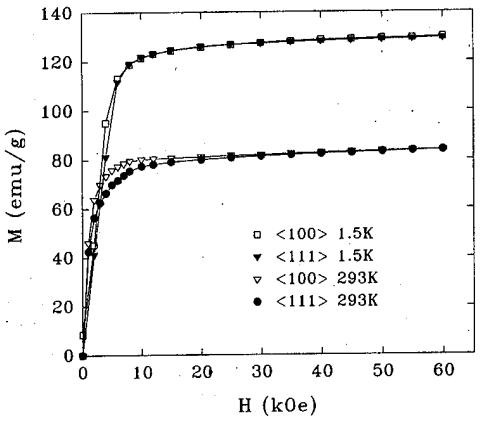


FIG. 2. Magnetic moment M vs applied field H of ⟨111⟩ and ⟨100⟩ single-crystal $Tb_{0.5}Dy_{0.5}(Fe_{0.9}Mn_{0.1})_2$ at 1.5 and 293 K.

the dramatic decrease of the dominant exchange interaction between Fe and Fe atoms.

Small single-crystal bars of $Tb_{0.5}Dy_{0.5}(Fe_{0.9}Mn_{0.1})_2$ cut in [111] and [100] directions in diameter of 1 mm and length of 5 mm were prepared for the measurements of magnetic moment versus applied magnetic field or temperature. Extracting sample magnetometer was used to measure the magnetization curves at 1.5 and 293 K and the curves of magnetic moment versus temperature. The magnetization curves of both the [111] and the [100] oriented samples at 1.5 and 293 K are shown in Fig. 2. It is very clear that the ⟨111⟩ direction is not a difficult magnetization direction at 1.5 K, nor is the ⟨100⟩ direction at 300 K. Therefore, it appears that magnetocrystalline anisotropy energy of the ⟨111⟩ direction is almost the same as that of the ⟨100⟩ direction. Saturation magnetic moment value of the two different directions is identical. In addition, the magnetic moments of $Tb_{0.5}Dy_{0.5}(Fe_{0.9}Mn_{0.1})_2$ and $Tb_3Dy_{0.7}Fe_2$ from 1.5 to 300 K were measured at applied field of 1 kOe as shown in Fig. 3. It can be seen that the magnetic moment values of $Tb_{0.5}Dy_{0.5}(Fe_{0.9}Mn_{0.1})_2$ which are oriented in the ⟨111⟩ and ⟨100⟩ directions show two inflections at the temperatures of 40 and 160 K, respectively. Moreover, the spin reorientation temperature (magnetocrystalline anisotropy compensation

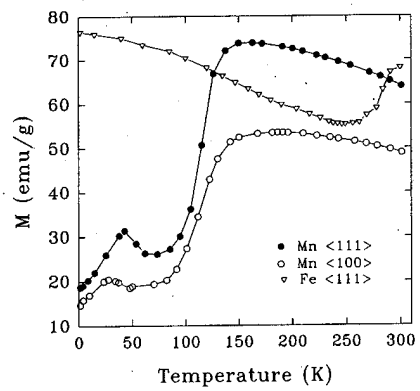


FIG. 3. Magnetic moment M vs temperature T of ⟨111⟩ single-crystal $Tb_{0.5}Dy_{0.5}(Fe_{0.9}Mn_{0.1})_2$ at applied field of 1 kOe.

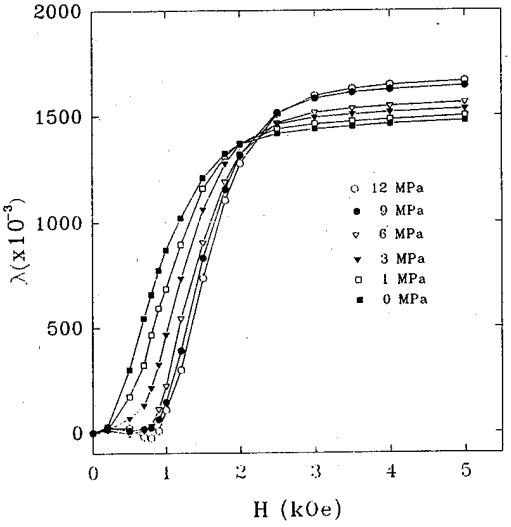


FIG. 4. Magnetostriction λ vs applied field H curves of $Tb_{0.5}Dy_{0.5}(Fe_{0.9}Mn_{0.1})_2$ with applied compressive stress from 0 to 12 MPa.

temperature, T_{comp}) of $Tb_{0.3}Dy_{0.7}Fe_2$ is 240 K at which magnetocrystalline anisotropy undergoes only one conversion. Its easy magnetization direction converts from the ⟨100⟩ below the T_{comp} to the ⟨111⟩ above the T_{comp}. However, the magnetic moment values of $Tb_{0.5}Dy_{0.5}(Fe_{0.9}Mn_{0.1})_2$ undergo the two conversions as mentioned above. It indicates that the substitution of Mn for Fe in $Tb_{0.5}Dy_{0.5}(Fe_{0.9}Mn_{0.1})_2$ remarkably affects the spin reorientation of this compound and further might influence the magnetocrystalline anisotropy of the rare-earth sites.

The rods of the [111]-oriented single crystals in the dimension of $4\times5\times15$ mm^3 were prepared for measuring magnetostriction with strain gauges at room temperature. Figure 4 shows the relation of the magnetostriction and the compressive axial prestress along the [111] direction. When compressive prestress increases from 0 to 12 MPa, saturation magnetostrictive coefficient, $\lambda_{[111]}$ (along ⟨111⟩ direction), increases from 1.48×10^{-3} to 1.67×10^{-3}, saturation field increases from 2.5 to 3.0 kOe, and the bias field needed to obtain the maximum value of $d_{33}(d\lambda/dH)$ also increases from 200 to 1000 Oe. Its magnetostriction coefficients $\lambda_{[111]}$ are far larger than those of the [112] oriented.[3] It is due to the fact that direction oriented along [111] is the largest direction of magnetostriction and the easiest magnetization direction, that the twin-free single-crystalline samples eliminate the impediment of twin boundaries which hinder the movement of magnetic domains. Moreover, when compressive stress is applied along [111], most magnetic moments must rotate toward [112]. The magnetostriction increases because magnetic moments increase contribution to magnetostriction when these magnetic moments rotate toward the [111] direction from the [112] direction. The increase of the bias field is due to the fact that the applied compressive stress makes domain energy of non-180 domain walls increase. Until the Zeaman energy is sufficient to surmount the anisotropy energy barrier and performs work required against the compressive stress, magnetic moment cannot rotate toward the [111] direction. The larger the applied compressive stress is,

the larger the anisotropy energy is. It indicates that the bias field increases with the compressive stress.

III. SUMMARY

Magnetization, Curie temperature, and room-temperature magnetostriction of ⟨111⟩-oriented twin-free single-crystalline samples of $Tb_{0.5}Dy_{0.5}(Fe_{0.9}Mn_{0.1})_2$ have been measured. The experimental results are as follows.

(1) It has been observed that Curie temperature decreased the lattice constant increased with Mn substituted for Fe in $Tb_{0.5}Dy_{0.5}(Fe_{0.9}Mn_{0.1})_2$.

(2) The magnetic moment values of $Tb_{0.5}Dy_{0.5}(Fe_{0.9}Mn_{0.1})_2$ show two inflections at 40 and 160 K, respectively. In the temperature range of 1.5–300 K, easy and difficult magnetization direction shows a dramatic difference from those of $Tb_{0.3}Dy_{0.7}Fe_2$. It suggests strongly that Mn atom substituting for iron remarkably influences magnetocrystalline anisotropy of the compound.

(3) Magnetostriction, $d\lambda/dH$, and the bias field increased with the increasing of applied compressive stress from 0 to 12 MPa. This result is far larger than those of [112].[3] It strongly suggested that [112] direction and twinned boundary influenced substantially the magnetostriction, d_{33} and the bias field.

It is the first time to report the experiment data of twin-free single crystals of $Tb_{0.5}Dy_{0.5}(Fe_{0.9}Mn_{0.1})_2$ as mentioned above.

[1] Sahashi, T. Kobayashi, and T. Funayama, "Magnetostriction and Magnetocrystalline Anisotropies of $Tb_xDy_{1-x}(Mn_yFe_{1-y})_2$. Pseudobinary Compounds," presented at the 10th International Workshop of Rare Earth Magnets and Their Applications, Koyoto, Japan, 16–19 May 1989.

[2] J. P. Teter, A. E. Clark, and O. D. McMasters, IEEE Trans. Magn. **MAG-26**, 1748 (1990).

[3] G. Wu, X. Zhao, J. Wang, J. Li, K. Jia, and W. Zhan, Appl. Phys. Lett. (to be published).

[4] E. Sayettat, J. Appl. Phys. **46**, 3619 (1975).

[5] E. Bertaut *et al.*, F. Tcheou Solid State Commun. **8**, 239 (1970).

Magnetic properties and magnetostriction of twin-free single-crystal $Tb_{0.27}Dy_{0.73}(Fe_{1-x}Al_x)_2$

Jinghua Wang, Guangheng Wu, Xuegen Zhao, Kechang Jia, and Wenshan Zhan
State Key Laboratory for Magnetism, Institute of Physics, CAS, P. O. Box 603, Beijing 100080, People's Republic of China

Magnetization curves, Curie temperature, and lattice constants of twin-free [111]-oriented single-crystal $Tb_{0.27}Dy_{0.73}(Fe_{1-x}Al_x)_2$ (x=0, 0.1) were investigated. It was observed that with the substitution of Al for Fe, Curie temperature and magnetocrystalline anisotropy decrease, and lattice constants increase. It is shown from the curves of magnetic moment versus temperature that the anisotropy compensation temperature of $Tb_{0.27}Dy_{0.73}(Fe_{0.9}Al_{0.1})_2$ is 280 K, which is higher than 260 K of $Tb_{0.27}Dy_{0.73}Fe_2$. Besides, the saturation magnetostriction λ_{111} of $Tb_{0.27}Dy_{0.73}(Fe_{0.9}Al_{0.1})_2$ was measured by using strain gauge method. The result indicates that λ_{111} increases from 1.01×10^{-3} to 1.54×10^{-3} as the compressive stress is increased from 0 to 12 MPa, and that the maximal $D_{33}(d\lambda/dH)$ is about 1.0. It is the first time to present the experimental data of the twin-free [111]-oriented single crystal of $Tb_{0.27}Dy_{0.73}(Fe_{0.9}Al_{0.1})_2$. © *1996 American Institute of Physics.*
[S0021-8979(96)66408-2]

I. INTRODUCTION

In view of the applications, it is necessary for good magnetostriction materials to have low anisotropy energy and large magnetostriction. Clark *et al.*[1,2] found out that compound $Tb_{0.27}Dy_{0.73}Fe_2$ (called Terfenol-D) possesses unusually large magnetostriction and magnetocrystalline anisotropy at room temperature (RT). Since then, many researchers have studied other element substitutions for Fe in $Tb_{0.27}Dy_{0.73}Fe_2$ to search for better materials. Among them, Zhong and Wang[3] found out that polycrystalline $Tb_{0.27}Dy_{0.73}(Fe_{1-x}Al_x)_2$ (x from 1.0 to 1.5) possess large saturation magnetostriction $\lambda_{\|}$ and low magnetocrystalline anisotropy. For instance, the saturation magnetostriction $\lambda_{\|}$ of $Tb_{0.27}Dy_{0.73}(Fe_{0.9}Al_{0.1})_2$ is 1.2×10^{-3} at 25 kOe, which is larger than that of $Tb_{0.27}Dy_{0.73}Fe_2$. Prajapati *et al.*[8] established that the substitution of Al for Fe in the ⟨112⟩ twin single crystals of $Tb_{0.27}Dy_{0.73}Fe_2$ produces a material with potential benefits for use in actuators: low magnetocrystalline anisotropy, and high d_{33}. On one hand, it is expected that the similar results can appear in single-crystal samples, on the other hand, considering that the magnetostriction of samples can be strongly affected by grain orientation and twin boundary, we decided to research on twin-free single crystals of $Tb_{0.27}Dy_{0.73}(Fe_{1-x}Al_x)_2$.

II. EXPERIMENT

The purity of the raw materials prepared for the growth of the single crystals of $Tb_{0.27}Dy_{0.73}(Fe_{1-x}Al_x)_2$ (x=0.0, 0.1) was as follows: for Tb and Dy, 99.95%, and for Fe and Al, better than 99.9%. The [111]-oriented single-crystal bars with approximately $2\times2\times10$ mm^3 were used as seeds. The crystals were grown in the MCGS-3 CZ apparatus by using Czochralski method.[14] As the result, the single crystals of $Tb_{0.27}Dy_{0.73}(Fe_{1-x}Al_x)_2$ (x=0.0, 0.1) with the [111] orientation were very well grown and their size is 6–10 mm in diameter and 50–80 mm in length.

Two resultant samples with different target compositions, $Tb_{0.27}Dy_{0.73}(Fe_{1-x}Al_x)_2$ (x=0.0, 0.1), were examined by chemical analyses. The results were given in Table I. The accuracy of the chemical analyses is ±0.01 for Al and Fe, and ±0.02 for Tb and Dy. As shown in Table I, the ratio of Tb/Dy was 0.39, which is higher than the corresponding one in the target compositions. It results from the preferential loss of Dy, because the vapor pressure of Dy is higher than that of Tb.

The twin-free single crystallinity of the crystals was determined by x-ray Laue spot photographs and metallographic observation. In addition, the characteristic diffraction peaks of (111), (222), and (333) were obtained solely by the x-ray diffraction experiments on the transverse sections of the crystals. The x-ray powder diffraction results indicate that all samples are in single phase of $MgCu_2$(C15) structure and possess high perfection.

In addition, the small single-crystalline bars of $Tb_{0.27}Dy_{0.73}(Fe_{1-x}Al_x)_2$ (x=0.0, 0.1), cut along [111] and [100] orientation and with the diameter of 1 mm and the length of 5 mm, were prepared for measuring magnetization curves and the curves of magnetic moment versus temperature by means of extracting sample magnetometer. Curie temperature was measured by vibrating sample magnetometer. The rods of the single crystal of $Tb_{0.27}Dy_{0.73}(Fe_{0.9}Al_{0.1})_2$ in the dimensions of $4\times5\times15$ mm^3 and with [111] orientation were prepared for measuring magnetostriction by strain gauge at RT.

TABLE I. Chemical composition, Curie temperature, lattice constant and saturature, magnetostriction of single-crystal $Tb_{0.27}Dy_{0.73}(Fe_{1-x}Al_x)_2$ (x =0.0, 0.1).

Sample	Chemical comp.	T_c(°C)	a(A)	λ_{111}
$Tb_{0.27}Dy_{0.73}Fe_2$	$Tb_{0.28}Dy_{0.72}Fe_{1.99}$	387	7.329	2.400×10^{-3}
$Tb_{0.27}Dy_{0.73}(Fe_{0.9}Al_{0.1})_2$	$Tb_{0.28}Dy_{0.72}(Fe_{0.9}Al_{0.1})_2$	267	7.539	1.010×10^{-3}

 0021-8979/96/79(8)/4668/3/$10.00 © 1996 American Institute of Physics

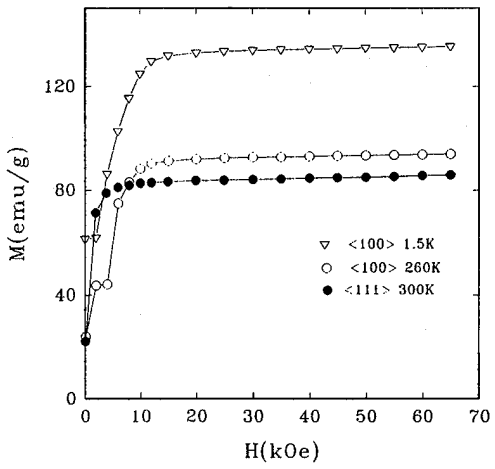


FIG. 1. Magnetization curves of ⟨100⟩ orientation rod of $Tb_{0.27}Dy_{0.73}Fe_2$ at 1.5, and 260 K, and ⟨111⟩ orientation rod at 300 K, respectively.

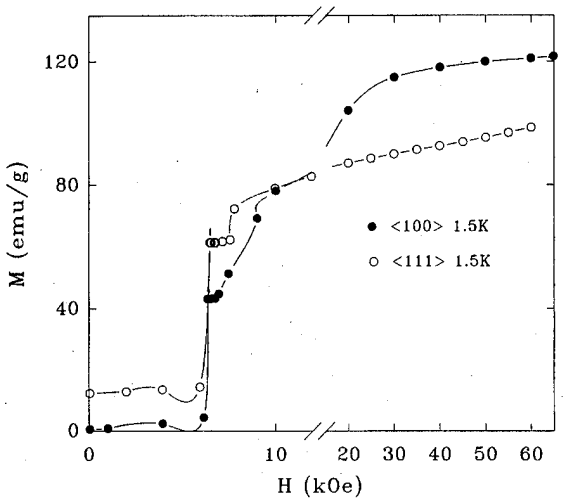


FIG. 2. Magnetic moment M vs applied field H of ⟨111⟩ and ⟨100⟩ single-crystal rods of $Tb_{0.27}Dy_{0.73}(Fe_{0.9}Al_{0.1})_2$ at 1.5 K.

III. RESULTS AND DISCUSSIONS

A. Lattice constants and Curie temperature

Because the half width of x-ray diffraction peaks of cubic Laves phase is very small at the crystal surface of (422),[5] and spontaneous magnetization influences all data of diffraction peaks except (422), the lattice constants listed in Table I are calculated by the (422) diffraction peak data.[6,7] In addition, it is observed in Table I that the Curie temperature decreases with Al doping in $Tb_{0.27}Dy_{0.73}Fe_2$. We believe that it results from the fact that average exchange interaction between Fe and Fe atoms decreases with the increase of the Al atoms in $Tb_{0.27}Dy_{0.73}(Fe_{1-x}Al_x)_2$.

B. Magnetization process

Magnetization curves of ⟨100⟩ orientation rod of $Tb_{0.27}Dy_{0.73}Fe_2$ at 1.5 and 260 K, and ⟨111⟩ orientation rod at 300 K, are shown in Fig. 1, respectively. It appears remarkably that the ⟨100⟩ direction is easy axis at 1.5 K. However, we cannot see clearly which axis is the easy one from the magnetization curves at 260 and 300 K, because the temperature of 260 or 300 K is already close to the anisotropy compensation temperature of the sample and its absolute value of magnetocrystalline anisotropy is smaller. The saturation magnetization M_s of the [100] oriented rod is 85 and 94 emu/g at 260 and 300 K, respectively. The magnetization curves of $Tb_{0.27}Dy_{0.73}(Fe_{0.9}Al_{0.1})_2$ at 1.5 K are shown in Fig. 2, while for 260 and 300 K, the curves are shown in Fig. 3. As shown in Fig. 3, the saturation magnetization for the [100] rod at 260 K and [111] rod at 300 K is 91 and 79 emu/g, respectively. Obviously, the saturation magnetization of $Tb_{0.27}Dy_{0.73}(Fe_{0.9}Al_{0.1})_2$ is less than that of $Tb_{0.27}Dy_{0.73}Fe_2$ at the same temperature. It is well known that the substitution of Al for Fe does not affect the absolute value of the magnetic moments of rare-earth sublattices. However, Al substitution for Fe may cause a deflection of the magnetic moments of the rare-earth sublattices with respect to the magnetizing direction, therefore, the average magnetic moment of every rare-earth atom decreases with the increase of Al content.

Furthermore, it is seen in Fig. 2 that magnetic moment almost does not change below the applied magnetic field of 6.5 kOe due to the pinning of magnetic domains. However, at the applied magnetic field of 6.5 kOe, the magnetic moment values of both the [100] and [111] oriented rods jump up suddenly. By contrast, this kind of jump does not occur for the samples of $Tb_{0.27}Dy_{0.73}Fe_2$ at 1.5 K, as shown in Fig. 2. The jump may result from either the pinning of domains by defects and intrinsic stress, or the occurrence of the macroscopic quantum effect of magnetization. In a word, the above results indicate that the Al substitution for Fe strongly affects the magnetic properties of $Tb_{0.27}Dy_{0.73}Fe_2$ at low temperature.

In Fig. 4 it is clear that both of the two curves of magnetic moment versus temperature for $Tb_{0.27}Dy_{0.73}(Fe_{1-x}Al)_2$ (x=0.0, 0.1) have an inflection at the temperature so-called anisotropy compensation temperature (T_{comp}). It indicates that magnetocrystalline anisotropy undergoes a transition when the easy direction of magnetization

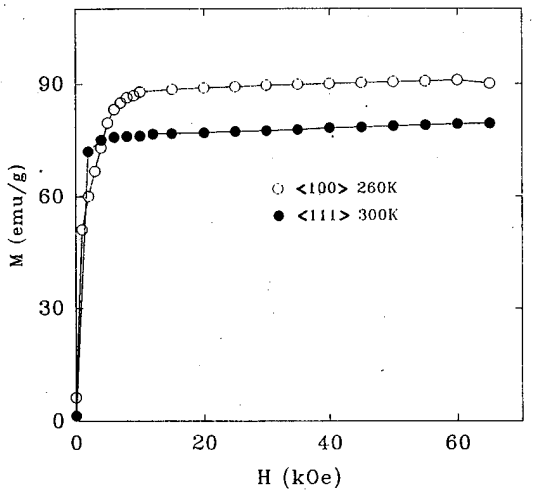


FIG. 3. Magnetic moment M vs applied field H of ⟨111⟩ and ⟨100⟩ single-crystal $Tb_{0.27}Dy_{0.73}(Fe_{0.9}Al_{0.1})_2$ at 260 and 300 K.

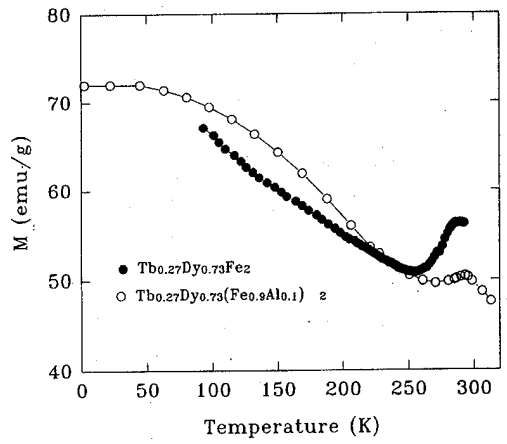


FIG. 4. Magnetic moment M vs temperature T of ⟨111⟩ single-crystal rods of $Tb_{0.27}Dy_{0.73}(Fe_{1-x}Al_x)_2$ (x=0.0, 0.1) at an applied field of 1 kOe.

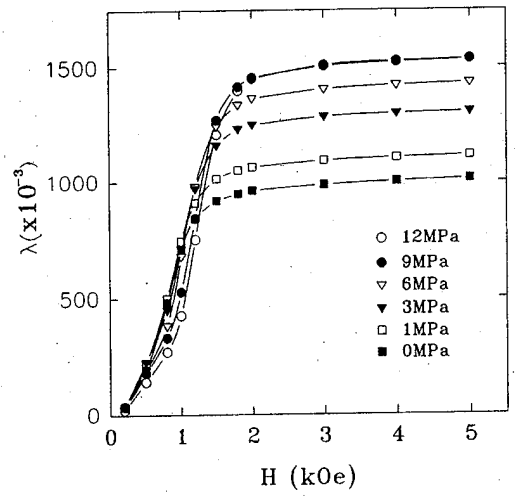


FIG. 5. Magnetostriction λ vs applied field H curves of $Tb_{0.27}Dy_{0.73}(Fe_{0.9}Al_{0.1})_2$ with applied compressive stress from 0 to 12 MPa.

is transited from ⟨100⟩ below the T_{comp} to ⟨111⟩ above the T_{comp}. In addition, it can also be seen in Fig. 4 that the T_{comp} of $Tb_{0.27}Dy_{0.73}(Fe_{0.9}Al_{0.1})_2$ is larger than that of $Tb_{0.27}Dy_{0.73}Fe_2$. Since the intrinsic anisotropy of $DyFe_2$ is larger than that of $TbFe_2$ while the Curie temperature of $TbFe_2$ is higher than that of $DyFe_2$, the increase of the T_{comp} for Al substitution is equivalent to the increase of the Dy content, or the decrease of Tb content. Therefore, it is reasonable to assume that the average magnetic moment of Tb atoms is affected more strongly by the Al substitution for Fe in $Tb_{0.27}Dy_{0.73}(Fe_{0.9}Al_{0.1})_2$ than that of Dy atoms. Similarly, we can also assume that the Al substitution decreases the intrinsic anisotropy of $TbFe_2$ more strongly than that of $DyFe_2$. Therefore, the magnetocrystalline anisotropy of $Tb_{0.27}Dy_{0.73}(Fe_{0.9}Al_{0.1})_2$ is decreased.

C. Magnetostriction

Figure 5 shows the relation of compressive axial stress and magnetostriction of the twin-free single-crystal $Tb_{0.27}Dy_{0.73}(Fe_{0.9}Al_{0.1})_2$. When the compressive stress is increased from 0 to 12 MPa, the saturation magnetostrictive coefficient along the [111] direction, λ_s increases from 1.01×10^{-3} to 1.54×10^{-3}, the saturation field increases from 1.8 to 2.3 kOe, and the maximum d_{33}=1.0 appears at the applied compressive stress of 12 MPa and magnetic fields from 1.0 to 2.0 kOe. These values are clearly better than those of ⟨112⟩-oriented twin single crystal under the same condition.[8] We believe that it is due to the fact that the [111] is the direction of the largest magnetostriction and the easiest magnetization, and that in the twin-free single-crystalline samples the impediment of the magnetic domain movement, such as twin boundaries, has been eliminated largely. Moreover, when the compressive stress is applied along [111] direction, most magnetic moments must rotate toward [112] direction. The reason for the increase is that the contribution of magnetic moments to magnetostriction is increased when the magnetic moments rotate toward the [111] from [112] direction. On the other hand, the applied compressive stress makes domain energy of non-180 domain wall increased, leading to the increase of the bias field. Until the Zeaman energy is sufficient to surmount the anisotropy energy barrier and performs work required against the compressive stress, magnetic moments cannot rotate towards the [111] direction. In fact, the larger the applied compressive stress is, the larger the anisotropy energy is. In a word, the bias field increases with the increase of the compressive stress.

IV. CONCLUSION

From the experimental results of the magnetic and magnetostrictive measurements on twin-free single-crystals $Tb_{0.27}Dy_{0.73}(Fe_{1-x}Al_x)_2$ (x=0.0, 0.1). We can obtain the following conclusions:

(1) The chemical analyses, the increase of lattice constant and the decrease of Curie temperature all confirm that Fe atoms have been substituted by Al atoms.

(2) With x increasing from 0 to 0.1, the anisotropy compensation temperature of $Tb_{0.27}Dy_{0.73}(Fe_{1-x}Al_x)_2$ increases slightly, while the magnetocrystalline anisotropy energy and the saturation magnetic moment decrease.

(3) The saturation magnetostriction coefficient λ_{111} in the [111] direction increases from 1.01×10^{-3} to 1.53×10^{-3} and d_{33} ($d\lambda/dH$) also increases when compressive stress increased from 0 to 12 MPa. These results are better than those of ⟨112⟩-oriented twin single crystal at the same conditions.

[1] A. E. Clark and H. S. Belson, AIP Conf. Proc. No. 10, Part I, 749 (1973).
[2] A. E. Clark, J. E. Cullen, O. D. McMasters, and E. B. Callen, AIP Conf. Proc. No. 29, 192 (1976).
[3] W.-D. Zhong and J. Wang, Proceedings of the 2nd International Symposium on Phys. of Magnetic Materials 1992, Vol. 1, p. 97.
[4] G. Wu, X. Zhao, J. Wang, J. Li, K. Jia, and W. Zhan, Appl. Phys. Lett. (to be published).
[5] V. Sima *et al.*, J. Phys. F **14**, 191 (1984).
[6] E. Sayettat, J. Appl. Phys. **46**, 3619 (1975).
[7] E. Bertaut *et al.*, F. Tcheou Solid State Commun. **8**, 239 (1970).
[8] K. Prajapati, A. G. Jenner, M. P. Schulze, and R. D. Greenough, J. Appl. Phys. **73**, 6171 (1993).

Perfect conductivity approximation: Modification for polyphase systems

K. V. Namjoshi, J. D. Lavers, and P. P. Biringer
Department of Electrical and Computer Engineering, University of Toronto, Toronto, Ontario, Canada

In this paper, we use an analytical model to investigate voltage drop across the conductors of a three-phase parallel wire planar transmission line carrying balanced currents. The expressions derived for the voltage drops are identical to those given by the perfect conductor model except for a term arising due to the propagation of fields inside the conductors. The voltage drops thus calculated yield different values for the two end conductors even when they are symmetrically placed with respect to the central conductor. The calculations show that the imaginary part of the correction term is of more significance than the real part. The results obtained show agreement with the measured values. © *1996 American Institute of Physics.* [S0021-8979(96)01408-1]

I. INTRODUCTION

In three-phase planar transmission lines carrying balanced currents, it is evident that the voltage drop values across the outer conductors are different from that across the central conductor as its relative position differs from that of the outer conductors. At a first glance it may appear that the outer conductors should have equal voltage drop values if they are symmetrically placed with respect to the central conductor. A numerical calculation by Cao and Biringer[1] has shown that this is not the case. There is a small but finite difference in the values of these two voltage drops. In two-dimensional problems involving single-phase currents, perfect conductivity approximation is frequently used in which the conductors are assumed to be perfectly conducting. Such a model gives quick and fairly acceptable results especially when the skin depth is small in comparison with the conductor cross sectional dimensions and the separation between the conductors. The conductors are assumed to be perfectly conducting for the calculation of the field variables and other related quantities. The power loss if desired is estimated by the knowledge of the surface magnetic field.[2] In this paper a calculation of voltage drop in a three phase transmission line is presented. The outer conductors of the line are equidistant from the central conductor. We use a model based on the perfect conductivity approximation and show that the model correctly predicts the small difference between the voltage drop values of the outer conductors provided one takes into account the effect caused by the propagation of fields inside the conductors. The voltage drop values thus calculated agree with the measured values.[1]

II. THEORY

A schematic of a three-phase parallel wire transmission line with conductors having a circular cross section is shown in Fig. 1. The conductors are nonmagnetic and carry balanced three-phase currents $\tilde{C}_1$, $\tilde{C}_2$, and $\tilde{C}_3$ such that $\tilde{C}_1$ leads $\tilde{C}_2$ by 120°. The resulting voltage drop across the conductors is obtained with the help of the vector potential at the surface of the conductors. In order to obtain the vector potential at any of the conductors, in the analysis below, the field variables are expressed in terms of local polar coordinates with the axis of the conductor as origin (Fig. 2). The other two currents are assumed to be filament currents. In the derivation ~ above a variable indicates the phasor representation. Absence of ~ indicates rms value.

A. Conductivity infinite

In this case the vector potential inside the conductors is zero. Vector potential A_Z outside the conductor due to a filament current $\tilde{C}$ at $(d,0)$ is given by[3]

$$A_Z=-\frac{\mu_0\tilde{C}}{4\pi}\log(d^2+\rho^2-2\rho d\cos\phi)-\frac{\mu_0\tilde{C}}{2\pi}\log\rho+\frac{\mu_0\tilde{C}}{4\pi}\log(a^4/d^2+\rho^2-2a^2\rho\cos\phi/d). \quad (1)$$

Therefore, the vector potential at the surface of conductor 2 A_{Z2} due to currents $\tilde{C}_1$, $\tilde{C}_2$, and $\tilde{C}_3$ is obtained as

$$A_{Z2}=-\frac{\tilde{C}_2\mu_0}{2\pi}\log a-\frac{\tilde{C}_1\mu_0}{2\pi}\log R-\frac{\tilde{C}_3\mu_0}{2\pi}\log R \quad (2)$$

or

$$A_{Z2}=-\frac{\tilde{C}_2\mu_0}{2\pi}\log a/R \quad (3)$$

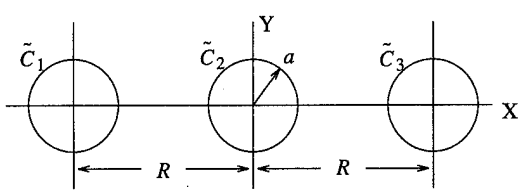


FIG. 1. A schematic of a three-phase transmission line with conductors having circular cross section. R is the distance between the conductors and a is the radius. $\tilde{C}_1$, $\tilde{C}_2$, and $\tilde{C}_3$ are the conductor currents.

 0021-8979/96/79(8)/4671/3/$10.00 © 1996 American Institute of Physics

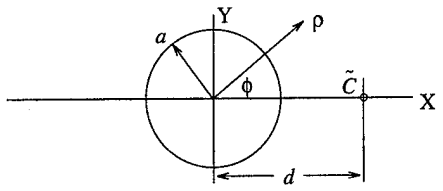


FIG. 2. The local coordinate system for any conductor showing current $\tilde{C}$ at $(d,0)$. The axis of the conductor under consideration is at the origin.

because $\tilde{C}_1+\tilde{C}_2+\tilde{C}_3=0$. Voltage drop per unit length, $\tilde{E}_{D2}$ for conductor 2 is obtained by

$$\tilde{E}_{D2}-j\omega\left[-\frac{\tilde{C}_2\mu_0}{2\pi}\log a/R\right]=0 \tag{4}$$

or

$$\tilde{E}_{D2}=-\frac{j\omega\tilde{C}_2\mu_0}{2\pi}\log a/R. \tag{5}$$

Similarly voltage drop across conductor 1, $\tilde{E}_{D1}$ and that across conductor 3, $\tilde{E}_{D3}$ are given by

$$\tilde{E}_{D1}=-\frac{j\omega\tilde{C}_1\mu_0}{2\pi}\log a/R-\frac{j\omega\tilde{C}_3\mu_0}{2\pi}\log 2 \tag{6}$$

or

$$\tilde{E}_{D1}=-\frac{j\omega\tilde{C}_1\mu_0}{2\pi}\left[\log a/R-\frac{1}{2}\log 2+j\frac{\sqrt{3}}{2}\log 2\right] \tag{6a}$$

and

$$\tilde{E}_{D3}=-\frac{j\omega\tilde{C}_3\mu_0}{2\pi}\log a/R-\frac{j\omega\tilde{C}_1\mu_0}{2\pi}\log 2 \tag{7}$$

or

$$\tilde{E}_{D3}=-\frac{j\omega\tilde{C}_3\mu_0}{2\pi}\left[\log a/R-\frac{1}{2}\log 2-j\frac{\sqrt{3}}{2}\log 2\right]. \tag{7a}$$

B. Conductivity finite

The conductors are solid. The vector potential is obtained by solving the field equations inside and outside the conductor and matching the fields at the interface. Vector potential due to a filament current $\tilde{C}$ at $(d,0)$ now given by Ref. 4. Outside the conductor at $\rho=a$,

$$A_Z=-\frac{\tilde{C}\mu_0}{2\pi\log R}+\frac{\tilde{C}\mu_0}{\pi ka}\sum_{n=1}^{\infty}(a/d)^n\frac{I_n(ka)}{I_{n-1}(ka)}\cos n\phi. \tag{8}$$

Inside the conductor at $\rho=a$,

$$A_Z=\frac{\tilde{C}\mu_0}{\pi ka}\sum_{n=1}^{\infty}(a/d)^n\frac{I_n(ka)}{I_{n-1}(ka)}\cos n\phi,$$
$$k=\sqrt{j\omega\sigma\mu_0}=(1+j)/\delta. \tag{9}$$

Here, δ is the skin depth, $\omega=2\pi f$ the frequency, σ the conductivity, and μ_0 is the permeability of the free space. I_n is the modified Bessel function of the first kind and order n. Using Eqs. (8) and (9), the vector potential across the conductor 2, A_{Z2}, is written as, inside the conductor at $\rho=a$,

$$A_{Z2}=-\frac{\tilde{C}_2\mu_0}{2\pi ka}\frac{I_0(ka)}{I_1(ka)}+\frac{\tilde{C}_1\mu_0}{\pi ka}\sum_{n=1}^{\infty}\left(\frac{a}{R}\right)^n\frac{I_n(ka)}{I_{n-1}(ka)}\cos n(\phi+\pi)+\frac{\tilde{C}_3\mu_0}{\pi ka}\sum_{n=1}^{\infty}\left(\frac{a}{R}\right)^n\frac{I_n(ka)}{I_{n-1}(ka)}\cos n\phi. \tag{10}$$

The first term on the right-hand side of Eq. (10) is due to the known current distribution.[5]

Outside the conductor at $r=a$,

$$A_{Z2}=-\frac{\tilde{C}_2\mu_0}{2\pi}\log a-\frac{\tilde{C}_1\mu_0}{2\pi}\log R-\frac{\tilde{C}_3\mu_0}{2\pi}\log R+\frac{\tilde{C}_1\mu_0}{\pi ka}\sum_{n=1}^{\infty}\left(\frac{a}{R}\right)^n\frac{I_n(ka)}{I_{n-1}(ka)}\cos n(\phi+\pi)+\frac{\tilde{C}_3\mu_0}{\pi ka}\sum_{n=1}^{\infty}\left(\frac{a}{R}\right)^n\frac{I_n(ka)}{I_{n-1}(ka)}\cos n\phi. \tag{11}$$

The potential drop $\tilde{E}_D$ across the conductor is given by

$$-j\omega\,Az\,\underset{\text{inside}}{}=\tilde{E}_D-j\omega\,Az\,\underset{\text{outside}}{}.$$

Therefore one gets for $\tilde{E}_{D2}$:

$$\tilde{E}_{D2}=-\frac{j\omega\mu_0}{2\pi}\left[\tilde{C}_2\log a+\tilde{C}_1\log R+\tilde{C}_3\log R-\tilde{C}_2\frac{I_0(ka)}{kaI_1(ka)}\right],$$

which after simplification leads to

$$\tilde{E}_{D2}=-\frac{j\omega\mu_0\tilde{C}_2}{2\pi}(\log a/R-T_s), \tag{12}$$

$$T_s=\frac{I_0(ka)}{kaI_1(ka)}, \tag{13}$$

$$T_s=\frac{(1-j)\delta}{2a}\ \text{at small}\ \delta/a. \tag{13a}$$

Equation (12) is similar to Eq. (5) except for a correction term, T_s. It is due to the contribution of the internal vector potential. The correction term depends only on the current distribution in the isolated conductor. Equation (13a) is obtained by using large argument approximation for Bessel functions.[6] Using a similar procedure, it can be shown that

$$\tilde{E}_{D1}=-\frac{j\omega\mu_0\tilde{C}_1}{2\pi}(\log a/R-T_s)-\frac{j\omega\mu_0\tilde{C}_3}{2\pi}\log 2 \tag{14}$$

or for small δ/a,

TABLE I. Voltage drops across the conductors. $a=1.1$ cm, $R=30$ cm, $f=400$ Hz, $\sigma=5.8\times10^7$ S/m, and current=1 kA.

E_D V/m	Phase angle of current	(12)–(15)		
		(5)–(7)	Attn. neglected	Attn. included
E_{D1}	120	1.861	1.877	1.949
E_{D2}	0	1.662	1.666	1.738
E_{D3}	−120	1.861	1.848	1.922

TABLE II. Voltage drops across the conductors. $a=1.1$ cm, $b=1.0$ cm, $R=30$ cm, $f=400$ Hz, $\sigma=5.8\times10^7$ S/m, and current=1 kA.

E_D V/m	Phase angle of current	(12)–(15)		
		Attn. neglected	Attn. included	Meas.
E_{D1}	120	1.901	1.921	1.936
E_{D2}	0	1.673	1.694	1.718
E_{D3}	−120	1.839	1.861	1.860

$$\tilde{E}_{D1}=-\frac{j\omega\tilde{C}_1\mu_0}{2\pi}\left(\log a/R-\frac{1}{2}\log 2-\frac{\delta}{2a}+j\frac{\sqrt{3}}{2}\log 2+j\frac{\delta}{2a}\right) \tag{14a}$$

and

$$\tilde{E}_{D3}=-\frac{j\omega\mu_0\tilde{C}_3}{2\pi}(\log a/R-T_s)-\frac{j\omega\mu_0\tilde{C}_1}{2\pi}\log 2 \tag{15}$$

or for small δ/a,

$$\tilde{E}_{D3}=-\frac{j\omega\tilde{C}_3\mu_0}{2\pi}\left(\log a/R-\frac{1}{2}\log 2-\frac{\delta}{2a}-j\frac{\sqrt{3}}{2}\log 2+j\frac{\delta}{2a}\right). \tag{15a}$$

It should be remembered that $\tilde{E}_{D1}$, $\tilde{E}_{D2}$, and $\tilde{E}_{D3}$ are voltage drops per unit length of the conductors.

III. DISCUSSION

In Eqs. (6) and (7), $\tilde{C}_1$ lags $\tilde{C}_3$ by 120°. It can be easily seen that E_{D1} and E_{D3} calculated using Eqs. (6) and (7) have equal magnitudes and they differ from that of E_{D2}. On the other hand, the magnitudes of E_{D1} and E_{D3} as given by Eqs. (14) and (15) are different because of the imaginary part of the correction term T_s in Eq. (13). Various values calculated using the expression derived above are given in Table I. Also given in the table are values which include only the imaginary or the quadrature component T_s. The real part or the attenuation part is not included. These also predict different values for E_{D1} and E_{D3}.

If the conductors are hollow instead of being solid, in Eqs. (12), (14), and (15), the correction term is modified to

$$T_s=\frac{1}{ka}\frac{I_0(ka)K_1(kb)+K_0(ka)I_1(kb)}{I_1(ka)K_1(kb)-K_1(ka)I_1(kb)}. \tag{16}$$

Here, a is the outer radius and b is the inner radius of the conductors. K_n is the modified Bessel function of the second and order n. Values obtained using Eq. (16) for T_s are given in Table II. Also shown in the table are measured values reported by Cao and Biringer.[1] The calculated values are in agreement with the measurement.

IV. CONCLUSIONS

The results presented in this paper indicate that the perfect conductivity model can still be used for three-phase or polyphase circuits provided a suitable correction term is included in the calculation. In the calculation above, the imaginary part of the correction term has a more significant effect than the real part.

[1] M. Cao and P. P. Biringer, IEEE Trans. Magn. **26**, 2768 (1990).
[2] R. L. Stoll, *The Analysis of Eddy Currents* (Clarendon, Oxford, UK, 1974), p. 62.
[3] P. M. Morse and H. Feshbach, *Methods of Theoretical Physics* (McGraw-Hill, New York, 1953), p. 1188.
[4] J. A. Tegopoulos and K. E. Kriezis, *Eddy Currents in Linear Conducting Media* (Elsevier, Amsterdam, The Netherlands, 1985), p. 127.
[5] R. L. Stoll, *The Analysis of Eddy Currents* (Clarendon, Oxford, UK, 1974), p. 24.
[6] H. B. Dwight, *Tables of Integrals and Other Mathematical Data*, 4th ed. (Macmillan, New York, 1965), p. 196.

Dual-complementary variational methods in eddy currents (abstract)

P. Lois, D. Baldomir, and J. Rivas
Departamento de Física Aplicada, Facultad de Física, University of Santiago de Compostela, Spain

Dual-complementary variational principles and their expressions in static electric and stationary magnetic fields fit quite well into computational methods.[1,2] We have got a very efficient computer graphics package exploiting these methods. But the main advantage with respect to other methods such as finite elements is that they are associated with the intuitive picture of lines of force for the fields. This enables the designer to use his physical intuition to lead him to practical improvements in the achievement need much less memory and CPU of a computer for most of the usual practical works. Actually our computer package was made on a cheap desk-top computer. Unfortunately these variational methods fail in eddy-current systems. The main reason is that eddy-current equations are equivalent to a diffusion equation which is not a self-adjoint differential operator. Nevertheless we have got to remove this difficulty[3] by changing the geometry associated to the conductor. Besides, to employ the exterior algebra of differential forms we get the best understanding of the basics of the mathematical problem. Finally, the paper gives a brief description of the new software that we introduce into this applied mathematical methods. © *1996 American Institute of Physics.*
[S0021-8979(96)80208-9]

[1] P. Hammond and J. K. Sykulski, *Engineering Electromagnetism: Physical Processes and Computation* (Oxford University, New York, 1994).
[2] J. K. Sykulski, *Computational Magnetics* (Chapman & Hall, London, 1995).
[3] D. Baldomar and P. Hammond, Proc. IEE **140**, 166 (1993).

 0021-8979/96/79(8)/4674/1/$10.00 © 1996 American Institute of Physics

Solution of induction heating problems involving media with hysteresis

A. A. Adly
Electric Power and Machines Department, Cairo University, Giza, Egypt

Induction heating is widely used in various industrial processes. In this paper, the Crank–Nicolson finite-difference approach is employed in the analysis of induction heating problems involving relatively long rods that exhibit hysteresis. The analysis is, thus, reduced to solving a 2D space-time electromagnetic field problem and exact B-H characteristics of rods are taken into account by utilizing Preisach-type models of hysteresis. A detailed numerical example is given in the paper and some sample simulation results covering different excitation frequencies and amplitudes are reported. © *1996 American Institute of Physics.* [S0021-8979(96)01508-8]

I. INTRODUCTION

Induction heating is widely used in various industrial processes such as those involving melting, alloying and hardening of metals (see, for instance, Ref. 1). In order to be able to predict and control the outcome of such processes, computations for estimating local field and flux density distributions as well as eddy current and hysteresis core may have to be performed. Such computations become complicated for media having nonlinear B-H characteristics and even more complicated for media exhibiting hysteresis.

In the past, several rigorous analytical formulations for problems dealing with nonlinear saturable magnetic media subject to time varying excitation have been developed (see, for instance, Refs. 2–5). By only considering reversible components of media B-H loops, these formulations may be used to simulate induction heating processes of media exhibiting hysteresis under high excitation currents and/or frequencies. This is because under such conditions hysteresis loss may be ignored in comparison to eddy current loss. Some attempts to account for the hysteresis phenomenon in similar problems have been also made (for example, refer to Refs. 3, 6, and 7). In most of these attempts the complex permeability principle was employed.[3,6] Though this approach leads to more accurate core loss calculations, it may not yield accurate local predictions. Other reported attempts to account for actual B-H characteristics have resulted in analytical and numerical formulations[7] that are too complicated to be easily utilized.

The purpose of this paper is to present a numerical approach for solving induction heating problems that involve media exhibiting hysteresis. In the paper, the Crank–Nicolson[8] finite-difference technique is used to analyze relatively long cylindrical rods with surface excitation along the azimuthal direction and exact B-H characteristics are taken into account by utilizing Preisach-type models of hysteresis.[9] Hence, the analysis is reduced to solving a 2D space-time electromagnetic field problem in which, for every row of nodes corresponding to the same rod radius, a separate Preisach model is used to keep track of its particular field variation history. No temperature rise effects, though, on media magnetic properties are considered in the presented analysis. Sample simulation results, covering different excitation frequencies and excitation amplitudes, for a specific example are given in the paper.

II. THE ANALYSIS APPROACH

The diffusion equation for the case of an infinitely long rod subject to time varying surface excitation along the azimuthal direction and having uniform conductivity σ can be given by

$$\frac{\partial^2 H_z(r,t)}{\partial r^2}+\frac{1}{r}\frac{\partial H_z(r,t)}{\partial r}=\sigma\frac{dB_z(r,t)}{dH_z(r,t)}\frac{\partial H_z(r,t)}{\partial t},\quad r\leqslant R, \tag{1}$$

where R is the rod radius while $H_z(r,t)$ and $B_z(r,t)$ are the axial field and flux density values corresponding to the radius r and time instant t, respectively. Defining h and p in a finite-difference scheme as the distance between adjacent nodes in space and the duration between successive considered instants, in order, r, R, and t may then be expressed by

$$\begin{aligned} &r=(i-1)h,\quad i=1,2,\ldots,M-1,\\ &R=(M-1)h,\quad \text{and } t=(k-1)p,\quad k=1,2,3,\ldots\ . \end{aligned} \tag{2}$$

Explicit and implicit finite-difference equations representing Eq. (1) can be derived using Taylor expansions about the nodes (i,k) and $(i,k+1)$, respectively. By alternately applying these explicit and implicit equations to successive time rows after shrinking the time step duration to half its value, the following Crank–Nicolson formulation of Eq. (1) can be obtained:

$$\begin{aligned} &iH_{i+1,k+1}+\{1-2i-(i-1)/a_{i,k+1/2}\}H_{i,k+1}\\ &\quad+(i-1)H_{i-1,k+1}\\ &=iH_{i+1,k}+\{1-2i-(i-1)/a_{i,k+1/2}\}H_{i,k}\\ &\quad+(i-1)H_{i-1,k}, \end{aligned} \tag{3}$$

where $H_{u,v}$ is the discrete field value at the mesh coordinates (u,v) and $B_{u,v}$ is the corresponding flux density. The values $H_{M,v}$ may be directly calculated from the surface excitation $J_s(v)$ and the term $a_{u,v}$ may be given by

$$a_{u,v}=p/[\sigma h^2(dB(H_{u,v})/dH_{u,v})]. \tag{4}$$

In Eq. (3), the predictor-corrector procedure is used for evaluating the appropriate value of the variable a. This means that, first, a half-time step Crank–Nicolson equation is computed using the values of $a_{i,k}$ in order to evaluate $H_{i,k+1/2}$ values. Then, values of $a_{i,k+1/2}$ are computed and, finally, substituted in Eq. (3) to give the field variations between time steps k and $(k+1)$.

 0021-8979/96/79(8)/4675/3/$10.00 © 1996 American Institute of Physics

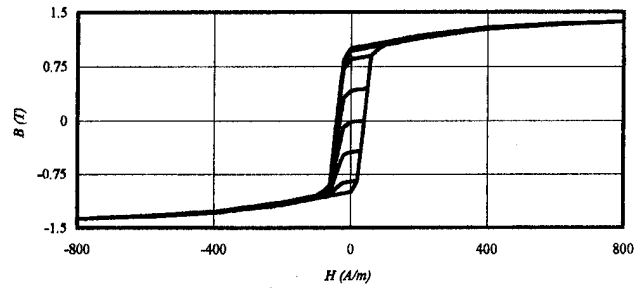


FIG. 1. Assumed B-H characteristics of the rod medium.

It should be pointed out that although the Crank–Nicolson formulation is stable for all values of h and p, it has a truncation error of the order (p^2+h^2) (refer to Ref. 8). This fact, as well as the anticipated skin depth, should be used as a guide while choosing a suitable grid discretization scheme for the finite-difference mesh of a particular problem.

Since media exhibiting hysteresis are the main focus of this study, it should be expected that the term (dB/dH) in Eq. (4) may widely vary for the same H value depending on previous history. For this reason, Preisach models of hysteresis[9] are utilized in the accurate evaluation of (dB/dH) and, consequently, of the variable a. This can be achieved using the expressions

$$B(H_{u,\nu})=-B_{\text{sat}}+\sum_{j=1}^{m-1}(B_{H_j,h_j}-B_{H_j,h_{j-1}})+(B_{H_m,H_{u,\nu}}-B_{H_m,h_{m-1}}), \tag{5}$$

$$B(H_{u,\nu})=-B_{\text{sat}}+\sum_{j=1}^{m-1}(B_{H_j,h_j}-B_{H_j,h_{j-1}})+(B_{H_{u,\nu},H_m}-B_{H_{u,\nu},h_{m-1}}), \tag{6}$$

and

$$(dB/dH)\approx\{[B(H+\Delta H)-B(H-\Delta H)]/[2\Delta H]\}. \tag{7}$$

In Eqs. (5) and (6) B_{sat} is the positive saturation flux density value, $B_{\alpha,\beta}$ is the flux density traced along an experimentally measured first-order-reversal curve corresponding to field value β and initiated from the main ascending branch of the hysteresis loop at the field α, while m, H_j, and h_j represent the number of field extrema, the jth local field maximum and the jth local field minimum stored by the model, respectively (see Ref. 9). Expression (5) applies to mesh locations experiencing a decrease in field values while Eq. (6) applies to those experiencing a field increase.

Knowing local field and flux density values corresponding to each time step k, and by the aid of Eq. (2), eddy currents $J_{i,k}$ as well as hysteresis losses P_h and eddy current losses P_e for a rod of unit length can be computed from

$$J_{i-1/2,k}\approx-\left(\frac{H_{i,k}-H_{i-1,k}}{h}\right),\quad i=2,3,\ldots,M, \tag{8}$$

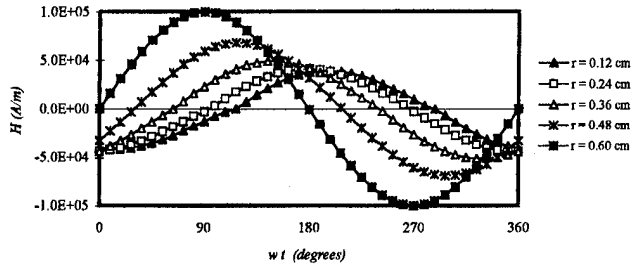


FIG. 2. Some local H waveforms for 10^5 A/m, 500 Hz surface excitation.

$$P_h\approx\sum_{i=2,3,\ldots,M}\pi h^2 f\{(i-1)^2-(i-2)^2\}\left[\sum_{\nu=k-N+1}^{k}(H_{i,\nu}+H_{i-1,\nu})(B_{i,\nu}+B_{i-1,\nu}-B_{i,\nu-1}-B_{i-1,\nu-1})/4\right], \tag{9}$$

where f is the frequency and N is the number of time intervals p per cycle and

$$P_e\approx\sum_{i=2,3,\ldots,M}\pi(2i-3)f\left[\sum_{\nu=k-N+1}^{k}p(J_{i,\nu}+J_{i-1,\nu})^2/(4\sigma)\right]. \tag{10}$$

III. A NUMERICAL EXAMPLE AND CONCLUSIONS

The proposed approach has been implemented and its digital computer code has been developed. Numerous simulations have been performed on a sample problem dealing with a silicon steel rod whose conductivity and radius are 2×10^6 Ω m and 0.6 cm, respectively. Only steady-state results are reported in this study. The set of first-order reversals shown in Fig. 1 was taken as the experimentally measured B-H characteristics of the rod material. For simplicity, these curves were assumed to be frequency independent.

Field computations were carried out using Eqs. (2)–(7) for various relatively high excitation frequencies and amplitudes, which are typical for induction heating processes. In order to obtain more accurate local field and power loss calculations, appropriate time and space discretizations were chosen to accommodate different frequencies and anticipated skin depths.

In Fig. 2 computed field waveforms at different radii under 500 Hz, 10^5 A/m surface excitation are shown. Two

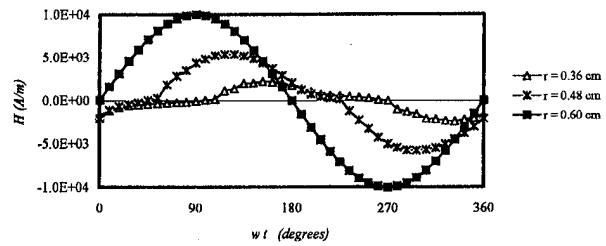


FIG. 3. Some local H waveforms for 10^4 A/m, 500 Hz surface excitation.

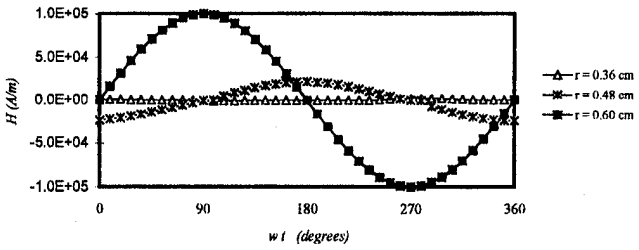


FIG. 4. Some local H waveforms for 10^5 A/m, 5000 Hz surface excitation.

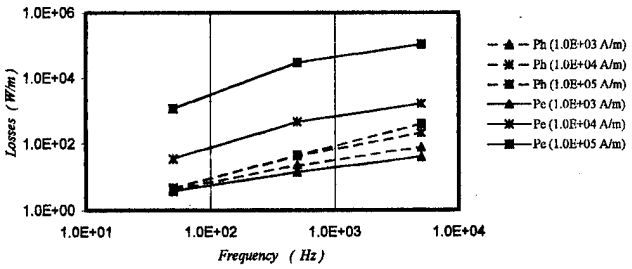


FIG. 5. Sample computed hysteresis (P_h) and eddy current (P_e) losses/unit length.

main results can be observed from these waveforms. First, the high excitation level drives the medium into saturation resulting in a low effective permeability and, consequently, a large skin depth δ (i.e., $\delta > R$). Second, the hysteresis phenomenon, which is accurately taken into account in the proposed analysis, has led to the phase differences between H waveforms corresponding to different rod radii. Those two observations are in total qualitative agreement with similar previously reported studies.[7]

Other waveform profiles for 500 Hz, 10^4 A/m and 5000 Hz, 10^5 A/m surface excitations, respectively, are shown in Figs. 3 and 4. By comparing Figs. 2 and 3 it can be deduced that for the same supply frequency the effective permeability varies with applied field level. This is typical for nonlinear magnetic materials and leads to a different skin depth δ ($\delta \approx 0.3\ R$ in this case). Figure 4, on the other hand, supports the expected result that for the same applied excitation level of Fig. 2, an increase in its frequency will lead to a decrease in skin depth ($\delta \approx 0.13\ R$). However, unlike for linear media, computed skin depths are no longer inversely proportional to the square root of excitation frequencies. Hysteresis and eddy current losses per unit length of the rod have been computed using Eqs. (8)–(10). Some results of these computations are shown in Fig. 5.

It can thus be concluded that, by incorporating Preisach models into the Crank–Nicolson finite-difference formulation, simulation of induction heating processes may be performed while accurately accounting for magnetic properties. Simulation results indicate that in such conditions the variation of local fields, hysteresis losses, and eddy current losses with respect to excitation amplitudes and frequencies may significantly deviate from linear media cases. This fact further highlights the importance of using the proposed technique. Even though effects of temperature rise resulting from heat dissipated in the magnetic material has not been taken into consideration, the proposed analysis can be integrated with thermodynamic models to account for this process. In this case, B will have to be calculated for any temperature using first-order reversals measured at the same temperature. Frequency effects on hysteresis loops may also be accounted for by utilizing dynamic Preisach models[9] or by the aid of other related studies (see, for example, Ref. 10).

[1] D. Melaab, O. Longeot, L. Krahenbuhl, L. Nicolas, and Ph. Wendling, IEEE Trans. Magn. **MAG-29**, 1558 (1993).
[2] P. D. Agarwal, Trans. IEE **78**, 169 (1959).
[3] J. F. Gieras, Proc. IEE **124**, 1098 (1977).
[4] I. D. Mayergoyz, F. M. Abdel-Kader, and F. P. Emad, J. Appl. Phys. **55**, 618 (1984).
[5] V. M. Machado, IEEE Trans. Magn. **MAG-30**, 4299 (1994).
[6] D. O'Kelly, J. Phys. D **8**, 568 (1975).
[7] K. Zakrzewski and F. Pietras, Proc. IEE **81**, 1679 (1971).
[8] R. L. Stoll, *The Analysis of Eddy Currents* (Clarendon, Oxford, 1974).
[9] I. D. Mayergoyz, *Mathematical Models of Hysteresis* (Springer, New York, 1991).
[10] D. C. Jiles, IEEE Trans. Magn. **MAG-30**, 4326 (1994).

Solution of magnetic field and eddy current problem induced by rotating magnetic poles (abstract)

Z. J. Liu and T. S. Low
Magnetics Technology Centre, National University of Singapore, 10 Kent Ridge Crescent, Singapore 0511

The magnetic field and eddy current problems induced by rotating permanent magnet poles occur in electromagnetic dampers, magnetic couplings, and many other devices. Whereas numerical techniques, for example, finite element methods can be exploited to study various features of these problems, such as heat generation and drag torque development, etc.,[1] the analytical solution is always of interest to the designers since it helps them to gain the insight into the interdependence of the parameters involved and provides an efficient tool for designing. Some of the previous work[2,3] showed that the solution of the eddy current problem due to the linearly moving magnet poles can give satisfactory approximation for the eddy current problem due to rotating fields. However, in many practical cases, especially when the number of magnet poles is small, there is significant effect of flux focusing due to the geometry. The above approximation can therefore lead to marked errors in the theoretical predictions of the device performance. Bernot *et al.*[4] recently described an analytical solution in a polar coordinate system where the radial field is excited by a time-varying source. A discussion of an analytical solution of the magnetic field and eddy current problems induced by moving magnet poles in radial field machines will be given in this article. The theoretical predictions obtained from this method is compared with the results obtained from finite element calculations. The validity of the method is also checked by the comparison of the theoretical predictions and the measurements from a test machine. It is shown that the introduced solution leads to a significant improvement in the air gap field prediction as compared with the results obtained from the analytical solution that models the eddy current problems induced by linearly moving magnet poles. © *1996 American Institute of Physics.* [S0021-8979(96)81808-3]

[1]T. W. Nehl *et al.*, IEEE Trans. Magn. **MAG-30**, 3000 (1994).
[2]M. P. Perry, IEEE Trans. Magn. **MAG-20**, 149 (1985).
[3]Z. J. Liu, A. Vourdas, and K. J. Binns, IEEE Proc. A 189 (1991).
[4]F. Bernot *et al.*, IEEE Proc. B **1**, 18 (1993).

 0021-8979/96/79(8)/4678/1/$10.00 © 1996 American Institute of Physics

Nonlinear flux diffusion and ac susceptibility of superconductors: Exact numerical results

Z. Koziol[a] and R. A. Dunlap
Department of Physics, Dalhousie University, Halifax, N.S., Canada B3H 3J5

The ac response of a slab of material with electrodynamic characteristics $E \sim j^{\kappa+1}$, $\kappa \geqslant 0$, is studied numerically. From the solutions of the nonlinear diffusion equation, the fundamental and higher-order components of the harmonic susceptibility are obtained. A large portion of the data for every κ can be scaled by a single parameter, $\xi \equiv t^{1/(\kappa+2)} \cdot H_0^{\kappa/(\kappa+2)}/D$, where t is the period of the ac field at the surface, H_0 is its amplitude, and D is the slab thickness. This is, however, only an approximate scaling property: The field penetration into a nonlinear medium is a more complex phenomenon than in the linear case. In particular, the susceptibility values are not uniquely defined by a set of only two parameters, such as κ and ξ, while one parameter, i.e., $t^{1/2}/D$, is sufficient to describe the electrodynamic response of a linear medium. © *1996 American Institute of Physics.* [S0021-8979(96)00408-X]

I. INTRODUCTION

The problem of nonlinear diffusion has recently attracted considerable attention in diverse fields of science. One example, which is considered in the present work, deals with the magnetization process of superconductors. In the case when the response of a superconductor to an applied ac field, $H = H_0 \exp(i\omega t)$, is linear, the electrodynamic properties in the superconducting state can be described in terms of the complex conductivity, $\sigma = \sigma_r + i\sigma_i$. In the flux-flow regime of high-T_c superconductors, which occurs in a broad $H-T$ range, it is usually justified to neglect the imaginary component of the complex conductivity. In that case, Maxwell's equations, $\nabla \times \mathbf{B} = 4\pi/c \cdot \mathbf{j}$ and $c\nabla \times \mathbf{E} = -\partial \mathbf{B}/\partial t$, provide the following result for the field penetration into a material filling half-space, $x>0$: $B = H_0\ \eta(x) \exp(i\omega t)$, with $\eta(x) = \exp(-\lambda x)$ and $\lambda^2 = 2i/\delta^2$, where $\delta^2 = c^2/(2\pi\omega\sigma_r)$. For a thin plate of thickness 2D, with the ac field parallel to the large surface of the plate, the following equations hold:[1]

$$4\pi\chi' = -1 + \frac{1}{a}\frac{\sinh(a)+\sin(a)}{\cosh(a)+\cos(a)},$$
$$4\pi\chi'' = \frac{1}{a}\frac{\sin(a)-\sinh(a)}{\cosh(a)+\cos(a)}, \tag{1}$$

where $a = 2D/\delta$. A maximum in χ'' results when $\delta(\sigma_r, \omega)$ is comparable to the sample size. Experimental results rarely show susceptibility curves which correspond to the flux-flow result of ohmic-like behavior. Rather, the effects are most often nonlinear. The dependence of the measured susceptibility curves on the excitation current and higher-order components in the harmonic susceptibilities are observed. In the limiting case of very strongly nonlinear response, the critical-state model may be used for the calculation of the ac susceptibility. Then, only one parameter is needed to construct the hysteresis curve for the magnetization, the field of the first full penetration to the sample center, H^*. It is assumed that the harmonic susceptibility components, χ'_m and χ''_m, are defined as Fourier components of the time-dependent magnetic hysteresis curve, $M(t)/D = \Sigma_m \chi'_m \cos(m\ \omega t) + \chi''_m \sin(m\ \omega t)$, where m is an integer. When, for instance, $H_0 < H^*$, $4\pi\chi'_1 = -(1 - H_0/2H')$ is obtained, then $4\pi\chi'_m = 0$ for every odd $m>1$, and $4\pi\chi''_m = 2H_0/3\pi m H^*$ for all odd $m>0$. To deal with situations which are more relevant to the description of real experimental results, it is necessary to investigate a nonlinear theory of the magnetic response which would bridge the two limiting cases observed: the linear response and the critical-state one. A fruitful approach to this problem is based on studies of the electrodynamic response of a medium characterized by a power-law current-voltage dependence, $j = \sigma(E)E = \sigma_0 E_0 (E/E_0)^{1/(\kappa+1)}$, where $\kappa \geqslant 0$. Using Maxwell's equations, the nonlinear diffusion equation describing the penetration of fields into a slab of thickness 2D lying in the yz plane[1-4] can be derived as

$$\frac{\partial \beta}{\partial \bar{t}} = \frac{\partial}{\partial \bar{x}}\left(\frac{\partial \beta}{\partial \bar{x}}\left|\frac{\partial \beta}{\partial \bar{x}}\right|^{\kappa}\right), \quad \bar{t} = \frac{t}{\tau_0}, \quad \bar{x} = \frac{x}{x_0}, \tag{2}$$

where $\beta = B/E_0$, $x_0 = c/(4\pi\sigma_0)$, and $\tau_0 = 1/(4\pi\sigma_0)$. Recently, studies of solutions of Eq. (2) have been carried out by many authors. The exact analytical description of the response of a superconductor to an abrupt change of external field[1,2] has been compared with the results of nonlogarithmic magnetization relaxation measurements on high-T_c materials.[5] Various aspects of the ac response of superconductors has been studied as well by Dorogovtsev[6] and van der Beek *et al.*[7] A vector generalization of the critical state model has been proposed by Mayergoyz.[8,9] Recent results of Gilchrist and Dombre[10] can be compared with numerical results described in the present work. The distinctive feature of solutions of Eq. (2) is that the flux-profile penetration resembles that in the models of the critical state. When a field change is applied, the profile of perturbation spreads out from the surface towards the sample center but a region exists where the field distribution is unchanged inside. If the response to a field change of H_0 is considered, the time after the front of the field change arrives to the center t^* is given by

[a]Electronic mail: zkoziol@is.dal.ca; http://is.dal.ca/~zkoziol/zkoziol.html

 0021-8979/96/79(8)/4679/3/$10.00 © 1996 American Institute of Physics

$$\frac{t^*}{\tau_0}=\frac{\kappa}{2(\kappa+1)}\,\frac{1}{(\kappa+2)}\left[\frac{\Gamma(1/\kappa+1)\Gamma(3/2)}{\Gamma(1/\kappa+3/2)}\right]^{\kappa}\left[\frac{\beta_0}{H_0}\right]^{\kappa}\left(\frac{D}{x_0}\right)^{\kappa+2}. \tag{3}$$

The initial magnetization, at $t<t^*$, is given by

$$4\pi M=-H_0\left(1-\left(\frac{t}{t^*}\right)^{1/(\kappa+2)}\frac{\Gamma(1/\kappa+3/2)}{\Gamma(1/\kappa+2)\Gamma(1/2)}\right). \tag{4}$$

Equations (3) and (4) imply that a single parameter, $\xi\equiv t^{1/(\kappa+2)}H_0^{\kappa/(\kappa+2)}/D$, can parametrize the short-time magnetization relaxation. It is informative to determine the extent to which this scaling relation is valid with respect to the ac susceptibility (with the replacement of t and H_0 by the ac field period and the field amplitude, respectively).

II. NUMERICAL MODELING OF NONLINEAR DIFFUSION

Most of the calculations of the nonlinear diffusion process presented here have been performed on an array of dimension 50×200, containing magnetic induction values B at 50 time intervals and 200 space intervals.[11] The magnetic field at the surfaces of the sample, $H_0\sin(\omega t)$, determines the boundary conditions. An average magnetic field $\langle B(t)\rangle$ in the sample has been computed from the magnetic field distribution, every 50 time steps. Next, a Fourier time analysis of $\langle B(t)\rangle$ has been performed and the coefficients of the fundamental and higher-order terms of the harmonic content have been found. The method of computation and its results have been carefully tested. First, the magnetization relaxation process after an abrupt change of the external field has been simulated and numerical results were compared with the known exact analytical expressions derived by Kozioł and de Châtel.[2] Then, the validity of the modeling of the ac response in the limit of linear diffusion on the ac susceptibility, as given by Eq. (1), was checked. It was confirmed also that the ac susceptibility converges towards the critical-state results for large κ. The time range for which the response to the ac field becomes periodic (the initial response at short time does not satisfies this condition) was also investigated. In most cases it is safe to analyze the data taken after the initial 50 000 steps in time evolution (this time depends on κ and H_0). An additional, more reliable, criterion of stable periodicity is based on the criterion that the dc or second harmonic components are not found. At large values of H_0, the calculations become unstable abruptly. It is possible to overcome this difficulty but at significant expense in computation time (the computation of one susceptibility point requires an average of about 3 h on an IBM-PC computer 486DX2-33 MHz). Therefore, we have concentrated on performing calculations for a larger number of points at lower fields.

III. RESULTS AND DISCUSSION

The penetration of an alternating field resembles, in some ways, the response to an abrupt change of external field; the amplitude of field changes diminishes gradually in the material and, if the field amplitude at the surface is not too large, there is no penetration to a volume separated by a certain distance from the sample surface. Whether the front of the flux profile in ac penetration propagates towards the center or not, is not an easy question to answer, since the initial very slow propagation which is observed might only be due to unstable initial conditions. Within the accuracy of calculations, the flux profile has a self-replicating shape of diminishing amplitude, with perfect periodicity in time at every point in space but with a phase shift which changes with the distance from the surface. This observation is consistent with the exact results found by Mayergoyz[8] for penetration of circularly polarized electromagnetic fields. The profiles obtained for one value of an ac field amplitude coincide with the profiles computed for another ac field amplitude, if the phase lag and spatial coordinates are shifted properly.

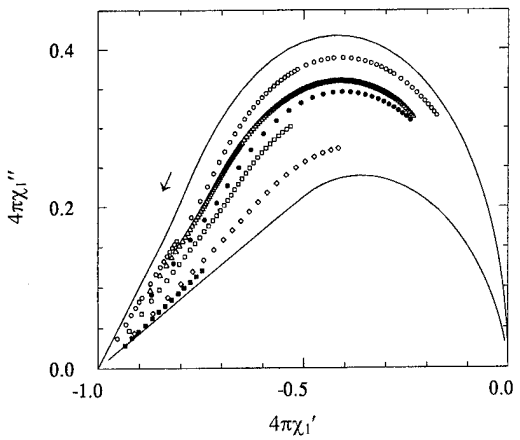


FIG. 1. The χ'' vs χ' plots of the ac susceptibility for different values of the nonlinearity parameter κ and different periods of the ac field t, (κ, t): (0.667, 25 000, ○), (0.667, 5000, △), (2, 12 500, ●), (2, 5000, □), (3, 10 000, ◇), (12, 6250, ■). Solid lines represent the critical-state and the linear-response limits for a thin plate. The difference between the data for $\kappa=2$ obtained for two different frequencies of the ac field should be noted. The direction of decreasing penetration depth is shown by the arrow.

Plots of χ'' vs χ' shown in Figs. 1 and 2 for different values of the nonlinearity parameter κ converge to the limit of linear diffusion for $\kappa\to0$ and to the limit given by the critical-state model for large $\kappa\gg1$. An important feature of the present results is seen in Fig. 1; susceptibility points computed for different frequencies of the ac field but the same value of κ, do not fall on the same curve. This is different from what it might be expected and seems to have been unnoticed in previous work.[10] In Fig. 3, we show that a simple scaling of the susceptibility with the amplitude of the ac field holds for the data obtained in the range of incomplete flux penetration, $\chi\sim H_0^{\kappa/(\kappa+2)}$. In Fig. 4, the real component of the first-harmonic susceptibility is drawn as a function of $H_0^{\kappa/(\kappa+2)}\,t^{1/(\kappa+2)}/D$, for different values of the field amplitude H_0, period of the field and for a few sample sizes. This latter scaling method is not perfect; small differences in the slopes of the data computed for various frequencies is found. This effect may be explained by the fact that flux profiles have a shape which depends on the time of field penetration.

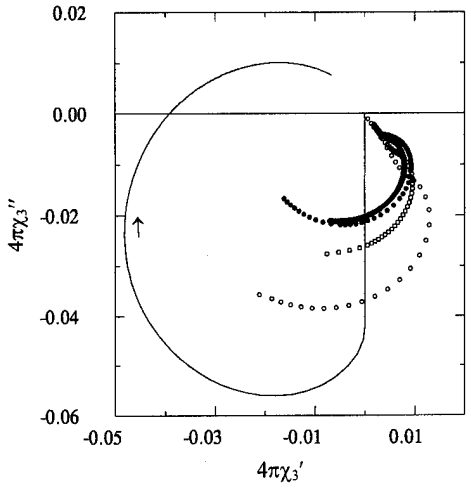


FIG. 2. The third-harmonic susceptibility χ_3'' vs χ_3' compared to the critical-state result represented by the solid line, for the following nonlinearity parameter κ and periods of the ac field t, (κ, t): (0.667, 25 000, ●), (0.667, 5000, ♦), (1, 5000, □), and (2, 12 500, ○). The direction of increasing amplitude of H_0 is shown by the arrow.

One should expect that the parameter $\xi = t^{1/(\kappa+2)} H_0^{\kappa/(\kappa+2)}/D$ will become an exact scaling variable only for the cases when all the parameters, t, H_0, and D, are simultaneously scaled by a constant λ in the following way: $D \rightarrow \lambda D$, $H_0 \rightarrow (\lambda H_0)^{\kappa/(\kappa+2)}$, and $t \rightarrow (\lambda t)^{1/(\kappa+2)}$.

IV. CONCLUSIONS

When the ac magnetic field does not penetrate to the sample center, the magnetic susceptibility is well described by a simple scaling relation: $\chi \sim \xi$, with

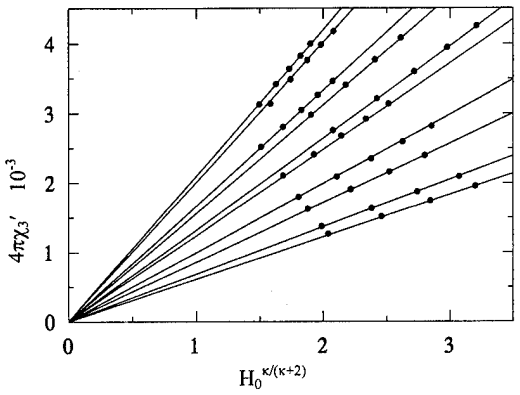


FIG. 3. The real component of the third-harmonic susceptibility as a function of the amplitude of the ac field, computed for an ac field of period equal to 25 000. The slope of solid lines decreases for increasing values of κ, which are the following: 0.667, 0.8, 1.2, 1.333, 1.667, 1.8, 2.333, 2.7, 3.35, 3.7. Similar scaling property is observed for the imaginary component of the third-harmonic susceptibility and for higher-order components as well.

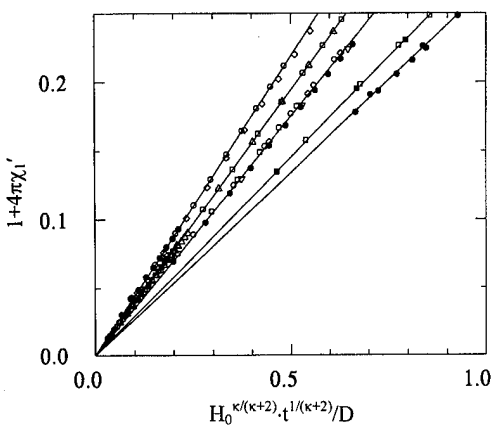


FIG. 4. Scaling of the flux penetration ($4\pi\chi_1' + 1$) by a function $H_0^{\kappa/(\kappa+2)}\, t^{1/(\kappa+2)}/D$, where H_0 gives the field amplitude, t gives the period, and D gives the sample thickness. Each of the solid lines passes through the data corresponding to the following values of the nonlinearity parameter κ: 0.667, 1, 2, 3, and 5, for lines with the smallest to largest slope. D is equal to 20 or 100 (there is no distinction between the symbols of the data corresponding to different values of D), while t is 2500 (○), 5000 (□), 6250 (◇), 10 000 (△), 12 500 (▽), 25 000 (●), and 100 000 (■).

$\xi = t^{1/(\kappa+2)}\, H^{\kappa/(\kappa+2)}/D$. For κ values close to 0, the overall dependence of $\chi''(\chi')$ closely resembles the dependence observed in the linear case. The conductivity, however, computed from $\chi''(\chi')$ data by using the assumption that the linear theory holds, will lead to false information and yield strongly overestimated values. An experimental criterion for detecting nonlinearity would be the observation of the amplitude dependence or the existence of higher order harmonics in the ac response. The susceptibility values of a nonlinear medium are not uniquely defined by a set of two parameters only, such as κ and ξ. For experimental purposes, however, treating ξ as a scaling variable offers a sufficiently accurate method of testing for nonlinear properties of materials.

ACKNOWLEDGMENTS

This work has been made possible due to the Killam Memorial Postdoctoral Fellowship awarded to Z. K. by Dalhousie University and a grant from the Natural Sciences and Engineering Research Council of Canada.

[1] Z. Kozioł, Ph.D. thesis, University of Amsterdam, 1994.
[2] Z. Kozioł and P. F. de Châtel, IEEE Trans. Magn. **30**, 1169 (1994).
[3] M. V. Vinokur *et al.*, Phys. Rev. Lett. **67**, 915 (1991).
[4] C. J. van der Beek *et al.*, Physica C **197**, 320 (1992).
[5] Z. Kozioł *et al.*, Physica C **212**, 133 (1993).
[6] S. N. Dorogovtsev, JETP Lett. **61**, 491 (1995).
[7] C. J. van der Beek *et al.*, Phys. Rev. B **51**, 15492 (1995).
[8] I. D. Mayergoyz, J. Appl. Phys. **75**, 6963 (1994).
[9] I. D. Mayergoyz, J. Appl. Phys. **76**, 6956 (1994).
[10] J. Gilchrist and T. Dombre, Phys. Rev. B **49**, 1466 (1994).
[11] The source code is available from the authors.

New method of evaluating the explicit magnetic-state-dependent energy of iron in semiempirical calculations

Genrich L. Krasko
Army Research Laboratory, Materials Directorate, AMSRL-MA-CC, Aberdeen Proving Ground, Maryland 21005-5069

The existing semiempirical methods for use in atomic computer simulations in iron (such as various modifications of the embedded atom method) have not explicitly taken account of the ferromagnetism *per se*. Rather, the adjustable parameters have simply been fitted to mechanical and thermal properties of bcc iron as a ferromagnetic phase. However, when the magnetic properties are essential in affecting localized atomic behavior (e.g., in the vicinity of crystal defects), these methods may be inadequate. To remedy the situation, a procedure is suggested for explicitly calculating the magnetic contribution to the energy of individual atoms, as a function of their atomic environment. The method uses the Stoner approach, as previously developed, and a data base obtained by the *ab initio* calculations on bcc Fe under hydrostatic and tetragonal deformations, and the (111) Fe free surface. The procedure may be incorporated in any semiempirical method: the ferromagnetic contributions to the bulk moduli, C_{11}, C_{12}, and C_{44} are easily calculated and may be used subsequently in adjusting the semiempirical method parameters. Preliminary testing shows a good agreement with the magnetic properties obtained by our *ab initio* calculations. [S0021-8979(96)04408-7]

I. INTRODUCTION

During the recent decade, iron has been the object of extensive study by various theoretical methods. Previous empirical and semiempirical approaches used in atomic computer simulations in iron have not explicitly allowed for magnetism *per se*. Rather, the ferromagnetic effects were taken into account indirectly, by fitting the model parameters to experimental data on bcc iron as a ferromagnetic phase. Obviously, such an approach will be inadequate for cases where the magnetic properties significantly change in the vicinity of crystal lattice defects. Numerous *ab initio* calculations do demonstrate significant changes in local magnetic moments both at point and two-dimensional defects (including grain boundaries and free surfaces). A possible way out is to attempt calculations of the magnetic contributions to the total energy separately, subsequently adding these contributions to the regular empirical potentials allowing for nonmagnetic contributions.

In this paper we suggest the procedure of explicitly calculating the ferromagnetic contribution to the energy of individual atoms (as well as the individual atoms' magnetic moments), as a function of their atomic environment. This procedure is based on the Stoner theory of itinerant ferromagnetism,[1] and uses the results of earlier *ab initio* calculations on iron.[2–5]

The plan of this paper is as follows. In Sec. II we briefly outline the Stoner model of itinerant ferromagnetism. In Sec. III we discuss the parametrization of the ingredient quantities to be used in semiempirical calculations. Section IV summarizes the procedure and discusses potential applications of the new method in empirical and semiempirical approaches.

II. THE STONER MODEL OF ITINERANT FERROMAGNETISM

The Stoner theory, first suggested in 1939,[1] has been successfully used in recent years in estimating both the equilibrium magnetization and magnetic energy of band electrons. This was made possible as a result of a rigorous formulation of the Stoner model as a perturbation approach in terms of microscopic electronic theory.[6–10] Particularly, the fundamental parameter of the theory, the Stoner exchange parameter **I** was understood in terms of density-functional characteristics.[8,9] In iron, the theory explained the metamagnetic behavior of the fcc phase.[1,6]

The Stoner approach in combination with self-consistent non-spin-polarized calculations enables one to perform the detailed analysis of ferromagnetic (FM) behavior, as well as identify all the possible magnetic stationary phases (both stable, metastable, and even unstable), and find the areas of their emergence. This analysis, using traditional spin-polarized calculations, is at present either too cumbersome or even practically impossible.

The Stoner model postulates that the change in energy upon forming a FM state with moment **m** consists of two parts. For a given **m**, the magnetic contribution to the total energy is[3]

$$E_m = 1/2 \int_0^{\mathbf{m}} \mathbf{m}'/N(\mathbf{m}')d\mathbf{m}' - 1/4\ \mathbf{I}\ \mathbf{m}^2. \tag{1}$$

The first term is the increase in the electron kinetic energy as a result of forming two subbands for spin up and down by flipping **m**/2 spin down electrons from just below the *NM* Fermi level into the unoccupied spin-up states just above the Fermi level. The second term is the exchange energy contribution, $-1/4\ \mathbf{I}\ \mathbf{m}^2$, where the exchange parameter **I** is a constant.

The procedure of "constructing" $N(\mathbf{m})$ is described in Ref. 10. The Stoner parameter **I** can be found from the perturbation theory analysis,[9] in terms of the *NM* system as a part of an *ab initio* calculation.

As follows from theory,[1,8,10] the criterion for appearing a stable (or a metastable) ferromagnetic state is

$$\mathbf{I}N(\mathbf{m})=1. \tag{2}$$

An important property of the function $N(\mathbf{m})$ is that, being multiplied by the d-electron band width W, it becomes virtually independent of volume, or the Wigner–Seitz (WS) radius s. Then Eq. (2) reads

$$\mathbf{N}(\mathbf{m})=W(s)/\mathbf{I}(s), \tag{3}$$

where $\mathbf{N}(\mathbf{m})=WN(\mathbf{m})$. The right-hand side of this equation does depend on s, and this dependence is important.

The Stoner parameter $\mathbf{I}$ has a very weak dependence on the volume and the crystal structure of the metal. On the other hand, both the magnetic energy, Eq. (1), the equilibrium magnetic moment $\mathbf{m}$ [as found from Eqs. (2) or (3)], and the equilibrium atomic volume, are rather sensitive to the values of $\mathbf{I}$. In papers[2–4] the value of $\mathbf{I}$, has been adjusted (by factor 1.075) so that the equilibrium WS radius s_0, for the FM bcc phase be equal to the experimental value.

In those papers *ab initio* (LMTO) calculations were performed for the body centered tetragonal (BCT) Fe for 12 c/a values: $1.0\leqslant c/a\leqslant\sqrt{2}$. For each c/a, self-consistent non-spin-polarized calculations were performed for nine values of the WS radius s (2.521 a.u. $\leqslant s\leqslant$2.788 a.u.). In each calculation, after convergence had been achieved, the "*ab initio*" Stoner parameters,[9] $\mathbf{I}_0(c/a,s)$, and then $\mathbf{I}=1.075\mathbf{I}_0$ were found, and the function $N(\mathbf{m})$ was generated. Then the Stoner equation, Eq. (3), was solved for the equilibrium magnetic moment $\mathbf{m}$ and the magnetic energy E_m, Eq. (1), calculated. The data base generated in this series of calculations will be used in our new method.

The above data, however, reflect only the hydrostatic and tetragonal deformation. An important ingredient of the new method, which is to be used in modeling grain boundaries and free surfaces, should be the information on free surfaces. The necessary data were provided by Dr. Ruqian Wu of CSU, at Northridge, CA.[5] In the next section we will describe in detail the parametrization of the data and discuss the algorithm of the method.

III. PARAMETRIZATION OF THE FIRST-PRINCIPLES DATA

Any semiempirical method has to be able to somehow describe the environment of the atom of interest. It is known from a vast experience of tight-binding calculations (see, e.g., Ref. 11), that the number of neighbors is an important parameter which plays a crucial role in band-structure calculations. We have chosen, therefore, to introduce the so-called "effective number of neighbors," Z_{eff}, to allow for the atomic environment. Since all the quantities are to be parametrized in terms of Z_{eff}, its definition is not very critical. It is important, however, that Z_{eff} should reflect the real atomic environment. We define

$$Z_{\text{eff}}=\sum (R_{\min}/R)^5 \exp[1-(R/R_{\min})^2], \tag{4}$$

where the summation is over atom coordinates R ($R_{\min}$ is the distance from a given atom to its nearest neighbor). No cutoff radius is introduced, but, in fact, the exponential in Eq. (4) provides a rather fast sum convergence. Figure 1 shows

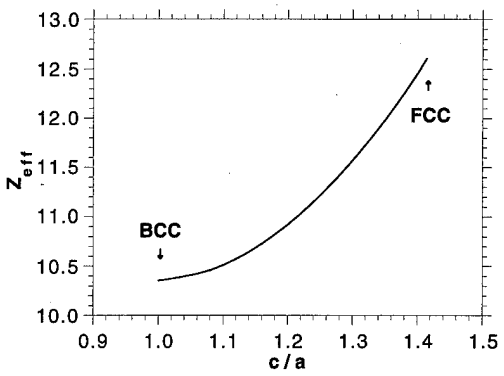


FIG. 1. $Z_{\text{eff}}(c/a)$ for BCT lattices.

the dependence of Z_{eff} on c/a in BCT lattices. One can see that Z_{eff} for bcc and fcc equal respectively to 10.37 and 12.63, while the corresponding nearest neighbor numbers are 8 and 12. The 10.37 number actually reflects the fact that the six second nearest neighbors in the bcc lattice are also situated rather close to the first nearest neighbors ($R_{2\text{nd}}/R_{1\text{st}}=1.155$); in the fcc lattice they are farther away ($R_{2\text{nd}}/R_{1\text{st}}=1.414$). Therefore the six second nearest neighbors in the fcc lattice are less important giving a smaller contribution to Z_{eff}.

Apart from the "environment" or "structure" parameter Z_{eff}, an important parameter is the volume per atom. In a perfect lattice the atomic volume, or, equivalently, the WS sphere of radius s, can be easily found. In a deformed crystal, or a crystal with defects, the atomic volume is difficult to define, and, in fact it is a "bad" parameter.

As was mentioned above, the left-hand side of Eq. (3), $\mathbf{N}(\mathbf{m})$, is virtually independent of volume. However, the right-hand side does depend on the local volume, where this dependence is mostly due to the d-electron band width, W.

It is known (see, e.g., Ref. 11), that in perfect crystals $W\sim 1/s^5$. Therefore, it is convenient to parametrize W in the form:

$$W=A(Z_{\text{eff}})\left(\sum 1/R^{10}\right)^{1/2}. \tag{5}$$

As a result, W has the right volume dependence.

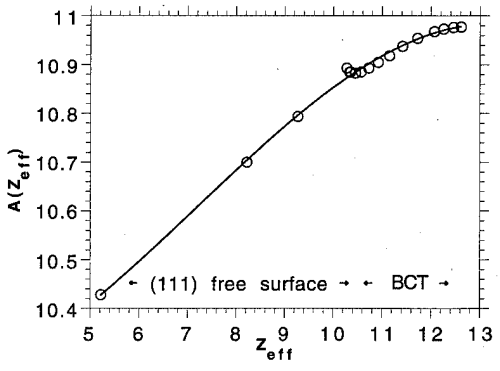


FIG. 2. Factor $A(Z_{\text{eff}})$.

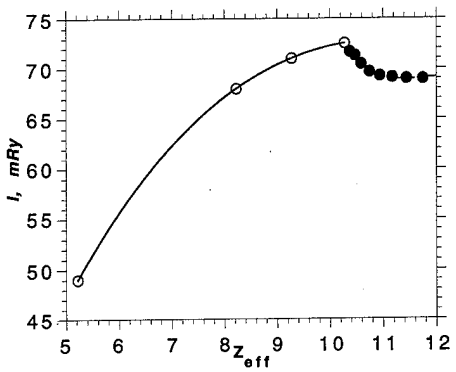


FIG. 3. The Stoner parameter, $\mathbf{I}(Z_{\text{eff}})$ (approximated by two polynomials).

The values of W are easily found as a byproduct of *ab initio* calculations: our data base comprises the values of W for a number of BCT lattices, as well as the bcc (111) free surface.[5] Figure 2 shows the results of fitting the function, Eq. (5) to the *ab initio* d-band widths W. The function $A(Z_{\text{eff}})$ is approximated by a polynomial in the interval $5.2 \leqslant Z_{\text{eff}} \leqslant 12.61$ [note the Z_{eff} values between 5.2 and 10.354 correspond to atoms in the vicinity of the (111) free surface].

We assume that the Stoner parameter $\mathbf{I}$ is only weakly volume dependent. However, it does depend on atomic environment, i.e., on Z_{eff}. We approximated the values of $\mathbf{I}$ (as found from the *ab initio* calculations, and augmented by factor 1.075) by two polynomials in Z_{eff} (Fig. 3).

Thus, if $N(\mathbf{m})$ is known, then, for a given Z_{eff} and W, Eq. (3) can be solved for the magnetic moment, $\mathbf{m}=\mathbf{m}(W/\mathbf{I})$. The next step is calculating E_{kin}, the kinetic energy contribution [the integral in Eq. (1); Fig. 4 shows E_{kin} vs $\mathbf{m}$ for three lattices], and then the total ferromagnetic energy, E_m.

Both the $N(\mathbf{m})$, $\mathbf{m}(x)$, $x=W/\mathbf{I}$, and $E_{\text{kin}}(\mathbf{m})$, calculated separately, can be directly introduced into the computer code as DATA statements. The three data sets are two-dimensional arrays, x and Z_{eff} being the variables.

It is known, that ferromagnetism is unstable beyond a definite range of atomic volume/structure values. This translates into a definite restriction for the values of $x=W/\mathbf{I}$.

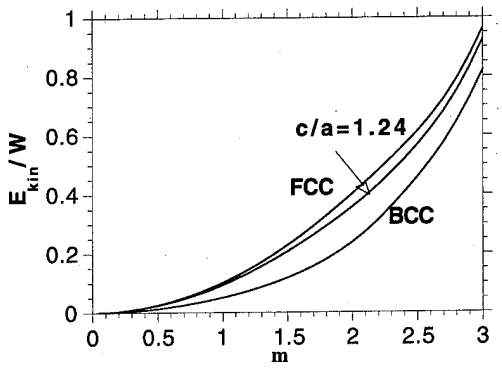


FIG. 4. The E_{kin}/W vs $\mathbf{m}$ for bcc, BCT with $c/a=1.24$, and fcc.

These are also found from *an initio* calculations and approximated by a polynomial in x.

IV. CONCLUSION

Following the above procedure, the computer code has been developed in the form of subroutine

STONER (**ni, ri, amag, emag**).

The calculation procedure is as follows. The subroutine STONER is called from a main program which generates ni and ri, the total number of neighboring atoms and their distances from the atom of interest (**ni** should include as many atoms as it may be necessary for the Z_{eff} to converge). The subroutine returns **amag** and **emag**, the magnetic moment on the atom of interest and its ferromagnetic energy. Wherever Eq. (3) does not have a ferromagnetic solution (the ferromagnetic solution is unstable), or E_m is positive (the ferromagnetic solution is metastable), the subroutine returns the values $\mathbf{m}=0$, and $E_m=0$.

The test runs of the subroutine for BCT lattices for $s=2.661$ (equilibrium volume for bcc Fe) from $c/a=1.0$ (bcc) through $c/a=1.32$ (at higher c/a's at this volume the ferromagnetic state is unstable) showed an excellent agreement between the values of $\mathbf{m}$ and E_m calculated by the new method and the results of our LMTO calculations.

The new procedure can be easily adopted by any semiempirical method. The most popular method, the embedded atom method, in its various modifications, fits some of the calculated quantities to their experimental values. In all EAM versions, among those quantities are the bulk modulus and the three elastic moduli: C_{11}, C_{12}, and C_{44}.

In order to implement the new procedure, a series of calculations for hydrostatic, tetragonal, and trigonal deformations of bcc Fe have to be performed, and the ferromagnetic contributions to the corresponding elastic moduli found. Then, this information is to be used in fitting the adjustable parameters in the corresponding EAM, provided that the magnetic contributions are calculated by the new method.

ACKNOWLEDGMENTS

The author is grateful to Dr. Ruqian Wu for providing his unpublished results of the electronic densities of states for the (111) free surface in Fe. Valuable discussions with Dr. R. J. Harrison are also acknowledged. The LMTO code used in our *ab initio* calculations was developed by Professor N. Christensen.

[1] E. C. Stoner, Proc. R. Soc. London, Ser. A **169**, 339 (1939).
[2] G. L. Krasko, Phys. Rev. B **36**, 8565 (1987).
[3] G. L. Krasko, Solid State Commun. **70**, 1099 (1989).
[4] G. L. Krasko and G. B. Olson, Phys. Rev. B **40**, 11536 (1989); J. Appl. Phys. **67**, 4570 (1990).
[5] R. Wu (unpublished).
[6] O. K. Andersen, J. Madsen, U. K. Paulsen, O. Jepsen, and J. Kollar, Physica B **86–88**, 249 (1977).
[7] S. H. Vosko and P. Perdew, Can. J. Phys. **53**, 1385 (1975).
[8] O. Gunnarsson, J. Phys. F **6**, 587 (1976).
[9] J. F. Janak, Phys. Rev. B **16**, 255 (1977).
[10] O. K. Andersen, O. Jepsen, and D. Gloetzel, in *Highlights of Condensed Matter Theory*, edited by F. Bassani, F. Fumi, and M. P. Tosi (North-Holland, New York, 1985), p. 59.
[11] D. G. Pettifor, in *Physical Metallurgy*, edited by R. W. Cahn and P. Hansen (North-Holland, New York, 1983), Part I, p. 73.

Three-dimensional modeling techniques applied to regions with small susceptibility variations (abstract)

R. J. Hill-Cottingham and J. F. Eastham
University of Bath, Claverton Down, Bath BA2 7AY, United Kingdom

I. R. Young and J. V. Hajnal
GEC/Hirst Research Centre, Elstree Way, Borehamwood, Herts WD7 1RX, United Kingdom

The article considers the modeling of regions where the susceptibility is 0.01–10 ppm different from the majority of the space of interest. These calculations are of use in MR imaging, for example, in one possible application, the susceptibility of an haemorrhagic deposit could be adduced. Two methods are considered. Firstly, the use of finite element modeling using double precision arithmetic in conjunction with carefully set convergence limits. Secondly, a method which considers the induced polarity in the region of enhanced susceptibility, and calculates the difference field. The work is validated initially by calculating analytically the field perturbation produced by a sphere of susceptibility of 1×10^{-8} and comparing the results with the two methods given above. It is shown that excellent agreement is obtained. As a further confirmation the field produced by a short cylindrical object was measured experimentally using a MR scanner and again the applicability of both modeling techniques was confirmed. © *1996 American Institute of Physics.*
[S0021-8979(96)80308-2]

An efficient three-dimensional demagnetizing field calculation scheme (abstract)

A. S. Kazmi and R. C. Giles
Department of Electrical, Computer, and Systems Engineering, Boston University, Boston, Massachusetts 022155

We present an efficient three-dimensional demagnetizing field calculation scheme for micromagnetic simulations of the domain walls in garnet-like materials. We take advantage of the fact that the domain wall is nearly planar and distribute computational power nonuniformly between the bulk of the material and the wall regions. We use fast Fourier convolutions along one dimension (approximately parallel to the domain wall) and a two-dimensional variant of Greengard's adaptive fast multipole method in the other dimensions.[1] Even a 2D nonadaptive multipole method has the time complexity of the order of N, for N points in contrast to full Fourier convolution ($N\log N$) or direct methods (N^2). The adaptive method is based on maintaining a point-to-point error bound which allows us to work at high resolution in the region of the domain wall and coarser resolution in the bulk material. In this case, the calculation scales proportional to the domain wall size rather than the sample volume. The error bound calculation is important for our method and it depends on the Gegenbauer's addition theorem for the modified Bessel functions.[2] Due to the complex nature of this addition theorem, we have relied on numerical methods, comparing our method to the direct calculations for small size samples. We have implemented this scheme on an SGI workstation and we are reporting the outcome of the 2D adaptive fast multipole method implementation. We have studied the relationship between error bounds, domain wall size, and actual time. We have also compared our results with that of M. Redjdal's method.[3] © *1996 American Institute of Physics.*
[S0021-8979(96)81908-2]

[1] L. F. Greengard, *ACM Distinguished Dissertations* (The MIT, Cambridge, MA, 1987).
[2] *Higher Transcendental Functions*, edited by A. Erdelyi (McGraw–Hill, New York, 1953), Vol. 2.
[3] M. Redjdal (private communication).

Computational calculations of magnetic relaxation and viscosity in small magnetic grains

J. M. Hernàndez, X. X. Zhang, and J. Tejada
Fac. Física, Universitat de Barcelona, Diagonal 647, Barcelona 08028, Spain

In this article we present a phenomenological model which simulates very well the magnetic relaxation behavior experimentally observed in small magnetic grains and single domain particles. In this model, the occurrence of quantum tunneling of magnetization below a certain temperature is taken into account. Experimental results for different materials are presented to illustrate the most important behavior deduced from our model. © *1996 American Institute of Physics.* [S0021-8979(96)79308-5]

The problem of magnetic relaxation is present in many situations of science and technology. In the last years, big efforts have been made with the aim to explain better; (a) the law governing the magnetic relaxation and the effects of energy barrier distributions,[1–4] (b) the temperature dependence of magnetic viscosity,[5–7] (c) the relation switching field distribution and magnetic noise in recording media.[8]

The simplest magnetic system for studying the dynamics of magnetization reversal is a single domain particle with uniaxial anisotropy. In the presence of an applied field opposite to the magnetization of the particle, the frequency of the magnetization reversal, at temperature T, is given by Ref. 9 $\Gamma=\omega\exp(-U/k_BT)$, where ω is the attempt frequency at an order of 1 GHz, and k_BT is the thermal energy. U is the energy barrier height to the magnetization reversal which is in the form of $U=KV[1-H/H_K]^{1/2}$ where K is the magnetic anisotropy constant, V is the volume of the magnetic switching unit (assumed to be the entire single domain particle) and H is the applied magnetic field. The anisotropy field, H_K, is defined in terms of K and the particle saturation magnetization M_s: $H_K=2K/M_s$.

We also incorporate to our model the effect of quantum tunneling under-barrier transitions of the magnetization below a certain crossover temperature, T_{CR},[10] which separates the classical and quantum regimes. Therefore the expression for the attempt frequency can be written as $\Gamma=\omega\exp[-U/k_BT_{ESC}(T)]$ where the escape temperature, $T_{ESC}(T)$, presents in magnetic systems, a temperature dependence characteristic of weak damping processes. Here we assume that $T_{ESC}(T)=T_{CR}\coth(T_{CR}/T)$, because this matches, qualitatively well, the behavior observed in both, magnetic systems and Josephson junctions.[11,12] In zero field, quantum transitions dominate below $T_{CR}(0)$. When an external magnetic field is applied, there is a reduction in the value of T_{CR} which depends on the magnetic field strength, H, and the anisotropy field, H_K (Refs. 10 and 13)

$$T_{CR}(H)=T_{CR}(0)\varepsilon^{1/2},\quad \text{where } \varepsilon=1-H/H_K. \tag{1}$$

As one applies a magnetic field H_1 on such a system consisting of N identical particles, the magnetic moment of the system, at its equilibrium state at temperature T, is $\mu_{eq}(H_1)=NM_sVg(H_1)$ with $g(H)=\tanh(M_sVH/k_BT)$. If the magnetic field is changed to a new value, H_2, the evolution of the magnetization moment to a new equilibrium state is governed by

$$\mu(t)=NVM_s\{g(H_2)+[g(H_1)-g(H_2)]\exp(-t\Gamma)\}. \tag{2}$$

If a size distribution of the particles $f(V)$ is taken into account in the model, as it does exist in a real physical material, then the magnetization (density of magnetic moment) relaxes as

$$M(t)=\frac{\int_0^\infty f(V)VM_s\{g(H_2)+[g(H_1)-g(H_2)]\exp(-t\Gamma(V))\}dV}{\int_0^\infty Vf(V)dV}. \tag{3}$$

In our computation process, it has been assumed that the distribution of volume, $f(V)$, have the form of the so-called log-normal distribution[14] given by $f(V)=(A/V)\exp[-\alpha\log^2(V/V_m)]$ where V_m is the average volume of the particles and α is related with the inverse of the distribution width.

Equation (3) is the basis of our calculations. This integral has been performed using numerical integration in the interval of volumes in which the distribution of sizes takes significant values.

Figure 1(a) shows the variation with time of the remnant magnetization in zero magnetic field at different temperatures, when previously the system has been saturated by an applied field H_1, much larger than the anisotropy field, H_K, and assuming $T_{CR}=0$. This M vs t data have been fitted using a time-logarithmic law

$$M(t)=[M(t=0)-M(t\to\infty)][B-S(T)\log(t)], \tag{4}$$

where $S(T)$ is the so-called magnetic viscosity, $M(t=0)$ is the initial magnetization and $M(t\to\infty)$ is the equilibrium

 0021-8979/96/79(8)/4686/3/$10.00 © 1996 American Institute of Physics

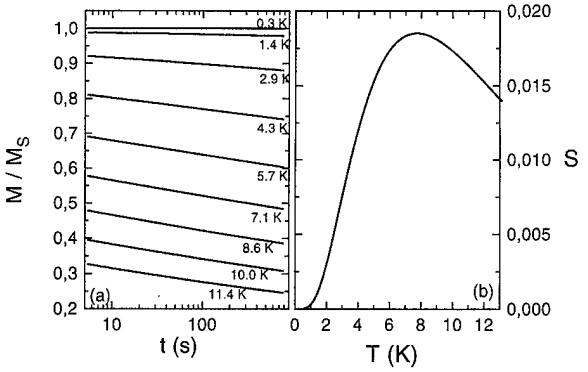


FIG. 1. (a) Relaxation of the magnetization for different temperatures from 0.3 to 11.4 K as a function of time in a logarithmic scale. (b) Temperature dependence of the magnetic viscosity deduced from (a).

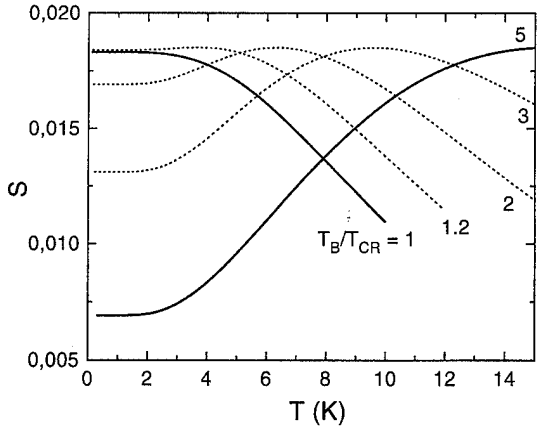


FIG. 2. Effect of the quantum tunneling in the dependence of the viscosity with the temperature for different values of the ratio between the blocking temperature and the crossover temperature.

magnetization at the second field, that is $M(t\rightarrow\infty)$ is equal to zero at zero applied field H_2. From Eq. (4), it is noted that the factor $[M(t=0) - M(t\rightarrow\infty)]$ have all the dependence of the relaxation process on the initial and the final equilibrium states. Therefore, the dependence of $S(T)$ on the temperature is perfectly characterizing the relaxation behavior of the particles.

Figure 1(b) shows the dependence of the magnetic viscosity obtained from Fig. 1(a) on temperature. A near perfect linear dependence of S on T is observed at temperatures much lower than the blocking temperature, which corresponds to the case that the relaxing fraction of the total magnetization is very small. The maximum of the viscosity appears at temperature near the theoretical expectation for the blocking temperature, $T_B = KV_m/[k_B \ln(t_{mes}\omega)]$, (7.14 K in this case) at which the inverse of the jumping frequency, Γ, for the mean volume particles equals the measuring characteristic time, t_{mes}. At temperatures higher that the blocking, the magnetic viscosity decreases because most of the barriers are overcome in a very short time and do not contribute to the slow relaxation processes.

Quantum tunneling processes are considered by introducing a nonzero value for the crossover temperature T_{CR}, below which the switching processes are independent of temperature. First we have computed the case when the transition temperature T_{CR} remains constant and the average volume of the grains (and therefore the average barrier height) is different. This situation corresponds to systems having different values for the ratio between the blocking temperature and the crossover temperature, T_B/T_{CR}. Both, crossover and blocking temperature scale with the anisotropy constant of the material, but while the crossover temperature does not depend on extensive parameters, blocking is proportional to the volume of the magnetic unit. Therefore the modification of the volume of the particles or grains under the assumption of constancy of the crossover temperature, induces only variations in the blocking temperature. It is, large particles may have large values for the ratio T_B/T_{CR}. In Fig. 2 we show different $S(T)$ curves for the situation when the ratio T_B/T_{CR} ranges from 5 to 1, with T_{CR} equals 3.3 K. The most remarkable fact is that the maximum of the viscosity disappears when T_B/T_{CR} is 1. This situation corresponds to the case when the system enters directly from the classical superparamagnetic regime onto a quantum superparamagnetic regime without any intermediate blocked state. This should be the ideal case to observe the resonance due to quantum coherence.[15]

In Fig. 3 we present the low temperature $S(T)$ values for the case when the applied field, H_2, modifies the crossover temperature between the classical and quantum regime, see Eq. (1). This corresponds to the case of a unique set of single domain particles or grains relaxing under the action of different values for the applied field. As the field values increase, the plateau in the viscosity appears at lower temperatures and the quantum viscosity values increase as a consequence of the reduction on the barrier heights.

The situation of Fig. 1 is compared with relaxation experiments performed on a CuCo granular material. Transmission electron patterns in similar systems suggest that this granular material has a log-normal size distribution in agreement with our assumption that the particles in the calculation have a log-normal size distribution. The zero field cooled (ZFC) magnetization vs temperature gives a blocking temperature $T_B = 8$ K.[16] The relaxation measurements were per-

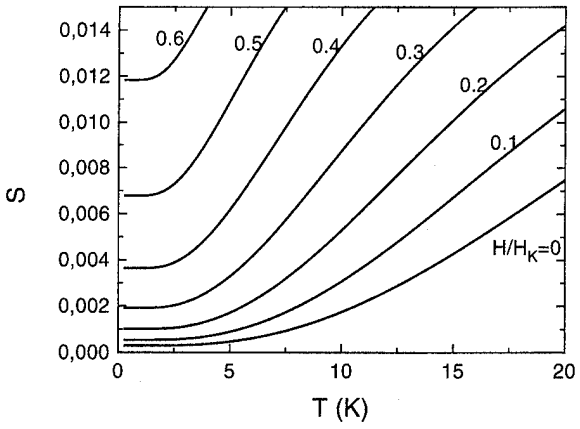


FIG. 3. Temperature dependence of the magnetic viscosity for different applied fields. The numbers near each curve indicate the ratio between the applied field and the anisotropy field.

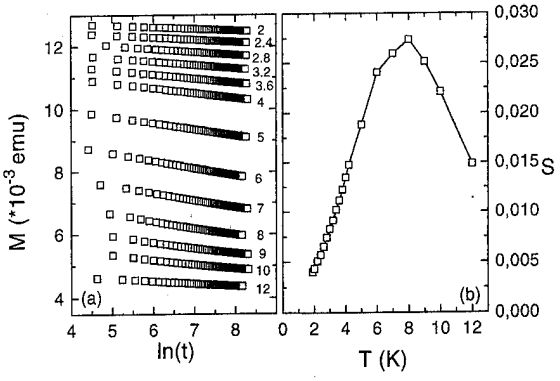


FIG. 4. (a) Magnetic relaxation in a particulate CuCo sample at different temperatures. (b) Dependence of the magnetic viscosity on temperature from (a).

formed from a field $H_1 = 100$ Oe, after which the field was removed, and then the variation of magnetization with time was measured during few hours. Figure 4(a) shows the relaxation of the remnant magnetization measured at different temperatures; a nearly perfect logarithmic time relaxation behavior is observed. The temperature dependence of magnetic viscosity is presented in Fig. 4(b), and has the same behavior as that shown in Fig. 1(b).

In case of the occurrence of quantum tunneling in the relaxation process, we can compare the experimental results obtained on CuDy granular material[17] which has different sizes with the calculated ones presented in Fig. 2. The temperature dependence of magnetic viscosity for samples with composition of Cu(100 Å)Dy(20 Å) and Cu(100 Å)Dy(40 Å) is shown in Fig. 5. The two samples have very similar anisotropy fields H_K and consequently the same value for the crossover temperature T_{CR}. We have also found, from ZFC and FC measurements, that these two systems have blocking temperatures of 2.4 K and 10 K, respectively, which corresponds to the different average size of the grains in the two samples. The theoretical predictions indicate that the transition temperature for these two systems is $T_{CR} = 3$ K. Therefore we are in a situation in which we have two different values for the ratio T_B/T_{CR}, 0.9 and 3, respectively. For the sample with $T_B = 2.4$ K (Cu(100 Å)Dy(20 Å)), we have observed, in agreement with the calculations, that there exists a direct transition from the thermal superparamagnetic behavior to the quantum regime.

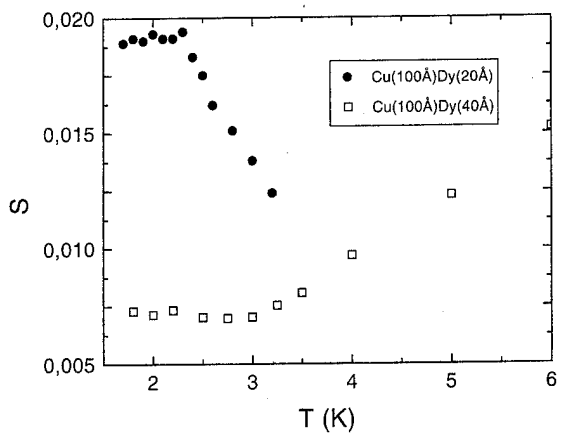


FIG. 5. Magnetic viscosity in two granular structured CuDy thin films: Cu(100 Å)(Dy(20 Å) (circles) and Cu(100 Å)Dy (40 Å) (squares).

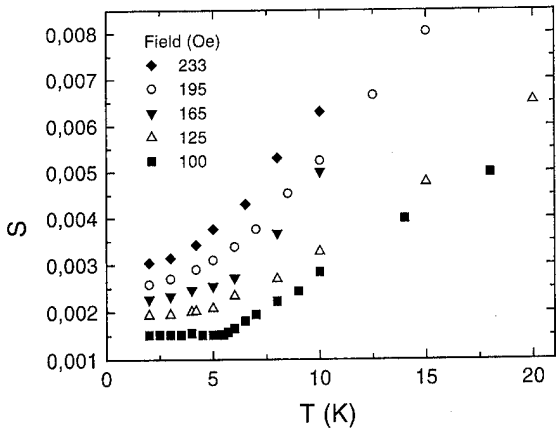


FIG. 6. Magnetic viscosity vs T for different applied fields in a TbFe random magnet.

In addition, the effect of applied field on the relaxation and quantum tunneling has been found in a TbFe random magnet.[18] The dependence of magnetic viscosity on the temperature obtained in relaxation measurements with different applied fields is shown in Fig. 6. It is clearly seen that the behavior of $S(T,H)$ in Fig. 6 is very similar to that in Fig. 3, although the experimental results obtained on the random magnetic thin film corresponds to a relaxation process due to the turning of magnetic moments in different clusters. However, this similarity is not surprising due to the fact that interactions between clusters do not affect the relaxation inside each cluster as a consequence of the large magnetic anisotropy values in these random magnets.

[1] U. Uehara and B. Barbara, J. Phys. (Paris) **47**, 235 (1986); D. V Berkov, J. Magn. Magn. Mater. **117**, 431 (1992).
[2] J. M. González and J. Tejada, Phys. Rev. B. **49**, 3867 (1994).
[3] D. K. Lottis, R. M. White, and E. Dan Dahlberg, Phys. Rev. Lett. **63**, 362 (1991).
[4] B. Barbara and L. Gunther, J. Magn. Magn. Mater. **128**, 35 (1993).
[5] J. Tejada, X. X. Zhang, and E. M. Chudnovsky, Phys. Rev. B **47**, 14977 (1993).
[6] S. H. Charap, J. Appl. Phys. **63**, 2054 (1988).
[7] R. W. Chantrell, J. Magn. Magn. Mater. **95**, 365 (1991) and references therein.
[8] W. M. Mularie and M. P. Sharrock, J. Appl. Phys. **69**, 4938 (1991), and references therein.
[9] L. Neel, Ann. Geophys. **5**, 99 (1949).
[10] E. M. Chudnovsky and L. Gunther, Phys. Rev. Lett. **60**, 661 (1988).
[11] H. Grabert, P. Olschowski, and U. Weiss, Phys. Rev. B **32**, 3348 (1985).
[12] X. X. Zhang, J. Tejada, A. Roig, O. N. Kolov, and E. Molins, J. Magn. Magn. Mater. **137**, L235 (1994).
[13] E. Chudnovsky, NATO Workshop Grenoble June 1994.
[14] C. G. Granqvist and R. A. Buhrman, Solid State Commu. **18**, 123 (1976).
[15] D. D. Awschalom, J. F. Smyth, G. Grinstein, D. P. Vincenzo, and D. Loss, Phys. Rev. Lett. **68**, 3092 (1992).
[16] X. X. Zhang *et al.* (unpublished).
[17] J. Tejada, X. X. Zhang, and C. Ferrater, Z. Phys. B: Condens. Matter **94**, 245 (1994).
[18] J. Tejada, X. X. Zhang, and Ll. Balcells, J. Appl. Phys. **73**, 6709 (1993).

Loss simulations in magnetostrictive actuators

G. Engdahl
Power Engineering, ABB Corporate Research, S-72178 Västerås, Sweden

A. Bergqvist
Electric Power Engineering, Royal Institute of technology, S-10044 Stockholm, Sweden

Power losses in a magnetostrictive actuator have been studied. The system consists of a cylindrical rod of Terfenol-D, a surrounding magnetic circuit to get a homogeneous flux, a mechanical load applied to the rod ends, and an electric coil. We consider transient operating conditions with time-varying driving voltage. Nonlinearity and hysteresis are handled by using a magnetomechanical hysteresis model as the constitutive law. Eddy currents and field constriction are taken into account by a finite difference representation of the diffusion equation for the active rod. Coil losses are trivially found through Ohm's law. The influence of laminations in the magnetostrictive rod on the eddy current loss is examined using finite element methods. © *1996 American Institute of Physics.* [S0021-8979(96)04308-0]

I. INTRODUCTION

The feasibility of utilizing highly magnetostrictive materials in various suggested applications depends strongly on the total efficiency of the electromechanical system. Numerous methods have been proposed regarding the modeling of specific loss processes such as eddy currents, hysteresis, etc., in highly magnetostrictive materials.[1,2] In this work, efforts have therefore been spent on the assembly of a simulation tool that simultaneously accounts for the main loss processes resistive heating in drive coils, eddy currents and hysteresis. The individual algorithms are described in more detail in Refs. 3–5. A specific actuator is used as an example to demonstrate the capability of the design tool.

II. MAGNETOSTRICTIVE ACTUATOR DEFINITION

The magnetostrictive actuator used as the demonstration object is visualized in Fig. 1 and is of a type described in Ref. 6. It comprises of NdFeB permanent magnets (coercivity 875 kA/m) that are traversed by the main dynamic component of the flux created by the driving coil (100 turns). No losses in the soft magnetic conductors (relative permeability 1000) are considered. This is a reasonable assumption if these parts consist of laminated silicon-iron.

In the demonstration example, the actuator is fed electrically by a voltage source in series with a capacitor tuned for obtaining series resonance. The actuator is mechanically biased by 25.5 MPa and loaded purely resistively by 25 kNs/m. The active material is considered either solid or laminated (four separate laminates), where a lower effective conductivity is assumed in the latter case.

III. MODELING PROCEDURES

In earlier works,[3,4] a two-dimensional model for magnetostrictive drive elements under transient conditions was developed. In the model, the behavior of the active Terfenol-D rod is represented using finite difference approximations for Newton's law of motion and the diffusion equation in axisymmetric coordinates. The interactions with the external electric circuit and mechanical load are described by additional sets of equations. Due to nonlinearity in the Terfenol-D, calculations are performed using time-stepping techniques rather than Fourier transforms, even under sinusoidal excitation.

An important aspect is the magnetomechanical constitutive law for the Terfenol-D. We have used two different types of material laws. In the first, a single-valued nonlinear relation entirely estimated from experiments is assumed. That is, strain S and flux density B are measured for a large number of values of field H and stress T. B and S can then be evaluated for any argument (H,T) by interpolation. In the second method, a recent hysteresis model[5] is used which is based on the following notions: Magnetization and strain are expressed as superpositions of contributions from a number of independent particles. The state of each particle is uniquely determined by its own magnetization and strain and its evolution is governed by the principle of entropy maximization. Hysteresis is assumed to be due to a friction-like resistance to any changes in the state which is represented by assuming that the free energy of individual particles has many densely distributed local minima. To characterize a material, the model uses a few parameters determining hysteretic properties in addition to the same anhysteretic database as the first method.

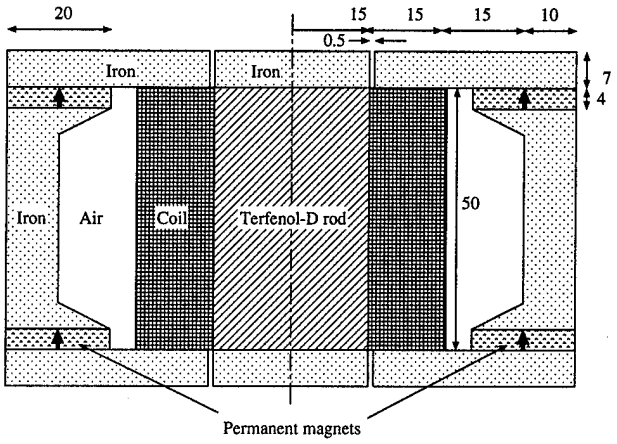


FIG. 1. Magnetic circuit of the considered actuator. All measures in mm.

 0021-8979/96/79(8)/4689/3/$10.00 © 1996 American Institute of Physics

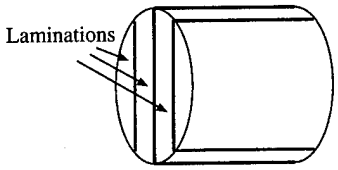


FIG. 2. Orientation of laminations in magnetostrictive rod.

IV. INITIAL CALCULATIONS

The influence of the external magnetic circuit is represented by using a reluctivity circuit parameter. This is done in order to avoid incorporating a finite element or finite difference representation of the entire magnetic circuit in the transient simulations since this would greatly slow down the computations. It has previously been established that this approach is a good approximation.[4] The reluctivity value was numerically calculated for the scheme shown under magnetostatic conditions using finite elements and found to be 5.0×10^6 A/V s.

Eddy currents in the active material can be reduced by using laminated magnetostrictive rods as shown in Fig. 2. In such a case, the system is strictly speaking not axisymmetric. However, to account for this, and calculate in three dimensions would be computationally very expensive and as an approximation, such a laminated rod may be treated as a homogeneous rod with reduced conductivity. In order to find the effective conductivity, we considered an infinitely long rod with laminations as shown and constant permeability and solved for the time-harmonic case with constant H-field amplitude along the border as boundary condition using an FE program. The use of laminations has the effect of both increasing the flux amplitude and decreasing the loss angle. It was found that if an effective conductivity in a homogeneous rod is chosen such that the loss angle is the same as for a laminated rod, the flux amplitude is different and vice versa. A useful compromise between fitting the loss angle and the flux amplitude, appears to be the rule

$$\sigma_{\text{eff}}=\sigma/(N+1)^2, \tag{1}$$

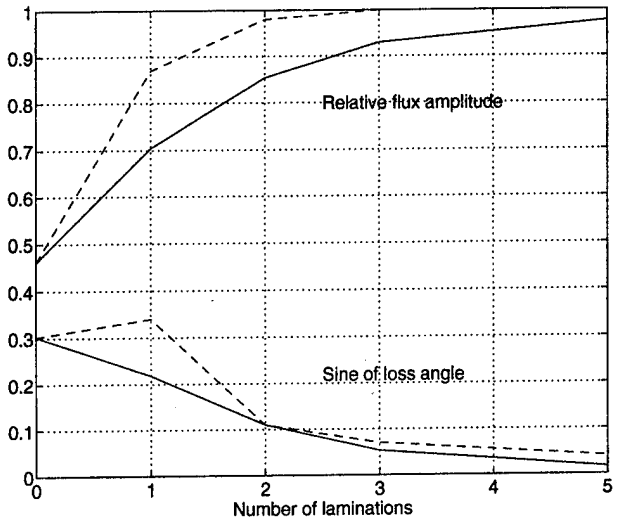


FIG. 3. Relative flux amplitude and sine of loss angle vs number of laminations N in an infinitely long cylindrical rod. Frequency=1000 Hz, relative permeability=5, conductivity $\sigma=1.67\times10^6$ Ω m, rod radius $r=15$ mm. Solid lines show calculations for a laminated rod. Dashed lines show calculations for a homogenous rod with conductivity $\sigma/(1+N)^2$.

where σ is the conductivity of Terfenol-D and N is the number of laminates. Figure 3 shows the error in flux magnitude and loss angle when this method is used.

V. RESULTS AND CONCLUSIONS

Simulations have been performed for frequencies $f=200$, 400, and 1000 Hz. We have compared the situations with and without laminations and with and without hysteresis in the active material, giving a total of twelve cases. The common external condition in all considered cases is that the driving voltage is sinusoidal with amplitude 8 V. We consider the average values over one period of the mechanical power P_{mech}, resistive loss P_{res}, eddy current loss P_{eddy}, and hysteresis loss P_{hyst}. The total power is

$$P_{\text{tot}}=P_{\text{mech}}+P_{\text{res}}+P_{\text{eddy}}+P_{\text{hyst}}. \tag{2}$$

TABLE I. Power parts in various simulation cases.

f (Hz)	η_{mech}	η_{res}	η_{eddy}	η_{hyst}	η_{err}
		Laminations, no hysteresis			
200	18.9	73.2	8.0	0	−4.9
400	47.2	38.3	14.5	0	0.2
1000	50.6	11.4	38.1	0	−18.7
		No hysteresis, no laminations			
200	5.6	37.2	57.2	0	−3.3
400	13.8	18.4	67.7	0	−7.2
1000	11.0	7.8	81.0	0	−5.9
		Hysteresis and laminations			
200	5.7	57.9	5.1	31.3	−17.8
400	30.8	36.4	10.4	22.3	−6.4
1000	30.8	13.0	20.4	35.8	−28.9
		Hysteresis, no laminations			
200	3.0	37.4	41.4	24.6	−6.4
400	10.3	25.5	56.0	8.3	2.5
1000	6.7	9.9	72.5	10.9	1.9

Table I shows the relative contributions of these terms defined as $\eta_{mech}=P_{mech}/P_{tot}$, $\eta_{res}=P_{res}/P_{tot}$, etc. Among these, η_{mech} is the efficiency of the device. The last column in the table gives an quantity η_{err} defined as

$$\eta_{err}=(P_{supp}-P_{tot})/P_{supp}. \tag{3}$$

Here P_{supp} is the average supplied electrical power over one period. Because of energy conservation, we should have $P_{sup}\equiv P_{tot}$. The fact that we do not, must therefore be an error which may have several causes. One is that the average mechanical power is a couple of magnitudes smaller than its positive and negative peak values. The estimate of its average value is therefore prone to significant numerical error. A different kind of error source is due to the constitutive law of the active material. In the nonhysteretic case, we should, due to energy conservation, have $\oint(BdH+SdT)\equiv 0$ for any closed cycle and at every point in space. Using Green's formula, this implies the Maxwell relation $\partial B/\partial T\equiv\partial S/\partial H$. However, the material data used in calculations showed some deviation from this relation. This could be due to an experiment error though it is then not clear which variables are incorrectly measured. It might also be due to how the anhysteretic curves are estimated from the hysteretic measured data. The same error is present in the hysteretic calculations, since the hysteresis model also used these data.

The inclusion of hysteresis in the simulations increased the computational time by a factor of 3–5 times. This was partly because each evaluation of B and S at a point in space and time took about five times longer and partly because in some cases a shorter time step was required to get convergence. We attempted the alternative method of estimating the hysteresis loss by performing the simulations without hysteresis and then subsequently using the hysteresis model with the resulting spatial average of the field and stress in the rod as input. Obviously, this will inevitably lead to an imbalance between input and output power. Furthermore, it turned out that the hysteresis loss computed in this manner greatly deviated from the one calculated with the hysteresis model incorporated in the simulation model, sometimes by a whole magnitude. The simplified method therefore seems dubious although it is not impossible that it could be useful under different conditions.

It is observed that eddy currents are very significant for nonlaminated rods, and that laminations considerably improve the overall efficiency at all frequencies, although this is partially offset by the fact that coil losses increase. With hysteresis, the eddy current loss will decrease which is due to the decrease in flux density amplitude. The efficiency is in all cases overestimated, when hysteresis is neglected, most notably for the case of $f=200$ Hz and a laminated rod.

A way to get around the imbalance of power could be to force the anhysteretic data to obey the Maxwell relation, overriding the experimentally measured values. For instance, instead of using direct measurements to find S as a function of H and T, it might be preferrable to determine it from measured values of H, T, and B as $S=\int(\partial B/\partial T)dH$

ACKNOWLEDGMENT

A. B. is supported by the Swedish Research Council for Engineering Sciences.

[1] T. Cedell, Ph. D. thesis, Lund University, 1995.
[2] I. D. Mayergoyz, *Mathematical Models of Hysteresis* (Springer, New York, 1991).
[3] L. Kvarnsjö and G. Engdahl, IEEE Trans. Magn. **27**, 5349 (1991).
[4] H. Tiberg, A. Bergqvist, and G. Engdahl, J. Appl. Phys. **73**, 5851 (1993).
[5] A. Bergqvist and G. Engdahl, MMM'95 Conference, Paper HD-07.
[6] H. Wakiwaka, T. Umezewa, and H. Yamada, IEEE Trans. Magn. **29**, 2443 (1993).

Analysis and optimization of synchronous magnetic couplings

E. P. Furlani
Imaging Research and Advanced Development, Eastman Kodak Company, Rochester, New York 14653-5305

Permanent magnet couplings made from rare-earth materials such as NdFeB render substantial torque, and are used in numerous applications that cannot be addressed with conventional materials. Moreover, formulas have been developed for designing and optimizing these devices. In this paper, the design formulas are summarized and demonstrated via optimization of practical coupling geometries. © *1996 American Institute of Physics.* [S0021-8979(96)01608-4]

I. INTRODUCTION

Synchronous magnetic couplings are used to transmit torque between two separated members with the most common applications involving the activation of devices in sealed containers. The two most common coupling configurations are radial and axial couplings. Rigorous torque predictions for either configuration require three-dimensional analysis, and while various numerical techniques such as the finite element analysis (FEA) are applicable, they tend to be awkward for the kind of parametric analysis that is often desired. To remedy this, formulas have been developed for predicting the torque of both types of couplings by Furlani *et al.*[1–3] These formulas, which are based on three-dimensional analytical analysis, apply to couplings made from materials such as NdFeB with a second quadrant constitutive relation of the form

$$B=\mu_0(H+M_s).$$

It is important to note that the analysis takes into account the magnets only, and does not (rigorously) apply when additional nonlinear materials are present (constituting a magnetic circuit). The formulas are expressed as finite sums of elementary functions, and are well suited for parametric analysis and optimization. Moreover, they have been verified using standard numerical methods as well as empirical data.[4,5] These formulas are summarized below and calculations are performed that demonstrate their effectiveness in the optimization of practical coupling geometries. In addition, the advantage of using sintered versus bonded NdFeB material is discussed.

II. AXIAL COUPLINGS

Axial couplings consist of two axially polarized, multipole disks that are constrained to rotate about a common axis (Fig. 1). One of the magnets is driven by an external source while the other is connected to a load. As the driven magnet rotates it imparts an axial force and torque to the load. The efficiency of the coupling is a function of several variables, including the material properties, number of poles, dimensions, separation distance, and the relative angular offset of the magnets. The force and torque are given by

$$F(\theta)=\frac{\mu_0}{4\pi}N_{\text{pole}}M_s^2\left\{\frac{\pi(R_2^2-R_1^2)}{N_{\text{pole}}N_rN_\theta}\right\}^2\sum_{m=0}^{2}\sum_{n=1}^{2}\sum_{i=1}^{N_{\text{pole}}}\sum_{j=1}^{N_r}\sum_{i'=1}^{N_\theta}\sum_{j'=1}^{N_r}\sum_{j'=1}^{N_\theta}\frac{(-1)^{(n+m)}\alpha_m h_m}{\{[r_i^2+r_{i'}^2-2r_ir_{i'}\cos(\theta_j-\theta_{j'}(n)]+h_m^2\}^{3/2}},\tag{1}$$

and

$$T(\theta)=\frac{\mu_0}{4\pi}N_{\text{pole}}M_s^2\left\{\frac{\pi(R_2^2-R_1^2)}{N_{\text{pole}}N_rN_\theta}\right\}^2\sum_{m=0}^{2}\sum_{n=1}^{2}\sum_{i=1}^{N_{\text{pole}}}\sum_{j=1}^{N_r}\sum_{i'=1}^{N_\theta}\sum_{j'=1}^{N_r}\sum_{j'=1}^{N_\theta}\frac{(-1)^{(n+m)}\alpha_m r_ir_{i'}\sin[\theta_j-\theta_j(n)]}{\{[r_i^2+r_{i'}^2-2r_ir_{i'}\cos(\theta_j-\theta_{j'}(n)]+h_m^2\}^{3/2}},\tag{2}$$

where θ is the relative angular offset of the two magnets (the torque is zero when $\theta=0$), N_{pole} is the number of poles, N_r and N_θ are "mesh" parameters that characterize the discretization of the "surface charge" on each magnet, and h_m and α_m are given by

$$h_m=h+mt_m \quad (m=0,1,2),$$

$h=$ separation of magnets (m),

$t_m=$ thickness of magnets (m),

and

$$\alpha_m=\begin{cases}1 & m=0\\ 2 & m=1,\\ 1 & m=2\end{cases}$$

respectively. These and the remaining variables are defined in detail in a previous paper.[1] Note that these formulas entail nested summations of elementary functions and are readily programmed. However, note that when programming multiple summations, a higher degree of accuracy can be achieved with fewer mesh points (i.e., lower values N_r and N_θ) if the total of a single summation over one index is

 0021-8979/96/79(8)/4692/3/$10.00 © 1996 American Institute of Physics

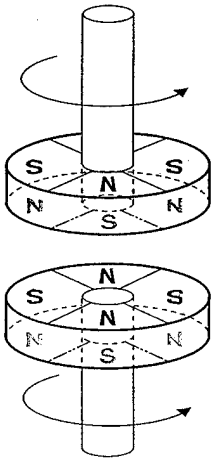


FIG. 1. Axial coupling.

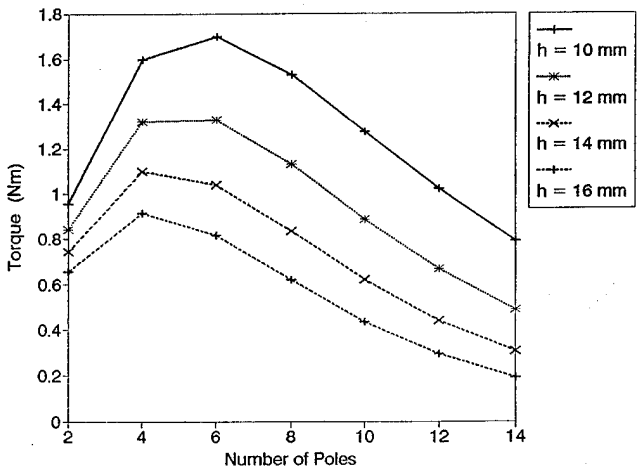


FIG. 3. Torque vs number of poles (axial coupling).

evaluated and saved separately (as an intermediate step), and then the totals of the successive summations are added together to obtain the final sum.

III. RADIAL COUPLINGS

Radial couplings consist of two coaxial, radially polarized, multipole cylinders that are constrained to rotate about a common axis (Fig. 2). Again, one of the magnets is driven while the other is connected to a load. The torque is given by

$$T(\theta)=\frac{2N_{\text{pole}}M_s^{\text{out}}h\tilde{R}}{N_z^{\text{out}}N_r^{\text{out}}}\sum_{p=0}^{N_z^{\text{out}}}\sum_{q=0}^{N_r^{\text{out}}}S_z(p)S_r(q)r(q)\times B_r^{\text{in}}\left[r(q),\theta+\frac{\pi}{N_{\text{pole}}},z(p)\right], \tag{3}$$

where M_s^{out} is the magnetization of the outer magnet, $B_r^{\text{in}}(r,\theta,z)$ is the field of the inner magnet, N_z^{out} and N_r^{out} are the discretization parameters for the outer magnet (numerical integration), $h=Z_2^{\text{out}}-Z_1^{\text{out}}$, $\tilde{R}=R_2^{\text{out}}-R_1^{\text{out}}$, and θ is the relative angular offset of the two magnets. Again, these and the remaining variables are described in previous work.[2]

IV. ANALYSIS

In this section, the coupling formulas are applied to the optimization of practical coupling geometries. The axial coupling is treated first. Consider an application that requires a torque of $T=1.0$ Nm to be transmitted through a 10 mm enclosure. To begin the analysis, choose the following nominal magnet dimensions:

$R_1=1$ cm (innder radius),

$R_2=4$ cm (outer radius),

$t_m=1.5$ cm (height).

The coupling is to be made from cold-pressed NdFeB with a 10% concentration of binder by volume. The author has found that a magnetization value of $M_s=4.3\times10^5$ A/m renders accurate data for this material (the corresponding value for 28 MGOe sintered NdFeB is $M_s=7.16\times10^5$ A/m). The analysis was performed on a Sun SPARCstation 10 with for-

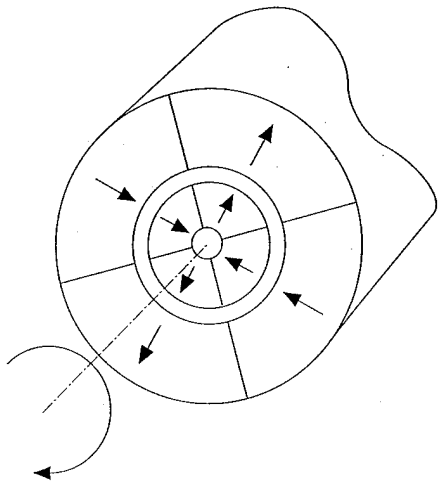


FIG. 2. Radial coupling.

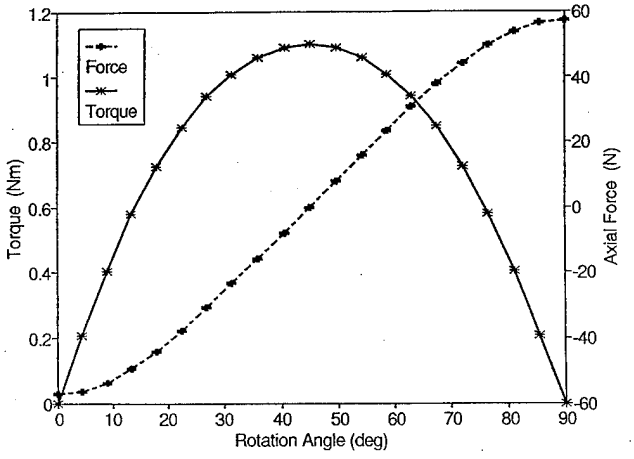


FIG. 4. Torque and force vs θ (axial coupling).

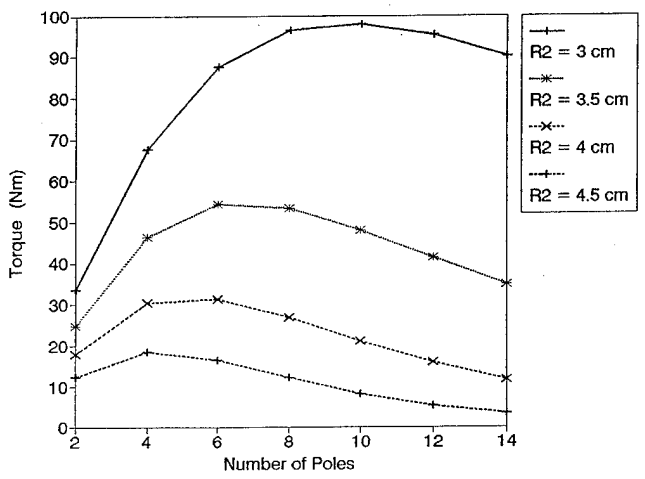


FIG. 5. Torque vs number of poles (radial coupling).

mulas (1) and (2) implemented in Fortran. The peak torque was computed as a function of the number of poles (N_{pole}) for a series of separations $h=10,12,14$, and 16 mm (Fig. 3). The analysis shows that the peak torque (which occurs at an angular offset of π/N_{pole}) occurs at 6, 6, 4, and 4 poles, respectively. In addition, the magnets can be separated by as much as 14 mm and still render the desired torque. To complete the analysis, the torque and force were computed as a function of θ for the 14 mm separation (Fig. 4). The maximum force is 60 N, and is attractive (negative) at $\theta=0°$ and repulsive (positive) at 90°. For this analysis the summation parameters N_r and N_θ were set to 12, and it took approximately 10 s to compute each torque value.

For the radial coupling consider an application that requires a torque of $T=90$ Nm to be transmitted through a 0.45 cm enclosure (i.e., the magnets, which are coaxial, must have a 0.45 cm radial gap between them). Assume that the magnets are to be made from cold-pressed NdFeB and have the following dimensions:

$R_1^{\text{in}}=1$ cm (inner radius of inner magnet),

$R_1^{\text{out}}=5$ cm (inner radius of outer magnet),

$R_2^{\text{out}}=8$ cm (outer radius of outer magnet),

$h=5$ cm (length).

The peak torque was computed as a function of the number of poles (N_{pole}) for a series of inner magnet, outer radial values $R_2^{\text{in}}=3$, 3.5, 4, and 4.5 cm (when R_2^{in} 4.5 cm there is a 0.5 cm radial gap between the inner and outer magnet). Note that the peak torque (which occurs at an angular offset of π/N_{pole}) occurs at 4,6,6, and 10 poles, respectively (Fig. 5). The analysis shows that a 10 pole coupling with $R_2^{\text{in}}=4.5$ cm is optimal for this application. For this analysis formula (3) was implemented in Fortran, and the summation parameters N_r, N_θ, and N_z were set to 10, 10, and 20, respectively.[2] It took approximately 5 s to compute each torque value. This is in sharp contrast to the hours it would take to perform a similar optimization using FEA.

Lastly, once torque calculations have been performed for a given value of magnetization M_s, the torque for any other value can be quickly determined because it is proportional to M_s^2. Thus, the torque obtained using 28 MGOe sintered NdFeB is 2.77 times greater than for cold-pressed NdFeB.

V. SUMMARY

Synchronous magnetic couplings can be readily designed and optimized for a given application using analytically based formulas. The analysis can be completed in a few minutes on a modern workstation and can completely eliminate costly and time consuming fabrication and testing.

[1] E. P. Furlani, IEEE Trans. Magn. **MAG-29**, 2295 (1993).
[2] E. P. Furlani, R. Wang, and H. Kusnadi, IEEE Trans. Magn. **MAG-31**, 2522 (1995).
[3] E. P. Furlani and T. S. Lewis, Int. J. Appl. Elect. Mech. **6**, 187 (1995).
[4] R. Wang, E. P. Furlani, and Z. J. Cendes, IEEE Trans. Magn. **MAG-30**, 2292 (1994).
[5] D. R. Huang, G. J. Chiou, Y. D. Yao, and S. J. Wang, J. Appl. Phys. **76**, 6862 (1994).

Irregular grain structure in micromagnetic simulation

D. G. Porter, E. Glavinas, P. Dhagat, J. A. O'Sullivan, R. S. Indeck, and M. W. Muller
Magnetics and Information Science Center, Department of Electrical Engineering, Washington University, St. Louis, Missouri 63130-4899

A randomized microstructure based on the Voronoi diagram is proposed for micromagnetic models. Simulations illustrate variability of extrinsic magnetic properties with microstructure, medium noise dependence on medium properties, and jitter dependence on trackwidth. © *1996 American Institute of Physics.* [S0021-8979(96)00508-6]

I. INTRODUCTION

Much research into the structural details of the magnetic patterns which store information in magnetic recording systems has been based on micromagnetic models of magnetic recording media.[1–4] Most of these models make use of a regular grain structure, tiling the medium plane with a spatially periodic array of hexagons or rectangles. Regular grain structures have a number of advantages, including the property that they form a space-filling partition of the medium plane. However, Miles has demonstrated that such microstructure regularity yields unphysical anisotropic properties,[5] and has proposed an alternative randomized grain geometry.[6,7] In the alternative strategy, grains are placed at random in the medium plane with care taken not to allow grain overlap. This strategy generates isotropic microstructures, but a multistage process is necessary to achieve an acceptable packing fraction.

In this paper we present a micromagnetic model with randomized microstructure as a generalization of regular microstructure models. The resulting grain geometry is irregular, and also forms a partition of the medium plane with no gaps between grains. The grain generation algorithm is built on the concept of the Voronoi diagram.[8]

II. IRREGULAR GRAIN GEOMETRY

Let $S \subset \mathbf{R}^2$ be a set of N planar points, $\{P_1,\ldots,P_N\}$. The Voronoi diagram of S, $\mathscr{V}(S)$, is the set of regions $\{R_1,\ldots,R_N\}$, where

$$R_k=\{x\in\mathbf{R}^2:\forall_{l\neq k}:\|x-P_k\|\leq\|x-P_l\|\}. \tag{1}$$

The computation of the Voronoi diagram is a well-studied problem in the field of computational geometry and can be performed using software available from The Geometry Center at the University of Minnesota.[9] When the set of initial points S is a lattice, the Voronoi diagram has a regular structure. Figure 1(a) illustrates the generation of a hexagonal grain structure as the Voronoi diagram of a lattice S. A generalization to irregular structures is achieved by choosing a randomly dispersed set of initial points S. Figure 1(b) illustrates the generation of an irregular grain structure as the Voronoi diagram of a set of points S generated by a Poisson point process.[10]

Because the Voronoi diagram is a partition of the medium plane, this method of generating randomized microstructure does not encounter the difficulty of a low packing fraction. In addition, Voronoi regions are an attractive grain model because they approximate the structure which results from crystal growth outward from nucleation sites represented by the points in S.

Three magnetic interactions are represented. Each grain exhibits uniaxial anisotropy with an easy axis chosen at random. The magnetic interactions are represented by dipole-dipole interactions computed at the centroids of the grains with moments proportional to grain area. This simple representation is accurate for long-range interactions. Short-range magnetostatic interactions are expected to be dominated by exchange interactions. Exchange interactions are computed in such a way as to split the exchange energy of a domain wall equally between each pair of grains which share an edge, following Muller and Indeck.[11] Therefore, the exchange interaction between two grains is proportional to the length of the edge they share. Grains are selected in a random sequence. The magnetization of each selected grain is rotated in the medium plane in response to its local field until it reaches a local minimum of magnetic energy. It has been demonstrated that the final magnetization state of this evolution algorithm is nearly sure to be a local minimum of total magnetic energy.[12]

III. SIMULATION RESULTS

To compute hysteresis loops, two 2 μm×2 μm medium patches were generated, one of hexagonal grains, the other of irregular grains. The grains were generated to have an average area of 2500 nm^2. Each patch was initialized to a state of negative saturation. Applied field values were stepped from -1.5 to 1.5 times the anisotropy field and back in steps of 0.03 times the anisotropy field, with a complete relaxation to a stable state at each step of the computation. The exact loop computed depends on the particular set of random easy axes selected. For each of the medium patches, Fig. 2 contains a plot of the average of five computed hysteresis loops, where each computed loop is based on a different random selection of easy axes. The values of remanence vary by as much as

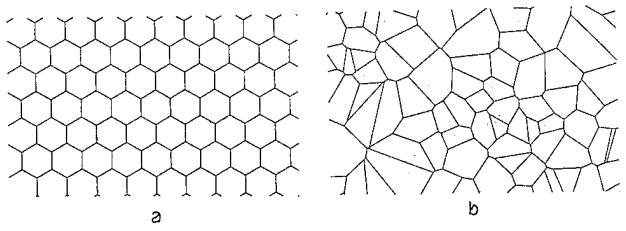


FIG. 1. Hexagonal (a) and irregular (b) grain structure.

 0021-8979/96/79(8)/4695/3/$10.00 © 1996 American Institute of Physics

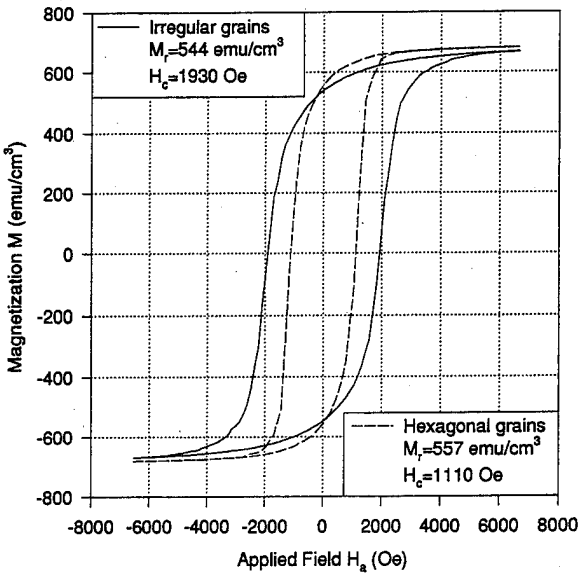


FIG. 2. Hysteresis loops for hexagonal and irregular grain structures.

3% from the average. Coercivity values vary as much as 11%. Significant differences in the extrinsic magnetic properties, particularly in the coercivity, arise from the different microstructures.

Figure 3 depicts a track of recorded information as represented by the model. The trackwidth is 1 μm, and the bit cell length is 150 nm, values sufficient to achieve an areal density of more than 4 Gbits per square inch. The thickness of the medium δ is 30 nm. The initial data pattern was directly set in the simulation; it was not generated by simulation of a recording process. The grey scale of the figure represents the component of magnetization parallel to the recorded track, with white representing magnetization fully saturated toward the left and black representing magnetization fully saturated toward the right.

The magnetic pattern which remains after the interacting grains have relaxed to a stable state depends on the medium properties. Figure 4 is the pattern after relaxation for medium A with properties selected to show very little corruption of the recorded pattern. Hysteresis loop computation for medium A yields a coercivity of 6800 Oe and a remanence of 531 emu/cm^3. Figure 5 is the pattern after relaxation for medium B with somewhat more realistic properties. Hysteresis loop computation for medium B yields a coercivity of 3100 Oe and a remanence of 535 emu/cm^3. The initial "recording" can easily be recovered visually from the corrupted magnetization of medium B by viewing Fig. 5 at a glancing angle from the bottom. Such a perspective approximates the integration across the trackwidth performed by a read head.

When corrupted magnetic patterns are read, the deviations of the resulting waveform from ideal are called medium noise. The read process was simulated using the Karlqvist model for an inductive read head. Figure 6 illustrates medium noise for an isolated transition recorded on both medium A and medium B, compared with the ideal pulse corresponding to an uncorrupted pattern.

One type of distortion caused by medium noise is the displacement of pulses from their intended locations.[13] This jitter has been theoretically and experimentally shown to de-

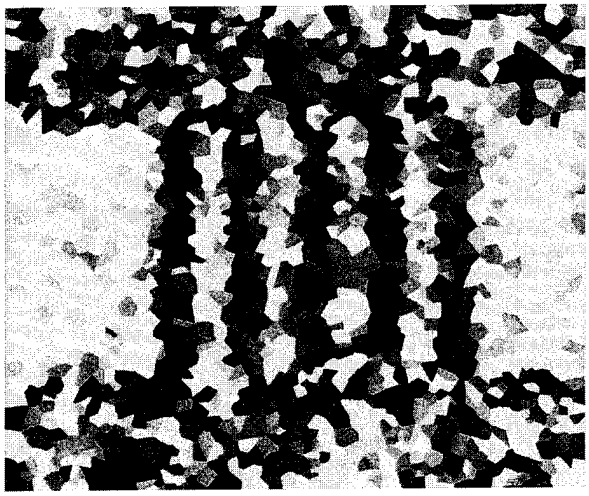


FIG. 4. Data pattern after relaxation for medium A. $M_r\,\delta$=1.59 memu/cm^2. H_c=6800 Oe.

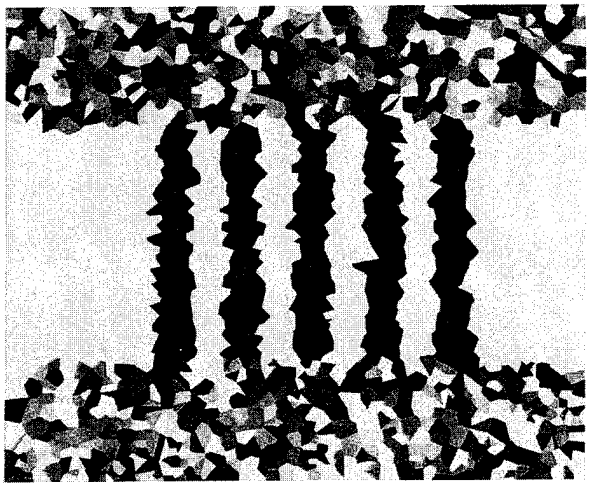


FIG. 3. High-density data pattern.

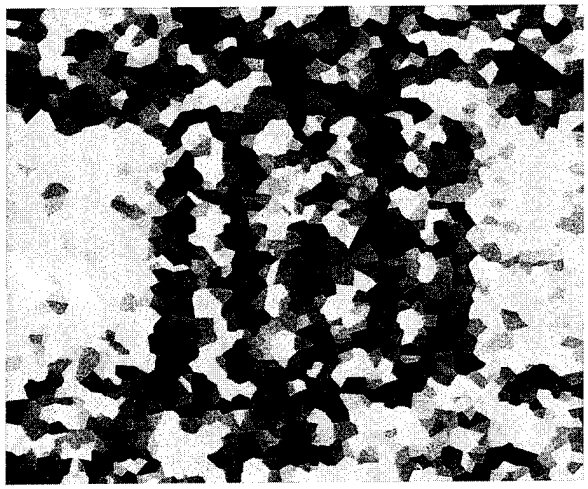


FIG. 5. Data pattern after relaxation for medium B. $M_r\,\delta$=1.61 memu/cm^2. H_c=3100 Oe.

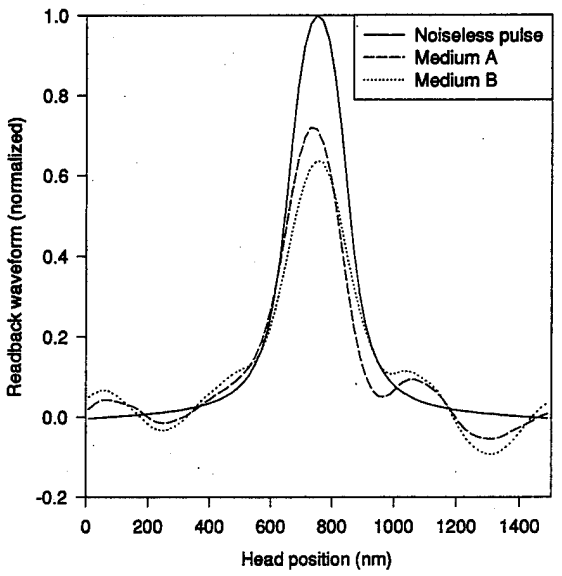


FIG. 6. Medium noise examples.

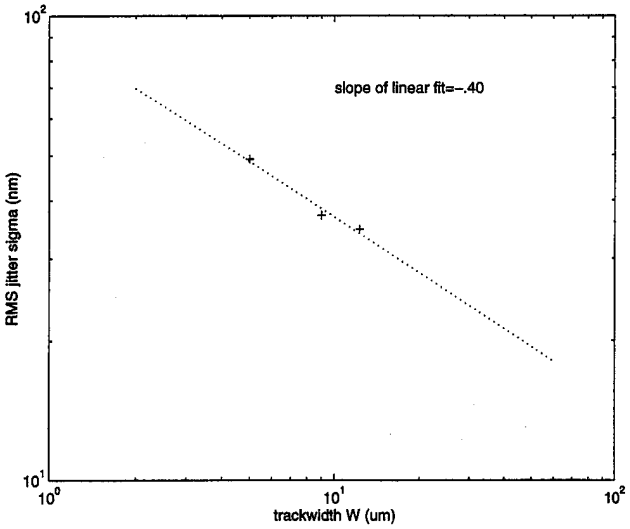


FIG. 8. Root-mean-square jitter vs trackwidth.

pend on the trackwidth of the read head.[14,15] For a trackwidth of W, the root-mean-square value of the jitter σ is predicted by theory to be

$$\sigma = CW^{-1/2}, \tag{2}$$

where C is a constant depending in part on the transverse coherence length and average grain size of the recording medium.

Simulations were performed to reproduce a set of experiments on a precision recording tester.[15] To simulate writing at many locations on a medium, 200 7.3 μm$\times$14 μm medium patches were generated with average grain area of 40 000 nm^2 and a thickness of 50 nm. Model parameters were selected to yield a coercivity of 1250 Oe and a remanence-thickness product of 4 memu/cm^2, matching the values of the medium in the experiments. The readback pulse waveforms from isolated transitions were computed for each patch for read heads and recorded tracks of width 5, 9, and 12.3 μm. The jitter values from these computed waveforms form the histograms of Fig. 7. As predicted by theory, a larger trackwidth yields a smaller value of root-mean-square jitter. Figure 8 is a log–log plot of σ vs W, with a slope of -0.40. The simulations were also performed without allowing the interacting grains to relax to a stable state. A corresponding slope of -0.63 was computed. Neither set of simulations closely matches the theoretically predicted value of $-1/2$. However, they are qualitatively consistent with it.

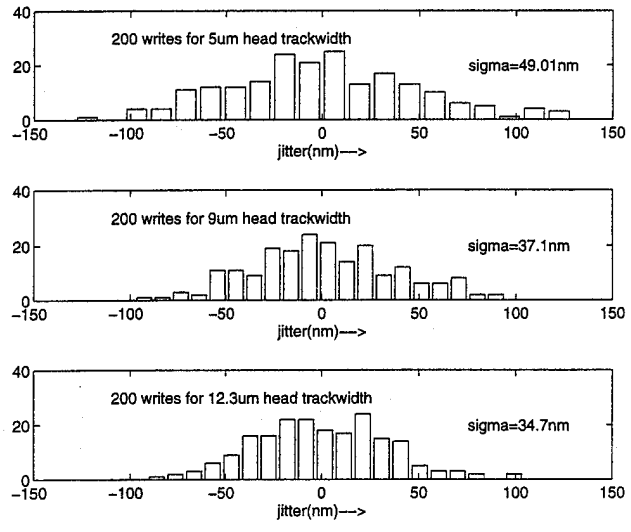


FIG. 7. Jitter histograms.

ACKNOWLEDGMENT

This work is supported in part by NSF Grants No. NCR-94-06197 and No. ECS-94-06198.

[1] G. F. Hughes, J. Appl. Phys. **54**, 5306 (1983).
[2] J.-G. Zhu and H. N. Bertram, J. Appl. Phys. **63**, 3248 (1988).
[3] M. Mansuripur and R. Giles, Comput. Phys. **4**, 291 (1990).
[4] J. J. Miles and B. K. Middleton, J. Magn. Magn. Mater. **95**, 99 (1991).
[5] J. J. Miles and B. K. Middleton, IEEE Trans. Magn. **26**, 2137 (1990).
[6] J. J. Miles, Ph.D. thesis, University of Manchester, 1990.
[7] J. J. Miles, M. Wdowin, J. Oakley, and B. K. Middleton, IEEE Trans. Magn. **31**, 1013 (1995).
[8] F. Aurenhammer, ACM Computing Surveys **23**, 345 (1991).
[9] C. B. Barber, D. P. Dobkin, and H. Huhdanpaa, submitted to the ACM Trans. on Mathematical Software (unpublished).
[10] D. L. Snyder and M. I. Miller, *Random Point Processes in Time and Space* (Springer, New York, 1991).
[11] M. W. Muller and R. S. Indeck, J. Appl. Phys. **75**, 2289 (1994).
[12] D. G. Porter, Ph.D. thesis, Washington University, St. Louis, MO, 1996, in preparation.
[13] E. Glavinas *et al.*, submitted to IEEE Trans. Magn. (unpublished).
[14] J. J. Miles and B. K. Middleton, J. Magn. Magn. Mater. **120**, 375 (1993).
[15] P. Dhagat, E. Glavinas, A. Jander, D. G. Porter, R. S. Indeck, and M. W. Muller, these proceedings.

Low temperature magnetic properties of a molecular compound (abstract)

J. L. Tholence and M. Novak
CRTBT, CNRS, BP 166, F38042 Grenoble cedex 09, France

D. Luneau and P. Rey
CENG, DRF, 17 Rue des Martyrs, F38054 Grenoble cedex 09, France

E. Belorisky
Laboratoire de Spectrométrie Physique, Université Joseph Fourier, BP 87, F38402 Saint Martin d'Hères cedex, France

In molecular compounds, the magnetic properties depend on the coupling between the magnetic moments of transition metal ions, rare earth ions, and/or free radicals. This coupling is often antiferromagnetic, but can give a high spin moment in some particular cases. When organic molecules form crystals, again the coupling between molecules can be antiferromagnetic or ferromagnetic like. In a few cases the ferromagnetism, only due to nitroxide radicals, has been observed at low temperature. We present here a more general case of a manganese(II) derivative of an "imidazole substituted nitronyl nitroxide" with complex behavior. The high temperature properties can be explained by ferrimagnetic coupling between the Mn and nitroxide spins. At low temperature a weak intermolecular coupling appears below 10 K, as well as a weak ferromagnetic component below 4.5 K. These low temperature properties might be due to the canting of antiferromagnetically coupled spins. © *1996 American Institute of Physics.*
[S0021-8979(96)59508-5]

 0021-8979/96/79(8)/4698/1/$10.00 © 1996 American Institute of Physics

An application of the wavelets to the magnetic field source searching

T. Doi and S. Yoshida
College of Engineering, Hosei University, Koganei, Tokyo 184, Japan

Y. Nakaya
Department of Nutrition, University of Tokushima, Tokushima, Tokushima 770, Japan

S. Hayano and Y. Saito
College of Engineering, Hosei University, Koganei, Tokyo 184, Japan

Recently, the wavelet analysis is being applied to the various fields, such as image data compression in informatics and spectrum analysis of the electrocardiogram. In the present article, we propose the two approaches, employing the wavelet analysis for the human heart diagnosis. One is the data base approach, and the other is an inverse approach searching for the magnetic field source of the human heart. The data base approach is an application of the data compression to the magnetocardiogram. Also, the magnetic field source searching is an application of the spectrum analysis to the magnetocardiogram. The results reveal that the data base approach makes it possible to identify the normal or abnormal heart, and the magnetic field source search is capable of estimating the current distribution of a distinct heart. © *1996 American Institute of Physics.* [S0021-8979(96)79408-1]

I. INTRODUCTION

Recent investigations concerning the magnetocardiogram (MCG) are establishing their possible use for human heart diagnosis, because the MCG data contain the activation current information of the human heart.[1] In order to utilize the MCG data for heart diagnosis, it may be classified by two approaches; one is a direct reading of the information from the MCG data, and the other is an inverse approach searching for the activation current in the heart. Direct application of the MCG data for diagnosis requires a great deal of experience and skillfulness for reading the information included in the MCG data. On the other hand, the inverse approach does not require intensive experience, but it is essential to exploiting a solution strategy for the inverse source problem.[2–4]

Recently, the wavelet analysis has been developed for the image data compression in informatics and for the spectrum analysis of the ECG.[5,6]

In the present article, we applied the wavelet analysis to the human heart diagnosis. The wavelet analysis is applied to the MCG data compression for the data base oriented diagnosis. This proposes an expert system employing the wavelet analysis. Further, the wavelet analysis is applied to the inverse approach searching for the current distribution in the heart.

As for results, the data base approach makes it possible to identify the normal or abnormal heart. Also, it is shown that the magnetic field source searching approach is capable of estimating the current distribution of the distinct heart.

Thus, we show that our approaches employing the wavelets are quite effective tools for MCG diagnosis.

II. APPLICATION OF THE WAVELET ANALYSIS TO MCG DIAGNOSIS

A. Discrete wavelet transform

In the present article, we employ Daubechie's analyzing wavelets. Let us consider the following linear transformation:

$$\mathbf{X}' = C\mathbf{X}, \tag{1}$$

where $\mathbf{X}$ is a data vector with order of n; n must be a power of 2; and C is

$$C=\begin{bmatrix}
c_0 & c_1 & c_2 & c_3 & 0 & 0 & \cdot & 0 & 0 & 0 & 0 \\
c_3 & -c_2 & c_1 & -c_0 & 0 & 0 & \cdot & 0 & 0 & 0 & 0 \\
0 & 0 & c_0 & c_1 & c_2 & c_3 & \cdot & 0 & 0 & 0 & 0 \\
0 & 0 & c_3 & -c_2 & c_1 & -c_0 & \cdot & 0 & 0 & 0 & 0 \\
\cdot & \cdot & \cdot & \cdot & \cdot & \cdot & \cdot & \cdot & \cdot & \cdot & \cdot \\
\cdot & \cdot & \cdot & \cdot & \cdot & \cdot & \cdot & \cdot & \cdot & \cdot & \cdot \\
\cdot & \cdot & \cdot & \cdot & \cdot & \cdot & \cdot & \cdot & \cdot & \cdot & \cdot \\
0 & 0 & 0 & 0 & 0 & 0 & \cdot & c_0 & c_1 & c_2 & c_3 \\
0 & 0 & 0 & 0 & 0 & 0 & \cdot & c_3 & -c_2 & c_1 & -c_0 \\
c_2 & c_3 & 0 & 0 & 0 & 0 & \cdot & 0 & 0 & c_0 & c_1 \\
c_1 & -c_0 & 0 & 0 & 0 & 0 & \cdot & 0 & 0 & c_3 & -c_2
\end{bmatrix}. \tag{2}$$

In Eq. (2), the first, third, fifth, and the other odd rows generate the components of data convolved with the coefficients c_0, c_1, c_2, c_3. This corresponds to a weighted integral operation. On the other side, the even rows generate the com-

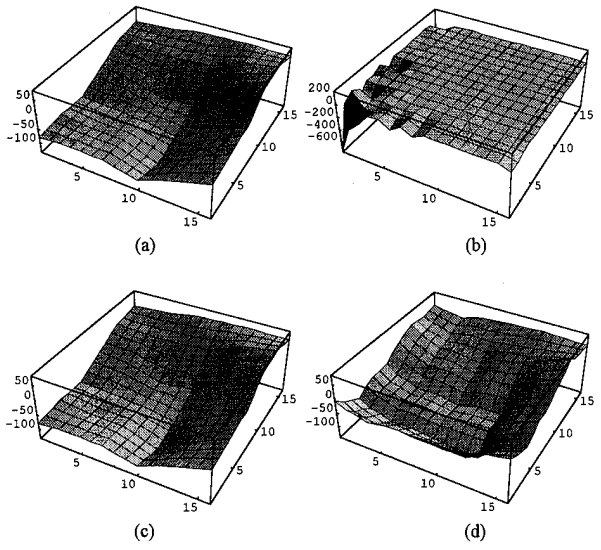


FIG. 1. An example of MCG data compression by means of the wavelet transformation. (a) An original MCG map, (b) a wavelet spectrum of (a), (c) a reproduced MCG map from the 100% spectrum in (b), and (d) the reproduced MCG map from the 6.25% spectrum in (b).

 0021-8979/96/79(8)/4699/3/$10.00 © 1996 American Institute of Physics

ponents of data convolved with the coefficients $c_3, -c_2, c_1, -c_0$. This corresponds to a weighted differential operation.

In order to carry out an inverse linear transformation, the coefficients c_0, c_1, c_2, c_3 should be determined by

$$C^T C = I, \tag{3}$$

where I is a nth order unit matrix and the superscript T refers to the transpose of matrix C^T in Eq. (3):

$$C^T = \begin{bmatrix} c_0 & c_3 & 0 & 0 & \cdot & 0 & 0 & 0 & 0 & c_2 & c_1 \\ c_1 & -c_2 & 0 & 0 & \cdot & 0 & 0 & 0 & 0 & c_3 & -c_0 \\ c_2 & c_1 & c_0 & c_3 & \cdot & 0 & 0 & 0 & 0 & 0 & 0 \\ c_3 & -c_0 & c_1 & -c_2 & \cdot & 0 & 0 & 0 & 0 & 0 & 0 \\ \cdot & \cdot & \cdot & \cdot & \cdot & \cdot & \cdot & \cdot & \cdot & \cdot & \cdot \\ \cdot & \cdot & \cdot & \cdot & \cdot & \cdot & \cdot & \cdot & \cdot & \cdot & \cdot \\ \cdot & \cdot & \cdot & \cdot & \cdot & \cdot & \cdot & \cdot & \cdot & \cdot & \cdot \\ 0 & 0 & 0 & 0 & \cdot & c_2 & c_1 & c_0 & c_3 & 0 & 0 \\ 0 & 0 & 0 & 0 & \cdot & c_3 & -c_0 & c_1 & -c_2 & 0 & 0 \\ 0 & 0 & 0 & 0 & \cdot & 0 & 0 & c_2 & c_1 & c_0 & c_3 \\ 0 & 0 & 0 & 0 & \cdot & 0 & 0 & c_3 & -c_0 & c_1 & -c_2 \end{bmatrix}. \tag{4}$$

From Eqs. (2)–(4), we have

$$c_0^2 + c_1^2 + c_2^2 + c_3^2 = 1, \qquad c_2 c_0 + c_3 c_1 = 0. \tag{5}$$

Equation (5) is composed of the two equations and has the four unknowns c_0, c_1, c_2, c_3. To determine the coefficients c_0, c_1, c_2, c_3, we have to consider the following conditions:

$$c_3 - c_2 + c_1 - c_0 = 0, \qquad 0c_3 - 1c_2 + 2c_1 - 3c_0 = 0. \tag{6}$$

From Eqs. (5) and (6), we have

$$c_0 = \frac{1+\sqrt{3}}{4\sqrt{2}}, \quad c_1 = \frac{3+\sqrt{3}}{4\sqrt{2}}, \quad c_2 = \frac{3-\sqrt{3}}{4\sqrt{2}}, \quad c_3 = \frac{1-\sqrt{3}}{4\sqrt{2}}. \tag{7}$$

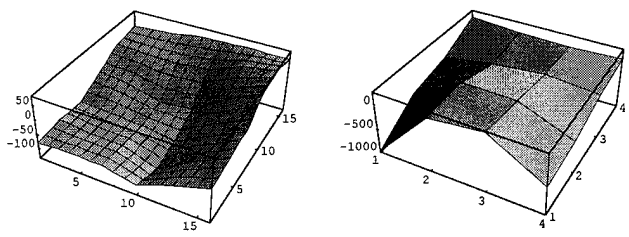
The set of coefficients c_0, c_1, c_2, c_3 in Eq. (7) is Daubechie's fourth-order analyzing wavelets.

For simplicity, let us consider a data vector $\mathbf{X}$ with the order of 16:

$$\mathbf{X} = [x_1\ x_2\ x_3\ x_4\ x_5\ x_6\ x_7\ x_8\ x_9\ x_{10}\ x_{11}\ x_{12}\ x_{13}\ x_{14}\ x_{15}\ x_{16}]^T. \tag{8}$$

In the case, the linear transformation using the matrix C_{16} yields

$$\mathbf{X}' = C_{16}\mathbf{X} = [s_1\ d_1\ s_2\ d_2\ s_3\ d_3\ s_4\ d_4\ s_5\ d_5\ s_6\ d_6\ s_7\ d_7\ s_8\ d_8]^T. \tag{9}$$



(a) Original MCG

(b) Compressed MCG in the form of wavelet spectrum

FIG. 2. The data compression of the MCG map of normal heart at QRS 30.0 (ms). (a) An original MCG map, and (b) the compressed MCG map in the form of wavelet spectrum.

The elements in vector $\mathbf{X}'$ are sorted by using the following matrix:

$$P_{16} = \begin{bmatrix} 1&0&0&0&0&0&0&0&0&0&0&0&0&0&0&0 \\ 0&0&1&0&0&0&0&0&0&0&0&0&0&0&0&0 \\ 0&0&0&0&1&0&0&0&0&0&0&0&0&0&0&0 \\ 0&0&0&0&0&0&1&0&0&0&0&0&0&0&0&0 \\ 0&0&0&0&0&0&0&0&1&0&0&0&0&0&0&0 \\ 0&0&0&0&0&0&0&0&0&0&1&0&0&0&0&0 \\ 0&0&0&0&0&0&0&0&0&0&0&0&1&0&0&0 \\ 0&0&0&0&0&0&0&0&0&0&0&0&0&0&1&0 \\ 0&1&0&0&0&0&0&0&0&0&0&0&0&0&0&0 \\ 0&0&0&1&0&0&0&0&0&0&0&0&0&0&0&0 \\ 0&0&0&0&0&1&0&0&0&0&0&0&0&0&0&0 \\ 0&0&0&0&0&0&0&1&0&0&0&0&0&0&0&0 \\ 0&0&0&0&0&0&0&0&0&1&0&0&0&0&0&0 \\ 0&0&0&0&0&0&0&0&0&0&0&1&0&0&0&0 \\ 0&0&0&0&0&0&0&0&0&0&0&0&0&1&0&0 \\ 0&0&0&0&0&0&0&0&0&0&0&0&0&0&0&1 \end{bmatrix}. \tag{10}$$

Thus, we have

$$P_{16}\mathbf{X} = P_{16}C_{16}\mathbf{X} = [s_1\ s_2\ s_3\ s_4\ s_5\ s_6\ s_7\ s_8\ d_1\ d_2\ d_3\ d_4\ d_5\ d_6\ d_7\ d_8]^T. \tag{11}$$

Further transformation to the elements $s_1, s_2, s_3, s_4, s_5, s_6, s_7, s_8$ in Eq. (11) yields

$$W^{(2)}\mathbf{X} = [S_1\ S_2\ S_3\ S_4\ D_1\ D_2\ D_3\ D_4\ d_1\ d_2\ d_3\ d_4\ d_5\ d_6\ d_7\ d_8]^T. \tag{12}$$

Similar transformation to s_1, s_2, s_3, s_4 in Eq. (12) yields

$$W^{(3)}\mathbf{X} = [\mathbf{S_1}\ \mathbf{S_2}\ \mathbf{D_1}\ \mathbf{D_2}\ D_1\ D_2\ D_3\ D_4\ d_1\ d_2\ d_3\ d_4\ d_5\ d_6\ d_7\ d_8]^T. \tag{13}$$

The transformation matrices used in Eqs. (12) and (13) are

$$W^{(2)} = (P'_{16}C'_{16})(P_{16}C_{16}), \quad W^{(3)} = (P''_{16}C''_{16})(P'_{16}C'_{16})(P_{16}C_{16}), \tag{14}$$

$$P'_{16} = \begin{bmatrix} P_8 & 0 \\ 0 & I_8 \end{bmatrix}, \quad C'_{16} = \begin{bmatrix} C_8 & 0 \\ 0 & I_8 \end{bmatrix},$$

$$P''_{16} = \begin{bmatrix} P_4 & 0 \\ 0 & I_{12} \end{bmatrix}, \quad C''_{16} = \begin{bmatrix} C_4 & 0 \\ 0 & I_{12} \end{bmatrix}. \tag{15}$$

Equation (13) is the finally obtained wavelet spectrum. The elements $\mathbf{S_1 S_2}$ in (13) are called the Mother Wavelet coefficients, and the others are called the wavelet coefficients at each level.

Inverse wavelet transform is carried out by

$$\begin{aligned} \mathbf{X} &= [W^{(3)}]^T W^{(3)}\mathbf{X}, \\ [W^{(3)}]^T &= [(P''_{16}C''_{16})(P'_{16}C'_{16})(P_{16}C_{16})]^T, \\ &= (P_{16}C_{16})^T(P'_{16}C'_{16})^T(P''_{16}C''_{16})^T, \\ &= C_{16}^T P_{16}^T (C'_{16})^T (P'_{16})^T (C''_{16})^T (P''_{16})^T. \end{aligned} \tag{16}$$

B. MCG data compression

Figure 1 shows an example of MCG data compression by means of the wavelet transformation. Figure 1(a) shows the original MCG map of the normal heart at QRS 30.0 (ms). Figure 1(b) shows a wavelet spectrum of Fig. 1(a). Figures

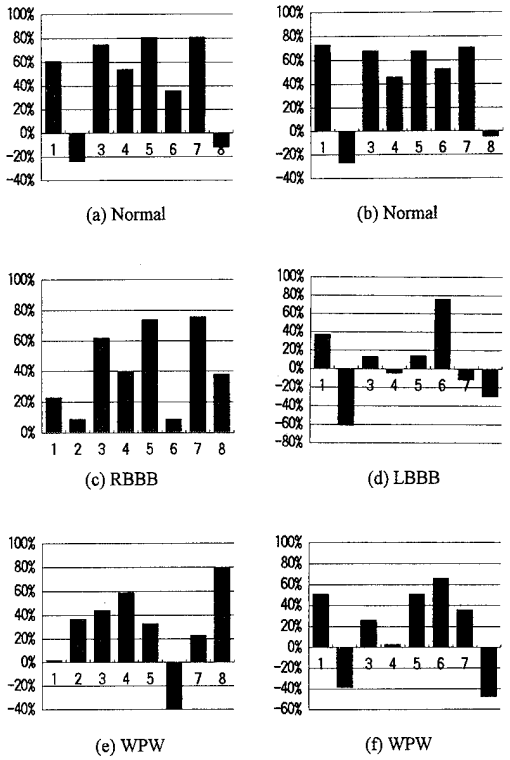


FIG. 3. Examples of the MCG diagnosis by means of the data base approach. (a) The correlative coefficient between the data base and normal heart. Similarly the correlative coefficients to the other normal (b), RBBB (c), LBBB (d), WPW syndromes (e), and the other WPW syndromes (f).

1(c) and 1(d) show the reproduced MCG map from the 100% and 6.25% spectrums in Fig. 1(b), respectively.

The results in Fig. 1 show that the wavelet transformation efficiently compresses the information included in the MCG map.

C. Data base approach

We applied the data compression by the wavelet transformation to the practical MCG maps.

Figures 2(a) and 2(b) show the original MCG map and its compressed wavelet spectrum (6.25%), respectively. We constructed the compressed data base using eight sets of the MCG data of normal hearts.

Figure 3(a) shows the correlative coefficients between the data base and the normal heart. Figures 3(b)–3(f) show the correlative coefficients to the other normal heart, right

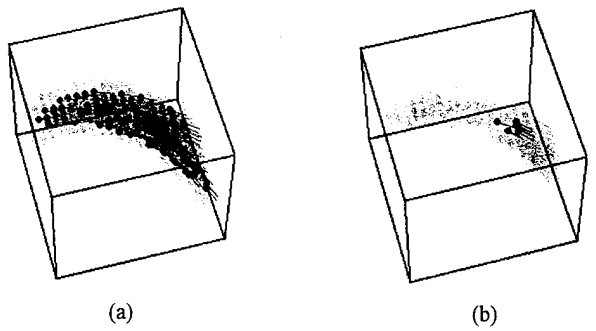


FIG. 4. Estimated current distribution in the case of normal heart at QRS 30.0 (ms). (a) An original current distribution, and (b) reproduced current distribution from the 1/16 times compressed data base.

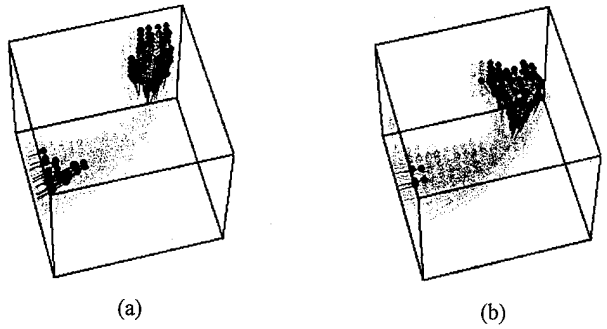


FIG. 5. Estimated current distribution in the case of WPW syndromes at QRS 30.0 (ms). (a) An original current distribution, and (b) reproduced current distribution from the 1/16 times compressed data base.

bundle branch block (RBBB), left bundle branch block (LBBB), Wolff–Perkinson–White (WPW) syndromes, and the other WPW syndromes, respectively.

Consideration of the results in Fig. 3 suggests that the data base approach makes it possible to identify the normal or not normal heart. Further, increasing a number of data bases may improve the accuracy of this approach.

D. Magnetic field source searching approach

In order to improve the data base approach, we evaluated the current distribution of heart from the compressed data base. Our searching strategy of the current distribution is called the sampled pattern matching method, which is a kind of generalized factor analysis.[2–4]

Figures 4(a) and 4(b) show an original current distribution and its reproduced current distribution from the 6.25% compressed data base, respectively. A similar example is shown in Fig. 5 for the WPW syndromes. Considering the results in Figs. 4 and 5, it is confirmed that the current distribution in the heart can be reproduced with sufficient accuracy from only the 1/16 times compressed data base. This means that further improvement of the heart diagnosis can be carried out by the inverse approach.

III. CONCLUSION

In the present article, we have applied the wavelet analysis to the MCG diagnosis.

At first, we proposed the data base approach using the MCG data compression by wavelet transformation. Using this data base approach, the normal and abnormal hearts could be read off.

Second, applying the magnetic field source searching approach to the compressed data base, the distinct current distribution reveals the details of heart condition. A further increase of the number of data bases should be carried out for the improvement of accurate diagnosis.

[1] H. Mori and Y. Nakaya, Biomagnetism **87**, 82 (1988).
[2] Y. Saito, E. Itagaki, and S. Hayano, J. Appl. Phys. **67**, 5830 (1990).
[3] H. Saotome, K. Kitsuta, S. Hayano, and Y. Saito, IEEE Trans. Magn. **29**, 1389 (1993).
[4] T. Doi, S. Hayano, I. Marinova, N. Ishida, and Y. Saito, J. Appl. Phys. **75**, 5907 (1994).
[5] M. Yamada, IEICE **76**, 518 (1993).
[6] N. V. Thakor, G. Xin-Rong, S. Yi-Chun, and D. F. Hanley, IEEE Trans. Biomed. Eng. **40**, 1085 (1993).

Published without author corrections

Functionalization and applications of nanosized γ-Fe_2O_3 particles

Qingxia Liu and Zhenghe Xu
Department of Mining and Metallurgical Engineering, McGill University, Montreal, P.Q., Canada H3A 2A7

A novel method to prepare nanosized γ-Fe_2O_3 particles containing reactive thio and/or disulphide groups using molecular self-assembly method is described. The monolayers are formed from self-assembled bolaamphiphiles, e.g., 16-mercaptohexadecanoic acid ($HS-C_{15}H_{30}-COOH$), and characterized using x-ray photoelectron spectroscopy. The magnetization of surfactant-coated particles is determined using a vibrating sample magnetometer. The potential uses of functionalized magnetic particles in recovering precious (Ag^+) and base (Cu^{2+}) metal ions from industrial effluent are examined. The modification of thiol on coated-magnetic particles by controlled oxidation is also described to extend the application of self-assembled organic monolayers to stabilizing ferrofluids.
© *1996 American Institute of Physics.* [S0021-8979(96)49508-7]

I. INTRODUCTION

Fine magnetic particles coated with thin organic films have found wide applications in raw material recovery,[1–3] biological cell separation,[4,5] waste remediation,[6] magnetic fluids,[7] magnetic ink, and magnetic memory media.[8] The organic thin films are often prepared by sol-gel silica coating followed by silanation,[9–10] formation of surfactant bilayers[11] and/or vesicles,[12] as well as polymer and ligand adsorption[13] on magnetic particles. These methods involve complex physical and interfacial chemistry, and the choice of preparation methods depends on the end-use of the prepared particles. The ease of synthesis, and control of the functionality and stability of the organic thin films are three major concerns.

The preparation of organic thin films on magnetic particles with reactive thio groups is of great interest due to their potential applications. It is well known that thio or disulphide groups are readily cross-linked to other incubated antibodies usually containing disulphides in the basic unit, forming tetrameric antibody complexes.[14–16] The simplicity of Langmuir-Blodgett deposition and self-assembly has made these methods useful in preparing various types of thin organic films.[17] In this communication, we report the preparation, characterization, and application of organic thin films containing reactive thio groups on nano-sized γ-Fe_2O_3 particles.

II. EXPERIMENT

A. Monolayer

γ-Fe_2O_3 powder (50 mg) purchased from Alpha Chemicals (20 nm) was gently mixed with 25 mL 16-mercaptohexadecanoic (MHA) solution (3 mM, perpared in chloroform) in a 40 mL vial while bubbling the nitrogen through the solution. The vial was then sealed and shaken for 24 h using a laboratory shaker. The treated particles were separated from solution by a hand magnet and rinsed repeatedly with chloroform, followed by dry hexane to remove unbound surfactant.

B. Oxidation of MHA monolayers

The reactive thio and/or disulphide groups on γ-Fe_2O_3 were further oxidized to produce different functionalities of sulphonate and/or sulphate. The oxidation experiment was conducted by bubbling ozone through the suspension of MHA-coated γ-Fe_2O_3 particles at a constant temperature of 0 °C for half an hour.

C. Characterization

X-ray photoelectron spectroscopy (XPS) and vibrating sample magnetometer (VSM) were used to characterize the γ-Fe_2O_3 particles with or without surfactant monolayer coatings. The experimental details in XPS spectrum acquisition were given elsewhere.[18] The VSM instrument was calibrated against a single crystal of nickel. The ζ potentials of γ-Fe_2O_3 particles with and without the treatment were also measured in 1 mM KCl solutions using a 501 Lazer-Zee Meter.

III. RESULTS AND DISCUSSION

A. Monolayer characterization

XPS spectra of γ-Fe_2O_3 particles with various treatments are shown in Fig. 1. The appearance of C_{1s} and S_{2p} bands on spectrum *b* (Figs. 1 and 2) for the samples contacted with MHA solutions, compared with spectrum a (untreated), suggests the self-assembly of MHA on γ-Fe_2O_3. In our previous report,[18] we have shown, from the semiquantitative XPS analysis using area ratio of bands Fe_{2p} to C_{1s}, that the magnetic particles immersed in MHA solution have a similar surface surfactant coverage to that obtained when γ-Fe_2O_3 is treated with a stearic acid solution. The Fourier transform infrared spectroscopic investigation confirmed that the carboxyl group of MHA is chemically anchored on γ-Fe_2O_3, leaving the thio group free for further reactions. The infrared spectra coupled with critical surface tensions derived from film flotation suggested the formation of a well-ordered and compact surfactant monolayer. It was also found that the MHA monolayer on γ-Fe_2O_3 was stable in acidic and alkaline media.

B. Metal ion loading characteristics

One of the important applications for the MHA coated γ-Fe_2O_3 particles containing reactive thio or disulphide groups is to recover precious (Ag) and base (Cu) metal ions or to remove toxic species from industrial effluents. It is well known that thio and disulphide groups have strong affinity to various metal ions, such as gold, silver, and copper.[19] The fabricated magnetic particles of large surface area can, there-

 0021-8979/96/79(8)/4702/3/$10.00 © 1996 American Institute of Physics

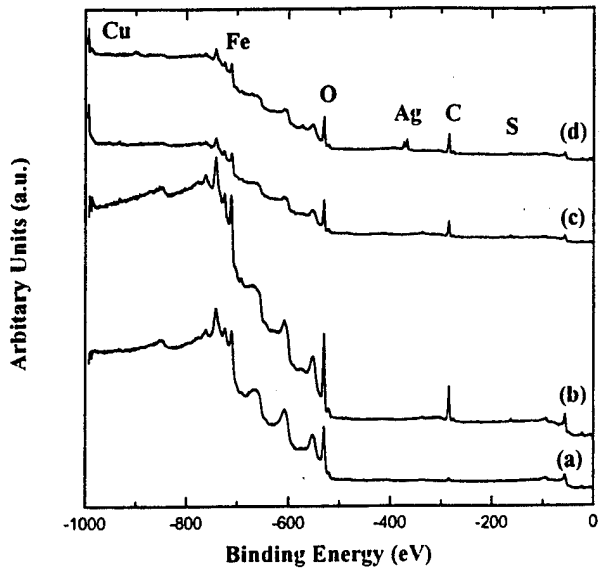


FIG. 1. XPS spectra of survey scans for γ-Fe_2O_3 surfaces with various treatments: (a) untreated; (b) MHA coated; (c) MHA coated with loaded Cu; and (d) MHA coated with loaded Ag.

fore, be used to capture silver or copper often present in industrial effluent. The metal-loaded magnetic particles can then be readily separated from effluent using magnetic separation.

To examine this application, the MHA-coated γ-Fe_2O_3 particles were brought to the contact with 10 mM $CuSO_4$ and AgCl solutions. The loaded particles were characterized using XPS spectroscopy and the spectra are included in Fig. 1. The bands centered at 934 and 954 eV on spectrum *c* (Fig. 2)

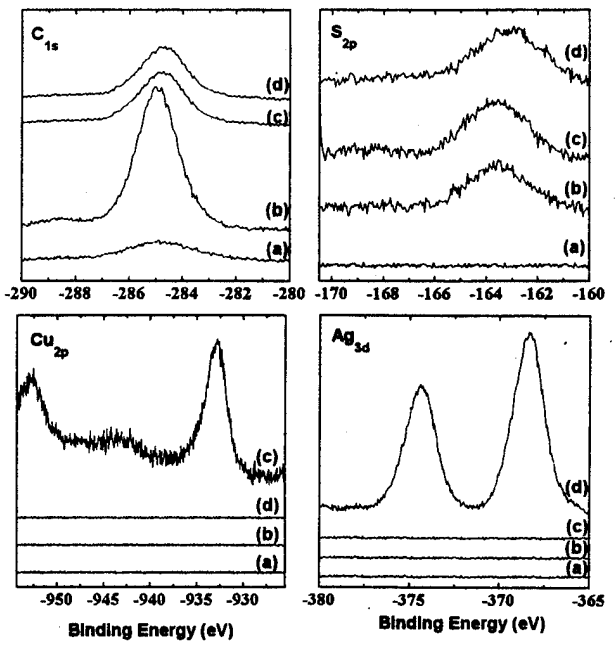


FIG. 2. XPS spectra of narrow scans for the elements of interests on γ-Fe_2O_3 surfaces with various treatments: (a) untreated; (b) MHA coated; (c) MHA coated with loaded Cu; and (d) MHA coated with loaded Ag.

are characteristic of copper ions, indicating the adsorption of copper from the solutions. The satellite band at 945 eV suggests that the majority of copper ions are in cupric form (Cu^{2+}) on MHA-coated γ-Fe_2O_3 particles. In addition, the area ratio of cupric satellite band to its $2P_{3/2}$ bands is lower than expected for pure cupric ions, suggesting that some of the copper ions are in a cuprous state. It appears that some cupric ions get reduced as a result of thiol oxidation to disulphide, sulphonate or sulphate, which accounts for the presence of an additional sulphur band of higher binding energy and low intensity (Fig. 2: S). In the case of silver-loaded particles, two bands at 368 and 374 eV are observed (Fig. 1: spectrum *d*; Fig. 2: Ag), suggesting that silver binds to MHA-coated γ-Fe_2O_3 particles.

The loading efficiency is evaluated by calculating the ratio of band area normalized by the element sensitivity factors. The calculation shows a 60% coverage of surface sulphur by copper ions and 80% by silver ions, demonstrating the potential use of MHA-coated γ-Fe_2O_3 particles in recovery of Ag and Cu from industrial effluent. The results suggest that each silver ion binds with one sulphur on MHA-coated γ-Fe_2O_3 particles. Whether each copper ion binds with two surface sulphurs is not clear. It appears that cuprous ions bind predominately with one while cupric ions bind with two sulphur atoms. This accounts for the low coverage of sulphur by copper ions (60%), yet higher than 50% as expected for a S:Cu coordination of 2:1.

C. Magnetic properties

The room temperature magnetization curve for the γ-Fe_2O_3 particles, obtained on a VSM, is shown in Fig. 3. A saturation magnetization of 52.7 emu/g at 1 Tesla was obtained for untreated γ-Fe_2O_3 particles, representing a strong magnetization. Only a marginal decrease in the saturation magnetization (2 emu/g) was observed when γ-Fe_2O_3 particles are coated with MHA. A common feature of these two magnetization curves is their small hysteresis and coercivity of magnetization, indicating that these particles are close to superparamagnetic at room temperature. It is also possible that the nanosized magnetic particles inverse magnetization by a rigid body rotation, contributing to an observed low coercivity. However, this is unlikely to be the case since the particles were pressed into a pellet form in our VSM experiments. Therefore, the observed low coercivity suggests that nano-sized γ-Fe_2O_3 particles do not become permanently magnetized after exposure to an external magnetic field. This property permits the particles to be redispersed without magnetic aggregation. Hence, the particles may be reused or recycled. It is also interesting to note that the thin organic film coatings do not affect the magnetization characteristics of fine magnetic particles for their use as magnetic memory media.

D. Electrokinetics

Another important application of thin organic film coating on fine magnetic particles is to stabilize magnetic particles in ferrofluid. The untreated γ-Fe_2O_3 particles exhibit an isoelectric point (iep) at *p*H ~5 as shown in Fig. 4 (down

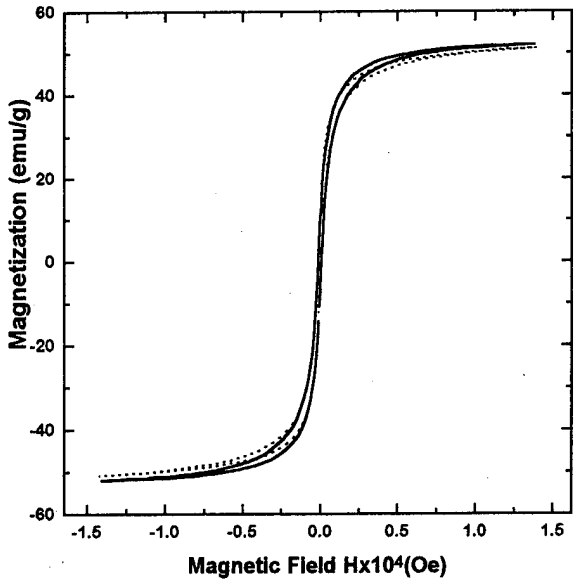


FIG. 3. Room temperature magnetization curve of γ-Fe_2O_3 obtained with vibrating sample magnetometer: solid line for untreated and dotted line for MHA-coated particles.

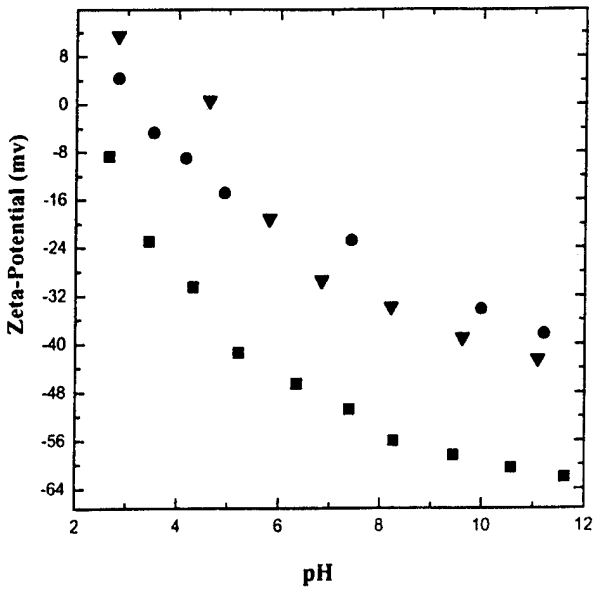


FIG. 4. Zeta potentials of γ-Fe_2O_3: down triangles for untreated particles; circle for MHA-coated particles; and square for MHA-coated particles but with further oxidation.

triangles). The particles tend to coagulate in neutral aqueous solution under the influence of molecular and magnetic attractive forces against the electrostatic double layer repulsive force which is minimal at solution *p*H's near the iep of the particles. This makes the stability of aqueous ferrofluids in neutral *p*H quite problematic, requiring the use of stabilizers. The presence of stabilizers may alter the magnetic properties of ferrofluids significantly. It has been shown that the presence of self-assembled thin organic films does not change the magnetization of γ-Fe_2O_3 particles. The ζ-potential measurement showed (Fig. 4: circles) that the iep remained the same while the ζ-potential becomes more negative above the iep when γ-Fe_2O_3 particles are coated with MHA. As a result, only marginal increase in electrostatic double layer repulsive force is expected. However, when the MHA monolayer on γ-Fe_2O_3 gets oxidized with ozone bubbling, the γ-Fe_2O_3 becomes negatively charged over the whole *p*H range studied (Fig. 4: squares). This may be attributed to the conversion of thiol or disulphide to sulphonate and/or sulphate which are the strong acids and readily dissociated. As a result, the surface retains a surface potential as high as -50 mV (so-called negative magnetic particles), inducing a strong electrostatic repulsive force between particles. This repulsive force can overcome the attractive molecular and magnetic forces. With additional short range hydration repulsion of sulphonate or sulphate groups, stable ferrofluids of high solid content can, therefore, be prepared for various industrial applications.

IV. CONCLUSIONS

The present work demonstrates that the self-assembly method can be used to prepare nanosized magnetic particles of a given functionality. The γ-Fe_2O_3 particles with reactive thio and/or disulphide groups were obtained by self-assembly of 16-mercaptohexadecanoic acid (MHA) from chloroform solutions. The presence of surfactant monolayers on γ-Fe_2O_3 has a marginal effect on its magnetization. The functionalized magnetic particles with reactive thio and/or disulphide groups are capable of capturing metal ions from aqueous solution, 80% and 60% of the sulfur being covered by silver and copper, respectively. The functionality of thiol on coated magnetic particles can be further modified by controlled oxidation to extend the application of self-assembled organic monolayers to stabilizing ferrofluids.

[1] J. Y. Huang, U.S. Patent 4,834,898 (1989); U.S. Patent 4,906,382 (1990).
[2] Q. Liu and F. J. Friedlaender, Mineral Eng. **7**, 449 (1994).
[3] Q. Liu and F. J. Friedlaender, IEEE Trans. on Magn. **30**, 4668 (1994).
[4] O. Olsvik, T. Popovic, E. Skjerve, K. S. Cudjoe, E. Hornes, J. Ugestad, and M. Uhlen, Clin. Microbiol. Rev. **7**, 43 (1994).
[5] S. V. Sonti and A. Rose, J. Colloid Interface Sci. **170**, 575 (1995).
[6] L. Nunez, B. A. Buchholz, and G. F. Vandegrift, Separation Sci. Technol. **30**, 1455 (1995).
[7] I. Enton, I. de Sabata, and L. Vekas, J. Magn. Magn. Mater. **85**, 219 (1990).
[8] P. Goldman, in *Electronic Ceramics: Properties, Devices and Applications*, edited by L. M. Levinson (Dekkee, New York, 1988).
[9] A. P. Philipse, M. P. B. van Bruggen, and C. Pathmamanoharan, Langmuir **10**, 92 (1994).
[10] R. K. Iler, in *The Chemistry of Silica* (Wiley, New York, 1979), p. 87.
[11] A. Wooding, M. Kilner, and D. Lambrick, J. Colloid Interface Sci. **149**, 98 (1992).
[12] C. Menager and V. Cabuil, J. Colloid Interface Sci. **169**, 251 (1995).
[13] J. Ugelstad, A. Berge, T. Ellingsen, R. Schmid, T. N. Nilsen, P. C. Mork, P. Stenstad, E. Hornes, and O. Olsvik, Prog. Polym. Sci. **17**, 87 (1992).
[14] C. K. Mathews and K. E. van Holds, *Biochemistry* (Benjamin/Cummings, Redwood City, CA, 1990), Chap. 14, p. 500.
[15] O. Olsvik, T. Popovic, E. Skjerve, K. S. Cudjoe, E. Hornes, J. Ugestad, and M. Uhlen, Clin. Microbiol. Rev. **7**, 43 (1994).
[16] T. E. Thomas, S. J. R. Abraham, E. W. Blackmore, and P. M. Lansdorp, J. Immunological Methods **154**, 245 (1992).
[17] A. Ulman, *An Introduction to Ultrathin Organic Film From Langmuir-Blodgett to Self-Assembly* (Academic, Boston, 1991).
[18] Q. Liu and Z. Xu, Langmuir **11**, 4617 (1995).
[19] C. H. Zhong and M. D. Poter, J. Am. Chem. Soc. **116**, 11616, (1994).

Catalytic activity of catalase under strong magnetic fields of up to 8 T

S. Ueno and M. Iwasaka
Institute of Medical Electronics, Faculty of Medicine, University of Tokyo, Tokyo 113, Japan

The question of whether or not magnetic fields affect enzymatic activity is of considerable interest in biomagnetics and biochemistry. This study focuses on whether magnetically related enzymatic activities can be affected by magnetic fields. We examined the effect of magnetic fields of up to 8 T on catalytic decomposition of hydrogen peroxide (H_2O_2). We observed changes in absorbance of reaction mixture of hydrogen peroxide and catalase at 240 nm, during and after magnetic field exposures. When the reaction mixture was not treated with nitrogen-gas bubbling, it was observed that the initial reaction rate of the reaction which was exposed to magnetic fields of up to 8 T was 50%–85% lower than the control data. This magnetic field effect was not observed, however, when the reaction mixture was bubbled with nitrogen gas to remove the dissolved oxygen molecules which were produced in the solution. We also measured concentration of dissolved oxygen which was produced by the decomposition of hydrogen peroxide. Dissolved oxygen concentration in the reaction mixture which was exposed to magnetic fields increased 20%–25% compared to the control solution. The results of the present study indicate that magnetic fields affect dynamic movement of oxygen bubbles which are produced in the reaction mixture by the decomposition of hydrogen peroxide, but not the catalytic activity of catalase itself. © *1996 American Institute of Physics.*
[S0021-8979(96)49608-3]

I. INTRODUCTION

The question of whether magnetic fields affect enzymatic activity or not is of considerable interest in biomagnetics and chemistry.

Catalase, which is an important heme protein in the body used to decompose toxic hydrogen peroxide, contains a ferric state (Fe^{3+}) iron atom, therefore its magnetic property shows paramagnetism.

It has been reported that magnetic fields of up to 6 T enhanced the activity of catalase 4.9%–52%.[1,2]

In our former study, however, we observed that magnetic fields of up to 1.0 T did not alter the rate of decomposition of hydrogen peroxide catalyzed by catalase.[3] Another group reproduced the negative results of catalase activity at 1.0 T.[4]

Oxygen molecules, which are produced by decomposition of hydrogen peroxide, are paramagnetic. We have reported that the oxygen absorption rates and desorption rates in a solution were modulated by the spatial distribution of oxygen gas in the air.[5] We have also reported that dissolved oxygen concentration was redistributed in magnetic fields of up to 8 T.[6]

In the present report, we examined the effect of magnetic fields of up to 8 T on catalytic decomposition of hydrogen peroxide (H_2O_2). Change in absorbance at 240 nm and dissolved oxygen concentration were measured.

II. METHOD

We used a horizontal type of superconducting magnet 700-mm long with a bore of 100 mm in diameter. The magnet produced 8 T at its center.

We investigated catalytic decomposition of hydrogen peroxide by catalase in a homogeneous magnetic field of 8 T, and in gradient magnetic fields where products of B and the gradient were 350–400 T^2/m.

A. Absorbance measurement

We carried out two types of experiments to evaluate the activity of catalase by changes in absorbance at 240 nm. The rate of disappearance of hydrogen peroxide was measured by observing the decrease in absorbance at 240 nm:

$$2H_2O_2 \xrightarrow{\text{catalase}} O_2 + 2H_2O. \quad (1)$$

First, absorbance of hydrogen peroxide was measured before and after an 8 T magnetic field exposure. In this case, low concentrations of catalase solutions were used. The reaction was started by the addition of 5 μl of catalase to 3 ml of hydrogen peroxide. Final concentration of catalase and hydrogen peroxide was 0.0125 μM and 10 mM, respectively. Reaction mixtures were exposed to a magnetic field of 8 T for 80 s at 30 °C±0.1 °C. After the mixture was removed from the magnetic fields, the absorbance of the mixture at 240 nm was immediately measured with a spectrophotometer.

The rate of reaction was evaluated by the reaction velocity constant $k=(1/t)\ln(c0/c1)$, where t is the reaction time, $c0$ the initial absorbance, and $c1$ the absorbance of the solution after t s.

Second, changes in the absorbance of hydrogen peroxide were measured during the 8 T magnetic field exposure. We made an absorbance measuring system in the superconducting magnet, as shown in Fig. 1. Rays from a deuterium lamp were introduced into the bore of the magnet. A reaction mixture in a cell with 1 cm optical path was kept in a temperature stabilized holder (25 °C±0.1 °C). Rays penetrated the cell and were introduced into an optical fiber which was connected to a monochromator.

Absorbance of the reaction mixture at 240 nm was continuously measured with and without nitrogen-gas bubbling. In order to de-gas oxygen bubbles and stir the reaction mixture, the nitrogen-gas bubbling was carried out by introduc-

 0021-8979/96/79(8)/4705/3/$10.00 © 1996 American Institute of Physics

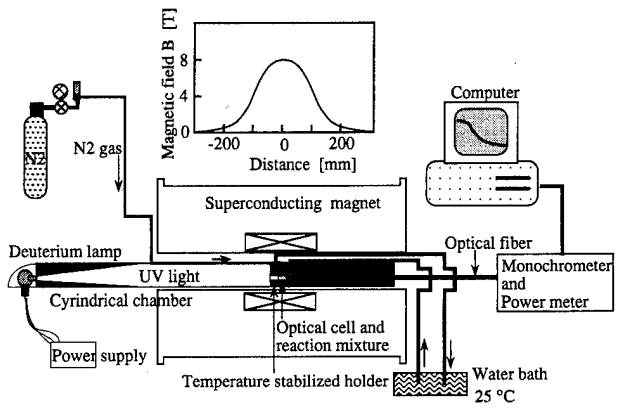


FIG. 1. Experimental setup to measure absorbance of a reaction mixture in magnetic field.

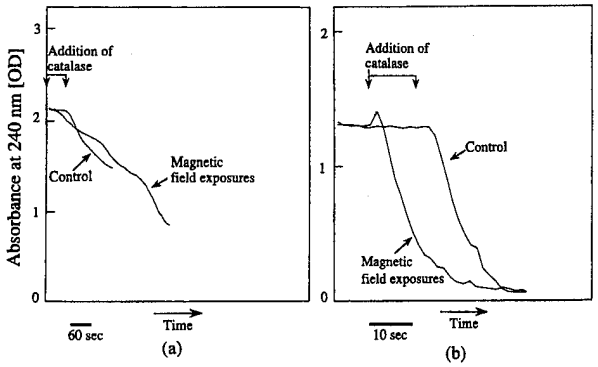


FIG. 3. Changes in the absorbance of hydrogen peroxide (a) without and (b) with nitrogen-gas bubbling. Catalase concentration was 0.03 μM. Hydrogen peroxide concentration was (a) 50 mM and (b) 20 mM.

ing nitrogen gas into the reaction mixture. Final concentration of catalase and hydrogen peroxide was 0.03–0.3 μM and 2.5–50 mM, respectively.

We also measured the decomposition of hydrogen peroxide by catalase in gradient magnetic fields where products of B and the gradient were 350–400 T^2/m.

B. Dissolved oxygen measurement

The rate of the decomposition of hydrogen peroxide by catalase was evaluated by the amount of dissolved oxygen concentration. A reaction mixture in a 50-ml beaker (30 ml hydrogen peroxide and 20 μl of catalase) was incubated in the thermal stabilization case, with and without an 8 T magnetic field. The final concentration of catalase and hydrogen peroxide was 3 nM and 30 mM, respectively. After 3–40 min of incubation at 25 °C±0.2 °C, a reaction mixture was taken out from the thermal stabilization case. Dissolved oxygen concentration was measured with a Clark type dissolved oxygen meter.

III. RESULTS AND DISCUSSION

The reaction velocity constant k of samples exposed to an 8 T magnetic field and control samples ($n=13$) was 1.2 ± 0.1[$\times 10^{-3}$] and 1.3±0.2 [$\times 10^{-3}$], respectively, as shown in Fig. 2.

Figure 3(a) shows the changes in the absorbance of hydrogen peroxide without nitrogen-gas bubbling. It was observed that initial reaction rate in magnetic fields of up to 8 T was 79% lower than the control. However, as shown in Fig. 3(b), this kind of positive effect of magnetic fields on initial reaction rate was not obtained in the condition with nitrogen-gas bubbling.

Figure 4 shows double reciprocal plots of the initial reaction rate v and the substrate concentration $[S]_0$ in the decomposition of hydrogen peroxide by catalase with and without nitrogen-gas bubbling. Similar to the results in Fig. 3, magnetic fields of up to 8 T affect the initial reaction rate v

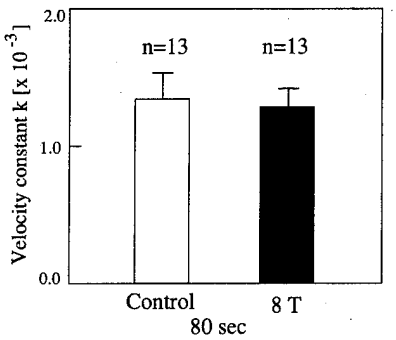


FIG. 2. Decomposition of hydrogen peroxide by catalase. Vertical line shows reaction velocity constant $k = (1/t)\ln(c0,c1)$, where t=80 s, $c0$ the initial absorbance, and $c1$ the absorbance of the solution after 80 s.

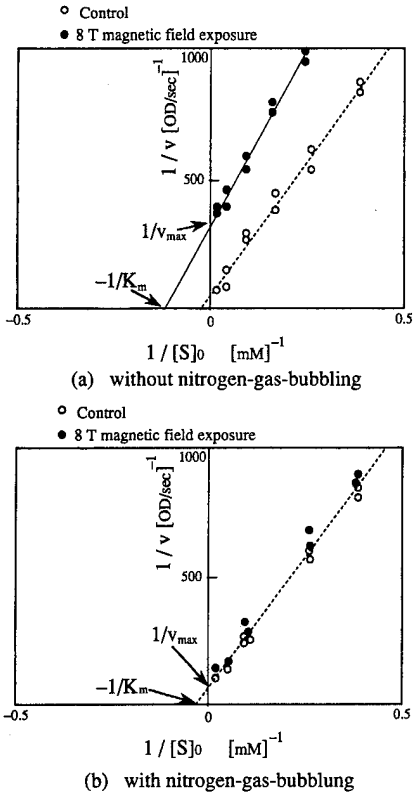


FIG. 4. Double reciprocal plots of the initial reaction rate v and the substrate concentration $[S]_0$ in the decomposition of hydrogen peroxide by catalase (a) without and (b) with nitrogen-gas bubbling. V_{max} is the maximum initial rate, and K_m is the Michaeris constant.

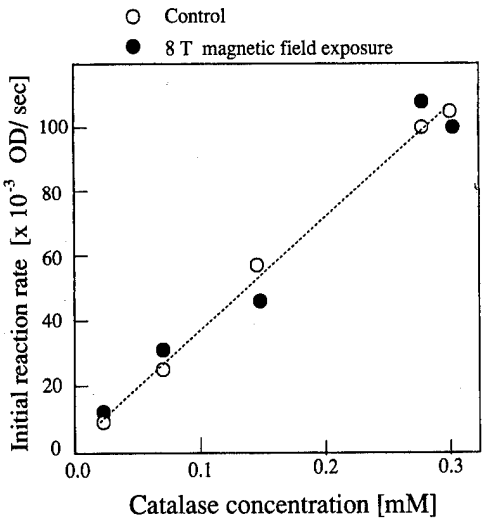


FIG. 5. Dependence of initial reaction rate on concentrations of catalase.

when the reaction proceeds without nitrogen-gas bubbling. The maximum initial rate V_{max} in magnetic fields is $\frac{1}{7}$ of the control.

In contrast, we obtained clear negative results with nitrogen-gas bubbling.

Dependence of initial reaction rate on concentrations of catalase is shown in Fig. 5. The data were obtained with nitrogen-gas bubbling. No significant effects were observed.

The results in Figs. 3 and 4 indicate that oxygen molecules which are produced by decomposition of hydrogen peroxide disturb the reaction significantly. Ejection of dissolved oxygen by nitrogen-gas bubbling removes the effects. There is a possibility that the magnetic fields restrain the evaporation of dissolved oxygen molecules from a reaction mixture.

It is necessary to investigate the changes in concentration of dissolved oxygen in reaction mixture. Figure 6 shows the results of dissolved oxygen measurement. No significant effects were observed during 3–5-min and 35–50-min period after the addition of catalase. On the other hand, dissolved oxygen concentration of the mixture which was exposed to an 8 T magnetic field increased 20%–25% compared to the control during a 10–20-min period.

We observed that the decomposition process of hydrogen peroxide catalyzed by a high concentration catalase generated visible oxygen bubbles. Aggregated visible oxygen bubbles can be attracted by strong magnetic fields with high gradients.[6] We have observed that dissolved oxygen concentration was redistributed in magnetic fields of up to 8 T.[6] We also observed that the oxygen desorption rate in a solution

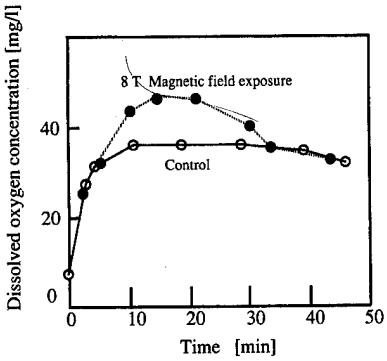


FIG. 6. Effect of magnetic field at 8 T on dissolved oxygen concentration which was generated by the decomposition of hydrogen peroxide by catalase.

was modulated by the spatial distribution of oxygen gas in the moist atmosphere.[5]

If a process of enzymatic reactions involve a radical pair, there is the possibility that magnetic fields affect the singlet-triplet conversion rate of radical pairs. The enzymatic reactions which involve photochemical processes are the most promising magnetically sensitive enzymatic reactions. The magnetic field effects on photochemical reactions were verified.[7–9]

Apart from the photochemical reactions, it is important to study the enzymatic reactions that involve radicals which are generated from nonphotochemical processes. It has been reported that magnetic fields of 0.10–0.15 T affected B_{12} ethanolamine ammonia lyase.[10]

The results of the present study indicate that magnetic fields of up to 8 T affect the dynamic movement of oxygen bubbles which are produced in the reaction mixture by hydrogen peroxide decomposition, but not the catalytic activity of catalase itself.

ACKNOWLEDGMENT

This work was supported in part by Grants from the Ministry of Education, Science and Culture.

[1] W. Haberditzl, Nature **213**, 72 (1967).
[2] L. M. Vainer, A. V. Podoplelov, T. V. Leshina, R. Z. Sagdeyev, and Yu. N. Molin, Biophysics (Biofizika) **23**, 2, 234 (1978).
[3] S. Ueno and K. Harada, IEEE Trans. Magn. **MAG-22**, 5, 868 (1986).
[4] K. Hummel, K. Martl, and M. G. Martl, J. Mol. Cat. **54**, L1 (1989).
[5] S. Ueno and K. Harada, IEEE Trans. Magn. **MAG-18**, 6, 1704 (1982).
[6] S. Ueno, M. Iwasaka, and T. Kitajima, J. Appl. Phys. **75**, 10, 7174 (1994).
[7] N. Hata, Chem. Lett. 547 (1976).
[8] Y. Tanimoto, H. Hayashi, S. Nagakura, H. Sakaguchi, and K. Tokumara, Chem. Phys. Lett. **41**, 267 (1976).
[9] K. Shulten, H. Staerk, A. Weller, H. J. Werner, and B. Nickel, Z. Phys. Chem. N. F. **101**, S371 (1976).
[10] T. T. Harkins and C. B. Grissom, Science **263**, 958 (1994).

Measurement of clottability of fibrin polymers using magnetic orientation

M. Iwasaka and S. Ueno
Institute of Medical Electronics, Faculty of Medicine, University of Tokyo, Tokyo 113, Japan

H. Tsuda
Clinical Laboratory, Kyushu University Hospital, Kyushu University, Fukuoka 812, Japan

Fibrin polymers, as a kind of diamagnetic material, are oriented parallel to the direction of magnetic fields. We investigated the polymerization of partially digested fibrinogens in an 8 T magnetic field in order to observe the clotting ability of various sizes of fibrinogen fractions using a magnetic orientation technique. We purified high-molecular weight fraction (F1) and low-molecular weight fraction from human fibrinogen (F2). Fibrin gels were formed in an 8 T magnetic field for 9 h, and transmittancies were measured to evaluate the degree of magnetic orientation. The results show that a lack at the C-terminal half of one Aα chain did not affect the magnetic orientation of fibrin. We also investigated the effect of the digestion of fibrinogen by plasmin on the magnetic orientation of fibrin. The result shows that partially digested fibrin molecules also orient in an 8 T magnetic field. However, the degree of magnetic orientation significantly decreases when fragment *X* and fragment *Y* appear. © *1996 American Institute of Physics.* [S0021-8979(96)49708-X]

I. INTRODUCTION

In the last process of blood coagulation, fibrinogen molecules change to fibrin monomers through the action of protease thrombin. Fibrin monomers are polymerized and form various sizes of fibers to become a gel. A fibrinogen molecule is a kind of diamagnetic material which has diamagnetic anisotropy. In the course of the polymerization process of fibrin, when a magnetic field of 10 to 20 T intensity is applied, the fibrin fibers orient parallel to the magnetic fields.[1–3] Some studies reported on the mechanisms of the polymerization process using the magnetic orientation of fibrin.[4–6] To investigate the fibrin structure and the mechanism of fibrin assembly, effects of coagulation factors such as Ca^{2+}, factor XIIIa, the fibrinopeptides on magnetic orientation of fibrin were clarified.[4,6] It was reported that ferromagnetic particles affected the magnetic orientation of fibrin polymers.[3] We have reported that magnetic orientation of fibrin fibers is observed in the fibrinolytic process.[7]

However, effects of degradation of fibrinogen molecules on magnetic orientation are not clear.

In this study, we investigated the polymerization of partially digested fibrinogens in an 8 T magnetic field in order to observe the clotting ability of various sizes of fibrinogen fractions using a magnetic orientation technique.

A fibrinogen molecule has three types of polypeptide chains. Each chain has the important role of binding other fibrin molecules. A simplified model of a fibrinogen molecule is shown in Fig. 1.[8] It is known that there are two types of fibrinogen fractions: high-molecular weight fractions and low-molecular weight fractions which lack the C-terminal half of one of the Aα chain that is one of three types of chains.[9] It is an interesting question whether the C-terminal half of one of the Aα chain has any effect on the magnetic orientation of fibrin.

II. MATERIALS AND METHODS

A. Magnetic field exposure system and measurement of magnetic orientation

We used a horizontal type of superconducting magnet 700 mm long with a 100 mm diameter bore. The magnet produced magnetic fields of up to 8 T at its center.

We used a spectrophotometer to observe the magnetic orientation of fibrin. Polarizing plates were placed before and after the optical cell holder, as shown in Fig. 2. The polarizing angle of the plate placed after the optical cell holder was

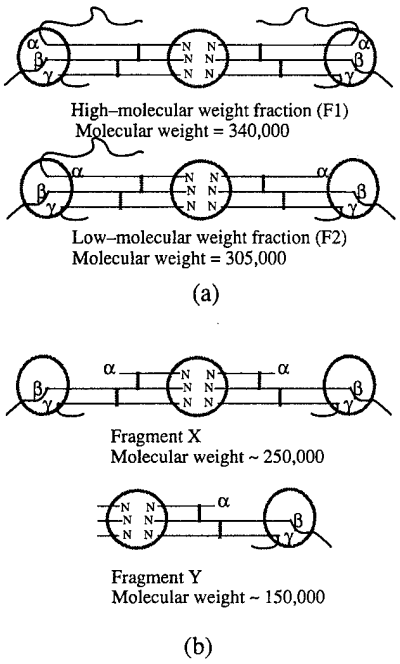


FIG. 1. Simplified model of a fibrinogen molecule and fractions. (a) Two types of fibrinogen fractions: high-molecular weight fractions and low-molecular weight fractions which lack the C-terminal half of one of the Aα chain that is one of three types of chains. (b) Fragment *X* and fragment *Y*.

 0021-8979/96/79(8)/4708/3/$10.00 © 1996 American Institute of Physics

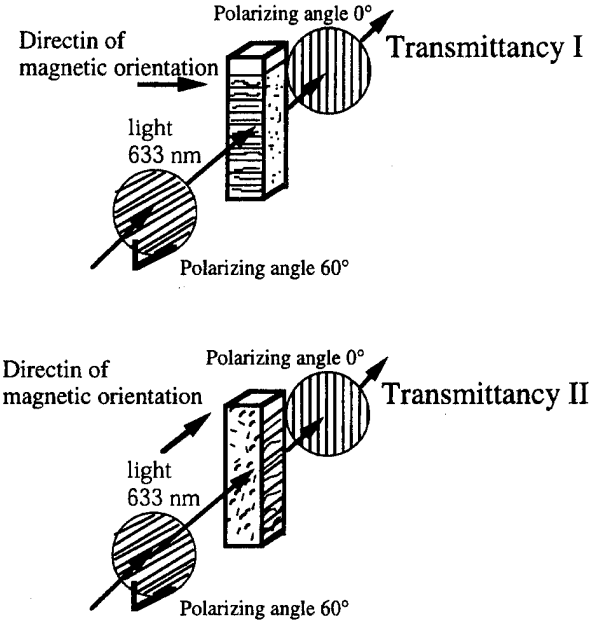


FIG. 2. Experimental setup to measure magnetic orientation of fibrin polymers.

0°, and the plate placed before the optical cell holder was 60°.

When fibrin polymers in an optical cell were oriented in a particular direction, optical anisotropy was observed as the difference of transmittancies (ΔT [%]) through two sides of the cell. This is a modulated method for measuring magnetic birefringence.[10] We measured two types of transmittancies of fibrin gel in a cell. One was the transmittance when the direction of light was parallel to the direction of the magnetic orientation of fibrin, and the other was the transmittancy when the direction of light was vertical to the direction of the orientation of fibrin. Fibrin gels were formed in an 8 T magnetic field for 9 h, and ΔT was measured to evaluate the degree of magnetic orientation.

B. Preparation of high- and low-molecular weight fraction from human fibrinogen

We purified high-molecular weight fraction (F1) and low-molecular weight fraction (F2) from human fibrinogen, according to the method reported by Hasegawa *et al.*[11]

C. Digestion of bovine fibrinogen with plasmin

We also investigated the effect of the digestion of fibrinogen by plasmin on the magnetic orientation of fibrin. Fibrinogen solutions (3.7, 1.5, and 0.66 mg/ml) were incubated with various concentrations of plasmin or without plasmin for 7 min at 37 °C. Each solution was mixed with 1 ml of tranexamic acid to stop the digestion of fibrinogen.[12] After fibrin gels were coagulated in an 8 T magnetic field, the ΔT of each gel was measured.

TABLE I. Magnetic orientation of two types of human fibrin. DT of F1 rich solution (F1:F2=9:1) and F2 rich solution (F1:F2=1.9).

Group	F1:F2	Concentration [mg/ml]	ΔT at 633 nm [%]
F1 rich	9:1	0.21	5.4
F2 rich	1:9	0.20	5.8

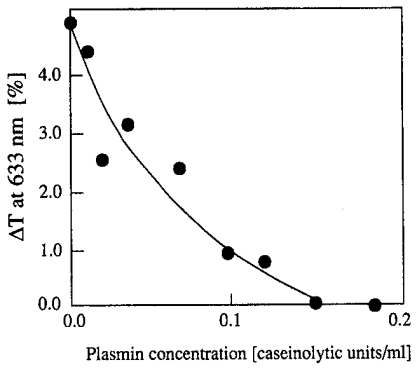


FIG. 3. Magnetic orientation of partially degraded bovine fibrin polymers. Concentration of fibrinogen was 3.7 mg/ml. Final concentration of plasmin varied from 0.016 to 0.16 [caseinolytic units/ml].

III. RESULTS AND DISCUSSION

Human fibrinogen solutions (0.2 mg/ml) were incubated with 5 μl of thrombin (5 NIH units/ml). ΔT of F1 rich solution (F1:F2=9:1) and F2 rich solution (F1:F2=1:9) was 5.4% and 5.8%, respectively, as shown in Table I. The results show that a lack of the C-terminal half of one Aα chain did not affect the magnetic orientation of fibrin.

Low-molecular weight fraction (F2) only lacks the C-terminal half of one of the Aα chain that is one of three types of chains. We investigated the magnetic orientation of bovine fibrinogen fractions which were further digested than the F2 fraction.

Figure 3 shows the results of magnetic orientation measurement of bovine fibrinogen fractions. It was observed that ΔT decreased depending on the amount of plasmin. When the final concentration of plasmin was more than 0.160 [caseinolytic units/ml], ΔT was zero.

Table II shows the results in the range of fibrinogen concentration from 0.66 mg/ml (C,D) to 1.45 mg/ml (A,B). Plasmin concentrations were 10 [$\times 10^{-3}$ caseinolytic units/ml] for A and C samples, 30 [$\times 10^{-3}$ caseinolytic units/ml] for B

TABLE II. Critical conditions for observing magnetic orientations of fibrin polymers. Fibrinogen–plasmin ratio shows the ratio of fibrinogen concentration [mg/ml] to plasmin activity [caseinolytic units/ml].

Sample	A	B	C	D
Fibrinogen concentration [mg/ml]	1.45	1.45	0.66	0.66
Plasmin concentration [caseinolytic units/ml]	0.01	0.03	0.01	0.05
Fibrinogen–plasmin ratio [mg/caseinolytic units]	145.0	48.3	66.0	13.2
ΔT at 633 nm [%]	3.9	1.4	2.3	0.1

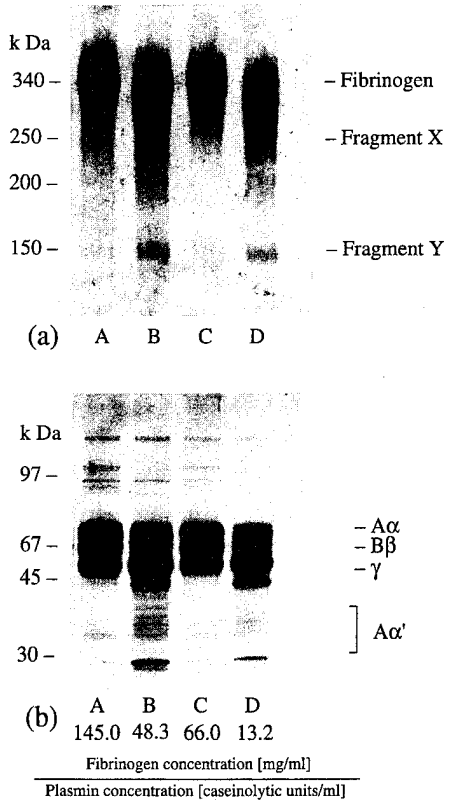


FIG. 4. SDS-PAGE of the degradation products of fibrinogen produced by plasmin. Same samples are shown in Table II. (a) Under nonreducing condition (4% gel), (b) under reducing condition (10% gel).

sample, and 50 [$\times 10^{-3}$ caseinolytic units/ml] for D sample. The fibrinogen–plasmin ratios show fibrinogen concentration [mg/ml]/plasmin activity [caseinolytic units/ml]. Depending on the fibrinogen–plasmin ratio, ΔT changed, and reached almost zero when the fibrinogen–plasmin ratio was 13 [mg/caseinolytic units]. This condition is critical in observing the magnetic orientation of partially digested fibrinogen.

Figure 4 shows the results of an SDS-PAGE (Polyacrylamide Electrophoresis) analysis of partially digested fibrinogens which were the same samples in Table II. Figure 4(a) shows the SDS-PAGE patterns of fibrinogen fractions under nonreducing conditions.

It was observed that magnetically oriented fibrinogens (A, and C samples) have a molecular weight of more than 200 kD. On the other hand, magnetically nonoriented fibrinogen molecules (D sample) also include so-called fragment X, and fragment Y. Although sample B included fragment X and fragment Y, concentration of sample B (1.45 mg/ml) is higher than in sample D (0.66 mg/ml). Degree of magnetic orientation of sample B (1.45 mg/ml) was lower than that of sample C (0.66 mg/ml). The results show that degree of magnetic orientation depends not only on the size of fibrinogen fractions, but also on fibrinogen concentration.

The electrophoresis pattern of fibrinogens under reducing conditions in Fig. 4(b) shows that fibrinogen fractions, which did not magnetically orient, mainly consisted of Aα', Bβ, or Bβ', and γ chains.

The result indicates the level of the size of digested fibrinogen fractions which oriented parallel to the direction of magnetic fields. Partially digested fibrin molecules oriented in an 8 T magnetic field. However, the degree of magnetic orientation decreased when the amount of fragment X and fragment Y, which are produced by degradation of fibrinogen, increased.

Usually, clottability of fibrinogen is evaluated by measuring absorbance of coagulating fibrin at 350 nm. We measured the absorbance of samples shown in Fig. 4 at 350 nm. However, the difference of absorbance in the samples were smaller than 0.01 [OD]. In our experimental setup, optical anisotropy ΔT is proportional to the degree of magnetic orientation. Table II and Fig. 4 indicate that degree of magnetic orientation varies inversely with the degradation of fibrinogen.

Results of the present study suggest that it is possible to estimate the size and function of fibrinogen fractions in a polymerization process using a magnetic orientation technique more sensitively than measuring absorbance changes at 350 nm.

IV. CONCLUSION

We investigated the magnetic orientation of degraded fibrinogen fractions which were produced by plasmin. We observed that optical anisotropy—the degree of magnetic orientation—decreased with the digestion of fibrinogen by plasmin.

Results of SDS-PAGE analysis indicate that the degree of magnetic orientation significantly decreases when fragment X and fragment Y appear.

ACKNOWLEDGMENT

This work was supported in part by Grants from the Ministry of Education, Science and Culture in Japan.

[1] J. Torbet, M. Freyssinet, and G. Hudry-Clergeon, Nature **289**, 91 (1981).
[2] A. Yamagishi, T. Takeuchi, T. Higashi, and M. Date, J. Phys. Soc. Jpn. **58**, 2280 (1989).
[3] S. Ueno, M. Iwasaka, and H. Tsuda, IEEE Trans. Magn. **29**, 3352 (1993).
[4] J. M. Freyssinet, J. Torbet, G. Hudry-Clergeon, and G. Maret, Proc. Natl. Acad. Sci. U.S.A. **80**, 1616 (1983).
[5] G. Hudry-Clergeon, J. M. Freyssinet, J. Torbet, and J. Marx, Ann. NY Acad. Sci. **408**, 380 (1983).
[6] J. Torbet, Biochem. J. **244**, 633 (1987).
[7] M. Iwasaka, S. Ueno, and H. Tsuda, IEEE Trans. Magn. **30**, 4695 (1994).
[8] S. V. Pizzo, J. Biol. Chem. **247**, 636 (1972).
[9] A. Nakashima, S. Sasaki, K. Miyazaki, T. Miyata, and S. Iwanaga, Blood Coagulation Fibrinolysis **3**, 361 (1992).
[10] G. Maret and G. Weill, Biopolymers **22**, 2727 (1983).
[11] N. Hasegawa and S. Sasaki, Thrombosis Res. **57**, 183 (1990).
[12] N. Aoki and P. C. Harpel, Seminars Thrombosis Hemostasis **10**, 24 (1984).

Analysis of extremely low frequency brain magnetic fields associated with short-term memory and recognition processes (abstract)

Hideki Yoshida
Department of Computer Science and Communication Engineering, Kyushu University, Fukuoka 812, Japan

Shoogo Ueno
Institute of Medical Electronics, Faculty of Medicine, University of Tokyo, Tokyo 113, Japan

Douglas Cheyne and Harold Weinberg
Brain Behavior Laboratory, Discovery Park at Simon Fraser University, Burnaby, British Columbia, V5A 1S6, Canada

One of the advantages of neural magnetic measurement using a dc-SQUID machine is to measure magnetic fields associated with the direct current or the extremely low frequencial components of neural electric activities. In this study, the order of four tones is memorized by the subject and compared with that of another four tones. The extremely slow magnetic fields were observed by using this paradigm. Two kinds of tones (two octaves apart: the 1046.5 Hz tone and the 261.6 Hz tone) were used. A male subject memorized the order of four tones chosen randomly. After 1.4 s rest, the other four tones were presented. The subject discriminated the order of the first tones from that of the last tones in the forward order. When another long (1 s) tone was presented 2.4 s later, the subject was to push either a true or a false button. Pushing the true button meant the order of the first four tones was the same as that of the last in the forward order. Pushing the false button meant the order was not the same. The whole-cortex 64 channels of MEG data were digitized with a sampling frequency of 125 Hz, and filtered (zero phase shift, low pass digital filter with a cutoff at 20 Hz). In comparison with the control wave, the wave during memorizing clearly includes very low frequency components. We observed that the intensities of the power spectral components at 0.5 Hz during memorizing and recognition is higher than that of the control power spectral components, and tried to make the topographies using the differences between the power spectral components at 0.5 Hz during memory and recognition and the control power spectral components. Because the memory processes affect the very low frequency components of MEG, the current dipole source models are made from the data filtered below 0.5 Hz. We observed that the memory processes affected the very low frequency components of MEG. We estimated the current dipole sources using MEG data below 0.5 Hz. © *1996 American Institute of Physics.* [S0021-8979(96)59608-4]

Artifacts in magnetic resonance imaging from metals

L. H. Bennett, P. S. Wang, and M. J. Donahue
National Institute of Standards and Technology, Gaithersburg, Maryland 20899

Metallic biomedical implants, such as aneurysm clips, endoprostheses, and internal orthopedic devices give rise to artifacts in the magnetic resonance image (MRI) of patients. Such artifacts impair the information contained in the image in precisely the region of most interest, namely near the metallic device. Ferromagnetic materials are contraindicated because of the hazards associated with their movement during the MRI procedure. In less-magnetic metals, it has been suggested that the extent of the artifact is related to the magnetic susceptibility of the metal, but no systematic data appear to be available. When the susceptibility is sufficiently small, an additional artifact due to electrical conductivity is observed. We present an initial systematic study of MRI artifacts produced by two low susceptibility metals, titanium (relative permeability $\mu_r \approx 1.0002$) and copper ($\mu_r \approx 0.99998$), including experimental, theoretical, and computer simulation results. © *1996 American Institute of Physics.* [S0021-8979(96)49808-4]

The recent report[1] of a fatal outcome when magnetic resonance imaging (MRI) was performed on the head of a patient having a ferromagnetic intracerebral aneurysm clip in place reemphasized the importance of the magnetic properties of clips or other surgical materials placed in the human body. Currently, most of the clips and many of the other implants are made of nonferromagnetic materials. Even so, when a patient with a "nonmagnetic" metal in the body is subjected to a MRI, an artifact is produced which causes a drop-out of signal near the metallic surface. This is an unfortunate circumstance, making it impossible to investigate a treated aneurysm, as the signal is degraded in precisely the region of most interest to the surgeon.

The artifacts produced in MRI by material magnetic susceptibility have been widely studied. For example, Patton[2] provides an overview of MR imaging and artifacts, and Lüdeke, Röschmann, and Tischler[3] give a particularly complete discussion of susceptibility related effects caused by (nonconducting) spheres and cylinders. A recent study[4] reports on the influence of small quantities of iron particles on MR images, and includes a comparison of the size of the artifact as a function of the particle mass. There has been less attention paid to MRI artifacts caused by eddy currents, but such effects have been observed.[5,6]

In this paper we report on artifacts in proton MR imaging produced by nonferromagnetic metals in an aqueous medium, including both experimental and theoretical results. In addition to an effect from the material susceptibility, we also observed an artifact caused by eddy currents in the metal. For materials with extremely low susceptibility (e.g., copper), the eddy current effect is the dominant artifact. For materials with a slightly larger susceptibility (e.g., titanium), both susceptibility and eddy current artifacts can be observed. The importance of the object's geometry on the extent of the susceptibility-induced artifact is also demonstrated. In particular, we show and explain how increasing the length of a Ti rod can decrease the MRI artifact (a similar effect was reported but not explained in Ref. 4), and give rise to a bimodal free induction decay frequency response.

The nuclear MR (NMR) imaging facility consists of a Bruker MSL-400 system with micro-imaging accessories. The spectrometer has a superconducting magnet of 9.394 T which corresponds to a ^{1}H resonant frequency of ≈400 MHz. A set of gradient coils generates field gradients of 9.785×10^{-2}, 3.549×10^{-2}, and 1.175×10^{-2} T/m along the x (reading), y (phase encoding), and z (slicing) axes, respectively. A 15-mm-wide by 30-mm-high rf coil was used for detecting nuclear spin-echo signals of the aqueous protons, with a $(\pi/2)$-τ-π-τ echo pulse sequence. More details on the experimental setup can be found elsewhere.[7]

We report here on experiments with 2-mm-diam copper and titanium rods of various lengths, submerged in water inside a 9-mm-inner-diam NMR tube. The applied field was shimmed initially for best response with the NMR tube and water alone. The shimming was left untouched for the rest of the experiments. Each rod was aligned with its long axis parallel to the static field (i.e., along the z-axis), and was held in place at the lower end with a teflon disk. The position of the lower end of each rod was the same, with the longer rods extending farther up the NMR tube. The magnetic resonance images were taken with the z-coordinate slice height in the center of the detection coil, about 7 mm from the rod's lower end.

We imaged copper rods of lengths between 4 and 25 mm. The (diamagnetic) susceptibility χ_v of the material was -2×10^{-5} (SI—Systeme Internationale), and the resistivity was 17 $\mu\Omega$ mm. The Fourier transform of the NMR free induction decay consisted of a single peak, and the MRI was essentially independent of the bar length. A representative image for a 15 mm Cu rod is shown in Fig. 1(a). The dark areas indicate the presence of water, so in the absence of any artifact the image would show the cross section of the copper rod as a 2 mm white disk centered inside a 9 mm black annulus of water. The white area here is larger than the rod, and has in particular a notable four-lobe asymmetry. The low susceptibility and high conductivity of the copper and this asymmetry led us to suspect the artifact was due to eddy currents in the copper.

To test this conjecture, we imaged titanium rods of various lengths. The susceptibility of the titanium was 2×10^{-4} (SI), and the resistivity was 530 $\mu\Omega$ mm. Compared to the copper, the titanium is paramagnetic with $|\chi_v|$ 10 times larger, and the resistivity is over 30 times greater. Figure 1(b)

 0021-8979/96/79(8)/4712/3/$10.00 © 1996 American Institute of Physics

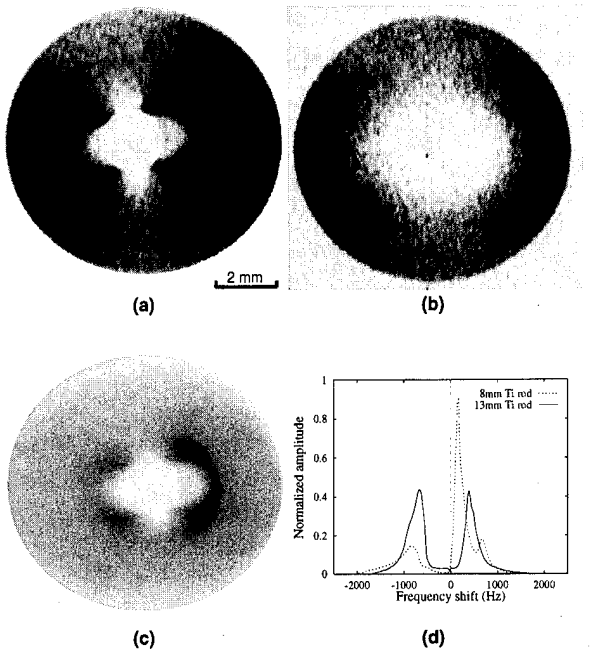


FIG. 1. Experimental results: (a) MR image cross section of a 15 mm Cu rod, (b) an 8 (mm) Ti rod, and (c) a 13 mm Ti rod; (d) Fourier transform of free induction decay for the 8 and the 13 mm Ti rods.

shows the MRI of an 8 mm Ti rod, at a cross-sectional height 1 mm below the top of the rod. Notice the circular susceptibility artifact (the white region is about 4.5 mm across, more than twice the diameter of the bar). Compare this to Fig. 1(c), which represents a cross section near the center of a 13 mm Ti rod. The artifact has a (this time dark) circular component, but exhibits mainly a four-lobe shape similar in size to that seen in the copper rod. We surmise that the symmetric susceptibility artifact is decreased because the slice is taken at a greater distance from the pole faces (i.e., the ends of the bar), and that the four-lobe artifact due to eddy currents is present in both the 8 and 13 mm Ti bar images, but is hidden in the former by the larger susceptibility artifact.

As discussed in the introduction, it is understood that material susceptibility will distort the field uniformity, and also that this can lead to a broadening of the free induction decay linewidth. We are apparently the first to report a splitting of the frequency response, as illustrated in Fig. 1(d), which is the Fourier transform of the free induction decay signal for the two Ti rod experiments. Both graphs show two peaks, but the second peak is more pronounced for the 13 mm rod. This phenomenon is examined in greater detail below.

These experimental results give strong evidence that metal objects produce MRI artifacts of two distinct natures, one due to the material's susceptibility and the second due to its conductivity. To explain these results in more detail, we developed a simple model, implemented that model as a computer simulation, and then compared the simulation results with the experiments. This model explains the observed artifacts by field inhomogeneities alone. It has two components, the first models material susceptibility effects and the second models eddy current effects. Alternately, these may be considered effects associated with the static field and the rf field, respectively.

The susceptibility effects are modeled by a pair of monopoles, one at each end of the cylindrical rod. For an applied static field of strength B_0 oriented along the positive z axis, the z component of the resultant field at point (x,y,z) is

$$B_z^{\text{static}} = B_0 + \frac{B_0 \chi_v R^2}{4}\left(\frac{z-z_t}{[x^2+y^2+(z-z_t)^2]^{3/2}} - \frac{z-z_b}{[x^2+y^2+(z-z_b)^2]^{3/2}}\right), \tag{1}$$

where χ_v is the material susceptibility, R is the radius of the bar, and z_t and z_b are the z coordinates of the top and the bottom of the bar, respectively. For nonferromagnetic materials the relative contributions of the in-plane components B_x and B_y are small enough to be neglected.

For this initial study we used a simplified eddy current model. First, replace the finite rod with an infinite cylinder, and then notice that at the frequencies of our rf pulse (400 MHz) the skin depth $\delta=(f\pi\mu\sigma)^{-1/2}$ for metals is in the micron range ($\delta_{\text{Cu}}=3.3$ μm, and $\delta_{\text{Ti}}=18$ μm). The eddy currents set up a magnetic field that exactly opposes the applied rf field below about one skin depth. Since the skin depth is negligible compared to the diameter of the rod (2 mm), our cylinder can be approximated by a cylinder that is uniformly magnetized directly equal but opposite to the applied rf pulse. For an applied pulse parallel to the y axis with amplitude $B^{\text{rf}}_{\text{applied}}$, the resultant field at position (x,y) has amplitude components

$$B_x^{\text{rf}} \approx -2xyB^{\text{rf}}_{\text{applied}}R^2(x^2+y^2)^{-2}, \tag{2}$$

$$B_y^{\text{rf}} \approx B^{\text{rf}}_{\text{applied}}[1+R^2(x^2-y^2)(x^2+y^2)^{-2}], \tag{3}$$

where R is again the radius of the bar. Note that unlike the equations for B^{static}, B^{rf} does not exhibit circular symmetry.

The static components of the field affect slice and line selection. Field inhomogeneities can shift the effective position (i.e., as seen by the reconstruction) of protons, increasing the apparent density in some regions and decreasing it in others. This effect is evident in Fig. 1(b), where the white artifact is a false indication of a decrease in the proton density, and in Fig. 1(c) where there are regions near the bar that are even darker than the undisturbed regions near the edge of the NMR tube. (For a detailed discussion of this effect see Ref. 3.) Conversely, B^{rf} does not affect slice or line selection, but rather only changes the strength of the rf pulse seen by each proton. If the rf pulse is optimized to give maximal response in the absence of eddy current counterfields, then this effect can only reduce the apparent density at any location. For a first approximation, we modeled the attenuation factor of the spin echo signal by

$$\alpha = -\sin(1.5|B^{\text{rf}}|\pi/B^{\text{rf}}_{\text{applied}})$$

for $\pi<1.5|B^{\text{rf}}|\pi/B^{\text{rf}}_{\text{applied}}<2\pi$, and 0 otherwise. For small deviations from $B^{\text{rf}}_{\text{applied}}$ this is the in-plane component of the nuclear magnetization moment resulting from a 1.5π rf pulse.

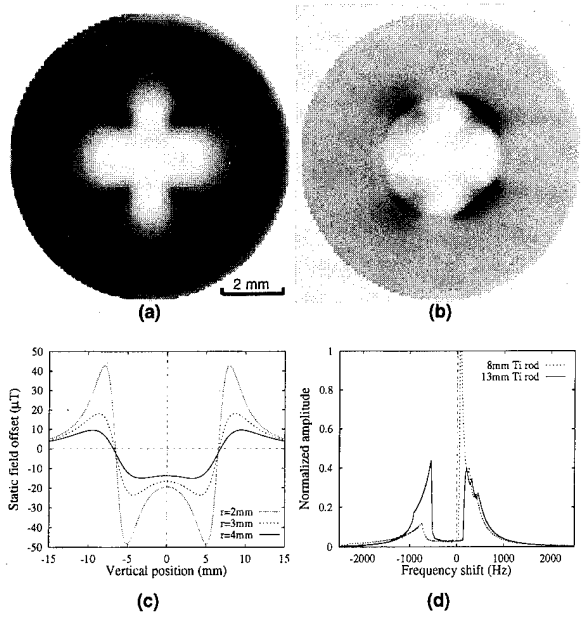


FIG. 2. Theoretical results: (a) Simulated MR image cross section of a 15 mm Cu rod, and (b) a 13 mm Ti rod; (c) field strength B^{static} for 13 mm Ti rod along lines parallel to the z axis at radial distances r=2, 3, and 4 mm; (d) simulated Fourier transform of free induction decay for 8 and 13 mm Ti rods.

The forward portion of the computer implementation (simulation of the MR data) was accomplished by partitioning the experimental volume into 0.1 mm cubic voxels, adjusting the proton densities of each voxel according to B^{rf} and the corresponding attenuation factor, and then using Eq. (1) to determine line slice (raysum) selection. Once the data were completely generated, the inverse portion of the simulation—the image reconstruction—was accomplished using a Bracewell convolution filter.[8]

Figures 2(a) and 2(b) show the resulting simulations corresponding to the 15 mm Cu and the 13 mm Ti rod experiments. A simulation of the 8 mm Ti rod experiment was also performed but is not shown. The simulations are all in qualitative agreement with the experiments. Furthermore, by running the simulation with either the susceptibility term or the eddy current term, we have verified that the four-lobe artifact is explained by eddy currents, and that the susceptibility artifact for an MR image taken in the middle of a rod will decrease with increasing rod lengths.

Let us now investigate the resonance splitting in the free induction decay observed in Fig. 1(d). If we use Eq. (1), fix $r = \sqrt{x^2+y^2}$ and allow z to vary, we obtain line profiles of the field strength along lines parallel to the z axis, as illustrated in Fig. 2(c) for a 13 mm Ti rod, where the applied field B_0 has been subtracted off. The field values at z heights near the center of the bar and also above and below the bar do not vary very much with in-plane distance r from the bar. The middle plateau corresponds to a field value of ≈ -15 μT, and the outside regions level off at ≈ 5 μT. These correspond to resonance frequencies of ≈ -640 and 210 Hz off the nominal resonant frequency of 400 MHz, not too different from the frequencies of the peaks seen in the experimental free induction decay frequency response curve of Fig. 1(d). A more accurate simulation based on Eq. (1) (taking into account, for example, the appropriate radial weighting) produces the curves presented in Fig. 2(d), and explains the relative size of the peaks as a function of the rod length.

We have shown, via both experiment and theory, that MRI artifacts from metallic objects have two distinct origins and manifestations. The first artifact source is inhomogeneity in the static field due to the material susceptibility, causing the MRI algorithm to mismap the reconstruction region. When the material susceptibility is small, a second type of artifact becomes important. This artifact type is a result of eddy currents set up in conductors by the high-frequency rf pulses, creating magnetic counterfields which change the effective amplitude of the rf pulses across the imaging region, thereby modifying the spin-echo signal and affecting the image reconstruction.

The susceptibility induced artifact has been extensively studied by others, and it is well understood that the magnitude of this effect scales with the material susceptibility. The importance of the object's geometry has perhaps not been properly appreciated, however. We show, for example, that the artifact produced in the center of a paramagnetic cylindrical rod is actually reduced by making the rod longer. Similarly, it has been understood that the susceptibility induced inhomogeneity can broaden the free induction decay resonance peak. We have shown that the field inhomogeneity from a simple rod can actually create a bimodal resonance response, and that this effect will vary with the length of the rod.

From a design standpoint, since the susceptibility induced artifact can be reduced by minimizing the susceptibility of the metallic part, one might hope to manage the eddy current induced effect by reducing the object's electrical conductivity. Note, however, that the magnitude of this effect scales with the object's width minus the skin depth. The skin depth at 400 MHz of even a relatively poor (for a metal) conductor like Ti is only 18 μm, so the impact of a metal's relative conduction on the size of the artifact is minimal.

We thank H. J. Brown for assistance with measurements and D. E. Mathews for assistance with sample preparation.

[1] R. P. Lucznik, D. A. Carrier, R. Pyka, and R. W. Haid, Radiology **187**, 855 (1993).
[2] J. A. Patton, RadioGraphics **14**, 1083 (1994).
[3] K. M. Lüdeke, P. Röschmann, and R. Tischler, Magn. Res. Imag. **3**, 329 (1985).
[4] A. Alanen, S. Bondestam, and M. Komu, Acta Radiol. **36**, 92 (1995).
[5] J. A. Malkoi, J. C. Hoffman, Jr., and P. J. Jarrett, Radiology **143**, 563 (1989).
[6] C. R. Camacho, D. B. Plewes, and R. M. Henkelman, J. Magn. Reson. Imag. (BEO) **5**, 75 (1995).
[7] P. S. Wang, S. G. Malghan, S. J. Dapkunas, K. F. Hens, and R. Raman, J. Mater. Sci. **30**, 1059 (1995); **30**, 1069 (1995); P. S. Wang (unpublished).
[8] R. N. Bracewell and A. C. Riddle, Astrophys. J. **150**, 427 (1967).

Magnetic phase transitions in perovskite-type anilinium-based tetrachlorocuprates

D. J. Nelson, K. Chan, F. Cervantes-Lee, and L. W. ter Haar
Department of Chemistry, University of Texas at El Paso, El Paso, Texas 79968

Our research efforts have expanded upon the work previously done on the molecular composites $(R\mathrm{NH_3})_2\mathrm{CuCl_4}$ (R=alkyl-) by utilizing various para-substituted anilines and anilinium derivatives as design tools. The resulting structures have the general formula $(R\mathrm{C_6H_4NH_3})_x\mathrm{CuCl_4}$ (R=methyl-, fluoro-, O_2N-, for $x=2$; R=H_3N-, $H_3NC_6H_4$- for $x=1$) and are similar to the aforementioned compounds, consisting of two-dimensional layers of corner-sharing $CuCl_6$ octahedra, resulting in a type of perovskite lattice. Equivalent magnetic sites are eclipsed between layers in the case of a small interleaving organic moiety, such as $H_3NC_6H_4NH_3$, but are otherwise staggered along one or more axes. Powder susceptibility data for representative compounds containing small anilinium derivatives reveal magnetic transitions at temperatures ranging from ~11.5 to ~7 K, depending upon the chemical nature of the anilinium substitution and the interlayer spacing. © *1996 American Institute of Physics.* [S0021-8979(96)49908-2]

I. INTRODUCTION

Research on the magnetostructural correlations of transition–metal ion clusters has been extensive over the past several years.[1] A significant area of this research has been the investigation of low-dimensional magnetic systems and how well these systems conform to present theory.[2] One area of this research that is still controversial is the nature of the low-temperature magnetic phase transitions occurring in two-dimensional ferromagnetic Heisenberg lattices.[3] The best synthetic examples of this theoretical system are the $(R\mathrm{NH_3})_x\mathrm{CuCl_4}$ perovskite compounds where R is an alkyl or alkylammonium group ($x=2$ or 1, respectively).[4] While this series of compounds appears to be exhaustively studied, we have wondered what magneto-optical properties these two-dimensional lattices would exhibit if organic dyes were used as the cationic spacers. Since most dyes are anilinium in nature, we decided to begin our investigations utilizing anilinium derivatives, some structures having already been solved.[4,5] This work deals with the structural and magnetic properties of the perovskite molecular composites $(R\mathrm{C_6H_4NH_3})_x\mathrm{CuCl_4}$ (R=methyl-, fluoro-, and nitro- for $x=2$; R=H_3N-, $H_3NC_6H_4$- for $x=1$), which represent the first compounds toward dye inclusions.

II. EXPERIMENT

The title compounds were synthesized via slow evaporation of solutions consisting of $CuCl_2\cdot 2H_2O$ and the appropriate aniline in a 2:1 molar ratio utilizing a solvent with variable proportions of 95% ethanol and concentrated HCl, dependent upon the aniline. All products crystallized out as small, light yellow platelets, with the exception of the 4-phenylenediaminium analog, which crystallized as dark yellow platelets, and the 4-nitroanilinium analog, which crystallized as green square platelets with two opposing corners of each platelet truncated. The crystal structures for the 4-nitroanilinium and phenylenediaminium analogs were determined at room temperature on a Siemens $R3m/V$ four-circle diffractometer with graphite monochromated Mo $K\alpha$ radiation (λ=0.71073 Å). The Siemens SHELXTL PLUS software package was used for structural refinement, utilizing the full-matrix least-squares method[6] (see supplementary material for solution and refinement parameters). Powder x-ray diffraction was utilized to characterize the similarities between the various compounds and to determine their interplanar spacings. The data were collected on a Rigaku D2000 at 298 K.

Magnetic susceptibility measurements were performed using a Quantum Design SQUID-based magnetometer utilizing modifications and procedures described elsewhere.[7] Field-dependent, temperature-dependent, and remnant magnetization powder measurements were performed on the 4-phenylenediaminium (**1**), benzidinium ($H_3NC_6H_4C_6H_4NH_3$)(**2**), 4-fluroranilinium (**3**), 4-toluidinium (4-methylanilinium) (**4**), and 4-nitroanilinium (**5**) analogs. The data were corrected for diamagnetism (**1**: -140×10^{-6} emu/mol; **2**: -153×10^{-6} emu/mol; **3**: -166×10^{-6} emu/mol; **4**: -183×10^{-6} emu/mol; and **5**: -176×10^{-6} emu/mol) using Pascal's constants for the diamagnetic contributions[8] and a TIP correction of 60×10^{-6} emu/mol per Cu(II) ion.

III. RESULTS AND DISCUSSION

A. Structure

The crystal structures of composites **1** and **5** are qualitively similar to their p-alkyl counterparts,[9] consisting of two-dimensional stacked arrays of corner-sharing $CuCl_6$ octahedra with the organic counterions acting as spacers between the layers. An example of one of the layers comprising the inorganic sublattice of compound **1** is illustrated in Fig. 1, which depicts the slight puckering of the tetrachlorocuprate layers.

Compound **1** possesses monoclinic symmetry and crystallizes in the $P21/c$ space group [a=10.019(2)Å, b=7.551(2)Å, c=7.164(2)Å, and β=93.17(2)°] while compound **5** possesses orthorhombic symmetry and crystallizes in the Pbca space group [a=7.065(2)Å, b=32.494(8)Å, and c=7.934(2)Å]. The presence of the nitro group in compound **5** effectively staggers successive layers in the a and c direc-

 0021-8979/96/79(8)/4715/3/$10.00 © 1996 American Institute of Physics

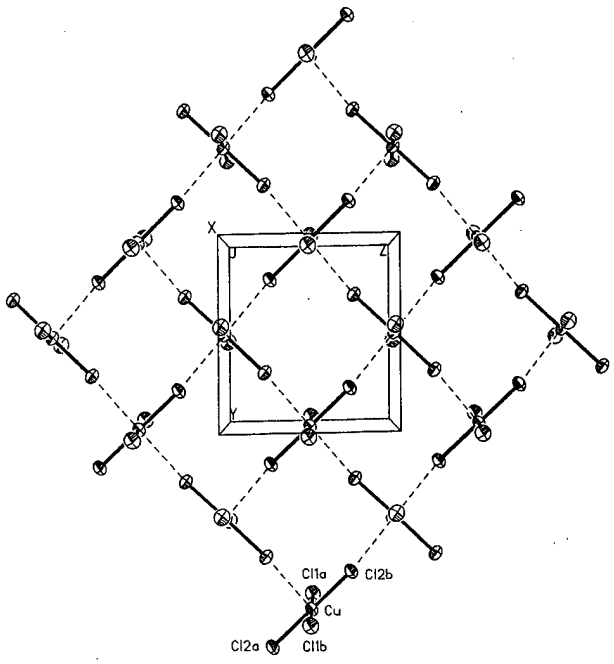


FIG. 1. Two-dimensional tetrachlorocuprate layer of compound **1**.

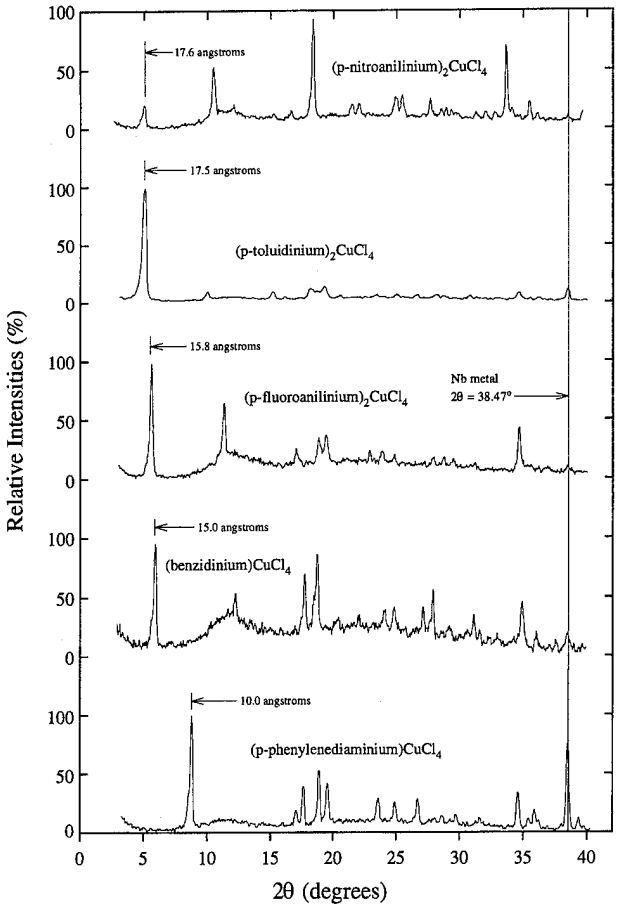


FIG. 2. Powder XRD spectra of compounds **1–5**. The spectra have been calibrated with Nb powder (2θ=38.47°) with appropriate d spacings shown (in Å).

tions, permitting only every other layer to be eclipsed as in $(CH_3NH_3)_2CuCl_4$,[3b] giving rise to the highly anisotropic unit cell (the a axis of compound **1** corresponds to the b axis of compound **5**). The ionic nature of the phenylenediaminium dication facilitates the smallest possible interlayer distance in the class of compounds under current investigation, with a d spacing of 10.0 Å (see Fig. 2). The bulkiness of the nitro and methyl substituents creates the largest d spacings of the compounds examined thus far, being 17.5 and 17.6 Å for analogs **4** and **5**, respectively. The other related materials with differing para-substituents are being investigated at this time.

B. Magnetism

Figure 3 depicts the molar susceptibility (χ_m), inverse molar susceptibility (χ_m^{-1}), and magnetic moment (μ_{eff}) for compound **1** over the temperature range 5–20 K. The data were collected at an applied field of 10 Oe, with the line through the data being an aid to the eye only, and not a fit to any magnetic model. The resultant curve exhibits a divergence in susceptibility which can be seen to be similar to the low-temperature magnetic data of related tetrachlorocuprate composites.[3b,c,10] The cusp in the molar susceptibility at 11.5 K is indicative of a magnetic phase transition. An important aspect of the molar susceptibility data is that the magnitude at the lowest measured temperature is approximately 67% of the magnitude at T_C=11.5 K. The curvature suggests that extrapolation to T=0 would have little effect on this ratio, implying that the critical temperature corresponds to the T_N of an LRO antiferromagnet. This conclusion is further supported by the eclipsed structure and short interplanar distance in this compound (see Table I), as has been noted in the antiferromagnetically ordering perovskite $(H_3NCH_2CH_2NH_3)CuCl_4$,[10a] and by magnetization measurements performed on compound **1** (not shown) which show saturation above 5000 Oe, a relatively large saturation field for this class of materials. High-temperature ($kT/J>1.5$—not shown) magnetic susceptibility data were collected at high field strengths (nominally 5000 Oe) and fit to the two-dimensional ferromagnetic Heisenberg model for S=1/2 put forth by Baker *et al.*,[11] where

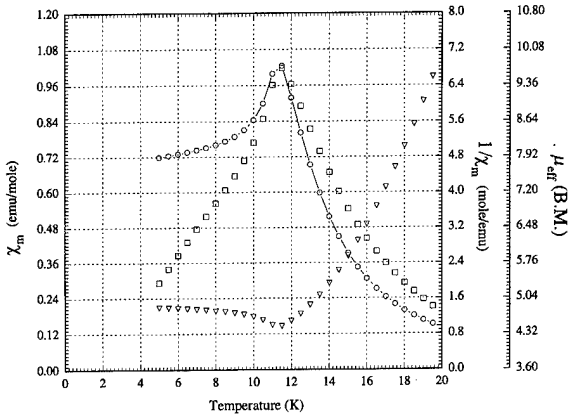


FIG. 3. Low-temperature magnetic data for compound **1**. (χ_m=○, χ_m^{-1}=▽, μ_{eff}=□).

TABLE I. Interplanar spacing and T_C values for compounds **1–5**.

Compound	Interplanar spacing (Å)	T_C (K)
(p-phenylenediaminium)$CuCl_4$ (**1**)	10.0	11.5
(benzidinium)$CuCl_4$ (**2**)	15.0	9.5
(p-fluoroanilinium)$_2CuCl_4$ (**3**)	15.8	9.3
(p-toluidinium)$_2CuCl_4$ (**4**)	17.5	8.5
(p-nitroanilinium)$_2CuCl_4$ (**5**)	17.6	6.8

$$\chi_m = \frac{Ng^2\beta^2 S(S+1)}{3kT}\left(1+\sum_{n\geq 1}\frac{\alpha_n}{2^n n!}x^n\right) \quad (1)$$

with $x=J/kT$ and the other symbols have their usual meaning (see Ref. 11 for the expansion coefficients). All of the compounds exhibit ferromagnetic exchange, with J values similar in magnitude (12–15 cm^{-1}) to their alkyl counterparts.[2]

The low-temperature data ($kT/J<1.5$—not shown) for the investigated compounds was collected with an applied field of 10 Oe, with the exception of compound **3**, which was subjected to a field of 1.75 Oe. All of the susceptibility curves displayed phase transitions, with the T_C values and corresponding interplanar spacings summarized in Table I. The observed trend is similar to the alkylammonium compounds, where the T_C is inversely related to the interplanar spacings. The first point to be made about this series is the similarity of the spacing between compounds **4** and **5** as compared to their significant T_C difference. This may be due to the staggering present in the p-nitroanilinium analog, leading to an ineffective interlayer exchange pathway. The other noticeable relationship is the similarity in the T_C values of composites **2** and **3**. The effect that the counterionic spacers have upon the T_C values in these composites becomes quite clear. The diverging susceptibility values, however, can be suggestive of either a lattice-dimensionality crossover, or a possible Kosterlitz–Thouless[12] ordering. The latter has been utilized to explain the low-temperature behavior in related complexes[2,3b] and is a definite possibility for this series. The behavior of compound **1**, however, is more likely attributable to a long range ordering owing to the reasons previously discussed.

IV. CONCLUSIONS

Using anilinium derivatives as counterions to form tetrachlorocuprate perovskite composites is remarkably successful, resulting in regularly modifiable structures. The only structural anomaly noted is composite **5**, owing to the nature of the nitro substituent. Perovskite compounds with similar anilinium substituents are currently being studied in order to study steric versus electrostatic effects on the proximity of the counterions. This series is currently being continued to include the other halogens as anilinium substituents, as well as aniline,[5b] 4-aminobiphenyl, and 4,4′-diamino-p-terphenyl [$H_2N(C_6H_4)_3NH_2$]. The latter composite possibility to date, however, has not been able to be synthesized by conventional means. Single-crystal studies are also underway on the five present compounds in order to further understand the nature of the magnetic phase transitions.

ACKNOWLEDGMENTS

Support from the Robert A. Welch Foundation and the National Science Foundation is gratefully acknowledged.

[1] For a review, see *Magnetostructural Correlations in Exchange Coupled Systems*, edited by R. D. Willett, D. Gatteschi, and O. Kahn, NATO ASI Series C140 (Reidel, Dordrecht, Netherlands, 1985), p. 400 and references therein.
[2] For a review, see *Physics and Chemistry of Materials with Low-Dimensional Structures*, edited by L. J. de Jongh (Kluwer, Dordrecht, Netherlands, 1990), Vol. 9, p. 1 and references therein.
[3] See, as examples, (a) R. Navarro and L. J. de Jongh, Physica B **84**, 229 (1976); (b) M. Aïn, J. Phys. Paris **48**, 2103 (1987); (c) H. von Känel, Physica B **96**, 167 (1979) and references therein.
[4] For a review, see P. Zhou, J. E. Drumheller, B. Patyal, and R. D. Willett, Phys. Rev. B **45**, 12365 (1992) and references therein.
[5] (a) M. Fareed Mostafa, M. M. Abdel-Kader, S. S. Arafat, and E. M. Kandeel, Phys. Scr. **43**, 627 (1991); (b) K. P. Larsen, Acta Chem. Scand. **A28**, 194 (1974).
[6] G. Sheldrick, SHELXTL, Siemens Analytical Instruments, Madison, WI, 1984.
[7] D. Nelson and L. W. ter Haar, Inorg. Chem. **32**, 182 (1992).
[8] E. A. Boudreaux and L. N. Mulay, *Theory and Applications of Molecular Paramagnetism* (Wiley, New York, 1976).
[9] L. J. de Jongh and A. R. Miedema, Adv. Phys. **24**, 1 (1974) and references therein.
[10] (a) L. O. Snively, P. L. Seifert, K. Emerson, and J. E. Drumheller, Phys. Rev. B **20**, 2101 (1979); (b) L. O. Snively, J. E. Drumheller, and K. Emerson, *ibid.* **23**, 6013 (1981).
[11] G. A. Baker, H. E. Gilbert, J. Eve, and G. S. Rushbrooke, Phys. Lett. A **25**, 207 (1967).
[12] J. M. Kosterlitz and D. J. Thouless, J. Phys. C **C6**, 1181 (1973).

$NiBr_2 \cdot 3H_2O$, a lower dimensional antiferromagnet

G. C. DeFotis, J. R. Goodey, A. A. Narducci, and M. H. Welch
Chemistry Department, College of William and Mary, Williamsburg, Virginia 23187

The trihydrate of nickelous bromide, $NiBr_2 \cdot 3H_2O$, is examined magnetically for the first time. A Curie–Weiss fit, $\chi_M = C/(T-\theta)$, to the susceptibility between 70 and 300 K yields $g = 2.31 \pm 0.01$ ($S=1$) and $\theta = 6.6 \pm 0.5$ K. Systematic curvature in χ^{-1} vs T is evident below 70 K. Despite the positive θ, $NiBr_2 \cdot 3H_2O$ appears to order antiferromagnetically at $T_c = 3.82 \pm 0.05$ K, somewhat below a maximum in $\chi(T)$ at $T(\chi_{max}) = 6.17 \pm 0.10$ K, with $\chi_{max} = 0.0900 \pm 0.0005$ emu/mol. The ratio $T_c/T(\chi_{max}) = 0.62 \pm 0.01$ suggests lower magnetic dimensionality. Between 4 and 12 K an acceptable fit with a two-dimensional Heisenberg model can be made, with $g = 2.58 \pm 0.01$, $J/k = -1.36 \pm 0.02$ K (assuming $\hat{H}_{ex} = -2J\Sigma_{i>j}\hat{\mathbf{S}}_i \cdot \hat{\mathbf{S}}_j$), and a correction for interlayer exchange $z'J'/k = -0.99 \pm 0.02$ K. Well above T_c the susceptibility is analyzed assuming axial and rhombic crystal field distortions, i.e., $D[\hat{S}_z^2 - S(S+1)/3]$ and $E[\hat{S}_x^2 - \hat{S}_y^2]$ spin Hamiltonian terms, with exchange included in a mean field approximation: $g = 2.33 \pm 0.02$, $D/k = 57.3 \pm 5.0$ K, $E/k = -24.9 \pm 3.0$ K, and $zJ/k = 5.28 \pm 0.20$ K. The parameters are provisional lacking single-crystal data, but the zero-field splitting is clearly quite large. Magnetization versus field isotherms depart only slightly from linearity for fields above 10 kG, and show a small hysteresis, even for temperatures above T_c. It is likely that ferromagnetically coupled $NiBr_2NiBr_2Ni\cdots$ chains are present, and that there are antiferromagnetic interactions between chains, such that strongly coupled layers occur, with weaker interactions between layers. © *1996 American Institute of Physics.* [S0021-8979(96)50008-2]

I. INTRODUCTION

The magnetic properties of $NiBr_2$ and certain of its hydrates have been studied, though not nearly as extensively as those of the corresponding chloride salts. $NiBr_2$ orders antiferromagnetically near 60 K,[1] the available data being too imprecise for greater exactness. $NiBr_2 \cdot 2H_2O$ is presumed to order antiferromagnetically (only the heat capacity has been measured at low temperatures) at 6.23 K, with a likely spin reorientation transition occurring at 5.79 K.[2] Most of the magnetic entropy is removed above the 6.23 K transition, suggesting that the material is of low magnetic dimensionality. $NiBr_2 \cdot 6H_2O$ has been more thoroughly studied and shown to order antiferromagnetically at 8.30 K,[3] rather than at 6.50 K as an earlier report had it.[4] The magnetism is clearly three dimensional and there are several detailed similarities with the behavior in isomorphous $NiCl_2 \cdot 6H_2O$.[5] However, heat capacity data for $NiCl_2 \cdot 6H_2O$ provide evidence for lower dimensional character.[6]

$NiCl_2 \cdot 4H_2O$ is well studied,[7,8] some indications of lower magnetic dimensionality being apparent. There is no known tetrahydrate of $NiBr_2$. Rather, for temperatures in the 36–60 °C range (where $NiCl_2 \cdot 4H_2O$ is obtained from aqueous solution of $NiCl_2$), $NiBr_2 \cdot 3H_2O$ is formed.[9] Nor is there a reported trihydrate of $NiCl_2$. In this paper the magnetic properties of $NiBr_2 \cdot 3H_2O$ are examined.

II. EXPERIMENT

$NiBr_2 \cdot 3H_2O$ was prepared by evaporating an aqueous solution of $NiBr_2$ to dryness at 40 °C and maintaining the solid at 50 °C for 24 h. Fine-grained yellow–green polycrystalline material was obtained. Exposure to atmospheric water vapor in handling of the material was minimized. Thermogravimetric analysis confirmed that trihydrate was obtained. An x-ray powder diffraction pattern showed many similarities with the known pattern of $NiBr_2 \cdot 2H_2O$,[10] but also significant differences. It seems likely that the structure of $NiBr_2 \cdot 3H_2O$, as yet unknown, is related to that of the dihydrate. Magnetic measurements were made with a vibrating sample magnetometer system[11] using a 0.1865 g sample. Susceptibilities are corrected for diamagnetism ($\chi_{dia} = -123 \times 10^{-6}$ emu/mol) and demagnetization.

III. MEASUREMENTS AND ANALYSIS

Figure 1 shows χ_M^{-1} vs T for polycrystalline $NiBr_2 \cdot 3H_2O$. A correction has also been applied for an assumed Van Vleck temperature-independent paramagnetic contribution of 240×10^{-6} emu/mol. This value follows from the expression[12] $\chi_{VV} = (N_0\mu_B^2/\lambda)(2-g)$ assuming an effective spin–orbit coupling constant $\lambda = -270$ cm^{-1}, somewhat smaller and typically so for octahedral Ni^{2+} systems than the free ion value $\lambda = -315$ cm^{-1}, and a g value of 2.25, also typical for Ni^{2+} compounds. For temperatures above 70 K good linearity is apparent in the plot; below 70 K deviations occur, and are fairly pronounced below 50 K. A Curie–Weiss fit [$\chi_M = C/(T-\theta)$, with $C = N_0g^2\mu_B^2S(S+1)/3k$ and $S=1$] in the 70–300 K range yields the mean g value and Weiss θ given in Fig. 1. The g value of 2.31 is plausible for a Ni^{2+} system. The positive θ means that ferromagnetic interactions predominate, even though the overall behavior is antiferromagnetic.

Figure 2 shows the susceptibility in the low-temperature regime in more detail. A rounded maximum is evident, with $T(\chi_{max}) = 6.17 \pm 0.10$ K and $\chi_{max} = 0.0900 \pm 0.0005$ emu/mol. Below $T(\chi_{max})$ a maximum in $\partial\chi/\partial T$, which it is plausible to identify with an antiferromagnetic transition,[13] occurs at $T_c = 3.82 \pm 0.05$ K. Both the broadness of the maximum and the relatively low ratio $T_c/T(\chi_{max}) = 0.62 \pm 0.01$ suggest that lower dimensional magnetic behavior is occurring. An up-

 0021-8979/96/79(8)/4718/3/$10.00 © 1996 American Institute of Physics

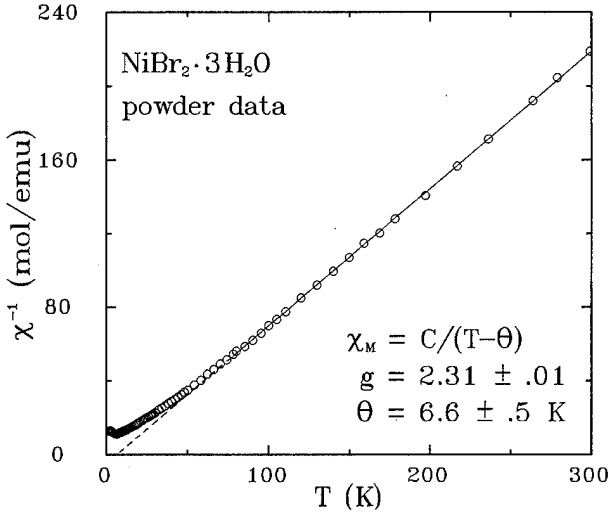


FIG. 1. Inverse molar magnetic susceptibility vs temperature for $NiBr_2 \cdot 3H_2O$ and Curie–Weiss fit.

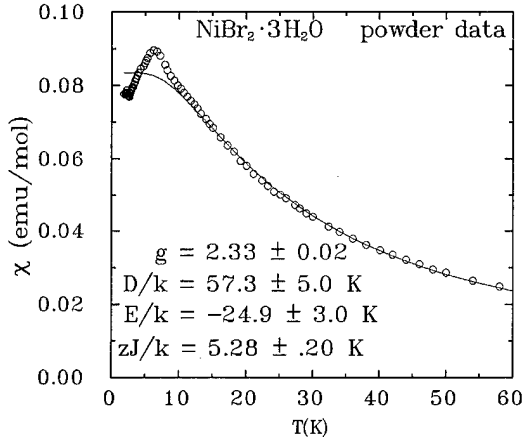


FIG. 3. Best fit to susceptibility data for $NiBr_2 \cdot 3H_2O$, with corresponding crystal-field and exchange parameters.

turn in $\chi(T)$ sets in near 2.55 K. Since this feature is somewhat sharp it is questionable whether paramagnetic impurities are responsible. However, no known hydrate of $NiBr_2$, or even $NiCl_2$ orders in this region.

Sufficiently above T_c, $\chi(T)$ for an ordering $S=1$ system can be analyzed including the effects of axial and rhombic crystal field distortions, which produce a zero-field splitting of the ^3A ground term. Including the Zeeman interaction the spin Hamiltonian is

$$\hat{H}=D[\hat{S}_z^2-S(S+1)/3]+E[\hat{S}_x^2-\hat{S}_y^2]+g\mu_B\mathbf{H}\cdot\hat{\mathbf{S}}. \quad (1)$$

Here g is assumed to be isotropic, as is often the case, or nearly so, in many Ni^{2+} systems. The eigenvalues in zero field correspond to three levels separated by $|D|-|E|$ and $2|E|$. Single-ion susceptibilities χ_x, χ_y, and χ_z can be calculated and the powder average susceptibility $(\chi_x+\chi_y+\chi_z)/3$ obtained,[14] an expression parametric in g, D, and E. The effects of exchange interaction, $\hat{H}_{ex}=-2J\,\Sigma_{i>j}\,\hat{\mathbf{S}}_i\cdot\hat{\mathbf{S}}_j$, must also be included, for which the mean field result is used,[15]

$$\chi^{ex}=\chi/[1-(2zJ/Ng^2\mu_B^2)\chi], \quad (2)$$

where J is a mean exchange interaction over z neighbors.

A mean field approximation cannot be applied close to T_c and, therefore, fits to the data were done for $T\geqslant 12$ K. A rather good fit appears in Fig. 3, with a rms deviation of 1.1% between 12 and 300 K for the parameters indicated; unshown data above 60 K are very well accounted for. The g value is close to that emerging from the Curie–Weiss fit. The D and E parameters are exceptionally large, but acquire physical plausibility from the fact that deviations from Curie–Weiss behavior appear as high as 70 K and are marked below 50 K. This suggests that for such temperatures kT is comparable with energy separations in the ground multiplet: $|D|/k-|E|/k=32.4$ K and $2|E|/k=49.8$ K. The value of zJ/k is in good agreement, within 7%, with the observed Weiss θ according to the mean field relation $\theta=2S(S+1)zJ/3k$. It should be noted that comparable quality fits could be obtained with negative D, e.g., $g=2.31$, $D/k=-72.1$ K, $E/k=\pm 17.1$ K, and $zJ/k=6.40$ K. Powder data do not permit an unambiguous determination of the sign of D; moreover, all fits are insensitive to the sign of E. However, in all high quality fits D and E were large, and despite many attempts to model the data using much smaller D and E values the result was invariably a much poorer quality fit, especially for $T<60$ K.

Given the lower dimensional characteristics in the data, already noted, attempts were made to fit $\chi(T)$ in the region between $\sim T_c$ and $\sim 4T_c$ with various lower dimensional models, using known high-temperature series expansions or exact results when available. Three-dimensional Heisenberg, XY, and Ising models were also tested and found inadequate, the observed susceptibility being more rounded in the vicinity of $T(\chi_{max})$ than the models permitted. A one-dimensional Heisenberg model yielded curves that were too broad for the observed susceptibility, as well as poor fits generally. Two-dimensional models clearly were capable of approximating

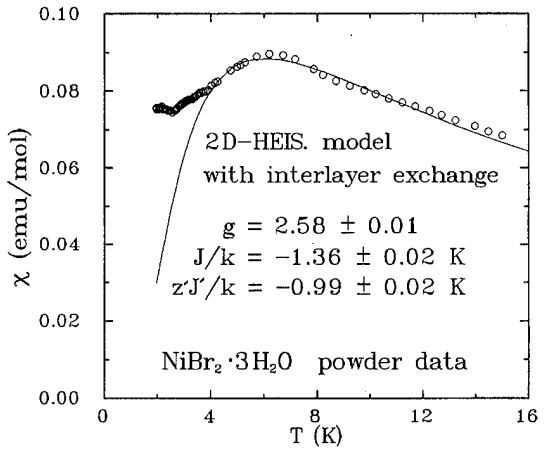


FIG. 2. Molar susceptibility vs temperature below 16 K for $NiBr_2 \cdot 3H_2O$; curve through data is a theoretical fit described in text.

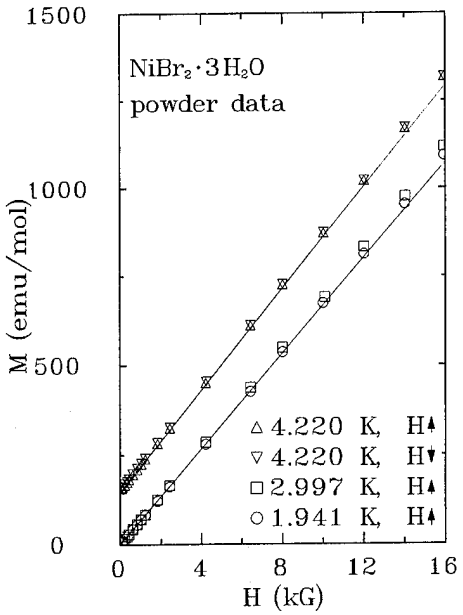


FIG. 4. Molar magnetization vs applied field at several temperatures for $NiBr_2 \cdot 3H_2O$; 4.220 K data are shifted up to 150 emu/mol for clarity.

the observed $\chi(T)$ more closely, and among these the 2D–Heisenberg model[16] succeeded best. This is not unexpected since Ni^{2+} systems generally exhibit Heisenberg model behavior. A fit to the data between 4.2 and 12 K (data above 12 K are also shown) appears in Fig. 2. It is excellent, with rms deviation 0.82% for the parameters indicated. Interlayer exchange must be included, via a mean field approximation of the form of Eq. (2), in order to obtain an adequate fit.

Figure 4 shows the molar magnetization versus applied field at various temperatures. No transitions are apparent up to 16 kG, but there are deviations from linear behavior above 10–12 kG for each isotherm. The extent of these deviations is similar at each temperature. Moreover, there is some small hysteresis present for each isotherm (shown only in the case of 4.220 K for clarity), and its size is similar at each temperature.

IV. DISCUSSION

The magnetic behavior of $NiBr_2 \cdot 3H_2O$ is distinctly different from that of the related $NiBr_2 \cdot 2H_2O$ and $NiBr_2 \cdot 6H_2O$, although as noted earlier lower dimensional character is suggested by heat capacity data on $NiBr_2 \cdot 2H_2O$.[2] A remarkable feature of $NiBr_2 \cdot 3H_2O$ is the large size of the zero-field splitting parameters D and E. A structure determination could be very helpful in assessing the strength of distortions in the coordination sphere of the Ni^{2+} ions, which should be substantial in order to produce D and E parameters of the size determined here. In the case of $NiBr_2 \cdot 2H_2O$ a fit to heat capacity data yielded a provisional estimate $D/k = -10$ K.[2] A much smaller $D/k = -1.5$ K value was estimated for $NiBr_2 \cdot 6H_2O$.[3] For the corresponding chloride materials, $NiCl_2 \cdot 2H_2O$ and $NiCl_2 \cdot 6H_2O$, reported parameters are $D/k = 1.1$ and -1.5 K, respectively,[17,5] with much smaller E values. For $NiCl_2 \cdot 4H_2O$ a rather larger magnitude value $D/k = -11.5$ K has been reported,[6] along with a small E.

While no clear trend is apparent it is likely that larger distortions occur in the Ni^{2+} environments of $NiCl_2 \cdot 4H_2O$ and $NiBr_2 \cdot 3H_2O$. And certainly the location of the third water in relation to what must be a presumed $[NiBr_4(OH_2)_2]$ coordination sphere in $NiBr_2 \cdot 2H_2O$ is important in this respect. It should also be noted that for isostructural complexes larger zero-field splittings are frequently found for bromide than for chloride homologues,[11,18] due to the greater covalency of the M–Br bond.[19]

There do remain certain puzzling features concerning the behavior of $NiBr_2 \cdot 3H_2O$, which probably cannot be fully resolved until a structure determination and single-crystal data are available. With very large zero-field splitting parameters and a moderate size exchange interaction it might be expected that ordering would not occur at finite temperature, according to theories which treat the effects of anisotropy and exchange on T_c,[20,21] and with large separations between the states of the ground triplet the success of an $S=1$ model in describing the low-temperature behavior is unexpected. As to the distribution of exchange interactions, it is most probable that ferromagnetically coupled $NiBr_2NiBr_2Ni\cdots$ chains occur, that for structural reasons these are coupled together antiferromagnetically into layers, and that antiferromagnetic interactions also occur between the layers. This accounts for the general results of the fittings.

ACKNOWLEDGMENTS

This work was supported by National Science Foundation-Solid State Chemistry Grant No. DMR-9213198. Acknowledgment is also made to the donors of The Petroleum Research Fund, administered by the ACS, for partial support of this research.

[1] I. Tsubokawa, J. Phys. Soc. Jpn. **15**, 2109 (1960).
[2] K. Kopinga and W. J. M. deJonge, Phys. Lett. A **43**, 415 (1973).
[3] S. N. Bhatia, R. L. Carlin, and A. P.-Filho, Physica B **92**, 330 (1977).
[4] R. D. Spence, H. Forstat, G. A. Khan, and G. Taylor, J. Chem. Phys. **31**, 555 (1959).
[5] A. I. Hamburger and S. A. Friedberg, Physica **69**, 67 (1973).
[6] W. K. Robinson and S. A. Friedberg, Phys. Rev. **117**, 402 (1960).
[7] J. N. McElearney, D. B. Losee, S. Merchant, and R. L. Carlin, Phys. Rev. B **7**, 3314 (1973).
[8] C. C. Becerra, N. F. Oliveira, A. P.-Filho, W. Figueiredo, and M. V. P. Souza, Phys. Rev. B **38**, 6887 (1988); S. S. Vianna and C. C. Becerra, *ibid.* **28**, 2816 (1983).
[9] J. W. Mellor, *A Comprehensive Treatise on Inorganic and Theoretical Chemistry* (Longmans Green, London, 1936), Vol. XV, p. 426.
[10] D. Weigel, Bull. Soc. Chim. (France) **10**, 2087 (1963).
[11] G. C. DeFotis, B. K. Failon, F. V. Wells, and H. H. Wickman, Phys. Rev. B **29**, 3795 (1984).
[12] M. Karnezos, D. L. Meier, and S. A. Friedberg, Phys. Rev. B **17**, 4375 (1978).
[13] M. E. Fisher, Philos. Mag. **7**, 1731 (1962).
[14] T. Haseda and M. Date, J. Phys. Soc. Jpn. **13**, 175 (1958).
[15] J. W. Stout and W. B. Hadley, J. Chem. Phys. **40**, 55 (1964).
[16] M. E. Lines, J. Phys. Chem. Solids **31**, 101 (1970).
[17] C. H. W. Swüste, A. C. Botterman, J. Mellenaar, and W. J. M. deJonge, J. Chem. Phys. **66**, 5021 (1977).
[18] D. V. Behere, S. K. Date, and S. Mitra, Chem. Phys. Lett. **68**, 544 (1979).
[19] W. deW. Horrocks and D. A. Burlone, J. Am. Chem. Soc. **98**, 6512 (1976).
[20] J. W. Johnson and Y.-L. Wang, Phys. Rev. B **24**, 5204 (1981); D. H.-Y. Yang and Y.-L. Wang, *ibid.* **12**, 1057 (1975).
[21] A. I. Nugmanov and L. R. Tagirov, J. Magn. Magn Mater. **111**, 301 (1992).

Magnetic field effect on interface profile between immiscible nonmagnetic liquids—Enhanced Moses effect

Hiroharu Sugawara, Noriyuki Hirota, Takuro Homma, Masayuki Ohta, and Koichi Kitazawa
Department of Applied Chemistry, Faculty of Engineering, University of Tokyo, 7-3-1, Hongo, Bunkyo-ku, Tokyo 113, Japan

Hiroyuki Yokoi, Yozo Kakudate, Shuzo Fujiwara, and Mitsutaka Kawamura
High Energy Density Laboratory, National Institute of Materials and Chemical Research, Tsukuba, Ibaraki 305, Japan

Shoogo Ueno and Masakazu Iwasaka
Institute of Medical Electronics, Faculty of Medicine, University of Tokyo, 7-3-1, Hongo, Bunkyo-ku, Tokyo 113, Japan

The change in the interface profile between immiscible nonmagnetic liquids was investigated quantitatively in a superconducting magnet with a large horizontal bore. The interface profile changed into concave down or up at the field center accordingly to the balance of magnetic susceptibilities between the lower and upper liquids. A flat interface was also demonstrated when the susceptibilities were balanced. It was found that modification of the interface profile was significantly amplified under an applied field as low as 1 T when the densities of the two liquids were quite close. The morphological change induced by the applied magnetic field can be used to remove a boundary, which initially separates two liquids without the field, and to initiate a mixing process or a chemical reaction between the two liquids. © *1996 American Institute of Physics.* [S0021-8979(96)50108-9]

Exploration of magnetism has been extended to nonmagnetic, i.e., dia- or paramagnetic, materials and living bodies since recent developments of superconducting magnet technology make it easier to access a high magnetic field. Indeed, it was observed that the surface of water bended downward under the field of 10 T or so at the center.[1,2] We have demonstrated that this phenomenon, which we called as Moses effect, is attributed to the diamagnetism of water. We then showed that the surface profile of aqueous solutions was systematically modified accordingly as their magnetic susceptibility varied from diamagnetic to paramagnetic values. However, the applied field should be high and steep enough in order to clearly observe these effects.

In this work, we employed more than two immiscible liquids to observe the field effect on the interface. We show that the interface profile is governed by susceptibility values of two liquids contiguous at the interface. The morphological changes may be clearly observed under a field even weaker than 1 T when the densities of the two liquids are adjusted quite close.

The magnet used in this study had a large horizontal open bore 200 mm in diameter and 1300 mm in length, and could produce magnetic field directed along the bore (x) axis. A narrow glass vessel of 10 mm width was fixed in the magnet, and the whole profile of the liquids inside the vessel could be monitored from outside by using a pair of mirrors, which could slide along the x direction.

Table I summarizes the sample liquids. The density ρ of each copper sulfate ($CuSO_4$) aqueous solution was determined by weight and volume measurements, and its magnetic susceptibility χ was estimated from the measured weight of its source materials ($CuSO_4 \cdot 5H_2O$ and H_2O) as well as their specific susceptibilities listed in the literature.[3] All the measurements were performed at room temperature.

Figure 1 shows a typical interface profile between two immiscible nonmagnetic liquids under various magnetic fields. The direction of the interface change, concave up or down, was dependent upon the specific combination of the sample liquids.

In Fig. 1(a), the lower liquid was sample A copper sulfate solution (blue), and the upper liquid was hexane (transparent). Here, hexane was added in sample A from the right side of the vessel under applied field of 8 T. The interface between sample A and hexane was flat, while the surface of sample A fell at the field center, and that of hexane moved up toward the right end of the vessel.

Figure 1(b) shows an interface between hexane (upper) and sample B (lower). Under the field of 3.8 T, the top surface of hexane fell by 9 mm, while the interface was raised by 24 mm. In Fig. 1(c) the upper liquid was substituted for

TABLE I. Specification of sample liquids. ρ density, χ volume magnetic susceptibility in SI units.

Sample		$\rho(10^3$ kg/m$^3)$	$\chi(10^{-6})$
$CuSO_4$ aq soln.	A	1.0071	7.116
	B	1.1328	8.584
	C	1.0132	−4.240
Hexane		0.662	−7.146
Monochlorobenzene		1.107	−8.653
Carbontetrachloride		1.603	−8.722
Water[a] (for reference)		0.9982	−9.02

[a]See Ref. 2.

 0021-8979/96/79(8)/4721/3/$10.00 © 1996 American Institute of Physics

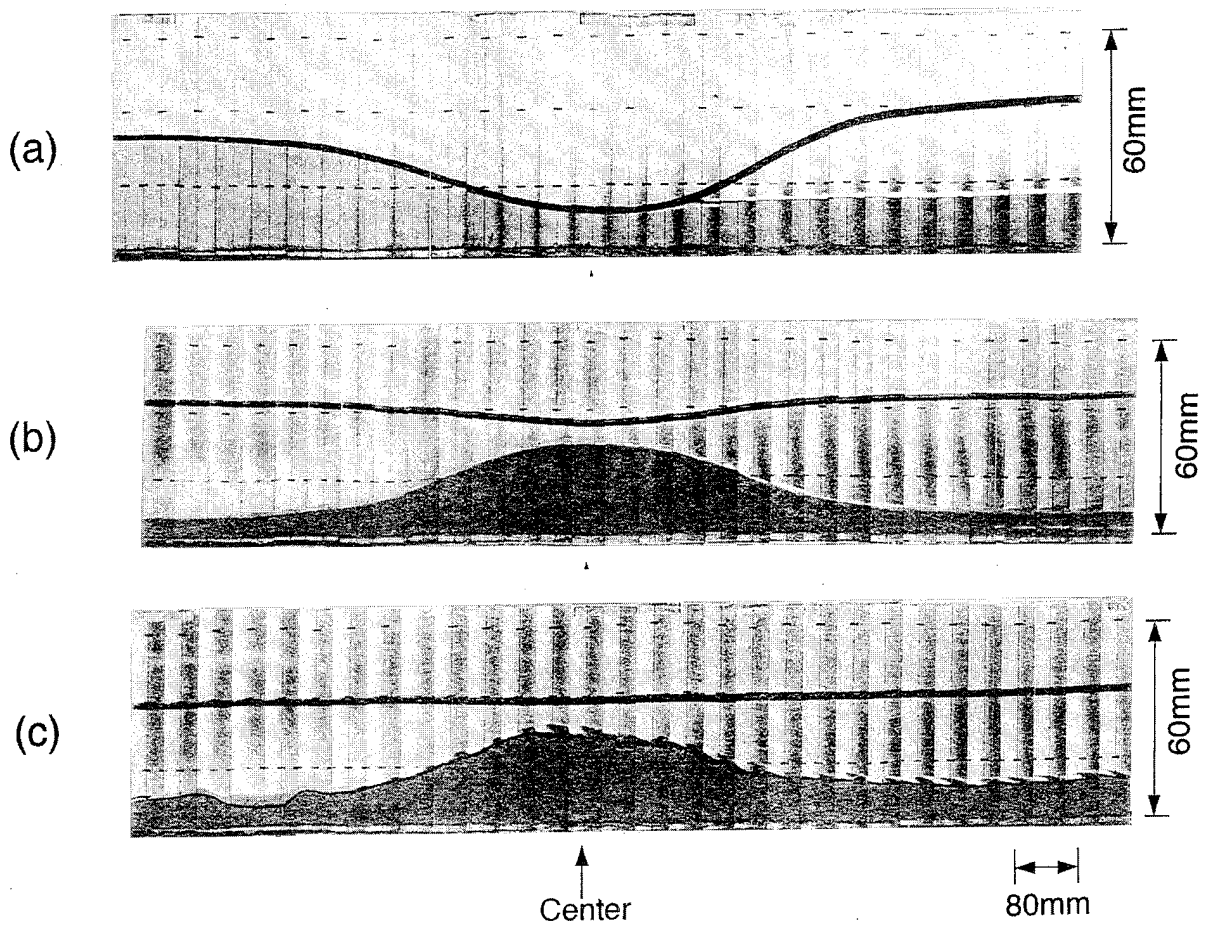


FIG. 1. Profile of the interface between an organic solvent (upper) and a copper sulfate aqueous solution (lower). The magnetic field was directed along the horizontal (x) axis. The sample liquids and the field strength at the center were (a) hexane and the solution A, 8 T; (b) hexane and the solution B, 3.8 T; (c) monochlorobenzene and the solution B, 0.9 T. The whole figure is a patchwork of 27–30 sectional photographs of which boundaries are seen as vertical shadows. The x direction is rescaled to $\frac{1}{4}$.

monochlorobenzene. When the field was reduced at 0.9 T, the interface was raised by 20.6 mm, though the top surface was almost flat.

It was also observed that the interface fell at the field center, as will be shown later in Fig. 2. Therefore, the interface profile may rise, fall, or be flat, depending on the combination of sample liquids. In addition, the interface profile can be enhanced: in Figs. 1(b) and 1(c), the height differences between the vertical interface level at the field center and that at the two ends of the vessel were both about 20 mm, being comparable to that of the water surface under 8 T.

Next, we show that the observed profiles are quantitatively explained by taking the magnetic volume energy into account.[2,4] The surface height y_2 is expressed as

$$y_2(x)=\frac{\chi_2}{\rho_2}\frac{(\mu_0 H(x))^2}{2g\mu_0}, \tag{1}$$

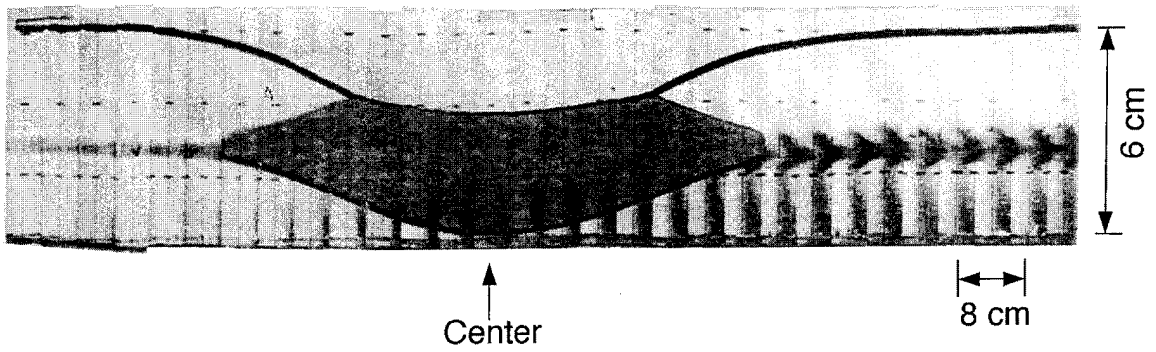


FIG. 2. Profile of the stack of three nonmagnetic liquids: hexane (upper), copper sulfate aqueous solution C (middle), and carbontetrachloride (lower). The applied magnetic field was 8 T at the center. The x direction is rescaled to $\frac{1}{4}$.

where the subscript 2 denotes the upper liquid, μ_0 the permeability in vacuum, and g the acceleration of the gravity. Equation (1) indicates that the surface height is proportional to $(\mu_0 H)^2$, and that the surface moves up or down at the field center, depending on the sign of χ_2.

The proportional coefficient $k(=\chi_2/2g\mu_0\rho_2)$ was evaluated to be 0.78 k_W, 1.20 k_W, and 0.86 k_W, for sample A, hexane, and monochlorobenzene, respectively, where $k_W=-3.66\times10^{-4}$ m/T^2 is the coefficient for water.[2] These values of k, being close to the value of water k_W, were why the height differences of their surfaces were comparable to that of water surface achieved under the same applied field.

In contrast, the interface height y_1 should be expressed as

$$y_1(x)=\frac{\chi_1-\chi_2}{\rho_1-\rho_2}\frac{(\mu_0 H(x))^2}{2g\mu_0}, \tag{2}$$

where the subscript 1 denotes the lower liquid.[5] Equation (2) indicates that the interface height is also proportional to $(\mu_0 H)^2$, and that the direction of the interface change depends on the balance of susceptibilities between the two liquids, $\Delta\chi=\chi_1-\chi_2$, because $\Delta\rho=\rho_1-\rho_2>0$. When the susceptibilities are balanced, the interface is kept flat as shown in Fig. 1(a); when $\chi_1>\chi_2$, the lower liquid rises, as shown in Figs. 1(b) and 1(c).

The proportional coefficient k may be enhanced in its magnitude by setting $|\Delta\chi|$ larger and/or $\Delta\rho$ smaller. The coefficient for Fig. 1(b) was evaluated to be $k=3.6\,|k_W|$, where both the values $|\Delta\chi|$ and $1/\Delta\rho$ were nearly twice the values $|\chi|$ and $1/\rho$ for water, respectively.

In particular, the enhancement is efficient when the densities of the two liquids are adjusted quite close: in Fig. 1(c), $\Delta\rho$ was set to be $\lesssim0.023$ g/cm^3, resulting in the coefficient $k=82\,|k_W|$. This is why we could observe the rise of interface as large as 20.6 mm even when the magnetic field was further reduced to 0.9 T.

Hence, Moses (fall) and reversed Moses (rise) effects can be significantly enhanced by designing an appropriate combination of sample liquids. We therefore call these significantly enhanced effects either an "enhanced Moses effect" or an "enhanced reversed Moses effect" depending on whether $\chi_2>\chi_1$ or $\chi_2<\chi_1$, respectively.

Nevertheless, be reminded that when $\Delta\rho$ becomes smaller the interfacial tension may compete with the enhanced Moses effect, and the interface profile may be modified. An example is seen in Fig. 1(c) as the irregular humps in the interface profile where the inner surface of the vessel once wet with one of the liquids hindered the further motion of the interface. A theoretical treatment of the enhanced Moses effect including the interfacial tension will be discussed elsewhere.[5]

Finally, we point out that morphological changes induced by the applied field may remove a boundary which initially separates two phases without the field.

Figure 2 shows interface and surface profiles of a stack of three nonmagnetic liquids: hexane, sample C copper sulfate aqueous solution, and carbontetrachloride. When the field was applied, the lower interface fell at the field center. Then, sample C deformed into a droplet, and floated on the bottom liquid, carbontetrachloride. At the same time, the upper liquid moved apart from the center. As a result, the top and bottom liquids were joined at the both ends of the vessel, gradually mixing into each other. Besides, the middle liquid, initially surrounded by the two liquids, was exposed at its top surface to air.

We consider that such kinds of morphological changes induced by an applied field can be used to initiate and terminate a mixing process or a chemical reaction between two liquids or between a liquid and the covering atmosphere.

We acknowledge the Advanced Chemical Processing Technology Research Association (ACTA) of Japan for permission of using the large bore superconducting magnet. N. H. thanks the Japan Society for Promotion of Science for partial financial support.

[1] S. Ueno and M. Iwasaka, J. Appl. Phys. **75**, 7177 (1994).
[2] N. Hirota, T. Homma, H. Sugawara, K. Kitazawa, M. Iwasaka, S. Ueno, H. Yokoi, Y. Kakudate, S. Fujiwara, and M. Kawamura, Jpn. J. Appl. Phys. **34**, L991 (1995).
[3] *Handbook of Chemistry and Physics*, edited by R. C. Wheast (CRC, Boca Raton, FL, 1978–79), 59th ed.
[4] See, for example, L. D. Landau and E. M. Lifshitz, *Electrodynamics of Continuous Media* (Addison–Wesley, Reading, MA, 1960).
[5] H. Sugawara, N. Hirota, T. Homma, M. Ohta, K. Kitazawa, M. Iwasaka, S. Ueno, H. Yokoi, Y. Kakudate, S. Fujiwara, and M. Kawamura (unpublished).

Ferromagnetic–insulator–ferromagnetic tunneling: Spin-dependent tunneling and large magnetoresistance in trilayer junctions (invited)

Jagadeesh S. Moodera and Lisa R. Kinder
Francis Bitter Magnet Laboratory, Massachusetts Institute of Technology, Cambridge, Massachusetts 02139

Tunneling between ferromagnet–insulator–ferromagnet (FM–I–FM) trilayer thin-film planar junctions has been successfully studied. Tunnel current was observed to be dependent on the relative orientation of the magnetization (M). Co, CoCr, CoFe, $Fe_{0.7}Pt_{0.3}$, and NiFe were tried as the FM electrodes with Al_2O_3 or MgO as the barrier layers for the above studies. Large magnetoresistance (MR) was observed as the M alignment of the two ferromagnets changed from being parallel to antiparallel orientation. At room temperature, the highest change in junction MR was 18%, field sensitivity factor reaching 5%/Oe in the best cases. The MR value increased to 25.6% at 4.2 K, and decreased as the dc bias was increased to a fraction of the barrier height. The angular dependence of MR varied nearly as the cosine of the relative angle of M, as predicted by Slonczewski's theory. The magnitude of MR agrees well with that given by Julliere's model, which predicts that the MR varies as the product of the conduction electron spin polarization of the FMs. These trilayer junctions can find application as high-density, nonvolatile storage media or as field sensors.
© *1996 American Institute of Physics.* [S0021-8979(96)50208-5]

INTRODUCTION

Spin-polarized tunneling experiments between a superconductor and a ferromagnet, performed 25 years ago,[1,2] led the way to the present field-dependent tunneling between FM films. Based on the earlier spin-polarized tunneling results, Julliere put forward a model for FM–I–FM tunneling,[3] assuming that spin is conserved in tunneling[2] and tunnel current is dependent on the density of states of the two electrodes. Due to the uneven spin distribution of conduction electrons at the Fermi level in the FMs, one can expect tunneling probability to be dependent on the relative magnetization orientation of the FM films. Analyzing the tunnel current, based on the spin density of states at the Fermi level of the two FM electrodes, Julliere showed the change in the tunnel conductance (ΔG) between antiparallel and parallel orientation of the two FMs as

$$\Delta G/G = 2P_1P_2/(1+P_1P_2), \tag{1}$$

where G is the conductance when the magnetizations are parallel, and P_1 and P_2 are the spin polarizations of the two FM electrodes. The change in the tunnel resistance can be written as

$$\Delta R/R = (R_A - R_P)/R_A = 2P_1P_2/(1+P_1P_2), \tag{2}$$

where R_A and R_P represent the junction resistances when the two FMs have their M antiparallel and parallel, respectively. *This latter definition is used in deducing the MR throughout the present work.*

Another theory of FM–I–FM tunneling proposed by Slonczewski analyzes the transmission of charge and spin currents through a rectangular barrier separating free-electron-like FM metals.[4] The orientation of the spins tunneling across the FM–I interface was strongly influenced by the barrier height, according to this theory. This affected the spin polarization and the exchange coupling between the FMs and was consistent with the low values of $\Delta R/R$ seen previously.[5–11]

The experimental values have come far short of the expected value according to Julliere's model, until very recently. For instance, in the case of Fe–I–Co tunnel junctions, with $P=40\%$ and $P=34\%$, respectively,[1,2] the expected junction MR should be 24%. Julliere studied Fe–Ge–Fe and Fe–Ge–Co junctions and obtained a change of 14% in the conductance at 4.2 K and zero bias.[3] This percentage dropped to less than 1% upon the application of several mV of dc bias to the junction. Various other groups, using mainly NiO, CoO, Gd_2O_3, and Al_2O_3 barriers, studied this effect and only small changes were seen—no more than 7% at 4.2 K.[5–11] In recent times, Miyazaki and his co-workers have improved the room-temperature results from 2.7% to 15.6% [according to the above definition, Eq. (2)].[12] However, the 15.6% value was seen in only one junction and was not reproducible. Using low-temperature deposition techniques, it was recently shown that reproducible results can be obtained using Al_2O_3 barriers with the highest change being 12% for CoFe/Al_2O_3/Co tunnel junctions at room temperature.[13]

Many limiting factors can reduce the MR effect: orange peel coupling between the FMs due to surface roughness,[14] interfacial and barrier spin scattering, FM surface degradation, domain walls, etc. By significantly overcoming some of these negative factors in the present work, values of $\Delta R/R$ have greatly improved to as high as 18% at room temperature and 25.6% at 4.2 K for CoFe/I/Co junctions. This is

 0021-8979/96/79(8)/4724/6/$10.00 © 1996 American Institute of Physics

close to the expected value of 27.6% predicted by Julliere's model. In the present work, a sensitivity factor of 5%/Oe is obtained for the tunnel junction devices.

EXPERIMENT

The thin-film planar junctions used for MR measurements were fabricated *in situ* through vacuum evaporation, in a system with a background pressure of 10^{-7} Torr. Glass substrates cooled to 77 K were covered with 1 nm thick Si (which serves as a nucleating layer beneath the first electrode). Then, the first FM base electrode, 8.0–15.0 nm thick and 0.2 mm wide, was deposited without or with an applied magnetic field (H) to align with an easy axis of magnetization. The base electrode deposition was followed by the evaporation of 1.2–2.0 nm of Al or Mg metal, covering the *entire* base electrode, to form the tunnel barrier.[15] The substrates were then warmed to room temperature and subjected to oxygen glow discharge to create an insulating layer of Al_2O_3 or MgO. Finally, the top FM electrode, 8.0–25.0 nm thick and 0.3 mm wide, was deposited. The FM materials used include Co, CoCr, CoFe, $Fe_{0.7}Pt_{0.3}$, and NiFe. The thickness was monitored by a quartz-crystal oscillator. In each run, a total of 72 junctions, each with an area of 6×10^{-4} cm^2, were prepared. The junction resistance (R_J) ranged from hundreds of ohms to tens of kilohms.

Junction MR was measured using a four-terminal ac or dc technique in fields up to ±0.5 T, in the temperature range of 4.2–325 K. For ac measurements, a Linear Research-400 ac resistance bridge with an accuracy of $\pm0.005\%$ was used and dc measurements also had similar accuracy. Measurements were done with H parallel or perpendicular to the junction plane. Several junctions were subjected to higher dc voltages to elucidate the bias dependence of the junction properties. These measurements were taken with voltages ranging from 0 to 0.8 V at 4.2, 77, and 295 K. Detailed temperature dependence of R_J, $\Delta R/R$, and tunnel current was measured between 4.2 and 295 K for some junctions. To control the temperature, the junctions were mounted on a sample probe with a heater. A platinum resistance thermometer, mounted adjacent to the sample, monitored the temperature. Angular dependence was measured at room temperature with the junction plane parallel to the field. R_J was recorded as the sample was rotated from 0° to 360°.

RESULTS

Several criteria were used to qualify the junctions for magnetotransport studies. As a first requirement, junctions with a resistance in the range of 1 kΩ to tens of kilohms were chosen for measurements. To prove that tunneling is the main source of conductance, $G(V)$ and $I(V)$ characteristics were taken for several junctions. Figure 1 shows the conductance of a CoFe/Al_2O_3/Co junction as a function of both low and high voltages at 4.2 K. At low bias, the conductance is nearly constant. However, at high bias nearly a parabolic dependence is observed. This behavior is expected for a good tunnel junction with a barrier height of above ~1 eV. At 4.2 K, a conductance dip was generally seen at zero bias,

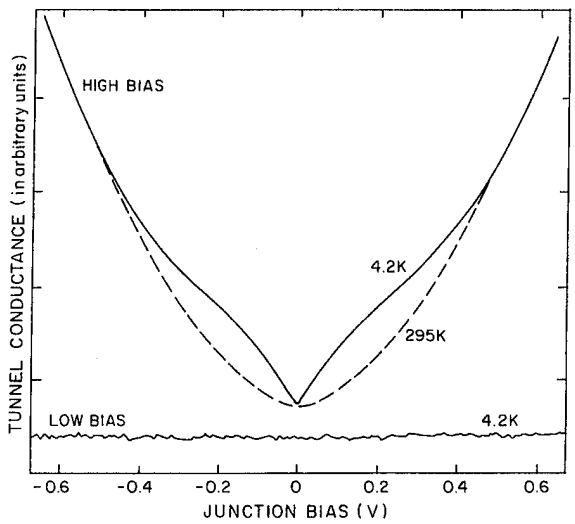


FIG. 1. Tunnel conductance as a function of dc bias for a CoFe/Al_2O_3/Co junction at 4.2 K. The lower curve was taken in the lower bias region and the upper curve is for the higher bias. The voltage scale for the lower curve should be divided by 500. For the higher bias region, data at 295 K are also shown.

whereas at 77 K and room temperature, the conductance dip was negligible. This feature will be discussed later.

$I-V$ curves taken from 0 to 0.8 V also confirm the quality of the junctions. At low bias, ohmic behavior was seen and higher bias showed parabolic dependence. Simmon's theory of tunneling was used to derive the barrier height (ϕ) and thickness (s) for several junctions.[16] For Al_2O_3 barriers, ϕ ranged from 1.8 to 3.5 eV. The corresponding barrier thicknesses varied from 1.8 to 1.2 nm. For the limited studies done with MgO barriers, values of $\phi\cong0.9$ eV and $s\cong2.1$ nm

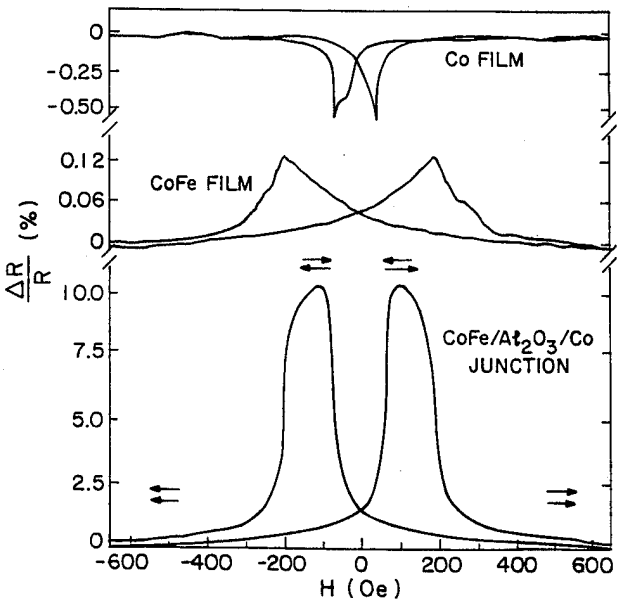


FIG. 2. Magnetoresistance of the tunnel junction and the two FM film electrodes as a function of applied magnetic field, taken at room temperature. The arrows indicate the direction of M in the two FMs, according to the FM–I–FM model of Julliere. (See Discussion).

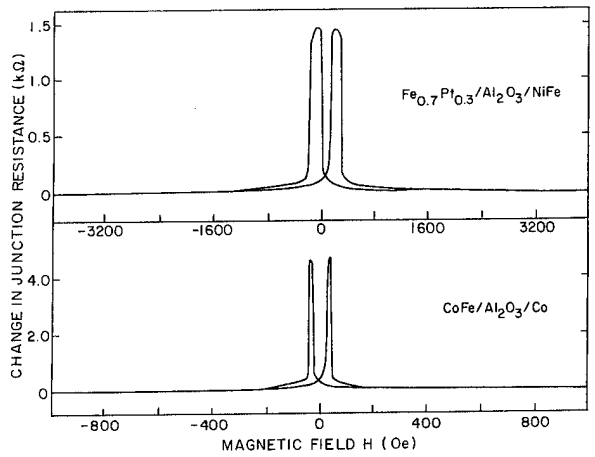


FIG. 3. Junction magnetoresistance vs applied magnetic field showing the variation in the higher field range for $CoFe/Al_2O_3/Co$ and $Fe_{0.7}Pt_{0.3}/Al_2O_3/NiFe$ samples. Note the field independence of MR at fields slightly beyond the peak.

were obtained. These barrier parameters are what is typically seen for standard Al_2O_3 and MgO tunnel barriers.

Good tunnel junctions with the above barrier parameters showed mostly a small temperature dependence of R_J. The junctions used in the present studies showed only a 10% to 30% increase in R_J as temperature was decreased from room temperature to 4.2 K. According to Simmon's and Stratton's tunneling theory, the tunnel current varies linearly with T^2.[17] This behavior was observed in the present junctions at temperatures <60 K. Also, these junctions withstood temperature cycling, high voltages (up to ± 0.8 V), and were stable in the ambient conditions.

MR measurements, displayed in Figs. 2 and 3, show a change in R_J as a function of applied field (H). At high field, the junction resistance is low, and it begins to increase as H decreases toward zero field. Upon reversing the field direction, R_J rapidly rises, showing a peak. With further increase in H,R_J drops to its original low value. *The ratio of the peak change to the absolute value at the peak is defined as* $\Delta R/R$. (This definition gives a lower value of the ratio as compared to the criteria used by others where the resistance change was divided by the low value of R_J at high H). In Fig. 2, the $CoFe/Al_2O_3/Co$ junction shows a $\Delta R/R$ of 10.6% at 300 K. Compared to the junction, the MR of the FM electrodes is also shown. The changes in the resistance for the full length of the strips are about 0.6% and 0.1% for Co and CoFe films, respectively. The junction area corresponds to only 1/30th of the length of the electrodes. In essence, the MR contribution of the FM film is negligible. Figure 3 shows the R_J vs H in the higher field range for two junctions at room temperature. The constancy of R_J as H increased beyond the peak value is evident.

MR effects were investigated with different FM electrodes like Co, CoCr, CoFe, $Fe_{0.7}Pt_{0.3}$, and NiFe and barriers of Al_2O_3 or MgO. Keeping CoFe as one electrode showed the highest percentage change. The maximum change was 25.6% at 4.2 K and 18% at room temperature for the $CoFe/Al_2O_3/Co$ trilayer. Many junctions consistently showed changes in the range of 14%–17% at room temperature. The

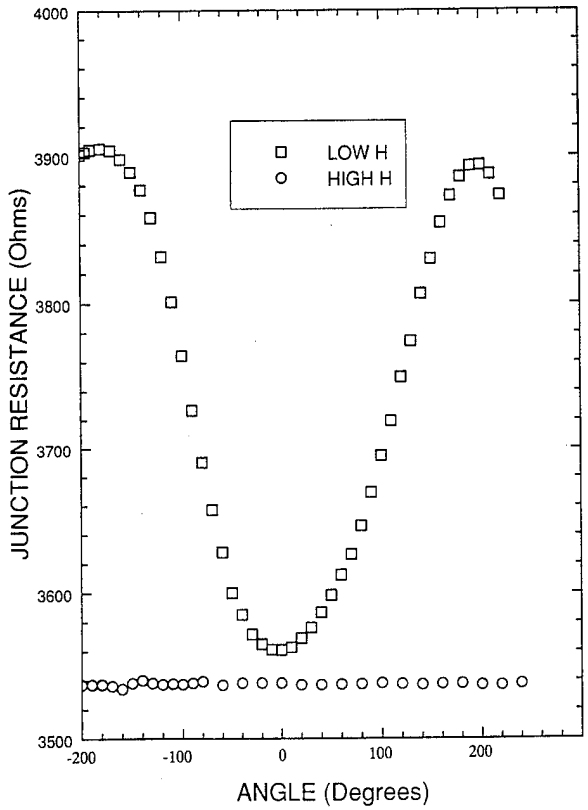


FIG. 4. Angular dependence of the junction magnetoresistance taken at low and high applied fields for a $CoFe/Al_2O_3/Co$ junction.

peak position at room temperature for various junctions occurred between 3 and 120 Oe. For example, $CoFe/Al_2O_3/Co$ and $CoFe/Al_2O_3/NiFe$ junctions deposited in the absence of H showed the peak at ± 120 Oe, whereas the peak for junctions prepared in an applied field occurred at ± 3 Oe. The peaks occurred at lower field values for thicker NiFe films and for films that were deposited in the presence of an applied field. The peak position and height did not change with field cycling. Also, upon reaching the maximum of R_J, when the field was turned off, the peak value of the resistance was maintained at $H=0$.

The angular dependence of MR was measured for several junctions, for a low and a high value of H, keeping H in the film plane. In order to perform this measurement, the junctions were subjected to a high field in the junction plane in one direction. Upon reversing the field, a low value of H was set (less than the peak field value). R_J was then recorded every 5°–10° as the sample was rotated with respect to the field. Seen in Fig. 4 is the periodic variation of R_J as a function of angle, showing cosine of the angle dependence (not shown in the figure) as discussed in Slonczewski's theory.[4] When similar measurements were done at a field value higher than the peak field, R_J remained constant (the lower curve in the figure). The maximum change in R_J (for low field) with respect to the angle nearly correlated with the $\Delta R/R$ observed in R vs H measurements.

In general, the MR of the junctions increased as the temperature was lowered. For example, in some cases, $\Delta R/R$

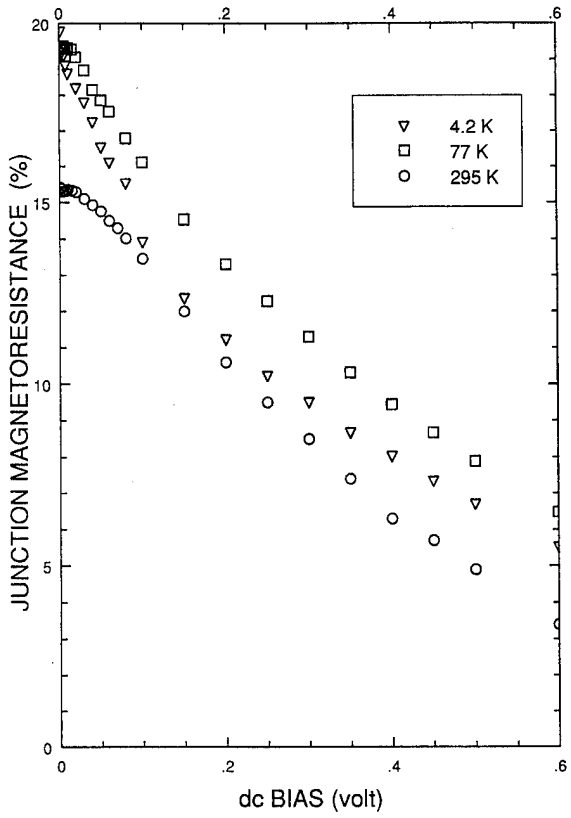


FIG. 5. The dc bias dependence of junction MR for a $CoFe/Al_2O_3/Co$ junction at 4.2, 77, and 295 K.

nearly doubled as the sample was cooled from room temperature to 77 K, and continued to increase as T decreased to 4.2 K. However, in certain cases, the $\Delta R/R$ slightly decreased upon cooling. This will be discussed later. Some junctions were warmed to 325 K and found to be stable. However, the $\Delta R/R$ value slightly decreased at higher temperatures.

The magnetoresistance dependence on the dc bias is displayed in Fig. 5 for a $CoFe/Al_2O_3/Co$ junction. As the dc bias increased, the $\Delta R/R$ increased slightly or remained constant at low bias. At higher voltages, the $\Delta R/R$ declined rapidly, reaching lower MR values. It is important to note that up to a few tens of mV, the decrease is not significant. Junctions with MgO barriers also displayed similar bias dependence of MR. Thicker Al junctions showed lower MR and the visible presence of unoxidized Al. The larger change in the R_J as a function of temperature and considerable asymmetry in the $G(V)$ curve indicated that for thinner barriers (below 1.4 nm), the base electrode was partially oxidized.

DISCUSSION

The junction magnetoresistance can be understood based on Julliere's model.[3] Referring to Fig. 2, at high fields, the two FM films have their M aligned in the applied H direction. (The M direction is indicated by arrows.) Upon reversing the field, the magnetization of the film with a lower coercive force (H_C) aligns itself in the new field direction. On the other hand, the second electrode, with a higher H_C, remains magnetized in the original field direction. In this configuration, the magnetization of the two films are antiparallel to each other. As the field is increased further, it becomes strong enough to align the M of the second FM electrode in the new field direction, resulting in parallel orientation. Thus, at high fields in either direction, the FM electrodes are saturated and parallel to each other. At intermediate fields, the electrodes are aligned antiparallel. According to the model presented in the introduction, when M are parallel, the tunneling probability is highest and tunneling current is maximum, thereby yielding a low R_J. In the antiparallel configuration, the tunneling probability and the current are lowest, resulting in higher R_J.

The MR curves of the two electrodes (see Fig. 2) clearly support the above interpretation. For instance, the extrema points of these curves indicate the coercive forces of the electrodes.[18] The peak in R_J is centered between the lower H_C of Co and the higher H_C of the CoFe film. Thus the peak position of the junction resistance is strongly correlated to the coercive fields of the FM electrodes. The H_C of the FM film is easily influenced by the film growth conditions: the presence of an applied magnetic field during film growth, substrate temperature, a nucleating layer, thickness of the film, etc.[19] $CoFe/Al_2O_3/$(NiFe or Co) junctions with the films deposited in the presence of an applied field showed a behavior different from those discussed above. For instance, the peak in R_J occurred at 3 Oe as compared to the peak in $CoFe/Al_2O_3/$(NiFe or Co) junctions, deposited in $H=0$, which occurred at about 120 Oe. Also, the peaks were extremely sharp, with a peak width of less than 3 Oe as compared to over 100 Oe in the other case. The sharpness and low H value of the peak position are directly the result of film growth in the presence of field, which reduces the H_C of the FM film and makes it sharper.[19] Thus, among many other factors, the sharpness and position of the H_C of two FM electrodes strongly influences the MR of the junction.

As pointed out in the previous section, the MR remained constant all the way to 0.5 T, beyond 2 or 3 times the peak value of the applied field (Fig. 3). During the oxidation of Al to form the Al_2O_3 barrier, it is possible that the top surface of the base electrode is partially oxidized as well, creating perhaps an antiferromagnetic (AF) oxide layer like CoO or FeO. In such a situation, one ends up with an FM/AF interface which can exhibit exchange anisotropy, perhaps detrimentally influencing the polarization of the electrons at the interfaces. The presence or absence of exchange anisotropy can be inferred by the shape of R_J vs H at high fields [20] and also by the displaced $M-H$ loop. As seen in Fig. 3, the near absence of MR at fields beyond ~0.05 T, and the symmetric $M-H$ loop observed point to the absence of exchange anisotropy caused by an AF oxide. The data in Fig. 3 were taken at room temperature. However, at 4.2 K, R_J vs H was slightly asymmetric, showing some MR effects even beyond 0.15 T. The $M-H$ loop was also asymmetric at 4.2 K showing the possible presence of an AF layer over the FM.[14]

The rotation of the magnetization of one FM with respect to the other also supports the FM–I–FM tunneling model. This is evident in the data shown for a $CoFe/Al_2O_3/Co$ junction in Fig. 4. At a field value higher

than the H_C of one electrode, when the sample is rotated in a magnetic field, the M of the softer film follows the field. This will change the relative orientation of M in the two FM films—switching from parallel to antiparallel orientation gradually. The tunneling probability is therefore affected, which is evidenced by the periodic variation of the R_J with the angle, as seen in this figure. The maximum value of the resistance corresponds to the antiparallel alignment of the relative magnetizations. The parallel orientation of M goes with the minimum of the curve. At field values higher than the H_C of both electrodes, if the above interpretation is correct, rotation of the sample in the field should maintain the parallel orientation of M (along the applied field) at all angles of H. In this case, the tunneling probability should be the highest and R_J should maintain a constant low value. This is exactly what is seen in the second curve which was taken at high field. Thus the angular dependence and the field dependence of R_J conclusively support the FM–FM tunneling model. The exact form of angular dependence of MR was not quite the cosine function predicted in Slonczewski's theory for the tunnel conductance.[4] The likely distribution of the H_C in the present FM films can contribute to this behavior.

The magnetoresistance behavior of the junction with applied magnetic field in the film plane and perpendicular to it was similar. In perpendicular field, the peaks were relatively broader and occurred at slightly higher field values. The latter peaks were several times broader than the peaks with H in the plane, if the films were deposited in a magnetic field parallel to the substrate plane. However, the MR of the junction remained the same. $M-H$ measurements showed that CoFe and Co films have their M in the film plane. So, when the field is perpendicular to the film plane, the film has to rotate toward the hard axis, thereby shifting the peaks to higher field values and also making them broader; the shift becomes even larger when the films are deposited in an applied magnetic field. Despite these variations, the tunneling model as discussed above is operative here, i.e., even when the magnetizations are perpendicular to the film plane.

Magnetoresistance, junction resistance, tunnel current, and peak position all varied with temperature. As the temperature decreased from 300 to 4.2 K, the MR nearly always increased. The H_C of the elemental FM increased more than that of the alloy FM as the temperature decreased. This allowed broader separation of H_C for the two FMs in some cases, if they were near each other at RT, creating a better antiparallel alignment (wider peaks). Also, at lower temperatures the $M-H$ loop of the FM films got sharper, with a higher value of H_C and remanent magnetization. This can give rise to larger MR effects and peaks shifting to higher H as T decreased. Room-temperature values for $\Delta R/R$ varied between 10% and 18% whereas at 4.2 K, the values went up to 21%–26%. Exceptions to the increase in $\Delta R/R$ with decreasing temperature occurred when the coercive fields of the two films changed such that they moved toward each other with decreasing temperature, creating a sharper peak and bringing down the MR effect. For instance, in the case of certain CoFe/Al_2O_3/NiFe junctions where the FM films were deposited in the presence of H, the H_C were so close to each other that the width of the peak was less than 3 Oe.

The R_J increased with a decrease in the temperature in all cases, the thinner barriers showing a higher percentage change. This is not unexpected since a thinner Al film barrier would allow possible oxidation of the base electrode, thus forming a temperature-dependent, semiconducting barrier at the interface. Such strongly paramagnetic oxide in the interface region can create spin scattering at RT, whereas at lower temperatures, magnetic ordering of this layer would reduce the spin scattering. If this is the case, MR can increase as temperature decreased.

The MR shows surprisingly strong decrease as the bias increased from 0 to 0.8 V. There was no change in $\Delta R/R$ for ac bias up to 1 mV. With dc bias, although $\Delta R/R$ initially showed a small increase or near constant value below ~10 mV at RT, overall it decreased with increasing dc bias. The decrease was small up to about 100 mV, and beyond which, it decreased faster. The value of $\Delta R/R$ at 0.8 V was about 1/5 of the low bias value; MgO barriers showed more decrease as compared to Al_2O_3 barriers. Also, if the $\Delta R/R$ at $V=0$ was lower, then the decrease with bias was larger. Irrespective of the starting $\Delta R/R$, the relative change was similar at 300, 77, and 4.2 K. Many causes can contribute to the decrease in the MR with bias. Among them, the bias dependence of the barrier height, creation of magnons, density of states effects in the FM, etc., may be responsible for the decrease in $\Delta R/R$. With the increase in dc bias, the effective barrier height decreases. MgO, with its smaller barrier height, is affected more than the Al_2O_3 barrier. This can increase the tunneling probability for the minority spins. The spin polarization of the tunneling current can then be expected to decrease, as discussed in Slonczewski's theory.[4] This might also explain strong bias dependence of the effect seen in Julliere's experiment.[3] The a-Ge (although exposed to oxygen) tunnel barrier which Julliere used is known to have a barrier height of 20–30 meV.[21] In this experiment, MR effects were only seen at helium temperatures below about 10 mV. This is the general trend that has been observed with other low barriers like NiO, Gd_2O_3, CoO, etc., where the junction MR effects were seen only at low temperatures and smaller bias.[5–11]

The presence of metal particles,[22] magnons,[23] magnetic impurities, localization effects, multistep tunneling, and states in the barrier or at the interface can adversely affect the spin polarizations of the tunneling electrons by causing spin flip scattering.[24] The dip in the conductance at $V=0$ observed at 4.2 K can be due to some combination of the above causes. One would expect by the presence of metal particles in the tunnel barrier (for example, unoxidized Al left in the barrier) a characteristic $G(0)$ vs T dependence below 4.2 K.[22] No measurable temperature dependence of $G(0)$ was observed between 1 and 4.2 K. However, if the metal particles are less than a few Å, then no significant temperature dependence can be expected.[22] In addition to a conductance dip, small features were observed in G vs V curves around 100 mV, especially in junctions with thinner barriers. This is consistent with the magnon formation as has been found in NiO by Tsui *et al.*,[23] causing spin flip during tunneling. Also, that the anomaly in G at $V=0$ is not the

cause of the MR is evident from the near independence of G vs V and large MR at room temperature, and only a small decrease in the effect at low bias (below ~100 mV), even at low temperatures.

The conduction electron spin polarization values that are used here were measured at the Fermi level. At high bias, one deals with the states away from the Fermi level which need not have the same spin polarization. If such is the case, then at higher bias, the effect ($\Delta R/R$) might decrease if the polarization is lower away from the Fermi level. Spin-polarization measurements at energies higher than at the Fermi level would be helpful. The magnitude of the MR effect can be calculated, for example, for CoFe/Al_2O_3/Co junctions according to Julliere's model [Eq. (2)]. The conduction electron spin polarization of 47% for CoFe was measured at 0.4 K using the spin-polarized tunneling technique as described in Refs. 1 and 2. Using a value of 34% for Co polarization,[2] one gets a calculated change of 27.6%, from Eq. (2). This compared well with the MR seen in the present junctions at 4.2 K.

CONCLUSIONS

Large magnetoresistance was observed in the FM–I–FM tunnel junctions (where FM=Co, CoCr, CoFe, FePt or NiFe, and I=MgO or Al_2O_3). This effect increased at lower temperatures. A significant decrease in MR was observed with increasing dc bias. At room temperature, MR values of 14%–17% were consistently obtained. The highest value of 18% was seen in CoFe/Al_2O_3/Co junctions. This value increased to 25.6% at 4.2 K which agrees well with the value of the MR estimated from the conduction electron spin polarization of the FMs, using Julliere's model. These trilayer devices and MR effects have potential as ultralow power field sensors or memory elements due to the small size, high R_J, independence of FM, barrier layer thickness, and field orientation.

ACKNOWLEDGMENTS

Many thanks to P. LeClair, T. M. Wong and G. Reynolds for their assistance and interest in this work. We are grateful to R. Meservey and P. Tedrow for helpful discussions. Comments by J. Slonczewski have been useful. L. R. Kinder thanks the Office of Naval Research for the Summer High School Apprenticeship (1995) and NSF for the High School Honors Program Sponsored through Boston University (Summer 1994). This research was supported by NSF Grant No. DMR-9423013 and ONR Grant No. N00014-92-J-1847.

[1] R. Meservey, P. M. Tedrow, and P. Fulde, Phys. Rev. Lett. **25**, 1270 (1970); P. M. Tedrow and R. Meservey, *ibid.* **26**, 192 (1971).
[2] P. M. Tedrow and R. Meservey, Phys. Rev. Lett. **27**, 919 (1971); P. Fulde, Adv. Phys. **22**, 667 (1973); R. Meservey and P. M. Tedrow, Phys. Rep. **238**, 174 (1994).
[3] M. Julliere, Phys. Lett. A **54**, 225 (1975); The idea of FM–I–FM tunneling originated in the 1960s (J. C. Slonczewski, R. C. Barker, and A. Yelon, private communication).
[4] J. C. Slonczewski, Phys. Rev. B **39**, 6995 (1989).
[5] S. Maekawa and U. Gäfvert, IEEE Trans. Magn. **MAG-18**, 707 (1982).
[6] Y. Suezawa and Y. Gondo, in *Proceedings of the International Symposium on Physics of Magnetic Materials, Sendai, 1987* (World Scientific, Singapore, 1987), p. 303; J. Magn. Magn. Mater. **126**, 524 (1993).
[7] R. Kabani, J. S. Moodera, P. M. Tedrow, and R. Meservey, Mater. Res. Soc. Extended Abstract (EA-21) (1990).
[8] J. Nowak and J. Rauluszkiewicz, J. Magn. Magn. Mater. **109**, 79 (1992).
[9] R. Nakatani and M. Kitada, J. Mater. Sci. Lett. **10**, 827 (1991).
[10] Y. Suezawa, F. Takahashi, and Y. Gondo, Jpn. J. Appl. Phys. **31**, L1451 (1992).
[11] P. LeClair, J. S. Moodera, and R. Meservey, J. Appl. Phys. **76**, 6546 (1994).
[12] T. Miyazaki, T. Yaoi, and S. Ishio, J. Magn. Magn. Mater. **98**, L7 (1991); T. Miyazaki, and N. Tezuka, *ibid.* **139**, L231 (1995).
[13] J. S. Moodera, L. R. Kinder, T. M. Wong, and R. Meservey, Phys. Rev. Lett. **74**, 3273 (1995).
[14] See, for example, A. Yelon, in *Physics of Thin Films,* edited by G. Hass, M. H. Francombe, and R. W. Hoffman (Academic, New York, 1971), Vol. 6, p. 205.
[15] C. J. Adkins, Philos. Mag. **8**, 1051 (1963); D. M. Burnell and E. L. Wolf, Phys. Lett. A **90**, 471 (1982).
[16] J. G. Simmons, J. Appl. Phys. **34**, 1793 (1963).
[17] J. G. Simmons, J. Appl. Phys. **35**, 2655 (1964); R. Stratton, J. Phys. Chem. Solids **23**, 1177 (1962).
[18] R. M. Bozorth, *Ferromagnetism* (Nostrand, New York, 1961), p. 745; M. B. Stearns, Mater. Res. Soc. Symp. Proc. **133**, 553 (1993).
[19] F. G. West, J. Appl. Phys. **35**, 1827 (1964); M. L. Cohen, in *Handbook of Thin Film Technology,* edited by G. I. Maissel and R. Glang (McGraw-Hill, New York, 1970), Chap. 17.
[20] We want to thank A. Chaiken for pointing this out to us.
[21] G. A. Gibson and R. Meservey, J. Appl. Phys. **58**, 1584 (1985).
[22] H. R. Zeller and I. Giaever, Phys. Rev. **181**, 789 (1969).
[23] D. C. Tsui, R. E. Dietz, and L. R. Walker, Phys. Rev. Lett. **27**, 1729 (1971).
[24] See, for instance, E. L. Wolf, in *Principles of Electron Tunneling Spectroscopy* (Oxford University Press, New York, 1985), Chap. 8.

Theory of spin-dependent tunneling and transport in magnetic nanostructures (invited)

S. Maekawa, J. Inoue, and H. Itoh
Department of Applied Physics, Nagoya University, Nagoya 464-01, Japan

We study the linear response theory of the electric transport in magnetic nanostructures. The conductance is expressed by using the wave functions of electrons on the Fermi level in the mean field theory at zero temperature. The theory is extended to the system with single resistive layer in which there exists electron–electron interaction and the conductance is derived in the single-site approximation. The theoretical results may be applied to a variety of magnetic nanostructures such as magnetic multilayers and ferromagnetic tunneling junctions. © *1996 American Institute of Physics.* [S0021-8979(96)50308-4]

I. INTRODUCTION

Spin-dependent transport phenomena have received much attention since the discovery of the giant magnetoresistance (GMR) in magnetic multilayers.[1] GMR was also observed in granular alloys.[2,3] In addition, there is growing interest in the study of magnetoresistance devices of magnetic nanostructures. These activities renewed the study of ferromagnetic metal/insulator/ferromagnetic metal tunneling junctions which were the first of the observation of magnetoresistance in the magnetic nanostructures.[4,5] The magnetoresistance in the tunneling junctions is called the tunneling magnetoresistance (TMR). Recent experiments have shown that TMR is as large as GMR in magnetic multilayers.[6,7] We note that TMR is also seen in magnetic granular semiconductors.[8,9]

Although interesting magnetoresistance phenomena have been observed in magnetic nanostructures, the theoretical study is far from complete. This is partly because it is not easy to take into account the nanostructure and random scattering potentials on an equal footing.

In this article, we formulate the conductance in magnetic nanostructures. Starting with the Kubo formula for the conductance, we find that the conductance depends only on the voltage at leads attached on the sample and does not depend on the detailed electric field distribution in it in the mean field theory at zero temperature, indicating that the theory for the nonlocal conductivity by Kane, Serota, and Lee[10] is valid in the magnetic systems as well. We extend this result and examine the transport in a system with single resistive layer in which there exists electron–electron interaction. In the single-site coherent potential approximation (CPA), we obtain a formula for the conductance due to electron–electron interaction.

Since the results obtained in this article are not limited in a particular model, they may be applied to a variety of magnetic nanostructures.

II. LINEAR RESPONSE THEORY

Let us first consider a magnetic multilayer at zero temperature. The thickness of each layer is of the order of 10 Å. The mean free path of an electron, which is the relaxation time of momentum × Fermi velocity, is estimated to be of the order of 100 Å from the value of the resistivity. Another important length scale is the spin-diffusion length, which is the relaxation time of spin memory × Fermi velocity. Although it is not easy to estimate it, this length is considered to be much longer than the mean free path. The above estimate indicates that the spin memory of an electron is conserved during the propagation through many layers. In other words, since each spin component of electrons contributes to the electric current almost independently, the so-called two-current model[11] works well. In the following, we study the conductance in the two-current model.

As seen in Fig. 1, the electric current is in the z direction and the total current (I) is given by integrating over the cross sectional area in the xy plane by

$$I=\int d\mathbf{S}(z)\int d\mathbf{r}'\sum_{\nu}\sigma_{z\nu}(\mathbf{r},\mathbf{r}')E_{\nu}(\mathbf{r}'), \tag{1}$$

$$\mathbf{E}(\mathbf{r}')=-\nabla' V(\mathbf{r}'), \tag{2}$$

with $\mathbf{E}$ and V being the electric field and electro-static potential, respectively. Here, the total current is independent of the position z because of the current conservation. The nonlocal conductivity[10] is given by the commutator of the current operator,

$$\sigma_{\mu\nu}(\mathbf{r},\mathbf{r}')=\lim_{\omega\to 0}\frac{1}{\omega}\int_0^{\infty}dt\,\exp(i\omega t)\langle[j_{\mu}(\mathbf{r},t),j_{\nu}(r',t)]\rangle, \tag{3}$$

$$\mathbf{j}(\mathbf{r})=\frac{e\hbar}{2im}\{\psi^{\dagger}(\mathbf{r})\nabla\psi(\mathbf{r})-[\nabla\psi^{\dagger}(\mathbf{r})]\psi(\mathbf{r})\}, \tag{4}$$

where $\langle\cdots\rangle$ denotes the expectation value in the ground state and e and m are the electric charge and the effective mass of an electron, respectively. The field operator $\psi(\mathbf{r})$ is expressed

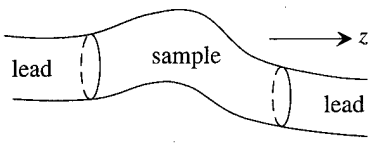


FIG. 1. Sample and leads for measuring conductance.

 0021-8979/96/79(8)/4730/3/$10.00 © 1996 American Institute of Physics

in the mean field theory by using the wave-function $\phi_{n\sigma}(\mathbf{r})$ and annihilation operator $c_{n\sigma}$ in the eigen-state n with spin σ as

$$\psi(\mathbf{r})=\sum_n \sum_\sigma \phi_{n\sigma}(\mathbf{r})c_{n\sigma}. \tag{5}$$

Inserting Eq. (5) into Eq. (4) and rewriting Eq. (3), we have

$$\sigma_{\mu\nu}(\mathbf{r},\mathbf{r}')=\pi\hbar e^2\sum_{m,n}\sum_\sigma J^\mu_{nm\sigma}(\mathbf{r})J^\nu_{mn\sigma}(\mathbf{r}') \times\delta(\epsilon_F-\epsilon_{n\sigma})\delta(\epsilon_F-\epsilon_{m\sigma}), \tag{6}$$

$$J^\mu_{nm\sigma}(\mathbf{r})=\frac{\hbar}{2im}\left[\phi^*_{n\sigma}(\mathbf{r})\frac{\partial}{\partial x_\mu}\phi_{m\sigma}(\mathbf{r}) -\left(\frac{\partial}{\partial x_\mu}\phi^*_{n\sigma}(r)\right)\phi_{m\sigma}(\mathbf{r})\right], \tag{7}$$

where ϵ_F and $\epsilon_{n\sigma}$ are the Fermi energy and eigen-value in the state n with spin σ, respectively. We note that the wave-function satisfies the Schrödinger equation,

$$\left(-\frac{\hbar^2}{2m}\nabla^2+U_\sigma(\mathbf{r})\right)\phi_{n\sigma}(\mathbf{r})=\epsilon_{n\sigma}\phi_{n\sigma}(\mathbf{r}), \tag{8}$$

where $U_\sigma(\mathbf{r})$ is the spin-dependent potential. As seen in Eq. (6), the conductivity is given by electrons on the Fermi level at zero temperature.

In one-dimension, examining the derivative, $dJ_{nm\sigma}/dz$, we find that the nonlocal conductivity is constant; $\sigma(z,z')=\sigma_0$. Then, we obtain

$$I=\sigma_0 V, \tag{9}$$

where V is the voltage between leads.

In three-dimension, examining the derivative, $\Sigma_\mu \partial J^\mu_{nm\sigma}(\mathbf{r})/\partial x_\mu$, we find

$$\sum_\mu \frac{\partial}{\partial x_\mu}\sigma_{\mu\nu}(\mathbf{r},\mathbf{r}')=\sum_\nu \frac{\partial}{\partial x'_\nu}\sigma_{\mu\nu}(\mathbf{r},\mathbf{r}')=0. \tag{10}$$

Therefore, integrating Eq. (1) by parts, changing the integral over the volume to that of the boundary of the sample and noting that the current flows out of the leads but not of insulating boundary, we obtain

$$I=V\int dxdy\int dx'dy'\sigma_{zz}(\mathbf{r},\mathbf{r}'), \tag{11}$$

where the total current depends on neither z nor z'. As seen in Eq. (11), the total current is independent of the detailed distribution of the electric field $\mathbf{E}$ in the sample but depends just on the voltage between leads as also shown in one-dimension.

The conductance in Eq. (11) is given by the wave-functions of electrons on the Fermi level, which depend on the nanostructure as well as magnetic structure in the sample. Once the geometry of the sample and the magnetic structure are given, the conductance is calculated. We note that the sample may include an insulating layer. Thus, Eq. (11) is applied to tunneling junctions as well.

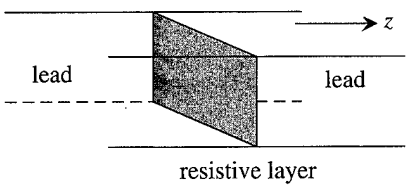


FIG. 2. Model of single resistive layer. Shaded layer denotes resistive layer.

III. EFFECTS OF ELECTRON–ELECTRON INTERACTION

In Sec. II, the conductance has been derived in the mean field theory. In this section, effects of the electron–electron interaction on the conductance is examined. For this purpose, we set up a model: we consider the tight binding model in a simple cubic lattice which contains a single resistive layer at $z=0$ as shown in Fig. 2. The z axis is chosen to be parallel to the (001) axis of simple cubic structure. In the layer, there exists the electron–electron interaction on each site given by the Hamiltonian,

$$H'=U\sum_l n_{l\uparrow}n_{l\downarrow}, \tag{12}$$

where $U>0$ and $n_{l\sigma}$ is the number operator with spin σ at site l in the layer.

We calculate the self-energy with spin σ, $\Sigma_\sigma(\epsilon_F+i0)$, in the single site coherent potential (or Hubbard) approximation (CPA). In the approximation, $\Sigma_\sigma(\epsilon_F+i0)$ is finite in the layer, independent of the momentum in the xy plane and diagonal in the spin space. Thus, the effective Hamiltonian may be written as

$$\hat{H}=-t\sum_{(i,j)}\sum_\sigma c^\dagger_{i\sigma}c_{j\sigma}+\sum_l\sum_\sigma \Sigma_\sigma c^\dagger_{l\sigma}c_{l\sigma}, \tag{13}$$

where t is the hopping parameter between nearest neighbor sites. Using the effective Hamiltonian [Eq. (13)], the transmission and reflection coefficients of electrons are calculated in the usual way[12] as

$$T^\sigma_{coh}=\frac{4t^2\sin^2\theta_{\mathbf{k}}}{(2t\sin\theta_{\mathbf{k}}+i\Sigma_\sigma)(2t\sin\theta_{\mathbf{k}}-i\Sigma^*_\sigma)}, \tag{14}$$

$$R^\sigma_{coh}=\frac{\Sigma_\sigma\Sigma^*_\sigma}{(2t\sin\theta_{\mathbf{k}}+i\Sigma_\sigma)(2t\sin\theta_{\mathbf{k}}-i\Sigma^*_\sigma)}, \tag{15}$$

where $\mathbf{k}=(k_x,k_y)$ is the wave number in the xy plane and $\theta_{\mathbf{k}}$ is defined as $-2t\cos\theta_{\mathbf{k}}=\epsilon_F+2t(\cos k_x+\cos k_y)$. Here, T^σ_{coh} and R^σ_{coh} are the coherent part of transmission and reflection coefficients, respectively. Since there exists the imaginary part in the self-energy in the resistive layer, electrons are caught in the layer and then diffuse from it. Such diffusive motion of electrons is incoherent. When the incoherent transmission and reflection coefficients are written as T^σ_{in} and R^σ_{in}, respectively, the current conservation is written as

$$T^\sigma_{coh}+R^\sigma_{coh}+T^\sigma_{in}+R^\sigma_{in}=1. \tag{16}$$

Following Stone and Lee,[13] we assume that electrons caught in the layer diffuse incoherently into the both sides equally and have

$$T_{\rm in}^{\sigma}=R_{\rm in}^{\sigma}=\tfrac{1}{2}(1-T_{\rm coh}^{\sigma}-R_{\rm coh}^{\sigma}). \tag{17}$$

Therefore, using the Landauer formula, we obtain the conductance as

$$\sigma_{zz}=\frac{e^2}{h}\sum_{\mathbf{k}}\sum_{\sigma}(T_{\rm coh}^{\sigma}+T_{\rm in}^{\sigma}), \tag{18}$$

$$T_{\rm in}^{\sigma}=\frac{it\sin\theta_{\mathbf{k}}(\Sigma_{\sigma}-\Sigma_{\sigma}^{*})}{(2t\sin\theta_{\mathbf{k}}+i\Sigma_{\sigma})(2t\sin\theta_{\mathbf{k}}-i\Sigma_{\sigma}^{*})}. \tag{19}$$

We can show that Eq. (18) is also derived from the Kubo formula [Eq. (1)] in the single site CPA (Ref. 12) without introducing the above assumption for the incoherent motions of electrons. In this case, the self-energy and vertex correction must be calculated consistently to satisfy the current conservation. When the single site CPA is used in the system with random scattering potentials, the elastic scattering is replaced by the inelastic one and the phase coherence of electrons is destroyed. However, it has been shown[12] that the conductance [Eq. (18)] agrees with that given by the numerical simulation with any strength of random scattering potentials. Therefore, the CPA may be used for the calculation of the conductance.

IV. DISCUSSION

We have studied the conductance in magnetic nanostructures. When the electron–electron interaction is neglected, the conductance depends only on the voltage between leads. Therefore, it is calculated once the nanostructure and magnetic structure are given in the sample. Although it is not easy to obtain the analytical solution of the conductance, the numerical simulation has been done extensively in a variety of the nanostructures.[14–16]

In the tunneling junctions, the insulating barrier is usually made by oxides so that the energy gap is caused by the electron correlation. We have introduced the electron–electron interaction in the single resistive layer and obtained the conductance due to the interaction. The application of Eq. (18) to the realistic junctions will be presented separately.

Finally, the theory obtained in this article is limited in the two-current model. Although the model works well at low temperatures, the spin-flip scattering will not be neglected as temperature increases. Effects of the scattering will also be studied separately.

ACKNOWLEDGMENTS

This work has been supported by Priority-Areas Grants from the Ministry of Education, Science and Culture of Japan, and the New Energy and Industrial Technology Development Organization (NEDO).

[1] M. N. Baibich, J. M. Broto, A. Fert, Nguyen Van Dau, F. Petroff, P. Etienne, G. Creuzet, A. Friederich, and J. Chazelas, Phys. Rev. Lett. **61**, 2472 (1988).
[2] A. E. Berkowitz, J. R. Mitchell, M. J. Carey, A. P. Young, S. Zhang, F. E. Spada, F. P. Parker, A. Hutten, and G. Thomas, Phys. Rev. Lett. **68**, 3745 (1992).
[3] J. Q. Xiao, J. S. Jiang, and C. L. Chien, Phys. Rev. Lett. **69**, 3220 (1992).
[4] M. Julliere, Phys. Lett. A **54**, 225 (1975).
[5] S. Maekawa and U. Gefvert, IEEE Trans. Magn. **MAG-18**, 707 (1982).
[6] T. Miyazaki and N. Tezuka, J. Magn. Magn. Mater. **139**, L231 (1995).
[7] J. S. Moodera *et al.*, Phys. Rev. Lett. **74**, 3273 (1995).
[8] H. Fujimori, S. Mitani, and S. Ohnume, Mater. Sci. Eng. B **31**, 219 (1995); S. Mitani *et al.* (to be published).
[9] J. Inoue and S. Maekawa (to be published).
[10] C. L. Kane, R. A. Serota, and P. A. Lee, Phys. Rev. B **37**, 6701 (1988).
[11] P. M. Levy, Solid State Phys. **47**, 367 (1994).
[12] H. Itoh, J. Inoue, and S. Maekawa (to be published).
[13] A. D. Stone and P. A. Lee, Phys. Rev. Lett. **54**, 1196 (1985).
[14] A. Oguri, Y. Asano, and S. Maekawa, J. Phys. Soc. Jpn. **61**, 2652 (1992).
[15] Y. Asano, A. Oguri, and S. Maekawa, Phys. Rev. B **48**, 6192 (1993).
[16] Y. Asano, A. Oguri, J. Inoue, and S. Maekawa, Phys. Rev. B **49**, 12831 (1994).

Spin-dependent tunneling effect and GMR in metal–nonmetal granular systems (invited) (abstract)

H. Fujimori and S. Mitani
Institute for Materials Research, Tohoku University, Sendai 980-77, Japan

S. Ohnuma
The Research Institute of Electric and Magnetic Materials, Sendai 982, Japan

Giant magnetoresistance (GMR, large negative and isotropic magnetoresistance) arising from a spin-dependent tunneling effect has been found in metal–nonmetal granular systems exhibiting extremely high electrical resistivities.[1] These granular materials are reactively sputtered Co–(Al, Si)–O and Fe–Mg–O thin films, having a two phase nanostructure consisting of the Co (or Fe) rich metallic and magnetic grains and the Al (or Si,Mg) oxide narrow intergrains. These films possess large specific electrical resistivities(ρ_0) of 10^4–10^6 $\mu\Omega$ cm at room temperature, and show remarkable magnetoresistance ($\Delta\rho/\rho_0$) whose values are about 8% in maximum at room temperature and at about 10 kOe of applied magnetic field. With decreasing temperature, $\Delta\rho/\rho_0$ and ρ_0 increase. The temperature dependence of ρ_0 can be expressed in terms of $\log \rho_0 \propto T^{-1.2}$, and the electrical current versus applied electrical voltage does not follow the ohmic low. We consider that a spin-dependent tunneling conductance in the path of magnetic grains–nonmetallic intergrains–magnetic grains is responsible for the observed GMRs accompanying high electrical resistivities. The details of these transport properties and the related magnetization and structural properties will be presented. © *1996 American Institute of Physics.* [S0021-8979(96)59708-3]

[1] H. Fujimori, S. Mitani, and S. Ohnuma, Mater. Sci. Eng. B **31**, 219 (1995).

 0021-8979/96/79(8)/4733/1/$10.00 © 1996 American Institute of Physics

Spin-dependent transmission of free electrons through ultrathin cobalt layers (invited)

H.-J. Drouhin, A. J. van der Sluijs, Y. Lassailly, and G. Lampel
Laboratoire de Physique de la Matière Condensée, Centre National de la Recherche Scientifique, Ecole Polytechnique, 91128 Palaiseau, France

We present an original technique to investigate spin-dependent electron interactions in ferromagnetic metals, and place it in the context of previous studies. Our technique is based on spin-polarized electron transmission through ultrathin, free-standing, metal foils. A longitudinally spin-polarized, quasimonoenergetic, free-electron beam impinges onto a ferromagnetic target consisting of a few atomic layers of cobalt sandwiched between gold layers, for an overall thickness of the order of 25 nm. It is remanently magnetized perpendicular to the film plane. The current transmitted through the foil is energy analyzed and its dependence on the relative orientation between the spin polarization of the primary beam and the magnetization direction of the cobalt layer is measured. The experiments are performed over a wide primary energy range, starting from the vacuum level of the target; the work function of the target can be lowered down to 2 eV by cesium deposition. We demonstrate a spin-filter effect, favoring the transmission of majority electrons. It is very large at low primary energy, when the electrons travel close to the 3*d* bands. Perspectives for compact and highly discriminative spin detectors are discussed. © *1996 American Institute of Physics.* [S0021-8979(96)50408-8]

I. INTRODUCTION

The physics of ultrathin magnetic layers is an active field of research, generally involving magnetoresistive and magneto-optical properties.[1,2] Novel magnetic sensors and heads are under development[3] and electron devices making use of "spin valve" effects are emerging.[4,5] We will consider a different but complementary approach, based on the spin-dependent transmission of free electrons through self-supported magnetic structures. Earlier accounts on this work can be found in Refs. 6–8.

Pioneering low-energy transmission experiments were performed by Kanter[9] who studied electron transmission through aluminum, gold, and silver foils to explore the energy dependence of the electron mean free path. Practically, free-standing foils can hardly be thinner than 20 nm and, because the electron mean free path is at most of the order of 2 nm, the transmitted intensity does not exceed a few 10^{-5} of the primary beam. It should be emphasized that such measurements are extremely difficult because the relevant parameter is this small transmission ratio, which can be affected by different factors, notably the foil quality. This type of measurement can also be compared to photoemission experiments: a substrate photoemission peak is selected and its attenuation is monitored as a function of a growing overlayer thickness. Whatever the technique, measuring electron mean free paths is intricate. Nevertheless, from the conductivity relaxation time, we know that, at very low energies, close to the Fermi level, the mean free path is long (tens of nm) whereas surface analysis techniques using electron beams demonstrate that, at much higher energies, the mean free path compares to the thickness of a few atomic layers. In all these experiments, the elastically emitted electrons can be unambiguously isolated, so that the mean free path which is measured is the *inelastic* mean free path. It characterizes the electron scattering out of the primary beam.

In this paper, we only consider the spin dependence of the transmitted intensity, which is a more reliable feature. The primary electron beam has a longitudinal spin polarization and impinges normally onto a cobalt layer sandwiched between gold layers, a ferromagnetic structure with a magnetization perpendicular to the film plane. We measure a transmission asymmetry between the incident electrons with spin parallel or antiparallel to the majority spin direction in the sample. Following Schönhense and Siegmann,[10] we can say that our structure acts as a "spin filter." Spin-dependent transmission has also been previously studied in photoemission experiments by the overlayer technique.[11] Generally, in these experiments, unpolarized electrons are injected from a substrate core level into the magnetic overlayer; due to spin-dependent transport a spin polarization builds up and the measured parameter is the spin polarization of the emitted beam. In an experiment closely related to our transmission technique, Gröbli *et al.*[12] studied the spin dependence of the current photoemitted from a gallium arsenide crystal covered with an Ag/Fe bilayer. There, by optical pumping, spin-polarized electrons are generated inside the semiconductor, with a spin polarization parallel to the direction of the exciting light, normal to the surface. The photoelectrons are subsequently extracted through the ferromagnetic overlayer. Such a solid-state structure, which associates the electron source to the magnetic target in a same device, is attractive, but the technology strongly constrains the experimental conditions: an Ag buffer layer has to be inserted to prevent interdiffusion and chemical reactions, and the magnetization has no perpendicular remanence so that the continuous application of a high magnetic field (± 1.6 T) is required to maintain the magnetization normal to the surface. A practical complication also arises due to the contribution of the metal layer itself to the photoemission current, which is responsible for a large background signal. A similar background contribution is present in all photoemission experiments and re-

 0021-8979/96/79(8)/4734/6/$10.00 © 1996 American Institute of Physics

stricts the study to a very precise range of metal thicknesses which does not allow one to discriminate between interface and bulk effects. Another device, called the "spin-valve transistor," has recently been elaborated.[5] It acts as a "hot-electron spectrometer" for the study of the magnetic interactions and possibly allows one to control the electron energy in the 0.3–3 eV range above the Fermi level. Generally speaking, in solid-state structures the effects may be more difficult to disentangle than in transmission experiments. A clear advantage of our technique is that we control the primary energy and polarization and can also analyze the transmitted beam, in energy and possibly in spin polarization. It is a very direct way to investigate spin-dependent interactions in ferromagnetic metals, a topic where the microscopic detail remains questioned. A transmission experiment is obviously restricted to electron energies exceeding the vacuum level, about 4 eV above the Fermi level for a clean gold surface, but a surface treatment by cesium deposition lowers it down to 2 eV. As magnetoresistance experiments probe the spin-dependent interactions at the Fermi level, and as some structures like the spin-valve transistor may cover intermediate energies, a complete investigation appears within reach.

Concerning applications, we will show that our spin-filtering foils constitute a new kind of spin detector, based on the exchange asymmetry. This has interesting implications because, if the electron spin is currently used as a probe of electronic and magnetic properties of solids, the spin measurement remains a bottleneck. In recent years, considerable effort has been put into the improvement of polarimeters, but an efficient, easy to use, spin detector remains to be found. Even now Au/Co/Au structures can compete with the best existing spin detectors.

II. BACKGROUND

For many years spin-polarized electron techniques have been intensively developed for the study of magnetic interactions.[13] Essentially, two types of experiments have to be distinguished: (i) experiments where the spin polarization of the beam after interaction with the ferromagnetic target is detected; (ii) experiments in which the primary beam is spin-polarized, and where the spin dependence of the electron current is the relevant parameter. Now, we will compare these two classes of experiments in the framework of a very simple model.

We assume that electrons are injected into a ferromagnetic foil and cross it to be reemitted into vacuum. The electron source emits a constant number of electrons $N=(n_+ + n_-)$ per unit of time and has a spin polarization $P_S=(n_+ - n_-)/(n_+ + n_-)$, where $n_+(n_-)$ is the number of electrons with spin up (down) with respect to a fixed reference axis, parallel to the magnetization direction; the absolute value of P_S is denoted as P. We only consider spin-dependent electron transport toward the surface and assume that the number of electrons reaching the surface with spin up (down) is $t_{\sigma+}n_+(t_{\sigma-}n_-)$; here $t_{\sigma+}(t_{\sigma-})$ are transport coefficients affected to up (down) spin and $\sigma=\pm$ indicates the majority spin direction in the ferromagnet. As the spin-dependent interactions depend only on the relative orientation of the incident spins with the majority spin direction in the ferromagnet, we have the symmetry relations $t_{++}=t_{--}$ and $t_{+-}=t_{-+}$; for simplicity, we will sometimes use the notation $t_{++}=T_+$ and $t_{+-}=T_-$. The spin polarization of the electrons reaching the surface, which we assume to be the emitted beam polarization, is $P_e=(P_S+a_\sigma)/(1+a_\sigma P_S)$, where a_σ is the spin asymmetry of the transport coefficients defined by $a_\sigma=(t_{\sigma+}-t_{\sigma-})/(t_{\sigma+}+t_{\sigma-})$. In the following, we will also speak of the asymmetry $a=a_+=(T_+-T_-)/(T_++T_-)$; we will see from general arguments that a should be positive. For analysis, it is convenient to define the parameters x_S and α_σ by the relations $P_S=\tanh x_S$ and $a_\sigma=\tanh \alpha_\sigma$. Then $P_e=\tanh(x_S+\alpha_\sigma)$, which allows its simple graphical determination, knowing the source polarization and the spin asymmetry of the transport process (see Fig. 1).

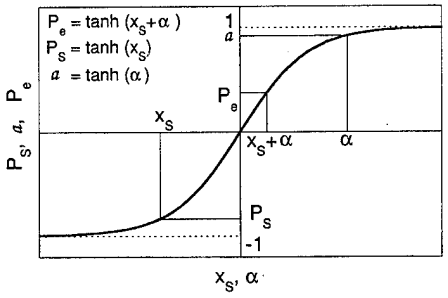


FIG. 1. Graphical determination of the emitted electron polarization.

To give an example, consider the work by Penn and co-workers:[14] an unpolarized electron beam impinges on a ferromagnetic glass with sufficient energy to excite a secondary electron cascade, with a spin polarization reflecting the bulk magnetization (about 0.2). The question was to explain the enhanced polarization of the low-energy secondaries (about 0.4 at the vacuum level). In this case, spin-polarized electrons are generated inside the ferromagnet by impact excitation and the polarized electron source with polarization $P_S=0.2$ lies within the ferromagnet. When the electrons are emitted at an energy not too far from the d bands, the lifetimes for majority and minority electrons differ. These lifetimes are interpreted as T_+ and T_-; this defines the spin asymmetry a for the emission process, and thus P_e. Here obviously, the spin polarization of the source cannot be reversed independently of the target magnetization.

Coming back to our experiment, we start with a *positive* spin polarization of the source and inject $n_+=(N/2)(1+P)$ electrons with spin up and $n_-=(N/2)(1-P)$ electrons with spin down, so that the transmitted beam intensity is $I_\sigma^+=(N/2)[t_{\sigma+}(1+P)+t_{\sigma-}(1-P)]$ for a given magnetization of the layer. Reversing the sign of the polarization, the transmitted intensity becomes $I_\sigma^-=(N/2)[t_{\sigma+}(1-P)+t_{\sigma-}(1+P)]$. The asymmetry in the transmitted intensity is then $\mathcal{A}_\sigma=(I_\sigma^+-I_\sigma^-)/(I_\sigma^++I_\sigma^-)=a_\sigma P$; we will note $\mathcal{A}=\mathcal{A}_+=aP$.

In this model, the spin polarization of the transmitted beam P_e and the asymmetry in the transmitted intensity $\mathcal{A}_\sigma$ are closely related. Nevertheless, the conditions in which the

experiments have to be performed are opposite: to determine the asymmetry a_σ of the transport process, an unpolarized source has to be preferred when performing spin-polarization measurements (case i), whereas a highly polarized source should be used if the spin-dependent intensity is measured (case ii). In real experiments, however, a strong change in the emitted beam polarization does not necessarily mean any related effect in the transmitted intensity: for instance, secondary electrons have a polarization which reflects the bulk magnetization but they may have no "memory" of the spin polarization of the primary beam. In fact, spin polarization and transmitted intensity measurements appear to be complementary.

When electrons travel through a ferromagnetic film of thickness d and only bulk effects are taken into account, it is usual to relate the spin-dependent transport coefficients to the spin-dependent inelastic mean free paths $\lambda_+(\lambda_-)$ for majority (minority) spin electrons through $T_\pm=\exp(-d/\lambda_\pm)$. Thus $a=\tanh[(d/2)(\lambda_-^{-1}-\lambda_+^{-1})]$; the transmission factor, the ratio of the transmitted (I) to the primary (I_0) intensity, takes the form $I/I_0=\cosh[(d/2)(\lambda_-^{-1}-\lambda_+^{-1})]\exp[-(d/2)(\lambda_-^{-1}+\lambda_+^{-1})]$. The spin asymmetry of the mean free path $(\lambda_+-\lambda_-)/(\lambda_++\lambda_-)$ is often considered and values ranging from 0.1 to 0.3 have been found at a few eV above the vacuum level for $3d$-transition metals.[10]

To go further in the analysis, we need a model to determine the spin-dependent transport coefficients. Because there is a larger number of empty states near the Fermi level for minority spin electrons, i.e., more relaxation channels, the majority spin electrons should be more easily transmitted. The simplest formulation was given by Schönhense and Siegmann.[10] For noble or transition metals these authors assume that the electron scattering cross section, which is proportional to the inverse of the electron mean free path, is directly related to the number of unoccupied states in the d band. This leads to different cross sections for majority and minority spin electrons, with the relation $\lambda_\pm^{-1}=\lambda_0^{-1}+\lambda_d^{-1}[5-(n\pm\Delta n)]$; here λ_0^{-1} and λ_d^{-1} are suitable coefficients and $n\pm\Delta n$ is the number of occupied states in the d band for majority and minority spin electrons. This simple theory gives fair agreement with presently available experimental data, at least for energies above the vacuum level. Yet many aspects remain to be cleared, for instance, the energy dependence of the scattering cross section or the comparison between different metals, because some results obtained in photoemission and in magnetoresistance experiments appear contradictory.[15] In our experiment, speaking in terms of mean free path, the measured asymmetry is directly related to $1/\lambda_--1/\lambda_+$, a physical quantity proportional to the magnetic moment. Unless performing absolute intensity measurements, which are extremely difficult, we cannot determine independently λ_- and λ_+. It will be useful in the following to write $1/\lambda_+=1/\lambda-1/\delta$ and $1/\lambda_-=1/\lambda+1/\delta$ which defines the spin-averaged mean free path λ by $1/\lambda=(1/2)[1/\lambda_-+1/\lambda_+]$. Then the spin asymmetry of the mean free path is λ/δ and, at energies above the vacuum level, we expect $\delta\gg\lambda$, with λ of the order of 1 nm.[10] The asymmetry a and the transmission ratio I/I_0 take simple forms, $a=\tanh(d/\delta)\sim(\lambda/\delta)(d/\lambda)$ and $I/I_0=\cosh(d/\delta)\exp(-d/\lambda)\sim\exp(-d/\lambda)$, for an ultrathin layer ($d\ll\delta$); in our experiment $d/\lambda\approx1$.

III. EXPERIMENT

The experimental setup has been described in detail elsewhere.[8] A longitudinally spin-polarized electron beam is obtained from a GaAs photocathode under optical pumping. This beam, whose polarization is modulated between +0.24 and −0.24, is focused on a ferromagnetic sample, remanently magnetized perpendicular to its surface. The current transmitted through the sample is energy-analyzed using a retarding-field analyzer (resolution 150 meV) and its polarization dependence is measured. Stray modulations are maintained at a relative level below a few times 10^{-4}. The sample's magnetization is reversed in the measurement configuration by a magnetic-field pulse. The sample holder can be cooled down to about 130 K by contact with a liquid–nitrogen cold finger. The primary electron energy E_P is continuously varied from the sample's vacuum level upward. Throughout the paper the energy is measured with respect to the Fermi level of the ferromagnetic structure.

We will present results on three nearly identical ferromagnetic structures, labeled A, B, and C. Each consists of a 1-nm-thick layer of cobalt sandwiched between gold layers: Au(21 nm, 22 nm, 22 nm)/Co(1 nm)/Au(2 nm) for structures A, B, and C, respectively. The primary beam impinges on the thicker gold layer. Details about the sample preparation can be found in Ref. 6. To obtain a free-standing sample, the Au/Co/Au films are evaporated on a float glass substrate with an intermediate layer of NaCl. Then the metal foil is lifted off in water and deposited onto a gold-plated copper sample holder with an aperture of about 3 mm diameter.

To explore a lower energy domain, we reduce the work function of the structures by cesium deposition, a well-known technique. Although cesium reacts with gold,[16] this is not of importance here as we are not concerned by the surface electronic structure. Practically, cesium is evaporated until a photoemission current is measured when the target is illuminated by a red laser diode, which means that the vacuum level has been lowered from 4 to about 2 eV above the Fermi level. The "activated" surface remains stable over a long time (several weeks). The amount of cesium deposited should be of the order of an atomic layer. Once deposited, cesium cannot be removed from the surface by subsequent treatment.

IV. THE SPIN-DEPENDENT TRANSMITTED CURRENT

A careful study of reference gold samples has been previously performed; the results and a comparative discussion with data by Kanter (Ref. 9) can be found in Ref. 8. Here we present results obtained at room temperature on Au/Co/Au structures with clean and cesiated surfaces; some results at lower temperature (130 K) are also given. The experimental curves are normalized to an incident current of 100 nA.

A. Principle of the measurement

The transmitted current measured as a function of the retarding potential at $E_P=3.8$ eV, from structure C with a

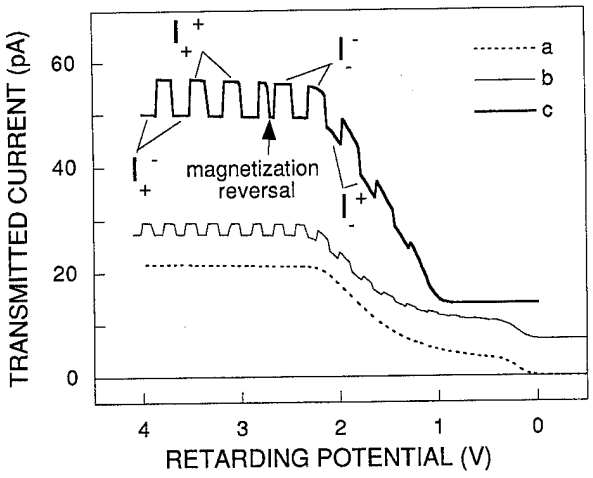


FIG. 2. Structure C, cesiated exit face. Transmitted current vs retarding potential for E_P=3.8 eV (curves a and b) and 2.9 eV (curve c). In the two upper curves, whose zero signal levels have been shifted for clarity, the spin polarization of the primary beam is switched periodically from +0.24 to −0.24 and the steps are the corresponding variations of the transmitted current.

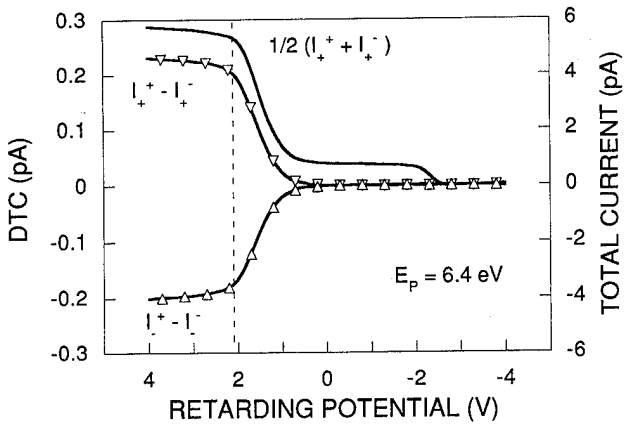


FIG. 3. Structure A with cesiated entrance and exit faces. Transmitted current (upper curve) and the corresponding DTCs for E_P=6.4 eV, for two opposite magnetizations of the cobalt layer.

cesiated exit surface, is shown in Fig. 2, curve (a). To understand this curve, remember that, for a retarding potential corresponding to a cutoff at energy E, the collected current is $I(E)=\int_E^{+\infty}\delta I(E')dE'$, where $\delta I(E')$ is the energy distribution of the transmitted current. Two main features are observed: a high-energy edge and a low-energy step. The high-energy edge, whose position varies linearly with E_P, corresponds to ballistic electrons or to electrons which experienced only small energy loss or momentum change throughout the foil ("quasielastic" part). The low-energy step ("inelastic" part) originates from electrons which have lost a notable part of their energy or from true secondary electrons, emitted with a negligible kinetic energy, at the surface vacuum level. The relative intensities of these two contributions depend on E_P; when E_P is close to the vacuum level, the elastic and inelastic parts cannot be separated. The total transmitted current is of the order of 10^{-4} of the primary beam. At higher E_P, the inelastic step is increased by a large amount, due to secondary electron generation. Information on the inelastic mean free path is contained in the high-energy edge, where true elastic electrons are detected.[8]

Information on the spin-dependent interactions is obtained from the difference in the transmitted intensity between both incident spin directions. The principle is made clear when looking at Fig. 2, curves (b) and (c), which visualize the transmitted intensity versus retarding potential at low primary energies [E_P=3.8 and 2.9 eV, respectively]. During the scan, the spin polarization of the source is switched periodically from +0.24 to −0.24 and the steps are the corresponding variation of the transmitted intensity, which is very large, especially at the lowest primary energy where the total transmitted intensity also increases due to the larger electron mean free path. At a given time, indicated by the arrow in curve (c), the magnetization of the film has been reversed by a pulse of field, so that the signal levels corresponding to the two incident spin orientations are exchanged.

As expected, the majority spin electrons are more easily transmitted. Practically, it is more convenient to use lock-in detection techniques to measure directly the intensity difference, that we call the spin-dependent differential transmitted current (DTC) $\Delta I_\sigma=\int_E^{+\infty}[\delta I_\sigma^+(E')-\delta I_\sigma^-(E')]dE'$, where $\delta I_\sigma^+(E')[\delta I_\sigma^-(E')]$ is the energy distribution of the transmitted current for incident electron spin polarization parallel (antiparallel) to the electron-beam propagation axis Oz and for majority spin in the ferromagnet parallel ($\sigma=+$) or antiparallel ($\sigma=-$) to Oz. In Fig. 3 (structure A, cesiated), the DTC measurements are shown for the two opposite magnetizations of the layer and the symmetry of the resulting curves with respect to the zero signal level is a test for the absence of instrumental asymmetry. As expected a zero DTC is measured when starting with a nonmagnetized structure. Then magnetic-field pulses are applied in order to saturate the DTC. Now, the intensity transmission asymmetry $\mathcal{A}$ and the spin asymmetry of the transport coefficients a depend on both E_P and on the transmitted electron energy E; we will explicitly state this energy dependence by writing $\mathcal{A}(E_P;E)$ and $a(E_P;E)$. At a fixed E_P, we numerically differentiate the collected current and the DTC to obtain the energy distribution of the transmitted current and its spin asymmetry. According to Sec. II, $\mathcal{A}_\sigma(E)=[\delta I_\sigma^+(E)-\delta I_\sigma^-(E)]/[\delta I_\sigma^+(E)+\delta I_\sigma^-(E)]$ and $\mathcal{A}(E)=\mathcal{A}_+(E)=a(E)P$.

B. Results and discussion

Because large effects are observed at low electron energy, we will first consider the effects of lowering the vacuum level. Figure 4 shows the energy distribution curve (EDC) of the transmitted current from structure C with a clean and with a cesiated exit surface. The "entrance" face had not been intentionally cesiated, but the possibility to inject electrons at energies as low as 2.6 eV indicates some cesium contamination. The low-energy end of each EDC is determined by the vacuum level cutoff, which appears to be reduced by 2 eV after cesiation, giving access to lower electron energies. We observe that the work-function reduction leaves the elastic peak almost unaffected while a large inelastic peak appears which becomes the dominant contribution to

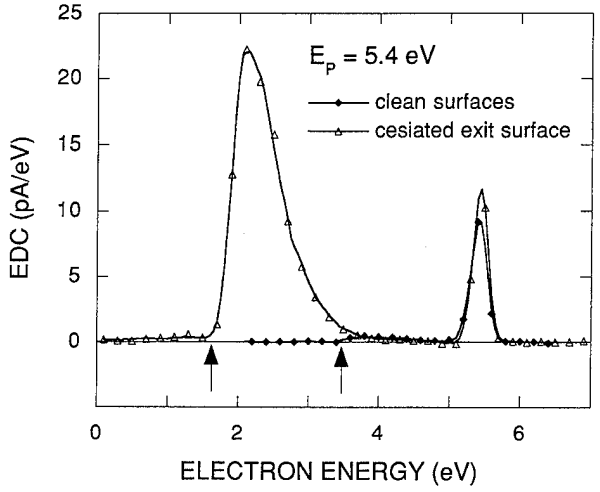


FIG. 4. Structure C with a clean surface (♦) and a cesiated exit surface (△). EDCs of the transmitted current obtained by numerical differentiation of the current collected after retardation for E_P=5.4 eV. The arrows indicate the locations of the vacuum level.

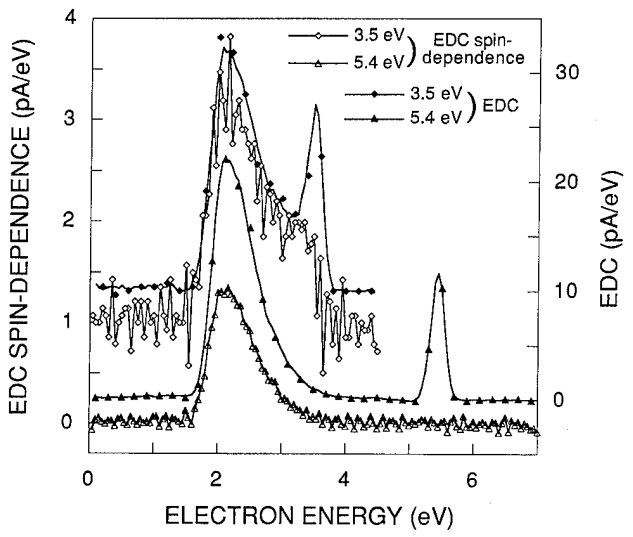


FIG. 5. Structure C, cesiated exit surface. EDC of the transmitted current (full symbols) and its spin dependence (open symbols) for E_P=3.5 eV (diamonds, single scan) and 5.4 eV (triangles, average of ten scans). For clarity, the base lines of the 3.5 eV curves have been shifted.

the transmitted current. At very low energy, the overall transmission is increased by more than an order of magnitude to reach 6×10^{-4}. In these conditions a spin asymmetry can be observed over an energy range of a few eV and it is possible to study precisely, at fixed E_P, the dependence of the transmission asymmetry on the transmitted electron energy E. Note that, at the Co layer, the initial conditions are well defined: in gold, the mean free path for spin relaxation is much longer than that for energy relaxation[17] and no significant secondary electron contribution is expected at low E_P, so that the spin polarization is conserved after passing the Au layer; cesium deposition should not affect the spin polarization.[12]

Figure 5 shows the EDCs of the transmitted current and their spin dependence (structure C, cesiated) for E_P=3.5 eV (upper curves) and 5.4 eV (lower curves). In the EDCs the elastic and inelastic peaks are well resolved. For E_P=5.4 eV, the spin-dependent curve closely follows the inelastic peak, no elastic contribution to the asymmetry being observed in these conditions; this is evidence that $a(E)$ remains constant over the inelastic peak. For E_P=3.5 eV, a small spin-dependent transmission is observed in the elastic peak and the spin-dependent signal is increased in the inelastic peak. In general, striking features are the large difference in transmission between the two incident spin orientations at low E_P and the sharp decrease of the spin dependence when increasing E_P. At the lowest primary energies, the incident electrons are transmitted at an energy close to the 3d bands, and spin-dependent transmission is observed whatever the emerging electron energy. At higher energies, spin-dependent transmission only appears at the inelastic peak. Lowering the temperature to about 130 K increases the transmitted current by about 50%. This fact was already mentioned by Kanter, who reported an exponential variation of the transmitted current versus temperature;[9] it was attributed to the temperature dependence of the electron–phonon interaction. The spin asymmetry is almost doubled in the elastic peak and does not change significantly in the inelastic peak. At 130 K, it became technically impossible to reverse the magnetization, because of a too large increase of the coercive field.

We will first discuss the elastic peak, where we measured a maximum asymmetry $a\approx0.13$ at $E_P\approx5$ eV for structure A with a clean surface. In this region, we use the inelastic mean free path model presented in Sec. II and we deduce that $T_+/T_-\approx1.3$; assuming a spin-averaged mean free path of the order of 1 nm in cobalt, this is also consistent with a mean free path asymmetry of about 0.13, a plausible value. However, further studies with other structures showed a sensitivity of the asymmetry in the elastic peak to the sample preparation. The analysis of these effects is under way. Now, because the asymmetry a is larger and constant over the inelastic peak we choose to plot its variation, as a function of E_P for structures A, B, and C, with clean or cesiated surfaces, at room temperature or at low temperature (Fig. 6). The results appear to be very reproducible and we see that a reaches extremely large values at low E_P and decreases rapidly with increasing E_P. The maximum value of a is about 0.6 which corresponds to $T_+/T_-=4$. Strictly speaking, here a mean free path model does not apply. Nevertheless, for a low E_P, it should yield a reasonable estimate of some mean free path average, between the vacuum level and E_P. Therefore, in Fig. 6, an additional point is indicated at the lowest E_P, where the elastic and inelastic peaks can no longer be resolved; on the total current we measure again $a\approx0.6$. Using this a value, we deduce a mean free path asymmetry of about 0.6, intermediate between the results obtained at a few eV above the clean surface vacuum level (0.25),[10] and those estimated at the Fermi level in magnetoresistance experiments (about 0.7).[15] Nevertheless, the detail of the electron transport in the inelastic part has to be analyzed prior to any more refined interpretation and at present a certain number of points remain unexplained, for instance, the very sharp decrease of the asymmetry with E_P, the larger asymmetry in the inelastic peak than in the elastic peak, even at ultralow

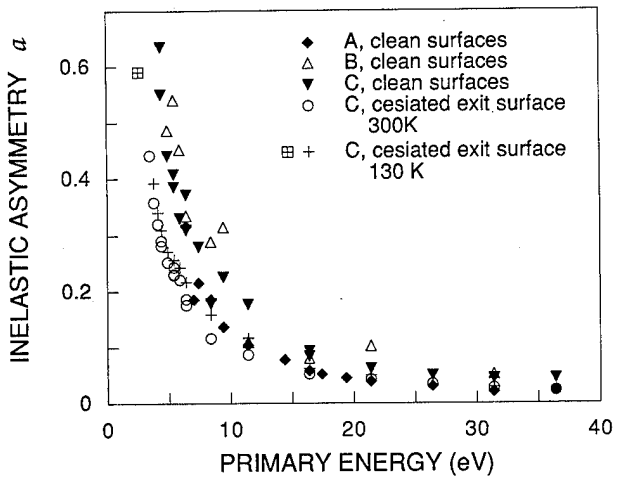


FIG. 6. Asymmetry a measured in the inelastic part of the transmitted current vs E_P for several structures and in various conditions. The point ⊞ is the asymmetry on the total transmitted current at $E_P=2.6$ eV, where the elastic and inelastic peaks are not resolved.

primary energy, and a small but reproducible reduction of the asymmetry, at given primary and analysis energies, after cesiation. It is clear that complementary experiments are necessary: let us mention the study of a structure where the primary beam impinges on the thinnest gold layer to clarify the role of the electron transport in the gold cap layers, the study of multilayers to discriminate between bulk and interface effects, and the spin analysis of the transmitted beam to determine the origin of the inelastic electrons.

V. CONCLUSION AND PERSPECTIVES

Magneto-optics and magnetoresistance are well established techniques which provide spectacular effects on (complicated) layered structures. Similar systems and also simple model structures, where many parameters are under control, can be studied by spin-polarized electron transmission, in a truly direct way. Our results show spin asymmetries which can be extremely large, but the technique is still in its infancy. We are convinced that, in a near future, it will yield new insight in the microscopic detail of spin-dependent electron interactions in ferromagnetic metals. Let us conclude with spin detectors. A polarimeter is generally characterized by the figure of merit $F=S^2I/I_0$, where $I(I_0)$ is the collected (incoming) current and S the Sherman function which expresses the scattering asymmetry. $1/F$ is almost proportional to the time needed to perform a polarization measurement with a given accuracy. For the traditional Mott polarimeter operating at an energy of 100 keV, S is typically 0.3 and F at best of the order of 10^{-4}. The data obtained on a cesiated Au/Co/Au sandwich (at low temperature) can be expressed in terms of spin detectors, identifying S to a: they correspond to $S=0.6$ and $F=1.7\times10^{-4}$; this figure of merit is one of the highest ever reported. A more detailed comparison with other recently developed detectors is given in Ref. 7. In our simple structure, only a small improvement (35%) of F can be expected by optimizing the thickness of the ferromagnetic layer. The expressions of a and I/I_0 given in Sec. II show that the figure of merit for the sole cobalt layer is of the order of $(\lambda/\delta)^2(d/\lambda)^2\exp(-d/\lambda)$, so that an optimum is reached for $d\sim2\lambda$ (about 2 nm), and in any case, we are restricted to thicknesses for which the magnetization remains perpendicular ($d\leqslant15$ Å). Because the transmitted current decreases exponentially over a characteristic length equal to the electron mean free path, i.e., about 2 nm, a much larger improvement can be expected from the improvement of I/I_0 when reducing even slightly the thickness of the gold layer. The use of cobalt multilayers should also be considered. When very small asymmetries have to be measured, the limiting factor is not the statistical noise but the sensitivity to instrumental asymmetries. Then, the high analyzing power that is expressed by a large S is a key feature and the detector quality cannot be reduced to an F value. The large Sherman function of our structure, the easy elimination of any instrumental asymmetry by magnetization reversal, and the possibility to operate in the electron counting mode make it very promising as a spin detector.

ACKNOWLEDGMENTS

We thank C. Marlière for his precious contribution in the early stage of the experiment, J.-P. Chauvineau for continuous support in sample growth and characterization, and F. Bridoux for his help with grazing incidence x-ray reflectometry. We are indebted to M. I. D'yakonov for many stimulating discussions. H.-J. D. thanks the "Direction de la Recherche et de la Technologie de la Délégation Générale pour l'Armement" for his support. A. J. v. d. S. acknowledges support from the European Community "Human capital and mobility" program.

[1] E. Vélu, C. Dupas, D. Renard, J.-P. Renard, and J. Seiden, Phys. Rev. B **37**, 668 (1988).
[2] D. Weller, H. Brändle, G. Gorman, C.-J. Lin, and H. Notarys, Appl. Phys. Lett. **61**, 2726 (1992).
[3] D. E. Heim, R. E. Fontana, Jr., C. Tsang, V. S. Speriosu, B. A. Gurney, and M. L. Williams, IEEE Trans. Magn. **30**, 316 (1993).
[4] M. Johnson, Phys. Rev. Lett. **70**, 2142 (1993).
[5] D. J. Monsma, J. C. Lodder, Th. J. A. Popma, and B. Dieny, Phys. Rev. Lett. **74**, 5260 (1995).
[6] Y. Lassailly, H.-J. Drouhin, A. J. van der Sluijs, G. Lampel, and C. Marlière, Phys. Rev. B **50**, 13054 (1994).
[7] A. J. van der Sluijs, H.-J. Drouhin, Y. Lassailly, G. Lampel, and C. Marlière, C. R. Acad. Sci. Paris II **319**, 753 (1994).
[8] H.-J. Drouhin, G. Lampel, Y. Lassailly, A. J. van der Sluijs, and C. Marlière, J. Magn. Magn. Mater. **151**, 417 (1995).
[9] H. Kanter, Phys. Rev. B **1**, 522 (1970).
[10] G. Schönhense and H. C. Siegmann, Ann. Phys. **2**, 465 (1993).
[11] D. P. Pappas, K.-P. Kämper, B. P. Miller, H. Hopster, D. E. Fowler, C. R. Brundle, A. C. Luntz, and Z.-X. Shen, Phys. Rev. Lett. **66**, 504 (1991).
[12] J. C. Gröbli, D. Guarisco, S. Frank, and F. Meier, Phys. Rev. B **51**, 2945 (1995).
[13] J. Kirschner, *Polarized Electrons at Surfaces*, Springer Tracts in Modern Physics No. **106** (Springer, Berlin, 1985).
[14] D. R. Penn, S. P. Apell, and S. M. Girvin, Phys. Rev. B **32**, 7753 (1985).
[15] B. A. Gurney, V. S. Speriosu, J.-P. Nozières, H. Lefakis, D. R. Wilhoit, and O. U. Need, Phys. Rev. Lett. **71**, 4023 (1993).
[16] W. E. Spicer, A. H. Sommer, and J. G. White, Phys. Rev. **115**, 57 (1959).
[17] F. Meier, G. L. Bona, and S. Hüfner, Phys. Rev. Lett. **52**, 1152 (1984).

The vibrating sample magnetometer: Experiences of a volunteer (invited)

S. Foner
Francis Bitter National Magnet Laboratory and Department of Physics, MIT, Cambridge, Massachusetts 02139

On its 40th anniversary, I describe how the vibrating sample magnetometer (VSM) was developed and, later, how the very low frequency VSM, a flux-integration device, was developed. The important features of the moving sample technique, detection coil symmetry, calibration, sensitivity, and image effects are discussed briefly. Some VSM adaptations discussed include operation at ^{3}He and dilution refrigerator temperatures, at high hydrostatic pressures, in superconducting, high-power water-cooled and hybrid magnets, for very low frequency ac susceptibility, and with SQUID detectors. © *1996 American Institute of Physics.* [S0021-8979(96)50508-4]

I. THE VIBRATING SAMPLE MAGNETOMETER (VSM)

The VSM and the Magnetism and Magnetic Materials Conference (M^3) are both celebrating their 40th anniversary. It is no surprise that the M^3 conference is still active and productive because magnetism continues to be important in basic science and in major industrial markets. However, the chance that a magnetic measurement instrument would continue to be popular is small, considering that often there appears to be more ways to measure magnetic properties than there are magneticians. Here I outline how two different VSMs were developed and discuss some of the many subsequent adaptations.

Science is not done in the logical manner presented in published papers. Often, chance or incidental factors lead to significant changes in direction. This was the case for the VSM. I arrived at Lincoln Laboratory during the early days of the Cold War. It was a classified laboratory, managed by MIT, that grew out of the war-time Radiation Laboratory at MIT and was dedicated to the US Electronic Air Defense. I was doing basic research in an applied physics group developing microwave ferrite devices for radar applications such as isolators, circulators, and Faraday rotators that capitalized on the gyrotropic properties of insulating ferrites in a magnetic field. The group, headed by Benjamin Lax, included Joseph Artman and Peter Tannenwald doing ferromagnetic resonance, and Kenneth Button, Stanley Autler, and Herbert Zeiger among others. At that time ferrites were fairly new and the magnetization of specific materials was needed for calculations of the microwave propagation in the devices. I had been involved in magnetism for my thesis and volunteered to measure the magnetization for these materials. First I used flux integration, detected by a coil surrounding the ferrite bar on reversal of the magnetic field. This required modifying a 12 in. Varian electromagnet by incorporating a time-delayed reversing switch. (The early magnets were sold for nuclear magnetic resonance which required a fixed, stable field. Our outstanding and large proportioned sales representative, "Tiny" Yewell of Yewell Associates, forwarded our magnet modifications and these often would appear sometime later in the Varian product line.) Then I built a modified classic Sucksmith ring balance[1] to measure the force on a small sample in a well-defined magnetic field gradient. The ring balance used two facing mirrors mounted on a very thin Cu–Be circular spring. The force on the spring deformed the ring so that the deflection of a light beam reflected between the mirrors was magnified when projected at some distance. This was a fairly rugged device. Then the group moved to new space in Bedford, MA and occupied a wooden radar field station, and anyone walking on the wooden floor caused the light beam to bounce erratically. Despite this limitation, data could be obtained. Just before the summer of 1955, we moved again, this time to a garage attached to the main building of the new laboratory and near a small lunch room on the next floor.

David J. Robbins, a bright young Harvard physics graduate student, joined the group for the summer to work with me on these measurements. Unfortunately, he was killed during a lunch break while testing a high-performance motorcycle on a nearby, new, unopened road. I remember the sad weekend at the end of the summer when my wife and I drove to New York for his funeral through the debris deposited just after the third of three successive hurricanes that chose routes through Boston on alternate weeks.

That summer we were living in a small farm-hand's house about 1 km from the laboratory and just off the runway at Hanscom Field, a Strategic Air Command (SAC) base at that time. While shaving one evening I decided to try ac induction for magnetic measurements. With some Duco cement, a small $2.00 (in 1955) replacement loudspeaker, a conical paper cup, and a paper straw (the latter components were light and conveniently available at night from the lunch room), the first working model VSM was assembled. Initial test of principle was made using a reduced amplitude 60 Hz line excitation of the speaker driver. A sketch of that VSM is shown in Fig. 1. For simplicity and convenience, operation in a conventional electromagnet required vibrating of the sample perpendicular to the applied magnetic field. It was not obvious at first, but general principles were developed for arrangements of even numbers of pickup coils to detect

 0021-8979/96/79(8)/4740/6/$10.00 © 1996 American Institute of Physics

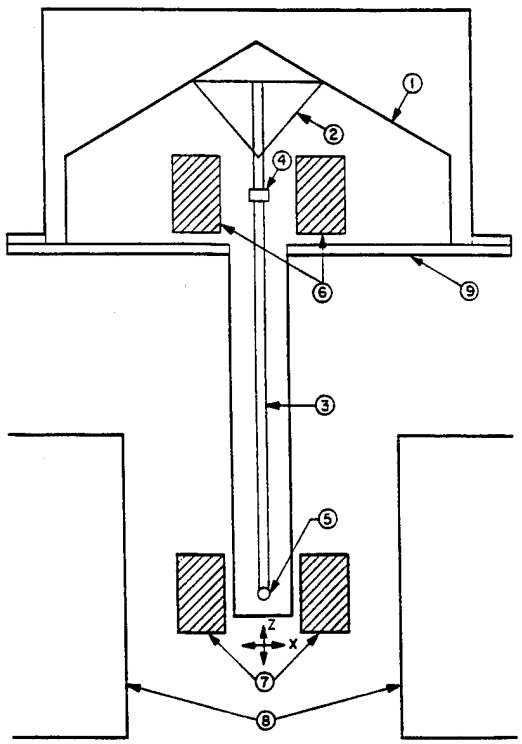


FIG. 1. First model of vibrating sample magnetometer (after Ref. 2).

the ac fields produced by the vibrating transverse moment while making the signal insensitive to sample position, vibration amplitude, and external field fluctuations to high order. Although generally inductive detection is used, any sensitive field sensor can be used; improved signal sensitivity can be expected for large transfer functions. Hall probes, magnetoresistors, and SQUIDs are largely frequency independent, whereas the inductive probe output is proportional to frequency. The symmetry arguments apply to all field sensors.

There were many new condensed matter physics problems to explore, and inexpensive war-surplus microwave equipment was available. These components were used for ferromagnetic, paramagnetic, and cyclotron microwave resonance programs pursued by the group. Field modulation combined with lock-in amplification was used routinely for signal processing. The lock-in amplifiers, originally developed at the Radiation Laboratory, were built in-house—no commercial instruments were available until the 1960s. The obvious way to enhance the signal-to-noise ratio of the VSM was to employ a lock-in amplifier, so I built one. The resulting simple magnetometer appeared to satisfy the requirements of convenience, versatility, and sensitivity and eliminated many of the shortcomings of other approaches. The first description of this VSM appeared in a short note[2] following one on megagauss pulsed field magnets,[3] another project for which I volunteered. Five-hundred reprints of this VSM note disappeared in a few months (copying machines were not ubiquitous then) and I received approval from MIT to patent the VSM, but at my expense. My wife was then in medical school, so we justified the expense as further education for me; the patenting process was indeed educational. I have continued to use both the VSM and high fields for

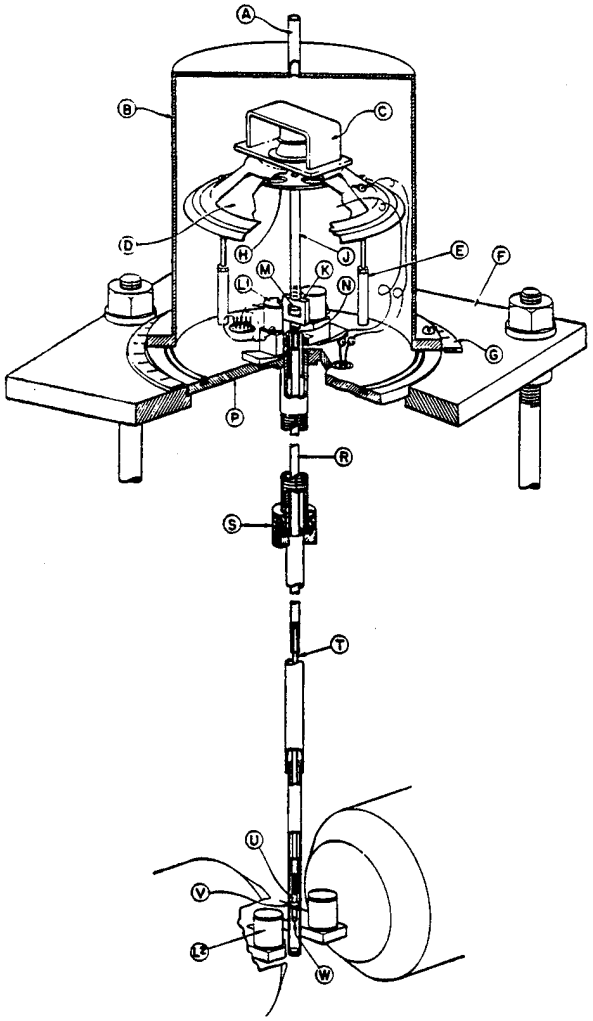


FIG. 2. Mechanical details of VSM (after Ref. 5).

research (not discussed here). The development of high-field magnets, the Francis Bitter National Magnet Laboratory (FBNML), and high-field superconductors are reviewed in a recent publication.[4]

Magnetism was fashionable in the US then and there were many practical magnetic devices developed. Visitors came to Lincoln Laboratory to see the operating VSM and to get more details. I was spending too much time repeating myself, so I wrote a detailed article[5] on the VSM that discussed the working model, Fig. 2. This led to further interest and 1000 reprints were exhausted in a short period. In the early 1960s I moved to the FBNML. There was a meeting in Boston at which Princeton Applied Research Corp. (PAR), at that time a startup instrument company, displayed a commercial lock-in amplifier (the JB-4) and I bought some for the Laboratory with the written proviso that they must meet the advertised specifications (they did). Later, when I inquired whether units could be purchased in quantity as an OEM product, I was invited to meet with the management to discuss the application. It is a long story, but I ended up assigning an exclusive license for the basic patent[6] to PAR so that they could develop and market the VSM. Several related VSM patents have been issued.[7] The commercial instrument continued to be produced by PAR (later as a subsidiary of

EG&G, Inc.) and recently the production was bought by LakeShore Cryotronics, Inc. The term VSM and Foner magnetometer have become somewhat generic in the literature, the original papers are rarely referenced, the VSM has been accepted as an ASTM Standard for magnetic measurements, the 1959 paper is cited as a Citation Classic,[8] and now several companies produce various forms of VSMs. Papers continue to appear with modifications and rediscoveries; some are improvements, and some take a step backward. (Commercial VSMs are not immune to this syndrome.) The availability of inexpensive digital computers, automation, and packaged systems has made measurements much less tedious, but there still is no substitute for understanding the limitations of the systems. New names such as torque VSM, vector VSM, and biaxial VSM have appeared recently to describe the ability to detect the vector component of the magnetization (not in the field direction) discussed earlier.[5] These are used, for example, for thin-film studies. Recently, some commercial SQUID instruments have added a VSM option.

The magnetic properties of a material are detected as a change in (1) magnetic flux, (2) force, or (3) by indirect techniques.[9] Space limitations do not permit a discussion here of the many magnetic moment measurement techniques. An excellent treatment of many methods is given by Zilstra.[10] Recent reviews are given in Refs. 11 and 12, where additional references are given. Here, I restrict my discussion largely to VSMs which use magnetic flux detection.

Almost all flux detection methods depend on the powerful benefits of sample motion to discriminate against contributions of the background flux. This includes the commercially available SQUID magnetometers, VSMs, and flux extraction; even ac susceptometers can take advantage of the moving sample principle. Moving the sample selects which part of the field distortion is due to the sample and also imparts externally controlled frequency, amplitude, and phase (wave form) information.

If a small sample is vibrated at a frequency f in a suitable detection coil array, the induced voltage E is given by

$$E=\sigma GA2\pi f\cos 2\pi ft, \tag{1}$$

where σ is the magnetic moment of the sample, G depends on the detection coil geometry, and A is the (small) amplitude of the sinusoidal vibration. A reference signal is generated by an element on the drive rod (attached to an electro- or permanent magnet or vibrating capacitor, etc.) which has the same amplitude and phase as the sample. If ratios of reference and sample signal are null-detected at the sensor input (the preferred mode), to first order, the null balance is independent of changes in A, f, amplifier gain or linearity, wave form, magnetoresistance of the detector coils, and small magnetic field instabilities. Otherwise these variables must be carefully controlled. E is made insensitive to position by choosing appropriate pickup coil configurations. The electronics acts as an ac bridge null detector. The first commercial instrument replaced the inductive reference sensor by a vibrating capacitor in the feedback balance arrangement.

The moving sample technique requires a well-designed drive mechanism. The electromagnetic transducer is driven far from resonance. This permits changing the loading on the drive rod without affecting the response appreciably. Dynamic out-of-phase damping and shock mounting minimizes transfer of momentum to the VSM support. A *single* washer, e.g., V in Fig. 2, serves as a centering element and sliding bearing; note that two sliding bearings would overspecify the mechanical arrangement leading to unwanted binding and noise. A convenient means for sample change is desirable.

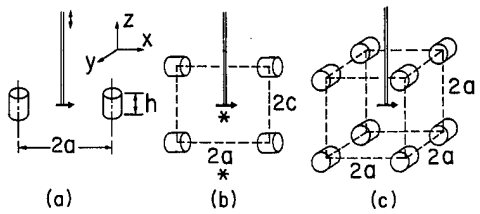


FIG. 3. Some examples of VSM coil configurations for vibration perpendicular to moment (after Ref. 13).

Practical detection coil arrangements for the VSM involve an even number of coils (or other detecting elements) in order to minimize sensitivity to sample position; for a dipole the signal varies as d^3 where d is the distance from the dipole. For the magnetization transverse to the vibration direction, no signal at frequency f is detected for coils with axes along the x, y, or z axis, for the coordinate system origin centered at the sample. Some examples of typical transverse detection coil configurations[13] are shown in Fig. 3 and the appropriate positions of the vibrating sample are indicated. Figure 3(a) shows a two-coil arrangement[2,3] and Fig. 3(b) shows a four-coil system by Mallinson.[14] For either coil arrangement, components of **M** along the y axis are obtained by either adding sets of coils rotated 90° about z, or by physically rotating the coils sets 90° about z. The eight-coil system by Bowden,[15] Fig. 3(c), intercepts components of **M** in the x, y, and z directions so that combinations of these coils can be used to detect the vector components of **M** along these axes. Similar results can be obtained by rotating the 8-coil set 90° (Bernards *et al.*[16]), and a 12-coil set was discussed by Bernards and Cramer.[17] The output is insensitive to position to first order because of symmetry for the sample centered as shown. Detection coil geometries and sensitivity functions (that give the proportionality constant for the magnetometer output of a unit dipole moment) are discussed by Zieba and Foner,[13] and Pacyna and Ruebenauer.[18] Sample geometry effects depend on relative sample size, given in terms of characteristic sample dimension versus coil radius. Calculations of these effects and experimental verification are given in Ref. 13 (see also special cases in Refs. 19 and 20) along with discussions of sensitivity and signal-to-noise of various coil configurations, sample position errors, sample support contributions, and related topics. The output for transverse moment detection coil systems cannot be calculated in closed form. Outputs of coil arrangements with axes along the vibration axis can be calculated in closed form, and these are employed for VSMs in axial fields produced by superconducting or other solenoids, where the moment is parallel to the vibration axis. However, for many studies an electromagnet using the transverse configuration is the best choice.

II. VERY LOW FREQUENCY VIBRATING SAMPLE MAGNETOMETER (VLFVSM)

In the mid-1960s Richard Frankel, now at California Polytechnic State University, was measuring the Pauli paramagnetism at high magnetic fields in Fe by the Mössbauer effect. I volunteered that we should be able to do much better with a VSM. Little did I know that it would be one of the most difficult experiments I had faced. The simplest approach was to use flux integration. The measurement involved detection of a very small change of a large quantity in the presence of field-dependent forces on the sample at high field in water-cooled magnets. High relative differential sensitivity was required, so that usually negligible systematic and instrumental errors became important. Richard Bozorth was experimenting at the Laboratory then and on hearing of our work decided to attempt this measurement. Of course, I told him that he was welcome to go first. Initially he used a galvanometer which was strongly affected by the fringe field of the magnets, so we furnished an integrating digital fluxmeter (a relatively new device at that time) that was insensitive to the fringing field. Bozorth adopted this device, but eventually decided to complete the work in a superconducting magnet.

Ed McNiff and I then returned to this problem. The solution came by indirection. My wife and I took a break at a local beach one weekend (a rare occurrence for us) and a simple solution occurred to me. Since it was not practical to position the sample sufficiently accurately in the pickup coils, the alternative was to avoid the issue; instead, move the sample beyond the centers of the coils and retrospectively determine where the centers were. We built a large-amplitude oscillating device which varied the frequency and amplitude of the sample displacement in the pickup coils and this became the heart of the VLFVSM.[21] In order to measure small differences of the large integrated signal at fixed field, most of the output was precisely subtracted and only the expanded difference was displayed on a strip-chart record. The time drift of the integrator was also averaged. (This mode of operation, where the sample is moved past the centers of the flux detection coils and retrospectively analyzed, now is used in many SQUID magnetometers.) The VLFVSM is actually a rugged differential low frequency *flux-integration* device. This device could be set up in any magnet and was used at FBNML for magnetization measurements in high fields for about 20 years. The first serious test of the VLFVSM involved measurement of the high-field susceptibility of Fe and Ni.

The results of the Fe and Ni measurements were reported by both groups at a session of the M^3 in 1965. We agreed to meet the previous evening to compare results; our experimental results differed. This was an interesting, lively, and very civilized get together; here I developed a great respect for Conyers Herring. These were difficult experiments and there were many possible sources of systematic errors. The theorists, Conyers Herring[22] then at AT&T Bell Laboratories and Arthur Freeman,[23] now at Northwestern University, presented the results for the respective groups, each with an appropriate model. A detailed paper that also discussed the possible sources of systematic errors was published subsequently.[24] More recently, René Pauthenet, in an invited paper at the 1981 M^3 Conference,[25] presented extensive high-field susceptibility data to 18 T (using water-cooled magnets and flux integration with a digital integrating fluxmeter) for Fe, Co, Ni, and YIG. His data for Fe and Ni were in good agreement with Ref. 24.

III. VSM MODIFICATIONS AND COMMENTS

The remainder of this paper discusses selected examples of modifications made to VSMs for special needs. Although most involve the axial configuration for high-field work, they can be adapted for the transverse mode. These illustrate the ease with which the VSM can be modified. Many commercial systems can be changed to suit specific needs, often with little effort, e.g., adding or replacing the detection coils. Our modified (commercial) VSMs have flexibility built in. All the drive rods are sectioned and connectors are installed so that various length drive rods can be added and interchanged. This allows us to use a magnetometer at several magnet stations with different geometries. A small moveable, variable-speed overhead hoist allows removal and replacement of the heavy drive head from the magnet, so that the VSM can be used at several locations. The bottom section of the commercial drive rod that supports the sample is replaced by components that minimize background contributions. (Many commercial sample holders have quite large masses that are satisfactory for large ferromagnetic moments, but contribute large backgrounds to small moment samples.) We also use relatively large access spaces for the pickup coils for general work. These coil arrangements can be replaced by more efficient ones for higher sensitivity, but despite the fact that most of our research involves nonferromagnetic materials, the added sensitivity is rarely needed. Our helium Dewars for superconducting magnets are all relatively short, only about 30 in. long so that the conventional ceiling clearance is adequate when removing the VSM. Magnets are chosen for minimum usable bores so they are inexpensive and economical to run—a 6 T magnet uses 3 ℓ/day of He and 5–6 ℓ for the first fill. Finally, the pickup coils, clamped to the inner bore, are interchangeable. The modifications for specific needs discussed below are clearly illustrated in detailed figures of the quoted references, but are not reproduced here because of space limitations.

A. Operation at ^{3}He

Some literature questioned whether the VSM could operate at ^{3}He temperatures because of the heat generated; the vibration amplitude is generally about 0.1–0.2 mm. Oliveira[26] demonstrated VSM operation down to 0.5 K with a modification of the tail section to support a small Dewar for the ^{3}He and a small surrounding ^{4}He Dewar. Both are inserted in the central bore in a superconducting magnet containing the axial coil form. Many other experiments also require thermal isolation with a minimal loss of working volume. This is particularly important because the sensitivity is a strong function of detection coil dimensions. In order to satisfy these needs small pumpable space-saving Dewars with a simple valve seal[27] are used, adding as little as 0.75 mm in radius.

B. High pressures

In order to measure magnetic properties under high hydrostatic pressures, Guertin[28] used a modification of the VSM in a superconducting magnet where a hydrostatic pressure clamp, containing the small sample and pressure calibrator (Sn), was attached to the bottom section of the drive rod. The clamp had about 500 times the moment of the sample, but its contribution was reduced by a factor of 200 because of its geometry in the pickup coils. These small, pure Be–Cu clamps produced hydrostatic pressures up to $P \approx 8$ kbar. By replacing the bottom section of the sheath with a space-saver Dewar and accommodating a slightly smaller diameter clamp, measurements were made in a controlled variable-temperature environment under pressure and in high fields.[29] The first axial vibrating *coil* magnetometer was developed by Smith[30] in order to measure magnetic properties in a pressure bomb.

C. Very low frequency ac susceptibility VSM

A novel adaptation of the VSM was used for measuring the very low frequency ($0.003 < f_0 < 0.03$ Hz$\ll f$) ac susceptibility, χ_{ac}, of spin-glass PrP_y by Guyot *et al.*[31] A small ac field was applied to the sample; the output of the VSM, which yielded the instantaneous response of M versus applied field, was recorded so that both the real and imaginary components of χ_{ac} were obtained. Of course lower values f_0 can be used with added patience.

D. Water-cooled and hybrid magnets

Early adaptation of the VSM to the high-power water-cooled magnets was examined and the electronics and mechanical components were modified by Hernan Praddaude and Ed McNiff. The VSM driving frequency was returned to minimize detection of the 6 Hz and harmonics from the dc generators, and the drive rod and the surrounding sheath was extended so that the electromechanical drive head was not exposed to high fields (e.g., drive rod lengths were extended to $\approx$5 ft for water-cooled magnets and 8 ft for the 31.8 T hybrid). The PAR drive operates far from resonance and the drive power was adequate despite the added load. Yaacov Shapira, now at Tufts University, was examining the magnetization steps in dilute magnetic semiconductors which occur at very high fields and low temperatures.[32] These measurements perform magnetic spectroscopy of the quantum mechanical level crossings, in, for example, antiferromagnetically coupled clusters.[33] The earliest magnetization step data[34] was obtained with the VLFVSM, but the point-by-point data taking was very time consuming for limited magnet time. (The data analysis was also time consuming, but that was off-line.) For more rapid data taking and for higher resolution, the VSM was the obvious choice so Shapira and McNiff installed the VSM as a Laboratory facility. For flexibility and good signal-to-noise, the axial pickup coils were mounted directly on the VSM sheath rather than clamped to the magnet. A three-coil axial arrangement (related to second-derivative coils) was used to minimize local field fluctuations. The standard VSM operated from 1.2 to 300 K. For operation down to 0.6 K, the bottom of the sheath including the pickup coils was immersed in liquid ^{3}He of a surrounding small space-saver Dewar arrangement. This VSM has been used for almost all the dc high-field magnetization measurements at FBNML for the last decade.

E. VSM operation at mK

A noteworthy recent adaptation extended VSM measurements to very low temperatures. Recently, plastic dilution refrigerators (PDR) have been developed that eliminate eddy current heating and allow operation in the mK range[35] in changing magnetic fields. The light weight and compactness of the PDR allowed demonstration of a practical VSM in that temperature range. The entire PDR tail section was attached to the drive rod and head of a commercial VSM vibrating at 82.7 Hz! With a dissipation <100 μW, operation below 50 mK was reported.[36]

F. SQUID VSM magnetometer

A SQUID (Superconducting Quantum Interference Device) magnetometer is a type of VLFVSM that incorporates a SQUID detector and electronics instead of a conventional integrating circuit. The SQUID generally operates at 4.2 K and is an extremely sensitive flux detector which must be carefully shielded. It is adequate to consider a SQUID a "black box" with a very low input impedance and very low noise, a very wide frequency response starting at dc, and a large transfer function. It matches the low impedance input to the room-temperature electronics. The sample is moved through the detector coils (usually restricted to a few turns total, separated by a few cm) for either peak detection or fitting the flux variation versus displacement of the sample. The point-by-point operation suffers from the same limitation of the above VLFVSM; it is point-by-point and slow. Unlike the inductive detector VSM whose output is proportional to frequency, the output of the SQUID detector is independent of frequency. Recently SQUID systems have been incorporating a VSM option (operating at a few Hz) for continuous data.

G. Calibration

The most convenient method of calibration of a VSM (and many other magnetometers) is to use a small standard reference comparison sample. Ni measured above technical saturation is recommended because it has a high and well-known moment so that large signals are obtained for a small sample, it is chemically stable, has a low saturation field, is inexpensive, is readily available in high purity, and even at 300 K is only slightly temperature sensitive.

H. Image effects

The flux distribution produced by a sample is distorted by any highly permeable medium (ferromagnetic or superconducting) in its neighborhood so the detected signal is affected. This effect is called the image effect. Observations of image effects of VSMs in superconducting magnets are discussed by Zeiba and Foner.[37] The superconducting magnet image effects can be subtle, and are influenced by whether the magnet is operated in the persistent mode or not,[38] and how densely it is wound.[37] The effect depends on the detailed geometry, increasing rapidly and nonlinearly as the

detection coils approach the high permeability medium because then they intercept more of the distorted flux of the sample. However, if the VSM or other device is calibrated with a known test sample, this image effect automatically is eliminated to first order, because both the flux from calibration and measured samples are affected in the same way. However, the measured values will be affected by the *field dependence of the image effect*. Both ferromagnets and superconducting wire show some field-dependent shielding changes. Recently, Zeiba[39] has given an extensive review of image and geometry effects of superconducting shields, flux transformers, and magnets in SQUID magnetometers. It should be noted that there is an additional image effect for large signals due to the currents in the flux transformer circuit, when using the *average flux-nulling* feedback mode. This effect can be eliminated by using a *current-nulling* feedback mode.

IV. SENSITIVITY

Despite statements to the contrary, lack of sensitivity is rarely an issue for the VSM, particularly for the MMM audience, and it can easily be improved by modifying the pickup coils or other detector so that they more effectively couple to the sample as discussed earlier.[40] For the same reasons, comparisons of sensitivity of different systems must be done with care because small changes in coil geometry can produce widely different sensitivities. For the axial configuration, as the coupling is increased, the signal-to-noise increases as $r^{-7/2}$ if limited by Johnson noise of the wire, and as r^{-5} if limited by field noise, where r is the pickup coil radius. As a demonstration for small samples, a change of magnetic moment of 1×10^{-9} emu at 1 T and 3×10^{-9} emu at 5 T could be detected in a (nonpersistent-mode) superconducting magnet[40] with the small detection coils clamped onto the VSM assembly.

Although not the purpose of this paper, I mention a few early M^3 memorable to me: (1) the second M^3 in Boston that took place in 1956; (2) the 1959 M^3, when the program committee rejected a paper by S. Autler as not relevant (it discussed use of superconductors in electromagnets and was the start of the first revolution in high-field superconductors, cf. Ref. 4, p. 123.); (3) the first evening symposium on magnetic measurement techniques,[9] chaired by R. M. Bozorth,[41] at the 1966 M^3 (the overflow audience was moved to the largest lecture hall; such symposia occur at intervals now); and (4) the first joint M^3 and International Conference of Magnetism in Boston in 1967. Of note was the evening champagne party at the Isabella Stewart Gardner Museum in Boston where antiphonal brass rang out across the balconies of this imported Italian villa. Several subsequent M^3 hosted evenings in local museums.

My experience was that each time I volunteered it led to new and interesting areas of activity for me and long-term dividends. Along the way I was fortunate to be involved in many areas and collaborations with many scientists and engineers; the list is too long to enumerate here. I wish to thank my many co-workers who made these enterprises so rewarding. The work at the Francis Bitter National Magnet Laboratory was funded by the National Science Foundation.

[1] W. Sucksmith, Philos. Mag. **8**, 158 (1929).
[2] S. Foner, Rev. Sci. Instrum. **27**, 548 (1956).
[3] S. Foner, Rev. Sci. Instrum. **27**, 547 (1956).
[4] S. Foner, IEEE Trans. Appl. Superconduct. **5**, 121 (1995).
[5] S. Foner, Rev. Sci. Instrum. **30**, 548 (1959).
[6] US Patent No. 2,946,948.
[7] US Patents No. 3,456,459, No. 4,005,358, No. 4,037,149; Germany Patent No. 2,656,838; Israel Patent No. 51,029.
[8] Citation Classic, ISI **26**, 14 (1985).
[9] See symposium on magnetic measurements, K. Dwight, J. Appl. Phys. **38**, 1505 (1967); S. Foner, *ibid.* **38**, 1510 (1967); and F. B. Humphrey, *ibid.* **38**, 1520 (1967).
[10] H. Zilstra, *Experimental Methods of Magnetism*, edited by E. P. Wohlfarth (Wiley, New York, 1967), Vols. 1 and 2.
[11] S. Foner, IEEE Trans. Magn. **MAG-17**, 3358 (1981).
[12] S. Foner, *Encyclopedia of Applied Physics*, edited by G. L. Trigg (VCH, New York, 1994), Vol. 9, p. 463; and P. J. Flanders and C. D. Graham, Rep. Prog. Phys. **56**, 431 (1993).
[13] A. Zieba and S. Foner, Rev. Sci. Instrum. **53**, 1344 (1982).
[14] J. Mallinson, J. Appl. Phys. **37**, 2514 (1966).
[15] G. J. Bowden, J. Phys. E **5**, 1115 (1972).
[16] J. P. C. Bernards, G. J. P. van Engelen, C. P. G. Schrauwen, H. A. J. Cramer, and S. B. Luitjens, IEEE Trans. Magn. **26**, 216 (1990).
[17] C. J. P. Bernards and H. A. J. Cramer, J. Magn. Magn. Mater. **123**, 141 (1993).
[18] A. W. Pacyna and K. Ruebenbauer, J. Phys. E **17**, 141 (1984).
[19] C. Johansson and M. Hanson, IEEE Trans. Magn. **30**, 1064 (1994).
[20] U. Ausserlechner, W. Steiner, and P. Kasperkovitz, IEEE Trans. Magn. **30**, 1061 (1995).
[21] S. Foner and E. J. McNiff, Jr., Rev. Sci. Instrum. **39**, 171 (1968).
[22] C. Herring, R. M. Bozorth, A. E. Clark, and T. R. McGuire, J. Appl. Phys. **37**, 1340 (1966).
[23] A. J. Freeman, N. A. Blum, S. Foner, R. B. Frankel, and E. J. McNiff, Jr., J. Appl. Phys. **37**, 1338 (1966).
[24] S. Foner, A. J. Freeman, N. A. Blum, R. B. Frankel, E. J. McNiff, Jr., and H. C. Praddaude, Phys. Rev. **181**, 863 (1969).
[25] R. Pauthenet, J. Appl. Phys. **53**, 8187 (1982).
[26] N. F. Oliveira, Jr. and S. Foner, Rev. Sci. Instrum. **43**, 37 (1972).
[27] S. Foner and E. J. McNiff, Jr., Rev. Sci. Instrum. **47**, 1304 (1976).
[28] R. Guertin and S. Foner, Rev. Sci. Instrum. **45**, 863 (1974).
[29] See, e.g., R. P. Guertin, *High-Pressure and Low-temperature Physics*, edited by C. W. Chu and J. A. Woollam (Plenum, New York, 1978), p. 97; M. S. Torikachvili, M. B. Maple, R. P. Guertin, and S. Foner, J. Appl. Phys. **53**, 2619 (1982); R. P. Guertin, S. Foner, and F. P. Missell, Phys. Rev. Lett. **37**, 529 (1976); D. W. Capone, II, R. P. Guertin, S. Foner, D. G. Hinks, and H.-C. Li, *ibid.* **51**, 601 (1983) and references therein.
[30] D. O. Smith, Rev. Sci. Instrum. **27**, 261 (1956); K. Dwight, N. Menyuk, and D. O. Smith, J. Appl. Phys. **29**, 491 (1958).
[31] M. Guyot, S. Foner, S. K. Hasanain, R. P. Guertin, and K. Westerholt, Phys. Lett. A **79**, 339 (1980).
[32] See reviews by Y. Shapira, J. Appl. Phys. **67**, 5090 (1990) and in *Semimagnetic Semiconductors and Diluted Magnetic Semiconductors*, edited by M. Averous and M. Balkanski (Plenum, New York, 1991), p. 121.
[33] See, for example, V. Bindilatti, T. Q. Vu, Y. Shapira, A. Agosta, E. J. McNiff, Jr., R. Kershaw, K. Dwight, and A. Wold, Phys. Rev. B **45**, 5328 (1992); Y. Shapira, Acta Phys. Polon. A **87**, 107 (1995) and references therein.
[34] Y. Shapira, S. Foner, D. H. Ridgley, K. Dwight, and A. Wold, Phys. Rev. **30**, 4021 (1984).
[35] R. Wagner and G. Frossati, Physica B **165**, 43 (1990); E. ter Harr, R. Wagner, C. M. C. M. van Woerkens, S. C. Steel, G. Frossati, L. Skrbek, M. W. Meisel, V. Bindilatti, A. R. Rodrigues, R. V. Martin, and N. F. Oliveira, Jr., J. Low Temp. Phys. **99**, 151 (1995), and E. ter Haar, thesis, Leiden University, April 1995.
[36] V. Bindilatti, E. ter Haar, A. R. Rodrigues, N. F. Oliveira, Jr., and G. Frassati, Physica B **194–196**, 37 (1994).
[37] A. Zieba and S. Foner, Rev. Sci. Instrum. **54**, 137 (1983).
[38] S. Foner, Rev. Sci. Instrum. **34**, 293 (1963).
[39] A. Zieba, Rev. Sci. Instrum. **64**, 3357 (1993).
[40] S. Foner, Rev. Sci. Instrum. **46**, 1425 (1975).
[41] His classic book, *Ferromagnetism*, has recently been reprinted and is available from IEEE Press.

Measurement of texture in magnetic recording media using a biaxial vibrating sample magnetometer

F. Schmidlin, P. R. Bissell, and J. A. Gotaas
Department of Physics and Astronomy, University of Central Lancashire, Preston PR1 2HE, United Kingdom

A method is described for the determination of the three dimensional easy axis distribution in recording media using a biaxial vibrating sample magnetometer and compensation for out-of-plane demagnetization field effects. Comparison of Lorentzian function fits to the data and measurement of orientation ratio with theoretical calculations indicates that the method gives a reasonable measure of the easy axis distribution. Examination of the theoretical relationship indicates that low values of orientation ratio are insensitive to distribution width indicating that it is necessary to make a full measure of easy axis distribution in-plane. However, out-of-plane distributions are generally narrower and it is often possible to estimate distribution width from a simple orientation ratio measurement. © *1996 American Institute of Physics.* [S0021-8979(96)79708-4]

I. INTRODUCTION

Orientation of magnetic particles in recording media has a major effect on magnetic properties and media recording performance. This is normally assessed by means of parameters such as squareness, orientation ratio (OR) and S^*. Although this gives an indication of the maintained properties and quality of a particular medium during production or development, it does have severe limitations and does not take into account the out-of-plane characteristics of media texture. In some advanced recording, the out-of-plane component can have a very important role in the properties and needs to be included in the media characterization. For example, metal evaporated tape has an inclined columnar structure which determines the structure of written bits; a longitudinal barium ferrite media can have an out-of-plane component which affects erasure properties. Furthermore, with the development of sophisticated micromagnetic models and their use to predict and interpret media behavior, full knowledge of the three dimensional easy axis distribution (EAD) is required. In this article we describe a technique which we have developed to measure the in-plane and out-of-plane distribution of easy axes in recording media using a biaxial vibrating sample magnetometer (VSM). Because the technique compensates for demagnetizing fields during measurement and gives a direct evaluation of the texture, it is equally applicable to any media irrespective of the texture axis direction or asymmetry in the distribution. However, in this article we concentrate on longitudinal particulate media.

The measurement may take considerable time (up to one day of automated measurement to obtain one out-of-plane EAD) and is therefore not suitable for routine characterization of media. However, curve fitting techniques are applicable to standard longitudinal media and our measurement technique can be used to assess the effectiveness of these fits and the suitability of the functions chosen.

II. METHOD

Techniques to determine the EAD in recording media have been described which use either torque[1] or VSM measurements.[2,3] It is assumed that when a large saturating field is applied at angle φ to the recording direction it will switch particle or grain moments so that, when returned to the remanent state, they occupy their easy axis directions closest to the field direction. If the field direction is now rotated to an angle $\varphi+\delta\varphi$ and the field application and removal repeated, the change in the vector remanence will be the result of moment switching for grains with easy axis directions between $\varphi+90°$ and $\varphi+\delta\varphi+90°$.[1] By repeating the measurement process for different values of φ from 0° to 180°, the easy axis distribution can be obtained in that plane of measurement.

We have extended the technique to out-of-plane measurements by using a biaxial VSM which allows for measurement of the sample magnetic moment to be made in the field direction and orthogonal to it with the ability to rotate the sample during the measurement process. A large magnetic field is applied to the sample at a particular direction and removed to leave the sample in a remanent state. This process can be used for in-plane and out-of-plane measurements although this step is more complex when out-of-plane. This is because the internal field must be kept in its original direction within the sample as the field is reduced to zero if a valid remanent state is to be created. Thus, for out-of-plane measurements, as the field is reduced constant calculation of the sample magnetization and rotation of the sample to adjust the internal field (applied plus demagnetizing) direction is required.[4]

By repeating in-plane and out-of-plane measurements, a full three dimensional description of the medium texture can be obtained which does not resort to function fitting, a technique[5] often used for media with longitudinal anisotropy but not applicable to tilted media.

The limitation of the technique is that out-of-plane measurements take considerable time even with a computer controlled VSM and it is necessary to use procedures to reduce the measurement time to a level which is acceptable for laboratory media characterization. The major difficulty is in maintaining the internal field, H_i, in a given direction, while reducing it from saturation to zero. For example, reducing the applied field, H_a, may cause the magnetization, $I(H_i)$, to decrease and rotate through a small angle. This in turn affects

 0021-8979/96/79(8)/4746/3/$10.00 © 1996 American Institute of Physics

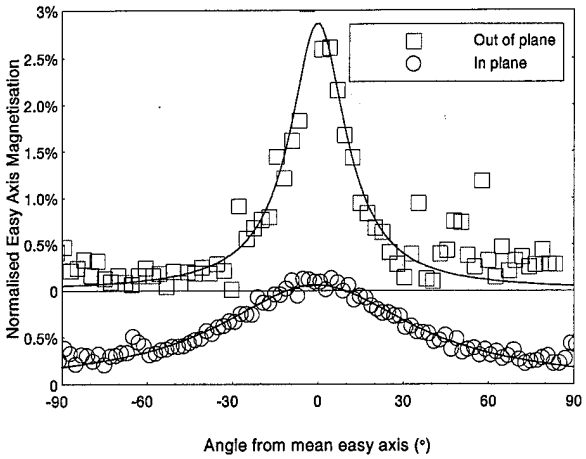


FIG. 1. In- and out-of-plane easy axis distribution for the γ-Fe_2O_3 sample.

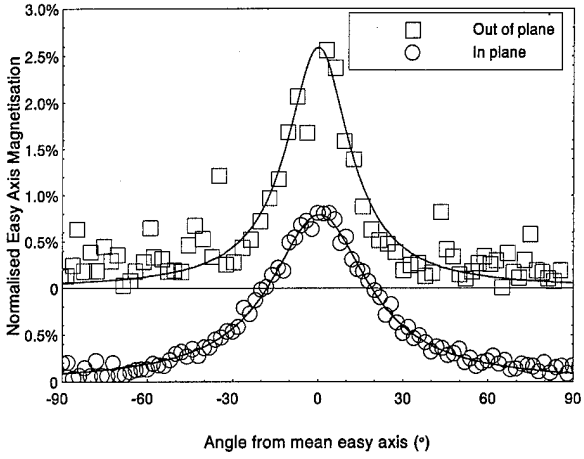


FIG. 3. In- and out-of-plane easy axis distribution for the metal particle sample.

the demagnetizing field, H_d, and hence the value and direction of H_i. If these changes are too large, irreversible switching of some moments may occur, invalidating the final remanent state. Thus, the measurement routine has to proceed cautiously, trying to predict what changes will occur in the magnetization strength and direction and to compensate for them.

To increase the speed of our EAD measurements, we assume that the sample response to field removal in two directions separated by a small angle will be similar. If we have mapped one such curve, we can use it to predict the second curve and select appropriate step sizes and angular rotations during the measurement. Additional adjustments are then made to correct for the small differences.

III. RESULTS AND DISCUSSION

Here we describe the use of our technique to measure three conventional longitudinal media: a CrO_2 hand spread, a γ-Fe_2O_3 audio tape and a Metal Particle Hi8 tape. These have been selected because they exhibit a range of different textures. It is essential to know true magnetization, rather than the magnetic moment usually measured by conventional VSM techniques, in order to calculate H_d. This was determined using the technique developed by Sollis *et al.*[6] which relies on the shift in the transverse susceptibility (χ_t) anisotropy peak produced by H_d when measurements are made out-of-plane.

Measured easy axis distributions in-plane and out-of-plane are shown in Figs. 1–3. It has to be stressed that the technique provides a direct measurement of the EAD. However, for analysis purposes the resulting easy axis distributions were fitted by a Lorentzian function

$$y = ab^2/(x^2+b^2), \tag{1}$$

where a is a normalizing factor and b gives the width of the distribution. The fits are shown with the data in Figs. 1–3. The choice of function follows the work of Templeton *et al.* who found it to be a good fit to longitudinal in-plane easy axis distributions,[3] with a tail out to 90°. It can be seen that in general the out-of-plane distribution is narrower than the in-plane which is not unexpected in particulate media given the coating process of production. Table I gives the measured widths of the fitted functions along with orientation ratios in and out-of-plane for the three samples.

The EAD width can be linked to the orientation ratio. Assuming a distribution $f(\alpha)$ about the mean easy axis ($\alpha=0$) and normalized to saturation, the squareness [Sq $=I(0)I(\infty)$] measured at an angle θ to the average easy axis will be the sum of all the moment components along θ so that:

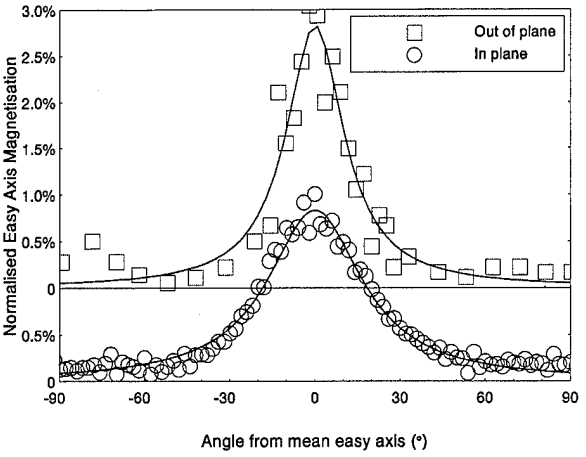


FIG. 2. In- and out-of-plane easy axis distribution for the CrO_2 sample.

TABLE I. Sample characteristics.

	Is (kA/m)	OR in plane	b in-plane (deg)	OR out of plane	b out-of-plane (deg)
γ-Fe_2O_3	70	1.5	32.1	2.9	12.3
CrO_2	107	3.0	19.8	4.0	12.6
MP	274	2.1	21.0	2.9	13.7

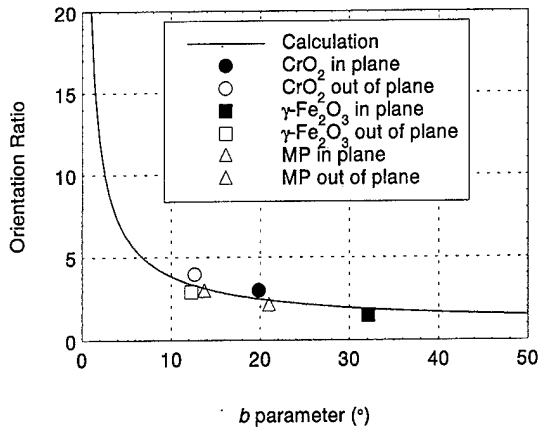


FIG. 4. Comparison between measured EAD width (b) and values calculated from the orientation ratio.

$$\mathrm{Sq}(\theta)=\int_{\theta-\pi/2}^{\pi/2} f(\alpha)\cos(\alpha-\theta)\,d\alpha + \int_{\pi/2}^{\pi/2+\theta} f(\alpha+\pi)\cos(\alpha-\theta)\,d\alpha. \quad (2)$$

OR is defined as $\mathrm{Sq}(0)/\mathrm{Sq}(\pi/2)$ so that the variation of OR can be calculated for different distribution widths, b, for a Lorentzian distribution. The calculated theoretical relationship is shown as a continuous line in Fig. 4. Data points are experimental measurements of OR and distribution widths for the three samples. Within an acceptable experimental error, data points lie close to the theoretical curve and indicate that the method of demagnetization field correction and curve fitting to the data gives a reasonable measure of the easy axis distribution.

Perhaps one of the most significant features of the theoretical curve is the insensitivity of the OR to the distribution width, b, for broad distributions. For values greater than $b \approx 20$, OR declines very slowly relative to the increase in b. This indicates that for wide distributions, OR is not an effective measure of the EAD. However, as OR increases it can be used to predict distribution widths more accurately. Since most in-plane orientation ratios of conventional longitudinal media fall into the low OR category, easy axis distributions can only be assessed accurately by a full measurement. However, since the OR is generally higher when measured out-of-plane, its use to assess the EAD in that direction is likely to be more accurate. Since the out-of-plane measurement is the one which is time consuming with its demagnetization corrections, it appears that a satisfactory assessment of the three dimensional easy axis distribution can be obtained for most longitudinal media by an EAD measurement in-plane and an OR determination out-of-plane. Since both these measurements can be made on a conventional VSM, although less conveniently than on a bidirection instrument, full 3D EAD characterization is possible in most measurement laboratories. However, each sample must be considered on its own merits and the applicability of the determination judged with reference to the curve in Fig. 4.

IV. CONCLUSION

We have demonstrated that it is possible to measure the easy axis distribution of recording media both in-plane and out-of-plane with a bidirectional VSM using demagnetization field compensation for out-of-plane measurements. However, the method is very lengthy and not suitable for normal magnetic characterization of media. A comparison of curve fits to experimental data and orientation ratio determination shows that, although OR is not sensitive to the width of the easy axis distribution for low OR values, it is capable of predicting distribution widths for narrow distributions. Since out-of-plane EADs are narrower than those in-plane, in some cases a satisfactory estimation of the 3D EAD can be obtained from a full EAD determination in-plane and an OR measurement out-of-plane. We emphasize that the applicability to each sample must be judged with respect to the theoretical curve of Fig. 4.

[1] P. J. Flanders and S. Shtrikman, J. Appl. Phys. **33**, 216 (1962).
[2] M. P. Sharrock, IEEE Trans. Magn. **26**, 225 (1990).
[3] T. L. Templeton, A. S. Arrot, and Y. Yoshida, IEEE Trans. Magn. **30**, 4263 (1994).
[4] J. P. C. Bernards and H. A. J. Cramer, IEEE Trans. Magn. **27**, 4873 (1991).
[5] M. El-Hilo, P. E. Kelly, K. O'Grady, and J. Popplewell, IEEE Trans. Magn. **26**, 210 (1990).
[6] P. Sollis and P. R. Bissell, J. Phys. D Appl. Phys. **24**, 1891 (1991).

Application of Barkhausen effect measurements for detection of near surface stress (abstract)

D. A. Kaminski and D. C. Jiles
Center for NDE, Iowa State University, Iowa

Barkhausen effect emissions have been shown to be dependent on stress in previous work.[1] This paper shows how the technique has been applied to evaluation of stress in automobile crankshafts. These components often fail prematurely due to residual tensile stress in the surface of the components, which leads to cracking and sudden fatigue failure. The measurements were made using an excitation frequency of 8 or 128 Hz with signal detection bandwidths of 3–15, 20–70, and 70–200 kHz. These corresponded to nominal magnetic field penetrations of 0.2, 0.07, and 0.02 mm. Results showed that measurements from the near surface (0.02 mm) were most sensitive to stress. A number of calibration experiments on different materials confirmed this result. In addition, it was found that low values of the root-mean-square Barkhausen voltage correlated with low tensile strength of the material. This measurement could, therefore, be used for detection of components that were likely to encounter early failure. A calibration of the Barkhausen voltage signal as a function of stress was obtained and this was in accordance with earlier theoretical calculations.[2] © *1996 American Institute of Physics.* [S0021-8979(96)59808-2]

[1]D. C. Jiles and L. Suominen, IEEE Trans. Magn. **30**, 4924 (1994).
[2]D. C. Jiles, L. B Sipahi, and G. Williams, J. Appl. Phys. **73**, 5830 (1993).

 0021-8979/96/79(8)/4749/1/$10.00 © 1996 American Institute of Physics

Nondestructive inspection of a fractured nickel bar by Barkhausen and magnetoacoustic emissions

C. C. Yu, C-D. Qin, and D. H. L. Ng[a)]
Department of Physics, The Chinese University of Hong Kong, Shatin, Hong Kong

Barkhausen emission (BE) and magnetoacoustic emission (MAE) measurements have been made on a nickel bar before and after it is torn apart by a tensile stress. The BE and MAE profiles obtained are all single-peaked. The peaks obtained after fracture are found at the lower field regions of the profiles, and this suggests that the field required for the domain wall motion in the fractured bar has been lowered. In the BE measurement, the signals show an increase of 44% (away from fracture end) to 144% (at fracture end); on the contrary, the MAE signals show a reduction of 43% (away from fracture end) to 14% (at fracture end). As the nickel bar is fractured, we find that in the broken pieces, the grains have been elongated in the stressed direction, and there is an increase of defects such as dislocations, voids and microcracks, especially near the fracture end of the bar. BE which is sensitive to these factors, has therefore been intensified. On the other hand, the plastically elongated grains, which have a lower absolute magnetostriction, enhance the reduction of MAE activity. The results measured from the nickel bar will be compared with those obtained from a fractured mild steel bar, which has different magnetostriction and other magnetic properties.
© *1996 American Institute of Physics.* [S0021-8979(96)50608-3]

I. INTRODUCTION

Barkhausen emission (BE) is the induced signal in the induction coil due to the change of magnetic flux in the magnetic sample, while magnetoacoustic emission (MAE) is the acoustic wave emitted when there is a change of magnetostrictive strain.[1] Both BE and MAE have been under development as techniques for the nondestructive evaluation of magnetic materials.[2] The possibilities of measuring stress,[3] detecting defects[4] and measuring sample thickness[5] have already been demonstrated. A practical application of BE and MAE to estimate the degree of damage in steel components have previously been reported.[6] In this article, we report both BE and MAE measurements taken from two different positions of a broken piece of a nickel bar resulting from a tensile loading. Our purpose is to find the dependence of the BE and MAE signals on the microstructures of the bar, which are observed as being different from one region to another. We have also compared the results with those reported from the previous study of a broken mild steel bar,[6] aimed at improving the understanding of the physical mechanism of the BE and MAE from fractured components of the two materials with similar metallic characteristics, but with different magnetic properties.

II. EXPERIMENTS

A nickel bar of dimensions 190 mm × 20 mm × 4 mm was annealed at 900°C before it was torn apart by a 300 kN Instron loading machine. The stress applied to break the bar was about 257 MPa. A 1 Hz magnetizing field of triangular wave form and peak-to-peak magnitude of 90 kA/m was produced by a c-core electromagnet. The field was applied parallel to the strained direction during the BE and MAE measurements. A flat induction coil placed underneath the c-core electromagnet was used to detect the BE signals from the surface of the sample, while the MAE signals were picked up by a nearby piezoelectric transducer. Both BE and MAE signals were amplified, rectified and filtered before they were plotted over half a hysteresis cycle. The BE and MAE measurements were taken at two positions of the broken bar, one near the fracture end, and the other one is 5 cm from the fracture end. The signals obtained were compared with those of the original bar. Hardness tests and optical microscopy were also performed at these two positions of the bar before and after it was fractured in order to measure the changes of the mechanical hardness and the microstructure of the bar.

III. RESULTS

The BE and MAE profiles of the original nickel bar are shown in Figs. 1(a) and 1(d) respectively, while the profiles obtained near the fracture end of one of the broken pieces of the bar are shown in Fig. 1(b) for BE, and Fig. 1(e) for MAE. At 5 cm away from the fracture end, the BE and MAE profiles obtained are shown in Figs. 1(c) and 1(f) respectively. The result shows that after the bar is torn, there is an overall increase of BE signals, but a reduction of MAE signals. The increase of BE is 144% at the fracture end and 44% away from the fracture end, while the reduction of MAE is 14% and 43% at these two positions. A summary of the BE and MAE signals normalized to the signals obtained from the original bar are shown in Table I. Results obtained from the optical microscopy show that the average diameter of the grains of the original bar before fractured is $\sim$ 60 μm, and the ratio of its long axis to the short axis, y/x, is about 1. In the hardness measurement, the Vicker's test is used as reference, the Vicker's hardness number (VHN) of the bar is 101. Such a number indicates that the bar is relatively soft, and we have therefore observed significant necking as the bar is strained beyond its elastic limit. The strain at break is measured to be 36%. After the bar is torn, the value of y/x and the VHN near the fracture end are measured, and are equal to 3 and 170 respectively. While, at the region 5 cm from the

a)Electronic mail: B108771@vax.csc.cuhk.hk

 0021-8979/96/79(8)/4750/3/$10.00 © 1996 American Institute of Physics

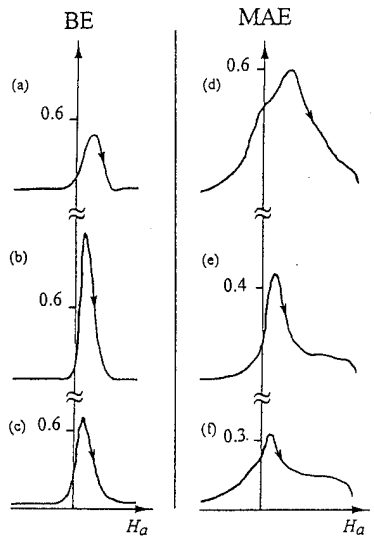


FIG. 1. BE profiles (a, b and c) and MAE profiles (d, e and f) as a function of an applied field H_a. Profiles a and d are obtained from the original nickel bar; profiles b and e are obtained from the broken bar with measurements made near the fracture end while profiles c and f are obtained at a position 5 cm from the fracture end. Both horizontal and vertical axes are of the same arbitrary scale for each profile.

fracture end, the value of y/x and the VHN are 2 and 154 respectively. These results are also tabulated in Table I.

IV. DISCUSSION

A. Barkhausen emission

As the nickel bar is torn, some of the major mechanical changes are: (i) numerous defects such as dislocations, microcracks and voids are created in the broken pieces of the bar, (ii) the grains are elongated in the strained direction, and (iii) the cross sectional area of the bar is no longer uniform. The first change is indicated by the increase of the VHN. The dislocations become less mobile as they are hindered by the defects created during the fracture, thus the VHN increases and indicates that the broken bar is hardened. This effect however does not reduce the mobility of the domain walls. We observed that the peaks of the BE profiles as well as the MAE profiles obtained from the broken bar are found at the lower field regions [Figs. 1(b) and 1(e)], this suggests that the field required for the motion of domain walls has been lowered. The facts that the dislocations formed during fracture are mostly lying perpendicular to the stressed direction and the field that applied to the bar is parallel to the stressed direction, as long as the walls are intersecting at some angle to the dislocations, the pinning effect is minimal and the domain wall motion has not been affected.[7] The optical microscopy reveals the elongation of the grains, which is another consequence of the fracture. The increase of the length of the grains in the y direction facilitate the domain wall motion as the magnetizing field is applied parallel to the strained axis, therefore the rate of change of magnetic induction, dB/dt, increases, thus a higher BE at the lower field region has been detected. Finally, the change of the cross sectional area of the bar can be easily observed by direct measurement. As the bar is strained, there has been a decrease of cross sectional area of the bar particularly at the necked region near the fracture boundary. Such a reduction has led to an increase of flux density inside the broken bar, and the BE signal which is proportional to dB/dt, has intensified accordingly.

We also observe that the largest increase of the BE signal is found near the fracture end. This variation of BE signals along the broken bar is due to the facts that the existence of relatively larger numbers of dislocations and microcracks, the most severe elongation of grains, and the smallest cross sectional area, are found at this region of the bar. All these factors contribute to the large BE response.

TABLE I. The peak values of BE and MAE normalized to the values obtained from the original nickel bar, VHN and y/x ratio measured from the bar before and after fractured, at positions near and 5 cm away from the fracture end.

		BE	MAE	VHN	y/x
Before Fractured		1.00	1.00	101	1/1
Fractured	Near	2.44	0.86	170	3/1
	Away	1.44	0.57	154	2/1

B. Magnetoacoustic emission

In contrast with the BE measurement of the fractured bar, the MAE activities decrease after the bar has been torn. One of the main factors leading to the overall reduction of the MAE signals is the decrease of the absolute magnetostriction of the elongated grains. In the presence of a tensile stress, the crystal lattice will be elongated in the stressed direction, nickel with a negative magnetostriction will have a smaller absolute strain.[8] Therefore after fracture, the nickel bar which has been plastically deformed, would have a smaller absolute magnetostriction. As the MAE activity is proportional to the magnitude of magnetostrictive strain, we have therefore observed that the MAE of the broken bar has decreased. At the same time, there are still some factors that would tend to enhance the MAE signals, which are the same as those that enhance the BE signals, such as the increase of flux density in the smaller cross section and the elongation of grains. However these factors appear not strong enough to make compensation for the overall loss of MAE activity due to the lowering of the absolute magnetostriction, nevertheless they are much more effectual at the position near the fracture end when compared with the situation at the far end. As a consequence, the reduction of MAE activity near the fracture end is less. It is also known that the closure domains which are mainly confined by the non-180° domain walls, always reside on grain boundaries, microcracks and voids, therefore the total area of the non-180° domain wall would increase as the defect density of the sample increases resulted from fracture. Since the MAE is generated by the motion of the non-180° domain wall, as a result MAE is relatively stronger in the fracture end where there are more non-180° walls. This also supports the fact that the decrease of MAE near the fracture end is smaller.

C. Comparison of nickel and mild steel

In the BE and MAE measurements of steel,[9] the profiles of both emissions usually contain two outer peaks, the initial peak represents domain wall nucleation while the final one is due to annihilation. This phenomena also applied to the situation in a fractured steel bar as we had reported in our earlier work.[6] However, in the BE and MAE profiles of the fractured nickel bar, a single peak is found at the low field region, which is a contribution of the domain wall motion. The fact that the central peaks do not appear in the BE and MAE profiles of mild steel but in nickel only, can be explained by the difference in the mobility of the domain walls in steel and nickel. It is known that the velocity of the wall is inversely proportional to the spontaneous magnetization M_s,[10] therefore in a material with a lower M_s such as nickel, the domain wall would be more mobile than that in steel. The existence of the strong central peak in the nickel profile confirms that the domain wall is easily unpinned in the low field. While in steel, the BE and the MAE activities contributed by the wall motion require a higher field, and is in the vicinity of where the annihilation process occurs, thus the two processes are superimposed into the final peak, and therefore only two outer peaks are found in the mild steel profiles.

Also in the mild steel results, the enormous increase of BE after the bar was fractured has also been reported. The above mentioned reasons used to explain the increase of BE in the nickel bar after fracture are also applicable to account for the mild steel case. However, the percentage increase of the BE signal in steel is 240%, and that in nickel is 144%. In order to explain the large difference, we consider the fact that in steel the rate of change of magnetization, dM/dt which is equal to $M_{\max} f$, is larger than that of nickel, where $M_{\max}$ is the maximum magnetization at the maximum applied field and f is the frequency of the magnetizing field of triangular wave form. In the MAE measurement obtained from the fractured steel bar, a reduction of 10% at the fracture end was reported, whereas 14% reduction is reported for the nickel bar. As the steel bar is hard and brittle, the elongation of the grains in the fracture bar is a lot smaller than that in the nickel bar which is more ductile.

Although the mechanical strain in the grain of steel is small, it still possesses a significant effect on the MAE signal due to the lowering of the absolute magnetostriction. This effect on steel has the same order of influence on nickel although nickel has a larger magnetostriction, it is because the mechanical strain in the grain of nickel is large. Therefore, there should not be a great difference in the amount of MAE reduction in the two fracture bars.

V. CONCLUSIONS

Significant changes occur in BE and MAE activities after tensile stress of rupture strength is applied on a nickel bar. From the study of the peak values of both signals at the fracture end and the far end of the broken nickel bar, we find that BE activity is intensified while MAE activity is suppressed. The changes of both BE and MAE activities are strongly related to the presence of defects and dislocations, the change of microstructures and the alternation of the physical dimensions of the broken bar. Employing these two techniques, we can realize the presence of stresses, structural defects and the relative values of dislocation and defect densities. A tremendous jump in BE signal indicates that the nickel component is severely damaged and plastically deformed. This can be reconfirmed by a slight decrease in MAE signal. With reference to both measurements, nondestructive investigation of nickel would be much more reliable.

ACKNOWLEDGMENT

This work was funded by the Research Grants Council of Hong Kong (RGC Earmarked Grant 1994/95, Ref: CUHK 310/94P).

[1] D. J. Buttle, C. B. Scruby, G. A. D. Briggs, and J. P. Jakubovics, Proc. R. Soc. London Ser. A **414**, 469 (1987).
[2] D. C. Jiles, NDT Int. **21**, 311 (1988).
[3] D. H. L. Ng, J. P. Jakubovics, C. B. Scruby, and G. A. D. Briggs, J. Magn. Magn. Mater. **104**, 355 (1992).
[4] D. H. L. Ng, J. P. Jakubovics, G. A. D. Briggs, and C. B. Scruby, J. Appl. Phys. **69**, 5868 (1991).
[5] D. H. L. Ng, C. C. H. Lo, S. C. Cheng, and J. P. Jakubovics, IEEE Trans. Magn. **30**, 4857 (1994).
[6] D. H. L. Ng, C. C. Yu, A. S. K. Li, and C. C. H. Lo, IEEE Trans. Magn. **31**, 3394 (1995).
[7] S. Tiitto, IEEE Trans. Magn. **12**, 855 (1976).
[8] B. D. Cullity, *Introduction To Magnetic Materials* (Addison-Wesley, Reading, 1972).
[9] D. H. L. Ng, C. C. H. Lo, and J. P. Jakubovics, J. Appl. Phys. **75**, 7009 (1994).
[10] H. J. Williams, W. Shockley, and C. Kittel, Phys. Rev. **80**, 1090 (1950).

A two-dimensional single sheet tester incorporating controlled magnetization direction

J. J. Dalton, J. Liu, A. J. Moses, D. H. Horrocks, and A. Basak
Cardiff School of Engineering, UWCC, Cardiff CF2 1XH, Wales, United Kingdom

The existence of magnetic anisotropy in electrical steels has long been known to designers of electrical machines. However the effect of this anisotropy in real devices has not to date been studied in any great depth. Finite element modeling software is proving useful for designing such electrical machines, however, the material models which form the heart of the process are based on limited data and indeed often make incorrect assumptions regarding the anisotropic nature of the machine core. This article discusses shortcomings of present anisotropic material models, suggests what is needed to overcome these shortcomings and presents one such two-dimensional magnetic test system capable of generating the materials data required. The method by which the data is obtained is described and measured results are presented, indicating some of the features of the system. © *1996 American Institute of Physics.* [S0021-8979(96)50708-X]

INTRODUCTION

The area of modeling of anisotropic electrical steels is receiving much attention presently. Grain oriented 3% silicon iron exhibits a high degree of anisotropy when magnetized out of its prominent rolling direction plane. This material is widely used as the core in power transformers and due to this magnetic anisotropy constitutes a source of large energy losses.[1]

Finite element modeling (FEM) techniques are increasingly being used as a design and analysis tool for electromagnetic machines. This numerical approach has as its nucleus a material model which is taken to characterize the magnetic properties of the material from which the electromagnetic core being designed is assembled. However these models suffer from several shortcomings which the system presented here attempts to overcome.

PROBLEMS OF CONVENTIONAL MAGNETIC ANISOTROPY MODELS

Conventional anisotropy models are based on one-dimensional $B-H$ relationships of the form

$$B_x=f_x(H_x), \quad B_y=f_y(H_y). \tag{1}$$

That is, the flux density component in the X or rolling direction is a function only of the field in the X direction. Similarly for the Y or transverse components. It can be easily shown that the approach given in Eq. (1) can be improved (ignoring a z component) by employing the following approach:

$$B_x=f_x(H_x,H_y), \quad B_y=f_y(H_x,H_y). \tag{2}$$

In order to construct the $B-H$ relationship shown in Eq. (1) or Eq. (2), the measured $B-H$ data from anisotropic magnetic materials is required. Conventional anisotropic models are formed from two measured $B-H$ curves (rolling and transverse directions), while using certain kinds of interpolation techniques to obtain intermediate curves.[2] These two measured $B-H$ curves do not reflect the full magnetic material behavior, especially when the direction of magnetization is away from the measured $B-H$ directions as happens in real machines.[3]

Generally for magnetic materials the $B-H$ constitutive relation can be stated as

$$\mathbf{B}=\mu_0\mathbf{H}+\mathbf{M}. \tag{3}$$

It is seen that vector **B** is the resultant of the magnetization vector **M** and field vector **H**. Depending on magnetization conditions it is therefore possible for the vectors **B** and **H** to be separate in space. This angle between **B** and **H** in practical cases creates regions of higher power losses in devices and so merits investigation.

The constitutive relation given in Eq. (3) is a one-dimensional relation, however it can be extended to yield a two-dimensional tensor relation. This tensor relation shows the mutual interlinking of the X and Y magnetizing directions. It is clear that to produce a more accurate model, the material data should reflect this dependence. What is in fact needed is measured $B-H$ data at intermediate magnetization angles. This data should include B- and H-total magnitude information as well as the instantaneous angular information of B and H total.

CONTROLLED DIRECTIONAL MAGNETIZATION SYSTEM

The magnetization system presented here is shown in Fig. 1 and is based on an orthogonal yoke arrangement for two-dimensional magnetization of electrical steel sheets 300 $\times$300 mm in dimensions. The flux density (B_xB_y) components and the field intensity (H_xH_y) components are obtained via B and H (calibrated) coils wound through, and on top of the sample, respectively. The excitation wave form generation and the sensor output signal analysis are all achieved by using a novel virtual instrumentation technique.[4] All the signal processing functions such as integration, filtering, spectral analysis, wave form analysis/reconstruction etc. are performed using software modules constructed within this environment.

On application of a magnetizing current to the rolling direction winding it is observed that besides the expected H_x

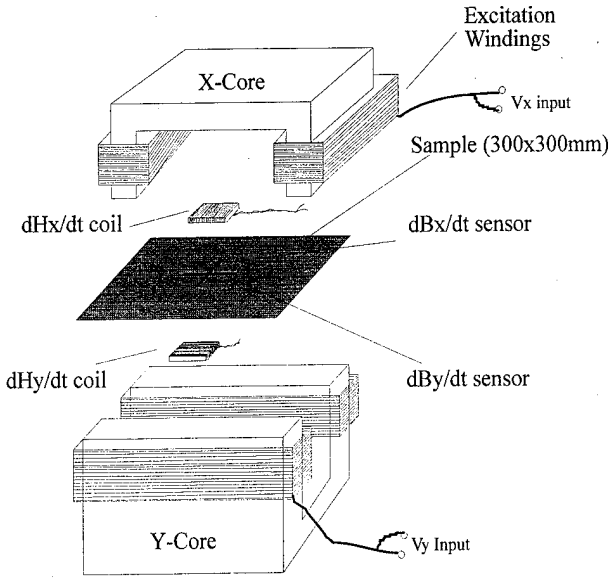


FIG. 1. The presented two-dimensional magnetizing system used showing excitation and measurement techniques.

component there exists a field in the transverse direction (H_y), and vice versa as reported by Nakata *et al.*[5] These H_x and H_y, and correspondingly B_x and B_y, components can be said to be "coupled" and thus the setting of a particular flux density at a given angle cannot be achieved simply by application of independent excitation waveforms to the X and Y excitation coils. These excitation waveforms must be generated according to measured B_x and B_y for the required magnetization conditions.

To achieve the required setting of the flux density components, an algorithm was developed which was based on the minimizing of the following objective function:

$$f=(B_{xm}-B_{x\text{ref}})^2+(B_{ym}-B_{y\text{ref}})^2, \tag{4}$$

where B_{xm} is the measured value of B_x and $B_{x\text{ref}}$ is the reference or desired value of B_x. Similarly for B_y. The reference values of B_x and B_y are calculated from

$$\begin{aligned} B_x&=B_t \cos \theta_B, \\ B_y&=B_t \sin \theta_B, \end{aligned} \tag{5}$$

where B_t represents the total flux density component, that is

$$B_t=\sqrt{(B_x^2+B_y^2)}. \tag{6}$$

The minimization function given in Eq. (4) was used as the controlling function for the direction setting algorithm. The minimization was performed as a sequential series of linear X and Y scans. Each scan involves stepping the output to either the X or Y excitation coil (whichever scan is being performed) while the output to the other coil is maintained constant. For each step the B_x and B_y signals are measured instantaneously and compared with the reference values $B_{x\text{ref}}, B_{y\text{ref}}$ for the required point and angle. After each X or Y scan the point (voltage input to the excitation coil windings, see Fig. 1) causing the function f to be a minimum is recorded and used as the constant input for the following scan. The ranges of both X and Y scans are cut or fine tuned

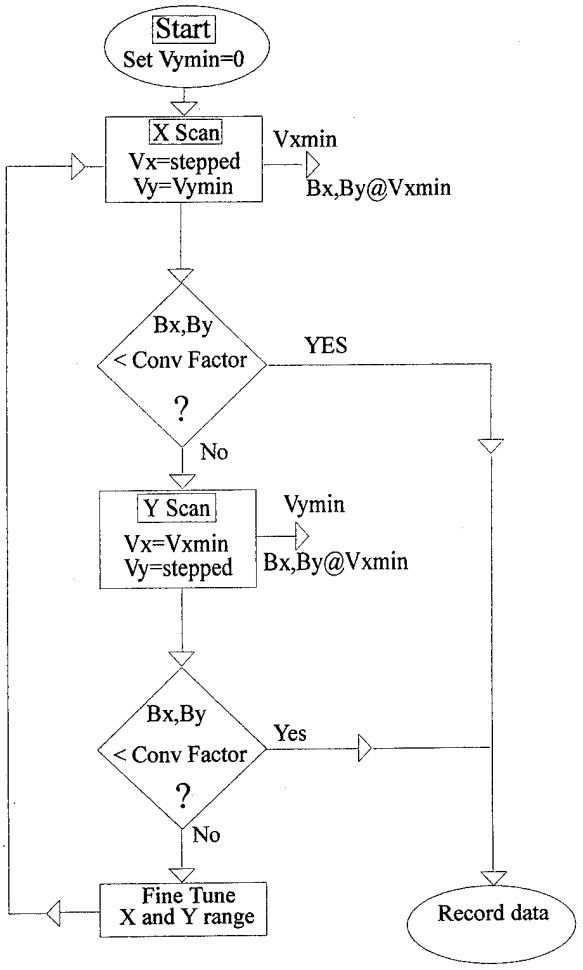


FIG. 2. Flowchart of objective function minimization scanning algorithm.

consecutively around the minimum points obtained from the scans, in a grid-reduction fashion. The process is equivalent to a two-dimensional surface scanning procedure which is based on distance minimization. The flowchart in Fig. 2 details the sequence.

This consecutive X and Y scanning is repeated in an iterative manner until the function f is found to be within a particular range of a designated accuracy number (convergence factor) for the required flux density and angle. This convergence factor is a number designating how small f should become before the required accuracy has been reached. When this convergence has been reached data can be recorded.

Due to the nonlinearity of the material the flux density in the sample was found to be highly distorted. For this reason the selection of the wave form instant on which to take the instantaneous component values is quite important to ensure stability of the scanning routine.

To this end it is desirable to have a monatonic decrease and increase up to and after a minimal point, respectively. This ideal response is shown in Fig. 3, which corresponds to a flux density of 0.5 T at 30° to the rolling direction of a sample of grain oriented silicon iron. Ripples on this response are to be avoided as the possibility of missing the

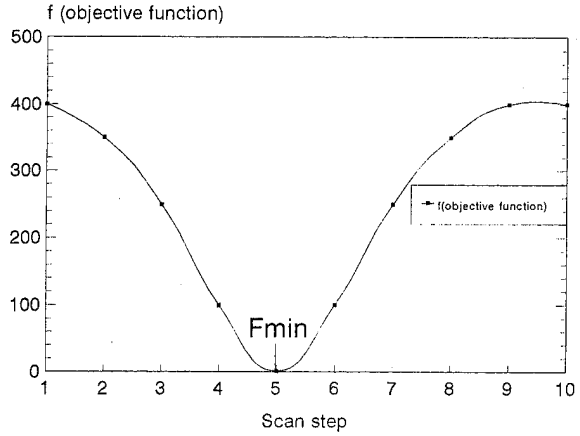


FIG. 3. The objective function change is plotted against scan steps for 30°, 0.5 T. This is an ideal response of f as it ensures algorithm stability.

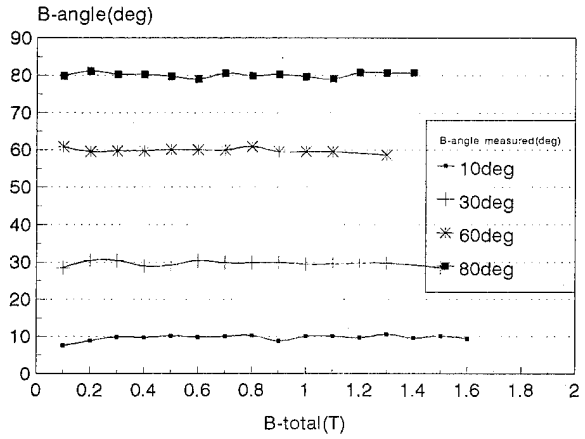


FIG. 5. The flux density set by the system is plotted against reference or ideal values at various angles (dotted lines).

required point and converging around the wrong point then becomes a reality. The four wave forms B_x, B_y, H_x, H_y were all instantaneously sampled at $|H_{\text{totalpeak}}|$ as it was found that this instant offered most stability in terms of the convergence routine. Note $|H_{\text{totalpeak}}| = \sqrt{(H_x^2+H_y^2)}$. The voltage inputs v_x and v_y to the excitation coils were uncontrolled in shape as reported previously.[6]

RESULTS AND DISCUSSION

The system was tested for various magnetization angles between 0° and 90°. The complete flux and field wave forms were recorded and the instantaneous angular information was recorded.

Figure 4 shows a typical $B-H$ curve for a sheet of 27 M4 grain oriented silicon and also the instantaneous H angular information for a magnetization angle fixed at 30° with respect to the rolling direction. It is seen that for lower flux density levels (<1.0 T), the H angle is close to 90°, while at higher flux densities (>1.0 T) the H angle drops steadily and eventually settles at around 56°–57°. This is significant as it shows that the measured results do not tie in with what the assumed results would have predicted. Figure 5 plots system accuracy for various magnetization angles in terms of angular accuracy. The accuracy was found to be in the range 97% for magnitude accuracy and 95% for angular accuracy, however due to high levels of flux wave form distortion, there was a practical upper limit to the level of flux density achievable at particular angles. These problems presented themselves worst between 40° and 60°, reflecting the anisotropic hard axis. This problem presently limits the system as to the maximum flux density it can achieve for any particular angle. However it is known[7] from early work that the flux density in real devices never reach these high levels anyway so in many ways, from a design point of view, it is not really necessary to have information for these higher levels. From a general knowledge point of view of course it is desirable to have this information and so it is an objective of the authors to pursue this. These experimental results will be reported later.

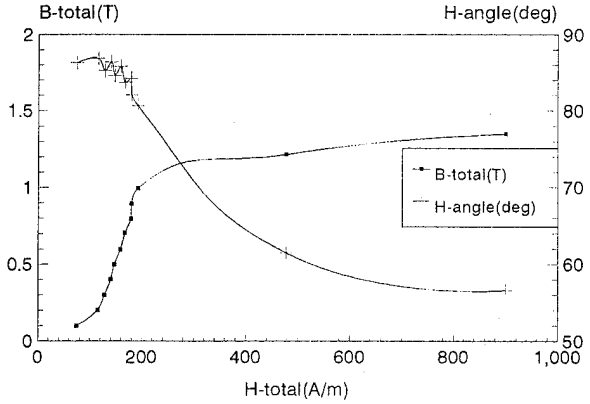


FIG. 4. A typical $B-H$ curve for a magnetization direction of 30° is shown. Also included is the H angular information.

CONCLUSION

A two-dimensional magnetic test system capable of magnetizing at user defined angles was successfully constructed. This information takes previous work a step further and allows the user to set up his own magnetization conditions based on flux density control. The complete B and H magnitude and angular information is now obtainable for any user defined magnetization angles thus facilitating us to take the anisotropic modeling process one step further.

[1] A. J. Moses, IEE Proc. A **137**, No. 5, Sep. (1990).
[2] A. D. Napoli and R. Paggi, IEEE Trans. Magn. **MAG-19**, 1557 (1983).
[3] A. J. Moses, Inter. J. Appl. Electromag. Mat. **3**, 193 (1992).
[4] J. J. Dalton, J. Liu, A. J. Moses, D. H. Horrocks, and A. Basak, International Symposium on Non-Linear Electromagnetic Systems (ISEM), Cardiff, September 1995 (unpublished).
[5] T. Nakata, F. Fujiwara, M. Nakano, and M. Okamoto, IEEE Trans. Magn. **30**, 3395 (1994).
[6] T. Nakata, N. Takahashi, K. Fujiwara, and M. Nakano, IEEE Trans. Magn. **29**, 3544 (1993).
[7] A. J. Moses, B. Thomas, and J. E. Thompson. IEEE Trans. Magn. **8** , 785 (1990).

A magnetoelastic torque transducer utilizing a ring divided into two oppositely polarized circumferential regions

I. J. Garshelis and C. R. Conto
Magnetoelastic Devices, Incorporated, P.O. Box 625, Pittsfield, Massachusetts 01202

Significant improvements in both transducer performance and constructional simplicity is achieved by dividing a single ring into two equal width regions having oppositely directed circumferential magnetizations. The square hysteresis loop associated with the uniaxial anisotropy in the ring enables this magnetization arrangement to be readily instilled by rotating the shaft/ring assembly in the dipole fields of a set of axially separated permanent magnets having opposing polarizations. Following the removal of the magnets, each such region effectively becomes a single domain separated from the other only by a centrally located 180° domain wall. Unchanging performance of the transducer throughout nearly 10^7 torque cycles, severe overloads, and a wide range of thermal environments attest to the stability of both the remanent magnetizations in each region and the position of the domain wall. © *1996 American Institute of Physics.* [S0021-8979(96)50808-6]

INTRODUCTION

We have previously described[1] a noncontact transducer wherein the torque carried by a shaft is indicated by the polarity and intensity of a magnetic field arising from a rigidly attached ring of circumferentially polarized, magnetostrictive material. We subsequently described[2] a transducer construction utilizing two contiguous rings having oppositely directed circumferential polarizations and showed that with this arrangement, ambiguous contributions to the torque responsive field, from ambient magnetic fields, could be effectively eliminated. It was clear from the analysis that this important improvement does not rely on the presence of two physically distinct rings, but derives instead from the difference in the responses of their respective magnetizations to torsional stress and to magnetostatic fields. Thus it is to be expected, and indeed it was suggested,[2] that a single ring, divided into two oppositely magnetized regions separated only by an encircling 180° domain wall, should mimic the performance of the two rings, at the same time providing a physically simpler construction.

Unlike the case with two separate rings wherein each ring can be readily magnetized in the desired circumferential direction by a coaxial current pulse *prior* to its assembly onto the shaft, the establishment of two oppositely polarized regions within a single ring clearly requires a different approach. In this article we show a simple means for simultaneously magnetizing two such regions and demonstrate that the resulting polarizations and location of the domain wall are stable over a wide range of environmental and operating conditions. Such stability is clearly crucial to the utility of the resulting torque transducer.

DESCRIPTION

Figure 1 shows the assembly of elements comprising a complete torque transducer. The ring, of magnetostrictive material, exhibits by its shape and typically also by a tensile "hoop" stress associated with its interference fit on the shaft, an effectively uniaxial magnetic anisotropy, K_u, having its easy axis in the circumferential direction. The ring is divided into two equal width regions, A and B, distinguished only by the opposite circumferential directions of their remanent magnetizations M_{rA} and M_{rB}. Because of the square $M-H$ loop associated with K_u, these remanent magnetizations approximate the saturation magnetization, M_s. The shaded transition region between A and B has no significant width; it is effectively a 180° domain wall encircling the ring and may in fact attain the structure and dimensions of an actual domain wall. Other than in these different details of magnetization and a few related consequences (to be discussed), operation of the device shown in Fig. 1 as a torque transducer follows the detailed description and analysis given in previous works.[1,2] Attention here is to the means of attaining the distinctly bordered, oppositely magnetized regions in a single ring.

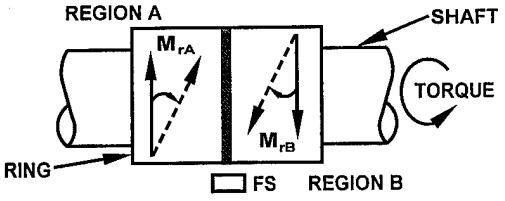


FIG. 1. Elements comprising the torque transducer. FS is field sensor.

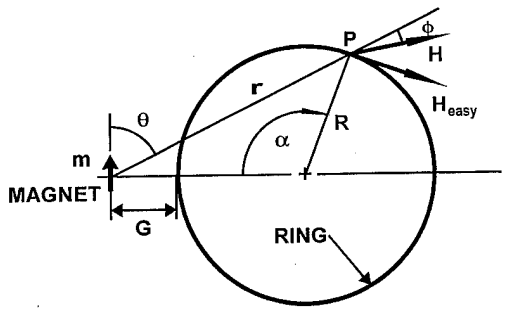


FIG. 2. Geometric considerations for determining the field, H_{easy} from a magnet of dipole strength m at any point P on the ring.

 0021-8979/96/79(8)/4756/3/$10.00 © 1996 American Institute of Physics

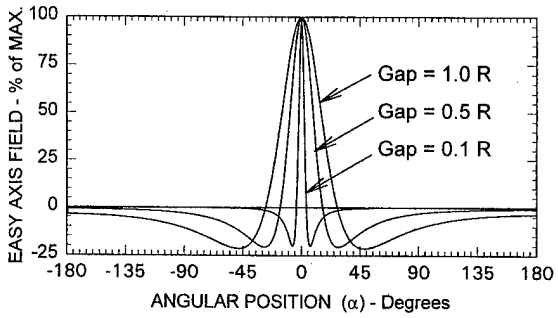


FIG. 3. Calculated easy axis field around ring for various magnet gaps.

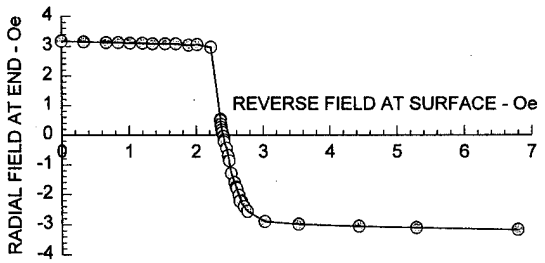


FIG. 5. Determination of H_c by disappearance of torque induced field.

PRINCIPLES OF MAGNETIZATION METHOD

While it is possible to use axial currents to polarize the two regions with the ring already in place on the shaft, magnetization by rotation through the fields from an antiparallel set of permanent magnets is a more practical method, allowing the same simple apparatus to be used with a wide range of shaft and ring sizes. The principles of this magnetizing method can be readily understood by considering first the action of the field from a *small* permanent magnet on a single region of the ring as the shaft is rotated on its axis. The location and orientation of the magnet, considered here as a simple dipole of moment m, relative to the ring are indicated in Fig. 2. The magnet is spaced from a thin (negligible radial thickness) ring of radius R by air gap G. The field H at any point P in the ring, distance r from the tangentially oriented dipole is readily found from[3]

$$H=\frac{m}{r^3}(3\cos^2\theta+1)^{1/2}, \tag{1}$$

where θ is the angle between m and the r vector. For any position angle α, r is found (from the Law of Cosines) as

$$r=[(R+G)^2+R^2-2(R+G)R\cos\alpha]^{1/2}. \tag{2}$$

H is seen to be directed at angle ϕ to r, where[3] $2\tan\phi=\tan\theta$.

With a small enough magnet, HM_s is at all points $<K_u$, hence only the tangential component of H, i.e., H_{easy}, can have any irreversible effects on the local direction of ring magnetization. From the geometry in Fig. 2 it is seen that,

$$H_{\text{easy}}=H\cos(\alpha-\theta-\phi). \tag{3}$$

The variations of H_{easy} with α, as found from Eqs. (1) to (3), are plotted in Fig. 3 (as percentages of their maximum values) for three values of G. In all three plots, H_{easy} is seen to cross zero (i.e., reverse direction) at relatively small angles on either side of $\alpha=0$, although these zero crossing angles are seen to depend significantly on G. The normalized peak reverse fields however, are seen to be notably insensitive to G, being always near 20% of the maximum H_{easy}.

If the shaft (ring) is now rotated (in either direction) for at least one full revolution, and if G and m are such that the peak negative value of $H_{\text{easy}}>H_c$ (the coercive force), all portions of the ring not situated in positive fields $>H_c$ will become magnetized in the negative direction, since such is the polarity of that field greater than H_c to which they were last exposed. The distribution of magnetization within the ring after such rotation (also while rotating) is shown in Fig. 4(a). If the field from the magnet is then sufficiently reduced (e.g., by insertion of a high permeability shield or "keeper" between the magnet and the ring) as to effectively eliminate the magnet's presence, the magnetization within the ring will relax to the distribution shown in Fig. 4(b). If the combined intensity of the demagnetizing field from the minor sector of the ring and the field acting on it from the major sector exceeds H_c, the magnetization within the minor sector will be reversed, thereby leaving the entire circumference of the ring magnetized in a single circular direction as shown in Fig. 4(c).

It should be clear that the field from m also extends axially and that, subject to the requirement that the peak negative values of $H_{\text{easy}}>H_c$, even a stationary magnet can polarize a ring wider than itself. Thus it should also be clear that, used in the manner described, a fixed array of two axially separated, oppositely polarized magnets of equal

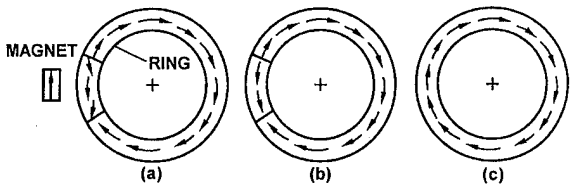


FIG. 4. Circumferential distribution of ring magnetization. (a) After full revolution. (b) Transiently, following magnet removal. (c) After polarity reversal within minor sector by fields at sector boundaries.

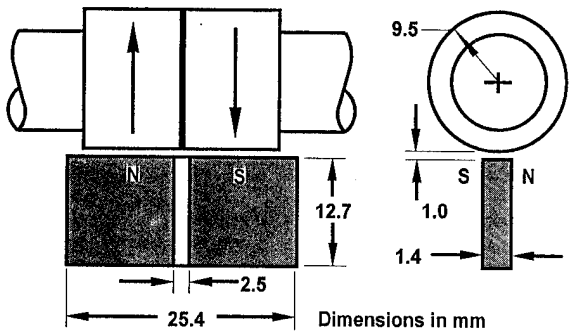


FIG. 6. Magnet arrangement used to simultaneously polarize two regions.

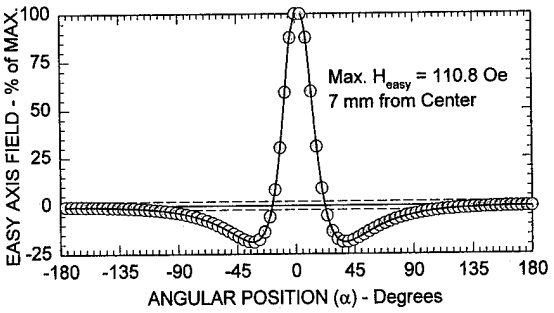


FIG. 7. Circumferential variations in easy axis field of actual magnet.

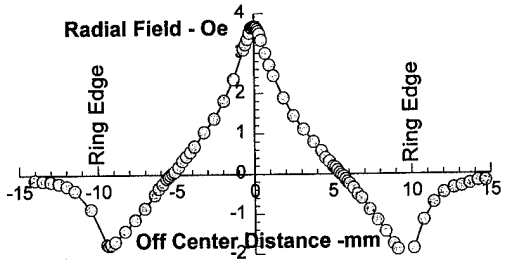


FIG. 9. Variation of radial field from 10 N m torque with position.

strengths will simultaneously create two regions on the same ring having antiparallel remanent magnetizations.

EXPERIMENT

The ring/shaft assembly used in this study was already described[2] in a previous work wherein the ring was uniformly magnetized over its entire 20 mm width in a single circular direction. Measurements were performed that provided a novel means of determining H_c of the ring *in situ*. Since operation as a torque transducer is based on the appearance of a field due to the torque induced tilting of an originally circumferential remanent magnetization, M_r, the polarity and magnitude of the field arising from the application of a fixed torque can be used to indicate the direction and relative magnitude of M_r. Thus when $M_r=0$, no field arises with torque. The experiment consisted of measuring the radial field near one end of the ring with an applied torque of 10 Nm following the passage, axially through the shaft (with zero torque), of successively larger currents having reversed polarity circular fields. The resulting data are plotted in Fig. 5.

The sharp critical field at 2.2 Oe reflects the expected dominant uniaxial anisotropy. The imperfect verticality of the subsequent reversal of M_r is also expected considering the finite thickness of the ring and the dependence of the internal circular field on radius. H_c is readily identified as 2.4 Oe. The somewhat sluggish approach to saturation (requiring nearly 7 Oe to reach 99.3%) is attributed to the gradual growth in hoop stress (hence, K_u) inward from the ends of the ring due to internal chamfers.

Two region polarization was accomplished by rotation in the fields of a proximate pair of bonded ferrite magnets,[4] sized and positioned as shown in Fig. 6. H_{easy} was found to vary with axial position along these magnets, reaching symmetrical maxima 7 mm from the axial centerline. Measured values of H_{easy} at one such location, around a 17 mm diam. circle, with the edge of the magnets 10.7 mm from the center are plotted as a percentage of the maximum value (110.8 Oe) in Fig. 7. The close resemblance of this plot to the Gap=0.5 R curve in Fig. 3 is especially striking in view of the areal distribution of dipoles in the actual magnets. The peak reverse fields, occurring at $\alpha=\pm 32°$, are seen to also approximate 20%. The variation of peak reverse field with axial position is plotted in Fig. 8. The transition zone between regions within which the reverse easy axis field exceeds H_c is seen to be $\approx$1 mm. While the status of magnetization and actual width of this zone are presently unknown it clearly acts effectively as a 180° domain wall.

Measured values along the ring of the radial component of the field arising with the application of a 10 N m torque to the shaft are plotted in Fig. 9. The variation in field is seen, as expected, to follow the form associated with an axial quadrupole, moderately modified by the demagnetizing effects of each region on the other. No significant variation in data of this kind was found after heating to 150 °C, cooling to −50 °C, each for several hours, immersion in liquid N_2, and more than 9×10^6 cycles of reversing torque. This attests to the stability of both the remanent magnetizations and the position of the wall separating them.

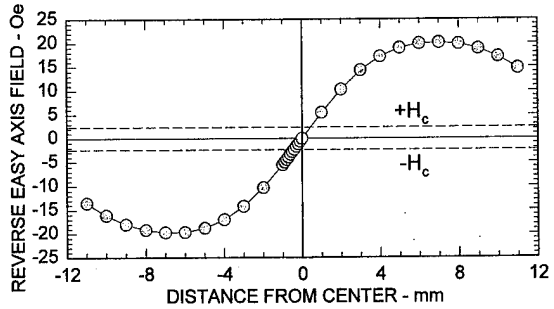


FIG. 8. Variation of peak reverse field with axial position.

DISCUSSION

Comparison of Fig. 9 with Fig. 5 in Ref. 2 shows that the single ring, two region construction provides a higher sensitivity (field per unit torque) than with two separate rings, attributable to the greater M_r attainable by magnetization *after* installation of the ring on the shaft.

[1] I. J. Garshelis, IEEE Trans. Magn. **28**, 2202 (1992).
[2] I. J. Garshelis and C. R. Conto, IEEE Trans. Magn. **30**, 4629 (1994).
[3] B. D. Cullity, *Introduction to Magnetic Materials* (Addison–Wesley, Reading, MA, 1972), p. 614.
[4] Plastiform MGO 1016, Arnold Engineering Co. Norfolk, NE 68702-1567.

Hall-effect characterization in semiconductor heterostructure junctions using polarized laser signal

Hoton How and Ta-Ming Fang
Massachusetts Technological Laboratory, Belmont, Massachusetts 02178

Feng Lu and Brian Ahern
RL/ERXE, Rome Lab., Hanscom AFB, Massachusetts 01731

We describe a new technique which exploits the ac Hall effect in the characterization of layered semiconductor structures. The method employs laser signals in the presence of a dc magnetic bias field. Upon incidence the polarization of the optical signal is rotated via a Lorentz force due to the ac Hall effect. As such, the reflected waves carry information on the Hall mobility of the charge carriers. The calculations show that ac Hall reflection warrants sufficient intensity to be measured. Our theory is complete in the sense that depth profiling has been explicitly incorporated in the formulation. © *1996 American Institute of Physics.* [S0021-8979(96)50908-X]

INTRODUCTION

Materials for present-day high-speed devices, such as high electron mobility transistors, often have many conducting layers incorporating semiconductor heterostructure junctions.[1] The straightforward dc Hall-effect techniques can be of only very limited use to analyze such materials. The problem is that the standard dc Hall-effect method measures only two parameters, resistivity ρ and Hall coefficient R_H, and thus is able to determine only two unknowns, the carrier concentration n and mobility μ, in a single layer. Extra information might be obtainable by measuring the magnetic-field dependencies of ρ and R_H upon which n and μ can be indirectly estimated for a two-layered structure.[2] Shortcomings for the current dc Hall-effect measurements are that they are not able to profile or characterize a semiconductor sample either horizontally or vertically. The present theory of the dc Hall effect always assumes limiting cases, adopting either the so-called two-band or the two-layer models.[3] In reality, space charges can accumulate/deplete across the sample layer boundaries depending on the relative strength of their respective electrochemical potentials. A new technique is presented in this paper which is able to provide local characterization of layered semiconductor samples. The technique exploits an ac Hall effect using laser signals in the presence of a dc bias magnetic field. The ac currents induced by the laser signal will experience a Lorentz force which deflects the electron/hole motion in the semiconductor, resulting in polarization rotation of the incident radiation. Therefore, by measuring the cross-polarized signals in the reflected and/or the transmitted optical beams, an ac Hall effect can be suitably characterized. Since no dc Hall voltage is measured, the method can be applied locally, with the scale limited only by the size of the incident laser beam. Most importantly, depth profiling of the semiconductor sample can be incorporated in this new technique. Since an electromagnetic wave propagates sequentially across the layers, the overall effect can be formulated provided that the respective parameters associated with each of the layers are known *a priori*. The predicted effects are of sufficient magnitude to warrant experimental interest.

FORMULATION

Analogous to the derivation of the gyromagnetic permeability, we first derive an expression for the tensor permittivity of a semiconductor medium in the presence of a dc bias magnetic field subject to Drude damping as[4]

$$\boldsymbol{\epsilon}=\epsilon_\infty\mathbf{1}-\frac{j}{\omega}\boldsymbol{\rho}^{-1}, \tag{1}$$

where

$$\boldsymbol{\rho}=\begin{pmatrix}\rho(1+j\omega\tau) & -R_HB & 0\\ R_HB & \rho(1+j\omega\tau) & 0\\ 0 & 0 & \rho(1+j\omega\tau)\end{pmatrix}.$$

ϵ_∞, after dividing by ϵ_0, the permittivity of vacuum, denotes the (optical) dielectric constant of the medium, and τ is the damping time constant. Electric resistivity and Hall coefficient are

$$\rho=-q(\mu_n n+\mu_p p)^{-1},\quad R_H=-rq\rho^2(\mu_p^2 p-\mu_n^2 n),$$

μ_p and μ_n are the mobilities, and p and n the concentrations for holes and electrons, respectively. The thermal statistic factor is absorbed in the parameter r which is defined as $r=\langle\tau^2\rangle/\langle\tau\rangle^2$, where $\langle A\rangle$ denotes the statistic average of quantity A over all the possible electronic states. For degenerate bands, $r=1$. Note that μ_p and μ_n may contain contributions from both processes arising from phonon and ionized impurity scattering.

Let the semiconductor structure consist of n layers. The zeroth and the $(n+1)$-th layers are both semi-infinite located above and below the semiconductor structure which can be the air or the substrate. The dc magnetic field is applied normal to the layered structure and the ac (optical) signal is considered to propagate along the magnetic-field direction (normal incidence), denoted as the z axis. The permittivity tensor can be diagonalized in terms of circularly polarized waves as

$$\epsilon^{\pm}=\epsilon_\infty+\frac{j}{\omega}\frac{1}{\rho(1+j\omega\tau)}\left(1\pm\frac{jR_HB}{\rho(1+j\omega\tau)}\right)^{-1}. \tag{2}$$

 0021-8979/96/79(8)/4759/3/$10.00 © 1996 American Institute of Physics

Denote the permittivities of the ith layer as $\epsilon_i^{\pm}$, $1 \leqslant i \leqslant n$, which can be evaluated from Eq. (2) by using the respective parameters of the layer, including resistivity, carrier concentration, and mobility, etc. The thickness of the ith layer is d_i, $1 \leqslant i \leqslant n$. The electromagnetic fields at the two sides of the layered structure can be related by a total transfer matrix[4]

$$\mathbf{T}^{\pm,\mathrm{tot}} = \prod_{i=1}^{n} \mathbf{T}^{\pm,i}(d_i) = \begin{pmatrix} a^{\pm} & b^{\pm} Z_0 \\ \dfrac{c^{\pm}}{Z_0} & d^{\pm} \end{pmatrix}, \tag{3}$$

such that

$$\begin{pmatrix} e_s^{\pm} \\ h_s^{\pm} \end{pmatrix} = \mathbf{T}^{\pm,\mathrm{tot}} \begin{pmatrix} e_0^{\pm} \\ h_0^{\pm} \end{pmatrix}. \tag{4}$$

Here the individual transfer matrix for each layer is[4]

$$\mathbf{T}^{\pm,i}(d_i) = \begin{pmatrix} \cos k_i^{\pm} d_i & -jZ_i^{\pm} \sin k_i^{\pm} d_i \\ -\dfrac{j}{Z_i^{\pm}} \sin k_i^{\pm} d_i & \cos k_i^{\pm} d_i \end{pmatrix}, \tag{5}$$

$$k_i^{\pm} = \sqrt{\mu \epsilon_i^{\pm}}\,\omega \quad \text{and} \quad Z_i^{\pm} = \sqrt{\frac{\mu}{\epsilon_i^{\pm}}},$$

and superscript $+(-)$ denotes right-hand (left-hand) polarization. We also have used subscript $i=0(s)$ to refer to the layer of air (substrate). The overall reflection and transmission coefficients of the structure are, respectively,[4]

$$r^{\pm} = \frac{-(a^{\pm}+b^{\pm})Z_0 + (c^{\pm}+d^{\pm})Z_s^{\pm}}{(a^{\pm}-b^{\pm})Z_0 - (c^{\pm}-d^{\pm})Z_s^{\pm}}, \tag{6}$$

$$t^{\pm} = \frac{2(a^{\pm}d^{\pm} - b^{\pm}c^{\pm})Z_s^{\pm}}{(a^{\pm}-b^{\pm})Z_0 - (c^{\pm}-d^{\pm})Z_s^{\pm}}. \tag{7}$$

Therefore, when the incident beam is polarized in the x direction, the reflected and transmitted beams in the cross-polarized (y) direction are

$$r_{\text{ac-Hall}} = j(r^{+} - r^{-})/2, \quad t_{\text{ac-Hall}} = -j(t^{+} - t^{-})/2. \tag{8}$$

The overall transfer matrices can be written in the form of Eq. (3) only if surface currents are absent from the layer boundaries. As such, the tangential magnetic fields vary continuously across the boundaries. If surface currents do exist, the above transfer matrix theory cannot be directly employed. Rather, the current sheet itself shall be treated as a separate semiconductor layer whose thickness is vanishingly small. That is, for a two-dimensional current sheet (2-DEG) one assumes d goes to zero. Thus n (or p) goes to infinity, with the product of d and n (or p) being finite. This results in finite surface carrier concentrations and finite surface resistance of the current sheet, denoted as n_s and R_s, respectively. As such, the transfer matrix associated with a 2-DEG sheet takes the following form:

$$\mathbf{T}^{\pm,\text{2-DEG}} = \begin{pmatrix} 1 & 0 \\ -[R_s(1 \mp r\mu_n B)]^{-1} & 1 \end{pmatrix}, \tag{9}$$

which can be then used in Eq. (3) for calculating $\mathbf{T}^{\pm,\mathrm{tot}}$.

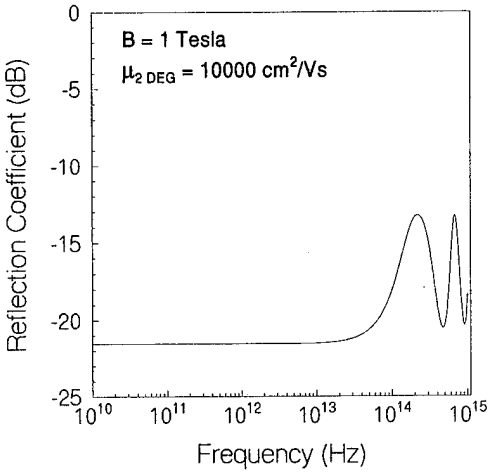


FIG. 1. The ac Hall reflection as a function of frequency.

RESULTS

We consider in this paper the calculation of the ac Hall reflection by a five-layered semiconductor heterostructural junction. The first layer is the cap material made of n^+-GaAs with carrier concentration 10^{18} cm^{-3} for ohmic contact purposes. The second layer is n-AlGaAs, which provides electrons to form a quasi-two-dimensional Fermi gas near the AlGaAs–GaAs interface. The dopant level here is 10^{18} cm^{-3}. However, due to electron diffusion into the 2-DEG sheet, the electron concentration in the second layer is about an order smaller than the dopant level (10^{17} cm^{-3}).[2] The third layer is an undoped AlGaAs layer, which serves as a spacer to separate the accumulated electrons in the 2-DEG sheet from their parent donor impurities in the second layer to enhance electron mobility. The fourth layer is the 2-DEG sheet whose default values in carrier concentration and mobility are 10^{12} cm^{-2} and 10 000 cm^2/V s, respectively. The fifth layer is the undoped GaAs material, which, due to its high electron affinity, attracts electrons from the n^+-AlGaAs layer to form the 2-DEG sheet. We consider the electron mobility to be 1000 cm^2/V s for the AlGaAs materials and 4000 cm^2/V s for the GaAs materials. The carrier concentration for the undoped materials (AlGaAs and GaAs) is 10^{14} cm^{-3}. The thicknesses of these layers are, respectively, 500, 500, 20, 0, and 1000 Å. We assume semi-insulating GaAs is used as the substrate, whose carrier concentration is 10^6 cm^{-3} and mobility is 1000 cm^2/V s. In the following calculations we consider the optical dielectric constant of GaAs and AlGaAs to be 10.9,[5] which differs from their dc value of 12.79.[5] The statistic factor r is taken to be 1, which corresponds to the degenerate case of the electronic states.

Figure 1 shows the ac Hall reflection for $\mu_{2\text{-DEG}} = 10\,000$ cm^2/V s and $B = 1$ T. In Fig. 1 oscillations appear at high frequencies ($>2\times10^{14}$ Hz), arising from internal reflections due to the layers' structural boundaries, say, the surface boundaries of the fifth layer of the undoped GaAs (thickness 1000 Å). Similar results are also obtained for higher $\mu_{2\text{-DEG}}$ and B values, which shows higher reflection coefficients, indicating that the magnitudes of ac Hall reflection are in the range which warrants accurate measurements.[4]

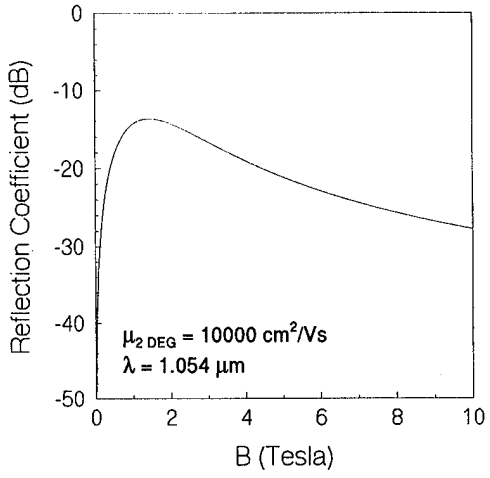


FIG. 2. The ac Hall reflection as a function of magnetic field.

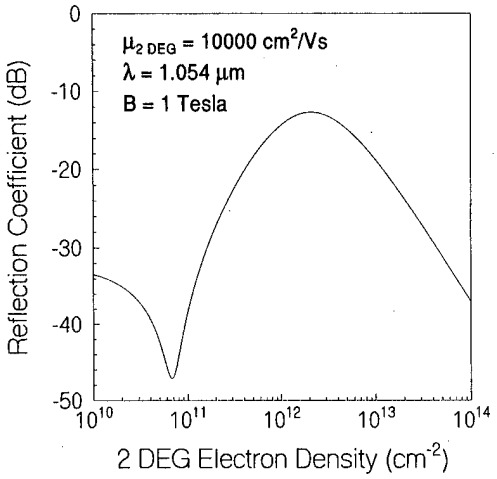


FIG. 3. The ac Hall reflection as a function of surface carrier concentration.

To be explicit, let us assume the ac signal is furnished by a Nd:YLF laser source providing light signals of wavelength $\lambda=1.054$ μm (for example, Quantronix 416). Figure 2 shows the calculated ac Hall reflection as a function of the applied magnetic field, B, for $\mu_{2\text{-DEG}}=10\,000$ cm^2/V s. It is seen in Fig. 2 that maximum reflection occurs at $B=1.194$ T, with a value of -13.87 dB. Similar results are found for $\mu_{2\text{-DEG}}=20\,000$ cm^2/V s, where the maximum occurs at $B=0.929$ T, with a value of -9.924 dB.[4] Therefore, by searching for optimal magnetic bias producing maximum ac Hall reflection, the magnitude of $\mu_{2\text{-DEG}}$ can be deduced.

Figure 3 shows the calculated reflection as a function of electron density in the 2-DEG sheet, n_s, assuming $\mu_{2\text{-DEG}}=10\,000$ cm^2/V s, $B=1$ T, and $\lambda=1.054$ μm. We showed elsewhere that[4] in Fig. 3 for $n_s>7\times10^{10}$ cm^{-2}, ac Hall reflection is attributed to Hall rotation in the 2-DEG sheet, identified as the larger (primary) peak in the reflection curve of Fig. 3. For $n_s<7\times10^{10}$ cm^{-2}, reflection from the cap layer dominates, appearing as the smaller peak (secondary) in Fig. 3. The ac Hall reflection due to the other layers (layers 2, 3, 4, and substrate) is almost invisible in Fig. 3, indicating that the considered semiconductor structure is essentially a two-layered system producing Hall rotation. This is called parallel conduction as reported in the dc Hall measurements.[2,3] Other properties of the layered structure are discussed in Ref. 4.

[1] R. Dingle, H. L. Stormer, A. C. Gossard, and W. Wiegmann, Appl. Phys. Lett. **33**, 665 (1978).
[2] D. C. Look, C. E. Stutz, and C. A. Bozada, J. Appl. Phys. **74**, 311 (1993).
[3] D. A. Syphers, K. P. Martin, and R. J. Higgins, Appl. Phys. Lett. **49**, 534 (1986).
[4] H. How and T. M. Fang (unpublished).
[5] SEMI International Standards, Materials Volume, Specifications M9–90, 1993.

Nature of the interlayer coupling in annealed $Ni_{80}Fe_{20}$/Ag multilayers

J. A. Borchers, P. M. Gehring, R. W. Erwin, and C. F. Majkrzak
Reactor Radiation Division, National Institute of Standards and Technology, Gaithersburg, Maryland 20899

J. F. Ankner
Research Reactor Facility, University of Missouri, Columbia, Missouri 65211

T. L. Hylton,[a] K. R. Coffey, M. A. Parker, and J. K. Howard
IBM Storage Systems Division, 5600 Cottle Road, San Jose, California 95193 .

Using x-ray and polarized neutron (PNR) reflectivity, we have measured the structural and magnetic depth profiles of annealed $Ni_{80}Fe_{20}$ (20 Å)/Ag (40 Å) multilayers. The x-ray data indicate that the interfaces are highly mixed. PNR measurements of the 335 °C annealed multilayer in small magnetic fields reveal a broad feature in the off-specular spin-flip scattering that is not present for the unannealed sample. The giant magnetoresistance is thus associated with antiferromagnetic correlations between micrometer-sized magnetic domains within the $Ni_{80}Fe_{20}$ layers. This spin ordering is consistent with a model in which weak dipolar forces lead to an antiparallel alignment of the domains across the Ag layers. © *1996 American Institute of Physics.* [S0021-8979(96)51008-4]

Sparked by the discovery of giant magnetoresistance (GMR),[1] studies of transition-metal multilayers have revealed complex correlations among their transport, magnetic, and structural properties. Neutron scattering has been important in determining the microscopic magnetic structure of these materials because one can obtain both the orientation and magnitude of the moment as a function of depth, independent of the sample volume. For example, Barthélémy *et al.*[2] used neutron techniques to prove that the peak in the resistivity for Fe/Cr multilayers is associated with antiparallel alignment of the ferromagnetic Fe layer moments. Subsequent diffraction studies[3] confirmed the oscillatory dependence of the exchange coupling on the nonmagnetic interlayer thickness.

We have applied polarized neutron reflectivity (PNR) techniques to the study of sputtered $Ni_{80}Fe_{20}$/Ag multilayers annealed at different temperatures. The as-grown multilayers show a change in resistivity $\Delta R/R_{sat}<0.3\%$ independent of the Ag layer thickness, though a maximum magnetoresistance change of $\approx 5\%$ is obtained after annealing at temperatures near 335 °C.[4,5] The measured saturation fields H_{sat} for the multilayers are smaller than 100 Oe, making them attractive candidates for magnetic sensor applications.

Cross-sectional transmission electron microscopy (XTEM) studies[6] indicate that annealing promotes the formation of Ag "bridges" spanning the $Ni_{80}Fe_{20}$ layers. Off-specular x-ray data suggest that annealing also reduces the lateral disorder through the interfacial region.[5] PNR measurements reveal that these structural modifications change the nature of the interlayer exchange coupling. Specifically, a broad peak at the half-order antiferromagnetic position is evident in transverse scans for the 335 °C annealed multilayer. The induced GMR is thus associated with antiferromagnetic correlations between the $Ni_{80}Fe_{20}$ layer moments along the growth axis, but the in-plane domains are small (≈ 1–5 μm). In agreement with previous suggestions,[4,7] we demonstrate that the strength of the field required to overcome the dipolar interaction between two finite plates is comparable to the saturation fields measured for the annealed samples.

For this study, four (111) textured multilayers of nominal composition Ta(100 Å)/Ag(20 Å)/[$Ni_{80}Fe_{20}$(20 Å)/Ag(40 Å)]$_4$/$Ni_{80}Fe_{20}$(20 Å)/Ag(20 Å)/Ta(40 Å) were sputtered onto silicon substrates under conditions described elsewhere.[4,6] Following growth, three of the multilayers were annealed at 305, 315, and 335 °C, respectively. $\Delta R/R_{sat}$ and H_{sat} were obtained from bulk transport and magnetization measurements, and their dependence on anneal temperature follows that described in a related study.

Using a double-axis x-ray spectrometer, we examined the samples at small angles to characterize the structural changes induced by annealing. Following subtraction of the background, superlattice peaks are visible only out to second order, as illustrated in Fig. 1 which shows the specular reflectivity for all four multilayers. From fits of the x-ray data we conclude that the $Ni_{80}Fe_{20}$ and Ag layers are strongly mixed along the growth-axis direction. (Details of these x-ray fits will be published elsewhere.[5]) The growth-plane averaged scattering[5] densities in the centers of the $Ni_{80}Fe_{20}$ and Ag layers differ by as much as 10% from their bulk values, indicating that Ag is present in the $Ni_{80}Fe_{20}$ layers (and vice versa) both prior to and after annealing. In Fig. 1 there is also a shift of the superlattice peaks to lower Q_z with increasing anneal temperature, suggesting that the bilayer thickness systematically increases. These data are not conclusive, however, because the bilayer spacings were not measured prior to annealing.

[a]Current address: Microunity Systems Engineering, Inc., 255 Caspian Drive, Sunnyvale, CA 94089.

 0021-8979/96/79(8)/4762/3/$10.00 © 1996 American Institute of Physics

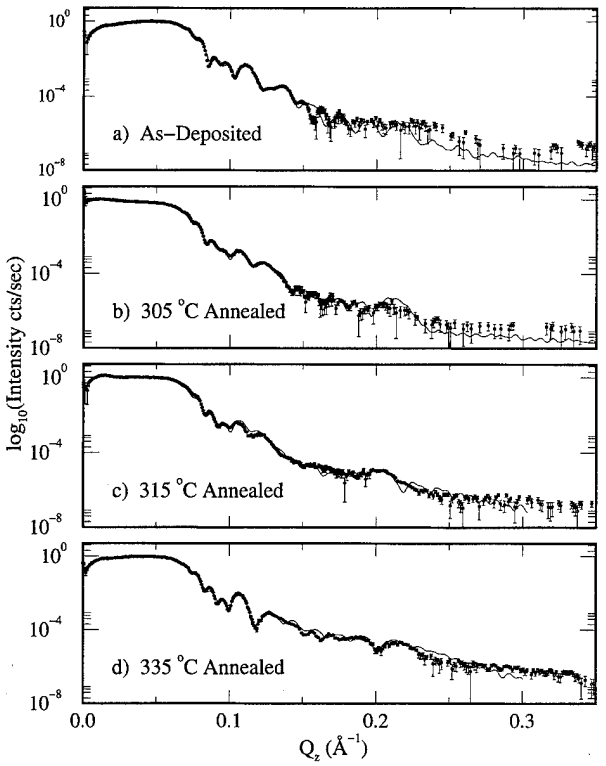


FIG. 1. Specular x-ray reflectivity of the $Ni_{80}Fe_{20}$/Ag multilayers. The circles correspond to the data and the solid lines are fits. The superlattice peaks in (d) are masked by interference fringes from the oxidized Ta base and cap layers.

The effects of annealing are seen principally in transverse x-ray scans, which are sensitive to the in-plane interfacial structure. At small values of Q_z, the Q_x scans have two distinct components centered at Q_x=0.0 Å^{-1}: a resolution-limited specular peak atop a broad diffuse peak.[5] The width of the diffuse component is inversely related to the coherence length ξ of the in-plane structural features. Crude estimates[6] of ξ vary between 3.5 and 5.5 μm, which is characteristic of grain boundaries, interfacial terracing, or other microscopic inhomogeneities within the sample plane. At all of the Q_z values considered, the width of the diffuse peak for the as-deposited sample is broader than that for the 335 °C annealed sample. Apparently ξ increases with anneal temperature as the in-plane structural domains coalesce. Combining these results with those of specular reflectivity and XTEM,[6] we propose that the Ag already present tends to conglomerate within the nominal $Ni_{80}Fe_{20}$ layers, possibly at the grain boundaries, and breaks the $Ni_{80}Fe_{20}$ into long, flat pancakes. This particulate structure seems to develop only in *sputtered* $Ni_{80}Fe_{20}$/Ag multilayers. As-grown epitaxial permalloy/Ag multilayers show no evidence of grain boundaries, though annealing does act to smooth the in-plane structure and expel Ag from the $Ni_{80}Fe_{20}$ layers.[10]

To characterize the magnetic structure, we performed PNR studies at the NIST Research Reactor using both specular and off-specular scattering geometries. The former provides a measure of the vector magnetization profile as a function of depth if the in-plane domains are large ($\gtrsim$50–100 μm). Details of the in-plane magnetic order can be obtained from off-specular analysis. For both geometries, we measured all four spin cross sections, (++), (−−), (+−), and (−+), as a function of field applied in-plane. (The + and − signs designate the parallel and antiparallel polarizations, respectively, of the incident and scattered neutrons relative to the applied field.) The (++) and (−−) non-spin-flip data are sensitive to both the nuclear and magnetic structures, their difference being related to the in-plane component of the magnetization parallel to the applied field. The (+−) and (−+) spin-flip data sense only the component of the magnetization perpendicular to the field.

We measured the specular reflectivity of the 335 °C annealed multilayer at its coercive field value of −4 Oe to probe the spin structure of the demagnetized state. The scans show *no* magnetic scattering at either the half-order or first-order superlattice peak position that would be characteristic of a net antiferromagnetic or ferromagnetic alignment, respectively, of the $Ni_{80}Fe_{20}$ interlayers.[5] The data for the as-deposited sample in a field of 0.6 Oe are similar. These featureless data imply that the ferromagnetic $Ni_{80}Fe_{20}$ layers order in discrete in-plane domains smaller than the coherence length of the incident neutrons (50–100 μm).

A picture of the magnetic structure emerges from transverse (Q_x) scans for the 335 °C annealed and as-deposited multilayers at Q_z values corresponding to the nominal half-order and first-order superlattice peak positions. Each sample was first studied in a saturation field of H=250 Oe and then in applied fields near their coercive values (−3.2 and −0.3 Oe, respectively), where the magnetoresistance is maximum. The data in Figs. 2(a)–2(d) are the difference between the low- and high-field spin-flip results, corrected for polarization efficiencies. A broad diffuse peak at Q_x=0.0 Å^{-1} is seen at half-order [Fig. 2(a)] for the 335 °C annealed multilayer, while the corresponding scan at first order [Fig. 2(b)] is flat. These data imply that the GMR arises from the formation of small, ferromagnetic $Ni_{80}Fe_{20}$ domains within the sample plane. That the scattering appears only at half-order suggests that some portion of these domains is antiferromagnetically coupled along the growth-axis direction. The remaining spins align either in in-plane domains that are uncorrelated from one bilayer to the next or in in-plane domains smaller than our detection limit ($\approx$ 1000 Å). From the full width at half-maximum of the diffuse spin-flip peak [Fig. 2(a)], we estimate an in-plane domain size of 1–5 μm, which is the same order of magnitude as the structural correlation length ξ obtained with x rays.

In contrast, the spin-flip-scan at the half-order position for the as-deposited multilayer shows no significant scattering when the field is lowered to its coercive value [Fig. 2(c)]. The corresponding data at the first-order position deviate slightly from background near the scan center [Fig. 2(d)], probably due to leakage of non-spin-flip scattering. Clearly, the low-field magnetic structure of the as-deposited multilayer is different from that of the 335 °C annealed sample.

Both the bulk magnetization[4] and PNR data for the as-deposited multilayer indicate that the coupling between the $Ni_{80}Fe_{20}$ layers is ferromagnetic. This coupling may be intrinsic or may result from the presence of $Ni_{80}Fe_{20}$ "pinholes" which connect the Ag layers.[9] (Such a structure is

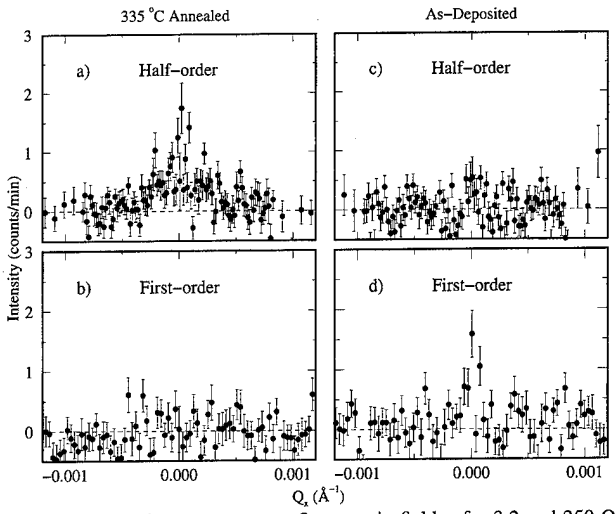


FIG. 2. Difference between neutron Q_x scans in fields of -3.2 and 250 Oe for the 335 °C annealed multilayer (a) half-order (Q_z=0.048 Å^{-1}) and (b) first-order (Q_z=0.091 Å^{-1}). The difference between scans in fields of -0.3 and 250 Oe for the as-deposited multilayer are shown in (c) at half-order (Q_z=0.052 Å^{-1}) and (d) at first-order (Q_z=0.099 Å^{-1}). The data represent an addition of the $(+-)$ and $(-+)$ cross sections.

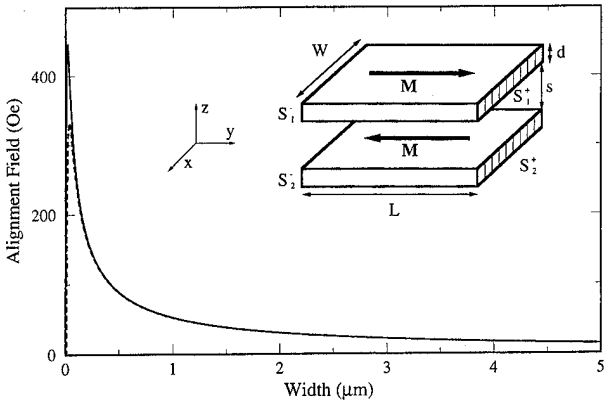


FIG. 3. Field $2H_c$ required to align blocks of spins calculated as a function of the in-plane domain width $W=L$. The dashed line represents the same calculation performed in the approximated case of $d,s \ll W,L$, as described in Ref. 6. The inset shows a schematic of the geometry used for these calculations.

difficult to detect using x-ray-diffraction techniques.) In addition to forming Ag bridges spanning the magnetic layers, the annealing process could also act to reduce the population of pinholes in the Ag layer. Theoretical descriptions[10] of such a system predict that the spin structure will change from ferromagnetic to antiferromagnetic as the defect density is decreased. This explanation of the magnetic changes is unlikely for our samples because it does not account for the emergence of micrometer-order, magnetic domains within the $Ni_{80}Fe_{20}$ layers.

In related discussions of these materials,[4,7] it was instead suggested that the formation of in-plane domains increases the strength of the dipolar coupling between neighboring magnetic layers relative to competing ferromagnetic interactions. We have calculated[5] the field required to overcome the dipolar force between two blocks separated by a distance s with antiparallel magnetization $\mathbf{M}$, as drawn in the inset of Fig. 3. Only the contributions of the magnetic flux from the ends of the block are significant for this configuration.

We consider blocks of equal height d, width W, and length L, though the expression can easily be generalized for other geometries. Integrating over the slab dimensions, we derive a general expression for the energy difference between the parallel and antiparallel configurations,

$$E_{\mathrm{diff}}=M^2\sum_{\alpha,\beta=1}^{4}\sum_{\delta,\gamma=1}^{2}\sigma_\delta\sigma_\gamma\Big\{|R_{\alpha,\beta,\delta,\gamma}|[\tfrac{1}{2}\epsilon_\beta X_\alpha^2+\tfrac{1}{2}\epsilon_\alpha Z_\beta \acute{Z}_\beta+\tfrac{1}{3}\epsilon_\alpha\epsilon_\beta R^2_{\alpha,\beta,\delta,\gamma}]+[X_\alpha^2\acute{Z}_\beta+\tfrac{1}{2}\epsilon_\alpha\acute{Z}_\beta(X_\alpha^2+Y^2_{\delta,\gamma})]\ln(|R_{\alpha,\beta,\delta,\gamma}|+Z_\beta)+[X_\alpha Z_\beta\acute{Z}_\beta+\tfrac{1}{2}\epsilon_\beta X_\alpha(Z_\beta^2+Y^2_{\delta,\gamma})]\ln(|R_{\alpha,\beta,\delta,\gamma}|+X_\alpha)-X_\alpha\acute{Z}_\beta|Y_{\delta,\gamma}|\tan^{-1}\left(\frac{X_\alpha Z_\beta}{|Y_{\delta,\gamma}||R_{\alpha,\beta,\delta,\gamma}|}\right)\Big\},\qquad(1)$$

where $\boldsymbol{\epsilon}=(-1,1,1,-1)$, $\boldsymbol{\sigma}=(1,-1)$, $\mathbf{X}=(-W,0,0,W)$, $Y_{\delta,\gamma}=(\sigma_\delta-\sigma_\gamma)L/2$, $\mathbf{Z}=(s,d+s,d+s,2d+s)$, $\acute{\mathbf{Z}}=(s,-d-s,-d-s,2d+s)$, and $R^2_{\alpha,\beta,\delta,\gamma}=X^2_\alpha+Y^2_{\delta,\gamma}+Z^2_\beta$. The field required to align the moments is $H_c=E_{\mathrm{diff}}/2MWLd$.

$2H_c$ is plotted as a function of W in Fig. 3 for $d=20$ Å, $d+s=60$ Å, and $M=760$ emu/cm^3. (The alignment field is multiplied by two because each layer couples to two adjacent layers.) The field decreases gradually with increasing domain width W. For $W\approx1.1$ μm, we calculate $2H_c=50$ Oe, which roughly matches the saturation field measured for the 335 °C annealed multilayer. The magnitude of the magnetostatic interactions among the 1–5 μm magnetic domains is thus of the same order as that of the antiferromagnetic coupling.

By design, the complex structure of annealed $Ni_{80}Fe_{20}$/Ag multilayers leads to low-field magnetic properties desirable for the fabrication of magnetic thin-film sensors. Using specular and off-specular PNR, we can directly probe the magnitude and direction of the magnetic moment as a function of depth and extract general features of the magnetic structure within the sample plane. We find that the in-plane magnetization of the $Ni_{80}Fe_{20}$ layers order in micrometer-sized domains after annealing and that antiferromagnetic correlations among these magnetic layers are responsible for the anomalous magnetoresistance in annealed multilayers.

[1] M. N. Baibich, J. M. Broto, A. Fert, F. Nguyen Van Dau, F. Petroff, P. Eitenne, G. Creuzet, A. Friederich, and J. Chazelas, Phys. Rev. Lett. **61**, 2472 (1988).

[2] A. Barthélémy, A. Fert, M. N. Baibich, S. Hadjoudj, F. Petroff, P. Etienne, R. Cabanel, S. Lequien, F. Nguyen Van Dau, and G. Creuzet, J. Appl. Phys. **67**, 5908 (1990).

[3] S. S. P. Parkin, A. Mansour, and G. P. Felcher, Appl. Phys. Lett. **58**, 1473 (1991).

[4] T. L. Hylton, K. R. Coffey, M. A. Parker, and J. K. Howard, Science **261**, 1021 (1993); J. Appl. Phys. **75**, 7058 (1994).

[5] J. A. Borchers, P. M. Gehring, C. F. Majkrzak, J. F. Ankner, T. L. Hylton, K. R. Coffey, M. A. Parker, and J. K. Howard, Mater. Res. Soc. Symp. Proc. **376**, 577 (1995); J. A. Borchers *et al.* (unpublished).

[6] M. A. Parker, T. L. Hylton, K. R. Coffey, and J. K. Howard, J. Appl. Phys. **75**, 6382 (1994).

[7] J. C. Slonczewski, J. Magn. Magn. Mater. **129**, L123 (1994).

[8] R. F. C. Farrow, R. F. Marks, T. A. Rabedeau, M. F. Toney, D. Dobbertin, R. Beyers, and S. S. P. Parkin, J. Appl. Phys. **76**, 3688 (1994).

[9] B. Dieny, V. S. Speriosu, S. Metin, S. S. P. Parkin, B. A. Gurney, P. Baumgart, and D. R. Wilhoit, J. Appl. Phys. **69**, 4774 (1991).

[10] J. F. Bobo, H. Fisher, and M. Piecuch, Mater. Res. Soc. Symp. Proc. **313**, 467 (1993).

Magnetization, magnetoresistance, and x-ray diffraction measurements of discontinuous [$Ni_{80}Fe_{20}$/Ag] multilayers (abstract)

T. Lorenz, M. Moske, A. Käufler, H. Geisler, and K. Samwer
Universität Augsburg, Memminger Str. 6, D-86135 Augsburg, Germany

Thin films for magnetic sensor application require a high sensitivity at low magnetic fields, for example, realized by Permalloy films. Promising candidates for a further improvement are discontinuous multilayers, first reported by Hylton *et al.*[1] In our study, we report on [2.5 nm $Ni_{80}Fe_{20}$/*y* nm Ag] multilayers with the spacer layer thickness *y* ranging from 1.2 nm to 6.0 nm. The multilayers were electron beam deposited in UHV at different temperatures. The substrates used are thermally oxidized silicon wafers. The magnetization is obtained using a vibrating sample magnetometer (VSM), the magnetoresistance is measured at room temperature with the Montgomery method. Low and high angle x-ray diffraction measurements are performed in a Siemens D-5000 diffractometer. The samples are annealed *ex situ* between room temperature and 340 °C. The magnetoresistance is maximal after annealing the samples at a specific temperature, which decreases with increasing Ag-spacer thickness *y*. Moreover, the GMR decreases if the multilayers are deposited at elevated temperatures (100–200 °C). We also report on the dependence of the GMR on the interface roughness ($\sigma \approx 0.5$ nm rms) which we deduce from the small angle x-ray diffraction measurements. For a characterization of the reliability, we also investigated the dependence of the GMR on aging at 100 °C for several hours. © *1996 American Institute of Physics.* [S0021-8979(96)59908-1]

Supported by the BMBF, Förderkennzeichen 13N6174.

[1] T. L. Hylton, K. R. Coffey, M. A. Parker, and J. K. Howard, Science **261**, 1021 (1993).

Exchange coupling in sputtered giant magnetoresistance NiFe/Cu/CoFe/Cu multilayers

M. T. Kief, J. Bresowar, and Q. Leng
Department of Physics, MINT, Box 870209, University of Alabama, Tuscaloosa, Alabama 35487-0209

We will report on the exchange coupling, magnetoresistance (MR) and film structure in the system NiFe/Cu/CoFe/Cu as a function of multilayer number (bilayers=6 to 20) and Cu spacing (5 to 31 Å). The multilayers were prepared by sputter deposition and investigated by x-ray diffraction (XRD), atomic force microscopy (AFM), vibrating sample magnetometry (VSM), ferromagnetic resonance (FMR), and standard MR methods. The exchange coupling, H_{ex}, and MR are shown to vary with Cu spacing. The XRD data indicates the multilayer structure is evolving through at least the first 20 bilayers. AFM measurements suggest subtle variations in interface quality and a rms roughness near 0.4 nm. These variations in structure are manifested in the FMR and MR. Multilayers with Cu spacers >11 Å generally show the expected two FMR peaks. Some multilayers show three peaks indicating defects within the multilayer. These defects can be viewed as the elusive "pinholes" which act to ferromagnetically short the magnetic layers together. This demonstrates that FMR provides very valuable information about defects in nonideal multilayers which is critical to our understanding and applications of giant magnetoresistance (GMR) systems. © *1996 American Institute of Physics.* [S0021-8979(96)79208-9]

MOTIVATION

Giant magnetoresistance (GMR) in multilayer systems requires that the magnetization in the magnetic layers alternate in different directions. Since the change in resistance varies as the $\cos(\theta)$, where θ is the relative angle between the magnetizations in alternate layers, the more closely the magnetizations orient antiparallel for zero applied field, the greater the magnitude of the GMR will be. The most common method to obtain this alternating variation in magnetization directions relies upon the oscillatory exchange coupling known to exist in such structures. It is often observed that changing the growth conditions can significantly alter the oscillatory coupling and thereby effect the GMR. It is commonly assumed that changes in multilayer microstructure such as surface roughness, interface mixing and thickness nonuniformity are responsible for the changes. However, the effect of these microstructures is not necessarily bad. For example, multilayers grown by sputtering often exhibit a decreased exchange coupling strength when compared to molecular beam epitaxy (MBE) prepared multilayers. For many applications (such as magnetic recording heads), a weak exchange coupling is very desirable. For this and many other reasons sputtering is often the method of choice.

Perhaps the most pervasive problem in all multilayers are defects which act to disrupt the desired antiparallel orientation. These defects, of various origins, are often called "pinholes" since they act as effective magnetic short circuits between alternate magnetic layers causing them to be pinned together due to strong ferromagnetic coupling. Although these "pinholes" are often blamed for poor results, it has been very difficult to verify the existence of them buried well within a multilayer and, in addition, to quantify their effects. In fact, the only direct observation that these authors are aware of is in simple magnetic sandwiches studied by Kerr microscopy.[1] There is a clear need to understand the role of microstructural nonidealities upon the exchange coupling in genuine multilayers and without requiring special sample preparation.

In this article we will report a study of exchange coupling in a GMR multilayer system prepared by sputter deposition. The purpose of this investigation has been to better understand these phenomena in multilayers with less than ideal microstructures. We hope that this system will serve a prototype of many others.

EXPERIMENTAL APPROACH

In order to understand the effect of structure upon the exchange coupling and the GMR it was necessary to devise a method to quantify these properties as well as the structure of the multilayer film itself. A direct measurement of the exchange coupling strength in both the ferromagnetic and antiferromagnetic coupling states is provided by ferromagnetic resonance (FMR). This technique has been employed by a few groups to determine the exchange coupling strength in MBE prepared trilayers[2–4] and sputter prepared trilayers.[5,6] A principle requirement to permit the determination of the coupling strength is that the magnetic layers must be magnetically distinct in order to break the degeneracy and permit the observation of both the acoustic and optical modes which occur at different applied magnetic fields. It is the separation of these modes which is related to the interlayer exchange coupling strength. A detailed discussion of the FMR technique and analysis will be published elsewhere.[7]

For the above reasons, we decided to investigate the system NiFe/Cu/CoFe/Cu. The target compositions were $Ni_{80}Fe_{20}$, Cu, and $Co_{90}Fe_{10}$. Since the saturation magnetization of $Co_{90}Fe_{10}$ is roughly twice that of $Ni_{80}Fe_{20}$, this assures a nondegenerate system for FMR characterization. FMR measurements were conducted on a homemade system at a Q-band frequency of 34.5 GHz.

The multilayer films were sequentially prepared by computer control of our Vac-Tec sputter system. The system base

 0021-8979/96/79(8)/4766/3/$10.00 © 1996 American Institute of Physics

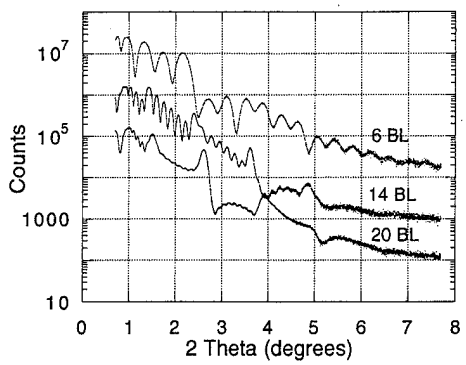


FIG. 1. Low-angle x-ray two-theta diffraction scans for 6, 14, and 20 BL with a Cu spacer layer thickness of 25 Å. Decreasing amplitude of the superlattice peaks indicates a loss of coherency with increasing BL number.

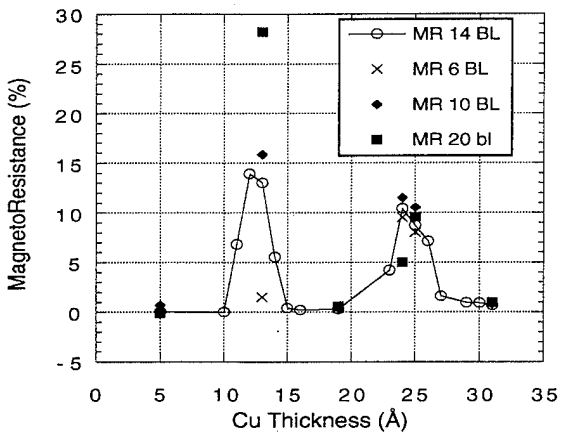


FIG. 2. Magnetoresistance for varying Cu spacer layer thicknesses and BL number. The two peaks near 13 and 25 Å indicate antiferromagnetic interlayer exchange coupling.

pressure is typically 2.0×10^{-7} mTorr. All films were deposited by dc (Cu) or dc-magnetron (NiFe, CoFe) sputtering at a pressure of 2.5×10^{-3} mTorr at ambient temperatures with deposition rates near 6 Å/s. All films were deposited upon Corning Glass #7059 glass substrates.

It is expected that the structure of the multilayers will depend upon the film thicknesses and the number of layers in the multilayer. In order to investigate the effects of the changing structure, we prepared sets of samples with varying Cu thickness (5 to 31 Å) and different layer number [6, 10, 14, and 20 magnetic/nonmagnetic bilayers (BL)]. The magnetic layer thicknesses were fixed at 15 Å, which was found to provide satisfactory results. (Other combinations were also investigated, but are not presented here.[7])

The structure of the films were characterized with low-angle and high-angle x-ray diffraction (XRD) and atomic force microscopy (AFM). The GMR was measured using the standard linear 4-point probe method. Vibrating sample magnetometry (VSM) and FMR were used to measure the magnetic properties.

RESULTS AND DISCUSSION

Figure 1 shows low angle XRD scans for 6, 14, and 20 BL with a Cu spacer thickness of 25 Å. The decreasing amplitude of the short period superlattice peaks indicates that the layering of the multilayers actually degrades with increasing multilayer number. A similar trend appears for other Cu thicknesses as well. Qualitatively these data suggest a loss of vertical coherency of the superlattice with increasing BL. Using the first and second Bragg peaks we estimate the BL period to be 36.5±1 Å, which is within 10% of the expected 40 Å period.

High angle XRD scans were also measured (not shown). All the multilayers are polycrystalline and show a ⟨111⟩ texture which sharpens with increasing BL number and increasing Cu thickness. The grain size is estimated by the Scherrer formula to be near 100 Å for the 14 BL multilayers. The position of the peak indicates the multilayer lattice spacing is between the bulk Cu and bulk Ni spacing.

AFM in air was used to investigate the surface topology and roughness of the multilayers. No significant trend was found with changing Cu thickness and BL number. However, for all samples measured a 1×1 μm scan had a typical roughness estimated to be 0.3 to 0.4 nm rms and 2 nm peak-to-peak. If we compare these values with the average film thickness (1 to 3 nm), it is conceivable that the interface roughness may have a significant influence upon the exchange coupling.

In summary, these GMR multilayers are polycrystalline with a small grain size and relatively rough interfaces, but probably not unlike many other sputter prepared multilayers. Further structural studies are currently underway.

The magnetoresistance as a function of Cu spacer thickness and BL number is shown in Fig. 2. Two peaks are observed near 13 and 24 Å of Cu in the 14 BL samples where the interlayer exchange coupling is expected to be antiferromagnetic. These thicknesses (13, 24 Å) and 5, 19, 25, and 31 Å are also shown for 6, 10, and 20 BL. In general, the MR at 6, 10, and 20 BL appears to follow the 14 BL curve but no simple trend with BL number can be confirmed. In particular note that the 14 BL data lies below both the 10 and 20 BL data at 13 Å of Cu. No known difference in preparation can account for this unexpected result other than the fact that the 14 BL samples were prepared first. The most likely cause is unknown impurities or background contamination which alter the microstructure, although none have been detected prior to this study. We will show below that the FMR results are consistent with this interpretation.

Figure 3 shows the FMR absorption signal for BLs having 25 Å Cu spacers. All these samples show two peaks except the 14 BL sample which shows three peaks. The low field peak (6500 Oe) and the high field peak (9000 Oe) may be thought of as the CoFe and NiFe uniform mode absorption signals, respectively. Strictly speaking, they correspond to the acoustic and optical modes of the system. The middle peak observed for the 14 BL sample it believed to be a third magnetic phase which we will discuss below. The shift in peak field position with BL number indicates a systematic decrease in the magnetic moment of the layers. This is consistent with the low-angle XRD data that indicates an increase in layer roughness with BL number.

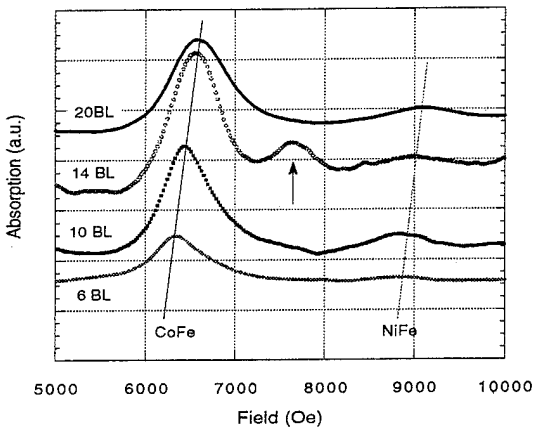


FIG. 3. Ferromagnetic resonance absorption spectra for 6, 10, 14, and 20 BL with a Cu spacer of 25 Å. Peaks near 6500 and 9000 Oe essentially correspond to absorption from the CoFe and NiFe layers, respectively. The separation of the peaks is due to the intrinsic difference in M_{sat} for the layers and the interlayer exchange coupling. The central peak indicated by an arrow for the 14 BL sample suggests absorption from a magnetic defect or "pinhole" (see text for discussion).

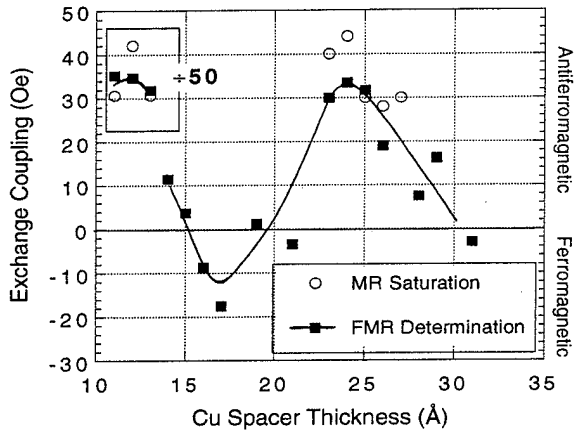


FIG. 4. The exchange coupling field determined by FMR and the saturation field of the MR is plotted versus Cu spacer layer thickness for 14 BL. The line is a guide to the eye following the FMR data. An oscillatory coupling is indicated with antiferromagnetic peaks near 13 and 25 Å, which is consistent with measured MR (Fig. 2). Note the 50-fold decrease in exchange coupling strength from 13 to 25 Å.

The separation of the FMR peaks, ΔH, is due to the difference in the effective saturation magnetization, M_{sat}, and the effective interlayer exchange coupling, J. Other studies have shown that for systems with nearly identical M_{sat}, $\Delta H=4J$.[2,3] In our system we must also account for the large differences in M_{sat} which produces a large intrinsic peak separation, $\Delta H_{intrinsic}$. $\Delta H_{intrinsic}$ was determined to have a value of 2300 Oe from separate experiments using 120 Å Cu spacers. Therefore, we can approximately relate the measured peak separation $\Delta H = \Delta H_{intrinsic} + 4J$.

Using this relation we can determine the interlayer exchange coupling in the multilayers directly. Figure 4 shows a plot of the exchange coupling versus Cu spacer thickness for 14 BL. In addition, we also show the saturation field determined from the MR profile for antiferromagnetically coupled multilayers. The agreement is good, especially considering the weak fields involved.

We now return to discussion of the middle FMR peak shown in 14 BL data of Fig. 3. It should be emphasized that this peak appears to be more the exception than the rule. Most of the samples do not show this peak. When the exchange coupling is small, as at 25 Å of Cu, the peak field position at which the absorption occurs is largely determined by the M_{sat} of the material. Therefore, the middle peak must arise from a component whose effective M_{sat} is approximately half way between CoFe and NiFe. We conclude that the middle peak should be assigned to a component acting as a strong ferromagnetically coupled or essentially alloyed CoFe/NiFe phase. This most likely arises from a "pinhole" in the Cu spacer layer which causes neighboring NiFe and CoFe layers to "short" together, disrupt the desired antiferromagnetic multilayer alignment and reduce the GMR. Numerical calculations of FMR absorption peaks also support this proposed interpretation.[7] Furthermore, the occurrence of these "pinholes" is not inconsistent with the multilayer structure and interface roughness as discussed above.

CONCLUSIONS

The structure of sputtered GMR multilayers evolves with BL number and Cu thickness. The MR varies with the microstructure and appears sensitive to subtle structural changes which are very difficult to observe by most methods. FMR is a simple and direct method to determine coupling strength and is consistent with MR estimates. FMR permits the measurement of local defects such as pinholes which have a significant effect upon the exchange coupling and MR in these structures. More work is needed to determine the origin of the defects.

ACKNOWLEDGMENT

This work was supported by the NSF-MRSEC Program under DMR-9400399.

[1] R. Schäfer, Proceedings of the 14th International Colloq. on Magnetic Films and Surfaces, Düsseldorf, Germany, 29 August–2 September 1994 (unpublished).
[2] B. Heinrich, S. T. Purcel, J. R. Dutcher, K. B. Urquhart, J. F. Cochran, and A. S. Arrott, Phys. Rev. B **38**, 12 879 (1988); B. Heinrich, Z. Celinski, J. F. Cochran, A. S. Arrott, K. Myrtle, and S. T. Purcell, *ibid.* **47**, 5077 (1993).
[3] J. J. Krebs, P. Lubitz, A. Chaiken, and G. A. Prinz, Phys. Rev. Lett. **63**, 1645 (1989); J. J. Krebs, P. Lubitz, A. Chaiken, and G. A. Prinz, J. Appl. Phys. **67**, 5920 (1990).
[4] Z. Zhang, L. Zhou, P. E. Wigen, and K. Ounadjela, Phys. Rev. B **50**, 6094 (1994).
[5] A. Layadi, J. O. Artman, B. O. Hall, R. A. Hoffman, C. L. Jensen, D. J. Chakrabarti, and D. A. Sanders, J. Appl. Phys. **64**, 5760 (1988); A. Layadi and J. O. Artman, J. Magn. Magn. Mater. **92**, 143 (1990).
[6] M. Pomerantz, J. C. Slonczewski, and E. Spiller, J. Magn. Magn. Mater. **54**, 781 (1986).
[7] Q. Leng, J. Bresowar, and M. T. Kief (to be published).

Spin polarized neutron scattering study of NiCo/Cu multilayers

Ming Mao, S. H. Nguyen, and B. D. Gaulin
Department of Physics and Astronomy, McMaster University, Hamilton, Ontario L8S 4M1, Canada

Z. Tun
AECL Research, Chalk River Laboratories, Chalk River, Ontario K0J 1J0, Canada

X. Bian, Z. Altounian, and J. O. Ström-Olsen
Center for the Physics of Materials and Department of Physics, McGill University, Montréal, Québec H3A 2T8, Canada

Spin polarized neutron reflectometry measurements were performed on $Ni_{80}Co_{20}$/Cu multilayers with a Cu spacer thickness of 20 Å, corresponding to the second oscillation peak in the magnetoresistance of the NiCo/Cu multilayer system. Measurements in a 15 Oe field indicate a nearly perfect antiferromagnetic stacking of the magnetic moments in successive $Ni_{80}Co_{20}$ layers. The existence of a small magnetic anisotropy in these magnetically soft multilayers leads to the canting of the magnetic moments at an angle of ~70° with respect to the neutron spin polarization. This interlayer antiferromagnetic coupling can be suppressed by an applied field of ~200 Oe.
© *1996 American Institute of Physics.* [S0021-8979(96)51108-8]

INTRODUCTION

Giant magnetic resistance (GMR) in magnetic multilayers is strongly correlated to magnetic ordering within the multilayers as the latter determines the nature of the spin dependent electron scattering. The magnetic order in the magnetic multilayer is maintained via RKKY-type exchange coupling[1] between adjacent magnetic layers across the nonmagnetic spacer thickness. The oscillatory behavior of GMR with increasing nonmagnetic spacer thickness results from an associated change in the exchange coupling from ferromagnetic (FM) to antiferromagnetic (AF).[2] $Ni_{80}Co_{20}$/Cu multilayers show a low-field GMR (~1%/Oe) (Ref. 3) at a regime where the magnetic exchange coupling between adjacent magnetic layers is assumed to be relatively weak. In this case, the magnetic anisotropy, which may arise from either substrate clamping or interface strains, could play an important role in determining the magnetic structure. The magnetic moments in neighboring magnetic layers could be oriented at 90° to each other, or even display random relative orientations. Understanding the low-field GMR in the NiCo/Cu system requires a detailed knowledge about its magnetic structure. Spin polarized neutron reflectometry has proved to be a powerful tool for this purpose.[4] It measures not only the nuclear and the magnetic scattering length profiles along the film growth direction but also provides information about the orientation profile of the average magnetization within the individual layers by distinguishing between two scattering processes. The nonspin-flip (NSF) scattering process probes the depth profile of the nuclear structure and the component of magnetic moment along the neutron spin polarization, while the spin-flip (SF) scattering process is solely attributed to the component of magnetic moment in the scattering plane.

EXPERIMENTAL TECHNIQUES

NiCo/Cu multilayers of structure Si/($Ni_{80}Co_{20}$)50 Å [Cu20 Å/($Ni_{80}Co_{20}$)15 Å]$_n$ with bilayer repeat n=12, 60 were prepared by dc magnetron sputtering at McGill University. The deposition of a 50 Å $Ni_{80}Co_{20}$ buffer layer was expected to improve the structural perfection and to reduce the in-plane magnetic anisotropy.

Spin polarized neutron reflectometry measurements were carried out on the C5 triple-axis spectrometer at AECL, Chalk River Laboratories. The (111) Bragg reflection of a Cu_2MnAl Heusler single crystal selected a narrow band ($\Delta\lambda$ =0.03 Å) of incident neutrons with a wavelength of 2.3705 Å and down-spin polarization **P**. A PG filter was placed at the incident side of the sample to eliminate the higher order contamination. The monochromated neutron beam was highly collimated, giving rising to an angular divergence of full width at half-maximum ~0.02° at the sample. A second identical Heusler crystal was used to analyze the energy and polarization of scattered neutrons. The beam path was covered with permanent magnets, serving as the guide field, **H**, to prevent the neutron spin from depolarizing. The guide field at the sample position was 15 Oe. When used as an applied field, the magnitude of the guide field at the sample position could be increased to a level as high as 250 Oe. Two Mezei-type[5] neutron spin flippers were installed in front of and after the sample in order to separate the NSF and SF scattering processes. The multilayer sample was first saturated under a magnetic field of 250 Oe before measurements were taken. The scattering intensities were measured in the usual θ–2θ mode with the multilayer surface normal bisecting the incident and scattered wavevectors. Diffuse scattering underneath the specular ridge was measured by $(\theta-\delta\theta)$–2θ scans with a small offset in θ.

RESULTS AND DISCUSSION

The specular reflectivities for NSF (R^{++},R^{--}) and SF (R^{+-},R^{-+}) channels were extracted from the measured scattering intensities after the corrections from nonspecular contributions, finite sample size, polarization and spin-flipping efficiencies.[6] Details will be described in a later publication. The reflectivities at 15 Oe field are shown in Fig. 1, where the two SF reflectivities, which are identical, have been added together to improve the statistics. While the data

 0021-8979/96/79(8)/4769/3/$10.00 © 1996 American Institute of Physics

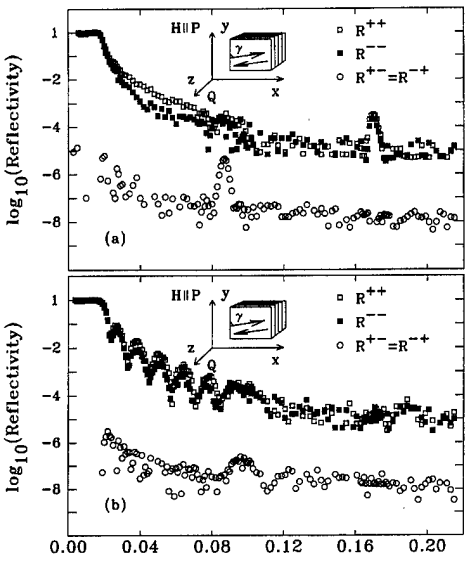


FIG. 1. Specular reflectivity for NSF (R^{++},R^{--}) and SF (R^{+-},R^{-+}) scattering processes at 15 Oe field for two $[(Ni_{80}Co_{20})15$ Å/Cu20 Å$]_n$ multilayers: (a) $n=60$, (b) $n=12$. The two SF reflectivities have been added and translated downwards by three orders of magnitude. The inset illustrates an antiferromagnetic stacking of magnetic moments (antiparallel arrows) in adjacent NiCo/Cu layers, which orient at an angle, γ, to y-axis, and the scattering geometry with the wavevector transfer, Q, lying within the xz plane and parallel to the z-axis.

for the 12 repeat sample clearly shows an oscillatory nature to the scattering due to interference between the scattering from the two interfaces of the multilayer of finite thickness, the data for the 60 repeat sample exhibits pronounced scattering peaks, characterizing the multilayer superlattice structure. The following discussion will therefore be focussed on the 60 repeat sample.

The NSF data, R^{++} and R^{--}, at 15 Oe field show total external reflection at $Q_c=0.017$ Å^{-1} and a Bragg reflection at $Q_B=0.17$ Å^{-1}, which corresponds to the bilayer periodicity of the multilayer, $\Lambda=d_{NiCo}+d_{Cu}$, 37 Å which is 2 Å larger than the nominal value. The total external reflection occurs at the same wave vector and the Bragg reflection shows the same intensity for the two NSF reflectivities. This indicates the absence of a ferromagnetic interlayer alignment for the 15 Oe applied field. Significant differences between the two NSF reflectivities, however, can be seen in the wave vector region, $Q\sim0.06$–0.08 Å, which may be ascribed to either the presence of an ~40 Å ferromagnetically ordered $Ni_{80}Co_{20}O_x$ oxide overlayer or most probably a few ferromagnetically coupled $Ni_{80}Co_{20}$ layers near the film surface. Further quantitative analysis on this phenomenon is in progress.

The SF data for the 15 Oe applied field do not show total external reflection. The reflectivity peaks at $Q=0.087$ Å^{-1} ($\sim Q_B/2$), indicating the existence of a periodic structure with twice the periodicity of the bilayer thickness in the multilayer. The fact that SF data are only sensitive to the component of magnetic moment, μ_x, within the scattering plane indicates an AF stacking of this component along the growth direction. An estimate from the preliminary model

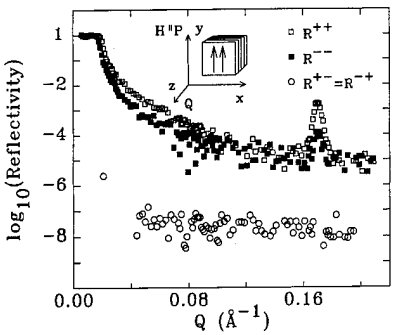


FIG. 2. Specular reflectivity for NSF (R^{++},R^{--}) and SF (R^{+-},R^{-+}) scattering processes at 230 Oe field for the 60 repeat sample. The inset shows that the magnetic moments (parallel arrows) in adjacent NiCo/Cu layers order ferromagnetically.

calculation gives a value of $\mu_x=(0.71\pm0.10)\mu_B$ per atom. Furthermore, the absence of Bragg scattering at Q_B is also indicative of zero net ferromagnetic order within the scattering plane at the 15 Oe field.

In addition to these major features, a very weak peak can also be seen at $Q_B/2$ on the NSF data. The periodicity and the weakness of this scattering implies that an AF alignment of a small component of magnetic moment (μ_y) along the neutron polarization direction (estimated at $0.25\mu_B$ per atom) exists. This can be attributed to the existence of a very weak magnetic anisotropy in the multilayers, which favors the alignment of the magnetic moments in adjacent $Ni_{80}Co_{20}$ layers at an angle of $\gamma\sim70°$ to the y-axis, as demonstrated by the inset in Fig. 1.

Upon increasing the guide field at the sample to 230 Oe, the most pronounced feature observed on the reflectivities is the disappearance of the half order peaks on all four scattering cross sections, as shown in Fig. 2. No scattering contribution from the SF process is seen within the background level. The critical wave vector for the total external reflection splits for the two NSF reflectivities as does the Bragg scattering intensity at Q_B. This indicates that the AF order has been destroyed at a field of 230 Oe. FM order forms as the applied field forces the magnetic domains to align along the field direction. Constructive and destructive interference between the nuclear and the magnetic Bragg scattering from a FM ordered interlayer structure gives rise to the asymmetry for the NSF data. The difference of the scattering intensity for the NSF data in the wavevector region from 0.06 to 0.08 Å^{-1}, as noticed above from the 15 Oe field data, remains unchanged at the 230 Oe field, confirming its ferromagnetic origin.

CONCLUSIONS

The low-field $Ni_{80}Co_{20}$/Cu multilayers at the chosen Cu spacer thickness of 20 Å possess a nearly perfect antiferromagnetic order along the film growth direction at a 15 Oe applied magnetic field. The total magnetic moment of the $Ni_{80}Co_{20}$ layer has been estimated to be $0.75\mu_B$ per atom, close to its bulk value of $0.82\mu_B$ per atom. The existence of a small magnetic anisotropy causes the magnetic moment to align along a direction of ~70° with respect to the neutron spin polarization.

The transition of the AF order to FM order is seen to be complete by a field of 230 Oe. It is expected that the ongoing neutron and x-ray scattering analysis will give more detailed information about the spatial distribution and coherency of the magnetic structure in $Ni_{80}Co_{20}$/Cu magnetic multilayers and shed more light on the complexity of the NSF data in the wavevector region from 0.06 to 0.08 $Å^{-1}$.

ACKNOWLEDGMENTS

We thank Dr. John F. Ankner for helpful discussions and AECL Chalk River Laboratories for providing facilities. We also acknowledge the financial support from the Natural Sciences and Engineering Research Council of Canada, Fonds FCAR du Québec and the Ontario Center for Materials Research.

[1] P. Bruno and C. Chappert, Phys. Rev. B **46**, 261 (1992).
[2] S. S. P. Parkin, N. More, and K. P. Roche, Phys. Rev. Lett. **64**, 2304 (1990).
[3] X. Bian, Ph.D Thesis, McGill University, Montreal, Canada, 1994.
[4] A. Schreyer, Th. Zeidler, Ch. Morawe, N. Metoki, H. Zabel, J. F. Ankner, and C. F. Majkrzak, J. Appl. Phys. **73**, 7616 (1993).
[5] O. Schäpf, *Neutron Spin Echo*, edited by F. Mezei (Springer, Berlin, 1980).
[6] C. F. Majkrzak, Handbook of Neutron Scattering, edited by W. Gläser (Springer, Berlin, in press).

Magnetic properties of epitaxial and polycrystalline Fe/Si multilayers

A. Chaiken and R. P. Michel
Materials Science and Technology Division, Lawrence Livermore National Laboratory, Livermore, California 94551

C. T. Wang
Department of Materials Science and Engineering, Stanford University, Palo Alto, California 94305

Fe/Si multilayers with antiferromagnetic interlayer coupling have been grown via ion-beam sputtering on both glass and single-crystal substrates. High-angle x-ray diffraction measurements show that both sets of films have narrow Fe peaks, implying a large crystallite size and crystalline iron silicide spacer layers. Low-angle x-ray diffraction measurements show that films grown on glass have rougher interfaces than those grown on single-crystal substrates. The multilayers grown on glass have a larger remanent magnetization than the multilayers grown on single-crystal substrates. The observation of magnetocrystalline anisotropy in hysteresis loops and (hkl) peaks in x-ray diffraction demonstrates that the films grown on MgO and Ge are epitaxial. The smaller remanent magnetization in Fe/Si multilayers with better layering suggests that the remanence is not an intrinsic property. © *1996 American Institute of Physics.* [S0021-8979(96)51208-4]

I. INTRODUCTION

The well-established picture of antiferromagnetic coupling in metal/metal multilayers would have to be extensively modified for coupling across insulating or semiconducting spacer layers, where the spacer does not possess a Fermi surface.[1,2] In particular the temperature dependence of the exchange coupling might be significantly different in ferromagnet/semiconductor multilayers where the exchange is mediated by thermally activated carriers.[1]

Unusual temperature-dependent magnetic properties have been reported for Fe/Si multilayers. For example, a large increase in the remanent magnetization has been observed at low temperature.[3] If the interlayer antiferromagnetic (AF) coupling increases with decreasing temperature, as in multilayers with metal spacers, one might expect the remanence instead to *decrease* at low temperature. Proper interpretation of the remanent magnetization in Fe/Si multilayers may therefore be important to understanding the origin of the interlayer coupling in this system. One way to explore the origin of the remanence is to compare films of different crystalline quality.

II. EXPERIMENTAL METHODS

The films used in this study were grown using ion-beam sputtering (IBS) in a chamber with a base pressure of 2×10^{-8} Torr. The deposition system is described in more detail elsewhere.[4] All samples used in this study were grown at a substrate temperature of 200 °C. All comparisons between films grown on glass and single-crystal substrates will be made on samples which were deposited *simultaneously* so as to eliminate any reproducibility issues.

The substrates used in this study were glass coverslips, MgO (001), Ge(001), and $Al_2O_3(11\bar{2}0)$. The MgO and Al_2O_3 substrates were cleaned according to a recipe reported by Farrow and co-workers.[5] The glass and Ge substrates were rinsed in solvents. All films are capped with a 200 Å Ge oxidation barrier. The magnetic and structural properties of the films are stable for at least one year.

III. STRUCTURAL CHARACTERIZATION

Figure 1 shows high-angle x-ray diffraction spectra for a purely (001)-oriented (Fe40 Å/Si14 Å)×60 multilayer grown on MgO(001) and a purely (011)-oriented multilayer grown simultaneously on glass. While multiple superlattice satellites are observed around the Fe(002) peak for the film grown on MgO, the film on glass has only one peak corresponding to (011)-textured growth. A single superlattice satellite is typically observed in multilayers on glass on the low-angle side in keeping with previous observations.[6] An estimate of the crystallite sizes in these films can be derived using the Scherrer formula. This analysis gives a coherence length of 165 Å for the film on glass and 188 Å for the film on MgO.

One possible explanation for the lack of satellite peaks in the film grown on glass might be different interference conditions in the (011) orientation. However, the diffraction spectrum of a (Fe40 Å/Si14 Å)×46 (011)-oriented multilayer grown on Al_2O_3 (not shown) has even stronger satellites than the (001)-oriented multilayers grown on MgO. The evidence therefore suggests that the presence of high-angle satellites in the film on MgO must be due to better layering, not better crystallinity or orientation. The small-angle x-ray scattering data shown in Fig. 2 confirm this hypothesis. The multilayer on MgO has four low-angle peaks, indicating a moderate degree of composition modulation. The multilayer on glass shows only two relatively broad peaks, indicating larger interfacial roughness and less order in the layering. The low-angle x-ray spectra are consistent with rocking curves which are only about 1° wide for films grown on MgO and Al_2O_3 but are typically 10° to 15° wide for films on glass. The bilayer periods determined from the low-angle peak positions are (41.0±0.1) Å for the MgO film and (40.9±0.2) Å for the glass film, the same within experimental error.

ϕ scans of the MgO and Fe [110] peaks for the film on the MgO substrate (not shown) demonstrate that it is oriented in-plane. While θ–2θ scans for (011)-oriented multilayers grown on Al_2O_3 substrates (not shown) also show multiple

 0021-8979/96/79(8)/4772/3/$10.00 © 1996 American Institute of Physics

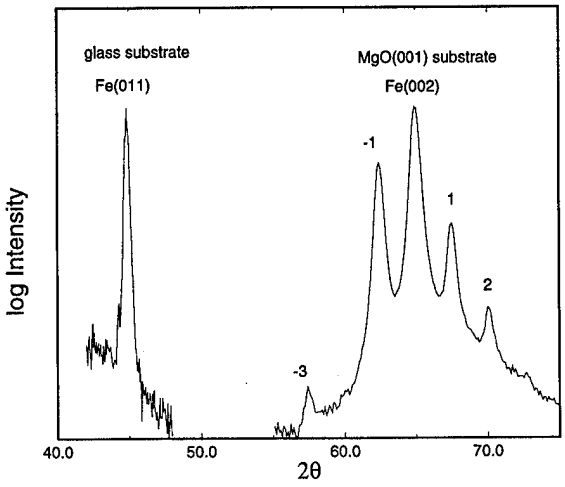


FIG. 1. High-angle x-ray diffraction spectra from two (Fe40 Å/Si14 Å)×60 multilayers grown on different substrates. High-angle x-ray peaks give information about lattice constants and stacking within the layers. The multilayer grown on MgO(001) has an Fe(002) peak with four satellites. The multilayer simultaneously grown on glass has only an Fe(011) peak.

high-angle superlattice satellites, the ϕ scans for this film indicate only weak orientation in-plane.

The shape of the high-angle peaks and their superlattice satellites are described by a well-known theory.[7] Application of this theory to the Fe/Si multilayers is difficult because the iron silicide lattice constant, the thickness of the remaining pure Fe, and the thickness of the iron silicide spacer can be estimated only roughly. A precise determination of the silicide lattice constant should make a quantitative analysis of these satellite features possible.

IV. MAGNETIC CHARACTERIZATION

Figure 3(a) shows magnetization curves for 60-repeat (Fe40 Å/Si14 Å) multilayers grown simultaneously on glass

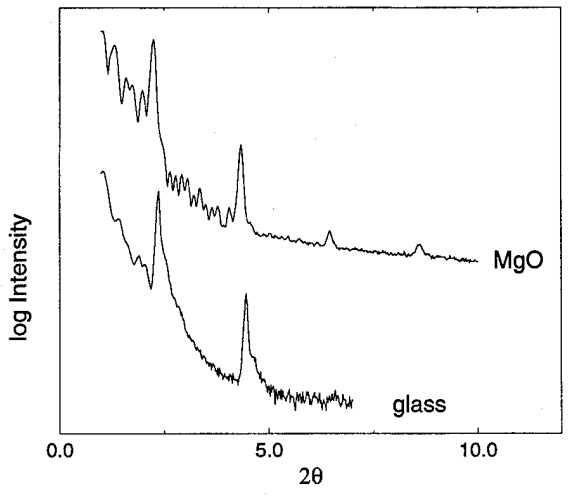


FIG. 2. Low-angle x-ray diffraction spectra for the same two (Fe40 Å/Si14 Å)×60 multilayers. Low-angle x-ray peaks give information about the bilayer period and layering of the multilayer. The multilayer grown on MgO has four relatively narrow peaks. The multilayer grown on glass has only two broad peaks, indicating a greater degree of interface roughness.

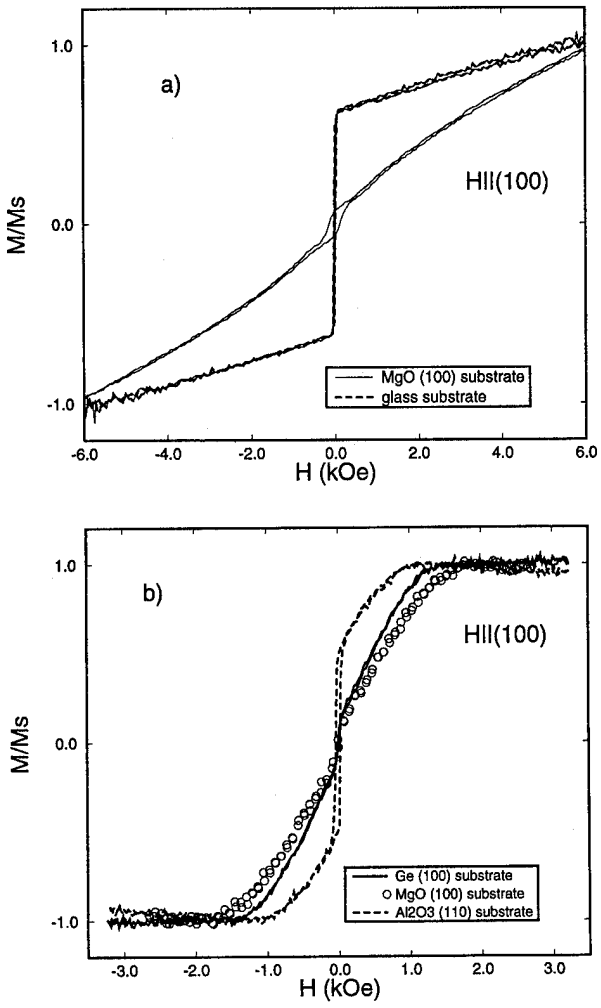


FIG. 3. Magnetization curves for Fe/Si multilayers grown on various substrates. The magnetization data is normalized to the highest measured value in order to facilitate comparison of the shape of the two data sets. (a) Hysteresis loops for the (Fe40 Å/Si14 Å)×60 multilayers simultaneously grown on MgO (001) and glass. The remanence is lower for the film grown on MgO. (b) Hysteresis loops for (Fe100 Å/Si14 Å)×2 multilayers (trilayers) grown on Al_2O_3 ($11\bar{2}0$), Ge(001), and MgO(001). All data are taken with the applied magnetic field along the Fe (100) easy direction.

and MgO(001). The saturation fields H_s appear to be similar for the two films. On the other hand, the remanent magnetization is 58% for the film on glass and 7% for the film grown on MgO. A remanence as low as 1% has been observed for other multilayers grown on MgO substrates. Superconducting quantum interference device (SQUID) magnetometer data taken up to higher fields gives a saturation field of 9.75 kOe for the multilayer on MgO at room temperature. Assuming for a moment that the interlayer coupling is purely bilinear in nature, a well-known formula relates the saturation field to the AF coupling strength: $A_{12}=H_sM_st_{Fe}/4$ where M_s is the saturation magnetization and t_{Fe} is the thickness of an individual Fe layer.[8] Use of this equation with $H_s=9.75$ kOe and the measured magnetization $M_s=1271$ emu/cm^3 gives $A_{12}=1.2$ erg/cm^2. This AF coupling value is comparable in size to the coupling measured in metal/metal multilayers.[9]

Figure 3(b) shows magnetization curves for Fe100 Å/Si14 Å/Fe100 Å trilayer films grown on Al_2O_3 $(11\bar{2}0)$, Ge(001), and MgO(001) substrates. All three of the magnetization curves in Fig. 3(b) were taken with the field applied along an Fe(100) easy direction. Significant in-plane anisotropy of the magnetization curves occurs for the films on the Ge and MgO substrates, similar to what has been observed for Fe/Cr/Fe trilayers.[8] The observation of magnetocrystalline anisotropy in the film on MgO but not in the film grown on Al_2O_3 is consistent with expectations from the ϕ scans, which show that the in-plane orientation of the film on MgO is much stronger.

Figure 3(b) once again demonstrates that the degree of remanence in Fe/Si multilayers is strongly related to the quality of layering. While the remanent magnetization of the epitaxial trilayers on Ge and MgO is only about 5% of the saturated value, the remanence of the polycrystalline trilayer on Al_2O_3 is close to 50%. The remanent magnetization of the trilayers on Ge and MgO is about 5% in the in-plane hard direction ($H\|$ Fe(110)) as well.

A SQUID magnetometer has been used to measure the magnetization curves of the IBS-grown Fe/Si multilayers at lower temperatures.[10] The temperature dependence of the remanent magnetization of these films is similar to that reported by other authors.[3]

V. DISCUSSION

At the moment it is not possible to tell why the in-plane ordering of the films grown on $Al_2O_3(11\bar{2}0)$ is inferior to that grown on the (001) MgO and Ge substrates. The difficulty with the Al_2O_3 growth may have to do with the 6° miscut of the substrates, or it may be due to an intrinsic difficulty with (011) growth of the Fe/Si multilayers. Previous work has shown that AF coupling in Fe/Si multilayers is dependent upon formation of a metastable iron silicide spacer layer phase.[4] The possibility exists that the spacer silicide does not grow well on Fe in the (011) orientation. This question can be answered only by further growth studies on better (011) substrates and careful structural characterizations.

A related question is whether the larger remanent magnet moment in the (011)-textured films might be due to a fundamental difference in magnetic properties from the (001)-textured films. Because a 46-repeat Fe/Si multilayer grown on Al_2O_3 has a remanence of only about 10%, this is unlikely. Undoubtedly the trilayer on Al_2O_3 has a higher remanence than the multilayer because the thinner film is more greatly impacted by the poor substrate surface quality. The staircase morphology caused by the 6° miscut of this Al_2O_3 substrate may lead to wavy interfaces between the Fe and iron silicide films or to pinholes through the silicide layers. Wavy interfaces can cause increased magnetostatic coupling or even biquadratic coupling,[11] both of which would tend to increase the remanence. The large remanence of the multilayers grown on glass substrates is likely also due to pinholes or magnetostatic coupling.

Pinhole-induced coupling may explain the unusual temperature dependence of the remanence. (Magnetostatic coupling is expected to be approximately temperature-independent.) Fe atoms in bridges through the silicide spacer layers are expected have a reduced Curie temperature. A larger remanence at low temperature therefore makes sense if the remanence is derived from pinhole coupling and is not an intrinsic effect. Low Curie temperature material may also be present in the iron silicide spacer layer or in at the iron/iron silicide interfaces.

By growing on a number of substrate materials and by using different deposition conditions, Fe/Si multilayers have been prepared with a varying degree of ordering. A large amount of accumulated evidence demonstrates that high remanence of the magnetization curves in Fe/Si multilayers is associated with interface roughness. The remanence is therefore not likely to be related to unusual exchange coupling but instead to originate from defects, perhaps pinholes through the silicide spacer layer. Since the remanent magnetization is caused by extrinsic effects, future studies should concentrate instead on measurements of the saturation field of the magnetization curves in order to learn more about the interlayer coupling.

ACKNOWLEDGMENTS

We would like to thank E. E. Fullerton, J. A. Borchers, R. M. Osgood III, and Y. Huai for helpful discussions, and B. H. O'Dell and S. Torres for technical assistance. Part of this work was performed under the auspices of the U. S. Department of Energy by LLNL under Contract No. W-7405-ENG-48.

[1] P. Bruno, Phys. Rev. B **49**, 13231 (1994).
[2] Z.-P. Shi, R. R. P. Singh, and B. M. Klein, Europhys. Lett. **29**, 585 (1995).
[3] J. E. Mattson, S. Kumar, E. E. Fullerton, S. R. Lee, C. H. Sowers, M. Grimsditch, S. D. Bader, and F. T. Parker, Phys. Rev. Lett. **71**, 185 (1993); K. Inomata, K. Yusu, and Y. Saito, Jpn. J. Appl. Phys. **33**, L1670 (1994).
[4] A. Chaiken, R. P. Michel, and M. A. Wall, Phys. Rev. B (submitted).
[5] R. F. C. Farrow, G. R. Harp, R. F. Marks, and T. A. Rabedeau, J. Cryst. Growth **133**, 47 (1993).
[6] C. L. Foiles, M. R. Franklin, and R. Loloee, Mater. Res. Soc. Proc. (to be published).
[7] E. E. Fullerton, I. K. Schuller, H. Vanderstraeten, and Y. Bruynseraede, Phys. Rev. **45**, 9292 (1992); J. A. Borchers, M. B. Salamon, R. W. Erwin, J. J. Rhyne, R. R. Du, and C. P. Flynn, Phys. Rev. B **43**, 3123 (1991).
[8] J. J. Krebs, P. Lubitz, A. Chaiken, and G. A. Prinz, Phys. Rev. Lett. **63**, 1645 (1989).
[9] S. S. P. Parkin, Phys. Rev. Lett. **67**, 3598 (1991).
[10] R. P. Michel and A. Chaiken (to be published).
[11] J. C. Slonczewski, Phys. Rev. Lett. **67**, 3172 (1991).

Anomalous temperature dependence of interlayer coupling in Fe/Si multilayers (abstract)

R. P. Michel, A. Chaiken, and M. A. Wall
Lawrence Livermore National Laboratory, Livermore, California 94550

J. W. Dykes
National Institute of Standards and Technology, Boulder, Colorado 80303

J. F. Ankner and H. Kaiser
University of Missouri-Columbia, Columbia, Missouri 65211

The magnetic coupling of the Fe layers in Fe/Si multilayers strongly depends on the morphology of the iron-silicide interlayer that forms during deposition. Antiferromagnetic interlayer coupling is only observed in Fe/Si multilayers with crystalline interlayers in the CsCl structure.[1] Recently, it has been shown that single layers of Fe–Si in the CsCl structure can be grown epitaxially on Si over a range of stoichiometries.[2] FeSi films are reported to be Kondo insulators below 50 K. We find evidence of a magnetic phase transition in antiferromagnetically coupled Fe/Si multilayers. M_s measured in a constant applied field of 50 kOe shows $T^{3/2}$ behavior down to 10 K. However, $M(T)$ at a lower constant field peaks around 50 K and decreases at lower temperature, indicating enhanced antiferromagnetic coupling or a phase transition. The remanent magnetization increases monotonically with decreasing temperature and has been explained by invoking thermally activated coupling. However, the saturation field also increases with decreasing temperature, indicating a stronger antiferromagnetic interaction. We explore the suggestion[3] that the interlayer coupling is biquadratic in nature. Polarized neutron reflectometry has also been used to get a clearer picture of the complicated magnetic behavior of this multilayer system. © *1996 American Institute of Physics.* [S0021-8979(96)60008-9]

Part of this work was performed under the auspices of the U. S. Department of Energy by LLNL under contract No. W-7405-ENG-48.

[1] R. P. Michel, A. Chaiken, and M. A. Wall, Mater. Res. Soc. Symp. Proc. (to be published).
[2] N. Onda, H. Sirringhaus, P. Steiner, and H. von Kanel, Mater. Res. Soc. Symp. Proc. **280**, 497 (1993).
[3] E. E. Fullerton and S. D. Bader (private communication).

 0021-8979/96/79(8)/4775/1/$10.00 © 1996 American Institute of Physics

Antiferromagnetic coupling in magnetic multilayers with a narrow gap semiconductor spacer

Zhu-Pei Shi and Barry M. Klein
Department of Physics, University of California, Davis, California 95616

Antiferromagnetic (AF) coupling has been observed in sputtered Fe/Si multilayers at room temperature, with thin spacers (<20 Å) which were claimed to be FeSi. To study the magnetic coupling in this system we extend the RKKY interaction approach to a temperature-dependent narrow gap semiconductor. The strong AF coupling at room temperature and weakly ferromagnetic (F) coupling at low temperatures observed in Fe/Si can be explained from this model. © *1996 American Institute of Physics.* [S0021-8979(96)51308-3]

The first evidence for AF coupling of magnetic multilayers via a transition-metal spacer was made in crystalline bcc (001) Fe/9 Å Cr/Fe sandwiches[1] using Brillouin light scattering and magneto-optical Kerr hysteresis loops. Interest in the Fe/Cr systems was heightened by the subsequent observation that the resistance of AF coupled (001) Fe/Cr multilayers[2] decreases enormously with the application of a magnetic field, a phenomenon called giant magnetoresistance. The oscillatory behavior of the magnetic coupling[3] has sparked tremendous interest in *metallic* multilayered structures. The oscillation periods of interlayer magnetic coupling have been successfully explained by applying RKKY-like interactions to the layered geometry and using the Fermi surface characteristics of the metal spacers.[4]

AF interlayer coupling was discovered in evaporated Fe/Si/Fe trilayers[5] and sputtered Fe/Si multilayers,[6] in which spacers are apparently *nonmetallic*. AF coupling in the multilayers was observed with crystalline spacer layer,[6] attributed to iron silicide (FeSi) formed in the interfaces, while in the trilayers the spacer was claimed to be amorphous semiconductor Si (a-Si).[5] The different spacers may originate from the differences in the preparation methods and the substrate temperatures used, because Fe and Si easily form an alloy. Inomata *et al.*[7] claimed that their Si spacer layers are an FeSi compound when the Si layer is less than 15 Å and is a combination of this silicide and amorphous Si when the Si spacer thickness is greater than 15 Å. Recently, Foiles *et al.*[8] used transmission electron diffraction to obtain direct evidence for iron silicides in sputtered Fe/Si multilayers. In this article we theoretically investigate the mechanism of AF coupling in sputtered Fe/Si multilayerers where the thin spacer is treated as ϵ-FeSi (rock-salt-like structure).

Band structure calculations predict a small semiconductor gap (67 meV in Ref. 9, 87 meV in Ref. 10, and 110 meV in Ref. 11) for ϵ-FeSi. Chainani *et al.*[12] reported high-resolution temperature-dependent photoemission spectra of ϵ-FeSi which show an extremely small gap of less than 5 meV. Here, we extend RKKY interaction theory between two magnetic moments in a semiconductor[13] to two magnetic sheets in a crystalline semiconductor with a narrow gap.

At finite temperatures, one may expect a considerable number of thermal electrons in the conduction band and holes in the valence band for a narrow gap semiconductor. Assuming the interaction between conduction electrons or holes and local spins has a form $H_{\rm int}=A\Sigma_i \sigma\cdot\mathbf{S}_i\delta(\mathbf{r}-\mathbf{r}_i)$, one obtains an RKKY coupling, in reciprocal space, as

$$j_{\rm RKKY}(\mathbf{q})=A^2\sum_{n_1,n_2,\mathbf{k}}\frac{f_{n_1\mathbf{k}}-f_{n_2\mathbf{k}'}}{\epsilon_{n_2\mathbf{k}'}-\epsilon_{n_1\mathbf{k}}}, \tag{1}$$

where $\mathbf{k}'=\mathbf{k}+\mathbf{q}+\mathbf{G}$ and $\mathbf{G}$ is a vector of the reciprocal lattice. $f_{n\mathbf{k}}$ is the Fermi distribution function for Bloch states $n\mathbf{k}$. For simplicity, we assume the free-electron gas approximation for the thermally activated electrons in the conduction bands and the holes in the valence bands. A simple conduction electron band for the spacer may be taken as

$$\epsilon_{\mathbf{k}}=\frac{\hbar^2k^2}{2m^*}+\frac{E_g}{2}, \tag{2}$$

where m^* is an effective mass, and E_g is an energy gap. According to Yafet's argument,[14] the RKKY coupling between two sheets of spins can be obtained directly by Fourier transforming Eq. (1), and is given as

$$J_{\rm RKKY}(z)=\frac{a}{2\pi}\int_0^\infty dq_z\, j_{\rm RKKY}(q_z)\cos(q_z z), \tag{3}$$

where $a=4.493$ Å is the lattice constant of ϵ-FeSi.

Given an energy gap and effective mass, the RKKY coupling can be estimated at finite temperatures from Eqs. (1)–(3). AF coupling can be obtained at finite temperatures in a narrow region of spacer thickness when the energy gap becomes very small. For example, we set $E_g=50$ K (4.3 meV, a possible extremely small gap[12]) and temperature $T=300$ K, and $J_{\rm RKKY}(z)$ for $m^*=m_e$, $2m_e$, and $4m_e$ are then obtained and plotted in Fig. 1, as a solid line, dashed line, and dotted line, respectively. We see that AF coupling occurs when the spacer thickness is 20 Å $<z<$35 Å, 14 Å $<z<$22 Å, and 10 Å $<z<$17 Å for $m^*=m_e$, $2m_e$, and $4m_e$, respectively. The result for the case $m^*=4m_e$ agrees well with experiments[6,7] where AF coupling at room temperature appears when the spacer thickness is between 11 and 17 Å.

Next we study the effect of energy gap at room temperature. Fixing the thickness of the spacer at $z=13$ Å, RKKY couplings for $m^*=m_e$, $2m_e$, and $4m_e$ are then obtained and plotted in Fig. 2, as a dotted line, dashed line, and solid line, respectively. We see that the AF coupling can be obtained for an energy gap up to 900 K for $m^*=4m_e$.

With decreasing temperature, experiments[6,7] indicated that the AF coupling at room temperature will disappear and the coupling in sputtered Fe/Si multilayers becomes *weakly*

 0021-8979/96/79(8)/4776/3/$10.00 © 1996 American Institute of Physics

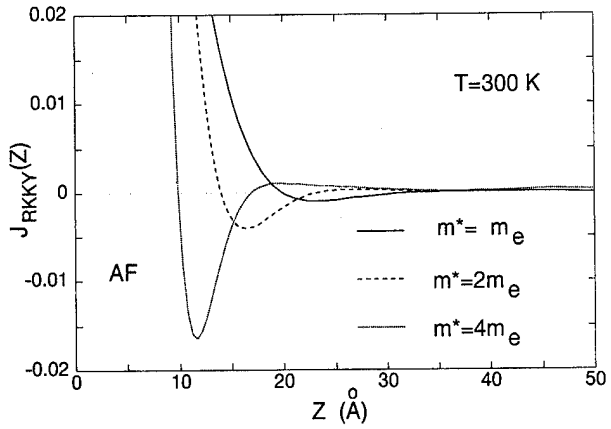


FIG. 1. Thickness dependence of RKKY coupling $J_{RKKY}(z)$ at temperature $T=300$ K and energy gap $E_g=50$ K. Solid line, dashed line, and dotted line are for effective mass $m^*=m_e$, $2m_e$, and $4m_e$, respectively. AF coupling occurs.

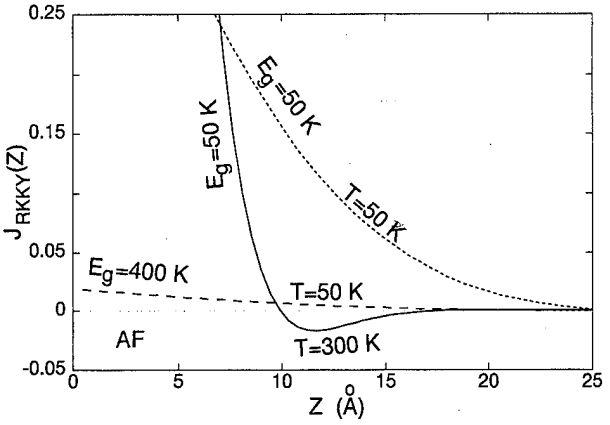


FIG. 3. RKKY coupling $J_{RKKY}(z)$ as a function of spacer thickness. A solid line with AF coupling is for $T=300$ K and $E_g=50$ K. Dotted line and dashed line are for $E_g=50$ K and $E_g=400$ K at $T=50$ K, respectively.

ferromagnetic (F) at low temperatures, e.g., $T=50$ K. We fix the values of the energy gap $E_g=50$ K and effective mass $m^*=4m_e$. The RKKY coupling $J_{RKKY}(z)$ at low temperature $T=50$ K is computed and plotted in Fig. 3, as a dotted line. We replot the result for $T=300$ K in Fig. 3, as a solid line, for comparison. For spacer thickness 11 Å $<z<17$ Å, the AF coupling at room temperature becomes *strong* F coupling at the low temperature $T=50$ K. This feature of the temperature dependence of the interlayer coupling is in contrast to the experimental observations[6,7] mentioned above. We conclude that the results of RKKY coupling based on a *rigid* small energy gap existing in the spacer cannot fully explain the interlayer magnetic coupling in sputtered Fe/Si multilayers.

It has been suggested that the transition-metal compound FeSi may belong to the class of strongly correlated materials known as Kondo insulators (hybridization semiconductor).[15] One of the salient features of a Kondo insulator is the temperature-dependent hybridization gap $E_g(T)$.[15] The energy gap at $T=0$ decreases with increasing temperature, and it becomes very small at relatively high temperatures.[16]

Fixing the values of $T=50$ K and $m^*=4m_e$, RKKY coupling $J_{RKKY}(z)$ for $E_g=400$ K is calculated and plotted in Fig. 3, as a dashed line. This coupling is weak F because of the relatively large energy gap as we expect. For spacer thickness 11 Å $<z<17$ Å, the desired (observed) coupling behavior in sputtered Fe/Si multilayers, in which the AF coupling at room temperature (solid line in Fig. 3) becomes very *weak* F at low temperatures, e.g., $T=50$ K (dashed line in Fig. 3), is obtained.

The model calculations we described above explain the experimental results for a crystalline spacer with a very narrow gap. But this model does not provide an AF coupling at room temperature or low temperatures for spacer materials with a much larger gap, e.g., a-Si ($E_g\approx0.4$ eV). The quantum interference approach with complex Fermi surface[17] produces an AF coupling at finite temperatures for spacers with a large energy gap. But this theoretical framework cannot explain the temperature-dependent AF coupling observed in experiments.[7,18] The mechanism of AF coupling through an a-Si spacer is still an open question, perhaps driven by defect states.

In conclusion, we modeled the spacer in sputtered Fe/Si multilayers as a *temperature-dependent narrow gap* semiconductor (ϵ-FeSi). We showed that the temperature-induced AF coupling at room temperature becoming weak F coupling at low temperatures for small thicknesses of the spacer in sputtered Fe/Si multilayers can be interpreted in terms of an RKKY-like interaction.

This research was supported by the University Research Funds of the University of California at Davis. Z. P. Shi would like to thank P. M. Levy, J. L. Fry, R. R. P. Singh, B. A. Jones, A. Chaiken, and R. P. Michel for very useful discussions.

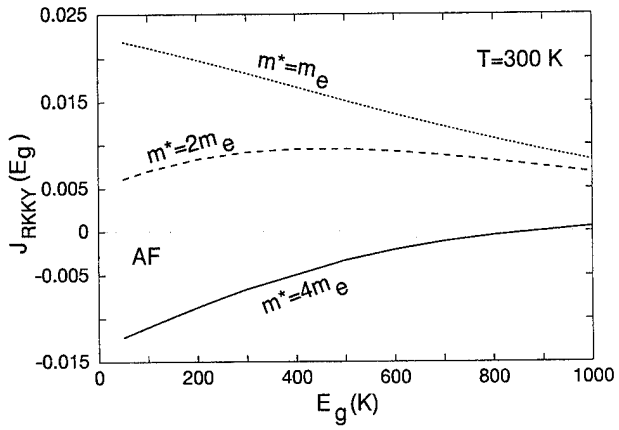


FIG. 2. RKKY coupling $J_{RKKY}(E_g)$ as a function of energy gap. Dotted line, dashed line, and solid line are for effective mass $m^*=m_e$, $2m_e$, and $4m_e$, respectively.

[1] P. Grünberg, R. Schreiber, Y. Pang, M. B. Brodsky, and H. Sowers, Phys. Rev. Lett. **57**, 2442 (1986).

[2] M. N. Baibich, J. M. Broto, A. Fert, F. Nguyen Van Dau, F. Pertroff, P. Eitenne, G. Crenzet, A. Friederich, and J. Chazelas, Phys. Rev. Lett. **61**, 2472 (1988).

[3]S. S. P. Parkin, N. More, and K. P. Roche, Phys. Rev. Lett. **64**, 2304 (1990).
[4]For a review, see, for example, B. Heinrich and J. F. Cochran, Adv. Phys. **42**, 523 (1993), and references therein.
[5]S. Toscano, B. Briner, H. Hopster, and M. Landolt, J. Magn. Magn. Mater. **114**, L6 (1992); B. Briner and M. Landolt, Phys. Rev. Lett. **73**, 340 (1994).
[6]E. E. Fullerton, J. E. Mattson, S. R. Lee, C. H. Sowers, Y. Y. Huang, G. Felcher, S. D. Bader, and F. T. Parker, J. Magn. Magn. Mater. **117**, L301 (1992); J. E. Matson, S. Kumar, E. E. Fullerton, S. R. Lee, C. H. Somers, M. Grimsditch, S. D. Bader, and F. T. Parker, Phys. Rev. Lett. **71**, 185 (1993).
[7]K. Inomata, K. Yusu, and Y. Saito, Phys. Rev. Lett. **74**, 1863 (1995).
[8]C. L. Foiles, M. R. Franklin, and R. Loloee, Mater. Res. Soc. Symp. Proc. **382** (1995).
[9]V. R. Galakhov, E. Z. Kurmaev, V. M. Cherashenko, Y. M. Yarmoshenko, S. N. Shamin, A. V. Postnikov, Stuhlenbrock, M. Neumann, Z. W. Lu, B. M. Klein, and Z. P. Shi, , J. Phys. Condensed Matter **7**, 5529 (1995).
[10]T. Jarlborg, Phys. Rev. B **51**, 11106 (1995).
[11]L. F. Matthesis and D. R. Hamann, Phys. Rev. B **47**, 13114 (1993).
[12]A. Chainani, T. Yokoya, T. Morimoto, T. Takahashi, S. Yoshii, and M. Kasaya, Phys. Rev. B **50**, 8915 (1994).
[13]W. Baltensperger and A. M. de Graaf, HPA **33**, 881 (1960).
[14]Y. Yafet, Phys. Rev. B **36**, 3948 (1987).
[15]G. Aeppli and Z. Fisk, Comments Condensed Mater. Phys. **16**, 155 (1992).
[16]C. Sanchez-Castro, K. S. Bedell, and B. R. Cooper, Phys. Rev. B **47**, 6879 (1993).
[17]P. Bruno, Phys. Rev. B **49**, 13231 (1994).
[18]M. Landolt and B. Briner, Appl. Phys. A **60**, 403 (1995).

Magnetic properties of $(1\bar{1}02)$ Dy/Y superlattices

K. Theis-Bröhl,[a] K. A. Ritley, and C. P. Flynn
Department of Physics, University of Illinois, 1110 West Green Street, Urbana, Illinois 61801-3080

K. Hamacher, H. Kaiser and J. J. Rhyne
Research Reactor Center, University of Missouri–Columbia, Columbia, Missouri 65211

Epitaxial $(1\bar{1}02)$ Dy/Y rare earth superlattices and a thick $(1\bar{1}02)$ Dy film, grown on sapphire with Y/Ta buffer layers, have been prepared by molecular beam epitaxy. Neutron diffraction and SQUID magnetization measurements on a single 200 nm thick $(1\bar{1}02)$ Dy layer showed nearly bulk behavior. However, for the $(1\bar{1}02)$ Dy/Y superlattices we found different magnetic behavior depending on the relative Dy to Y-layer thickness. The superlattices exhibit both ferromagnetic and helical phases, but with the Néel and Curie temperatures significantly different from bulk Dy. These results differ from previous findings in Dy/Y superlattices grown along [0001]. © *1996 American Institute of Physics.* [S0021-8979(96)79108-2]

Extensive studies of the magnetism of (0002) Dy/Y superlattices (SLs) show a long-range indirect exchange coupling of the heavy rare-earth Dy through the Y spacer material.[1] Deviating from the bulk behavior of Dy (which shows a ferromagnetic phase with a Curie temperature at 85 K and a helimagnetic phase with a Néel temperature at 185 K)[2] the ferromagnetic phase in the (0002)Dy/Y superlattices is completely suppressed by epitaxial strain. Neutron diffraction scans of the (0002)Dy/Y superlattices showed only helical antiferromagnetism down to 5 K.[1] Studies of Dy/Y superlattices grown in *a*- and *b*-orientation (*c*-axis in the film plane) show a similar phase diagram to the *c*-axis grown superlattices;[3,4] however, only single-layer ordering was observed and the long-range 3D-magnetic ordering was destroyed. The observed weak coupling was attributed to the directional dependence of the conduction electron response.

This paper reports results on a series of $(1\bar{1}02)$Dy/Y superlattices and films for which the angle between the growth orientation and the *c*-axis is close to 45°. Coupling between successive planes should therefore be affected by this angle. Due to the off *c*-axis growth direction the magnetic domain size within the (0002) plane has to be limited by the Dy-layer thickness.

The samples were grown at the University of Illinois. A $(1\bar{1}00)$ sapphire substrate with an 1.5° miscut along the $[11\bar{2}0]$ orientation was used to avoid the growth of a second $(1\bar{1}02)$Dy/Y structural domain.[5] The sapphire was annealed for 1 h at 1200 °C before depositing a 75 nm thick Ta(211) buffer (growth temperature 960 °C). A 100 nm thick $(1\bar{1}02)$Y buffer layer was grown on the Ta at a growth temperature of 500 °C, and was found to grow tilted at an angle of about 5° to the Al_2O_3 and to form facets.[5] On the Y buffer we have grown the Dy/Y superlattice at a growth temperature that avoids interdiffusion. Finally, we protected our superlattices with a 15 nm thick Y toplayer.

To confirm the quality of the samples and to find the superlattice periodicities, we analyzed our samples with small and high angle x-ray scattering. Typical rocking widths for the Dy/Y have been found to about 0.5° which are larger than for the superlattices grown in the [0001] orientation. Unfortunately, the very high quality of the *c*-axis grown superlattices could not be completely reached in the superlattices grown along $[1\bar{1}02]$.

To illustrate the magnetic behavior we present the results of 3 superlattices and one 200 nm thick Dy layer grown in the same way as the superlattices. In the superlattices the Dy individual layer thickness was varied and the Y layer thickness was held nearly constant (see Table I). SQUID magnetometry and neutron diffraction measurements were used to analyze the superlattices and the Dy layer. Figure 1 shows a typical zero field cooled SQUID measurement at a magnetic field of 100 Oe. The data show a peak at 95 K that indicates the occurrence of a ferromagnetic phase. An additional peak at 170 K reflects the Néel temperature T_N of the helical magnetic phase. The SQUID data of the 200 nm thick Dy show a behavior close to bulk Dy with the first peak at 85 K (ferromagnetic Curie temperature) and a second peak due to the Néel temperature at 188 K. Field cooled measurements in the 200 nm thick Dy layer confirm that the phase transition to the ferromagnetic phase is more gradual than the first-order transition in bulk. For the superlattices the ferromagnetic peak was found at slightly higher temperatures than for the 200 nm thick Dy layer (see Table I), and the second (helical antiferromagnetic) peak was found at lower temperatures than in bulk which decrease with decreasing Dy layer thickness (see Table I).

The neutron diffraction measurements were performed at the Research Reactor Center of the University of Missouri–Columbia. Neutron data were taken on a triple-axis spectrometer using 2.35 Å wavelength neutrons from a silicon monochromator and (002) pyrolitic graphite analyzer. Slit collimators with $54'-40'-40'-40'$ acceptance angles were used before and after the monochromator and analyzer, respectively. The *c*-axis of the superlattices which has an angle of 42.2° to the out-of-plane $[11\bar{2}0]$ film orientation was oriented parallel to the scattering vector. This configuration allowed continuous scans in Q along the $(000l)$ orientation, which is also the propagation direction of the incommensurate helimagnetic order.

On both sides of the (0002) nuclear peak we found magnetic peaks caused by the helical antiferromagnetism in all

[a]Present address: Institut für Experimentalphysik/Festkörperphysik, Ruhr-Universität Bochum, D-44780 Bochum, Germany.

 0021-8979/96/79(8)/4779/3/$10.00 © 1996 American Institute of Physics

TABLE I. Results of SQUID and neutron diffraction measurements.

Sample	SL individual layer thicknesses (in monolayers)	SQUID: 1.peak	SQUID 2.peak	Neutron diffraction: max. temperature for magnetic peaks
SL A	$[Dy_{33}/Y_{15}]_{30}$	100 K	175 K	175 K
SL B	$[Dy_{21}/Y_{20}]_{34}$	95 K	170 K	165 K
SL C	$[Dy_{9}/Y_{17}]_{30}$	95 K	150 K	150 K
Dy layer	200 nm Dy	85 K	188 K	not measured

samples (see Fig. 2 for superlattice A). In the case of superlattice C with a 9 ML thick Dy layer thickness these peaks were very weak. Figure 3 shows the temperature dependence of the average turn angle of the helimagnetic spiral weighted between Dy and Y layers, found from the $(0002)^{\pm}$ peak positions. The behavior is very much like the samples grown in [0001] orientation. In the superlattices the helimagnetic phase is observed down to 10 K. The turn angles show an almost linear behavior above 100 K but lock into constant values below 100 K. With decreasing Dy layer thickness the turn angles were larger. This particular behavior is expected because the nominal Y turn angle is larger than that of Dy. We could not extract the turn angles of the Dy layers separately because of the different orientations of the superlattice periodicity and the magnetic propagation axis and furthermore because of the lack of superlattice harmonics on one side of the helimagnetic peaks. The turn angles of the thick Dy are similar to bulk behavior and exhibit a lower turn angle than for the superlattice. In the case of the thick Dy layer no helimagnetic phase peaks were found below the Curie temperature.

For the superlattices with the thicker Dy layers (superlattice A and superlattice B) the magnetic satellite peaks show harmonics (only one side can be distinguished in the data of Fig. 2) due to the superlattice periodicity. Since we have grown the superlattices in $[1\bar{1}02]$ orientation but the scan is along [0001], we observe only the projection of the superlattice periodicity on the magnetic peaks in the [0001] orientation. To show that the superlattice harmonics of the magnetic peaks have their maxima in orientations parallel to $[1\bar{1}02]$, we carried out additional scans along $[\delta\ \bar{\delta}\ 0\ l+2\delta]$ across the magnetic peaks (area scans). The insets of Fig. 2 present such scans. The scans cross the [0001] axis at $l=1.822$ ($Q_l=2.018$ Å^{-1}, $(0002)^-$ peak) and at $l=2.171$ ($Q_l=2.426$ Å^{-1}, $(0002)^+$ peak). The superlattice harmonics are clearly resolved in these measurements and their Q separation agrees with our measured superlattice periodicity.

Aside from the orientational effects on the harmonics of the $(1\bar{1}02)$Dy/Y superlattices the neutron results for the helimagnetism are qualitatively similar to the (0002)Dy/Y superlattices. However, the spin coherence range is much more restricted. The coherence lengths of the helimagnetic spirals varys for the $(1\bar{1}02)$ superlattices from 12.0 to 24.0 nm. Taking into consideration the superlattice periodicity and its projection to the [0001] orientation, these values for the coherence length are equivalent to about two periods of each (Dy/Y) superlattice in the [0001] orientation.

More striking, however, is the simultaneous observation of a ferromagnetic phase in the $(1\bar{1}02)$ superlattices that was not seen in (0002) superlattices. Additional (0002) peak intensity was found below room temperature in superlattices A and B reflecting this ferromagnetism. This is shown in Fig. 4 for superlattice A where we plot the square root of the excess integrated intensity of the (0002) peak normalized by the nuclear-only intensity. This value is proportional to the ferromagnetic moment component. The figure also shows the

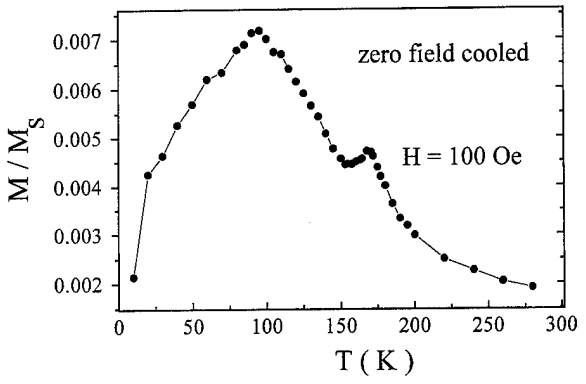


FIG. 1. Zero field cooled SQUID measurement for the superlattice $[Dy_{21}/Y_{20}]_{34}$ (superlattice B). The measurement was performed with increasing temperature from 10 K at a magnetic field of 100 Oe.

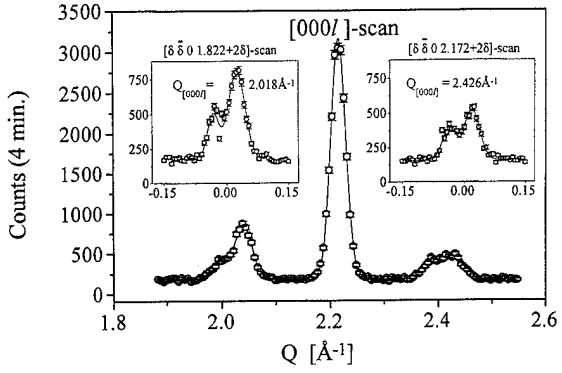


FIG. 2. Neutron diffraction scan along [000l] direction in $[Dy_{33}/Y_{15}]_{30}$ (superlattice A). The measuring temperature was 100 K. The solid line represents a fit to the data using a Voigt function for the (0002) nuclear peak and Gaussians for the $(0002)^{\pm}$ magnetic peaks. The split of the [000l] magnetic peaks is caused by the superlattice harmonics which have their maxima in an orientation parallel to the growth direction (only one side of the harmonics can be distinguished). The insets show neutron diffraction scans across the $(0002)^-$ and $(0002)^+$ magnetic peaks in orientations parallel to the growth direction. The scans are along the $[\delta\ \bar{\delta}\ 0\ 1.822+2\delta]$ and the $[\delta\ \bar{\delta}\ 0\ 2.172+2\delta]$ orientations at $Q_l=2.018$ Å^{-1} and $Q_l=2.426$ Å^{-1}, respectively.

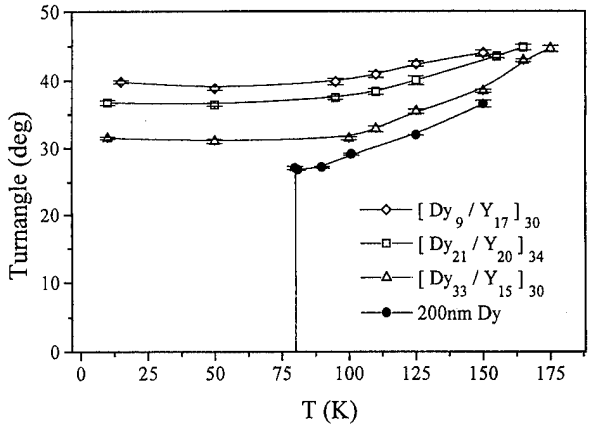


FIG. 3. Temperature dependence of interplane turn angles of the helimagnetic spiral for superlattice $[Dy_{33}/Y_{15}]_{30}$. The values are weighted averages of the turn angles of the Dy and the Y layers.

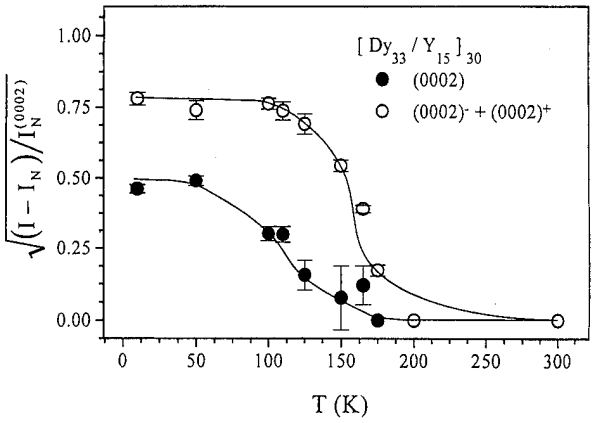


FIG. 4. Temperature dependences of the magnetic peak relative intensities. The solid circles represent the ferromagnetic moment component derived from the square root of the excess integrated intensities of the (0002) peak at different temperatures normalized by its average value above T_N. The open circles represent the helimagnetic component derived from the square root of the integrated intensity of the $(0002)^-$ and the $(0002)^+$ helimagnetic satellites normalized to the (0002) nuclear peak intensity.

square root of the total integrated intensity of the helimagnetic satellite peaks again normalized to the intensity of the (0002) peak above T_N.

Dy/Lu(0002) superlattices[6] also show ferromagnetic order. Lu is a spacer material that compresses the Dy basal plane (2.4% lattice mismatch), favoring ferromagnetism, as opposed to the large Y lattice that favors helimagnetism. In the $(1\bar{1}02)$Dy/Y superlattices one a-axis must be found in the film plane and should undergo an expansion similar to that in the (0002)Dy/Y superlattices. However, the other two a-axes do not lie in the film plane and undergo a different expansion due to the anisotropic lattice strain epitaxy. This may be the mechanism responsible for the mixed magnetic behavior in the $(1\bar{1}02)$ superlattices A and B.

In conclusion we have grown $(1\bar{1}02)$Dy/Y superlattices and found a coexistence of a helimagnetic phase and a ferromagnetic phase. The average turn angles measured down to 10 K are similar to (0002)Dy/Y superlattices. The coherence length of the helimagnetic spiral was limited to about two superlattice periods. In the $[Dy_9/Y_{17}]_{30}$ superlattice with a thin Dy layer thickness separated by thick Y spacers only the helimagnetic phase was observed.

This work was supported by the Deutsche Forschungsgemeinschaft through Br 1466/2-1, by ONR N00014-94-1-1146 and by NSF DMR 91-21888.

[1] J. J. Rhyne, R. W. Erwin, J. Borchers, S. Sinha, M. B. Salamon, R. Du, and C. P. Flynn, Physica B **159**, 111 (1989).
[2] M. K. Wilkinson, W. C. Koehler, E. O. Wollan, and J. W. Cable, J. Appl. Phys. **32**, 48 (1961).
[3] F. Tsui, C. P. Flynn, M. B. Salamon, R. W. Erwin, J. Borchers, and J. J. Rhyne, Phys. Rev. B **43**, 13320 (1991).
[4] C. P. Flynn, F. Tsui, M. B. Salamon, R. W. Erwin, and J. J. Rhyne, J. Phys.: Condens. Matter **1**, 5997 (1989).
[5] R. Du and C. P. Flynn, J. Phys.: Condens. Matter **2**, 1335 (1990).
[6] R. S. Beach, A. Matheny, M. B. Salamon, C. P. Flynn, J. A. Borchers, R. W. Erwin, and J. J. Rhyne, J. Appl. Phys. **73**, 6901 (1993).

Structural, field, and temperature dependence of noncollinear magnetic coupling in Fe/Cr(001) superlattices (abstract)

J. F. Ankner,[a] H. Kaiser,[a] and K. Hamacher[a]
Missouri University Research Reactor, Columbia, Missouri 65211

A. Schreyer, Th. Zeidler, and H. Zabel
Ruhr Universität Bochum, 44780 Bochum, Germany

C. F. Majkrzak
NIST, Gaithersburg, Maryland 20899

M. Schäfer and P. Grünberg
Forschungszentrum Jülich, 52425 Jülich, Germany

Utilizing the magneto-optic Kerr effect (MOKE) in conjunction with x-ray and neutron reflectometry (NR) and diffraction, we have studied the magnetic coupling of Fe/Cr(001) superlattices grown at room temperature and 250 °C. Only the samples grown at elevated temperature exhibit noncollinear coupling of 5.0 nm Fe layers across 1.7 nm Cr interlayers. The noncollinear samples feature a less-disordered in-plane interfacial structure than those grown at room temperature. Using x-ray diffuse reflectivity, we have measured a length scale of 10 nm for these in-plane features. We have also observed, via NR, a remanent noncollinear coupling angle of 50° and, via MOKE and NR, a gradual approach to saturation at upwards of 7 kOe. These features can be explained qualitatively by the proximity magnetism model of Slonczewski. We will compare the predictions of both the proximity and bilinear/biquadratic models with our data and present the results of ongoing neutron measurements of the temperature dependence of the coupling. © *1996 American Institute of Physics.* [S0021-8979(96)60108-8]

[a]Supported by ONR N00014-94-1-1146.

 0021-8979/96/79(8)/4782/1/$10.00 © 1996 American Institute of Physics

Structural and magnetic properties of fcc Pt/Fe(111) multilayers

Ruqian Wu and Lujun Chen
Department of Physics and Astronomy, California State University, Northridge, California 91330-8268

Nicholas Kioussis
Institute of Materials Science, NCSR "Demokritos," 15310 Ag. Paraskevi, Athens, Greece
and Department of Physics and Astronomy, California State University, Northridge, California 91330-8268

The structural, electronic, and magnetic properties of the 2Pt/5Fe/2Pt(111) system were investigated using the total energy full-potential linearized augmented-plane-wave method. The interplanar relaxation, determined by the atomic force approach, was found to be large between the nearest Pt–Fe and Fe–Fe distances, thus altering the electronic and magnetic properties of the system. We find an enhancement of the spin and orbital Fe magnetic moment (2.44 μ_B) at the interface, and a large induced magnetic moment (0.27 μ_B) at the interfacial Pt site, which is relatively short ranged. The effects of the interface on the contact hyperfine fields is evaluated: The (negative) core-polarization contribution is found to scale with the moment, but the valence contribution changes from negative in the interior to *positive* at the interface. The trend of the calculated layer-by-layer hyperfine fields agrees well with experiment. © *1996 American Institute of Physics.* [S0021-8979(96)51408-X]

I. INTRODUCTION

Recent experiments have revealed that (Co,Fe)/(Pd,Pt) multilayers where the ferromagnetic layers are only a few monolayers thick show perpendicular magnetic anisotropy; combined with the large magneto-optical Kerr rotation, these multilayers appear to be promising candidates for high-density magneto-optical storage media.[1,2] It is well known that Pd and Pt are considered to be "nearly magnetic" with anomalously large susceptibility. A small percentage (0.1 at. %) of Fe in bulk Pd induces magnetic moments on the surrounding Pd atoms giving rise to giant magnetic moments of 10 μ_B per Fe atom. Similarly, Pd or Pt atoms at an Fe/Pd or Fe/Pt interface are strongly polarized by the Fe atoms.[3,4] Magnetization measurements on Fe/Pt multilayers have shown an enhanced magnetization by about 15% over the bulk Fe value for Fe thicknesses larger than 12 Å.[15] Recent magnetization and Mössbauer measurements[6] on Fe/Pt multilayers have shown a strong enhancement of about 15% of the hyperfine field in the second Fe monolayer below the interface, which fades out in a damped oscillation within 6–10 Fe monolayers. A similar trend of the layer-by-layer hyperfine field was observed for the Fe/Pd multilayers.[7]

In order to understand the changes in electronic structure induced at the Fe/Pt interface, and their effects on modifying the atomic magnetic moments and hyperfine fields as compared to the corresponding bulk values, we have carried out a series of self-consistent spin-polarized local-spin-density total energy calculations with the use of the full-potential linearized augmented-plane-wave (FLAPW) method.[8] Because of the high density of states at the Fermi level in Pt and the sensitivity of the number of the Fe majority spin holes on the local environment,[3] structural changes should reflect themselves in the magnetic response of the Fe and Pd atoms near the interface and in the interlayer magnetic coupling. Thus a well determined atomic structure is always a prerequisite for obtaining reliable predictions of the electronic and magnetic properties—especially for those systems with strong overlayer–substrate hybridization.

II. COMPUTATIONAL METHOD AND RESULTS

In this article, the structural properties of the 2Pt/5Fe/2Pt(111) sandwich were determined using the atomic force approach,[9] which yields a well-optimized atomic structure. The Pt/Fe(111) system is simulated by a slab consisting of five layer of Fe and two layers of Pt on each side. We have carried out two sets of electronic structure calculations with the in-plane lattice constant frozen to either that of bulk fcc Pt (a_{Pt}=5.243 a.u.) or to the value of a=5.063 a.u., which is about the average of the bulk Fe and Pt interatomic distances. The interplanar distances of *all* layers in the slab are adjusted efficiently according to the calculated forces.[9] In the FLAPW approach, no shape approximations are made to the charge densities, potentials, and wave functions. The Kohn–Sham equations are solved self-consistently with an energy cutoff of 13 Ry for the variational plane-wave basis set. Within the muffin-tin spheres (r_{Fe}=2.15 a.u. and r_{Pt}=2.45 a.u.), lattice harmonics with angular momentum l up to 8 are employed to expand the charge density, potential, and wave functions. Summations over 18 k points in the $\frac{1}{12}$ irreducible 2D Brillouin zone are employed for k-space integrations. When the mean-root-square difference between the input and output charge and spin densities in the semirelativistic iterations is converged to better than 1.0×10^{-4} e/(a.u.)^3, the spin–orbit coupling is invoked as a perturbation in a second variational way.[10]

Calculated results for the layer-by-layer vertical atomic positions, spin and orbital magnetic moments, and Fermi contact hyperfine fields broken down into valence ($H_{CF,v}$) and core contributions $H_{CF,c}$ are listed in Table I, for the two values of the in-plane lattice constant. The structure with the bulk fcc Pt in-plane lattice constant is found to be the most stable (lowest total energy). Large multilayer relaxations are found for the Pt–Fe and Fe–Fe interplanar distances which play an important role on the electronic and magnetic properties of the system. The interlayer Fe–Fe distance, 3.26 a.u. in the interior region and 3.23 a.u. in the interfacial region, is much smaller than the corresponding Pt–Pt interlayer dis-

TABLE I. Calculated layer-by-layer vertical atomic positions, z (in a.u.), spin and orbital magnetic moments, M and L_z (in μ_B), Fermi contact hyperfine fields H_{CF} broken down into valence ($H_{CF,v}$) and core ($H_{CF,c}$) contributions (in kG), and the ratios $H_{CF,c}/M$ in (kG/μ_B) for Fe/Pt(111), for two values (a=5.243 a.u. and a=5.063 a.u.) of the in-plane lattice constant.

Atom	Fe(C)	Fe(I-1)	Fe(I)	Pt(I)	Pt(S)
a=5.243 a.u.					
z	0.00	3.26	6.49	10.03	14.27
M	2.07	2.11	2.44	0.27	0.05
L_z	0.04	0.07	0.12	0.08	0.01
H_{CF}	−315	−328	−275	···	···
$H_{CF,v}$	−30	−39	+60	···	···
$H_{CF,c}$	−285	−289	−335	···	···
$H_{CF,c}/M$	−137.7	−137.6	−137.6	···	···
a=5.063 a.u.					
z	0.00	3.30	6.57	10.19	14.52
M	1.95	2.00	2.32	0.25	0.07
L_z	0.04	0.05	0.10	0.06	0.02
H_{CF}	−308	−319	−282	···	···
$H_{CF,v}$	−39	−43	+36	···	···
$H_{CF,c}$	−269	−276	−318	···	···
$H_{CF,c}/M$	−137.9	−138.0	−137.4	···	···

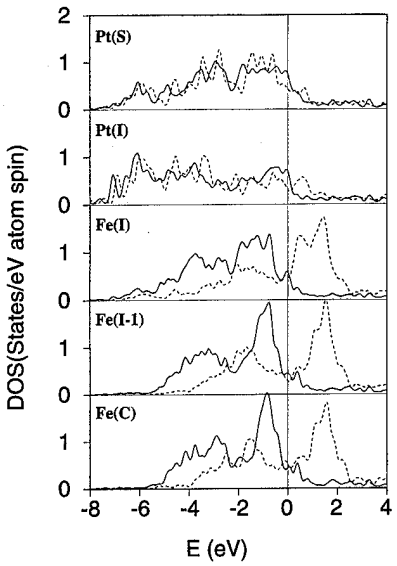


FIG. 2. Calculated layer-by-layer density of states for Pt/Fe(111). Solid and dashed lines stand for majority and minority spin parts, respectively. Energies are measured with respect to the Fermi energy.

tance of 4.28 a.u. in bulk fcc Pt. This is expected, of course, since the size of Fe atoms is much smaller than that of Pt atoms. Nevertheless, the Fe–Fe interatomic distance of 4.45 a.u. is still smaller by about 5% than that of 4.69 a.u. in bcc Fe. This shrinkage of the Fe–Fe distance can be attributed (i) to interfacial effects and (ii) to the failure of the local density approximation (LDA) imposed on the density functional theory which is known for underestimating the lattice constants of 3d transition metals by about 3%.[11] Note that while there is, as expected, an expansion of the interlayer distances for the smaller (5.063 a.u.) in-plane lattice constant, the Fe–Fe interatomic distance remains almost intact (within 1%). For both sets of calculations, the Pt–Fe and Pt–Pt interatomic distances are 4.65 and 5.22 a.u., respectively. These results clearly indicate that metal atoms tend to preserve their volumes upon slight changes of local environment. Surprisingly, while the Pt–Fe distance shrinks by 6.5% compared to the average of the bond lengths in bulk Fe and Pt, no relaxation (<1%) is found between the Pt–Pt layers, despite the presence of the surface and the interface on either side of the Pt layers.

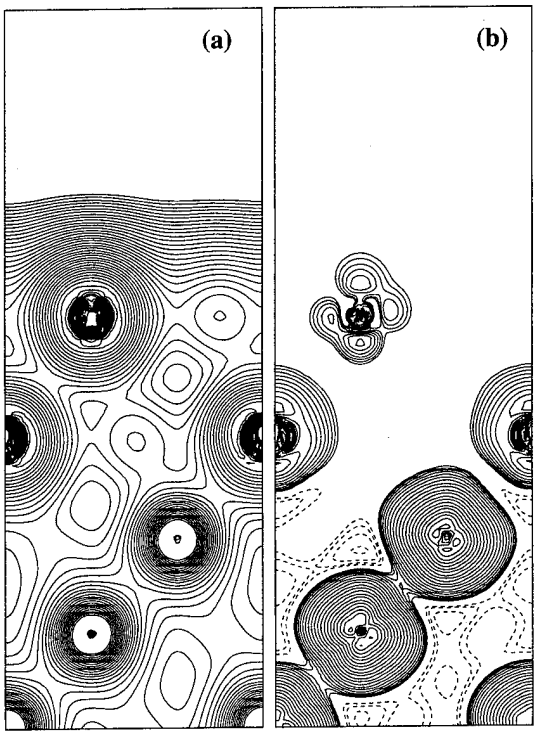


FIG. 1. Calculated charge and spin densities for Pt/Fe(111). Contours start from $\pm 1\times10^{-3}e$/a.u.^{3} and increase successively by a factor of $\sqrt{2}$. Solid (dotted) lines in (b) denote the positive (negative) spin density, respectively.

The charge density of the Pt/Fe(111) is presented in Fig. 1(a). The charge density in the interfacial region between Fe and Pt is greater than that between Pt and Pt atoms, indicating a strong Fe–Pt bonding. The strong interfacial interaction between the magnetic Fe overlayer and the Pt substrate can be seen more clearly in Fig. 2, where the layer-by-layer density of states (DOS) of the majority and minority spin are plotted. The profile of the DOS of the interface Fe(I) atom differs substantially from that of the central Fe(C) atom and even from that of the subinterface Fe(I-1) atom. Strong hybridization can be seen especially in the energy range of −6 to −4 eV and around the Fermi level for the majority spin, and around +1 eV and below −4 eV for the minority spin. As a result, the 5d bands of the interface Pt(I) and even of the surface Pt(S) are spin polarized. Note also that the d bands of the interfacial Fe(I) and Pt(I) layers are broadened, corresponding to the strong overlayer–substrate hybridization.

The spin density of the Pt/Fe(111) is shown in Fig. 1(b). The solid (dashed) lines label the positive (negative) contours. We find that (i) the Fe layers adopt ferromagnetic coupling in the distorted fcc structure; (ii) the induced magneti

zation of the Pt(I) site is parallel to that of Fe; and (iii) the magnetic disturbance in the Pt layers is short ranged [the volume associated with the positive spin density around Pt(S) becomes very small]. As can be seen more quantitatively in Table I, the spin magnetic moments of the Fe(C) and Fe(I-1) are 2.07 and 2.11 μ_B, respectively. These values are well below the calculated magnetic moment of 2.25 μ_B for bcc bulk Fe using the experimental lattice constant (a =5.425 a.u.), but close to that of 2.06 μ_B obtained using the LDA optimized lattice constant (a=5.225 a.u.). By invoking the spin–orbit coupling, small orbital magnetic moments, 0.03 and 0.05 μ_B, are found for the Fe(C) and Fe(I-1), respectively. From the DOS curves in Fig. 2, we see that there is a smaller number of majority spin d holes for the Fe(I) atom compared to that for the other Fe atoms. As a result, there is an enhancement of the Fe(I) magnetic moment (2.44 μ_B), which indicates the important role of the Pt–Fe interfacial hybridization on the Fe magnetization. The orbital magnetic moment of the Fe(I) is also found to be large, 0.1 μ_B. It is desirable to have experimental measurements using the magnetic circular dichroism technique to verify our theoretical predictions. The magnetic perturbation in the Pt layers is a shorter range effect since the induced spin (orbital) moment decreases quickly from 0.27 (0.08) μ_B in the Pt(I) layer to 0.05 (0.01) μ_B in the surface Pt(S) layer. It is important to note that the magnetic moments listed in Table I for the two values of the lateral lattice constants differ markedly, even though the interatomic distances remain almost unchanged. Clearly, this shows that the magnetism in Pt/Fe(111) is very sensitive to the details of the geometry, and thus a well-optimized atomic structure appears to be very important.[12]

The magnetic hyperfine interaction, which describes the interaction of the electronic spin moment with the nuclear magnetic moment, provides an important tool for the study of interface magnetism. Table I presents the calculated layer-by-layer Fermi contact hyperfine fields broken down into valence and core contributions. As established for many magnetic systems,[3] the core contribution (negative in sign) is proportional to the local Fe magnetic moment. The ratio of the core-hyperfine-field and the magnetic moment (137.5 kG/μ_B) is independent of the value of the in-plane lattice constant, and is very close to that obtained for other systems, 130–140 kG/μ_B.[3] While our results for the Fe(I) layer do show an enhancement of the interfacial magnetic moment, the total calculated H_{CF} is smaller in magnitude (−275 kG) due to the large *positive* (+60 kG) valence contribution, which, however, is localized to the interface; the subinterface valence contributions are again negative. Thus, as in previous calculations,[3] we find that while the core contribution is dominant, the valence contribution is very sensitive to the local environment. The trend of the calculated layer-by-layer H_{CF} agrees well with recent Mössbauer experiments;[6] i.e., the total H_{CF} is relatively smaller at the Fe(I), increases by 8.5% at the Fe(I-1), and then decreases again by 4% at the Fe(C). However, due to the small Fe–Fe interlayer distances found in our calculations, the results for the total hyperfine fields and magnetic moments are about 8%–10% smaller than the measured values.[12]

ACKNOWLEDGMENTS

Work supported by the ONR (Grant No. N00014-95-1-0489), the NSF (DMR-89-18887), and by a computing grant at the Arctic Region Supercomputing Center. N. K. would like to thank A. Simopoulos and T. Tsakalakos for enlightening comments and discussions.

[1] See review papers in *Magnetism in the Nineties*, edited by A. J. Freeman and K. A. Gschneidner, Jr. (Elsevier Science, Amsterdam, 1991).
[2] S. Hashimoto, H. Matsuda, and Y. Ochiai, Appl. Phys. Lett. **56**, 1069 (1990); F. J. A. M. Greidanus, W. B. Zeper, F. J. A. den Broeder, W. F. Godlieb, and P. F. Carcia, *ibid.* **54**, 2481 (1989); W. B. Zeper, F. J. A. M. Greidanus, P. F. Carbia, and C. R. Fincher, J. Appl. Phys. **65**, 4971 (1989).
[3] A. J. Freeman and R. Q. Wu, J. Magn. Magn. Mater. **100**, 497 (1991).
[4] B. Heinrich, A. S. Arrott, J. F. Cochran, Z. Celinski, and K. Myrtle, in *Science and Technology of Nanostructured Magnetic Materials*, edited by G. C. Hadjipanyasis and G. A. Prinz (Plenum, New York, 1991), p. 15.
[5] T. Katayama, Y. Suzuki, Y. Nishihara, T. Sugimoto, and M. Hashimoto, J. Appl. Phys. **69**, 5658 (1991).
[6] E. Devlin, V. Psycharis, A. Simopoulos, D. Niarchos, A. Jankowski, T. Tsakalakos, H. Wan, and G. Hatzipanayis, J. Magn. Magn. Mater. **120**, 236 (1993); E. Devlin, A. Kostikas, A. Simopoulos, A. Jankowski, M. Croft, and T. Tsakalakos (to be published).
[7] G. Kisters, Ch. Sauers, E. Tsymball, and W. Zinn, Hyperfine Interactions **92**, 285 (1994).
[8] E. Wimmer, H. Krakauer, M. Weinert, and A. J. Freeman, Phys. Rev. B **24**, 864 (1981), and references therein.
[9] Defined as the first derivative of the total energy with respect to the atomic position, the force in FLAPW approach contains both the Hellman–Feynman term and the Pulay correction terms. See also for bulks: J. M. Soler and A. R. Williams, Phys. Rev. B **40**, 1560 (1989); R. Yu, D. Singh, and H. Krakauer, *ibid.* **43**, 6411 (1992).
[10] D. S. Wang, R. Wu, and A. J. Freeman, Phys. Rev. Lett. **70**, 869 (1993).
[11] K. B. Hathaway, H. J. F. Jansen, and A. J. Freeman, Phys. Rev. B **31**, 7603 (1985); C. S. Wang, B. M. Klein, and H. Krakauer, Phys. Rev. Lett. **54**, 1852 (1985).
[12] Since LDA tends to underestimate the lattice constant of the 3d transition metals, calculations using the measured Fe–Fe interlayer distances will be carried out for quantitative comparison with experiment.

Magnetic properties and magnetization reversal in Co/Au multilayers (abstract)

Z. S. Shan, J. X. Shen,[a] R. D. Kirby, and D. J. Sellmyer
Behlen Laboratory of Physics and Center for Materials Research and Analysis, University of Nebraska, Lincoln, Nebraska 68588-0113

We report studies of magnetic properties in CoX Å/Au60 Å multilayers (X=5,6,7,8,12,20 Å), which were prepared by sputtering on Si(111) substrates, with emphasis on the magnetization reversal. Magnetization reversal was investigated by measurements of initial magnetization curves, minor loops, coercivity as a function of the maximum field of minor loops, temperature dependence of magnetic properties using Kronmüller's model,[1] time decay of Kerr rotation angle Θ_K, and the field-sweep speed dependence of coercivity $H_c(dH_a/dt)$ at room and/or low temperature. It is found that (1) the thermal activation volumes determined by $H_c(dH_a/dt)$ increase from $\sim 2.0\times10^{-17}$ to $\sim 9.9\times10^{-17}$ cm^3 as X varies from 5 to 20 Å, which corresponds to a cylindrical activation volume with ~800 Å diameter. (2) A Kronmüller analysis together with the initial magnetization curves, etc., for a Co5 Å/Au60 Å sample at room and low temperature indicates that wall pinning with small pinning sites is the major coercivity mechanism. The interaction between grains was studied with the so-called ΔM method: samples with thin Co layers (X=5,6,7 Å), which show perpendicular anistropy, exhibit negative ΔM or dipolar interactions, while samples with a thick Co layer (e.g., X=20 Å), which show in-plane anisotropy, exhibit positive ΔM or ferromagnetic exchange interactions. © *1996 American Institute of Physics.* [S0021-8979(96)60208-9]

Research supported by NSF-DMR 9222976.

[a]Present address: Applied Magnetics, 75 Robin Hill Road, Goleta, CA 93117.

[1]H. Kronmüller, K. D. Durst, and M. Sagawa, J. Magn. Mater. **74**, 291 (1988).

 0021-8979/96/79(8)/4786/1/$10.00 © 1996 American Institute of Physics

Coordinated RHEED, XRD, and FMR investigations of MBE grown Co–Cu (100) superlattices

R. A. Lukaszew and R. Naik
Department of Physics and Astronomy, Wayne State University, Detroit, Michigan 48202

K. R. Mountfield and J. O. Artman
Department of Electrical and Computer Engineering, Carnegie Mellon University, Pittsburgh, Pennsylvania 15213-3890

A sequence of fcc, ⟨100⟩ oriented, [Co (50 Å)–Cu (X)] superlattices with X=25–200 Å, was grown by molecular beam epitaxy on Cu(100)/Si(100) substrates. In-plane 33.4 GHz ferromagnetic resonance (FMR) data were analyzed to determine the perpendicular uniaxial magnetic anisotropy field (H_u) and cubic anisotropy field contributions. The H_u values were found to be negative, indicating that the film normal is a magnetic hard axis. The magnitude of H_u depended on the Cu layer thickness. Superlattice x-ray-diffraction and reflection high-energy electron-diffraction patterns were analyzed. The measured strain data for Co superlattice layers, in combination with known elastic and magnetostriction constants for bulk fcc Co, yield calculated strain-induced H_u values which agree well with those obtained from the FMR. The observed H_u values, which are affected by the Cu layer thickness, approach a constant for Cu thickness >100 Å. © *1996 American Institute of Physics.* [S0021-8979(96)51508-6]

INTRODUCTION

We report here our coordinated strain-dependent magnetic anisotropy studies of Co–Cu (100) superlattices using reflection high-energy electron diffraction (RHEED), x-ray diffraction (XRD), and ferromagnetic resonance (FMR). Many phenomena observed in magnetic multilayers are strongly affected by structural and interfacial perfection of the films and the presence of strains.[1] Recently we studied strained Ni–Cu(100) superlattices of varying Ni and Cu layer thicknesses using in-plane and out-of-plane FMR.[2] The observed uniaxial perpendicular magnetic anisotropy was found to be solely strain induced and depended not only on the layer thickness of Ni but also on that of Cu. In 1968 Jesser and Matthews[3] used transmission electron microscopy studies to show that ultrahigh vacuum evaporated deposits of Co on a (001) Cu surface at room temperature have fcc structures and are elastically strained so as to match the Cu lattice across the Co–Cu interface. For Co film thicknesses larger than 20 Å long dislocations were generated to accommodate part of the difference between the lattice parameters of fcc Co and Cu. Jesser and Matthews observed an increase in the density of misfit dislocations as the thickness of Co film was further increased. Heinrich *et al.*,[4] using FMR, have investigated magnetic anisotropy in ultrathin films of metastable fcc Co(001) films grown on a bulk Cu(001) single crystal and covered by a Cu(001) film. A large negative uniaxial perpendicular anisotropy field was observed, a consequence of the tetragonal distortion induced in a Co(001) lattice grown on Cu(001).

EXPERIMENT

A sequence of Co–Cu (100) superlattices was prepared in an ultrahigh vacuum using a molecular beam epitaxy deposition system with a base pressure $<1\times10^{-10}$ Torr. The superlattices were grown on a 1200 Å thick Cu(100) seed layer deposited on Si(100) substrates etched with a 10% hydrofluoric acid solution. Co and Cu were evaporated from two independent electron-beam evaporators with computer-controlled pneumatic shutters and at deposition rates of ~0.5 Å/s. Further details of the deposition system, the growth of Cu(100) seed layers on hydrogen-terminated Si(100), and the growth of epitaxial Co(100) layers on Cu(100) layers are described elsewhere.[5,6] In order to determine the effect of the Cu thickness on the strain and magnetic anisotropy, four different superlattices were prepared, each with a constant Co layer thickness of 50 Å alternated with Cu layers of thicknesses of 25, 50, 100, and 200 Å, respectively. The total thickness of Co in each superlattice was kept at 500 Å. All films had a 50 Å Cu cap layer for protection from oxidation.

During the deposition of the film, RHEED scans were continuously recorded (up to 30 scans per second) using a CCD camera. RHEED scans were subsequently analyzed to determine the in-plane strains of the superlattice layers. Standard θ–2θ XRD scans were performed with Cu $K\alpha$ radiation. A one-dimensional x-ray scattering model, which includes discrete layer thickness fluctuations and interface diffusion in the kinematic approximation, was used to determine the periodicity of the superlattice as well as the strains in the Co and Cu layers.[7]

RESULTS AND DISCUSSION

Sharp and elongated spotty RHEED patterns were observed during the growth of all Co-Cu superlattice films indicating epitaxial but three-dimensional growth. The full fourfold azimuthal symmetry of the ⟨100⟩ orientation for the Co–Cu superlattices was clearly observable for all the films. The mismatch between the Cu and fcc Co bulk value lattice spacings (3.617 and 3.548 Å, respectively) is 1.9%. This is small enough that strained, epitaxial growth can be anticipated for the Co–Cu superlattice films. Figure 1 shows the in-plane lattice spacings, d_{200}, obtained from the recorded horizontal line scans of the RHEED pattern observed during the growth of first two bilayers of a [Co(50 Å)–Cu(200 Å)]

 0021-8979/96/79(8)/4787/3/$10.00 © 1996 American Institute of Physics

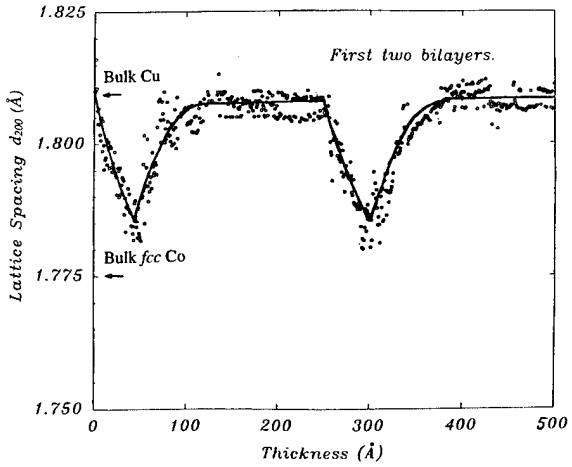


FIG. 1. In-plane lattice spacings of Co and Cu layers obtained from RHEED scans during the growth of first two bilayers of the [Co(50 Å)–Cu(200 Å)] superlattice. The solid line is only a guide to the eyes.

superlattice grown on a 1200 Å thick Cu(100) seed layer deposited on a Si(100) substrate. The data indicate that the Co lattice is initially stretched to match the bulklike Cu lattice but relieves its strain, perhaps by formation of dislocations.[3] It is interesting to note that the Co lattice remains stretched at a thickness of 50 Å with a residual in-plane strain of ~0.6%. Further growth of Cu on Co shows that the Cu lattice initially gets compressed to match the Co lattice and then approaches bulk Cu lattice spacing for a Cu thickness ~100 Å. Hence, for superlattices with Cu layer thicknesses <100 Å, it is expected that Co and Cu layers are coherently strained and that the strain in Co layers is affected by the Cu layer thickness. Figure 2 shows the lattice spacings, d_{200}, of Co and Cu layers during the growth of the first three bilayers of a [Co (50 Å)–Cu(50 Å)] superlattice. The Co layers in the second and third bilayers are strained to a lesser extent compared to the first Co layer which is grown on a bulklike Cu seed layer. These results correlate with XRD measurements as explained below.

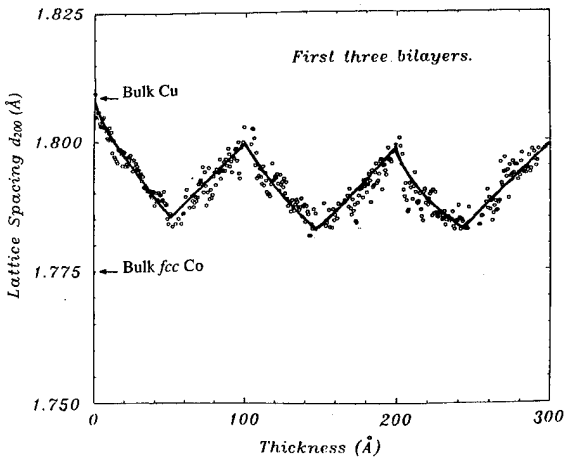


FIG. 2. In-plane lattice spacings of Co and Cu layers obtained from RHEED scans during the growth of first three bilayers of the [Co(50 Å)–Cu(50 Å)] superlattice. The solid line is only a guide to the eyes.

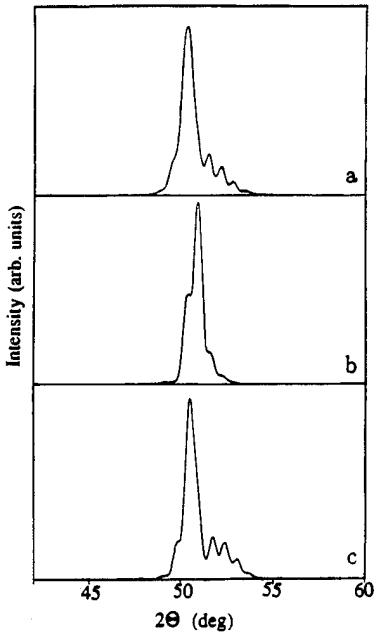


FIG. 3. (a) The high-angle XRD scan for the [Co(50 Å)–Cu(100 Å)] superlattice. Simulations of the XRD intensities for this superlattice (b) with bulk Co(200) and Cu(200) lattice spacings of 1.774 and 1.808 Å; (c) and with Co(200) and Cu(200) lattice spacings of 1.747 and 1.815 Å.

High-angle x-ray-diffraction measurements on all of the samples confirm ⟨100⟩ oriented growth of the Co–Cu superlattices with no trace of the ⟨111⟩ texture. Figure 3(a) shows the XRD scan for a Co–Cu superlattice with a Co layer thickness of 50 Å and a Cu layer thickness of 100 Å. Comparisons of the simulated XRD patterns to the observed peak patterns for the Co–Cu superlattices indicate a strong dependence upon the lattice spacing modulations and a relative insensitivity to composition modulations, very similar to the observations on Ni–Cu(100) (see Ref. 3) and Co–Cu(111) (see Ref. 7) superlattices. Figure 3(b) shows the simulated XRD intensities for the above superlattice with bulk Co(200) and Cu(200) lattice spacings of 1.774 and 1.808 Å, respectively. Obviously, these simulated XRD intensities do not reproduce the experimental pattern. On the other hand, Fig. 3(c) shows the simulated XRD intensities for strained Co(200) and Cu(200) lattices with spacings of 1.747 and 1.815 Å, respectively. Although we use a single average value for the lattice spacing for each component of the superlattice (contrary to the RHEED observations), Fig. 3(c) represents a reasonable simulation of the experimental XRD pattern. The $d_{\perp}(=d_{200})$ spacings for both Co and Cu in these superlattices are determined from the best fit of the simulations to the experimental XRD data (see Table I) and clearly show that the Co lattices are contracted while the Cu lattices are dilated along the growth direction. This is consistent with the RHEED results since an expansion of the Co lattice in the direction parallel to the film plane leads to a contraction of the lattice perpendicular to it. The observed tetragonal distortion (see Table I) for Co amounts to a few percent as reflected by the negative values of $(\epsilon_{\perp}-\epsilon_{\parallel})$, where $\epsilon_{\perp}$ and $\epsilon_{\parallel}$ are the perpendicular and parallel strains, respectively. $\epsilon_{\perp}=(d_{\perp}-d_0)/d_0$ and $\epsilon_{\parallel}$ is evaluated using the relation

TABLE I. XRD and FMR results for Co–Cu(100) superlattices.

t_{Co} (Å)	t_{Cu} (Å)	Co d_{200}(Å)	Cu d_{200}(Å)	Co $(\epsilon_\perp-\epsilon_\parallel)$[a]	$4\pi M_{eff}$ (kG)	$2K_1/M_s$ (kOe)	H_u (FMR)[b] (kOe)	H_u (Calc.) (kOe)
50	25	1.757	1.827	−0.0168	22.0	−1.0	−3.7	−3.7
50	50	1.752	1.820	−0.0217	23.3	−1.1	−5.0	−4.8
50	100	1.747	1.815	−0.0266	23.6	−1.2	−5.3	−5.8
50	200	1.747	1.810	−0.0266	23.7	−1.2	−5.4	−5.8

[a]$\epsilon_\parallel=-\epsilon_\perp(1-\nu)/2\nu$ where ν is the Poisson ratio. $\nu=0.4$ for fcc Co.
[b]$H_u=4\pi M_s-4\pi M_{eff}$ where $4\pi M_s=18.3$ kG for bulk fcc Co. H_u (Calc.) obtained from strain data. Uncertainties: $d_{200}\pm0.002$, $(\epsilon_\perp-\epsilon_\parallel)\pm0.0024$, $4\pi M_{eff}\pm0.5$, $2K_1/M_s\pm0.05$, H_u (FMR)±0.5, H_u (Calc.)±0.6.

$\epsilon_\parallel=\epsilon_\perp(1-\nu)/2\nu$, where d_0 is the undistorted Co spacing and the Poisson ratio $\nu=0.4$ for Co.[4] Although the Co layer thickness is kept same (50 Å) in all the superlattices, we note that the tetragonal distortion of the Co lattice is sensitive to the Cu layer thickness.

The FMR data were taken at room temperature in a 33.4 GHz, TE_{011} cylindrical cavity system. At this microwave frequency the requisite resonance magnetic field is sufficient to magnetically saturate the samples. Typical FMR samples were 2 mm×2 mm and were aligned along cleavage faces of the Si substrate. Resonance fields for in-plane FMR measurements on all films exhibit an oscillatory angular dependence with respect to a ⟨100⟩ crystallographic direction in the film reflecting the fourfold symmetry of the Co layers. From fits to the angular dependence[5] of the experimental resonance data, the effective demagnetization field $4\pi M_{eff}$ and the cubic anisotropy contribution $2K_1/M_s$ are determined (see Table I) where K_1 is the fourth-order cubic anisotropy constant and M_s is the saturation magnetization. The presence of any perpendicular magnetic anisotropy H_u can be numerically determined from the relationship $H_u=4\pi M_s-4\pi M_{eff}$. The bulk Co values of $g=2.13$ and $4\pi M_s=18.3$ kG have been utilized in the calculations.[8,9]

Utilizing the measured strain $(\epsilon_\perp-\epsilon_\parallel)$ from XRD data, we have calculated the contribution to the strain-induced magnetic anisotropy due to inverse magnetostriction using the following expression:[10]

$$H_u=(3/M_s)\lambda_{100}(C_{11}-C_{12})(\epsilon_\perp-\epsilon_\parallel). \quad (1)$$

Here λ_{100} is the linear magnetostriction constant along ⟨100⟩, and C_{11} and C_{12} are the cubic elastic constants. For bulk fcc Co values of[4,9] $M_s=1460$ emu/cm^3, $\lambda_{100}=1.3\times10^{-4}$, $C_{11}=2.42\times10^{12}$ dyn/cm^2, and $C_{12}=1.6\times10^{12}$ dyn/cm^2, Eq. (1) gives H_u values between −3.7 and −5.8 kOe for the superlattices; see Table I. The magnitude of H_u depends on the Cu layer thickness and approaches a constant value for Cu thickness >100 Å. These values agree reasonably well with the values derived from FMR measurements. We note that the observed values of $2K_1/M_s$ for Co–Cu superlattices are similar to those of single-layered Co(100) samples.[4]

In summary, our coordinated studies on Co–Cu (100) superlattices using RHEED, XRD, and FMR measurements have shown that the strain in the Co lattice is affected by the thickness of Cu layers and that magnetostriction plays a significant role in determining the magnetic anisotropy. The observed H_u values depend on the Cu layer thickness and approach a constant for Cu thickness >100 Å.

ACKNOWLEDGMENT

This work was supported by the National Science Foundation Grants No. DMR-9321127 and No. ECD 8907068.

[1] See various articles in "Magnetic Thin Films, Multilayers and Surfaces," edited by H. Hopsters, S. S. P. Parkin, G. Prinz, J.-P. Renard, W. Zinn, Materials Research Society Symposium Proceedings, 1991, Vol. 231.
[2] R. Naik, A. Poli, D. McKague, A. Lukaszew, and L. E. Wenger, Phys. Rev. B **51**, 3549, 1995.
[3] W. A. Jesser and J. W. Matthews, Phil. Mag. **17**, 461 (1968).
[4] B. Heinrich and J. F. Cochran, Advances in Physics, **42**, 523 (1993).
[5] R. Naik, C. Kota, J. S. Payson, and G. L. Dunifer, Phy. Rev. B **48**, 1008 (1993).
[6] B. G. Demczyk, R. Naik, G. Auner, C. Kota, and U. Rao, J. Appl. Phys. **75**, 1956 (1994).
[7] F. J. Lammellas, H. He, and R. Clarke, Phys. Rev. B **43**, 12296 (1991).
[8] R. Krishnan, S. Sakakima, J. F. Cochran, B. Heinrich, C. Myrtle, R. W. Qiao, and C. E. Patton, J. Mag. Mag. Mat. **67**, 88 (1987).
[9] H. P. Myers and W. Sucksmith, Proc. Roy. Soc. (London) **A207**, 427 (1951); W. D. Doyle and P. J. Flanders, Proc. of the International Conf. on Mag. Nottingham, 1964, p. 751.
[10] S. Chikazumi and S. H. Charap, *Physics of Magnetism* (Wiley, New York, 1964).

Studies of the magnetic anisotropies of Co(1$\bar{1}$00)/Cr(211) and Co(11$\bar{2}$0)/Cr(100) multilayers

J. C. A. Huang, F. C. Tang, W. W. Fang, R. L. Liu, and Y. M. Hu
Physics Department, National Cheng–Kung University, Tainan, Taiwan 70101

C. K. Lo, Y. Liou, Y. D. Yao, W. T. Yang, C. P. Chang, and S. Y. Liao
Institute of Physics, Academia Sinica, Taipei, Taiwan 70101

Co(1$\bar{1}$00)/Cr(211) and Co(11$\bar{2}$0)/Cr(100) multilayers have been simultaneously prepared on MgO(110) and MgO(100) substrates, respectively, by molecular beam epitaxy. They show however distinct magnetic anisotropic behavior which coincides with their magneto–crystalline anisotropy. Magneto–optical Kerr effect shows the existence of a unique easy axis and strong in-plane uniaxial magnetic anisotropy in Co(1$\bar{1}$00)/Cr(211) multilayers, which is induced by the well-defined hexagonal crystalline of the Co(1$\bar{1}$00) layers. For Co(11$\bar{2}$0)/Cr(100) multilayers, on the other hand, an in-plane biaxial magnetic anisotropy is found due to the bicrystalline structure of the Co(11$\bar{2}$0) layers. © *1996 American Institute of Physics.* [S0021-8979(96)51608-X]

I. INTRODUCTION

The magnetism of thin metallic films and multilayers has attracted much attention in recent years for both fundamental research and advanced technological applications. It is noted that magnetism in these systems can often be characterized by specific magnetic anisotropies. For example, the perpendicular surface (interface) anisotropy can exist in ultra thin magnetic films (multilayers) as a consequence of symmetry breaking in the surface (interface).[1] There also has been an increasing interest in understanding the relationship between the magnetic anisotropies and the crystal structures. It is found that the magnetic anisotropies of the thin films may depend strongly on the underlying templates (substrates or buffer layers).[2–5]

Co-related system is suitable for studying the correlation between structure and magnetism owing to the abundance of the its structural and magnetic properties. The bulk phase of Co is known as hexagonal close packed (hcp) at room temperature. It undergoes a Martinsitic structural transformation to face centered cubic (fcc) phase at ~400 °C.[6] In the form of thin films it can also be epitaxially stabilized as body centered cubic (bcc) structure.[7] Co/Cr multilayers are of our high interest because of the remarkable structural and magnetic properties, and possible applications in magnetic or magneto–optical recording. Previous studies[8–11] on Co/Cr multilayers have been, however, restricted to polycrystalline, textured, or semiepitaxial samples, making the understanding of the structural and magnetic properties and their interplay much difficult.

In this article we report the magneto-optical Kerr effect (MOKE) studies of the magnetic anisotropies of high-quality Co(1$\bar{1}$00)/Cr(211) and Co(11$\bar{2}$0)/Cr(100) multilayers grown by molecular beam epitaxy (MBE). Longitudinal and polar MOKE configurations were used to determine the magnetic easy and hard axes, and their connection with the crystal structures. We demonstrate here the novel control of the orientation and crystalline structure, and hence the magnetic anisotropies (uniaxial or biaxial) of Co layers by using proper crystal plane of the underlying Cr layers.

II. FILM PREPARATION AND MEASUREMENTS

We have indeed grown more than 30 samples of Co/Cr(211) and Co/Cr(100) multilayers. The results presented here mainly focus on the general and common features of these samples. The specific Co/Cr samples discussed here posses 17 bilayers periods with 40 Å Co and 20 Å Cr in each bilayer: $[Co(40\ Å)/Cr(20\ Å)]_{17}$. The Co/Cr(211) and Co/Cr(100) multilayers were simultaneously prepared on epitaxial grade MgO(110) and MgO(100) substrates, respectively. Details of the growth procedures were described elsewhere.[14]

The crystal structure and quality were characterized by reflection high-energy electron-diffraction (RHEED) and x-ray diffraction (XRD). The correlation between the structural and magnetic properties were investigated by MOKE technique. Polar (magnetization lies in the scattering plane and perpendicular to the film surface) and longitudinal (magnetization lies both in the scattering plane and the film surface) configurations of MOKE were employed to determine the out-of-plane and in-plane magnetization loops of the samples. The MOKE measurements were carried out at room temperature in a magnetic field H up to 2 kOe. Note that the penetration depth[12] of the (He–Ne) laser light for MOKE experiment is of ~150–200 Å, only top three Co/Cr bilayers (of the multilayers) can be probed by MOKE.

III. RESULTS AND DISCUSSIONS

For Co/Cr multilayers on grown Mo buffer layers on MgO(110) substrates studied here, we have determined the following orientational relationships (ORs):

Co(1$\bar{1}$00)‖Cr(211)‖Mo(211)‖MgO(110),

Co[11$\bar{2}$0]‖Cr[$\bar{1}$11]‖Mo[$\bar{1}$11]‖MgO[$\bar{1}$10],

Co[0001]‖Cr[0$\bar{1}$1]‖Mo[0$\bar{1}$1]‖MgO[001];

while on MgO(100) substrates the ORs are:

Co(11$\bar{2}$0)‖Cr(100)‖Mo(100)‖MgO(100),

Co[1$\bar{1}$00]‖Cr[011]‖Mo[011]‖MgO[010],

 0021-8979/96/79(8)/4790/3/$10.00 © 1996 American Institute of Physics

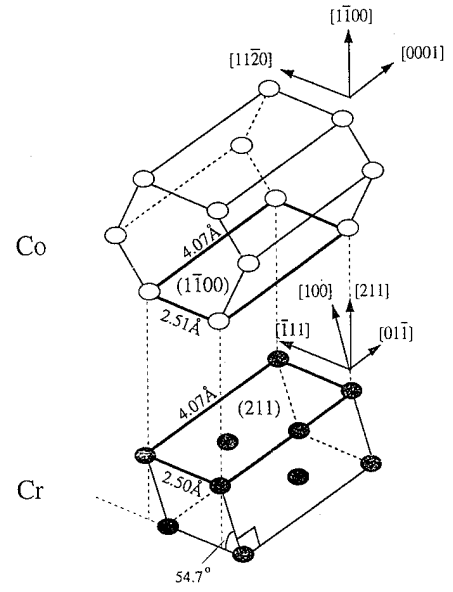


FIG. 1. Schematic diagrams showing the geometry, unit cell (indicated by bold lines) and epitaxial relationship of the hcp Co(1$\bar{1}$00) and bcc Cr(211).

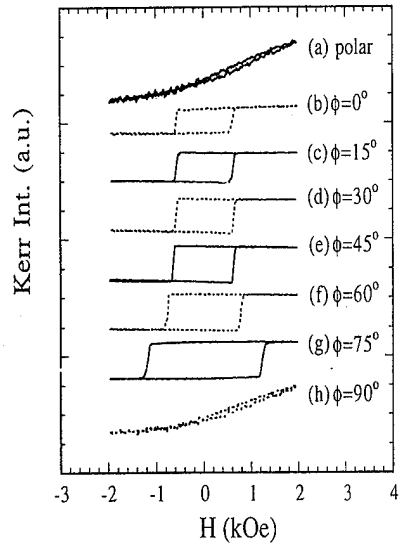


FIG. 3. The MOKE hysteresis loops for the Co(1$\bar{1}$00)/Cr(211) multilayer: (a) polar Kerr loop; (b)–(h) longitudinal Kerr loops as a function of the azimuthal angle ϕ.

Co[0001]‖Cr[0$\bar{1}$1]‖Mo[0$\bar{1}$1]‖MgO[001]

(or

Co[0001]‖Cr[011]‖Mo[011]‖MgO[010],

and

Co[1$\bar{1}$00]‖Cr[0$\bar{1}$1]‖Mo[0$\bar{1}$1]‖MgO[001]

due to the bicrystalline structure, as discussed below). The epitaxial relationships were confirmed by RHEED and XRD studies. Part of the structural analysis related to these multilayers were or to be published elsewhere.[13–15] We present here mainly about their magnetic properties and the effect of crystal structure upon magnetic anisotropies, as investigated by MOKE.

Figure 1 and Fig. 2 display the schematic diagrams of the geometry and the unit cells of Co(1$\bar{1}$00)/Cr(211) and Co(11$\bar{2}$0)/Cr(100) multilayers, respectively. Although Co (hcp) and Cr (bcc) possess distinct bulk structures, Co(1$\bar{1}$00) and Cr(211) planes match extremely well in lattice parameters and symmetry (both are twofold). As illustrated in Fig. 1, the unit cell of Co(1$\bar{1}$00), 4.07 Å×2.51 Å, matches perfectly with that of Cr(211), 4.07 Å×2.50 Å. This provides us an opportunity to synthesize high-quality heterostructural superlattices. For Co(11$\bar{2}$0)/Cr(100) system, on the other hand, the unit cell of Co(11$\bar{2}$0), 4.07 Å×4.34 Å, match poorly in

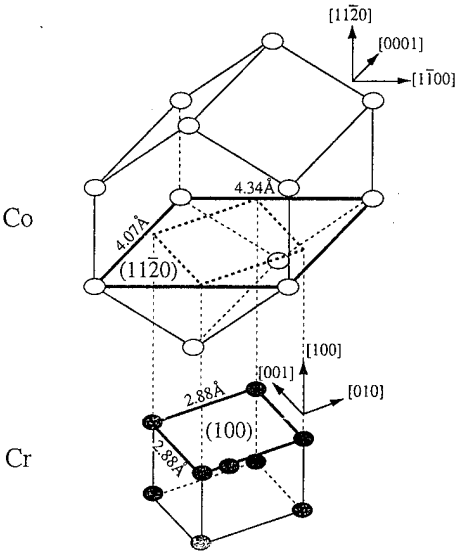


FIG. 2. Schematic diagrams showing the geometry, unit cell (indicated by bold lines) and epitaxial relationship of the hcp Co(11$\bar{2}$0) and bcc Cr(100).

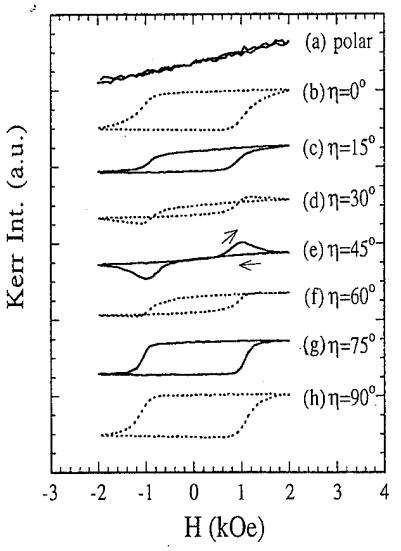


FIG. 4. The MOKE hysteresis loops for the Co(11$\bar{2}$0)/Cr(100) multilayer: (a) polar Kerr loop; (b)–(h) longitudinal Kerr loops as a function of the azimuthal angle η.

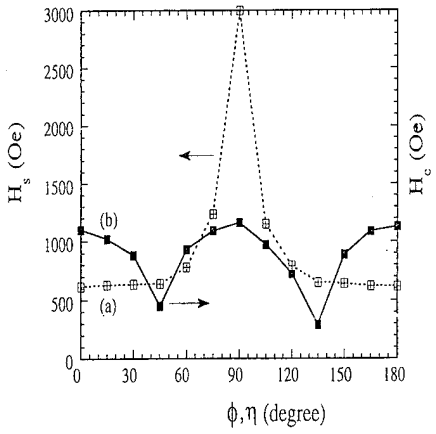


FIG. 5. (a) Saturation field H_s is shown as a function of the azimuthal angle ϕ for the Co(1$\bar{1}$00)/Cr(211) multilayer. (b) Coercive field H_c is plotted as a function of the azimuthal angle η for the Co(11$\bar{2}$0)/Cr(100) multilayer.

one direction (Co[1$\bar{1}$00]) with the rotated cell of Cr(100), 4.07 Å×4.07 Å, where 4.07 Å(=$\sqrt{2}$×2.88 Å) is the diagonal spacing of the original cell. Indeed, Cr(100) possesses fourfold crystal symmetry while Co(11$\bar{2}$0) has only twofold symmetry. The symmetry and lattice-spacing mismatches between Co(11$\bar{2}$0) and Cr(100) cells result in the bicrystalline structure of the Co(11$\bar{2}$0) layers. That is, the Co[0001] axis can be either parallel to the Cr[011] or Cr[01$\bar{1}$].

Shown in Figs. 3(a) and 4(a) are the polar MOKE hysteresis loops of the Co/Cr(211) and Co/Cr(100) multilayers, respectively. It is clear that both multilayers are hard to be magnetized along the out-of-plane directions. For Co/Cr(211) sample, Figures 3(b)–3(h) show a series of in-plane magnetization loops as a function of the azimuthal angle ϕ, where ϕ is defined as the angle between the MgO[$\bar{1}$10](∥Cr[01$\bar{1}$]∥Co[0001]) axis (see Fig. 1) and the direction of the applied field. Similar measuring procedures of the MOKE hysteresis loops for Co/Cr(100) multilayers are displayed in Figs. 4(b)–4(h), where in this case the azimuthal angle η is the angle between the in-plane MgO[001](∥Cr[01$\bar{1}$]) axis (see Fig. 2) and the direction of the field.

Although both multilayers are difficult to be magnetized along the out-of-plane directions, they show however quite distinct in-plane azimuthal anisotropies. For Co/Cr(211) sample, square hysteresis loops were observed from ϕ=0° (H∥Co[0001]) to 75° with gradual increase of the saturation field as the angle ϕ is turned (experimentally done by in-plane rotation of the sample with the field direction fixed). While continuously varying magnetization curves were observed for field along ϕ=90° (H∥Co[11$\bar{2}$0]), as shown in Figs. 3(b)–3(h). The saturation field H_s here is defined as the field when the magnetization is 90% saturated during magnetization reversal process. It is obvious that the magnetic hard axis lies in the (in-plane) Co[11$\bar{2}$0] direction perpendicular to the easy axis Co[0001] (see Figs. 1 and 3). Very similar hysteresis loops and saturation fields were found for field directed along the azimuthal angles ϕ and (180−ϕ) [as well as (ϕ+180) and −ϕ], suggesting the existence of a uniaxial magnetic anisotropy for the Co/Cr(211) sample. This can be clearly seen by plotting H_s as a function of the azimuthal angle ϕ, as shown in Fig. 5(a). The relatively large saturation fields of >500 Oe in the easy direction is likely resulted from the Cr spacer layers.[16]

For Co/Cr(100) sample, on the other hand, the in-plane magnetization loops are more complicated. As shown in Fig. 4(b), squarelike hysteresis loops were observed for η=0°. By turning the azimuthal angle η from 0° to 45°, the hysteresis loops shift from one type to another with gradual decrease of the coercive field. Similar hysteresis loops and coercive fields were found for field directed along the azimuthal angles η and (90−η). The MOKE patterns in Figs. 4(b)–4(h) repeat for η from 90° to 180° (and every other 90°). Figure 5(b) shows the coercive field H_c as a function of the azimuthal angle η. As can be determined from Fig. 5(b) and Figs. 4(b)–4(h), the easy axes are along η=0° (∥Cr[01$\bar{1}$]) and η=90° (∥Cr[011]), and the hard axis along η=45° (∥Cr[010]) and η=135° (∥Cr[001]), indicating the existence of a biaxial magnetic anisotropy for the Co/Cr(100) sample. Note that the two magnetic easy axes (along Cr[01$\bar{1}$] and Cr[011]) coincide with the Co[0001] axes of the bicrystalline Co layers, as discussed above.

Similar magnetic anisotropic properties mentioned above have been detected in single bilayer films of Co/Cr(100) and Co/Cr(211). Furthermore, we have observed relatively strong (weak) anisotropic effect in magnetoresistance measurements for the latter (former) case.[15] It appears that the anisotropic effect dominates in the Co/Cr(211) multilayers, in marked contrast to the other multilayer systems which show stronger coupling effect and isotropic (and giant) magnetoresistance effect. The mechanism of magnetization reversal processes, including the minor loop behaviors, of the Co/Cr(211) and Co/Cr(100) films will be published in the forthcoming articles.

[1] L. Neel, J. Phys. **15**, 225 (1954).
[2] J. J. Krebs, B. T. Jonker, and G. A. Prinz, J. Appl. Phys. **61**, 2596 (1986).
[3] J. M. Florczak and E. Dan Dahlberg, J. Appl. Phys. **67**, 7520 (1990).
[4] J. M. Florczak, E. Dan Dahlberg, J. N. Kuznia, A. M. Wowchak, and P. I. Cohen, J. Appl. Phys. **69**, 4997 (1991).
[5] N. Metoki, Th. Zeidler, A. Stierle, K. Brohl, and H. Zabel, J. Magn. Magn. Mater. **118**, 57 (1993).
[6] See, e.g., CRC *Handbook of Chemistry and Physics*, 69th ed., edited by R. C. Weast, M. J. Astle, and W. H. Beyer (Chemical Rubber, Boca Raton, Florida, 1988–1989).
[7] G. A. Prinz, Phys. Rev. Lett. **54**, 1051 (1985).
[8] D. Wang and D. J. Sellmyer, J. Appl. Phys. **69**, 4541 (1991).
[9] M. B. Sterns, C. H. Lee, and T. L. Groy, Phys. Rev. B **40**, 8256 (1989).
[10] M. B. Sterns, Y. Cheng, and C. H. Lee, J. Appl. Phys. **67**, 5925 (1990).
[11] Y. Henry, C. Meny, A. Dinia, and P. Panissod, Phys. Rev. B **47**, 15037 (1993).
[12] We have studied various Co/Cr bilayers with Cr(50–300 Å) grown on top of thick Co layers. The Kerr intensities were completely suppressed for Cr films thicker than 200 Å.
[13] J. C. A. Huang, Y. Liou, H. L. Liu, and Y. J. Wu, J. Cryst. Growth **139**, 363 (1994).
[14] Y. Liou, J. C. A. Huang, Y. D. Yao, C. H. Lee, K. T. Wu, C. L. Lu, S. Y. Liao, Y. Y. Chen, N. T. Liang, W. T. Yang, C. Y. Chen, and B. C. Hu, J. Appl. Phys. **76**, 6516 (1994).
[15] J. C. A. Huang, Y. Liou, Y. D. Yao, W. T. Yang, C. P. Chang, S. Y. Liao, and Y. M. Hu, Phys. Rev. B **52**, R13 110 (1995).
[16] We have observed a trend that H_s decreases with the decreasing of the Cr thickness for a fixed Co thickness in the multilayers. For pure Co films on MgO substrates, the measured saturation fields are of only ~50–100 Oe.

Reorientational transition of the magnetic anisotropy and antiferromagnetic coupling of Co/Cr(001) superlattices

Th. Zeidler, F. Schreiber, and H. Zabel
Experimentalphysik/Festkörperphysik, Ruhr-Universität Bochum, 44780 Bochum, Germany

We have measured the magnetic anisotropy of high quality Co/Cr(001) superlattices as a function of the Co thickness using the magneto-optical Kerr effect (MOKE) and a torsion magnetometer. The samples grown by molecular beam epitaxy exhibit a reorientational transition of the easy axis from in-plane for large Co thicknesses ($t_{Co} \geq 14$ Å) to out-of-plane for 10 Å$\leq t_{Co} \leq$14 Å and back again to the in-plane orientation for $t_{Co} \leq 10$ Å. We provide evidence that this reorientational transition of the magnetization direction is due to a sign change of the interface anisotropy constant induced by a concomitant structural phase transition of the Co layers from hcp to bcc with decreasing Co layer thickness. We have observed antiferromagnetic alignment of the Co layer magnetization both for in-plane and perpendicular magnetic anisotropy. The first maximum of the antiferromagnetic interlayer interaction occurs at $t_{Cr}=6$ Å, which is in a good agreement with the results for Fe/Cr(001). In order to theoretically describe the spin structure of the antiferromagnetic coupled multilayers we have performed absolute minima calculations of the angle dependent anisotropy energy. In contrast to trilayer systems we found highly asymmetric spin structures in the superlattices during the remagnetization process. © *1996 American Institute of Physics.* [S0021-8979(96)51708-6]

One of the important issues in the field of magnetic superlattices is the investigation of magnetic interface anisotropies. The crystal structure of the superlattices and sharp interfaces are of crucial importance for understanding of these anisotropies. In Co/Cr(001) superlattices the Co layers exhibit a continuous structural phase transition from hexagonal close packed (hcp) to body centered cubic (bcc) with decreasing Co layer thickness.[1] Therefore the magnetic properties of Co/Cr(001) superlattices are expected to be strongly influenced by this structural phase transition. The ideal bcc structure is, however, never realized even down to $t_{Co}=5$ Å. Furthermore, concerning the oscillatory interlayer exchange coupling and the appertaining spin structure, a comparison between the similar systems Co/Cr(001) and Fe/Cr(001) is highly interesting.

The magnetic anisotropy as measured via magneto-optical Kerr effect (MOKE) hysteresis curves [Figs. 1(a) and 1(b)] and ferromagnetic resistance (FMR) (Ref. 2) for Co thicknesses $t_{Co} \geq 14$ Å exhibits a typical $1/t_{Co}$ behavior indicating the presence of a perpendicular interface anisotropy in Co/Cr(001) superlattices with an extrapolated critical Co thickness $t_C \approx 13.5$ Å for perpendicular magnetic anisotropy.[3] From the slope we obtain an interface anisotropy constant of $K_S \approx -0.65$ mJ/m^2 using the reduced value of magnetization $M_S=1000$ kA/m as determined by a Faraday balance. This rather large value of K_S is comparable with results for Co/Pd and Co/Pt.[4,5] The reduced magnetization M_S arises from a small interdiffusion zone at the interface between adjacent Co and Cr layers which is estimated to be <2 Å.

The magnetic anisotropy energy per Co unit volume E_A of the system Co/Cr(001) can be expressed as

$$NE_A = \sum_{n=1}^{N} \frac{1}{2}\mu_0 M_S^2 \cos^2\theta_n - \sum_{n=1}^{N} \mu_0 M_S H \cos(\theta_n - \theta_H) + \sum_{n=1}^{N} K_1 \cos^2\theta_n + \sum_{n=1}^{N} K_2 \cos^4\theta_n + \sum_{n=1}^{N} \frac{1}{t_{Co}} 2K_S \cos^2\theta_n, \quad (1)$$

including Zeeman energy, shape anisotropy, crystal anisotropy terms of Co hcp K_1 and K_2 and the interface anisotropy contribution K_S. The angle θ_n ($n=1,\ldots,N$, N=number of Co layers) is defined by the angle between the sample normal and the magnetization **M**. The magnetic field H is aligned perpendicular to the surface ($\theta_H=0$).

Taking into account the experimental values for K_S and M_S we have calculated the magnetocrystalline anisotropy constants K_1 and K_2 by a fit to the data points shown by the solid lines in Figs. 1(a) and 1(b). Best results are obtained with the values $K_1=2.1\times10^5$ J/m^3 and $K_2=1.1\times10^5$ J/m^3. These data are in a good agreement with literature values[6–8] for bulk Co.

For Co thicknesses 14 Å$\geq t_{Co} \geq$12 Å polar MOKE hysteresis curves as displaced in Fig. 1(c) exhibit a reduced remanent magnetization which indicates that perpendicular alignment of the magnetization is not reached. The corresponding longitudinal MOKE curve in Fig. 1(g) exhibits a mixture of polar and longitudinal contributions indicating a slanted easy axis with respect to the surface normal.

For Co thicknesses <12 Å we observe a switching of the magnetic moments back into the in-plane orientation [Fig. 1(d)]. Direct observations of the easy axis of the superlattices were performed by a simplified torque magnetometer. The easy axis of the sample is oriented parallel to the applied

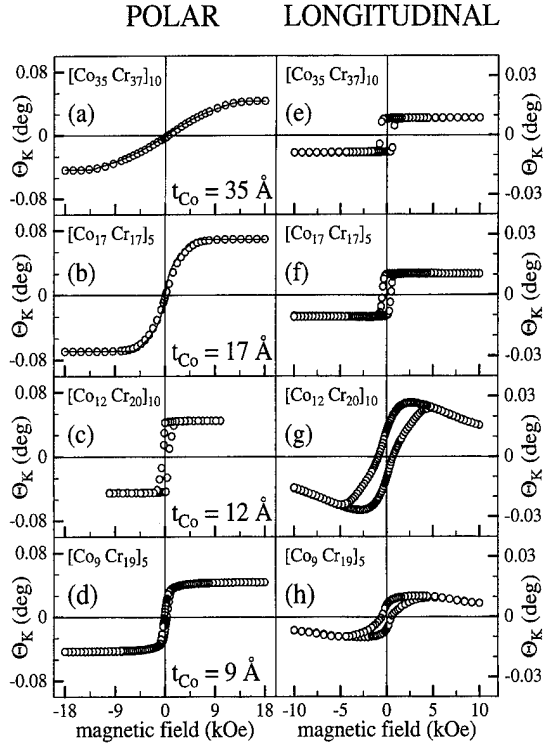


FIG. 1. MOKE hysteresis loops of Co/Cr superlattices as a function of Co layer thickness: (a)–(d) for polar configuration (out-of-plane) and (e)–(h) longitudinal (in-plane) configuration. The solid lines (a) and (b) are fits to the data points using Eq. (1).

magnetic field and the angle between the magnetic field and the sample normal corresponds to the easy axis orientation. To eliminate any influence from the torque by the attachment wire the position of the sample has to be the same with and without magnetic field. The experimental data are shown in Fig. 2. The easy axis exhibits a continuous rotation from the in-plane orientation of $\theta_M=\pi/2$ for thick Co layers to a nearly perpendicular direction ($\theta_M=0$) with decreasing Co layer thickness at $t_{Co}=12$ Å. For $t_{Co}<12$ Å the magnetic anisotropy rotates back from the perpendicular to the in-plane orientation in a good agreement to our MOKE data.

A reorientation has also been observed in Cu/Ni/Cu trilayers.[9] However, in contrast to the present work, this reorientation is related to a coherent–incoherent growth mode. Normally one would expect a complete switching of the easy axis from an in-plane to a perpendicular orientation within a thickness range of $\Delta t_{Co}\approx 2$ Å around the critical thickness. The dashed line in Fig. 2 represents the expected behavior of the easy axis according to the model as described by Eq. (1). The experimental results indicate that new anisotropy contributions have to be taken into account for small Co layer thicknesses.

We believe that the reorientation of the easy axis is strongly affected by the continuous structural phase transition of the Co layers from hcp to bcc. The experimental results can be explained by a change of the interface anisotropy from a negative value for hcp Co to a positive value for Co in the bcc structure prefering an in-plane orientation of the magnetization. The interface anisotropy of bcc Co appears to be opposite to the hcp interface anisotropy.

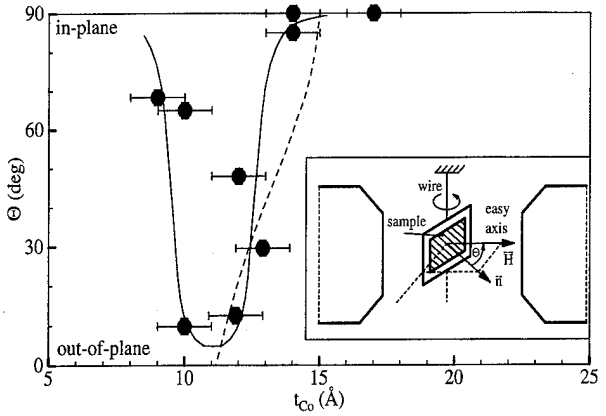


FIG. 2. Easy axis of the magnetization as a function of the Co layer thickness. The solid line is a guide to the eye. The broken line is calculated using Eq. (1) with $H=0$. The experimental "torque" arrangement is shown in the inset. The in-plane component of the easy axis is aligned horizontally.

The observed epitaxial strain of $e_1=+7\%$, $e_2=-4\%$, and $e_3=+0.2\%$ for $t_{Co}=10$ Å gives rise to strong magneto–elastic contributions. Model calculations according to Mason[10] lead to a perpendicular magneto–elastic contribution of $K_{ME}\approx 6$ kOe. This value of K_{ME} is not big enough to overcome the in-plane contributions K_1, K_2, and the shape anisotropy. On the other hand, it is not small enough to be neglected in the lower Co-thickness regime.

The magnetization of the samples is not significantly reduced down to $t_{Co}=9$ Å, indicating sharp interfaces and interdiffusion of not >2 Å. Therefore we can exclude decreasing magnetization effects as described for Co/Pt (Ref. 4) for ultrathin Co thicknesses.

In contrast to the out-of-plane results described so far, the in-plane anisotropy of the superlattices is independent of the Co layer thickness for $t_{Co}\leqslant 16$ Å. Depending on the crystal domain structure[1] we observe uniaxial or fourfold in-plane magnetic anisotropies.

To study the antiferromagnetic interlayer exchange coupling, we have grown by molecular beam epitaxy (MBE) methods Co/Cr(001) superlattices with varying Cr thicknesses $t_{Cr}\approx 5$–23 Å and with Co thicknesses of $t_{Co}\approx 10$, 12, and 22 Å. We obtain antiferromagnetic coupled superlattices with either a slanted easy axis or with an in-plane alignment of the magnetization, depending on t_{Co}. For $t_{Co}\approx 12$ Å (out-of-plane anisotropy) and a Cr thickness of 10 Å we observe antiferromagnetic hysteresis curves as shown in Fig. 3, whose shape can be explained by a spin structure as described further below. As shown in Fig. 4 the first maximum of the antiferromagnetic coupling occurs at $t_{Cr}=6$ Å, which is in a good agreement to the results of Fe/Cr(001).[11] The samples are not saturated in this Cr thickness regime up to 18 kOe, implying an antiferromagnetic coupling strength of $|J_1|>0.5$ mJ/m^2. Neither a second maximum nor a two monolayer oscillation of the interlayer coupling as known for the system Fe/Cr(001) (Ref. 12) has been observed so far.

For $t_{Co}=22$ Å (in-plane anisotropy) we observe an antiferromagnetic coupling as well. The first maximum appears

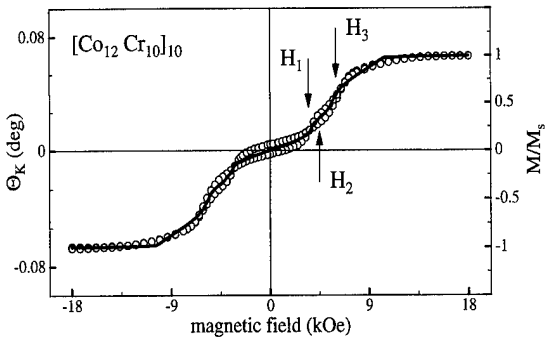


FIG. 3. Experimental polar MOKE hysteresis loop and the magnetization curve according to the theory (solid line). More details are given in the text.

to occur at the same Cr thickness as in the previous case. Again neither a second maximum nor a monolayer oscillation was observed.

In order to theoretically describe the hysteresis curves and spin structures of the antiferromagnetically coupled superlattices we add to the anisotropy energy E_A in Eq. (1) the bilinear exchange coupling term J_1 and a new uniaxial anisotropy term K_u using

$$NE_A' = NE_A + \sum_{n=1}^{N} K_u \cos^2(\theta_n - \theta_u) - \sum_{n=1}^{N-1} \frac{1}{t_{Co}} 2J_1 \cos(\theta_n - \theta_{n-1}). \quad (2)$$

The angle θ_u defines the orientation of the easy axis with respect to the sample normal direction. The origin of the intermediate anisotropy term K_u is not quite clear at the present time, but necessary for a phenomenological description of the anisotropy and coupling behavior at Co layer thickness <14 Å. The introduction of K_u is phenomenologically justified for the slanted easy axis. Taking into account the anisotropy constants K_1, K_2, and K_S and using

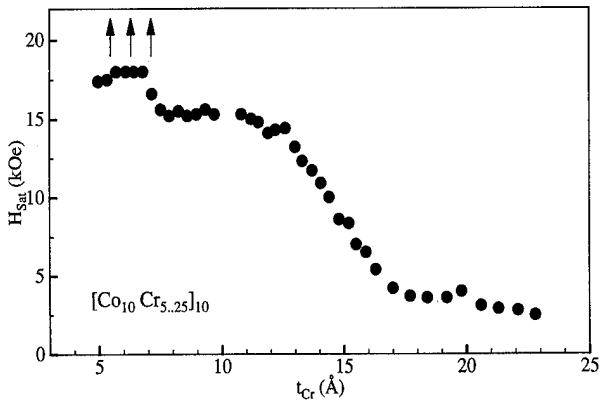


FIG. 4. Saturation field as a function of the Cr layer thickness. The arrows in the thickness regime of 6 Å indicate that the samples were not saturated up to 18 kOe.

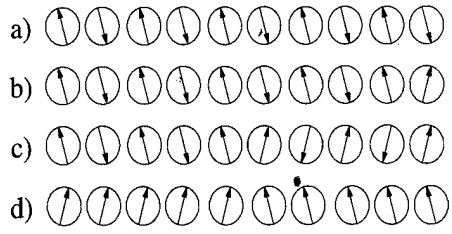


FIG. 5. Spin structure as determined from absolute minima calculations using Eq. (2). To simplify the presentation, the spin orientation in the individual Co layers are plotted side by side.

$K_u = 2\times10^5$ J/m^3 and $\theta_u = 54°$ as parameters, we have performed absolute minima calculations of Eq. (2) to determine J_1 at $t_{Co} = 12.5$ Å from a fit to the MOKE hysteresis data points as shown in Fig. 3. The calculated magnetization curve in Fig. 3 (solid line) agrees very well to the data points using $J_1 = -0.31$ mJ/m^2.

In contrast to bilayer systems the remagnetization process of the Co/Cr(001) superlattices exhibit strong asymmetric spin structures. The rather complicated hysteresis loop in Fig. 3 can be explained as follows: In remanence the magnetic moments are oriented antiparallel along the easy axis direction [Fig. 5(a)]. A surface spin flip transition with domain wall nucleation at H_1 (Fig. 3) leads to an asymmetric spin structure [Fig. 5(b)]. At slightly higher fields H_2 we observe "domain wall" motion to a more stable state with a symmetric spin structure in respect to the center of the superlattice [Fig. 5(c)]. At higher fields ($H > H_3$) we observe a switching of the spins into the direction of the magnetic field [Fig. 5(d)]. Afterwards coherent rotation of the layer spins occurs until saturation will be achieved. The two outermost Co layers differ slightly in their orientation from the inner layers, because they are only coupled to one neighbor.

The crossed MOKE curve in Fig. 3 can be explained by the fact that the top Co layer provides a stronger contribution to the Kerr signal than the inner layers. The slight difference in the saturation regime is not yet well understood.

We would like to thank J. Podschwadek and W. Oswald for their technical assistance. This work was supported by the Deutsche Forschungsgemeinschaft through SFB 166.

[1] N. Metoki, W. Donner, and H. Zabel, Phys. Rev. B **49**, 17351 (1994).
[2] F. Schreiber, Z. Frait, Th. Zeidler, N. Metoki, W. Donner, H. Zabel, and J. Pelzl, Phys. Rev. B **51**, 2929 (1195).
[3] Th. Zeidler, F. Schreiber, W. Donner, N. Metoki, and H. Zabel, Phys. Rev. B (in press).
[4] B. N. Engel, C. D. England, R. A. Van Leeuwen, M. H. Wiedmann, and C. M. Falco, Phys. Rev. Lett. **67**, 1910 (1991).
[5] C. J. Lin, C. H. Lee, R. F. C. Farrow, E. E. Marinero, H. V. Do, H. Notarys, and C. J. Chien, J. Magn. Magn. Mater. **93**, 194 (1991).
[6] D. M. Paige, B. Szpunar, and B. K. Tanner, J. Magn. Magn. Mater. **44**, 239 (1984).
[7] F. Ono, J. Phys. Soc. Jpn. **50**, 2564 (1981).
[8] Z. Frait, Brit. J. Appl. Phys. **15**, 993 (1964).
[9] M. T. Johnson, R. Jungblut, P. J. Kelly, and F. J. A. den Broeder, J. Magn. Magn. Mater. **148**, 118 (1995).
[10] W. P. Mason, Phys. Rev. B **96**, 304 (1954).
[11] S. Democritov, J. A. Wolf, and P. Grünberg, Europhys. Lett. **15**, 881 (1991).
[12] J. Unguris, R. J. Celotta, and D. T. Pierce, Phys. Rev. Lett. **67**, 140 (1991).

Spin-resolved density of states of 3*d* magnets

A. K. See and L. E. Klebanoff[a)]
Department of Chemistry and Zettlemoyer Center for Surface Studies, Lehigh University, Bethlehem, Pennsylvania 18015

Spin-resolved x-ray photoelectron spectroscopy and high-resolution x-ray photoelectron spectroscopy studies of the valence electronic structure of ferromagnetic Fe, Co, $Co_{66}Fe_4Ni_1B_{14}Si_{15}$, and Ni are reported, and compared with theoretical densities of states. Agreement between theory and experiment is very good for ferromagnetic Fe and $Co_{66}Fe_4Ni_1B_{14}Si_{15}$. For metallic Co, experiment agrees poorly with theory incorporating a 1.5 eV exchange splitting, suggesting a reduced (1.2 eV) exchange splitting attributable to valence electron correlation in Co metal. Ferromagnetic Ni shows poor agreement between experiment and theory, particularly in the ↑-spin channel. © *1996 American Institute of Physics.* [S0021-8979(96)16908-6]

I. INTRODUCTION

Previous x-ray photoelectron spectroscopy (XPS) studies of the valence-band density of states (DOS) of the 3*d* ferromagnetic metals have been spin-integrated experiments.[1] This article presents spin-resolved x-ray photoelectron spectroscopy (SRXPS) studies of the DOS of Fe, Co, a Co-based magnetic glass $Co_{66}Fe_4Ni_1B_{14}Si_{15}$, and Ni. Complementary spin-integrated high-energy-resolution x-ray photoelectron spectroscopy (HRXPS) spectra are also reported for these metals with a higher energy resolution than previously attained. The SRXPS and HRXPS data are compared with majority-spin (↑-spin) and minority-spin (↓-spin) theoretical DOS for these ferromagnetic metals, as recently calculated by Moruzzi.[2]

II. EXPERIMENT

The SRXPS instrumentation and measurement process has been described in detail elsewhere.[3] Details of sample preparation and characterization can be found in Ref. 4. Briefly, the Fe sample was a 80-Å-thick single-crystal Fe(011) film prepared by evaporating high-purity iron onto a W(011) substrate. The cobalt-glass $Co_{66}Fe_4Ni_1B_{14}Si_{15}$ sample was an amorphous metallic ribbon. The Co-metal sample was a thick (in excess of 60 Å) polycrystalline film prepared by evaporation of high-purity Co onto the cobalt-based magnetic glass. The Ni sample was a Ni(011) single crystal that was cleaned by standard procedures. A Cu sample used for control SRXPS experiments was a thick polycrystalline film prepared by evaporating high-purity Cu onto the Ni(011) single crystal.

SRXPS allows the decomposition of an XPS spectrum into separate majority-spin ($N\uparrow$) and minority-spin ($N\downarrow$) contributions, respectively, in a manner described previously.[3] All samples were studied in remanent saturated magnetization.

The HRXPS measurements employed a SCIENTA ESCA-300 x-ray photoelectron spectrometer, which is described in detail elsewhere.[5] A variety of samples was used for the HRXPS studies. The Fe and Co metal samples were high-purity polycrystalline foils that were cleaned by argon-ion sputtering. The Ni sample was a Ni(011) single crystal, cleaned in the standard fashion. The amorphous metallic Co-glass sample was a sputter-cleaned thin strip of composition $Co_{66}Fe_4Ni_1B_{14}Si_{15}$. The sample temperature during all SRXPS and HRXPS measurements was ~298 K.

III. RESULTS AND DISCUSSION

SRXPS spectra for Fe, Co, the Co–glass $Co_{66}Fe_4Ni_1B_{14}Si_{15}$, Ni, and a Cu control sample are compared with theoretical DOS for these metals in Fig. 1. All theoretical DOS presented in this article have been calculated[2] using augmented spherical waves (ASW) in the "atomic sphere" and local density approximations. For comparison with photoemission spectra, the theoretical ↑-spin and ↓-spin and *l*-resolved DOS are adjusted with calculated atomic σ_{4s}, σ_{4p}, and σ_{3d} cross sections.[6] The variation of the valence-band cross section with energy was accounted for using Shevchik λ_{4s}, λ_{4p}, and λ_{3d} values[7] calculated from the theoretical *l*-resolved DOS for each spin. The resulting (fully corrected) *l*-resolved DOS are then added together, truncated with the Fermi-Dirac distribution, and convoluted with a Gaussian of appropriate width to simulate the instrumental energy resolution of SRXPS or HRXPS (1.6 eV FWHM or 0.34 eV FWHM, respectively). Cross section and Shevchik parameters used for modification of theoretical DOS are given in Ref. 4.

The comparison of theoretical DOS with SRXPS and HRXPS spectra is clearly valid for the polycrystalline samples. Previous work[8–10] on phonon-assisted nondirect valence transitions, and the angular acceptances used in the SRXPS and HRXPS instrumentation, indicate that contributions from wave-vector-conserving transitions would be negligible for the Ni(011) and Fe(011) single-crystal samples.

a)Author to whom correspondence should be addressed.

 0021-8979/96/79(8)/4796/3/$10.00 © 1996 American Institute of Physics

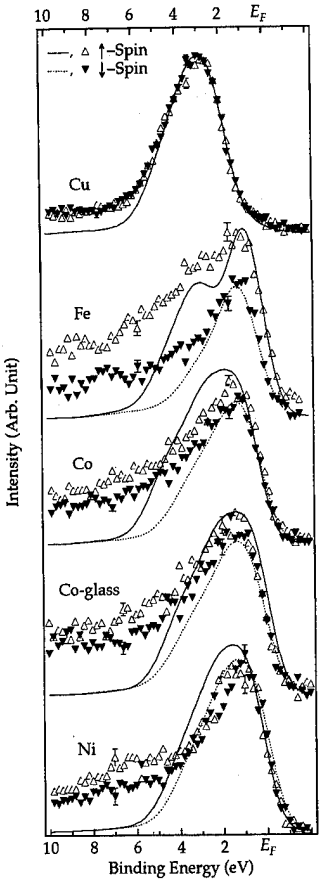


FIG. 1. Comparison of raw SRXPS spectra of Cu, Fe, Co, $Co_{66}Fe_4Ni_1B_{14}Si_{15}$, and Ni with the ↑-spin DOS and the ↓-spin DOS as calculated by Moruzzi.

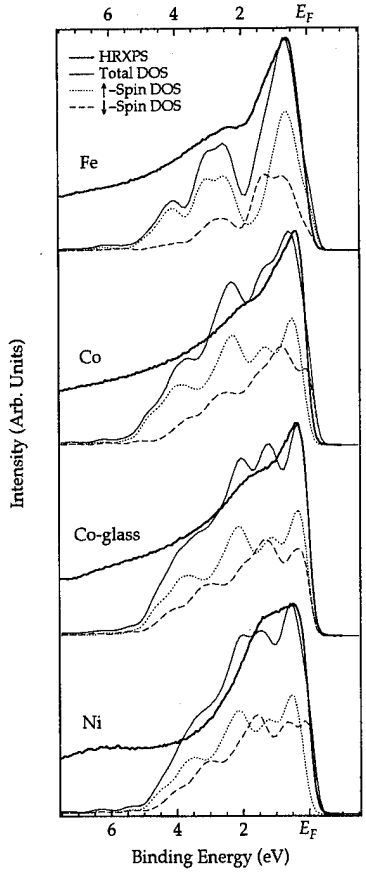


FIG. 2. Comparison of raw HRXPS spectra of Fe, Co, $Co_{66}Fe_4Ni_1B_{14}Si_{15}$ and Ni with the ↑-spin DOS, the ↓-spin DOS, and the total (↑-spin+↓-spin) DOS.

Since there is no calculated DOS available for $Co_{66}Fe_4Ni_1B_{14}Si_{15}$, a DOS derived from Co metal was used. This somewhat crude derivation involved rigidly shifting the spin-resolved Co metal DOS towards each other to reflect a t_{2g} ($\Gamma_{25'}$) exchange splitting of 0.88 eV. This accounts for the fact that the Co atoms in the glass have a smaller magnetic moment (1.0 μ_B) than the Co atoms in Co metal (1.72 μ_B).[11] Since the flat bands near Γ contribute strongly to the DOS, the modification should provide a reasonable first-order approximation to the true DOS of $Co_{66}Fe_4Ni_1B_{14}Si_{15}$.

A SRXPS valence-band spectrum of nonmagnetic Cu is shown at the top of Fig. 1. The $N\uparrow$ and $N\downarrow$ spectra for a nonmagnetic sample should overlap. Thus, the Cu result serves as a control, indicating our ability to measure zero spin polarization given the limited statistical condition of the SRXPS data.

For all of the comparisons shown in Fig. 1 between SRXPS experiment and theory, one of the theoretical DOS curves is normalized to the corresponding SRXPS data at the maximum of the valence-band intensity. However, the same normalization is applied to both spin-resolved DOS, so that the relative intensities of the ↑-spin and ↓-spin DOS accurately reflect the theoretical prediction.

The $N\uparrow$ and $N\downarrow$ Fe SRXPS spectra are compared with theoretical ↑-spin and ↓-spin Fe DOS in Fig. 1. The SRXPS spectra reveal that at low ($<\sim 2$ eV) binding energy, the Fe valence-band spectrum consists of a large ↑-spin component accompanied by a ↓-spin component shifted to slightly larger binding energy. These results are in good accord with the theory of Moruzzi (Fig. 1), and are also supported by the comparison of the Fe HRXPS spectrum with theory in Fig. 2. The main Fe HRXPS valence-band peak at 0.65 eV in Fig. 2 possesses an unresolved shoulder toward high binding energy. Comparison with theory in Fig. 2 suggests the shoulder is predominantly ↓ spin.

The Fe SRXPS data also reveal a poorly resolved feature at ~3 eV in the valence-band spectrum which has a large ↑-spin polarization, in agreement with the theoretical ↑-spin Fe DOS. The $N\downarrow$ peak at 1.1 ± 0.1 eV and the poorly resolved $N\uparrow$ shoulder at 3.0 ± 0.2 eV correspond to a wave-vector-averaged exchange splitting of 1.9 ± 0.2 eV, in general agreement with theory (2.0 eV).[2] Spin-resolved UPS studies[12] of Fe report a t_{2g} ($\Gamma_{25'}$) exchange splitting of 2.2 eV.

The SRXPS valence-band spectrum of Co metal is shown in Fig. 1. Although the $N\downarrow$ Co SRXPS spectrum agrees well with the ↓-spin theoretical DOS, especially toward smaller binding energy, the width and mean energy of the $N\uparrow$ Co SRXPS spectrum is poorly accounted for the ↑-spin Co theoretical DOS. This is also apparent in the comparison of Co metal HRXPS with theory in Fig. 2.

We attribute the overall poor agreement between Co experiment and theory to a reduced exchange splitting for Co metal. Prior UPS studies[13] of Co(0001) have reported a t_{2g} exchange splitting of the $3d$ electrons of 1.2 eV, smaller than the 1.5 eV predicted by theory.[2] More recently, spin-resolved UPS studies of fcc Co films grown on Cu(111) report an exchange splitting of 1.4 eV,[14] although the $\Gamma_{25'}$ ↑-spin peak position was not obvious from the data. The HRXPS spectrum of Co metal in Fig. 2 compares more favorably to a theoretical DOS in which the ↑-spin and ↓-spin DOS have been shifted toward each other to reflect a reduced t_{2g} exchange splitting of 1.2 eV.[4] This crude modification of the theory leads to better agreement with HRXPS experiment for the large Co peak at 0.42 eV, and better energy agreement for the hump at 1.75 eV. The relative intensities within the valence band are, however, not accurately predicted.

The SRXPS data of $Co_{66}Fe_4Ni_1B_{14}Si_{15}$ in Fig. 1 are in good agreement with the theoretical DOS that were "synthesized" from the Co-metal DOS. The position and relative intensities of the main $Co_{66}Fe_4Ni_1B_{14}Si_{15}$ $N\uparrow$ and $N\downarrow$ SRXPS peaks near ~1.5 eV agree well with their theoretical spin-resolved counterparts.

The agreement in Fig. 2 between the HRXPS data for $Co_{66}Fe_4Ni_1B_{14}Si_{15}$ and the theoretical DOS for the glass synthesized from the DOS of Co metal is better than for Co metal itself. The first peak at 0.40 eV in the HRXPS spectrum is very accurately reproduced by the theoretical DOS. The spectral hump at 1.50 eV in the HRXPS spectrum would seem to be a composite of the two DOS peaks at 1.30 and 2.11 eV in the theory. The HRXPS spectrum and theory are in good agreement regarding the relative intensity and location of this hump, suggesting that this feature is strongly determined by the reduced $3d$-exchange splitting in the glass.

Interestingly, the agreement between theoretical and experimental DOS is better for $Co_{66}Fe_4Ni_1B_{14}Si_{15}$, for which there is increased delocalization of the Co $3d$ bands due to hybridization with the metalloid components,[11] than for Co metal. Similarly, the agreement between experimental and theoretical DOS is better for Fe, which has a more delocalized $3d$ band structure, than for Co metal. The agreement between experiment and theory for $Co_{66}Fe_4Ni_1B_{14}Si_{15}$ and Fe suggest that the poor agreement for Co metal is due to narrow-band electron correlation in Co metal that acts to reduce the effective exchange interaction and decrease the Co valence bandwidth. These correlation effects should be smaller for the more delocalized $3d$ bands of Fe and $Co_{66}Fe_4Ni_1B_{14}Si_{15}$. Interestingly, these correlations in Co do not lead to discrete satellite structure in valence-band or core-level photoemission from Co metal,[11] as they do for Ni metal.[15]

Prior UPS data[16] suggest that the exchange splitting in Ni is 0.31 eV, smaller than the 0.60 eV splitting predicted by band theory.[2] Kamper *et al.*[17] using spin-resolved UPS, have shown that the Ni exchange splitting varies with e_g and t_{2g} character. The exchange splitting of e_g states is 0.16 eV, while that for t_{2g} states is 0.33 eV. The average exchange splitting is 0.24 eV. The SRXPS spectrum of Ni is shown in Fig. 1. Band theory gives a particularly bad account of the $N\uparrow$ component, in a manner consistent with a reduced exchange splitting. Previous theory[15] has assigned narrow-band correlations in Ni as the cause of the reduced Ni exchange splitting. The 6 eV satellite displays strong ↑-spin polarization. The origin of this spin polarization has been discussed,[18] and will not be considered here.

ACKNOWLEDGMENTS

This article is based upon work supported by the National Science Foundation under Grant No. CHE-9117138. We thank Dr. V. L. Moruzzi for providing extensive ASW calculations of the DOS. The assistance of A. C. Miller in the SCIENTA ESCA Laboratory of Lehigh University is appreciated.

[1] H. Höchst, S. Hüfner, and A. Goldmann, Phys. Lett. **57** A, 265 (1976), and references therein.
[2] V. L. Moruzzi, private communication.
[3] L. E. Klebanoff, D. G. Van Campen, and R. J. Pouliot, Rev. Sci. Instrum. **64**, 2863 (1993).
[4] A. K. See and L. E. Klebanoff, Surf. Sci. **340**, 309 (1995).
[5] U. Gelius, B. Wannberg, P. Baltzer, H. Fellner-Feldegg, G. Carlsson, C.-G. Johansson, J. Larsson, P. Munger, and G. Vegerfors, J. Electron. Spectrosc. Relat. Phenom. **52**, 747 (1990).
[6] J. H. Scofield, J. Electron. Spectrosc. Relat. Phenom. **8**, 129 (1976).
[7] N. J. Shevchik, Phys. Rev. B **13**, 4217 (1976).
[8] Z. Hussain, C. S. Fadley, S. Kono, and L. F. Wagner, Phys. Rev. B **22**, 3750 (1980).
[9] R. C. White, C. S. Fadley, M. Sargurton, and Z. Hussain, Phys. Rev. B **34**, 5226 (1986).
[10] L. E. Klebanoff and D. G. Van Campen, Phys. Rev. B **46**, 9744 (1992).
[11] L. E. Klebanoff, D. G. Van Campen, and R. J. Pouliot, Phys. Rev. B **49**, 2047 (1994).
[12] E. Kisker, K. Schroder, M. Campagna, and W. Gudat, Phys. Rev. Lett. **52**, 2285 (1984).
[13] F. J. Himpsel and D. E. Eastman, Phys. Rev. B **21**, 3207 (1980).
[14] U. Alkemper, C. Carbone, E. Vescovo, W. Eberhardt, O. Rader, and W. Gudat Phys. Rev. B **50**, 17496 (1994).
[15] L. C. Davis, J. Appl. Phys. **59**, R25 (1986).
[16] F. J. Himpsel, J. A. Knapp, and D. E. Eastman, Phys. Rev. B **19**, 2919 (1979).
[17] K. P. Kamper, W. Schmitt, and G. Guntherodt, Phys. Rev. B **42**, 10696 (1990).
[18] A. K. See and L. E. Klebanoff, Phys. Rev. B **51**, 11002 (1995).

Electronic structure and exchange interactions in fcc Fe

M. van Schilfgaarde, V. P. Antropov,[a] and B. N. Harmon[a]
SRI International, 333 Ravenswood Avenue, Menlo Park, California 94025

We apply a new first principles approach for evaluating the spin dynamics for arbitrary magnetic systems. The method is implemented within the local density approximation and applied to γ-Fe, a frustrated system where we obtain new low-energy magnetic configurations. © *1996 American Institute of Physics.* [S0021-8979(96)35408-X]

As is well known for magnetic systems, density functional (DF) theory has yielded theoretical results for ground-state properties in agreement with experiment.[1] Detailed calculations for excited state properties, or thermal properties are less satisfactory, although a number of conceptual models and some methods for the treatment of such properties have been available for some time. Nevertheless questions still abound concerning physical phenomena above the Curie temperature. For example, what is the nature of the short range order, or what is the temperature dependence of the local magnetic moments and band splitting? Recently, we formulated[2] a general method to evaluate the "slow" spin dynamics in the framework of *ab initio* DF. In this article, we present more complete results for the ground state of fcc Fe, a typical frustrated system, and obtain many new magnetic structures.

The fcc Fe and related systems (Ni–Fe, Fe–Mn) have been studied for many years[3] as part of the "invar" problem. It also serves as a prototype model for a frustrated magnetic system. Earlier "static" calculations for fcc Fe[4,5] have shown a dependence of the magnetic ordering on volume. Near the equilibrium volume fcc Fe was found to be nonmagnetic, but with increasing volume the antiferromagnetic (AFM) state first becomes stable and then spin spiral (SS) and finally ferromagnetic (FM) ordering appears.[5] With our SD formalism we allow the spin system much more freedom to choose an equilibrium structure, and have found new and complex spin configurations with lower energies. We considered a unit cell consisting of 32 atoms with independent local moments. To calculate the electronic structure we used the linear-muffin-tin orbital method[6] with and without spin-orbital coupling. Initially the spins were frozen in a random orientation and the self-consistent electronic structure determined. Then the MM were allowed to relax along the direction of the "forces."

It is known that the local-density approximation underestimates the lattice constants of the transition metals, especially for the $3d$ series. The gradient corrections dramatically reduce the error (though they tend to overestimate the MM by about 10%). Since gradient-corrected calculations are probably much better predictors of the ground state, we give results of simulations using a local density functional, and corresponding simulations for the gradient-corrected functional of Perdew and Wang.

Figure 1 shows the evolution of the spins for two different lattice constants, $a=3.59$ Å and $a=3.73$ Å, as calculated within the local-density approximation using the functional of Barth and Hedin. For the $a=3.59$ Å simulation, the energy dropped smoothly and the spins ordered into the four-atom/cell "triple-**k**" (3**k**) structure (all spins oriented along $[\pm1\pm1\pm1]$ directions), with the MM about $1.6\mu_B$ (Fig. 1). For $a=3.73$ Å, the evolution of the spins was more complex, relaxing into a nearly stable structure of 16 atoms/cell, and then finding a slightly more stable configuration with spins

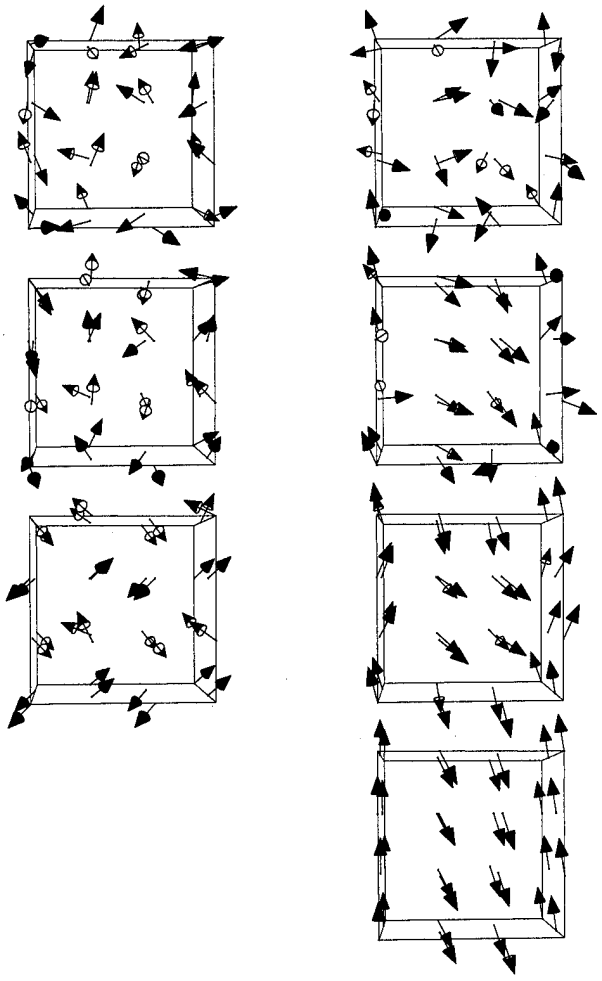


FIG. 1. The left column shows the evolution of spins in a 32-atom cell of fcc Fe with $a=3.59$ Å. Top: the starting random configuration; middle: after 75 steps; bottom: after 200 steps. This last configuration is close to a 3**k** structure, the minimum-energy structure allowed by the simulation (no SS allowed). The right column is similar, but for $a=3.73$ Å. Spin configurations after 0, 20, 75, and 220 steps are shown, the last being close to the ↑↑↓↓ structure.

[a]Ames Laboratory, Department of Physics & Astronomy, Iowa State University, Ames, IA 50011.

 0021-8979/96/79(8)/4799/3/$10.00 © 1996 American Institute of Physics

ordered in a ↑↑↓↓ pattern along [001] and a moment of about $2.3\mu_B$ (Fig. 1).

Subsequent static calculations for the **2k**, **3k**, FM, and ↑↑↓↓ magnetic configurations, and similar configurations with a SS superimposed, showed that the energetically most favorable configuration exhibited a complex volume dependence. Considering first only cases with no SS (as no SS was accessible to the simulation), we find the system to be magnetically ordered at the theoretical equilibrium volume (a = 3.44 Å), in a **3k** structure with small MM ($0.8\mu_B$). At that volume the **3k** is nearly degenerate with nonmagnetic Fe, being only 0.9 meV/atom more stable. The **2k** is also very close in energy, lying only 1.2 meV above the **3k**. With increasing lattice constant the lowest-energy structure is overtaken by the AFM ↑↑↓↓ [001] structure for $a>3.59$ Å, and is in turn overtaken by FM ordering for $a>3.73$ Å. Including spin–orbit coupling increased the binding energy by approximately 5 meV/atom, but did not alter the relative energies of the various magnetic configurations.

It has been proposed[5] that the minimum energy configuration for some range of volume of fcc Fe is an incommensurate (0,0,q) SS, evolving into the FM structure for large lattice constants. Accordingly, we considered various magnetic configurations with a (0,0,q) SS superimposed (without spin–orbital coupling), and indeed the **3k**, **2k**, and FM structures were further stabilized by an incommensurate SS with $1/q \approx 5-6a$. The equilibrium configuration is a **3k**+SS at $a=3.44$ Å and $1/q \approx 6a$, the SS stabilizing the normal **3k** structure by 1.8 meV; this is 2.0 meV lower than nonmagnetic Fe at its own equilibrium lattice constant (3.43 Å). With increasing volume the optimal $1/q$ evolves slowly from $\approx 6a$ at $a=3.44$ Å to $\approx 5a$ at $a=3.55$ Å in both the **3k** and **2k** configurations. At $a=3.55$ Å the **2k**+SS overtakes the **3k**+SS. For $a>3.61$ Å, ↑↑↓↓ [001] is the most stable structure; it is in turn overtaken by FM ordering for $a>3.73$ Å. Remarkably, the simple (0,0,q) SS is never the most stable structure, though at $a=3.59$ Å it is only 1 meV higher energy than the **2k**+SS and ↑↑↓↓ structures.

When the local functional of Vosko was used in place of the Barth–Hedin functional, essentially similar results were obtained. Corresponding calculations with the gradient-correction of Perdew and Wang shared some features in common with local-density results, namely, a very strong dependence of magnetic moment on lattice constant and the favoring of complex noncollinear orderings at small lattice constants, the ↑↑↓↓ ordering at intermediate lattice constants, and FM ordering at large lattice constants. Apart from these general tendencies, gradient corrections dramatically change the results. Simulations with gradient corrections were prosecuted at $a=3.57$ Å, $a=3.61$ Å, and $a=3.65$ Å. The latter two evolved to the ↑↑↓↓ configuration, although the evolution to ↑↑↓↓ for $a=3.65$ Å was rather tortuous, owing to the existence of other nearly degenerate orderings. The $a=3.57$ Å simulation evolved to a noncollinear eight-atom configuration shown in Fig. 2. This antiferromagnetic configuration has two inequivalent atoms (a low-spin state marked "L" and a high-spin state marked "H"), and may be viewed as a four-atom structure with a commensurate (0,1/2,0) SS superimposed. For $a<3.48$ Å, the angle ϕ in Fig. 2 is $\pi/2$, so that

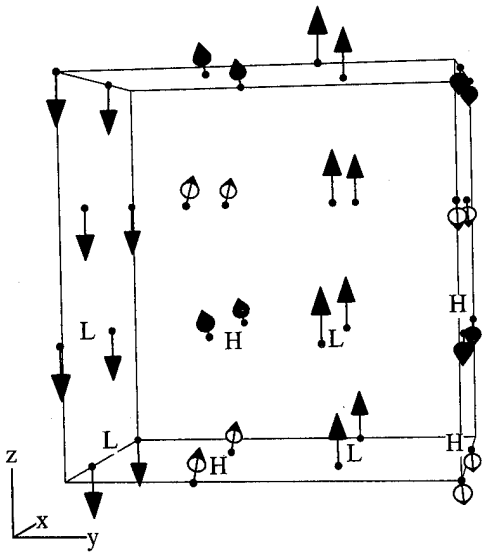


FIG. 2. Eight-atom cell found by the simulation. "H" marks the high-spin moments; "L" marks the low-spin moments. All moments are oriented in the $x-z$ plane. For small a, H lie along the x axis. For increasing $a>3.50$ Å, the H spins rotate smoothly in the $x-z$ plane, increasing to an orientation where all NN angles are approximately 0°, 60°, or 120°.

all spins are aligned at 0°, 90°, or 180°. For increasing $a>3.48$ Å, ϕ smoothly decreases to a value where every angle is approximately 60° or 120°). This configuration is the most stable one we found for $a<3.54$ Å (Fig. 3). For 3.54 Å$<a<$3.65 Å, which includes the global minimum energy at $a=3.61$ Å, the ↑↑↓↓ is the most stable. For $a>3.65$ Å, fcc Fe ordered ferromagnetically. Once again, the SS was never the stable structure, though it is nearly degenerate with the eight-atom configuration (Fig. 1).

The low-energy magnetic configurations are generally different stacking sequences along [001] planes, with all spins lying perpendicular to the stacking. Moreover, with the

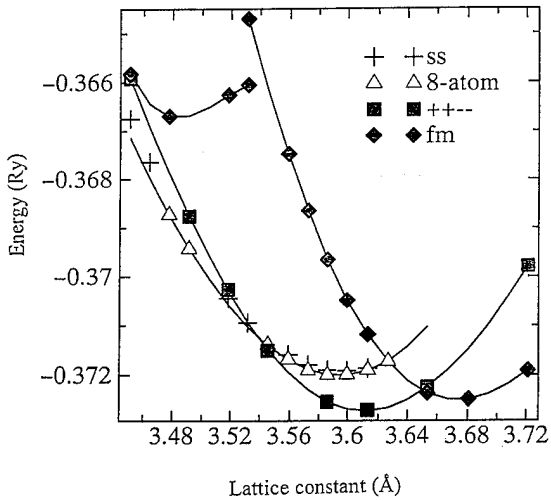


FIG. 3. Total energies as a function of a for several configurations. The global minimum-energy structure is the ↑↑↓↓ structure. For small a, the eight-atom configuration is lowest in energy; for large a, the FM configuration is lowest. Note the two distinct energy-volume curves for the FM configuration, corresponding to a low-spin and a high-spin state.

exception of the eight-atom structures, the remaining structures had all spins within a plane and were ferromagnetically aligned. To investigate of the effective exchange coupling parameters we consider an effective planar Hamiltonian coupling neighboring planes along the [001] direction, with spins in each plane aligned ferromagnetically in the plane. The coupling may be decomposed as a Fourier series of the rotation angle $\phi_i - \phi_j$ between plane i and j. To determining the coupling parameters, we consider a cell of four independent planes. By considering a continual rotation starting from a FM $(++++)$ configuration to the AFM $(+--+)$, and another from the FM to the $++--$ configuration, there is information to extract two parameters, namely the first- and second-neighbor couplings J^1 and J^2. (More distant-neighbor coupling is neglected.) The effective exchange Hamiltonian may then be written

$$H_{\text{eff}} = \sum (J_k^1 \cos k\varphi_1 + J_k^2 \cos k\varphi_2). \tag{1}$$

By construction, this Hamiltonian fits the FM-AFM and FM-$(++--)$ energy difference exactly. We mention in passing that the MM depends rather strongly on the configuration, so any attempt to construct it by small displacements about some starting configuration is doomed to fail. The J for the bilinear biquadratic and bicubic terms are listed in Table I. It is seen that the NN bilinear coupling rapidly evolves from nearly zero at $a = 3.59$ Å to a large negative value. Near the point where it becomes comparable to the 2NN bilinear term, there is a transition from a the AFM $(+--+)$ configuration to the FM. The rather large (and more slowly varying) 2NN bilinear term accounts for configurations favoring second neighbors antiferromagnetic. When the first NN bilinear term is very small, higher-order terms such as the biquadratic become relatively important, explaining why noncollinear ordering is found there.

TABLE I. Exchange parameters according to Eq. (1) (in mRy).

	Bilinear		Biquadratical		Bicubic	
a (a.u.)	J^1	J^2	a^1	J^2	J^1	J^2
3.59	−0.22	1.89	0.39	−0.49	−0.15	−0.17
3.65	−2.65	1.42	0.22	−0.58	−0.12	−0.04
3.72	−4.34	1.16	0.14	−0.60	−0.17	0.01

M.vS. gratefully acknowledges support from ONR, Contract No. N00014-89-K-0132. This work was partially carried out at the Ames Laboratory, which is operated for the U.S. Department of Energy by Iowa State University under Contract No. W-7405-82. This work was supported by the Director for Energy Research, Office of Basic Energy Sciences of the U.S. Department of Energy.

[1] R. O. Jones and O. Gunnarsson. Rev. Mod. Phys. **61**, 689 (1985).
[2] V. P. Antropov, M. I. Katsnelson, M. van Schilfgaarde, and B. N. Harmon, Phys. Rev. Lett. **75**, 729 (1995).
[3] E. F. Wasserman, Phys. Scr. **T25**, 209 (1989); Y. Tsunoda, Prog. Theor. Phys. Suppl. **101**, 133 (1990).
[4] J. Kübler, Phys. Lett. **81A**, 81 (1980).
[5] O. Mriasov, A. I. Liechtenstein, L. Sandratskii, and V. A. Gubanov, J. Phys. Condens. Matter **3**, 7683 (1991); M. Uhl, L. Sandratskii, and J. Kübler, Phys. Rev. B **50**, 291 (1994).
[6] O. K. Andersen, M. Pawlowska, and O. Jepsen. Phys. Rev. B **34**, 5253 (1986).

Critical dynamics at the spin-density-wave transition of chromium

B. J. Sternlieb, J. P. Hill, T. Inami,[a] and G. Shirane
Department of Physics, Brookhaven National Laboratory, Upton, New York 11973

W.-T. Lee and S. A. Werner
Department of Physics, University of Missouri, Columbia, Missouri 65211

Eric Fawcett
Department of Physics, University of Toronto, Toronto, Ontario M5S 1A7, Canada

Neutron scattering measurements of the critical fluctuations associated with the spin-density-wave transition at the Néel temperature, $T_N \approx 312$ K, in a single-**Q** chromium crystal are reported. Critical fluctuations are observed emanating from allowed magnetic satellite positions and from satellite positions, corresponding to *absent* magnetic domains, at which no elastic scattering occurs. The inelastic scattering from these "silent satellites" grows rapidly with increasing temperature, becoming equal to the allowed single-**Q** satellite scattering at T_N. The line shapes of the inelastic scattering at both the allowed and silent satellites are found to be intrinsically asymmetric, reflecting the underlying nesting geometry of the Fermi surface. Energy scans at the silent satellite positions reveal a weakly temperature dependent, characteristic energy below which the observed scattering intensity falls rapidly to zero. © *1996 American Institute of Physics.* [S0021-8979(96)17008-0]

Of the electrons responsible for the magnetism of the transition metals Cr, Mn, Fe, Co, and Ni, those of chromium have the most itinerant character. In contrast to local moment systems, the experimental and theoretical properties of the magnetic critical dynamics associated with this itineracy remain poorly understood.[1,2] In 1960, Overhauser first demonstrated that the spin-density-wave (SDW) state presents a plausible ground state of the free electron gas, and further suggested that such a state might be responsible for the magnetism observed in chromium below its Néel temperature, $T_N \approx 312$ K.[3] Direct evidence of the itinerant, SDW character of the magnetism in chromium[2] is observed in elastic magnetic neutron scattering experiments, where allowed magnetic Bragg peaks are observed at momenta, $\mathbf{Q}_\pm = (1 \pm \delta, 0, 0)$, corresponding to the "nesting" of electron and hole elements of the Fermi surface as shown in the insert to Fig. 1. The magnetic excitations associated with this ordered, SDW state have an unusually steep dispersion, $v \approx 850$ meV Å,[4] which is also consistent with an energy scale set by the Fermi energy. Near T_N, observation of the critical fluctuations which drive the transition from an orthorhombic magnetic phase to the high temperature, cubic, paramagnetic state, is complicated by the presence of three degenerate magnetic domains in the ordered state. However, by first cooling through the Néel transition with a large field applied along a [100] axis, a single-domain or single-**Q** sample can be produced which remains unaffected by the subsequent removal of the applied field for temperatures $T < T_N$.[5] Recent high resolution neutron scattering measurements[6] have demonstrated that the critical fluctuations associated with T_N arise at both the allowed satellite positions corresponding to the single-**Q** state, $\mathbf{Q}_\pm = (1 \pm \delta, 0, 0)$, and, surprisingly, at the "silent" satellite positions, associated with the magnetic domains excluded by single-**Q** crystal preparation; $\mathbf{Q}^S_\pm = (0, 1 \pm \delta, 0), (0, 0, 1 \pm \delta)$. In this article we extend these measurements to higher resolutions and smaller energy transfers. These data indicate that the inelastic line shapes associated with both the allowed and the silent satellite scattering have an intrinsic asymmetry about $\mathbf{Q}_\pm$, consistent with the q-dependence of the Fermi surface nesting. The temperature dependence of the observed silent satellite scattering at energy transfers of $\Delta E = 0.35$ meV peaks more sharply, and at a temperature closer to T_N, than our earlier $\Delta E = 0.5$ meV data. The corresponding q-widths associated with these data also demonstrated a more marked minima at T_N than observed earlier. However, at all temperatures the data remain far from resolution limited in q. Efforts to measure the energy dependence of the silent satellite scattering at $T = 140$, 230, 280, and 300 K are also reported. These data indicate that the silent satellite scat-

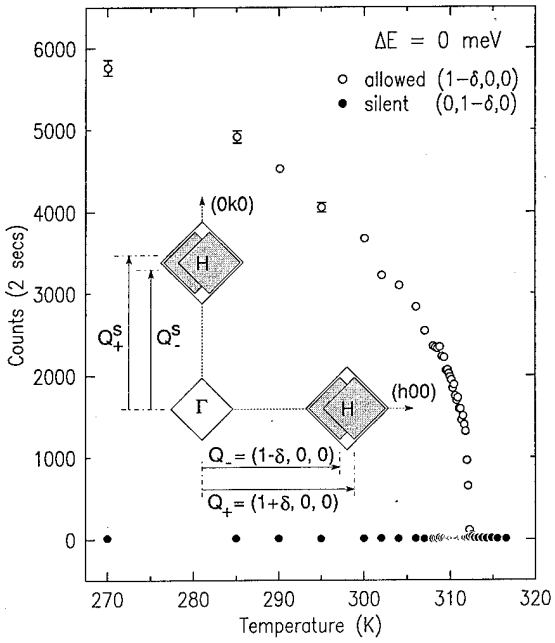


FIG. 1. (Top) temperature dependence of the elastic scattering in Cr#10 at allowed, (○) and silent, (●), satellite positions. (insert) ($hk0$) scattering plane illustrating the nesting of the electron Fermi surface octahedron at $\Gamma = (000)$ with the slightly larger hole octahedron at $H = (100)$. The shaded nesting shown corresponds to the allowed, single-**Q** state.

 0021-8979/96/79(8)/4802/3/$10.00 © 1996 American Institute of Physics

tering has a characteristic energy, $E_{ss} \approx 5$ meV, that softens weakly with increasing temperature.

The high resolution measurements presented below were performed at the HFBR H-9 triple-axis spectrometer using a 60′-40′-60′-*S*-80′-80′ collimation configuration and unpolarized neutrons with a fixed incident energy of $E_i = 4.0$ meV. The (002) reflection of pyrolytic graphite was used to monochromate and analyze the incident and scattered neutrons. Cold beryllium was used to filter higher order (λ/n) contamination from the incident beam. Additional measurements involving larger energy transfers were performed at the H-7 spectrometer using fixed final energy neutrons ($E_f = 14.7$ meV), a pyrolytc graphite filter in the scattered beam, and a 40′-40′-*S*-40′-40′ collimation configuration. Prior to both sets of measurements, Cr#10, an irregularly shaped 25.6-g single crystal with a 0.73° mosaic, was prepared in a single domain or single-**Q** magnetic state by cooling through the Néel transition to room temperature with a magnetic field of $|\mathbf{H}| = 20$ T applied along the (h00) crystal axis. After removing the field, the samples was mounted in a closed cycle He^4 refrigerator with the (00l) axis normal to the scattering plane. Two sets of satellites are accessible in this geometry: the $(1 \pm \delta,0,0)$ and $(\pm\delta,1,0)$ satellites, corresponding to the allowed magnetic reflections of the prepared single-**Q** state, and the $(0,1 \pm \delta,0)$ and $(1, \pm \delta,0)$ "silent satellites" of the absent $\mathbf{Q}^S_{\pm} = (0,1 \pm \delta,0)$ magnetic domain (Fig. 1 insert). After cooling to a starting a temperature of $T = 100$ K, all subsequent elastic and inelastic measurements were made with monotonically increasing temperature.

The temperature dependences of the elastic peak intensities observed at equivalent allowed, $\mathbf{Q}_- = (1-\delta,0,0)$ and silent, $\mathbf{Q}^S_- = (0,1-\delta,0)$, satellites are shown in Fig. 1. The ratio of these intensities, or the single-**Q** ratio, is greater than 200:1 for all temperatures below T_N, indicating that the bulk of the sample is characterized by a single magnetic do-main. The sharp fall off of the magnetization just below T_N, and the measured value of the Néel temperature, $T_N = 312.12(2)$ K, are constant with the established, weakly first-order character of the SDW transition in pure chromium.[7]

Representative longitudinal elastic scans through the allowed and silent satellite positions, at $T = 311.95$ K ($= T_N - 0.17$ K), are shown in the top panels of Fig. 2. The peak in the allowed satellite data reflects the finite-order parameter present below T_N. The observed q-width of this scattering is entirely attributable to the finite instrument resolution: $\Delta q^{\text{meas.}} = \Delta q^{\text{res}} = 0.011$ Å^{-1}. The absence of elastic scattering at the silent satellite position indicates that the single-**Q** character of the sample remains intact at temperatures approaching T_N. The lower panels of the figure show equivalent scans taken at finite energy transfer, $\Delta E = 0.35$ meV. The strong inelastic scattering visible at the silent satellite position, which is nearly comparable to the allowed satellite scattering at this temperature, demonstrates that fluctuations at the silent satellite nesting vectors play an important role in the dynamics at $T \rightarrow T_N$. This strong dynamic response in the absence of an underlying static magnetization is an intrinsic feature of the critical dynamics of chromium and cannot be attributed to any selection rules associated with the magnetic scattering measurements. In contrast to the

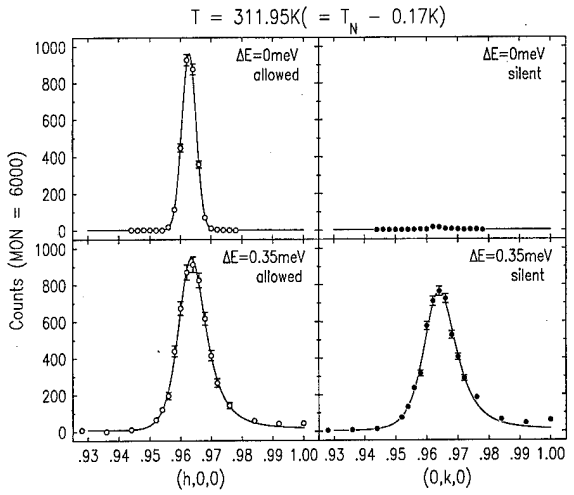


FIG. 2. $T = 311.95$ K$(= T_N - 0.17$ K). (Top left) allowed elastic scattering at $(1-\delta,0,0)$. (Top right) elastic scattering at the silent satellite position $(0,1-\delta,0)$ (bottom panels) corresponding inelastic, $\Delta E = 0.35$ meV, scans.

elastic data, the q-widths of both the allowed and silent inelastic scans are roughly twice the instrument resolution. The corrected widths reflect a real-space, dynamic correlation length on the order of a few spin-density-wave periods ($\sim 45 \times a$). Another notable feature of the both the allowed and silent inelastic data is the asymmetry of the measured scattering intensities about their respective nesting vectors. Trial fits indicate that this is not the result of resolution related contamination from the neighboring satellite positions, but is rather an inherent feature of the inelastic SDW scattering. This asymmetry is related to the slightly better nesting that occurs for small displacements of the optimal nesting vector towards, rather than away from, the commensurate position, $\tau_m = (100)$ (see Fig. 1). We note that the energy dependence of this asymmetry has not been explored, and may well complicate arguments concerning the presence or absence of a distinct, commensurate source of scattering at higher energies where poorer instrument resolutions hinder the clear separation of contributions to the observed scattering intensities.

The temperature dependences of the allowed and silent satellite scattering at $\Delta E = 0.35$ meV are presented in Fig. 3. Critical scattering is observed at both the allowed and silent satellite positions. The peak intensities at the two satellites, shown in the top panel, agree above T_N as required by the cubic symmetry of the paramagnetic state. Below T_N, fluctuations associated with the silent satellite fall off rapidly, while the corresponding allowed satellite intensities fall to the finite level maintained by the magnetic "spin-wave" excitations of the ordered single-**Q** state. The associated momentum widths are presented in the lower panel of the figure. The temperature dependence of the allowed satellite scattering q-width is monotonic and smoothly varying through T_N. This width remains broader than the instrument resolution at all temperatures down to $T = 270$ K, where the scattering is entirely due to spin waves. The spin-wave velocity, $v \approx 850$ meV Å, is too sharp to be responsible for the width of this scattering, which suggests that this broadening in q is due to the damped nature of these excitations. At the silent satel-

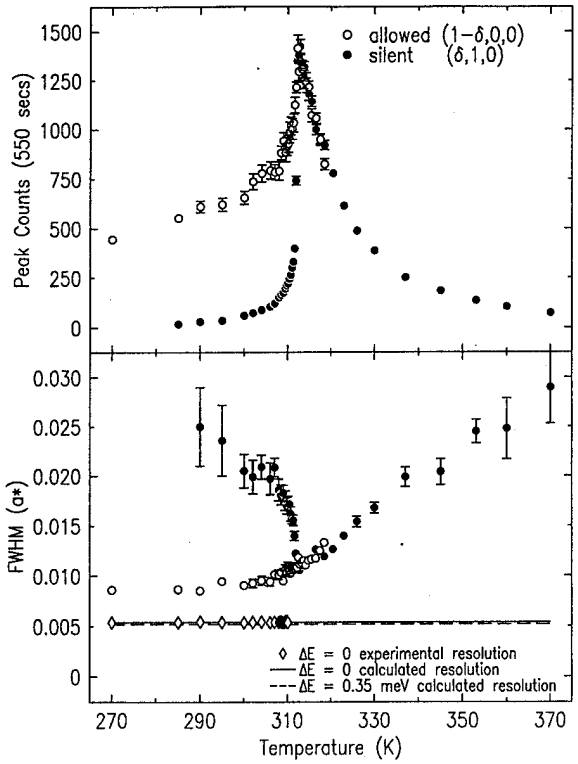


FIG. 3. (Top) temperature dependence of the peak inelastic, $\Delta E = 0.35$ meV, intensities at the allowed, (○), and silent, (●), satellite positions. (bottom) Corresponding scan widths plotted with measured and calculated instrument resolutions.

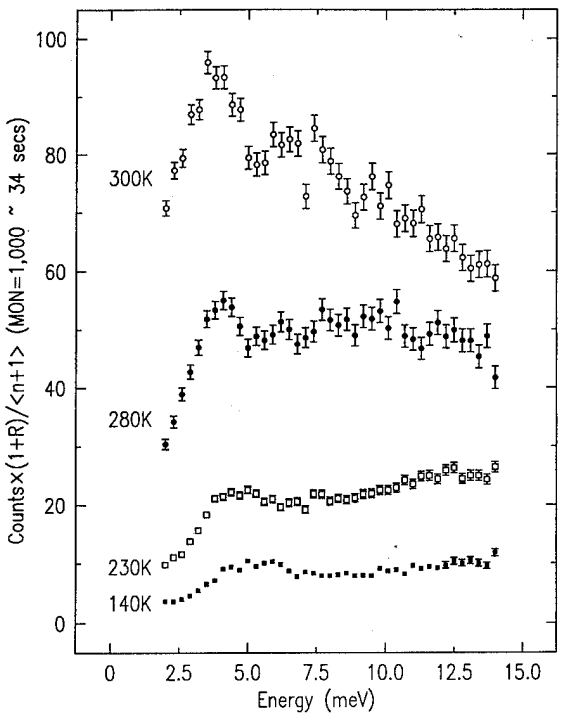


FIG. 4. Energy scans at the silent satellite position $(1,\delta,0)$ at $T = 300$, 280, 230, and 140 K. These intensities have been corrected for both instrument and Bose thermal factors.

lites, the q-width of the observed scattering has a sharp minimum at $T \approx T_N$. This width is observed to broaden more rapidly with decreasing than increasing temperatures about T_N. However, in contrast to local moment systems, the width of this scattering remains anomalously narrow at temperatures far from T_N.

To investigate whether the dynamics observed at the silent satellite positions possess a characteristic frequency, energy dependent measurements were performed at $\mathbf{Q}^S_- = (0,1-\delta,0)$ at $T = 140$, 230, 280, and 300 K. These data, shown in Fig. 4, demonstrate a peak in the spectral density, E_{ss}, below which the observed scattering falls off rapidly. Substantial spectral weight is also observed at higher energies. At $T = 140$ K, this peak energy is $E_{ss} \approx 5$ meV. With increasing temperature, the peak becomes more pronounced while softening somewhat in energy ($E_{ss} \approx 3.8$ meV at $T = 300$ K). In addition, the spectral weight at energies above E_{ss} appears to shift down in energy as well.

The results presented in this paper demonstrate that the SDW to paramagnetic transition in single-**Q** chromium is driven by critical fluctuations arising at all six satellite positions about the nominal antiferromagnetic zone center: $(1, \pm\delta, 0, 0)$, $(1, \pm\delta, 0)$ and $(1, 0, \pm\delta)$. These high resolution measurements have also revealed that the line shapes associated with the dynamics at both the allowed and silent satellite positions possess an asymmetry which reflects the underlying nesting geometry of the Fermi surface. The energy dependence of the silent satellite scattering, and particularly the characteristic "cutoff" energy, E_{ss}, introduces a new puzzle in the understanding of SDW behavior. Efforts to quantitatively study the temperature dependence of this energy and its possible relation to other characteristic parameters of chromium (i.e., δ) are currently underway. The low energy scale of E_{ss} may be a clue useful in determining the polarization of the silent satellite fluctuations as our most recent measurements have revealed that the longitudinal excitations that dominate the low temperature dynamics at energies below $\Delta E \approx 9$ meV, also play an important role at temperatures approaching T_N. A superior single-**Q** sample, currently in preparation, should allow a more quantitative and systematic study of the temperature, energy, and **q**-dependence of this novel scattering.

We wish to thank Dr. Lawrence G. Rubin of the Francis Bitter National Magnet Laboratory for his help and advice during our efforts to field-cool our crystals. Invaluable technical assistance was provided by R. Rothe, J. Biancarosa, and R. J. Liegel. Work at Brookhaven National Laboratory was carried out under Contract No. DE-AC0276CH00016, Division of Materials Science, U.S. Department of Energy. WTL and SAW would like to acknowledge the support of the NSF through Grant No. NSF-PHY 9024608, and EF the Natural Sciences and Engineering Council of Canada.

[1] M. F. Collins, *Magnetic Critical Scattering* (Oxford University Press, Oxford, England, 1989).
[2] E. Fawcett, Rev. Mod. Phys. **60**, 209 (1988).
[3] A. W. Overhauser, Phys. Rev. Lett. **4**, 226 (1960).
[4] S. K. Sinha *et al.*, Phys. Rev. B **15**, 1415 (1977).
[5] T. J. Bastow and R. Street, Phys. Rev. B **88**, 935 (1966).
[6] B. J. Sternlieb *et al.*, Phys. Rev. Lett. **75**, 541 (1995).
[7] A. Arrott, S. A. Werner, and H. Kendrick, Phys. Rev. Lett. **14**, 1022 (1965).

Theory of non-Heisenberg exchange: Results for localized and itinerant magnets

O. N. Mryasov and A. J. Freeman
Department of Physics and Astronomy, Northwestern University, Evanston, Illinois 60208-3112

A. I. Liechtenstein
Max Plank Institut FKF, Heisenberg Strasse 1, D-70569 Stuttgart, Germany

A general formulation of intersite (layer) exchange coupling in bulk (multilayer) materials is proposed based on the treatment of the spin (layer) rotation as a perturbation in terms of the force theorem and multiple scattering theory. The expansion of the intersite (layer) exchange interaction energy gives expressions for the bilinear and biquadratic exchange. For metals, the approach is illustrated by linear muffin-tin orbital calculations of exchange coupling constants in the ferromagnetic $3D$-metals and the fcc phase of bulk Fe. Long range oscillations of strongly volume dependent exchange coupling in fcc Fe appears to be the origin of the spin-density-wave instability in this metastable phase. The correctness of expressions for the limit of localized magnets is demonstrated by calculations for the antiferromagnetic insulator NiO. In contrast with other theories, this method can be used for both nonmagnetic and magnetic spacers in metallic multilayers, as is illustrated by calculations of the interfacial and interlayer exchange in Fe/Mn and Co/Mn. © *1996 American Institute of Physics.* [S0021-8979(96)17108-7]

While most theoretical models of order in magnetic materials are based on the Heisenberg Hamiltonian, the basis for this theory of the exchange coupling is not as definite as its wide use may suggest. There are a variety of magnets for which the Heisenberg Hamiltonian is definitely not adequate. Detailed studies of the exchange mechanisms for ions with more than one unpaired electron[1–3] gives an effective spin Hamiltonian

$$H_{ij}^{\mathrm{ex}} = -J_1^{ij}(\mathbf{s}_i \cdot \mathbf{s}_j) - J_2^{ij}(\mathbf{s}_i \cdot \mathbf{s}_j)^2 - \cdots \tag{1}$$

with bilinear (J_1) and biquadratic (J_2) terms.[4] In fact, the situation is even more complicated if conduction electrons are present, in which case the effective Hamiltonian may be a rather complicated function of the spin variables, $\mathbf{s}_i$.[5,6]

One of the interesting recent discoveries is that the oscillatory exchange coupling between ferromagnetic (FM) films separated by nonmagnetic or antiferromagnetic spacer layers can be quite complicated, simultaneously displaying oscillations as well as regions of 90° coupling.[7] The energy of the exchange coupling between layers was found[7] to be expandable as

$$E_s = C - J_1 \cos\Theta - J_2 \cos^2\Theta, \tag{2}$$

where J_1 is considered bilinear and J_2 biquadratic exchange and Θ is the angle between sublayer magnetizations. Metallic magnets with itinerant electrons may naturally exhibit strong non-Heisenberg exchange interactions[5] and the definition of exchange is not so obvious. However, for small variations of the spin density, the classical Heisenberg[8] Hamiltonian may be generalized in the form

$$H_{ij}^{\mathrm{ex}} = -\sum_n J_n^{ij}(\mathbf{e}_i \cdot \mathbf{e}_j)^n, \tag{3}$$

where e_i is a unit vector in the direction of the magnetic moment on site i and the J_n^{ij} are bilinear, biquadratic, and higher order exchange coupling constants.

Thus, there is uncertainty about the applicability of a particular model used for exchange interaction in a given system. Sometimes, and even more importantly, it may not be clear how many exchange constants should be taken into account in a theoretical model of a material, because it is not known *a priori* over what range significant interactions occur. The peculiarities of the exchange coupling are controlled by details of the electronic structure, chemical bonding, and hybridization and can be treated nowadays on the basis of modern *ab initio* methods relatively accurately.

All these factors stimulated our efforts to study exchange interactions in bulk and multilayer materials using (i) the local spin density (LSD) treatment of the many-body problem and (ii) multiple scattering theory. We consider an infinitesimal angle of rotation of the magnetic moments as a perturbation in the scope of multiple-scattering theory and the force theorem[9] and use a generalization of this approach for the non-Heisenberg form of the exchange interaction Hamiltonian [Eq. (3)]. The expressions obtained for bilinear and biquadratic exchange turn out to have a convenient and physically transparent[10] form for *ab initio* calculations. Elements of this theory were presented first in Ref. 11. An important feature of this infinitesimal angle rotation approach is that it allows a unified theory to be applied, in principle, for itinerant and localized bulk and multilayered magnetic systems, even with magnetic spacers.

In this paper, we summarize some of our recent results obtained in the scope of this approach for $3D$ ferromagnetic metals, localized magnets like NiO, and metallic multilayers. One of the general questions addressed is whether the theory captures the peculiarities of the exchange coupling for different magnetic substances. Now, in localized magnets, biquadratic exchange is expected to be small compared with bilinear; here $J_2/J_1 \sim (t_{ij}/U)^2$, where t_{ij} are transfer integrals for insulators (~0.1–0.5 eV) and U is the on-site Coulomb correlation energy (5–10 eV).[1] In the case of metallic multilayers, J_2/J_1 is observed to be about 0.15 and to occur between

 0021-8979/96/79(8)/4805/3/$10.00 © 1996 American Institute of Physics

TABLE I. The ratio of the sum of bilinear $\Sigma_{j=1}^{NN} J_1^{0j}$ and biquadratic $\Sigma_{j=1}^{NN} J_2^{0j}$ coupling with NN nearest-neighbor shells in bcc Fe, fcc Co, and fcc Ni. The spin-wave-stiffness constants D (meV Å^2) are presented in comparison with experimental data (D^{exp}).

	NN	$\Sigma_{j=1}^{NN} J_2^{0j}/\Sigma_{j=1}^{NN} J_1^{0j}$	D	D^{exp}
Fe bcc	17	0.10	214	281[a]
Co fcc	12	0.12	360	384[b]
Ni fcc	8	0.14	527	555[c]

[a]Reference 17: neutron scattering measurements at room temperature.
[b]Reference 18: neutron scattering measurements at room temperature.
[c]Reference 19: room temperature measurements.

well-defined ferromagnetic layers. There are no measurements available for $3D$ metals for which exchange occurs between not so well-defined spin momenta in contrast with multilayer materials.

Further, as is known, the effective exchange interaction constants in metals control the energy of spin waves. In particular, in the long-wave limit the dispersion relation has the form

$$\omega_{\mathbf{q}} = D|\mathbf{q}|^2, \tag{4}$$

where D is the spin-wave stiffness constant which may be expressed through bilinear exchange interaction constants (J_1^{ij}) between sites i,j with α, β-Cartesian coordinates of the distance vector $\mathbf{r}_{ij}$ and magnetic moment (m) as[9]

$$D = \frac{1}{m} \sum_{\alpha,\beta} \sum_{j} J_1^{ij} \cdot r_{ij}^{\alpha} \cdot r_{ij}^{\beta}. \tag{5}$$

This sum provides a natural criterion for the number of nearest shells that have to be taken into account to get a converged result for spin-wave stiffness constants.

Results of our calculations for Fe, Co, and Ni, i.e., sums of bilinear and biquadratic exchange as well as spin-wave stiffness constants, are summarized in Table I. As can be seen, this sum is converged for bcc Fe at about 16–18 neighbors, for fcc Co 10–12, and for fcc Ni about 6–8. Thus, for the ferromagnetic $3D$-metals the biquadratic term is seen to be fairly large.

In addition to spin waves, the effective exchange coupling controls the energy of noncollinear configurations. As is known from band structure calculations, fcc Fe shows a tendency to form a noncollinear ground state.[12–15] In contrast with the well-known spin-density-wave instability of Cr that is driven by Fermi surface nesting features, from an analysis of the band structure of noncollinear configurations fcc Fe is likely an example of a frustrated system.[13] The direct proof of this suggestion may be reached on the basis of *ab initio* calculations of the exchange coupling constants. From the calculated bilinear and biquadratic terms, we determined the energy of spin spiral magnetic configurations with distribution

$$\mathbf{m}_i = m_i(\sin\Theta\cos(\phi_i), \sin\Theta\sin(\phi_i), \cos\Theta), \tag{6}$$

with $\phi_i = \mathbf{q}\cdot\mathbf{r}_i$ for $\mathbf{q} = q(0,0,1)$ and $\Theta = \pi/2$.

In Fig. 1 we show the dependence of the total energy of spin spiral configurations calculated using the Heisenberg

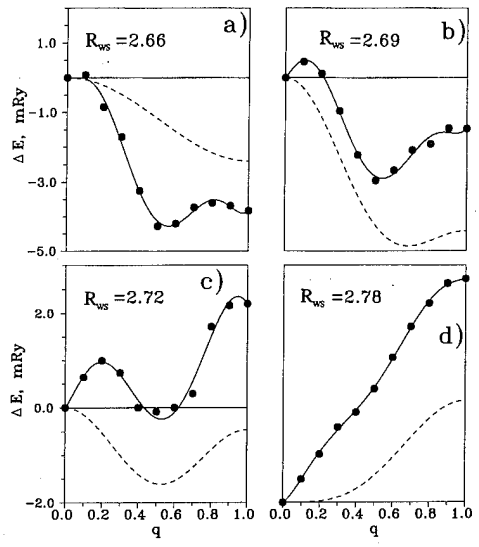


FIG. 1. Total energy of spin spiral noncollinear configurations ($\Theta = \pi/2$, $\mathbf{q} = q\cdot(0,0,1)$) calculated directly by the LMTO-SS method for fcc Fe at different volumes corresponding to Wigner–Seitz radii (R_{ws}) (a) 2.66, (b) 2.69, (c) 2.72, and (d) 2.78 A.U. Solid line with filled circles are results of direct self-consistent LMTO-SS calculations and dashed lines are Heisenberg model results obtained with exchange parameters determined for five nearest shells in the FM state.

model and the LMTO-SS method.[12] Calculations were performed for different volumes since fcc Fe shows a strong and nontrivial dependence of the exchange coupling on volume.[16] We found for both the high-spin and low-spin states that taking into account the biquadratic exchange determined in the ferromagnetic state does not make a qualitative difference in terms of the tendency of fcc Fe to a form noncollinear magnetic structure. However, a comparison of the Heisenberg model and self-consistent LMTO-SS calculations shows clearly that the leading contribution to the noncollinearity of fcc Fe in high-spin state is a competition of ferro- and antiferromagnetic exchanges which are strongly volume dependent. As can be seen in Fig. 1, the Heisenberg model with exchange coupling parameters determined for five nearest-neighbor shells in the ferromagnetic state fails to reproduce the spin spiral structure as being preferable in the low-spin state. This discrepancy may be explained by strong configurational dependence of the exchange parameters of the low-spin state driven by transformation to the high-spin state with the introduction of noncollinear magnetic ordering.[12,13]

The calculation of the exchange coupling in $3D$ metals is probably too hard a test of the theory because of the configurational dependence. The opposite extreme case is that of localized magnetic insulators with relatively well defined spin momenta. We calculated the bilinear and biquadratic contributions to the superexchange interaction between nearest Ni atoms through oxygen in the localized magnetic insulator NiO. The exchange parameters were determined for the antiferromagnetic ground state of type AF II. As expected,[22] LDA gives an underestimated gap (~0.65 eV) and the magnetic moment is about 1.0 μ_B. Results presented in Table II clearly show that the theory correctly describes the limiting

TABLE II. Estimate of bilinear J_1 (in K) and biquadratic J_2 (in K) terms on the superexchange for the localized antiferromagnetic insulator NiO.

	J_1	J_2/J_1
Theory	−78	0.05
Expt.[a]	−88	···
Expt.[b]	−222	···

[a]Reference 20.
[b]Reference 21.

case of a localized magnetic insulator; the ratio J_2/J_1 is predicted to be about 0.05.

Magnetic multilayers are also an example of magnets where theory may work relatively well compared with bulk metallic magnets. Hence, we applied the theory for Fe/Mn and Co/Mn metallic multilayers. The following features of this type of magnets attracted our attention: (i) large biquadratic exchange; (ii) a relatively strong magnetic spacer. Calculations performed using the LMTO-ASA method for ferromagnetic alignment of Fe layers give the results summarized in Table III. As can be seen, large biquadratic exchange is likely a peculiarity of the Co/Mn superlattice, since Fe_3/Mn_5 does not show large biquadratic exchange. We found that ferromagnetic exchange of two interfacial atoms, Co-Mn, is stronger (and enhanced in comparison with bulk Co) than Fe-Mn; another interesting peculiarity is an in-plane (Mn-Mn) antiferromagnetic exchange in Fe/Mn superlattices.

TABLE III. Interlayer, interfacial, and in-plane exchange coupling (mRy) for Co_3/Mn_5, Fe_3/Mn_5 superlattices.

Type of exchange	Term	Co_3/Mn_5	Fe_3/Mn_5
Interlayer (Fe-Fe)	J_2/J_1	0.75	0.04
Interface (Co-Mn)	J_1	1.61	···
Interface (Fe-Mn)	J_1	···	0.65
In plane (Mn-Mn)	J_1	0.15	−0.22

Work at Northwestern University was supported by the U.S. Office of Naval Research (Grant No. N00014-94-1-0030) and a grant of computer time at the Arctic Region Supercomputer Center. We are grateful to R. Sabiryanov for help in developing the code to J. Kudrnovsky, I. V. Solovyev, and M. I. Katsnelson for stimulating discussions.

[1] P. W. Anderson, Solid State Phys. **14**, 99 (1963).
[2] C. Herring, Rev. Mod. Phys. **34**, 631 (1962).
[3] N. Fuchikami and Y. Tanabe, J. Phys. Soc. Jpn. **47**, 505 (1979).
[4] Note that while the true Hamiltonian should contain small spin dependent contributions such as spin–orbit coupling, we consider only isotropic classical non-Heisenberg Hamiltonian in this paper.
[5] E. L. Nagaev, Sov. Phys. Usp. **1**, 31 (1982), and references therein.
[6] M. I. Auslender and M. I. Katsnelson, Teor. Mat. Fiz. **51**, 436 (1982).
[7] M. Ruhrig *et al.*, Phys. Status Solidi A **125**, 635 (1991).
[8] R. E. Prange and V. Korenman, Phys. Rev. B **19**, 4691 (1979).
[9] A. I. Liechtenstein, M. I. Katsnelson, and V. A. Gubanov, J. Phys. F **14**, L125 (1984), and reference therein.
[10] O. N. Mryasov, A. I. Liechtenstein, and A. J. Freeman (to be published).
[11] O. N. Mryasov and A. J. Freeman, Bull. Am. Phys. Soc. **39**, N.1, 528 (1994).
[12] O. N. Mryasov *et al.*, J. Phys: Condensed Matter **3**, 7683 (1991).
[13] O. N. Mryasov, V. A. Gubanov, and A. I. Liechtenstein, Phys. Rev. B **45**, 12330 (1992).
[14] M. Uhl, L. M. Sandratski, and J. Kubler, J. Magn. Magn. Mater. **45**, 314 (1992).
[15] V. P. Antropov, *et al.*, Phys. Rev. Lett. **75**, 729 (1995).
[16] R. F. Sabiryanov, S. Bose, and O. N. Mryasov, Phys. Rev. B **51**, 8958 (1995).
[17] S. Shirane, U. J. Minkiewitz, and R. Nathans, J. Appl. Phys. **39**, 383 (1968).
[18] S. J. Pickart *et al.*, Phys. Rev. B. **156**, 623 (1967).
[19] H. A. Mook *et al.*, Phys. Rev. Lett. **30**, 156 (1973).
[20] J. S. Smart, *Evaluation of Exchange Interactions from Experimental Data, in Magnetism,* edited by G. T. Rado, H. Suhl (Academic, New York, 1963), Vol. 3, p. 63.
[21] M. T. Hatchings *et al.*, Solid. State Commun. **9**, 1011 (1971).
[22] K. Terakura *et al.*, Phys. Rev. B **30**, 4734 (1984).

Local density approximation of magnetocrystalline anisotropy: An approach for narrowband materials

R. P. Erickson
Department of Physics, Oregon State University, Corvallis, Oregon 97331-6507

We exploit the purely magnetocrystalline response associated with the Goldstone excitation of a spontaneously magnetized system in order to describe, within a local density approach, the ground state interaction between a local magnetic moment and its surroundings, whose origin is in strong short-range (on-site) electron interactions and the hybridization of localized states. The idea is to consider an applicable form for the ground state energy, and therefore the magnetic anisotropy energy, beyond the local spin density approximation, which might be inferred from existing models of narrowband materials. © *1996 American Institute of Physics.* [S0021-8979(96)41708-5]

I. INTRODUCTION

An oscillating magnetic field of radio frequency is often used in conjunction with a uniform static field to probe the Goldstone mode of a spontaneously magnetically ordered sample in order to extract information about the strength and directional character of the magnetic anisotropy and the field-induced strain, or magnetostriction. The radio frequency field is tuned to resonate with the precessional frequency of the sample's average magnetization, which rotates about the direction of the uniform field. This represents a dynamical means of gleaning information about the way in which the spin angular momentum of the sample's magnetically active electrons is coupled to the crystalline environment via the electrons' orbital angular momentum. Since it costs no exchange energy to excite the Goldstone mode, this magnetocrystalline response is obtained separately from specific information about the manner in which individual electrons are correlated.

Early attempts to calculate magnetocrystalline effects were summarized by Van Vleck,[1] who pointed out the need to account for the coupling of orbital angular momenta of neighboring atoms of itinerant systems. Stimulated by this work, Brooks[2] utilized band theory to make order of magnitude estimates of the intrinsic anisotropy of Fe and Ni, and refinements of his study can be found in the literature.[3] More recently, within a density functional approach, Daalderop and co-workers[4] calculated the magnetic anisotropy energy (MAE) of bulk Fe, Co, and Ni. Similar calculations have been performed for YCo_5,[5] for example.

Industrial application of rare-earth and transition-metal compounds has sustained interest in the prediction of the magnetic properties of these materials, both in the bulk and in multilayer structures. Contemporary studies of these systems have centered on first-principle calculations, using density functional theory, within the framework of the local spin density (LSD) approximation, as in Refs. 4 and 5. Within this method, difficulties can exist in calculating the magnetic moment per atom and, particularly, the MAE. For example, the easy-axis prediction for fcc Ni, in Ref. 4, differs from experiment. It has been suggested by these authors that numerical precision may be the cause of the discrepancy; Jansen[6] has theorized that the atomic orbital energy, or orbital polarization, which is associated with Hund's rules, should be incorporated into any such calculation. More recent results for the local magnetic moments of YCo_5 (Ref. 7) appear to support this assessment.

Present LSD approaches, like those mentioned above, intrinsically calculate single-electron Bloch states to study magnetic properties. For example, with regard to Fe, Co, and Ni, such Bloch state descriptions successfully reproduce, to a high degree of accuracy, the observed magnitude of the local moment in these metals. Ultimately, this is a testament of band theory: the *d*-like bands of Fe, Co, and Ni, and the position of the Fermi level with respect to these states, are essential to explaining the ferromagnetism in these metals. But particularly in the oxides of these metals, other Mott insulators, and rare-earth compounds, the short-range correlations of localized *d* or *f* electrons are more difficult, perhaps impossible, to address within the local density approximation, and modifications based on the Hubbard model,[8] and the periodic Anderson model[9] have been proposed.

The purpose of the present discussion is to consider how, if at all possible, one might incorporate the salient features of strong short-range interactions and hybridization of localized states into a local description of the ground state energy, and therefore MAE, of a narrowband material. While a discussion of anisotropy energy is perhaps a secondary consideration when addressing the basic nature of the ground state energy of these systems, it should be remembered that the effect of spin-orbit coupling is inextricably linked, via Hund's rules, to the multiplet character of the ground state itself. In fact, as outlined in Sec. II, the explicit dependence of the Hamiltonian on the spin-orbit interaction can be exploited, via magnetocrystalline response theory, to give a local description of the strongly correlated system. In Sec. III, we consider an example of how one might formulate an approximation to the ground state energy using this approach.

II. PRELIMINARY DISCUSSION

As mentioned, one way to measure magnetocrystalline properties is to cause the average magnetization $\mathbf{M}(t)$ of a sample of volume Ω to precess in an applied field. In this section, we relate the ground state energy to the equation of motion of $\mathbf{M}(t)$—in the zero-field, time-independent (steady-state) limit—equivalent to a virtual rotation of the average magnetization $\mathbf{M}$. In this way, magnetic anisotropy response can be addressed specifically, and the ground state can be resolved to be in magnetic equilibrium. To maintain simplic-

 0021-8979/96/79(8)/4808/3/$10.00 © 1996 American Institute of Physics

ity, we consider only the response associated with intrinsic anisotropy, neglecting shape anisotropy in addition to striction effects, and we confine our discussion to the absolute zero of temperature. We assume dissipation effects to be negligible—those associated with the relativistic origin of spin-orbit coupling, which tend to cause the magnitude of $\mathbf{M}$ to vary with its direction $\hat{M}$.

We adopt a nonrelativistic approach, letting the magnetic moment operator be $\mathbf{m} = -\mu_B(\mathbf{L} + 2\mathbf{S})$, where $\mathbf{L}$ and $\mathbf{S}$ are the total orbital and spin angular momentum of the system, respectively, and μ_B is the Bohr magneton. At the absolute zero of temperature let a ground state be $|\hat{M}\rangle$—dependent on $\hat{M}$, which is aligned with the axis of quantization and referenced from the principal axes of the crystal. The true magnetic ground state corresponds to an easy-axis direction $\hat{M}_0$.

The time rate of change of $\mathbf{M}(t)$ is related to the way in which the free energy per volume varies with change in $\hat{M}$. At zero temperature, neglecting dissipation, and in the steady state [i.e., $d\mathbf{M}(t)/dt|_0 \equiv 0$], we have

$$\gamma^{-1}\frac{d}{dt}\mathbf{M}(t)|_0 = -\frac{1}{\Omega}\frac{\partial}{\partial \hat{M}}E_G(\hat{M})|_{\hat{M}=\hat{M}_0} \equiv 0, \tag{1}$$

where $E_G(\hat{M})$ is a ground state energy, and $\gamma = g\mu_B/\hbar$ is a gyromagnetic ratio. The equal sign holds for all (virtual fluctuations) $\hat{M}$ while the equivalence sign is true for $\hat{M} = \hat{M}_0$, only—precisely the zero-torque constraint satisfied by the true ground state energy.

Consider the magnetic moment $\mathbf{m}(t)$ within a volume $V \leq \Omega$. With q_N representing the $3N$ spatial degrees of freedom of an N-particle system, (i.e., $q_1 \equiv \mathbf{x}$ is the position of one particle), the local magnetization is

$$\mathbf{M}(q_1,t) = \int dq_{N-1}\langle \hat{M}|q_N\rangle\langle q_N|\mathbf{m}(t)|q_N\rangle\langle q_N|\hat{M}\rangle, \tag{2}$$

where a sum over all relevant quantum numbers is implied. As always, $\mathbf{m}(t) = \int_V dq_1 \mathbf{M}(q_1,t)$, and

$$\frac{d}{dt}\mathbf{m}(t) = \int_V dq_{a1}\frac{\partial}{\partial t}\mathbf{M}(q_1,t) \tag{3}$$

indicates how the time rate of change of $\mathbf{m}(t)$ is related to the time rate of change of $\mathbf{M}(q_1,t)$.

Now suppose $\mathbf{M}(t)$ is aligned with an easy axis, and consider the rotation of $\mathbf{M}(q_1,t)\,\delta V$ away from the moment distribution associated with $\mathbf{M}(t)$, where δV is an infinitesimal volume element whose location is referenced by q_1. There must be a restoring torque that tends to reduce the spin-orbit energy of δV, bringing $\mathbf{M}(q_1,t)\,\delta V$ back into the original moment configuration of the easy-axis magnetization. This is not the only torque exerted, however, because the rotation of $\mathbf{M}(q_1,t)\,\delta V$ away from the easy-axis configuration also augments exchange energy. The tendency of exchange energy to increase must be compensated via a second restoring torque exerted on $\mathbf{M}(q_1,t)\,\delta V$ by the surrounding magnetic environment.

Thus, in the presence of spin-orbit coupling, the torque on $\mathbf{M}(q_1,t)\,\delta V$ necessarily consists of these two parts, which can be quantified by writing the Hamiltonian as $\mathbf{H}(\hat{M}) = \mathbf{H}_0 + \mathbf{V}_{so}(\hat{M})$. Here, $\mathbf{H}_0$ describes the kinetic energy of N electrons and their Coulomb interactions with the ions of the lattice and with each other, while the spin-orbit term $\mathbf{V}_{so}(\hat{M})$ imposes on the total Hamiltonian, and therefore the ground state energy, a dependence on $\hat{M}$ via the intrinsic spin. For concreteness, we assume $\mathbf{V}_{so}(\hat{M}) = \lambda\mathbf{L}\cdot\mathbf{S}(\hat{M})$.

Having separated $\mathbf{H}(\hat{M})$ into these two parts, we write the steady-state expression $\gamma^{-1}\partial\mathbf{M}(q_1,t)/\partial t|_0 = \mathbf{P}_0(\hat{M};q_1) + \mathbf{Q}_0(\hat{M};q_1)$, where

$$\mathbf{P}_0(\hat{M};q_1) = -i\int dq_{N-1}\langle \hat{M}|q_N\rangle\langle q_N|[\mathbf{S}(t),\mathbf{H}_0]|q_N\rangle \times\langle q_N|\hat{M}\rangle|_0 = -\nabla_1\cdot\overleftrightarrow{\mathbf{j}}_0(\hat{M};q_1), \tag{4}$$

$$\mathbf{Q}_0(\hat{M};q_1) = -i\int dq_{N-1}\langle \hat{M}|q_N\rangle\langle q_N|[\mathbf{S}(t),\mathbf{V}_{so}(\hat{M})]|q_N\rangle \times\langle q_N|\hat{M}\rangle|_0 = -\partial\epsilon(\hat{M};q_1)/\partial\hat{M}. \tag{5}$$

Note, for example, that the intrinsic spin operator does not commute with $\mathbf{H}_0$ in Eq. (4) since it is a time-dependent operator, in the Heisenberg picture. However, in passing to a steady-state limit, we necessarily treat this operator as time independent. In this way, the excitation of the local magnetization that is described by Eqs. (4) and (5) is defined to be a virtual excitation. In Eq. (4), $\mathbf{S}$ (now regarded as time independent) commutes with electrostatic contributions to $\mathbf{H}_0$ since these are spin independent. The commutation of $\mathbf{S}$ with the kinetic energy operator is described by the spin-flip current density, which (with m an electron mass) is given by

$$\overleftrightarrow{j}_0(\hat{M};q_1) = -\frac{\hbar^2}{2im}\lim_{q_1'\to q_1}(\nabla_1 - \nabla_{1'})\mathbf{S}(\hat{M};q_1,q_1'),$$
$$\mathbf{S}(\hat{M};q_1,q_1') = \int dq_{N-1}\langle \hat{M}|q_1 q_{N-1}\rangle\mathbf{S}\langle q_1' q_{N-1}|\hat{M}\rangle. \tag{6}$$

Equation (5) is expressed in terms of a derivative of the local energy density:

$$\epsilon(\hat{M};q_1) = \int dq_{N-1}\langle \hat{M}|q_N\rangle\langle q_N|\mathbf{H}(\hat{M})|q_N\rangle\langle q_N|\hat{M}\rangle. \tag{7}$$

This follows by differentiating Eq. (7) with respect to $\hat{M}$, with total electron number density held fixed,[10] i.e., replacing $\mathbf{H}(\hat{M})$ by $\partial\mathbf{V}_{so}(\hat{M})/\partial\hat{M} = -\lambda\mathbf{L}\times\mathbf{S}(\hat{M}) = i[\mathbf{S},\mathbf{V}_{so}(\hat{M})]$.

Putting the above definitions together, the steady-state limit of $\partial\mathbf{M}(q_1,t)/\partial t$ satisfies

$$\gamma^{-1}\frac{\partial}{\partial t}\mathbf{M}(q_1,t)|_0 + \nabla_1\cdot\overleftrightarrow{j}_0(\hat{M};q_1) = -\frac{\partial}{\partial\hat{M}}\epsilon(\hat{M};q_1), \tag{8}$$

which is the analog of Eq. (1) for an infinitesimal volume element. In the presence of spin-orbit coupling, the divergence term is necessarily indicative of an anisotropic exchange interaction between the local magnetization and the surrounding magnetic environment.

III. EXAMPLE

To make a connection between the previous section and LSD, and also the motivations of Refs. 8 and 9, we consider the following scenario: Let V be the volume of a primitive cell of a perfect crystal and assume a set of magnetically active states is localized within each cell, within a volume $V_{\rm loc} < V$, contributing a moment $\mathbf{m}_{\rm loc}^{(i)}$ to the total moment of the ith cell. Then suppose a virtual rotation is applied to each local moment $\mathbf{m}_{\rm loc}^{(i)}$ so that the average magnetization is made to vary as $\Sigma_i \mathbf{m}_{\rm loc}^{(i)}/\Omega$, where the sum is over all unit cells. According to Eq. (1), we then have

$$\gamma^{-1}\sum_i \frac{d}{dt}\mathbf{m}_{\rm loc}^{(i)}(t)|_0 = -\frac{\partial}{\partial \hat{M}}E_G(\hat{M}). \tag{9}$$

Now let $\mathbf{m}$ represent the total moment in some unit cell, say the ith cell. Noting that $\mathbf{m}$ varies as $\mathbf{m}_{\rm loc}^{(i)}$, we have $d\mathbf{m}(t)/dt|_0 = d\mathbf{m}_{\rm loc}^{(i)}(t)/dt|_0$, so that upon substituting Eq. (8) into the steady-state limit of Eq. (3) and applying Gauss's Law, we obtain

$$-\gamma^{-1}\frac{d}{dt}\mathbf{m}_{\rm loc}^{(i)}(t)|_0 = \frac{\partial}{\partial \hat{M}}\int_{V_i} dq_1 \epsilon(\hat{M};q_1) + \mathbf{j}_0^{(i)}(\hat{M}), \tag{10}$$

where $\mathbf{j}_0^{(i)}(\hat{M}) = \int_{A_i} d\mathbf{A}_i \cdot \overleftrightarrow{j}_0(\hat{M};q_1)$. Here, A_i is the surface bounding the volume $V_{\rm loc}$ of the ith cell, with $d\mathbf{A}_i$ directed outwardly normal to A_i. Substituting Eq. (10) into Eq. (9) and integrating,

$$E_G(\hat{M},[\rho_\sigma]) = \int_\Omega dq_1 \epsilon(\hat{M},[\rho_\sigma];q_1) + \sum_i \int_{\hat{M}_0}^{\hat{M}} \mathbf{j}_0^{(i)}(\hat{M}')\cdot d\hat{M}'. \tag{11}$$

In Eq. (11), we have inserted the functional dependence of the ground state energy on electron number density ρ_σ ($\sigma = \uparrow,\downarrow$)—if $\mathbf{j}_0^{(i)}(\hat{M}')$ is to describe purely the rotation of $\mathbf{m}_{\rm loc}^{(i)}$ it will not vary with ρ_σ since the magnitude of $\mathbf{m}_{\rm loc}^{(i)}$ will remain fixed. Equation (11) describes the energy of a manifold of virtually excited magnetic states. The second term on the right of Eq. (11) represents exchange energy incurred through the rotation of local moments with respect to their true ground state orientation.

We can separate $\epsilon(\hat{M},[\rho_\sigma];q_1)$ into a LSD part and a strong short-range interaction part, where the polarization direction of the LSD Bloch states can be taken to be along $\hat{M}$ while that of the localized states of the ith cell is along $\hat{m}_{\rm loc}^{(i)}$, which is most easily referenced from $\hat{M}$. Of course, $\hat{M}$ itself depends on the orientations of the various local moments, and one is therefore inclined to choose an amenable ansatz for the set of orientations $\{\hat{m}_{\rm loc}^{(i)}\}$, such as through the imposition of a supercell geometry, not unlike earlier LSD studies of antiferromagnetic Cr.[11]

To determine the true (real ground state within a density functional context, we must vary Eq. (11), not only with respect to number density—to obtain the usual Kohn–Sham equations, but also with respect to $\hat{M}$, i.e., we must impose the constraint $\partial E_G/\partial \hat{M} = 0$, setting Eq. (1) to zero. Thus, in addition to the Kohn–Sham equations, we have the local magnetic torque (energy gradient) constraints

$$\frac{\delta}{\delta \hat{m}_{\rm loc}^{(i)}}\int_{V_i} dq_1 \epsilon(\hat{M},[\rho_\sigma];q_1) + \mathbf{j}_0^{(i)}(\hat{M}) = 0, \tag{12}$$

which taken together with the Kohn–Sham equations, represent an extended set of equations that must be solved self-consistently.

The spin-flip current $\mathbf{j}_0^{(i)}(\hat{M})$ of Eq. (12) assumes fully the significance of describing the interactions between the various local moments—via the hybridization between the localized states and the Bloch states of the LSD approximation. Thus, for example, if we were to imagine approximating $\epsilon(\hat{M},[\rho_\sigma];q_1)$ by a LDA+U scheme,[8] the noncollinear arrangement of local moments implicit in Eq. (11) could naturally and self-consistently account for spin-flip processes, processes that are not inherent in LDA+U itself. Clearly, even a simpler approximation of $\epsilon(\hat{M},[\rho_\sigma];q_1)$, by standard LSD techniques alone, could incorporate spin-flip processes in this way.

The spin-flip current has been utilized in model descriptions of the Ruderman–Kittel-type interaction of magnetic multilayers, for example.[12] Specific application of Eqs. (11) and (12) within the context of a self-consistent density functional calculation is presently being studied.

ACKNOWLEDGMENTS

Discussions with H. Jansen, G. Schneider, and S. Fox were much appreciated. Support was provided by the Office of Naval Research, through Contract N00014-9410326.

[1] J. H. Van Vleck, Phys. Rev. **52**, 1178 (1937).
[2] H. Brooks, Phys. Rev. **58**, 909 (1940).
[3] G. C. Fletcher, Proc. Phys. R. Soc. (London) A **67**, 505 (1954); K. Merkle, Z. Naturforsch **14a**, 938 (1959); J. C. Slonczewski, J. Phys. Soc. Jpn. **17**, Suppl. B-1, 34 (1962); N. Mori, *ibid.* **27**, 307 (1969); E. I. Kondorskii and E. Straube, Sov. Phys. JETP **36**, 188 (1973); N. Mori, Y. Fukuda, and T. Ukai, J. Phys. Soc. Jpn. **37**, 1263 (1973); N. Mori, T. Ukai, and H. Yoshida, *ibid.* **37**, 1272 (1973).
[4] G. H. O. Daalderop, P. J. Kelly, and M. F. H. Schuurmans, Phys. Rev. B **41**, 11 919 (1990).
[5] G. H. O. Daalderop, P. J. Kelly, and M. F. H. Schuurmans, J. Magn. Magn. Mater. **104-107**, 737 (1992).
[6] H. J. F. Jansen, J. Appl. Phys. **67**, 4555 (1990).
[7] L. Nordström, M. S. S. Brooks, and Börje Johansson, J. Magn. Magn. Mater. **104-107**, 1942 (1992).
[8] V. I. Anisimov, J. Zaanen, and O. K. Anderson, Phys. Rev. B **44**, 943 (1991); V. I. Anisimov, I. V. Solovyev, M. A. Korotin, M. T. Czyżyk, and G. A. Sawatzky, *ibid.* **48**, 16 929 (1993).
[9] M. M. Steiner, R. C. Albers, D. J. Scalapino, and L. J. Sham, Phys. Rev. B **43**, 1637 (1991); M. M. Steiner, R. C. Albers, and L. J. Sham, *ibid.* **45**, 13 272 (1992).
[10] The assumption that the total number density is independent of $\hat{M}$ is consistent with the neglect of dissipation effects, and consistent with the approximations made in the calculations of MAE in Refs. 4 and 5, for example.
[11] J. Kübler, J. Magn. Magn. Mater. **20**, 277 (1980); H. L. Skriver, J. Phys. F Metal. Phys. **11**, 97 (1981).
[12] R. P. Erickson, K. B. Hathaway, and J. R. Cullen, Phys. Rev. B **47**, 2626 (1993).

Magnetic properties of melt-quenched Ni-rich amorphous and bcc Zr–Ni alloys (abstract)

László F. Kiss, Lajos K. Varga, and Imre Bakonyi
Research Institute for Solid State Physics, Hungarian Academy of Sciences, H-1525 Budapest, POB. 49, Hungary

It has been demonstrated recently[1] that the structure of melt-quenched Zr–Ni ribbons in the vicinity of 90 at. % Ni was strongly dependent on the quenching rate: at the highest quenching rate, the alloys $Zr_{10}Ni_{90}$ and Zr_9Ni_{91} could be prepared with an amorphous structure whereas at lower quenching rates the Zr_9Ni_{91} alloy was prepared as a solid solution of Zr in Ni with a body-centered cubic (bcc) structure. In a preliminary measurement[2] we have established a Curie point (T_c) of 66 K for the a-Zr_9Ni_{91} ribbon which was much smaller than the value T_c=235 K reported[3] for an a-$Zr_{10}Ni_{90}$ ribbon. This discrepancy has motivated us to perform the present detailed magnetization study in the temperature range 5 to 300 K. It was also of interest to compare the Curie point of the amorphous and bcc phase with the same chemical composition. The real component χ' of the AC susceptibility as well as the magnetization isotherms up to H=18.5 kOe have been investigated. The measurements of χ' yielded T=41, 66, and 70 K for a-$Zr_{10}Ni_{90}$, a-Zr_9Ni_{91}, and bcc-Zr_9Ni_{91} ribbons, respectively. The para-ferromagnetic transitions were found to be fairly sharp although in some of these samples several transitions differing by a few degrees only could be observed. In some of the samples, however, very faint magnetic transitions indicated by a small broad peak could also be detected around 250 K. This feature can be attributed to some residual phases of either an unknown Zr–Ni intermetallic compound or of Ni(Zr) solid solution precipitates. The close coincidence of this peak with the Curie temperature reported by Kaul[3] suggests that his value (T_c=235 K) cannot be representative of the amorphous Zr–Ni matrix but it rather may originate from ferromagnetic precipitates. The magnetization isotherms for the amorphous and bcc-Zr_9Ni_{91} alloy indicated the development of a significant magnetization around the T_c values deduced from χ'. The saturation magnetization at the lowest temperature amounted to about 7 emu/g in both structural modifications. This value is reasonable in view of the reduction of T_c with respect to pure fcc-Ni. The present T_c data indicate that the critical concentration for the onset of magnetic ordering in the Zr–Ni system should be slightly below 90 at. % Ni. It can be concluded from this study that the magnetic behavior of Zr–Ni alloys at about 90 at. % Ni content is characteristic for very weak itinerant ferromagnets and the results will be analyzed in this framework with the help of Arrott plots. © *1996 American Institute of Physics.* [S0021-8979(96)42208-5]

[1] Á. Cziráki, B. Fogarassy, G. Van Tendeloo, P. Lamparter, M. Tegze, and I. Bakonyi, J. All. Comp. **210**, 135 (1994).
[2] J. Tóth, I. Bakonyi, and G. Hilscher, Europhys. Lett. **24**, 379 (1993).
[3] S. N. Kaul, Phys. Rev. B **27**, 6923 (1983).

Specific heat and magnetization of $Co_{2-x}Sc_{1+x}Sn$

Z. W. Chen,[a] C. L. Lin, and T. Mihalisin
Department of Physics, Temple University, Philadelphia, Pennsylvania 19122

J. T. Wang
Department of Physics, Southern University and A&M College, Baton Rouge, Louisiana 70813

X. Q. Wang
Department of Materials Science and Engineering, University of Pennsylvania, Philadelphia, Pennsylvania 19104

Co_2ScSn crystallizes with the cubic L_{21} Heusler structure and is an itinerant ferromagnet with T_c=238 K. X-ray diffraction measurements show that $Co_{2-x}Sc_{1+x}Sn$ retains the L_{21} crystal structure with an essentially unchanged lattice constant for $0 \leqslant x \leqslant 0.15$. However, T_c determined from the magnetization measurements decreases monotonically with increasing Sc concentration from 238 K for x=0 to 40 K for x=0.11, and then remains at 40 K from x=0.11 to 0.14. The electronic specific heat coefficient γ is enhanced from 13 mJ/mole-K^2 for Co_2ScSn (x=0) to 30 mJ/mole-K^2 for x=0.13 ($Co_{1.87}Sc_{1.13}Sn$). In addition, the C/T versus T^2 plot shows a leveling-off behavior at low temperatures for the x=0.13 sample. The γ enhancement and level-off behavior observed when a system approaches a magnetic instability are discussed in terms of the self-consistent renormalization theory of spin fluctuations for weak itinerant ferromagnets and nearly magnetic systems. © *1996 American Institute of Physics.* [S0021-8979(96)17208-3]

INTRODUCTION

Co_2ScSn crystallizes with the cubic L_{21} Heusler structure and is an itinerant ferromagnet with a saturation moment of 0.51 μ_B per Co atom.[1,2] We have shown[2] from magnetization measurements at low applied magnetic fields that the system undergoes a transition from a paramagnetic state to a helimagnetic state at T_c=238 K, and exhibits spin glass behavior below 100 K. The application of high magnetic fields suppresses the helimagnetic state and the spin glass behavior, and Co_2ScSn becomes a simple ferromagnet. We have also shown[3] that the substitution of Ni for Co in $(Co_{1-x}Ni_x)_2ScSn$ decreases T_c linearly with increasing Ni concentration and that T_c approaches zero in the vicinity of 40% Ni substitution (x=0.4). The electronic specific heat coefficient γ is enhanced from 13 mJ/mole-K^2 for Co_2ScSn (x=0) to 58 mJ/mole-K^2 for x=0.4 and x=0.5. In addition, for the x=0.4 and x=0.5 samples the specific heat divided by temperature (C/T) vs T^2 plot shows a leveling-off behavior at low temperatures, instead of the typical straight line behavior. γ enhancements and upturn behavior in C/T have been previously observed in f-electron systems, e.g. $(Ce,Gd)Sn_3$[4] and $(Y,U)Pd_3$,[5,6] when these systems are close to a magnetic instability. This behavior is also consistent with the predictions of self-consistent renormalization (SCR) theory[7] of spin fluctuations for nearly magnetic and weak itinerant magnetic systems.

Another way to drive the system towards a nonmagnetic state which does not involve the introduction of another element into the Co_2ScSn system is to depart from the 2 to 1 Co to Sc ratio, that is to make the $Co_{2-x}Sc_{1+x}Sn$ system. This system retains the L_{21} crystal structure for $x \leqslant 0.15$. The temperature dependence of the magnetization and specific heat and the T_c variation for this system are presented for $0 \leqslant x \leqslant 0.15$.

EXPERIMENT

Polycrystalline $Co_{2-x}Sc_{1+x}Sn$ samples were prepared in an inert atmosphere arc furnace with appropriate care taken to compensate for the weight loss of the more volatile Sn. The samples were wrapped in Ta foils and were annealed under high vacuum at 800 °C for 8 weeks. This long period of annealing is necessary since we have shown[2,3] that the crystal structure and physical properties of Co_2ScSn and its related systems are significantly influenced by heat treatment. Powdered x-ray diffraction and high power, high-resolution electron microscopy measurements at room temperature were used to check sample homogeneity and crystal structure. The results indicated that $Co_{2-x}Sc_{1+x}Sn$ retains the cubic L_{21} Heusler structure with an essentially unchanged lattice constant of 6.190 Å for $0 \leqslant x \leqslant 0.15$. The magnetization was measured from 1.8 to 400 K at various magnetic fields up to 5.5 T using a commercial superconducting quantum interference device (SQUID) magnetometer. The specific heat was measured from 1.2 to 25 K in zero field and applied magnetic fields up to 4 T using a semiadiabatic heat pulse method.

RESULTS AND DISCUSSION

We have shown using magnetization, electrical resistivity, and ^{119}Sn Mossbauer measurements[2,8] that the ferromagnetic transition occurs at T_c=238 K for Co_2ScSn. Shown in Fig. 1 curve (a) is the temperature dependence of the magnetization of Co_2ScSn measured in an applied field of 20 Oe. It can be seen that the magnetization increases rapidly below 238 K. Below T_c, down to 100 K, the magnetization is essentially unchanged. This behavior of constant magnetization can be explained in terms of the helical magnetic state,[2] and

[a]Present address: Department of Materials Science and Engineering, University of Southern California.

 0021-8979/96/79(8)/4812/3/$10.00 © 1996 American Institute of Physics

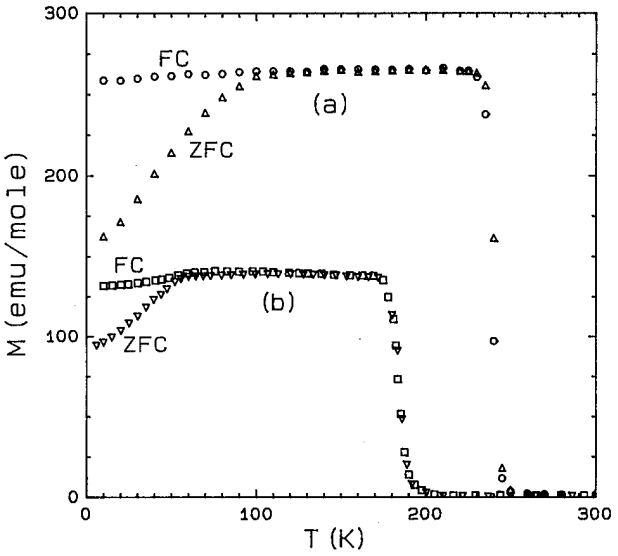


FIG. 1. The temperature dependence of the magnetization measured at $H=20$ Oe for (a) Co_2ScSn and (b) $Co_{1.97}Sc_{1.03}Sn$. ZFC: zero field cooled data, and FC: field cooled data.

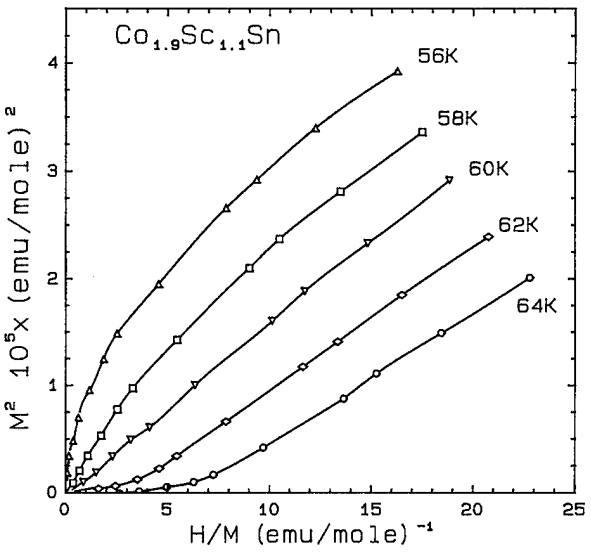


FIG. 2. Arrot plots (M^2 vs H/M) at $T=56$, 58, 60, 62, and 64 K for $Co_{1.9}Sc_{1.1}Sn$.

has also been observed for other itinerant magnets, e.g., MnSi and $Fe_{1-x}Co_xSi$.[9–11] Below 100 K the zero field cooled (ZFC) data increases monotonically with increasing temperature, but the field cooled (FC) data do not vary with temperature. This hysteretic behavior indicates that Co_2ScSn undergoes a second transition to a spin glass like state at low temperatures, i.e., below 100 K. We have also shown[2] that the helical magnetic state and spin glasslike behavior are suppressed by the application of high magnetic fields, and Co_2ScSn becomes a simple ferromagnet.

We have shown[3] that T_c decreases linearly with decreasing Co concentration in the $(Co_{1-x}Ni_x)_2ScSn$ system, and approaches zero in the vicinity of 40% Ni substitution for Co ($x=0.4$). We have also measured the temperature and magnetic field dependence of the magnetization for the $Co_{2-x}Sc_{1+x}Sn$ system with $0\leqslant x\leqslant 0.15$. The magnetization measured at low applied fields for the samples with lower Co concentrations, i.e., $0<x\leqslant 0.15$, shows a similar behavior to that shown in Fig. 1 curve (a). Curve (b) in Fig. 1 shows the FC and ZFC magnetization for $Co_{1.97}Sc_{1.03}Sn$ ($x=0.03$), also measured at $H=20$ Oe. It can be seen, however, that T_c and the spin glass transition for this sample occur at lower temperatures, i.e., 190 and 55 K, respectively. Again, the helical magnetic state and spin glass behavior for these samples with lower Co concentrations can be also suppressed by the application of high magnetic fields (not shown), and the samples then become simple ferromagnets.

In order to extract the ferromagnetic transition temperature T_c, we have measured M versus H for several temperatures near T_c for every sample reported here. Arrott plots (M^2 versus H/M) for $Co_{1.9}Sc_{1.1}Sn$ ($x=0.1$) at various temperatures are shown in Fig. 2. T_c is determined as the temperature for which a linearly extrapolated curve on the Arrott plot goes through the origin. We find a T_c value of 60 K from this plot for this sample. T_c determined from Arrott plots is in good agreement with T_c defined as the temperature where $|dM/dT|$ is maximum.

Shown in Fig. 3 is T_c versus Sc concentration $(1+x)$ for the $Co_{2-x}Sc_{1+x}Sn$ system. T_c decreases monotonically with decreasing Co concentration (increasing Sc content $1+x$) from $T_c=238$ K for Co_2ScSn ($x=0$) to 40 K for $x=0.11$. It is interesting that T_c remains almost the same (40 K) for the samples with even higher Sc concentrations in the region between $(1+x)=1.11$ and 1.14. One might argue that Co content can not be lowered below 1.89 (or that the true maximum value of $(1+x)$ is 1.11), and that is why T_c stays unchanged for $0.11<x\leqslant 0.15$. For the following reasons we rule out this speculation. First, for the samples with $0.11<x\leqslant 0.15$ no detectable extra phases are seen via the x-ray diffraction measurements. Second, we did not find a contribution to the magnetization from free Co metal or magnetic impurity phases. Third, we observe that the value of the mag-

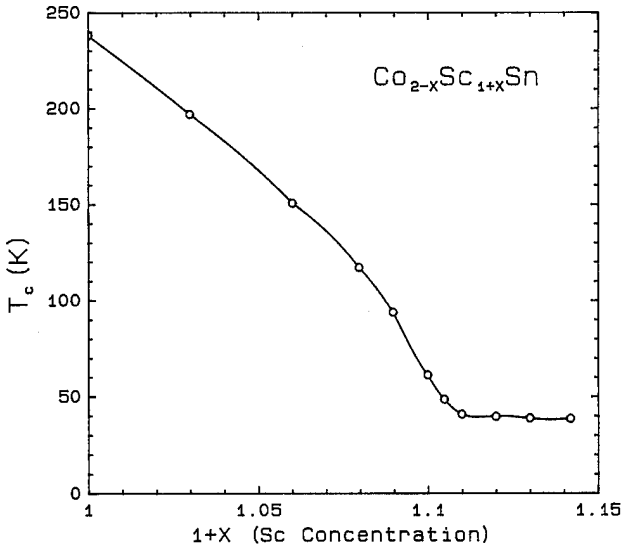


FIG. 3. T_c as a function of Sc concentration $(1+x)$ for the $Co_{2-x}Sc_{1+x}Sn$ system with $0\leqslant x\leqslant 0.15$.

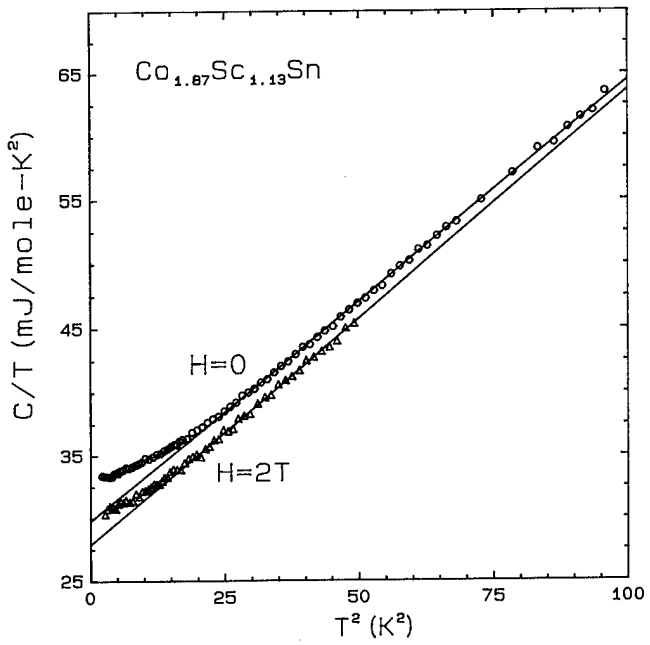


FIG. 4. C/T vs T^2 plot measured at applied fields $H=0$ and $H=2$ T for $Co_{1.87}Sc_{1.13}Sn$. The straight line indicates a linear fit to higher temperature data from $T=5$ to 10 K.

netization at low temperatures decreases monotonically as one lowers the Co content across the entire regime, including $0.11<x\leqslant 0.15$.

As mentioned earlier, the variation of γ as the system approaches a magnetic instability is of primary interest. Shown in Fig. 4 is the C/T versus T^2 data measured at $H=0$ and 2 T for $Co_{1.87}Sc_{1.13}Sn$. For $H=0$ γ values of 33.5 and 30 mJ/mole-K^2 are obtained from C/T at $T=1.4$ K and from a linear fit of higher temperature data ($T=5$–10 K), respectively. Either of the γ values mentioned above for $Co_{1.87}Sc_{1.13}Sn$ is larger than that of Co_2ScSn, i.e., $\gamma=13$ mJ/mole-K^2. This enhanced γ behavior when the system approaches a magnetic instability has been reported previously for many f- and d-electron systems. For example, γ is greatly enhanced for 10% Gd, 20% U, and 60% Co in the $(Ce_{1-x}Gd_x)Sn_3$,[4] $(Y_{1-x}U_x)Pd_3$,[5,6] and $(Co_{1-x}Ni_x)_2ScSn$[3] systems, respectively.

It is clear that the C/T versus T^2 plot for $Co_{1.87}Sc_{1.13}Sn$ shown in Fig. 4 shows a leveling-off behavior at lower temperatures. This is behavior has also been observed in the cases of heavy fermion f-electron systems,[4–6] enhanced paramagnetic itinerant d-electron systems[12] and weakly magnetic d-electron systems.[13] We do not believe that the leveling-off behavior seen in C/T versus T^2 for $Co_{1.87}Sc_{1.13}Sn$ is due to the presence of a spin glass transition for two reasons. First a plot of T_g (spin glass transition temperature) versus $1+x$ (not shown here) shows that T_g goes to zero for $1+x\sim 1.07$. Second this type of C/T versus T^2 behavior is not seen for samples which have a spin glass transition namely pure Co_2ScSn and $Co_{2-x}Sc_{1+x}Sn$ with $1+x<1.07$. The self-consistent renormalization (SCR) theory of spin fluctuations[7] can explain the magnetic, electric, and thermodynamic properties of nearly magnetic and weakly magnetic itinerant systems. According to the prediction of the SCR theory, an additional contribution of the form $T[\ln(T/T_{sf})]$ should be added to the specific heat resulting in a leveling-off behavior in a C/T versus T^2 plot at low temperatures. Although the applied field of 2 T reduces the specific heat over the entire temperature range, it is not sufficiently strong to suppress the spin fluctuations, and thus the leveling-off behavior in $H=2$ T remains similar to that in zero field. That is, one expects that T_{sf} is considerably larger than 2 K which would correspond to the field of 2 T.

In conclusion, we have measured the magnetization and specific heat of the $Co_{2-x}Sc_{1+x}Sn$ system with $0\leqslant x\leqslant 0.15$. T_c decreases monotonically with decreasing Co concentration from 238 K for $x=0$ to 40 K for $x=0.11$ and then remains at 40 K between $x=0.11$ and $x=0.14$. The specific heat data for $Co_{1.87}Sc_{1.13}Sn$ show that γ is enhanced to 30 mJ/mole-K^2 and the C/T versus T^2 plot exhibits a leveling-off behavior at low temperatures.

ACKNOWLEDGMENTS

C. L. Lin and T. Mihalisin acknowledge support from the Materials Research Center at Temple University and DOD-AFOSR under Grant No. F49620-93-1-0018. X. Q. Wang of the University of Pennsylvania acknowledges support from NSF-MRL under Grant No. DMR91-20668.

[1] S. K. Malik, P. L. Paulose, R. Nagarajan, A. E. Dwight, P. P. Vaishnava, and C. W. Kimball, Hyperfine Inter. **34**, 427 (1987).
[2] C. L. Lin, T. Mihalisin, and N. Bykovetz, J. Magn. Magn. Mater. **116**, 355 (1992).
[3] C. J. Fuller, Z. W. Chen, N. Anbalagan, C. L. Lin, and T. Mihalisin, J. Appl. Phys. **73**, 5427 (1993).
[4] C. L. Lin, T. Yuen, G. Y. Jiang, and T. Mihalisin, J. Appl. Phys. **70**, 6092 (1991).
[5] C. L. Seaman, M. B. Maple, R. W. Lee, S. Ghamaty, M. S. Torikachvili, J. S. Kang, L. Z. Liu, J. W. Allen, and D. L. Cox, Phys. Rev. Lett. **67**, 2882 (1991).
[6] B. Andraka and A. M. Tsvelik, Phys. Rev. Lett. **67**, 2886 (1991).
[7] T. Moriya, in *Spin Fluctuations in Itinerant Electron Magnetism*, Springer Series in Soild State Sciences 56, (Springer, Berlin, 1985).
[8] Z. W. Chen, C. L. Lin, T. Mihalisin, and N. Bykovetz, J. Appl. Phys. **73**, 6974 (1993).
[9] K. Shimizu, H. Maruyama, H. Yamazaki, and H. Watanabe, J. Phys. Soc. Jpn. **59**, 305 (1990).
[10] J. Beille, J. Voiron, F. Towfiq, M. Roth, and Z. Y. Zhang, J. Phys F **11**, 2153 (1981).
[11] J. Beille, J. Voiron, and M. Roth, Solid State Commun. **47**, 399 (1983).
[12] M. Shiga, K. Fujisawa, and H. Wada, J. Phys. Soc. Jpn. **62**, 1329 (1993).
[13] C. J. Fuller, C. L. Lin, T. Mihalisin, F. Chu, and N. Bykovetz, Solid State Commun. **83**, 863 (1992).

On the conduction band polarization in metallic systems with a periodic array of localized magnetic moments

A. Hernando and J. M. Rojo
Instituto de Magnetismo Aplicado and Departamento Física de Materiales, Universidad Complutense, Las Rozas, P.O. Box 155, Madrid 28230, Spain

J. C. Gómez Sal
Instituto de Magnetismo Aplicado and Departamento de Materia Condensada, Universidad de Cantabria, Spain

J. M. Novo
Instituto de Magnetismo Aplicado and Departamento de Matemática Aplicada y Computación, Universidad de Valladolid, Spain

It is shown that the indirect exchange between magnetic moments distributed in a periodic array and carried out through the conduction band results from the balance of a ferromagnetic component, static effect, and an antiferromagnetic one, polarization effect. The sign of the coupling mainly depends on the density of states at the Fermi level. For filled bands only the antiferromagnetic component exists (metallic superexchange) and, in particular, only for free electrons both components exactly compensate to each other, remaining the typical Ruderman–Kittel–Kasuya–Yosida ripple due to the oscillating character of the polarization. © *1996 American Institute of Physics.* [S0021-8979(96)17308-X]

I. INTRODUCTION

In spite of increasing activity in the last few years, much controversy still remains about the role of conduction electrons in promoting indirect exchange in localized arrays of magnetic moments. This concerns, as a key subject, the physics of alternating layers of magnetic and nonmagnetic materials in which many current experiments are not particularly consistent with each other and corresponding theoretical efforts are at stake.[1] Some other long standing problems, such as the indirect exchange of magnetic ions in rare earth ternary compounds,[2] also want a good explanation of the general trends in the polarization sign. In all these cases the so called Ruderman–Kittel–Kasuya–Yosida (RKKY) interaction has been invoked without much detailed analysis of other contributions, that can, however, in some cases play a crucial role.[3] In the present article we make a general analysis of the dominant contributions arising from conduction band indirect exchange. We show that two independent components exist and that their balance can be shown to explain the experimental data concerning the polarization sign of ferromagnetic arrays in both rare earth compounds and alternating multilayers.

II. FIRST AND SECOND ORDER SUPEREXCHANGE PERTURBATION

The model most calculations refer to[4] consists of an array of magnetic moments, that act as a source of magnetic field and are supposed to be fixed, immersed in band of conduction electrons. The response of the electron band to the localized magnetic moments is calculated by perturbating the conduction band hamiltonian with a term of the form $\mathbf{H}'=\mu_B\Sigma_i\sigma_i\cdot\mathbf{H}$, where the sum in units of Bohr magneton is extended to all electron spins σ_i. This model applies to the case of multilayers composed by alternating layers of ferromagnetic and nonmagnetic metal (for example, Co/Cu), where the array consists of finite width regions (Co) of constant magnetic field $\mathbf{H}$ separated by other regions (Cu) in which the magnetic response is included in terms of a non local susceptibility χ. It does also apply to ternary compounds involving rare earths metals, in which case the array consists of the rare earth magnetic ions, the rest of the components in the material acting only as electron suppliers.

Most of the recent work has been centered in discussing the role of the nondiagonal second order perturbation terms of $\mathbf{H}'$, leading to polarization of the electron gas. A well known result, the so called RKKY interaction, is the appearence of decaying oscillations of the polarization gas as a function of the distance to a fixed magnetic moment. It is clear that one should add to the latter the result of the diagonal first order perturbation correction, the so called static contribution, arising from the redistribution of spins to minimize the energy of the system, a term first discussed by Fröhlich and Nabarro and later, by Zener.[5] It was shown[6] that *for free electrons*, the static contribution could be directly obtained by including the zeroth order Fourier components ($q=0$) in the second order perturbation. Since then, most authors have simply ignored the static contribution by keeping the $q=0$ term in the second order computation.

We believe that this procedure, whereas perfectly correct in the free electron approximation, may lead to error in real systems, in which band effects are relevant. Band effects have been considered previously[7] but, mostly, in view of correcting the RKKY second order results. We argue in the following that static and polarization effects are independent (except in the very special case of free electrons) and that seldom will the static one cancel the dc value of the polarization oscillation.

III. FERRO- VERSUS ANTIFERROMAGNETIC CONTRIBUTIONS

To be precise, we discuss now the exchange interaction between two magnetic moments that are immersed in an electron background corresponding to a given band. In order

to arrive at our main clonclusion we argue in succesive steps. First we consider a completely filled band not overlaping with other bands. As there are not unoccupied states within a small energy range from the uppermost occupied level, there cannot be Pauli-like electron spin flip and the only result is a second-order deformation of the electron wavefunctions leading to antiferromagnetic interaction between the magnetic moments. We want to remark that the energy difference between the ferro and antiferromagnetic states due to the second order deformation, E'_{SO}, does indeed oscillate as a function of the distance between spins but that oscillation takes place around a dc value of $E'_{SO} > 0$, i.e., in spite of the oscillation, the lowest energy configuration is always antiferromagnetic. This behavior has been derived in previous works carried out for unidimensional periodic arrays of magnetic moments.[3,8,9] We present in the Appendix a simple argument which illustrates the origin of the antiferromagnetic character of the indirect exchange due to polarization.

Now we discuss the general case of a partially filled band. For the purpose of our argument we can divide that bands in two regions: the one, far from the Fermi level, in which the spins cannot flip and that can be considered as a filled band and the other, in the neighborhood of the Fermi level, in which, in order to decrease the energy of the system, electron spins tend to jump to unoccuppied states with their spins parallel to the external magnetic moments. From the first region an antiferromagnetic contribution is expected (corresponding to second order perturbation) whereas a ferromagnetic one (corresponding to first order) arised from the second. The ferromagnetic contribution, which corresponds to first order perturbation of the electron hamiltonian $\mathbf{H}'$ is obviously very sensitive to the density of state at the Fermi level, $N(E_F)$, in much the same way as the Pauli paramagnetism is. The overall response of the system depends on a detailed balance between the above contributions, that are not related to each other. One can think in terms of the positive polarization displacing the zero level of the negative polarization oscillation. We want to remark that unless this positive displacement cancels the mean negative value of the second order oscillation the overall behavior of the system will not switch from ferro to antiferromagnetic as a function of distance between magnetic moments. The overall behavior will be conditioned by the dominating zeroth order contribution.

Two special cases are worth discussing further. First, an experimental observation: oxides having a well defined electron gap, such as nickel oxide, are well known to have an antiferromagnetic behavior based on indirect electron exchange. We can easily explain it on the grounds that these materials have completely filled bands that prevent Pauli-like spin reorientation and allow only wavefunction redistribution. That is equivalent to think of a vanishing density of states at the Fermi level. Second, a theoretical result: in a *free electron* gas the dc mean value of the second order antiferromagnetic contribution has been shown to exactly compensate the first order ferromagnetic one (see the Appendix). *Only* in systems whose behavior can be approximated by a free electron gas, the second order oscillation takes place around the zero dc value resulting in a global oscillation of antiferromagnetic versus ferromagnetic behavior as a function of distance.

IV. RARE EARTH COMPOUNDS

Rare earth, R, compounds can be described as a periodic array of $R\ 3^+$ ions with well localized magnetic moments, $\mu_b g_J J$, inmersed in a conduction band electron sea. In order to avoid both crystalline field effects or competing localized-itinerant magnetism considerations, we focus our discussion on GdM equiatomic systems, where M is a transition metal which does not contribute to the localized magnetism, as is the case for M=In, Ag, Cu, Ni, Zn, Cd, Ga, etc.[2] The M ions act on the conduction band by changing $N(E_F)$. Some of these compounds are ferromagnetic (RNi, RZn, RGa) while others exhibit antiferromagnetism (RCu, RIn, and RAg). The study of the corresponding diluted ternary compounds $RM_xM'_{1-x}$ shows the evolution from one behavior to another. In this sense, for the $GdNi_{1-x}Cu_x$ orthorhombic compounds[10] a change from a ferromagnetic collinear structure (for $x=0$) to an antiferromagnetic one (for $x>0.5$) is observed. Similar behavior has been found for $RZn_{1-x}Cu_x$ or $RZn_{1-x}Ag_x$ cubic alloys.[11,12] This overall behavior can be understood on the light of the considerations we have outlined in this article. Recent band calculations[13] have shown that $N(E_F)$ is much larger for GdZn than for GdCu. This fact would support the idea that for small $N(E_F)$, as is the case for GdCu, the antiferromagnetic coupling due to electron band polarization overcomes the ferromagnetic component associated to the static effect. As Cu is partially substituted by an increasing amount of Ni, $N(E_F)$ increases resulting in a net indirect ferromagnetic coupling. It is important to notice that the influence of the interatomic distances, quite often invoked as cause of sign change for indirect exchange, can be ruled out after considering recent results in $Ho_{1-x}Y_xNi$ series.[14] These series present cell volume changes slightly larger than in $GdNi_{1-x}Cu_x$, however, all of them are ferromagnetic. In this case, in spite of the variations of distance between magnetic ions, the magnetic coupling does not exhibit sign switch because $N(E_F)$ has not been modified, as Y and Ho atoms provide the same number of electrons to the conduction band.

V. CONCLUSIONS

In a periodic array of magnetic moments described by a conduction electron exchange hamiltonian, first (static) and second order (polarization) perturbing effects do not, in general, cancel out their mean values as function of distance between the magnetic moments in the array. The overall ferromagnetic versus antiferromagnetic behavior depends, therefore, on the balancing of those effects and, particularly, on the density of states at the Fermi level. This effect is much stronger that other often considered components such as refined RKKY corrections, correlation effects, etc. A wealth of experimental data are shown to be explained on these simple grounds, particularly the ferromagnetic versus antiferromagnetic behavior of ternary compounds including rare earth ions.

APPENDIX

Let us show that the second order perturbation term leads to an antiferromagnetic coupling. For completely filled bands or orbitals the first order vanishes and therefore only a second term contribution is expected. (This is the case for superexchange in oxides). According to Ref. 4, E'_{SO} becomes

$$E'_{SO}=E_{\text{ferr}}-E_{\text{ant}}=\Sigma\chi_q h_q^{2\ \text{ant}}-\Sigma\chi_q h_q^{2\ \text{ferr}}, \tag{A1}$$

where h_q^{ant} and h_q^{ferr} are the Fourier components of the polarizing effective field, $\mathbf{H}^{\text{ant}}(x)$ and $\mathbf{H}^{\text{ferr}}(x)$, corresponding to the antiferromagnetic and ferromagnetic configurations of the localized moment, respectively. χ_q is the q-th Fourier component of the nonlocal susceptibility $\chi(x-x')$. *It can be shown with generality that E'_{SO} is positive and can be labelled as superexchange term.* The basic idea is that in a filled band one half of the electrons has spin up whereas the other half has spin down. As it has been shown for periodic arrays, $m(x)$ oscillates with the same wavelength than $H(x)$ even though it presents superimposed a shorter wavelength RKKY ripple.[3,8,9] Consider the case of a simple cubic lattice of localized moments with interatomic distance a. If the localized moments lie in a ferromagnetic configuration $m(x)$ would oscillate with wavelength a. However, for the antiferromagnetic configuration $m(x)$ should oscillate with wavelength 2a. In general, since χ_q varies proportionally to $\Sigma_k\{1/(E_k-E_{k+q})\}$, it decreases with increasing q, thus $\chi(2\pi/2a)>\chi(2\pi/a)$ and thereby E'_{SO} is positive. This general trend can be understood by considering that the wave function deformation, which gives rise to $m(x)$, requires an extra second order kinetic energy to be achieved. In other words the shorter the wavelength of the magnetic configuration the higher the second order kinetic energy required to produce $m(x)$ with the same periodicity. Hence, the polarization amplitude decreases as the wavelength of $H(x)$ decreases. Therefore the magnetic energy reduction due to the spin polarization becomes more effective as larger is the $H(x)$ wavelength.

For any band the difference between the ferro and antiferromagnetic energy configurations must also include the static contribution and according to Ref. 4 becomes

$$\Delta E=E_{\text{ferr}}-E_{\text{ant}}=-\mu_B^2 N(E_F)h_0^2+E'_{SO}. \tag{A2}$$

For the particular case of a parabolic and infinitely wide band (free electrons) the positive E'_{SO} exactly counterbalances, except for the RKKY ripple, the negative $-\mu_B{}^2N(E_F)h_0^2$ static term. But, for example, in a finite parabolic band filled up to the top it is verified that $\Delta E = E'_{SO} > 0$ and therefore the indirect exchange is antiferromagnetic.

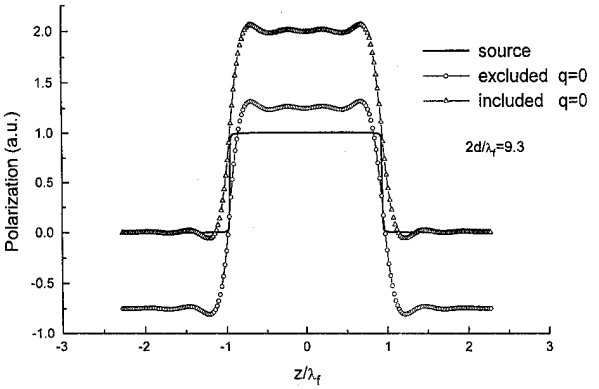


FIG. 1. Free electron spin polarization. It is shown that the antiferromagnetic background due to terms $q\neq0$ is exactly compensated by the ferromagnetic contribution coming from the term $q=0$. The source wavelength is 9.3 times the Fermi wavelength of the free electron system.

Figure 1 shows the spin polarization profile of a free electron system polarized by a periodic source as that described in the same figure. Calculation were performed by using the Fourier terms of the free electron susceptibility[4] in the expression $m(x)=\Sigma\chi_q h_q\{\exp(iqx)\}$, with and without including the term $q=0$.[3]

[1] Y. Yafet, in *Magnetic Multilayers*, edited by L. H. Bernett and R. E. Watson (World Scientific, to be published); Z. P. Shi, P. M. Levy, and J. L. Fry, Phys. Rev. B **49**, 15159 (1994).

[2] H. R. Kirchmayr and C. A. Poldy, in *Handbook on the Physics and Chemistry of Rare Earths*, edited by K. A. Gschneider and L. Eyring (North-Holland, Amsterdam, 1979) Vol. 1, Chap. 14.

[3] A. Hernando, J. J. Moreno, and J. M. Rojo, 2nd International Symposium on Metallic Multilayers, 1995, Cambridge, UK.

[4] For a review see C. Kittel, in *Solid State Physics*, edited by F. Seitz, D. Turnbull, and H. Ehrenreich (Academic, New York, 1968), Vol. 22, p. 1.

[5] H. Frohlich and F. R. Nabarro, Proc. R. Soc. London Ser. A **175**, 382 (1940); C. Zener, Phys. Rev. **81**, 440 (1951).

[6] K. Yoshida, Phys. Rev. **106**, 893 (1957); see important discussion on the $q=0$ subject by J. H. Van Vleck, Rev. Mod. Phys. **34**, 681 (1962).

[7] L. Roth, H. J. Zeiger, and T. A. Kaplan, Phys. Rev. **149**, 519 (1966).

[8] N. García and A. Hernando, J. Magn. Magn. Mater. **99**, L12-L19 and L20-L24 (1991).

[9] G. M. Genkin and M. V. Sapzhnikov, J. Magn. Magn. Mater. **139**, 179 (1995).

[10] J. A. Blanco, J. C. Gómez Sal, J. Rodriguez Fernández, D. Gignoux, D. Schmitt, and J. Rodriguez Carvajal, J. Phys. Condensed Matter **4**, 8233 (1992).

[11] K. Takei, Y. Ishikawa, N. Watanabe, and K. Tajima. J. Phys. Soc. Jpn. **47**, 888 (1979).

[12] U. Kobler, J. Schweizer, P. Chieux, and W. Zinn. J. Physique, Coll. C8 **49**, 1099 (1988).

[13] A. V. Posnikov, V. P. Antropov, and O. Jepsen, J. Phys. Condensed Matter **4**, 2475 (1992).

[14] J. A. Blanco, J. Rodriguez Fernández, J. C. Gómez Sal, J. Rodriguez Carvajal, and D. Gignoux, J. Phys. Condensed Matter **7**, 2843 (1995).

Electronic and magnetic properties of the 4*d* itinerant ferromagnet $SrRuO_3$

David J. Singh
Complex Systems Theory Branch, Naval Research Laboratory, Washington, DC 20375

Density functional calculations are used to elucidate the electronic and magnetic structure of $SrRuO_3$. Itinerant ferromagnetic behavior is found both in the cubic perovskite and the actual orthorhombic structure. The calculated moment is 1.59 μ_B. Unusually strong hybridization is evident in both the electronic structure and magnetism. The Fermi velocities indicate significant spin differentiation of the transport properties. [S0021-8979(96)17408-6]

INTRODUCTION

Although known for some time,[1–5] there has been a recent revival of interest in the ferromagnetic (FM) perovskite, $SrRuO_3$.[6–16] This is driven partially by technological applications for metallic perovskite substrates.[6,7] However, $SrRuO_3$ also has attracted considerable interest in its own right. First of all, 4*d* FM is rare, occurring only in a handful of compounds and certain low-dimensional systems. Second, metallic FM perovskites are of current interest due to the discovery of colossal magnetoresistance (CMR) in (La,Ca) MnO_3. Finally, superconductivity has recently been reported in the next member ($n=1$) of the $Sr_{1+n}RuO_{3+n}$ series,[17] and this material shows interesting similarities to the high critical temperature cuprates.[18–19]

$SrRuO_3$ occurs in an orthorhombic, Pbnm, $GdFeO_3$ type structure with four formula units per cell, similar to $LaMnO_3$. Interestingly, $SrRuO_3$ also has the same nominal *d* electron count as $LaMnO_3$, although it is a FM metal rather than an antiferromagnetic (AF) insulator in its ground state. In the perovskite structure crystal field, transition metal *d* orbitals are split into a lower lying t_{2g} level, and a higher e_g level. These are also exchange split in magnetic perovskites. In $LaMnO_3$ the distortion from the cubic perovskite structure has been rationalized as due to the electron count, i.e., the remaining electron, after occupation of the majority spin t_{2g} level enters the double degenerate majority e_g orbital, leading to a Jahn–Teller (JT) instability. First principles calculations[20,21] show that $LaMnO_3$ is a FM metal in the cubic perovskite structure, and takes its AF ground state when the distortion occurs. In contrast, $SrRuO_3$ is a FM metal, with a considerably reduced moment (relative to $LaMnO_3$) in its ground state. Unlike $LaMnO_3$ the distortion in $SrRuO_3$ involves mostly rotation of O octahedra, with only slight changes in the Ru–O bond lengths; this suggests different origins for the instability in the two materials. However, neither $BaRuO_3$ nor $CaRuO_3$ are known to be FM ($CaRuO_3$ is AFM[4]), indicating magneto-structural coupling.

Certain interesting differences are expected between 4*d* and 3*d* magnets. Generically, one expects greater itinerancy, less atomiclike character, and less important Coulomb correlation effects in 4*d* materials. The higher atomic numbers are expected to lead to stronger spin-orbit splittings, which will manifest themselves in stronger magneto-crystalline anisotropies. This is confirmed[22] in $SrRuO_3$. The weak FM ($M\sim1.5$ μ_B) implies occupation of both minority and majority spin t_{2g} orbitals. Longo and co-workers[4] have presented a picture of itinerant 4*d* magnetism due to an instability of a 2/3 full, hybridized t_{2g} manifold.

This article elucidates the electronic and magnetic structure of $SrRuO_3$ using local spin density (LSD) calculations.

METHOD

Calculations were performed using a local orbital extension of the linearized augmented plane wave (LAPW) method.[23] Sphere radii of 2.05 a.u. and 1.55 a.u. were used for the cations and anions, respectively. Well converged sets of approximately 650 basis functions were used for the cubic perovskite structure, while four times this number were employed for the quadrupled orthorhombic cell. Brillouin zone averaging was done using special **k** points. 120 **k** points in the irreducible wedge of the zone were used for the cubic perovskite structure, while a similar mesh density, resulting in 144 **k** points, was used for the orthorhombic structure. The orthorhombic calculations were performed for the structure of Jones *et al.*[5] A slightly different alternate structure is given by Kobayashi *et al.*,[8] who also studied the variation with composition. Calculations for the cubic perovskite structure were at a lattice parameter of 3.923 Å, which yields the same volume per atom.

STRUCTURE AND MAGNETISM

A FM moment of 1.17 μ_B was obtained in the cubic structure. This FM state was 40 meV lower in energy than the constrained paramagnetic solution. The wide experimental range of 1.0–1.55 μ_B has been ascribed, at least in part, to the difficulty in obtaining saturation in this material.[9,22] Kanbayashi[22] performed an extensive series of measurements on $SrRuO_3$ leading to the conclusion that this is due to the large magneto-crystalline anisotropy in this 4*d* compound. Some experimental determinations are 1.27 μ_B from the magnetization in 5.5 T at 6 K,[22] 1.4 μ_B from neutron diffraction,[4] and 1.55 μ_B from magnetization in pulsed fields.[4] Calculations with the actual orthorhombic structure yield a FM solution of the LSDA equations, with a moment per Ru atom of 1.59 μ_B and a further energy lowering (relative to cubic FM) of 140 meV per formula unit, indicating that the energetics associated with the rotations of the oxygen octahedra are higher than the magnetic energies. Although the moment is higher than most quoted values of the experimental moment, it is quite consistent with experiment given the difficulty in saturating the material. Another impor-

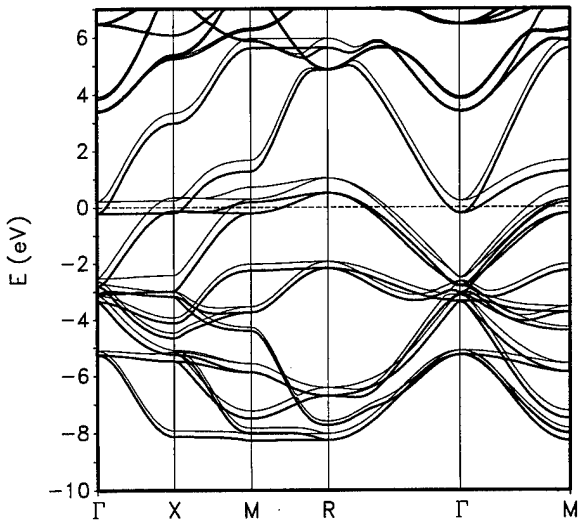


FIG. 1. Band structure of cubic perovskite structure $SrRuO_3$. The heavy (light) lines denote majority (minority) spin.

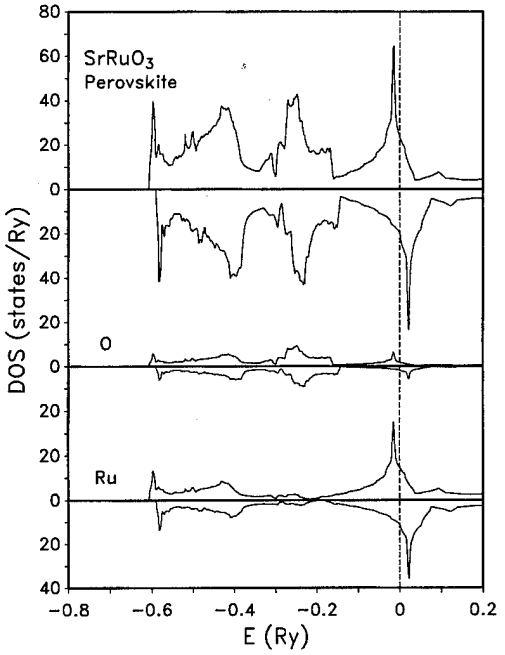


FIG. 2. Total and projected DOS for cubic perovskite $SrRuO_3$. The projections are onto LAPW spheres and are on a per atom basis. Majority (minority) spin is shown as positive (negative). The dashed vertical line denotes E_F.

tant factor that could affect the moment is stoichiometry, which is a problem generic to perovskite materials, and would be anticipated to affect the moments in a (moderately) weak itinerant FM. Finally (see below), the magnetism arises from strongly hybridized itinerant Ru–O bands, leading to substantial O contributions to the moment. These will affect the fit of neutron scattering data and should be taken into account. For the actual orthorhombic structure, the moment in the Ru sphere, which approximates the $4d$ contribution, was 1.01 μ_B (64%), while each O sphere contributed 0.13 μ_B (total of 24%). The remaining interstitial magnetization contains both Ru $4d$ and O $2p$ contributions, although due to the small O sphere radius and the extended character of $O^{2-}p$ orbitals, the O contribution is probably dominant in this region. In any case, O contributions are large, and reflect the strongly hybridized bands near E_F.

Calculations were performed as a function of lattice parameter for the cubic perovskite structure. The moment was found to increase with increasing volume, with a slope of 0.06 $\mu_B/\text{Å}^3$ about the experimental volume. This value suggests that the moments are quite robust, although this slope should not be compared with experiment because of the assumed cubic structure. Neumeier and co-workers measured the pressure dependence of the Curie temperature, T_C finding a moderate slope, −5.7 K/GPa.[9]

ELECTRONIC PROPERTIES

The calculated band structure and projected density of states (DOS) of perovskite structure $SrRuO_3$ are shown in Figs. 1 and 2, respectively. The DOS for the orthorhombic structure is given in Fig. 3. These show a complex of very strongly hybridized Ru(d)-O(p) bands extending from −8 to +4 eV relative to the Fermi energy. This complex narrows to a width of less than 6 eV at the Γ point where p-d mixing is suppressed by symmetry and is broadest along the zone boundaries, consistent with a picture of strong p-d hybridization.

The DOS for paramagnetic $SrRuO_3$ (not shown) has a large peak, slightly (23 meV; 0.2 e for cubic) above the Fermi level, E_F. This peak arises from flat bands near E_F. These bands originate with a pure Ru $4d$ e_g symmetry state at Γ. On each of the three orthogonal planes, $k_x=0$, $k_y=0$, and $k_z=0$ there is a band of this strong $4d$ character showing almost no dispersion in the plane, but dispersing upwards away from it due to p-d mixing. These sheets of flat bands lead to a large $N(E_F)$ (112 Ry^{-1} in the cubic structure). This

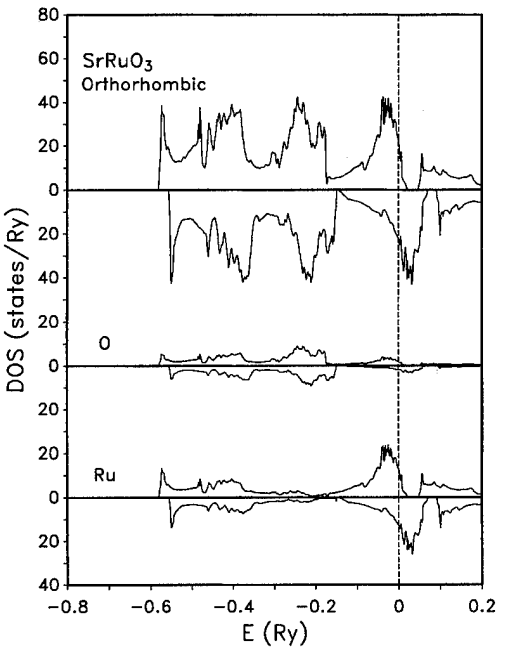


FIG. 3. DOS (per formula unit) for orthorhombic $SrRuO_3$ as in Fig. 2.

provides an itinerant Stoner mechanism for FM. The energy is lowered by exchange splitting this peak. The peak occurs in both structures, although it is broadened in the orthorhombic structure where there is some p component allowed in previously d-like bands. The exchange splitting (0.65 eV near E_F for the orthorhombic structure) reduces the Fermi level DOS to $N_\uparrow(E_F)=24\ \mathrm{Ry}^{-1}$ and $N_\downarrow(E_F)=20\ \mathrm{Ry}^{-1}$ in the cubic structure and similar values of 23 and 22 Ry^{-1}, respectively, on a per Ru basis for the orthorhombic structure.

A 0.35 eV gap is present in both spin channels above E_F for the orthorhombic structure. E_F would lie in the majority spin gap if the moment were enhanced to 2 μ_B/Ru, in which case half metallic behavior would be obtained. Effective half metallic FM is present in the (La,Ca)MnO_3 system, and this may be important for the CMR effect.[20] It is unclear what modification, if any, could enhance the moment of $SrRuO_3$ by 0.40 μ_B.

As mentioned the magnetization density has considerable O(p) character reflecting the strong hybridization, which at the Fermi energy is mostly from dispersive bands like those dispersing upwards from -3 eV to cross E_F along Γ-R in the perovskite structure. Near E_F, approximately one quarter of the projection of these bands is p-like on the O spheres.

There are several sheets of Fermi surface for the cubic structure. These are flat planar sections of majority spin electrons along the $k_z=0$, $k_y=0$, and $k_z=0$ planes plus additional sections in both spins derived from dispersing p-d hybridized bands. The folding and distortion associated with the orthorhombic structure results yields quite complex Fermi surfaces with several sheets. The Fermi velocities in the orthorhombic structure are isotropic to within 10% in both spins. The average velocities, $\langle V_F\rangle_x \approx \langle V_F\rangle_y \approx \langle V_F\rangle_z$ are 0.85×10^7 cm/s and 1.65×10^7 cm/s, for majority and minority spin, respectively. This implies significant spin differentiation in the transport properties, even though the $N(E_F)$ are similar (ρ often depends on $N(E_F)^{-1}\langle V_F\rangle^{-2}$ although there can be complications). If suitable chemical modifications were found to increase the exchange splitting, this differentiation would also increase becoming maximum when the half metallic state is reached and majority spin conduction is cut off.

SUMMARY

LSDA electronic structure calculations for $SrRuO_3$ show it to be a band FM due to a Stoner mechanism. The electronic structure shows very strong $4d$-$2p$ hybridization through the valence band region. This reflects the extended (relative to $3d$ and $4f$ magnets) $4d$ orbitals of Ru as well as the fact that center of the $4d$ orbitals is only 1.9 eV higher than that of the O $2p$ orbitals as measured by the band positions at Γ (there is no mixing at Γ). The largest energy scale derives from the hybridization, which sets the width of the p-d manifold (12 eV). The crystal field splittings are 3 and 2.5 eV for Ru d and O p, respectively (Γ); the exchange splittings depend on the relative p-d weights of the band, but are approximately 0.65 eV near E_F. The spin moment per Ru atom is 1.59 μ_B although due to hybridization, a substantial fraction of this is O p like. Strong hybridization differentiates $SrRuO_3$ from most $3d$ or $4f$ magnets. This difference, the high magneto-crystalline anisotropy, the metallic conduction and the spin differentiation make $SrRuO_3$ a particularly interesting material for further study.

Note added in proof: P. B. Allen and co-workers have recently reported LSD calculations with similar conclusions (P.B. Allen preprint).

ACKNOWLEDGMENTS

I am grateful to W. E. Pickett for numerous helpful discussions. Work at the Naval Research Laboratory is supported by the Office of Naval Research. Computations were performed at the DoD computing center at CEWES.

[1] J. J. Randall and R. Ward, J. Am. Chem. Soc. **81**, 2629 (1959).
[2] R. J. Bouchard and J. L. Gillson, Mater. Res. Bull. **7**, 873 (1972).
[3] A. Callaghan, C. W. Moeller, and R. Ward, Inorg. Chem. **5**, 1572 (1966).
[4] J. M. Longo, P. M. Raccah, and J. B. Goudenough, J. Appl. Phys. **39**, 1327 (1968).
[5] C. W. Jones, P. D. Battle, P. Lightfoot, and W. T. A. Harrison, Acta Crystallogr. C **45**, 365 (1989).
[6] C. B. Eom, R. J. Cava, R. M. Fleming, J. M. Phillips, R. B. van Dover, J. H. Marshall, J. W. P. Hsu, J. J. Krajewski, and W. F. Peck, Science **258**, 1766 (1992).
[7] X. D. Wu *et al.*, Appl. Phys. Lett. **62**, 2434 (1993).
[8] H. Kobayashi, M. Nagata, R. Kanno, and Y. Kawamoto, Mater. Res. Bull. **29**, 1271 (1994).
[9] J. J. Neumeier, A. L. Cornelius, and J. S. Schilling, Physica B **198**, 324 (1994).
[10] V. Giannakopoulou *et al.*, Solid State Commun. **93**, 579 (1995).
[11] L. Klein, J. S. Dodge, T. H. Geballe, A. Kapitulnik, A. F. Marshall, L. Antognazza, and K. Char, Appl. Phys. Lett. **66**, 2427 (1995).
[12] A. Gulino *et al.*, Phys. Rev. B **51**, 6827 (1995).
[13] J. L. Martinez *et al.*, J. Magn. Magn. Mater. **140-144**, 179 (1995).
[14] M. Itoh, M. Shikano, and T. Shimura, Phys. Rev. B **51**, 16432 (1995).
[15] D. Kirillov, Y. Suzuki, L. Antognazza, K. Char, I. Bozovic, and T. H. Geballe, Phys. Rev. B **51**, 12825 (1995).
[16] S. C. Gausepohl, M. Lee, K. Char, R. A. Rao, and C. B. Eom, Phys. Rev. **52**, 3459 (1995).
[17] Y. Maeno, H. Hashimoto, K. Yoshida, S. Nishizaki, T. Fujita, J. G. Bednorz, and E. Lichtenberg, Nature **372**, 532 (1994).
[18] T. Oguchi, Phys. Rev. B **51**, 1385 (1995).
[19] D. J. Singh, Phys. Rev. B **52**, 1358 (1995).
[20] W. E. Pickett and D. J. Singh, Phys. Rev. B **53**, 1146 (1996).
[21] D. D. Sarma *et al.*, Phys. Rev. Lett. **75**, 1126 (1995).
[22] A. Kanbayashi, J. Phys. Soc. Jpn. **44**, 108 (1978), and references therein.
[23] D. J. Singh, *Planewaves Pseudopotentials and the LAPW Method* (Kluwer, Boston, 1994), and references therein.

Magnetic and transport properties of Na doped $SrRuO_3$ and $CaRuO_3$

M. Shepard, G. Cao, S. McCall, F. Freibert, and J. E. Crow
National High Magnetic Field Laboratory, Florida State University, Tallahassee, Florida 32306

The magnetic susceptibility $\chi(T)$ ($2 \leqslant T \leqslant 400$ K) and electrical resistivity $\rho(T)$ ($2 \leqslant T \leqslant 300$ K) of undoped and Na doped $SrRuO_3$ and $CaRuO_3$ single crystals were measured. These two perovskites are orthorhombic with space group Pbnm. While both of the undoped systems exhibit metallic conductivity, $SrRuO_3$ is ferromagnetic with $T_c \leqslant 160$ K, but $CaRuO_3$ is paramagnetic. When a small concentration of Na ($\leqslant 12\%$) replaces Sr in the structure, $SrRuO_3$ becomes an insulator with a depressed ferromagnetic response. In contrast, Na doped $CaRuO_3$ ($\leqslant 5\%$) remains metallic with the appearance of antiferromagnetism below 70 K. The dramatic changes in magnetic and transport properties resulting from Na replacement of Sr and Ca reflects the very subtle differences driving the magnetism in $SrRuO_3$ and $CaRuO_3$. © *1996 American Institute of Physics.* [S0021-8979(96)17508-2]

I. INTRODUCTION

In the past few years, there has been a renewed interest in $3d$-electron transition metal perovskite and "perovskite-like" oxides. This interest has been driven by the discovery of a variety of exotic, highly correlated electron ground states, e.g., superconductivity,[1] spin-Peierls phase,[2] and other unusual magnetic ground states, depending on the anisotropy, the spin of the system, coupling to the lattice, and electron-spin correlations. More recently, additional interest has been stimulated by the observation of an unusually large magnetoresistance in rare-earth manganates[3] which is propelled by the enormous potential of these systems in magnetic information storage and retrieval systems and in other magnetic sensors applications. However, physical properties of the $4d$ and $5d$ metal oxides, though drawing moderate attention recently, remain largely unexplored.

One class of oxides that has attracted renewed interest is strontium ruthenium oxide, $SrRuO_3$, and its calcium analog, calcium ruthenium oxide, $CaRuO_3$.[4–6] Both of these systems have a perovskite structure and metallic-like conductivity. $SrRuO_3$ is a ferromagnetic metal with a Curie temperature $T_c \leqslant 160$ K. $CaRuO_3$ is also metallic, but its magnetic ground state is a little more controversial with some reports indicating a lack of long range magnetic order[7] and others reporting suggestive evidence for an antiferromagnetic ground state with a Neel temperature $T_n \sim 110$ K.[5] Results have been presented on the series $Sr_{1-x}Ca_xRuO_3$,[8] where the system remains metallic with increasing Ca concentrations, but the ferromagnetic transition, T_c, is shifted to lower temperatures. In this article, we report results on Na doped $SrRuO_3$ and $CaRuO_3$ compounds where drastic changes in magnetic and transport properties are observed.

II. EXPERIMENTAL DETAILS AND RESULTS

The pure and doped single-crystal samples were grown in different manners. Undoped $SrRuO_3$ and $CaRuO_3$ single crystals were grown from a seeded flux mixture. First, polycrystalline samples were prepared from stoichiometric ratios of $CaCO_3$ or $SrCO_3$ and RuO_2. The ground polycrystalline $SrRuO_3$ ($CaRuO_3$) sample was then mixed with $SrCl_2$ ($CaCl_2$) in the ratio 20:1 (flux:sample).[6] The mixture was placed into an alumina crucible, heated to 1350 K for 5 h, cooled at a rate of 5 °C /h to 1100 °C and then rapidly cooled to room temperature. The Na doped samples were prepared by mixing stoichiometric ratios of $SrCO_3$ ($CaCO_3$) with RuO_2 in a Na-rich flux of Na_2CO_3 and the mixture was cooked using a similar temperature profile to that used for the undoped samples.

X-ray powder diffraction patterns along with SEM (scanning electron microscopy) revealed that samples were all single phase and crystal structures with lattice constants similar to those previously reported. The amount of Na in the doped crystals was determined using EDX (energy dispersive x ray). Magnetic susceptibility was measured from 1.8 K$\leqslant T \leqslant$400 K with a magnetic field of $H \leqslant 7T$ using a standard commercial SQUID magnetometer. Electrical resistivity measurements from 2 K$\leqslant T \leqslant$300 K were made using a standard four probe dc technique. Gold leads were attached to the samples with silver epoxy; the leads were baked at 300 °C for 1 h to reduce lead contact resistance.

The resistivities, $\rho(T)$, versus temperature of $SrRuO_3$ and $Sr_{0.88}Na_{0.12}RuO_3$ single crystals were measured [see Fig. 1(a)]. $SrRuO_3$ is a metal with resistivity values on the order of 200 $\mu\Omega$ cm, whereas (Sr,Na)RuO_3, (Na=12%) becomes insulating with a resistivity on the order of 10^6 Ω cm. A kink in the $SrRuO_3$ resistivity curve in the vicinity of 130 K is indicative of the ferromagnetic transition and, thus, the reduction of spin scattering. Figure 1(b) shows a typical Fisher–Langer cusp-like anomaly that appears in the derivative of the resistivity due to changes in the short-range fluctuations of the spins near the ferromagnetic transition.[9]

Susceptibility measurements [Fig. 2(a)] give a clear indication of the presence of ferromagnetism in both systems. $SrRuO_3$ exhibits a ferromagnetic transition at 130 K, while $Sr_{0.88}Na_{0.12}RuO_3$ shows a suppressed ferromagnetic response at 70 K. Previous work on the pressure dependence of the ferromagnetic transition of $SrRuO_3$ shows that the transition temperature decreases as the applied pressure increases. This is similar to the response noted when systematic concentrations of the smaller divalent ion Ca replaced Sr in $SrRuO_3$.[10] Our experimental results indicate that the addition of monovalent Na ions into $SrRuO_3$ also decreases the transition temperature. A fit of the paramagnetic region to the modified Curie–Weiss law, i.e., $\chi(T) = \chi_0 + C/(T+\theta)$,

 0021-8979/96/79(8)/4821/3/$10.00 © 1996 American Institute of Physics

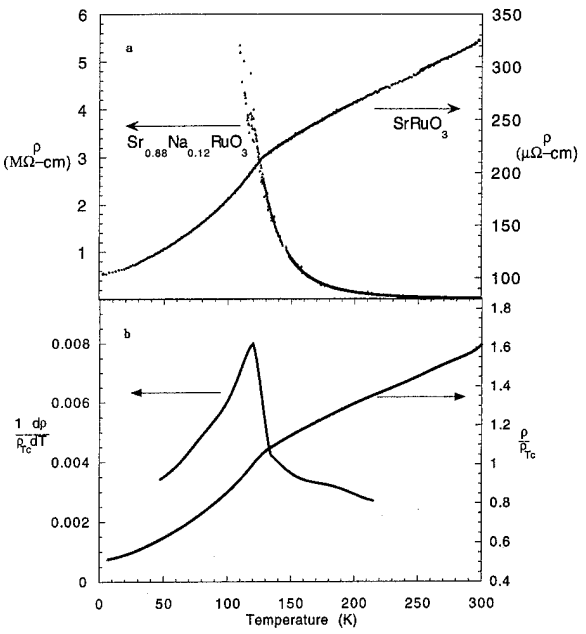


FIG. 1. (a) Electrical resistivity vs temperature for $SrRuO_3$ and $Sr_{0.88}Na_{0.12}RuO_3$. (b) A polynomial fit of the electrical resistivity of $SrRuO_3$ in (a) normalized to ρ_{T_c} and the derivative of the fitted function showing a cusp-like anomaly at the ferromagnetic transition.

(shown in Fig. 3) gives values of $T_c = 126$ K and $\mu_{eff} = 2.8$ μ_B for $SrRuO_3$ and, for $Sr_{0.88}Na_{0.12}RuO_3$ $T_c = -80$ K and $\mu_{eff} = 1.9$ μ_B. The Hund's rule value for $SrRuO_3$ gives $\mu_{eff} = 2.8$ μ_B, assuming that $g = 2$. The consistency of the measured value with the Hund's rule value indicates that Ru is indeed in the low-spin state, i.e., $S = 1$.

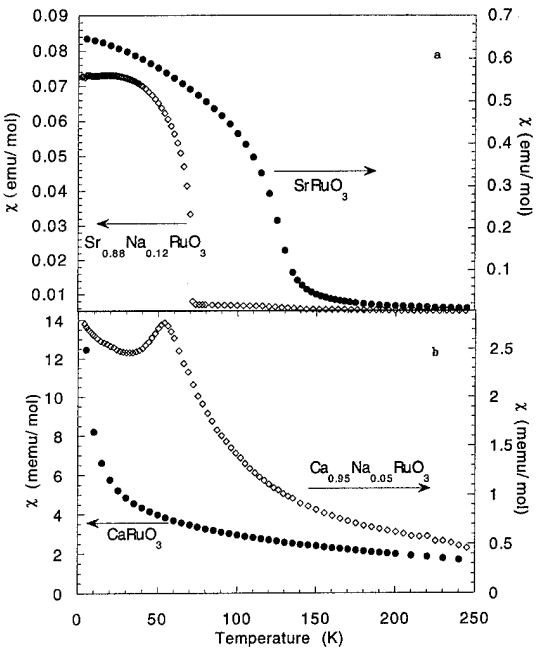


FIG. 2. Magnetic susceptibility vs temperature for (a) $SrRuO_3$ and $Sr_{0.88}Na_{0.12}RuO_3$ indicating the suppression of the ferromagnetic transition response with Na doping, and for (b) $CaRuO_3$ and $Ca_{0.95}Na_{0.05}RuO_3$ showing the onset of antiferromagnetism resulting from Na doping.

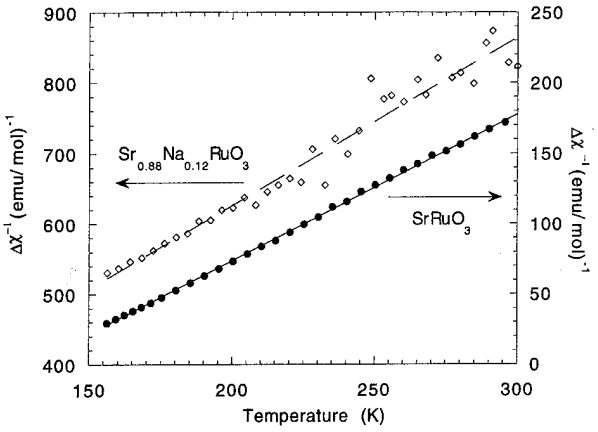


FIG. 3. Inverse susceptibility vs temperature $[\Delta\chi = \chi(T) - \chi_0]$ for $SrRuO_3$ and $Sr_{0.88}Na_{0.12}RuO_3$ above the ferromagnetic transition.

The resistivities of $CaRuO_3$ and $Ca_{0.95}Na_{0.05}RuO_3$ have been measured, although they are not shown here. $CaRuO_3$ is metallic, with a resistivity value similar to $SrRuO_3$ (~400 $\mu\Omega$ cm). $Ca_{0.95}Na_{0.05}RuO_3$, remains metallic with almost the same temperature dependence as that of the pure sample, but the magnitude of the resistivity has increased slightly with doping (~2 mΩ cm). No anomaly is discerned in the temperature range measured. Susceptibility measurements for $CaRuO_3$ and $Ca_{0.95}Na_{0.05}RuO_3$ are shown in Fig. 2(b). $CaRuO_3$ exhibits a paramagnetic response whose $1/\Delta\chi$ versus T behavior (Fig. 4) results in $\theta = T_N = 65$ and $\mu_{eff} = 1.8$ μ_B. When Na is doped into $CaRuO_3$, an apparent antiferromagnetic transition which is not present in the undoped compound appears in the vicinity of 55 K. A fit of $\chi(T)$ to the modified Curie–Weiss behavior for $Ca_{0.95}Na_{0.05}RuO_3$ yields $\theta = T_N = 122$ K and $\mu_{eff} = 1.0$ μ_B.

$SrRuO_3$ and $CaRuO_3$, systems with similar resistivities but different magnetic properties, are shown to respond quite differently to Na doping. While $Sr_{0.88}Na_{0.12}RuO_3$ remains ferromagnetic with a depressed T_c, $Ca_{0.95}Na_{0.05}RuO_3$ induces antiferromagnetism. The difference in the behaviors of these two doped systems can be related to the behavior of the undoped structures. $SrRuO_3$ and $CaRuO_3$ both possess col-

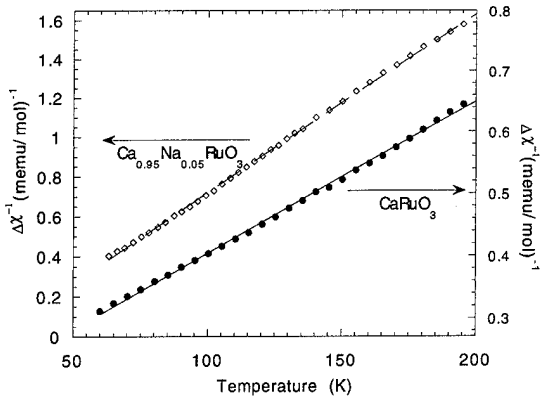


FIG. 4. Inverse susceptibility vs temperature $(\Delta\chi = \chi(T) - \chi_0)$ for $CaRuO_3$ and $Ca_{0.95}Na_{0.05}RuO_3$ above the antiferromagnetic transition of $Ca_{0.95}Na_{0.05}RuO_3$.

lective and localized $4d$ electrons. It has been suggested that the appearance of ferromagnetism in $SrRuO_3$, but not $CaRuO_3$, could be attributed to the greater strength of the overlap of Sr($4d$)-Ru($4d$) energy bands, compared to Ca($4d$)-Ru($4d$) overlap, and to the greater distortion from a cubic lattice in $CaRuO_3$ due to the difference in ionic radii.[4,5,11] Similar behavior has been reported for (RE)MnO_3 where an extreme sensitivity of T_c and $\rho(T,H)$ is reported for very subtle changes in the RE ionic radii.[12] This extreme sensitivity to the $A-O$ versus $B-O$ bond distance in ABO_3, where B is a transition metal ion, may be a universal property of these systems.

The suppressed T_c in $Sr_{0.88}Na_{0.12}RuO_3$ indicates that the reduced size of the Na cation compared to that of Sr changes the collective-electron interactions. This behavior is similar to pressure studies, both physical and chemical substitution, which indicate that, as the cell volume is decreased, T_c is also decreased. The ferromagnetic response is sensitive to the Ru–O–Ru bond distance. $CaRuO_3$ was first been reported to be antiferromagnetic.[5] Although a magnetic response might be anticipated due to the presence of ferromagnetism in $SrRuO_3$, no evidence of a magnetic transition is seen for $CaRuO_3$ in this study, or in recent reports by other groups.[7] However, $Ca_{0.95}Na_{0.05}RuO_3$ does show an antiferromagnetic response. The doping of Na into the distorted $CaRuO_3$ perovskite appears to change the overlap of the Ru–O–Ru bond sufficiently to lead to the support of antiferromagnetism.

In both cases, the resistivity of the doped crystal has increased from the undoped crystal. The introduction of Na ions into $SrRuO_3$ distorts this crystal structure and may thus localize charge carriers. The substitution of Na for Sr in $SrRuO_3$ leads to a reduction of μ_{eff}, 2.8 μ_B ($SrRuO_3$)>1.9 μ_B ($Sr_{0.88}Na_{0.12}RuO_3$), which may be an indication of a magnetic spin dilution. The resistivity of $Ca_{0.95}Na_{0.05}RuO_3$ is similar to the undoped $CaRuO_3$. The effective moment μ_{eff} of the doped crystal is less than the undoped system, 1.8 μ_B ($CaRuO_3$)>1.0 μ_B ($Ca_{0.95}Na_{0.05}RuO_3$), once again a possible indication of magnetic spin dilution.

The doping of Na into the well-characterized systems of $SrRuO_3$ and $CaRuO_3$ have revealed the richness of magnetic and transport properties. The most striking feature is that a small Na concentration drastically changes mechanisms of electron scattering and magnetic spin interactions for $SrRuO_3$ and $CaRuO_3$, respectively. The difference in the sensitivity of these physical properties to the introduction of Na reflects a difference in conduction band and spin interactions between these two compounds. Further work is, therefore, necessary to fully explore the physical properties in these oxides.

[1] See, for example, *High Temperature Superconductivity*, edited by J. W. Lynn (Springer, New York, 1990).
[2] M. Hase, I. Terasake, and K. Uchinokura, Phys. Rev. Lett. **70**, 3651 (1993).
[3] R. von Helmholt, J. Wecker, B. Holzapfel, L. Schultz, and K. Samwer, Phys. Rev. Lett. **71**, 2331 (1993); S. Jin, T. H. Tiefel, M. McCormack, R. A. Fastnacht, R. Ramesh, and L. H. Chen, Science **264**, 413 (1994).
[4] A. Callaghan, C. W. Moeller, and R. Ward, Inorg. Chem. **5**, 1572 (1966).
[5] J. M. Longo, P. M. Raccah, and J. B. Goodenough, J. Appl. Phys. **39**, 1327 (1968).
[6] R. J. Bouchard and J. L. Gillson, Mater. Res. Bull. **7**, 873 (1973).
[7] G. L. Catchen, T. M. Rearick, and D. G. Schlom, Phys. Rev. B **49**, 318 (1994).
[8] J. J. Neumeier, A. L. Cornelius, and J. S. Schilling, Physica B **198**, 324 (1994).
[9] P. L. Rossiter, in *The Electrical Resistivity of Metals and Alloys*, edited by R. W. Cahn, E. A. Davis, and I. M. Ward (Cambridge University Press, Cambridge 1987).
[10] M. Shikano, T. Huang, Y. Inaguma, M. Itoh, and T. Nakamura, Solid State Commun. **90**, 115 (1994).
[11] P. A. Cox, R. G. Edgell, J. B. Goodenough, A. Hamnett, and C. C. Naish, Solid State Phys. **16**, 6221 (1983).
[12] S. W. Cheong, H. Y. Hwang, P. G. Radaelli, D. E. Cox, M. Marezio, B. Batlogg, P. Schiffer, and A. P. Ramirez, to appear in Proc. of the Physical Phenomena at High Magnetic Fields II, edited by World Scientific.

Goldstone modes of incommensurate chromium alloys

R. S. Fishman
Solid State Division, P.O. Box 2008, Oak Ridge National Lab., Oak Ridge, Tennessee 37831-6032

S. H. Liu
Physics Department, University of California, San Diego, California 92093

The spin excitations about the two incommensurate wavevectors of the spin-density-wave (SDW) state in Cr are studied for the first time within the random-phase approximation. Transverse spin-wave (SW) modes and longitudinal phason modes are associated with the rotational and translational symmetries of Cr. While both mode frequencies vanish at the SDW ordering wavevectors, only the SW mode with linear dispersion and mode velocity $c=v_F/\sqrt{3}$ is undamped for nonzero frequencies. As in a local-moment system, the SW mode corresponds to the rigid rotation of the local magnetic moments. The phason modes have a nearly linear dispersion at low frequencies with velocity $c_{ph}<c$. As T approaches T_N, c_{ph} approaches c. Phason modes have been observed in the longitudinally polarized SDW state below 120 K in pure Cr and are responsible for a 60 meV peak in the cross sections midway between the satellites. © *1996 American Institute of Physics.* [S0021-8979(96)17608-9]

Transition-metal antiferromagnets bare some striking similarities to their rare-earth cousins but also display some important differences. Unlike the local magnetic moments of rare earths, the spin-density wave (SDW) of transition-metal antiferromagnets consists of bound electron-hole pairs. Because the itinerant magnetic moments can fluctuate, the dynamics of transition-metal antiferromagnets are of great interest. Of the two known transition-metal antiferromagnets, only Cr alloys have been observed in an incommensurate (I) state[1] where the periodicity of the SDW is incommensurate with the lattice. Unlike the single SDW of commensurate (C) alloys with wavevector $G/2=2\pi/a$, the magnetization of I Cr alloys superimposes two ISDWs with wavevectors $Q'_{\pm}$ on either side of $G/2$. Until recently,[2] very little has been known theoretically about the unique dynamics of the I phase. In this article, we present some recent results for the low-frequency Goldstone modes of I Cr alloys.

Chromium and its dilute alloys are susceptible to the formation of a SDW because of the almost perfectly nested electron a and slightly larger hole b Fermi surfaces.[1] For pure Cr, the mismatch ∂ of the nesting wavevectors $Q_{\pm}=(G/2)(1\pm\partial)$ is about 0.036. As Cr is doped with Mn, the electron surface grows and this mismatch decreases; doping with V enlarges the hole surface and increases ∂. The Coulomb attraction between electrons and holes produces a SDW consisting of electron-hole pairs in a spin-triplet state with order parameter g. In order to minimize the nesting free energy on both sides of the Fermi surfaces,[3] the actual SDW wavevectors are given by $Q'_{\pm}=(G/2)(1\pm\partial')$, where $0\leq\partial'<\partial$. Doping with more than 0.2% Mn stabilizes the CSDW state with $\partial'=0$. Pure Cr and CrV alloys are in an ISDW state with $\partial'>0$. The three domains for the SDW wavevectors $\mathbf{Q}'_{\pm}$ correspond to the possible directions for the nesting wavevectors $\mathbf{Q}_{\pm}$. In this article, we choose the SDW wavevectors to lie along the $\hat{z}$ direction. Then in units of $2\pi/a$, the SDW wavevectors are $(0,0,1\pm\partial')$.

Because the two ISDW wavevectors are distinct, I Cr alloys have two condensates of electron-hole pairs: the $ab\pm$ condensates contain electrons with wavevector $\mathbf{k}$ and holes with wavevector $\mathbf{Q}'_{\pm}-\mathbf{k}$. Since each $ab\pm$ electron-hole pair carries net momentum $\mathbf{Q}'_{\pm}$, the condensate must consist of an equal number of $ab+$ and $ab-$ pairs with total momentum equal to a multiple of $\mathbf{Q}'_{+}+\mathbf{Q}'_{-}=G\hat{z}$. Correspondingly, the magnetization must sum the ISDWs at $\mathbf{Q}'_{+}$ and $\mathbf{Q}'_{-}$ with equal weights.

The spin associated with each ISDW at site $\mathbf{R}$ is

$$\mathbf{S}_{\pm}(\mathbf{R})=\hat{m}\alpha_s g\ \exp\{i(\mathbf{Q}'_{\pm}\cdot\mathbf{R}+\theta_{\pm})\}, \tag{1}$$

where the phase constants $\theta_{\pm}$ may be different for the two ISDWs and α_s is a constant. Of course, the total spin is given by $\mathbf{S}(\mathbf{R})=\mathbf{S}_{+}(\mathbf{R})+\mathbf{S}_{-}(\mathbf{R})$. The low-frequency Goldstone modes of I Cr alloys are associated with the invariance of the free energy under translations and rotations of the ISDW state in Eq. (1). While transverse spin-wave (SW) modes are associated with the free energy's rotational invariance, longitudinal phason modes are associated with its translational invariance. Both the SW and phason modes evolve from the SDW ordering wavevectors $\mathbf{Q}'_{\pm}$.

We recently studied[2] the excitations about the ISDW states within the random-phase approximation (RPA). Although the RPA is the simplest formalism to study the spin dynamics of a conventional antiferromagnet, applying the RPA to an itinerant antiferromagnet was a challenging task. Unlike the spin dynamics of a local-moment system, the spin dynamics of an itinerant antiferromagnet are driven by quasiparticle transitions. Because the nesting on one side of the Fermi surface is affected by the mismatch on the other side, a three-band model is required for the quasiparticle energies. In contrast to the simpler two-band model developed by Fedders and Martin,[4] the three-band model introduced by Young and Sokoloff[5] allows quasiparticle transitions between the $ab+$ and $ab-$ condensates.

Since I Cr has two ordering wavevectors, its spin susceptibility contains two sets of contributions centered around each wavevector:

$$\chi_t(\mathbf{q},\omega)=2(\chi_{-}(\mathbf{q}-\mathbf{w},\omega)+\chi_{-}(-\mathbf{q}-\mathbf{w},\omega)), \tag{2}$$

$$\chi_l(\mathbf{q},\omega)=\chi_{+}(\mathbf{q}-\mathbf{w},\omega)+\chi_{+}(-\mathbf{q}-\mathbf{w},\omega), \tag{3}$$

 0021-8979/96/79(8)/4824/3/$10.00 © 1996 American Institute of Physics

$$\chi_{\pm}(\mathbf{q},\omega)=-\frac{2}{V}+\frac{1}{t_{1\pm}(\mathbf{q},\omega)+it_{2\pm}(\mathbf{q},\omega)}, \tag{4}$$

where $\mathbf{w}=(2\pi\partial'/a)\hat{z}$ and $V>0$ is the attractive Coulomb interaction between the electrons and holes. In Eqs. (2) and (3), the wavevector $\mathbf{q}$ is measured from $(G/2)\hat{z}$. Hence, the crystal momentum $\mathbf{p}$ associated with fluctuations of wavevector $\mathbf{q}$ is $\mathbf{p}=\mathbf{q}+(G/2)\hat{z}$. For simplicity, we only consider spin fluctuations with $\mathbf{q}$ along the $\hat{z}$ direction. In Eq. (4), $t_{1\pm}$ and $t_{2\pm}$ are real functions of $\mathbf{q}$ and ω whose lengthy expressions are given elsewhere.[2] For this discussion, we shall be primarily concerned with their analytic properties. The transverse and longitudinal cross sections are proportional to the imaginary parts of $\chi_t(\mathbf{q},\omega)$ and $\chi_l(\mathbf{q},\omega)$.

While the first terms in Eqs. (2) and (3) produce the satellite at $\mathbf{Q}'_+$, the reflected terms with $\mathbf{q}\rightarrow-\mathbf{q}$ produce the satellite at $\mathbf{Q}'_-$. Above the Néel temperature, $t_{1+}=t_{1-}$ and $t_{2+}=t_{2-}$. Consequently, $\chi_t=2\chi_l$ and the spin fluctuations are isotropic. Below the Néel temperature, the collective modes are given by the zeroes of the denominator $t_{1\pm}+it_{2\pm}$. By summing the contributions from each SDW, Eqs. (2) and (3) distinguish the collective modes about one SDW from the collective modes about the other. Hence, the collective modes about $\mathbf{Q}'_{\pm}$ are not affected by the spin excitations about $\mathbf{Q}'_{\mp}$.

Nonetheless, the dynamics of the two SDWs are *not* independent. To preserve the total momentum of the condensate, excitations must maintain the same number of $ab+$ and $ab-$ pairs. So a fluctuation which transfers a hole from the $ab+$ to the $ab-$ condensates is prohibited. But a fluctuation which transforms an $ab+$ pair into an $ab-$ pair and then back to an $ab+$ pair with no net change in momentum is allowed. Processes such as this one, which are absent in the two-band model, dynamically couple the two ISDWs.

A rich spectrum of collective excitations is produced by the complex quasiparticle energies of I Cr alloys. In this article, we concentrate on the Goldstone modes which evolve from the SDW wavevectors. At zero frequency, both the longitudinal and transverse susceptibilities have poles at $\mathbf{Q}'_{\pm}$ with $t_{1\pm}(0,0)=t_{2\pm}(0,0)=0$. At nonzero frequencies, these poles develop into the transverse SW modes and the longitudinal phason modes. Other modes associated with the oscillation of the SDW amplitude $\alpha_s g$ in Eq. (1) are discussed in a more lengthy treatment.[2]

The transverse SW modes have linear dispersion $\omega=c|q\pm w|$ with the same mode velocity $c=v_F/\sqrt{3}\approx1500$ meV Å as in the C regime.[6] Due to the large size of this mode velocity, the splitting of each satellite into sidepeaks is difficult to observe experimentally. Measurements in the C phase,[7,8] however, indicate that the SW velocity is about 30% smaller than predicted. But as discussed in Ref. 2, the effective SW velocity may be shifted by the background of incoherent excitations.

Because the magnetic moments of an itinerant system are not fixed by any conservation law, there has been some question[9] whether the SWs in Cr alloys are similar to those in a local-moment system. We find that the two SWs with frequency ω and crystal momentum $p=\pm Q'_{\gamma}+\omega/c(\gamma=\pm)$ have poles of equal strength. This suggests that the spin deviation at site $\mathbf{R}$ should be written

$$\delta S(\mathbf{R},t)\propto S_{\gamma}(\mathbf{R})\exp[i(\mathbf{p}\mp\mathbf{Q}'_{\gamma})\cdot\mathbf{R}-i\omega t], \tag{5}$$

which corresponds to the rigid rotation of each spin just as in a rare-earth antiferromagnet. In an itinerant antiferromagnet, the nodes of each static SDW with $S_{\gamma}(\mathbf{R})=0$ are not affected by the propagating SWs.

Phason modes are produced by the dynamics of the phases $\theta_{\pm}(\mathbf{R},t)$ in Eq. (1). Supposing θ_0 to be the equilibrium phase and setting $\delta\theta(\mathbf{R},t)=\theta_{\pm}(\mathbf{R},t)-\theta_0$, the change in spin is given by

$$\delta\mathbf{S}_{\pm}(\mathbf{R},t)=\hat{m}i\alpha_s g\,\delta\theta(\mathbf{R},t)\exp\{i(\mathbf{Q}'_{\pm}\cdot\mathbf{R}+\theta_0)\}, \tag{6}$$

which is parallel to the spin polarization direction $\hat{m}$. Hence, phasons are longitudinal excitations which evolve from the ISDW wavevectors at $\mathbf{Q}'_{\pm}$. Because the CSDW state is not translationally invariant (shifting the phase changes the magnitude of the spin at every site), phason modes do not appear[6] in the C phase of Cr alloys.

Since the zero-frequency pole in the longitudinal susceptibility is damped at any nonzero frequency, the dispersion of the phason modes is determined by the condition $t_{1+}(\mathbf{q},\omega)=0$ but $t_{2+}(\mathbf{q},\omega)<0$. For small frequencies, the phasons evolve linearly with mode velocity $c_{ph}<c$. As shown in Fig. 1, the phason mode velocity approaches the SW velocity as $T\rightarrow T_N$. The phason velocity is also an increasing function of the incommensurability energy $z_0=4\pi\partial v_F/\sqrt{3}a$, which grows linearly with the V concentration in CrV alloys. In the $z_0\rightarrow\infty$ limit, our results agree with Psaltakis,[10] who found that $c_{ph}=c$ for a one-dimensional ISDW with $\mathbf{Q}'_{\pm}=\mathbf{Q}_{\pm}$.

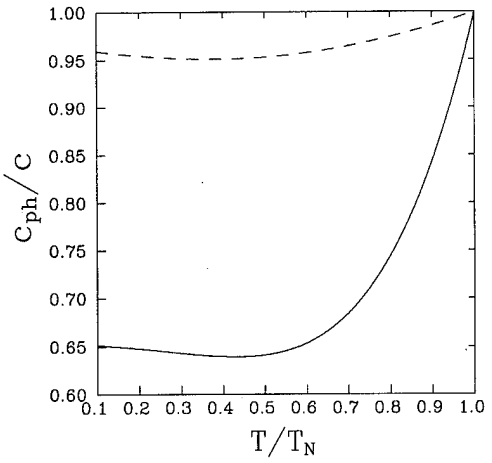


FIG. 1. The phason mode velocity c_{ph} normalized by the SW velocity versus T/T_N for $z_0/T_N^*=4.7$ (solid) or 7.0 (dashed).

In Fig. 2, we graph the SW and phason modes evolving from the two ISDW satellites. The energy scale $T_N^*\approx80$ meV is the Néel temperature of perfectly nested Cr with $\partial=0$. The two satellites lie at $cq=\pm cw\approx\pm1.903\,T_N^*$. As shown, the phason modes evolve linearly up to a frequency of about 0.4 $T_N^*\approx32$ meV. Above 0.75 $T_N^*\approx60$ meV, the phason modes are overdamped and disappear. At this frequency, the inner

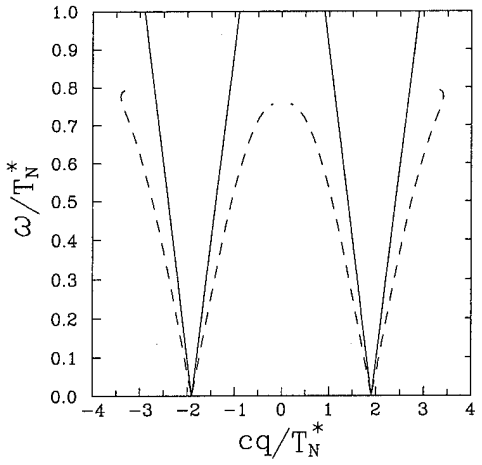


FIG. 2. The normalized frequency ω/T_N^* vs wavevector cq/T_N^* for the transverse SW (solid) and longitudinal phason (dashed) modes with $z_0/T_N^* = 4.7$ and $T/T_N = 0.5$.

phasons smoothly join another damped longitudinal excitation discussed in Ref. (2). The intersection of the inner phason modes with $q=0$ was recently observed by Fukuda *et al.*[11] as a 60 meV peak in the $G/2$ cross section. The inner phasons also bend the SW cones towards $G/2$, as first observed by Fincher *et al.*[12]

Because they evolve from the satellite wavevectors and have velocities of order v_F, phason modes have often been mistaken for SWs. In the longitudinally polarized (L) SDW state below 120 K for pure Cr, the pinning energies[13] constrain the spin fluctuations parallel to $\hat{m}$ and $\mathbf{Q}'_{\pm}$. So the low-frequency, longitudinal excitations observed by Burke *et al.*[13] were actually phason modes.

Since the incoherent background of quasiparticle excitations is suppressed at low temperatures, experiments in the LSDW state may be able to observe the temperature dependence of the phason mode velocity. The dependence of c_{ph} on V doping may also be observable: as the phason velocity increases, the 60 meV peak in the $G/2$ cross section will move to higher energies.

One of us (RF) would like acknowledge support from the U.S. Department of Energy under Contract No. DE-FG06-94ER45519 and under Contract No. DE-AC0584OR21400 with Lockheed Martin Energy Research Corporation. SL would like to thank Prof. L. Sham and Prof. R. Dynes for their hospitality at UCSD. Useful conversations with E. Fawcett, B. Sternlieb, and V. S. Viswanath are also gratefully acknowledged.

[1] For comprehensive reviews of Cr alloys, see E. Fawcett, Rev. Mod. Phys. **60**, 209 (1988) and E. Fawcett, H. L. Alberts, V. Yu. Galkin, D. R. Noakes, and J. V. Yakhmi, *ibid.* **66**, 26 (1994).
[2] R. S. Fishman and S. H. Liu (unpublished).
[3] R. S. Fishman and S. H. Liu, Phys. Rev. B **48**, 3820 (1993).
[4] P. A. Fedders and P. C. Martin, Phys. Rev. **143**, 8245 (1966).
[5] C. Y. Young and J. B. Sokoloff, J. Phys. F **4**, 1304 (1974).
[6] R. S. Fishman and S. H. Liu, Phys. Rev. B **50**, 4240 (1994).
[7] S. K. Sinha, S. H. Liu, L. D. Muhlestein, and N. Wakabayashi, Phys. Rev. Lett. **23**, 311 (1969); S. K. Sinha, G. R. Kline, C. Stassis, N. Chesser, and N. Wakabayashi, Phys. Rev. B **15**, 1415 (1977).
[8] J. Als-Nielsen, J. D. Axe, and G. Shirane, J. Appl. Phys. **42**, 1666 (1971).
[9] S. H. Liu, Phys. Rev. B **13**, 3962 (1976); J. Magn. Magn. Mater. **25**, 97 (1981).
[10] G. C. Psaltakis, Solid State Commun. **51**, 535 (1984).
[11] T. Fukuda, Y. Endoh, K. Yamada, M. Takeda, S. Itoh, M. Arai, and T. Otomo (preprint).
[12] C. R. Fincher, G. Shirane, and S. A. Werner, Phys. Rev. B **24**, 1312 (1981).
[13] S. K. Burke, W. G. Stirling, K. R. A. Ziebeck, and J. G. Booth, Phys. Rev. Lett. **51**, 494 (1983).

Magnetic hardening of melt-spun nanocomposite $Nd_2Fe_{14}B$/Fe magnets

I. Panagiotopoulos, L. Withanawasam, A. S. Murthy, and G. C. Hadjipanayis
Department of Physics and Astronomy, University of Delaware, Newark, Delaware 19716

E. W. Singleton and D. J. Sellmyer
University of Nebraska, Lincoln, Nebraska 68588-0111

Coercivity optimization studies were done on melt-spun nanocomposite $Nd_4R_2Fe_{87-x}NbT_xB_6$ (R=Nd,Y,Dy; T=Ag,Cu) isotropic ribbon samples. The maximum attainable coercivities, after adjusting the annealing time, were found to be very sensitive to the annealing temperatures. The optimum magnetic properties [H_C=3.9 kOe, $(BH)_{max}$=10 MGOe] were obtained by annealing at 750–775 °C for a few minutes. Optimization by flash annealing gave similar results. Microstructural studies show that the grain size is greater than the theoretically predicted grain size for optimum coupling between the hard and the soft phase. With the annealing conditions used, $Nd_4Dy_2Fe_{87}NbB_6$ samples gave moderate coercivities and in $Nd_4Y_2Fe_{87}NbB_6$ samples the coercivity was reduced more than the expected reduction in the anisotropy field due to the presence of Y. © *1996 American Institute of Physics.* [S0021-8979(96)37708-2]

INTRODUCTION

Nanocomposite magnets consisting of a fine mixture of magnetically soft and hard phases can lead to large reduced remanences (M_r/M_s), relatively high coercivities, and high energy products due to the exchange coupling between the hard and soft phases.[1–3] Our previous studies in Nd–Fe–B ribbons showed a reduced remanence of 0.78 and a coercivity of 2.7 kOe resulting in an energy product of 14.45 MGOe.[4] However microstructural studies in these samples show that the grain size is larger than the optimum size predicted by theoretical calculations[1–3] to be of the order of the domain wall width of the hard phase (~10 nm).

In this article we present data on optimization studies of $Nd_4R_2Fe_{87-x}NbT_xB_6$ (R=Nd,Y,Dy; T=Ag,Cu) isotropic ribbon samples. To increase the coercivity Nb and other elements (Ag,Cu) are introduced in order to prevent grain growth and help achieve small grain sizes. Substitution of Nd with other rare earth elements influences the magnetic properties in two ways: it changes the anisotropy of the hard phase which is supposed to affect the optimum grain size and therefore the maximum coercivity and also raises the crystallization temperature of the amorphous alloy.[5]

EXPERIMENT

$Nd_4R_2Fe_{87-x}NbT_xB_6$ ingots were prepared by arc-melting the constituent elements in an argon atmosphere. Pieces of these ingots were melt-spun from a quartz tube having an orifice diameter ~1 mm at high wheel speeds (60 m/s). These overquenched ribbon samples were then annealed at different times and temperatures to optimize the magnetic properties. After annealing, the samples were quenched in liquid nitrogen. Some of these samples were also flash annealed in high vacuum at currents of 0.2–1 A for time intervals 5–240 s. The properties of the annealed ribbons are very sensitive to the current. After finding a suitable annealing current, more fine optimization could be achieved by varying the annealing time. Hysteresis loops were measured in a vibrating sample magnetometer (VSM) with a maximum field of 20 kOe. The field was applied in the plane of the ribbons and along the ribbon axis to minimize demagnetizing effects. Transmission electron microscopy (TEM) studies were carried out using a Jeol JEM-2000FX microscope.

RESULTS

The magnetic properties were optimized by annealing for various time intervals at various temperatures. The effects of the annealing conditions to the magnetic properties are shown in Figs. 1–3 for $Nd_6Fe_{87}NbB_6$, $Nd_6Fe_{86.9}Ag_{0.1}NbB_6$, and $Nd_6Fe_{86.9}Cu_{0.1}NbB_6$ ribbon samples, respectively. When annealed at 650 °C the magnetic properties are far from op-

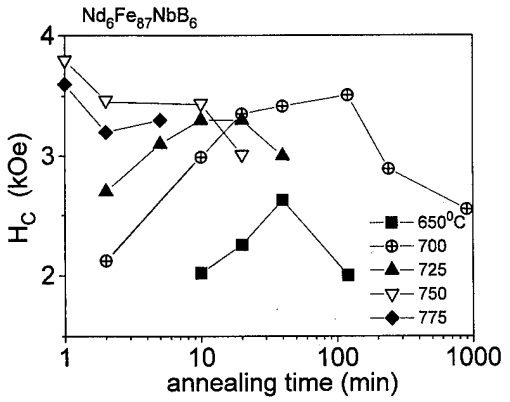


FIG. 1. Coercivity as a function of annealing time at various annealing temperatures for a $Nd_6Fe_{86.9}NbB_6$ sample.

 0021-8979/96/79(8)/4827/3/$10.00 © 1996 American Institute of Physics

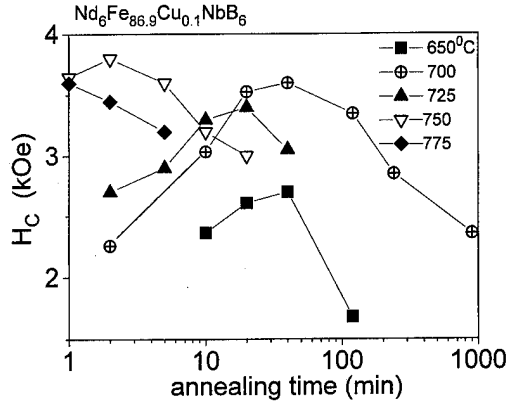


FIG. 2. Coercivity as a function of annealing time at various annealing temperatures for a $Nd_6Fe_{86.9}Ag_{0.1}NbB_6$ sample.

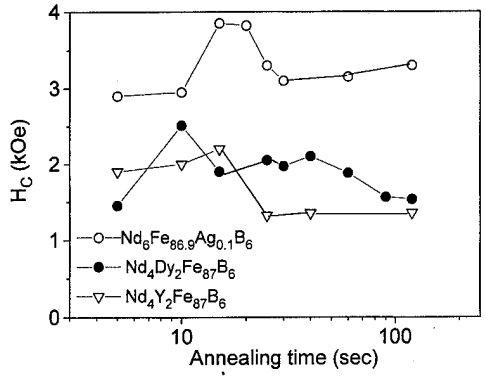


FIG. 4. Coercivity as a function of annealing time for flash annealed ribbons. (a) $Nd_6Fe_{86.9}Ag_{0.1}NbB_6$ at a current of 0.75 A. (b) $Nd_4Dy_2Fe_{87}NbB_6$ at a current of 0.45 A. (c) $Nd_4Y_2Fe_{87}NbB_6$ at a current of 0.60 A.

timum; at this temperature the crystallization does not lead to the formation of the 2:14:1 phase. At 700 °C the optimum coercivity (~3.5 kOe) is reached after 1–2 h of annealing for all the samples. At temperatures 750–775 °C the optimum annealing time is reduced to few minutes and coercivities ~3.9 kOe are obtained. These differences in coercivities can be attributed to the different dependence of the nucleation and growth rates on the annealing temperature[6] resulting in different kinds of microstructure. For even higher temperatures the optimum annealing time would probably be <1 min. For this reason flash annealing was done in one of the samples. The optimum annealing time found is of the order of only 15–20 s (Fig. 4) and the optimum value of coercivity is slightly higher than that obtained by conventional annealing on the same sample.

The grain size of these optimized $Nd_6Fe_{86.9}Ag_{0.1}NbB_6$ ribbons was of the order of 30–50 nm which is greater than the size predicted by theory for optimum exchange coupling (Fig. 5). The critical dimension of the soft phase below which the soft and hard phases are optimally coupled is predicted by theory to be of the order of the Bloch wall width of the hard phase δ given by

$$\delta = \pi (A/K)^{1/2},$$

where A is the exchange stiffness constant and K is the first order anisotropy constant of the hard phase. The ratio of the actual to the optimum grain size defines the ratio H_C/H_K (Refs. 1 and 4), where H_K is the anisotropy field of the hard phase.

By substituting Nd with Dy, which has higher anisotropy field, one would expect to get higher coercivities. The anisotropy constant K of Dy on the other hand is close to that of Nd so that the critical dimension for the soft phase is not expected to be very different. However in the $Nd_4Dy_2Fe_{87}NbB_6$ sample only moderate coercivities were obtained as shown in Fig. 4 where H_C is plotted as a function of annealing time. This can be attributed to the fact that Dy increases the crystallization temperature of the 2:14:1 phase[5] requiring annealing conditions unfavorable to keeping the grain size of the soft phase close to the optimum size.

When substituting Nd with the nonmagnetic Y, the anisotropy of the hard phase is reduced. This of course is expected to lower the attainable coercivity but on the other hand δ and consequently the optimum grain size, will now be increased to values closer to the actual one. As shown in Fig. 4 for the $Nd_4Y_2Fe_{87}NbB_6$ sample H_C is reduced by more than the expected reduction in anisotropy when substituting 1/3 of Nd atoms by Y. In both cases it seems that the effect of the substitutions on the kinetics of the crystallization process does not permit a direct interpretation of the data in terms of

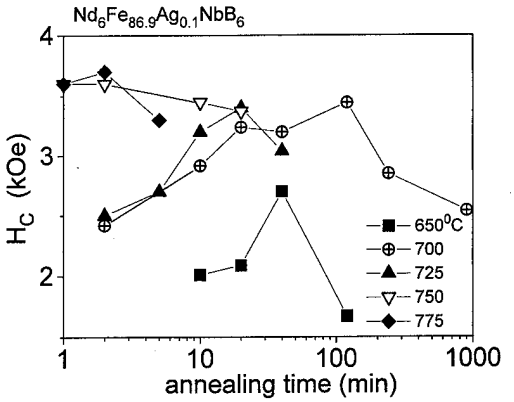


FIG. 3. Coercivity as a function of annealing time at various annealing temperatures for a $Nd_6Fe_{86.9}Cu_{0.1}NbB_6$ sample.

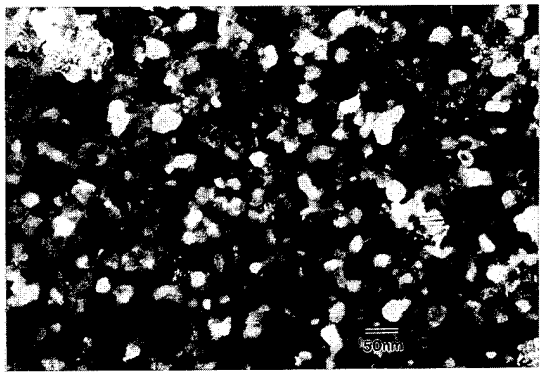


FIG. 5. TEM micrograph of a flash annealed $Nd_6Fe_{86.9}Ag_{0.1}NbB_6$ sample.

the expected changes in the anisotropy of the hard magnetic phase.

CONCLUSION

The optimum magnetic properties in $Nd_6Fe_{86.9}T_{0.1}NbB_6$ samples were obtained by annealing at 750 °C for a few minutes. Flashed annealed samples for shorter times gave similar results. However microstructural studies show that the grain size in these samples is greater than the theoretically predicted grain size for optimum coupling between the hard and the soft phase. Therefore one can expect even better properties in these samples by proper control of the crystallization procedure that would lead to smaller grain sizes.

ACKNOWLEDGMENTS

This work was supported by the DOE DE-FG02-86ER45262 and DE-FG02-90ER45413.

[1] E. F. Kneller and R. Hawig, IEEE Trans. Magn. **27**, 3588 (1991).
[2] R. Skomski and J. M. D. Coey, Phys. Rev. B **48**, 15812 (1993).
[3] T. Schrefl, H. Kronmüller, and J. Fidler, J. Magn. Magn. Mater. **127**, L273 (1993).
[4] L. Withanawasam, G. C. Hadjipanayis, and R. F. Krause, J. Appl. Phys. **75**, 6646 (1994).
[5] L. Withanawasam, A. S. Murthy, G. C. Hadjipanayis, and R. F. Krause, J. Magn. Magn. Mater. **140–144**, 1057 (1995).
[6] V. E. Martin, J. Bernaldi, J. Fidler, F. Cebollada, and J. M. Conzalez, J. Alloys Compounds **191**, 127 (1993).

Microstructural control of NdFeB cast ingots for achieving 50 MGOe sintered magnets

D. W. Scott, B. M. Ma, Y. L. Liang, and C. O. Bounds
Rhône-Poulenc, Rare Earths and Gallium, CN 7500, Cranbury, New Jersey 08512

The combination of chemical composition and microstructure of cast alloy has been found to be critical to the performance of NdFeB sintered magnets. Maximizing the amount of $Nd_2Fe_{14}B$ phase (or minimizing the amount of secondary phase) by reducing the Nd content more closely to the stoichiometric composition appears to be essential for obtaining high BH_{max} magnets. However, α-Fe precipitation has been found to increase with decreasing Nd content and severely hinders the development of high BH_{max} magnets. A two-step method, incorporating ingot casting and isothermal annealing, has been developed to minimize the amount of precipitated α-Fe in low Nd content alloys. This method provides a drastic improvement in the B_r and BH_{max} of sintered magnets obtained. By decreasing the Nd content to 13 at. % in the cast alloy, incorporating better particle control during fine milling, and controlling grain growth during sintering; magnets with a B_r of more than 14.5 kG and a BH_{max} of 50 MGOe have been consistently obtained. Furthermore, because of the reduction in the amount of Nd-rich grain boundary phase, a significant improvement in the corrosion resistance of magnets was also observed. © *1996 American Institute of Physics.* [S0021-8979(96)37808-9]

I. INTRODUCTION

NdFeB-type permanent magnets are currently being used in an extensive array of applications where strong magnetic characteristics are required. With the rapid progression of technology, magnet manufacturers have expressed a desire to produce NdFeB magnets possessing a BH_{max} in excess of 45 MGOe.[1–3] While the chemical composition of a magnet is vital to obtaining optimum magnetic performance and corrosion resistance, microstructure is also important in dictating the magnet's overall quality. Recent trends have been aimed at adjusting the overall alloy composition from the original $Nd_{15}Fe_{79}B_6$ toward a more stoichiometric $Nd_2Fe_{14}B$ composition. By maximizing the amount of $Nd_2Fe_{14}B$ phase, manipulating grain alignment of the $Nd_2Fe_{14}B$ crystals, controlling grain growth via sintering, magnets exhibiting a BH_{max} greater than 45 MGOe can be produced in production.[4]

While the use of a lower total rare earth content tends to improve the corrosion resistance of the magnet due to a reduction of the Nd-rich phase, it also allows for more α-Fe precipitation during solidification based on the Nd/B-Fe phase diagram.[5,6] Precipitated α-Fe in the cast alloy makes powder reduction difficult in addition to hindering grain alignment, thus it could be detrimental to magnetic performance. In addition, α-Fe precipitation creates Nd-rich regions which are extremely susceptible to oxidation attack and magnet degradation. Controlling the amount of precipitated α Fe through improved casting techniques and isothermal annealing has become an important issue in alloy casting and magnet processing in order to achieve a BH_{max} of 50 MGOe.

In this article, we will quantify the amount of precipitated α Fe and other secondary phases in the cast alloys and relate them to the chemical composition and corrosion resistance in the sintered magnets. We will also present the effects of the amount of secondary phases on the energy product of sintered magnets.

II. EXPERIMENT

A set of three alloys cast to $Nd_xFe_{94-x}B_6$ ($x=13,14,15$) were prepared by conventional vacuum induction melting and casting. Each alloy was isothermally annealed at 1050 °C for 8 h. Microstructure and isothermal magnetic analyses (ITMA), used to measure α-Fe precipitation, were evaluated for both as-cast and annealed ingots.[6] The magnets used in this study were prepared and tested using the procedures detailed in previous reports.[7,8]

III. RESULTS AND DISCUSSION

Figure 1 presents optical micrographs for NdFeB cast ingots at $Nd_xFe_{94-x}B_6$ ($x=13,14,15$). Columnar grain growth in the cast ingots diminished as the total rare earth (TRE) content decreased from $x=15$ to $x=13$ as more precipitated α Fe appeared. This was most likely attributed to the increased residence time in the *liquid*+Fe phase region of the pseudo binary Fe-Nd-B phase diagram.[9] In order to produce sintered NdFeB permanent magnets in excess of 50 MGOe, several secondary phases must be minimized by shifting the alloy composition toward a more stoichiometric $Nd_2Fe_{14}B$. These secondary phases were identified as the Nd-rich grain boundary phase,[5] $Nd_{1+\epsilon}Fe_4B_4$ boron rich phase,[10] neodymium oxide phases,[3] and the α-Fe precipitation previously noted. Isothermal annealing was effective in reducing the amount of α-Fe precipitation in the cast alloy. Table I indicates the reduction in α-Fe precipitation for all three alloys. During isothermal annealing, α Fe reacts with the Nd-rich and $Nd_{1+\epsilon}Fe_4B_4$ phases to form $Nd_2Fe_{14}B$ which may explain the increase in the amount of the $Nd_2Fe_{14}B$ grains as shown in Fig. 2.

After maximizing the $Nd_2Fe_{14}B$ matrix phase in the cast ingot, focus was directed at powder preparation and grain alignment to further increase magnetic remanence (B_r) and ultimately, energy product (BH_{max}). B_r was increased by

 0021-8979/96/79(8)/4830/3/$10.00 © 1996 American Institute of Physics

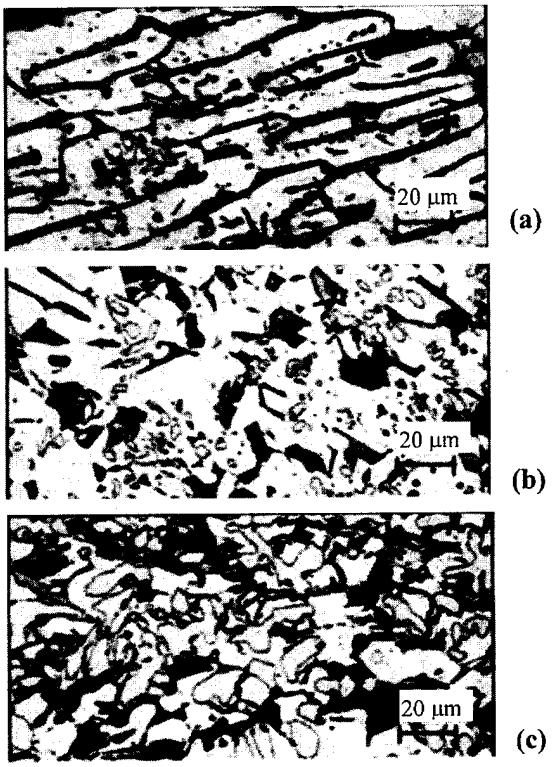


FIG. 1. Optical micrographs of $Nd_xFe_{94-x}B_6$ as-cast ingots at 500× where (a) $x=15$, (b) $x=14$, and (c) $x=13$.

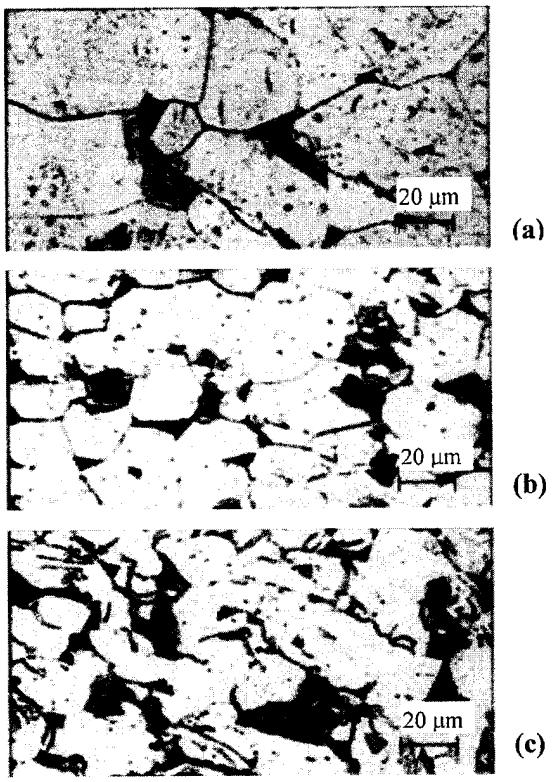


FIG. 2. Optical micrographs of $Nd_xFe_{94-x}B_6$ annealed ingots at 500× where (a) $x=15$, (b) $x=14$, and (c) $x=13$.

minimizing powder oxidation and grain alignment (texture) as cited by several individuals as an important factor in achieving higher B_r and subsequently, higher BH_{max} in the final magnets.[11–13]

Magnetic characterization was performed on the three sintered magnets listed in Table I and shown in Fig. 3. The inverse relationship between B_r and H_{ci} can be seen for magnets of varying TRE content. B_r increased steadily from 13.2 to 14.5 kG as TRE content decreased from $x=15$ to $x=13$. Microstructural evaluation and image analysis for the three magnets, shown in Fig. 4, explained the magnetic characteristics obtained for each magnet. The decrease in TRE content not only yielded a steady increase in BH_{max} but also drastically changed the magnet's microstructure. At $x=15$, a larger amount of secondary phase was present. Image analysis determined that the total secondary phases comprised nearly 30% of the entire sintered magnet with an average grain size of 10 μm as listed in Table I. Decreasing TRE content ($x=14$) generated a corresponding decrease in secondary phases. Image analysis measured the secondary phases to account for 21% of the total sintered magnet with an average grain size of 9 μm. This trend continued with a further decrease in TRE ($x=13$) as the total secondary phases were calculated to be 17% of the magnet with an average grain size of 8 μm. It was critical to note that Nd content may be directly related to the average grain size in the sintered magnet. A decrease in Nd content, and consequently a reduction in the amount of Nd-rich grain boundary phase, may reduce the diffusion rate between grains which would minimize grain growth.

Chang expressed the importance of evaluating the texture for the cross section of a polished, sintered magnet by examining the x-ray diffraction pattern. Texture can be quantified by comparing the relative intensity ratio of the (006) peak to the (105) peak as shown in Fig. 5. Higher ratios are generally associated with optimum grain alignment. Optimization of texture is obtained by a combination of various steps: (1) increasing the percentage of $Nd_2Fe_{14}B$ phase by composition control, (2) decreasing particle size and particle size distribution of the precursor alloy powders, (3) minimizing grain growth. The ratio of the (006) to (105) peaks were calculated to be 1.50 for the 41 MGOe magnet, 1.55 for the

TABLE I. Characteristics of $Nd_xFe_{94-x}B_6$ ingots and sintered magnets.

Nd content ($x=$)	α-Fe precipitation (wt %)		B_r	H_c	H_{ci}	BH_{max}	H_k	Part. size	Grain size	Secondary phase	Bulk corrosion
	As-cast	Annealed	(kG)	(kOe)	(kOe)	(MGOe)	(kOe)	(μm)	(μm)	(%)	(mg/cm^2)
15	7.1	0.8	13.2	9.1	11.2	41.3	8.4	3.2	10	29.8	51.4
14	12.0	1.6	13.8	7.8	8.3	45.0	7.4	3.2	9	21.2	6.2
13	16.0	1.9	14.5	7.8	8.1	50.0	7.1	3.3	8	17.6	0.0

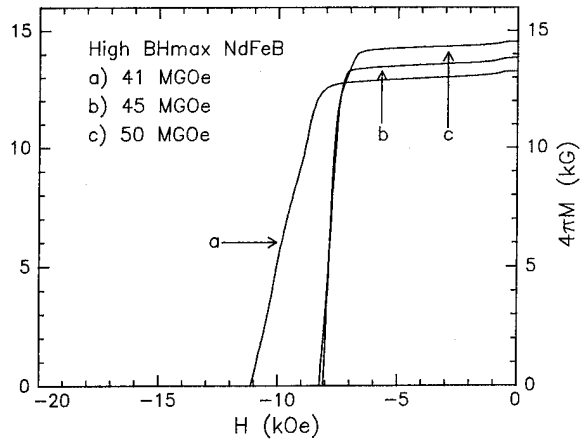


FIG. 3. Hysteresis loops for 41, 45, and 50 MGOe sintered magnets.

45 MGOe magnet, and 1.57 for the 50 MGOe magnet.

Accelerated corrosion testing was also conducted on the three sintered magnets. The decrease in TRE content and minimization of the Nd-rich grain boundary phase tremendously reduced the regions for oxidation to occur as bulk corrosion resistance greatly improved for lower TRE containing magnets as shown in Table I. At $x=15$, bulk corrosion was measured to be 51.4 mg/cm^2. Continuous improvements in bulk corrosion occurred with the decrease in Nd content to $x=14$ where corrosion was measured to be 6.2 mg/cm^2 with a further decrease to 0.0 mg/cm^2 at $x=13$.

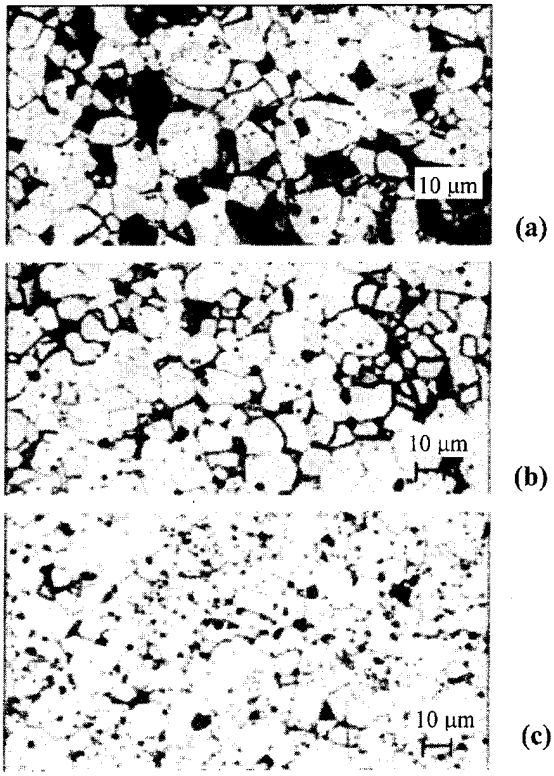


FIG. 4. Optical micrographs of NdFeB sintered magnets where (a) 41 MGOe, (b) 45 MGOe, and (c) 50 MGOe.

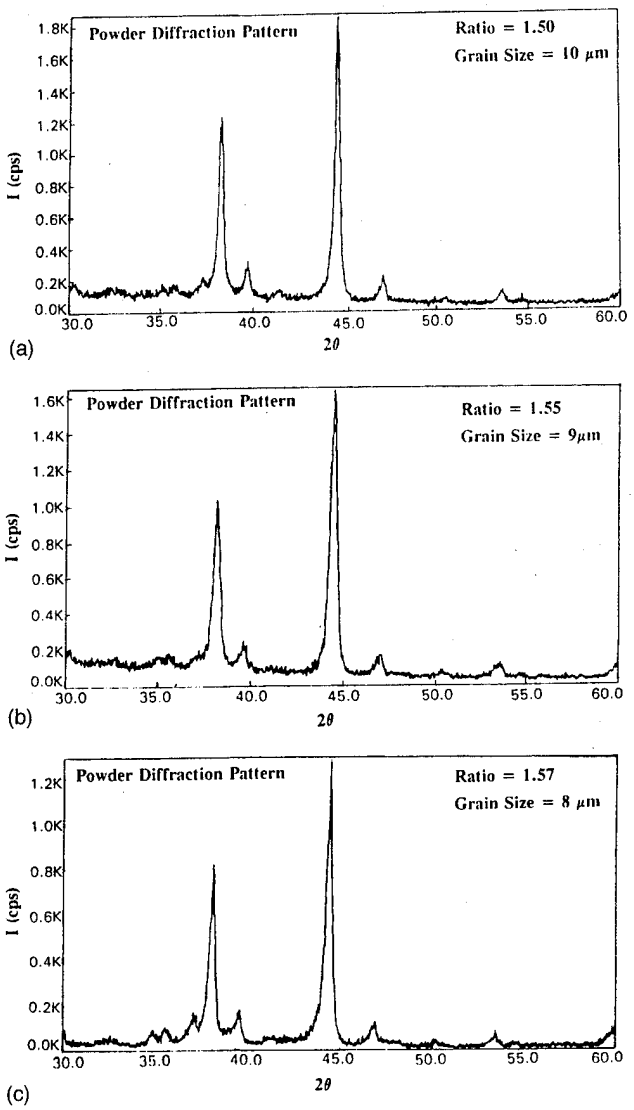


FIG. 5. X-ray diffraction patterns for (a) 41, (b) 45, and (c) 50 MGOe sintered magnets.

[1] T. Minowa, M. Yoshikawa, and M. Honshima, IEEE Trans. Magn. **25**, 3776 (1989).
[2] K. Tokuhara and S. Hirosawa, J. Appl. Phys. **69**, 5521 (1991).
[3] A. S. Kim and F. E. Camp, J. Mater. Eng. **13**, 175 (1991).
[4] Y. Kaneko and N. Ishigaki, JMEPEG **3**, April 1994.
[5] Y. Matsura, S. Hirosawa, H. Yamamoto, S. Fujimura, M. Sagawa, and K. Osamura, Jpn. J. Appl. Phys. **24**, L635 (1985).
[6] W. L. Liu, Y. L. Liang, B. M. Ma, and C. O. Bounds, IEEE Trans. Magn. **28**, 2154 (1992).
[7] B. M. Ma, Y. L. Liang, D. W. Scott, W. L. Liu, and C. O. Bounds, 13th International Workshop on Rare-Earth Magnets and their Applications, Birmingham, UK, 1994, pp. 309–318.
[8] B. M. Ma, D. W. Scott, Y. L. Liang, W. L. Liu, and C. O. Bounds, Proceedings of the 9th Conference on Magnetism and Magnetic Tech., 1994, pp. 142–149.
[9] H. H. Stadelmaier, G. Schneider, and E. Henig, *Hard and Soft Magnetic Materials*, edited by J. A. Salsgiver (American Society for Metals, Metals Park, OH, 1987), pp. 45–50.
[10] Y. L. Chang and Y. R. Qing, Phys. Status Solidi **93**, 573 (1986).
[11] M. Sagawa and H. Nagata, IEEE Trans. Magn. **29**, 2747 (1993).
[12] T. Kawai, B. M. Ma, S. G. Sankar, and W. E. Wallace, J. Appl. Phys. **67**, 4610 (1990).
[13] W. C. Chang, T. B. Wu, and K. S. Liu, J. Appl. Phys. **63**, 3531 (1988).

Formation of $Nd(Fe_{1-y}Co_y)_2$ in rapidly quenched $Nd_{13.75}(Fe_{1-x}Co_x)_{80.25}B_6$ ($x=0-0.5$) alloys

Er. Girt, M. Koknaeva, and Z. Altounian
Centre for the Physics of Materials, Department of Physics, McGill University, 3600 University Street, Montréal, Québec H3A 2T8, Canada

X-ray diffraction patterns of overquenched $Nd_{13.75}(Fe_{1-x}Co_x)_{80.25}B_6$ ($x=0-0.5$) ribbons show fine grains of the 2–14–1 phase in an amorphous matrix. The ribbons, subsequently annealed at 975 K for 5 min, were investigated using quantitative x-ray structural analysis. The results indicate that in addition to the main 2–14–1 phase, all the samples have approximately 1 vol % of the γ-Nd phase. The existence of the $Nd(Fe_{1-y}Co_y)_2$ phase is established for $x \geqslant 0.25$ and its amount reaches up to 5.4 vol % for higher Co concentrations. From an interpolation of the measured lattice parameters of the 1–2 phase, the Co content is estimated to vary from $y=0.38$ to $y=0.58$ for this series of alloys. Using differential scanning calorimetry (DSC) the enthalpy of formation of the 1–2 phase in overquenched $Nd_{13.75}(Fe_{0.7}Co_{0.3})_{80.25}B_6$ ribbons is found to be about 3 kJ/mol. The activation energy necessary for the formation of the 1–2 phase, for the same composition, as determined from the Kissinger relation is 2.2±0.1 eV. © *1996 American Institute of Physics.* [S0021-8979(96)37908-5]

INTRODUCTION

The rapid solidification technique of melt spinning has been used to obtain Nd–Fe–B magnetic materials based on the 2–14–1 structure. Compositions which yield melt-spun ribbons with optimum magnetic properties are nonstoichiometric and are Nd rich.[1] This excess of Nd causes the formation of a suitable secondary phase, with a relatively low melting point, which plays a critical role in the magnet fabrication process. Apart from the excess of Nd, the Nd–Fe–B magnets often contain a certain amount of Co substituted for Fe to enhance the magnetic properties. It has been observed that for high Co concentrations ($x \geqslant 0.3$) in the R-rich $R-Fe_{1-x}Co_x-B$ alloys (R=Nd,Pr) the $Nd(Fe,Co)_2$ phase appears.[2–4] The $NdCo_2$ structure is a stable phase while the $NdFe_2$ is a high pressure phase which could be formed as a result of rapid solidification.[5] In this study, we investigate the formation of the $Nd(Fe,Co)_2$ phase in melt-spun $Nd_{13.75}(Fe_{1-x}Co_x)_{80.25}B_6$ ($x=0-0.5$) samples.

EXPERIMENTAL TECHNIQUE

The overquenched $Nd_{13.75}(Fe_{1-x}Co_x)_{80.25}B_6$ ($x=0-0.5$) ribbons were kindly supplied by C. D. Fuerst of General Motors. The ingots were prepared by induction melting in an argon atmosphere followed by melt spinning under argon using a wheel surface speed of 30 m/s. The ribbons were crushed and sieved to ensure that uniform flakes are selected. X-ray diffraction patterns of these flakes show very fine grains of the 2–14–1 phase as well as a large amount of the amorphous phase.[6] A comparison of the enthalpy of formation of these ribbons with fully amorphous ribbons shows that the overquenched ribbons contain about 20% of crystalline 2–14–1 phase. Crystallization of $Nd_{13.75}(Fe_{1-x}Co_x)_{80.25}B_6$ ($x=0-0.5$) flakes was investigated using differential scanning calorimetry (DSC). Quantitative phase analyses of the ribbons before and after annealing were done using quantitative x-ray structural analysis. The x-ray measurements were done on a Nicolet–Stöe powder diffractometer using graphite monochromated Cu Kα radiation.

RESULTS AND DISCUSSION

The $Nd_{13.75}(Fe_{1-x}Co_x)_{80.25}B_6$ ($x=0-0.5$) flakes were crystallized by annealing at 970 K for 5 min. For quantitative analyses, the x-ray patterns of the annealed samples were fitted to the 2–14–1, γ–Nd (also known as the Nd-rich phase) and $Nd(Fe_{1-y}Co_y)_2$ structures. The results of the fitting for all compositions ($x=0-0.5$) indicate that besides the main 2–14–1 phase, all the samples have approximately 1 vol % of the γ-Nd phase. The formation of the $Nd(Fe_{1-y}Co_y)_2$ phase, however, is found to depend critically on the overall Co content of the ribbons. The volume fraction and lattice constants of the 1–2 phase obtained from the fitting are presented in Fig. 1. The existence of the 1–2 phase in the annealed samples is established for $x \geqslant 0.25$ and its amount seems to saturate at 5.4 vol % for $x \geqslant 0.3$. This is not unexpected as the Nd content is constant for all compositions

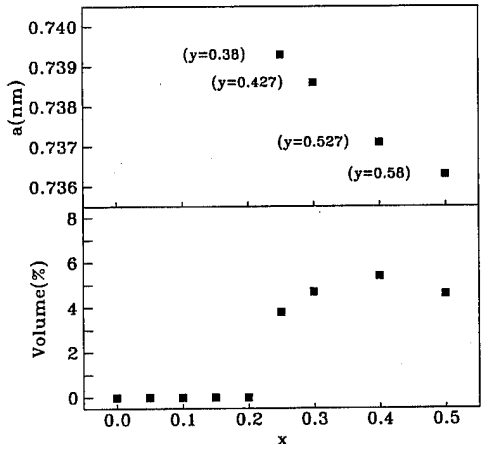


FIG. 1. The volume fraction and lattice constants of the $Nd(Fe_{1-y}Co_y)_2$ phase obtained from the fitting of the x-ray data of crystallized $Nd_{13.75}(Fe_{1-x}Co_x)_{80.25}B_6$ ($x=0-0.5$) ribbons. The concentrations of Co and y were estimated from the change in the lattice constants.

 0021-8979/96/79(8)/4833/3/$10.00 © 1996 American Institute of Physics

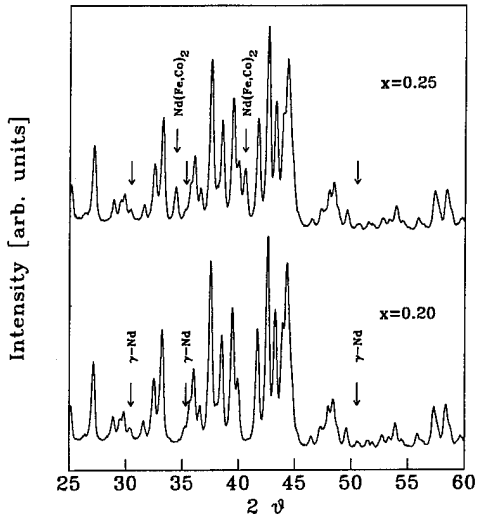


FIG. 2. X-ray diffraction scans of crystallized $Nd_{13.75}(Fe_{1-x}Co_x)_{80.25}B_6$ ribbons with $x=0.2$ and $x=0.25$.

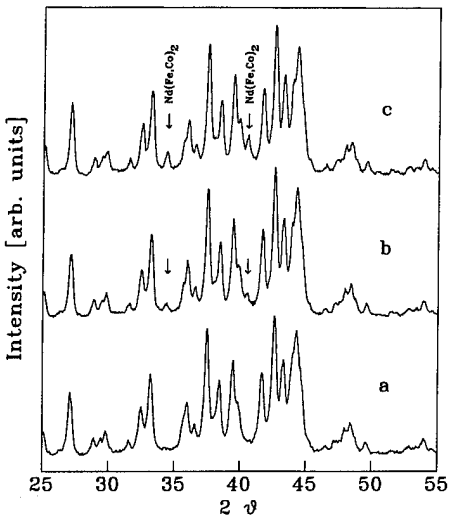


FIG. 4. X-ray diffraction scans obtained after heating the sample in the DSC at a rate of 40 K/min to (a) 900, (b) 920, (c) 940 K and subsequently cooled at a rate of 320 K/min.

and the amount of γ-Nd is found to be independent of x. The lattice constant of the 1–2 phase decreases nearly linearly with increasing Co concentration. From an interpolation of the measured lattice constants of the $NdFe_2$ and $NdCo_2$ phases,[5,7] we find that the Co content in $Nd(Fe_{1-y}Co_y)_2$ varies from a minimum of $y=0.38$ to a maximum of $y=0.58$ for this series of alloys. The x-ray patterns for the $Nd_{13.75}(Fe_{1-x}Co_x)_{80.25}B_6$ samples ($x=0.2$ and 0.25) are shown in Fig. 2. For $x=0.25$, the presence of the $Nd(Fe_{0.62}Co_{0.38})_2$ phase is clearly seen.

Figure 3 shows the DSC thermoscan of the $Nd_{13.75}(Fe_{0.7}Co_{0.3})_{80.25}B_6$ ribbon sample heated at 40 K/min. Besides the crystallization of the amorphous phase at T_{x1} into the 2–14–1 phase, the DSC measurements show another exothermic reaction at T_{x2}. The inset of Fig. 3 gives an expanded view of the region where T_{x2} occurs. For structural studies, the $Nd_{13.75}(Fe_{0.7}Co_{0.3})_{80.25}B_6$ sample was heated at a rate of 40 K/min to the temperatures indicated by the letters a, b, and c in the inset of Fig. 3, and subsequently cooled at 320 K/min. X-ray diffraction results, displayed in Fig. 4, show that the 1–2 phase forms in the temperature region between a and c. Therefore, the exothermic reaction at T_{x2} represents the formation of the $Nd(Fe_{0.57}Co_{0.43})_2$ phase. From the enthalpy of the exothermic process at T_{x2} and the calculated amount of the 1–2 phase for $Nd_{13.75}(Fe_{0.7}Co_{0.3})_{80.25}B_6$ deduced from the quantitative x-ray analysis, we obtain a value of about 3 kJ/mol for the enthalpy of formation of the 1–2 phase. For the purpose of measuring the activation energy for the formation of the 1–2 phase, $Nd_{13.75}(Fe_{0.7}Co_{0.3})_{80.25}B_6$ samples were heated at different heating rates in the DSC. Using the Kissinger method,[8] a value of 2.2 ± 0.1 eV for the activation energy of the 1–2 phase was obtained. It is worth mentioning that the amount of the 1–2 phase in the $Nd_{13.75}(Fe_{0.75}Co_{0.25})_{80.25}B_6$ sample diminishes after additional heating at 1170 K for 1 h. For the samples with high Co concentrations ($x\geq0.3$) the 1–2 phase is stable at 1170 K.

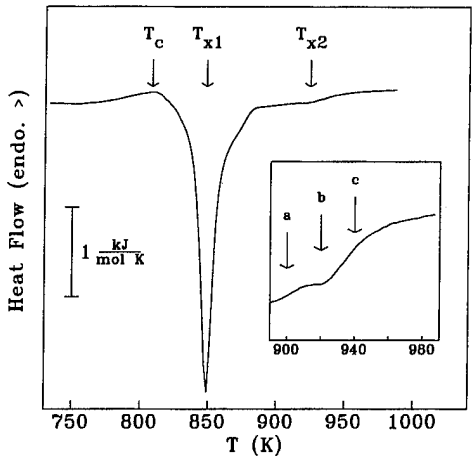


FIG. 3. DSC scans, at 40 K/min, for $Nd_{13.75}(Fe_{0.7}Co_{0.3})_{80.25}B_6$ ribbons. T_c is the curie temperature of the $Nd_2(Fe_{0.7}Co_{0.3})_{14}B$ phase, T_{x1} is the crystallization temperature of the $Nd_2(Fe_{0.7}Co_{0.3})_{14}B$ phase, and T_{x2} is the formation temperature of the $Nd(Fe_{0.573}Co_{0.427})_2$ phase. The inset represents an enlarged region from 890 to 990 K.

CONCLUSION

The rapidly quenched $Nd_{13.75}(Fe_{1-x}Co_x)_{80.25}B_6$ ($x\geq0.25$) samples contain the $Nd(Fe,Co)_2$ phase after annealing at 975 K for 5 min. The amount of the $Nd(Fe,Co)_2$ phase increases with the Co concentration and saturates at 5.4 vol % for $x=0.4$. The $Nd(Fe,Co)_2$ phase forms after the crystallization of the $Nd_2(Fe,Co)_{14}B$ phase for the rapidly quenched $Nd_{13.75}(Fe_{0.7}Co_{0.3})_{80.25}B_6$ samples. The enthalpy and activation energy of formation of the $Nd(Fe,Co)_2$ phase in the $Nd_{13.75}(Fe_{0.7}Co_{0.3})_{80.25}B_6$ sample are 3 kJ/mol and 2.2 ± 0.1 eV, respectively.

ACKNOWLEDGMENT

The research was supported by grants from the Natural Sciences and Engineering Research Council of Canada, and Fonds pour la Formation de Chercheurs et l'Aide à la Recherche, Québec.

[1] J. J. Croat, J. F. Herbst, R. W. Lee, and F. E. Pinkerton, Appl. Phys. Lett. **44**, 148 (1984); J. Appl. Phys. **55**, 2078 (1984).

[2] H. Yamamoto, S. Hirosawa, S. Fujimura, K. Tokuhara, H. Nagata, and M. Sagawa, IEEE Trans. Magn., **MAG-23**, 2100 (1987).

[3] C. D. Fuerst and J. F. Herbst, J. Appl. Phys. **63**, 3324 (1988).

[4] J. Wecker and L. Schultz, Appl. Phys. Lett. **54**, 393 (1989).

[5] L. X. Liao, Z. Altounian, and D. H. Ryan, J. Appl. Phys. **67**, 4821 (1990).

[6] C. D. Fuerst and E. G. Brewer, J. Appl. Phys. **73**, 5751 (1993).

[7] *Pearson's Handbook*, edited by P. Villars and L. D. Calvert (American Society for Metals, Metals Park, OH, 1985).

[8] H. E. Kissinger, Anal. Chem. **29**, 1702 (1957).

Hard and soft magnetic properties of nanocrystalline Fe–Nd–Zr–B alloys containing intergranular amorphous phase (abstract)

A. Inoue, A. Kojima, A. Takeuchi, and T. Masumoto
Institute for Materials Research, Tohoku University, Sendai 980-77, Japan

A. Makino
Alps Electric Company, Ltd., Nagaoka, 940, Japan

The nanoscale crystalline and amorphous phases obtained by partial crystallization of an amorphous phase in rapidly solidified $Fe_{90}Nd_{7-x}Zr_xB_3$ alloys were found to exhibit rather good hard magnetic properties in the composition range below 3 at. % Zr and good soft magnetic properties in the range above 4 at. % Zr. The hard magnetic alloys consist of nanoscale bcc–Fe and bct–$Fe_{14}Nd_2B$ particles surrounded by the remaining amorphous phase, while the soft magnetic alloys are composed of bcc–Fe and remaining amorphous phases. The particle size is measured to be about 20 nm for the bcc–Fe phase and 15 nm for the $Fe_{14}Nd_2B$ phase for a the former alloys and about 10 nm for the bcc–Fe phase for the latter alloys. The volume fraction of the remaining amorphous phase is evaluated to be about 20 to 30 at. % and the Nd and Zr contents are much higher than the nominal concentrations for the hard and soft magnetic alloys from the high-resolution TEM images and nanobeam compositional analyses. The remanence (Br), intrinsic coercivity (iHc), and maximum energy product are 1.24 T, 200 kA/m, and 88 kJ/m^3, respectively, for the nanocrystalline $Fe_{90}Nd_5Zr_2B_3$ alloy annealed for 180 s at 1023 K, while the saturation magnetization (Bs), coercivity (Hc), and permeability at 1 kHz are 1.63 T, 16 A/m, and 7000, respectively, for the nanocrystalline $Fe_{90}Nd_2Zr_5B_3$ alloy annealed for 180 s at 923 K. The high Br and Bs values are presumably due to the magnetic coupling between bcc–Fe particles via the ferromagnetic intergranular amorphous phase and the large iHc for the alloy containing more than 4 at. % Nd is due to the exchange magnetic interaction betweeen $Fe_{14}Nd_2B$ particles via ferromagnetic bcc–Fe and amorphous phases. The appearance of the rather good hard and soft magnetic properties for the same alloy series containing the high Fe content is extremely important for future development of manocrystalline hard and soft magnetic materials. © *1996 American Institute of Physics.* [S0021-8979(96)63808-0]

 0021-8979/96/79(8)/4836/1/$10.00 © 1996 American Institute of Physics

Melt-spun $Pr_2Co_{14}B$/Co nanocomposite magnets

L. Withanawasam, I. Panagiotopoulos, and G. C. Hadjipanayis
Department of Physics and Astronomy, University of Delaware, Newark, Delaware 19716

We have successfully prepared a new nanocomposite magnet consisting of a mixture of a magnetically hard $Pr_2Co_{14}B$ phase and a soft Co phase using the technique of melt spinning. The final microstructure with the above phases is formed after annealing the melt-spun ribbons through an intermediate transformation to the metastable $TbCu_7$-type structure. Optimum coercivity of 4.3 kOe was observed in a sample with the composition $Pr_8Co_{83}Nb_1B_8$ after heating above 775 °C.
© *1996 American Institute of Physics.* [S0021-8979(96)38008-X]

INTRODUCTION

Recently, the new concept of nanocomposite magnets consisting of a fine mixture of magnetically hard and soft phase has attracted much attention because of its potential use for high performance, low cost permanent magnets.[1–5] The high reduced remanences and relatively high coercivity observed in melt-spun $Nd_4Fe_{77}B_{19}$ ribbons containing mostly soft Fe_3B with some hard $Nd_2Fe_{14}B$ led to the realization of this new material concept.[6,7] A distinctive feature of such isotropic magnets is the observation of reduced remanence $[M_r/M_s]$ greater than 0.5 which is a consequence of exchange coupling among the hard and soft grains. Previously, we have investigated and reported the properties of $R_2Fe_{14}B/\alpha$-Fe nanocomposite magnets prepared by melt spinning.[8,9]

In the present study, we have investigated the Pr–Co–B alloys consisting of $Pr_2Co_{14}B$ and Co phases. $Pr_2Co_{14}B$ with a high uniaxial anisotropy (H_A=100 kOe) and a saturation magnetization of 125 emu/g, and Co, with saturation magnetization of 160 emu/g, are suitable candidate phases for nanocomposite magnets. Despite the lower saturation magnetizations of $Pr_2Co_{14}B$ and Co compared to those of $Pr_2Fe_{14}B$ and Fe, the nanocomposites of $Pr_2Co_{14}B$/Co showed a great potential for high temperature applications due to the higher Curie temperatures of $Pr_2Co_{14}B$(720 °C) and hcp Co (1100 °C).

EXPERIMENT

Ingots with different compositions given by $Pr_xCo_{99-x-y}Nb_1B_y$ (x=6,8 and y=6,8) were prepared by arc melting the constituent elements in argon atmosphere. These compositions were selected to achieve a nanocomposite material in which the hard $Pr_2Co_{14}B$ phase content is higher than 50 wt %. Pieces of the ingot were melt-spun from a quartz tube having an orifice diameter of about 1 mm. Wheel speeds in excess of 45 m/s were used. The resulting ribbons were studied using differential scanning calorimetry (DSC) and differential thermal analysis (DTA) for possible phase transformations. X-ray diffraction (Cu K_α) was used to identify the phases present. The hysteresis loops were measured in a vibrating sample magnetometer (VSM) with a maximum field of 20 kOe. Selected samples were also measured in a SQUID magnetometer with a maximum field of 55 kOe. The coercivity of the samples was optimized through annealing at temperatures in the range of 650–900 °C and times between 4 and 60 min.

RESULTS AND DISCUSSION

X-ray diffraction was used to determine the structure of as-spun ribbons. The diffraction patterns showed that the ribbons with Co content less than 85% were amorphous/nanocrystalline in structure. The ribbons containing more than 85 at. % of Co were crystalline with strong reflections due to fcc Co.

Calorimetric studies were performed on the as-spun samples using differential thermal analysis to determine the phase transformation temperatures. Two such thermal scans on ribbons with composition $Pr_8Co_{83}Nb_1B_8$ and $Pr_8Co_{85}Nb_1B_6$ are shown in Fig. 1. These traces consist of three exothermic peaks; a broad peak with T_{peak}<600 °C, a sharp exotherm near 645 °C, and another peak at T_{peak}>760 °C. The low-temperature exotherms are due to the amorphous to crystalline structural transformations.

Samples annealed at temperatures close to 650 °C were examined through x-ray diffraction and revealed the pattern shown in Fig. 2. The major reflections of this pattern can be indexed to a hexagonal structure of the type $TbCu_7$. Thus, after crystallization the samples contain a majority phase of the $TbCu_7$-type along with some minority phases as indicated by the XRD pattern including fcc cobalt.

When these samples were annealed at temperatures above the higher temperature exotherms (T_{peak}=760 and 775 °C), the metastable $TbCu_7$-type structure transformed to

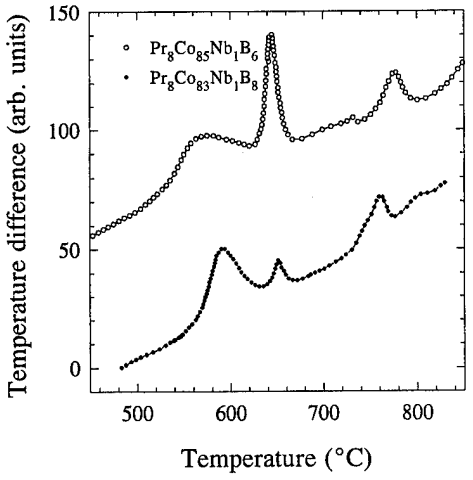


FIG. 1. DTA traces obtained for as-spun $Pr_8Co_{83}Nb_1B_8$ and $Pr_8Co_{85}Nb_1B_6$ samples at a scanning rate of 10 °C/min showing three exothermic peaks.

 0021-8979/96/79(8)/4837/3/$10.00 © 1996 American Institute of Physics

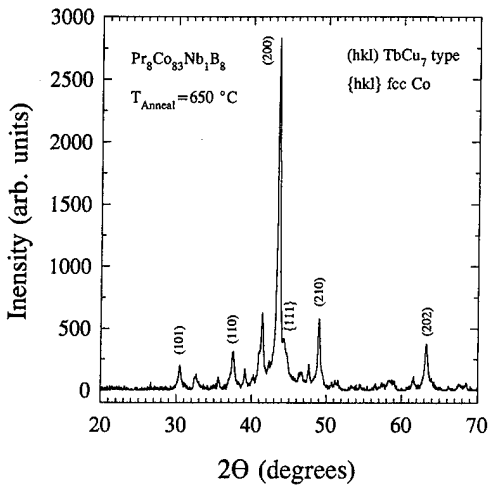


FIG. 2. XRD pattern of a $Pr_8Co_{83}Nb_1B_8$ sample annealed at 650 °C indicating the presence of $TbCu_7$-type and fcc Co structures.

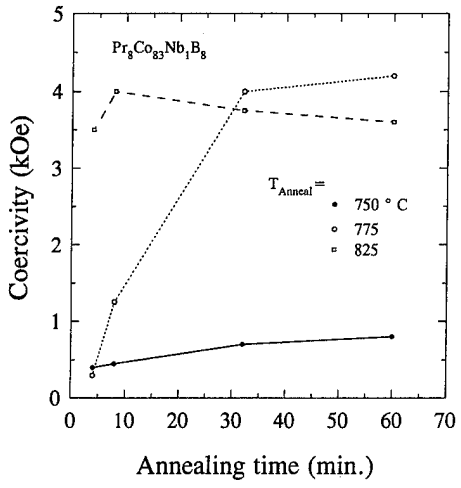


FIG. 4. Coercivity of $Pr_8Co_{83}Nb_1B_8$ as a function of annealing time at different annealing temperature.

the intended mixture of $Pr_2Co_{14}B$+Co (both fcc and hcp) phases. This is evident from the XRD pattern of a $Pr_8Co_{83}Nb_1B_8$ sample annealed at 775 °C shown in Fig. 3. Hence, we establish that a mixture of $Pr_2Co_{14}B$ and Co phases can be prepared by the conventional metallurgical process of rapid quenching.

Magnetic hysteresis studies showed that the as-spun samples are soft and develop a coercivity of about 500 Oe after annealing at 650 °C (to the metastable $TbCu_7$-type structure). The development of coercivity with annealing temperature and time was further investigated. A summary of these results are presented in Figs. 4 and 5 for the $Pr_8Co_{83}Nb_1B_8$ and $Pr_8Co_{85}Nb_1B_6$ samples, respectively. As mentioned before, the coercivity is negligible for annealing at temperatures below 775 °C due to the absence of the hard $Pr_2Co_{14}B$ phase. When the annealing temperature is raised above 775 °C, large coercivities develop after a relatively long annealing time of the order of an hour. This time can be reduced by increasing the annealing temperature to attain coercivities close to those resulting from the 775 °C anneal. This behavior is quite different from what we have observed in the Pr–Fe–Nb–B system. Namely, the optimum annealing time is lower than 10 min, and the optimum temperature is as close to the transition temperature at which the hard phase appears. Furthermore, in the Fe system even a small excess of temperature and time leads to a considerable degradation of the coercivity in contrast to the behavior observed in $Pr_2Co_{14}B$/Co samples.

The hysteresis loop of a coercivity optimized $Pr_8Co_{83}Nb_1B_8$ with a coercivity of 4.3 kOe is shown in Fig. 6. The magnetization measured under a maximum field of 20 kOe is 90 emu/g with a reduced remanence of 0.60. The observation of such coercivity and reduced remanence are believed to be a consequence of exchange coupling between the hard and soft phases of the magnet.[7]

In a nanocomposite magnet the coercivity depends on the ratio of hard to soft phase content as well as on the microstructure. The above data seem to indicate that for the

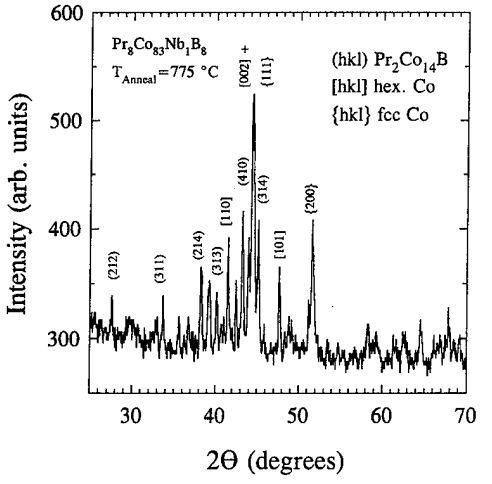


FIG. 3. XRD pattern of a $Pr_8Co_{83}Nb_1B_8$ sample annealed at 775 °C indicating the presence of $Pr_2Co_{14}B$+Co phases.

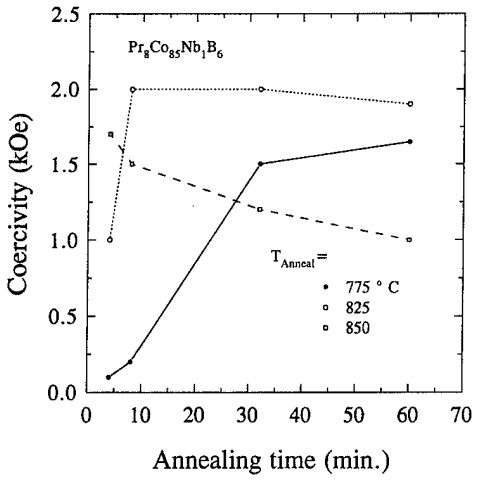


FIG. 5. Coercivity of $Pr_8Co_{85}Nb_1B_6$ as a function of annealing time at different annealing temperatures.

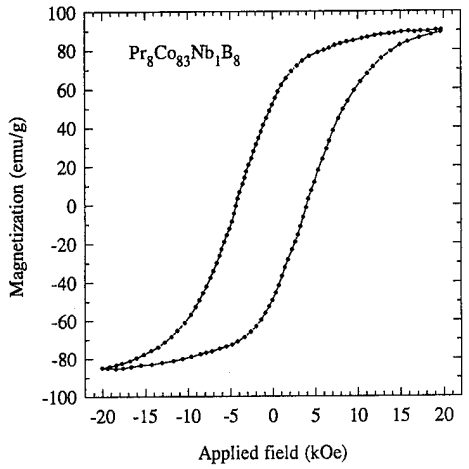


FIG. 6. Hysteresis loop of a coercivity optimized $Pr_8Co_{83}Nb_1B_8$ sample showing a room temperature coercivity of 4.3 kOe.

Pr–Co–B system a microstructural development preceding the structural transformation (from soft $TbCu_7$-type to $Pr_2Co_{14}B$) is required to optimize coercivity. However, the above premise has to be verified through microstructural investigations.

Samples containing 6 at. % of Pr resulted in moderate coercivities of only 2.0 kOe. The existence of a large crystalline fraction (Co) in the as-spun ribbons of these samples may be responsible for this poor coercivity.

CONCLUSION

We have successfully prepared a melt-spun composite magnet consisting of a mixture of $Pr_2Co_{14}B$ and Co phases having coercivities as high as 4.5 kOe.

ACKNOWLEDGMENT

Work supported by the Army Research Office.

[1] H. A. Davis, A. Manaf, M. Leonawicz, and P. Z. Zhang, Nanostru. Mater. **2**, 197 (1993).
[2] J. Ding, P. G. McCormick, and R. Street, J. Magn. Magn. Mater. **124**, 1 (1993).
[3] Ralph Skomski and J. M. D. Coey, Phys. Rev. B **48**, 15812 (1993).
[4] T. Schrefl, J. Fidler, and H. Kornmuller, Phys. Rev. B **49**, 6100 (1994).
[5] H. Fukunaga and H. Inoue, Jpn. J. Appl. Phys. **31**, 1347 (1992).
[6] R. Coehroon, D. B. De Mooji, and D. De Waard, J. Magn. Magn. Mater. **80**, 101 (1989).
[7] E. F. Kneller and R. Hawig, IEEE Trans. Magn. **MAG-27**, 3588 (1991).
[8] L. Withanawasam, G. C. Hadjipanayis, and R. F. Krause, J. Appl. Phys. **75**, 6646 (1994).
[9] L. Withanasam, A. S. Murthy, G. C. Hadjipanayis, and R. F. Krause, J. Appl. Phys. **76**, 7065 (1994).

Hydrogen induced corrosion mechanism in NdFeB magnets

A. S. Kim, F. E. Camp, and T. Lizzi
Crucible Research Center, Crucible Materials Corporation, 6003 Campbells Run Road, Pittsburgh, Pennsylvania 15205-1022

An investigation was conducted comparing the corrosion behavior of NdFeB magnets in flowing hydrogen and in the heat and humidity of an autoclave. The results show that corrosion is both macroscopically and microscopically similar in both environments. In both cases, the corrosion progressed most rapidly in those areas where the magnetic orientation of the $Nd_2Fe_{14}B$ matrix grains was perpendicular to the outer surface. A corrosion mechanism involving the reaction of hydrogen—either as a pure gas or as a by-product of the decomposition of water vapor—with the neodymium-rich grain boundary phase is proposed. © *1996 American Institute of Physics.* [S0021-8979(96)38108-6]

I. INTRODUCTION

The corrosion of Nd–Fe–B-type magnets has long been associated with exposure to humidity.[1–4] It is expected that the water vapor reacts with the Nd-rich grain boundary phase to cause the corrosion.[3] Thus, the application of moisture barriers such as epoxy or metallic coatings have proven effective in reducing the rate of corrosion of Nd–Fe–B magnets.[2–4] Further, the corrosion resistance is improved by stabilization of the Nd-rich grain boundary phase by the addition of alloying elements.[4–7] However, the mechanism involved in the corrosion of Nd–Fe–B-type alloys on exposure to humidity has not been settled. The present paper deals with an investigation into humidity-related corrosion mechanism.

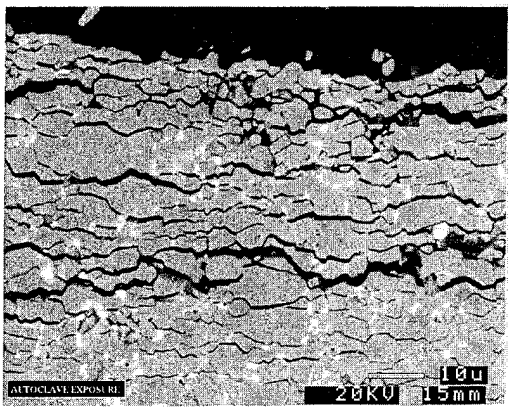
II. EXPERIMENT

The magnets used in this study were prepared by standard powder metallurgical sintering techniques from an alloy having a chemical analysis of (weight percent): 30.8 Nd, 3.33 Dy, 64.6 Fe, 1.09 B, 0.07 Al, 0.08 C, and 0.04 O. The sintered magnets were machined to disks approximately 14 mm diameter by 7 mm thick. Two types of environmental corrosion testing were performed on unmagnetized samples. Autoclave tests were used to expose the magnets to a hot, humid environment. In these tests, the magnets were placed in autoclaves where a pool of water was vaporized to produce a pressure of 10–15 psi and a temperature of 110–115 °C. This method has proven to be a convenient way of estimating the susceptibility of NdFeB magnets to atmospheric corrosion.[1,2] Hydrogen exposure testing was accomplished by placing the magnets in laboratory glassware under flowing hydrogen at atmospheric pressure at room temperature. Corroded samples were mounted and cross-sectioned parallel to the magnetic direction. The samples were metallographically polished and then examined by light microscopy and by scanning electron microscopy (SEM).

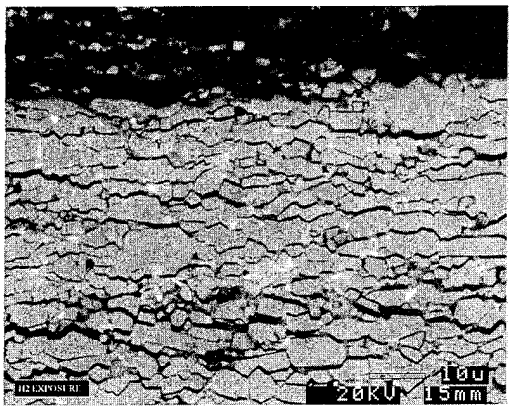
III. RESULTS AND DISCUSSION

The magnets in this study were subjected to either flowing hydrogen or to a 110–115 °C humid atmosphere in a 96 h autoclave test. Figure 1 shows that the corrosion was intergranular, i.e., along the Nd-rich grain boundary phase, for both the hydrogen and the humidity exposure test samples.

Also, for both testing conditions, the resulting corrosion occurred primarily on the pole faces of the magnets. The corrosion progressed in the direction of the magnetic orientation as shown in Fig. 2. These results agree with the observation of McGuiness *et al.*[8] that both hydrogen and humidity induced corrosion progressed along the magnetic direction from the pole faces in aligned samples but occurred generally from all surfaces on isotropic samples.



(a)



(b)

FIG. 1. SEM micrographs of (Nd–Dy)–Fe–B magnets subjected to (a) autoclave test and (b) hydrogen exposure. Magnetic orientation is normal to the magnet outer surface.

 0021-8979/96/79(8)/4840/3/$10.00 © 1996 American Institute of Physics

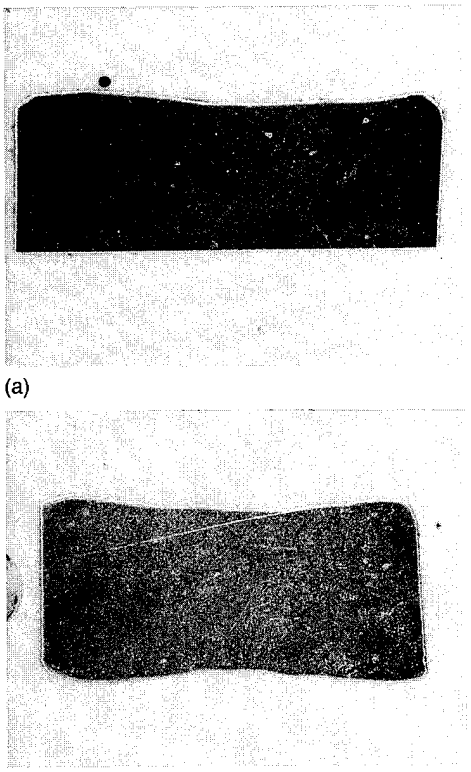


FIG. 2. Cross section of the (Nd–Dy)–Fe–B magnets subjected to (a) autoclave test and (b) hydrogen exposure. Magnetic orientation is in the vertical direction.

Metallographic examination reveals that the corrosion was related to the local orientation of the matrix $Nd_2Fe_{14}B$ grains as illustrated in Fig. 3. The reason for this is related to the morphological arrangement of the $Nd_2Fe_{14}B$ matrix grains. The matrix grains are of a tetragonal structure whose magnetic axis is along the *c* axis. As is evident in Fig. 1, the matrix grains are generally rectangular or brick shaped in cross section with the *c* axis several times shorter than the *a* axis. In magnetically aligned samples, the matrix grains become arranged in a more or less layered pattern. This results in the Nd-rich grain boundary phase also being arranged in layers. During corrosion or decrepitation, the transformation of the Nd-rich grain boundary phase to a hydride causes it to expand creating local stresses. The mechanical effect of the expansion is greatest along the continuous layers of the Nd-rich phase. Thus,the disadhesion of the matrix grains occurs in layers and the corrosion progresses along the local direction of magnetization as these layers spall off.

The similarities between the corrosion caused by exposure to the two types of atmospheric conditions tested infers a common corrosion mechanism. Since the hydrogen exposure presents hydrogen as the sole reactant species, it is logical that hydrogen would be involved in a common corrosion mechanism. Hydrogen may be generated in the autoclave testing from the decomposition of water vapor:

$$3H_2O+Nd\rightarrow Nd(OH)_3+3H.$$

The hydrogen may then diffuse into the magnet and become a reactant with the Nd-rich grain boundary phase causing the

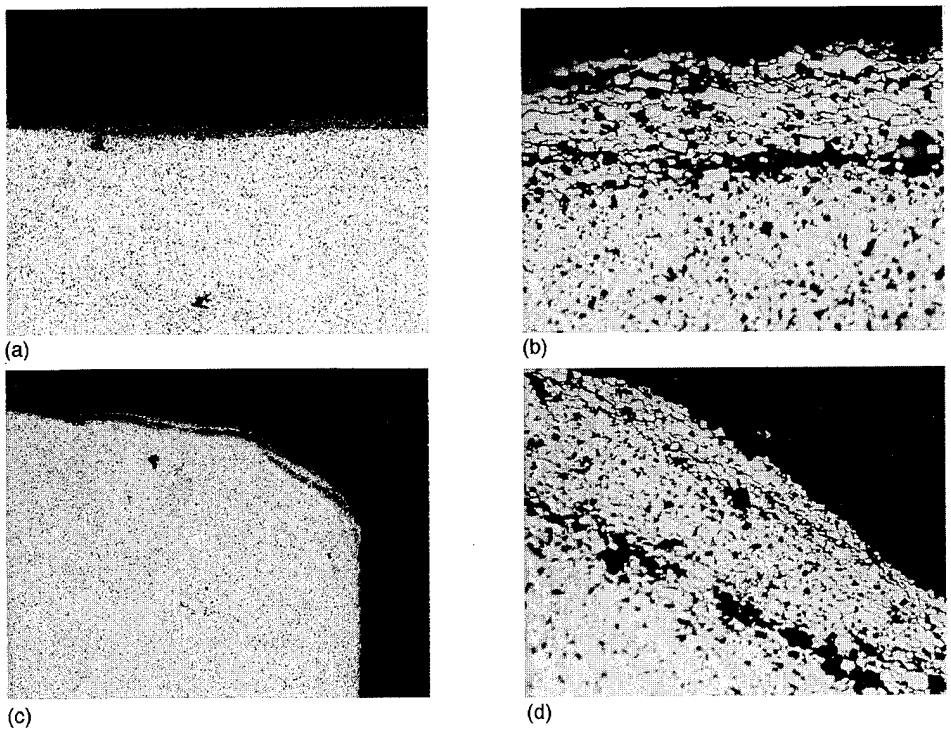


FIG. 3. Illustrations of how the corrosion followed the local orientation of the matrix grains in a similar fashion in both autoclaved and hydrogen exposure samples. (a), (b) Area of autoclaved sample at two magnifications; (c), (d) area of hydrogen exposed sample at two magnifications.

observed corrosion:

$$Nd+3H \rightarrow NdH_3.$$

Thus, the corrosion mechanism for NdFeB magnets in the heat and humidity of the autoclave test starts with a surface reaction of water vapor with the Nd-rich grain boundary phase. Then, as the hydrogen diffuses along the grain boundaries into the interior of the magnet, the hydrogen reacts with the Nd-rich grain boundary phase to cause a volume expansion of the grain boundary phase. This results in the dislodging of the $Nd_2Fe_{14}B$ matrix phase grains and decrepitation occurs. This same phenomenon also occurs with the exposure of the magnets to pure hydrogen, except that the initial reaction of the moisture to form the hydrogen is replaced by a dissociation of molecular hydrogen.

Hydrogen is also known to enter into the $Nd_2Fe_{14}B$ matrix phase.[9] However, as Harris has noted,[10] elevated temperatures or pressures are necessary for this to occur. Unless the rate of the exothermic reaction of the hydrogen with the Nd-rich phase is sufficient to locally raise the temperature to the necessary level, matrix phase adsorption of hydrogen, although not unimportant, would probably not dominate in humidity-related corrosion.

On the other hand, there is collaborative data supporting the conclusion that the hydrogen reaction with the Nd-rich grain boundary phase is the predominant mechanism in the humidity-related corrosion of Nd–Fe–B-type magnets. First, a strong correlation has been established between an increase in the total rare earth level—and, therefore, an increase in the amount of Nd-rich phase—and an increase in the corrosion rate.[11] Also, as noted earlier, alloying additions to the Nd-rich grain boundary phase can greatly reduce the bulk corrosion rate.

IV. CONCLUSIONS

The corrosion of NdFeB magnets in hot, humid autoclave and flowing hydrogen environments was found to be similar both macroscopically and microscopically. In both cases, the corrosion progressed most rapidly in those areas where the magnetic orientation of the $Nd_2Fe_{14}B$ matrix grains was perpendicular to the outer surface. Hydrogen, introduced either as a gas or as a product of a reaction of water vapor with the Nd, diffuses along the grain boundaries and reacts with the Nd-rich grain boundary phase. This reaction causes an expansion of the Nd-rich grain boundary phase which in turn dislodges the NdFeB matrix phase grains leading to magnet decrepitation. Observations of the effect of various alloying elements supports the supposition that the hydrogen reaction which causes the corrosion is primarily with the Nd-rich grain boundary phase.

[1] J. Jacobson and A. Kim, J. Appl. Phys. **61**, 3763 (1987).
[2] C. J. Willman and K. S. V. L. Narasimhan, J. Appl. Phys. **61**, 3766 (1987).
[3] A. S. Kim, F. E. Camp, and S. Constandinides, *Corrosion of Electronic and Magnetic Materials*, edited by P. J. Peterson (ASTM, Philadelphia, PA, 1992), pp. 68–79.
[4] K. Tokuhara and S. Hirosawa, J. Appl. Phys. **69**, 5521 (1991).
[5] H. Nakamura, A. Fukuro, and T. Yoneyama, Proceedings of 10th International Workshop on Rare Earth Magnets and Application (II), Kyoto, Japan, 1989, pp. 315–322.
[6] A. S. Kim, F. E. Camp, and E. J. Dulis, IEEE Trans. Magn. **26**, 1936, (1990).
[7] S. K. Besenicar, J. Holic, G. Drazic, and B. Saje, IEEE Trans. Magn. **30**, 693 (1994).
[8] P. J. McGuiness, L. Fitzpatick, V. A. Yarrtys, and I. R. Harris, J. Alloys Compounds **206**, L7 (1994).
[9] O. Isnard, W. B. Yelon, S. Miraglia, and D. Fruchart, J. Appl. Phys. **78**, 1892 (1995).
[10] I. R. Harris and P. J. McGuiness, Proceedings of the 11th International Workshop on Rare Earth Magnets and Application, 1990, p. 29.
[11] B. M. Ma, Y. L. Liang, D. W. Scott, W. L. Liu, and C. O. Bounds, 13th International Workshop on Rare Earth Magnets and Application, 1994, p. 309.

Magnetic properties and transmission electron microscopy microstructures of exchange coupled $Nd_{12-x}Fe_{82+x}B_6$ melt spun ribbons

W. C. Chang and D. M. Hsing
Department of Physics, National Chung Cheng University, Ming-Hsiung, Chia-Yi, Taiwan, Republic of China

The nanocomposite melt spun ribbons of the alloys $Nd_{12-x}Fe_{82+x}B_6$ ($x=0$, 2.5, 3, and 4) have been prepared by rapid quenching and/or post heat treatment. In the alloy with $x=0$, homogeneous grain morphologies were obtained at the lower wheel speed (18 m/s≤Sw≤25 m/s) to result in a strong exchange coupling effect between $Nd_2Fe_{14}B$ and α-Fe grains, the magnetic properties of Br=9.6 kG, iHc=7.7 kOe, and (BH)max=18 MGOe was achieved. In the alloys with $x=2.5$, 3, and 4, exchange coupling effect is also found and the best magnetic properties of Br=11.4 kG, iHc=6.3 kOe, and (BH)max=19 MGOe are achieved in the alloy ribbons with $x=2.5$ quenched at a wheel speed of 18 m/s without any post heat treatment. Inasmuch as the crystallization temperature of the ribbons increased with decreasing the Nd content, the microstructures, the size and volume fraction of the α-Fe and $Nd_2Fe_{14}B$ phases evaluated by transmission electron microscopy observation, of the above alloy ribbons were dominated by the Nd content, the wheel speed and the heat treatment temperature apparently. As a result, the exchange coupling effect and the magnetic properties of the ribbons were strongly affected. © *1996 American Institute of Physics.* [S0021-8979(96)38208-2]

I. INTRODUCTION

Recently, nanocomposite magnets with a soft magnetic phase embedded in hard magnetic matrix phase have been of interest due to their high magnetization without excessive loss of coercivity.[1,2] In the $Nd_2Fe_{14}B$ type nanocomposite magnets, two type of composites, α-Fe/$Nd_2Fe_{14}B$,[3] and $Fe_3B/Nd_2Fe_{14}B$,[1,4] have been widely studied. In this article, we have studied the alloys around the composition of $Nd_2Fe_{14}B$, i.e., $Nd_{12-x}Fe_{82+x}B_6$, to determine the effect of Nd content on the microstructure, the exchange coupling effect and the magnetic properties of the nanocomposite ribbons. Finally, the relationship between the size and volume fraction between α-Fe and $Nd_2Fe_{14}B$ phases, identified with transmission electron microscopy (TEM), and the magnetic properties of the ribbons will be presented and discussed.

II. EXPERIMENT

The starting materials of the $Nd_{12-x}Fe_{82+x}B_6$ ($x=0$, 2.5, 3, and 4) ingots, 250 g for each, were prepared by a vacuum induction furnace. The composition and alloy abbreviation of each alloy is listed in Table I. The ingots were crushed and small pieces of each (about 2 g) were used for melt spinning. The wheel speed of the melt spinner was set in the range from 18 to 35 m/s during preparation of the melt spun ribbons. The crystallization temperature for each over-quenched alloy ribbon was measured with a differential thermal analyzer (DTA). The ribbons were subsequently heated treated at 700 or 750 °C for 10 to 30 min in order to improve the microstructures and magnetic properties. The crystallinity of the as-quenched ribbons and the heated treated ribbons were investigated by a x-ray diffractometer with Cu $K\alpha$ radiation. The ribbons were first magnetized with a pulse magnetic field of 60 kOe, and then the magnetic properties were measured by a vibrating sample magnetometer (VSM) with an applied field of 12 kOe. The microsctructures of the ribbons were observed by a transmission electron microscope; the grain size of the α-Fe and $Nd_2Fe_{14}B$ phases and their volume fractions were measured from TEM photographs for correlating with their magnetic properties.

TABLE I. The $Nd_{12-x}Fe_{82+x}B_6$ alloy formula and their abbreviation in this study.

X	Formula	Alloy abbrev.
0	$Nd_{12}Fe_{82}B_6$	$N1$
2.5	$Nd_{9.5}Fe_{84.5}B_6$	$N2$
3	$Nd_9Fe_{85}B_6$	$N3$
4	$Nd_8Fe_{86}B_6$	$N4$

III. RESULTS AND DISCUSSION

Table II exhibits the glass formation temperature (Tg) of the over-quenched $N1$, $N2$, $N3$, and $N4$ alloy ribbons measured from the DTA curves. It shows that the value of Tg increases with decreasing the Nd content of the ribbons. Due to the difference of the glass formation temperature in those four alloy ribbons, the first two alloy ribbons in this study, $N1$ and $N2$, were heat treated at 700 °C, while the latter two alloy ribbons, $N3$ and $N4$, were heat treated at 750 °C for various times to obtain suitable grain sizes and also proper magnetic properties. From phase diagram, the possible phases for the $N1$ ribbon after crystallization are α-Fe and $Nd_2Fe_{14}B$, whereas a small amount of Fe_3B might appear in $N2$, $N3$, and $N4$ ribbons. However, from our x-ray diffraction patterns and TEM micrographs, it is rather difficult to

TABLE II. The crystallization temperature of the over-quenched $N1$, $N2$, $N3$, and $N4$ ribbons.

Alloys	$N1$	$N2$	$N3$	$N4$
Tg (°C)	630	650	710	720

 0021-8979/96/79(8)/4843/3/$10.00 © 1996 American Institute of Physics

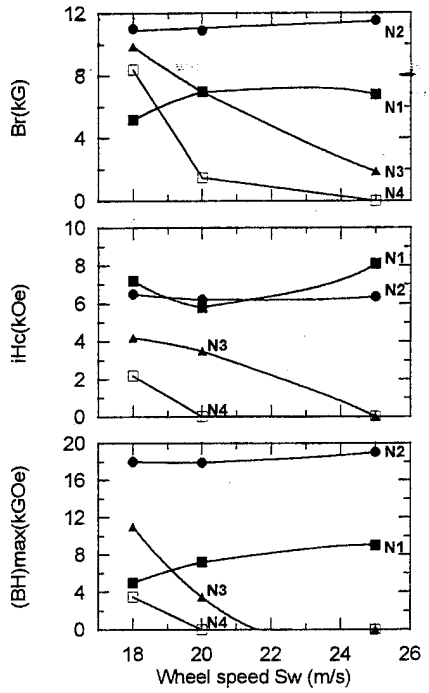


FIG. 1. The magnetic properties of the as-spun alloy ribbons melt quenched at different wheel speed.

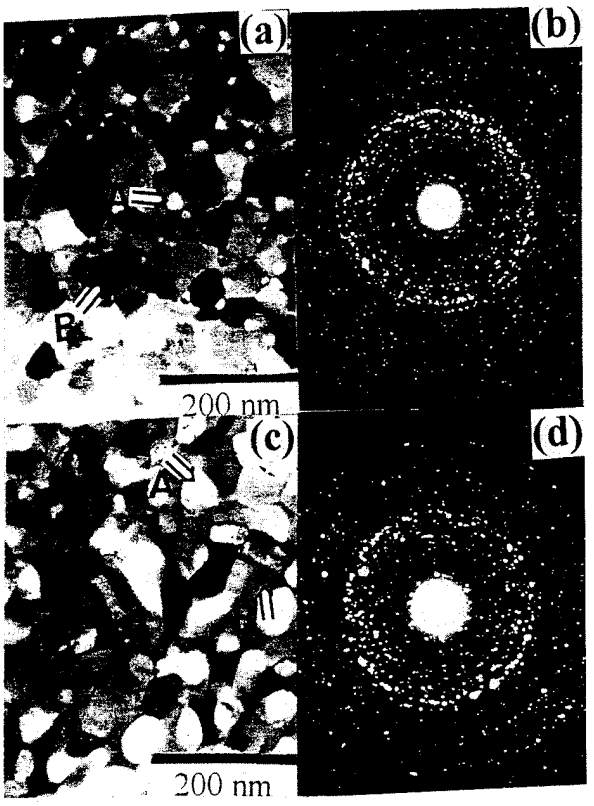


FIG. 3. TEM micrographs and the selected area diffraction (SAD) patterns of the $N1-25$ m/s ribbon heat treated at 700 °C for 30 min [(a) and (b)] and the $N4-25$ m/s ribbon heat treated at 750 °C for 30 min [(c) and (d)].

prove the existence of Fe_3B phase in these ribbons. The difficulty may be due the very small volume fraction of Fe_3B, so that one cannot detect it easily.

A. Magneties properties of the ribbons

The magnetic properties of the as-quenched ribbons are strongly dependent upon the alloy composition and the wheel speed (Sw) during melt spinning. The Br, iHc, and (BH)max are shown in Fig. 1. Note that worse magnetic properties were measured on the $N3$ and $N4$ alloy ribbons quenched at or exceeding 20 m/s since they were amorphous, which was confirmed with x-ray diffraction analysis. On the other hand, the $N1$ and $N2$ alloy ribbons might be well crystallized already at a wheel speed equal to or less than 25 m/s resulting in a quite excellent magnetic properties, especially for the case of $N2$ alloy ribbons. For example, the magnetic properties of Br=11.4 kG, iHc=6.3 kOe, and (BH)max=19 MGOe was achieved in the $N2$ ribbons quenched at a wheel speed of 25 m/s, these values are higher than the values of the commercial NdFeB MQ powders. From the higher remanence than 8 kG, the maximum Br value of isotropic $Nd_2Fe_{14}B$ phase that predicted from a Stoner–Wohlfrth model, one can easily conclude the existence of the exchange coupling effect between the hard magnetic phase, $Nd_2Fe_{14}B$, and soft magnetic phase, α-Fe.[3]

After a suitable heat treatment, the magnetic properties of $N1$, $N3$, and $N4$ alloy ribbons were drastically improved. However, heat treatments did not improve but deteriorated slightly the magnetic properties of $N2$ alloy ribbons. As it is known that the magnetic properties of the nanocomposite ribbons are strongly dependent upon the size and the volume fraction of the soft and hard magnetic phases,[5,6] one can speculate that the grain sizes are very fine after melt spinning of $N1$, $N3$, and $N4$ alloys. The subsequent heat treatment improves their microstructures and therefore enhances their magnetic properties. In the case of $N2$ ribbons, owing to the grain sizes are already well established after melt spinning at or lower than 25 m/s, further heat treatment may promote α-Fe grains, also $Nd_2Fe_{14}B$ grains, growing beyond the critical size, i.e., $d \approx 10.4$ nm,[7] of the best exchange coupling interaction. Figure 2 shows the best magnetic properties of the above four alloy ribbons after their best heat treatment ($N1$, $N3$, and $N4$) or without any subsequent treatment ($N2$). From Fig. 2 it can be seen that the magnetic properties, especially iHc and (BH)max, have a sharp transition

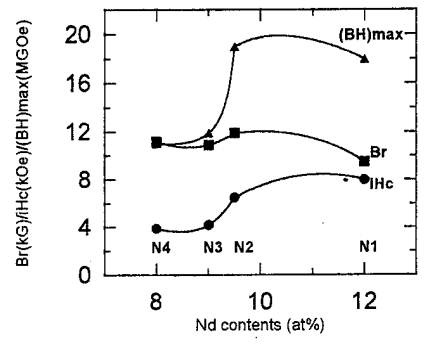


FIG. 2. The best magnetic properties of the $Nd_{12-x}Fe_{82+x}B_6$ (x=0, 2.5, 3, and 4) alloy ribbons under various condition of heat treatment.

TABLE III. The grain size and vol. fraction of α-Fe and $Nd_2Fe_{14}B$ phases and the magnetic properties of various alloy ribbons subjected different heat treatment.

Alloy	Sw (m/s)	Heat treatment	$D_{\alpha\text{-Fe}}/D_{2:14:1}$ (nm/nm)	α-Fe (vol %)	Br (kG)	iHc (kOe)	(BH)max (MGOe)
$N1$	25	700 °C, 30 min	20/70	8	9.5	8	18
$N1$	30	700 °C, 30 min	40/120	8	7.8	7.3	9.4
$N2$	18	···	15/50	15	11	6.3	18
$N2$	35	700 °C, 20 min	50/250	15	9	2.8	7.2
$N3$	18	750 °C, 20 min	35/70	25	10.9	4.1	11.7
$N4$	25	750 °C, 30 min	50/80	35	9.9	2.8	7.8

from $N2$ to $N3$. For $N1$ and $N2$ alloy ribbons, (BH)max over 18 MGOe can be achieved, but only 12 and 11 MGOe were obtained in $N3$ and $N4$ alloy ribbons, respectively. The reason of this big difference in magnetic properties will be studied from their microstructure observation as follows.

B. Microstructure analysis of the ribbons

The microstructures of various alloy ribbons with or without heat treatment have been studied. Two special cases are shown in Fig. 3. Figures 3(a) and 3(b) are the TEM micrographs and the selected area diffraction (SAD) patterns of alloy ribbon $N1$ quenched at 25 m/s then followed with 700 °C heat treating for 30 min, and Figs. 3(c) and 3(d) are that of the alloy ribbon $N4$ quenched at 25 m/s followed with 750 °C heat treating for 30 min. For the former alloy ribbon, the size of the α-Fe phase (as arrow A indicates) is quite small, also the volume fraction of it is low in comparison with that of $Nd_2Fe_{14}B$ phase (as arrow B indicates). For the latter alloy ribbon, the size and volume fraction of the α-Fe phase apparently increase. The size of the α-Fe phase is almost identical to that of $Nd_2Fe_{14}B$ phase. As mentioned previously, the Fe_3B phase is the third phase that is most likely to form in this alloy; unfortunately, it is not easy to distinguish between Fe_3B, if any, and α-Fe phases simply from their shape and from their compositions analyzed with energy dispersive x-ray analyzer.

Table III lists the grain size and volume fraction ratio of the α-Fe and $Nd_2Fe_{14}B$ phases, evaluated from TEM micrographs, and the magnetic properties of various alloy ribbons subjected different heat treatment. It can be found that a small α-Fe grain size ($\leqslant$20 nm) is accompanied with a high Br, iHc, and (BH)max for the ribbons of $N1$–25 m/s and $N2$–18 m/s, even though it is larger than 10.4 nm of the calculated critical size for strongest exchange coupling. The grain size of $Nd_2Fe_{14}B$ (50–70 nm) in these two ribbons seems not to affect the magnetic properties. The increases in grain size of both the α-Fe and $Nd_2Fe_{14}B$ phases in the ribbons of $N1$–30 m/s and $N2$–35 m/s due to heat treatment results in the reduction of Br, iHc, the squareness of the 2nd quadrant demagnetization curve and (BH)max drastically. Since reducing the Nd content in the alloy ribbons may retard the crystallization tendency, a higher heat treatment temperature is needed for the low Nd containing alloy ribbons, $N3$ and $N4$, to crystallize, leading to very rapidly growing α-Fe grains (50 nm for $N4$–25 m/s ribbon annealed at 750 °C for 30 min). Also, the volume fraction of α-Fe increases with the decrease of Nd content, the exchange coupling effect between α-Fe and $Nd_2Fe_{14}B$ phases is therefore rapidly decreased.[6] This is the reason why we could not easily obtain excellent magnetic properties of melt spun ribbons in the low Nd containing alloys, i.e., $N3$ and $N4$.

IV. CONCLUSION

The nanocomposite melt spun ribbons of the alloys $Nd_{12-x}Fe_{82+x}B_6$ (x=0, 2.5, 3, and 4) can be prepared by direct rapid quenching with or without a proper post heat treatment. The crystallization temperature of the ribbons increases with decreasing the Nd content of the alloy so that their microstructures and magnetic properties are affected. For the alloys with x=0 and 0.25, a microstructure with fine α-Fe, $\leqslant$20 nm, embedded in $Nd_2Fe_{14}B$ grains can be easily obtained, the magnetic properties of Br=11.4 kG, iHc=6.3 kOe, and (BH)max=19 MGOe result. For the alloys with x=3 and 4, a microstructure with a larger volume fraction and coarser α-Fe, $\geqslant$50 nm, coexisting with coarser $Nd_2Fe_{14}B$ grains is easily seen when the ribbons subjected to subsequent heat treatment. The exchange coupling effect between magnetic hard and soft phases is drastically decreased.

ACKNOWLEDGMENT

The kind support from Dr. B. M. Ma and Dr. C. O. Bounds, Rhone-Poulenc Rare Earths and Gallium, and from T. S. Chin, Tsing Hua University, Taiwan, is acknowledged.

[1] R. Coehoorn, D. B. de Mooij, J. P. W. B. Duchateau, and K. H. Buschow, J. Phys. (Paris) Colloq. **49**, C8-669 (1988).
[2] J. Ding, P. G. McCormick, and R. Street, J. Magn. Magn. Mater. 124, L1 (1993).
[3] A. Manaf, R. A. Buckley, and H. A. Davis, J. Magn. Magn. Mater. **128**, 302 (1993).
[4] S. Hirosawa and H. Kanekiyo, IEEE Trans. Magn. **29**, 2863 (1993).
[5] T. Schrefl, H. Kronmuller, and J. Fidler, J. Magn. Magn. Mater. **127**, L273 (1993).
[6] T. Schrefl, R. Fischer, J. Fidler, and H. Kronmuller, J. Appl. Phys. **76**, 7053 (1994).
[7] E. F. Kneller and R. Hawig, IEEE Trans. Magn. **27**, 3588 (1991).

Microstructure of flash and conventionally annealed melt spun NdFeB (abstract)

M. V. P. Altoé
Universidade de São Paulo, Brazil, Department of MSME, University of California at Berkeley, Berkeley, California 94720,
and Lawrence Berkeley Laboratory, 1 Cyclotron Road, Berkeley, California 94720

M. Chandramouli and G. Thomas
Department of MSME, University of California at Berkeley, Berkeley, California 94720
and Lawrence Berkeley Laboratory, 1 Cyclotron Road, Berkeley, California 94720

Spring magnets consist of a mixture of exchanged coupled, hard and soft magnetic phases and exhibit improved energy products and remanence. In this study, magnets containing a mixture of $Nd_2Fe_{14}B$ and Fe_3B have been fabricated using melt spinning under either Ar or He atmospheres.[1] In addition, samples have been heat treated using conventional (furnace) annealing and flash annealing techniques. Magnetic measurements using VSM confirm good spring magnet behavior for all the conventionally annealed samples and for samples flash annealed for $t<30$ s and $T<750$ °C. X-ray diffraction reveals that α–Fe, Fe_3B, and $Nd_2Fe_{14}B$ are present in different amounts depending on the annealing conditions. Transmission electron microscopy shows differences in grain size, crystallinity, and phase distribution. Lorentz electron microscopy reveals the influence of the microstructure on the magnetic domain structure. These results are correlated with the observed magnetic properties. © *1996 American Institute of Physics.* [S0021-8979(96)63908-9]

This research was supported by the Director, Office of Energy Research, Office of Basic Energy Sciences, Materials Sciences Division of the U.S. Department of Energy under Contract No. DE-AC03-76SF00098. M. V. P. Altoé acknowledges the support of FAFESP Brazil.

[1] M. Altoé, M. Lancarotte, H. Rechenberg, F. Missell, and J. Gonzalez, AD-06 presented at INTERMAG 95, San Antonio, Texas, 18–21 April, and to be published in the proceedings.

 0021-8979/96/79(8)/4846/1/$10.00 © 1996 American Institute of Physics

A metallurgical approach toward alloying in rare earth permanent magnet systems (abstract)

D. J. Branagan
Ames Laboratory, United States Department of Energy and Materials Science and Engineering Department, Iowa State University, Ames, Iowa 50011

K. W. Dennis and M. J. Kramer
Ames Laboratory, United States Department of Energy, Iowa State University, Ames, Iowa 50011

R. W. McCallum
Ames Laboratory, United States Department of Energy and Materials Science and Engineering Department, Iowa State University, Ames, Iowa 50011

In bulk permanent magnets, the extrinsic properties relating to the microstructure determined the level of hard magnetic properties that is actually achieved. Many researchers have worked on the microstructure property relationships in the $Nd_2Fe_{14}B$ (2-14-1) system but, in general, the approach has been to analyze the microstructure of materials which have been shown to have good magnetic properties rather than to study the effect of alloy additions on the metallurgical properties of the system. The microstructure which is obtained under a given set of processing conditions is highly dependent on the solidification behavior of the alloy, as well as grain growth phenomena. Alloy additions which effect the solidification behavior of the melt and then form precipitates which pin grain boundaries, and therefore control grain size, should be valuable in producing the uniform microstructure required for good magnetic properties. A number of refractory metal carbides perform both of these functions. The carbides have a reasonable degree of solubility in the 2-14-1 melt and, under conditions of reasonable rapid solidification, a degree of metastable solubility in the 2-14-1 phase. However, there is very limited equilibrium solid solubility in the 2-14-1 phase so that the intrinsic magnetic properties are not effected. The addition of these materials to 2-14-1 results in a factor or three reduction of the quench rate required to produce amorphous material. In addition, the crystallization temperature of the glass is enhanced leading to enhance nucleation and finer grain size during crystallization. Finally refractory metal carbide precipitates decorate the grain boundaries of the crystallized material inhibiting grain growth. Transition metal carbide formation, solid and liquid solubility, effects on solidification, nucleation, and grain growth will be discussed. © *1996 American Institute of Physics.* [S0021-8979(96)64008-3]

This work was performed at the Ames Laboratory, Iowa State University and supported by the Director of Energy Research, Office of Basic Science, U.S. Department of Energy under Contract No. W-7405-ENG-82.

Microstructure and composition in rapidly quenched NdFeB-based hard magnet alloys

Tai D. Nguyen and Kannan M. Krishnan
National Center for Electron Microscopy, Lawrence Berkeley Laboratory, University of California, Berkeley, California 94720

Laura Henderson Lewis, Yimei Zhu, and David O. Welch
Department of Applied Science, Brookhaven National Laboratory, Upton, New York 11973

A detailed study of the microstructure and composition in hot-pressed (MQ-2) and die-upset (MQ-3) magnet alloys based on the $Nd_2Fe_{14}B$ composition, utilizing high resolution and analytical transmission electron microscopy, is reported. The initial magnetic properties of the two samples show different behaviors, which are attributed to the difference in the anisotropy of the grain structure and the grain boundaries. The hot-pressed sample shows faceted grains of the 2-14-1 phase, while die-upset sample shows plate-like grains, together with larger equiaxed grains that contain a speckling of precipitates in the grain interior. The grain structure and composition remain rather similar in the two samples. The grain boundary phase averages ~1–>10 nm in width. The thicker grain boundaries are Nd-rich, while the thinner grain boundaries in the hot-pressed sample exhibit an Fe-rich composition near that of the $NdFe_3$ phase. Nd-rich phases are found at the grain boundary junctions of both samples, with the Nd:Fe ratio near 7:3 in the die-upset sample, and up to 3:2 in the hot-pressed sample. The significance of the microstructure and the grain boundary phases on the magnetic behavior in the two samples is discussed. © *1996 American Institute of Physics.* [S0021-8979(96)38308-9]

INTRODUCTION

Dependence of the magnetic properties in melt-quenched and die-upset magnet alloys on the microstructure and composition is well known; mechanisms for demagnetization in these alloys however is still an area of active debate. Models that have been proposed to explain the behavior of die-upset magnetic alloys include strong pinning model,[1,2] nucleation model,[3] and microcrystalline model.[4] A review of these models is given by Herbst.[5] Observation of the domain structures of a thin die-upset magnet sample in an electron microscope using the Lorentz technique indicates that magnetization proceeds by domain wall motion restricted by pinning at grain boundaries,[6] while investigations on interaction mechanisms by analysis of the time-dependent magnetizing curves after thermal demagnetization agrees with the nucleation-controlled mechanism.[7] Preliminary microstructural studies of die-upset NdFeB samples with the nominal composition $Nd_{13.75}Fe_{80.25}B_6$ show the presence of an Fe-rich phase at the grain boundaries.[8,9] It was proposed that this phase provides possible exchange coupling between grains and potential reversed domain nucleation sites. In this article, we present microstructure and phase analyses of hot-pressed (MQ-2) and die-upset (MQ-3) magnet alloys studied by transmission electron microscopy (TEM). The relationship between the observed microstructure and magnetic properties, and the effects of the secondary and grain boundary phases on the reversal mechanisms in these materials are discussed.

EXPERIMENTAL TECHNIQUES

The magnet alloys were obtained from the General Motors Research and Development Center. Overquenched melt-spun ribbons were consolidated at 750 °C to form the hot-pressed sample; and further deformed at 800 °C to produce the oriented die-upset magnet.[10–12] The magnetic measurements were performed with a quantum design SQUID magnetometer of thermally demagnetized samples.[8] For TEM examination, the materials were ultrasonically cut into 3 mm discs, mechanically thinned and dimpled, and then ion-milled at liquid nitrogen temperature until transparent to the electron beam. They were studied in JEOL 200CX microscopes, operating at 200 kV. The electron beam size used for microanalysis ranged from 10 to 15 nm in diameter.

RESULTS

Comparison of the magnetic data of the two samples measured at 77 °C (350 K) is shown in Figs. 1(a) and 1(b). In general, while both samples display a linear increase in properties with applied field, the die-upset sample acquires its saturation magnetization M_s at lower maximum field than does the hot-pressed sample [Fig. 1(a)]. The initial susceptibility of the hot-pressed sample is substantially lower than that of the die-upset sample, indicating that it is much more difficult to magnetize the former. The hot-pressed sample reaches a much higher coercivity value, but the remanence is poor.

The microstructure of the hot-pressed sample is shown in Fig. 2. It exhibits mostly faceted 2-14-1 nm-sized grains with low-contrast grain boundary regions typically on the order of 2–3 nm [Fig. 2(a)]. Transmission electron diffraction does not reflect any preferred orientations in the grains, similar to results from transmission neutron scattering and transmission x-ray diffraction of similar samples.[13] Shown in the inset is a typical energy dispersive x-ray (EDX) spectrum from the main 2-14-1 phase. Since boron could not be detected with this technique, the ratio of Nd to Fe in this phase is 1:7. EDXs analysis of the thin grain boundary regions indicates an Fe-rich phase with Nd:Fe ratio between 1:4 and

 0021-8979/96/79(8)/4848/3/$10.00 © 1996 American Institute of Physics

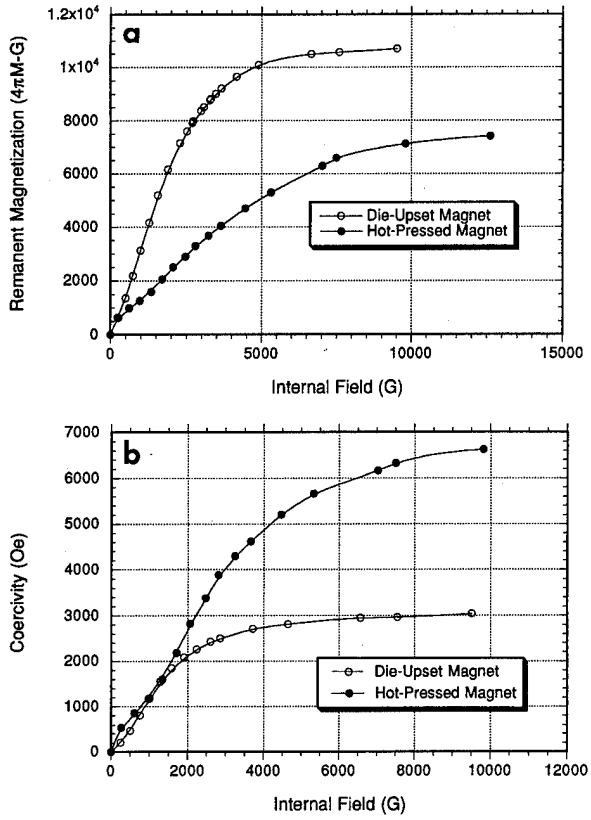


FIG. 1. Development of (a) remanent magnetization B_R and (b) coercivity H_{ci}, with internal field at $T=77$ °C (350 K).

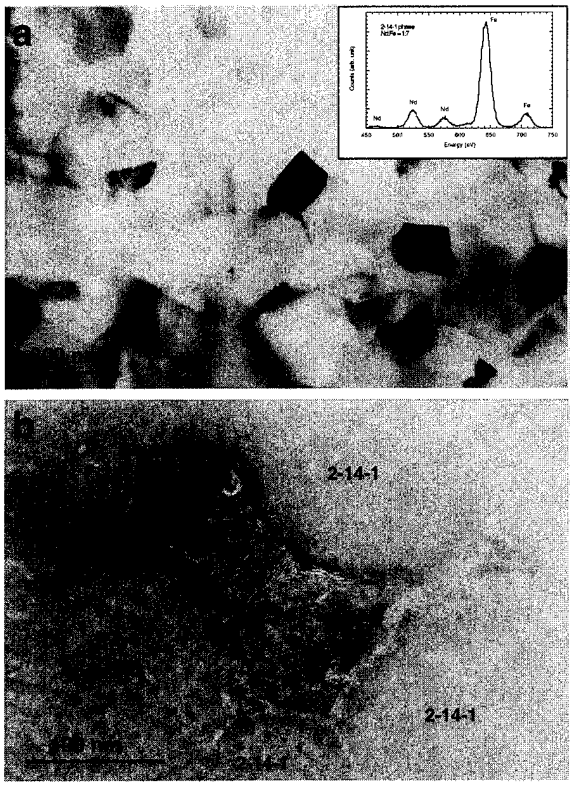


FIG. 2. (a) Grain structure of the hot-pressed sample. The inset shows the EDX spectrum of the 2-14-1 main phase, and (b) high magnification TEM image of a grain boundary junction.

1:5, as has been reported in previous studies on related die-upset magnets.[8,9] The microstructure also contains pockets of noticeably different contrast with sizes up to 10 nm at the junctions between many grains, suggestive of a different phase material. Figure 2(b) shows a high-resolution image of such a grain junction; it has a nanocrystalline structure, a signature of possible recrystallization of this unidentified phase, and a Nd:Fe atomic ratio ranging from 2:3 to 3:2.

The microstructure of the die-upset sample is shown in Fig. 3. It consists of platelike grains, ~600 nm in length by 150 nm in width, together with larger equiaxed grains that contain a speckling of precipitates in the grain interior [Fig. 3(a)]. A second phase, similar to that found in the hot-pressed sample, is also observed at the grain junctions in both the platelike and equiaxed regions of this sample. It too possesses a nanocrystalline structure and a Nd-rich composition, with a Nd:Fe ratio up to 3:1, close to that determined by Mishra.[6,14] Figure 3(b) shows a higher magnification of a platelike region with many of the second-phase pockets. Strong strain contrast is visible around these pockets, which may indicate an incoherent interface between the main 2-14-1 grains and the second-phase grains. The boundaries along the length of the plate-grains are usually free of a grain boundary phase, although it has also been observed that the second phase at the grain junctions in some cases extends into the grain boundaries, but decreases in thickness and eventually diminishes. The exact composition of the materials found in the thin grain boundary region (in the order of 1–2 nm) is in question due to the spreading of the electron beam through both the main-phase grains and the grain boundary phase. EDX spectra show either composition of the main 2-14-1 phase, or of a phase that is rich in Nd compared to the grains.

DISCUSSION

Although the microstructures of the two samples are quite different—the hot-pressed sample has an isotropic structure while the die-upset sample has an anisotropic platelike grain structure—the grain boundary structure and composition remain rather similar. Information obtained during the course of the study can be divided into two categories: that obtained from meso-scale (10 nm range) features and that obtained from fine-scale (1–3 nm range) features. In general, materials in the thinner grain boundary regions are found to be Fe-rich in the hot-pressed microstructure and remain indeterminate in the die-upset microstructure.

The presence of second phases, in the grains and at the grain boundaries and grain boundary junctions, is thought to be responsible for the reversal mechanisms in these magnetic alloys.[1–6] The role that these second phases play however is difficult to ascertain because different studies of similar materials have reported different structures and phase constitution. Mishra and his colleagues reported finding of a bcc structure with a lattice parameter close to that of β-Nd,[15] and Nd-rich phases,[6,14–16] including Nd oxides,[14] in a Nd-rich B-deficient rapidly quenched alloy, while in Nd-rich B-rich alloys, Chu *et al.* reported finding of $Nd_5Fe_2B_6$ grains and amorphous Nd-rich grain boundaries in rapidly quenched

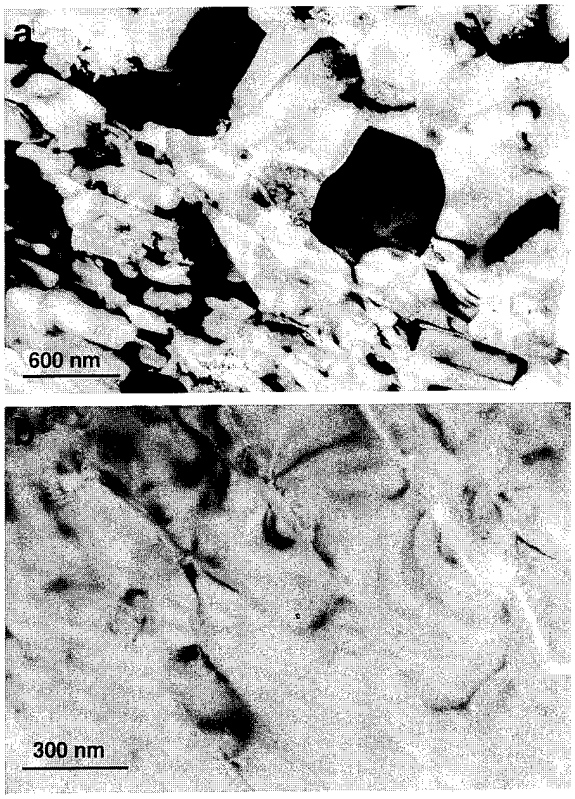


FIG. 3. (a) Grain structure of the die-upset sample showing both platelike and equiaxed grains, and (b) high magnification TEM of the platelike grains showing the strain contrast around the second phase pockets.

samples, and hexagonal structured Nd-rich intragranular precipitates in the hot-pressed samples.[16] Clearly the microstructures and phase constituents are very dependent upon composition and the processing conditions. The effect that these two parameters have upon microstructure, and hence magnetic properties, is not well understood and still is an active area of debate.

In the case of the two related magnets studied here, differences in the magnetic behavior can be explained by microstructural differences, because both the thicker and the thinner intergranular regions were found to have roughly the same composition and structure in both magnets. The grain boundary junctions were observed in both samples, although those in the die-upset sample seem to have a higher Nd:Fe ratio than those in the hot-pressed sample. The higher coercivity in the hot-pressed sample most likely stems from the difficulty in magnetizing randomly oriented grains rather than from the smaller grain size in this case. A finer grain size would be expected to yield a higher coercivity by either (i) reversal by rotation if the particle is too small to sustain a domain wall, or (ii) impedance (pinning) of domain walls by grain boundaries or grain boundary phases. Reversal by rotational processes is unlikely since the grains in the hot-pressed material are not single-domain particles due to magnetostatic and exchange interactions. There is no clear evidence from room-temperature magnetic data for pinning-controlled coercivity; the linear approach to both coercivity and remanence are characteristic of nucleation-controlled reversal.[17] The poor remanence in the hot-pressed sample is thus due to the approximately random orientation of the grains, and alignment of the grains upon die-upsetting is responsible for the increase in the remanence.

The presence of excess iron in the grain boundary phase has several important consequences with regards to intergrain interactions. One result is that it is possible that the grains are exchange-coupled as well as magnetostatically coupled by the presence of a ferromagnetic grain boundary phase. The amount of this intergranular phase found in these magnets however is too small (1–2 vol %) to produce an observable enhanced remanence.[18] However it may allow for the existence of lower-anisotropy sites for the nucleation of reverse domains while reducing the probability of domain wall pinning at the intergranular phase.

CONCLUSIONS

Transmission electron microscopy was used to study the microstructure and composition in hot-pressed (MQ-2) and die-upset (MQ-3) $Nd_2Fe_{14}B$-based magnet alloys. The hot-pressed sample with the nominal composition $Nd_{13.75}Fe_{80.25}B_6$ shows faceted grains of the 2-14-1 phase, while die-upset NdFeB samples having the same bulk composition show platelike grains, together with larger equiaxed grains that contain a speckling of precipitates in the grain interior. The thinner grain boundaries exhibit a Fe-rich composition near that of the $NdFe_3$ phase, while the thicker intergranular phases are Nd-rich. Nanocrystallites with Nd:Fe ratio near 7:3 are also found at the grain junctions in the equiaxed grain regions of the die-upset samples. The initial magnetic properties of the two samples are different, which is attributed to the difference in the anisotropy of the grain structure. The high coercivity and low remnance of the hot-pressed sample result from the random orientation of the grains. The Fe-rich phase at the grain boundaries in both samples could provide exchange-coupling between the grains and sites for possible reverse magnetization nucleation.

[1] Gaunt, Philos. Mag. B **48**, 261 (1983).
[2] F. D. Pinkerton and C. D. Fuerst, J. Appl. Phys. **69**, 5817 (1991).
[3] M. Gronnefeld and H. Kronmuller, J. Magn. Magn. Mater. **88**, L267 (1990).
[4] J. D. Livingston, in *Soft and Hard Magnetic Materials with Applications*, edited by J. A. Salsgiver, K. S. V. L. Narasimhan, P. K. Rastogi, H. R. Sheppard, and C. M. Maucione (ASM, Metals Park, OH, 1986).
[5] J. F. Herbst, Rev. Mod. Phys. **63**, 819 (1991).
[6] R. K. Mishra and R. W. Lee, Appl. Phys. Lett. **48**, 733 (1986).
[7] L. Folks, R. Street, and R. C. Woodward, J. Appl. Phys. **75**, 6271 (1994).
[8] L. H. Lewis, Y. Zhu, and D. O. Welch, J. Appl. Phys. **76**, 6235 (1994).
[9] Y. Zhu, J. Tafto, L. H. Lewis, and D. O. Welch, Philos. Mag. Lett. **71**, 297 (1995).
[10] R. W. Lee, Appl. Phys. Lett. **46**, 790 (1985).
[11] C. D. Fuerst and E. G. Brewer, J. Appl. Phys. **73**, 5751 (1993).
[12] C. D. Fuerst, E. G. Brewer, R. K. Mishra, Y. Zhu, and D. O. Welch, J. Appl. Phys. **75**, 4208 (1994).
[13] L. H. Lewis *et al.* (unpublished).
[14] R. K. Mishra, Appl. Phys. Lett. **62**, 967 (1987).
[15] R. K. Mishra, J. Magn. Magn. Mater. **54-57**, 450 (1986).
[16] T.-Y. Chu, L. Rabenberg, and R. K. Mishra, J. Appl. Phys. **69**, 6046 (1991).
[17] G. C. Hadjipanayis and A. Kim, J. Appl. Phys. **63**, 3310 (1988).
[18] L. H. Lewis (private communication).

Explosive compaction of Magnequench Nd–Fe–B magnetic powders

S. Guruswamy, M. K. McCarter, and J. E. Shield
University of Utah, Salt Lake City, Utah 84112

V. Panchanathan
Magnequench, Delphi(E), General Motors Corp., Anderson, Indiana 46013

Magnequench NdFeB powders having high and low rare earth contents were explosively compacted to obtain cylindrical magnets. The magnetic properties were found to be isotropic and were superior to conventionally consolidated isotropic magnets. The $(BH)_{max}$ was 14.7 MGOe and the remanence was 8.7 kG for the explosively compacted magnet with lower rare earth content. X-ray diffraction patterns confirm the explosively compacted magnet to be crystalline and the predominant phase to be the 2-14-1 phase. Transmission electron microscopy examination showed a microstructure to consist of 20–25 nm size equiaxed grains consistent with the magnetic measurements. © *1996 American Institute of Physics.* [S0021-8979(96)38408-5]

I. INTRODUCTION

High $(BH)_{max}$, use of less strategic Nd, and high concentration of low cost Fe and B have made NdFeB alloys extremely attractive for many high-performance permanent magnet applications.[1–5] With higher $(BH)_{max}$, high power levels and high magnetic fields can be obtained using smaller magnets and consequently the use of NdFeB magnets, with $(BH)_{max}$ in the range of 35–40 MGOe, has resulted in revolutionary developments in the miniaturization of motors, actuators and sensors, and other devices critical to a wide range of industries and technologies.

The Magnequench division of General Motors produces NdFeB magnetic powders by melt spinning ribbons of NdFeB alloy followed by comminution. These powders are used to make polymer bonded magnets, hot pressed isotropic magnets, and hot deformed anisotropic magnets.[1–4] The microstructure developed by these processes consists of grains of the hard magnetic phase $Nd_2Fe_{14}B$ separated by a nonmagnetic grain boundary phase.[1,5–7]

Powders can also be consolidated with shock waves in the appropriate pressure range and duration for a given powder.[8–12] The shock waves may be generated by detonating shaped explosive charge in contact with the powder container or by impact with a high velocity projectile. The pressures in the shock front that moves through the powder are several times the flow stress of the material, typically several GPa. Consolidation occurs by particle deformation followed by extrusion in to the void space. The material near the surface of the particle will see temperature pulses exceeding the melting point over durations that range from microseconds to milliseconds but quickly quenched by heat flow in to the bulk of the powder particle. Thus it is possible to nearly preserve the original microstructures that have been obtained by the rapid solidification processing of the powder. Densities approaching theoretical density can be achieved by a proper choice of pressure and pulse duration. Also effective breakup of adherent oxide film can be achieved minimizing the tendency to fracture along prior particle boundaries.

University of Utah in collaboration with Magnequech is carrying out explosive compaction studies of isotropic and anisotropic powders to obtain full density. This article examines the influence of explosive compaction on the magnetic properties and microstructures of two isotropic NdFeB powders. The two powders, one containing lower amount of rare earth and the other containing an higher amount of rare earth, are examined. The explosively compacted magnets were characterized using x-ray diffraction, scanning electron microscopy and transmission electron microscopy. The magnetic properties were examined with a vibrating sample magnetometer.

II. EXPERIMENTAL WORK

Two isotropic powders used in this study were MQP-A powder and MQP-B powder. The nominal composition of the MQP-A powder was Fe-30.5 wt % total rare-earth-0.9 wt % B and that of powder MQP-B was Fe-5 wt % Co-27.5 wt % total rare-earth-0.9 wt % B. The rare earth component consisted of mainly Nd with 0.5% (max) of Pr and 0.2 wt % (max) of other rare earths. The powders were packed in a copper tube closed at one end with a tight-fitting steel rod. The open end of copper tube was then sealed with a steel cap. The packed density of the powder was ~55%. The cop-

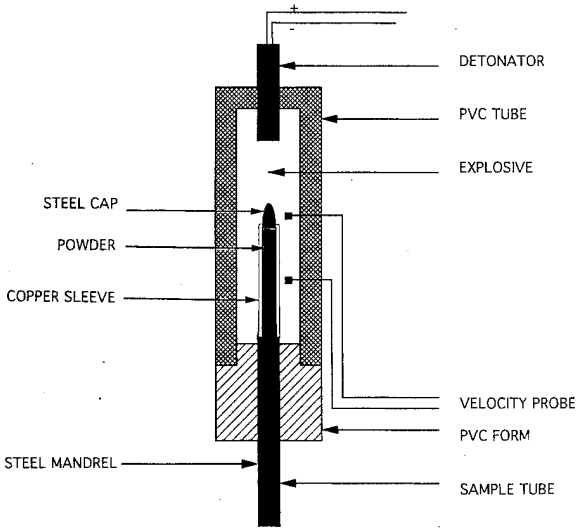


FIG. 1. Explosive container assembly for explosive compaction of NdFeB powders.

 0021-8979/96/79(8)/4851/3/$10.00 © 1996 American Institute of Physics

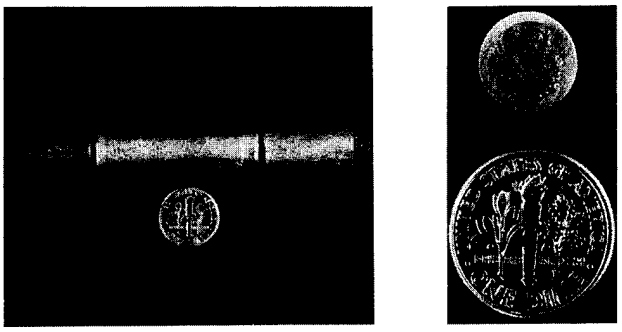


FIG. 2. (a) An explosively compacted NdFeB magnet and (b) micrograph of a cross section of the FeNdB magnet piece shown in (a).

per tube assembly containing the powder was placed centrally in an explosive charge container as shown in Fig. 1. The cylindrical detonator fuse was inserted in the snugly fitting hole in the cap of the PVC container. The liquid-slurry explosive Dyno Nobel 207X was prepared by mixing the two components, perchlorate-base liquid component A and an aluminum-based component B. The mixture was then poured into the container, which was closed with the cap assembly containing the compacted copper tube. The weight of the explosive charge used for the compaction experiments was ~350 g.

Explosive compaction using large amounts of explosive charges as indicated above were performed at the Dyno Nobel facilities just outside of Salt Lake City. The shock wave velocity was measured in several explosive experiments using two triggers placed at different locations of the container. Typical shock wave velocities achieved in these experiments were ~4300 m/s. The detonation velocity is related to the compaction pressure by the following relation,[13]

$$DP=2.325\times10^{-7}\rho(VOD)^2,$$

where VOD is the velocity of detonation in ft/s, DP is the detonation pressure in kbar, and ρ is the density of the explosive mix in g/cc. The resulting compaction pressure was ~6 GPa. The explosively compacted specimens prepared from MQP-A powder and MQP-B powder are hereafter referred to as EC-A and EC-B, respectively.

Optical microscopy and scanning electron microscopy techniques were used to examine the porosity and crack size distribution in EC-A and EC-B specimens. The microstructure was examined by transmission electron microscopy (TEM) using a Jeol 2000 FX II STEM. X-ray diffraction was performed using a Siemens D5000 diffractometer. Differential thermal analysis was carried out using a Perkin Elmer DTA^{-7} system. Specimens 4.5 mm×4.5 mm×4.5 mm in size were used for the magnetic measurements using a vibrating-sample magnetometer (VSM).

III. RESULTS AND DISCUSSION

Figure 2(a) shows an optical micrograph of one of the explosively compacted piece and Fig. 2(b) shows a cross section of the compacted piece. The sample shows in general excellent compaction with some cracking. A central hole is

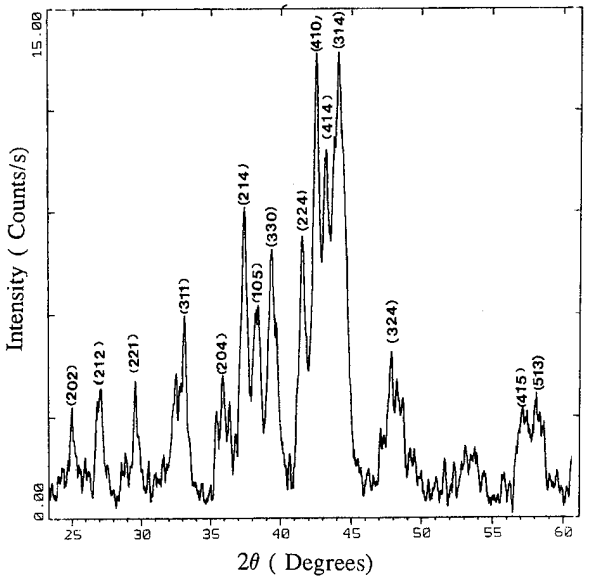


FIG. 3. X-ray diffraction pattern of explosively compacted EC-B magnet.

observed along the axis of the cylindrical piece and this arises from the melting and ejection of material under the focussed energy of the shock waves near the center. The hole is called the Mach stem and results from an excessive consolidation pressure.[9] The size of the hole was observed to decrease in the direction of shock wave propagation and was not observed in over a 5 mm length at the other end. This hole can be eliminated by lowering the detonation pressure or by having an additional copper tube sleeve surrounding the tube that contains the powder.[10,14] The cracks observed arise from the tensile component of the reflected shock waves. These can be minimized or eliminated by controlling the ratio of the explosive charge to the powder, the detonation pressure and the use of a two tube design as mentioned earlier. No significant variation in the porosity distribution

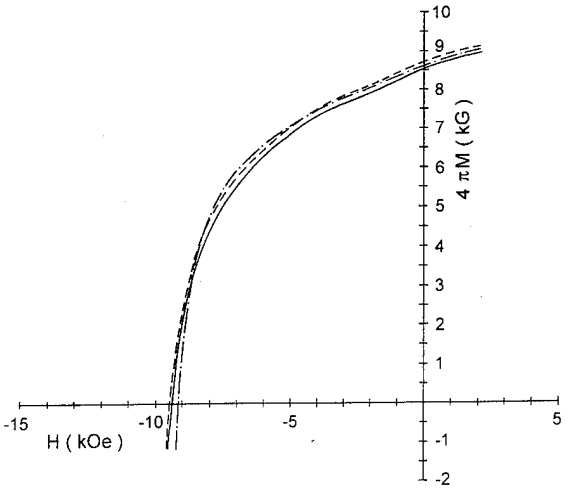


FIG. 4. Demagnetization curves for three orthogonal directions in EC-B magnet.

TABLE I. Magnetic properties of EC-A and EC-B magnet.

Specimen orientation	M_s (kG)	B_r (kG)	H_{ci} (kOe)	BH_{max} (MGOe)
	EC-A magnet			
z-direction	8.6	7.63	14.57	11.41
x-direction	7.94	7.51	14.51	11.03
y-direction	8.00	7.59	14.46	11.53
	EC-B magnet			
z-direction	8.96	8.54	9.41	14.05
x-direction	9.11	8.72	9.47	14.72
y-direction	9.02	8.64	9.17	14.58

and cracking was observed along the length of the compact. The density of specimen EC-A was 7.2 g/cc while the density of EC-B was 7.3 g/cc.

Figure 3 shows an x-ray diffraction pattern obtained for explosively compacted MQP-B powder. The peaks observed correspond to 2-14-1 phase. This confirms that the material is still crystalline and contains predominantly the hard 2-14-1 phase. The amount of other possible phases was small and could not be identified from this pattern. The differential thermal analysis of the compacts revealed a major peak at 1172 °C, corresponding to the melting of the 2-14-1 phase.

Demagnetization curves determined using a VSM in three orthogonal directions showed that the magnetic properties were isotropic in both EC-A and EC-B magnets. Figure 4 shows the demagnetization curves for EC-B magnet. Table I summarizes the values of B_r, H_{ci}, and BH_{max} for the two specimens obtained from the demagnetization curve which shows essentially no difference in magnetic properties measured along the three orthogonal directions. This is expected as the explosive compaction occurs under nearly isostatic compressive pressure conditions and the microstructure of the ribbons are nearly preserved. In Table II, the magnetic properties of bonded isotropic magnets, and hot pressed magnets are compared with the explosively compacted magnets. The BH_{max} values observed are higher and comparable to hot pressed magnets.[3,4] The densities observed in the present EC-A and EC-B specimens are ~95%. The explosive compaction could achieve nearly 100% density

TABLE II. Comparison of magnetic properties of EC-A and EC-B magnets with bonded and hot pressed magnets.[3,4]

Sample	B_r (kG)	H_{ci} (kOe)	BH_{max} (MGOe)
EC-A magnet	7.6	14.5	11.3
EC-B magnet	8.6	9.4	14.5
MQ1-A isotropic magnet	6.3	15.0	9.0
MQ1-B isotropic magnet	6.9	9.0	10.0
MQ2 isotropic hot pressed magnet	8.0	18.0	14.0

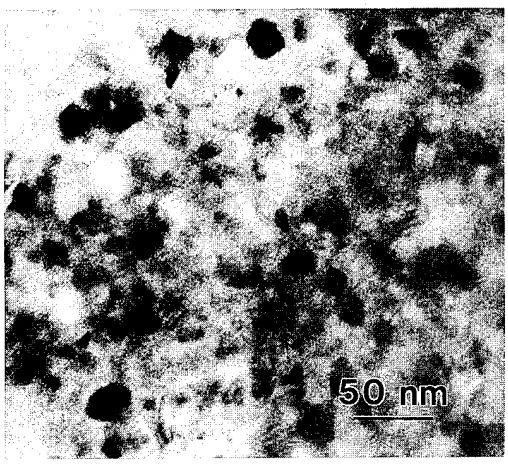


FIG. 5. A TEM micrograph of an EC-B specimen.

and hence a >10% increase in BH_{max} is possible by this processing route which makes this approach very attractive.

Figure 5 shows a TEM image of an EC-B specimen. The microstructure consists of equiaxed grains on the order of 20–25 nm. This microstructure is similar to that observed in the original ribbon. The equiaxed microstructure observed is consistent with the isotropic properties observed for specimens EC-A and EC-B. It is very important to note that the explosive compaction has preserved the rapidly solidified ribbon microstructure and therefore do not have any adverse effects of grain growth. Further TEM work is in progress to understand the enhancement in magnetic properties by explosive compaction.

ACKNOWLEDGMENTS

The support of this work by GM–Magnequench and Dyno Nobel through the provision of materials, experimental facilities, and personnel for the explosive compaction experiments is gratefully acknowledged.

[1] J. J. Croat and J. F. Herbst, Mater. Res. Soc. Bull. **XIII**, 37 (1988).
[2] J. F. Herbst, Rev. Mod. Phys. **63**, 819 (1991).
[3] V. Panchanathan, J. Mater. Eng. **11**, 51 (1989).
[4] J. J. Croat, IEEE Trans. Magn. **MAG-25**, 3550 (1989).
[5] M. Sagawa, S. Hirosawa, H. Yamamotto, S. Fujimura, and Y. Matsuura, Powder Metall. **35**, 785 (1992).
[6] R. K. Mishra, Mater. Sci. Eng. B **7**, 297 (1991).
[7] A. Hutten, J. Met. **44**, 11 (1992).
[8] R. N. Wright, G. E. Korth, and J. E. Flinn, Adv. Mater. Proc. **132**, 56 (1987).
[9] L. E. Murr and K. P. Staudhammer, in *Shock Waves For Industrial Applications*, edited by L. E. Murr (Noyes, Park Ridge, NJ, 1988), pp. 1–57.
[10] M. A. Meyers, N. N. Tadhani, and L. H. Yu, in Ref. 9, pp. 265–334.
[11] *Metals Handbook*, 10th ed. (ASM, Metals Park, OH, 1984), Vol. 7, pp. 305 and 692.
[12] R. Prummer, in *Explosive Welding, Forming and Compaction*, edited by T. Z. Blazynski (Applied Science, New York, 1983), pp. 369–389.
[13] *Explosives and Rock Blasting* (Atlas Powder Company, Dallas, TX, 1987), p. 18.
[14] A. Ferreira and M. A. Meyers, in *Shock-Wave and High-Strain Rate Phenomena in Materials*, edited by M. A. Meyers, L. E. Murr, and K. P. Staudhammer (Marcel Dekker, New York, 1992), pp. 361–370.

The protective coatings of NdFeB magnets by Al and Al(Fe)

C-D. Qin, A. S. K. Li, and D. H. L. Ng
Department of Physics, The Chinese University of Hong Kong, Shatin, Hong Kong

NdFeB permanent magnets are coated by two different methods, dip coating and evaporation coating, with Al. It is found that an intermetallic reaction has occurred and formed a dominant phase of $FeAl_{2.5}B_x$ at the interface between the Al coating and the magnet material. Such reaction enhances strong bonding between the coating and the magnet. When Al(Fe) is used for the coating, no detectable intermetallic phase is observed, and therefore the amount of magnet material is conserved. We have studied the effect of the intermetallic phase on corrosion protection of the magnet. It is found that this phase is less resistive towards HNO_3 solution than pure Al; but it is more resistive towards NaOH and NaCl. The investigation of the changes of microstructures of the coatings under different tempering conditions have also been carried out. The results show that the heat treatment at 500 °C for 10 min for a ~ 2 μm thick Al coating by evaporation can produce an optimal layer of intermetallics. If the temperature is too low, the coating will not adhere to the magnet or if too high, it will fully react with the magnet and produce a rough coating surface.
© *1996 American Institute of Physics.* [S0021-8979(96)38508-1]

I. INTRODUCTION

It is well known that NdFeB type permanent hard magnets possess excellent magnetic properties. However, their large scale commercial applications are hindered partly by their poor corrosion resistance.[1] To improve the corrosion resistance of the magnets, methods such as doping[2,3] and surface coatings by plastic resin, Al or Ni have been employed.[4,5] Whereas the previous works have demonstrated the effectiveness of various coatings under corrosion tests, the microstructure and chemical interaction between the coatings and the magnetic materials have not been fully studied. To carry out further study on the mechanisms of the metallic coatings for corrosion protection of the magnets, we have the NdFeB magnets coated by two different methods, dip coating and evaporation coating, with either Al or Al(Fe) alloy. The interfacial reactions are studied and the intermetallic compounds have been identified. The effect of the various coatings under different processing conditions are evaluated against different corrosion tests.

II. EXPERIMENTAL PROCEDURES

Commercial $Nd_{15}Fe_{77}B_8$ cast ingot was cut into 3 mm × 3 mm × 8 mm blocks. The large surface of each block was polished. These blocks were then coated by two different techniques. In the dip coating method, the sample was dipped either into molten Al or molten Al(3wt%Fe) up to 60 sec at 750 °C. In the evaporation method, the blocks were placed in a vacuum of 3×10^{-5} mbar with vaporized Al. The coated samples were then treated with different tempering conditions in a vacuum of 5×10^{-5} mbar in order to find a suitable tempering condition to produce strong bonding between the coating and the magnet. The final products were cut, polished and tested with different corrosive solutions such as HNO_3, $HCl+10H_2O$, and NaCl and NaOH saturated solution at room temperature. In order to examine the rates of corrosion of the outer layer of Al, the intermetallic phases and the magnetic matrix, we have used a dip coated magnet with relatively thick Al and intermetallic layers (~0.5 mm each) as a result of being heat treated for 30 min at 600 °C for the corrosion test. The sample was corroded in the NaCl+NaOH saturated solution, and its weight was continuously measured by a thermogravimetric analyzer so that the rate of corrosion (which is proportional to the rate of weight loss) can be deduced. Scanning electron microscopy (SEM) and electron probe microanalysis (EPMA) were also employed in this study.

III. RESULTS AND DISCUSSION

A. Heat treatment and microstructures

1. Evaporation coated samples

The evaporation coated magnet with Al is smooth and reflective as a mirror. The coating has a thickness of ~2 μm. When the coated sample is heat treated at 300 °C for 10 min, the Al coating will fall off from the magnet material. One of the possible reasons is because of the differences between the coefficients of thermal expansion of Al and the NdFeB magnet. When the temperature of sample is changed, thermal stresses will build up and destroy the weak interfacial bonding. From the SEM inspections of the fallen Al layer and the magnet substrate, there is no trace of interfacial reaction product. This indicates that the heat treatment of such temperature cannot induce any intermetallic reactions. When a heat treatment at 400 °C was used, the debonding of the Al layer did not occur even though no intermetallic layer was observed as shown in Fig. 1. However, the bonding is weak as indicated by the presence of a groove at the interface. At or above 500 °C, the heat treatment produces an intact magnet coated with Al. Here, we observed that there are intermetallic phases between the coating and the magnet as an evidence to the occurrence of the interfacial reactions. Figures 2(a) and 2(b) show from the top of the evaporation coated Al magnets after the heat treatments of 500 °C and 600 °C for 10 min, respectively. In the former, the intermetallic reaction has not consumed all the Al of the coating. However, the Nd segregated at the grain boundaries of the magnet, is particularly high, has reacted actively with the Al coatings, and the product of the reaction pushed its way up to

 0021-8979/96/79(8)/4854/3/$10.00 © 1996 American Institute of Physics

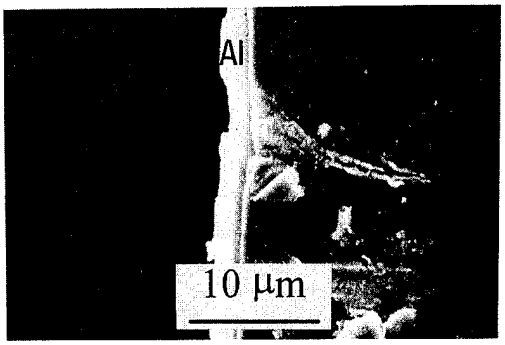


FIG. 1. A cross-sectional view shows no observable intermetallic layer between the Al coating (indicated with mark Al) and the NdFeB magnet (on the right).

the surface and appears as the grain boundary-like pattern as seen in Fig. 2(a). It was determined this intermetallic reaction product to be $Nd_{23\pm3}Fe_{4.5\pm0.4}Al_{73\pm3}$ while the composition of the adjacent Al coating was $Nd_{3\pm0.1}Fe_{18\pm1}Al_{79\pm1}$. The high content of Fe up to 18 at.% found in the Al coating suggested that the solubility of Fe in Al is enhanced by the presence of Nd. For the heat treatment of 600 °C, most of the Al coating is consumed in the intermetallic reaction, thus the surface of the magnet shows the white intermetallic phase as shown in Fig. 2(b). Its composition is found to be $Nd_{4\pm0.5}Fe_{27.5\pm0.5}Al_{68\pm0.5}$, or $FeAl_{2.5}$ for simplicity (the composition of boron cannot be determined by EPMA). On the

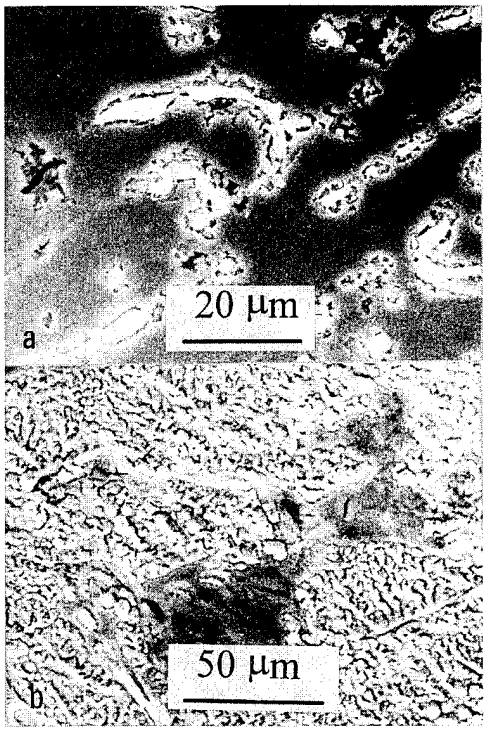


FIG. 2. Two top views of the evaporation coated Al magnet after the heat treatment of 500 °C and 600 °C for 10 min respectively. (a) The bright area are the intermetallic product from the reaction of the Al layer and the Nd segregated at the grain boundary of the magnet. (b) Most of the Al has been reacted with the Nd of the magnet and therefore the coating surface is converted to rough intermetallic phases. Some pieces of Al coating still remain and appear as dark patches.

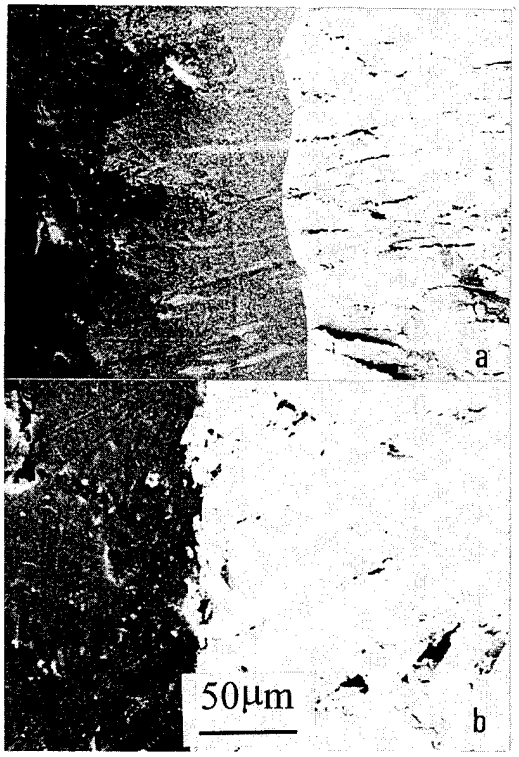


FIG. 3. (a) and (b) are the cross-sections of dip coated samples in Al and Al(3wt%Fe), respectively. The magnet is in bright contrast while the Al and Al(Fe) are in dark contrast.

magnet surface, however, there exist some pieces of reacted Al coating (appears dark in the picture) which have the composition of $Nd_{3\pm0.3}Fe_{20\pm1}Al_{77\pm1.5}$, and are similar to those found in the surface of the 500 °C heat treated samples. This highly reacted coating is not suitable for corrosion protection because its surface is rough and not uniform.

2. Dip coated sample

For the dip coated magnet by molten Al at 750 °C for 30 s, the intermetallic reaction product is $Nd_{3\pm2}Fe_{28\pm1}Al_{69.7\pm1}$, or $FeAl_{2.5}$ for simplicity.[6] As the intermetallic reactions involve an extensive amount of Fe, it is expected that the use of Al(Fe) alloy for coating will reduce the consumption of Fe from the NdFeB magnet, thus the content of the magnet elements can be preserved. To show the different intermetallic reactions for the two coating materials, Al and Al(3wt%Fe), the coating procedures were performed in identical furnace conditions at 750 °C for 1 min. Figure 3(a) shows that an intermetallic phase of ~ 92 μm thick has been formed for Al coating, while Fig. 3(b) shows no obvious intermetallic phase at the interface of the coating and the magnet for the magnet coated by Al(Fe). Nevertheless, both figures show that there is no groove at the interface. However, it is possible that some extent of intermetallic reactions did occur at the interface in the Al(Fe) coated magnet, but has not been resolved by the SEM. Such a result thus shows that Al alloyed with Fe can significantly reduce the consumption of magnet materials. It is recommended that Al

alloyed with Fe should be used for the coating of NdFeB type magnets; or at least it should be used as an intermediate coating layer for Al coating to the magnets.

B. Corrosion tests of the dip coated magnets

When the dip coated magnet is tested in the HNO_3+4H_2O solution, the intermetallic phase appears very stable even after the magnet itself has been fully dissolved by the acid. This shows that such a coating of Fe-Al intermetallic phases can be used for corrosion protection. However, we also find that Al itself is more corrosion resistant to acid dissolution than the Fe-Al phases. Thus, in protecting the NdFeB magnets in the HNO_3 environment Al coating is much more appropriate. In the corrosion test using HCl $+10H_2O$, it is found that the corrosion resistance is in the order of: intermetallic phases > Al > magnet, this is assessed by measuring the relative thickness of each material being dissolved. The results thus suggest that thicker intermetallic phases, produced by higher temperature and longer tempering time of Al coated magnet, is an advantage for the NdFeB magnet being used in the HCl type acidic environment. When the dip coated magnet is tested in the saturated NaOH and NaCl solution, the results show that the corrosion resistance is in the order of: magnet > intermetallic phases > Al. Their rates of weight loss measured by the thermogravimeter are 2.5, 12.7 and 17.3 g/cm^2/min, respectively. Therefore, in the NaOH and NaCl environment, the magnet should be coated with extra thick Al.

IV. CONCLUSIONS

In this paper, we have reported that both evaporation coated and dip coated Al are suitable for the corrosion protective coatings for the NdFeB magnets. It is found that intermetallic reactions at the interface of the coating and the magnet are essential for the firm adhesion of Al layer to the NdFeB magnet materials. The minimum temperature required for the occurrence of a significant intermetallic reaction is around 500 °C for the evaporation coated Al. The intermetallic phases are mainly $FeAl_{2.5}$ based for both evaporation and dip coated coatings. When the magnet is dip coated by Al, large scale intermetallic reaction occurs. As the Al(3wt%Fe) is used for the coating, it is found that there is no observable intermetallic reaction, and the magnet materials have not been disturbed. The corrosion tests show that in HNO_3 solution the order of corrosion resistance is: Al > intermetallic phase > magnet, while in HCl solution it is: intermetallic phase > Al > magnet, and in NaOH+NaCl saturated solution it is: magnet > intermetallic phase > Al.

ACKNOWLEDGMENTS

We thank N. C. Ku, W. Y. Lee, and C. C. Yu for their technical support.

[1] J. M. le Breton and J. Teillet, J. Magn. Magn. **101**, 347 (1991).
[2] M. Shimotomai, Y. Fukuda, A. Fujita, and Y. Ozaki, IEEE Trans. Magn. **26**, 1939 (1990).
[3] K-W Kang, B-C Kim, and J-T Song, J. Mater. Sci.: Mater. Electron. **6**, 4 (1995).
[4] T. Minowa, H. Yoshikawa, and M. Honshima, IEEE Trans. Magn. **25**, 3776 (1989).
[5] P. Mitchell, IEEE Trans. Magn. **26**, 1933 (1990).
[6] *Binary Alloy Phase Diagrams*, edited by T. B. Massalski, J. Murrar, L. H. Bennett, H. Baker, and L. Kacprzak (American Society of Metals, Metals Park, OH, 1986).

Twin screw extrusion of a metal particle dispersion

H. Göktürk[a] and K. Maki
Kao Corporation, Recording and Imaging Science Laboratory, 2606, Akabane, Ichikaimachi, Haga, Tochigi, 321-34, Japan

Twin screw extruder is employed as a mechanical dispersion tool in the processing of particulate media incorporating high specific surface area (SSA) pigments. In this study, the effectiveness of a typical screw configuration used in the processing of formulations containing acicular iron particles of SSA=50 m^2/g was experimentally investigated. During a steady state mixing operation, the extruder was brought to a dead stop, the screws were pulled out and material samples were collected from nine different screw sections. These samples were analyzed to determine the progress of the mixing process as the dispersion flows from section to section. Using SEM micrographs of the material samples, magnetic particle distributions corresponding to different screw sections were identified. The microstructure was observed to change from a granular appearance of aggregates and voids to a coagulated but relatively more uniform distribution of magnetic particles. The state of the dispersion was also magnetically evaluated by probing the magnetostatic interaction in the dispersion samples. Both hysteresis curves and remanence curves of the samples were utilized for this purpose. Interaction parameters associated with the hysteresis curves, such as coercivity, did not exhibit clear trends from section to section. The remanence curves were found to be more appropriate to analyze the state of the dispersion. Peak ΔM values calculated from the remanence curves followed the changes that were observed in the microstructure. It was concluded from the overall results that the extrusion process could be further improved by changes in the screw configuration. © *1996 American Institute of Physics.* [S0021-8979(96)80408-1]

INTRODUCTION

Particulate recording media consist of magnetic particles dispersed in a polymeric binder. Magnetic particles commonly available are gamma iron oxide, cobalt doped iron oxide, chromium oxide, barium ferrite, or metal (mainly iron) powders.[1–3] During the course of development of the particulate media, there has been a shift from iron oxides towards metal particles which are more attractive because of their higher coercivities and higher magnetizations. For example, digital audio tape, one of the newest tape products, employs metal particles. This trend from iron oxides to metal particles has necessitated concomitant improvements in the dispersion preparation methods because metal particles are smaller in size, they have higher specific surface areas and they are more difficult to disperse. One of these improvements is the introduction of a mechanical dispersion method by means of a twin screw extruder.[4] Metal particle dispersion containing a high loading level of the solids is kneaded by the extruder. High shear force deformations generated within the extruder are believed to help break up the aggregates. The motivation of this study is to analyze the twin screw kneading process to understand the dispersive mixing brought about by the extruder and to investigate improvements that can be implemented for pigments presenting greater difficulty of dispersion. Such pigments are considered for the purpose of increasing the recording densities further.[2,5]

MATERIALS AND PROCESSING

The magnetic dispersion used in the study was prepared by using acicular iron particles of length: 180 nm, diameter: 20 nm, specific surface area: 50 m^2/g, and saturation magnetization: 125 emu/g. Carbon black and alumina were also included in the dispersion in small amounts. The binder consisted of a combination of polyvinyl chloride and urethane polyester polymers. The polymers were dissolved in a solvent mixture which included cyclohexanone, toluene, and methyl ethyl ketone. The solids content of the dispersion was 80% by weight and the pigment to polymer ratio was about 5.

The operation of the twin screw extruder involves the selection of a number of parameters including the screw configuration, the rotation rate of the screws, the flow rate of the material, and the process temperatures of different zones. The screw configuration, being the most important parameter in the functioning of the extruder, was chosen as the main subject of the analysis. As the material flows from one section of the extruder into the next, it goes through changes in

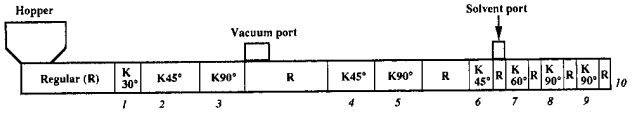


FIG. 1. Scaled schematic view of the screw configuration; screw sections consisting of kneading disks are marked as K and the angle of stagger of the disks is indicated.

[a]On leave of absence from Highly Filled Materials Institute at Stevens, Hoboken, NJ 07030.

 0021-8979/96/79(8)/4857/3/$10.00 © 1996 American Institute of Physics

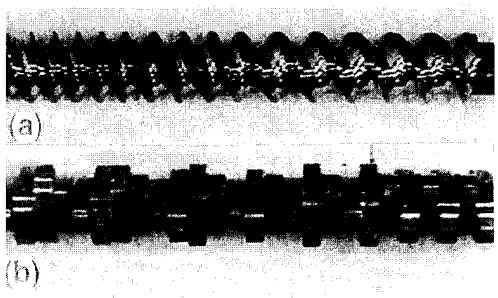


FIG. 2. Examples of (a) regular and (b) kneading screw sections.

terms of the distribution of the ingredients. The objective of the analysis is to understand the effect of different kneading sections on the state of the dispersion.

During a kneading run, the extruder was brought to a dead stop after reaching steady state operation, the screws were pulled out and material samples were collected from nine different kneading sections. Samples of the extrudate (labeled as 10 in Fig. 1) were also included in the study. All the samples were analyzed in terms of their microstructure and macroscopic properties to evaluate the state of the dispersion. The volatiles within the material samples, unavoidably, evaporated during the sample collection, therefore the solids content of the analyzed samples were all the same although the distributions of the constituents were different.

MICROSCOPIC CHARACTERIZATION

The microstructure analysis of the material samples collected from the extruder was based on scanning electron micrographs (SEM) obtained by using a Hitachi SEM, model S-4000. Figure 3(a) shows a sample micrograph of material samples from kneading section 1. The material has a granular appearance consisting of particles and voids. Some of the particles are clumped together in aggregates; individual particles are also observable. Comparison of the microstructure of the samples from kneading section 1 [Fig. 3(a)] with that of kneading section 5 shown in Fig. 3(b) indicates that they have similar features. Microstructure of samples from kneading sections 2 to 4 (not shown) also look like those from kneading sections 1 and 5. These kneading sections occupy a considerable portion of the screw length, yet, the micrographs do not suggest a noticeable change occurring in the microstructure of the dispersion during dry kneading.

A micrograph of the material samples from kneading section 7 is shown in Fig. 3(c). The microstructure is distinctly different from those of sections 1 to 5. The voids seem to disappear, the magnetic particles tend to a coagulated state and their spatial distribution becomes more homogenous. The micrographs of the samples from kneading sections 8 and 9 (not shown) are very similar to that of kneading section 7. The introduction of the solvent into the dispersion between kneading sections 6 and 7 seems to cause a significant change in the microstructure of the material. Section 6 is behind the solvent port, but the material in section 6 also gets affected by the solvent pumped into the extruder.

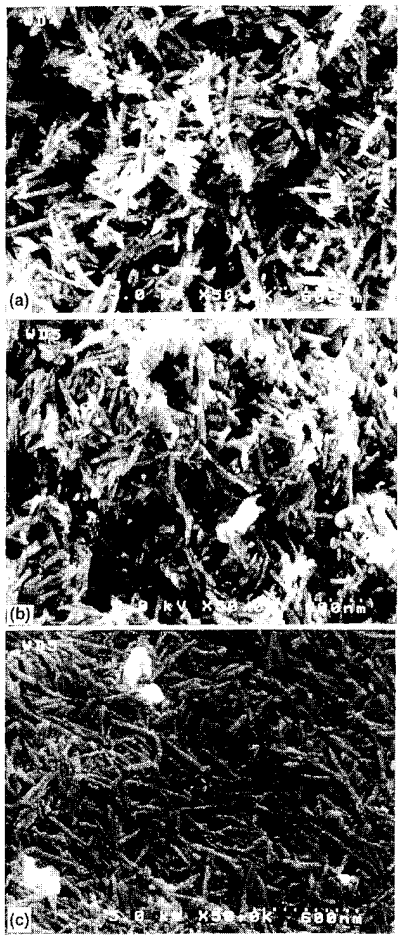


FIG. 3. Micrographs of material samples from kneading sections (a) 1, (b) 5, and (c) 7.

Cutaway views of the material samples, exposed by cutting the samples with the knife accessory of the SEM, were also obtained to see the internal structure. The micrographs of the cutaway sections show that the distribution of the solvent within the dispersion is not uniform in section 7 as indicated by a lack of coagulation in some parts. The solvent distribution improves in sections 8 and 9.

MAGNETIC MEASUREMENTS

Evaluation of the state of the dispersion from a magnetic point of view is very desirable since the dispersion of the study is intended for a magnetic function. The approach that is selected in this study is based on the magnetostatic interaction that exist between the particles of the dispersion. The magnetostatic interaction is inversely related to the separation between the magnetic particles. It is expected that during the kneading process the average inter particle distance would change due to attrition of the aggregates and spatial rearrangements of the particles. Variations in the inter particle spacing would give rise to changes in the intensity of particle interactions. By measuring magnetic parameters which are influenced by inter particle interactions in a well known manner, one can assess the state of the dispersion.

The experimental investigation of magnetic inter particle interactions was performed by measuring the hysteresis and remanence curves of the material samples collected from dif-

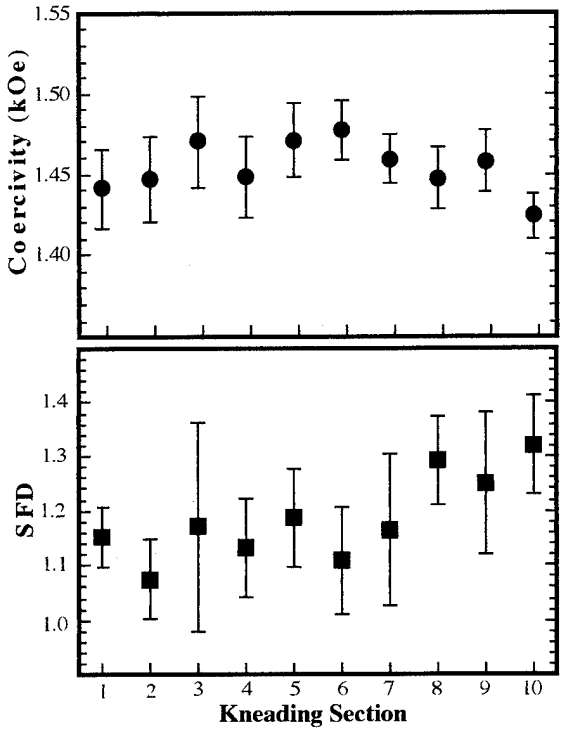


FIG. 4. Variation of the coercivity and the switching field distribution SFD as a function of the kneading section; six samples per data point.

ferent kneading sections by means of a vibrating sample magnetometer, model BHV55 made by Riken Denshi Company of Japan. The material samples from the kneading sections were irregular shapes of solid like texture owing to their relatively high solids content. It was necessary to shape the material in order to ensure that samples placed in the uniform magnetic field of the VSM would also have uniform fields inside. It is known from analytical studies that ellipsoidal shapes satisfy this requirement well. Therefore the samples for magnetic measurements were prepared, by cutting and filing, as low aspect ratio (<10) ellipsoids.

The parameters chosen from the hysteresis curves to understand the intensity of particle interactions included coercivity H_c and switching field distribution SFD. The variation of these parameters with the intensity of inter particle interactions had been studied extensively.[1,3,8,9] For randomly oriented acicular particles, increasing intensity of particle interactions decrease coercivity and broaden SFD. The chosen parameters are plotted in Fig. 4 as a function of the kneading section. The error bars shown in all of the figures represent 95% confidence intervals of the Student's-*t*-Distribution. The hysteresis curve parameters exhibit weak trends from section to section. For example the average coercivity increases about 3% from section 1 to 6 then decreases by the same amount up to section 9. The average SFD values are about the same from sections 1 through 7, whereas, those of sections 8 to 10 have about 10% higher values. Higher SFD values imply increased intensity of inter particle interactions due to smaller inter particle spacing. The size of the error bars generally conceal the trends, but it is clear that sections 6 and 7, where the solvent is introduced, serve as a demarcation point.

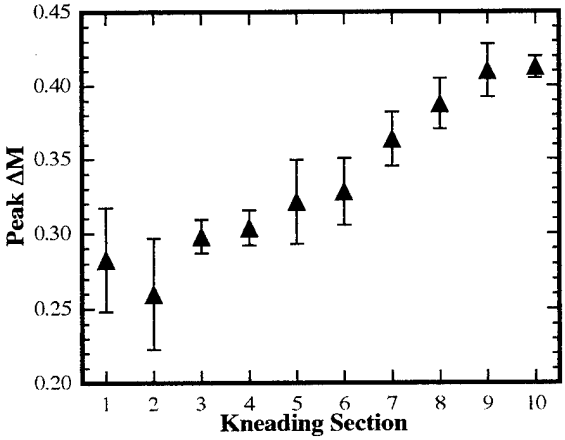


FIG. 5. Variation of the peak ΔM values as a function of the kneading section; six samples per data point.

Inter particle interactions can be also investigated from remanence curves.[3,9,10] The isothermal remanence and the demagnetization remanence curves of the material samples were measured and the ΔM function was calculated from these curves. For randomly oriented acicular particles ΔM is a negative, bell shaped curve with a single maximum. Since ΔM function shows the degree of deviation of the dispersion from the hypothetical case of non interacting particles, the peak value of ΔM was selected as an interaction parameter. The measured peak ΔM values of the material samples are plotted in Fig. 5 as a function of the kneading section. The following information can be deduced from the data: Peak ΔM values pertaining to kneading sections 1 to 5 are very nearly equal. This result confirms the observation that changes in the microstructure of material samples from these sections are not noticeable. Peak ΔM values of kneading sections affected by the solvent addition, i.e., sections 6 to 9, increase regularly. The increase in the intensity of interactions can be anticipated from the coagulation observed in the micrographs. Peak value of ΔM serves as an indicator of the degree of coagulation, which is difficult to quantify from the micrographs. The increase in the peak ΔM values does not level off towards the end of the extruder. The change in peak ΔM from kneading section 7 to 8 and 8 to 9 are about equal. Likewise, the size of the error bars are about the same in sections 7, 8, and 9. These results suggest that the mixing performed after the solvent addition might be incomplete.

[1] G. Bate, Proc. IEEE **74**, 1513 (1986).
[2] M. P. Sharrock, IEEE Trans. Magn. **25**, 4374 (1989).
[3] E. Köster and T. C. Arnoldussen, in *Magnetic Recording Handbook, Technology and Applications,* edited by C. D. Mee and E. D. Daniel (McGraw-Hill, New York, 1990), pp. 101–257.
[4] D. H. Davies, in *Technological Applications of Dispersions, Surfactant Science Series, Vol. 52,* edited by R. McKay (Dekker, New York, 1994), pp. 443–456.
[5] H. J. Richter (preprint of invited paper at Intermag 1995).
[6] D. M. Kalyon and H. Sangani, Polym. Eng. Sci. **29**, 1018 (1989).
[7] D. M. Kalyon, C. Jacob, and P. Yaras, Plast. Rub. Comp. Proces. Appl. **16**, 193 (1991).
[8] A. R. Corradi and E. P. Wohlfart, IEEE Trans. Magn. **14**, 861 (1978).
[9] G. W. D. Spratt, N. Kodama, H. Inoue, Y. Uesaka, and M. Katsumoto, IEEE Trans. Magn. **27**, 4660 (1991).
[10] D. E. Speliotis and W. Lynch, J. Appl. Phys. **69**, 4496 (1991).

Preparation of acicular iron nanoparticles by the reduction of ferrous salt in the presence of tubular lecithin assemblies

Jason L. Cain and David E. Nikles
Department of Chemistry and Center for Materials for Information Technology, University of Alabama, Tuscaloosa, Alabama 35487-0336

Ferromagnetic α-Fe particles were prepared by reduction of Fe^{2+} in the presence of tubular lecithin assemblies found in lecithin/cyclohexane/water association colloids. The particles consisted of both large single- and multi-domain acicular rods, 0.25–5 μm in length with a length to width ratio of at least 6:1, encapsulated in lecithin. The coercivity depended on the reaction medium and ranged from 7 to 131 Oe. The highest coercivity particles were obtained in the cyclohexane-rich region of the ternary phase diagram. © *1996 American Institute of Physics.* [S0021-8979(96)07108-3]

INTRODUCTION

There are many reports of the preparation of nanometer size magnetic particles formed in reverse micelles. Magnetite particles were prepared by precipitation of mixtures of $FeCl_2$ and $FeCl_3$ in aerosol OT (AOT)/water/isooctane[1] or AOT/water/cyclohexane[2] microemulsions. Barium ferrite nanoparticles were prepared by coprecipitation of precursor carbonates in cetyltrimethylammonium bromide (CTAB)/water/butanol/octane microemulsions, followed by calcining.[3] Cobalt[4] or iron[5] nanoparticles were prepared by sodium borohydride reduction of Co^{2+} or Fe^{2+} solubilized in AOT/water/hydrocarbon microemulsions.

Our objective is to prepare acicular iron particles with a particle size of 50 nm and a coercivity of greater than 2000 Oe. The approach is to use association colloids as templates to control the size and shape of iron particles formed in their presence. Reverse micelles are mixtures of surfactant, oil, and water where a monolayer of surfactant separates the water from the oil. Of the many ternary systems that have been shown to form reverse micelles, the one of most interest to this work is the lecithin/cyclohexane/water system, Fig. 1.[6,7] When water is added to hydrocarbon solutions of soybean lecithin until the value of w (the molar ratio of water to surfactant) exceeds 1, there is a huge increase in solution viscosity.[8] Light scattering and neutron diffraction experiments have shown that the lecithin forms long, flexible tubes with an aspect (length to diameter) ratio approaching 100.[9] We have reported that reduction of Fe^{2+} in these tubes led to chains of spherical α-Fe particles trapped in the tubular assemblies.[10] Here we report our attempts to control the reduction process in order to prepare acicular iron particles.

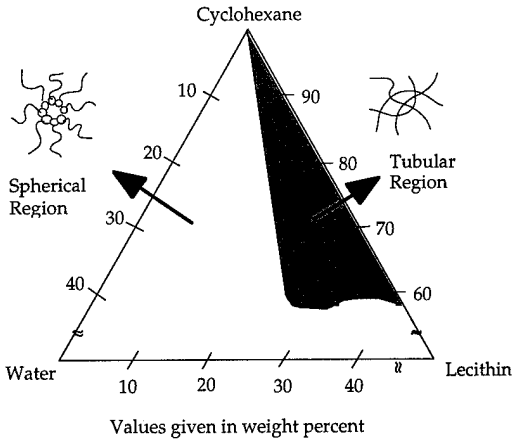


FIG. 1. A portion of the lecithin/cyclohexane/water ternary phase diagram (Refs. 1 and 2).

EXPERIMENT

Soybean lecithin (purified grade, Fisher Scientific) was dissolved in cyclohexane (HPLC grade, Fisher Scientific) by stirring for 12 h. The next day a 0.15 M solution of ferrous chloride in water was added to the lecithin/cyclohexane solution. The volume of solution was selected to control the composition of water in the colloid. This mixture was allowed to stir vigorously for 15 min, then gently for 3 h, to assure the solution was completely mixed. The solution was allowed to equilibrate for two days after stirring. Over the two day period the mixture separated into two phases. The upper phase, yellow and transparent, consisted of cyclohexane and lecithin, and was discarded. The viscous, turbid,

TABLE I. Summary of coercivity data for iron particles prepared in lecithin/cyclohexane/water association colloids.

Trial	Lecithin	Cyclohexane	w	H_c (Oe)
1	6.76	83.33	40.58	29
2	8.31	79.18	41.65	28
3	9.75	75.00	43.30	7
4	11.57	71.07	41.50	48
5	12.70	66.67	44.96	131
6	13.85	63.08	46.11	56
7	14.93	59.70	47.03	31
8	16.30	56.16	46.73	42
9	17.13	52.80	48.56	39
10	17.57	50.00	51.08	17
11	17.86	47.08	54.33	40
12	8.05	76.69	52.42	12
13	9.92	72.73	48.42	20
14	11.20	68.80	49.40	29
15	12.40	65.12	50.15	55
16	13.06	61.57	53.75	23
17	15.38	54.55	54.08	39

 0021-8979/96/79(8)/4860/3/$10.00 © 1996 American Institute of Physics

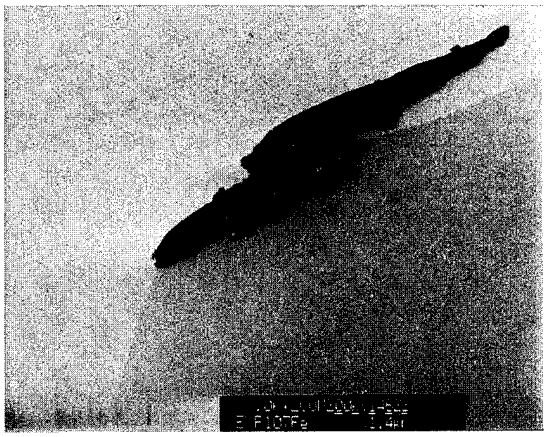


FIG. 2. Acicular iron particles made in trial 5.



FIG. 4. Acicular iron particles made in trial 3.

lower phase was used for reduction experiments. Sodium borohydride was added to the lower phase in the presence of an applied magnetic field of 1200 G, whereupon a black precipitate immediately formed. The supernatant liquid was decanted from the particles and the particles were rinsed three times with cyclohexane, then twice with ethanol. The particles were dried in an oven under ambient atmosphere at 125 °C overnight. Residual lecithin coated the particles and somewhat protected them from air oxidation. This allowed a day or so to obtain structural or magnetic data, before the particles corroded. After drying, the particles were characterized by vibrating sample magnetometry, x-ray diffraction, and transmission electron microscopy.

RESULTS AND DISCUSSION

Reduction of Fe^{2+} in lecithin/cyclohexane/water ternary systems gave iron particles that were either superparamagnetic or ferromagnetic, depending on the reaction conditions. X-ray diffraction showed only one peak: the α-Fe (110) reflection at $d=202.7$ pm. The data in Table I shows the effect of reaction conditions on the magnetic properties of the iron particles. Trials 4 and 5 gave ferromagnetic hysteresis loops, while the other trials gave loops that the showed superparamagnetic and ferromagnetic components. Transmission electron micrographs, Figs. 2–4, show the structures of the resulting iron particles. Figures 2 and 3 show micrographs of the highest coercivity iron particles prepared in trial 5. These were large acicular structures with diameters from 150 to 800 nm and length to width ratios of at least 10:1. Particles generated from trial 3, Fig. 4, were large, acicular, multidomain iron structures and agglomerates surrounded by tubular lecithin assemblies. These lecithin tubules had diameters of approximately 100 nm, with micrometer lengths. These structures were commonly found for the samples having a high superparamagnetic fraction. Most trials yielded particle structures very similar to those found in trial 3.

We were surprised that the reduction in a magnetic field led to acicular iron particles. This result was in contrast to our earlier report[10] of the formulation of chains of iron spheres by the same procedure, in the absence of a magnetic field. There has been a report of high coercivity Fe/Co alloy particles formed by borohydride reduction in aqueous solutions in the presence of a magnetic field;[11] those particles consisted of chains of spheres. In all our trials there was a significant fraction of spherical iron particles, not shown in the TEM photographs. The presence of the spherical particles indicates that we do not have adequate control of the particle formation. Future work will be directed at achieving control of the process, so that we can prepare acicular particles with a 50 nm size.

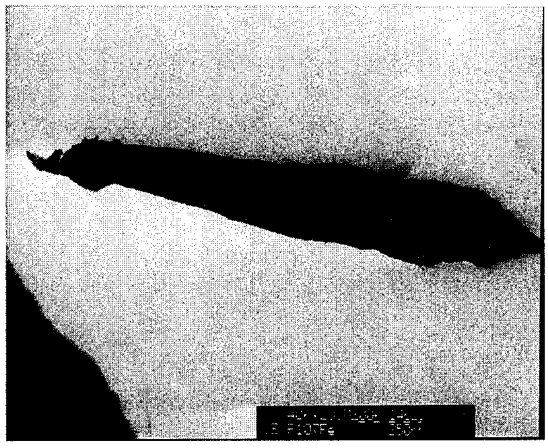


FIG. 3. Acicular iron particle made in trial 5.

ACKNOWLEDGMENT

This work was supported primarily by the MRSEC Program of the National Science Foundation under Award Number DMR-9400399.

[1] M. Gobe, K. Kon-No, K. Kandori, and A. Kitahara, J. Colloid Interfac. Sci. **93**, 293 (1983).

[2] K. M. Lee, C. M. Sorensen, K. J. Klabunde, and G. C. Hadjipanayis, IEEE Trans. Magn. **28**, 3180 (1992).

[3] V. Pillai, P. Kumar, M. S. Multani, and D. O. Shah, Colloids Surfaces A **80**, 69 (1993).

[4] J. P. Chen, K. M. Lee, C. M. Sorensen, K. J. Klabaunde, and G. C. Hadjipanayis, J. Appl. Phys. **75**, 5876 (1994).

[5] J. Rivas, M. A. Lopez-Quintela, J. A. Lopez-Perez, L. Liz, and R. J. Duro, IEEE Trans. Magn. **29**, 2655 (1993).
[6] P. Schurtenberger and C. Cavaco, Langmuir **10**, 101 (1994).
[7] P. Schurtenberger, Q. Peng, M. E. Leser, and P.-L. Luisi, J. Colloid Interfac. Sci. **156**, 46 (1993).
[8] R. Scartazzini and P. L. Luisi, J. Phys. Chem. **92**, 829 (1988).
[9] P. Schurtenberger, L. J. Magid, S. M. King, and P. Lindner, J. Phys. Chem. **95**, 4173 (1991).
[10] J. L. Cain, S. R. Harrison, J. A. Nikles, and D. E. Nikles, J. Magnet. Magn. Mater. (in press).
[11] A. Watanabe, T. Uehori, S. Saitoh, and Y. Imaoko, IEEE Trans. Magn. **17**, 1455 (1981).

Iron particle surface chemistry and corrosion protection by amine-quinone polyurethanes

Antony P. Chacko and David E. Nikles
Department of Chemistry and Center for Materials for Information Technology, The University of Alabama, Tuscaloosa, Alabama 35487-0336

The ability of amine-quinone polyurethanes to protect iron particles from corrosion was shown to depend on the polymer composition and on the particle surface chemistry. The amine-quinone polyurethanes were prepared from 2,5-bis(*N*-2-hydroxyethyl-*N*-methylamino)-1,4-benzoquinone (AQM-1), tolylene diisocyante and polytetrahydrofuran diol (average molecular weight 650). The AQM-1 content was varied from 20 to 40 wt % (AQPU-15); the polymer with 40 wt % AQM-1 had the highest affinity for the iron surface and showed the best corrosion protection. AQPU-15 had a higher affinity for the commercial iron particle having a aluminum-rich surface, than for a commercial particle having a silicon-rich surface. Tape samples containing AQPU-15 and the particles having the Al-rich surface showed excellent corrosion resistance, maintaining 98% of the initial saturation magnetization after 48 h exposure to *p*H 2 aqueous buffer. Samples containing AQPU-15 and the particles having the Si-rich surface completely corroded after 2 h exposure. The presence of aluminum on the iron surface served to enhance the adsorption of AQPU-15 and improve the corrosion resistance. © *1996 American Institute of Physics.*
[S0021-8979(96)07208-X]

INTRODUCTION

Organic coatings protect metals from corroding through interposition of a continuous, adherent, high resistance film between the metal surface and its environment, to achieve a mechanical exclusion of the environment from the metal surface. However this mechanical exclusion is never achieved practically since all continuous organic films are permeable to some degree to moisture and many coatings have occasional physical defects or acquire them in service. Another practical way of corrosion protection is by the use of corrosion inhibitors.[1] Organic compounds such as amines, acetylenic alcohols, and heterocyclic compounds have been used as inhibitors for industrial applications. The corrosion inhibition efficiency of an organic compound is mostly dependent on its adsorption onto the metal surface. This adsorption involves replacement of moisture by the organic inhibitor at the interface between coating and metal surface. The adsorption of these organic compounds is influenced by the presence of functional groups such as =NH, -N=N-, -CHO, R-OH and R=R in the inhibitor molecule.[2] Slavcheva *et al.*[3] found a definite relation between protective action and the variation of the chemical structure in a given reaction series. For effective corrosion protection, these compounds should

(i) be polymeric,
(ii) form a compact barrier film,
(iii) chemisorb onto metal surfaces, and
(iv) have high adsorption energy on the surface.[2]

The discovery of the excellent adhesion of quinone amine polymers to iron surfaces and the further demonstration of their corrosion protection have been reported by Erhan and coworkers.[4–6] Muralidhran *et al.* investigated in detail recently the corrosion inhibiting property of an amine quinone oligomer (M_n=1150) made by electropolymerization.[7,8] They demonstrated the corrosion inhibition of iron and steel by these polymers. We have demonstrated that polyurethane binders containing a 2,5-diamino-1,4-benzoquinone functional group in the polymer chain, amine-quinone polymers, inhibit the corrosion of commercial iron particles.[9] In this study amine-quinone polymers were further evaluated for their corrosion protection properties. The influence of polymer structure and metal particle surface chemistry on corrosion protection was investigated in an ongoing effort to understand the corrosion protection mechanism of metal particles by amine-quinone polymers.

EXPERIMENT

Three different amine-quinone polymers were prepared by melt polymerization of the three monomers 2,5-bis(*N*-2-hydroxyethyl-*N*-methylamino)-1,4-benzoquinone (AQM-1), tolylene diisocyante (TDI), and polytetrahydrofuran diol (Terathane® 650, average molecular weight 650). The polymers differed by the AQM-1 content; AQPU-13 contained 20 wt % percent, AQPU-15 contained 40 wt %, while AQPU-16 contained 30 wt %. Details of the polymer synthesis and physical properties were reported earlier.[10] Two different commercial polyvinylchloride wetting binders, PVC-1 and PVC-2, were used for comparison. Commercial iron particles from two different vendors, MP-1 (specific surface area 54 m^2/g, H_c 1500 Oe, and σ_s 122 emu/g) and MP-2 (specific surface area 48 m^2/g, H_c 2000 Oe, and σ_s 145 emu/g), were obtained. Electron microprobe analysis showed MP-1 to contain 96% Fe, 3.7% Al and 0.2% Si. MP-2 had 80% Fe, 12.8% Co, 2.9% Ni, and 3.8% Si. The microprobe was not sensitive to the oxygen in the particles and the reported composition does not include the oxygen content.

The adsorption behavior of the amine-quinone polyurethanes onto metal particles was studied by exposing the metal particles to solutions of the polymers in tetrahydrofuran (THF) for a period of seven days with continuous agitation. After seven days, the dispersion of metal particles in polymer solution was allowed settle for a day, the superna-

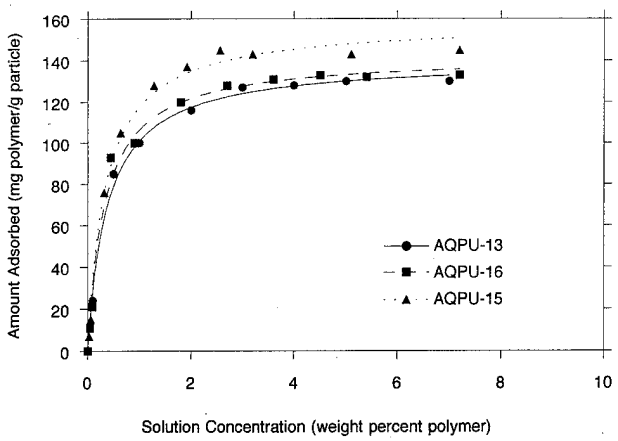


FIG. 1. Adsorption isotherms for amine-quinone polymer adsorption from THF solution onto commercial iron particles, MP-1.

tant solution decanted from the particles, the solution filtered through a 2.0 μm pore size filter to remove any suspended particles. The concentration of polymer remaining in the supernatant solution was determined by spectrophotometry. The amount of polymer adsorbed onto the iron particles was calculated from the initial volume and concentration of the polymer solution and the concentration of the supernatant solution.

MP samples were prepared by dispersing the iron particles in a cyclohexanone solution of a polymer, either an amine-quinone polymer or a polyvinylchloride. The dispersions were cast onto polyester base films using a hand drawdown apparatus that longitudinally oriented the particles. The coatings were dried in a convection oven at 60 °C overnight. The MP tape samples were exposed to *p*H 2.00 aqueous buffer (sulfamic acid/potassium phthalate buffer) or to 80 °C and 80% relative humidity in a Tenney Th Jr. temperature/humidity chamber. The samples consisted of 6-mm-diameter circles punched from the hand-drawn coatings. They were exposed for a period of time, the saturation magnetization determined by vibrating sample magnetometry (14 kOe saturation field), and then returned for more exposure.

RESULTS AND DISCUSSION

The amine-quinone polymers have a two-phase microstructure consisting of a discrete, crystalline hard segment phase in a continuous, amorphous soft segment phase.[11] The amine-quinone monomer is in the hard segment phase and the degree of phase segregation increases with increasing AQM-1 and content. Our model for corrosion protection of iron particles by amine-quinone polymers is the strong adsorption of the amine-quinone functional group to the particle surface. This leads to a crystallization of the hard segment around the particle surface, providing a crystalline barrier against diffusion of oxygen and moisture to the surface.

The AQM-1 content in the amine-quinone polymers has an influence on the adsorption behavior of the polymers to the iron particles, MP-1. The adsorption isotherms, Fig. 1, show that AQPU-13 and AQPU-16 had a similar adsorption behavior, while AQPU-15 had an increased adsorption capacity. The isotherms obeyed the Langmuir model, Eq. (1), and fits of the equation to the data gave the Langmuir parameters of capacity (A) and affinity (B) in Table I. The Langmuir affinity for the three polymers were similar, however the Langmuir capacity was highest for AQPU-15. Repeated attempts to measure adsorption isotherms for adsorption of the commercial polyvinyl chlorine wetting binders gave irreproducible results and we have chosen not to report the data here.

TABLE I. Langmuir parameters for adsorption of amine-quinone polyurethanes onto MP-1 iron particles from THF solution.

Polymer	AQM-1 content	Capacity (A)	Affinity (B)
AQPU-13	20%	140±2	2.59±0.23
AQPU-15	40%	158±3	2.91±0.31
AQPU-16	30%	142±3	3.00±0.40

$$\theta = A\,\frac{BC}{1+BC} \tag{1}$$

Commercial iron particles have a ceramic surface coating that serves to inhibit sintering during particle synthesis and also passivates the particles against corrosion. The particles used in this work had very different ceramic compositions. MP-1 was aluminum-rich with very little silicon, while MP-2 was silicon-rich with no detectable aluminum. Adsorption isotherms for adsorption of AQPU-15 from THF solution showed a very different behavior for the two particles. These two particles had different specific surface areas and for comparison the amount of polymer adsorbed was expressed per specific area of the particle. MP-1 had a Langmuir capacity, $A = 6.00 \pm 0.00$ mg/m^2 and a Langmuir affinity coefficient, $B = 0.98 \pm 0.00$, while MP-2 had $A = 4.14 \pm 0.35$ mg/m^2 and $B = 0.77 \pm 0.21$. AQPU-15 had a preferential affinity towards MP-1, which had an aluminum-rich surface oxide.

Metal particle tapes prepared using amine quinone polymers and commercial metal particles were exposed to different corrosive environments to study the corrosion protection capability of these polymers. For comparison purposes, MP tape samples containing commercial polyvinylchloride wetting binders were also studied. Two accelerated corrosion conditions, *p*H 2 aqueous buffer and 80 °C and 80% relative humidity were selected. The extent of corrosion of iron pigment was determined by measuring the relative loss in bulk magnetic properties as a function of time exposed to the corrosive conditions. Figure 2 is a plot of relative saturation magnetization as a function of exposure time. The MP sample made with commercial polyvinyl chloride wetting binders, PVC-1 and PVC-2, completely corroded (complete loss of bulk magnetic properties) after only 2 h exposure to *p*H 2 buffer. The MP samples containing amine-quinone polymers showed excellent stability in *p*H 2 aqueous buffer solution for many hours. A similar, though less, dramatic trend in corrosion protection was found for MP samples exposed to 80 °C and 80% relative humidity, Fig. 3. MP tapes containing amine-quinone polymers showed better retention

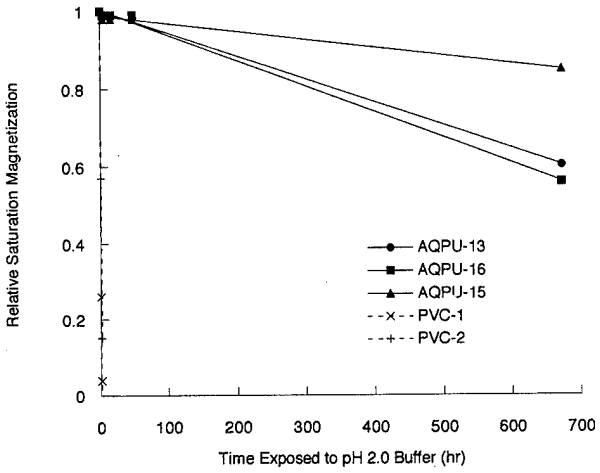


FIG. 2. Plot of relative saturation magnetization as a function of exposure time for MP tapes exposed to *p*H 2.0 aqueous buffer.

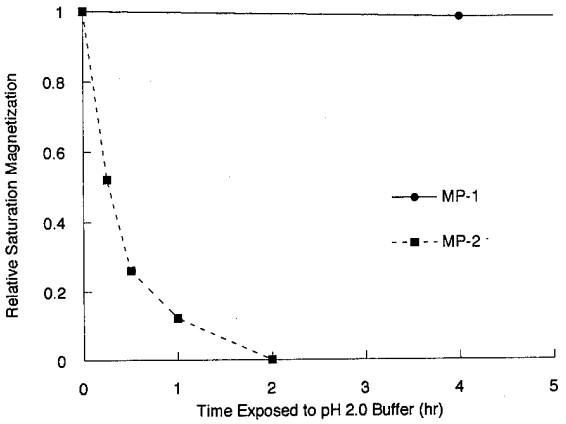


FIG. 4. Plot of relative saturation magnetization as a function of exposure time for MP tapes exposed to *p*H 2.0 aqueous buffer.

of magnetic properties than MP tapes prepared from the polyvinylchloride wetting binders. Among the amine-quinone polyurethanes, MP samples prepared from AQPU-15 (having 40% AQM-1 and the highest affinity for the particle surface) showed the best corrosion protection, while AQPU-13 (having 20% AQM-1 and a lower affinity for the particle surface) showed least corrosion protection. This better coverage of particle surface afforded by AQPU-15 led to better protection of particle surface from corrosive *p*H 2 aqueous buffer solution.

MP samples containing AQPU-15 and either MP-1 or MP-2 showed very different corrosion behavior when exposed to *p*H 2 buffer, Fig. 4. MP-1 particles having an aluminum-rich surface and a higher Langmuir capacity for AQPU-15, had an excellent stability against corrosion. MP-2 particles having a silicon-rich surface and a much lower Langmuir capacity for AQPU-15, completely corroded after 2 h exposure. This difference in the ability of the amine-quinone polymer to protect the iron particles from corrosion may be due to the difference in surface sites, arising from the different ceramic coatings. However, we can not rule out the possibility that this difference may be due to the presence of Co and Ni in MP-2, which may make this particle intrinsically more susceptible to corrosion. This question will be addressed when we obtain iron particles, having the same ceramic surface chemistry, but different levels of Co and Ni.

Our early success in inhibiting the corrosion of commercial iron particles, MP-1, by using amine-quinone polymers led us to expect that amine-quinone polymers would protect all grades of iron particles from corrosion. The results clearly showed that both the adsorption behavior and corrosion protection were influenced by the composition of metal particles. Clearly the amine-quinone polymers have a preference for iron particles having aluminum in their surface ceramic layer.

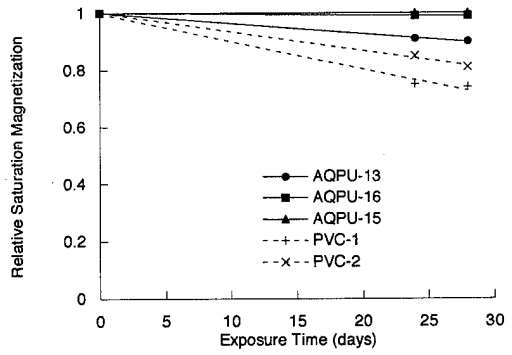


FIG. 3. Plot of relative saturation magnetization as a function of exposure time for MP tapes exposed to 80 °C and 80% relative humidity.

ACKNOWLEDGMENTS

This work was supported in part by the Sponsors of the Center for Materials for Information Technology and by the Department of Defense Advanced Research Projects Agency through a grant administered by the National Storage Industry Consortium.

[1] M. Sratman, R. Feser, and A. Leng, Electrochim. Acta **39**, 1207 (1994).
[2] S. Sathyanarayan, K. Balkrishnan, S. K. Dhawan, and D. C. Trivedi, Electrochim. Acta **39**, 831 (1994).
[3] E. Slavcheva, E. Sokolova, and S. Raicheva J. Electroanal. Chem. **360**, 271 (1993).
[4] K. Kaleem, F. Chertok, and S. Erhan, Prog. Org. Coating **15**, 63 (1987).
[5] S. Erhan, U. S. Patent 4,882,413, 1989.
[6] T. A. Reddy and S. Erhan, J. Appl. Polym. Sci. **51**, 1591 (1994).
[7] K. L. N. Phani, S. Pitchumnani, S. Muralidharan, S. Ravichandran, and S. V. K. Iyer, J. Electroanal. Chem. **353**, 315 (1993).
[8] S. Muralidharan, K. L. N. Phani, S. Pitchumnani, S. Ravichandran, and S. V. K. Iyer, J. Electrochem. Soc. **142**, 1478 (1995).
[9] J.-L. Liang and D. E. Nikles, IEEE Trans. Magn. **29**, 3649 (1993).
[10] R. I. Webb, A. P. Chacko, and D. E. Nikles, Polymer Preprints **35**, 769 (1994).
[11] D. E. Nikles, J.-L. Liang, J. L. Cain, A. P. Chacko, R. I. Webb, and K. Belmore, J. Polym. Sci. A **33**, 2881 (1995).

Synthesis and magnetic properties of electrodeposited metal particles on anodic alumite film

Xiaohua Bao,[a] Feiyue Li, and Robert M. Metzger
Department of Chemistry and Center for Materials for Information Technology, University of Alabama, Tuscaloosa, Alabama 35487-0209

Elongated metal particles have been prepared by depositing transition metals into the pore channels of anodic aluminum oxide (alumite), with well-defined pores that build up into uniform and parallel channels. The highest coercivity for freshly prepared α-Fe particles in the alumite substrate reached 2700 Oe in the easy direction. The remanance curves of alumite films containing electrodeposited metals (Fe and Co) were measured to study the magnetostatic interaction of the particles. The possible reversal mechanisms of the metal particles in the alumite substrates were examined by the rotational hysteresis integral and the angular variation of the coercivity. © *1996 American Institute of Physics.* [S0021-8979(96)06808-6]

I. INTRODUCTION

Needle-shaped α-Fe or metal alloy particles, prepared by electrodeposition of metal into the parallel micropores of anodized aluminum substrate, have been considered as potential candidates for both perpendicular magnetic recording media[1,2] and high-quality particulate magnetic media.[3] Anodizing an aluminum sample in acidic solution (sulfuric, oxalic, chromic, or phosphoric acids) forms a thin layer of well-defined microporous structure, ideally consisting of hexagonal close-packed cells (Fig. 1). The shape of the particles assembled in the film ensures a large perpendicular anisotropy. The pore density and the pore diameter of the sample depend upon the acid used and the applied anodizing voltage. The micropores formed by anodization can also be widened to any desired value, by treating the sample with dilute phosphoric acid for different times. The metal particles formed by electrodeposition can be freed from the substrate by dissolving the alumite with a mixture of chromic acid and phosphoric acid.

Magnetostatic interactions among the magnetic particles influence their magnetization reversal. Several theoretical models for magnetic particle interactions have been studied.[4–6] In an electrodeposited anodic alumite sample the metal particles are embedded in parallel pore channels, which provides a simple geometry for theoretical calculations. The perpendicular anisotropy energy of an Fe-electrodeposited alumite film was calculated theoretically by Masuda[7] (who studied hexagonal arrays of cylinders 1–1.3 μm long, 33–57 nm diameter, 115 nm distant center to center) and by Daimon *et al.*[8] In this article, the magnetostatic interaction of the particles was studied by measuring the remanence curves; the reversal mechanisms of the particles were examined by the rotational hysteresis integral and the angular variation of the coercivity.

II. EXPERIMENTAL DETAILS

An aluminum sheet ($1\times2\times0.025$ cm^3) was treated with 5% NaOH solution at 60–70 °C, then neutralized in 50% HNO_3 and rinsed with deionized water. This surface-treated aluminum sample was anodized at 50 V in 15% H_2SO_4 solution at room temperature, using another Al sheet as cathode. The pores of the anodic alumite were widened by immersing the sample in dilute phosphoric acid (0.085 M). Transition metals (Fe and Co) were electrodeposited by ac electrolysis into the pore channels by using the corresponding electrolyte (either 50 g/L $FeSO_4 \cdot 7H_2O$ or 30 g/L $CoSO_4$, plus 25 g/L boric acid). Metal deposition was carried out at 16 V, 60 Hz, with a graphite counterelectrode.

The morphologies of the alumite films and the metal particles were observed by a transmission electron microscope (Hitachi H-800 200 kV TEM). The magnetic properties of the metal electrodeposited films and the metal particles were measured in a vibrating sample magnetometer (digital measurement systems VSM) with a maximum applied field of 14 kOe.

III. RESULTS AND DISCUSSION

The cell diameter and the pore diameter of the anodic alumite sample (anodized in 15% H_2SO_4), measured from a TEM micrograph, were 35 and 18 nm, respectively. A typical region of the anodized alumite film is shown in Fig. 2. TEM images of α-Fe particles, freed from the substrate by dissolving the alumite with H_3PO_4/H_2CrO_4, were also obtained (Fig. 3); the average lengths were 250–500 nm (depending on deposition times); the diameter was 16 nm. All of the

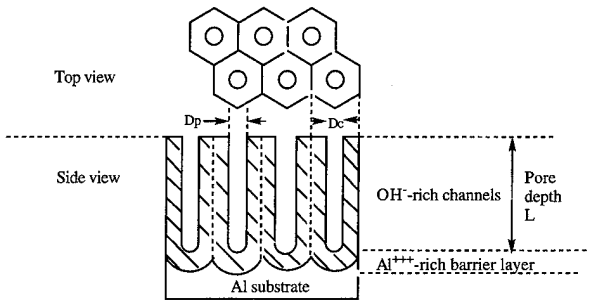


FIG. 1. Schematic diagram of alumite film, indicating the cell diameter, pore diameter and pore length.

[a]Present address: Indium Corporation of America, 1676 Lincoln Ave., Utica, NY 13502.

 0021-8979/96/79(8)/4866/3/$10.00 © 1996 American Institute of Physics

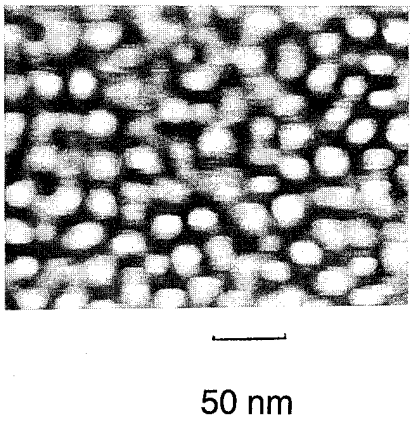


FIG. 2. TEM image of an anodized alumite film, showing the open pores (light areas).

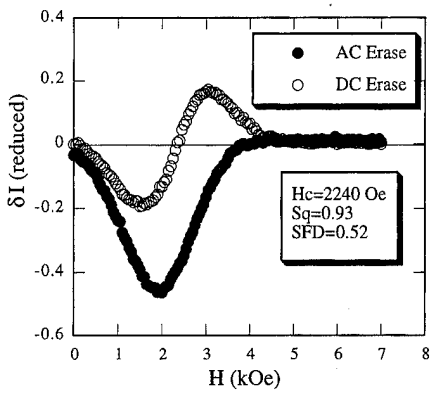


FIG. 4. Modified Henkel plots of alumite samples with pores filled with electrodeposited Fe (dc erase and ac erase; the coercivity, squareness, and switching field distribution for the sample are shown in the box).

metal (Fe and Co) electrodeposited anodic alumite samples showed strong perpendicular anisotropy. Typically, coercivities in the easy direction are (for fresh samples) H_c=2300–2700 Oe for α-Fe, and 1400 Oe for Co. To our knowledge, the coercivity of 2700 Oe is the highest value measured for pure α-Fe particles.

Oxidation in the channels occurs slowly: α-Fe samples that are several days old have H_c=2100–2200 Oe. When fresh α-Fe electrodeposited samples were heated in boiling water (to seal the pores), or reduced under hydrogen gas at 450 °C, their coercivity after several days was 300–400 Oe higher than that of untreated samples.

In an attempt to make high-moment acicular α''-$Fe_{16}N_2$ containing particles, α-Fe particles imbedded in the alumite matrix (the bottom Al metal sheet was removed by treating with Br_2/MeOH) were nitrided under ammonia and hydrogen mixed gas at 700 °C and quenched by immersion in liquid nitrogen.[9] The nitrided sample was characterized with VSM and powder x-ray diffraction: γ'-Fe_4N was detected for high NH_3:H_2 ratios, but no α''-$Fe_{16}N_2$ phase has been detected so far in the nitrided samples.

The remanence curves of these samples were measured to study the particle–particle interactions in the films. Figures 4 and 5 show the modified Henkel plots (δI vs applied field H) of the Fe and Co containing alumite samples, respectively; δI is defined by $\delta I = I_d - (1 - 2 \times I_r)$, where I_r is the reduced isothermal remanence [i.e., the isothermal remanence divided by $I_r(\infty)$, its value at saturation], and I_d is the reduced dc demagnetization remanence. In general, positive δI values are ascribed to particle–particle interactions which tend to stabilize the magnetized state, while negative δI values come from mutual particle–particle demagnetization.[10] For Fe particles or Co particles in alumite, the modified Henkel plots (Figs. 4 and 5) show that ac erasure can randomize the particle moments, while dc erasure cannot. Since the demagnetization interaction fields were found to be similar for all the samples, they are clearly due to the parallel arrangement of the particles in two dimensions; this also causes a larger switching field distribution (SFD=0.52 for Fe and 0.95 for Co).

The reversal mechanisms of the metal particles in the alumite substrates were also examined by the rotational hysteresis integral [$R = \int (W_r/I_s) d(1/H)$, Fig. 6], where W_r is

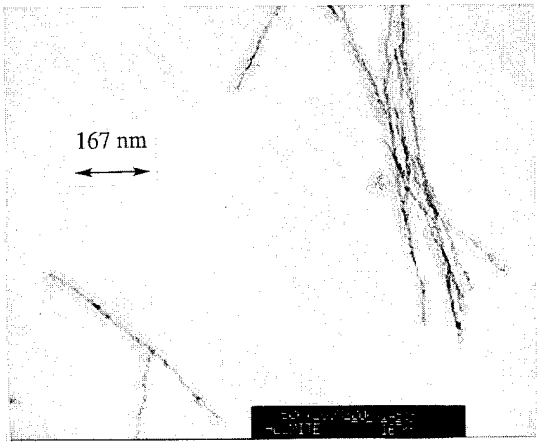


FIG. 3. TEM image of α-Fe particles (length=500 nm, diameter 16 nm) freed from the substrate by dissolving the alumite with H_3PO_4/H_2CrO_4.

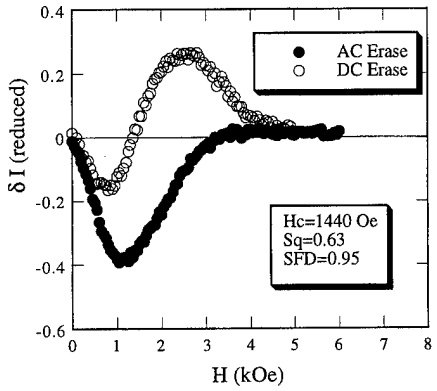


FIG. 5. Modified Henkel plots of alumite samples with pores filled with electrodeposited Co (dc erase and ac erase; the coercivity, squareness, and switching field distribution for the sample are shown in the box).

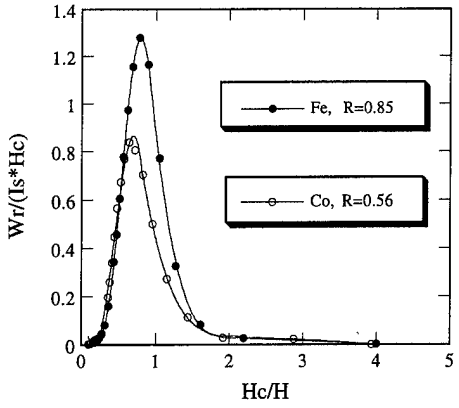


FIG. 6. Plot of the rotational hysteresis integrand $W_r/(I_s{}^*H_c)$ as a function of (H_c/H), the reciprocal of the applied field H multiplied by the coercivity H_c, for the alumite films electrodeposited with Fe (closed circles) and with Co (open circles). The insets show the values of the rotational hysteresis integral R (0.85 for Fe, 0.56 for Co).

the work per unit volume needed to rotate the sample by 360° in a fixed magnetic field, and I_s is the saturation magnetization, and also by the angular variation of the coercivity (Fig. 7).

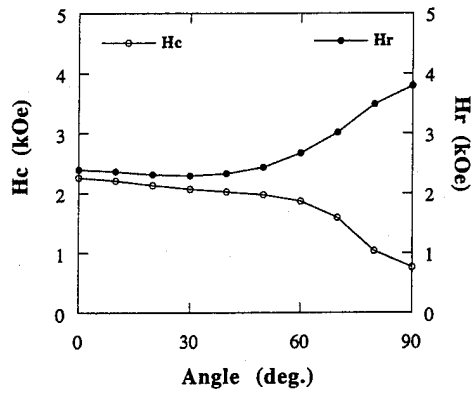


FIG. 7. Variation of coercivity H_c and of remanence coercivity H_r with the angle between the particle axis and the applied magnetic field.

TABLE I. Values of R, the rotational hysteresis integral for different reversal models.[11]

	Coherent rotation		Incoherent rotation		
	Stoner–Wohlfarth model		fanning model		curling model
Wall motion	aligned	random	aligned	random	aligned
4.0	0.415	0.380	1.54	1.02	2.6

For different reversal models the R values can be predicted theoretically, as shown in Table I.[11] The measured values $R=0.85$ for aligned Fe particles in alumite (Fig. 6), and $R=0.56$ for aligned Co particles in alumite (Fig. 6) include the particle–particle interactions, and suggest that the reversal mechanism is, to a first approximation, closer to the Stoner–Wolfarth model ($R=0.41$) than to other models. This assumption is also supported by the angular dependence of the coercivity (Fig. 7).

ACKNOWLEDGMENTS

We are grateful for the kind assistance of Mr. Lin He and the advice of Professor Hideo Fujiwara and Professor William D. Doyle. This work was supported in part by the NSIC-ARPA advanced tape program.

[1] S. Kawai, Proceedings of the Symposium on Electrochemical Technology Electronics, 1987, [Proc. Electrochem. Soc. **88-23**, 389 (1988)].
[2] J. W. Diggle, T. C. Downei, and C. W. Coulding, Chem. Rev. **69**, 365 (1969).
[3] D. AlMawlawi, N. Coombs, and M. Moskovits, J. Appl. Phys. **70**, 4421 (1991).
[4] E. Kneller, J. Appl. Phys. **39**, 945 (1968).
[5] E. Kneller, IEEE Trans. Magn. **MAG-16**, 36 (1980).
[6] E. Köster, IEEE Trans. Magn. **MAG-11**, 1185 (1975).
[7] M. Masuda, Jpn. J. Appl. Phys. **26**, 1680 (1987).
[8] H. Daimon, O. Kitakami, O. Inagoya, and A. Sakamoto, Jpn. J. Appl. Phys. **30**, 282 (1991).
[9] X. Bao, R. M. Metzger, and M. Carbucicchio, J. Appl. Phys. **73**, 6734 (1993).
[10] R. W. Chentrell and K. O'Grady, in *High Density Digital Recording*, edited by K. H. J. Buschow *et al.* (Kluwer Academic Dordrecht, 1993) pp. 101–135.
[11] M. Prutton, *Thin Ferromagnetic Films* (Butterworths, London, 1964) p. 116.

Published without author corrections

Lanthanide and boron oxide-coated α-Fe particles

Feiyue Li, Xiaohua Bao,[a] and Robert M. Metzger
Department of Chemistry and Center for Materials for Information Technology, University of Alabama, Tuscaloosa, Alabama 35487-0209

Massimo Carbucicchio
INFM, Department of Physics, Università di Parma, Viale delle Scienze, I-43100 Parma, Italy

To increase the coercivity of α-Fe particles, needlelike goethite crystals were first coated with different Ln^{3+} ions (Ln=La,Nd,Sm,Gd,Dy,Eu) plus B^{3+}, then reduced to α-Fe under H_2. The magnetic moment of the particles depends upon the Ln and B contents and temperature. Both powder x-ray diffraction and Mössbauer spectra indicate the existence of a crystalline FeO phase; the FeO content decreased as the reduction temperature increased. A phase with no hyperfine splitting was also detected in the Mössbauer spectra, which may be superparamagnetic α-Fe or amorphous iron oxide; the amount of this phase decreased as the reduction temperature increased. The temperature dependence of the coercivity of these B- and Ln-coated particles was steeper than for particles coated with silica: this suggests a coercivity mechanism other than shape anisotropy.
© *1996 American Institute of Physics.* [S0021-8979(96)06708-X]

I. INTRODUCTION

High-density magnetic recording requires the development of media with ever higher coercivity and magnetic moment. Fine acicular particles of α-Fe or alloys are suitable and widely used media materials. Several methods have been investigated to prepare acicular metal particles: decomposition of carbonyls[1] or oxalates,[2] reduction of ferrous salts in aqueous solution with $NaBH_4$,[3] deposition from the vapor phase,[4] and the conventional method of reducing acicular geothite (α-FeOOH) particles under H_2 gas.[5]

Miyahara and Kawakami reported a coercivity enhancement of α-Fe particles by a surface coating of Nd and B.[6] This coercivity enhancement was attributed to a possible coupling between the amorphous iron oxide layer with a special microstructure, and the iron core.[6] In this article, α-Fe particles were coated with boron and several rare-earth elements; the magnetic properties and the phases present in the samples were studied by powder x-ray diffraction and Mössbauer spectroscopy.

II. EXPERIMENTAL DETAILS

Acicular goethite (α-FeOOH) particles were synthesized by passing air for at least 20 h through an aqueous solution (volume=100 mL) of 0.018 mol $FeSO_4 \cdot 7H_2O$ and the additives $NiSO_4 \cdot 6H_2O$ (atom ratio Ni/Fe=0.01) and NaH_2PO_4 (atom ratio P/Fe=0.01) mixed with 0.072 mol NaOH. The Ni^{2+} and PO_4^{3-} additives are known to increase the aspect ratio and improve the size distribution of the goethite particles.[7,8] The particle size and the aspect ratio of the goethite particles depend upon the Ni^{2+} and PO_4^{3-} concentration. After optimizing the reaction conditions (Ni and P contents, dehydration temperature, reduction temperature, and reaction time), the aspect ratio of the goethite particle reached about 17:1; the average particle length was about 0.2 μm.

The goethite particles were coated with different Ln^{3+} ions (Ln=La,Nd,Sm,Gd,Dy,Eu) and B^{3+} (by using the appropriate aqueous solutions of nitrate salts and H_3BO_3), then washed, dried, reduced to α-Fe under H_2, then slowly exposed to air under toluene. For instance, freshly prepared α-FeOOH particles were dispersed in 100 mL of a solution of Ln $(NO_3)_3$ (atom ratio Ln/Fe=0.05) and of H_3BO_3 (atom ratio B/Fe=0.18); the pH of the slurry was adjusted to pH 8 with ammonia solution, so that the hydroxides of Ln and B could coat the surfaces of the α-FeOOH particles. The coated particles were dried at 130 °C in air, and then reduced to α-Fe particles by passing H_2 gas at high temperatures (specified below) for 4 h. The coated α-Fe particles were then immersed in toluene and dried in air at room temperature. A sample coated with silica (instead of borides and lanthanides) was also prepared, for comparison.

The morphologies of particles (goethite and α-Fe) were observed by transmission electron microscopy (Hitachi H-800 TEM). The magnetic properties of the metal particles were measured on a vibrating sample magnetometer (Digital Measurement Systems) with a maximum applied field of 14 kOe. The presence and the contents of different phases in the reduced particles were identified by powder x-ray diffraction (Rigaku DXG-2B) using Cu K_α radiation and by transmission Mössbauer spectroscopy.

TABLE I. Magnetic properties (saturation magnetization σ_s, coercivity H_c, and squareness S_q) of α-Fe particles coated with various lanthanide oxides and boron oxide, and reduced at 510 °C.

Coating	σ_s (emu/g)	H_c (Oe)	S_q
La_2O_3–B_2O_3	32	1947	0.50
Nd_2O_3–B_2O_3	46	1800	0.49
Sm_2O_3–B_2O_3	44	1776	0.48
Eu_2O_3–B_2O_3	46	1751	0.49
Gd_2O_3–B_2O_3	39	1938	0.50
Dy_2O_3–B_2O_3	42	1941	0.49

[a]Current address: Indium Corporation of America, Utica, N.Y.

 0021-8979/96/79(8)/4869/3/$10.00 © 1996 American Institute of Physics

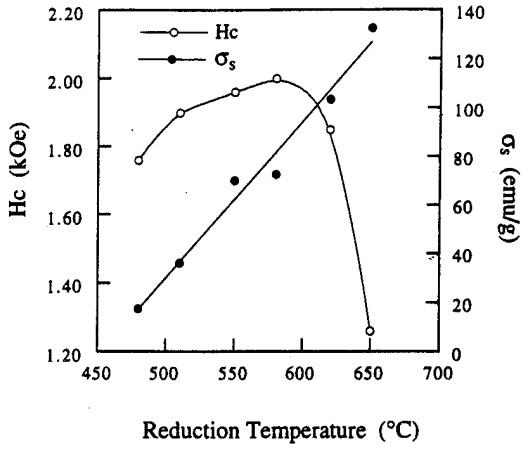


FIG. 1. Magnetic moment (σ_s) and coercivity (H_c) of the La- and B-coated particles as a function of the reduction temperatures.

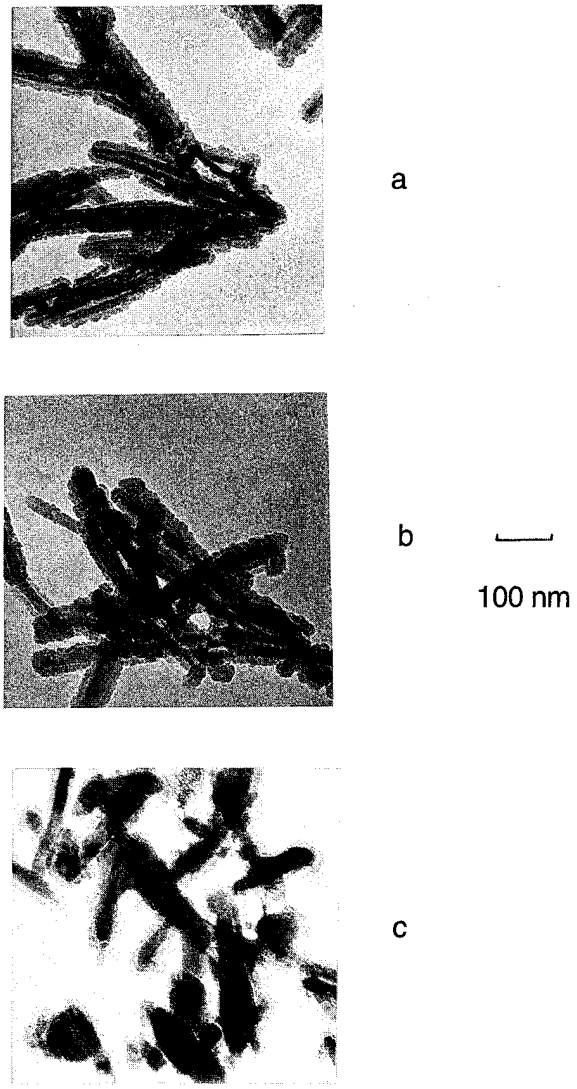


FIG. 2. Transmission electron micrographs of α-Fe particles coated with La and B oxides, after reduction in H_2 gas at (a) 480 °C (b) 550 °C, and (c) 650 °C. Sintering increases with increasing reduction temperatures.

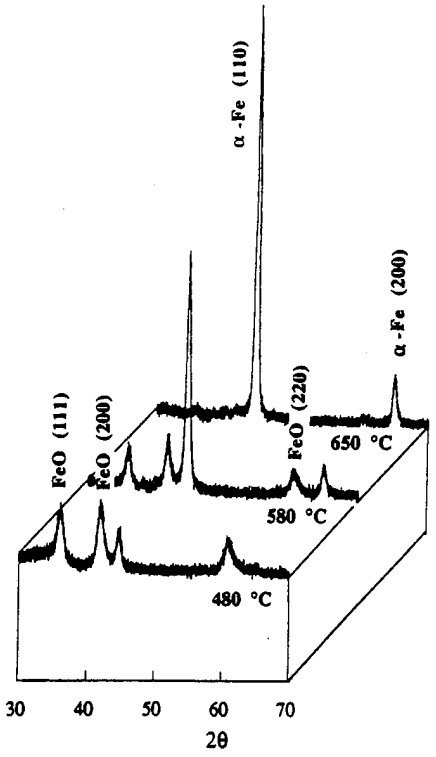


FIG. 3. Powder x-ray diffraction spectrum of La- and B-coated samples reduced at different temperatures.

III. RESULTS AND DISCUSSION

The coercivity of the rare-earth and boron-coated α-Fe particles varied from 1750 to 1950 Oe. Varying the rare-earth elements did not have a large or systematic effect on the magnetic properties (see Table I). The magnetic moment of the particles depends slightly on which lanthanide was used (see Table I), and strongly on the reduction temperature: Fig. 1 shows the magnetic moment (σ_s) and coercivity (H_c) of La and B-coated particles as a function of the reduction temperature. As the reduction temperature increased from 480 to 580 °C, the coercivity of the particles increased from 1750 to 2100 Oe. When the reduction temperature was further increased to 650 °C, the coercivity of the sample dropped to 1250 Oe, because significant particle sintering was seen by TEM (see Fig. 2) for particles reduced at 650 °C. The magnetic moment of the particles increased monotonically with the reduction temperature. The other lanthanide coatings were not studied as a function of reduction temperature.

The existence of a crystalline FeO phase was confirmed by both powder x-ray diffraction (see Fig. 3) and Mössbauer spectra (see Fig. 4) of the La and B-coated particles. In particular, the Mössbauer spectra show a four-line contribution due to nonstoichiometric ferrous oxide: two absorption lines at 1.47 and 1.30±0.01 mm/s (with respect to α-Fe), due to Fe^{++} ions in stoichiometric wustite structure, and two at 0.80 and 0.43±0.01 mm/s, due to Fe^{++} ions located near clusters of vacancies.[9] The FeO content decreased as the reduction temperature increased (see Fig. 5), which is consistent with the increase in magnetic moment. A phase with no hyperfine splitting was also detected in the Mössbauer spec-

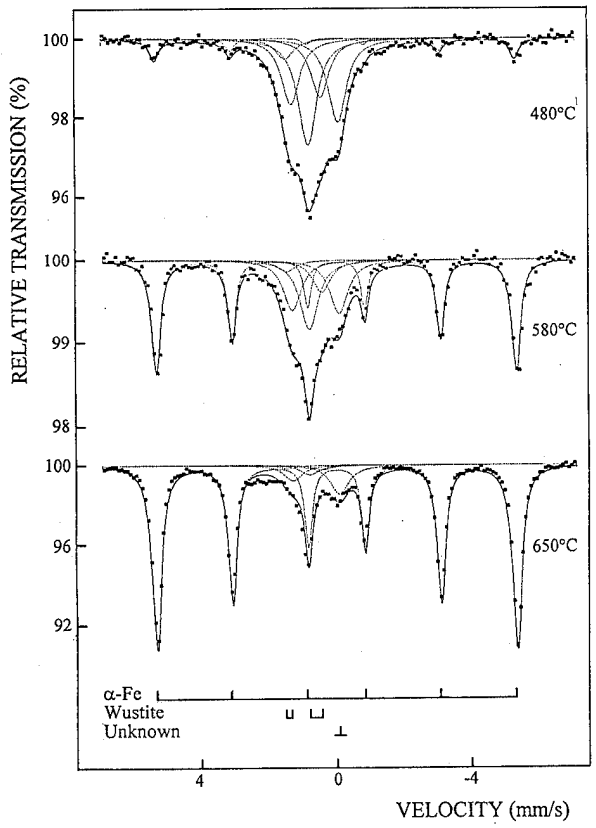


FIG. 4. Transmission Mössbauer spectrum of La- and B-coated samples reduced at different temperatures.

tra (see Fig. 4), which may be γ-austenite (unlikely), isolated superparamagnetic α-Fe, or an amorphous iron oxide in the passivation layer. The relatively small amount of this phase decreased slightly as the reduction temperature increased (see Fig. 5).

The temperature dependence of the coercivity of these B- and La-coated particles was steeper than for Si-coated

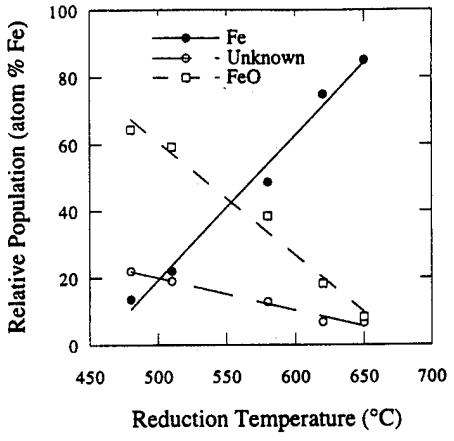


FIG. 5. Mössbauer Fe atom fraction of α-Fe, FeO, and the unknown phase, as a function of the sample reduction temperature.

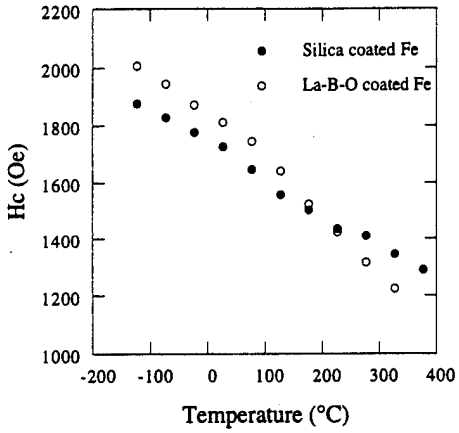


FIG. 6. The temperature dependence of the coercivity of B- and La-coated particles and Si-coated particles.

particles, for which shape anisotropy is thought to be dominant (see Fig. 6): this suggests that for the B- and La-coated particles the coercivity may be determined by surface anisotropy rather than by shape anisotropy.

In our laboratory, α-Fe particles coated with silica, and prepared by reduction in H_2 at around 400–450 °C have typical moments of 120 emu/g and coercivities of up to 2000 Oe; they tend to sinter at around 500 °C. The Ln oxide-B oxide particles prepared here achieve maximum coercivity of 2000 Oe and a moment of about 75 emu/g at the optimum reduction temperature of 580 °C: therefore equivalent coercivities (but lower moments) are attained using higher reduction temperatures and tolerating higher sintering temperatures than Si-coated particles.

IV. CONCLUSION

Replacing the silica coating of α-Fe particles by a coating of boron and any lanthanide requires higher reduction temperatures and provides a small gain in coercivity. The relatively high coercivity even at low reduction temperatures suggests that the coercivity is not simply due to shape anisotropy.

ACKNOWLEDGMENT

Supported in part by the NSIC-ARPA Advanced Tape Program.

[1] J. R. Thomas and J. B. Lavinge, US Patent No. 3,284,358 (8 Nov. 1966).
[2] W. J. Schule, J. Phys. Chem. **63**, 83 (1959).
[3] A. L. Oppegard, F. J. Darnell, and H. C. Miller, J. Appl. Phys. **32**, 184 (1961).
[4] T. Tanaka and N. Tamagawa, Jpn. J. Appl. Phys. **6**, 1096 (1967).
[5] E. H. Carman, Brit. J. Appl. Phys. **6**, 426 (1955).
[6] T. Miyahara and K. Kawakami, IEEE Trans. Magn. **MAG-23**, 2887 (1987).
[7] K. Yamada, T. Harato, O. Takagi, Y. Hamaguchi, and T. Ashitani, Jpn. Patent No. 61,141,627 (28 June 1986).
[8] E. Schwab, V. Volker, R. Feser, and B. Meyer, Ger. Patent No. 3,732,526 (6 April 1989).
[9] L. F. Checherskaya, V. P. Romanov, and P. A. Tatsienko, Phys. Status Solidi A **19**, K177 (1973).

Time effects in exchange anisotropy-affected metal-evaporated tapes

G. Bottoni, D. Candolfo, and A. Cecchetti
INFM-Dipartimento di Fisica, Università, 44100 Ferrara, Italy

The time-dependent magnetic behavior in metal evaporated tapes for high-density magnetic recording is studied at low temperatures, where the coupling between the ferromagnetic Co and the antiferromagnetic CoO, in the obliquely evaporated CoNiO film, induces a unidirectional exchange anisotropy, and it is compared with the effects obtained at room temperature, where no coupling occurs. At low temperature a contraction of the hysteresis loop as a function of the number of repeated cycles N is observed, with a remarkable decrease of the measured coercive field. No contraction occurs at room temperature. The time dependence of the magnetization is larger at low temperatures, with increase of magnetic viscosity and thermal fluctuation field, than at room temperature. The observed anomalous increase of thermal instability of magnetization and coercivity with the decrease of the temperature is imputed to the presence of exchange coupling between the ferromagnetic and antiferromagnetic phases at low temperature and to the effect that such coupling can exert on the reversal of the magnetization in the ferromagnetic grains. © *1996 American Institute of Physics.* [S0021-8979(96)07308-6]

I. INTRODUCTION

Metal-evaporated (ME) tapes are Co-Ni obliquely evaporated thin films, which are considered among the most notable of the high density magnetic storage media, and which are now used in high-band 8 mm video cassettes. The tape consists of one or more layers where Co (80%) and Ni (20%) fine ferromagnetic particles are aligned in columns with an angle to the film plane. The deposition takes place in the presence of a flow of oxygen gas, which has a number of beneficial effects on the film properties and on the preparation process, among which are the improvement of coercivity, corrosion resistance and signal-to-noise ratio.[1,2] The presence of oxygen during the film deposition gives rise to the formation of oxides of the metals, primarily CoO, among the ferromagnetic grains and in the film surface layers. The CoO is antiferromagnetic with a Néel temperature practically coinciding with room temperature (T_N=293 K). Below this temperature, the effect of the coupling between the ferromagnetic Co and the antiferromagnetic CoO is significant, and we observed a shift of the hysteresis loop along the field axis in the tapes cooled from room temperature to lower temperatures in the presence of an applied magnetic field or in the remanent state[3] (no displacement of the hysteresis occurs when the tape is cooled demagnetized and in zero field). We observed also an anomalous behavior of these ME tapes at low temperature in the presence of rotational magnetic field, with a monotonic increase of the rotational hysteresis energy losses with the applied field, which do not show any tendency to decrease at least up to fields as high as 18 kOe (i.e., substantially larger than the anisotropy field of these materials).[4] These effects are originated in the exchange coupling between the ferromagnetic and antiferromagnetic phases, which gives rise to the unidirectional "exchange anisotropy" when the system is cooled through the Néel temperature of the antiferromagnet, and which was observed in different systems, since 1956.[5] The presence of exchange anisotropy in ME tapes was proved also by the analysis of the torque curves, which show a superposition of uniaxial and unidirectional anisotropies at low temperatures.[4]

In this work, we have studied the time-dependent magnetic behavior of these ME tapes at low temperatures, where the two magnetic phases are exchange coupled with the macroscopic effects we described, and we have compared it with the behavior at room temperature, where no coupling occurs.

II. EXPERIMENT

Several types of different commercial ME tapes have been analyzed. The behavior is similar in all samples and in this paper two of them have been chosen to represent the magnetic behavior of all them. The two tapes are indicated with the letters A and B. The hysteresis loops have been measured with a total sweep time of 5 min in all the reported experiments. At room temperature the hysteresis is symmetrical with coercivity $H_c \approx 1100-1150$ Oe and saturation magnetization about 500 emu/cm^3. When cooled from room temperature in presence of an applied field (H=10 kOe) or in the remanent state the hysteresis is displaced, with different values of the coercivities in the two branches of the hysteresis loop, H_c' and H_c''. At 80 K H_c' = 3350 Oe (A and B tapes), H_c'' = 2420 Oe (A) and 2020 Oe (B). When the demagnetized tapes are cooled in zero field, no displacement of the hysteresis occurs, and $H_c' = H_c'' = 2600-2500$ Oe. The remanent magnetization lightly decreases with the decrease of temperature: at 295 K $M_r \approx 400$ emu/cm^3, at 80 K $M_r \approx 380$ emu/cm^3.

The above-reported values are the coercivities obtained in the first cycle after cooling. If the cycle at 80 K is repeated, the magnetization values change: the hysteresis loops are not superimposed, but they show a contraction which increases with the number of cycles N. The absolute values of both the coercivities, H_c' and H_c'', decrease with increasing N. The H_c variation rate decreases when the number of cycles increases, and the contraction seems to proceed towards a saturation. Figure 1 shows the hysteresis contraction of tape A in the first five cycles after cooling. The observed effect is large: the variation $\Delta H_c' \cong 700$ Oe after 15 cycles. The lower coercivity H_c'' exhibits a smaller decrease: $\Delta H_c''$

 0021-8979/96/79(8)/4872/3/$10.00 © 1996 American Institute of Physics

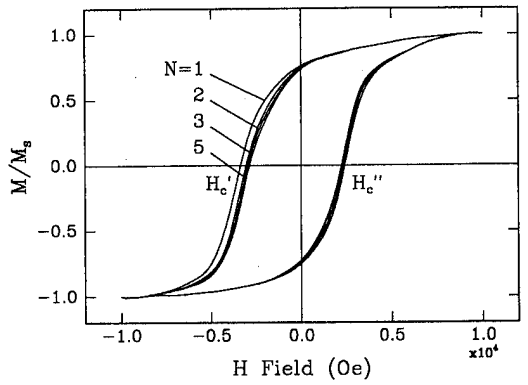


FIG. 1. Hysteresis loops of tape A at 80 K in the first five cycles after cooling. N is the number of cycles.

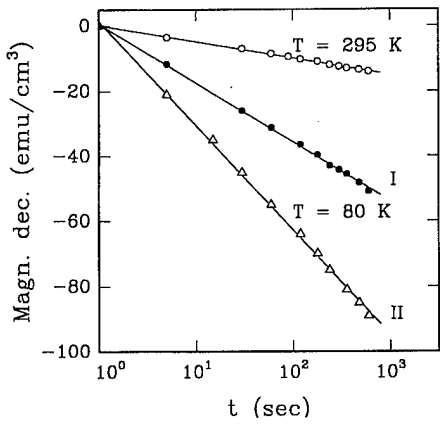


FIG. 3. Magnetization decay of tape A at 295 and 80 K (I: tape cooled demagnetized in zero field, II: tape cooled in presence of magnetic field).

$\cong$ 200 Oe (in 15 cycles). On the contrary, no noticeable contraction occurs in repeated cycles at room temperature.

The dependence of H_c on the number of cycles N is almost linear with $1/\sqrt{N}$, as it is shown in Fig. 2, and it can be described by the equation:[6]

$$H_c(N)=H_c(\infty)+\frac{K}{\sqrt{N}}, \tag{1}$$

where K is a constant and $H_c(\infty)$ should be the value of coercivity obtained after an infinite number of cycles. As we see in Fig. 2, $H_c'(\infty) \neq H_c''(\infty)$ in both tapes, which means that, even when deducted this contraction effect, a dissimmetry between the coercivities in opposite directions persists. This indicates the different origin of the hysteresis displacement (exchange anisotropy) than that of the coercivity reduction with repeated cycles, which we can impute to time effects.

In the same ME tapes we also measured the time dependence of the magnetization: the samples were saturated with the application of a strong magnetic field, then an opposite field H was applied and the decrease of the magnetization with time in the presence of a constant field H has been measured. The magnetization decay has been evaluated both at room temperature and at 80 K. At this low temperature, the measurement has been performed in tapes cooled demagnetized in zero field (I) and in tapes cooled in presence of a magnetic field (II). Figure 3 shows the obtained magnetization decay of tape A in the three cases. Tape B and all of the other ME tapes we measured showed similar behavior. The decay is much faster at 80 K than at room temperature, and the samples cooled in the presence of H (shifted loops) have larger decay than the samples cooled as demagnetized (symmetrical loops). This result is surprising: at low temperature the thermal energy effect is larger than at higher temperature. As a consequence the coefficient of magnetic viscosity S,[7] which is the rate of variation in the dependence of M on $\ln(t)$, increases when the temperature decreases. Figure 4 reports the dependence of S on reduced field at room temperature and 80 K. The maximum value of S, which is reached at applied field $H \cong H_c$, increases from $\sim$2.5 emu/cm^3 at room temperature to values as high as $\sim$16 emu/cm^3 at 80 K. From the magnetic viscosity it is possible to deduce the thermal fluctuation field $H_f = S/\chi_{\text{irr}}$, the magnetic field which will have on the magnetization the same effect of the thermal agitation.[8] Also H_f is larger at 80 K than at room temperature, as it is shown in Fig. 5, and it increases from $\sim$10 to

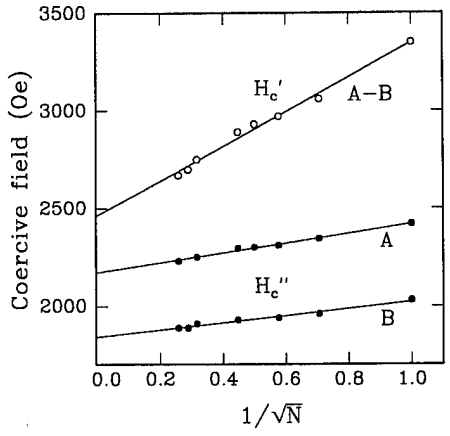


FIG. 2. Coercive fields in opposite directions of tapes A and B as a function of $1/\sqrt{N}$, with N number of cycles.

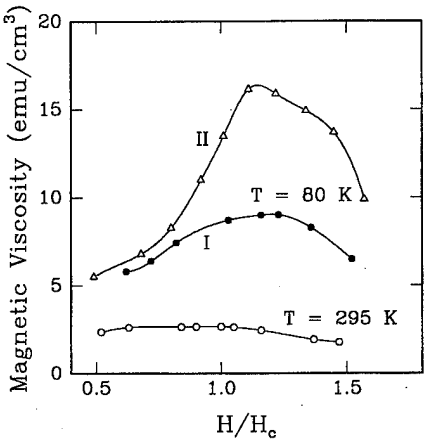


FIG. 4. Magnetic viscosity vs reduced applied field of tape A at 295 and 80 K.

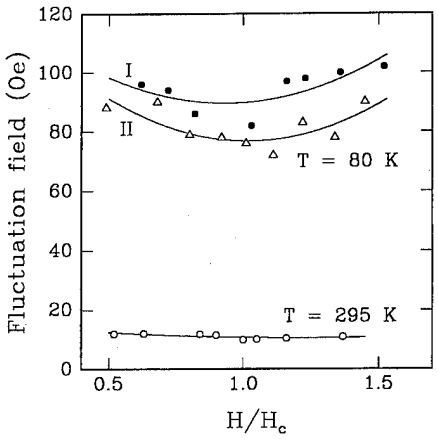


FIG. 5. Thermal fluctuation field vs reduced applied field of tape A at 295 and 80 K.

~100 Oe. The irreversible susceptibility χ_{irr} decreases from ≈0.23 to ≈0.17 emu/cm^3 Oe cooling from 295 down to 80 K.

III. DISCUSSION

The experimental results show that in the ME tapes the thermal stability of the magnetization is weakened by the decrease of temperature, with increase of magnetization decay, magnetic viscosity and thermal fluctuation field. This evolution is accompanied by a contraction of hysteresis in repeated cycles at low temperatures, with a diminishing of coercive field in successive cycles, which does not occur at room temperature.

As discussed above, in these Co-Ni-CoO systems an exchange anisotropy appears at low temperatures, and the physical origin of this particular property can perhaps explain the unusual increase of time effects with decreasing temperature. The exchange anisotropy is due to the exchange coupling between the adjacent layers of ferromagnetic and antiferromagnetic phases. When the system is cooled through the Néel temperature of the CoO in the presence of a magnetic field, the consequent orientation of the spins in the antiferromagnet gives rise to the unidirectional anisotropy in the coupled ferromagnetic grains.

At room temperature, and in general above the Néel temperature of the antiferromagnet, no magnetic order exists in the Co oxide, and thus no exchange coupling with the ferromagnet. Below the Néel temperature, the CoO is antiferromagnetically ordered, but the action of an applied field, in conjunction with that of the thermal energy, opposes the antiparallelism of the elementary magnetic moments, which can result in partial misalignment (canting). The magnetic spins of the adjacent layers of ferromagnetic Co grains which are exchange coupled with the canted spins of the antiferromagnet are also misaligned, even with respect to the other layers of magnetic moments in the ferromagnetic Co grains. Such region of different magnetic orientation can act as centers of nucleation for the reversal of the magnetization in the particles. In such condition the magnetization switching is modified and made easier than it would be if such misaligned regions did not exist. Consequently the particles are magnetically less stable: the total magnetization of the material markedly decreases with the time and the coercivity is progressively reduced.

The macroscopic effects of this evolution of magnetization reversal mode therefore are just the experimental results we observed: at low temperature, where Co is exchange coupled with CoO, the magnetization decay and viscosity will be anomalously larger than at room temperature and the coercivity in successive multiple cycles will decrease, as a further consequence of the enhancement of time effects on the magnetization.

ACKNOWLEDGMENT

This work was supported by the Italian Ministero dell'Università e della Ricerca Scientifica e Tecnologica.

[1] J. Hokkyo, T. Suzuki, K. Chiba, K. Sato, Y. Arisaka, T. Sasaki, and Y. Ebine, J. Magn. Magn. Mater. **120**, 281 (1993).
[2] J. S. Gau, R. G. Spahn, and D. Majumdar, IEEE Trans. Magn. **MAG-22**, 582 (1986).
[3] G. Bottoni, D. Candolfo, and A. Cecchetti, IEEE Trans. Magn. **30**, 3945 (1994).
[4] G. Bottoni, D. Candolfo, and A. Cecchetti, MRM '95 Conference (Paper BQ04), Oxford, UK, 1995, J. Magn. Magn. Mater. (to be published).
[5] W. H. Meiklejohn and C. P. Bean, Phys. Rev. **102**, 1413 (1956).
[6] D. Paccard, C. Shlenker, O. Massenet, P. Montmory, and A. Yelon, Phys. Status Solidi **16**, 301 (1966).
[7] E. P. Wohlfarth, J. Phys. F **14**, L155 (1984).
[8] R. Street and J. C. Woolley, Proc. Phys. Soc. **62**, 562 (1949).

The archival stability of metal evaporated tape for consumer digital VCRs

Seiichi Onodera, Tsutomu Takeda, and Takahiro Kawana
Sendai Technology Center, Sony Corporation 3-4-1 Sakuragi, Tagajo-shi, Miyagi-ken 985, Japan

A new metal evaporated (ME) tape was released for consumer digital VCRs. It has greatly improved its recording characteristics and durability compared with conventional Hi-8ME tape. Demagnetization of the new ME tape has been studied using accelerated and ambient conditions. Demagnetization of saturation magnetization follows the cubic law, and it was found that the estimated archival lifetime is about 60 years. Moreover, we have investigated characteristics such as dropout, carrier-to-noise ratio, and error rate, and we confirmed that the new ME tape has enough stability for practical applications. © *1996 American Institute of Physics.*
[S0021-8979(96)14108-1]

I. INTRODUCTION

Co–(Ni)–O obliquely metal evaporated (ME) tape has characteristics suitable for high density recording and low noise properties. Consequently, ME tape was introduced into the consumer video market for a high-band 8 mm VCR in 1989.[1]

A new metal evaporated tape was released for digital consumer VCRs. Some of its properties such as recording characteristics and durabilities are greatly improved compared with conventional Hi-8ME tape due to material engineering for the magnetic material, and the adoption of a multilayer structure for the magnetic film, and a carbon protective layer applied on the top surface. It shows about 4.5 dB higher output at a wavelength 0.5 μm.[2]

There are several investigation of metal evaporated tape on its corrosion properties.[3,4] In this paper, the archival stability of this new metal evaporated tape is discussed particularly in demagnetization, and characteristics needed for practical application in terms of reproduced output, carrier to noise ratio, dropout, and error rate.

II. EXPERIMENTAL PROCEDURE

Magnetic layers were deposited on PET film using web-coater-type vacuum evaporation equipment. The degradation of magnetic properties was measured by a VSM (vibrating sample magnetometer). The applied saturation magnetic field was 1.19 (MA/m). Specimens for the accelerated measurement were kept in each environmental condition up to 100 days as wound cassettes. Table I shows the experimental aging conditions. The recording characteristics were measured with a MIG head with an effective gap length of 0.2 μm, B_s of 1.1 T, a track width of 13 μm, and a head-to-tape relative velocity of 10.2 m/s.

TABLE I. Accelerate experimental condition.

	Temperature (°C)	Humidity (%RH)
I	30	90
II	50	90
III	65	90

III. RESULTS AND DISCUSSION

Figure 1 shows the time aging dependence of demagnetization (ϕs) in each accelerating environmental condition, where the ratio of demagnetization is defined as follows: demagnetization $X(\%)=[\Delta\phi/\phi(0)]\times 100$, $\Delta\phi=\phi(0)-\phi(t)$. Each line shows almost the same slope. This slope shows the same values as the Hi-8ME tape we discussed previously.[5] It indicates that demagnetization (ϕs) of the new ME tape for consumer digital VCRs, almost follows the cubic law.[6] Thus, demagnetization X will be expressed as

$$X^n = kt, \quad n=3. \tag{1}$$

From these results, the constant of rate constant k, is derived, and moreover as shown in Fig. 2, from the relation between $\ln(k)$ and $1/T$ for each condition the activation energy in the Arrhenius part is derived as 1×10^2 (kJ/mol). This value is almost the same as the values in the Hi-8ME tape.[5] It means that the new ME tape for consumer VCRs has the same temperature dependence as the Hi-8ME tape.

Figure 3 shows the time aging dependence of demagnetization (ϕr) in each accelerating environmental condition. The reproduced output depends on the remanent magnetization.

Figure 4 shows long-term demagnetization at room-temperature storage. The demagnetization also nearly fol-

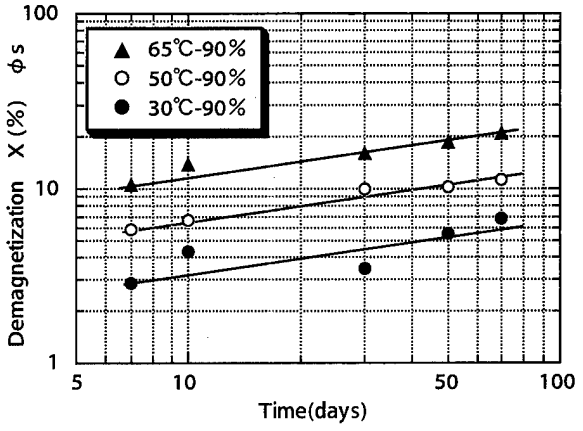


FIG. 1. Time aging dependence of demagnetization (ϕs) in accelerating condition.

 0021-8979/96/79(8)/4875/3/$10.00 © 1996 American Institute of Physics

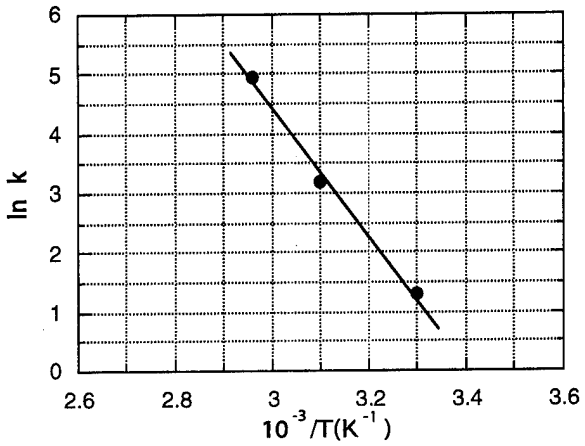


FIG. 2. Temperature dependence of the logarithmic rate constant.

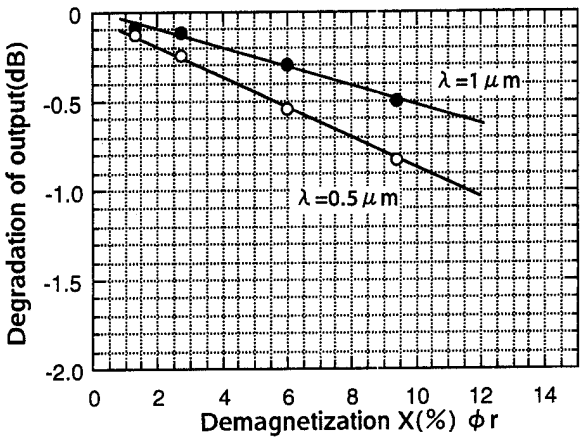


FIG. 5. Magnetization dependence of reproduced output.

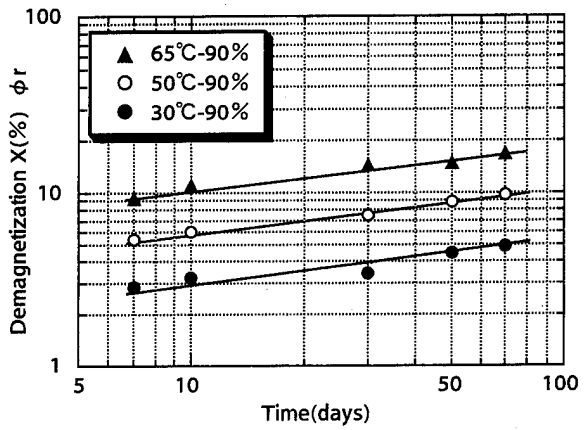


FIG. 3. Time aging dependence of demagnetization (ϕr) in accelerating condition.

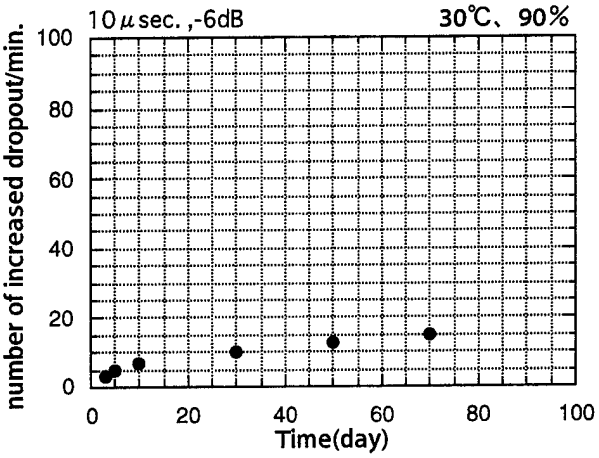


FIG. 6. Time aging dependence of dropout.

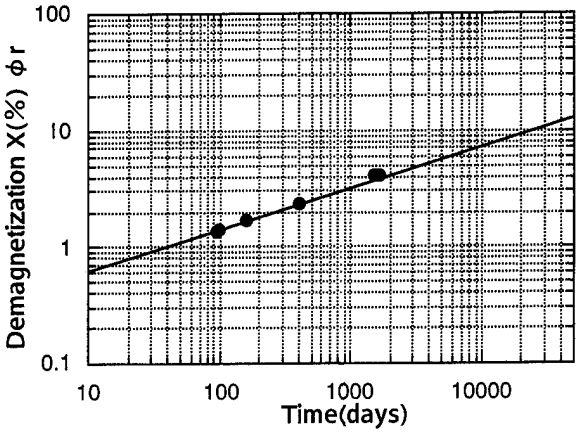


FIG. 4. Time aging dependence of demagnetization in ambient condition.

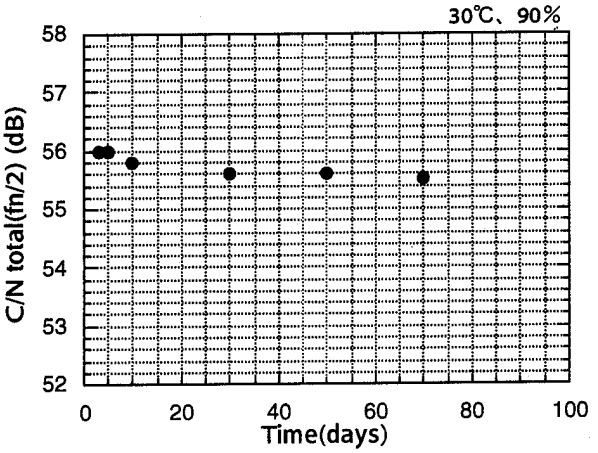


FIG. 7. Time aging dependence of carrier-to-noise ratio.

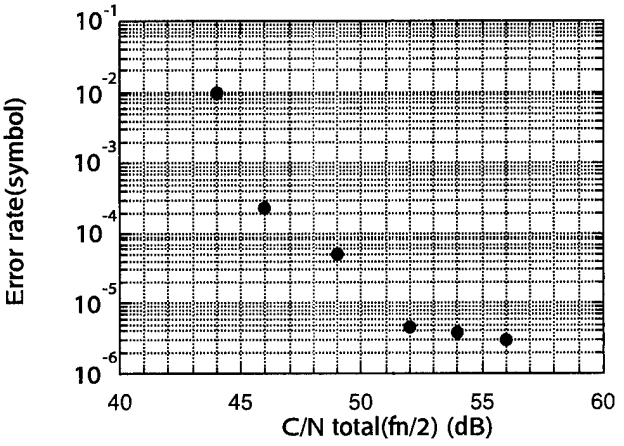


FIG. 8. Error rate dependence of carrier-to-noise ratio.

lows the cubic law like in the accelerated environmental conditions and Hi-8ME in long-term storage at room temperature.

In order to estimate the archival life, we examined the relation between demagnetization and the decrease of reproduced output. Figure 5 shows the effect of the decrease in remanent magnetization on reproduced output at recording wave lengths of 1 and 0.5 μm, respectively. The reproduced output is normalized to the initial value of the tape. A linear decrease in reproduced output in dB was observed against the decrease of remanent magnetization. From Figs. 4 and 5, we can estimate the archival lifetime in ambient atmosphere for a decrease in reproduced output of -1 dB at each recording wavelength. At 0.5 μm recording wavelength, the lifetime has been estimated to be about 60 years at room temperature.

On the other hand, characteristics for reliability in practical application such as dropout, carrier-to-noise ratio, and error rate are also important matters. We describe the changes of these properties at a typical condition of 30 °C, 90%.

Figure 6 shows an increase in dropout number. The dropout is measured by SHIBASOKU VH06AZ, as the number of defects defined by a threshold of 10 μs in length and -6 dB in output, per minute in a recording wavelength is about 1 μm($fn/2$). With the passage of storage time, the number of dropouts increases slightly but that number is less than the specification for consumer digital VCRs.

Figure 7 shows the time aging dependence of the carrier to noise ratio. Carrier frequency is around 10 MHz (recording wave length=1 μm, RBW=30 kHz, VBW=300 Hz). The noise level is defined as the average of the amplitudes in two frequencies which are +2 MHz from the carrier frequency. The carrier to noise ratio is about 56 dB, and it decreases slightly with increasing storage time. The decrease in reproduced output is the dominant factor for this result, and the increase of the noise level is not significant through the storage.

The effect of the decrease in carrier-to-noise ratio which will be made to the error rate was investigated, as shown in Fig. 8. Every decreased carrier-to-noise ratio was produced by adding white noise to the reproduced signal. From this result, the error rate will change as the carrier-to-noise ratio change.

IV. CONCLUSION

It was found that the demagnetization (ϕs) of a new ME tape for consumer digital VCRs follows the cubic law, by measurement at accelerated and ambient conditions. The Arrhenius activation energy was determined to be 1×10^2 (kJ/mol). This is the same value that is determined for the Hi-8ME tape. The estimated lifetime at ambient conditions to decrease the reproduced output for -1 dB (λ=0.5 μm) is about 60 years. The degradation of carrier to noise ratio with increasing storage time is mainly caused by the decrease of reproduced output. For a 4 dB change in carrier to noise ratio, the change in error rate will be about 1 decade. A sizable increase in dropouts with storage time was not observed; consequently, this new ME tape is reliable enough for practical applications.

[1] K. Chiba, K. Sato, Y. Ebine, and T. Sasaki, IEEE Trans. Consumer Electron. **CE-35**, 421 (1989).
[2] T. Kawana, S. Onodera, and T. Samoto, Intermag'95 EA-03 (1995) (to be published).
[3] D. Speliotis, IEEE Trans. Magn. **26**, 124 (1990).
[4] P. J. Sides, G. Spratt, and J. P. Kampf, IEEE Trans. Magn. **30**, 4059 (1994).
[5] T. Kawana, T. Takeda, T. Uchimi, and K. Sato, MRM '95 (1995) (to be published).
[6] N. F. Mott, Trans. Faraday Soc. **35**, 1175 (1939); *ibid.* **36**, 472 (1939).

Effects of Cr_2O_3 or Y_2O_3 doping in barium ferrite thin-film medium for high-density recording

Y. J. Chen and M. H. Kryder
Data Storage Systems Center, Dept. of Electrical and Computer Engineering, Carnegie Mellon University, Pittsburgh, Pennsylvania 15213

The effects of Cr_2O_3 or Y_2O_3 doping on the surface morphology and magnetic properties in barium ferrite thin films have been studied. Thin films were deposited by co-sputtering a barium ferrite target with a Cr_2O_3 or Y_2O_3 target. The deposited amorphous films were homogenized at a temperature of 600 °C for over 10 h followed by annealing at 800 °C in a tube furnace. It was observed that, whereas stoichiometric barium ferrite shows 5000 Å×500 Å acicular grainlike features, films doped with Cr_2O_3 or Y_2O_3 had equiaxed topographic features with an average size of 500 Å. Magnetic studies showed that the coercivity of the doped films was over 3500 Oe and was larger than that of stoichiometric films. A weak magnetostatic interaction was found in all the films. Studies of the magnetic after effect indicated excellent thermal stability in all the films. © *1996 American Institute of Physics.* [S0021-8979(96)06908-2]

I. INTRODUCTION

The goal of achieving areal density of 10 Gb/in.^{2} and beyond in magnetic recording imposes many challenges on the recording medium. The medium must have coercivity above 3000 Oe[1] in order to record bits with very narrow transition length. The medium cannot utilize a thick overcoat for protection from mechanical wear or chemical erosion because of the demand of lower flying height by the recording head. The signal-to-noise ratio at such high recording density requires that the grains of the recording medium be less than 100 Å in size, and yet magnetically isolated from each other to minimize the transition noise.

Barium hexaferrite thin-film recording media are promising for this application. Stoichiometric barium ferrite thin films typically have coercivity of 3000–4000 Oe. The mechanical hardness and chemical stability of barium ferrite may furthermore eliminate the need for a protective overcoat. The magnetic interactions between grains in barium ferrite thin films are believed to be magnetostatic.[2] Magnetostatic coupling usually gives rise to lesser transition noise than does exchange coupling, however stoichiometric barium ferrite films have grain sizes of 3000–5000 Å, which is too large to achieve reasonable SNR in high-density magnetic recording.

CoTi doping in barium ferrite thin films was investigated by Sui *et al.*[3] and Wong *et al.*[4] It was observed, however, that CoTi doping reduced not only the grain size, but also the coercivity. In their study, a CoTi doped film which had an average grain size of 160 Å was found to have a coercivity below 1000 Oe. It is desirable to obtain reduced grain size, but still maintain high coercivity.

Hylton *et al.*,[5] reported small grain size and high coercivity barium ferrite films by inclusion of small amounts of Cr_2O_3, yttrium stabilized zirconia (YSZ), ZrO_2, and other additives. The purpose of the present study is to further pursue the effects of doping on the microstructural and magnetic properties of barium ferrite thin films, particularly when Cr_2O_3 or Y_2O_3 are used as the dopants.

II. EXPERIMENTAL PROCEDURES

The barium hexaferrite films were deposited by rf sputtering in a Leybold Z-650 sputtering system by co-sputtering of two 3 in. targets. A $Ba_{1.25}Fe_{12}O_{19}$ target was used as the primary target. Cr_2O_3 or Y_2O_3 targets were used as the secondary target. In order to achieve as small as 1% volumetric addition of the dopants in the barium ferrite films, the path between the secondary target and the substrate palette was blocked by a plate with an adjustable slot opening. During the sputtering process, oxidized Si substrates on a rotating substrate palette were exposed to the targets alternately. The amount of doping was adjusted by controlling the slot opening and by changing the sputtering powers of both targets. In this study, the sputtering power of the secondary target was fixed at 50 W, and a sputtering power of 75 W or 125 W was used for the barium ferrite target. The total Ar/O_2 gas flow rate was 120 sccm with an O_2 flow rate of 20 sccm. The thicknesses of all the films were 1000 Å.

One batch of the as-deposited amorphous films (A1, B1, C1) was annealed for 15 min in a tube furnace preheated to 800 °C. Another batch of amorphous films (A2, B2, C2) was soaked at 600 °C for 10 h and then annealed at 800 °C for 15 min in the same furnace. The magnetic properties of the films were studied on an alternating gradient magnetometer (AGM). From the magnetic hysteresis loops of the samples, M_s, H_c, and squareness were determined. The doping and sputtering conditions of these films, as well as their magnetic properties, are listed in Table I.

TABLE I. In-plane magnetic properties.

Sample	Dopant	BaFe sputtering power (W)	M_s (emu/cc)	H_c (Oe)	Sq.	S^*
A1	···	75	266	3250	0.65	0.55
A2	···	75	250	3080	0.67	0.59
B1	Cr_2O_3	75	271	3230	0.69	0.53
B2	Cr_2O_3	75	289	3550	0.70	0.52
C1	Y_2O_3	125	230	3165	0.47	0.34
C2	Y_2O_3	125	238	3210	0.49	0.30

 0021-8979/96/79(8)/4878/3/$10.00 © 1996 American Institute of Physics

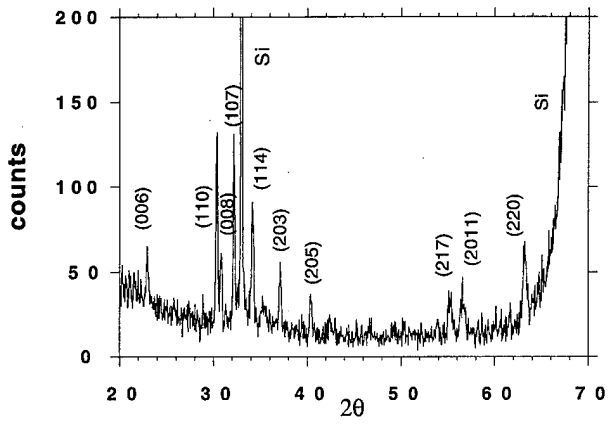


FIG. 1. X-ray diffraction spectrum of sample B2.

III. RESULTS

Typical X-ray diffraction patterns shown in Fig. 1 indicate that the majority of the grains have their c axes oriented randomly in the plane of the films as suggested by the strong (110) and (220) peaks. However, other peaks appearing in the diffraction pattern indicate a considerable volume of the film with out-of-plane orientation of the c axis.

The surface morphologies of the films were characterized using an atomic force microscope (AFM). It was observed that the samples which were annealed at 800 °C had acicular grainlike features typically 5000 Å in length. The AFM image of sample A1 is shown in Fig. 2. In samples B1 and C1, which were doped with Cr_2O_3 and Y_2O_3, respectively, similar equiaxed features were observed.

The AFM images of the doped samples, which had been soaked at 600 °C prior to annealing at 800 °C, showed a very different surface morphology. Sample B2 has only fine equiaxed features, as indicated in Fig. 3. The average feature size of sample B2 is about 500 Å. Sample C2 has even finer

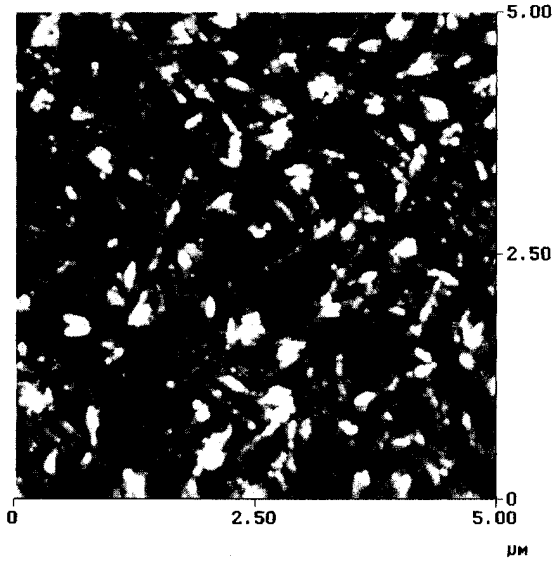


FIG. 2. AFM image of the undoped sample A1 which was annealed at 800 °C.

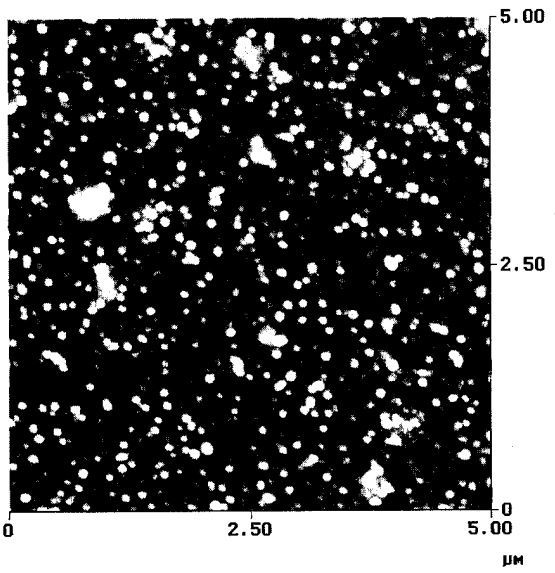


FIG. 3. AFM image of the Cr_2O_3 doped sample B2 which was soaked at 600 °C for 10 h prior to annealing at 800 °C.

equiaxed features yet there are still some traces of large acicular grainlike features. The surface morphological structure of the undoped sample A2, which had been soaked at 600 °C prior to annealing at 800 °C, remained similar to the surface morphology of sample A1.

The in-plane hysteresis loops of the films were measured using an AGM. The results are listed in Table I. The coercivity of sample B2 is 3550 Oe, about 10% greater than samples A1 or B1. The squarenesses of samples A1, A2, B1, and B2 range from 0.65 to 0.7, whereas the squareness of samples C1 and C2 is approximately 0.5.

Values of ΔM[6,7] were also measured for the films. The results for samples A1 and B2 are plotted in Fig. 4 as a function of applied field. Both samples show a small positive interaction among the grains at low field and a small negative interaction at high field.

The thermal stability of the films was studied by measurements of the magnetic viscosity[8] at room temperature. A

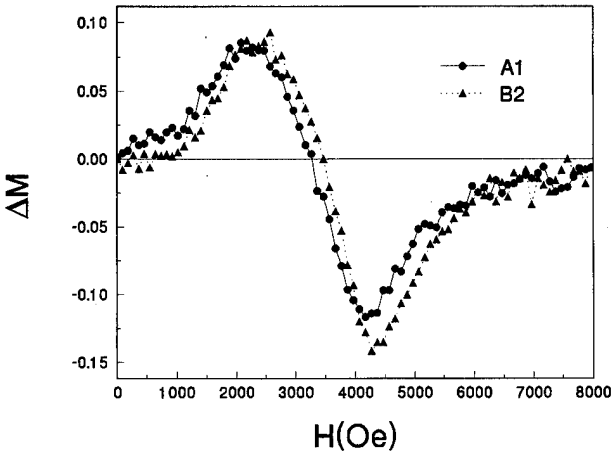


FIG. 4. Plots of ΔM for samples A1 and B2.

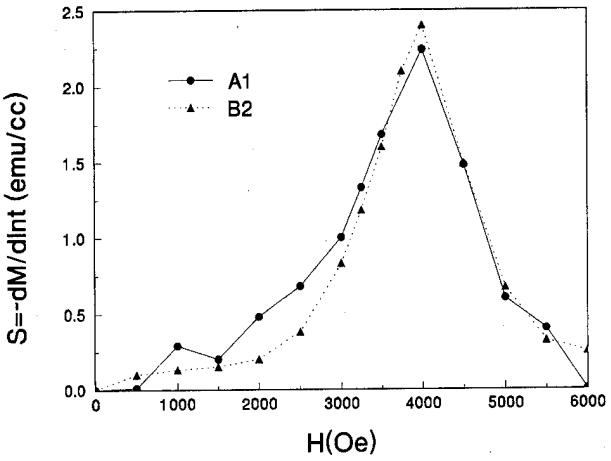


FIG. 5. Magnetic viscosity $S=-dM/\ln t$ plotted vs field for samples A1 and B2.

12 000 Oe magnetic field was first applied to saturate the samples and was subsequently reversed in direction and held at H during the measurement. The process was repeated for various values of H. The time dependences of the magnetization were then measured for up to 200 s. The magnetic viscosity S $(=|dM/d\ln t|)$ was extracted through linear regressions of the M vs $\ln t$ plots. There were small variations of S in different time regimes. The linear regressions of data were carried out at 100 s for consistency. The data of samples A1 and B2 are shown in Fig. 5. Both samples have a similar field dependence of magnetic viscosity. There is no thermal decay observed at $H=0$ for either sample. The magnetic viscosity S of sample B2 is less than 0.2 emu/cc at $H<2000$ Oe.

IV. DISCUSSION AND CONCLUSIONS

The imperfection of the c-axis in-plane orientation as indicated by the x-ray diffraction spectra in Fig. 1 may be due to the high sputtering power used on the barium ferrite target. Sui *et al.*[9] previously showed that the c-axis in-plane orientation could be enhanced by using low sputtering power. However, low sputtering power results in a low sputtering rate of about 2 Å/min for barium ferrite and a long sputtering time >8 h for a 1000 Å thick film.

From the studies of the topographic structure, it is concluded that doping of barium ferrite with Cr_2O_3 or Y_2O_3, followed by proper annealing, results in changes in the surface morphology of the films. The doped and annealed samples exhibit a finer and more equiaxed surface morphology than the undoped samples. This surface morphology is in fact very similar to the grain structure observed previously by transmission electron microscopy (TEM) in CoTi doped samples,[4] and it is believed that the Cr_2O_3 and Y_2O_3 doped films also have a fine grain structure, although this has not yet been confirmed by TEM.

The small increase of H_c in both the Cr_2O_3 and Y_2O_3 doped films contrasts with the reduction in H_c previously observed in CoTi doped films.[4] CoTi doping is known to reduce the anisotropy of barium ferrite. Hence the reduction of H_c in that case is expected. The increase in coercivity for Cr_2O_3 and Y_2O_3 doping may be related to the observed changes in topography, actual changes in grain size or shape,[10] or to nonmagnetic phases introduced by the Cr_2O_3 or Y_2O_3.

The values of squareness of samples A1, A2, B1, and B2 bear the characteristics of 2D randomly oriented single domain particles. The smaller values of squareness of samples C1 and C2 are believed to be caused by the more random c-axis orientation, due to the greater sputtering power used as indicated by x-ray diffraction spectra. It is noted that the squareness value of 0.5 corresponds to the squareness expected from a random array of noninteracting particles.

The small positive portion of the ΔM curve is believed to be caused by positive magnetostatic interaction between stacked grains. The values of ΔM become negative at larger fields, presumably because of negative magnetostatic interactions of adjacent grains. The transition occurs when about half of the grains or grain clusters have switched their magnetization direction.

The small thermal decay found in the magnetic viscosity measurements indicates that the films are thermally stable.

ACKNOWLEDGMENT

This work was supported by the National Science Foundation under Grant No. ECD-8907068.

[1] E. S. Murdock, R. F. Simmons, and R. Davidson, IEEE Trans. Magn. **MAG-28**, 3078 (1992).
[2] Y. J. Chen, X. Sui and M. H. Kryder (to be published).
[3] X. Sui and M. H. Kryder, IEEE Trans. Magn. **MAG-30**, 4044 (1994).
[4] B. Wong, X. Sui, D. E. Laughlin, and M. H. Kryder, J. Appl. Phys. **75**, 5966 (1994).
[5] T. L. Hylton, M. A. Parker, M. Ullah, K. R. Coffey, and J. K. Howard, J. Appl. Phys. **75**, 5960 (1994).
[6] E. P. Wohlfarth, J. Appl. Phys. **29**, 595 (1958).
[7] P. E. Kelly, K. O'Grady, P. I. Mayo, and R. W. Chantrell, IEEE Trans. Magn. **MAG-25**, 3881 (1989).
[8] R. Street and J. C. Wooley, Proc. Phys. Soc. London, Sect. A **62**, 562 (1949).
[9] X. Sui and M. H. Kryder, Appl. Phys. Lett. **63**, 1582 (1993).
[10] E. Kneller and F. E. Luborsky, J. Appl. Phys. **34**, 656 (1963).

Sputtered hexagonal Ba-ferrite films for high-density magnetic recording media

Akimitsu Morisako and Mitsunori Matsumoto
Deptartment of Information Engineering, Shinshu University, 500 Wakasato, Nagano 380, Japan

Masahiko Naoe
Department of Physical Electronics, Tokyo Institute of Technology, 2-12-1 O-okayama, Meguro-ku 152, Japan

Ba-ferrite (BaM) thin films were prepared by both a facing targets sputtering (FTS) system and dc magnetron sputtering (DCMS) at room temperature. They were successively annealed to crystallize. The films prepared by FTS system were crystallized at 650 °C, while those prepared by DCMS system were crystallized at 700 °C. Saturation magnetization, coercivity, and squareness ratio of the films prepared by FTS are 210 emu/cc, 3.3 kOe, and 0.7 in perpendicular direction, respectively, after the annealing at 650 °C. It was found that oxidized Fe is partially reduced to metallic Fe by high-temperature annealing. © *1996 American Institute of Physics.* [S0021-8979(96)07408-2]

I. INTRODUCTION

High-density recording medium should have an excellent mechanical durability as well as moderate hard magnetism. Oxide films have a big advantage in chemical stability and mechanical durability as compared with a metal thin film. The authors have been studying hexagonal Ba-ferrite (BaM) films prepared by a sputtering[1] and sol-gel method[2] for high-density perpendicular magnetic recording media. In order to prepare BaM films with c-axis orientation, the substrate temperature should be elevated to about 620 °C,[1] but such a high temperature is not suitable for the practical fabrication of recording media. The authors have already reported that a Pb addition is effective to lower the substrate temperature to 550 °C.[3] It is still recommended to lower the substrate temperature for the practical fabrication. Recently, a few studies on the postannealing effects for amorphous BaM films prepared by a conventional diode sputtering system have been reported.[4,5]

In this study, in order to develop a new fabrication technique for BaM thin films, BaM ferrite films have been prepared at room temperature by using both a facing target sputtering (FTS) system and a conventional dc magnetron sputtering (DCMS) system at room temperature. These films were successively annealed in air and their crystallographic characteristics and magnetic properties have been studied.

II. EXPERIMENT

The films were prepared by using a FTS system[6] and DCMS system at room temperature. In the FTS system, a pair of permanent magnets are installed behind both targets. The magnetic field from these magnets confines the plasma between the targets. Consequently, the films can grow without disturbance from the plasma because the substrate is located out of the plasma.

After evacuating the chamber to a pressure below 2×10^{-6} Torr for both sputtering systems, argon and oxygen gases were introduced and working gas pressure was set at 3 mTorr. The targets used in this study were sintered ferrite disks (8 cm diameter) with stoichiometric composition of BaM (i.e., $BaFe_{12}O_x$). The substrates were thermally oxidized silicon wafers and the substrate temperature was set at room temperature. The thickness of the films was about 1500 Å.

The deposited films were annealed at 600–900 °C for 5 h in air. The crystal structure was determined by x-ray diffractometry (Cu $K\alpha$). The chemical shift for Fe in the BaM films were evaluated by x-ray photoelectron spectroscopy (XPS).

III. RESULTS AND DISCUSSION

All of the films prepared by FTS and DCMS systems at room temperature were amorphous. The compositions of the films prepared by the FTS system were $Ba_{0.9}Fe_{12}O_x$, while those prepared by DCMS were $Ba_{0.6}Fe_{12}O_x$. The large deficiency of Ba in the films prepared by DCMS is mainly caused by the bombardment of the high-energy particles, which are recoiled discharge gas atoms and γ electrons emitted from the target.

Figure 1 shows x-ray diffraction diagrams of BaM films annealed at various temperatures (Ta). The films prepared by the FTS system were crystallized after they were annealed at

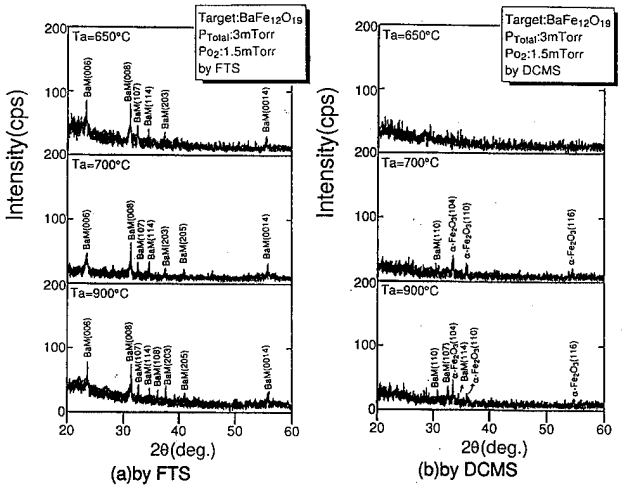


FIG. 1. X-ray diffraction diagrams of the film prepared by FTS (a) and DCMS (b).

 0021-8979/96/79(8)/4881/3/$10.00 © 1996 American Institute of Physics

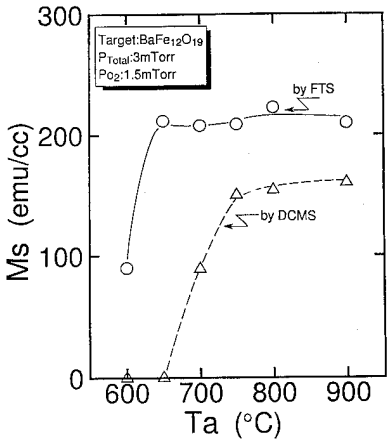


FIG. 2. Dependence of saturation magnetization on the annealing temperature.

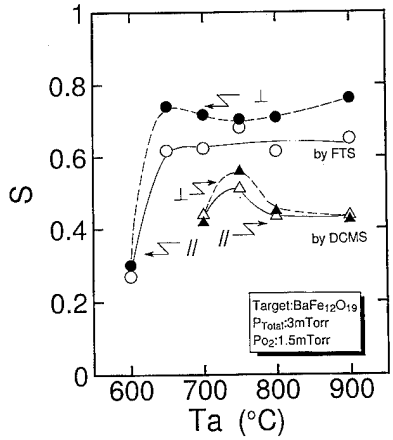


FIG. 4. Dependence of squareness ratio on the annealing temperature.

650 °C, while those prepared by DCMS system were crystallized at above 700 °C of Ta, as shown in Fig. 1. It was found that the crystallization of the films prepared by FTS begins at lower temperature. The diffraction lines for the annealed films prepared by the FTS system are only from the M phase and various planes in hexagonal crystallite are observed. This suggests that magnetic properties of annealed films prepared by FTS are almost isotropic. In contrast with these results the diffraction lines from both the BaM and α-Fe_2O_3 phase are observed for the annealed films prepared by the DCMS system. This is due to the deficiency of Ba in the films as mentioned above.

Figure 2 shows the dependence of saturation magnetization (Ms) for the annealed films on Ta. Ms for the films prepared by the FTS system was almost zero after annealing at 550 °C. The Ms increases from 90 to 210 emu/cc with increase of Ta from 600 to 650 °C and exhibits constant value of 210 emu/cc for further elevation of Ta. The Ms for the films prepared by DCMS increases from zero to 150 emu/cc, with an increase of Ta up to 750 °C, and exhibits almost constant value of 160 emu/cc for further elevation of Ta up to 900 °C. The Ms for the films prepared by DCMS is lower than that of the films prepared by the FTS system. This is caused by the coexistence of the nonmagnetic α-Fe_2O_3 phase, as shown in Fig. 1.

Figure 3 shows the dependence of coercivity (Hc) on Ta. The Hc were measured at both in-plane direction (∥) and perpendicular direction (⊥). The films prepared by the FTS and DCMS systems show the hysteresis loop after the annealing at Ta at above 600 °C and above 700 °C, respectively. The $Hc_{\parallel}$ and $Hc_{\perp}$ have almost same value for the films prepared by the FTS system and increase from about 0.3 to 3.4 kOe with the increase of Ta from 600 to 650 °C and gradually increase with increasing of Ta higher than 650 °C. The $Hc_{\parallel}$ and $Hc_{\perp}$ for the films prepared by the DCMS system are from 1.0 to 1.8 kOe and considerably lower than those of the films prepared by the FTS system.

Figure 4 shows the dependence of the squareness ratio (S) in the directions both in-plane and perpendicular to the film plane on Ta. The squareness ratio in both directions for the films prepared by the FTS system increases with the increase of Ta from 600 to 650 °C and exhibits almost constant values at Ta of above 650 °C. The squareness ratio in perpendicular direction is about 0.7 and slightly higher than those of in-plane direction for the films prepared by the FTS system, while those for the films prepared by DCMS take the maximum values of about 0.5 at Ta of 750 °C.

Figure 5 shows the XPS spectra for the films prepared by the FTS system [see Fig. 5(a)] and DCMS [see Fig. 5(b)].

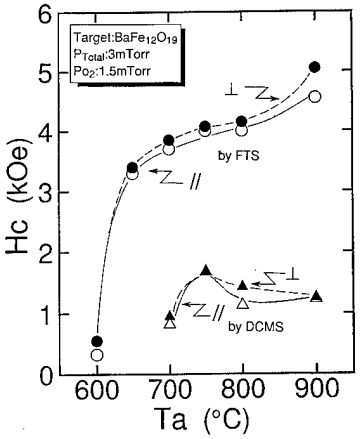


FIG. 3. Dependence of coercivities on the annealing temperature.

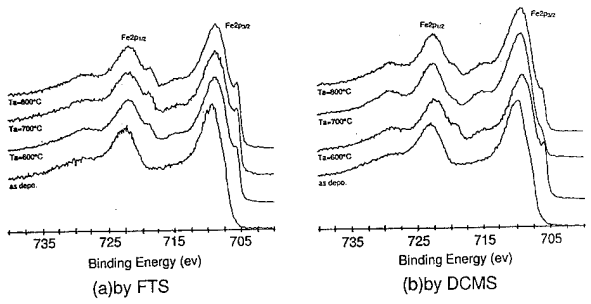


FIG. 5. XPS spectra of the films prepared by FTS (a) and DCMS (b) systems.

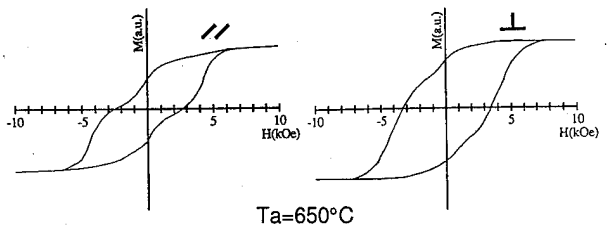


FIG. 6. M–H loops for the film prepared by the FTS system after annealing at 650 °C.

Two spectra are observed in as-deposited films. These are from the α-Fe_2O_3 phase. The extra spectrum around 705 eV corresponds to metallic Fe and can be observed for the annealed films. This means that oxidized Fe is reduced to metallic Fe by high-temperature annealing in air. In order to suppress the reduction of oxidized Fe, the oxygen gas pressure should be controlled during the annealing.

Figure 6 shows the M–H loops of the films prepared by the FTS system after annealing at 650 °C. The loops at perpendicular and in-plane directions are almost similar in shape and seem to be composed of two phases. From the x-ray diffraction diagrams, the phase synthesized in the annealed films is only BaM, as shown in Fig. 1. Although it is not clear to date what kind of magnetic phase is necessary for coexistence, reduced metallic Fe, as mentioned above, seems to affect the shape of M–H loops. These shapes should be improved for high-density magnetic recording media.

IV. CONCLUSION

In this study, BaM films were prepared by the FTS and DCMS systems and they were successively annealed in air to crystallize. It was found that the films prepared by the FTS system are crystallized at lower temperature as compared with the films prepared by the DCMS system. Any preferential crystal orientation was not observed after the annealing of the films prepared by both systems. The annealed films prepared by the FTS system consist of a single BaM phase, while those prepared by DCMS consist of a BaM and nonmagnetic α-Fe_2O_3 phase. Although the reason why the crystallization begins at lower temperature for the films prepared by the FTS system is not clear to date, it suggests that the FTS system has the advantage of practical mass production for the recording medium in comparison to the DCMS system. The magnetic properties for the annealed films are almost isotropic and the values of Hc for the films prepared by the FTS system are from 3 to 5 kOe and higher than those of the films prepared by the DCMS system. Although it is required to control the value of Hc, these values seem to be suitable for ultrahigh density recording media. From the results of XPS measurement it was found that oxidized Fe is reduced to metallic Fe by the high-temperature annealing. This means that partial oxygen gas pressure should be controlled during the annealing process. To clarify the differences in the crystallization process for the films prepared by the FTS and DCMS systems, further experiments should be necessary.

ACKNOWLEDGMENTS

This work was sponsored in part by a Grant-in-Aid for Developmental Scientific Research (Contract No. 06655093) from the Ministry of Education, Science, Sport, and Culture of Japan and the Takayanagi Foundation for Electronics Science and Technology.

[1] A. Morisako, M. Matsumoto, and M. Naoe, IEEE Trans. Magn. **MAG-23**, 2358 (1987).
[2] M. Matsumoto, A. Morisako, and T. Haeiwa, Advances in Ferrites (Proceedings of ICF-5, Bombay, India), 1989, p. 533.
[3] A. Morisako, H. Nakanishi, M. Matsumoto, and M. Naoe, J. Appl. Phys. **75**, 5969 (1994).
[4] A. Morisako, M. Matsumoto, and M. Naoe, Ferrites (Proceedings of ICF-6, Tokyo and Kyoto, Japan), 1992, p. 436.
[5] T. L. Hylton, M. A. Parker, K. R. Koffey, R. Umphress, and J. K. Howard, J. Appl. Phys. **75**, 5960 (1994).
[6] M. Naoe, S. Yamanaka, and Y. Hoshi, IEEE Trans. Magn. **MAG-16**, 646 (1980).

Recording characteristics of Co-γFe_2O_3 perpendicular magnetic recording media

S. Yamamoto, T. Andou, H. Kurisu, and M. Matsuura
Faculty of Engineering, Yamaguchi University, Tokiwadai, Ube 755, Japan

T. Doi and K. Tamari
R&D Division, Toda Kogyo Corporation, Meiji-shinkai, Otake, Hiroshima 739-06, Japan

The recording characteristics of Co-γFe_2O_3 perpendicular magnetic recording hard disk media were investigated. Sliding contact recording was performed to evaluate the intrinsic high-density recording performance of the media with using a metal-in-gap-type ring head. The half-voltage density D_{50} of 176 kFRPI and low-density reproduced voltage E_p of 143 $nV_{p\text{-}p}$/[turn μm (m/s)] were obtained for the optimal medium whose Co-γFe_2O_3 layer thickness was 0.13 μm and perpendicular coercivity was 1800 Oe. The pass wear durability test was performed at 2 m/s, or at a disk rotation of 830 rpm. The reproduced voltage did not decrease with time, and scratches and damage were not observed on the tested track even after 18 000 000 passes. The Co-γFe_2O_3 medium is one of the candidates for ultrahigh-density recording media because of its specific advantages; superior high density recording performance and hardness tolerable for sliding contact use.
© *1996 American Institute of Physics.* [S0021-8979(96)14508-7]

I. INTRODUCTION

After the invention of perpendicular magnetic recording, various types of perpendicular magnetic recording media were proposed.[1–7] It has been proven experimentally that an extremely high density recording exceeding 500 kFRPI is possible in perpendicular magnetic recording using a Co–Cr perpendicular media.[8,9] Contact recording is essential to achieve such a high density recording with suppressing spacing loss. There are two ways to achieve contact recording: One is to develop superior overcoat materials, and the other is to develop magnetic thin films for recording layers with sufficient hardness. In the case of Co–Cr medium, an overcoat layer, such as amorphous carbon and SiO_x, is necessary for contact recording because of its insufficient hardness. Oxidized magnetic material is expected to be one of the candidates in the latter approach described above because it is essentially harder than the metallic magnetic materials.

We have already reported that the spinel Co-γFe_2O_3 films obtained by annealing the sputtered CoO/Fe_3O_4 multilayers have a large perpendicular magnetic anisotropy, which originates from preferential crystalline orientation of the [100] axis.[10,11] The perpendicular coercivity of these Co-γFe_2O_3 films can be controlled in the wide range from 0.8 to 5.0 kOe. From the viewpoint of magnetic properties, the Co-γFe_2O_3 films are applicable to perpendicular magnetic recording media. However, the recording performance for the Co-γFe_2O_3 recording media fabricated by this process has never been measured.

In this study, therefore, the feasibility of these films as perpendicular magnetic recording hard disk media in contact recording use was investigated with respect to recording characteristics and pass-wear durability.

II. EXPERIMENT

In the fabrication of Co-γFe_2O_3 perpendicular magnetic recording hard disk media, at first, a 0.2 μm thick NiO layer was deposited on 2.5 in. glass substrate by reactive rf sputtering. Successively, CoO/Fe_3O_4 multilayers were deposited on the NiO underlayer at a substrate temperature of 200 °C. Finally, the disks were annealed at the temperatures from 280 to 350 °C to obtain perpendicular anisotropy.[11] No overcoat layers were prepared on any of the disks.

The specification of the tested Co-γFe_2O_3 hard disks is shown in Table I. In sample series A, the thickness of Co-γFe_2O_3 recording layer δ, varies from 0.10 to 0.17 μm. In series B, perpendicular coercivity $H_{c\perp}$, varies from 1472 to 2506 Oe. The metal-in-gap (MIG) ring heads with a gap length of about 0.2 μm designed for the Hi-band 8 mm VCR were used to measure the recording characteristics. The sliding contact method was introduced to evaluate the intrinsic high-density recording performance of the media.[12]

III. RESULTS AND DISCUSSION

The thickness and perpendicular coercivity dependence of recording characteristics was measured using series A and B samples, respectively, to optimize the media parameters. For all the media, the isolated reproduced pulse shape was di-pulse showing that the perpendicular magnetization mode was realized.

TABLE I. Specification of Co-γ Fe_2 O_3 perpendicular magnetic recording hard disks.

		δ (μm)	$H_{c\perp}$ (Oe)
Series A	Sample A1	0.10	1930
	Sample A2	0.13	1861
	Sample A3	0.17	1900
Series B	Sample B1	0.13	1472
	Sample B2	0.13	1630
	Sample B3	0.13	1710
	Sample B4	0.13	1861
	Sample B5	0.13	2323
	Sample B6	0.13	2506

 0021-8979/96/79(8)/4884/3/$10.00 © 1996 American Institute of Physics

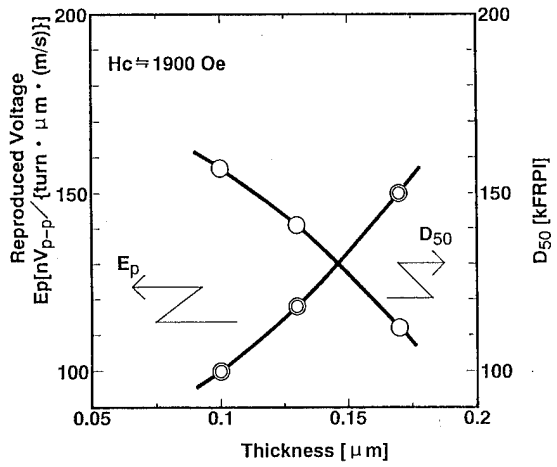


FIG. 1. Co-γFe_2O_3 layer thickness dependence of half-voltage density (D_{50}) and low density reproduced voltage E_p.

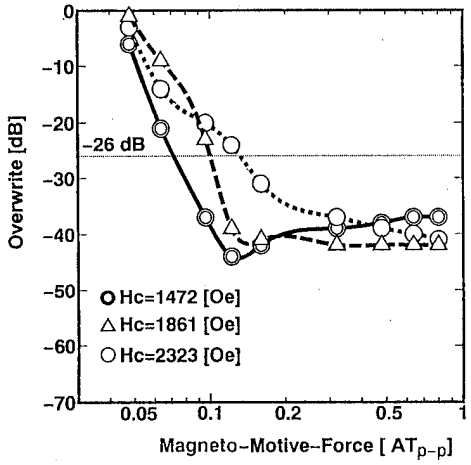


FIG. 3. Overwrite characteristics for 0.13 μm thick Co-γFe_2O_3 disks.

The Co-γFe_2O_3 layer thickness dependence of the D_{50} and E_p is shown in Fig. 1. As the Co-γFe_2O_3 layer thickness decreases from 0.17 to 0.1 μm, the half-voltage density D_{50}, increases. On the other hand, the peak voltage of the isolated reproduced pulse E_p, decreases with decreasing Co-γFe_2O_3 layer thickness. It is necessary to optimize the Co-γFe_2O_3 layer thickness according to the density because a tradeoff relation exists between D_{50} and E_p. At densities over 100 kFRPI (kilo flux reversals per inch), the highest reproduced voltage was obtained by using a 0.13 μm thick Co-γFe_2O_3 disk.

The perpendicular coercivity dependence of the D_{50} and E_p is shown in Fig. 2. These data were obtained using 0.13μm thick Co-γFe_2O_3 disks. Both for the D_{50} and E_p, the maximum value obtained at the perpendicular coercivity was about 1700 Oe.

Overwrite characteristics were also measured for the 0.13 μm thick Co-γFe_2O_3 disks to check the performance for saturation recording. The 36 kFRPI signal was overwritten by a 58 kFRPI signal. Overwrite value, which is defined as the ratio of the 36 kFRPI reproduced signal voltage after and before overwrite operation, was plotted against the recording magnetomotive force in Fig. 3. For all the disks with perpendicular coercivity from 1750 to 2338 Oe, the ultimate overwrite value becomes close to −40 dB. This result shows that the recording magnetic field generated by the MIG head is strong enough to perform saturation recording on the 0.13 μm thick disks.

The bit density response curves were shown in Fig. 4. For comparison, the commercialized 2.5-in. longitudinal recording hard disk was also tested. In the longitudinal hard disk, a CoNi recording layer and the 20 nm thick overcoat layer were deposited on a glass substrate. The longitudinal coercivity and the remanent magnetization and thickness product $M_{r\delta}$, of the CoNi layer were 1370 Oe and 2.5×10^{-3} emu/cm^2, respectively. The D_{50} of 176 kFRPI and E_p of 143 $nV_{p\text{-}p}$/[turn μm (m/s)] were obtained for the Co-γFe_2O_3 perpendicular hard disk whose Co-γFe_2O_3 thickness was 0.13 μm and perpendicular coercivity was 1800 Oe. These values of D_{50} and E_p were 1.9 and 1.2 times higher than those of the CoNi longitudinal disk.

The pass wear durability test was performed at 2 m/s, or

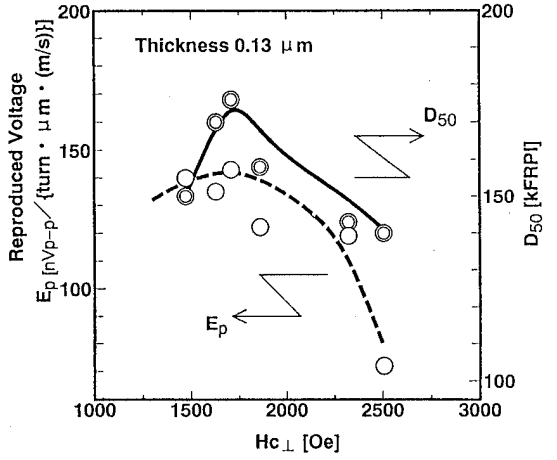


FIG. 2. Perpendicular coercivity dependence of D_{50} and E_p.

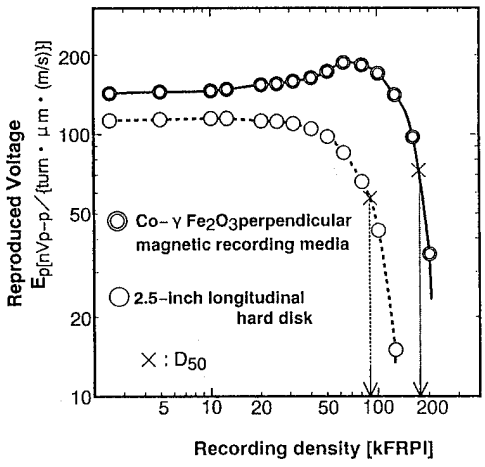


FIG. 4. Bit density response curves for Co-γFe_2O_3 perpendicular magnetic recording disk (◎) and CoNi longitudinal magnetic recording disk (○).

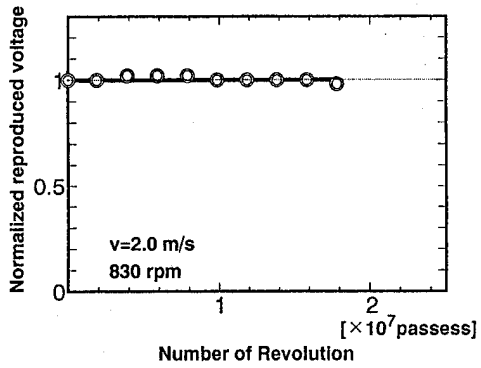


FIG. 5. Pass wear durability test.

a disk rotation of 830 rpm. The liquid lubricant was applied on the Co-γFe_2O_3 disk. After the 50.7 kFRPI signal was recorded, reproduction operation was continued with monitoring the reproduced signal voltage. In Fig. 5, the reproduced signal voltage was plotted against the number of disk revolutions. For comparison, a sputtered Co–Cr perpendicular hard disk without an overcoat layer was also tested. The Co–Cr disk was damaged just after the pass wear test started. On the contrary, for the Co-γFe_2O_3 hard disk, deviation of the reproduced voltage from the initial state was within a few percent, and no scratches or damage were observed even after 18 000 000 passes.

IV. CONCLUSION

A D_{50} of 176 kFRPI and E_p of 143 $nV_{p\text{-}p}$/[turn μm (m/s)] have been obtained for the Co-γFe_2O_3 hard disk with optimized thickness and coercivity. It was found that the Co-γFe_2O_3 disk has pass wear durability over 18 000 000 revolutions in spite of no overcoat.

From these experimental results, it is concluded that the Co-γFe_2O_3 medium is one of the candidates for ultrahigh-density recording media because of its specific advantages; superior high density recording performance and hardness tolerable for sliding contact use.

[1] S. Iwasaki and Y. Nakamura, IEEE Trans Magn. **MAG-13**, 1272 (1977).
[2] O. Kubo, T. Ido, and H. Yokoyama, IEEE Trans. Magn. **MAG-18**, 1122 (1982).
[3] Y. Ota, N. Tani, M. Ishikawa, T. Yamada, K. Nakamura, and A. Itoh, IEEE Trans. Magn. **MAG-20**, 768 (1984).
[4] J. R. Desserre and D. Jeanniot, IEEE Trans. Magn. **MAG-19**, 1647 (1983).
[5] Y. Hoshi, M. Matsuoka, and M. Naoe, IEEE Trans. Magn. **MAG-21**, 1459 (1985).
[6] Y. Ohtani, Trans. IEICE Jpn. **J68-C**, 818 (1985).
[7] J. K. Lin, J. M. Sivertsen, and J. H. Judy, IEEE Trans. Magn. **MAG-21**, 1462 (1985).
[8] S. Yamamoto, Y. Nakamura, and S. Iwasaki, IEEE Trans. Magn. **MAG-23**, 2070 (1987).
[9] S. Yanase, T. Kiya, N. Honda, and K. Ouchi, Tech. Rep. IEICE Jpn. **MR95-14**, 15 (1995).
[10] K. Tamari, T. Doi, and N. Horiishi, Appl. Phys. Lett. **63**, 3227 (1993).
[11] T. Doi and K. Tamari, 40th Annual Conference on MMM (1995).
[12] Y. Nakamura, J. Magn. Soc. Jpn. **15**, 497 (1991).

Preparation and the magnetic properties of Co-γ-Fe_2O_3 perpendicular magnetic films on NiO underlayer

T. Doi and K. Tamari
R&D Division, Toda Kogyo Corporation, 1-4 Meiji-shinkai, Ohtake, Hiroshima 739-06, Japan

The NiO underlayer, which had ⟨100⟩ orientation, with NaCl-like structure could be prepared onto the glass substrate by reactive rf sputtering at ambient temperature. The CoO/Fe_3O_4 multilayers were grown epitaxially on the underlayer at 200 °C; the Fe_3O_4 and CoO on the NiO grew along the ⟨100⟩ axis independent of the bilayer thickness Λ, though those on the glass substrate did not show the ⟨100⟩ orientation for $\Lambda > 100$ Å. Followed by annealing of the multilayers in air at 280–350 °C, the ⟨100⟩-oriented Co-γ-Fe_2O_3 perpendicular magnetic films were obtained. The (400) of the Co-γ-Fe_2O_3 on the (200) of the NiO has tensile stress at the interface because of the smaller (400) spacing than the (200) spacing normal to the film plane. Therefore, the (400) spacing measured parallel to the film plane (2.072 Å) was smaller than that of bulk, 2.086 Å. The magnetic properties of the Co-γ-Fe_2O_3 films on the NiO, Co-γ-Fe_2O_3/NiO, obtained above were evaluated. The squareness compensated by a demagnetization coefficient of Co-γ-Fe_2O_3/NiO were more than 0.94, though those of the Co-γ-Fe_2O_3 on the glass substrate, Co-γ-Fe_2O_3/glass, were about 0.85. The anisotropy energy of Co-γ-Fe_2O_3/NiO was estimated 3.3×10^6 ergs/cm^3, which value was larger than that of Co-γ-Fe_2O_3/glass (2.5×10^6 ergs/cm^3). Coercivity of the perpendicular hysteresis loop of Co-γ-Fe_2O_3/NiO increased with Co contents and could be controlled in the region of 0.8–5.0 kOe, although H_c of Co-γ-Fe_2O_3/glass were 5.0 kOe constantly. The columnar grains of the Co-γ-Fe_2O_3, whose diameter is 300–500 Å, grew continuously along the columnar grains of NiO.
© *1996 American Institute of Physics.* [S0021-8979(96)07508-9]

I. INTRODUCTION

Continuous thin films composed of γ-Fe_2O_3 with a spinel crystal structure have been noted as magnetic recording media because of their high chemical stability, corrosion resistance, large coercivity, and durability due to high hardness. In particular, the perpendicular magnetic films, e.g., the Os doped γ-Fe_2O_3 films obtained by the annealing of the films in an external magnetic field,[1] have been investigated for high-density recording media.

In our previous studies, we have found the preparation method to obtain the Co containing γ-Fe_2O_3, Co-γ-Fe_2O_3, perpendicular magnetic films by control of the crystalline orientation;[2] For the CoO/Fe_3O_4 multilayers of the bilayer thickness $\Lambda < 80$ Å on the glass substrate, the multilayers indicate ⟨100⟩ orientation, and ⟨100⟩-oriented Co-γ-Fe_2O_3 films can be obtained by annealing of the multilayers in air at 400 °C. The Co-γ-Fe_2O_3 films have a large perpendicular magnetic anisotropy energy, which is induced with the preferential crystalline orientation of ⟨100⟩ axis.

In the present study, we researched the underlayer that promotes ⟨100⟩ orientation of the Co-γ-Fe_2O_3. Numerous works show that cubic spinel type crystal can be grown epitaxially on cubic NaCl-like structural materials such as rock salt,[3,4] single-crystal MgO,[5,6] CoO on rock salt,[7] and NiO on single-crystal MgO.[8] From this point of view, we tried to prepare ⟨100⟩-oriented NiO films on the glass substrate, not on the single-crystal substrates, as the underlayer. Furthermore, the magnetic properties of the Co-γ-Fe_2O_3 films prepared onto the NiO underlayer were investigated in comparison with the Co-γ-Fe_2O_3 films on the glass substrate. The microstructures of the Co-γ-Fe_2O_3 films on the NiO were also investigated.

II. EXPERIMENT

NiO films were prepared in Ar+O_2 mixed gas (O_2 pressure, P_{O_2}, was 0.07–0.09 mTorr) onto the glass substrate (HOYA N5) by reactive rf sputtering. The NiO film growth rate was 40 Å/min. CoO/Fe_3O_4 multilayers were prepared onto the NiO film and the glass substrate in Ar+O_2 mixed gas (P_{O_2} was 0.09–0.11 mTorr) at 200 °C by reactive rf sputtering. The multilayers growth rate was 40 Å/min. For the sputtering targets, Ni, Fe, and Co metal disks with 3 in. in diameter were used, respectively. In order to transform the multilayers to Co-γ-Fe_2O_3 films, the heat treatment was carried out in air at 280–350 °C for 1–3 h. The film thicknesses were measured with a surface roughness instrument. The crystal structures and Λ were examined by x-ray diffraction (Fe $K\alpha$). The magnetic properties were measured with a vibrating sample magnetometer at 20–75 °C. The composition and the depth distribution of composition in the films were analyzed by inductively coupled plasma atomic emission spectroscopy and electron spectroscopy for chemical analysis (ESCA), respectively. Microstructures of the Co-γ-Fe_2O_3 films on the NiO were observed by scanning electron microscope (SEM).

III. RESULTS AND DISCUSSION

NiO films prepared at 25 °C showed ⟨100⟩ orientation [Fig. 1(a)], though the films at 200 °C had ⟨111⟩ orientation. It revealed that the ⟨100⟩-oriented NiO could be obtained at lower temperature than other NaCl-like structural oxide such as ⟨100⟩-oriented MgO which were prepared at 310–750 °C.[9] Figure 2 shows the relationship between the NiO film thickness, δ_{NiO}, and the intensity ratio, $I_{(200)}/I_{(111)}$, in the x-ray diffraction spectra of NiO. For the

 0021-8979/96/79(8)/4887/3/$10.00 © 1996 American Institute of Physics

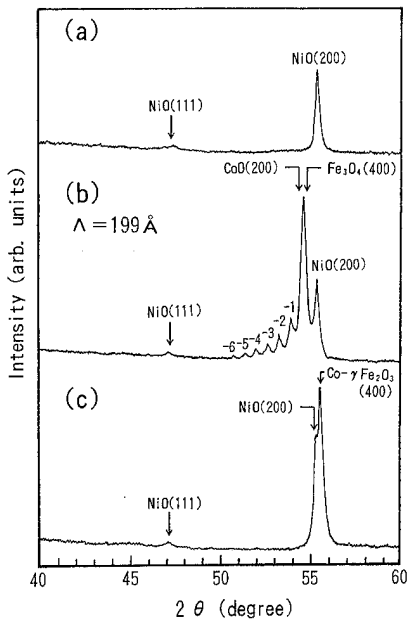


FIG. 1. X-ray diffraction spectra (Fe $K\alpha$) of ⟨100⟩-oriented NiO film of 1200 Å in thickness prepared onto the glass substrate at 25 °C (a), CoO/Fe_3O_4 multilayer ($[CoO(34\ Å)/Fe_3O_4(165\ Å)]_{10}$) prepared onto the ⟨100⟩-oriented NiO (b) and Co-γ-Fe_2O_3 on the ⟨100⟩-oriented NiO obtained by annealing the multilayer at 350 °C for 2 h (c).

films of $\delta_{NiO} \geqslant 800$ Å, $I_{(111)}$ were the same value, about 10 cps, as shown in Fig. 1(a). It is assumed that there is random oriented initial growth layer of 800 Å in thickness, thus the films of $\delta_{NiO} \geqslant 1000$ Å were used as the underlayer in subsequent experiments.

X-ray diffraction spectrum of as-deposited CoO/Fe_3O_4 multilayer prepared for $\Lambda = 199$ Å onto the NiO underlayer is shown in Fig. 1(b). This indicates the multilayers are grown epitaxially on the NiO; The Fe_3O_4 and CoO on the NiO grew along the ⟨100⟩ axis independent of Λ, though those on the glass substrate did not show the ⟨100⟩ orientation for $\Lambda > 100$ Å.[2] The epitaxial growth of these crystals is attributed to good lattice match. The distances between the oxygen atoms in the fcc lattices of NiO, Fe_3O_4, and CoO along ⟨100⟩ direction were 2.089, 2.099, and 2.130 Å, respectively. These

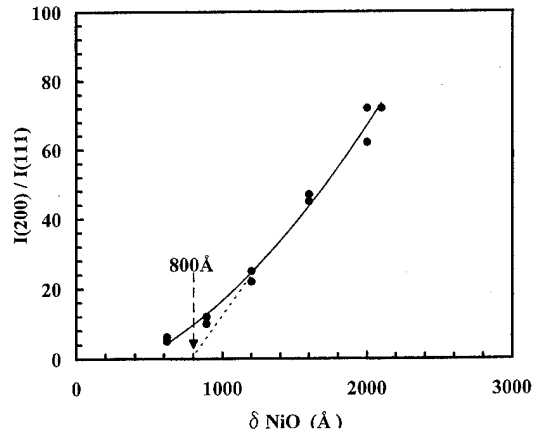


FIG. 2. Dependence of intensity ratio, $I_{(200)}/I_{(111)}$, in the x-ray diffraction spectra on film thickness, δ_{NiO}, of the NiO prepared at 25 °C.

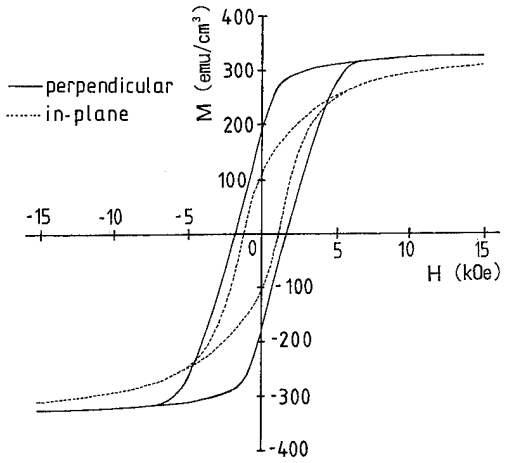


FIG. 3. Magnetic hysteresis loops of ⟨100⟩-oriented Co-γ-Fe_2O_3 of 1300 Å in thickness with Co/Fe=0.03 on NiO underlayer.

dimensions represent a lattice mismatch between NiO and Fe_3O_4 of 0.48%, between Fe_3O_4 and CoO of 1.46%, all are within 1.5% of one another.

The Co-γ-Fe_2O_3 films obtained by annealing the multilayers on the NiO had ⟨100⟩ orientation as shown in Fig. 1(c). The (400) spacing of the Co-γ-Fe_2O_3 measured parallel to the film plane, $d_{(400)}$, was 2.072 Å. This value is smaller than that of bulk, 2.086 Å, because the (400) of the Co-γ-Fe_2O_3 on the (200) of the NiO has tensile stress at the interface due to smaller (400) spacing than (200) spacing normal to the film plane. Diffusion of Ni atoms in the NiO layer into the Co-γ-Fe_2O_3 was not observed.

The ⟨100⟩-oriented Co-γ-Fe_2O_3 films on the NiO, Co-γ-Fe_2O_3/NiO, with the Co-γ-Fe_2O_3 film thicknesses varied from 500 to 2600 Å, were perpendicular magnetic films as shown in Fig. 3. The squareness compensated by a demagnetization coefficient of Co-γ-Fe_2O_3/NiO were more than 0.94, while those of the Co-γ-Fe_2O_3 on the glass substrate, Co-γ-Fe_2O_3/glass, were about 0.85. It is considered that a departure of the magnetic easy axis of Co-γ-Fe_2O_3/NiO from a perpendicular direction is smaller than that of Co-γ-Fe_2O_3/glass, reflecting the importance of

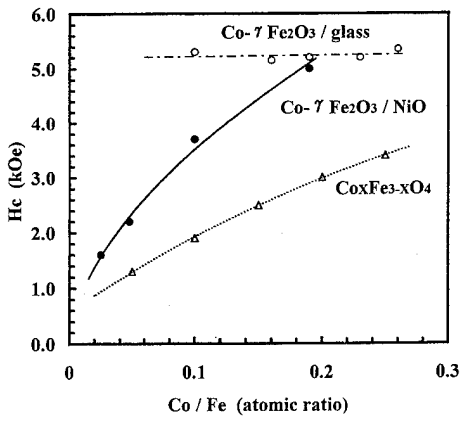


FIG. 4. Coercivity of the perpendicular hysteresis loop, H_c, vs atomic ratio for ⟨100⟩-oriented Co-γ-Fe_2O_3 on NiO underlayer, ⟨100⟩-oriented Co-γ-Fe_2O_3 on the glass substrate, and cobalt ferrite films.

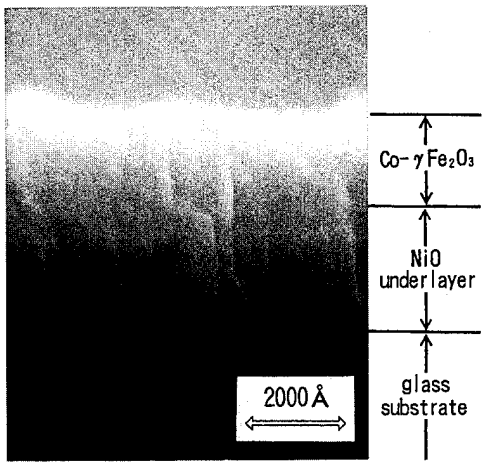


FIG. 5. SEM observation of cross section of ⟨100⟩-oriented Co-γ-Fe_2O_3 film on NiO underlayer obtained by annealing at 300 °C for 2 h.

the ⟨100⟩ orientation. For the films having the coercivity of perpendicular hysteresis loop, H_c, of 5.0 kOe, the anisotropy energy of Co-γ-Fe_2O_3/NiO was estimated 3.3×10^6 ergs/cm^3 from the initial in-plane magnetization curve, which was larger than that of Co-γ-Fe_2O_3/glass (2.5×10^6 ergs/cm^3), because of the tensile stress described above. H_c of Co-γ-Fe_2O_3/NiO increased with Co contents and could be controlled in the region of 0.8–5.0 kOe, although those of Co-γ-Fe_2O_3/glass were 5.0 kOe constantly (Fig. 4). Additionally, the same H_c could be obtained from Co-γ-Fe_2O_3/NiO films with about one-third the Co content of the cobalt ferrite films prepared onto the glass substrate.[10] It seems that the larger H_c for Co-γ-Fe_2O_3/NiO relative to the cobalt ferrite is caused mainly by a higher extrinsic stress-induced anisotropy due to the larger tensile stress. Temperature dependence of H_c, dH_c^*/dT (here dH_c^* is dH_c divided by H_c measured at room temperature), for Co-γ-Fe_2O_3/NiO was −0.266%/°C which was smaller than Co-surface modified γ-Fe_2O_3 powder used for magnetic tapes, −0.32%/°C.[11]

SEM observation of the cross section of Co-γ-Fe_2O_3/NiO is shown in Fig. 5. The columnar grains of the Co-γ-Fe_2O_3, whose diameter is 300–500 Å, grew continuously along the columnar grains of the NiO.

Co-γ-Fe_2O_3/NiO have the possibilities to be a high-density magnetic recording media, e.g., Co-γ-Fe_2O_3/NiO have a large coercivity, a chemical stability, and high hardness tolerable for sliding contact use with no overcoat, i.e., "0" spacing. Further investigations are now in progress.[12]

ACKNOWLEDGMENTS

The authors are grateful to Professor Y. Miura at Okayama University for his technical assistance in the ESCA analysis. We would also like to acknowledge the useful discussions with a member of Toda Kogyo Corporation.

[1] S. Ohta and A. Terada, Thin Solid Films **143**, 73 (1986).
[2] K. Tamari, T. Doi, and N. Horiishi, Appl. Phys. Lett. **63**, 3227 (1993).
[3] Y. Bando, S. Horii, and T. Takada, J. Appl. Phys. **17**, 1037 (1978).
[4] T. Shigematsu, H. Ushigome, Y. Bando, and T. Takada, J. Cryst. Growth **50**, 801 (1980).
[5] N. N. Evtihiev, N. A. Economov, A. R. Krebs, N. A. Zamjatina, V. D. Baurin, and V. G. Pinko, IEEE Trans. Magn. **MAG-12**, 773 (1976).
[6] M. Sakamoto, M. Asano, T. Fujii, T. Nanba, A. Osaka, Y. Miura, and J. Takada, Proceedings of The Sixth International Conference on Ferrites, Japan, 1992 (unpublished), p. 872.
[7] T. Terashima and Y. Bando, Thin Solid Films **152**, 455 (1987).
[8] See, for example, D. M. Lind, S. D. Berry, G. Chern, H. Mathias, and L. R. Testardi, Phys. Rev. B **45**, 1838 (1992).
[9] K. Kamata, Y. Shibata, and Y. Kishi, J. Mater. Sci. Lett. **3**, 423 (1984).
[10] H. Torii, E. Fujii, and M. Hattori, Proceedings of the Sixth International Conference on Ferrites, Japan, 1992 (unpublished), p. 464.
[11] A. Eiling, R. A. Pott, and H. Kathrein, IEEE Trans. Magn. **MAG-22**, 741 (1986).
[12] S. Yamamoto, H. Kurisu, M. Matsuura, T. Doi, and K. Tamari (these proceedings).

Determination of local order in the amorphous precursor to Ba-hexaferrite thin-film recording media

J. E. Snyder, V. G. Harris, B. N. Das, and N. C. Koon
Code 6342, Naval Research Laboratory, Washington, DC 20375

X. Sui
Seagate Technology, Bloomington, Minnesota 55435

M. H. Kryder
Data Storage Systems Center, Carnegie Mellon University, Pittsburgh, Pennsylvania 15213

Ba-hexaferrite thin films for recording media applications are often fabricated by a two-step process: sputter deposition of an amorphous precursor, followed by annealing to crystallize the $BaFe_{12}O_{19}$ phase. The magnetic anisotropy of the crystalline films can be either in-plane or perpendicular, depending on the sputtering process used in the first step. However, conventional structural characterization techniques have not been able to distinguish between different as-sputtered films. Using polarization-dependent extended x-ray absorption fine structure (PD-EXAFS), we have observed anisotropic local structure around both Ba and Fe atoms in the amorphous precursor films. Comparison of the results suggests that the amorphous films consist of networks of Fe atoms surrounded by their O nearest neighbors, with Ba atoms fitting into in-between spaces as network modifiers (there might also be some minor Fe network modifying contribution). The local structural anisotropy of the amorphous films appears to determine the orientation of the fast-growing basal plane directions during annealing, and thus the directions of the *c* axes and the magnetic anisotropy.
© *1996 American Institute of Physics.* [S0021-8979(96)14208-8]

Sputtered barium hexaferrite ($BaFe_{12}O_{19}$) thin films show considerable promise for both longitudinal and perpendicular recording media applications. They can be produced with magnetic easy axes distributed randomly in-plane,[1] or aligned perpendicularly,[2] depending on the sputtering process. The films can either be grown as polycrystalline films by using high substrate temperatures,[3,4] or deposited as amorphous films, then crystallized by postdeposition annealing.[1,2] In the two-step process, the crystalline texture and magnetic anisotropy of the crystallized film depend on the sputtering process used to deposit the amorphous precursor. However, x-ray diffraction, electron diffraction, and transmission electron microscopy cannot distinguish between different amorphous films that will crystallize with different magnetic anisotropies.

In a previous paper, we reported the first measurements of local structure and structural anisotropy in amorphous precursor Ba–Fe–O films, using polarization-dependent extended x-ray absorption fine structure (PD-EXAFS).[5] This technique provides an element-specific probe of local atomic structure, weighted in the direction of the x-ray electric polarization vector. Results show that the as-sputtered films are not completely disordered, but rather have an ordered local structure around the Fe atoms. That structure consists of two main features: a peak corresponding to Fe–O nearest neighbors (comparable in amplitude to that of the crystallized films), and a second peak, corresponding predominantly to Fe–Fe neighbors. In addition, the local structure shows significant anisotropy: the films which will crystallize with perpendicular anisotropy show more crystalline-like order in the in-plane direction than perpendicular, and those which will crystallize with in-plane anisotropy show more order in the out-of-plane direction. These results suggest that the direction of greater order determines the direction in which the fast-growing basal planes form upon crystallization, thus determining the crystalline texture and magnetic anisotropy which develop.

In the present work, we report new PD-EXAFS results on the local structure around Ba in as-sputtered and crystallized Ba–Fe–O films, compare them with our previously reported results for Fe, and discuss what can be concluded about the structure of sputtered amorphous Ba–Fe–O films.

The films of this study were sputter deposited from sintered oxide targets onto SiO_2/Si substrates at ambient temperature. Films which crystallize with perpendicular anisotropy were deposited by conventional rf magnetron sputtering; in-plane anisotropy films were deposited by reactive rf diode sputtering. Some films were then crystallized by annealing in air at 800 °C for 3 h (see Refs. 1 and 2 for more details).

For each sample, PD-EXAFS data were collected for the Fe *K* edge and Ba L_{III} edge, using total-electron-yield detection on the X-23B beam line at the National Synchrotron Light Source (NSLS). Spectra were collected using both grazing incidence geometry (which probes structure perpendicular to the film plane) and normal incidence (which probes in-plane structure). For comparison, data were also collected for powder samples of Ba-hexaferrite, Ba-monoferrite ($BaFe_2O_4$), and BaO (used as empirical standards). The data were analyzed by standard EXAFS analysis procedures,[6] to obtain Fourier transforms of the EXAFS spectra. In this format, peaks correspond to "shells" of neighbors around the absorbing atoms: the radial coordinate (r) corresponds to distance from the absorbing atom (plus a photoelectron phase shift of 0.3–0.5 Å); the amplitude is related to the number and type of neighbor atoms present at that distance and their atomic disorder.

Fourier-transformed Ba EXAFS spectra for as-sputtered

 0021-8979/96/79(8)/4890/3/$10.00 © 1996 American Institute of Physics

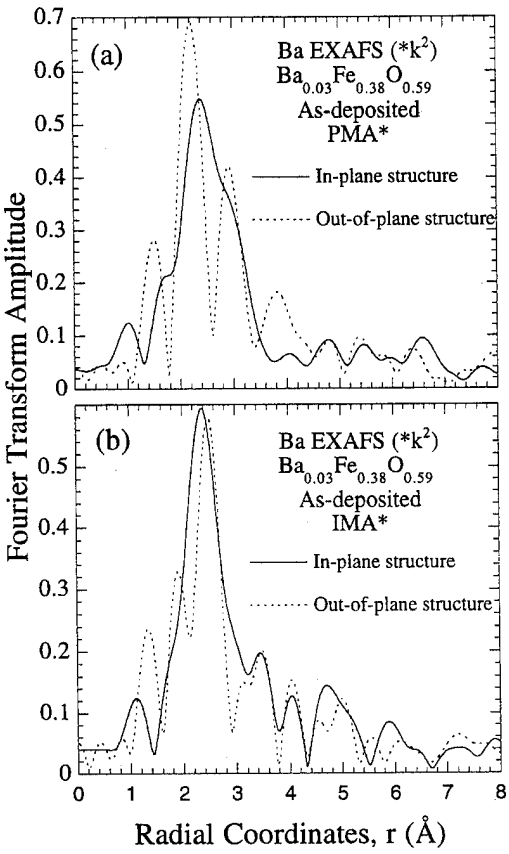


FIG. 1. Fourier-transformed Ba EXAFS results for as-sputtered $Ba_{0.03}Fe_{0.38}O_{0.59}$ films that will crystallize with (a) perpendicular magnetic anisotropy (PMA*); (b) in-plane magnetic anisotropy (IMA*).

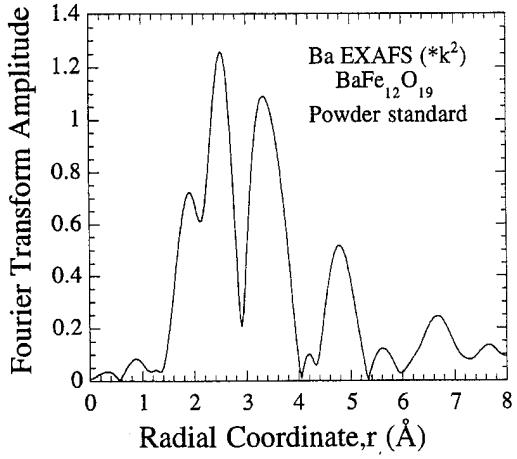


FIG. 2. Fourier-transformed Ba EXAFS results for the $BaFe_{12}O_{19}$ powder standard.

films are shown in Fig. 1. The results show that there is significant local ordered structure around Ba in the amorphous films. In each spectrum, two or three main features can be observed. Comparison with the standard spectra showed them most closely related to features in the $BaFe_{12}O_{19}$ standard (and not a good match to the spectra of either BaO or $BaFe_2O_4$). The first peak in Figs. 1(a) and 1(b) (centered at 2.2–2.5 Å) can be identified from comparison to the $BaFe_{12}O_{19}$ standard (Fig. 2), as corresponding to Ba–O nearest neighbors. It is a factor of 2–3 times smaller than it is in the spectra from the crystallized films (Fig. 3), indicating that the relative order around Ba is much less in the amorphous films. The first peak is also shifted to lower r in the amorphous film spectra, indicating that the O nearest neighbors are packed in closer. In the film which will crystallize with perpendicular anisotropy [Fig. 1(a)], it is at 2.4 Å for in-plane structure, and 2.2 Å for out-of-plane structure. In the film which will crystallize with in-plane anisotropy [Fig. 1(b)], it is at 2.4 Å for in-plane structure, and 2.5 Å for out-of plane structure. In all the crystalline samples (films or powder), it is at 2.5 Å.

The second structural feature in the Ba EXAFS results can be identified as Ba–Fe neighbors. This peak also shows considerably reduced amplitude, and in some cases, large shifts in r. In the as-sputtered film which will crystallize with perpendicular anisotropy [Fig. 1(a)], it is at about 2.9 Å for both in-plane and out-of-plane structure. For the film which will crystallize with in-plane anisotropy [Fig. 1(b)], the out-of-plane structure shows a split peak, with maxima at 3.5 and 3.1 Å. The in-plane structure shows it split even more strongly: one peak is at 3.5 Å; the remainder is seen as a shoulder on the first peak, at about 2.9 Å. In the powder standard, this peak appears at 3.3 Å (Fig. 2); in the crystalline films it is at 3.2 or 3.5 Å (Fig. 3).

The film that will crystallize with perpendicular anisotropy [Fig. 1(a)], shows a third feature (centered at 3.8 Å) in the out-of-plane structure. This would appear to correspond to Ba–2nd Fe neighbors, which in the crystal, are at 4.8 Å (Fig. 2).

Ba and Fe appear to play quite different roles in the structure of the as-sputtered films. In the Fe EXAFS of the amorphous films, the Fe–O peak is comparable in amplitude and at the same r as in crystalline $BaFe_{12}O_{19}$.[5] This indicates that the number and position of O nearest neighbors around Fe atoms is, on average, quite similar to that in the crystal. The structure around Ba, however, shows considerable differences. In the Ba EXAFS of the amorphous films, the Ba–O peak is only 1/2–1/3 as large as the corresponding $BaFe_{12}O_{19}$ crystalline peak, and in some of the spectra, it is shifted to lower r. Thus, the Ba atoms in the as-sputtered films do not have as many nearest neighbors as they would have in the $BaFe_{12}O_{19}$ crystal(12); nor do those neighbors have the structure (slightly distorted hexagonal close packed) that they would have in the crystal. Similarly, for the second structural feature: In the Fe EXAFS of the amorphous films, the Fe–Fe peak has reduced amplitude and splitting, but is at the same position as that of the crystal.[5] The Ba EXAFS, on the other hand show either a Ba–Fe peak shifted to much lower r, or two different small Ba–Fe peaks, one shifted and one not. It appears that the structure of the as-sputtered films is made up of networks whose individual units consist of Fe atoms surrounded by their O nearest neighbors. Ba atoms appear to fit into spaces where some of the Fe–O nearest-neighbor units can pack in around them. Thus, it appears that the Fe atoms play the role of network formers, and the Ba atoms the role of network modifiers (although there might

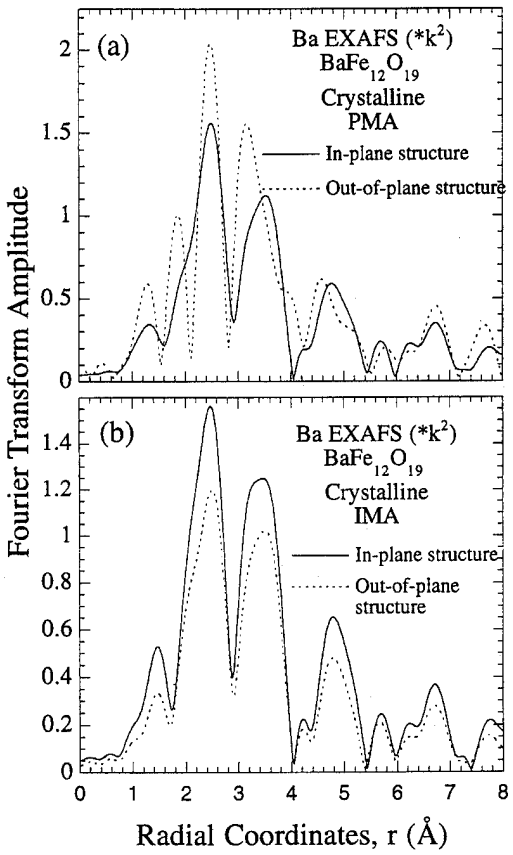


FIG. 3. Fourier-transformed Ba EXAFS results for crystallized $BaFe_{12}O_{19}$ films which have (a) perpendicular magnetic anisotropy; (b) in-plane anisotropy.

also be some minor Fe network-modifying contribution). This agrees with what is known about their roles in some glasses,[7] and in Ba monoferrite.[8]

When Ba has less than the full complement of O nearest neighbors, it appears that the O atoms can pack in closer. This agrees with the observations of the standards. In $BaFe_{12}O_{19}$, Ba has 12 O nearest neighbors and the Ba–O peak is at 2.5 Å. In $BaFe_2O_4$, Ba has 7 or 11 O nearest neighbors, and the Ba–O peak is at 2.4 Å. In BaO, Ba has 6 O nearest neighbors and the Ba–O peak is at 2.2 Å. Since Ba^{2+} is a little smaller than O^{2-},[9] perhaps the O atoms interfere with each other in the structures with more nearest neighbors. It also appears that when Ba has fewer O nearest neighbors, units of two joined Fe-nearest-neighbor O polyhedra (observed in the Fe EXAFS) can pack in closer. This would appear to explain the big shift of the Ba-2nd Fe neighbor peak in Fig. 1(a).

Local structural anisotropy can also be observed in the Ba EXAFS of the as-sputtered films. In the film which will crystallize with perpendicular anisotropy [Fig. 1(a)], the out-of-plane structure shows a Ba–O nearest-neighbor peak, a Ba–Fe peak, and a Ba-2nd Fe peak all shifted to much lower r than in the crystal. The in-plane structure shows the Ba–O nearest-neighbor peak at an r value much closer to that of $BaFe_{12}O_{19}$, and no low-r Ba-2nd Fe peak. The in-plane structure thus has more crystalline-like order. In the film which will crystallize with in-plane anisotropy [Fig. 1(b)], the in-plane structure shows a Ba–O nearest-neighbor peak shifted to lower r with an amplitude of only about 1/3 that of the crystallized film, and part of the Ba–Fe correlation shifted to much lower r. The out-of-plane structure shows a Ba–O nearest-neighbor peak in the same position as the crystallized film, with a much larger relative amplitude (1/2 that of the crystallized film), and the Ba–Fe correlation has only a small splitting. For this film, the out-of-plane structure appears more crystalline-like. These directions of more crystalline-like order agree with those determined from the Fe-EXAFS.[5] Apparently during annealing, the fast-growing basal planes form along these pre-existing directions of more crystalline-like order, thus setting up the crystalline texture and resulting magnetic anisotropy.

Local structure has been observed around both Ba and Fe atoms in as-sputtered amorphous Ba–Fe–O films, using PD-EXAFS measurements. Results suggest that the amorphous films consist of networks of Fe atoms surrounded by their O nearest neighbors, with Ba atoms fitting into in-between spaces as network modifiers (there might also be a minor Fe network modifying contribution). The local structure around Ba shows evidence of structural anisotropy, with the indicated directions of more crystalline-like order agreeing with those determined from the Fe-EXAFS. The results suggest that the local structural anisotropy of the amorphous films determines the orientation of the fast-growing basal plane directions during annealing, and thus the directions of the c axes and the magnetic anisotropy.

We would like to thank K. M. Kemner for collecting the Ba EXAFS data for the $BaFe_2O_4$ powder standard. This research was carried out in part at the National Synchrotron Light Source, which is sponsored by the U.S. Department of Energy. One of the authors (J.E.S.) was supported by the National Research Council Associateship Program. This research was also supported in part by the National Science Foundation under Grant No. ECD-8907068.

[1] X. Sui and M. H. Kryder, Appl. Phys. Lett. **63**, 15821 (1993).
[2] X. Sui, M. H. Kryder, B. Y. Wong, and D. E. Laughlin, IEEE Trans. Magn. **29**, 3751 (1993).
[3] A. Morisako, M. Matsumoto, and M. Naoe, IEEE Trans. Magn. **23**, 56 (1987).
[4] P. Gerard, E. Lacroix, G. Marest, B. Blanchard, G. Rolland, and B. Bechevet, Solid State Commun. **71**, 57 (1989).
[5] J. E. Snyder, V. G. Harris, N. C. Koon, X. Sui, and M. H. Kryder, IEEE Trans. Magn. **31**, 3844 (1995).
[6] D. E. Sayers and B. A. Bunker, in *X-Ray Absorption*, edited by D. C. Koningsberger and R. Prins (Wiley, New York, 1988).
[7] C.-K. Lee and R. F. Speyer, J. Mater. Sci. **29**, 1348 (1994).
[8] H. Mitsuda, S. Mori, and C. Okazaki, Acta Crystallogr. B **27**, 1263 (1971).
[9] L. Pauling, *The Nature of the Chemical Bond* (Cornell University Press, Ithaca, 1960).

Fabrication and magnetic properties of metal/cobalt ferrite composite thin films

J. G. Na
Division of Metals, Korea Institute of Science and Technology, Sungbuk, Seoul 136-791, Korea

To improve the saturation magnetization (M_s) of cobalt ferrite thin films, metal/cobalt ferrite composite thin films were prepared by controlling the sputtering conditions such as oxygen concentration in sputtering gas, substrate temperature, composition of the thin films. With decreasing the oxygen ratio from 50% to 5% in sputtering gas and increasing the substrate temperature from room temperature to 400 °C, the M_s of the thin films was increased and the coercivity (H_c) decreased. The result was attributed to deposition of the metal/cobalt ferrite thin films. With increasing the metal ratio in the thin films, preferred orientation of (111) of cobalt ferrite was worsened in the thin films. The metal deposited in the thin films was identified as cobalt with (002) preferred orientation. In higher cobalt content than the stoichiometric composition of $CoFe_2O_4$, the thin films with high M_s and H_c could be deposited in the wide substrate temperature range of 200–400 °C. We can prepare the metal/cobalt ferrite composite thin films with M_s about 580 emu/cm^3 and H_c 1700 Oe by controlled the sputtering conditions. The thin films are thought to be applicable to the magnetic recording media with high recording density. © *1996 American Institute of Physics.* [S0021-8979(96)07608-5]

I. INTRODUCTION

Cobalt ferrite thin films are very promising materials for magnetic recording media because they exhibit high crystalline anisotropy energy, good chemical stability and mechanical wear.[1,2] The excellent magnetic properties of the cobalt ferrite are known to be mainly attributed to the Co ions in a spinel lattice.

Cobalt ferrite has an inverse spinel structure, with half of the Fe^{+3} ions on tetrahedral sites (A sites) and the rest, together with Co^{+2} ions, on octahedral sites (B sites) at room temperature. According to the one-ion crystalline-field model, the strong anisotropy of Co^{+2} ion on the B site originates from incompletely quenched angular momentum, which is attributed to the interaction of the electronic structure of Co^{+2} ions with the crystal field.[3]

Although the cobalt ferrite thin films have the superior properties for the magnetic recording media, there are some weak points to be solved before their application can be realized. The low saturation magnetization (M_s) of the thin films, less than half of the metallic thin films, is one of them.

In this study, the metal/cobalt ferrite composite thin films were prepared to improve M_s by controlling the sputtering conditions such as oxygen concentration in sputtering gas, substrate temperature, composition of the thin films. Also was investigated the relationship between the microstructures and the magnetic properties of the thin films.

II. EXPERIMENTAL PROCEDURE

Cobalt ferrite thin films were prepared by a reactive sputtering method using a facing targets-sputtering unit. The sputtering gas was the mixture of Ar and O_2 and each gas was introduced into the chamber independently. Targets were composed of 6-cm-diam iron disks (99.9 at. % purity) and cobalt chips (99.9 at. % purity). The cobalt content of ferrite thin films was controlled by adjusting the number of cobalt chips attached on the iron disks. Thermally oxidized Si wafers were used as substrates. Prior to deposition, the targets were presputtered at 1 mTorr for 30 min. Typical sputtering conditions are summarized in Table I.

Structure analysis of the films was done by x-ray diffraction (XRD). The composition and the thickness of the thin films were measured by using an electron probe microanalyzer and a surface profiler (Tencor P-1, Tencor Instruments, CA).

Magnetic properties of the thin films were measured by using a vibrating sample magnetometer (VSM-5, Toei Ind. Co., Japan).

III. RESULTS AND DISCUSSION

Figure 1 shows the variation of magnetic properties of the thin films with oxygen concentration in the sputtering atmosphere. Because the *V-I* characteristics of the sputtering unit and the deposition rate of the thin films were changed with the oxygen ratio in the sputtering atmosphere, we deposited the thin films in the rate of 200 Å/min by controlling the electrical input power. As can be seen in Fig. 1, the thin films can be divided into three regions. The thin films in the region I represent high M_s and low H_c, while those of the region III low M_s and high H_c. The thin films in the region II show regions characteristics intermediate to I and III. Typical hysteresis loops of the thin films deposited in the sputtering atmosphere of (a): (5% O_2+Ar), (b): (10% O_2+Ar), and (c): (50% O_2+Ar) are shown in Fig. 2. The

TABLE I. Sputtering conditions for the magnetic thin films.

Background pressure	less than 5×10^{-6} Torr
Sputtering pressure	1×10^{-3} Torr
Sputter gas	10% O_2+Ar
Composition	33.7 at. % Co–Fe
Substrate temperature	300 °C
Input power	0.8 Å×580 V dc
Film thickness	0.2 μm

 0021-8979/96/79(8)/4893/3/$10.00 © 1996 American Institute of Physics

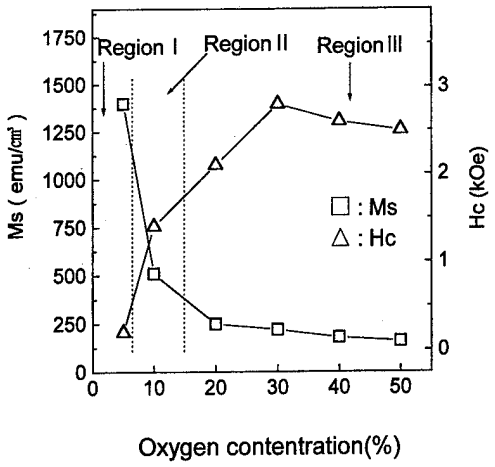


FIG. 1. The variation of magnetic properties of the thin films with oxygen concentration in the sputtering atmosphere.

hysteresis loops of the thin films (a) and (c) represent the loop shapes of conventional metallic and ferrite thin films, respectively. The hysteresis loops of the thin film (b) shows shapes intermediate to those of the thin films (a) and (c).

Figure 3 represents XRD patterns of the thin films shown in Fig. 2. For the thin film (c), only the peaks corresponding to cobalt ferrite were detected and for the thin films (a) and (b), the peaks corresponding to cobalt ferrite and cobalt metal were detected, which indicates that those films are composed of the ferrite and the cobalt. The higher intensity of the Co peaks of the thin film (a) than those of the thin

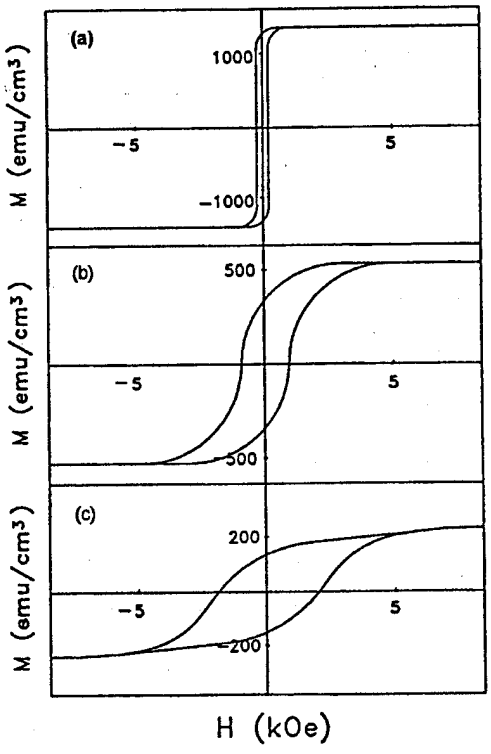


FIG. 2. The typical hysteresis loops of the thin films deposited in the sputtering atmosphere of (a): (5% O_2+Ar), (b): (10% O_2+Ar), and (c): (50% O_2+Ar).

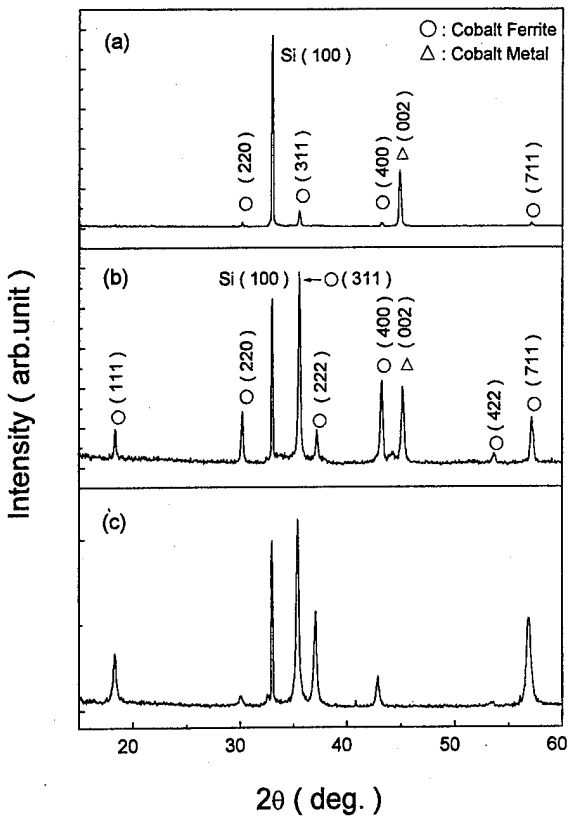


FIG. 3. XRD patterns of the thin films deposited in the sputtering atmosphere of (a): (5% O_2+Ar), (b): (10% O_2+Ar), and (c): (50% O_2+Ar).

film (b) reveals that the thin film (a) contains more cobalt metal than the thin film (b) and the result leads to the M_s increase of the thin films in the regions I and II shown in Fig. 1. One can see that the preferred orientation of (111) of the cobalt ferrite is worsened with decreasing the oxygen concentration in the sputtering atmosphere.

It is noteworthy from Fig. 3 that the metal deposited in the metal/ferrite composite thin films was identified as cobalt with preferred orientation of (002), which might be attributed to cobalt being more noble than iron in the oxidization-reduction series.[4] The result, together with worsening the preferred orientation of (111) of cobalt ferrite in the metal/ferrite thin film with decreasing the oxygen concentration in the sputtering atmosphere, might lead to the decrease of coercivity of the thin films shown in Fig. 1 because the direction of easy magnetization of the cobalt metal and cobalt ferrite vary as ⟨001⟩ and ⟨110⟩, respectively.[5]

Figure 4 shows the variation of magnetic properties of the thin films with the composition of the thin films and the substrate temperature. Three compositions, 28.5, 33.7, and 37.8 metal at. % Co-Fe of the thin films shown in Fig. 4 were chosen as the hypostoichiometric, stoichiometric, and hyperstoichiometric compositions of cobalt ferrite in the order of listing. As can be seen in Fig. 4, the M_s of the thin films increases with increasing the substrate temperature, while the H_c of the thin films decreases. The result agrees with the result of Fujii *et al.*[6] They reported that the oxidation degree of iron oxide thin films was dependent on deposition parameters, e.g., substrate temperature and oxygen partial pressure,

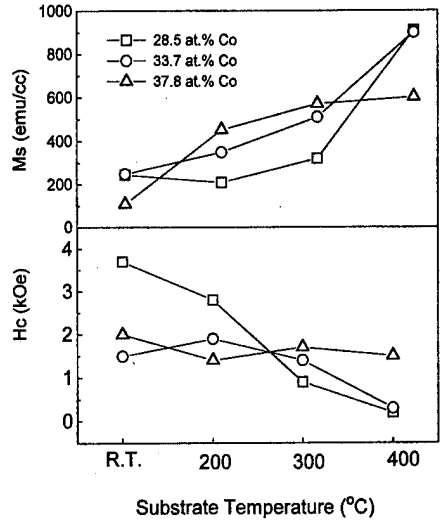


FIG. 4. The variation of magnetic properties of the thin films with the composition of the thin films and the substrate temperature.

and more-oxidized phases were deposited at low substrate temperature. They explained that the result may be attributed to the ratio of chemisorbed O_2 molecules and condensed Fe atoms on the surface of growing film. The substrate temperature influenced the chemisorption in such a way that oxygen partial pressure was effectively raised at lower substrate temperature.

In Fig. 4, one can see that the variation of magnetic properties of the thin films is different with the composition of the thin films. For the hyperstoichiometric composition of 38.8 at. % Co–Fe, the metal/ferrite composite thin films with M_s about 580 emu/cm^3 and H_c about 1700 Oe, which might be applicable to the magnetic recording media with high recording density, can be prepared in the wide substrate temperature range of 200–400 °C. The M_s value of metal/ferrite thin films is two to three times higher than that of the conventional cobalt ferrite thin films and the H_c value is comparable to the conventional metallic thin films.[7,8] For the near stoichiometric or hypostoichiometric compositions of 33.7 and 28.5 at. % Co–Fe, however, the metal/ferrite composite thin films with the predominant magnetic properties for the magnetic recording media can be prepared in the narrow substrate temperature range around 300 °C. As can be seen in Fig. 3, the metal/ferrite composite thin films are composed of the cobalt ferrite and the cobalt metal. The deposition of the cobalt metal in the metal/ferrite thin films may be one of the causes of the wide substrate range for the deposition of the thin films of the hyperstoichiometric composition. The result is thought to be important for the reproducibility of the metal/ferrite composite thin films.

IV. CONCLUSIONS

The metal/cobalt ferrite composite thin films with M_s about 580 emu/cm^3 and H_c about 1700 Oe can be prepared by controlled the sputtering conditions such as oxygen concentration in sputtering gas, substrate temperature, and composition of the thin films with a deposition rate of 200 Å/min. With decreasing the oxygen ratio from 50% to 5% in sputtering gas and increasing the substrate temperature from room temperature to 400 °C, the M_s of the thin films was increased and the H_c decreased. With increasing the metal ratio in the thin films, preferred orientation of (111) of cobalt ferrite was worsened. The metal deposited in the metal/ferrite composite thin films was identified as cobalt with preferred orientation of (002). In higher cobalt content than the stoichiometric composition of $CoFe_2O_4$, the thin films with high M_s and H_c could be deposited in the wide substrate temperature range of 200–400 °C.

[1] N. Matsushita, K. Noma, S. Nakagawa, and M. Naoe, Proceedings of 6th International Conference on Ferrites, 1992, p. 428.
[2] A. N. Okuno, S. Hashimoto, and K. Inomata, J. Appl. Phys. **71**, 5926 (1992).
[3] J. C. Slonczewski, Phys. Rev. **110**, 1341 (1958).
[4] D. R. Lide, *CRC Handbook of Chemistry and Physics* (CRC, Boca Raton, 1993), pp. 8–21.
[5] B. D. Cullity, *Introduction to Magnetic Materials* (Addison–Wesley, Menlo Park, CA, 1972), p. 207.
[6] T. Fujii, M. Takano, R. Katano, Y. Bando, and Y. Isozumi, J. Appl. Phys. **66**, 3168 (1989).
[7] J. W. D. Martens, J. Appl. Phys. **59**, 3820 (1986).
[8] J. C. Milaan and R. D. Fisher, IEEE Trans. Magn. **MAG-23**, 122 (1987).

Co–Cr films prepared by sputtering using electron cyclotron resonance microwave plasma

S. Yamamoto, K. Sato, H. Kurisu, and M. Matsuura
Faculty of Engineering, Yamamaguchi University, Tokiwadai, Ube 755, Japan

The sputtering deposition using an electron cyclotron resonance (ECR) microwave plasma was tried to use in the fabrication of the Co–Cr perpendicular magnetic recording media. As the Ar sputtering gas pressure increased from 4×10^{-2} to 8×10^{-2} Pa, the Co(002) x-ray diffraction peak intensity increased and the half-value width of the rocking curve $\Delta\theta_{50}$ decreased. This result implies that Co–Cr films with high perpendicular orientation and good crystallinity are achieved at high Ar gas pressure. The Co–Cr films deposited at a target to substrate distance of 230 mm had a good preferred crystal orientation ($\Delta\theta_{50}$ less than 4°), high perpendicular magnetic anisotropy (H_k higher than 4 kOe), and high perpendicular coercivity over 1400 Oe even though the Co–Cr thickness is as small as about 50 nm, and no underlayers were introduced. Thus, the ECR sputtering has high potential in the deposition of the Co–Cr films for ultrahigh density recording media. © *1996 American Institute of Physics.* [S0021-8979(96)14608-3]

I. INTRODUCTION

An extremely high density recording exceeding 500 kFRPI has already been achieved in perpendicular magnetic recording using a Co–Cr perpendicular media.[1–3] It has been proven that such a high recording resolution of Co–Cr films is originated from the compositional separation into Co- and Cr-rich regions in the size range of a few nanometers.[4–6] In order to improve the recording resolution further, it is necessary to develop the film deposition technology by which the compositional separation is controlled more precisely.

Recently, an electron cyclotron resonance (ECR) microwave plasma has been developed, and used in the thin-film deposition processing. Compared with the conventional diode sputtering, the ECR sputtering features: (1) generation of dense plasma even at Ar gas pressure as low as 10^{-2} Pa, (2) generation of highly ionized plasma, and its controllable irradiation to the substrate.[7,8]

Up to now, there have been only a few attempts concerning the application of the ECR sputtering to the Co–Cr film deposition.[9] Hirono and co-workers[10] have succeeded in reducing the grain size of Co–Cr films with a compositionally separated microstructure, while maintaining high grade magnetic properties by using the ECR sputtering method.

In this study, we have tried the deposition of the Co–Cr films for high density perpendicular magnetic recording media by using the ECR sputtering, focusing on the effects of Ar gas pressure, and substrate location on the crystallographic and magnetic properties.

II. EXPERIMENT

The ECR plasma sputtering deposition apparatus used in this experiment is shown in Fig. 1. The discharge chamber was designed as a TE_{113} resonance cavity. The main coils are arranged around the periphery of the discharge chamber. The magnetic field of 875 G satisfying the ECR condition is generated in this chamber by these coils. The 2.45 GHz microwave was introduced into the chamber perpendicularly to the chamber sidewall through the waveguide. This waveguide/discharge chamber geometry enables the continuous deposition of the conductive films. Under the ECR condition, high density plasma is generated at Ar gas pressure as low as 10^{-2} Pa. In this discharge chamber/substrate configuration shown in this figure, the plasma stream occurs from the discharge chamber toward the substrate along the magnetic lines of force. A cylindrical target to which the negative voltage, V_a, of -100 V was applied, was placed at the end of the discharge chamber. The composition of the target was $Co_{80}Cr_{20}$ wt %. The input microwave power was 300 W. The Co–Cr films with a thickness from 0.025 to 0.35 μm were deposited on the 30 μm thick polyimide substrate at the substrate temperature T_{sub}, of 100° in centigrade. The Ar gas pressure was varied in the range from 3×10^{-2} to 9×10^{-2}

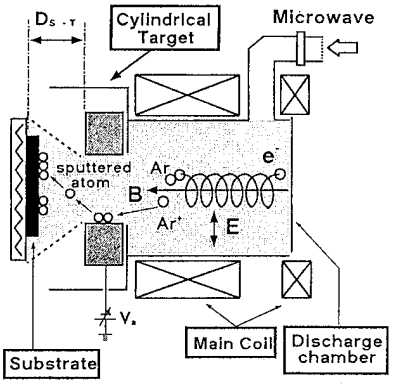


FIG. 1. Cross-sectional view of ECR plasma sputtering deposition apparatus.

 0021-8979/96/79(8)/4896/3/$10.00 © 1996 American Institute of Physics

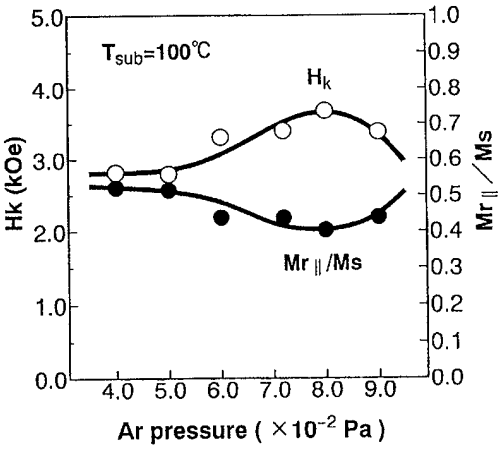


FIG. 2. Ar gas pressure dependence of perpendicular magnetic anisotopy field H_k, and in-plane squareness $M_{r_\parallel}/M_s$.

Pa. The substrate-to-target distance D_{s-t} was varied from 170 to 230 mm. The plasma with the electron temperature from 5 to 12 eV, and the electron density from 0.6×10^9 to 1.6×10^9 cm^{-3}, was achieved in the above described experimental condition. The deposition rate in our experiments varies from 1.5 to 7.2 nm/min according to Ar gas pressure and target to substrate distance.

The crystallographic and magnetic properties were measured using an x-ray diffractometer and a vibrating sample magnetometer, respectively.

III. RESULTS AND DISCUSSION

At first, the Ar sputtering gas pressure dependence of crystallographic and magnetic properties was investigated for a substrate-to-target distance D_{s-t} of 170 mm. As the Ar gas pressure increased from 4×10^{-2} to 8×10^{-2} Pa, the Co(002) x-ray peak intensity drastically increased, and the half-value width of the rocking curve $\Delta\theta_{50}$, became a half, showing that the crystallinity and perpendicular orientation of Co c axis has been improved. The Ar gas pressure dependence of perpendicular magnetic anisotropy field H_k, and in-plane squareness, $M_{r_\parallel}/M_s$, are shown in Fig. 2. The maximum H_k and the minimum $M_{r_\parallel}/M_s$ were obtained at an Ar gas pressure of 8×10^{-2} Pa. The maximum of perpendicular coercivity $H_{c_\perp}$, and the minimum of in-plane coercivity $H_{c_\parallel}$, were also achieved at Ar gas pressure of 8×10^{-2} Pa. These results show that the highly perpendicularly oriented Co–Cr films with high perpendicular orientation and magnetic properties desired for high density perpendicular recording have been prepared at relatively high Ar gas pressure of 8×10^{-2} Pa using ECR sputtering.

To clarify this phenomenon, the probe diagnosis for the ECR plasma was performed. From the $V-I$ characteristics, it was found that both the floating potential of the substrate V_f, and the plasma potential V_s, decrease with increasing Ar gas pressure. Some of the Ar ions in the plasma are accelerated by the voltage difference between V_s and V_f, i.e., V_s-V_f, and move along the magnetic lines of force, and finally bombard the substrate. It is surmised that the excessive amount of Ar ion bombardment to the substrate at low Ar gas pressure disturbs the crystal orientation, and consequently, the H_k and $H_{c_\perp}$ are low.

In the next step, optimization of the substrate-to-target distance D_{s-t} was performed at an Ar gas pressure of 8×10^{-2} Pa. The D_{s-t} was varied from 170 to 230 mm. The Co–Cr films with half-value width of the rocking curve $\Delta\theta_{50}$, less than 4° were obtained around D_{s-t} of 170 and 230 mm. However, the in-plane M–H hysteresis loops of the films are different in each other as shown in Fig. 3. The in-plane M–H loop for the film deposited at D_{s-t} of 170 mm

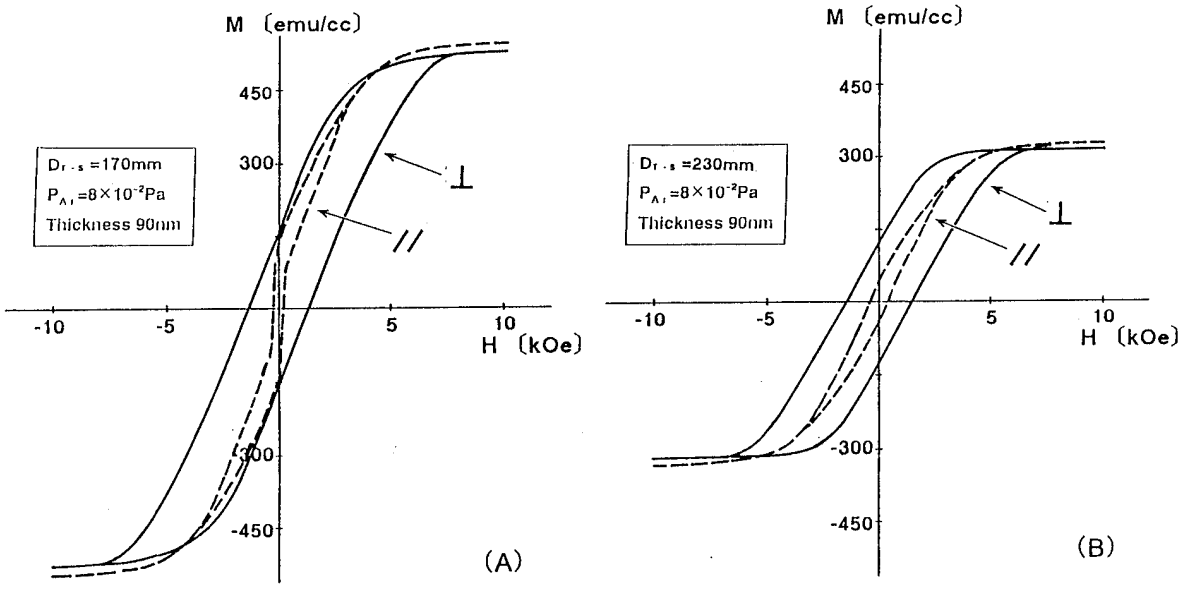


FIG. 3. M–H hysteresis loops of Co–Cr films in perpendicular direction (solid line) and in-plane direction (dashed line); (a) is for deposition at substrate-to-target distance D_{s-t}, of 170 mm, and (b) for deposition at D_{s-t} of 230 mm.

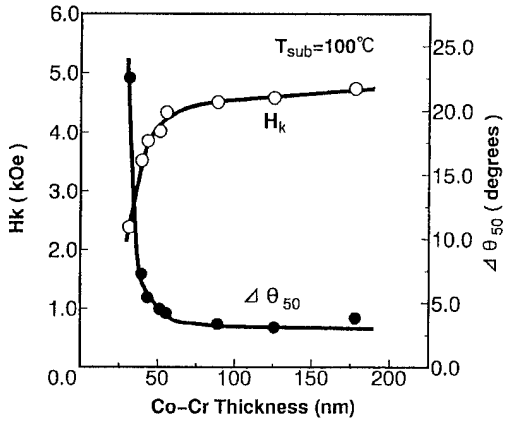


FIG. 4. Thickness dependence of $\Delta\theta_{50}$ and H_k of Co–Cr films deposited at optimal condition, i.e., D_{s-t} of 230 mm and Ar gas pressure of 8×10^{-2} Pa.

has jump at low magnetic field as shown by the broken line. This jump is caused by the existence of a low coercivity initial layer in which the Co c axis does not align in perpendicular direction.[11,12] In the conventional diode sputtering methods, it is difficult to eliminate this nonoriented initial layer unless the underlayer such as Ti and Cr are introduced. On the other hand, for the films deposited by the ECR sputtering at D_{s-t} of 230 mm, no jumps are observed as shown by the solid line because the Ar ion bombardment during deposition is so small that the crystallinity and crystal orientation are not disturbed.

The thickness dependence of the $\Delta\theta_{50}$ and H_k is shown in Fig. 4. These Co–Cr films are deposited at D_{s-t} of 230 mm and at an Ar gas pressure of 8×10^{-2} Pa. As the Co–Cr thickness increases from 27 to 50 nm, the $\Delta\theta_{50}$ drastically decreased and reached a near plateau value of around 3° at a thickness of 90 nm. H_k increased sharply in the thickness range 27 to 50 nm and showed a relatively small increase about 90 nm. Surprisingly, very small $\Delta\theta_{50}$ of 3.1° was obtained at a thickness of 90 nm.

The thickness dependence of the perpendicular coercivity, $H_{c_\perp}$, is shown in Fig. 5. The open circles are for the films

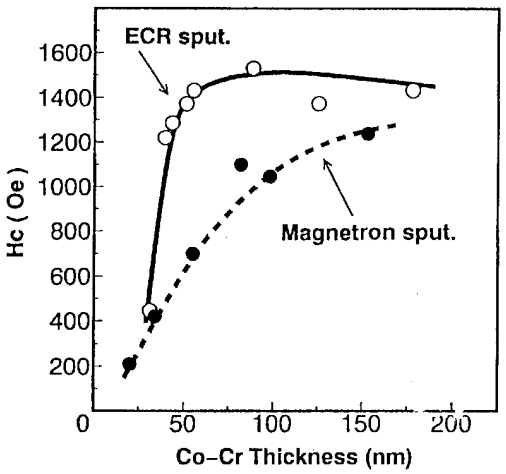


FIG. 5. Perpendicular coercivity $H_{c_\perp}$, as a function of Co–Cr film thickness. Open circles are for ECR sputtering deposition, and solid circles are for magnetron diode sputtering deposition.

deposited by the ECR sputtering condition tuned at D_{s-t} of 230 mm and at Ar gas pressure of 8×10^{-2} Pa. For comparison, the data for the Co–Cr films prepared by magnetron diode sputtering at the optimal sputtering condition, i.e., Ar gas pressure of 5×10^{-1} Pa, are plotted by solid circles. In both sputtering depositions, the same polyimide substrate was used, and the underlayers which play a role to control the Co crystal orientation were not introduced. Although the films prepared by conventional magnetron sputtering needs at least 100 nm thickness to achieve perpendicular coercivity higher than 1000 Oe, in the ECR sputtering, only 50 nm thickness is enough to realize 1400 Oe coercivity. This is considered by the authors as the specific advantage of the ECR sputtering over the diode sputtering for the Co–Cr films for perpendicular recording.

IV. CONCLUSION

The ECR sputtering deposition technique was used in the fabrication of the Co–Cr perpendicular magnetic recording media. The Co–Cr films with superior crystallinity, perpendicular orientation, and magnetic properties desirable for high density recording were achieved at a high Ar gas pressure of 8×10^{-2} Pa. The Co–Cr films deposited at a target to a substrate distance of 230 mm showed good crystal orientation ($\Delta\theta_{50}$ less than 4°) high perpendicular magnetic anisotropy (H_k higher than 4 kOe), and high perpendicular coercivity over 1400 Oe even when the Co–Cr thickness was as small as about 50 nm. We conclude that the ECR sputtering has high potential in the deposition of the Co–Cr films for ultrahigh density recording media.

ACKNOWLEDGMENTS

We are grateful to Dr. S. Hirono of NTT Interdisciplinary Research Laboratories for his valuable discussion and advice, and T. Nakamura for his experimental assistance in VSM measurements. This research was supported by a Grant-in-Aid for Scientific Research (C) and by the Electric Technology Research Foundation of Chugoku.

[1] S. Iwasaki and Y. Nakamura, IEEE Trans. Magn. **MAG-13**, 1272 (1977).
[2] S. Yamamoto, Y. Nakamura, and S. Iwasaki, IEEE Trans. Magn. **MAG-23**, 2070 (1987).
[3] S. Yanase, T. Kiya, N. Honda, and K. Ouchi, Tech. Rep. IEICE **MR95-14**, 15 (1995).
[4] Y. Maeda, S. Hirono, and M. Asahi, Jpn. J. Appl. Phys. **24**, L951 (1985).
[5] Y. Maeda and M. Asahi, J. Appl. Phys. **61**, 1972 (1987).
[6] Y. Maeda, K. Takei, S. Yamamoto, and Y. Nakamura, J. Magn. Soc. Jpn. **15**, 457 (1991).
[7] T. Ono *et al.*, Jpn. J. Appl. Phys. **23**, L534 (1984).
[8] M. Matsuoka and K. Ono, J. Vac. Sci. Technol. A **6**, 25 (1988).
[9] C. Takahashi, M. Kiuchi, K. Ono, and S. Matsuo, J. Vac. Sci. Technol. A **6**, 2348 (1988).
[10] S. Hirono, M. Igarashi, and Y. Maeda, Tech. Rep. IEICE **MR94-60**, 41 (1994).
[11] Y. Nakamura and S. Iwasaki, IEEE Trans. Magn. **MAG-23**, 153 (1987).
[12] M. Yasumura, K. Ouchi, and S. Iwasaki, IEEE Trans. Magn. **MAG-23**, 2794 (1987).

Magnetic viscosity and switching volumes of annealed Fe/Pt multilayers

C. P. Luo, Z. S. Shan, and D. J. Sellmyer
Behlen Laboratory of Physics and Center for Materials Research and Analysis, University of Nebraska, Lincoln, Nebraska 68588-0113

Magnetic viscosity and the phenomenon of the sweep-rate dependence of the coercivity are important for the characterization of magnetic recording media. The activation volume of magnetization reversal or switching volume is directly related to medium noise. The magnetic viscosity behavior of annealed Fe/Pt multilayers was studied and the switching volumes were obtained by both measurements of the sweep-rate dependence of coercivity and time dependence of magnetization. It is found that samples with larger coercivities have smaller switching volumes, and an estimate of the magnetic grain diameter is about 9 nm. The coercivity mechanisms are also discussed. © *1996 American Institute of Physics.* [S0021-8979(96)07808-8]

I. INTRODUCTION

Magnetic viscosity parameters are directly associated with the microscopic structure of materials and with the processes responsible for magnetization. The analysis of magnetic viscosity may allow a better understanding of magnetization reversal and coercivity mechanisms. For magnetic recording media, the activation volume of reversal or switching volume is an essential parameter which is related to the media noise. Previously, we have reported that annealed Fe/Pt multilayers with fct structure have large in-plane coercivities and fine grain sizes,[1] which suggests potential applications in future ultrahigh-density magnetic recording. In this work, we studied the magnetic viscosity properties and the switching volumes of the annealed Fe/Pt multilayers.

II. MAGNETIC VISCOSITY

The phenomenon of magnetic viscosity has its origins in thermal agitation of magnetic moment over energy barriers. In many materials it is found experimentally that

$$M(H,t)=M(H,t_0)-S(H)\ln(t), \tag{1}$$

where $S(H)$ is the viscosity coefficient. According to Street and Woolley,[2]

$$S(H)=\chi_{\rm irr}(H)H_f(H), \tag{2}$$

where $\chi_{\rm irr}$ is the irreversible susceptibility characterizing the barrier hopping and H_f the fluctuation field which is defined by

$$H_f(H)=k_BT/[V^*(H)M_s], \tag{3}$$

where $V^*(H)$ is the activation volume of reversal, k_BT the Boltzmann energy, and M_s the magnetic moment per unit volume.

Another aspect of the time-dependent behavior is the sweep-rate (dH_a/dt) dependence of the coercivity. Higher sweep-rate measurements generally give larger values of H_c than lower sweep-rate measurements. Under certain assumptions, the coercivity varies linearly with respect to $\ln(dH_a/dt)$:[3]

$$H_c=k_BT/(V^*M_s)[\ln(dH_a/dt)+\text{const}]. \tag{4}$$

The activation volume V^* can be obtained from the slope of the $H_c\sim\ln(dH_a/dt)$ plot.

III. SAMPLES AND MEASUREMENTS

Fe/Pt multilayers were deposited by rf and dc sputtering on cover glasses and annealed at 300 °C for 30 min. The base pressure of the sputtering system was 2×10^{-7} Torr and the Ar pressure was 5 mTorr during deposition. All magnetic measurements were made using a Micromag-2900 alternating gradient force magnetometer. For each measurement of the time dependence of magnetization, the sample was initially saturated with a positive field of 10 kOe, and then a constant negative test field was applied. In order to obtain the $\chi_{\rm irr}(H)$ curves, the dc demagnetization (DCD) and the isothermal remanence magnetization (IRM) curves were measured.

IV. RESULTS AND DISCUSSIONS

A. Magnetic parameters

The hysteresis loops of the annealed Fe/Pt multilayers with different bilayer thickness (d_b) were measured with applied field in the film plane. All of the measured samples had the same composition and a total thickness of 150 Å. The magnetic parameters such as coercivity (H_c) and squareness (M_r/M_s) are listed in Table I. Rather square hysteresis loops have been obtained for all samples. The table also shows that the coercivities are strongly dependent on d_b, which will be discussed later.

Figure 1 shows the $\chi_{\rm irr}(H)$ curves of the examined samples, which were obtained by differentiating the DCD and IRM curves, respectively. According to O'Grady[4] and Donnet *et al.*,[5] the IRM differential $(\chi^i_{\rm irr})$ measures the distribution of energy barriers to wall motion; while the DCD differential $(\chi^d_{\rm irr})$ measures the energy barrier to domain nucleation in the first instance and then examines the mechanism by which reversal proceeds. Thus, both quantities provide direct information about magnetization reversal, and their relations to coercivity and activation volume will be discussed later.

B. Magnetic viscosity properties

1. Sweep rate dependence of H_c

Measurements of the coercivities as a function of sweep rates were carried out for samples A, B, C, and D with sweep rates varying from 10 to 1000 Oe/s. The results shown in

 0021-8979/96/79(8)/4899/3/$10.00 © 1996 American Institute of Physics

TABLE I. The magnetic parameters and switching volumes of the annealed Fe/Pt multilayers.

Samples[a]	A	B	C	D	E
d_b (Å)	15	30	37.5	50	75
H_c (Oe)[b]	934	2220	2560	3140	1140
M_r/M_s	0.85	0.89	0.87	0.87	0.85
$V^*(\times 10^{-18}\ \text{cm}^3)$[c]	6.96	1.42	1.93	1.20	···
$V^*(H_c)(\times 10^{-18}\ \text{cm}^3)$	2.03	1.51	1.33	1.25	2.42

[a]Samples are: A: (Fe 8.2 Å/Pt 6.8 Å)$_{10}$; B: (Fe 16.4 Å/Pt 13.6 Å)$_5$; C: (Fe 20.2 Å/Pt 17.3 Å)$_4$; D: (Fe 27.4 Å/Pt 22.6 Å)$_3$, and E: (Fe 40.4 Å/Pt 34.6 Å)$_2$. All samples are the same total thickness and were annealed at 300 °C for 30 min.
[b]H_c was measured at a sweep rate of 250 Oe/s.
[c]V^* was determined from the measurement of the sweep-rate dependence of coercivity.
[d]$V^*(H_c)$ is the switching volume when the applied field equals to H_c.

Fig. 2 are that H_c linearly depends on $\ln(dH_a/dt)$. So Eq. (4) can be applied to analyze the results and the switching volumes are obtained, as listed in Table I. A small switching volume of 1.2×10^{-18} cm^3 has been measured for sample D which has a coercivity of 3.14 kOe. As the total film thickness h is 150 Å, the magnetic grain size which is defined as $(V^*/h)^{1/2}$ is about 90 Å.

2. Time dependence of magnetization

Logarithmic time decays have been observed for all samples under constant negative applied fields. As an example, Fig. 3 shows the magnetization varying linearly with $\ln(t)$ for sample C under different applied fields. From these plots the viscosity coefficients $S(H)$ were obtained, as shown in Fig. 4. The variation of S with H essentially mirrors the behavior of $\chi_{\text{irr}}(H)$ which gives a measure of irreversible processes in the film.

From $S(H)$ and $\chi_{\text{irr}}(H)$, $V^*(H)$ can be obtained, as shown in Fig. 5. Clearly, $V^*(H)$ is not a constant. It depends on the applied fields. This arises from the fact that the applied field may affect both the height and the distribution of energy barriers. In the low-field region, both A and E have much larger V^* than the other samples, while in the high-field region, all samples tend to have the same V^*. At each sample's coercive field, the sample with larger H_c shows smaller $V^*(H_c)$. The values of $V^*(H_c)$ are matched very well with V^* obtained from the sweep-rate dependence measurement of coercivity except for sample A, for which V^* is a little larger than $V^*(H_c)$.

Both H_c and V^* are related to the magnetization reversal mechanisms which depend on the microstructure. Figure 1 reflects how the distribution of energy barriers varies with d_b. In the low-field region, for samples A and E, the nucleation field is greater than the domain-wall-pinning field as can be seen from the $\chi_{\text{irr}}(H)$ curves. Hence, following the

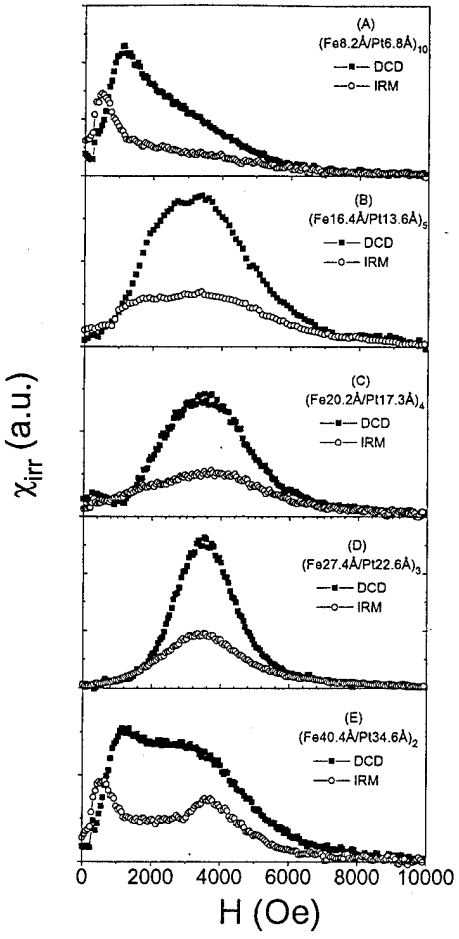


FIG. 1. Differentiated remanence curves for annealed Fe/Pt multilayers.

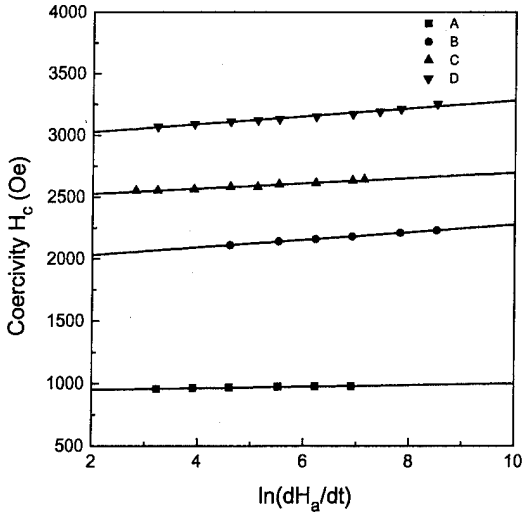


FIG. 2. The variation of H_c with sweep rate dH_a/dt.

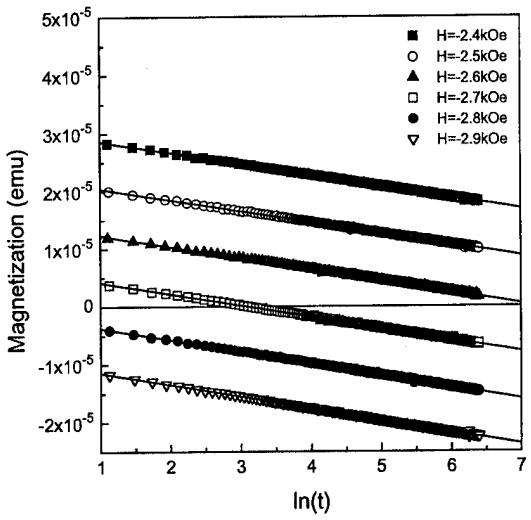


FIG. 3. Time decay of magnetization in the presence of constant magnetic fields in the direction opposite to the initial magnetization for sample C.

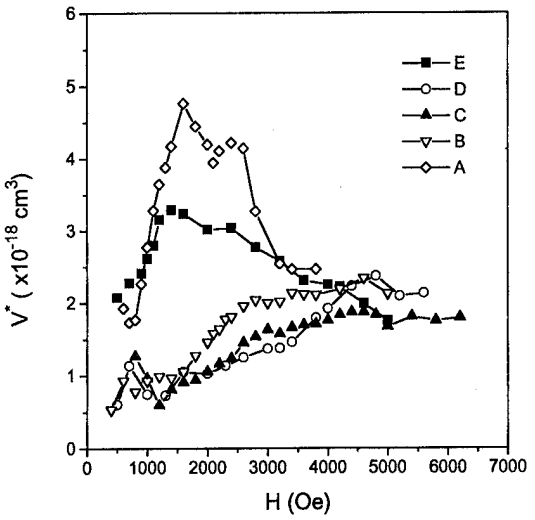


FIG. 5. The variation of activation volumes with applied field.

analysis of O'Grady,[4] once the domain is nucleated it expands quickly, causing a sharp increase in switching volumes. And then the decrease of activation volume with applied field may be associated with the pinning of the movement of the nucleated domain walls.

The coercivity is also related to the exchange coupling between grains. Generally the coercivity increases with the reduction of exchange coupling.[6] For a system without interaction, $\chi^d_{\rm irr}$ and $\chi^i_{\rm irr}$ should be identical with $\chi^d_{\rm irr} = 2\chi^i_{\rm irr}$. This suggests that the grains are more strongly exchange coupled for samples A and E, for which the $\chi^i_{\rm irr}$ curves increase at lower field than the $\chi^d_{\rm irr}$ curves.[7] The exchange coupling appears to be reduced for samples B, C, and D as the $\chi^i_{\rm irr}(H)$ and $\chi^d_{\rm irr}(H)$ curves are centered at the same position. High-resolution transmission electron microscopy (TEM) data on these samples show grain sizes of about 15 nm. The large value of H_c in sample D presumably is connected with a smaller exchange coupling, but the correlation of this with details of the nanostructures awaits further TEM studies.

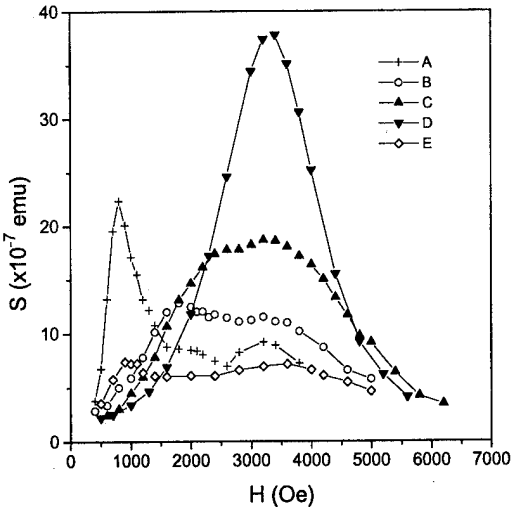


FIG. 4. The variation of viscosity coefficient S with applied field H.

V. SUMMARY

Through the study of magnetic viscosity behavior of the annealed Fe/Pt multilayers, their activation volumes of reversal were obtained. Films with larger coercivities have smaller switching volumes. Given the small estimated value of the magnetic grain size (~90 Å) and the large and controllable coercivities, these films may have potential as new ultra-high-density recording media.

ACKNOWLEDGMENTS

This research was supported by NSF under Grant No. DMR-9222976 and by the CMRA.

[1] C. P. Luo and D. J. Sellmyer, IEEE Trans. Magn. **31**, 2764 (1995).
[2] R. Street and J. C. Woolley, Proc. Phys. Soc. London Sect. A **62**, 562 (1949).
[3] P. Bruno, G. Bayreuther, P. Beauvillain, C. Chappert, G. Lugert, D. Renard, J. P. Renard, and J. Seiden, J. Appl. Phys. **68**, 5759 (1990).
[4] K. O'Grady, T. Thomson, and S. J. Greaves, J. Appl. Phys. **75**, 6849 (1994).
[5] D. M. Donnet, V. G. Lewis, J. N. Chapmant, K. O'Grady, and H. W. van Kesteren, J. Phys. D **26**, 1741 (1993).
[6] I. L. Sanders, T. Yogi, J. K. Howard, S. E. Lambert, G. I. Gorman, and C. Hwang, IEEE Trans. Magn. **MAG-25**, 3869 (1989).
[7] K. O'Grady, R. W. Chantrell, and I. L. Sanders, IEEE Trans. Magn. **29**, 286 (1993).

Seed layer induced (002) crystallographic texture in NiAl underlayers

Li-Lien Lee, David E. Laughlin, and David N. Lambeth
Data Storage Systems Center, Carnegie Mellon University, Pittsburgh, Pennsylvania 15213

The magnetic properties of Co alloy thin films are strongly dependent on their crystallographic texture and microstructure which in turn can be controlled by the texture of the underlayer. For Co alloy longitudinal recording media with Cr underlayers, it is desirable to have (002) textured Cr underlayers. Since NiAl has the $B2$ structure and has a lattice constant similar to that of Cr, NiAl has the potential to be an alternative underlayer to Cr. However, the (002) crystallographic texture of the NiAl films is difficult to obtain. It is found that the (002) texture in NiAl underlayers can be achieved by employing a seed layer of either (002) textured Cr or MgO. Because of the improved texture a significant increase of the in-plane coercivity in CoCrPt/NiAl films was obtained. © *1996 American Institute of Physics.* [S0021-8979(96)07908-4]

NiAl is an ordered phase with the $B2$ structure. It has a similar crystal structure and lattice constant as that of Cr. It has been shown by the authors that sputter-deposited NiAl films can be used as underlayers for HCP Co alloy longitudinal recording media.[1,2] Sputter deposited NiAl underlayers tend to induce good in-plane c-axis texture in the overlying Co films through the NiAl (112) preferred oriented film planes. An often asked question is: can the crystallographic texture of the NiAl underlayer be altered?

One of the frequently sought after crystallographic textures for Cr underlayers is (002). It has been argued by Zhu[3] that the (002) textured Cr underlayers may render a high signal-to-noise ratio in the HCP Co alloy thin film recording media. Since NiAl and Cr are structurally similar, a (002) textured NiAl may impart a similar benefit. We have tried to raise the substrate temperature during the sputtering of NiAl, a practice often used to achieve the (002) texture in Cr. However, this approach fails to produce the (002) texture in the NiAl film. Other means have to be found. A simple solution to this is by making use of a proper seed layer. A seed layer (sometimes called a precoating) is a thin-film layer that is deposited between the substrate and the underlayer. Seed layers are used for (1) the facilitation of infrared heating of glass substrates, (2) the modification of the topography of the disk substrates for tribological purpose, and (3) inducing preferred crystallographic texture to underlayers.

For longitudinal recording media, seed layers such as Al,[4] Ti,[5] Ni_3P, $TiSi_2$, Cr, C,[6] Ta, W, and Zr[7] have been used. Varying degrees of success have been reported, however, the industry is still in the process of searching for a better seed layer. Because of the similarity in crystal structures of NiAl and Cr, employment of a (002) Cr seed layer, which can be achieved by sputter depositing on to a heated substrate, is another approach to inducing the crystallographic texture of NiAl to (002). Another kind of seed layer which may do the same is MgO.

MgO is an ionic crystal with the $B1$ (NaCl-type) crystal structure with a lattice constant of 0.421 nm. It has been shown by Nakamura and Futamoto[8] that a Cr film deposited on a single-crystal (002) MgO tends to have its (002) plane lying parallel to the film plane due to heteroepitaxial growth. It is easy to obtain a sputter-deposited MgO film with a (002) texture because the (002) plane has the lowest surface energy.[9] Here, the authors have found that, similar to Cr, NiAl deposited on a MgO seed layer can have the (002) texture.

All films were deposited by rf diode sputtering. The deposition conditions were the same as that of the previous papers by the authors.[1,2] The MgO films were deposited by rf sputtering of a 99.95 at. % pure MgO bulk target and the deposition rate was 4 nm/min. The HCP Co alloy films used in this study were obtained by sputtering from a CoCr target

TABLE I. The in-plane magnetic properties of the CoCrPt (40 nm)/NiAl(100 nm) films on MgO seed layers of various thickness.

MgO thickness	H_c (Oe)	S^*	S	Mrt (memu/cm^2)
0nm	1862	0.87	0.84	1.4
2nm	2558	0.92	0.86	1.1
5nm	2811	0.92	0.87	1.2
8nm	3283	0.92	0.88	1.1
10nm	3238	0.91	0.87	1.0
20nm	3236	0.86	0.84	1.0
50nm	3182	0.82	0.87	1.0

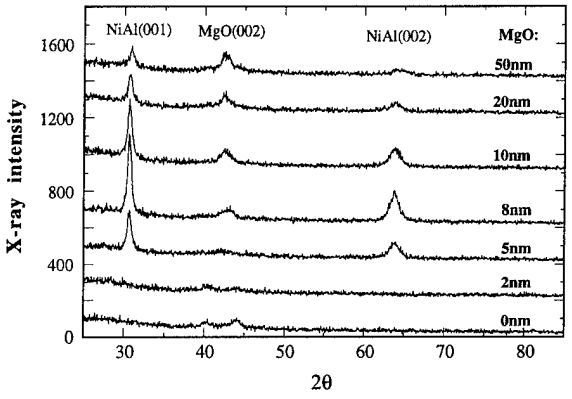
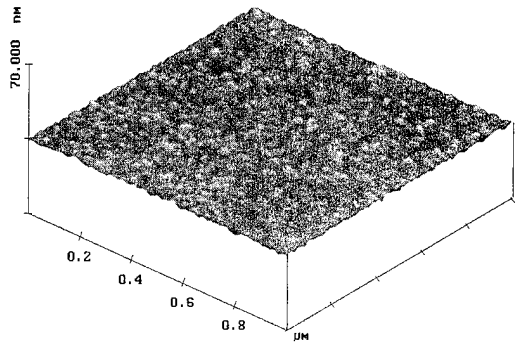
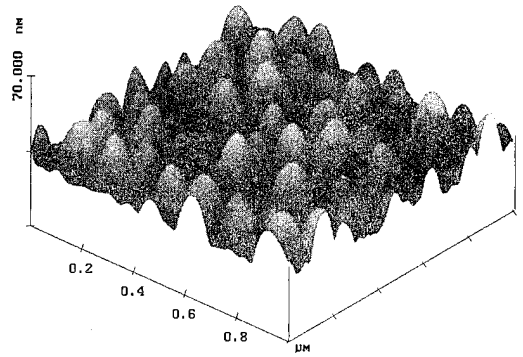


FIG. 1. X-ray diffraction spectra of CoCrPt(40 nm)/NiAl(100 nm) films on various thicknesses of MgO seed layers.

 0021-8979/96/79(8)/4902/3/$10.00 © 1996 American Institute of Physics



(a) NiAl,100nm/MgO,10nm/glass



(b) NiAl,100nm/MgO,20nm/glass

FIG. 2. AFM surface plots of 100 nm NiAl films with MgO seed layers of (a) 10 nm and (b) 20 nm on smooth glass substrates.

with bonded Pt chips. Substrates were biased at −100 V with respect to the target during the deposition of CoCrPt films. EDX analysis of the magnetic CoCrPt film determined the composition to be $CoCr_{10}Pt_{18}$. Smooth glass substrates were used. Film thicknesses were determined by profilometry. Surface morphology of the films were checked by atomic force microscopy (AFM). Transmission electron microscopy (TEM) was performed on studying the films' plane-view microstructure. In-plane magnetic properties were measured by vibrating sample magnetometry (VSM). Crystallographic textures were studied by x-ray diffractometry with Cu $K\alpha$ radiation.

TABLE II. The in-plane magnetic properties of the 40 nm CoCrPt films on 100 nm NiAl, 100 nm Cr, and 100 nm NiAl/10 nm Cr underlayers.

Underlayer	H_c (Oe)	S^*	S	Mrt (memu/cm^2)
NiAl	2221	0.79	0.81	0.81
Cr	2228	0.74	0.85	0.83
NiAl/Cr	3153	0.78	0.85	0.84

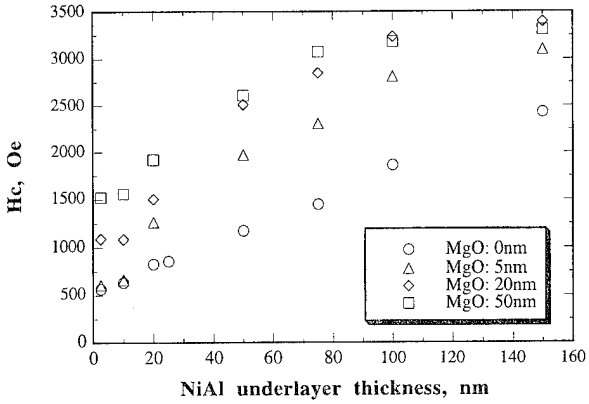


FIG. 3. Coercivity values of the 40-nm-thick CoCrPt vs their NiAl underlayer thickness for MgO seed layers of 0, 5, 10, 20 nm thick.

Table I lists the VSM measurements of the 40-nm-thick CoCrPt films on 100 nm NiAl underlayers on MgO seed layers of various thicknesses. The coercivity increases rapidly and then levels off as the MgO seed layer thickens. The maximum coercivity of 3280 Oe occurs at a MgO thickness of 8 nm. The crystallographic texture of these 40 nm CoCrPt/100 nm NiAl films on MgO seed layers revealed by x-ray diffraction spectra are plotted in Fig. 1. The (002) MgO peak continuously becomes stronger as the MgO layer thickens. However, the intensity of the (002) NiAl peak is not proportional to the MgO thickness. The maximum coercivity film in Table I corresponds to the film with the strongest (002) NiAl crystallographic texture.

AFM studies of the films showed little increase in surface roughness as the MgO seed layer is increased from 2 to 10 nm. However, there is a dramatic increase of the surface roughness as the MgO seed layer reaches 20 nm which is believed to be the main cause for the apparent deterioration of the epitaxy between NiAl and MgO. Figure 2 shows the AFM surface topography plots of 100 nm NiAl films on 10 and 20 nm MgO seed layers on glass substrates. A 20 nm MgO seed layer can roughen the film considerably to form

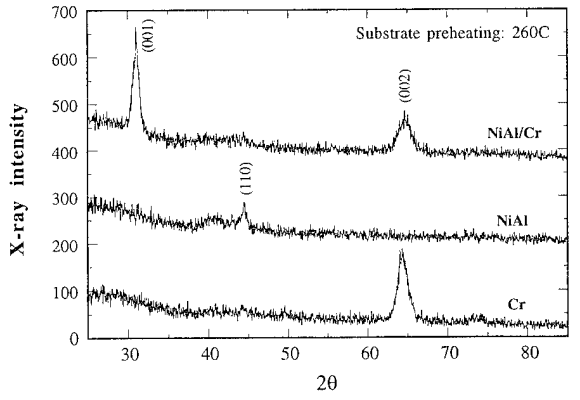


FIG. 4. X-ray diffraction spectra of the CoCrPt(40 nm)/Cr(100 nm) film and CoCrPt(40 nm)/NiAl(100 nm) films with and without a 10 nm Cr seed layer. These films were all deposited with 260 °C substrate preheating.

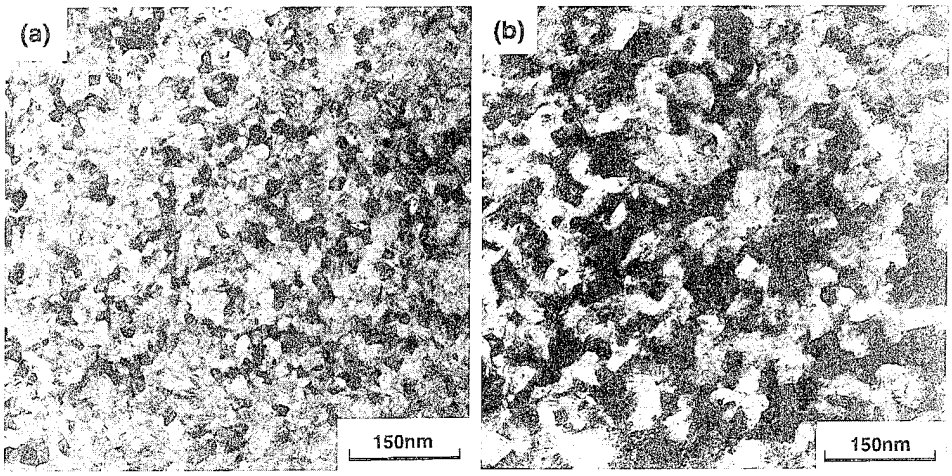


FIG. 5. Bright-field TEM micrographs of CoCrPt(40 nm)/NiAl(100 nm) films (a) on a 5 nm MgO seed layer and (b) on a 10 nm Cr seed layer.

surface bumps of up to ~150 nm in diameter and ~25 nm in height. Because a low flying height is necessary for future high-density recording media, this surface roughening may be problematic. On the other hand, to avoid the stiction of the head slider to the smooth disk the surface of the disk substrate is generally roughened by mechanical and/or chemical texturing. For glass disks, a sputtered texture is often used.[10] With the MgO seed layer the roughness can be tailored by controlling the MgO layer thickness or fine tuning the sputtering process.

Figure 3 is a plot of four sets of coercivity data of the 40-nm-thick CoCrPt films versus their NiAl underlayer thicknesses for MgO seed layers of 0, 5, 20, and 50 nm.

Likewise, a 10 nm Cr seed layer when prepared on a 260 °C preheated substrate induces (002) texture in a subsequent NiAl layer. Figure 4 plots the x-ray diffraction spectra of 40 nm CoCrPt/100 nm NiAl films with and without a 10 nm Cr seed layer and a 40 nm CoCrPt/100 nm Cr film. For comparison, these films were all deposited onto 260 °C preheated substrates. The substrate preheating helps to bring out the (002) texture in the NiAl underlayer with a Cr seed layer as well as the standard pure Cr underlayer. However, no (002) peak is observed in the film with only the pure NiAl underlayer. Table II lists the in-plane bulk magnetic properties of the specimens depicted in Fig. 4. It shows the coercivity of the CoCrPt film on the NiAl underlayer is significantly increased due to the incorporation of the Cr seed layer, similar to the MgO seed layer. However, lower coercivity squareness and $M_r t$ were observed in the film with a Cr seed layer. With a similar (002) texture, the NiAl underlayer appears to induce a higher coercivity in the CoCrPt film than the Cr underlayer.

Figure 5 compares the TEM bright-field micrographs of 40 nm CoCrPt/100 nm NiAl films on 5 nm MgO and 10 nm Cr seed layers. Although these plane-view micrographs show overlapping NiAl and Co grains, it is obvious that the grain size of the film with a Cr seed layer is more than twice the grain size (180 Å) of the film with a MgO seed layer.

In summary, seed layers of Cr and MgO which can induce the (002) crystallographic texture in the NiAl underlayers were shown to be beneficial to the in-plane coercivity of the CoCrPt films. While Cr seed layers require substrate heating, MgO seed layers do not. Therefore, films on a MgO seed layer have finer grains. Surface roughness can also be tailored by using a MgO layer which can provide sputtered texture to smooth substrates to reduce the stiction of the head to the smooth disk.

This work was supported in part by the DSSC of CMU under a NSF Grant No. ECD-8907068 and an ARPA Contract No. MDA972-93-1-0009. The government has certain rights to this material.

[1] L.-L. Lee, D. E. Laughlin, and D. N. Lambeth, IEEE Trans. Magn. **MAG-30**, 3951 (1994).
[2] L.-L. Lee, D. E. Laughlin, and D. N. Lambeth, IEEE Trans. Magn. **MAG-31**, 2728 (1995).
[3] J. Zhu and X. Ye, Digests of Intermag 95, Paper FA03, (1995).
[4] H. S. Chang, K. H. Shin, T. D. Lee, and J. K. Park, IEEE Trans. Magn. **MAG-31**, 2731 (1995).
[5] T. Kogure and S. Katayama, J. Appl. Phys. **67**, 4701 (1990).
[6] X. Tang, B. Reed, and R. Zubeck, IEEE Trans. Magn. **MAG-30**, 3963 (1994).
[7] H. Kataoka, T. Kanbe, H. Kashiwase, E. Fujita, Y. Yashisa, and K. furusawa, Intermag 95 Paper BC03, IEEE Trans. Magn. **MAG-31**, 2734 (1995).
[8] A. Nakamura and M. Futamoto, Jpn. J. Appl. Phys. **32**, L1414 (1993).
[9] P. W. Tasker, Adv. Ceram. **10**, 176 (1984).
[10] M. Mirzamaani and C. V. Jahnes, IEEE Trans. Magn. **MAG-28**, 3090 (1992).

Plastic substrate preembossed 100 kbpi, 3.4 μm track width magnetic disk (abstract)

O. Ishizaki, T. Ohnuki, and K. Adachi
Engineering Research Laboratory, Hitachi Maxell Ltd., 6-20-1 Kinunodai, Yawara-mura, Tsukuba-gun, Ibaraki 300-24, Japan

K. Akagi, H. Momiji, and O. Komoda
Central Research Laboratory, Hitachi Ltd., 1-280 Higashi-koigakubo, Kokubunji, Tokyo 185, Japan

N. Ohta
Engineering Research Laboratory, Hitachi Maxell Ltd., 6-20-1 Kinunodai, Yawara-mura, Tsukuba-gun, Ibaraki 300-24, Japan

To achieve higher areal recording density and at the same time very low cost magnetic media, a preembossed disk is proposed in which servo marks, header signals, and ROM data are formed on a plastic substrate by an injection method.[1,2] Those media give very attractive features to reduce track pitch comparable to optical disks. A very expensive and low throughput servo writer is not necessary by using such preembossed servo marks. To realize the preembossed disk, a magnetic layer should be prepared by low-temperature deposition. In this paper, we studied the sputtering process and suitable magnetic materials such as CoCrPt/Cr film on plastic substrate. Plastic substrate was made by amorphous polyolefin (APO). The under layer (Cr), magnetic layer (CoCrPt), protective layer (C) are formed by magnetron sputtering without substrate heating. Effects of Pt content, thicknesses of magnetic layer, and under layer were investigated. Results showed that coercivity was achieved to 1900 Oe at Pt about 20 at. %, 30-nm-thick magnetic layer and 200-nm-thick under layer. Recording characteristics of the disk were measured by an MR head. The head has a track width of 3.4 μm and a shield distance of 0.35 μm. The results were D_{50}=100 kfci, C/N=47 dB (at 75kfci), and a resulting density of 0.7 Gb/in^2. The signal output from the prepit shows 80% maximum value compared with conventional magnetic bits. © *1996 American Institute of Physics.* [S0021-8979(96)45608-4]

[1] S. Yonezawa, SPIE/SPSE Symposium on Electronic Imaging, Feb. 11, 1990.
[2] K. Watanabe, T. Takeda, K. Okada, and H. Takino, IEEE Trans. Magn. **29**, 4030 (1993).

Nonlinear partial erasure and its correlation with transition noise in longitudinal thin-film media

Jian-Gang Zhu, Terence Lam, Yansheng Luo, and Xiao-Guang Ye
MINT, Department of Electrical Engineering, University of Minnesota, Minneapolis, Minnesota 55455

Nonlinear partial erasure and the supralinear noise enhancement at high recording densities are the two critical factors limiting linear recording density in longitudinal thin-film disk media. In this paper, via spin stand measurements, nonlinear partial erasure was studied in terms of medium magnetic parameters, such as M_rT, H_c and orientation ratio, and recording conditions, such as fly height and write current optimization. It is found that the nonlinear partial erasure and the supralinear noise increase always occur at the same recording density, independent of media magnetic properties and recording condition. © *1996 American Institute of Physics.* [S0021-8979(96)14308-4]

I. INTRODUCTION

At high recording densities, longitudinal thin-film media exhibit nonlinear amplitude reduction, referred to as nonlinear partial erasure, in addition to nonlinear bit shift.[1] Since all of the advanced data recovery channels, such as PRML, are based on linear superposition, severe partial erasure can present a significant limitation on the linear recording density. Another recording density limiting factor is the transition noise at high recording densities where the noise rises faster than the initial linear increase.[2,3] With the introduction of magnetoresistive heads, the recording channel can become medium noise dominated. In this paper, we report a systematic experimental study on the correlation between nonlinear partial erasure and medium noise.

II. EXPERIMENTAL AND ANALYTICAL METHOD

The measurements of nonlinear partial erasure were performed on a high precision air-bearing spin stand tester. In order to avoid head nonlinearity, inductive thin-film heads instead of MR heads were used for all the measurements, even for disks with low M_rT values used in MR applications. To distinguish the nonlinear partial erasure from nonlinear transition shift, all "1"s patterns were recorded on thin-film disks so that the deterministic relative position shift in between adjacent transitions is absent. The nonlinear transition shift becomes a block shift and the intertransition interval is exactly the same as the data pattern of the write current. The nonlinear amplitude reduction is usually referred to as the ratio between the amplitude of an actually recorded all "1"s patterns and the amplitude of all "1"s patterns formed by superimposing isolated voltage pulses at the same intertransition interval. Here, in order to eliminate the impact of electronic noise, this ratio was actually measured in frequency domain using a spectrum analyzer with the method briefly described as the follows.

Assuming the linear superposition holds, the signal spectrum of a recorded all "1"s pattern can be written as

$$V(k)=2k_0V(k)\sum_{n=\text{odd.}}\delta(k-nk_0),$$

where $k=2\pi/\lambda$ is the wave number, $k_0=2\pi/\lambda_0=\pi/B_0$ is the fundamental wave number while B_0 is the recording bit length, and $V(k)$ is the Fourier transform of the isolated voltage pulse. The third harmonic for a recording density at $D_1=1/B_1$ is

$$V_{D_1}(k=3k_1)=2k_1V(3k_1).$$

The first harmonic for a recording density three times higher $D_3=3D_1$ is

$$V_{D_3}(k=k_3)=2k_3V(k_3)=2\times3k_1V(3k_1).$$

Thus, if the linear superposition holds, we have

$$V_{D_3}(\text{first harmonic})=3V_{D_1}(\text{third harmonic}).$$

We define the ratio

$$P=\frac{V_{D_3}(\text{first harmonic})}{3V_{D_1}(\text{third harmonic})}.$$

If the density $D_1=D_3/3$ is low enough where superposition still holds, P becomes a measure of the nonlinear partial erasure at density D_3 and is closely equal to the nonlinear amplitude reduction of the voltage wave form. A more detailed description of the method can be found in Ref. 4. In this paper, P is referred to as the nonlinear partial erasure and is always plotted as a function of recording density D_3.

A magnetic force microscope, made by Digital Instruments, was used to image the recorded transition patterns. MFM tips were coated with CoCrTa film for imaging. The resonant frequency of the tips is in the range of 30–70 kHz. The magnetic images were obtained using the frequency detection mode.

A set of selected disks with a range of coercivity and area magnetic moment density were used in the measurement. The magnetic hysteresis parameters are listed in Table I. Thin-film heads with gap length $g=0.21$ μm, fly height

TABLE I. List of film disks.

Disks	H_c (Oe)	M_rT (memu/cm^2)	OR
Disk A	2200	0.79	1.0
Disk B	1500	2.8	2.5
Disk C	1400	2.7	1.0
Disk D	1650	2.5	1.0
Disk E	1750	1.3	1.0
Disk F	1400	2.7	1.0

 0021-8979/96/79(8)/4906/3/$10.00 © 1996 American Institute of Physics

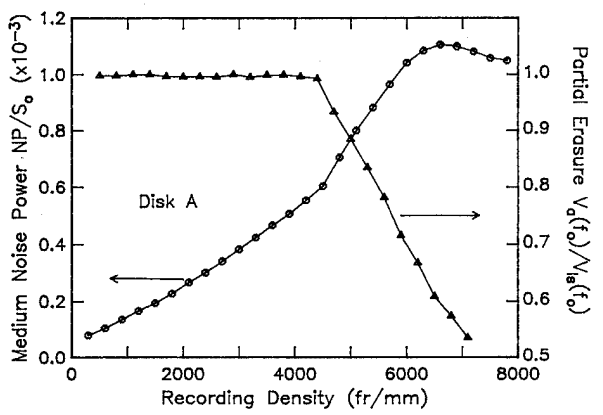


FIG. 1. Measured nonlinear partial erasure P and integrated medium noise power vs recording density.

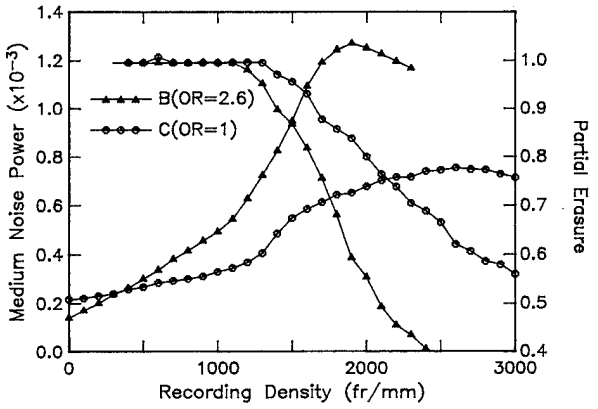


FIG. 3. Measured partial erasure P and integrated noise power as functions of recording densities for a highly oriented disk (disk B), and an isotropic disk (disk C).

$d_f = 2.5$ μm, and a track width of 4.5 μm were used for all the recording measurements except cases mentioned otherwise. The write current was optimized for voltage amplitude at high linear densities. The medium noise is normalized by the peak amplitude of the isolated voltage pulse.

III. RESULTS AND DISCUSSIONS

A. Partial erasure, transition noise, and percolation

Figure 1 shows the measured medium noise power and measured partial erasure as functions of recording density for disk A. Both the supralinear noise increase and nonlinear partial erasure are well pronounced. The onset of the supralinear noise increase and the onset of the nonlinear partial erasure occur at the exact same recording density. Beyond this density, the partial erasure ratio decreases almost linearly with increasing recording density.

The coincident of the onset density for the two measurement quantities is not accidental. Repeated measurements of over 20 different disks using various thin-film heads at various recording conditions show that the two onsets always occur at the same recording density. A magnetic force microscopy image, shown in Fig. 2, taken at densities in the supralinear noise increase region, clearly shows the onset of the percolation between adjacent transitions that also coincide with the onsets of partial erasure and the supralinear noise increase. Figure 2 shows the transition image at relatively high density and the intertransition percolation apparently has become well pronounced. From these experimental results, it is concluded that the intertransition percolation is the cause for both the nonlinear partial erasure and the supralinear transition noise increase.

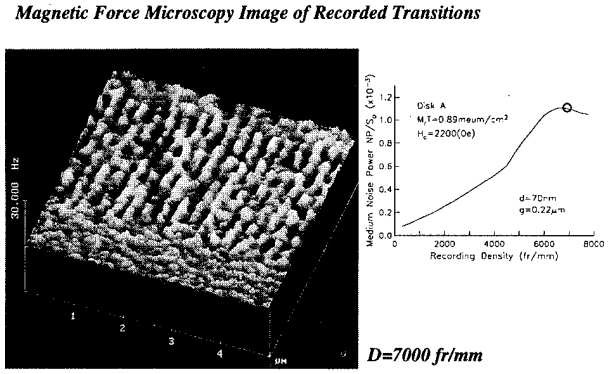


FIG. 2. MFM images of recorded transitions at recording density $D = 7000$ fr/mm for disk A.

B. Effect of medium orientation ratio

Disks B and C have similar magnetic area moment density and similar coercivity, but with a quite different orientation ratio. Disk B is highly oriented with an orientation ratio of 2.8 while disk C is essentially isotropic. Figure 3 shows the measured partial erasure and medium noise power for both disks B and C. At low densities, the oriented disk exhibits lower medium noise than that of the isotropic disk. At high recording densities, however, the supralinear noise increase for the oriented disk becomes much more pronounced than that for the isotropic disk. The partial erasure of the oriented disk exhibits a significantly steeper slope than that of the isotropic disk.

C. Effect of medium *MrT*

Disks D and E have similar coercivity, but very different magnetic area moment values: $MrT = 2.5$ memu/cm^3 for disk D and 1.3 for disk E. Figure 4 shows the measured partial erasure and medium noise power for disks D and E as functions of recording density. The onset of the partial erasure and supralinear noise increase for the higher moment disk occurs at significantly lower density than that of the lower moment disk. The slopes of the noise increase at low and high recording densities are significantly greater for the higher moment disk than that for the lower moment disk. Such behavior has been observed experimentally[3] and also predicted by micromagnetic simulations.[4] Reducing medium MrT brings the advantage of narrower transition lengths which result in shifting the onset of the partial erasure and supralinear noise increase toward higher recording densities.

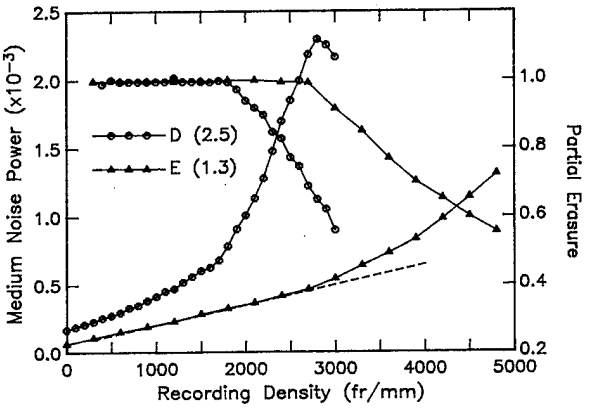


FIG. 4. Measured partial erasure P and integrated noise power as functions of recording densities for two disks with different moment densities: disk D ($M_rT=2.5$ memu/cm^3) and disk E ($M_rT=1.3$ memu/cm^3).

D. Effect of recording fly height

Recording fly height can also significantly affect the partial erasure and the medium noise. In order to study the effect of fly height, two thin-film heads were used, one with a conventional slider and the other with a tripad slider. The recording measurements were performed on disk A. The head-medium magnetic separation is approximately $d=75$ nm for the head on the conventional slider and $d=25$ nm for the tripad slider. The two thin-film heads have similar gap length, $g\approx 0.21$ μm and same track width $W=4.5$ μm. Figure 5 shows the measurements for the two fly heights. The partial erasure starts at a density, $D=4400$ fr/mm, for the higher flying height case and at $D=6000$ fr/mm for the lower flying case. The slopes of the medium noise increase at both linear and supralinear regimes are significantly higher for the higher flying case than those for the lower flying one.

E. Effect of write current

Apart from the fly height, write current is another factor which can affect the behavior of both partial erasure and transition noise. Figure 6 shows the measurements for disk F which has relatively low coercivity. At a write current of 6 mA at which the high frequency output was optimized, the onset of the partial erasure occurs at $D=2400$ fr/mm while at a write current of 30 mA, the partial erasure occurs at a much lower density: $D=1500$ fr/mm. The shift of the onset density of the partial erasure is likely due to broader transitions created by the poor head field gradient.

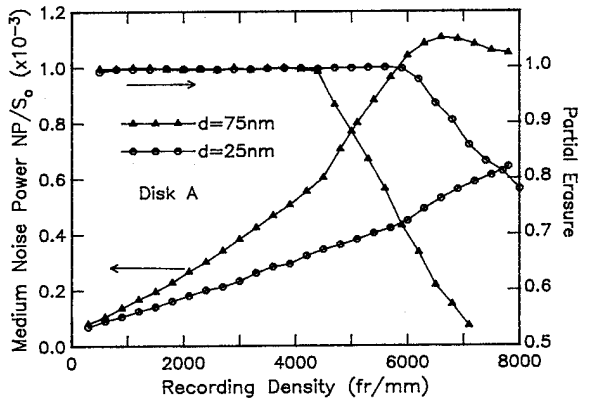


FIG. 5. Measured partial erasure P and integrated medium noise power vs recording densities for recording at two different fly heights.

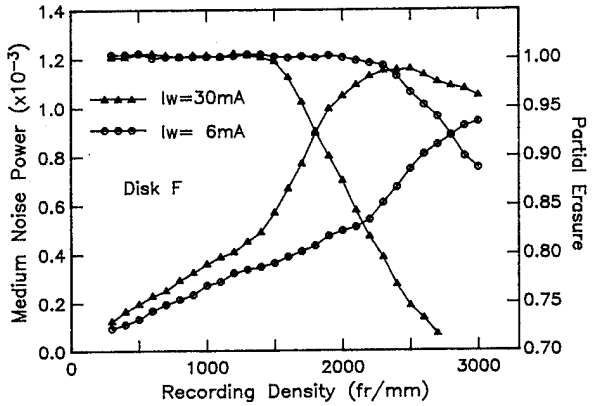


FIG. 6. Measured partial erasure P and integrated medium noise power vs recording densities for recording at two different write current amplitudes.

IV. REMARKS

It is concluded that the onset of the partial erasure is essentially determined by the transition length parameter which is a function of medium magnetic parameters, such as area moment density M_rT, and coercivity H_c, and the recording conditions, such as fly height and recording current. Reducing either the medium M_rT or the recording fly height reduces the transition length parameter, thereby shifting the onset of the partial erasure towards higher densities.

At high recording densities, nonlinear partial erasure can dominate the medium nonlinearity. Conventional measurement technique of nonlinear transition shift, such as the fifth harmonic elimination method, cannot distinguish the nonlinear partial erasure from the nonlinear transition position shift. At high densities, write precompensation not only compensates for the nonlinear transition position shift, in fact also compensates the nonlinear partial erasure by moving the adjacent transitions further apart.

ACKNOWLEDGMENTS

This research is supported in part by the National Science Foundation Young Investigator Award under Grant No. ECS9358309, NIST/ATP-NSIC High Density Disk Program, and IBM Faculty Development Award. The authors would like to thank Dr. Ken Johnson, Dr. Marry Doerner from IBM for providing some of the disk media used in these measurements.

[1] See, e.g., H. Takano, T. Lam, J.-G. Zhu, and J. H. Judy, IEEE Trans. Magn. **29**, 3709 (1993).
[2] N. R. Belk, P. K. George, and G. S. Mowry, J. Appl. Phys. **59**, 557 (1986).
[3] N. R. Belk, P. K. George, and G. S. Mowry, IEEE Trans. Magn. **21**, 1350 (1985).
[4] J.-G. Zhu, IEEE Trans. Magn. **27**, 5040 (1991).
[5] X. Che, IEEE Trans. Magn. **31**, 3021 (1995).

Magnetic force microscopy study of submicron track width recording in thin-film media

Yansheng Luo, Terence T. Lam, and Jian-Gang Zhu
MINT, Department of Electrical Engineering, University of Minnesota, Minneapolis, Minnesota 55455

Hua-Ching Tong and Robert Rottmayer
Read-Rite Corp., 44100 Osgood Road, Fremont, California 94539

The magnetic force microscopy (MFM) technique is used to investigate the writing properties of a set of thin-film heads with track widths ranging from 2 to 0.5 μm. MFM images show that track edge percolation occurs at lower densities than on-track intertransition percolation. Track edge percolation results in track edge fluctuations and effective track width reduction. As the head track width is reduced to the near-micron or submicron ranges, the track edges become dominant portions of the track and consequently cause severe degradation of the recording tracks. Track edge percolation is caused by a poor edge field gradient and is possibly enhanced by pole tip corner saturation. In order to achieve high-density narrow track recording, high moment writing heads become necessary. © *1996 American Institute of Physics.* [S0021-8979(96)08008-9]

I. INTRODUCTION

Rapid increase of track density requires a much improved understanding of the recording properties for narrow track recording heads. As the track width narrows down to the near-micron or submicron range, not only the properties of the erased band become significant, but also the on-track recording characteristics near the track edges become more and more important.[1–3] For conventional thin-film heads, head saturation at the corners of the pole tips does not present a serious problem and has always been neglected since the track width is sufficiently wide. At near-micron or submicron track widths, the head corner saturation phenomenon will be severe and will affect the recording properties more significantly.

To address the above issues, we present a magnetic force microscopy (MFM) study of the recording properties of narrow track thin-film heads. The heads have track widths ranging from 2 to 0.5 μm. The emphasis is to investigate the impact of head width reduction on the writing characteristics, both on-track and at track edges.

II. EXPERIMENT

The recording heads used in this study were fabricated from a set of identical thin-film heads with advanced air bearing (tripad) designs for achieving low flying heights. Using a high precision focused ion beam (FIB) etching technique, the pole tips of these heads were trimmed from the air bearing surface to obtain very narrow track widths. The track widths obtained are 2, 1, 0.75, and 0.5 μm. Figure 1(a) shows the picture of a head before FIB trimming and Fig. 1(b) shows the picture of a trimmed head with 1 μm track width. The trimming depth is 1 μm, approximately the same as the head throat height. The heads all have a gap length $g=0.22$ μm and a flying height less than 1 μin.

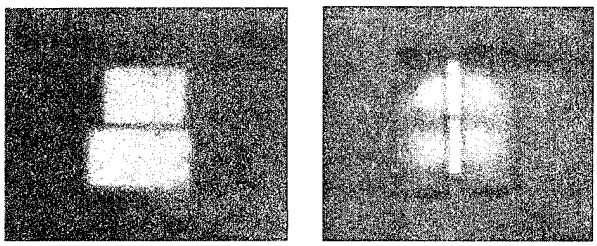
Recording experiments were performed on a precision air-bearing spin stand. The magnetic disk used in this study was a planar isotropic thin-film disk with $Mrt=0.79$ memu/cm^2 and $H_c=2200$ Oe. The disk was in a dc erased state prior to recording. The heads all have 42 turns and the recording current used is 10 mA zero to peak at which the overwrite performance was optimized.

A Digital Instruments Nanoscope III TAFM was used to obtain high-resolution images of the recording tracks. MFM tips were coated with CoCrTa alloy for magnetic imaging. The resonant frequency of the tip is in the range of 30–70 kHz. The magnetic images were obtained in the frequency detection mode.

III. RESULTS AND DISCUSSION

A. Properties at low recording densities

Figure 2 shows an MFM image of a track recorded with the 1-μm-wide recording head. The linear density is 2000 fr/mm. As shown in this image, the transitions are well defined both in the on-track region and in the track edge region. The track width is about 0.62 μm measured from the image. In the side regions of the track, the medium remains in the dc erased state. Since these heads are trimmed from the air bearing surface, two shoulders are created on both sides [see Fig. 1(b)]. However, the MFM image in Fig. 2 shows, for the heads we used, 1 μm trimming depth is sufficient to suppress



(a) (b)

FIG. 1. Optical microscope images from the ABS for the (a) untrimmed TF head, and (b) trimmed 1-μm-wide TF head.

 0021-8979/96/79(8)/4909/3/$10.00 © 1996 American Institute of Physics

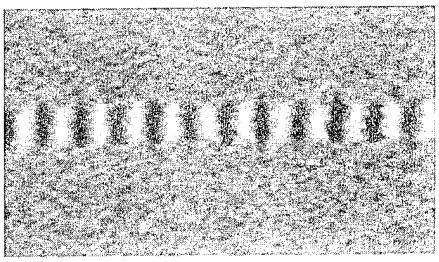


FIG. 2. MFM images of an isolated track recorded with the 1-μm-wide head at linear density of 2000 fr/mm.

the influence of the fringing fields from the shoulders. The well-recorded transitions and clear track edges indicate the success of the trimming process.

B. Properties at high recording densities

Figure 3(a)–3(d) show the MFM images of the recording tracks at a linear density of 5000 fr/mm. The head widths are 2, 1, 0.75, and 0.5 μm, respectively. For all the four heads, the on-track portion of the transitions are well defined. The transitions near the track edges, however, become much more irregular than that at low densities as shown in Fig. 2. Such irregularity near the track edges becomes more critical

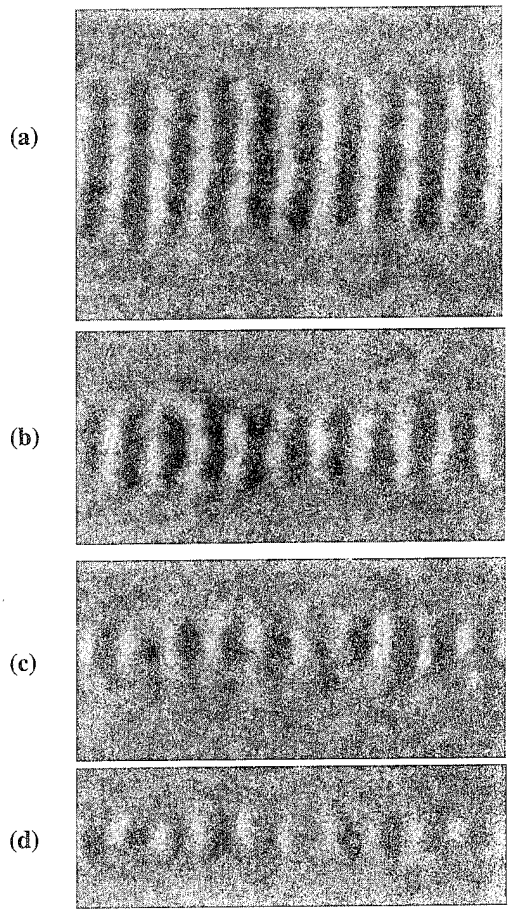


FIG. 3. MFM images of isolated tracks at linear density of 5000 fr/mm. The widths of the recording heads are: (a) 2 μm, (b) 1 μm, (c) 0.75 μm, and (d) 0.5 μm.

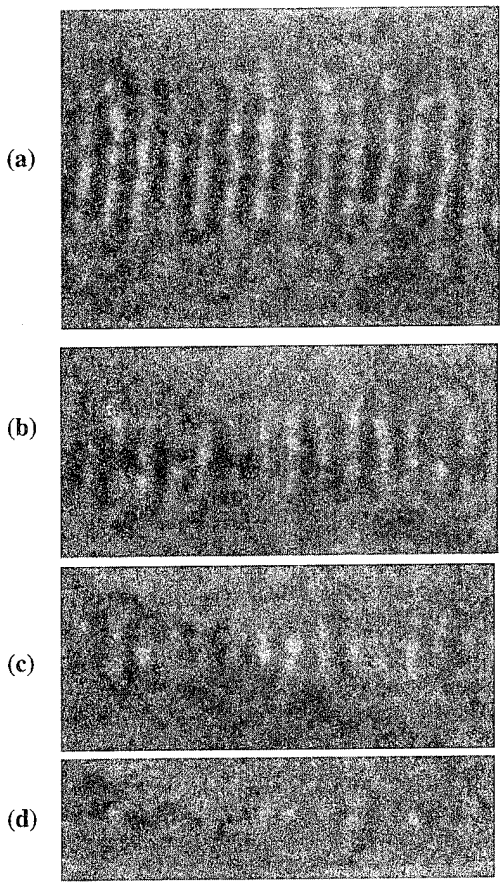


FIG. 4. MFM images of isolated tracks at linear density of 7000 fr/mm. The widths of the recording heads are: (a) 2 μm, (b) 1 μm, (c) 0.75 μm, and (d) 0.5 μm.

for the narrower tracks. For the 0.5-μm-wide track, the spatial scale of the irregularity is comparable to a significant portion of the track width. The transition fluctuations near the track edges result in effective track width reduction which shows as a form of partial erasure in spin-stand recording measurement.[4] The edge transition fluctuations are likely to be caused by the relatively poor head field gradient near the track edges. The presence of any pole tip corner saturation, which could be the situation here, will worsen this effect.

Figures 4(a)–4(d) show the MFM images of the recording tracks at a higher linear recording density: 7000 fr/mm. At this density, for the 2 μm track, the intertransition percolation near the track edges becomes much more pronounced as shown in Fig. 4(a), while the intertransition percolation for the on-track portion is much less severe than that near the track edges. For the 1, 0.75, and 0.5 μm tracks, the percolation has extended from the track edges into significant portion of the entire track. In particular, for the 0.5-μm-wide track, percolation has caused complete self erasure of some of the transitions.

The above MFM images clearly demonstrate that the track edge percolation occurs at lower recording densities than the on-track percolation. For head widths in the near-micron or submicron range, the recording properties near the track edge become dominant. It is likely that the severe track

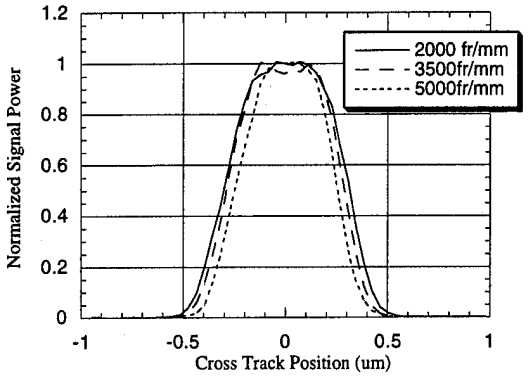


FIG. 5. The cross track signal power profiles of three tracks recorded with the 1 μm head at 2000, 3500, 5000 fr/mm linear densities.

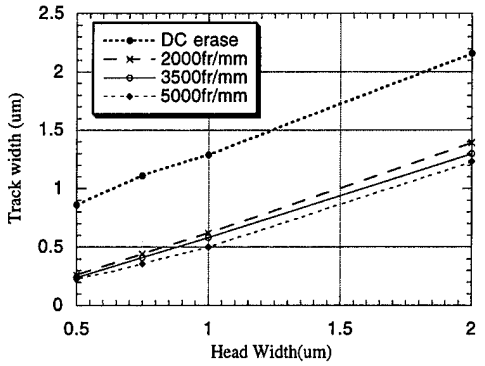


FIG. 6. The track width as a function of head width. The tracks are recorded at: 2000, 3500, and 5000 fr/mm. The dc erase track width is also shown. As recording density increases, track width decreases.

edge percolation at high recording densities for the narrow track heads is closely related to the head saturation at the pole tip corners. Since the heads are trimmed from wide track heads, the flux to the pole tips must be in excess. In practice, it is believed that pole tip corner saturation always occurs and has been demonstrated by various head field modeling.[5] Therefore, high moment write heads are necessary for high-density narrow track recording to ensure good field gradient at track edges.

C. Isolated track width and dc erase track width measurement

Using a technique similar to Ref. 6, we have measured the track widths for the trimmed heads at different densities. First, a series of single isolated tracks were recorded on a dc erased disk. Then the cross track signal power profiles were calculated from MFM images of these tracks. The track width is defined as the width of the region where the signal power is above half of the on-track amplitude. Figure 5 shows the obtained cross track profiles of 1 μm head recorded tracks. The recording densities are 2000, 3500, and 5000 fr/mm, respectively. The on-track signals are normalized to the same magnitude so that the track widths at different densities can be compared. The track widths measure 0.62, 0.58, and 0.50 μm for 2000, 3500, and 5000 fr/mm, respectively. As the recording density increases, the track width decreases.

Figure 6 summarizes the isolated track widths and dc erase track widths for the four trimmed narrow track heads. The linear curves indicate similar side writing characteristics of the four heads. The side writing is more related to the gap length and pole geometry rather than the pole width. For all heads, similar track width reduction at high recording density is observed. The difference between the isolated track width and dc erase track width approximately equals twice the edge erase band. For these narrow heads, the dc erase track width is about 0.6 μm greater than the isolated track width which gives an erase band width of 0.3 μm. To further reduce the erase band and increase track packing density, it is also desirable to use high moment heads for generating high gradient head fields.

IV. CONCLUSIONS

We have studied the write properties of a series of very narrow thin-film heads with track widths ranging from 2 to 0.5 μm. We have experimentally shown 1-μm-deep pole trimming is sufficient to suppress the interference of the side fringing fields from the etched shoulders. It is found that track edge percolation occurs at lower densities than on-track intertransition percolation. Track edge percolation causes track edge fluctuations and effective track width reduction. As the track width is reduced to the near-micron or submicron ranges, the track edges become dominant portions of the track and consequently cause severe degradation of the recording tracks. Track edge percolation is caused by poor edge field gradients and is possibly enhanced by pole tip corner saturation. In order to achieve high-density narrow track recording, high moment heads become necessary.

[1] C. Tsang, H. Santimi, D. McCown, J. Lo, and R. Lee, TMRC 95.
[2] M. H. Kryder and W. Y. Lai, IEEE Trans. Magn. **MAG-30**, 3873 (1994).
[3] J. Su, K. Ju, J. Lo, and G. Countryman, IEEE Trans. Magn. **MAG-26**, 2463 (1990).
[4] T. L. Lam, Y. S. Luo, and J. G. Zhu, these proceedings.
[5] J. Justy (private communication).
[6] Y. S. Luo, T. L. Lam, and J. G. Zhu, INTERMAG 95, paper HQ01.

Magnetic force microscopy images of ultrahigh-density bit patterns recorded on high-coercivity longitudinal and perpendicular thin-film media

Xing Song, John Sivertsen, and Jack Judy[a)]
The Center for Micromagnetics and Information Technologies (MINT), Department of Chemical Engineering and Materials Science, University of Minnesota, MPLS, Minnesota 55455

Magnetic bit patterns recorded on high-coercivity longitudinal thin-film media (L1: H_c=2500 Oe, L2: 2850 Oe), and perpendicular thin-film media (P1: H_c=2830 Oe, P2: H_c=3780 Oe) were investigated using magnetic force microscope (MFM). For the longitudinal media, insufficient writing is responsible for limiting the detectable density. By reducing the head fly height from 3 to 2 microinches, the maximum detectable density of L1 is increased from 7000 to 10 500 fr/mm. At this density the well-defined track edge disappears and a complete bit collapse occurs as the bit length becomes much smaller than the average domain size observed in the dc-saturation remanent state. In the case of perpendicular media, contact recording provides sufficient writing and a well-defined track edge at densities above 10 000 fr/mm for both media. A maximum detectable density about 12 000 fr/mm is obtained in both media. At higher recording densities, domain refinement takes place but magnetic interactions within the track also cause the formation of large domains which eventually destroys the bit periodicity. © *1996 American Institute of Physics.* [S0021-8979(96)08108-5]

I. INTRODUCTION

In order to achieve an ultrahigh recording density of 10 Gbits/in.^{2}, longitudinal media should have high coercivity (2500–3500 Oe) and low remanent magnetization-thickness product (0.5–1.0 memu/cm^2).[1] Furthermore, it has been suggested that a possible way to realize even higher areal densities is to utilize perpendicular magnetic recording media.[2,3] Some magnetic force microscopy (MFM) studies on thin-film recording media with coercivities below 2500 Oe have been reported.[4,5] The purpose of this paper is to compare MFM images of ultrahigh-density bit patterns recorded on high-coercivity longitudinal and perpendicular thin-film media and investigate the effects of coercivity, remanent magnetization-thickness product, average domain size, head fly height, and formation of large domains on the recorded patterns.

II. EXPERIMENT

The two longitudinal media used in this experiment are CoCrPt/Cr thin films with different coercivities and remanent magnetization-thickness products: L1, H_c=2500 Oe, $Mr\delta$ =0.65 memu/cm^2; L2, H_c=2850 Oe, $Mr\delta$=0.55 memu/cm^2. The two perpendicular media with 7-μm-thick NiFe underlayer used in this experiment are: P1, a 550 Å single-layer CoCrTaPt film with H_c=2830 Oe; P2, a multilayer 20×(7.5 Å Pd/3.5 Å Co) film with H_c=3781 Oe. An air-bearing spin stand tester was used for the recording measurements. The media were erased to dc-saturation remanent state before recording. For the longitudinal media, recording was done using an FeTaN head with B_s~18 kG, gap length ~0.29 μm, and track width ~5.30 μm at a fly height of ~3 microinches unless otherwise stated. For the perpendicular media, contact recording was realized using a CoNbZr single-pole head with track width ~5.27 μm. Magnetic force microscope images of the recorded bit patterns were obtained using a Nanoscope III in a "tapping-lift" mode with a CoCrTa/Cr-coated tip magnetized in the vertical direction.

III. RESULTS AND DISCUSSION

A. Recording measurements

Figure 1 shows the roll-off curves of the four media. The reproduced voltages for the longitudinal media are almost constant below 4000 fr/mm and drop sharply above 4500 fr/mm. The signals for the perpendicular media start to drop above 3000 fr/mm. A D_{50} of about 5000 fr/mm is obtained in all cases. Signal is undetectable above 7000 fr/mm for the longitudinal media, whereas second peaks around 10 000 fr/mm are obtained for the two perpendicular media.

Noise measurements indicate a smaller integrated medium noise for L2 and P2 compared with L1 and P1, respectively (not shown). It is also observed that P2 suffers from significant larger PW_{50} than P1 (P1: 17.7 microinches, P2: 32.3 microinches).

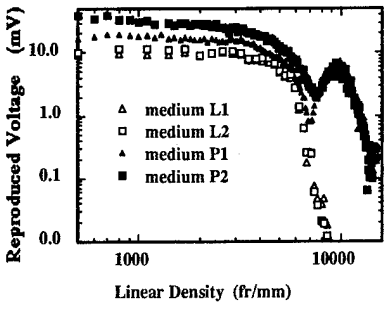


FIG. 1. Reproduced voltage vs linear density of the four media.

[a)]Department of Electrical Engineering.

 0021-8979/96/79(8)/4912/3/$10.00 © 1996 American Institute of Physics

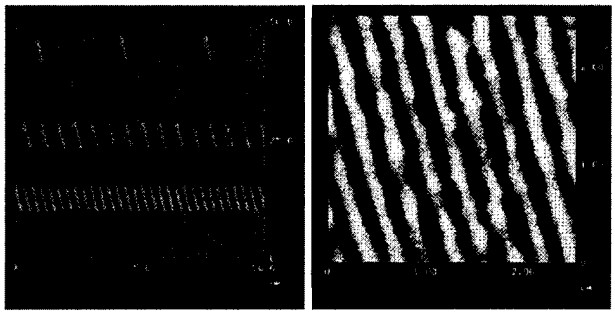


FIG. 2 (a) FIG. 2(b)

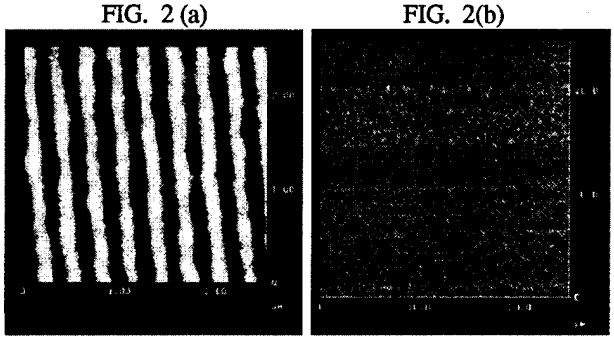


FIG. 2 (c) FIG. 2 (d)

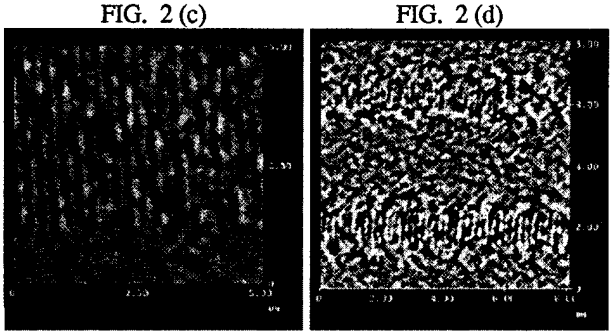


FIG. 2 (e) FIG. 2 (f)

FIG. 2. MFM images of bit patterns recorded on medium L1 and L2. (a) L1: 100, 500, and 1000 fr/mm. (b) L1: 7000 fr/mm. (c) L2: 7000 fr/mm. (d) L2: 8000 fr/mm (top) and 9000 fr/mm (bottom). (e) L2: 8000 fr/mm [a zoom-in image of the top portion of (d)]. (f) L1: 9500 fr/mm (bottom) and 10 500 fr/mm (top), recorded at a fly height of 2 microinches.

B. MFM images of high-coercivity longitudinal media

Figure 2 shows tracks recorded on L1 and L2 at different densities. The same tip was used to obtain these images. The tip lift scan height was set at 40 nm. The general features of the recorded bit patterns of the two longitudinal media are similar at low densities. Figure 2(a) shows the MFM images of bit patterns recorded on L1 at three different low densities. These recorded tracks exhibit sharp bit transitions and well-defined track edges.

The average domain size observed in the dc-erased background of these media is ~270 nm for L1 and ~200 nm for L2. Domains of the same size exist within the recorded bits in each medium. Smaller domains are indication of smaller magnetic exchange interaction and the smaller exchange coupling within L2 explains its smaller integrated medium noise observed in the recording measurement.

As the recording density increases and the bit length approaches or becomes smaller than these average domain sizes, zig-zag transitions become more significant and percolation starts to take place. Figures 2(b) and 2(c) show 7000 fr/mm tracks recorded on these media. L2 suffers less from bit transition degradation and exhibits a larger maximum detectable density of 8000 fr/mm [Fig. 2(e)] compared with 7000 fr/mm of L1 because of the lower $Mr\delta$ and smaller domain size in L2. Figure 2(d) shows two tracks recorded at 8000 and 9000 fr/mm on L2. Figure 2(e) is a zoom-in image around the 8000 fr/mm track. The 9000 fr/mm track is not distinguishable from dc-erased background even by a closer inspection with a higher magnification and smaller tip-to-sample separation (not shown).

In order to improve the magnetic interaction between the head and the medium, bit patterns were recorded on L1 using a head with track width of 2 μm at a lower fly height of 2 microinches. Figure 2(f) shows the tracks with linear densities of 9500 and 10 500 fr/mm recorded on L1. It is clear that a much higher detectable density on L1 is achieved as the head fly height is reduced. Similar improvement of the detectable density in L2 is expected.

At these ultrahigh densities the effective track width is reduced from 2 to 1.3 μm and well-defined track edge no longer exists. Magnetic interaction between the recorded track and the dc-erased background causes the formation of some magnetic domains slightly larger than the average size at the track edges and severe percolation takes place within the tracks. As the write density increases further, bit pattern collapse completely because of a bit length much smaller than the average domain size and can not be resolved.

C. MFM images of high-coercivity perpendicular media

Figure 3 shows several tracks recorded on P1 and P2 at different densities. All images were obtained using the same tip with the tip lift scan height set at 80 nm. Writing is sufficient for these high-coercivity media due to a contact recording mode and a reduced demagnetizing field at high density (indicated by straight track edges). A maximum detectable density of 12 000 fr/mm is obtained on both media.

As mentioned in Sec. III A, recording measurements indicate that P2 has a smaller integrated medium noise and a larger PW_{50} than P1. The MFM images shown in Fig. 3. provide insight understanding of these results. As shown in Fig. 3(a), magnetic domains having ~250 nm in average size are clearly observed in both the dc-erased background and within the bits for P1. In the case of P2 shown in Fig. 3(c), magnetic domains can be hardly seen although the frequency scale of the two images is the same (z range: 100 Hz). By reducing the frequency scale, magnetic domains with the size ~130 nm can be resolved (not shown). It is observed that zig-zag transitions are present within the track on P2 at density as low as 1000 fr/mm, which develop into magnetic interference at intermediate density as shown in Fig. 3(d). From the recording results and these observations, it is concluded that P2 has a smaller integrated medium noise because of a smaller exchange coupling (indicated by its smaller magnetic domain size) and the magnetic irregularities present at bit transitions account for its large PW_{50} detected in the recording measurement.

Figure 3(e) shows a 12 000 fr/mm track on P1. A domain refinement phenomenon is observed. After applying and re-

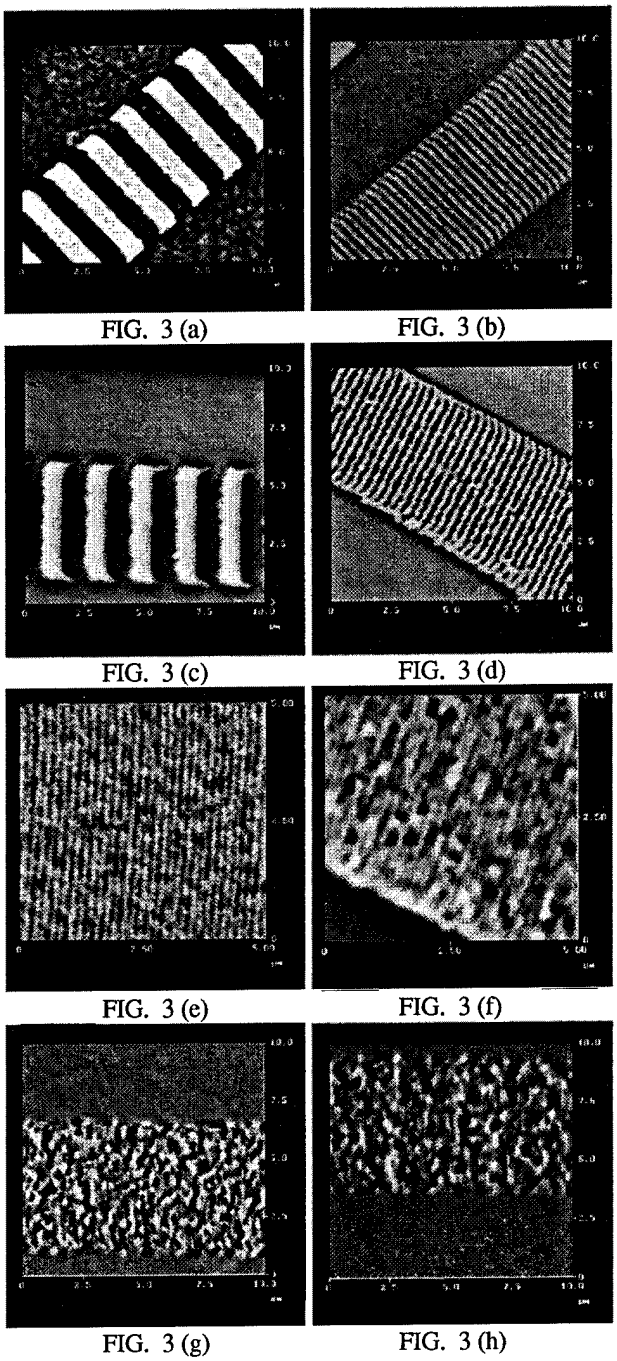


FIG. 3. MFM images of bit patterns recorded on medium P1 and P2. (a), (b) P1: 1000 and 5000 fr/mm. (c), (d) P2: 1000 fr/mm and 5000 fr/mm. (e) P1: 12 000 fr/mm. (f), (g), (h) P2: 11 000, 12 000, 14 000 fr/mm.

moving the high-frequency write field, domains with original size of ~250 nm in the dc-erased state break into smaller domains of ~80 nm. At some locations along the bits, local magnetic domains reverse their polarities with respect to their neighbors' and these magnetization discontinuities lead to signal loss at this density. Figure 3(f) shows a 11 000 fr/mm track recorded on P2. Magnetic domains crossing several bit lengths distribute randomly within the track although individual bits can still be resolved indicating the domain refinement phenomenon. The formation of these domains are caused by magnetic interactions within the track after the high-frequency write signal is removed. Figures 3(g) and 3(h) show tracks recorded on P2 at even higher densities. 12 000 and 14 000 fr/mm. The large domains formed within the track grow in number and in size as the write density increases. Signal peak at 166 nm wave length corresponding to 12 000 fr/mm write density is observed in the spatial frequency domain of Fig. 3(g). As the write density increases to 14 000 fr/mm, domains of 200–700 nm in size form within the track and no signal peak corresponding to this density can be resolved in the frequency domain.

IV. CONCLUSIONS

(1) Ultrahigh-density bit patterns high-coercivity of 10 500 and 12 000 fr/mm are resolved in MFM images of longitudinal and perpendicular media, respectively. Smaller integrated medium noise is obtained from media with smaller average domain size in both kinds of media.

(2) In the longitudinal recording, well-defined track edge disappears and severe percolation destroys the signal written within the track at ultrahigh densities. The detectability of the recorded tracks is dominantly limited by insufficient writing and average domain size observed in the dc-saturation remanent state of the media.

(3) In the perpendicular recording, because of a contact recording mode, the writing is sufficient even for a medium with coercivity as high as 3780 Oe. At ultrahigh densities, domain refinement takes place and local magnetization reversal leads to a reduced signal to noise ratio. Formation of large domains with in the track ultimately destroys the signal.

(4) A less severe zig-zag transition is observed in the medium with a smaller $Mr\delta$ in the longitudinal recording. The zig-zag transition and magnetic interference observed in P2 contribute to a large PW_{50}.

ACKNOWLEDGMENTS

The authors would like to thank Dr. S. Bhatia (IBM) and Dr. A. Payne (Censtor) for providing the media used in this study. We further thank Dr. T. Arnoldussen (IBM) for carrying out low fly height recording on L1.

[1] E. S. Murdock, R. F. Simons, and R. Davison, IEEE Trans. Magn. **28**, 3079 (1992).
[2] S. Yamamoto, Y. Nakamura, and S. Iwasaki, IEEE Trans. Magn. **23**, 2070 (1987).
[3] J. K. Howard, J. Magn. Soc. Jpn. **18**, 59 (1994).
[4] M. Futamoto and Y. Honda, J. Magn. Soc. Jpn. **18**, 485 (1994).
[5] P. Glier, K. Sin, J. Sivertsen, and J. Judy, J. Magn. Soc. Jpn. **18**, 571 (1994).

The effect of physical structure on δI curves of longitudinal thin film (abstract)

N. S. Walmsley, A. Hart, and D. A. Parker
Department of Mathematics and Statistics, University of Central Lancashire, Preston, Lancashire, PR1 2HE, United Kingdom

C. Dean and R. W. Chantrell
Department of Physics, University of Keele, Keele, Staffordshire, ST5 5BG, United Kingdom

Conventionally, the simulation of thin films has been carried out using an HCP structure to represent its physical structure. Such an idealized structure has been shown to overestimate the effect of interparticle coupling by using an homogeneous exchange coupling scheme.[1] A more realistic approach to represent physical structure has been undertaken by generating a system of grains which lie on a radially isotropic structure and have a nonuniform volume distribution. Interaction effects can be shown by computing δI curves formed through the comparison of the remanence curves using the Wohlfarth relation. To generate an isothermal remanence curve (IRM), a realistic ac erased state is necessary which has been carried out by using a simulated annealing technique.[2] A comparison has been made to determine the effect of physical structure on the bulk properties by computing hysteresis loops, remanence curves, and δI curves. To reduce statistical error these have been averaged over four different sets of easy axes. The loops indicate that an irregular physical structure leads to an increase in the coercivity and decrease in the squareness. The dc-demagnetization curves show an increase in remanent coercivity; this can be attributed to the random physical structure decreasing the size of magnetically correlated regions within the microstructure. The effect of the physical microstructure on the δI curves will be discussed in full in the paper. © *1996 American Institute of Physics.* [S0021-8979(96)45708-3]

[1] N. S. Walmsley, A. Hart, D. A. Parker, R. W. Chantrell, and J. J. Miles, to be presented at MRM 1995 (accepted for J. Magn. Magn. Mater.).
[2] C. Dean, R. W. Chantrell, A. Hart, D. A. Parker, and J. J. Miles, IEEE Trans. Magn. **27**, 4769 (1991).

Micromagnetic studies of inhomogeneous CoPtCr bicrystal thin-film media

Qingzhi Peng and H. Neal Bertram
The Center for Magnetic Recording Research, University of California at San Diego, La Jolla, California 92093

Mary Doerner
IBM Storage Systems Division, 5600 Cottle Road, San Jose, California 95193

The effects of medium inhomogeneities in microstructure and exchange configuration are studied by using micromagnetic simulation. Two types of media are studied: one has a uniform bicrystal structure and another has a partial bicrystal structure with 20% random nonbicrystal sites. The comparison of magnetic (M-H loops) and recording properties (transition profiles and noise) for these two types of media are made under two cases with homogeneous or inhomogeneous intergranular exchange coupling. It is found that the introduction of random nonbicrystal sites reduces the medium noise in the case with homogeneous intergranular exchange, while medium noise is barely affected in the case with inhomogeneous intergranular exchange. © *1996 American Institute of Physics.* [S0021-8979(96)07008-7]

I. INTRODUCTION

Current high-density recording utilizes polycrystalline thin films as recording media. It is important to understand the medium noise mechanism and its dependence on microstructure. Suitable epitaxial growth conditions can give rise to bicrystal microstructure, where a polycrystalline thin film consists of bicrystal clusters.[1,2] Each bicrystal cluster consists of subcrystallites that possess two possible orthogonal easy axis. Due to their unique microstructure, bicrystal media have been studied, and proposed as possible candidate media for future ultrahigh density recording.[3,4] Experimental evidence (e.g., x-ray diffraction and TEM images) indicates that there exist nonbicrystal sites in a bicrystal thin film. It is the purpose of this work to further explore (following the work of Ref. 4) the implication of such inhomogeneity on medium magnetic and recording properties by using micromagnetic simulation.

II. MODELING

In this study, we use a 256×128 planar hexagonal array to model the actual medium. Each hexagon corresponds to a Co alloy subcrystallite which is assumed to be single domain and to possess a uniaxial c axis. A grain, which can be either bicrystal or nonbicrystal, is represented by using a cluster of a hexagon subcrystallite and its six nearest neighbors. The height to diameter aspect ratio of a single hexagon subcrystallite is 3:1 in order to keep the aspect ratio of the grains to be unity ($\delta/D=1$). The diameter of bicrystal cluster is assumed to be 18 nm. Within a bicrystal grain, the c axis of subcrystallites are along two mutually orthogonal orientations in the film plane. Among bicrystal grains, their c axis are randomly oriented. In an individual nonbicrystal grain, all subcrystallites have the same direction of c axes. The c axis are 3D randomly oriented among nonbicrystal grains. The modeling of bicrystal and nonbicrystal clusters is illustrated in Fig. 1.

The magnetostatic interaction is described by a scaled constant $h_m=M_s/H_k$, where M_s is the saturation magnetization and $H_k=2K/M_s$ is the anisotropy field. A fixed magnitude is assumed for each subcrystallite's anisotropy field H_k. In this article, an intrinsic anisotropy energy constant $K\sim1.5\times10^6$ erg/cc and saturation magnetization $M_s\sim360$ emu/cc are utilized throughout the study, which yields $h_m\sim0.04$. The exchange coupling between neighboring subcrystallites is described by the normalized parameter $h_e=A^*/KD^2$, where A^* is the effective intergranular exchange constant. Two different exchange constants, h_e^{in} and h_e^{out} were used. The term h_e^{in} describes the coupling between the Co alloy subcrystallites within a grain, while h_e^{out} gives the coupling between neighboring grains, as shown in Fig. 1. It is assumed that bicrystal grains and nonbicrystal grains have similar exchange features.

The dynamics of magnetization reversal is solved by using the Landau–Lifshitz equations.[5] The hysteresis and recording dynamics are simulated. The following recording parameters are used: head medium spacing $d'+\delta/2=25$ nm and recording gap $g=0.35$ μm. The playback signals are obtained by convolving the recorded magnetization transition profile with the playback magnetoresistance (MR) head field, where the Potter approximation[6] is used. The shield-to-shield spacing G for the MR head is 0.2 μm. The width of the MR element, which defines the playback track width, is 0.5 μm.

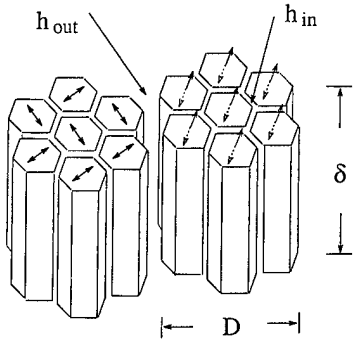


FIG. 1. Modeling of a subgrain cluster, where seven subcrystalline grains are utilized for computation use Ref. 3. The cluster on the left corresponds to a bicrystal cluster. The cluster on the right is a nonbicrystal cluster.

 0021-8979/96/79(8)/4916/3/$10.00 © 1996 American Institute of Physics

TABLE I. Summary of the simulated media with different microstructures and exchange configurations.

	Microstructure	h_{in}	h_{out}
Type A (Case I)	Uniform bicrystal	0.16	0.16
Type B (Case I)	20% Random nonbicrystal	0.16	0.16
Type A (Case II)	Uniform bicrystal	0.31	0.056
Type B (Case II)	20% Random nonbicrystal	0.31	0.056

TABLE II. The simulated magnetic and recording properties.

	S	H_c (Oe)	a/D	SNR
Type A (Case I)	0.87	2440	1.04	25.6
Type B (Case I)	0.82	2470	1.14	27.6
Type A (Case II)	0.88	2240	0.89	31.5
Type B (Case II)	0.81	2510	0.93	31.8

The MR element thickness is assumed to be much smaller than G.

III. RESULTS AND DISCUSSIONS

Two types of media are investigated. Type A has a uniform bicrystal structure where all grains possess bicrystal microstructure. Type B has a partial bicrystal structure where there are 20% random nonbicrystal sites. We further divide our studies into two cases according to the characteristics of exchange interaction. In case I, uniform intergranular exchange is used. In case II, inhomogeneous exchange interactions are used, where a strong exchange interaction within the bicrystal cluster and a relatively weak exchange between the bicrystal clusters are chosen. The microstructures and micromagnetic parameters used in the simulation are summarized in Table I. The terms h_{in} and h_{out} are chosen to keep the coercivity of type B medium in case I and II around 2500 Oe.

The comparisons of simulated M-H loops of type A and type B media for case I and case II are plotted in Figs. 2(a) and 2(b), respectively. The remanent squareness and coercivity are listed in Table II. In case I, type A medium has a coercivity of 2440 Oe, very close to the coercivity of type B, which is 2470 Oe. Type B medium has slightly smaller remanence squareness S of 0.82, compared with type A medium with $S\sim0.87$. In case II, type A medium has a coercivity of 2240 Oe and $S\sim0.88$. The introduction of 20% random nonbicrystal sites increases the coercivity of type B medium to 2510 Oe and reduces its S to 0.81.

The transition profiles and noise distributions of the type A and type B media are simulated and shown in Fig. 3(a) for case I and in Fig. 3(b) for case II. The simulated transition parameters and signal-to-noise ratio (SNR) [at a recording density of 100 kfci] are listed in Table II. In case I, the simulated transition parameter a/D of type A medium is ~1.04. The transition of type B medium is broadened with larger transition parameter $a/D\sim1.14$. Compared with the type A medium, the transition noise of type B is reduced due to the existence of random nonbicrystal sites, as shown in Fig. 3(a). The type B medium yields approximately 2 dB better SNR than type A. In case II, the transition profile of type B with $a/D\sim0.93$ is slightly broadened from the type A medium with $a/D\sim0.89$, even though type B has a larger coercivity than type A. The introduction of 20% random nonbicrystal sites has little effect on medium noise in case II. In this case, the type B medium has approximately the same noise level as type A, as seen from Fig. 3(b).

By comparing case I and II, it is found that media in case II generally have sharper transitions and lower noise than in case I. The physical origins lie in two aspects. First of all,

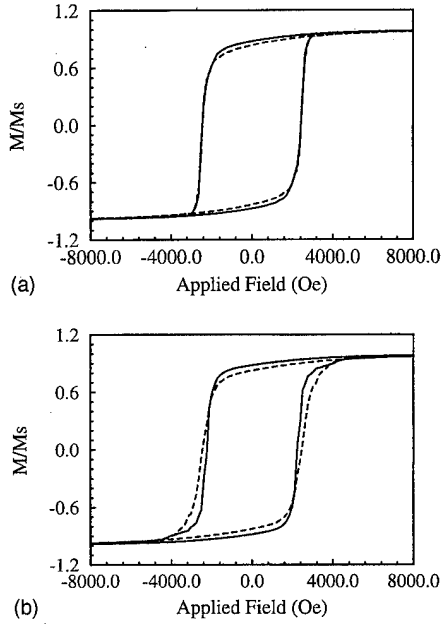


FIG. 2. Comparisons of M-H loops of type A (solid) and type B media (dashed), (a) with homogeneous exchange interactions (case I), (b) with inhomogeneous exchange interactions (case II).

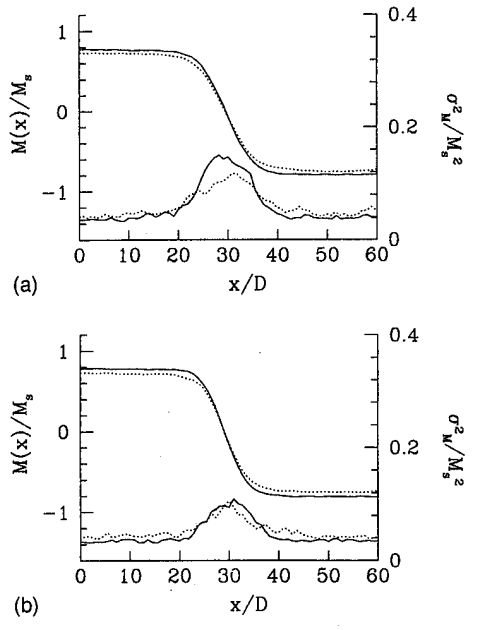


FIG. 3. Comparisons of transition profiles and noise of type A (solid) and type B (dotted) media, (a) for case I with $h_{in}=h_{out}=0.16$, (b) for case II with $h_{in}=0.31$ and $h_{out}=0.056$.

media in case II have smaller h_{out}, which governs the exchange interaction between clusters. This will result in a better decoupling between clusters, which will lower the transition noise and reduce the transition width. Furthermore, as discussed in Ref. 4, another important physical phenomena is the fluctuation of the "effective" anisotropy energy constant of a magnetic grain, which consists of tightly coupled subcrystallites. In the "tightly coupling" case, the effective anisotropy energy constant can be approximated by $K_{eff}=(1-A_{\|}/A_{\perp})/(1+A_{\|}/A_{\perp})\cdot K$, where $A_{\|}/A_{\perp}$ is the relative area percentage ratio of the mutually orthogonal subcrystallite axes and K is the intrinsic anisotropy. The variation of the effective H_k from grain to grain will lower the medium noise further by reducing the effect of exchange coupling between the neighboring grains.[7] The nonbicrystal grain in the type B medium will possess an effective anisotropy $K_{eff}\simeq K$, which explains the increase of coercivity for the type B medium in case II. In addition, due to the existing effective H_k fluctuation, the randomness induced by the 20% nonbicrystal sites will have little effect on medium noise. However, the situation is different for case I, where the tight coupling approximation is no longer valid due to the homogeneous exchange coupling. In this case, the 20% random nonbicrystal grains that exist in the type B medium will induce noticeable new randomness that will reduce the effect of exchange coupling and lower the noise.

It is still unclear which case of I and II is closer to the medium in reality. Further experimental and theoretical works are needed to clarify this complication. There are two main mechanisms that can cause the weakening of exchange interactions between the grains, either the existence of voids or significant Cr segregation at the grain boundary. In some most recent CoPtCr bicrystal media, TEM images reveal no clear voids between the grain boundaries.[4] Recently, electron spectroscopic imaging analysis of the compositional inhomogeneity in CoTaCr indicates Cr segregation at the grain boundaries and intra grains.[8]

IV. CONCLUSIONS

The effects of inhomogeneities in microstructure and exchange configuration are studied by using micromagnetic simulation. The introduction of partial random nonbicrystal sites reduces the medium noise in the case with homogeneous intergranular exchange. It has little effect on medium noise in the case with inhomogeneous intergranular exchange.

ACKNOWLEDGMENTS

The IBM corporation is to be thanked for a research award to support this work. This work was also supported in part by NSIC/ARPA under Grant No. MDA972-93-009 and the NSF/MRG fund (NSF-DMR 90-10908). The authors wish to thank the San Diego Supercomputer Center for continuing support for their studies.

[1] M. Mirzamaani, C. V. Jahnes, and M. A. Russak, J. Appl. Phys. **69**, 5169 (1991).
[2] T. P. Nolan, R. Sinclair, and T. Yamashita, J. Appl. Phys. **73**, 5566 (1993).
[3] X. G. Ye and J. G. Zhu, J. Appl. Phys. **75**, 6135 (1994).
[4] Q. Z. Peng, H. N. Bertram, N. Fussing, M. Doerner, M. Mirzamaani, D. Margulies, R. Sinclair, and S. Lambert, IEEE Trans. Magn. **MAG-31**, 2821 (1995).
[5] H. N. Bertram and J. G. Zhu, Solid State Phys. **46**, 271 (1992).
[6] R. I. Potter, IEEE Trans. Magn. **MAG-10**, 502 (1974).
[7] X. D. Che and H. N. Bertram, J. Appl. Phys. **75**, 6779 (1994).
[8] Y. Yahisa, K. Kimoto, K. Usami, Y. Matsuda, J. Inagaki, K. Furusawa, and S. Narishige, IEEE Trans. Magn. **MAG-31**, 2836 (1995).

Multilevel master equation for bicrystal clusters

I. Klik and Y. D. Yao
Institute of Physics, Academia Sinica, NanKang, Taipei, Taiwan, Republic of China

C. R. Chang
Department of Physics, National Taiwan University, Taipei, Taiwan, Republic of China

A bicrystal film is modeled as an ensemble of clusters of four particles which interact via short-range exchange coupling. Their easy axes are oriented pairwise along two randomly chosen orthogonal directions and the relaxational dynamics of the resultant clusters are described in terms of a multilevel master equation. The randomly deposited bicrystal film is compared with a randomly deposited film of uniaxial clusters. The relaxational properties of the entire array are determined by the easy axes arrangement and by the nature of coupling within the cluster. In particular, for ferromagnetic coupling the occurrence probability of fully magnetized bicrystal cluster states is high and we propose that in conjunction with the highly isotropic coercivity this property leads to a sharp transition between film regions magnetized in opposite directions. © *1996 American Institute of Physics.* [S0021-8979(96)08208-1]

Bicrystal films have recently attracted considerable attention,[1–3] both from the point of view of material science[4,5] and of applications to information storage.[6,7] They combine the beneficial properties of highly oriented and isotropic films, being distinguished, in particular, by coercivity squareness which approaches unity[6] and by low noise levels[7] at high recording density. It was suggested that these desirable qualities result from the fourfold symmetry of the film microstructure: A nanocrystalline film, e.g., the Cr(100)/Co-alloy($11\bar{2}0$) epitaxial structure, with randomly oriented bicrystal clusters shows a better recording performance than an ordered bicrystal film.[2] Both the (oriented) bicrystal[6] and the (globally disordered) nanocrystalline films[2] have been proposed, at least micromagnetically, as suitable media for high-density recording up to 10 Gbits/in.^{2}, yet their thermal stability has not been, to date, studied. Here we use previously developed multilevel master equation formalism[8] to analyze the relaxation properties of locally coupled four particle clusters. We find that the relaxational properties of the cluster array are determined by the arrangement of easy axes within the cluster and by the nature of the local coupling: For negative exchange (ferromagnetic) coupling the occurrence probability of fully magnetized cluster configurations is found to be very high and insensitive to temperature. We expect these properties to lead to a sharp transition between the regions magnetized in opposite directions.

We assume that each configuration of the N locally interacting constituent particles has a definite arrangement of easy axes; here we set $N=4$ and adopt the biaxial symmetry shown in Fig. 1. Also shown there is a cluster of four aligned particles whose properties and stability we shall compare with the biaxial model. In either case the clusters are deposited in the $x-y$ plane and their orientation with respect to the in-plane applied field $\mathbf{H}=(H,0,0)$ is random. For simplicity of calculation (see below) we further assume that all constituent particles are identical. Parametrizing their magnetization vectors as $\mathbf{M}_i=M_s(\cos\phi_i,\sin\phi_i,0)$, $\phi\in\langle 0,2\pi)$ and M_s is the saturation magnetization, we obtain the expression

$$E=KV\sum_{i=1}^{2}[\sin^2(\phi_{2i-1}-\beta)+\cos^2(\phi_{2i}-\beta)]$$
$$-V\sum_{i=1}^{4}\mathbf{M}_i\cdot\mathbf{H}+E_{\text{int}} \tag{1}$$

for the total energy of the biaxial cluster, and similarly also for the uniaxial one whose anisotropy energy is given by the sum $KV\Sigma_i^4\sin^2(\phi_i-\beta)$. The random inclination angle $\beta\in\langle 0,\pi/2\rangle$ is defined in the sketch of Fig. 1; K is anisotropy constant, V activation volume, and M_s saturation magnetization. In the absence of mutual interactions the two species of constituent particles have identical nucleation fields, $H_n(\beta)/H_n(0)=[\cos^{2/3}\beta+\sin^{2/3}\beta]^{-3/2}$, $H_n(0)=2K/M_s$, easily obtained by solving the coupled equations $\partial E/\partial\phi_i=\partial^2E/\partial\phi_i^2=0$. We assume that local interactions within the clusters are exchange dominated[2] and in order to avoid a proliferation of adjustable parameters we set

$$E_{\text{int}}=\rho\sum_{i\neq j=1}^{4}\mathbf{M}_i\cdot\mathbf{M}_j \tag{2}$$

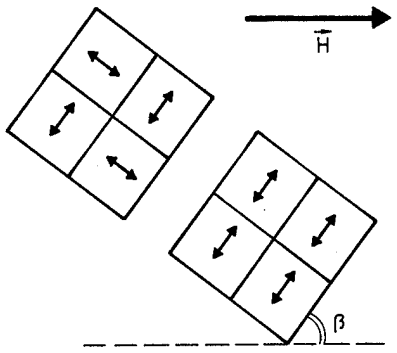


FIG. 1. The two species of four particle clusters considered in text. Easy axes of the constituent particles are depicted by doubleheaded arrows; the upper left cluster thus has biaxial and the lower right uniaxial symmetry. The inclination angle β and the orientation of the applied field $\mathbf{H}$ correspond to Eq. (1).

 0021-8979/96/79(8)/4919/3/$10.00 © 1996 American Institute of Physics

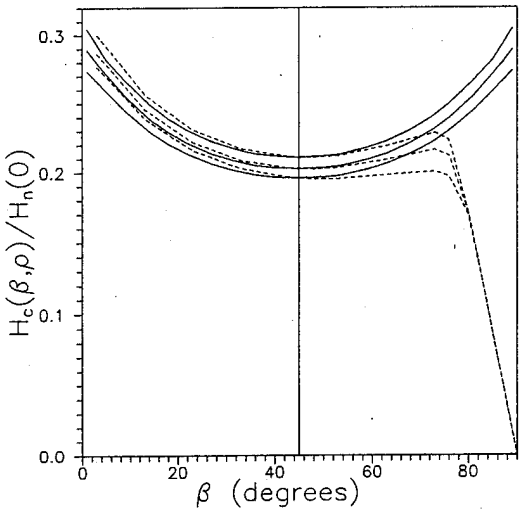


FIG. 2. The angular dependence of coercivity for the biaxial (solid lines) and uniaxial (dashed lines) clusters. Coupling strength $\rho M_s^2/KV=-10^{-2}$ (uppermost curves), 0 (middle curves) and 10^{-2} (lowermost curves).

so that the detailed cluster geometry becomes in this approximation irrelevant. The (global) weak interactions between separate clusters may be modeled within the mean field theory,[9] where $\mathbf{H}\rightarrow\mathbf{H}_{\text{eff}}=\mathbf{H}+\alpha\langle\mathbf{M}\rangle$ in Eq. (1), $\langle\mathbf{M}\rangle$ is the instantaneous magnetization of the entire array, and α a phenomenological parameter. By assumption the mean field $\alpha\langle\mathbf{M}\rangle$ is weaker than the interaction field (2) and in this paper, where we do not carry out averaging over the inclination angle β, we disregard it altogether. If included, the mean field will slightly deform and shift[9] the resultant hysteresis loops without introducing any qualitatively new features into the model.

It has recently been shown[8] that the thermally activated evolution of an array of interacting single-domain particles, as represented here by Eqs. (1) and (2), may be described by the master equation

$$\frac{dn_i}{dt}=-\sum_{i=1}^{\mathcal{N}} R_{ij}n_j \tag{3}$$

for the probabilities n_i that the $\mathcal{N}\leqslant 2^N$ distinct metastable minima of the total energy (1) are occupied, i.e., that the cluster finds itself in a particular magnetic configuration. The elements R_{ij} are the rates of thermally activated transitions between these metastable minima (configurations). For arbitrary coupling strength ρ they are expressed[10] in terms of the minima and saddle point energies of Eq. (1). This poses, however, a formidable extremal problem[11] and for this reason we adopt here the weak coupling limit[8] in which E_{int} is treated as a small perturbation of the total energy (1). This limit excludes simultaneous reversals of two or more particles within the cluster and the admissible single particle reversals take place in a local field defined by the magnetizations of the partner (nonreversing) particles which are assumed to be frozen at their respective local energy minima in each of the $\mathcal{N}$ possible metastable configurations. Each particle has a nonzero reversal probability in every one of the $\mathcal{N}$ possible configuration of the entire cluster and the transition elements R_{ij} are then expressed as linear combinations of the $N\times\mathcal{N}$ single particle relaxation rates. For not too large $\mathcal{N}$ the master Eq. (3) is easily solved numerically using the stable backward Euler method.[12]

The biaxial cluster of Fig. 1 has $\mathcal{N}=10$ distinct metastable configurations whereas for the uniaxial cluster $\mathcal{N}=5$. In considering the stability of the cluster we could, in principle, analyze the occurrence probability $n_i(t)$ of every possible metastable configuration but it is more convenient to define the probabilities $p_n(t)$, $n=0$, 1, and 2, that either n or $4-n$, particles have reversed by the time t. Note that for an isolated particle $p_0(t)\equiv 1$ at all times since the particle either did or did not reverse and no third possibility exists.

At a given inclination angle β we subject both cluster species to a periodic applied field $H(t)=H_n(0)\cos 2\pi ft$ of frequency $f=0.5$ Hz and calculate the major hysteresis loop. In our model calculation we set $KV/k_BT=42$ and for the prefactor of thermal decay rate[8,10,11] we choose the value $f_0=e^{25}$ Hz $\approx 7.2\times 10^{10}$ Hz. The chosen temperature is relatively very high, corresponding to an isolated particle lifetime of about nine months. The angular dependence of the coercivity $H_c(\beta,\rho)$ is primarily determined by the axes orientation within the cluster while the influence of interactions between the constituent particles is relatively minor. The variation of coercivity with orientation, however, is significantly smaller for the more isotropic biaxial model than for the uniaxial model and this, in particular, implies a smaller dispersion of single particle switching events in a randomly deposited sample (see Fig. 2).

Even though interparticle interactions have, in the present model, only minor influence on coercivity, they do *significantly affect* the stability of partially magnetized clusters in which one (or three) resp. two particles have reversed with probabilities $p_1(t)$ resp. $p_2(t)$ by the time t. According to Eq. (2) positive exchange interactions ($\rho>0$) favor the formation of configurations with antiparallel alignment of single particle magnetization vectors, i.e., they stabilize partially magnetized clusters. Negative coupling, on the other hand, inhibits the formation of such configurations and increases the stability of fully magnetized states in which all or no particles have reversed with probability $p_0(t)$. In Fig. 3 we plot, for selected values of β, the nonequilibrium magnetization $M[H(t)]$ of the biaxial cluster together with the corresponding probabilities $p_2[H(t)]$. The figure shows that even small *negative* coupling significantly decreases the probability p_2 (and similarly also for p_1) that the cluster will find itself in one of the partially demagnetized configurations anytime during the hysteresis process. The effect is even more pronounced at lower temperatures. In particular, for $KV/k_BT>46$ and $\rho M_s^2/KV=-10^{-2}$, we obtain $p_0(t)\approx 1$ at all times and the partially demagnetized states become all but absent from the hysteresis process. At the same time, the switching field distribution $\chi[H(t)]=\partial M[H(t)]/\partial H(t)$ becomes more sharply peaked as the intermediate states are suppressed. Similar conclusions may be also reached about the thermal stability of uniaxial clusters; in this case, however, the probabilities $p_1(t)$ and $p_2(t)$ lack the striking isotropy displayed by the plots of Fig. 3.

In summary, we find that even very small negative (fer-

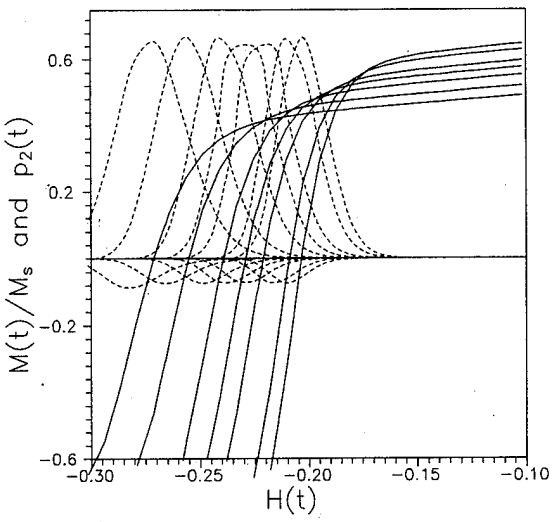


FIG. 3. The nonequilibrium magnetization $M(t)$ of the biaxial cluster measured along the applied field (solid lines) together with the probabilities $p_2(t)$. Inclination angle $\beta=5°$ (leftmost curves), 9°, 14°, 18°, 22°, 31°, and 40° (rightmost curves). The magnetization curves are plotted for $\rho=0$, the probabilities plots are for $\rho M_s^2/KV=-10^{-2}$ (with plots inverted, $p_2\rightarrow -p_2$, for clarity) and 10^{-2}. Note that the values of p_2 (here max $p_2\approx 0.08$ for $\rho<0$ and max $p_2\approx 0.65$ for $\rho>0$) are highly isotropic.

romagnetic) exchange forces significantly inhibit the formation of partially demagnetized configurations of four particle clusters for all technically relevant values of the ratio KV/k_BT. This finding is of interest to magnetic recording technology since the high probability of finding a fully magnetized cluster leads one to expect a sharp boundary between film regions magnetized in opposite directions. This feature, moreover, is quite insensitive to the orientation of a biaxial cluster (see Fig. 3). This may be of benefit to manufacture of hard disks where uniaxial clusters have to be aligned with the tangential direction. Randomly oriented biaxial clusters form a highly homogeneous, stable recording medium whereas an array of randomly oriented uniaxial clusters is highly inhomogeneous, with a substantial fraction of the clusters likely to be found in one of the possible partially demagnetized states.

This research was in part supported by Grant No. NSC85-2112-M-001-020 of the National Science Council of The Republic of China.

[1] Tu Chen, R. Ranjan, D. Wachenschwanz, J. Chen, C. Ross, and T. Yamashita, InterMag'95, FA-02, San Antonio, Texas, 1995.
[2] J.-G. Zhu and X.-G. Ye, InterMag'95, FA-03, San Antonio, Texas, 1995.
[3] X.-G. Ye and J.-G. Zhu, IEEE Trans. Magn. **28**, 3087 (1992).
[4] T. P. Nolan, R. Sinclar, R. Ranjan, and T. Yamashita, J. Appl. Phys. **73**, 5566 (1993).
[5] M. Mirzamaani, C. V. Jahnes, and M. A. Russak, J. Appl. Phys. **69**, 5169 (1991).
[6] J.-G. Zhu, X.-G. Ye, and T. C. Arnoldussen, IEEE Trans. Magn. **29**, 324 (1994).
[7] J. Ding and J.-G. Zhu, IEEE Trans. Magn. **30**, 3978 (1994).
[8] I. Klik and C. R. Chang, Phys. Rev. B **52**, 3540 (1995).
[9] D. L. Atherton, IEEE Trans. Magn. **26**, 3059 (1990); J. S. Yang, C. R. Chang, and I. Klik, Phys. Rev. B **51**, 15203 (1995).
[10] P. Hänggi, P. Talkner, and M. Borkovec, Rev. Mod. Phys. **62**, 251 (1990).
[11] Its solution is known only for a particle pair; see W. Chen, S. Zhang, and H. N. Bertram, J. Appl. Phys. **71**, 5579 (1992); I. Klik, J. S. Yang, and C. R. Chang, *ibid.*, **76**, 6493 (1994).
[12] W. H. Press, B. P. Flannery, S. A. Teukolsky, and W. T. Vetterling, *Numerical Recipes* (FORTRAN Version) (Cambridge University, Cambridge, 1990), Sec. 15.6.

Coercivity mechanism in CoPt alloy films with perpendicular magnetic anisotropy (abstract)

Th. Kleinefeld and J. Heimel
Universität Duisburg, FB10/Angewandte Physik, D-47048 Duisburg, Germany

D. Weller
IBM Almaden Research Center, San Jose, California 95120-6099

The coercivity is one of the key parameters for defining a suitable magneto-optic recording material. In order to get insight into coercivity mechanisms we have studied the magnetization reversal processes by means of magneto-optic methods in CoPt alloy films. These films were prepared in UHV by coevaporation with a typical composition ratio of $Co_{28}Pt_{72}$ and show excellent perpendicular magnetic anisotropy at elevated substrate temperatures during deposition. STM and x-ray measurements reveal characteristic grain size of about 15–20 nm and dispersion of crystallite axis of the order of 0.5°, respectively, which varies only slightly with total film thicknesses of 5–50 nm. The magnetization reversal processes are investigated by using polar Kerr microscopy and were found to be dominated by domain formation and domain wall propagation. A micromagnetic model was developed which describes the film as an ensemble of single domain particles. The size of these single domain particles was chosen to be of the order of the average grain size. In the numerical simulation we include dipolar interaction and domain wall energy contribution. The comparison of the results of the simulation with the experimental results clearly points out that the microstructure is responsible for the magnetization reversal behavior. A thermal as well as thermally activated magnetization processes contribute to the reversal mechanism. The coercivity is predominantly determined by pinning on grain boundaries. © *1996 American Institute of Physics.*
[S0021-8979(96)45808-2]

This work is supported by the Deutsche Forschungsgemeinschaft/SFB166.

 0021-8979/96/79(8)/4922/1/$10.00 © 1996 American Institute of Physics

Grain morphology and magnetic properties of CoCrPt/Cr(Si,Ti) films sputtered at room temperature

G. Choe
Materials Research Corporation, Route 303, Orangeburg, New York 10962

CoCrPt films were deposited on Cr-Si and Cr-Ti underlayers at room temperature with variations in Si and Ti concentration. Magnetic properties including H_c and S^* were improved by Cr-Si and Cr-Ti underlayers. CoCrPt films deposited on a Cr-Si underlayer showed uniformly grown Co grains without large chains of grouped fine grains that were observed for the films deposited on a Cr underlayer, thus resulting in the increased S^*. The Cr-Ti films showed changes in crystallography with increasing Ti content and thus affected the growth texture of Co grains. It is suggested that high performance CoCrPt recording media can be fabricated at room temperature by modifying the Cr underlayer films. © *1996 American Institute of Physics.* [S0021-8979(96)08308-8]

I. INTRODUCTION

High-density longitudinal recording media require low noise and high coercivity. Previous reports indicated that media noise could be significantly reduced by the decreased magnetic exchange coupling.[1–4] Several methods including voided Co alloy with thick Cr underlayer[1–3] or Cr segregated Co alloy[4] are reported to be effective in achieving an exchange decoupling. Most previous studies to reduce media noise and enhance coercivity were performed using Co alloy thin films sputtered onto a heated substrate for the purpose of achieving a preferred orientation of c axis and also promoting Cr segregation. However, the heating prior to deposition may complicate the disk manufacturing process, since the aluminum substrate can be thermally distorted and the amorphous Ni-P can be crystallized. In the present study, grain morphology and magnetic properties of CoCrPt films sputtered on Cr-Si and Cr-Ti underlayer films at room temperature were investigated. This paper reports that alloying of the Cr underlayer controls the grain growth of CoCrPt films deposited without substrate heating and thus improves the magnetic properties of CoCrPt.

II. EXPERIMENTS

$Co_{68}Cr_{14}Pt_{18}$ thin films on a Cr underlayer were deposited onto glass substrates at room temperature by rf magnetron sputtering. The thicknesses of the Cr underlayer and CoCrPt layer were 1500 and 500 Å, respectively. The Cr layer was deposited at 5 mTorr of argon pressure, while the CoCrPt layer was deposited at 10 mTorr. The compositions of Si and Ti in the Cr layer were varied using Si and Ti chips placed on the Cr target and were analyzed by energy dispersive spectroscopy (EDS) using a transmission electron microscope (TEM). Magnetic properties including coercivity (H_c), magnetization (M_s), squareness (S), and coercive squareness (S^*) were measured using vibrating sample magnetometer (VSM) and microstructural characterization was performed by TEM using plane and cross-sectional observation. The crystallography was investigated using x-ray diffraction (XRD) with Cu $K\alpha$ radiation.

III. RESULTS AND DISCUSSION

Figure 1 shows plane-view TEM micrographs of CoCrPt films deposited on a Cr underlayer at different substrate temperatures. The CoCrPt films deposited at 200 °C exhibited Co grains separated from neighboring grains by void boundaries and the grain size was uniform. A magnetic coercivity (H_c) of 1880 Oe was observed with high coercive squareness (S^*) of 0.88. However, the CoCrPt films deposited without substrate heating showed remarkably different grain morphology from the films deposited with substrate heating, as shown in Fig. 1(b). The Co grain diameter ranged widely from 60 to 120 Å, and the fine grains were coupled in the shape of large chains. This effect possibly resulted in low S^* of 0.71 for the films deposited at room temperature, although H_c remained nearly constant at 1900 Oe due to the well isolated Co grains. Thus, in the present study, CoCrPt films were deposited on a Cr-Si or Cr-Ti underlayer that is expected to modify the morphology and/or crystallography of pure Cr to attempt to change the Co grain morphology and crystallography, thereby improving S^*.

Figure 2(a) shows the effect of a Cr-Si underlayer on the magnetic properties of CoCrPt films sputtered at room temperature as a function of increasing Si concentration. The CoCrPt films deposited on a Cr-Si underlayer showed higher H_c and S^* than the films deposited on a Cr underlayer. H_c increased linearly with increasing Si content and was maximized (2600 Oe) at 5.8 at. % Si, but slightly decreased with

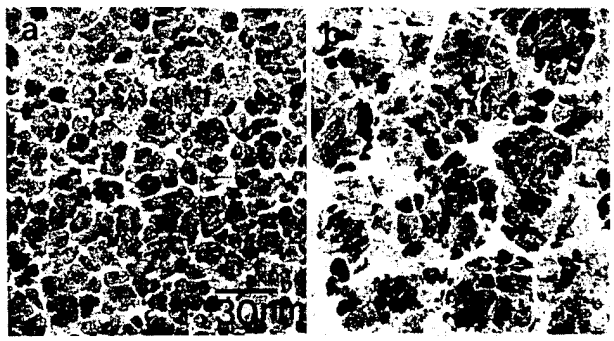


FIG. 1. Plane view of TEM micrographs of CoCrPt films sputtered on a Cr underlayer at (a) 200 °C and (b) room temperature.

 0021-8979/96/79(8)/4923/3/$10.00 © 1996 American Institute of Physics

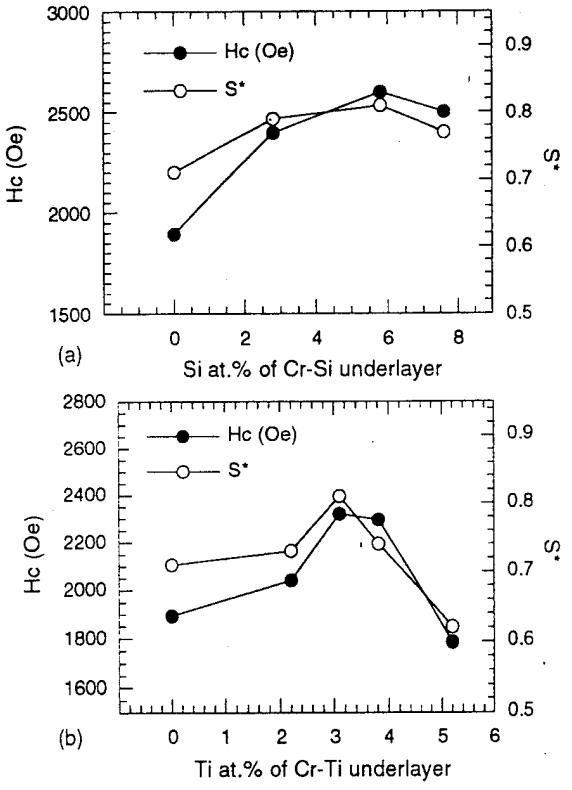


FIG. 2. Magnetic properties of CoCrPt films deposited on (a) Cr-Si and (b) Cr-Ti underlayers as a function of Si and Ti concentration.

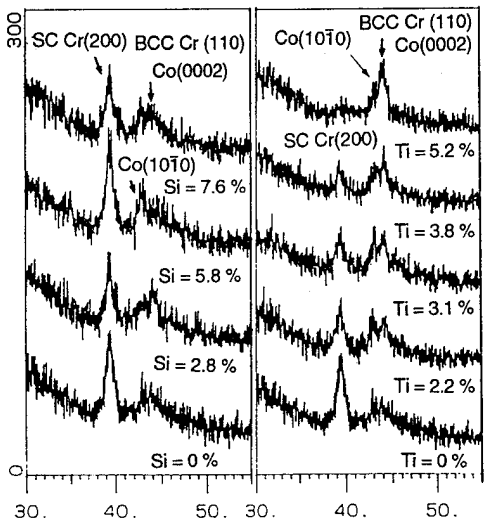


FIG. 3. Change in x-ray diffraction spectra of CoCrPt films sputtered on (a) Cr-Si and (b) Cr-Ti underlayers with increasing Si and Ti concentration.

further increase in Si content. In addition, S^* increased up to 0.80 with increasing Si content in the Cr-Si underlayer. The Cr-Si underlayer significantly improves magnetic properties (H_c,S^*) of CoCrPt films sputtered at room temperature. Figure 2(b) shows magnetic properties of CoCrPt films deposited onto a Cr-Ti underlayer as a function of Ti concentration. The effect of the Cr-Ti underlayer on H_c and S^* of CoCrPt films was similar to that of the Cr-Si underlayer. With increasing Ti content, H_c initially increased to a maximum value of 2320 Oe at 3.1 at. % Ti, and then decreased to 1800 Oe with further increase in Ti content. S^* increased to 0.81 at 3.1 at. % Ti but decreased to 0.62 at 5.1 at. % Ti. The appropriate amount of Ti addition to the Cr underlayer appears to enhance both H_c and S^* of CoCrPt films. This result is consistent with Shiroishi *et al.*'s report,[5] although the optimum Ti concentration for improving magnetic properties is much higher in their report than in this study.

The origin of the H_c and S^* enhancement caused by Cr-Si and Cr-Ti underlayers was investigated by observing the grain morphology and crystallography using TEM and XRD. Figures 3(a) and 3(b) display the x-ray diffraction patterns of CoCrPt films sputtered on Cr-Si and Cr-Ti films at room temperature. For the Cr-Si films, independent of Si concentration, preferred orientation of Cr was almost constant, while the FWHM of the (200) peak became wider with increasing Si content, indicating a decreasing grain size. This result is further confirmed by TEM grain morphology of Cr-Si films. The Cr-Si and Cr films sputtered at room temperature showed a predominant (200) texture of simple cubic structure mixed with a minor (110) peak of body centered cubic (bcc) structure, contrary to a frequently reported texture of bcc (110) at room temperature or low substrate temperature,[6,7] while the Cr films sputtered at 200 °C showed only (110) texture. This effect is possibly due to the difference in quenching rate of Cr adatoms resulting in metastable simple cubic (200) by altered surface mobility and diffusion. However, as the Ti content of Cr-Ti films increased, the (200) peak diminished and the bcc (110) peak intensity increased. Accordingly, the crystallography of the CoCrPt films altered with increasing Ti concentration in the Cr-Ti underlayer. With increasing Ti content in the Cr-Ti underlayer, the Co(10$\bar{1}$0) texture appears to increase by the enhanced epitaxial growth of Co crystallites whose c axis aligns to the film plane, resulting in the increased H_c and S^*, as above shown in Fig. 2(b).

The plane-view TEM micrographs (Fig. 4) show the important effect of Si addition in Cr-Si films on grain morphology. As shown in diffraction patterns, crystallography was not affected by Si concentration of Cr-Si films. The Cr films sputtered at room temperature showed irregularly shaped grains with voided boundaries, although the films sputtered at 200 °C exhibited highly oriented, uniform grains. This difference in Cr grains with substrate heating temperature is

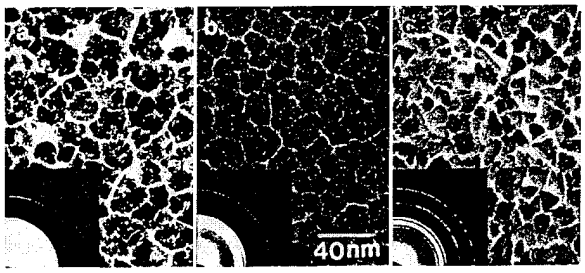


FIG. 4. Plane view of TEM micrographs of (a) Cr, (b) $CrSi_{5.8}$, and (c) $CrTi_{3.1}$ films sputtered at room temperature.

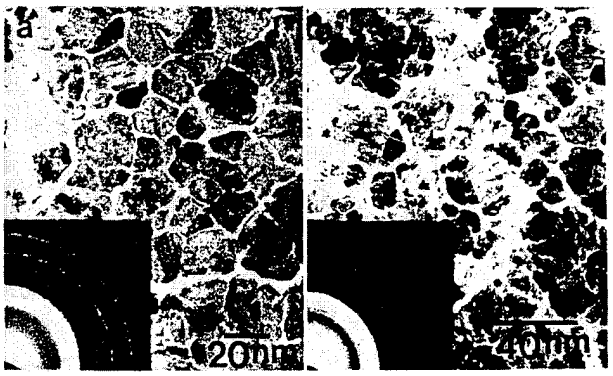


FIG. 5. Plane view of TEM micrographs of CoCrPt films sputtered on (a) $CrSi_{5.8}$ and (b) $CrTi_{3.1}$ underlayers at room temperature.

considered to result in the low S^* of CoCrPt films sputtered at room temperature. However, the grain morphology of Cr-Si films became more uniform than that of Cr films and the grain size slightly reduced. It is noted that fine subgrains ($\approx$50 Å) inside the large grains are clearly seen in Cr-Si films, possibly indicating segregation of Si atoms at subgrain boundaries. This result is supported by the XRD pattern showing no change in lattice parameter of Cr(200) with Si content. The grain morphology of Cr-Ti films was similar to that of Cr films but, as shown in the XRD pattern, the preferred orientation of electron diffraction pattern changed from sc (200) to bcc (110).

Figures 5(a) and 5(b) show TEM micrographs of CoCrPt films sputtered on Cr-Si and Cr-Ti underlayers. The CoCrPt films grown on a Cr-Si underlayer exhibit Co grains well separated from neighboring grains without large chains of grouped fine grains that were observed for the CoCrPt films deposited on a Cr underlayer. This effect is possibly associated with the increased S^* of CoCrPt films deposited on Cr-Si underlayers, independent of the preferred orientation of Co grains. The CoCrPt films deposited on a Cr-Ti underlayer, however, showed similar grain morphology like the films deposited on a Cr underlayer. This result is due to the different grain morphology of Cr-Si and Cr-Ti underlayer films that control the film growth of CoCrPt. Cross-sectional TEM micrographs (Fig. 6) also indicate that, for the CoCrPt films deposited on a Cr underlayer, the Co grains grow nonuniformly with irregular shapes. On the other hand, the Co grains of CoCrPt films grown on Cr-Si underlayers appear to be more uniform and better aligned along the growth direction than those of CoCrPt films deposited on a Cr underlayer. The fine Co grains of CoCrPt films deposited on a Cr-Ti underlayer appear to grow on a single Cr-Ti column. It is concluded that the modifed grain morphology or crystallographic orientation of Cr underlayer by Si or Ti alloying plays an important role in changing the Co grain morphology as well as the preferred orientation, thereby offering the possibility of fabrication of high performance recording media at room temperature.

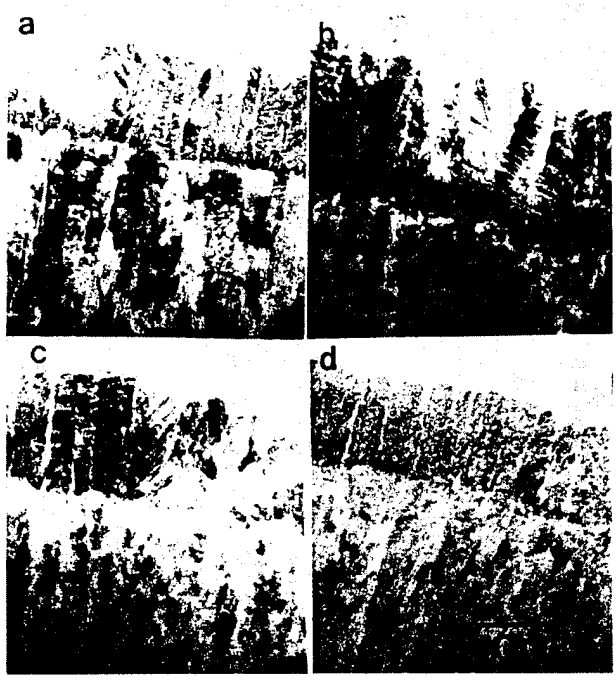


FIG. 6. Cross-sectional TEM micrographs of (a) CoCrPt/Cr (200 °C), (b) CoCrPt/Cr (room temperature), (c) CoCrPT/$CrSi_{5.8}$ (room temperature), and (d) CoCrPT/$CrTi_{3.1}$ (room temperature).

[1] T. Chen and T. Yamashita, IEEE Trans. Magn. **24**, 2700 (1988).
[2] T. Yogi, G. L. Gorman, C. Hwang, M. A. Kakalec, and S. E. Lambert, IEEE Trans. Magn. **24**, 2727 (1990).
[3] R. Ranjan, J. A. Christner, and D. P. Ravipati, IEEE Trans. Magn. **26**, 322 (1990).
[4] M. F. Doerner, T. Yogi, D. S. Parker, and T. Nguyen, IEEE Trans. Magn. **29**, 3667 (1993).
[5] Y. Shiroishi, Y. Hosoo, A. Ishikawa, Y. Yahisa, Y. Sugita, H. Suzuki, T. Ohno, and M. Ohura, J. Appl. Phys. **73**, 5569 (1993).
[6] S. L. Duan, J. O. Artman, B. Wong, and D. E. Laughlin, IEEE Trans. Magn. **26**, 1587 (1990).
[7] D. E. Laughlin, Y. C. Feng, L. L. Lee, and B. Wong, Mater. Res. Soc. Symp. Proc. **343**, 327 (1994).

Ultrahigh vacuum SQUID magnetometry study of the magnetic properties of Co/Co-oxide thin films

S. Spagna[a] and M. B. Maple
Institute for Pure and Applied Physical Sciences, University of California, San Diego, La Jolla, California 92093

R. E. Sager
Quantum Design Inc., San Diego, California 92121

Exchange coupling between Co and Co-oxide in bilayer and trilayer thin-film structures has been studied using a recently developed ultrahigh vacuum SQUID magnetometer (UHVSQM) system. Using this novel technique, newly deposited Co films from a separate molecular beam epitaxy facility were transported into the UHVSQM without breaking vacuum and magnetically characterized before and after *in situ* room temperature oxidation. Field-cooled hysteresis measurements performed at low temperatures indicate the presence of a complex antiferromagnetic Co-oxide domain structure as a result of oxidation. The stability of the magnetic structure is determined by competition between frustration generated at the interface when the ferromagnetic Co moments are reversed and stabilizing antiferromagnetic anisotropy which becomes large only at low temperatures (<150 K). © *1996 American Institute of Physics.* [S0021-8979(96)66508-9]

Exposure of thin Co films at room temperature to large quantities of oxygen, or even diluted oxygen in the form of air, results in partial oxidation of the film which passivates the surface forming a well-defined thin oxide layer approximately 20 Å thick.[1–3] Due to the low magnetic moments of the Co^{2+} ions within the thin Co oxide layer, the long-range antiferromagnetic (AF) order that is known to occur in the bulk Co oxide[4] is extremely difficult to study directly in this thin passivating layer. However, information about the magnetic ordering of the Co^{2+} ions can be obtained from the exchange coupling of the Co^{2+} ions in the oxide to the metal Co atoms. In Co/Co-oxide magnetic structures, exchange coupling is manifested in a dramatic increase in coercivity and displacement of the hysteresis loop along the field axis for samples that have been cooled in an applied magnetic field to a temperature at which the anisotropy of the Co oxide is large.[5,6] This complex of anomalies is commonly associated with the phenomenon of "exchange anisotropy."

In this paper, we demonstrate the application of a general purpose ultrahigh vacuum (UHV) compatible SQUID magnetometer (UHVSQM) system[7] we have developed to obtain magnetic information regarding the thin AF Co-oxide layers via exchange coupling to the ferromagnetic (FM) Co film on which the Co-oxide forms. In using this system, polycrystalline Co thin-film samples, grown by electron-beam evaporation on Si(100) substrates in a molecular beam epitaxy (MBE) facility (base pressure $\sim 1\times10^{-10}$ Torr), are transported to the UHVSQM without breaking vacuum and characterized magnetically. The magnetic characterization consists of magnetization versus magnetic field hysteresis measurements in fields up to one tesla, down to 20 K, and in a variable vacuum environment to pressures as low as 10^{-10} Torr. Comparison of the magnetic properties obtained from the low-temperature magnetization versus applied magnetic field hysteresis loops, before and after oxidation, yields useful information concerning exchange anisotropy and, in turn, the underlying Co-oxide magnetic structure.

Figure 1 shows the striking effect of the oxidation process after cooling in a field of 1 T and measuring magnetization versus magnetic field hysteresis loops of an 80 Å Co/Si(100) sample at 20, 50, and 150 K. A number of important features can be identified. Before oxidation, the magnetization curves are symmetric and exhibit small coercive fields, reflecting negligible anisotropy of the virgin FM Co films. After oxidation, the hysteresis loops are markedly broadened and shifted along the field axis. These observations provide evidence that the spins of the Co^{2+} ions within the oxide film act as pinning sites, impeding the free-spin rotation of neighboring FM Co atoms, thus increasing the overall coercivity of the sample. The overall coercivity is defined as $H_c = 1/2|H_c^l - H_c^r|$, where H_c^l and H_c^r are the coercive fields corresponding to the left and right of the hysteresis loops. The field offset is best described in terms of an effective internal "exchange field"[5,6] H_E, defined as $H_E = 1/2|H_c^l + H_c^r|$, which arises from the AF interface and acts in the same direction as the previously applied magnetic field. As any amount of oxidation results in a shift of the hysteresis loop, these measurements indicate that prior to the oxidation treatment no substantial contamination occurred from the time the sample was grown until the completion of the first set of hysteresis loops (a period of approximately 5 h).

Because the interface is the source of the exchange field,

[a]Quantum Design Inc., San Diego, CA 92121.

0021-8979/96/79(8)/4926/3/$10.00
© 1996 American Institute of Physics

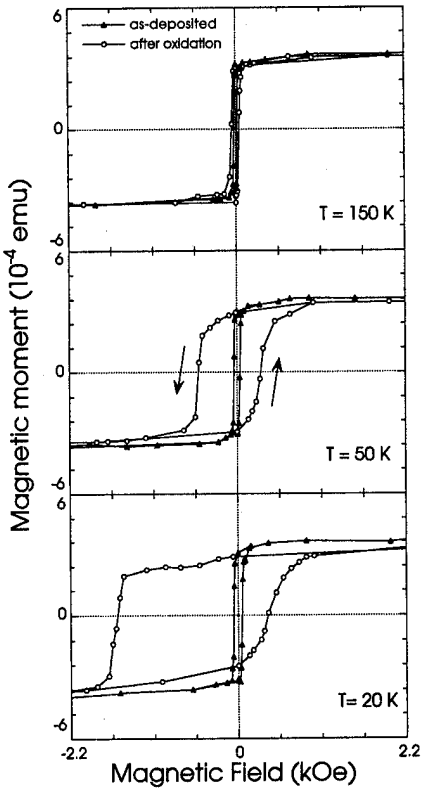


FIG. 1. One tesla field-cooled hysteresis loops measured at 20, 50, and 150 K for a 80 Å Co/Si(100) sample.

a detailed understanding of the AF Co-oxide magnetic structure requires a combination of measurements which probe the morphology of the metal-oxide interface as well as its magnetic properties. A depth profiling technique, employing Auger electron spectroscopy (AES) in conjunction with 1 keV Ar^+ ion sputter etching was utilized to characterize the morphology of the oxidized samples. The profiles were reproducible apart from minor thickness variations (±5 Å) due to deposition nonuniformities. Figure 2 shows the normalized Auger peak height for the strongest Co(*LMM*), O(*KLL*), and Si(*LMM*) transitions for an oxidized 80 Å Co/Si(100) sample. Qualitatively, the growth of the Co-oxide layers deduced from these measurements produces separate spatially well defined regions. The first region (shown in white in Fig. 2), results from an oxidation reaction front in which oxygen molecules dissociatively chemisorb to the oxide, trap electrons, and finally combine with the metal ions to form an oxide layer approximately 23 Å thick. This first region terminates at the metal-oxide interface, adjacent to the Co metal layers shown in gray in Fig. 2. If this interface were atomically flat, cooling of the bilayer in a large applied magnetic field would result in alignment of the Co spins (↑) in the metal film, forming a single magnetic domain. By the same interaction, the spins (↑) of the AF oxide next to this interface would also align ferromagnetically, creating an "uncompensated" spin configuration (where an interfacial energy difference $\Delta\sigma$ per unit area favoring a specific FM orientation is created in the cooling process) as schematically shown in the inset of Fig. 2. Below the Néel temperature of the oxide, the next spin plane (⇓) in the AF Co-oxide layers nucleate so as to be oppositely directed to the first plane. Once the oxide spins are arranged in this configuration, and the anisotropy of the AF is strong, the FM spins tend to be locked in the field cooling direction thus resulting in a shift along the field axis. Although this model, involving a simplified AF magnetic structure comprised of alternating ferromagnetically coupled planes, qualitatively reproduces the features of exchange coupling, the Auger depth profile indicates a relatively broad and atomically rough metal-oxide interfacial region. There is increasing evidence[8–10] that roughness and chemical inhomogeneity on an atomic scale between the metal and oxide layers results in nonuniform exchange interactions creating a complex AF magnetic structure. Within this framework, when the FM forms a single domain during magnetic field cooling, the random exchange field transferred across the interface causes the AF to break up into lateral domains to minimize the random interfacial field energy. However, evidence for a domain structure from hysteresis loop measurements of Co/Co-oxide bilayers is difficult to obtain because of the small thickness of the oxide layers formed at room temperature. Comparison of the magnetic properties, before and after oxidation (Fig. 3, upper panel), indicates that exchange coupling effects after oxidation develop gradually and become large only at low temperatures. The loss of exchange field above 150 K can be attributed to the metastability of the thin AF magnetic structure which is strongly affected by destabilizing forces that are generated upon rotation of the Co spins within the metal film. This result is consistent with previous work on oxide passivated Co fine particles,[12,13] where it was concluded that the underlying cause of the AF "magnetically soft" domain state may be attributed to a crossover to superparamagnetic behavior due to the extremely thin nature of the oxide layers. The gradual recovery of the saturation moment of the Co^{2+} ions in the oxide layers at high temperature (Fig. 3, lower panel) supports this prediction indicating that the frustration generated at the interface during hysteresis measurements is sufficiently high to suppress AF long-range ordering and induce a crossover to superparamagnetic behavior.

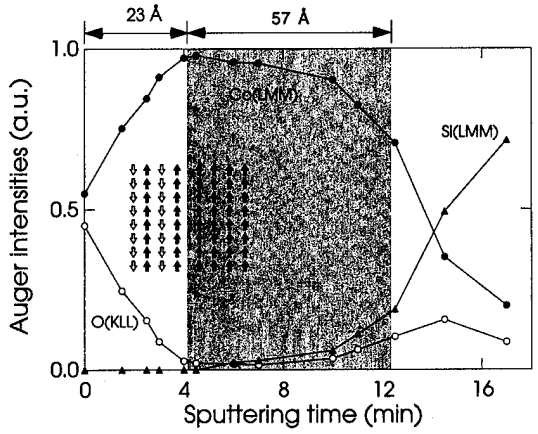


FIG. 2. AES depth profile of a 23 Å Co-oxide/67 Å Co bilayer structure. The inset shows a simplified spin planar model for at an atomically flat AF-FM interface.

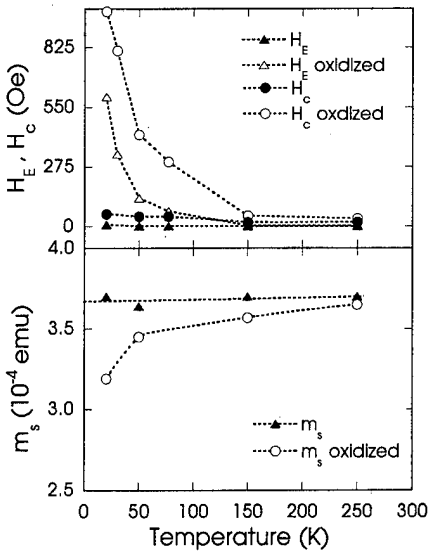


FIG. 3. Temperature dependence of coercive force H_c, exchange field H_E, and saturation moment m_s (lower panel) before (▲), and after (○), complete oxidation of a 80 Å Co/Si(100) thin-film sample.

Figure 4 compares 1 T field-cooled hysteresis loops measured at 50 K, before and after a 150 Å Co deposition on a 25 Å Co-oxide/100 Å Co bilayer. The dramatic enhancement of the coercive and exchange fields that results suggests an increased effectiveness of the oxide layer. Furthermore, in contrast to the bilayer, the shape of the hysteresis loop for the trilayer structure is considerably different, reminiscent of two superimposed unequal loops shifted toward opposite sides of the field axis. These findings seem to suggest that the spin distribution in the oxide is nonuniform on a macroscopic scale but more effectively "frozen" during the hysteresis measurements. Figure 5 shows the Auger depth profile for the trilayer structure which reveals two metal-oxide interfaces which separate an oxide layer (~50 Å thick), sandwiched between two Co metal layers 100 Å in thickness. Apparently, the additional deposition results in a partial oxidation of the Co atoms impinging on the oxide surface, producing a thicker and magnetically more stable oxide film. The inset of Fig. 5 depicts a simplified planar model for the AF structure deduced from these measurements. Assuming a random field at the interface, when the FM forms a single domain [shown by a global (↑) FM moment] in an external field, it is energetically favorable for the AF to break up into domains (↑, ⇓) to minimize the net interfacial anisotropy energy. The presence of a domain state, coupled with a coercivity mechanism within the AF which anchors the domain state in place, leads to the exchange anisotropy effects. The resultant hysteresis loop is then the sum of oppositely magnetized AF domains which produce two shifted loops in opposite directions along the magnetic field axis. Evidence of a domain pattern has also been obtained using the magneto-optic Kerr effect in thick Co/CoO bilayers.[11]

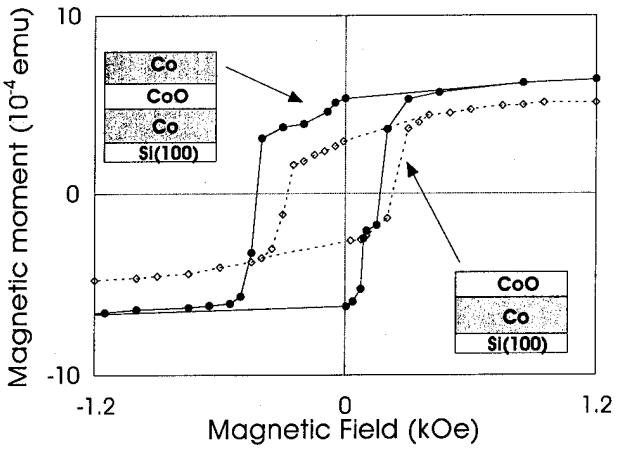


FIG. 4. Comparison of hysteresis loops of (a) 25 Å Co-oxide/100 Å Co bilayer, and (b) 100 Å Co/50 Å Co-oxide/100 Å Co trilayer structures.

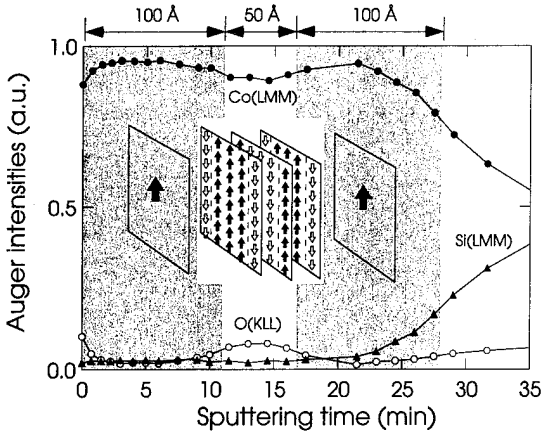


FIG. 5. AES depth profile for 100 Å Co/50 Å Co-oxide/100 Å Co trilayer structure. The inset shows a simplified AF domain planar structure arising from a random field at the metal-oxide interfaces.

We acknowledge useful discussions with J. Herrmann and M. T. Simnad. This research was supported by the U.S. Department of Energy under Grant No. DE-FG03-86ER45230. Some equipment used in this research was provided by the Center for Interface and Materials Science and funded by the W. A. Keck Foundation.

[1] V. M. Jiménez, A. Fernàndez, J. P. Espinòs, and A. R. Gonzàlez-Elipe, J. Electron. Spectrosc. **71**, 61 (1995).
[2] L. Duò, M. Finazzi, F. Ciccacci, and L. Braicovich, Phys. Rev. B **47**, 15848 (1993).
[3] N.-Li Wang, U. Kaiser, O. Ganschow, L. Wiedmann, and A. Benninghoven, Surf. Sci. **124**, 51 (1983).
[4] C. G. Shull, W. A. Strauser, and E. O. Wollan, Phys. Rev. **83**, 333 (1956); W. L. Roth, J. Phys. Chem. Solids **25**, 11 (1964).
[5] W. H. Meiklejohn and C. P. Bean, Phys. Rev. **102**, 1413 (1956).
[6] W. H. Meiklejohn, J. Appl. Phys. **29**, 454 (1958); J. Appl. Phys. Suppl. **33**, 1328 (1962).
[7] S. Spagna, R. E. Sager, and M. B. Maple, Rev. Sci. Instrum. (submitted).
[8] T. J. Moran, J. Gallego, and I. K. Shuller, J. Appl. Phys. (in press).
[9] D. Mauri, H. C. Siegmann, P. S. Bagus, and E. Kay, J. Appl. Phys. **62**, 3047 (1987).
[10] A. P. Malozemoff, Phys. Rev. B **37**, 7673 (1988); J. Appl. Phys. **63**, 3874 (1988); Phys. Rev. B **35**, 3679 (1987).
[11] M. Takahashi, A. Yanai, S. Taguchi, and T. Suzuki, Jpn. J. Appl. Phys. **6**, 1093 (1980).
[12] X. Lin, G. C. Hadjipanayis, and S. I. Shah, J. Appl. Phys. **75**, 6676 (1994).
[13] L. Smardz, U. Kobler, and W. Zinn, Vacuum **42**, 283 (1991).

Ferromagnetic resonance of sputtered Co/Mn multilayers

D. Spoddig, F. Schreiber,[a] J. Pflaum, and J. Pelzl
Institut f. Experimentalphysik III, Ruhr-Universität, 44780 Bochum, Germany

Q. Wang and H. Zabel
Institut f. Experimentalphysik IV, Ruhr-Universität, 44780 Bochum, Germany

Co/Mn multilayers were prepared by rf sputtering onto single-crystal MgO(001) and $Al_2O_3(11\bar{2}0)$ substrates resulting in, respectively, (001)- and (111)-oriented layers. The structure was thoroughly analyzed by x-ray scattering in various geometries. For the magnetic investigations, ferromagnetic resonance (FMR) was applied. Complementary measurements employed the magneto-optical Kerr effect and Faraday balance magnetometry. Results for the in-plane anisotropy, the surface anisotropy, the magnetization, and the FMR linewidth are presented. The comparison with other Co-based multilayer system indicates that both the structural and the magnetic properties of the Co/Mn system are more complicated than in the case of systems with a presumably weaker electronic interaction at the interface. © *1996 American Institute of Physics.* [S0021-8979(96)66608-6]

I. INTRODUCTION

Thin and ultrathin magnetic layers offer fascinating possibilities for studying structure and magnetism in low dimensions and for manipulating material properties in a way which is not accessible in the bulk. Many epitaxial systems have been studied within the last years. Some of these turned out to be suitable as model systems (e.g., Co/Cu in different orientations) while others exhibit a more sophisticated and specific behavior such as, e.g., Co/Cr(001).[1] In the more complicated systems one may find changes of the structural phase accompanied by a change of the magnetic properties of the ferromagnetic material or an impact on the magnetism of, e.g., Co caused by the nontrivial spin structure of its epitaxial partner.

Due to its unusual bulk properties, Mn can be suspected to be an extremely interesting but also difficult candidate for thin-film investigations. Several remarkable aspects have been pointed out in the pioneering work of Ounadjela and co-workers on Co/Mn superlattices grown by evaporation on Ru(0001).[2] Mn is the only transition metal which has no simple bulk phase (fcc, bcc, or hcp) at room temperature. Four different structures are found as a function of temperature with a wide range of atomic volumes and also magnetic order is possible.

In this contribution, we present ferromagnetic resonance (FMR) measurements on rf-sputtered Co/Mn multilayers on MgO and sapphire substrates. We concentrate on the (001)-oriented samples in this report on our first results. The data are compared to those obtained for the (111) orientation on sapphire.

II. SAMPLE PREPARATION AND EXPERIMENTAL

The Co/Mn multilayers were prepared by rf sputtering on MgO(001) and $Al_2O_3(11\bar{2}0)$ substrates with Co as the first layer. The thicknesses of the Co layers, t_{Co}, cover a range from 10 to 50 Å and the thickness of the Mn layers ranges from 5 to 35 Å. The samples consist of ten superlattice periods. For both Co and Mn, the sputtering rates were 0.1 Å/s at a substrate temperature of 100 °C. The structural properties of the layers were thoroughly characterized by x-ray diffraction in various configurations.[3] As in the rest of the paper, we concentrate on the (001)-oriented samples. Both Co and Mn were found to exhibit the (metastable) strained fcc (fct) structure. The total roughness was relatively high (about 5–8 Å). By diffuse scattering it was found that the larger fraction of the roughness was correlated so that one may still speak of a well-defined superlattice structure. More details about our x-ray investigations can be found in Ref. 3.

All samples were measured at room temperature by FMR as a function of the external field orientation (with the in-plane angle ϕ and the out-of-angle θ) in a 9 GHz cavity. Complementary measurements were performed at 17 and 69 GHz in a shortened waveguide setup. The maximum magnetic field available was 31 kG. In most of the measurements the limiting factor for the accuracy of the determination of the magnetic parameters was the linewidth of the resonance curves (see below; for remarks on the absolute accuracy of the apparatus and measurements on samples exhibiting broad lines see, e.g., Ref. 4). Additionally, the magnetic investigations included magneto-optical Kerr-effect (MOKE) measurements and Faraday balance magnetometry.[3]

III. RESULTS AND DISCUSSION

The results of the angular dependent FMR measurements are analyzed using the energy density formalism for the resonance condition.[5] For the (001)-oriented films, the external field energy($-\mathbf{M}\cdot\mathbf{H}$), the cubic magnetocrystalline anisotropy $\{-(K_1/2)\cos^4\Theta - (K_1/8)\sin^4\Theta[3+\cos(4\phi)]\}$, and the effective out-of-plane anisotropy energy as a sum of demagnetizing energy and surface anisotropy K_s are the relevant contributions.[6] For the resulting resonance relations,

[a]Also with Academy of Sciences, Institute of Physics, 18040 Prague 8, Czech Republic.

 0021-8979/96/79(8)/4929/3/$10.00 © 1996 American Institute of Physics

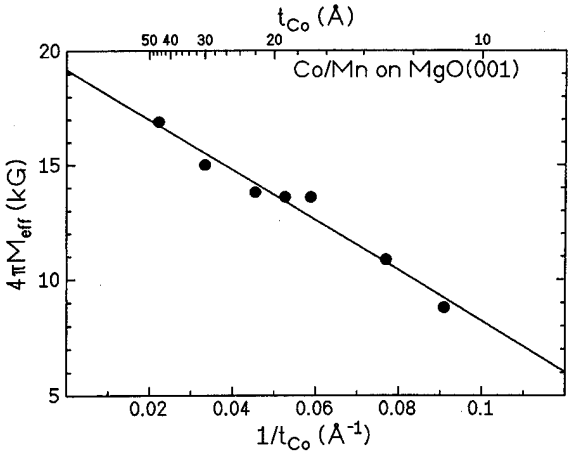


FIG. 1. Effective out-of-plane anisotropy versus $1/t_{Co}$ for the series on MgO(001).

the reader is referred to the above references. As done by many authors, the effective magnetization is defined as

$$4\pi M_{\text{eff}} = 4\pi M - 2\frac{2K_s}{Mt_{\text{Co}}}. \tag{1}$$

In Fig. 1, we plot $4\pi M_{\text{eff}}$ as a function of the inverse thickness. The slope of the straight line is 110 kG Å which corresponds to $K_s = 0.4 \pm 0.1$ erg/cm^2 assuming the bulk value for M (1430 emu/cm^3). However, in our magnetization measurements with a Faraday balance we found the magnetization to be thickness dependent (see below), so that the real K_s value is reduced.

The thickness dependence of the out-of-plane resonance field for the (111)-oriented samples (not shown) yielded a surface anisotropy of $K_s = 0.35 \pm 0.15$ erg/cm^2 (again assuming $M = 1430$ emu/cm^3). The K_s values are in the range of that reported by Ounadjela *et al.* for the layers prepared by evaporation ($K_s = 0.5$ erg/cm^2).[2] If one tries to compare these results to Co/Cu which was also investigated in the (001) and in the (111) orientation it is worth remarking that for Co/Mn, K_s has the same (positive) sign for both orientations while for Co/Cu the sign is different, i.e., K_s favors out-of-plane magnetization for Co/Cu(111) and in-plane magnetization for Co/Cu(001).[7]

For the *in-plane* anisotropy, it is often much more difficult to extract a clear thickness dependence. In the series of the (001)-oriented layers, the magnetocrystalline anisotropy field parameter $2K_1/M$ was found in the range of about 0.6–0.8 kG, apparently without systematic t_{Co} dependence for the thicker layers. A sample with $t_{Co} = 45$ Å is shown in Fig. 2. In contrast, for t_{Co} below 15 Å, the anisotropy was less than half of this value.

We think that this behavior is connected rather with the growth and the structural characteristics than with intrinsic surface effects. At low thicknesses, the structure may not be fully developed and interdiffusion effects which are not negligible in the present samples may play an important role. This may also be consistent with the magnitude of $2K_1/M$ for thicker samples which is still slightly reduced in comparison with, e.g., those obtained on Co/Cu(001).[7]

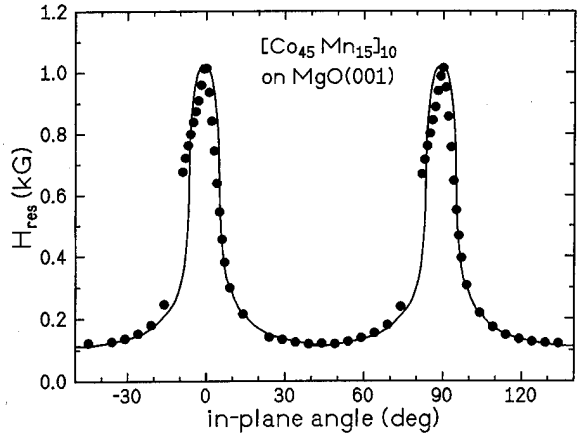


FIG. 2. In-plane angular dependence of the resonance field for $[Co_{45}Mn_{15}]_{10}$ grown on MgO(001).

In Fig. 3, we show an example of the (111)-oriented layers. The 60° (sixfold) symmetry is obvious with a difference of the resonance field between hard and easy axis of the order of 25 G. This corresponds to values of about 0.3 G for the parameter K_4/M if described in terms of the hexagonal anisotropy energy $[K_4 \sin^6 \Theta \cos(6\phi)]$.[8] In comparison to our investigations of molecular beam epitaxy (MBE) grown Co/Cu(111) superlattices on the same substrates (sapphire),[9] the anisotropy is weaker in the present samples. However, the fact that it is clearly resolved can still be taken as an indication of a good structural in-plane coherence.[9]

In addition to the magnetocrystalline anisotropy, several samples also exhibited a uniaxial in-plane contribution $[K_u \sin^2 \Theta \cos^2(\phi - \phi_u)]$ which is quite often found in thin films. As the magnitude of the corresponding effective field $2K_u/M$ was small (of the order of 10 G) and no simple systematic behavior was found we do not focus on this point.

As already indicated above, the resonance lines were relatively broad in some cases. For the (001)-oriented samples, the linewidth values were found between about 150 and 460 G for the in-plane easy axis and between 250 and 470 G for the hard axis at X-band frequencies with the general tendency of broader lines for lower thicknesses. The

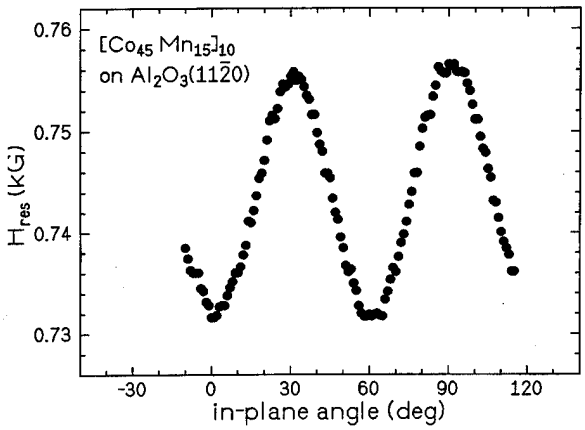


FIG. 3. In-plane angular dependence of the resonance field for $[Co_{45}Mn_{15}]_{10}$ grown on sapphire.

linewidths are higher at higher frequencies due to the intrinsic (Gilbert) damping but there are significant nonintrinsic broadening contributions (see also Refs. 6, 7, and 10). The linewidths of the (111) layers were lower, without significant angular dependence. As it was found in Ref. 2 for MBE-grown Co/Mn on Ru(0001), the lines in perpendicular orientation were usually broader.

Besides the roughness of the interface and other structural imperfections [maybe particularly important in the strongly anisotropic (001)-oriented layers] also a significant strain[3] may contribute to the line broadening in the present superlattices.

Unfortunately, because of the linewidth limiting the accuracy for all extracted parameters, it was not possible yet to determine the g-factor g with a precision sufficient to decide whether g deviates from the bulk value or not. This can be tried in future experiments using additional frequencies up to 92 GHz, and it should be particularly interesting as in systems with the partner of the ferromagnetic metal having an only partially filled $3d$ band, the electronic interaction at the interface may be expected to give rise to changes in the bandstructure which influence g (see also Ref. 4).

Our Faraday balance measurements which are reported in more detail in Ref. 3 yielded a reduction of the magnetization with respect to the bulk value corresponding to the moment of about two or three monolayers of Co. No evidence was found for a ferromagnetic contribution of Mn.

In conclusion, we have presented ferromagnetic resonance measurements on sputtered Co/Mn in the (001) and (111) orientation. The surface anisotropy K_s was determined. If compared to the Co on Cu which can also be prepared in both orientations with Co in the fcc phase, the results for the thickness dependence of the in-plane anisotropy and also the linewidth and the reduced magnetization may indicate that Co on Mn is a much more complicated system as it was pointed out also in Ref. 2. More data seem to be required for this epitaxial system. It should also be kept in mind that CoMn alloys exhibit invar properties which may play a role under certain conditions, e.g., very thin layers and high interdiffusion. This will be addressed in future investigations.

ACKNOWLEDGMENTS

The authors wish to thank Dr. Z. Frait (Prague) for helpful discussions and complementary measurements in his laboratory. This work was supported by the Deutsche Forschungsgemeinschaft (SFB 166).

[1] W. Donner, N. Metoki, A. Abromeit, and H. Zabel, Phys. Rev. B **48**, 14745 (1993); N. Metoki, W. Donner, and H. Zabel, *ibid* **49**, 17351 (1994).

[2] K. Ounadjela, P. Vennegues, Y. Henry, A. Michel, V. Pierron-Bohnes, and J. Arabski, Phys. Rev. B. **49**, 8561 (1994); K. Ounadjela, Y. Henry, M. Farle, and P. Vennegues, J. Appl. Phys. **75**, 5601 (1994), and references therein.

[3] Q. Wang, N. Metoki, Ch. Morawe, Th. Zeidler, and H. Zabel, J. Appl. Phys. **78**, 1689 (1995).

[4] F. Schreiber, Z. Frait, Th. Zeidler, N. Metoki, W. Donner, H. Zabel, and J. Pelzl, Phys. Rev. B **51**, 2920 (1995).

[5] J. Smit and H. G. Beljers, Philips Res. Rep. **10**, 113 (1955); J. O. Artman, Phys. Rev. **105**, 62 (1957).

[6] B. Heinrich and J. F. Cochran, Adv. Phys. **42**, 523 (1993).

[7] B. Heinrich, J. F. Cochran, M. Kowalewski, J. Kirschner, Z. Celinski, A. S. Arrott, and K. Myrtle, Phys. Rev. B **44**, 9348 (1991); M. Kowalewski, C. M. Schneider and B. Heinrich, *ibid* **47**, 8748 (1993).

[8] We may remark that here we use the hexagonal energy system only for the *description* of the experimental in-plane data. This does not mean that the cubic system and its transformation to the (111) plane may not be used. For further discussion of this point see Ref. 9 and also J. O. Artman, J. Appl. Phys. **77**, 5484 (1995); F. Schreiber, A. Soliman, P. Bödeker, R. Meckenstock, K. Bröhl, J. Pelzl, and I. A. Garifullin, *ibid.* **77**, 5486 (1995). It should be noted that the problem of twinned structure and the resulting overall sixfold symmetry as discussed in the latter reference is also relevant for the present Co/Mn samples.

[9] F. Schreiber, A. Soliman, P. Bödeker, R. Meckenstock, K. Bröhl, and J. Pelzl, J. Magn. Magn. Mater. **135**, 215 (1994).

[10] F. Schreiber, J. Pflaum, Z. Frait, Th. Mühge, and J. Pelzl, Solid State Commun. **93**, 965 (1995).

Structural and magnetocrystalline anisotropy contributions to the blocking temperatures of $Ni_xCo_{(1-x)}O$ exchange couples (abstract)

Kentaro Takano and Ami E. Berkowitz
Department of Physics and Center for Magnetic Recording Research, CMRR-0401, University of California, San Diego, La Jolla, California 92093-0401

Wei Cao and Gareth Thomas
Department of Material Science and Mineral Engineering, University of California, Berkeley, California 94720

The simple spin and crystal structure of the antiferromagnetic (AF) monoxide $Ni_xCo_{1-x}O$ facilitates structural characterization and modeling of its magnetic properties $Ni_xCo_{1-x}O$ is also receiving technological attention for biasing magnetoresistive sensors as a robust alternative to FeMn. In this work, we studied the thickness dependence of the AF layer on the exchange field created through interfacial exchange coupling between $Ni_xCo_{1-x}O$ and $Ni_{81}Fe_{19}$ films. The $Ni_xCo_{(1-x)}O$ films were reactively sputtered on silicon substrates and capped with a 300 Å $Ni_{81}Fe_{19}$ layer. An additional silver layer was deposited as an oxidation barrier. An exchange field was observed on all the exchange couples with the $Ni_xCo_{(1-x)}O$ thickness ranging from 25 to 1000 Å. The exchange couples were characterized using transmission electron microscopy (TEM) to yield information on the orientation, structure, and size of the crystallites. The films were polycrystalline with columnar grains. For oxide thicknesses below 300 Å, the film was randomly oriented but developed a texture with a preferred orientation for thicker films. We found that the blocking temperature, at which the exchange field goes to zero, decreases with decreasing oxide thickness. The blocking temperature is relatively thickness independent for higher thicknesses but decreases rapdily below a certain thickness. The decrease in the blocking temperature does not appear to be consistent with a finite size scaling law.[1] Instead we modeled this behavior to take into account the temperature dependence associated with the changing microstructure of the AF layer with thickness, in particular the size of the crystallites. In thick oxide films, the blocking temperature corresponds to the AF ordering temperature, the Néel temperature. The decrease of the blocking temperature below the Néel temperature suggests at the competing magnetic and thermal energies necessary for exhibiting unidirectional anisotropy. The thickness sensitivity of the blocking temperatures of the AF monoxides are found to be strongly dependent on their magnetocrystalline anisotropy. © *1996 American Institute of Physics.* [S0021-8979(96)67408-4]

[1] S. Parkin and V. Speriosu, in *Magnetic Properties of Low Dimensional Systems, Proceedings of the Second Workshop, San Luis Potosi, Mexico, 23–26 May 1989* (Springer, Berlin, 1990), pp. 110–120.

 0021-8979/96/79(8)/4932/1/$10.00 © 1996 American Institute of Physics

Rotatable anisotropy in radio frequency diode sputtered iron thin films

W. Win, E. J. Yun, and R. M. Walser
I/UCR Center for Magnetics, The University of Texas at Austin, Austin, Texas 78712

Iron films deposited by rf diode sputtering exhibited a robust, rotatable hysteresis loops with nearly perfect squareness; i.e., ~100% of M_s rotates to any in-plane direction x, following the application of $H_x > H_c$, and exhibits a stable uniaxial hysteresis for further variations in H_x. The rotatable anisotropy (RA) observed is highly reproducible on various substrates (glass, silicon, and alumina), and is unaffected by variations in; substrate temperature (to 300 °C), deposition rate (15–300 Å/min), in-plane orienting magnetic fields (to 200 Oe), and annealing at temperatures to 370 °C in a large magnetic field (to 1.3 kOe). RA was absent only in films deposited in higher Ar pressures.
© *1996 American Institute of Physics.* [S0021-8979(96)66708-1]

I. INTRODUCTION

Rotatable anisotropy (RA) has been observed in iron films prepared by rf diode sputtering. In these films, a rectangular easy axis hysteresis loops with abrupt transitions and high remanence can be observed in an arbitrary in-plane direction by applying a field that exceeds the typical coercivity of ≈10–12 Oe. The rotatable anisotropy of these films is extremely robust and highly reproducible.

There are no previous reports of RA in Fe thin films deposited by rf diode sputtering. RA has been observed in evaporated, negative magnetostrictive Fe thin films that exhibit stripe domains.[1–3] However, the RA associated with stripe domains is markedly different from that observed in rf diode sputtered films. In addition, Fe films obtained by rf diode sputtering are markedly different from those recently obtained by rf magnetron,[4,5] dc diode,[5] and dual ion beam[6] sputtering. The purpose of this article is to discuss the results of experiments to characterize RA in rf diode sputtered Fe films. Experiments aimed at determining the origin of the observed RA will be presented elsewhere.

II. EXPERIMENT

The iron films described in this article were deposited by rf diode sputtering from a 5 in. iron target with a purity of 99.95%. The base pressure of the system was below 2.5×10^{-7} Torr and the Ar pressure during sputtering was between 5 and 30 mTorr. Films were deposited in both the static and rotational deposition modes. In the rotational deposition mode, the substrates were rotated under the Fe target at 6 rpm. Substrate bias in the range from −40 to −50 V was occasionally applied during deposition. The static and rotational deposition rates were ~270–300 Å/min, and ~15–18 Å/min, respectively. Films with 1000 Å thickness were deposited on cover glass slides, silicon wafers, and alumina substrates. The Fe films were deposited either at ambient, or at 300 °C substrate temperatures. In-plane bias magnetic fields of 200 Oe were applied during the deposition of some films. The effect of temperature on RA was investigated by annealing a film to 370 °C in a vacuum of 4.5×10^{-6} Torr. The effect of applying a large (1.3 kOe) in-plane field parallel to a predetermined axis during annealing was also investigated.

The $B-H$ loops of the films were obtained, at room temperature, using either a low field hysteresis loop tracer (drive field ≤100 Oe) or a vibrating sample magnetometer (VSM). The room temperature resistivity was measured with a four-point probe method.

III. RESULTS AND DISCUSSION

The rotatable anisotropy in the rf diode sputtered iron films was characterized by measuring their in-plane hysteresis loops as a function of the orientation and amplitude of in-plane driving fields. A typical hysteresis loop of a ~1000 Å thick Fe film deposited on glass is shown in Fig. 1. When a field $H_x > 10$ Oe was applied in an arbitrary in-plane direction x, the magnetization of this film rotated to that direction,

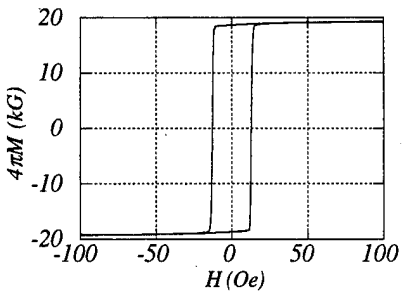


FIG. 1. Hysteresis loop of Fe film deposited on glass substrate (10 mTorr Ar). The magnetic field was applied along an arbitrary direction.

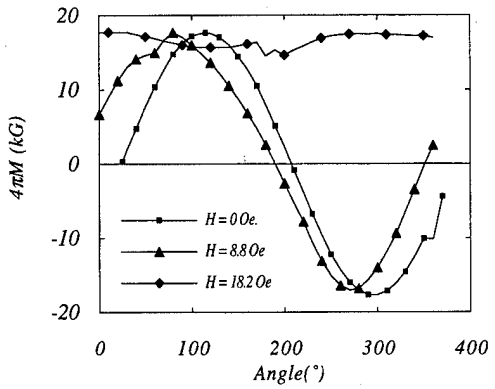


FIG. 2. Variations in film magnetization with the angle ϕ (see text) that a saturated Fe film is rotated in fields; $H=0$, $H<H_c$, and $H>H_c$.

 0021-8979/96/79(8)/4933/3/$10.00 © 1996 American Institute of Physics

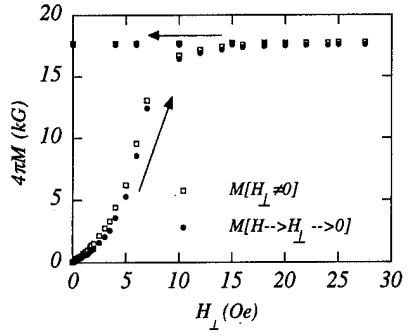


FIG. 3. Magnetization observed during (□), and following (●), the application of $H_\perp$ perpendicular to a direction of prior saturation.

where it exhibited a stable square hysteresis loop for further variations in H_x. Independent of the orientation of the film, the squareness ratio M_r/M_s was typically between 0.95 and 0.98.

Figure 2 illustrates the RA in a 1000 Å iron film with $H_c \approx 12$ Oe. The sample magnetization was first saturated along an arbitrarily selected axis x. A stationary dc field was then applied along this axis, and the sample rotated so that the axis of initial saturation made an angle ϕ with the direction of the applied field. Figure 2 plots the variations in the film magnetization along the axis of initial saturation with ϕ, for applied fields of $H_x=0$, $H_x=8.8$ Oe$<H_c$, and $H_x=18.2$ Oe$>H_c$. For $0<H_x<H_c$, the magnetization exhibited a uniaxial anisotropy. The rotatable anisotropy was evidenced by the near independence of the magnetization on the rotation angle, when a field $H_x>H_c$ was applied.

The rotation of the easy axis was confirmed by measuring the magnetization perpendicular to a previously saturated direction as a function of the applied field. In this experiment, a dc field large enough to saturate the sample, was applied in the VSM along an arbitrary direction in the film plane. The sample was then rotated 90° around the film normal to a new direction. The in-plane magnetization in the new direction was initially zero as expected. The magnetization was measured (Fig. 3) with the field applied along the 90° direction ($H_\perp$); first while it was increased from zero to above H_c, and then (as shown by the arrows) while it was increased to zero. Figure 3 plots the magnetization measured

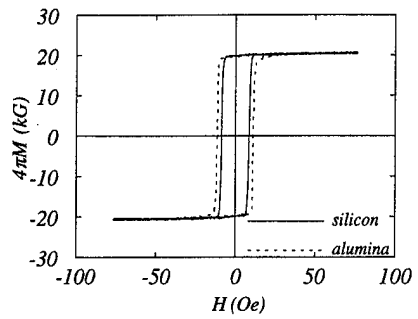


FIG. 4. Hysteresis loops of Fe films deposited on silicon (solid) and alumina (dashed) substrates. (The hysteresis loop of an Fe film deposited on a glass substrate is shown in Fig. 1.)

TABLE I. Substrate dependence of the magnetic properties of Fe films with thickness ≈1000 Å.

Substrate	M_s (G)	H_c (Oe)	ρ ($\mu\Omega$ cm)
Glass	21 204	9	14.9
Si	20 711	8	15.5
Alumina	20 840	12	14.8

while $H_\perp$ was present (open squares), and the remanent magnetization after $H_\perp$ was removed (solid circles). The remanence of these minor hysteresis loops were observed to be typically >95%. When $H_\perp$ exceeded H_c, the $M=M_s$ and the $M_r \approx M_s$, indicating that the magnetization and uniaxial hysteresis had completely rotated to the new direction.

For dc and ac magnetic fields larger than H_c, the in-plane magnetization rotated to the field direction independent of the initial film orientation. However, for $H_{ac}<H_c$, the rotatable hysteresis loop collapsed into a horizontal line with zero slope, and remained at zero when the sample was rotated. Hence, the hard-axis minor loop was not observable with H_{ac}. A finite slope along the hard axis was observed for dc magnetic fields in the range $0<H_{dc}<H_c$. $M(0)=0.98$ $M(H_{dc})$ was observed throughout this H_{dc} range. When $H_{dc} \geq H_c$, the magnetization remained aligned with the direction of H_{dc}, when the sample was rotated.

The robustness of the RA was investigated by: (a) varying the substrate material, (b) applying a magnetic bias field during deposition, (c) heating the substrate, and (d) annealing the as-deposited films. Fe films were deposited by rf diode sputtering onto cover glass slides, silicon wafers, and alumina substrates. RA was observed in the films deposited on all of these substrates. Furthermore, the coercivity, squareness ratio, and resistivity were nearly independent of the substrate. The hysteresis loops of Fe films deposited on silicon and alumina substrates are shown in Fig. 4 to illustrate the similarity in their hysteresis loops. The typical magnetic properties of films deposited on these substrates are summarized in Table I.

Rotatable anisotropy was observed in Fe films with, or without, a 200 Oe bias magnetic field applied in-plane during the deposition. The properties are summarized in Table II.

After annealing at 370 °C in vacuum in the presence of a strong in-plane field (1.3 kOe), a slight increase in M_s (from 21 181 to 21 432 G) was accompanied by small decreases in H_c (from 12 to 10 Oe) and resistivity (from 16 to 13.6 $\mu\Omega$ cm). However, the rotatable anisotropy was completely unaffected by this annealing process. The RA was also unchanged in films deposited on substrates held at elevated temperatures to 300 °C.

TABLE II. Magnetic properties of ≈1000 Å thick Fe films deposited with and without H_{ext} field.

H_{ext} (Oe)	M_s (G)	H_c (Oe)	ρ ($\mu\Omega$ cm)
0	21 181	12	16.03
200	21 486	12	14.4

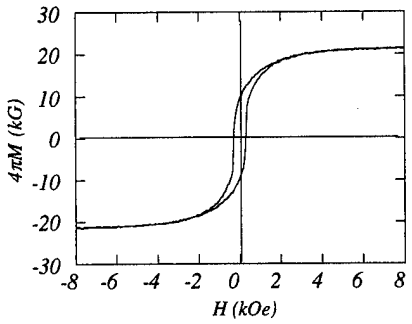


FIG. 5. Isotropic hysteresis loop of rf diode sputtered 1000 Å Fe film deposited with Ar pressure=30 mTorr. (See Fig. 1 for hysteresis loop of Fe film deposited with Ar pressure=10 mTorr.)

RA could be eliminated in the rf diode sputtered Fe films only by increasing the Ar pressure (to 30 mTorr). As shown in Fig. 5, the resulting films were isotropic with $H_c \approx 300$ Oe. The dependences of the magnetic properties and electrical resistivity of the Fe films on Ar pressure are shown in Figs. 6(a) and 6(b). The increase in Ar pressure was believed to increase the film porosity, reduce M_s, and increase H_c and the resistivity. The RA vanished in these films and the in-plane hysteresis loops were isotropic.

IV. SUMMARY

Fe films deposited by rf diode sputtering exhibit a previously unobserved, and exceptionally robust, rotatable anisotropy. The rf diode sputtered films were very high quality with resistivity and M_s values that were within $\pm 1\%$ of pure bulk iron. The hysteresis loops of these films were very square with $\sim 100\%$ remanence and sharp magnetization reversal transitions. The rotatable anisotropy was reproducible and unaffected by the substrate material, the application of an in-plane bias field during deposition, substrate heating, and postdeposition annealing. RA was not detected in rf diode sputtered Fe films only when they were sputtered at Ar pressures high enough to eliminate the uniaxial anisotropy. Similar RA was observed in films deposited in static and rotating deposition modes with a tenfold variation in deposition rate. The insensitivity of RA to variations in deposition

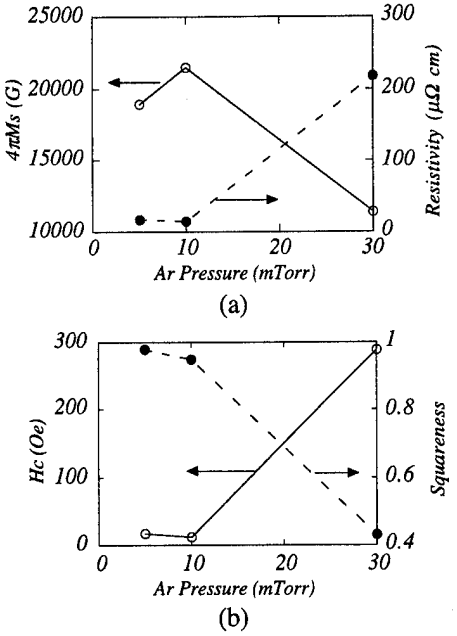


FIG. 6. Variations in; (a) $4\pi M_s$ and resistivity and (b) H_c and squareness, with Ar sputter gas pressure.

parameters suggests that the random interfacial morphology produced by rf diode sputter deposition is the important structural feature responsible for RA in Fe thin films. Investigations to confirm this are in progress.

ACKNOWLEDGMENTS

This work was sponsored by the Industry/University of Texas Cooperative Research Center for Magnetics, and by the Texas Advanced Technology Program under Grant No. 257.

[1] Y. Sugita, H. Fujiwara, and N. Saito, J. Phys. Soc. Jpn. **19**, 782 (1964); **20**, 469 (1965).
[2] H. Fujiwara, Y. Sugita, and N. Saito, Appl. Phys. Lett. **4**, 199 (1964).
[3] N. Saito, H. Fujiwara, and Y. Sugita, J. Phys. Soc. Jpn. **19**, 1116 (1964).
[4] Y. K. Kim and M. Oliveria, J. Appl. Phys. **74**, 1233 (1993).
[5] M. Hong, E. M. Gyorgy, R. B. van Dover, S. Nakahara, D. D. Bacon, and P. K. Gallagher, J. Appl. Phys. **59**, 551 (1986).
[6] M. Naoe, M. Yamaga, and N. Terada, IEEE Trans. Magn. **MAG-21**, 1900 (1985).

Coupling effects in Fe/CoNbZr and Fe/Ag/CoNbZr sandwiches studied by magneto-optical techniques

M. C. Contreras, J. F.-Calleja, M. O. Gutiérrez, and M. Rivas
Departamento de Física, Universidad de Oviedo, 33007 Oviedo, Spain

R. Krishnan
Laboratoire de Magnétisme et d'Optique de Versailles, C.N.R.S., 92195 Meudon Cedex, France

Experimental characterization of magnetic anisotropy, coercive field, and anisotropy dispersion of sputtered Fe/CoNbZr and Fe/Ag/CoNbZr sandwiches were carried out by transverse biased initial susceptibility (TBIS) measurements with a magneto-optic Kerr effect at both film/air and glass/film interfaces. Three different behaviors have been observed depending on the range of magnetization fluctuation. The results indicate that Fe grains play a fundamental role in the type of the dispersion (long range or short range). The results obtained from the coercive field and from x-ray diffractograms agree with those obtained by TBIS. © *1996 American Institute of Physics.* [S0021-8979(96)66808-8]

INTRODUCTION

The study of ferromagnetic double-layered and sandwiched films is the basis for understanding multilayered systems. The magnetic and magneto-optical properties of the ferromagnetic sandwiched films are strongly influenced by the coupling at the interfaces. However the origin of this coupling mechanism is as yet unclear. Several investigators have suggested that a positive coupling is caused by an exchange interaction through pinholes[1] in the intermediate layer. Others[2–4] have proposed the interaction between domain walls or by the ripple stray fields of ferromagnetic layers.

In this article we investigate Fe/CoNbZr and Fe/Ag/CoNbZr sandwiches by performing transverse biased initial susceptibility (TBIS) measurements and several magnetostatic techniques. As is well known, TBIS measurements have their foundation in the application of a small alternating field h_{ac} and an orthogonal steady field H_{dc}, both in the film plane. Then, the susceptibility in a direction parallel to h_{ac} is measured as a function of H_{dc}. In the following, the transverse susceptibility will be called $\chi_t(\beta)$, with β the angle between the easy axis of induced anisotropy and the direction of H_{dc}.

EXPERIMENTAL PROCEDURE

The layers were prepared by sequential rf sputtering using a system which was first pumped to a pressure of 4×10^{-7} Torr. The targets were pure Fe, Ag, and and an alloy of Co–Nb–Zr (CNZ). The deposition parameters were a rf power of 80 W and an Ar pressure of 6 mTorr. A water cooled glass substrate was used.[5,6] All the sandwiches have a Fe layer in contact with the substrate.

The saturation magnetization M_s was measured with a vibrating sample magnetometer. M_s in the sandwiches ranging from 1000 to 1100 emu cm^{-3} and the in-plane $M-H$ loops were measured by magneto-optical Kerr effect (MOKE) and a hysteresis graph.

Morphological and crystallographic structure of the films were examined by standard x-ray diffraction (XRD) of Cu $K\alpha$ radiation. All the films except the CoNbZr layer showed a polycrystalline structure. The amorphous structure of the CoNbZr layer was confirmed by XRD, as no evidence of the crystalline order on a scale of more than a few Å was detected.

We have studied the magnetic behavior of these sandwiches by using the MOKE system to perform TBIS measurements at both film/air (f/a) and glass/film (g/f) interfaces in two different configurations: with the dc field applied along the easy axis and along the hard axis. Note that the optical penetration depth in our case is approximately 400 Å, which allows us to probe the top and the under layer of the bilayers and sandwiches in those cases in which their thickness is smaller than 400 Å. It is noteworthy that TBIS measurement is more sensitive than the measurement of the hysteresis loop: It allows us to determine very precisely the easy axis and the anisotropy field (H_k) and moreover to quantify the anisotropy dispersion distinguishing between short- and long-range magnetization fluctuations in the plane of the film whose origin is different.

H_k is obtained from the linear extrapolations to the value $\chi_{t,\beta}^{-1}=0$ in the $\chi_{t,\beta}^{-1}$ vs H curves from the high field range, β being the angle between the dc applied field and the easy axis of the film.

In real films these extrapolations for $\beta=0$ and $\beta=\pi/2$ cut the abcissa at asymmetrical points separated by $2H_k$. We denote this asymmetry by ΔH_k. The normalized value $\Delta H_k/H_k$ is phenomenologically related with the magnetization dispersion.

The H_c/H_k ratio provides information about the prevalent mechanism in the magnetization reversal process. If this ratio is small compared to unity the dominating magnetization reversal process is characterized by nucleation of a small number of opposite domains followed by subsequent wall propagation. On the other hand, if $H_c/H_k \geq 1$ the reversal mechanism becomes more complicated, involving incoherent rotation and the nucleation of a large number of small opposite domains, spread over the whole film area.

RESULTS AND DISCUSSION

Three different behaviors are observed.

Figure 1 shows $\chi_{t,\beta}^{-1}$ vs H curves obtained for the as-prepared Fe film. Both curves present a minimum and cut the

 0021-8979/96/79(8)/4936/3/$10.00 © 1996 American Institute of Physics

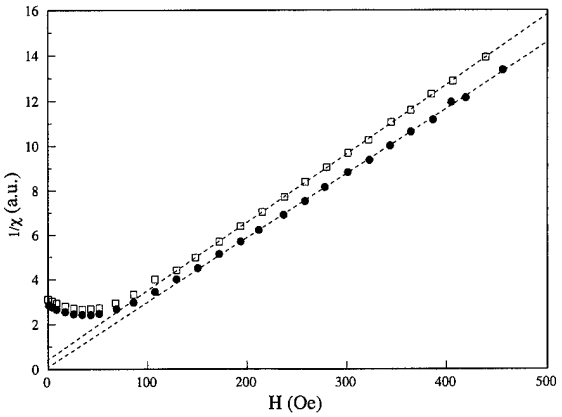


FIG. 1. Experimental curves of $\chi(\beta)^{-1}$ vs H and linear extrapolations for the Fe layer. Squares represent $\beta=0$ and circles $\beta=\pi/2$.

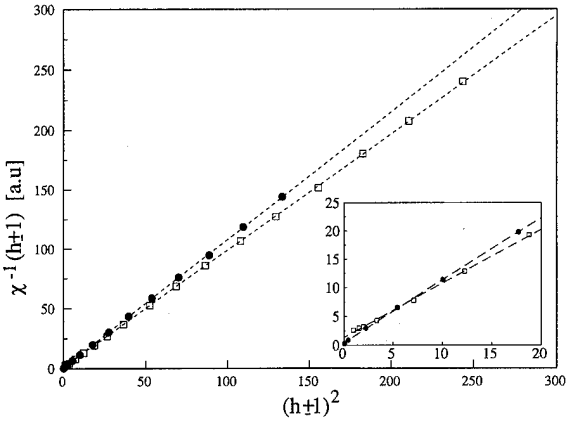


FIG. 3. Experimental curves of $\chi(\beta)^{-1}(h\pm1)$ vs $(h\pm1)^2$ and linear extrapolations for sample 5. Squares represent $\beta=\pi/2$ and circles $\beta=0$.

abcissa at negative values, which indicate that this film is quasi-isotropic, as expected. For this film we obtain $\Delta H_k/H_k=1.6$. From x-ray diffractograms it was concluded that the Fe layer has a bcc structure with a (110) and (200) texture [the (211) reflection was absent].

In the case of CoNbZr, layer inverse susceptibility follows the law

$$\chi^{-1}=\frac{H_k}{M_s}[(h\pm1)+b(h\pm1)^{-1/4}], \tag{1}$$

where $h=H_{dc}/H_k$.

This can clearly be seen in Fig. 2, which shows that $\chi^{-1}(h\pm1)^{1/4}$ vs $(h\pm1)^{5/4}$ follows a linear law. The parameter b is known as the ripple parameter[7,8] and represents local short-range fluctuations of magnetization. In this case $b=0.21$. Different values of H_k obtained at both interfaces may be explained by an oxidation of Zr in the film/air interface.

For the rest of the layered samples the inverse of the transverse susceptibility follows the law

$$\chi^{-1}=\frac{H_k}{M_s}[(h\pm1)+c(h\pm1)^{-1}]. \tag{2}$$

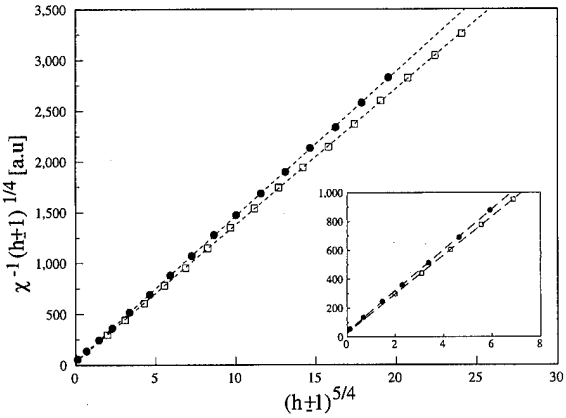


FIG. 2. Experimental curves of $\chi(\beta)^{-1}(h\pm1)^{1/4}$ vs $(h\pm1)^{5/4}$ and linear extrapolations for the CoNbZr layer. Squares represent $\beta=\pi/2$ and circles $\beta=0$.

This has been checked by plotting $\chi^{-1}(h\pm1)$ vs $(h\pm1)^2$ as shown in Fig. 3. Parameter c represents skew or long-range fluctuation of magnetization in the plane of the sample, that is to say, this effect implies a much higher dispersion of anisotropy than ripple effect.[9] Due to the locally different easy direction in a particular grain, the magnetization, lying in the plane of the film, rotates with respect to the magnetization in the surroundings.

Table I reports values of b and c for the samples with the first two behaviors previously mentioned.

Table II reports values of H_k, H_c, and $\Delta H_k/H_k$ for all the samples under study. In those cases in which the thickness is larger than the penetration depth we give the values for both f/a and g/f interfaces. From XRD profiles of Fe/CoNbZr sandwiches only one peak was observed corresponding to Fe(110) texture. The peak becomes sharper when the thickness of Fe is larger, which suggests a larger grain size in samples 3 and 6, probably due to diffusion of Fe at the interfaces. The existence of the interdifussion layer was shown by conversion Mössbauer spectroscopy.[6] This leads to a very small value of H_k and a high $\Delta H_k/H_k$ at both interfaces that justifies the hypothesis. In the other cases this behavior has been observed mainly at the g/f interface corresponding to a Fe deposit.

The coercive fields of individual Fe and CoNbZr are 17 and 0.5 Oe, respectively, and the H_c/H_k ratio is in the first case much higher than unity and in the second case much

TABLE I. Values of b amd c for the samples.

Sample	No.	b	c
Fe	1	...	...
CoNbZr	2	0.21	...
Fe/CNZ	3	...	0.4
Fe/CNZ	4	...	0.2
Fe/CNZ	5	...	0.7
2×(Fe/CNZ)	6	...	0.9
Fe/Ag/CNZ	7	...	0.5
Fe/Ag/CNZ	8	...	0.7
Fe/Ag/CNZ	9	...	0.9

TABLE II. Magnetic properties of the films. When two values are given they are in the order (f/a)/(g/f).

Sample	No.	t (nm)	H_k (Oe)	$\Delta H_k/H_k$	H_c (Oe)
Fe	1	50	5.1	1.6	17.0
CoNbZr	2	160	14.6/11.8	0.21/0.17	0.5
Fe/CNZ	3	80/80	7.2/5.5	0.14/0.27	5.1
Fe/CNZ	4	30/30	12.4/11.6	0.10/0.13	6.0
Fe/CNZ	5	20/20	11.9	0.21	5.8
2×(Fe/CNZ)	6	2×(20/20)	8.7/8.3	0.18/0.28	4.5
Fe/Ag/CNZ	7	20/6/20	14.4/12.3	0.21/0.28	10.3
Fe/Ag/CNZ	8	20/3/20	12.4/11.0	0.23/0.17	11.6
Fe/Ag/CNZ	9	20/1.5/20	12.2/12.0	0.23/0.25	8.7

smaller than unity, strengthening the idea of a quasi-isotropy for Fe. In the rest of the samples the H_c/H_k ratio approximates unity.

According to the experimental results the addition of Fe layers increases the coercivity. In all cases according to the experimental results the repeated nucleation of Fe grains leads to an increase of coercivity and these values are close at both interfaces.

Samples 7–9 are sandwiches with a nonmagnetic intermediate layer. XRD analysis indicated a broad diffraction peak with a low intensity identified as bcc Fe(110). The H_k values are similar in these films to those without an intermediate layer from which we may deduce that ferromagnetic coupling between Fe and CoNbZr layers occurs through a nonmagnetic layer up to 60 Å thick. The ferromagnetic coupling also gives a value of magnetization similar to those Fe/CoNbZr alloys. In these samples there is a substantial increase in coercive force indicating a less strong coupling between the ferromagnetic layers. In these cases a contribution to the coercive force may arise from pinning of the wall at the interfaces.

CONCLUSIONS

To summarize, TBIS measurements by MOKE give an indication of anisotropy field and different local fluctuations of magnetization over the sample in the case of polycrystalline Fe/CoNbZr and Fe/Ag/CoNbZr sandwiches. $\chi_{t,\beta}^{-1}$ vs H has been found to be sensitive to small changes of the dispersion and the quality of the dispersion and XRD and H_c results agree with results found by TBIS measurements.

ACKNOWLEDGMENTS

This work was partially supported by the Comisión Interministerial de Ciencia y Tecnología (CICYT) MAT93-1431 and by the University of Oviedo DF/95-214-3.

[1] O. Massenet, F. Biragnet, H. Juretschke, R. Montmory, and A. Yelon, IEEE Trans. Magn. **MAG-2**, 553 (1966).
[2] M. Okon and H. Hoffmann, IEEE Trans. Magn. **MAG-9**, 563 (1973).
[3] H. Niedoba, L. J. Heyderman, H. O. Gupta, I. B. Puchalska, and A. Hubert, J. Appl. Phys. **69**, 5865 (1991).
[4] F. W. A. Dirne, F. J. A. den Broeder, J. A. M. Tolboom, H. J. de Wit, and C. H. M. Witmer, Appl. Phys. Lett. **53**, 2386 (1988).
[5] R. Krishnan and J. Eymery, J. Magn. Magn. Mater. **104**, 1893 (1992).
[6] R. Zuberek, H. Szymckak, R. Krishnan, and M. Tessier, J. Magn. Magn. Mater. **133**, 490 (1994).
[7] G. Suran, H. Ouahmane, I. Iglesias, M. Rivas, J. A. Corrales, and M. C. Contreras, J. Appl. Phys. **76**, 1749 (1994).
[8] M. C. Contreras, M. Rivas, I. Iglesias, J. A. Corrales, R. Krishnan, and M. Tessier, IEEE Trans. Magn. **29**, 3885 (1993).
[9] M. Rivas, J. F.-Calleja, I. Iglesias, M. C. Contreras, M. Guyot, M. Porte, V. Cagan, and R. Krishnan, J. Magn. Magn. Mater. (to be published).

Low-energy ion beam-assisted deposition of giant magnetoresistive thin films

S. J. Guilfoyle, R. J. Pollard,[a] and P. J. Grundy
Joule Laboratory, Department of Physics, University of Salford, Salford M5 4WT, United Kingdom

Granular and multilayer Co-Ag and NiFe-Ag thin films have been prepared by magnetron sputtering and by concurrent low-energy (0–500 eV) ion radiation-assisted deposition. The ion beam bombardment slightly increased the giant magnetoresistance of granular films and then progressively decreased it. X-ray data revealed a change in the crystalline structure of these films, dependent on the energy of the beam. Examination using transmission electron microscopy (TEM) also highlighted differences between the as-sputtered and the ion beam-assisted films. For multilayer films, TEM and x-ray analysis shows changes in the interfacial and crystal structure induced by the ion beam. © *1996 American Institute of Physics.* [S0021-8979(96)66908-4]

I. INTRODUCTION

Since the discovery of giant magnetoresistance (GMR) in antiferromagnetically coupled multilayers,[1] there has been intense interest in the electrical and microstructural properties of such films.[2,3] More recently, GMR has been found to occur in granular systems consisting of a magnetic phase dispersed in a nonmagnetic host.[4] It is known that for multilayer films the magnetic layer and spacer layer thicknesses are critical for the GMR effect to be maximized.[5] For the case of granular films, post-deposition annealing and deposition onto heated substrates affect the nucleation and grain size. These conditions also affect the GMR of such films. Therefore, it appears that in a similar way to multilayers, the size and spacing of the magnetic regions strongly influences the GMR in granular samples.

Ion beam-assisted deposition (IBAD) can alter the growth mechanisms and atomic arrangements in thin films. The crystal structure, grain size, resistivity, and surface topography can all be affected by the additional surface energy.[6] These effects are not necessarily duplicated by thermal treatment such as annealing. Hence, IBAD is a convenient way to explore the dependence of GMR on microstructure in heterogeneous thin films.

II. EXPERIMENT

Films were deposited by magnetron sputtering from separate Co, Ag, and NiFe targets onto precleaned glass and silicon substrates at ambient temperature. Sputter pressures of 3 mTorr and a background pressure of 3×10^{-7} Torr were used. Granular films were approximately 60 nm thick, multilayers were of the order of 90 nm. The ion beam source used was a broad beam Kaufman type, no substrate heating effects from the ion beam were observed. Energies of up to 500 eV were used, with a spread of incident flux between 10^{14} and 10^{15} ions cm^{-2} s^{-1}, and beam currents of typically 2–3 mA. Samples deposited on glass were cut for electrical measurements and films on silicon were dimpled and ion milled for transmission electron microscope (TEM) examination. All measurements were taken at room temperature. Composition and thickness details were obtained using a JEOL JSM 6400 scanning electron microscopy (SEM). A JEOL 3010 TEM was used for microstructural examination.

III. RESULTS AND DISCUSSION

Initially a series of Co-Ag and NiFe-Ag granular films was sputtered with concurrent application of the ion beam source at various energies. Straightforward sputtered samples (no IBAD) had compositions 67% Ag and 56% Ag, respectively. All the sputtering conditions remained constant. The GMR values were calculated according to $\Delta\rho/\rho = [\rho_{max} - \rho(H_{max})]/\rho(H_{max})$. For all these samples, the fields applied (2 T) produced GMR loops which were some way from saturation.

Figure 1 shows the variation of the electrical properties $(\rho,\Delta\rho,\Delta\rho/\rho)$ with ion beam voltage. There is a slight increase in the GMR for both film types at low energies and a subsequent decrease at higher energies. A possible explanation for the increase is that the additional energy could be causing enhanced surface mobility leading to segregation of the magnetic regions. The resultant size and dispersion of the mag-

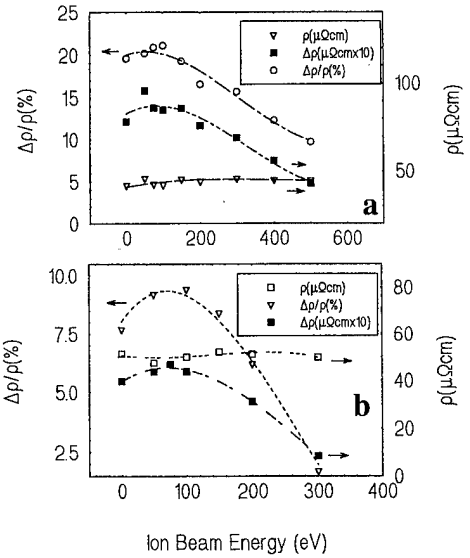


FIG. 1. Electrical properties of (a) Co-Ag and (b) Ag-NiFe alloys as a function of ion beam energy.

[a]Now at Dept. of Pure and Applied Physics, the Queen's University of Belfast, Belfast BT7 1NN, United Kingdom.

 0021-8979/96/79(8)/4939/3/$10.00 © 1996 American Institute of Physics

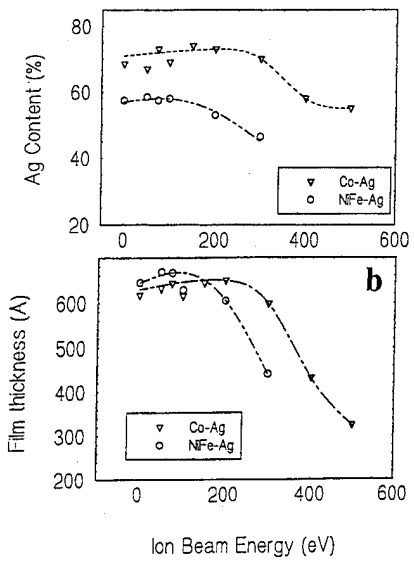


FIG. 2. (a) Ag content and (b) film thickness as a function of ion beam energy.

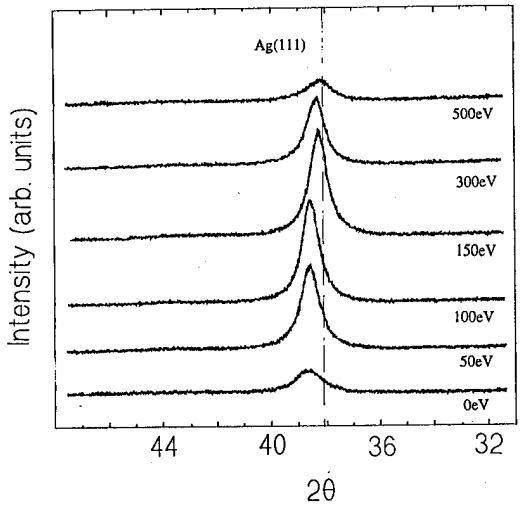


FIG. 3. High-angle x-ray (Cu $K\alpha$) diffraction of Co-Ag granular alloys.

netic particles would be more suitable for electron scattering. The zero-field resistivity remains virtually constant with energy, implying that significant numbers of extended defects are not being created, which would be the case for thermal treatments such as annealing.

There are several possible reasons why the GMR progressively decreases at higher beam energies. Firstly, the beam may continue to cause growth and segregation, leading to a decreased scattering cross section which is detrimental to the GMR. There is also the possibility of Ar incorporation in the film. Argon atoms could lodge in grain boundaries thus hindering the electron transport properties and growth mechanisms. However, again this is not an important factor as the resistivity has not increased. Finally, the ion beam may preferentially etch the Ag at higher energies, as the sputter yield is significantly higher (approximately 2.8 atoms/ion for Ag and 1.1 for Co at 500 eV, and 0.6 and 1.5 atoms/ion, respectively, at 200 eV).[7] It is known that GMR is strongly compositionally dependent[8] so even a small change in the stoichiometry could affect the GMR. Compositional examination using SEM did not detect any significant Ar, though a drop in the Ag content and film thickness (Fig. 2) was highlighted, indicative of preferential sputtering. This compositional change could adequately explain the drop in GMR, though the drop in GMR has been found to be almost independent of film thickness, at least for the thicknesses considered here.[9] Magnetization curves for films deposited at low energy are generally superparamagnetic in shape with similar M_s values. Increasing the ion beam energy leads to slightly more square loops due to the larger percentage of magnetic material. Preliminary measurements reveal that M_s remains relatively constant for energies less than 150 eV, at higher energies both the NiFe content and the M_s value increase. However, M_s for a film deposited with 500 eV ion beam assistance is significantly less than for a sputtered film with the same composition. This is indicative of a different magnetization process, perhaps the ion beam is affecting the dilution of the magnetic material in the Ag.

X-ray diffraction of a straightforward sputtered Co-Ag film (33% Co) [Fig. 3(a)] using Cu $K\alpha$ radiation shows only one peak at 38.7°, which corresponds to a d spacing of 2.32 Å. This can be interpreted as that of 111 Ag (2.36 Å) contracted by the presence of the smaller Co atoms. Increasing ion energy causes an increase in the intensity of this peak up to 150 eV [Figs. 3(b)–3(d)]. This correlates with the increase in GMR, as a result of growth and crystallization of Ag grains to form a more ordered structure. Further increasing the beam energy [Figs. 3(e)–3(f)] could hinder strong diffraction by causing some structural imperfections through increased atomic displacements and through the incorporation of impurities in the film. A slight shift (1.5%) towards the bulk Ag 111 d-spacing value was seen at energies above 100 eV, good evidence of elemental segregation.

Electron micrographs of sputtered films reveal a structure consisting of spherical 10–30 nm particles [Fig. 4(a)] whereas IBAD films at higher energies are composed of regions segregated into channels [Fig. 4(b)]. The photograph in Fig. 4(b) is taken from near the edge of the thinned sample. It seems possible from the contrast in the micrograph that the film is amorphous near the Si/film interface. That is, the ion beam is promoting an amorphous metastable structure which crystallizes on segregation.

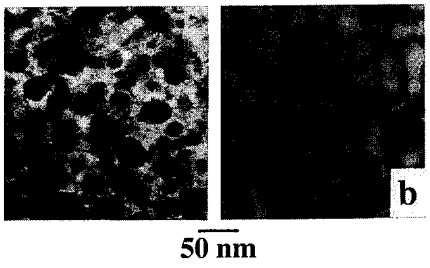


FIG. 4. TEM micrographs of Co-Ag sample (a) without ion beam assistance and (b) with ion beam (500 eV) assistance.

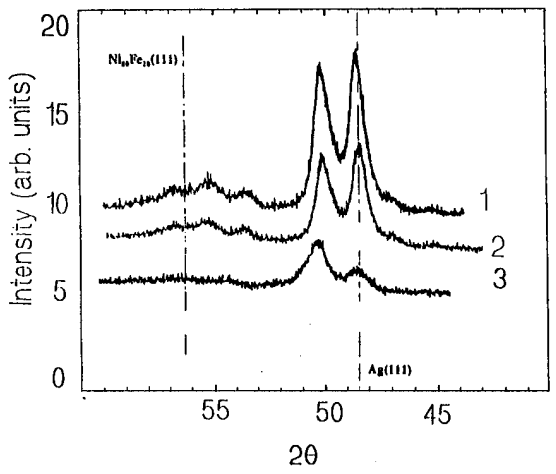


FIG. 5. High-angle x-ray diffraction of (Fe $K\alpha$) AgNiFe multilayers. Film 1 is as-sputtered, 2 has 2 min of substrate etch at 500 eV, and 3 has been continually ion beam-assisted throughout deposition.

A series of multilayer films [15×(30 Å NiFe, 30 Å Ag)] was deposited from alternately shuttered targets. Film 1 was deposited without ion beam modification. The substrate of film 2 was pre-etched at 500 eV for 2 min. The ion beam was applied at 250 eV during the entire course of deposition (500 s) of film 3 on a pre-etched substrate.

Although these films do not have suitable layer thicknesses for large GMR values, their structural modification is of interest in comparison with that of granular films. Figure 5 shows the high-angle x-ray diffraction (XRD) patterns (Fe $K\alpha$) for these films. Film 1 exhibits a clear Ag(111) peak at 48.5°. There are several other small maxima, one of which corresponds to the bulk NiFe(111) maximum at 56.3°. The peak at 50.1° is likely to be either a (111) satellite maxima, or originates from strained material at the interface of each layer. Further evidence for the superlattice structure is provided by electron microscopy and electron diffraction (to be published). For film 2, the diffracted intensity is slightly reduced, possibly indicating that the ion beam has roughened the substrate, resulting in a less-perfect crystal structure [i.e., a decrease in the preferred (111) texture] and increased scattering defects. This is quantified by a slight increase in the film resistivity. The Ag(111) peak is smaller for film 3, this is as a consequence of the IBAD energy being enough to sputter the film, resulting in thinner layers and less material. Also, the superlattice maxima intensity is further reduced for film 3, this could indicate that the constant IBAD affects the crystal structure, causing a further decrease in the texture and increased mixing at the interfaces. Initial low-angle measurements (to be published) are commensurate with this.

TEM micrographs of films 1 and 3 are shown in Fig. 6. The multilayer structure of the first film is clearly visible with well-defined NiFe and Ag layers. The orientation of the Ag and NiFe appears to be strongly influenced by the Si

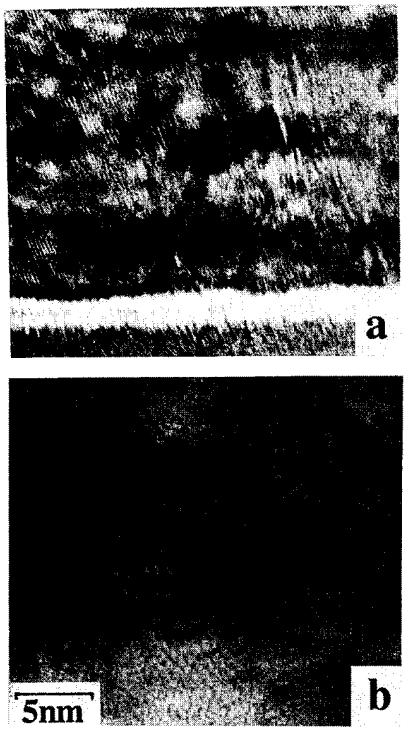


FIG. 6. TEM micrographs of AgNiFe multilayers (a) with and (b) without ion beam assistance. The Si substrate is visible in (a) but not in (b).

substrate, further indication of the superlattice structure. The structure of film 3 is somewhat different. The ion beam appears to have caused layer intermixing, leading to a structure which is reminiscent of the granular materials, with poorly defined layers and little preferred orientation. Further investigation of such materials is underway, including a comparison of this type of film to granular films formed by the annealing of multilayers.

ACKNOWLEDGMENTS

B. Ashworth is acknowledged for TEM sample preparation. The support of SERC/EPSRC through Grant No. GR/H65320 is acknowledged.

[1] M. N. Baibich, J. M. Broto, A. Fert, F. Nguyen Van Dau, F. Petroff, P. Etienne, G. Creuzet, A. Friederich, and J. Chazelas, Phys. Rev. Lett. **61**, 2472 (1988).
[2] M. E. Tomlinson, R. J. Pollard, D. G. Lord, and P. J. Grundy, J. Magn. Magn. Mater. **111**, 79 (1992).
[3] T. L. Hylton, K. R. Coffey, M. A. Parker, and J. K. Howard, Science **261**, 1021 (1992).
[4] A. E. Berkowitz, J. R. Mitchell, M. J. Carey, A. P. Young, S. Zhang, F. E. Spada, F. T. Parker, A. Hutten, and G. Thomas, Phys. Rev. Lett. **68**, 3745 (1992).
[5] S. S. P. Parkin, N. Moore, and K. P. Roche, Phys. Rev. Lett. **64**, 2304 (1990).
[6] S. M. Rossnagel and J. J. Cuomo, Vacuum **38**, 73 (1988).
[7] J. P. Biersack and W. Eckstein, Appl. Phys. A **34**, 73 (1984).
[8] J. A. Barnard, A. Waknis, M. Tan, E. Haftek, M. R. Parker, and M. L. Watson, J. Magn. Magn. Mater. **144**, L230 (1992).
[9] J. R. Mitchell and A. E. Berkwitz, J. Appl. Phys. **75**, 6192 (1994).

Dynamic hysteresis of two-dimensional magnetic islands with uniaxial anisotropy

C. N. Luse[a] and A. Zangwill
School of Physics, Georgia Institute of Technology, Atlanta, Georgia 30332

Frequency-dependent hysteresis for two-dimensional magnetic islands with uniaxial anisotropy is studied with a nearest-neighbor spin-one Ising model in the Bethe–Peierls approximation. A characteristic frequency for magnetization reversal is identified that depends on the island morphology only through the ratio θ/p of the coverage to the mean island perimeter roughness as measured by the density of unsaturated near-neighbor bonds. As a result, dissimilar hysteresis is predicted for large versus small and compact versus fractal islands. © *1996 American Institute of Physics.* [S0021-8979(96)67008-7]

Growth-induced surface roughness can influence magnetization processes in ultrathin films in a profound way. Hysteresis measurements of both perpendicular[1] and in-plane[2] anisotropy systems document this fact and so provide support for the notion that the behavior of magnetic moments at poorly coordinated step and edge sites can control magnetic response if the surface-to-volume ratio is not small. Although *quantitative* control of the two-dimensional (2D) roughness of an ultrathin film is difficult to achieve, scanning tunneling microscopy studies reveal that one can manipulate the *one-dimensional* edge roughness of 2D epitaxial islands deposited onto a single-crystal substrate since island size[3] and morphology[4] (fractal versus compact) depend sensitively on growth conditions. This suggests the likely value of a study of the hysteretic response of a collection of 2D magnetic islands deposited on a nonmagnetic substrate at temperatures well below the superparamagnetic blocking temperature. That the requisite magnetic islands can indeed be formed has been demonstrated by Elmers *et al.*[5] for the Fe/W(110) system.

We report here model mean field calculations of the frequency-dependent hysteresis from a system of 2D islands with specified perimeter-to-area ratio. We assume a strong uniaxial anisotropy (either perpendicular or in-plane) and focus on effects associated with the reduction of the net exchange experienced by edge moments rather than the different anisotropy they experience.[6] The problem then is equivalent to a spin *one* Ising model in a time-dependent field with total energy

$$E=-J\sum_{\langle ij\rangle} s_i s_j - H_0 \cos\,\omega t \sum_i s_i, \tag{1}$$

where J is a nearest-neighbor exchange energy, H_0 measures the external field strength, and the variables $s_i=0,\pm 1$ label whether the site i of a square lattice is unoccupied or occupied by an atom with spin up or down. The Bethe–Peierls approximation (BPA)[7] to this system replaces The complex set of N spin variables $\{s_i\}$ by seven quantities: the number densities of single sites occupied by up and down spins: n_+ and n_-, and the number densities of *pairs* of adjacent sites with all combinations of up spin, down spin, and unoccupied nearest neighbors: n_{++}, n_{--}, n_{+-}, n_{+0}, and $n_{-,0}$. From these, the coverage $\theta = n_+ + n_-$, magnetization density $m = n_+ - n_-$, perimeter density $p = n_{+0} + n_{-0}$, domain wall density $q=n_{+-}$, and island pair magnetization density $g=n_{++}-n_{--}$ are defined and assigned to the components of a vector $\mathbf{x}$. For $\omega=0$, the BPA yields a well-defined free energy $F(\mathbf{x})$ from which equilibrium properties are obtained by minimization.[7]

To treat $\omega\neq 0$, we adopt a kinetic Bethe–Peierls approximation (KBPA)[8] and let $\mathbf{x}(t)$ denote the statistical expectation value of the (now) time-varying variable set defined above. The time evolution of each $x_k \in \mathbf{x}(t)$ is determined from

$$\tau\frac{d}{dt}x_k(t)=\sum_{\Delta}\Delta_k\sum_{\mathbf{p}\in\Delta} n[\mathbf{p}|\mathbf{x}(t)]e^{-E(\mathbf{p})/k_BT}, \tag{2}$$

where Δ is a vector of integers that specifies the change $\mathbf{x}\rightarrow\mathbf{x}+\Delta/N$ in the state of the system associated with a spin flip event. An isolated spin is presumed to flip spontaneously in zero field after a mean time τ while the configuration-dependent energy barrier $E(\mathbf{p})$ to flip an arbitrary spin is estimated from the BPA to Eq. (1). The combinatoric factor $n[\mathbf{p}|x(t)]$ is the BPA to the number density of sites with local arrangements of spins $\mathbf{p}$ compatible with Δ given that the system average is fixed at $\mathbf{x}(t)$. The sum over $\mathbf{p}$ indicates that several spin configurations generally are consistent with a given value of Δ. Our calculations regard the coverage θ and island roughness p as independent free parameters. The remaining variables $m(t)$, $q(t)$, and $g(t)$ are determined from a numerical solution to the coupled nonlinear set (2) using Gear's method[9] for stiff differential equations. We judge that steady state has been achieved when $|[x_k(t) - x_k(t+2\pi/\omega)]/x_k(t)|\leq 10^{-5}$ for all three variables and compute hysteresis loop areas from $m(t)$ and $H(t)$ using the formula $A=\oint m dH$. All the results reported here use the fixed values $J/k_BT = 1.0$ and $H_0/k_BT = 1.5$.

To appreciate the origin of *static* hysteresis in this model, the inset to Fig. 1 shows the BPA free energy as a function of m at $H=0$ and low temperature. Application of a field $+H_0$ tips the curve so that the absolute minimum occurs at the saturation magnetization $+m_0$. The curve rocks to the left and $-m_0$ eventually becomes the absolute minimum as the field is reduced and then reversed adiabatically. A square hysteresis loop results because the magnetization

[a]Present address: ExecuTrain, Inc., 1000 Abernathy Road, Atlanta, GA 30328.

 0021-8979/96/79(8)/4942/3/$10.00 © 1996 American Institute of Physics

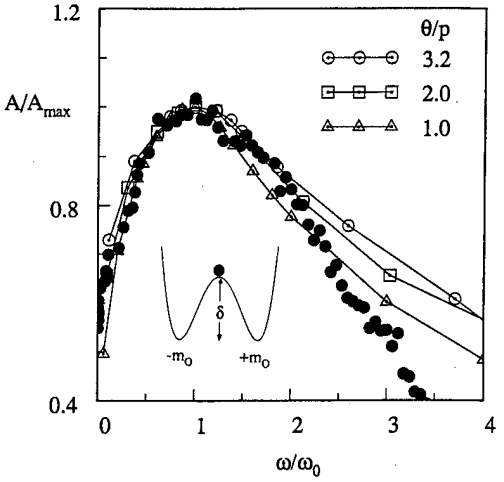


FIG. 1. Scaled hysteresis loop areas plotted vs scaled frequency for several values of θ/p. Different choices of θ and p yield curves exactly coincident with those shown so long as their ratio is fixed. The filled circles are experimental data for Co/Cu(001) from Ref. 10. Inset: effective BPA free energy $F(m|H)$ when $H=0$. The parameters δ and m_0 vary with θ and p. The text discusses the instantaneous magnetization (black dot) as a Newtonian particle that slides along this curve.

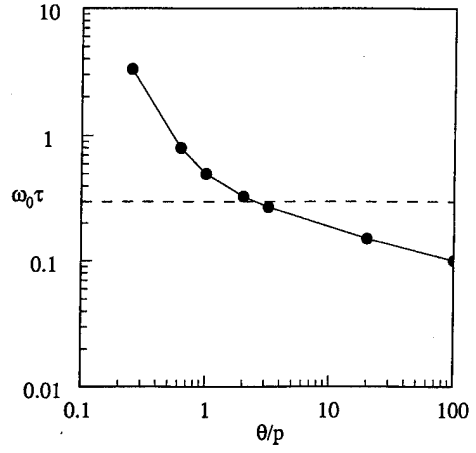


FIG. 2. Calculated dependence of the dimensionless resonant frequency $\omega_0\tau$ on the scaling parameter θ/p (solid curve). Dashed line is drawn at $\omega\tau=0.3$.

takes the final abscissa value of a classical particle that slides down to the nearest local minimum of this energy curve. In fact, the barrier between the two minima in Fig. 1 is an artifact of the mean field approximation and there is no true thermal activation. We thus are free to *reinterpret* the asymmetric double-well structure of $F(m|H)$ as arising from the presumed uniaxial anisotropy well below the superparamagnetic blocking temperature. Any change in "temperature" in Eq. (2) merely renormalizes H_0 and the magnitude of an effective anisotropy constant related to J. In this language, all the effects we report below arise from the parametric dependence of the BPA free energy on the coverage and perimeter density.

Figure 1 shows normalized loop areas $A(\omega)$ calculated for several values of the ratio of the coverage θ to the edge roughness p for our problem along with Kerr-effect data of Jiang *et al.*[10] for ~3 monolayers of Co/Cu(001). The agreement may well reflect the fact that the top of an as-grown ultrathin magnetic film is well described as a collection of two-dimensional islands. But each theoretical point on this diagram corresponds to results obtained from many different choices of θ and p. That is, the curves of $A(\omega)$ are *identical* so long as the ratio θ/p is held fixed. The latter thus can be chosen to parameterize both the shape of the curves and the value of the frequency ω_0 at which the loop area maximum occurs (Fig. 2).

At fixed coverage, the calculated loop areas exhibit a nontrivial dependence on p (Fig. 3) for different values of the frequency. The static loop area (see caption for frequency labeling) decreases with increasing roughness and vanishes above a coverage-dependent critical value of perimeter density p_c. $A(p)>0$ and is monotone decreasing at the lowest frequencies but develops a simple maximum as the frequency increases. At still higher values of ω, a discontinuity appears in $A(p)$ that eventually evolves to a cusp singularity. At the largest frequencies investigated, the cusp occurs precisely at p_c and $A(p)$ is composed of two parabolic arcs.

To interpret these results, it is useful to regard the frequency response of the amplitude and phase of the magnetization $m(t)$ with respect to the magnetic field $H(t)$ as analogous to the corresponding quantities for the displacement of a damped, driven oscillator with respect to its driving force. So long as $\omega<\omega_0$, the magnetization makes large amplitude excursions between the two minima at $\pm m_0$ in Fig. 1. One checks that the loop area increases in this regime simply because the phase of $m(t)$ progressively lags the phase of $H(t)$ as ω increases. The area is maximal at $\omega=\omega_0$ when the phase lag is $\pi/2$ and decreases thereafter as the excursions of $m(t)$ from zero become smaller and smaller with increasing frequency.

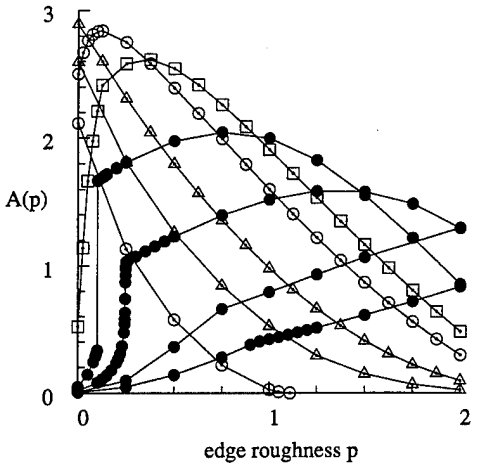


FIG. 3. Calculated hysteresis loop areas $A(p)$ at $\theta=1/2$ plotted versus perimeter density p for different values of dimensionless sweep frequency $\omega\tau$. Beginning at the bottom of the figure at $p=1$ and moving upward in order, the curves labeled with open symbols correspond to $\omega\tau$ values of 0.0 (circles), 0.03 (triangles), 0.1 (triangles), 0.3 (circles), and 0.5 (squares). Beginning at the top of the figure at $p=1$ and moving downward in order, the curves labeled with closed circles correspond to $\omega\tau=1.0$, 2.0, 5.0, and 10.0.

The resonant frequency ω_0 can be identified with the inverse of the characteristic time for the 'particle' in the inset to Fig. 1 to slide from the unstable maximum to one of the minima of the effective free energy. The variation of ω_0 depicted in Fig. 2 then suggests that either δ or m_0 or both decrease as θ/p decreases. To connect this notion more directly with the surface morphology, we offer two alternative spatial interpretations of our mean field theory. Consider a two-dimensional island composed of S atoms. The fractal dimension d_f and perimeter dimension d_p of the island are defined by the relations $S \propto R^{d_f}$ and $P \propto R^{d_p}$, where R is the radius of a circle that completely encloses the island and P is the total number of perimeter atoms. It follows that $R^{d_f-d_p}=\theta/p$ and $N=\theta/R^{d_f}$, where N is the total island number density. Now suppose the total coverage is held fixed. For compact islands, the resonant frequency decreases monotonically as the average island size increases. Alternatively, for fixed θ and fixed N, the resonant frequency increases monotonically as the fractal character of each island increases. In either case, the value of ω_0 correlates with the average coordination number of occupied lattice sites.

This idea is sufficient to develop a qualitative understanding of the behavior seen in Fig. 3. The magnetization $m(t)$ is nearly π out-of-phase with $H(t)$ at the highest frequencies where ω is larger than any value of ω_0. The details of the effective potential are not important in this regime, but the mere fact that $d\omega_0/dp>0$ (so that $\omega-\omega_0$ decreases) guarantees that $dA/dp>0$ since the phase shift, in turn, retreats toward $\pi/2$. The latter is achieved when $\omega=\omega_0$ so $A(p)$ exhibits a maximum whenever a horizontal line drawn at the sweep frequency ω intersects the curve in Fig. 2. Of course, $m(t)$ and $H(t)$ are nearly in-phase when ω is smaller than any value of ω_0 and the smallest loops will arise when δ and m_0 are minimal. The fact that this occurs for maximal edge roughness (so that $dA/dp<0$) is most clear from the static case since the BPA to the Ising model[7] exhibits no spontaneous magnetization for coordination numbers less than two.

The discontinuity and kink features are a bit more subtle. Suppose the relevant feature occurs at the frequency dependent value p_0. It turns out that the hysteresis loops at fixed ω are asymmetric, i.e., centered about a nonzero value of magnetization, for all $p<p_0$ but are symmetric with respect to $m=0$ for all $p>p_0$. The "capture" of $m(t)$ in one well (asymmetric case) in not unreasonable since the discontinuity/kink anyway occurs only when $\omega \gg \omega_0$ and the total excursion of $m(t)$ is not large. The decrease in δ that accompanies increased edge roughness then makes the "escape" of the magnetization (symmetric case) readily explicable if not its signature as a nonanalyticity in $A(p)$.

In conclusion, we have presented the results of Bethe–Peierls-type mean field calculations for the dynamic magnetic hysteresis expected from a collection of two-dimensional islands after deposition onto a nonmagnetic substrate. The islands are assumed to be superparamagnetic and maintained at low temperature so that thermal magnetization reversal does not occur. The frequency-dependent loop areas and resonant frequencies were found to depend only on the ratio of the coverage to the mean island perimeter density in this approximation. The systematic variations we predict are amenable to direct experimental test because variations in substrate temperature and deposition flux permit (nearly) independent control of both the total island number density and the island edge roughness.

ACKNOWLEDGMENTS

This work was supported by the U.S. Department of Energy under Grant No. DE-FG05-88ER45369. The authors thank the authors of Ref. 10 for permission to reproduce some of their unpublished data.

[1] P. Bruno, G. Bayreuther, P. Beauvillain, C. Chappert, G. Lugert, D. Renard, J. P. Renard, and J. Sieden, J. Appl. Phys. **68**, 5759 (1990).
[2] Y.-L. He and G.-C. Wang, J. Appl. Phys. **76**, 6446 (1994).
[3] J. A. Stroscio and D. T. Pierce, Phys. Rev. B **49**, 8522 (1994).
[4] R. Q. Hwang, C. Günther, J. Schröder, S. Günther, E. Kopatzki, and R. J. Behn, J. Vac. Sci. Technol. A **10**, 1970 (1992); M. Bott, T. Michely, and G. Comsa, Surf. Sci. **272**, 161 (1992).
[5] H. J. Elmers, J. Hauschild, H. Höche, U. Gradmann, H. Bethge, D. Heuer, and U. Köhler, Phys. Rev. Lett. **73**, 898 (1994).
[6] A. S. Arrott and B. Heinrich, J. Magn. Magn. Mater. **93**, 571 (1991).
[7] K. Huang, *Statistical Mechanics*, 2nd ed. (Wiley, New York, 1987). See also, F. Ducastelle, Prog. Theo. Phys. Suppl. **115**, 255 (1994).
[8] Y. Saito and R. Kubo, J. Status Phys. **15**, 233 (1976). See also Y. Saito and H. Müller-Krumbhaar, J. Chem. Phys. **70**, 1078 (1979).
[9] W. C. Gear, *Numerical Initial Value Problems in Ordinary Differential Equations* (Prentice–Hall, Englewood Cliffs, NJ, 1971).
[10] Y.-L. He and G.-C. Wang, Phys. Rev. Lett. **70**, 2336 (1993); Q. Jiang, H.-N. Yang, and G.-C. Wang (unpublished).

Uniaxial magnetic anisotropy of iron thin films deposited by oblique incidence of deposition particles

Y. Hoshi and E. Suzuki
Faculty of Engineering, Tokyo Institute of Polytechnics, Atsugi, Kanagawa 243-02, Japan

M. Naoe
Faculty of Engineering, Tokyo Institute of Technology, Oh-okayama, Meguro-ku, Tokyo 152, Japan

Uniaxial magnetic anisotropy induced in iron thin films by the oblique incidence of deposition particles was investigated by computer simulation. In the simulation, the self-shadowing effect was considered mainly to explain changes in the magnetic anisotropy of iron films with the incident angle. The simulated grain shape in the film changes significantly with the incident angle of deposition particles. Grains elongated in a direction normal to the incidence direction of depositing particles were clearly observed in simulated film deposited with an incidence angle around 60°. However, the film deposited at an incidence angle of 80° had columnar grains separated from each other and inclined to the incidence direction. Changes in the uniaxial magnetic anisotropy of the film can be qualitatively explained by the shape anisotropy of these grains in the film. The decrease in saturation magnetization of these films with incident angle seems to be mainly caused by the formation of a porous film. © *1996 American Institute of Physics.* [S0021-8979(96)67108-6]

I. INTRODUCTION

Many reports on the computer simulation of microstructures in film treated by the oblique incidence of deposition have appeared in the literature.[1–12] The formation of inclined columnar structures in film is mainly caused by the self-shadowing effect in growing films.

It is well known that iron film deposited by the oblique incidence of particles has in-plane uniaxial magnetic anisotropy[13,14] and its easy axis changes from the normal to the parallel direction of incidence particles as incident angle increases from 60° to 80°.[13] These changes in the direction and energy of magnetic anisotropy are thought to be caused by changes in the microstructure of the film due to the incident angle of deposition particles.[2,4,13,14] However, it was still not clear how the grain structure in the film plane changes with the incident angle of particles as a result of the self-shadowing effect, since the dimensions of simulated film used were too small. In this study, we investigated the self-shadowing effect on the in-plane microstructure of the film by using three-dimensional Monte Carlo simulation based on a simple hard sphere model that showed that changes in the uniaxial magnetic anisotropy of iron film with an incident angle were mainly caused by changes in the grain shapes in the film.

II. SIMULATION MODEL

In this study, a Monte Carlo simulation model similar to the one Henderson *et al.* reported[1] were used, e.g., we assumed that the depositing atoms were hard spheres and allowed to relax to the extent that each moved to the nearest position where it was able to make contact with three atoms (zero migration case). The direction of incidence of depositing atoms on the substrate was in the x-z plane as shown in Fig. 1. In the calculation, atoms with a radius 1.26 Å were deposited on a 725 Å×725 Å substrate. Although the total lack of relaxation in the adatom was not physically realistic, it was set at a limit where the self-shadowing effect became the most pronounced.

When the migration of the adatom was taken into consideration, incident atoms migrated across the surface jumping from site to site as shown in Fig. 1. When the adatom reached a site where it contacts with more than four atoms during migration, the adatom was assumed to be fixed in that position.

III. RESULTS AND DISCUSSION

It is well known that the uniaxial magnetic anisotropy of iron thin films deposited by the oblique incidence of particles changes significantly with the incidence angle as shown in Fig. 2.[13] Films deposited at an incidence angle below 70° have uniaxial magnetic anisotropy with its easy axis normal

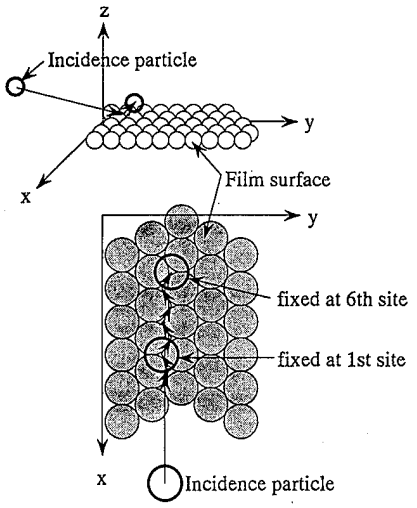


FIG. 1. Hard sphere deposition model used in this study. Adatom migration length was changed as shown in the figure.

 0021-8979/96/79(8)/4945/3/$10.00 © 1996 American Institute of Physics

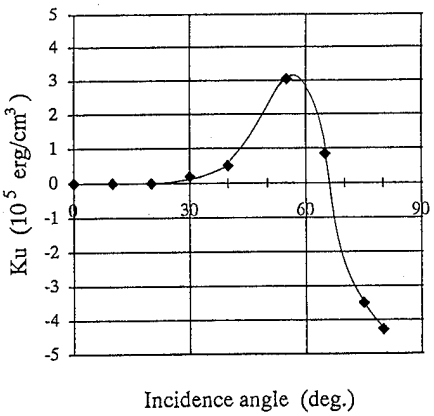


FIG. 2. Changes in uniaxial magnetic anisotropy energy K_u of iron film with incidence angle reported by West (Ref. 13).

to the direction of incidence. However, films deposited at an incidence angle above 80° have uniaxial magnetic anisotropy with its easy axis parallel to the plane of incidence.

Figure 3 shows the film structures: (a), (c), (e): cross section [parallel to plane of incidence (x-z plane)] and (b), (d), (f): in-plane section [parallel to substrate (x-y plane)]

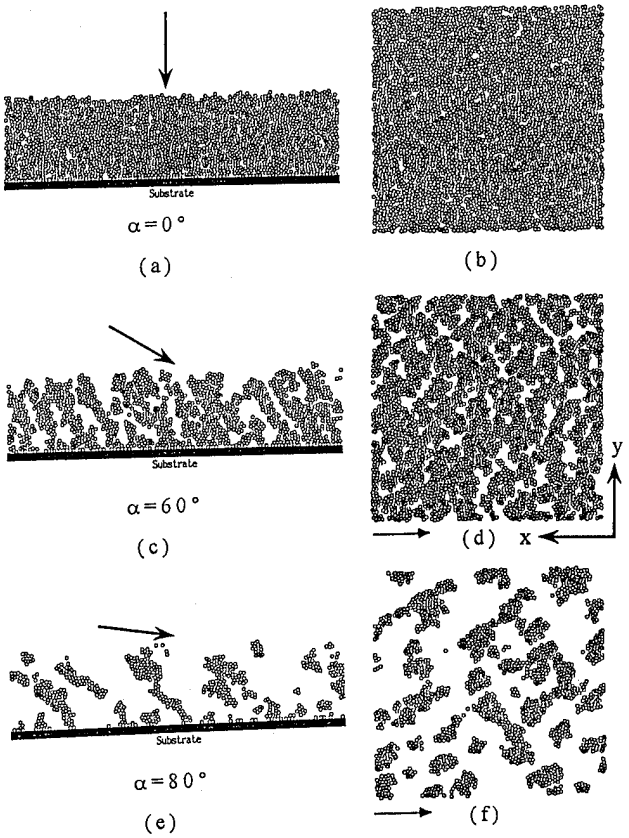


FIG. 3. Structures of simulated films produced at incidence angles 0°: (a), (b), 60°: (c), (d), and 80°: (e), (f). (a), (c), and (e) are cross sections of the film parallel to the plane of incidence (x-z plane) and (b), (d), and (f) are in-plane sections parallel to the substrate (x-y plane).

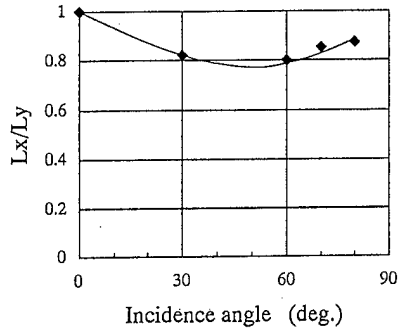


FIG. 4. Changes in grain shapes L_x/L_y with incidence angle, where L_x and L_y are mean grain size in x and y direction, respectively.

calculated for various oblique incidence angles of deposited particles. In calculation, surface migration of deposited atoms was not considered. It is evident from the figure that films deposited at an oblique angle around 60° have clear elongated grains. This grain can create large uniaxial shape magnetic anisotropy in film with its easy axis normal to the incident direction of deposited particles. To clarify how changes in grain shape are related to incident angle, the ratio of L_x to L_y was calculated, where L_x and L_y were mean grain size in the x and y directions, respectively. Figure 4 shows changes in the L_x/L_y ratio with incidence angle α. It is clear from the figure that ratio L_x/L_y assumes a minimum value at an incidence angle around 60°. This indicates that elongated grains in the y direction were formed in the film. This result can be explained as follows: grains in the film lose continuity in the parallel direction much more easily than in the normal direction to the incident direction of particles, since the shadow region for depositing particles only expands in a direction parallel to the plane of incidence. Therefore, increase in uniaxial magnetic anisotropy energy with increase in incidence angle α from 0 to 60° is due to the formation of elongated grains shown in Figs. 3(c) and 3(d).

Further increases in incident angle causes the shadowing region on the film surface to extend greatly so that the continuity of grains even in the normal direction will be lost due to the self-shadowing effect. As a result, film deposited at an

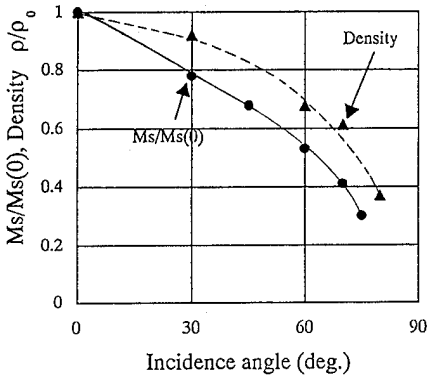


FIG. 5. Changes in saturation magnetization $M_s/M_s(0)$ of iron films with incidence angle reported by Hashimoto *et al.* (Ref. 14). Changes in density $\rho/\rho(0)$ of simulated films with incidence angle are also shown.

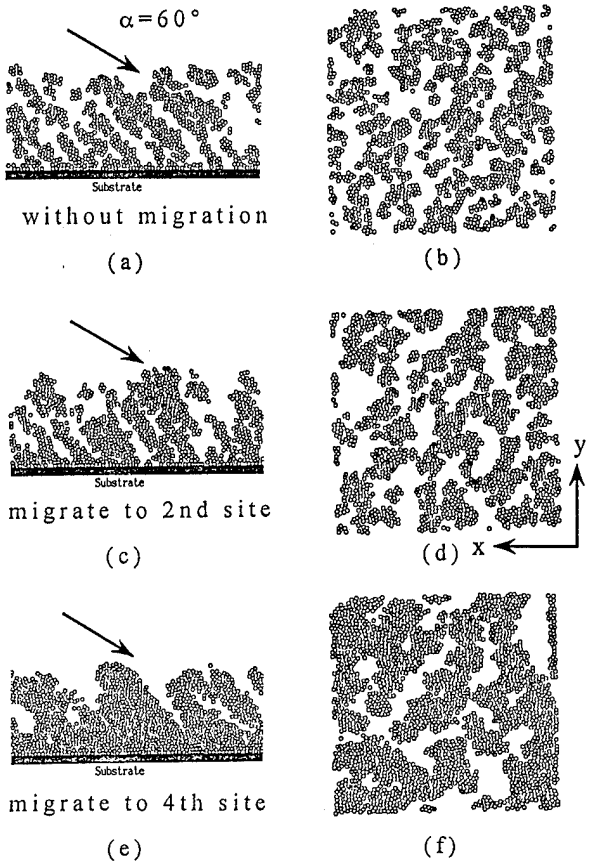


FIG. 6. Simulated films structures produced at incidence angle of 60° for three kinds of adatom migration length [(a)(b): fixed at first site, (c)(d): fixed at second site, and (e)(f): fixed at fourth site as shown in Fig. 1].

incidence angle of 80° is composed of inclined columnar grains that are separated from each other as shown in Figs. 3(e) and 3(f). This kind of film structure induces uniaxial magnetic shape anisotropy with its easy axis parallel to the plane of incidence of deposition particles.

A change in saturation magnetization M_s of iron films with the incidence angle shown in Fig. 5 was reported by Hashimoto *et al.*[14] Changes in density in the simulated film due to incidence angle are also shown in Fig. 5. M_s and density decreases in similar manner with incident angle. This suggests that the decrease in M_s of iron film due to incidence angle was mainly caused by a reduction in film density.

Figure 6 shows simulated film structures calculated for various surface migrations of deposited adatoms. It is clear from the figure that both film density and grain size increase monotonously as surface migration increases. The grain shape in the x-y plane (L_x/L_y ratio), however, barely changes when the migration length of the deposition particle increases from two to four steps.

IV. CONCLUSIONS

To explain uniaxial magnetic anisotropy induced in iron films deposited by oblique evaporation, film structures were simulated using Monte Carlo simulation by depositing atoms on a 725 Å×725 Å substrate. In the simulation, the self-shadowing effect was the only mechanism responsible for formation of voids in the film. The shape of simulated grain in the film changed significantly with the incident angle of deposition particles. Changes in the uniaxial magnetic anisotropy of the film deposited by oblique incidence can be qualitatively explained by changes in the shape anisotropy of these grains in the film. The decrease in saturation magnetization of iron film due to the incident angle agreed well with the decrease in film density. Therefore, the self shadowing effect is the most important mechanism causing uniaxial magnetic anisotropy in iron film deposited by oblique evaporation.

[1] D. Henderson, M. H. Brodsky, and P. Chaudhari, Appl. Phys. Lett. **25**, 641 (1974).
[2] A. G. Dirks and H. J. Leamy, Thin Solid Films **47**, 219 (1977).
[3] S. Kim, D. J. Henderson, and P. Chaudhari, Thin Solid Films **47**, 155 (1977).
[4] H. J. Leamy, G. H. Gilmer, and A. G. Dirks, Current Topics Mater. Sci. **6**, 311 (1980).
[5] L. Bangjun and H. A. Macleod, SPIE **540**, 150 (1985).
[6] K.-H. Muller, J. Appl. Phys. **58**, 2573 (1985).
[7] K.-H. Muller, J. Vac. Sci. Technol. A **4**, 184 (1986).
[8] B. J. Bartholomesz, SPIE **821**, 174 (1987).
[9] D. J. Smith, SPIE **821**, 120 (1987).
[10] J. S. Gau and B. Liao, Thin Solid Films **176**, 309 (1989).
[11] S. Muller-Pfeiffer, H. J. Amklam, and W. Haubenreisser, Phys. Status Solidi B **49**, 491 (1990).
[12] S. Muller-Pfeiffer, H. van Kranenburg, and J. C. Lodder, Thin Solid Films **213**, 143 (1992).
[13] F. G. West, J. Appl. Phys. **35**, 1827 (1964).
[14] T. Hashimoto, K. Hara, K. Okamoto, T. Hashimoto, and H. Fujiwara, J. Phys. Soc. Jpn. **43**, 1415 (1973).

Complex anisotropies in sputtered $Co_{90}Fe_{10}$ alloy thin films (abstract)

E. J. Yun, W. Win, and R. M. Walser
I/UCR Center for Magnetics, The University of Texas at Austin, Austin, Texas 78712

Among all the known magnetic materials with vanishingly small magnetostriction, alloys with the composition $Co_{90}Fe_{10}$ have the highest magnetization at 300 K. Despite this combination of useful properties, thin films of these alloys have been little studied. This study investigated the magnetic characteristics of $Co_{90}Fe_{10}$ alloy thin films deposited by rf diode sputtering. The hysteresis loops of nominal 1000-Å-thick $Co_{90}Fe_{10}$ films deposited in $\approx$150 Oe planar field exhibited complex biaxiality. Two, orthogonal easy axis loops with different coercivities were observed. The direction corresponding to the hysteresis loops with the smallest (largest) coercivity are referred to as the soft (easy) axis. Dual hard axes were found at $\pm 68°$ on either side of the easy axis. Similar biaxial hysteresis loops were observed in $Co_{90}Fe_{10}$ films deposited by sequential sputtering from pure Co and Fe targets on static or rotating substrates, and in films deposited from a $Co_{90}Fe_{10}$ alloy target on stationary substrates. The magnetization and resistivity of the sequentially sputtered films were 19.66 kG and 18.4 $\mu\Omega$ cm, while those deposited from the alloy target were 19.00 kG and 14.5 $\mu\Omega$ cm. The biaxiality was sensitive to a number of parameters which appeared to destabilize the soft axis state compared to the hard axis states. With increasing film thickness (to 3400 Å), the biaxiality disappeared, and films deposited under similar conditions exhibited rotatable anisotropy. The biaxiality could also be reduced, and the coercivity increased, by increasing the magnetic bias applied during deposition. Films annealed at 370 °C became uniaxial when a 1.3 kOe field was applied parallel to the easy axis, and became isotropic when the field was parallel to the hard axis. The biaxiality was enhanced, and H_c reduced, by depositing 1000-Å-thick $Co_{90}Fe_{10}$ films onto a 500 Å 80Ni20Fe underlayer. In all cases, whenever the biaxiality was eliminated, the films exhibited a rotatable uniaxial anisotropy. The biaxiality of these films likely has its origin in the coupling of two uniaxial anisotropies as previously analyzed.[1] The deposited films are highly polycrystalline. In addition, the symmetries of the planar magnetic state obtained were the same for crystalline and amorphous substrates. Thus, it is unlikely that either uniaxial anisotropy is due to magnetocrystallinity, but are probably induced. The experimental trends observed in the study can in principle be understood in terms of a two layer model in which a rotatable, stress induced uniaxial anisotropy in an underlayer, is exchange coupled to the field induced uniaxial anisotropy of an overlayer. In this model the complex biaxiality is modified by experimental parameters which modify the relative strength and coupling strength of these anisotropies. © *1996 American Institute of Physics.* [S0021-8979(96)67508-3]

[1] E. J. Torok, H. N. Oredson, and A. L. Olson, J. Appl. Phys. **35**, 3469 (1964); A. Yelon, *ibid.* **38**, 325 (1967).

 0021-8979/96/79(8)/4948/1/$10.00 © 1996 American Institute of Physics

Ferromagnetic resonance studies of noble metals based sandwiches

Y. D. Wang, L. Y. Chen, Y. X. Sui,[a] S. M. Zhou, Y. Wang, Y. X. Zheng, Y. H. Qian, and Q. Y. Jin

T.-D. Lee Physics Laboratory and Department of Physics, Fudan University, Shanghai 200433, People's Republic of China

In this paper we have prepared Fe/Cu, Ag, Au/Fe sandwiches by ion beam sputtering and studied the interlayer coupling behavior by ferromagnetic resonance technique. In these sandwiches the Fe and noble metal layers are polycrystalline in the textures of (110) and (111), respectively. It is found that the in-plane resonance field and the linewidth oscillate as a function of nonmagnetic layer thickness in a period of about 1.0 nm for Fe/Cu, Au/Fe structures, and 1.4 nm for Fe/Ag/Fe system. It is suggested that the interlayer coupling strength between the ferromagnetic layers oscillates in the same period with the resonance field. An in-plane anisotropy was found in Fe/Ag/Fe system.
© *1996 American Institute of Physics.* [S0021-8979(96)67208-1]

I. INTRODUCTION

The interlayer coupling between ferromagnetic layers separated by nonmagnetic metal spacer layers has attracted much attention because of its importance in basic research and in applications. For example, the antiferromagnetic coupling can induce giant magnetoresistance.[1] Because the Fermi surfaces for Cu, Ag, and Au are simpler and similar to each other they are usually used as spacer layers.[2] Furthermore, many experiments have shown that the noble metal based multilayers can exhibit large magnetoresistance changes.[1] For sandwich structures, many methods have been employed to investigate the interlayer coupling behavior, such as ferromagnetic resonance (FMR),[3] Brillouin light scattering,[4] surface magneto-optical Kerr effect (SMOKE),[5] magnetoresistance (MR), and vibrating sample magnetometer. With FMR technique, both the strength and the sign of the interlayer coupling can be known. Moreover, it is usually used to study the anisotropy in layered structures. In this paper we will study the interlayer coupling behavior in Fe/Cu, Ag, Au/Fe sandwiches with FMR technique. It is interesting to find that the in-plane resonance field and the linewidth oscillate as a function of nonmagnetic layer thickness.

II. EXPERIMENTS AND DISCUSSIONS

All samples were deposited onto Si(100) slices by ion beam sputtering technique from iron, copper, silver, and gold targets with an area of 8×10 cm^2, in the structure order of X(1.0 nm)/Fe(4.0 nm)/X/Fe(4.0 nm)/X(10.0 nm)/Si, where X refers to Cu, Ag, and Au, respectively. The top layer was used to avoid oxidation. The background pressure was 7×10^{-5} Pa and the Ar pressure 2×10^{-2} Pa during deposition. The deposition rates of Fe, Cu, Ag, and Au were 0.08, 0.15, 0.18, and 0.15 nm/s, respectively. The layer thicknesses were controlled through the rotation of target holder and shutters by a microcomputer. X-ray diffraction showed that for these samples the Fe and noble metal layers are polycrystalline in the textures of bcc (110) and of fcc (111), respectively.

The electronic paramagnetic resonance spectrometer of model ER-200D-SRC was used to measure the room-temperature FMR spectra with a microwave frequency of 9.78 GHz under an applied magnetic field parallel to the film plane.

As shown in Figs. 1 and 2, for Fe/Cu/Fe and Fe/Au/Fe structures the resonant field H_{res} in the parallel geometry showed oscillation as a function of nonmagnetic layer thickness with a period of about 1.0 nm, for Fe/Ag/Fe system the period is 1.4 nm, as presented in Fig. 3. The resonance linewidth ΔH also oscillates in the same period as the resonance field. According to theoretical model proposed by Cochran *et al.*[6] it can be considered that the oscillation of H_{res} is due to the interlayer coupling oscillation. In fact, the oscillation of the resonant field might be produced by the oscillation of anisotropy energies due to interface effect. The interface effect originates from the interlayer coupling. So we can suggest that the oscillation of the resonant field is a result of the oscillation of the interlayer coupling strength. Moreover, the oscillation of the resonance field has also been observed in Fe-Ni/Cr/Fe-Ni systems[7] and the correlated oscillations between the resonance field and the linewidth have been also observed in previous work about Fe-Ni/Cu multilayers by

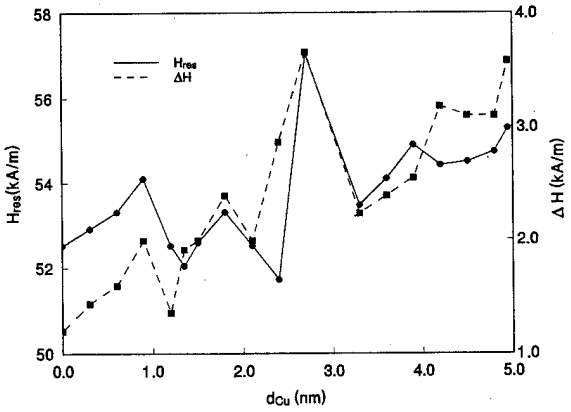


FIG. 1. The d_{Cu} dependence of the resonance field H_{res} and the resonance linewidth ΔH in the parallel geometry for Fe(4.0 nm)/Cu/Fe(4.0 nm) sandwiches.

[a]Center for Materials Analysis and Measurement, Nanjing University, Nanjing 210093, People's Republic of China.

 0021-8979/96/79(8)/4949/2/$10.00 © 1996 American Institute of Physics

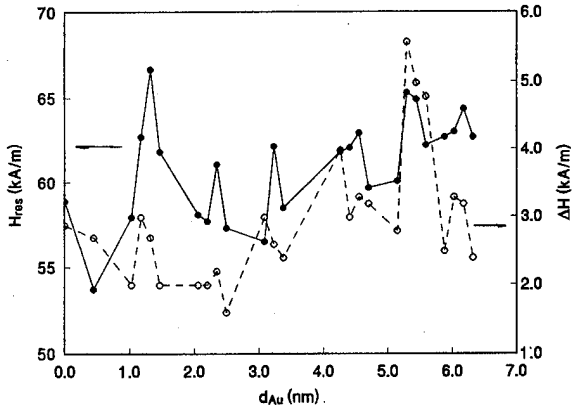


FIG. 2. The d_{Au} dependence of the resonance field H_{res} and the resonance linewidth ΔH in the parallel geometry for Fe(4.0 nm)/Au/Fe(4.0 nm) sandwiches.

Zhou *et al.*[8] They were all attributed to the oscillatory interlayer coupling strength.

In the early stages, the oscillatory coupling was explained as a RKKY-like interaction. Recently several studies showed that the quantum well states exist in noble metal films deposited on ferromagnetic substrates,[9] that is to say, the s,p-like quantum well states in Cu, Ag, and Au layers were found by the inverse photoemission in Cu, Ag, or Au/Fe structures. The spin-polarized quantum well states in noble metal layers have been proposed to be carriers of the oscillatory interlayer coupling.[10–13] For the quantum well states, the oscillation period $\Lambda = \pi/|k_F - k_{BZ}|$, where k_F and k_{BZ} are wave vectors on the Fermi surface and at the FBZ in the oriented normal direction in nonmagnetic layers. For Cu, Ag, and Au in the texture of (111), Λ is found to be 0.95, 1.4, and 1.0 nm.[2] It is obvious that the observed oscillation periods in the above series of sandwiches are close to the corresponding calculated data. It is noted that the interface roughness acts as a low-pass filter for the oscillation frequency[14] and does not play any role on the long oscillation period for (111) direction of Ag layers. In addition to the resonant field,

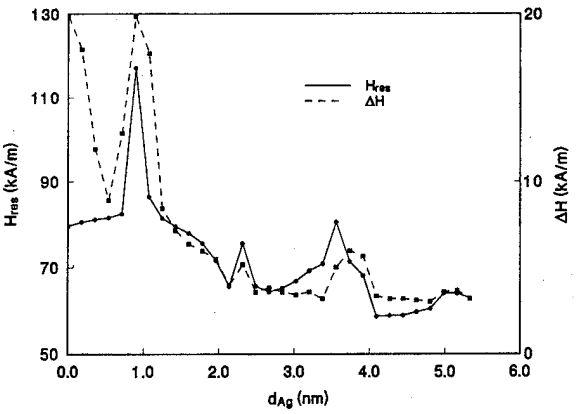


FIG. 3. The d_{Ag} dependence of the resonance field H_{res} and the resonance linewidth ΔH in the parallel geometry for Fe(4.0 nm)/Ag/Fe(4.0 nm) sandwiches.

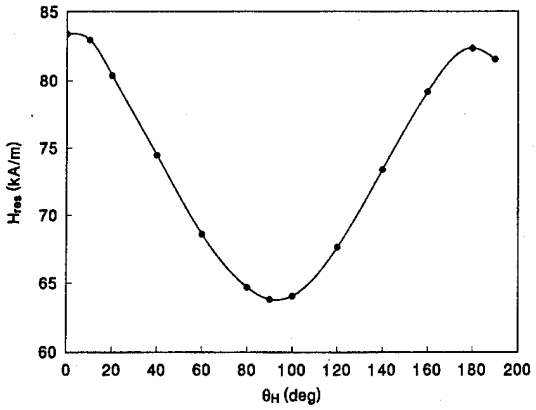


FIG. 4. The angle dependence of the in-plane resonance field in the range of 0–180° for Fe/Ag/Fe sandwiches, which begins at an arbitrary position.

for above structures the polar Kerr rotation and ellipticity were also observed to oscillate respectively in a same period as the resonant field with the variation of the nonmagnetic layer thickness, which will be discussed elsewhere.

We have also studied the behavior of the in-plane anisotropy in Fe/Ag/Fe structures. As shown in Fig. 4 the resonance field has a maximum in the angle range of 180°. This in-plane anisotropy might depend on the condition in sputtering process, including the energies of Ar^+ and incident angle. However this parameters influence the anisotropy needs further detailed work.

In conclusions, we have prepared three series of Fe/Cu/Fe, Fe/Ag/Fe, and Fe/Au/Fe sandwiches by ion beam sputtering and studied the interlayer coupling behaviors with FMR technique. It is interesting to find that for these samples, the in-plane resonant field and the linewidth oscillates with the same periods of 1.0, 1.4, 1.0 nm, respectively. It is suggested that the interlayer coupling oscillates in strength as a function of nonmagnetic layer thickness.

ACKNOWLEDGMENTS

This work was supported by State Education Commission, NSF of China, Chia Tai Groups fellow and Shanghai Research Center for Applied Physics.

[1] B. Dieny, J. Magn. Magn. Mater. **136**, 335 (1994).
[2] P. Bruno and C. Chappert, Phys. Rev. Lett. **67**, 1602 (1991).
[3] Z. Celinski and B. Heinrich, J. Magn. Magn. Mater. **99**, L25 (1991).
[4] B. Heinrich, Z. Celinski, J. F. Cochran, W. B. Muir, J. Rudd, Q. M. Zhong, A. S. Arrott, K. Myrtle, and J. Kirschner, Phys. Rev. Lett. **64**, 673 (1990).
[5] M. T. Johnson, S. T. Purcell, N. W. E. Mcgee, R. Coehoorn, J. aan de Stegge, and W. Hoving, Phys. Rev. Lett. **68**, 2688 (1992).
[6] J. F. Cochran, B. Heinrich, and A. S. Arrott, Phys. Rev. B **34**, 7788 (1986); H. Yamazaki, J. Magn. Magn. Mater. **125**, 272 (1993).
[7] J. S. S. Whiting, M. L. Watson, A. Chambers, J.-C. S. Levy, D. Mercier, I. B. Puchalska, and H. Niedoba, J. Magn. Magn. Mater. **115**, 174 (1992).
[8] S. M. Zhou, H. R. Zhai, H. Y. Zhang, A. Hu, R. W. Peng, G. Feng, Y. H. Liu, X. D. Ma, L. Y. Chen, and H. B. Huang, Phys. Status Solidi A **143**, 405 (1994).
[9] J. E. Ortega and F. J. Himpsel, Phys. Rev. Lett. **69**, 844 (1992); J. E. Ortega, F. J. Himpsel, G. J. Mankey, and R. F. Willis, Phys. Rev. B **47**, 1540 (1993).
[10] S. N. Okuno and K. Inomata, Phys. Rev. Lett. **72**, 1553 (1994).
[11] D. M. Edwards *et al.*, Phys. Rev. Lett. **67**, 493 (1991).
[12] B. A. Jones and C. B. Hanna, Phys. Rev. Lett. **71**, 423 (1993).
[13] M. V. Schilfgaarde and W. A. Harrison, Phys. Rev. Lett. **71**, 3870 (1993).
[14] Y. Wang, P. M. Levy, and J. L. Fry, Phys. Rev. Lett. **65**, 2732 (1990).

Finite temperature magnetization reversal in ultrathin magnetic films

S. T. Chui
Bartol Research Institute, University of Delaware, Newark, Delaware 19716

We study the magnetization reversal of Heisenberg spins in a two-dimensional plane under an external reversing field at finite temperatures. In the Ising limit dominated by uniaxial anisotropy and exchange, we observe nucleation of domains in Monte Carlo simulations. Analysis of the probability distribution in the energy provides for an estimate of the free energy for domain nucleation that is much smaller than that obtained from the wall energy at zero field because the energy of the nucleus approaches zero at the threshold of coherent rotation. The coercive field depends linearly on the temperature. When the dipolar interaction becomes important, reversed spins domains form quickly but do not grow. There is an intermediate regime when most spins are aligned parallel to the plane. © *1996 American Institute of Physics.* [S0021-8979(96)67308-4]

Stimulated by the possibility of integrating the semiconductor microelectronics technology with magnetic elements[1] there has been much interest recently in understanding the fundamental physics of magnetic films from 1 to 100 layers.[2] Depending on material parameters, the magnetization can lie parallel or perpendicular to the plane.[3,4]

A question of importance is how the spins reverse itself under the presence of an external field. This issue has been much studied at zero temperature in "thick" films[5] but very little work was done at finite temperature in ultrathin films where nucleation of domains through thermal fluctuation becomes possible.

In this article we study the magnetization reversal of Heisenberg spins in a 2D plane interacting with long-range dipolar, short-range exchange, and uniaxial anisotropy (perpendicular to the film) interactions at finite temperatures. In real systems, impurity[6] and edge effects can also be important. To elucidate the physics of this complex phenomenon it is important to understand one effect at a time. For this reason impurity and edge effects are not considered in this paper. Our results provide for new physical pictures in this largely unexplored area and are summarized in the abstract. We now describe our results in detail.

We choose our coordinates so that the film is in the xy plane. The total energy of the system is $E_T=E_0-H\Sigma_i S_{zi}$, where the "internal" interaction energy between the spins is $E_0=0.5\Sigma_{ij=xyz,RR'}V_{ij}(R-R')S_i(R)S_j(R')$. The sum is over the 2D positions R, R' of the spins in the plane. The potential $V=V_d+V_e+V_a$ is the sum of the dipolar energy $V_{dij}(R)=g(\delta_{ij}/R^3-3R_iR_j/R^5)$; the exchange energy $V_e=-J\delta(R=R'+d)\delta_{ij}$, and the anisotropy energy $V_a=-2K\delta(R=R')\delta_{iz}\delta_{jz}$. Here d denotes the nearest neighbors. The simulation reported here follows our earlier work on the equilibrium finite temperature studies of the phase diagram in ultrathin magnetic films,[3] where $H=0$. The long-range dipolar potential is summed with the Ewald sum technique. In the present study, we start with the magnetization upward along the z direction and study the system in the presence of a reversing magnetic field. We have assumed that we are dealing with block spins[4,5] with renormalized couplings so that the formation of domains can be observed in a reasonable size system.

We first describe our results in the Ising-like limit ($g=0$). For experimental films involving rare-earth elements the site anisotropy is large. This Ising limit is a reasonable approximation. In Fig. 1 we show a typical intermediate Monte Carlo configuration which clearly demonstrates the spin reversal through domain formation. An estimate of the coercive field can be determined from the threshold at which nucleation occurs during the finite simulation time (2000 MC steps/spin).

An estimate of the free energy of nucleation ΔF can be obtained from the total number of configurations, $P(E_0,t)$, of different "internal" interaction energy E_0 accumulated from the initial time up till time t. This "probability distribution" accumulated till a time near the completion of the magnetization reversal is illustrated by the dashed line in Fig. 2 for $J=-2$, $K=-1$, $g=0$. The normalization of P is arbitrary. Since E_0 does not include contributions due to interactions with the external field, increasing E_0 corresponds to increasing domain wall length. As time increases and domain walls are formed, E_0 is increased. Thus different E_0 corresponds to different times where the contributions to the total accumulated distribution are generated. The peak at around $E_1=549$ corresponds to configurations where domains are absent and most of the spins are lined up, as we can see from the fact that the average z magnetization $|M_z(E_0)|$, shown as the dotted curve in Fig. 2, is still close to

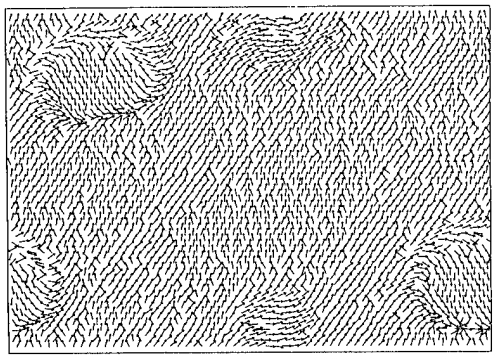


FIG. 1. The orientation of the spins with respect to the z axis (the vertical direction shown) for an Ising-like system near the threshold for coherent rotation at an intermediate time. The location of the spins are in the xy plane. The orientation of the spins here is not in the xy plane. The xy orientation of the spins is not shown.

 0021-8979/96/79(8)/4951/3/$10.00 © 1996 American Institute of Physics

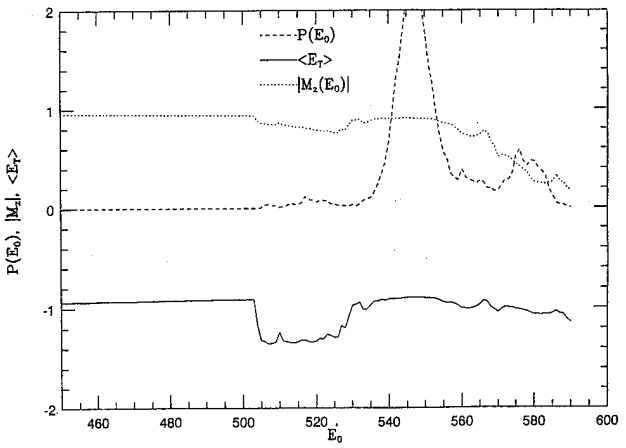


FIG. 2. Probability distribution $P(E_0t)/2\times10^5$, the total energy $E_T/2\times10^4$ and the absolute value of the average magnetization as a function of E_0 for an Ising-like system.

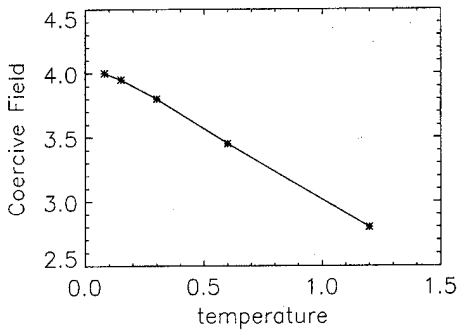


FIG. 3. The coercive field as a function of temperature for $J=4$, $K=2$, and $g=0$.

one. These configurations occur at the early history of the reversal process. As time increases eventually a critical nucleus is formed near $E_2\approx568$, where $P(E_2)$ is at a minimum. As the domain grows, the domain wall length is increased and E_0 increases. At the same time the net magnetization in the z direction decreases. This metastable phase with a domain corresponds to the second smaller peak around 580. Eventually when all the spins are reversed another peak corresponding to the final state develops. This occurs at an energy of 480 and is not shown in this figure. From Boltzman's distribution, we expect $P(E_1)/P(E_2)=\exp(-\Delta F/kT)$. We thus estimate the free energy of nucleation by $\Delta F=T\ln[P(E_1)/P(E_2)]\approx1.5$ in units with $k=1$. The total energy, which includes that of the external magnetic field, is shown by the solid line.

The nucleation energy from conventional theory is $E_n=\pi\tau^2/2H$, where τ is the domain wall energy per unit length. We estimated τ at zero field numerically[10] and found that $E_n\approx50$, much larger than ΔF.

When $H>H_r=2K$, the spins can be reversed by coherent rotation so that all the spins rotated together as a whole. The formula for the nucleus and the domain wall energy discussed in the previous paragraph is derived in zero magnetic field. When the field is included, near the threshold for coherent rotation τ approaches zero as $\tau\propto(H-H_r)^2$.[7–9] Thus at finite temperatures coherent rotation is always preceded by nucleation. When the nuclei first formed the spins inside are only rotated by an angle θ_F of the order $\cos^{-1}[(H-K)/K]$. The sum of the anisotropy energy and the magnetic field energy is approximately the same at θ_F and at $\theta=0$.

An intermediate configuration close to the onset of coherent rotation ($K=1$, $H=1.9$, $T=0.15$) is illustrated in Fig. 1. There is large scale fluctuation where the spins are tilted slightly. In addition we also see three nuclei at the upper left, lower right, and lower middle. For the nuclei in the lower middle the spins are not completely rotated inside. As we discussed earlier this is the rule for small nuclei. Inspection of an earlier configuration shows that when the nuclei at the upper left and lower right first formed, the spins inside them are not completely rotated either.

In Fig. 3 we show the temperature dependence of the coercive field for $J=4$, $K=2$, and $g=0$. H_c depends approximately linearly on T. This is in contrast with the case of small particles where one expects a temperature dependence of the form $\sqrt{1-T/T_B}$ for some constant T_B. This linear temperature dependence can be understood as follows. The energy of a nucleus consists of a sum of a wall energy and an interior contribution. We expect the interior contribution to be small because, as we argued above, in the interior the spins have only turned by a small amount θ_F and their energy change is small. The domain wall energy consists of a sum of two parts: the wall bending energy and the energy per unit length τ for flat walls. Thus the wall energy of a circular nucleus of radius R is approximately $E_n=\tau2\pi R+\beta/R$ for some elastic constant β. We optimize E_n with respect to R and get $R=\sqrt{\beta/2\pi\tau}$. For the small particle case, the size of the nucleus is not a function of H. In the present case, it is. Substituting this value of R into E_n, we obtain a nucleation energy $E_n\approx2\sqrt{2\pi\tau\beta}$. At a finite temperature the nucleation energy is comparable to the temperature at the coercive field, i.e., $E_n=\gamma T$ for some constants γ of the order of unity. Recall that $\tau\propto(H-H_r)^2$. Substituting in the value of E_n, we obtain a linear temperature dependence for the coercive field. We next turn our attention to the case where the dipolar interaction is no longer zero.

Monte Carlo simulations were carried out with a nonzero dipolar interaction. A typical configuration is displayed in Fig. 4 where we show the projection of the spin on the xy plane at an intermediate time for $J=-2$, $K=-1$, $g=-0.1208$, $T=0.4$, $h=0.7$. There are now intermediate configurations where nearly all the spins are along the xy plane with pockets of spin rotated domains (empty-like spaces) in between. The reversal mechanism seems different from the Ising case.

Examination of histories of spin configurations indicates that the pockets of spin down domains form very quickly. When all spins are along the z axis, the uniaxial anisotropy is reduced by the dipolar interaction to $K'=K-g/g_1$, where $1/g_1=0.75\ \Sigma_R1/R^3=0.128$.[3] The energy to create a domain wall is reduced from $\sqrt{KJ}$ to $\sqrt{K'J}$. Thus it becomes easier to create spin down domain. The domain wall width is now increased to $\sqrt{J/K'}$. When the pockets of spin down domains

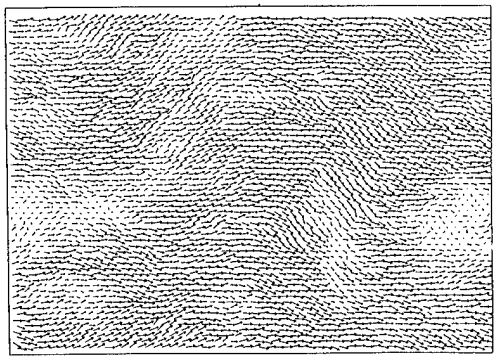


FIG. 4. The projection of the spins interacting with an additional dipolar interaction onto the xy plane sin $\theta(\cos\theta,\ \sin\theta)$ at an intermediate time. The orientation of the spins shown are in the same plane as the location of the spins. This is different from Fig. 1.

are created, the domain walls from different nuclei now overlap so that there is a large fraction of spins along the xy plane. When this happens, the effective anisotropy field is no longer K' but is increased back up to close to K. Also, it becomes more difficult for the spin reversed domains to grow because the local dipolar field created by the other spins in the xy plane make it more difficult to flip the spins at the boundary from the xy plane to the negative z direction. Thus the spins along the xy plane remain locked in. Instead the remaining spin up electrons gets flipped into the xy plane. This picture of spin reversal is different from that in the Ising-like case.

In conclusion, we present here some examples of new phenomena and insights that can happen in finite temperature spin reversals in ultrathin films. There are many interesting questions that wait to be studied. Finite temperature fluctuation of the domain walls is very important in ultrathin films. Whereas in three-dimensional situations, domain walls are flat, recent experimental and theoretical results[6,11] indicate that walls in ultrathin films are not flat. The effect of these on the dynamics of spin reversal is not completely clarified.

There is a similarity between coherent rotation and spinodal decomposition. In both cases the barrier against a continuous change of the order parameter approaches zero. Just as in the case of spinodial decomposition, there may be a scaling relationship for the structure factor of the magnetization in the long time limit near the onset of coherent rotation. A detailed relationship between the two is not clear at the moment and remains to be investigated.

ACKNOWLEDGMENT

This work was supported by the Office of Naval Research under Contract No. N00014-94-1-0213.

[1] G. Prinz, Science **1092**, 250 (1990).
[2] B. Heinrich and J. F. Cochran, Adv. Phys. **42**, 524 (1993).
[3] For a recent summary from a theoretical perspective, see S. T. Chui, Phys. Rev. B **50**, 12559 (1994).
[4] S. T. Chui, Phys. Rev. Lett. **74**, 3896 (1995).
[5] See, for example, H. Neal Bertram and J. G. Zhu, in *Solid State Physics*, edited by H. Ehrenreich and D. Turnbull (Academic, New York, 1992), Vol. 46, p. 271.
[6] S. T. Chui, Phys. Rev. B **51**, 250 (1995).
[7] S. T. Chui, J. Appl. Phys. (to be published).
[8] A. Aharoni, Phys. Rev. **119**, 127 (1960).
[9] J. S. Broz, H. B. Braun, O. Brodbeck, W. Baltensperger, and J. S. Helman, Phys. Rev. Lett. **65**, 787 (1990).
[10] We construct a triangular lattice of 400 spins with half of the spins up on the left and half of the spins down on the right. We then minimize the energy of the system by allowing the spins to relax numerically with a quasi-Newton method. We find for zero external field, $J=-2$ and $K=-1$, an energy τ of 5.5 per lattice constant.
[11] A. Berger, U. Linke, and H. P. Oepen, Phys. Rev. Lett. **68**, 839 (1992); J. Pommier, P. Meyer, G. Penissard, J. Ferre, P. Bruno, and D. Renard, *ibid.* **65**, 2054 (1990).

The growth of magnetic Fe overlayers on sulphur passivated GaAs(100)

G. W. Anderson,[a] M. C. Hanf,[b] and P. R. Norton
Interface Science Western, The University of Western Ontario, London, Ontario N6A 5B7, Canada

M. Kowalewski, K. Myrtle, and B. Heinrich
Department of Physics, Simon Fraser University, Burnaby, British Columbia V5A 1S6, Canada

This paper describes a new approach for producing epitaxial Fe overlayers on GaAs(100), which prevents the intermixing of the semiconductor elements in the overlayer. This is accomplished by sulphur passivation of the substrate surfaces in an aqueous ammonium sulphide solution prior to Fe deposition. bcc Fe(100) is observed to grow epitaxially on S/GaAs(100) substrates, with most of the S floating out as an ordered overlayer. No evidence of semiconductor interdiffusion into the Fe overlayer is observed. The Fe overlayers are observed to be ferromagnetic, with easy axes along the [010] directions. A uniaxial in-plane anisotropy is observed, in addition to the expected fourfold anisotropy, which is attributed to the bonding geometry at the interface. The saturation magnetization of these overlayers is found to be close to that of bulk Fe. © *1996 American Institute of Physics.* [S0021-8979(96)70908-X]

The growth of magnetic overlayers and multilayers on semiconductors has attracted considerable attention due to the potential for integrating the desired magnetic properties of these systems with computer circuitry. However, in practice, the growth of transition metals on semiconductor substrates is difficult, generally resulting in the intermixing of the semiconductor elements into the overlayer. In the case of the growth of Fe overlayers on GaAs(100), a significant amount of As has been observed to interdiffuse into the overlayer.[1–3] This has been shown to result in a significant decrease in the magnetization of these systems.[3] This paper describes a new approach for producing epitaxial Fe overlayers on GaAs(100), which prevents the intermixing of the semiconductor elements in the overlayer: the use of sulphur passivated substrates.

It has been recently shown that many semiconductor surfaces (including InP, GaAs, and Ge) can be effectively passivated by treatment in an aqueous ammonium sulphide solution.[4–13] These surfaces are thought to be composed of 1 ML of S atoms bridge bonded to the semiconductor surface, essentially continuing the bulk lattice positions.[4–13] This configuration results in all of the semiconductor dangling bonds being saturated, producing a chemically passive surface that is extremely resistant against oxidation by air. When such samples are placed into vacuum, they show clean, well-ordered surfaces.

We have investigated the use of S-passivated substrates for the growth of Fe overlayers as a potential means of preventing As interdiffusion into the Fe overlayer. In this investigation Auger electron spectroscopy (AES), low energy electron diffraction (LEED), reflection high energy electron diffraction (RHEED), and static secondary ion mass spectrometry (SSIMS) measurements have been used to examine the structure and check for As interdiffusion in the overlayers deposited at 25 °C. Magnetic characterization of the system has been accomplished utilizing the magneto-optic Kerr effect (MOKE) and ferromagnetic resonance (FMR) techniques.

Two separate UHV systems were utilized in this investigation. The first system, located at the University of Western Ontario, consists of a diffusion pumped UHV growth/analysis chamber (base pressure $<1\times10^{-10}$ Torr) which is connected to a turbo-pumped UHV loadlock chamber (base pressure 2×10^{-10} Torr) equipped with a remote sample transfer arm. The loadlock chamber is also equipped with a MOKE apparatus for the magnetic characterization of the samples. The main growth/analysis chamber is equipped with a liquid nitrogen shrouded Fe evaporation source, a four-grid retarding field analyzer for LEED measurements, a CLAM electron energy analyzer (Fisons Instruments) for AES measurements, and a SSIMS system consisting of a Hiden quadrupole mass spectrometer and a Kimball Physics Cs^+ ion gun. It is also interfaced to a 2.5 MV Van de Graaff accelerator which was utilized for a Rutherford backscattering calibration of the evaporation rate onto an Al substrate.[14]

The second UHV system utilized is a multiple chamber MBE system, consisting of growth, analysis and sample introduction chambers, designed and located at Simon Fraser University. This system is equipped with a double-pass cylindrical mirror analyzer (PHI-10–360, equipped with an OMNI lens) for XPS measurements, a PHI-06-190 RHEED system to monitor the quality of the Fe growth, and a quartz crystal thickness monitor to monitor the Fe coverage.

Additional magnetic characterization of the samples was accomplished by *ex situ* FMR measurements on samples capped with 20 ML of Au. Ferromagnetic resonance (FMR) measurements were carried out using a magnetic microwave spectrometer operating at 24 GHz which has been previously described.[15] The FMR measurements were carried out on 6, 9, 20, 25, and 30 ML thick Fe films.

The S-passivated GaAs(100) samples were prepared *ex situ* by treatment in an aqueous sulphide solution. *n*-type GaAs(100) wafers [aligned to within 0.5° of the (100) direction] from Bertram Laboratories were utilized in these investigations. The GaAs(100) samples were degreased in hot

[a]Present address: Department of Physics, University of California, Davis, CA 95616.
[b]Present address: Faculté, des Sciences et Techniques, Laboratoire de Physique et de Electronique, 4 rue des Frères Lumière, 68093 Mulhouse, France.

 0021-8979/96/79(8)/4954/3/$10.00 © 1996 American Institute of Physics

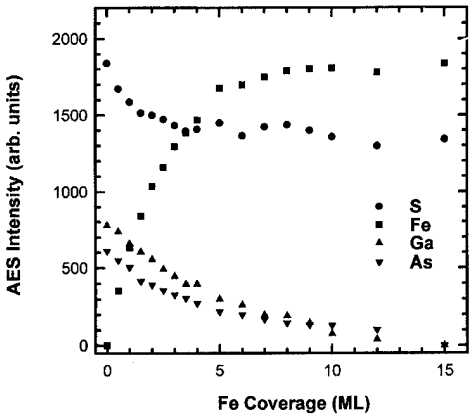


FIG. 1. The Intensity of the Fe, S, Ga, and As AES transitions as Fe is deposited.

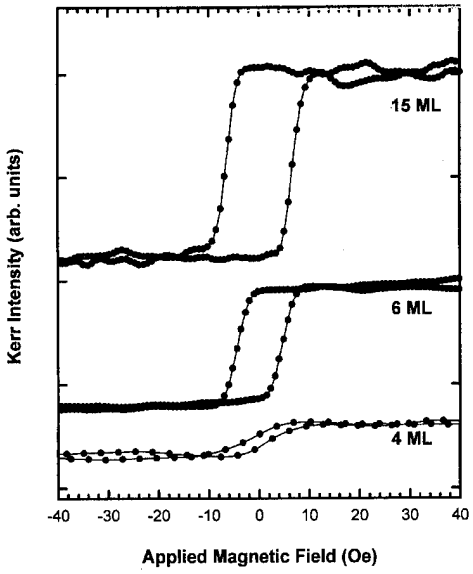


FIG. 2. MOKE hysteresis loops for various Fe/S/GaAs(100) overlayers. The applied magnetic field is along the Fe[010] easy axis.

(50–60 °C) methanol and then treated for 20 min. at 65 °C, in an aqueous ammonium sulphide $[(NH_4)_2S]$ solution. After this treatment the samples were rinsed with running deionized water and methanol for about 5 min, blown dry with He and inserted into the loadlock chamber. A new sample was utilized for each experiment.

Upon insertion into the vacuum system the samples showed a poor (1×1) LEED pattern and a small amount of C contamination. The samples were annealed to 450 °C prior to Fe deposition to desorb any remaining contaminants and improve the surface order. After this thermal treatment, a sharp (2×1) LEED pattern was observed and the C contamination had been removed. The (2×1) reconstruction is due to the dimerization of the adjacent S rows.

AES and SSIMS measurements were utilized to investigate the presence of As interdiffusion during the growth of the Fe overlayers. Figure 1 shows the variation of the Fe (703 eV), S (152 eV), Ga (1070 eV), and As (1228 eV) AES intensities during Fe deposition. The Fe AES signal initially increases steadily with Fe coverage, leveling off at a coverage of about 7 ML [where 1 ML is the surface atomic density of Fe(100)]. The S AES signal shows an initial decrease, but then levels off and is still at about 70% of its initial intensity at Fe coverage of 20 ML. This persistence of the S signal means that some of the S is floating out on top of the Fe film, as the S electrons would not penetrate a 20 ML film.

Both the Ga and As AES signals decrease in an exponential manner, being undetectable by a coverage of 15 ML. Fitting these data yielded values of 14.3 and 18.9 Å for the Ga and As AES electron mean free paths. These values are in good agreements with the calculated values of 17 and 19 Å,[16] suggesting that the Fe film is uniform and that neither Ga or As is interdiffusing through the overlayer.

SSIMS measurements were utilized to look for As interdiffusion at lower levels, due to the high sensitivity of SIMS for As. SSIMS measurements of the S/GaAs(100) substrate showed strong S and As signals. Fe overlayers of 2, 4, and 6 ML were also analyzed. In all cases, Fe and S signals were clearly visible, with As never being observed. Taking into account the sensitivity of SSIMS for As, this means that the upper limit for the amount of As interdiffusion is 0.01 ML.

The quality of the Fe overlayers was investigated by LEED and RHEED measurements. During the initial phase of deposition, the substrate LEED pattern is observed to fade into a rising background, disappearing completely by an Fe coverage of about 1.5 ML. As deposition continues, an overlayer pattern is observed to begin forming at a coverage of about 3 ML, and continues to increase in intensity as deposition continues. The pattern observed was identified as being due to $c(2\times2)$ S/Fe(100),[17] indicating that the S floats out in an ordered overlayer on the Fe surface.

RHEED experiments were utilized to provide further information on the substrate and growth morphology. The substrate RHEED pattern showed a laterally well-ordered surface, but also showed that the surface had a strong three-dimensional nature (i.e., it is hilly). As Fe is deposited, the substrate RHEED pattern disappears into a ring of diffuse intensity, indicating that the Fe is polycrystalline. As further Fe is deposited a (2×2) S/Fe(100) RHEED pattern is observed to begin forming at 2.3 ML, with the ring completely disappearing by a coverage of 4.5 ML. The Fe pattern also exhibits the same type of three dimensionality as the substrate, suggesting that the overlayer retains the morphology of the substrate.

The magnetic properties of the Fe/S/GaAs(100) system were investigated by MOKE and FMR measurements. The MOKE measurements showed that for Fe coverages <4 ML, the samples did not show ferromagnetic behavior. This suggests that the disordering/islanding in the initial interfacial region is sufficient to prevent the development of ferromagnetic ordering. For higher coverages, clear ferromagnetic hysteresis loops are observed, which increase in strength as further material is deposited (see Fig. 2). The rounding observed in these loops likely indicates the presence of some defects in the Fe overlayers, which are pinning the magnetization.

The FMR measurements revealed the presence of uniaxial and fourfold in-plane anisotropies. The fourfold anisotropy had its easy axes along the {001} crystallographic

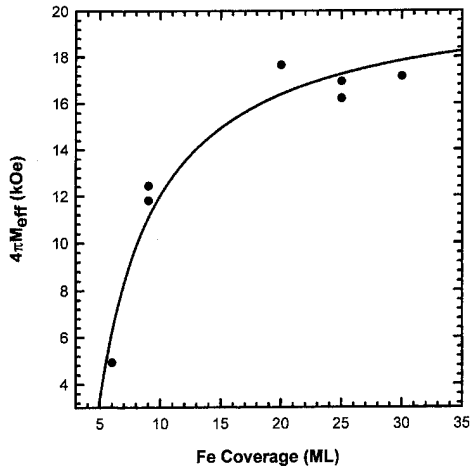


FIG. 3. The effective magnetization as a function of Fe overlayer thickness. The solid line represents the two term fit to the data.

directions, the uniaxial anisotropy had its easy axis along $[0\bar{1}1]$. The in-plane uniaxial anisotropy was strongly dependent on the sample thickness. For the 6 ML thick sample the strength of the uniaxial anisotropy was found to be $2K_u/M_s=0.1$ kOe, and it decreased to 0.4 kOe in the thickness range of 30 ML. The fourfold anisotropy was increasing with an increasing Fe film thickness: the strength of the fourfold anisotropy $2K_1/M_s$ was close to zero for the 6 ML thick sample, and 0.4 kOe for the 30 ML thick film. The thickness dependence of the in-plane anisotropies was otherwise scattered sufficiently so that no attempt was made to fit the measured results.

The effective magnetization $(4\pi M_{\text{eff}}=4\pi M_s-H_u)$ is shown in Fig. 3 as a function of Fe coverage. The solid line is a fit to the data, obtained using a constant plus $1/d$ term. The constant and $1/d$ terms were found to be 20.7 kG and -86.9 kG/ML, respectively. The constant term is very close to the saturation induction of bulk Fe (21.55 kG), showing that the measured film reached nearly bulk properties at a very low Fe coverage. On the contrary, the films deposited directly on GaAs(001) substrate showed significantly decreased saturation magnetization in the thin-film limit due to a severe interdiffusion of As into the Fe overlayer.[3] The undiminished saturation magnetization of films deposited on S-passivated GaAs(001) is in agreement with the previously discussed structural studies, which show no penetration of As into the Fe. The $1/d$ term is most likely associated with the presence of a well-defined perpendicular uniaxial anisotropy. The effective uniaxial surface anisotropy is $K_s=1.1$ erg/cm^2 with the easy axis perpendicular to the film surface.

The FMR lines have symmetric peaks, with the linewidths depending on the Fe film thickness. A 25 ML film possessed very narrow FMR linewidths: 60 and 100-Oe for the hard and easy in-plane magnetic axis, respectively. The FMR linewidth was observed to increase with decreasing film thickness. The 6 ML overlayer exhibited FMR linewidths of 210 and 400 Oe for the hard and easy magnetic axes, respectively. The magnetic properties across the sample were not always homogeneous. The FMR peaks for 9 and 25 ML samples exhibited a large splitting (separated by 2–5 FMR linewidths for the easy and hard axes, respectively) indicating that there was either a problem with the Au capping layer or the samples were inhomogeneous in thickness.

We have shown a new procedure for the growth of Fe overlayers on GaAs(100), the use of S-passivated substrates, that prevents the interdiffusion of the As into the overlayer. Fe(100) has been shown to grow on this substrate, with a layer of ordered S floating out on top of the overlayer. The S acts as a surfactant, holding the Fe on top of the substrate,[17] and not allowing semiconductor interdiffusion into the overlayer. Samples with Fe coverages greater than about 4 ML exhibit ferromagnetic behavior. These samples show the expected fourfold in-plane anisotropy, as well as an additional uniaxial anisotropy. The presence of this uniaxial anisotropy has been previously observed for Fe/GaAs(100)[3,18] and was attributed to the surface bonding geometry. The effective magnetization can be fit with two terms: a constant term (20.7 kG) and a $1/d$ surface term. The constant term is very close to the saturation induction of bulk Fe (21.55 kG). Thus, the bulk atomic layers in the overlayer behave as expected for bulk Fe. There is no indication of the reduction in magnetization previously attributed to interdiffused As.[3]

The support of the Natural Sciences and Engineering Research Council of Canada (NSERCC) is gratefully acknowledged. M.C.H. also acknowledges the receipt of a NSERCC International Fellowship.

[1] J. R. Waldrop and R. W. Grant, Appl. Phys. Lett. **34**, 630 (1979).
[2] S. A. Chambers, F. Xu, H. W. Chen, I. M. Vitomirov, S. B. Anderson, and J. H. Weaver, Phys. Rev. B **34**, 6605 (1986).
[3] J. J. Krebs, B. T. Jonker, and G. A. Prinz, J. Appl. Phys. **61**, 2596 (1987).
[4] C. J. Sandroff, R. N. Nottenburg, J. C. Bischoff, and R. Bhat, Appl. Phys. Lett. **51**, 33 (1987).
[5] Y. Tao, A. Yelon, E. Sacher, Z. H. Lu, and M. J. Graham, Appl. Phys. Lett. **60**, 2669 (1992).
[6] Z. H. Lu, M. J. Graham, X. H. Feng, and B. X. Yang, Appl. Phys. Lett. **62**, 2932 (1993).
[7] Z. H. Lu and M. J. Graham, Phys. Rev. B **48**, 4604 (1993).
[8] H. Xia, W. N. Lennard, G. R. Massoumi, J. J. J. van Eck, L. J. Huang, W. M. Lau, and D. Landheer, Surf. Sci. **324**, 159 (1995).
[9] M. Tanimoto, H. Yokoyama, M. Shinohara, and N. Inoue, Jpn. J. Appl. Phys. **33**, L279 (1994).
[10] T. Ohno and K. Shiraishi, Phys. Rev. B **42**, 11194 (1991).
[11] T. Ohno, Surf. Sci. **255**, 229 (1991).
[12] G. W. Anderson, M. C. Hanf, P. R. Norton, Z. H. Lu, and M. J. Graham, Appl. Phys. Lett. **66**, 1123 (1995).
[13] O. L. Warren, G. W. Anderson, M. C. Hanf, K. Griffiths, and P. R. Norton, Phys. Rev. B **52**, 2959 (1995).
[14] G. W. Anderson and P. R. Norton, Surf. Sci. **336**, 267 (1995).
[15] B. Heinrich, in *Ultrathin Magnetic Structures II*, edited by B. Heinrich and J. A. C. Bland (Springer-Verlag, New York, 1994), p. 204.
[16] S. Tanuma, C. J. Powell, and D. R. Penn, Surf. Sci. **192**, L849 (1987).
[17] G. W. Anderson, M. C. Hanf, and P. R. Norton, Phys. Rev. Lett. **74**, 2764 (1995).
[18] B. T. Jonker, Proc. SPIE **2140**, 118 (1994).

Epitaxial ferromagnetic MnAs thin films grown on Si (001): The effect of substrate annealing

K. Akeura, M. Tanaka,[a] T. Nishinaga, and J. De Boeck[b]
Department of Electronic Engineering, The University of Tokyo, 7-3-1 Hongo, Bunkyo-ku, Tokyo 113, Japan

We have studied two different types of epitaxial ferromagnetic MnAs thin films on Si (001) substrates grown by molecular beam epitaxy. When the Si substrates were annealed at a relatively high temperature (~900 °C) and then MnAs was grown, we obtained epitaxial MnAs films with twofold crystal symmetry (type I). In contrast, when the thermal cleaning of the Si substrate was done at a lower temperature (~600 °C), epitaxial MnAs thin films had fourfold crystal symmetry (type II). The growth plane in both types of MnAs thin films was the $(\bar{1}101)$ of the hexagonal MnAs. The type I MnAs films are single domain with strong magnetic anisotropy, whereas the type II MnAs films are double domain with the lack of strong magnetic anisotropy. © *1996 American Institute of Physics.* [S0021-8979(96)71008-9]

Epitaxial ferromagnetic metallic thin films on semiconductors are very attractive as a new class of electronic materials,[1] because it is expected that such artificial structures can lead to the integration of magnetism with semiconductor electronics, giving the unprecedented opportunities for new device applications. So far, we have successfully grown epitaxial ferromagnetic MnAs thin films on GaAs (001) substrates by molecular beam epitaxy (MBE) and have found that the starting surface reconstructions and stoichiometry play a critical role in determining epitaxial orientations and magnetic properties.[2–4] Furthermore, very recently, we have successfully grown ferromagnetic MnAs on Si (001) substrates.[5] The combination of ferromagnetic materials with Si is obviously important for many potential applications, because most of the existing LSI circuitry is based on Si technologies. In the MBE growth of MnAs on Si (001), it was found that supplying As_4 flux first without Mn flux on Si was necessary to obtain MnAs films with good magnetic properties, whereas supplying Mn flux without As flux on Si led to polycrystalline MnAs.

In this paper, we extend this study on MnAs/Si, and show that two types of MnAs thin films with different structural and magnetic properties are epitaxially grown on Si (001), depending on the thermal cleaning temperature of the Si substrates prior to the growth of MnAs.

MBE growth was performed with a conventional III–V MBE machine (ULVAC MBC-508) with a Mn effusion cell. We used Si (001) substrates (p-type, boron doped) misoriented 1° towards [110]. After being etched with HF solution and dried with N_2 gas, the Si substrates were introduced into the MBE growth chamber. Watching reflection high energy electron diffraction (RHEED), we annealed the substrates at the temperature T_a(=600–1000 °C) for a few minutes to turn the hydrogen-terminated (1×1) Si surface to the clean surface of (2×2)-(001) Si, as shown in Fig. 1(a), which was taken with [110] Si incidence. It is known that the HF etching is very effective to passivate the Si surface, making the annealing temperature dramatically lower to obtain clean surfaces.[6] This (2×2) Si surface was first exposed to the As_4 flux, and then the substrate temperature was cooled to 300 °C. After this process, Si surface is terminated with 1 monolayer (ML) of As atoms, showing clear (2×2) reconstruction in the RHEED patterns. With the As_4 flux kept on, MnAs epitaxial growth was started by supplying the Mn flux with a growth rate of 0.1–0.4 μm/h. During the growth the substrate temperature was kept at 300 °C and the pressure of As_4 flux was about 1×10^{-5} Torr.

Here, we have found that the annealing temperature T_a

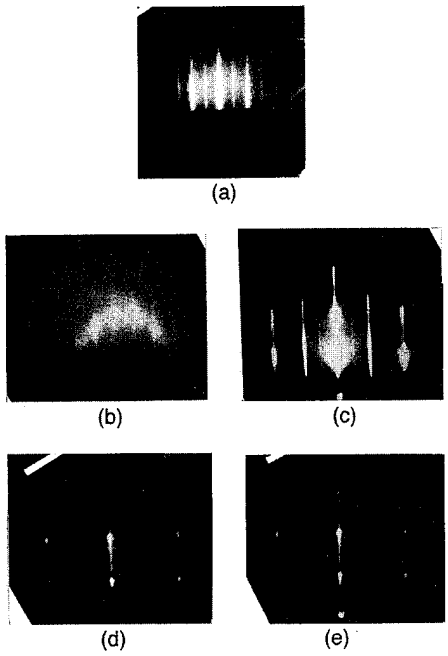


FIG. 1. (a) A RHEED pattern taken from the (2×2)–(001) Si surface after annealing at T_a=600 °C with the incident electron beam along the Si $[\bar{1}10]$, normal to the misorientation direction. Almost the same RHEED pattern is observed after annealing at T_a>900 °C. (b), (c), (d), and (e) are RHEED patterns of the type I and type II MnAs thin films with two different electron beam azimuths. (b) Type I, electron beam azimuth//Si $[\bar{1}10]$ ⊥ misorientation direction; (c) type I, electron beam azimuth//Si [110] ∥ misorientation direction; (d) type II, electron beam azimuth//Si $[\bar{1}10]$ ⊥ misorientation direction; (e) type II, electron beam azimuth//Si [110] ∥ misorientation direction.

[a]Also PRESTO (Sakigake 21), JRDC, 4-1-8 Honcho, Kawaguchi, Saitama 332, Japan; Electronic Mail: Masaaki@ee.t.u-tokyo.ac.jp.
[b]Interuniversity Microelectronics Center (IMEC), 75 Kapeldreef, B3001 Leuven, Belgium.

 0021-8979/96/79(8)/4957/3/$10.00 © 1996 American Institute of Physics

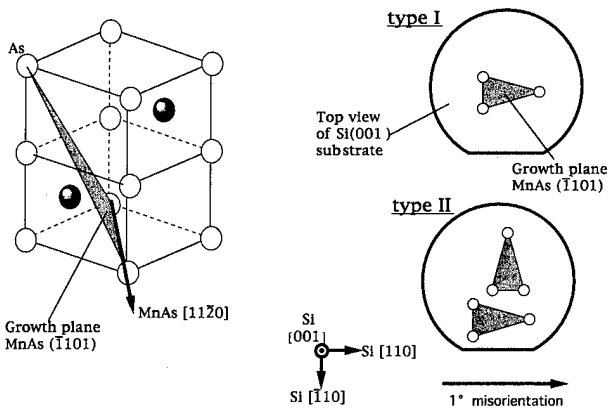


FIG. 2. Crystal structure of the hexagonal MnAs and the ($\bar{1}$101) plane are shown on the left-hand side. Top view of the epitaxial relationships of the MnAs/Si(001) system is shown on the right-hand side. The type I MnAs consists of a single domain, in which the axis of MnAs [$\bar{1}\bar{1}$20] is along the Si [$\bar{1}$10]. The type II MnAs has double domains, in which one domain has the MnAs [$\bar{1}\bar{1}$20] axis along the Si [$\bar{1}$10] and the other domain has the MnAs [$\bar{1}\bar{1}$20] axis along the Si [110], 90° different with respect to the substrate plane.

of the Si substrate prior to the growth of MnAs plays an essential role in determining structural and magnetic anisotropy in the MnAs/Si system. When we annealed the substrate at a relatively high temperature (T_a~900 °C) and started the growth of MnAs in the way described previously, we obtained MnAs thin films with the structure of twofold crystal symmetry, which we refer to as type I, as shown by Figs. 1(b) and 1(c) taken from a 1.4 μm thick MnAs thin film. For the type I MnAs thin films, the RHEED pattern with the incident electron beam along the Si [$\bar{1}$10] [Fig. 1(b)] is clearly different from that with the incident electron beam along the Si [110] [Fig. 1(c)]. Here we define the [110] and [$\bar{1}$10] of Si as the direction parallel and normal to the misorientation direction, respectively. The intervals of the streaks in the RHEED patterns of Figs. 1(b) and 1(c) are in good agreement with the lattice constants along the MnAs [1$\bar{1}$02], [$\bar{1}\bar{1}$20] axes, respectively. In contrast, when we annealed the Si substrate at about 600 °C, which is high enough to obtain the Si (2×2) reconstruction [Fig. 1(a)], we obtained MnAs thin films with fourfold structural symmetry, which we refer to as type II, as shown in Figs. 1(d) and 1(e) taken from a 0.3 μm thick MnAs thin film. Note here that despite the different annealing temperature, very clear (2×2)–(001) Si surface was obtained for both types, indicating that the starting Si surface has little disorder or contamination. For the type II MnAs, the RHEED pattern of Fig. 1(d) (along the Si [$\bar{1}$10] azimuth) is very similar to that of Fig. 1(e) (along the Si [110] azimuth). X-ray diffraction measurements (θ-2θ method) were done on both types of MnAs films, and it was found that the growth plane of both types was the ($\bar{1}$101) of hexagonal MnAs.

From the RHEED and x-ray results, the epitaxial relationships of the two types of MnAs grown on Si (001) are determined and summarized as shown in Fig. 2. The type I MnAs consists of a single domain in terms of crystallographic orientation, in which the [$\bar{1}\bar{1}$20] axis of MnAs is parallel to the [$\bar{1}$10] axis of Si. In contrast, the fourfold symmetry of the type II MnAs is due to the existence of double domains; in one domain the MnAs [$\bar{1}\bar{1}$20] is parallel to the Si [$\bar{1}$10] just like the type I, and in the other domain the MnAs [$\bar{1}\bar{1}$20] is parallel to the Si [110], 90° different with respect to the substrate plane.

As shown in Fig. 2, the experimental fact that the uniaxial anisotropy in the type I MnAs films always correlates with the misorientation direction of the Si substrate indicates that atomic steps on the Si surface plays an essential role. We speculate that the difference between the type I and type II MnAs arises from the difference in the initial step structure of the Si misoriented surfaces before growing MnAs. The direction of the Si dimers on the Si (001) substrate and/or the As dimers of the As prelayer seems to determine the alignment of the [$\bar{1}\bar{1}$20] axis of MnAs. Although it is difficult to obtain a single-domain Si (2×1) surface on 1° misoriented substrates, it is likely that when we annealed the substrate at high temperature (T_a~900 °C), one domain that has Si dimers arranged parallel to the step edge of the Si substrate becomes more or less dominant, compared with the other domain having Si dimers normal to the step edges. Thus, the MnAs thin films grown on this surface tend to have the structure with twofold symmetry (type I). In contrast, when the annealing temperature T_a is relatively low (600 °C), the direction of the Si dimers on the substrate surface, either parallel or normal to the step edges, is equally distributed. Therefore, in this case, the MnAs films grown on this surface tend to have double domains, showing the fourfold symmetry in RHEED.

Although in some samples a little polycrystalline character was seen in the RHEED [e.g., Fig. 1(d)], we rule out the possibility that this kind of disorder causes the lack of uniaxial anisotropy in the type II, because the disorder appears in both type I and type II samples. Since the initial (2×2) Si surfaces for both types have no difference in the RHEED properties exhibiting well-ordered reconstruction, this partially disordered character appeared during the epitaxial growth of MnAs, probably due to the the the lack of uniformity of the substrate temperature over the 2-in. wafers. Further refinements of the growth conditions are needed to obtain better quality.

To investigate the magnetic properties of the type I and type II MnAs on Si (001), we have performed magnetization measurements by alternating gradient force magnetometry (AGFM),[7] on 300 nm thick MnAs thin films of both types. We applied the magnetic field H in various directions and found that the easy axis of the magnetization in both types of MnAs is in-plane. Figures 3(a)–3(d) show the in-plane M-H characteristics at room temperature of type I [(a),(b)] and type II [(c),(d)] MnAs thin films, with H normal [(a),(c)] and parallel [(b),(d)] to the misorientation direction of the Si substrates. A squarelike M-H hysteresis curve was recorded with H// Si [110], normal to the misorientation direction [Fig. 3(a)], while only a little hysteresis was observed with H// Si [110], parallel to the misorientation direction [Fig. 3(b)]. Therefore, the type I MnAs has strong magnetic anisotropy in the substrate plane. Considering the epitaxial orientation (see Fig. 2), the easy magnetization axis of the type I MnAs/Si is the MnAs [$\bar{1}\bar{1}$20], which is parallel to the Si

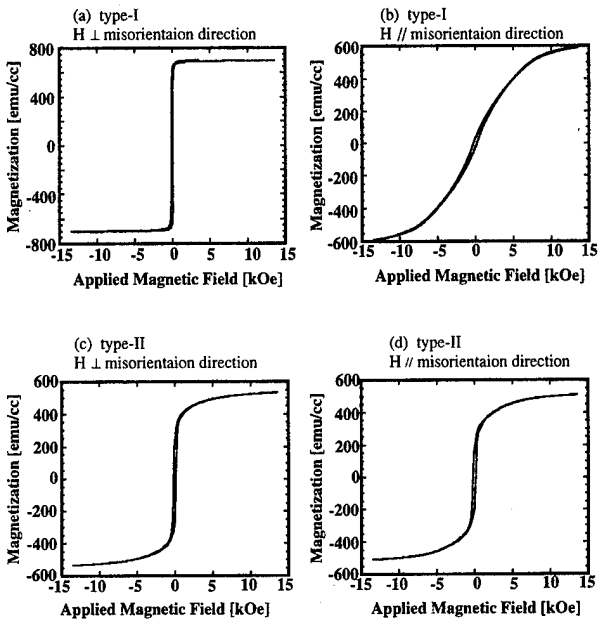


FIG. 3. Room-temperature $M-H$ curves of 300 nm thick type I and type II MnAs films grown on Si. The applied magnetic field H was in-plane. (a) type I, H//Si $[\bar{1}10]\perp$ misorientation direction; (b) type I, H//Si [110] misorientation direction; (c) type II, H//Si $[\bar{1}10]\perp$ misorientation direction; (d) type II, H//Si [110] misorientation direction.

$[\bar{1}10]$. When H is along the easy axis, the saturation magnetization (M_s), remnant magnetization (M_r), and coercive field (H_c) of this 300 nm thick type I MnAs is 690 emu/cc, 625 emu/cc, and 94 Oe, respectively. In contrast, the M-H curves of the type II MnAs on Si showed some hysteresis when H was applied both along the Si $[\bar{1}10]$ and along the Si [110] as shown in Figs. 3(c) and 3(d). The M_r and H_c values of Figs. 3(c) and 3(d) are 217 emu/cc and 124 Oe, and 162 emu/cc and 148 Oe, respectively, similar to each other. This indicates that the type II MnAs films consist of two crystallographic domains; in one domain the MnAs $[\bar{1}\bar{1}20]$ axis (the easy magnetization axis) is along the Si $[\bar{1}10]$, and in other domain the MnAs $[\bar{1}\bar{1}20]$ is along the Si [110]. The existence (type I) and the lack (type II) of strong magnetic anisotropy in type I and type II are consistent with the structural analysis.

In conclusion, we have grown two types of ferromagnetic MnAs thin films on Si(001) by MBE. The two types of MnAs have different crystal symmetry, caused by the different annealing temperature of the misoriented Si substrates. In-plane magnetic anisotropy was characterized for both types of MnAs on Si, consistent with the structure analysis. This result indicates the importance of the starting surface in controlling the structure and magnetic properties in the epitaxial MnAs/Si system.

The authors wish to thank Y. Matsunaga for useful discussions on the MBE growth on Si substrates. Thanks are also due to the cooperation of M. Ueki at the initial stage of this work. This work was partly supported by the PRESTO Project of JRDC and by a Grant-in-Aid for Scientific Research from the Ministry of Education, Science and Culture, Japan. One of the authors (M.T.) acknowledges the partial financial support from the Yazaki Foundation and Inamori Foundation.

[1] G. Prinz, Science **250**, 1092 (1990).
[2] M. Tanaka, J. P. Harbison, T. Sands, T. L. Cheeks, V. G. Keramidas, and G. M. Rothberg, J. Vac. Sci. Technol. B **12**, 1091 (1994).
[3] M. Tanaka, J. P. Harbison, M. C. Park, Y. S. Park, T. Shin, and G. M. Rothberg, Appl. Phys. Lett. **65**, 1964 (1994).
[4] M. Tanaka, J. P. Harbison, M. C. Park, Y. S. Park, T. Shin, and G. M. Rothberg, J. Appl. Phys. **76**, 6278 (1994).
[5] K. Akeura, M. Tanaka, M. Ueki, and T. Nishinaga, Appl. Phys. Lett. **67**, 3349 (1995).
[6] T. Takahagi, I. Nagai, A. Ishitani, H. Kuroda and Y. Nagasawa, J. Appl. Phys. **64**, 3516 (1988); T. Takahagi, A. Ishitani, H. Kuroda, Y. Nagasawa, H. Ito, and S. Wakao, J. Appl. Phys. **68**, 1 (1990).
[7] P. J. Flanders, J. Appl. Phys. **63**, 3940 (1988); Rev. Sci. Instrum. **61**, 839 (1990).

Thickness dependence of effective magnetic anisotropy

Ching-Ray Chang
Department of Physics, National Taiwan University, Taipei, Taiwan, Republic of China

Taking into account the occurrence probability of holes and imperfections we derive the nonlinear thickness dependence of the product Kt in very thin films. We predict both the usual $1/t$ and the recently observed $1/t^2$ dependence of the effective magnetic anisotropy K from the stochastic model. Agreement between theory and published experimental data is very good. © *1996 American Institute of Physics.* [S0021-8979(96)71108-5]

The surface properties of ultrathin films have recently attracted considerable interest. One of the most appealing new features, both from the point of view of fundamental physics[1–3] and of potential applications to information storage,[4,5] is magnetic anisotropy induced by symmetry breakdown at the film surfaces. Magnetic anisotropy in bulk ferromagnets differs considerably from that in thin films,[6] it is often written[7,8] as $E_A=KV\sin^2\theta$ where θ is an angle between the magnetization direction and the normal to the film, V is the film volume, and K is effective anisotropy energy density. Its deviation from the bulk value usually varies with the film thickness t as $1/t$ and is therefore attributed to the two film surfaces:

$$K=K_V+\frac{2K_S}{t}, \tag{1}$$

where K_V is the magnetic volume anisotropy which includes shape and crystalline contributions and K_S is the magnetic surface anisotropy (MSA). The influence of the surfaces (or interfaces) can be large enough to change the preferential orientation of magnetization in the film from in-plane to perpendicular.[9]

The physical origin of MSA has been studied qualitatively before and several possible mechanisms were proposed. A series of first-principles calculations on Co-based multilayers shows the order of the magnetic anisotropy is 1 meV/Co and it is simply related to the spin-orbit interaction.[3,10–12] Despite these advances in our understanding there remain some features of MSA in multilayers which could not until now be explained even qualitatively, to wit, most data exhibit a kink in the t dependence of the product Kt and a peculiar $1/t^2$ dependence of the effective magnetic anisotropy K has also been reported.[8,13] However, most of the first-principles calculations are based more on the situation of the perfect interface and neglect the roughness and imperfection of the interface. Indeed, roughness reduces the magnitude of K_S, especially for the sputtered samples[14] and the growth imperfection will result in a reduction of K_S from its intrinsic value of an ideal plane. When the interface is very rough, the effective areas of the interface reduces and the measured K_S also decreases.[15]

Some experimental results suggest that islandlike structures form on ultrathin films.[4] Magnetostatic[16] and strain calculations[17] also indicate that film imperfections can result in nonlinear t dependence of the product Kt. However, the influence of the imperfection film was largely ignored in most theoretical studies which concentrated for simplicity on continuous films; to understand it we must first consider the actual film growth mechanism during which the imperfections arise. This is a difficult problem involving complicated many-body effects, our goal here is to develop a simple independent column growth model covering the most essential features. Here we do not intend to simulate the real, complicated epitaxial system, we only want to demonstrate the imperfection film existing even in our simple model, and its possible dependence on the film thickness. The basic idea is that atoms to be deposited on the substrate are highly energetic and form, in effect, an ideal gas of Brownian particles. After adsorption they undergo redistribution, but on a cold, rapidly quenching substrate the adsorbed atoms are not free to move around and can, therefore, be approximately treated as randomly deposited. Within this simple model of rapidly quenched Brownian particles we develop a stochastic description of the surface area covered during film deposition and then employ a heuristic argument to take into account the effects of redistribution.

The film growth is modeled as a process of random deposition of M atoms over N sites so that the average thickness of the film is $t=\mathrm{M/N}$ layers. An exact combination expression for the occupation probability of a chose site is, of course, available but a simple geometric argument illustrated in Fig. 1 shall suffice for sufficiently large $\mathrm{N}<\mathrm{M}$. The probability of at least one of the N sites being empty is then $P_0^{(1)}\sim 1/t$ while the effective area ratio P_f^1, the probability of

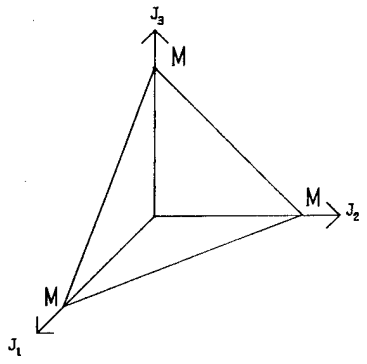


FIG. 1. There are $\mathrm{N}=4$ sites over which $\mathrm{M}\gg 4$ atoms are distributed, and the film thickness $t=\mathrm{M/N}$. The occupation numbers of each of the four sites are J_1, J_2, J_3, and $J_4=\mathrm{M}-J_1-J_2-J_3$, respectively, with the subsidiary condition $J_1+J_2+J_3\leqslant\mathrm{M}$. The number of all possible configurations is approximately equal to the simplex volume and the number of configurations with at least one site empty approximately equal to its surface area. The surface to volume ratio is then $\mathrm{N}'/\mathrm{M}\cdot[\mathrm{N}'+\sqrt{\mathrm{N}'}]\sim 1/t$, where $\mathrm{N}'=\mathrm{N}-1$.

 0021-8979/96/79(8)/4960/3/$10.00 © 1996 American Institute of Physics

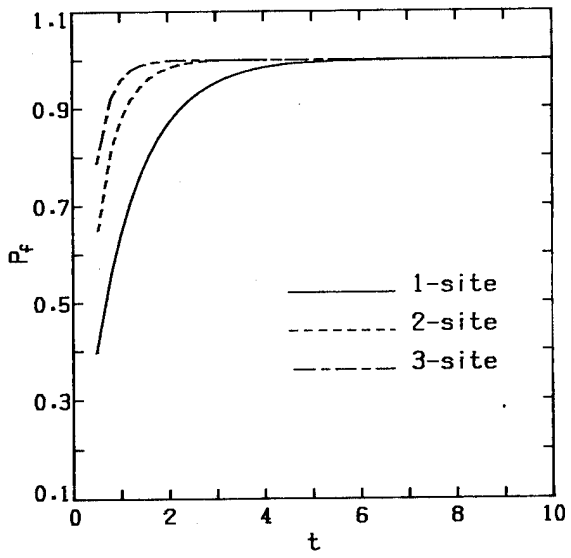


FIG. 2. The probabilities $P_f^1(t)$, $P_f^2(t)$, and $P_f^3(t)$ that a film formed by random deposition of $5000t$ Brownian particles over 5000 sites does not have at least a single site hole, at least a 2-site contiguous hole and at least a 3-site contiguous hole respectively. Note that contiguous holes are extremely rare. The plots show results of numerical simulations.

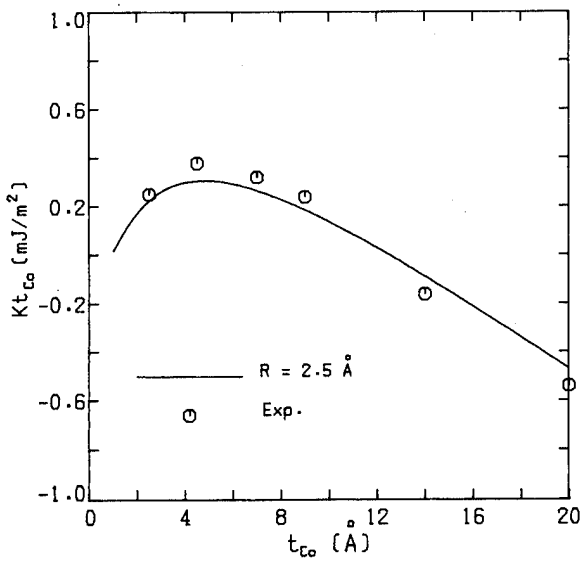


FIG. 3. Comparison between experimental data (Ref. 4) and the proposed Eq. (2).

the film being free of holes, equals $1-P_0^{(1)}$. To verify this expression we used a Monte Carlo simulation in which five hundred samples of $M=5000t$ atoms were randomly distributed over 5000 sites and averaged. The simulation results (Fig. 2) confirm the $1/t$ dependence of $P_f^{(1)}(t)$ for large enough t.

Adsorbed atoms have a certain probability of undergoing redistribution by means of surface diffusion. It is a reasonable assumption that interatomic attractive forces shall preferentially remove small holes which were initially randomly distributed in the film.[18] The probability of at least two neighboring deposition sites being empty is $P_0^{(2)}=O(1/t^2)$ and $P_f^{(2)}=1-P_0^{(2)}$ therefore represents the occupation probability after redistribution which, by assumption, removed single-site holes. We simulated the probability $P_f^{(2)}$ of the film not having a small (at least two sites) contiguous hole. Figure 2 shows that $P_f^{(2)}$ deviates from unity only for very thin films and, as predicted, $P_0^{(2)}\sim 1/t^2$ for sufficiently large t. By extension, on a very warm substrate only larger, n-site holes survive redistribution with probability $P_0^{(n)}(t)=0(1/t^n)$ (see Fig. 2 for $n=3$).

After the film growth and redistribution processes, there are still certain chances, e.g., $P_0(t)$, that the film can have holes, and the effective area ratio of the interface is not unity, i.e., $P_f(t)$. On the average, the film still can have a well-defined surface anisotropy K_S, however, its magnitude should be proportionally decreasing because of holes. Usually, thinner film results in the larger holes and the films may even break up into patches when it is very thin (Fig. 2). However, some thick films also tend to form columnar structures because of the geometrical self-shadowing effects[15] which are not included in our independent column growth model.

According to Eq. (1) the anisotropy energy within the volume $V=St$ of a film of surface area S is $E_A=(K_V V+2K_S S)\sin^2\theta$ but our previous considerations show that the surface area S should be modified by the effective area ratio $P_f(t)$ that there exists a film surface at all:

$$Kt=K_V t+2K_S P_f(t). \tag{2}$$

This modification of Eq. (1) is our key result. An explicit expression for the probability $P_f(t)$ is likely to be very complicated, because of the redistribution effect. All $1/t^n$ terms should appear at $P_f(t)$ simultaneously and we propose here the heuristic, single parameter formula $P_f(t)=\exp(-R/t)=1-R/t+o(R/t)$. Exponential functional form is chosen to exhibit all $1/t^n$ terms and R is an adjusting parameter. For $K_V<0$ a kink (maximum) appears in the plot of the product Kt while for large enough t the usual formula (1) is recovered. In Fig. 3 we show the plot of Kt_{Co} for the experimental data of Ref. 4 together with the best fit according to Eq. (2). Using the reported volume anisotropy energy,[4,5] $K_V=-0.72$ MJ/m^3, the best fit gives $K_S=0.55$ mJ/m^2 and $R=2.5$ Å. The fitted magnetic surface anisotropy is the same as reported value of K_S for Co/Pt multilayers.[19] It is interesting to point out that R is about one atomic layer of Co and is very close to the reported surface roughness of Co film[7] ($\approx$2 Å). This result suggests that the parameter R of our heuristic formula is related to surface roughness, but we cannot provide any rigorous proof.

As mentioned above, a $1/t^2$ thickness dependence of the effective anisotropy constant K has been reported for ultrathin films with perpendicular magnetization, such as fcc Fe/Cu[13] and Au/Co/Au(111) multilayers.[8] Within our model we expect such films to have holes with probability $P_0^{(1)}\sim 1/t$ so that $K=O(1/t^2)$ by Eq. (2). Our heuristic formula was also successfully used in interfacial curling model explaining the enhanced coercivity of coated particles.[20] We cannot substantiate our conjecture that redistribution effects lead to higher order thickness dependence since there exist, to the

best of our knowledge, no experimental data relating the effective anisotropy K to surface diffusion rate.

Although the independent column growth model is quite simple, however, it covers the most fundamental features of the film growth process and reveals the facts of the imperfection of the interface. Any more realistic simulations should still be manifested as the similar form of the Eq. (2). We wish to emphasize that the proposed modification of surface properties, i.e., their intrinsically stochastic nature, does not effect only MSA but every other surface related quantity.

The author would like to thank Ivo Klik for useful discussions. This research has been partially supported by NSC Grant NSC-85-2112-M002-030, Republic of China.

[1] J. G. Gay and R. Ritcher, Phys. Rev. Lett. **56**, 2728 (1986).
[2] F. J. A. den Broeder, D. Kuiper, A. P. van de Mosselaer, and W. Hoving, Phys. Rev. Lett. **60**, 2769 (1988).
[3] G. H. O. Daalderop, P. J. Kelly, and F. J. A. den Broeder, Phys. Rev. Lett. **68**, 682 (1992).
[4] W. B. Zeper, F. J. A. M. Greidanus, P. F. Carcia, and C. R. Fincher, J. Appl. Phys. **65**, 4971 (1989).
[5] H. J. G. Graaisma, W. J. M. de Jonge, and F. J. A. den Broeder, J. Magn. Magn. Mater. **66**, 351 (1987).
[6] C.-J. Lin, G. L. Gorman, C. H. Lee, R. F. C. Farrow, E. E. Marinero, H. V. Do, H. Notarys, and C. L. Chien, J. Magn. Magn. Mater. **93**, 194 (1991).
[7] C. Chappert and P. Bruno, J. Appl. Phys. **64**, 5736 (1988).
[8] P. Bruno and J.-P. Renard, Appl. Phys. A **49**, 499 (1989).
[9] P. F. Cargia, A. D. Meinhardt, and A. Suna, Appl. Phys. Lett. **47**, 178 (1985).
[10] R. H. Victora and J. M. Maclaren, Phys. Rev. B **47**, 11583 (1993).
[11] K. Kyuno, R. Yamamoto, and S. Asano, J. Phys. R. Jpn. **61**, 2099 (1992).
[12] C. Li, A. J. Freeman, H. J. F. Jansen, and C. L. Fu, Phys. Rev. B **42**, 5433 (1990).
[13] C. Liu, E. R. Moog, and S. D. Bader, Phys. Rev. Lett. **60**, 2422 (1988).
[14] M. T. Johnson, R. Jungblut, P. J. Kelly, and F. J. A. den Broeder, J. Magn. Magn. Mater. **148**, 118 (1995).
[15] M. T. Johnson, J. J. de Vries, N. W. E. McGee, J. aan de Stegge, and F. J. A. den Broeder, Phys. Rev. Lett. **69**, 3575 (1992).
[16] C. R. Chang, J. Appl. Phys. **72**, 596 (1992).
[17] C. R. Chang, Phys. Rev. B **48**, 15817 (1993).
[18] C. Uebing and R. Gomer, J. Chem. Phys. **95**, 7626 (1991).
[19] F. J. A. den Broeder, W. Hoving, and P. J. H. Bloemen, J. Magn. Magn. Mater. **93**, 562 (1991).
[20] J. S. Yang and C.-R. Chang, Phys. Rev. B **49**, 11877 (1994).

Uniaxial and planar magnetic anisotropy of thin transition-metal films (abstract)

R. Lorenz and J. Hafner
Institut für Theoretische Physik and Center for Computational Materials Science, Technische Universität Wien, A 1040 Wien, Austria

We present a novel approach to the calculation of the spin structures and magnetic anisotropies in crystals and thin films. Our technique is based on self-consistent real-space recursion calculations on a tight-binding linear muffin-tin orbital (TB LMTO) Hubbard Hamiltonian including spin–orbit coupling and allowing for arbitary orientations of the local spin-quantization axes. It allows one to scan the magnetic energy continuously as a function of the orientation of the magnetic moment and thus to avoid the computational problems that plague other techniques. Applications are presented for bulk iron and for thin Fe overlayers on Cu (111) and Cu (100) substrates. For monolayer coverage, we predict a perpendicular direction of the magnetic moment for Fe/Cu(100) an in-plane orientation of the spins for Fe/Cu(111), with anisotropies of the order of 1–2 meV. For Fe/Cu(100) we present a detailed investigation of the variation of the spin structures and of the change from perpedicular to in-plane anisotropy with increasing thickness of the Fe films. © *1996 American Institute of Physics.* [S0021-8979(96)67608-7]

 0021-8979/96/79(8)/4963/1/$10.00 © 1996 American Institute of Physics

Structural and magnetic properties of face-centered-cubic Fe films grown on Co(100)

Ernesto J. Escorcia-Aparicio, R. K. Kawakami, and Z. Q. Qiu
Department of Physics, University of California at Berkeley, Berkeley, and Materials Science Division, Lawrence Berkeley National Laboratory, Berkeley, California 94720

A rich variety of magnetic and structural properties have been found in fcc Fe films grown on Cu(100). In order to better comprehend the relation between the magnetic and structural properties of fcc Fe, we investigated fcc Fe films grown by molecular beam epitaxy on fcc Co(100). Structural characterization by low-energy electron diffraction and reflection high-energy electron diffraction indicate that the structural properties of fcc Fe films grown on Co(100) at room temperature are very similar to those of fcc Fe on Cu(100), exhibiting three distinct regions (fct, fcc, and bcc), with characteristic reconstructions at the boundaries. Magnetic measurements with *in situ* surface magneto-optic Kerr effect (SMOKE) reveal in-plane magnetization at room temperature for the three regions. Regions I and III are ferromagnetic, while region II has a small Kerr signal which is constant throughout the region. Cusps in the coercivity of the SMOKE loops are found to correspond to transitions between the three regions. Oxygen absorption experiments performed at room temperature revealed no change in the magnetization of region II, suggesting that the live layers responsible for the magnetic signal in this region are not at the surface. © *1996 American Institute of Physics.* [S0021-8979(96)71208-1]

Films of fcc Fe grown on Cu(100) at room temperature exhibit three regions with distinct structural and magnetic properties. Low-energy electron diffraction (LEED) and reflection high-energy electron diffraction (RHEED) measurements yield a fct phase for Fe thickness (d_{Fe})<5 ML, a fcc phase for d_{Fe}~5–11 ML, and a bcc phase for d_{Fe}>11 ML.[1–6] Characteristic LEED reconstruction patterns associated with each phase have also been identified.[1–6] It has been shown that the fct phase is ferromagnetic[2,3,7–9] and the fcc phase is antiferromagnetic with a live magnetic surface layer.[8,9] Both phases have out-of-plane magnetization with the ordering temperature below room temperature.[2,3,7–9] The bcc phase is bulklike ferromagnetic with in-plane magnetization.[2,3,7–9] Cusps in the coercivity of the magnetic hysteresis loops coincide with the transitions between the structural phases.[8,9] These results have led to the conclusion that there is a strong correlation between the structural and magnetic properties of Fe/Cu(100).[1–4,7] In light of this, the natural avenue to pursue is to ascertain which of the magnetic properties of the films are more susceptible to modification through structural changes by studying which magnetic properties are more closely tied to the structure.

In this paper, we shall report on experiments performed on ultrathin Fe films grown by molecular beam epitaxy (MBE) on fcc Co(100). The Co(100) substrate was obtained by growing a few monolayers (ML) of Co on a Cu(100) single crystal. Since Co has magnetic properties of its own, we wished to create a substrate that would structurally be similar to Cu(100), with added magnetic properties, in the hope that we would be able to separate which effects were due to structure and which ones to magnetic effects.

All samples were epitaxially grown in an ultrahigh vacuum (UHV) chamber with a base pressure of $\sim 2\times10^{-10}$ Torr. The UHV system is equipped with effusion cells, thickness monitor, RHEED, LEED, Auger electron spectroscopy (AES), Ar^+ ion sputtering, and an *in situ* surface magneto-optic Kerr effect (SMOKE) setup with both longitudinal and polar configurations. A sample manipulator provides a temperature range of 120–900 K and permits the use of all the above techniques at different stages of a single chamber.

The single-crystal Cu(100) substrate was mechanically polished down to 0.25 μm diamond paste and finished with vibration polishing using 0.05 μm Al_2O_3 powder. The substrate was then cleaned in UHV with cycles of Ar^+ ion sputtering at 2–5 keV and annealing at 650 °C. AES was used to ensure the cleanliness of the surface. For the growth of Fe on a dirty substrate, we observed as many as 40 RHEED oscillations accompanied by a 2×2 reconstruction in the LEED pattern, consistent with the report of Li *et al.*[9]

For all of the specimens reported here, a 6 ML fcc Co(100) film was epitaxially grown at room temperature onto the Cu(100) to form the substrate. The pressure during growth remained below 6×10^{-9} Torr. The Fe film was grown on top of the Co(100) either with a uniform thickness to study the LEED reconstruction and RHEED oscillations, or with a wedge shape to facilitate the thickness dependence study.

The structural properties of the room-temperature growth Fe/Co(100) system were investigated by RHEED and LEED. RHEED intensity was monitored during film growth and is shown in Fig. 1. Three regions can be identified: a region of erratic oscillations, followed by a region with fairly periodic and constant oscillations which gives way to a region where the oscillations disappear and the RHEED intensity is greatly decreased. The RHEED patterns for regions I and II are consistent with a fcc-like crystal structure, while the pattern for region III is consistent with bcc islandlike growth. Studies performed on the Fe/Cu(100) system[2,3,7–9] have yielded similar RHEED oscillation patterns. Other studies performed on the Fe/Cu system have shown that there, region I has a pseudo-fct crystal structure, while regions II and III are fcc and bcc, respectively.[1–6] The great similarity between the RHEED patterns and oscillations of the Fe/Cu and Fe/Co systems is consistent with the assertion that regions I, II, and III have, respectively, fct, fcc, and bcc crystal structures in both systems.

 0021-8979/96/79(8)/4964/3/$10.00 © 1996 American Institute of Physics

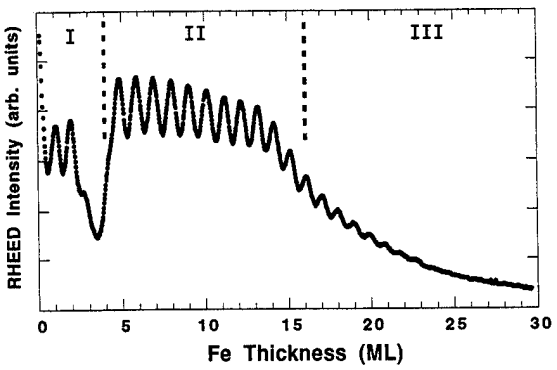


FIG. 1. Typical RHEED intensity variations during Fe deposition on fcc Co(100). Samples were grown at room temperature with a growth pressure $<6\times10^{-9}$ Torr. Different oscillatory behaviors identify three distinct regions, which are indicated. RHEED and LEED patterns show no difference between the Fe/Co(100) and Fe/Cu(100) systems.

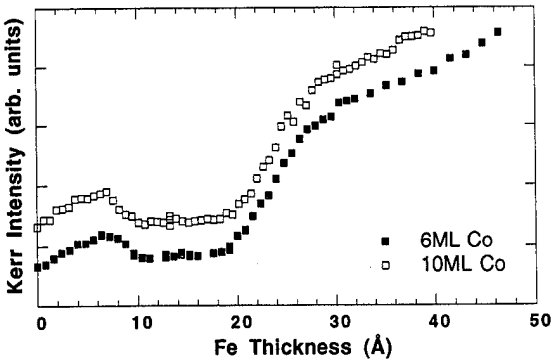


FIG. 2. Longitudinal Kerr signals of Fe wedges grown on different thicknesses of fcc Co(100) at room temperature. A study of the effect of Co thickness on the Fe/Co(100) system was performed by growing identical Fe wedges on different thicknesses of fcc Co(100). Two typical curves for 6 and 10 ML of Co are shown. Only in-plane magnetization was found in these samples throughout the whole thickness range.

A sample in which layers of Fe were uniformly grown on top of Co(100) was used to study reconstruction between regions I and II, taking a LEED picture after each successive growth. In particular, LEED patterns for pure Co and 2, 3.5, and 6 ML of Fe on Co were carefully studied. The pure Co and 2 ML of Fe (region I), showed a sharp 1×1 structure. The LEED pattern for 3.5 ML of Fe (transition between regions I and II), showed a 4×1 or 5×1 reconstruction. Finally, the pattern for 6 ML Fe coverage (region II) showed a 1×1 or a weak 2×1 reconstruction. Wedge samples of Fe on Co(100) yielded similar results. Experiments performed on the Fe/Cu(100) system yield a 1×1 reconstruction for region I, $4-5\times1$ reconstruction for the transition region between regions I and II and a 2×1 reconstruction for region II. The similar structural behaviors of the Fe/Cu and Fe/Co systems suggest that the structural properties of the fcc Fe are purely determined by the underlayer crystal structure, and are independent of the magnetic properties of the substrate.

Magnetic measurements were performed using the *in situ* SMOKE technique. Each of the three structural regions was observed to have a distinct magnetic behavior. In contrast to the room-temperature growth Fe/Cu(100) system, where the magnetization is out-of-plane in the first two regions with an ordering temperature below room temperature,[2,3,7–9] the room-temperature growth Fe/Co(100) system exhibits in-plane magnetization throughout the thickness range with an ordering temperature well above room temperature. Since both Co and Cu produce the same crystal structure for the Fe overlayer, we attribute the different magnetic behavior of the Fe/Co systems to the magnetic nature of the Co substrate.

We first studied the effect of the Co layer thickness on the magnetization of the Fe by growing identical Fe wedges on a different thickness of Co (2–20 ML). The results of two of these experiments, for 6 and 10 ML of Co are shown in Fig. 2. The two curves have a similar shape, but are offset from each other due to contribution from the Co. If the Co Kerr signal is subtracted from both, as in Fig. 3, both curves coincide precisely. Therefore, 6 ML of Co is enough for all the features of the Fe/Co system to be present. The choice of 6 ML as the Co thickness for most of our experiments was purely arbitrary.

Region I, which goes from 0 to 10 Å (6 ML) of Fe, is ferromagnetic with the Kerr intensity proportional to d_{Fe}. The Kerr signal drops to a small and constant level in region II, which goes from 10–20 Å (6–11 ML) of Fe. In region III, the Kerr signal increases and again acquires a ferromagnetic character. Since all three regions exhibit in-plane magnetization, we are able to compare directly the magnitudes of the Kerr signals in these three regions. It is interesting to note that the magneto-optic responses for regions I and III fall roughly on the same line, suggesting that the Fe film retains the magnitude of the magnetic moment as its structure

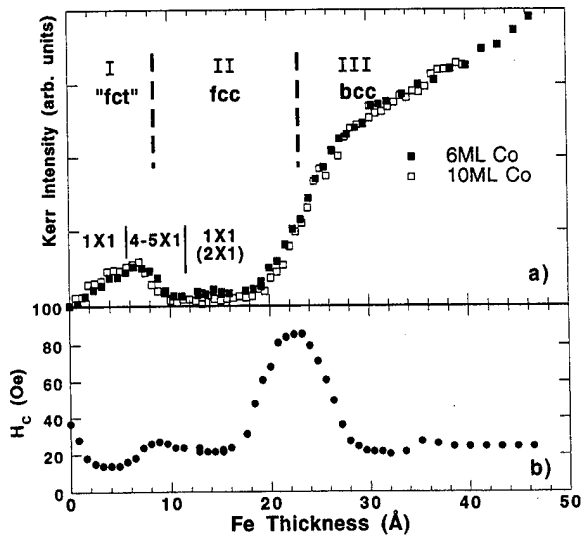


FIG. 3. (a) The same Kerr signals as in Fig. 2 with the Co backgrounds subtracted. The curves are identical for both Co thicknesses. Measurements were taken at room temperature. Note that the magneto-optic response in regions I and III falls roughly on the same line. (b) Cusps in the coercivity of the SMOKE loops were observed to correspond to the transition between regions.

changes from fcc to bcc. We attribute the different magnetic behavior between the Fe/Co and Fe/Cu systems to the ferromagnetic nature of the Co layer. We believe that it is the direct polarization of the Fe by the Co moment at the interface that causes the in-plane magnetization and the enhanced ordering temperature in the Fe/Co system as compared to the Fe/Cu system. To support our idea about direct coupling between Fe and Co, we investigated the shape of the magnetic hysteresis loop of the Fe/Co film. If the Fe overlayer were not coupled to the Co underlayer, a hysteresis loop for a Fe/Co film would have a step at the fields corresponding to the coercivities of Fe and Co. What we observe, however, is a single square loop with the coercitivity shifted from that of Co to a new value as d_{Fe} increases. The coercivity of the Fe/Co system versus d_{Fe} is shown in Fig. 3. Just as in the Fe/Cu system, as reported by Li *et al.*,[8] we observed cusps in the coercivity at the transitions between the three structural regions.

Region II seems to be the most interesting of the regions in this system. The fact that the Kerr signal is constant throughout the whole region, seems to imply that there are only a few layers that are magnetically live. A similar live layer was also found in the Fe/Cu system below room temperature and seems to come from the surface layer of the Fe film. Since the live layer in our Fe/Co system was observed at room temperature and there exists a direct magnetic coupling between Fe and Co, we speculate that the live layer in the Fe/Co system originates from the interface of Fe and Co instead of the surface layer of the Fe. To determine this, an Fe wedge grown on 6 ML Co was prepared and SMOKE measurements were performed just as described previously. A small amount of oxygen was leaked into the chamber so that it would react with the surface of our sample (a few minutes at 10^{-7} Torr). In principle, the oxygen would react with a few surface layers of our sample and if the magnetic live layers of the fcc region were located at the surface, we would see a change in the Kerr signal. A complete SMOKE scan across the wedge was performed after the oxygen absorption. The results of the SMOKE scans both before and after oxygen absorption are shown in Fig. 4. The most salient result is that the Kerr signal in region II remains the same, implying that the magnetic live layers for this region are not located at the surface. It can also be observed that region I and the transition to region II are shifted to regions of greater d_{Fe}, while the transition to region III seems virtually unaffected. The shift can be explained by realizing that if the oxygen removes magnetic layers from the surface, the thickness of Fe is effectively diminished. Also, since the fct and fcc phases are metastable, it is not inconceivable that the introduction of an oxide phase on the surface would cause a shift in the transition region, especially for regions so thin that surface effects are easily felt in the rest of the film. The fact that the transition to region III does not shift can be attributed to the fact that taking off layers in the surface cannot prevent the shift to the more stable bcc phase.

In conclusion, we have been able to grow fcc Fe on fcc Co(100). Structurally, the Fe/Co(100) system has been shown to be very similar to Fe/Cu(100). The basic magnetic features for both systems have been found to be very similar.

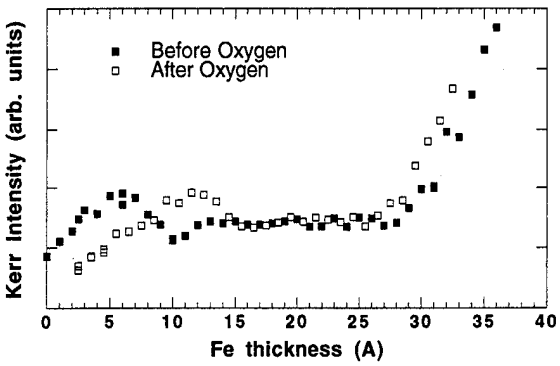


FIG. 4. Oxygen absorption experiment performed to ascertain the origin of the magnetic live layers in region II. SMOKE scans before and after oxygen absorption are shown. The shift in region I is evidence that the oxygen reacted with the surface. The magnitude of the Kerr signal in region II remains unchanged after absorption, implying that the magnetic live layers in this region are not at the surface.

Both initially have a ferromagnetic region for low coverage with a fct crystal structure. A second region is fcc and has only a few magnetic live layers. The third region is bcc and is again ferromagnetic. We believe that the difference in the plane of polarization and the ordering temperature for both systems is due to the Co polarizing the Fe moments at the interface. For both cases, cusps in the coercivity of SMOKE loops are observed. Li *et al.*[8,9] have reported that the fcc region for the Fe/Cu(100) system is antiferromagnetic with a ferromagnetic surface layer and that the antiferromagnetic coupling oscillation period is 2.6 ML. This noninteger period would seem to indicate the presence of spin-wave effects. Our experiments with oxygen absorption show that there is no live layer at the surface for the Fe/Co(100) system. We have seen evidence of the polarization of the Fe moments at the interface which would seem to indicate that the magnetic live layers are at the interface. Further work should concentrate on trying to determine whether there are antiferromagnetic coupling oscillations at lower temperatures. Also, the use of different growth conditions for this system should help further delineate the differences between the Fe/Cu(100) and the Fe/Co(100) systems.

This work supported in part by the U.S. DOE under Contract No. DE-AC03-SF00098.

[1] P. Xhonneux and E. Courtens, Phys. Rev. B **46**, 556 (1992).
[2] J. Thomassen, F. May, B. Feldman, M. Wuttig, and H. Ibach, Phys. Rev. Lett. **69**, 3831 (1992).
[3] M. Wuttig and J. Thomassen, Surf. Sci. **282**, 237 (1993).
[4] S. Müller, P. Bayer, A. Kinne, P. Schmailzl, and K. Heinz, Surf. Sci. **322**, 21 (1995).
[5] S. Müller, P. Bayer, C. Reischl, K. Heinz, B. Feldmann, H. Zilgen, and M. Wuttig, Phys. Rev. Lett. **74**, 765 (1995).
[6] H. Magnan, D. Chandesris, B. Villete, O. Heckman, and J. Lecante, Phys. Rev. Lett. **67**, 859 (1991).
[7] K. R. Heim, S. D. Healy, Z. J. Yang, J. S. Drucker, G. G. Hembree, and M. R. Scheinfein, J. Appl. Phys. **74**, 7422 (1993).
[8] D. Li, M. Freitag, J. Pearson, Z. Q. Qui, and S. D. Bader, Phys. Rev. Lett. **72**, 3112 (1994).
[9] D. Li, M. Freitag, J. Pearson, Z. Q. Qiu, and S. D. Bader, J. Appl. Phys. **76**, 6425 (1994).

Galvanomagnetic properties and magnetic domain structure of epitaxial MnAs films on GaAs(001)

M. C. Park, Y. Park, T. Shin, and G. M. Rothberg
Department of Materials Science and Engineering, Stevens Institute of Technology, Hoboken, New Jersey 07030

M. Tanaka
Department of Electrical Engineering, The University of Tokyo, 7-3-1 Hong, Bunkyo-ku, Tokyo 113, Japan

J. P. Harbison
Bellcore, 331 Newman Spring Road, Red Bank, New Jersey 07701

Epitaxial MnAs films on GaAs(001) in the thickness range 20–200 nm were studied. Using ordinary and extraordinary Hall effect data to determine the field required for perpendicular saturation and saturation magnetizations reported elsewhere, we determined the shape anisotropy constant in the basal plane of the hexagonal structure to be $3.7(0.6)\times10^5$ erg/cm^3 and the surface anisotropy constant to be $-1.3(0.4)$ erg/cm^2. The negative sign indicates thin enough films will be perpendicularly magnetized. By magnetic force microscopy of a 100 nm film we found stripe domains with 180° Bloch walls, thereby avoiding the hard c axis. The widths of the domains and the walls are 4.0(0.3) μm and 95(6) nm, respectively. In magnetoresistance, we observed behavior similar to other ferromagnets, namely peaks centered around the positive and negative coercive fields, and at fields beyond the coercive field a linear dependence on magnetic field. The electrical resistance showed rapid increase with temperature beginning about 5° below the Curie temperature (40 °C) caused by the change in crystal structure from hexagonal to orthorhombic. The resistivities are, respectively, 300(24) and 375(30) $\mu\Omega$ cm. Comparison with bulk values indicates the large lower temperature value is partly due to the presence of some orthorhombic phase observed in x-ray studies. © *1996 American Institute of Physics.* [S0021-8979(96)71308-8]

INTRODUCTION

Recently we reported initial results on the molecular beam epitaxy (MBE) growth of MnAs films on GaAs substrates,[1] and showed that they have excellent magnetic properties with almost square hysteresis loops, relatively high remanent magnetization (M_r=301–567 emu/cm^3) and relatively low coercive field (H_c=65–926 Oe).[2]

MnAs/GaAs is a new, epitaxial, ferromagnetic system with potentially useful magnetic properties. As such, it is worthwhile to measure a variety of properties to obtain an overall view. Here, we report galvanomagnetic properties (magnetoresistance, Hall effect, electrical resistance) obtained using a four-point probe method and magnetic domain structure using magnetic force microscopy (MFM). Additional structural and magnetization studies will be reported elsewhere.

EXPERIMENT

MnAs films with thicknesses of 20, 50, 100, and 200 nm grown on GaAs(001) substrates were used in this work. The easy axis is in the film plane in the [−1,−1,2,0] direction. The c axis is a hard axis also in the film plane in type A films and 39° out of the plane in type B. The films are hexagonal, but type A contains some paramagnetic orthorhombic phase near the substrate interface.[2] The magnetoresistance and Hall effect of these films were measured at room temperature using an ac four-point probe technique.[3] The frequency of the ac current was varied in the range from 400 to 1000 Hz while its amplitude was kept constant at 1 mA. Electrical resistance was measured at temperatures from 25 to 60 °C.

The domain structure of a 100 nm type B film was investigated by means of MFM using a commercial atomic force microscope.[4] The noncontact mode of operation was used to measure the forces between a magnetic tip and the magnetostatic stray field of the sample. Typically the tip was rastered 50–100 nm above the surface.

RESULTS AND DISCUSSION

The longitudinal magnetoresistance (MR) of a 100 nm MnAs film is displayed in Fig. 1(a). Here the field is in the easy direction parallel to the current in the plane of the sample. In Fig. 1(a) the linear part of the curve beyond the coercive field H_c (VSM value ±324 Oe) is due to s-d electron scattering as explained by Mott.[5] The peaks in Fig. 1(a) occur at the transition region observed in the vicinity of H_c in the VSM hysteresis loop and are centered at about H_c. The peaks are attributed to electron scattering from the domain walls.[6] Figure 1(b) shows the thickness dependence of the longitudinal magnetoresistance ratio, defined as resistance at zero field minus resistance at maximum field (±1400 Oe) divided by resistance at zero field.

The extraordinary Hall effect (EHE) voltage or resistance is linearly proportional to the component of the magnetization perpendicular to the plane of the film. Figure 2(a) shows the field dependence of the Hall resistance R_{xy} of a 20 nm film. Below the saturation field H_s the linear slope is related to the EHE and above H_s it is related to the ordinary Hall effect, which is much smaller. The data are fit to two straight lines whose intersection is taken to be H_s, which in this case is ~5500 Oe. The magnitude of H_s is given by

 0021-8979/96/79(8)/4967/3/$10.00 © 1996 American Institute of Physics

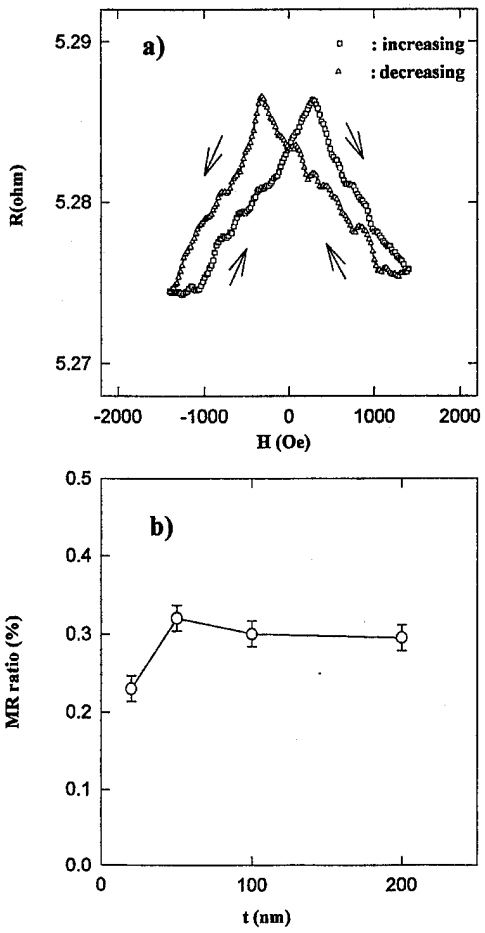


FIG. 1. (a) Resistance variation with applied field in the longitudinal geometry, 100 nm film. (b) Magnetoresistance ratio as a function of thickness from 20–200 nm.

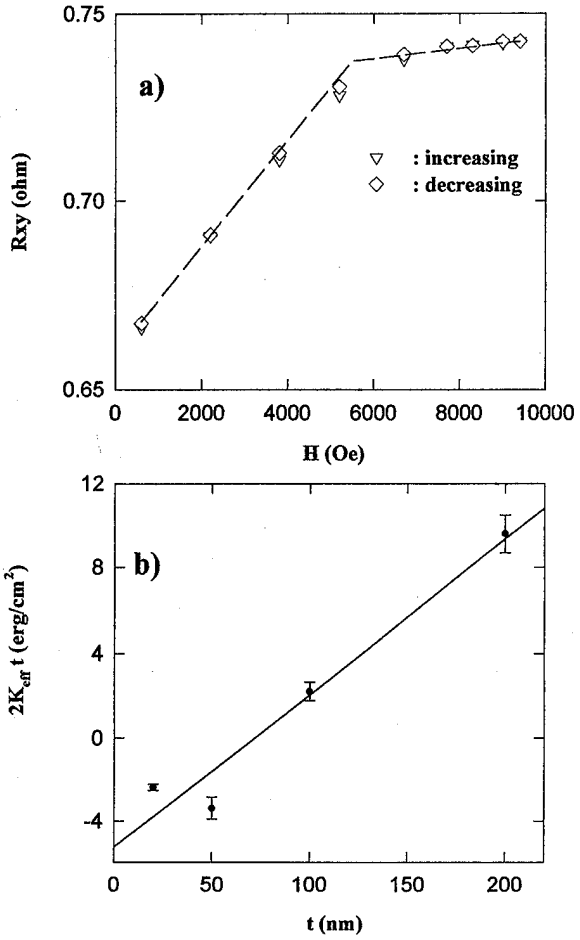


FIG. 2. (a) Hall resistance vs applied perpendicular field, 200 nm film. (b) Effective anisotropy constant times thickness as a function of thickness from 20–200 nm.

$H_s = 4\pi M_s + 2K_{\text{eff}}/M_s$, where K_{eff} is the effective anisotropy constant. K_{eff} can be written as $K_v + 2K_s/t$. Here, K_v is the shape anisotropy constant for the crystal plane perpendicular to the c axis, i.e., the basal plane of the MnAs structure, which in type A is also perpendicular to the film plane and t the thickness of the film. K_s is the surface anisotropy constant. Using the VSM values of M_s and the Hall effect values of H_s we find the effective anisotropy constant shown in Fig. 2(b) versus film thickness. The straight line is a least-squares fit yielding $K_v = 3.7(0.6) \times 10^5$ erg/cm^3. The c-axis anisotropy constant is about ten times larger. The fit gives $K_s = -1.3(0.4)$ erg/cm^2, the negative sign causing K_{eff} to become negative below about 75 nm, favoring perpendicular magnetization, which is opposed by the demagnetization energy. A thin enough film will show perpendicular magnetization.

Figure 3 shows the electrical resistance of a 200 nm film over the temperature range of 25–60 °C. Beginning about 5° below the Curie temperature (40 °C) the electrical resistance shows a rapid increase with temperature, which is caused by the change in crystal structure from hexagonal to orthorhombic that occurs in this temperature region, as observed by us in unpublished x-ray studies. See also Ref. 7 for x-ray results on bulk MnAs. We have measured the resistivity of the 200 nm film using the van der Pauw method,[8] which gives a directional average. Its value at 25 °C, 300(24) $\mu\Omega$ cm, is ~1.5 times greater than that of the bulk hexagonal phase[9] (~180 $\mu\Omega$ cm) along the c direction. A number of factors, such as strains, the presence of some orthorhombic phase,

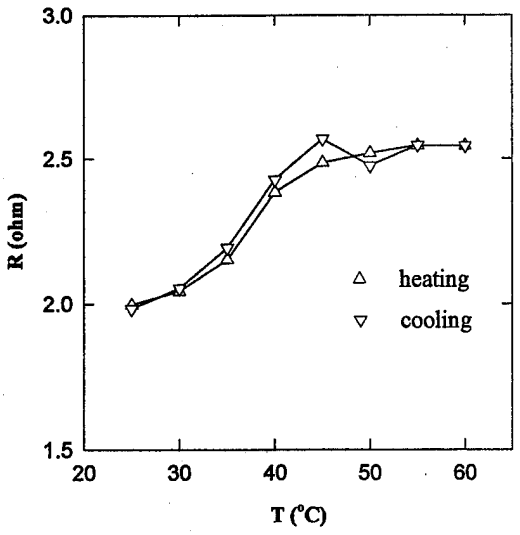


FIG. 3. Resistance variation with temperature, 200 nm film.

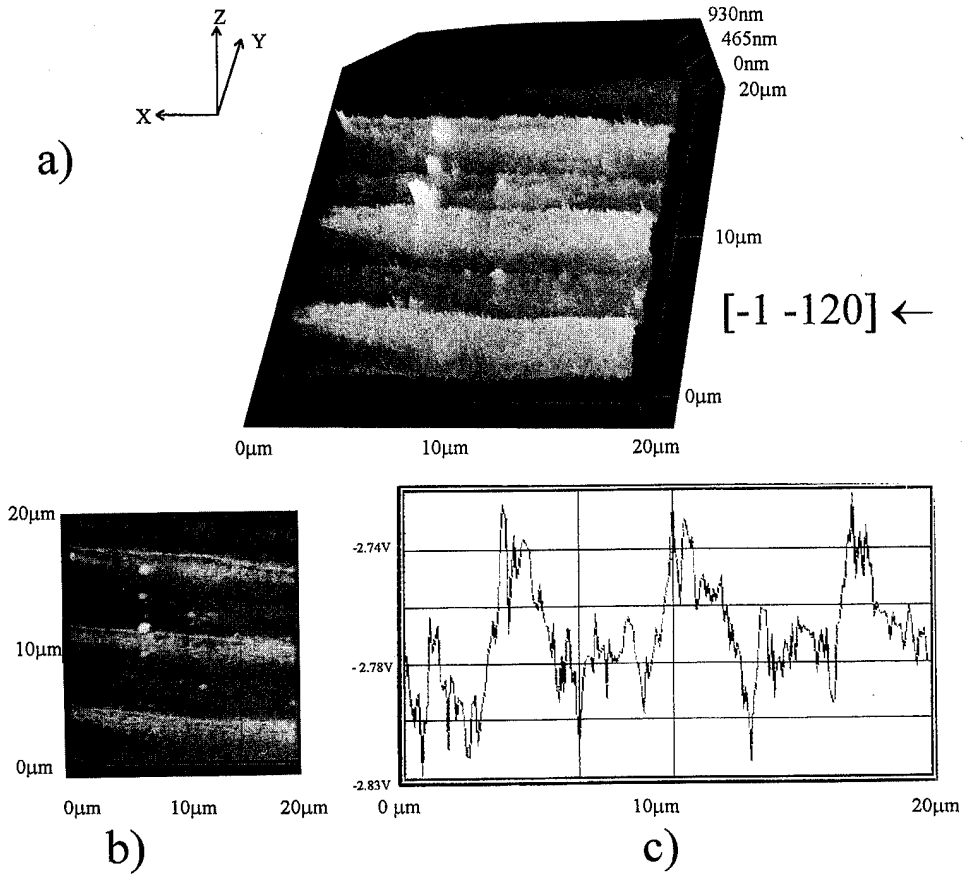


FIG. 4. MFM images of 100 nm film. x and y dimensions 20 μm. (a) z distance is proportional to force derivative. Arrow shows easy axis [−1−120]. (b) Brightness is proportional to force derivative; (c) line scan along path shown in (b).

and scattering at the interfaces, could account for the higher film resistivity. At 60 °C we find 375(30) $\mu\Omega$ cm to be compared with the bulk orthorhombic value of ~360 $\mu\Omega$ cm.[9] The closer agreement is expected since the film at 60 °C is single phase. Resistivity measurements in the bulk are difficult and poorly reproducible due to thermal fracturing of the samples, which is absent in our films.

Figure 4 shows MFM images of a 100 nm type B film in its demagnetized state. This film has an easy axis in-plane and hard c-axis tilted up 39°. In Fig. 4(a) the z direction (out of the film plane) shows not film height, but the vertical gradient of magnetic force. In Fig. 4(b) the force gradient is shown only by color variations. The broad bands are the domains, and as indicated in the figures their magnetizations lie along the easy axis in alternate directions. The vertical spikes are due to noise. In Fig. 4(b) it can be seen that alternate domain walls show a bright or dark line. The bright line indicates direction of magnetization perpendicularly up from the film, and the dark line shows the reverse. Thus the domain walls are 180° Bloch type. We believe this is the first MFM image of in-plane magnetized stripe domains. This shape is expected since the domains will avoid the very hard c axis. We find the average domain width is 4.0(0.3) μm and the domain wall width is 95(6) nm as given by the lines at the domain walls.

To better understand the brightness variation from one domain to another in Fig. 4(b) we have done the line scan shown in Fig. 4(c) along a path across the domains as shown in Fig. 4(b). This result agrees with the line scan calculated by Mamin *et al.*[10] corresponding to a tip having equal longitudinal and transverse components of its magnetization.

[1] M. Tanaka, J. P. Harbison, T. Sands, T. I. Cheeks, V. G. Keramidas, and G. M. Rothberg, J. Vac. Sci. Technol. B **12**, 1091 (1994).
[2] M. Tanaka, J. P. Harbison, M. C. Park, Y. S. Park, T. Shin, and G. M. Rothberg, J. Appl. Phys. **76**, 6278 (1994).
[3] F. L. A. Machado, B. L. da Silva, S. M. Rezende, and C. S. Martins, J. Appl. Phys. **75**, 6563 (1994).
[4] *Non-Contact and High Amplitude Resonance AFM User's Manual* (Topometrix, Santa Clara, CA 1993).
[5] N. F. Mott, Proc. Phys. Soc. London Ser. A **153**, 699 (1936).
[6] R. A. Hajjar, M. Mansuripur, and H. P. Shieh, J. Appl. Phys. **69**, 7067 (1991).
[7] R. H. Wilson and J. S. Kasper, Acta Crystallogr. **17**, 95 (1964).
[8] *Annual Book of ASTM Standards*, Vol. 10-05(F-76) (ASTM, 1995), p. 92.
[9] S. Haneda, N. Kazama, Y. Yamaguchi, and H. Watanabe, J. Phys. Soc. Jpn. **42**, 1201 (1977).
[10] H. J. Marmin, D. Rugur, J. E. Stern, B. D. Terris, and S. E. Lambert, Appl. Phys. Lett. **53**, 17 (1988).

GMR properties of spin valves using multilayered $Co_{90}Fe_{10}$ for free magnetic layer

Koichi Nishioka
Data Storage and Retrieval System Division, Hitachi Ltd., Kozu, Odawara, 256 Japan

Takayuki Iseki
Central R&D Center, JVC, 58-7, Shinmei-cho, Yokohama, 239 Japan

Hideo Fujiwara and Martin R. Parker
Center for Materials for Information Technology, The University of Alabama, Tuscaloosa, Alabama 35487-0209

To achieve higher GMR ratios in spin valves, $Co_{90}Fe_{10}$ films were used as the free and the pinned layer. A single layer of CoFe 100 Å and a multilayer of CoFe 18 Å/(Cu 8 Å/CoFe 18 Å)$_5$ were used as the free layer. Although the single layer CoFe showed large coercivities of 58 Oe along the easy axis and 40 Oe along the hard axis, the multilayer CoFe 18 Å/(Cu 8 Å/CoFe 18 Å)$_5$ showed smaller coercivities of 10 Oe along the easy axis and 1.5 Oe along the hard axis on a 100 Å thick Ta underlayer. The anisotropy field of the multilayer was 20 Oe. The film structures of the free layer were evaluated and it was found that the multilayer had higher oriented (111) texture than the single layer. The reason why the multilayer had higher oriented (111) texture was that the Cu layers between CoFe layers helped to have highly oriented (111) texture. To reduce the anisotropy field, the film was annealed in a magnetic field perpendicular to the initial easy axis at several temperatures. As the result, the anisotropy field was reduced to 3 Oe and the coercivity was 4 Oe after annealing at 140 °C. The GMR ratio of the spin valve of Ta 100 Å/CoFe 18 Å/(Cu 8 Å/CoFe 18 Å)$_4$/Cu 24 Å/CoFe 30 Å/FeMn 150 Å/Ta 50 Å was 7% after the annealing. © *1996 American Institute of Physics.* [S0021-8979(96)71508-0]

I. INTRODUCTION

Spin valves which consist of a free and a pinned magnetic layer with a nonmagnetic spacer layer[1] are prime candidates for read heads in future magnetic recording systems. Spin valves with NiFe in the magnetic layers show 3%–4% GMR ratio. In order to achieve higher performance in spin valves, higher GMR ratio is preferable. It is reported that utilizing Co as the pinned and the free-magnetic layer gives higher GMR ratio than utilizing NiFe because the Co layer gives larger spin dependent scattering at the interface.[1,2] However, it is difficult to use Co film as the free layer because it does not show soft magnetic properties. The coercivity is more than 30 Oe.[3] If Co or Co-based films gives soft magnetic properties, higher performances can be achieved in spin valves. In this study, we have tried to achieve soft magnetic properties in Co-based alloy films by making the films into multilayers and we have used this multilayer as the free layer of our spin valve. We also explored how annealing in a field affects the magnetic properties of the Co-based free layer and the pinned layer.

II. EXPERIMENTAL PROCEDURE

Films were sputter deposited on glass (Corning No. 7059) in a uniform dc field.[4] $Co_{90}Fe_{10}$ alloy target was used for the deposition of the magnetic layer because the content gave zero magnetostriction. The magnetic properties of single layer CoFe and multilayer CoFe with Cu interlayers were investigated. Spin valve films were prepared and GMR versus field curves were evaluated. The standard structure of the spin valve films (except for the free layer) was of Ta(100 Å)/free layer/Cu(24 Å)/CoFe(30Å)/FeMn(150 Å)/Ta(50 Å). The microstructures of the CoFe films were evaluated by x-ray diffractometry using Cu $K\alpha$ x-ray and atomic force microscope (AFM). Annealing and cooling in a magnetic field was also performed. The magnetic field during the annealing and the cooling was 100 Oe and was perpendicular to the initial easy axis and the initial pinned direction. Samples were kept for 1 h at the annealing temperature.

III. EXPERIMENTAL RESULTS

A. GMR and magnetic properties

Figures 1(a) and 1(b) show the GMR versus field curves

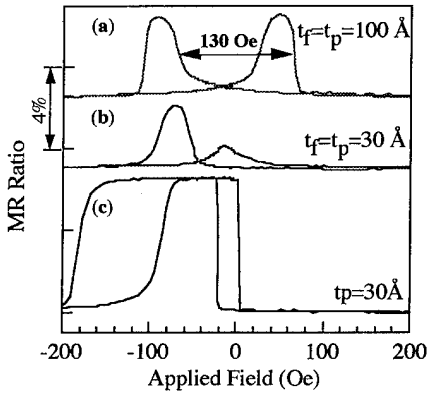


FIG. 1. (a) and (b) are GMR vs field curves of spin valves with single layer CoFe for the free and the pinned magnetic layer. The film structure is of Ta 100 Å/CoFe t_f Å/Cu 24 Å/CoFe t_p Å/FeMn 150 Å/Ta 50 Å. (c) is a GMR vs field curve of a spin valve with a multilayer of CoFe 18 Å/(Cu 8 Å/CoFe 18 Å)$_4$ for the free magnetic layer. The film structure is of Ta 100 Å/the free layer/Cu 24 Å/CoFe 30 Å/FeMn 150 Å/Ta 50 Å.

 0021-8979/96/79(8)/4970/3/$10.00 © 1996 American Institute of Physics

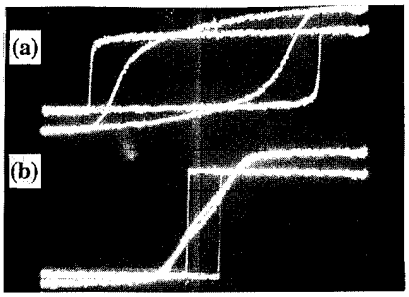


FIG. 2. The hysteresis loops of (a) a 100 Å thick CoFe single layer and (b) a multilayer of CoFe 18 Å/(Cu 8 Å/CoFe 18 Å)$_5$ on a 100 Å thick Ta underlayer.

of spin valves using single-layer CoFe for both the free and the pinned layer. The applied field was parallel to the pinned direction. When the thickness of both the CoFe free and pinned layers is 100 Å (a), there appears a large hysteresis about 130 Oe at the magnetic reversal of the free layer. The hysteresis of the pinned layer is also much larger than 100 Oe. The hysteresis of the free layer is so large that the GMR property is not suitable as a magnetic field sensor. When the thickness of both the CoFe free and pinned layers is 30 Å (b), the GMR curve shows two peaks and one of the peaks is much smaller than the other, which is not suitable as a magnetic field sensor. The hysteresis curve ($B-H$ curve) of this sample was also evaluated and it was found that this peak imbalance occurred because the magnetic reversals of the free and the pinned layer occurred at almost the same field when the applied field increased from a negative value to a positive value. Since the reason for the overlap of the magnetic reversals was caused by the small pinning field of 40 Oe, a larger pinning field was needed.

In order to improve the magnetic properties of the CoFe free layers, first, the thickness dependence of the coercivity of CoFe was investigated. As a result, the coercivity decreases from 58 to 12 Oe on decreasing the thickness from 100 to 30 Å, which means a thinner free layer is effective in achieving low coercivity. However, a 30 Å thin free layer showed only a small pinning field and a poor GMR versus field curve as shown in Fig. 1. Therefore we tried to make the free layer into a multilayer using Cu as the interlayers. Figure 2 shows the hysteresis loops of a 100 Å thick CoFe single layer and a multilayer of CoFe 18 Å/(Cu 8 Å/CoFe 18 Å)$_5$, on a 100 Å thick Ta underlayer. In the figure, hysteresis loops along the easy and the hard axis are shown. Both of the coercivities along the easy and the hard axis decrease drastically, from 58 to 8 Oe along the easy axis and from 40 to 1.5 Oe along the hard axis by the multilayering. The dispersion angles α_{50} were also evaluated, which was 35° in the single layer and 2° in the multilayer. The anisotropy field in the multilayer was about 20 Oe, which is relatively large comparing NiFe film.

Utilizing the multilayer as the free layer, spin vale films were deposited. The structure was: Ta 100 Å/CoFe 18 Å/(Cu 8 Å/CoFe 18 Å)$_4$/Cu 24 Å/CoFe 30 Å/FeMn 150 Å/Ta 50 Å. The GMR versus field curve is shown in Fig. 1(c). There are two discrete loops coming from the magnetic reversal of the free layer and the pinned layer. Comparing the GMR curve of the spin valve which have a 30 Å thick single layer CoFe for the free layer, the pinning field increased up to 140 Oe. The coercivity of the free layer is about 10 Oe, which is much smaller than that of the 100 Å thick CoFe spin valve of Fig. 1(a). The reason we chose this CoFe thickness (18 Å) for the free layer was that CoFe thickness smaller than 20 Å gave smallest coercivity in the free layer, but the thickness smaller than 15 Å gave smaller pinning field. As for the Cu thickness (8 Å), larger Cu thickness gave worse squareness in the magnetic reversal of the free layer.

B. Structural study of the free layer

To investigate the microstructure of the free layer, we made a 630 Å thick single layer film of CoFe and a multilayer film of CoFe 18 Å/(Cu 8 Å/CoFe 18 Å)$_{34}$ on a 100 Å thick Ta underlayer. In these films, the total CoFe thicknesses were the same. Although these films were thicker than the actual free layer of spin valves, they showed similar magnetic properties to the actual thick free layer, which meant that the multilayer film of CoFe 18 Å/(Cu 8 Å/CoFe 18 Å)$_{34}$ showed much smaller coercivity (10 Oe) and much smaller dispersion α_{50} (4°) than those of the single layer CoFe film (the coercivity was 35 Oe and the dispersion α_{50} was 12°). In the x-ray spectra (θ–2θ scan) of these films, there appeared fcc (111) peak in both of the films. The peak height of the multilayer film was four times of the height of the single layer. The half-height width of the multilayer was smaller than that of the single layer and the estimated grain sizes from the half-height widths were 180 Å for the multilayer and 120 Å for the single layer.

In the rocking curves of the fcc (111) peaks of these films, the half-height width of the multilayer was 8.2° and was much smaller than that of the single layer (12.1°), which meant that (111) planes in the multilayer were much more oriented than those in the single layer. To find the reason why the multilayer had a more highly oriented (111) texture, we investigated the crystal growth of Cu on a CoFe layer. 630 Å thick Cu layers were deposited on a film of Ta 100 Å/CoFe 18 Å and on a film of Ta 100 Å. The rocking curves of the Cu(111) peak of these samples were measured. The half-height width of the Cu layer on a 18 Å thick CoFe layer was much smaller than that of the Cu layer on Ta. From these results, a Cu layer on a CoFe layer tends to have a much more highly oriented (111) texture than a CoFe layer and as a result, the multilayer of CoFe and Cu had a more highly oriented texture than the CoFe single layer.

AFM images of the multilayer CoFe 18 Å/(Cu 8 Å/CoFe 18 Å)$_{34}$ on Ta underlayer and the single layer CoFe 630 Å were observed. The grain size of the multilayer from the image was about 400 Å, which was larger than that of the single layer (≅300 Å). The grain sizes obtained from the AFM image were almost double those obtained from the half-height widths of x-ray spectra, but these results of AFM images and x-ray spectra were consistent qualitatively. However, it was not fully understood why the multilayer showed much smaller coercivity than the single layer. The magnetic properties might be related to the texturing of the film.

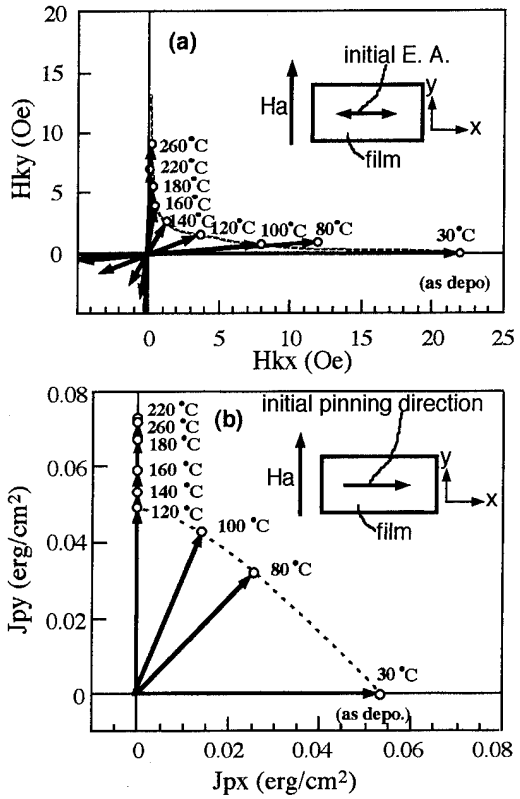


FIG. 3. Vector figures of (a) the anisotropy field of the free layer and (b) the coupling constant between the pinned layer and the antiferromagnetic layer after annealing for 1 h at several temperatures. A field of 100 Oe was applied perpendicular to the initial easy axis and the initial pinned direction during annealing and cooling.

C. Annealing effect

As shown in Fig. 2, the as-deposited anisotropy field H_k of the CoFe multilayer was still relatively large. In order to reduce the anisotropy field of the free layer, we investigated how annealing affects the anisotropy field in the free layer and the pinning field in the pinned layer. A magnetic field of 100 Oe was applied perpendicular to the initial easy axis and the initial pinning direction during the annealing and the cooling down.

Figure 3(a) shows how the anisotropy field changes with annealing. Increasing the annealing temperature, the direction of the anisotropy field rotates from the initial easy axis to a direction perpendicular to the initial easy axis. The magnitude of the anisotropy decreases from 22 to 3 Oe with increasing annealing temperature to 140 °C and it increases with increasing the temperature from 140 °C. Figure 3(b) shows the pinning direction and the coupling constant between the pinned layer and the antiferromagnetic layer after annealing at several temperatures. The direction of the arrows shows the pinning direction and the length of the arrows shows the coupling constant between the pinned layer and the antiferromagnetic layer. The pinning direction rotates from the initial direction toward the direction of the applied field during annealing. The pinning direction rotates by 50° away from the initial direction when the annealing temperature is 80 °C. It becomes parallel to the direction of the applied field during annealing when the temperature is higher than 120 °C. The coupling constant decreases with increasing the temperature from RT to 120 °C and it increases with increasing temperature from 120 to 220 °C.

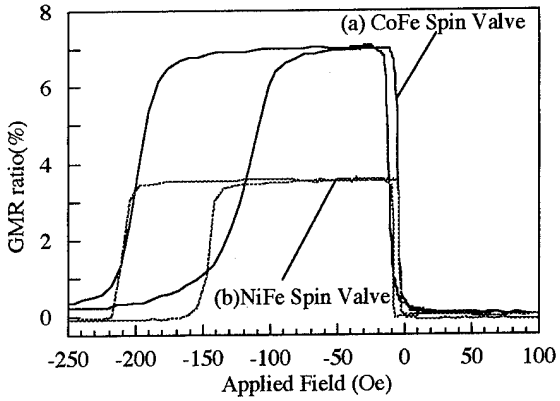


FIG. 4. GMR vs field curves of a CoFe spin valve and a NiFe spin valve. The samples are of (a) Ta 100 Å/CoFe 18 Å/(Cu 8 Å/CoFe 18 Å)$_4$/Cu 24 Å/CoFe 30 Å/FeMn 150 Å/Ta 50 Å after annealing at 140 °C and (b) Ta 100 Å/NiFe 100 Å/Cu 24 Å/NiFe 75 Å/FeMn 150 Å/Ta 50 Å.

Figure 4 shows the GMR versus field curve after annealing at 140 °C, which gives the smallest anisotropy field in the free layer. In the same figure, a curve of a NiFe lower case spin valve is also shown for comparison.[4] The coercivity of the CoFe spin valve is 4 Oe, which is of comparable value of that of the NiFe spin valve. The slope at the magnetic reversal of the free layer is almost the same as that of the NiFe lower case spin valve.

ACKNOWLEDGMENTS

The authors would like to thank Dr. Mark T. Kief and Dr. Jian X. Shen for AFM measurements.

[1] B. Dieny *et al.*, J. Appl. Phys. **69**, 4774 (1991).
[2] B. Dieny *et al.*, *Magnetism and Structure in Systems of Reduced Dimension, NATO ASI Series, Series B: Physics* (Plenum, New York, 1993), vol. 309, p. 2790.
[3] B. Dieny *et al.* U.S. Patent, 5159513 (1992).
[4] K. Nishioka *et al.*, IEEE Trans. Magn. (to be published).

Micromagnetics of uneven ultrathin film trilayers

A. S. Arrott
Simon Fraser University, Burnaby, British Columbia V5A 1S6 Canada

For ferromagnetic sandwiches where two iron layers are separated by a middle layer, the strength of the coupling sharply varies with each change in the thickness of the middle layer. If the interfaces were sharp on the atomic scale, one could observe this directly, or else one can use micromagnetics to take into account the actual morphology of less than ideal interfaces as shown by Slonczewski. As an approximation the average magnetization in each layer is found from a phenomenological energy that contains the competition between bilinear and biquadratic exchange constants that depend on surface roughness. More detailed micromagnetic calculations using relaxation methods to treat spatial variations of the magnetization in each layer are given for Fe–Cr–Fe sandwiches. The approximate calculations give jumps in the magnetization at critical fields, but these are smeared out in the more detailed calculations. For the special case of equivalent layers, the phenomenological expression for the energy can be used to obtain analytic expressions for the field dependence of the magnetization. © *1996 American Institute of Physics.* [S0021-8979(96)71608-7]

Two ferromagnetic ultrathin films separated by a nonferromagnetic ultrathin film is called a trilayer sandwich. The ferromagnetic layers can be treated as magnetic units that couple to each other in a way that depends on the properties of the middle layer and its two interfaces. Theory and experiment show that the variation of the thickness by one atomic layer d_0 is sufficient to make large changes in that coupling, sometimes reversing the sign with each additional atomic layer.[1] If interfaces were perfect one could determine $U_0(nd_0,\theta_1,\theta_2)$, the dependence of the coupling energy per unit area for perfectly flat layers, and how it changes with the thickness of the middle layer, $d=nd_0$, and the angles of the moments in the ferromagnetic layers. But interfaces are not perfect. The measured quantities depend on averaged interactions which depend on averaged angles, averaged layer thicknesses $\langle n\rangle$, and the range of layer thicknesses Δn. If the films are such that at most, three thicknesses of the interlayer are present it is possible to deconvolute the interlayer exchange from experiments on less than perfect samples.[2]

The foundations for this subject have been well set by Slonczewski.[3] To a first approximation

$$U_{\text{eff}}(\langle n\rangle,\Delta n,\theta_1,\theta_2)=J_1(\langle n\rangle,\Delta n)\cos(\theta_1-\theta_2) - J_2(\langle n\rangle,\Delta n)\sin^2(\theta_1-\theta_2) \quad (1)$$

where J_1 is called the bilinear exchange and J_2 is called the biquadratic exchange. These depend on the interlayer exchange and the surface roughness. To obtain the magnetic response to a field H applied in the plane of the sandwich, one must add the anisotropy energy and the Zeeman energy. The total energy per unit area is

$$U=U_{\text{eff}}-\sum_{i=1}^{2} H\sigma_{si}\cos\theta_i+K_i\sin^2\theta_i\cos^2\theta_i, \quad (2)$$

where σ_{si} is the magnetic moment and K_i is the fourfold, in-plane, magnetic anisotropy energy, both per unit area, for the two ferromagnetic layers, $i=1$ and 2. Both σ_s and K depend on the thickness of the given layer. In a proper experiment σ_s and K would be known for each of the layers from previous experiments on individual layers. The layers should be thin enough that the exchange coupling produces a high degree of alignment of moment directions through the thickness. Equation (1) describes the situation where the interfaces are atomically flat except for islands that are one atom rises or one atom depressions called mesas or antimesas. The model is applicable when the mean separation of the mesas is comparable to or smaller than the exchange length.

In analyzing experimental results one can use Eq. (1) with its two parameters J_1 and J_2, or one can go back to the calculus of variations that underlies the model to determine the spatially varying magnetization in each of the two layers where the parameters are the desired $J(n)$ for perfect layers. The latter is computationally intensive with a relaxation calculation needed for each point on a curve of the field dependence of the magnetization; an example is given below for a sandwich of 20 atomic layers of Fe coupled to 40 atomic layers of Fe through Cr. It is much less work to compute the magnetization from Eqs. (1) and (2). In the simplest case where the two ferromagnetic layers are indistinguishable, there are analytic solutions for the magnetization which are given below. This case is explored in detail in that it provides a road map for exploration of more realistic models.

A straightforward approach, using Eqs. (1) and (2), is to calculate the energy for all pairs of angles for a series of fields, following a local minimum from one field to the next. Local minima become inflection points at critical fields. For each local minimum there can be upper and/or lower critical fields. A particular example for equivalent layers is shown in Fig. 1, where the lower energy contours are shown for four fields $H\sigma_s/(2J_1)=0.35$, 0.5, 0.7, and 0.85 for $K=J_1$ and $J_2=0.2J_1$. The darker regions in Fig. 1 have higher energy. The corresponding magnetizations are discussed below.

For this special case of equivalent layers, analytical results follow by introducing the normal coordinates, $\bar{\theta}=(\theta_1+\theta_2)/2$ and $\Delta=(\theta_1-\theta_2)/2$. For $\bar{\theta}=0$, the moments in the two layers rotate in opposite senses. For $\Delta=0$, the moments are locked together. For the ranges of field for which $\bar{\theta}=0$ is an equilibrium solution, the energy is given by

$$U=2[(-2J_2+K)\cos^4\Delta+(J_1-2J_2+K)\cos^2\Delta - \sigma_s H\cos\Delta]-J_1. \quad (3)$$

 0021-8979/96/79(8)/4973/3/$10.00 © 1996 American Institute of Physics

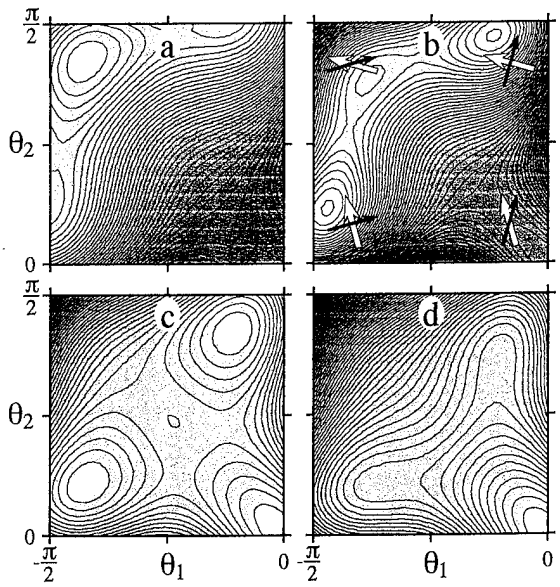


FIG. 1. For the case of equivalent layers, contours of equal energy for $-\pi/2<\theta_1<0$ and $0<\theta_2<\pi/2$ for Eqs. (1) and (2) with $K=J_1>0$ and $J_2=0.2J_1$. In (a), (b), (c), and (d), $H\sigma_s/(2J_1)=0.35$, 0.52, 0.70, and 0.85, respectively. The local minimum that starts in (a) near $\theta_1=-\pi/2$, $\theta_2=\pi/2$ moves along the diagonal toward the fully aligned state at $\theta_1=\theta_2=0$ without falling into the deep minima on either side; see (c). If K is slightly decreased, the path is through one of the side minima.

The relation between $m_x\equiv\cos\Delta\cos\bar{\theta}=\cos\Delta$, the magnetization relative to saturation, and the field is given by

$$\frac{H\sigma_s}{2J_1}=\left[\frac{K-2J_2}{J_1}(1-2m_x^2)+1\right]m_x. \tag{4}$$

From Eqs. (3) and (4), it can be seen that the biquadratic exchange is equivalent to a fourfold anisotropy when $\bar{\theta}=0$. The field dependence of m_x is shown in Fig. 2 for a range of effective anisotropy $K_{\text{eff}}\equiv(K-2J_2)$. For $0.2J_1>K_{\text{eff}}>-J_1$, the m_x curves are completely reversible. For $K_{\text{eff}}>0.2J_1$, m_x jumps to saturation with a decrease in energy as seen in the lower portion of Fig. 2, which shows $U-U_s$, where U_s is the energy for the saturated state at the particular field. For $K_{\text{eff}}<-J_1$, m_x jumps on reversal. In real materials there are many nucleation sites with the result that the magnetization often finds a route to the lowest energy state. Thus, there are reversals in very small reverse fields and jumps to saturation at less than the critical fields. For $K_{\text{eff}}>0.2J_1$, the jumps to saturation would then occur close to the fields for which $U-U_s$ goes through zero (see Fig. 2).

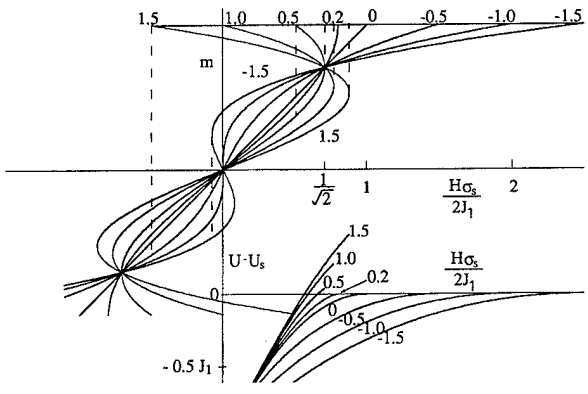


FIG. 2. Field dependence of (a) the relative magnetization, m, and (b) the energy, $U-U_s$, for symmetric configurations with $\theta_1=-\theta_2$. U_s is the energy of the saturated state in the same field. The normalized effective anisotropy, $K_{\text{eff}}/J_1\equiv(K-2J_2)/J_1$ varies as noted from curve to curve. In (a) the thin lines correspond to unstable equilibria and the dotted lines to jumps at instability points. It can be seen in (b) that, when $K_{\text{eff}}/J_1>0.2$, the energy is greater than at saturation for a range of fields below the instability field. For $H=\sqrt{2}J_1/\sigma_s$, $m=1/\sqrt{2}$ independent of K_{eff}.

In addition to the saturated states and the states with counter-rotating magnetizations, there are states where σ_{x1} and σ_{x2} differ. In the ranges of J_2 and H for which $\bar{\theta}\neq0$, the relation between H and $m_x\equiv\cos\Delta\cos\bar{\theta}$ is given parametrically as a function of $\bar{\theta}$. As the function contains two square roots, there are four combinations of the signs in front of the radicals. There are ranges of $\bar{\theta}$ for which there are no solutions of the equation that relates Δ and $\bar{\theta}$; these ranges depend on J_1/K and J_2/K. In terms of $x\equiv\cos\Delta\equiv\cos[(\theta_1-\theta_2)/2]$ and $y\equiv\cos\bar{\theta}\equiv\cos[(\theta_1+\theta_2)/2]$, the energy is

$$\begin{aligned}U=&-J_1(1-2x^2)-J_2[1-(1-2x^2)^2]-2\sigma_sHxy\\&+2K[x^2(1-x^2)-8x^2y^2(1-x^2)(1-y^2)\\&+y^2(1-y^2)].\end{aligned} \tag{5}$$

Minimizing with respect to Δ and $\bar{\theta}$, produces analytical expressions for the dependence of H and x on y:

$$\frac{H\sigma_s}{2K}=\frac{y}{x}(-2y^2+1)(8x^4-8x^2+1), \tag{6}$$

$$x^2=\frac{Y_a^{\pm}\sqrt{Y_a^2-8KY_by^2(2y^2-1)}}{4Y_b}, \tag{7}$$

$$Y_a=-J_1+2J_2+K(8y^4-1),$$

$$Y_b=2J_2+K(4y^2-1). \tag{8}$$

The relative magnetization is given by $m_x=xy$.

One can only begin to catalog the range of behaviors encompassed by these equations for $\bar{\theta}\neq0$ along with the saturated and symmetric solutions, $\Delta=0$ and/or $\bar{\theta}=0$. Here, it helps to be specific. The case investigated is that of Fig. 1 where $J_1=K$ and $J_2=0.2J_1$, for which $(K-2J_2)=0.6J_1$. The dependence of m_x and U on H is shown in Fig. 3. In low fields the lowest energy states have $\bar{\theta}=0$. The magnetization is reversible on path I($Opqr$). The state with $\bar{\theta}=0$ becomes unstable at r, where the saturated state and the state on path II($abcd$) with $\bar{\theta}\neq0$ have almost the same energy. If one looks with sufficient precision, the state maintains $\bar{\theta}=0$ as m_x jumps to saturation. In Fig. 1, one can see the small local minimum sneaking along the divide between the two deep minima. With a slight change in the parameters, or with a slight rotation of the field direction, the configuration jumps to path II with $\bar{\theta}\neq0$, even though this reduces m_x slightly. Path II is stable between point a, where on decreasing fields it jumps to path I, and point d, where on increasing fields it jumps to the saturated state.

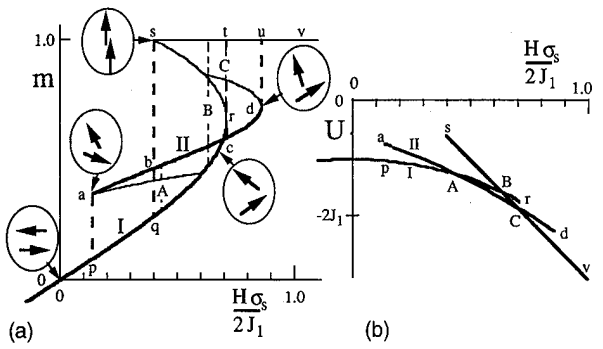


FIG. 3. Field dependence of (a) the relative magnetization, m, and (b) the energy U, for the case, $K=J_1>0$ and $J_2=0.2J_1$, illustrated in Fig. 1.

At the field corresponding to A in Fig. 3, the energy is the same on both paths. If there is nucleation, this is where the jump might occur. One could speculate on what might happen on nucleation from a high field. Is the jump from saturation to path I or to path II? Such questions are answered in more realistic models where the magnetizations in the two sublattices adjust suitably at critical points. In terms of Eq. (1), J_2 is field dependent near the critical fields.

An example of a more realistic calculation is given for a sandwich of Fe–Cr–Fe with one atom high variations in the thickness of the middle layer from place to place on a scale comparable to the exchange length. Now the exchange interactions $A_i[(dM_{ix}/dx)^2+(dM_{iy}/dx)^2+(dM_{ix}/dx)^2+(dM_{iy}/dx)^2]$ for $i=1,2$ come into the calculation explicitly. [They are already included in the derivation of Eq. (1).] The exchange between the layers is described by a local interaction directly across the middle layer $U(x,y)=J(x,y)(M_{1x}M_{2x}+M_{1y}M_{2y})$. In the middle layer there are islands (mesas) of greater thickness for which $J(x,y)=-J$ (ferromagnetic) imbedded in a matrix (plains) of lower thickness where the $J(x,y)=J$ (antiferromagnetic).

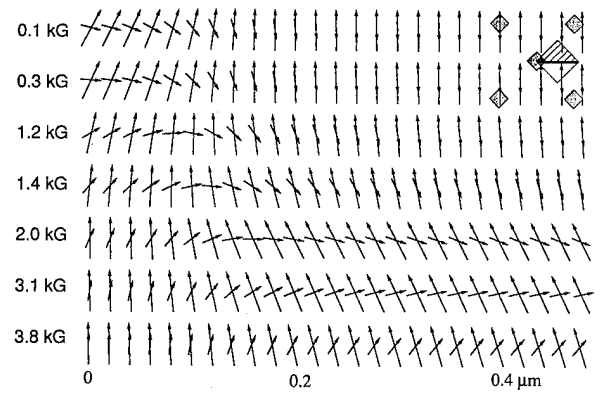


FIG. 4. The variation of the magnetization along a line from the center of a mesa where the coupling is ferromagnetic to the middle of the region of antiferromagnetic coupling between the mesas, a distance of 50 nm which is about 3 exchange lengths. Note, that in low fields the antiferromagnetic coupling penetrates well into the ferromagnetic mesa. The mesas are illustrated in the upper-right-hand side corner. The derivatives of the magnetization vanish on the boundaries of the shaded triangle used for calculation.

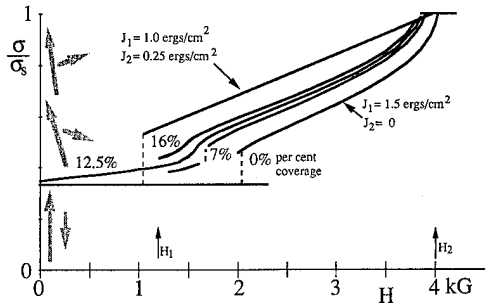


FIG. 5. The field dependence of the magnetization for the simulation of a sandwich of 20 atomic layers of Fe separated by 11 atomic layers of Cr from 40 atomic layers of Fe. The mean spacing of the mesas is 70 nm as determined by electron diffraction. The area fraction covered by the mesas is varied from curve to curve as indicated. The model assumes that the interlayer exchange J oscillates in sign with each additional atomic layer in the interface. The interlayer exchange $J=J_1=1.5$ erg/cm^2 is chosen to match a measured upper critical field H_2. As the area of the mesas of ferromagnetic coupling, $J=-J_1$, is increased, the lower transition approaches the measured lower critical field H_1. The upper curve is calculated from Eq. (2) using the known anisotropies and magnetizations for 20 and 40 layers of Fe and choosing $J_1=1.0$ erg/cm^2 and $J_2=0.25$ erg/cm^2. It does not give the curvatures found in the relaxation model and in the experimental results.

In low fields, the two layers will be coupled close to parallel in the mesas and close to antiparallel in the plains. In between, $M_{ix}(x,y)$ and $M_{iy}(x,y)$ change with position. It is assumed for simplicity that the islands are periodic in x and y; see upper-right-hand side corner of Fig. 4. The calculation was originally meant to simulate a real experiment[4] which had 20 atomic layers of Fe separated by 11 atomic layers of Cr from an Fe whisker substrate. The choice of 40 atom layers for the base layer in the model was to emulate the bulk by replacing it by an effective strongly coupled layer. In the experiment there were two fields, H_1 and H_2, where the magnetization showed changes of state (see Fig. 5). The anisotropy, magnetization, and exchange constants in each layer are known. The only adjustable parameters in the calculation were J and the area of coverage by mesas of ferromagnetic coupling. The mesa separation was ~70 nm.

A relaxation method[5] is used to solve for the magnetization patterns at a series of fields. The magnetization along a line joining second neighbor mesas is shown in Fig. 4. The magnetization of the thicker layer remains close to the field direction for all fields. The magnetization of the thinner layer remains close to antiparallel until a critical field ~1.5 kG, where they turn to ~90 with respect to the field. This is discontinuous at low coverage and continuous for higher coverage. The dotted lines in Fig. 5 indicate the fields where two different configurations have the same energy.

The suppression of discontinuous jumps is a major difference between the more realistic relaxation calculation and the model with biquadratic exchange independent of field.

[1] J. Urguris, R. J. Celotta, and D. T. Pierce, Phys. Rev. Lett. **67**, 140 (1991); S. T. Purcell *et al.*, Phys. Rev. Lett. **67**, 903 (1991).
[2] B. Heinrich *et al.*, Phys. Rev. B **47**, 5077 (1993).
[3] J. C. Slonczewski, Phys. Rev. Lett. **67**, 3172 (1991).
[4] B. Heinrich *et al.*, J. Magn. Magn. Mater. **140–144**, 545 (1995).
[5] A. S. Arrott, J. Appl. Phys. **69**, 5212 (1991).

Magnetization of two-dimensional *XY* magnets with symmetry breaking fields: Relevance to ultrathin magnetic films (abstract)

J. Rothman and P. C. W. Holdsworth
Laboratoire de Physique Théorique ENSLAPP, URA 14-26 du CNRS, Ecole Normale Supérieure de Lyon, 69364 Lyon, France

S. T. Bramwell
Department of Chemistry, University College London, London WC1H OAJ, United Kingdom

The magnetization of ultrathin films shows a power law dependence on temperature with an exponent β that depends on the spin anisotropy. Experimentally it is found that films with easy-axis anisotropy show $\beta=1/8$, characteristic of the two-dimensional Ising model, while those with dominant easy-plane anisotropy show $\beta=0.23$. We recently discussed the finite size magnetization of the *XY* model and showed that this system has universal behavior which leads to the exponent $\beta=0.23$. A number of authors have therefore interpreted their results in terms of the finite size two-dimensional *XY* model. The success of these explanations implies that the four- and sixfold anisotropy fields present in real films are irrelevant in determining the critical behavior of the magnetization. In the sixfold case this observation agrees with theoretical expectations, while in the fourfold case the situation is unclear, as the renormalization group analysis of José *et al.* shows the fourfold field to be a marginally relevant variable which gives rise to nonuniversal exponents. This theoretical result, however, pertains to the thermodynamic limit and is not necessarily relevant to real finite systems. We investigate the effect of symmetry breaking fields on the magnetic behavior of idealized finite size *XY* models by means of Monte Carlo simulation. We find that the fourfold field is indeed irrelevant for the system sizes of interest, and may only become relevant for system sizes beyond the physical domain. We also confirm that the sixfold field is both qualitatively and quantitatively irrelevant, and notice a number of novel features connected with the behavior of finite size models which cannot be observed in the thermodynamic limit. © *1996 American Institute of Physics.* [S0021-8979(96)67708-3]

Characterization of iron-oxide films grown on Cu(001) and Ag(001) (abstract)

L. Scipioni and B. Sinkovic
Department of Physics, New York University, New York, New York 10003

Ultrathin films of different phases of iron oxide have been grown in UHV on Cu(001) and Ag(001) substrates by reactive evaporation and their structural and magnetic properties measured. By varying the oxygen partial pressure during growth, the oxide stoichiometry was varied from Fe/O=2/3 (fully oxidized) to Fe/O=3.5, as measured by AES and XPS, spanning: FeO, α-Fe_2O_3, Fe_3O_4, and oxide+metal films. LEED patterns and STM images reveal that all of the films grow with a (111) surface orientation with two domains rotated 90° from each other. Films with Fe/O>1 exhibit a 16×1 superstructure induced by the presence of Fe-metal atoms localized at oxide/substrate interface, as found by XPD measurements. Their net magnetization is perpendicular to the film plane, while the films without an interfacial Fe-metal layer exhibit in-plane magnetization. The fully oxidized films (α-Fe_2O_3) exhibit an antiferromagnetic behavior. Temperature dependences of MOKE signal from thin Fe_3O_4 films indicate enhancement of Verwey transition. © *1996 American Institute of Physics.* [S0021-8979(96)67808-X]

 0021-8979/96/79(8)/4976/1/$10.00 © 1996 American Institute of Physics

Thickness dependence of magneto-optical properties in face-centered-cubic Co/Cu(001) ultrathin films

K. Nakajima and T. Miyazaki
Department of Applied Physics, Faculty of Engineering, Tohoku University, Sendai 980-77, Japan

Magneto-optical Kerr spectra of ultrathin Co films grown on Cu(001) surfaces have been measured *in situ*. The growth mode and the crystal structure have been investigating by reflection high-energy electron diffraction observation. A 20-Å-thick fcc Co grown on Cu(001) had a lateral lattice constant of 3.59±0.01 Å, which was about 1.4% expanded compared with that of the bulk fcc Co. There was a remarkable difference above 4 eV in $\omega\sigma_{yz}$ spectra between 20- and 1000-Å-thick films. $\omega\sigma_{yz}$ spectra for 20-Å-thick Co film showed a resonance-type structure at around 5 eV. It is considered that the structure is caused by the lower energy shift of the 1→6 interband transitions due to the narrowing of the 3*d* bands. © *1996 American Institute of Physics.* [S0021-8979(96)71708-6]

The magnetic properties of ultrathin film and multilayer systems with Co have received much attention in recent years due to the fundamental interest in these properties and their potential applications. These multilayers exhibit novel and unique properties in their magneto-optical properties.[1,2] Recently, Weller *et al.* have presented the polar Kerr spectra of thick fcc Co film.[3] There is a clear difference in polar Kerr spectra between the fcc and hcp phases. It is considered that the unique magneto-optical properties in the multilayers are relevant to the crystal structure of the magnetic layers. In addition, a strong dependence of the magnetic properties of fcc Co films on their structure and growth conditions has been found.[4,5] However, there are few studies aimed at exploring the effect of the influence of the structure on the magneto-optical properties of fcc Co films. In this article, we report the results of the *in situ* observation of magneto-optical Kerr effect spectra during the epitaxial growth of fcc Co on the Cu(001) surface.

The samples were prepared by means of electron beam heating. The base pressure of the deposition chamber was below 5×10^{-11} Torr. A polished MgO single crystal was used as a substrate. After a heat treatment of the substrate at 830 °C, a Ag buffer layer, 1000 Å thick, was deposited to alleviate the lattice mismatch between Cu and MgO and then a 2000-Å-thick Cu seed layer was deposited. The Co layers were grown on this seed layer at room temperature. The thickness of the film was measured by a calibrated quartz thickness monitor. The growth rate of Co was 2 Å/min. The growth mode and crystal structure were monitored during the deposition by a reflection high-energy electron diffraction (RHEED) apparatus with a digital camera system.

After the deposition, the sample was transferred from the deposition chamber to another connected measurement chamber and ellipsometric measurements were performed *in situ*. The angle of incident was set at 55.7°. The complex Kerr effect $\phi_k+i\eta_k$ was measured by the Faraday-cell modulation method. The complex optical constant $n+ik$ was measured by the rotating analyzer method. All experiments were carried out in the photon energy range of 1.7–5.1 eV at room temperature in a remanent state in order to reduce the Faraday effect in vacuum windows. The measurement was repeated after each Co layer deposition in an angstrom step up to 20 Å. The entire measurement time required for each sample was less than 1 h in a background pressure of 1×10^{-9} Torr.

RHEED patterns observed during the growth of 1000 Å Co essentially maintained the same fourfold symmetry as that of the Cu(001) surface. A conventional x-ray diffraction scan for 1000-Å-thick Co showed only a fcc(002) peak with an interlayer spacing of 1.768 Å. It shows good agreement with the lattice constant found in bulk fcc Co (a=3.5447 Å).[6] The specular reflected RHEED intensity recorded during the deposition is shown in Fig. 1(a). RHEED intensity oscillation is observable with an average period of 1.8 Å. The oscillation means that fcc Co grows in a manner of layer-by-layer growth on the Cu(001) surface. However, the first, second, and third periods are longer than 1.8 Å. It is considered that the irregular oscillation periods with an initial decrease of intensity are due to cobalt agglomeration, which makes the growth mode deviate from the ideal layer-by-layer growth.[7–9] Figure 1(b) shows the thickness dependence of the in-plane lattice constant estimated from intervals between (01) and $(0\bar{1})$ streaks along [100] direction. Obviously, the first adsorbed Co layer has a different lateral lattice constant than that of the Cu substrate. The lattice constant for layers up to 20 Å thick takes a nearly constant value of 3.59±0.01 Å, which is about 0.6% less than that for the Cu substrate and is also about 1.4% greater than that of the bulk fcc Co. Above 20 Å, the lattice constant approaches the intrinsic value of the bulk fcc Co asymptotically.

The Kerr effect was observed first at 6 Å (3.3 ML) with the in-plane easy axis. No perpendicular magnetic anisotropy was observed in the entire range of measurements. It agrees with other experimental results.[5,10] The complex Kerr spectra for 6- to 20-Å-thick films exhibited essentially the same features. The Kerr ellipticity spectrum had a broad peak at around 4 eV. The Kerr rotation spectrum was correspondingly dispersive at the energy and had another broad peak at 4.8 eV. Figure 2 shows spectra of the off-diagonal elements of the conductivity tensor $\omega\sigma_{yz}$ for 20- and 1000-Å-thick fcc Co. The inset to Fig. 2 shows the Re σ_{xx} spectra for those films. The conductivity tensor was calculated from the measured value of the complex Kerr effect $\phi_k+i\eta_k$ and the complex optical constant $n+ik$ using suitable equations. Apparently, there is a remarkable difference between the spectra

 0021-8979/96/79(8)/4977/3/$10.00 © 1996 American Institute of Physics

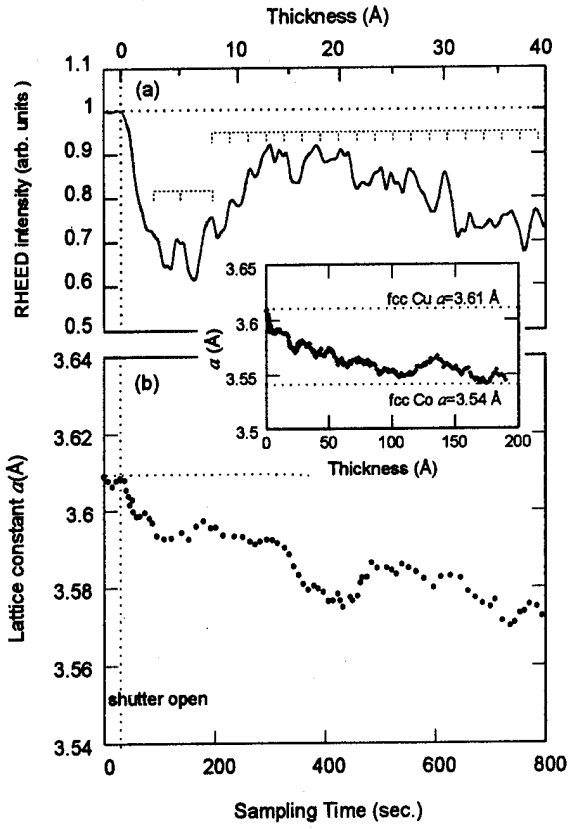


FIG. 1. (a) Specularly reflected RHEED intensity during the growth of Co films on Cu(001) surface. The electron beam is incident to 0.7° with an energy of 20 keV. The intensity is normalized to the value of the Cu surface. The upper horizontal axis shows the mass thickness of the film measured by the quartz thickness monitor. (b) Lateral lattice constant a as a function of the film thickness.

for 20-Å and 1000-Å-thick films. For 20-Å-thick film, the $\omega\sigma_{yz}$ spectra exhibit a resonance-type structure at around 5 eV. The Re $\omega\sigma_{yz}$ spectrum has a broad peak at around 4.8 eV. The Im $\omega\sigma_{yz}$ spectrum is correspondingly dispersive and changes its sign at 5.0 eV. On the other hand, for 1000-Å-thick film, the Im $\omega\sigma_{yz}$ still has not changed its sign at the energy. Theoretical calculations predicted that the Im $\omega\sigma_{yz}$ spectrum of bulk fcc Co took its sign, reversed from positive to negative, at 5.7 eV.[11] The interband transitions 1→6 in both spin bands are responsible for it.[12–15] Halicov *et al.*[11] argued that the 1→6 transition was of the character for the 3*d* transition metals. The transitions occur between the $s-d$ subbands located at the bottom of the 3*d* band and the higher $s-p$ subbands above the Fermi level. Thus, the zero-crossing point of the Im $\omega\sigma_{yz}$ spectrum is roughly in proportion to the 3*d*-band width.

We consider that the marked resonance structure at 5 eV for 20-Å-thick film is caused by the same 1→6 transitions with shifting to the lower energy side due to the larger lateral lattice constant. Without any tetragonal distortion normal to the lattice planes, the larger lateral lattice constant causes a narrowing of the 3*d*-band width. Our RHEED experiments cannot provide any information about the perpendicular distances. However, recent low-energy electron diffraction analysis showed that the intermediate layers of Co/Cu(001)

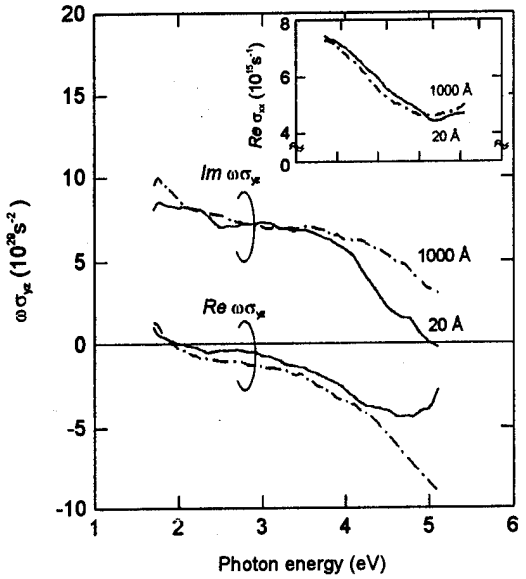


FIG. 2. $\omega\sigma_{yz}$ spectra of Co films deposited on the Cu(001) surface. The solid and dotted-dashed curves correspond to 20- and 1000-Å-thick films, respectively. The inset shows the Re σ_{xx} spectra of the films.

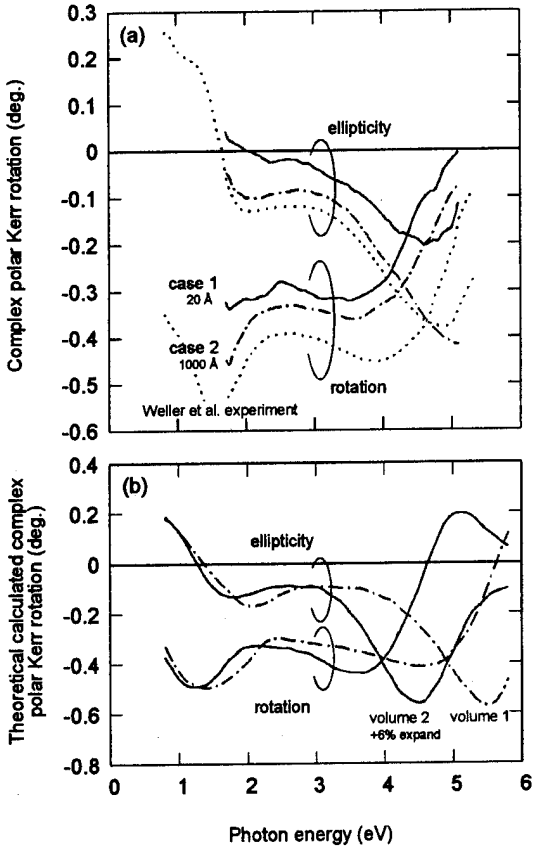


FIG. 3. (a) Evaluated complex polar Kerr spectra for bulk fcc Co. The solid and dotted-dashed curves correspond to cases 1 (using the conductivities for 20-Å-thick Co) and 2 (for 1000 Å), respectively. The dotted curves represent the experimental polar Kerr spectra for the 1000-Å-thick fcc Co film presented by Weller *et al.* (Ref. 3). (b) Theoretical calculated spectra for bulk fcc Co presented by Gasche *et al.* (Ref. 17). The solid and dotted-dashed curves correspond to volumes 1 (11.18 Å/atom), and 2(13.22 Å/atom; 18% expanded compared with volume 1), respectively.

films that were a few monolayers thick had an interlayer spacing of 1.74±0.01 Å, a decrease by about 2% compared with the bulk fcc Co.[9,16] If we obediently combine the value of $c=3.48$ Å with the lateral lattice constant $a=3.59$ Å, we get a value of 11.21 Å^3/atom as the atomic volume. It is increased by about 1% compared with that of the bulk fcc Co ($a=3.54$ Å; 11.09 Å/atom).

Recently, Gasche *et al.*[17] calculated the complex polar Kerr spectra of the bulk fcc Co as a function of the lattice parameter. In order to compare our results with their theoretical calculations, we evaluated the complex Kerr spectra of the bulk fcc Co from the obtained conductivities. In Fig. 3(a) the evaluated polar Kerr spectra are shown. Cases 1 and 2 correspond to the 20- and 1000-Å-thick Co, respectively. The dotted lines show the experimental result for the 1000-Å-thick fcc Co film presented by Weller *et al.*[3] It is clearly seen that the high energy peak in the ellipticity spectrum in case 2 shifts to lower energy compared to the peaks of case 1 and Weller's data. Figure 3(b) shows the theoretical calculations by Gasche *et al.*[17] In the calculation, they took volumes 1 and 2 to be 11.18 and 13.22 Å/atom, respectively. The former corresponds to the experimental lattice constant of $a=3.54$ Å and the latter to the case where the lattice constant is 6% larger than that of the experiment. The ellipticity spectrum for volume 1 shows a broad peak at 5.4 eV. And strikingly, the high energy peak shifts to the low energy side at about 4.4 eV for volume 2. They also calculated the magnetic moments for each case. It was shown that the 18% expansion in atomic volume caused a 10% enhancement in the magnetic moment. Their results clearly confirmed that the center position of the $1\rightarrow6$ transitions strongly depends on the $3d$-band width. From these results, it is satisfactory to say that the observed lateral lattice expansion in the 20-Å-thick Co may modify the electronic structure, narrowing the $3d$-band width, as it appears to effect its magneto-optical properties.

In conclusion, in the 20-Å-thick fcc Co film, we found that the Im $\omega\sigma_{yz}$ spectra for the 20-Å-thick film changed its sign at 5 eV. Theoretical calculations predicted that the Im $\omega\sigma_{yz}$ spectrum of bulk fcc Co took its sign, reversed from positive to negative, at 5.7 eV. It is considered that the observed lower energy shift of the zero-crossing point of Im $\omega\sigma_{yz}$ is due to the expanded lateral lattice constant that leads to the narrowing of $3d$ bands.

This work was supported in part by a Grant-in-Aid for Japanese Junior Scientists from the Ministry of Education, Science, Sports and Culture of Japan.

[1] W. B. Zeper, F. J. A. M. Greidanus, P. F. Carsia, and C. R. Fincher, J. Appl. Phys. **65**, 4971 (1989).
[2] S. Hashimoto, Y. Ochiai, and K. Aso, Jpn. J. Appl. Phys. **28**, L1824 (1989).
[3] D. Weller, G. R. Harp, R. F. C. Farrow, A. Cebollada, and J. Stichit, Phys. Rev. Lett. **72**, 2097 (1994).
[4] C. M. Schneider, P. Bressler, P. Schuster, J. Kirchner, J. J. de Miguel, and R. Miranda, Phys. Rev. Lett. **64**, 1059 (1990).
[5] J. J. de Miguel, A. Cebollada, J. M. Gallego, R. Miranda, C. M. Schneider, P. Schuster, and J. Kirchner, J. Magn. Magn. Mater. **93**, 1(1991).
[6] C-A. Chang, J. Magn. Magn. Mater. **109**, 243 (1992).
[7] H. Li and B. P. Tonner, Surf. Sci. **237**, 141 (1990).
[8] S. Ferrer, E. Vlieg, and I. K. Robinson, Surf. Sci. Lett. **250**, L363 (1991).
[9] A. Clarke, G. Jennings, R. F. Willis, R. J. Rous, and J. B. Pendry, Surf. Sci. **187**, 327 (1987).
[10] B. Heinrich, J. F. Cochran, M. Kowalewski, J. Kirchner, Z. Celenski, A. S. Arrot, and K. Myrtle, Phys. Rev. B **44**, 9348 (1991).
[11] S. V. Halikov and Y. A. Uspenski, J. Phys. Condens. Matter **2**, 6137 (1990).
[12] M. Singh, C. S. Wang, and J. Callaway, Phys. Rev. B **11**, 287 (1975).
[13] Y. Kubo and S. Wakoh, J. Phys. Soc. Jpn. **50**, 835 (1981).
[14] D. K. Misemer, J. Magn. Magn. Mater. **72**, 267 (1988).
[15] C. S. Wang and J. Callaway, Phys. Rev. B **9**, 4897 (1974).
[16] E. Navas, P. Schuster, C. M. Schneider, J. Kirchner, A. Cebollada, C. Ocal, R. Miranda, J. Cerda and P. de Andres, J. Magn. Magn. Mater. **121**, 65 (1993).
[17] T. Gasche, M. S. S. Brooks, and B. Johansson, Proceedings of the Magneto-Optics Recording Media International Symposium '94, 1995, p. 303.

Investigation of magnetic coupling in sputtered epitaxial Fe/Cr and Co/Cu wedged structures

X. Bian
IBM Almaden Research Center, 650 Harry Road, San Jose, California 95120-6099

H. T. Hardner
Department of Physics, University of Illinois at Urbana–Champaign, Urbana, Illinois 61801

S. S. P. Parkin
IBM Almaden Research Center, 650 Harry Road, San Jose, California 95120-6099

We explore the magnetic interlayer exchange coupling in single-crystalline Fe/Cr and Co/Cu wedged multilayers prepared by magnetron sputtering on two orientations of MgO—(100) and (110). Structural examination shows that high quality epitaxial films are obtained in both systems using seeded epitaxy growth techniques. Oscillatory interlayer coupling is observed in Cr-wedged samples grown on both MgO(100) and MgO(110) with similarly long oscillation periods of ~18 Å. These results are comparable to earlier work for molecular beam epitaxy and sputter-deposited epitaxial Fe/Cr structures. Long-period oscillatory coupling is also observed in sputtered Co/Cu(110) for the Cu-wedged structures. Studies of the dependence of magnetic coupling on the thickness of the magnetic layers for fixed Cr layer thickness provides no evidence of any nonmonotonic dependence. © *1996 American Institute of Physics.* [S0021-8979(96)71808-2]

Since the discovery of antiferromagnetic (AF) coupling between ferromagnetic layers across a nonmagnetic spacer layer[1] and its oscillatory nature,[2] interlayer exchange coupling has attracted extensive theoretical and experimental studies for a wide variety of structures. Oscillation in exchange coupling as a function of nonmagnetic layer thickness has been demonstrated to be a general property for most magnetic/nonmagnetic transition and noble-metal multilayers.[3] Long periods of 8–12 Å—with the exception of Cr (~18 Å)—have been identified in sputtered polycrystalline multilayers.[3] Additional short-period oscillations have been found in molecular-beam epitaxy (MBE) grown single-crystalline wedges.[4,5] Of particular interest is the dependence of the interlayer exchange coupling strength on the thickness of the ferromagnetic layer. There have been far fewer studies on this property and the nature of this dependence, whether oscillatory[6,7] or not, remains an open question.

Sputter epitaxy is a useful technique for the growth of oriented epitaxial films since it readily allows for the exploration of diverse materials and thin film structures. This technique has had limited application to the study of the magnetic and transport properties of epitaxial metallic thin film structures.[8–10] In this article, we study the interlayer exchange coupling in wedged Fe/Cr(100), (211), and Co/Cu(110) sandwiches and multilayers prepared by magnetron sputtering. Results are presented for well-defined long-period oscillations in wedged structures as well as the consequences of significant in-plane magnetic anisotropy. These studies were, in large part, carried out using longitudinal magneto-optical Kerr measurements.

A number of Fe/Cr and Co/Cu wedged multilayers, with either a wedged nonmagnetic layer or ferromagnetic layers, were grown by magnetron sputter deposition in an ultrahigh vacuum chamber equipped with six 2 in. dc magnetron sputtering sources. The base pressure prior to deposition was typically 2.0×10^{-9} Torr, the sputter pressure was usually 3.0×10^{-3} Torr Ar and the deposition rates were 2.0 Å/s for all sputtered metals. For Fe/Cr, a Cr seed layer, at least 100 Å thick was deposited at temperatures ranging up to 525 °C onto polished, chemically cleaned single-crystal MgO(100) and (110) substrates to establish the epitaxy. Subsequent layers were deposited at 150–180 °C and were capped with a thin Cr layer. For Co/Cu a seed layer of 50 Å Pt was deposited at 500–525 °C and the Co/Cu structure was grown near room temperature. The wedged layers were formed by moving a precision-controlled shutter during the deposition. Usually related nonwedged multilayers with fixed layer thicknesses were deposited under similar conditions to allow for detailed x-ray and superconducting quantum interference device magnetometry studies. The structural characterization of the films was performed using x-ray diffraction with Cu K_α radiation. The magnetic properties were studied with longitudinal magneto-optic Kerr effect (MOKE). Using computer-controlled precision motion stages Kerr hysteresis loops were collected as a function of position along a wedge and azimuthal orientation of the wedge with regard to the applied magnetic field.

The crystallographic orientation of the films was examined by x-ray diffraction on nonwedged multilayer samples. Figure 1 shows the high-angle specular θ–2θ scan for a [Fe15 Å/Cr 28 Å]$_7$ multilayer grown on 100 MgO. Figure 1 also shows that the film is of a single-crystallographic orientation and is oriented along (100). Only the MgO(200), MgO(400), and Fe/Cr(200) reflections and the associated superlattice satellites are observed. The Fe/Cr(200) rocking curve full width at half-maximum (FWHM) is only 1.30° as shown in the inset of Fig. 1, indicating a high degree of crystal orientation. The high-angle specular scan for a corresponding Fe/Cr multilayer grown on 110 MgO similarly shows evidence of a single-crystalline orientation. In this case Bragg peaks corresponding to MgO(220) and Fe/Cr(211) and its associated superlattice peaks are found. Rocking curves about the Fe/Cr(211) reflection have a typical FWHM of 1.40°. These values compare favorably with rocking curves from typical comparable MBE-grown

 0021-8979/96/79(8)/4980/3/$10.00 © 1996 American Institute of Physics

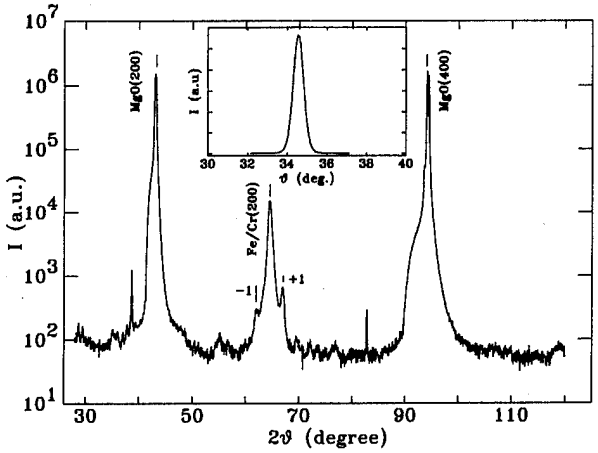


FIG. 1. High angle x-ray specular scan for a Fe/Cr multilayer of the form, MgO(100)/Cr 100 Å/[Fe 15 Å/Cr 28 Å]$_7$/Fe 15 Å/Cr 40 Å. The inset shows the rocking curve at the Fe/Cr(200) Bragg reflection.

multilayers.[11] The in-plane structure and epitaxial orientation were also studied by asymmetric diffraction scans on selected samples.

As an indirect structural characterization, we studied the magnetocrystalline anisotropy on a wedged multilayer to verify its epitaxial crystal structure. Such an experiment was carried out by measuring the MOKE hysteresis loops at a particular Cr thickness for which the magnetic layers are ferromagnetically coupled for various azimuthal angles. Figure 2 shows the dependence of the in-plane remanent magnetization as a function of azimuthal angle for typical (100)- and (211)-oriented Fe/Cr samples. The remanent moment is defined as a proportion of the saturation magnetization of the film. The remanence will show maxima along the easy axis and minima along the hard axis. As shown in Fig. 2 the (100)-oriented sample displays a fourfold magnetic anisotropy, whereas the (211)-oriented sample has a twofold mag-

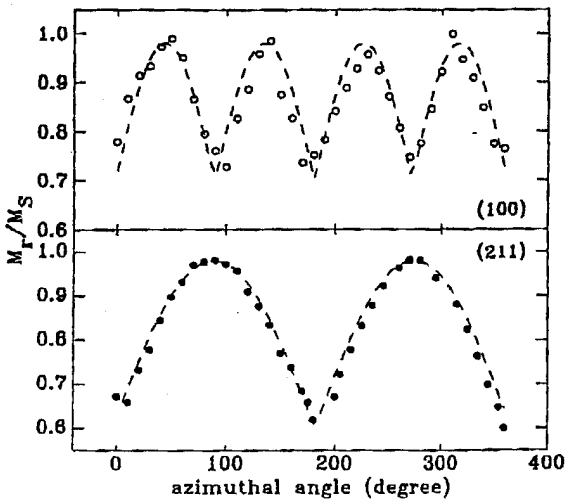


FIG. 2. The dependence of remanent magnetization as a function of azimuthal angle for wedged Fe/Cr multilayers with Cr thickness ~20 Å, for (100) orientation, and (211) orientation.

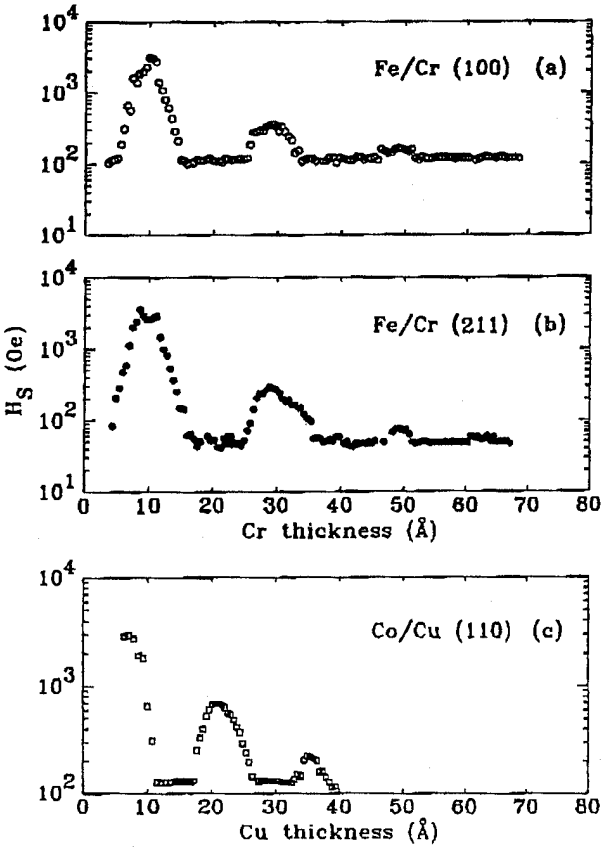


FIG. 3. The dependence of saturation (75%) field H_S on the nonmagnetic layer thickness for: (a) MgO(100)/Cr 100 Å/[Fe 15 Å/Cr (4–70) Å]$_5$/Fe 15 Å/Cr 40 Å; (b) MgO(110)/Cr 100 Å/[Fe 15 Å/Cr (4–70) Å]$_5$/Fe 15 Å/Cr 40 Å; and (c) MgO(110)/Pt 100 Å/Cu 50 Å/[Co 10 Å/Cu (5–40) Å]$_5$/Co 10 Å/Cu 10 Å/Pt 15 Å.

netic anisotropy as expected from the corresponding crystal symmetries. The dashed lines shown in Fig. 2 are straightforward calculations of the idealized remanence, which is proportional to the cosine of the angle between the measurement direction and the nearest easy axis.[9,12] For the (211) oriented multilayer there is excellent agreement between the calculated and measured remanence indicative of a strong in-plane uniaxial anisotropy. For the 100 sample slight deviations from the calculated curve may be due to the finite coercivity of the film.[9]

The interlayer exchange coupling was investigated at room temperature by measuring magnetic hysteresis loops at various positions along a wedge using the MOKE magnetometer. Fe/Cr and Co/Cu wedged structures were studied for which either the nonmagnetic layer Cr and Cu layer thicknesses or the ferromagnetic layer Fe and Co thicknesses were varied. In order to enhance the Kerr signal the structures were multilayered and typically comprised five wedged layers. Figure 3 shows typical plots of the saturation field as a function of nonmagnetic layer thickness for Fe/Cr(100), (211) and Co/Cu(110). The saturation field is defined arbitrarily as the field at which the moment corresponds to 75% of the saturation magnetization, except where otherwise specified. To properly include effects of in-plane crystalline anisotropy the angular dependence of the magnetic properties was first explored to find the magnetic easy and hard

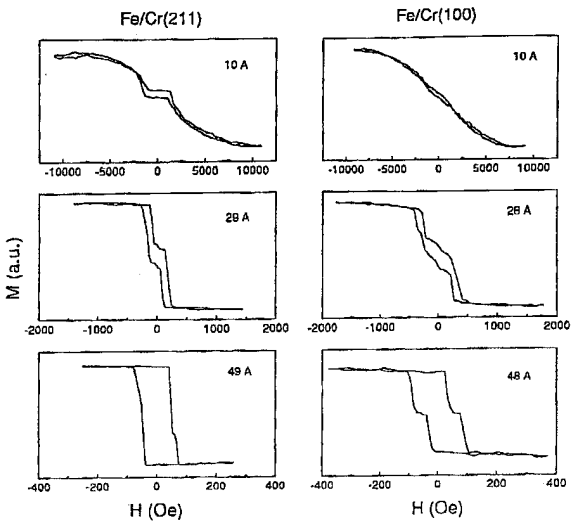


FIG. 4. Typical MOKE hysteresis loops for sputter-epitaxy grown (110) and (100) Fe/Cr wedged multilayers at the first three AF-coupled Cr peak positions. The samples are the same as those shown in Figs. 3(a) and 3(b).

axes. Scans along the wedge were subsequently performed along these or related directions which correspond to particular crystal directions. The MOKE apparatus allows the sample to be placed at an arbitrary angle with respect to the external field. As shown in Figs. 3(a) and 3(b), three well-defined peaks in the saturation field are observed for Fe/Cr(100) and Fe/Cr(211) wedged multilayers at room temperature. Note that each set of data in Fig. 3 was obtained from two wedged samples which span successive Cr thickness ranges for each orientation. An expected long-period oscillation with a Cr period of ~18 Å is found. For both orientations, the coupling strength and phase are nearly identical, and are similar to previous results found for epitaxial Fe/Cr structures.[4,8] Although no clear short-period oscillations are seen for these sputtered wedges, there is structure (a twin peak) within the first and second peaks shown in Fig. 3 which may be associated with the presence of a short-period oscillatory coupling. Figure 3(c) shows the saturation field as a function of Cu thickness for an epitaxial Co/Cu(110) wedged multilayer. Three peaks in the saturation field are readily identified in a single-wedged multilayer corresponding to an oscillation period similar to that found in MBE-grown Co/Cu wedges.[5]

Figure 4 shows typical room-temperature magnetic hysteresis loops measured on 100 and (211) Fe/Cr wedged multilayers at three Cr thicknesses (10, 29, and 48 Å) corresponding to the three AF peaks in Figs. 3(a) and 3(b). Note that the corresponding 100 and (211) samples were deposited simultaneously on substrates placed side by side to ensure otherwise identical samples. The hysteresis loops are measured along the in-plane magnetic easy axes for each orientation. The shape and detailed structure of the magnetic hysteresis loops reflects a competition between the AF interlayer coupling between the Fe layers and the magnetic anisotropy of the Fe layers. As the Cr thickness is increased the AF coupling strength decreases rapidly, whereas the anisotropy varies less. Depending on the relative strength of the AF coupling and the magnetic anisotropy a spin–flop transition is observed in some cases, as evidenced by an abrupt change in the magnetization at a particular field. Similarly a plateau in magnetization for the (211)-oriented Fe/Cr wedges at low fields results from a large in-plane magnetic anisotropy compared to strength of the AF coupling. The different shapes of the hysteresis loops for the (211) and 100 samples suggest that the in-plane magnetocrystalline anisotropy is weaker for the (100)-oriented samples as compared to that of the (211) orientation. The magnetization behaviors for these oriented wedge structures are similar to these found for oriented superlattices.[8]

Using high quality crystalline wedged multilayers the dependence of the AF coupling strength on the ferromagnetic layer thickness has been explored for a number of structures. In contrast to recent results from Fe/Cr multilayers grown by ion beam sputtering,[6] our data show no clear evidence of an oscillatory dependence of coupling strength on the thickness of Fe, t_{Fe}, in 100 Fe/Cr structures. By contrast, the saturation field, H_S, is found to decrease monotonically with increasing Fe thickness simply as $1/t_{\mathrm{Fe}}$. The same functional dependencies of H_S on $1/t_{\mathrm{Fe}}$ were found in a series of 100 Fe/Cr superlattices prepared by similar sputter epitaxy techniques.[13]

The current study demonstrates that sputter epitaxy is a technique capable of producing a wide range and large number of structures quickly and relatively inexpensively. This allows the ready exploration of magnetic and other properties which are sensitive to crystal orientation. It is particularly useful to prepare high quality single-crystalline wedged structures which, as previously demonstrated in MBE studies, can be quickly measured using simple Kerr magnetometry allowing the extraction of both interlayer coupling strengths and in-plane magnetic anisotropies.

We wish to thank K. P. Roche, M. Hart, and D. C. Miller for technical support. One of us (X.B.) is greatly indebted to the Natural Sciences and Engineering Research Council of Canada for support through a post-doctoral Fellowship.

[1] P. Grünberg, R. Schreiber, Y. Pang, M. B. Brodsky, and H. Sowers, Phys. Rev. Lett. **57**, 2442 (1986).
[2] S. S. P. Parkin, R. Bhadra, and K. P. Roche, Phys. Rev. Lett. **66**, 2152 (1991).
[3] S. S. P. Parkin, Phys. Rev. Lett. **67**, 3598 (1991).
[4] J. Unguris, R. J. Celotta, and D. T. Pierce, Phys. Rev. Lett. **67**, 140 (1991).
[5] M. T. Johnson, R. Coehoorn, J. J. de Vries, N. W. E. McGee, J. aan de Stegge, and P. J. H. Bloemen, Phys. Rev. Lett. **69**, 968 (1992).
[6] S. N. Okuno and K. Inomata, Phys. Rev. Lett. **72**, 1553 (1993).
[7] P. J. H. Bloemen, M. T. Johnson, M. T. van de Vorst, R. Coehoorn, J. J. de Vries, R. Jungblut, J. ann de Stegge, A. Reinders, and W. J. M. de Jonge, Phys. Rev. Lett. **72**, 764 (1994).
[8] E. E. Fullerton, M. J. Conover, J. E. Mattson, C. H. Sowers, and S. D. Bader, Phys. Rev. B **48**, 15755 (1993).
[9] G. R. Harp and S. S. P. Parkin, Appl. Phys. Lett. **65**, 3063 (1994).
[10] B. J. Daniels and B. M. Clemens, Appl. Phys. Lett. **66**, 520 (1995).
[11] J. C. A. Huang, R. R. Du, and C. P. Flynn, Phys. Rev. Lett. **66**, 341 (1991).
[12] R. W. Tustison, T. Varitimos, J. Van Hook, and E. F. Schloemann, Appl. Phys. Lett. **51**, 285 (1987).
[13] X. Bian, F. de Aguiar, and S. S. P. Parkin (unpublished).

Enhancement of orbital magnetism at surfaces: Co on Cu(100) (abstract)

M. Tischer, F. May, and K. Baberschke
Institut für Experimentalphysik, Freie Universität Berlin, Arnimallee 14, D-14195, Germany

O. Hjortstam, D. Arvanitis, J. Hunter Dunn, J. Trygg, B. Johansson, and O. Eriksson
Physics Department, Uppsala University, Box 530, S-75121 Uppsala, Sweden

J. M. Wills
Theoretical Division, Los Alamos National Laboratory, Los Alamos, New Mexico 87545

By combining MCXD experiments with first principles electronic structure calculations, we demonstrate that the orbital contribution to magnetism can be strongly enhanced at surfaces. This effect is illustrated for Co grown on a Cu(100) surface. The MCXD measurements were performed using the SX 700 plane grating monochromators at BESSY. The Co films were evaporated and characterized *in situ*, for their cleanness, thickness (1.6–50 ML), and structural order.[1] For a film thickness up to 2.2 ML, measurements of the ac MCXD susceptibility response at a fixed photon energy allowed one to measure the critical temperature, *Tc*, of the films and their critical properties were characterized *in situ*.[1] For several samples the MCXD response as a function of the x-ray incidence angle was investigated as well. This allows one to quantify and correct saturation effects that can occur in the measurements.[2] Data were taken in a temperature range between 40 and 350 K, and for many samples measurements were performed at several reduced temperatures, *T/Tc*. The first layer of Co on the Cu(100) surface shows an enhanced orbital moment, in contrast to the subsequent layers where the orbital moment is bulklike. The lowering of the symmetry, the enhanced spin moment, and the increased value of the density of states at the Fermi level are factors that combine to give the observed enhancements. © *1996 American Institute of Physics.*
[S0021-8979(96)679608-0]

[1] M. Tischer *et al.*, J. Magn. Magn. Mater. **135**, L1 (1994).
[2] J. Hunter Dunn *et al.*, J. Phys. C **7**, 1111 (1995).

Critical phenomena in the two-dimensional *XY* magnet Fe(100) on W(100)

H. J. Elmers, J. Hauschild, G. H. Liu, and U. Gradmann
Physikalisches Institut, TU Clausthal, D 38678 Clausthal-Zellerfeld, Germany

We experimentally investigated the magnetic phase transition of the in-plane magnetized double-layer Fe on W(100). This epitaxial system approximates the theoretical two-dimensional (2D) *XY* model to a large extent because of its pseudomorphic growth and structural stability. We measured the magnetization of W(100)/Fe in the vicinity of the Curie temperature T_C using the diffraction of spin polarized electrons and the magnetization of W(100)/Fe/Ag in a wider temperature interval using conversion electron Mössbauer spectroscopy. The temperature dependence of the spontaneous magnetization follows a power law with an exponent $\beta=0.22\pm0.03$ in the temperature regime $0.3\leqslant T/T_C\leqslant 0.99$. The susceptibility $\chi(T>T_C)$ can be fitted alternatively by a power law with an unusually large exponent $\gamma\approx 5$ or by an exponential law $\chi\propto\exp(b/\sqrt{T-T_C})$, as predicted for the 2D *XY* model, with $b=1.6$. © *1996 American Institute of Physics.* [S0021-8979(96)71908-9]

The magnetic phase transition in ultrathin films of two-dimensional (2D) symmetry is a subject of intensive research. Whereas the Mermin–Wagner theorem[1] predicts an absence of long range order in isotropic 2D systems, a magnetic second-order phase transition has been found in several ultrathin films on nonmagnetic substrates.[2–4] One generally believes that the magnetic anisotropy is responsible for the existence of magnetic order in these ultrathin films. For an anisotropy of twofold (uniaxial) symmetry theoretical considerations result in a phase transition which has the character of the well-known 2D Ising model.[5,6] For in-plane magnetized films in the (100) crystallographic orientation it is easy to show that the twofold anisotropy term vanishes. The character of phase transition in these films without uniaxial anisotropy is not well understood. Whereas the persistence of the 2D *XY* model, if anisotropies of sixfold symmetry are included, is a matter of fact,[7] it is a guess for the fourfold case. The 2D *XY* model on a lattice of infinite size predicts an absence of spontaneous order.[8] Recently, Bramwell and Holdsworth[9] suggested that finite size effects can stabilize magnetic order in the 2D *XY* model. Experiments on ultrathin magnetic films approximating the theoretical model are of particular interest as they can test the theoretical predictions.

Experimental studies of ultrathin films approximating the 2D *XY* model (i.e., in-plane magnetization without uniaxial anisotropy) Au(100)/Fe(100),[10,11] Cu(100)/Ni(100),[12] and Cu(111)/Ni(111)[13] confirm the effective exponent $\beta=3\pi^2/128\approx 0.23$, predicted in Ref. 9. Considerable errors (>20%) for the magnetization exponent show up in previous studies,[11,13] which in part might be caused by structural defects. The critical behavior of the magnetic susceptibility has not been analyzed yet for this class of ultrathin films.

In this article we study the bilayer Fe(100) on W(100). We choose this system because the structure approximates theoretical model systems to a large extent. The free surface enthalpy of W $\gamma_W=3.4\ \mathrm{J\,m^{-2}}$ is larger than that of Fe $\gamma_{Fe}=2.9\ \mathrm{J\,m^{-2}}$. Therefore the Fe adsorbate wets the W substrate, forming thermodynamically stable and pseudomorphic films consisting of large area islands. A detailed structural study of the bilayer Fe(100) on W(100) is given in Refs. 14 and 15. In contrast to the case of noble metal substrates the *d*-band electrons of Fe and W hybridize to some extent. *Ab initio* calculations[16] result in magnetic moments of Fe atoms directly at the W interface (1.7 μ_B/atom) and Fe atoms in the second layer (2.4 μ_B/atom), whereas the polarization of W atoms at the interface ($-0.2\mu_B$/atom) is negligible. We present experimental data both for the spontaneous magnetization and for the magnetic susceptibility. We will show that the experimental data are consistent with the theoretical picture of the 2D *XY* model given in Ref. 9. Two sets of experiments were performed in separate vacuum chambers with similar preparation conditions. The spontaneous magnetization of the Ag-covered bilayer Fe on W(100) was determined using conversion electron Mössbauer spectroscopy (CEMS).[17] The magnetization as a function of temperature and external field for the uncovered W(100)/Fe(100) bilayer was investigated by spin polarized low-energy electron diffraction (SPLEED).[15,18]

Using CEMS in zero external field[17] we measured the magnetic hyperfine field $B_{hf}(T)$ as a function of temperature for the Ag-covered Fe bilayer on W(100). B_{hf} measures the local spontaneous magnetization independent of the magnetic domain state and is proportional to the magnetization with respect to its temperature dependence even far away from T_C.[19] Results of $B_{h,f,i}(T)$ for a Fe film of thickness $\Theta=2.2$ monolayers (ML) deposited at 300 K are plotted in Fig. 1. Below T_C, the CEMS spectra of the double layer showed three components of different hyperfine fields $B_{hf,i}$ = $a-c$. The three components belong to Fe atoms placed in different atomic environments.[20] Fe atoms directly at the W surface and covered by Fe atoms (a) produce component $B_{hf,a}$ Fe atoms in the second layer and covered by Ag (b) produce component $B_{hf,b}$. Finally, Fe atoms in the second layer and covered by Fe atoms or Fe atoms in the third layer (c) produce the component $B_{hf,c}$. Figure 1 shows power law fits to the temperature dependence of the three components. All three components show the same temperature dependence and can be fitted in the total available temperature interval 88 K$\leqslant T\leqslant T_C$ by a power law $B_{hf,i}(T) = B_{hf,i}(0)(1 - T/T_C)^{\beta}$ with the same Curie temperature $T_C=306$ K and the same effective exponent $\beta=0.22\pm0.01$. The common

 0021-8979/96/79(8)/4984/3/$10.00 © 1996 American Institute of Physics

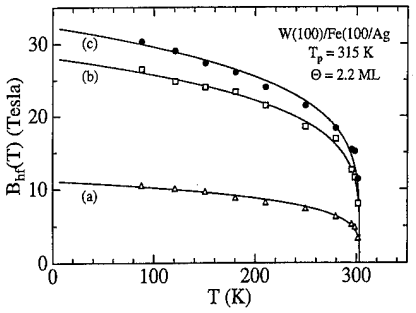


FIG. 1. Temperature dependence of the magnetic hyperfine field B_{hf} for a film of Fe(100) on W(100) having a thickness of $\Theta=2.2$ ML, deposited at $T_p=315$ K, and coated by Ag. The spectra consists of three components, corresponding to Fe atoms at the Fe/W interface [(a), △], Fe atoms in the second layer at the Fe/Ag interface [(b), □], and Fe atoms in the second or third layer of triple-layer islands [(c), ●]. The solid lines represent power law fits with a unique Curie temperature $T_C=306$ K and critical exponent $\beta=0.22\pm0.01$.

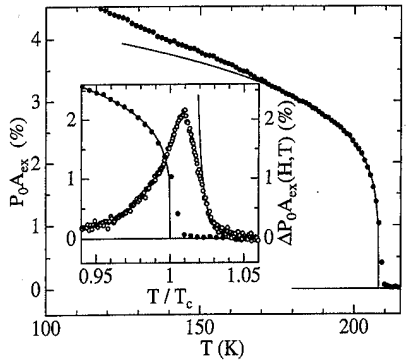


FIG. 2. Exchange asymmetry $P_0A_{ex}(T)$ (●) in the remanent state for a film of Fe(100) on W(100) having a thickness of $\Theta=1.6$ ML, deposited at 300 K and subsequently annealed at $T=550$ K. The power law (solid line) $P_0A_{ex}\propto(T_C-T)^{\beta}$ [$\beta=0.217\pm0.002$, $T_C=(207.8\pm0.1)$ K] is fitted in the interval $[0.9T_C, 0.99T_C]$. The inset shows $P_0A_{ex}(T)$ and the increase of asymmetry $\Delta P_0A_{ex} = P_0[A_{ex}(H,T) - A_{ex}(0,T)]$ for external field $H_1=0.63$ Oe (○). The exponential law $\Delta P_0A_{ex} \propto \exp(b/\sqrt{T/T_C}-1)$ (solid line) was fitted to the data for fixed $T_C=207.8$ K, resulting in $b=1.6$.

temperature dependence allows the conclusion that no magnetically independent clusters exist in the sample (i.e., monolayer and double-layer patches) and that no spin–wave components perpendicular to the film with a wave vector $k_\perp\neq0$ are excited. Hence the magnetic behavior of the double layer is truly 2D.

For the uncovered bilayer Fe on W(100) we measured the magnetization $M(H,T)$ as a function of external magnetic field ($H<2$ Oe) and temperature T using SPLEED (see Refs. 15 and 18). With this method one determines the asymmetry P_0A_{ex} of specular reflected electrons for spin polarization $|\mathbf{P}_0|=0.2$ parallel or antiparallel to the direction of magnetization.[21] P_0A_{ex} shows the same temperature and field dependence as the magnetization component M along the quantization axis.[11,22] The quantization axis was directed along one of the two in-plane easy axes—[001] or [010].[23] In contrast to the temperature dependence of the hyperfine field $B_{hf}(T)\propto M(T)$, the proportionality $P_0A_{ex}(H,T)\propto M(H,T)$ only holds in the direct vicinity of T_C, i.e., for reduced temperature ($|t|=|1-T/T_C|<0.1$). Figure 2 shows the experimental results for the temperature dependence of $P_0A_{ex}(0,T)$ of a Fe film having a thickness of $\Theta=1.6$ ML, deposited at 300 K and subsequently annealed at 550 K. We observed a reversible temperature dependence of $P_0A_{ex}(T)$. Therefore we conclude that the film stays in a homogeneous single-domain magnetic state. A single-domain state is not uncommon for ultrathin films of the (100) symmetry class. Single-domain states were observed directly by SEMPA studies for Co/Cu(100).[24] For a single-domain state $P_0A_{ex}(H=0,T)$ is proportional to the spontaneous magnetization. We fitted our data to the power law $P_0A_{ex}(T)\propto(1-T/T_C)^{\beta}$ in the temperature interval $0.9\leqslant T/T_C\leqslant0.99$ with T_C and β as fitting parameters. The fit interval is limited by the onset of the tail at $T=0.99T_C$, where the experimental data deviate considerably from the power law (see Fig. 2). This frequently observed tail above T_C is attributed to finite size effects which broaden the transition. Note that the tail covers a temperature region of $\Delta T/T_C\approx0.5\%$ only. Usually 3%–5% of the tails are observed for ultrathin films.[3] The theoretical value for the tail width is $\Delta T/T_C\approx a/l$,[3] where a is the lattice parameter and l is the length scale of the coherent regions of the film. This implies a finite size scale of $l\approx400$ Å. The power law fit results in $T_C=207.8$ K and $\beta=0.217\pm0.002$. The power law is further characterized by the straight line of data points in a log–log plot (see Fig. 3).

It should be mentioned that the statistical error of β from the fit (0.1%) is far less than the variance resulting from deviating temperature intervals used for the fit.[3] Since the critical region for which the power law should be valid is not known exactly we varied the fit interval within reasonable limits (see Ref. 3). Taking into account this uncertainty, we finally attain $\beta=0.22\pm0.03$. We performed similar fits for three films in the thickness region 1.6 ML$\leqslant\Theta<$2.0 ML, resulting in a unique value of the effective exponent $\beta=0.22\pm0.03$, which we then identify with the unique exponent of the double layer.

The magnetic susceptibility was derived from the field dependence of the asymmetry, $\chi(T)\propto\Delta P_0A_{ex}(H,T)$, where $\Delta A_{ex}(H,T)=A_{ex}(H,T)-A_{ex}(0,T)$. $\Delta A_{ex}(H,T)$ was mea-

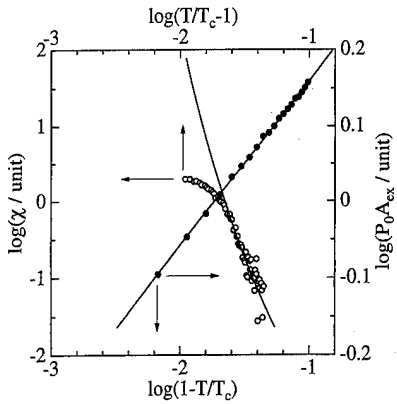


FIG. 3. Double logarithmic plot of susceptibility χ(○) and spontaneous magnetization M(●) vs reduced temperatures (data from Fig. 2). The full lines represent fits to the power law and to the exponential law, respectively (see Fig. 2).

sured for $H_1=0.6$ Oe and $H_2=1.3$ Oe. Figure 2 shows the experimental data of $\Delta P_0 A_{ex}(H_1,T)$ for the same bilayer as discussed above.

In a temperature regime directly at T_C, $0.98<T/T_C<1.02$, the difference $\Delta A_{ex}(H,T)$ showed a sublinear increase with H. In this temperature regime $\Delta A_{ex}(H,T)$ provides a lower limit for $\chi(T)$, only. We find a maximum value of $\Delta A_{ex}(H,T)$ at $T=210$ K$=1.01T_C$. A direct determination of the absolute value of χ is not possible. However, a rough estimate can be made by deriving the proportionality constant $\alpha=M/P_0A_{ex}$ from the low temperature extrapolation. Then the lower limit for the susceptibility maximum is $\chi(1.01T_C)>1\times10^4$ (in SI units). Following Farle *et al.*,[25] $\chi=l/t$ can be related to the length scale l of homogeneous islands in the film of thickness t. In this model the maximum value of χ would correspond to $l>30$ μm in sharp contrast to the small value of l estimated from the tail of $M(0,T)$. We would rather guess that the giant susceptibility is an indication of a structurally induced superparamagnetic susceptibility, as discussed for Fe films on W(110).[26]

For $T>1.02T_C$, we observed a linear increase of $\Delta A_{ex}(H,T)$ with H, resulting in the temperature dependence of $\chi(T)$. Figure 3 shows a double logarithmic plot of $\chi(T>1.02T_C)$ using $T_C=207.8$ K. The logarithmic plot reveals the steep increase of $\chi(T)$ upon approaching T_C from the paramagnetic region. Assuming a power law divergence $\chi(T)\propto(T-T_C)^{-\gamma}$, the linear section of the slope would correspond to an unusually large value of the exponent $\gamma\approx5$. Instead we show in Fig. 3 a fit using the exponential law predicted for the 2D *XY* model, $\chi(T)\propto\exp(b/\sqrt{T/T_C}-1)$.[8] The fit results in the parameter $b=1.6\pm0.1$, which is of the order of magnitude predicted for the pure 2D *XY* model ($b=2.6$).[8] Note that $\chi(T)$ also increases considerably upon approaching T_C from temperatures below T_C.

In summary we measured the critical behavior of the spontaneous magnetization and of the magnetic susceptibility for the double-layer Fe(100) and W(100). Our results are consistent with a finite size 2D *XY* model. A quantitative comparison of theory and experiment obviously requires further research involving experimental samples and theoretical models.

[1] N. D. Mermin and H. Wagner, Phys. Rev. Lett. **17**, 1133 (1966).
[2] *Ultrathin Magnetic Structures*, edited by J. A. C. Bland and B. Heinrich (Springer, Berlin, 1994).
[3] Z. Q. Qiu, J. Pearson, and S. D. Bader, Phys. Rev. B **49**, 8798 (1994).
[4] H. J. Elmers, Int. J. Mod. Phys. B **9**, 3115 (1995).
[5] M. Bander and D. L. Mills, Phys. Rev. B **38**, 12015 (1988).
[6] K. Binder and D. P. Landau, Phys. Rev. B **13**, 1140 (1976).
[7] J. V. José, L. P. Kadanoff, S. Kirkpatrick, and D. R. Nelson, Phys. Rev. B **16**, 1217 (1977).
[8] J. M. Kosterlitz, J. Phys. C. Solid State Phys. **7**, 1046 (1974).
[9] S. T. Bramwell and P. C. W. Holdsworth, Phys. Rev. B **49**, 8811 (1994).
[10] C. Rau, Appl. Phys. A **49**, 579 (1989).
[11] W. Dürr, M. Taborelli, O. Paul, R. Germar, W. Gudat, D. Pescia, and M. Landolt, Phys. Rev. Lett. **62**, 206 (1989).
[12] F. Huang, G. J. Mankey, M. T. Kief, and R. F. Willis, J. Appl. Phys. **73**, 6760 (1993).
[13] C. A. Ballentine, R. L. Fink, J. Araya-Pochet, and J. L. Erskine, Phys. Rev. B **41**, 2631 (1990).
[14] M. Plihal, D. L. Mills, H. J. Elmers, and U. Gradmann, Phys. Rev. B **51**, 8193 (1995).
[15] H. J. Elmers and J. Hauschild, Surf. Sci. **320**, 134 (1994).
[16] R. Wu and A. J. Freeman, Phys. Rev. B **45**, 7532 (1992).
[17] J. Korecki and U. Gradmann, Phys. Rev. Lett. **55**, 2491 (1985).
[18] H. J. Elmers, J. Hauschild, and U. Gradmann, J. Magn. Magn. Mater. **140–144**, 671 (1995).
[19] G. Lugert and G. Bayreuther, Phys. Rev. B **38**, 11068 (1988).
[20] S. M. Dubiel and W. Zinn, Phys. Rev. B **30**, 3784 (1984).
[21] S. F. Alvarado, R. Feder, H. Hopster, F. Ciccacci, and H. Pleyer, Z. Phys. B **49**, 129 (1982).
[22] R. Feder and H. Pleyer, Surf. Sci. **117**, 285 (1982).
[23] D. Venus and H. L. Johnston, Phys. Rev. B **50**, 15787 (1994).
[24] H. P. Oepen, J. Magn. Magn. Mater. **93**, 116 (1991).
[25] M. Farle, K. Baberschke, U. Stetter, A. Aspelmeier, and F. Gerhardter, Phys. Rev. B **47**, 11571 (1993).
[26] H. J. Elmers, J. Hauschild, H. Fritzsche, G. Liu, U. Gradmann, and U. Köhler, Phys. Rev. Lett. **75**, 2031 (1995).

In situ Brillouin light scattering from ultrathin epitaxial Fe/Ag(100) films with Cr and Ag overlayers

R. J. Hicken, A. Ercole, S. J. Gray, C. Daboo, and J. A. C. Bland
Cavendish Laboratory, Madingley Road, Cambridge CB3 0HE, United Kingdom

We have studied the magnetic properties of ultrathin epitaxial Fe/Ag(100) films by means of *in situ* Brillouin light scattering (BLS) in an ultrahigh vacuum chamber equipped with magneto-optic Kerr effect, low energy electron diffraction, and reflection high energy electron diffraction instruments. Our novel *in situ* BLS system allows us to perform measurements rapidly, in order to avoid surface contamination, and hence to observe the evolution of the spin-wave frequency with increasing film thickness. Good reproducibility is observed between different growth runs. The direction of the applied field within the film plane has been varied revealing that the magnetocrystalline anisotropy has cubic symmetry and that there is no observable in-plane uniaxial anisotropy. From the values of the hard and easy axis spin wave frequencies we have determined the values of the in-plane fourfold anisotropy and effective demagnetizing fields during the growth of 13.9 monolayer (ML) Fe films. The evolution of the fourfold anisotropy is in reasonable agreement with that reported by other researchers. The effect of depositing Cr and Ag overlayers onto the completed 13.9 ML film has also been studied. We have deduced values for the surface anisotropy constants for the Fe/Ag and Fe/vacuum interfaces and we compare these with previously reported values. A qualitatively different evolution of the spin wave frequency with overlayer thickness is observed for the deposition of Cr and Ag, which may be related to the magnetic properties of the Cr overlayer. © *1996 American Institute of Physics.* [S0021-8979(96)72008-3]

We have recently developed a novel *in situ* Brillouin light scattering (BLS) apparatus that allows us to make measurements both quickly and routinely during the growth of ultrathin film samples. In this paper we report first upon our results for the growth of epitaxial Fe films on Ag(100) substrates and second upon the effect of depositing Ag and Cr overlayers on to 13.9 monolayer (ML) thick Fe layers. Both the cubic magnetocrystalline and surface anisotropy constants may be determined as the film thickness is increased in submonolayer steps. It is well known that high quality epitaxial Fe(100) films can be stabilized on the Ag(100) substrate and an excellent review of the structural and magnetic properties of this system has recently been given.[1] The growth of the first few ML of Fe was found to be complicated and subject to the detailed growth conditions. As the Fe thickness, d, is increased the magnetization reorients from an out of plane to an in-plane configuration and there is some variation in the value of d at which the magnetization reorientation has been reported to occur.[1–3] However it is believed that as d is increased above a value of about 5 ML a stable growth mode is obtained.[1]

A value of $d=13.9$ ML was chosen for experiments in which overlayers of either Ag or Cr were deposited because the magnetic properties of the completed Fe layers were found to be well reproduced between different growth runs and because the measured spin wave frequencies were found to still be sensitive to the overlayer coating. The use of Ag overlayers allows us to obtain symmetric boundary conditions for the Fe film and hence to determine the values of the surface anisotropy constants for both the Fe/vacuum and Fe/Ag interfaces. The use of Cr is motivated by the recent observation of a large moment in Cr overlayers and by the fact that the ordering of successive layers of Cr moments in the ultrathin limit is subject to debate.[4] We show here that Ag and Cr overlayers have a qualitatively different effect on the magnetic properties of the underlying Fe layer.

The commercially obtained single crystal Ag(100) substrate was mechanically polished and then chemically polished and electropolished. Cycles of 500 eV Ar^+ sputtering and annealing were used to clean the substrate and to remove the deposited film at the end of each growth run. The base pressure in the chamber was better than 2×10^{-10} mbar, rising to no more than 5×10^{-10} mbar during deposition. Reflection high energy electron diffraction (RHEED) intensity oscillations were observed during the homoepitaxial growth of Ag on our crystal. This allowed us to calibrate a quartz crystal oscillator placed in the sample position and the Fe and Cr rates were then calibrated using this same crystal oscillator. Deposition of the Fe, Ag, and Cr was carried out at ambient temperature using a typical rate of 1 Å per minute. Figure 1 shows typical RHEED patterns obtained from the surfaces of a clean Ag crystal and a 13.9 ML Fe film. These show that the substrate is flat and well ordered and confirm the epitaxial nature of the Fe film. A detailed structural study using low energy electron diffraction (LEED) and RHEED will be described elsewhere.

We are able to perform both BLS and longitudinal magneto-optic Kerr effect (MOKE) measurements *in situ* without moving the sample from the main growth position. Instead a Fe core electromagnet with a maximum field of 2.1 kOe is moved so that the sample lies between its pole pieces. The sample holder possesses azimuthal rotation so that the magnetic field may be applied along any direction within the plane of the film. The novel feature of the BLS system is that the *f*/No. 2 objective lens is located in a re-entrant tube, mounted on a bellows, that can be moved close to the sample whenever it is required. Further details of our system will be given elsewhere.

 0021-8979/96/79(8)/4987/3/$10.00 © 1996 American Institute of Physics

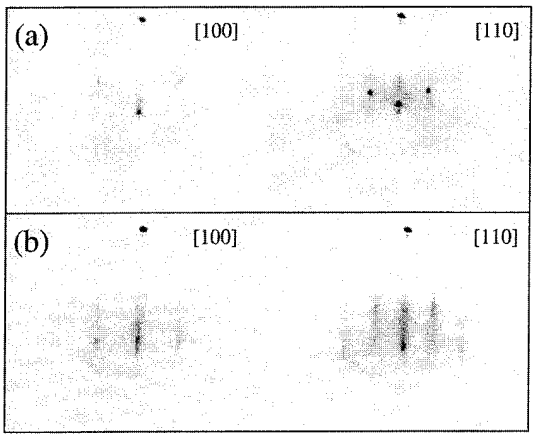


FIG. 1. Negative RHEED images at a beam energy of 15 keV and angle of incidence of ~3° are shown for (a) the Ag(100) substrate, and (b) a 13.9 ML Fe(100) film. The beam direction indicated in each case corresponds to a crystallographic axis of the Ag substrate.

For Fe layer thicknesses greater than 3 ML we find, from MOKE and BLS measurements, that the magnetic anisotropy is fourfold with any in-plane uniaxial anisotropy being negligibly small. The magnetic free energy per unit area of the Fe(100) film may be written in the form

$$E = d[-\mathbf{M}\cdot\mathbf{H} + K_1^{\parallel}(u_y^4 + u_z^4) + K_1^{\perp}u_x^4 + 2\pi DM^2u_x^2] + (K_s^{(1)} + K_s^{(2)})u_x^2, \quad (1)$$

in which u_x, u_y, and u_z are the direction cosines of the magnetization, $\mathbf{M}$, relative to the crystallographic axes of the film, with the x axis being taken as the surface normal. $\mathbf{H}$ is the applied magnetic field vector, $K_1^{\parallel}$ and $K_1^{\perp}$ are the magnetocrystalline volume anisotropy contants,[1] and $K_s^{(1)}$ and $K_s^{(2)}$ are the surface anisotropy constants for the two surfaces of the film. If the magnetization lies in the film plane, as is the case in this study, then in-plane MOKE and BLS are sensitive only to the value of $K_1^{\parallel}$ and so we will refer to the value of $K_1^{\parallel}$ simply as K_1. A factor D has been included in the demagnetizing energy term to take account of the reduced demagnetizing field that occurs in ultrathin films due to the discrete nature of the lattice. We have taken D to have the form $1-0.425/N$ where N is the thickness of the Fe film in monolayers.[1] We have not included a volume type uniaxial perpendicular anisotropy energy in Eq. (1) because this is believed to be negligible for Fe/Ag(100).[1]

Enhanced moments in ultrathin Fe/Ag(100) films have been both predicted[5] and observed.[6] However, since we are not able to measure the Fe moment directly *in situ*, in this study we assume that the Fe magnetization is thickness independent and equal to the bulk value of 1710 emu/cm^3. All BLS calculations also assume the bulk Fe values of 2.09 for the g factor and 2×10^{-6} erg/cm for the exchange constant. The spin wave frequencies observed by BLS are determined largely by the values of two quantities, the cubic anisotropy field $2K_1/M$ and the effective demagnetizing field

$$(4\pi M)_{\text{eff}} = 4\pi DM - 2(K_s^{(1)} + K_s^{(2)})/Md. \quad (2)$$

By measuring the spin wave frequency with the field applied parallel to the easy [001] and hard [011] in-plane

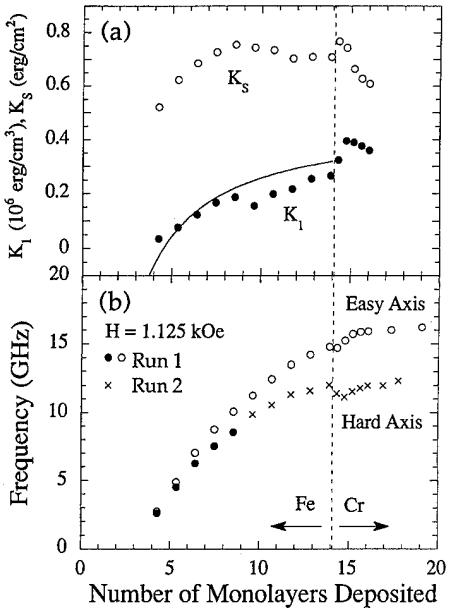


FIG. 2. (a) Values of the surface anisotropy constant K_S and the cubic anisotropy constant K_1 calculated from the data in (b) are shown. The solid curve is an empirical curve for K_1 from Ref. 1. (b) Easy and hard axis BLS frequencies measured in two experiments in which a 13.9 ML Fe film was capped with Cr are plotted. The frequency error bars are smaller than the symbols used.

axes, we may deduce the values of both K_1 and $(K_s^{(1)}+K_s^{(2)})/2$, the average surface anisotropy constant, henceforth referred to as K_S.

Experiments were performed to verify that surface contamination can be neglected in our studies. Repeated growth runs then showed that there was some scatter in the BLS frequencies measured at small Fe thicknesses, but that for larger thicknesses these frequencies were highly reproducible. No magnetic signal was ever observed with MOKE or BLS for Fe thicknesses less than about 3 ML. Even if the remanent magnetization was oriented normal to the film plane one would still expect to observe some signal in both the MOKE and BLS experiments as the applied field pulls the magnetization towards the film plane. Alternatively these films may not be ferromagnetic at room temperature. Since other researchers have observed ferromagnetism at room temperature even in 1 ML films,[2] we are presently performing a detailed structural analysis in order to determine whether our Fe films are continuous for thicknesses less than 3 ML.

In Fig. 2 we have combined data from two growth runs to form one data set from which we have calculated the values of K_1 and K_S as a function of the film thickness. We note that both the easy and hard axis frequencies show a small reduction with the initial deposition of Cr and that this is reflected in the small peak in K_S that is observed at this point. Interestingly the deposition of Cr seems to lead to a significant increase in the value of K_1. However, for a Fe film that was ~15 ML thick, the thickness is uncertain because the Fe rate became unstable during the growth, the deposition of Cr was again found to produce a peak in the calculated value of K_S but no increase in the

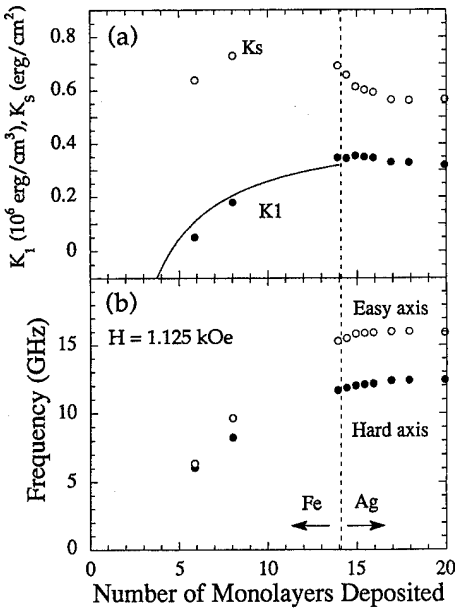


FIG. 3. (a) Values of the surface anisotropy constant K_S and the cubic anisotropy constant K_1 calculated from the data in (b) are shown. The solid curve is an empirical curve for K_1 derived in Ref. 1. (b) The easy and hard axis BLS frequencies measured in an experiment in which a 13.9 ML Fe film was capped with Ag are plotted. The frequency error bars are smaller than the symbols used.

value of K_1 was observed. Figure 3 shows the spin wave frequencies measured in a growth run for which Ag was deposited on to a 13.9 ML Fe film. The values of the calculated anisotropy constants are again shown. Comparing Figs. 2 and 3 we see that the effects of capping with Ag and Cr are qualitatively different since the spin wave frequency increases monotonically for the case of Ag but not for Cr.

We now compare the values obtained for K_1 and K_S with those obtained by other authors. The relationship $2K_1^{\parallel}/M=(0.55-2.5/N)$ was previously found[1] to give a good fit to the value of the in-plane cubic anisotropy field (measured in kOe). We have plotted this curve in Figs. 2(b) and 3(b) and see that it is in reasonable agreement with our experimental data. We note that in Fig. 2(b) the small jump in the value of K_1 between 8 and 9 ML of Fe is probably an artefact since this is the point at which the two sets of hard axis BLS data have been pasted together. The apparent enhancement of the value of K_1 when Cr is deposited onto the 13.9 ML film is intriguing but further experiments are required in order to confirm this effect. From Fig. 3(b) we see that capping of the 13.9 ML film with Ag has little effect upon the value of K_1 which is in agreement with reports that the value of K_1 is insensitive to the material deposited at the upper interface.[1]

From Figs. 2(b) and 3(b) we see that the value of K_S for an uncoated Fe film is approximately equal to 0.70 erg/cm^2 for Fe thicknesses greater than or equal to 6 ML, but that it appears to decrease for smaller Fe thicknesses, in qualitative agreement with previous studies.[1] From Fig. 3(b) we see that approximately 3 ML of Ag must be deposited before the value of K_S becomes saturated at about 0.56 erg/cm^2. Further work is required to determine whether this gradual change in K_S results from the growth mode of the Ag, the effects of strain, or is purely an electronic effect. If we assume that the upper and lower Fe/Ag interfaces are identical in terms of their surface anisotropy constant, and this need not be the case,[7] then we deduce surface anisotropy values of 0.56 erg/cm^2 for the Fe/Ag interface and 0.84 erg/cm^2 for the Fe/vacuum interface. These values are somewhat smaller than those of 0.81 and 0.96 erg/cm^2 reported in Ref. 1 for the Fe/Ag and Fe/vacuum interfaces, respectively. From Fig. 2(b) we see that, with the deposition of Cr, K_S increases to 0.77 erg/cm^2 before decreasing to 0.61 erg/cm^2. This nonmonotonic behavior of K_S corresponds to the small dip seen in both the hard and easy axis spin wave frequencies, which has been observed in all of our experiments. This may be associated with the antiferromagnetic ordering of successive layers of Cr moments, although detailed structural studies are required in order to determine the effects of interfacial roughness.

In conclusion, we have shown how *in situ* BLS may be used to quickly obtain information on the evolution of magnetic anisotropies during the growth of ultrathin ferromagnetic films. We have observed the development of the magnetic interface anisotropy during the deposition of submonolayer quantities of Ag and Cr onto 13.9 ML Fe films and have shown that Ag and Cr have a qualitatively different effect. We suggest that the Cr moment may be effective in determining the interface anisotropy constant at the Fe/Cr interface.

We would like to acknowledge the help of E. Gu and E. Ahmed in the preparation of the Ag single crystal substrate, and the financial support of the EPSRC and the DRA.

[1] B. Heinrich and J. F. Cochran, Adv. Phys. **42**, 523 (1993).
[2] J. Chen, M. Drakaki, and J. L. Erskine, Phys. Rev. B **45**, 3636 (1992).
[3] Z. Q. Qiu, J. Pearson, and S. D. Bader, Phys. Rev. Lett. **70**, 1006 (1993).
[4] C. Turtur and G. Bayreuther, Phys. Rev. Lett. **72**, 1557 (1994).
[5] S. Ohnishi, M. Weinert, and A. J. Freeman, Phys. Rev. B **30**, 36 (1984); C. L. Fu, A. J. Freeman, and T. Oguchi, Phys. Rev. Lett. **54**, 2700 (1985).
[6] C. L. Wooten, J. Chen, A. Mulhollan, J. L. Erskine, and J. T. Markert, Phys. Rev. B **49**, 10 023 (1994).
[7] P. J. Schurer, Z. Celinski, and B. Heinrich, Phys. Rev. B **51**, 2506 (1995).

Magneto-optical investigation of the fcc–bcc phase transition of Fe wedges sandwiched between CuNi alloys (abstract)

H. Theuss,[a] D. Weller, and A. Carl[b]
IBM Almaden Research Center, 650 Harry Road, San Jose, California 95120-6099

We report a systematic investigation of the fcc–bcc structural phase transition of thin Fe films sandwiched between CuNi alloys. The structures were of the type substrate/20 nm Pt/10 nm CuNi/0–2 nm Fe wedge/1 nm CuNi/2 nm Pt. All films were deposited in high vacuum by electron beam evaporation at temperatures ranging from 400 °C (Pt seed layer) to 100 °C (CuNi alloy layers and Fe wedge) to 20 °C (Pt cap layer). The CuNi composition ratio was varied in 10 at. % steps in order to vary its lattice constant from a=0.3607 nm (Cu) to 0.3517 (Ni) nm, which encompasses the value of gamma Fe (fcc low spin state). X-ray diffraction measurements reveal strong (111) texturing with an alignment of the Pt ⟨111⟩ axis better than 5 deg (rocking curve width) of the completed structures. Kerr loops in fields ±18 kOe were recorded as function of the Fe-wedge position with a spatial resolution of about 0.8 mm, corresponding to 0.1 nm Fe thickness resolution. These hysteresis loops reveal the saturation Kerr angle (0.1 mdeg resolution), the saturation field (anisotropy field) and a paramagnetic slope, which are all analyzed as function of the Fe thickness and the CuNi composition. Clear evidence for the formation of paramagnetic Fe is found for Cu-rich CuNi alloys, where a Kerr rotation below the resolution limit of our apparatus extends up to >2 nm Fe thickness. The transition thickness from fcc to bcc Fe, as characterized by the onset of a linear uptake of the Kerr rotation, shows a pronounced maximum near about 25 at. % Ni, indicating that a small compression of the Fe lattice constant (about −2%) leads to the nonferromagnetic fcc Fe state. A similar study, using CuAu alloys with the aim of characterizing the high spin ferromagnetic fcc Fe phase, is in progress.[1] © *1996 American Institute of Physics.* [S0021-8979(96)68008-0]

---

[a]On leave from Max-Planck-Institut für Metallforschung, Heisenberg str. 1, 70569 Stuttgart, Germany.
[b]Present address: Universitaet-GH-Duisburg, Labor für Teiftemperaturphysik, Lotharplatz 1, 47048 Germany.

[1] See, e.g., S. Mitani, A. Kida, and M. Matsui, J. Magn. Magn. Mater. **126**, 76 (1993).

 0021-8979/96/79(8)/4990/1/$10.00 © 1996 American Institute of Physics

Dependence of structural and magnetic properties on deposition angle in electron-beam evaporated Co/Pt multilayer thin films

Ki-Seok Moon and Sung-Chul Shin
Department of Physics, Korea Advanced Institute of Science and Technology, Kusung-Don, Yusung-Gu, Taejon 305-701, Korea

The effects of deposition angle on the structural and magnetic properties of e-beam evaporated Co/Pt multilayer thin films prepared on tilted substrates were examined. It was found that the [111] crystallographic orientations of the multilayer thin films were not aligned with columnar growth orientations and that they remained normal to the substrate planes, irrespective of deposition angle, even though the deposition angle was severely oblique up to 60°. Interestingly enough, the magnetic easy axis orientation was nearly aligned with the substrate normal, irrespective of deposition angle, which suggested that surface anisotropy was a major reason for the perpendicular anisotropy in Co/Pt multilayer thin films. © *1996 American Institute of Physics.* [S0021-8979(96)72108-7]

I. INTRODUCTION

Co-based multilayer thin films have been the subject of considerable investigation because of their novel properties and potential technological applications. In particular, the application of these materials to magneto-optic (MO) recording is of great interest today due to superior environmental stability and a larger Kerr effect at short wavelength (<500 nm) compared to the current choice for MO media—rare-earth–transition metal (RE–TM) alloy thin films.[1] In particular, Co/Pt multilayer thin films have been reported as the best choice owing to a large spin–orbit coupling.[2]

The magnetic properties of Co/Pt multilayer thin films were reported to be very sensitive to preparation methods and condition, as well as to sublayer and total film thicknesses: sputtering gas[3] and pressure[4] in sputtering, and vacuum pressure and substrate temperature in evaporation.[5] In this article, we report the effects of deposition angle on the structural and magnetic properties of Co/Pt multilayer thin films.

II. EXPERIMENT

Co/Pt multilayer thin films were prepared on glass substrates by e-beam evaporation in a vacuum system maintained at about 6×10^{-6} Torr. To achieve oblique deposition, the substrates were mounted on tilted substrate holders making the angle of incident vapor beam 0°, 15°, 30°, 45°, and 60° with respect to each substrate normal. The multilayer structure was achieved by alternatively exposing the substrate to two sources via a rotating substrate holder. The substrate holder was placed 25 cm above the sources. The dwelling time spent by the substrate above each source could be controlled by a computer interfaced to a stepping motor which drove the substrate holder. Two sources were physically separated by stainless-steel shields to prevent the cross contamination of their fluxes. The sources were screened with a shutter driven by a stepping motor in order to prevent deposition to the substrates during rotation of the substrate holder. Typical deposition rates of 0.28 Å/s for Co and 0.25 Å/s for Pt, monitored by two corresponding quartz crystal sensors, were kept constant within a 10% fluctuation to achieve the same modulation wavelength in all samples. All samples were designed to have the same total thickness of 300 Å, consisting of a 4-Å-thick Co and 9.2-Å-thick Pt sublayer. Since a series of samples with different angles of incidence was prepared in the same run under identical conditions, possible variations of preparation conditions between different runs were eliminated.

The film structure was examined by low- and high-angle x-ray diffractometry and the growth morphology of the film was investigated by microfractography. A preferred orientation and degree of texture of the film was studied from the measurements of a rocking curve and pole figure. Magnetization was investigated using a vibrating-sample magnetometer. The magnetic anisotropy was determined from analysis of a torque curve measurement of an applied field of 10 kOe.

III. RESULTS AND DISCUSSION

All samples in this study developed low-angle x-ray diffraction peaks irrespective of the deposition angle, which suggests the existence of a multilayer structure in those samples. High-angle x-ray diffraction experiments revealed that the films were polycrystalline grown along the [111] crystallographic orientation having a d_{111} spacing of 2.201 Å.

Figure 1 shows the typical cross sections of the samples examined by a scanning electron microscope in order to examine the growth morphology depending on the angle of incidence. A columnar structure was observed for all samples. This columnar microstructure has been commonly observed for deposited atoms having low mobility.[6] In the initial stages of film formation a random distribution of small crystallites is created on the substrate and each crystallite acts as a nucleus for further growth. The region of the substrate behind a growing crystallite is prevented from receiving metal vapor because this region is in the shadow of the crystallite. When the rate of migration of atoms in the deposited regions to the shadowed ones is smaller than the rate of void formation via shadowing, column formation occurs during deposition. Therefore, the void region becomes larger and the columns become more tilted with an increasing angle of incidence. The relation between the columnar growth orientation β and the angle of incidence α is plotted for Co/Pt

 0021-8979/96/79(8)/4991/3/$10.00 © 1996 American Institute of Physics

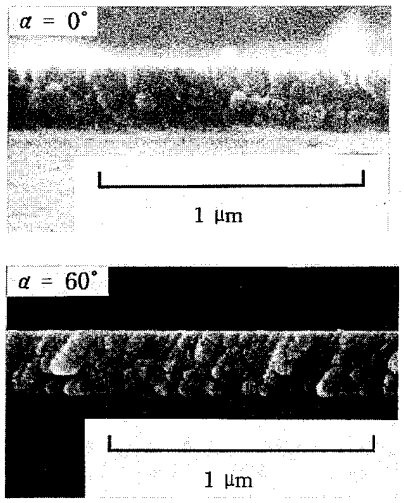


FIG. 1. Cross-sectional scanning electron micrographs of (4 Å Co/9.2 Å $Pt)_{152}$ prepared at the incidence angles α=0° and α=60°.

multilayer thin films in Fig. 2. One can see that Co/Pt multilayer thin films generally follow the tangential rule, $\tan\alpha = 2\tan\beta$.[8]

Interestingly enough, the [111] growth orientation remains normal to the substrate plane even for the samples fabricated at large α's. Figure 3 shows x-ray rocking curves along the substrate normal for (4 Å Co/9.2 Å $Pt)_{152}$ with various α's. As seen in Fig. 3, the peak becomes smaller and the full width at half-maximum widens with increasing α. But the peak position does not nearly change with α. Thus, one would imagine that the [111] growth orientation remains nearly aligned with the substrate normal, irrespective of deposition angle. This fact was also confirmed by examining x-ray pole figures. Figure 4 shows a typical [111] pole figure for the sample prepared at α=45°. The center of the plot and

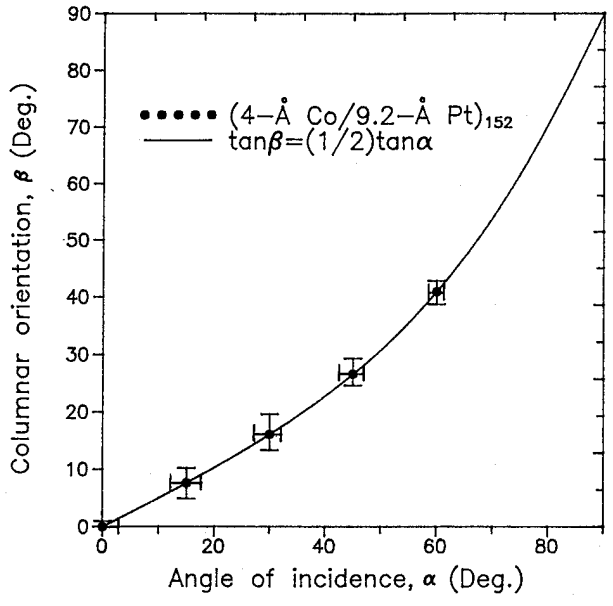


FIG. 2. Columnar growth orientation, β, vs the angle of incident vapor beam, α, in Co/Pt multilayer thin films. Here, α and β are measured from the substrate normal.

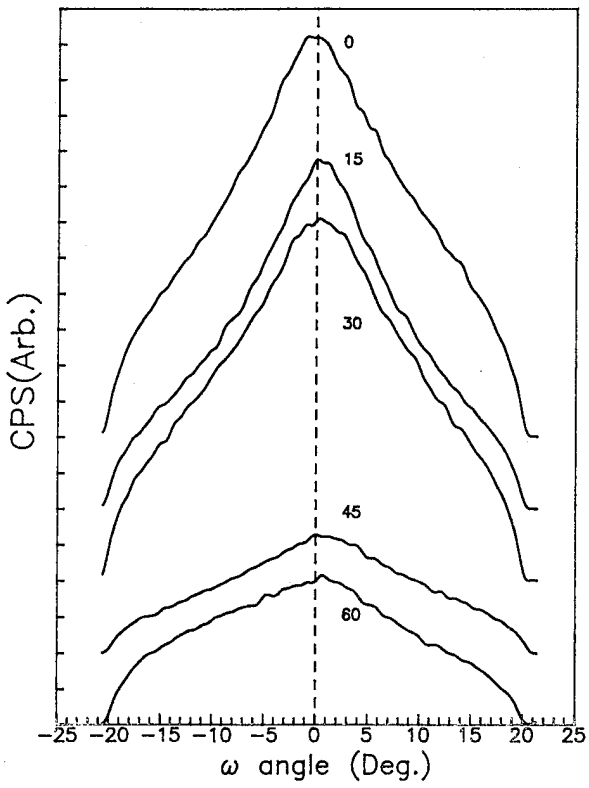


FIG. 3. X-ray rocking curves along a fcc [111] texture for (4 Å Co/9.2 Å $Pt)_{152}$ with various α's.

the cross indicate the substrate normal and the direction of the incident vapor beam, respectively. The pole density is expressed by numerical values in the given regions and has been normalized by the average value. One can clearly see that the [111] direction lies almost along the direction of the substrate normal. A similar result was observed for the sample prepared at α=60°. Therefore, it may be concluded that the [111] crystallographic orientation is not aligned with columnar growth orientation in evaporated Co/Pt multilayer thin films.

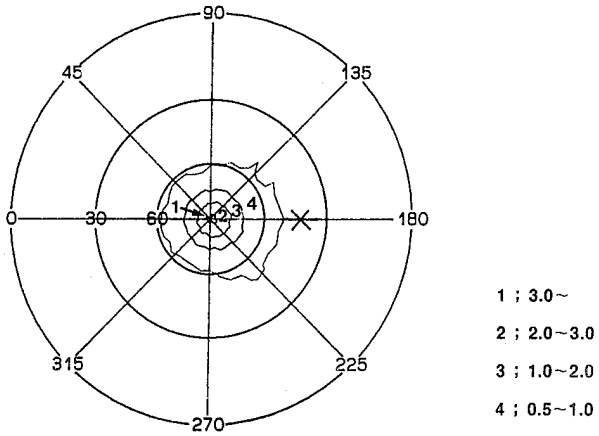


FIG. 4. The [111] pole figure of (4 Å Co/9.2 Å $Pt)_{152}$ prepared at deposition angle α=45°.

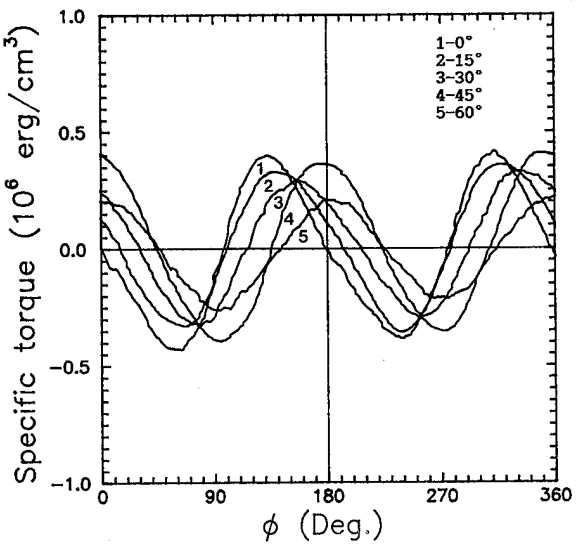


FIG. 5. Variation of the torque curve with the incidence angle of (4 Å Co/9.2 Å Pt)$_{23}$.

We also measured the dependence of the saturation magnetization M_s per Co volume on α. The M_s of the film at α=0° is 1260 emu/cc (87.5% of a Co bulk magnetization) and there is a monotonic decrease with increasing α. The result is believed to probably be caused by an increase of the porous region due to the enhancement of the shadowing effect for a higher α.

Figure 5 shows the variation of the torque curve with varying α's. As noted in Fig. 5, the specific torque τ_p becomes smaller and ϕ_0, the angle where the torque is zero in the first quadrant of ϕ, becomes larger. To estimate the intrinsic anisotropy energy and the easy axis orientation, torque curves were analyzed by a simple model described as follows.[7] We assume that a film has a uniaxial anisotropy with a single easy axis making an angle δ from the substrate normal. We consider only the first-order anisotropy energy constant K_u and ignore any higher order terms. Then

$$K_u^2 = K_s^2 + \tau_p^2 + 2K_s\tau_p \cos(2\phi_0), \tag{1}$$

$$\delta = \phi_0 - (1/2)\tan^{-1}\left(\frac{K_s \sin(2\phi_0)}{K_2 \cos(2\phi_0) + \tau_p}\right), \tag{2}$$

where K_s is the shape anisotropy energy of $2\pi M_s^2$ and M_u is the first-order anisotropy energy constant.

In Table I, we summarize the calculated results according to Eqs. (1) and (2). A monotonic decrease of K_u with increasing α is believed to be closely correlated with the structural change of the sample. The K_u associated with an interface is phenomenologically described as $K_u = 2K_{\text{int}}/t_{\text{Co}} + K_V$, where K_{int} is the surface anisotropy originating from the interface per unit area. t_{Co} is the Co thickness, and K_V is the volume anisotropy consisting of the shape anisotropy, magnetocrystalline anisotropy, and magnetoelastic anisotropy. Since the texture and interface of a film become poor with increasing α, the magnetocrystalline and the surface anisotropies are expected to decrease with α. The shape anisotropy is also decreased with α due to a smaller M_s for a higher α. In Table I, it is very interesting to note that the easy axis orientation remains nearly normal even for the sample prepared at α=60°. This is in sharp contrast in comparison to ferromagnetic single-layer films.[8] In those systems, the easy axis orientation was reported to be dependent on the direction of the incident vapor beam and thus, the growth-induced anisotropy of the columnar structures was believed to be a major source of the magnetic anisotropy. However, the fact that the easy axis orientation is insensitive to columnar growth orientation in Co/Pt multilayer thin films implicitly implies the importance of the surface anisotropy in this system.

TABLE I. Magnetic parameters of (4 Å Co/9.2 Å Pt)$_{23}$ prepared at oblique incidence. Here, τ_p is the specific torque, ϕ_0 is the angle where the torque is zero in the first quadrant of ϕ, K_s is $2\pi M_s^2$, K_u is the first-order anisotropy energy constant, and δ is the easy axis orientation measured from the substrate normal.

α (deg)	τ_p (10^6 dyn cm/cm^3)	ϕ_0 (deg)	K_s (10^6 ergs/cm^3)	K_u (10^6 ergs/cm^3)	δ (deg)
0	1.7	0.0	9.8	11.5	0.0±0.1
15	1.5	8.2	9.7	11.2	1.1±0.1
30	1.2	20.0	7.7	8.8	2.6±0.3
45	1.2	41.5	6.5	6.8	5.1±0.5
60	0.7	45.0	4.0	4.0	4.9±0.6

IV. CONCLUSIONS

We have studied the effects of deposition angle on the structural and magnetic properties of e-beam evaporated Co/Pt multilayer thin films on the tilted substrates. The [111] crystallographic orientation of samples was not aligned with the columnar growth orientation and remained normal to the substrate planes, in spite of increasing deposition angle. Also, it was found from the torque curve that the magnetic easy axis orientation was nearly aligned with the substrate normal, irrespective of deposition angle.

ACKNOWLEDGMENTS

This work was supported by the Korea Science and Engineering Foundation under Grant No. 941-0200-031-2.

[1] S. Hashimoto, Y. Ochiai, and K. Aso, J. Magn. Magn. Mater. **88**, 211 (1990).
[2] K. H. J. Buschow, P. G. V. Engen, and R. Jongebreur, J. Magn. Magn. Mater. **38**, 1 (1983).
[3] P. F. Carcia, S. I. Shah, and W. B. Zeper, Appl. Phys. Lett. **56**, 2345 (1990).
[4] S.-C. Shin, J.-H. Kim, and D.-H. Ahn, J. Appl. Phys. **69**, 5664 (1991).
[5] S. M. Paik, S. Kim, and I. K. Schuller, Phys. Rev. B **43**, 1843 (1991).
[6] H. J. Leamy and A. G. Dirks, J. Appl. Phys. **49**, 3430 (1978).
[7] S.-C. Shin and C.-S. Kim, IEEE Trans. Magn. **27**, 4852 (1991).
[8] K. L.Chopra, *Thin Film Phenomena* (Krieger, Malabar, FL, 1969), p. 629.

Simulations of inhomogeneous magnetization processes in ultrathin films with growth-induced roughness (abstract)

A. Moschel and A. Zangwill
School of Physics, Georgia Institute of Technology, Atlanta, Georgia 30332

M. D. Stiles
Electron Physics Group, National Institute of Standards and Technology, Gaithersburg, Maryland 20899

Magnetization in ultrathin films depends in a very sensitive way on the morphology of the surface of the films. Using a X–Y model with enhanced anisotropy at the step edges, we have calculated hysteresis loops in different directions at zero temperature for nominally vicinal and flat films with growth-induced surface roughness. For the vicinal films the influence of the width of the terraces and the strength of the anisotropy at the edges is studied. For the "flat" films the influence of the shape and the size of 2D and 3D island roughness is investigated. Some interesting properties of the coercive field and the remanent magnetization are discussed and compared to some experimental results. © *1996 American Institute of Physics.* [S0021-8979(96)82008-6]

 0021-8979/96/79(8)/4994/1/$10.00 © 1996 American Institute of Physics

Measurement of the crystalline anisotropy in sputtered single-crystal FeTaN thin films

L. Varga and W. D. Doyle
Department of Physics and Astronomy and Center for Materials for Information Technology, The University of Alabama, Tuscaloosa, Alabama 35487-0209

FeTaN single-crystal thin films were grown in order to investigate the dependence of the crystalline anisotropy constant, K_1, on the Ta and nitrogen content. Films with 5 and 10 wt % Ta and different nitrogen contents were prepared by dc sputtering on MgO(100) substrates at elevated temperatures. The film/substrate orientation was (100)‖(100) and [100]‖[110]. The values of K_1 were determined by measuring the in-plane angular dependence of the ferromagnetic resonance spectra and agreed very well with the values obtained from torque measurements, indicating that the total volume was biaxial cubic material. The hysteresis loops were characteristic of biaxial anisotropy and the anisotropy fields estimated from magnetization curves were consistent with the resonance and torque data. In Fe, K_1 was $(4.8\pm0.1)\times10^5$ ergs/cc in good agreement with the bulk value. In FeTa, K_1 decreased to $(4.4\pm0.1)\times10^5$ and $(3.5\pm0.1)\times10^5$ ergs/cc for 5 and 10 wt % Ta content, respectively, and further to $(2.7\pm0.1)\times10^5$ and $(2.1\pm0.1)\times10^5$ ergs/cc in $(Fe_{95}Ta_5)N$ depending on the nitrogen content. The nitrogen addition to $Fe_{90}Ta_{10}$ resulted in the formation of epitaxial $(FeTa)_4N$ which is an fcc structure with a negative K_1 of $(-1.5\pm0.2)\times10^5$ ergs/cc. © *1996 American Institute of Physics.* [S0021-8979(96)08408-4]

I. INTRODUCTION

The optimization of the soft magnetic properties of FeXN high magnetization alloys for recording head applications will require the knowledge of the crystalline anisotropy K_1, and the magnetostriction which impact the ripple structure.[1,2] The crystalline anisotropy of FeXN alloys has been assumed to be the same as bulk Fe,[2,3] based on the magnetic properties of $Fe_{16}N_2$,[4] and their soft properties were widely believed to originate only from their nanocrystalline structure.[2,3] In this work we report the direct measurement of K_1 in single-crystal Fe, FeTa, and FeTaN films.

II. EXPERIMENTAL METHOD

MgO single-crystal platelets with (100) orientation were chosen as the substrate material for epitaxial growth based on earlier work[5,6] which found the film/substrate orientation to be Fe(100)‖MgO(100) and Fe[100]‖MgO[110] with a lattice mismatch of −3.8%. FeTaN films of different Ta and nitrogen content were sputtered from hot pressed Fe, $Fe_{95}Ta_5$, and $Fe_{90}Ta_{10}$ targets at a total argon-nitrogen pressure of 4 mTorr, and fixed sputtering power of 50 W onto commercially obtained, epitaxially polished substrates at temperatures of 150–200 °C. The nitrogen content was varied by controlling the flow rate of the N_2 gas during deposition. The deposition rates were 1–2 Å/s and the film thickness ranged from 800 to 2000 Å.

After preparation, film thicknesses were determined by a Dektek Profilemeter and used to calculate the volume of the samples measured in the magnetometer and torquemeter. The structural analysis was carried out on a Rigaku D/Max-2BX thin-film diffractometer with Cu K_a radiation. Diffraction patterns in the $2\Theta-\Theta$ and 2Θ modes were used to determine the structure, the lattice parameter, and the orientation of the films with respect to the substrate.

The values of K_1 were obtained by measuring the angular dependence of the ferromagnetic resonance (FMR) using a spectrometer with a 34.48 GHz cylindrical TE_{011}-mode resonant cavity. A static field, up to 18 kOe, was rotated in the plane of the film. From the fit to the theoretical model[6,7] the saturation magnetization M_S, and K_1 were determined. The torque was recorded as a function of angle and applied field up to 10 kOe in the plane of the films. The maximum torque above the anisotropy fields and the total volume of the sample were used to calculate the anisotropy constant in sup-

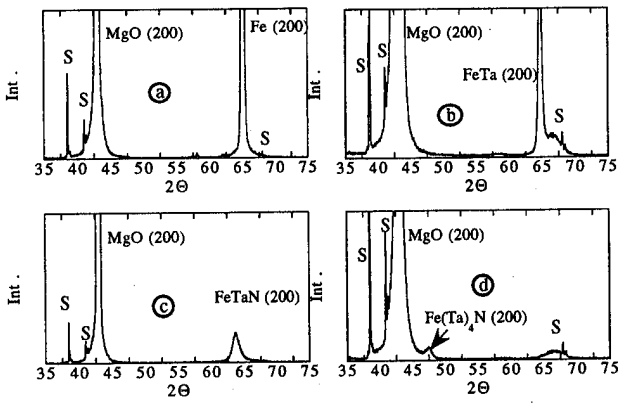


FIG. 1. X-ray spectra of (a) Fe, (b) FeTa, (c) FeTaN, and (d) $(FeTa)_4N$ sputtered films in the $2\Theta-\Theta$ mode. The peaks indexed by (*S*) are from the MgO substrate.

 0021-8979/96/79(8)/4995/3/$10.00 © 1996 American Institute of Physics

TABLE I. Measured magnetization, anisotropy constant, thickness, and lattice parameter of Fe, FeTa, FeTaN, and $(FeTa)_4N$ sputtered films.

Sample	M_S emu/cc (±5%) VSM	M_S emu/cc (±1%) FMR	K_1 10^5 (±1%) ergs/cc FMR	K_1 10^5 (±2%) ergs/cc TRQ	H_K Oe (±5%) VSM	K_1 10^5 ergs/cc VSM	Thick Å	a_0 Å
Fe	1650	1720	4.8	5.0	570	4.7	1390	2.87
$Fe_{95}Ta_5$	1520	1620	4.4	4.3	550	4.2	1100	2.88
$Fe_{90}Ta_{10}$	1500	1500	3.5	3.6	430	3.2	2140	2.90
$Fe_{95}Ta_5N$	1600	1440	2.7	2.8	400	3.2	1040	2.90
$Fe_{95}Ta_5N$	1590	1560	2.1	2.2	350	2.7	1220	2.94
$(FeTa)_4N$	1140	1350	−1.5	−0.7	260	−1.1	1610	3.83

port of the FMR data. The hysteresis loops were measured along [100], [110], [010], and [1$\bar{1}$0] directions of the substrate. The anisotropy field $H_K=2K_1/M_S$ was estimated from the saturation field in the hard direction.[8]

III. RESULTS AND DISCUSSION

The x-ray diffraction patterns (Fig. 1) in the 2Θ−Θ mode for Fe, FeTa, and FeTaN showed only a strong (200) peak consistent with the expected growth orientation of Fe(100)||MgO(100). No evidence of a randomly oriented polycrystalline component was observed although if a small intensity (110) diffraction peak were present, it would be hidden under the right shoulder of the MgO(200) diffraction peak at ~44.5°. The (200) peaks of FeTa and FeTaN [Figs. 1(b), 1(c)] were shifted toward smaller angles relative to the Fe(200) peak consistent with the expected lattice expansion of the α-Fe. The lattice parameters were determined from the d spacing of the (200) planes (Table I). The calculated nitrogen content[9] for the two $(Fe_{95}Ta_5)N$ samples were 2.9 and 8.6 at %. The linewidth of the (200) film peak increased and its intensity decreased relative to the MgO(200) peak with the addition of Ta and nitrogen, suggesting a decrease in the degree of crystallinity or an increase in nonuniform strain. To collect information about the orientation relationship of the substrate and the film, the 2Θ mode was used. When the sample was aligned such that the low angle incident beam, the normal of the film and the [100] direction of MgO were in the same plane, a diffraction peak corresponding to the (112) planes of the film appeared on the spectra [Figs. 2(a), and 2(b)] which disappeared with a slight rotation in the plane (<5°). This again is consistent with the expected orientation of [110]||[100]. For the FeTa and FeTaN compared to Fe, a low intensity peak [Fig. 2(b)], whose amplitude did not change with rotation, was observed at an angle consistent

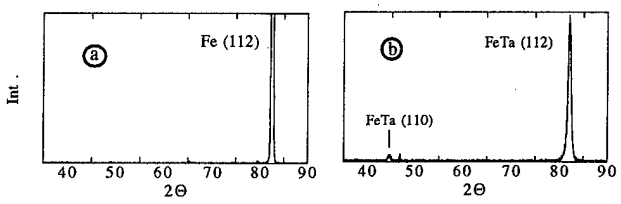


FIG. 2. X-ray spectra of (a) Fe and (b) FeTa films in the 2Θ mode.

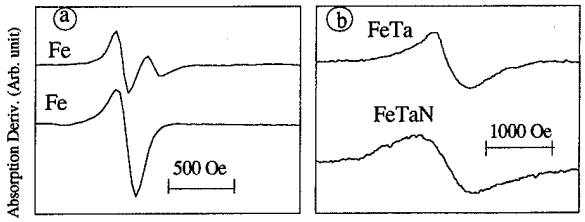


FIG. 3. Ferromagnetic resonance lines for (a) two different Fe and (b) FeTa and FeTaN sputtered films.

with a reflection from the (110) planes. This suggests that some amount of polycrystalline material with a (200) texture is also present.

When the nitrogen flow rate was increased to 0.7 sccm for the $Fe_{90}Ta_{10}$ target from the maximum of 0.3 sccm used for $Fe_{95}Ta_5$, the phase structure completely changed from bcc α-Fe to fcc $(FeTa)_4N$ [Fig. 1(d)].

The FMR spectra for several films are shown in Fig. 3. The narrowest line occurred in the Fe films and varied from 90 to 140 Oe [Fig. 3(a)], which is in the range reported by others (50–400 Oe).[5,10] It increased to ~500 Oe in FeTa and ~1000 Oe in FeTaN [Fig. 3(b)], consistent with the decrease in degree of crystallinity suggested by the increased x-ray linewidth. Also, in some of the resonance spectra, extra resonance lines were observed [Fig. 3(a)] close to the main (i.e., highest amplitude) line, possessing the same biaxial symmetry (Fig. 4), with essentially the same value of K_1 but a slightly smaller (~5%) value of M_S. This is not consistent with a surface oxide layer which would be expected to have a much lower value of M_S. At the present time the extra resonance cannot be explained.

The angular dependence of the main resonance in the plane (Fig. 5) could be fitted very well with a simple biaxial anisotropy in all cases. For the α-phase films K_1 was positive; i.e., the easy axis was along the [100]. The values of K_1 and M_S obtained from the fit are listed in Table I. For Fe, the results are in good agreement with the bulk values.[6] Both K_1 and M_S decreased in the FeTa and further in FeTaN. The magnetization values for all the α-phase films were in good agreement with those obtained from the vibrating sample magnetometer (VSM) measurement and values reported for polycrystalline films,[9] showing that the magnetization is rela-

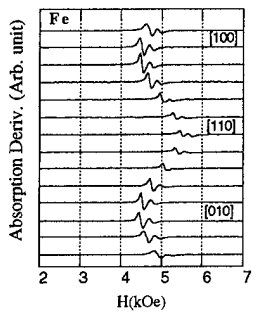


FIG. 4. Ferromagnetic resonance spectra of Fe in the film plane. The directions denote approximately the film directions and the applied field was changed by 10° steps.

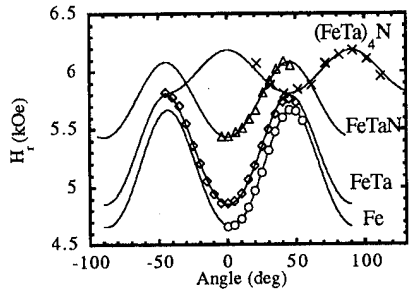


FIG. 5. Angular dependence of the ferromagnetic resonance field in the (100) plane of Fe (○), FeTa (◇), FeTaN (△), and $(FeTa)_4N$ (×). The angle is measured with respect to the [110] direction of the substrate.

tively constant throughout the films. In the $(FeTa)_4N$, K_1 changed sign and decreased in absolute magnitude, consistent with the expectation for fcc Fe_4N. The magnetization obtained from the VSM for $(FeTa)_4N$ was ~15% less than the FMR value which means that a significant fraction of the film was not contributing to the biaxial resonance. This could be a polycrystalline, lower moment nitride phase, which did not appear in the x-ray spectra.

The angular dependence of the torque in the (100) plane (Fig. 6) showed a pure biaxial behavior and crystal symmetry in agreement with the FMR measurements. The torque curves below the anisotropy field [Fig. 6(a)] fit a simple biaxial, Kondorsky-type switching.[11,12] At fields higher than the anisotropy field [Fig. 6(b)], the maximum torque in the (100) plane was independent of field, characteristic of a uniform anisotropy. The values of the anisotropy calculated from the maximum torque and the total volume of the

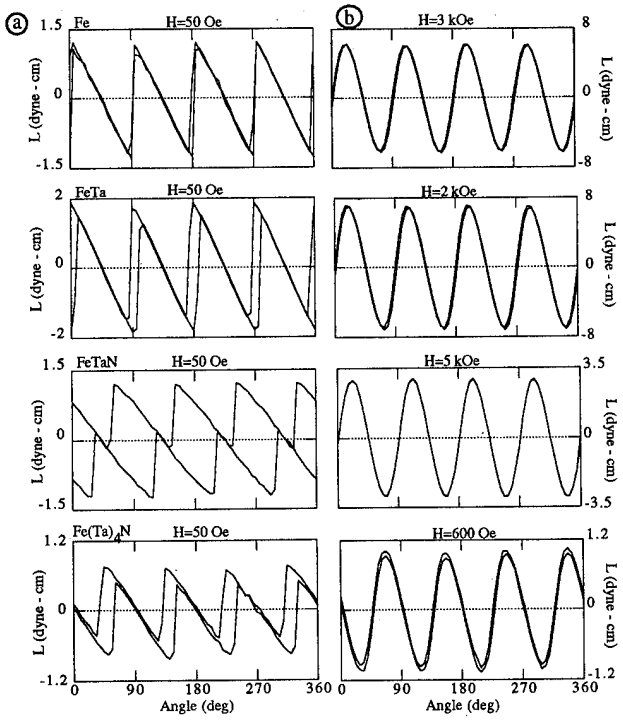


FIG. 6. Torque curves (a) below and (b) above the anisotropy field for Fe, FeTa, FeTaN, and $(FeTa)_4N$ in the film plane.

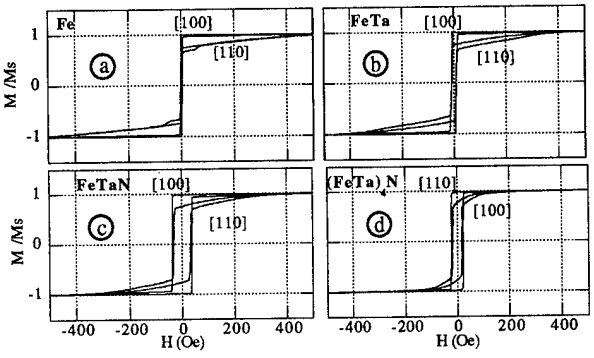


FIG. 7. Magnetization curves for (a) Fe, (b) FeTa, (c) FeTaN, and (d) $(FeTa)_4N$ sputtered films along [100] and [110] directions of the films.

samples were in very good agreement with the FMR data for Fe, FeTa, and FeTaN (Table I), again confirming that the films were well oriented, single phase, single crystals.

The M-H loops also showed biaxial symmetry in the plane in all cases (Fig. 7), in agreement with FMR and torque data. The addition of Ta and nitrogen caused an increase in the coercivity implying a decrease in the homogeneity of the films, consistent with the x-ray and FMR data. The value of K_1 extracted from M_S and H_K confirmed the FMR and torque results (Table I).

IV. CONCLUSION

The crystalline anisotropy of Fe is reduced by the addition of Ta and nitrogen. FeTa films with 10 wt % Ta have smaller K_1 than samples with 5 wt % Ta. The value of K_1 in α-phase $(Fe_{95}Ta_5)N$ single-crystal films was found to be $\sim 2-3\times10^5$ erg/cc, roughly half the value in pure Fe. This alone is not sufficient to explain the soft properties of FeTaN, and so the answer must be related to the magnetostriction and the nanocrystalline structure of these materials. In fcc-phase $(FeTa)_4N$ single-crystal films, K_1 changed sign and decreased to -1.5×10^5 ergs/cc. This suggests the possibility of further optimizing the soft properties of FeTaN for recording head applications by preparing a mixed phase polycrystalline system with zero effective crystalline anisotropy.

ACKNOWLEDGMENT

This work was supported in part of a grant from the U.S. department of Commerce administered by NSIC.

[1] H. Hoffman, Thin Solid Films **58**, 223 (1979).
[2] E. Haftek, L. Varga, W. D. Doyle, and J. A. Barnard, IEEE Trans. Magn. **31**, 3773 (1995).
[3] M. Takahashi and T. Shimatzu, IEEE Trans. Magn. **26**, 1485 (1990).
[4] Y. Sugita, K. Mitsuoka, N. Komuro, H. Hoshiya, Y. Kozono, and M. Hanazono, J. Appl. Phys. **70**, 5977 (1991).
[5] *Single-Crystal Films*, edited by M. H. Francombe and H. Sato (Wiley, New York, 1964), p. 215.
[6] O. Kohmoto and C. Alexander, Jpn J. Appl. Phys. **31**, 2101 (1992).
[7] J. G. Wright, Philos. Mag. **24**, 271 (1971).
[8] E. W. Pugh, Proc. Intermag (1963).
[9] V. R. Inturi and J. A. Barnard, IEEE Trans. Magn. **31**, 2660 (1995).
[10] J. J. Krebs, B. T. Jonker, and G. A. Prinz, J. Appl. Phys. **61**, 3744 (1987).
[11] E. Kondorsky, J. Phys. (U.S.S.R.) **2**, 161 (1940).
[12] W. D. Doyle, IEEE Trans. Magn. **2**, 68 (1966).

Magnetic properties and crystal structure of FeTaAlN soft magnetic materials for MIG head (abstract)

Yiqun Li, Bingchu Cai, Xianglin Zeng, and Dong Xu
Information Storage Research Center, Shanghai Jiao Tong University, Shanghai 200030, People's Republic of China

Fe-based nitride films have been expected as promising head core materials used for high-density magnetic recording MIG head due to their large saturation flux density combined with excellent soft magnetic properties. Recent studies found that the addition of 8–13 at. % Ta in Fe–N resulted in a remarkable improvement of thermal stability.[1] It was also reported that small amount of Al appeared to inhibit the formation of γ'-Fe_4N phase and to prevent the grain growth during annealing.[2] In this paper, the magnetic properties and crystal structure of a new Fe–M–N soft magnetic film, FeTaAlN, has been reported. FeTaAlN films about 3 μm thick were prepared on glass substrate by dc magnetron sputtering method in $Ar+N_2$ plasma and then annealed in vaccum. The films generally present high $4\pi M_s$ (15–20 kG). X-ray diffraction results show that both as-deposited and annealed films have only two phases, an α-Fe phase with perfered (110) axis orientation and a Ta_3N_5 phase. Annealing is essential in lowering H_c without seriously diminishing $4\pi M_s$ of the films; the film with the lowest H_c (about 0.5 Oe) has a $4\pi M_s$ of above 15 kG. The peak broadenings of both the α-Fe phase and the Ta_3N_5 phase are observed as annealing temperature increases. Meanwhile, the (110) peaks of α-Fe shift slightly to higher 2θ value. This indicates that the interstitial nitrogen atoms come out of α-Fe lattice when the films are annealed and a part of b.c.t. α-Fe is transferred into b.c.c. α-Fe, which causes the broadening of α-Fe peak. On the other hand, the segregated nitrogen atoms may react with Ta atoms that dissolved substitutionally in α-Fe to form fine Ta_3N_5 particles and make the Ta_3N_5 peak broadened. Thus, it is thought that the decrease of H_c is mainly due to the reduction of internal stress. The magnetostrictions of the films are on the order of 10^{-6}. FeTaAlN film presents high saturation flux density and good soft magnetic properties even after annealing at 500 °C, and it is potentially a superior substitute for the core materials of high-density recording MIG head. © *1996 American Institute of Physics.* [S0021-8979(96)45308-7]

[1] N. Ishiwata, C. Wakabayashi, and H. Urai, J. Appl. Phys. **69**, 5616 (1991).
[2] M. H. Kryder, S. Wang, and K. Rock, J. Appl. Phys. **73**, 6212 (1993).

 0021-8979/96/79(8)/4998/1/$10.00 © 1996 American Institute of Physics

Magnetic domain control of thick Fe-M(Zr,Ta)-N films for digital VCR metal in gap heads

M. Uchizawa, J. Fujita, H. Kobayashi, and S. Tanabe
Advanced Technology R&D Center, Mitsubishi Electric Corporation, 8-1-1 Tsukaguchi-Honmachi, Amagasaki, Hyogo 661, Japan

Magnetic domain structures of thick and small area ($45\times45\times5$ μm^3) Fe-M(Zr or Ta)-N films were observed by a scanning Kerr-effect microscope (SKEM). The important factors in controlling the magnetic domains are the magnetostriction and the uniaxial anisotropy. By changing the N content in bcc Fe and the Ar pressure during sputtering, the saturation magnetostriction constant λ_s and the anisotropy field H_k were controlled in the range of 3×10^{-6}–6×10^{-6} and 10–130 A/m, respectively. Clear and consecutive changes in the domain structures were observed by varying the film's λ_s, H_k, and stress σ, and the observed structures agree qualitatively with the structures predicted by theoretical calculations. The wall structure where Bloch-like rotations and the Neel-like rotations are combined was observed by SKEM. The metal in gap heads using different λ_s and H_k films were fabricated and the output at 20 MHz was measured. A lower H_k is not necessarily better for obtaining a higher output in high-frequency ranges. The head output depends on the film's magnetic domain structure, and the structure can be controlled by changing the λ_s and H_k. © *1996 American Institute of Physics.* [S0021-8979(96)08508-0]

I. INTRODUCTION

About 10 μm or less track width and the same order gap depth are required for digital VCR metal in gap (MIG) heads.[1] The metal films at both sides of the gap must be thick in order to obtain sufficient recording properties.[2] The aspect ratio of the track width to the film thickness is 3:1 to 2:1. In order to obtain higher output in high-frequency ranges, the permeability in the direction of the film thickness and the magnetic domain structure are important.[3] The magnetic domain structures of these kind of thick "film" are completely different from the domain structures of wide area films and typical thin films. Wide area Fe-Zr-N film domain structures have been reported and the film has a clear domain structure even for isotropic films as compared to Sendust (FeSiAl) film domain structures.[4] However, small size thick Fe-Zr-N film domain structures have not been reported. The magnetic domain structure was observed using small scale samples, $45\times45\times5$ μm^3 by scanning Kerr-effect microscope (SKEM) in this work. The important factors in controlling the magnetic domains of this shape of Fe-M(Zr or Ta)-N film are the saturation magnetostriction constant λ_s and anisotropy field H_k. The relation between those parameters and the domain structures was observed by SKEM, and the observed structures were compared with the structures predicted by theoretical calculations considering each energy term (exchange, anisotropy, magnetoelastic, and magnetostatic energy). The magnetostatic energy for each shape and each magnetization distribution was calculated using a three-dimensional finite element method (3D-FEM). Furthermore, a wall structure where Bloch-like rotations and surface Neel-like rotations are combined was observed. This domain structure was predicted theoretically[5] but had not been observed in a real soft magnetic film. Finally, MIG heads using different λ_s and H_k films were fabricated and the outputs at 20 MHz were compared.

II. EXPERIMENTAL METHODS

The *S*-polarized longitudinal mode of the SKEM (Phase Metrics) was used in the observation. As shown in Fig. 1(a), a 200 kHz sinusoidal field is applied to the sample in the transverse direction. A polarized argon laser beam is injected at an oblique angle, and the magnetization variation synchronized at 200 kHz in longitudinal and perpendicular directions is picked up by a lock-in amplifier. The selected signal magnitude and phase are graphically represented. The lines in an image do not show the walls themselves but show the movement of the walls. Two opposite phase 90° walls' movement appears as in Fig. 1(b). That is, when the applied magnetic field in the direction from left to right is increased, the shaded part of the magnetization in the longitudinal direction is increased and the hatch part magnetization is decreased. This magnetization magnitude and phase information is pictured as white and black lines along the walls.

The samples were prepared using an ion beam sputtering (IBS) deposition method on $CaTiO_3$ or nonmagnetic ferrite

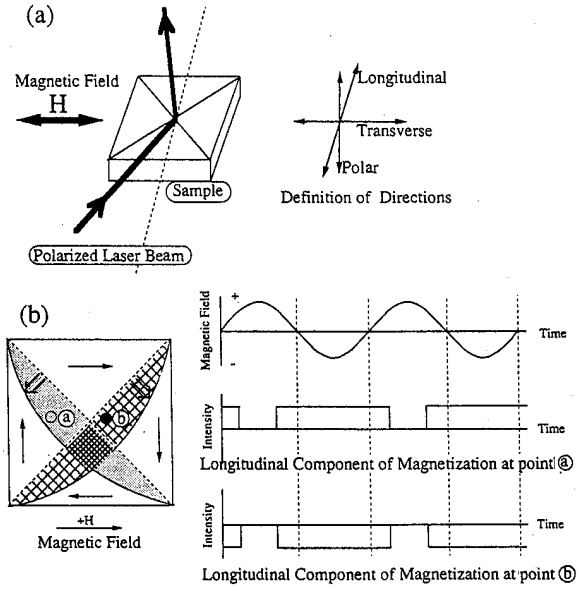


FIG. 1. (a) Principle of the SKEM observation and definition of the directions. (b) Explanation of why white and black lines appear along walls.

 0021-8979/96/79(8)/4999/3/$10.00 © 1996 American Institute of Physics

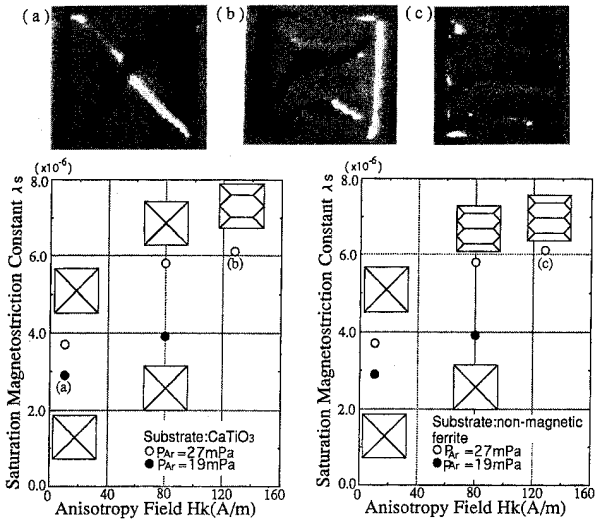


FIG. 2. Variation of the magnetic domain structures for different λ_s and H_k samples on $CaTiO_3$ substrates.

substrates. An $Fe_{90}Zr_{10}$ target was used and N_2 gas flowed across the substrate. The as-deposited Fe-Zr-N amorphous films were annealed at 530 °C without applying a magnetic field in order to obtain fine crystalline Fe-Zr-N films. Some films were annealed again at 250 °C in a 6400 A/m applied field in order to induce uniaxial anisotropy. By changing the N_2 pressure during deposition, the λ_s and H_k were controlled in the range of 3×10^{-6}–6×10^{-6} and 10–130 A/m, respectively. The deposited and annealed 5-μm-thick samples were machined into a $45\times45\times5$ μm^3 plate.

III. RESULTS AND DISCUSSION

Figure 2 shows the variation of the magnetic domain structures for different λ_s and H_k film samples on $CaTiO_3$ and nonmagnetic ferrite. The thermal linear expansion coefficients α of $CaTiO_3$ and nonmagnetic ferrite are 115×10^{-7} and 85×10^{-7} $(1/K)$, respectively. The α of the annealed Fe-Zr-N film is close to that of $CaTiO_3$. That is, a larger tension is applied to the film in-plane directions on nonmagnetic ferrite substrate and the magnetization is easy to direct in-plane because λ_s is positive. The magnetic domains are separated by 90° walls in the case of a small λ_s and H_k film. As λ_s and H_k increase, 180° walls appear. 180° walls appear at a smaller H_k in the films on nonmagnetic ferrite because of the stronger in-plane tension. When a magnetic ferrite was

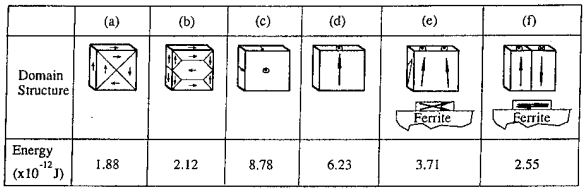


FIG. 3. Total energy of each domain structure for a $45\times45\times5$ μm^3 sample. When uniaxial anisotropy increases over a threshold value (a) shape changes to (b) shape. (c), (d) shape energies are large because of the large magnetostatic energy. However, when the films are deposited on magnetic substrates, the energy decreases drastically even without closure domains.

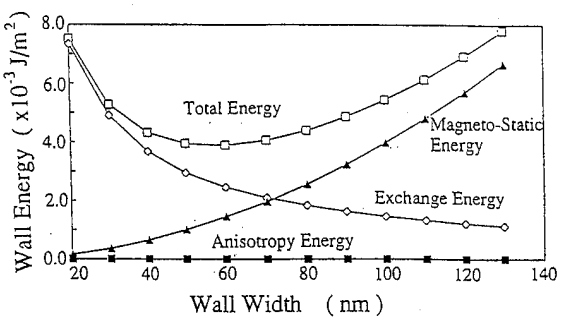


FIG. 4. Calculated wall energy density vs wall width.

used as a substrate as in an MIG head, the domain structure could not be observed. We assumed that the magnetic ferrite substrate reduced the magneto-static energy on the boundary when the magnetization was directed perpendicularly. Therefore, the magnetization dispersion including the perpendicular direction is increased, and this increase of the dispersion makes the domain structures unclear.

Figure 3 shows the total energy (exchange, anisotropy, and magnetostatic) for each domain structure. The total wall energy was estimated using a well-known simple elliptic cylinder model. This model was explained briefly in LaBonte's paper.[5] In his model, the wall energy density E_w is expressed as follows:

$$E_w=\frac{a}{2}K_u+\frac{1}{a}\pi^2A+\frac{1}{4\mu_0}\frac{a^2}{a+D}M_s^2, \tag{1}$$

where a, K_u, A, μ_0, M_s, and D represent the wall width, anisotropy energy density, exchange stiffness constant, permeability for free space, saturation magnetization, and thickness, respectively. We used the following values for Fe-Zr-N films:

$$K_u=64(\mathrm{J/m^3})(H_k=80\ \mathrm{A/m}),\quad A=1.49\times10^{-11}(\mathrm{J/m})\times(\text{the value for Fe}),$$

$$M_s=1.6(\mathrm{T}),\quad D=5\times10^{-6}(\mathrm{m}).$$

Figure 4 shows the calculated wall energy density E_w versus wall width. The minimum value is about 3.9×10^{-3} (J/m^2) at about 60 nm wall width. The energy density for 90° walls is assumed to be 1/2 of that for 180° walls. The magnetostatic energies for (c)–(f) structures were calculated by 3D-FEM. The $45\times45\times5$ μm^3 magnetic film was divided into about 5000 finite elements, and the demagnetizing field Hd_i at each element which is magnetized in one direction was calculated. The magnetostatic energy E_m, of the whole film is obtained as follows:

$$E_m\sum^{i} M_sHd_iV_i, \tag{2}$$

where V_i is the volume of each finite element. If the films are deposited on a magnetic ferrite substrate, the total energy is lowered without producing well-defined domains and closure domains.

In the above simple calculations for the wall energy, the threshold value of H_k for moving from (a) to (b) in Fig. 3, which is the value obtained from the calculation, (the energy of a)=(the energy of b), is about 350 (A/m)(4.4 Oe) although

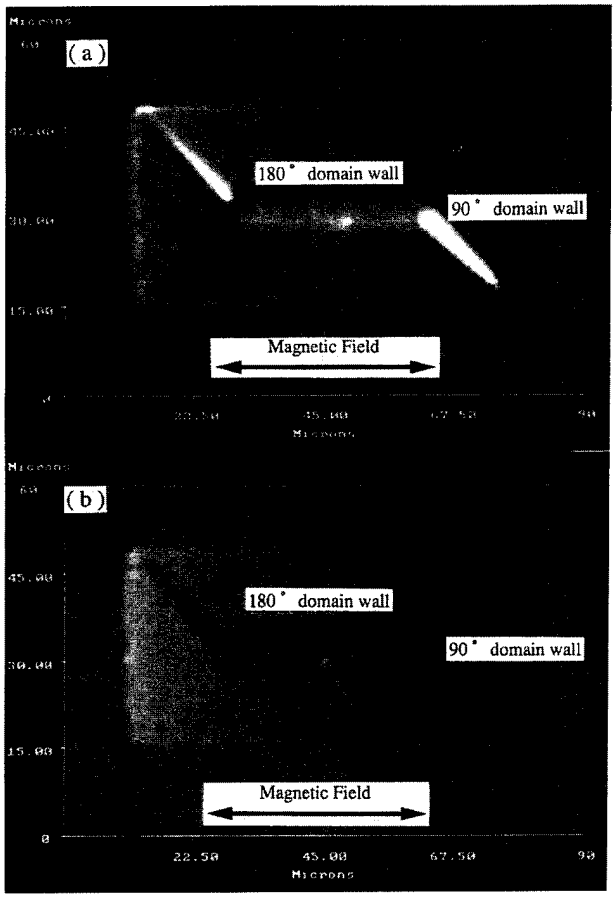


FIG. 5. Domain and wall movements for a re ctangular shape ($35\times65\times5$ μm^3) film. (a) Observed in Longitudinal mode. 180° walls separate in white and black portions. (b) Observed in polar mode. 180° walls appear in monotone.

the threshold is about 130 (A/m)(1.6 Oe) H_k in real films as shown in Fig. 2. We thought that the reason for this quantitative disagreement between the calculated value and the observed value is in the model for the calculation of wall energy density. As LaBonte pointed out in his paper,[5] the reversal must be more nearly like Neel walls on the top and bottom surfaces in order to decrease the magnetostatic energy. According to his paper, the wall energy density for a film thicker than 200 nm is less than 1/3 of that calculated from the simple elliptical cylinder model.

TABLE I. Fabricated heads specifications, measure conditions, and results.

Magnetic film	Anisotropy field (A/m)	Anisotropic 130	Isotropic 10
Heads	gap length (μm)	0.22	0.22
	gap depth (μm)	11	11
	track width (μm)	10	12
	coil turns	15	15
Measurement	tape	metal evaporated tape	
	coercive force (A/m)	144 000	
	medium thickness (μm)	0.2	
	relative velocity (m/s)	10.2	
	normalized output voltage at 20.4 MHz [nV/(μm turn m/s)]	215 (0 dB)	174 (−1.8 dB)

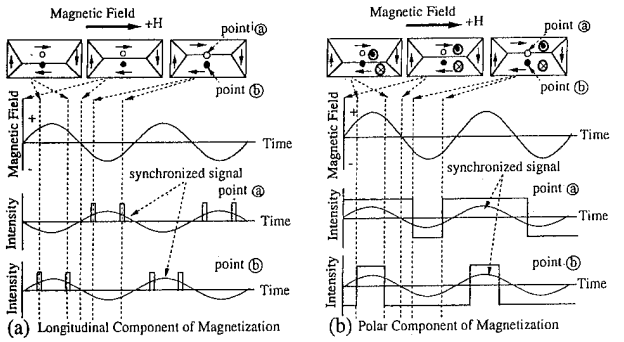


FIG. 6. Explanations for Fig. 4 photos. (a) The movement of longitudinal magnetization with applied field is in-phase in the upper half and out of phase in lower half. (b) The movement of polar magnetization is in-phase with the applied field.

Figure 5 shows the domain (wall) movement for a rectangular plate film ($35\times65\times5$ μm^3) observed by polar mode and longitudinal mode. In the photo taken in the longitudinal mode (a), the phases of the field and the magnetization are the same in the upper half and opposite in the lower half. However, in the photo taken in the polar mode (b), the boundary of the domains along the 180° wall appears as a monotone line which means the field and magnetization phases are the same at all times. In order to explain these results, we conclude the following:

(1) On the top surface, the magnetization in a wall has a longitudinal component and no perpendicular component, that is, the reversal is similar to a Neel wall. Therefore, the movement of the magnetization in the longitudinal direction is in-phase with the field variation in the upper half and out-of-phase in the lower half as shown in Fig. 6(a). This is the reason that white and black parts appear in a line in the longitudinal mode.

(2) The domains have a small perpendicular component as shown in Fig. 6(b), therefore, the movement of the magnetization in the polar direction is in-phase with the field variation throughout the whole region. This is the reason that the line is monotone in polar mode.

In order to confirm the relationship between the domain structure and the output level of a MIG head, we fabricated MIG heads using different H_k films around the gap. The permeability in the thickness direction of the film is important in obtaining higher output from an MIG head. In order to obtain high permeability in the thickness direction at high frequency, the magnetization process should be rotational and the magnetization of the film must be in-plane. Therefore, we chose an almost isotropic film, (a) in Fig. 2, and an anisotropic one, (b) in Fig. 2. Table I shows fabricated MIG heads specifications, measurement conditions, and results. As predicted above, the output of the head using an anisotropic film is larger than the head using an isotropic film by 1.8 dB.

[1] S. M. C. Borgers, W. A. L. Heijnemans, E. de Niet, and P. H. N. de With, IEEE Trans. Consd. Electron., **34**, 597 (1988).
[2] G. Vinson Kelley, IEEE Trans. Magn. **MAG-24**, 2392 (1988).
[3] S. Muraoka, H. Hasegawa, K. Takahashi, and E. Sawai, The Institute of IEICE, Japan, Spring meeting, 1989 (in Japanese), pp. 5–47.
[4] A. Hosono and S. Tanabe, IEEE Trans. J. Magn. Jpn. **8**, 475 (1993).
[5] A. E. LaBonte, J. Appl. Phys. **40**, 2450 (1969).

Contact magnetoresistive head for perpendicular magnetic recording

Ken-ichi Takano, Hiroaki Muraoka, and Yoshihisa Nakamura
Research Institute of Electrical Communication, Tohoku University, 2-1-1 Katahira, Aoba-ku, Sendai 980-77, Japan

Contact-type magnetoresistive (MR) inductive head designs and recording characteristics have been discussed in perpendicular magnetic recording. The shielded-type MR head offered a high D_{50} of 100–135 kFRPI, and the unshielded MR head had the largest output in a low density region. However when the recorded bit length became shorter than the shield-to-shield spacing, the shield had little effect and the output of the shielded head was no longer almost equal to that of the unshielded MR head. In result, the shielded-type and even unshielded-type MR heads have good high density recording characteristics in the head-to-medium contact state. © *1996 American Institute of Physics.* [S0021-8979(96)08608-7]

I. INTRODUCTION

Magnetoresistive (MR) head technology makes it possible to perform high areal density magnetic recording over 1 Gbit/in.^{2} (Refs. 1 and 2). The MR head is expected to offer a high density response as well as the large output for the sensor in future high linear and track density recording system. In a high linear density recording design, the low head-to-medium clearance and a high resolution medium have to be developed. On the other hand, extremely high resolution recording over 600 kFRPI has been characterized by using a perpendicular medium and a single-pole head in the head-to-medium contact state.[3] Consequently the introduction of the contact perpendicular recording is expected to be an important technology in the high density design. A MR head for perpendicular recording is also a key element to a sensitive read head. However a few reports[4,5] have been presented on readback performance of a MR head combined with a perpendicular medium. In this work the characteristics of perpendicular magnetic recording are described, obtained by the combination of contact MR heads and a perpendicular double-layered disk.

II. HEAD DESIGN

Generally a conventional MR head is optimized for longitudinal recording, which is combined with an inductive ring head and has a shielded MR element for the improvement of high density response.[6] When a MR head is adopted for the read element in perpendicular magnetic recording, the single-pole head is preferable to the ring head from the view point of the write performance. Moreover the shield effect in the MR head is not sufficiently investigated for the perpendicularly recorded mode. Consequently the MR head for perpendicular recording has to be newly designed. Here we designed and fabricated three kinds of contact MR heads for perpendicular recording.

The schematic cross sections of the MR heads and the illustrations for the read/write elements used in the following experiments, are shown in Fig. 1. These heads have a writing single pole, an auxiliary core, and a read MR element. The auxiliary core is wounded with a 26 turn coil, and the read/write elements are connected with the core.

Each MR element has a 25-nm-thick Ni_{80}–Fe_{20} film biased by a soft adjacent layer (SAL). The sensor height of a conventional flying MR head is typically 1–2 μm for high read sensitivity. However a sliding contact hard disk system[7] gives rise to the wear of the air bearing surface (ABS) due to the head-to-disk contact, and here every MR sensor height is adjusted to approximately 10 μm. The sense current was set at 20 mA (current density: 0.3×10^7 A/cm^2) in accordance with the output wave form asymmetry.

A. Unshielded-type MR head

The unshielded-type MR head Fig. 1(a) is composed of a MR read element and an inductive write element. These elements are arranged at intervals of 50 μm and magnetically separated from each other. The write pole is made of 0.4-μm-thick Co–Zr–Nb amorphous film. This pole, the MR element, and the lead line are exposed on the ABS. The track width of the MR read sensor is 3 μm, and the height is 10 μm.

B. Shielded-type MR head

The head shown in Fig. 1(b) has a MR element shielded on both sides. The shields made of Co–Zr–Nb film are 0.4

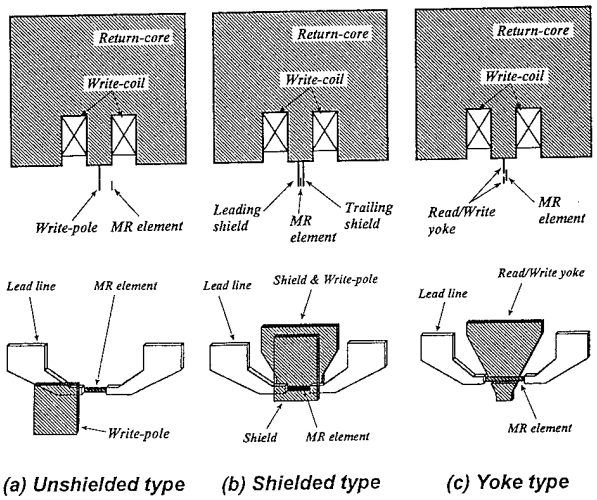


FIG. 1. The upper figures are the schematic cross sections of contact MR heads for perpendicular magnetic recording. The lower figures are schematic illustrations of the read/write elements of the MR heads.

 0021-8979/96/79(8)/5002/3/$10.00 © 1996 American Institute of Physics

TABLE I. Properties of the double-layered hard disk for the experiments.

Parameters	Values
Thickness of Co–Cr	50 nm
M_S of Co–Cr	496 emu/c
$H_{c(\perp)}$ of Co–Cr	1480 Oe
Thickness of Ni–Fe–Nb	0.5 μm
Thickness of SiO_2	4 nm
Substrate	Glass

μm thick, and are thinner than that of a conventional MR head. The trailing shield plays a part in the recording as an inductive write pole and defines the write track width. The shield-to-shield spacing, without the thickness of the MR and the SAL films, is 0.7 μm. The shields are also exposed on the ABS in addition to the MR element and lead line. The read width and height of the MR sensor are 3 and 10 μm, respectively.

C. Yoke-type MR head

A MR sensor is inserted into the yoke of the head shown in Fig. 1(c). The head construction is simple since the yoke performs the read and write operations as a flux guide, all in one. The yoke material is Fe–Si/SiO_2 multilayered film, and the yoke is only exposed on the ABS. The front yoke, whose thickness and width are 0.25 and 10 μm, respectively, guides the medium surface flux through the MR sensor. Both the front yoke width and height are 10 μm, and this track width is wider than those of the above-described MR heads.

III. MEASUREMENT CONDITIONS

The contact MR heads were evaluated on a Co–Cr/Ni–Fe–Nb double-layered hard disk. Table I shows properties of the medium for the following experiments. The disk was fabricated by sputtering a Cr underlayer, a Ni–Fe–Nb backlayer, a Co–Cr recording layer, and a SiO_2 protective layer on a flat glass substrate. The surface was given a coat of liquid lubricant (PFPE), which kept the electric insulation between the exposed MR element, the lead lines, and the disk surface. The measurements were performed at a relative velocity of 2 m/s, then the head-to-disk clearance was 30 nm.

Every head had adequate write performance, and especially in the shielded type, good overwrite characteristics were obtained since the leading shield operates as a shield from the stray field of the prewritten region.[8] The readback performance of the MR heads was tested after the saturation recording. The mechanical rubbing noise and the thermal asperity were not detected in the contact state combined with the medium.

IV. READBACK PERFORMANCE

Figure 2 shows readback wave forms of the three types of heads at 10 kFRPI density. These wave forms were different from the one produced by longitudinal recording. Even in the unshielded MR head Fig. 2(a), the output had a very sharp slope at the rear side of a magnetic transition, and was

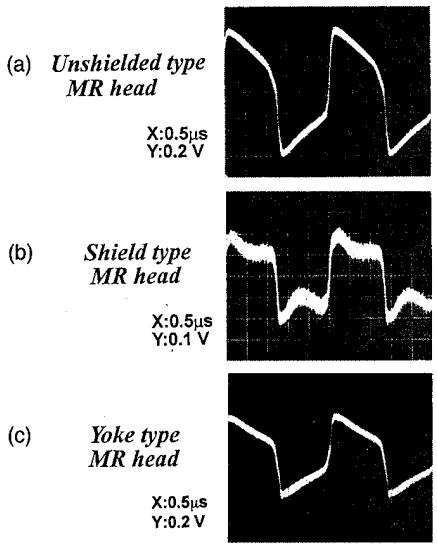


FIG. 2. Readback wave forms of MR heads at a linear density of 10 kFRPI. (a) Unshielded-type, (b) shielded-type, and (c) yoke-type.

gradually attenuated after the peak due to the medium demagnetization state and the high passage filter of 20 kHz cutoff frequency in the read amplifier.

On the other hand, the shielded MR head Fig. 2(b) had the wave form emphasized not only at the rear but also at the front of a transition. Since the surface demagnetization field is relieved in the vicinity of the transition, the peak appears at the front of the transition, too.

The yoke-type MR head Fig. 2(c) had almost the same wave form as the unshielded type, since the head did not have a shield. The wave form did not have the peak at the front side of the transition like the unshielded type head because of the stray field from the neighboring recorded region. These wave forms are related to the medium demagnetization state and the surface field gathering range by each contact MR head. However every wave form approached sine waves with increasing recording density.

We also measured the recording density characteristics. The rolloff curves differed according to the type of MR head, as shown in Fig. 3. In the unshielded-type head, the largest output of low density was obtained. This is because the MR sensor is situated on the medium surface and gathers the

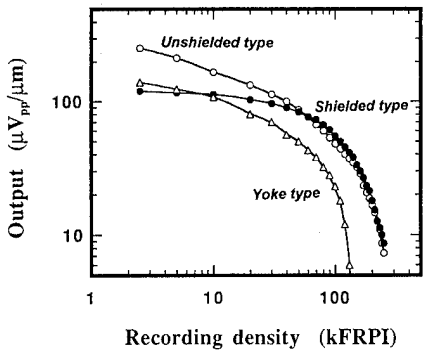


FIG. 3. Density rolloff curves of MR heads with a sense current of 0.3×10^7 A/cm^2.

medium field widely. This stray field decreased and the output gradually decreased with increasing recording density. However this output decrease was smaller than the theoretical MR height loss,[9] considered just nonmagnetic space. The actual MR height loss must be quite tiny.

On the other hand, the shielded-type MR head gathered only the medium surface field of the shield-to-shield region and the output was lower than that of the two heads in low density. However the head showed the highest D_{50} of 100 kFRPI, and it was increased to 135 kFRPI by adopting a 0.5 μm shield-to-shield spacing. However the experimental result was not in agreement with the theory characterized by spacing loss and gap loss, and the output of the shielded head was almost equal to that of the unshielded MR head in high density region. This is because the shielded MR head cannot be always regarded as two back-to-back ring heads,[6] and the MR element must operate independently, particularly in high density region.

The yoke-type MR head also gathered the surface stray field far from the recorded region and showed large output in low density, though its MR element was remote from the medium surface. However the output decreased gradually in low density and rapidly in the range over 50 kFRPI with increasing recording density, because of the yoke thickness loss and the decrease of the stray field. The thinner front yoke must be adopted for high density response.

Both the shielded- and unshielded-type MR heads have high read sensitivity in a high density recording region. In fact, the 500 kFRPI signal was confirmed in these MR heads.

V. SUMMARY

We designed and fabricated the newly developed contact MR heads for perpendicular magnetic recording. They were evaluated with a double-layered hard disk in order to examine the operation of the MR element and the shield in the contact state. The shielded-type, unshielded-type, and yoke-type heads offered square waves with the sharp slope at the transition. Though the construction of the yoke-type MR head was simple, the head showed poor high density resolution because of the yoke thickness loss. In contrast, each read element of the unshielded and shielded MR heads is so thin that the thickness loss can be practically negligible. The shielded-type and even unshielded-type MR head had good high density characteristics. The shield, which was considered necessary for a high density response, had little effect when the recorded bit length became shorter than the shield-to-shield spacing. The output of the shielded-type head was almost as large as that of the unshielded type in the high density region in the case of the head contact, because of the independent operation of the MR element in both heads. We conclude that the combination of a contact MR head and a perpendicular medium offers the possibility of a future high density storage system.

[1] C. Tsang, M. Chen, T. Yogi, and K. Ju, IEEE Trans. Magn. **26**, 1689 (1990).
[2] M. Futamoto, F. Kugiya, M. Suzuki, H. Takanor, Y. Matsuda, N. Inaba, Y. Miyamura, K. Akagi, T. Nakao, H. Sawaguchi, H. Fukuoka, T. Munemoto, and T. Takagaki, IEEE Trans. Magn. **27**, 5280 (1991).
[3] S. Yamamoto, Y. Nakamura, and S. Iwasaki, IEEE Trans. Magn. **23**, 2070 (1987).
[4] D. J. Seagle, M. A. Meiniger, T. J. Beaulieu, and C. J. Spector, IEEE Trans. Magn. **26**, 2160 (1990).
[5] H. Mitsuhashi, O. Morita, K. Oniki, S. Terada, A. Matsuzono, and H. Takino, J. Magn. Soc. Jpn. **18**, 421 (1994).
[6] R. I. Potter, IEEE Trans. Magn. **MAG-10**, 502 (1974).
[7] Y. Nakamura, K. Ouchi, S. Yamamoto, and I. Watanabe, IEEE Trans. Magn. **26**, 2436 (1990).
[8] H. Muraoka, S. Ohki, and Y. Nakamura, IEEE Trans. Magn. **30**, 4272 (1994).
[9] R. P. Hunt, IEEE Trans. Magn. **MAG-7**, 150 (1971).

Magnetostriction and thin-film stress in high magnetization magnetically soft FeTaN thin films

M. K. Minor, B. Viala, and J. A. Barnard
Department of Metallurgical and Materials Engineering and The Center for Materials for Information Technology, The University of Alabama, Tuscaloosa, Alabama 35487-0202

Domain structures in thin-film heads can be significantly influenced by magnetoelastic anisotropy. In this study we have undertaken systematic measurements of magnetostriction and stress in as-deposited and annealed states in FeN and FeTaN single-layer thin films with varying nitrogen contents. Magnetostriction was positive for FeN films, increased with increasing nitrogen content, and shifted toward negative values after annealing. Stress in as-deposited FeN films was tensile and decreased (became more compressive) with increasing nitrogen content. Annealing the FeN films resulted in significant stress relief. By contrast, magnetostriction was found to be negative for simple FeTa (zero nitrogen) and increased linearly with increasing nitrogen content to positive values. The magnetostriction in FeTaN did not change significantly after annealing at 200 and 250 °C. FeTaN film stresses were compressive in the as-deposited state and increased in magnitude (became more compressive) with increasing nitrogen content. After annealing these stresses were relieved slightly. Ta has been found to be very effective in enhancing the thermal stability of the FeN films. © *1996 American Institute of Physics.* [S0021-8979(96)08708-3]

I. INTRODUCTION AND EXPERIMENTAL METHODS

An extremely important factor in optimizing the performance of thin-film recording heads is the control of domain structures. Domain structures in thin films are controlled by the magnetoelastic anisotropy which is proportional to the product of the film stress (σ_f) and saturation magnetostriction. The relationship between domain structures and magnetoelastic anisotropy in FeTaN thin films has recently been studied.[1–3] In this article, film stress and magnetostriction in both FeN and FeTaN films have been studied as a function of nitrogen content for as-deposited and annealed states.

Nanocrystalline, single-layer FeN and FeTaN films were deposited at ambient temperature by dc magnetron reactive sputtering in a Vac-Tec Model 250 Sputtering System. The films were grown on oxidized silicon wafers with a ⟨100⟩ orientation in an aligning field of ~70 Oe to induce uniaxial anisotropy. 4″ diameter Fe and Fe-10 w/o Ta targets were used. The 10 w/o target produced films with ~3.2 a/o Ta. All films were grown at a fixed power of 220 W and a fixed Ar pressure of 3 mTorr. Nitrogen content was controlled by varying the flow rate (sccm) of a 90 Ar-10 N_2 gas mixture. These conditions produced growth rates of ~640 Å/min with the pure Fe target and ~730 Å/min with the Fe-10 Ta target. Films ranged from 4600 to 6000 Å thick. Films were vacuum annealed for 30 min at 200 and 250 °C in a 200 Oe aligning field in a vacuum ($<5\times10^{-6}$ Torr). Film stress was measured on a Flexus 2320 thin-film stress measurement system. Film structure was studied using x-ray diffraction (XRD) performed on a Rigaku D/Max-2BX XRD system. Coercivities were measured on a SHB Instruments Model 106 loop tracer. Saturation magnetostriction was measured in an ac magnetostriction tester.[4]

II. EXPERIMENTAL RESULTS AND DISCUSSION

X-ray diffraction revealed that the as-deposited and annealed FeN and FeTaN films have the α-Fe structure with a (110) growth texture. This corresponds to a single-phase bcc film structure with N dissolved interstitially and Ta dissolved substitutionally.[5,6] No evidence was found by XRD for the existence of iron nitride or tantalum nitride phases but small volume fractions would be difficult to detect using XRD. TaN phases were identified by means of transmission electron microscopy (TEM) cross-sectional examinations in both as-deposited and annealed FeTaN films. The early stage of the homogenous nucleation of fcc TaN coherent particles (10 Å) has been observed around 2.5 sccm N_2 flow rate in as-deposited FeTaN films. Annealing temperatures higher than 300 °C have been found to promote the nucleation and growth of this phase. TaN phases also have been observed in similar materials by others.[1]

Figure 1 shows the d spacing of (110) planes, d_{110}, versus nitrogen flow rate for the FeN and FeTaN films in the as-deposited and annealed states. Several features stand out in Fig. 1. At zero nitrogen, d_{110} is larger in magnitude for FeTa than for Fe. This lattice expansion can be explained by the presence of substitutional Ta atoms, according to Vegard's law. In liquid FeTa alloys, the measured lattice dilation (56.28×10^{-4}/at. % Ta) is within 10% of Vegard's Law prediction.[7] Our measurement is in good agreement with this result. Figure 1 also indicates that d_{110} increases as nitrogen flow rate increases. This result is expected because when more nitrogen is available in the sputtering plasma, more nitrogen is incorporated into the interstitial lattice sites during growth. Increased interstitial nitrogen results in the lattice expansion. Figure 1 also indicates that d_{110} decreases upon annealing. This is due to stress relief and/or defect annihilation in the films. The FeN films undergo significantly greater lattice contraction than their FeTaN counterparts. This indicates that Ta stabilizes the lattice structure.

Another clear feature is that the FeTaN films incorporate more nitrogen than the FeN films for the same sputtering conditions, i.e., the rate of increase of d spacing with N_2 flow is higher for FeTaN than FeN films. The FeTa lattice has a

 0021-8979/96/79(8)/5005/3/$10.00 © 1996 American Institute of Physics

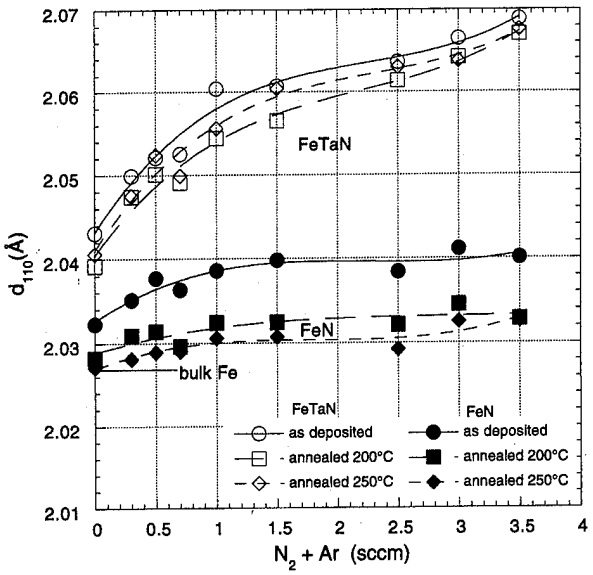


FIG. 1. Dependence of lattice spacing d_{110} on nitrogen flow rate for FeN and FeTaN films in the as-deposited and annealed (200 and 250 °C) states.

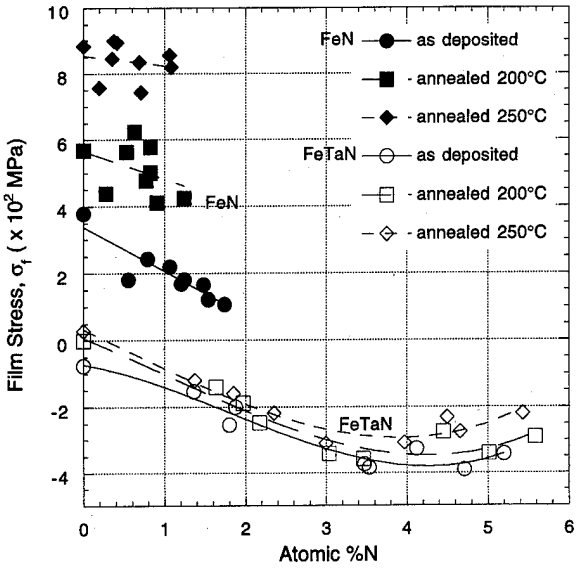


FIG. 3. Film stress vs at. % N for FeN and FeTaN films in the as-deposited and annealed (200 and 250 °C) states.

higher affinity for nitrogen than the pure Fe lattice. The solubility of nitrogen in a number of binary liquid alloys has been extensively studied.[8] Refractory metals such as Ti, Zr, Va, and Ta markedly increase the solubility of nitrogen in liquid iron. Nitrogen "roughly" obeys Sievert's law in Fe sputtered in nitrogen-rich plasma, a/o $N \propto P(N_2)^{0.5}$, where $P(N_2)$ represents the nitrogen partial pressure in the sputtering gas environment. An estimate of the nitrogen concentration in the films was made on the basis of the measured lattice expansion using published data.[9] Extending this line of reasoning, the nitrogen incorporation in the presence of 10 w/o Ta has been evaluated using the interaction coefficient for Ta, $e^{Ta}(N) = -0.034$, measured in the liquid alloy.[8] Experimental results shown in Fig. 2 reveal a good agreement with the predicted nitrogen content up to 1 sccm N_2 flow rate for FeTaN. Higher nitrogen flows leads to a discrepancy which is consistent with the observed onset of nucleation of TaN phases.

Average grain sizes were estimated from the FWHM of the (110) peak (not shown). The grain size was found to decrease with increasing nitrogen content. The average grain sizes ranged from 110 to 83 Å for the FeN films and from 160 to 100 Å for the FeTaN films. Average grain size in the FeN films increased 25%–45% after annealing at 200 °C and 30%–55% after annealing at 250 °C. On the other hand, the FeTaN films showed less than 10% average grain size increase after annealing at 200 °C and no appreciable growth

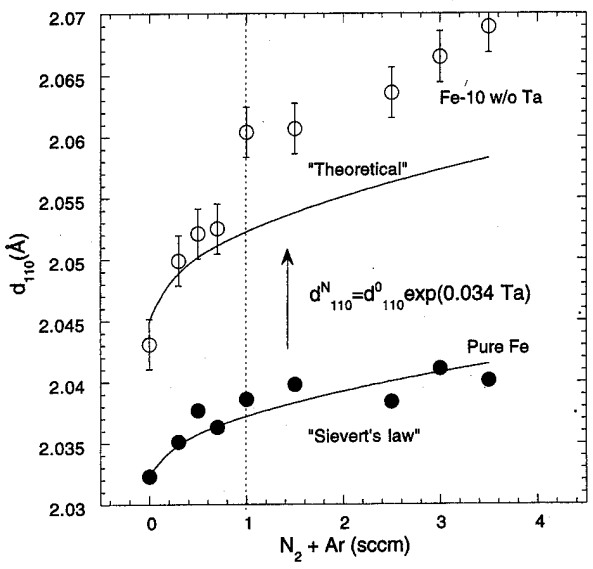


FIG. 2. Theoretical and experimental dependence of lattice spacing d_{110} on nitrogen flow rate in Fe-10 w/o TaN.

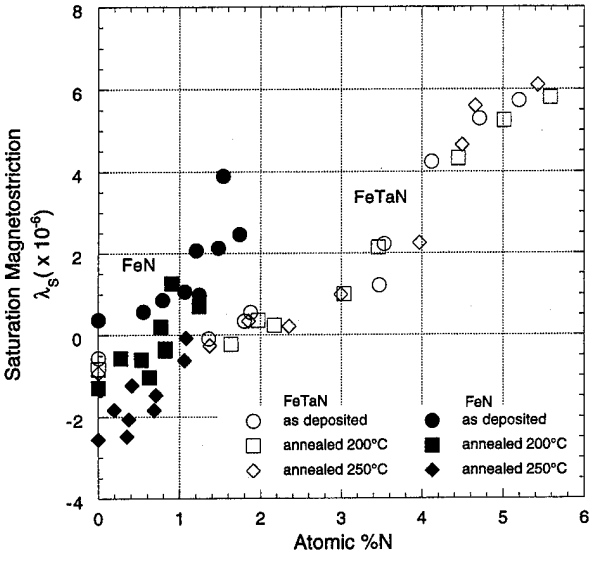


FIG. 4. Magnetostriction vs at. % N for FeN and FeTaN films in the as-deposited and annealed (200 and 250 °C) states.

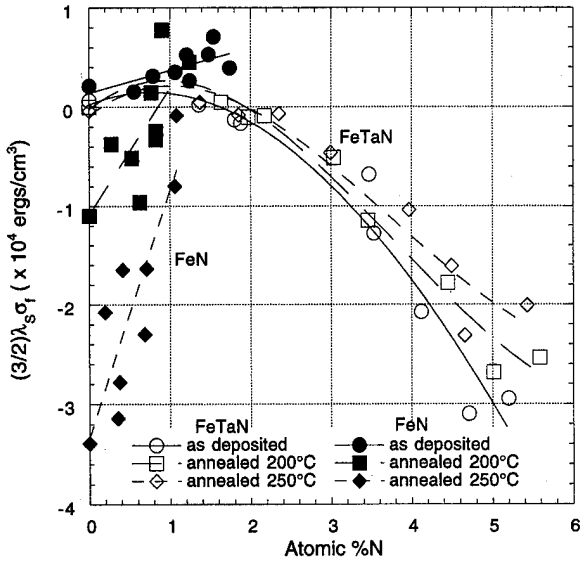


FIG. 5. Magnetoelastic anisotropy vs at. % N for FeN and FeTaN films in the as-deposited and annealed (200 and 250 °C) states.

after the second anneal at 250 °C. This is another indication of the stabilizing effect of Ta.

Figure 3 shows film stress versus N content for FeN and FeTaN films. FeTaN films contain about three times as much interstitial nitrogen as FeN films grown under the same conditions. All as-deposited FeN films were in a state of tension and the magnitude of the tensile stress increased substantially with annealing. By contrast, as deposited FeTaN films were in a state of compression and while annealing resulted in stress relaxation, the sign of the stress remained compressive. Ta is a larger atom than Fe (~16% larger) and its substitution into the Fe lattice causes lattice strains which result in a more compressive stress state compared to FeN. Although N is incorporated interstitially in both the FeN and FeTaN, both the interstitial N and substitutional Ta act to expand the lattice in the FeTaN and this generally makes the FeTaN more compressive than the FeN. FeN films undergo much more stress relaxation after annealing than the FeTaN films, as another indication of the stabilizing effect of Ta.

Figure 4 shows saturation magnetostriction λ_S versus at. % N for as-deposited FeN and FeTaN films in both as deposited and annealed states. (After annealing the FeN films at 200 and 250 °C, λ_S could not be achieved because the films could not be saturated. λ_S values reported for FeN films after annealing are taken at 60 Oe.) The FeN films have a more positive λ_S than the FeTaN films in the as-deposited state. Upon annealing, the values of λ_S for the FeN films become more negative. This change is consistent with the growth of the (110)-oriented grains which have an average negative λ_S. The values of λ_S for the FeTaN films increase from negative to positive with increasing nitrogen content as reported previously.[10] These values do not change appreciably after annealing at 200 and 250 °C. The general increase in λ_S with N content is consistent with our previous work.[2,10] Here again, Ta clearly stabilizes the lattice structure and increases the thermal stability.

Figure 5 shows magnetoelastic anisotropy, (3/2) λ_S σ_f, versus at. % N for the FeN and FeTaN films in both the as-deposited and annealed states. The as deposited FeN films have a positive magnetoelastic anisotropy due to both positive stress and magnetostriction. The magnetoelastic anisotropy for the FeN films changes dramatically after annealing. The values become negative and all annealed FeN films exhibit M-H loops characteristic of stripe domains. This is due to a favored perpendicular anisotropy component resulting from the increasing tensile stress and decreasing magnetostriction. The FeTaN films exhibit a curve which is negative for the as-deposited state and does not change significantly with annealing. The high nitrogen, ~5 a/o, FeTaN films exhibited M-H loops characteristic of stripe domains, however, no stripe domains were evident after annealing at 250 °C. The combination of the linear increase of the positive magnetostriction with the increase of the compressive stress leads to an increasingly negative magnetoelastic anisotropy with nitrogen incorporation for FeTaN. It has been observed that the FeTaN films exhibit a well defined columnar structure which becomes finer as nitrogen is added, leading to a decrease of the shape anisotropy. In these conditions, a perpendicular anisotropy component appears promoting the formation of stripe domains, experimentally observed in the range of 5 a/o N in as-deposited and 200 °C annealed FeTaN films. After annealing at 250 °C, the stripe domains disappear mainly because of the reduction of the magnetoelastic anisotropy due to the decrease of the compressive stress.

ACKNOWLEDGMENT

This work was supported primarily by the MRSEC Program of the National Science Foundation under Award No. DMR-9400399.

[1] N. Ishiwata, Y. Takeshima, T. Konehari, and H. Urai, presented at the 6th International Conference on Ferrites (in press).
[2] J. C. Cates, C. A. Alexander, Jr., E. Haftek, and J. A. Barnard, IEEE Trans. Magn. (submitted).
[3] J. C. Cates, G. Qiu, E. Haftek, C. A. Alexander, Jr., and J. A. Barnard, Mater. Res. Soc. Symp. Proc. **313**, 345 (1993).
[4] A. Tam and H. Schroeder, IEEE Trans. Magn. **MAG-25**, 2629 (1989).
[5] G. Qiu, E. Haftek, J. C. Cates, C. A. Alexander, Jr., and J. A. Barnard, Mater. Res. Soc. Symp. Proc. **313**, 339 (1993).
[6] G. Qiu, E. Haftek, and J. A. Barnard, J. Appl. Phys. **73**, 6573 (1993).
[7] E. P. Abrahamson and S. L. Lopata, Trans. Metall. Soc. AIME **236**, 76 (1966).
[8] D. B. Evans and R. D. Pehkle, Trans. Metall. Soc. AIME **233**, 1620 (1965).
[9] H. A. Wriedt, N. A. Gokeen, and R. H. Nafziger, Bull. Alloy Ph. Diag. **8**, 355 (1987).
[10] V. R. Inturi and J. A. Barnard, IEEE Trans. Magn. (submitted).

Exchange coupling between NiO and NiFe thin films

J. X. Shen and M. T. Kief[a)]
Department of Physics and Astronomy, P.O. Box 870324, University of Alabama, Tuscaloosa, Alabama 35487-0324

NiO/NiFe bilayer thin films were prepared by rf reactive and dc magnetron sputtering, respectively. The exchange coupling strength between NiO and NiFe as a function of NiO texture and interface roughness was investigated by using different sputtering pressures, Au, and Cu buffer layers. The experimental results show that the exchange coupling field strongly depends on the NiO/NiFe interface roughness. In addition, we found the exchange coupling is largest for the (200) texture compared to the (111)-texture films. This is surprising since the bulk spin structure of NiO predicts the (200) plane to be compensated while the (111) plane is to be uncompensated. © *1996 American Institute of Physics.* [S0021-8979(96)14408-0]

I. INTRODUCTION

Investigations of exchange coupling between antiferromagnetic and ferromagnetic thin films have been carried out for several decades because of the interest both in physics and technology (for example, the magnetoresistive recording head).[1–5] However, many questions concerning this exchange coupling remain unanswered. In particular, the simplest models predict an exchange coupling strength typically 100 times greater than that observed in experiments. Recently, two models have been proposed by Mauri[6] and Malozemoff[7] to quantitatively explain this phenomenon. In Mauri's model, the antiferromagnetic film forms a domain wall along the interface to minimize the free energy of the system during the reversal of the ferromagnetic film under an applied magnetic field. In order to have exchange coupling, parallel spin configuration in the antiferromagnetic film at the interface is assumed. In Malozemoff's model, the antiferromagnetic film breaks up into domains due to the roughness at the interface and the domain walls are perpendicular to the interface. In this case, a completely parallel (uncompensated) spin configuration at the interface is not necessary and the roughness in the interface is very important. In this paper, we report how the texture and interface roughness of the antiferromagnet (NiO) affects the exchange coupling in the NiO/NiFe system.

II. EXPERIMENT

All films in this study were prepared in our Vac-Tec four-cathode sputter system with a base pressure of 5×10^{-7} Torr. All samples were prepared as follows: Substrate [Corning Glass 7059, Si(111) wafer]/buffer layer (if used)/NiO/NiFe. NiO was deposited by rf reactive ion sputtering from a Ni target in the mixture of O_2 and Ar gases. The ratio of the O_2 to Ar was regulated by two mass flow controllers and confirmed by residual gas analyzer. Single-phase NiO thin films, as evidenced by x-ray diffraction measurements, could be obtained with the O_2 to Ar ratio of 6%–20%. However, maximum exchange coupling between NiO and NiFe occurred for the films sputtered at an 8% O_2–Ar ratio. $Ni_{80}Fe_{20}$, Au, and Cu thin films were prepared by dc sputtering with 99.99% pure Ar at a pressure of 2.5 mTorr. A permanent magnet which produced a magnetic field of ~80. Oe along the substrate surface was present during the deposition process. This field produced an easy axis in the NiFe film and defined the exchange coupling axis. X-ray diffraction was used to characterize the crystalline properties of the films and the roughness was determined by atomic force microscopy (AFM). The magnetic properties were measured using both a vibrating sample magnetometer (VSM) and a B-H loop tracer. All the measurements were conducted on the as-deposited samples. The exchange coupling field defined by the asymmetric shift of the ferromagnet hysteresis loop from zero applied field was determined after many cycling of measurements to ensure that no noticeable aftereffect was present.

III. RESULTS AND DISCUSSION

Figure 1 shows the exchange coupling field (H_E) of 200 Å NiFe films deposited on 300 Å NiO thin films with glass substrate as a function of NiO sputtering pressure. The H_E increases rapidly with decreasing sputtering pressure of O_2

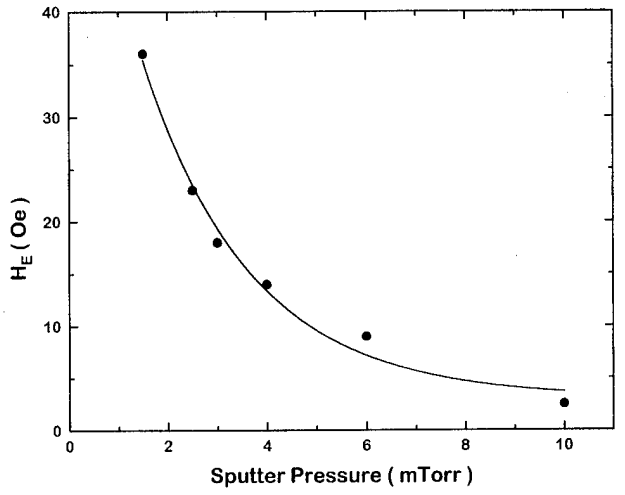


FIG. 1. Exchange coupling field of glass/NiO 300 Å/NiFe 200 Å as a function of NiO sputtering pressure.

[a)]Author to whom correspondence should be addressed.

 0021-8979/96/79(8)/5008/3/$10.00 © 1996 American Institute of Physics

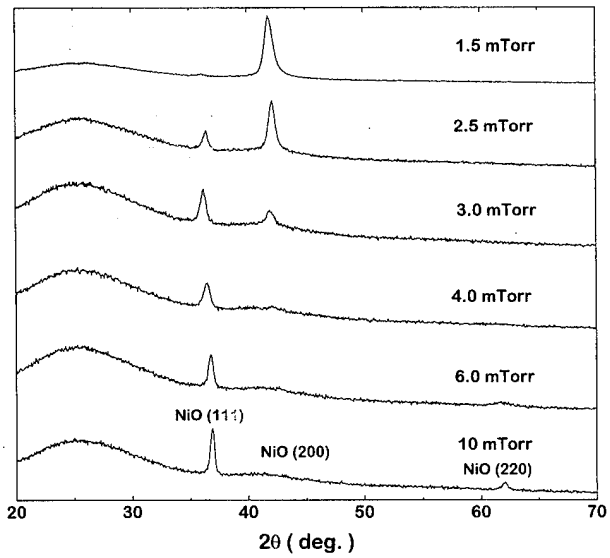


FIG. 2. X-ray diffraction patterns for glass/NiO 300 Å films prepared at different sputtering pressures.

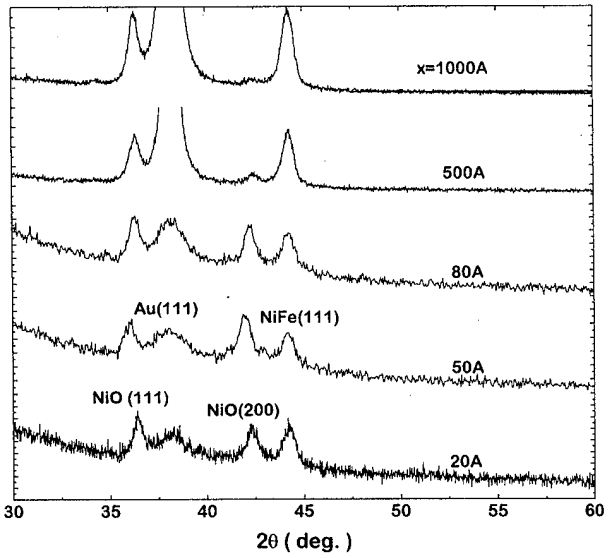


FIG. 3. X-ray diffraction patterns for glass/Au*x* Å/NiO 300 Å/NiFe 200 Å thin films.

and Ar. The AFM measurements of NiO films prepared at the same time as the above films show that the roughness of the NiO surface increases with increasing sputtering pressure. The rms roughness determined by AFM over an area of 500 nm^2 varied from 7 to about 14 Å when the sputtering pressure increased from 1.5 to 10 mTorr, respectively. Therefore, the exchange coupling was found to increase with decreasing rms roughness of NiO interface. Unfortunately, the texture of the NiO thin films also changes with the sputtering pressure. Figure 2 shows the high angle x-ray diffraction patterns of NiO films sputtered at different pressures. At 10 mTorr, there is a strong (111) diffraction peak and no (200) peak is detectable. With decreasing Ar/O sputtering pressure, the NiO (111) peak gradually decreases and by 1.5 mTorr, the (111) diffraction peak has almost totally disappeared. The NiO (200) diffraction peak gradually increases with decreasing sputtering pressure. For NiO sputtered at 1.5 mTorr, the texture of the NiO is almost totally (200). These data show that the increase of H_E with decreasing sputtering pressure could be due to the decreasing roughness of the NiO interface (Fig. 1) or due to the increase of the NiO (200) texture (Fig. 2) or both. This result is somewhat surprising, when we consider that the spin structure of bulk NiO (Ref. 8) predicts the NiO (100) plane is the spin compensated plane (i.e., no net in-plane moment), while the NiO (111) is the spin uncompensated plane (i.e., maximum in-plane moment). Neglecting roughness, Mauri's model would predict that the exchange coupling would be zero for the NiO (200) orientation. Of course, this prediction assumes perfectly flat and abrupt interfaces which the AFM shows to be a poor description of the real films. In order to investigate the independent effects of texture and roughness on the exchange coupling further one must separate these two factors. In order to vary the roughness and texture independently, we used Au buffer layers to promote the (111) texture of NiO and Cu buffer layers to alter the roughness of the NiO while maintaining the (200) texture.

Sputtered Au generally has a strong (111) texture and the lattice mismatch of Au(111) and NiO(111) is modest (2.2%). Therefore, it can be expected that the texture of the NiO may copy the texture of the Au buffer layer. Figure 3 shows the x-ray diffraction pattern of glass/Au*x* Å/NiO 300 Å/NiFe 200 Å thin films with the Au buffer layer thickness x varying from 20 to 1000 Å. The sputtering pressure of NiO is 2 mTorr. Two features are worth noting: (i) the NiFe and Au(111) diffraction peaks increase with increasing Au buffer layer thickness. (ii) The NiO(111) diffraction peak of NiO increases relative to the (200) diffraction peak with increasing Au buffer layer thickness. The NiO films change from weak texture for a very thin Au buffer layer to almost complete (111)-texture for a very thick Au buffer layer, possibly due to the epitaxy of the NiO on the Au. Figure 4 plots the exchange coupling field as a function of the ratio of (111) diffraction intensity to (200) diffraction intensity. Surpris-

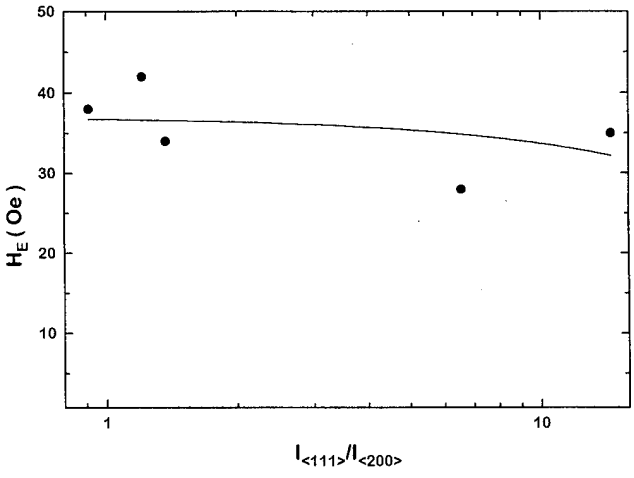


FIG. 4. Exchange coupling field as a function of NiO (111) and (200) diffraction peak intensity ratio, for the samples of Fig. 3.

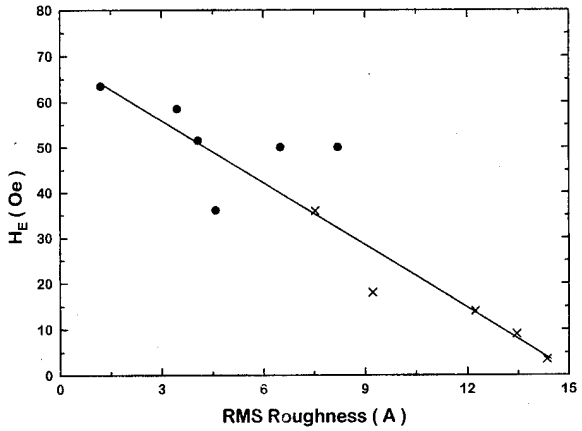


FIG. 5. Exchange coupling field of NiO 300 Å/NiFe 200 Å as a function of rms roughness of NiO thin film. (●) Si/Cu 500 Å/NiO 300 Å/NiFe 200 Å, in which NiO prepared under 1.5 mTorr and 150 W. (×) Glass/NiO 300 Å/NiFe 200 Å, in which NiO prepared at different sputter pressure.

ingly, H_E barely changes with the change of the texture of NiO. Similar results were found in the FeF_2–Fe exchange coupling system.[9]

Next we investigated the role of the interface roughness for nearly constant texture. A 500 Å Cu buffer layer was sputtered on Si(111) with varying sputtering pressure. The surface of the Cu buffer layer is expected to change from very smooth at lower sputtering pressure to very rough at high sputtering pressure. A 300 Å NiO film was deposited onto the Cu buffer layer at a pressure of 1.5 mTorr and power of 150 W to produce a NiO (200) texture. Since the lattice mismatch between Cu and NiO is quite large, the change of texture in the Cu buffer layer should not strongly affect the texture of the NiO films. Finally, 200 Å NiFe film is deposited onto the NiO/Cu/Si samples. The x-ray diffraction pattern confirms that NiO has the desired (200) texture and this texture appears nearly independent of the Cu buffer layer. The roughness of the NiO increases with Cu sputter pressure from 1.5 to 15 mTorr, as measured by AFM. Without the Cu buffer, very smooth and almost featureless NiO surfaces can be realized, with rms roughness of ~1 Å over a 1 μm^2. With the Cu buffer layer, the NiO is much rougher, reaching a maximum rms roughness of 8.4 Å for the Cu sputtered at 15 mTorr. Figure 5 plots the exchange coupling H_E, as a function of the rms roughness for these NiFe/NiO/Cu/Si samples (circles) and the NiFe/NiO/glass for varying sputter pressures (crosses). The NiO texture varies from entirely (200) for the smoothest films to entirely (111) for the roughest films. Figure 5 indicates that the highest H_E are obtained for the smoothest NiO. Recalling Fig. 4 which showed the very weak or no dependence of H_E on NiO texture, we are led to conclude that H_E is dominated by the interface roughness for the NiO/NiFe system. Presently, we cannot say if this conclusion is fundamental or practical in origin. In other words, roughness may always be the controlling factor in determining H_E or it may be experimentally difficult to produce flat NiO films with (111) texture. Further experiments to answer this question are underway.

IV. CONCLUSIONS

We have shown that the exchange coupling between NiO and NiFe is strongly dependent on the interface roughness. Although this result is not unexpected, it is surprising that H_E is found to be much larger for the compensated (200)-textured NiO film then the uncompensated (111)-textured NiO film. Finally, it should be emphasized that future models of antiferromagnet/ferromagnet exchange coupling must include more realistic representations of the interface topology, most interfaces have large features comparable to the AFM domain wall width (~100 nm), not simply atomic vacancies or defects.

ACKNOWLEDGMENTS

This work was supported in part by DOD-ARO Grant No. DAAH-04-94-G 0251 and the NSIC-ATP Heads Program.

[1] W. H. Meiklejohn and C. P. Bean, Phys. Rev. B **102**, 1413 (1957).
[2] M. J. Carey and A. E. Berkowitz, Appl. Phys. Lett. **60**, 3060 (1992).
[3] S. S. P. Parkin and V. R. Deline, Phys. Rev. B **42**, 10583 (1990).
[4] C. Tsang and K. Lee, J. Appl. Phys. **53**, 2605 (1982).
[5] O. Allegranza and M. M. Chen, J. Appl. Phys. **73**, 6218 (1993).
[6] D. Mauri, H. C. Siegmann, P. S. Bagus, and E. Key, J. Appl. Phys. **62**, 3047 (1987).
[7] A. P. Malozemoff, Phys. Rev. B **35**, 3679 (1987).
[8] W. L. Roth, Phys. Rev. B **110**, 1333 (1958).
[9] J. Nogues, D. Lederman, and I. K. Schuller (unpublished).

Search for high moment soft magnetic materials: FeZrN (abstract)

A. Chakraborty, G. H. Bellesis, K. R. Mountfield, D. N. Lambeth, and M. H. Kryder
Data Storage Systems Center, Carnegie Mellon University, Pittsburgh, Pennsylvania 15213-3890

FeN materials exhibiting high moment, low coercivity and small magnetostriction have previously been reported. Zr has been known to reduce the magnetostriction in other Fe alloys. The criteria for an ideal recording head pole material as well as shields for magnetroresistive sensors include high moment, low coercivity, high permeability, and zero magnetostriction. We present here the properties of half micrometer thick rf sputtered FeZrN films on glass coupons. The films were deposited at a pressure of 3 mTorr using a Perkin–Elmer sputtering system. The target was composed of Fe with Zr chips covering approximately 2% of the surface area. The properties were measured as a function of the N_2 partial pressure. The saturation magnetization of the as-sputtered films was approximately 20 kG. The easy axis and the hard axis coercivities show minima at approximately 7%–10% N_2 partial pressure of approximately 1.8 and 0.6 G, respectively. The magnetic anisotropy is approximately 5 G yielding a dc permeability of approximately 4000 along the hard axis. X-ray data reveal a systematic change in the ratio of α-Fe and γ-Fe_4N; the amount of the γ-Fe_4N phase increases with increasing N_2 flow rate. The magnetostriction increases with increasing N_2 content crossing zero at approximately 6%. The grain size as probed by atomic force microscopy is an increasing function of the N_2 partial pressure, from a few nm for a N_2 partial pressure of 5% to as large as 50 nm for a N_2 partial pressure of 15%. © *1996 American Institute of Physics.* [S0021-8979(96)45408-3]

Magnetic properties of CoFeB sputtered films for high Bsat applications (abstract)

Durga Ravipati, Hua-Ching Tong, and Lena Miloslavsky
Read Rite Corporation, Fremont, California

High density recording requires pole material with a large saturation magnetization and high permeability. To realize the high data rate and high frequency (in the range of 40–100 mHz) applications in thin film heads, high resistivity materials are desired.[1] Amorphous materials such as CoZrNb, CoHfNb, etc., and crystalline materials such as FeAlN, FeN, etc., were studied for high Bsat applications.[2–4] CoFeB films were rf sputter deposited on Al2O3–TiC substrates. The as-deposited Hce (easy axis coercivity), Hch (hard axis coercivity) anisotropy field Hk and magnetiostriction λs were measured to be 0.05–0.10, 0.19–0.31, 16–21 and -6.5×10^{-7}, respectively, with a saturation magnetization of 15.4 kG. The as-deposited magnetic anistropy Hk was reduced to 2.5 Oe by vacuum annealing the wafers in a rotating external magnetic field of ~6000 Oe at 200 °C. Reduction of Hk by RFA can be attributed to magnetic field thermally induced pair ordering. A 1 μm thick CoFeB film exhibited resistivity of 66 $\mu\Omega$ cm compared to 22 $\mu\Omega$ cm for NiFe plated films. The high resitivity helps in reducing eddy current losses which do impede the uniform reversal of magnetization in the films. The amorphous structure was observed to be stable to 250–275 °C and changes to crystalline structure above 300 °C. Details on corrosion properties and x-ray diffraction data will be presented. © *1996 American Institute of Physics.* [S0021-8979(96)45508-X]

[1] H. Takano *et al.*, presented at Intermag '95 in San Antonio (unpublished).
[2] Y. Shimada, Phys. Status Solidi 255 (1984).
[3] S. Wong *et al.*, J. Appl. Phys. **69**, 5625 (1991).
[4] H. L. Hu *et al.*, IEEE Trans. Magn. **30**, 3870 (1994).

Exchange coupling of sputter deposited NiCo–O/NiFe thin films

Minshen Tan, Hua-Ching Tong, Swie-In Tan, and Robert Rottmayer
Read-Rite Corporation, 44100 Osgood Road, Fremont, California 94539

NiCo–O serving as the exchange layer in a spin valve structure has the advantage of being corrosion resistant and unable to shunt sensing current in the read element. In this work, NiCo–O/NiFe thin films are studied. The films are deposited on Si wafers using rf sputtering. The antiferromagnetic NiCo–O films were reactively sputtered from alloy targets; one has a 55 at. % of Co and the other 60 at. % of Co. The chamber atmosphere is an Ar/O_2 mixture containing ~10% O_2. For films with optimal structures, the exchange strength is around 40–45 Oe. The coercivity of the pinned layer is between 18–26 Oe. The exchange strength and coercivity as a function of NiCo–O thickness (with NiFe thickness fixed at 200 Å) and NiFe thickness (with NiCo–O fixed at 250 Å) are examined. The exchange field is found to increase with the antiferromagnet thickness initially and then flatten out or drop slightly when the antiferromagnet thickness is beyond 200–250 Å. Blocking temperature of the bilayer films is also measured, and is found to increase with NiCo–O thickness. NiCo–O with lower Co content shows slightly higher blocking temperature. © *1996 American Institute of Physics.* [S0021-8979(96)08808-X]

I. INTRODUCTION

The demand for ever-increasing storage density in the data storage industry calls for new recording technology. Spin valve/giant magnetoresistive (GMR) read head is the next generation beyond magnetoresistive (MR) heads, which operates on a magnetic anisotropy mechanism. The spin valve/GMR effect occurs mostly in a layered structure consisting of at least a sandwich with one conducting spacer (S) separating two ferromagnetic (FM) layers. The conduction electrons preserve their spin orientation of the magnetization in the original magnetic layer where they are from when they move across the spacer and enter into the neighboring magnetic layer. Depending on the magnetization orientation in the new layer, the electrons can be either highly scattered if the spin orientation has a large angle with respect to the local magnetization, or lightly scattered if the aforementioned angle is small. The film structure's electrical resistance will then be different. In a spin valve head with a structure of AFM/FM1/S/FM2 the magnetization of FM1 is fixed at one direction by the exchange coupling with an antiferromagnetic layer attached to it. The other magnetic layer (FM2) will have a uniaxial anisotropy perpendicular to FM1. The electrical resistance, and ultimately the signal output, of the sensor is then a function of the cosine of the relative angle between the two magnetization vectors as it dictates the spin dependent scattering of the conduction electrons. Large exchange coupling strength between the so-called "pinned" ferromagnet FM1 and the "pinning" antiferromagnet (AFM) has then become one of the core technologies in the spin valve heads. The exchange pinning layer has received extensive study.[1–5] In the early stage of spin valve head development, antiferromagnetic alloy materials such as FeMn, NiMn, and TbCo were used as the exchange pinning layer, partially inherited from the exchange biasing scheme in MR technologies. However, the poor corrosion properties of these alloys posed serious problems for head manufacturing. To address the corrosion resistance, nonconducting oxide materials emerge as the choice for pinning materials.[1,3,4] Most studied are oxides of ferromagnetic metals and alloys, such as NiCo–O, Ni–O, or Co–O. These oxide materials possess excellent corrosion resistance and, because they are nonconducting, the current shunting effect during read process is also minimized and the signal output is enhanced. In this article, the sputter deposition of NiCo–O of different NiCo compositions will be discussed. Magnetic properties of NiCo–O/NiFe exchange coupled films will be investigated, together with the microstructural and crystal structure of the films.

II. EXPERIMENT

NiCo–O/NiFe thin films were deposited by sputtering in a rf diode system. The bilayer films were deposited on 3 in. Si wafers. NiCo–O was reactively sputtered from NiCo alloy targets, one with 55 at. % Co, and the other with 60 at. % Co. The Ar/O_2 mixture contained roughly 10% vol. O_2, maintained by mass flow controllers. A downstream pressure control system was used to maintain the set chamber pressure. The pressure for NiCo–O deposition was kept at 2 mTorr. The base pressure of the system was $(2–3)\times10^{-7}$ Torr.

The exchange field, H_{ex}, and coercivity, H_c, were measured by an SHB 108 loop tracer. A Lakeshore 7300 vibrating-sample magnetometer (VSM) equipped with a low vacuum heating furnace was used to measure the blocking temperature of the NiCo–O/NiFe bilayer exchange couples. Hysteresis loops could also be obtained while the sample was heated. An x-ray diffractometer (XRD) was used to obtain microstructure and crystal structure information.

III. RESULTS AND DISCUSSIONS

A. NiCo–O *t* Å/NiFe 200 Å films

In this series of samples, NiCo–O (Co 55 at. % and 60 at. %) was reactively sputtered, and the thickness varied from 100 to 400 Å with 50 Å increment. NiFe films were fixed at 200 Å thick. The exchange field and coercivity of the samples were listed in Table I, and the exchange field versus NiCo–O thickness data were plotted in Fig. 1. It agreed with previous work that exchange field initially increased with

 0021-8979/96/79(8)/5012/3/$10.00 © 1996 American Institute of Physics

TABLE I. Magnetic properties of NiCo–O t Å/NiFe 200 Å.

t_{NiCo-O} (Å)	Co 55 at. %		Co 60 at. %	
	Hex (Oe)	Hc (Oe)	Hex (Oe)	Hc (Oe)
100	34.2	29.3	15.3	47.1
150	44.4	26.6	27.4	44.6
200	41.5	24.9	37.6	39.2
250	42.5	20.5	36.4	33.0
300	41.3	20.3	32.7	30.4
350	41.5	21.4	32.6	28.2
400	42.5	18.5	32.3	27.7

antiferromagnet thickness and this tendency flattened out when the AFM thickness reached around 200 Å and beyond. The slight fluctuation (within a few Oe) of the exchange field beyond that thickness is believed to be due to the sample fluctuations and measurement precisions. Extrapolating to the thin thickness side, the exchange strength quickly "dies out" when antiferromagnet thickness drops below 50 Å, as revealed by other researchers.[2,3] However, although the exchange field was small at the thin NiCo–O end, the high coercivity indicated that the AFM/FM interaction still exists. While it is not very surprising to see that, in general, Co 60% films result in smaller H_{ex} and higher H_c throughout the spectrum of NiCo–O thickness compared with Co 55% samples, it is interesting to note that coercivity to exchange field ratio is much more undesirable for Co 60% films than those for Co 55%. For t_{NiCo-O} up to 200 Å, Co 60% samples have coercivity larger than the exchange strength. Cobalt's high anisotropy constant is believed to be the cause for higher coercivity in the Co-rich samples. It is also interesting to note that in both series of the samples coercivity actually decreased while the exchange field became larger. This will be discussed further in Sec. III C.

B. NiCo–O 250 Å/NiFe t Å films

Another series of NiCo–O/NiFe samples were made by fixing the NiCo–O thickness at 250 Å. The NiFe layer thickness was changing from 50 to 200 Å at an increment of 50 Å. The exchange field strength sharply increased as the NiFe thickness reduced, as predicted by Malozemoff[6] in Eq. (1),

$$H_{ex}=\Delta\sigma/2M_F t_F, \tag{1}$$

in which H_{ex} is the exchange field strength, $\Delta\sigma$ is the energy difference per unit area at the FM/AFM interface, and M_F and t_F are the magnetization and thickness of the ferromagnetic material. The coercivity of the films also increased drastically with thinner NiFe layers. It seemingly outpaced the increase of H_{ex} as the NiFe thickness was as thin as 50 Å. This rapid increase in coercivity is believed to be due to the films being less continuous, less crystalline, for thinner NiFe films. The data were shown in Fig. 2.

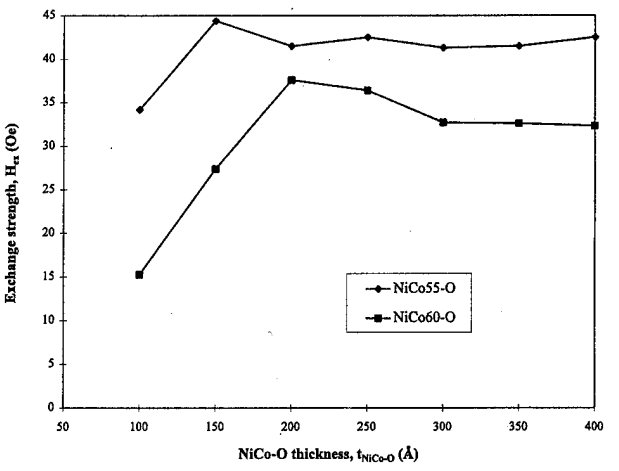


FIG. 1. Exchange field vs NiCo–O thickness for NiCo–O Å NiFe 200 Å films.

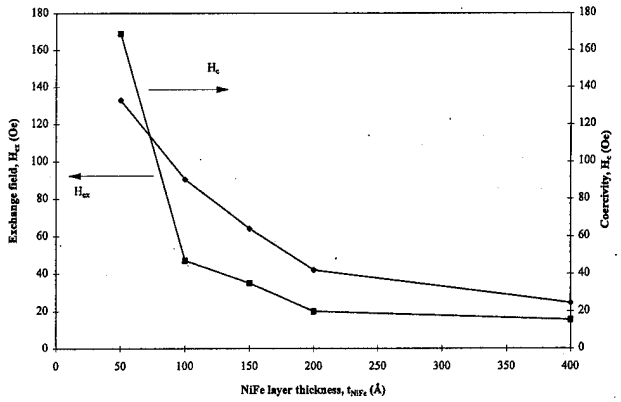


FIG. 2. Exchange field vs NiFe thickness for NiCo–O 250 Å/NiFe Å films.

C. Blocking temperature of the NiCo–O/NiFe films

The Lakeshore 7300 VSM with a heating tube was used to measure the blocking temperature, T_b, of the exchange coupled films. Heating was conducted under vacuum to prevent oxidation of the films. Hysteresis loops were recorded at each temperature and exchange field and coercivity were measured from the loops. Blocking temperature is determined at the point when the coercivity of the film was close to what a typical NiFe film is supposed to be, ~1.5–2 Oe, and the loop is symmetric. It was found for the NiCo55-O/NiFe 200 Å series that blocking temperature increases monotonically with the NiCo–O thickness. And the Co 55% sample has a higher blocking temperature than Co 60% sample. The results are shown in Fig. 3. Although exchange coupling is an interfacial phenomenon, it is obvious from what was described here in the blocking temperature versus NiCo–O thickness data, as well as what was previously shown in Table I and Fig. 1, that the whole antiferromagnet layer exerts its influence on the interfacial behaviors of NiCo–O/NiFe films. These behaviors are more complicated than H_{ex} vs NiFe thickness, which is relatively well understood by Eq. (1). While the Néel temperature is a characteristic of a particular material, the blocking temperature is associated with the Néel temperature ($T_b<T_N$) but may vary depending on different process and processing parameters. As the thickness of NiCo–O increases, the grains grow and, as a result, magnetic interactions become more coherent

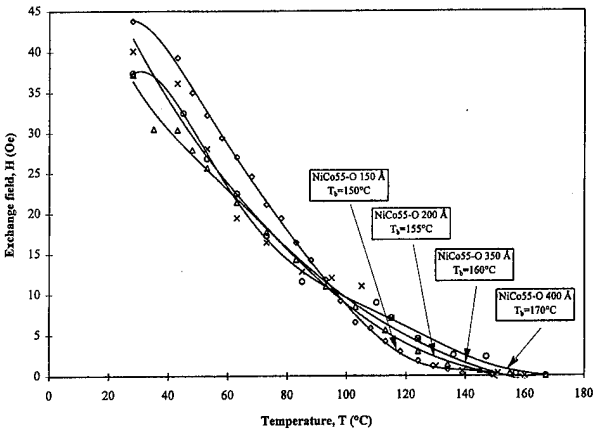


FIG. 3. Blocking temperature vs NiCo–O thickness.

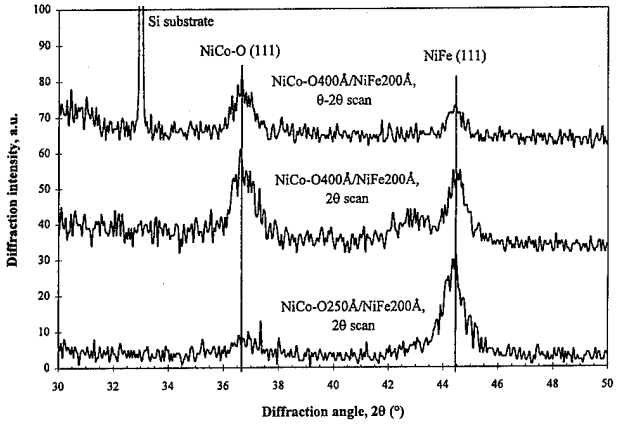


FIG. 4. XRD scans for NiCo–O/NiFe films.

among the grains and domains. This is most likely the reason behind the $T_b - t_{\mathrm{NiCo-O}}$ relationship demonstrated in Fig. 3.

D. Microstructural analysis by XRD

X-ray diffraction was performed on selected samples. Overall, the films showed a broad, weak NiFe(111) peak in the θ–2θ scan, an indication of a weakly textured structure of the films. Weakly textured NiCo–O(111) was seen only in the sample with NiCo–O thickness of 400 Å. The NiFe texture was stronger in samples with thicker NiCo–O underneath than those with thinner NiCo–O films. Figure 4 shows both the 2θ (i.e., the grazing angle scanning mode for thin films) and θ–2θ scans of the NiCo–O 400 Å/NiFe 200 Å sample and the 2θ scan of the NiCo–O 250 Å/NiFe 200 Å sample. The grain size is estimated by using Scherrer's formula[7]

$$t = 0.9\lambda_x/(\Delta 2\theta)\cos\,\theta_B, \tag{2}$$

where t is the grain size, λ_x is the wavelength of the incident x-ray beam, $\Delta 2\theta$ is the full width at half maximum (FWHM) of the diffraction peak, and θ_B is the Bragg's angle of the particular diffraction plane. For the sample with NiCo–O thickness of 250 Å, NiCo–O and NiFe grain sizes are estimated as 59 and 107 Å, respectively; and for the NiCo–O 400 Å sample, they are 92 and 143 Å, respectively.

IV. CONCLUSIONS

NiCo–O/NiFe thin films were prepared by rf sputtering. NiCo–O was reactively sputtered. NiCo55-O outperforms NiCo60-O in terms of larger exchange strength, smaller coercivity, as well as thermal stability. Higher blocking temperature in samples with thicker NiCo–O films (NiFe thickness fixed) is probably due to the fact that the NiCo–O in these thicker films has larger grain size and a more coherent microstructure, as indicated by x-ray diffraction results. Although exchange strength quickly reduces as the NiCo–O thickness drops below 200 Å, the interaction between NiCo–O and NiFe still exists even for the thinnest samples in this work, evidenced by the higher coercivity present in the samples.

ACKNOWLEDGMENT

The authors would like to thank Raminder Garcha for technical assistance in film deposition and part of the VSM measurements.

[1] M. J. Carey and A. E. Berkowitz, Appl. Phys. Lett. **60**, 3060 (1992).
[2] S. Soeya *et al.*, J. Appl. Phys. **74**, 6297 (1993).
[3] A. Devasahayam and M. Kryder (in press).
[4] K. Ha, L. Rea, and Y. K. Kim (in press).
[5] C. Tsang, N. Heiman, and K. Lee, J. Appl. Phys. **53**, 2605 (1982).
[6] A. P. Malozemoff, J. Appl. Phys. **63**, 3874 (1988).
[7] B. D. Cullity, *Elements of X-ray Diffraction*, 2nd ed. (Addison-Wesley, Reading, MA, 1978), Chaps. 3 and 7.

Preparation of soft magnetic Fe/Ta and Fe:N/Ta:N multilayered films with large magnetization for inductive recording head

Masahiko Naoe and Shigeki Nakagawa
Department of Physical Electronics, Tokyo Institute of Technology, 2-12-1 O-okayama, Meguro, Tokyo 152, Japan

Fe/Ta multilayered films were deposited on Si substrates by ion beam sputtering (IBS) by alternately using separate Fe and Ta targets. Thickness of Fe and Ta layers ℓ_{Fe} and ℓ_{Ta} bilayers $\ell_{Fe}+\ell_{Ta}$ in specimen films and total thickness of multilayers films with 10 bilayers were constant at 100 and 1000 Å, respectively. For as-deposited films, coercivity H_c took minimum value of 0.15 Oe at ℓ_{Fe} of 88 Å and ℓ_{Ta} of 12 Å, where saturation magnetization $4\pi M_s$ was 18.3 kG. Films postannealed at 500 °C exhibited $4\pi M_s$ of 19.1 kG, H_c of 0.05 Oe and μ_r of 1820. Fe:N/Ta:N multilayered films with N content of ~10 at. % were deposited by bombarding N ions extracted from the subgun while the films were being grown. For as-deposited films, H_c took minimum value of 0.07 Oe and μ_r took maximum value of 1310 at $\ell_{Fe:N}$ of 93 Å and $\ell_{Ta:N}$ of 7 Å, where $4\pi M_s$ was 20.5 kG. Films postannealed at 500 °C exhibited $4\pi M_s$ of 21.2 kG, H_c of 0.03 Oe and μ_r of 2380. Consequently, Fe/Ta and Fe:N/Ta:N multilayered films may be very suitable for magnetic cores in inductive heads for ultrahigh density recording. © *1996 American Institute of Physics.* [S0021-8979(96)14708-X]

I. INTRODUCTION

It has been reported that the multilayered films, such as Fe/Al and Fe/Si multilayers, exhibit excellent soft magnetism.[1,2] Inductive heads with high magnetic field for ultrahigh density recording need very soft magnetic thin films with sufficiently large saturation magnetization $4\pi M_s$ as magnetic cores in them. The Fe–Ta:N films postannealed at 500 °C exhibited $4\pi M_s$ of 19.7 and H_c of 0.05 Oe, respectively.[3] Since Fe and Fe_8N exhibited $4\pi M_s$ as large as 21.4 and 29.0 kG,[4] respectively, and Ta atoms are very insoluble into Fe layers, Fe/Ta multilayered films as well as Fe:N/Ta:N ones seemed to be hopeful for magnetic cores in the recording heads. Also, it is known that ion beam sputtering (IBS) is very useful in making multilayered films, since it can form continuous films with thickness as small as a few atomic layers. In this study, these multilayered films were deposited by using IBS apparatus and the relationship of their magnetic characteristics, the film construction and preparation condition was investigated.

II. EXPERIMENT

The dual ion beam sputtering (IBS) apparatus used in this study has a Kaufman-type of two guns with two grids. Ar and N_2 as pure as 99.999% at the pressure of 1.5×10^{-4} Torr was introduced through the main gun and subgun, respectively, as the working gas. Planar targets of Fe and Ta were sputtered by a uniform beam at an acceleration voltage for main gun and subgun of 500 and 100 V and extraction current of 3 and 1 mA, respectively. The deposition rates of Fe and Ta layers were ~15 and 10 Å/min, respectively.

At first, Fe/Ta multilayered films were deposited on Si wafers at room temperature by sputtering alternately with separate Fe and Ta targets. Thickness of Fe and Ta layers, ℓ_{Fe} and ℓ_{Ta}, respectively, were strictly controlled in the range between 0 and 100 Å. Thickness of Fe/Ta bilayers $\ell_{Fe}+\ell_{Ta}$ and total thickness of the multilayered films with 10 bilayers were set at constant values of about 100 and 1000 Å, respectively. Second, Fe:N/Ta:N multilayered films with N content of ~10 at. % were deposited by bombarding N ions extracted from subgun on the surface of growing films by using the dual IBS apparatus. The postheating treatment for improving soft magnetic characteristics of the as-deposited films was carried out at the annealing temperature T_A of 500 °C for 1 h in vacuum at residual gas pressure below 2×10^{-6} Torr.

The saturation magnetization $4\pi M_s$ and the coercivity H_c were determined on M–H hysteresis loops measured by using a vibrating sample magnetometer. The relative permeability μ_r was determined by using a vector impedance meter at the frequency of 5 MHz.

III. RESULTS AND DISCUSSION

A. Saturation magnetization $4\pi M_s$

Figure 1 shows the dependence of $4\pi M_s$ on the thickness of Fe and Ta layers ℓ_{Fe} and ℓ_{Ta}, respectively, for the as-deposited and postannealed Fe/Ta multilayered films. The

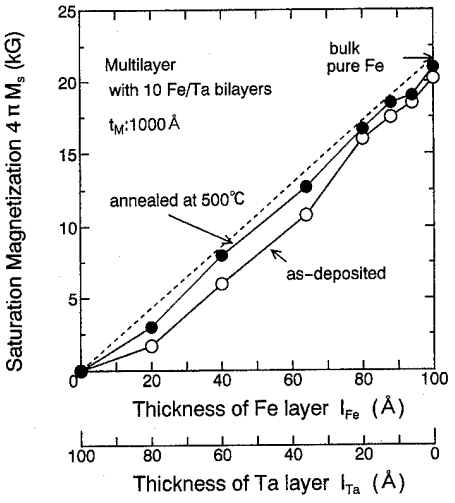


FIG. 1. Dependence of saturation magnetization $4\pi M_s$ of Fe/Ta multilayer on layer thickness ℓ_{Fe}, ℓ_{Ta}.

 0021-8979/96/79(8)/5015/3/$10.00 © 1996 American Institute of Physics

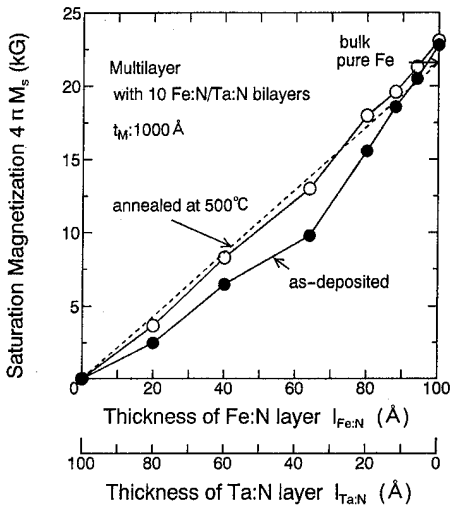


FIG. 2. Dependence of saturation magnetization $4\pi M_s$ of Fe:N/Ta:N multilayer on layer thickness $\ell_{Fe:N}$, $\ell_{Ta:N}$.

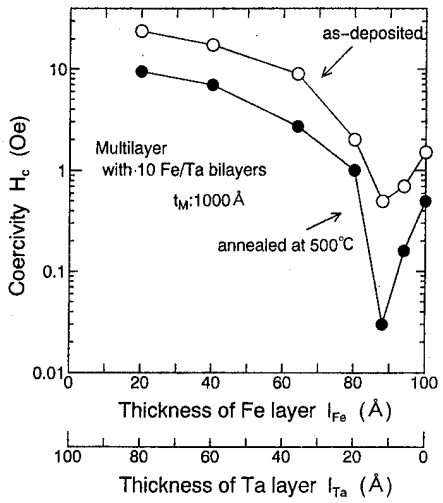


FIG. 3. Dependence of coercivity H_c of Fe/Ta multilayer on layer thickness ℓ_{Fe}, ℓ_{Ta}.

saturation magnetization of both, as-deposited films and postannealed films, decreased from 20.1 to 0 kG nearly in proportion with the decrease of ℓ_{Fe} and increase of ℓ_{Ta}. The postannealed films exhibited significantly larger $4\pi M_s$ than the as-deposited ones for same ℓ_{Fe}.

Figure 2 shows the dependence of $4\pi M_s$ on $\ell_{Fe:N}$ and $\ell_{Ta:N}$ for the Fe:N/Ta:N multilayered films. The saturation magnetization of the films decreased from 22.7 to 0 kG nearly in proportion with decrease of $\ell_{Fe:N}$ and $\ell_{Ta:N}$. The postannealed films exhibited apparently larger $4\pi M_s$ than the as-deposited ones for the same $\ell_{Fe:N}$ in the range of 40–80 Å. The as-deposited and postannealed Fe:N single layer films possessed larger $4\pi M_s$ of 22.5 and 22.7 kG, respectively, than that of bulk pure Fe (21.3 kG). It was found that the increase of $4\pi M_s$ after postannealing might be attributed to the increase in the size of Fe and Fe:N crystallites in the multilayers, since the value of crystallite size estimated by the half value width of x-ray diffraction peaks increased by a factor of 1.5–1.8 after postannealing.

B. Coercivity H_c

Figure 3 shows the dependence of H_c on ℓ_{Fe} and ℓ_{Ta} for the as-deposited and postannealed Fe/Ta multilayered films. H_c of both as-deposited and postannealed films decreased with increase of ℓ_{Fe} in the range of 20–88 Å and increased with increase of ℓ_{Fe} from 88 to 100 Å. The postannealed films exhibited remarkably lower H_c than the as-deposited ones for same ℓ_{Fe}. H_c of the as-deposited and postannealed films took the minimum values of 0.15 and 0.05 Oe, respectively, at ℓ_{Fe} of 88 Å.

Figure 4 shows the $\ell_{Fe:N}$ dependence of H_c for the Fe:N/Ta:N multilayered films. H_c of both films decreased with increase of $\ell_{Fe:N}$ in the range of 40–93 Å and increased with increase of $\ell_{Fe:N}$ from 93 to 100 Å. Also, the postannealed Fe:N/Ta:N multilayered films exhibited much lower H_c than the as-deposited ones for same $\ell_{Fe:N}$. H_c of the as-deposited and postannealed films took the minimum values of 0.07 and 0.03 Oe, respectively.

C. Relative permeability μ_r

Figure 5 shows the dependence of μ_r on ℓ_{Fe} and ℓ_{Ta} for the as-deposited and postannealed Fe/Ta multilayered films. μ_r of both as-deposited and postannealed films increased with increase of ℓ_{Fe} in the range of 0–88 Å and decreased remarkably with increase of ℓ_{Fe} from 88 to 100 Å. The postannealed films exhibited about two times higher μ_r than the as-deposited ones for same ℓ_{Fe}. μ_r of the as-deposited and postannealed films took the maximum values of 1180 and 1820, respectively, at ℓ_{Fe} of 88 Å.

Figure 6 shows the ℓ_{Fe} dependence of μ_r for the Fe:N/Ta:N multilayered films. μ_r of both films increased drastically with increase of $\ell_{Fe:N}$ from 64 to 80 Å and decreased remarkably with increase of $\ell_{Fe:N}$ from 93 to 100 Å. Also, the postannealed Fe:N/Ta:N multilayered films exhibited about two times higher μ_r than the as-deposited one for same $\ell_{Fe:N}$. μ_r of the as-deposited and postannealed films took the maximum values of 1200 and 2380, respectively, at $\ell_{Fe:N}$ of 93 Å. The improvement of soft magnetism such as H_c de-

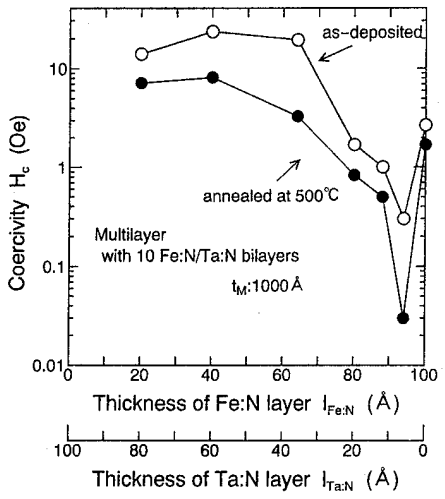


FIG. 4. Dependence of coercivity H_c of Fe:N/Ta:N multilayer on layer thickness $\ell_{Fe:N}$, $\ell_{Ta:N}$.

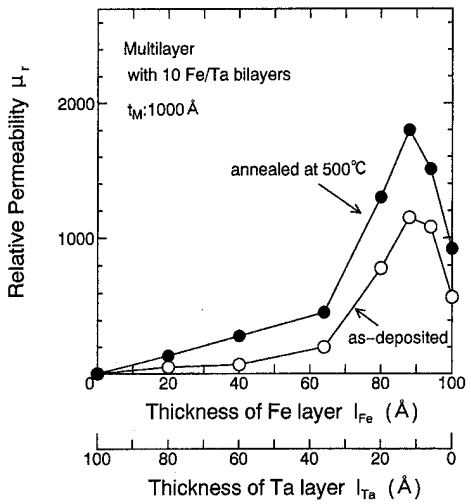


FIG. 5. Dependence of relative permeability μ_r of Fe/Ta multilayer on layer thickness ℓ_{Fe}, ℓ_{Ta}.

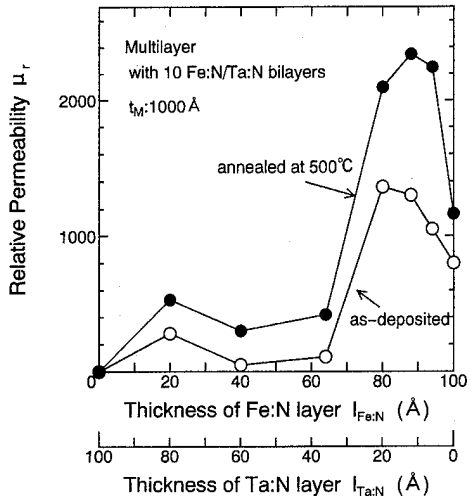


FIG. 6. Dependence of relative permeability μ_r of Fe:N/Ta:N multilayer on layer thickness $\ell_{Fe:N}$, $\ell_{Ta:N}$.

crease and μ_r increase seemed to be caused due to decrease in internal stress, since the degree in curvature of the specimens with very thin fused quartz substrates decreased drastically after postannealing.

IV. CONCLUSION

In this study, the Fe/Ta and Fe:N/Ta:N multilayers were deposited with the bilayer thickness of 100 Å and the total thickness of 1000 Å by using the dual ion beam sputtering apparatus. The relationship between their magnetic characteristics and the film construction and preparation condition was investigated. The obtained results are as follows:

(1) For the as-deposited Fe/Ta multilayers, the coercivity H_c took the minimum value of 0.15 Oe and the relative permeability μ_r took the maximum value of 1180, where the saturation magnetization $4\pi M_s$ was 18.3 kG.

(2) These Fe/Ta multilayers exhibited $4\pi M_s$ of 19.1 kG, H_c of 0.05 Oe, and μ_r of 1820, after postannealing at 500 °C.

(3) For the as-deposited Fe/Ta multilayers, H_c took the minimum value of 0.07 Oe and μ_r took the maximum value of 1310, where $4\pi M_s$ was 20.5 kG.

(4) This Fe:N/Ta:N exhibited $4\pi M_s$ of 21.2 kG, H_c of 0.03 Oe, and μ_r of 2380, after postannealing at 500 °C.

Consequently, the Fe:N/Ta:N multilayers postannealed at proper temperature may be the most suitable for soft magnetic cores which are required to possess large $4\pi M_s$.

[1] M. Nagakubo, T. Yamamoto, and M. Naoe, J. Appl. Phys. **64**, 5751 (1988).
[2] K. Kubota, M. Nagakubo, and M. Naoe, IEEE Trans. Magn. **MAG-26**, 2335 (1990).
[3] N. Ishiwata, C. Wakabayashi, and H. Urai, J. Appl. Phys. **69**, 5616 (1991).
[4] Y. Sugita, H. Takahashi, M. Komuro, K. Mitsuoka, and A. Sakuma, J. Appl. Phys. **70**, 6637 (1994).

Cr\(CoPtCr,CoPt$_x$) layered film studies for hard bias applications

A. Tsoukatos, S. Gupta, and D. Marx
Materials Research Corporation, 560 Route 303, Orangeburg, New York 10962

Cr\(CoPtCr,CoPt) films were deposited on oxidized Si ⟨100⟩ substrates via dc magnetron sputtering. Process parameters, such as deposition rates, number of bilayers, and bias voltage, were varied to achieve the hard magnetic properties without thermal processing of the films. Coercivities in the range of 2000 Oe, with corresponding squareness of about 0.8–0.9, and remanent magnetization in the range (3–3.6) memu/cm^3, were achieved by identification of the optimum conditions. © *1996 American Institute of Physics.* [S0021-8979(96)08908-6]

I. INTRODUCTION

CoPt-based alloys are well-established hard magnetic materials.[1–4] However, the hard magnetic phase associated with these type of alloys is heat induced and the deposition processes for magnetoresistive head elements require ambient temperatures in the range of 100 °C. This range of temperatures is well below the range required for the precipitation of the CoPt face center tetragonal (fct) hard magnetic phase (i.e., >450 °C).[5] Therefore, the development of hard magnetic films with CoPt-based alloys has been undertaken using process parameters, and adjacent metallic layers that can induce exchange coupling that results in hard magnetic behavior. The magnetic properties of these films may be improved by biasing the constituent underlayer, but this is a technique more appropriate for the development of media, for which the Cr underlayer is significantly thicker.[6] The hard magnetic properties in correlation to the excellent oxidation resistance associated with these materials make them ideal candidates for media and MR head applications. The usefulness of the Cr\(CoPtCr,CoPt) films for hard bias component in the former application is the focus of our experiments.

II. EXPERIMENTAL PROCEDURES

Cr\(CoPtCr,CoPt) layered films were sputter deposited via dc rotating magnetron from 10 in. high-purity targets. The films were deposited on thermally oxidized silicon ⟨100⟩ 6 in. wafers. Deposition rates varied as a function of applied dc power (1–5 kW) and argon pressure (1–15 mTorr). The thickness of the Cr underlayer varied between 50 and 1000 Å, while the magnetic layer thicknesses ranged between 50 and 700 Å. Film samples ($0.25<A<0.4$ cm^2) were subsequently evaluated in terms of their magnetic properties, using a vibrating sample magnetometer. The type of magnetic interactions present in these films were qualitatively studied via isothermal remanence curves, using a vibrating sample magnetometer.

The particular combinations of the Cr\magnetic layer structures studied were initially defined by an experimental design, which was used to statistically generate the range of process parameters, which were successively adjusted so as to achieve the optimum process. Additional experiments were performed using as a guide the bilayered structure ($n=1$), which involved multilayered structures of (Cr\CoPtCr)$_n$ with $n>1$, and that resulted in achieving the desired magnetic properties while maintaining the total thickness within a comparable range to the bilayer.

In addition to the multilayered structures rf biasing of the individual layers was successfully utilized to improve the magnetic properties of the bilayered structures.

The crystal structure of the films was determined via x-ray diffraction. Low-angle x-ray diffraction (XRD) was also used to quantify the integrity of the thinner layers deposited at higher deposition rates.

III. RESULTS AND DISCUSSION

In Table I the magnetic properties are shown with reference to the deposition rate (power) of the magnetic layer. The thickness of the magnetic component was found directly proportional to the resulting M_rt values. However, a more complicated interaction is involved in the thickness/deposition rate (power) effect on the coercivity of the magnetic component. Figure 1 shows a surface plot of the coercivity as a function of magnetic layer thickness and deposition power, as deposited at 3 mTorr, with a 200 Å Cr underlayer deposited at 3 mTorr and 5 kW.

The combined results of the above experiments have lead to the conclusion that, given the experimental conditions, it is difficult to maximize coercivity and magnetization simultaneously, at magnetic layer thicknesses below the 500 Å range, without rf biasing of the individual layers during deposition. Therefore, an alternative route was investigated that would allow simultaneous maximization of the magnetic features, with no significant changes of the process parameters but rather of the resulting film structure. The bilayer structure was changed to a (Cr/CoPtCr)$_n$ structure with $n=2,4,10$. A limitation was encountered in the number of n,

TABLE I. The effect of the magnetic layer deposition rates on the coercivity, squareness, and remanent magnetization per cm^2. The Cr underlayer was at 125 Å, and the deposition pressure was at 3 mTorr for the CoPtCr films, with the Cr at 150 Å and the deposition pressure at 5 mTorr for the CoPt films.

Deposition rate (Å/s) CoPtCr/CoPt	H_c (Oe) CoPtCr/CoPt	SQ CoPtCr/CoPt	M_rt (memu/cm^2) CoPtCr/CoPt
23/25	1540/1683	0.77/0.82	3.20/4.40
46	1436	0.79	3.40
69/75	1605/1715	0.75/0.86	2.90/3.70
115/125	1706/1722	0.78/0.85	3.0/3.45
161/175	1742/1922	0.79/0.91	3.0/2.5

 0021-8979/96/79(8)/5018/3/$10.00 © 1996 American Institute of Physics

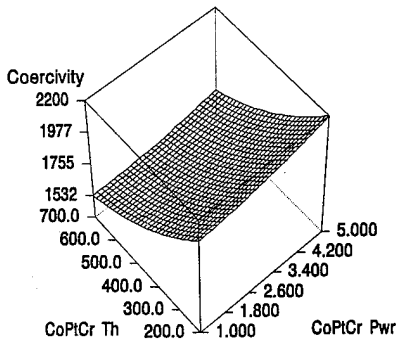


FIG. 1. Coercivity as a function of process conditions for a Cr\CoPtCr bilayer with constant Cr thickness at 200 Å.

since the overall structure thickness needs to be below the 1500 Å range in order to avoid excessive noise generation. The magnetic layer thicknesses used were at 50, 100, 250, 350, and 400 Å, while the underlayer was at 50, 100, 200, and 250 Å. Figure 2 shows the results for the $n=2$ structures (total structure thickness=1000–1300 Å). Although the combined thickness of the magnetic component became as high as 800 Å the resulting coercivity is of the order of 1900 Oe, with corresponding magnetic moment of 3.3 memu/cm^2. Furthermore, by reducing the underlayer thickness to 200 Å the coercivity of the structure is maintained in the 1800 Oe range while the value of the magnetic moment is 3.55 memu/cm^2.

The Rutherford Backscattering spectroscopy results for a $n=2$ structure are shown in Fig. 3. The effective layering of

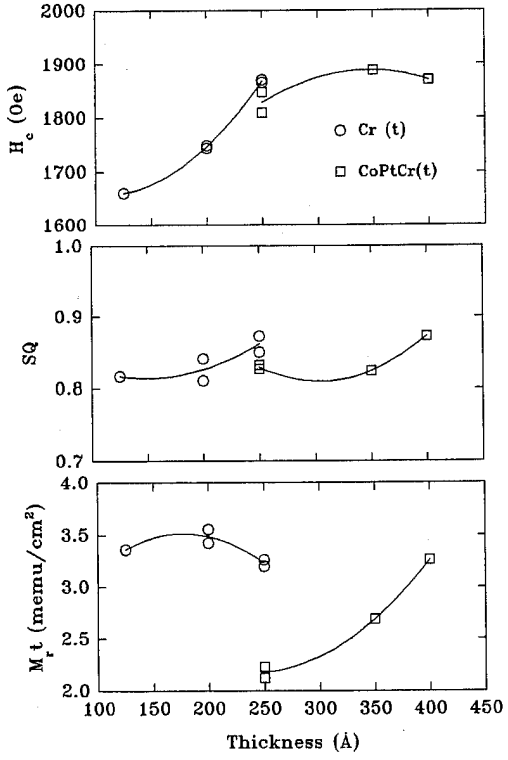


FIG. 2. Magnetic properties of $(Cr\backslash CoPtCr)_n$ bilayers as a function of thickness of the Cr (CoPtCr, $t=400$ Å) and CoPtCr (Cr, $t=200$ Å) components.

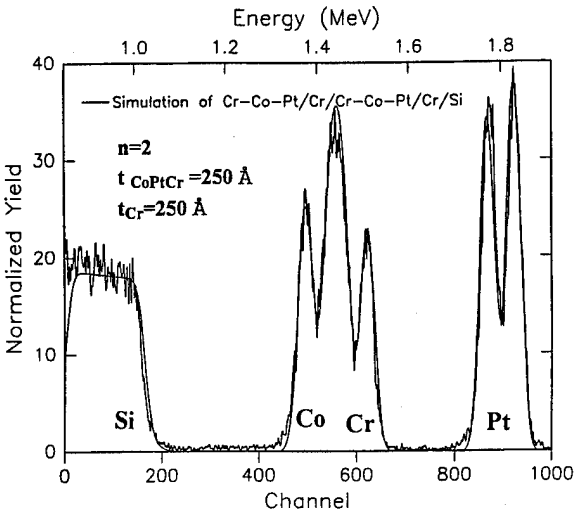


FIG. 3. Rutherford backscattering spectra of a Cr\CoPtCr films for $n=2$.

the $n=2$ structure is clearly indicated by the two characteristic peaks for Pt ($Z=78$). Due to the proximity of the Z numbers for Co ($Z=28$) and Cr ($Z=24$), there is overlapping of their characteristic peaks, and, therefore, it is not possible to differentiate by visual observation. However, the least-squares techniques used to fit the spectrum quantifies the actual structure present. Figure 4 shows the low-angle x-ray diffraction spectrum of a Cr\CoPtCr multilayer with measured bilayer thickness of 152±5 Å. The film structure was sputtered at high deposition power and the individual layer thicknesses were chosen so as to quantify the integrity of the layered structures at such deposition rates (Table I).

Similar high coercivity/high remanent magnetization combinations were also obtained by supplying rf bias to the substrate during the individual layer deposition. Figure 5 shows the plots of the magnetic data as a function of the layer thickness as deposited with rf bias conditions.

X-ray diffraction studies of these films provided limited information regarding the crystal structures present, due to

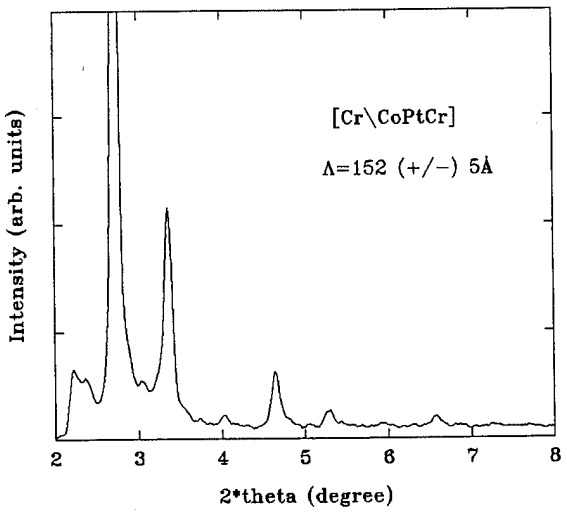


FIG. 4. Low-angle x-ray diffraction data for a [Cr-100\CoPtCr-50] multilayer with $n=10$.

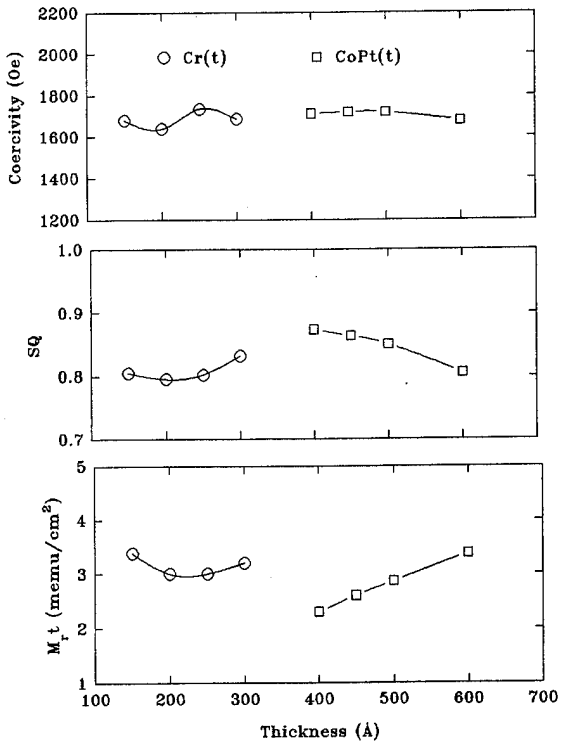


FIG. 5. Magnetic data for Cr\CoPt bilayers as deposited under the influence of substrate bias and as a function of layer thickness for each of the bilayer components.

the restricted resolution imposed by the films thicknesses. Figure 6 shows the spectrum of a Cr\CoPt film with total film thickness of about 850 Å. The characteristic (110) Cr line is present, although broadened due to the layer thickness (150 Å), with the two other peaks identified as components of the magnetic phase mixture consisting of $CoPt_3$, and Co [(111) fcc line]. However, more detailed crystal structure investigation is required via transmission electron microscopy (TEM), considering the film thicknesses in this study.

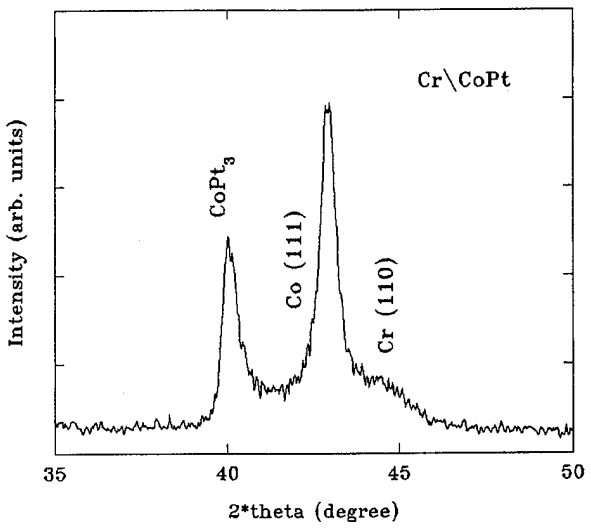


FIG. 6. X-ray diffraction spectrum for a Cr\CoPt film of total thickness of about 850 Å.

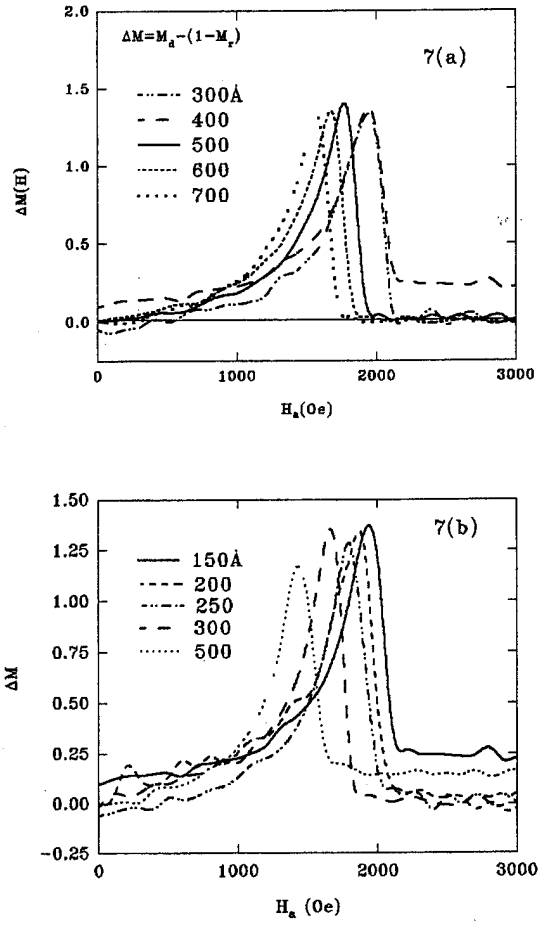


FIG. 7. ΔM curves indicative of positive interactions for Cr\CoPt bilayers as a function of (a) magnetic layer thickness, and (b) of Cr underlayer thickness.

The type of magnetic coupling present was identified via isothermal magnetic remanence curves. The concave down Henkel plots indicate positive interactions,[7] which is in agreement with the results of the differentiated magnetizing and demagnetizing curves of these films that are indicative of positive exchange coupling. Figure 7(a) shows the ΔM curves for Cr\CoPt films at 150 Å Cr underlayer and varying magnetic layer thickness, with the corresponding ΔM curves as a function of underlayer thickness shown in 7(b), signifying the switching field strength relative to the film structure.

ACKNOWLEDGMENTS

The authors would like to thank Dr. L. Withanawasam, I. Werasekera, and Dr. P. Swann for their helpful contribution in the development of this manuscript.

[1] A. S. Darling, Plat. Metals Rev. **7**, 96 (1961).
[2] R. A. MacGuire and P. Gaunt, Philos. Mag. **13**, 567 (1966).
[3] J. A. Aboaf, S. R. Herd, and E. Klokholm, IEEE Trans. Magn. **MAG-19**, 1514 (1983).
[4] A. Tsoukatos, H. Wan, G. C. Hadjipanayis, Y. J. Zhang, M. Waite, and S. I. Shah, J. Magn. Magn. Mater. **118**, 387 (1993).
[5] E. Gephard and W. Koster, Z. Metallkunde **32**, 253 (1940).
[6] P. Glijer, J. M. Sivertsen, and J. H. Judy, IEEE Trans. Magn. **MAG-30**, 5070 (1994).
[7] P. I. Mayo, K. O'Grady, P. E. Kelly, J. Cambridge, I. L. Sanders, T. Yogi, and R. W. Chantrell, J. Appl. Phys. **69**, 4733 (1993).

Early development of neutron scattering by magnetic materials (invited) (abstract)

C. G. Shull
Department of Physics and Nuclear Reactor Laboratory, Massachusetts Institute of Technology, Cambridge, Massachusetts 02139

Neutron scattering has established itself as an important tool in studying magnetic materials. The early history of this development will be outlined, ranging from the earliest studies of paramagnetic materials to those of ferromagnetic and antiferromagnetic materials. © *1996 American Institute of Physics.* [S0021-8979(96)68108-7]

 0021-8979/96/79(8)/5021/1/$10.00 © 1996 American Institute of Physics

Magnetic scattering of neutrons (invited) (abstract)

R. M. Moon[a)]
Solid State Division, Oak Ridge National Laboratory, Oak Ridge, Tennessee 37831

Ever since the pioneering work of C. G. Shull and E. O. Wollan in the early 1950s, neutron scattering has played a crucial role in expanding our understanding of magnetic materials. Neutrons have been the preferred tool to reveal the most detailed information on the magnetic structure and dynamics of the full range of materials exhibiting magnetic properties. Some highlights of the substantial body of work during the first 45 years of magnetic scattering will be presented. Topics include magnetic structures, magnetic form factors, magnetic phase transitions, and magnetic excitations. © *1996 American Institute of Physics.* [S0021-8979(96)68308-X]

[a)]Retired; present address: 865 West Outer Drive, Oak Ridge, TN 37830.

Neutron scattering as a probe of unconventional superconductivity in $YBa_2Cu_3O_7$ (invited) (abstract)

B. Keimer
Department of Physics, Princeton University, Princeton, New Jersey 08544

We have carried out a variety of neutron scattering experiments on the high temperature superconductor $YBa_2Cu_3O_7$ which elucidate the unconventional microscopic properties of the cuprates and illustrate the power and versatility of neutron scattering as a probe of novel materials. Small angle magnetic neutron diffraction is thus far the only technique capable of revealing the structure of the vortex lattice in the cuprate superconductors in magnetic fields of several tesla. We have shown that in $YBa_2Cu_3O_7$ the vortex lattice in this field range has an oblique structure when the field is applied along the c axis (perpendicular to the CuO_2 layers).[1] Recent theoretical work has attributed this unusual structure to the unconventional (d-wave) pairing state realized in the cuprates. We will also discuss the rich behavior of the vortex lattice when the field is tilted with respect to the c axis. We have used inelastic neutron scattering to elucidate the magnetic and lattice vibrational excitations in $YBa_2Cu_3O_7$. Magnetic and phonon scattering were separated both by detailed calculations of phonon dynamical structure factors and by neutron polarization analysis. A novel resonant magnetic excitation at wave vector $\mathbf{q}=(\pi/a,\pi/a)$ and energy $\hbar\omega=40$ meV appears in the superconducting state.[2] The simplest model for this resonance relies on quasiparticle pair creation and implies a sign reversal of the energy gap function on the Fermi surface. Alternative models will also be discussed. We have also observed a strongly wave vector dependent renormalization of the energy and lifetime of a specific phonon in the superconducting state of $YBa_2Cu_3O_7$.[3] Since the phonon self-energy is sensitive to the anisotropies of the energy gap and Fermi surface via the electron–phonon interaction, our data contain important information about these parameters. © *1996 American Institute of Physics.* [S0021-8979(96)68408-6]

[1]B. Keimer, W. Y. Shih, R. W. Erwin, J. W. Lynn, F. Dogan, and I. A. Aksay, Phys. Rev. Lett. **73**, 3459 (1994).
[2]H. F. Fong, B. Keimer, P. W. Anderson, D. Reznik, F. Dogan, and I. A. Aksay, Phys. Rev. Lett. **75**, 316 (1995).
[3]D. Reznik, B. Keimer, F. Dogan, and I. A. Aksay, Phys. Rev. Lett. **75**, 2396 (1995).

 0021-8979/96/79(8)/5022/1/$10.00 © 1996 American Institute of Physics

Strong magnetic fluctuations in transition metal oxides (invited)

C. Broholm
Department of Physics and Astronomy, The Johns Hopkins University, Baltimore, Maryland 21218 and National Institute of Standards and Technology, Gaithersburg, Maryland 20899

G. Aeppli
AT&T Bell Laboratories, Murray Hill, New Jersey 07974

S.-H. Lee and W. Bao
Department of Physics and Astronomy, The John Hopkins University, Baltimore, Maryland 21218

J. F. DiTusa
Department of Physics and Astronomy, Louisiana State University, Baton Rouge, Louisiana 70803

Most magnets have long-range magnetic order when the thermal energy is less than the local magnetic exchange energy ($T<|\Theta_{CW}|$). Effects such as reduced dimensionality and frustration, however, can suppress the ordering transition and lead to unusual cooperative paramagnetic phases at low temperatures. We review neutron scattering experiments exploring such short-range-ordered phases in insulating transition metal oxides. We discuss $(V_{1-x}Cr_x)_2O_3$, in which orbital fluctuations appear to limit spin correlations to within small "molecular" clusters, $SrCr_{9p}Ga_{12-9p}O_{19}$, in which geometrical frustration allows local anitferromagnetic constraints to be fulfilled without long-ranged order, and Y_2BaNiO_5, in which magnetic interactions occur only within chains of spins which are unable to order because of the Haldane effect. Emphasis is placed on the common features of exchange interactions in these oxides and the important role which magnetic neutron scattering has played in understanding the unusual magnetic phenomena. © *1996 American Institute of Physics.*
[S0021-8979(96)72208-6]

I. INTRODUCTION

A common structural unit in magnetism is a transition series cation surrounded by six oxygen ions at the vertices of an octahedron.[1] This unit, for example, is the source of interacting magnetic moments in classical three-dimensional antiferromagnets such as MnO, FeO, CoO, NiO, Fe_2O_3, and Cr_2O_3. Adjoining octahedra, however, can also build periodic structures whose connectivity is not conducive to the development of conventional long-ranged order, and therefore may give rise to novel cooperative magnetic phenomena. In this article we review experiments examining such magnetic oxides which have strong magnetic fluctuations and short-ranged spin correlations even at low temperatures ($T\ll\Theta_{CW}$).

The neutron scattering techniques pioneered by Shull and Brockhouse are irreplaceable tools for elucidating spin correlations in these systems, much as they were for conventional Néel antiferromagnets.[2] The measured quantity is the probability that a neutron with a wave vector $\mathbf{k}_i$ is scattered into a final state with wave vector $\mathbf{k}_f$ through its interaction with the sample. Under suitable conditions this scattering process may be treated in the Born approximation, and in this case the scattering probability distribution is proportional to the neutron scattering cross section, which depends only on wave vector transfer, $\mathbf{Q}=\mathbf{k}_i-\mathbf{k}_f$, and energy transfer, $\hbar\omega=(\hbar^2/2m)(k_i^2-k_f^2)$. Here we consider only the magnetic part of the scattering cross section, which is proportional to

$$I_m(\mathbf{Q},\omega)=\sum_{\alpha\beta}(\delta_{\alpha\beta}-\hat{Q}_\alpha\hat{Q}_\beta)S^{\alpha\beta}(\mathbf{Q},\omega), \tag{1}$$

where $S^{\alpha\beta}(\mathbf{Q},\omega)$ is the dynamical spin correlation function,

$$S^{\alpha\beta}(\mathbf{Q},\omega)=|F(Q)|^2\frac{(g\mu_B)^2}{2\pi\hbar}\int dt e^{i\omega t}\times\frac{1}{N}\sum_{\mathbf{RR}'}\langle S^\alpha_{\mathbf{R}}(t)S^\beta_{\mathbf{R}'}(0)\rangle e^{-i\mathbf{Q}\cdot(\mathbf{R}-\mathbf{R}')}, \tag{2}$$

which contains unique information about magnetic correlations in the sample. In this expression $F(Q)$ is the magnetic form factor, a property of the $3d$ orbitals.[17]

For powder samples the information available from magnetic neutron scattering is less specific than for single crystals, because the scattered intensity only depends on $Q=|\mathbf{k}_i-\mathbf{k}_f|$ and is proportional to the spherically averaged dynamic spin correlation function

$$\langle S(Q,\omega)\rangle=\int\frac{d\Omega_{\hat{Q}}}{4\pi}\frac{1}{2}I_m(\mathbf{Q},\omega). \tag{3}$$

Nonetheless, as we shall see, important results may still be extracted, especially in the small Q limit or when we are interested in Brillouin zone averaged quantities.

For comparison with bulk measurements, and between different neutron scattering experiments, we have in most cases measured scattering cross sections in absolute units. The scale factor between the detector count rate and the quantities of Eqs. (1)–(3) were determined by normalizing to count rates associated with known nuclear scattering cross sections of the samples.

II. ORBITAL FLUCTUATIONS IN $(V_{1-x}Cr_x)_2O_3$?

V_2O_3 can be insulating or metallic and antiferromagnetic or paramagnetic depending on temperature, pressure, and exact stoichiometry,[3] and consequently the material has been a testing ground for theories of electronic correlations and

 0021-8979/96/79(8)/5023/6/$10.00 © 1996 American Institute of Physics

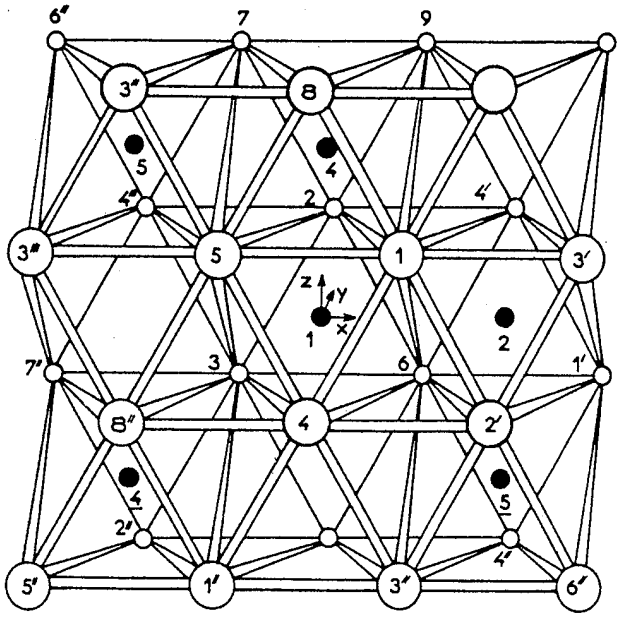


FIG. 1. Crystalline structure of $(V_{1-x}Cr_x)_2O_3$. The trivalent cations (filled circles) are surrounded by O^{2-} ions (open circles) on the vertices of trigonally distorted octahedra. (From Ref. 11.)

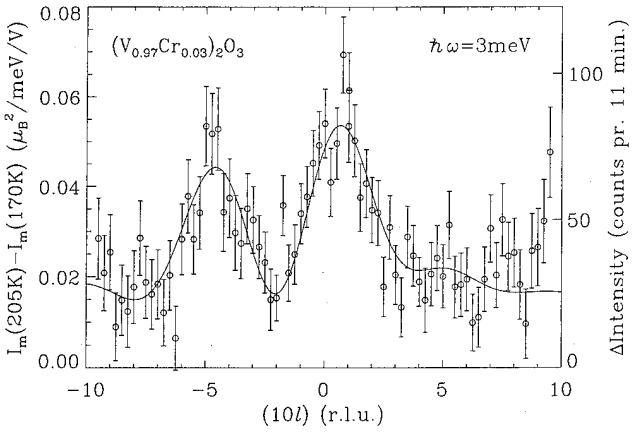


FIG. 2. **Q** dependence of inelastic scattering at $\hbar\omega=3$ meV and $T=205$ K in the paramagnetic insulating phase of $(V_{0.97}Cr_{0.03})_2O_3$. The 170 K data from the antiferromagnetic phase are a good measure of background and were subtracted from the 205 K data. The data were taken on BT2 at NIST with $E_f=13.7$ meV and collimations 60′–40′–40′–60′ around the PG(002) monochromator and analyzer. A 1-in.-thick PG filter followed the sample.

magnetism for decades.[4,5] Here we shall confine our attention to the insulator $(V_{0.97}Cr_{0.03})_2O_3$ whose antiferromagnetism defies explanation in terms of a conventional Heisenberg spin Hamiltonian.

Figure 1 shows a sketch of the corundum structure of V_2O_3. The trivalent cation sites, which are surrounded by six oxygen atoms on the vertices of trigonally distorted octahedra, form puckered honeycomb layers stacked in such a way that each vanadium site has a nearest neighbor above or below it. V^{3+} has only two $3d$ electrons which occupy the crystal field triplet t_{2g}. The t_{2g} orbitals have significant overlap only with their counterparts on neighboring vanadium atoms and this has two important consequences: (1) V_2O_3 is a Mott insulator as opposed to a charge transfer insulator. (2) Direct cation–cation overlap between in-plane nearest neighbors and the one out-of-plane nearest neighbor are the dominant sources of magnetic exchange interactions.[1] Even though these interactions would appear to yield a three-dimensional nonfrustrated antiferromagnet, the magnetic transition which takes place at $T_N=180$ K, is unusual because (1) it occurs far below $|\Theta_{CW}|=350$ K, (2) it involves an antiferromagnetic structure[6] which is unique for corundum transition metal oxides[2,7,8], (3) it is accompanied by a lattice distortion, and (4) it is a first order transition.

To explore this unusual magnetic phase transition, we have examined spin correlations in the paramagnetic phase by inelastic magnetic neutron scattering. Figure 2 shows the wave vector dependence of neutron scattering at $T=205$ K and $\hbar\omega=3$ meV. For **Q** along the (10l) direction we find two well-defined peaks which, in being almost as wide as the projection of the first Brillouin zone in that direction, imply that magnetic correlations involve only nearest neighbors. The data are qualitatively different from those derived from paramagnetic scattering in conventional three-dimensional antiferromagnets, not only because the correlations are so short ranged for $T/T_N-1=0.08$, but also because coherent scattering dominates over incoherent scattering despite the very short correlation lengths. Correlations are so short ranged, in fact, that we can fit the data to a truncated lattice sum which neglects all but the correlations between nearest neighbors,

$$S(\mathbf{Q})=\sum_{\mathbf{RR}'}\langle S_{\mathbf{R}}S_{\mathbf{R}'}\rangle\exp[i\mathbf{Q}\cdot(\mathbf{R}-\mathbf{R}')]. \tag{4}$$

The best fit, which also describes $(h,0,-5)$ and $(h01)$ scans at $\hbar\omega=3$ meV, is shown as a solid line in Fig. 2. From the fit we obtain values for nearest-neighbor spin correlations: $\langle\mathbf{S}_{[0,0,0]}\cdot\mathbf{S}_{\langle 0,0,1/6+\delta\rangle}\rangle=0.6(3)$, $\langle\mathbf{S}_{[0,0,0]}\cdot\mathbf{S}_{\langle 1/3,2/3,\delta\rangle}\rangle=-0.19(8)$, $\langle\mathbf{S}_{[0,0,0]}\cdot\mathbf{S}_{\langle 1/3,2/3,\delta-1/6\rangle}\rangle=0.18(8)$, and $\langle\mathbf{S}_{[0,0,0]}\cdot\mathbf{S}_{\langle 1/3,2/3,1/6\rangle}\rangle=-0.09(3)$ where $\delta=0.026$. These values were normalized so that $\langle\mathbf{S}_{[0,0,0]}\cdot\mathbf{S}_{[0,0,0]}\rangle=1$. Figure 3 shows that it is not a lack of interactions that prevents longer-ranged correlations from developing. The full widths at half-maximum (FWHM) of constant–$\hbar\omega$ scans along the (10l) direction through the peak at $\mathbf{Q}\approx(101)$ are almost indistinguishable from those at $\hbar\omega=3$ meV, for energy transfers, $\hbar\omega$, as high as 18 meV. Also the nearly $\hbar\omega$-independent peak amplitudes indicate that these correlations may persist to even higher energies.

The **Q** dependence of paramagnetic scattering from $(V_{1.97}Cr_{0.03})_2O_3$ resembles that of energy integrated scattering from isolated spin clusters in dilute magnets.[9] However, the energy spectrum is continuous indicating that we are dealing with excitations in a macroscopic physical system. A possible explanation for this unusual behavior was recently proposed by Rice.[10] His idea is that orbital fluctuations in the paramagnetic phase of $(V_{1-x}Cr_x)_2O_3$ inhibit long-ranged spin correlations through their effect on exchange interactions. In his description, which is based on the work of Castellani *et al.*,[11] one d electron is occupied in covalent bonding with the out-of-plane nearest neighbor while the other must choose which of the three in-plane vanadium neighbors to bond with. Pairs which bond have ferromagnetic spin–spin

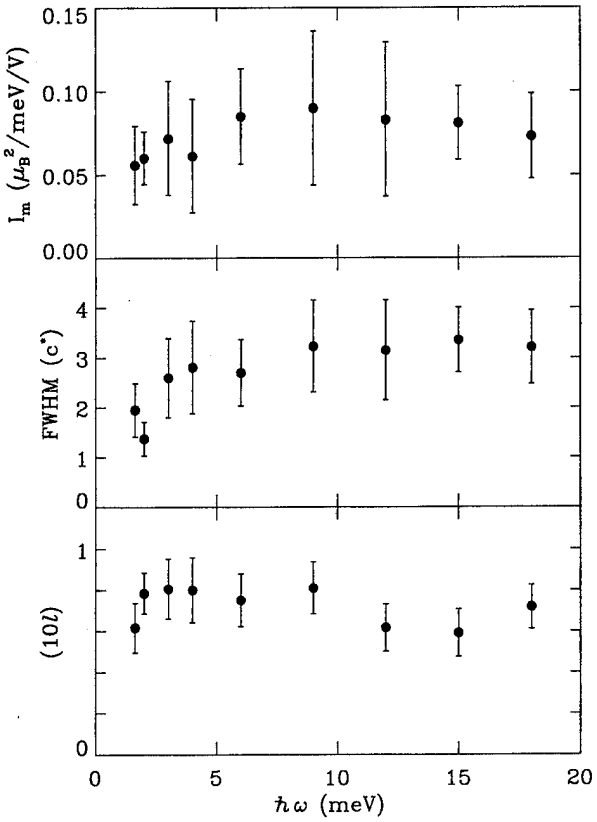


FIG. 3. $\hbar\omega$ dependence of inelastic scattering for $\mathbf{Q}\approx(101)$ at $T=205$ K in $(V_{0.97}Cr_{0.03})_2O_3$ as derived from Lorentzian fits to constant $\hbar\omega$ scans along the $(10l)$ direction. The top frame is the amplitude of the modulated component, the middle frame is the FWHM, and the bottom frame is the peak position.

interaction whereas those which do not interact antiferromagnetically, and this leads to an effective spin–orbit coupling which cannot be accounted for by a conventional spin Hamiltonian. In this theory the coupling of the spin system to orbital fluctuations is what inhibits the development of spin order for $T\approx|\Theta_{CW}|$ and the magnetic transition is actually driven by an orbital ordering transition. In particular, the orbital order enables the development of long-ranged spin order by establishing an ordered array of spin exchange interactions. Further neutron scattering experiments probing the effects of orbital fluctuations on spin fluctuations both in the low and high temperature phases are underway to test this hypothesis.

III. ISOLATED SPIN PAIRS AND FRUSTRATION IN $SrCr_{9p}Ga_{12-9p}O_{19}$

$SrCr_{9p}Ga_{12-9p}O_{19}$ is a more complicated substance than most condensed matter physicists are normally willing to consider. Nonetheless, the unique magnetic properties of this insulating oxide do warrant attention. The bulk properties which called our attention to $SrCr_{9p}Ga_{12-9p}O_{19}$ were (1) a magnetic susceptibility which follows Curie–Weiss behavior with $\Theta_{CW}=-500$ K down to $T\approx100$ K,[12] (2) the absence of static order until a spin-glass-like transition at $T_g=3.5$ K$\ll|\Theta_{CW}|$,[13] and (3) low temperature specific heat data,

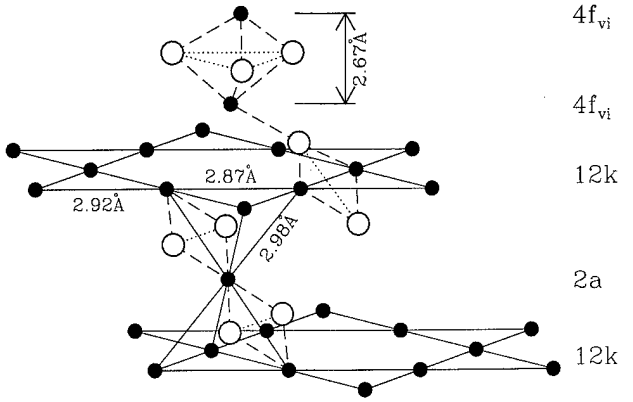


FIG. 4. Chromium ions (solid circles) and part of their distorted O^{2-} octahedral coordination in $SrCr_{9p}Ga_{12-9p}O_{19}$. (From Ref. 16.)

$C(T)$, which in being proportional to T^2 resembles a long-range ordered two-dimensional magnet more than a conventional spin glass for which $C\propto T$.[13]

The aspects of the crystal structure which are relevant for this discussion are shown in Fig. 4. As in V_2O_3, the trivalent magnetic cation, in this case Cr^{3+}, is surrounded by a distorted octahedron of oxygen atoms. The cation lattice is however more complicated in this case, encompassing three distinct sites which are denoted $12k$, $2a$, and $4f_{vi}$. The $12k$ layer is a slightly distorted Kagomé lattice whereas the $2a$ and $4f_{vi}$ layers are triangular lattices. The Cr^{3+} ions in the $12k-2a-12k$ block form corner-sharing tetrahedra, as in three-layer (111) slabs of the trivalent cation sites in the cubic pyrochlore[14,15] and spinel structures.

Neutron scattering experiments have enabled us to derive a comprehensive model of magnetic interactions in this material, and to identify the three-layer $12k-2a-12k$ slab as the origin of the two-dimensional frustrated magnetism in $SrCr_{9p}Ga_{12-9p}O_{19}$.[16] Figure 5 shows wave vector integrated inelastic neutron scattering, $S(\omega)$, at $T=1.3$ K from a powder sample of $SrCr_{9p}Ga_{12-9p}O_{19}$ with $p=0.92(5)$. Apart

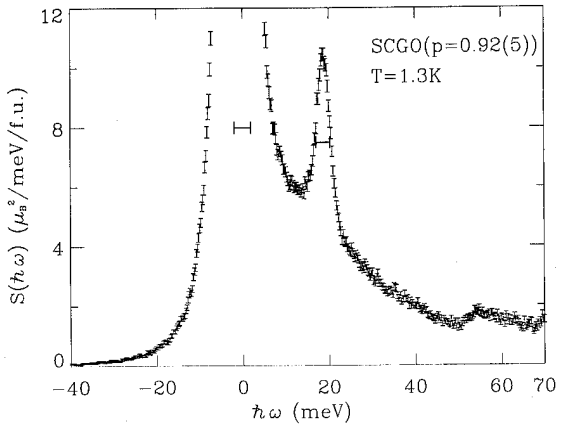


FIG. 5. Energy dependence of wave-vector-integrated magnetic neutron scattering $S(\hbar\omega)=\int[I(Q,\omega)/|F(Q)|^2]Q^2dQ/\int Q^2dQ$ from $SrCr_{9p}Ga_{12-9p}O_{19}$, $p=0.92(5)$ at $T=1.3$ K. The data were obtained from 1139 μA h of beam time on the HET instrument at ISIS with $E_i=100$ meV using slit pack C rotating at 100 Hz. The horizontal bars show the FWHM of the instrumental resolution. (From Ref. 16.)

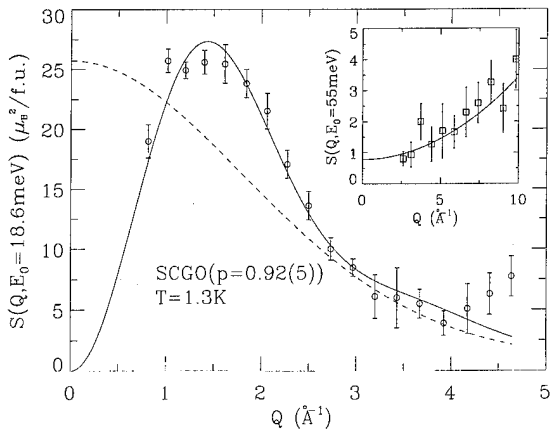


FIG. 6. Q dependence of the integrated intensity of the 20 meV excitation in $SrCr_{9p}Ga_{12-9p}O_{19}$, $p=0.92(5)$ at $T=1.3$ K. The dashed line is the magnetic form factor squared for chromium (Ref. 17), the solid line was calculated for 0.7(1) antiferromagnetically interacting pairs of spins per formula unit. The inset identifies the 55 meV feature visible in Fig. 5 as a vibrational in origin because the integrated intensity rises with wave vector transfer. The data were obtained using the MARI instrument at ISIS (Ref. 16).

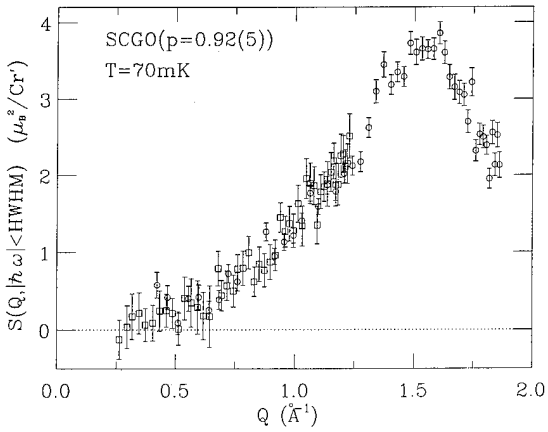


FIG. 7. Q dependence of elastic magnetic scattering from $SrCr_{9p}Ga_{12-9p}O_{19}$, $p=0.92(5)$ at $T=70$ mK. The data were obtained by subtracting elastic peak intensities at $T=20$ K from the same at $T=70$ mK. The experiment was performed on the IRIS instrument at ISIS using both its PG(002) analyzer (open circles) and its MICA(004) analyzer (open squares). (From Ref. 20.)

from the incoherent elastic peak and a broad spectrum of magnetic scattering visible from 0 to 40 meV, we notice a resolution limited peak at $\hbar\omega=18.6$ meV. Because the peak is sharp in wave-vector-integrated data, it must be associated with a nondispersive excitation and is therefore likely to arise from single atoms, or small clusters of atoms, which are decoupled from the rest of the system. From the Q dependence of the energy-integrated intensity of the ridge, shown in Fig. 6, we can exclude that it arises from (i) a local vibrational excitation, because the intensity decreases with Q and (ii) a crystal field excitation on a single chromium atom, because the Q dependence is distinguishable from the magnetic form factor for chromium.[17] Instead, the Q dependence of the scattering closely resembles that from an isolated pair of antiferromagnetically interacting spins,[9] shown as a solid line in Fig. 6. Such spin pairs also provide a detailed account for the energy and temperature dependence of the data, including a peak in $S(\omega)$ at $\hbar\omega=37.2$ meV which only appears for $T>100$ K.[16]

Considering also the values of the two fitting parameters which went into calculating the solid line in Fig. 6 and the position of the peak in Fig. 5, we conclude that there are 0.7(1) isolated spin pairs per formula unit in $SrCr_{9p}Ga_{12-9p}O_{19}$ $[p=0.92(5)]$. Spins of a pair are separated by $R\approx2.68(7)$ Å and interact antiferromagnetically with an exchange coupling constant $J=18.6(1)$ meV. Since $4f_{vi}$ spins are the only spins which each are part of a unique spin pair, and since there are 0.78 $4f_{vi}$–$4f_{vi}$ spin pairs per formula unit separated by 2.681(3) Å in our sample, it is likely that the $4f_{vi}$ Cr^{3+} ions are the ones forming isolated spin pairs in Sr $Cr_{9p}Ga_{12-9p}O_{19}$.

The oxygen octahedra of chromium ions in adjacent $4f_{vi}$ planes share a common face whereas the oxygen octahedra of neighboring $4f_{vi}$ and $12k$ sites share a corner. The exact same environment exists in corundum Cr_2O_3 where it has been established[18] that the exchange constant between Cr^{3+} ions with corner sharing oxygen octahedra is only 0.2 meV because occupied $3d$ orbitals in Cr^{3+} do not overlap oxygen orbitals.[1] Occupied orbitals of Cr^{3+} ions in face sharing octahedra, however, have appreciable direct overlap which in Cr_2O_3 gives rise to a 15 meV antiferromagnetic exchange coupling. This number, being close to the 18.6 meV exchange constant for spin pairs in SCGO $[p=0.92(5)]$, supports our comparison to Cr_2O_3 and our conclusion that $4f_{vi}$ spin pairs form isolated singlets in $SrCr_{9p}Ga_{12-9p}O_{19}$.

Having accounted for the $4f_{vi}$ chromium sites we are left with the quasi-two-dimensional magnet consisting of a triangular lattice ($2a$) sandwiched between two Kagomé lattices ($12k$). Alternatively this lattice can be described as a three-layer (111) slab of the trivalent cation sites in the cubic pyrochlore or spinel structures. The oxygen octahedra of nearest neighbors within this spin system all share an edge and exchange interactions are therefore expected to be comparable in magnitude. Fitting high temperature bulk susceptibility data to the sum of the susceptibility of the $4f_{vi}$ spin pairs and a Curie–Weiss term to account for the pyrochlore slab, we extract a value of 9.5(5) meV for the average exchange constant within the slab. It is satisfying that this number is close to the value of 6.7(4) meV measured for the exchange constant between chromium ions whose octahedra share an edge in Cr_2O_3.[18]

Evidently it is the reduced dimensionality and unique connectivity within this three-layer magnetic which give rise to the unusual cooperative magnetic properties of $SrCr_{9p}Ga_{12-9p}O_{19}$. We have performed a number of neutron scattering experiments to explore these properties.[19] Our most interesting data are perhaps those establishing the Q dependence of elastic magnetic scattering in the spin glass phase.[20] The data, shown in Fig. 7, were obtained by subtracting elastic scattering at $T=20$ K$>T_g$ from the same at $T=70$ mK. Since the half-width at half-maximum (HWHM) of the energy resolution function in this experiment was 7.5 μeV (circles) and 2.25 μeV (squares) this measurement probes magnetic correlations which persist on the nanosecond time scale. From the wave vector integral of the data we

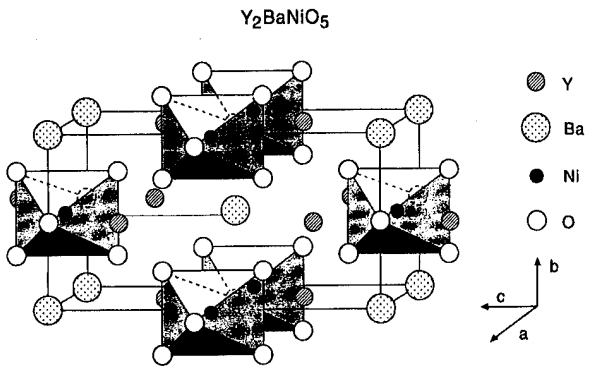


FIG. 8. Structure of Y_2BaNiO_5. The oxygen ion which is a member of the octahedral coordination of two nickel ions mediates superexchange along the spin chain. (From Ref. 31.) Holes reside on this atom for $Y_{1.90}Ca_{0.10}BaNiO_5$.

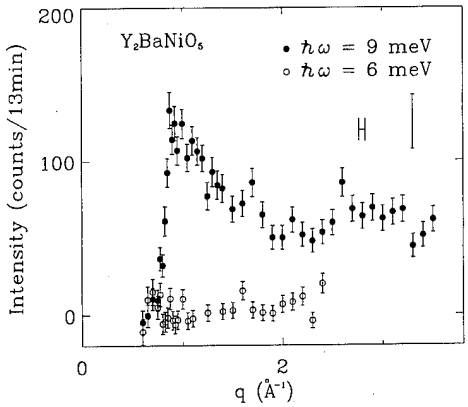


FIG. 9. Q dependence of inelastic magnetic scattering from a powder sample of Y_2BaNiO_5 at $T=10$ K for $\hbar\omega=6$ meV (open circles) and $\hbar\omega=9$ meV (filled circles). Background was measured for each of these scans at $\hbar\omega=-6$ and -9 meV, respectively, and subtracted. The horizontal bar corresponds to the FWHM Q resolution. The experiment was performed on the thermal neutron triple axis spectrometer BT2 at NIST with $E_i=40.3$ meV and collimations 60′–20′–42′–44′ around the PG(002) monochromator and analyzer. A 2-in.-thick PG filter preceded the monochromator. (Adapted from Ref. 32.)

conclude that the frozen moment in this system is only $1.9(2)\mu_B$, which is less than half of the frozen moment in a conventional Neél state formed by $S=3/2$ Cr^{3+} ions and thus implies that quantum spin fluctuations are strong in this insulating magnet. The elastic magnetic scattering is also unusual in that although we are dealing with a concentrated magnet with only weak structural disorder, there are no sharp peaks in the data, implying that long-ranged magnetic correlations are absent. Instead the broad peak at wave vector $Q\approx1.5$ Å^{-1} indicates the presence of short-range antiferromagnetic correlations. Since the width of the peak is comparable to its displacement from $Q=0$ static magnetic correlations are only maintained between nearest neighbors. Nonetheless, $S(Q)$ appears to vanish as $Q\rightarrow0$. A vanishing forward cross section is very significant, because it implies that there exists a decomposition of the frozen spin state into subgroups of spins which possess net spin zero. The zero spin subgroups could be pairs, triangles, or tetrahedra of nearest-neighbor Cr^{3+} ions. Although such a spin configuration in principle could be concocted on most lattices, it appears to be the unique connectivity of the pyrochlore slab which makes such a spin configuration energetically favorable by allowing for all antiferromagnetic interactions to be satisfied without establishing long-ranged order. In this respect the frozen spin configuration in $SrCr_{9p}Ga_{12-9p}O_{19}$ resembles the ground state of the weakly diluted classical Kagomé antiferromagnet which Shender *et al.*[21] have found to obey a "rule of satisfied triangles."

IV. HALDANE GAP AND HOLE DOPING IN Y_2BaNiO_5

The combination of low dimensionality and a low integer spin quantum number ($S=1$) causes Y_2BaNiO_5 to be a rare example of a transition metal oxide which evades magnetic order down to temperatures as low as 50 mK.[22] One dimensionality in this material comes about because oxygen octahedra, which coordinate Ni^{2+}, share a corner only for Ni^{2+} ions displaced along the a axis. Because Ni^{2+} ($3d^8$) has more than three $3d$ electrons, the superexchange interactions between such magnetic cations are strong,[1] and by dominating over all other exchange interactions, yield a one-dimensional antiferromagnet (see Fig. 8).

The consequences of this microscopic solid state chemistry for the magnetic properties of the material are quite astonishing. Figure 9, for example, shows the Q dependence of inelastic neutron scattering from a powder sample for $T=10$ K$\ll|\Theta_{CW}|$ K[23] and $\hbar\omega=9$ meV$\ll k_B|\Theta_{CW}|$. In this low T and $\hbar\omega$ regime, neutron scattering from a conventional three-dimensional Heisenberg antiferromagnetic is strongest at low energies and always peaked for Q in the vicinity of magnetic Bragg peaks. For Y_2BaNiO_5, however, inelastic scattering is only visible in the higher energy Q scan ($\hbar\omega=9$ meV) and only beyond a sharp onset at $Q=0.85$ Å$^{-1}\approx\pi/a$. Beyond this value no pronounced Q dependence is visible in the data except for a gradual decrease in intensity as Q increases. The absence of well-defined peaks in constant energy scans implies that long-ranged three-dimensional spin correlations do not exist in this material. However, the resolution limited onset of scattering as a function of Q distinguishes this magnet from conventional short-range ordered paramagnets, and indicates the presence of some form of long-ranged one-dimensional coherence.[24]

The unusual absence of inelastic scattering at $\hbar\omega=6$ meV was further explored through a constant $Q=1.1$ Å^{-1} scan (Fig. 10) which shows clear evidence of a 9 meV gap in the magnetic excitation spectrum. The single ion anisotropy of octahedrally coordinated Ni^{2+} cannot account for the gap, which instead appears to be an experimental example of the so-called Haldane gap[25] which characterizes the excitation spectrum of integer spin, one-dimensional antiferromagnets.[26,27] It is interesting to note that this quantum many-body effect actually prevents magnetic order from taking place at any temperature in real materials such as Y_2BaNiO_5 and NENP[28] in which residual three-dimensional interactions do not exceed the threshold required to drive the gap to zero as they do in $CsNiCl_3$.[26]

What sets Y_2BaNiO_5 apart from other quasi-one-dimensional magnets previously studied is that holes may be

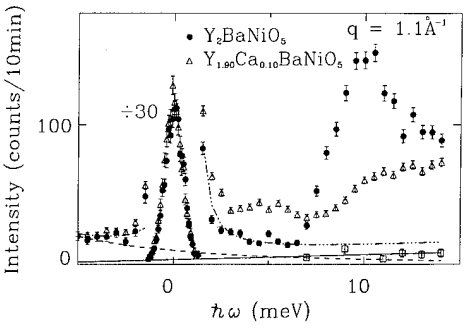


FIG. 10. $\hbar\omega$ dependence of inelastic neutron scattering at wave vector transfer $Q=1.1$ Å$^{-1}=0.65a^*$ and temperature, $T=10$ K. Solid circles are for Y_2BaNiO_5, open triangles for $Y_{1.90}Ca_{0.10}BaNiO_5$, a material where holes are placed on the superexchange mediating oxygen ions with a mean separation of 10 nickel sites. The data were obtained on the thermal neutron triple axis spectrometer BT2 at NIST with $E_f=14.7$ meV and collimations 60′–20′–42′–44′ around the PG(002) monochromator and analyzer. A 1-in.-thick PG filter followed the sample. The solid line is the background measured with analyzer turned 10° from reflection. The dashed line is the background resulting from $\lambda/2$ neutrons in the unfiltered incident beam. The dashed–dotted line shows the tails of the elastic signal superimposed on the previously mentioned background contributions. The sharp peak centered at $\hbar\omega=0$ comes from incoherent elastic nuclear scattering. Adapted from (Ref. 29.)

placed on the superexchange mediating oxygen atoms of the $(NiO_5)^{8-}$ chains by substituting Ca^{2+} for Y^{3+}.[29] This leads to a simple yet novel many-body system: Charge carriers interacting with a quantum spin liquid. The open triangles in Fig. 10 show that hole doping both introduces a subgap resonance in the excitation spectrum and shifts spectral weight above the gap to higher energies. Whereas the latter effect is also seen in samples where the average chain length is reduced by replacing Ni^{2+} by Zn^{2+}, the subgap resonance is peculiar to hole-doped samples. The simplest model which may be relevant for understanding the subgap resonance treats holes as static perturbations in the superexchange. In the analogous phonon problem a localized perturbation of interactions leads to a bound state or localized "optical" mode. A recent theoretical analysis of such a model has indeed identified a subgap resonance pinned to the middle of the Haldane gap when the impurity bond strength modulation exceeds a certain threshold.[30]

ACKNOWLEDGMENTS

We would like to acknowledge our collaborators in this work M. A. Adams, C. J. Carlile, S. A. Carter, C. T. Chen, S.-W. Cheong, B. Hessen, J. M. Honig, T. J. L. Jones, P. Metcalf, J.-H. Park, T. G. Perring, A. P. Ramirez, T. F. Rosenbaum, J. Spalek and, S. F. Trevino. We also thank the ISIS facility at the Rutherford Appleton Laboratory, and the National Institute of Standards and Technology for providing the experimental facilities which enabled the research, and the National Science Foundation which funded work at JHU through Grant Nos. DMR-9302065, DMR-9357518, and DMR-9453362.

[1] J. B. Goodenough, Phys. Rev. **117**, 1442 (1960), Prog. Solid State Chem. **5**, 145 (1972).
[2] C. G. Shull, W. A. Strauser, and E. O. Wollan, Phys. Rev. **83**, 333 (1951).
[3] D. B. McWhan, A. Menth, J. P. Remeika, W. F. Brinkman, and T. M. Rice, Phys. Rev. B **7**, 1920 (1973).
[4] N. F. Mott, *Metal Insulator Transitions* (Taylor & Francis, London, 1974).
[5] W. F. Brinkman and T. M. Rice, Phys. Rev. B **2**, 4302 (1970).
[6] R. M. Moon, Phys. Rev. Lett. **25**, 527 (1970).
[7] D. E. Cox, W. J. Takei, and G. Shirane, J. Phys. Chem. Solids **24**, 405 (1963).
[8] E. F. Bertaut, Compt. Rend. Acad. Sci. **252**, 76 (1961).
[9] A. Furrer and H. U. Güdel, J. Magn. Magn. Mater. **14**, 256 (1979).
[10] T. M. Rice (unpublished).
[11] C. Castellani, C. R. Natoli, and J. Ranninger, Phys. Rev. B **18**, 4945, (1978).
[12] X. Obradors, A. Labarta, A. Isalgue, J. Tejada, J. Rodriguez, and M. Pernet, Solid State Commun. **65**, 189 (1988).
[13] A. P. Ramirez, G. P. Espinosa, and A. S. Cooper, Phys. Rev. Lett. **64**, 2070 (1990); Phys. Rev. B **45**, 2505 (1992).
[14] M. J. Harris, M. P. Zinkin, Z. Tun, B. M. Wanklyn, and I. P. Swainson, Phys. Rev. Lett. **73**, 189 (1994).
[15] J. N. Reimers, J. E. Greedan, R. K. Kremer, E. Gmelin, and M. A. Subramanian, Phys. Rev. B **43**, 3387 (1991); J. E. Greedan, J. N. Reimers, C. V. Stager, and S. L. Penny, *ibid.* **43**, 5682 (1991).
[16] S.-H. Lee, C. Broholm, G. Aeppli, T. G. Perring, B. Hessen, and A. Taylor (unpublished).
[17] A. J. Freeman and R. E. Watson, Acta. Crystallog. **14**, 231 (1961).
[18] E. J. Samuelsen, M. T. Hutchings, and G. Shirane, Physica **48**, 13 (1970).
[19] C. Broholm, G. Aeppli, G. P. Espinosa, and A. S. Cooper, Phys. Rev. Lett. **65**, 3173 (1990); J. Magn. Magn. Mater. **69**, 4968 (1991).
[20] S.-H. Lee, C. Broholm, G. Aeppli, A. P. Ramirez, T. G. Perring, C. J. Carlile, M. A. Adams, T. J. L. Jones, and B. Hessen (unpublished).
[21] E. F. Shender, V. B. Cherepanov, P. C. W. Holdsworth, and A. J. Berlinsky, Phys. Rev. Lett. **70**, 3812 (1993).
[22] A. P. Ramirez, S.-W. Cheong, and M. L. Kaplan, Phys. Rev. Lett. **72**, 3108 (1994).
[23] B. Batlogg, S.-W. Cheong, and L. J. W. Rupp, Jr., Physica **194–196B**, 173 (1994).
[24] M. den Nijs and Koos Rommelse, Phys. Rev. B **40**, 4709 (1989).
[25] F. D. M. Haldane, Phys. Rev. Lett. **50**, 1153 (1983).
[26] Z. Tun, W. J. L. Buyers, R. L. Armstrong, K. Hirakawa, and B. Briat, Phys. Rev. B **42**, 4677 (1990).
[27] L. P. Regnault, J. Rossat-Mignod, J. P. Renard, M. Verdaguer, and C. Vettier, Physica (Amsterdam) **156–157B**, 247 (1989); S. Ma, C. Broholm, D. H. Reich, and B. J. Sternlieb, Phys. Rev. Lett. **69**, 3571 (1992).
[28] O. Avenel, J. Low Temp. Phys. **89**, 547 (1992).
[29] J. F. DiTusa, S.-W. Cheong, J.-H. Park, G. Aeppli, C. Broholm, and C. T. Chen, Phys. Rev. Lett. **73**, 1857 (1994).
[30] Z.-Y. Lu, Z.-B. Su, and L. Yu, Phys. Rev. Lett. **74**, 4297 (1995); other relevant theoretical papers are E. Sørensen and I. Affleck, Phys. Rev. B **51**, 16115 (1995); S. Fujimoto and N. Kawakami, *ibid.* **52**, 6189 (1995); K. Penc and H. Shiba, *ibid.* **52**, R715 (1995); E. Dagotto, J. Riera, A. Sandvik, and A. Moreo (unpublished).
[31] D. J. Buttrey, J. D. Sullivan, and A. L. Rheingold, J. Solid State Chem. **88**, 291 (1990).
[32] J. F. DiTusa, S.-W. Cheong, C. Broholm, G. Aeppli, L. W. Rupp, Jr., and B. Batlogg, Physica B **194–296**, 181 (1994).

Overview of Nd–Fe–B magnets and coercivity (invited)

J. Fidler and T. Schrefl
Institut für Angewandte und Technische Physik, T.U. Wien, Wiedner Hauptstrasse 8-10, A-1040 Vienna, Austria

High performance $Nd_2Fe_{14}B$-based permanent magnets are produced with different composition and various processing techniques. The composition and the processing route influence the complex, multiphase microstructure of the magnets, such as grain size, alignment, and distribution of phases. Grain sizes in the range between 10 and 500 nm are obtained by melt spinning, mechanical alloying, and the HDDR process. Sintered and hot worked magnets exhibit grain sizes above 1 μm. The coercive field is determined by the high uniaxial magnetocrystalline anisotropy as well as the magnetostatic and exchange interactions between neighboring hard magnetic grains. The dipolar interactions between misaligned grains are more pronounced in large-grained magnets, whereas exchange coupling reduces the coercive field in small grained magnets. Transmission electron microscopy has been used to study the influence of substituent and dopant elements on microstructure, coercivity, and corrosion resistance of advanced (Nd,S1)–(Fe,S2)–B:(M1,M2) magnets. The replacement of the Nd-rich intergranular phase by secondary phases formed after doping by M1 and M2 type elements improves the corrosion resistance, especially in large-grained magnets. Secondary, nonmagnetic phases reduce the remanence and the energy product. In addition to the characterization of the microstructure, special attention has been paid to the computer modeling of the interaction between microstructure and coercivity. The simulation of the magnetization reversal process based on the real microstructure reveals a good agreement with experimental values. It is shown that the coercive field depends on grain size, distribution, and misorientation of grains. A strong exchange coupling between hard magnetic grains is desired in nanostructured magnets in order to improve the remanence. This effect is further increased by secondary, soft magnetic phases. Nanocrystalline, composite Nd–Fe–B based magnets show a remanence enhancement, both in experiments and in model calculations. © *1996 American Institute of Physics.* [S0021-8979(96)38608-2]

I. INTRODUCTION

Different types of rare-earth permanent magnets, which show excellent hard magnetic properties, are based on $SmCo_5$, Sm_2Co_{17}, $Nd_2Fe_{14}B$, and $Sm_2Fe_{17}N_x$ alloys with a high magnetocrystalline anisotropy of the hard magnetic phase.[1] Recent developments on iron-rare-earth magnets have been made in order to increase coercivity and corrosion resistance and to decrease material and production costs. Attempts are made to change the composition and to optimize the various preparation techniques, such as the powder metallurgical sintering process, the melt-spinning route, the mechanically alloying process and the hot working technique, in order to obtain $Nd_2Fe_{14}B$-based permanent magnets with high remanence, coercivity, and energy product. In addition to the primary hard magnetic phase, various secondary phases also occur, depending on the composition and the processing conditions. This is because of the complex phase relations and phase diagrams involved. The multicomponent composition of the magnets leads to the formation of nonmagnetic and soft magnetic phases. Generally, two types of substituent elements, which replace the rare-earth element or the transition element sites in the hard magnetic phase, and two types of dopant elements are distinguished.[2] Substituent elements mainly change the intrinsic properties, such as spontaneous magnetic polarization, Curie temperature, and magnetocrystalline anisotropy.[3] Depending on the type, the dopant elements, which show a low solubility within the hard magnetic phase, form additional intergranular rare-earth-containing or boride phases. These phases change the coupling behavior between the hard magnetic grains. Nonmagnetic intergranular phases eliminate the direct exchange interaction and also reduce the long-range magnetostatic coupling between the hard magnetic grains,[4] both effects lead to an increase of the coercive field. On the other hand, the decrease of the volume fraction of the hard magnetic phases within the magnet decreases the remanence. Insufficient temperature stability and poor corrosion resistance are the main factors limiting applications of $Nd_2Fe_{14}B$-based magnets. Secondary nonmagnetic phases, which replace the Nd-rich intergranular phase, considerably improve the corrosion resistance and are of great technological interest.

The activities in permanent magnetism are mainly concentrated on the improvement of the magnetic energy density product, the corrosion resistance and the temperature coefficient of the coercive field of Nd–Fe–B-based magnets. The optimization of nitrided magnets, bonded magnets, and composite nanocrystalline magnets are prospective activities.[5]

 0021-8979/96/79(8)/5029/6/$10.00 © 1996 American Institute of Physics

The main emphasis of this paper is to distinguish different types of $Nd_2Fe_{14}B$-based magnets and to show the influence of the microstructure on the coercivity.

II. MICROSTRUCTURE OF (Nd,S1)-(Fe,S2)–B:(M1,M2) MAGNETS

Nd–Fe–B-based permanent magnets exhibit a complex multiphase microstructure. According to the ternary phase diagram at least three equilibrium phases occur: the hard —magnetic $Nd_2Fe_{14}B$ phase (ϕ), the boride phase $Nd_{1+\epsilon}Fe_4B_4$, and the low melting Nd-rich phase (n). Other phases, such as Fe rich and Nd oxides, and pores are found depending on the composition and processing parameters.[6] Selected substituent elements replace the Nd atoms (S1 =Dy,Tb) and the Fe atoms (S2=Co,Ni,Cr), respectively, in the hard magnetic ϕ phase and considerably change intrinsic properties, such as the spontaneous polarization, the Curie temperature, and the magnetocrystalline anisotropy. The formation of intermetallic, soft magnetic Nd–(Fe,S2) phases, such as the Laves-type $Nd(Fe,S2)_2$-phase,[7–9] deteriorate the coercivity of the magnets. If dopant elements M1 or M2 are added to Nd–Fe–B, in some cases the coercivity is increased and the corrosion resistance is improved. Our previous, systematic transmission electron microscopy studies performed on sintered, melt spun, mechanically alloyed, and hot worked magnets have shown that two different types of dopants can be distinguished independently of the processing route. Both types influence the microstructure in a different way.[10–15] (i) *Type 1 dopants* (M1=Al, Cu, Zn, Ga, Ge, Sn) ⇒ form binary M1-Nd or ternary M1-Fe–Nd phases, (ii) *Type 2 dopants* (M2=Ti, Zr, V, Mo, Nb, W) ⇒ form binary M2-B or ternary M2-Fe–B phases.

The main difference between substituent and dopant elements is the solubility range within the $Nd_2Fe_{14}B$ phase. The doping changes the microstructure of Nd–Fe–B sintered magnets in the following way: If a solubility exists at the high temperature (1100 °C), the dopant element is partly dissolved in the hard magnetic $Nd_2Fe_{14}B$ phase (ϕ). This is the case for most of the M1-dopant elements (Al and Ga). The dopant element replaces the Fe atoms and therefore changes the spontaneous polarization, Curie temperature, and anisotropy field.[3] If the solubility at sintering temperature is low, precipitation within the ϕ-phase occurs.[16] This is mainly the case with M2 dopants. The main effect of the addition of dopant elements is the formation of new intergranular phases.[2]

In order to understand the formation of the microstructure and the enhancement of coercivity, various Dy- and Co-free Nd–Fe–B magnets containing a combination of type 1 and type 2 additives, such as (Ga,Nb)[10] and (Cu,Nb),[11] were prepared by the conventional powder metallurgical route from hydrogen decrepitated (HD) powder and were investigated by means of transmission electron microscopy (TEM) after the magnetic characterization. In order to compare these results, we also studied the influence of the (Al,V) and (Al,Mo) additions on the microstructure of Nd–(Fe,Co)–B and (Nd,Dy)–(Fe,Co)–B magnets, respectively.

Type 1 dopants influence the wetting behavior of the liquid phase during the sintering or the hot working process



FIG. 1. TEM micrograph of the intergranular region between hard magnetic grains in the sintered $Nd_{15.5}Fe_{67.5}Co_5B_7Al_2Mo_3$ magnet showing the boride phase $(Mo,Fe)_3B_2$ (iB) and the Nd_3Co-phase (iNc).

and therefore affect the magnetic decoupling of the grains. After cooling from high temperature, the formation of additional Nd-containing intergranular phases like $Nd_6Fe_{13}M1_1$ [for M1= Al,Ga,Cu (δ phase)], $Nd_3(Ga,Fe)+Nd_5(Ga,Fe)_3$, and NdCu or $NdCu_2$ occurs. The better separation and decoupling of the hard magnetic grains leads to the enhancement of the coercivity of the magnets. The replacement of the Nd-rich intergranular phase by new dopant-containing phases improves the corrosion resistance of the magnet. *Type 2 dopants* like V and Mo as well as W and Nb show a low solubility within the hard magnetic phase and form precipitates within the ϕ phase and intergranular borides, such as $(V,Fe)_3B_2$, $(Mo,Fe)_3,B_2$, NbFeB, and WFeB, Ti and Zr doping lead to TiB_2[17] and ZrB_2 precipitates, respectively. In Nd–(Fe,Co)–B:M1-doped magnets the magnetic properties of the $Nd(Fe,Co,M1)_2$ phases are changed and the coercivity is increased.[18] In Nd–(Fe,Co)–B: M2-doped magnets the formation of the soft magnetic $Nd(Fe,Co)_2$ phase is suppressed and the intergranular Nd-rich phase is partly replaced by the Nd_3Co phase. This main effect of this addition is to improve the coercivity and the corrosion resistance.

The TEM micrograph of Fig. 1 shows a typical two-phase intergranular region in the sintered $Nd_{15.5}Fe_{67.5}Co_5B_7Al_2Mo_3$ magnet. The Nd-rich phase is replaced by the Nd_3Co phase (iNc) and by the intergranular boride $(Mo,Fe)_3B_2(iB)$. In addition to these phases the $Nd_6Fe_{13}Al_1$ phase was also identified as an intergranular phase. A more detailed investigation of this magnet revealed the influence of the Al content on the coercivity and the formation of the Nd_3Co phase.[19] A similar and comparable microstructure was previously observed by TEM investigations of the Nd–(Fe,Co)–B:(Al,V) sintered magnet.[15] Various additional phases were identified in the intergranular region in the sintered $Nd_{18}Fe_{74}B_6Ga_1Nb_1$ (Ref. 10) and $Nd_{15.4}Fe_{75.7}Be_{6.7}Cu_{1.3}Nb_{0.9}$ (Ref. 11) magnets, such as Ga- or Cu-containing Nd phases and Nb-containing boride phases. In accordance with the binary Ga–Nd phase diagram, the two phases were characterized as eutectoidal mixture of $Nd_3(Ga,Fe)$ and $Nd_5(Ga,Fe)_3$. A similar result was obtained in the $Nd_{15.4}Fe_{7.57}B_{6.7}Cu_{1.3}Nb_{0.9}$ magnet. Individual NbFeB

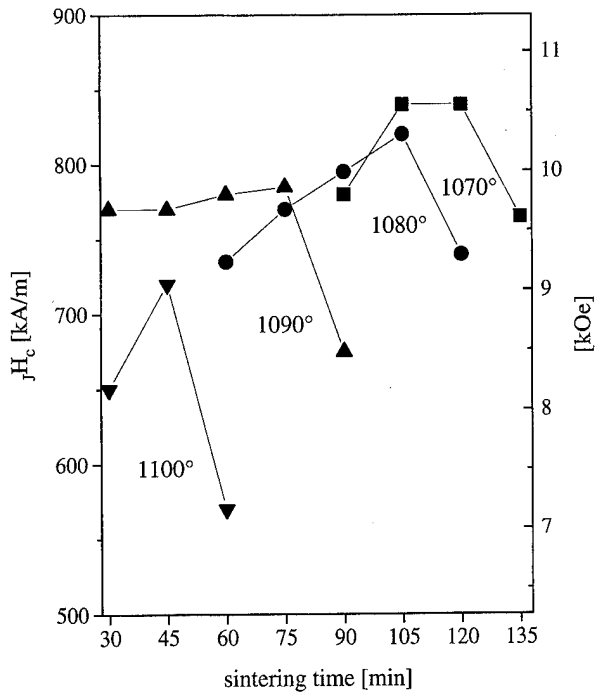


FIG. 2. Dependence of the coercive field on the sintering temperature and time of optimized $Nd_{15.1}Fe_{78.4}B_{6.1}Ga_{0.1}Cu_{0.3}$ magnets with high remanence (1.38 T) and energy density product (360 kJ/m^3) (Ref. 20).

precipitates with diameters of less than 100 nm were identified within the grain interior of the ϕ phases of both magnets. Large NbFeB precipitates occur in the intergranular region between the hard magnetic grains. The combination of (Ga,Nb)- and (Cu,Nb)-doping shows both of types 1 and 2 microstructural changes. The advantage of the Nb addition is avoidance of the formation of α-Fe, which easily occurs in Ga- and Cu-doped magnets due to their phase relationship in the ternary phase diagram M1–Fe–Nd.

The processing route of the magnet strongly influences the grain size and grain size distribution. Optimized, sintered magnets with a maximum density exhibit an average grain size in the order of 5–10 μm. The coercive field strongly depends on the sintering parameters, such as temperature and time (Fig. 2).[20] Nanocrystalline and submicron magnets show a grain size in the range of 10–500 nm and are obtained by the melt-spinning route,[21] or by mechanically alloying,[22] or by the HDDR (hydrogenation, disproportionation, desorption, and recombination) process.[23] TEM investigations of Nd–Fe–B ribbons show that the microstructure and the magnetic properties sensitively depend on the composition and the quench rate (wheel speed). The electron micrographs of Fig. 3 show the inhomogeneous grain size distribution from the free to the wheel surface side of the ribbon. For ribbons of the thickness of about 30 μm the average grain size of 20 nm near the wheel side increases to 500–700 nm near the free side. For low quenching rates different morphologies of the ϕ grains are observed. Preferential orientation of the grains is only found in equiaxed small grains and disappears for very large grains, as well as for dentritic structures. The most evident texture is observed in columnar grains which crystallized with the c-axis perpendicular to the ribbon plane.[24] The formation of intergranular phases between the hard magnetic $Nd_2Fe_{14}B$ grains is more pronounced in the large grained regions of the ribbon.[25] A magnetically anisotropic behavior has been found in HDDR processed, Co-substituted and Ga-, Zr-doped magnets.[26] The mechanism for the preferential orientation of $Nd_2(Fe,Co)_{14}B$ grains with an average diameter of about 300 nm after recombination is not yet clear. It is suggested that finely dispersed undecomposed $Nd_2(Fe,Co)_{14}B$ particles play an important role by acting as nuclei for the growth or recrystallization of the hard magnetic phase during the desorption process.[27] These particles can be formed under controlled hydrogenation conditions together with additives to decelerate the decomposition.

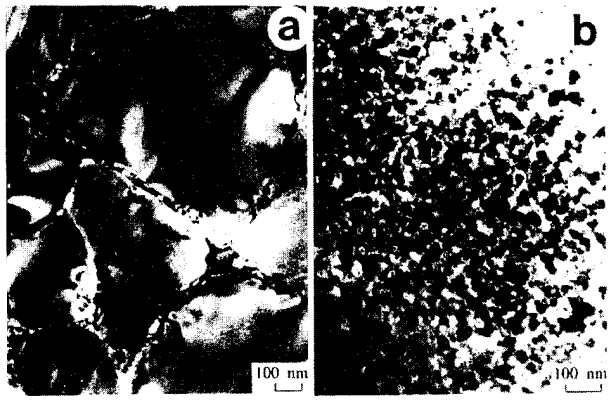


FIG. 3. Inhomogeneous grain size distribution across a $Nd_{15}Fe_{76}B_9$ ribbon. TEM micrograph taken (a) near free surface side and (b) wheel side.

III. COERCIVITY

In $Nd_2Fe_{14}B$ based magnets, prepared by the sintering, the melt spinning, the mechanically alloying, or the hot working processing route the hard magnetic grains behave like single domain particles after magnetic saturation. The nucleation and the expansion of reversed magnetic domains control the coercive field during the magnetization reversal process. Micromagnetic calculations by Brown showed that the coercive field of an ideal, homogeneously magnetized material is given by the nucleation field expressed by[28]

$$H_n=\frac{2K_1}{J_s}-(N_{\parallel}-N_{\perp})\frac{J_s}{\mu_0} \tag{1}$$

where K_1 and J_s are the first anisotropy constant and the spontaneous magnetic polarization, respectively, and $N_{\parallel}$ and $N_{\perp}$ denote the demagnetization factors parallel and perpendicular to the rotational symmetry axis of an ellipsoidal particle.

Several authors have shown that the experimental results for the temperature dependence of the coercive field $H_c(T)$ of $Nd_2Fe_{14}B$ based magnets can be described independently by the processing route by the equation[29–31]

$$H_c(T)=cH_A(T)-n\frac{J_s(T)}{\mu_0}, \tag{2}$$

where H_A is the anisotropy field, which is 5340 kA/m for $Nd_2Fe_{14}B$ at room temperature.[32] The temperature indepen-

dent constants c and n take into account the deteriorating effects of the real microstructrue. A typical value of 0.2–0.5 was found for the parameter c, depending on the composition and processing parameters of the magnet. The parameter n (0.8–1.7) is related to the local demagnetizing field arising from free stray fields at internal phase and grain boundaries. The angular and the temperature dependence of H_c of sintered, melt spun and hot worked $Nd_2Fe_{14}B$ based magnets has been described by Givord and co-workers[33] by a different model. These authors consider that the magnetization reversal is initiated in a volume equal to the activation volume V_a determined from magnetic viscosity measurements. The coercive field is given by

$$H_c = c' \frac{\sigma_w}{V_a^{1/3} \mu_0 J_s} - n \frac{J_s}{\mu_0} - \frac{25kT}{\mu_0 J_s V_a}, \tag{3}$$

where σ_w is the domain wall energy and k is the Boltzmann constant.

A detailed micromagnetic treatment of the nucleation field was carried out by Kronmüller *et al.*[34,35] and leads to the equation

$$H_n = \alpha_K \alpha_\psi \frac{2K_1}{J_s} - N_{\text{eff}} \frac{J_s}{\mu_0}, \tag{4}$$

where α_K describes the inhomogeneity of the magnetocrystalline anisotropy in grain boundary regions with anisotropy lower than that of the matrix phase and in which reverse domain nucleation is supposed to occur. α_ψ accounts for misaligned grains, and N_{eff} is an average effective local demagnetization factor. Experimental measurements[36] of the angular dependence of H_c of oriented sintered $Nd_2Fe_{14}B$ magnets showed that the factor α_ψ differs from the predictions of the Stoner–Wohlfarth theory[37] of noninteracting, single domain particles. MQI and MQIII types of magnets show a similar magnetization reversal behavior and temperature dependence of H_c compared with sintered magnets.[55] A classical domain wall pinning behavior has not been found in such magnets. An increase of the magnetocrystalline anisotropy of the hard magnetic phase leads to an enhancement of the coercive field according to Eqs. (1), (2), and (4). Substituting Nd by Dy by a small amount considerably increases the anisotropy field and slightly decreases the spontaneous polarization.[35]

A conventional, ideal, anisotropic Nd–Fe–B magnet consists of well-aligned grains which are completely separated by a nonmagnetic intergranular phase. Two conditions must be fulfilled for a complete surrounding of the hard magnetic grains. First, the dihedral angle,[39] which was found to be in the order to 10°–30° and decreases with the amount of doping,[6] must become zero. Second, the volume fraction of the liquid phase during sintering must exceed a certain value (≈20%). Both criteria are not fulfilled in Nd–Fe–B magnets. Thus, the typical microstructure consists of two types of grain boundaries, one containing intergranular phases especially at grain junctions and corners and one in direct contact to each other. Our studies are in good agreement with the theoretical consideration of the liquid phase sintering process.[39] The incomplete separation of the hard magnetic ϕ grains by a low-melting intergranular phase, lead to the fact that even in doped Nd–Fe–B magnets the ϕ grains are not completely magnetically decoupled. These magnetic interactions therefore consist of long range *magnetostatic or dipolar interactions* and of the short range *exchange coupling* between misaligned grains. Both interactions determine the *coercivity* of $Nd_2Fe_{14}B$-based magnets.[40] The contribution of exchange coupling between misaligned grains becomes more dominant with decreasing grain size.

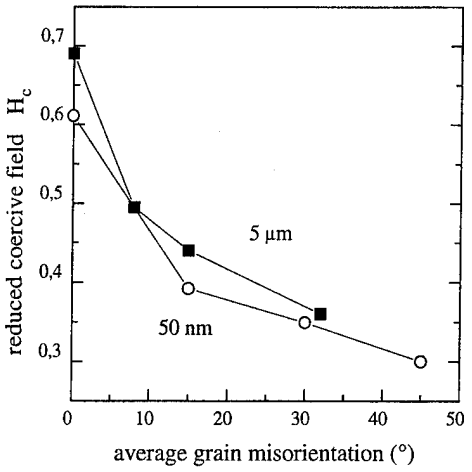


FIG. 4. Finite element calculation of the coercive field normalized by $2K_1$ J_s as a function of the average misorientation angle of $Nd_2Fe_{14}B$ grains with different diameter (64 grains).

IV. ROLE OF MICROSTRUCTURE ON COERCIVITY

Computer simulation of the magnetization reversal process has become an important tool for the investigation of microstructural effects on coercivity.[41–44] The lack of the hysteresis models based on Eqs. (1)–(4) lies in the fact that they describe the behavior of angular and temperature dependence of the coercive field of magnets, but do not allow any predictions of the influence of a certain, real microstructure on the coercivity. Moreover, for a complete understanding of the influence of the microstructure on coercivity it is important to know the effect of microstructural parameters, such as grain size, shape of grains, misalignment of grains, etc., and of different distributions of these parameters on the coercive field. For the two- and three-dimensional, micromagnetic, finite element calculations a realistic grain structure was built by the assumption of different models of grain nucleation and growth.[41,45] Corresponding to electron micrographs (Figs. 1 and 3) a real homogeneous or inhomogeneous distribution of phases and grain diameters was assumed for the calculations. The method of minimizing the total magnetic Gibb's free energy with respect to the magnetic polarization has been described previously.[46,47] The creation of the microstructure starts with a random or preferential seeding for the nucleation of grains, followed by a uniform grain growth in all directions or a preferred growth in one direction, the triangulation of the grains for finite element calculation, and the distribution of hard, soft, and nonmagnetic grains. In our calculations, the total structure of 30–64 grains is divided into 20 000 meshes.

Figure 4 shows the calculated dependence of the coercive field as a function of the average misorientation of the hard magnetic $Nd_2Fe_{14}B$ grains. The deviation of the misalignment from the average value is in the order of ±5°.

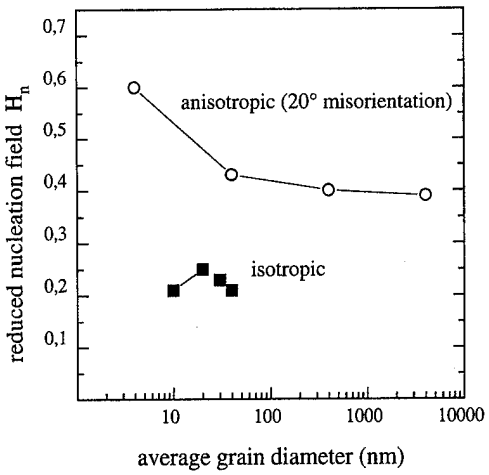


FIG. 5. Numerical calculation of the dependence of the nucleation field on the grain diameter of $Nd_2Fe_{14}B$ magnets.

Similar results are obtained for small (50 nm) and large (5 μm) grained magnets. The upper limit for the coercive field of a real magnet with about 20° misorientation is only 1/3 of the maximum theoretical value of the anisotropy field. From theoretical considerations it is obvious that an improvement of the alignment by changing the processing steps increases both the remanence and coercive field.[48] The dependence of the nucleation field on the average grain diameter is shown in Fig. 5. The nucleation field is defined at the field $H_n(|H_n| \leq |H_c|)$ at which irreversible magnetization reversal processes first occur after saturation. The nucleation field increases with decreasing grain diameter. This observation corresponds to coercive fields obtained after varying sintering temperatures and times (Fig. 2). The calculations predict that in an isotropic mechanically alloyed or melt-spun magnet the maximum coercive field is obtained for a mean grain diameters of 20 nm. The effect of an inhomogeneous distribution of grains with different diameter, simulating the case of the cross section of a melt-spun ribbon with different grain sizes at the wheel and free surface side (Fig. 3) is shown in Fig. 6. The demagnetization curve of the inhomogeneous microstructure shows a lower coercive field compared to the homogeneous one (Fig. 7). The current and previous numerical micromagnetic calculations reveal that the interplay of the magnetostatic and exchange interactions between neighboring grains limit the coercive field considerably. Nanocrystalline, single phase Nd–Fe–B magnets with isotropic alignment show an enhancement of remanence. Soft magnetic grains in composite permanent magnets cause a high polarization, and hard magnetic grains induce a large coercive field provided that the particles are small and strongly exchange coupled.[49–53] Micromagnetic calculations, which were obtained for a composite material of nanocrystalline $SmCo_5$, $Nd_2Fe_{14}B$, and $Sm_2Fe_{17}N_{2.7}$ grains, and α-Fe as soft magnetic phase, show that remanence, coercivity, and coercive squareness sensitively depend on microstructural features, such as the grain size and the volume fraction of the soft magnetic phase.[47,54] Interparticle exchange interactions enhance the remanence by about 60% with respect to noninteracting particles for a mean grain size of 10–20 nm. The

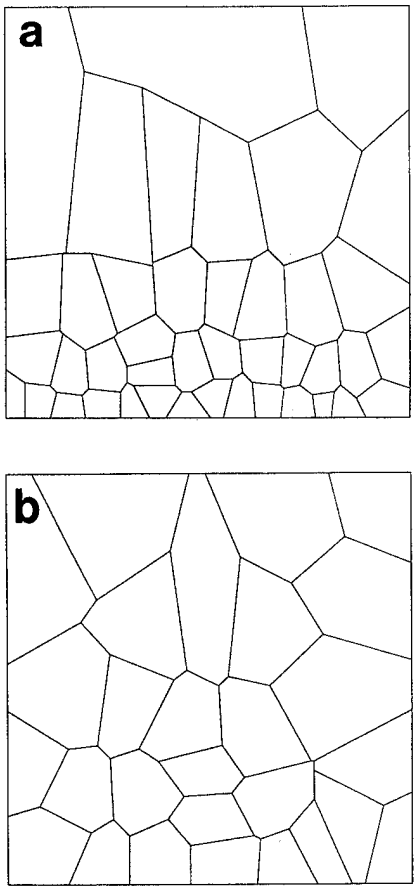


FIG. 6. Computer generated microstructure of $Nd_2Fe_{14}B$ melt spun ribbons with inhomogeneous grain size distribution. The grain sizes range from (a) 17 to 146 nm and from (b) 40 to 114 nm (Ref. 45).

remanence enhancement and energy produce increases with decreasing grain size and increases with increasing α-Fe content. Because of their remarkably high magnetocrystalline anisotropy, novel nitrided intermetallic compounds have a large potential for composite permanent magnets.

V. CONCLUSIONS

Rare earth permanent magnets exhibit a complex, multiphase microstructure, which considerably influences the coercivity and the remanence of the magnets. $Nd_2Fe_{14}B$ based hard magnets can be distinguished by different processing routes, by microstructural differences, or by the kind of elemental substitution or addition. There exist metallurgical reasons for long range dipolar interaction and short range exchange coupling between neighboring hard magnetic grains. The doping of elements changes the phase relation and favors the formation of new phases. Additional secondary nonmagnetic intergranular phases decrease the remanence and interrupt the magnetic interactions between the grains, thereby improving the coercivity of large grained sintered or hot worked magnets. Soft magnetic secondary phases, such as α-Fe, destroy coercivity in large grained magnets. The additional intergranular phases partly replace the Nd-rich phase and considerably improve the corrosion resistance of the magnet. Numerical, micromagnetic calculations have shown that microstructural parameters, such as

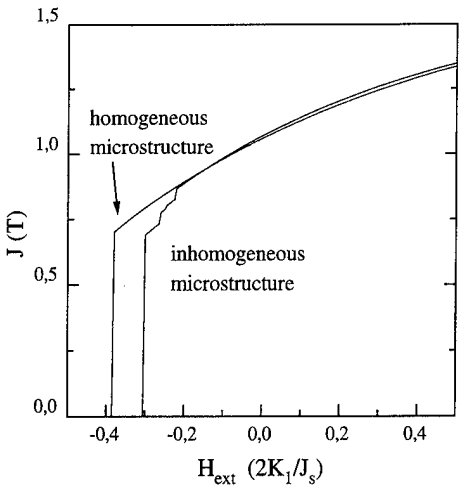


FIG. 7. Calculated demagnetization curves of the inhomogeneous microstructure of Fig. 6(a) and of the homogeneous microstructure of Fig. 6(b).

grain size, misorientation, and distribution of grains and phases control coercive field. The dipolar interactions considerably reduce the coercive field of ideally oriented particles by about 20% with respect to ${}_iH_c$ of an isolated particle, and exchange coupling between misaligned grains drastically reduces the coercive field to about 30%–40% of the ideal nucleation field. Contrary to the situation found in large-grained magnets, the strong coupling between the hard magnetic grains is desired in nanostructured, composite rare earth permanent magnets. The excellent hard magnetic properties of isotropically oriented grains are attributed to intergrain exchange interactions, which enhance the remanence by more than 40% as compared to the remanence of noninteracting particles, if the grain size is in the order of 10–30 nm. The content of soft magnetic phases up to 20% is favorable for increased remanence enhancement and sufficient high coercive fields. The advantage of the nitrided Sm_2Fe_{17}, compared to $Nd_2Fe_{14}B$, is the better temperature stability of the permanent magnetic properties.

ACKNOWLEDGMENTS

This work was supported by the Austrian Science Foundation FWF through Grant No. P10511-NAW and by the BRITE/ERUAM EC Project BREU-150.

[1] H. H. Stadelmaier, J. Mater. Eng. **12**, 185 (1990).
[2] J. Fidler, Proceedings of the Seventh International Symposium on Magnetic Anisotropy & Coercivity in RE-TM Alloys, edited by B. Street, The University of Western Australia, (unpublished), pp. 11.
[3] W. Rodewald and W. Fernengel, IEEE Trans. Magn. **MAG-24**, 1638 (1988).
[4] H. Kronmüller and T. Schrefl, J. Magn. Magn. Mater. **129**, 66 (1994).
[5] J. D. M. Coey, J. Magn. Magn. Mater. **140-144**, 1041 (1995).
[6] J. Fidler and K. G. Knoch, J. Magn. Magn. Mater. **80**, 48 (1989).
[7] J. Fidler, C. Groiss, and M. Tokunaga, IEEE Trans. Magn. **26**, 1948 (1990).
[8] S. Hirosawa, K. Tokuhara, S. Mino, T. Matsui, K. Morii, and Y. Nakayama, Mater. Res. Soc. Symp. Proc. **232**, 275 (1991).
[9] S. Szymura, H. Bala, Yu. M. Rabinovich, V. V. Sergeev, and G. Pawlowska, J. Magn. Magn. Mater. **94**, 113 (1991).
[10] J. Bernardi, J. Fidler, M. Seeger, and H. Kronmüller, IEEE Trans. Magn. **29**, 2773 (1993).
[11] J. Bernardi and J. Fidler, J. Appl. Phys. **76**, 6241 (1994).
[12] J. Fidler, K. G. Knoch, H. Kronmüller, and G. Schneider, J. Mater. Res. **4**, 806 (1989).
[13] S. F. Parker, P. J. Grundy, and J. Fidler, J. Magn. Magn. Mater. **66**, 74 (1987).
[14] J. Fidler and J. Bernardi, J. Appl. Phys. **70**, 6456 (1991).
[15] J. Bernardi, J. Fidler, and F. Födermayr, IEEE Trans. Magn. **28**, 2127 (1992).
[16] W. Rodewald and B. Wall, J. Magn. Magn. Mater. **80**, 57 (1989).
[17] Y. Kotano, J. Shimomura, and M. Shimotomai, J. Appl. Phys. **69**, 6055 (1991).
[18] I. Sakai, A. Tsutai, M. Sahashi, and K. Inomata, IEEE Trans. Magn. **26**, 2616 (1990).
[19] E. Estevez, J. Fidler, F. Feijen, and K. H. J. Buschow (unpublished).
[20] W. Winkler, Diploma thesis, TU Vienna, Austria, 1995.
[21] J. Wecker, Z. Metallkde. **81**, 159 (1990).
[22] L. Schultz, *Supermagnets, Hard Magnetic Materials*, edited by G. J. Long and F. Grandjean (Kluwer Academic, The Netherlands, 1991), p. 573.
[23] I. R. Harris, *Proceedings of the XII International Workshop on Rare Earth Magnets and Their Applications*, edited by B. Street (The University of Western Australia, Perth, Australia, 1992), p. 347.
[24] A. Zaluska, Y. Xu, Z. Altounian, J. O. Ström-Olsen, R. Allem, and G. L. L'Esperance, J. Mater. Res. **6**, 724 (1991).
[25] C. Koestler, R. Ramesh, C. J. Echer, G. Thomas, and J. Wecker, Acta. Mettal. **37**, 1945 (1989).
[26] R. Nakayama, T. Takeshita, M. Itakura, N. Kuwano, and K. Oki, J. Appl. Phys. **76**, 412 (1994).
[27] M. Uehara, H. Tomizawa, S. Hirosawa, T. Tomida, and Y. Maehara, IEEE Trans. Magn. **29**, 2770 (1993).
[28] W. F. Brown, Jr. Rev. Mod. Phys. **17**, 15 (1945).
[29] S. Hirosawa, K. Tokuhara, Y. Matsuura, H. Yamamoto, S. Fujimura, and M. Sagawa, J. Magn. Magn. Mater. **61**, 363 (1986).
[30] R. Grössinger, X. C. Kou, R. Krewenka, H. R. Kirchmayr, and M. Tokunaga, IEEE Trans. Magn. **26**, 1954 (1990).
[31] A. Fukuno, K. Hirose, and T. Yoneyama, J. Appl. Phys. **67**, 4750 (1990).
[32] S. Hock, Ph.D. thesis, University of Stuttgart, Germany, 1988.
[33] D. Givord, P. Tenaud, and T. Viadieu, IEEE Trans. Magn. **MAG-24**, 1921 (1988).
[34] H. Kronmüller, Phys. Status Solidi B **144**, 385 (1987).
[35] H. Kronmüller, K.-D. Durst, and M. Sagawa, J. Magn. Magn. Mater. **74**, 291 (1988).
[36] H. F. Schmidts, G. Martinek, and H. Kronmüller, J. Magn. Magn. Mater. **104–107**, 1119 (1992).
[37] E. C. Stoner and E. P. Wohlfarth, Philos. Trans. R. Soc. London **240**, 599 (1984).
[38] K. Fritz, J. Guth, B. Grieb, E.-T. Henig, and G. Petzow, Z. Metallkd. **83**, 11 (1992).
[39] N. German, *Liquid Phase Sintering* (Plenum, New York, 1985).
[40] T. Schrefl, H. F. Schmidts, J. Fidler, and H. Kronmüller, J. Magn. Magn. Mater. **124**, 251 (1993).
[41] T. Schrefl and J. Fidler, J. Magn. Magn. Mater. **111**, 105 (1992).
[42] Y. Uesaka, Y. Nakatani, and N. Hayashi, J. Magn. Magn. Mater. **123**, 209 (1993).
[43] M. Grönefeld and H. Kronmüller, J. Magn. Magn. Mater. **80**, 223 (1989).
[44] H. F. Schmidts and H. Kronmüller, J. Magn. Magn. Mater. **94**, 220 (1991).
[45] B. Habiger, Diploma thesis, TU Vienna, Austria, 1995.
[46] T. Schrefl, J. Fidler, and H. Kronmüller, J. Magn. Magn. Mater. **138**, 15 (1994).
[47] T. Schrefl, J. Fidler, and H. Kronmüller, Phys. Rev. B **49**, 6100 (1994).
[48] A. S. Kim, F. E. Camp, and H. H. Stadelmaier, J. Appl. Phys. **76**, 6265 (1994).
[49] H. A. Davies, A. Manaf, M. Leonowicz, P. Z. Zhang, S. J. Dobson, and R. A. Buckley, *Nanostructured Materials* (Pergamon, New York, 1993), Vol. 2, p. 197.
[50] R. W. McCallum, A. M. Kadin, G. B. Clemente, and J. E. Keem, J. Appl. Phys. **61**, 3577 (1987).
[51] R. Coohorn, D. B. Mooij, and C. D. E. Waard, J. Magn. Magn. Mater. **80**, 101 (1989).
[52] G. C. Hadjipanayis and W. Gong, J. Appl. Phys. **64**, 5559 (1988).
[53] J. Ding, P. G. McCormick, and R. Street, J. Magn. Magn. Mater. **124**, 1 (1993).
[54] T. Schrefl, R. Fischer, J. Fidler, and H. Kronmüller, J. Appl. Phys. **76**, 7053 (1994).
[55] M. Grönefeld and H. Kronmüller, J. Magn, Magn. Mater. **88**, L267 (1990).

High performance NdFeB magnets (invited)

A. S. Kim and F. E. Camp
Crucible Research Center, A Division of Crucible Materials Corporation, 6003 Campbells Run Road, Pittsburgh, Pennsylvania 15205-1022

Although the production and applications of NdFeB magnets have increased enormously in the last decade because of their outstanding magnetic properties at room temperature, some applications were limited because of poor thermal stability and corrosion resistance. To address these problems, there have been many efforts and much progress. In many instances, the alloy modifications produced an improvement of some characteristics but only at the expense of other characteristics. It is therefore necessary to find a method (or alloy) for improving the thermal stability, coercivity, and corrosion resistance without sacrificing performance. We have found that the proper control of very small amounts of Cu, Co, and O in (Nd, Dy)FeB alloys substantially improves the coercivity, high-temperature capabilities, and corrosion resistance without a reduction of remanence. As a result, a high performance NdFeB magnet with excellent temperature stability and corrosion resistance was developed. © *1996 American Institute of Physics.* [S0021-8979(96)38708-1]

I. INTRODUCTION

NdFeB magnets were discovered in 1983 with outstanding magnetic properties at room temperature.[1,2] In the initial stage of development, the maximum energy product of sintered NdFeB magnets was close to 30 MGOe.[1] Since then, this value has become considerably improved. In 1985, Narashimhan[3] reported 45 MGOe and in 1993 Kaneko *et al.*[4] reported 54.2 MGOe. The maximum energy product commercially available today is about 45 MGOe. Because of this high energy product, applications have increased enormously in the last decade. Current applications include consumer electronics, computer peripherals, acoustics, office automation, and magnetic resonance image. However, some applications were limited because of poor thermal stability (low T_c and high-temperature coefficient of B_r and H_{ci}) and corrosion resistance. To address this problem, there have been many efforts and much progress. In many instances, the alloy modifications produced an improvement of some characteristics but only at a cost of impairing other characteristics.

For example, the addition of cobalt[5,6] to Nd(Dy)FeB increases the Curie temperature and reduces the temperature coefficient of residual magnetization (B_r), but because the coercivity is decreased by its addition, the temperature stability is not actually improved. To overcome cobalt's negative effect and to enhance the coercivity, various elements have been added to NdFeB. Substitution of Nd by heavy rare earth (HRE) elements[6] such as Dy or Tb increases the anisotropy and thus increases the coercivity. However, these HREs decrease the saturation magnetization and thus reduce the remanence and energy products.

The addition of grain boundary modifying elements[7–9] such as Al, Ga, and Sn was also found to effectively increase the coercivity. The effect of the additives in the intergranular phase is to form nonmagnetic compounds that can magnetically isolate the grains of the main phase during sintering. However, most additives have the unfavorable property of decreasing the magnetization of the main phase, and thus reduce the remanence and energy products.

Refractory elements[10–12] such as Nb, Mo, V, W, Cr, Zr, Ti, etc., were also found to enhance the coercivity. Those additives suppress the formation of α-Fe to some extent, inhibit grain growth during sintering and may form borides in the grain boundary and/or within the main $Nd_2Fe_{14}B$ phase. By forming nonmagnetic phases, they largely reduce the remanence and energy products.

Since the addition of alloying elements such as those described above usually accompanies unfavorable decreases of remanence and energy product, the increase in coercivity (or improvement in temperature stability) was traded off at the expense of magnetic performance. Therefore, it is necessary to find a method (or alloy) for improving the thermal stability (T_c and/or H_{ci}) without such reduction.

Because the remanence and energy product are reduced by (1) the reduction of M_s value of the $Nd_2Fe_{14}B$ phase with the addition of heavy rare earth elements such as Dy or Tb, or of grain boundary modifiers such as Al, Ga, or Sn, (2) the formation of a nonmagnetic boride phase such as $(M,Fe)_3B_2$ with refractory elements such as those described above, it is necessary to design a microstructure having only nonmagnetic grain boundaries without such B_r reducing factors for enhancing coercivity. It is also necessary to increase the T_c of the $Nd_2Fe_{14}B$ phase without changing the M_s and H_A values in order to improve the temperature stability. If we design such a magnet based on this assumption, it will have higher T_c and H_{ci} without B_r reduction.

For improving the corrosion resistance, it is necessary to change the Nd-rich grain boundary from a reactive to a nonreactive phase. Adding Co[13,14] to this alloy changes the grain boundary phase from Nd-rich (Nd–Fe) to a Nd_3Co or $Nd(Fe,Co)_2$ phase. These additions improve the corrosion resistance but at the expense of coercivity. Therefore, it is necessary to change this Co-containing ferromagnetic grain boundary phase to a nonmagnetic phase in order to enhance the coercivity as well as the corrosion resistance.

Based on this design, we attempted to develop an alloy which improves not only the thermal stability (T_c and H_{ci}) and corrosion resistance but also the magnetic performance (B_r and BH_{max}).

 0021-8979/96/79(8)/5035/5/$10.00 © 1996 American Institute of Physics

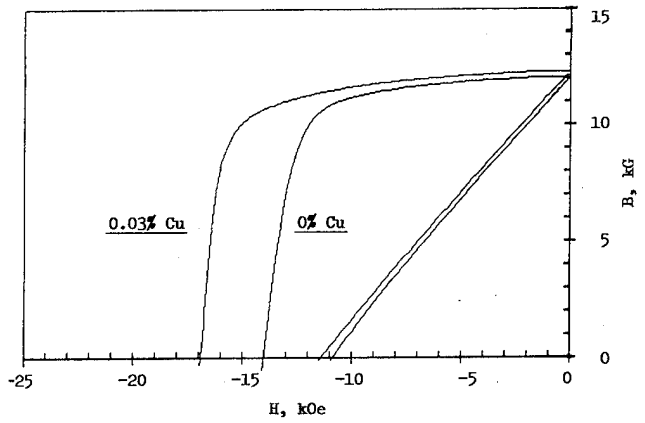


FIG. 1. Demagnetization curves of (Nd,Dy)FeB magnets with and without Cu addition.

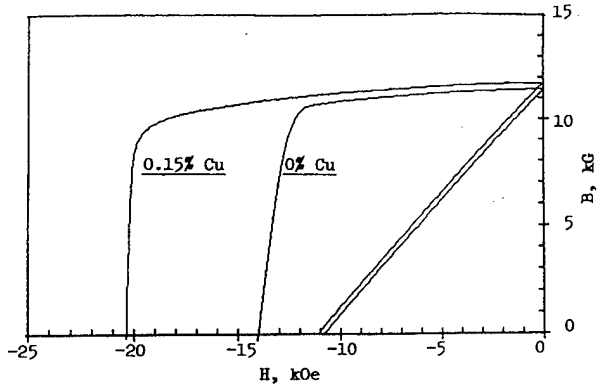


FIG. 3. Demagnetization curves of 30.5Nd–2.5Dy–1.1B–1.2Co–bal Fe magnets with and without Cu addition.

II. EXPERIMENTAL PROCEDURE

The R–(Fe,Co)–B magnets used in this study were prepared by the conventional powder metallurgy process. The material was produced by vacuum introduction melting of a prealloyed charge of high purity elements and master alloys to produce a molten mass of the desired alloy composition. The molten mass was poured into a cooper book mold or atomized into fine powders with argon gas. The case ingot or atomized powder was hydrided at 1–30 atm. The cast ingot was crushed and pulverized into coarse powders. The pulverized powder or atomized powder was then ground into fine powders by jet milling with an inert gas such as Ar or N_2 gas. The average particle size of the milled powders was in the range of 1–5 μm by Fisher subsieve sizer measurements.

The prepared powders were placed in a rubber bag, aligned in a magnetic field, and compacted by cold isostatic pressing. The pressed compacts were then sintered to approximately their theoretical density in a vacuum furnace at between 900 and 1100 °C for 1–4 h. The sintered magnets were further heat treated at about 800–900 °C for 1 h and then aged at between 450 and 700 °C. The magnets were ground and sliced into cylindrical shapes (6 mm thick×15 mm diam).

The magnetic properties of the ground magnets were measured with a hysteresigraph equipped with a high-temperature search coil. The irreversible loss was estimated by measuring the flux difference with a Helmholtz coil before and after exposing the magnet at elevated temperatures (up to 250 °C) for 1 h. The permeance coefficient was one. The oxygen content of the sintered magnet was analyzed by a Leco oxygen analyzer (Model No. TC436AR).

The corrosion rate was determined by measuring the weight loss after exposing the magnets to an autoclave at 110–115 °C and at 10–15 psi steam pressure for 96 h.

III. RESULTS AND DISCUSSION

A. Effect of minor elements such as Cu and Co

It was found that the coercivity of a (Nd,Dy)FeB magnet was substantially increased by very small additions of copper (as low as 0.03% Cu) as shown by the demagnetization curves in Fig. 1. Therefore, we investigated the effect of copper variation on the magnetic properties of (Nd,Dy)FeB and (Nd,Dy)(Fe,Co)B alloys.

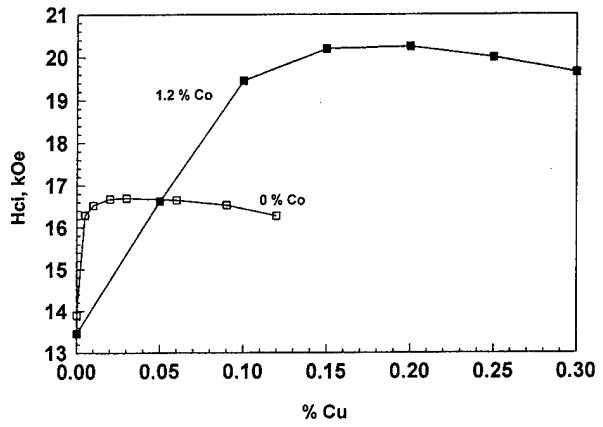


FIG. 2. Effect of Cu content on the coercivity of 30.5Nd–2.5Dy–bal (Fe,Co)–1.1B alloy.

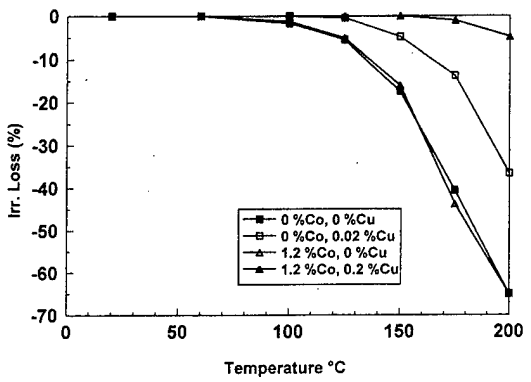


FIG. 4. Irreversible losses of 30.5Nd–2.5Dy–1.1B–bal (Fe,Co,Cu) magnets as a function of Cu and Co content.

TABLE I. Corrosion rates (wt. losses) of 33Nd–1.1B–XCo–YCu–bal Fe magnets after autoclave tests at 110–115 °C for 96 h.

% Co	% Cu	Wt. loss (mg/cm^2)
0	0	203.3
5.0	0	17.5
0	0.15	18.3
1.2	0.15	0.15

Figure 2 shows the H_{ci} variations as a function of copper content in (Nd,Dy)FeB and (Nd,Dy)(Fe,Co)B alloys. The coercivity of the (Nd,Dy)FeB alloy rapidly increases up to 0.005% Cu, reaches a maximum of 0.02% Cu, and then remains the same with further increases in copper content up to 0.12%. Therefore, a very small amount (as low as 0.005%) of copper is sufficient to increase the coercivity of (Nd,Dy)FeB alloys. On the other hand, the coercivity of the (Nd,Dy)(Fe,Co)B alloy continuously rapidly increases up to 0.1% Cu, slowly reaches a maximum at 0.2% Cu, and then starts to slowly decrease with further increases in copper content. The degree of coercivity increase in the (Nd,Dy)(Fe,Co)B alloy is much larger than that in the (Nd,Dy)FeB alloy. The average remanence remains the same up to 0.2% Cu in the (Nd,Dy)(Fe,Co)B alloy. Since Co additions increase the T_c without changing the M_s and H_A values, the combined additions of Co and cu increase not only H_{ci} but also T_c without reducing B_r.

Figure 3 compares demagnetization curves of identical 30.5Nd–2.5Dy–1.2Co–1.1B-bal Fe magnets with 0% and 0.15% copper addition. The coercivity is substantially increased (~6 kOe) with a small addition (0.15%) of copper while the remanence slightly increases. This may be due to grain boundary modification without affecting the matrix phase. Because the very small additions of copper do not sacrifice either the remanence or Curie temperature, they can overcome the negative effect of cobalt in NdFeB magnets and further enhance the coercivity.

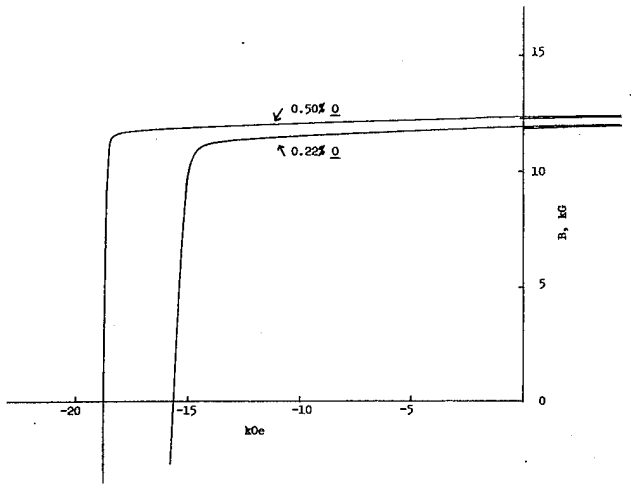


FIG. 6. Demagnetization curves of 30.5Nd–2.5Dy–1.2Co–1.1B–63.4Fe magnets with and without oxygen doping.

Because of the dramatic increase in coercivity by the combined addition of cobalt and copper in (Nd,Dy)FeB alloys, the temperature stability is also substantially improved. As shown in Fig. 4, the irreversible loss of a 30.5Nd–2.5Dy–1.1B–bal Fe magnet is not changed by the addition of cobalt, is reduced by the very small addition of copper (0.02%), and is substantially reduced by the combined addition of cobalt and copper. The magnet operating temperature has increased by about 25 °C for the single addition of copper and by about 75 °C for the combined addition copper and cobalt. Therefore, the temperature stability of (Nd,Dy)FeB can be significantly improved without B_r reduction by small additions of Co and Cu.

The corrosion resistance of a (Nd,Dy)FeB magnet is also improved by the combined addition of Co and Cu. As shown in Table I, the weight loss from autoclave testing is substan-

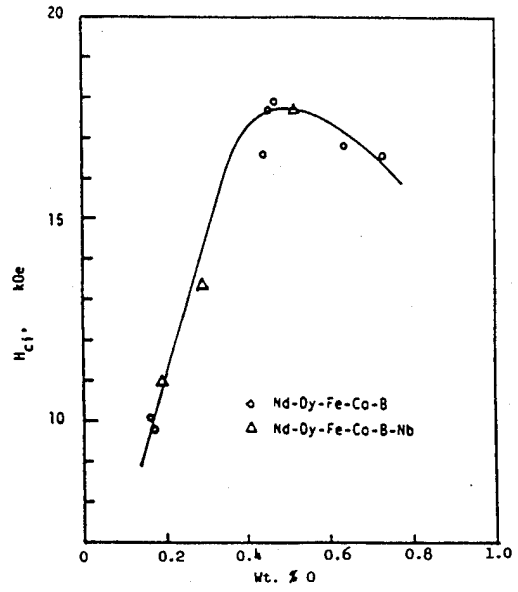


FIG. 5. Variation of H_{ci}, for 29Nd–4Dy–bal Fe–5Co–1.15B–M alloys, as a function of oxygen content.

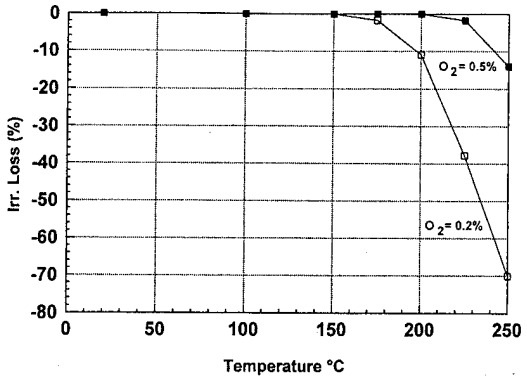


FIG. 7. Comparison of irreversible losses (PC=1.0) of 28Nd–6Dy–1.1B–2.5Co–0.15Cu–bal Fe magnets with and without oxygen doping.

TABLE II. Magnetic properties of 28Nd–6Dy–1.1B–2.5Co–0.15Cu–bal Fe alloy with and without oxygen doping at 20 and 150 °C.

	0.2% O_2	0.5% O_2
B_r, kG at 20 °C	10.45	10.65
B_r, kG at 150 °C	9.1	9.3
α, %/°C	−0.099	−0.098
H_{ci}, kOe at 20 °C	24.1	27.2
H_{ci}, kOe at 150 °C	8.1	11.5
β, %/°C	−0.511	−0.444

tially (about one magnitude) reduced by the addition of either Cu or Co. When Cu and Co are added together, the weight loss approaches zero. This indicates that the corrosion resistance is also significantly better by the combined addition of Cu and Co than from any single addition. Therefore, improved corrosion resistance of NdFeB magnets can be obtained without sacrificing magnetic performance by the very small additions of cobalt and copper.

B. Effect of oxygen

Since oxygen is inevitably introduced into the sintered NdFeB magnets during the process, it is necessary to systematically determine the effect of oxygen on the magnetic properties and to define the proper content range. We examined the magnetic properties of (Nd,Dy)(Fe,Co)B alloys containing various levels of oxygen.

As shown in Fig. 5, the coercivity of a cobalt containing (Nd,Dy)(Fe,Co)B magnet initially increases rapidly with increasing oxygen content up to about 0.4% and then starts to decrease with further increases in oxygen content. The optimum oxygen content for the peak coercivity varies depending on the total rare earth content and other minor phases. We made magnets from the same (Nd,Dy)(Fe,Co)B alloy with and without oxygen doping, and compared their magnetic properties. As shown in Fig. 6, both B_r and H_{ci} are increased by oxygen doping. The coercivity improvement will be discussed under microstructural analysis.

Since the coercivity of a (Nd,Dy)(Fe,Co)B alloy is improved by proper oxygen doping, we compared the irreversible losses of the same 28Nd–6Dy–1.1B–2.5Co–0.15Cu–bal Fe with and without oxygen doping. As shown in Fig. 7, the irreversible loss is greatly improved by oxygen doping, where the operating temperature of the higher oxygen magnet is increased by as much as 50 °C.

We also measured the magnetic properties of both magnets at 20 and 150 °C and compared the temperature coefficients as shown in Table II. With oxygen doping the remanences are slightly increased at both temperature levels. The coercivities at 20 and 150 °C are substantially increased with oxygen doping. The temperature coefficient of coercivity has improved from −0.51%/°C to −0.44%/°C. Since the temperature coefficient of the same alloy without Co and Cu is about −0.65%/°C, the temperature coefficient of H_{ci} was substantially improved by the combined addition of Co and Cu, and further improved by oxygen doping.

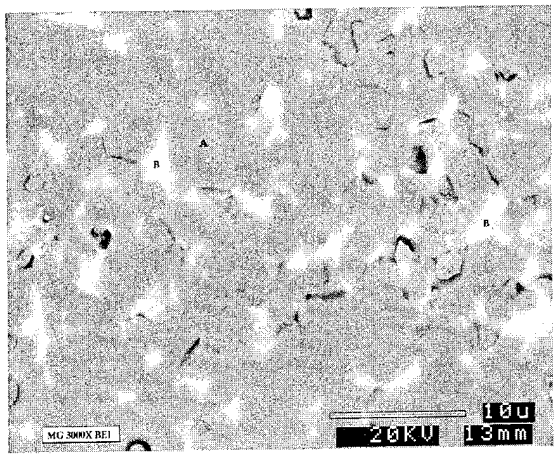


FIG. 8. SEM micrograph of 28Nd–6Dy–1.1B–2.5Co–0.15Cu–bal Fe magnet.

Thus, the temperature stability and corrosion resistance of (Nd,Dy)(Fe,Co)B magnets can be substantially improved, without a reduction of remanence, by the combined addition of cobalt and copper. A proper oxygen doping of this alloy system further improves the temperature stability without B_r reduction (or with improved remanence).

C. Microstructural study

A magnet made from a (Nd,Dy)(Fe,Co,Cu)B alloy was examined in a SEM with EDS. As shown in Fig. 8, the microstructure reveals a grey (matrix) phase and a white (Nd-rich) grain boundary phase without discernable other (boride) phases. The EDS spectra on the white phase identifies it as mainly $(Nd,Dy)_{15}Co_4Cu$. These results indicate that the addition of small amounts of Cu and Co to (Nd,Dy)FeB alloys modifies the grain boundary phase from Nd-rich (Nd–Fe) to $(Nd,Dy)_{15}Co_4Cu$ without forming any nonmagnetic grains or changing the matrix phase. This fulfills the requirements of microstructural design suggested in the Introduction. The $(Nd,Dy)_{15}Co_4Cu$ phase, which is being further investigated, is assumed to be nonmagnetic because the coercivity is dramatically enhanced.

The effect of oxygen doping of the (Nd,Dy)(Fe,Co)B magnet on the microstructure was examined in a TEM. The TEM micrographs of magnets with and without oxygen doping exhibit an equiaxed grain structure as shown in Fig. 9. The grains in the magnet without oxygen doping appear to be uniformly decorated with a 50 nm thick intergranular phase. There are numerous defects. In the magnet with oxygen doping, the grain size becomes finer, and the intergranular phase appears to be largely confined to the triple junctions. The grain boundaries in this sample are very smooth without apparent defects, leading to better coercivity. As reported by Choi *et al.*,[14] the reduction of Laves phase $Nd(Fe,Co)_2$, in the grain boundary from oxygen doping may also contribute to the increase in coercivity, because Co additions to the (Nd,Dy)FeB alloy usually forms the magnetically soft Laves phase which reduces the coercivity.



FIG. 9. TEM micrograph of 30.5Nd–2.5Dy–1.1B–1.2Co–0.15Cu–bal Fe magnets with (b) and without (a) oxygen doping.

IV. CONCLUSION

The very small addition of copper (as low as 50 ppm) to (Nd,Dy)FeB alloys has substantially increased the coercivity without reducing B_r. The combined small addition of copper and cobalt to these alloys dramatically increased the coercivity without B_r reduction. This may be due to the formation of nonmagnetic grain boundary phases without forming nonmagnetic grains or without decreasing saturation magnetization. The proper amount of oxygen doping in these (Co and Cu containing) alloys further increases the coercivity with a slight increase in remanence. This may be due to grain growth inhibition, grain boundary cleaning, and/or grain orientation enhancement. Such additions also substantially reduce both temperature coefficient of coercivity and the irreversible temperature loss. Because of the increased coercivity and reduced temperature coefficient of coercivity, the temperature stability has improved enormously without a sacrifice of (or with improved) magnetic performance. The combined small additions of copper, cobalt, and oxygen have also improved the corrosion resistance. Therefore, a high performance, temperature stable, and corrosion resistant magnet is developed by the combined small addition of Co, Cu, and O to (Nd,Dy)FeB alloys.

ACKNOWLEDGMENTS

The authors wish to acknowledge R. A. Hohowski, F. S. Snyder, and T. W. Sloan for their technical assistance. They also wish to thank Dr. W. B. Eisen, R. A. Zoglmann, and S. Gaiffi for their enthusiastic support and encouragement. This work was supported by the Crucible Magnetics Division.

[1] M. Sagawa, S. Fujimura, N. Togawa, H. Yamamoto, and Y. Matsuura, J. Appl. Phys. **55**, 2083 (1984).
[2] J. J. Croat, J. F. Herbst, R. W. Lee, and F. E. Pinkerton, J. Appl. Phys. **55**, 2078 (1984).
[3] K. S. V. L. Narasimhan, J. Appl. Phys. **57**, 4081 (1985).
[4] Y. Kaneko and N. Ishigaki, J. Mater. Eng. Perf. **3**, 228 (1994).
[5] B. Ma, Mater. Res. Soc. Symp. Proc. **96**, 43 (1987).
[6] M. Sagawa, S. Fujimura, H. Yamamoto, Y. Matsuura, and K. Hiraga, IEEE Trans. Magn. **20**, 1584 (1984).
[7] A. Kim, J. Appl. Phys. **63**, 3975 (1988).
[8] M. Tokunaga, H. Kogure, M. Endoh, and H. Harada, IEEE Trans Magn. **23**, 2287 (1987).
[9] P. Schrey and M. Velicescu, J. Magn. Magn. Mater. **101**, 417 (1991).
[10] S. Hirosawa, H. Tomizawa, S. Mino, and A. Hamamura, IEEE Trans. Magn. **26**, 1960 (1990).
[11] M. Sagawa, P. Tenaud, F. Vial, and K. Hiraga, IEEE Trans. Magn. **26**, 1957 (1990).
[12] A. S. Kim and F. E. Camp, IEEE Trans. Magn. **28**, 2151 (1992).
[13] F. E. Camp and A. S. Kim, J. Appl. Phys. **70**, 6348 (1991).
[14] S. D. Choi, W. Y. Lee, and C. J. Yang, J. Korean Inst. Met. **28**, 531 (1990).

Anisotropic Nd–Fe–B bonded magnets made from HDDR powders (invited)

T. Takeshita and K. Morimoto
Materials Research Laboratories, Central Research Institute, Mitsubishi Materials Corporation, 1-297, Kitabukuro-cho, Omiya, Saitama 330, Japan

Anisotropic Nd–Fe–B magnet powders can be produced by the hydrogenation-decomposition-desorption-recombination (HDDR) process from Nd–Fe–B–Co–M (M = Ga, Zr, Nb, Hf, and Ta) alloys. The present status of those HDDR powders and the bonded magnets made from them are reviewed with regards to the powder particle size dependence of their magnetic properties, their magnetic thermal stability, and their magnetization behavior. The results of a mechanistic study on the recombination step are also presented. The magnetic properties of the anisotropic HDDR powder depend relatively little on the powder particle size. Bonded magnets with a density of ~6.20 g/cm^3 and a BH_{max} of 18.5–20.5 MGOe can be produced from anisotropic HDDR powders with particle sizes of below 300 μm diam. The temperature coefficient of the intrinsic coercive force $_iH_c$, of the bonded magnet is −0.55%/°C in the temperature range from 25 to 100 °C. The magnetization force needed for full magnetization of the bonded magnet is about twice the coercive force of the magnet, indicating that the magnetization mechanism is different from that of the rapidly solidified isotropic Nd–Fe–B magnet. In the early stage of the recombination step of the HDDR process (1 min desorption), three phases are produced, i.e., α-(Fe,Co), spherical NdH_2 and rimlike $Nd_2(Fe,Co)_{14}B$ surrounding the NdH_2 particle. Further desorption makes the $Nd_2(Fe,Co)_{14}B$ phase grow. © *1996 American Institute of Physics.* [S0021-8979(96)38808-0]

I. INTRODUCTION

Resin-bonded Nd–Fe–B magnets made from rapidly solidified magnet powders have been increasingly used in many applications. The maximum energy products (BH_{max}) of these magnets are 12 MGOe at the most, since they are magnetically isotropic. The development of anisotropic bonded magnets possessing a larger maximum energy product than the isotropic magnets are, therefore, desired in the Nd–Fe–B magnet system.

The hydrogenation-decomposition-desorption-recombination (HDDR) process has been shown to induce a large coercivity in the Nd–Fe–B magnet system.[1–3] This process utilizes the phase transformation of the intermetallic $Nd_2Fe_{14}B$ compound with hydrogen. $Nd_2Fe_{14}B$ decomposes into NdH_2, α-Fe and Fe_2B in hydrogen atmosphere at elevated temperatures, and then this decomposed mixture recombines to form the original $Nd_2Fe_{14}B$ compound in the subsequent hydrogen desorption step.[3] By this process, original large crystalline grains of $Nd_2Fe_{14}B$ in the cast ingot are transformed into fine crystalline grains of about 0.3 μm diam, which is close to a size of a single magnetic domain of $Nd_2Fe_{14}B$.[3] This fine microstructure is thought to be related to high coercivities of the HDDR magnet powders. The application of the HDDR process produces almost isotropic magnet powders in ternary Nd–Fe–B alloys. On the other hand, the substitution of Fe with Co and the addition of elements such as Ga, Zr, Nb, Hf, and Ta induces magnetic anisotropy in HDDR magnet powders.[4–6] The appearance of magnetic anisotropy in the HDDR powders is due to the correlated c-axes orientation of the fine $Nd_2(Fe,Co)_{14}B$ crystalline grains in each powder particle.[6] The anisotropic HDDR magnet powder is now commercially available, and bonded magnets with maximum energy products larger than 15 MGOe are now available.[7]

In this report, the current status of anisotropic HDDR magnet powders and the bonded magnets made from them are presented. Also included are some results of the microstructural study on the Nd–Fe–Co–B–Zr alloy system in the desorption step of the HDDR process in order to understand the origin of the preferred alignment of the crystalline c-axes of the recombined $Nd_2(Fe,Co)_{14}B$ crystalline grains.

II. EXPERIMENT

The alloy ingots of various compositions close to the $Nd_2(Fe,Co)_{14}B$ stoichiometry, i.e., $Nd_{12-13}Fe_{bal}B_{5-8}Co_{10-20}M_{0.1-1}$ (M = Ga,Zr), were prepared by arc-melting constituent elements in an Ar gas atmosphere. The alloy ingots were subsequently homogenized at 1120 °C for 20 h in an argon atmosphere, and then were crushed into blocks of sizes less than 20 mm×20 mm×20 mm. Those blocks were subjected to HDDR processing with the following condition: first heated up in atmospheric hydrogen gas from room temperature to 830 °C, kept at this temperature for 10 min, evacuated for about 40 min reaching a high vacuum (10^{-5} Torr), and then quenched by Ar gas to room temperature. After this HDDR processing, the alloy blocks were crushed into powders of less than 420 μm diam for the bonded magnet production. Anisotropic bonded magnets were prepared in the following manner: The magnet powders were mixed with a resin binder, and the powders were placed in a mold and were aligned with a magnetic field of 24 kOe and pressed into a green compact, and finally the green compact was hardened at 100–170 °C for 1 h. The densities of bonded magnets so prepared are from 6.0 to 6.2 g/cm^3. The magnetic properties of the powders and those of the bonded magnets were measured by a vibrating sample magnetometer (VSM) and a B–H tracer. The VSM data were corrected for the demagnetizing fields. The powder specimens for the mea-

 0021-8979/96/79(8)/5040/5/$10.00 © 1996 American Institute of Physics

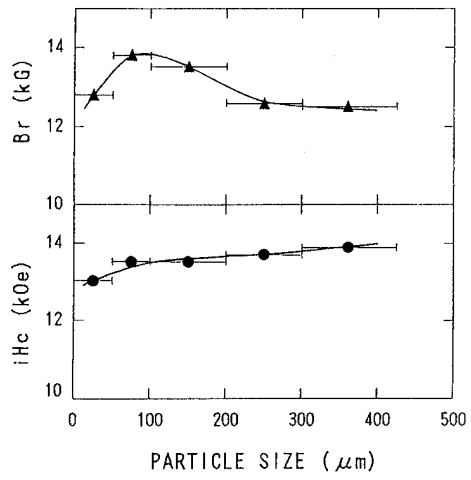


FIG. 1. Particle size dependence of B_r and ${}_iH_c$ of the anisotropic HDDR magnet powder.

surements were aligned with a magnetic field of 15 kOe and then consolidated into bricks with paraffin wax. Unless otherwise stated, the bonded magnets were magnetized in a pulsed magnetic field of 70 kOe before the measurement. In the long-term aging tests at elevated temperatures, the samples were periodically cooled to room temperature and their open-circuit remanent flux was measured with a digital fluxmeter. The microstructures of the sample powders were examined with a transmission electron microscope (TEM). The TEM specimens were prepared by molding the powders in resin, cutting it into a plate with a thickness less than 0.1 mm, and thinning it by the ion milling technique.

III. RESULTS AND DISCUSSION

A. Powder particle size dependence of magnetic properties

Figure 1 shows the powder particle size dependence of the residual induction, B_r, and intrinsic coercive force, ${}_iH_c$, of the anisotropic HDDR powder of Nd–Fe–B–Co–Zr–Ga system. The largest value of B_r is obtained for magnet powders with diameters of 50–200 μm. These particle sizes are roughly the same as those of the original crystalline grain sizes of $Nd_2(Fe,Co)_{14}B$ phase in the starting alloy ingots. This suggests that the crystalline c-axis orientation of the original $Nd_2(Fe,Co)_{14}B$ grains of the alloy ingots may be maintained during the HDDR processing. The coercive force ${}_iH_c$ is almost constant and about 14 kOe for magnet powders with diameters of 50–420 μm. In magnet powders with diameters of less than 50 μm, the B_r and ${}_iH_c$ are smaller than those of larger particles by 1 kG and 1 kOe, respectively. This is considered to be due to the deterioration of these properties by the surface oxidation of the powder particle and also may be due to the stress introduced during the crushing operation in the powder production stage. This particle size dependence of magnetic properties is, however, relatively small, and magnet powder with a wide particle size distribution can be used for bonded magnet production. It is well known that a wide distribution of particle sizes helps to produce a dense green compact, and this is favorable for the production of bonded magnets of high density and consequently with large BH_{max}.

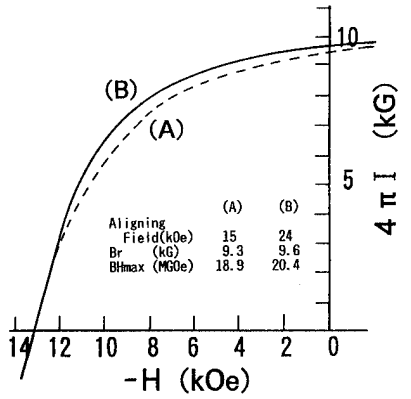


FIG. 2. Demagnetization curves of the anisotropic bonded magnets made by using aligning magnetic fields of (A) 15 kOe and (B) 24 kOe, respectively.

Figure 2 shows the demagnetization curves of bonded magnets made from the anisotropic HDDR powder of Fig. 1 with particle diameters less than 300 μm. Raising the density of green compacts to 6.2 g/cm^3 by applying a compacting pressure of 6 ton/cm^2, bonded magnets with BH_{max} of 18.5–20.5 MGOe were obtained. The value of BH_{max} depends mainly on the aligning field strength.

B. Temperature dependence of magnetic properties

Figure 3 shows temperature dependent demagnetization curves of the bonded magnet made from the anisotropic HDDR magnet powders in Fig. 1. The magnetic properties of the magnet at room temperature were: B_r = 8.5 kG, ${}_iH_c$=12.5 kOe, and BH_{max} = 16.0 MGOe. The temperature coefficients of B_r and ${}_iH_c$ in the temperature range of 25–100 °C were −0.10 and −0.55%/°C, respectively. The absolute value of the latter parameter is larger than that of an isotropic Nd–Fe–B bonded magnet made from the rapidly

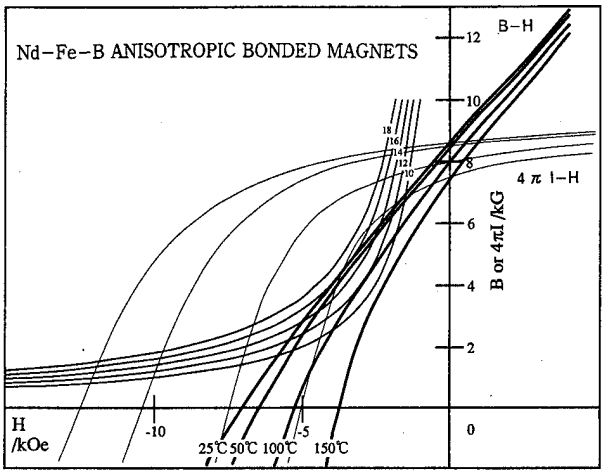


FIG. 3. Temperature dependence of demagnetization curve of the anisotropic bonded magnet.

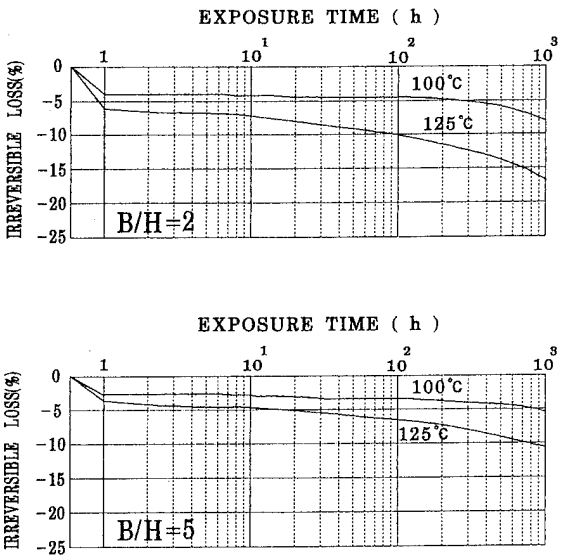


FIG. 4. Change in open-circuit remanent flux of the anisotropic bonded magnets during long-term aging tests.

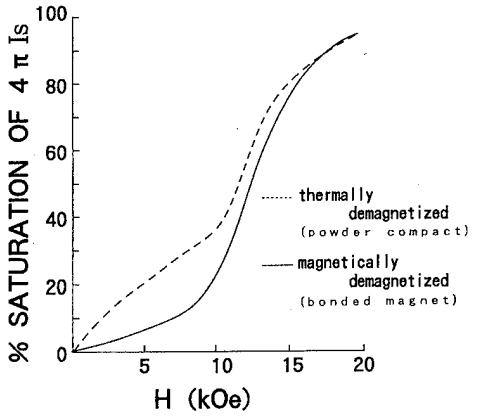


FIG. 5. Magnetization curves of the specimens made from the anisotropic HDDR magnet powder.

solidified magnet powder (−0.45%/°C), but still lower than that of sintered Nd–Fe–B magnets (−0.65%/°C). These differences may be related to their different microstructures. The rapidly solidified powder is made of very small $Nd_2Fe_{14}B$ crystalline grains of about 50 nm diam and an amorphous boundary phase.[8] The sintered magnet consists of $Nd_2Fe_{14}B$ crystalline grains of 10–50 μm diam and a nonmagnetic Nd-rich boundary phase.[9] In contrast to those microstructures, the HDDR magnet powder contains $Nd_2(Fe,Co)_{14}B$ crystalline grains of about 0.3 μm diam, which is comparable to that of the single magnetic domain of $Nd_2Fe_{14}B$, and essentially does not contain a boundary phase(s).[6] This unique microstructure of the HDDR powder may affect its temperature coefficient of ${}_iH_c$ as well as its coercivity mechanism.

Figure 4 shows the change in the open-circuit remanent flux of the HDDR bonded magnets during long-term aging tests. The magnetic properties of the samples used in this test are the same as those shown in Fig. 3. Before the test, the magnets were coated with epoxy resin for protecting the samples against oxidation. After exposure to the air at 100 °C for 1000 h, the irreversible magnetic flux losses of the magnets with the permeance coefficients (B/H) of 2 and 5 are 8% and 5%, respectively. The flux losses of these samples were increased to 17% and 11% as the environmental temperature was raised to 125 °C. Although the irreversible flux loss of the bonded magnets partly depends on the magnet production conditions such as the types of resin binders, the surface treatment of the powders and others, these aging test results suggest that the upper limit of operating temperatures for bonded magnets based on the anisotropic HDDR magnet powders is around 100 °C.

C. Magnetization behavior of the HDDR magnet powder

Figure 5 shows the magnetization curve of an anisotropic HDDR powder compact thermally demagnetized and that of an anisotropic bonded magnet demagnetized by a dc magnetic field antiparallel to the aligning field. The powder compact specimen was prepared by aligning the magnet powder without any resin binder, pressing the powder into a green compact and heating the compact to 550 °C for the thermal demagnetization. The specimen demagnetized by a dc field shows a smooth "S" shape magnetization curve with low permeabilities. On the other hand, the specimen thermally demagnetized exhibits a magnetization curve which slowly rises at low fields, and shows an inflection point around 10 kOe and then steeply rises at higher fields. These magnetization behaviors suggest that the magnetic domain structure of the anisotropic HDDR powder in the thermally demagnetized state is different from that of the one in the magnetically demagnetized state, and that the magnetic domain wall motion determines the magnetization behavior of this magnet powder. This magnetization behavior is quite different from that of rapidly solidified magnets or that of sintered magnets, and suggests that the coercivity mechanism would also be unique, i.e., neither the pinning type of rapidly solidified powder nor the nucleation type of sintered magnet.

Figure 6 shows the magnetizing field dependence of magnetic properties of the anisotropic bonded magnet with a high ${}_iH_c$ of 13 kOe (type H) which has been shown in the previous figures, and those of the magnet with a low ${}_iH_c$ of 10 kOe (type L). The type-L magnet is made from the anisotropic HDDR powder, the additives content of which is lower than that of the type-H magnet powder. The magnetic remanence (B_r) and the maximum energy product (BH_{max}) of both types of magnets are typically 9.0 kG and 17.5 MGOe, respectively, although the strength of their coercivities are different. The magnetic field strength required for full magnetization is about twice the intrinsic coercive force for both types of magnet, i.e., 30 kOe for the type-H magnet and 20 kOe for the type-L magnet. Although the reduction of the coercive force may be thought to restrict the range of operating temperature, the type-L magnet is a good candidate for many applications where the magnetization is difficult

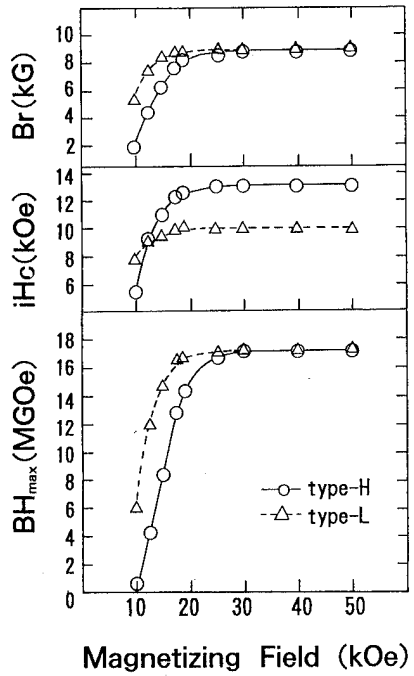


FIG. 6. Magnetizing field dependence of magnetic properties of the anisotropic bonded magnets with ${}_iH_c$'s of 13 kOe (type H) and 10 kOe (type L), respectively.

because of the physical arrangement, typically radially oriented ring magnets with multiple poles.

D. Microstructural change in the desorption step

The microstructures of both the isotropic Nd–Fe–B and the anisotropic Nd–Fe–B–Co–M (M = Zr or Ga) HDDR powders are the same with regards to the size and morphology of their crystalline grains, and their boundary region structures. The only difference is the crystallographic orientations of the fine $Nd_2Fe_{14}B$ and $Nd_2(Fe,Co)_{14}B$ crystalline grains. In order to understand the appearance of a preferred crystallographic orientation of the fine grains in the anisotropic magnet powder, the microstructural change of the Nd–Fe–Co–B–Zr alloy in the desorption step of the HDDR process was studied with TEM. Figure 7 shows TEM bright field images of the $Nd_{12.6}Fe_{bal.}Co_{11.6}B_{6.0}Zr_{0.1}$ alloy taken during the desorption operation. The condition of the desorption was as follows: The alloy was first heated up in atmospheric hydrogen gas to 830 °C and hydrogenated at 830 °C for 10 min in 1 atm H_2, and desorbed at this temperature for each period of time (1, 10, and 20 min), and subsequently quenched by Ar gas. The microstructure of the 1 min desorption consists of three phases: (1) spherical particles of about 20 nm diam (A,B,C,and J), (2) matrix phase (E,H,and I), and (3) rimlike phase of thickness of 30–50 nm (D,F, and G) which surround the spherical phase. The electron diffraction pattern indicates that the type (1) is NdH_2 of the fcc structure, and the type (2) is α-(Fe,Co) of the bcc structure. The type (3) can be attributed to $Nd_2(Fe,Co)_{14}B$ or a related phase based on the energy dispersive x-ray analysis as well. After a 10 min desorption, the rimlike phase grows to 50–100 nm in thickness and can be clearly identified as

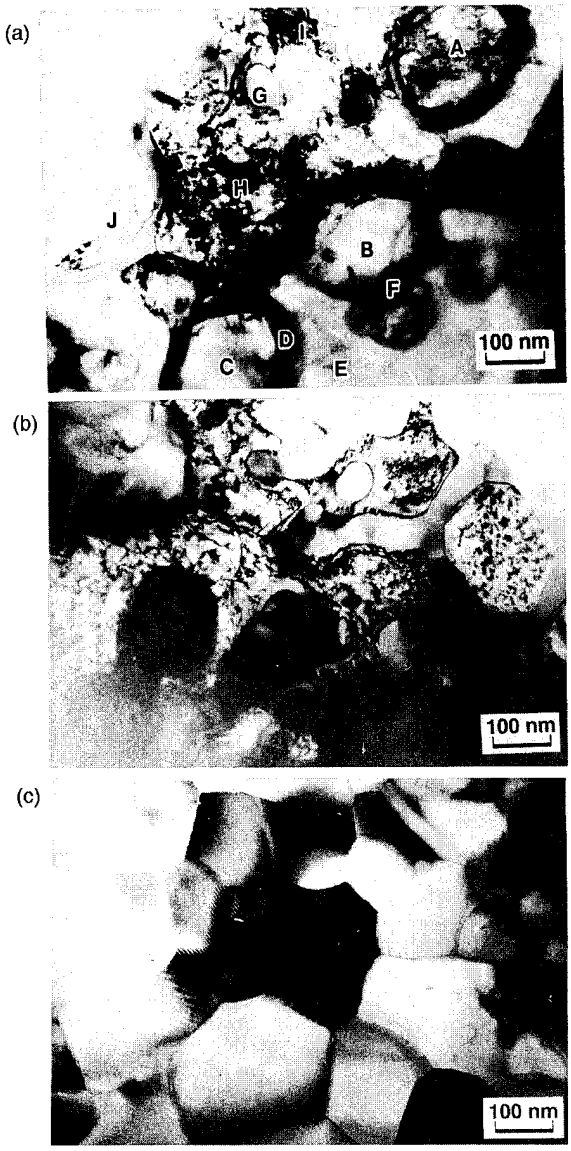


FIG. 7. TEM bright field images of the $Nd_{12.6}Fe_{bal.}Co_{11.6}B_{6.0}Zr_{0.1}$ alloy hydrogenated at 830 °C for 10 min at 1 atm H_2, desorbed for each period of time and subsequently quenched by Ar gas: (a) after 1 min, (b) after 10 min, and (c) after 20 min.

$Nd_2(Fe,Co)_{14}B$ by the electron diffraction pattern. After a 20 min desorption, the recombination of the decomposed phases is completed, and the product is made of only fine grains of $Nd_2(Fe,Co)_{14}B$ of about 300 nm diam. These observations show that in the desorption step the recombination reaction proceeds as the rimlike phase grows, and the rimlike $Nd_2(Fe,Co)_{14}B$ phase may carry the direction of the c axis of the original large crystalline grain to the recombined fine crystalline grains. Uehara and co-workers reported that the fine undecomposed $Nd_2(Fe,Co)_{14}B$ particles exist in the hydrogenated Nd–Fe–Co–B–Ga and Nd–Fe–Co–B–Ga–Zr alloys, and they proposed that these undecomposed particles should act as nuclei for the growth or recrystallization of the $Nd_2(Fe,Co)_{14}B$ phase with a preferred crystallographic orientation during the desorption step.[10,11] The TEM results of this study, however, cannot rule out the possibility of the formation of the rimlike $Nd_2(Fe,Co)_{14}B$ phase by a rapid

recombination reaction after the complete decomposition, and it is still not clear whether the rimlike $Nd_2(Fe,Co)_{14}B$ phase originates from the original crystalline grain without any transformation or it is formed by the recombination of the decomposed products after the complete decomposition. In order to clarify this question, it is necessary to compare the ternary Nd–Fe–B system and the Nd–Fe–Co–B–Zr–(Ga) system(s) more thoroughly regarding their microstructural changes in the HDDR process and crystallographic relationships of the decomposed products.

IV. CONCLUSION

The magnetic properties of anisotropic Nd–Fe–B bonded magnets made from HDDR powders are reported. The results of recent microstructural studies on the appearance of the crystallographic orientation during the HDDR process are also described. The anisotropic bonded magnets are now commercially available and are used in several applications such as the automatic-iris mechanism of VTR cameras and other actuators. In order to extend the application areas of this magnet, research and development on further improvements of magnetic thermal stabilities and magnetization characteristics of the HDDR magnet powders are being conducted. Besides this, basic studies for clarifying the mechanism of the induction of high coercivities and the preferred crystallographic orientation in the HDDR powders are also in progress.

ACKNOWLEDGMENTS

We would like to express appreciation to Professor K. Oki, Professor N. Kuwano, and Dr. M. Itakura of Department of Materials Science and Technology, Graduate School of Engineering Sciences, Kyushu University, for their TEM observations and valuable discussions.

[1] T. Takeshita and R. Nakayama, Proceedings of the 10th International Workshop on Rare-Earth Magnets and their Applications, Kyoto, Japan, 1989, Vol. 1, p. 551.
[2] R. Nakayama, T. Takeshita, M. Itakura, N. Kuwano, and K. Oki, J. Appl. Phys. **70**, 3770 (1991).
[3] R. Nakayama and T. Takeshita, J. Appl. Phys. **74**, 2719 (1993).
[4] T. Takeshita and R. Nakayama, Proceedings of the 11th International Workshop on Rare-Earth Magnets and their Applications, Pittsburgh, PA, 1990, Vol. 1, p. 49.
[5] R. Nakayama and T. Takeshita, J. Alloys Compounds **193**, 259 (1993).
[6] R. Nakayama, T. Takeshita, M. Itakura, N. Kuwano, and K. Oki, J. Appl. Phys. **76**, 412 (1994).
[7] J. J. Croat and M. E. Hughes, The 9th International Conference on Nd-Fe-B Magnets-95, San Diego, CA, February 26–28, 1995.
[8] R. K. Mishra, J. Magn. Magn. Mater. **54–57**, 450 (1986).
[9] M. Sagawa, S. Fujimura, H. Yamamoto, Y. Matsuura, and K. Hiraga, IEEE Trans. Magn. **MAG-20**, 1584 (1984).
[10] M. Uehara, H. Tomizawa, H. Hirosawa, T. Tomida, and Y. Maehara, IEEE Trans. Magn. **MAG-29**, 2770 (1993).
[11] M. Uehara, P. Choi, T. Tomida, H. Tomizawa, H. Hirosawa, and Y. Maehara, in Digests of the Intermag Conference, San Antonio (April 18–21, 1995, p. BD-02).

Sm_2Fe_{17} interstitial magnets (invited)

K.-H. Müller, Lei Cao,[a] N. M. Dempsey,[b] and P. A. P. Wendhausen[c]
Institut für Festkörper- und Werkstofforschung Dresden e.V., 01171 Dresden, Germany

Various processing routes for making permanent magnets based on interstitially modified Sm_2Fe_{17} have been recently developed. Zn bonding of coarse grained $Sm_2Fe_{17}N_3$ gives coercivities $\mu_0 J H_c$ as high as 2.2 T. Effective methods to prepare highly coercive $Sm_2Fe_{17}N_3$ powders for polymer bonding are mechanical alloying and rapid quenching. With the very simple method of additional milling of coarse grained nitrided powders we achieved $\mu_0 J H_c \approx 1.5$ T. A coercivity up to 3.5 T has been achieved by a modified HDDR procedure, reducing the particle size of the starting material by milling prior to the hydrogenation–disproportionation–desorption–recombination (HDDR) treatment. This is attributed to a better control of two critical parameters, namely grain size and the amount of unrecombined α-Fe accompanying the intermediate $TbCu_7$ structure-type phase. Resin bonded HDDR-$Sm_2Fe_{17}N_3$ magnets show an unexpected high initial susceptibility. This may be due to a strong magnetic interaction of the grains. To develop coercivity in $Sm_2Fe_{17}C_{y>1}$ obtained by gas–solid reactions of Sm_2Fe_{17} the same methods as those applied to $Sm_2Fe_{17}N_3$ can be successfully used. Fully dense magnets with a coercivity up to 1.5 T were made from the interstitially as well as substitutionally modified compound $Sm_2Fe_{15}Ga_2C_2$ by hot pressing of highly coercive powders. © *1996 American Institute of Physics.* [S0021-8979(96)38908-7]

I. INTRODUCTION

The discovery of the excellent properties of $Nd_2Fe_{14}B$ in 1983 and its subsequent commercial success inspired a search for still improved ternary rare-earth iron compounds. A promising way to do that was to modify R_2Fe_{17} which is the most iron-rich binary rare-earth iron intermetallic compound but it is unsuitable for permanent magnets because its Curie temperature is too low and its magnetocrystalline anisotropy is easy plane. A remarkably higher $T_c = 253$ °C was found for $Sm_2Fe_{17}H_2$,[1] but this interstitially modified compound still has an unsuitable magnetic anisotropy and the hydrogen desorbs at about 300 °C.[2] A similar increase of T_c and a uniaxial magnetic anisotropy were achieved by introducing carbon into the melt,[3] which yields $Sm_2Fe_{17}C_x$ ($x \leq 1.5$). However, these compounds have not been able to match the intrinsic properties of $Nd_2Fe_{14}B$. An essential step was taken, when the interstitial compounds $Sm_2Fe_{17}N_x$ and $Sm_2Fe_{17}C_x$ ($x = 2$–3) were prepared by low-temperature solid–gas reactions.[4,5] The carbon and nitrogen atoms occupy octahedral interstitial sites in the rhombohedral 2:17 structure. There are two main effects of the interstitial atoms: (i) an increase of T_c and of the spontaneous polarization J_s, caused by a lattice expansion resulting in a change in the electronic structure of the Sm_2Fe_{17} sublattice,[6] and (ii) the formation of a strong uniaxial magnetic anisotropy, because the positions of the C and N atoms are very close to the rare-earth atoms and therefore create a strong crystalline electric field at the site of the $4f$ electrons.[7–9] The Sm_2Fe_{17} interstitial compounds have intrinsic properties comparable to or even better than those of $Nd_2Fe_{14}B$ (see Table I). The problem was then to develop coercivity and to find processes for making good permanent magnets. High-temperature powder metallurgy could not be used because the interstitial compounds mentioned above disproportionate when heated above about 600 °C.[10] One strategy to overcome this difficulty was to imitate sintering with a low-melting metal where most encouraging results were obtained with zinc.[11–14] Successful methods for making fine grained coercive $Sm_2Fe_{17}N_x$ or $Sm_2Fe_{17}C_x$ powders for polymer bonded magnets are mechanical alloying,[15] melt spinning,[16] intense milling after the interstitial modification,[17] and hydrogenation-disproportionation-desorption-recombination (HDDR).[2,18] Weak points of the interstitially modified Sm_2Fe_{17} magnets, so far, are their low values of remanence B_r and energy density $(BH)_{max}$, which is due to (i) the presence of nonmagnetic phases,[10] (ii) low densities, and (iii) missing grain alignment in nanostructured powders. A very interesting result is that the substitutionally modified compounds $Sm_2Fe_{17-y}Ga_yC_2$ ($y \leq 3$) can be prepared by melting and are stable at quite high temperatures (see Table I).[19] This enables the application of heat treatments for magnetic hardening[20] as well as hot pressing to get fully dense magnets, as will be shown in this paper. The values of B_r and $(BH)_{max}$ may also

TABLE I. Intrinsic properties of some compounds. T_c: Curie temperature, J_s: spontaneous polarization, H_A: anisotropy field (easy axis), and T_s: temperature limiting thermal stability.

Compound	T_c (°C)	J_s (T)	$\mu_0 H_A$ (T)	T_s (°C)
$Nd_2Fe_{14}B$	315	1.6	9	>1000
Sm_2Fe_{17}	115	1.05	easy plane	>1200
$Sm_2Fe_{17}H_2$	253	1.35		300[2]
$Sm_2Fe_{17}C$	290	1.2	6	>1150[3]
$Sm_2Fe_{17}C_3$	395	1.45	16	600[10]
$Sm_2Fe_{17}N_3$	475	1.55	22	600[10]
$Sm_2Fe_{15}Ga_2C_2$	362	1.05	13	>1150[19]
$Sm_2Fe_{14}Ga_3C_2$	356	0.95	9	>1150[19]

[a]Permanent address: State Key Laboratory of Magnetism, Institute of Physics, Chinese Academy of Sciences, Beijing 100080, People's Republic of China.
[b]Permanent address: Department of Pure and Applied Physics, Trinity College, Dublin 2, Ireland.
[c]Permanent address: LABMAT, Universidade Federal de Santa Catarina, 88045 Florianopolis, Brazil.

 0021-8979/96/79(8)/5045/6/$10.00 © 1996 American Institute of Physics

be increased by the effect of so-called remanence enhancement caused by magnetic interaction of the interstitial 2:17 phase with a soft magnetic phase (e.g., α-Fe) in nanostructured two-phase materials.[21] The coercivity of Zn bonded coarse grained $Sm_2Fe_{17}N_3$ magnets is mainly controlled by nucleation of reverse domains.[22,23] On the other hand, the magnetization processes in fine grained interstitial magnets is not yet well understood.[24]

II. INTERSTITIAL AND SUBSTITUTIONAL MODIFICATION OF Sm_2Fe_{17}

Table I compares the intrinsic magnetic properties, Curie temperature T_c, room-temperature values of spontaneous polarization J_s, and anisotropy field H_A, of some modified Sm_2Fe_{17} compounds with those of $Nd_2Fe_{14}B$. Obviously, only $Sm_2Fe_{17}N_3$ and $Sm_2Fe_{17}C_3$ match the properties of $Nd_2Fe_{14}B$ and they have even higher Curie temperatures. The temperature T_s also given in Table I represents a stability limit for the considered phases, which is due to melting, disproportionation, or desorption. A disadvantage of $Sm_2Fe_{17}N_3$ and $Sm_2Fe_{17}C_3$ is their low value of T_s, which excludes high-temperature methods for magnetic hardening or consolidation. As an encouraging result the thermal stability of $Sm_2Fe_{17}C_x$ ($x>1.5$) could be considerably improved by a partial substitution of Fe by Ga (see Table I).

In the 2:17 structure three $9e$ octahedral interstitial sites per formula unit can be occupied by C or N atoms. In most practical cases, however, the net concentration x in $Sm_2Fe_{17}N_x$ or $Sm_2Fe_{17}C_x$ is less than 3 and there is a controversial discussion whether partially nitrogenated or carbonated Sm_2Fe_{17} is single phase or not.[10] We have also investigated this problem. $Sm_2Fe_{17}N_x$ ($x<3$) material was prepared by a gas-interstitial modification of coarse Sm_2Fe_{17} powder which was exposed to N_2 gas under 10^5 Pa at 450 °C for different times in order to get different degrees of nitrogenation. The magnetic domain structure of the powder particles was observed by the Bitter technique. The local x concentration was measured along various lines by electron probe microanalysis (EPMA). Figure 1 shows typical results for a nonfully nitrided Sm_2Fe_{17} particle. Due to incomplete nitrogenation we find three regions of the particle: (i) a non-nitrided core, (ii) a fully nitrided outer shell, and (iii) a smooth transition region a few microns thick. It should be noted that the heterogeneous material shown in Fig. 1 is far from thermal equilibrium. To get more insight into the phase structure of partially nitrided samples in thermal equilibrium we homogenized them at 450 °C in a small sealed quartz tube and analyzed them by differential scanning calorimetry (DSC). As shown in Fig. 2, all samples with $0.3 \leqslant x \leqslant 3$ are characterized by only one exothermal peak indicating the presence of only one phase which decomposes at a certain temperature depending on x. Similar results were found for partially carbonized samples.

III. MAGNETIC HARDENING

A. Rapid quenching

Nanocrystalline Sm–Fe alloys have successfully been produced by rapid quenching.[16] Besides the well-known

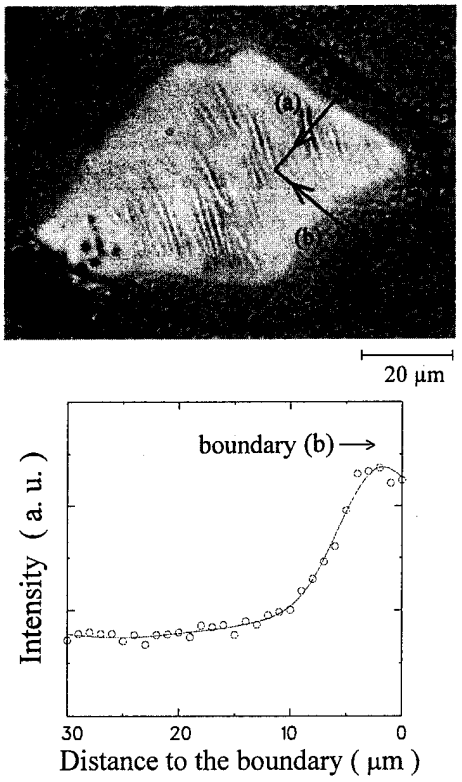


FIG. 1. Domain pattern (Bitter technique) of a non-fully-nitrided Sm_2Fe_{17} particle and nitrogen concentration in the diffusion layer measured by EPMA in a scan along line (b).

equilibrium phases of the binary Sm–Fe system, a hexagonal $TbCu_7$-type phase shows up in melt spun ribbons. Nitrogenation leads to an overall improvement of the hard magnetic properties. To get optimum properties it is necessary to avoid the $TbCu_7$ structure.[16]

B. Mechanical alloying

Mechanical alloying was the first successful method for making highly coercive $Sm_2Fe_{17}N_x$ magnets.[15] Powders of Sm and Fe are cold worked in a ball mill to yield an intimate mixture of nanocrystalline iron and an amorphous Sm–Fe alloy. This is then heat treated at 730 °C to induce crystallization of Sm_2Fe_{17}. The powder is then nitrogenated or car-

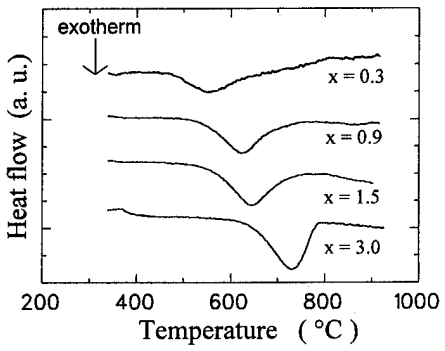


FIG. 2. DSC curves for the decomposition of $Sm_2Fe_{17}N_x$ homogenized at 450 °C for 160 h (heating rate 10 K/min).

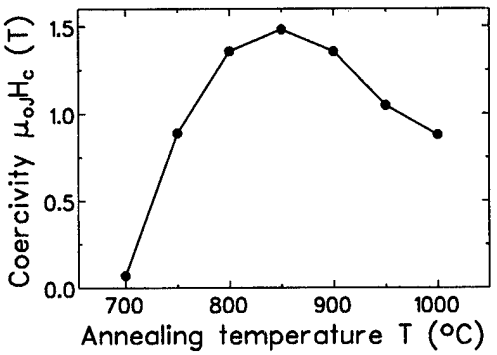


FIG. 3. Coercivity vs annealing temperature for a mechanically alloyed $Sm_2Fe_{17}Ga_2C_2$ magnet (annealing time: 1 h).

bonated by a solid–gas reaction in N_2 or C_2H_2 atmospheres at 450–500 °C to yield material with extremely high coercivity, up to $\mu_0 J_c = 3$ T. We used mechanical alloying to prepare coercive nanocrystalline $Sm_2Fe_{15}Ga_2C_2$ powder. Elemental Sm, Fe, and Ga were milled together with a Fe–C prealloy in a planetary ball mill (Retsch 400 M) for 60 h. The formation of material with the Th_2Zn_{17}-type structure was confirmed by x-ray diffractometry and DSC. As shown in Fig. 3 an optimum value of coercivity of about 1.5 T was achieved by a heat treatment at 850 °C (for 1 h). Similar results are reported in Ref. 20.

C. Milling subsequent to nitrogenation or carbonation

Ball milling is a widely used technique for magnetic hardening of rare-earth transition-metal compounds. Here, we will present results on milling of the material after the interstitial modification.

The coercivity $\mu_0 J_c$ of $Sm_2Fe_{17}N_3$ prepared by gas–solid reactions, can be remarkably increased by milling from about 0.3 to 1.5 T.[17] As shown in Fig. 4 domain structures are clearly visible in particles of a not additionally milled powder, but in the additionally milled state they can hardly be seen. This indicates that the seemingly large particles in Fig. 4(b) are in reality agglomerates of small particles or cold-welded single-domain crystallites isotropically distributed. Obviously in such a microstructure no classical domain structure can be formed. Enhancement in coercivity by fragmentation of big particles into smaller ones is a well-known effect of milling. We have also prepared nanostructured $Sm_2Fe_{15}Ga_2C_2$ powders by intense milling of homogenized ingots, with the Th_2Zn_{17}-type structure, and a subsequent annealing. As shown in Fig. 5 an optimum coercivity $\mu_0 J_c$ of 1.2 T was achieved by a heat treatment for 15 min at 700 °C.

D. Hydrogenation-disproportionation-desorption-recombination (HDDR)

The HDDR process is a well-established method to produce highly coercive fine grained powders for bonded Nd–Fe–B permanent magnets. In this section we will present some results on the adaptation of HDDR for magnetic hardening of interstitially modified Sm_2Fe_{17} compounds.[2] At room temperature the amount of hydrogen absorbed can

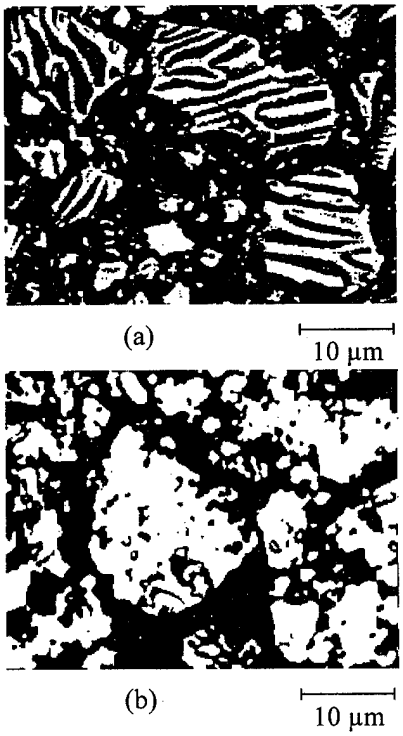


FIG. 4. Optical micrographs (Bitter technique) for two resin bonded $Sm_2Fe_{17}N_3$ powders: (a) not additionally milled, (b) additionally milled for 600 min.

reach about 5 atoms per unit formula. This results in strong volume expansion of about 3 vol % causing the material to become friable or even to decrepitate. With increasing temperature, hydrogen is desorbed and at 500 °C its content is almost zero. For a hydrogen pressure of 10^5 Pa the disproportionation of Sm_2Fe_{17} into SmH_x and Fe occurs above 520 °C. Hydrogen desorbs completely from SmH_x when the material is heated above 570 °C under vacuum and the intimate mixture of Sm and Fe reverts to fine grained Sm_2Fe_{17}. This recombination process was studied using x-ray diffractometry (see Fig. 6). At low temperatures the material tends to crystallize in the $TbCu_7$-type structure characterized by the absence of superstructure reflections. At higher temperatures the superstructure reflections start appearing, indicating the

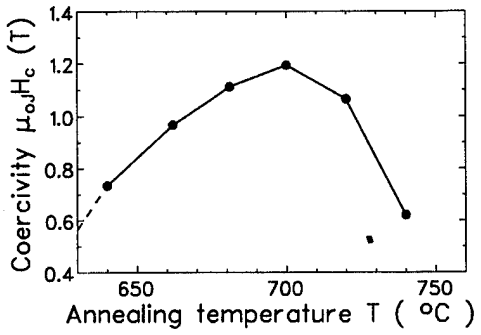


FIG. 5. Coercivity vs annealing temperature for a $Sm_2Fe_{15}Ga_2C_2$ powder annealed after ball milling.

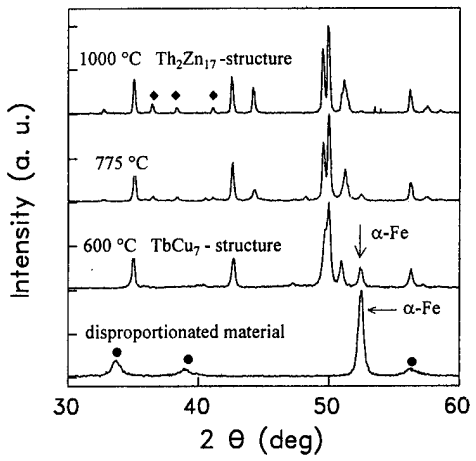


FIG. 6. X-ray patterns of Sm_2Fe_{17} in the disproportionated state [(●) nearly amorphous SmH_x] and recombined for 1 h at different temperatures, showing the transition from the $TbCu_7$ structure to the Th_2Zn_{17} structure which is characterized by the superstructure reflections (♦).

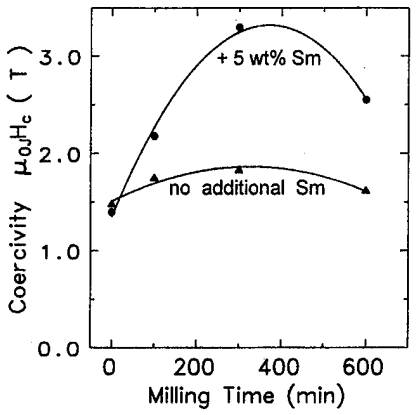


FIG. 8. Coercivity of HDDR $Sm_2Fe_{17}N_3$ as a function of duration of milling prior to the hydrogenation.

presence of the Th_2Zn_{17}-type structure, but only for temperatures as high as 1000 °C where the sharp superstructure reflections show up. As expected, the recombined material shows grain sizes much smaller than those of the parent alloy. This is shown in Fig. 7 where it can also be seen that the final grain size strongly depends on temperature and duration of the recombination step. After proper nitrogenation the coercivity of the HDDR material will strongly depend on the recombination conditions. For our conditions, optimum values of coercivity $\mu_0 J_c$ up to 1.7 T were achieved for material recombined at a temperature of about 750 °C for 1 h. Such a material shows grain sizes of about 500 nm. As shown in Fig. 8 the coercivity $\mu_0 J_c$ of nitrogenated HDDR Sm_2Fe_{17} has been increased from 1.5 to 3.5 T by milling prior to the HDDR treatment with an addition of excess Sm. Figure 9 shows an optical micrograph of HDDR Sm_2Fe_{17} which was recombined at a too high temperature (1000 °C). The material has an inhomogeneous microstructure consisting of large grains coexisting with much finer grains. The larger grains are concentrated in the core of the particles while the finer grains form an outer shell. A possible reason for this is that material in this outer shell remains in the disproportionated state as long as the flow of hydrogen, being desorbed from within the core, can prevent recombination. As a consequence of this, the earliest formed grains within the core have longer time to grow. By milling the material before the HDDR treatment, shorter times are needed for complete hydrogen desorption and subsequent recombination and therefore grain growth can be better controlled. The enhancement in coercivity achieved by adding

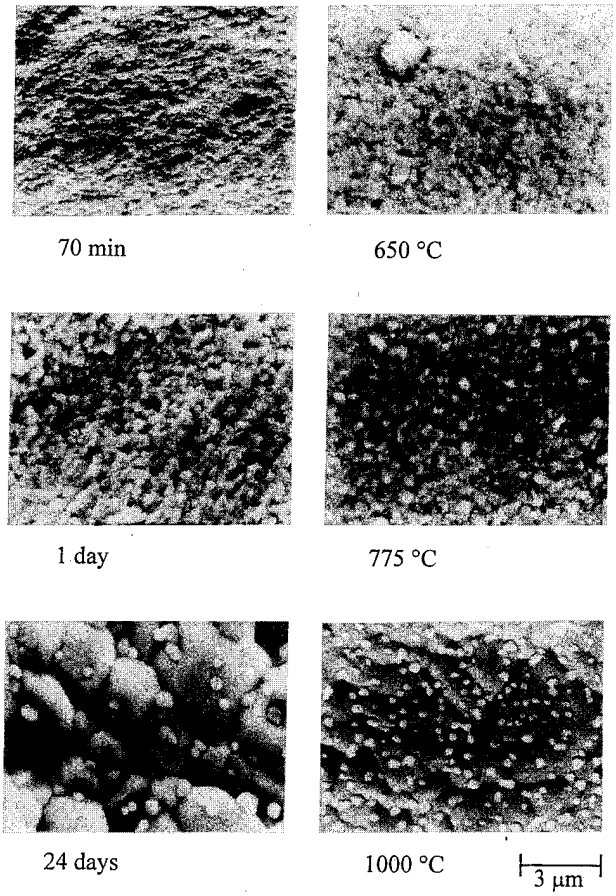


FIG. 7. SEM micrographs showing the microstructure of HDDR Sm_2Fe_{17} recombined at 700 °C for different times (left-hand side column) and for 1 h at different temperatures (right-hand side column).

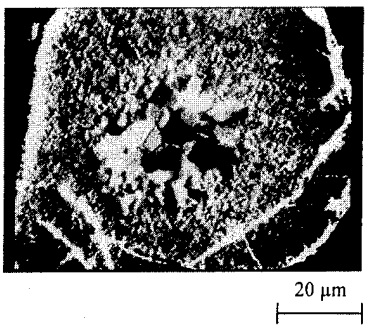


FIG. 9. Optical micrograph of a big HDDR Sm_2Fe_{17} particle recombined for 30 min at 1000 °C, showing a core of large grains surrounded by a shell of fine grains.

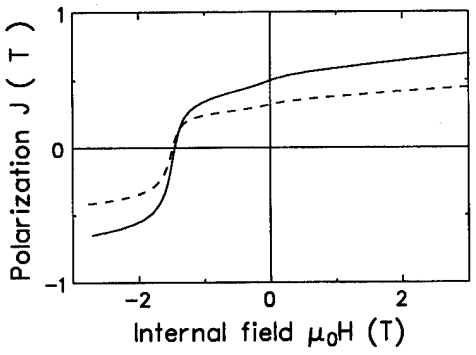


FIG. 10. Demagnetization curves of mechanically alloyed $Sm_2Fe_{15}Ga_2C_2$ (----): annealed for 1 h at 850 °C and cold pressed, (—): annealed for 30 min at 850 °C and hot pressed.

excess Sm is mainly attributed to the suppression of α-Fe. Furthermore, the formation of additional minority phases cannot be excluded.

E. Zinc bonding

The original idea of Zn bonding of $Sm_2Fe_{17}N_3$ or $Sm_2Fe_{17}C_3$ was to use a low melting metal which might wet and separate the hard magnetic grains, thus imitating liquid-phase sintering.[11–14] Coercivities $\mu_0 J_c$ as high as 2.2 T have been achieved up to now. However, we found that liquid Zn does not play an important role. The main effect of Zn is to form paramagnetic intermetallic phases around the 2:17 particles, which decouple them magnetically, smooth them, and remove α-Fe. Though Zn-bonded coarse $Sm_2Fe_{17}(N,C)_x$ powders were successfully textured, their energy density $(BH)_{max}$ did not exceed 80 kJ/m^3, which is caused by a relative low density and the presence of nonmagnetic phases. Zinc bonding was also successfully combined with other methods of magnetic hardening. For HDDR Sm_2Fe_{17} which was nitrogenated and then Zn bonded we achieved $\mu_0 J_c$=3 T. A value of 4.4 T is reported for mechanically alloyed Sm_2Fe_{17} which was Zn bonded after nitrogenation.[25]

IV. REMANENCE AND ENERGY DENSITY

In principle, the remanence B_r can be increased by (i) grain alignment, (ii) consolidation, (iii) avoiding nonferromagnetic phases, and (iv) exploiting the effect of remanence enhancement due to magnetic interaction. The best combination of grain alignment, high density, and small content of nonmagnetic phases has been reported in Ref. 26. A remanence of 0.9–1.0 T and an energy density of about 160 kJ/m^3, both related to the real density, were achieved for compression-molded (epoxy bonded) $Sm_2Fe_{17}N_3$. Remanence enhancement has been achieved by producing a coherent nanocrystalline structure in mechanically alloyed, isotropic Sm_7Fe_{93}-nitride powders consisting of α-Fe and $Sm_2Fe_{17}N_3$.[21]

We have increased the density of the mechanically alloyed $Sm_2Fe_{15}Ga_2C_2$ described in Sec. III B (see Fig. 3) by hot pressing. This is possible because the material is stable up to high temperatures (see Table I). Hot pressing resulted in a density of 7.6 g/cm^3, i.e., 97% of the full density. As shown in Fig. 10 the remanence of the hot-pressed material is nearly half of the spontaneous polarization of $Sm_2Fe_{15}Ga_2C_2$.

V. MAGNETIZATION PROCESSES

For compounds such as $Sm_2Fe_{17}N_x$ or $Sm_2Fe_{17}C_x$ ($1<x$) the domain-wall width δ ranges from 2 to 5 nm and the critical single-domain particle size D_c from 200 to 500 nm. The grain size D of typical fine grained magnets, made from these compounds by rapid quenching, mechanical alloying, intense milling, or HDDR, lies between these two characteristic lengths, $\delta \ll D \leq D_c$. Therefore, a classical domain structure with 180° domain walls cannot be formed and the concepts of nucleation-type magnets or pinning-type magnets, successfully used to analyze coercivity of coarse grained materials such as Zn-bonded $Sm_2Fe_{17}N_3$ or Sm_2Co_{17}-type magnets, will fail. The details of the coercivity mechanisms as well as the domain structures in fine grained materials are not well understood and represent an important area for further research. In a reasonable approximation, these materials can be considered as systems of interacting single-domain particles where the type and strength of the interaction is controlled by the structure, the thickness, and the composition of the grain boundaries. The magnetization direction of a given grain will not only depend on the applied field and on the magnetic prehistory of that grain but also on the magnetization state of its neighboring grains. For melt-spun Nd–Fe–B it was shown that the interaction may result in magnetic structures called interaction domains.[27] Two well-known methods to study the interaction by means of magnetic measurements are (i) Wohlfarths remanence analysis, and (ii) an analysis of initial magnetization curves measured on samples with different magnetic prehistories.[24] In the following we will present some results obtained by method (ii) for two different types of fine grained $Sm_2Fe_{17}N_3$. The samples were prepared by milling after nitrogenation for 600 min and by HDDR. As shown in Fig. 11, the demagnetization curves of both materials are similar with coercivities $\mu_0 J_c$ of about 1.5 T, but their initial magnetization curves are very different. The susceptibility $\chi \sim dJ/dH(H \rightarrow 0)$ of the milled material does not depend on the magnetic prehistory, as predicted for systems of noninteracting single-domain particles. The HDDR sample shows a behavior similar to that of nucleation controlled magnets:[22] the susceptibility is much larger in the thermally demagnetized state than in the field demagnetized state. This result is not yet well understood. Possibly there is a strong exchange interaction between the grains, resulting in interaction domains similar to those reported in Ref. 27. The investigation of the domain structure in the HDDR material are in progress.

VI. CONCLUSIONS

Various processing routes are now established for developing coercivity above 1.5 T for interstitial 2:17 materials: mechanical alloying, rapid quenching, different milling procedures, HDDR, metal bonding, and combinations of these

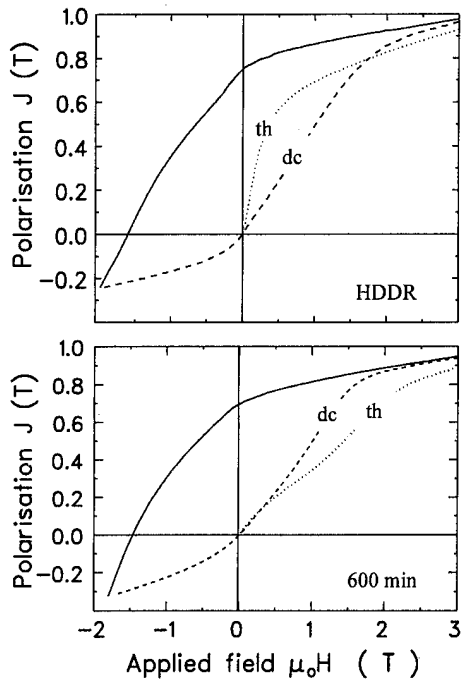


FIG. 11. Demagnetization curves (—) and initial magnetization curves measured after thermal demagnetization (th) and dc field demagnetization (dc) for resin bonded $Sm_2Fe_{17}N_x$ powders prepared by HDDR (recombination for 1 h at 775 °C) or by additional milling after nitrogenation for 600 min.

methods. The highest values of $\mu_0 J H_c$, reported so far, are 3.5 T for HDDR $Sm_2Fe_{17}N_3$ and 4.4 T for Zn bonded mechanically alloyed $Sm_2Fe_{17}N_3$. The prospects of interstitially modified Sm_2Fe_{17} will depend on the development of effective processing routes for magnets with appropriate values of B_r and $(BH)_{max}$ which are now limited by the presence of nonmagnetic phases, pores, and missing grain alignment (in the case of fine grained materials). The highest value of $(BH)_{max}$, reported so far, is 160 kJ/cm^3 for compression-molded epoxy-bonded $Sm_2Fe_{17}N_3$ (with $\rho \approx 5.9$ g/cm^3, $B_r \approx 0.98$ T $\mu_0 J H_c = 0.8$ T). There are prospects for enhancing $(BH)_{max}$ by (i) stabilizing the interstitial compounds by a partial substitution of Fe by elements such as Ga, and (ii) exploiting the phenomenon of remanence enhancement in fine grained two phase materials. Interstitially modified Sm_2Fe_{17} materials, in particular those prepared by HDDR, show interesting aspects of magnetization processes connected with nonconventional domain structures.

ACKNOWLEDGMENTS

L. C. would like to thank the Alexander von Humboldt Foundation for financial support. N.M.D. would like to thank CEAM for the provision of an HCM fellowship. P.A.P.W. is grateful for a research scholarship provided by CNPq. The authors are grateful to Professor J. M. D. Coey, Professor I. R. Harris, Professor L. Schultz, D. Eckert, A. Handstein, S. Wirth, M. Wolf, and J. Edelmann for helpful discussions.

[1] X. Z. Wang, K. Donnelly, J. M. D. Coey, B. Chevalier, J. Etorneau, and T. Berlureau, J. Mater. Sci. **23**, 329 (1988).
[2] P. A. P. Wendhausen, B. Gebel, N. M. Dempsey, K.-H. Müller, and J. M. D. Coey, in Proceedings of the 13th International Workshop on RE Magnets and their Applications, Birmingham 1994, p. 831.
[3] D. B. de Mooij and K. H. J. Buschow, J. Less-Common Met. **142**, 349 (1988).
[4] J. M. D. Coey and H. Sun, J. Magn. Magn. Mater. **87**, L251 (1990).
[5] H. Sun, Y. Otani, and J. M. D. Coey, J. Magn. Magn. Mater. **104–107**, 1439 (1992).
[6] Q. N. Qi, H. Sun, R. Skomski, and J. M. D. Coey, Phys. Rev. B **45**, 278 (1992).
[7] K. H. J. Buschow, J. Alloys Comp. **193**, 223 (1993).
[8] R. Skomski, M. D. Kuz'min, and J. M. D. Coey, J. Appl. Phys. **73**, 6934 (1993).
[9] M. Wolf, S. Wirth, P. A. P. Wendhausen, D. Eckert, and K.-H. Müller, J. Magn. Magn. Mater. **140–144**, 995 (1995).
[10] J. M. D. Coey, Proceedings of the 6th International Conference on Ferrites (ICF6), Kyoto 1992, p. 1064.
[11] ?. Otani, Y. A. Moukarika, H. Sun, J. M. D. Coey, E. Devlin, and I. R. Harris, J. Appl. Phys. **69**, 6735 (1991).
[12] P. A. P. Wendhausen, A. Handstein, P. Nothnagel, D. Eckert, and K.-H. Müller, Phys. Status Solidi A **127**, K121 (1991).
[13] M. Q. Huang, L. Y. Zhang, B. M. Ma, Y. Zheng, J. Elbichi, W. E. Wallace and S. G. Sankar, J. Appl. Phys. **70**, 6027 (1991).
[14] W. Rodewald, M. Velicescu, B. Wall, and G. W. Repel, in Proceedings of the 12th International Workshop on RE Magnets and their Application, Canberra 1992, p. 191.
[15] K. Schnitzke, L. Schultz, J. Wecker, and M. Katter, Appl. Phys. Lett. **57**, 2853 (1990).
[16] M. Katter, J. Wecker, and L. Schultz, J. Appl. Phys. **70**, 3188 (1991).
[17] P. A. P. Wendhausen, B. Gebel, D. Eckert, and K.-H. Müller, J. Appl. Phys. **75**, 6018 (1994).
[18] C. N. Christodolou and T. Takeshita, J. Alloys Comp. **196**, 155 (1993).
[19] B. G. Shen, F. W. Wang, L. S. Kong, L. Cao, and H. Q. Guo, J. Magn. Magn. Mater. **127**, L267 (1993).
[20] J. Ding, P. G. McCormick, R. Street, B. G. Shen, and F. W. Wang, Proceedings of the 13th International Workshop on RE Magnets and their Application, Birmingham, 1994, p. 787.
[21] J. Ding, P. G. McCormick, and R. Street, J. Magn. Magn. Mater. **124**, 1 (1993).
[22] K.-H. Müller, P. A. P. Wendhausen, D. Eckert, and A. Handstein, Proceedings of the 7th International Symposium on Magnetic Anisotropy and Coercivity in RE-TM Alloys, Canberra, 1992, p. 34.
[23] X. C. Kou, E. H. C. P. Sinnecker, R. Grössinger, G. Wiesinger, W. Rodewald, and H. Kronmüller, Proceedings of the 13th International Workshop on RE Magnets and their Applications, Birmingham, 1994, p. 753.
[24] D. Eckert, P. A. P. Wendhausen, B. Gebel, M. Wolf, Ll. M. Martinez, and K.-H. Müller, Proceedings of the 13th International Workshop on RE Magnets and their Applications, Birmingham, 1994, p. 743.
[25] C. Kuhrt, K. O'Donnell, M. Katter, J. Wecker, K. Schnitzke, and L. Schultz, Appl. Phys. Lett. **60**, 3316 (1992).
[26] T. Iriyama, T. Katsumata, and R. Mitsui, Trans. Mater. Res. Jpn. **14B** (1994).
[27] G. C. Hadjipanayis and W. Gong, J. Magn. Magn. Mater. **66**, 390 (1987).

Disorder and noncollinear magnetism in permanent-magnet materials (invited)

R. Lorenz and J. Hafner[a)]
Institut für Theoretische Physik, Technische Universiät Wien, Wiedner Hauptstrasse 8-10, A-1040 Wien, Austria

We report calculations of the noncollinear magnetic structures and of the magnetic anisotropies of $YFe_{12-x}Mo_x$ permanent magnets with the $ThMn_{12}$ structure, using a novel variant of a spin-polarized tight-binding-linear-muffin-tin-orbital technique allowing for local spin-quantization axes on each site and considering spin–orbit coupling. The ternary $YFe_{12-x}Mo_x$ compounds crystallize in the tetragonal $ThMn_{12}$ structure which can be stabilized only by the partial substitution of Fe by an early transition metal like Mo. We show that the substitutional disorder leads to canted spin-structures at low Mo content ($x\sim1$) and to spin-glass-like behavior at higher Mo content ($x\sim3$). We also find that the character of the anisotropy changes from uniaxial to planar with higher Mo content. © *1996 American Institute of Physics.* [S0021-8979(96)39008-1]

Permanent magnet materials are of highest technological importance. The properties that characterize a good permanent magnet are high Curie temperature, a large saturation magnetization, and a large uniaxial anisotropy. In recent years, it has been shown that rare-earth-transition-metal compounds of the type $REFM_{12-x}M_x$ (RE=Y, Gd, Nd, Sm; TM=Fe, Co; M=Ti, V, Cr, Mo) with the body-centered tetragonal $ThMn_{12}$ structure have a high-potential as permanent magnets.[1–11] Their properties can even be improved by nitrogenation. The problematic point is that at least a partial substitution of Fe or Co by a transition element with an only partially filled *d* band or by silicon is necessary to stabilize the $ThMn_{12}$ structure of the otherwise metastable $REFe_{12}$ or $RECo_{12}$ compound. This substitution leads to a reduction of magnetization (although the compounds remain magnetically ordered up to $x=4$), and in the RE–Fe compounds possibly also to the formation of noncollinear spin structure.

X-ray[1] and neutron[2] diffraction as well as Mössbauer experiments[7] show that the *M* atoms occupy preferrently the (8*i*) sites of the tetragonal $ThMn_{12}$ structure. Both magnetization measurements[8,9] and Mössbauer studies[7,8] show a decreasing moment with increasing *x*. However, it turns out that the average hyperfine fields derived from the Mössbauer spectra cannot be converted to magnetic moments with a constant (i.e., independent of *x*) scaling factor. This suggests that with increasing *M*-metal content (and hence increasing disorder) a noncollinear (canted) spin-structure develops. The assumption of a noncollinearity of the magnetic moments is supported by low-field magnetization and coercivity measurements in YFe_9Mo_3 indicating spin-glass behavior.[8] Investigations of the magnetic anisotropy[10,11] have bee interpreted in terms of a change from uniaxial to planar anisotropy. Spin-polarized electronic structure calculations for hypothetical ordered $YFe_{12-x}Mo_x$ ($x=0,4$) compounds[3,6] and for supercells simulating disordered $YFe_{12-x}Mo_x$ ($x=1,2,3,4$) alloys[8] predict the existence of magnetic order up to $x=4$, but the calculated moment decreases much more slowly than observed. This again compatible with noncollinearity of the magnetic moments.

The possible reason for the appearance of noncollinear spin structures in disordered $YFe_{12-x}Mo_x$ lies in frustrated competing ferro- and antiferromagnetic exchange interactions. It is well known that the distance-dependence of the Fe–Fe exchange interactions follows a Slater–Néel curve with a zero close to $d_{Fe-Fe}\sim2.45$ Å. In the $YFe_{12-x}Mo_x$ compounds, the Fe–Fe nearest-neighbor distances vary between 2.38 Å and 2.65 Å. Hence, the exchange coupling is antiferromagnetic in the Fe–Fe pairs with the shortest bond lengths and ferromagnetic at larger distances. It has been pointed out [12] that the existence of strong antiferromagnetic interactions is very important for the high Curie-temperatures and large anisotropies of the $YFe_{12-x}M_x$ and Y_2Fe_{17} compounds. Collinear ferromagnetic ordering is possible only if the antiferromagnetic coupling is overweighted locally by stronger ferromagnetic interactions. This is possible only in the perfect crystal. Substitutional disorder breaks the balance and leads to the formation of canted magnetic moments. In principle, the situation is similar to the case of asperomagnetic phases in Fe-rich amorphous alloys.

In recent years, several attempts have been made to adapt existing codes for band-structure calculations in the local-spin-density approximation to noncollinear spin structures.[13,14] However, these generalizations of the augmented-spherical-wave (ASW) and linear-muffin-tin-orbital (LMTO) codes are applicable only to systems with a small number of degrees of freedom in the spin structure.

Recently, two of us have proposed a novel approach based on the mapping of the LSDA Hamiltonian onto a real-space tight-binding Hubbard Hamiltonian:[15]

$$\mathbf{H}=\mathbf{H}_{band}+\mathbf{H}_{exch}+\mathbf{H}_{so} \tag{1}$$

where $\mathbf{H}_{band}$ describes the nonmagnetic part of the band structure, $\mathbf{H}_{exch}$ the magnetic exchange splitting, and $\mathbf{H}_{so}$ the spin–orbit coupling. The two-center tight-binding Hamiltonian $\mathbf{H}_{band}$ is constructed via a canonical transformation from the selfconsistent scalar-relativistic LMTO Hamiltonian in the atomic sphere approximation.[16] The formulation of the

[a)]Corresponding author. Electronic-mail: jhafner@tph.tuwien.ac.at; FAX: +43-1-5867760; Tel.: +43-1-58801-5676.

 0021-8979/96/79(8)/5051/5/$10.00 © 1996 American Institute of Physics

TABLE I. Absolute values of average local magnetic moments $|\mu_i|$ (in Bohr magnetons) in substitutionally disordered $YFe_{12-x}Mo_x$ alloys and magnetic moment $\bar{\mu}$ per formula unit. (a) Mo atoms are substituted only on the $8i$ sites, (b) Mo atoms are distributed over the $8i$ and $8f$ sites (cf. text). The results given in the lines marked with an asterisk refer to the collinear calculations (Ref. 8), the results in the lines marked with a double asterisk give the results obtained by Coehoorn (Ref. 3) in the limiting cases of the ordered compounds.

(a)

	$\lvert\mu_i\rvert$					$\bar{\mu}$	
x	Y (a)	Mo(i)	Fe(i)	Fe(j)	Fe(f)	Theor.	Expt.[a]
0**	−0.39	···	2.32	2.26	1.86	24.1	
1	−0.38	−0.58	2.28	2.09	1.61	18.7	23.7
1*	−0.37	−0.66	2.46	2.11	1.55	21.1	
2	−0.35	−0.43	2.27	1.94	1.55	10.3	14.2
2*	−0.37	−0.53	2.28	2.01	1.62	17.7	
3	−0.30	−0.34	2.04	1.93	1.39	9.5	3.6
3*	−0.32	−0.42	2.03	1.89	1.50	14.0	
4	−0.23	−0.23	···	1.52	1.02	8.9	1.7
4*	−0.27	−0.28	···	1.40	1.23	10.8	
4**	−0.17	−0.21	···	1.34	1.23	8.9	

(b)

	$\lvert\mu_i\rvert$					$\bar{\mu}$	
x	$Y(a)$	Mo(i,j)	Fe(i)	Fe(j)	Fe(f)	Theor.	Expt.[a]
3	−0.12	−0.27	2.60	2.32	1.16	3.8	3.6
4	−0.16	−0.20	2.39	2.15	1.04	2.8	1.7

[a]Reference 8.

exchange part is based on the assumption that the local exchange splitting Δ_{il} is proportional to the local spin polarization,

$$\Delta_{il}=I\mu_{il}, \tag{2}$$

with an effective Stoner parameter I, leading to

$$\mathbf{H}_{\text{exch}}=-\frac{1}{2}\sum_{ilm}\Delta_{il}\sum_{ss'}X_{\zeta i,ss'}c^{\dagger}_{ilms}c_{ilms'}, \tag{3}$$

where

$$\mathbf{X}_{\zeta i}=\mathbf{D}_{\zeta i}\sigma_z\mathbf{D}^{\dagger}_{\zeta i} \tag{4}$$

is the local Pauli spin-matrix σ_z referring to the local quantization axis ζ_i, rotated to a global spin axis (the $\mathbf{D}_{\zeta i}$ are the rotation matrices). The ansatz equation (3) for the exchange part of the Hamiltonian is based on the observation that the proportionality equation (2) holds exactly, with a universal value $I=(0.95\pm0.015)$ eV for all $3d$- and $4d$-metals, if the local exchange splitting Δ_{il} is defined in terms of the difference in the position of the center of gravity of the spin-up and spin-down bands[17] (for a general discussion of the mapping of the LSDA exchange-correlation potential on Hubbard-(or Stoner-)type models, see, e.g., Anisimov *et al.*,[18] here we only note that in our case the effective Stoner I has to be identified with Hund's rule exchange). A local effective Stoner-parameter I_{il} can be derived from the ab initio LMTO calculations in the collinear limit. For the $YFe_{12-x}Mo_x$ compounds, we find that the calculated I_{il}'s agree very well with the universal value. The spin–orbit-coupling term is given by

$$\mathbf{H}_{\text{so}}=\sum_i \xi_i\sigma_i\cdot\mathbf{L}_i, \tag{5}$$

where ξ_i is the spin–orbit-coupling matrix element calculated with the self-consistent scalar relativistic wavefunctions.

The self-consistent spin-structure is then calculated using an iterative real-space recursion algorithm. Starting with a random distribution of the local spin-quantization axes ζ_i, for each atomic site i the local spin-polarized partial densities of state $n_{ilms}(E)$ for spins parallel and perpendicular to ζ_i are calculated using the recursion method.[19] Integrating the $n_{ilms}(E)$ up to the Fermi level defines the updated local magnetic moment μ_{ilm}. In general, μ_{ilm} will have transverse components with respect to ζ_i and the new local quantization axis ζ_i' must be rotated into the direction of the moment. The calculation is iterated until the directions are stabilized and selfconsistency according to Eq. (2) has been achieved. The main advantage of this technique is that in essence we calculate the magnetic force that rotates the moment into the direction of easy magnetization. Our technique is similar in spirit to the method proposed by Krey *et al.*[20,21] However, Krey *et al.* used an empirical TB-Hamiltonian for the band-part, and treated the Stoner parameter (they call it a Hubbard U, somewhat misleadingly) as an adjustable parameter. In contrast, our approach is parameter-free. Our technique has been used to treat spero- and asperomagnetism in amorphous Fe and Fe–Zr, Fe–Y alloys,[22] as well as spin-glass behavior in CuMn solid solutions.[23] The technique is also very useful in the absence of competing exchange interactions because it immediately predicts the easy axis of magnetization and allows, by repeating the calculation in the presence of a magnetic field perpendicular to the easy axis, to determine the value of the anisotropy constant without calculating very small energy differences.[22] Here, we concentrate on the non-collinearity induced by the substitutional disorder, but it is

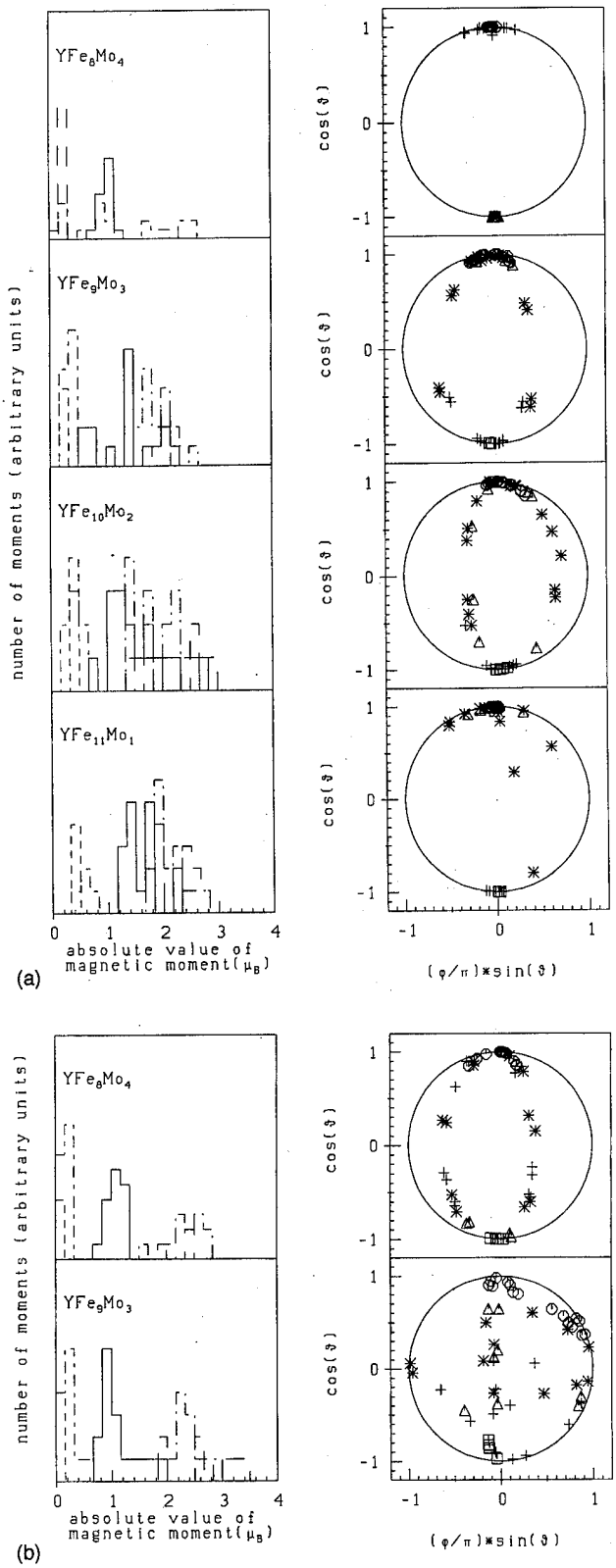


FIG. 1. Distribution of the local magnetic moments in disordered $YFe_{12-x}Mo_x$ alloys. Left column: distribution of the absolute values $|\mu_i|$ in the form of a histogram [full line—Fe($8i$), dashed line—Fe($8j$), dash–dot—Fe($8f$), dotted–Y, dash–dot–dot—Mo]. Right column—polar diagram for the orientation of the moments [star—Fe($8i$), triangle—Fe($8j$), circle—Fe($8f$), cross—Mo, square–Y]. Part (a) represents the case where the Mo-atoms occupy only $8i$ sites, part (b) the case where one Mo-atom per formula unit was placed on an $8j$ site.

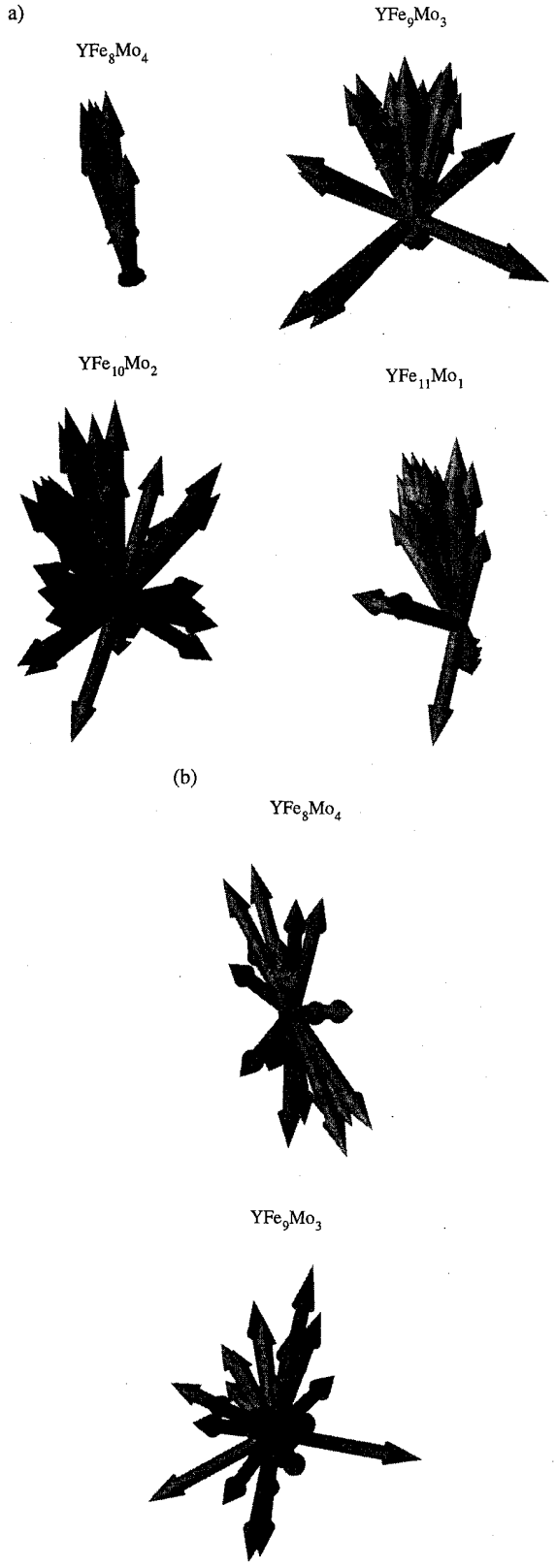


FIG. 2. Vector models representing the spin-structures in disordered $YFe_{12-x}Mo_x$ alloys. Part (a) refers to Mo-substitution on the Fe($8i$)-sites only, part (b) to Mo-substitution on the ($8i$) and ($8j$) sites (cf. text).

important to include the local anisotropies arising form the spin–orbit coupling in the calculations.

The calculations have been performed for a periodically repeated supercell containing 52 atomic sites (four formula

units or two $ThMn_{12}$ unit cells). In a first series, Mo was substituted only on randomly selected $8i$-sites (note that in this case YFe_8Mo_4 is again a fully ordered intermetallic compound). In a second series, for $x=3$ and $x=4$, one Mo-atom per formula unit was placed on an $8j$-site instead of an $8i$-site. The local spin-polarized DOS, local moments and spin splittings are calculated selfconsistently on all 52 sites, using 25 recursion steps for d-states and 9 recursion steps for s- and p-states. The results for the absolute values of the local moments (averaged over the crystallographically equivalent sites) and for the average moment per formula unit are given in Table I. If the Mo-atoms occupy only the $8i$ sites, we find a reduction of the calculated macroscopic magnetization compared to the collinear case, whereas the absolute values of the local moments are only little affected. This reduction is 12% for $x=1$, 40% for $x=2$, and 30% for $x=3$, whereas for $x=4$ a collinear configuration is retained as expected. This means that for larger Mo content these calculations do not reproduce the observed reduction of the magnetic moment. If for $x=3,4$ some Mo atoms are put on the $8j$ sites, the macroscopic magnetization drops dramatically and is now in good agreement with experiment. Occupation of the $8j$ sites occurs only for high global Mo concentrations. It is important to emphasize that although due to the disorder the global magnetization is strongly reduced, the local magnetic moments are even increased on the $8i$- and $8j$-Fe sites and only slightly reduced on the $8f$-Fe sites. The negative moments carried by the Y and Mo atoms is only induced by the strong covalent coupling of the Y and Mo d bands to the minority-spin band of Fe. Hence, the Y and Mo local moments are also only weakly affected by the disorder. Hence, the reduction of the magnetization results from the disorder in the directions of the local moments.

This is illustrated in Fig. 1 where we show the distributions of angles of the absolute values $|\mu_i|$ of the local moments and the distribution of the orientations in the form of a polar diagram. Figure 2 shows the orientation of the spins in the form of a vector model. For $YFe_{11}Mo_1$, we find that most moments are concentrated along the z direction, only two Fe($8i$) moments are oriented almost perpendicular to the preferred direction. For $YFe_{10}Mo_2$, the moments fan out in a wide angle, but again we observe (in the polar diagram as well as in the vector model), a preference of some Fe moments for an orientation in a plane perpendicular to the direction of the global magnetization. This is even more pronounced in YFe_9Mo_3 (and Mo on the $8i$ sites only) where the eight Fe($8i$) moments lie in pairs in a plane perpendicular to the other Fe-spins which show only a slight canting from the easy axis. This is the classical solution for antiferromagnetic moments in an almost uniform field resulting from the other Fe atoms. YFe_8Mo_4 is again a simple collinear ferromagnet (That our figures still show some canting is an artifact: we start from a completely random spin-configuration and to arrange all spins exactly parallel would require extremely long computer runs). If one Mo-atom per formula unit is put on the $8j$ sites, the character of the spin-structure changes [Figs. 1(b) and 2(b)] completely: YFe_9Mo_3 now shows spin-glass-like behavior of the Fe-moments, whereas in YFe_8Mo_4 the Fe-moments are arranged in a plane perpendicular to the z direction. Hence, the calculations show not only that the substitutional disorder can lead to the formation of noncollinear—in the extreme case almost spin-glass-like—spin-structures, it also indicates that the character of the anisotropy changes from uniaxial to planar with higher Mo-contents. In principle, the anisotropy can be calculated quantitatively by repeating the calculations in applied fields of varying strength and varying geometry. However, this will require a very high additional computational effort.

In summary, we have shown that the calculation of noncollinear magnetic structures is now possible even for very complex compounds with substitutional disorder and that this leads to deep insights into the physical mechanisms determining the composition-dependence of the magnetic properties of permanent-magnet materials. The noncollinearity has to be attributed to competing ferro- and antiferromagnetic exchange interactions. Further increase of x however reduces the degree of noncollinearity (note that for $x=4$, all $8i$ sites are occupied by Mo so that the structure is again ordered), and although the resulting magnetization is smaller than in the collinear calculations, it is still appreciably larger than the experimental values. If we assume that for $x \geqslant 3$ some Mo-atoms occupy also other Fe-sites ($8j$ or $8f$), the calculations predict an almost spin-glass-like magnetic structure for $x=3$, while for $x=4$ the disorder in the spin directions is again reduced. The calculated magnetization is now in very good agreement with experiment.[8] At the same time, the calculated spin-structures indicate that around $x \sim 2$, the character of the anisotropy changes from uniaxial to planar. This would confirm recent experimental observations.[10,11]

Work at the Technical University Vienna has been supported by the Austrian Ministry for Science and Research under Project No. 45.378/2-IV/6/94 ("Magnetism on the nanometer scale") within the framework of the Materials Research Program.

[1] D. B. de Mooij and K. H. J. Buschow, J. Less Common Metals **136**, 207 (1988).
[2] Hong Sun, Y. Morii, H. Fujii, M. Akayama, and S. Funahashi, Phys. Rev. B **48**, 13333 (1993).
[3] R. Coehoorn, Phys. Rev. B **41**, 11 790 (1990).
[4] S. S. Jaswal, Y. G. Ren, and D. J. Sellmyer, J. Appl. Phys. **67**, 4564 (1990).
[5] A. S. Fernando, J. P. Woods, S. S. Jaswal, D. Welipitiya, B. M. Patterson, and D. J. Sellmyer, J. Appl. Phys. **75**, 6303 (1994).
[6] S. Ishida, S. Asano, and S. Fujii, Physica B **193**, 66 (1994).
[7] M. Anagnostou, E. Devlin, V. Psycharis, A. Kostikas, and D. Niarchos, J. Magn. Magn. Mater. **131**, 157 (1994).
[8] I. A. Al-Omari, S. S. Jaswal, A. S. Fernando, D. J. Sellmyer, and H. H. Hamdeh, Phys. Rev. B **50**, 4564 (1994).
[9] Hong Sun, M. Akayama, K. Tatami, and H. Fujii, Physica B **183**, 33 (1993).
[10] Hong Sun, M. Akayama, and H. Fujii, Phys. Stat. Solidi A **140**, K107 (1993).
[11] Y. Z. Wang, B. P. Hu, L. Song, K. Y. Wang, G. C. Liu, J. Phys. Condens. Matter **6**, 7085 (1994).
[12] J. Kübler, K. Höck, J. Sticht, and A. R. Williams, J. Phys. F **18**, 469 (1988).
[13] O. N. Mryasov, A. I. Liechtenstein, L. M. Sandratskii, and V. A. Gubanov, J. Phys. Condens. Matter **3**, 7683 (1991).
[14] R. Lorenz and J. Hafner, J. Magn. Magn. Mater. **139**, 209 (1995).
[15] O. Jepsen and O. K. Andersen, Phys. Rev. Lett. **53**, 2571 (1984).

[16]I. Turek, Ch. Becker, and J. Hafner, J. Phys. Condens. Matter **4**, 7257 (1992); Ch. Becker and J. Hafner, Phys. Rev. B **50**, 3933 (1994).
[17]V. I. Anisimov, J. Zaanen, and O. K. Andersen, Phys. Rev. B **44**, 943 (1991).
[18]R. Haydock, V. Heine, and M. J. Kelly, J. Phys. C **8**, 2591 (1975).
[19]U. Krey, S. Krompiewski, and U. Krauss, J. Magn. Magn. Mater. **86**, 85 (1990).
[20]U. Krey, U. Krauss and S. Krompiewski, J. Magn. Magn. Mater. **103**, 37 (1992).
[21]R. Lorenz and J. Hafner, J. Phys. Condens. Matter **7**, L253 (1995).
[22]M. S. Anagnostou, I. Panagiotopoulos, A. Kostikas, D. Niarchos, and G. Zouganelis, J. Magn. Magn. Mater. **130**, 57 (1994).
[23]C. Becker and J. Hafner, J. Magn. Magn. Mater. (to be published).

Long range order in 2-D arrays of nanometer-sized Fe islands on CaF_2/Si(111) (invited) (abstract)

M. R. Scheinfein, K. E. Schmidt, K. R. Heim, and G. G. Hembree
Department of Physics and Astronomy, Arizona State University, Tempe, Arizona 85287-1504

The effective magnetic moment was measured as a function of Fe island size during the initial stages of Fe growth on CaF_2/Si(111) in an ultrahigh vacuum scanning electron microscope equipped with an *in situ* SMOKE analysis chamber. This substrate was selected for its wide bandgap, chemical inertness, viability of integration into an Si based technology and the availability of nanopatterning using electron beams for producing devices. Fe grown at room temperature initially nucleates into a monodisperse distribution of 3-D islands at very high nucleation densities ($8\times10^{12}/cm^2$). Increased Fe coverages lead to 2-D island growth. A room temperature superparamagnetic to ferromagnetic phase transition occurs as a function of Fe island radius. Mean field and Monte Carlo calculations illustrate that three distinct magnetic phases exist as a function of island diameter. Ferromagnetic order is present at room temperature when $r>3$ nm, superparamagnetism is favored when 2 nm $< r <3$ nm, and a frustrated random antiferromagnetic phase exists when $r<2$ nm. Further depositions of Ag on superparamagnetic Fe island arrays produce Ag islands which couple the covered Fe island moments in-plane, implying that the Ag mediates the magnetic exchange between individual Fe islands within an Ag island. Implications for 2-D giant magnetoresistance devices will be discussed. © *1996 American Institute of Physics.* [S0021-8979(96)62908-7]

Supported by ONR Grant No. N00014-93-1-0099.

 0021-8979/96/79(8)/5056/1/$10.00 © 1996 American Institute of Physics

Fabricating nanoscale magnetic mounds using a scanning probe microscope

K. Bessho, Y. Iwasaki, and S. Hashimoto
Sony Corporation Research Center, 174 Fujitsuka-cho, Hodogaya-ku, Yokohama 240, Japan

Nanometer-scale mounds were fabricated by applying voltage pulses between a substrate and an atomic force microscope cantilever coated with magnetic material. Mounds were formed on both insulator and conducting substrates. Magnetic force microscopy (MFM) observations of the fabricated mounds were performed, and the contrast was turned over by reversing the magnetization of the tip, which is convincing proof that the mounds are magnetic. The MFM images also suggest that the mounds are perpendicularly magnetized. These results demonstrate that scanning probe microscope based nanofabrication is a promising method to fabricate nanoscale magnetic dots on any kind of substrates. © *1996 American Institute of Physics.* [S0021-8979(96)40008-2]

I. INTRODUCTION

Magnetic thin films, magnetic thin wires, and magnetic fine particles, which are expected to show quite different intriguing properties from the bulk material, are now being actively investigated. Especially, periodic arrays of isolated single domain ferromagnetic mounds are of technological as well as scientific interest because they represent a possible future ultrahigh density recording medium.[1] To obtain such an array, it is necessary to reproducibly fabricate mounds which are only a few tens of nanometers in size. However, the preparation of such an array with well-controlled size and spacing is much more difficult than for example thickness control of thin films with molecular beam epitaxy.

Several methods have been presented, such as electron beam lithography,[2] islandlike growth of thin films,[3] and scanning probe microscope (SPM) based nanofabrication.[4] SPM based methods have the advantage that sufficiently small mounds can be fabricated and their positions can be controlled. We have already reported controlled fabrication of metallic PtIr mounds in air by field evaporation of material from a scanning tunneling microscope (STM) tip.[5] In the present work we applied this method to fabricate an array of nanoscale magnetic mounds.

In general, magnetic materials are not favorable for a STM tip in air, because they are easily oxidized which causes the tunneling current to be unstable. An alternative idea is to perform the fabrication in an ultrahigh vacuum (UHV) chamber, or invoke an atomic force microscope (AFM), which does not require the tunneling current in the servo system.

In this work, we focus on the fabrication of magnetic mounds with AFM. The mounds were characterized with magnetic force microscopy (MFM).

II. PROCEDURE AND RESULTS OF MOUND FABRICATION

The AFM based nanofabrication was carried out in ambient conditions by applying voltage pulses between a metal coated AFM cantilever and a substrate, following Imura *et al.* who fabricated Au mounds reproducibly on the Si/SiO_2 substrate.[6] We used a Digital Instruments' (DI's) MultiMode AFM (Nanoscope III), both in contact mode and in TappingMode™.[7] Commercial Si cantilevers, sputter coated with CoCr by DI, which were originally for MFM observation, were used in the expectation that coated CoCr should be field evaporated and deposited onto the substrate. The spring constant of the CoCr coated cantilevers was around 5 N/m. Co or Fe were evaporated on the MFM cantilevers, which were also used in order to fabricate Co and Fe mounds.

Both insulators and metals were used as substrates. The insulator was a piece of Si wafer with a chemically oxidized SiO_2 layer on the surface (Si/SiO_2 substrate), which was prepared by boiling in acid (the usual 4:1:1 mix of water, peroxide, hydrochloric acid) after removing the nature oxide layer in hydrofluoric acid. The thickness of the SiO_2 layer is estimated to be 2 nm by ellipsometry. The metal substrates will be described later.

Figure 1 shows mounds fabricated using (a) CoCr coated, (b) Co coated, and (c) Fe coated cantilever, by applying (a) -7 V, 0.5 ms, (b) -8 V, 0.5 ms, and (c) -9 V, 0.5 ms pulse voltage to the Si/SiO_2 substrate. (a) and (b) were done in contact mode, and (c) in TappingMode. The diameter and the height of the fabricated mounds were about (a) 70 and 10 nm, (b) 140 and 5 nm, and (c) 175 and 55 nm, respectively. These mounds are expected to be composed of coated magnetic material emitted from the cantilever surface toward the substrate by field evaporation.

Figure 2 shows an array of mounds fabricated by repeatedly applying $+12$ V, 900 ms pulses to a Si/SiO_2 substrate using a CoCr coated cantilever. In this way, nanometer scale mounds were fabricated reproducibly using an AFM cantilever coated with magnetic material.

III. MFM OBSERVATION OF THE MOUNDS

We used MFM (in dynamic mode, Nasoscope III) to confirm that the fabricated mounds are really composed of magnetic material. In dynamic-mode MFM the shift of a cantilever resonant frequency due to the magnetic dipole interaction is detected, but the observation of this interaction is often impeded by other external force such as the resistance by the atmosphere, so-called air damping. We carried out the observation in low pressure (500 mTorr) in order to reduce this air damping, because this noisy effect is liable to stand

 0021-8979/96/79(8)/5057/3/$10.00 © 1996 American Institute of Physics

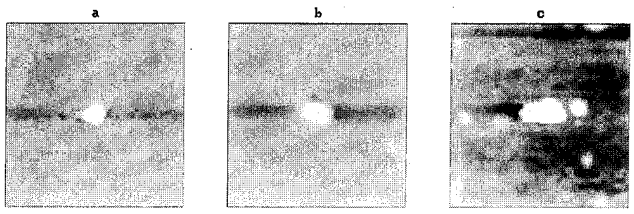


FIG. 1. Mounds fabricated using a (a) CoCr coated, (b) Co coated, and (c) Fe coated cantilever, by applying (a) −7 V, 0.5 ms, (b) −8 V, 0.5 ms, and (c) −9 V, 0.5 ms pulse voltage to the Si/SiO_2 substrate [500 nm×500 nm scan for (a), 750 nm×750 nm scan for (b) and (c)]. The diameter and the height of the fabricated mounds were about (a) 70 nm and 10 nm, (b) 140 and 5 nm, and (c) 175 and 55 nm, respectively.

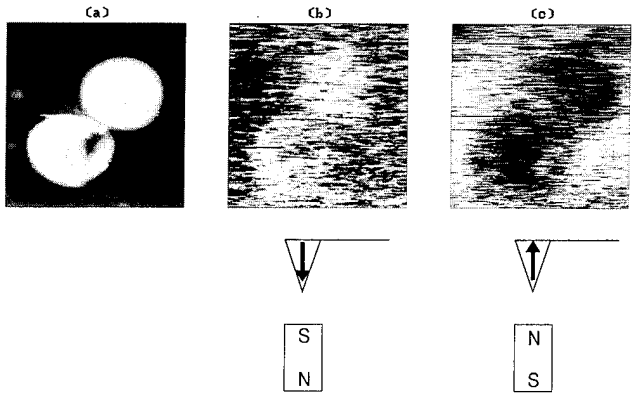


FIG. 3. (a) An AFM image of mounds fabricated with Co coated cantilever (750 nm×750 nm scan). The diameter and the height of the upper mound is 300 and 60 nm, respectively. (b) A MFM image of the mounds observed simultaneously with the AFM image, taken with a new CoCr cantilever magnetized in the bottom-to-apex direction. (c) A MFM image of the mounds observed simultaneously with the AFM image, taken with a cantilever magnetized in the apex-to-bottom direction.

out in observing a steep mound around its foot. A new CoCr coated MFM cantilever, with spring constant $k=5$ N/m and resonant frequency $f_0=67$ kHz, was used.

Figure 3(a) shows an AFM image of mounds fabricated with a Co coated cantilever. The diameter and the height of the upper mound is 300 and 60 nm, respectively. Figure 3(b) shows the MFM image of the mounds observed simultaneously with the AFM image. The MFM cantilever (tip), which had been magnetized in the bottom-to-apex direction in about 3 kOe field using a permanent magnet, was lifted 100 nm during observation. After being taken off from the MFM unit and magnetized in the opposite direction with the permanent magnet again, the tip was used to observe the interaction with the same mounds, as is shown in Fig. 3(c). The contrast for the MFM image has been turned over by reversing the direction of the tip magnetization, which is a convincing proof that the interaction between the tip and the mounds is actually magnetic.

Figure 3 also suggests that the mounds are perpendicularly magnetized. The contrast by the mounds and the substrate was estimated to be a 3.6° shift in phase of cantilever vibration, and corresponds to the interaction force gradient $\partial F_z/\partial z = 3.0 \times 10^{-3}$ N/m. A simple calculation to estimate the interaction force gradient was also carried out using Mathematica™. To represent the tip magnetization, a $(50\ \text{nm})^3$ cubic magnet magnetized perpendicular to the substrate was assumed at the position of the tip apex, for the thickness of CoCr is around 50 nm.[7] Recorded bits on Co/Pt multilayer film were observed in order to estimate the tip magnetic moment, and 2.44×10^{-22} Wb m was obtained by comparing the contrast from the MFM image and the calculation using the saturation magnetization $M_s=0.5$ T, the thickness $t=18$ nm and the diameter of the bit $d=3000$ nm for the Co/Pt film. With these data, the calculation based on the integral of magnetic dipole interaction between small volume elements in a perpendicularly magnetized Co mound and in the cubic tip resulted in $\partial F_z/\partial z=2.3\times10^{-3}$ N/m, which is quite comparable to that obtained in the actual observation. If we assume that the mounds are magnetized in-plane, the estimation of the force gradient resulted in values 10 times larger than in the perpendicular case. Therefore, this is further evidence that the mounds are magnetized perpendicularly.

IV. MOUND FABRICATION ON A METALLIC SUBSTRATE

In addition to insulator (Si/SiO_2) substrates, mounds were fabricated on metallic substrates by two different methods. One is to apply pulses in TappingMode AFM, so that the electric field can be generated when the cantilever is not touching the surface. A piece of Pt wire was melted and

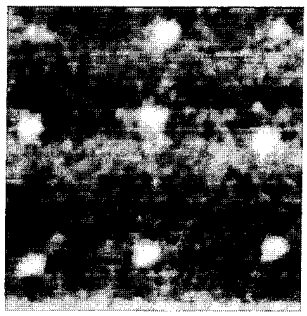


FIG. 2. An array of CoCr mounds on a Si/SiO_2 substrate (550 nm×550 nm scan). Each mound was fabricated by applying a voltage pulse of +12 V for 900 ms. The size of a mound is typically 40 nm in diameter and 2 nm in height.



FIG. 4. The fabricated mounds on a Pt (111) substrate by repeatedly applying +13 V 500 ms pulses to the substrate with TappingMode AFM (350 nm×350 nm scan). The size of a mound ranges 40–50 nm in diameter and 3–10 nm in height.

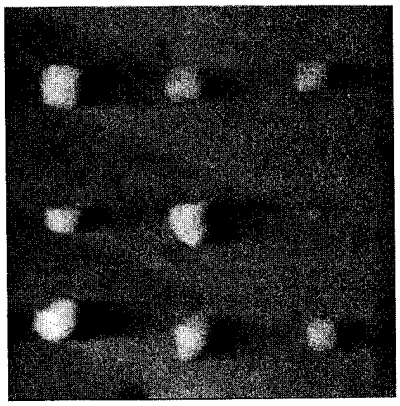


FIG. 5. An array of mounds fabricated by repeatedly applying +2.1 V, 0.3 ms pulses to the Pt thin-film substrate (300 nm×300 nm scan). The size of a mound ranges 10–40 nm in diameter and 3–25 nm in height.

cooled to give a Pt ball with (111) facets on its surface, a chosen facet of which was used as a conducting substrate.

Figure 4 shows the fabricated mounds on a Pt (111) substrate by repeatedly applying +13 V, 500 ms pulses to the substrate.

Another way is to apply pulses between a STM tip and a substrate in UHV, as mentioned in the introduction. Much purer mounds are expected in this method. The fabrication was performed in vacuum less than 5×10^{-10} Torr at room temperature. The STM was a commercial one (Unisoku USM-501) and tips were made of electrochemically etched 0.25 mm diam Ni wire. The substrate was epitaxial Pt thin film evaporated onto MgO (100) single crystal. After pulsing, the substrate surface was observed again with the same tip.

By repeatedly applying +2.1 V, 0.3 ms pulses to the substrate, an array of mounds were fabricated as shown in Fig. 5. The diameter of the mounds was in the range 10–40 nm, which is sufficiently small to be a single domain particle.

V. SUMMARY

Nanoscale mounds of CoCr, Co, or Fe were fabricated on the Si/SiO_2 substrate using AFM based nanofabrication techniques. Using TrappingMode AFM or UHV-STM, mounds of CoCr or Ni were also formed on a conducting platinum substrate.

MFM observations of the fabricated Co mounds were performed. The contrast was turned over by reversing the magnetization of the tip, which is a convincing proof that the mounds are indeed magnetic. The MFM images also suggest that the mounds are perpendicularly magnetized. These results demonstrate that SPM based nanofabrication is a promising method to fabricate nanoscale magnetic dots on any kind of substrate.

ACKNOWLEDGMENTS

We would like to acknowledge K. Ryu for preparing substrates and Y. Tanaka and N. Nakayama for ellipsometry measurements.

[1] S. Y. Chou, M. S. Wei, P. R. Krauss, and P. B. Fischer, J. Appl. Phys. **76**, 6673 (1994).
[2] R. M. H. New, R. F. W. Pease, and R. L. White, J. Vac. Sci. Technol. B **13**, 1089 (1995).
[3] D. D. Chambliss, R. J. Wilson, and S. Chiangn, J. Vac. Sci. Technol. B **9**, 933 (1991).
[4] A. D. Kent, S. von Molnar, S. Gider, and D. D. Awschalom, J. Appl. Phys. **76**, 6656 (1994).
[5] K. Bessho and S. Hashimoto, Appl. Phys. Lett. **65**, 2142 (1994).
[6] R. Imura, H. Koyanagi, M. Miyamoto, A. Kikukawa, T. Shintani, and S. Hosaka, Microelectron. Eng. **27**, 105 (1995).
[7] K. Babcock, V. Elings, M. Dugas, and S. Loper, IEEE Trans. Magn. **30**, 4503 (1994).

Magnetic properties of nanometer-size CoPt particles

S. H. Liou
Behlen Laboratory of Physics and Center for Materials Research and Analysis, University of Nebraska, Lincoln, Nebraska 68588-0111

Y. Liu
Department of Mechanical Engineering and Center for Materials Research and Analysis, University of Nebraska, Lincoln, Nebraska 68588-0656

S. S. Malhotra, M. Yu, and D. J. Sellmyer
Behlen Laboratory of Physics and Center for Materials Research and Analysis, University of Nebraska, Lincoln, Nebraska 68588-0111

We have prepared nanometer-size, isolated CoPt particles. The particles in the range of 100–300 nm in diameter were formed by annealing thin films in the temperature range of 550–800 °C. Films with magnetic coercivity as high as 30 kOe were achieved. The results indicate that the high magnetic coercivity was obtained because the crystallite size approaches that of noninteracting single-domain particles. © *1996 American Institute of Physics.* [S0021-8979(96)04508-3]

I. INTRODUCTION

One of the requirements for practical applications of magnetic devices, such as high-density magnetic recording media, magnetic bias films of magneto resistive elements, and magnetic tips for magnetic force microscopy, is high magnetic coercivity (H_c).[1,2] It is known that an assembly of very fine noninteracting high anisotropy magnetic particles is magnetically hard; i.e., it has a large coercivity. This effect is due to the fact that the particles are single domains and that magnetization reversal takes place only by rotation of M_s vectors against strong anisotropy forces. For randomly distributed single-domain particles, the H_c will be as high as $0.98K/M_s$, where K is the anisotropy constant and M_s is the saturation magnetization.[3]

The CoPt binary alloy is an excellent system because it has both chemical stability and high magnetic anisotropy. CoPt alloy thin films have received significant attention as possible magneto-optic recording media owing mainly to the existence of ordered intermetallic phases with exceptional magnetic properties.[4,5] CoPt compounds are known for their hard magnetic properties. In the bulk form, it shows a high magnetocrystalline anisotropy (4×10^7 ergs/cm^3) and a relatively large saturation magnetization $M_s=800$ emu/cm^3.[6,7] From the calculation using the above equation, one would expect an H_c of 48 kOe in the CoPt alloy. However, early studies showed H_c values of less than 6 kOe in a CoPt binary alloy.[6–8] Recently, Qiu *et al.* have shown that a maximum intrinsic coercivity of about 4.3 kOe was obtained in a mixture of ordered and disordered phases after annealing the rapidly solidified CoPt alloy at 700 °C for 30 min.[9] In thin films, as reported by Tsoukatos *et al.* the maximum H_c observed in CoPt films is of the order of 6.8 kOe.[10] It is known that the hard magnetic behavior of the CoPt alloy is related to the crystal phase transition. The as-cast alloy has a disordered fcc structure which transforms into an ordered fct structure with $c/a=0.98$ after annealing at a temperature below 835 °C. The magnetic hardness of permanent magnets are also influenced by the size of the particles and the interaction between the particles. In order to have a better understanding of magnetic properties of small particles in the CoPt alloy system, we need to prepare films which consist of desired nanostructures.

In this paper, we report a method to prepare films containing nanometer-size particles and show the development of coercivity as high as 30 kOe in CoPt alloy films.

II. EXPERIMENT

The CoPt alloy films were prepared on fused quartz substrates with dc magnetron sputtering. The film thickness was in the range of 10–300 nm. The substrate was fused quartz. The target was made by sintering high-purity Co (99.9%) and Pt (99.99%) powder with 1:1 atomic ratio at 1050 °C for 24 h. The base pressure before introducing the Ar gas was 3×10^{-8} Torr. In order to improve the ordering and to control the crystallite size, the CoPt films were annealed under one atmosphere of Ar/H_2 in the temperature range of 550–800 °C, and the range of annealing time was from 30 min to 40 h. The magnetic properties of the films were measured by SQUID magnetometry. The crystal structure and particle sizes were examined by high-resolution transmission electron microscopy (HRTEM), selected-area diffraction (SAD), nanodiffraction, and atomic force microscopy (AFM).

III. RESULTS AND DISCUSSION

Particle growth on a substrate is dependent on the strength of interaction between the atoms of the growing film and the atoms of the substrate. As shown by Pashley, particles as small as 10 nm can be formed in the early nucleation stage.[11] If we choose suitable substrates and growth conditions, CoPt films with well separated particles can be produced. One would expect that particles in the range of 10–500 nm can be prepared by controlling the thickness of films and substrate temperatures.

In this study, we prepared CoPt films with the thickness of 10, 20, and 320 nm on quartz substrates and then annealed them in the temperature range of 550–800 °C. Most metals do not wet insulating surfaces such as quartz, so that the particles are expected to form after the thermal treatment.

As shown in Fig. 1, the H_c of CoPt films is in the range of 2–22 kOe, depending on the film thickness and annealing

 0021-8979/96/79(8)/5060/3/$10.00 © 1996 American Institute of Physics

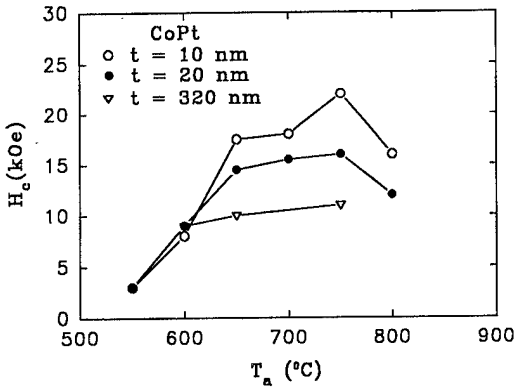


FIG. 1. The evolution of H_c vs the annealing temperature for films with thickness of 10, 20, and 320 nm.

temperature. These films were annealed in the temperature range of 550–800 °C for 30 min in Ar/H_2 atmosphere. The H_c was measured at 300 K with the film surface perpendicular to the magnetic field. The as deposited films regardless of their thickness has a H_c less than 100 Oe. The H_c increases with the increasing annealing temperature. The highest H_c of 22 kOe was observed for 10-nm-thick films annealed at 750 °C. For films annealed at 800 °C, the value of H_c decreased. The H_c of the film with a thickness of 320 nm after annealing at 800 °C also decreased. This datum is not shown in Fig. 1, because it was not prepared in the same sputtering run.

In the CoPt binary system, a disordered fcc and a tetragonal CuAu type structure can coexist in the concentration near 50 at. % Co. This system exhibits excellent hard magnetic properties that depend strongly on the concentration and the degree of crystalline order of the alloy.

As shown in Fig. 2, HRTEM images show that all the as-deposited CoPt films are continuous and composed of 5–10 nm crystallites. The corresponding SAD ring pattern can be indexed using a disordered fcc structure model. After annealing at 750 °C, the crystal structure of the films transforms to the fct structure as identified by the nanodiffraction. The 320-nm-thick film remains continuous after annealing and has crystallite sizes of 50–100 nm. For films of nominal thickness on the order of 10 nm, the alloy forms 50–300 nm particles which grow discontinuously on the substrate. Dark-field images show that there are several crystallites in the large particles. The particles are clearly observed by using atomic force microscopy. As shown in Fig. 3, the CoPt film with a thickness of 10 nm after annealing at 750 °C for 30 min formed many particles with a size range of 50–300 nm. The particle height is in the range of 30–70 nm. This indicated that the film area near the particle was cleaned during the formation of particles.

The observed microstructure is consistent with the early studies that the formation of the tetragonal crystallite and the growth of the crystallite after annealing at high temperature is partly responsible for the increase of H_c.[8–10] It is known that the film annealed at high temperature increases the size of the crystallite which is clearly observed in HRTEM image.



FIG. 2. (a) HRTEM image of as-deposited film. (b) Dark-field image for film annealed at 750 °C for 30 min.

For films annealed at 800 °C, the reduction of H_c may be due to the further crystallite growth which results in the formation of multidomain. In comparison with earlier studies, one of the major differences is possibly that the particle size and the interaction between the particles in these samples prepared by different groups are not the same. In our films, the separated nanometer size particles form a nearly noninteracting system which leads to very high H_c values. This conclusion is also supported by our thickness dependence of the H_c in the films which were prepared from the same sputtering run and annealed together at the same temperature and time duration. Under this preparation condition, the ordering and the size of the crystallite in these films should be the same. One of the major differences between the thin and the thick films is the separation of the particles, i.e., the interactions between the particles is not the same as in these films when they have different thickness. As shown in Fig. 1, the value of H_c of the 10-nm-thick film is about two times higher than that of the 320-nm-thick films.

In order to further understand the effect of the ordering on the H_c, we have examined a series of samples with 10 nm thickness which were annealed at 750 °C for 30 min to 40 h.

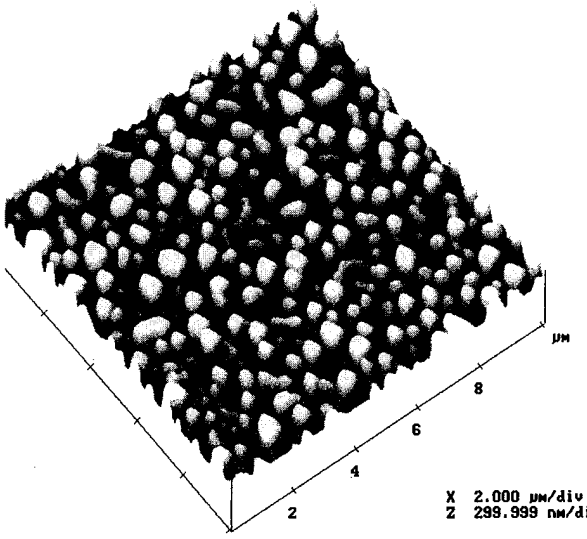


FIG. 3. The atomic force microscopy picture of a nominal 10-nm-thick CoPt film annealed at 750 °C for 30 min.

The result is shown in Fig. 4. The magnetic coercivity of CoPt films dramatically increases upon annealing at 750 °C for 3 h, and then decreases to roughly 24–25 kOe after 20 h annealing. The hysteresis loop of the film with the highest H_c measured at 300 K is shown in Fig. 5. The measured intrinsic coercivity in this film is 30 kOe. Here we should note that the measured value may not be the actual H_c due to the low applied magnetic field (5.5 T). The ordering of the crystallites should improve after a long annealing time, so the H_c of the film should also improve if the ordering is the most important factor. The reduction and the leveling off of the H_c in the films after long annealing indicates that the crystallite growth is more important than the further ordering in these films. The increase of H_c at the beginning of the annealing stage is likely due to the growth of the crystallites which reach the size of a magnetic single domain. After further annealing, the drop in H_c of the films may be due to the increase in the crystallite size which results in multidomain formation.

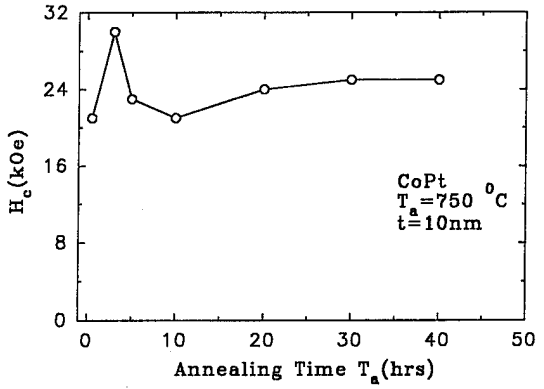


FIG. 4. The H_c of CoPt films with a nominal 10 nm thickness annealed at the temperature of 750 °C for 30 min to 40 h.

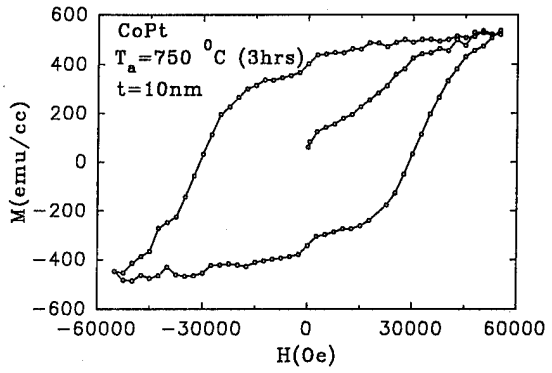


FIG. 5. The hysteresis loops of a CoPt film with a nominal 10 nm thickness that was annealed at 750 °C for 3 h.

IV. SUMMARY

As revealed by high-resolution transmission electron microscopy and atomic force microscopy, we have prepared well separated and nanometer-size CoPt particles (in the range of 100–300 nm). The smaller particles form a nearly noninteracting system and have dimensions close to the single-domain particle size which leads to a very high coercivity value of about 30 kOe. This value is about five times higher than the early studies which show coercivity values of less than 6 kOe and is close to the theoretical estimate of 48 kOe for the CoPt alloy.

ACKNOWLEDGMENT

This Research was supported by NSF under Grant No. OSR-9255225.

[1] E. S. Murdock, IEEE Trans. Magn. **28**, 3078 (1992).
[2] K. Babcock, V. Elings, M. Dugas, and S. Loper, IEEE Trans. Magn. **30**, 4503 (1994).
[3] B. D. Cullity, *Introduction to Magnetic Materials* (Addison–Wesley, Reading, MA, 1972), p. 338.
[4] D. Weller, H. Brandle, G. Gorman, C.-J. Lin, and H. Notarys, Appl. Phys. Lett. **61**, 2726 (1992).
[5] M. R. Visokay and R. Sinclair, Appl. Phys. Lett. **66**, 1692 (1995).
[6] A. S. Darling, Plat. Met. Rev. **7**, 96 (1963).
[7] R. A. MacGuire and P. Gaunt, Philos. Mag. **13**, 567 (1966).
[8] G. Hadjipanayis and P. Gaunt, J. Appl. Phys. **50**, 2358 (1979).
[9] N. Qiu, J. A. Teubert, R. A. Overfelt, and J. E. Wittig, J. Appl. Phys. **70**, 6137 (1991).
[10] A. Tsoukatos, H. Wan, G. C. Hadjipanayis, Y. J. Zhang, and M. Waite, J. Magn. Magn. Mater. **118**, 387 (1993).
[11] D. W. Pashley, Adv. Phys. **14**, 327 (1965).

Oxidation states and magnetism of Fe nanoparticles prepared by a laser evaporation technique

B. J. Jönsson, T. Turkki, V. Ström, M. S. El-Shall,[a] and K. V. Rao
Royal Institute of Technology, Department of Condensed Matter Physics, 100 44 Stockholm, Sweden

Nanoparticles of iron and iron oxide have been prepared in a thermal diffusion cloud chamber using pulsed laser evaporation. SEM/TEM studies of these particles reveal a size distribution with a mean diameter of about 60 Å. This is consistent with the mean particle size estimated from the magnetic data. The oxidation levels of these nanoparticles prepared at different partial oxygen pressures were investigated using FTIR. All the samples are found to exhibit superparamagnetism with blocking temperatures ranging from 50 K to above room temperature. Magnetic anisotropy constants are calculated from the frequency dependence of the blocking temperatures are found to be one quarter of magnitude higher than is known for the bulk. © *1996 American Institute of Physics.* [S0021-8979(96)40108-1]

I. INTRODUCTION

Ultrafine or nanoparticles have been the subject of intense research in recent years. Nanoparticles have unique properties in comparison with the bulk: large surface to volume ratio, discrete electron energy levels which can be easily tuned over a wide range of compositions, etc. Magnetic nanoparticles become single domain below a certain size and exhibit superparamagnetism. Interest in magnetic nanoparticles remains high because of the wide range of potential applications, including information storage, ferrofluids, permanent magnets and pigments in paints. Iron oxide nanoparticles are also expected to have properties as high performance catalysts.

In this paper, we present the magnetic properties of iron and iron oxide nanoparticles produced by pulsed laser evaporation in different oxygen partial pressure atmosphere. The superparamagnetic properties of these nanoparticles are also presented.

II. EXPERIMENT

Iron oxide samples were prepared in a modified upward thermal diffusion cloud chamber.[1,2] A sketch of the chamber is shown in Fig. 1. The iron target was set on the bottom plate. The chamber was filled with desired amount of oxygen and further filled with helium to 800 Torr. The top plate was cooled down to −100 °C while the bottom plate was at room temperature. Metal was vaporized using Nd:YAG laser (532 nm, 20 Hz, and 20 mJ/pulse). In the present investigations the partial oxygen pressure was varied from 0 to 500 Torr while keeping the total pressure at 800 Torr.

SEM and TEM micrographs were taken with JEOL SM 840 and JEOL 2000 EX instruments, respectively. The infrared absorption spectra were recorded on a Nicolet 750 Magna Fourier transform spectrophotomer under atmospheric pressure. dc magnetic measurements were performed using Quantum $MPMS_2$ SQUID magnetometer. The zero field cooled measurements were performed by cooling the sample to 5 K at zero field and then applying 20 G field for the warming up scan. Hysteresis loops were measured at selected temperatures. Between every loop the sample was warmed up to 300 K and the remanence field was minimized. ac magnetic measurements were performed using a home-built two-position ac susceptometer with a three-coil mutual inductance bridge. The driving field was 3 Oe for all measurements and the frequency was varied from 4 Hz to 4 kHz.

III. RESULTS AND DISCUSSION

For brevity we label the samples Fe-0, Fe-10... allowing the number to denote the partial oxygen pressure, in Torr, during preparation. The color of the samples goes from very dark brown, almost black (the color of FeO and Fe_3O_4) to reddish brown (the color of γ-Fe_2O_3) with increasing oxygen pressure. TEM bright field images (Fig. 2) show the samples to consist of very small particles with mean diameter of about 60 Å. Some larger particles with sizes 50–500 nm are also present. No significant difference in particle size distribution is observed between different samples. The size of the particles is found to be controlled by the total pressure, temperature gradient, and the partial pressure of the metal vapor. These parameters were kept the same for every preparation. The diffuse TEM electron diffraction patterns indicate the presence of FeO, Fe_3O_4, and γ-Fe_2O_3 phases in all samples.

Because of the high surface to volume ratio the activity at the surface of the nanoparticles would be significantly different from that of the bulk. From the Fourier transformed, FTIR absorption data we find that in these particles the chemisorption of CO_2 increases with the partial oxygen pressure. At oxygen partial pressures below 200 Torr the samples are found to consist mainly of Fe_3O_4 with some γ-Fe_2O_3 contamination. The γ-Fe_2O_3 peak at 450 cm^{-1} is barely visible. At higher partial oxygen pressures the sample stoichiometry appears to be close to the γ-Fe_2O_3 form.

The iron and iron oxide particles prepared in this study, have sizes within the single domain particle regime (about 200 Å for Fe). Their magnetic behavior is well described in terms of superparamagnetism. For a superparamagnet the relaxation time τ is given by.[3]

$$\tau = \tau_0 e^{KV/k_B T}, \quad (1)$$

[a]Permanent address: Virginia Commonwealth University, Department of Chemistry, Richmond, VA 23284-2006.

 0021-8979/96/79(8)/5063/3/$10.00 © 1996 American Institute of Physics

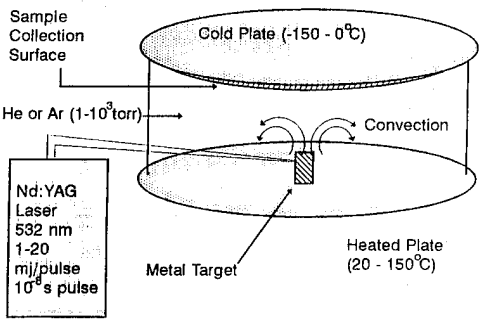


FIG. 1. A sketch of the diffusion cloud chamber.

where K and V are the anisotropy constant and the particle volume, respectively, and τ_0 is of the order of 10^{-9} s. The superparamagnetic behavior is observed above the blocking temperature T_B. Below T_B the particles are magnetically frozen and hysteresis appears.

The in-phase ac susceptibility χ' was measured for five samples prepared at different partial oxygen pressures (Fig. 3). χ' is found to increase monotonically with temperature for the Fe-0 sample. This behavior is consistent with expected blocking temperature[4] of 300 K for iron particles in the size range 60–80 Å. When the particles consist of iron oxide instead of iron, there is a dramatic change in behavior. A clear cusp is seen at about 65 K in sample Fe-10. Increasing the oxidation of iron, as in Fe-50, gives rise to another cusp around 110 K which then dominates in Fe-200. Finally, we observe only one cusp in the Fe-500 sample.

There is a sudden increase in coercivity below the blocking temperature (Fig. 4). The coercivity does not fall to zero above T_B as expected for a purely superparamagnetic sample. This is probably due to the existence of the few large-size particles (50–500 nm) seen in the TEM micrographs.

The magnetization of a paramagnet follows a Langevin function:

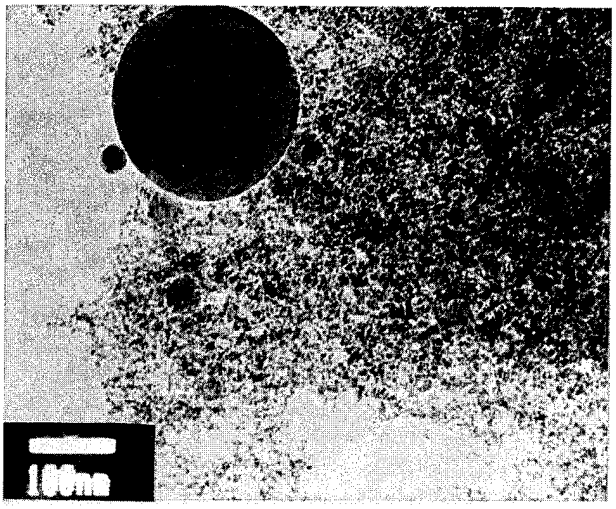


FIG. 2. TEM micrograph of the Fe-10 sample.

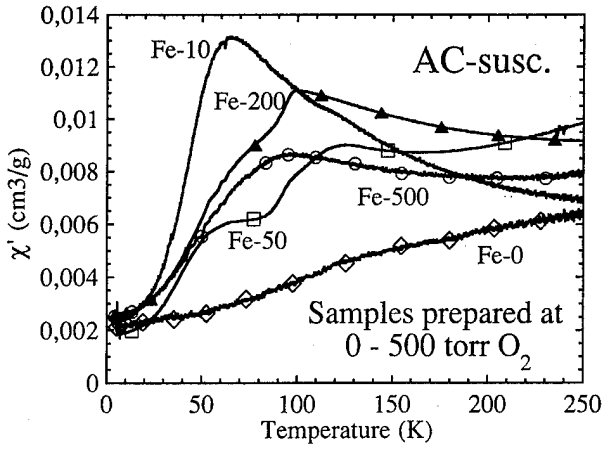


FIG. 3. In-phase ac susceptibility as a function of temperature.

$$\frac{M}{M_s} = L(a) = \coth a - \frac{1}{a}, \qquad a = \frac{\mu H}{k_B T}. \tag{3}$$

Since the Langevin function is a linear function for small arguments, $L(a) \approx a/3$, this will hold for superparamagnetic particles of different sizes at low fields. Thus, measuring M/H loops and taking the slope around zero field gives us a means of calculating the mean-magnetic moment of our particles and therefore, a mean-particle diameter.

The mean-magnetic moment per particle for sample Fe-10 is found to be 5100 μ_B. Assuming the dominant phase to be Fe_3O_4, which has 4.1 μ_B per molecule, eight molecules per unit cell and a lattice constant of 8.39 Å, we estimate the mean-particle diameter to be around 60 Å, in good agreement with the TEM observations.

Knowing the mean volume of our particles we can now estimate K_1. We measured χ' at six different frequencies between 4 and 4000 Hz and included a SQUID measurement with a measuring time of about 100 s. Taking the maximum of χ' to be the blocking temperature and plotting $1/T_B$ vs $\ln(f)$, f being the driving frequency, we get a straight line (Fig. 5). The slope of this line is equal to $-k_B(|K_1|V)^{-1}$, according to Eq. (1).

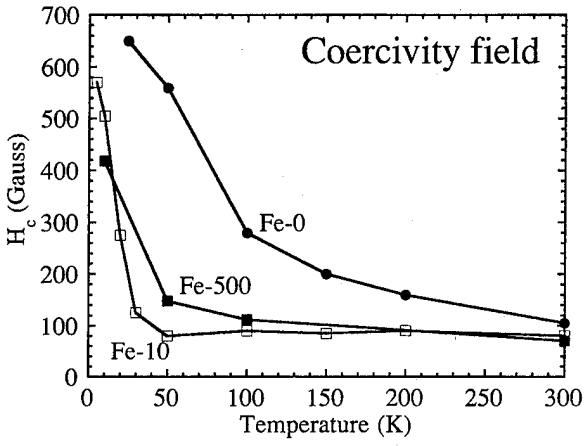


FIG. 4. Coercivity field as a function of temperature for samples showing one single cusp.

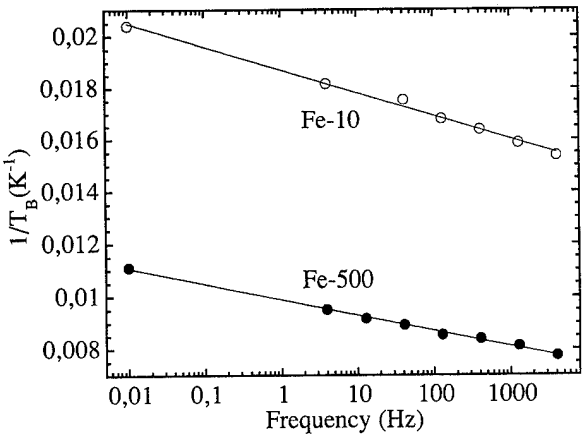


FIG. 5. Plot showing the blocking temperature as a function of measuring frequency for samples Fe-10 and Fe-500.

In the case of a cubic structure with the easy direction along $\langle 111 \rangle$, K_1 is replaced[5] by $K_1/12$. We thus get an anisotropy constant $|K_1| = 2.1 \times 10^6$ ergs/cm^3 for sample Fe-10. If we assume the mean size to be equal in all samples we get $|K_1| = 3.1 \times 10^6$ ergs/cm^3 for the sample Fe-500. Those values for $|K_1|$ are an order of magnitude larger than the values for bulk Fe_3O_4 and γ-Fe_2O_3, but agrees well with values reported in literature[6] for small particles.

Since all samples have about the same size distribution it is the difference in composition that determines the different magnetic behavior. The sample Fe-0 has a high blocking temperature due to the anisotropy barrier being higher for iron than for its oxides. In iron the easy directions are along the cube sides $\langle 100 \rangle$ and K_1 should be replaced by $K_1/4$ and not $K_1/12$. When the core of the nanoparticles is Fe_3O_4 the anisotropy barrier is reduced and the blocking temperature falls to about 50 K. With increasing oxidation, the fraction of γ-Fe_2O_3 increases and since its anisotropy barrier is slightly higher than that for Fe_3O_4, a new cusp develops at about 110 K. As the γ-Fe_2O_3 fraction further increases this cusp dominates and is the only one observed in the sample Fe-500.

IV. CONCLUSIONS

We have demonstrated a simple technique to prepare nanoparticles of iron and iron oxide. By varying the partial oxygen pressure in preparation we have been able to change the oxidation state of Fe. Particles prepared at low oxygen pressure consist mainly of FeO and Fe_3O_4 while those prepared at higher oxygen pressure consist of γ-Fe_2O_3. As a consequence the magnetic behavior changes in a rather complex way. The magnetic properties, analyzed in terms of superparamagnetism, are found to be consistent with the implications from the particle size and structure. Magnetic anisotropy constants calculated from our experimental data agree well with the expected values for small particles.

ACKNOWLEDGMENTS

It is a pleasure to acknowledge many valuable discussions with Professor Dan E. Dahlberg during his visit with us. T. Turkki is most obliged to colleagues at the Department of Chemistry at VCU for their hospitality and financial support during her stay at VCU. This research has been partially supported by the Swedish National Cluster Consortium, and NSF Grants DMR 9207433 and CHE 9311643, in the United States.

[1] M. S. El-Shall, W. Slack, W. Vann, D. Kane, and D. Hanley, J. Phys. Chem. **98**, 3067 (1994).
[2] M. S. El-Shall, W. Slack, W. Vann, D. Hanley, and D. Kane, Mater. Res. Soc. Symp. Proc. **351**, 369 (1994).
[3] L. Néel, Ann. Geophys. **5**, 99 (1949).
[4] S. Gangopadhayay, G. S. Hadjipanayis, B. Dale, C. M. Sorenson, K. J. Klabunde, V. Papaefthymiou, and A. Kostikas, Phys. Rev. B **45**, 9778 (1992).
[5] B. D. Cullity, *Introduction to Magnetic Materials* (Addison-Wesley, Reading, MA, 1972), pp. 410–418.
[6] S. Mørup and H. Topsøe, Appl. Phys. **11**, 63 (1976).

65 Gbits/in.^{2} quantum magnetic disk (abstract)

Stephen Y. Chou and Peter R. Krauss
NanoStructure Laboratory, Department of Electrical Engineering, University of Minnesota, Minneapolis, Minnesota 55455

Quantum magnetic disk (QMD), proposed recently, offers a new paradigm for ultrahigh density magnetic recording.[1] In a QMD, each bit is represented by a prepatterned nanoscale single-domain magnetic pillar or bar that was uniformly embedded in a nonmagnetic material on a disk. The size and shape of each bit is well controlled during the fabrication to ensure single magnetic domain formation, therefore the magnetic moment of each bit has only two quantized states: equal in magnitude but opposite in direction. Compared to conventional magnetic disks, the QMD offers many unique advantages in writing, reading, and tracking. In this article, we report the fabrication of both longitudinal and perpendicular magnetization QMDs and their investigation with scanning electron microscopy, atomic force microscopy, and magnetic force microscopy. Both QMDs were fabricated using electron beam nanolithography, reactive ion etching, and chemical mechanical polishing. We will also discuss QMD fabrication techniques which do not involve conventional lithography. The perpendicular QMD structure consists of 50-nm-diam nickel pillars uniformly embedded in 200 nm thick SiO_2 with a surface roughness of 0.5 nm rms. The pillar array has a period of 100 nm which corresponds to a magnetic storage density of 65 Gbits/in^2—over two orders of magnitude greater than the current state-of-the-art magnetic storage density. © *1996 American Institute of Physics.* [S0021-8979(96)80508-0]

Partially supported by ARPA N00014-93-1-0648 and ONR N00014-93-0256.

[1] S. Y. Chou, M. S. Wei, P. R. Krauss, and P. B. Fischer, J. Vac. Sci. Technol. B **12**, 3695 (1994).

Quantized writing processes in quantum magnetic disks (abstract)

Usman Suriono and Stephen Y. Chou
NanoStructure Laboratory, Department of Electrical Engineering, University of Minnesota, Minneapolis, Minnesota 55455

It has been suggested that the writing process in quantum magnetic disks (QMDs) is quantized: a write head either writes perfectly the entire bit which is a discrete single-domain element isolated from other bits with nonmagnetic materials, or it does not write the bit at all.[1] This article presents the micromagnetics demonstration of this quantized writing process. In the simulation, each QMD bit is assumed to be a polycrystalline cobalt bar of 700 nm long, 50 nm wide, and 30 nm thick, and to be oriented parallel to the disk surface. To obtain the dynamic motion of the magnetization structure of the bit, iterative energy minimization algorithm and the Landau–Lifshitz–Gilbert equation were used. The write head field is assumed to be parallel to the long axis of the bar and uniform with a strength of 2.5 times the bar coercivity. The write field has a width the same as that of the bar but a length that is only three-quarters of the cobalt bar length. It was found that even though the writing field size was smaller than the size of the bar, the magnetic moment of the entire single-domain bar can be switched from one direction to another, giving a perfect writing. The switching process occurred roughly in two stages. First, the magnetic moments got reversed in the region where the write field was applied. Second, driven by exchange force and shape anisotropy, the reversal propagated out of the write field region and reached the entire bit. It was also found that if the overlap of the writing field with the bar was less than one-quarter of the bar length in the bar long axis or four-fifths of the bar width in the bar short axis, the writing field would only temporarily perturbs the magnetic moment distribution of the bar. When the write field was removed from the bar, the magnetic moment of the bar would return to its original state. The quantized writing process in the QMD will allow the use of a smaller and therefore faster write head, can avoid the errors due to misplacement and fringing field, hence is suitable for ultrahigh-density storage. © *1996 American Institute of Physics.* [S0021-8979(96)82108-3]

[1] S. Y. Chou, M. S. Wei, P. R. Krauss, and P. B. Fischer, J. Vac. Sci. Technol. B **12**, 3695 (1994).

 0021-8979/96/79(8)/5066/1/$10.00 © 1996 American Institute of Physics

Nonmonotonic length dependence of switching field of nanolithographically defined single-domain nickel and cobalt bars (abstract)

Linshu Kong and Stephen Y. Chou
NanoStructure Laboratory, Department of Electrical Engineering, University of Minnesota, Minneapolis, Minnesota 55455

Previously, the switching field of nanolithographically defined single-domain permalloy and nickel bars was found to increase monotonically as the bar aspect ratio increases[1] or as the bar width decreases.[2] In this work, we will show, for the first time, that when the bar width is fixed, the switching field of nanolithographically defined single-domain nickel and cobalt bars changes nonmonotonically with the bar length (hence the aspect ratio). The isolated Ni and Co bars were fabricated using electron-beam lithography and a lift-off process, and have a thickness of 35 nm, a fixed width of 100 nm, and a length varying from 200 nm to 5 μm. The magnetic force microscopy (MFM) showed that all the as-fabricated bars, except for the Ni bars with a length less than 500 nm, are single domain. The switching field of the single-domain bars was found to increase with the bar length first, then decrease after reaching a peak. The peak switching field and corresponding bar length are 640 Oe and 1 μm for Ni, and 1250 Oe and 2 μm for Co. This behavior, which clearly deviates from Stoner-Wohlfarth model, suggests that two different mechanisms should be responsible for the magnetization reversal process in different bar lengths. When the bar length is small, the exchange energy can be much larger than the magnetostatic energy to keep the bar switching quasicoherently and the switching field increases with the bar length. However, when the bar length is large, the exchange energy cannot overweigh the magnetostatic energy for quasi-coherent switching and therefore the lowest switching energy state would be incoherent switching which involves multidomain (or vortex) reversal leading to an decrease of switching field. The detailed analysis will be presented in the paper. © *1996 American Institute of Physics.* [S0021-8979(96)82208-4]

Partially supported by ARPA N00014-93-1-0648 and ONR N00014-93-0256.

[1] J. F. Smyth *et al.*, J. Appl. Phys. **69**, 5262 (1991).
[2] M. S. Wei and S. Y. Chou, J. Appl. Phys. **76**, 6679 (1994).

Ultramicro fabrications on Fe-Ni alloy films using electron-beam writing and reactive-ion etching (abstract)

I. Nakatani
National Research Institute for Metals, Tsukuba 305, Japan

Microfabrication techniques are successfully used for semiconducting materials, while they are limited for the application to magnetic materials. For the magnetic materials, useful RIE (reactive-ion-etching) process that is essential for high-resolution microlithography has not yet been successful. In this work, RIE method useful for permalloy (80%Ni-4.5%Mo-Fe) has been newly constructed. High-resolution electron-beam writing was followed by the RIE process, leading to 250 nm line and space patterns in the permalloy film with 10 nm accuracy. In order to achieve a high-resolution electron-beam writing, amorphous carbon film was use between the resist layer and SiO_2 film overlaid on the permalloy film. There are four levels in the process. Most critical step in the fabrication of magnetic material is RIE process using a rf discharged plasma of NH_3-CO mixed gas. Maximum etching rate of 35 nm/min and highly anisotropic etching for the permalloy was obtained at the composition of 50 mol % NH_3-CO at the pressure of 2.4×10^{-3} Torr. The etching selectivity ratio of permalloy to SiO_2 employed as a mask was about 10. By this method, nanostructures of permalloy with highly anisotropic profile were fabricated. This method shows prominent features still for Co-Cr alloy films. © *1996 American Institute of Physics.* [S0021-8979(96)80608-X]

Structural and magnetic study of submicronic single crystal cobalt box arrays

M. Hehn, K. Ounadjela, S. Padovani, J. P. Bucher, and J. Arabski
IPCMS, 23 rue du Loess, 67037 Strasbourg Cedex, France

N. Bardou, B. Bartenlian, and C. Chappert
IEF, Bat 220, Université, Paris Sud, 91405 Orsay Cedex, France

F. Rousseaux, D. Decanini, F. Carcenac, E. Cambril, and M. F. Ravet
L2M/CNRS, 196 avenue Henri Ravera, 92225 Bagneux, France

We present a study of magnetic dot arrays fabricated in Ru(5 nm)/Co/Ru(32 nm) films with cobalt thickness varying from 10 to 500 nm. Large array areas up to 5×5 mm^2 have been obtained with lateral dot size and spacing of 0.5 μm. The magnetization curves are characteristic of a perpendicular magnetized multidomain structure. Lateral size reduction does not drastically change the domain structure but has immediate consequences on the nucleation and saturation fields. A magnetic force microscopy study confirms the perpendicular multidomain structure and provides intrinsic magnetic characteristics. © *1996 American Institute of Physics.* [S0021-8979(96)40208-1]

The magnetization orientation in Co films depends strongly on the film thickness. By growing ultrathin Co(0001) layers, the surface anisotropy, combined with the strong crystalline anisotropy, allows Co to retain its magnetization direction perpendicular to the film despite the large magnetostatic energy. Such perpendicular anisotropy has been clearly evidenced in several systems as Co/Au(111)[1] or Co/Ru(0001).[2] When the Co thickness is increased, the surface contribution is reduced and is not anymore sufficient to overcome the demagnetizing energy. Consequently, the magnetization lies in plane.

For thicker films, there must be one additional crossover predicted by Kittel[3] for which the magnetization turns from in-plane to out-of-plane. This prediction based on a classical model taking into account the magnetic anisotropies, the dipolar energy and the energies of the boundary surfaces between domains foresees that the crossover thickness (t_{cr}) for which the magnetization turns out of plane is about 30 nm for a perfect hcp structure.[4]

The objective of our work is to favor a perpendicular single domain magnetization structure for large Co thicknesses by stabilizing a (0001) hcp cobalt structure which gives rise to a large perpendicular magnetocrystalline anisotropy ($K_{MC}=5.2\times10^6$ erg/cm^3). In this paper, we have identified the crossover thickness above which the magnetization is perpendicularly oriented in the domain structure. Moreover, we have determined the average domain size of the order of 100–200 nm. A possibility to quantify the domains density down to a limit for which the system behaves like a single domain structure would be to reduce the lateral dimensions below a critical length of the order of the domain size in the continuous film. Considering this idea, we have studied in this paper the relationships between the film thickness and the reduction of the geometric lateral dimensions on the magnetic properties and the domain structure.

Ru(5 nm)/Co(t_{Co})/Ru(20 nm) films with cobalt thickness (t_{Co}) varying from 10 to 500 nm were prepared by molecular-beam epitaxy at 400 °C on Al_2O_3 ($11\bar{2}0$) substrates. The RHEED patterns obtained during the sample growth reveal well-defined rods which suggest good crystalline quality. $\theta/2\theta$ x-ray diffraction scans of the (222)fcc/(0004) hcp Bragg peak revealed a peak located at the expected angle for the hcp stack.

Patterning was performed using synchrotron x-ray lithography in the L2M lithography station implemented on the Super-ACO storage ring. Large array areas up to 5×5 mm^2 have been obtained with lateral dot size of 0.5 μm and array periodicity of 1 μm. Details on the different processes can be found elsewhere.[5]

Magnetization measurements at room temperature were carried out in an alternating gradient force magnetometer with the field applied perpendicular and parallel to the substrate plane. Two types of magnetic behavior have been observed depending on the Co thickness as expected from the Kittel prediction.[3] This allows to identify the crossover thickness t_{cr} at about 25 nm.

Below t_{cr}, for both films and arrays, the magnetization curves are characteristic of samples which have their magnetic moments confined along the film plane.[4] In the parallel configuration, the introduction of reduced lateral dimensions change the shape of the curves: the saturation field H_s is larger for dots because domains must be expelled from the dot instead of moving through the film. This effect gives rise to a decrease of the curve slope before saturation.[4] The increase of the saturation field results from the nonzero value of the in-plane component of the demagnetizing field in contrast with the continuous films. In the perpendicular configuration, the saturation field value of about 11.5 kOe for the 10-nm-thick Co film allows the evaluation of the magnetocrystalline anisotropy (4.6×10^6 erg/cm^3). This value confirms the good crystalline quality of the hcp cobalt phase.

Above t_{cr}, the magnetization curves, for both films and arrays, are characteristics of samples which have their magnetic moments perpendicular to the film plane (Figs. 1 and 2). This result is confirmed by the domain imaging. In the following, we will first present the results obtained on the continuous Co films and then discuss the consequences of the reduction of the lateral dimensions of the films.

 0021-8979/96/79(8)/5068/3/$10.00 © 1996 American Institute of Physics

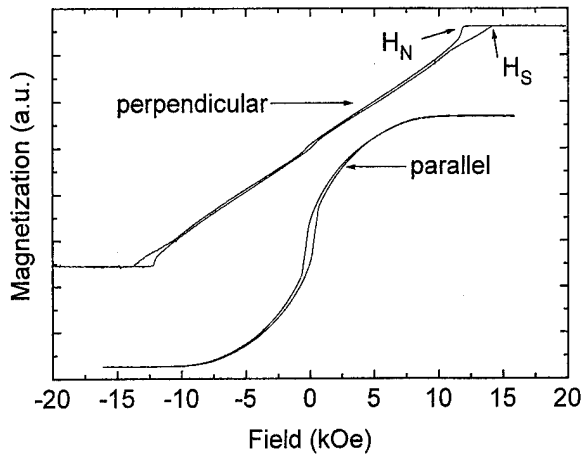


FIG. 1. Perpendicular and parallel $M-H$ curves for a 150-nm-thick cobalt layer. The values for which the saturation (H_s) and nucleation (H_n) fields have been estimated are indicated with the arrows.

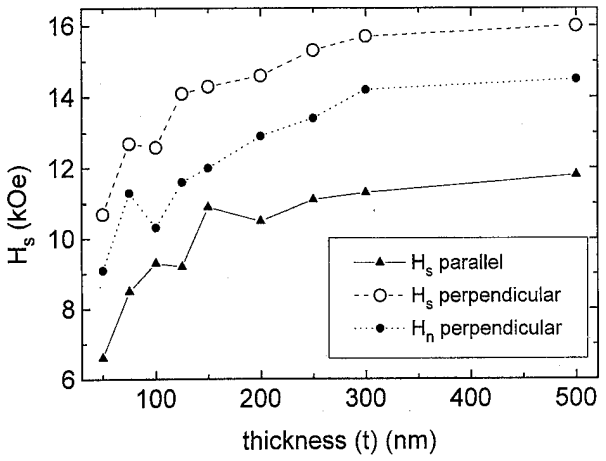


FIG. 3. Perpendicular nucleation field H_n, perpendicular and parallel saturation field H_s vs cobalt film thickness.

Continuous cobalt films: In the perpendicular direction (Fig. 1), the experimental magnetization curves[4] display shapes very similar to those computed for bubbles and stripes domain lattices[6] which strongly suggests that the magnetization states of the films consist of magnetic domains with perpendicular magnetization. The $M-H$ curve slope, from zero up to near H_s, remains constant and results from a competition between pressures acting on the wall. The saturation field H_s (respectively, nucleation field H_n) (as shown in Fig. 1) increases from 12.6 (respectively, 10.3) kOe for t_{Co} of 100 nm to 16 (respectively, 14.6) kOe for 500 nm as shown in Fig. 3. Such an increase is related to the variation of the demagnetizing factor with the film thickness. This is presumably due to changes of the interaction between the charges at both surfaces within each domain.

The singularity in the decreasing field shown in Fig. 1 indicates the nucleation of domain walls followed by the wall motion. In the parallel configuration, H_s increases with film thickness as shown in Fig. 3. Walls are not submitted to a magnetic pressure from the magnetic field, and in consequence a coherent rotation is responsible of the magnetization reversal. Along this hypothesis, the saturation field in the parallel orientation can be described by the expression $H_{s\parallel}=(2/M_s)\times(K_1+2K_2)-H_{d\perp}(t_{Co})$ where K_1 and K_2 are the first and second order magnetocrystalline anisotropies and $H_{d\perp}(t_{Co})$ is the perpendicular demagnetizing field. This expression derived for a single domain structure, shows that for a 500-nm-thick Co film, using $K_1=5.2\times10^6$ erg/cm^3 and $K_2=1.6\times10^6$ erg/cm^3 (Ref. 7) of the bulk cobalt, $H_{d\perp}(t_{Co})$ must be neglected to fit the experimental value of $H_{s\parallel}=11.75$ kOe. These negligible $H_{d\perp}(t_{Co})$ values, compared to the demagnetizing field for perpendicular single domain films ($4\pi M_s$), arise from the presence of magnetic domains of sufficiently small aspect ratio favorable to decrease the demagnetizing field to values close to zero. As the film thickness decreases (Fig. 3), $H_{s\parallel}$ decreases due to a small increase of $H_{d\perp}(t_{Co})$.

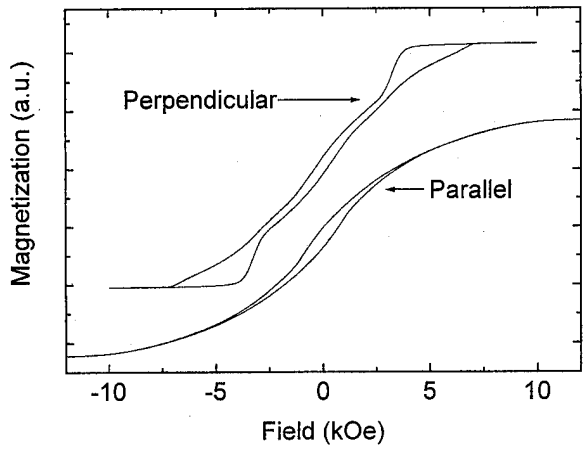


FIG. 2. Perpendicular and parallel $M-H$ curves for a 150-nm-thick dot array.

The domain structure has been observed in zero field by magnetic force microscopy (MFM) using a Nanoscope III from Digital Instruments with a magnetic tip in the tapping/lift mode. Figure 5(a) shows a typical domain structure observed on an epitaxial Co thin film. The MFM image of a 100-nm-thick cobalt film shows a demagnetized domain pattern consisting of stripes of about 100 nm domain width. The black and white contrast are related to domains oriented antiparallel. We found regular 180° domains with the magnetization vector pointing along the surface normal. Moreover, a systematic study of the domain width (W) with the film thickness (t_{Co}) has shown a linear relationship between W^2 and t_{Co}.[4]

Cobalt dots array: The results obtained on the magnetic dots indicate that, by reducing the geometric lateral dimensions, the magnetic properties are strongly affected although the experimental magnetization curves measured for the dot arrays above t_{cr} are very similar to those one obtained for the continuous films (Fig. 2). One can expect that the magnetization structure has not drastically changed with the lateral size reduction. However, the major magnetic parameters as the coercive, saturation, and nucleation fields show strong differences.

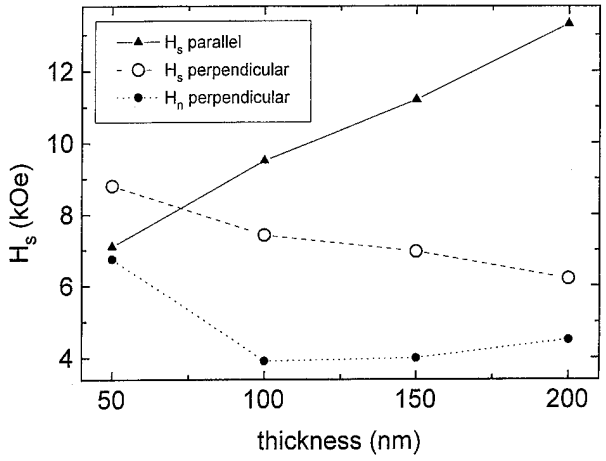


FIG. 4. Perpendicular nucleation field H_n, perpendicular and parallel saturation field H_s vs cobalt dot thickness.

In the perpendicular geometry, the consequences of the lateral size reduction are immediate (Fig. 4): H_s (respectively, H_n) decreases from 8.8 (respectively, 6.7) kOe for t_{Co} of 50 nm to 6.2 (respectively, 4.5) kOe for 200 nm instead of increasing. This is related to the reduction of the perpendicular demagnetizing factor $N_\perp$, with the increase of the aspect ratio. For a perpendicular multidomain structure, the perpendicular $H_s(H_s^m)$ can theoretically be evaluated, for a thick dot, from $H_s^m = N_\perp M_s$ while, for a single domain structure, it is equal to $H_s^s = N_\perp M_s - (2K_1/M_s)$. The result of the numerical evaluation for a 500-nm-thick dot with a lateral size of 700 nm gives $H_s^s \approx 0$ (square loop) and $H_s^m = 7.3$ kOe. This last value, close to the experimental one (6.8 kOe), gives a first proof of the existence of domains in dots. The decrease of H_n can be related to the size of the first nucleated domain. As indicated previously, the width of the domain increases with the film thickness. Consequently, for thicker dots, the energy required for nucleating large domains will increase and therefore decrease H_n. This has been confirmed by the MFM study. Indeed, the domain structure, as shown in Fig. 5(b) for the 50-nm-thick dots array, consists of stripes and bubbles domains with a domain width ($W = 70$–75 nm) very similar to the one observed on the continuous films.

In the parallel geometry, the saturation field increases from 7.1 kOe for t_{Co} of 50 nm to 13.3 kOe for t_{Co} of 200 nm.

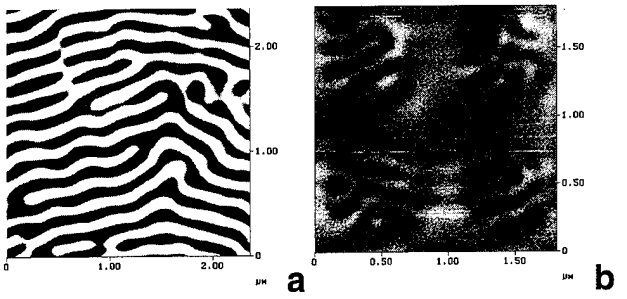


FIG. 5. MFM image of a demagnetized (a) 100-nm-thick continuous cobalt film and (b) 50-nm-thick array of dots.

For a single domain structure, the saturation field is equal to $H_s = (2/M_s)(K_1 + (N_\parallel - N_\perp)M_s^2 + 2K_2)$ and should vary from 2 to 6 kOe for, respectively, 50 and 200 nm thicknesses. The large difference between the experimental and calculated values shows that $N_\perp$, affected by the domain structure (already discussed in the case of continuous films), is much smaller than in the case of the single domain structure while $N_\parallel$ remains the same. The saturation field evaluated, in a first approximation using $N_\perp = 0$ gives a quite good agreement with the experimental data.

In summary, we have evidenced a crossover thickness at about 25 nm for epitaxial (0001) hcp cobalt films, above which the magnetization is perpendicularly oriented with a stripe and bubble domain structure. The MFM images have shown that the domain width of the stripes increases with the cobalt thickness. The lateral reduction of the cobalt films in dots of 500-nm-linewidth arrays have shown that the intrinsic magnetic characteristic have been strongly affected whereas the domain structure shows similar features.

This work was supported in part by the European Capital and Mobility Programme "Mesoscopic Magnetic Nanostructures". M. H. and K. O. thank Dr. H. van den Berg for fruitful discussions.

[1] C. Chappert, Phys. Rev. B **34**, 3192 (1986); R. Allenspach *et al.*, Phys. Rev. Lett. **65**, 3344 (1990).
[2] K. Ounadjela *et al.*, Phys. Rev. B **45**, 7768 (1992).
[3] C. Kittel, Phys. Rev. **70**, 965 (1946).
[4] M. Hehn *et al.* (unpublished).
[5] F. Rousseaux *et al.*, J. Vac. Sci. Technol. B (to be published).
[6] J. A. Cape and G. Lehman, J. Appl. Phys. **42**, 5732 (1971).
[7] D. M. Paige *et al.*, J. Magn. Magn. Mater. **44**, 239 (1984).

High field irreversibility in $NiFe_2O_4$ nanoparticles (abstract)

R. H. Kodama and A. E. Berkowitz
Physics Department, University of California, San Diego, La Jolla, California 92093 and Center for Magnetic Recording Research, University of California at San Diego, La Jolla, California 92093

E. J. McNiff, Jr. and S. Foner
Francis Bitter National Magnet Laboratory, MIT, Cambridge, Massachusetts 02139

Several anomalous magnetic properties of organic coated $NiFe_2O_4$ nanoparticles have been reported previously by Berkowitz *et al.*[1] These properties included low magnetization with a large differential susceptibility at high fields, shifted hysteresis loops after field cooling below 50 K, and Mössbauer spectra indicating a fraction of the material being magnetically ordered but not responsive to applied fields. It was suggested that a "strongly anisotropic phase" was present on the particles surface, and that the organic coating was responsible for producing high local anisotropy fields on the surface atoms. The present study extends the original work in several ways. We find that the lack of saturation in high fields is accompanied by irreversibility up to 20 T, in some cases. We have confirmed the previously reported behavior, in addition to observing similar behavior in samples prepared without the organic surfactant. This implies that we are observing a finite size effect. We have recently reported time dependence of the remanent magnetization which persists down to 0.4 K and does not appear to follow a thermally activated law. Instead, the viscosity becomes temperature independent below 2 K.[2] The model we propose for the high field irreversibility as well as the previously reported behaviors, is that there is a layer of spins at the surface which are spin glass-like, and that these spins can be reoriented irreversibly by a field or by thermal activation. The effect of surface spin interactions on magnetization relaxation will be discussed. © *1996 American Institute of Physics.* [S0021-8979(96)63008-1]

This work was supported in part by the MRSEC Program of the NSF under Award No. DMR-9400439. The FBNML is supported by the NSF.

[1] A. E. Berkowitz, J. A. Lahut, and C. E. VanBuren, IEEE Trans. Magn. **MAG-16**, 184 (1980).
[2] R. H. Kodama, C. L. Seaman, A. E. Berkowitz, and M. B. Maple, J. Appl. Phys. **75**, 5639 (1994).

Sputter deposited Co/CoO composite materials

J. Y. Yi, C. L. Platt, M. L. Rudee, A. E. Berkowitz, and T. L. Cheeks
University of California, San Diego, California 92039

Magnetic composites consisting of ultrafine particles of Co and CoO were prepared by dc reactive magnetron sputtering in a $Ar+O_2$ gas mixture. The films were composed of 60–140 Å particles of hcp Co and fcc CoO. The magnetization, coercivity, and particle size were found to be dependent on the O_2 partial pressure, such that the magnetization decreased and the coercivity increased to a maximum value of 1000 Oe with increasing O_2 partial pressure. A shift in the hysteresis loop was observed for several samples, indicating exchange coupling between the Co and CoO. © *1996 American Institute of Physics.* [S0021-8979(96)04608-X]

I. INTRODUCTION

Recently, composite thin films consisting of two insoluble metals or a metal embedded within an insulator have been the subject of an intense study due to their potential applications in magnetic and magneto-optic recording as well as other applications.[1–3] Metal-metal composites such as Co-Ag, Co-Cu, and metal-oxide composites such as Fe-SiO_2, Co-Al_2O_3 and Co-CoO are of interest because of their GMR effects, large coercivities, and exchange anisotropy.[4–6] Particularly interesting are thin-film metal-oxide composites in which the metal, a ferromagnet, is embedded within an antiferromagnetic oxide. These materials are known to exhibit exchange anisotropy such that the hysteresis loop shifts when the specimen is cooled down in a strong magnetic field. It is well known that the unidirectional exchange anisotropy exists in the bulk Co/CoO system.[7]

Thin films of Co/CoO have shown excellent properties such as high coercivity, perpendicular anisotropy, enhanced Kerr rotation, and exchange anisotropy.[8,9] The films typically consisted of fine particles of hcp Co and fcc CoO. The Neel temperature of CoO is about 293 K. Thin films of the composite material have been prepared using two different techniques, namely, rf reactive sputtering of Co in a $Ar+O_2$ gas mixture and reactive electron beam evaporation in which Co was evaporated in an O_2 environment.[10,11] In general, the microstructure of the films consisted of columnar grains with chains of fine Co particles surrounded by CoO particles. The magnetic properties, such as the saturation magnetization and the coercivity were found to be dependent on the O_2 partial pressure. Loop shifts of 1.6 kOe due to the exchange anisotropy were observed in 9000 Å sputter deposited films cooled to 120 K.[10]

In this study, we have prepared Co/CoO composite materials using dc reactive magnetron sputtering with a single Co target in a $Ar+O_2$ gas mixture. We discuss the influence of oxygen partial pressure on the microstructure and magnetic properties of these films.

II. EXPERIMENTAL DETAILS

Thin films of Co/CoO were prepared by dc reactive magnetron sputtering using a $Ar+O_2$ gas mixture. Prior to deposition the base pressure was better than 10^{-7} Torr and the total pressure during deposition did not exceed 2 mTorr. During deposition the Ar gas flow rate was fixed at 5 sccm and the O_2 flow rate was systematically adjusted to obtain the desired Co/CoO composition. The typical deposition conditions were a dc power of 20 W and a total pressure of 1.6 mTorr. A preliminary series of thin films were deposited to determine the deposition parameters, i.e., power, pressure, and $Ar+O_2$ mixture that resulted in Co/CoO thin films. The parameters were chosen to obtain the Co and CoO rather than Co_2O_3 or Co_3O_4 phases.

The films (5000 Å) were deposited onto glass substrates at a deposition rate of about 200 Å/min. The substrates prior to deposition were at room temperature, however, during deposition a slight increase in temperature of about 30 °C was observed. Presputtering of the Co target was performed using Ar followed by presputtering in the $Ar+O_2$ gas mixture used during film deposition.

The composition and microstructure of the films were investigated using x-ray diffraction (XRD) and transmission electron microscopy (TEM). The magnetic properties were measured using a vibrating sample magnetometer (VSM) and a SQUID magnetometer.

III. RESULTS AND DISCUSSION

Figure 1 shows the x-ray diffraction analysis (Co $K\alpha$, λ=1.7902 A, 1.8 kW) for 5000-Å-thick films deposited on glass substrates using Ar plus increasing partial pressure of O_2. The spectra show that the films deposited using pure Ar were hcp Co as indicated by the x-ray diffraction peaks of the (002), (101), and (100) planes. With increasing O_2 partial pressure the amplitude of the Co peaks decrease and the (111), (200) peaks of CoO gradually increase. Above a critical O_2 partial pressure (0.082 mTorr), the (111) peaks of Co_3O_4 begin to appear. The x-ray diffraction results show that Co/CoO films can be controllably obtained between 0.062 and 0.074 mTorr O_2 partial pressure. Beyond this partial pressure window, the films consist of mostly CoO or the Co_3O_4 phase.

A suggested mechanism for cobalt oxide formation has been described by Hecq *et al.*[12] Hecq suggests that when the oxygen partial pressure P_{O_2} is below a certain critical value P^* ($P_{O_2} < P^*$), the atoms sputtered from the target are metallic Co. The atoms are subsequently partially oxidized on the substrate resulting in a film composed of Co and CoO. When the oxygen partial pressure is between the critical value and 10% of the total pressure ($P^* < P_{O_2} < 10\%$ of the total pressure), the target surface oxidizes gradually and the

 0021-8979/96/79(8)/5072/3/$10.00 © 1996 American Institute of Physics

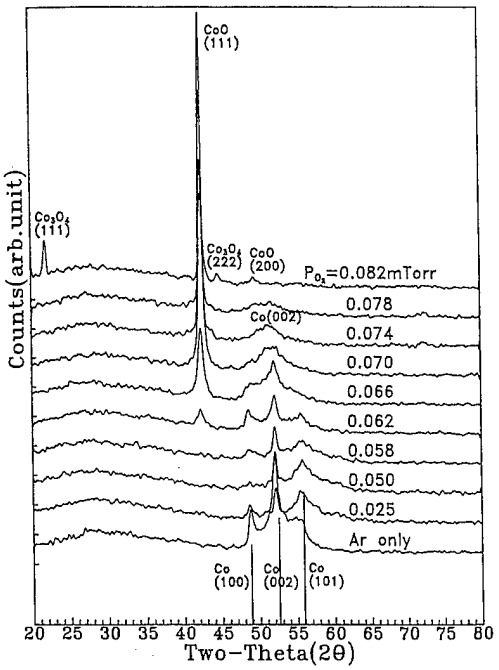


FIG. 1. X-ray diffraction spectra of Co/CoO thin films deposited using 20 WDC, Ar+ increasing O_2 partial pressure.

sputtered atoms are CoO rather than Co. The additional oxidation at the substrate surface results in both CoO and Co_3O_4 films. When $P_{O_2} > 10\%$ of the total pressure, the deposited film is entirely Co_3O_4 because the target surface is fully oxidized. Thus, the overall composition of the deposited films is expected to be dependent on oxygen partial pressure.

The x-ray results reported here confirm that the film composition is dependent on both the O_2 partial pressure and the input power. Since the O_2 partial pressure probably influences the oxidation rate of the target and the substrate, it is expected that at a given input power the oxide formation increases with increasing O_2 partial pressure. When the O_2 partial pressure exceeds a certain value, Co_3O_4 is expected to form. The input power should influence the sputter rate of the target material such that at a constant O_2 partial pressure and increasing input power, the target sputter rate will exceed the oxidation rate. This should result in formation of less CoO and more Co.

Transmission electron microscopy was performed on a series of samples deposited at 20 W and an O_2 partial pressure ranging from 0.050 to 0.074 mTorr. For the samples deposited at 0.050 and 0.070 mTorr, the microstructure consisted of fine equiaxed grains of Co and CoO that appear to extend throughout the film thickness. The electron diffraction patterns were consistent with the x-ray diffraction measurements confirming the formation of hcp Co and fcc CoO.

Figures 2(a)–2(c) show the bright-field TEM images obtained from 400-Å-thick films deposited at 0.050, 0.070, and 0.074 mTorr, respectively. The particle size was estimated from both bright-field and dark-field images. The particles size for samples deposited at 0.050 mTorr O_2 partial pressures were about 60 Å, while the particle size for the samples deposited at the higher O_2 partial pressures were about 140 Å. Also, the samples deposited at 0.050 mTorr appeared to

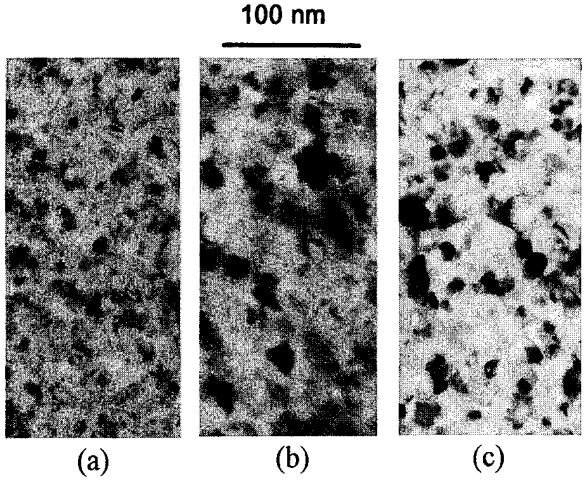


FIG. 2. Bright-field electron micrographs of Co/CoO films deposited at 20 W and O_2 partial pressure of (a) $P_{O_2} = 0.05$ mTorr, (b) $P_{O_2} = 0.07$ mTorr, and (c) $P_{O_2} = 0.074$ mTorr. The scale bar represents 100 nm.

have amorphous regions between the crystalline particles while those deposited at 0.074 mTorr were fully crystalline. It should be noted that the fine equiaxed Co/CoO grains reported here differ significantly from previous reports of larger columnar microstructures with mutually parallel chains of fine Co and CoO particles. The reason for the differences in microstructure may be related to the deposition conditions and is currently under investigation.

The coercivity (H_C) and saturated magnetization (M_S) measured parallel to the film plane as a function of increasing O_2 partial pressure are shown in Fig. 3. The saturated magnetization of pure Co films measured 1400 emu/cm^3 a value comparable to the bulk Co value of 1420 emu/cm^3. Figure 3 shows that the M_s remained fairly constant at low values of O_2 partial pressure. As the partial pressure increases above 0.050 mTorr a more dramatic decrease in the M_s is observed. The decrease in magnetization with increasing O_2 partial pressure is most likely due to the increasing

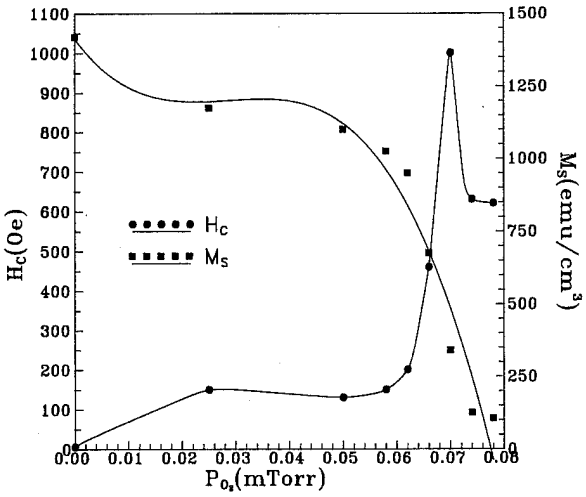


FIG. 3. Saturation magnetization and coercivity of Co/CoO films at room temperature as a function of O_2 partial pressure.

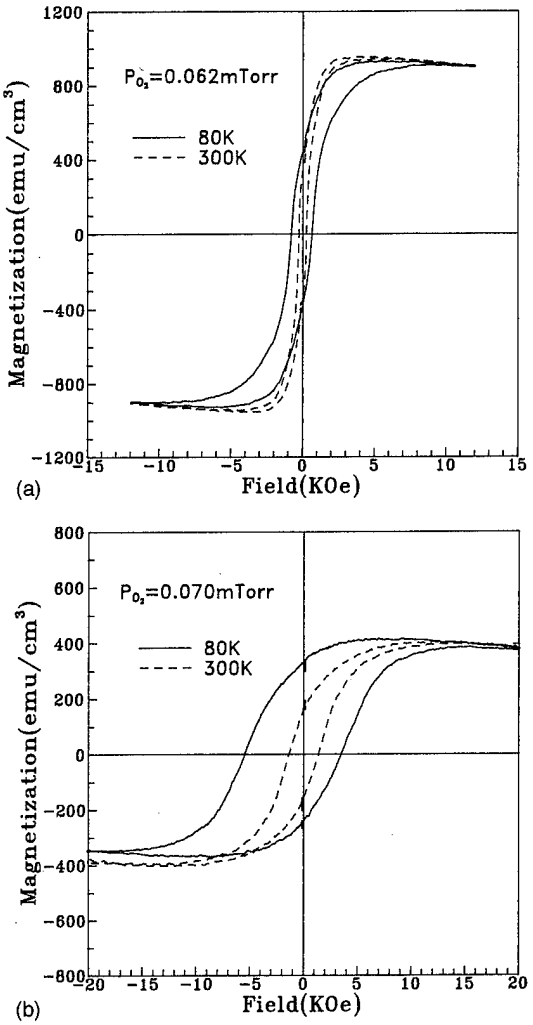


FIG. 4. Magnetic hysteresis loops of Co/CoO films at 80 K. (a) O_2 partial pressure of 0.062 mTorr and (b) O_2 partial pressure of 0.070 mTorr. Solid loops were measured after cool down to 80 K in a strong field.

amount of antiferromagnetic CoO within the film as confirmed by x-ray measurements. Above 0.078 mTorr, the M_s approaches zero, which corresponds to the Co_3O_4 phase transformation.

The H_c of the deposited films (Fig. 3) shows an initial increase to about 150 Oe with increasing O_2 partial pressure from 0.010 to 0.060 mTorr. As the O_2 partial pressure increases from 0.060 to 0.070 mTorr, the H_c increased substantially to a maximum value of 1000 Oe. Further increase in the O_2 partial pressure results in a slight reduction in H_c to about 650 Oe. The maximum H_c value obtained here is similar to the values obtained from previous work. The main difference is that the measurements were obtained from the magnetization parallel to the film plane rather than perpendicular to the film plane.[10]

A distinguishing property of Co/CoO composite films is its exchange anisotropy. The hysteresis loop shifts were measured parallel to the film plane after the specimen was cooled down to 80 K in a 20 kOe field. Figure 4 shows the magnetic hysteresis loops for two Co/CoO thin films deposited at two different partial pressure of O_2. The figure shows that the films deposited at the higher oxygen partial pressure, i.e., CoO rich, had a larger loop shift than the films deposited at the lower oxygen partial pressure. The loop shift value for a higher O_2 partial pressure was 1000 Oe while the value for the lower O_2 partial pressure was 85 Oe. These results show that the exchange anisotropy exists in these films and that it is very sensitive to the O_2 partial pressure, i.e., the Co to CoO ratio. The exchange field or loop shift is comparable to previously reported values, however, it is difficult to compare the Co to CoO ratio for a direct comparison. Further studies to determine the extent of the exchange anisotropy as a function of O_2 partial pressure, Co to CoO, ratio and particle size/volume fraction are currently underway.

IV. SUMMARY

We have successfully fabricated Co/CoO composite thin films using dc reactive magnetron sputtering in a $Ar+O_2$ gas mixture. The films exhibit a fine grained equiaxed microstructure that appear to extend throughout the film thickness. The particle sizes ranged from 60 to 140 Å and were found to be dependent on the O_2 partial pressure. Both the magnetization and coercivity are dependent on the O_2 partial pressure and a maximum coercivity value of 1000 Oe is measured. In addition to controlling the Co/CoO ratio over a fairly wide range of O_2 partial pressures, exchange anisotropy is observed in the films. This suggests that a strong interaction between of Co and CoO exists within these sputter deposited thin films.

ACKNOWLEDGMENT

This work was supported by the National Science Foundation Grant No. DMR-9400439.

[1] A. Garvin and C. L. Chien, J. Appl. Phys. **67**, 938 (1990).
[2] Y. Ota, T. Asaka, S. Asari, K. Nakamura, and A. Itoh, IEEE Trans. Magn. **MAG-20**, 1030 (1984).
[3] G. Xiao and C. L. Chien, Appl. Phys. Lett. **51**, 1280 (1987).
[4] M. J. Carey, A. P. Young, A. Starr, D. Rao, and A. E. Berkowitz, Appl. Phys. Lett. **61**, 2935 (1992).
[5] J. Q. Qing and G. Xiao, Phys. Rev. B **49**, 3982 (1994).
[6] S. H. Liou and C. L. Chien, J. Appl. Phys. **63**, 4240 (1988).
[7] W. H. Meiklejohn and C. P. Bean, Phys. Rev. **102**, 1413 (1956).
[8] X. Lin, G. C. Hadjipanayis, and S. I. Shah, J. Appl. Phys. **75**, 6676 (1994).
[9] M. Ohkoshi, K. Tamari, S. Honda, and T. Kusuda, J. Appl. Phys. **57**, 4043 (1985).
[10] M. Ohkoshi, K. Tamari, S. Honda, and T. Kusuda, IEEE Trans. Magn. **MAG-20**, 788 (1984).
[11] K. Yoshida and T. Takayama, J. Magn. Magn. Mater. **82**, 228 (1989).
[12] M. Hecq, A. Hecqet, and J. Van Cakenberghe, Thin Solid Films **42**, 97 (1977).

High-resolution observation of magnetization processes in 2 μm × 2 μm × 0.04 μm permalloy particles

K. Runge, Y. Nozaki, Y. Otani, and H. Miyajima
Department of Physics, Faculty of Science and Technology, Keio University, Hiyoshi 3-14-1, Kohoku, Yokohama 223, Japan

B. Pannetier
Centre de Recherches sur les Très Basses Températures, CNRS, BP 166, 38042 Grenoble Cedex 9, France

T. Matsuda and A. Tonomura
Advanced Research Laboratory, Hitachi Ltd., Hatoyama, Saitama 350-03, Japan

The magnetization process in an array of 2 μm × 2 μm × 0.04 μm permalloy particles fabricated on a 100 nm carbon membrane was investigated by means of high-resolution Lorentz microscopy and electron holography in magnetic fields parallel and perpendicular to the film surface. For perpendicular fields, the magnetization reversal was found to begin with the nucleation of a vortex which gradually transformed into a closure domain configuration. At the remanent state, the flux closure was achieved with the generation of a new type of doubled domain wall. © *1996 American Institute of Physics.* [S0021-8979(96)01708-0]

I. INTRODUCTION

Recent progress in microfabrication techniques now enables us to produce a variety of magnetic microstructures. An array of micron-size permalloy particles, for example, may be used as a device for applying in submicron scale spatially modulated magnetic fields on an underlying layer. According to the domain observation of submicron rectangular permalloy particles by Hefferman *et al.*,[1] the magnetic state of such particles can be easily controlled by a small external magnetic field less than 5 mT and their domain structures are extremely reproducible. We have tested this idea by fabricating a permalloy square particle array on a two-dimensional superconducting niobium film.[2,3] The superconducting properties of the underlying niobium film were significantly influenced by the modulated local fields created by the array, revealing peculiar behaviors such as quantum oscillations in the magnetoresistance and flux guide effects which stabilize the superconducting state.[3,4] Although qualitative explanations of the origin of these behaviors were given in previous studies,[3–5] there are still unsolved problems associated with the magnetic state of the particles. Properties of magnetic domain walls and their movements in the particles are therefore a key to fully clarify the origin of these phenomena.

In this study, our aim is to directly observe the domain structures inside the micron-size particles and the flux distribution outside the particles under magnetic fields parallel and perpendicular to the sample surface by means of high-resolution Lorentz microscopy and electron holography.

II. EXPERIMENTAL PROCEDURE

The magnetic particle array was fabricated by electron beam lithography and conventional sputtering techniques on top of a 30 nm carbon membrane. The array consists of 2×10^5 permalloy $Fe_{20}Ni_{80}$ square particles with an edge length of 2 μm and a thickness of 40 nm, sandwiched by Mo protecting and buffer layers of 10 nm. The total thickness of the sample is only 90 nm so that the sample is transparent for an electron beam. The structure of the array is a square lattice with the lattice constant of 4 μm, which gives the maximum dipole field of 0.3 mT in the homogeneously magnetized state. The particles are thus considered as more or less isolated. The magnetocrystalline anisotropy is negligible for $Fe_{20}Ni_{80}$, and the in-plane easy axes are mainly determined by the shape anisotropy of the particles. The estimated in-plane anisotropy field is 0.9 T.

The Lorentz micrographs reveal the domain walls as dark or light lines due to the divergence or overlap of the electron beams after passing magnetic domains with different magnetization directions. On the other hand, the electron holograms contain the amplitude and phase of the electron beam transmitted through the sample. The optically reconstructed image interfered with a planar comparison wave reveals contour fringes of constant phase, that is, the flux distribution.

A 300 kV field emission microscope (Hitachi Co. Ltd.) was used for the observation at 4.2 K in parallel fields. For the observation in perpendicular fields, a 200 kV microscope (Hitachi Co. Ltd.) was operated only at room temperature. Perpendicular fields up to 1.6 T were applied by adjusting the current supplied to the objective lens. Obtained images were recorded on either video tapes or films.

III. RESULTS AND DISCUSSION

Initial studies were made in parallel fields at 4.2 K using the defocused mode of Lorentz microscopy. A field profile of typical domain structures observed in permalloy particles together with inferred domain structures are shown in Fig. 1. The parallel field $\mu_0 H_\parallel$ was applied along a direction tilted by ~30° from the vertical axis as indicated in the figure. When $\mu_0 H_\parallel$ is zero, flux closure was achieved within the particles by four-closure domain (left particle) or seven-closure domain (right particle) configuration segmented by 90° and 180° domain walls. Bright and dark domain walls were observed according to the circulation of the magnetization in either clockwise or anticlockwise direction, respectively. Some of the particles exhibited distorted seven-

 0021-8979/96/79(8)/5075/3/$10.00 © 1996 American Institute of Physics

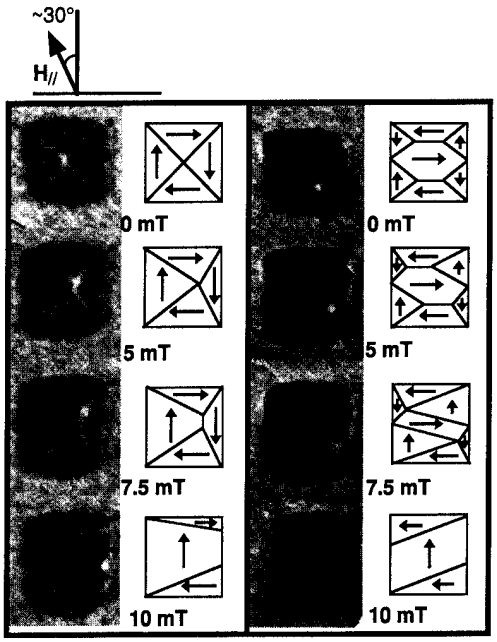


FIG. 1. Parallel field profile of four-closure domain and seven-closure domain configurations observed by means of Lorentz microscopy together with the inferred domain structures.

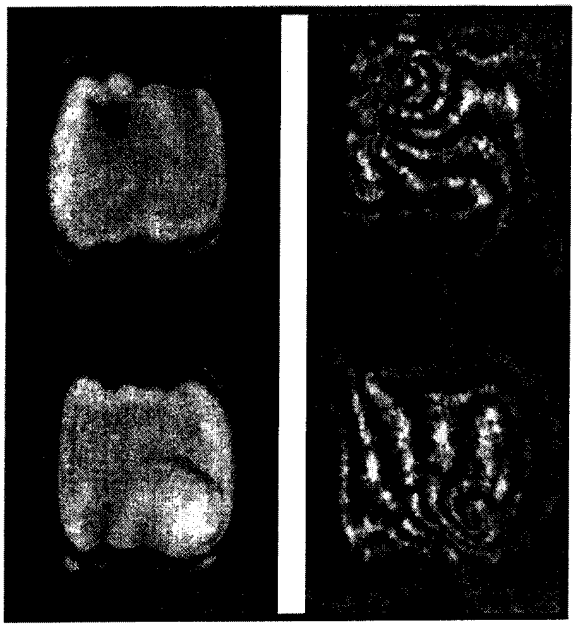


FIG. 2. Lorentz micrograph and flux line maps taken under a field of 0.16 T applied perpendicular to the particle surface.

closure domain configurations, in which one of the circulation dominated. This may be due to the domain wall pinning by irregularities found along the edges of the particles.

As $\mu_0 H_\parallel$ is increased, domains with magnetization directions close to the external field direction grow. This results in a shift of the intersection of the 90° domain walls in the four-closure domain configuration toward the corner of the particle (left column in Fig. 1). The initial movement of the intersection agrees well with the trajectory calculated by minimizing the free energy composed of the magnetic energy, the magnetostatic energy, and the domain wall energy.[6] The intersection first moves perpendicular to the applied field direction and gradually approaches the corner of the particle. When the parallel field is increased above 7 mT, the intersection splits into two with the generation of 180° domain wall. Further increase of the field sweeps this wall towards the right side of the particle, leading to a rather simple nonsolenoidal domain structure with two 90° walls.

In the case of the seven-closure domain configuration (right column in Fig. 1), with an increase of $\mu_0 H_\parallel$, two triangular segments with the magnetization direction along the external field grow until the vertices reach the edges of the particle accompanied by the annihilation of 180° domain walls. Above 8 mT, the central domain is gradually squashed by the growing triangular segments, resulting in a nonsolenoidal structure as observed in the four-closure domain structure. In the demagnetizing process, some of the seven-closure domain configurations are found to transform abruptly to four-closure domain configurations within a transition time of less than 100 ms. This suggests that the four-closure domain configuration is energetically favorable relative to the seven-closure domain configuration.

Measurements in perpendicular fields $\mu_0 H_\perp$ were performed at room temperature by means of Lorentz microscopy and electron holography. Prior to the measurements, the sample was magnetized perpendicular to the film plane in a magnetic field of 1.2 T and the images were captured while the applied field was decreased from 1.2 T to zero. When the field is in the range of $1.2\ \mathrm{T} \geqslant \mu_0 H_\perp \geqslant 0.6$ T, the particles are uniformly magnetized perpendicular to the film plane. Interestingly, dark or bright dots began to appear in the particles at $\mu_0 H_\perp = 0.4$ T, reflecting the vortex formation associated with the nucleation of magnetization reversal. This can clearly be seen in Fig. 2 which shows a Lorentz micrograph of two particles soon after the nucleation together with flux line maps taken by electron holography. The bright and dark dots correspond to the vortices with anticlockwise and clockwise circulation, respectively. The intensity analysis of the central part of the vortex in the Lorentz micrograph based on Fuller and Hale's method[7] shows that the intensity distribution reflects an exponential decay of the perpendicular magnetization component which is characteristic of the vortex.[8] This fitting yields the exchange length of 5 nm. The magnetization at the center of the vortex therefore directs opposite to the external field direction, gradually changes its direction into the film plane within the exchange length and then toward the external field direction. The flux line map also supports the above mentioned feature of the vortex. The density of the fringes, that is, the in-plane magnetization intensity is lower at the edges of the particles than in the vicinity of the vortex center.

In most cases, the vortices are located at the corner of the particles. This can be understood from the fact that the strongest demagnetizing field is exerted on the edge of the particle for a perpendicularly magnetized thin plate. At the initial stage of the reversal, the magnetization tends to rotate into the film plane because of the large demagnetizing field

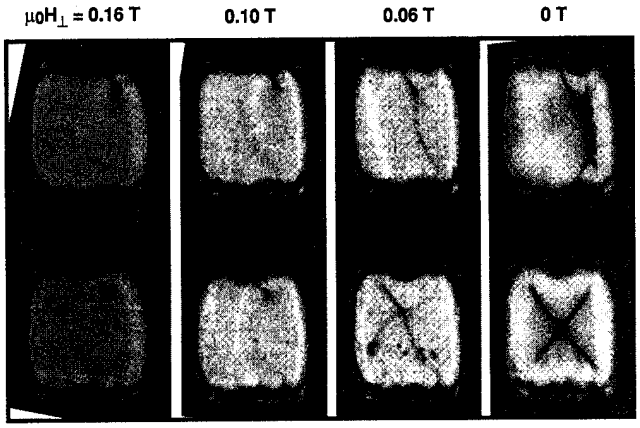


FIG. 3. Perpendicular field profile of the development of the vortices observed by means of Lorentz microscopy.

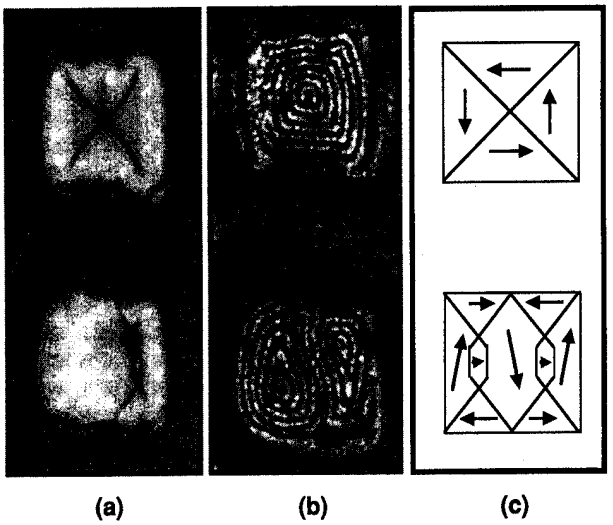


FIG. 4. (a) Lorentz micrograph, corresponding (b) flux line map, and (c) the inferred magnetization distribution of the four-closure domain and the seven-closure domain configurations in the remanent state.

and then forms a vortex to avoid the volume and surface charges. The initial size and location of the vortex may be closely related with the shape of the rounded corner as is expected from the van den Berg's approach.[9] In addition, the presence of the flux lines between the particles clearly shows that there is a dipole interaction although it is difficult to quantify its strength. This is also an important factor that determines the location of the vortices.

Figure 3 shows a field profile of the vortices taken by Lorentz microscopy. The vortices, initially nucleated at the corner of the particle, steadily move toward the center with decreasing $\mu_0 H_\perp$ to 0.10 T. In the figure, there is observed a small sign of the pinned domain walls which seem to restrict the movement of the vortices. When $\mu_0 H_\perp$ reaches 0.06 T, a significant difference is observed in the domain configuration between the top and bottom particles. The vortex in the top particle stays in the vicinity of the corner whereas the vortex in the bottom particle stays near the center of the particle. This difference results in a seven-closure domain configuration for the top particle and a four-closure domain configuration for the bottom particle in the remanent state. Figure 4 shows a Lorentz micrograph, corresponding flux line maps and inferred magnetization distributions for the four-closure domain and the seven-closure domain configurations. In the case of the four-closure domain configuration, complete flux closure seems to be achieved. Since the period of the fringes is equivalent to one flux quantum ($\phi_0 = 4.14 \times 10^{-15}$ Wb), the in-plane magnetization is evaluated as 0.83 T from the relation $n\phi_0/S$, where $n(=8)$ is the number of the fringes and S ($=4 \times 10^{-14}$ m^2) is the cross-sectional area which the circulating magnetization passes through. The obtained value coincides well with the saturation magnetization of bulk permalloy, and this proves that the magnetization lies in plane. More interesting is the seven-closure domain configuration. One should notice that there is a double wall in between the triangular segments in the Lorentz micrograph. In the corresponding flux line map, the in-plane flux density of the upper left and the lower right part of the particle is less, suggesting that the magnetization stands out of the film plane. As shown in the schematic domain structure, the double wall consists of a kind of combined 90° domain walls, in which the magnetization changes its direction at the expense of magnetostatic energy due to the surface charge. It should also be noted that the remainders of the vortices can be recognized in the flux line map. The reason of the appearance of the seven-closure domain type configuration may be related to the creation of the vortex with counter circulation.

ACKNOWLEDGMENTS

The authors would like to thank J. P. Nozières, LLN CNRS, for permalloy sputtering. One of us (K.R.) would like to thank the Commission of the European Community for financial support.

[1] S. J. Hefferman, J. N. Chapman, and S. McVitie, J. Magn. Magn. Mater. **95**, 76 (1991).
[2] O. Geoffroy, D. Givord, Y. Otani, B. Pannetier, and F. Ossart, J. Magn. Magn. Mater. **121**, 223 (1993).
[3] Y. Otani, B. Pannetier, J. P. Nozières, and D. Givord, J. Magn. Magn. Mater. **126**, 622 (1993).
[4] Y. Otani, Y. Nozaki, H. Miyajima, B. Pannetier, M. Ghidini, J. P. Nozières, G. Fillion, and P. Pugnat, Physica C **235–240**, 2945 (1994).
[5] Y. Nozaki, Y. Otani, K. Runge, H. Miyajima, B. Pannetier, and J. P. Nozières (unpublished).
[6] K. Runge, Y. Nozaki, Y. Otani, H. Miyajima, B. Pannetier, T. Matsuda, and A. Tonomura (unpublished).
[7] H. W. Fuller and M. E. Hale, J. Appl. Phys. **31**, 238 (1960).
[8] J. Miltat, in *Applied Magnetism*, edited by R. Gerber *et al.*, Nato ASI Ser. 253 (Kluwer, the Netherlands, 1994), pp. 221–308.
[9] H. A. M. van den Berg, J. Appl. Phys. **57**, 2168 (1985).

Neutron diffraction determination of the nuclear spin ordering in Cu and Ag at nano- and subnano-K temperatures (invited)

M. Steiner, A. Metz, and K. Siemensmeyer
Hahn Meitner Institut, Berlin, Glienicker Str. 100, 14109 Berlin, Germany

O. V. Lounasmaa, J. T. Tuoriniemi, K. K. Nummila, and R. T. Vuorinen
Low Temperature Laboratory, Helsinki University of Technology, Otakaari 3A, 02150, Espoo, Finland

K. N. Clausen and K. Lefmann
Risø National Laboratory, Physics Department, P.O. Box 49, 4000 Roskilde, Denmark

F. B. Rasmussen
Niels Bohr Institute, University of Copenhagen, 2100 Copenhagen, Denmark

The spontaneous nuclear spin ordering in the simple diamagnetic metals Cu and Ag has been studied by neutron diffraction using the spin dependent part of the nuclear cross section. Simple antiferromagnetic ordering of type I has been found in zero field for these fcc-systems below 60 and 560 pK for Cu and Ag, respectively. The ordering in an applied field has been investigated and the phase diagrams have been determined: a very complex phase diagram with different magnetic structures, strong hysteresis, and time dependence was found for Cu, while in Ag the phase diagram is very simple. Comparison with *ab initio* calculations allows a rather deep insight into the interactions leading to the ordering. © *1996 American Institute of Physics.*
[S0021-8979(96)39108-8]

I. INTRODUCTION

The weakest interaction in solids is between nuclear spins: it can be smaller than the interaction between electronic moments by 10 to 15 orders of magnitude! To study these interactions is therefore a very interesting and challenging problem for theory and experiment. For such studies, the determination of the ordered ground state is the crucial experiment. The only way to achieve this is by neutron diffraction. But, due to the smallness of the nuclear moments, the magnetic cross section of the neutrons cannot be used. Fortunately, the nuclear cross section has a spin dependent part, which can be used to study the ordered nuclear ground state. Suitable systems have to be chosen bearing in mind, that the smallness of the interaction results in an extremely low transition temperature and that any electronic magnetism will overrule any tendency of the nuclear spin system to order spontaneously. Thus, only such systems are of interest, of which one knows, that they can be cooled to extremely low temperatures and that they are ideal electronic diamagnets. The simple metals Cu and Ag fulfill these requirements ideally. Systematic investigations by nuclear magnetic resonance (NMR) and susceptibility measurements on Cu and Ag have given strong evidence, that there is spontaneous nuclear ordering below 60 nK and 560 pK, respectively.[1] From such measurements, it was concluded that the ordering should be antiferromagnetic, but no firm proof could be given by these techniques.

In the temperature range of interest particular phenomena and properties of a solid become key issues: it is most likely that the interactions are simple and tractable by *ab initio* calculations [dipolar and Rudermann, Kittel, Kasuya, Yosida (RKKY) interactions]; the nuclear system is "completely" decoupled from the surrounding electronic and lattice system, talking between these systems occurs through the very slow spin lattice relaxation only with typical time constants of hours. No temperature measurement in the usual sense is possible in this situation. Since cooling is by adiabatic demagnetization, ordering takes place at constant entropy S. In this situation phenomena can be studied, which are very difficult or impossible to study in electronic magnets: A prominent example is the antiferromagnet on the fcc-lattice, where the topological frustration competes with antiferromagnetism, in which situation electronic magnets tend to change the structure at the ordering temperature to break the frustration. A further advantage of the extraordinary low energy scale of nuclear magnets is the corresponding long time scales for onset of order or changes of order. In conclusion, many phenomena not accessible experimentally in electronic magnets are at the experimentalist's hands in nuclear magnets.

In this paper, the results of our intense studies of Cu and Ag by neutron diffraction will be presented. Not only will it be shown, that neutron experiments are feasible at extremely low temperatures, but that new and exciting phenomena of general interest were found, too, as a reward for the efforts necessary to perform such experiments.

II. EXPERIMENT

It is appropriate to shortly discuss some properties of the neutron cross section used in the experiments to be discussed, for more details see Ref. 2. The nuclear polarization $\langle P_N \rangle$ enters the structure factor as $\langle P_N \rangle (b^+ - b^-)$, in analogy to the electronic magnetic scattering length, $(b^+ - b^-)$ being the spin dependent part of the nuclear scattering

 0021-8979/96/79(8)/5078/3/$10.00 © 1996 American Institute of Physics

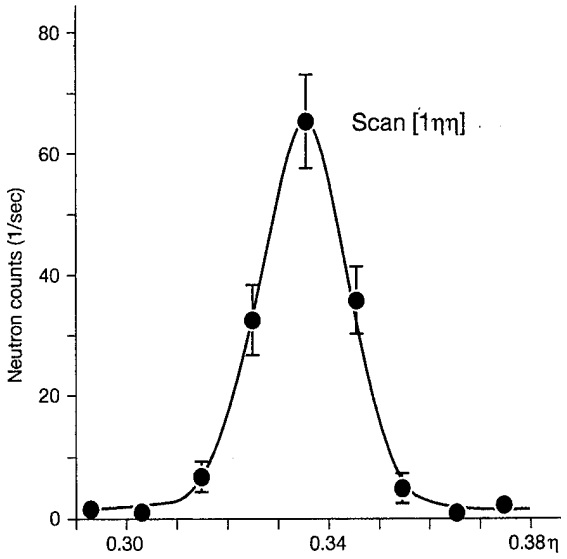


FIG. 1. Scan along $[1\eta\eta]$ at $T \ll 60$ nK in Cu. The width of the observed peak at $\eta = 1/3$ is determined by the resolution.

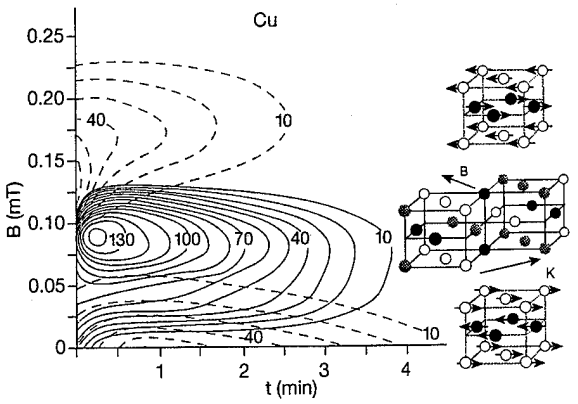


FIG. 2. The magnetic phase diagram of the nuclear spin ordering in Cu. The corresponding structures are indicated. Note the very strong coexistence of the different phases especially at low fields. The numbers given in the diagram are intensities in arbitrary units.

length. However, since the scattering is due to nuclear forces, there is no interaction vector or sin α-term as in electronic magnetism. Therefore, the determination of the moment direction in nuclear magnets can not be performed by a systematic measurement of different Bragg-reflections as in electronic magnets, but needs experiments with polarized neutrons and polarization analysis. As $b,(b^+ - b^-)$ does not show any Q dependence, an obvious way to separate nuclear from electronic magnetic scattering. $(b^+ - b^-)$ is comparable in size to b for many isotopes. Otherwise, the procedure for the magnetic structure determination is the same for the nuclear magnets as for electronic magnets. It is worth mentioning that not only the scattering, but the absorption may depend on $\langle P_N \rangle$, giving yet another way to measure $\langle P_N \rangle$ by neutrons.

Obviously the biggest hurdle to be passed in such studies is to reach the necessary low temperatures. It is generally true, that there is no technique to achieve continuous cooling in the sub-mK range. All further cooling has to be done by adiabatic demagnetization.[3] For the studies of Cu and Ag, a two stage adiabatic demagnetization procedure was used: the first stage is a large polycrystalline piece of copper, which is demagnetized into the μK range, the electronic and the lattice system being in thermal equilibrium with the nuclear system. This powerful stage cools the second stage, the actual sample (Cu or Ag-single crystal), to the corresponding temperature. From there this stage and only the nuclear system of it is demagnetized to zero field, hopefully ending up in the ordered regime of the nuclear system. It is clear, that at the end of such a cooling cycle the nuclear system, now completely decoupled from its lattice and electronic system, will warm up according to the external heat leak into it. Therefore, the heat leak must be minimized to a point where the neutron beam determines the heat load. In Cu the time for experiments in the ordered phase was about 6 min, while in Ag more than 30 min were achieved. This difference is due to the different spin-lattice relaxation times. The time needed to prepare the system for these short periods, i.e., for the cooling procedures was between one and two days.

III. RESULTS

A. Copper

The neutron diffraction experiments have been performed at the DR3-reactor of Risø National Laboratory using a two axis diffractometer. Guided by theoretical predictions[4] a (1,0,0) reflection was found in zero field below $T_N = 60$ nK demonstrating, that the ordering of the nuclear spin system is of type I for this fcc system. Its width was resolution limited. When applying an external magnetic field the (1,0,0)-peak disappeared around 0.08 mT and reappeared at 0.12 mT until at 0.25 mT the field had completely destroyed the antiferromagnetic ordering. Again guided by theory, scans along the $[1,\eta,\eta]$ direction have been performed at intermediate fields, yielding a peak at $\eta = 1/3$ as shown in Fig. 1. From such measurements, a complete phase diagram has been mapped out as shown in Fig. 2.[5] It must be noted that the (1, 1/3, 1/3) type of structure has never been observed for such fcc antiferromagnets before.

A striking feature of this phase diagram is the strong coexistence of the different phases along the phase boundaries. A very strong time and history dependence accompanied every passage through the phase diagram.[6] As there was no way to determine the thermodynamic parameters, entropy S or T, mainly because of the strong hysteresis in the phase diagram, the temperature coordinate had to be replaced by a time coordinate where $t = 0$ represents the end of the demagnetization. Measurements with the field direction along different crystallographic direction have lead to another phase diagram shown in Fig. 3. It is obvious that with field along [1,0,0] and [0,1,1] there are the three phases as in Fig. 2, but that for field along [1,1,1] the high field (1,0,0) phase is missing. Whether there is no ordering in this situation or whether there is another, not yet discovered type of ordering is not clear.[7]

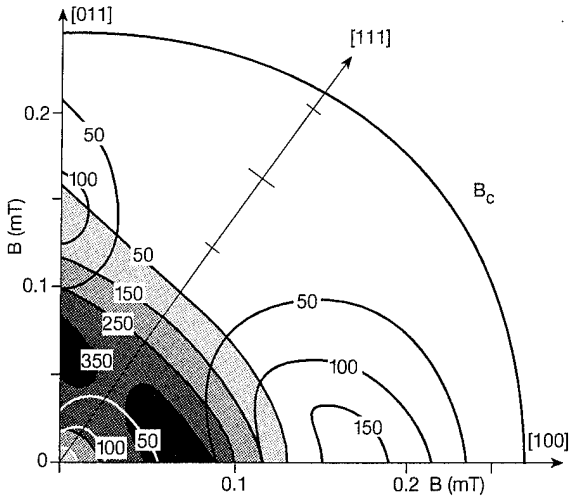


FIG. 3. The magnetic phase diagram of Cu for a field along different directions. Note the missing high field phase around [111].

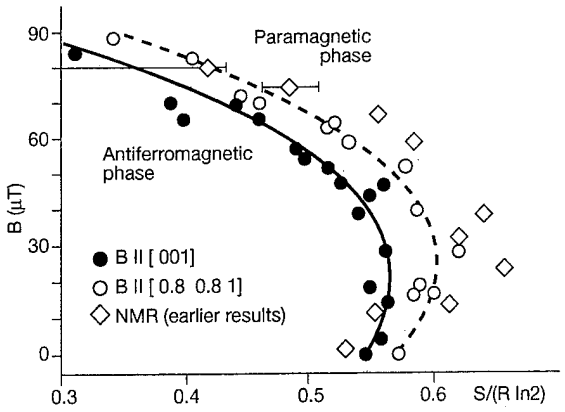


FIG. 4. The H,S phase diagram of the nuclear spin system in Ag for two field directions. The lines are guides for the eye. The phase transition appears to be continuous all along the phase boundaries.

B. Silver

Again guided by theory, in zero field below $T_N=560$ pK (Ref. 8), the same structure was found as in Cu, namely type I for the fcc lattice. When applying a magnetic field no new phase was observed, yielding the simple phase diagram shown in Fig. 4. This phase diagram resembles very closely the phase diagram of an extremely weakly anisotropic antiferromagnet, yet no additional phase boundary has been detected. No hysteresis nor any time or history dependencies have been observed. However, a very selective occurrence of the three degenerate domains of the (1,0,0) structure has been observed: for example, demagnetization along [0,0,1] resulted in the occurrence of the (0,0,1) domain only and no particular time dependence was observed. Thus, this is definitely a single-k structure. No evidence for the predicted multi-k structure in finite fields has been obtained. In these investigations the entropy S could be determined at each measurement and thus the phase diagram of Fig. 4 is presented as H,S diagram. This was achieved by using the spin dependent part of the absorption, which without any calibration yields the direct nuclear polarization, from which S can be deduced. By this technique, it was found that at finite fields inside the ordered phase a significant direct polarization of the nuclei coexists with the antiferromagnetic polarization. The corresponding susceptibility $\langle P_N\rangle/H$ was found to be 0.36 and independent of S.

IV. CONCLUSION

The neutron scattering studies on the simple metals Cu and Ag have uniquely proven the existence of a long range antiferromagnetic ground state of the respective nuclear spin systems. A new antiferromagnetic structure for fcc systems was found at 0.1 mT in Cu. The determination of the magnetic unit cells is only a part of a complete magnetic structure determination: the direction of the magnetic moments with respect to the crystallographic axis remains to be determined. The phase diagrams are surprisingly different, perhaps an indication of the influence of the size of the spin: Cu has $I=3/2$, while in Ag $I=1/2$, which makes Cu a classical and Ag a quantum system. The assumed and calculated structures seem to agree with experiment; in Cu in particular, the agreement covers the whole phase diagram, while in Ag at present agreement is limited to zero field. Again this might be a consequence of $I=1/2$. In both cases, dipol–dipol and RKKY interaction suffice to describe the structures found. Although *ab initio* calculations are feasible, the identification of the true ground state is difficult due to the high degree of degeneracy in these topologically frustrated fcc antiferromagnets. The remarkable stability of the one domain created during demagnetization in Ag should be noted as well. In Cu various time dependent phenomena have been observed. Whether they are due to the restriction $S=$const during ordering or whether they reflect the slow ordering remains to be clarified by further investigations. In any case, it has become clear that nuclear magnets are not just another class of magnets, but represent systems whose properties add new interesting and fundamentally important phenomena to our knowledge of magnetic ordering. This outcome balances the enormous efforts necessary to perform such experiments successfully.

[1] M. T. Huiku and M. T. Loponen, Phys. Rev. Lett. **49**, 1288 (1982). P. J. Hakonen and S. Yiu, J. Low Temp. Phys. **85**, 25 (1991). M. Steiner, Int. J. Mod. Phys. B **7**, 2909 (1993).

[2] M. Steiner, Physica Scripta **42**, 367 (1990).

[3] O. V. Lounasmaa, *Experimental Principles and Methods Below 1K* (Academic, London, 1974).

[4] P.-A. Lindgård, X.-W. Wang, and B. N. Harmon, J. Magn. Magn. Mater. **545–547**, 1052 (1986).

[5] K. Siemensmeyer, M. Steiner, H. Weinfurter, K. N. Clausen, P. A. Lindgård, A. J. Annila, O. V. Lounasmaa, A. S. Oja, and J. T. Tuoriniemi, Physica B **180&181**, 29 (1992).

[6] A. J. Annila, K. N. Clausen, A. S. Oja, K. Siemensmeyer, M. Steiner, J. T. Tuoriniemi, and H. Weinfurter, Physica B **165&166**, 783 (1990).

[7] K. Siemensmeyer and M. Steiner, Z. Phys. B: Condens. Matter **89**, 305 (1992).

[8] J. T. Tuoriniemi, K. K. Nummila, R. T. Vuorinen, O. V. Lounasmaa, A. Metz, K. Siemensmeyer, M. Steiner, K. Lefmann, K. N. Clausen, and F. B. Rasmussen, Phys. Rev. Lett. **75**, 3744 (1995).

Critical properties of the spin Peierls transition in $CuGeO_3$

M. D. Lumsden, B. D. Gaulin, and H. Dabkowska
Department of Physics and Astronomy, McMaster University, 1280 Main St. West, Hamilton, Ontario L8S 4M1, Canada

The spin-Peierls transition in $CuGeO_3$ has been studied using x-ray diffraction techniques. The order parameter of the (1/2,5,1/2) superlattice reflection has been measured with a temperature stability of ± 5 mK. Careful analysis has been performed fitting the order parameter to both an ordinary power law in the reduced temperature as well as to a power law with the first correction to scaling term included in an attempt to determine a consistent value of the critical exponent β. We obtain a value of β of 0.36 ± 0.03 at a transition temperature of 14.06 ± 0.02 K. This value of β is consistent with conventional three-dimensional Heisenberg or *XY* behavior and clearly inconsistent with the tricritical values reported previously. © *1996 American Institute of Physics.* [S0021-8979(96)39208-4]

INTRODUCTION

The spin-Peierls transition occurs in one-dimensional $S=1/2$ Heisenberg spin chains in which the spins couple to the phonons of the lattice. Below some transition temperature, the lattice undergoes a structural dimerization which is driven by magnetic interactions within the chain. The magnetic susceptibility falls isotropically to zero due to the presence of a magnetic energy gap separating the nonmagnetic singlet ground state from the triplet excited states. This transition had previously only been found in a few organic compounds until the discovery, by Hase *et al.*,[1] of such a transition in the inorganic insulator $CuGeO_3$. Hase *et al.*[1] observed the characteristic magnetic susceptibility drop below a temperature of 14 K. Since this time, many other characteristic properties of the spin-Peierls transition have been found in this material. For instance, the magnetic energy gap has been observed using neutron scattering[2] and the singlet to triplet nature of the excitations have been demonstrated by such measurements in the presence of a magnetic field.[3] In addition, the characteristic dimerization of the chains has been observed using x-ray and neutron diffraction.[4]

One question which remains unclear is what the true value for the critical exponent β describing the order parameter is for the transition in this material. Neutron scattering results seem to yield an exponent consistent with tricritical behavior[5] while thermal expansion measurements yield a value consistent with conventional three-dimensional (3D) behavior.[6] This uncertainty motivated us to carefully measure the order parameter using x-ray scattering techniques.

EXPERIMENTAL DETAILS

The lattice parameters of $CuGeO_3$ at room temperature are $a=4.81$ Å, $b=8.47$ Å, and $c=2.941$ Å and the linear chains consist of $S=1/2$, Cu^{2+} ions stacked along the c axis. Below a temperature of 14 K, there is a dimerization along this chain which is accompanied by slight displacements of the $O(2)$ atoms[7] yielding a doubling of the unit cell along the a axis. Consequently, we find superlattice reflections with indices $(h/2,k,l/2)$ with h and l odd and k odd or even. This has been observed in electron diffraction,[8] x-ray and neutron scattering[4] and later neutron diffraction[7] studies. We have chosen to measure the order parameter of the (1/2,5,1/2) superlattice reflection due to its relative strength and to allow for a direct comparison with other studies where the identical reflection was measured.

A single crystal of $CuGeO_3$ was grown from self flux by the slow cooling method with approximate dimensions $2 \times 1 \times 0.5$ mm^3. The sample was mounted in a Be can in the presence of a He exchange gas. This can was then connected to the cold finger of a closed cycle He refrigerator. Within the temperature range of interest, a temperature stability of ± 5 mK was obtained. Cu $K\alpha$ radiation from an 18 kW rotating anode x-ray generator, further monochromatized via the (0,0,2) reflection of a focusing pyrolitic graphite (PG) crystal, was used as the incident radiation in these measurements. No analyzer crystal was employed.

RESULTS AND ANALYSIS

The data obtained for the peak intensity as a function of temperature at the (1/2,5,1/2) superlattice reflection is shown in Fig. 1. The peak intensity at the ordering wave vector is proportional to the square of the order parameter. Prior to performing the measurements, the effect of changes in lattice parameters,[5,7] was carefully investigated. Both transverse and longitudinal scans were performed at several temperatures, some near T_{sp} and some far below T_{sp}. With our relatively low resolution configuration, no change in peak position, or line shape, could be detected. Thus, the measurements were performed by varying the temperature in 5 mK increments and monitoring the intensity at $(\frac{1}{2},5,\frac{1}{2})$.

Despite an extensive search, no critical scattering was observed above T_{sp}. However, the best fit to the data, represented by the solid line in Fig. 1 is systematically lower than the data in the immediate vicinity of T_{sp}. This may suggest the presence of weak critical scattering very close to the transition temperature.

The critical behavior of the order parameter has been determined by fitting the intensity to an ordinary power law in the reduced temperature:

$$\text{Intensity} = I_0 t^{2\beta} + \text{Background}, \tag{1}$$

where the reduced temperature t is $(T_{sp}-T)/T_{sp}$. This expression is expected to be valid in the asymptotic region where $T \to T_{sp}$. In addition to this, another form of the same equation was used

 0021-8979/96/79(8)/5081/3/$10.00 © 1996 American Institute of Physics

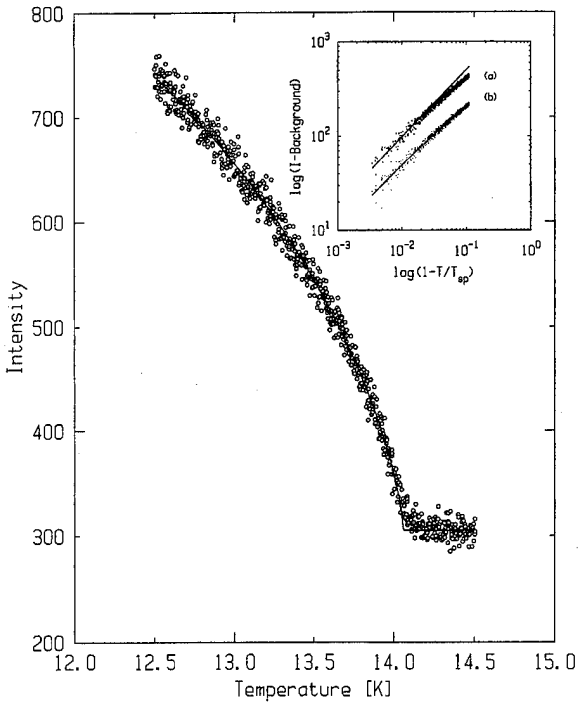


FIG. 1. X-ray scattering peak intensity as a function of temperature at the (1/2,5,1/2) ordering wave vector. The solid line represents the best fit to a power law with correction-to-scaling included. The insert shows the same data on a logarithmic scale (a and b are displaced vertically). The solid line (b) represents the same fit with correction-to-scaling included while the solid line (a) represents a fit to a straight power law with the same value of β.

$$\text{Intensity} = I_0 t^{2\beta}(1 + A t^{\Delta}) + \text{Background}, \tag{2}$$

where Δ is approximately 0.5.[9] This form includes the first *correction-to-scaling confluent singularity* term, which is the first-order correction for deviations of the data from the asymptotic region. The fits were performed using data in the region $0.004 < t < 0.11$.

The fit shown in Fig. 1 represents the best fit to Eq. (2) yielding a value of $\beta = 0.36 \pm 0.03$ at a transition temperature of 14.06 ± 0.02 K. The insert (b) shows the same fit but on a logarithmic scale while insert (a) show a fit to the straight power law equation (1) with the same value of β. One can qualitatively see that the fit only agrees at small values of t and the data clearly deviate from the fit at larger values of t when the straight power law is used.

We were therefore motivated to more carefully examine the dependence of the fit on the inclusion of points far from the transition temperature. Fits were performed as a function of starting point using both the straight power law equation (1) and the power law with correction-to-scaling included Eq. (2) and the resulting plot of β as a function of initial temperature is shown in Fig. 2. Both fits were carried out using a fixed value of T_{sp}. The value of β is independent of starting point when the power law with correction to scaling is used. However, when the straight power law is used, β changes over the entire temperature range. The curves become progressively closer to agreement as $T \rightarrow T_{sp}$ but could not be extended beyond a $T_{initial}$ of 13.8 K due to a lack of good statistics over such a small temperature interval. Nonetheless, there is quite reasonable agreement between the two values near T_{sp} and the analysis with the correction to scaling term included seems to be quite robust.

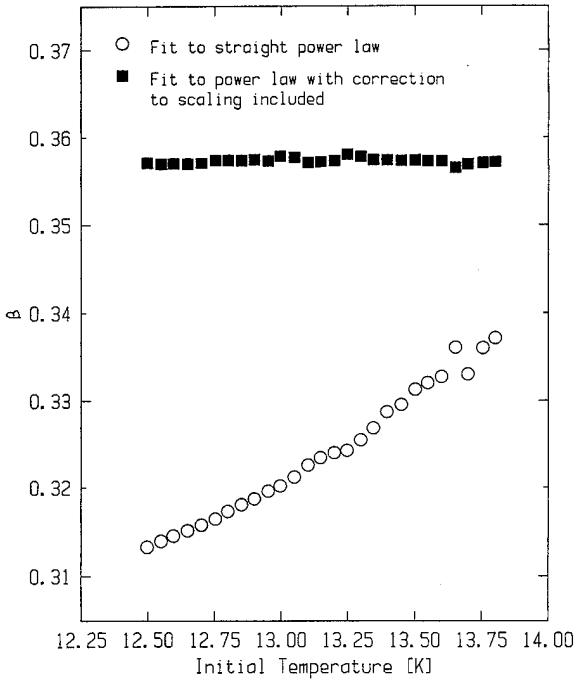


FIG. 2. The dependence of β on the temperature at which the fit was initialized for both the straight power law and the power law with correction-to-scaling included. Both curves use a constant fixed value of T_{sp}.

The value of the critical exponent β is also strongly influenced by the choice of T_{sp} and this dependence was also examined in detail. Figure 3 shows a plot of the goodness-of-fit parameter χ^2 and the critical exponent β as a function

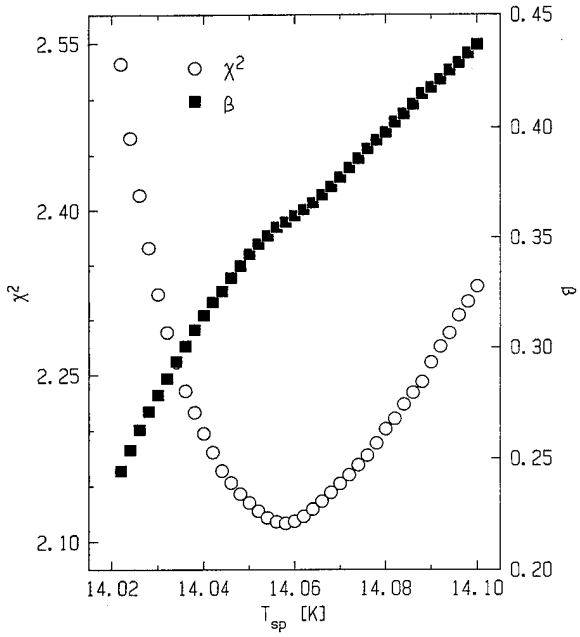


FIG. 3. The dependence of the goodness-of-fit parameter $\chi^2 = \Sigma_i [\log(I_{calc}(T_i)) - \log(I_{obs}(T_i))]^2$ on T_{sp} along with the corresponding variation of the critical exponent β.

of the chosen value of T_{sp} from a fit to the power law with correction to scaling included. There is a pronounced minimum in the χ^2 curve at a T_{sp} of 14.06 K with a corresponding β value of 0.36.

CONCLUSIONS

Following this careful measurement and analysis, we conclude that the spin-Peierls transition in $CuGeO_3$ is a continuous transition which is characterized by a transition temperature of 14.06 ± 0.02 K and a critical exponent β of 0.36 ± 0.03. This value of β is in agreement with conventional 3D behavior but is in closest agreement with 3D Heisenberg and XY behavior (predicted values of β: 3D Ising=0.326, 3D XY=0.345, and 3D Heisenberg=0.367[10]). It is important to note that this value of β differs substantially from the value of 0.26 (consistent with tricritical behavior) obtained from previous neutron diffraction work.[5] We believe that this difference can be attributed to improper consideration of the effect of the inclusion or removal of data points well away from T_{sp}. Indeed, if we use data from a similar range of reduced temperature as was used by Harris *et al.*,[5] we obtain a similar estimate of β. However, such a fit produces a clear deviation from the data near the transition temperature.

ACKNOWLEDGMENTS

This work was supported in part by the Natural Sciences and Engineering Research Council of Canada and by the Ontario Centre for Materials Research.

[1] M. Hase, I. Terasaki, and K. Uchinokura, Phys. Rev. Lett. **70**, 3651 (1993).
[2] M. Nishi, O. Fujita, and J. Akimitsu, Phys. Rev. **50**, 6508 (1994).
[3] O. Fujita, J. Akimutsu, M. Nishi, and K. Kakurai, Phys. Rev. Lett. **74**, 1677 (1995).
[4] J. P. Pouget, L. P. Regnault, M. Ain, B. Hennion, J. P. Renard, P. Veillet, G. Dhalenne, and A. Revocolevschi, Phys. Rev. Lett. **72**, 4037 (1994).
[5] Q. J. Harris, Q. Feng, R. J. Birgeneau, K. Hirota, K. Kakurai, J. E. Lorenzo, G. Shirane, M. Hase, K. Uchinokura, H. Kojima, I. Tanaka, and Y. Shibuya, Phys. Rev. B **50**, 12606 (1994).
[6] H. Winkelmann, E. Gamper, B. Büchner, M. Braden, A. Revcolevschi, and G. Dhalenne, Phys. Rev. B **51**, 12884 (1995).
[7] K. Hirota, D. E. Cox, J. E. Lorenzo, G. Shirane, J. M. Tranquada, M. Hase, K. Uchinokura, H. Kojima, Y. Shibuya, and I. Tanaka, Phys. Rev. Lett. **73**, 736 (1994).
[8] O. Kamimura, M. Terauchi, M. Tanaka, O. Fujita, and J. Akimitsu, J. Phys. Soc. Jpn. **50**, 6508 (1994).
[9] A. Aharony and G. Ahlers, Phys. Rev. Lett. **44**, 782 (1980).
[10] M. F. Collins, *Magnetic Critical Scattering* (Oxford University Press, New York, 1989).

Evidence for crossover effects in the spin dynamics of the two-dimensional antiferromagnet $Sr_2CuO_2Cl_2$ from ^{35}Cl nuclear magnetic resonance

B. J. Suh
Ames Laboratory and Department of Physics and Astronomy, Iowa State University, Ames, Iowa 50011

F. Borsa
Ames Laboratory and Department of Physics and Astronomy, Iowa State University, Ames, Iowa 50011 and INFM-Dipartimento di Fisica "A. Volta," Universitá di Pavia, I-27100 Pavia, Italy

L. L. Miller, D. C. Johnston, and D. R. Torgeson
Ames Laboratory and Department of Physics and Astronomy, Iowa State University, Ames, Iowa 50011

M. Corti
INFM-Dipartimento di Fisica "A. Volta," Universitá di Pavia, I-27100 Pavia, Italy

^{35}Cl nuclear magnetic resonance (NMR) and relaxation measurements have been performed in stacked $Sr_2CuO_2Cl_2$ single crystals with Néel temperature $T_N=257$ K for two crystal orientations with respect to the applied field: $\mathbf{H}\|\mathbf{c}$ and $\mathbf{H}\perp\mathbf{c}$. All the parameters of ^{35}Cl NMR are found to exhibit a strong orientation dependence varying in temperature. In particular, the unconventional anisotropy and strong temperature dependence of the ^{35}Cl nuclear spin–spin relaxation rate, T_2^{-1}, are presented and discussed in terms of a crossover of the Cu^{2+} spin dynamics from Heisenberg to XY-like correlation for $T\rightarrow T_N^+$. The onset of anisotropic broadening and shift of the ^{35}Cl NMR line was observed well above T_N, which is in agreement with the previous results. © *1996 American Institute of Physics.* [S0021-8979(96)39308-0]

I. INTRODUCTION

The undoped layered perovskite system $Sr_2CuO_2Cl_2$ represents a very good model system for the spin $S=1/2$ two-dimensional (2D) square-lattice Heisenberg antiferromagnet (2DSLHA) with weak easy-plane anisotropy.[1] Recent neutron scattering studies[2] and ^{35}Cl NMR and susceptibility studies[3–5] provide a quantitative comparison of theory and experiments regarding the temperature dependence of the intraplanar correlation length (ξ) of the Cu^{2+} spins above the Néel temperature $T_N=257$ K and the crossover effects associated with the XY anisotropy and the anisotropy induced by an external magnetic field.[5] In particular, the ^{35}Cl nuclear spin-lattice relaxation rate T_1^{-1} (NSLR) in single crystals with $\mathbf{H}\|\mathbf{c}$ has revealed a divergent behavior for $T\rightarrow T_N^+$, indicating a crossover of the Cu^{2+} spin dynamics from Heisenberg to **XY**-like correlation at $T\approx 290$ K.

In this paper, we present additional evidence for the crossover effect obtained from measurements of ^{35}Cl nuclear spin–spin relaxation rate (T_2^{-1}). Furthermore, we present new data for the anisotropic broadening and shift of the ^{35}Cl NMR line occurring above T_N which agree with previous results[4] and confirm the presence of field-induced two dimensional short range ordering above T_N.

II. EXPERIMENTAL RESULTS

The ^{35}Cl NMR experiments were carried out on a stack of single crystals of $Sr_2CuO_2Cl_2$ having a common tetragonal c axis using coherent Fourier transform spectrometers at 4.7 and 8.2 T (see Ref. 5 for experimental details). The ^{35}Cl ($I=3/2$) resonance line refers to the central transition only ($+1/2\leftrightarrow -1/2$).[5]

The results for the temperature dependence of the shift of the ^{35}Cl line with respect to NaCl aqueous solution are shown in Fig. 1 for two magnetic field intensities and two orientations. The results for the ^{35}Cl linewidth at half maximum are shown in Figs. 2(a) and (b). The measurements for $\mathbf{H}\perp\mathbf{c}$ are not reported for $T<T_N$ since the ^{35}Cl resonance line becomes very broad. The decay of the spin-echo signal was measured as a function of separation τ between two radio frequency (rf) pulses in an ordinary pulse sequence, $(\pi/2)_x-\tau-(\pi)_y$, with $\tau_{\pi/2}=2.5$ μs. The shape of the spin-echo decay was not a simple form such as a single exponential or a single Gaussian but could be fit by the product of two functions, an exponential, and a Gaussian:

$$M(t)=M(0)\exp\left(-\frac{t}{T_L}\right)\exp\left[-\left(\frac{t}{T_G}\right)^2\right]. \tag{1}$$

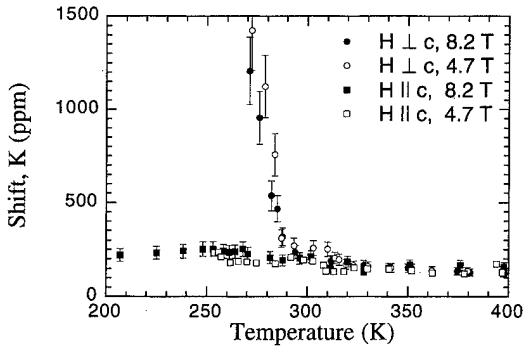


FIG. 1. ^{35}Cl NMR shift, K, vs temperature in stacked $Sr_2CuO_2Cl_2$ single crystals for two intensities and two orientations of the external magnetic field $\mathbf{H}$ with respect to the crystal c axis.

 0021-8979/96/79(8)/5084/3/$10.00 © 1996 American Institute of Physics

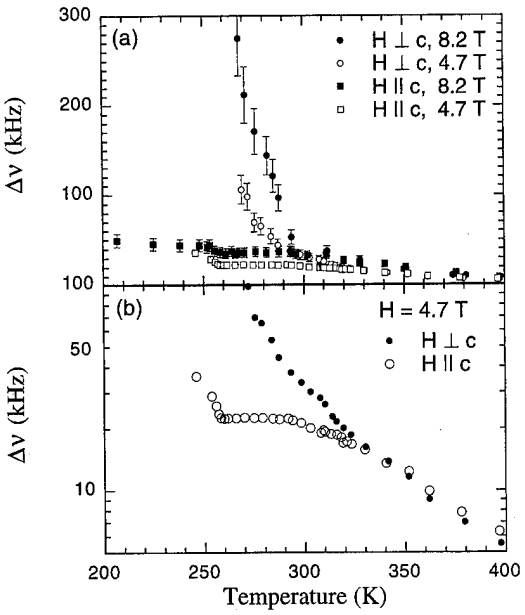


FIG. 2. ^{35}Cl NMR linewidth $\Delta\nu$ at half maximum height vs temperature in stacked $Sr_2CuO_2Cl_2$ single crystals: (a) Linear-scale plot of $\Delta\nu$ for two magnetic field intensities. (b) Semilog plot of $\Delta\nu$ for $H=4.7$ T.

The results for the temperature dependence of the exponential component, T_L^{-1}, and of the Gaussian component, T_G^{-1}, of the spin-echo decay are shown in Figs. 3(a) and (b), respectively.

III. DISCUSSION

First, as can be seen from Fig. 3(b), the Gaussian contribution, T_G^{-1}, to the spin–spin relaxation rate is anisotropic and practically temperature independent. An approximate calculation of the Van Vleck second moment[6] due to homonuclear ^{35}Cl nuclear dipolar interaction yields $(1/T_2)_{\rm dip}=(\langle\Delta\nu^2\rangle/2)^{1/2}=43\ {\rm s}^{-1}$ for $\mathbf{H}\perp\mathbf{c}$ and $(1/T_2)_{\rm dip}=63\ {\rm s}^{-1}$

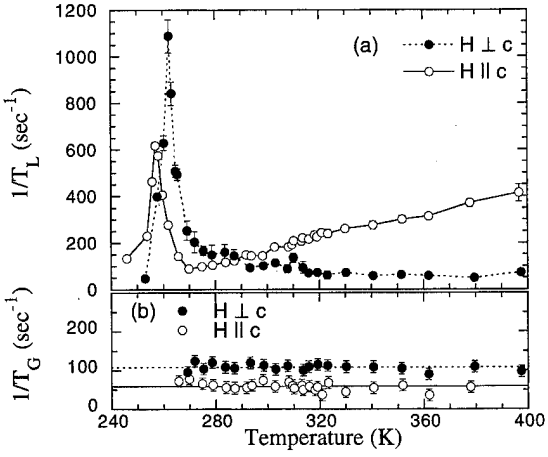


FIG. 3. Plots of the ^{35}Cl nuclear spin–spin relaxation rate components for $H=4.7$ T. (a) The exponential component (T_L^{-1}) vs T. The curves are only guides for the eye. (b) The Gaussian component (T_G^{-1}) vs T. The lines are the average values of T_G^{-1}; (dashed line) $(T_G^{-1})_{ab}=107\ {\rm s}^{-1}$, and (solid line) $(T_G^{-1})_c=58\ {\rm s}^{-1}$.

for $\mathbf{H}\perp\mathbf{c}$ in the case of a simple Gaussian shape of the spin-echo decay. The calculated values agree both in magnitude and in sign of the anisotropy with the experimental results. We conclude that the temperature independent Gaussian component of the spin-echo decay [see Eq. (1)] is due to nuclear dipolar interaction, i.e., $T_G^{-1}\equiv(1/T_2)_{\rm dip}$. On the other hand, the exponential component of the spin-echo decay, T_L^{-1}, [see Fig. 3(a)] is indicative of a contribution due to the ^{35}Cl nucleus-Cu^{2+} electron spin interaction modulated by the fast Cu^{2+} spin dynamics and thus can give information on crossover effects. For weak time dependent fluctuations of the local field and in a time dependent perturbation theory, one can write for this contribution[6]

$$\frac{1}{T_L}=\frac{1}{2}\gamma^2\int\langle h_z(t)\cdot h_z(0)\rangle dt+\frac{1}{2T_1}, \tag{2}$$

where $h_z(t)$ is the component of the local field parallel to $\mathbf{H}$ at the ^{35}Cl site due to the Cu^{2+} magnetic moments. As it was discussed previously[4,5] the dominant contribution to the ^{35}Cl hyperfine interaction comes from the dipolar and/or contact interaction of the ^{35}Cl nucleus with the first neighbor Cu^{2+} magnetic moment at distance d along the c axis. Thus, we can write for the hyperfine field

$$\mathbf{h}=\mathbf{h}_{\rm dip}+\mathbf{h}_{\rm cont}=\frac{1}{d^3}(-\mu_a\hat{a}-\mu_b\hat{b}+2\mu_c\hat{c})$$
$$+A(\mu_a\hat{a}+\mu_b\hat{b}+\mu_c\hat{c}), \tag{3}$$

where $\hat{a}$, $\hat{b}$, and $\hat{c}$ are the unit vectors of the crystal axes reference frame and $\mu_{a,b,c}$ are the instantaneous components of a Cu^{2+} nearest neighbor magnetic moment to a given ^{35}Cl nucleus and A is the contact hyperfine constant. By combining Eqs. (2) and (3), one has

$$\left(\frac{1}{T_L}\right)_c=\left(\frac{1}{2T_1}\right)_c+\frac{\gamma^2}{2d^6}\cdot 4J_{\parallel}(0)+\frac{\gamma^2A^2}{2}J_{\parallel}(0)\qquad(\mathbf{H}\parallel\mathbf{c}),$$
$$\left(\frac{1}{T_L}\right)_{ab}=\left(\frac{1}{2T_1}\right)_{ab}+\frac{\gamma^2}{2d^6}\cdot J_{\perp}(0)+\frac{\gamma^2A^2}{2}J_{\perp}(0)\quad(\mathbf{H}\perp\mathbf{c}), \tag{4}$$

where $J_{\perp}(0)\equiv J_{aa}(0)=J_{bb}(0)$, $J_{\parallel}(0)\equiv J_{cc}(0)$, and $J_{\alpha\beta}(0)=\int_{-\infty}^{+\infty}\langle\mu_\alpha(t)\mu_\beta(0)\rangle dt$. Comparing the data in Fig. 3(a) with the values of $T_1^{-1}=2W$ in Ref. 5 one has $T_L^{-1}\gg T_1^{-1}$ above T_N which implies $J_{\alpha\beta}(0)\gg J_{\alpha\beta}(\omega_L)$,[5] where ω_L is the nuclear resonance frequency. Thus, by neglecting the first term in Eq. (4), one has $(T_L^{-1})_c=(4\gamma^2/2d^6+\gamma^2A^2/2)J_{\parallel}(0)$ and $(T_L^{-1})_{ab}=(\gamma^2/2d^6+\gamma^2A^2/2)J_{\perp}(0)$. Figure 4 shows the direct ratio $(T_L^{-1})_c/(T_L^{-1})_{ab}$ vs temperature. The saturating value of the ratio $(T_L^{-1})_c/(T_L^{-1})_{ab}\cong 5.5\pm 1$ well above T_N is consistent with Eq.(4) for a relatively small contact hyperfine interaction A. As $T\to T_N^+$, $(T_L^{-1})_c$ decreases in agreement with the behavior expected if the longitudinal out-of-plane fluctuations, $J_{\parallel}(0)$, are progressively suppressed with decreasing temperature [see Figs. 3(a) and 4]. We conclude, consistent with the conclusion previously inferred from NSLR measurements,[5] that the Cu^{2+} spin system crosses over from Heisenberg to XY-like behavior upon cooling toward T_N. Very close to T_N the NSLR is strongly enhanced.[5] Thus, the

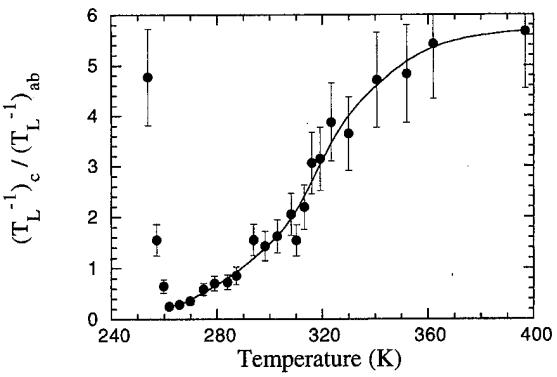


FIG. 4. The ratio $(T_L^{-1})_c/(T_L^{-1})_{ab}$ vs T. The curve is only a guide for the eye.

first term in Eq. (4) is no longer negligible and $(T_L^{-1})_{c,ab}$ are also enhanced. The fact that $T_L^{-1} \gg T_1^{-1}$ [i.e., $J_{\alpha\beta}(0) \gg J_{\alpha\beta}(\omega_L)$] well above T_N probably contains important information about the type of correlated spin-order in the system but it cannot be presently understood. One could speculate that very low frequency modes are present contributing to T_L^{-1} but not to T_1^{-1} or that the critical modes in this low-dimensional system have a diffusive character with consequent logarithmic divergence of the spectral density as $\omega \to 0$.[7]

The results for the ^{35}Cl NMR line shift and width are shown in Figs. 1 and 2, respectively. The linewidths, $\Delta\nu$, are in good agreement with previous results.[4] Regarding the shifts, K, vs T, we can see a field independent enhancement of K in Fig. 1 for the applied field in the ab plane which could not be observed previously[4] due to poorer quality of the single crystal stack available previously. As discussed previously,[4] the enhancement and the anisotropy of $\Delta\nu$ cannot be explained by demagnetization effects nor by random ferromagnetic impurities. Also, the magnetic susceptibility displays a weak temperature dependence with no enhancement close to T_N; thus, the observed enhancement of $\Delta\nu$ and of K cannot be simply the result of the paramagnetism of the Cu^{2+} magnetic moments. On the other hand, the results could be explained qualitatively if one assumes that the application of the magnetic field in the ab plane stabilizes static two-dimensional short range order of the Cu^{2+} moments.[4] It is interesting to note that the onset of the anisotropy in the line broadening occurs around the temperature at which $(T_L^{-1})_c$, i.e., the out-of-plane fluctuations, $J_{\|}(0)$, decrease most rapidly (see Fig. 4).

Finally, the magnitudes of the broadening, of the shift, of the NSLR, and spin–spin relaxation rates are too large to be accounted for by a "bare" dipolar interaction between ^{35}Cl and Cu^{2+} magnetic moments as in Eq. (4). It is quite likely that the partial covalent Cl–Cu bond induces an enhanced pseudodipolar interaction which we infer to be almost one order of magnitude larger than the "bare" dipolar interaction in order to explain the data.

ACKNOWLEDGMENTS

Ames Laboratory is operated for the U.S. Department of Energy by Iowa State University under Contract No. W-7405-Eng-82. The work at Ames Laboratory was supported by the Director for Energy Research, Office of Basic Energy Sciences.

[1] For reviews, see D. C. Johnston, J. Magn. Magn. Mater. **100**, 218 (1991); E. Manousakis, Rev. Mod. Phys. **63**, 1 (1991).
[2] M. Greven, R. J. Birgeneau, Y. Endoh, M. A. Kastner, B. Keimer, M. Matsuda, G. Shirane, and T. R. Thurston, Phys. Rev. Lett. **72**, 1096 (1994); Z. Phys. B **96**, 465 (1995).
[3] F. Borsa, M. Corti, T. Goto, A. Rigamonti, D. C. Johnston, and F. C. Chou, Phys. Rev. B **45**, 5756 (1992).
[4] M. Corti, F. Borsa, L. L. Miller, and A. Rigamonti, J. Appl. Phys. **75**, 7146 (1994).
[5] B. J. Suh, F. Borsa, L. L. Miller, M. Corti, D. C. Johnston, and D. R. Torgeson, Phys. Rev. Lett. **75**, 2212 (1995).
[6] A. Abragam, *Principles of Nuclear Magnetism* (Oxford, New York, 1961).
[7] See, for example, H. Benner and J. P. Boucher, in *Magnetic Properties of Layered Transition Metal Compounds*, edited by L. J. de Jongh (Kluwer, The Netherlands, 1990), p. 323.

Magnetic and nonmagnetic glass transitions in the Blume–Emery–Griffiths model with competing biquadratic interactions (abstract)

Daniel P. Snowman and Susan R. McKay
Department of Physics and Astronomy, University of Maine, Orono, Maine 04469-5709

The Blume–Emery–Griffiths model, a spin-1 Ising model with bilinear (J), biquadratic (K), and crystal field (Δ) terms, provides a general system for the analysis of both density and magnetic fluctuations. Using a Monte Carlo hard-spin mean-field approach,[1] we have calculated the phase diagrams resulting from a random bimodal distribution of biquadratic interactions, $K_{ij}=\pm K$, with equal probabilities. The quenched disorder in K competes with the propagation of long-range magnetic order and leads to two types of glassy ordered phases, magnetic and nonmagnetic. The variance in the site density over the lattice serves as an order parameter for the transition to these glassy phases. We compare the structure and overlaps of their low lying energy states with those of the three-dimensional Ising spin glass, determined using the same method.[2] The magnetic glass exhibits a much more gradual loss of overlap with its low-temperature state than the spin glass. The form of the overlap versus temperature curve in the vicinity of the critical temperature for the magnetic glass suggests that the system is fluctuating between a pair of ordered states, with one obtained from the other by flipping all spins, rather than sampling many different states. © *1996 American Institute of Physics.* [S0021-8979(96)64108-X]

[1] R. R. Netz and A. N. Berker, Phys. Rev. Lett. **66**, 377 (1991).
[2] E. A. Ames and S. R. McKay, Bull. Am. Phys. Soc. **39**, 385 (1994); D. P. Snowman, E. A. Ames, and S. R. McKay, University of Maine (preprint).

The three-dimensional RFIM: Existence of a tricritical point? (abstract)

Laura Hernandez and H. T. Diep
Groupe de Physique Statistique, Université de Cergy Pontoise, 49 Av. des Genottes, BP 8428, 95006 Cergy Pontoise, Cedex, France

The critical behavior of the RFIM has been a subject of controversy for a long time. After the qualitative analysis of Imry and Ma[1] and the rigorous proof given by Imbrie,[2] it is nowadays accepted that the lower critical dimension of the system is $d_1=2$. Though some general results exist in the mean field approach,[3,4] the nature of the transition for the real system for $d>2$ remains less clear. In this work we study, using the Monte Carlo histogram technique and finite size scaling, the three-dimensional RFIM with a symmetric bimodal field distribution. Our results strongly suggest the existence of a tricritical point where the transition crosses over from a second-order transition at low but finite fields to a first-order transition for high fields, in contradiction with previous suggestions issued from standard Monte Carlo simulations.[5] © *1996 American Institute of Physics.* [S0021-8979(96)64208-9]

[1] Y. Imry and S. K. Ma, Phys. Rev. Lett. **35**, 1399 (1975).
[2] J. Imbrie, Phys. Rev. Lett. **53**, 1747 (1984).
[3] A. Aharony, Phys. Rev. B **18**, 3318 (1978).
[4] D. Andelman, Phys. Rev. B **27**, 3079 (1983).
[5] A. P. Young and M. Nauenberg, Phys. Rev. Lett. **54**, 2429 (1985).

$m=3$ Ashkin–Teller-like cubic model on an FCC lattice

Ronald Fisch
Department of Physics, Washington University, St. Louis, Missouri 63130

Monte Carlo simulations have been used to study a model consisting of three Ising models with nearest neighbor exchange J on a face-centered-cubic lattice, which are coupled together by a constraint. The constraint requires that the vector sum of the four spins located at the corners of any elementary tetrahedron of the lattice not add to zero. Finite-size scaling analysis of the Monte Carlo results for $L\times L\times L$ lattices with $L=16$, 32, and 64 has been used to find that $T_c/J=10.84\pm0.01$. The finite-size scaling functions for the magnetization and magnetic susceptibility near T_c are consistent with standard $m=3$ Heisenberg critical exponents, as predicted by renormalization group theory. Strengthening the four-spin constraint increases the value of the effective negative Ashkin–Teller four-spin coupling, and drives T_c to infinity. © *1996 American Institute of Physics.* [S0021-8979(96)39408-7]

The role of topological defects in low-temperature phases which possess a spontaneously broken continuous symmetry is a subject of long-standing and continuing interest.[1,2] One way to learn about the effects of these defects is to study toy models in which they have been reduced in number or removed altogether.[3–8] Completely removing the string defects from a three-dimensional XY model[3,4,8] or the point defects from a three-dimensional Heisenberg model[5,6] forces the system to remain in the broken-symmetry phase at all temperatures.

A point demonstrated nicely by the model of Kamal and Murthy[7] is that the inability of the system to get out of the broken-symmetry phase without creating defects does not prove that these defects drive the phase transition. Kamal and Murthy showed that in a three-dimensional Heisenberg model where nearest-neighbor pairs of point defects were allowed the transition to the high temperature paramagnetic phase did occur. These nearest-neighbor defect dipoles do not change the long-range topological properties of the system. Thus, we cannot properly attribute the failure to reach the symmetry-restored phase when defects are prohibited to the topological aspect of the problem.

The way in which the defects are removed from a model is by attaching a large (or infinite) energy to each spin configuration which contains a defect. It is inevitable that this procedure also induces strong interactions between the spin-wave excitations. Thus, from a renormalization-group perspective, varying the defect fugacity is essentially equivalent to varying the four-spin interaction potential. (In the context of the two-dimensional XY model, these two quantities are related through a duality transformation.[9])

In order to make this point explicit, in the work presented here we will show that by directly varying the strength of a four-spin interaction for a three-dimensional three-component spin model, we can achieve results which are similar to those found when the defect fugacity is varied. Furthermore, we can obtain qualitatively similar results in a four-component spin model,[10] for which there are no topological defects.

The Hamiltonian we study is of the form

$$H=-J\sum_{\langle ij\rangle}\mathbf{S}_i\cdot\mathbf{S}_j-J_4\sum_{\text{tetr}}f(|\mathbf{S}_i+\mathbf{S}_j+\mathbf{S}_k+\mathbf{S}_l|^2), \tag{1}$$

where each $\mathbf{S}$ is a classical fixed-length three-component spin variable which can assume the eight values $(\pm1,\pm1,\pm1)$. The sites i form a face-centered cubic (fcc) lattice, $\langle ij\rangle$ is a sum over neighbor pairs, and tetr is a sum over sets of four spins which form an elementary tetrahedron of the lattice. We assume that J and J_4 are positive.

Equation (1) is qualitatively similar to the $m=3$ Ashkin–Teller model studied by Grest and Widom,[11] although the form of the four-spin coupling is different. For simplicity, we choose our four-spin potential to have a hard-core form. Define

$$r_4=\left|\sum_{i=1}^{4}\mathbf{S}_i\right|^2. \tag{2}$$

Then we choose $f(r_4)$ to be of the form

$$f(r_4)=\infty \text{ if } r_4\leq R \text{ and } 0 \text{ otherwise.} \tag{3}$$

When $R<0$ (or $J_4=0$), the model reduces to three decoupled Ising models. The critical temperature of the Ising model on an fcc lattice[12] is approximately $T_c/J=9.7969$. The form of Eq. (3) forces the magnetization, and therefore T_c, to be a monotonically increasing function of R.

Because the model restricts each $\mathbf{S}$ to eight vectors corresponding to the corners of a cube, r_4 can only assume a finite set of integer values: {0,4,8,12,...,48}. The number of different states of four spins is $8^4=4096$. The number of these which have $r_4=0$ is 216, and the number which have $r_4=4$ is 864. Thus, setting $R=0$ gives a rather weak perturbation of the Ising model, but $R=4$ is substantially stronger.

As R is increased the entropy of a paramagnetic phase, which has no long range order, is reduced relative to the entropy of a ferromagnetic phase. For $R=4$ the paramagnetic phase is only stable at very high T. For $R=8$ there is never a stable paramagnetic phase. In this case, there is a first order phase transition at about $T/J=12.9$, to a phase in which one of the spin components becomes almost completely ordered, while the remaining components are disordered. This phase is called phase III by Grest and Widom,[11] and occurs for negative values of the four-spin coupling in the standard Ashkin–Teller model. When one spin component is fully ordered, then r_4 must be ≥16. In the large m limit of our model, phase III becomes more stable than the paramagnetic

 0021-8979/96/79(8)/5088/3/$10.00 © 1996 American Institute of Physics

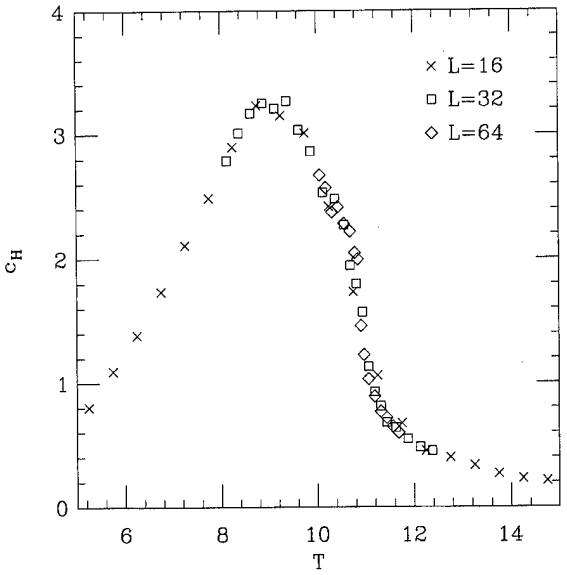


FIG. 1. Specific heat for the $m=3$ cubic model with $R=0$ on $L\times L\times L$ fcc lattices.

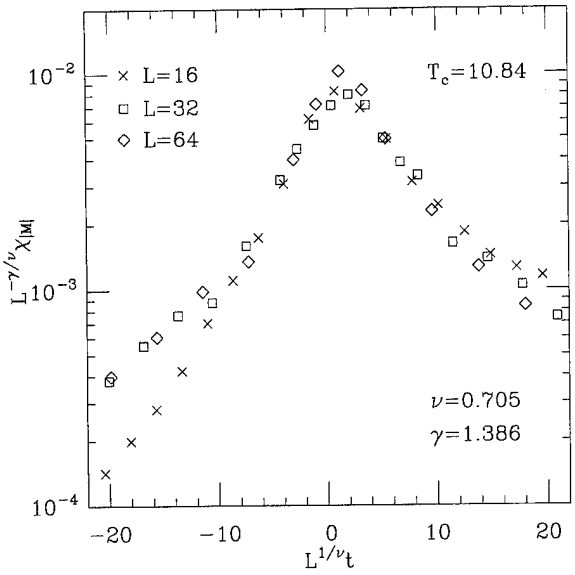


FIG. 3. Finite-size scaling of the longitudinal susceptibility for the $m=3$ cubic model with $R=0$ on $L\times L\times L$ fcc lattices. The vertical axis is scaled logarithmically, $t=T/10.84-1$, $\nu=0.705$, and $\gamma=1.386$.

phase at high T when $R=16$. Having one component ordered allows the remaining components to ignore the four-spin potential. The net result of this is that phase III has a higher entropy than the paramagnetic phase in this range of R. Of course, when R becomes very large all of the components must remain ordered at all T, and the model becomes uninteresting.

Although there is no precise correspondence, increasing the value of R is similar to increasing the hedgehog fugacity in the model of Lau and Dasgupta.[5,6] We could increase the similarity by allowing each **S** to assume all values on the surface of a sphere, so that r_4 would have a continuous range of values. That, however, is not the path we will follow here.

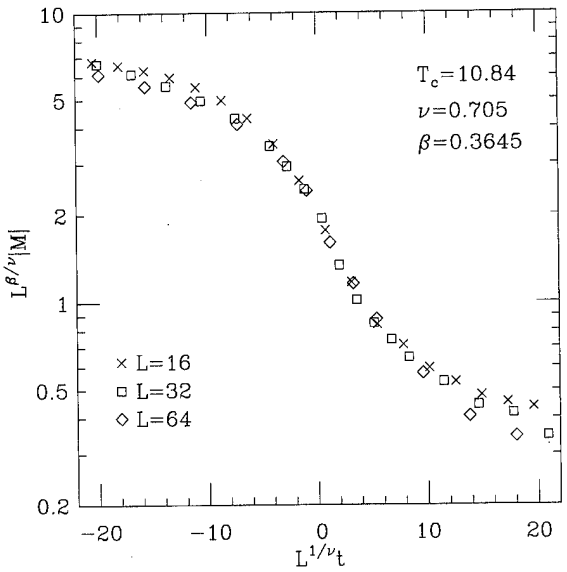


FIG. 2. Finite-size scaling of the magnetization for the $m=3$ cubic model with $R=0$ on $L\times L\times L$ fcc lattices. The vertical axis is scaled logarithmically, $t=T/10.84-1$, $\nu=0.705$ and $\beta=0.3645$.

In the remainder of this work we will describe the results of a detailed Monte Carlo study of the discretized model for the case $R=0$.

A renormalization group analysis[13–15] predicts that Eq. (1) with a weak ferromagnetic four-spin term like the one we get for $R=0$ should have a ferromagnetic critical point which is the universality class of the $m=3$ Heisenberg fixed point. This prediction has been verified experimentally.[16] A Monte Carlo study can give detailed information which is not easy to obtain in a laboratory experiment.

The computer program used was a simple adaptation of the standard Metropolis Monte Carlo algorithm. All of the energies in the problem are integers, which allows for efficient computation. An attempt to flip a spin consisted of the following procedure. First, one of the eight possible states of a spin was chosen using a pseudorandom number generator. If this state was identical to the existing state of the spin being tested, a different state was chosen. Then, a decision between the existing state and the proposed state was made using the Metropolis algorithm with a second, different random number generator. One Monte Carlo step (MCS) consisted of a sweep through the entire lattice using this procedure. The spin lattice was stored as an $L\times L\times L$ integer array in which only alternate sites were used. Although this might seem wasteful, the actual size of the array was small enough so that convenience was the overriding factor. The sizes used were $L=16$, 32, and 64. Averaging was typically carried out over 10 000 MCS at each temperature, after allowing time for equilibration. Somewhat longer runs were used for the $L=64$ case near T_c.

Since a crossover from Ising to Heisenberg critical behavior is involved, it is not necessarily true that the lattice sizes accessible to the computer will show the $m=3$ behavior. This requires that the strength of the four-spin term be enough to shift the behavior far enough away from the Ising case so that the crossover scale is not too large. Setting $R=0$

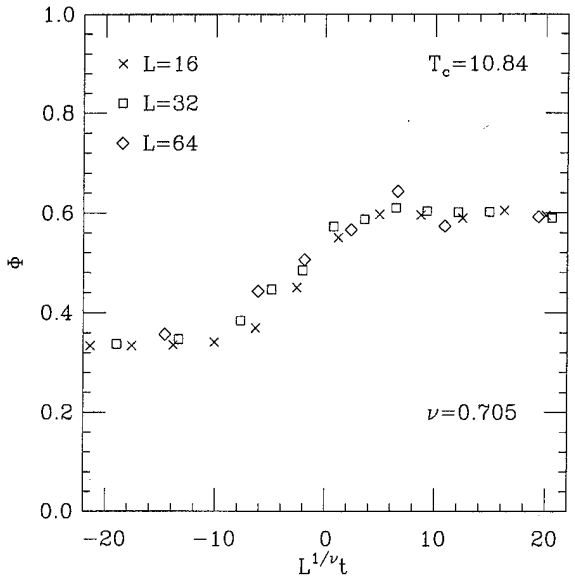


FIG. 4. Finite-size scaling of the cubic anisotropy function Φ defined in Eq. (6), for the $m=3$ cubic model with $R=0$ on $L\times L\times L$ fcc lattices. $t=T/10.84-1$ and $\nu=0.705$.

is satisfactory for this purpose. It turned out that $L=16$ was the smallest useful lattice size, because of the crossover.

Figure 1 shows the specific heat for the three lattice sizes. Most of the specific heat is contained in a broad peak centered at $T/J\approx 9$. This peak may be thought of as the remanent of the Ising behavior. As L gets large, we see a shoulder develop at T_c, which is approximately 10% above the Ising T_c. In order to study the critical properties, we will use finite-size scaling theory.[17] As we can see from Fig. 1, most of the specific heat is in the broad background. Thus, we would need data from even larger lattices to get useful information about critical behavior from the specific heat.

The finite-size scaling functions[17] for the magnetization and the (longitudinal) magnetic susceptibility (per spin) are given by

$$M(L,T)=L^{-\beta/\nu}Q_M(tL^{1/\nu}) \tag{4}$$

and

$$\chi(L,T)=L^{\gamma/\nu}Q_\chi(tL^{1/\nu}), \tag{5}$$

where $t=T/T_c-1$. The values of the critical exponents were set equal to the standard renormalization group field theory values[18] for the $m=3$ Heisenberg critical point. Thus, the only adjustable parameter is T_c, which is estimated to be $10.84\pm 0.01\ J$. The scaling forms, Eq. (4) and Eq. (5), are used to display the data from the $L=16$, 32, and 64 lattices in Figs. 2 and 3, respectively. We see that the overlap of the data for different values of L is good in a fairly broad region near T_c. The breakaway of the $L=16$ data at low temperatures is caused by the crossover from Ising behavior.

In order to study the angular distribution of the magnetization, we calculate the function

$$\Phi(L,T)=\frac{L^3}{2}\sum_{\alpha=1}^{3}\left(\sum_i S_i^\alpha\right)^4 \Bigg/ \left(\sum_{\alpha=1}^{3}\left(\sum_i S_i^\alpha\right)^2\right)^2. \tag{6}$$

For large L, Φ goes to 1/3 for $T<T_c$ and 3/5 for $T>T_c$. As demonstrated in Fig. 4, the transition region near T_c has a width proportional to $L^{-1/\nu}$. Therefore, the correlation length exponent for transverse fluctuations is the same as for longitudinal fluctuations. We do not find a new critical exponent associated with Φ, and two exponents suffice for the description of the asymptotic critical behavior.

Overall, we can say that the data are entirely consistent with the prediction that the critical behavior for $R=0$ is described by the $m=3$ Heisenberg critical point. In work which will be described elsewhere,[10] we have also verified the prediction[13–15] that the critical behavior of the $m=4$ case of Eq. (1) is described by a stable $m=4$ cubic fixed point.

[1] P. W. Anderson, *Basic Notions of Condensed Matter Physics* (Benjamin-Cummings, Menlo Park, CA, 1984).
[2] B. I. Halperin, in *Physics of Defects, Les Houches 1980*, edited by R. Balian, M. Kleman, and J.-P. Poirier (North-Holland, Amsterdam, 1981), p. 813.
[3] G. Kohring, R. E. Shrock, and P. Wills, Phys. Rev. Lett. **57**, 1358 (1986).
[4] G. Kohring and R. E. Shrock, Nucl. Phys. B **288**, 397 (1987).
[5] M.-h. Lau and C. Dasgupta, J. Phys. A **21**, L51 (1988).
[6] M.-h. Lau and C. Dasgupta, Phys. Rev. B **39**, 7212 (1989).
[7] M. Kamal and G. Murthy, Phys. Rev. Lett. **71**, 1911 (1993).
[8] R. Fisch, Phys. Rev. B **52**, 12 512 (1995).
[9] J. V. Jose, L. P. Kadanoff, S. Kirkpatrick, and D. R. Nelson, Phys. Rev. B **16**, 1217 (1977).
[10] R. Fisch (unpublished).
[11] G. S. Grest and M. Widom, Phys. Rev. B **24**, 6508 (1981).
[12] J. Adler, J. Phys. A **16**, 3585 (1983).
[13] A. Aharony, in *Phase Transitions and Critical Phenomena*, edited by C. Domb and M. S. Green (Academic, London, 1976), Vol. 6, p. 357.
[14] E. Domany and E. K. Riedel, J. Appl. Phys. **50**, 1804 (1979).
[15] K. E. Newman and E. K. Riedel, Phys. Rev. B **25**, 264 (1982).
[16] M. Seeger, S. N. Kaul, H. Kronmüller, and R. Reisser, Phys. Rev. B **51**, 12585 (1995).
[17] M. N. Barber, in *Phase Transitions and Critical Phenomena*, edited by C. Domb and J. L. Lebowitz (Academic, London, 1983), Vol. 8, p. 145.
[18] J. C. Le Guillou and J. Zinn-Justin, Phys. Rev. B **21**, 3976 (1980); J. Phys. Lett. (Paris) **46**, L137 (1985).

Phase transitions in disordered systems: Exactly solvable model

D. Nicolaides and A. A. Lisyansky
Department of Physics, Queens College of CUNY, Flushing, New York 11367

The critical behavior at phase transitions of random systems is studied within the framework of an exactly solvable model which takes into account interactions of fluctuations with equal and opposite momenta. Using the replica method, the dimensional reduction by 2 for the ϕ^4 model with a quenched random field is explicitly shown. Phase transitions in systems with two interacting order parameters which in addition are coupled to two independent random fields are also studied. In the absence of random fields the model demonstrates fluctuation induced phase transitions of the first order for spacial dimension $d<4$. In random systems with only one quenched random field present, second order phase transitions are restored. Two random fields suppress any phase transitions for $d<4$. For interaction of an infinite range, the model demonstrates the mean field critical asymptotics independently of dimensionality or the presence of random fields. © *1996 American Institute of Physics.* [S0021-8979(96)39508-3]

Within the last two decades there has been considerable interest in the critical behavior of systems with quenched disorder.[1–6] In the present paper, we investigate such systems within the framework of an exactly solvable model that takes into account interaction of fluctuations with equal and opposite momenta. This model is very convenient to use in investigating critical phenomena in complex systems. Even though in its simplest version it has the same critical asymptotics as the spherical model,[7,8] it explicitly demonstrates major qualitative results that have been obtained within renormalization group theory including fluctuation induced first order phase transitions.[9,10] The renormalization group and the model lead to a similar critical behavior for phase transitions in orthorombic high T_c superconductors with d pairing[11] and for oxygen ordering near a structural phase transition in Y–Ba–Cu–O.[12] Below we show that the model also demonstrates a dimensional crossover[1–4] for systems under a random quenched field. Also, we show that the fluctuation induced first order phase transition in systems with coupled order parameters[10] is replaced by a continuous one in the presence of a random field.

We consider a system described by the Ginzburg–Landau functional

$$H=\frac{1}{2}\int d^dx\Big[\tau S^2(\mathbf{x})+c(\nabla S(\mathbf{x}))^2+\frac{g}{4}S^4(\mathbf{x})-hS(\mathbf{x})-h(\mathbf{x})S(\mathbf{x})\Big] \tag{1}$$

where $S(\mathbf{x})$ is a scalar order parameter, $\tau\propto T-T_c$, h, and $h(\mathbf{x})$ are constant and random fields, respectively. The free energy averaged with respect to a distribution of the random field can be evaluated with the help of the replica method.[13,14] Assuming that $h(\mathbf{x})$ is a δ-correlated random variable, $\langle h(\mathbf{x})h(\mathbf{x}')\rangle=B\delta(\mathbf{x}-\mathbf{x}')$, and $\varphi(\mathbf{x})$ is a replicated n-component vector order parameter, we derive an effective functional $H_{\text{eff}}[\varphi]$,

$$H_{\text{eff}}=\frac{1}{2}\int d^dx\Big[\tau|\varphi(\mathbf{x})|^2+c(\nabla\varphi(\mathbf{x}))^2+\sum_{i=1}^{n}\Big[\frac{g}{4}\varphi_i^4(\mathbf{x})-h\varphi_i(\mathbf{x})\Big]-B\Big(\sum_{i=1}^{n}\varphi_i(\mathbf{x})\Big)^2\Big]. \tag{2}$$

The free energy can be calculated exactly if we split interaction terms in Eq. (2) as follows:

$$\int d^dx\varphi_i^4(\mathbf{x})\to\frac{1}{V}a^2[\varphi_i],\quad a[\varphi_i]=\int d^dx\varphi_i^2(\mathbf{x}). \tag{3}$$

Equation (3) implies that the model considers interactions of fluctuations with equal and antiparallel momenta only, and transfers the φ^4 model into the universality class of the spherical model.[7,8] The model then uses a transformation analogous to that of Hubbard–Stratonovich so the partition function is read

$$Z=\int\prod_{i=1}^{n}(D\varphi_{i\mathbf{q}}\,dx_i\,dy_i)\exp\Big[-\frac{V}{2}\sum_{i=1}^{n}\Big(\tau x_i+\frac{g}{4}x_i^2-x_iy_i-\frac{h}{V}\varphi_{i0}\Big)-\frac{1}{2}\sum_{i=1}^{n}\sum_{\mathbf{q}}|\varphi_{iq}|^2(y_i+cq^2-B)+\frac{B}{2}\sum_{\mathbf{q}}\sum_{i\neq j}^{n}\varphi_{i\mathbf{q}}\varphi_{j-\mathbf{q}}\Big]. \tag{4}$$

After the diagonalization with respect to indices i and j functional integrals in Eq. (4) can be calculated as

$$Z=\int\Big(\prod_{i=1}^{n}dx_i\Big)dy\,\exp\Big[-\frac{V}{2}F(x_i,y,h)\Big], \tag{5}$$

$$F(x_i,y,h)=\sum_{i=1}^{n}\Big[tx_i+\frac{g}{4}x_i^2-yx_i\Big]-(1-n)f_d(y;c)+f_d(y-nB;c)-\frac{nh^2}{y-nB}, \tag{6}$$

where t is the renormalized trial critical temperature given by $t=\tau+g/2\,S_d(2\pi)^{-d}\theta_d(\Lambda)$,

 0021-8979/96/79(8)/5091/3/$10.00 © 1996 American Institute of Physics

$$\theta_d(\Lambda)=\frac{S_d}{(2\pi)^d}\begin{cases}\dfrac{\Lambda^{d-2}}{c(d-2)}, & d\neq 2\\ \dfrac{1+\ln(c\Lambda^2)}{2c}, & d=2\end{cases}$$

$$f_d(y;c)$$

$$=\frac{S_d}{(2\pi)^d}\begin{cases}\dfrac{\pi y^{d/2}}{dc^{d/2}\sin(\pi d/2)}\equiv\kappa(c)y^{d/2}, & d\neq\text{even}\\ \dfrac{1}{d}\left(-\dfrac{y}{c}\right)^{d/2}\ln y, & d=\text{even}\end{cases}\tag{7}$$

Λ is the cutoff momentum, and S_d the surface area of a d-dimensional sphere. In the thermodynamic limit, $V\to\infty$, the saddle point of the integrals in Eq. (5) gives an exact solution for the partition function.

The disorder averaged free energy and the order parameter Φ are given, respectively, by the expressions

$$F_{\rm av}=\lim_{n\to 0}\frac{1}{n}F(x_i,y,h),\quad \Phi=-\frac{\partial F_{\rm av}}{\partial h}=\lim_{n\to 0}\frac{h}{y(h)},\tag{8}$$

with x_i and y defined by the equations $\partial F/\partial x_i=0$ and $\partial F/\partial y=0$. This system of $n+1$ equations can be reduced to just one equation for y. The latter equation should be expanded in powers of n up to the first order. The resulting equation for y can be written in terms of Φ when Eqs. (8) are used:

$$\Phi^2+\frac{2t}{g}-\frac{2}{g}\frac{h}{\Phi}+\frac{(-1)^{d/2}}{c^{d/2}}\left(\frac{h}{\Phi}\right)^{(d-2)/2}\left[\frac{1}{d}+\frac{1}{2}\ln\left(\frac{h}{\Phi}\right)\right]$$
$$-\frac{(-1)^{d/2}B(d-2)}{2c^{d/2}}\left(\frac{h}{\Phi}\right)^{(d-4)/2}\left[\frac{1}{d}+\frac{1}{d-2}\right.$$
$$\left.+\frac{1}{2}\ln\left(\frac{h}{\Phi}\right)\right]=0,\quad d=\text{even},\tag{9a}$$

$$\Phi^2+\frac{2t}{g}-\frac{2}{g}\frac{h}{\Phi}+\frac{\kappa(c)}{2}\left(\frac{h}{\Phi}\right)^{(d-2)/2}-\frac{B}{4}\kappa(c)(d-2)$$
$$\times\left(\frac{h}{\Phi}\right)^{(d-4)/2}=0,\quad d=\text{noneven}.\tag{9b}$$

When $t=0$ it becomes obvious from Eqs. (9) that in the limit $h\to 0$ there are no solutions for Φ when $d\leqslant 4$. When $4<d<6$ the third and fourth terms in Eq. (9b) can be omitted because they become of a smaller order in h compared to the last term. After this the equation gives the same critical asymptotics as the "pure" model with the lower dimension $2<d'(=d-2)<4$. Namely, for critical exponents β and δ we have $\beta=1/2$, $\delta=(d'+2)/(d'-2)$. When $d>6$ in the limit $h\to 0$ only the first three terms in Eqs. (9) survive, and we arrive at the mean field critical exponents. Finally, for $d=6(d'=4)$ Eq. (9a) provides logarithmic corrections to the field asymptotic of the order parameter, $\Phi\propto[h\ln(ch)]^{1/3}$. So, the model explicitly demonstrates the dimensional crossover in the presence of quenched random fields.[1-4] It may seem contradictory that the model with the one-component order parameter has a lower critical dimension $d_c=4$. Indeed, functional (1) corresponds to the random-field Ising model with $d_c=2$. However, after the reduction equation (3), the model belongs to the spherical model universality class which has $d_c=4$.

Parameter $c^{1/2}$ represent the radius of interactions in the original system. Setting $c\to\infty$ (or $\kappa=0$) we suppress fluctuations. In this case, one can see from Eqs. (9) that a second order phase transition is restored and critical exponents become the same as the mean field ones independently of dimensionality or the presence of random fields.

Now, we consider the critical behavior of systems with two coupled scalar order parameters, which also are under the influence of two random fields. The Ginzburg–Landau functional is

$$H[S_1,S_2]=\frac{1}{2}\int d^dx\left\{\sum_{i=1}^{2}\left[\tau_iS_i^2(\mathbf{x})+c_i(\nabla S_i(\mathbf{x}))^2\right.\right.$$
$$\left.+\frac{1}{4}g_iS_i^4(\mathbf{x})\right]+\frac{1}{2}wS_1^2(\mathbf{x})S_2^2(\mathbf{x})$$
$$\left.-2\sum_{i=1}^{2}[h_iS_i(\mathbf{x})+h_i(\mathbf{x})S_i(\mathbf{x})]\right\}.\tag{10}$$

After following steps similar to those described above, we find two equations for the n-dimensional ($n\to 0$) order parameter Φ_i ($i=1,2$):

$$\Phi_i^2-\frac{2g_i}{\Delta}\frac{h_i}{\Phi_i}+\frac{2g_{i'}t_i}{\Delta}-\frac{2wt_{i'}}{\Delta}+\frac{2w}{\Delta}\frac{h_{i'}}{\Phi_{i'}}+\begin{cases}\dfrac{d}{2}\kappa(c_i)\left(\dfrac{h_i}{\Phi_i}\right)^{(d-2)/2}\\ \dfrac{(-c)^{-d/2}}{d}\left(\dfrac{h_i}{\Phi_i}\right)^{(d-2)/2}\left[1+\dfrac{d}{2}\ln\left(\dfrac{h_i}{\Phi_i}\right)\right]\end{cases}$$
$$+\begin{cases}\dfrac{-d(d-2)\kappa(c_i)}{4}B_i\left(\dfrac{h_i}{\Phi_i}\right)^{(d-4)/2}\\ \dfrac{(-c)^{-d/2}}{d}B_i\left(\dfrac{h_i}{\Phi_i}\right)^{(d-4)/2}\left[d-1+\dfrac{d(d-2)}{4}\ln\left(\dfrac{h_i}{\Phi_i}\right)\right]\end{cases}=0\quad\text{for}\quad\begin{cases}d=\text{noneven}\\ d=\text{even}\end{cases}\tag{11}$$

where $i\neq i'$, $\Delta\equiv g_1g_2-w^2$ and $\kappa(c)$ is defined by Eq. (7). In case $B_1=B_2=0$ and $2<d<4$, Eqs. (11) give a jumplike solution for Φ_i when $\Delta<0$ and $h_i=0$,[10] so one has a fluctuation-induced first-order phase transition. When both B_1 and B_2 are not equal

to zero no solutions of Eqs. (11) exist when $h_i \to 0$ for $2<d\leqslant 4$. So, the long range order is destroyed. Let us consider the case when there is only one random field, say $B_1=0$, $B_2\neq 0$. For the sake of simplicity, we set $d=3$. The solutions of Eqs. (11) when $h_1=h_2=0$ are $\Phi_2=0$ and

$$\Phi_{i\pm}^2=\frac{3w|\kappa(c_2)|}{2g_1}\left[-\frac{3|\kappa(c_2)|\Delta}{8g_1}\right.$$
$$\left.\pm\sqrt{\left(\frac{3\kappa(c_2)\Delta}{8g_1}\right)^2+t_2-\frac{wt_1}{g_1}}\right]-\frac{2t_1}{g_1}$$
$$\mp\frac{3w|\kappa(c_2)|B_2}{4g_1\sqrt{\left(\frac{3\kappa(c_2)\Delta}{8g_1}\right)^2+t_2-\frac{wt_1}{g_1}}}. \tag{12}$$

The solution Φ_{1+} corresponds to the lowest free energy. When $B_2=0$ and $\Delta<0$ a nonzero value of Φ_{1+} appears by a jump at the temperature defined by the equation $[3\kappa(c_2)\Delta/8g_1]^2+t_2-wt_1/g_1=0$. However, as long as $B_2\neq 0$, the dependence of Φ_{1+} on the temperature is no longer jumplike. Even though the solution of the equation $\Phi_{1+}^2=0$ is very cumbersome, it can be shown that near it Φ_{1+}^2 increases linearly from zero with decreasing temperature. Besides, a nonequilibrium free energy corresponding to the functional equation (10) calculated in the framework of the model exhibits a dependence on the order parameter which is typical to second order phase transitions. So, in a system with two coupled order parameters the presence of a random field conjugated with one of them restores a phase transition of the second order.

[1] Y. Imry and S.-K. Ma, Phys. Rev. Lett. **35**, 1399 (1975).
[2] G. Grinstein, Phys. Rev. Lett. **36**, 944 (1976).
[3] A. Aharony, Y. Imry, and S.-K. Ma, Phys. Rev. Lett. **37**, 1364 (1976).
[4] A. P. Young, J. Phys. C **10**, L247 (1977).
[5] S. Singh and Jr. Banavar, Phys. Rev. Lett. **55**, 2220 (1985).
[6] D. I. Uzunov, E. R. Korutcheva, and Y. T. Millev, Physica A **129**, 535 (1985).
[7] T. Schneider, E. Stoll, and H. Beck, Physica A **34**, 436 (1975).
[8] Yu. M. Ivanchenko, A. A. Lisyansky, and A. E. Filippov, Theor. Math. Phys. **67**, 413 (1986).
[9] Yu. M. Ivanchenko, A. A. Lisyansky, and A. E. Filippov, Phys. Lett. A **119**, 55 (1986).
[10] A. A. Lisyansky and D. Nicolaides, Phys. Lett. A **173**, 179 (1993).
[11] Yu. M. Ivanchenko, A. A. Lisyansky, and A. E. Filippov, Sov. Phys. Solid State **31**, 1767 (1989).
[12] Yu. M. Ivanchenko, A. A. Lisyansky, and A. E. Filippov, Phase Transitions **22**, 31 (1990).
[13] V. J. Emery, Phys. Rev. B **11**, 239 (1975).
[14] S. F. Edwards and P. W. Anderson, J. Phys. F **5**, 965 (1975).

Effect of exchange anisotropy on susceptibility of one-dimensional spin 1/2 ferromagnets

Ying Liu and John E. Drumheller
Physics Department, Montana State University, Bozeman, Montana 59717

We have studied several quasi-one-dimensional spin 1/2 ferromagnets ranging from Heisenberg to Ising anisotropy to test the Johnson and Bonner prediction that the low temperature thermodynamic behavior of these systems in external fields depends on the exchange anisotropy and that there are certain ranges of the anisotropy and fields in which bound magnons or spin waves dominate thermodynamic properties. The experimental results confirm that for the samples tested bound magnons dominate susceptibility across available range of the anisotropy ($\gamma<1.05$) and for fields up to 9 T near the Heisenberg limit. © *1996 American Institute of Physics.* [S0021-8979(96)39608-X]

INTRODUCTION

Nonlinear magnetic excitations called bound magnons[1] (BMs) have been shown by Johnson and Bonner (JB) theory[2] and earlier experiments[3] to play an important role in determining the low temperature thermodynamic properties of the one-dimensional ferromagnetic system. The Hamiltonian is given by

$$H=-J\sum_{i}^{N}\left[S_i^zS_{i+1}^z+\gamma(S_i^xS_{i+1}^x+S_i^yS_{i+1}^y)\right]$$

$$-g\mu_B h\sum_{i}^{N}S_i^z,$$

where J is the exchange interaction along a chain, and γ is an exchange anisotropy parameter which varies between the Ising limit ($\gamma=0$) and the isotropic Heisenberg limit ($\gamma=1$). The elementary excitations of this system, more easily identified in the Heisenberg case, are spin waves (SWs) with bound magnons resulting from nonlinear interactions between the spin waves. In particular, Johnson and Bonner[2] predicted that the low-T thermodynamic behavior of the system in external fields depends on the exchange anisotropy of the systems. There are several regions in field-anisotropy ($h-\gamma$) parameter space in which BMs or SWs dominate thermodynamic properties. The dominant behavior of the susceptibility is shown by Fig. 1. It can be seen that BMs are predicted to dominate over SWs throughout the range $0<\gamma<1$ and in most of the range of fields, except at very high fields. It is interesting to note that JB also predicted that for specific heat the situation is very different: spin waves give the main contribution in most of the range of $h-\gamma$ space and dominance of BMs only occurs in the range $0<\gamma<0.6$ with small fields.[2] In this paper, we present the experimental susceptibility results of several quasi one-dimensional spin 1/2 ferromagnets and compare these results to the JB prediction.

EXPERIMENTS AND RESULTS

The best example of a one-dimensional spin 1/2 Heisenberg ferromagnetic system reported up until now, as so far we know, is $(C_6H_{11}NH_3)CuCl_3$ (CHAC)[4] and its bromine analog $(C_6H_{11}NH_3)CuBr_3$ (CHAB)[4], both of which have strong intrachain exchange J of about 70 K and weak interchain coupling $J'/J\sim10^{-4}$. Compounds $(C_4H_8SO)CuCl_2(TMSO)$[5] and $(CH_3)_4NCuCl_3(TMCuC)$[6] have middle range intrachain exchange of 40–50 K, and interchain $J'J\sim10^{-4}$. The compound $[(CH_3)_3NH]CuCl_3\cdot2H_2O(FeTAC)$[3] has small J and J'/J, with Ising anisotropy. Anisotropy values γ of CHAB, CHAC, TMSO, TMCuC, and FeTAC are 1.05, 0.995, 0.975, 0.92, and 0.05 (Ising), respectively.[3–6] The preparation and structural analysis of these compounds have been previously reported.[3–6] Most of the samples were provided by R. Willett, Chemistry Department, Washington State University.

The magnetic ac susceptibilities of crystal samples of CHAB, CHAC, TMSO, and powdered crystal sample of TMCuC were measured from 4.2 to 35 K in an ac field $h=10$ Oe, frequency $f=80$ Hz and dc magnetic fields h of 0, 1, 2, 3, 4, and 5 T with both the applied fields along the easy-axis direction, which is perpendicular to the chain direction. All measurements were performed on the LakeShore Model 7225 AC Susceptometer/DC magnetometer. Measurements were fully calibrated and performed automatically through

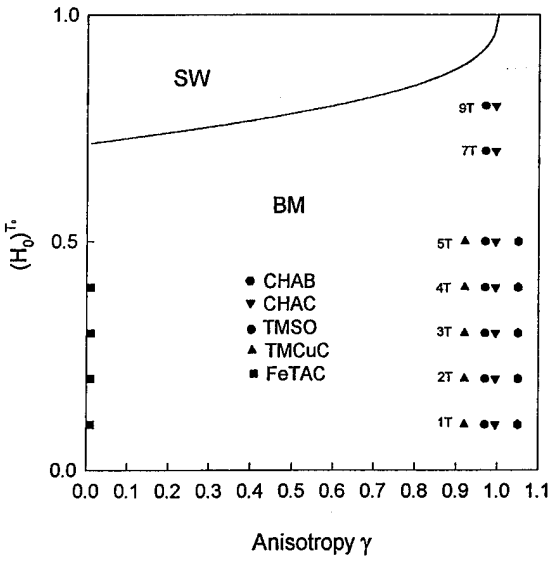


FIG. 1. Regions and corresponding crossover boundary (Ref. 2) which determine bound magnon (BM) and spin wave (SW) dominance on susceptibility as a function of field h and anisotropy γ, where $H_0=h/\gamma J$, $T_0=T/\gamma J$. Dots represent experimental results.

 0021-8979/96/79(8)/5094/2/$10.00 © 1996 American Institute of Physics

data acquisition and control software packages. The system accuracies for both ac and dc measurements are $\pm 1\%$, and the temperature accuracy is ± 0.2 K. The high-field ac susceptibilities of crystal sample of TMSO and CHAC were measured in a ac field $h=10$ Oe, frequency $f=80$ Hz, and in high dc magnetic fields h of 7 and 9 T at the LakeShore laboratory, Westerville, Ohio. The ac susceptibility of FeTAC at fields 1, 2, 3, and 4 T was measured and reported earlier[3] and high-field data were not available.

Temperature dependences of the ac susceptibilities of CHAB, CHAC, TMSO, TMCuC, and FeTAC all show typical rounded peaks of bound magnon effects as predicted by the JB theory. All the data are analyzed in term of contributions of BMs and SWs, by using the JB susceptibility model.[2] Fitting results show that BMs dominate over SWs on susceptibility in all of these compounds. The experimental results extracted from ac susceptibility data are plotted at fields $h=1$, 2, 3, 4, 5, 7, and 9 T and $\gamma=1.05$, 0.995, 0.975, 0.92, and 0.05, in the field-anisotropy parameter space in Fig. 1. Figure 1 shows that BMs dominate susceptibility across available range of γ ($\gamma<1.05$) and for fields up to 9 T near the Heisenberg limit, confirming the prediction of JB over this range.

ACKNOWLEDGMENT

This work was supported by the NSF Grant No. DMR-93-10967. We would like to thank Brad Dodrill for help with the high-field ac susceptibility data.

[1] H. A. Bethe, Z. Phys. **71**, 205 (1931); M. Wortis, Phys. Rev. **132**, 85 (1963).
[2] J. D. Johnson and J. C. Bonner, Phys. Rev. B **22**, 251 (1980).
[3] D. N. Haines and J. E. Drumheller, Phys. Rev. Lett. **58**, 2702 (1987); K. Ravindran, D. N. Haines, and J. E. Drumheller, J. Appl. Phys. **67**, 5481 (1990); D. N. Haines, K. Ravindran, and J. E. Drumheller, J. Phys. Colloq. **49**, C8-1483 (1988); Phys. Rev. B **45**, 3122 (1992).
[4] K. Kopinga, A. M. Tinus, and W. J. de Jonge, Phys. Rev. B **25**, 4685 (1982).
[5] D. D. Swank, C. P. Landee, and R. D. Willett, Phys. Rev. B **20**, 2154 (1979).
[6] C. P. Landee and R. D. Willett, Phys. Rev. Lett. **6**, 463 (1979).

Effects of randomness in gapped antiferromagnetic quantum spin chains

Kun Yang
Department of Electrical Engineering, Princeton University, Princeton, New Jersey 08544

R. A. Hyman
Physics Department, Indiana University, Bloomington, Indiana 47405

R. N. Bhatt
Department of Electrical Engineering, Princeton University, Princeton, New Jersey 08544

S. M. Girvin
Physics Department, Indiana University, Bloomington, Indiana 47405

The effects of bond randomness are studied for spin chains with excitation gaps in the pure case. Systems with enforced topological structure like the spin-1/2 chain with enforced dimerization and spin-1 chain in the Haldane gapped phase appear very stable against randomness. On the other hand, systems with spontaneously generated topological order like the spin-1/2 chain with spontaneous dimerization are found to be unstable even for weak randomness despite the gap. © *1996 American Institute of Physics.* [S0021-8979(96)39708-6]

Theoretical work[1–4] on random quantum magnetic systems has shown that systems which behave critically in the absence of randomness are unstable against weak randomness. At low temperature these systems are in the so called random singlet (RS) phase,[1,3] in which spins far apart in space form weakly bound singlet pairs in a random manner. The low-temperature thermodynamic properties of these systems are dominated by the weakly bound pairs and are universal,[1–3] e.g., the susceptibility diverges as $[T \log^2 T]^{-1}$ at low T, for the Heisenberg or XXZ spin-1/2 chain, independent of the details of the randomness.[3] The disorder averaged spin–spin correlation functions also exhibit power law with universal exponents.[3] There has been, however, very little work on effects of bond randomness on gapped antiferromagnets. We address this issue in the present paper.

Examples of gapped antiferromagnetic spin chains include integer spin chains in the Haldane phase,[5] dimerized spin-1/2 chains,[6] and spin chains with spontaneous dimerization.[7] Naively one would expect such systems to be stable against weak randomness due to the existence of a gap, while strong enough randomness might drive them to a random singletlike phase. We find, however, this is not the case. The behavior of these systems depends *crucially* on their *topological structure*. Systems with enforced topological order, like the dimerized spin-1/2 chain and spin-1 chain in the Haldane phase, are found to be very stable and the topological order parameter survives even *strong randomness*. The low temperature thermodynamics is *nonuniversal* (as is seen experimentally[8]) in these systems, in contrast to the random singlet phase. On the other hand, systems with spontaneously generated topological order (like the spontaneously dimerized spin-1/2 chain) are unstable and are driven to the RS phase by weak randomness, even though such chains have gaps separating their ground and excited states.

We start with the spin-1/2 chain with spontaneous dimerization, and for convenience focus on the Majumdar–Ghosh (MG) model in the presence of weak randomness:[7]

$$H=\sum_i (J_i \mathbf{S}_i\cdot\mathbf{S}_{i+1}+K_i \mathbf{S}_i\cdot\mathbf{S}_{i+2}), \tag{1}$$

with J's random but distributed near 1 and K's near 1/2. When $J_i=1$ and $K_i=1/2$, this is the usual MG model with two degenerate spontaneously dimerized ground states and an excitation gap. We can separate H into two parts: $H=H_0+H'$, with

$$H_0=\sum_i K_i(\mathbf{S}_i\cdot\mathbf{S}_{i+1}+\mathbf{S}_i\cdot\mathbf{S}_{i+2}+\mathbf{S}_{i+1}\cdot\mathbf{S}_{i+2}), \tag{2}$$

$$H'=\sum_i \delta_i \mathbf{S}_i\cdot\mathbf{S}_{i+1}, \tag{3}$$

where $\delta_i=J_i-K_i-K_{i-1}$. The ground states of H_0 are the same as the ground states of the pure MG Hamiltonian, again with a double degeneracy, labeled as $|L\rangle$ and $|R\rangle$. H', however, breaks the degeneracy and each term in it favors one state or the other. Hence, it is energetically favorable to separate the system into domains of $|L\rangle$ and $|R\rangle$ where they are favored by H'. In doing so, however, one creates domain walls which are unpaired edge spins. There is a finite energy cost (gap) from H_0 but the energy gain from H' always wins since it grows with the length of the domains as $|\delta|\sqrt{L}$, where $|\delta|$ is the typical strength of δ_i and L is the typical length of the domains. The energy gain is proportional to $\sqrt{L}$ because δ_i is random. We, hence, find in the weak randomness limit the typical size of domains diverges as $L\sim 1/\delta^2$ and the density of domain walls is $N_d\sim\delta^2$. These unpaired spins in the domain walls dominate the low T thermodynamics since the bulk excitations within the domains are gapped. They are expected to have weak and random (due to the fluctuations in domain length) antiferromagnetic interactions. Hence, the low temperature thermodynamics should have the same form as the random Heisenberg chain with nearest neighbor interaction which is in the random singlet phase,[3] for example, the susceptibility *diverges* at low T: $\chi\sim\delta^2/T|\log T|^2$. This should be contrasted with the pure case where χ *vanishes* exponentially at low T due to the existence of a gap. We, hence, find that the spontaneously

 0021-8979/96/79(8)/5096/3/$10.00 © 1996 American Institute of Physics

dimerized spin-1/2 chains are unstable against *weak* randomness, due to the facts that the ground state has a double degeneracy and the spinons carried by domain walls are weakly interacting and unconfined.

We next consider the dimerized spin-1/2 chain, where we find very different physics. The Hamiltonian for random antiferromagnetic XXZ chain is

$$H=\sum_i J_i[S_i^x S_{i+1}^x+S_i^y S_{i+1}^y+\Delta S_i^z S_{i+1}^z], \tag{4}$$

where S_i^α are spin-1/2 operators, J_i are (random) positive coupling constants, and $0\leqslant\Delta\leqslant 1$. It can be shown that any $\Delta<1$ flows to $\Delta=0$ under renormalization group transformation.[3] We hence concentrate on the cases of XX chain ($\Delta=0$) and Heisenberg chain ($\Delta=1$). In the presence of dimerization the distribution of the couplings J_i depends on whether i is even or odd. We write the distribution functions for even and odd J's as $P_e(J,J_0)$ and $P_0(J,J_0)$, respectively. Here J_0 is the cutoff in the distribution function corresponding to the strongest bond in the system.

A powerful method to study such random antiferromagnets is the real space decimation renormalization group (RG) introduced by Dasgupta and Ma.[1] (See also Ref. 2). In this real space RG procedure we pick the bond in the system with the largest J (i.e., the strongest bond), say, J_{23}, between spins 2 and 3. Since this is such a strong bond, spins 2 and 3 are likely to form a singlet pair in the low energy (on scales much smaller than J_{23}) states of the system and become inert. The major physical effect of the existence of spins 2 and 3 is to mediate an effective coupling between their neighboring spins 1 and 4. For the XX chain, $\tilde{H}_{1-4}=\tilde{J}_{14}(S_1^x S_4^x+S_1^y S_4^y)$ where $\tilde{J}_{14}=J_{12}J_{34}/(J_{23})+O(1/J_{23}^2)$. And for the Heisenberg chain, $\tilde{H}_{1-4}=\tilde{J}_{14}\mathbf{S}_1\cdot\mathbf{S}_4$ where $\tilde{J}_{14}=J_{12}J_{34}/(2J_{23})+O(1/J_{23}^2)$. The energy cutoff is then lowered to $\Omega=\max\{\tilde{J}\}$. The generated coupling is still between two nearest neighbor spins (since we have decimated spins 2 and 3 so spins 1 and 4 become nearest neighbors), so the renormalized Hamiltonian has the same form as the original one, except that the distribution of bonds is slightly different and the cutoff is lower. Thus, we can repeat this procedure and continue lowering the energy scale (cutoff) and renormalizing the bond distribution. As shown by Fisher,[4] in the absence of dimerization ($P_e=P_0$), the distribution $P(J)$ flows toward an energy scale dependent universal random singlet (RS) fixed point distribution in the low energy limit

$$P(J,\Omega)=\frac{\alpha}{\Omega}\left(\frac{J}{\Omega}\right)^{-1+\alpha} \tag{5}$$

where Ω is the energy cutoff and $\alpha=1/\log(J_0/\Omega)$ which goes to zero logarithmically. Hence, the distribution becomes more and more singular at $J=0$ as the energy scale decreases, implying that the decimated bonds are more and more likely to be *much* stronger than their neighbors, and the whole decimation procedure becomes asymptotically exact in the low energy limit. The consequence of this universal fixed point distribution is that the low temperature thermodynamics and long distance spin–spin correlation function are universal for the undimerized random spin-1/2 chain.[3]

The situation is totally different when there is a small difference in the distributions for even and odd bonds, i.e., dimerization. We find that dimerization is a *relevant* perturbation at the RS fixed point, with eigenvalue $+1$,[9] indicating that the difference in distributions *grows* as the energy scale decreases. Physically this is easy to understand. Assume that, on average, the odd bonds are slightly stronger than the even bonds. Thus, an odd bond is somewhat more likely to get decimated in the real space RG decimation procedure. This also results in decimation of two intermediate strength neighboring even bonds and generation of a *much weaker even bond.* Consequently, the even bond distribution picks up weight near $J=0$ faster than the odd bond distribution and the over all strength of even bonds decreases faster than the odd bonds. Thus, in the low energy limit, the system can be viewed as a trivially soluble collection of uncoupled spin pairs (isolated odd bonds). We refer to this phase as the random dimer (RD) phase.

After renormalization, the distribution of odd bonds takes the form

$$P_0(J)=\frac{\alpha}{\Omega_0}\left(\frac{J}{\Omega_0}\right)^{-1+\alpha}\Theta\left(1-\frac{J}{\Omega_0}\right), \tag{6}$$

where Ω_0 is the energy scale at which the difference in strength of the even and odd bonds becomes significant. From the eigenvalue of the relevant perturbation we find for weak dimerization $\log(J_0/\Omega_0)\sim 1/\delta$, where δ parameterizes the strength of dimerization, and $\alpha=1/\log(J_0/\Omega_0)\propto\delta\ll 1$. Knowing the distribution of odd bonds and treating the even bonds as unconnected, the thermodynamic properties in the low temperature limit can be easily calculated. As the temperature goes to zero, the spin susceptibility diverges like $\chi\sim T^{-1+\alpha}$, and the specific heat goes to zero like $C_v\sim T^\alpha$. They are qualitatively similar to those in the RS phase but nevertheless *nonuniversal.* The averaged spin–spin correlation function is short ranged, with the correlation length (distance between spins) $\xi\sim|\delta|^{-\nu}$ and $\nu=2$. The existence of a divergent magnetic susceptibility away from the critical point is characteristic of a Griffiths phase. The divergent susceptibility arises from magnetically active gapless excitations. The random singlet phase, discussed by Fisher,[3] also exhibits a divergent susceptibility. However, in the case of the random singlet state, the averaged spin–spin correlation function decays as $1/R^2$ at long distances so the system is critical and a divergent susceptibility is expected. If the initial dimerization is large, the flow begins far from the RS phase and the bond distribution of the stronger bonds does not flow to a power law and the gap does not close up. When this is the case, thermodynamic properties will depend strongly on the initial distribution and the susceptibility will remain finite.

The dimer phase has a novel kind of topological order that measures the dimerization of the chain, manifested in the following "string-topological correlation function" similar to that discussed in the context of spin-1 chain:[10]

$$T_{ij}=\langle\Psi_0|S_i^z \exp\left[i\pi\sum_{i<k<j} S_k^z\right]S_j^z|\Psi_0\rangle, \tag{7}$$

where $|\Psi_0\rangle$ is the ground state. For a completely dimerized ground state (where all the even bonds or all the odd bonds are set to be zero) $T_{ij}=-1/4$ if i is a left spin of a dimer and j is the right spin of a (possibly different) dimer. This is because every spin between i and j in the completely dimerized model is paired up with another spin between i and j. $T_{ij}=0$ otherwise. Therefore, this special topological correlation function is long-ranged even though the ordinary spin–spin correlation function is short-ranged. For a general spin-1/2 chain with randomness, we introduce a topological order parameter

$$T=\lim_{j-i\to\infty}(\overline{T_{2i,2j-1}}-\overline{T_{2i+1,2j}}), \tag{8}$$

where the overbar stands for average over randomness. Obviously T vanishes in the absence of dimerization. In the presence of dimerization, T measures the probability that the two end spins have survived decimation until the dimerization becomes large, and the low energy physics becomes that of the completely dimerized chain. We find[9] for small δ, T scales like

$$T\sim-|\delta|^{2\beta}\,\mathrm{sgn}(\delta), \tag{9}$$

with $\beta=\nu=2$, and $\mathrm{sgn}(\delta)$ is positive if even bonds are stronger and negative if odd bonds are stronger.

It is important to notice that the topological order is not a spontaneous order like the spontaneous magnetization in a ferromagnet; it is actually dynamically *enforced* by the Hamiltonian. For example, the sign of the order parameter is determined by the sign of the dimerization, unlike spontaneous magnetization which can take any direction allowed by the symmetry. It reflects the fact that the Hamiltonian favors singlet pairs to be formed over even bonds, if the even bonds are stronger in general. In the absence of odd bonds the ground state is a trivial collection of singlet pairs over even bonds and the dimer or topological order is perfect. In the presence of odd bond couplings (but weaker than even bonds in general) both quantum and statistical fluctuations generate regions where singlet pairs are formed over odd bonds. Between regions of different topological structures there has to be a spin unpaired to its neighbors (a soliton). In the presence of dimerization, the energy cost of the "wrong region" (the area having singlets formed over the odd bonds in this case) is proportional to its length (at least at long enough length scales); hence, the unpaired spins are confined by a linear confining potential.[11] The confinement length in the weak dimerization limit is the length scale at which dimerization becomes significant under RG, which is also the spin–spin correlation length. We hence find that although the gap vanishes in the presence of strong randomness, the dimer phase is stable and the topological order persists due to the confinement of unpaired spins. This should be contrasted with the case of spontaneous dimerization. In that case the two degenerate ground states also have finite topological order parameter, but it is a *spontaneous* order associated with the spontaneously broken translation symmetry, and is immediately killed upon introducing weak randomness and hence unconfined domain walls (solitons).

Our results for the dimerized spin-1/2 chain are likely to be applicable to the spin-1 chain in the Haldane phase. In the absence of randomness, they exhibit similar physical properties and can be connected to each other without closing the gap, implying they belong to the same phase.[12] It is natural to expect that they behave similarly in the presence of randomness.[9] An explicit example that provides strong support to the above conjecture is the random version of the Affleck–Kennedy–Lieb–Tasaki model:[13]

$$H=\sum_i J_i\left[\mathbf{S}_i\cdot\mathbf{S}_{i+1}+\frac{1}{3}(\mathbf{S}_i\cdot\mathbf{S}_{i+1})^2\right], \tag{10}$$

where $J_i>0$. The exact ground state of this random model is identical to that of the pure model,[13] i.e., a valence bond solid. Its excitation spectrum and thermodynamic properties will certainly depend on the distribution of J_i, yet the perfectly topologically ordered ground state (with short range spin–spin correlation function) is completely unaffected by randomness.

In summary, we have shown that the effects of randomness on gapped spin chains depend crucially on the topological structure of the system. Systems with enforced topological order like the dimerized spin-1/2 chain and the spin-1 chain in the Haldane phase are very stable, while systems without such enforced order like the spin-1/2 chain with spontaneous dimerization is unstable against weak randomness despite the gap.

We thank D. Fisher, D. Haldane, and S. Sachdev for stimulating discussions and important suggestions. This work was supported in part by NSF Grants No. DMR-9224077, No. DMR-9416906, and No. DMR-9400362. R.N.B. is also supported in part by a Guggenheim fellowship.

[1] C. Dasgupta and S. K. Ma, Phys. Rev. B **22**, 1305 (1979).
[2] R. N. Bhatt and P. A. Lee, Phys. Rev. Lett. **48**, 344 (1982); J. Appl. Phys. **52**, 1703 (1981).
[3] D. S. Fisher, Phys. Rev. B **50**, 3799 (1994).
[4] D. S. Fisher, Phys. Rev. B **51**, 6411 (1995).
[5] F. D. M. Haldane, Phys. Lett. A **93**, 464 (1983); Phys. Rev. Lett. **50**, 1153 (1983).
[6] For recent work, see, for example, R. R. P. Singh, M. P. Gelfand, and D. A. Huse, Phys. Rev. Lett. **61**, 2484 (1988).
[7] C. K. Majumdar and D. K. Ghosh, J. Math. Phys. **10**, 1388, 1399 (1969); J. Phys. C **3**, 911 (1970); F. D. M. Haldane, Phys. Rev. B **25**, 4925 (1982).
[8] L. C. Tippie and W. G. Clark, Phys. Rev. B **23**, 5846 (1981).
[9] R. A. Hyman, Kun Yang, R. N. Bhatt, and S. M. Girvin, Phys. Rev. Lett. **76**, 839 (1996).
[10] K. Rommelse and M. den Nijs, Phys. Rev. Lett **59**, 2578 (1987); S. M. Girvin and D. P. Arovas, Phys. Scr. T **27**, 156 (1988).
[11] This is known in the case of integer spin chains as confinement of spinon excitations. See N. Read and S. Sachdev, Phys. Rev. Lett. **62**, 1694 (1989).
[12] K. Hida, Phys. Rev. B **45**, 2207 (1992).
[13] I. Affleck, T. Kennedy, E. H. Lieb, and H. Tasaki, Phys. Rev. Lett. **59**, 799 (1987).

Competition between spin-Peierls phase and three-dimensional antiferromagnetic order in $CuGe_{1-x}Si_xO_3$

J. P. Renard, K. Le Dang, and P. Veillet
Institut d'Electronique Fondamentale, CNRS URA 022, Université Paris-Sud, 91405 Orsay Cedex, France

L. P. Regnault
CEA/Département de Recherche Fondamentale sur la Matière Condensée, SPSMS/MDN, Centre d'Etudes Nucléaires, 38054 Grenoble Cedex 9, France

G. Dhalenne and A. Revcolevschi
Laboratoire de Chimie du Solide, CNRS URA 446, Université Paris-Sud, 91405 Orsay Cedex, France

The effect of substitution of Si to Ge in $CuGe_{1-x}Si_xO_3$ single crystals has been studied by magnetic susceptibility, Cu nuclear magnetic resonance, and neutron scattering measurements. The phase diagram in the (x,T)-plane is characterized by an initial rapid decrease of the spin-Peierls temperature, T_{SP}, on increasing x and by the occurrence of a three-dimensional long range ordered antiferromagnetic phase at $T=T_N$ in the range $0.005 \leqslant x \leqslant 0.05$. This phase diagram is qualitatively discussed. The neutron scattering data for $x=0.007$ show that the dimerization which takes place below T_{SP} is not suppressed below T_N. © *1996 American Institute of Physics.* [S0021-8979(96)39808-2]

I. INTRODUCTION

One-dimensional antiferromagnets (1D-AF) with isotropic short range interactions are of current interest because they exhibit large quantum effects. In particular, for the spin value $S=1/2$, the quantum fluctuations and the magnetic energy can be reduced by the dimerization of the chain, if the latter can be easily distorted. The resulting exchange alternation gives rise to a singlet ground state separated from the first excited states by a gap. As the temperature is reduced, a spin-Peierls (SP) transition from a uniform phase to a dimerized phase (SP phase) occurs at a well defined temperature, T_{SP}. The recent discovery of a simple inorganic spin-Peierls compound, $CuGeO_3$ (Ref. 1) which can be grown in large single crystals and can accept various substitutions has renewed the field of experiments on the spin-Peierls transition. $CuGeO_3$ has an orthorhombic structure composed of linear chains of Cu^{2+} ions running along the c axis, and well separated from each other by Ge–O chains.[2] The $S=1/2$ Cu^{2+} spins in a chain are equally spaced at high temperature and strongly coupled by antiferromagnetic intrachain interaction. The spin-Peierls transition which occurs at $T_{SP}=14.3$ K is evidenced by a kink in the magnetic susceptibility.[1,3] The structural transition to the dimerized state at T_{SP} has been revealed by x-ray and elastic neutron scattering.[3,4] A rather attractive feature of $CuGeO_3$ is its ability to accept substitutions on the cationic sites. Investigations of such substituted materials have been carried out on samples containing either divalent ions substituted for Cu^{2+} such as Zn, Mg, Ni, and Mn,[5–8] or Si substituted to Ge.[9] We discuss here the effect of Si substituted for Ge on the phase diagram of $CuGe_{1-x}Si_xO_3$.

II. PHASE DIAGRAM OF $CuGe_{1-x}Si_xO_3$

The experimental investigation by susceptibility, Cu nuclear magnetic resonance and neutron scattering was carried out on $CuGe_{1-x}Si_xO_3$ with $0 \leqslant x \leqslant 0.1$ single crystalline samples cleaved along the (100) plane from large single crystals several cm long, grown from the melt by a floating zone method associated with an image furnace.[10,11] Details about the crystal growth and the Si concentration determination have been reported in a previous article.[9]

The temperature behavior of magnetic susceptibility of $CuGe_{1-x}Si_xO_3$ for $x \geqslant 5\times10^{-3}$ strongly differs from that of pure $CuGeO_3$. In the concentration range 5×10^{-3} to 10^{-2}, when lowering the temperature, both χ_c and χ_b exhibit first a decrease, reminiscent of a spin-Peierls transition followed by an increase. Below a certain temperature T_N that we attribute to the onset of three-dimensional antiferromagnetic (3D-AF) order, χ_c exhibits a sharp drop and decreases toward zero whereas χ_b continues to increase but with a smaller slope. In the concentration range $2–5\times10^{-2}$, no indication of the SP transition can be detected from the temperature dependence of susceptibility whereas the transition to 3D-AF phase remains very clear. From these susceptibility data, the Néel temperature T_N at which χ_c vs T shows a sharp peak and the spin-Peierls temperature T_{SP} corresponding to inflection point above T_N have been determined and plotted as a function of x, leading to the phase diagram of Fig. 1. The Cu NMR experiments performed at 2 K in a dc magnetic field of 11 kOe applied along the c crystal axis have revealed a striking difference between the samples with $x=0$ and 0.0025, and the samples with $x \geqslant 0.005$.[9] While the first ones show one narrow line for each Cu isotope, the second ones show broad spectra splitted by the Cu hyperfine fields, corresponding to the antiferromagnetic long range order with the Cu spin direction along the c axis. Neutron scattering studies (Sec. III) and ultrasonic velocity measurements[12] performed on large single crystals with $x=7\times10^{-3}$ are consistent with this phase diagram. The drastic initial decrease of T_{SP} with increasing x is well described by $T_{SP}(x)/T_{SP}(0)=1-\alpha.\,x$ with $\alpha \approx 50$. For comparison a coefficient $\alpha \approx 14$ was found for Zn doping.[5] In a wide range of Si concentrations, $5\times10^{-3} \leqslant x \leqslant 5\times10^{-2}$, the 3D-AF phase is observed at low temperature. T_N exhibits a maximum at $T_{N\max} \approx 5$ K for $x=0.015$.

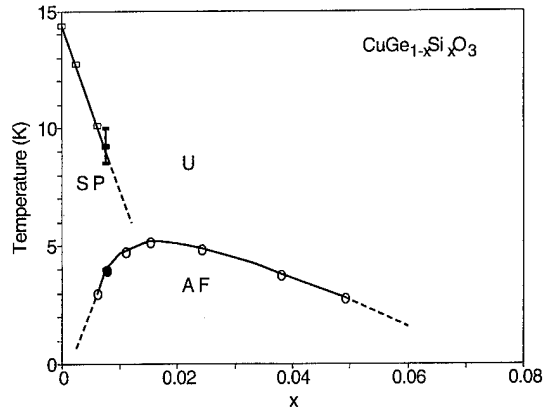


FIG. 1. (x,T)-plane phase diagram of $CuGe_{1-x}Si_xO_3$ obtained from magnetic susceptibility measurements performed on single crystals. The three different regions limited by the phase separation lines correspond to the uniform phase (U) at high T, the spin-Peierls phase (SP) at low x and T, and the 3D long range ordered antiferromagnetic phase (AF) at low T and intermediate x values. The neutron determination of T_{SP} and T_N for $x=7.10^{-3}$ (Sec. III) is indicated by black square and circle.

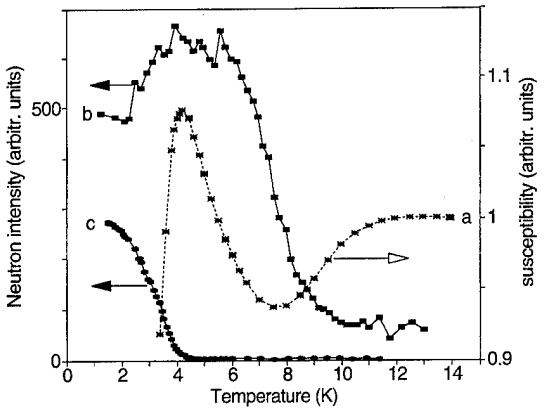


FIG. 3. Magnetic susceptibility and neutron scattering peak intensities vs the temperature, T, in a single crystal of $CuGe_{0.993}Si_{0.007}O_3$. Curves a, b, and c, respectively, correspond to χ_c, intensity of the dimerization peak (1/2, 3,1/2) and intensity of the 3D-AF Bragg peak (0,1,1/2).

III. NEUTRON SCATTERING STUDY OF $CuGe_{0.993}Si_{0.007}O_3$

The neutron scattering experiments were performed using three-axis spectrometers, DN1, installed on a thermal neutron beam of the Siloe reactor at CEN-Grenoble and IN12, installed on a cold neutron guide of the High Flux Reactor at ILL. In both cases, collimations $60'-60'-60'$ were used and the incident neutron wave vectors were fixed at $k_i=2.62$ and 1.5 $Å^{-1}$, respectively. Neutron diffraction experiments performed on the DN1 spectrometer have clearly demonstrated the existence of superlattice peaks indexed with the propagation vector $\mathbf{k_{SP}}=(1/2,0,1/2)$, as in pure $CuGeO_3$.[3] Figure 2 depicts Q-scans along the c direction across scattering vector $\mathbf{Q}=(1/2,3,1/2)$, recorded at temperatures $T=11$, 4, and 1.5 K, which show the appearance of a resolution-limited peak below roughly 10 K. The temperature dependence of intensity at the maximum is given in Fig. 3 (curve b). Two remarks can be made concerning this curve.

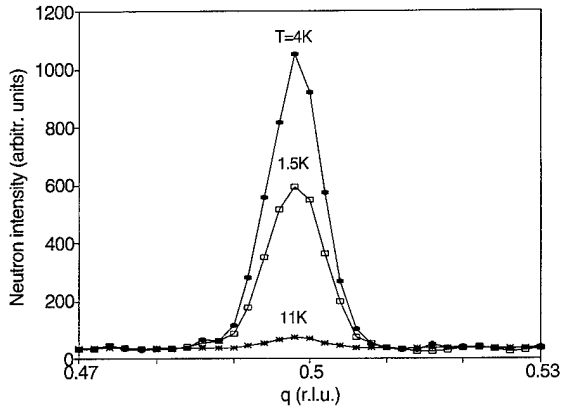


FIG. 2. Elastic neutron scattering scans around the dimerization peak (1/2, 3,1/2) at 1.5 K ($T \ll T_N$), 4 K ($T \cong T_N$), and 11 K ($T > T_{SP}$) in $CuGe_{0.993}Si_{0.007}O_3$. The persistence of the dimerization below the Néel temperature, T_N, of 3D-AF long range order is clearly observed.

First, the transition is relatively "smooth" and is characterized by an up-turned curvature, probably due to a distribution of transition temperature in the sample. Our experimental data are consistent with a transition temperature ranging from 8.5 to 10 K, with an average value of 9.2 K in good agreement with susceptibility measurements on the same sample, Fig. 3 (curve a). This broadening is very likely related to a small inhomogeneity in the Si content, which amounts from our data to $x=0.007\pm0.001$. More interestingly, the intensity of dimerization peaks increases continuously down to about 4 K, below which the signal starts to decrease slightly. This is precisely the temperature at which χ_c exhibits a maximum, reflecting the appearance of 3D-AF long range ordering, Fig. 3. This interpretation has been further confirmed by studying the temperature dependence of superlattice peak (0,1,1/2), which in fact corresponds to the minimum in energy of the excitation spectrum in pure $CuGeO_3$. Figure 3 (curve c) shows the variation on temperature of the (0,1,1/2) peak, obtained with the IN12 spectrometer. Quite unambiguously, a magnetic Bragg peak appears below $T_N \approx 4$ K, characteristic of a 3D *antiferromagnetic* ordering described by the wave vector $\mathbf{k_{AF}}=(0,1,1/2)$. Above T_N, quasi-1D correlations subsist, which *coexist* with the dimerized phase up to T_{SP}, above which a more classical magnetic behavior is recovered. So, below T_N the dimerized phase persists (at least partly), coexisting with the 3D antiferromagnetic phase. The important point is that these two phases seem to coexist *independently one from each other*, as if a true "phase separation" was present in the system. Within this interpretation, the slight decrease of the (1/2,3,1/2) intensity observed below T_N may be associated with a decrease of the population of dimerized domains. Inelastic neutron scattering experiments[13] have confirmed this interpretation, by showing that the spin-Peierls gap associated with the dimerized phase is unchanged when crossing T_N, whereas the intensity of this mode increases slightly.

IV. DISCUSSION

The phase diagram of Fig. 1 clearly reflects the competition between the SP gap, Δ, which tends to induce a nonmagnetic SP phase and the interchain interaction, J', which tends to induce a long-range ordered 3D-AF phase. The stable phase at $T=0$ is determined by a balance between Δ and the effective 3D interaction, $E'=zJ'\xi_0/d$ where z is the number of neighboring chains, ξ_0 the 1D correlation length, and d the chain parameter. The effect of Si substitution is to reduce Δ, as evidenced by the drastic decrease of T_{SP} and by inelastic neutron scattering data on $CuGe_{0.993}Si_{0.007}O_3$:[13] $\Delta=1.4$ meV instead of 2.1 meV in pure $CuGeO_3$.[14,15] Since ξ_0 is expected to be inversely proportional to Δ, the ratio E'/Δ should increase as $1/\Delta^2$ which strongly favors the 3D-AF phase. Indeed a maximum value of T_N is observed for $x=0.02$ which corresponds to the vanishing of the gap, $\Delta(x)$, for a linear dependence on x. With further increase of x, one can expect that the lattice defects reduce ξ_0 and thus reduce T_N.[16] This simple physical picture can be applied to other kinds of substituents like Zn. This explains the striking similarity between the observed phase diagrams for Si and Zn doped $CuGeO_3$, the relevant difference being in the $\Delta(x)$ dependence. It is also supported by recent calculations on a two-dimensional array of chains with alternating intrachain exchange.[17] These calculations show that the dimerized phase can undergo long range AF order when the exchange alternation parameter which governs the size of the gap lies below a critical value. This is in agreement with the neutron experiments showing the persistence of the chain dimerization below T_N.

In summary, we have shown that Si substitution in $CuGeO_3$ has a drastic effect on the spin-Peierls transition. At low temperature, a long range ordered antiferromagnetic phase is observed in a wide range of Si concentrations, in good agreement with the theoretical predictions. Its existence has been confirmed by neutron scattering experiments on a $CuGe_{0.993}Si_{0.007}O_3$ single crystal, which have shown that the dimerization is not suppressed below T_N.

ACKNOWLEDGMENTS

The authors thank P. Monod for interesting discussions, M. Poirier for a preprint on Si doped $CuGeO_3$, and NEDO for financial support.

[1] M. Hase, I. Terasaki, and K. Uchinokura, Phys. Rev. Lett. **70**, 3651 (1993).
[2] H. Völlenkle, A. Wittmann, and H. Nowotny, Monatsh. Chem. **98**, 1352 (1967).
[3] J. P. Pouget, L. P. Regnault, M. Ain, B. Hennion, J. P. Renard, P. Veillet, G. Dhalenne, and A. Revcolevschi, Phys. Rev. Lett. **72**, 4037 (1994).
[4] K. Hirota, D. E. Cox, J. E. Lorenzo, G. Shirane, J. M. Tranquada, M. Hase, K. Uchinokura, H. Kojima, Y. Shibuya, and J. Tanaka, Phys. Rev. Lett. **73**, 736 (1994).
[5] M. Hase, I. Terasaki, Y. Sasago, K. Uchinokura, and H. Obara, Phys. Rev. Lett. **71**, 4059 (1993).
[6] M. Hase, Y. Sasago, K. Uchinokura, G. Kido, and T. Hamamoto, J. Magn. Magn. Mater. **140-144**, 1691 (1995).
[7] S. B. Oseroff, S. W. Cheong, B. Aktas, M. F. Hundley, Z. Fisk, and L. W. Rupp, Phys. Rev. Lett. **74**, 1450 (1995).
[8] J. G. Lussier, S. M. Coad, D. F. McMorrow, and D. McK Paul, J. Phys. Condens. Matter **7**, L325 (1995).
[9] J. P. Renard, K. Le Dang, P. Veillet, G. Dhalenne, A. Revcolevschi, and L. P. Regnault, Europhys. Lett. **30**, 475 (1995).
[10] A. Revcolevschi and R. Collongues, C. R. Acad. Sci. (Paris) **266**, 1767 (1969).
[11] A. Revcolevschi, Rev. Int. Htes Temp. **7**, 73 (1970).
[12] M. Poirier, R. Beaudry, R. Castonguay, M. L. Plumer, G. Quirion, F. S. Razavi, A. Revcolevschi, and G. Dhalenne, Phys. Rev. B (unpublished).
[13] L. P. Regnault (unpublished).
[14] M. Nishi, O. Fujita, and J. Akimitsa, Phys. Rev. B **50**, 6508 (1994).
[15] L. P. Regnault, M. Ain, B. Hennion, G. Dhalenne, and A. Revcolevschi, Physica B (in press).
[16] C. Dupas and J. P. Renard, Phys. Rev. B **18**, 401 (1978).
[17] N. Katoh and M. Imada, J. Phys. Soc. Jpn. **63**, 4529 (1994).

Domain structure in NiO biasing layers (abstract)

R. W. Erwin and J. A. Borchers
Materials Science and Engineering Laboratory, National Institute of Standards and Technology, Gaithersburg, Maryland 20899

D. M. Lind, E. Lochner, K. A. Shaw, B. Singer, P. Stoyonov, and R. C. DiBari
Florida State University, Tallahassee, Florida

S. D. Berry
Limestone College, Gafney, South Carolina

Fe_3O_4/NiO multilayers exhibit long-range antiferromagnetic order with the magnetite ferrimagnetic correlations confined to a single layer due to stacking faults of the spinel structure at the interfaces.[1] We are studying the field dependence of the interlayer coupling and magnetic structure in a series of Fe_3O_4/NiO multilayers using neutron diffraction. Both NiO and Fe_3O_4 thin films were included in the measurements for comparison. In a single thick Fe_3O_4 film, intensity changes with magnetic field are consistent with the alignment of the net ferrimagnetic moment parallel to the applied field. In a single thick NiO film, we observe no intensity changes with magnetic field. For multilayers where the ratio of NiO to Fe_3O_4 is far from unity, the field dependence approximates that of the thick film of the majority constituent. However, for a Fe_3O_4 (68 Å)/NiO (34 Å) multilayer the NiO antiferromagnetic intensity decreases with increasing field, applied parallel to a [110] axis in the film plane. This indicates a domain repopulation in the NiO, concomitant with the magnetization of the magnetite, where the antiferromagnetic modulation direction prefers the [111] axes that are closest to the applied field direction. A broadening of the NiO peak shows that the repopulated domains are smaller. We are pursuing a complete measurement of the domain populations by measuring a series of NiO antiferromagnetic diffraction peaks. © *1996 American Institute of Physics.* [S0021-8979(96)42308-0]

[1] J. A. Borchers, R. W. Erwin, S. D. Berry, D. M. Lind, J. F. Ankner, E. Lochner, K. A. Shaw, and D. Hilton, Phys. Rev. B **51**, 8276 (1995).

 0021-8979/96/79(8)/5102/1/$10.00 © 1996 American Institute of Physics

Exchange biasing in MBE grown Fe_3O_4/CoO bilayers: The antiferromagnetic layer thickness dependence

P. J. van der Zaag,[a] A. R. Ball, L. F. Feiner, and R. M. Wolf
Philips Research Laboratories, Prof. Holstlaan 4 5656 AA Eindhoven, The Netherlands

P. A. A. van der Heijden
Department of Physics, Eindhoven University of Technology (EUT) 5600 MB Eindhoven, The Netherlands

Exchange biasing has been studied for a series of [100] and [111] oriented, epitaxial Fe_3O_4/CoO bilayers grown by oxidic MBE. The low-temperature exchange biasing versus CoO layer thickness is compared to theoretical models for exchange biasing. We argue that the Malozemoff random field model does not apply to this system. The exchange biasing calculated according to the Meiklejohn–Bean model, assuming nearest-neighbor exchange coupling across a flat and magnetically uncompensated interface, differs for [100] oriented bilayers by a factor of ≃8 from the experimental value. © *1996 American Institute of Physics.* [S0021-8979(96)17708-5]

I. INTRODUCTION

When a system, consisting of an antiferromagnet (AF) and a ferro- or ferrimagnet (F), is field cooled through the Néel temperature, T_N, of the AF, exchange anistropy can shift the hysteresis loop along the field axis. This phenomenon is called exchange biasing.[1] Recently, the interest in this effect revived,[2–5] due its application in magneto-resistive sensors.[6] Still, the microscopic origin of this effect is poorly understood. In the extensively studied Ni-Fe/Fe-Mn system the magnitude of the loop shift or bias field, H_{eb}, is smaller by more than two orders of magnitude than calculated according to the original interpretation.[4,6] In this interpretation the biasing is caused by a unidirectional anisotropy arising from nearest-neighbor exchange coupling across a perfectly flat interface which is magnetically uncompensated at the AF side.[1] If the ferromagnet is made single domain by a large applied field above T_N of the AF component, field cooling through T_N results in alignment of the AF interface spins to the aligned F interface spins. If the anisotropy energy of the AF is larger than the energy of this exchange coupling, reversing the F magnetization direction below T_N costs twice the energy associated with the exchange bonds across the interface. This requires an extra field, H_{eb}. Balancing the Zeeman energy with the exchange energy per F–AF bond, leads to:

$$H_{eb}=\frac{n2J_{ex}|S_F||S_{AF}|}{a^2\mu_0 M_F t_F} \tag{1}$$

with a the lattice parameter and n/a^2 the number of exchange coupled bonds across the AF–F interface per unit area, J_{ex} the exchange constant, S_i the spin of either F or AF, μ_0 the vacuum permeability, M_F the magnetization of the F layer and t_F the thickness of the F layer. Since Eq. (1) fails to describe the magnitude of H_{eb} in Ni-Fe/Fe-Mn, alternative models have been proposed, involving either planar domain walls[7] or perpendicular domain walls due to interface roughness[8] in the AF layer.

One of the problems in the study of exchange biasing is the lack of simple model systems. AF alloy systems such as FeMn have a complicated, noncollinear spin structure. Oxidic AF materials such as CoO have a simple collinear spin structure. Moreover, (bulk) properties of magnetic oxides are well documented.[9,10] In addition, CoO has an experimentally convenient T_N of 291 K. Since molecular beam epitaxial (MBE) growth of magnetic oxidic multilayers of Fe_3O_4 and CoO or NiO has been demonstrated,[11] we decided to examine exchange biasing in MBE grown Fe_3O_4/CoO bilayers.

II. RESULTS AND DISCUSSION

Fe_3O_4/CoO bilayers were deposited on (0001) α-Al_2O_3 substrates[12] and on (100) $SrTiO_3$ substrates by oxidic MBE. In a limited oxygen partial pressure range $\approx 8.5\times10^{-5}$ mbar it is possible to grow both CoO and Fe_3O_4.[13] RHEED and x-ray diffraction show that the deposition on $SrTiO_3$ results in epitaxial [100] oriented bilayers with a rocking curve of ≈1.3° (FWHM). To study the exchange biasing, the bilayers were field cooled from 350 K in a 4400 kA/m field in a SQUID (Quantum Design MPMS5). After correction for the substrate's diamagnetic contribution, hysteresis loops as the one shown in Fig. 1 were obtained.

Two aspects of Fig. 1 are noteworthy. First of all, the M_S value is 473±24 kA/m at 5 K, where the inaccuracy is mainly caused by the 2%–5% of precision with which the Fe_3O_4 thickness is determined by x-ray fluorescence (XRF). On average we find from all our bilayers M_S=476±49 kA/m at 5 K for [100] oriented Fe_3O_4/CoO bilayers on $SrTiO_3$ with $t_{Fe_3O_4}$ = 120 ± 10 Å. This is below the bulk M_S of 510 kA/m of Fe_3O_4 at 5 K, but higher than M_S≃370 kA/m reported by other groups for [100] Fe_3O_4/CoO[11] and Fe_3O_4/NiO[14] multilayers with comparable Fe_3O_4 thickness. Also in our [111] oriented bilayers, some of which were grown simultaneously with the [100] bilayers, M_S is lower.[12] A second interesting aspect of Fig. 1 is that we do observe a hysteresis loop shifted by the exchange bias field, H_{eb}, along the field axis, despite the fact that the (100) CoO plane forms a magnetically compensated plane, see Fig. 2(a). The most straightforward explanation of this observation is that the magnetic lattice parameter of the Fe_3O_4 to player is twice that of CoO. Hence exchange coupling across the interface occurs only to Co spins in one of the two magnetic sublattices, see Fig. 2(b).

In Fig. 3 we have plotted H_{eb} versus temperature, T, for

[a]Author for correspondence.

 0021-8979/96/79(8)/5103/3/$10.00 © 1996 American Institute of Physics

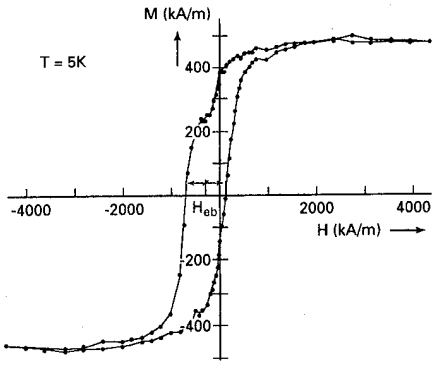


FIG. 1. Field cooled hysteresis loop at 5 K of an [100] oriented Fe_3O_4/CoO bilayer with Fe_3O_4 thickness, $t_{Fe_3O_4}$ of 114 Å and CoO thickness, t_{CoO} of 30 Å. The loop is shifted or exchange biased by H_{eb}.

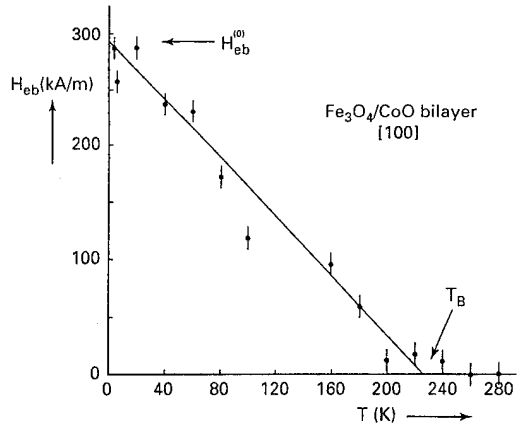


FIG. 3. The exchange biasing field, H_{eb}, vs temperature, T, for the [100] Fe_3O_4/CoO bilayer with $t_{Fe_3O_4}$ = 114 Å and t_{CoO}=30 Å. Note the linear dependence of H_{eb} on T. The biasing vanishes at the blocking temperature, T_B=230±10 K. For $T\rightarrow 0$ H_{eb} extrapolates to $H_{eb}^{(0)}$.

the same bilayer that gave the 5 K hysteresis loop of Fig. 1. The data are taken from the first loop after field cooling, because the training[15] of the hysteresis loop was only 7% over the first ten hysteresis cycles at 5 K. This is to be compared to the ≈65% training effect over the first nine hysteresis cycles in sputtered Ni-Fe/Fe-Mn bilayers at 10 K.[15] H_{eb} is seen to depend linearly on T, consistent with our earlier data for [111] Fe_3O_4/CoO bilayers[12] and those of other antiferromagnetic oxides.[2] In the bilayer in Fig. 3 the CoO thickness, t_{CoO}, is 27.8±1.4 Å and the temperature at which H_{eb} vanishes, the blocking temperature, T_B, is 230±10 K, well below T_N of bulk CoO of 291 K. As can be seen from Fig. 4, where T_B is plotted versus t_{CoO} for both [111] and [100] bilayers, the reduction of T_B below T_N of CoO appears to occur for t_{CoO}<50 Å, independent of the bilayer orientation. Similar to the reduction of T_B for FeMn thinner than 100 Å in $Ni_{80}Fe_{20}$/FeMn bilayers,[16] the data in Fig. 3 can be described by a finite-size scaling formula:[16]

$$\frac{T_N - T_B(t_{AF})}{T_N} \propto t_{AF}^{-\delta}, \tag{2}$$

where t_{AF} is the antiferromagnetic layer thickness, with δ≃1.2, which is comparable to δ=1.6±0.3 found for $Ni_{80}Fe_{20}$/FeMn bilayers.[16] This would imply that for t_{CoO}<50 Å the magnetic correlation length becomes limited by the film thickness. We note that a recent study of the CoO thickness influence on T_B in NiO/CoO/$Ni_{80}Fe_{20}$ trilayers, suggests that for t_{CoO}<50 Å the CoO T_B becomes sensitive to the NiO underlayer.[2] However, it remains to be proven whether the reduction of T_B below 50 Å is the result of an actual reduction of T_N in ultrathin CoO layers.

Since H_{eb} depends on T, discussions of biasing as well as comparisons to theoretical predictions of the magnitude of H_{eb} are best made with respect to the biasing data extrapolated to 0 K, $H_{eb}^{(0)}$.[12] Therefore, we have plotted $H_{eb}^{(0)}$ versus t_{CoO} in Fig. 5 for both [111] and [100] oriented Fe_3O_4/CoO bilayers. The data for the [111] oriented bilayers are taken from Ref. 12. Figure 5 shows a very small t_{CoO} of ≈4 Å for the onset of biasing. This suggests that the CoO roughness is

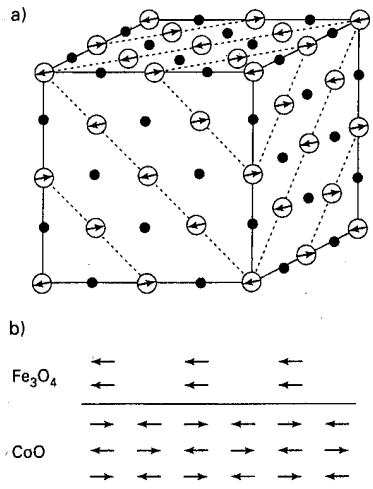


FIG. 2. (a) Schematic representation of the bulk spin structure of CoO. Oxygen atoms are represented by (●). The dotted lines connect the spins within identical (111) planes. For simplicity the Co spins are drawn parallel to the (111) plane. Note that the cube faces, the (100) planes are compensated, i.e., within them the net magnetization is zero. (b) Schematic illustration of the double magnetic lattice parameter of Fe_3O_4 with respect to CoO.

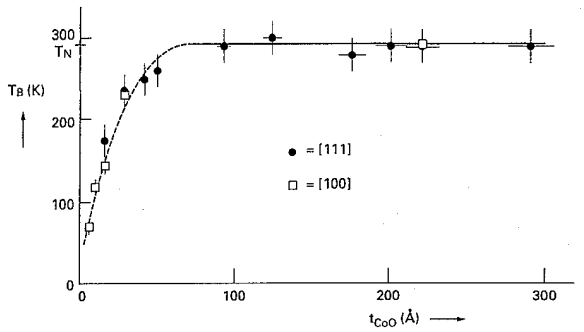


FIG. 4. The blocking temperature, T_B vs t_{CoO} for [111] and [100] oriented Fe_3O_4/CoO bilayers. For t_{CoO}<50 Å T_B is lower than the CoO Néel temperature, T_N=291 K.

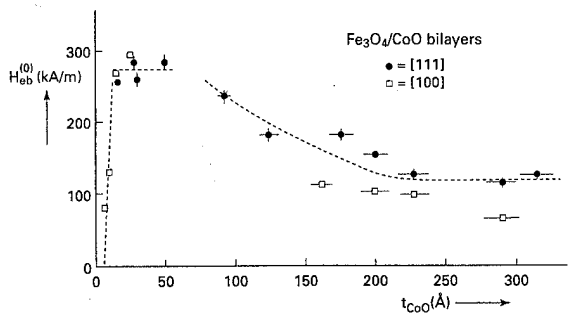


FIG. 5. The exchange biasing at 0 K, $H_{eb}^{(0)}$ vs t_{CoO} for a series of [111] and [100] oriented Fe_3O_4/CoO bilayers. The [100] oriented bilayers were grown on (100) $SrTiO_3$; the [111] oriented bilayers were grown on (0001) α-Al_2O_3 substrates (Ref. 12). The Fe_3O_4 thickness is ≈120 Å. The onset of biasing occurs at t_{CoO}≈4 Å. $H_{eb}^{(0)}$ is maximum for t_{CoO} between 16–50 Å. The dashed curve is a guide to the eye through the [111] data.

≈4 Å and that it is be possible to assess this roughness directly from exchange biasing data at low T.

Figure 5 shows that the dependence of $H_{eb}^{(0)}$ on t_{CoO} is roughly the same for the [100] and [111] orientation. Despite the qualitative similarity to the dependence predicted by Malozemoff's theory (viz., a regime where $H_{eb}\sim 1/t_{AF}$ followed by a regime, where H_{eb} is constant, see Fig. 5 of Ref. 8), we do not believe that this theory applies to the present system. First, the constant part is an artefact of the nonanalytic approximation to the random-field energy, which disappears when an analytic expression is used.[17] After this correction the agreement with Fig. 5 is no longer obvious. Secondly, Malozemoff's model predicts a critical thickness above which biasing should disappear:[8]

$$t_{A,\mathrm{crit}}=\frac{f_i\sqrt{A/K}}{4\sqrt{\pi}} \tag{3}$$

with f_i a parameter in the order of 1,[8] A the exchange stiffness and K the uniaxial anistropy constant of the AF. If $t_{A,\mathrm{crit}}$ is calculated for the present case of an Fe_3O_4/CoO bilayer, one finds, using $K_{CoO}=1.1\times10^7$ J/m^3 (Ref. 18) that $t_{A,\mathrm{crit}}\leqslant 2$ Å. Clearly, this is inconsistent with our experimental observations.

Finally, it is interesting to note that the Meiklejohn–Bean model works better in the present case than in metallic systems. $H_{eb}^{(0)}$ calculated from Eq. (1) by counting the number of Co-O-Fe superexchange bonds through a perfectly flat interface, using as estimate for $|J_{ex}|=2.5\cdot10^{-22}$ J from similar bonds in spinels[10] and M_F≈476 kA/m, yields $H_{eb}^{(0)}$≈1500–3000 kA/m, depending on the interface model. The maximum value found for $t_{CoO}<50$ Å in a [100] oriented bilayer is 294 kA/m, which is smaller by a factor of ≈8. In Table I we have given the presently available low-temperature unidirectional anisotropy constants $K_{eb}^{(0)}=\mu_0 M_S H_{eb}^{(0)} t_F$[12,19] with the ratio of the experimental and [from Eq. (1)] calculated $H_{eb}^{(0)}$. Table I shows that the [100] oriented Fe_3O_4/CoO bilayer system is closest to the straightforward ideas concerning exchange biasing proposed by Meiklejohn and Bean,[1] whereas $H_{eb}^{(0)}$ of MBE grown $Ni_{80}Fe_{20}$/FeMn still differs considerably from this calculated value. This suggests that exchange biasing in metal alloy systems is indeed more complex than in [100] oriented Fe_3O_4/CoO bilayers. The latter system may be a good model system to elucidate factors influencing exchange biasing, such as growth.

TABLE I. The low-temperature unidirectional anisotropy constant $K_{eb}^{(0)}=\mu_0 M_S H_{eb}^{(0)} t_F$ and the ratio Δ of the biasing calculated from Eq. (1) and the experimentally found $H_{eb}^{(0)}$ for three MBE grown F/AF bilayers.

F/AF system	Interface	$K_{eb}^{(0)}$ (mJ/m^2)	Δ
Fe_3O_4/CoO	(100)	2.11	8
Fe_3O_4/CoO	(111)	1.43	35
$Ni_{80}Fe_{20}$/FeMn	(111)	0.22	73

III. CONCLUSION

We have shown that oxidic [100] oriented Fe_3O_4/CoO bilayers grown on $SrTiO_3$ exhibit exchange biasing, despite the magnetically compensated (100) CoO interface. Exchange biasing is found up to 300 Å of CoO underlayer thickness, which is inconsistent with the predictions of Malozemoff's random field model, when applied to this system. The maximum value of exchange biasing extrapolated to 0 K, $H_{eb}^{(0)}$ is 294 kA/m, which is only a factor of ≈8 smaller than calculated on the basis of nearest-neighbor exchange across a perfectly flat interface. Compared to metal alloy systems such as $Ni_{80}Fe_{20}$/FeMn, [100] oriented Fe_3O_4/CoO bilayers may be a good model system to study exchange biasing.

[1] W. H. Meiklejohn and C. P. Bean, Phys. Rev. **105**, 904 (1957).
[2] M. J. Carey and A. E. Berkowitz, Appl. Phys. Lett. **60**, 3060 (1992); M. J. Carey, A. E. Berkowitz, J. A. Borchers, and R. W. Erwin, Phys. Rev. B **47**, 9952 (1993).
[3] S. Soeya, S. Tadokoro, T. Imagawa, M. Fuyama, and S. Narishige, J. Appl. Phys. **74**, 6297 (1993).
[4] R. Jungblut, R. Coehoorn, M. T. Johnson, J. aan de Stegge, and A. Reinders, J. Appl. Phys. **75**, 6659 (1994).
[5] T. Lin, D. Mauri, N. Staud, C. Hwang, J. K. Howard, and G. L. Gorman, Appl. Phys. Lett. **65**, 1183 (1994).
[6] V. S. Speriosu, D. A. Herman, I. L. Sanders, and T. Yogi, IBM J. Res. Develop. **34**, 884 (1990).
[7] D. Mauri, H. C. Siegmann, P. S. Bagus, and E. Kay, J. Appl. Phys. **62**, 3047 (1987).
[8] A. P. Malozemoff, Phys. Rev. B **37**, 7673 (1988).
[9] J. Smit and H. P. J. Wijn, *Ferrites* (Philips Technical Library, Eindhoven, 1959).
[10] A. Broese van Groenou, P. F. Bongers, and A. L. Stuyts, Mater. Sci. Eng. **3**, 317 (1968/1969).
[11] T. Terashima and Y. Bando, Thin Solid Films **152**, 455 (1987); D. M. Lind, S. D. Berry, G. Chern, H. Mathias, and L. R. Testardi, Phys. Rev. B **45**, 1838 (1992).
[12] P. J. van der Zaag, R. M. Wolf, A. R. Ball, C. Bordel, L. F. Feiner, and R. Jungblut, J. Magn. Magn. Mater. **148**, 346 (1995).
[13] R. M. Wolf, A. E. M. De Veirman, P. van der Sluis, P. J. van der Zaag, and J. B. F. aan de Stegge, Mater. Res. Soc. Symp. Proc. **341**, 23 (1994).
[14] S. D. Berry, D. M. Lind, G. Chern, and H. Mathias, J. Magn. Magn. Mater. **123**, 126 (1993).
[15] C. Schlenker, S. S. P. Parkin, J. C. Scott, and K. Howard, J. Magn. Magn.Mater. **54-57**, 801 (1986).
[16] S. S. P. Parkin and V. S. Speriosu, in *Magnetic Properties of Low-Dimensional Systems II*, edited by L. M. Falicov, F. Mejía-Lira, and J. L. Morán-López, (Springer, Berlin, 1990), Chap. 13.
[17] L. F. Feiner (unpublished).
[18] J. Kanamori, in *Magnetism*, edited by G. T. Rado and H. Suhl (Academic, New York, 1963), Vol. 1, pp. 198–199.
[19] P. J. van der Zaag, R. Jungblut, and A. Reinders (unpublished).

Magnetic properties of exchange-coupled Fe/FeO bilayers

D. V. Dimitrov, A. S. Murthy and G. C. Hadjipanayis
Department of Physics and Astronomy, University of Delaware, Newark, Delaware 19716-2570

C. P. Swann
Bartol Research Institute, Newark, Delaware 19716

The magnetic, structural and microstructural properties of sputtered Fe thin films and Fe\Fe–O bilayers were studied as a function of the Fe layer thickness, the type of the Fe oxide and the substrate used. Two different ways to prepare the oxide layers were used; postdeposition oxidation and reactive sputtering. Postdeposition oxidation produced films with mixed Fe–oxides (FeO, Fe_3O_4, Fe_2O_3); however reactive sputtering led to bilayers with controlled stoichiometry, Fe\FeO, Fe\$Fe_3O_4$, and Fe\$Fe_2O_3$, respectively. The coercivity of both the Fe films and Fe\Fe–O bilayers, deposited on substrates with or without Cr buffer layer, was found to increase with decreasing Fe film thickness. The coercivity of the samples deposited on a Ag buffer layer was much lower and did not change substantially with the Fe film thickness. The presence of the Fe–oxide layer led to a large increase of coercivity. This is attributed to the higher anisotropy of the oxide and to exchange coupling of Fe–oxide with the softer Fe layer. © *1996 American Institute of Physics.* [S0021-8979(96)17808-1]

INTRODUCTION

Iron oxide thin films have been studied extensively for the last few decades, mainly because of their application in magnetic recording media. Recently antiferromagnetic oxide films have been used to create exchange bias in spin valves.[1] However, it was found that the exchange coupling to the oxide layer deteriorates the properties of the soft magnetic layer.[2] Different kinds of deposition methods including magnetron dc and rf sputtering, molecular beam epitaxy and evaporation have been used[3–7] to prepare films. The stoichiometry, magnetic and microstructural properties were found to depend substantially on the deposition parameters, substrates used, film thickness, and postdeposition annealing.[3–7]

In contrast, relatively little attention has been paid to iron–iron oxide systems.[8–10] Schneider *et al.*[8] found smooth hysteresis loops in evaporated Fe\Fe_2O_3\Fe sandwiches with coercivity of a few hundred Oe. They also observed columnar structure and perpendicular anisotropy. In contrast Ruf and Gambino[9] observed very soft behavior with a coercivity ~5 Oe and planar anisotropy. Our previous studies[10] on passivated fine Fe particles showed substantial increase in the coercivity due to the exchange coupling between the iron core and the iron oxide shell.

In this work we have extended our studies on small passivated Fe particles to Fe\Fe–O bilayers and we studied the effect of exchange coupling between the iron and iron oxide thin layers on the magnetic properties of the bilayers.

EXPERIMENT

Thin Fe films and Fe\Fe–O bilayers were prepared by dc magnetron sputtering in an atmosphere of 5 mTorr Ar on water cooled substrates. Carbon coated transmission electron microscopy (TEM) grids, aluminum foils, Kapton, glass slides, and carbon sheets were used as substrates. Two different methods were used to prepare the Fe\Fe–O bilayers; postdeposition oxidation in 500 mTorr of O_2 for 2 h or reactive sputtering in a mixture of Ar and O_2. Samples were deposited either directly on substrates or on substrates with 30 nm Ag (Cr) buffer layers. All samples were covered with a 30 nm Ag layer for protection against further oxidation. The thickness of the Fe layer was varied between 5 and 40 nm, but the thickness of the reactively sputtered oxide was kept at 5 nm. The microstructure of the films was studied by TEM, using a Jeol JEM-2000 FX microscope. The thickness of the Fe films was determined by low angle x-ray diffractometry (XRD). The thickness of Fe oxide layers was determined by x-ray photoelectron spectroscopy for oxides made by postdeposition oxidation and Rutherford backscattering spectrometry (RBS) for oxides prepared by reactive sputtering. The stoichiometry of the oxide was determined by XRD and selected area diffraction (SAD). The magnetic properties were studied by a superconducting quantum interference device (SQUID) magnetometer in fields as high as 50 kOe and in the temperature range 10–300 K.

RESULTS AND DISCUSSION

All films were polycrystalline and quite uniform. The grains were small, typically 10 nm in size. Figure 1 shows a bright field micrograph of an oxidized 10 nm Fe film deposited on a Cr buffer layer. Unfortunately, the SAD patterns for Fe, Ag, and Cr are so close that they practically overlap, making it impossible to get separate dark field images of the buffer layer (Ag or Cr) and Fe film by itself.

Postdeposition oxidation produced an oxide layer, ~5 nm thick, consisting of a mixture of different oxides, FeO, Fe_3O_4, and Fe_2O_3. In contrast, by using reactive sputtering in a mixture of Ar and O_2, it was possible to make oxides with a determined stoichiometry. Figure 2 shows the XRD spectra for films sputtered with oxygen to Argon ratios 0.5%, 1%, and 4%. It is seen that under these conditions pure FeO, Fe_3O_4, and α-Fe_2O_3 are formed. RBS proved to be a very useful supplementary tool to XRD, allowing the relative amount of oxygen to iron to be estimated quite accurately. Figure 3 shows both a RBS and low angle XRD spectra of 15 nm Fe film deposited on glass. Analysis of the RBS spec-

 0021-8979/96/79(8)/5106/3/$10.00 © 1996 American Institute of Physics

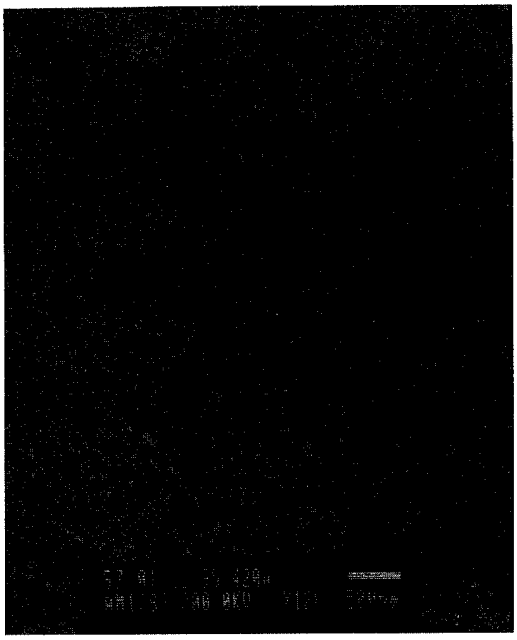


FIG. 1. Bright field micrograph of 10 nm thick Fe\Fe–O bilayer prepared by postdeposition oxidation.

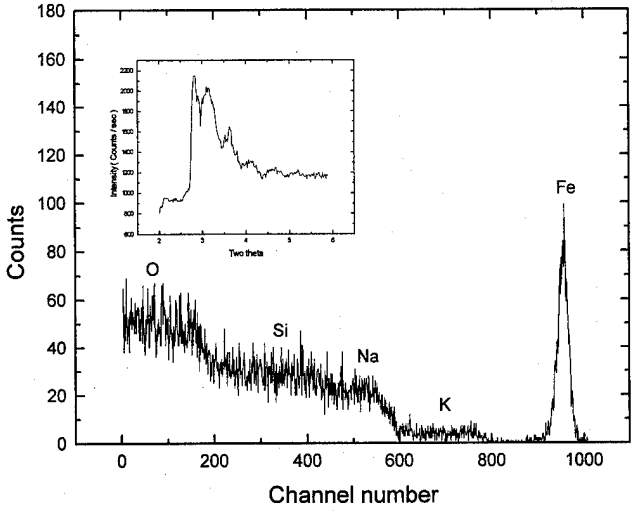


FIG. 3. RBS spectrum and low angle XRD insert for 15 nm Fe film on glass substrate.

tra was done using the computer program RUMP.[11] From the theoretical fit of RBS spectrum one obtains the number of atoms per unit area in the film. Low angle XRD allows the thickness of the film to be calculated. For pure Fe films, combining the results from RBS with low angle XRD spectra we estimated that the density of Fe films was about 90% of the bulk. The result was very reproducible, with a dispersion $<2\%$.

In order to understand the effect of exchange coupling between Fe and Fe–oxides on the magnetic properties of bilayers it was necessary to study the properties of pure Fe films first. The coercivity of the samples deposited directly on substrates, or on substrates with a Cr buffer layer, showed a very strong thickness dependence, in contrast to the samples deposited on a Ag buffer layer (Fig. 4). We believe that the reason for the different trend is the microstructure, which is different for the two kinds of films. It is well known that Cr layers are not smooth, but very rough with many voids. Because of this the Fe film resembles more of a particulate medium (isolated grains) than a continuous film. Another reason could be the formation of Fe–O in the interface between the underlayer and the film. This is also the case in films deposited directly on Al substrate. The saturation magnetization of the films was close to 1550 emu/cc, at 10 K, and did not change substantially with thickness for samples with a buffer layer. The result is similar to the one obtained from Kim and Oliveria.[12] The M_S value is lower than the bulk value of 1750 emu/cc, at 10 K, but is in excellent agreement with the estimated density (90% of bulk) of sputtered Fe films. The lack of any evidence for Fe oxides in XRD, SAD, and RBS spectra supports the idea that the lower value

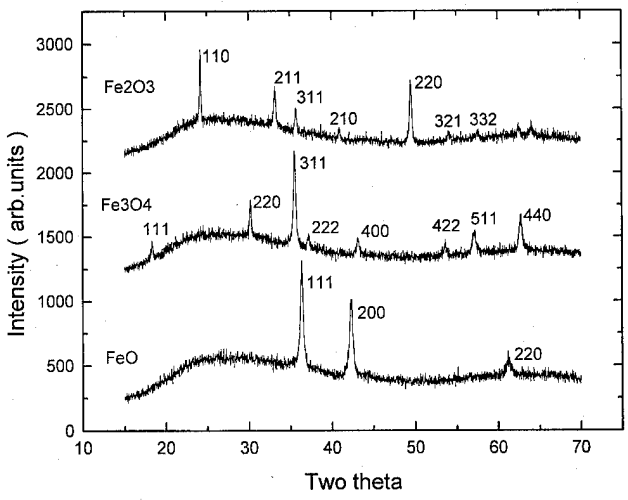


FIG. 2. X-ray diffraction spectra for thin oxide films prepared by reactive sputtering. The oxygen to argon partial pressure is 0.5% for FeO, 1% for Fe_3O_4, and 4% for Fe_2O_3.

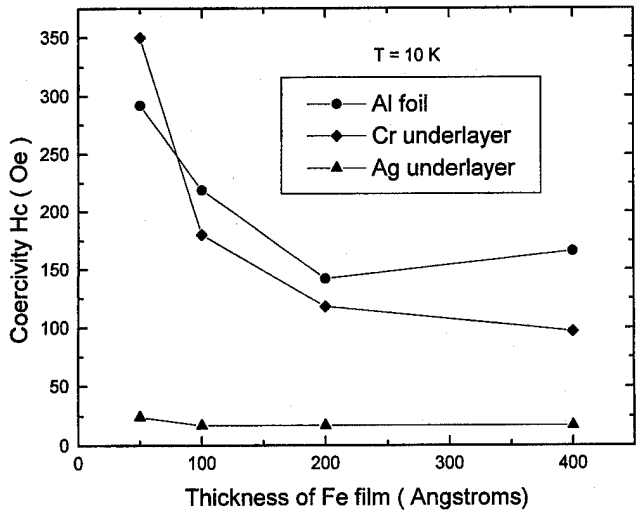


FIG. 4. Thickness dependence of coercivity for pure Fe films on three different substrates.

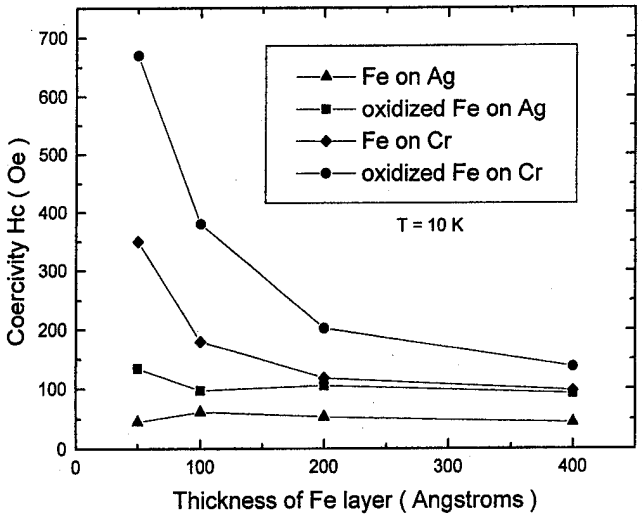


FIG. 5. Effect of the oxide layer on the coercivity: comparison between pure Fe films and Fe\Fe–O bilayers prepared by postdeposition oxidation.

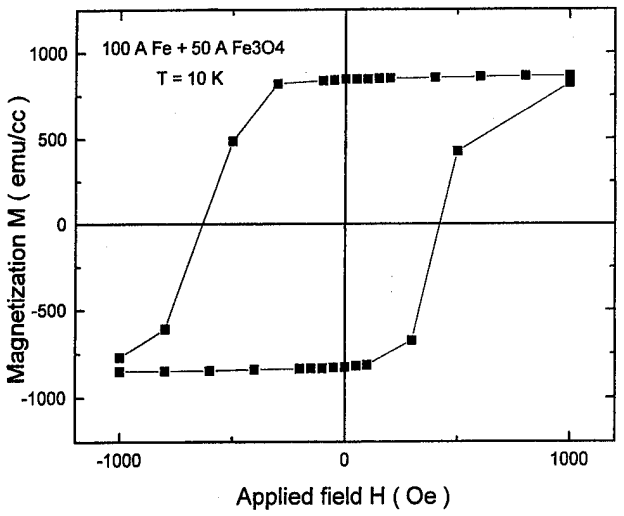


FIG. 6. Shifted hysteresis loop observed in Fe\Fe_3O_4 bilayer.

for the saturation magnetization is due to the lower density. For films deposited directly on Kapton and Al foil, a decrease of the saturation magnetization with decreasing thickness was found. A number of reasons could be responsible for this trend; these include partial oxidation because of the oxide layer on top of Al foil, iron atoms diffusing into Kapton (because it is very porous) or noncollinear spin structures on the surface of the film.

The oxide layer led to an increase in the coercivity for almost all the samples. The only exceptions were the thinnest samples deposited directly on Kapton. Figure 5 shows the effect for samples prepared by postdeposition oxidation. It is seen that the increase in the coercivity is most pronounced for the thinnest films. This result is analogous to the one observed in passivated Fe particles.[9] It is attributed to the fact that for the thinnest samples, the relative number of Fe atoms exchange coupled to the Fe–oxide layer is the largest.

The trend seen in Fig. 5 is also representative of the samples prepared by reactive sputtering. The effect is strongest in the thinnest Fe\$Fe_3O_4$ bilayer deposited directly on Al foil, with an increase from 300 to 700 Oe at 10 K. For Fe\FeO and Fe\$Fe_2O_3$ bilayers the increase is smaller, from 300 to 515 Oe for Fe\FeO and to 490 Oe for Fe\$Fe_2O_3$. Shifted hysteresis loops for field cooled samples were observed in all bilayers, prepared by postdeposition oxidation and by reactive sputtering, confirming the presence of exchange coupling between Fe and Fe–O layers. Figure 6 shows the shifted loop for Fe\$Fe_3O_4$ bilayer with 10 nm Fe layer with a shift of 200 Oe. It is well known[13] that the coercivity of soft materials can be increased by exchange coupling with a higher anisotropy material. FeO and α-Fe_2O_3 in bulk are known to be antiferromagnetic with low anisotropy. However, recent reports suggest a large surface anisotropy in Fe–oxides.[14] Also our recent results on thin FeO films show a ferromagnetic behavior with significant magnetic hysteresis a coercivity >5 kOe at 10 K and saturation magnetization ~220 emu/cc. Both of these results indicate that the oxide layers may behave as strongly anisotropic, pinning the interface spins of the soft Fe layer and leading to high coercivity. We are studying these possibilities and the results will be reported soon.

In summary, the magnetic properties of Fe\Fe–O bilayers indicate the presence of a strong exchange coupling between the Fe film and Fe–O surface layer, resulting in a substantial increase in Hc. These results suggest a large anisotropy for the surface Fe–O oxides. The details of this interaction are presently being studied.

ACKNOWLEDGMENT

This work has been supported by NSF DMR-9307676.

[1] B. Dieny, J. Magn. Magn. Mater. **136**, 335 (1994).
[2] C. Schlenker and R. Buder, Czech. J. Phys. B **21**, 506 (1971).
[3] Y. K. Kim and M. Oliveria, J. Appl. Phys. **75**, 431 (1994).
[4] Zeng-Jun Zhou and Jun-Jue Yan, J. Magn. Magn. Mater. **115**, 87 (1992).
[5] C. Hwang, Mao-Min Chen, and G. Castillo, J. Appl. Phys. **63**, 3272 (1988).
[6] J. K. Lin, J. M. Sivertsen and J. H. Judy, J. Magn. Magn. Mater. **54**, 1659 (1986).
[7] S. Ohta and A. Terada, Thin Solid Films **143**, 73 (1986).
[8] J. W. Schneider, A. M. Stoffel, and G. Trippel, IEEE Trans. Magn. **9**, 183 (1973).
[9] R. Ruf and R. J. Gambino, J. Appl. Phys. **55**, 2628 (1984).
[10] S. Gangopadhyay, G. C. Hadjipanayis, S. I. Shah, C. M. Sorensen, K. M. Klaubunde, V. Papaefthymiou, and A. Kostikas, J. Appl. Phys. **70**, 5888 (1991).
[11] L. R. Doolittle, in Proceedings of the Seventh International Conference on Ion Beam Analysis, Berlin, Germany, 1985 [Nucl. Instrum. Methods B **15**, 227 (1986)].
[12] Y. K. Kim and M. Oliveria, J. Appl. Phys. **74**, 1233 (1993).
[13] R. Skomski and J. M. D. Coey, Phys. Rev. B **48**, 15 812 (1993).
[14] J. M. D. Coey and I. V. Shvets, J. Appl. Phys. **73**, 6742 (1993).

Effects of cooling field strength on exchange anisotropy at permalloy/CoO interfaces

Timothy J. Moran[a] and Ivan K. Schuller
Physics Department 0319, University of California–San Diego, La Jolla, California 92093

We have studied exchange anisotropy at ferromagnet/antiferromagnet (FM-AFM) interfaces as a function of cooling field in $Ni_{80}Fe_{20}$ (permalloy) films deposited on bulk single-crystal CoO substrates. Hysteresis loops measured after cooling through the antiferromagnetic ordering temperature in different magnetic fields show that the exchange bias has little dependence on cooling field. Large cooling fields produced hysteresis loops with larger remanent magnetization and larger coercivity. These trends can be explained using a model that assumes that the FM anisotropy axis directions can be influenced by the magnetic history of the AFM. Large cooling fields also led to larger CoO susceptibility, which implies rotation of the CoO spin axes. The simultaneous rotation of the FM anisotropy axes and the AFM spin axes suggests perpendicular coupling at the FM-AFM interface. © *1996 American Institute of Physics.* [S0021-8979(96)17908-8]

Exchange anisotropy, which is magnetic anisotropy caused by the interaction of two neighboring magnetic materials, has been studied in many systems. These include permalloy/FeMn,[1] permalloy/TbCo,[2] and permalloy/$Co_xNi_{1-x}O$.[3] This interest is partly due to the potential for application in the field of magnetoresistive sensors.[4] Recent work has explored the interfacial structure dependence of exchange anisotropy.[5,6] Here we report on a different aspect of the problem, studying how the magnitude of the cooling field affects the interface coupling. The results indicate cooling in large magnetic fields causes the FM anisotropy axes to be oriented parallel to the cooling field and the AFM spin axes to be perpendicular to the cooling field. Taken together, these results suggest a perpendicular coupling between the FM and AFM spins.[7]

The sample preparation is described elsewhere.[5] Briefly, bulk single crystals of CoO with (111) or (100) orientation were given various surface treatments such as sanding, polishing, heating, and ion bombardment. $Ni_{80}Fe_{20}$ (permalloy) films, 100 or 200 Å thick, were deposited at room temperature using a Riber MBE system with a typical pressure of better than 5×10^{-9} Torr during deposition.

The magnetic measurements were performed with a Quantum Design SQUID magnetometer, making use of the magnet reset option to reduce the magnetic field offset in the sample space. The field was applied in the plane of the film. Before each measurement the samples were heated to 400 K, which is above the ordering temperature of CoO (T_N=291 K), but low enough that the heating is unlikely to cause large structural changes.[8] The samples were then cooled to 50 K in a magnetic field, $H_{cooling}$. Hysteresis loops were then measured over the range (−1500 Oe, 1500 Oe). For each hysteresis loop a large linear background due to the CoO susceptibility χ(AFM) had to be subtracted.

Figure 1 shows two hysteresis loops for a permalloy/CoO sample for two different cooling fields. Both loops exhibit a shift toward the negative field direction. This shift, known as the exchange bias (H_E), is defined as the field halfway between the two field axis intercepts. The coercivity (H_C) is defined as the average magnitude of the two field axis intercepts. The remanence (m_r) represents the average of the two zero field moment values. The reduced remanence (m_r/m_s) is calculated by dividing average zero field moment by the saturation moment, where the saturation moment was determined by averaging over several loops. Understanding the exchange bias magnitude has been the main goal of previous exchange anisotropy studies. However, this report will focus on the other effects visible in Fig. 1, which are that the $H_{cooling}$=70 kOe loop has larger remanence and larger coercivity.

Figure 2 shows the exchange bias, coercivity, reduced remanence, and CoO susceptibility χ(AFM), for two different samples as a function of the magnitude of the cooling field. We will discuss the FM behavior first and then the AFM behavior. The exchange bias changed very little (<5 Oe) for different cooling fields for all samples measured. For some samples the exchange bias decreased for larger cooling fields while in others it increased or remained constant. The remanence increased with larger cooling fields for seven out of eight samples measured. In most cases, the coercivity also

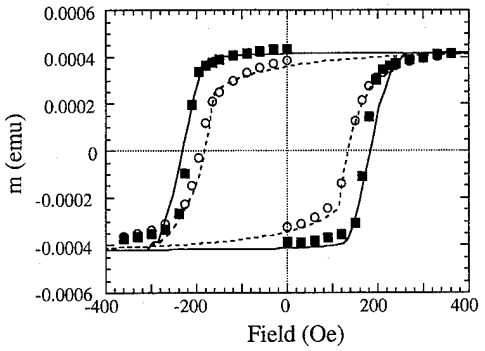


FIG. 1. Magnetization data for a 200 Å permalloy/CoO sample at T=50 K, taken after cooling through two different fields, $H_{cooling}$=10 kOe (circles) and $H_{cooling}$=70 kOe (squares). The lines are fits to the model described in the text, where θ_{fan}=10° was used for the solid line and θ_{fan}=35° was used for the dashed line.

[a]Current location: Physics Department, University of Minnesota, Minneapolis, MN 55455.

 0021-8979/96/79(8)/5109/3/$10.00 © 1996 American Institute of Physics

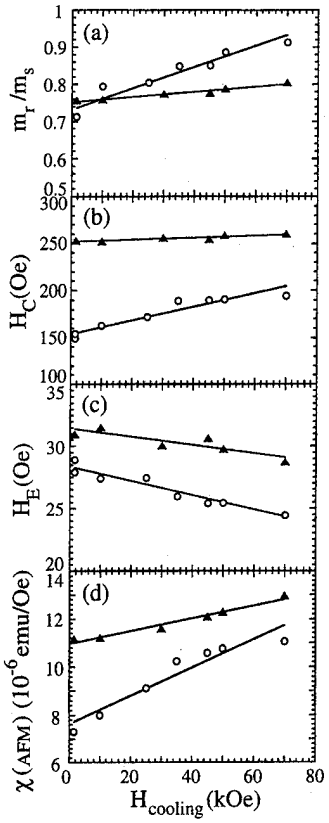


FIG. 2. (a) Reduced remanence (m_r/m_s), (b) coercivity (H_C), (c) exchange bias (H_E), and (d) CoO susceptibility χ(AFM) measured at $T=50$ K as a function of cooling field magnitude ($H_{cooling}$) for two different samples: (circles) 200 Å permalloy/CoO(111), (triangles) 200 Å permalloy/CoO(100). The lines are guides to the eye.

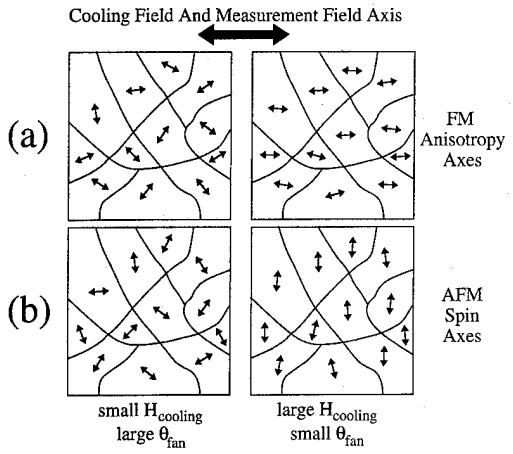


FIG. 3. Illustration of model described in the text, showing a top view of FM regions having various anisotropy axes. Large cooling fields produce FM anisotropy axes which are parallel to the cooling field, and AFM spin axes which are perpendicular to the cooling field.

increased for larger cooling fields, although this data contained some scatter. These results were reversible with cooling field; in other words the values in Fig. 2 did not vary depending on the order of the measurements. The same trends were observed for samples cooled in positive or negative magnetic fields.

The trends toward higher coercivity and remanence are similar to the behavior expected for a ferromagnet having a uniaxial anisotropy axis which changes its direction relative to the applied field. For a single domain FM with uniaxial anisotropy, hysteresis loops will have higher remanence and coercivity if the anisotropy axis is more parallel to the applied field.[9] Therefore the variation in magnetic properties with different cooling fields is possibly due to changes in direction of the anisotropy axes governing the FM behavior.

For this model [Fig. 3(a)], the FM has uniaxial anisotropy but is divided into different regions, each having different directions for the anisotropy axis. The low cooling field state has a wide distribution of anisotropy axes, while for the high cooling field state the anisotropy axes are more parallel to the field direction. To test this model theoretical hysteresis curves were calculated and compared to the data. For the calculation the anisotropy axes were assumed to follow a Gaussian distribution $W(\theta_K)\alpha \exp[-(\theta_K)^2/2(\theta_{fan})^2]$, where $W(\theta_K)$ is the weighting function, θ_K is the angle between the anisotropy axis and the field axis, and θ_{fan} is the angular spread of the axes.

Figure 1 shows calculated hysteresis curves with exchange bias, saturation moment, and FM anisotropy set at $H_E=24$ Oe, $m_s=0.00042$ emu, and K(FM)$=110\,000$ ergs/cc, respectively to match the data. The only difference between the calculated curves is the angular spread of the axes, θ_{fan}, which changes from 10° to 35°. The agreement with the data implies that the physical properties of the sample are not changing, only the spread in the anisotropy axes.

The most likely source of this change is the magnetic structure in the AFM, which has been changed by heating the sample above the AFM ordering temperature and cooling in a different magnetic field. It is important to note that for these samples the FM coercivity is strongly influenced by interactions with the AFM.[5] The low-temperature coercivity, typically 200 Oe, is much larger than the room temperature coercivity, typically 30 Oe, with a sharp rise near the ordering temperature of the CoO, $T_N=291$ K. A 200 Å permalloy film deposited under the same conditions onto silicon had coercivities that were smaller (<5 Oe) and did not change with temperature (up to 400 K) or cooling field (up to 7 T). Therefore the mechanism driving the cooling field effects in Figs. 1 and 2 are very likely related to changes in the AFM.

Fortunately the AFM susceptibility data in Fig. 2 provides information about the spin structure in the AFM. Figure 2(d) shows that the low field CoO susceptibility, measured at $T=50$ K with $|H|<1.5$ kOe, increases for larger cooling fields. This change in the susceptibility indicates that the spin axes of the CoO are more perpendicular to the field if the AFM has been exposed to large magnetic fields. (See Fig. 3) This is because the AFM susceptibility is largest when the spin axis is perpendicular to the applied field. Rotation of AFM spin axes toward directions perpendicular to large magnetic fields has been observed previously in MnO[10] and MnF_2.[11]

To recap, the change in FM remanence and coercivity

implies that the FM anisotropy axes are more parallel to the applied field after cooling in large magnetic fields [Fig. 3(a)]. The change in AFM susceptibility implies that the AFM spin axes are more perpendicular to the applied field after cooling in large magnetic fields [Fig. 3(b)]. If one assumes that the FM spins have an energy advantage to align perpendicular to the AFM spins, the FM anisotropy axis rotation can be easily explained. Under this assumption of perpendicular coupling, the large cooling field causes the AFM spin rotation, which then causes the FM anisotropy axis rotation. If perpendicular coupling does exist, it may be related to the perpendicular coupling that has been observed recently between ferromagnetic Fe layers separated by thin Cr layers.[7] Recent work in our laboratory indicates that perpendicular coupling also occurs in the ferromagnet–antiferromagnet system Fe/FeF_2.[12] Other workers have discussed possible perpendicular coupling at permalloy/FeMn interfaces.[13]

In conclusion, we have discovered changes in the behavior of an FM layer adjacent to an AFM, which are due to cooling through T_N in large magnetic fields. The data can be explained by a model where different FM regions have different anisotropy axes, and the distribution of these axes is altered by cooling through different magnetic fields. Susceptibility data from the AFM indicate that the AFM spin axes are also influenced by large cooling fields. Together these two trends suggest that the FM spins and AFM spins may have perpendicular coupling.

This work was supported by the US National Science Foundation and Department of Energy. We thank J. G. Gallego, D. Lederman, and J. Nogués for useful discussions.

[1] R. D. Hempstead, S. Krongelb, and D. A. Thompson, IEEE Trans. Magn. **14**, 521 (1978); C. Tsang, N. Heiman, and K. Lee, J. Appl. Phys. **52**, 2471 (1981); R. Jungblut, R. Coehoorn, M. T. Johnson, J. aan de Stegge, and A. Reinders, *ibid.* **75**, 6659 (1994).
[2] W. C. Cain, W. H. Meiklejohn, and M. H. Kryder, J. Appl. Phys. **61**, 4170 (1987); N. Smith and W. C. Cain, *ibid.* **69**, 2471 (1991).
[3] M. J. Carey and A. E. Berkowitz, Appl. Phys. Lett. **60**, 3060 (1992); J. Appl. Phys. **73**, 6892 (1993).
[4] B. Dieny, J. Magn. Magn. Mater. **136**, 335 (1994).
[5] T. J. Moran, J. M. Gallego, and I. K. Schuller, J. Appl. Phys. **78**, 1887 (1995).
[6] J. Nogués, D. Lederman, T. J. Moran, and I. K. Schuller (to be published).
[7] M. Ruhrig, R. Schafer, A. Hubert, R. Mosler, J. A. Wolf, S. Demokritov, and P. Grunberg, Phys. Status Solidi A **125**, 635 (1991).
[8] A. K. Kao and P. Kasiraj, IEEE Trans. Magn. **27**, 4452 (1991).
[9] B. D. Cullity, *Introduction to Magnetic Materials* (Addison-Wesley, Reading, MA, 1972), p. 336.
[10] F. Keffer and W. O'Sullivan, Phys. Rev. **108**, 637 (1957); D. Bloch, J. L. Feron, R. Georges, and I. S. Jacobs, J. Appl. Phys. **38**, 1474 (1967).
[11] I. S. Jacobs, J. Appl. Phys. **32**, 61S-62S (1961).
[12] J. Nogués, T. J. Moran, D. Lederman, and I. K. Schuller (to be published).
[13] R. Jungblut, R. Coehoorn, M. T. Johnson, C. Sauer, P. J. van der Zaag, A. R. Ball, T. G. S. M. Rijks, J. aan de Stegge, and A. Reinders, J. Magn. Magn. Mater. **148**, 300 (1995).

The role of interface crystalline and magnetic structure in exchange anisotropy (abstract)

J. Nogués, D. Lederman,[a] and Ivan K. Schuller
Department of Physics, University of California—San Diego, La Jolla, California 92093-0319

K. V. Rao
Royal Institute of Technology, Stockholm, Sweden

Large exchange bias effects were measured in antiferromagnetic FeF_2-ferromagnetic Fe bilayers. The interface spin structure and roughness was controlled by using different substrates and growth temperatures. The samples were characterized *ex situ* using low and high angle x-ray diffraction, in-plane x-ray diffraction, and atomic force microscopy. We discovered that the exchange bias is largest in the (110) FeF_2 spin-compensated surface films, in contradiction with simple models that predict a low exchange anisotropy for spin-compensated surfaces. For these samples, the exchange anisotropy decreases as the interface roughness increases. © *1996 American Institute of Physics.* [S0021-8979(96)42408-8]

This work was supported by the U.S. Department of Energy, Grant No. DE-FG03-87ER-45332.

[a]Present address: Physics Dept., West Virginia University, Morgantown, WV 26505-6315.

 0021-8979/96/79(8)/5112/1/$10.00 © 1996 American Institute of Physics

Topological coupling in magnetic multilayer films

J. Zhang and R. M. White
Data Storage Systems Center, Department of Electrical and Computer Engineering, Carnegie Mellon University, Pittsburgh, Pennsylvania 15213

The role of topological coupling, the magnetostatic coupling associated with interfacial roughness in magnetic sandwich/multilayer structures, was studied both analytically and experimentally. We report the first controlled measurements of such topological coupling. A coupling field of the order of 10 Oe between magnetic layers was observed in Co/Cu/Co sandwich structures fabricated with an artificially controlled in-phase roughness of variable amplitude with a fixed period of 3.5 μm. The coupling field was compared with the value predicted by a first-order approximation model and correlated with the geometry of the structure. Scale invariance of the coupling field allows the results to be extended to ultrathin giant magnetoresistance/spin valve structures. © *1996 American Institute of Physics.* [S0021-8979(96)18008-2]

I. INTRODUCTION

Coupling between magnetic layers separated by nonmagnetic interlayers has attracted enormous interest and has been studied with accelerated vigor since the discovery of the giant magnetoresistance (GMR) effect.[1] This coupling may align the magnetization in adjacent magnetic layers parallel or antiparallel. Various mechanisms have been proposed to explain the coupling. In the case where the spacer layer is thin and conducting, exchange-like coupling can occur through conduction electrons. The sign of this coupling is predicted to oscillate with the interlayer thickness and this has been observed in various systems.[2] Since this coupling has an exchange origin, it is usually strong. Another important mechanism, which is of magnetostatic origin and was first suggested by Néel,[3] is the magnetostatic coupling caused by magnetic free poles induced by interfacial roughness. The roughness at the interfaces is generally correlated in the case of as-deposited multilayers due to the propagation of the roughness profile from layer to layer. This kind of coupling exists in structures with both thick and thin interlayers, as long as roughness exists, and is generally small. However, its importance can not be overestimated, especially in weakly coupled low field GMR/spin valve materials,[4,5] which are critical for device applications such as high density magnetic recording read heads and magnetoresistive random access memories,[4] etc.

A lot of work has been done for exchange-based coupling. However, not as much was done for magnetostatic coupling, especially topological coupling. The reasons are twofold. First, the roughness in ultrathin multilayers is uncontrolled. Second, it is difficult to distinguish magnetostatic coupling from exchange coupling when the spacer thickness is on a nanometer scale. Although results on topological coupling have been reported,[6] no study has ever been done with controlled roughness. The purpose of this study is not only to demonstrate the existence of topological coupling, but also to study it in a controlled way, and to consider the implications for ultrathin GMR/spin valve structures.

II. THEORETICAL ANALYSIS

The origin of the topological coupling can be seen from Fig. 1(a). Assuming a uniform magnetization in the films, magnetic free poles are induced at the interfaces due to interfacial roughness. When the roughness at adjacent interfaces is in-phase, which is generally the case for as-deposited films, the magnetizations of the two magnetic layers tend to align with each other to achieve a low energy state, giving a ferromagnetic coupling.

The first calculation of topological coupling was carried out by Néel.[3] His analytical analysis assumed semi-infinite magnetic layers with a correlated sinusoidal interface roughness and a distribution of induced surface magnetic charge distribution projected onto a smooth surface. A closed form expression for surface interaction energy was obtained. Using a numerical approach, we have extended Néel's model to consider the roughness with an arbitrary phase difference (i.e., not necessarily correlated) and a finite magnetic layer thickness. The geometry used in the model is shown in Fig. 1(a). The sinusoidal roughness has a peak–peak amplitude of h, period p, magnetic layer thickness is t with magnetization M, and spacer thickness is d. As a first-order approximation, an in-plane uniform magnetization was assumed. This assumption holds as long as the magnetic layer has an in-plane uniaxial anisotropy and the roughness amplitude h is much smaller than the period p. Both top and bottom interfaces of two magnetic layers (A,B,A',B') were included in the interaction energy calculation due to the finite thickness of the

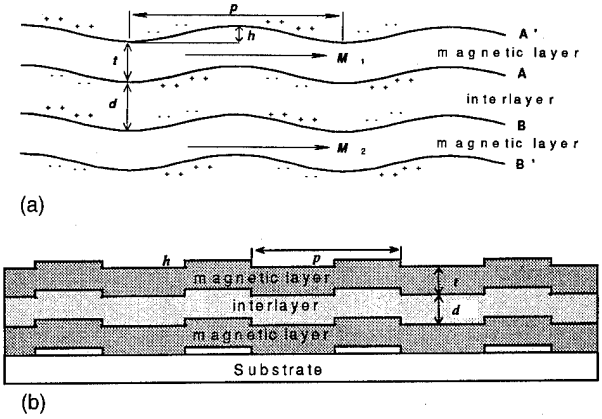


FIG. 1. (a) In-phase sinusoidal interface roughness in multilayers. (b) In-phase step interface roughness in multilayers. The structure shown in (b) was actually fabricated.

 0021-8979/96/79(8)/5113/3/$10.00 © 1996 American Institute of Physics

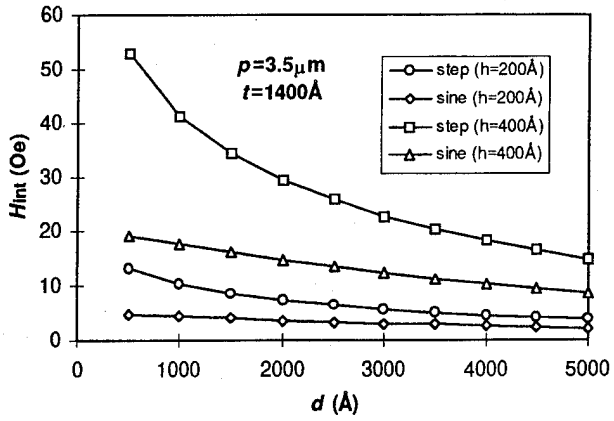


FIG. 2. Ferromagnetic coupling field due to two inner interfaces A-B only for in-phase sinusoidal and step roughness with dimensions used in experiments (p=3.5 μm, h=200–400 Å, d=1000–5000 Å, t=1400 Å, magnetization of Co is 1400 emu/cm^3).

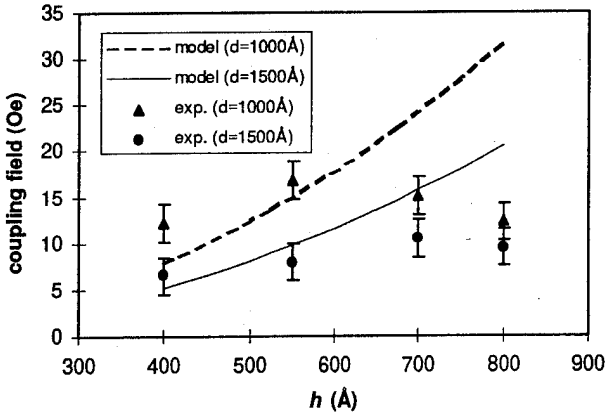


FIG. 3. Model predicted H_{int} and measured $\Delta H_c/p$ in Co/Cu/Co sandwich structures with the step roughness for variable roughness amplitudes h=400–800 Å.

magnetic layers. It was found that the surface interaction energy was proportional to cos φ, where φ is the roughness phase. For the special case of φ=0 (in-phase roughness), a negative interaction exists for magnetizations shown in Fig. 1(a) and indicates a ferromagnetic coupling, while for $\varphi=\pi$ (out-of-phase roughness), an antiferromagnetic coupling exists. We will concentrate on the in-phase case in this paper. The coupling field can be obtained by $H_{\text{int}}=E_{\text{int}}/Mt$, where t is the thickness of the magnetic layer. It can be shown that the coupling field is scale invariant; i.e., the coupling field is independent of the actual size of the structure as long as the aspect ratio remains the same. This prompted us to study topological coupling by using structures on a larger scale.

The interaction energy for an arbitrary roughness profile can be obtained by a Fourier decomposition. One simple and interesting case of the in-phase roughness is the step roughness as shown in Fig. 1(b), since it can be easily fabricated and controlled experimentally. The same geometrical parameters, h, p, t and d were used as in the sinusoidal case. For clarity, the coupling field due to two inner interfaces (A-B) only is plotted in Fig. 2 for both sinusoidal and step roughness with geometries used in Sec. III. (We assume Co is used for the magnetic layer). It is clear that the coupling field for the step roughness is larger than that of the sine roughness, and it decreases more quickly as interlayer thickness increases. The total surface interaction energy is the algebraic sum of the interaction energy for all interfaces, namely, A-B, A'-B', A-B', and A'-B. The first two contribute to a ferromagnetic coupling, the latter two give rise to a smaller antiferromagnetic component. Thus we expect structures with an in-phase step roughness to be dominated by ferromagnetic coupling. The total coupling field for Co/spacer/Co structures with the step roughness as shown in Fig. 1(b) is plotted in Figs. 3 and 4 for variable roughness amplitude h and interlayer thickness d. Markers are experimental data, as will be discussed in Sec. III. It can be seen that the coupling field given by the model increases as d decreases and h increases. The coupling field is also expected to be proportional to the magnetization M.

If the magnetic layers have square hysteresis loops (S=1) and the same coercivity, the ferromagnetic coupling will appear as an increase of the coercivity of the bilayers H_{c2} compared to that of a single layer H_{c1}. The coupling field is then given by $H_{\text{int}}=H_{c2}-H_{c1}$.

III. EXPERIMENT

Co/Cu/Co sandwich structures with correlated artificial step roughness were fabricated on Si substrates. The material and the dimension of the structure were chosen to make the coupling observable and films with good magnetic properties possible to fabricate. The artificial surface roughness was created by an array of nonmagnetic Cu strips fabricated using a standard lift-off process. The amplitude (varied from 400 Å to 800 Å) and the period (fixed at 3.5 μm) of the roughness were individually controlled by the thickness and the width of the metallic strips, respectively. An atomic force microscope (AFM) image of the Si substrate with such step roughness is shown in Fig. 5. The fine grooves were determined to be the original roughness on the substrate and its amplitude is less than 50 Å (pk-pk), which is small compared to the artificial roughness. A 1500 Å Cu seed layer was de-

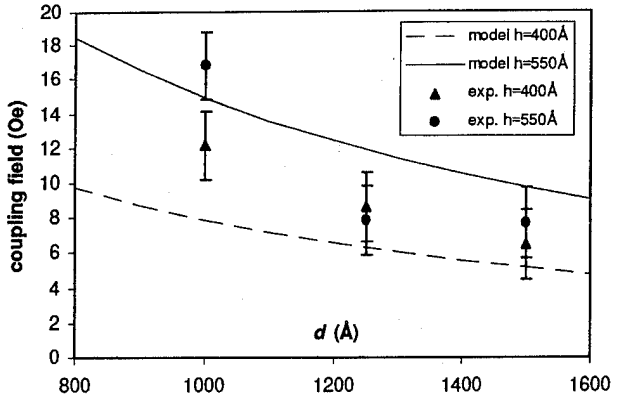


FIG. 4. Model predicted H_{int} and measured $\Delta h_c/p$ for variable interlayer thickness d=1000–1500 Å.

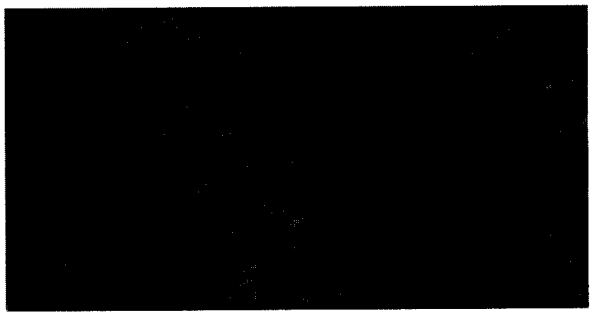


FIG. 5. AFM image of artificially created step roughness. The z axis is highly exaggerated to show details ($h=400$ Å, $p=3.5$ μm).

posited, followed by a Co/Cu/Co sandwich structure deposition in a Perkin–Elmer 2400-8L sputtering system without breaking the vacuum. The base pressure was below 2×10^{-7} Torr. A magnetic field perpendicular to the stripes was used to create an in-plane uniaxial anisotropy. The Cu seed layer was used to assure that two Co layers were symmetric and have the same magnetic properties. The Cu interlayer thickness ranges from 1000 Å to 1500 Å, which is thick enough so that exchange coupling is negligible. The artificial roughness on the substrate was found to propagate after the deposition, as expected.

The sample thus made was then cut in half. One half was sputter etched to peel off the top magnetic layer. The other half was also mounted in the etching chamber, but masked, to avoid any possible thermal effect on the film magnetic properties. The hysteresis loop was measured on a B-H looper, and a coercivity increase of the order of 10 Oe for bilayer structures was observed compared with single layers, as shown in Fig. 6, indicating a ferromagnetic coupling. The increase of the apparent coercivity $\Delta H_c=H_{c2}-H_{c1}$ is defined as the measured coupling field.

Another set of films was made using the same procedure but on flat substrates. No coupling was observed. This confirmed that exchange coupling does not exist, and the coupling observed in structures with roughness was totally due to magnetostatic coupling.

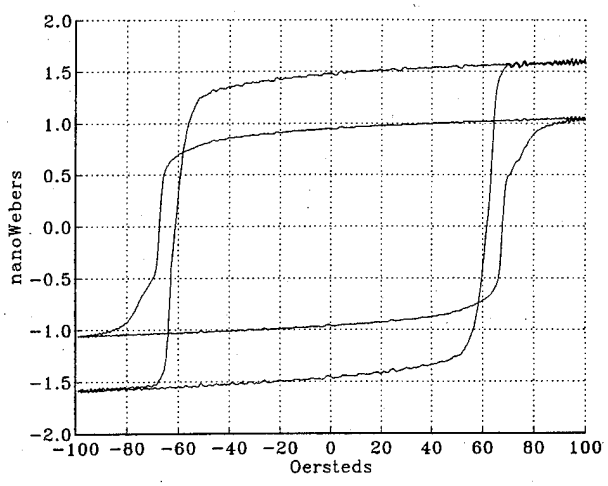


FIG. 6. Typical B-H loops for bilayers and single layers deposited on substrates with step artificial roughness.

IV. RESULTS AND CONCLUSION

As shown in part II, when squareness $S=1$, the apparent coercivity of a sandwich increases by H_{int}. However, as can be seen in Fig. 6, the loops were not perfectly square. Before correlating the measured coupling field, the nonsquare shape of hysteresis loops must be taken into account. When $S\neq1$, the free magnetic poles available in bilayers near H_{c1} (coercivity of single layer) are less than that at saturation. Thus we define $p=M_2(H_{c1})/M_{s2}$ as a parameter that characterizes this reduction, where $M_2(H_{c1})$ is the magnetization of bilayers at the coercivity of single layers, and M_{s2} is the saturation magnetization of bilayers. Assuming that two magnetic layers switch simultaneously and uniformly, we expect that the measured coupling field ΔH_c is smaller than in films with $S=1$, given approximately by pH_{int}. This means $\Delta H_c/p$ should correlate to the modeled H_{int}. The measured $\Delta H_c/p$ is plotted for variable roughness amplitude h and interlayer thickness d in Figs. 3 and 4, respectively. It can be seen for small roughness amplitude, $\Delta H_c/p$ is close to the coupling field predicted by the model. However, when the roughness amplitude increases, the demagnetizing field associated with the roughness increases and results in domain formation, especially near the edges of the steps, which invalidates the assumption of uniform switching and reduces the coupling field. The dependence of the coupling field on interlayer thickness is in much better agreement with the model. The discrepancy between the measured and predicted values is due to approximations in the model, measurement error and film deposition nonuniformity.

Scale invariance allows us to apply the above results to ultrathin GMR/spin valve structures although the exchange coupling might be important in this range. Topological coupling could be used to create the coupling in GMR/spin valve films,[5,7] in which antiparallel alignment of magnetic moments is essential. For device applications, a low saturation field, i.e., very weak coupling, is required. The existence of ferromagnetic topological coupling could be used to partially cancel an antiferromagnetic exchange coupling and thereby reduce the net coupling.[5] On the other hand, if magnetostatic coupling is dominant, it could be reduced by obtaining uncorrelated rough interfaces using thermal annealing.[7]

ACKNOWLEDGMENT

This work was supported by the National Science Foundation under Grant No. ECD-8907086. The U.S. Government has certain rights to this material.

[1] M. N. Baibich, M. Broto, A. Fert, F. Nguyen Van Dau, F. Petroff, P. Etienne, G. Greuzei, A. Frederick, and J. Chazelas, Phys. Rev. Lett. **2472**, 61 (1989).
[2] S. S. P. Parkin, N. More, and K. P. Roche, Phys. Rev. Lett. **64**, 2304 (1990).
[3] L. Néel, C. R. Acad. Sci. **255**, 1545 (1962).
[4] J. M. Daughton and Y. J. Chen, IEEE Trans. Magn. **29**, 2705 (1993).
[5] M. R. Parker, S. Hossain, D. Seale, J. A. Barnard, and M. Tan, H. Fujiwara, IEEE Trans. Magn. **30**, 358 (1994).
[6] E. W. Hill, S. L. Tomlinson, and J. P. Li, J. Appl. Phys. **73**, 5978 (1993).
[7] E. Y. Chen, S. C. Loper, J. M. Haugen, J. M. Anderson, and J. M. Daughton, Digest of Intermag **AC-07** (1995).

Surface roughness in Cu(100)/[Co/Cu]$_n$ systems grown by ion-beam sputtering

Timothy J. Minvielle[a] and Robert L. White
Department of Materials Science, Stanford University, Stanford, California 94305

Robert J. Wilson
IBM, Almaden Research Center, San Jose, California 95120

The development of surface roughness in Co/Cu systems was investigated through the use of *in situ* scanning tunneling microscopy. Multilayers and single layers of cobalt and copper were sequentially grown on a Cu(100) substrate. We show that the growth mode of cobalt on copper is quite different from that of copper on cobalt. We characterize these differences by looking at the lateral variations and obtaining a mean measure of island length. The cobalt tends to nucleate in small (<5 nm) islands. An overlayer of copper broadens this length scale while maintaining approximately the same peak-to-peak roughness of 5 monolayers. These growth mechanisms are shown to affect the way in which roughness propagates through multilayers. The impact of deposition temperature is also examined and seen to alter the degree of roughness in these samples. We conclude by discussing the implications for the magnetoresistance of these structures. © *1996 American Institute of Physics.* [S0021-8979(96)22608-3]

I. INTRODUCTION

The effect known as giant magnetoresistance (GMR) has generated much interest in magnetic multilayered structures.[1–3] At the heart of the phenomenon is the spin dependent scattering of carriers by thin magnetic layers separated by nonferromagnetic spacers. The Co/Cu system is worth noting because of its large value of magnetoresistance in both multilayer and spin valve systems. Since the effect depends strongly on the oscillatory antiferromagnetic coupling and surface roughness, it is important to obtain a clear understanding of the growth mechanisms of the individual layers. We have examined the surface evolution of a number of Co/Cu films through *in situ* scanning tunneling microscopy (STM). These films were grown with the goal of ascertaining the impact that each material has on the development of roughness in multilayers.

II. EXPERIMENT

The films were grown via ion-beam sputtering (IBS) at a pressure of 2.5×10^{-4} Torr of argon. Background pressures were low ($<5\times10^{-10}$ T) throughout the study. The deposition rate was 0.1 Å/s for cobalt and 0.2 Å/s for copper. Rate measurements and thickness determinations were performed using an *in situ* quartz crystal. The substrate used was a Cu(100) crystal that was sputter etched and annealed prior to each deposition. Each sample was measured with an *in situ* STM[4] at 1–4 nA of tunneling current. X-ray photoemission spectroscopy (XPS) measurements indicated that contaminant levels were negligible. All samples were, unless otherwise noted, grown at room temperature at a beam voltage of 1000 V.

In this surface study, we needed a useful way to characterize the in-plane, lateral variations of the films we grew. The horizontal dimensions of layers at the same atomic height varied greatly depending on the order in which the various materials were deposited. Since auto-correlation and Fourier techniques proved too sensitive to substrate steps, we instead used mean island length as an indicator of lateral roughness.

Low-energy electron diffraction (LEED) patterns revealed that the samples were epitaxial with evidence of twinning. Similar observations have been made[5] in related systems where twinning was found to have an effect on the coupling between ferromagnetic Co layers.

III. RESULTS AND DISCUSSION

A. The growth modes of cobalt and copper

The way in which cobalt/copper layers form during dc magnetron sputtering has been described elsewhere.[6] In general, copper is thought to act as a "smoothing agent" when grown on cobalt. This behavior may help explain the variation in the strength and type of coupling with the number of layers in multilayered films. We found that the way in which copper acts to reduce roughness in IBS-grown films on single crystals is confined primarily to the lateral dimension. The peak-to-peak roughness proved fairly insensitive to the amount of copper grown on cobalt. Instead, the in-plane characteristic lengths varied greatly with the amount of copper deposited. The STM indicated that this is the most distinguishing form of roughness in these films.

First we describe the way in which cobalt grows on copper as illustrated in Fig. 1 (all figures are 600 Å wide). This sequence initiates much of the roughness seen in these films. The initial layer of cobalt is seen to grow via island nucleation with the second layer beginning before the first is finished. Growth beyond the first several layers is essentially cobalt on cobalt. The cobalt progresses via this mechanism to develop a rough surface on the copper substrate. Small, numerous islands indicate that cobalt has a low mobility on copper. Peak-to-peak roughness is 4–5 monolayers at 21 Å.

Note the small lateral lengths in these images. It is quite clear that the growth of the cobalt is not layer by layer and

[a]Electronic mail: tjm@leland.stanford.edu

 0021-8979/96/79(8)/5116/3/$10.00 © 1996 American Institute of Physics

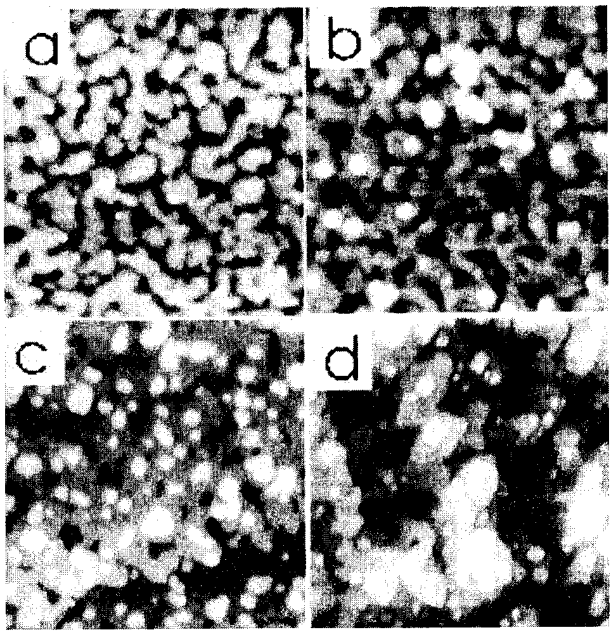


FIG. 1. Roughness development in films of the form: Cu(100)/Co (n Å) for (a) $n=1$, (b) $n=3$, (c) $n=10$, and (d) $n=21$. Full width is 600 Å.

that the horizontal dimensions of contiguous, same-height areas is small. A typical characteristic length is 40 Å after 21 Å of vertical growth. In this sense, cobalt on copper demonstrates a high lateral roughness.

The growth of copper on cobalt proceeds in a very different fashion. As shown in Fig. 2, even a few angstroms of copper is sufficient to show its larger surface mobility. The copper acts to smooth the surface in the lateral dimension. Peak-to-peak roughness remains fairly constant throughout various thicknesses, however. A typical characteristic length for these films is 150 Å after 21 Å of vertical growth.

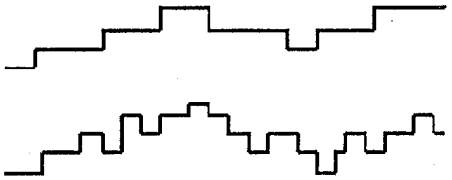


FIG. 3. Copper (top layer) decreases the lateral roughness of cobalt (bottom layer) due to its higher mobility.

If we contrast Figs. 1 and 2 we see what the effects of copper are on these depositions. The peak-to-peak roughness remains largely unaffected even with increasing thicknesses of copper, while the lateral roughness increases dramatically. These concepts are illustrated in Fig. 3 where it is shown how two layers with the same peak-to-peak roughness can exhibit marked differences in the lateral direction.

B. Bilayer progression

We next investigated roughness at the bilayer level. These structures are of interest in relation to the GMR effect. The way in which the atomic level roughness develops through the first bilayer is important for both spin valves and multilayers. We used our results for the effects on roughness from copper and cobalt on these thicker structures. Several samples of the form Cu(100)/[Co(21 Å)/Cu(21 Å)]$_n$ were grown and the results are shown in Fig. 4.

For clarity, we used the smoothing effects of copper to examine the roughness for 1, 2, and 5 bilayers by always looking at the top copper layer. The roughness is fairly evi-

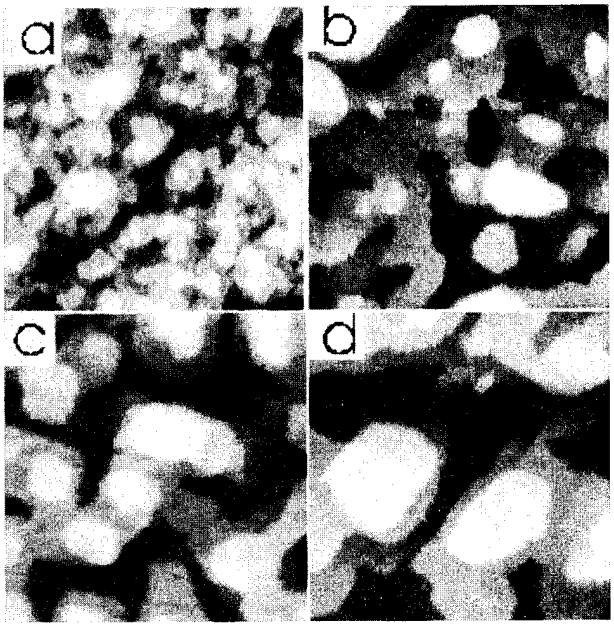


FIG. 2. Roughness development in films of the form: Cu(100)/Co (21 Å)/Cu(n Å) for (a) $n=1$, (b) $n=5$, (c) $n=21$, and (d) $n=40$. Full width is 600 Å.

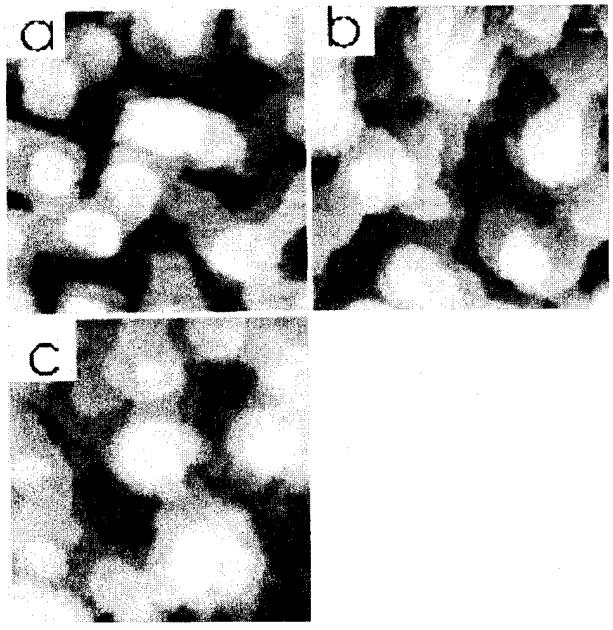


FIG. 4. Bilayer roughness in films of the form: Cu(100)/[Co(21 Å)/Cu(21 Å)]$_n$ for (a) $n=1$, (b) $n=2$, (c) $n=5$. Full width is 600 Å.

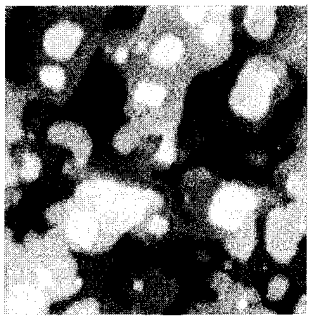


FIG. 5. (a) Cu(100)/Co(21 Å) grown at $T=150$ °C. Full width is 600 Å.

dent with up to 6 or 7 monolayers of roughness visible in a multilayer composed of 5 bilayers. There is not a great deal of change with increasing number of bilayers. Instead, the degree of roughness seems fairly well set with the completion of the first or second bilayer.

The implications for GMR in these films are not good because of the high peak-to-peak roughness. To account for any uncontrolled variability in deposition rate, we grew multilayered wedges where the copper thickness was varied by as much as 15 Å. Magnetoresistive measurements indicated no (<1%) change in resistance over the entire sample for fields up to several thousand oersted. The hysteresis loops of the film were also measured using the magneto-optic Kerr effect (MOKE) and no antiferromagnetic coupling was present.

C. Temperature effects

It is known[7] that cobalt and copper do not interdiffuse more than a few monolayers at room temperature. To illustrate the effect of elevated temperatures on cobalt mobility and consequently roughness, 21 Å of cobalt was grown at 150 °C. It is immediately apparent (see Fig. 5) that the lateral scale of the islands is much larger than for room temperature. Comparing Fig. 5 with Fig. 1(d) suggests that the difference in temperature seems to have given the cobalt atoms a much greater mobility that allowed for more layered growth. Note that the peak-to-peak roughness is still similar.

A bilayer formed at this temperature shows [see Fig. 6(b)] a great deal more smoothness in the lateral direction than an identical structure grown at room temperature [see Fig. 6(a)]. The enhanced copper mobility has clearly resulted in a film whose lateral variation is quite reduced in comparison to a film grown at room temperature. Even more striking is the same film grown at −50 °C [see Fig. 6(c)]. At this low temperature, the characteristic lateral lengths have been clearly reduced. This occurred despite the presence of 21 Å of copper which, as we have seen, ordinarily provides for longer lengths.

IV. CONCLUSIONS

With the STM we see that the evolution of roughness in IBS-grown Co/Cu films depends strongly on the growth

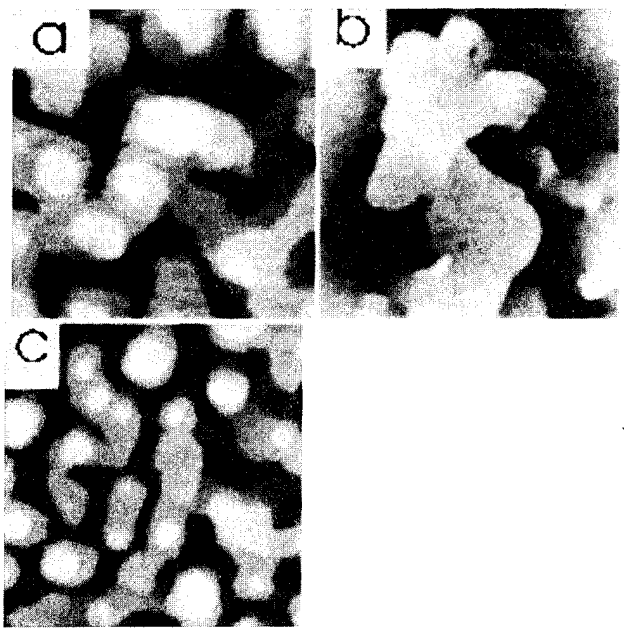


FIG. 6. Cu(100)/Co(21 Å)/Cu(21 Å) grown at (a) room temperature, (b) at $T=150$ °C and (c) at $T=-50$ °C. Full width is 600 Å.

mechanisms of each component. Although usually viewed in peak-to-peak terms, roughness throughout this study varied more in the horizontal length scales. Cobalt tends to grow in small islands that produce rough coverage, meaning that the length scales that are characteristic in these surfaces are small (<50 Å). Due to its larger mobility, copper extends the lateral dimensions of the surface without strongly influencing peak-to-peak roughness.

The cumulative effects of these growth modes on bilayer progression are that the degree of roughness for Cu(100) substrates is mostly set by the first two bilayers and increases only slightly beyond that. This effect is consistent with the absence of GMR in these structures.

Finally, the mobilities of copper and cobalt can be altered by changing the growth temperature. This results in enhanced characteristic lengths at higher temperatures and diminished ones for lower temperatures.

ACKNOWLEDGMENTS

This work has been supported by the Department of Commerce on Contract No. 70NANB2H1239 through the National Storage Industry Consortium. The authors would also like to thank Bruce Melior for technical support.

[1] M. N. Baibich *et al.*, Phys. Rev. Lett. **61**, 2472 (1988).
[2] S. S. P. Parkin, R. Bhadra, and K. P. Roche, Phys. Rev. Lett. **66**, 2152 (1991).
[3] B. Dieny *et al.*, J. Magn. Magn. Mater. **93**, 101 (1991).
[4] S. Chiang and R. J. Wilson, IBM J. Res. Dev. **30**, 515 (1986).
[5] J. Camarero *et al.*, Phys. Rev. Lett. **73**, 2448 (1994).
[6] Th. Eckl *et al.*, J. Appl. Phys. **75**, 362 (1994).
[7] G. R. Harp *et al.*, Mater. Res. Soc. Symp. Proc. **313**, 41 (1993).

^{59}Co nuclear magnetic resonance studies of the effect of annealing molecular beam epitaxy grown Co/Cu(111) multilayers

T. Thomson and P. C. Riedi
Department of Physics and Astronomy, University of St. Andrews, St. Andrews, Fife, United Kingdom

B. J. Hickey
Department of Physics, University of Leeds, Leeds, United Kingdom

^{59}Co NMR, magnetotransport and grazing incidence x-ray scattering studies have been undertaken on a series of Co/Cu(111) multilayers, grown by molecular beam epitaxy (MBE), and subsequently annealed. Magnetotransport measurements showed that the magnetoresistance ($\Delta\rho/\rho$) decreased only slightly as the annealing temperature was increased, but both the resistivity ρ and the change in resistivity $\Delta\rho$ doubled. NMR measurements showed that the strain in the interior of the Co layers relaxed slightly as a result of annealing while the strain at the interfaces remained constant. A small increase in the ratio of the area under the main NMR line to the area under the interface line, together with a reduction of interface line area, suggests a slight deterioration in the quality of the interfaces as a result of annealing. These observations are consistent with the model that MBE grown multilayers require good quality interfaces for large magnetoresistance (MR). Data from x-ray measurements showed that the increase in resistivity could be explained as a result of alloying between the top Cu layer of the multilayer and the Au capping layer. © *1996 American Institute of Physics.* [S0021-8979(96)18108-9]

I. INTRODUCTION

Co/Cu(111) multilayer films exhibiting grant magnetoresistance (GMR) are still currently receiving much attention[1–3] both at a fundamental level and for applications in magnetic recording systems. In this work we report on the effect of thermal annealing a series of molecular beam epitaxy (MBE) grown Co/Cu(111) multilayer films using the complementary techniques of ^{59}Co NMR and x-ray scattering, together with magnetotransport measurements. This article is mainly concerned with the investigation of these materials using spin echo NMR spectroscopy and correlating the results obtained with magnetotransport and x-ray scattering measurements. A more comprehensive discussion of the x-ray results and magnetotransport measurements may be found in Ref. 4.

NMR is essentially a microscopic probe of the local atomic environments. When excited by the applied radio frequency field the nucleus precesses in an effective magnetic field (hyperfine field) determined by the atomic environment. The atomic environment can be modified by the inclusion of different atoms in the vicinity of the atom containing the probe nucleus. This can occur as a result of alloying and at interfacial regions in multilayer materials. Hence at ideally flat, planar interfaces in the fcc Co/Cu(111) system one would expect an atomic environment of 9×Co nearest neighbors (NN) and 3×Cu NN.[6,7] Structural imperfections such as grain boundaries can also lead to a change in the effective magnetic field at the nucleus. If the material under investigation is strained, then the hyperfine field changes as a result of the change in interatomic distance. In these MBE grown films strain results from the lattice mismatch (Co=3.54 Å, Co=3.61 Å) between Co and Cu.

II. EXPERIMENT

A single multilayer film was grown at the MBE facility in Leeds. A base pressure of 3×10^{-11} mbar was obtained in the MBE chamber, and a high degree of uniformity across the sample was ensured by rotating the sample at 1 Hz throughout the grown process. The film was grown on a polished single crystal sapphire substrate of dimensions 12×10×1 mm oriented normal to the $(1\bar{1}20)$ direction. A buffer layer, consisting of Nb 60 Å deposited at 950 °C followed by Cu 30 Å, was grown on the sapphire prior to the multilayer. The multilayer consisted of Co 11.5 Å/Cu 7 $Å_{\times 20}$, a Au cap of 38 Å was deposited to inhibit oxidation.

The final film was cut into 8×2 mm sections using a diamond saw. The resulting identical samples were annealed in a stream of oxygen-free nitrogen for 45 min at 200, 260, 290, and 320 °C. A fifth sample was left unannealed as a control.

The ^{59}Co NMR spectra were measured in a phase detected, swept frequency spin echo spectrometer[8,9] with the samples in a tuned circuit. During the course of the experiments only the tuning and matching of the sample coil were changed, so any errors due to mismatches and standing waves in the instrument are identical in all the spectra measured. Corrections for ω^2 and variations in the spin–spin relaxation time (T^2) with frequency were made in the usual way.[6] All spectra were measured at 4.2 K.

Magnetoresistance (MR) measurements were carried out using a standard four probe method with collinear, pressure type electrical contacts. All MR measurements were performed at 4.2 K in applied fields up to 4 T using a geometry with the current and applied field parallel, and in the plane of the film. The resistivities ρ were obtained assuming a uniform current throughout the cross section of the films.

III. RESULTS AND DISCUSSION

The results obtained from the magnetoresistance measurements are detailed in Table I. Table I shows a decrease in MR at higher annealing temperatures, and that the resistivity and the change in resistivity in the presence of a magnetic

TABLE I. Magnetoresistance measurements at $T=4.2$ K for a series of annealed MBE grown [Co(11.5 Å/Cu7 Å]$_{x20}$/Au(38 Å) multilayers films. The term ρ_s is the saturation resistivity at 4 T and $\Delta\rho$ the change in resistivity between zero applied field and saturation.

Annealing conditions	ρ_s (Ω cm)	$\Delta\rho$ (Ω cm)	MR(%)
Unannealed	8.2	3.0	36.6
200 °C for 45 min	9.0	3.4	37.8
260 °C for 45 min	12.0	4.4	36.7
290 °C for 45 min	14.4	4.7	32.6
320 °C for 45 min	18.6	5.8	31.1

field doubled for the highest annealing temperature. It is these results that the structural determination using NMR and x-ray scattering should seek to explain.

The ^{59}Co NMR spectra for the unannealed and the most heavily annealed (320 °C for 45 min) MBE grown Co/Cu(111) samples are shown in Fig. 1. It is immediately apparent that no gross changes have occurred as a result of annealing. This is somewhat surprising and demonstrates that Co/Cu(111) multilayers, prepared with a careful choice of substrate and buffer layer structure, are resistant to change up to temperatures in excess of 300 °C. The larger of the two peaks (~215 MHz) in Fig. 1 is the NMR line associated with Co surrounded by 12 Co nearest neighbors (the main line). The smaller peak (~168 MHz) in Fig. 1 is the ideal planar interface line where three of the nearest-neighbor Co atoms are substituted by Cu. The intensity between these lines is mostly due to substitution of one or two nearest-neighbor Cu atoms in the interior of the Co layers, although grain boundaries may also contribute to the observed signal in this region. As can be seen from Fig. 1 the main line is shifted to the low-frequency side of the spectrum compared to the value expected for multidomain fcc Co powder. This shift is due to an extensive strain in the plane of the film caused by the lattice mismatch of 2% between Co($a=3.54$ Å) and Cu($a=3.61$ Å).

Although no gross changes occurred as a result of annealing these Co/Cu multilayers, closer examination of the NMR spectra reveals some smaller effects. In order to quantify these effects the experimental data is fitted with a series of Gaussian functions. In the region of interest—150 to 250 MHz—we fit the data with a total of four Gaussians representing the bulk (12 NN Co) first (11 Co+1 Cu) second (10 Co+2 Cu), and third (9 Co+3 Cu) Cu substituted atomic environments. As the first and second substituted environments are not very well defined, due to the lack of intensity, we ensure a consistency of fit over the region by keeping the width, the center position, and the relationship between the amplitudes of these two Gaussian functions constant. In this way we obtain an amplitude scaling parameter that characterizes small differences in the volume of the samples. Hence we are able not only to compare the ratio of the areas under the main and planar interface lines from a single spectrum, but are also able to compare the intensities of the main and planar interface lines between spectra. As the area under a line is directly related to the number of atoms in the particular environment, it is possible to examine how the number of atoms in both the bulk and planar interface line change as a result of annealing. This assumes, as is the case here, that the spectrometer is in an identical configuration for each spectrum.

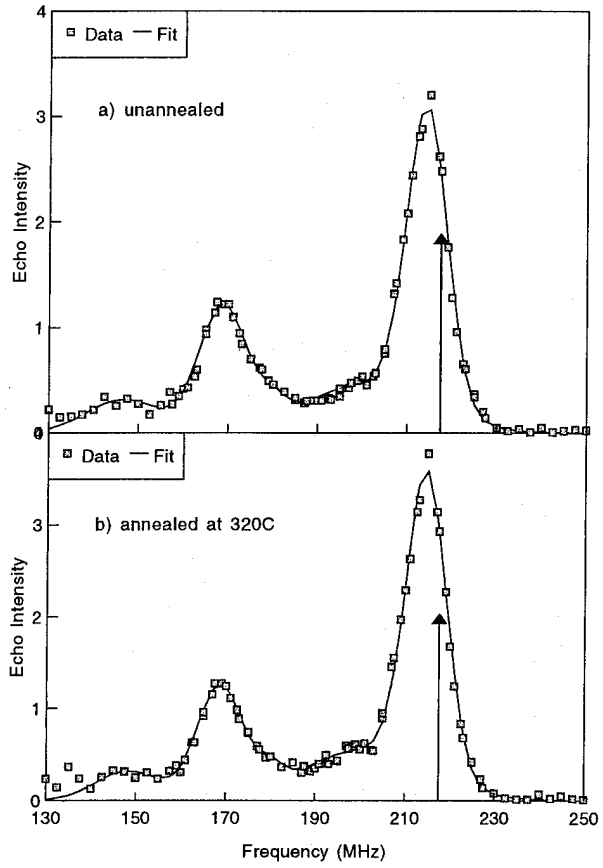


FIG. 1. ^{59}Co spin echo spectra for Co/Cu(111) multilayer films with structure sapphire/Nb(60 Å)/Cu(30 Å)/[Co(11.5 Å/Cu7 Å]$_{x20}$/Au(38 Å) (a) unannealed (b) annealed at 320 °C for 45 min. All data taken at 4.2 K and corrected for ω^2 and variations in the spin–spin relaxation time T^2. The arrow marks the position of the center of the NMR line from unstrained fcc Co powder.

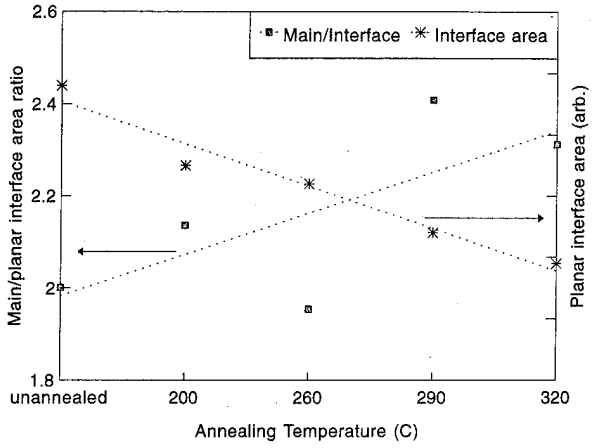


FIG. 2. Ratio of main to planar interface line intensity, and the normalized interface line area as a function of annealing temperature. The trend in the ratio is clear and shows a decrease in the number of atoms in the ideal atomic environment relative to the bulk. This interpretation is confirmed by the decrease in the area under the interface line.

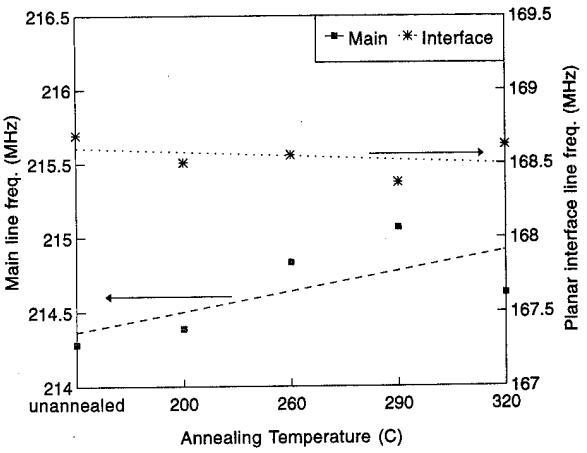


FIG. 3. Center frequency of the main and planar interface NMR lines changes as a function of annealing temperature. The interface line frequency remains constant whereas the main line frequency increases. It is worth pointing out that this increase in frequency is independent of the details of the model used to fit the spectra. The uncertainty in the fit of the center frequency is 50 kHz.

Figure 2 shows both the main/planar interface line ratio and the integrated area under the planar interface line as a function of annealing temperature. The ratio of the main/planar interface line increases with annealing temperature. This could be due to either an increase in the relative number of atoms in the bulk environment or a decrease in the number of atoms in the planar interface environment. Examination of the intensities of the interface line shows that the later is true. The area under the main line does not systematically change and remains approximately constant. Thus we conclude that some small deterioration of interfacial quality has occurred as a result of annealing.

Changes in the position of the main and planar interface lines are shown in Fig. 3. The planar interface line remains constant whereas the main line shows a trend towards higher frequencies at higher annealing temperatures reflecting changes in strain in the interior of the Co layers. The effect of lattice strain can be estimated from high-pressure measurements on fcc Co powder which show that the NMR frequency is increased by 0.106 ± 0.01 MHz/kbar. As mentioned in the introduction the Co lattice will be extensively strained in the plane, although the shift in frequency is never as great as would be predicted for a uniform volume expansion in three dimensions.[6] This is presumably because of contraction normal to the film plane. The shift in the NMR main line can be expressed in terms of an equivalent hydrostatic pressure, as shown in Table II.

The results in Table II show a clear trend in that all the samples show less strain following annealing. This is consistent with the finding that the amount of planar interface reduces with annealing, as less planar interface implies less

TABLE II. ^{59}Co NMR main line frequency and equivalent hydrostatic pressure as a function of annealing temperature. Unstrained fcc Co powder has a center frequency of 217.4 MHz.

Annealing conditions	Main line frequency (MHz)	Equivalent hydrostatic pressure (kbar)	Pressure change on annealing (kbar)
Unannealed	214.28	−29.4	0
200 °C for 45 min	214.39	−28.4	1.0
260 °C for 45 min	214.84	−24.2	5.2
290 °C for 45 min	215.07	−22.0	7.4
320 °C for 45 min	214.63	−26.2	3.2

epitaxial registry and so less strain in the interior of the Co layers. A similar strain relaxation, following annealing, has been observed in sputtered Co/Ag multilayers[10] although the effects in this material were substantially larger.

Details of the x-ray work on these samples is presented elsewhere,[4] and in this article we shall be content to quote the major results. The x-ray data show no dramatic changes in the specular reflectivity profile. This is consistent with the NMR data where no gross changes were found in any of the spectra. The x-ray data showed significant changes in the Au capping layer as the annealing temperature approached 300 °C, in that a AuCu alloy formed between the Au and the top Cu layer of the multilayer. In order to confirm that a AuCu alloy that formed, a further multilayer with a Co capping layer was grown and annealed at 320 °C. The x-ray scattering data from this sample showed very little change as a result of annealing. The formation of this alloyed capping layer with its higher resistivity accounts for the large changes in measured resistivity. These changes occur because the resistance of this layer both adds in series to the resistance of the multilayer, and is spin dependent (Ref. 4).

ACKNOWLEDGMENT

The support of the U.K. Engineering and Physical Sciences Research Council is gratefully acknowledged.

[1] M. N. Baibich, J. M. Broto, A. Fert, F. Nguyen van Dau, F. Petroff, P. Etienne, G. Creuzet, A. Friederich, and J. Chazelas, Phys. Rev. Lett. **64**, 2472 (1988).
[2] S. S. P. Parkin, R. Bhadra, and K. P. Roche, Phys. Rev. Lett. **66**, 2152 (1991).
[3] D. Grieg, M. J. Hall, C. Hammond, B. J. Hickey, H. P. Ho, M. A. Howson, M. J. Walker, N. Wiser, and D. G. Wright, J. Magn. Magn. Mater **110**, L239 (1992).
[4] H. Laidler, I. Pape, C. I. Gregory, B. J. Hickey, and B. K. Tanner, J. Appl. Phys. (in press).
[5] B. J. Hickey (unpublished).
[6] T. Thomson, P. C. Riedi, and D. Greig, Phys. Rev. B **50**, 10319 (1994).
[7] T. Thomson, P. C. Riedi, K. Bröhl, and P. Bödeker, J. Magn. Magn. Mater **148**, 34 (1995).
[8] T. Dumelow and P. C. Riedi, Hyper. **35**, 1061 (1987).
[9] J. S. Lord and P. C. Riedi, Meas. Sci. Technol. **6**, 149 (1995).
[10] E. A. M. Van Alphen, P. A. A. Vanderheijden, and W. J. M. DeJonge, J. Magn. Magn. Mater, **140–144**, 609 (1995).

Field dependent resonance frequency of hysteresis loops in a few monolayer thick Co/Cu(001) films

Q. Jiang, H.-N. Yang, and G.-C. Wang
Department of Physics, Applied Physics, and Astronomy, Rensselaer Polytechnic Institute, Troy, New York 12180-3590

Dynamic responses of magnetic hysteresis loops in a few monolayer (ML) thick Co/Cu(001) films were studied using surface magneto-optic Kerr effect (SMOKE). For a fixed external field strength H_0, the hysteresis loop area increases as a function of frequency with a power law and reaches a maximum at a resonance frequency Ω_0. This Ω_0 depends on the external periodic field strength as well as the thickness and roughness of the films. The thickness and roughness parameters were measured quantitatively using high-resolution low-energy electron diffraction. For a fixed film thickness, the Ω_0 in the low field region is highly dependent on H_0, which is consistent with the prediction from the mean field model. For two Co films with an equivalent thickness but different degrees of film roughness, the resonance frequency Ω_0 is lower for the rougher films in all the field strengths studied. For a fixed field strength, the value of Ω_0 decreases as Co film roughness increases in a few ML regime. The roughness dependency in Ω_0 indicates that the slowing down in the magnetization reversal process is due to the increased film roughness. © *1996 American Institute of Physics.* [S0021-8979(96)18208-5]

In recent years, the subject of nonequilibrium phenomena associated with hysteresis responses of a magnetic system under an external oscillating magnetic field has received attention both in theory[1–5] and in experiment.[6,7] Effect of surface roughness on hysteresis responses and coercivity is also an interesting topic.[8–10] In particular, the value of coercivity H_c depends on the time scale of the relaxation process and film roughness. In the past, the dynamic behavior of frequency dependent coercivity or hysteresis loss had been studied for metallic glasses, ferrites, and others.[11–14] The study on dynamic behavior in ultrathin ferromagnetic films has only begun recently. For Co/Cu(001) films in a few ML thick regime, it was observed that this system belongs to the Ising spin system and the hysteresis loop area scales with the field strength H_0 and frequency Ω as $A \sim H_0^{\alpha}\Omega^{\beta}$ with $\alpha=\beta=2/3$ in the low field and low frequency regimes.[7]

In this paper, we will present experimental results of the resonance frequency Ω_0 in a few ML thick Co films and its dependence on the applied field strength and film roughness. At Ω_0 the hysteresis loop area reaches a maximum and beyond it the loop area decreases. At Ω_0, the delay time τ corresponds to a phase lag $\pi/2$ between the magnetization and the applied field, therefore the loop area is a maximum. In the low field regime, the obtained relationship between Ω_0 and H_0 are consistent with the prediction derived from the mean-field theory.[3] The decrease in Ω_0 for the rough film compared with the smooth film is consistent with the observation obtained by magneto-optic Faraday rotation images for ≈6 ML thick Co/Au(001) films.[15]

All experiments were performed in an ultrahigh vacuum (UHV) chamber equipped with high-resolution low-energy electron diffraction (HRLEED),[16] SMOKE,[17] Auger electron spectroscopy (AES), and a sputter ion gun. The Co atoms evaporation, the determination of thickness and deposition rate as well as the calibration of the effective magnetic field have been described.[7] We deposited Co films on a smooth Cu(001) and a slightly rough Cu(001) substrate. The smooth Cu(001) substrate was obtained by sputtering at room temperature and then annealing at ≈875 K for 30 min. The slightly rough Cu(001) substrate was obtained after light sputtering (0.22 μA/cm^2) without annealing.

For 2.5 ML thick Co films grown on a smooth Cu(001) substrate, the frequency dependent hysteresis loop area A was plotted in Fig. 1 for selected field strengths H_0. The values of different H_0 noted in the figure are external field strengths H_0 near zero frequency, or the dc field. The insets (a), (b), and (c) in Fig. 1 are measured hysteresis loops for 20 Hz, 75 Hz and 450 Hz at H_0=31.1 Oe, respectively. When the sweeping frequency increases, the loop shape changes from a squarelike [$\Omega<\Omega_0$, inset (a)] to a rounded square at the four corners [$\Omega\sim\Omega_0$, inset (b)], then to a distorted parallelogram ($\Omega>\Omega_0$, not shown), and finally to a nearly straight line at high frequencies with the average magnetization $\langle M\rangle$ near its initial magnetization status [$\Omega\gg\Omega_0$, inset (c)]. At Ω_0, the hysteresis loop shapes at three different field strengths H_0 shown in Fig. 1 are all squarelike but rounded at the four corners [inset (b)]. When H_0 increases, the Ω_0 shifts rapidly from a low value=34 Hz at a low field strength H_0 (20.7 Oe) to a higher value=125 Hz at a high field strength H_0 (82.8 Oe) as shown in Fig. 2 (filled circles). A similar increase in Ω_0 with the increasing H_0 was observed for the slightly rough Co/Cu(001) film at 2.5 ML equivalent thickness (open circles). This phenomenon can be explained by the following Ising-like model.

The dynamics of hysteresis in a one-component Ising-like system is governed by the time dependent Ginzburg-Landau equation where a double well potential barrier is assumed. When spatial fluctuation is neglected, the time-dependent magnetization M under an external sinusoidal field $H(t)=H_0\sin(\Omega t)$ can be described by a mean field model[1]

$$\tau\frac{dM}{dt}=-(rM+uM^3)+H_0\sin(\Omega t), \tag{1}$$

 0021-8979/96/79(8)/5122/3/$10.00 © 1996 American Institute of Physics

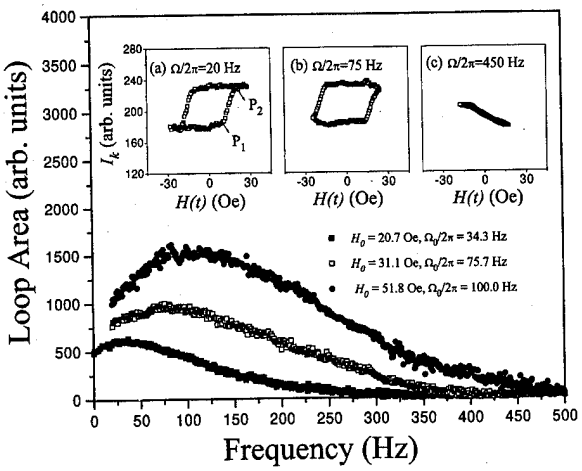


FIG. 1. Hysteresis loop area vs frequency at selected field strengths H_0 for ≈2.5 ML thick Co films grown on a smooth Cu(001) substrate. The H_0 near dc field and the Ω_0 at different H_0 are indicated in the figure. The insets: hysteresis loop shapes for 20 Hz (a), 75 Hz (b), and 450 Hz (c) when H_0=31.1 Oe.

where $rM+uM^3$ ($r<0$ and $u>0$) originates from a double well potential due to the anisotropy energy. In the low frequency regime, $0\leq\Omega\leq\Omega_0$, the dynamic coercivity H_c has been derived analytically[3] from Eq. (1) as

$$H_c=H_{c0}+K_1[\Omega^2(H_0^2-H_{c0}^2)]^{1/3}, \tag{2}$$

where K_1 is a constant and $H_{c0}=\sqrt{-4r^3/27u}$ is the static coercivity which can be obtained under adiabatic condition ($\Omega\to 0$). Where the magnetization in an Ising-like system is approximately a constant, the loop A can thus be derived as $A\approx 4\,M_0\,H_c$, i.e.,

$$A=A_0+K[\Omega^2(H_0^2-H_{c0}^2)]^{1/3}, \quad H_0>H_c, \tag{3}$$

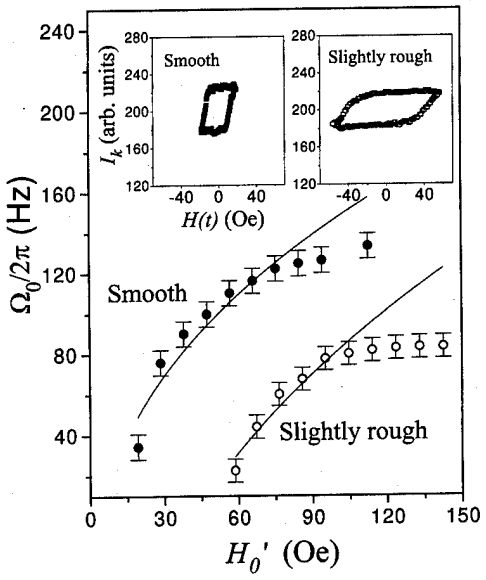


FIG. 2. Resonance frequency Ω_0 vs the effective field strength H_0' for ≈2.5 ML thick Co films grown on a smooth Cu(001) substrate (filled circles); grown on a slightly rough Cu(001) substrate (open circles). Solid curves are fits using Eq. (4). The insets: the hysteresis loops at 4 Hz for the smooth film (filled squares) and the slightly rough film (open squares).

where K is a constant and A_0 is the static loop area. The assumption of the constant magnetization is consistent with our observation in the scaling regime for a few monolayer thick Co films/Cu(001).[7]

Equation (2) indicates that the threshold H_c is a function of H_0 and Ω. At a fixed H_0, the threshold H_c will increase from the static value H_{c0} by an amount proportional to a 2/3 power law of the frequency Ω.[18] By continuously increasing Ω, the dynamic coercivity H_c may pass the H_0 limit; thus, the loop area will reach a maximum value at the resonance frequency $\Omega=\Omega_0$. When Ω increases further, the loop area will decrease because the applied external field strength is not high enough ($H_0<H_c$) within its time scale to overcome the double well barriers and reverse the magnetization. Replacing H_c by H_0 in the left hand side of Eq. (2), the field dependence of the resonance frequency can be expressed in the following form

$$\Omega_0=\frac{(H_0-H_{c0})^{3/2}}{C\sqrt{H_0^2-H_{c0}^2}}, \tag{4}$$

where $C=K_1^{3/2}$. Note that when $H_0\sim H_{c0}$, the $\Omega_0\sim H_0-H_{c0}$ shows a linear relationship with H_0. In practice, one must consider the modification of H_0 by the eddy current effect. This correction can be made as the effective field strength H_0', which equals H_0 times a calibration factor $g(\Omega)$. Replacing H_0 by the effective field strength H_0', we used Eq. (4) to fit our resonance frequency data for both smooth and slightly rough films shown as solid curves in Fig. 2.

In the low field and low frequency regimes, Eq. (4) indicates that the value of Ω_0 is dependent on the applied field strength H_0 and static coercivity H_{c0}. For 2.5 ML thick films, at $\Omega/2\pi$=4.0 Hz, the dynamic coercivity H_c(40.0 Oe) is larger in the slightly rough film (open squares in the inset of Fig. 2) than that (15.0 Oe) on the smooth film (filled squares in the inset of Fig. 2). The static coercivity H_{c0} can be obtained by extrapolating Ω_0 to Ω_0=0 of the solid lines, the static coercivities H_{c0} are 4.3 Oe and 40.5 Oe for the smooth film and rough film, respectively. The change in the static coercivity H_{c0} value results in the difference in values of Ω_0 between the smooth and slightly rough films shown in Fig. 2, which is consistent with the description of Eq. (4). Note that in both 2.5 Co/Cu(001) films, the hysteresis loop shapes shown in the insets of Fig. 2 indicate a narrow distribution of coercivity H_c over islands ($H_c\pm 3.0$ Oe for the smooth film and $H_c\pm 6.0$ for the rough film). If we assume that the distribution of H_{c0} is the same as that of H_c, the fit values of Ω_0 displayed in Fig. 2 will be affected by ±5.0 Hz. In addition to the static coercivity H_{c0}, the surface roughness of the deposited film may play a role in the value of Ω_0 and is discussed in later paragraphs.

The plot of Ω_0 vs H_0 in the high field strength region deviates from the fit curves (solid curves) using Eq. (4) (see Fig. 2). This may be due to the fact that the scaling law described by Eq. (3) is not valid at high field strength and high frequency regions.[7]

Note that the magnitude of the value of resonance frequency Ω_0 is quite different from that of the switching frequency Ω_s, which is equal to the inverse of t_s, the time period required for the magnetization M (or magnetic induc-

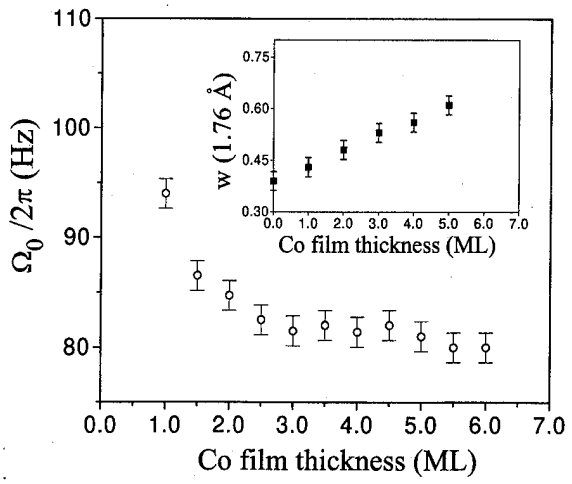


FIG. 3. Resonance frequency Ω_0 vs Co films thickness (open circles). These films were grown on a slightly rough Cu(001) substrate. The external field strength was fixed at a dc equivalent field H_0=103.0 Oe for all measurements. The inset: the interface width w (filled squares) as a function of Co film thickness.

tion B) to change from 0.1 to 0.9 of the total change ΔM (or ΔB).[19] Roughly speaking, t_s is the time period for M to jump from P_1 to P_2 as shown in the inset (a) of Fig. 1. Switching speed study usually requires a dc bias field H_b to be added to a pulse field system to allow the higher coercivity samples to be switched from saturation to zero remanence.[20] The Ω_0 defined in our study is related to the inverse of the time period in which magnetization responds to a sinusoidal periodic magnetic field when the magnetic field changes in a complete cycle of $-H_0 \rightarrow 0 \rightarrow H_0 \rightarrow 0 \rightarrow -H_0$. The physical significance of the Ω_0 is that there is a symmetry breaking of the average magnetization at the $\Omega=\Omega_0(H_0)$, i.e., $\langle M(t)\rangle=0$ for $\Omega<\Omega_0(H_0)$ changes to $\langle M(t)\rangle\neq 0$ for $\Omega>\Omega_0(H_0)$; within the time period of $1/\Omega_0$, the magnetization can still make excursions between two minimum states without losing its amplitude, and beyond it the average magnetization is a nonzero value ($\Omega>\Omega_0$) and the magnetization prefers to stay near its initial magnetic status ($\Omega\gg\Omega_0$).[7]

For a few ML thick Co films grown on a slightly rough Cu(001) substrate, the Ω_0 value under a dc equivalent field H_0=103.0 Oe shown in Fig. 3 (filled circles) decreases rapidly from 94 Hz at 1.0 ML to 83 Hz at 3.0 ML, and then decreases further to 80 Hz at 6.0 ML. The measured coercivity H_c is nearly constant (40.0 Oe) in this thickness regime.[18] This implies that the change in Ω_0 as a function of thickness for the slightly rough film may not be caused by H_c. Note that in this thickness regime, the surface roughness parameters do change their values and may relate to the change in Ω_0. We extracted the changes in roughness parameters in a few ML Co films, i.e., the interface width w, roughness exponent α, and the lateral correlation length ξ[18,21] by the analysis of the energy dependent angular profiles ($I-V$) of the (00) beam using HRLEED. The result is shown in the inset of Fig. 3. The interface width w (filled squares) increases from $0.39t$ for a slightly rough but clean Cu(001) surface to $0.61t$ for a 5.0 ML thick Co film, where t is a single step height (1.76 Å for the Co film). The change in the α value with Co film thickness also exhibits a continuous drop from 0.57±0.02 at 1.0 ML to 0.44±0.02 at 5.0 ML thick (not shown). A smaller value of α corresponds to a more locally rugged surface. The lateral correlation length ξ shows only a small change from 218±5 Å on a slightly rough Cu(001) surface to 182±5 Å for Co films at 3.0 ML thick (not plotted). Another observation is that, for 2.5 ML thick Co films shown in Fig. 2, the maximum Ω_0 (85 Hz) in the slightly rough film ($w=0.52t$, $\alpha=0.49$, $\xi=190$ Å, open circles) is lower than that (125 Hz) in the smooth film ($w=0.49t$, $\alpha=0.61$, $\xi=250$ Å, filled circles). These data in Figs. 2 and 3 indicate that the resonance frequency Ω_0 decreases when surface roughness increases.

In submonolayer regime, a recent magnetic lattice gas model calculation of dynamic hysteresis of magnetic islands predicts that the value Ω_0 depends on the lacunarity of each magnetic island.[22] The results of the model indicate that the net exchange energy associated with the edge moments in magnetic islands affects the value of Ω_0. Extension of this model to several monolayer thick ferromagnetic films is highly desired. In addition to the changes in the exchange energy, local defects can also modify the magnetic anisotropy energy, thus these defects create hard magnetic centers in which the magnetization reversal process slows down and manifests itself through the increased coercivity and reduced Ω_0. The slowing down of the magnetization reversal in ≈6 ML thick Co/Au(001) rough films was also observed by magneto-optic Faraday rotation images in which a lacunar domain structure evolved slowly towards a uniformly reversed magnetic state.[15]

This work was supported by ONR. We deeply appreciate K. Liang for the loan of the Cu(001) crystal. We also acknowledge the use of the HRLEED from Leybold Vacuum Products.

[1] M. Rao, H. R. Krishnamurthy, and R. Pandit, Phys. Rev. B **42**, 856 (1990).
[2] C. N. Luse and A. Zangwill, Phys. Rev. E **50**, 224 (1993).
[3] P. Jung, G. Greg, R. Roy, and P. Mandel, Phys. Rev. Lett. **65**, 1873 (1990).
[4] D. Dhar and P. Thomas, J. Phys. A **25**, 4967 (1992).
[5] A. M. Somoza and R. C. Desai, Phys. Rev. Lett. **70**, 3279 (1993).
[6] Y.-L. He and G.-C. Wang, Phys. Rev. Lett. **70**, 2336 (1993).
[7] Q. Jiang, H.-N. Yang, and G.-C. Wang, Phys. Rev. B **52**, 14911 (1995).
[8] Y.-L. He and G.-C. Wang, J. Appl. Phys. **76**, 6446 (1994).
[9] S. Z. Wu, G. J. Mankey, F. Huang, and R. F. Willis, J. Appl. Phys. **76**, 6434 (1994).
[10] M. Donath, G. Schönhense, K. Ertl, and V. Dose, Appl. Phys. A **50**, 49 (1990); R. Allenspach, M. Taborelli, M. Landolt, and H. C. Siegmann, Phys. Rev. Lett. **56**, 953 (1986).
[11] S. U. Jen and C. J. Weng, J. Appl. Phys. **64**, 4627 (1988).
[12] K. Shirae, J. Appl. Phys. **50**, 7618 (1979).
[13] J. J. Lu, H. L. Huang, and I. Klik, J. Appl. Phys. **76**, 1726 (1994).
[14] H. B. Jiang and C. P. Bean, Rev. Sci. Instrum. **66**, 3284 (1995).
[15] J. Pommier, P. Meyer, G. Pénissard, J. Ferré, P. Bruno, and D. Renard, Phys. Rev. Lett. **65**, 2054 (1990).
[16] U. Scheithauer, G. Meyer, and M. Henzler, Surf. Sci. **178**, 441 (1986); J.-K. Zuo, R. A. Harper, and G.-C. Wang, Appl. Phys. Lett. **51**, 250 (1987).
[17] J.-P. Qian and G.-C. Wang, J. Vac. Sci. Technol. A **8**, 4117 (1990).
[18] Q. Jiang, H.-N. Yang, and G.-C. Wang (unpublished).
[19] B. D. Cullity, *Introduction to Magnetic Materials* (Addison-Wesley, Reading, MA, 1972).
[20] W. D. Doyle, L. He, and P. J. Flanders, IEEE Trans. Magn. **29**, 3634 (1993).
[21] H.-N. Yang, G.-C. Wang, and T.-M. Lu, *Diffraction From Rough Surfaces and Dynamic Growth Fronts* (World Scientific, Singapore, 1993).
[22] A. Zangwill, these proceedings.

Fe adsorption and film growth on GaAs(001) (2×4)-As (abstract)

E. Kneedler, P. M. Thibado, B. T. Jonker, B. R. Bennett, L. J. Whitman,
B. V. Shanabrook, and J. J. Krebs
Naval Research Laboratory, Washington, DC 20375-5343

We have examined the initial interface formation and subsequent film growth for Fe films on the As-terminated (2×4) reconstructed surface of GaAs(001) in an effort to correlate the initial adsorption sites and film growth with the magnetic anisotropy. The growth and surface studies were performed in a four chamber ultrahigh vacuum system which incorporates UHV sample transfer between the chambers for III–V semiconductor growth, metal growth, photoelectron diffraction (PED), and scanning tunneling microscopy (STM). After coating with a thin film of Au (40 Å) at room temperature, the samples were removed from the system for postgrowth characterization, which included ferromagnetic resonance and magnetometry. The GaAs(001) surface was prepared via homoepitaxial growth by MBE, with the growth terminated in a manner which resulted in a well-ordered As-dimer terminated (2×4) reconstructed surface as revealed by reflection high energy electron diffraction and STM. Fe deposition was performed in a second MBE chamber for coverages which ranged from 0.1 ML to several tens of monolayers at a substrate temperature of 175 °C. The sample was then transferred under UHV to either the PED or STM chamber to determine the initial adsorption sites, growth mode, and evolution of film structure with increasing coverage. For the lowest coverages studied (0.1 ML), we obtain evidence for preferential adsorption at As-dimer sites. At a coverage of 1 ML, two-dimensional islands form approximately 20 Å in size, but elongated along the missing dimer rows with an aspect ratio of 2:1. At high coverages (>40 Å), we observe three-dimensional mounds or clusters with an average in-plane diameter of approximately 100 Å and a narrow size distribution. Even at this coverage, the monolayer terraces of the GaAs substrate are clearly visible in the STM image, with the Fe film uniformly growing on each terrace. Photoelectron diffraction in the forward scattering regime (high electron kinetic energy) is utilized to determined the growth mode. At low kinetic energy, information on the adsorption site is obtained from Auger electron diffraction and compared with the results of the real space STM images. [S0021-8979(96)42508-9]

This work was supported by the Office of Naval Research.

 0021-8979/96/79(8)/5125/1/$10.00 © 1996 American Institute of Physics

Magnetic properties and Pd–H miscibility gap in Ni/Pd composite fine particles

Takashi Manago, Yoshichika Otani,[a] and Hideki Miyajima
Department of Physics, Faculty of Science and Technology, Keio University, Hiyoshi 3-14-1, Kohoku, Yokohama 223, Japan

Etsuo Akiba
National Institute of Materials and Chemical Research, Tsukuba, Ibaraki 305, Japan

The magnetic and structural properties of Ni fine particles coated with Pd were investigated in hydrogen atmospheres by means of *in situ* magnetometry and *in situ* x-ray diffractometry. The x-ray diffraction patterns in hydrogen atmospheres show that the width of the plateau in the Pd–H phase boundary (miscibility gap) narrows with decreasing Pd thickness, which is reminiscent of nano-crystalline Pd. At room temperature, the magnetization in hydrogen atmospheres shows a steep saturation and a small decrease in the residual magnetization, indicating that the interface magnetic anisotropy is reduced by the hydrogenation. © *1996 American Institute of Physics.* [S0021-8979(96)18308-1]

I. INTRODUCTION

The susceptibility χ of Pd is the largest in the $4d$ transition metal series.[1] This is due to a high exchange enhancement. The Stoner enhancement factor is 9.3.[2] Though Pd is a paramagnet, it is nearly a ferromagnet. If an additional strong exchange enhancement acts on Pd, the paramagnetic Pd may turn ferromagnetic.[3] Also, Pd metal absorbs a large amount of hydrogen and χ depends on the hydrogen concentration. Specifically, χ decreases with increasing hydrogen concentration and goes to zero at $PdH_{0.6}$. Further increase of hydrogen results in a negative susceptibility.[1] This is because the donor electrons from H atoms enter the $4d$ band of Pd, and χ is thereby depressed.

The properties of the hydride PdH_x, characterized by the pressure-concentration isotherms, the so-called $p-x-T$ curves, show a phase separation between the solid solution (α) and the hydride (β) and a plateau at the phase boundary (miscibility gap). The $p-x-T$ curves of the PdH_x were believed to be independent of the particle size. However, recent studies on nanocrystalline Pd particles demonstrated that the plateau was narrowed by diminishing the size of the particles.[4–6] This suggests that the narrowing of the plateau is somehow associated with the increased contribution of the surface relative to the volume.

We have been investigating the magnetic and structural properties of spherical Ni particles coated with Pd. The average diameter of Ni sphere is 0.7 μm and the thickness of the Pd shell is a few tens of nm. Previous studies[7,8] showed that the Pd shell seemed magnetically polarized through the exchange coupling with Ni at the interface, whereby weakly ferromagnetic properties appeared in the Pd shell at low temperatures. There was also observed a remarkable effect of hydrogenation that depressed the above mentioned ferromagnetic behavior of the Pd shell.

In this study, we performed *in situ* magnetization and x-ray diffraction measurements in hydrogen atmospheres so as to obtain more detailed information on magnetic and structural properties of the Ni/Pd particles.

II. EXPERIMENTAL PROCEDURE

Five samples with different weight of Pd (5, 10, 15, 20, and 30 wt %) were prepared by chemical reduction method.[7] Hereafter, we call these samples, according to their Pd wt %, NP05, NP10, NP15, NP20, and NP30, respectively. The average thickness of the Pd shell for each sample is tabulated in Table I. For comparison, the coarse-powdered Pd (C–Pd) was also prepared.

The change in the lattice parameter of Pd shell was measured under hydrogen pressure from 0.1 to 30.0 atom at 295 K by means of *in situ* x-ray diffractometry (XRD) using CuK_α radiation (λ=0.1542 nm). The sample was mounted inside a pressure chamber with beryllium windows. While evacuating the chamber, we first measured diffraction patterns in the angular range $36° \leqslant 2\theta \leqslant 56°$, which include the (111) reflection from the Pd shell and the (200) reflection from the Ni core. Hydrogen gas (7N) was then introduced into the pressure chamber until the pressure rose to 30.0 atm. The pressure decreased by about 0.1% because of the hydrogen absorption of the Pd shell and finally achieved its equilibrium after about 5 min. Then x-ray diffraction patterns were obtained in the same angular range. The hydrogen pressure was then reduced to the desired pressure and was kept for about 5 min. The same experimental routine was repeated for the different samples.

TABLE I. Weight percent of the Pd and average thickness of the Pd layer of the Ni/Pd composite particles. The average diameter of Ni particles is (0.7 ±0.2) μm.

Sample No.	Weight of Pd (wt %)	Average thickness of Pd (nm)
NP05	5.39	4.8
NP10	11.05	10.2
NP15	15.95	15.4
NP20	21.83	21.0
NP30	32.35	36.6

[a]Present address: Department of Materials Science, Faculty of Engineering, Tohoku University, Sendai 980, Japan.

 0021-8979/96/79(8)/5126/3/$10.00 © 1996 American Institute of Physics

Magnetization measurements were carried out in a hydrogen atmosphere using a vibrating sample magnetometer (VSM) at room temperature (298 K) in magnetic fields up to 12 kOe. The vibrating rod, specially constructed for the *in situ* magnetometry, consists of a glass tube connected to a copper tube and a nonmagnetic sample holder made of synthetic resin (Dyfreon). Through the vibrating rod, the hydrogen gas can be introduced into the sample space during the magnetization measurement. In order to subtract a signal from the sample holder, each sample was measured in both hydrogen and dry air atmospheres.

In order to study the miscibility gap, the $p-x-T$ curve was measured for NP15 and C–Pd at 373 K in the hydrogen gas pressure up to approximately 10 atm.

III. RESULT AND DISCUSSION

In the previous work,[7] the lattice parameter of Pd in the Ni/Pd composite particles was unchanged by hydrogenation. There are two possible explanation for this result; one is that there is an isovolumetric constraint during hydrogenation and the other is that the absorbed hydrogen desorbs even at the room temperature as soon as the particles are exposed into the air. Our recent electrical resistivity measurements in a hydrogen atmosphere support the latter explanation. The equilibrium state was achieved within 5 min, suggesting that the surface barrier inhibiting the desorption of the hydrogen is very low. A significant portion of the hydrogen stored in the Pd shells must have desorbed during the x-ray diffraction measurements. In order to clarify this point, we performed the *in situ* x-ray diffraction measurement in hydrogen atmosphere.

The XRD patterns show no trace of any mixing of Ni and Pd at the interface. Before hydrogenation, the lattice parameter of the Pd layer is 0.3889 nm, which is the same as that of the C–Pd. The XRD patterns for NP15 under various hydrogen pressures are shown in Fig. 1. No shift was observed in the position of the diffraction peaks from the Ni core, indicating that Ni core hardly absorbs any hydrogen. On the other hand, the Pd shell transforms into the β–Pd phase, and the Pd lattice dilates about 3%–4%. By reducing the hydrogen pressure to zero, the lattice parameter of the Pd shell returned to the value before hydrogenation. A linear relationship between the Pd lattice parameter and logarithm of the hydrogen pressure was obtained as shown in Fig. 2. Interestingly, the change in the lattice parameter depends on the thickness of the Pd shells, and the lattice parameter is smaller for the thinner shells. The hydrogen concentration x in the Pd shell was determined from the linear relation between the lattice parameter of the Pd and the hydrogen concentration. According to Schirber and Morosin,[9] the lattice parameter a is given by $a(x)=0.4025(1+0.044(x-0.6))$ nm. The hydrogen concentration evaluated from the above relation is indicated on the upper axis in Fig. 2. The figure clearly shows that the width of the plateau at the Pd–H phase boundary significantly narrows as the thickness of Pd shell diminishes. The $p-x-T$ curve for NP15 and C–Pd also show that the amount of the hydrogen in the β phase is reduced, that is, the width of the plateau of NP15 becomes narrower than that of C–Pd.

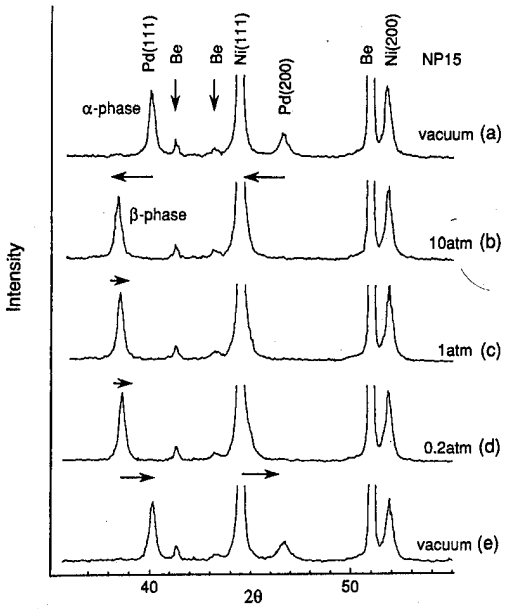


FIG. 1. XRD pattern of one of the samples, NP15, in hydrogen pressures, wherein the reflection from Be is due to the Be sample holder. The XRD measurement was performed sequentially from (a) to (e).

The above mentioned hydrogenation characteristics is quite similar to that observed in nanocrystalline PdH_x, the surface of which plays an important role in determining the width of the plateau.[6] Monte Carlo simulation[6] of the $p-x-T$ curves of nanometer-size Pd clusters under hydrogen loading showed that the surface was first loaded with hydrogen and then the interior. This resulted in the narrowed plateau. Considering the large surface area of the Pd shells of the Ni/Pd composite particles, we may apply the same explanation to our case.

The magnetization curves of Ni/Pd particles in dry air and hydrogen atmospheres are shown in Fig. 3, together with the difference of the magnetization $\Delta M = M_{(\text{hydrogen})}\text{-}M_{(\text{dry air})}$ as a function of magnetic field. The difference in magnetization ΔM approaches zero and become slightly negative with increasing magnetic field. That

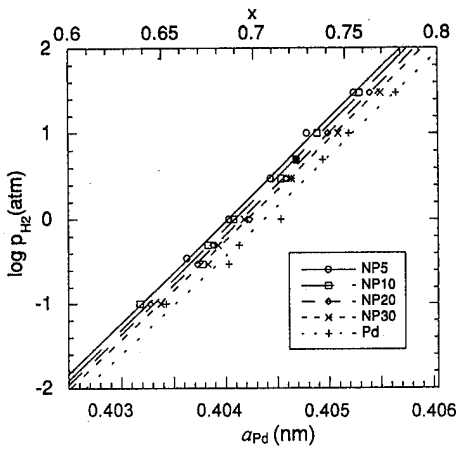


FIG. 2. Hydrogen pressure dependence of the Pd lattice parameter (lower x-axis) and the hydrogen concentration (upper x-axis).

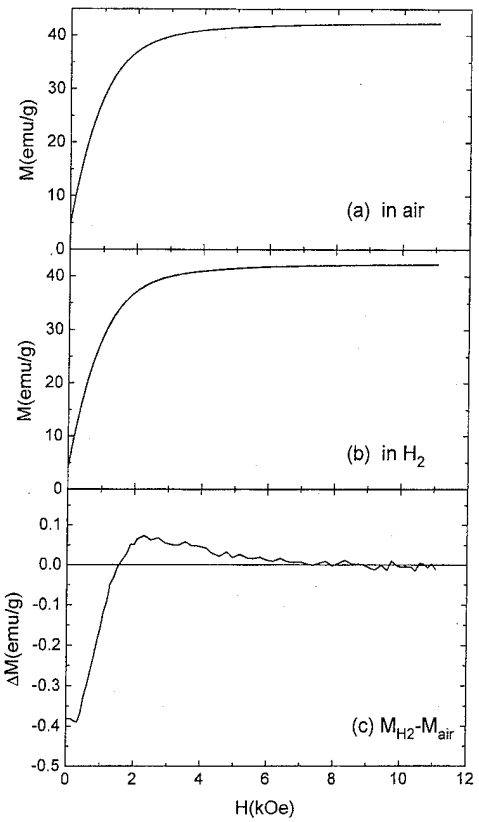


FIG. 3. Magnetization curves of Ni/Pd particles (NP15) in a dry air (a) and in a hydrogen atmosphere (b). The magnetization difference between the magnetization taken in a dry air and in a hydrogen atmosphere, $\Delta M = M_{(\text{hydrogen})} - M_{(\text{dry air})}$ (c).

is, the saturation magnetization of Ni/Pd composite particles after hydrogenation is smaller than before hydrogenation. However, the contribution from the magnetically polarized Pd shell to the magnetization is small at room temperature. The magnetization curve of the hydrogenated Ni/Pd particles exhibits a steep increase toward saturation and the residual magnetization is decreased by about 0.3–0.4 emu/g.

These results imply that the interface anisotropy between the Ni core and the Pd shell is suppressed by the hydrogenation since the Ni core hardly absorbs hydrogen at the low pressure of a few tens of atm. The evaluated change in magnetic anisotropy energy per unit area from the difference between two magnetization curves, ΔK, is about $-(2\text{–}2.5)\times10^{-2}$ erg/cm^2, which is independent of the thickness of Pd shell, as shown in Fig. 4. The change of the magnetic anisotropy may be closely related to the change in the elastic energy at the interface, coupled with the Pd lattice expansion due to the hydrogenation. Further investigations are required in order to clarify the effect of the hydrogen on the interface anisotropy.

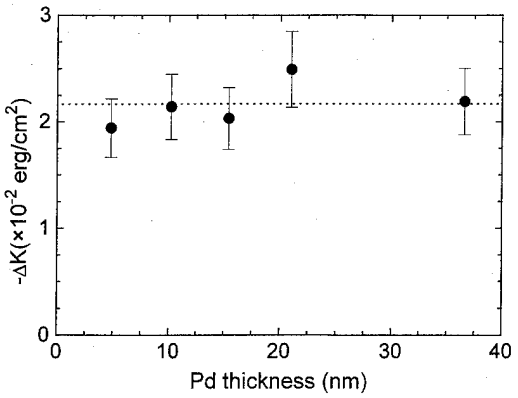


FIG. 4. Pd thickness dependence of the change in the magnetic anisotropy energy, ΔK, per unit interface area between the Ni core and the Pd shell.

ACKNOWLEDGMENTS

We would like to express our gratitude to H. Sakamoto, Tanaka Kikinzoku, Inc., for giving us detailed information about the Ni/Pd composite particles. We also thank M. Yoshida, Hitachi Chemical Co. Ltd., for his assisting in *in situ* x-ray diffraction measurements. This work was partly supported by the Grant-in-aid for Scientific Research from the Ministry of Education, Science, Sport and Culture in Japan.

[1] H. C. Jamieson and F. D. Manchester, J. Phys. F: Metal Phys. **2**, 323 (1972).
[2] *Magnetic Properties of Metals. d-Element, Alloys and Compounds*, edited by H. P. J. Wijn (Springer-Verlag, Berlin, 1991), p. 63.
[3] A. J. Freeman and Ru-qian Wu, J. Magn. Magn. Mater. **100**, 497 (1991).
[4] T. Mütschel and R. Kirchheim, Scr. Metall. **21**, 1101 (1987).
[5] J. A. Eastman, L. J. Thompson, and B. J. Kestel, Phys. Rev. B **48**, 84 (1993).
[6] R. J. Wolf, M. W. Lee, and J. R. Ray, Phys. Rev. Lett. **73**, 557 (1994).
[7] Y. Otani, H. Miyajima, M. Yamaguchi, Y. Nozaki, A. J. Fagan, and J. M. D. Coey, J. Magn. Magn. Mater. **135**, 293 (1994).
[8] Y. Otani, H. Miyajima, M. Yamaguchi, Y. Nozaki, T. Manago, A. J. Fagan, and J. M. D. Coey, J. Magn. Magn. Mater. **140–144**, 403 (1995).
[9] E. Wicke and H. Brodowsky, in *Topics in Applied Physics*, edited by G. Alefeld and Völkl (Springer-Verlag, Berlin, 1978), Vol. 29, p. 78.

Magnetic impurities and clusters on Ag, Pd, and Pt surfaces (abstract)

V. S. Stepanyuk
MPI für Mikrostrukturphysik Halle, Germany

K. Wildberger, P. Lang, R. Zeller, and P. H. Dederichs
Institut für Festkörperforschung, Forschungszentrum Jülich GmbH, Germany

The modern STM technique allows to manipulate the structure of small clusters on surfaces and to produce one- or two-dimensional nanostructures. It can be speculated that due to the reduction of coordination number many of these clusters containing transition elements are magnetic. In this paper we will show that small clusters of 3*d*, 4*d*, and 5*d* atoms are magnetic on different substrates. Our calculations are based on density functional theory and a newly developed KKR Green's function method for defects at surfaces.[1] We calculate the magnetic properties of several linear chains (*C*) and plane islands (*I*) of 4*d* and 5*d* adatoms. In particular we consider linear chains of 2 (dimers, *C*2), 3 and 4 adatoms (*C*3 and *C*4), being oriented in (110) direction, as well as three compact islands with 4, 5, and 9 adatoms (*I*4, *I*5, and *I*9). The moments of the dimers are in general reduced by the interaction in comparison to the moments of single adatoms.[1] In most cases both a ferromagnetic and an antiferromagnetic configuration exist, with the ferromagnetic one being more stable at the end and the antiferromagnetic one at the beginning of the series. For the linear chains quite large moments are obtained, but the behavior with size is nonregular. The large moments obtained for all four chain structures indicate that also infinite chains of these atoms should show appreciable moments. For compact islands (*I*4, *I*5, and *I*9) the hybridization effects within the cluster are even larger. For Ag(001) we find only appreciable moments for the Ru and Rh nanostructures. © *1996 American Institute of Physics.* [S0021-8979(96)42608-8]

[1] P. Lang *et al.*, Solid State Commun. **92**, 755 (1994).

 0021-8979/96/79(8)/5129/1/$10.00 © 1996 American Institute of Physics

High-frequency magnetic properties in metal–nonmetal granular films (invited)

S. Ohnuma
The Research Institute of Electric and Magnetic Materials, Sendai 982, Japan

H. Fujimori, S. Mitani, and T. Masumoto
Institute for Material Research, Tohoku University, Sendai 980-77, Japan

The structure and properties of Co–N and Co–O based films, prepared by rf magnetron reactive sputtering using nitrogen or oxygen and argon gases, have been studied. Transmission electron microscopy (TEM) observation reveals that each Co–(Al or Si)–(N or O) film is a typical film with granular structure, with grain size less than 5 nm. It is found by micro-focused energy-dispersive x-ray and electron energy loss spectroscopy analysis that the grains are mainly composed of Co and the intergranular regions are ceramics of N or O. In Co–N based films, soft magnetic properties are found in both Si and Al containing films over a wide range of film preparation conditions and compositions. Only the films with Al show soft magnetic properties in Co–O based films, which have ρ of 500–1000 $\mu\Omega$ cm, H_k of about 80 Oe and B_s of about 10 kG. By adding about 10 at. % Pd, the soft magnetic properties and H_k of Co–O based films are significantly improved, with H_k more than 180 Oe. These films exhibit a remarkable constant frequency response of the permeability up to around 500 MHz, which is approximately explained by the Landau–Lifshitz formula.
© *1996 American Institute of Physics.* [S0021-8979(96)28808-7]

I. INTRODUCTION

Recent improvements in electronic devices have led to a demand for further miniaturization and higher frequency operation of magnetic devices. One of the important properties of magnetic materials required for such applications is the frequency (f) response of permeability (μ), which is limited by eddy current loss and resonance. According to the modified Landau–Lifshitz equation, which predicts the μ-f response, large values of saturation magnetization (M_s), electrical resistivity (ρ) and anisotropy field (H_k) are required for magnetic materials to show an excellent μ-f response.[1] Soft magnetic films studied to date have large B_s, but exhibit a poor frequency response, assuming sufficient film thickness (d) for such applications, primarily due to their low ρ and H_k.[2–4]

A well-known method for reducing eddy current loss is to laminate soft magnetic thin films with insulating layers, i.e., constructing multilayers.[5] However, the μ-f response of multilayers is not improved as much as expected for the thickness of the isolated magnetic layers. Another method is to increase ρ of the magnetic film. Recently, Fe-based films with a two-phase hetero-amorphous or granular structure have been found to possess both large ρ and soft magnetic properties.[6–8] Unfortunately, these films also show a poorer μ-f response than expected from their large ρ. The reason is the low values of H_k in the films. There has not been any consideration of H_k in preparing these soft magnetic materials. Hence, if soft magnetic films which possesses high ρ and B_s as well as reasonably large H_k could be realized, they can be expected to exhibit an excellent μ-f response and prove to be the most suitable material for the above applications.

To realize such films, we have tried to synthesize Co based films with granular structure.[9,10] The advantage of a granular film is that the particle size, and consequently the magnetic properties, can be tailored by adjusting the method of deposition and the preparation conditions. And the interparticle material may also be controlled by considering the values of the heat of formation for the substances both of the particles and the interparticle regions. Cobalt based alloys are known to exhibit zero magnetostriction[11] and an induced magnetic anisotropy.[12] Then, if the size of the particles and the thickness of the interparticle region for Co based granular films can be controlled arbitrarily, we can prepare soft magnetic films with large B_s, H_k, and ρ.

In this article, we will describe the results of synthesizing a variety of Co based granular films, expected to have large H_k and ρ and to be magnetically soft, and emphasize the relationship between the structure and magnetic properties, in particular, a high-frequency response of permeability.

II. EXPERIMENT

Granular metal films have been produced by a variety of means, including evaporation, co-sputtering of a metal, and an insulator, and sequential sputtering of a metal and an insulator.[13] Each method has advantages and disadvantages. All of the films discussed in this work were prepared by sputtering an alloy target in a reactive gas. Such a reactive sputtering method using an alloy target is best for controlling closely the concentration of gas elements and for obtaining films with homogenous composition. However, in this method there are some compositional limitations on the films, attributable to the preparation of the alloy target. The

 0021-8979/96/79(8)/5130/6/$10.00 © 1996 American Institute of Physics

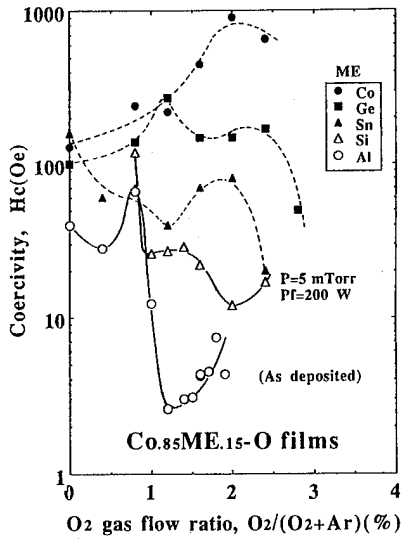


FIG. 1. Curves of the coercivity for as-deposited Co–ME–O films vs O_2 gas flow ratio in a sputtering gas (target: $Co_{85}ME_{15}$, ME=Co, Al, Ge, Si, Sn).

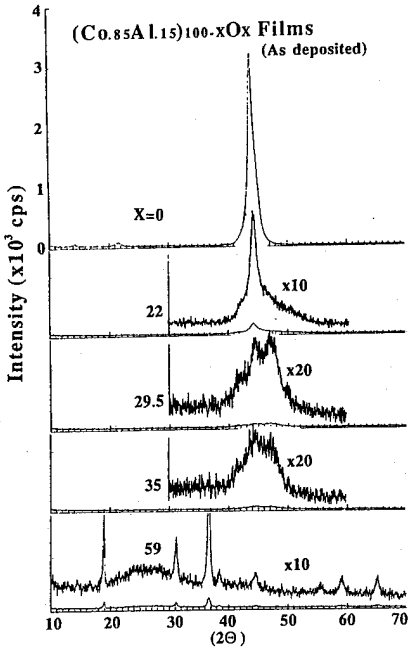


FIG. 2. X-ray diffraction patterns of the granular $(Co_{.85}Al_{.15})$–O films with varying O concentration.

composition of our alloy targets has been mainly selected by consideration of the difference of the heats of formation between the Co–(N or O) compound and the oxide or nitride of the second elements (ME). Therefore, Co–ME (ME=Al, Si, B, Ge, or Sn) alloy plates were used as targets.

Films were prepared by rf reactive magnetron sputtering with (O_2 or N_2)+Ar gases in a background pressure better than 3×10^{-7} Torr. During sputtering, a static magnetic field of about 100 Oe was applied parallel to the substrate plane in order to induce an in-plane uniaxial anisotropy in the films. The composition of films was mainly measured by Rutherford backscattering spectrometry (RBS) with He^{2+} ions of 2 MeV energy. Film structures were investigated by x-ray diffraction (XRD) and micro-focused high-resolution transmission electron microscopy (HRTEM), with energy dispersive x-ray analysis (EDX) and electron energy loss spectroscopy (EELS). Magnetization vs field was measured with a vibrating-sample magnetometer (VSM). The permeability from 1 to 500 MHz was determined by both figure of eight and parallel line methods.[14] The electrical resistivity was measured by the conventional four-point probe method. As substrate materials, glassy carbon plate, NaCl single-crystal and Corning #7059 glass (0.5 mm in thickness) were used for RBS analysis, TEM observation, and other measurements, respectively.

III. RESULTS AND DISCUSSION

A. Effects of ME elements

In order to find the suitable ME elements to show soft magnetic properties at high frequency, films have been systematically prepared under varying sputtering conditions (mainly, sputtering gas pressure and gas flow ratio of O_2 or N_2 in Ar), and changing target compositions. Figure 1 illustrates the variation in H_c for Co–ME–O films with changing O_2 gas flow ratio in the sputtering gas. It is noted that only the films containing Al show soft magnetic properties in a limited range of O_2 ratio, and H_c of other films is over 10 Oe. In the case of N based films, on the other hand, the films with not only Al but also Si show soft magnetic properties over a wider N concentration range than that of O based films. These results may be related to the microstructure of the films and, consequently, to the difference of the heat of formation between Co–(N or O) and ME–(N or O) compounds.[15]

In what follows, attention is mainly focused on films containing Al, which show soft magnetic properties in both Co–N and Co–O films, and have the largest difference of heat of formation between Co–(N or O) and Al–(N or O) compounds in this series.

B. Microstructure

Figure 2 shows the x-ray diffraction patterns of Co–Al–O films with different oxygen concentrations. The structure of soft magnetic films is basically fcc phase (α-Co), while hcp phase (γ-Co) is observed in Co–ME–O films not showing soft magnetic properties. The width of the diffraction peaks becomes wider and the peak height decreases drastically with increasing O content in films between 20 and 50 at. % O. From the Scherrer formula,[16] the particle size can be estimated from the x-ray diffraction patterns, and the results suggest that a granular structure may be realized in films in this range of O content. With a further increase of oxygen content above 50%, Co–O phase with considerably coarse particle size was observed.

To reveal the structure variation of these films more clearly, we performed TEM observation of Co–(N or O) based films. TEM is an ideal tool for the investigation of the size and shape distributions of the particles in a granular sample. A micrograph of the particle structure of Co–Al–O

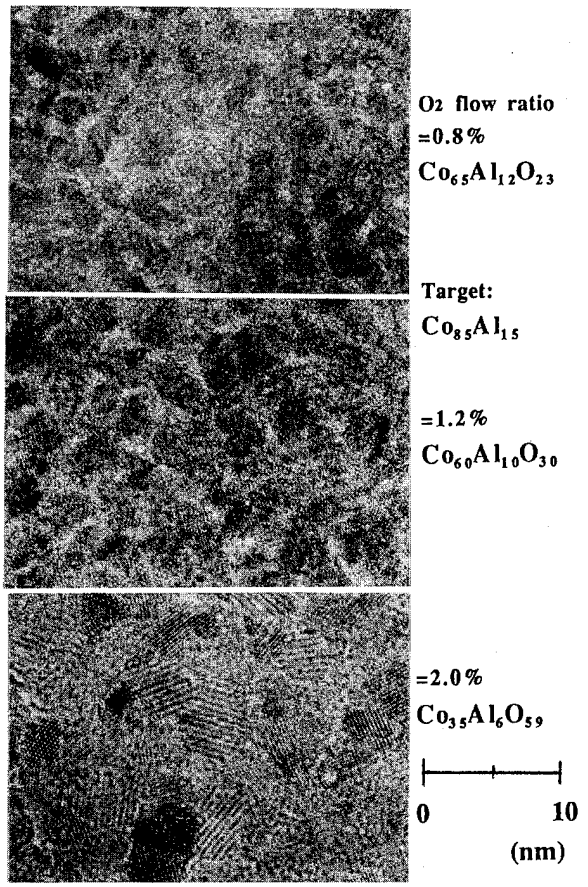


FIG. 3. TEM images of the Co–Al–O granular films containing different amounts of O (target: $Co_{85}Al_{15}$).

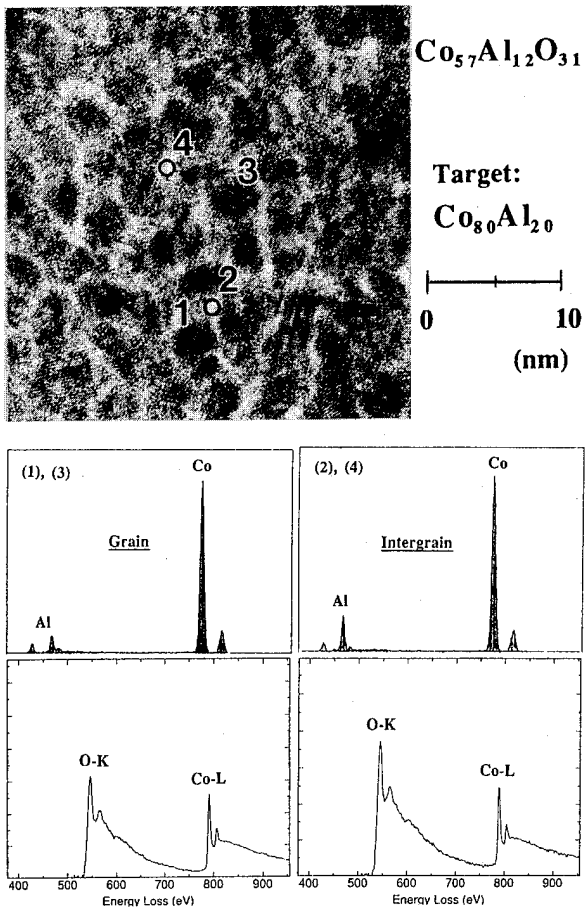


FIG. 4. TEM image and EDX and EELS spectra of grain (1,3) and intergrain (2,4) regions for Co–Al–O granular film.

films deposited from a $Co_{85}Al_{15}$ target is shown in Fig. 3. A clear granular structure is observed in the films with a considerable amount of oxygen (30–50 at. % O). The particles are seen to be of relatively narrow size distribution, to be roughly spherical in shape and to be under 50 Å in diameter. The films containing more than 50 at. % O are seen to consist of an oxide phase with large lattice constants and particle diameters. Electron diffraction ring patterns were observed, and found to be in good agreement with the x-ray diffraction results. The interparticle materials seem to become clearer with increasing concentration ratio of ME/Co in the target, which suggests the existence of ME ceramics in the interparticle regions.

The same tendency of structure is observed in the Co–Al–N films, where the particle–interparticle interface is not as clear as that for Co–O based films, as reported earlier. It is also observed in Co–N based films that the interparticle regions are more or less in the amorphous state, while the particles contain more clearly a microcrystalline phase.[17]

Of considerable interest is the compositional difference between the particle and interparticle materials for these films. The local compositions of several positions marked in Fig. 4 have been investigated by micro-focus EDX and EELS, where the spot diameter is about 2 nm. By comparing the results for the interparticle and particle regions, it is clear that there is considerable compositional difference between them. Specifically, the Al concentration is low in the particle but high in the interparticle region; consequently, the Co concentration is high in the particle, but low in the interparticle region. Moreover, the O concentration is high in the interparticle region and low in the particle. These results contain information from not only the spot but also from a little of its surroundings, because the spot size of the electron beam is large compared to the width of the interparticles regions and electrons are scattered by the surface roughness of the film. Therefore, the actual composition of the particle and interparticle regions are thought to be more clearly separated than shown in Fig. 4; that is, the particles consist mainly of a Co based alloy and the interparticle regions of (O or N) ceramics. Analysis of the local composition of Co–N based films is more difficult than that of Co–O based films, as the interface between the particle and the interparticle regions is not as clear and the size of particles is smaller than that of Co–Al–O films. This analysis has not yet been performed.

These results for the local composition support the previous hypothesis about the preferential oxidation of Al during deposition and the formation of Al–O materials in the interparticle regions. And these hypotheses are also useful when considering the explanation for the high electrical resistivity and magnetic properties of the present films, as will be discussed later.

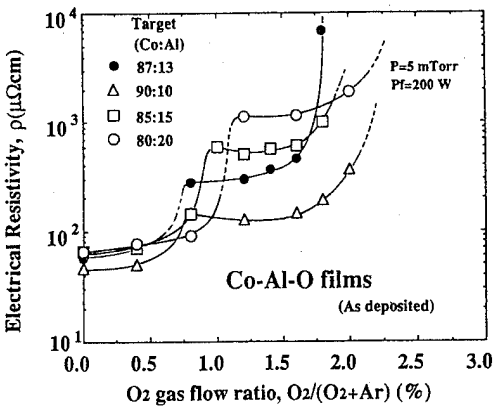


FIG. 5. Relationship between electrical resistivity and O_2 gas flow ratio in sputtering gas for various Co–Al–O films (targets of Co:Al=90:10, 87:13, 85:15, 80:20).

C. Transport properties

We measured the electrical resistivity at room temperature of each series of samples. The result of these measurements is shown in Fig. 5 for Co–Al–O granular films as a function of the flow ratio of O_2 gas. As one expects, there are two steps of the increment of the resistivity versus O_2 ratio, that is, metal–to–nonmetal transitions. The first increment, at lower O content, corresponds approximately to the formation of the granular structure, which is attributed to the preferential oxidation of Al. In well-known granular materials, it is called the percolation threshold,[18] where metal particles become so dilute that they no longer form a conducting path. In the case of this series, the value of ρ is under 10^3 $\mu\Omega$ cm, since the Al concentration of the targets is substantially lower than that of common granular materials where there may be some conducting path because of their much smaller interparticle layer thickness. On the other hand, for Al concentrations higher than 20 at. % in the target, the value of the resistivity for the films is higher than 10^4 $\mu\Omega$ cm. These results also support the existence of Al–O materials in the interparticle regions. The reason for the second rapid increment of ρ may be the oxidation of Co, and the value exceeds 10^8 $\mu\Omega$ cm. Almost the same results are observed in the case of Co–Al–N films. The first increment of ρ is sharper than that of Co–Al–O films,[17] but its magnitude is not as high. The difference in the ρ values between the O and N systems is attributed to the differences in the morphologies and the interparticle materials of the two systems.

To reveal the relationship between ρ and composition, contours of ρ in the ternary Co–Al–O system films are shown in Fig. 6. As one can see, a large ridge of resistivity is found near 17 at. % Al. It is worth noting that the composition of this ridge is almost the same as the Al_2O_3 stoichiometric chemical composition. In Co–Al–N films, a ridge of ρ is observed at the stoichiometoric composition AlN (1:1). These results also support the belief that the interparticle regions mainly consist of Co and Al based ceramics in these granular films, and are in agreement with Ref. 18, which reports that the chemical shift of the Al^{2P} peak is largest when the ρ of films is maximum.

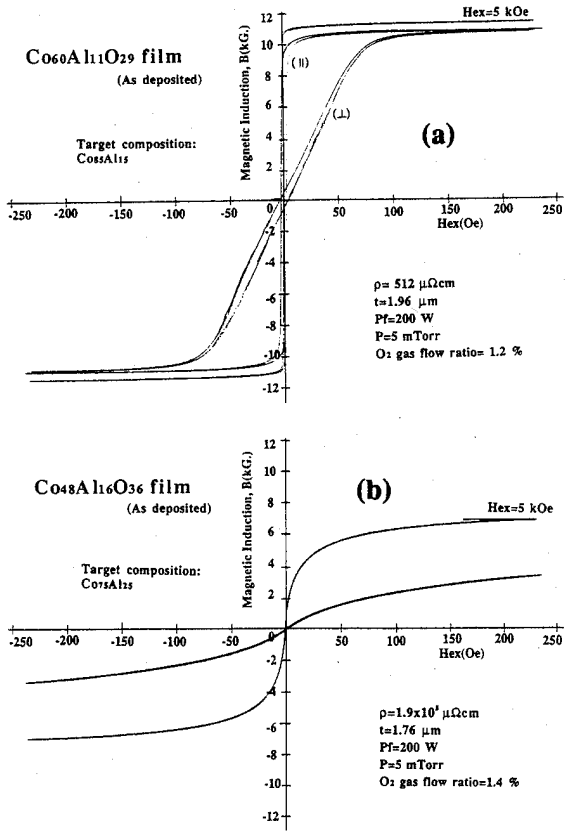


FIG. 6. Contours of the electrical resistivity for Co–Al–O films (dashed line: Al_2O_3 composition).

D. Magnetic properties

Typical magnetic hysteresis loops of Co–Al–O granular films measured at RT are shown in Fig. 7, where Fig. 7(a) is the result using a $Co_{85}Al_{15}$ target, and Fig. 7(b), using $Co_{75}Al_{25}$. Keeping in mind that H_c of a pure Co film is about 50 Oe due to magnetic multidomain structure, we find that the granular Co based film has H_c as low as 5 Oe for $Co_{85}Al_{15}$–O films. The change of H_c with O concentration is similar to the result for ρ shown in Fig. 5. Namely, in films

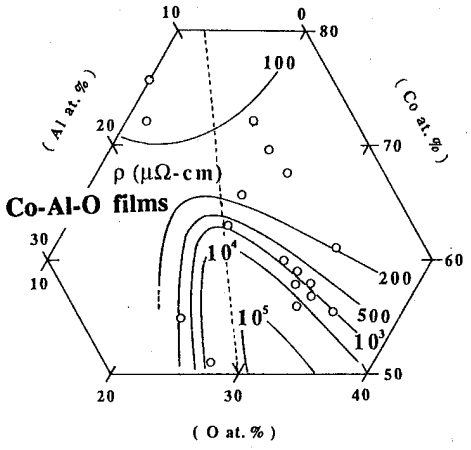


FIG. 7. Magnetization curves of Co–Al–O film in the as-deposited state [targets: (a) $Co_{85}Al_{15}$, (b) $Co_{75}Al_{25}$].

with a small amount of O, where selective oxidation starts to occur, perpendicular anisotropy with large H_c is observed. On the other hand, films which contain a considerable amount of O and have a ridge of ρ, show soft magnetic properties. Such soft magnetic films have been found across a wide range of preparation conditions for Co–Al–N films. The small value of H_c is attributed to (1) the existence of some magnetic interaction among the particles, the percolation effect, and (2) the phase of particles. Approaching the percolation threshold, the formation of a connecting network of small particles starts to occur. Under such conditions, the particles would prefer a magnetic closure-domain structure due to dipolar interaction, and effectively the system behaves as a multidomain structure even though individual particles still remain single domain. As a result, the magnetic properties are similar to soft magnets.[19] Another reason is the phase of the particles. All the films which exhibit soft magnetic properties are composed entirely of fcc phase with (111) preferred orientation, for which the anisotropy energy is reported to be the lowest.[20]

As seen in Fig. 7(a), a larger anisotropy field than 80 Oe is attained. The H_k is considered to be induced by the magnetic field during deposition. However, no difference of morphology perpendicular and parallel to the direction of the applied field is detected by TEM observation or an electrical resistivity measurement. An H_k value of 35 Oe at the most is also observed in Co–Al–N films, and is necessary to improve the frequency response of the permeability, as will be discussed later.

For films prepared from targets with Al concentration above 20 at. %, the magnetization does not saturate even in a field of 5 kOe [see Fig. 7(b)]. In such a film, magnetic granular particles seem to be isolated and protected by the nonmagnetic matrix. These ultrafine particles can be considered as an noninteracting assembly of single domain particles or superparamagnetic particles. Almost all the existing models assume free-standing particles dispersed in a nonbonding medium and predict an H_c higher than 1000 Oe for a moderate value of volume fraction of particles. In fact, the films with H_c more than 1000 Oe have been reported.[21]

In our case, however, the H_c of the granules are extremely small compared with results reported previously. For an assembly of noninteracting single domain particles, the predicted coercivity for coherent rotation is given by $H_c = 0.96\ K/M_s$ for uniaxial anisotropy K. For α-Co this amounts to coercivity $H_c = 2700$ Oe. The low values of coercivity in as-sputtered films are believed to be the results of (1) the small anisotropy energy of fcc phase with (111) preferred orientation, mentioned before, and of (2) particle sizes much smaller than the single domain particle size, which is estimated to be 53 nm, leading to incoherent magnetization processes.

There are considerable differences of B_s and H_k between soft magnetic Co–N and Co–O based films. The B_s and H_k of Co–N based films are about 8 kG and 30 Oe, respectively. On the other hand, B_s and H_k of Co–O based films are 10 kG and 80 Oe, respectively. The difference in B_s is attributed to the difference of the ratio of Co/Al between Co–N and Co–O based alloys, and the difference of heat of formation between Al–N and Al–O compounds. The reason for the difference in H_k may be due the difference of morphology of particles. Further investigation is required to give a full account of the phenomenon.

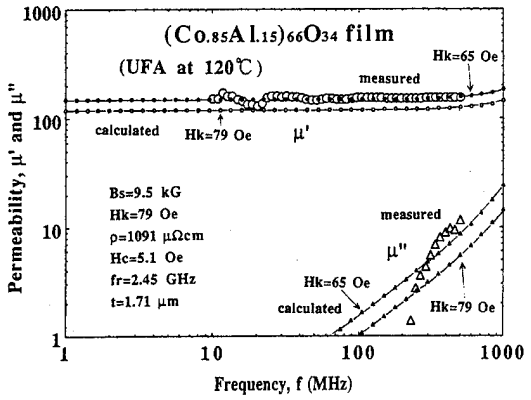


FIG. 8. Measured and calculated frequency characteristics of permeability for Co–Al–O granular films in the as-deposited state.

According to calculations based on the Landau–Lifshitz equation, as mentioned above, the frequency characteristics of the permeability in magnetic films are known to be improved by increases not only in ρ but also in the magnitudes of B_s and H_k. Large values of ρ, B_s, and H_k in soft magnetic Co–(Si,Al)–N and Co–Al–O films are advantageous to the μ-f characteristics. Figure 8 is a typical example of the μ-f characteristics of as-deposited $Co_{85}Al_{15}$–O films. Despite the film thickness being nearly 2 μm, the real part (μ') of permeability is flat up to 500 MHz and almost consistent with the calculations based on the experimental values for M_s, H_k, ρ, and d. However, the experimental result of the imaginary part (μ'') near 500 MHz is in poor agreement with the calculated one. One reason may be that the calculation neglects the effect of local eddy currents, which occur due to impedance associated with capacitance between metallic particles separated by insulating interparticles regions. An improvement of the theory, taking into account such effects, is now in progress. Another reason is the magnitude of the damping factor. In the case of the films shown in Fig. 7(b), their μ-f response is extremely poor. Also giant magnetoresistance characteristics have been observed;[22] however, they will not be discussed further in this article.

Co–O based films are advantageous in having high B_s and ρ; however, they show soft magnetic properties in a more limited composition range, compared with the results of Co–N based films. Consequently, the addition of other elements has been investigated for improving the soft magnetic properties of Co–O based films. Only Pd and Ni were found to improve the Co–O films, by causing them to be magnetically soft and also enhancing the anisotropy field.[23] Figure 9 shows typical magnetization hysteresis loops of as-deposited Co–Si–Pd–O films. Co–Si–O films do not show soft magnetic properties, as described above. Fairly soft magnetic properties and also a large H_k are observed in this system.

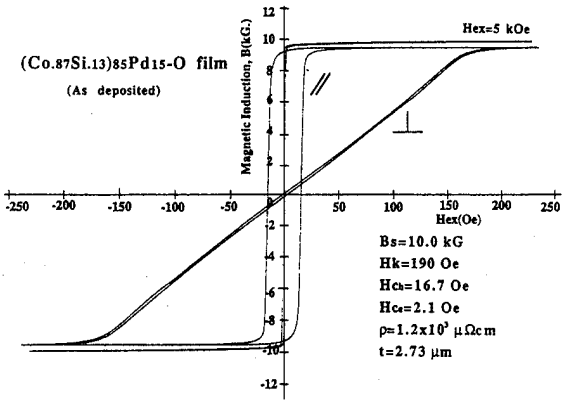


FIG. 9. Magnetic hysteresis loop of Co–Si–Pd–O granular films in the as-deposited state.

Another effective method for improving μ-f response is heat treatment. Recently, the μ-f characteristics at higher frequencies for Co–N based films were found to be improved by annealing at about 250 °C in a uniaxial magnetic field (UFA).[24] Annealing in magnetic field is also effective for Co–Pd–O based films with large H_k. The value of H_k decreases monotonically with increasing annealing temperature during rotational field annealing (RFA), and is almost O Oe near 250 °C. Therefore, films with any magnitude of H_k can be obtained by the combined use of RFA and UFA.

IV. CONCLUSIONS

We can point out that granular alloys with high electrical resistivities, saturation magnetizations, and anisotropy field can be made by rf reactive magnetron sputtering of Co–(Al or Si)–N and Co–Al–O films. Control of the metal volume fraction of Co/(Al or Si), the difference in the heat of formation between Co–(O or N) and Si–N, Al–(O or N) compounds, and the presence of fcc Co granules are essential for making such films. They represent a new type of high-frequency thin-film magnetic material, which may operate in the high-frequency range beyond 100 MHz with high μ' and low μ''. They are promising thin-film materials for applications such as high-frequency thin transformers and inductors, as well as thin-film heads for high-density magnetic recording.

ACKNOWLEDGMENTS

The authors would like to thank S. Yamaguchi, S. Nagata, and K. Takahiro of the Institute for Material Research, Tohoku University, for RBS analysis, and N. S. Kazama and E. Suzuki of Sendai Lab., YKK Co., for TEM observations.

[1] A. Hosono and Y. Shimada, J. Magn. Soc. Jpn. **12**, 295 (1988).
[2] N. Hasegawa and M. Saito, IECE Tech. Report No. MR89-121989, 19-- (unpublished).
[3] K. Terunuma *et al.*, J. Magn. Soc. Jpn. **14**, 257 (1990).
[4] S. Suwabe, Y. Yoshizawa, and T. Nishiyama, Digest of Intermag. Conf. BA-09, 1990 (unpublished).
[5] H. Fujimori *et al.*, J. Appl. Phys. **55**, 1769 (1984).
[6] H. Karamon, J. Appl. Phys. **63**, 4306 (1988).
[7] H. Matsuyama, H. Eguchi, and H. Karamon, J. Appl. Phys. **69**, 5123 (1990).
[8] E. Sugawara, F. Matsumoto, H. Fujumori, and T. Masumoto, J. Magn. Soc. Jpn. **16**, 247 (1992).
[9] M. Hayashide *et al.*, J. Magn. Soc. Jpn. **15**, 379 (1991).
[10] S. Ohnuma *et al.*, J. Magn. Soc. Jpn. **17**, 391 (1993).
[11] S. Ohnuma and T. Masumoto, *Rapidly Quenched Metals III*, edited by B. Cantor (The Metals Society, London, 1978), p. 197.
[12] H. Fujimori and T. Masumoto, Trans. Jpn. Inst. Met. **17**, 175 (1976).
[13] R. W. Cohen and B. Abeles, Phys. Rev. **168**, 444 (1967); L. G. Feinstein and R. D. Hutteman, Thin Solid Films **20**, 103 (1974); E. M. Logothetis *et al.*, J. Appl. Phys. **60**, 2548 (1986).
[14] T. Kimura *et al.*, J. Magn. Soc. Jpn. **17**, 497 (1993).
[15] J. F. Elliott and M. Gleiser, *Thermochemistry for Steelmaking* (Addison-Wesley, Reading, MA, 1960), Vol. 1.
[16] B. D. Cullity, *Elements of X-ray Diffraction*, 2nd ed. (Addison-Wesley, Reading, MA, 1978) p. 102.
[17] S. Ohnuma *et al.*, J. Magn. Soc. Jpn. **18**, 303 (1994).
[18] B. Abeles, H. I. Pinch, and J. J. Gittleman, Phys. Rev. Lett. **35**, 247 (1975).
[19] H. Hoffmann, J. Appl. Phys. **35**, 1790 (1964); G. Herzer, IEEE Trans. Magn. **MAG-25** 3327 (1989).
[20] A. Hosono and Y. Shimada, J. Appl. Phys. **67**, 6981 (1990).
[21] G. Xiao and C. L. Chien, Appl. Phys. Lett. **51**, 1280 (1987).
[22] H. Fujimori, S. Mitani, and S. Ohnuma, Mater. Sci. Eng. B **31**, 219 (1995).
[23] S. Furukawa *et al.*, Abstracts of Jpn. Inst. Met. **113**, 264 (1993).
[24] S. Ohnuma, S. Mitani, H. Fujimori, and T. Masumoto, J. Magn. Soc. Jpn. **19**, 425 (1995).

Published without author corrections

Giant magnetoimpedance effect in soft and ultrasoft magnetic fibers

P. Ciureanu
Engineering Physics Department, Ecole Polytechnique, P.O. Box 6079, Sta. Centre-ville, Montreal PQ H3C 3A7, Canada

P. Rudkowski and G. Rudkowska
Physics Department, McGill University, 3600 University, Montreal PQ H3A 2T8, Canada

D. Menard, M. Britel, and J. F. Currie
Engineering Physics Department, Ecole Polytechnique, P.O. Box 6079, Sta. Centre-ville, Montreal PQ H3C 3A7, Canada

J. O. Ström-Olsen
Physics Department, McGill University, 3600 University, Montreal PQ H3A 2T8, Canada

A. Yelon
Engineering Physics Department, Ecole Polytechnique, P.O. Box 6079, Sta. Centre-ville, Montreal PQ H3C 3A7, Canada

Soft NiFe-Permalloy fibers and ultrasoft NiCo-based amorphous fibers, having a circular cross section with 30–40 μm in diameter, have been cast by melt extraction. The fibers have been driven by a sinusoidal current with 20 mA_{pp} constant amplitude and frequencies from 0.1 to 100 MHz. Both longitudinal and transverse giant magnetoimpedance effects have been observed in these fibers. The longitudinal GMI effect at 30 MHz was 60% in ultrasoft $(NiCo)_{70}FeSiBMn$ fibers for a saturating field of about 7 kA/m. The same effect was found at 10 MHz frequency for Permalloy fibers for a larger saturating field (20 kA/m). The transverse GMI effect was smaller (≈35% for NiCo and ≈20% for NiFe), and showed a maximum at low frequency (3 MHz). The magnetic field responses of the fibers are quadratic. An inverse effect of 10%–30% was observed for both types of fibers in longitudinal as well as in transverse field responses at high current frequency and low field strength. All of the observed effects could prove to be very useful for a new generation of high-sensitivity magnetic field sensors. © *1996 American Institute of Physics.*
[S0021-8979(96)28908-3]

Recent reports of large magnetoinductive and magnetoimpedance effects in Unitika amorphous wires[1–3] have prompted us to investigate whether soft and ultrasoft magnetic fibers show similar effects. These fibers have been obtained through melt extraction, a newly improved casting method,[4] which uses a rotating wheel to extract solid fibers directly from the melt. The heat is removed along the contact line between the wheel and the melt, thus promoting frozen tensile stresses in the fiber, directed from the contact line towards the opposite surface, which is the last to solidify. This stress distribution produces a uniaxial anisotropy with a domain structure consisting mainly of domains perpendicular to the fiber length, and of longitudinal and, possibly, circumferential closure domains at the fiber surface. A simple model regards these fibers as assemblies of thin films, having in-plane anisotropy and fanning around the contact line. (A more exact geometrical description would be "thin wedges".) Each film contains the contact line and all the fiber columns making the same angle to a reference horizontal axis.[5] The anisotropy easy axis is parallel to the fiber for negative magnetostriction materials, and perpendicular for positive magnetostriction ones. Except for thin films, fibers are the magnetic elements with the lowest cross-sectional area, which makes them very suitable for sensing purposes. Radial solidification with respect to the extracting wheel, causing transverse stress and uniaxial anisotropy in the fiber, is the main feature of all fibers cast by melt extraction.

The domain structure of negative magnetostriction Co-rich wires, showing an inner core with longitudinal domains and an outer shell with ring-like domains,[3] is very different from the transverse domain distribution in NiCo and NiFe fibers. Their as-cast diameter is also different (125 μm wires vs 30–40 μm fibers). However, we measured almost identical GMI responses in near-zero, as well as in slightly negative and positive magnetostriction fibers.

Soft Permalloy fibers, having compositions of 80%wtNi/20%wtFe, 81Ni/19Fe, and 82Ni/18Fe, and positive, near-zero and negative magnetostriction,[6] as well as ultrasoft amorphous 45Ni25Co6Fe9Si13B2Mn fibers, have been prepared and measured. The resistivity of NiFe fibers was about 30 $\mu\Omega$cm, while NiCo fibers showed a resistivity of 150 $\mu\Omega$cm. Samples of 80/20 Permalloy fibers have been vacuum annealed for several hours at 960 °C in order to relax the quenched-in stresses. Their resistivity increased to 60 $\mu\Omega$cm and the fiber showed voids and unhomogeneities. All fibers were 20 mm long, quite homogeneous in properties and 30–40 μm in diameter. The measuring set-up consisted of a rf signal generator driving the fiber in series with a low value resistor. The output level of the generator was adjusted at each frequency so as to keep constant the voltage drop across the resistor. The current through the fiber was thus maintained at 20 mA_{pp} in amplitude. The GMI response is defined as:[6]

$$\Delta Z/Z \approx \Delta U/U = [U_f(H_{sat}) - U_f(H=0)]/U_f(H=0),$$

 0021-8979/96/79(8)/5136/3/$10.00 © 1996 American Institute of Physics

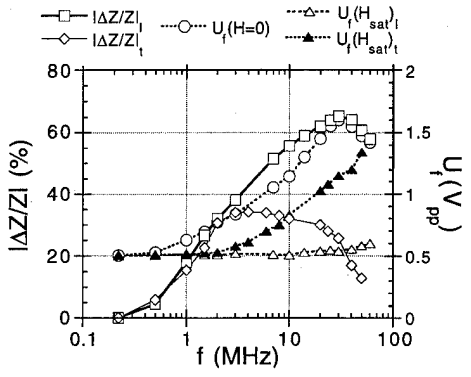


FIG. 1. The longitudinal and transverse GMI effects and the voltage drops across the amorphous NiCo fibers in zero and saturating fields vs the frequency of the driving current.

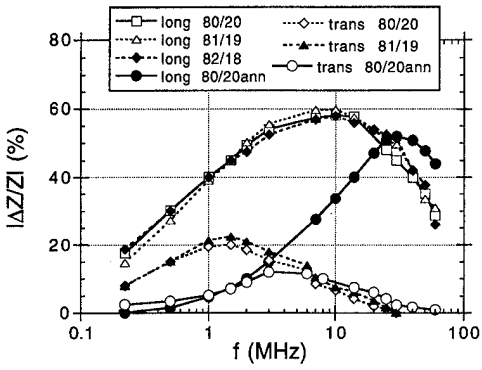


FIG. 3. The longitudinal and transverse GMI effects of several Permalloy fibers with different NiFe composition versus the frequency of the driving current.

where H_{sat} is the longitudinal or transverse saturating field, applied using a pair of Helmholtz coils, and U_f is the voltage drop across the fiber.

Both longitudinal ($|\Delta Z/Z|_l$) and transverse ($|\Delta Z/Z|_t$) GMI effects are negative. The frequency behavior of these effects and of U_f in zero and saturating fields for NiCo amorphous fibers are shown in Fig. 1. The impedance of the fiber in zero field increases with increasing frequency up to a maximum at 30 MHz, then drops at higher frequency. When a 7 kA/m saturating longitudinal field is applied, U_f becomes almost frequency independent, as for a copper fiber. In transverse fields, the voltage drop across the fiber in "saturating" fields of about 20–30 kA/m increases with frequency. The maximum in $|\Delta Z/Z|_l$ is larger than 60% at 30 MHz, while the maximum in $|\Delta Z/Z|_t$ is 35% at 3 MHz, due to the different frequency behavior of $U_f(H_{sat})$. Figure 2 shows the fiber responses as functions of the strength of longitudinal and transverse fields. $|\Delta Z/Z|_l$ has larger sensitivity and saturates at higher field for higher frequency. The field variation of $|\Delta Z/Z|_t$ is not as steep, and shows a low field inverse effect, which reaches 10% at 1.5 MHz.

The GMI effects in Permalloy fibers are also negative. The longitudinal effect shows a maximum of 60% at 10 MHz, while the transverse effect has a maximum of about 20% at 1.5 MHz (Fig. 3). It is likely that we have not saturated the fiber in the transverse direction, where a maximum demagnetization occurs, using the Helmholtz coils. The GMI effect is the same for all three compositions of the NiFe alloy, even if the magnetostriction changes from positive to negative. The behavior of Permalloy fibers is almost identical to that of NiCo amorphous fibers, the only difference being the displacement toward lower frequency of the maximum GMI effect. In fact, the 20% value of $|\Delta Z/Z|_l$ appears at 1 MHz in case of amorphous fibers, and at only 220 kHz in case of Permalloy fibers. The latter case is more favorable when using fibers as magnetic field sensors.

Unlike the NiCo fibers, the NiFe fibers at saturation do not show a constant voltage drop as a function of frequency (Fig. 4). Both $U_f(H_{sat})$ and $U_f(H=0)$ increase with frequency, and the frequency variation of $\Delta Z/Z$ is determined by their different rates of variation. The increase of $U_f(f)$ with frequency was previously reported for Unitika amorphous wires.[3] In our case, this increase may be simply caused by the unsaturated state of the fiber. Figures 3 and 4 also show the frequency behavior of the GMI effects and of the voltage drops for annealed Permalloy fibers, which are assumed to be stress free. The maximum in $|\Delta Z/Z|_l$ is only slightly lower than those of as-cast fibers. However, the maximum in $|\Delta Z/Z|_t$ is half of the original value and both maxima are displaced toward higher frequency. The variation

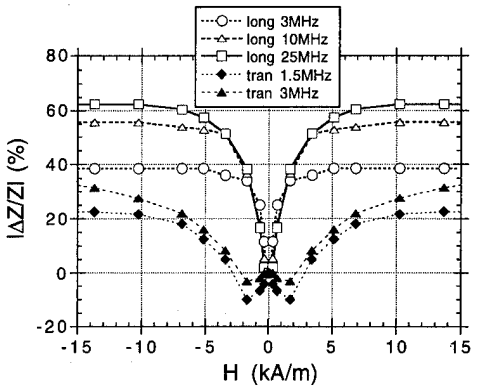


FIG. 2. The longitudinal and transverse magnetic field responses of the amorphous NiCo fibers for different frequencies of the driving current.

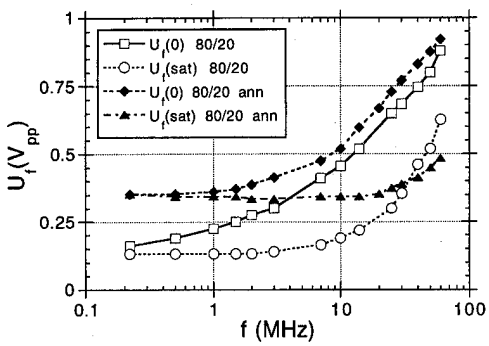


FIG. 4. The voltage drops across the as-cast and annealed 80Ni/20Fe Permalloy fibers in zero and saturating fields vs the frequency of the driving current.

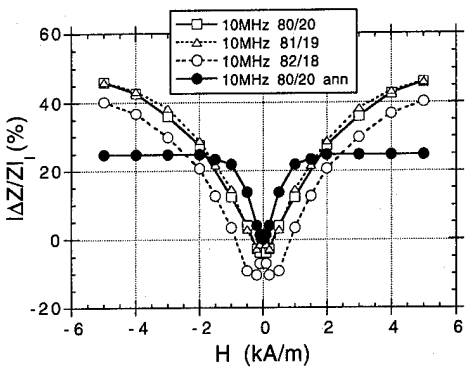


FIG. 5. The longitudinal magnetic field responses of several Permalloy fibers with different NiFe composition.

in voltage drops remains unaltered, and only the magnitude of U_f is larger due to the increase in fiber resistivity after annealing.

The longitudinal GMI responses of as-cast Permalloy fibers show that the saturating field is considerably higher than that of amorphous fibers (Fig. 5). However, the annealed 80Ni/20Fe fibers seem to be softer than the as-cast fibers with the same composition. The inverse effect is present for all compositions, being the largest for 82Ni/18Fe. The fact that this effect disappears from the response of the stress-free annealed fiber, suggests that the inverse effect may be related to the magnitude of the quenched-in stresses. The transverse GMI responses of Permalloy fibers show little sensitivity and quite large saturating fields (50 kA/m).

A surprising similarity in the magnitude and frequency behavior of longitudinal and transverse GMI effects was found for ultra soft NiCo amorphous fibers and for soft NiFe fibers with slightly negative, near-zero and positive magnetostriction. The longitudinal effect is quite similar to that reported for Unitika amorphous wires, even if fibers are very different from wires in terms of geometry, composition, and quenched-in stress distribution. It seems that GMI is a general effect, not limited to a very particular type of magnetic sample. Whatever the origin of GMI, soft and ultra soft magnetic fibers have the potential to be used as sensing elements for a new generation of magnetic field sensors. Depending on the application, the sensitivity of the fiber can be changed by adjusting the frequency of the driving current such as to obtain optimized sensing devices.

This work was supported by the National Sciences and Engineering Research Council of Canada.

[1] K. V. Rao, F. B. Humphrey, and J. L. Costa-Krämer, J. Appl. Phys. **76**, 6204 (1994).
[2] R. S. Beach and A. E. Berkowitz, J. Appl. Phys. **76**, 6209 (1994).
[3] L. V. Panina, K. Mohri, K. Bushida, and M. Noda, J. Appl. Phys. **76**, 6198 (1994).
[4] P. Rudkowski and J. O. Ström-Olsen, U. S. Patent 5,003,291, March 26, 1991.
[5] P. Ciureanu, P. Rudkowski, G. Rudkowska, and J. O. Ström-Olsen, IEEE Trans. Magn. **29**, 2251 (1993).
[6] P. Rudkowski, P. Ciureanu, G. Rudkowska, M. Britel, D. Menard, J. O. Ström-Olsen, and A. Yelon, *The 12th Conference on Soft Magnetic Materials (SMM12)*, Cracow, Sept. 1995, to be published in J. Magn. Magn. Mater.

Giant magneto-impedance effects in Metglas 2705M

R. L. Sommer[a] and C. L. Chien
Department of Physics and Astronomy, The Johns Hopkins University, Baltimore, Maryland 21218

Giant magneto-impedance (GMI) results for Metglas 2705M have been studied in two measuring geometries in several field annealed samples. A rich variety of peak features in GMI, all within a small field range, have been observed. The various features in the GMI are discussed in terms of magnetic susceptibility and microstructural properties of the amorphous ribbon. © *1996 American Institute of Physics.* [S0021-8979(96)29008-8]

The observation of giant magneto-impedance (GMI) in amorphous alloys with negligible magnetostriction[1–3] has attracted a great deal of attention for fundamental and technological interest. The origin of the effect appears to be the field dependence of the effective differential susceptibility of the soft amorphous materials. The GMI effect is better understood in the case of wires,[2] but many aspects remain to be unraveled in the case of ribbons. Very recently,[4] a rich variety of peak features in GMI within a small field range have been observed in suitably annealed amorphous samples of CoFeSiB alloy. The aspects of annealing and measuring geometries in the GMI effects in commercial amorphous ribbons remain to be resolved. In this work, the GMI effects in commercial Metglas 2705M (nominal composition $Co_{69}Fe_4Ni_1Mo_2B_{12}Si_{12}$) ribbons have been studied in two geometries (longitudinal and transverse) for several field-annealed samples with frequencies up to 100 kHz and currents in the range $0.1<I<20$ mA. The rich variety of GMI spectra observed can be accounted for by using a simple model.

The samples were cut from the middle sections of a commercial Metglas 2705M ribbon (nominal thickness of 20 μm and resistivity of about 150 $\mu\Omega$ cm) with dimensions of about 10 mm×1 mm. The leads were made by using In solder and the GMI was detected via a two-channel lock-in amplifier. For the four probe measurements, a low-noise current source provided sinusoidal currents between 0.1 and 20 mA. The probe current frequency range used in these experiments was $0.1\ \text{Hz}\leqslant f\leqslant 100$ kHz. During all data acquisition, the quasi-static dc field was swept between −150 and +150 Oe and back, although only the data of the increasing field part are displayed. The GMI results are expressed as $\Delta Z/Z_{dc}=[Z(H)-Z(5\ \text{kOe})]/R_{dc}$, $\Delta R/R_{dc}=[R(H)-R(5\ \text{kOe})]/R_{dc}$, or $\Delta X/R_{dc}=[X(H)-X(5\ \text{kOe})]/R_{dc}$, where Z is the impedance, R the resistance, X the reactance, and R_{dc} the dc resistance. Similar to those in Ref. 4, the samples were subjected to four different annealing geometries: as-cast (AC); annealed in zero field (ZFA); longitudinally annealed (LA) with a 2 kOe field oriented parallel to the long direction of the sample; transversely annealed (TA) with a transverse field of 2 kOe. All annealing took place at $T_A=300$ °C for 15 min in an Ar atmosphere. Two geometries for the measurement were adopted. In the longitudinal magneto-impedance (LMI) measurements, the probe current and the external dc field were applied along the long direction of the sample. In the transverse magneto-impedance (TMI) measurements, the probe current was parallel to the long direction of the sample but the field was applied perpendicular to the current and remained in the ribbon plane.

In Fig. 1, the LMI measurements at frequency $f=100$ kHz under a 20 mA peak value for the probe current for the samples subjected to four different field annealing geometries are shown. The as-cast sample exhibits a 15% MI effect [see Fig. 1(a)] and a width of about 10 Oe with little structure. Annealing in zero field [see Fig. 1(b)] decreases somewhat the effect size and the width. Substantial changes occur after field annealing, which causes significantly larger widths of about 30 Oe. The LA sample [see Fig. 1(c)] shows a much smaller effect, whereas the TA sample [see Fig. 1(d)] gives the largest effect of the four samples with a more interesting structure consisting of four peaks. The intricate peak structure of the TA sample is better displayed in the insets of Fig. 2 for both reactance (ΔX) and resistance (ΔR), where the two shoulder peaks (a,d) and the two central peaks (b,c) are labeled.

In Fig. 2, the magnitudes of the four peaks of ΔR and ΔX are plotted as a function of frequency. At the same frequency, the effect size of ΔX is larger than that of ΔR. Between the shoulder and the central peaks, there is a very different frequency dependence in both resistance and reactance, indicating that they are of different origins. Depending on the relative size of the sample thickness (t) and the skin depth (δ_m), a frequency dependence of approximately f or

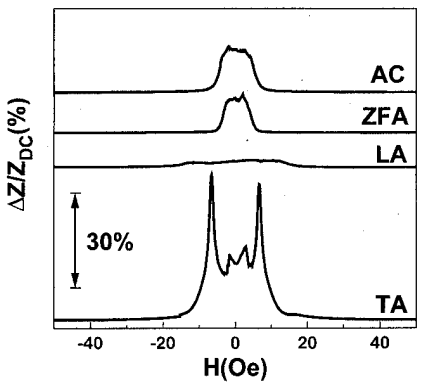


FIG. 1. Longitudinal magneto-impedance (LMI) at 100 kHz and 20 mA of Metglas 2705M samples subjected to different annealing conditions: as-cast (AC), annealed at 300 °C in zero field (ZFA), longitudinal field (LA) of 2 kOe, and transverse field (TA) of 2 kOe.

[a]Permanent address: Depto. de Física, UFSM, 97119-900 Santa Maria RS, Brasil.

 0021-8979/96/79(8)/5139/3/$10.00 © 1996 American Institute of Physics

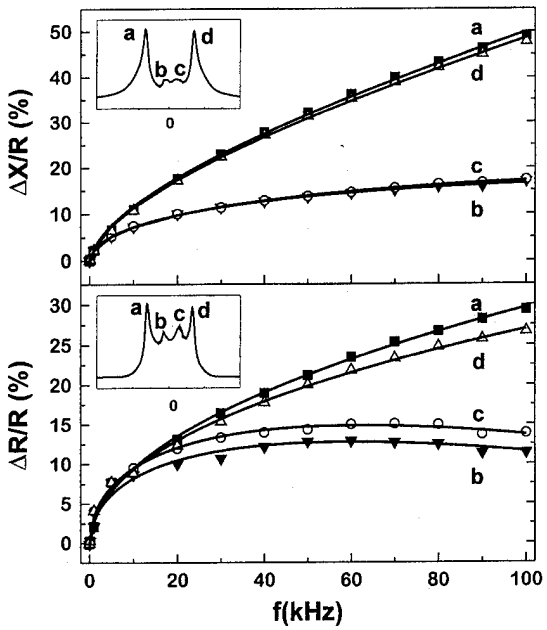


FIG. 2. Intensities of various peaks (a, b, c, and d) vs frequency in longitudinal magneto-impedance (LMI) of a Metglas 2705M sample annealed in a transverse field. The insets show the reactance (X) and resistance (R) vs H curves.

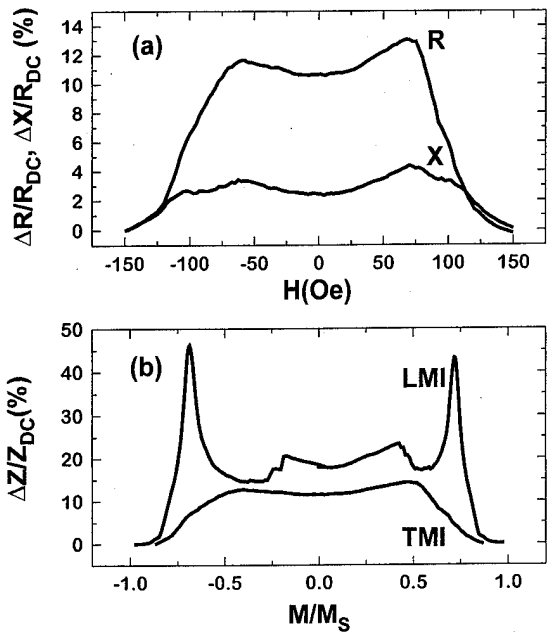


FIG. 3. (a) Transverse magneto-impedance (TMI) at 100 kHz and 20 mA of a Metglas 2705M sample annealed in a transverse field. The $\Delta R/R$ and $\Delta X/R$ results are shown. (b) LMI and TMI as a function of the reduced magnetization (M/M_s).

$f^{1/2}$ may be realized.[2] Since δ_m depends on the permeability value, which is not known beforehand, the applicable regime cannot be ascertained *a priori*. We find the experimental results can be well described by using $pf + qf^{1/2}$ with two parameters p and q. In most frequency ranges, particularly at high frequencies, the $f^{\frac{1}{2}}$dependence dominates as it should. However, the p and q values needed to fit shoulder and center peaks are different.

In Fig. 3(a), the transverse magneto-impedance measurements (TMI) for the TA sample are shown. TMI is a new measuring geometry; previous studies failed to have observed a substantial effect due to the lack of higher field measurements.[1,3] Comparing the results of TMI and LMI of the TA sample, the resolution of the TMI is clearly inferior; the TMI exhibits a broad plateau without discernible peak structure. It should be noted that the principal difference between LMI and TMI is that the width of TMI is about ten times *larger* than that for LMI.

The observed results of different measuring geometries (LMI and TMI) and different field annealing can be understood by recognizing the appropriate components of the susceptibility, the roles of anisotropy and field annealing, and the demagnetizing factor due to the ribbon sample shape. First of all, since the probe current is always along the ribbon direction, the field H_{ac} generated by the probe current is always perpendicular to the ribbon direction. Consequently, in the *longitudinal* GMI (LMI), where H is along the ribbon direction, it is the *transverse* susceptibility (χ_T) that contributes. In the *transverse* GMI (TMI), where H is perpendicular to the ribbon direction, it is the *longitudinal* susceptibility (χ_L) that contributes.

For amorphous alloys with nearly zero magnetostriction, it is well known that field annealing can induce an anisotropy. This is due to the random nature of the magnetic anisotropy in the as-cast materials and the absence of appreciable magnetoelastic contribution to the effective anisotropy. Annealing with the longitudinal field induces an anisotropy in the longitudinal direction, and transverse annealing induces an transverse anisotropy. It is also well known that magnetic annealing greatly enhances the permeability, which is the underlying mechanism for the GMI effects.

We first discuss the LMI results, where the H field is applied along the ribbon direction. In the as-cast sample, the absence of peak structure suggests negligible anisotropy, which is somewhat different from those found in other amorphous materials.[5] As a result, there are only small differences between the LMI spectra of the as-cast and the zero field annealed samples. In the LA sample, the average magnetization and the induced anisotropy axis are along the ribbon direction, which is perpendicular to H_{ac}. The small magnitude of H_{ac} is incapable of appreciably altering the magnetization along the ribbon direction, hence a very small effect, as shown in Fig. 1(c). In the TA sample, the easy axis, described by the effective anisotropy field H_K, is perpendicular to the ribbon direction and parallel to the H_{ac} produced by the probe current. This results in a much larger effect, as shown in Figs. 1(d) and 2. The peak structure (labeled a, b, c, and d in the inset of Fig. 2) is due to two different magnetization processes excited by the probe current. The shoulder peaks, or the outer peaks (labeled a and d in the inset of Fig. 2), located at ± 6.5 Oe, as shown in Fig. 1(d), are caused by the rotation of the magnetization against the anisotropy field. The peak location of 6.5 Oe marks the value of $H_i = H - 4\pi D_L M \approx H_K$, and corresponds to the peak observed in the transverse differential susceptibility.[6,7] The cen-

tral peaks, or the inner peaks (labeled b and c in Fig. 2), as shown in Fig. 1(d), are probably due to the movement of a transverse domain wall (DW) structure. These domain walls would move under the combined action of H_{ac} and H fields for $H<H_K$. Eventually a coercive field for such a domain wall motion can be defined where the maximum in the susceptibility associated with the DW motion occurs.

For the TMI results, the relevant susceptibility now is the longitudinal susceptibility (χ_L). However, the demagnetization effects, which are negligible in the LMI case, now become important. As a result, the relevant longitudinal susceptibility has an *apparent* value of

$$\chi_L^{\text{app}}=\frac{\chi_L}{1+4\pi\cdot D_T\chi_L},$$

which is χ_L corrected for demagnetization effects and D_T is the demagnetization factor in the transverse direction. Because of the large value of χ_L, hence $4\pi\cdot D_T\gg 1$ and the apparent susceptibility is given by $\chi_L^{\text{app}}\approx 1/4\pi\cdot D_T$, i.e., the longitudinal susceptibility is *clamped* by the demagnetization factor, not reflecting its own field dependence. Consequently, the TMI results exhibit a plateau with no resolvable peak structure, as shown in Fig. 3(a). Furthermore, by the same token, the internal field $H_i=H-4\pi\cdot D_T M$ is also very different from the applied field H. Hence, the TMI effects occur over a much wider field values than those of LMI, as shown in Fig. 3(a).

For the reasons given above, one cannot compare the TMI and LMI within the same field range, which disregards the effects of the demagnetization factor. Instead, the TMI and LMI results should be compared at the same magnetization value. This is shown in Fig. 3(b), where we show the LMI and TMI results at 100 kHz and 20 mA. While the LMI result shows the intricate peak structure, the TMI result is essentially featureless, because the relevant susceptibility has been limited by the demagnetization factor. The main GMI effect, in both LMI and TMI, occurs in *different* field ranges but in the *same* magnetization range. Under a sufficiently large external field, which saturates the magnetization, there is no GMI effect. The "clamping" effect of the demagnetization factor on the TMI is clearly shown in Fig. 3(b). This comparison also vividly illustrates that the LMI in the TA sample provides most information concerning the GMI effects.

In Fig. 4, we show the LMI vs H curves for the TA sample at selected frequencies from 1 Hz to 100 kHz. At very low frequencies [e.g., at 1 Hz as shown in Fig. 4(a)], one essentially measures the dc resistance curve. For this ferromagnetic alloy, there is small (0.02%) and negative anisotropic magnetoresistance (AMR) as expected. Even at a low frequency of 100 Hz [Fig. 4(b)], the larger and positive GMI effect (with a double-peak structure) has overridden the smaller and negative AMR effect. When the frequency is further increased, the magnitude of the GMI effects increases, and the structure becomes more resolved. For intermediate frequencies [e.g., Figs. 4(b) and 4(c)], the inner peaks are larger than the outer ones. For higher frequencies, the outer peaks clearly dominate. One also observes that as the frequency is increased, the locations of the peaks shift to higher values. This is a general property of the transverse susceptibility.[7] The effect of the magnitude of the probe current on the LMI at 100 kHz has also been studied. It is observed that the inner peaks are better defined only when the probe current has exceeded 5 mA, beyond which the spectra appear to be essentially independent of the probe current.

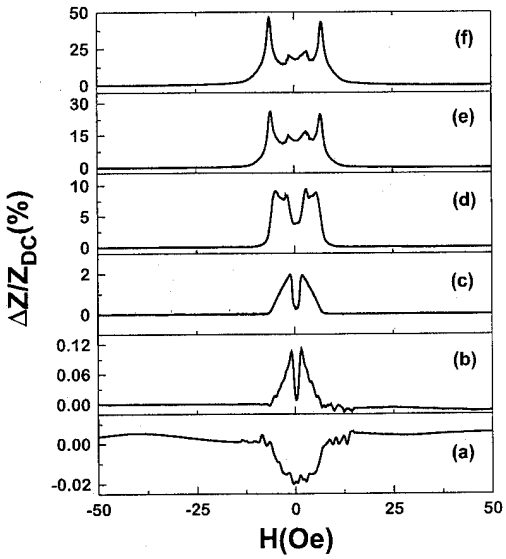


FIG. 4. Longitudinal magneto-impedance (LMI) at 20 mA of a Metglas 2705M sample annealed in a transverse field and measured at various frequencies: (a) 1 Hz, (b) 100 Hz, (c) 1 kHz, (d) 10 kHz, (e) 25 kHz, and (f) 100 kHz.

In summary, a rich variety of GMI results have been observed in Metglas 2705M, a commercially available amorphous ribbon. We show that transverse field annealing is crucial in bringing out the detailed features of the GMI spectra. The TMI is hampered by the demagnetization effects, whereas the LMI reveals the intricate peak structure. We show that rotation against the anisotropy field and domain wall motion are the two main factors controlling the GMI effects.

The authors thank Dr. R. Hasegawa from Allied Corp. for kindly supplying the samples. This work has been supported by ONR Grant No. N00014-91-J-1633 and CNPq of Brazil.

[1] F. L. A. Machado, C. S. Martins, and S. M. Rezende, Phys. Rev. B **51**, 3926 (1995).
[2] L. V. Panina, K. Mohri, T. Uchiyama, and M. Noda, IEEE Trans. Magn. **MAG-31**, 12 (1995).
[3] R. S. Beach and A. E. Berkowitz, Appl. Phys. Lett. **64**, 3652 (1994).
[4] R. L. Sommer and C. L. Chien, Appl. Phys. Lett. **67**, 857 (1995).
[5] R. L. Sommer and C. L. Chien, these proceedings.
[6] H. Hoffmann, Phys. Status Solidi **33**, 175 (1969).
[7] W. D. Doyle, X. He, and P. Tang, J. Appl. Phys. **73**, 5995 (1993).

Barkhausen noise in FeCoB amorphous alloys (abstract)

G. Durin and G. Bertotti
IEN Galileo Ferraris, GNSM and INFM, C.so Massimo d'Azeglio 42, 10125 Torino, Italy

In recent years, the Barkhausen effect has been indicated as a promising tool to investigate and verify the ideas about the self-organization of physical complex systems displaying power law distributions and $1/f$ noise. When measured at low magnetization rates, the Barkhausen signal displays $1/f^{\alpha}$-type spectra (with $\alpha=1.5\div 2$) and power law distributions of duration and size of the Barkhausen jumps.[1] These experimental data are quite well described by the model of Alessandro *et al.*[2] which is based on a stochastic description of the domain wall dynamics over a pinning field with brownian properties. Yet, this model always predicts a $1/f^2$ spectrum, and, at the moment, it is not clear if it can take into account possible effects of self-organization of the magnetization process. In order to improve the power of the model and clarify this problem, we have performed a thorough investigation of the noise spectra and the amplitude distributions of a wide set of FeCoB amorphous alloys. The stationary amplitude distribution of the signal is very well fitted by the gamma distribution[2] $P(v)=v^{c-1}\exp(-v)/\Gamma(c)$, where v is proportional to the domain wall velocity, and c is a dimensionless parameter. As predicted in Ref. 2, this parameter is found to have a parabolic dependence on the magnetization rate. In particular, the linear coefficient is related to the amplitude of the fluctuations of the pinning field, a parameter which can be measured directly from the power spectra. In all measured cases, the power spectra show α exponents less than 2, and thus poorly fitted by the model. Actually, the absolute value of the high frequency spectral density is not consistent with the c parameter determined from the amplitude distribution data. This discrepancy requires to introduce effects not taken into account in the model, as the propagation of the jumps along the domain wall.[3] This highly enhances the fit of the data and indicates effects of propagation on the scale of a few millimeters. These results are analyzed in terms of new descriptions of the statistical properties of the pinning field based on fractional brownian processes. © *1996 American Institute of Physics.* [S0021-8979(96)64308-2]

[1] G. Durin, G. Bertotti, and A. Magni, Fractals **3**, 351 (1995).
[2] B. Alessandro, C. Beatrice, G. Bertotti, and A. Montorsi, J. Appl. Phys. **68**, 2901 (1990).
[3] G. Durin, C. Beatrice, and G. Bertotti, IEEE Trans. Magn. **30**, 464 (1994).

 0021-8979/96/79(8)/5142/1/$10.00 © 1996 American Institute of Physics

Magnetism and microstructure of nanocrystalline nickel

H. Kisker
Information Storage Materials Laboratory, Toyota Technological Institute, Nagoya 468, Japan,
Institut für Theoretische und Angewandte Physik, Universität Stuttgart, Stuttgart, Germany

H. Kronmüller
Max-Planck-Institut für Metallforschung, Stuttgart, Germany

H.-E. Schaefer
Institut für Theoretische und Angewandte Physik, Universität Stuttgart, Stuttgart, Germany

T. Suzuki
Information Storage Materials Laboratory, Toyota Technological Institute, Nagoya 468, Japan

In order to study the influence of the nanocrystalline microstructure on the magnetic properties of pure nanocrystalline metals, *in situ* magnetic measurements of high-purity nanocrystalline nickel, prepared by a gas-condensation technique with subsequent compaction at various pressures have been performed. The approach to ferromagnetic saturation indicates free volumes in the nanocrystalline system of the size of individual missing crystallites as well as internal stresses. While the saturation polarization of the nanocrystalline Ni samples appears to be unchanged compared to coarse-grained Ni the coercive field and magnetic domains are strongly influenced by the nanocrystalline structure. The shape of the domains with sizes of 10–200 μm much larger than the crystallite size depends on the annealing state of the specimen. The initial coercive field increases with the compaction pressure during preparation. Upon annealing it further increases to a maximum value at $T_a = 500$ °C and decreases at higher annealing temperatures. Additionally, the effect of oxygen located in the grain boundaries has been studied. © *1996 American Institute of Physics.* [S0021-8979(96)29108-4]

I. INTRODUCTION

The magnetic properties of nanocrystalline materials were investigated intensively over the last few years due to a high potential for future technical applications. In order to study the influence of the microstructure on the magnetic properties of nanocrystalline materials, nanocrystalline Ni as a model system of a pure nanocrystalline ferromagnetic metal has been investigated recently by several groups.[1–4] Because impurities such as oxygen contamination play an important role in the magnetic properties of these ultrafine grained materials, *in situ* magnetic measurements have been performed in the present work by exclusively handling the specimens in vacuum.

II. PREPARATION AND CHARACTERIZATION

Nanocrystalline Ni samples have been produced by the inert gas-condensation technique[5] with subsequent compaction at various pressures (0.5–2 G Pa). The mass density of the nanocrystalline samples was about 80% the bulk value. *In situ* nuclear reaction analysis for the determination of the oxygen contents in specimens handled in vacuum or after exposure to air yield 0.5 at. % or 6 at. % of oxygen, respectively. From *in situ* x-ray line broadening a mean crystallite size of 10 nm and internal strains of $\langle e^2 \rangle^{\frac{1}{2}} = 0.4$–$0.9\%$ are deduced. This average crystallite size is consistent with the observation by transmission electron microscopy. Upon isochronal annealing (1 h) the mean crystallite size slowly increases with increasing annealing temperature with strong crystallite growth starting at an annealing temperature of 300 °C. The internal strains decrease to 50% of the initial value upon annealing at 100 °C.

III. APPROACH TO FERROMAGNETIC SATURATION AND SPONTANEOUS POLARIZATION

Measurements of the magnetic moment m as a function of temperature and applied field were performed with a superconducting quantum interference device (SQUID) magnetometer at temperatures between 5 and 320 K and in external fields $-7\ \text{T} < \mu_0 H_{ex} < 7\ \text{T}$.

The analysis of the approach to ferromagnetic saturation then carried out is based on the magnetoelastic coupling between internal stresses caused by defects and the spontaneous magnetization J_s. These measurements of the approach to ferromagnetic saturation therefore yield information on the geometry, the size, and the concentration of the defects. The high-field polarization can be described in general as

$$J(T,\mu_0 H) = J_s(T) - \sum_{i=1}^{n} a_i (\mu_0 H)^{p_i}, \tag{1}$$

where $J_s(T)$ describes the spontaneous polarization at a constant temperature T and p_i the exponents of the field terms with amplitudes a_i. Spin inhomogeneities with a typical field dependence as $p = -\frac{1}{2}$ are characteristic for point defects[6] or nonmagnetic inclusions,[7,8] whereas the term with $p = 1$ describes dislocation dipoles[9–11] and the term with $p = 2$ is typical for separate edge dislocations. At higher temperatures the thermal energy causes an additional field dependence as $p = -\frac{1}{2}$, which is known as para effect.[12]

In situ measurements of the approach to ferromagnetic saturation in high-purity nanocrystalline Ni indicate that the field dependence of the polarization of the as-prepared specimens can be well described by

 0021-8979/96/79(8)/5143/3/$10.00 © 1996 American Institute of Physics

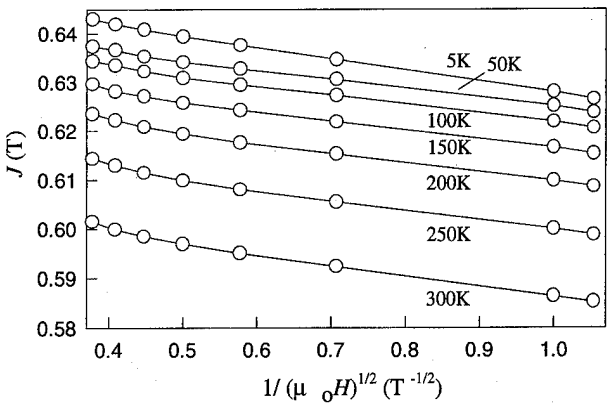


FIG. 1. Polarization J vs $1/(\mu_0 H)^{1/2}$ of high-purity nanocrystalline Ni according to Eq. (2). The deviation from a linear behavior at high external fields is due to the para effect.

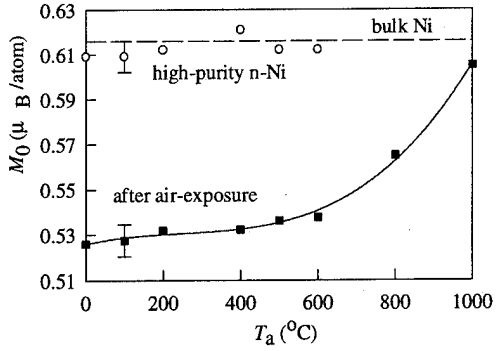


FIG. 2. Variation of the saturation magnetization M_0 upon isochronal annealing ($t_a = 1$ h) without (○) or after air exposure of the samples (?). The value of bulk Ni is indicated by a dashed line (---).

$$J(\mu_0 H) = J_s - a_{-\frac{1}{2}} \frac{1}{\sqrt{\mu_0 H}} \tag{2}$$

at high fields, above $\mu_0 H_{ex} = 0.9$ T (see Fig. 1) with $a_{-\frac{1}{2}}$ being constant. This field dependence may result from stress fields due to point defects or the magnetostatic contribution of spherical nonmagnetic inclusions, such as nanovoids. This only holds if the defect radii are smaller than the exchange length ℓ_{ex} and the distances between the defects are larger than ℓ_{ex}. Therefore the upper limit of the defect density N_{max} is given by

$$N_{max} = \frac{3}{4\pi} \frac{1}{\ell_{ex}^3}. \tag{3}$$

For nonmagnetic inclusions such as nanovoids the microstructural constant $a_{-\frac{1}{2}}$ is given by[7,8]

$$a_{-\frac{1}{2}} = \frac{\sqrt{2}\pi^2 J_s^{\frac{5}{2}}}{27\sqrt{\mu_0 A_{ex}}} r_0^4 N, \tag{4}$$

where r_0 describes the radius and N the density of the spherical nonmagnetic inclusions. Taking the maximum density of defects [see Eq. (3)], we may estimate a minimum radius r_0 applying Eq. (4). With J_s and $a_{-\frac{1}{2}}$ derived by fitting Eq. (2) to the experimental data and with A_{ex} of bulk Ni, we obtain a minimum radius of the voids of $r_0 = 6.5$ nm which is about the size of individual missing crystallites. Smaller voids with $r_0 = 2.1$ nm in nanocrystalline Fe were reported by Hirscher *et al.*, applying the same technique of analyzing the approach to ferromagnetic saturation.[13]

Upon annealing for 1 h at 100 °C, the field dependence significantly changes and an additional field term $1/(\mu_0 H_{ex})^2$ is required for a good fit to describe the approach to ferromagnetic saturation. This field term may be ascribed to long-range internal stress fields[14] with

$$a_{-2} = \frac{3}{5} \frac{\mu_0^2 \lambda_s^2}{J_s} \sigma_i^2. \tag{5}$$

With the constant a_{-2} and the magnetization J_s derived by fitting Eq. (1) to the experimental data we obtain the value of the internal stresses $\sqrt{\sigma_i^2} \approx 0.85$ G Pa being of the same order of magnitude as the internal stresses which can be derived from the strains detected by x-ray line broadening.

The temperature variation of the spontaneous magnetization $J_s(T)$ was determined analyzing the approach to ferromagnetic saturation [see Eq. (1)] at various temperatures. Extrapolation of $J_s(T)$ to zero temperature yields the saturation polarization J_0. Figure 2 shows the variation of the saturation polarization J_0 with increasing annealing temperature T_a for high-purity nanocrystalline Ni as well as of nanocrystalline Ni with 6 at. % oxygen in the grain boundaries after air exposure. Whereas the saturation polarization of the high-purity n–Ni samples is unchanged compared to bulk Ni, oxygen contamination of the samples significantly reduces J_0. No Ni oxide was observed by x-ray diffraction analysis in the specimens containing 6 at. % of oxygen.

IV. DOMAIN STRUCTURE AND COERCIVE FIELD

The magnetic domain structure of nanocrystalline Ni samples (n-Ni) was studied by means of magneto-optic Kerr microscopy. A fine and irregular domain structure with a mean domain size of 12 μm was found in the as-prepared samples indicating a strong decrease of the effective crystal anisotropy which can be explained by the random anisotropy model[15] if the crystallite size is smaller than the exchange length ℓ_{ex}. After annealing the specimens for 1 h at 100 °C, elongated domain structures of a mean width of 30 μm appeared (see Fig. 3), which is typical for a material with an anisotropy dominated by internal stresses. This change in the magnetic domain structure can be explained by a transition from a system with very small crystal anisotropy to that with dominating magnetoelastic anisotropy due to the long-range internal stress fields induced upon annealing (analogs to the observations of the approach to ferromagnetic saturation).

The magneto-optic Kerr studies at various external magnetic fields along with *in situ* measurements of the coercive field H_c, indicate that the magnetization process in nanocrystalline Ni is dominated by domain wall movements. The coercive field in n-Ni of some 10 mT, much higher than in bulk Ni (0.01 mT) has been measured, indicating that the

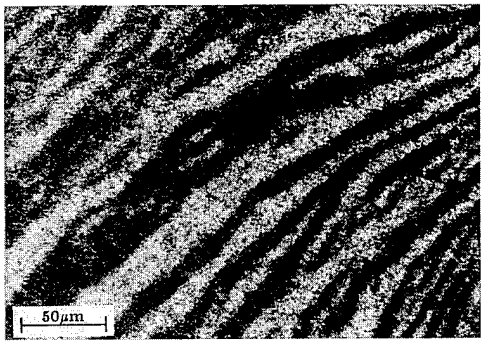


FIG. 3. Elongated domains in nanocrystalline Ni after annealing at 100 °C for 1 h.

magnetization process is impeded by pinning of the domain walls in the nanocrystalline structure. In a simple model of domain wall movement in an uniaxial sinusoidal stress field, the temperature variation of the coercive field can be written as[16,17]

$$\mu_0 H_c \approx \frac{\lambda_s \Delta\sigma}{M_s}\left(\frac{\lambda}{\delta_B}\right), \tag{6}$$

where λ_s, M_s, and $\Delta\sigma$ denote the isotropic magnetostriction constant, the spontaneous magnetization, and the amplitude of the stress field, respectively, if the wavelength of the stress field λ is smaller than the domain wall width δ_B. Fitting Eq. (6) to the experimental data and assuming a wavelength λ of the stress field equal to the mean crystallite size (10 nm) in the as-prepared nanocrystalline samples, we obtain the amplitude of the stress field of $\Delta\sigma$=0.32 G Pa or 1 G Pa for compaction during preparation at 1 G Pa or 2 G Pa, respectively. These values are of the same order of magnitude as the internal stresses obtained from x-ray diffraction line broadening as well as from the analysis of the approach to ferromagnetic saturation.

V. CONCLUSION

Internal stresses are found to strongly influence the magnetic properties of compaction prepared nanocrystalline nickel. The stress fields in the nanocrystalline specimens have been detected by x-ray line broadening. The value of these stresses increases with increasing compaction pressure during preparation. However, by analyzing the approach to ferromagnetic saturation the stress field can only be detected after annealing of the samples. Additionally, the magnetic domain structure changes upon annealing from initially diffuse domains, typical for a small effective crystal anisotropy, to elongated domains which can be ascribed to dominating magnetoelastic anisotropy in the annealed state. This change upon annealing can be explained by structural relaxation increasing the wavelength of the stress field. The temperature variation of the coercive field in the nanocrystalline Ni samples can be described by domain wall movement in an uniaxial stress field of the same order as determined by x-ray diffraction and by analyzing the approach to ferromagnetic saturation.

ACKNOWLEDGMENTS

This work was supported by the Deutsche Forschungsgemeinschaft (Contract No. Scha428/8-1). One of the authors (H.K.) acknowledges the award of the Graduiertenförderung of the state of Baden-Württemberg.

[1] H.-E. Schaefer, H. Kisker, H. Kronmüller, and R. Würschum, Nanostruc. Mater. **1**, 523 (1992).
[2] U. Erb, A. M. El-Sherik, G. Palumbo, and K. T. Aust, Nanostruc. Mater. **2**, 385 (1993).
[3] L. Daróczi, D. L. Beke, G. Posgay, and M. Kis-Varga, Nanostruc. Mater. **6**, 981 (1995).
[4] H. Kisker, T. Gessmann, R. Würschum, H. Kronmüller, and H.-E. Schaefer, Nanostruc. Mater. **6**, 925 (1995).
[5] H. Gleiter, Prog. Mater. Sci. **33**, 223 (1989).
[6] H. Kronmüller, N. Lenge, and H.-U. Habermeier, Phys. Lett. A **101**, 439 (1984).
[7] H. Kronmüller, Z. Phys. **168**, 478 (1962).
[8] H. P. Chang, R. Herz, and H. Kronmüller, Appl. Phys. **22**, 155 (1980).
[9] H. Kronmüller, M. Fähnle, M. Domann, H. Grimm, R. Grimm, and B. Gröger, J. Magn. Magn. Mater. **13**, 53 (1979).
[10] H. Kronmüller, IEEE Trans. Magn. **MAG-15**, 1218 (1979).
[11] H. Grimm and H. Kronmüller, Phys. Status Solidi B **117**, 663 (1983).
[12] T. Holstein and H. Primakoff, Phys. Rev. **58**, 1098 (1940).
[13] M. Hirscher, R. Reisser, R. Würschum, H.-E. Schaefer, and H. Kronmüller, J. Magn. Magn. Mater. **146**, 117 (1995).
[14] E. Kneller, *Ferromagnetismus* (Springer, Berlin, 1962).
[15] R. Alben, J. J. Becker, and M. C. Chi, J. Appl. Phys. **49**, 1653 (1978).
[16] A. H. Morrish, *The Physical Principles of Magnetism* (Krieger, Malabar, FL, 1965).
[17] E. Kondorsky, Phys. Z. Sowjet Union **11**, 597 (1937).

Small-angle neutron scattering behavior of $Fe_{91}Zr_9$ glass under magnetic field

L. Fernández Barquín and J. C. Gómez Sal
CITIMAC, U. Cantabria, Santander 39005, Spain

S. N. Kaul
School of Physics, U. Hyderabad, Hyderabad 500046, India

J. M. Barandiarán and P. Gorría
Dept. Elec. Electrónica, UPV, Bilbao 48080, Spain

J. S. Pedersen
Dept. Sol. St. Phys., Risoe Nat. Lab., Roskilde 4000, Denmark

R. Heenan
ISIS Facility, RAL, Chilton, Didcot, OX11 0QX, United Kingdom

Zero-field and in-field small-angle neutron scattering measurements over a wide Q range are presented for the $Fe_{91}Zr_9$ metallic glass in the 10–290 K range. Two transitions observed at 210 K and around 60 K are related to Tc and reentrant transition temperature, respectively. The spectra ($0.003\ Å^{-1}<Q<0.5\ Å^{-1}$) reveal the existence of an important contribution at the lowest Q values and at least two humps in the entire curves. The application of the magnetic field results in an anisotropic signal, and a global decrease of intensity. The magnetic field drastically reduces $I(Q)$ in the region for $Q<0.04\ Å^{-1}$, but not so strongly at larger Q values (even at $H=4$ T), becoming more evident a remaining hump. Its origin can so far be uniquely explained by the models dealing with the existence of clusters embedded in a ferromagnetic matrix. © *1996 American Institute of Physics.* [S0021-8979(96)29208-0]

I. INTRODUCTION

Fe_xZr_{100-x} glasses ($x\approx 90$) have attracted considerable attention because of their striking magnetic properties. The magnetic phase diagram exhibits reentrant spin glass (RSG), ferromagnetic (FM), and paramagnetic (PM) regimes depending on the composition and temperature.[1] The existing explanations are controversial and based on diverse physical views. On the one hand, some authors suggest a mixed phase with ferromagnetic order in the z direction coexisting with spin glass in xy directions, i.e., transverse spin freezing (TSF).[1] On the other, there are approaches dealing with magnetic clusters embedded in a matrix, being the coupling inside the cluster antiferromagnetic (AFM-FM)[2] and ferromagnetic (FM–FM).[3] The basic origin of the clusters is different for the latter two, caused by chemical and density fluctuations in the structure, respectively. In addition, a superparamagnetic behavior has been put forward to explain magnetization[4] and χ_{ac}.[5] During the last few years, the FM–FM model has been supported by an increasing evidence of ferromagnetic resonance (FMR),[6] bulk magnetization (BM),[3] and Mössbauer (MS) results.[3] However, Ren and Ryan[7] have explained recently some of the existing results, using a wide compositional range, in terms of the TSF model.

It is clear that a direct experimental evidence of the existence or not of the clusters in these alloys is of paramount interest. SANS technique is a tool for such a purpose and in fact several studies have already been carried out using Fe–Zr alloys by Rhyne *et al.*,[8] who pointed out the inhomogeneous magnetism in the alloys. Recently, Mergia *et al.*[9] have extended the study using in-field SANS, and showing dependencies of $I(Q)$ on the field. The conclusions of these studies are somewhat indefinite and an even more complete study should be desirable. Partial uncertainty came from the fact that the SANS for these alloys may include several contributions, some of which could be manifested especially in the very low Q region and then are blurred if an insufficient large Q range is covered.

As a consequence of these considerations, we have undertaken an intensive study of the SANS on $Fe_{91}Zr_9$, employing a range extended to lower Q values and under magnetic fields up to 4 T. In this communication, the initial SANS results are presented. Use of a wide Q range will help to ascertain any hidden contribution while the application of magnetic fields will affect the contributions to SANS intensity coming from magnetic origin.

II. EXPERIMENT

Ribbons 1.5 mm wide and 0.02 mm thick were cast by melt spinning under argon atmosphere. X-ray diffraction showed no crystallinity in both ribbon faces. SANS between 15 and 300 K was performed in LOQ instrument ($0.006\ Å^{-1}<Q<0.2\ Å^{-1}$) in the Rutherford–Appleton Laboratory, and in a SANS diffractometer in Risoe ($0.003\ Å^{-1}<Q<0.5\ Å^{-1}$). Samples were wrapped in a rectangular shape Al foil, which was placed vertically. In Risoe, fields up to 4 T were applied vertically along the longitudinal ribbon direction, while in LOQ, a horizontal field (0.26 T) was used. Usual corrections were performed.[10]

III. RESULTS AND DISCUSSION

Figure 1 shows $I(Q)$ behavior (in Log–Log scale) in $H=0$ T field for temperatures in the three magnetic phases:

 0021-8979/96/79(8)/5146/3/$10.00 © 1996 American Institute of Physics

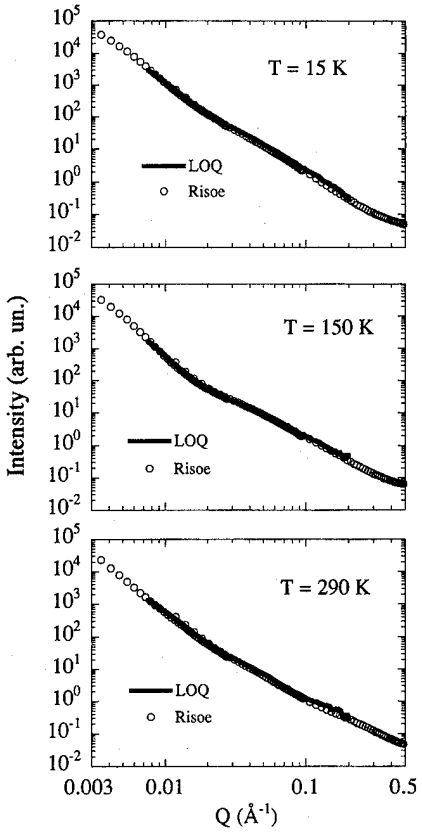


FIG. 1. $I(Q)$ in Log–Log scale for sets of data obtained in LOQ and Risoe instruments. LOQ data have been normalized to the Risoe data.

RSG (15 K), FM (150 K), and PM (290 K), for LOQ and Risoe runs. It is clear that both sets show the same results, though the Risoe data extend down to very low Q values. In fact, in these latter, an intensity increase is observed. The data in this Q region must be considered for any fitting evaluation, and it is expected that it will alter the previous SANS results.[8,9] Moreover, it is important to note that the $I(Q)$ in the PM regime is unusually large, which could be a sign of persistence of inhomogeneties above Tc (clustering or short-range magnetic correlations). It is also interesting that in the FM and RSG regimes, an enhancement of at least two humps is building up centered around 0.004 and 0.05 Å^{-1}. In Figure 2, the $I(T, Q=\text{fixed})$ behavior is shown to check for any transitions. As observed in Refs. 8 and 9, there is a cusp around Tc (210 K for $Fe_{91}Zr_9$) in agreement with BM, MS,

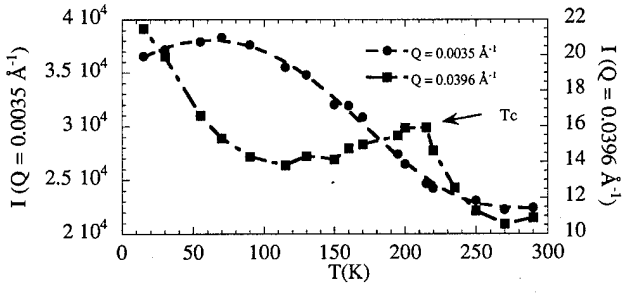


FIG. 2. $I(Q=\text{fixed}, T)$ for two Q values in zero-field configuration.

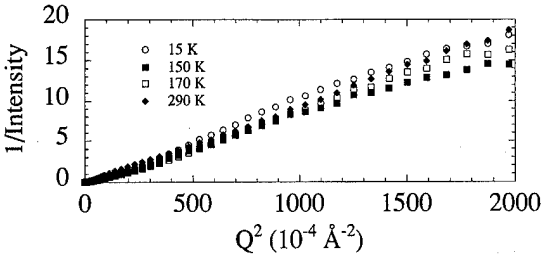


FIG. 3. $I(Q)^{-1}$ vs Q^2 for a few characteristic temperatures.

etc. Another feature is the steady increase of signal, significantly when $T<80$ K, towards the RSG state. At the lowest Q value, it is detected in a broad maximum close to T_{RSG} (around 60 K).

SANS from a normal ferromagnet is described by a Lorentzian (L1), whereas for the systems with random anisotropy, a Lorentzian+(Lorentzian)^2 (L2) behavior of $I(Q)$ has been proposed.[11] Plots to check the L1 behavior are too far to be linear in the studied Q range (see Fig. 3). So, a pure ferromagnetic behavior must be ruled out.[8] L2 fittings do not account for the results because more than two contributions could be extracted from the curves, as seen in Fig. 1. Then, it would be valuable to include an extra term for the fittings, as in the following expression:

$$I(Q)=\frac{A}{Q^2+\kappa_1^2}+\frac{B}{(Q^2+\kappa_2^2)^2}+\frac{C}{(Q^2+\kappa_3^2)^2}\,. \qquad (1)$$

Equation (1) has been used to fit $I(Q)$ in the overall Q range. If any of these contributions is negligible, the corresponding coefficient (A, B, or C) must tend to zero. The calculations reveal that Eq. (1) yields the lowest χ^2. The variation of the fitted coefficients and correlation lengths ($\zeta_1=1/\kappa_1$, $\zeta_2=1/\kappa_2$, and $\zeta_3=1/\kappa_3$) are presented in Fig. 4. The main contribution to $I(Q)$ stems from the Lorentzian term, which is expected to include magnetic scattering from the ferromagnetic matrix. In addition, the SANS signal should also contain an underlying structural scattering and this contribution is still large above Tc. Parameter ζ_1 shows an enhancement in the FM region. Regarding to the B contribution, it is more important at $T<T_{RSG}$, revealing the existence of the RSG state. This term is small for $T>T_{RSG}$, whereas the correlation length increases in the ferromagnetic region, as corresponds to the long-range alignment of the moments. The third contribution is small and rather constant, but fading away for $T>$Tc. To derive more information, it is helpful to deal with the magnetic scattering only. For this, the PM signal has been subtracted from the FM and RSG intensities. I(RSG)-I(PM) leads to an entirely positive magnetic contribution for all Q values, but I(FM)-I(PM) results in negative values around the central Q values. This is important as it is witnessing the large PM intensity. Preliminary calculations show that in this case Eq. (1) still improves the quality of fittings. Though all the scattering coefficients decrease with respect to those in Fig. 4, this effect is especially intense in the Lorentzian coefficient (ten times smaller), confirming that this term contains a structural contribution. On the other hand, the variations of the fitting parameters resemble those in Fig. 4.

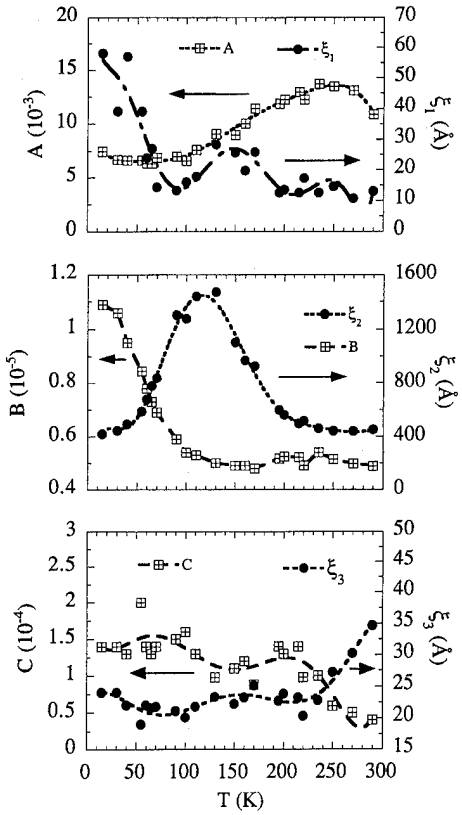


FIG. 4. Thermal dependence of the fit parameters in the expression (1).

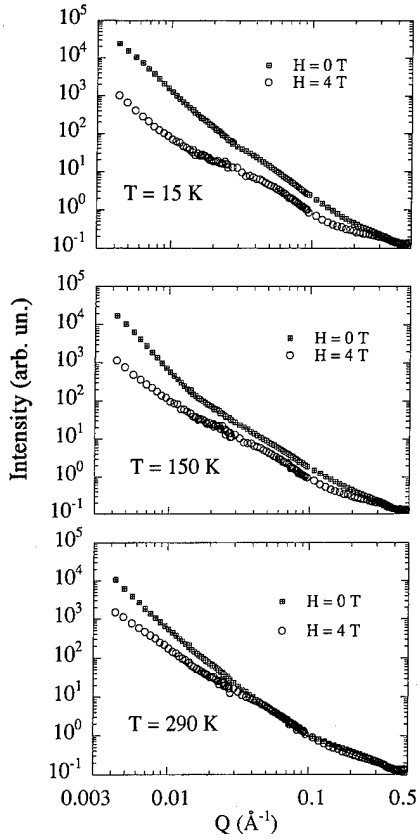


FIG. 5. Comparison between zero-field and in-field (4 T) SANS intensity for a given temperature in the PM, FM, and RSG states.

When a magnetic field is applied, the contour intensity patterns become anisotropic due to the moment alignment along the field direction. A low 0.26 T field is sufficient to origin these anisotropic contours and result in a decrease of the entire intensity. Larger fields result in a slightly further decrease of the intensity. In Fig. 5, the comparison of zero- and in-field measurements for the three regimes is presented. The most important effect is observed in the lower Q values, being more pronounced in the RSG regime. While for 290 K curves the signals coincide for $Q > 0.04$ Å^{-1}, this is not the case in the magnetic regimes. An enhancement of the humps around 0.04 Å^{-1} is clear at lower temperatures. These results could be interpreted as the alignment of the matrix magnetic moments, destroying the spin-glass state, and then reducing the intensity in the lower Q range. In addition, this alignment is also detected in the PM regime. However, the magnetic field does not affect the central hump of the curves in the three temperatures. Then, this remaining hump needs the existence of SANS centers to be understood, and not influenced by magnetic fields of such magnitude. The closest physical picture to explain this is that related to the existence of clusters in these alloys.

Although these results and discussions must be considered as preliminary, signs of the existence of ferromagnetic clusters have been detected in the wide Q-range spectra, which are encouraging a deeper analysis. Indeed, the key point is to separate the magnetic and structural contributions; two ways are open for such a purpose: an extensive fitting procedure for the subtracted FM-PM and RSG-PM spectra, considering more temperatures and new theoretical approaches, and a complete evaluation of the anisotropic signal in the in-field experiments. Both studies are already being carried out.

ACKNOWLEDGMENTS

L.F.B., J.C.G.S., J.M.B., and P.G. acknowledge O. Nielsen (Lyngby) and R. Ibarre (Zaragoza) for help in the samples preparation. CEC-LIP grant for Risoe experiments and CICYT MAT93-0691 for funding.

[1] D. H. Ryan, J. M. D. Coey, E. Batalla, Z. Altounian, and J. O. Strom-Olsen, Phys. Rev. B **35**, 8630 (1987).
[2] M. Saito, H. Hiroyoshi, K. Fukamichi, and Y. Nakagawa, J. Phys. F **16**, 911 (1986).
[3] S. N. Kaul, J. Phys.: Condens. Matter **3**, 4027 (1991); S. N. Kaul, V. Siruguri, and G. Chandra, Phys. Rev. B **45**, 12343 (1992).
[4] L. F. Kiss, T. Kemeny, I. Vincze, and L. Granasy, J. Magn. Magn. Mater. **135**, 161 (1994).
[5] S. N. Kaul, J. Appl. Phys. **61**, 451 (1987); N. Hegman, L. F. Kiss, and T. Kemeny, J. Phys.: Condens. Mater. **6**, L427 (1994).
[6] S. N. Kaul and V. Siruguri, J. Phys: Condens. Mater. **4**, 505 (1992).
[7] H. Ren and D. H. Ryan, Phys. Rev. B **51**, 15885 (1995).
[8] J. J. Rhyne, R. W. Erwin, J. A. Fernandez-Baca, and G. E. Fish, J. Appl. Phys. **63**, 4080 (1988).
[9] K. Mergia, S. Messoloras, G. Nikolaides, D. Niarchos, and R. J. Stewart, J. Appl. Phys. **76**, 6380 (1994).
[10] J. S. Pedersen, J. Phys. IV (Paris) Coll. C8 **3**, 491 (1993).
[11] G. Aeppli, S. M. Shapiro, R. J. Birgeneau, and H. S. Chen, Phys. Rev. B **28**, 5160 (1983).

Time-temperature-transformation study of a nanocrystalline $Fe_{91}Zr_7B_2$ soft magnetic alloy

K. Suzuki, J. M. Cadogan,[a] and V. Sahajwalla
School of Materials Science and Engineering, the University of New South Wales, Sydney 2052, Australia

A. Inoue and T. Masumoto
Institute for Materials Research, Tohoku University, Sendai 980-77, Japan

The structure, soft magnetic properties, magnetostriction, grain size and volume fraction of the residual amorphous phase have been studied for an amorphous $Fe_{91}Zr_7B_2$ alloy annealed for periods of 60 s–1080 ks, at temperatures of 823–973 K. The highest permeability (at 1 kHz and 0.4 A/m) 31,000 and smallest coercivity 4.2 A/m are obtained for the sample annealed at 923 K for 60 s, where a small grain size (≈12 nm) and about 35% of the residual amorphous phase are measured. The coercivity of the nanocrystalline alloy varies as the 3^{rd} power of the grain size, corresponding to the case where the magnetically coupled region has a dimensionality between two and three. This slightly low dimensionality is presumed to be due to the alignment of the magnetization in the sample plane. © *1996 American Institute of Physics.* [S0021-8979(96)29308-7]

I. INTRODUCTION

Nanocrystalline soft magnetic alloys consisting of bcc nano crystallites embedded in an amorphous matrix have been produced[1–5] by primary crystallization of melt-spun amorphous ribbons. Among the nanocrystalline soft magnetic alloys, the $Fe_{91}Zr_7B_2$ alloy is particularly attractive because of its high saturation magnetization (≈1.7 T)[3].

The magnetic softness of the nanocrystalline Fe–Zr–B alloys depends strongly on annealing conditions such as annealing temperature and heating rate.[6] However, in most of the previous reports on Fe–M–B (M=Zr, Hf, and Nb) alloys,[7] the nanocrystalline phase was obtained by isochronal annealing for 3.6 ks and no systematic study of the annealing conditions with different annealing times has been reported. In this study we have examined the structure, volume fraction of the residual amorphous phase, grain size, magnetostriction, and soft magnetic properties of the amorphous $Fe_{91}Zr_7B_2$ alloy annealed for periods ranging from 60 s to 1080 ks, at several temperatures ranging from 823 to 973 K, with the intention of clarifying the dominant factor as well as the optimum annealing condition to obtain magnetic softness.

II. EXPERIMENTAL PROCEDURE

An amorphous $Fe_{91}Zr_7B_2$ alloy was prepared in an argon atmosphere by single-roller melt spinning. Since a homogeneous nanostructure with good magnetic softness has been prepared[6] at a high heating rate (>1 K/s) in the Fe–M–B (M=Zr, Hf, and Nb) systems, the amorphous samples were vacuum sealed in quartz tubes and annealed by using a salt bath; the heating rate was ≈3 K/s. The mean grain size (D) and the volume fraction of the residual amorphous phase (V_{am}) were evaluated from the peak width of the (110) x-ray reflection and ^{57}Fe Mössbauer results, respectively. To avoid the effect of surface crystallization products on D, the annealed samples were polished. The evaluation of V_{am} was made by assuming the same recoil-free fractions for the bcc and amorphous phases and that the Fe content of the bcc phase is 98 at. %, which has previously been reported[8] for the nanocrystalline $Fe_{90}Zr_7B_3$ alloy, using atom-probe field ion microscopy. Coercivity (H_c) and saturation magnetostriction (λ_s) were measured using a dc B-H tracer and a capacitance bridge, respectively. The effective permeability (μ_e) was measured at 1 kHz and 0.4 A/m.

III. RESULTS AND DISCUSSION

A. Soft magnetic properties and nanostructure

Figure 1 shows the annealing time (t_a) and temperature (T_a) dependence of H_c for the amorphous $Fe_{91}Zr_7B_2$ alloy. The annealed structures determined by x-ray diffractometry and Mössbauer spectroscopy are also shown in Fig. 1. A small H_c (<5 A/m) is obtained in a relatively high T_a range (923–973 K) in a very short t_a range (>100 s). The optimum t_a for obtaining low H_c shifts toward longer time periods with decreasing T_a. As shown in Fig. 2, a similar dependence of magnetic softness on t_a and T_a is observed from the change in μ_e.

The onset of primary crystallization for the amorphous $Fe_{91}Zr_7B_2$ alloy was measured to be 830 K at a rate of 3.3 K/s by using a differential scanning calorimeter. Furthermore, it was confirmed that the crystallization reaction is

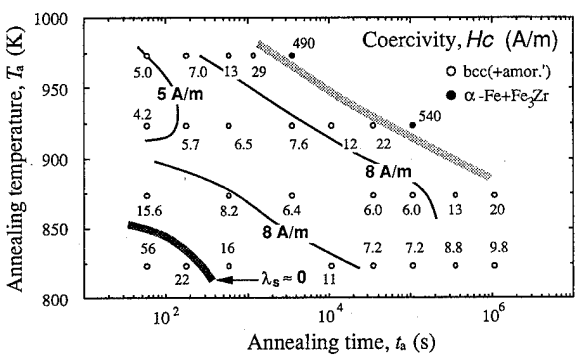


FIG. 1. Annealing time and temperature dependence of coercivity (H_c).

[a]School of Physics, The University of New South Wales.

 0021-8979/96/79(8)/5149/3/$10.00 © 1996 American Institute of Physics

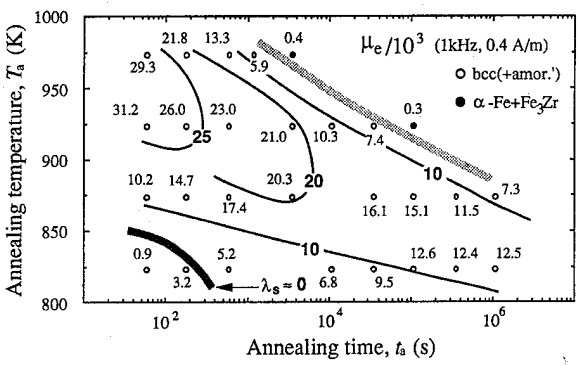


FIG. 2. Annealing time and temperature dependence of permeability (μ_e).

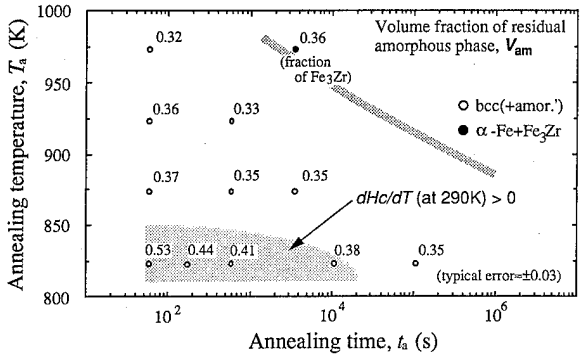


FIG. 4. Annealing time and temperature dependence of volume fraction of the residual amorphous phase (V_{am}).

virtually complete by 920 K. Accordingly, the evolution of the nanoscale bcc phase takes place isochronally at $T_a = 923$ and 973 K, and isothermally at $T_a = 823$ K. Therefore, an isochronal heating at a high heating rate is more appropriate for the formation of the nano structure with good soft magnetic properties rather than a low-temperature isothermal annealing.

In Figs. 1 and 2, the zero magnetostrictive line on which the λ_s value becomes virtually zero is also shown. It is clear that the t_a and T_a for obtaining the optimum magnetic properties do not agree with those for the zero magnetostrictive line, revealing that the magnetic softness in the nanocrystalline $Fe_{91}Zr_7B_2$ alloy is governed by factors other than magnetostriction. It is well established[9] that the apparent magnetic anisotropy ($\langle K \rangle$) of nanocrystalline materials depends on intergranular magnetic interactions as well as the grain size. Furthermore, the H_c of the nanocrystalline alloys increases with temperature toward the Curie temperature (T_c) of the residual amorphous phase, because the intergranular exchange coupling is inhibited by the nonmagnetic intergranular region. Given the low T_c of Fe-rich amorphous alloys, the temperature dependence of H_c (i.e., dH_c/dT) at room temperature may become positive for the sample in which the residual amorphous phase dominates the magnetic softness through the effectiveness of the intergranular coupling.

Figure 3 shows the relation between the mean grain size of the bcc phase (D) and the annealing conditions (t_a and T_a) for the $Fe_{91}Zr_7B_2$ alloy. Although a small D (<13 nm) is obtained at $t_a = 60$ s for all the annealing temperatures, D increases up to ≈20 nm with t_a even before the nanocrystalline bcc structure begins to decompose into α-Fe+Fe_3Zr. The increase in D in Fig. 3 corresponds to the increase in H_c in Fig. 1, indicating that the grain growth of the nanocrystalline bcc phase is responsible for the degradation of the soft magnetic properties in the longer t_a range. However, high H_c values of 10–60 A/m are seen in a short t_a range ($<10^4$ s) where a small D (<13 nm) is confirmed, suggesting that the magnetic softness in the short t_a range is dominated by the intergranular magnetic coupling. Figure 4 shows the relation between V_{am} and the annealing conditions (t_a and T_a). The region where a positive temperature dependence of H_c was confirmed at room temperature is also shown in Fig. 4. It is evident that the area for which high V_{am} values above 0.4 are obtained corresponds to that of high H_c values and furthermore a positive dH_c/dT is confirmed in this area. Consequently, we conclude that the magnetic softness is mostly dominated by D and V_{am} and good soft magnetic properties are obtained for samples with $D < 13$ nm and $V_{am} \approx 0.35$.

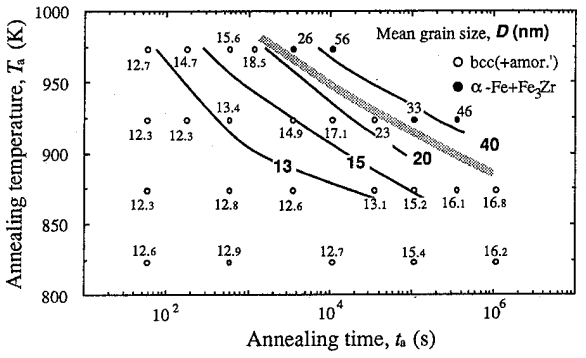


FIG. 3. Annealing time and temperature dependence of mean grain size (D).

B. Random anisotropy model or Ripple theory?

Two theoretical models, the random anisotropy model[9] and magnetic ripple theory,[10] have been applied to nanocrystalline materials having small D less than the ferromagnetic exchange length ($L_{ex} \approx \sqrt{A/K}$). In both models, a magnetically coupled region in which the effects of magnetocrystalline anisotropy (K) are statistically averaged out is assumed and an expansion of the coupled region or a decrease in the grain size promotes the averaging effect leading to small H_c. The random anisotropy model gives

$$H_c \propto K[D/(A/K)^{\frac{1}{2}}]^{2n/(4-n)}, \quad (1)$$

where A is the exchange stiffness and n is the dimensionality of the coupled region. Since only the exchange interaction is considered as the intergranular interaction in this model, the shape of the coupled region is uniform and is independent of the direction of the magnetic moment. To evaluate the exponent $x[=2n/(4-n)]$ for the present Fe–Zr–B alloy, the data on H_c and D in Figs. 1 and 3 are replotted in Fig. 5. The data points with $H_c > 8$ A/m in the short t_a range and those

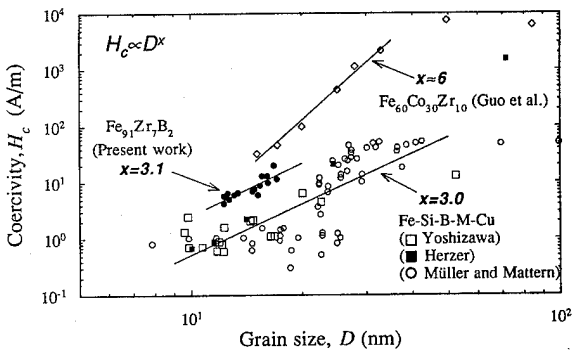


FIG. 5. Relation H_c and D for the nanocrystalline $Fe_{91}Zr_7B_2$ alloy. Data replotted from previous reports on Fe–Si–B–M–$Cu_{2,5,11}$ and $Fe_{60}Co_{30}Zr_{10}^4$ alloys are also shown for comparison.

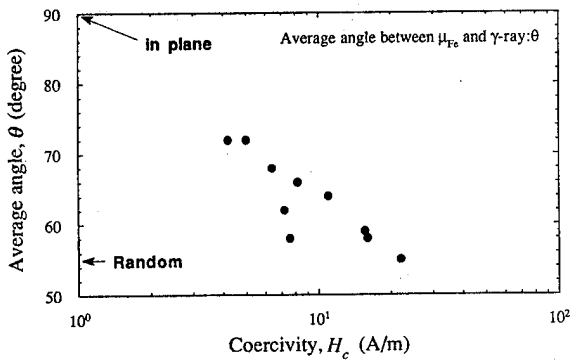


FIG. 6. Average angle between the Fe magnetic moment and incident γ-ray evaluated from ^{57}Fe Mössbauer measurements as a function of H_c.

for the samples containing the Fe_3Zr compound are excluded to avoid the influences of parameters other than D. The data from the previous reports on the Fe–Si–B–M–Cu (M=IVa to VIa metal)[5,9,11] and $Fe_{60}Co_{30}Zr_{10}^4$ alloys are also plotted in the Fig. 5 for comparison. The exponent x derived from least-squares fitting of the data points in a range $D<L_{ex}$ (≈35 nm) is about 3 for both the Fe–Zr–B and Fe–Si–B–M–Cu alloys, implying that the magnetically coupled region is nonuniform in three-dimensional space ($n<3$). Given the thickness of the ribbon samples (≈20 μm), which is large enough to provide the uniform three-dimensional coupling ($n=3$), this result cannot be explained by Eq. (1).

Unlike the random anisotropy model, the dipole–dipole interaction as well as the exchange interaction is considered in the ripple theory, and thus the shape of the coupled region depends on the direction of the magnetic moment. This theory gives a two-dimensional ellipsoid for the coupled region in thin-film materials, in which the magnetization is fully aligned in the plane. Although the ripple theory for bulk materials has not been established, the theory suggests that the shape of the coupled region in the ribbon samples can be nonuniform ($n<3$) due to the contribution of the dipole–dipole effect originating from the magnetic texture along the sample plane. To clarify the presence of the magnetic texture in the Fe–Zr–B samples, the average angle between the Fe magnetic moments and the incident γ-ray direction (θ) was evaluated from the ^{57}Fe Mössbauer results. As can be seen in Fig. 6, the magnetic moment tends to align in the ribbon plane with decreasing H_c, reflecting that the shape anisotropy dominates the direction of the magnetic moment in samples with low $\langle K \rangle$. Accordingly, the dipole–dipole effect of reducing the dimensionality of the coupled region is presumed to be significant in low H_c samples. This is consistent with the results in Fig. 6 in which a high exponent $x \approx 6$, corresponding to $n \approx 3$, is limited to the $Fe_{60}Co_{30}Zr_{10}$ alloy having relatively high H_c values. Thus, the sample shape can be responsible for the D^3 dependence in the present Fe–Zr–B alloy. An extension of the ripple theory to three-dimensional materials is needed for quantitative discussion.

ACKNOWLEDGMENTS

One of the authors, K.S., would like to thank Dr. H. S. Li and Dr. N. Hasegawa for valuable discussions.

[1] Y. Yoshizawa, S. Oguma, and K. Yamauchi, J. Appl. Phys. **64**, 6044 (1988).
[2] G. Herzer, IEEE Trans. Magn. **MAG-25**, 3327 (1989).
[3] K. Suzuki, N. Kataoka, A. Inoue, A. Makino, and T. Masumoto, Mater. Trans. JIM **31**, 743 (1990).
[4] H. Q. Guo, T. Reininger, H. Kronmüller, M. Rapp, and V. K. Skumrev, Phys. Status Solidi A **127**, 519 (1991).
[5] M. Müller and N. Mattern, J. Magn. Magn. Mater. **136**, 79 (1994).
[6] K. Suzuki, A. Makino, A. Inoue, and T. Masumoto, Sci. Rep. Res. Inst. Tohoku Univ. Ser. A **39**, 133 (1994).
[7] K. Suzuki, A. Makino, A. Inoue, and T. Masumoto, J. Appl. Phys. **74**, 3316 (1993).
[8] K. Hono, Y. Zhang, A. Inoue, and T. Sakurai, Mater. Trans. JIM **36**, 909 (1995).
[9] G. Herzer, Phys. Scr. T **49**, 307 (1993).
[10] H. Hoffmann, IEEE Trans. Magn. **MAG-9**, 17 (1973).
[11] Y. Yoshizawa, Doctoral thesis, Tohoku University, 1993.

Soft magnetic properties of Fe–Zr–B thin films (abstract)

N. B. Shevchenko, J. A. Christodoulides, X. Meng-Burany, A. S. Murthy, and G. C. Hadjipanayis
Department of Physics and Astronomy, University of Delaware, Newark, Delaware 19716

The Fe–Zr–B system has been shown to exhibit superior soft magnetic properties in melt-spun ribbons.[1] These ribbons with composition $Fe_{87}Zr_7Cu_3B_3$ had very low coercivity (0.02 Oe) and high magnetization (190 emu/g) after crystallization at 540 °C from the amorphous state. We have recently extended these studies to thin films with similar composition. These films were prepared by dc magnetron sputtering from a solid alloy target. Transmission electron microscopy and differential scanning calorimetry were used to study the evolution of the microstructure upon annealing. Magnetic measurements were taken with a hysteresigraph. Unlike the as-spun ribbon samples, the as-sputtered films showed 10 nm crystallities. Selected area diffraction patterns indicated a two phase microstructure, with the bcc phase which gave rise to the soft magnetic properties in the ribbons, coexisting with a second phase leading to degraded soft magnetic properties ($H_c = 20$ Oe and $M_s = 150$ emu/g). Subsequent annealing of the thin film samples enhanced the formation of the second phase and further degraded the soft magnetic properties. Work is currently underway to determine a means of suppressing the formation of the secondary phase while preserving the phase with superior soft properties. © *1996 American Institute of Physics.* [S0021-8979(96)64408-9]

Work supported by the National Science Foundation under Contract No. NSF DMR-9307676.

[1]N. B. Shevchenko, Y. J. Zhang, and G. C. Hadjipanayis, J. Appl. Phys. **73**, 5601 (1993).

 0021-8979/96/79(8)/5152/1/$10.00 © 1996 American Institute of Physics

The change of magnetic properties in nanocrystalline $Fe_{88}Zr_7B_4Cu_1$ alloy by cooling rate

K. S. Kim, V. Ström, J. Wittborn, and K. V. Rao
Deptartment of Condensed Matter Physics, Royal Institute of Technology, S-10044 Stockholm, Sweden

K. Y. Kim and T. H. Noh
Division of Advanced Materials, Korea Institute of Science and Technology, Seoul 136-791, Korea

S. C. Yu
Department of Physics, Chungbuk National University, Cheongju 360-763, Korea

We have investigated the effect of cooling rate, followed immediately after the isothermal annealing, on the magnetic properties of melt-spun $Fe_{88}Zr_7B_4Cu_1$ alloy. As the cooling rate is increased, the effective permeability, 2×10^4, improved by 50% on annealing at around 650 °C. The remanence ratio is also found to concomitantly decrease with the increasing cooling rate. The increase of permeability and decrease of remanence ratio are consistent with the expected suppression of the induced magnetic anisotropy. From an analysis of the transmission electron microscopy micrographs, and the x-ray diffraction spectral intensities, we find that the volume fraction of the amorphous matrix to that of the nanocrystallized magnetic entities to be about 20%, at which the permeability has the maximum value for this system. Scanning electron microscopy and antiferromagnetic investigations show a much smoother surface morphology with a finer grain distribution in the rapidly quenched sample. © *1996 American Institute of Physics.* [S0021-8979(96)29408-3]

During recent years there has been of considerable interest in Fe-based rapid quenched materials which, upon annealing, nanocrystallize into a state with ultrafine bcc-Fe grains. Numerous studies about soft magnetic nanocrystalline materials have been published,[1,2] including the dependence of the functional properties on annealing conditions. The reason for the good soft magnetic properties of these nanocrystalline materials is understood to be a consequence of the reduction in the effective magnetocrystalline anisotropy on forming ultrafine grains.[3] In amorphous alloys it is well known that induced magnetic anisotropy can be effectively suppressed by controlling the quench rate or by annealing the same in a rotating magnetic field.[4] From the point of view applications, it is thus useful to know how the cooling rate after annealing influences the soft magnetic properties of nanocrystalline alloys. In this article, we investigate and discuss the effect of cooling rate after annealing $Fe_{88}Zr_7B_4Cu_1$ nanocrystalline alloys which are known to exhibit soft magnetic properties with high saturation magnetization and permeability.[5] Scanning electron microscopy (SEM) and atomic force microscopy (AFM) surface morphology characterizations shows a finer grain distribution and much smoother surface in the rapidly quenched sample, resulting in low coercivity and good soft magnetic properties.

Amorphous $Fe_{88}Zr_7B_4Cu_1$ alloy ribbons were prepared by the well-known single roller melt spinning technique. The ribbons obtained were 20 μm thick and about 2 mm wide. They were wound into toroidal cores and annealed for 1 h above their crystallization temperatures T_{x1} in N_2 gas atmosphere. The structure of the samples was examined by x-ray diffractometer using Cu $\kappa\alpha$ radiation and transmission electron microscopy (TEM). The cooling rate after annealing was varied by carrying out two different methods: (a) by slow cooling a vacuum-sealed specimen to ambient conditions, and (b) by water quenching the sample in an Ar gas atmosphere after vacuum annealing. The effective permeability was measured at 1 kHz and 0.8 A/m with an impedance analyzer. The magnetic induction at 800 A/m and coercive force were measured with a dc hysteresis loop tracer. The saturation magnetization measurements were carried out by means of a superconducting quantum interference device (SQUID) magnetometer in a field of 1 T in the temperature range 5–300 K. The features of surface quality of the ribbon were investigated with SEM and AFM.

The amorphous $Fe_{88}Zr_7B_4Cu_1$ alloy was annealed at various temperatures above the first crystallization temperature, 471 °C, in order to form nanocrystallites. Figure 1 show the effective permeability (μ_e) and magnetic coercivity (H_c) of $Fe_{88}Zr_7B_4Cu_1$ alloy as a function of the annealing temperature. The effective permeability of the alloys increased with annealing temperatures. Especially, as the cooling rate

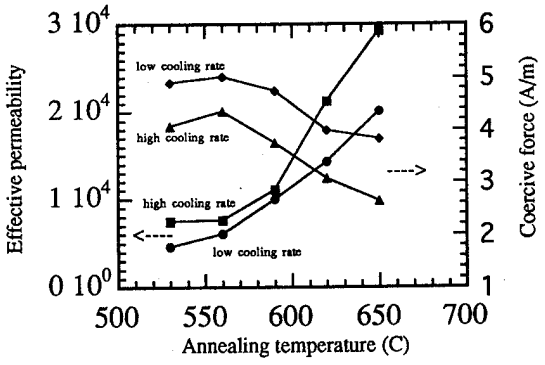


FIG. 1. The effective permeability (μ_e) at 1 kHz and magnetic coercivity (H_c) as a function of annealing temperature for $Fe_{88}Zr_7B_4Cu_1$ alloy on fast and slow cooling, respectively.

 0021-8979/96/79(8)/5153/3/$10.00 © 1996 American Institute of Physics

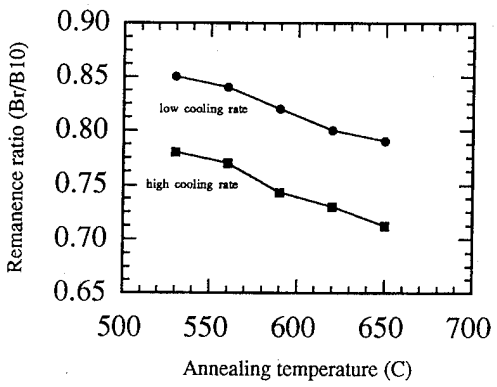


FIG. 2. The remanence ratio (Br/B_{10}) as a function of annealing temperature for $Fe_{88}Zr_7B_4Cu_1$ alloy on fast and slow cooling, respectively.

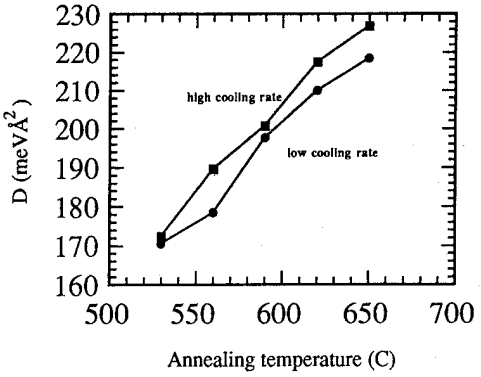


FIG. 3. The spin-wave stiffness (D) as a function of annealing temperature for $Fe_{88}Zr_7B_4Cu_1$ alloy fast and slow cooling, respectively.

increased, the effective permeability, 2.1×10^4, improved by 50% on annealing at 650 °C. On the other hand, although not shown in the figure, μe values decrease drastically on annealing the samples above 650 °C. The coercive field is found to be consistently smaller for samples processed with a higher cooling rate at all annealing temperatures and reaches values as low as 3 A/m (~38 mOe). Notice from high that H_c decreases monotonically with increasing annealing temperatures. It is useful to point out that on annealing above 650 °C, H_c is found to increase drastically. This is consistent with the TEM morphology studies, which show larger grain growth and intergranular structures on annealing above 650 °C (see Fig. 4 which will be discussed later).

Figure 2 shows the remanence ratio (B_r/B_{10}) as a function of annealing temperature. The remanence ratio is a measure of the distribution of domain orientation and is strongly correlated with the induced magnetic anisotropy. In ribbon-type amorphous and nanocrystalline materials, most of the spontaneous magnetization is aligned in the direction of the ribbon axis because the self-induced magnetic anisotropy is considered to form along this direction due to stress effects during the casting of the ribbons. Notice that the remanence ratios for the samples cooled at the higher rate are all smaller than those for the more slowly cooled samples, suggesting that the rapid cooling suppresses the induced anisotropy. The above studies thus show consistently that higher cooling rate has an advantage in obtaining higher permeability and good soft magnetic properties. Furthermore, because of rapid cooling from the higher annealing temperature a fine scale random distribution of the nanostructured particles is obtained. This decreases further the effective local anisotropy and hence results in lower H_c and higher μ_e.

In a nanocrystallized sample the temperature dependence of the magnetization would reflect the effect of annealing on the stiffness constant of the amorphous matrix as well as that of the nanocrystallized magnetic entities. This is specially so because it is well known that the spin-wave stiffness constant in an amorphous material is half of that for the crystalline analog. At low temperatures, the magnetization $M(T)$ is well described in terms of the spin-wave approximation

$$[M(T)-M(0)]/M(0)=BT^{3/2}+CT^{5/2}. \quad (1)$$

The Bloch coefficient B, which is the thermal average of the total contribution arising from spin waves of all wavelengths, is related to the spin-wave stiffness, D, through the expression[6]

$$D=\xi(3/2)^{2/3}[g\mu_B/M(0)B](k_B/4\pi), \quad (2)$$

where $\xi(3/2)$ is the Riemann zeta function and g is the spectroscopic splitting g factor. Figure 3 shows the spin-wave stiffness, D, as a function of annealing temperature for the two different cooling rates. The values of D were determined from a fit to the SQUID magnetic data in the temperature range within 5–200 K. As seen in Fig. 3, it is found that the

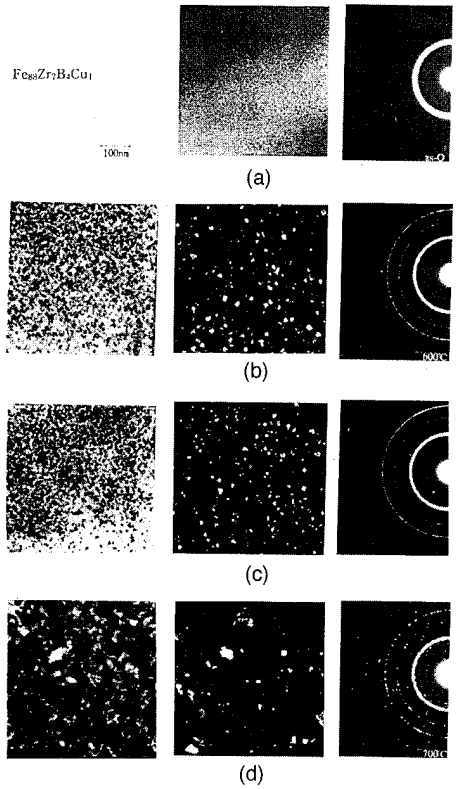


FIG. 4. The bright- and dark-field electron micrograph and selected-area electron diffraction for $Fe_{88}Zr_7B_4Cu_1$ alloy as a function of annealing temperature. The annealing conditions are (a) as-quenched, (b) 600 °C, (c) 650 °C, and (d) 700 °C.

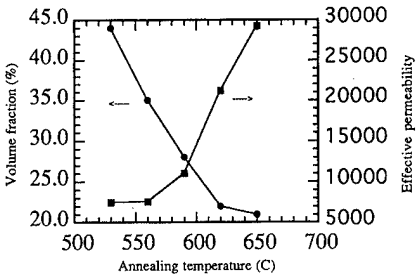


FIG. 5. The volume fraction of residual amorphous phase and effective permeability for the sample cooled at the higher rate as a function of annealing temperatures for $Fe_{88}Zr_7B_4Cu_1$ alloy.

values for D change from 172.3 meV Å^2 to as much as 226.8 meV Å^2 on fast cooling from 650 °C. Furthermore, the value of D is consistently higher for the fast quenched state and for the 650 °C annealed sample the difference is as much as about 4%. From the observed changes in the value of D on annealing we estimate volume fraction of the nano crystal assuming the value of D for pure Fe from literature.[7] In Figure 4 is shown the bright and dark field electron micrograph and selected-area electron diffraction pattern of the samples as a function of annealing temperature. Clearly, while nanocrystallized particle size, 7–12 nm, does not change very much on annealing the sample up to 650 °C, drastic changes in the morphology along with intergranular effects are observed on annealing at higher temperature.

In order to evaluate the fraction of the residual amorphous phase, we used TEM analysis as well as the XRD data. We used line fitting pattern of crystalline and amorphous peaks of the samples obtained by x-ray diffraction pattern and the ratio between crystallites and amorphous matrix in TEM micrographics. We estimate the amorphous phase correlates well with a simple evaluation using the magnetic data taking into consideration independent contributions to the magnetization from the amorphous matrix and the nanocrystals. Figure 5 represents the volume fraction of the residual amorphous phase and the effective permeability for the sample cooled at the higher rate. Our previous studies[8] on these samples show that the saturation magnetostriction of $Fe_{88}Zr_7B_4Cu_1$ alloy also has a minimum value of nearly zero when annealed in the temperature regime around 620–650 °C. Furthermore, over the same annealing temperature interval the volume fraction of the residual amorphous phase is found to remain nearly the same. However, the permeability for the sample annealed at 650 °C is higher than that observed for the 620 °C annealed sample. Hence, this result shows that low saturation magnetostriction is not the only important factor for obtaining soft magnetic properties. In this case we argue that the permeability is limited by magnetocrystalline anisotropy and that it can be suppressed by a high cooling rate after annealing.

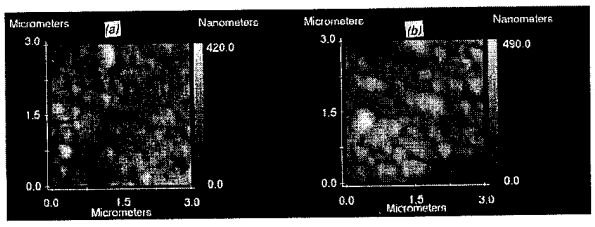


FIG. 6. The AFM surface morphology of the samples' different cooling rates after nano crystallizing $Fe_{88}Zr_7B_4Cu_1$ alloy at 650 °C with (a) high cooling rate and (b) low cooling rate.

The surface microstructures arising from the different cooling rates after annealing have been investigated using SEM and AFM. Figure 6 shows the AFM images for samples with two cooling rates. It can be noticed that the surface morphology is significantly smoother after cooling at the higher rate. Furthermore, from a chemical analysis energy-dispersive x ray (EDX), we find that the surface of the slowly cooled sample has an increasing tendency to oxidize. Thus the slow cooled sample with a rougher more inhomogeneous grain distribution appears to provide additional domain pinning centers and result in higher coercivity values. Undoubtedly more detailed comparison to establish the relationship of the microstructure to the obtained coercivity values would be desirable.

In summary, we have studied the magnetic properties of nanocrystalline $Fe_{88}Zr_7B_4Cu_1$ alloy cooled at different rates after annealing. The increase of permeability, decrease of remanence ratio, as well as decrease in the magnetic coercivity H_c to values as low as 3 A/m are consistent with the expected suppression of the induced magnetic anisotropy. From TEM microstructural analysis and XRD peak we estimate the volume fraction of the amorphous matrix to that of the nanocrystallized magnetic entities. Finally, SEM(EDX) and AFM surface morphology studies are shown to evidence a random distribution of fine nanocrystalline entities and a much finer surface profile for the sample rapidly cooled directly from the annealing temperatures.

This research has been supported by the National Funding Agencies in Sweden and Korean Science and Engineering Foundation under Grant No. 941-0200-0330-2.

[1] Y. Yoshizawa, S. Oguma, and K. Yamauchi, J. Appl. Phys. **64**, 6044 (1988).
[2] K. Suzuki, A. Makino, A. Inoue, and T. Masumoto, J. Appl. Phys. **70**, 6232 (1991).
[3] G. Herzer, IEEE Trans. Magn. **26**, 1397 (1990).
[4] H. Sakakima, H. Senno, Y. Yanagiuchi, and E. Hirota, J. Appl. Phys. **52**, 2480 (1981).
[5] K. Suzuki, M. Kikuchi, A. Makino, A. Inoue, and T. Masumoto, Mater. Trans. JIM **32**, 961 (1991).
[6] F. Keffer, in *Encyclopedia of Physics* (Springer, Berlin, 1966), Vol. XVII-2.
[7] R. J. Birgeneau, J. A. Tarvin, G. Shirane, E. M. Gyorgy, R. C. Sherwood, H. S. Chen, and C. L. Chien, Phys. Rev. B **18**, 2192 (1978).
[8] K. S. Kim, S. C. Yu, K. Y. Kim, T. H. Noh, and I. K. Kang, IEEE Trans. Magn. **29**, 2679 (1993).

Improvement of soft magnetism of $Fe_{90}Co_{10}$ sputtered films by addition of N and Ta

Shigeki Nakagawa, Satoshi Tanaka, Katsumi Suemitsu, and Masahiko Naoe
Deptartment of Physical Electronics, Tokyo Institute of Technology, Meguro, Tokyo 152, Japan

The addition of Ta and N into sputtered $Fe_{90}Co_{10}$ alloy films was performed to attain soft magnetism with large saturation magnetization $4\pi M_s$. Addition of Ta below 8 at. % to $Fe_{90}Co_{10}$ films improved their crystallinity and the lattice constant of Fe crystallites was expanded. These films revealed relatively large $4\pi M_s$ of about 21 kG. The deposition of Fe–Co and Fe–Co–Ta films at N_2 partial pressure P_{N2} below 0.1 m Torr was so effective as to cause fine granulation in the film. $Fe_{84.6}Co_{8.4}Ta_7$:N films deposited at P_{N2} of about 0.2 mTorr and postannealed at 150 °C revealed $4\pi M_s$ and relative permeability μ_r of about 16 kG and 1500, respectively. © *1996 American Institute of Physics.* [S0021-8979(96)29508-X]

I. INTRODUCTION

Magnetic thin films with large saturation magnetization $4\pi M_s$ deposited on thin polymer sheet substrate are regarded as promising candidates for many applications, such as core materials in micromagnetic devices and the backlayers in double layered media for perpendicular magnetic recording.[1] The important requirements for these thin films are that they exhibit large $4\pi M_s$ and high relative permeability μ_r. Furthermore, they should be deposited at low substrate temperature T_s because of low heat resistance of the substrates. Although thin films of Fe–Ni and Fe–Si–Al alloys have been used as the soft magnetic layers, $4\pi M_s$ of them were relatively small below 12 kG. $Fe_{90}Co_{10}$ alloy has an extremely large $4\pi M_s$ of about 24 kG. However, $Fe_{90}Co_{10}$ alloy has a bcc crystalline phase and large saturation magnetostriction constant λ_s of about 1.5×10^{-5}. Then, it is required to reduce λ_s and grain size of the films in order to improve the soft magnetism of $Fe_{90}Co_{10}$ thin films. Iron nitride Fe–N thin films were widely investigated as soft magnetic thin films for many applications mentioned above.[2] In addition, Fe–Ta–N thin films were also found as the soft magnetic core layers in MIG-type VTR heads with high performance of recording characteristics.[3,4] In this study, N and Ta were added into $Fe_{90}Co_{10}$ thin films during sputtering in order to improve the soft magnetism through the effects of reduction of grain size.

II. EXPERIMENTAL PROCEDURE

Specimen films were deposited by the facing targets sputtering apparatus. $Fe_{90}Co_{10}$ alloy plates were used as targets. Fe–Co–N and Fe–Co–Ta–N films were deposited by reactive sputtering method using mixture gas of N_2 and Kr. Total pressure of the mixture gas was set at 1 m Torr, and the N_2 partial pressure P_{N2} was adjusted to control the N contents in deposited films. Ta was added into $Fe_{90}Co_{10}$ films by using the composite targets in which Ta sheet plates were placed on $Fe_{90}Co_{10}$ targets. The films were deposited on polyethylene naphthalate (PEN) tape substrates at room temperature. Si wafers were also used as the substrates for investigating postannealing effect. Thickness of the films was about 200 nm. Annealing treatments were performed at a temperature of 150 °C in an evacuated chamber for 1 h. Film composition was analyzed by inductively coupled plasma (ICP) analysis. Crystallographic and magnetic characteristic were analyzed by x-ray diffractometry (XRD) and the vibrating-sample magnetometer (VSM), respectively.

III. RESULTS AND DISCUSSION

From x-ray diffraction (XRD) patterns, $Fe_{90}Co_{10}$ films revealed a bcc-Fe crystalline phase with (110) orientation, but the crystalline phase was degraded monotonically with increase of N_2 partial pressure P_{N2}. The addition of N to $Fe_{90}Co_{10}$ films seemed effective to enhance the fine granulation of crystallites in the films and to expand the lattice parameter. The formation of γ-Fe_4N phase was not observed in these films.

Figure 1 shows the variation of XRD patterns of $(Fe_{90}Co_{10})_{100-x}Ta_x$ films for various Ta content x. Addition of Ta up to 10% improved the crystallite growth and caused the significant shift of peak in XRD patterns. It was not clarified whether the peak shift toward the lower side of the diffraction angle means the expansion of lattice of α-Fe crystallites or the appearance of other phases, such as Fe_7Ta_3 and Fe_2Ta. Excessive Ta content above 9 at. % caused the degra-

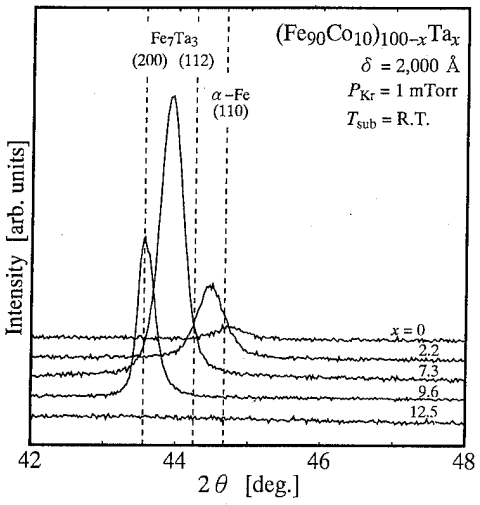


FIG. 1. X-ray diffraction patterns of $(Fe_{90}Co_{10})_{100-x}Ta_x$ films for various Ta content x.

 0021-8979/96/79(8)/5156/3/$10.00 © 1996 American Institute of Physics

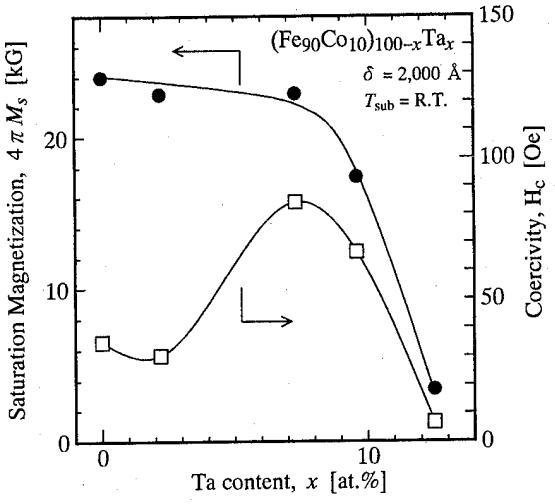


FIG. 2. Changes of $4\pi M_s$ and H_c of $(Fe_{90}Co_{10})_{100-x}Ta_x$ films as a function of Ta content x.

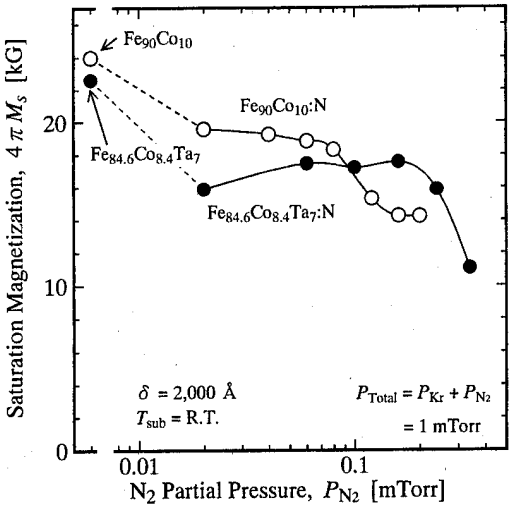


FIG. 4. $4\pi M_s$ of $Fe_{90}Co_{10}$:N and $Fe_{84.6}Co_{8.4}Ta_7$:N films as a function of P_{N2}.

dation of crystallinity. Figure 2 shows the changes of $4\pi M_s$, and coercivity H_c of $(Fe_{90}Co_{10})_{100-x}Ta_x$ films as a function of Ta content x. $Fe_{90}Co_{10}$ films exhibited a large $4\pi M_s$ of about 24 kG. Such a large $4\pi M_s$ decreased gradually to about 22 kG with increase of Ta content x up to about 8 at. %. Although excessive Ta content above 8 at. % caused the significant degradation of $4\pi M_s$, $(Fe_{90}Co_{10})_{91}Ta_9$ films exhibited relatively large $4\pi M_s$ of about 17 kG. These films with such a large $4\pi M_s$ are suitable for practical applications as soft magnetic flux path. However, these films exhibited relatively high coercivity H_c of about several tenths Oe. Such high coercivity seemed to be originated from the crystalline anisotropy because crystallite growth was observed in the films, as shown in Fig. 1. Since it seemed necessary for attaining good soft magnetism to cause fine granulation of crystallites in $Fe_{90}Co_{10}$ films, the addition of N to $(Fe_{90}Co_{10})_{100-x}Ta_x$ was investigated.

From XRD patterns, it was observed that the addition of N into $Fe_{84.6}Co_{8.4}Ta_7$ films caused a drastic decrease in height and broadening of the peak, which means fine granulation. Furthermore, peak shift was also observed for films deposited at higher P_{N2}. Figure 3 shows the P_{N2} dependence of diffraction intensity I_p and crystallite size $\langle D \rangle$ of $Fe_{90}Co_{10}$:N and $Fe_{84.6}Co_{8.4}Ta_7$:N films evaluated on the XRD patterns, as shown in Fig. 2. The addition of a small amount of N caused a drastic decrease of I_p and $\langle D \rangle$, especially for Fe–Co–Ta films. However, crystalline phase was observed in Fe–Co:N films even at P_{N2} as high as about 0.1 m Torr. This crystalline phase seems to correspond to α-Fe or ϵ-$Fe_{2-3}N$ phases. On the contrary, such crystalline phase was not observed in $Fe_{84.6}Co_{8.4}Ta_7$:N films deposited at P_{N2} around 0.1 m Torr, so that they looked amorphouslike.

Figure 4 shows the changes of $4\pi M_s$ of $Fe_{90}Co_{10}$:N and $Fe_{84.6}Co_{8.4}Ta_7$:N films as a function of P_{N2}. Deposition at

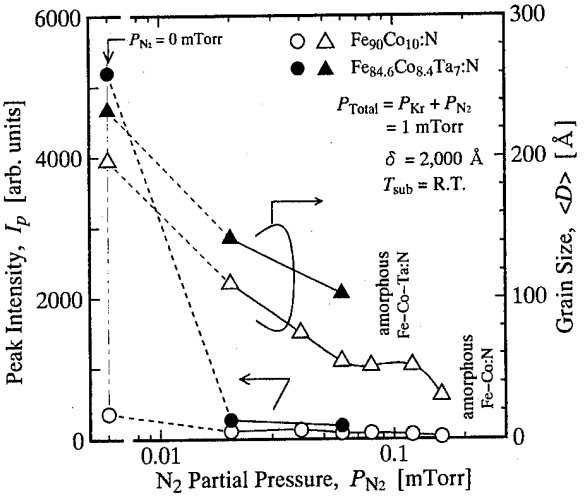


FIG. 3. P_{N2} dependence of diffraction intensity I_p and grain size $\langle D \rangle$ of $Fe_{90}Co_{10}$:N and $Fe_{84.6}Co_{8.4}Ta_7$:N films.

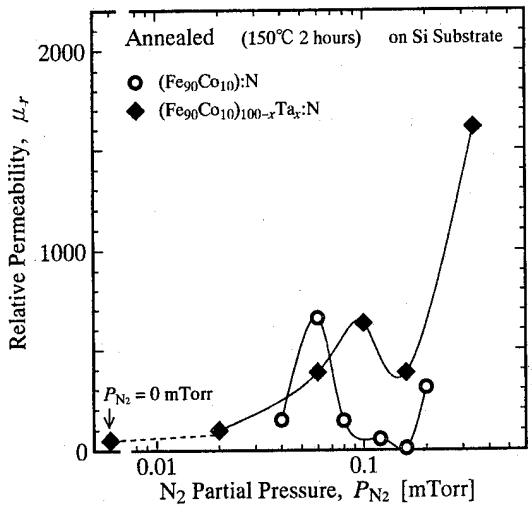


FIG. 5. Change of μ_r of $Fe_{90}Co_{10}$:N and $Fe_{84.6}Co_{8.4}Ta_7$:N films after post-annealing at 150 °C as a function of P_{N2}.

P_{N2} as low as 0.02 m Torr caused the decrease of $4\pi M_s$ from 24 to 20 kG and from 22 to 17 kG for $Fe_{90}Co_{10}$:N and $Fe_{84.6}Co_{8.4}Ta_7$:N films, respectively. The decrease of $4\pi M_s$ from 18 to 15 kG was also observed at P_{N2}, higher than 0.1 m Torr for $Fe_{90}Co_{10}$:N films. The decrease seemed to originate from the existence of $Fe_{2-3}N$ crystallites in the films. On the contrary, $4\pi M_s$ of $Fe_{84.6}Co_{8.4}Ta_7$:N films was around 17 kG at P_{N2} up to 0.2 mTorr. All of as-deposited films, however, exhibited their permeability μ_r of about 200 in spite of the addition of nitrogen.

The annealing process at the relatively low temperature of 150 °C significantly improved the soft magnetism. Figure 5 shows the change of μ_r of $Fe_{90}Co_{10}$:N and $Fe_{84.6}Co_{8.4}Ta_7$:N films postannealed at 150 °C as a function of P_{N2}. Although a slight increase of μ_r for $Fe_{90}Co_{10}$:N films was observed at P_{N2} around 0.06 m Torr, μ_r of $Fe_{90}Co_{10}$:N films were relatively low. On the contrary, $Fe_{84.6}Co_{8.4}Ta_7$:N films exhibited relatively high μ_r of about 500 at P_{N2} around 0.1 m Torr. Furthermore, $Fe_{84.6}Co_{8.4}Ta_7$:N films deposited at P_{N2} of about 0.3 mTorr exhibited high μ_r of about 1600. These films with such a high μ_r may be applicable for core materials in micromagnetic devices and the backlayers in recording media. These results seemed to originate from both the fine granulation of Fe–Co crystallites by nitridation and the drastic decrease of saturation magnetostriction constant λ_s of $Fe_{84.6}Co_{8.4}Ta_7$:N films. Although λ_s of $Fe_{90}Co_{10}$ films is about 1.5×10^{-5}, it was successfully decreased to the order of 10^{-6} by the addition of Ta and N to Fe–Co films.

IV. CONCLUSION

The addition of Ta and N to $Fe_{90}Co_{10}$ alloy films sputter-deposited on polymer tape substrate was investigated to attain soft magnetism with large $4\pi M_s$ and high μ_r. The results obtained in this study were summarized as follows:

(1) Addition of Ta atoms to $Fe_{90}Co_{10}$ enhanced the crystallite growth and caused lattice expansion of Fe crystallites while Ta content is below 8 at. %. These films exhibited relatively large $4\pi M_s$ of about 22 kG. Excessive Ta content above 8 at. % caused degradation of crystallinity and decrease of $4\pi M_s$.

(2) Introduction of a small amount of N_2 into the reactive sputtering chamber was so effective as to cause fine granulation of crystallites in Fe–Co films, and especially in Fe–Co–Ta ones.

(3) $Fe_{84.6}Co_{8.4}Ta_7$:N films deposited at P_{N2} of about 0.2 m Torr and postannealed at 150 °C exhibited $4\pi M_s$ and μ_r about 16 kG and 1500, respectively.

Consequently, these Fe–Co–Ta:N films may be applicable to the practical applications, especially to the backlayers in double layered magnetic tapes.

[1] S. Iwasaki, Y. Nakamura, and K. Ouchi, IEEE Trans. Magn. **MAG-15**, 1456 (1979).

[2] M. Takahashi, H. Shoji, and T. Wakiyama, J. Magn. Soc. Jpn. **13**, Suppl. S1, 585 (1989).

[3] N. Ishiwata, C. Wakabayashi, and H. Urai, J. Appl. Phys. **69**, 5616 (1991).

[4] T. Okumura, A. Osaka, N. Ishiwata, M. Kitamura, and H. Urai, IEEE Trans Magn. **MAG-28**, 2121 (1992).

Effect of nitrogen interstitial in α-Fe crystalline on the magnetic soft properties of FeTaN thin films

W. C. Chang and D. C. Wu
Department of Physics, National Chung Cheng University, Ming-Hsiung, Chia-Yi, Taiwan, Republic of China

J. C. Lin and C. J. Chen
Materials Research Laboratories, Industrial Technology Research Institute, Chutung, Hsinchu, Taiwan, Republic of China

The effect of nitrogen interstitial in α-Fe crystalline on the magnetic soft properties of $Fe_{87.5}Ta_{12.5}Nx$ films has been investigated. The magnetic soft properties can be improved by carefully controlling the nitrogen flow ratio during sputtering and the postannealing to result in a film with fine grain size and low magnetostriction. Using x-ray diffraction technique, the nitrogen content in the α-Fe crystalline of FeTaN film can be estimated from the effect of lattice expansion of α-Fe crystalline due to nitrogen interstitial. It is found that the film with about 7.5 at. % N_2 in α-Fe crystalline exhibits the best magnetic soft properties of $Br=1.6$ T, $Hc=0.2$ Oe and $\mu_i(1\ \text{MHz})=3400$, respectively. X-ray diffraction analysis is found to provide a proper and an easy way to identify the suitable condition for growing excellent magnetic soft FeTaN thin films. © *1996 American Institute of Physics.* [S0021-8979(96)29608-6]

I. INTRODUCTION

Magnetic soft FeTaN thin films have been reported to be good candidates, superior to sendust (FeAlSi), to act as a metallic layer in metal-in-gap head for increasing the gap field while writing a high coercivity recording media. The virtues of FeTaN films include high saturation magnetization, very low coercivity, and high permeability in the high-frequency region.[1,2] Their excellent magnetic soft properties are primarily contributed by the formation of TaN phase during annealing treatment to prevent α-Fe grains from growing over nanometer scale, so-called nanocrystalline structure.[3] The nanometer scale α-Fe grains can effectively reduce their magnetic anisotropy energy through the micromagnetic interaction among them.[4] The key factor is that one should introduce a suitable content of nitrogen atom to the film during sputtering to meet the above purpose[2,5] and also a certain amount of magnetostriction intrinsic to the microcrystalline magnetic soft film is necessary to ensure high permeability.[4] The suitable nitrogen content needed inside the film is normally dependent upon the content of Ta in the film, where the nitrogen content of the films were usually identified with electron spectroscopy for chemical analysis (ESCA) or Auger spectrometer. To the best of our knowledge, it seems that no article has ever mentioned the effect of nitrogen in α-Fe crystalline on the magnetic properties of FeTaN films. In this study, we have paid very special attention to the effects of nitrogen flow and annealing temperature on the variation of α-Fe (110) lattice spacing and on the nitrogen content in α-Fe, evaluating the same from x-ray diffraction analysis. Finally, their relationship with the magnetic properties of the $(Fe_{87.5}Ta_{12.5})N_x$ films will be discussed.

II. EXPERIMENT

The target material with the normal composition $Fe_{87.5}Ta_{12.5}$ was melted from 99.9 wt % Ta and 99.999 wt % Fe metal with vacuum induction furnace, and then the melt was cast in a copper mold 2 in. in diameter. The $(Fe_{87.5}Ta_{12.5})N_x$ films were sputtered on recrystallized glass, 1 cm×1 cm×0.05 cm in size, using a dc sputtering apparatus. The surfaces of the target and substrate are parallel while the distance was kept at 6 cm. In order to obtain FeTaN films with various nitrogen content, argon gas, 10 and 15 sccm, in combination with nitrogen gas, flow ratio $(R(N_2)=F(N_2)/[F(Ar)+F(N_2)])$ in the range from 8% to 15%, was regulated and flown into the vacuum chamber for reactive sputtering. After sputtering, a thin SiO_2 film, about 100 Å thick, was sputtered on the FeTaN film in order to prevent oxidation during the subsequent annealing process. Annealing treatment was performed at 425–500 °C for 30 min. An x-ray diffractometer with Cu $K\alpha$ radiation was adopted to analyze the crystallinity of the as-sputtered and postannealed films. Lattice constant of the α-Fe crystal of the postannealed films was calculated from their α-Fe(110) lattice spacing. The magnetic properties of the films were measured with a vibrating-sample magnetometer (VSM) and with a LCR meter. The N_2 content in the α-Fe crystal of the films was estimated from the relationship of α-Fe(110) lattice spacing versus the amount of nitrogen interstitial reported by Kusumi *et al.*[7]

III. RESULTS AND DISCUSSION

Figure 1 exhibits the diffraction patterns of the as-deposited and postannealed, from 425 to 500 °C, $(Fe_{87.5}Ta_{12.5})N_x$ films sputtered under 15 sccm Ar and 8% N_2 atmosphere. For the as-deposited film, no diffraction peak arising from the film has been found, confirming that the film is in the amorphous state. After annealing at 425 °C or higher temperature, a broad but low intensity α-Fe (110) peak appears reflecting that the grain size of α-Fe is quite small. The diffraction peak of TaN phase is also not found due to its small size. One thing to be noted is that the 2θ position of those α-Fe (110) peaks is lower than 44.2°, which is lower than 44.7° of a pure α-Fe (110) peak, implying that the lattice spacing of α-Fe crystal is expanded. In other words, the co-sputtered N atoms were not all combined with

 0021-8979/96/79(8)/5159/3/$10.00 © 1996 American Institute of Physics

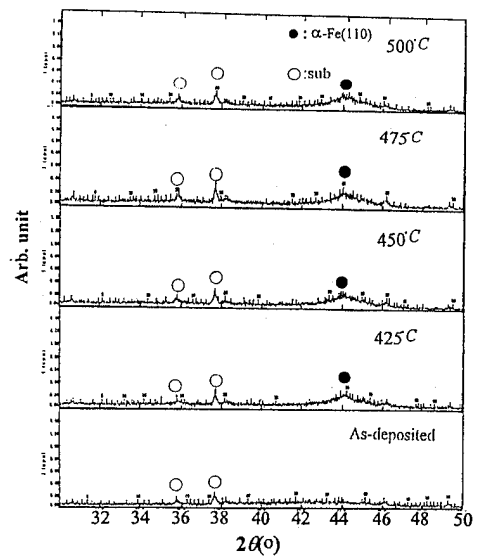


FIG. 1. X-ray diffraction patterns of the films sputtered under 15 sccm argon gas and 8% nitrogen gas flow ratio (500 °C anneal).

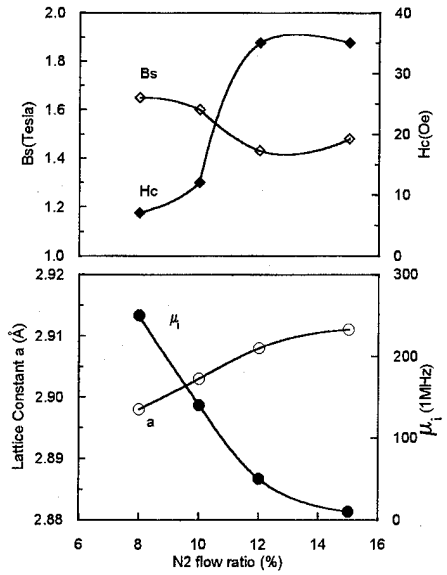


FIG. 3. The variation of B_r, H_c, μ_i and lattice constant, a, with nitrogen flow ratio for the films (0.6 μm thick) sputtered under 15 sccm argon gas.

Ta to form TaN to impede α-Fe grains from growing; instead many of them were interstitialed in α-Fe crystal after crystallization. The value $\Delta(2\theta)$, defined as $44.7°-(2\theta)_{\alpha\text{-Fe}(110)}$, corresponds to the nitrogen content inside the α-Fe crystal. The larger the $\Delta(2\theta)$ the higher the nitrogen interstitial in the α-Fe crystal is. Figure 2 shows the variation of 2θ position of α-Fe (110) peak of the films sputtered under different atmosphere and followed by 450 and 500 °C annealing. It can be seen that the value of 2θ is obviously decreased with increasing quantity of Ar flow and the N_2 flow ratio. However, increasing the annealing temperature results in a slight increase of 2θ in high N_2 flow ratio ($\geq$12%) region, but a large increase in low N_2 region (<12%). In other words, too large N_2 flow during sputtering is always accompanied by an over-quantity nitrogen atom interstitial in the α-Fe phase after crystallization, and this might result in the increase of its magnetostriction[6] and deteriorate the magnetic soft properties rapidly. Accordingly, except for supplying enough nitrogen to form TaN phase to impede α-Fe grains from over growing, controlling the suitable nitrogen flow to prevent excessive nitrogen interstitial in α-Fe crystalline should also be considered.

Figures 3 and 4 demonstrate the effect of nitrogen flow ratio on the α-Fe lattice constant, a, and the magnetic properties, B_s, H_c, and μ_i(1 MHz), of the films sputtered under 15 and 10 sccm argon gas flow, respectively. For the former, it is clear that lattice constant a and coercivity H_c increase and in reverse B_s and μ_i decrease with increasing N_2 flow ratio. The magnetic soft properties, especially H_c and μ_i, are still not magnetic soft in this case. For the latter, the trend of a, H_c, B_s, and μ_i changing with N_2 flow ratio is almost the same as that in the previous case, however, after reducing the argon gas flow from 15 to 10 sccm, an excellent magnetic

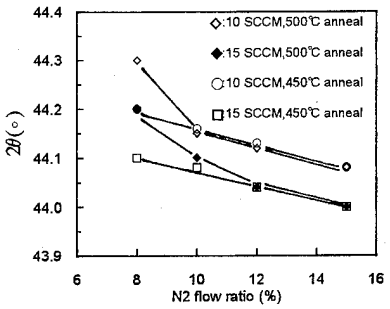


FIG. 2. The variation of 2θ position of α-Fe(110) peak with nitrogen flow ratio in various films.

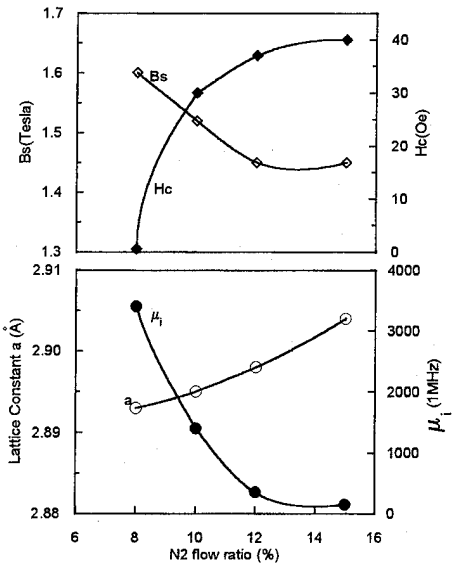


FIG. 4. The variation of B_r, H_c, μ_i, and lattice constant, a, with nitrogen flow ratio for the films (0.6 μm thick) sputtered under 10 sccm argon gas.

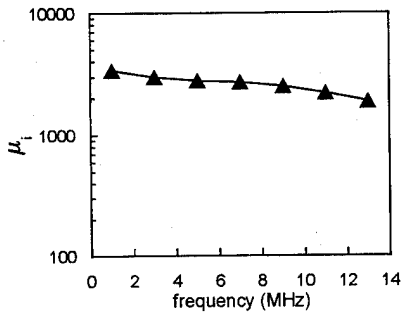


FIG. 5. The frequency response of μ_i of the film with the best magnetic soft properties in this study (10 sccm Ar, 8% N_2 flow ratio and 500 °C anneal).

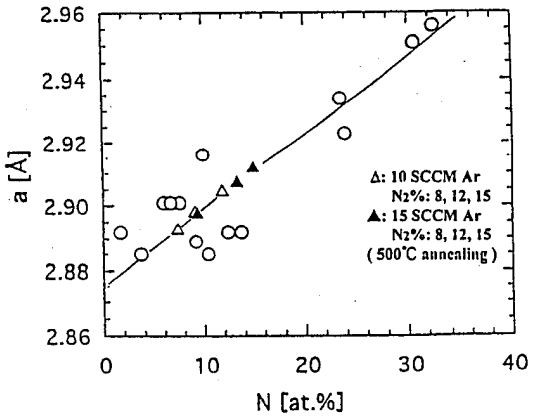


FIG. 6. Intra fitting of the α-Fe lattice constant of some studied films on the figure of lattice constant vs nitrogen content of the $Fe_{1-x}N_x$ films plotted by Kusumi *et al.*[7]

soft property, $B_s = 1.6$ T, $H_c = 0.2$ Oe, and $\mu_i(1\text{ MHz}) = 3400$, is achieved in the film sputtered at 8% N_2 flow ratio. In this film, the lattice constant, a, has already reduced to 2.893 Å, while it is still larger than 2.876 Å, the value of a nitrogen free α-Fe crystal. Figure 5 shows its frequency response of μ_i indicating that the permeability of the film is also very stable in the high-frequency region.

As mentioned before, too many nitrogen interstitials in α-Fe grains may deteriorate the magnetic soft properties of FeTaN films, whereas the nitrogen content of the films can only be detected more precisely with ESCA and Auger spectroscopy. Due to the large spot size of the electron beam in the above two spectroscopy and also too small grain size of the α-Fe and TaN phases, a true nitrogen content in α-Fe crystal can hardly be precisely detected individually. However, if one knows the variation of α-Fe (110) lattice spacing with the nitrogen concentration in it, the interstitial nitrogen content in α-Fe crystal of the FeTaN films can be evaluated. Fortunately, Kusumi *et al.* had established a relationship concerning the dependence of lattice constant of α-Fe (110) crystal with the nitrogen concentration in $Fe_{1-x}N_x$ films in their latest study.[7] Although the data have much scatter, a linear relationship between the lattice constant of α-Fe and the nitrogen concentration in the film was found. After intra fitting our experimental results of the films sputtered with various atmosphere and followed by 500 °C annealing in their figure, as shown in Fig. 6, the nitrogen content in the α-Fe crystalline of the studied FeTaN films can be estimated. It was found that about 7.5 at. % nitrogen, after the formation of TaN phase, is estimated existing in α-Fe crystal of the $(Fe_{87.5}Ta_{12.5})N_x$ film with the best magnetic soft properties (film sputtered under 10 sccm Ar and 8% nitrogen flow ratio then followed by 500 °C annealing). Excess nitrogen content in α-Fe crystalline would lead to the increment of magnetostriction to deteriorate the magnetic soft properties of the films rapidly. From the above results, in addition to the control of the grain size of α-Fe crystal, controlling the content of nitrogen interstitial in α-Fe crystal by x-ray diffraction analysis might be a proper and an easy way to justify the suitable condition for growing excellent magnetic soft FeTaN thin films.

ACKNOWLEDGMENT

The research supported by Materials Research Laboratories, Industrial Technology Research Institute Taiwan, Republic of China under Grant No. 35P2320-1 is acknowledged.

[1] N. Ishiwata, C. Wakabayashi, and H. Urai, J. Appl. Phys. **69**, 5616 (1991).
[2] K. Nago, H. Sakakima, K. Ihara, and K. Osano, IEEE Trans. Magn. **28**, 2943 (1992).
[3] E. Haftek and J. A. Barnard, IEEE Trans. Magn. **30**, 3915 (1994).
[4] M. Takahashi, T. Shimatsu, and H. Shoji, Proceedings of the 6th International Conference on Ferrite, 1992 (unpublished), p. 1483.
[5] J. C. Lin, L. J. Chen, and C. J. Chen, IEEE Trans. Magn. **30**, 3912 (1994).
[6] J. C. Cates, C. Alexander, Jr., E. Haftek, and J. A. Barnard, IEEE Trans. Magn. **29**, 3105 (1993).
[7] K. Kusumi, H. Miyajima, and Y. Otani, J. Magn. Soc. Jpn. **18**, 241 (1994).

Giant magnetoresistance induced by spin-correlation scattering in magnetic thin films and other compounds

Liang-Jian Zou
Institute of Solid State Physics, Academia Sinica, P.O. Box 1129, Hefei 230031, China

X. G. Gong and Qing-Qi Zheng
CCAST (World Laboratory), P.O. Box 8730, Beijing, 100080 and Institute of Solid State Physics, Academia Sinica, P.O. Box 1129, Hefei 230031, China

C. Y. Pan
Physics Department, Center of Magnetism in Information Technology, Utah State University, Logan, Utah 84332

We present the study of the giant magnetoresistance effect in ferromagnetically ordered thin film and bulk based on the Hund's rule coupling between the mobile d electron and the core spin of Mn ions. It has been shown that the resistivity is proportional to the spin–spin correlation functions, a maximum resistivity appears near the critical point in absence of magnetic field and an applied field drives the resistivity peak to higher temperature and reduces the peak value, which is in agreement with the experiments. The giant magnetoresistance effect in thin film is attributed to the spin-correlation-dependent scattering and the low-dimensional character. © *1996 American Institute of Physics.* [S0021-8979(96)51808-2]

I. INTRODUCTION

Recently negative magnetoresistance (MR) has been found in perovskitelike ferromagnetic semiconductive thin films, such as in the films of $La_{1-x}Ba_xMnO_3$,[1] $La_{1-x}Sr_xMnO_3$,[2] $La_{1-x}Ca_xMnO_3$ (Ref. 3) and $Nd_{1-x}Sr_xMnO_3$.[4] Their MR ratios $[(R_B-R_0)/R_B]$ reported are much larger than those found in magnetic multilayers. Especially, in epitaxial $La_{1-x}Ca_xMnO_3$ and $Nd_{1-x}Sr_xMnO_3$ thin films, MR ratios are found to be $\sim 10^3$–10^4 under magnetic field $B=6$ T. More recently a giant MR ratio is also found to be in excess of 10^2 for polycrystalline La–Y–Ca–Mn–O compounds.[5] These remarkable findings can provide promising industrial applications in devices. It also brings us an interesting problem, namely, the mechanism of exhibiting such a giant MR in these ferromagnetic transition-metal–oxide compounds.

Some mechanisms[1–8] have been suggested to explain the experimental findings. These studies provide in depth investigations for the problem of interest. However, it seems to us that these proposed mechanisms do not provide a satisfactory answer. The double exchange and magnetic polaron transfer mechanism suggested by some authors[1–5] can explain qualitatively the semiconductive behavior in conduction and the negative temperature coefficient of the resistivity above T_c in the $La_{1-x}R_xMnO_3$ compounds. However, as pointed out by Millis *et al.*,[6] there exist crucial quantitative discrepancies between the experiments and the theory for the resistivity behavior in an external field, besides, it seems to be hard to form magnetic polaron in the heavy doped La–R–Mn–O and Nd–R–Mn–O systems. In the spin-disorder scattering mechanism,[7] the huge MR ratio is attributed to the alignment of the canting of manganese spins in the strong external field. However, as indicated by the experiments,[3,4] the magnetization saturates in a not large magnetic field, and increasing magnetic field further does not change the spin configurations any more, so the spin-disorder scattering mechanism is not responsible for the change of resistivity by several orders in magnitude under the high magnetic field.

In this article, we present another possible mechanism of the giant MR in these ferromagnetic semiconductive materials. The model and formalism is described in Sec. II, the theoretical curves is calculated in Sec. III, the discussion and conclusion is given in Sec. IV.

II. MODEL HAMILTONIAN

In the La–R–Mn–O or Nd–R–Mn–O compounds, the three $3d$ electrons of Mn^{+4} ions at the low level, t_g, can be considered as the localized spin S_i of the ferromagnetic background, the outer-shell $3d$ electron of Mn^{+3} ions at the high level, e_g, can hop and transfer between different Mn sites as an itinerant one, and is responsible for the electric conduction. In such a model, the outer d electron interacts with the core localized spin through the Hund's rule coupling, the Hamiltonian can be expressed as

$$H=H_0+V, \tag{1}$$

$$H_0=\sum_{k\sigma}(\epsilon_k-\sigma\mu_B B)c^{\dagger}_{k\sigma}c_{k\sigma}-\sum_{\langle ij\rangle}A\mathbf{S}_i\cdot\mathbf{S}_j - \sum_i g\mu_B B S^z_i, \tag{2}$$

$$V=-\frac{J}{N}\sum_{ikq}\sum_{\mu\nu}e^{i\mathbf{q}\cdot\mathbf{R}_i}\mathbf{S}_i\cdot c^{\dagger}_{k+q\mu}\sigma_{\mu\nu}c_{k\nu}. \tag{3}$$

Here ϵ_k is the energy spectrum of conduction electrons with respect to the chemical potential μ, A the effective ferromagnetic exchange constant between manganese ions, and only

 0021-8979/96/79(8)/5162/3/$10.00 © 1996 American Institute of Physics

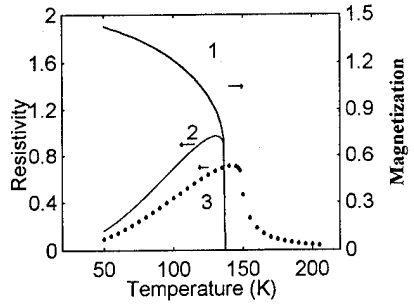


FIG. 1. Magnetization and resistivity of La–Sr–Mn–O bulks with respect to temperatures under different magnetic fields, here $J=300$ K $T_c=140$ K. (1) Magnetization in $B=2$ T, (2) resistivity in $B=6$ T, and (3) resistivity in $B=8$ T.

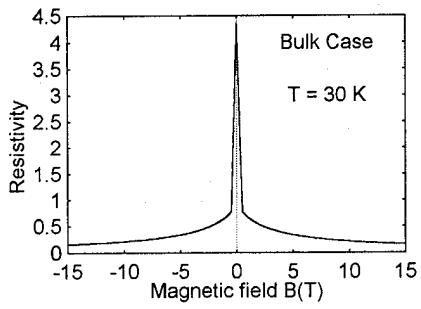


FIG. 2. Magnetoresistance of La–Sr–Mn–O bulks, theoretical parameters are chosen as $J=300$ K, $T_c=140$ K, $T=70$ K.

the nearest-neighbor interaction is considered, $g\mu_B B$ is Zeemann energy of the Mn ions in the magnetic field B; the conduction electron is scattered from state $\mathbf{k}$ spin ν to state $\mathbf{k}+\mathbf{q}$ spin μ by the localized spin $\mathbf{S_i}$ of the magnetic Mn ions. J denotes the coupling between the itinerant electron and the localized spin of Mn $3d$ electrons. One notes that under the external magnetic field and in the internal molecular field of ferromagnetically ordered state, the band of the itinerant electrons will split, this splitting will shift the position of the conduction band with respect to the chemical potential. The spectrum of the conduction electrons with state $\mathbf{k}\sigma$ is $\epsilon_{k\sigma}=\epsilon_k-\sigma(\mu_B B+J\langle S^z\rangle)$. The scattering rate of the conduction electrons scattered by the localized spins is[9]

$$\omega=\frac{2\pi}{\hbar}\sum_m |\langle f|V|m\rangle|^2\delta(E_f-E_m), \tag{4}$$

where $|f\rangle$ refers to the final equilibrium state and $|m\rangle$ the intermediate state of the system during the scattering process. Summing over all the intermediate states at a temperature of T, one gets

$$\omega=\frac{\pi}{\hbar}\frac{J^2D(0)}{4}\sum_{kq\sigma} f_{k\sigma}(1-f_{k\sigma})f_{k+q\bar{\sigma}}(1-f_{k+q\bar{\sigma}})$$
$$\times[\langle S_q^- S_{-q}^+\rangle+\langle S_q^+ S_{-q}^-\rangle+8\langle S_q^z S_{-q}^z\rangle], \tag{5}$$

where $D(0)$ is the density of states of the conduction electrons near the chemical potential, $f_k=1/[e^{\beta(\epsilon_k-\epsilon_F)}+1]$ is the Dirac–Fermi distribution function. The lifetime of the conduction electron between two scatterings is $\tau=\omega^{-1}$, and the resistivity can be obtained by the Drude formula, $\rho=m^*/ne^2\tau=m^*\omega/ne^2$, where n denotes the carrier density, m^* the effective mass of carriers. One could obtain the temperature–and field-dependent resistivity $\rho(T,B)$ as

$$\rho(T,B)=\sum_q F(q,T,B)[\langle S_q^- S_{-q}^+\rangle+\langle S_q^+ S_{-q}^-\rangle$$
$$+8\langle S_q^z S_{-q}^z\rangle], \tag{6}$$

where the factor $F(q,T,B)$

$$F(q,T,B)=\frac{\pi D(0)m^*J^2}{4\hbar ne^2}\sum_{k\sigma} f_{k\sigma}(1-f_{k\sigma})f_{k+q\bar{\sigma}}$$
$$\times(1-f_{k+q\bar{\sigma}}). \tag{7}$$

$F(q,T,B)$ depends on the temperature T and the magnetic field B. Accordingly, for specific doped concentration, x, the effective mass and the concentration of carriers are fixed, the resistivity is determined by the spin-correlation functions and the factor F.

III. RESULTS

In order to obtain quantitative results, the concrete forms of the transverse and the longitudinal spin–spin correlation functions over all the temperature range and in any magnetic field are needed. However, such an exact correlation function is not available for two- and three-dimensional Heisenberg ferromagnets. In this article, the approximate forms of the longitudinal and transverse correlation functions ($T<T_c$) (Ref. 8) and the longitudinal correlation function ($T>T_c$) (Ref. 9) are adopted. The resistivity and the magnetization are measured in reduced units.

A. For three-dimension cases

We first consider the bulk material of La–R–Mn–O, the lattice constant $a=3.8$ Å, and the coordinate number z is 6. The theoretical curves are evaluated for La–Sr–Mn–O compounds.

In the three-dimension case, the order–disorder transition occurs within a narrow temperature range. When approaching the critical point T_c, the spin–spin correlation function changes dramatically from the long-range correlation to short-range one. The temperature dependence of magnetization, the resistivity and the MR in the bulk La–Sr–Mn–O with the magnetic filed $B=8$ T is shown in Fig. 1, these quantities exhibit step fall when temperature (T) exceeds the Curie point T_c, which can be attributed to the weaken of the spin–spin correlation and the reduction of spin-correlated fluctuation scattering. The MR exhibits a maximum, which is similar to results of Fisher *et al.*[10]

The field-dependence of the MR below Curie temperature is shown in Fig. 2. The MR decreases monotonously with increasing magnetic field. The MR ratio in the bulk case is 1600% for $B=8$ T. The behavior of the MR above and below T_c does not agree with the experiment very well.[11] That indicates that some other scatterings are needed to be considered.

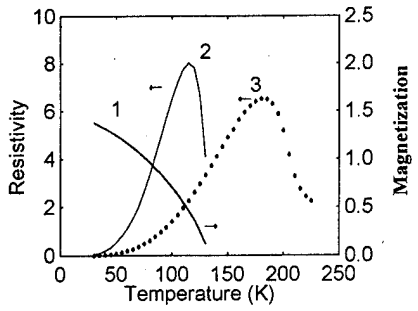


FIG. 3. Temperature dependence of magnetization and resistivity under different magnetic fields for La–Sr–Mn–O thin films where $J=500$ and $T_c=345$ K. (1) Magnetization in $B=1$ T, (2) resistivity in $B=1$ T, and (3) resistivity in $B=10$ T.

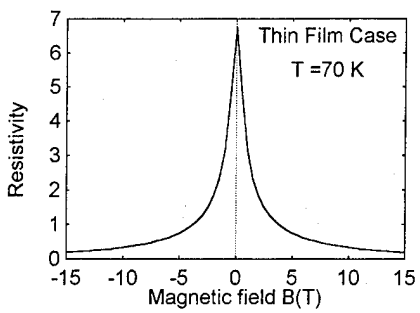


FIG. 4. Field dependence of resistivity for La–Sr–Mn–O thin films. Theoretical parameters: $T_c=240$, $J=500$, and $T=30$ K.

B. For two-dimension cases

In the quasi-two-dimensional systems, such as in thin films, the lattice constant is chosen to be the same as in the three-dimensional case, and the coordinate number is $z=4$. The temperature dependence of the magnetization and the resistivity in La–Sr–Mn–O thin film are shown in Fig. 3. The magnetization is calculated self-consistently under an external magnetic field $B=1$ T. Because of the reduction of the dimension, the transition temperature is broaded. The spin order–disorder transition occurs within a wide range (see Fig. 3). Correspondingly, the resistivities under different magnetic fields exhibit maxima within the transition region, since the spin-correlation scattering rate ω is very large near the transition point. When the magnetic field is increased, the resistivity peak moves to higher temperature and the maximum value is reduced (see curves 2 and 3 in Fig. 3). This could be interpreted as that a strong field aligns all spins in the systems and suppresses the correlation between spin at different sites, thus reduces the spin-correlated fluctuation scattering between the conduction electrons and the localized spins. These theoretical results agree with the experiments very well.[1–4]

The field-dependence of the MR for a quasi-two-dimension system is shown in Fig. 4. One can see that the magnetoresistance also decreases monotonously with increasing field in the strong field region. This fact coincides with the experiments.[1–4] The MR ratio $\Delta R_B/R_B$ in field $B=6$ T can be as high as 1000%.

IV. DISCUSSION AND CONCLUSION

The resistivity due to the interaction Eq. (3) was studied for bulks by Fisher *et al.*[11] Fisher's work doesn't consider the spin-splitting of the conduction electrons caused by the external magnetic field and the internal molecular field, which may be important for the MR effect in an external magnetic field and magnetically ordered state. Our study has shown that the spin correlation scattering is essential in the thin films and should be responsible for the giant MR near T_c where the long-range or the short-range spin–spin correlations and the spin fluctuation are large.

From this study we can summarize several results. (a) If the measurement temperature is below or above far away from the critical point T_c, the MR change ΔR_B is small. However, the MR behaviors below and above T_c may be dramatically different since the former is dominated by the fluctuation scattering of the long-range spin-correlation, the latter is by that of short-range correlation. (b) If the critical transition range is wide, a giant MR could be observed within a wide temperature range, this property is useful for the applications. It suggests us that if we want to find a new kind of material which could be used in room temperature for magnetic recording and sensitive detect, then the Curie critical point of this material should be near the room temperature, and it should be in a low-dimension system, such as in thin film. It also indicates that in the case of magnetic multilayers, if measured temperatures near T_c, a more high giant MR may be found. Further experiments are extremely desired to verify these predictions.

ACKNOWLEDGMENTS

This work is financially supported by the Grants of the NNSF of China and the LWTZ of CAS. One of the authors (Q.-Q. Z.) is grateful for support from the CMIT at Utah State University.

[1] R. M. Kusters, J. Singleton, D. A. Keen, R. McGreevy, and W. Hayes, Physica B **155**, 362 (1989).
[2] R. Von Helmolt, J. Wecker, B. Holzapfeil, L. Schultz, and K. Samwer, Phys. Rev. Lett. **71**, 2331 (1993); R. Von Helmolt, J. Wecker, K. Samwer, L. Hampt, and K. Barner, J. Appl. Phys. **76**, 6925 (1994).
[3] S. Jin, T. H. Tiefel, M. McCormack, R. A. Fastnacht, R. Ramesh, and L. H. Chen, Science **264**, 413 (1994); J. Appl. Phys. **76**, 6929 (1994); M. McCormack, S. Jin, T. H. Tiefel, R. M. Fleming, J. M. Phillips, and R. Ramesh, Appl. Phys. Lett. **64**, 3045 (1994).
[4] G. C. Xiong, Q. Li, H. L. Ju, S. N. Mao, L. Senpati, X. X. Xi, R. L. Greene, and T. Venkatesan, Appl. Phys. Lett. **66**, 1427 (1995).
[5] S. Jin, H. M. O'Bryan, T. H. Tiefel, M. McCormack, and W. W. Rhodos, Appl. Phys. Lett. **66**, 382 (1995).
[6] A. J. Millis, P. B. Littlewood, and B. I. Shraiman, Phys. Rev. Lett. **74**, 5144 (1995).
[7] N. Furukawa, J. Phys. Soc. Jpn. **63**, 3214 (1994).
[8] R. M. White, *Quantum Theory of Magnetism*, Springer Series (McGraw–Hill, New York, 1970).
[9] R. A. Tahir-Kheli, *Phase Transition and Critical Phenomena*, edited by C. Domb and M. S. Green (Academic, New York, 1975), Vol. 5B.
[10] M. E. Fisher and J. S. Langer, Phys. Rev. Lett. **20**, 665 (1968).
[11] A. Urushibara, Y. Moritomo, T. Arima, A. Asamitsu, G. Kido, and Y. Tokura, Phys. Rev. B **51**, 14 103 (1995).

Giant magnetoresistive memory effect in $Nd_{0.7}Sr_{0.3}MnO_z$ (abstract)

G. C. Xiong, Q. Li, H. L. Ju, R. L. Greene, T. Venkatesan, M. Dominguez, S. E. Lofland, and S. M. Bhagat

Department of Physics, Center of Superconductivity Research, University of Maryland, College Park, Maryland 20742-4111

A novel giant magnetoresistance memory effect has been observed in epitaxial $Nd_{0.7}Sr_{0.3}MnO_z$ thin films which have previously been found to exhibit a linear increase in conductivity on first application of a magnetic field *(B)*. Here we reported that the conductivity of the films depends not only on the applied field but also on the magnetic history. At T well below the temperature T_p where the zero-field resistivity has a peak, the film enters a high conductivity state $[(\Delta R/R_B) > 10^3]$ upon application of a magnetic field which persists even when B is reduced to zero. The original "zero" field state is not recovered until the sample is warmed to $T \sim T_p$. Surprisingly, the dc magnetization exhibits only a weak irreversibility while the magnetoconductivity is markedly hysteretic. That is, while the remanent magnetization is small the remanent magnetic resistivity is 10^{-3} times the initial zero-field-cooled resistivity. A possible explanation based on a two-component model of semiconducting matrix with embedded shunting paths of ferromagnetic material will be presented.
© *1996 American Institute of Physics.* [S0021-8979(96)60308-5]

Ferromagnetic resonance and intrinsic properties of $La_{0.67}Ba_{0.33}MnO_z$

S. E. Lofland, S. M. Bhagat, H. L. Ju, G. C. Xiong, T. Venkatesan, and R. L. Greene
Department of Physics, University of Maryland, College Park, Maryland 20742-4111

S. Tyagi
Department of Physics, Drexel University, Philadelphia, Pennsylvania 19104

Systematic magnetization and ferromagnetic resonance (FMR) measurements have been performed on thin-film samples of $La_{0.67}Ba_{0.33}MnO_z$ (T_C~340 K). It is found from the FMR data that as-grown films show broad lines whose width Γ increases to nearly 1 kOe as T reduced to 77 K. The increase roughly follows the increase in the magnetization suggesting magnetic inhomogeneity as the main cause for the rise in Γ. However, when films were properly annealed in O_2, we obtained narrow lines (Γ~200 Oe at 10 GHz). Γ was effectively independent of temperature and linearly dependent upon microwave frequency, both of which are strong signs that, we have succeeded in obtaining a *uniform, homogeneous manganite* sample. Having gotten a uniform material, we have measured the intrinsic properties of this system. © *1996 American Institute of Physics.* [S0021-8979(96)51908-9]

Ferromagnetic resonance (FMR) linewidths provide a very sensitive probe of the magnetic homogeneity of a sample. The mixed manganites such as $La_{1-x}Ba_xMnO_3$, which have attracted a great deal of attention recently, are very susceptible to variations in local chemistry. Thus non-uniformity and inhomogeneity are serious concerns. We demonstrate how FMR was used to confirm magnetic homogeneity, or lack thereof, in thin film samples and discuss some of the characteristics of the nearly homogeneous films obtained by a long-anneal procedure. Here we focus on the magnetic properties, the transport properties are discussed elsewhere.[1]

Films of $La_{0.67}Ba_{0.33}MnO_z$ (LBMO) were produced by pulsed-laser deposition (PLD) onto $LaAlO_3$ (LAO) substrates. After deposition, some of the films were annealed, at 1000 °C in an atmosphere of O_2 with a flow rate of ~40 cc/min for several days, and some were left as grown. The thickness of the films is 4000 Å, nominally. Rutherford backscattering (RBS), ion-channeling and x-ray diffraction showed that the films had very good crystallinity. Direct current magnetization was measured with a quantum interference device (SQUID) magnetometer in fields of 0–10 kOe applied parallel to the film plane.

FMR measurements were performed at 3.5, 10, 22, and 36 GHz, using conventional modulation and lock-in detection techniques[2] over a temperature range of 77–360 K. Data were taken in both the parallel ($H_\parallel$ film plane) and perpendicular ($H_\perp$ film plane) geometries.

It is well known that ferromagnetic resonance lines are well described by the Landau–Lifshitz–Gilbert equation.[3] For large linewidths, a correction must be applied to determine the true resonance fields.[4] For the narrow lines observed here, detailed lineshape calculations[3] based on the Landau–Lifshitz–Gilbert equation justify the use of the Kittel resonance equations

$$\frac{\omega}{\gamma}=[H_\parallel(H_\parallel+4\pi M_{\rm eff})]^{1/2}, \tag{1a}$$

$$\frac{\omega}{\gamma}=H_\perp-4\pi M_{\rm eff}, \tag{1b}$$

where ω is the microwave frequency, $\gamma=(g\mu_B/\hbar)$ the gyromagnetic ratio, $H_\parallel$ and $H_\perp$ the resonance fields in the parallel and perpendicular geometries, respectively, and $M_{\rm eff}$ the effective magnetization. $H_\parallel$, $H_\perp$, and $M_{\rm eff}$ may be influenced by the anisotropy torques, if any.

FMR data from as-grown films are rather hard to interpret meaningfully. At 300 K, the resonance is quite sharp, the peak-to-peak linewidth Γ_{pp} being 0.2 kOe and Γ_{pp} increases rapidly when T is lowered (squares, Fig. 1). At low temperatures several lines besides the main resonance appear, especially in the perpendicular geometry. This is a clear indication of inhomogeneity. Although the x-ray and RBS data point to a homogeneous material, the FMR clearly suggests otherwise. This sample we designate LBMO-I where I stands for inhomogeneous.

Whereas it is not fruitful to offer quantitative explanations for the T variation of the inhomogeneously broadened linewidths, it is useful to note that the increase in Γ_{pp} follows closely that of $4\pi M_{\rm eff}(T)$ (circles, Fig. 1) obtained from Eq. (1a) using $g=2.00$. This fact suggests that the observed $4\pi M$ is an average value and that a distribution of M values should be invoked to account for the linewidth data.

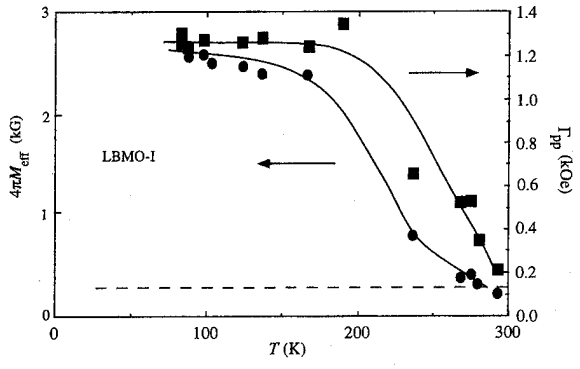
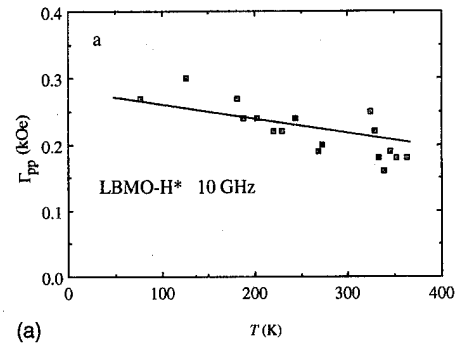


FIG. 1. Measured linewidth Γ_{pp} (squares) vs T for LBMO–I*. The full line is a guide to the eye. The dashed line represents the expected T dependence of Γ_{pp} for a uniform ferromagnet. $4\pi M_{\rm eff}$ (circles) vs T for LBMO–I from 10-GHz data. Notice that Γ_{pp} follows $4\pi M_{\rm eff}$.

 0021-8979/96/79(8)/5166/3/$10.00 © 1996 American Institute of Physics



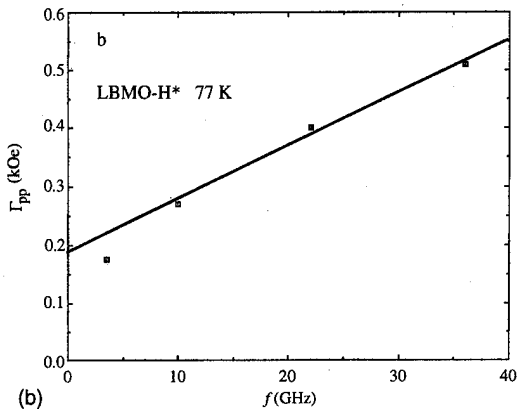


FIG. 2. (a) Γ_{pp} vs T for LBMO–H^* at 10 GHz. The line is a guide to the eye. Γ_{pp} is nearly independent of T, as expected for a homogeneous ferromagnet. (b) Γ_{pp} vs f for LBMO–H^*. The linear dependence of Γ_{pp} is as expected of a uniform ferromagnet, although the nonzero intercept suggests some remaining inhomogeneity.

In contrast to that of as-grown films, the FMR response of highly annealed films is quite satisfactory. The T dependence of Γ_{pp} for the parallel geometry is displayed in Fig. 2(a) for 10 GHz, and one notes that Γ_{pp} is effectively independent of T, as expected for a simple ferromagnet.[5] As a further check of the validity of this interpretation, consider the frequency (f) dependence of Γ_{pp} at 77 K. As seen in Fig. 2(b), Γ_{pp} increases linearly with f. However, as also found in amorphous ferromagnets,[4] extrapolation of Γ_{pp} has a nonzero value at $f=0$, indicative of a residual magnetic

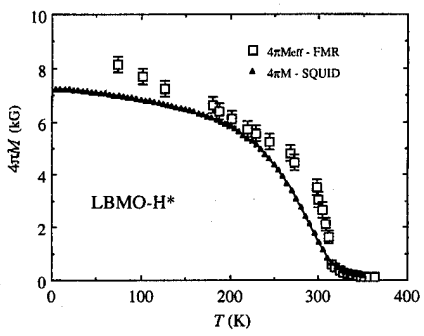


FIG. 3. $4\pi M_{\text{eff}}$ and $4\pi M$ vs T for LBMO–H^* derived from 10-GHz FMR data and SQUID magnetometry, respectively. The difference between $4\pi M_{\text{eff}}$ and $4\pi M$ is ascribed to strains in the film.

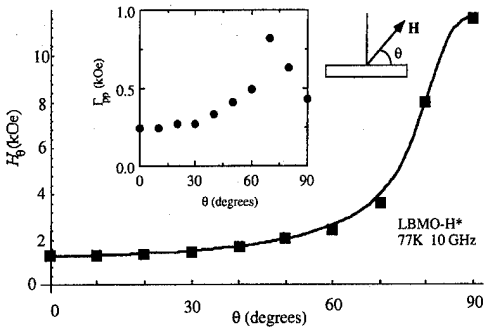


FIG. 4. Resonance field H_θ vs θ for LBMO–H^* at 77 K and 10 GHz. The full line is a solution to the resonance equations as a function of θ for $4\pi M=8.15$ kOe and $g=2.00$. The inset is Γ_{pp} vs θ. Γ_{pp} is largest near the point where $dH_\theta/d\theta$ is a maximum.

inhomogeneity within the sample. This film we designate LBMO–H^*, where H^* stands for nearly homogeneous.

Now that we have a fairly uniform sample we can measure its intrinsic magnetic properties. Consider the value of the effective magnetization $4\pi M_{\text{eff}}$ (squares, Fig. 3) obtained from FMR. This is to be compared with the SQUID data (triangles, Fig. 3). It is clear that the difference is ~1 kOe, increasing somewhat with reducing T. Most likely, this arises from anisotropy caused by strains and a non-zero magnetostriction in the films.

Figure 4 shows the variation of the resonance field H_θ and linewidth (inset) as the applied field is rotated from the parallel ($\theta=0°$) to the perpendicular configuration at 77 K. The full line was calculated using a straightforward generalization of the Kittel equations with $4\pi M_{\text{eff}}=8.15$ kOe and $g=2.00$. The close agreement shows that, in this film, the anisotropy is uniaxial with the symmetry (hard) axis being normal to the film plane. The variation of Γ_{pp} with θ serves as a consistency check on the validity of the resonance equations. $\Gamma_{pp}(\theta)$ should be maximal where $[dH_\theta(\theta)/d\theta]$ is largest, as we observe.

Writing $(4\pi M_{\text{eff}}-4\pi M)=2K_u/M$, one obtains the T variation of the anisotropy constant K_u shown in Fig. 5. The magnitude of K_u is not unreasonable. Simple theory[6] would give $K_u \sim (3/2)\lambda_m \sigma$ where λ_m is the magnetostriction constant and σ the stress in the film. A λ_m value of 10^{-5} seems credible, giving $\sigma \sim 10^{10}$ erg/cm^3. This implies strains of

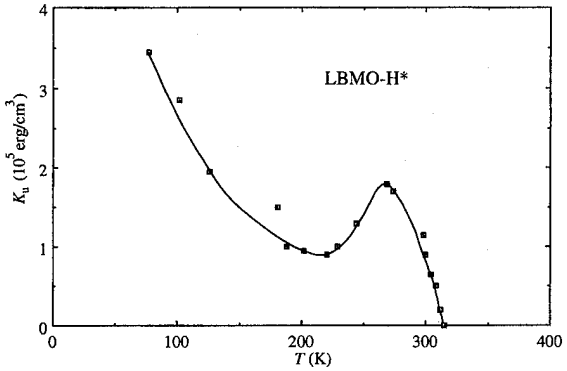


FIG. 5. Anisotropy constant K_u vs T derived from $4\pi M_{\text{eff}}$ and $4\pi M$. The line is a guide to the eye. The nonmonotonic behavior may be the result of magnetostriction.

$\sim 10^{-2}$, which are not unusual for a film grown on a substrate with a lattice mismatch of ~3%. Also, Perekalina *et al.*[7] measure $K_u \sim 10^5$ erg/cm^3 in $La_{1-x}(Sr, Pb)_xMnO_{3+\gamma}$ crystals ($x=0.1$ and 0.3) by torque measurements. The T dependence of K_u is not understood at this time, although nonmonotonic T dependences of magnetostriction have been reported.[8] It would be surprising if strain-induced fields did not also contribute to the line broadening. Part of the intercept observed in Fig. 2(b) could arise from this source.

In conclusion, it has been found that as-grown thin-film samples of $La_{0.67}Ba_{0.33}MnO_z$, which appear to be quite uniform by other techniques, show wide FMR lines, suggestive of sizeable magnetic inhomogeneity. Using a proper annealing treatment of thin films, behavior symptomatic of a uniform, homogeneous ferromagnet was observed in both the frequency and temperature dependence of the FMR linewidths. The present FMR linewidths are the narrowest observed in any giant magnetoresistance manganite system. It seems reasonable to claim that the heat treatment used here, although not fully optimized, yields the most homogeneous manganite films studied so far. This can be expected to become a benchmark for further work on these interesting systems.

We thank M. A. Manheimer for use of the 3.5 GHz spectrometer and M. Dominquez and R. P. Sharma for a fruitful discussion.

[1] S. E. Lofland, S. M. Bhagat, H. L. Ju, G. C. Xiong, T. Venkatesan, and R. L. Greene, Phys. Rev B **52**, 15 058 (1995).
[2] S. M. Bhagat, in *Techniques of Metal Research*, edited by E. Passaglia (Interscience, New York, 1974), Vol. VI, Part 2, Chap. 8.
[3] S. M. Bhagat, ASTM Handbook **10**, 267 (1986).
[4] D. J. Webb and S. M. Bhagat, J. Magn. Magn. Mater. **42**, 109 (1984).
[5] S. M. Bhagat, S. Haraldson, and O. Beckman, J. Phys. Chem. Solids **38**, 593 (1977).
[6] A. H. Morrish, *Physical Principles of Magnetism* (Wiley, New York, 1965).
[7] T. M. Perekalina, I. É. Lipin'ski, V. A. Timofeeva, and S. A. Cherkezyan, Sov. Phys. Solid State **32**, 1827 (1991).
[8] K. P. Belov and Z. P. Sirota, Zhurn. Eksp. Teor. Fiz. **36**, 1058 (1959).

Role of epitaxy and polycrystallinity in the magnetoresistance and magnetization of $La_{0.8}Sr_{0.2}MnO_3$ thin films

Kannan M. Krishnan, A. R. Modak, and C. A. Lucas
Materials Sciences Division, Lawrence Berkeley National Laboratory, Berkeley, California 94720

R. Michel
Lawrence Livermore National Laboratory, Livermore, California 94551

H. B. Cherry
Materials Science and Mineral Engineering, University of California, Berkeley, California 94720

$La_{0.8}Sr_{0.2}MnO_3$ thin films were simultaneously deposited by pulsed laser ablation on silicon (Si) and $LaAlO_3$ (LAO) substrates. Films on Si were polycrystalline while those on LAO were (100) epitaxial with an in-plane correlation length of ≈10 nm. The magnetization and magnetoresistance behavior of these two films were significantly different. Both films exhibit antiferromagnetic–ferromagnetic transitions—at different temperatures [180 K (LAO); 230 K (Si)]—and their magnetic moments at 10 K were significantly different (Si—0.0035 emu; LAO—0.0022 emu). However, both films showed significant high field slope in magnetization at 10 K. Significant fractions of both films remain antiferromagnetic at low temperatures and hence net susceptibilities, dependent on the direction of the applied magnetic field, are different for the epitaxial (LAO) and randomly oriented polycrystalline (Si) films. The magnetoresistance peak, corresponding to the semiconductor–metal transition is observed at 170 and 130 K for the epitaxial (LAO) and polycrystalline (Si) films, respectively. Moreover, their resistance values are two orders of magnitude different (Si—MØhms; LAO—KOhms). These properties can be interpreted in terms of the major role of grain boundaries in determining the scattering as well as possible differences in O_2 stoichiometry. © *1996 American Institute of Physics.* [S0021-8979(96)52008-8]

INTRODUCTION

The magnetic and electronic transport properties of alkaline earth substituted manganese oxides, $La_{1-x}A_xMnO_3$ (A =Ca, Sr, or Ba), with perovskite structure are quite well known.[1,2] In particular, for $0.1<x<0.5$, they order ferromagnetically near room temperature and the mixed Mn^{3+}/Mn^{4+} content resulting from divalent substitution leads to quasimetallic conductivity. The fundamental mechanism governing their galvanomagnetic properties and magnetization behavior is, as yet, not clearly understood—traditionally, treatments have focused on the "double exchange" interaction[3] whilst more recently, explanations involving polaron effects due to a strong electron–phonon coupling arising from a Jahn–Teller splitting of the Mn^{3+} ion have been proposed.[4] On the other hand, the very large negative magnetoresistance observed in these materials[5–7] has attracted much recent attention because of their potential application in information storage and other field sensing devices. It is claimed[7] that these properties are dependent on the optimization of the conditions of growth and annealing, composition, oxidation state, epitaxy, and the overall microstructure. In order to address these latter issues we have grown $La_{0.8}Sr_{0.2}MnO_3$ (LSMO) films by laser ablation simultaneously on $LaAlO_3$ (LAO) and silicon (Si) substrates, characterized their crystallography and measured their magnetic/transport properties.

EXPERIMENTAL DETAILS

LSMO thin films were synthesized by pulsed laser deposition using a 248 nm KrF excimer laser (Lambda Physik, Lextra 200) with a 30 ns pulse width and output energy of 400 mJ. The laser was operated at 3 Hz for 15 min producing films ~2000 Å thick. A sintered $La_{0.8}Sr_{0.2}MnO_3$ target was used. The ejected plume of material was deposited simultaneously onto polished $LaAlO_3$ [100] and Si [100] (with native oxide) substrates maintained at 675 °C. The base pressure in the chamber was 2×10^{-6} Torr. During the deposition the oxygen pressure in the vacuum chamber was maintained at 100 mTorr by flowing oxygen at 50–70 sccm. After deposition, the films were cooled to room temperature at 5 °C/min in an oxygen pressure between 500 and 600 Torr.

X-ray diffraction measurements were made using a four-circle Huber diffractometer based on a 12 kW Rigaku rotating-anode source. Cu $K_{\alpha 1}$ x-rays were selected and collimated using a graphite monochromator crystal, scattered from the sample and then detected by a scintillation counter after passing through a resolution-defining slit. In this mode of operation the instrumental resolution is relatively poor ($\sim1\times10^{-2}$ Å^{-1}) but the incident x-ray intensity is higher than in a high resolution mode.[8]

Magnetization and resistance measurements were performed in a Quantum Design SQUID based magnetometer system. A modified sample holder equipped with electrical leads was used for the resistance measurements. The leads were attached using pressed indium contacts. In all measurements, the field was applied in the plane of the film and the current was applied parallel to the field.

RESULTS AND DISCUSSION

For the sample grown on the Si substrate, the dominant feature in a θ–2θ x-ray scan was the (004) Si Bragg reflection and this was accompanied by several other weak peaks which could be indexed to the perovskite film. As the film

 0021-8979/96/79(8)/5169/3/$10.00 © 1996 American Institute of Physics

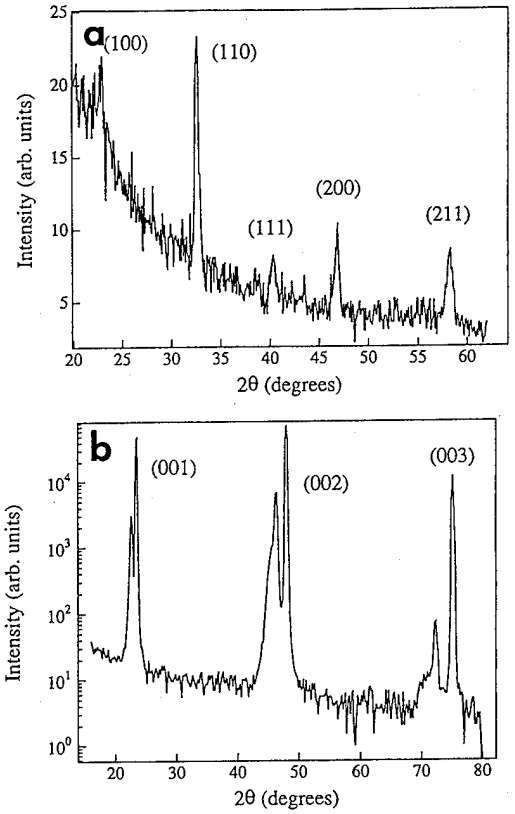


FIG. 1. (a) 2θ x-ray scan at fixed θ angle (8°) for the LSMO (80/20) film grown on a Si substrate. (b) $\theta-2\theta$ scan for the LSMO (80/20) film grown on a $LaAlO_3$ substrate.

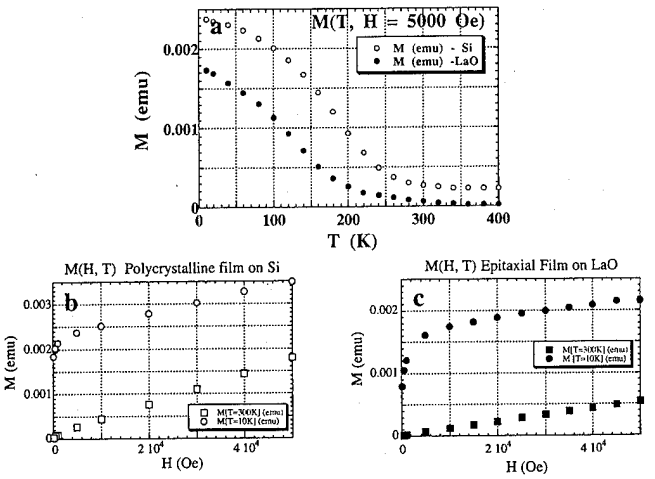


FIG. 2. (a) $M(T, H=5$ kOe) for polycrystalline (Si) and epitaxial (LAO) films. M(H) behavior at $T=10$ K and 300 K for the films are shown in (b) and (c).

Bragg peaks showed no specific orientation dependence in rocking scans (i.e., the film is polycrystalline), a 2θ scan was performed at a fixed θ angle (8°) to remove the Si Bragg reflection. The result is shown in Fig. 1(a). Assuming a cubic structure for the perovskite film allows the peaks to be indexed as shown in Fig. 1, and the lattice constant is determined to be $a=3.88\pm0.05$ Å.

Figure 1(b) shows a $\theta-2\theta$ scan for the film grown on the $LaAlO_3$ substrate ($a=3.78$ Å). Again the peaks are indexed according to the cubic notation. The two peaks at each position correspond to the substrate (higher intensity) and the perovskite film. A rocking scan through the $LaAlO_3$ peak gives a full-width-half-maximum (FWHM) of ~0.18° which is merely the limit of the instrumental resolution. This compares to a FWHM of the perovskite peak of 1.1°. The position of the perovskite peak corresponds to a cubic surface-normal lattice constant, $c=3.92$ Å. Measurement of in-plane Bragg reflections, e.g., (111), gave a smaller lattice mismatch and implies that there is some in-plane lattice matching causing a tetragonal distortion in the film. In Fig. 2 there also appears to be a shoulder on the low angle side of the film peak. This feature is an order of magnitude smaller than the principal peak and may be due to regions of the film that are perfectly lattice matched, in-plane to the substrate, thus leading to a larger tetragonal distortion. Finally a rocking scan through the in-plane (200) perovskite Bragg reflection gave a Lorentzian lineshape with a FWHM of 1.32°. This corresponds to an in-plane correlation length of ~100 Å. Transmission electron microscopy (TEM) observations are also in progress to corroborate these deductions.

A comparison of the magnetic moments of the two films, that have identical volumes (since the films have identical area as well as thickness), in an applied field of 5000 Oe as a function of temperature is shown in Fig. 2(a). The ferromagnetic transition temperatures are $\sim T_c=180$ K and $T_c=230$ K for the films deposited on $LaAlO_3$ and Si, respectively. Both films show a room temperature $M(H)$ that is linear with applied field consistent with antiferromagnetism [Figs. 2(b) and 2(c)]. However, the magnetic moment at 5 T for the polycrystalline film (≈0.0035 emu) is higher than that observed for the epitaxial film (≈0.0022 emu). Both films showed a significant high field slope at 10 K even at applied fields as high as 5 T.

The temperature and field dependent resistance values of the two films were quite different. The overall resistance of the polycrystalline films on Si was 2–3 orders of magnitude greater than that of the single crystal film on $LaAlO_3$. The resistance of the polycrystalline film increased monotonically with decreasing temperature except for a small bump observed around 130 K [Fig. 3(a)]. At roughly the same temperature, a rather broad peak in the magnetoresistance was observed: the peak magnetoresistance was 125% in a field of 5 T. The zero field resistance of the single crystal film peaked (at 185 K) more sharply than the polycrystalline films, and dropped as temperature decreased further indicating a semiconductor to metal transition [Fig. 3(b)]. In this case, the peak in magnetoresistance is correlated reasonably well with the onset of the magnetic transition: the peak magnetoresistance of the single crystal was 140% in a field of 5 T, at a temperature of 170 K, which is slightly below the magnetic transition.

The distinct difference in the behavior of the polycrystalline and epitaxial (LSMO) films of the same composition (except for oxygen stoichiometry) and thickness is evidence of the significant dependence of the magnetotransport properties on the nature of crystallinity. The magnetic properties

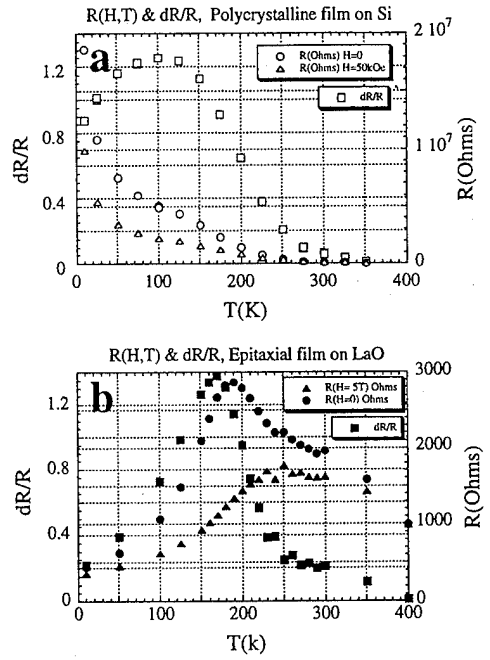


FIG. 3. $R(H=0)$, $R(H=5\text{ T})$, and $[R(0)-R(5\text{ T})]/R(0)$ vs T for the polycrystal (Si) films (a) and epitaxial (LAO) films (b).

can then be rationalized in relation to the microstructure.

The high-field susceptibility of the polycrystalline LSMO films in the antiferromagnetic state (at room temperature) is higher than in the epitaxial films. This fact may be understood in terms of the crystal structure. It is known that in single crystal LSMO alternate (001) planes are antiferromagnetically ordered.[2] In each (001) plane the moments are ferromagnetically ordered along either the (010) or the (100) directions. Hence for the epitaxial film, with the field applied in the plane of the film, the measured susceptibility is: χ epitaxial$=1/2\ (\chi_{\|}+\chi_{\perp})$, where $\chi_{\|}$ and $\chi_{\perp}$ are the susceptibilities parallel and perpendicular to the spin alignment. This assumes that the distribution of domains corresponding to the two possible orientations is statistically equivalent, and the crystal anisotropy is large enough so that the domains do not flip at low field and align perpendicular to the applied field. At the same time, for the polycrystalline film, the measured susceptibility is χ polycrystalline$=1/3\ (\chi_{\|}+2\chi_{\perp})$ assuming random orientation.[9] Below the Neel temperature it is reasonable to assume that $\chi_{\|}$ decreases with decreasing temperature and $\chi_{\perp}$ remains constant, and that in general $\chi_{\|}<\chi_{\perp}$. Thus the polycrystalline film is expected to have a higher measured susceptibility than the (100) epitaxial film. Our measurements show a $\chi_{\|}\approx 5.3\times10^{-3}$ and $\chi_{\perp}\approx 3.6\times10^{-3}$ at room temperature.

Both the Curie temperature and the ferromagnetic magnetization of the epitaxial film are lower than those of the polycrystal implying that the ferromagnetic moment per Mn atom is smaller in the single crystal than in the polycrystal. In these films the relative atomic fraction of both Sr and O affect the tetravalent Mn content. Further, the change in the ferromagnetic moment per Mn atom with the fraction of tetravalent Mn is particularly large close to 20% Mn^{4+}, which would be expected in the composition corresponding to 20 at % Sr.[2] Since the total number of La, Sr, and Mn atoms in the two films are nominally equal, the difference in the moments could arise mainly from differences in oxygen stoichiometry. The interdiffusion of oxygen would be much faster along grain boundaries than in the bulk and hence, the polycrystal would have a higher equilibrium oxygen content than the single crystal. Future (EELS) measurements may help to clarify the issue relating to the relative oxygen stoichiometries in the two films.

The absolute resistance of the polycrystalline film is higher than the epitaxial film due to the additional scattering from defects and grain boundaries as well as the differences in oxygen stoichiometry. This is to be expected considering the small grain size observed in the polycrystalline films (0.1–0.2 μm) from TEM studies.[10] The slightly larger magnetoresistance of the epitaxial film as compared to the polycrystalline film, however, is not yet completely understood. Both the proposed mechanisms, i.e., double exchange and polaron effects, would be significantly affected by structural irregularities at grain boundaries leading to a reduction in intergranular conductivity. The effect of grain boundaries would be particularly significant in these materials due to their uniquely coupled magnetic and conductive properties. Note that the magnitude of the magnetoresistance of polycrystalline films is similar to that observed for the epitaxial films although the resistance versus temperature curves show a largely insulatorlike behavior (except for the very small bump at 130 K). Only the temperature dependence of the MR is significantly affected. This indicates that although the semiconductor–metal transition is closely associated with the MR effect, it does not influence the magnitude significantly. The polycrystallinity increases the resistance of the film while maintaining the percentage magnetoresistance.

Overall, the results confirm the important role of the microstructure in determining the properties of LSMO films and suggest the need to make measurements on well defined grain boundaries, e.g., films grown on bicrystal substrates. Such experiments would permit an understanding of the influence of grain boundaries on the double exchange interactions, in addition to magnetoresistance properties.

ACKNOWLEDGMENTS

This work was supported by the Director, Office of Energy Research, Office of Basic Energy Sciences, Materials Sciences Division of the U.S. Department of Energy under Contract No. DE-AC03-76SF00098.

[1] G. H. Jonker and J. H. van Santen, Physica **16**, 337 (1950).
[2] E. O. Wollan and W. C. Koehler, Phys. Rev. **100**, 545 (1955).
[3] C. Zener, Phys. Rev. **82**, 403 (1951).
[4] A. J. Mills, P. B. Littlewood, and B. I. Shraiman, Phys. Rev. Lett. **74**, 5144 (1995).
[5] K. Chahara, T. Ohno, M. Kasai, and Y. Kozono, Appl. Phys. Lett. **63**, 1990 (1993).
[6] R. von Helmholt, J. Wecker, B. Holzapfel, L. Scultz, and K. Samwer, Phys. Rev. Lett. **71**, 2331 (1993).
[7] S. Jin, T. H. Tiefel, M. McCormak, R. A. Fastnacht, R. Ramesh, and L. H. Chen, Science **264**, 413 (1994).
[8] C. A. Lucas, Acta Cryst. A **45**, 416 (1989).
[9] B. D. Cullity, *Introduction to Magnetic Materials* (Addison–Wesley, Reading, 1972).
[10] A. R. Modak and K. M. Krishnan (unpublished).

Magnetic exchange and charge transfer in mixed-valence manganites and cuprates

Gerald F. Dionne
Lincoln Laboratory, Massachusetts Institute of Technology, Lexington, Massachussetts 02173

Metallic resistivity occurs at cryogenic temperatures in insulators with small carrier trap energies, e.g., superconducting cuprates. A similar metallic regime has been reported for the lanthanide (RE) manganites $(RE^{3+}_{1-x}A^{2+}_{x})MnO_3$. To interpret the anomalous resistivity ρ as a function of temperature and magnetic field in these compounds, a model constructed from the relation for mobility activated semiconduction and the Brillouin–Weiss theory of ferromagnetism has been developed. The resistivity maximum occurs at the susceptibility peak slightly above the Curie temperature T_C and its magnitude is related to the hopping electron trap energy E_{hop} by $\exp(E_{hop}/kT_C)$. Where $T<T_C$, ρ is metallic because E_{hop} is small due to the collinear polarization of spins. For $T\geqslant T_C$, E_{hop} increases to a value ~0.1 eV equal to the decrease in stabilization energy of the transfer electrons caused by the transition from spin alignment to disorder. The magnetoresistance sensitivity $d\rho/dH$ at $T=T_C$ is controlled by T_C through $(1/T_C)\exp(E_{hop}/kT_C)$. The relative sensitivity $(1/\rho)d\rho/dH$, however, is proportional to $1/T_C^2$. These results also reinforce the concept that metallic resistivity in the superconducting cuprates occurs because of the frustration of antiferromagnetism. © *1996 American Institute of Physics.* [S0021-8979(96)52108-4]

I. INTRODUCTION

Recent observations of anomalous reductions in electrical resistivity of lanthanide perovskite $(RE^{3+}A^{2+})MnO_3$ films in strong magnetic fields[1] have prompted a reexamination of the seminal work on the properties of these mixed-valence manganites. Original magnetic studies were reported by Jonker and Van Santen in 1950.[2] A follow-up note[3] reported the characteristic peak in resistivity at the Curie temperature, similar to that observed in the films.

In this article, the magnetic and electronic data are discussed in terms of the conventional theories and a phenomenological model of magnetoresistance is developed and used to interpret reported measurements. To place the low temperature metallic electrical behavior in a broader context, the charge transfer mechanisms of the $Mn^{3+}\leftrightarrow Mn^{4+}+e^-$ combination are compared with those of $Cu^{2+}\leftrightarrow Cu^{3+}+e^-$ in the p-type high-T_c superconducting cuprates.[4]

II. MAGNETIC PROPERTIES OF $(RE^{3+}A^{2+})MnO_3$

In the generic $(RE^{3+}A^{2+})MnO_3$ system, three oxidation states of Mn can occur, offering a variety of 180° superexchange interactions. For the cubic octahedral oxygen coordination, crystal-field effects dictate that the t_{2g} orbital states are of lower energy and are half-filled to satisfy the Hund's rule spin polarization requirement for each of $Mn^{2+}(d^5)$, $Mn^{3+}(d^4)$, and $Mn^{4+}(d^3)$. For all combinations of ionic pairs, the t_{2g} electrons provide weak antiferromagnetism via π bonding through the O^{2-} anions, e.g., Mn^{4+}–O^{2-}–Mn^{4+}. For the Mn^{2+} and Mn^{3+} ions, the exchange is determined more by the stronger σ-bonding e_g states. A single electron in the e_g states (Mn^{3+} case) can be stabilized by a static Jahn–Teller (JT) orthorhombic distortion that splits energy levels as shown in Fig. 1. Exchange couplings expected for the various ion combinations are well documented.[5]

According to Curie temperature T_C data[2] for $(RE^{3+}_{1-x}A^{2+}_{x})Mn^{3+}_{1-x}Mn^{4+}_{x}O_3$, ferromagnetism dominates in the regime up to $x=0.5$, with a peak near $x=0.3$. As Mn^{4+} ions are introduced, parallel spin alignments occur through a combination of factors: (i) the Mn^{3+}–O^{2-}–Mn^{4+} couplings produce ferromagnetism through charge transfer between half-filled and empty orbital states, and (ii) the anticipated antiferromagnetism from the collective Mn^{3+}–O^{2-}–Mn^{3+} couplings in a static JT effect are converted to ferromagnetism possibly by the vibronic-induced JT effect proposed by Goodenough *et al.*[6] that blurs the e_g bands and allows the Mn^{3+} e_g electrons to transfer into empty orbital states.

For a random distribution of Mn^{4+} ions, the exchange energy E_{ex} of a spin $\mathbf{S}_i$ surrounded by z spins $\mathbf{S}_j$ is given by the Hamiltonian $\mathscr{H}_{ex}=2\Sigma_j J_{ij}\mathbf{S}_i\cdot\mathbf{S}_j=2zJS^2\cos\theta$, and

$$E_{ex}=2z[J_{33}S_3^2(1-x)^2+2J_{34}S_3S_4x(1-x)+J_{44}S_4^2x^2]\cos\theta, \quad (1)$$

where J is the average J_{ij} coefficient; the average $S=(1-x)S_3+xS_4$, and θ is the average angle between adjacent spins. The variation in E_{ex} with x may be inferred

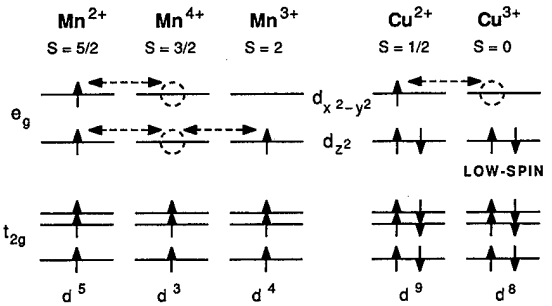


FIG. 1. Crystal-field splittings and ground-state orbital occupancies of Mn and Cu ions in orthorhombically distorted oxygen octahedra. Delocalization exchange with ferromagnetic spin polarization are indicated.

 0021-8979/96/79(8)/5172/3/$10.00 © 1996 American Institute of Physics

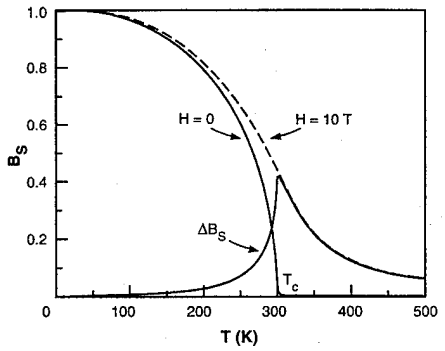


FIG. 2. Curves of B_S and ΔB_S vs T for $H=0$ and 10 T and $T_C=300$ K.

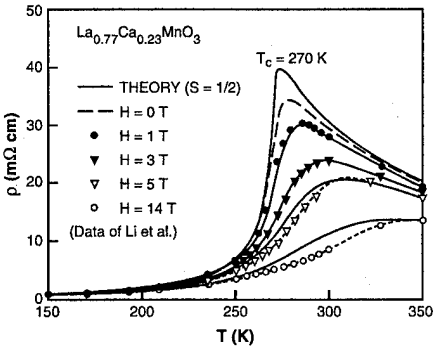


FIG. 3. Comparison of theory with experiment for ρ vs T (data of Ref. 14). The $B_{1/2}$ model was used with $N=719$ mol/cm^3.

directly from the T_C data,[2] which register a peak above 300 K at $x\approx0.3$. An empirical model[7] is used to sort out the contributions of the individual terms in Eq. (1). To relate E_{ex} to T_C we employ the standard expression $kT_C=2zJS(S+1)/3=E_{ex}(S+1)/3S$. Calculations based on Eq. (1) were scaled to fit $kT_C=0.025$ eV ($T_C=300$ K) with a maximum at $x=0.3$. From this exercise, J_{33} peaks at 0.0022, while $J_{34}=0.0030$, and $J_{44}=-0.00074$ eV. It is therefore concluded that the relative importance of the terms of Eq. (1) is weighted towards the charge transfer J_{34} component.

The temperature dependence of the magnetic moment per mole $M(T)$ may be described by the Brillouin–Weiss molecular field theory which models the degree of spin collinearity, i.e., cos θ, by a Brillouin function $B_S(y)$ according to $M(T)=M(0)B_S(y)$, where $M(0)=g\mu_B S\mathcal{N}$, $\mathcal{N}$ is Avogadro's number, and $y=E_{ex}/kT$. In a magnetic field H, $E_{ex}=g\mu_B S(H_{ex}+H)$, where g is the gyromagnetic ratio (=2), μ_B is the Bohr magneton, and $H_{ex}=NM$,[7] with N the molecular field coefficient in mol/cm^3. N is related to the exchange constant J (in ergs) through $N=2zJ/g^2\mu_B^2\mathcal{N}$. For $T_C=300$ K, B_S and ΔB_S are calculated by means of a numerical iterative procedure and plotted as a function of T for H values of 0 and 10 T in Fig. 2.

An alternative approach that allows the use of the $B_{1/2}$ function is to ignore the Russell–Saunders rule and to sum the exchange contributions from uncoupled spins. In this case, $s=1/2$ and $JS^2\cos\approx J^iS^2\cos$, where J^i is the resultant exchange constant from the orbitals of the individual spins.

III. MAGNETORESISTIVE PROPERTIES OF $(RE^{3+}A^{2+})MnO_3$

The electrical conductivity of mixed-valence oxides obeys the standard relation with activated mobility,[8,9] where $\sigma=ne(eD/kT)\exp(-E_{hop}/kT)$. The factor (eD/kT) is the Einstein diffusion mobility, n is the carrier density, and D the diffusion constant which equals the ratio of the square of the hop distance to the carrier lifetime d^2/τ. In previous studies of the normal state of the cuprate superconductors,[10,11] this relation was refined and expressed as a resistivity:

$$\rho=C(kT)[(1-x)/x]\exp(E_{hop}/kT), \qquad (2)$$

where the effective number of carriers per formula unit $x(1-x)=nV$, V is the volume of a formula unit ($\sim a^3$) based on lattice parameter a (=4 A), and $C=V/e^2d_{min}{}^2\nu_{hop}$. The hopping frequency $\nu_{hop}(=1/\tau)$ is equated to the Debye frequency $\nu_D=(k/h)\Theta_D\approx5\times10^{12}$ Hz for a Debye temperature $\Theta_D\approx250$ K. The $(1-x)$ factor in the numerator of Eq. (2) arises from a correction to the effective hop distance d ($\propto a$) which increases with x according to $d_{min}/(1-x)$. By Eq. (2), ρ passes through a minimum at $T=E_{hop}/k$ and assumes a metallic slope that approaches the linear function $C(kT)[(1-x)/x]$.

The principal source of the activation energy E_{hop} is the reduction in stabilization energy[11,12] of the electron carrier in the e_g orbitals that covalently link the Mn^{3+} and Mn^{4+} ions. This loss in binding energy represents the additional (thermal) energy required to effect the carrier transfer and occurs because of spin canting. Since B_S represents the z-axis projection of spins within a cone of half-angle θ, $(1-B_S)$ approximates the fractional loss in binding energy as a function of temperature and magnetic field.

The activation energy may then be expressed as $E_{hop}=E^0_{hop}+E^{ex}_{hop}(1-B_S)$, where E^0_{hop} is the trap energy from electrostatic and elastic factors (typically <0.01 eV for the high-T_c cuprates[4]), and E^{ex}_{hop} is the exchange contribution that reaches its full value at $T\geq T_C$.[7] For the manganite system, $E^{ex}_{hop}\approx0.1$ eV. This estimate for E^{ex}_{hop} is justified by equating $E^{ex}_{hop}\approx2zJ_{34}S_3S_4=0.106$ eV for $z=6$, $J_{34}=0.0030$ eV, $S_3=2$, and $S_4=3/2$.

In Fig. 3, ρ vs T data of Li *et al.*[13] for a composition estimated as $(La^{3+}_{0.77}Ca^{2+}_{0.23})MnO_3$ subjected to H fields of 0, 1, 3, 5, and 14 T are fitted by curves generated from Eq. (2), employing in this case the $s=1/2$ approximation which provided a slightly better fit to the data than that obtained with the average spin model.[7] Except for the $H=0$ curve, which did not reach its full peak probably due to the inhomogeneously broadened tail of the M vs T curve, theory and data agree quite closely. For these and all subsequent computations, $C=6$ mΩ cm/eV, $E^0_{hop}=0.004$ eV, and $E^{ex}_{hop}=0.1$ eV.

Since E^{ex}_{hop} is a constant of the transfer ions, the peaks of ρ at $H=0$ should theoretically touch the $(kT)\exp(E_{hop}/kT)$ envelope at the appropriate T_C values. This is confirmed by the average spin model calculations in Fig. 4. From these results, the sharp increase in ρ at T_C is enhanced by almost

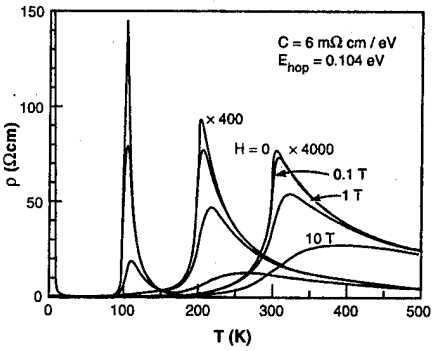


FIG. 4. Curves of ρ vs T for materials with T_C=100, 200, and 300 K, computed from the B_S model. Numerical results are listed in Table I.

four orders of magnitude between 300 and 100 K. The ρ_{max} (H=0) values listed in Table I are in general agreement with data reported in the literature, which are typically $\sim 10^2$ Ω cm at T_C=100 K.

Consistent with the behavior of ρ, $d\rho/dH$ at $T=T_C$ is shown to be proportional to $(1/T_C)\exp(E_{hop}/kT_C)$ and

$$(1/\rho)d\rho/dH = -g\mu_B S(S+1)E_{hop}^{ex}\mathcal{F}/3(kT_C)^2, \qquad (3)$$

where $\mathcal{F}$ is a Lorentzian-type broadening function that accounts for the paramagnetic tail at $T>T_C$.[7] In the ideal limit as $H\rightarrow 0$, Eq. (3) states that $(1/\rho)d\rho/dH$ is inversely proportional to T_C^2. This dependence is suggested by the computed values listed in Table I for $T=T_C$ and dH=1 Oe.

IV. $Mn^{3+(4+)}$ AND $Cu^{2+(3+)}$ ELECTRON TRANSFER

Metallic resistivity in transition-metal oxides also occurs in situations where one of the transfer ions is in a zero-spin state.[11] Unlike the Mn^{3+}–O^{2-}–Mn^{4+} case where ferromagnetic spin polarization removes the exchange trap, however, E_{hop}^{ex} is absent from systems with S=0 ions because there are no internal polarization requirements. In addition, charge transfer from these mobile nonmagnetic cations causes breakdowns of the regional antiferromagnetic couplings and can eventually reduce the Néel temperature T_N to zero.[12]

TABLE I. Parameter values at $T=T_C$ from Fig. 4.

T_C (K)	x	N (mol/cm^3)	ρ_{max} (H=0) (Ω cm)	$(1/\rho)d\rho/dH$ (dH=1 Oe) (Oe)$^{-1}$
77	0.04	26	4770	-4.7×10^{-3}
100	0.05	34	145	-3×10^{-3}
200	0.15	71	0.233	-1×10^{-3}
300	0.30	114	0.020	-2×10^{-4}

The most remarkable of these situations is seen in the p-type metallic conductivity of Cu^{2+}–O^{2-}–Cu^{3+} couplings in the perovskite structure. For the Cu^{3+} ion, the S=0 state arises from a low-spin configuration (see Fig. 1) that occurs because of a large splitting of the e_g doublet.[14] Here the splitting of $d_{x^2-y^2}$ and d_{z^2} occurs more from the pronounced tetragonal/orthorhombic symmetry of the layered perovskites than from the JT effect that is required to create the splitting in the manganites. The influence of antiferromagnetic exchange on the $Cu^{2+(3+)}$ conductivity is to deter the formation of large polarons that are necessary for the coherent activationless charge transfer of superconductivity. The presence of only 5% of zero-spin Cu^{3+} is sufficient to frustrate the antiferromagnetic ordering and create the metallic phase that allows the onset of superconductivity (the Néel temperature T_N and T_c=0 condition).[11,12]

V. DISCUSSION AND CONCLUSIONS

The principal insights gained from the magnetoresistance analysis are the following.

(1) The magnetic condition may be unique to Mn cations covalently linked in octahedral sites with 180° bonds.
(2) The resistivity maximum $\rho_{max}\sim(kT_C)\exp(E_{hop}/kT_C)$ at H=0 and occurs at the susceptibility peak slightly above $T=T_C$.
(3) The maximum of $d\rho/dH$ occurs at $T=T_C$ and is proportional to $(1/T_C)\exp(E_{hop}/kT_C)$.
(4) The maximum of $(1/\rho)d\rho/dH$ occurs at $T=T_C$ and is proportional to $1/T_C^2$.
(5) E_{hop}^{ex} is fixed by the local exchange energy $2zJ_{34}S_3S_4$ and is estimated from theory and experiment at 0.1 eV.
(6) $E_{hop}^{ex}/kT_C\approx 6J_{34}S_3S_4/JS(S+1)$ and is therefore dependent mainly on the exchange energy of the individual Mn^{3+}–O^{2-}–Mn^{4+} couplings.

[1] S. Jin, T. H Tiefel, M. McCormack, R. A. Fastnacht, R. Ramesh, and L. H. Chen, Science **264**, 413 (1994).
[2] G. H. Jonker and J. H. Van Santen, Physica **XVI**, 337 (1950).
[3] J. H. Van Santen and G. H. Jonker, Physica **XVI**, 599 (1950).
[4] G. F. Dionne, M. I. T. Lincoln Laboratory Techn. Report No. 1024, 1995, AD-A297287.
[5] J. B. Goodenough, *Magnetism and the Chemical Bond* (Wiley, New York, 1963).
[6] J. B. Goodenough, A. Wold, N. Menyuk, and R. J. Arnott, Phys. Rev. **124**, 373 (1961).
[7] G. F. Dionne, M. I. T. Lincoln Laboratory Techn. Report No. 1029, 1996 (in press).
[8] R. J. D. Tilley, *Defect Crystal Chemistry and Its Applications* (Blackie, London, 1987), Chap. 6.
[9] R. R. Heikes and W. D. Johnston, J. Chem. Phys. **26**, 582 (1957).
[10] G. F. Dionne, J. Appl. Phys. **69**, 4883 (1991).
[11] G. F. Dionne, M. I. T. Lincoln Laboratory Techn. Report No. 885, 1992, AD-A253975.
[12] G. F. Dionne, J. Appl. Phys. **69**, 5194 (1991).
[13] Y.-Q. Li, J. Zhang, S. Pombrik, S. DiMascio, W. Stevens, Y. F. Yan, and N. P. Ong, J. Mater. Res. **10**, 2166 (1995).
[14] J. B. Goodenough, G. Demazeau, M. Pouchard, and P. Hagenmuller, J. Solid State Chem. **8**, 325 (1973).

Correlation between magnetovolume and giant magnetoresistance effects in doped $La_{2/3}Ca_{1/3}MnO_3$ perovskites

J. M. De Teresa, J. Blasco, M. R. Ibarra, J. García, C. Marquina, P. Algarabel, and A. del Moral

Departamento de Física de la Materia Condensada e Instituto de Ciencia de Materiales de Aragón, Universidad de Zaragoza-CSIC, 50009-Zaragoza, Spain

$La_{0.62}Tb_{0.05}Ca_{0.33}MnO_3$ and $La_{0.6}Y_{0.07}Ca_{0.33}MnO_3$ have been studied in order to probe into the mechanisms responsible for the giant magnetoresistance ratios observed in this kind of compound. The experiments have shown a strong connection between the magnetotransport and magnetovolume properties. A large volume effect appears above T_c which collapses with applied magnetic field or when the long range magnetic order sets in. Above T_c the magnetostriction and magnetoresistance isotherms are highly correlated. Charge localization with local distortion appears to be responsible for the transport and volume properties at zero field. Charge mobility and a more normal volume dependence on temperature are restored by applying high enough magnetic fields.
© *1996 American Institute of Physics.* [S0021-8979(96)52208-0]

I. INTRODUCTION

A lot of experimental and theoretical effort is currently being devoted to understand the intriguing behavior of $R_xB_{1-x}MnO_3$ (R=rare earth, B=Ca,Sr,Ba,Pb) and related compounds.[1–10] The main interest of some of these compounds is the exhibition of giant magnetoresistance (GMR) ratios across a wide range of temperatures. The understanding of the relevant mechanisms which produce the GMR in these perovskitelike materials is of great importance due to the vast technological applications of GMR devices.

Recent works on $Pr_{1/2}Sr_{1/2}MnO_3$ (Refs. 5 and 11) have given evidence for charge ordering accompanied by a first-order change of the lattice parameters which strongly increases the resistivity. In this article we study the volume change of doped $La_{2/3}Ca_{1/3}MnO_3$ across the temperature range where GMR ratios are observed. In these compounds the resistance shows a maximum at around T_c, when the ferromagnetic long-range order sets in, marking the crossover from a nonmetallic state to a metallic one. The highest GMR ratios appear around T_c. The presence of lattice distortions above T_c was assumed to be a signal of charge localization.[12] Consequently resistance and volume effects would be highly correlated in this region. Simultaneous measurements of resistance and linear thermal expansion have been carried out to check this possibility. The effect of applying a magnetic field on the transport and volume properties has also been measured through magnetoresistance (MR) and magnetostriction (MS) experiments up to 12 T. The collapse of the charge-ordering state under applied magnetic field in $Pr_{1/2}Sr_{1/2}MnO_3$ has recently been reported[5] and consequently the GMR ratios in doped $La_{2/3}Ca_{1/3}MnO_3$ can be connected with the collapse of the localized-charge state under applied magnetic field.

II. EXPERIMENT

The samples were prepared using a gel precursor in order to obtain well-mixed reagents. Stochiometric amounts of La_2O_3, Tb_4O_7 (Y_2O_3 in the yttrium-doped compound), $CaCO_3$, and $MnCO_3$ with nominal purities >99.9%, were dissolved in concentrated nitrid acid resulting in a light solution. Afterwards, citric acid and ethylene glycol were added in a ratio of 4 g citric acid to 1 ml ethylene glycol and 1 g metal nitrates. The solution was heated and the excess nitrid acid and water were boiled off giving a brown (yellow–brown in the yttrium-doped compound) gel. The gel was heated to give a black–brown (brown in the yttrium-doped compound) powder. This precursor was calcined at 1173 K overnight. The remaining black powder was cold pressed to 4 kbar and sintered at 1273 K for 3 h with intermediate grindings. Finally the pellet was sintered at 1573 K for 8 h resulting in a hard black ceramic material. The samples were analyzed by means of x-ray powder diffraction resulting in a single phase with a perovskitelike structure.

A superconducting coil was used to produce steady magnetic fields up to 12 T. Both resistance (MR) and thermal expansion (MS) were simultaneously measured in two different pieces of the same sample in order to correlate both properties. Resistance (MR) was measured with the standard four points technique; the contacts were done with silver paste on bar-shaped samples. The magnetic field was applied parallel to the current. Linear thermal expansion ($\Delta L/L$) was measured using the strain–gauge technique. The volume thermal expansion ($\Delta V/V$) was calculated as three times the linear thermal expansion. For the MS results the strain parallel ($\lambda_\parallel$) and perpendicular ($\lambda_\perp$) to the applied field was measured. Volume magnetostriction (VMS) and anisotropic magnetostriction (AMS) are straightforwardly calculated as $\omega=\lambda_\parallel+2\lambda_\perp$ and $\lambda_t=\lambda_\parallel-\lambda_\perp$, respectively.

Magnetization and initial magnetic susceptibility (χ_{ac}) under applied fields up to 5 T were carried out with a quantum interference device magnetometer (SQUID).

III. RESULTS AND DISCUSSION

Magnetization measurements (not presented here) gave ferromagnetic order at $T_c \approx 220$ K for the terbium-doped compound and $T_c \approx 160$ K for the yttrium-doped compound. These temperatures coincide with the maxima of the resistance at zero field shown in Fig. 1. Consequently the onset of ferromagnetism makes the samples leave the nonmetallic

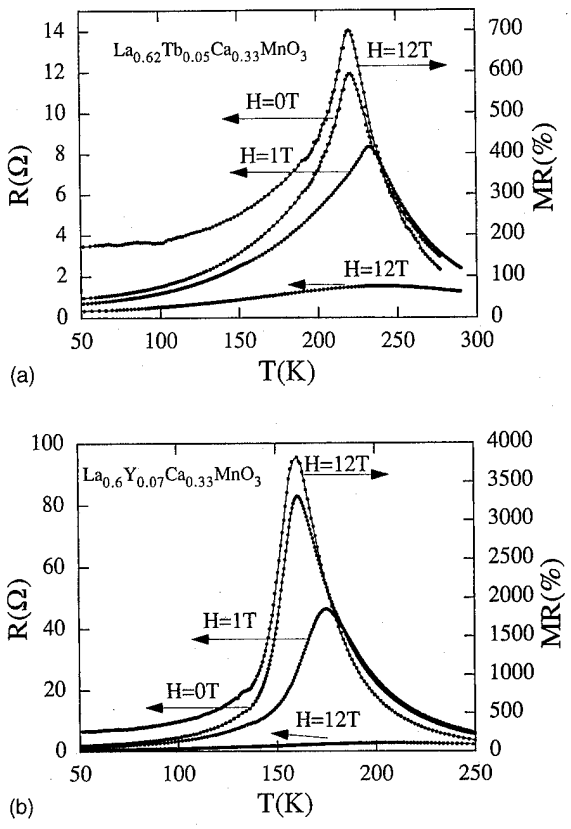


FIG. 1. Resistance vs temperature at 0, 1, and 12 T and MR(%) at 12 T of (a) $La_{0.62}Tb_{0.05}Ca_{0.33}MnO_3$ and (b) $La_{0.6}Y_{0.07}Ca_{0.33}MnO_3$.

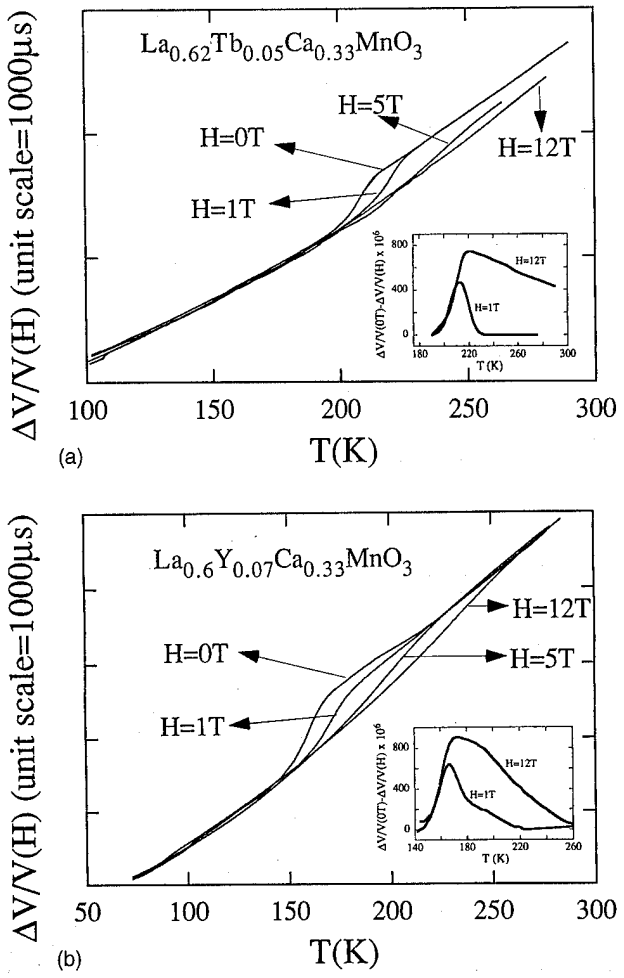


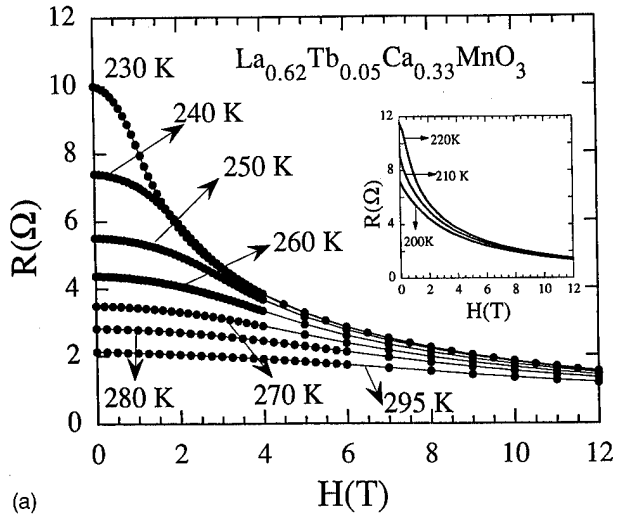
FIG. 2. Volume thermal expansion vs temperature at 0, 1, 5, and 12 T of (a) $La_{0.62}Tb_{0.05}Ca_{0.33}MnO_3$ and (b) $La_{0.6}Y_{0.07}Ca_{0.33}MnO_3$. The insets show the difference of the relative volume $\Delta V/V(0\ \mathrm{T})-\Delta V/V(1\ \mathrm{T})$ and $\Delta V/V(0\ \mathrm{T})-\Delta V/V(12\ \mathrm{T})$ obtained from these measurements.

state and enter the metalliclike state. This transition has recently been considered to be a first-order insulator–metal transition.[9] It has been proposed[9] that an abrupt increase in b (the matrix element which describes the electron hopping ratio between Mn sites) at T_c is a possible mechanism for the crossover from one state to the other.

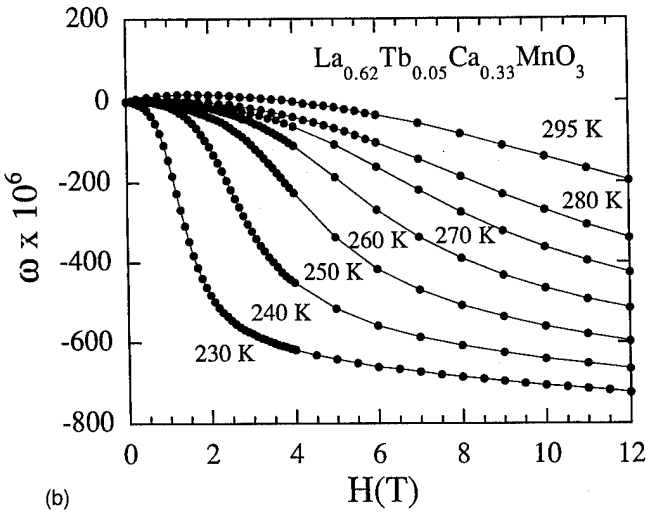
The effect of applying a magnetic field is twofold (see Fig. 1). First the transition is shifted to higher temperatures and second the resistance values are strongly diminished in all temperatures. It brings about large MR values at 12 T ($\mathrm{MR}(\%)=100\{[\rho(0)-\rho(H)/\rho(H)\}$) which are shown in Fig. 1. At around T_c, MR(%) reaches values of ≈700 for the terbium-doped compound and ≈3800 for the yttrium-doped compound. A strong connection between T_c values and MR ratios has been observed in other work:[4,9,10] for lower T_c values, larger MR ratios are obtained.

The connection between resistance and volume effects is of great interest because it can give a new insight into the problem. In Fig. 2 we show the volume thermal expansion versus temperature under different magnetic fields. The insets show the differences obtained between the curves under zero and applied magnetic field. The volume thermal expansion curve under 12 T (this field has almost supressed the nonmetallic state) is similar to the usual anharmonic lattice contribution. Under zero field (simultaneously with the strong resistance effect) an extra contribution appears. At $\sim T_c$ a strong lattice contraction (≈0.8%) accompanies the crossover from the nonmetallic to the metallic behavior. This rather steep change of the lattice parameters at T_c can be related to the abrupt change of b claimed by Hwang *et al.*[9] The extra contribution to the volume thermal expansion above T_c can be due to the progressive charge localization with decreasing temperature of the e_g Mn electrons[13] until T_c is reached. This localization can cause a local distortion of the lattice. At T_c the insulator–metal transition accompanied by volume change would delocalize the e_g electrons and the metallic behavior would take place.

In Fig. 3 we show the isotherms of MR and VMS at different temperatures for the Tb-doped compound. Although GMR exists below and above T_c, the resistance isotherms have different shape in both regions. Below T_c [see inset of Fig. 3(a)] the curvature is always positive and a rapid change of resistance takes place at low fields. Above T_c the curvature changes from negative to positive at a field (H_c) which moves upwards with increasing temperatures. Below H_c the resistance is rather flat, evolving rapidly above H_c towards a tendency to saturation. The VMS (ω) and AMS (λ_t) versus temperature at the maximum field (12 T) are shown in Fig. 4. The AMS is the typical of a ferromagnet: zero above T_c and small below T_c. The VMS is intriguing: zero below T_c and very large above T_c. This unusual volume effect has its



(a)



(b)

FIG. 3. (a) Resistance vs applied magnetic field at temperatures $>T_c$. The inset shows the results at temperatures below T_c. (b) Volume MS as a function of applied magnetic field at temperatures above T_c.

maximum value at T_c and rapidly vanishes when the insulator–metal transition takes place. In Fig. 3(b) the shape of the VMS isotherms above T_c can be seen. The VMS isotherms are extremely similar to the MR isotherms. It seems evident that above T_c the transport and volume properties are intimately related with each other. It appears that both, the charge localization and the local distortion which take place at zero field, are released by applying a magnetic field, causing large MR and VMS effects. These effects are also visible

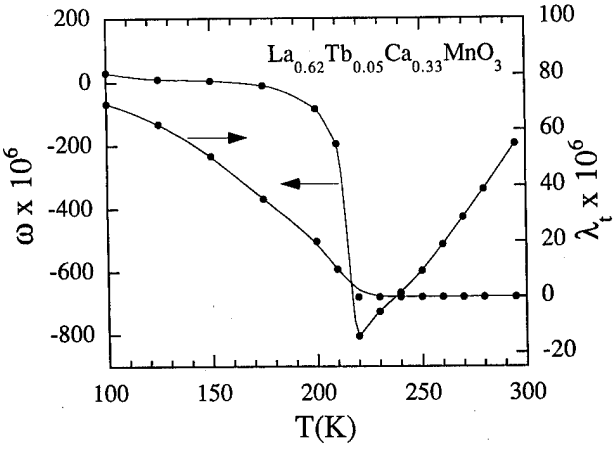


FIG. 4. Volume (ω) and anisotropic (λ_t) MS at 12 T vs temperature.

in the pure $La_{2/3}Ca_{1/3}MnO_3$ compound and will be published elsewhere.

In summary, MR and MS measurements have revealed a tight relationship between the transport and volume properties of doped $La_{2/3}Ca_{1/3}MnO_3$ above T_c suggesting a charge localization which causes a volume effect. These phenomena disappear at T_c, when the long range magnetic order sets in, where a large volume contraction takes place (0.8%), or by applying high enough magnetic fields, bringing about GMR ratios and large VMS values above T_c.

[1] M. McCormack, S. Jin, T. H. Tiefel, R. M. Fleming, J. M. Phillips, and R. Ramesh, Appl. Phys. Lett. **64**, 3045 (1994).
[2] S. Jin, H. M. O'Bryan, T. H. Tiefel, M. McCormack, and W. W. Rhodes, Appl. Phys. Lett. **66**, 382 (1995).
[3] J. Z. Liu, I. C. Chang, S. Irons, P. Klavins, R. N. Shelton, K. Song, and S. R. Wasserman, Appl. Phys. Lett. **66**, 3218 (1995).
[4] V. Caignaert, A. Maignan, and B. Raveau, Solid State Commun. **95**, 357 (1995).
[5] Y. Tomioka, A. Asamitsu, Y. Moritomo, H. Kuwahara, and Y. Tokura, Phys. Rev. Lett. **74**, 5108 (1995).
[6] A. Urushibara, Y. Moritomo, T. Arima, A. Asamitsu, G. Kido, and Y. Tokura, Phys. Rev. B **51**, 14 103 (1995).
[7] Y. Moritomo, A. Asamitsu, and Y. Tokura, Phys. Rev. B **51**, 16 491 (1995).
[8] A. J. Millis, P. B. Littlewood, and B. I. Shraiman, Phys. Rev. Lett. **74**, 5144 (1995).
[9] H. Y. Hwang, S.-W. Cheong, P. G. Radaelli, M. Marezio, and B. Batlogg, Phys. Rev. Lett. **75**, 914 (1995).
[10] J. M. De Teresa, J. Blasco, M. R. Ibarra, J. García, C. Marquina, P. Algarabel, and A. del Moral, Solid State Commun. **96**, 627 (1995).
[11] K. Knízek, Z. Jirak, E. Pollert, F. Zounová, and S. Vratislav, J. Solid State Chem. **100**, 292 (1992).
[12] M. R. Ibarra, P. A. Algarabel, C. Marquina, J. Blasco, and J. García, Phys. Rev. Lett. **75**, 3541 (1995).
[13] For a discussion on the Mn electronic configuration in these compounds see for instance Ref. 6.

Pressure effect on the resistivity in GMR $La_{0.60}Y_{0.07}Ca_{0.33}MnO_3$ compound (abstract)

Z. Arnold and K. Kamenev
Institute of Physics, AVCR, Cukrovarniká 10, 16200 Praha 6, Czech Republic

M. R. Ibarra, P. A. Algarabel, C. Marquina, J. Blasco, and J. García
Departamento de Física de la Materia Condensada e Instituto de Ciencia de Materiales de Aragón, Universidad de Zaragoza-CSIC, Facultad de Ciencias, 50009 Zaragoza, Spain

The substitution of La^{+3} by smaller Y^{+3} ions in mixed valence Mn^{+3}–Mn^{+4} perovskites $La_{0.67-x}Y_xCa_{0.33}MnO_3$ gives rise to a decrease of the order temperature ($T_c=160\pm5$ K for $x=0.07$ and $T_c=240$ K for $x=0$). One of the most relevant features found in this compound was the extremely large magnetoresistance observed in bulk polycrystals ($\approx-10\,000\%$) near T_c.[1] This huge effect was associated with the reduction of the lattice parameter. In order to have an insight into the influence of volume change on transport properties in this compound, we have performed measurement of the thermal dependence of the resistivity under hydrostatic pressure up to 8 kbar. At ambient pressure a peaklike anomaly in the resistivity is observed at T_c. Under the former assumptions, one would expect an increase of the resistivity value at the maximum as well as a decrease of T_c. However, we have found a shift toward higher temperatures and a drastic decreasing of the maximum in the resistivity for increasing pressures. At a pressure of 7.5 kbar the anomaly in the resistivity almost disappears and consequently the GMR effect. As a consequence, the effect of pressure seems to be identical to the effect of the applied magnetic field. Ibarra *et al.*[2] recently observed a large spontaneous magnetovolume effect at T_c with an extra contribution to the lattice thermal expansion. This extra contribution was found to be suppressed by an applied magnetic field. From these preliminary results it seems that the interplay between magnetostrictive deformations and the shrinkage of the lattice by external pressure could be in the origin of the observed behavior.
© *1996 American Institute of Physics.* [S0021-8979(96)60408-1]

This work has already been published in Appl. Phys. Lett. **67**, 2875 (1995).

[1] S. Jin, H. M. O'Bryan, T. H. Tiefel, M. MacCormack, and W. W. Rhodes, Appl. Phys. Lett. **66**, 382 (1995).
[2] M. R. Ibarra, P. A. Algarabel, C. Marquina, J. Blasco, and J. García, these proceedings.

 0021-8979/96/79(8)/5178/1/$10.00 © 1996 American Institute of Physics

Hall effect and giant magnetoresistance in lanthanum manganite thin films

J. E. Núñez-Regueiro,[a] D. Gupta, and A. M. Kadin
Department of Electrical Engineering, University of Rochester, Rochester, New York 14627

Magnetoresistance and Hall coefficient have been investigated as a function of temperature in patterned thin films of La–Ca–Mn–O. Our data on magnetoresistance show a maximum magnetoresistance ratio $\Delta\rho/\rho(0)$ of $\approx -60\%$ at 1.5 T and 240 K. The Hall coefficient indicates that the carriers are predominantly holes, with apparent density that varies as a function of temperature. Although changes in mobility were also observed, our results indicate that changes in carrier density become more important than changes in mobility at temperatures lower than the Curie temperature. We interpret our data in terms of a simple picture that includes two parallel contributions to the carrier density and the conductivity. © *1996 American Institute of Physics.*
[S0021-8979(96)52308-7]

The correlation between electric and magnetic properties of manganese oxides has drawn a good amount of attention for more than 40 years.[1–4] Lanthanum manganite, $LaMnO_3$, has a perovskite crystalline structure and exhibits a range of magnetic phases when divalent atoms (Ca, Ba) are substituted on the La site. As the temperature is lowered, most manganites exhibit a nonzero spontaneous magnetization at a temperature T_c, indicating that some sort of ferromagnetic coupling is present. Interest in these mixed valence compounds has been revived recently in connection with giant negative magnetoresistance in ferromagnetic thin films[5–12] with compositions such as $La_{0.67}Ca_{0.33}MnO_3$ (LCMO). Upon application of a large magnetic field, the electrical resistance of such films can drop by a factor of more than 1000, at a temperature somewhat below the ferromagnetic transition.[5] The origin of this effect is not well understood, although qualitative explanations involving magnetic polaron scattering, double exchange, and metal–insulator transitions have been discussed.[1,6]

A necessary condition for the electric conduction is the presence of mobile carriers. As was shown by Jonker and van Santen,[2] this is satisfied when the Mn ions are in a mixed +3/+4 valence. They showed that in the case of $LaMnO_3$, substitution of x atoms of trivalent La by divalent Ca forces x Mn atoms to become tetravalent. In the ideal case, each Mn^{+4} ion contributes one hole to the total number of carriers. However, doping is not the only mechanism by which carriers are induced. The fact that these compounds behave like antiferromagnetic semiconductors at both ends of the composition diagram ($LaMnO_3$–$CaMnO_3$) (Ref. 2) is a good indication that thermal ionization of some Mn^{3+} ions is also possible. Based on the assumption that the carrier density would yield information about the nature of the transition in perovskite-type manganites, we investigated the Hall coefficient as a function of temperature in patterned thin films of LCMO. Our results indicate that changes in carrier density become more important than changes in mobility at temperatures lower than the Curie temperature.

Our 6000 Å films were deposited by rf sputtering from a powdered target with composition $La_{2/3}Ca_{1/3}MnO_3$ onto $LaAlO_3$ (100) substrates, using a process[13] that had been optimized for the high-T_c perovskite superconductor $YBa_2Cu_3O_7$ (YBCO). Sputtering gases were Ar and O_2, with partial pressures of 10 and 5 mTorr, respectively. The substrates were held at 630 °C during deposition, and cooled down in 100 Torr O_2. X-ray diffraction analysis at room temperature indicates that as-deposited films grew epitaxially on the $LaAlO_3$ substrate with a perovskite-type cubic structure, with lattice parameter $a=3.84$ Å.

The inset in Fig. 1 shows the pattern used for measuring both the Hall voltage and the longitudinal resistance. The bias current terminals are labeled $I+$, $I-$, the longitudinal voltage was read between V_{1+} and $V_{1-}(V_L=V_{1+}-V_{1-})$, and the transverse voltage was taken between V_{t+} and $V_{t-}(V_t=V_{t+}-V_{t-})$. The distance w between transverse voltage electrodes was 4.2 mm. This pattern was photolithographically defined and etched with a 50 H_2O_2: 1 H_2SO_4: 1000 H_2O solution. The resistivity of patterned samples seemed to be unaffected by the etching process, as compared to their unpatterned counterparts. Indium contacts were soldered onto the film. Samples were mounted in a temperature controlled cryostat cooled by liquid N_2 flow, surrounded by a superconducting solenoid capable of generating homogeneous magnetic fields of up to 4 T. Both longitudinal resis-

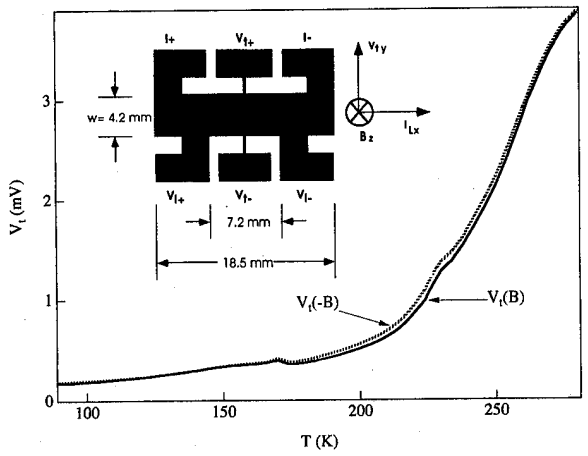


FIG. 1. Transverse voltage vs T for the positive $[V_t(B)]$ and negative $[V_t(-B)]$ sense of magnetic field. $B=1.5$ T. The inset shows the pattern used for Hall effect measurements. A magnetic field pointing into the page is defined positive.

[a]Electronic mail: nunez@ee.rochester.edu

 0021-8979/96/79(8)/5179/3/$10.00 © 1996 American Institute of Physics

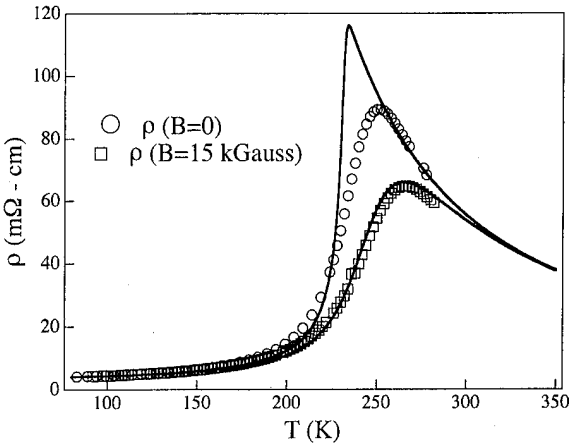


FIG. 2. ρ vs T for an LCMO thin film, for $B=0$ and 1.5 T. The solid lines are fits to Eq. (1), for parameters $\alpha=223$ S/cm, $\beta=243$ S/cm, $T_c=232$ K, $E_0/k=790$ K, and $M_s=350$ emu/cm^3, as discussed in Ref. 7.

tance and transverse voltage were measured under constant current bias ($I_L=1$ mA) as a function of temperature and applied magnetic field. The direction of the field was normal to the substrate, therefore at right angles with the current. The sense of the field was reversed in different runs. In order to avoid errors arising from longitudinal heat flow, the sample was thermally sunk to a temperature controlled copper block, and the current leads were wound around thermal binding posts. All measurements were repeated under slow cool-down and slow warm-up, yielding the same results. These results were also reproduced in subsequent runs for different values of magnitude and sense of I_L.

Samples studied show a sharp peak in the longitudinal resistivity which indicates a transition from a thermally activated semiconducting-like region ($d\rho_L/dT<0$) to a metallic-like region ($d\rho_L/dT<0$). Both the abscissa and ordinate of the peak in the ρ_L vs T curve are strongly affected by externally applied magnetic fields. As the field is increased the amplitude of the peak is reduced and the maximum shifts to higher temperatures. Figure 2 shows a plot of ρ_L vs T of a typical sample with and without an applied field of 1.5 T. The symbols are the experimental data, the solid lines are their corresponding fit to the phenomenological expression:[7]

$$\rho_L=1/\sigma_L=1/\{\alpha[M/M_S]^2+\beta\ \exp(-E_0/kT)\}, \qquad (1)$$

where σ_L is the longitudinal conductivity, M represents the microscopic magnetization of spins within a magnetic domain, M_s is the saturation magnetization ($M_s=350$ emu/cm^3),[7] and α and β are constants. $M=M(B,T)$ was determined from the mean-field expression[14] for an average spin of 1.83 for the Mn ions. In fitting Eq. (1) to the data of Fig. 2, the values of α and M_s are fit to the low temperature data; those for β and E_0 are determined by fitting to the high-temperature data. The only other parameter is T_c, which is close to the temperature of the maximum resistance for $B=0$. In this way, we obtained the curves also shown in Fig. 2, using $\alpha=223$ S/cm, $\beta=243$ S/cm, $T_c=232$, and $E_0/k=790$ K. Here, T_c represents the effective magnetic transition temperature of a large portion of the material, even if some portions have higher transitions. Equation (1) predicts a giant magnetoresistance (MR), defined here as $\mathrm{MR}=[\rho_L(1.5\ \mathrm{T})-\rho_L(0)]/\rho_L(0)$, at just below T_c. In our case, MR was $\sim -60\%$ at 240 K. Equation (1) was found to fit data from other thin films and single crystals, with similar values of the fitting parameters.[7] In particular, we could account for the "colossal" MR observed in some samples[12] merely by lowering the value of T_c to 90 K.

Although the fit of Eq. (1) is very good in the large field, the zero-field peak is lower and more rounded in the experiments than in the model. We believe this is a consequence of an inhomogeneous distribution of Curie temperatures, which is suggested by a broadened magnetization curve near T_c in preliminary data on this sample,[7] comparable to that in other similar thin films. This would tend to show up more strongly in the zero-field resistance than that at higher fields, or in the magnetization itself. That is because the resistance should change sharply below T_c, and the current will tend to follow the path of least resistance. Hence even a relatively small percentage of a higher-T_c material could have a disproportionate effect on $\rho_L(T)$. In larger fields, since $M(T)$ does not change as sharply, the variation in ρ among inhomogeneous regions should be reduced, and hence the deviation from homogeneous behavior should be much less.

The MR has sometimes been attributed to changes in scattering rates, but the "colossal" changes in the manganites seem to be more suggestive of a metal–nonmetal transition where the carrier density changes. For conduction by carriers of a single type and sign, the conductivity can be expressed within a Fermi liquid picture as a product of the carrier density p and the mobility μ: $\sigma_L=pe\mu$, where we are anticipating that the carriers will be holes with charge $+e$. One can then determine the carrier density from the transverse Hall field $\mathbf{E}_H=-\mathbf{v}\times\mathbf{B}=(-1/pq)\ \mathbf{J}\times\mathbf{B}$. In a Cartesian coordinate system, where I_L, V_t, and B are, respectively, parallel to the x, y, and z-directions, $p=J_xB_z/eE_H$, where J_x is the current density.

It is worth noting that the extraction of information from Hall effect measurements in materials showing appreciable magnetization is not straightforward.[15] A complete analysis of the Hall effect in magnetic materials normally requires measurement up to large magnetic fields to separate the "anomalous" Hall effect (associated with skew scattering) from the "ordinary" Hall effect associated with the carrier density). In the present case, however, going up to very large fields would be expected to change the effective carrier density, the very parameter that we want to measure. To avoid such confusion in these preliminary measurements, we have taken a deliberately naive approach, and treated the entire Hall voltage (at the moderate field of 1.5 T) as arising from the ordinary Hall effect. This should be reasonably accurate for $T>T_c$, but would be much less so for $T\ll T_c$, when M becomes fairly large. With this proviso, we continue with our analysis.

We used the Hall effect in order to attempt to separate out the effects of both carrier density and mobility. In this experiment, it is important to note that the measured trans-

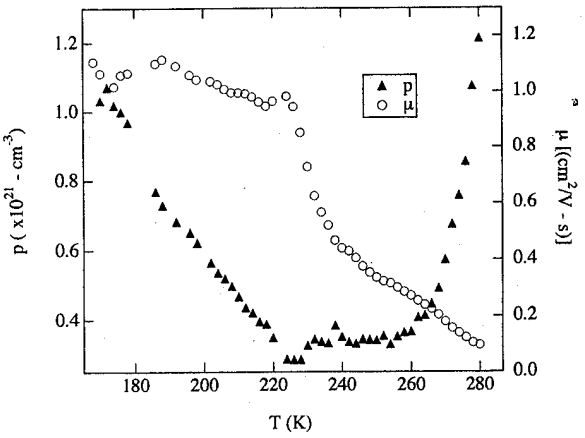


FIG. 3. Temperature dependence of hole density (p) and mobility (μ) for an LCMO thin film in a field of 1.5 T.

verse voltage does not consist simply of the Hall voltage (as it would in the ideal situation), but rather is dominated by a superimposed component of the longitudinal voltage, as is illustrated in Fig. 2. We separate these two parts by their response to a change in the sign of B: a magnetoresistive component should be unchanged if B is reversed, while the Hall voltage should be reversed. Thus, we determine the true Hall voltage as the odd part of the measured transverse voltage, or the Hall field as $E_H=[V_t(B)-V_t(-B)]/2w$. If the difference becomes very small (as it does below 160 K), then the determination of the Hall field becomes uncertain. In our case, E_H was measured at 1.5 T, using the configuration shown in Fig. 1. The possibility that E_H arose from variations in the applied magnetic field in different runs, or from other artifacts, was ruled out since the observed longitudinal voltage did not show significant changes $[V_L(B)\approx V_L(-B)]$.

Once p is known, μ can then be estimated from $\mu=1/\rho_L ep$, where ρ_L is the measured longitudinal resistivity. Figure 3 is a plot of the effective carrier density and the effective mobility versus temperature of a typical sample. Our results show that majority carriers are of positive sign. As the temperature is reduced, the apparent carrier density decreases, then turns around and increases again sharply. Since the unit cell volume is $\sim 5.7\times10^{-23}$ cm^3, the carrier density falls from 0.07 carriers/unit-cell at room temperature to 0.02 holes/unit cell at the resistance peak (T_{peak}), levels off and starts rising again at T_c, approaching 0.06 holes/cell at 165 K. Below T_c the carrier density is expected to grow as the number of ferromagnetic ions increases. Based on stoichiometry, the estimated carrier density of a $La_{2/3}Ca_{1/3}MnO_3$ sample may be expected to approach 0.33 holes/cell as the temperature approaches $T=0$. Changes in mobility were also observed, but they appear to become significant in the region $T_c<T<T_{peak}$, where the carrier density shows little variation. This temperature range coincides with the region in temperature where the strongest MR changes are usually reported.[9,12] When $T>T_{peak}$, changes in both carrier density and mobility seem to affect the conductivity.

The data for carrier density and mobility can be qualitatively understood in the following manner: In the high temperature semiconducting state, as the temperature is cooled, the carriers freeze out, and in addition the mobility increases somewhat (due in part to decreased scattering from carriers). In the low temperature metallic phase, the mobility increases a bit more and then saturates, due perhaps to decreased spin-flip scattering as the material orders magnetically. However, since this correlates with the strength of the magnetization in the ferromagnetic state, the carrier density reverses direction in the metallic phase, and continues to increase as the temperature is cooled further.

We have investigated magnetoresistance and Hall coefficient as a function of temperature in patterned thin films of La–Ca–Mn–O. We found that our data can be interpreted in terms of a simple picture that includes two parallel contributions to the carrier density. This picture is also consistent with most of the experimental results reported to date on giant negative magnetoresistance in both thin films and single crystals of perovskite type manganites.

The Hall coefficient indicates that the carriers are predominantly holes, with apparent density that varies as a function of temperature. Although changes in mobility were also observed, our results indicate that changes in carrier density become more important than changes in mobility for $T<T_c$. It appears that the carrier density might be expressed as the sum of two terms as in Eq. (1), and the mobility is another factor that multiplies this to obtain the conductivity. A more quantitative description will require a more complete set of measurements, including determination of the anomalous Hall effect that may be associated with skew scattering. Future work will analyze p and μ for a range of applied fields as well as temperatures, and will attempt to incorporate both of these phenomena into a more complete phenomenological equation.

One author (J.E.N.R.) acknowledges financial support from CONICIT, Venezuela. Another author (D.G.) acknowledges the Frank J. Horton fellowship. This work was supported in part by NSF Grant DMR-9122727.

[1] P. G. de Gennes, Phys. Rev. **118**, 141 (1960).
[2] G. Jonker and J. Van Santen, Physica **16**, 337 (1950).
[3] E. Wollan and W. Koehler, Phys. Rev. **100**, 545 (1955).
[4] C. Zener, Phys. Rev. **82**, 403 (1951).
[5] S. Jin, T. H. Tiefel, M. McCormack, R. A. Fastnacht, R. Ramesh, and L. H. Chen, Science **264**, 413 (1994).
[6] R. von Helmolt, J. Wecker, K. Samwer, L. Haupt, and K. Bärner, J. Appl. Phys. **76**, 6925 (1994).
[7] J. E. Núñez-Regueiro and A. M. Kadin (unpublished).
[8] G. Xiong, Q. Li, H. Ju, R. Greene, and T. Venkatesan, Appl. Phys. Lett. **66**, 1689 (1994).
[9] S. Jin, M. McCormack, T. Tiefel, and R. Ramesh, J. Appl. Phys. **76**, 6929 (1994).
[10] H. Ju, J. Gopalkrishnan, J. Peng, Q. Li, G. Xiong, T. Venkatesan, and R. Greene, Phys. Rev. B **51**, 6143 (1995).
[11] G. Xiong, Q. Li, H. Ju, S. Mao, L. Senapati, X. X. Xi, R. Greene, and T. Venkatesan, Appl. Phys. Lett. **66**, 1427 (1995).
[12] M. McCormack, S. Jin, T. Tiefel, R. Fleming, J. Phillips, and R. Ramesh, J. Appl. Phys. **64**, 3045 (1994).
[13] J. K. Truman, W. R. White, P. H. Ballentine, D. S. Mallory, and A. M. Kadin, IEEE Trans. Supercond. **3**, 1679 (1993).
[14] C. Kittel, *Introduction to Solid State Physics*, 6th ed. (Wiley, New York, 1986).
[15] C. M. Hurd, *The Hall Effect in Metals and Alloys* (Plenum, New York, 1972).

Magnetic properties of colossal magnetoresistive manganese oxides

J. Fontcuberta, B. Martínez, A. Seffar, S. Piñol, A. Roig, E. Molins, and X. Obradors
Institut de Ciència de Materials de Barcelona, CSIC Campus U.A.B., Bellaterra 08193, Catalunya, Spain

J. Alonso and J. M. González-Calbet
Departimento Química Inorgánica, Universidad Complutense, Madrid 28040, Spain

The effects of isovalent substitution into the lanthanide sites in $La_{1-x}Y_xCa_{0.30}MnO_{3-\delta}$ oxides is presented. We report on the electrical and magnetic properties of these materials for $x=0-0.25$. We have found that the ferromagnetic ordering temperature *decreases* and the cusp of the resistivity occurring at this temperature *increases* when the smaller lanthanide Y is introduced into the lattice. We will provide evidence that a key signature of the magnetic properties of these oxides is the presence of an unusual long tail in the magnetization versus temperature curves $M(T)$, extending up to $3T_M$ and which is very sensitive to the applied magnetic field and becomes increasingly important with the concentration of Y in the lattice. These features signal a strong polarizability of the spin clouds in these materials as our Mössbauer experiments will clearly demonstrate. Finally, we will show that the magnetoresistance of these compounds can be well-described in terms of a spin-disorder scattering mechanism. © *1996 American Institute of Physics.*
[S0021-8979(96)71408-4]

I. INTRODUCTION

The dynamics of charges in systems having strong electron correlations and near the Mott transition have received a renewed interest since the discovery of high-temperature superconductivity in the cuprate oxides. One of the most remarkable features of these systems is that a strong spin-charge coupling can exist and the dynamics of carriers is expected to be strongly dependent on the spin arrangement. The recent discovery of dramatic magnetoresistive effects in manganese perovskites is a very spectacular example of this strong interplay between itinerant carriers and localized magnetic moments.[1–3]

It was known long ago that $LaMnO_3$ and $CaMnO_3$ are antiferromagnetic (AF) insulators;[1,4] however, when a solid solution $La_{1-x}Ca_xMnO_3$ is formed, the existence of both $Mn^{3+/4+}$ ions has profound effects on the crystal structure, the spin arrangement and the transport properties. For $x\approx 0.2-0.4$ the compounds are metallic and ferromagnetic. It is close to the transition from the paramagnetic state to the ferromagnetic state where a cusp in the resistivity has been observed. Application of an external magnetic field of a few teslas suppresses the resistive cusp. Magnetoresistivity values as high as a 10^6% have been reported.[3]

Although a detailed microscopic understanding of such huge magnetoresistive effect is not yet available, the simple observation of the fact that a high field is required to suppress a scattering channel immediately suggests that we are dealing with the internal, atomiclike exchange fields of these materials. This is just the opposite behavior as observed in metal-based giant-magnetoresistive materials which require fields of only a few Oe to show the maximal change of resistivity (although much smaller $\approx$100%!![5]). The appearance of a metallic ferromagnetic state on doping has been explained by the mechanism of the double exchange.[6] Due to the Hund rule, the Mn^{3+} ions in $LaMnO_3$ have three electrons in the t_{2g} orbitals and a single electron in the e_g orbital. Because the Hund rule and the on-site Coulomb repulsion between e_g electrons, $LaMnO_3$ is an AF insulator. The substitution of La atoms by divalent ions (Ca^{2+},Sr^{2+},Ba^{2+}) leads to a depletion of the e_g orbitals which now become available for electrons of the surrounding Mn^{3+} ions to jump into the empty states as long as the hopping electron has its spin parallel to the t_{2g}^3 spins. This means that the magnetic moments of the Mn^{3+} and Mn^{4+} should be parallel for metallic conduction. The AF coupling between the $Mn^{3+/4+}$ ions should be overcome by the gain of kinetic energy of the itinerant electrons in order to stabilize a metallic and ferromagnetic state.[6] It is clear that AF is controlled by the hopping integral t_{ij} between ionic sites which thus should be strongly dependent on the overlapping of the $3d$ orbitals. Therefore, one can expect that distortion of the Mn–O–Mn bond should result in a severe change of the coupling between itinerant carriers and localized spins.[7]

In this letter, we will explore some effects of introduction of a smaller trivalent lanthanide (Y^{3+}) in the La sites.

II. EXPERIMENT

Ceramic samples of $La_{0.7-x}Y_xCa_{0.3}MnO_3$ ($x=0-0.25$) composition were prepared by solid state reaction of precursor oxides. Appropriate amounts of La_2O_3, CaO, Mn_2O_3 and Y_2O_3 were mixed and heated in air at 900 °C for 24 h with intermediate grinding. A final sintering process step was carried out at 1400 °C. The as-prepared materials were characterized by x-ray diffraction. They are single phase and have an orthorhombic perovskite structure (Pbnm). The lattice parameters are found to vary linearly with the Y concentration.[7] Plasma, chemical, and ATD analysis have been used to check the sample composition and stoichiometry. Within the context of this letter the relevant results of such analysis are that the oxygen contents of the samples does not vary significantly with the Y composition and the measured ratio Y/La follows the expected changes.[8] Magnetoresistivity measurements have been performed under fields up to 5.5 T by conventional four-probes method with the current parallel to the applied field. Magnetic properties have been measured by

 0021-8979/96/79(8)/5182/3/$10.00 © 1996 American Institute of Physics

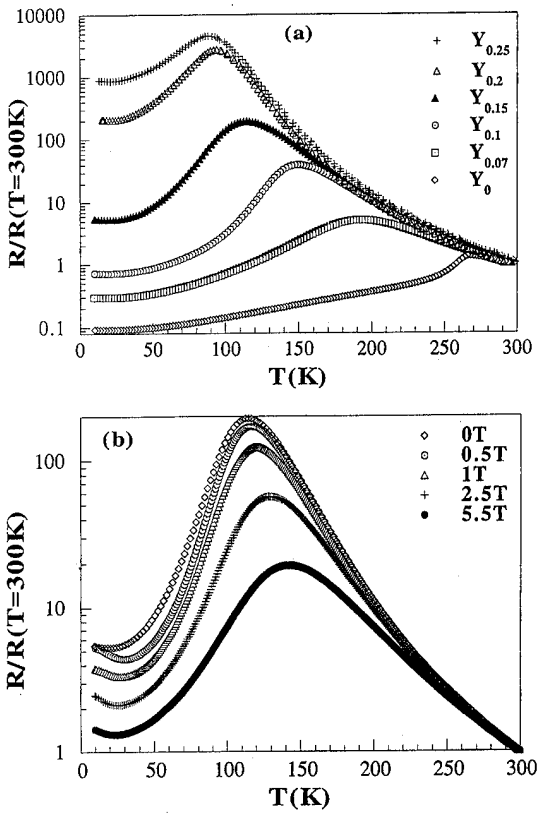


FIG. 1. (a) Normalized resistivity vs temperature for $La_{1-x}Y_xCa_{0.33}MnO_{3-\delta}$ ($x=0-0.25$). (b) Normalized resistivity vs temperature for $x=0.15$ at several applied magnetic fields.

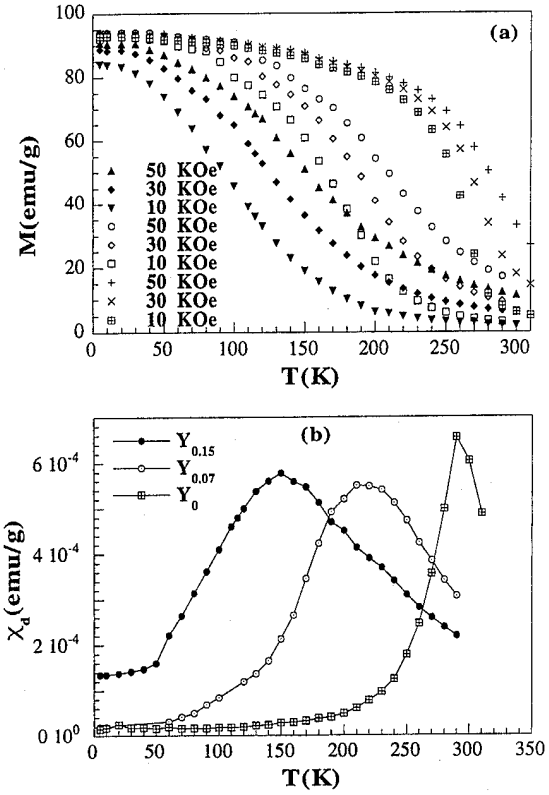


FIG. 2. (a) Temperature dependence of the magnetization of the $x=0$, 0.07, and 0.15 samples at several fields. (b) High-field differential susceptibility for the same samples as a function of temperature.

using a QD SQUID magnetometer up to 5.5 T. Mössbauer experiments were performed on ^{57}Fe doped samples (2%) by using a ^{57}CoRh source. Spectra were recorded at several temperatures. When necessary a magnetic field of 0.3 T was applied to the sample and perpendicular to the γ-ray beam.

III. RESULTS AND DISCUSSION

Figure 1(a) shows the zero-field temperature dependence of the resistivity of some of the samples. A giant resistive peak develops at low temperature. Its amplitude $\Delta R(T)/R=[R_{\max}-R(300\ \text{K})]/R(300\ \text{K})$ is as high as 5×10^5%for $L=Y_{0.25}$. At temperatures well below the resistivity peak, a metalliclike behavior is almost recovered. The most remarkable results of Fig. 1(a) are the lowering of the temperature T_M where the maximum resistance ($R_{\max}$) occurs when increasing the Y concentration, and the systematic enhancement of $R_{\max}$. The application of a magnetic field strongly reduces the resistivity as shown in Fig. 1(b). The magnetoresistance $\Delta R(H)/R=[R_{\max}(H)-R(5\ \text{K},\ 5\ \text{T})]/R(5$ K,5 T) reaches its maximum at temperatures close to T_M, decreasing above and below T_M.

From the structural point of view, the Y substitution is expected to enhance the buckling of the MnO_6 octahedra, thus leading to a reduction of the Mn–O–Mn bond. As a consequence, the transfer interaction of e_g electrons should be reduced. Therefore, our results indicate that a reduction of t_{ij} produces a lowering of T_M and an enhancement of the magnetoresistance.[7]

We turn now to the magnetic properties. In Fig. 2(a) we present some of the magnetization versus temperature curves measured at several fields. ($H=10$, 30, and 50 kOe) for samples having $x=0$, 0.07, and 0.15. Several aspects of these data should be pointed out. First, the drop of magnetization at the ferromagnetic ordering temperature T_M closely coincides with the temperature were the cusp in the resistivity is observed. Both temperatures decrease with increasing the Y concentration into the lattice. At $T\ll T_M$ the saturated magnetization is of about 3.7 μ_B in accordance with the classical value expected for e_g electrons (0.7/f.u.) fully polarized by the t_{2g} localized spins ($S=3/2$). The weak dependence of the 0 K magnetization on the Y concentration could reflect the existence of some noncollinear spin arrangement. Notice that at 5 T this difference is further reduced. It should also be noticed in Fig. 2(a) that at T_M, for the $x=0.15$ sample, a field of 5 T induces a magnetization which reaches about 75% of its saturated value at this temperature. Such an extraordinary magnetic polarizability is a key feature of these ferromagnetic manganites. Data of Fig. 2(a) displays a characteristic long tail extending up to the highest measured temperature (300 K) and which becomes more pronounced as the Y concentration increases. Comparison of the resistivity and magnetization curves reveals that it is along this long tail that resistivity rises when lowering temperature. As shown by data of Fig. 2(a), the magnetization in the tail is very sensitive to the applied magnetic field and so the magnetoresistivity is relevant in this temperature range. Figure 2(b), where we show the high field susceptibility of the samples as

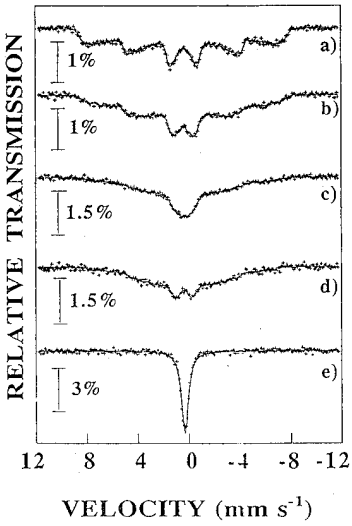


FIG. 3. Temperature dependence of transmission Mössbauer spectra of ^{57}Fe: $La_{1-x}Y_xCa_{0.33}MnO_{3-\delta}$ ($x=0.07$) sample. (a) 69 K, (b) 80 K (c) 90 K (d) 90 K and $H=3$ kOe, and (e) 100 K.

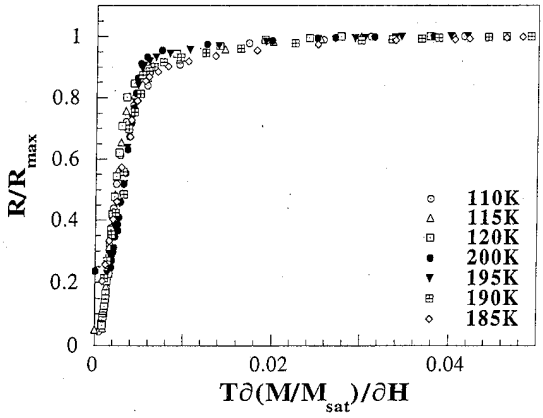


FIG. 4. Magnetorestitivity of the $x=0.07$ and $x=0.15$ samples as a function of the differential susceptibility at several temperatures.

a function of temperature, clearly reflects the strong polarizability of the system, which is particularly relevant close to T_M.

Further evidence of the magnetic ordering and polarizability can be gained by using Mössbauer spectroscopy, which is a local probe of the magnetic ordering. In Fig. 3, we present the Mössbauer spectra recorded at various temperatures for the $x=0.07$ sample. From room temperature down to 100 K a singlet is observed: That means that in this temperature range the nuclear magnetic moment is rapidly precessing. At lower temperatures, as spontaneous magnetic order sets in, the magnetic moments become blocked and the typical 6-finger pattern of ^{57}Fe becomes apparent. At temperatures close to T_M (for instance 90 and 80 K in Fig. 3) the hyperfine splitting of the spectra gradually appears. In this letter we focus our attention to this temperature region. At $T<90$ K the spectra can be fitted to a distribution (ΔH) of hyperfine fields which become progressively narrower when reducing temperature. At $T=90$ K, the distribution ΔH extends up to 500 kOe. At this point it should be mentioned that introduction of $Fe^{3+/4+}$ ions into the Mn sites, even at the low concentration used (2% ^{57}Fe) in principle can produce severe disturbances on the establishment of the ferromagnetic order and the metallic state. For instance the electronic Fe:$3d^{5/4}$ configuration can reduce electron jumping into this position thus resulting in a reduction of the kinetic energy and consequently the ferromagnetic state could be depressed. Our data of Fig. 3 seem to suggest that this is indeed the case as T_M is reduced from $T_M \approx 110$ K ($x=0.07$) to $T_M \approx 90$ K in the ^{57}Fe doped sample. In spite of this effect, the system still remains highly polarizable as will be seen in the following. We have recorded Mössbauer spectra under a magnetic field. In Fig. 3 we include the spectra collected at 90 K under an $H=3$ kOe field. Comparison of the spectra taken with and without field clearly reveals the more prominent development of the hyperfine sextet which reveals the strong field-induced polarizability. Notice that $H=3$ kOe is much smaller than the hyperfine field (up to 500 kOe).

The appearance of a giant resistive peak close to T_M suggests that spin-disorder scattering is a dominant scattering channel in these systems. Due to the fact that the resistivity at the cusp is much higher than the resistivity well above and below T_M, we can simply analyze the field dependence of the resistivity neglecting all other factors contributing to the overall resistivity and considering simply the spin-scattering term. The spin-disorder scattering term is expected to be a function of the differential susceptibility $\chi(T,H)$ and should increase with temperature. Therefore, we can write: $\rho(T,H) \propto F[T,\chi(T,H)]$ where F is some function. In Fig. 4, we plot the resistivity data for samples $x=0.07$ and 0.15 at temperatures close to the cusp of $\rho(T,H)$ as a function of $T\cdot\chi(T,H)$. It is very significant that data for samples having very distinct critical temperatures and values of the maximal resistivity (see Fig. 1) collapse onto a single function. This means that a common scattering mechanism is operating on all samples and the field dependence of the resistivity is simply given by a function of the susceptibility.

In summary we have shown that the giant magnetoresistivity response in these manganites is accompanied by an unusual magnetic polarizability of the electronic clouds. Both effects appear to be controlled by the mean size of the lanthanides, that is the concentration of the smaller Y ion into the lattice.

We would like to acknowledge financial support by the CICYT-MIDAS (MAT94-1924-CO2), DGICYT (PB92-0849) Projects and the Generalitat de Catalunya. A. S. is grateful to the Instituto de Cooperación con el Mundo Arabe for a grant.

[1] G. H. Jonker and J. H. van Santen, Physica **19**, 120 (1953).
[2] R. von Helmolt *et al.*, Phys. Rev. Lett. **71**, 2331 (1993).
[3] S. Jin *et al.*, Science **264**, 413 (1994).
[4] E. O. Wollan and W. C. Koehler, Phys. Rev. **100**, 545 (1955).
[5] M. N. Baibich *et al.*, Phys. Rev. Lett. **61**, 2472 (1988); A. E. Berkowitz *et al.*, Phys. Rev. Lett. **68**, 3745 (1992).
[6] P. G. de Gennes, Phys. Rev. **118**, 141 (1960).
[7] J. Fontcuberta *et al.*, Phys. Rev. Lett. **76**, 1122 (1996).
[8] J. Fontcuberta *et al.* (unpublished).

Magnetic and magnetoresistance studies on radio frequency sputtered La–Pb–Mn–O films

G. Srinivasan, T. E. Brusca, and A. S. Fisher
Department of Physics, Oakland University, Rochester, Michigan 48309-4401

V. Suresh Babu and M. S. Seehra
Department of Physics, P.O. Box 6315, West Virginia University, Morgantown, West Virginia 26506-6315

Results on structural and magnetic characterization of radio frequency sputtered thin films of $La_{0.74}Pb_{0.26}MnO_z$ on (100) Si are presented. Stoichiometric films with a thickness of 0.6 μm showing (110) textured growth were deposited in a mixed argon–oxygen atmosphere. The low temperature magnetization is 10% smaller than the expected value for a collinear ferromagnetic order in the oxide. Zero-field resistivity data show a metal-to-semiconductor transition centered at T_{ms}=250 K. Data on magnetoresistance (MR)=$[\rho(0)-\rho(H)]/\rho(0)$ versus temperature reveal the following important features: (i) a maximum value of 22% for H=2 T at the metal-to-insulator transition temperature, (ii) MR value of 15%–22% over the entire temperature range 4.2–300 K, and (iii) a substantial MR, ~10% even at temperatures as high as 380 K, well above the Curie temperature. Data on the temperature dependence of ferromagnetic resonance linewidth at 9.4 GHz show a discontinuity at T_{ms}. © *1996 American Institute of Physics.* [S0021-8979(96)52408-3]

Jonker and co-workers,[1] about four decades ago, discovered ferromagnetism in a series of Mn and Co based perovskite compounds with the composition $La_{1-x}(Ca,Ba,Sr)_x(Mn,Co)O_3$. Zener attributed the ferromagnetic order to the double exchange (DE) interaction between Mn^{3+} and Mn^{4+} or Co^{3+} and Co^{4+} ions and the oxides are therefore known as DE ferromagnets.[2] Recent reports on the observation of a giant magnetoresistance (GMR) in the Mn-based perovskite oxides have generated a considerable interest in DE ferromagnets for useful technologies.[3–5] A large MR, ~60% at room temperature, was observed in thin films of $La_{0.67}Ba_{0.33}MnO_z$.[3] Thin films of La–Ca–Mn–O prepared by ion beam sputtering were found to show a maximum MR of 53%.[4] A colossal MR, on the order of 127 000% in inflationary units, was reported for thin films of $La_{0.67}Ca_{0.33}MnO_z$.[5] The very large MR, however, occurs at very high applied magnetic fields H=5–8 T, and is suggested to arise from a metal-to-semiconductor type transition, DE assisted processes and magnetic polaron scattering.[3–5] Studies on single crystals of La–Sr–Mn–O reveal, in addition to GMR, a rich variety of phenomena including external field induced crystallographic transitions and giant magnetostriction.[6]

Here we report a similar GMR effect in thin films of $La_{1-x}Pb_xMnO_z$.[7] Structural and magnetic properties of single crystals of the oxides with x=0.25–0.45 were reported in the late 1960s by Morrish and co-workers.[8–11] The oxides order ferromagnetically with the Curie temperature T_C ranging from 315 to 350 K. Data on temperature dependence of the resistivity show a metallic to semiconductor transition at a certain temperature T_{ms}, and T_{ms} is dependent on x and is slightly smaller than T_C. The observation of a relatively large MR at ambient temperature, ~20% at T_{ms} for a field of 1 T could be of importance for potential device applications for the oxides.[9,10] In this study films of $La_{0.74}Pb_{0.26}MnO_z$ with (110) orientation were deposited on (100) Si by rf sputtering in a mixed O_2–Ar atmosphere, and were characterized by magnetization, ferromagnetic resonance (FMR) and MR measurements. The low temperature magnetization for the film was ~10% smaller than the value expected for collinear ferromagnetic ordering of Mn moments. Data on FMR linewidth show a discontinuity at the metal-to-semiconductor transition at T_{ms}=250 K. A maximum MR=$[\rho(0)-\rho(H)]/\rho(0)$ of 22% was observed at T_{ms} for H=2 T. Details on these studies are provided in the following sections.

The technique of rf sputtering was used to prepare films of La–Pb–Mn–O. For film preparations a polycrystalline sintered target with the composition $La_{0.67}Pb_{0.33}Mn_{0.75}O_z$ prepared by standard ceramic techniques from powders of La_2O_3, PbO, and $MnCO_3$ was mounted in a magnetron gun. The sputtering was carried out in a 20% oxygen and 80% argon atmosphere at a pressure of 40 mTorr and a rf power of 50 W at 13.6 MHz. Films were deposited on (100) Si substrates mounted on a heated platform placed at a distance of 6 cm below the target. Samples with thickness 0.6 μm were obtained for a sputtering duration of 24 h. The film composition determined by energy dispersive x-ray spectroscopy techniques was $La_{0.74}Pb_{0.26}MnO_z$.

As-deposited films were amorphous and annealing at 700–1000 °C was necessary to crystallize the films. X-ray diffraction measurements performed on annealed films showed (110) orientation with a lattice constant a=3.861 ±0.004 A and a film–substrate lattice mismatch on the order of 0.5%.

Magnetization measurements were performed with a Faraday balance and a high field superconducting quantum interference device (SQUID) magnetometer. X-band ferromagnetic resonance data were obtained using a reflection type cavity. Magnetoresistance studies were carried out using the four-probe technique.

Films sputtered at a substrate temperature of 500 °C were amorphous, paramagnetic at room temperature, and did not order magnetically down to 80 K. Magnetization (M) measurements showed evidence for a long range order in films annealed in air or oxygen at T_a=600–1000 °C. In Fig.

 0021-8979/96/79(8)/5185/3/$10.00 © 1996 American Institute of Physics

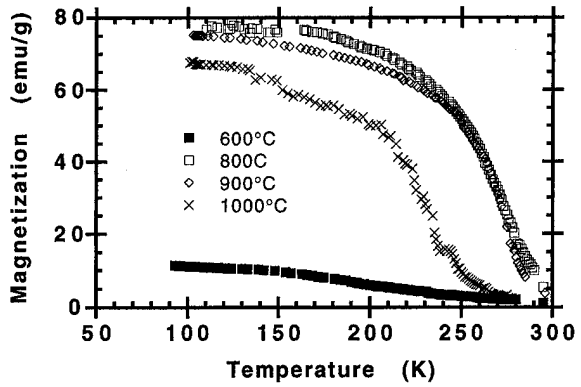


FIG. 1. Magnetization as a function of temperature for a series of annealing temperatures for La–Pb–Mn–O films sputtered in a pure argon temperature.

1, M vs T data are shown for a static in-plane field of 5 kOe for a film sputtered in pure argon. The data indicate an increase in the low temperature M value with increase in T_a. However, M is found to decrease for $T_a = 1000$ °C, possibly due to the loss of Pb from the film. We also studied the effects of sputtering parameters such as the atmosphere and pressure on M. Both pure argon and oxygen–argon sputtered films showed same M value, but T_C for argon sputtered films were smaller than for films sputtered in oxygen–argon. An increase in the sputtering pressure, from 5 to 40 mTorr, resulted in an increase in M and T_C and could be due to changes in the film composition.

In this article, the focus is on magnetic properties of films sputtered in 20% oxygen–80% argon at 40 mTorr and annealed at 800 °C in oxygen. Figure 2 shows the dependence of M on temperature. The measurements were done for an in-plane static field of 5 kOe. The Curie temperature obtained by linear extrapolation of high temperature M data is ~325 K and is in excellent agreement with the single crystal value of 319–328 K.[9] One observes a long tail in the M vs T data close to T_C. The M value at 5 K is 73 emu/g and is 10% smaller than the value of 80.5 emu/g expected for a collinear ferromagnetic ordering of Mn moments and for Mn^{3+} and Mn^{4+} concentrations estimated from the composition. The discrepancy could be due to either a smaller than expected concentration of Mn^{3+} in the film or due to a canted ferromagnetic order. The presence of competing magnetic interactions in DE ferromagnets, i.e., positive double exchange and negative superexchange, could lead to canted ferromagnetism for certain compositions.[12] However, M data for single crystals provide no evidence for a canted spin structure.[9] Thus it is quite likely that the film contains a larger than expected tetravalent Mn ions. Further studies are required for an understanding of the cause of reduction in M in the film. Figure 3 shows data on the static field dependence of M at 5 and 250 K the temperature at which resistivity ρ shows a maximum. In the ferromagnetic state, saturation of M occurs at $H = 100$–500 Oe. The coercive field increases with decreasing T. The data show a relatively small slope at fields above saturation as expected for ferromagnets.

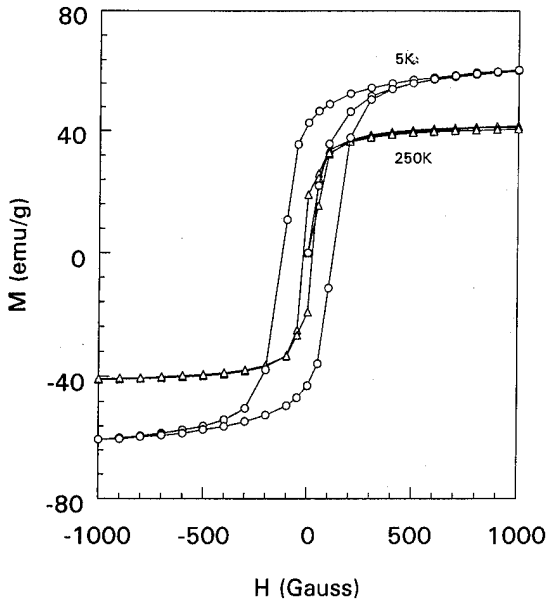


FIG. 3. M vs H data for the film at 5 and 250 K. The field was applied parallel to the film plane.

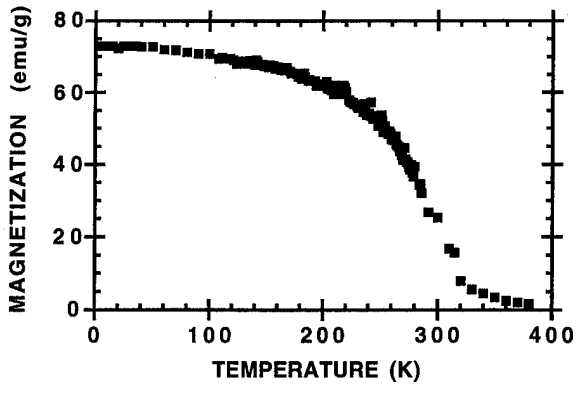


FIG. 2. Magnetization measured with an in-plane static field of 5 kOe vs temperature data for a film of $La_{0.74}Pb_{0.26}MnO_z$ sputtered in mixed argon–oxygen atmospheres and annealed at 800 °C in oxygen. The Curie temperature is 325 K.

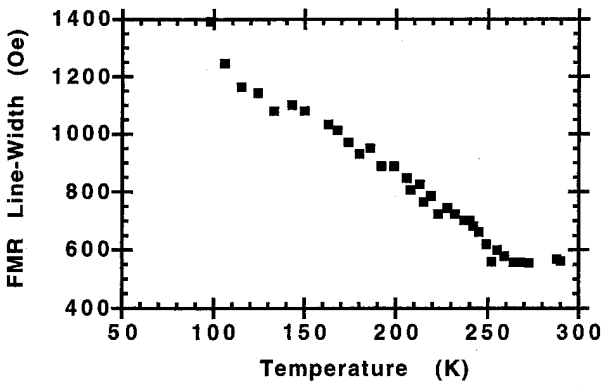


FIG. 4. Temperature dependence of the ferromagnetic resonance linewidth at 9.3 GHz for the film. The static magnetic field was applied parallel to the film plane. The data show a discontinuity at the metal to semiconductor transition at $T_{ms} = 250$ K.

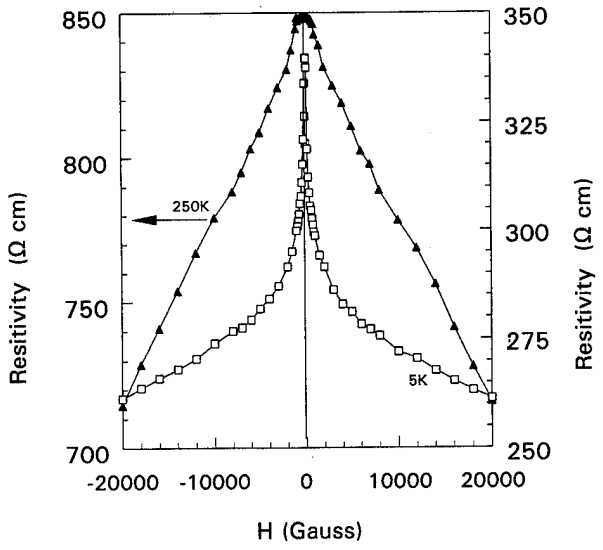


FIG. 5. Variation of resistivity ρ with the applied field H for a series of temperature.

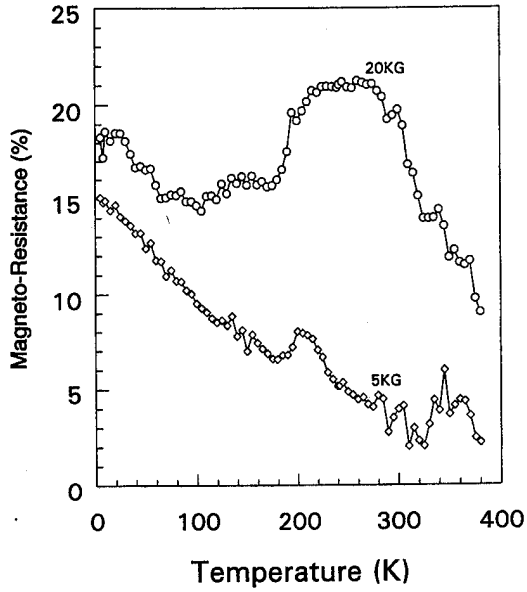


FIG. 6. Magnetoresistance $[\rho(0)-\rho(H)]/\rho(0)$ vs temperature data for the film for applied fields of 0.5 and 2 T.

Ferromagnetic resonance measurements were done at 9.3 GHz as a function temperature for H both parallel and perpendicular to the film plane. The g value at room temperature estimated from the resonance fields is 2.18. In single crystals, the g value remained constant at 1.97 and was independent of x in the paramagnetic state where as in the ordered state it ranged from 2.07 (for $x=0.45$) to 2.15 (for $x=0.26$) and the strong dependence of g on x was suggested to arise from the formation of a spin polarized conduction band.[10] The g value for the film is in very good agreement with the single crystal value of 2.15.[10] Figure 4 shows the variation of FMR linewidth ΔH with T for the static field parallel to the film plane. A linear decrease in ΔH, from 1200 Oe at 100 K to 600 Oe at 250 K is observed when T is increased from 100 to 250 K. A temperature independent ΔH is measured for $T \geq 250$ K, a region in which the sample shows a semiconductorlike behavior. In single crystals ΔH dropped rapidly with T, showed a minimum at the metal-to-semiconductor transition temperature T_{ms}, and increased with further increase in T.[10] The increase in ΔH below T_{ms} is attributed to an efficient spin–lattice relaxation process via the lattice orbitals of band electrons.[10]

The electrical resistivity ρ and its field dependence were measured using the four-probe configuration and a high field superconducting magnet. The static field was applied parallel to the film plane. For $H=0$, a metallic-type behavior with a maximum in ρ at 250 K was observed. With further increase in T, ρ decreased. Thus the transition from metallic to semiconductor type conduction occurs at $T_{ms}=250$ K, ~75 K below the Curie temperature. However, in single crystals T_{ms} is 30 K above T_C.[10] In the presence of an external static field, ρ is found to decrease. Figure 5 shows ρ vs H data for a series of temperature. The largest decrease in ρ is observed at T_{ms}. The magnetoresistance $[\rho(0)-\rho(H)]/\rho(0)$ was determined for $H=0.5$ and 2 T and are plotted as a function of temperature in Fig. 6. For $H=0.5$ T, MR decreases linearly with T, from 15% at 5 K to 2% at T_C. When the field is increased to 2 T the data show a maximum value of 22% at the metal-to-semiconductor transition temperature. Magnetoresistance values of 15%–22% are observed over the entire temperature range 5–300 K. A substantial MR is observed for $T>T_C$, ~10% at 380 K. The observation of a large MR over a wide temperature interval could be of importance for useful applications. The MR values are in agreement with results for single crystals and textured (100) La–Pb–Mn–O films on single crystal $LaAlO_3$ substrates.[10,13]

The authors acknowledge the Donors of The Petroleum Research Fund, administered by the American Chemical Society, for the support of the research at Oakland University.

[1] G. H. Jonker and J. H. Van Santen, Physica **16**, 337 (1950); **19**, 120 (1953); **22**, 707 (1956).
[2] C. Zener, Phys. Rev. **82**, 403 (1951).
[3] R. von Helmolt, J. Wecker, B. Holzapfel, L. Schultz, and K. Samwer, Phys. Rev. Lett. **71**, 2331 (1993).
[4] K. Chahora, T. Ohno, M. Kasai, and Y. Kozono, Appl. Phys. Lett. **63**, 1990 (1993).
[5] S. Jin, M. McCormack, T. H. Tiefel, and R. Ramesh, J. Appl. Phys. **76**, 6929 (1994).
[6] A. Asamitsu, Y. Moritomo, Y. Tomioka, T. Arima, and Y. Tokura, Nature **373**, 407 (1995).
[7] G. Srinivasan, V. Suresh Babu, and M. S. Seehra, Appl. Phys. Lett. **67**, 2090 (1995).
[8] A. H. Morrish, B. J. Evans, J. A. Eaton, and L. K. Leung, Can. J. Phys. **47**, 2691 (1969).
[9] L. K. Leung, A. H. Morrish, and C. W. Searle, Can. J. Phys. **47**, 2697 (1969).
[10] C. W. Searle and S. T. Wang, Can. J. Phys. **47**, 2703 (1969); **48**, 2023 (1970).
[11] M. J. Oretzki and P. Gaunt, Can. J. Phys. **48**, 346 (1970).
[12] P.-G. De Gennes, Phys. Rev. **118**, 141 (1960).
[13] S. Sundar Manoharan, N. Y. Vasanthacharya, M. S. Hegde, K. M. Satyalakshmi, V. Prasad, and S. V. Subramanyam, J. Appl. Phys. **76**, 3929 (1994).

Composition dependence of giant magnetoresistance in $(La_{1-x}Y_x)_{2/3}Ca_{1/3}MnO_\delta$ $(0 \leqslant x \leqslant 1)$

Zisen Li, X. T. Zeng, and H. K. Wong[a)]
Physics Department, The Chinese University of Hong Kong, Shatin, Hong Kong

We have prepared a series of polycrystalline bulk samples of $(La_{1-x}Y_x)_{2/3}Ca_{1/3}MnO_\delta$ $(0 \leqslant x \leqslant 1)$, and studied their magnetization M, resistivity ρ, and low-field magnetoresistance (MR) in the temperature range $10 \leqslant T \leqslant 300$ K. The ferromagnetic transition temperature of the samples T_c decreases with increasing x. For each sample, both ρ and MR have peak values at a temperature close to T_c. The peak value of ρ increases rapidly with increasing x while the peak value of MR has a maximum at $x \sim 0.4$. We observed MR value [defined as $[\rho(0)-\rho(B)]/\rho(0)$] as high as 91% at $B=0.85$ T. Some of the results could be explained by the semicovalent exchange theory of Goodenough [Prog. Solid State Chem. **5**, 145, (1971)]. © *1996 American Institute of Physics.* [S0021-8979(96)52598-3]

I. INTRODUCTION

Nonparallel spin alignment is a prerequisite of the giant magnetoresistance (GMR) effects.[1] The dramatic change in resistivity in an external magnetic field is due to a spin-dependent scattering mechanism. In magnetic multilayers that exhibit GMR, there exists an antiferromagnetic (AFM) coupling between the otherwise ferromagnetic layers.[1] Similar AFM spin configuration can be found in many compounds that were previously studied in great depth. A typical example is the lanthanum manganites whose spin structures depend on the composition.[2] Chahara *et al.*[3] noticed that in $La_{1-x}Ca_xMnO_3$ (LCMO), the Mn spins are coupled antiferromagnetically when $x<0.2$.[2] They prepared LCMO thin films of this composition and observed a large MR $\approx$53% for $B=1$ T. Here we define MR$=[\rho(0)-\rho(B)]/\rho(0)$. At almost the same time, von Helmolt *et al.*[4] observed GMR$\approx$60% for $B=7$ T in $La_{2/3}Ba_{1/3}MnO_3$ (LBMO) thin films and McCormack *et al.*[5] obtained a colossal MR$\approx$99.9% for $B=6$ T in an epitaxial $La_{2/3}Ca_{1/3}MnO_3$ thin film. The last two compounds, $La_{2/3}Ba_{1/3}MnO_3$ and $La_{2/3}Ca_{1/3}MnO_3$, are purely ferromagnetic and the AFM coupling does not exist. Furthermore, special annealing treatments on these films must be done for the GMR effects to appear. It appears that high quality of crystallinity in the thin-film structures is tied to the GMR properties; however, manganite single crystals were available as early as in 1969: Leung, Morrish, and Searle grew $La_{1-x}Pb_xMnO_3$ single crystals and measured their electric and magnetic properties including the magnetoresistance; however, they did not observe a very large MR effect.[6] This indicates that the crystal quality should not be a prerequisite for the GMR effect. In fact, Jin *et al.*[7] reported recently that MR$\approx$99% at $B=6$ T can be obtained in sintered bulk samples of $La_{0.60}Y_{0.07}Ca_{0.33}MnO_\delta$ and attributed the improvement to a decrease of lattice constant. To gain further insight to this finding, we prepared a series of $(La_{1-x}Y_x)_{2/3}Ca_{1/3}MnO_\delta$ $(0 \leqslant x \leqslant 1)$ (LYCMO), and studied their electric and magnetic properties. We found that these properties depend on x, the doping level of yttrium. A very high GMR value (MR $\approx$91%) was observed in samples with $x \approx 0.4$ using only a low magnetic field ($B=0.85$ T).

II. SAMPLE PREPARATION

Polycrystalline samples of $(La_{1-x}Y_x)_{2/3}Ca_{2/3}MnO_\delta$ with $x=0\%$, 10%, 30%, 40%, 50%, 60%, and 100% were prepared by standard ceramic process. Stoichiometric amounts of La_2O_3, Y_2O_3, $CaCO_3$, and MnO_2 were intimately mixed and ground in a small amount of alcohol for 48 h by a ball mill. The resultant slurry was dried and then prefired at 1000 °C for 8 h. The powder was ground again, pressed into small pellets, sintered at 1350 °C for 8 h in oxygen, and then cooled slowly to room temperature in air. All samples were made using identical procedures.

III. CHARACTERIZATION

Some of the samples were fractured and then investigated by a scanning electron microscope. Their grain morphology varied dramatically for different x. The grain sizes in most samples (including $x=100\%$) were about 5 μm and the grains were well connected. The samples with $x=40\%$ and $x=50\%$ had elongated grains and were more porous than the other samples.

Their crystallographic structure was studied with an x-ray powder diffractometer at room temperature. It should be noted that the structures of the two end compounds $La_{2/3}Ca_{1/3}MnO_\delta$ (LCMO) and $Y_{2/3}Ca_{1/3}MnO_\delta$ (YCMO) were studied before. LCMO has a nearly cubic perovskite structure[2] while YCMO is orthorhombic.[8] We reproduced these results and also found that for increasing x, the LYCMO structure varied gradually from a nearly cubic perovskite structure to an orthorhombic structure with decreasing lattice constants.

IV. MAGNETIC PROPERTIES

The magnetization of the samples were measured by an EG&G PAR vibrating sample magnetometer equipped with a 10 K closed-cycle refrigerator. Typical hysteresis loops at $T=10$ K are shown in Fig. 1. For larger x, the saturation field is also higher and the saturation magnetization smaller. The temperature dependence of the magnetization M (magnetic

a)Author to whom correspondence should be addressed.

 0021-8979/96/79(8)/5188/3/$10.00 © 1996 American Institute of Physics

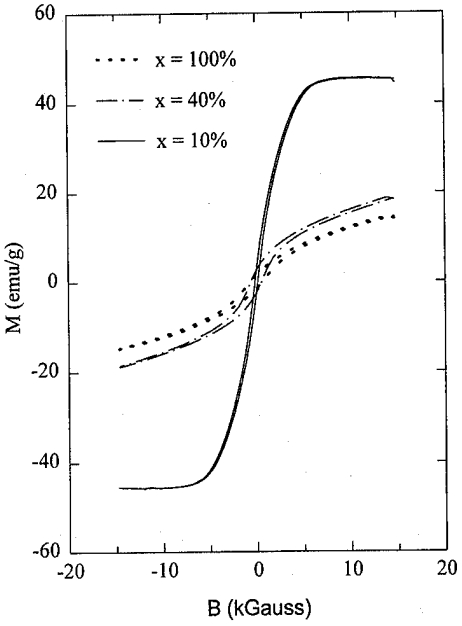


FIG. 1. Hysteresis loops for LYCMO.

moment per unit mass) is shown in Fig. 2. Care should be exercised in determining the Curie temperature T_c of these polycrystalline ceramics. Since most samples do not have a sharp transition, the Arrott plot method or similar approach is not appropriate. We determined the Curie temperatures by an extrapolation procedure described by Leung and co-workers.[6] The results obtained by this method match the metal–semiconductor transition temperatures as summarized in Table I.

V. RESISTIVITY AND MAGNETORESISTANCE

The bulk materials were sliced with a diamond saw into thin sheets of approximately 8.5 mm in length, 2 mm in width, and 0.7 mm in thickness for electrical transport measurements. The electrical resistance and magnetoresistance were measured by the four-point probe technique in a temperature range of 10 K $\leqslant T \leqslant$ 300 K and magnetic field $B<1$ T. In view of practical applications, such a low field range is of much importance. The contacts were made by depositing silver pads on the thin specimens. For samples with high resistivity, a Keithley 610 C electrometer had to be used. The resistivity for each sample as a function of temperature was measured using the same measurement current.

All samples except the ones with $x=100\%$ and $x=60\%$ showed a metal–semiconductor transition. At a fixed temperature, the resistivity increased rapidly with increasing doping level x as shown in Fig. 3. In contrast, the MR value has only a moderate x dependence. The highest value of MR was obtained for the sample with $x=40\%$ as shown in Fig. 4. At zero field, this sample has a sharp metal–semiconductor transition at $T\approx 57.7$ K. At $B=0.85$ T, the transition shifts to $T\approx 67$ K but with a broad cusp. The MR value peaks at $T=53$ K and has a remarkable value of about 91% for a low magnetic field $B=0.85$ T. In comparison, Jin *et al.* obtained 99% for $B=6$ T.[7] The field dependence of the resistivity exhibits a hysteresis effect as illustrated in Fig. 5. Table I lists the major properties of our samples. It is interesting to note

TABLE I. Properties of $(La_{1-x}Y_x)_{2/3}Ca_{1/3}MnO_\delta$. MR_{max}: peak value of MR measured at $B=0.85$ T; ρ_{max}: peak value of resistivity; a: lattice constant. MR_{max} and ρ_{max} occur at temperatures T_1 and T_2, respectively.

Composition x (%)	a (Å)	T_1 (K)	MR_{max} $[\Delta\rho/\rho(0)]$ (%)	T_2 (K)	ρ_{max} (kΩ cm)
10	7.6936	161	64.3	181.2	9.40×10^{-4}
30	7.6870	65.8	79.2	70.8	13.0
40	7.6712	53.1	90.9	57.7	60.8
50	7.6610	39.7	73.6	35.0	12.5×10^{4}

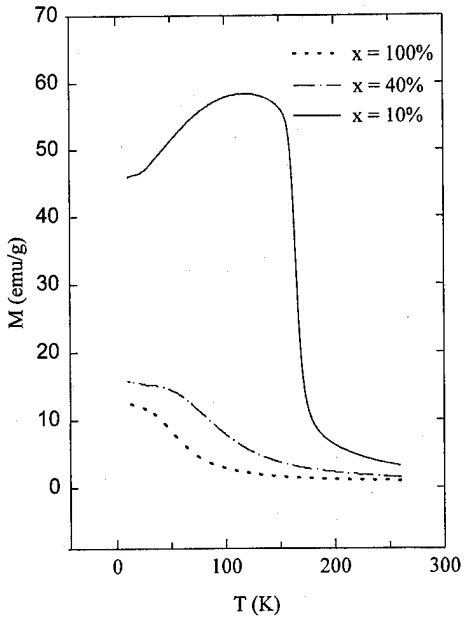


FIG. 2. Temperature dependence of magnetization.

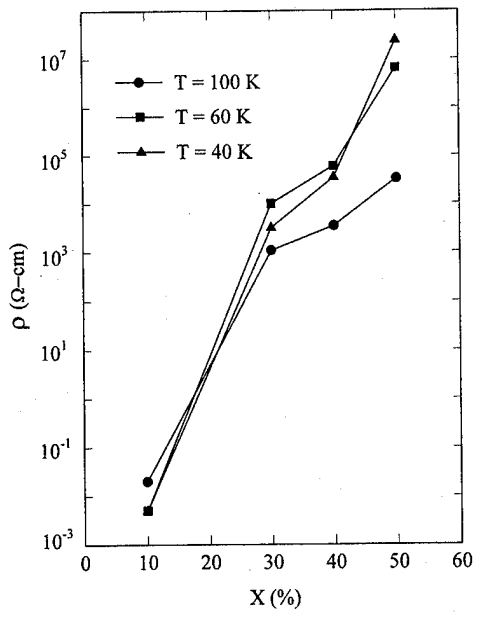


FIG. 3. Composition dependence of resistivity at different temperatures.

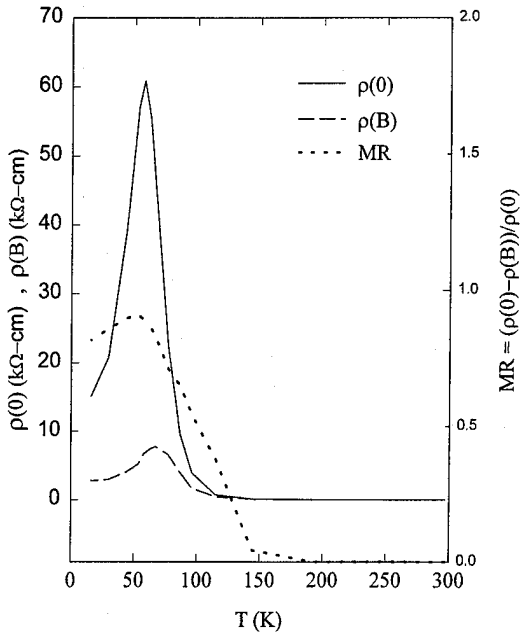


FIG. 4. Temperature dependence of $\rho(0)$, $\rho(B)$, and MR for LYCMO (x =40%); B=0.85 T.

that the samples with x=40% and x=50% show relatively strong MR effect but they are porous. The results may suggest that the grain boundaries play a major role in this property.

VI. DISCUSSION

Substitution of La by Y in LCMO must influence the lattice structure and their properties. Goodenough discussed the large cation effect based on his semicovalent exchange theory.[2] Because Ca has a smaller ionic size than Sr and Ba, $La_{1-x}Ca_x MnO_3$ forms solid solutions of perovskite structure throughout the entire composition range: $0 \leqslant x \leqslant 1$.[9] Since La, Ca, and Y occupy the same lattice sites and the Y^{3+} ionic size $\approx Ca^{2+}$ ionic size $< La^{3+}$ ionic size, we expect that the $(La_{1-x}Y_x)_{2/3}Ca_{1/3}MnO_\delta$ lattice contracts gradually for increasing x, in agreement with our experimental results. In addition, replacing La by Y should not change the Mn^{4+}/Mn^{3+} ratio but the difference in ionic size affects the covalent-bond formation. This may explain why we found a smaller Curie temperature and thus larger resistivity for larger x.

It is of interest to note that for the sample with x=0.4, the magnetic transition is quite broad and the resistivity is relatively high. These are two common features which can be found also in other samples reported to have very large MR.[4,5,7] The broad transition indicates some magnetic inhomogeneity. Our x-ray results cannot tell us how the three ions, La, Y, and Ca, arrange in the lattice. If they form clusters, then one may use the model of Gubkin and Perekalina[10] to understand the very large MR effect. If it is the case, then the ferromagnetic tunnel junctions[11] may be effective at the grain boundaries. This may explain why the porous samples (x=0.4, and 0.5) have higher MR than other compositions.

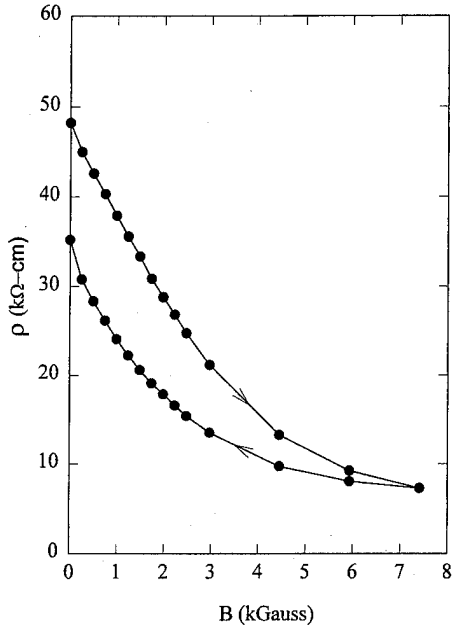


FIG. 5. Hyseteresis of the resistivity $\rho(B)$ with applied magnetic field; T=53 K.

VII. SUMMARY

A series of polycrystalline bulk samples of $(La_{1-x}Y_x)_{2/3}Ca_{1/3}MnO_\delta$ were made by standard ceramic process. It is found that the crystallographic structure changes gradually from cubic perovskite to orthorhombic and the lattice constants become smaller for larger x. The change of lattice structure affects the electrical and magnetoresistance effect. The maximum MR was observed for $x \sim 0.4$ with peak MR =91% at B=0.85 T.

ACKNOWLEDGMENTS

This work was partially supported by grants from the Hong Kong Research Grant Council and Croucher Foundation.

[1] P. M. Levy, Solid State Phys. **47**, 367 (1994).
[2] J. B. Goodenough, Prog. Solid State Chem. **5**, 145 (1971).
[3] K. Chahara, T. Ohno, M. Kasai, and Y. Kozono, Appl. Phys. Lett. **63**, 1990 (1993).
[4] R. von Helmolt, J. Wecker, B. Holzapfel, L. Schultz, and K. Samwer, Phys. Rev. Lett. **71**, 2331 (1993).
[5] M. McCormack, S. Jin, T. H. Tiefel, R. M. Fleming, J. M. Phillips, and R. Ramesh, Appl. Phys. Lett. **64**, 3045 (1994).
[6] L. K. Leung, A. H. Morrish, and C. W. Searle, Can. J. Phys. **47**, 2697 (1969).
[7] S. Jin, H. M. O'Bryan, T. H. Tiefel, M. McCormack, and W. W. Rhodes, Appl. Phys. Lett. **66**, 382 (1995).
[8] E. Pollert, S. Krupicka, and E. Kuzmicova, J. Phys. Chem. Solids **43**, 1137 (1982).
[9] J. B. Goodenough, Phys. Rev. **100**, 564 (1955).
[10] M. K. Gubkin and T. M. Perekalina, JETP Lett. **60**, 747 (1994).
[11] J. S. Moodera, L. R. Kinder, T. M. Wong, and R. Meservey, Phys. Rev. Lett. **74**, 3273 (1995).

Effects of high-temperature annealing on the optical absorption of Ca:YIG films

R. E. Bornfreund and P. E. Wigen
Department of Physics, The Ohio State University, 174 West 18th Avenue, Columbus, Ohio 43210

The effect of high-temperature annealing on the optical properties of a calcium doped yttrium iron garnet (Ca:YIG) film were studied. The optical absorption was examined for a film of $Ca_{0.18}$:YIG reduced in an atmosphere of N_2 at temperatures above 900 °C. During the annealing, the optical absorption initially decreased below the as-grown value as expected, but subsequently increased to a value greater than that for the as-grown film as the annealing temperatures were increased. The changes observed in the optical absorption are believed to be due to the introduction of oxygen vacancies in the film as a result of the annealing. Initially, the added oxygen vacancies simply compensate the Ca^{2+}, while successive annealings introduce excess vacancies which lead to a new absorption mechanism. The results of this study and the expected mechanism for the effect are reported. © *1996 American Institute of Physics.* [S0021-8979(96)14808-6]

I. INTRODUCTION

Ca:YIG films are currently being investigated as a possible alternative to the dilute magnetic semiconductors. Ca:YIG has many of the properties of a magnetic semiconductor, having resistivities as low as 300 Ω cm and activation energies of 0.2–0.4 eV. The wide variety of ions which can be substituted into the garnet structure allow for a tailoring of both the optical and magnetic properties.

At present, the electrical compensation associated with the doping of Ca^{2+} for Y^{3+} is not fully understood. In previous studies, Ca:YIG was subjected to high-temperature annealings in a reducing atmosphere to promote charge compensation by the creation of oxygen vacancies.[1] The previous high-temperature annealing studies observed broad changes in the lattice constant, magnetization, and resistivity of Ca:YIG. Upon annealing in a reducing atmosphere, the room-temperature magnetization has been reported to decrease by as much as 50%, the lattice constant to decrease by as much as 0.032 Å, and the room-temperature resistivity to increase by several orders of magnitude. These changes have been associated with the formation of oxygen vacancies within the film upon reduction.

A complementary study has been performed to determine the effects of the annealing on the optical properties of the material. In the present study, the optical absorption was examined in a sample annealed in N_2 at temperatures above 900 °C. Previous optical studies[2] of the effects of annealing have limited themselves to temperatures below 900 °C. The present work will show that unexpected changes in the optical absorption occur only when annealing temperatures are above 900 °C. While unexpected, the changes are consistent with the previous study on the other material properties.

II. EXPERIMENT

The sample under study is a thin garnet film of composition $Ca_{0.18}$:YIG. It was grown on a [111] oriented gadolinium gallium garnet (GGG) substrate by liquid phase epitaxy (LPE). The growth was performed in a $PbO–B_2O_3$ based melt. The thickness of the film was measured by an optical interference method,[3] which yielded a thickness for the film of 8.06 μm.

Absorption measurements were performed in a Perkin-Elmer Lambda 19 optical spectrometer. All measurements were performed at room temperature. The optical absorption was measured from 190–2500 nm. The annealings were performed in an Accutherm furnace. The sample was annealed successively in a reducing atmosphere of N_2 at 900, 930, 960, and 1000 °C. The annealing was performed for 7 h and the flow rate of the N_2 within the furnace was 2 SCFH. The absorption spectra for the annealings are shown in Fig. 1. For comparison, a second film from the same substrate was annealed in O_2 at 1000 °C under the same flow and time conditions. Only insignificant changes in the optical absorption

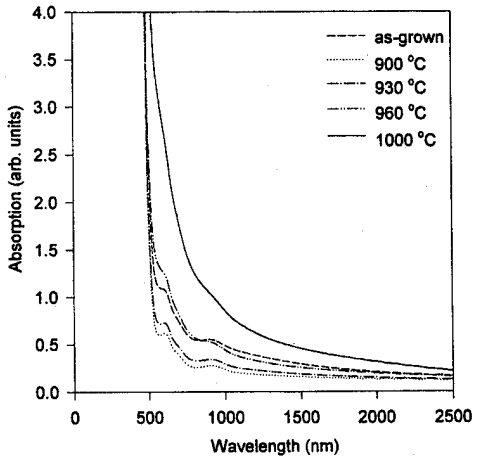


FIG. 1. Optical absorption of $Ca_{0.18}$:YIG for a film successively annealed for 7 h at the indicated temperatures in a N_2 atmosphere.

 0021-8979/96/79(8)/5191/2/$10.00 © 1996 American Institute of Physics

compared to the as-grown spectra were found and therefore, this spectrum was left off the graph for the sake of clarity.

III. RESULTS AND DISCUSSION

The optical absorption spectra shown in Fig. 1 have two features at roughly 607 and 910 nm. These features have been identified in YIG as crystal field transitions.[4,5] The transition at 607 nm is the ${}^6A_1({}^6S) \rightarrow {}^4T_1({}^4G)$ transition occurring within the tetrahedral iron crystal field levels, while the other feature occurring at 910 nm is the ${}^6A_{1g}({}^6S) \rightarrow {}^4T_{1g}({}^4G)$ transition occurring within the octahedral crystal field levels. No shift in the position of these transitions is observed during the course of the annealing study.

Upon annealing the sample, only shifts in the background absorption A, are observed. With a wavelength of 1000 nm chosen as a reference, A decreases roughly 50% upon annealing at 900 °C in N_2. Subsequent annealings at higher temperatures resulted in an overall increase in A. An annealing in N_2 at 930 °C resulted in A increasing to 75% of the original sample's value. The optical absorption continued to increase when the film was annealed at 960 °C, with the value of A close to that of the as-grown film. Of note is the observation that the value of A for the 960 °C annealing goes from being smaller in magnitude than the as-grown value at wavelengths longer than 850 nm to larger than the as-grown value at wavelengths smaller than 850 nm. Annealing in 1000 °C results in an increase in A of 76% over the as-grown value at 1000 nm and the introduction of a broad tail to the optical band edge.

The initial decrease in A with reduction is consistent with previously reported decreases in A upon reduction in a boiling $FeCl_2$ solution.[2] This is due to the formation of a sufficient number of oxygen vacancies to optically and electrically compensate the absorption center associated with the holes produced by Ca^{2+} doping in YIG. The subsequent increase in A would seem to be due to the dominance of a new absorption mechanism due to the additional oxygen vacancies.

As mentioned earlier, the transitions at 607 and 910 nm do not shift in position or broaden with annealing. The introduction of a broad tail to the band edge and the introduction of oxygen vacancies with annealing suggests a modification of the $2p$ valence band, but details of the new absorption center are not known at this time.

In order to eliminate the possibility that thermal migration of the ions produced the observed effects, a second film was annealed in O_2 at 1000 °C for 7 h. Although not shown for the sake of clarity, little change was observed in the absorption spectra of the oxidized sample compared to its as-grown state. This is in agreement with previous measurements of the magnetization, electrical resistivity, and lattice constant in which insignificant changes were observed.[1]

IV. CONCLUSIONS

Unexpected shifts in the absorption spectra have been observed in Ca:YIG films reduced in a N_2 atmosphere at temperatures above 900 °C. The shifts in the optical absorption are observed in association with the formation of oxygen vacancies within the crystal lattice through the high-temperature reduction. A broadening of the band edge for the sample reduced at 1000 °C can be attributed to a modification of the valence band structure due to the excess oxygen vacancies introduced.

ACKNOWLEDGMENT

This work was supported by Army Research Organization Grant No. DAAH 04-95-1-0115.

[1] Y. J. Song, G. B. Turpin, R. E. Bornfreund, H. Aoyama, and P. E. Wigen, these proceedings.

[2] R. C. LeCraw, E. M. Gyorgy, R. D. Pierce, J. W. Neilsen, S. L. Blank, D. C. Miller, and R. Wolfe, Appl. Phys. Lett. **31**, 243 (1977).

[3] M. Wöhlecke, Appl. Phys. Lett. **30**, 395 (1977).

[4] S. H. Wemple, S. L. Blank, J. A. Seman, and W. A. Biolsi, Phys. Rev. B **9**, 2134 (1974).

[5] C. Javanovic, S. Sure, E. Clausing, C. Schafschwerdt, M. Neumann, H. Alwes, K. Lorenz, H. Dötsch, W. Tolksdorf, and P. Willich, J. Appl. Phys. **71**, 436 (1992).

Determination of Mn composition in $Zn_{1-x}Mn_xSe$ from Faraday rotation analysis

Yu-Xiang Zheng, Liang-Yao Chen, Shi-Ming Zhou, Ya-Dong Wang, Yu Wang, and You-Hua Qian
T.-D. Lee Physics Laboratory and Department of Physics, Fudan University, Shanghai 200433, People's Republic of China

Jie Wang, Cai-Xia Jin, and Xun Wang
Surface Physics Laboratory, Fudan University, Shanghai 200433, People's Republic of China

In $Zn_{1-x}Mn_xSe$, Mn^{2+} $d \rightarrow d^*$ transitions were found to induce giant Faraday rotation, and peaks of the Faraday rotation spectra were red-shifted linearly with increasing Mn composition. Through studying the magneto-optical transition variation with Mn composition, the Mn composition can be determined. Results from the Faraday rotation analysis were compared with the x-ray diffraction data and were found in good agreement with each other. © *1996 American Institute of Physics.* [S0021-8979(96)14908-2]

I. INTRODUCTION

The diluted magnetic semiconductor $Zn_{1-x}Mn_xSe$ is formed by random substitution of Mn for Zn atoms. It shows some interesting magnetic and magneto-optical properties,[1] such as the giant Faraday rotation.[1–3] This made it a promising candidate for fabricating some magneto-optical devices, such as magnetic field sensors, magneto-optical isolators, etc., and much attention has been paid to the study of the material in recent investigations.

The magneto-optical properties and lattice parameter of $Zn_{1-x}Mn_xSe$ are tunable by varying the Mn composition. Yoder-short, Debska, and Furdyna[4] had quantitatively given the data and equations for the lattice parameter as a function of Mn composition x by using both electron probe microanalysis and x-ray diffraction methods which can be used to determine the Mn composition precisely. In terms of equations of Ref. 4, therefore, in most cases the Mn composition can be simply determined by measuring the lattice parameter through the x-ray diffraction technique.

In this paper, we provide a new method to determine the Mn composition in $Zn_{1-x}Mn_xSe$. We found that the giant Faraday rotations are actually induced by Mn^{2+} $d \rightarrow d^*$ transitions and peaks of Faraday rotation spectra are linearly red-shifted with Mn composition. Here, an empirical formula about the variation of Mn^{2+} $d \rightarrow d^*$ transitions with composition is presented, and the Mn composition can be readily determined from the Faraday rotation data for these samples. Results were compared with those obtained from x-ray diffraction data.

II. EXPERIMENT AND RESULTS

$Zn_{1-x}Mn_xSe$ film samples in this experiment were grown on (100)-oriented GaAs by the molecular beam epitaxy method (MBE) at the temperature of 280 °C. Using the equation given in Ref. 4, Mn compositions were determined by x-ray diffraction measurements. The x-ray diffraction was performed with copper radiation and the diffraction pattern was measured in 2θ from 60° to 70°. The spectra of Faraday rotation were measured at room temperature and 10 kG magnetic field with a rotating analyzer type Kerr apparatus,[5] since GaAs is opaque in the visible range and thin $Zn_{1-x}Mn_xSe$ films are almost transparent in the photon energy range below the interband energy gap. The photon energy was scanned from 1.5 to 3.5 eV with 0.01 eV interval, and the incidence angle of light was about 2°.

$Zn_{1-x}Mn_xSe$ alloys have many phases. They exhibit zinc-blende structure for $x<0.30$ and wurtzite structure for $0.30<x<0.57$. When x is higher than 0.57, multiple phases coexist in the alloys. Both zinc-blende and wurtzite structures are tetrahedrally coordinated, and the local environment of the tetrahedron formed by like atoms is identical so it is meaningful to consider the mean cation-cation distance d_c over the entire range of existence of $Zn_{1-x}Mn_xSe$.[4] The cation-cation distance d_c is a function of composition x, which can be written as

$$d_c = 4.005 + 0.1748x. \tag{1}$$

Figure 1 shows x-ray diffraction patterns of the $Zn_{1-x}Mn_xSe$ films grown on (100) GaAs substrates. The right sharp peak corresponds to (400) plane of GaAs, and the weaker one to that of $Zn_{1-x}Mn_xSe$ films. From Bragg reflection formula, we have

$$2d_{400} \sin\theta = \lambda, \tag{2}$$

where d_{400} is the interplanar distance between (400) planes, θ is the diffraction angle, and λ is the wavelength of copper radiation and is equal to 1.5406 Å. The cation-cation distance d_c is related to d_{400} by the following equation:

$$d_c = 2\sqrt{2}d_{400}, \tag{3}$$

so it is easy to determine the Mn composition by Eqs. (1)–(3).

Figure 2 shows the spectra of Faraday rotation Θ_F for the $Zn_{1-x}Mn_xSe$ samples. There are two observable peaks labeled as E_a at energy of 2.4 to ~2.55 eV, and E_b at ~2.6 eV for all samples, and another peak labeled as E_c with an energy of ~2.72 eV for the sample having higher composition. With increasing Mn composition, the positions E_a, E_b, and E_c shift to the lower energy end. The peaks at E_a and E_b come close to each other, and finally combine into a single broad peak.

We assign E_a, E_b, and E_c to the Mn^{2+} $d \rightarrow d^*$ multiplet transitions.[2] E_a corresponds to ${}^6A_1({}^6S) \rightarrow {}^4T_2({}^4G)$ transi-

 0021-8979/96/79(8)/5193/2/$10.00 © 1996 American Institute of Physics

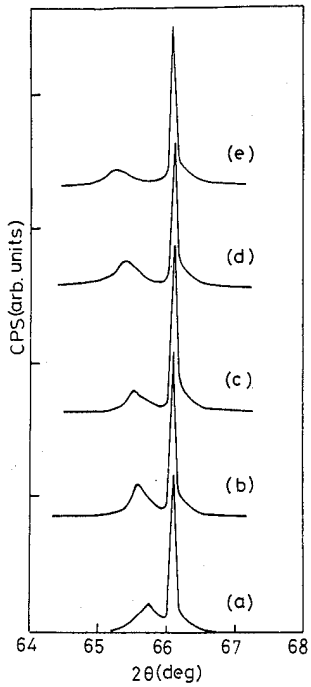


FIG. 1. X-ray diffraction patterns of the $Zn_{1-x}Mn_xSe$ film samples a, b, c, d, and e grown on (100)-oriented GaAs. The sharp peaks correspond to (400) plane of GaAs, and the broad ones correspond to that of $Zn_{1-x}Mn_xSe$ films. Mn concentrations determined by the broad peaks of $Zn_{1-x}Mn_xSe$ films for a, b, c, d, and e samples are 0.06, 0.11, 0.14, 0.17, and 0.21, respectively.

tion, E_b to ${}^6A_1({}^6S)\rightarrow[{}^4A_1({}^4G),{}^4E({}^4G)]$, and E_c to ${}^6A_1({}^6S)\rightarrow{}^4T_2({}^4P)$. The red-shifts of E_a and E_b in $Zn_{1-x}Mn_xSe$ were clearly found to be linear with composition, which can be expressed as

$$E_a(300\ \text{K})=(2.6132-1.1370x)\ \text{eV}, \tag{4}$$

$$E_b(300\ \text{K})=(2.6934-0.6200x)\ \text{eV}, \tag{5}$$

while E_c at ~2.72 eV varies less with composition. The disappearing of the E_c peak for lower composition samples

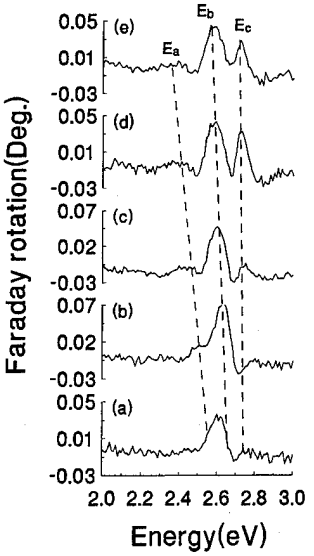


FIG. 2. The spectra of Faraday rotation Θ_F of the $Zn_{1-x}Mn_xSe$ film samples a, b, c, d, and e measured at room temperature and 10 kG magnetic field. Mn concentrations determined by the E_b peaks of $Zn_{1-x}Mn_xSe$ films for a, b, c, d, and e samples are 0.05, 0.10, 0.15, 0.18, and 0.21, respectively.

TABLE I. The comparison of Mn composition obtained from the x-ray diffraction technique and Faraday rotation analysis for $Zn_{1-x}Mn_xSe$ film samples a, b, c, d, and e.

Samples	a	b	c	d	e
x-ray diffraction	0.06	0.11	0.14	0.17	0.21
Faraday analysis	0.05	0.10	0.15	0.18	0.21

was due to the stronger interband absorption occurring at the interband gap energy E_g that is $\leqslant E_c$ to make Faraday rotation spectra be cutoff at E_g. As we have known, the interband gap E_g also varies with composition. For $Zn_{1-x}Mn_xSe$, $E_g(x)$ at room temperature it can be written as

$$E_g(300\ \text{K})=(2.71+0.19x)\ \text{eV}. \tag{6}$$

Unlike E_a and E_b, E_g shows bowing effects, i.e., shifts to lower then higher energies with increasing Mn concentration as indicated in Ref. 1. From Eqs. (4)–(6), it is obvious that E_a and E_b are always lower than E_g in the entire composition range, but E_c(~2.72 eV) will be higher than E_g for lower composition samples. The E_c transition will be masked by E_g transitions for these samples, resulting in the disappearance of the E_c peak.

The Faraday rotation peak at E_b is considerably large and sharp. Therefore, if the position of E_b can be measured precisely, the composition can be determined relatively easily by using Eq. (5). In our experiment, the $Zn_{1-x}Mn_xSe$ samples were characterized by both the x-ray diffraction technique and Faraday rotation analysis method. Mn compositions were determined by using Eqs. (1)–(3) with x-ray diffraction data and by using Eq. (5) with Faraday rotation data, respectively. The results from the two methods are compared and are shown to be in good agreement as seen in Table I.

III. CONCLUSION

In this experiment, we found that the giant Faraday rotation induced by Mn^{2+} $d\rightarrow d^*$ multiplet transitions in $Zn_{1-x}Mn_xSe$ can be used as a method to determine Mn composition. The Faraday rotation peak at E_b(~2.6 eV) is considerably strong and sharp at room temperature, and $E_b(x)$ is found to be given by $2.6934-0.6200x$ eV. The precise E_b data can be readily obtained from Kerr apparatus, and then the compositions are immediately obtained. The compositions determined from both x-ray diffraction technique and Faraday rotation analysis were compared and were in good agreement with each other.

This work was supported by the NSF of the People's Republic of China.

[1] A. Twardowski, T. Dietl, and M. Demianiuk, Solid State Commun. **48**, 845 (1983).
[2] C. Benecke, W. Busse, and H.-E. Gumlich, J. Cryst. Growth **101**, 931 (1990).
[3] D. U. Bartholomew, J. K. Furdyna, and A. K. Ramdas, Phys. Rev. B **34**, 6943 (1986).
[4] D. R. Yoder-short, U. Debska, and J. K. Furdyna, J. Appl. Phys. **58**, 4056 (1985).
[5] J. K. Furdyna, J. Appl. Phys. **64**, R29 (1988).

Microstructural properties of (ZnSe/FeSe) and (ZnSe/MnSe) diluted magnetic semiconductor superlattices (abstract)

K. Park[a] and L. Salamanca-Riba
Department of Materials and Nuclear Engineering, University of Maryland, College Park, Maryland 20742

B. T. Jonker
Naval Research Laboratory, Washington, DC 20375

Recently, there has been increased research activity on Fe-, Mn-, and Co-based diluted magnetic semiconductors (DMS) because of their interesting magneto-optical properties. Potential applications of DMS usually require thin films with a high degree of structural perfection, and high quality single crystal epilayers of $Zn_{1-x}Fe_xSe$ and $Zn_{1-x}Co_xSe$ have been grown by molecular beam epitaxy (MBE).[1,2] In this work, the microstructural properties of (ZnSe/FeSe) and (ZnSe/MnSe) DMS superlattices grown on (001) GaAs substrates by MBE have been investigated using transmission electron microscopy. High-quality (ZnSe/FeSe) superlattices were grown by introducing a ZnSe buffer layer on the GaAs substrate prior to the growth of the superlattice. In contrast, nominal (ZnSe/FeSe) superlattices grown directly without a buffer layer on the substrate showed evidence for interdiffusion between the constituent layers of the superlattice. Chemical ordering of the Zn and Fe atoms was also observed in the resultant $Zn_{1-x}Fe_xSe$ alloys along the [001] and [110] directions. This ordered structure corresponds to the CuAu–I type structure. In contrast, the (ZnSe/MnSe) superlattices did not show interdiffusion, but contained many microtwins and 60°-type misfit dislocations. The MnSe layer in the (ZnSe/MnSe) superlattices existed as a zinc-blende structure. © *1996 American Institute of Physics.* [S0021-8979(96)46908-7]

---

[a]Present address: Division of Metals, Korea Institute of Science and Technology, P.O. Box 131, Cheongryang, Seoul, Korea.

[1] B. T. Jonker, J. J. Krebs, G. A. Prinz, X. Liu, A. Petrou, and L. Salamanca-Young, Mater. Res. Soc. Symp. Proc. **151**, 151 (1989).
[2] B. T. Jonker, J. J. Krebs, S. B. Qadri, and G. A. Prinz, Appl. Phys. Lett. **50**, 848 (1987).

 0021-8979/96/79(8)/5195/1/$10.00 © 1996 American Institute of Physics

Polaron-polaron interactions in diluted magnetic semiconductors

P. A. Wolff
NEC Research Institute and MIT, Cambridge, Massachusetts 02139

R. N. Bhatt and A. C. Durst
Department of Electrical Engineering, Princeton University, Princeton, New Jersey 08544

The bound magnetic polaron (BMP) is the characteristic collective state of diluted magnetic semiconductors. Isolated BMP are well understood, but their interactions are only beginning to be explored. Recent polaron magnetization experiments on p-ZnMnTe suggest a *ferromagnetic* polaron-polaron interaction, in contrast to the invariably *antiferromagnetic* impurity exchange interaction in conventional semiconductors. To investigate this question theoretically, we have developed a simplified model of polaron pairs whose central feature is competition between the usual, antiferromagnetic, virtual-hopping interaction, and the loss of carrier-magnetic ion exchange energy, by intermediate ions, when the polaron moments are antiferromagnetically aligned. The model is sufficiently simple that its partition function can be calculated in detail. With reasonable parameters, it predicts a ferromagnetic polaron-polaron interaction at low temperatures. © *1996 American Institute of Physics.* [S0021-8979(96)15008-7]

The bound magnetic polaron (BMP) is the characteristic collective state of diluted magnetic semiconductors (DMS). BMP is created by the exchange interaction of localized carriers with magnetic ions (often Mn^{2+} in II–VI semiconductors) within the carrier orbit.[1] To date, BMP studies have generally been done on dilute samples where polaron-polaron interactions are negligible. Recently, however, polaron magnetization experiments on heavily doped, p-type ZnMnTe have given hints of a weak *ferromagnetic* polaron-polaron interaction,[2] whereas in conventional nonmagnetic semiconductors impurity-impurity interactions are invariably antiferromagnetic.[3] To explain this unexpected result, we have studied a simplified model of polaron pairs whose central feature is competition between the usual, antiferromagnetic interaction due to virtual hopping of carriers, and the loss of carrier-Mn^{2+} exchange energy by intermediate magnetic ions when the polaron moments are antiferromagnetically aligned. With reasonable parameters, the model predicts a ferromagnetic polaron-polaron interaction at low temperatures. This result suggests the possibility of polaron ferromagnetism in heavily doped (albeit insulating), p-type II–VI DMS.

The BMP problem is complicated, theoretically, by the fact that the exchange field experienced by a Mn^{2+} ion is proportional to the square of the carrier wave function at its site—therefore, varies rapidly with Mn^{2+} ion position. This spatial variation precludes an exact, quantum mechanical evaluation of the single polaron partition function, and makes the polaron pair problem intractable. To avoid this difficulty we have extended an exactly soluble model of the single polaron, developed by Ryabchenko and Semenov (RS),[4] to the polaron pair case. RS make the seemingly drastic approximation of replacing the spatially varying wave function by a constant for $r \leqslant R_0$ and zero for $r > R_0$. The carrier-Mn^{2+} exchange interaction then takes the simple form

$$H = K \sum_{(R_i < R_0)} (s \cdot S_i) = K(s \cdot S) \equiv \frac{K}{2}[(s+S)^2 - S^2 - s^2], \tag{1}$$

where S_i is the Mn^{2+} spin at site R_i, s is the carrier spin (assumed to be 1/2) and $S = \Sigma_i(S_i)$. Here, S^2, s^2, and $(s+S)^2$ are constants of the motion so, for a given S, Eq. (1) immediately gives the energies. For $s = 1/2$ there are two levels corresponding to $|S+s| = (S \pm 1/2)$ with energies $E_+ = KS/2$ and $E_- = -K(S+1)/2$. When $S \gg 1$, the most probable situation for polarons at low temperature, these states are highly degenerate because there are many ways of combining the Mn^{2+} spins (with $R_i < R_0$) to give total spin S. The degeneracies are lifted when the carrier wave function varies in space so, in detail, the eigenfunctions of the RS model are quite different from those of the true Hamiltonian. Nevertheless, when averaged over possible values of S, Eq. (1) gives an excellent approximation to the BMP partition function[5] if the parameters K and R_0 are determined with the Feynman variational theorem.[6]

Granting that the RS model gives a good description of the single polaron, how can it be extended to treat the polaron pair? We assume, as in Liu's experiments, that polarons are far apart (spacing d) compared to the Bohr radius (a^*) of the localized carrier states. It is then natural, as illustrated in Fig. 1, to divide Mn^{2+} spins into three categories—those associated with polaron 1 ($|R_i - R_1| < R_0$), those associated with polaron 2 ($|R_i - R_2| < R_0$), and intermediate Mn^{2+} spins that feel a weaker exchange field from *both* carriers. In the spirit of the RS model we then choose a Hamiltonian for the pair problem of the form

$$H = K[(s_1 \cdot S_1) + (s_2 \cdot S_2)] + K'[(s_1 + s_2) \cdot S_3] + J(s_1 \cdot s_2). \tag{2}$$

The first term in this equation describes two polarons without interaction, the second is a polaron-polaron coupling induced by intermediate Mn^{2+} (with total spin S_3) that can be ferromagnetic if the carrier spins are in a triplet state. Finally, $J(s_1 \cdot s_2)$ is the standard, antiferromagnetic interaction induced by virtual hopping of carriers from one site to the other. In the limit we are considering ($a^*/d \ll 1$), the parameters K' and J are both exponentially smaller than K. For acceptor BMP in ZnMnTe, $K \simeq 2$ meV. K' and J are of order

 0021-8979/96/79(8)/5196/3/$10.00 © 1996 American Institute of Physics

POLARON PAIR MODEL

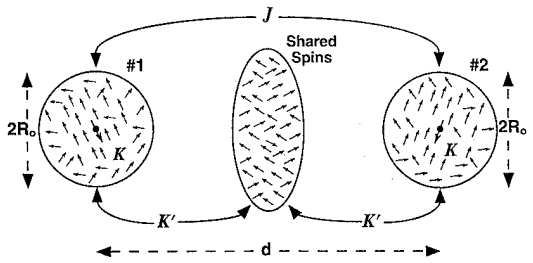


FIG. 1. Schematic of polaron pair model.

$$K' \cong K e^{-d/a^*} \quad \text{and} \quad J \cong \frac{e^2 a^*}{\epsilon d^2}\,(e^{-2d/a^*}). \tag{3}$$

To lowest order (ignoring K' and J terms) the two polaron problem has four, highly degenerate energy levels: $E=(K/2)(S_1+S_2)$, $E=(K/2)[S_1-(S_2+1)]$, $E=-(K/2)[(S_1+1)-S_2]$, and $E=-(K/2)[(S_1+1)+(S_2+1)]$. At low temperatures, where the most probable values of S_1 and S_2 are sizable, these manifolds are separated from one another by energies of order 20–30 meV,[7] with only the last one having substantial occupation. Off-diagonal matrix elements of the K' and J operators between these manifolds produce only weak, second order perturbations. Thus, in calculating the effect of the K' and J operators, we need only include matrix elements *within* the ground state manifold.

BMPs have many degrees of freedom—of order $(6)^N$ where N is the number of Mn^{2+} ions involved. Thus, even at low temperatures, their properties are statistically determined. For that purpose we need the partition function of the model Hamiltonian. A fully quantum mechanical calculation is complicated, but unnecessary at low temperatures. In that limit (below about 20 K in ZnMnTe) the individual polarons have fully formed by aligning all Mn^{2+} spins within their orbits. Each has a sizable spin; $\langle (S_1)\rangle = \langle (S_2)\rangle \simeq 50$. Intermediate Mn^{2+} spins (those in S_3) are only partially aligned but, because there are many of them, fluctuations produce a sizable value of $\sqrt{\langle S_3^2\rangle} \approx \sqrt{N_3}$. Thus, the three spin populations all have large total spin, implying that a classical approximation can be used in calculating averages over $\mathbf{S}_1$, $\mathbf{S}_2$, and $\mathbf{S}_3$. Henceforth, we integrate over these variables in evaluating the partition function, but retain the quantum mechanical properties of the two carrier spins (s_1 and s_2).

In this semiclassical approximation the wave functions of the unperturbed polaron pair (assuming $K'=J=0$) are: $\alpha_1(1)\alpha_2(2)$, $\alpha_1(1)\beta_2(2)$, $\beta_1(1)\alpha_2(2)$, $\beta_1(1)\beta_2(2)$, where $\alpha_{1,2}$ and $\beta_{1,2}$ are spinors whose quantization axes are parallel to $\mathbf{S}_1$ and $\mathbf{S}_2$, respectively. The state $\varphi_0=\beta_1(1)\beta_2(2)$ with (classical) energy $-K(S_1+S_2)/2$ corresponds to the ground state manifold previously discussed. It is the only state occupied at low temperature, so the effects of the K' and J perturbations are determined, as discussed above, by the diagonal matrix elements

$$M_{K'} = \langle \varphi_0 | H_1 | \varphi_0 \rangle = \frac{-K'}{2}\left[\frac{S_2\mathbf{S}_1 + S_1\mathbf{S}_2}{S_1 S_2}\right]\cdot \mathbf{S}_3 \tag{4}$$

and

$$M_J = \langle \varphi_0 | H_2 | \varphi_0 \rangle = \frac{J}{4}\left(\frac{S_1\cdot S_2}{S_1 S_2}\right) = \frac{J\mu_{12}}{4}. \tag{5}$$

Here, μ_{12} is the cosine of the angle between $\mathbf{S}_1$ and $\mathbf{S}_2$. The partition function then takes the form $Z = Z_P(6)^{N_{\text{ext}}}$ where N_{ext} is the number of Mn^{2+} ions external to the interaction region and the polaron pair partition function is

$$Z_P = \int\int\int \left\{ D_{N_1}(S_1) D_{N_1}(S_2) D_{N_3}(S_3) e^{\beta K/2(S_1+S_2)} \times (e^{-\beta J \mu_{12}/4}) \exp\left[\beta K'/2\,\frac{|S_2\mathbf{S}_1 + S_1\mathbf{S}_2|}{S_1 S_2}\,\mu_3 S_3\right]\right\} \times d^3S_1\, d^3S_2\, d^3S_3. \tag{6}$$

Here, $D(S)$ is the number of ways of combining N Mn^{2+} spins to give total spin S. Integrating over $d\mu_3$ and using the fact

$$\frac{|S_2\mathbf{S}_1 + S_1\mathbf{S}_2|}{S_1 S_2} = \sqrt{2}(1+\mu_{12})^{1/2}, \tag{7}$$

we find

$$Z_P = 4\pi \int\int\int \left\{ D_{N_1}(S_1) D_{N_1}(S_2) D_{N_3}(S_3) e^{\beta K/2(S_1+S_2)} \times (e^{-\beta J \mu_{12}/4}) \frac{\sinh \dfrac{[\beta K'(1+\mu_{12})^{1/2} S_3]}{\sqrt{2}}}{\dfrac{[\beta K'(1+\mu_{12})^{1/2} S_3]}{\sqrt{2}}} \right\} \times d^3S_1\, d^3S_2 S_3^2\, dS_3. \tag{8}$$

The dS_3 integration is simplified by the relation

$$2\pi S_3 D(S_3) = -\frac{d}{dS_3}[D_z(S_3)], \tag{9}$$

where $D_z(S_3)$ is the number of ways of combining N_3 Mn^{2+} spins to give total $S_z = S_3$. This formula is the classical analog of a quantum mechanical relation derived by Kasuya and Yanase.[8] After integrating by parts, Eq. (8) takes the form

$$Z_P = 2\int\int\int \left\{ D_{N_1}(S_1) D_{N_1}(S_2) D_z(S_3) e^{\beta K/2(S_1+S_2)} \times e^{-\beta J \mu_{12}/4} \cosh\left[\frac{\beta K'(1+\mu_{12})^{1/2}}{\sqrt{2}}\right]\right\} d^3S_1\, d^3S_2\, dS_3. \tag{10}$$

Here

$$D_z(S) \equiv Tr\left\{ \delta\left[S - \sum_{j=1}^{N} (S_{jz})\right]\right\}, \tag{11}$$

and the dS_3 integration can be evaluated via the method described in Ref. 1. The result is

$$Z_P = 2(6)^{N_3} \int \int \left\{ D_{N_1}(S_1) D_{N_1}(S_2) e^{\beta K/2(S_1+S_2)} e^{-\beta J \mu_{12}/4} \times \left[F\left(\frac{\beta K'}{\sqrt{2}} \sqrt{1+\mu_{12}} \right) \right]^{N_3} \right\} d^3S_1 \, d^3S_2$$

$$= 2\pi Z_1 Z_2 (6)^{N_3} \int_0^{\sqrt{2}} e^{-\beta J/4(x^2-1)} \left[F\left(\frac{\beta K' x}{\sqrt{2}} \right) \right]^{N_3} x \, dx, \tag{12}$$

where we have made the change of variables $\mu_{12}=(x^2-1)$. Z_1 and Z_2 are the partition functions of polarons 1 and 2 without interaction. F is one sixth the single Mn^{2+} ion partition function

$$F(y) \equiv \frac{1}{6} \left[\frac{\sinh(3y)}{\sinh(y/2)} \right]. \tag{13}$$

We now have an analytic approximation to the partition function from which one can determine all thermodynamic properties, such as $\langle \mu_{12} \rangle$. To evaluate it, note that the integrand of Eq. (12) is the relative probability of finding $\mu_{12}=(x^2-1)$. Therefore

$$\langle \mu_{12} \rangle = \frac{\int_0^{\sqrt{2}} e^{-\beta J/4(x^2-1)} \left[F\left(\frac{\beta K' x}{\sqrt{2}} \right) \right]^{N_3} (x^2-1) x \, dx}{\int_0^{\sqrt{2}} e^{-\beta J/4(x^2-1)} \left[F\left(\frac{\beta K' x}{\sqrt{2}} \right) \right]^{N_3} x \, dx}. \tag{14}$$

Equation (14) has been evaluated for representative values of the ratio, (K'/J) and number (N_3) of intervening Mn^{2+} ions, as a function of temperature. Figure 2 shows a typical result of these calculations. The various curves in this figure reflect different degrees of competition between the K' and J interactions. When $(K'/J)=0$ there is no competition so that the polaron spins are antiferromagnetically aligned, $\langle \mu_{12} \rangle < 0$, at all temperatures.

As this ratio increases, the polaron pair behaves ferromagnetically in an increasing range of temperatures above $T=0$. For intermediate values of (K'/J), the crossover from ferromagnetic to antiferromagnetic behavior is at $kT \simeq \frac{1}{6}(N_3 K')^2/J$.

We propose a simplified, soluble model of a pair of BMP, designed to capture the essence of the interaction between polarons in diluted magnetic semiconductors. We are able to analytically calculate the partition function of the model at low temperatures where each carrier polarizes Mn^{2+} spins within its orbit, but the interpolaron interaction may be large or small compared to the temperature. Our calculations are approximate in two ways. The more important of the two is the constant wave function approximation, as used by RS for the single polaron problem. For the single polaron it has been tested and shown to give results within 10% of those measured.[5] Preliminary results using optimized Hamiltonians for the polaron pair problem suggest that Hamiltonian (2) is a reasonable approximation to it as well.[9] Moreover, it is encouraging that, with reasonable parameters,

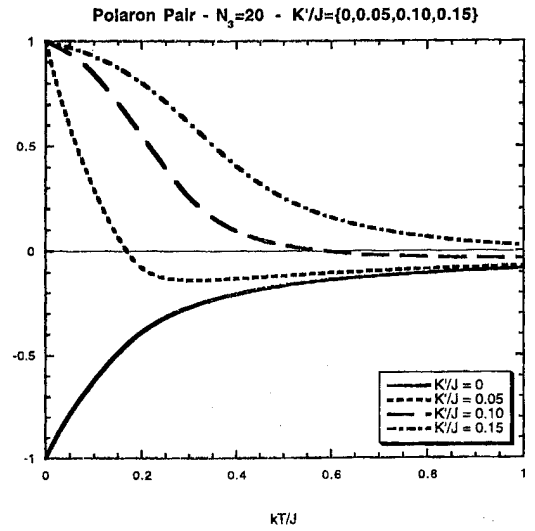


FIG. 2. Plots of the thermal average of the cosine of the angle between polaron spins, $\langle \mu_{12} \rangle$, vs temperature for $N_3=20$ and several values of the ratio (K'/J).

the model favors a ferromagnetic polaron-polaron interaction whose size is not inconsistent with Liu's results.

The second approximation is our neglect of next-nearest-neighbor Mn^{2+}–Mn^{2+} exchange interactions. Nearest-neighbor interactions are included by the use of an effective Mn^{2+} concentration $\bar{x}=x(1-x)$.[12,1] Next-nearest-neighbor interactions become important at about 1 K. Thus, polaron interaction effects should be partially suppressed when the carrier-Mn^{2+} exchange field falls below 1 K. For the intervening Mn^{2+} ions this effect becomes important when

$$\frac{2(bN_0)}{\pi N_0 (a^*)^3} e^{-d/a^*} \cong 10^{-4} \text{ eV}, \tag{15}$$

where (bN_0) is the hole-Mn^{2+} exchange interaction, about 1.2 eV in ZnMnTe. With $a^*=10^{-7}$ cm, Eq. (15) predicts that suppression begins for $(d/a^*)>6$, which is close to the most probable interpolaron distance ratio $(d/a^*=7)$ in a sample containing 7×10^{17} acceptors per cc. We conclude that our neglect of next-nearest-neighbor Mn^{2+} interactions is barely justified in Liu's experiments. It is probable, therefore, that the weak ferromagnetic polaron-polaron interaction he observes is due to a fraction of the pairs whose separation is smaller than the average, but with a substantially larger value of K'.

[1] BMP is discussed in *Semiconductors and Semimetals*, edited by J. K. Furdyna and J. Kossut (Academic, San Diego, 1988), Vol. 25, p. 413.
[2] J. Z. Liu, G. Lewen, P. Becla, and P. A. Wolff, Bull. Am. Phys. Soc. **39**, 402 (1994).
[3] R. N. Bhatt and P. A. Lee, Phys. Rev. Lett. **48**, 344 (1982), and references therein.
[4] S. M. Ryabchenko and Yu. G. Semenov, Sov. Phys. JETP **57**, 825 (1983).
[5] P. A. Wolff, in *Semimagnetic and Diluted Magnetic Semiconductors*, edited by M. Averous and M. Balkanski (Plenum, New York, 1991).
[6] R. P. Feynman, *Statistical Mechanics* (W. A. Benjamin, Reading, MA, 1972), p. 67.
[7] M. Bugajski, P. Becla, P. A. Wolff, D. Heiman, and L. R. Ram-Mohan, Phys. Rev. B **38**, 10512 (1988).
[8] T. Kasuya and A. Yanase, Rev. Mod. Phys. **40**, 684 (1968).
[9] A. C. Durst, R. N. Bhatt, and P. A. Wolff (unpublished).

Hybrid pole pieces for permanent magnets

M. G. Abele and J. H. Jensen
Department of Radiology, New York University School of Medicine, New York, New York 10016

Highly uniform magnetic fields for nuclear-magnetic-resonance imaging require accurate design of the pole pieces of a permanent magnet structure. We present a mathematical theory of pole pieces viewed as filters that eliminate selected harmonics of an expansion of the field distortion. Previous work has discussed two types of filters: active pole pieces and passive pole pieces. These are reviewed and a third type of filter, the hybrid pole piece, is introduced. The hybrid pole piece provides distinct advantages by combining features of both active and passive pole pieces. © *1996 American Institute of Physics.* [S0021-8979(96)52608-6]

I. INTRODUCTION

Permanent magnets can be designed to generate highly uniform fields for nuclear-magnetic-resonance imaging in medicine. Sophisticated design approaches[1] are required not only to minimize the size and weight of a magnet, but also to compensate for the poor tolerances of the magnetic characteristics of available materials. This article presents a hybrid design for the pole pieces of a magnet that acts as a filter to eliminate the spatial harmonics of the field distortion. The design follows a precise mathematical formulation that applies to the design phase as well as to the final shimming of the magnet.

II. FILTER EQUATIONS

Figure 1 shows the schematic of a permanent magnet. The interface between the two pole pieces and the gap are assumed to be parallel plane surfaces at a distance $2y_0$ from each other. Assume a reference cylinder of radius r_i that contains the region of interest where the field must satisfy the required uniformity condition. If the two plates are composed of a material of infinite permeability, the magnetostatic potential within the reference cylinder can be expanded in the series[2]

$$\Phi(r,\psi,y)=\Phi_2+\frac{y_0+y}{2y_0}\Phi_0 + \sum_{m,n} I_m\left(n\pi\frac{r}{2y_0}\right)\sin\left(n\pi\frac{y_0+y}{2y_0}\right) \times(a_{m,n,1}\cos m\psi+a_{m,n,2}\sin m\psi), \quad (2.1)$$

where r,ψ,y are cylindrical coordinates with the axis y being coaxial to the reference cylinder, and I_m is the modified Bessel function of the first kind. Φ_0 is the potential difference between the two plates, and Φ_2 is the potential of the plate located at $y=-y_0$. The first two terms on the right-hand side of Eq. (2.1) correspond to a uniform field oriented along the axis y, and the series over the m,n harmonics of amplitudes $a_{m,n,1}$ and $a_{m,n,2}$ is the field distortion. In most cases, $a_{m,n,1}$ and $a_{m,n,2}$ decrease rapidly with increasing m and n, and the distortion is primarily due to just a small number of low-order harmonics.

The elimination of the unwanted harmonics of the spectrum defined by Eq. (2.1) is provided by a filter structure located on the two plates outside the reference cylinder. The principle of the design of the filter is an alteration of the potentials of the plates in the region between concentric circles of radii r_i and r_e. With a proper choice of this alteration, the harmonics of the field distortion in Eq. (2.1) may be cancelled.

Let $\delta\Phi_+(r,\psi)$ by the potential shift on the upper plate from the value $\Phi_2+\Phi_0$, and let $\delta\Phi_-(r,\psi)$ be the shift on the lower plate from Φ_2. The shifts required to cancel the field distortion satisfy, to a good approximation, the system of integral equations[2]

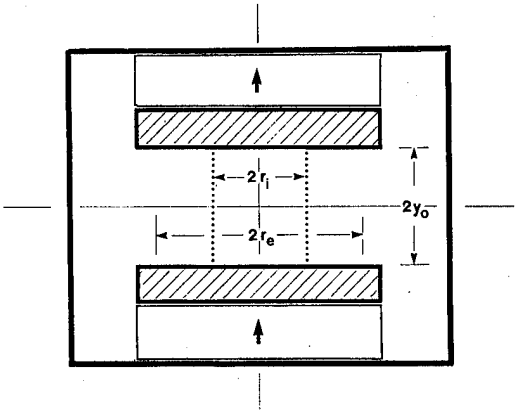


FIG. 1. Schematic of a permanent magnet. The shaded regions are the pole pieces, the arrows indicate the direction of magnetization in the magnetic material, and the heavy external line represents the yoke.

 0021-8979/96/79(8)/5199/3/$10.00 © 1996 American Institute of Physics

$$\frac{\pi}{8y_0^2}(-1)^n n\int_0^{2\pi} d\psi \int_{r_i}^{r_e} rK_m\left(n\pi\frac{r}{2y_0}\right)$$

$$\times[\delta\Phi_+(r,\psi)-(-)^n\delta\Phi_-(r,\psi)]\begin{pmatrix}\cos m\psi\\ \sin m\psi\end{pmatrix}dr$$

$$=(1+\delta_{m0})\begin{pmatrix}a_{m,n,1}\\ a_{m,n,2}\end{pmatrix}, \tag{2.2}$$

for $m = 0,1,2,\ldots$ and $n = 1,2,3,\ldots$, and where K_m is the modified Bessel function of the third kind. The filter equations (2.2) are exact in the limit that the radial dimension of the plates tends to infinity. K_m behaves asymptotically as

$$K_m(x)\sim\left(\frac{2}{\pi x}\right)^{1/2} e^{-x} \quad (x\gg 1). \tag{2.3}$$

Because of this rapid decrease of K_m with increasing values of its argument, Eq. (2.2) implies that the larger the value of n is for a harmonic the more its cancellation will tend to be dominated by the behavior of the shifts $\delta\Phi_\pm$ close to $r = r_i$.

III. FILTER STRUCTURES

The filter equations (2.2) do not have a unique solution. A solution is determined by selecting a geometry for the filter structure. Consider, as an example, an axisymmetric magnet whose geometry is independent of ψ and is symmetric with respect to the plane $y=0$. Assume, to begin with, perfect geometrical and magnetic characteristics of the materials, in which case the two plates acquire equal and opposite potentials, i.e.,

$$\Phi_2 = -\tfrac{1}{2}\Phi_0, \tag{3.1}$$

and the potential shifts may be assumed to obey the condition

$$\delta\Phi_+(r) = -\delta\Phi_-(r). \tag{3.2}$$

As a consequence, the expansion (2.1) reduces to the $m=0$, $n=2,4,6,\ldots$ terms.

A solution of the filter equations (2.2) intended to cancel a given number of harmonics l is obtained by dividing the interval between $r = r_i$ and $r = r_e$ on both plates into l concentric rings each with a potential shift $\pm\delta\Phi_k$, $k = 1,\ldots,l$ (+ for the upper plate and − for the lower plate). Equation (2.2) then reduces to

$$\frac{\pi}{2y_0}\sum_{k=1}^{l} C_{n,k}\delta\Phi_k = a_{0,n,1}, \quad n=2,4,\ldots,2l. \tag{3.3}$$

The coefficients $C_{n,k}$ are given by

$$C_{n,k} = r_k K_1\left(n\pi\frac{r_k}{2y_0}\right) - r_{k-1}K_1\left(n\pi\frac{r_{k-1}}{2y_0}\right), \tag{3.4}$$

where r_k is the inner radius of the kth ring with $r_k < r_{k-1}$ and $r_0 \equiv r_e$. An optimization of the l ring filter structure results in a radial dimension $\Delta r_k \equiv r_{k-1} - r_k$ for each ring,

$$\Delta r_k \sim \frac{y_0}{k\pi}. \tag{3.5}$$

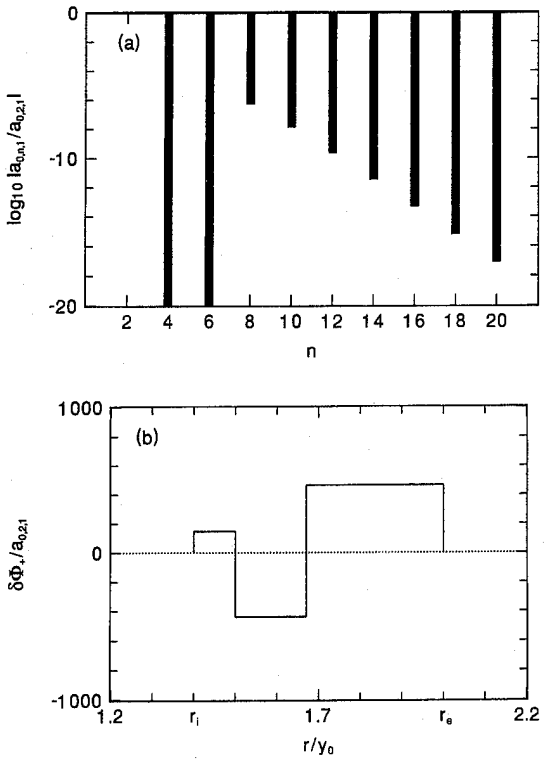


FIG. 2. (a) Spectrum of the field generated by an axisymmetric three-ring filter designed to cancel the $n=2$ harmonic without generating $n=4,6$ harmonics (the odd-order harmonics are zero by symmetry and are not shown). (b) $\delta\Phi_+$ in the three rings.

By virtue of Eq. (3.5), the radial dimension of the filter structure diverges for $l = \infty$. This is a consequence of the fact that the filter should enclose completely the region of interest in order to cancel the full spectrum of the field distortion. Therefore, the filter must be limited to the cancellation of a finite number of harmonics, usually chosen to be the lowest order in n.

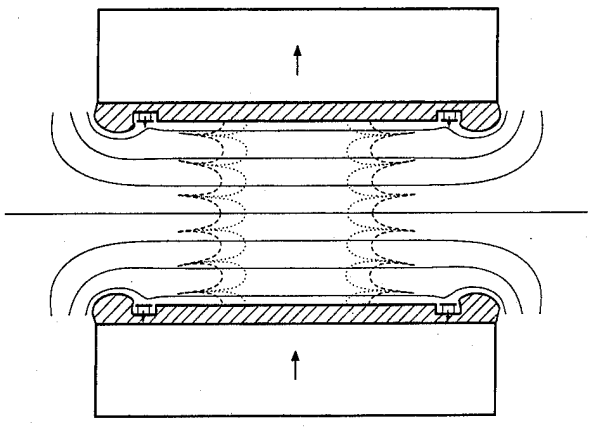


FIG. 3. A hybrid pole piece (shaded region) designed to cancel the $n=2,4$ harmonics. Each pole piece has one active ring, which are magnetized in the direction shown by the small arrows. The dashed line is the boundary of region of 100 ppm uniformity, and the dotted line is the boundary of the region of 10 ppm uniformity. The solid lines between the pole pieces represent equipotential surfaces.

Figure 2(a) shows the spectrum of the field within a cylinder of radius $r_i = 1.4y_0$ generated by a three-ring filter designed to cancel the $n=2$ harmonics without generating $n=4,6$ harmonics. The distribution of $\delta\Phi_+$ in the rings is plotted in Fig. 2(b), showing a sign inversion of $\delta\Phi_+$ in adjacent rings. Such a sign inversion is typical of filters designed to cancel a single harmonic and is a result of all the coefficients $C_{n,k}$ being positive.

For an active pole piece, the filter is constructed by embedding magnetic material into the plates. In particular, to generate the uniform shifts $\pm\delta\Phi_k$ determined by Eqs. (3.3), magnetic material is sandwiched between the main body of the plate and magnetically insulated concentric plates of high permeability material with dimensions corresponding to the l rings.[2–4] This arrangement permits the shifts to be easily adjusted by altering the amount of magnetic material for each ring.

In a traditional magnet design, the compensation of the field distortion is provided by the geometry of the pole pieces, which are equipotential in the ideal limit of infinite magnetic permeability.[5] The geometry of such passive pole pieces is obtained from the same solution obtained with Eqs. (3.3) by considering the equipotential surfaces whose potentials $\pm\Phi_p$ satisfy the condition $\Phi_p \leqslant \Phi_{\min}$, where $\Phi_{\min}$ is the minimum of the magnitude of the ring potentials. By transforming these two equipotential surfaces into surfaces of infinite magnetic permeability, a pair of massive pole pieces is generated that entirely enclose the original plates.[2]

If $\Phi_p > \Phi_{\min}$, the equipotential surfaces $\pm\Phi_p$ do not completely enclose the plates. The transformation of the equipotential surfaces $\pm\Phi_p$ into surfaces of ferromagnetic material then results in hybrid pole pieces that leave a part of the filter region of the plates exposed. The potential shifts required on this exposed portion of the plates can be produced by embedding magnetic material in the plates, as for an active filter. An example of hybrid pole pieces is shown in Fig. 3, where Φ_p is equal to the potential $\Phi_0/2$ of the top plate inside the reference cylinder of radius r_i; the filter structure consists of two rings designed to cancel the $n=2,4$ harmonics. Figure 3 also shows the boundaries of the regions of 10^{-4} and 10^{-5} field uniformity.

As previously stated, fabrication tolerances introduce odd order n and $m \neq 0$ harmonics, whose amplitudes are expected to be small compared to the amplitudes of the even-order harmonics generated by an ideal magnet. The components of the filter structure designed to cancel odd order n harmonics can be chosen to satisfy the condition

$$\delta\Phi_+(r) = +\delta\Phi_-(r). \tag{3.6}$$

Consider, for instance, a ring designed to cancel an $n=1$ harmonic. Following the same optimization procedure that leads to Eq. (3.5), the radial dimension of such a ring should be $2y_0/\pi$, which is about the same as the combined radial dimension of the three rings that cancel the $n=2,4,6$ harmonics. Therefore, the cancellation of this odd-order harmonic can be achieved by modifying the potential of a group of rings designed to cancel even order harmonics. In general, the cancellation of the harmonics introduced by the tolerances may be achieved without introducing additional rings, and the shimming or adjustment of the distribution of $\delta\Phi_\pm$ in the filter elements is provided from the solution of the filter equations (2.2) with the right-hand side terms $(a_{m,n})_{1,2}$ being obtained from a measurement of the field of the assembled magnet. Hence, the design and shimming of a magnet are achieved with a unified approach.

As shown in the example of Fig. 3, the cancellation of the cylindrical harmonics provides a quasi-cylindrical region of field uniformity extending over the entire distance between the pole pieces. This property implies that the required geometrical precision inside the reference cylinder is much higher than that outside the cylinder. In particular, the precision inside the cylinder may have to be as small as a few microns to achieve uniformities of the order of 10^{-5} or higher.

Because of these precision requirements, a passive pole piece with a nonplanar surface inside the reference cylinder may be difficult to fabricate. Furthermore, a passive pole piece, being a rigid structure, requires additional components in order to shim the magnet. A hybrid pole piece designed for $\Phi_p = \Phi_0/2$ can more easily satisfy the precision requirements inside the reference cylinder and, because it contains active elements, has the flexibility needed for shimming. In addition, the hybrid structure is more compact. The advantage of a hybrid over a fully active pole piece is that it allows a significant amount of magnetic material to be eliminated, particularly in the external ring which usually requires the largest potential shift.

IV. CONCLUDING REMARKS

The analytic approach to the design of filter structures presented in this article provides a replacement for the iterative numerical methods that are conventionally used in the design of magnet pole pieces. Both the design and shimming of a magnet can be accomplished by following a unified, systematic procedure based on the expansion (2.1) and the filter equations (2.2). With a single computation, the designs for passive, active, and hybrid pole pieces are obtained. Hybrid pole pieces, which include both magnetic and ferromagnetic materials, may be easier to fabricate than either passive or active pole pieces, while having the flexibility required for a magnet's shimming.

[1] M. G. Abele, *Structures of Permanent Magnets* (Wiley, New York, 1993).
[2] M. G. Abele, J. H. Jensen, and H. Rusinek, in the 13th International Workshop on Rare-Earth Magnets and their Applications, Birmingham, U.K., September 1994, pp. 167–176.
[3] M. G. Abele, H. Rusinek, F. Bertora, and A. Trequattrini, J. Appl. Phys. **75**, 6990 (1994).
[4] M. G. Abele, J. Appl. Phys. **76**, 6247 (1994).
[5] T. Miyamoto, H. Sakurai, and M. Aoki, in the 10th International Workshop on Rare-Earth Magnets and their Applications, Kyoto, Japan, May 1989, pp. 121–130.

Method based on the saturation approach law for monitoring the quality of texture in 3% Si–Fe

M. Birsan and J. A. Szpunar
Metallurgical Engineering, McGill University, 3450 University Street, Montréal PQ H3A 2A7, Canada

The magnetic saturation of a polycrystalline material is achieved as a result of rotation of the magnetization vector toward the direction of the applied magnetic field, against the magnetocrystalline energy. The magnetization rotation process in a grain-oriented material depends on the values of anisotropy constants, on the distribution of grain orientations, and on the direction of magnetization. Based on the magnetization rotation process, a simple instrument was devised and tested to monitor the differences of texture strength in grain-oriented 3% Si–Fe laminates. The simplicity and robustness of this instrument are remarkable and it can easily work on line. © *1996 American Institute of Physics.* © *1996 American Institute of Physics.* [S0021-8979(96)52708-2]

INTRODUCTION

When the magnetic-field strength gradually increases toward the value of the saturation field, the magnetization vector rotates toward the direction of the applied field against the magnetocrystalline energy. This is the saturation approach process, and it reflects the magnetic anisotropy of the material. The magnetic torque measured under these conditions provides information about the orientation of the magnetization vector with respect to the easy magnetization direction of the sample.

In grain-oriented 3% Si–Fe, the magnetization curve from saturation to remanence is primarily determined by the crystallographic texture. In this range of the hysteresis curve, the displacements of domain walls have already been completed and the magnetization occurs by rotation magnetization.

In a previous article,[1] a model-based method was developed to correlate texture and the coefficient representing the contribution of the magnetic anisotropy to the rotation process. It has been shown that, in a textured ferromagnetic material, the saturation approach law of the magnetization in the direction of the field is given by

$$I=I_s\left(1-\frac{|\overline{C^2}|}{2I_s^2H^2}\right), \tag{1}$$

where the information concerning the influence of texture on the magnetization rotation is fully contained in the C^2 coefficient. Using the procedure of averaging a crystal property in a polycrystalline sample,[2] we calculated[1] the mean square value of the coefficient C over the crystal orientation distribution,

$$|\overline{C^2}|=K_1^2\left(\frac{16}{105}-\frac{1}{9n_4\sqrt{\pi}}\frac{1}{9}F_4(\chi,\eta)+\frac{1}{13n_6\sqrt{\pi}}\frac{1}{275}F_6(\chi,\eta)+\frac{1}{17n_8\sqrt{\pi}}\frac{1}{4}F_8(\chi,\eta)\right),$$

where

$$F_8(\chi,\eta)=\frac{1}{\sqrt{2}}C_8^{11}\overline{P_8^0}(\chi)+C_8^{12}\overline{P_8^2}(\chi)\cos 2\eta+C_8^{13}\overline{P_8^4}(\chi)\cos 4\eta+C_8^{14}\overline{P_8^6}(\chi)\cos 6\eta+C_8^{15}\overline{P_8^8}(\chi)\cos 8\eta,$$

$$F_6(\chi,\eta)=\frac{1}{\sqrt{2}}C_6^{11}\overline{P_6^0}(\chi)+C_6^{12}\overline{P_6^2}(\chi)\cos 2\eta+C_6^{13}\overline{P_6^4}(\chi)\cos 4\eta+C_6^{14}\overline{P_6^6}(\eta)\cos 6\eta,$$

$$F_4(\chi,\eta)=\frac{1}{\sqrt{2}}C_4^{11}\overline{P_4^0}(\chi)+C_4^{12}\overline{P_4^2}(\chi)\cos 2\eta+C_4^{13}\overline{P_4^4}(\chi)\cos 4\eta. \tag{2}$$

In the above equation, χ and η are the spherical angular coordinates of the direction of the magnetization in the sample coordinate system, $P_l^n(\chi)$ are the normalized associated Legendre functions, and C_l^{nm} are the texture coefficients calculated from standard x-ray pole figure measurements. Thus, Eq. (1) illustrates that the magnetization rotation process in a grain-oriented material depends on the value of cubic anisotropy constant K_1, on the distribution of grain orientations (texture), and on the direction in which the specimen is magnetized. This process was analytically described and experimentally tested.[1] Agreement between the experimental data and the predicted values was strong, demonstrating that the crystallographic texture controls the magnetization process from the knee of the magnetization curve to saturation. These theoretical findings were used to build an instrument evaluating the texture quality, and which can be implemented for on-line texture inspection.

TEXTURE QUALITY INSPECTION

In a constant magnetic field, strong enough to align the magnetic moments in each crystallite in one direction, the direction of the sample magnetization is determined by its crystallographic texture through the magnetic anisotropy energy. Based on this theoretical background, we devised a simple instrument which gives information about the quality of the texture by measuring the angle between the direction of magnetization in the sample and the direction of a fixed applied field. The measurement is indirect because, instead of the angular displacement of the magnetization vector, the

 0021-8979/96/79(8)/5202/3/$10.00 © 1996 American Institute of Physics

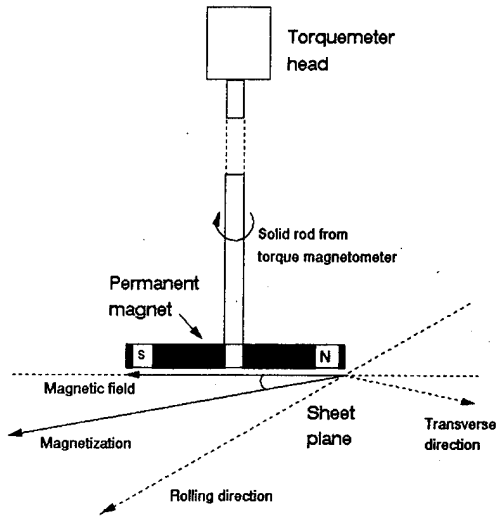


FIG. 1. Experimental setup for monitoring the quality of texture.

instrument measures the torque exerted by the sample magnetization on the external field produced by a permanent magnet.

The instrument is a modified torque magnetometer of the same type as the one described by Aldenkamp, Marks, and Zijlstra.[3] The orientation of the magnetization vector relative to the magnetic field can be determined as follows: When a disk-shaped specimen is placed in a magnetic field H parallel to its plane, the torque exerted on the disk by the increasing field gradually increases with the strength of the field. The magnetization rotates from the sample easy magnetization direction toward the direction of the field, and the path followed by the magnetization **I** can be determined from the equilibrium condition

$$I\,H\sin(\eta_0-\eta)=-\frac{\partial\overline{E_a}}{\partial\eta}, \tag{3}$$

where η is the angle between an easy magnetization direction and the magnetization vector, η_0 is the angle between the same easy magnetization direction and the magnetic field, and E_a is the magnetic anisotropy energy. The transducer measured the torque exerted by the magnetic field on the sample magnetization.

This arrangement could be reversed: A magnet producing the horizontal field is fixed relative to the sample which is placed in front of the magnet with the normal direction (ND) perpendicular to the field. In this case, the magnetometer records the torque produced by the sample magnetization acting on the fixed permanent magnetic field. The electromagnet was removed and the new setup is illustrated in Fig. 1. A strong permanent Nd–Fe–B magnet ($H_c=480\times10^3$ A/m=6000 Oe) attached to the magnetometer rod magnetized the sample above the value of the magnetization knee. If the magnetic field is not oriented along the easy direction of magnetization, the magnetization direction in the sample does not coincide with the direction of the field due to the magnetocrystalline energy. For a magnetic field of constant direction and magnitude, strong enough to magnetize the sample above the magnetization knee, the direction of magnetization depends only on the texture of the sample, as was previously illustrated.[1]

The material used for analysis is a coarse grain-oriented metal sheet placed horizontally underneath the permanent magnet which is hung through the glass rod on the lower suspension of the torquemeter head. The material thickness is 9 mil (=0.21 mm) and, therefore, we assume that the overall magnetization is confined to the sheet plane, minimizing the magnetostatic energy caused by free magnetic poles on the sheet surfaces. The magnetic-field vector **H** and the magnetization vector **I** are, therefore, coplanar, i.e., the magnetization rotation occurs in the sheet plane.

The magnetic anisotropy of grain-oriented 3% Si–Fe materials is associated with a crystallographic {110}⟨001⟩ texture. As has been demonstrated,[1] when the applied field lies between $\eta=0°$ and $\eta=45°$ directions of the sample, a higher value of the lag angle between the magnetization and magnetic field corresponds to a better orientation of the crystallite easy magnetization directions along the sample rolling direction. Since the torque measures the sine of the angle between the magnetization and the magnetic field, it provides information about the perfection of grain orientation in the sample.

The permanent magnet produces a constant magnetic field, which is a function of the distance between the permanent magnet and the sample plane. To obtain comparable information about the texture quality of different materials, the tests must be performed at constant magnetic field, which means a constant distance between the permanent magnet and the surface of the sample. The large dimensions of the metal sheet, practically infinite size in comparison with the dimensions of the permanent magnet, exclude the possibility of the free magnetic poles appearing inside the sample, so that the demagnetizing field can be considered zero.

The instrument was experimentally tested in the laboratory on two pieces of grain-oriented metal sheets of different texture quality. We call these two specimens OR-A (good quality) and OR-B (poor quality). The OR-A specimen has a smaller dispersion angle of the ⟨001⟩ directions around the rolling direction than specimen OR-B. The material texture is represented using the orientation distribution function (ODF). To illustrate the texture differences, Figs. 2(a) and 2(b) present the $\varphi_2=0°$ section of the orientation distribution function (ODF) for the two samples.

The objective of the laboratory test was to identify the optimum position of the magnet relative to the sample rolling direction and to evaluate the sensitivity of the method. Starting from a position where the direction of the magnetic field coincides with the rolling direction (RD), the metal sheet was rotated 45°, and the signal proportional to the torque was recorded by the instrument in 2.5° steps. The results obtained for the two samples are shown in Fig. 3. The difference in torque value between the two specimens is significant when the permanent magnet is situated at approximately 12° from the rolling direction. For the two examples considered here, the difference in magnetic torque corresponds to approximately 1000 N m/m^3.

The shape of these curves is less important for our pur-

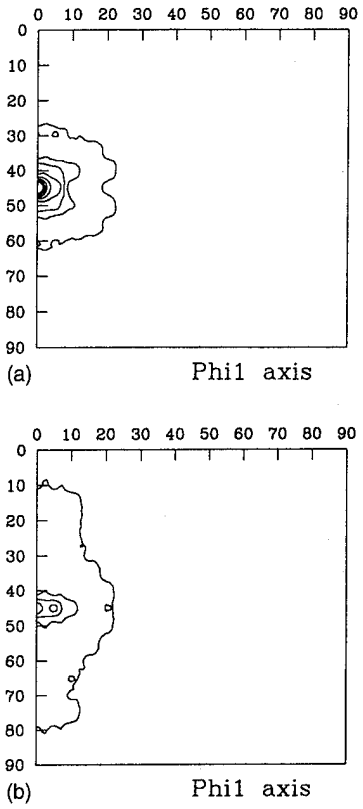


FIG. 2. $\phi_2=0°$ ODF sections for (a) sample OR-A and (b) sample OR-B.

poses; however, one has to emphasize that the curve shape does not reflect the sample symmetry, but it is a result of the interaction between the sample magnetization and the permanent magnet. To illustrate this, we deduce a qualitative expression for the torque obtained using the presented instrument.

If the magnetic field **H** is oriented in a direction lying in the sheet plane, and with an angle η_0 to the sample easy magnetization direction, the magnetization direction in the sample plane is determined by the equilibrium condition (3), where the torque $L(\eta)=\partial E_a/\partial\eta$ is a function of the texture coefficients of the material.[2]

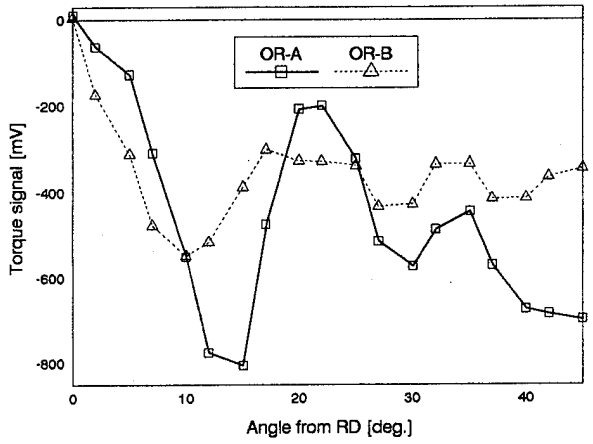


FIG. 3. Torque signal recorded from the two grain-oriented samples.

Let us assume that the relative permeability of the sample in the direction $(90°,\eta)$ is $\mu(\eta)$. The problem of permeability variation with the angle from the easy magnetization direction of the sample is discussed elsewhere.[4,5] Here, we consider[6,7] that the permeability is described, to the first approximation, as a linear function of $F_4(\eta)$, defined in Eq. (2), and, as a result, one can write

$$\mu(\eta)\approx\mu_2\cos 2\eta+\mu_4\cos 4\eta, \tag{4}$$

where μ_2 and μ_4 are material constants.

The magnetization in direction $(90°,\eta)$ is related to the component of the magnetic field in this direction through the relationship

$$I(\eta)=\mu(\eta)H(\eta_0)\cos(\eta_0-\eta). \tag{5}$$

Substituting Eqs. (4) and (5) in Eq. (3), we obtain

$$\begin{aligned}L(\eta)&=\tfrac{1}{2}\mu(\eta)H^2(\eta_0)\sin 2(\eta_0-\eta)\\&\approx L_0+L_4'\cos 4\eta+L_4''\sin 4\eta\\&\quad+L_6'\cos 6\eta+L_6''\sin 6\eta+\cdots,\end{aligned} \tag{6}$$

where the coefficients of the series are functions of η_0, H, and texture coefficients. The presence of the sine functions in the above equation shows that the symmetry of the torque curve is not orthorhombic (sample symmetry). From this point of view, the instrument is not appropriate for obtaining texture information. What is important is that the experimental curves reflect the differences in texture between the two materials.

In the proposed industrial application of the instrument, the direction of the magnetic field created by the permanent magnet should be constant relative to the rolling direction, for example, at 12.5° where the difference in torque signal is maximum. The instrument must be calibrated using materials of known texture.

The simplicity and robustness of this instrument are remarkable. This instrument could be readily implemented to monitor the quality of the grain-oriented materials on line. When implemented on the processing line, the designed instrument would indicate the variation in the texture of the final product.

CONCLUSIONS

The approach to saturation law has offered us the theoretical background for obtaining information about the quality of material texture. A method to evaluate texture was devised and tested using a modified torquemeter. The variations in texture quality were easily detected. This method can be implemented on line and may be of practical importance to the grain-oriented steels industry.

[1] M. Birsan and J. A. Szpunar, J. Appl. Phys. **78**, 3293 (1995).
[2] H. J. Bunge, *Texture Analysis in Materials Science* (Butterworths, London, 1982).
[3] A. A. Aldenkamp, C. P. Marks, and H. Zijlstra, Rev. Sci. Instrum. **31**, 544 (1960).
[4] M. Birsan and J. A. Szpunar, Mater. Sci. Forum **157**, 1543 (1994).
[5] M. Birsan and J. A. Szpunar, J. Appl. Phys. (to be published).
[6] W. B. Hutchinson and J. G. Swift, Texture **1**, 117 (1972).
[7] P. R. Morris and J. W. Flowers, Texture Cryst. Solids **4**, 129 (1981).

Construction of novel magnets for generating astatic fields in x-ray topography

Tetsuo Nakajima
Photon Factory, National Laboratory for High Energy Physics, Oho 1-1, Tsukuba, Ibaraki 305, Japan

Masami Yoshizawa
Saitama Institute of Technology, Fusaiji, Okabe, Saitama 369-02, Japan

Superconducting (*S*-type) and normal-conducting (*N*-type) magnets, which can freely change the direction and strength of the fields, were constructed due to an incidental requirement concerning x-ray diffraction. Both magnets comprise three pairs of solenoids, the axes of which intersect orthogonally at the central point. Each pair of solenoids is independently excited by bipolar electric power sources. Alternating and direct current magnetic fields applied to an arbitrary direction $[h_1k_1l_1]$ in a single crystal can be varied to another direction $[h_2k_2l_2]$, parallel to an arbitrary curved surface. The components ($\mathbf{H}_x$, $\mathbf{H}_y$, and $\mathbf{H}_z$) from each solenoid were simultaneously measured using three Hall elements. The prescribed magnetic field ($\mathbf{H}$) was accurately synthesized by computer control of the electric power sources through the direction cosines, H_i/H ($i=x$, y, and z). The magnet was used to take synchrotron radiation x-ray topographs of α-Fe-3% Si in magnetic fields swept in the (110) plane from [002] via $[2\bar{2}2]$, $[1\bar{1}0]$, $[2\bar{2}\bar{2}]$, and $[00\bar{2}]$ to [002]. In the *S* type, an inner metal Dewar having a transmittable part of an x-ray beam made of a confocal beryllium cylinder was installed in order to generate temperatures higher than 4.2 K. © *1996 American Institute of Physics.* [S0021-8979(96)52808-7]

I. INTRODUCTION

In x-ray diffraction, samples set on a four-circle goniometer, used for determining the crystal structure, can be irradiated by the incident beam into an arbitrary direction $[hkl]$ of a crystal. However, the direction of the magnetic fields rigidly fastens onto either the pole direction or the axis of the solenoid. To make the magnetic field direction goniometrically controllable, two original types of the *S*- and *N*-type magnets were constructed, in which the direction of the magnetic fields generated by a set of three pairs of independent solenoids, regardless of the direction of the solenoid axes, can be goniometrically controlled by three bipolar electric-power sources. The axes of the three pairs of coils intersect orthogonally at the central point in both the *S* and *N* types. Differing from the usual type magnet, the direction of the fields are *unsettled*, i.e., *astatic*. Hence, alternating or direct current magnetic fields applied to a crystal can vary from one direction $[h_1k_1l_1]$ to another $[h_2k_2l_2]$ while remaining parallel to an arbitrary curved surface. A test measurement of the SR x-ray topography of α-Fe-3% Si is described.

II. INSTRUMENTATION

A. Three-channel gaussmeter

The components ($\mathbf{H}_x$, $\mathbf{H}_y$, and $\mathbf{H}_z$) of the magnetic fields were simultaneously measured using a three-channel gaussmeter (series-9900 made by F. W. Bell Inc., USA). Knowledge of the components is essential for controlling the strength and direction of the magnetic fields. The direction cosines (H_i/H, $i=x$, y, and z) correspond to the Miller indices $[hkl]$ in a single crystal, respectively. [Here, H is equal to $(H_x^2 + H_y^2 + H_z^2)^{1/2}$]. An assembly of two Hall generators, in which two are the plate type with an active area of approximately $0.040''\phi$ and one is a cylinder type with an active area of approximately $0.020''\phi$, is used to measure $\mathbf{H}_x$, $\mathbf{H}_y$, and $\mathbf{H}_z$.

Neglecting the resistive voltage, the coupling between coils, and the oscillations with current changes, the bipolar power supplies act as ac power sources. Therefore, a modified simple circuit as shown in Fig. 1 for three pairs of solenoids with three bipolar electric-power sources has been used.

Both astatic magnets were excited by three bipolar electric power sources. The rated output of power supplies were ±16 V, ±82 A and ±43 V, ±82 A for SPEC-88703 and SPEC-88704, respectively. Diodes (Toshiba 60JC15 or Nihon Inter 20M60) and rheostats (1 Ω, with a 60 amp current capacity) were attached as guard circuits against quenching of the superconducting coils. Variations of each component of the magnetic fields are controlled through a GPIB interface to a computer. The fields are increased or decreased by choosing a plus or minus current increment defined by the total current (164 amp) divided by 1000. Hence, the fields change by a stepwise cyclic pace of $\mathbf{H}_x$, $\mathbf{H}_y$, and $\mathbf{H}_z$, closely paralleling the desired path. Adjusting the coincidence between the directions of the fields and the orientation of the Hall generators was carefully done.

B. Three axial split magnet

1. The S-type magnet

Figure 2 shows a cross-sectional view of the layout of the *S*-type magnet (A), together with the outer (B) and inner (C) Dewars. The coils, wound with single-strand NbTi, wire comprise a compound winding, and are identical in size. The

 0021-8979/96/79(8)/5205/3/$10.00 © 1996 American Institute of Physics

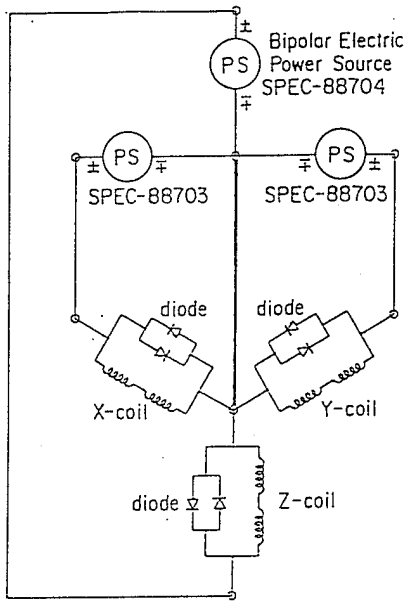


FIG. 1. Circuit of three pairs of X, Y, and Z coils and three bipolar electric-power sources.

coil constants lie between 0.01268 and 0.01259 T A^{-1}. The strength of the magnetic field at the central point is about 0.5 T with a homogeneity of 24% within a 10 mmϕ spherical volume. Thus, the resultant maximum field is nearly equal to about 0.86 T, parallel to the [111] direction at about 40 A. Photographs giving a general view of the S-type magnet and a bird's eye view of Dewar's top flange are shown in Figs. 3(a) and 3(b), respectively. The outer metal Dewar shown in Fig. 2 has four twofold x-ray transmission windows, which consist of two different sizes of beryllium plates: 80 mmϕ

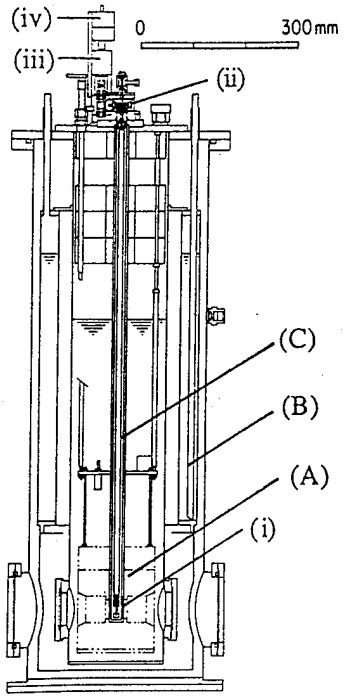
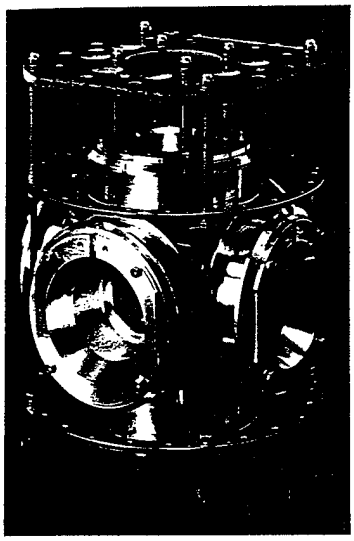


FIG. 2. Cross-sectional view of the layout of the S-type magnet.

(a)



(b)

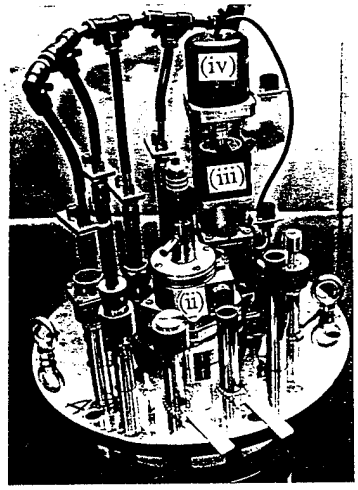


FIG. 3. Photographs of a general view of the S-type magnet (a) and a bird's eye view of Dewar's top flange (b).

$\times$0.5 mm thick sealed by an indium-coated *helicoflex* metal O ring on the inside windows of liquid helium container, and 140 mm$\phi\times$1.2 mm thick sealed by a neoprene O ring on the outside windows at room temperature. The aperture angle in each window is set to be $\pm$15.0°. The duration of operation with 16 ℓ of liquid helium is about 15 h. The warning level is monitored by a liquid helium level meter.

The low part of the confocal walls of the inner Dewar (i) in Fig. 2 was made of two beryllium cylinders with a diameter of 30 and 20 mm and length of 30 mm which formed the vacuum jacket. The sample holder is connected to an accurate θ-rotation stage (ii) driven by a stepping motor (iii), which has an angular resolution of 1×10^{-4} deg per pulse, independently confirmed by encorder (iv). Generally, the full width at half maximum (FWHM) of the diffraction pattern gives $\pm\ \Delta\mathbf{q}_{\parallel}$ parallel to the scattering vector $\mathbf{q}$, which expresses any fluctuation of the length in the periodicity and the FWHM from the rocking curve gives $\pm\Delta\mathbf{q}_{\perp}$ perpendicu-

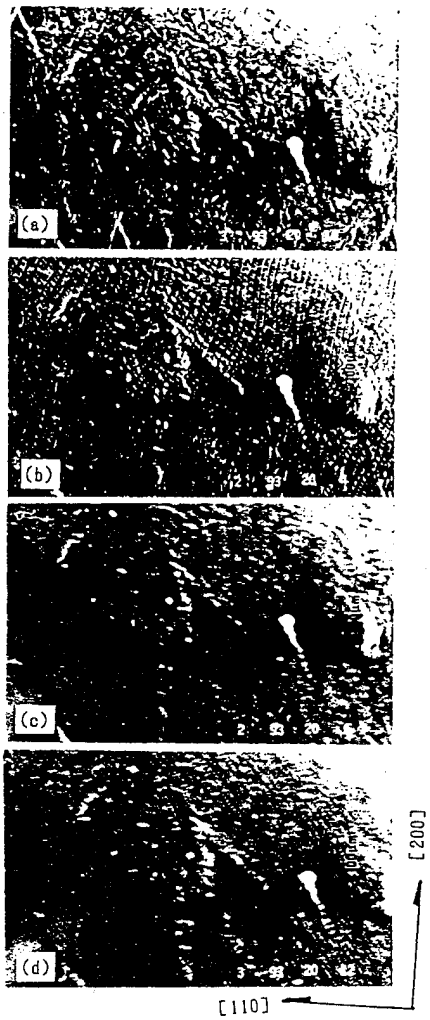


FIG. 4. Topographs of (110) Laue spots of α-Fe-3% Si single crystal: (a) (110) at H=0 Oe, (b) 320 Oe ∥ [002], (c) 320 Oe ∥ [$2\bar{2}2$], (d) 320 Oe ∥ [$00\bar{2}$].

lar to **q**, which expresses any fluctuation of the direction in periodicity. Both quantities are complementary, which is important for gaining a better understanding of the crystal structure based on topographs.

2. N-type magnet (Ref. 1)

The three pairs of coils for the N-type magnet have three different sizes. The maximum fields are up to about 337 Oe at 30 A for the smallest and medium coils and the same field at 60 A in the largest one. The maximum heat generations are about 165, 800, and 2400 W, respectively. Thus, in order to cool the coils, the maximum flow rates of water are 0.4, 2, and 4 ℓ per min, respectively. The field homogeneity of each coil is typically one part in 1×10^{-4} within a 10 mmϕ spherical volume at the central point.

III. EXPERIMENTAL RESULTS AND REMARKS

White SR x-ray topographs of an α-Fe-3% Si single crystal in magnetic fields swept by the N-type magnet in (110) from [002] via [$2\bar{2}2$], [$1\bar{1}0$], [$\bar{2}\bar{2}2$], [$00\bar{2}$], to [002] were taken using SR x-ray beams of 6 mm×2 mm. To take topographs with $2\theta_B = 90°$, SR x-ray beams were injected into the specimen of a thin plate parallel to (110) at an angle of 45°, which is the Bragg angle (θ_B). Magnetic fields were swept in the (110) plane through the above-mentioned path. These procedures are only feasible using this type of the magnet. Topographs were taken by using Ilford nuclear emulsion plates L4. The axis of easy magnetization in α-Fe-3% Si is in the [200] direction. Figures 4(b) and 4(d) show the magnetic domain structures nearly parallel to [002] and to [$00\bar{2}$], respectively. In Figs. 4(a) and 4(c), no clear geometrical pattern of the magnetic domain structure could be observed.

The astatic magnet is applicable not only to SR x-ray diffraction and solid state physics, but also as a novel insertion device for an SR light source. The insertion device would consist of several two-axis astatic magnets in series. The main characteristics resulting from using the astatic magnetic fields as insertion device are as follows: ease of (1) rapid production of polarized electromagnetic waves from linear polarization via elliptical polarization to circular polarizations by control of the power sources, (2) arbitrary rotation of the polarization plane in linear polarization, and (3) switching from left-circular light to right-circular light, and vice versa, in circular polarization.

[1] T. Nakajima, M. Yoshizawa, and Cao Zhuoliang, Physica B **194-196**, 143 (1944).

Automized magnetic hysteresis measurement system

Rolf Disselnkötter
ABB Corporate Research, P. O. Box 10 13 32, D-69003 Heidelberg, Germany

Modeling and design of magnetic components require primary data on material hysteresis properties. In this article a flexible and highly automized system is described, which is suited for the characterization of the low frequency soft magnetic behavior (≈5 Hz–2 kHz) of ferromagnetic samples. The apparatus consists of a PC with the control program, a modular data acquisition/signal generation system, and a remotely controllable power amplifier to which the sample is connected. Integration of the secondary output voltage is performed digitally. The system operates in current control mode, and the user can select from a variety of adjustable excitation functions and even complex measurement procedures. It is possible to perform stationary or transient measurements of major and minor loops, initial magnetization and commutation curves, to do automatic demagnetization, and to output specific parameters which are necessary for sample characterization or model calibration. Amplitude selection and autoscaling of the measurement sensitivity can proceed within wide dynamic ranges. Sample, signal parameter, output, and characteristic data can be printed or plotted, edited, saved, reloaded, or changed in format. A number of different options for measurement and postprocessing are available. Instead of $B(H)$ also $M(H)$ or $\mu(H)$ curves or time signals can be displayed. Future software versions will also support the voltage control mode (which is already provided in the amplifier), and the measurement of the anhysteretic curve. A selection of example measurements obtained for two samples and with different types of excitation signals indicates the suitability of the system for various applications. © *1996 American Institute of Physics.* [S0021-8979(96)52908-5]

I. INTRODUCTION

Modeling and design of magnetic components often require more information on the hysteresis properties than usually available from the suppliers. This holds in particular for applications when (apart from nonlinearity and loss) signal symmetry (minor loops) and transient response are of importance.[1] Experimental characterization of the complex hysteresis behavior of soft magnetic materials may be either rather tedious or it requires a very flexible tool.

Former approaches of programmable hysteresis loop tracers[2–4] are often tailored to specific applications in that they either do not support core modeling, are restricted to a small frequency range, or (without reprogramming) to a few fixed test procedures and excitation signals.

In this article a hysteresis measurement system is described, which has been developed for the measurement of the low frequency response (≈5 Hz–2 kHz) of soft ferromagnetic samples to "arbitrary" periodic or transient signals. Also complex measurement functions can be performed. The apparatus is computer-automized, while the user is still given full control of all its functions at the same time. Characteristic hysteresis parameters necessary for sample characterization and model calibration can be extracted.

II. DESCRIPTION OF THE HARDWARE

The schematic diagram of the hysteresis loop system is shown in Fig. 1. It consists of mainly four components, which are an IBM compatible PC with the software for control and data evaluation, an external modular system with plug in boards for data acquisition and signal generation, the power amplifier to which the sample is connected, and the power supplies for the amplifier.

The sample may be either of toroidal or stripe shape (with known demagnetization factor). It must be provided with two appropriate windings (for primary current and secondary voltage) which are connected to the amplifier by four screw terminals.

Nearly all the functions of the power amplifier can be both controlled by the front panel or by PC (via the digital I/O port of the modular system). It can be operated either with current (ranges 0.25, 2.5, and 25 A) or voltage control (gains 1 or 4.5) with a maximum output voltage of ±48 V. Input voltage for full range output current is ±10 V. Offset can be fine-adjusted manually. Maximum bandwidth of the amplifier is 30 kHz. For the reduction of internal losses the supply voltage can be controlled from the PC with an 8-bit resolution. Two analog output voltage signals corresponding to the primary current and the secondary voltage of the sample are connected to the data acquisition system.

The modular data acquisition/signal generation system (MUSYCS/IMC) is internally synchronized; however, all its functions are programmed from the PC via a serial interface. The current and voltage signals are sampled with a maximum total rate of 1 MHz, converted with 12-bit resolution and stored in the local 4 MB-RAM before they are transferred to the PC for further processing. For frequencies below 100 Hz the horizontal resolution is limited to 2000 samples per signal period by the software (this is reduced at higher frequencies). Input ranges can be set from ±50 mV up to ±50 V. Acquisition is triggered by a pulse from the four-channel synthesizer board (±10 V, 12-bit, common time base of maximum 1 MHz per channel with a depth of 8000 samples each) which at the same time starts generating the amplifier input signal. By means of an integrated programmable attenuator it is possible to use the full 12-bit

 0021-8979/96/79(8)/5208/3/$10.00 © 1996 American Institute of Physics

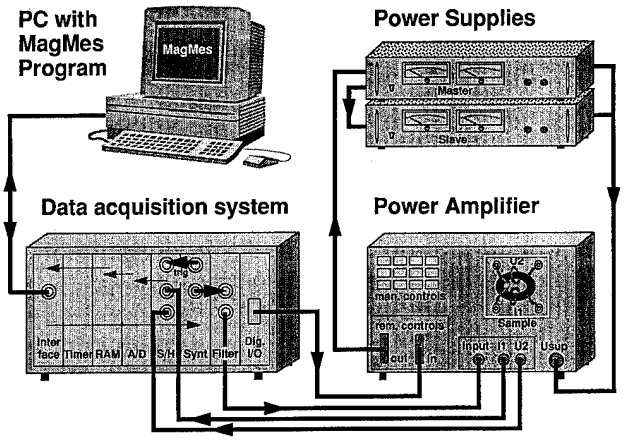
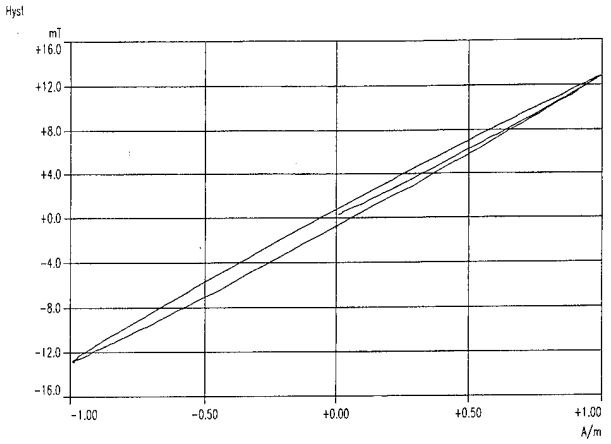


FIG. 1. Schematic diagram of the computer controlled hysteresis measurement system. The sample is provided with two windings which are connected to the power amplifier by screw terminals.

resolution with small amplitude signals. Before the output is transmitted to the amplifier it is first routed through a programmable low pass filter in order to reduce digital noise. Control of the amplifier modes and ranges is performed by a digital I/O board with 24 output channels.




```
[Hysteresis curve values]

H_tip (A/m)     =     0.996
Hc (A/m)        =     0.040
B_tip (T)       =     0.013
Br (T)          =     0.001
μd_i            = -9.1339E+01
μd_r            = 8.1472E+03
μd_c            = 1.2587E+04
μ_tip           = 1.0205E+04

[Power losses]

Pd/V (W/m^3)    = 1.12E+00
Pd/m (W/Kg)     = 2.05E-04
Pd/f (W/Hz)     = 1.64E-09
Pd (W)          = 1.64E-06
Pa (Var)        = 5.89E-05
Loss angle (°)  =  88.4

[Signal]

Signal type : Sine Standard
Freq (Hz)       =  1000

Input filter cutoff frequency [Hz] = 20000
```

FIG. 2. 1 kHz initial magnetization curve and Rayleigh loop (1 A/m) of a *T*38 ferrite ringcore. Dependent on the type of measurement characteristic values of fields, inductions, permeabilities, and power loss of the curve are calculated and can be printed out.

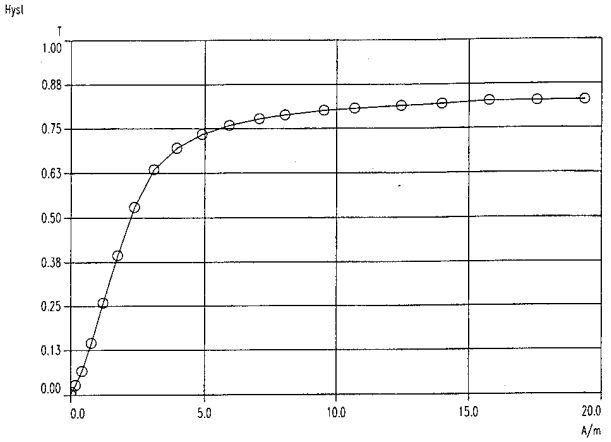
III. DESCRIPTION OF THE SOFTWARE

The "MagMes" system software is a menue structured FRAME program using MUSYCS and FAMOS functions. It runs under MS-WINDOWS.

The measurement system is controlled from the main dialogue. It contains two curve windows which typically display the measured $I1(t)$ and $U2(t)$ time signals and the $B(H)$ hysteresis curve (the latter is obtained by digital integration!). Further, there are controls for triggering a new (autoscaled!) measurement and for on-line adjustment of signal amplitude and power supply voltage. Signal type, amplitude, and frequency as well as the sample name are also displayed. Other functions can be called by referring to the pull down menue bar on top of the dialogue window:

The functions of the "Sample Menue" allow to edit, print, save, and load those parameters of the device under test, which are necessary for calculation of secondary data or for correct demagnetization and excitation. Apart from the winding numbers and areas, the core geometry and demagnetization factor, the saturation field and the number of signal cycles necessary to reach a stationary magnetic state of the sample can be defined.

Likewise, there is a "Signal Menue," which allows to edit, store, and load signal parameters. There are different types of signals which can be selected: periodic signals (like sine, square, or triangle), nonperiodic (sine with linearly or exponentially varying amplitude, "arbitrary" steady signals composed of sine half-waves), and more complex procedures like the measurement of commutation and anhysteretic curves (will be implemented in the next version). For each of




```
[Hysteresis curve values]

H_tip (A/m)     =    19.366
B_tip (T)       =     0.829
μd_i            = 3.0828E+05
μd_tip          = 9.2338E+02
μ_tip           = 3.4056E+04

[Power losses]


[Signal]

Signal type : Commutation Curve
Freq (Hz)       =     5

Input filter cutoff frequency [Hz] =   100
```

FIG. 3. 5 Hz commutation curve of an Ultraperm F80 ringcore. In an automatic procedure every point of the curve is measured at least with the number of cycles necessary to reach the stationary state of the core.

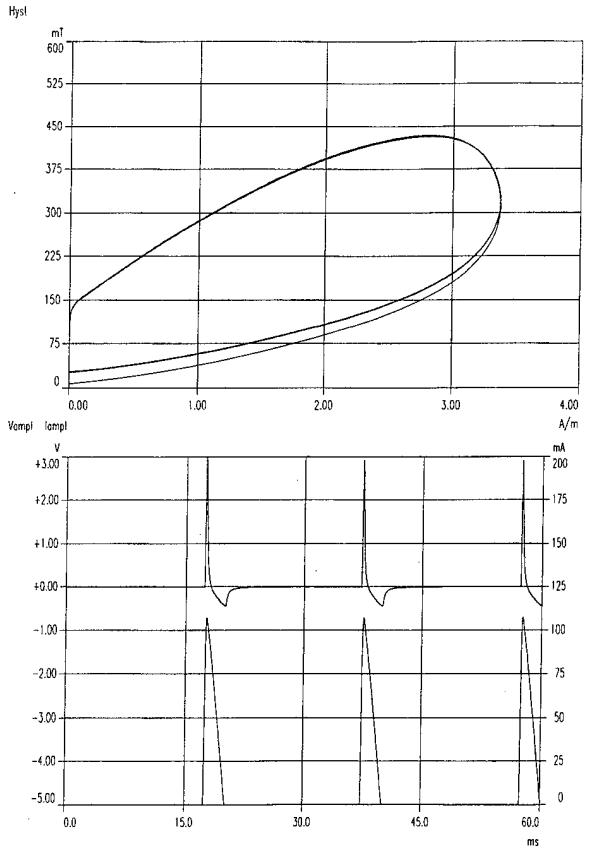


FIG. 4. Response of an Ultraperm F80 ringcore to a series of unipolar 50 Hz sine pulses cut at 135° (test for residual current transformers).

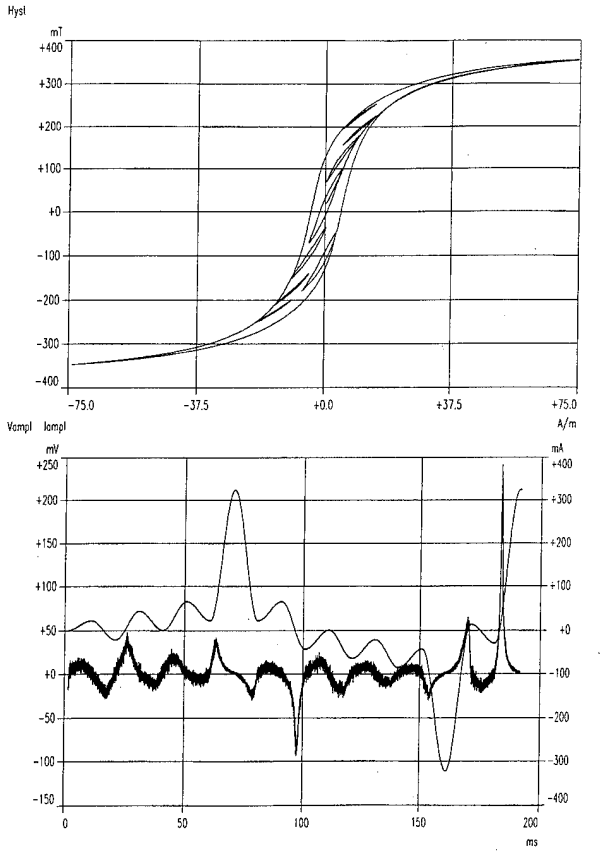


FIG. 5. Minor loops located at any point within the major loop can be constructed by "arbitrary" signals composed of sine half-waves.

the signal types there is a "Parameter Menue," in which amplitude, frequency, offset, duty factor, and other parameters can be defined. For sine-type signals in particular, one of the subtypes "standard, half-bridge, full bridge, phase control or pulse" can be chosen. The possibility of outputting just a few signal cycles enables the generation of high field amplitudes without causing thermal problems. The signal waveform data are calculated and transmitted to the synthesizer immediately before the measurement.

In the "Measurement Menue" it is possible to select options for measurement, data evaluation, curve display, and data output. Further, a set of numerical results for the current curve can be displayed. Optionally, automatic sample demagnetization voltage- or B-offset compensation, and input signal filtering can be performed. The kind and format of the curve display [$B(H)$ vs $M(H)$ or $\mu(H)$; $H(t)$ and $B(t)$ vs $I(t)$ and $U(t)$] as well as the file format for data output (ASCII or adapted to the MagCAD preprocessor used for model calibration) are selectable. In other menues it is possible to load, print, or plot data.

Up to now, MagMes only supports current control, though the amplifier can work both with I and U control.

IV. EXAMPLE MEASUREMENTS

The following figures show only some examples of measurements which are possible with MagMes. In Fig. 2 the initial magnetization curve and Rayleigh loop measured on a demagnetized $T38$ ferrite ringcore with two cycles of a 1 kHz standard sine signal are displayed together with the automatically calculated numerical results. Apart from amplitude permeability and other characteristic hysteresis parameters also some values of the differential permeability at different locations on the curve are given.

Figure 3 shows the results of a low frequency commutation curve measurement performed on a highly permeable strip wound core. The individual points on the curve are determined with selectable resolution in a stepwise automatic procedure.

Figures 4 and 5 show hysteresis curves resulting for special types of the excitation waveform: A 135° cut unipolar sine signal is used for tests on pulse sensitive residual current circuit breakers. Due to the decrease of remanence during $H=0$ larger values of B (and thus of the output voltage) are obtained! With a composed signal like in Fig. 5 the properties of minor loops located anywhere within the major loop are accessible.

[1] Von E. Gerecke, Bull. SEV/VSE **67**, 407 (1976).
[2] P. T. Jowett and D. I. MacInnes, Computerized Magnetic Test and Evaluation of Hysteretic Materials, Conf. Rec. IEEE IAS Annual Meeting, San Diego, Oct. 1989, (unpublished), p. 285.
[3] A. R. Eichmann, M. K. Devine, D. C. Jiles and D. A. Kaminski, IEEE Trans. Magn. **28**, 2462 (1992).
[4] T. Kulik, H. Savage, and A. Hernando, J. Appl. Phys. **73**, 6855 (1993).

Alternating current-excited magnetoresistive sensor

P. Ripka[a)]
Czech Technical University, Faculty of Electrical Engineering, Department of Measurement, 166 27 Praha 6, Czech Republic

Thin-film anisotropic magnetoresistors are superior to semiconductor magnetic field sensors. ac excitation of the sensor bridge reduced the noise level to 10 nT p-p. The offset reduction and sensor characteristic stabilization was achieved by periodical flipping by means of 100 mA/100 μs current pulses into a 400 turns coil wound across the sensor perpendicular to the sensitive axis. The use of the flipping mechanism can significantly improve the performance of the permalloy anisotropic magnetoresistors: long-term offset stability of 10 nT, hysteresis below 100 ppm FS and 5 nT p-p noise can be achieved with low-power sensor electronic circuits. The array of eight magnetoresistors was used in a contactless dc current meter. A sensitivity of 0.1 mA and high geometrical selectivity was obtained. © *1996 American Institute of Physics.* [S0021-8979(96)53008-7]

Commerically available thin-film anisotropic magnetoresistor bridges such as Philips KMZ or Planartechnik KMY are superior to semiconductor magnetic field sensors. Their bridge structure is schematically shown in Fig. 1; individual resistors have a meander shape to increase the effective length. The "barber pole" structure made of aluminum strips on the permalloy surface causes the deflection of the current direction by 45° from the field sensitive axis (y), and thus linearizes the sensor characteristics.[1] The sensors should be premagnetized in perpendicular (x) direction along the strip length. Afterward the x-direction field should be kept low to avoid possible distortion of the characteristics.

Sensor sensitivity can be further increased: Veith *et al.*[2] reached values of more than 100 mV/V/mT by 2.5-mm-long sensor, Smith *et al.*[3] reported sensitivity of 400 mV/V/mT using thin-film flux concentrators. The sensors may have resolutions of 10 nT which is sufficient for compass applications, contactless current sensing, and proximity sensing applications. A single magnetoresistor compass was described by Paperno and Kaplan.[4]

The measurements reported in the present article were performed on a Philips KMZ10A1 sensor. The sensor sensitivity for 5 V dc bridge supply was 70 V/T; the magnetometer output fluctuations are thus caused not only by fluctuations of the magnetoresistance, but also by input amplifier $1/f$ noise at ultralow frequencies and even by bridge thermal noise.[5] Significant improvement can be observed when the bridge is excited by an ac signal. Using 10 V p-p squarewave excitation and lock-in amplifier for the signal processing, we observed no change in the sensitivity for excitation frequencies from the 150 Hz to 15 kHz. Figure 2(a) shows how the low-frequency sensor noise was reduced: the power spectral density at 1 Hz was 3.6 and 1/6 nT/$\sqrt{\text{Hz}}$ for dc and squarewave supply, respectively. The instrumentation noise level was below 0.1 nT/$\sqrt{\text{Hz}}$ (measured for the excitation switched off). Figure 2(b) is the time plot for the ac supplied sensor output: the p-p noise is 10 nT.

The main disadvantage of the permalloy magnetoresistors is the danger of distortion of their characteristics by a field in perpendicular (x) direction. Figure 3 shows the sensor characteristic for the measured field declined by 10° from the y axis. The field component in x direction causes the change of the magnetization in easy direction so that for higher field values, the characteristic changes its polarity.

The mentioned flipping effect can be used for stabilization of the sensor characteristic. The permanent magnetization in the easy direction was changed by current impulses into the 5-mm-long, 6-mm-i.d. coil of 400 turns wound across the sensor (Fig. 1). Figure 4 shows the sensor characteristics for changing the polarity and amplitude of the flipping pulses: 100 mA current impulses which create a maximum field of about 4 kA/m in the coil center guarantee stable operation.

The electronic circuit which was developed generates flipping pulses of 100 μs duration and 800 μs repetition rate with successively altering polarity. The sensor output is read by a gated integrator for 100 μs in between each of the flipping pulses. The resulting characteristic is shown in Fig. 5. Sensor modulation reduces the offset by one order of magnitude to below 1 mT, hysteresis to below 100 ppm FS and long-term offset variations to below 10 nT; the temperature coefficient of the sensitivity (10^{-3} K^{-1}) remained unchanged.

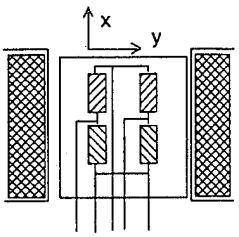


FIG. 1. Permalloy magnetoresistive sensor. The bridge consists of four resistors with "barber pole" structure. The sensor measures magnetic field in the "y" direction.

[a)]Electronic mail: ripka@feld.cvut.cz

 0021-8979/96/79(8)/5211/3/$10.00 © 1996 American Institute of Physics

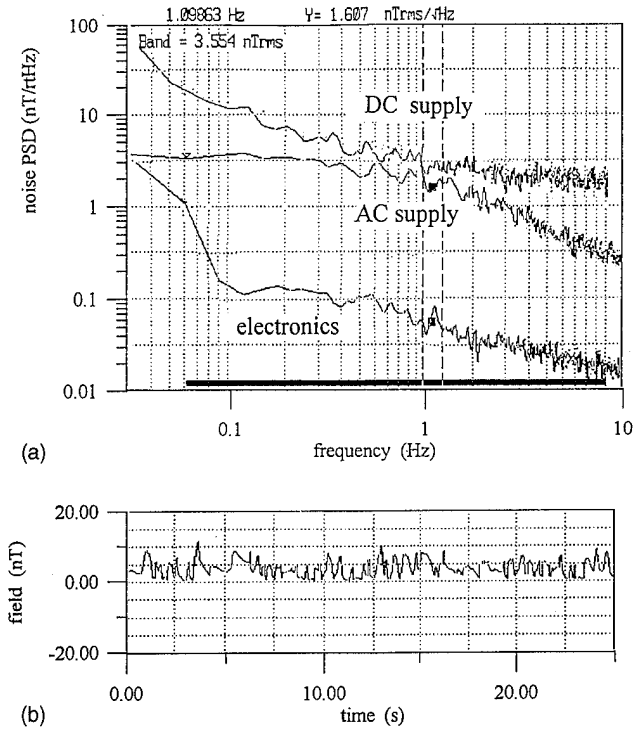


FIG. 2. Noise of the KMZ 10A1 magnetoresistor: (a) Power spectral density for dc and ac supply and own noise of the magnetometer electronics. (b) Time plot of the ac-supplied sensor output in zero field.

A sensor array of eight dc supplied magnetoresistors has been used in a contactless dc current meter. The sensors are mounted to follow the flux lines of the measured current (Fig. 6). The Earth's field and the disturbing fields caused by an error current flowing outside the sensor are partially suppressed: 5 A false current located 10 cm from the sensor

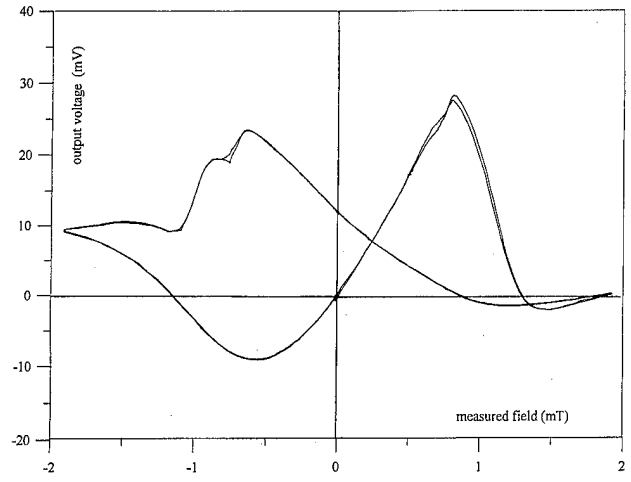


FIG. 3. Characteristic of the dc supplied magnetoresistor for field direction 10° from "y".

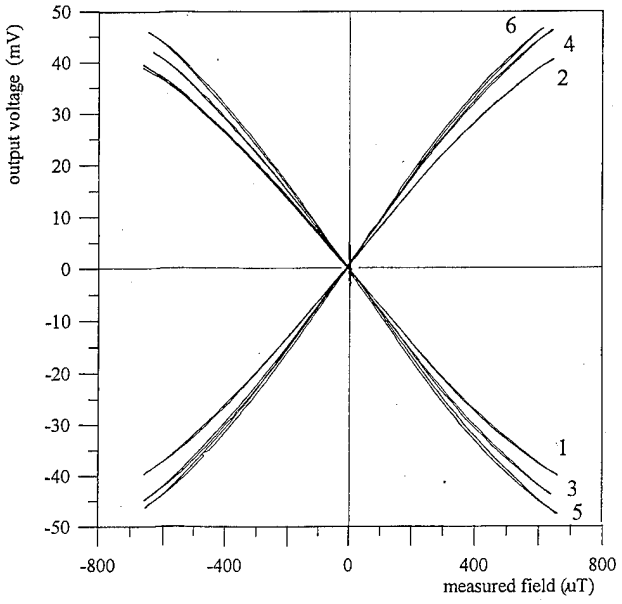


FIG. 4. Sensor characteristics for various amplitude and polarity of the (single) flipping current pulses: minimum flipping current of ±40 mA (curves 1,2), ±100 mA (3,4), and ±1 A (5,6).

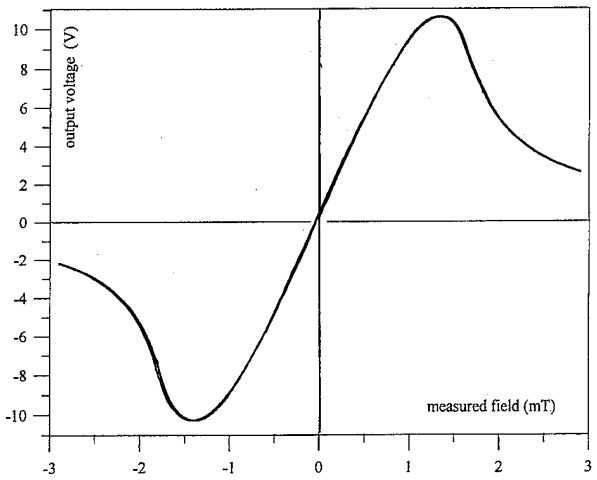


FIG. 5. Sensor characteristics with flipping field of 4 kHz created by ±100 mA pulses into 400 T coil (max. field of 4 kA/m).

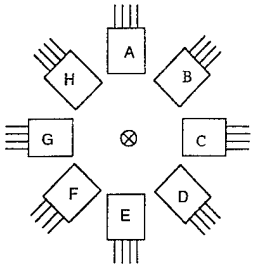


FIG. 6. Array of eight magnetoresistors for the contactless measurement of current through the conductor in their center.

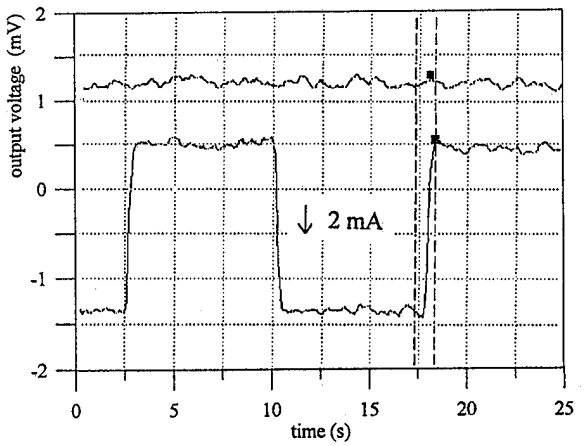


FIG. 7. Output noise of the current meter from Fig. 6: zero output in shielding (upper trace) and response to 2 mA current step (lower trace).

array axis causes a maximum error of 20 mA depending on the angular position. The Earth's field caused a maximum error of 15 mA. Most of this error is due to the sensor array imbalance caused by tolerances of individual sensor sensitivities, which were from 1.08 to 1.29 mV/A. Further improvement is expected to be achieved by adjusting the individual sensor sensitivities and by the use of flipping for the stabilization. The current resolution achieved is shown in Fig. 7: The sensor's own noise is equivalent to 0.1 mA p-p. This makes the sensor worth further development, as the commercially available dc current clamps using Hall sensors in the air gap have only 10 mA resolution.

This work was supported by the Grant Agency of the Czech Republic under No. 102/93/1197.

[1] J. P. J. Groenland, C. J. M. Eijkel, J. H. J. Fluitman, and R. M. de Ridder, Sensors Actuators A **30**, 89 (1992).
[2] M. Vieth, H. Berg, and W. Bartsch, IEEE Trans. Magn. **30**, 939 (1994).
[3] N. Smith, F. Jeffers, and J. Freeman, J. Appl. Phys. **69**, 5082 (1991).
[4] E. Paperno and B. Z. Kaplan, Proc. Imeko TC-4 Symposium, Prague 1995, p. 123.
[5] P. Ripka, Sensors Actuators A **42**, 394 (1994).

Magnetic field distribution caused by a notebook computer and its source searching

T. Doi, S. Hayano, and Y. Saito
College of Engineering, Hosei University, Koganei, Tokyo 184, Japan

Previously, we have proposed a method of solution for the inverse problems, and successfully applied it to the biomagnetic fields. In the present article, we apply our inverse approach to the leakage magnetic field source searching for the notebook computers. As a result, it is found that our inverse approach is quite effective in searching for the leakage magnetic field source. The validity of our solutions is carefully examined by comparing the measured and calculated magnetic field distributions. © *1996 American Institute of Physics.* [S0021-8979(96)53108-4]

In order to prevent the misoperation and mutual action among the electronic devices, a magnetic shielding is one of the key techniques in the electromagnetic compatibility (EMC) field. Searching for the magnetic field source from locally measured magnetic fields is reduced into the solution of an inverse problem. Inverse problems are classified into two major categories, i.e., one is the inverse parameter problem[1] and the other is the inverse source problem.[2–4] In order to shield the leakage electromagnetic field from the electronic devices effectively, it is essential to solve the inverse field source problem.

Previously, we have proposed the sampled pattern matching method as a method of solution for the inverse problems, and we have applied it to the biomagnetic fields as well as conventional nondestructive testing problems.[1–4]

In the present article, we measure the magnetic field above the keyboard of a notebook computer as well as a typical example of electronic devices. And we apply our inverse approach to the leakage magnetic field source searching of the notebook computers.

Most of the inverse problem in the electromagnetic fields reduces to solving for a following governing equation

$$\mathbf{X}_p = \int_v G\mathbf{Y}_s dV, \tag{1}$$

where $\mathbf{X}_p$, $\mathbf{Y}_s$, G, and V are the known field vector, unknown source vector, Green's function or its space derivative, and volume containing the unknown source vector, respectively.

In the sampled pattern matching (SPM) method, we assume that the magnitude of a field source at each position can be represented by the space occupying rate of unit source. This means that the governing Eq. (1) is assumed to be modified into

$$\mathbf{X}_p^{[N]} = \int_p G^{[N]} \boldsymbol{\delta} dP, \tag{2}$$

where superscript $[N]$ refers to the normalized quantities. Also, $\boldsymbol{\delta}$ and P are the vector delta function representing the source vector $\mathbf{Y}_s$ and $(|G|/|\mathbf{X}_P|)V$, respectively.

Physically, this transformation corresponds to the pulse width modulation (PWM) technique in power electronic engineering. Representation of the space occupying rate of unit source is one of the key ideas of the sampled pattern matching method.

Discretizing Eq. (2), we have

$$\mathbf{X}_p^{[N]} = \sum_{i=1}^{m} \Delta P_i \mathbf{G}_i^{[N]} = D\mathbf{P} \tag{3a}$$

$$\begin{bmatrix} \Delta X_{p1} \\ \Delta X_{p2} \\ \vdots \\ \Delta X_{pn} \end{bmatrix} = \begin{bmatrix} G_{11} & G_{12} & \cdots & \cdots & G_{m1} \\ G_{21} & G_{22} & \cdots & \cdots & G_{m2} \\ \vdots & \vdots & \ddots & & \vdots \\ G_{n1} & G_{n2} & \cdots & \cdots & G_{nm} \end{bmatrix} \begin{bmatrix} \Delta P_1 \\ \Delta P_2 \\ \vdots \\ \vdots \\ \Delta P_m \end{bmatrix}, \tag{3b}$$

where m denotes a number of subdivisions of the field source existing space. Denoting n as a number of field measured points (i.e., the order of vector $\Delta\mathbf{X_P}$), D becomes an n by m rectangular system matrix composed by the column vectors $\mathbf{G}_i^{[N]}(i=1,2,\cdot,m)$, and $\mathbf{P}$ is a mth order PWM field source vector whose element is $\Delta P_i(i=1,2,\cdot,m)$.

In order to evaluate the vector $\mathbf{P}$ in a least-squares sense, multiplication of D^T to both sides of Eq. (3a) yields

$$D^T \Delta\mathbf{X}_\mathbf{P}^{[N]} = D^T D\mathbf{P} \tag{4}$$

or

$$\mathbf{P} = |D^T D|^{-1} D^T \Delta\mathbf{X}_\mathbf{P}^{[N]}. \tag{5}$$

From Eq. (5), it seems able to evaluate the solution vector $\mathbf{P}$. But, this is practically difficult, because the column vectors $\mathbf{G}_i^{[N]}(i=1,2,\cdot,m)$ constituting the system matrix D are not linear independent. In other words, the elements of matrix D have been obtained by discretizing the same continuous function G, so that the matrix D^TD becomes a singular matrix. Thus, it is difficult to evaluate the vector $\mathbf{P}$ by means of the conventional least-squares fit.

Consideration of the matrix D^TD in (4) reveals that the diagonal elements take 1 but the other elements are always less than 1 because each of the column vectors $\mathbf{G}_i^{[N]}(i=1,2,\cdot,m)$ in D is normalized. Thereby, the matrix D^TD may be regarded a unit matrix with order m. This assumption means that Eq. (4) yields an approximate solution of $\mathbf{P}$, which coincides with those of a factor analysis. Further consideration of Eq. (4) suggests that the elements in (4) take values between -1 and 1. Namely, the elements $\Delta P_i,(i=1,2,\cdot,m)$ in the vector $\mathbf{P}$ are

$$\Delta P_i = \mathbf{X}_p^T \cdot \mathbf{G}_i / [\|\mathbf{X_p}\| \ \|\mathbf{G}_i\|], \quad i=1,2,\cdots,m, \tag{6}$$

where the elements $\Delta P_i(i=1,2,\cdot,m)$ of $\mathbf{P}$ are called the *pattern matching figures.*

 0021-8979/96/79(8)/5214/3/$10.00 © 1996 American Institute of Physics

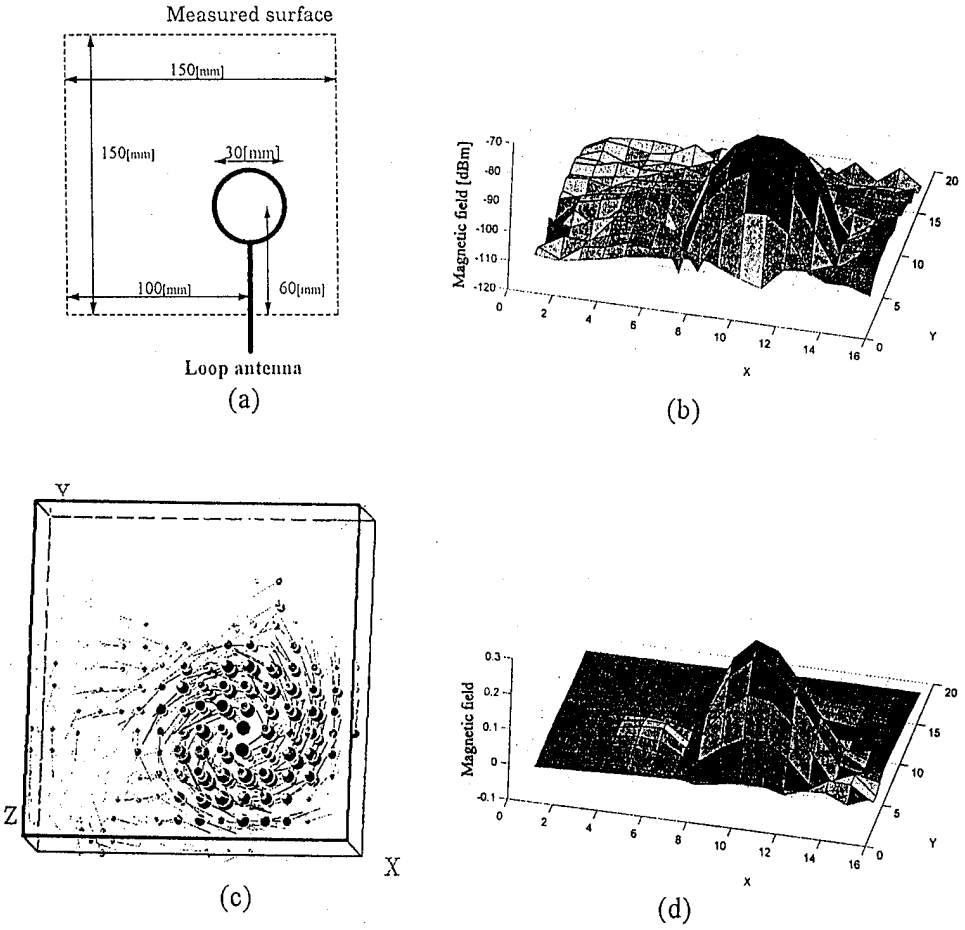


FIG. 1. An experimental result of the field source searching. (a) Schematic diagram of a loop antenna, (b) measured magnetic field distribution above the loop antenna, (c) estimated current distribution, and (d) reproduced magnetic field distribution by the currents in (c).

Since we have to decide the existence of vector delta function δ in (2) by the least-squares sense, the SPM method assumes that only one element taking the maximum pattern matching figure in Eq. (6) has a unit vector delta function. If the ΔP_h takes the maximum, then this point h is the *first pilot point* and its associated pattern vector $\mathbf{G}_h$ is called the *first pilot pattern.*

The second pilot point is decided as the maximum element of

$$\Delta P_{hi}=\mathbf{X}_p^T\cdot(\mathbf{G}_h+\mathbf{G}_i)/[\|\mathbf{X}_\mathbf{p}\|\ \|\mathbf{G}_h+\mathbf{G}_i\|],$$
$$i=1,2,\cdots,m;i\neq h. \tag{7}$$

The similar processes of Eqs. (6) and (7) are continued until the peak value of the pattern matching figure is obtained. Finally, the field source $\mathbf{Y}_\mathbf{s}$ is transformed into the PWM field source pattern $\mathbf{P}$.

As shown above, one of the merits of the SPM method is that the SPM method gives a most dominant solution against a locally measured field pattern. For further details of the SPM method, see Refs. 1–4.

One of the problems of the field source searching is the validity of the solutions. In order to check the validity of solutions, a simple experimental example demonstrates the validity of the SPM method.

First, we measured the magnetic field having 75 MHz frequency above the loop antenna. Figures 1(a) and 1(b) show the schematic field distribution, respectively. The magnetic field above the loop antenna was measured with the spectrum analyzer. The 75 MHz current flows in the loop antenna. The magnetic fields at 256 (16×16) equispaced locations above the loop antenna were measured. Second, we applied the SPM method to this magnetic field. Figures 1(c) and 1(d) show the obtained current distribution from the locally measured magnetic field in Fig. 1(b) and the reproduced magnetic field distribution calculated from the currents in Fig. 1(c), respectively.

Obviously, the results in Fig. 1 suggest that the SPM method is capable of estimating the global magnetic field source distribution. Thus, the SPM method is a useful solution strategy for the leakage magnetic field source searching from the electronic devices.

We measure the leakage magnetic fields for the two types of notebook computers. One is operating at 75 MHz, and the other is operating at 100 MHz CPU frequency. Both the computers equipped the INTEL DX4 CPU.

The magnetic fields above the keyboards were measured with a spectrum analyzer under the full CPU condition.

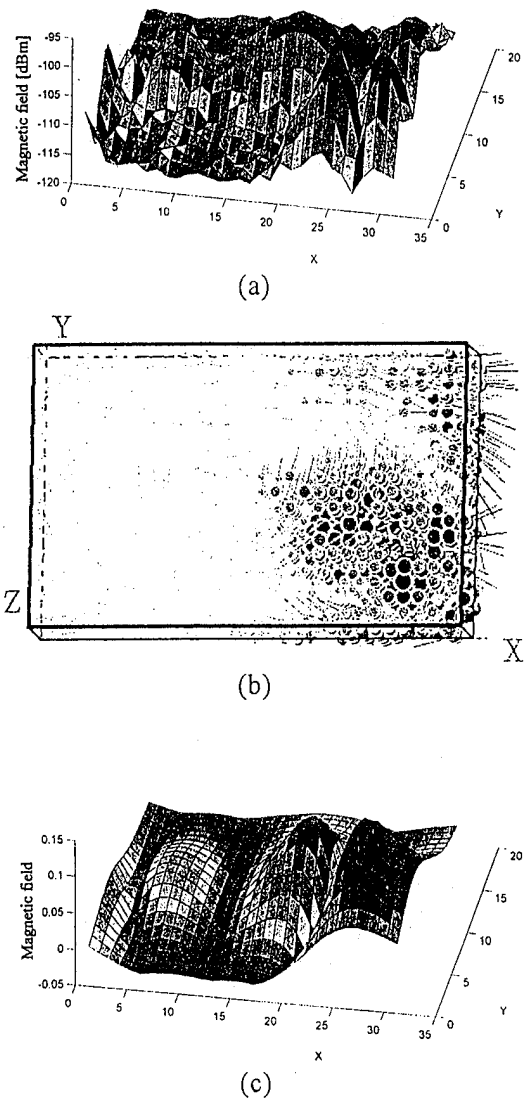


FIG. 2. The leakage magnetic field source distribution searching of the notebook computer operating at 75 MHz CPU frequency. (a) The measured magnetic field distribution, (b) the estimated current distribution, and (c) the reproduced magnetic field distribution calculated by the currents in (b).

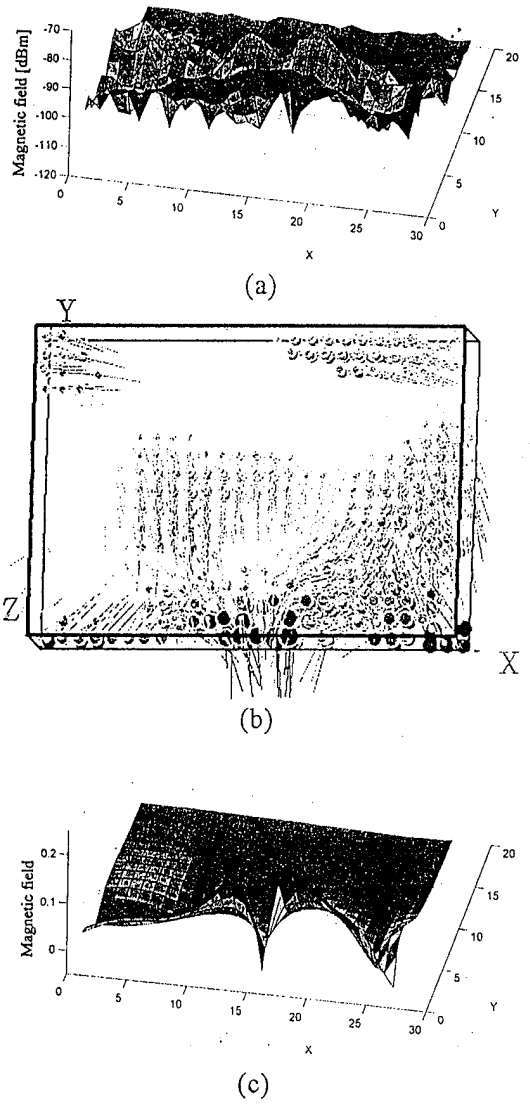


FIG. 3. The leakage magnetic field source distribution searching of the notebook computer operating at 100 MHz CPU frequency. (a) The measured magnetic field distribution, (b) the estimated current distribution, and (c) the reproduced magnetic field distribution calculated by the currents in (b).

Figure 2(a) shows the measured magnetic field distribution having 75 MHz. Figures 2(b) and 2(c) show the estimated current distribution and the reproduced magnetic field distribution calculated by the currents in Fig. 2(b), respectively. The results in Fig. 2 suggest that the magnetic field source measured above the keyboard is roughly classified into two parts; one is the CPU and the other is the power supplier. Thus, the magnetic shielding should be carried out mainly to these two parts.

Figure 3(a) shows the measured magnetic field distribution having 100 MHz. Figures 3(b) and 3(c) show the estimated current distribution and the reproduced magnetic field distribution calculated by the currents in Fig. 3(b), respectively.

The results in Fig. 3 suggest that the magnetic field source measured above the keyboard is mainly caused by two parts: one is the power supplier and the other is the signal flowing line to the display. Thus, the magnetic shielding of this computer should be carried out mainly to the power supplier and the line connecting from the CPU to the display.

In the present article, the validity of our inverse solution method has been carefully checked by means of the simple loop antenna. Further, it has shown that the different parts become the leakage magnetic field source depending on the circuit structure, and the common leakage magnetic field source of the two types of computers is the power supplier. This means that the magnetic shielding of any notebook computers should be carried out to the power supplier.

[1] T. Doi, S. Hayano, I. Marinova, N. Ishida, and Y. Saito, J. Appl. Phys. **75**, 5907 (1994).
[2] Y. Saito, E. Itagaki, and S. Hayano, J. Appl. Phys. **67**, 5830 (1990).
[3] H. Saotome, K. Kitsuta, S. Hayano, and Y. Saito, IEEE Trans. Magn. **MAG-29**, 1389 (1993).
[4] H. Saotome, T. Doi, S. Hayano, and Y. Saito, IEEE Trans. Magn. **MAG-29**, 1861 (1993).

Highly sensitive magneto-optic transverse Kerr effect measurement system for the detection of perpendicular anisotropy and magnetic phases in thin films

J. A. Corrales, M. Rivas, J. F.-Calleja, I. Iglesias, and M. C. Contreras
Departamento de Física, Universidad de Oviedo, 33007 Oviedo, Spain

Transverse biased initial susceptibility (TBIS) measurements were made using a magneto-optical Kerr effect system on samples that exhibited an in-plane and a perpendicular anisotropy. A change in the slope of both the inverse transverse susceptibility and the hysteresis loop is observed at a certain value of the applied in-plane field H_s. At values of the applied field higher than H_s the magnetization lies in the plane of the film; at values lower than H_s an out-of-plane component appears. By performing TBIS measurements we can also detect different micromagnetic phases magnetically uncoupled with different values of the anisotropy field. The occurrence of a downwards curvature in the inverse susceptibility when the dc field is applied along the hard axis together with the multiple minima when the dc field is applied along the easy axis can be explained by the existence of weakly coupled micromagnetic phases. © *1996 American Institute of Physics.* [S0021-8979(96)53208-7]

INTRODUCTION

Reflection magneto-optical effects are useful for obtaining information about the magnetization process that occurs on the sample surface.[1,2] In the case of thin films thinner than 1000 Å in which there is no appreciable variation of the magnetic structure through the thickness, the magneto-optical effects provide complete information.

Magnetic films often show magnetic uniaxial anisotropy. The origin of such an anisotropy depends on the physical structure of the sample and in some cases it is a source of controversy, because there are several factors that can influence it simultaneously (magnetostriction, stresses, inhomogeneities, etc.).

It is experimentally observed that such a uniaxial behavior is not uniform all over the sample. There are macroscopical anisotropy fluctuations, that intuitively would correspond to macroscopically uniaxial regions of the sample for which the magnitude as well as the easy direction of the anisotropy changes from one region to the other. This long-range fluctuation is known as "skew" and can be studied from the transverse susceptibility.[3,4]

Also, in polycrystalline and amorphous soft thin films the direction of local magnetization fluctuates from place to place. This short-range dispersion is caused by microscopical local anisotropy mainly due to structural and composition inhomogeneities and is known as "ripple." This ripple is predicted by the micromagnetic theories and observed experimentally by Lorentz microscopy.[5] In the case of polycrystalline films this would correspond to the fact of being constituted by crystallites whose size is about a few hundreds of Å and in the case of amorphous films to the presence of slight local variations in the composition, in regions whose size goes from tens to hundreds of Å. The magnitude of the ripple can be studied from the transverse susceptibility.[3]

In conclusion, to understand the relationship between the physical structure and the magnetic properties of thin films it is very useful to use an experimental system that provides as much information as possible about the processes that take place in real films.

PRINCIPLES OF THE EXPERIMENTAL TECHNIQUE

In a first-order approximation, the transverse Kerr effect consists of a small change in the reflectivity of p-polarized light proportional to the part of the magnetization that runs on the plane of the sample and perpendicular to the plane of the incident light. So any change of this component of the magnetization induces a proportional change in the intensity of the reflected light that can be detected by a photodiode with a linear response.

Transverse susceptibility is measured by applying two magnetic fields in the plane of the film: a dc bias field H_{dc} parallel to the plane of incidence of light from 10 H_k (to ensure saturation) to 0 and a sinusoidal field h_{ac} of small amplitude perpendicular to H_{dc}. The modulated Kerr signal is proportional to the component of the magnetization parallel to h_{ac}, δM. For the signal to be proportional to the initial susceptibility the amplitude of h_{ac} must be chosen small enough to ensure that we are working in the Rayleigh region of the sample, where the magnetization process is reversible and linear. In that case the variation of δM follows a sinusoidal law of the same frequency as h_{ac}. Typically we have $h_{ac} \approx 1\%\ H_k$. The working frequency was chosen to be different from that typical of electrical noise and its harmonics, in our case 127 Hz.

The light source was a halogen lamp (12 V, 50 W). The diameter of the spot on the sample was 3 mm.

The measured Kerr signal U is proportional to the transverse susceptibility: $U = k\chi_t$ with k a proportionality constant.

For the quantitative evaluation of the microscopic local anisotropy fluctuations, the dynamic differential susceptibility measurement proposed by Hoffmann is used.[3] The inverse of the Kerr signal obtained experimentally is expressed as

 0021-8979/96/79(8)/5217/3/$10.00 © 1996 American Institute of Physics

$$U^{-1}(\beta)=k(\beta)\frac{H_k}{M_s}[(h\pm 1)+b(h\pm 1)^{-1/4}+c(h\pm 1)^{-1}], \tag{1}$$

where the plus sign corresponds to $\beta=0$ (dc bias field applied along the easy axis) and the minus sign to $\beta=\pi/2$ (dc bias field applied along the hard axis) and $h=H_{dc}/H_k$. The first term in Eq. (1) corresponds to the coherent rotation process (Stoner–Wohlfarth model), the second describes the contribution of the ripple related to short-range fluctuations of the magnetization, and the third term is the "skew" term caused by long-range fluctuations of the magnetic anisotropy.

These coefficients are given by[3]

$$b=\left(\frac{1}{4\pi\sqrt{2}}\right)S^2M_s\sqrt{t}/(AK_u)^{5/4}, \tag{2}$$

$$c=3\langle\theta^2\rangle \tag{3}$$

with $\langle\theta^2\rangle$ the mean square value of the skew angle.

Here, M_s, t, A, and K_u are the saturation magnetization, film thickness, exchange constant, and uniaxial magnetic anisotropy of the films, respectively. S is called the structure constant, which corresponds to the magnitude of short-period local anisotropy fluctuations.

All the films under study in this work were deposited by sputtering. All of them present an in-plane uniaxial anisotropy.

EXPERIMENTAL RESULTS

In certain alloys in which different magnetic phases may appear it is not certain that Hoffmann's model for transverse susceptibility can be successfully applied. In other cases, the occurrence of a perpendicular component of the magnetization may also provoke the failure of the theory.

However, we can still use the magneto-optical Kerr effect (MOKE) to measure the transverse bias initial susceptibility (TBIS). It is noteworthy that the TBIS measurement is more sensitive than the measurement of the hysteresis loop: The easy axis and the anisotropy field can be determined very precisely and moreover short- and long-range magnetization fluctuations can be distinguished and quantified.

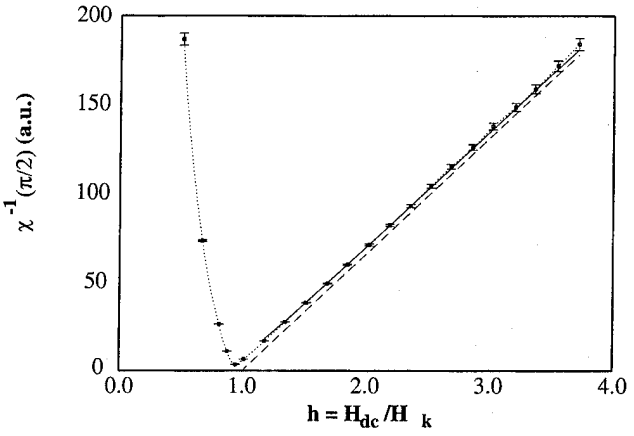


FIG. 1. $\chi^{-1}(\pi/2)$ vs h curves. Squares correspond to the experimental data; the solid line corresponds to the theoretically predicted curve with $b=0.06$ and $c=0$; the dashed line corresponds to the prediction from the coherent rotation model. The dotted line is a guide for the eye.

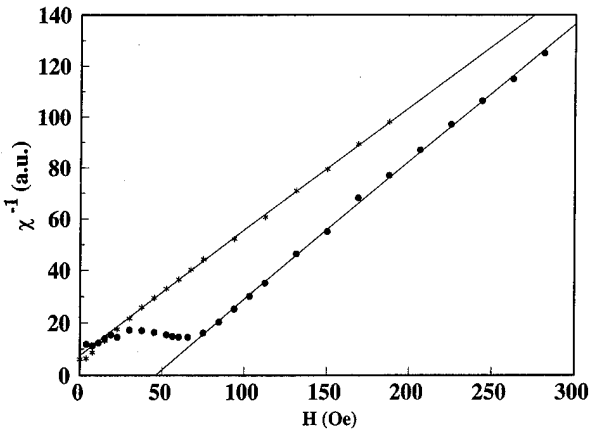


FIG. 2. Experimental $\chi_{t,\beta}^{-1}$ vs H and linear extrapolations for $Ni_{91}Y_9$. Circles represent $\beta=\pi/2$ and asterisks $\beta=0$.

Figure 1 shows the behavior of the inverse of the transverse susceptibility of a film that obeys the theory proposed by Hoffmann with negligible skew.[6] In Fig. 2 we report the inverse of the transverse susceptibility for a film of $Ni_{91}Y_9$ that shows a gradient in composition across the sample area. Figures 3 and 4 correspond to two different zones of the same sample named A and B.

This behavior may be phenomenologically justified by a model in which the basic hypothesis is the existence of micromagnetically ordered regions isolated in a nonmagnetic matrix. Each region must have an easy direction of the magnetization and an anisotropy constant K_R. The spatial distribution of the easy directions is aleatory, all directions are equally probable, and there is no appreciable magnetic interaction among regions, so the global behavior of the transverse susceptibility of the sample may be analyzed from the individual contributions of each ordered region. In such a case the film would present an isotropic behavior, existing a linear relation between χ_t^{-1} and bias field H for H high enough (strictly for $H\to\infty$) and a maximum in the susceptibility for a value of H close to $H_{kR}=2K_R/M_{sR}$ (M_{sR} being

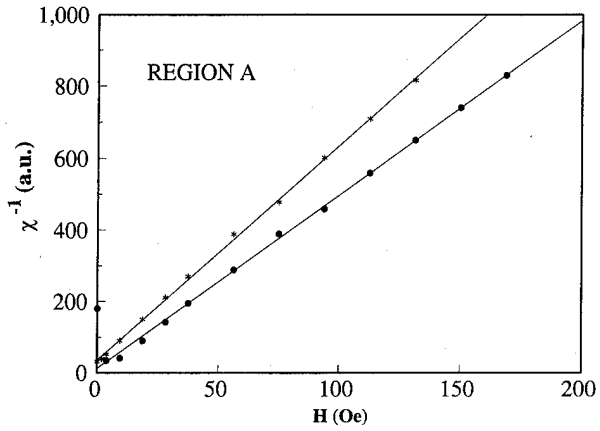


FIG. 3. Experimental $\chi_{t,\beta}^{-1}$ vs H and linear extrapolations for the more isotropic region of the film $Ni_{91}Y_9$. Circles represent $\beta=\pi/2$ and asterisks $\beta=0$.

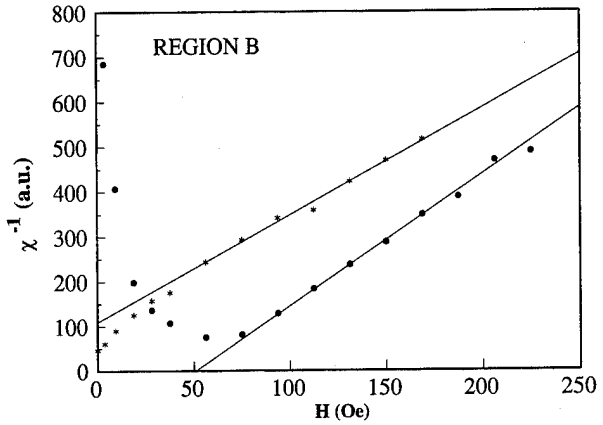


FIG. 4. Experimental $\chi_{t,\beta}^{-1}$ vs H and linear extrapolations for the more anisotropic region of the film $Ni_{91}Y_9$. Circles represent $\beta=\pi/2$ and asterisks $\beta=0$.

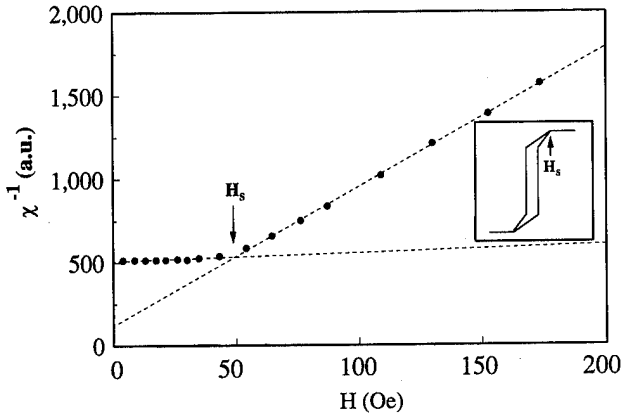


FIG. 5. χ^{-1} vs H for a film with perpendicular anisotropy. The inset shows the hysteresis loop.

the saturation magnetization of each micromagnetic region). This is due to the contribution to total susceptibility measured in any direction of the region in which the easy axis is perpendicular to the applied field H.

Real films are not always isotropic but present an anisotropic behavior that must be associated to a macroscopic anisotropy in each region induced by the fabrication process.

In Fig. 2 both $\chi_{t\pi/2}^{-1}$ and χ_{t0}^{-1} vs H curves show a minimum at different values of the bias field. The occurrence of the downwards curvature of χ_{t0}^{-1} in the range of low magnetic fields, together with the multiple minima in $\chi_{t\pi/2}^{-1}$ (regions A and B) can be explained by two micromagnetic phases weakly coupled. The two regions show two different values of H_k. These values are $H_k=45.9$ Oe corresponding to an anisotropic region (Fig. 4) and $H_k=6.9$ Oe for a more isotropic one (Fig. 3); the latter shows large magnetization dispersion, i.e., linear extrapolations asymmetrically cut the abscissa and both χ_{t0}^{-1} and $\chi_{t\pi/2}^{-1}$ show a minimum at nearly the same value of the bias field.

The occurrence of a uniaxial anisotropy whose easy axis is normal to the plane of the film is a fact often observed in magnetically ordered thin films. Above a certain critical value of the thickness[7] and depending on the existence of stresses, magnetostriction, etc., magnetic films may present a domain structure with stripe domains in which the local magnetization has components of alternating sign normal to the plane of the film in addition to in-plane component.

Kerr magnetometers have been suggested as a good substitute for conventional magnetometers for measuring perpendicular anisotropy.[2,8,9] TBIS measurements can be used as an alternative technique, as we will show.

Let us describe in a phenomenological way the influence of a perpendicular component of magnetization on the behavior of transverse susceptibility.

In these cases characteristic loops present a change in the slope for $H=H_s$. Figure 5 represents the inverse of the susceptibility versus the bias field for a film with perpendicular anisotropy and the associated hysteresis loop. Here we can see that at high values of dc bias field the magnetization is kept in the plane until the field is reduced below the saturation field, H_s. From this we may see that H_s can be estimated from the change in the slope of this representation as well as from the hysteresis loop with the important advantage that the TBIS measurement is much more sensitive than the measurement from the loop.

This behavior can be explained by the combination of two effects: On one side, the decrease of the magnitude of the magnetization in-plane component, as H decreases below the saturation field, H_s. H_s corresponds to the value of H above which the magnetization lies in the plane of the film and so the existence of the stripe domains and related phenomena disappear. On the other hand the effect of the anisotropy related to the direction of the stripe domain structures characterized by an out-of-plane component of the local magnetization must increase when H is diminished below H_s. Both effects contribute to the change in the slope of $\chi_{t\beta}^{-1}$ for $H=H_s$ and are difficult to separate *a priori*.

To summarize, TBIS measurements by MOKE can be used to detect different amorphous micromagnetic phases in a film allowing us to measure the anisotropy field of each separately. In the case of the existence of perpendicular anisotropy this technique can be used as an alternative technique to estimate a value of the perpendicular anisotropy field.

ACKNOWLEDGMENTS

This work was partially supported by the Comisión Interministerial de Ciencia y Tecnología (CICYT) MAT93-1431 and the University of Oviedo DF/95-214-3.

[1] M. Corke, A. W. J. Dawkins, and R. B. Inwood, J. Phys. E Sci. Instrum. **15**, 251 (1982).
[2] R. Carey, D. M. Newman, and B. W. J. Thomas, J. Phys. D Appl. Phys. **26**, 839 (1993).
[3] H. Hoffmann, Phys. Status Solidi **33**, 175 (1969).
[4] J. M. Alameda, M. C. Contreras, and H. Rubio, Phys. Status Solidi A **85**, 511 (1984).
[5] H. W. Fuller and M. E. Hale, J. Appl. Phys. **31**, 238 (1960).
[6] G. Suran, H. Ouahmane, I. Iglesias, M. Rivas, J. A. Corrales, and M. C. Contreras, J. Appl. Phys. **76**, 1749 (1994).
[7] Y. Murayama, J. Phys. Soc. Jpn. **21**, 2253 (1966).
[8] D. J. Mapps, N. Mahvan, and S. Warner, IEEE Trans. Magn. **MAG-23**, 2590 (1987).
[9] W. Geerts, C. Lodder, and T. Popma, J. Magn. Magn. Mater. **137**, 224 (1994).

First-order magnetic phase transition in (Er, Tb)M_2(M=Co, Ni) (abstract)

A. Y. Takeuchi, F. Garcia, and S. F. da Cunha
Centro Brasileiro de Pesquisas Físicas-CBPF/CNPq, r. Dr. Xavier Sigaud 150, CEP-22290-Rio de Janeiro,RJ-Brazil

The rare-earth intermetallic compounds RCo_2, cubic Laves phases, are very suitable to study the magnetism of the 3*d*. Depending on the R magnetism we have an induced moment for the Co. For R=Dy, Ho, or Er the magnetic transition is of first order, whereas for Gd and Tb it is of second order. This behavior has been observed in this work by electrical resistivity and dc magnetization measurements in function of concentration in the system $(Er_{1-x}Tb_x)Co_2$ where the internal field of the nearest R neighbors can induce the Co moment. Magnetization measurements of field cooling (FC) and zero field cooling (ZFC) samples are different for $T<T_c$. This difference collapses for higher applied magnetic fields. The minimum[1] for T just above T_c in ρ vs T curves disappears for $x=0.2$ with the onset of the second-order transition up to $x=1.0$. This minimum can result from the conduction electrons scattering on the spin fluctuations, enhanced by the 4*f* moments and the scattering by phonons. The idea of the metamagnetism of Co moments in the origin of this minimum is discarded. From our results we can conclude that a small amount of Tb in $ErCo_2$ changes the first-order to second-order transition. Since the localization of the Fermi energy in the density of state of the 3*d* band is very important, a comparison study has been done with the system $(Er_{1-x}Tb_x)Ni_2$. The concentration dependence of the lattice parameter differs a little from Vegard's law. Here we can infer from our results that all the magnetic transitions are second-order type. © *1996 American Institute of Physics.* [S0021-8979(96)42708-7]

[1]N. H. Duc *et al.*, J. Phys. F: Met. Phys. **18**, 275 (1988).

 0021-8979/96/79(8)/5220/1/$10.00 © 1996 American Institute of Physics

Magnetism in URhSi

K. Prokeš, E. Brück, K. H. J. Buschow, and F. R. de Boer
Van der Waals-Zeeman Institute, University of Amsterdam, 1018 XE Amsterdam, The Netherlands

V. Sechovský and P. Svoboda
Department of Metal Physics, Charles University, 12116 Prague 2, The Czech Republic

X. Hu and H. Maletta
BENSC, Hahn-Meitner Institute GmbH, 14109 Berlin 39, Germany

T. J. Gortenmulder
Kamerlingh Onnes Laboratory, University of Leiden, 2300 RA Leiden, The Netherlands

Our neutron-powder-diffraction experiment revealed that URhSi crystallizes in the orthorhombic TiNiSi (space group *Pnma*) structure and orders ferromagnetically at low temperatures with the U magnetic moments of 0.11 μ_B aligned along the c axis. Anomalies in the temperature dependence of the magnetic susceptibility, specific heat and electrical resistivity indicate that URhSi orders below 9.5 K. The enhanced C_p/T value (extrapolated to 0 K) of 186 mJ/mol K^2 can be partially reduced in magnetic fields, which indicates a considerable magnetic contribution even at very low temperatures. The ferromagnetic ground state is documented also by magnetization measurements at low temperatures. The high-field magnetization data obtained on oriented powder reveal a strong magnetocrystalline anisotropy. All the results obtained on polycrystalline samples classify URhSi as an itinerant $5f$ ferromagnet with very reduced U magnetic moments. © *1996 American Institute of Physics.* [S0021-8979(96)18408-8]

I. INTRODUCTION

The literature reports for URhSi either the $CeCu_2$ type structure[1,2] (space group *Imma*) or its ordered version of the TiNiSi type[3] (*Pnma*) similar to a number of other equiatomic ternary UTX (T=transition metal, X=Si or Ge) compounds.[4] The differences between the x-ray or neutron-diffraction patterns for the two types of structures can be sometimes easily overlooked because the extra reflections, which appear for the ordered ternary version, are usually very weak. In both structures, the U atoms are coordinated in zigzag U chains within which each U atom has two nearest U neighbors at a distance of d_{U-U}~350 pm. In Hill's classification,[5] such a value of d_{U-U} means that these compounds are situated in a critical region between localized and itinerant $5f$ electron behavior. The present contribution involves the determination of the type of the crystal structure and the magnetic ground state in the context of magnetic, transport and thermal properties.

II. EXPERIMENT

A polycrystalline sample of URhSi has been prepared by arc-melting stoichiometric amounts of the constituting elements of at least 99.9% purity under an argon atmosphere and subsequently annealed for four weeks at 900 °C under vacuum. The purity and the composition homogeneity were checked by x-ray diffraction and by electron-microprobe analysis. The average composition of the major phase in the sample is deviating from the stoichiometric composition by less than 0.9 at. %. Nevertheless, a slight amount of URh_2Si_2 could be traced by the electron-microprobe analysis.

The magnetic susceptibility (M/H) in the temperature region 10–300 K and the low-temperature (down to 2 K) magnetization curves were measured in a Quantum Design SQUID magnetometer in magnetic fields up to 5 T on a fine-powder sample with grains fixed in random orientation by diamagnetic glue.

The specific heat was measured by a standard semiadiabatic method in the temperature region 1.6–250 K and compared with the previous results[3] from the temperature region 1.3–40 K.

The electrical resistivity was measured on a small bar-shaped sample by standard ac four-point method. Assuming large errors in the geometrical factor (in addition to the expected influence of internal microcracs) only the normalized electrical resistivity $\rho/\rho_{300\ K}$ is presented.

Neutron-diffraction data at 2.8, 24, and 80 K were obtained using the neutron powder diffractometer E6 installed at the Hahn–Meitner Institute using an incident neutron wavelength of 2.386 Å. For these measurements URhSi was powdered and encapsulated into a vanadium container under He atmosphere. The recorded spectra were analyzed by means of the Rietveld profile procedure[6] using the program FULLPROF.[7] The neutron-scattering lengths were taken from Sears[8] and uranium magnetic form factor from Delapalme.[9]

III. BULK MEASUREMENTS

The susceptibility (Fig. 1) is nearly field independent above 30 K. Below this temperature, the magnetization curves (Fig. 2) become progressively curved reflecting increasing ferromagnetic correlations.

The $1/\chi$ vs T dependence above 150 K is nearly linear and satisfies Curie–Weiss (CW) law

$$\chi = C/(T-\Theta_p) \tag{1}$$

with $C=(1.268\pm0.008)\cdot10^{-5}$ m^3/mol K ($\mu_{\text{eff}}=2.84\pm0.01$ μ_B/U atom) and $\Theta_p=-164.3\pm0.9$ K.

 0021-8979/96/79(8)/5221/3/$10.00 © 1996 American Institute of Physics

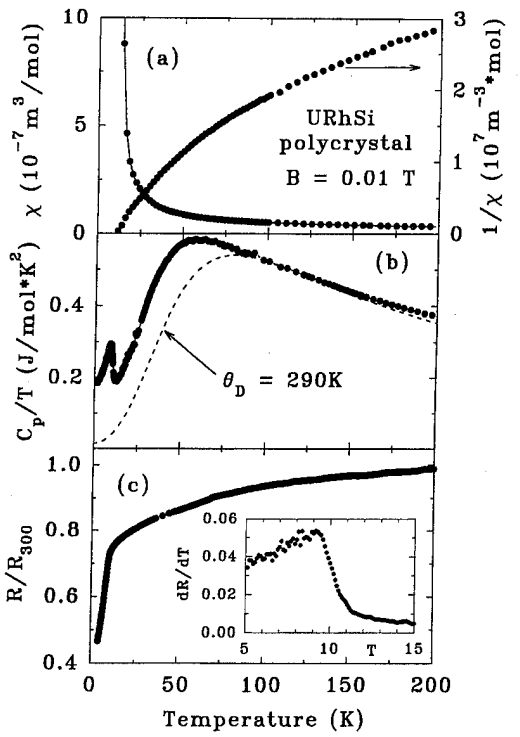


FIG. 1. Temperature dependences of the magnetic susceptibility measured in 0.01 T together with its reciprocal value (a), the specific heat in the representation C_p/T vs T (b) and the electrical resistivity of URhSi together with the temperature derivative of the electrical resistivity in the inset (c).

The strongly nonlinear part between 20 and 150 K can be roughly approximated by a modified CW law including a temperature independent term χ_0

$$\chi = C/(T-\Theta_p)+\chi_0 \tag{2}$$

with significantly lower value of Curie constant, a positive paramagnetic Curie temperature of 9.7 K and $\chi_0 \sim 10^{-8}$ m^3/mol. Although, the applicability of both approaches for polycrystalline data of an anisotropic material is rather questionable some tentative conclusions can be made. The value

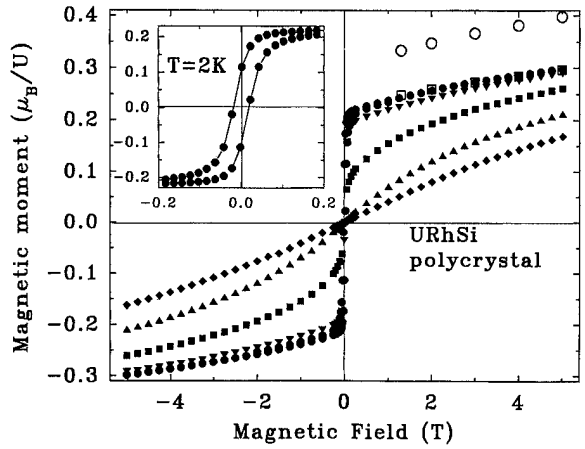


FIG. 2. Field dependence of the magnetization of the fixed powder of URhSi at various temperatures: 2 K (●), 5 K (▼), 10 K (■), 15 K (▲), and 20 K (◆). Some of the previous data measured at 4.2 K are also shown: free powder (○) and fixed powder (□).

of the effective moment from the high temperature fit, which can be taken as the upper limit in this material is much lower compared to free ion U^{3+} or U^{4+} expectation values in localized systems. We can take it as a good evidence of delocalization of $5f$ moments in the present system. The drastically different Θ_p values from the high- and low-temperature region point to very strong magnetocrystalline anisotropy in the paramagnetic range.

The magnetic ordering at T_C=9.5 K is reflected by a relatively broad peak in the C_p/T vs T curve [Fig. 1(b)]. No other anomalies are seen between 1.6 and 250 K. The linear extrapolation of C_pT vs T^2 from the region 1.6–8 K to T=0 K gives a tentative γ value of 185.6±1.3 mJ/mol K^2. A much better fit can, however, be obtained by the formula

$$C/T = \gamma+\beta^*T^2+\delta^*T^2\ \ln(T) \tag{3}$$

which involves the contribution of spin fluctuations through the additional logarithmic term. For the temperature region 1.6–9 K, the fitting parameters: γ=180.9±0.6 mJ/mol K^2, β^*=2.4±0.1 mJ/mol K^4 and δ^*=−0.5±0.05 mJ/mol K^4 ln K were obtained. To estimate the magnetic entropy we tried to subtract the Debye function with a probable value of Debye temperature Θ_D. This task turns out to be very difficult. It seems impossible to assign one single value of Θ_D. The best agreement in the high-temperature part can be obtained for Θ_D=290 K together with the assumption of γ=20 mJ/mol K^2. In this way, we obtained by integrating $(C/T-C_{\text{Debye}}/T)$ in the temperature region 0–100 K, a value of 9.1 J mol^{-1} K^{-1} for the magnetic entropy. This means a value of 1.58 R ln 2 or, through the expression R ln$(2J+1)$, a value for J of 1.0. In fact, this value represents the estimated upper limit. The magnetic entropy connected with the magnetic transition is only a very small fraction of this value, the rest originates most probably from magnetic fluctuations.

The onset of magnetic ordering at T_C=9.5 K is reflected also by the maximum in the temperature derivative of the electrical resistivity [Fig. 1(c)] near this temperature. The resistivity in the paramagnetic range is slightly decreasing with lowering temperature. It drops significantly below T_c, where also a quadratic temperature dependence with normalized parameters ρ_0=0.4088±0.0004 and the quadratic coefficient A=3.292±0.009·10^{-3} K^{-2} is observed.

The high-field magnetization[6] measured at 4.2 K up to 35 T on a field-aligned powder sample saturates slowly and at 35 T it reaches 0.67 μ_B/f.u. (M_{free}). A value of 0.31 μ_B/f.u. is obtained by extrapolation to zero magnetic field. For a powdered sample with randomly oriented grains, somewhat smaller values of 0.52 μ_B/f.u. (M_{fix}) and 0.23 μ_B/f.u., respectively, are recorded. Although the magnetization is by far not yet saturated in 35 T the ratio $M_{\text{free}}/M_{\text{fix}}$=0.78 can be taken as a supporting indication for an easy-plane anisotropy.

The low-field magnetization measured at different temperatures on a fixed-powder sample are shown in Fig. 2, where also some points from the previous high-field magnetization measurements (big open points) are displayed. It is clear that both data sets compare well and that hysteresis effects set in at low temperatures, as can be seen from the inset in Fig. 2 yielding a value of the remanent magnetization of 0.10 μ_B/f.u.

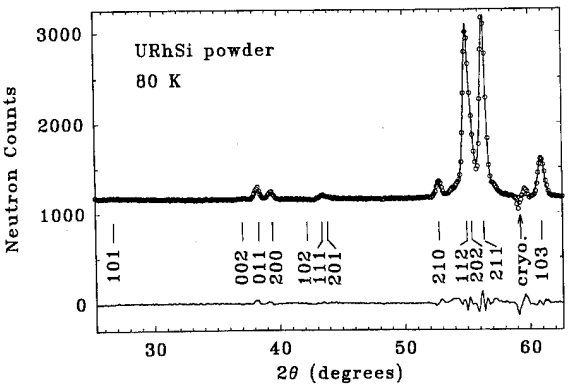


FIG. 3. Neutron-diffraction spectrum recorded at 80 K together with the best fit. The full line at the bottom represents the difference between the experimental data and the fit.

TABLE I. The refined structural parameters of URhSi at 80 K.

Space group		*Pnma*		T=80 K
U	4c	X_U 1/4 Z_U	X_U=0.000 61 (115)	Z_U=0.185 42 (116)
Rh	4c	X_{Rh} 1/4 Z_{Rh}	X_{Rh}=0.145 53 (192)	Z_{Rh}=0.572 10 (157)
Si	4c	X_{Si} 1/4 Z_{Si}	X_{Si}=0.784 15 (228)	Z_{Si}=0.610 84 (231)

Lattice parameters		R factors
a=702.256±0.103 pm		R_p=3.63%
b=412.104±0.075 pm		R_{wp}=5.04%
c=745.842±0.079 pm		R_B=2.35%
	χ^2=0.954	

IV. NEUTRON DIFFRACTION RESULTS

Two possible crystallographic structures were considered: the $CeCu_2$ type of structure (space group *Imma*) and its ordered version TiNiSi (space group *Pnma*). The neutron-diffraction patterns obtained above the transition temperature, namely at 80 K (Fig. 3) and 24 K, can be indexed using the orthorhombic TiNiSi type of structure. Note that the lines indexed as 102, 111, 201, and 210 would be not present for the $CeCu_2$ type. The structural parameters determined at 80 K are summarized in Table I. The absence of any unindexed reflection proofs the very low content of the URh_2Si_2 secondary phase indicated by the electron microprobe. A considerable improvement of fit is achieved by introducing a slightly higher fraction of U (0.9%) and a slightly lower atomic fraction of Rh (−0.8%). This is in a good agreement with the electron-microprobe analysis.

The spectrum recorded at 2.8 K (well below T_C inferred from bulk experiments) contains no additional reflections, but only additional magnetic contributions to the 101, 011, 200, 112, 202, and 211 nuclear Bragg reflections. This is consistent with identical magnetic and crystallographic unit cells. The magnetic structure was determined by fitting to the models possible within the experimental constrain. The best agreement was obtained for the model with all U moment parallel to the c axis, i.e., for the ferromagnetic model with the size of magnetic moments 0.11±0.02 μ_B/U atom.

V. CONCLUSIONS

URhSi crystallizes in the orthorhombic TiNiSi-type of structure (space group *Pnma*) and orders ferromagnetically below 9.5 K with ordered U moments of about 0.11 μ_B. This rather small value in comparison with most *UTX* compounds together with magnetization, susceptibility, specific-heat, and resistivity behavior suggests that the magnetism in URhSi is governed by strongly delocalized uranium 5f electron states. The origin of this itinerant behavior can be found mainly in the strong 5f-ligand hybridization.

The ordered U moment determined by the neutron-diffraction is much smaller that the value obtained from the high-field magnetization experiment. This fact points to field-induced moments in the latter experiment. The presence of magnetic fluctuations which play an important role at zero field even well above the transition temperature can be inferred from the bulk measurements. Studies on single-crystalline URhSi are highly desirable to get more specific information on substantial issues of magnetism in URhSi as are the magnetocrystalline anisotropy, orbital and spin moments, etc.

ACKNOWLEDGMENTS

This work was sponsored by the "Stichting voor Fundamenteel Onderzoek der Materie" (FOM), and The Grant Agency of the Czech Republic (Project No. 202/93/0184). Support to K. P. in the framework of the E. C. funded training program HC & M is acknowledged. The work of V.S. and P.S. at HMI Berlin was supported by program PECO.

[1] R. Troc and V. H. Tran, J. Magn. Magn. Mater. **73**, 389 (1988).
[2] E. Brück, Ph.D. thesis, University of Amsterdam, 1991.
[3] B. Lloret, Ph.D. thesis, University of Bordeaux, 1988.
[4] V. Sechovský and L. Havela, in *Ferromagnetic Materials*, edited by E. P. Wolfarth and K. H. J. Buschow (North-Holland, Amsterdam, 1988), Vol. 4, Chap. 4, pp. 309–491.
[5] H. H. Hill, in *Plutonium and Other Actinides*, edited by W. N. Miner (AIME, New York, 1970), p. 2.
[6] H. M. Rietveld, J. Appl. Cryst. **2**, 65 (1969).
[7] J. Rodrigues-Carvajal, FULLPROF, version 2.6, October 1, 1994, ILL (unpublished).
[8] V. F. Sears, Neutron News **3**, 26 (1992).
[9] A. Delapalme, Rapport Interne CEA-CNRS/DPh. G. SDN/LLB/85/59.
[10] F. R. de Boer, E. Brück, J. C. P. Klaasse, H. Nakotte, K. H. J. Buschow, L. Havela, V. Sechovský, P. Nozar, E. Sugiura, M. Ono, M. Date, and Y. Yamagishi, J. Appl. Phys. **69**, 4702 (1991).

Magnetic and crystallographic properties of $CrAs_{1-x}S_x(0 \leqslant x < 1)$

Takanobu Suzuki and Hideaki Ido
Faculty of Engineering, Tohoku Gakuin University, Tagajo 985, Japan

S substitution for As of CrAs compound has been successful up to 90 at. % for the first time in this work. The x-ray powder patterns and magnetic susceptibility curves have been observed for the compounds $CrAs_{1-x}S_x(0 \leqslant x \leqslant 0.6)$ in the temperature region from 80 K to 1100 K. It was found that the crystallographic transition from the orthorhombic MnP to the hexagonal NiAs type structure occurs with increase of temperature in the composition region $x \leqslant 0.5$. From the temperature dependence of lattice parameters, large spontaneous magnetostriction is found to occur mainly along the B axis of the compounds with small x. The magnetostriction decreases with x and disappears at $x=0.35$. The Neel temperature have also been determined. The magnetic moments per Cr atom in the compounds with $x=0.3$, 0.4, and 0.5 have been found to be within $2.95 \pm 0.10\ \mu_B$, in the temperature region of the NiAs type structure. These data are compared with the previous ones of similar compounds. © *1996 American Institute of Physics.* [S0021-8979(96)18508-4]

I. INTRODUCTION

It has been well known that the compound CrAs is a typical itinerant antiferromagnet with a double spiral magnetic order and shows a discontinuous change of the lattice parameters at the Neel temperature T_N(265 K).[1,2] It is also very interesting that the compound undergoes the crystallographic transition from an orthorhombic MnP type to a hexagonal NiAs type at $T_t = 1100$ K.[3] In our previous works,[4,5] we studied the magnetic and crystallographic properties of a lot of substituted CrAs compounds by $3d$ elements and some pnictogen elements, and we found that T_N of the substituted compounds decreases drastically with the substitution except for the cases of Mn and Sb. Recently, we are successful for the first time to prepare *S*-substituted CrAs and investigated the magnetic and crystallographic properties of the samples with sulphur concentration x less than 0.2.[6] In the present work, the substitution of sulphur is extended to $x=0.9$ and x-ray and magnetic measurements have been performed for substituted compounds to compare the sulphur substitution effects with the other cases mentioned above.

II. SAMPLE PREPARATION

Compounds $CrAs_{1-x}S_x$ with various values of x between 0 and 0.9 were prepared by heating the mixture of desired masses of powdered Cr, As, and S in vacuum at 300 °C for three days, and then at 800 °C for three days. After quenching into water, they were crushed and mixed and heated again at 1000 °C for five days and then annealed at 300 °C for another two weeks. The crystal structure at room temperature has been found to be of the orthorhombic MnP type for the samples with $x \leqslant 0.4$ and of the hexagonal NiAs type in the case of $x > 0.4$ by powder x-ray methods. The relationship between MnP and NiAs type structures is explained in Fig. 1.

III. RESULTS AND DISCUSSION

The powder x-ray diffraction patterns were observed for the samples at various temperatures between 80 and 800 K in order to obtain the temperature dependence of lattice parameters A, B, and C and the crystallographic phase transition temperature T_t from MnP to NiAs type structure. The lattice parameters were calculated by applying the least squares method to the observed patterns. The crystallographic transition temperature T_t has been determined by observing the temperature variation of the intensities of diffraction lines (210), (112), and (103) which disappear when the positional parameters u, v, x, and w become 0. Temperature dependencies of A, B and C axes of some representative samples are shown together with T_t in Figs. 2, 3, and 4, respectively.

As seen in Fig. 2, a discontinuous change of A axis, which means the negative spontaneous magnetostriction,[6] occurs at T_N in the cases of $x=0.0$ and 0.1, and the discontinuous change disappears for the samples with x larger than 0.16.

It is seen from Fig. 3 that B axis of CrAs ($x=0$) shows a discontinuous change at T_N, which means the positive spontaneous magnetostriction of 3.8%. The magnetostriction decreases linearly with x and changes its sign between $x=0.3$ and 0.4 as seen in Fig. 3, where the negative striction is seen for the curve with $x=0.4$.

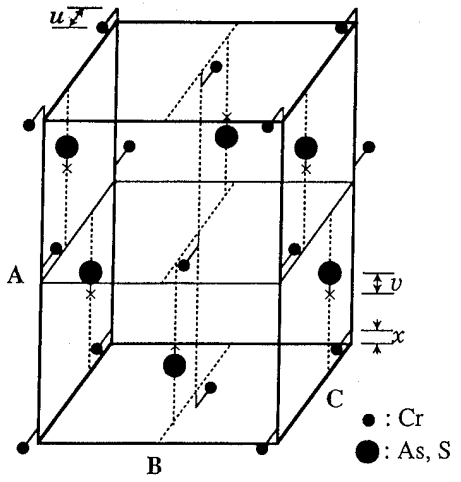


FIG. 1. Crystal structure of MnP type. This structure becomes the hexagonal NiAs type, if the positional parameters u, v, x, w (w is not shown in the figure) disappear and the distortion parameter $\delta = C/\sqrt{3}B$ becomes 0.

 0021-8979/96/79(8)/5224/3/$10.00 © 1996 American Institute of Physics

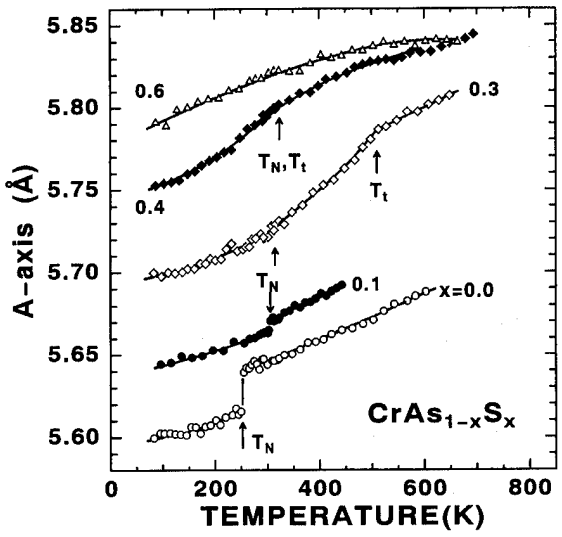


FIG. 2. Temperature dependence of A axis for some representative samples.

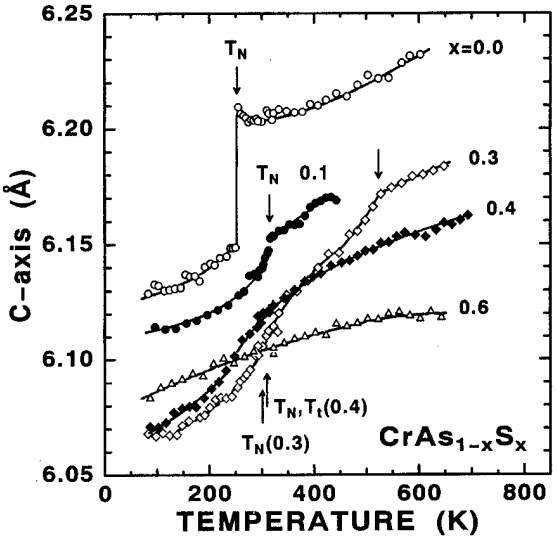


FIG. 4. Temperature dependence of C axis for some representative samples.

Temperature dependence of C axis shown in Fig. 4 is similar to that of A axis in Fig. 2, and the magnitude of negative magnetostriction of C axis at T_N is about 1/4 of that of B axis in the case of $x=0$. The temperature dependence of the unit cell volume $V=A\cdot B\cdot C$ shown in Fig. 5 reflects mainly the temperature dependence of B axis.

The phase diagram of this system (Fig. 6) has been constructed on the basis of the results of crystallographic measurements mentioned above as well as the results of magnetic measurements which will be shown below. As shown in Fig. 6, the crystallographic transition temperature T_t decreases linearly with increase of x, while the Neel temperature T_N increases gradually with increase of x. Therefore, the temperatures T_t and T_N in the composition range $x\geqslant 0.38$ are considered to have the same value.

The temperature variations of magnetic susceptibility have been measured for several samples with different sulphur content in the temperature region between 80 and 1100 K. The reciprocal susceptibility vs temperature curves are shown in Fig. 7. The kink at 320 K and the broad minimum at around 800 K of the curve for $x=0.16$ correspond to T_N and T_t, respectively, shown in Fig. 6. The gradual decrease of $\chi^{-1}-T$ curve for $x=0.16$ between T_N and T_t is considered to be caused mainly by the decrease of the atomic positional parameters in MnP type structure.[7] The curve for $x=0.3$ is similar to that of $x=0.16$. In the case of $x=0.5$, T_N and T_t are considered to coincide with each other, which is consistent with phase diagram shown in Fig. 6. The broad peak at around 120 K for $x=0.5$ cannot be explained at the present time. The $\chi^{-1}-T$ curve above T_t seems to be explained by the Curie–Weiss law, from which we obtained the magnetic moment per Cr atom μ_{Cr} ($=2S_{Cr}$, where S_{Cr} is the chromium atomic spin) and the paramagnetic Curie tempera-

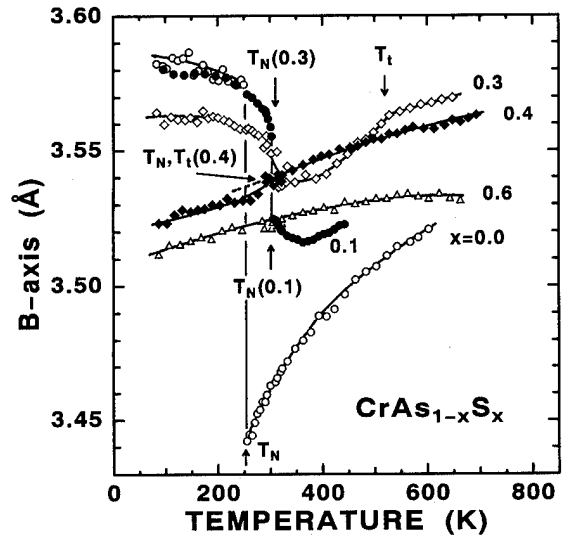


FIG. 3. Temperature dependence of B axis for some representative samples.

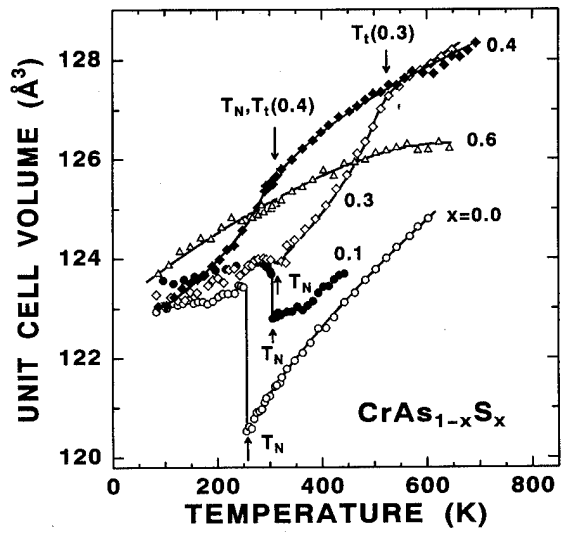


FIG. 5. Temperature dependence of the unit cell volume for some representative samples.

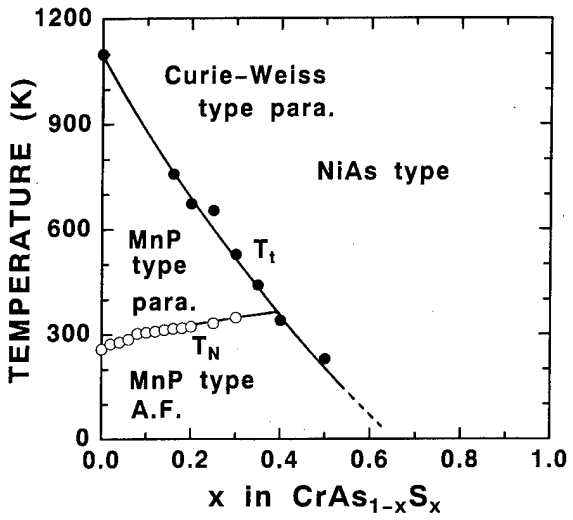


FIG. 6. The crystallographic and magnetic phase diagram of the system $CrAs_{1-x}S_x$.

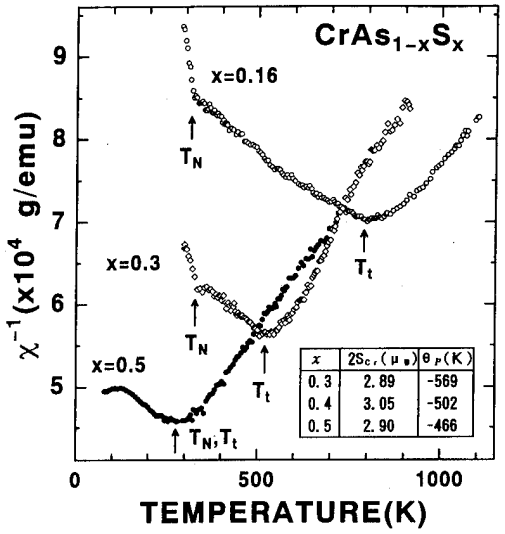


FIG. 7. Temperature dependence of the inverse magnetic susceptibility for some representative samples.

ture θ_p as shown in the table in Fig. 7. In the case of the sample with $x=0.3$, the Curie–Weiss law seems to hold in the temperature region above 700 K, from which we obtained the values of $2S_{Cr}$ and θ_p in the same table. The anomalous behavior of $\chi^{-1}-T$ curve between T_t and $T=700$ K is difficult to explain at present. The $\chi^{-1}-T$ curve for $x=0.16$ in the temperature region above T_t is similar to $\chi^{-1}-T$ curve of $x=0.3$ between T_t and 700 K, therefore we did not apply the Curie–Weiss law in the case of $x=0.16$. The values of $2S_{Cr}$ and θp for $x=0.4$ are also given in the table in Fig. 7, though the $\chi^{-1}-T$ curve is not shown in Fig. 7. The magnetic moment per Cr atom obtained by the magnetic susceptibility measurements have been reported for the systems $CrAs_{1-x}Sb_x$,[8] $CrAs_{1-x}Se_x$,[9] $Cr_{1-x}Ti_xAs$ (Ref. 3) and $Cr_{1-x}Mn_xAs$.[7] According to them, the Cr moment is in the range from 2.7 to 3.2 μ_B in the temperature region where the compounds take the NiAs type structure. The values shown in the inset of Fig. 7 are also in that range. On the other hand, the magnetic moment per Cr in CrAs at 4.2 K is 1.7 μ_B.[10] The enormous difference in the Cr magnetic moment is believed to be caused by the crystal structure difference as well as the spin fluctuation effect.[11]

[1] K. Selte, A. Kjekshus, W. E. Jamison, A. F. Andresen, and J. E. Engebresen, Acta Chem. Scand. **25**, 1703 (1971).
[2] N. Kazama and H. Watanabe, J. Phys. Soc. Jpn. **30**, 1319 (1970).
[3] T. Suzuki and H. Ido, J. Appl. Phys. **55**, Part IIA, 2042 (1984).
[4] T. Suzuki and H. Ido, J. Appl. Phys. **69**, 4624 (1991).
[5] T. Suzuki and H. Ido, J. Appl. Phys. **73**, 5686 (1993).
[6] T. Suzuki and H. Ido, J. Mag. Mag. Mater. **140–144**, 149 (1995).
[7] H. Ido, J. Mag. Mag. Mater. **70**, 205 (1987).
[8] T. Suzuki and H. Ido, J. Mag. Mag. Mater. **55**, 936 (1986).
[9] A. Kjekshus and W. E. Jamison, Acta Chem. Scand. **25**, 1139 (1971).
[10] A. Kallel, H. Boller, and E. F. Bertaut, J. Phys. Chem. Solids **35**, 1139 (1974).
[11] K. Motizuki and K. Katoh, J. Phys. Soc. Jpn. **53**, 735 (1984).

Impact of criticality and phase separation on the spin dynamics of the one-dimensional $t-J$ model

Shu Zhang and Gerhard Müller
Department of Physics, The University of Rhode Island, Kingston, Rhode Island 02881-0817

Joachim Stolze[a)]
Physikalisches Institut, Universität Bayreuth, 95440 Bayreuth, Germany

The recursion method is used to determine the $T=0$ spin dynamic structure factor $S_{zz}(q,\omega)$ in the Luttinger liquid state and in the phase-separated state of the one-dimensional $t-J$ model. As the exchange coupling increases from zero, the dispersions and line shapes of the dominant spin excitations are observed to undergo a major metamorphosis between the free-fermion limit and the onset of phase separation. The familiar two-spinon spectrum of the Heisenberg antiferromagnetic chain emerges gradually in the strongly phase-separated state. © *1996 American Institute of Physics.* [S0021-8979(96)18608-0]

The $t-J$ model for strongly correlated electrons has been widely used as a prototypical system for the study of the interplay between charge and spin degrees of freedom.[1] For a one-dimensional (1D) lattice of N sites the Hamiltonian reads

$$H_{t-J}=-t\sum_{\sigma=\uparrow,\downarrow}\sum_{l=1}^{N}\{\tilde{c}^{\dagger}_{l,\sigma}\tilde{c}_{l+1,\sigma}+\tilde{c}^{\dagger}_{l+1,\sigma}\tilde{c}_{l,\sigma}\}+J\sum_{l=1}^{N}\left\{\mathbf{S}_l\cdot\mathbf{S}_{l+1}-\frac{1}{4}n_l n_{l+1}\right\} \tag{1}$$

with $\tilde{c}_{l,\sigma}=c_{l,\sigma}(1-n_{l,-\sigma})$, $n_l=n_{l,\uparrow}+n_{l,\downarrow}$, $n_{l,\sigma}=c^{\dagger}_{l,\sigma}c_{l,\sigma}$, $S^z_l=(n_{l,\uparrow}-n_{l,\downarrow})/2$, and $S^+_l=\tilde{c}^{\dagger}_{l,\uparrow}\tilde{c}_{l,\downarrow}$. Here we consider the quarter-filled-band case ($N_e=N/2$ electrons).

The hopping term amounts to an effectively repulsive force between electrons on nearest-neighbor sites,[2] and the exchange term represents an attractive force if these two electrons have opposite spins. As the exchange interaction increases from zero, the ground state of H_{t-J} undergoes a transition, at $J/t\simeq 3.2$, from a Luttinger liquid state to a phase-separated state.[3–5] In the Luttinger liquid state, both the charge correlations (at $q=\pi$) and the spin correlations (at $q=\pi/2$) are critical. The transition, which is driven by the spin coupling, produces charge long-range order (at $q=0$) combined with a new type of spin criticality (at $q=\pi$).

The focus of this study is on the frequency-dependent spin fluctuations of H_{t-J} as they manifest themselves in the $T=0$ spin dynamic structure factor

$$S_{zz}(q,\omega)=\frac{1}{N}\sum_{l,m}e^{-iqm}\int_{-\infty}^{+\infty}dt\,e^{i\omega t}\langle S^z_l(t)S^z_{l+m}\rangle. \tag{2}$$

For the calculation of this quantity, we employ the recursion method[6] in combination with a *strong-coupling continued-fraction analysis*.[7,8] The recursion method in the present context is based on an orthogonal expansion of the wave function $|\Psi^z_q(t)\rangle=S^z_q(-t)|G\rangle$, where $S^z_q=N^{-1/2}\Sigma_l e^{iql}S^z_l$ is the spin fluctuation operator, and $|G\rangle$ is the finite-size ground-state wave function of Eq. (1). After some intermediate steps, the algorithm produces a sequence of continued-fraction coefficients $\Delta^z_1(q)$, $\Delta^z_2(q)$,... for the relaxation function,

$$c^{zz}_0(q,z)=\cfrac{1}{z+\cfrac{\Delta^z_1(q)}{z+\cfrac{\Delta^z_2(q)}{z+\cdots}}}, \tag{3}$$

which is the Laplace transform of the symmetrized correlation function $\Re\langle S^z_q(t)S^z_{-q}\rangle/\langle S^z_qS^z_{-q}\rangle$. The $T=0$ spin dynamic structure factor (2) is then obtained from Eq. (3) via the relation

$$S_{zz}(q,\omega)=4\langle S^z_qS^z_{-q}\rangle\Theta(\omega)\lim_{\epsilon\to 0}\Re[c^{zz}_0(q,\epsilon-i\omega)]. \tag{4}$$

In a previous paper[9] we have used the recursion method together with a *weak-coupling continued-fraction analysis* for a study of the charge dynamic structure factor in the Luttinger liquid phase of the $t-J$ model. The spin dynamics poses a far greater challenge. Very few explicit results seem to exist.[10] One key spin dynamical property in the Luttinger liquid phase can be inferred from the asymptotic behavior of the static spin correlations as proposed in previous work:[4,5]

$$\langle S^z_lS^z_{l+m}\rangle\sim B_1\frac{1}{m^2}+B_2\frac{\cos(\pi m/2)}{m^{\eta_\rho/4+1}}, \tag{5}$$

where η_ρ is the exponent which also governs the algebraic decay of the $(q=\pi)$ oscillations, $\sim\cos(\pi m)/m^{\eta_\rho}$, in the static charge correlation function $\langle n_ln_{l+m}\rangle$. This exponent is known to assume the value $\eta_\rho=2$ in the free-fermion limit $(J/t=0^+)$. It increases linearly, $\Delta\eta_\rho\simeq 0.40\,J/t$, in the weak-coupling regime,[3,9] assumes the value $\eta_\rho\simeq 3.4$ at $J/t=2$ (supersymmetric case),[11] and diverges at the endpoint, $J/t\simeq 3.2$, of the Luttinger liquid state.[3]

The oscillatory term in Eq. (5) implies that the dynamically relevant excitation spectrum of $S_{zz}(q,\omega)$ is gapless at $q=\pi/2$. The spectral-weight distribution of the spin dynamic structure factor at this critical wave number can then be predicted (under mild assumptions) to have a singularity of the form

$$S_{zz}(\pi/2,\omega)\sim\omega^{\eta_\rho/4-1}. \tag{6}$$

The infrared exponent starts out negative in the free-fermion limit, $\sim\omega^{-1/2}$, increases monotonically with increasing J/t,

[a)]Permanent address: Institut für Physik, Universitat Dortmund, 44221 Dortmund, Germany.

 0021-8979/96/79(8)/5227/3/$10.00 © 1996 American Institute of Physics

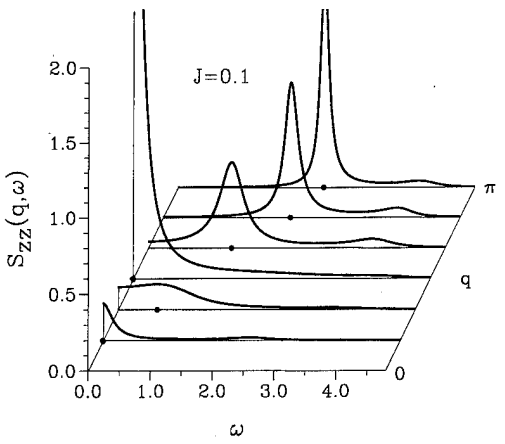


FIG. 1. Spin dynamic structure factor $S_{zz}(q,\omega)$ at $T=0$ for $q=2\pi l/12$, $l=0,\ldots,6$ of the 1D $t-J$ model with $t=1$ and $J=0.1$ in the Luttinger liquid phase near the free-fermion limit.

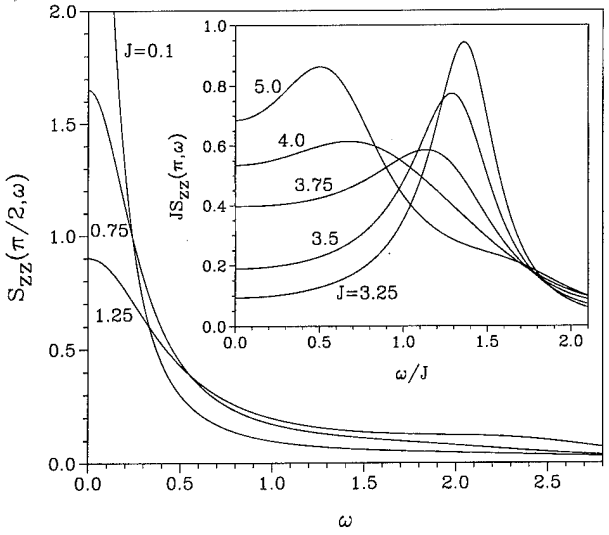


FIG. 2. Line shape at $q=\pi/2$ of the spin dynamic structure factor $S_{zz}(q,\omega)$ at $T=0$ for various values of J in the Luttinger liquid state of the 1D $t-J$ model with $t=1$ (main plot). Line shape at $q=\pi$ for various values of J in the phase-separated state (inset).

and then diverges at $J/t\simeq 3.2$, where phase separation sets in. A landmark change in $S_{zz}(\pi,\omega)$ is expected to occur at the point where the infrared exponent switches sign (from negative to positive). This happens for $\eta_\rho=4$, which corresponds to the coupling strength $J/t\simeq 2.3$.

Our results for $S_{zz}(q,\omega)$ indicate that the Luttinger liquid phase of the $t-J$ model can be divided into two regimes with distinct spin dynamical properties. As a representative result of the first regime ($0<J/t\lesssim 1$), we show in Fig. 1 $S_{zz}(q,\omega)$ as a continuous function of ω and a discrete function of the q values realized in a system of $N=12$ sites with coupling strength $J/t=0.1$.

All results presented here have been calculated via a strong-coupling continued-fraction reconstruction from the coefficients $\Delta_1,\ldots,\Delta_6$ and a Gaussian terminator. The Δ_k's have been extracted via the recursion method from the ground-state wave function for $N=12$, which in turn has been computed via the conjugate-gradient method. The entire procedure was explained in Ref. 7.

Throughout the Brillouin zone except at small q we observe a well-defined dynamically relevant spin mode with a $|\cos q|$-like dispersion as indicated by the full circles. Near the critical wave number, $q=\pi/2$, the function $S_{zz}(q,\omega)$ may exhibit a power-law divergence of the form $\sim [\omega^2 - c^2(\pi/2-q)^2]^{(\eta_\rho/4-1)/2}$, similar to what has been observed at the critical wave number in other Luttinger liquids.[12] At long wavelengths the spectral weight in $S_{zz}(q,\omega)$ is concentrated at fairly low frequencies. Data for longer chains will be needed for a quantitative analysis of the spin dispersions at small q in this regime.

As the exchange coupling increases toward $J/t\simeq 1$, the following changes in the spectral-weight distribution of $S_{zz}(q,\omega)$ can be identified:

(i) The amplitude of the $|\cos q|$-like dispersion grows with increasing J/t. The gradual upward shift of the peak position in $S_{zz}(q,\omega)$ is accompanied by a significant increase in linewidth. For the $q=\pi$ spin mode this is contrary to what one expects under the influence of an antiferromagnetic exchange interaction of increasing strength. That trend changes at stronger coupling as we shall see.

(ii) The intensity of the central peak in $S_{zz}(\pi/2,\omega)$ weakens gradually. This is illustrated in the main diagram of Fig. 2. The peak turns shallow and then vanishes altogether. This property of our data reflects the gradual weakening and ultimate disappearance of the power-law divergence (6), given the (approximately known) J/t dependence of the infrared exponent.

As the coupling strength increases past the value $J/t\simeq 1$, the spin modes which dominate $S_{zz}(q,\omega)$ in the first regime of the Luttinger liquid phase broaden rapidly and lose their distinctiveness. There is a crossover region between the first and second regimes, which roughly comprises the coupling range $1\lesssim J/t\lesssim 2$. Over that range, the spectral weight in $S_{zz}(q,\omega)$ is distributed over a broad structure with rapidly shifting peaks.

At the end of the crossover region, a new type of spin mode with an entirely different kind of dispersion has gained prominence in $S_{zz}(q,\omega)$, and it stays dominant throughout the remainder of the Luttinger liquid phase. This is illustrated in Fig. 3 by a plot of $S_{zz}(q,\omega)$ for a J/t value near the onset of phase separation. The representation is the same as in Fig. 1 except for the different frequency scale.

The dispersion of these new spin modes, as shown by the full circles, does no longer have a soft mode at $q=\pi/2$. At $J/t\sim 2.0$ the dispersion has a $|\sin(q/2)|$-like shape, i.e., a smooth maximum at $q=\pi$ and a tendency to approach zero linearly as $q\to 0$. As J/t increases toward the transition point, the peak positions in $S_{zz}(q,\omega)$ gradually shift to lower values of ω/J (with t held fixed). The shift proceeds more rapidly at q near π than at smaller q, which has the consequence that the maximum in the dynamically relevant spin dispersion starts to move away from $q=\pi$ toward $q=\pi/2$.

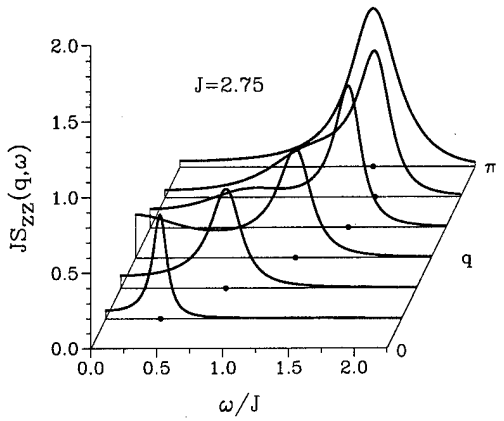


FIG. 3. Spin dynamic structure factor $S_{zz}(q,\omega)$ at $T=0$ for $q=2\pi l/12$, $l=0,\ldots,6$ of the 1D $t-J$ model with $t=1$ and $J=2.75$ in the Luttinger liquid phase near the onset of phase separation.

This trend from a $|\sin(q/2)|$-like toward a $|\sin q|$-like dispersion persists in the phase-separated state ($J/t>3.2$).

The evolution of the spectral-weight distribution in $S_{zz}(\pi,\omega)$ from a well-defined mode at $\omega/J\simeq 1.4$ near the onset of phase separation toward a soft mode in the strongly phase-separated state is shown in the inset to Fig. 2. By contrast, the spectral weight in $S_{zz}(\pi/2,\omega)$, which has been slowly shifting toward lower values of ω/J in the second regime of the Luttinger liquid phase, now starts to move back out to higher frequencies in the phase-separated state (not shown here). The single-peak structure grows taller, the linewidth shrinks somewhat, and the peak position settles at $\omega/J\simeq 1.57$.

All these properties and trends reflect or foreshadow the much better understood $T=0$ dynamical properties of the 1D $s=1/2$ Heisenberg antiferromagnet—the end product of the $t-J$ model in the completely phase-separated state. The spin dynamic structure factor $S_{zz}(q,\omega)$ under these circumstances is known to be dominated by a continuum of two-spinon excitations with a lower boundary $\epsilon_L(q)=(\pi/2)J|\sin q|$, where the spectral-weight distribution has a divergent singularity, and an upper boundary $\epsilon_U(q)=\pi J|\sin(q/2)|$, where the spectral-weight distribution becomes very small.[7,8,13]

This work was supported by the U.S. National Science Foundation, Grant No. DMR-93-12252. Computations were carried out on supercomputers at the National Center for Supercomputing Applications, University of Illinois at Urbana-Champaign.

[1] F. C. Zhang and T. M. Rice, Phys. Rev. B **37**, 3759 (1988); C. Gros, R. Joynt, and T. M. Rice, Phys. Rev. B **36**, 381 (1987).
[2] At $J/t=0$ it is more likely that the site adjacent to an electron is occupied by a hole than by another electron.
[3] M. Ogata, M. U. Luchini, S. Sorella, and F. F. Assaad, Phys. Rev. Lett. **66**, 2388 (1991).
[4] F. F. Assaad and D. Würtz, Phys. Rev. B **44**, 2681 (1991).
[5] C. S. Hellberg and E. J. Mele, Phys. Rev. Lett. **67**, 2080 (1991).
[6] R. Haydock, Solid State Physics **35**, 215 (1980); M. H. Lee, Phys. Rev. B **26**, 2547 (1982); E. R. Gagliano and C. A. Balseiro, Phys. Rev. B **38**, 11766 (1988).
[7] V. S. Viswanath and G. Müller, *Recursion Method—Application to Many-Body Dynamics*, Lecture Notes in Physics, Vol. m 23 (Springer-Verlag, New York, 1994).
[8] V. S. Viswanath, S. Zhang, J. Stolze, and G. Müller, Phys. Rev. B **49**, 9702 (1994).
[9] V. S. Viswanath, S. Zhang, G. Müller, and J. Stolze, Phys. Rev. B **51**, 368 (1995).
[10] J. Deisz, K.-H. Luk, M. Jarrell, and D. L. Cox, Phys. Rev. B **46**, 3410 (1992); T. Tohyama, P. Horsch, and S. Maekawa, Phys. Rev. Lett. **74**, 980 (1995).
[11] N. Kawakami and S.-K. Yang, Phys. Rev. Lett. **65**, 2309 (1990).
[12] A. Luther and I. Peschel, Phys. Rev. B **12**, 3908 (1975); H. C. Fogedby, J. Phys. C **11**, 4767 (1978).
[13] G. Müller, H. Thomas, H. Beck, and J. C. Bonner, Phys. Rev. B **24**, 1429 (1981).

Rapid loss of magnetic order in Ni on alloying with Cr, Mo, Re, and Si

V. Suresh Babu, A. S. Pavlovic, and Mohindar S. Seehra[a)]
Physics Department, West Virginia University, Morgantown, West Virginia 26506-6315

In this article, the variation of the Curie temperature T_c and the magnetic moment μ of Ni in the fcc alloys $Ni_{1-x}M_x$ (M=Cr, Mo, Re, and Si) are reported for concentrations x between 0 and 15 at. %. The decrease of T_c and μ with x reported earlier for NiCr alloys are also observed for the NiMo, NiRe, and NiSi alloys. The initial rates of decreases are about 60 K/at. % for T_c and 0.05 μ_B/at. % for μ, leading to critical concentration $x_c \simeq 13\%$ above which ferromagnetism disappears. Qualitatively, these decreases may be understood in terms of transfer of outer shell electrons of M atoms to the $3d\downarrow$ band of Ni in the alloys. However, a quantitative calculation of x_c is not yet available. © *1996 American Institute of Physics.* [S0021-8979(96)18708-7]

INTRODUCTION

In this paper, we present experimental results on the variation of the Curie temperature T_c and magnetic moment μ of Ni as it is alloyed with Cr, Mo, Re, and Si for concentrations up to 15 at. % of the dopants. The variations of the T_c's of $Ni_{1-x}Cr_x$ alloys have been reported by a number of research groups[1–5] and the results have also been discussed theoretically.[6–9] However results presented here for the Mo, Re, and Si alloys are new and they provide an opportunity to examine in further detail the theoretical interpretations advanced for the NiCr alloys. Details of these investigations are presented below.

EXPERIMENTAL PROCEDURES

The binary alloys $Ni_{1-x}M_x$ (M=Cr, Mo, Re, and Si) were prepared by arc melting from four nine pure materials for the compositions x=3, 6, and 9 at. % for Si and x=5, 8, 10, 12, and 15 at. % for Cr, Mo, and Re using oxygen-free argon atmosphere. All samples were homogenized by remelting and turning over several times, followed by annealing in argon for 120 h at 1000 °C. Samples were then cut for x-ray diffraction (XRD), magnetic measurements, and for measurements of thermal expansion for temperatures to 1000 °C. Results of the thermal expansion and their comparison with the results from molecular dynamics simulations have been reported elsewhere.[10] Here we concentrate on the magnetic properties of these materials. XRD patterns were recorded using a Rigaku/DMax diffractometer (Cu K_α radiation) in the 2θ range of 20°–90° at a scan speed of 1°/min and a sampling interval of 0.02°. Magnetic studies reported here were carried out using a SQUID magnetometer (Quantum Design model MPMS) with samples in the shape of square discs with masses of about 10–80 mg and magnetic fields applied in the plane of the discs. The magnetic susceptibilities $\chi = M/H$ were measured in H=50 Oe in most cases.

RESULTS AND DISCUSSION

Only samples with single fcc phase as determined by XRD were investigated further. The lattice constant a measured from the XRD peaks using the standard iterative method[11] is plotted against the concentration x of the various alloys in Fig. 1. From the linear fits in Fig. 1, the atomic radii calculated assuming close packing are 1.246, 1.290, 1.382, and 1.401 Å for Ni, Cr, Re, and Mo, respectively. These results are in excellent agreement with the literature values,[12] suggesting that in the alloys, Cr, Re, and Mo occupy substitutional positions. On the other hand, for the Si case, there is no significant change in the lattice constant with concentration suggesting perhaps interstitial occupancy.

In Fig. 2, we show on a semilog scale the temperature variations of χ (50 Oe) for Ni and representative alloys where the solid line for Ni is a fit to the Curie–Weiss law $\chi = C/(T-T_c)^\gamma$ and where T_c was determined by linear extrapolation of the data[13] from above and below the transition. Our measured values for Ni are $T_c = 632 \pm 2$ K and $\gamma \simeq 1.25 \pm 0.02$, in good agreement with the reported values of $T_c \simeq 630$ K and $\gamma \simeq 1.35 \pm 0.02$.[1] This good agreement of T_c values at these high temperatures provides a good check on the temperature calibration of our magnetometer whereas γ values might have been affected by the nonspherical shapes of our samples. The latter fact can affect the magnitudes of low field χ near T_c due to demagnetization factors when χ approaches unity. In any case, the emphasis of the present work is on the variation of T_c and saturation magnetization M_0 as a function of the atomic concentration x in $Ni_{(1-x)}M_x$.

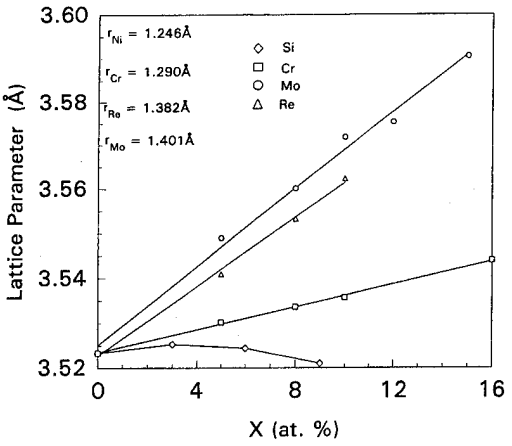


FIG. 1. Measured lattice parameter of the fcc phase is plotted against x in $Ni_{1-x}M_x$ for M=Si, Cr, Mo, and Re. The straight line fits yield the listed atomic radii assuming close packing.

a)Corresponding author.

 0021-8979/96/79(8)/5230/3/$10.00 © 1996 American Institute of Physics

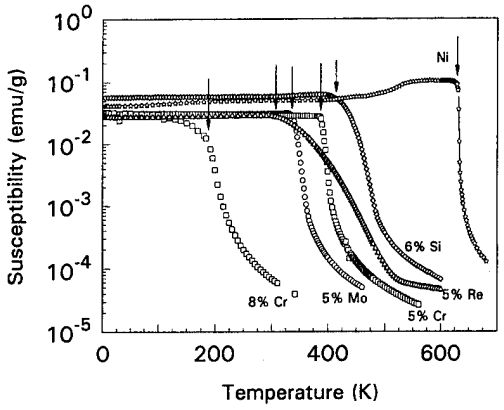


FIG. 2. Measured magnetic susceptibility $\chi = M/H$ (H=50 Oe) vs temperature for representative samples. The arrows point to the estimated T_c.

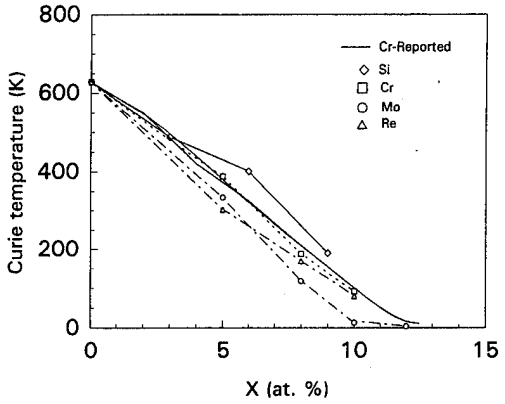


FIG. 4. Variation of the Curie temperature T_c with concentration x for different alloys. The solid line is for the $Ni_{1-x}Cr_x$ system based on literature values whereas lines joining the points are for visual aid.

For some samples near the critical x for ferromagnetism, a definite kink in low-field χ vs T is not observed. In those cases, we used the Arrott plots of M^2 vs H/M (Fig. 3) to estimate T_c by linear extrapolation from the high H/M values (at T_c, the extrapolated curve passes through the origin).[1] A plot of T_c's so evaluated versus the concentration x is shown in Fig. 4 where we have also included data from the literature on the NiCr system. Our observed variations of T_c with x for NiCr alloys are in excellent agreement with those reported by Besnus *et al.*[2] and Simpson *et al.*[5] (solid line in Fig. 4) yielding critical concentration $x_c \simeq 13\%$. For the NiSi, NiRe, and NiMo alloys, T_c vs x curves are essentially similar to that for the NiCr alloys in that in all cases T_c falls toward zero at a rate of about 60 K/at. % although there are clearly slight differences between the different cases. For $x > 10\%$ there are deviations from this linearity as also noted by Besnus *et al.*[2] and $x_c \simeq 13\%$.

Next we consider the variation of saturation magnetization M_0 or equivalently the magnetic moment μ on the Ni atom as a function of x. M_0 was estimated from the M vs H plots carried out to 20 kOe at 5 K, and in some cases with low T_c compositions at 2 K. For a Ni wafer, our measured value of $M_0 = 60.55$ emμ/g translates into $\mu = 0.636\ \mu_B$, in excellent agreement with the reported value of 0.642 μ_B.[1] The variation of μ vs x is plotted in Fig. 5 for all our samples as well as those reported in literature.[2,4] Again the drop in μ with increasing x at a rate of about 0.05 μ_B/at. % is obvious, with substantial drop in this rate of decrease for $x > 10\%$. From the data in Figs. 4 and 5, it is clear that alloying of Ni with Cr, Re, Mo, and Si affects the magnetic moment μ and T_c of Ni in essentially similar fashion, viz., rapid lowering of μ and T_c as x is increased, so that above the critical concentration $x_c \simeq 13\%$, magnetic order is absent at a nonzero temperature.

There are small yet noticeable differences between the different systems investigated here. For example, T_c for the Re and Mo alloys tend to be somewhat lower than those for the Si and Cr alloys for the same x (Fig. 4) whereas μ for the Si alloys for the same x is lower than the other cases. Of course, Re and Mo are larger atoms and they produce larger change in the lattice constants (Fig. 1) so that these observations may be related. A plot of M_0^2 vs T_c yields essentially a linear behavior (Fig. 6) for high T_c compositions whereas the points for samples with $x > 10\%$ show a significant deviation from this linearity, as also noted by Besnus *et al.*[2]

The band theory of the ferromagnetism of Fe, Co, and Ni has been the subject of discussion for several decades[6–9] and a simple picture is presented by Kittel.[12] The exchange-split

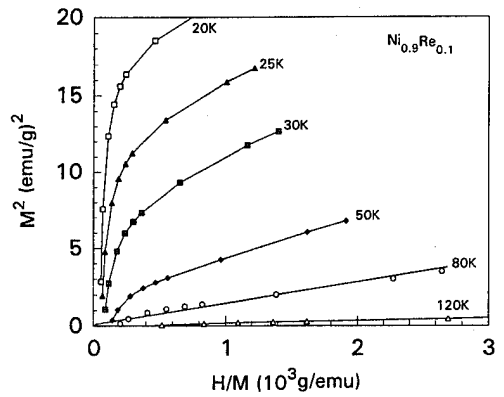


FIG. 3. The Arrott plot of M^2 vs H/M for the $Ni_{0.9}Re_{0.1}$ alloy. A $T_c = 80$ K is estimated as discussed in text.

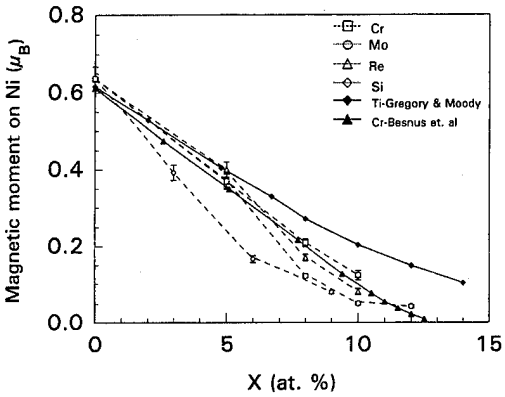


FIG. 5. Variation of the magnetic moment μ with concentration x for different alloys where data from literature on the NiCr and NiTi systems are also included. The lines are drawn through the points for visual aid.

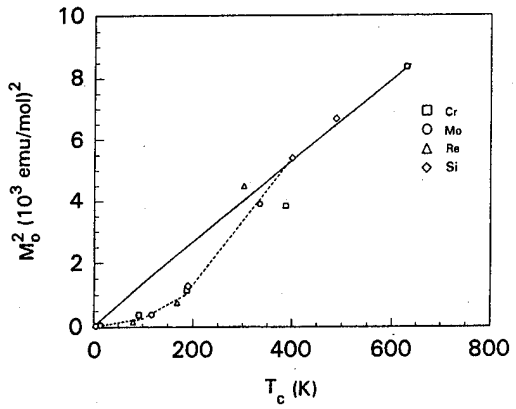


FIG. 6. A plot of M_0^2 against T_c. Departures from linearity are observed for compositions close to x_c.

$3d\downarrow$ and $3d\uparrow$ bands below T_c leads to 0.54 holes/atom of $3d\downarrow$ band of Ni to agree with the experimental value of μ. Qualitatively the alloying of Ni with Cr, Re, Mo, and Si may result in the partial transfer of the outer shell electrons of these atoms into the empty $3d\downarrow$ band, thus lowering both μ and, consequently, T_c. To the best of our knowledge, a theoretical calculation to explain the experimental result of $x_c \simeq 13\%$ observed here for the four alloy systems is not yet available. Hopefully, these experimental results would stimulate such a calculation.

ACKNOWLEDGMENTS

This work was supported in part by the NSF/WV EPSCoR program.

[1] J. S. Kouvel and M. E. Fisher, Phys. Rev. A **136**, 1626 (1964).
[2] M. J. Besnus, Y. Gottehrer, and G. Munschy, Phys. Status Solidi **49**, 597 (1972).
[3] R. Chiffey and T. J. Hicks, Phys. Lett. A **34**, 267 (1971).
[4] I. P. Gregory and D. E. Moody, J. Phys. F **5**, 36 (1975).
[5] M. A. Simpson and T. F. Smith, Aust. J. Phys. **35**, 307 (1982); A. B. Kaiser and T. F. Smith, Physica B **160**, 33 (1989).
[6] See the review by E. P. Wohlfarth, in *Ferromagnetic Materials*, edited by E. P. Wohlfarth (North-Holland, New York, 1980), pp. 1–70.
[7] H. Hasegawa and J. Kanamori, J. Phys. Soc. Jpn. **33**, 1599 (1972).
[8] R. Caudron, R. Caplain, J.-J. Meunier, and P. Costa, Phys. Rev. B **8**, 5247 (1973).
[9] D. M. C. Nicholson and R. H. Brown, Phys. Rev. Lett. **70**, 3311 (1993).
[10] A. S. Pavlovic, V. Suresh Babu, and M. S. Seehra, J. Phys.: Condensed Matter (in press).
[11] H. P. Klung and L. E. Alexander, *X-ray Diffraction Procedures*, 2nd ed. (Wiley, New York, 1974), pp. 628–633.
[12] See, e.g., C. Kittel, *Introduction to Solid State Physics*, 6th ed. (Wiley, New York, 1986), p. 76.
[13] C. G. Robbins, H. Claus, and P. A. Beck, J. Appl. Phys. **40**, 2269 (1969).

Magnetic properties of the $SmMn_2(Ge_{1-x}Si_x)_2$ system

Shibaji Saha and Naushad Ali
Department of Physics and Molecular Science Program, Southern Illinois University at Carbondale, Carbondale, Illinois 62901

Magnetization and thermal expansion measurements have been carried out on the polycrystalline $SmMn_2(Ge_{1-x}Si_x)_2$ system ($x=0.00$, 0.01, 0.02, 0.03, 0.05, 0.08, 0.10, 0.12, and 0.15) to study its magnetic properties. It is found that the temperature range of stability of the antiferromagnetic region increases with the increase of Si content. This behavior is explained as a decrease in the Mn–Mn intralayer separation. Ferro- to antiferromagnetic (T_2) and antiferro- to ferromagnetic (T_1) transitions are found to be first order for all the samples up to $x=0.10$. For $x=0.15$ sample the antiferro- to ferromagnetic (T_1) transition is of first order while the ferro- to antiferromagnetic (T_2) transition appears to be second order. A magnetic phase diagram of $SmMn_2(Ge_{1-x}Si_x)_2$ has been determined. © *1996 American Institute of Physics.* [S0021-8979(96)18808-3]

INTRODUCTION

Intermetallic ternary compounds, RMn_2X_2 (R=rare earths and X=Si, Ge),[1,2] have attracted considerable attention. The compounds are body centered tetragonal and form in $ThCr_2Si_2$ crystal structure. The structure is formed by stacking of atomic layers perpendicular to the c axis following the sequence $\cdots R\text{–}X\text{–Mn}\text{–}X\text{–}R\cdots$. The magnetic properties of RMn_2X_2 compounds are very sensitive to Mn–Mn intralayer distance, $R^a_{\text{Mn–Mn}}$. Compounds with $R^a_{\text{Mn–Mn}} \leqslant 0.2865$ nm are antiferromagnetic while they are ferromagnetic for $R^a_{\text{Mn–Mn}} \geqslant 0.2865$ nm. Among these compounds, $SmMn_2Ge_2$ exhibits the most interesting properties, mainly because its $R^a_{\text{Mn–Mn}}$ value is close to the critical value. $SmMn_2Ge_2$ is ferromagnetic with a Curie temperature of 340 K. As the sample is cooled below 340 K, the ferromagnetic phase persists down to 150 K, at which point it reorders antiferromagnetically. This antiferromagnetic phase is retained down to 100 K. As the sample is cooled below 100 K, it enters to a ferromagnetic phase. The antiferromagnetic phase is thought to be very sensitive to the Mn–Mn intralayer separation.[3]

In an effort to understand the nature of the magnetic properties in $SmMn_2Ge_2$, Duraj *et al.*[4,5] have studied $Sm_{1-x}Gd_xMn_2Ge_2$ and $Sm_{1-x}Y_xMn_2Ge_2$. It has been observed that with the increase of Y and Gd content, the temperature range of stability of the ferromagnetic phase decreases while that of the antiferromagnetic phase increases. This effect has been related to a decrease in intralayer distance, $R^a_{\text{Mn–Mn}}$, with increasing concentration of Gd or Y. Another study by Duraj *et al.*[6] on $Sm_{0.09}Nd_{0.1}Mn_2Ge_2$ shows that with the increase of external pressure, it is possible to regain the "lost" antiferromagnetic phase. All the above studies show that transition from the ferro- to the antiferromagnetic phase is strongly coupled with interatomic distance ($R^a_{\text{Mn–Mn}}$).

Recently, we made an effort[7] to replace the Mn content partially with Cr in $SmMn_2Ge_2$. Our study shows that by the addition of 5% Cr in place of Mn, the antiferromagnetic region in $Sm(Mn_{1-x}Cr_x)_2Ge_2$ system disappears. In the present study, we have tried to partially replace the nonmagnetic contributor, Ge, in $SmMn_2Ge_2$ by Si. Magnetization and thermal expansivity measurements have been performed on $SmMn_2(Ge_{1-x}Si_x)_2$ for $x=0.00$ to $x=0.15$. Magnetization measurements as a function of temperature and magnetic field have been utilized to determine the magnetic phase diagram of the $SmMn_2(Ge_{1-x}Si_x)_2$ system.

EXPERIMENTAL DETAILS

Samples were synthesized by arc melting in an Ar atmosphere of the proper amounts of the constituent elements. An excess amount of Mn was added to compensate for its weight loss due to volatility during melting. The purity of the elements were 99.9% for Sm, 99.99% for Mn and Cr, and 99.999% for Ge. During the melting process the ingots were turned over and remelted 4 to 5 times to ensure homogeneity. Samples were then wrapped in Ta foil and annealed under vacuum ($\sim 10^{-7}$ Torr) at 800 °C for 7 days. Magnetization measurements were carried out by means of a SQUID magnetometer (Quantum Design, CA) over the temperature range of 5–395 K and in an applied magnetic field range of 0.1–55 kG. Thermal expansion measurements were made using a capacitance dilatometer over the temperature range of 5–290 K.

EXPERIMENTAL RESULTS AND DISCUSSION

The temperature dependence of magnetization of $SmMn_2(Ge_{1-x}Si_x)_2$ for $x=0.00$ to 0.15 in an applied field of 100 G is shown in Fig. 1. The samples were cooled down from room temperature in zero applied magnetic field before magnetization measurements. For $x=0.00$, i.e., for $SmMn_2Ge_2$, the transition temperatures are found to be at $T_c=339$ K for the para- to ferromagnetic transition, at $T_2=158$ K for the ferro- to antiferromagnetic transition, and at $T_1=103$ K for the reentrant ferromagnetic transition. For $x=0.00$ sample we also notice that there is a clear sharp peak at 148.5 K. This behavior was reported previously[7,8] and the temperature was labeled as spin-reorientation temperature (T_{SR}). It was explained as a spin reorientation of the Mn moments from the c axis ⟨001⟩ direction to the basal plane ⟨110⟩ direction, which appears as a stable antiferromagnetic phase down to T_1. This T_{SR} is also observed clearly for the $x=0.01$ sample. This spin-reorientation behavior persists for all the samples up to $x=0.15$. The inset of Fig. 1 shows the spin-reorientation transition for some of the samples. It

 0021-8979/96/79(8)/5233/3/$10.00 © 1996 American Institute of Physics

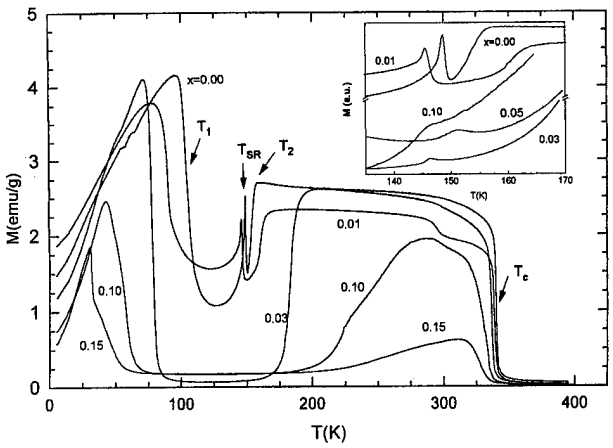


FIG. 1. Magnetization of $SmMn_2(Ge_{1-x}Si_x)_2$ ($x=0.00$–0.15) samples as a function of temperature at 100 G. Inset shows magnified view of the spin-reorient transitions.

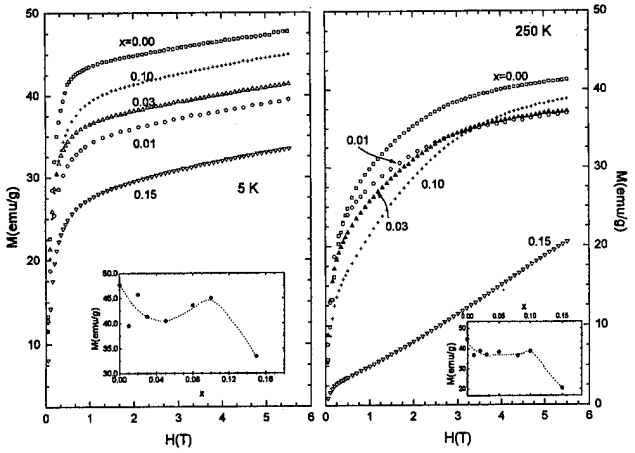


FIG. 2. Magnetization as a function of applied magnetic field at 5 K (a) and at 250 K (b). Insets show the magnetization values at the maximum field (5.5 T) as a function of Si concentration.

shows that the T_{SR} does not change significantly with increasing Si concentration, but that transition is not as sharp in higher concentration Si samples as that of pure $SmMn_2Ge_2$. From Fig. 1 what we also notice is that the increase of Si content in $SmMn_2(Ge_{1-x}Si_x)_2$ has the effect of increasing the temperature range of the antiferromagnetic phase. For example, the 55 K temperature range of the antiferromagnetic phase for the sample with $x=0.00$ increases to about 220 K for sample with $x=0.15$. The other thing to notice is that the ferro- to antiferromagnetic transition (T_2) becomes broader instead of sharp transitions observed for the samples with lower Si content.

Fujii *et al.*[3] suggested in the study of single crystal $SmMn_2Ge_2$ that at the ferro- to antiferromagnetic transition, (T_2) the R^a_{Mn-Mn} distance becomes smaller than the critical value of 0.2865 nm. This is why the sample transforms from the ferromagnetic to antiferromagnetic phase. For $SmMn_2Ge_2$ it has been demonstrated[9] by the application of external pressure on the temperature-dependent ac susceptibility measurements that ferro- to antiferromagnetic (T_2) and antiferro- to ferromagnetic (T_1) transitions are very sensitive to the intralayer distance. What Duraj *et al.*[9] have found is that, with the increase of external pressure, the temperature range of the antiferromagnetic phase of $SmMn_2Ge_2$ widens. Another study,[4] in which chemical pressure was used by substituting Gd for Sm in $SmMn_2Ge_2$, also shows the broadening of the antiferromagnetic region. In the case of $SmMn_2Ge_{1-x}Si_x)_2$, it is very likely that increasing the Si content effectively reduces the Mn–Mn in-plane distance. Consequently, as the Si content in $SmMn_2(Ge_{1-x}Si_x)_2$ is increased, the antiferromagnetic coupling becomes stronger. This effect results in a wider temperature range of the antiferromagnetic phase of $SmMn_2(Ge_{1-x}Si_x)_2$.

Figure 2(a) shows the magnetic field dependence of magnetization at 5 K of $SmMn_2(Ge_{1-x}Si_x)_2$ compounds for $x=0.00$ to $x=0.15$. For all the samples magnetization increases sharply up to about 0.5 T. Above 1.0 T magnetization increases linearly up to the maximum applied field of 5.5 T and never saturates. Magnetization values at the maximum applied field (5.5 T) are plotted against Si content in the inset of Fig. 2(a). It shows that magnetization does not change much for the samples up to $x=0.10$ and then drops fast.

Figure 2(b) shows the magnetic field dependence of magnetization of $SmMn_2(Ge_{1-x}Si_x)_2$ at 250 K for $x=0.00$ to $x=0.15$. The temperature 250 K falls in the high-temperature ferromagnetic phase (from M vs T data). Changes in magnetization for samples up to $x=0.10$ are broad for applied magnetic field up to 3.0 T and then increase slowly for field up to 5.5 T. Magnetization is not saturated for any sample at the maximum applied field of 5.5 T. The M vs H behavior at 250 K of $x=0.15$ sample shows its proximity in the antiferromagnetic phase. The magnetization values at the maximum applied field (5.5 T) are plotted against Si content in the inset of Fig. 2(b). It shows that magnetization decreases very slowly with the increase of Si content for up to $x=0.10$ then drops faster.

To know how the thermal expansion varies with temperature for different samples of $SmMn_2(Ge_{1-x}Si_x)_2$ and to know the order of the phase transitions, thermal expansion measurements were performed. Results are plotted in Fig. 3.

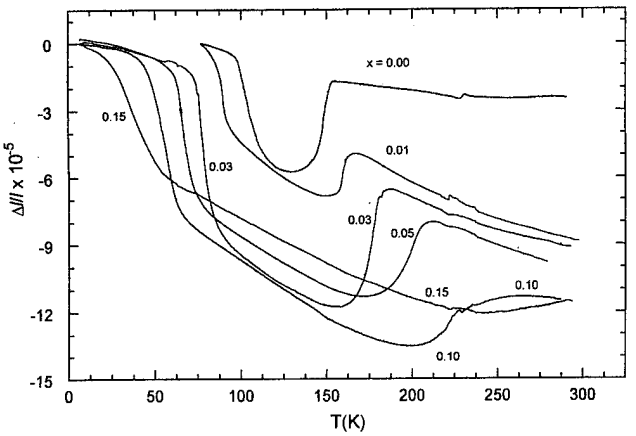


FIG. 3. Relative thermal expansivity $\Delta l/l$ of $SmMn_2(Ge_{1-x}Si_x)_2$ samples as a function of temperature for $x=0.00$ to 0.15.

Thermal expansion behavior of the samples reflects the corresponding magnetic properties (Fig. 1). Also, the transition temperatures (T_1 and T_2) found from magnetization and thermal expansion measurements agree for every sample. The antiferro- to ferromagnetic transitions (T_1) for samples with $x=0.00$ to $x=0.15$ shows a step change in thermal expansion measurements. This implies that the type of the phase transition at T_1 is first order. Similarly, ferro- to antiferromagnetic transitions (T_2) are of first order for $x=0.00$ to $x=0.10$ samples. However, for $x=0.15$ sample, the slope change at the phase transition suggests that the antiferro- to ferromagnetic phase transition (T_2) is most likely of second order. The anomalies found for all the samples in the temperature range 220 to 235 K came from the background. Thermal expansion data could also indicate the change in lattice parameters. The largest change in thermal expansion data occurs at the two first order phase transitions. Actual lattice parameters of $SmMn_2Ge_2$ and $Sm_{1-x}Gd_xMn_2Ge_2$ at different temperatures were determined by x-ray studies.[9,4] For both compounds it was found that at the ferro- to antiferromagnetic (T_2) and antiferro- to ferromagnetic transitions (T_1) the lattice constant a goes through a discontinuity. In the present study, the step changes in thermal expansion data (at T_1 and T_2 temperatures) of $SmMn_2(Ge_{1-x}Si_x)_2$ suggest a discontinuity in the lattice constant "a."

A phase diagram of $SmMn_2(Ge_{1-x}Si_x)_2$ is shown in Fig. 4. It shows that T_c essentially remains constant with increasing Si concentration. The ferro- to antiferromagnetic transition temperature (T_2) increases almost linearly with the increase of Si concentration. The antiferro- to ferromagnetic transition temperature (T_1) decreases almost linearly with the increase of Si concentration. The range of the antiferromagnetic phase increases sharply with increasing Si content. Temperature range of both ferromagnetic phases decrease with the increase of Si content. The spin-reorientation temperature T_{SR} does not change significantly for any of the samples.

SUMMARY

We have studied the magnetic and thermal properties of polycrystalline $SmMn_2(Ge_{1-x}Si_x)_2$ system for $x=0.00$ to $x=0.15$. It is found that the temperature range of stability of the antiferromagnetic phase increases with the increase of Si content. This behavior is explained as a consequence of the possible decrease in the in-plane Mn–Mn distance. We have demonstrated again that the magnetic properties of $SmMn_2Ge_2$ and the related compounds are very sensitive to the interatomic distances. We have determined the magnetic phase diagram of $SmMn_2(Ge_{1-x}Si_x)_2$.

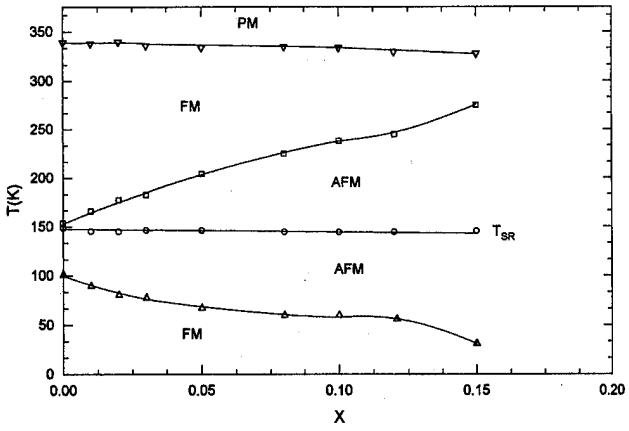


FIG. 4. Magnetic phase diagram of $SmMn_2(Ge_{1-x}Si_x)_2$. It shows the different magnetic phases, e.g., paramagnetic (PM), ferromagnetic (FM), and antiferromagnetic (AFM), that are present at different temperatures.

[1] A. Szytula, J. Alloys Comp. **178**, 1 (1992).
[2] A. Szytula and J. Leceijewicz, Handb. Phys. Chem. Rare Earths **12**, 133 (1989).
[3] H. Fujii, R. Okamato, T. Shigeoka, and N. Iwata, Solid State Commun. **53**, 715 (1985).
[4] M. Duraj, R. Duraj, and A. Szytula, J. Magn. Magn. Mater. **79**, 61 (1989).
[5] M. Duraj, R. Duraj, and A. Szytula, J. Magn. Magn. Mater. **82**, 319 (1989).
[6] R. Duraj, M. Duraj, and A. Szytula, J. Magn. Magn. Mater. **132**, 67 (1994).
[7] N. Ali, and S. Saha, J. Alloys Comp. **227**, 49 (1995).
[8] S. Saha and N. Ali (unpublished).
[9] M. Duraj, R. Duraj, A. Szytula, and Z. Tomkowicz, J. Magn. Magn. Mater. **73**, 240 (1988).

Remanent magnetization in the linear chain antiferromagnet $(CH_3NH_3)Mn_{1-x}M_xCl_3\cdot 2H_2O$, M=Cd or Cu

A. Paduan-Filho and C. C. Becerra
Instituto de Física, Universidade de São Paulo, CP 66318, São Paulo, SP, Brazil

F. Palacio
Instituto de Ciencia de Materiales de Aragon, CSIC, Universidad de Zaragoza, E-50009, Spain

The substitution of small amounts of Mn^{2+} by Cu^{2+} or Cd^{2+} ions in the linear chain antiferromagnet $(CH_3NH_3)MnCl_3\cdot 2H_2O$ ($T_N=4.12$ K) leads to the appearance of a remanent magnetic moment in the substituted compound. Magnetization measurements carried out in single crystals revealed that the remanent magnetization (M_r) appears along the direction of the easy axis when the sample is cooled through the ordering temperature in the presence of an axial magnetic field as low as few millioersteds. Samples with $x\sim 0.01$ of Cu and $x=0.008$ of Cd were investigated. The measured magnetization $M=M_r+\chi_{\|}H_{\text{axial}}$ observed at applied axial fields $H_{\text{axial}}=0.8$ Oe in both crystals is almost entirely due to the contribution of M_r since $\chi_{\|}H_{\text{axial}}$ is very small. Hysteresis curves were also obtained for the Cd diluted system and the results shows that at $T=1.5$ K a reversal in the direction of M_r is obtained for H_{axial} around 200 Oe. A comparison with previous recent observations in some three-dimensional diluted antiferromagnets is made. © *1996 American Institute of Physics.* [S0021-8979(96)18908-X]

The compound $(CH_3NH_3)MnCl_3\cdot 2H_2O$ (MMC) is a quasi-one-dimensional Heisenberg-like antiferromagnet.[1] A three-dimensional ordering of the linear chains occurs at $T_N=4.12$ K. From the value of the spin–flop field at $T=0$ in the magnetic phase diagram a ratio of the anisotropy to the exchange field $H_A/H_E=4\times 10^{-3}$ was estimated.[2] In this paper we describe the effects of the substitution of the Mn^{2+} ion by Cu^{2+} and Cd^{2+} in the magnetic properties of this system at low field. We measured the magnetization with a vibrating sample magnetometer (VSM) in the presence of very small axial fields (H_{axial}) provided by a copper solenoid mounted coaxally with the pick-up coils of the VSM.

Figure 1 shows the temperature dependence of the magnetization data for powder samples of MMC with 1% of Cu and 0.8% of Cd (percentages were obtained from relative concentration of the metallic ions in the growing solutions of the crystals). The samples were cooled through T_N in the presence of a magnetic field H_{axial} of 0.8 Oe applied along the axis of the detecting coils. The principal characteristic of the data is the appearance of a spontaneous magnetic moment. This moment is much higher in the Cd substituted compound than in the Cu one. The measured moment can be described by $M=M_r+\chi H_{\text{axial}}$, where M_r is the spontaneous moment and χ is the susceptibility of the compound. In both cases χH_{axial} is much smaller than M_r. Within the resolution of the VSM, no moment was detected in the measurements performed on undiluted ($x=0$) powder samples of MMC. In the Cu doped compound the spontaneous moment develops at a temperature $T=4.5$ K, which is slightly higher than the ordering temperature of pure MMC. In the sample with Cd the moment appears at $T=3.9$ K.

Figure 2 shows the M vs T curves obtained for a single crystal of MMC with 0.8% of Cd. The magnetization was measured along the antiferromagnetic easy axis, in the presence of six different axial fields H_{axial} ranging from 0.08 Oe to 8 Oe which were applied along the easy axis of the crystal. No magnetic moment was detected in measurements made along a direction perpendicular to the easy axis. Thus, the occurrence of the spontaneous magnetization in the Cd doped crystal is restricted to the direction of the easy axis. This excludes a canting of the antiferromagnetic sublattices as the origin of this effect. At least two important features should be pointed out in the data: (a) the spontaneous magnetization saturates at low axial fields (at 4.8 Oe it is almost saturated in the curves shown in Fig. 2), and (b) there is a region, just below T_N, where the moment appears to be saturated at fields as low as 80 mOe. As for the powder samples the measured magnetization can be described by $M(T)=M_r(T)+\chi_{\|}H$, where $\chi_{\|}$ is the parallel susceptibility. The term $\chi_{\|}H$ is here also much smaller than M_r. The saturated value of M_r at 1.5 K is about 0.6% of the value of the

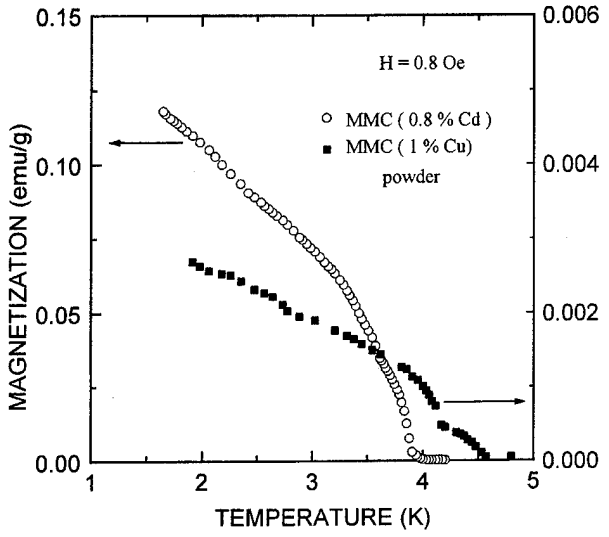


FIG. 1. Temperature dependence of the magnetization of powder samples of MMC with: 0.8% of Cd substitution (○) and 1% of Cu substitution (■). Note the difference in the right-hand scale (for Cu doping) and left-hand scale (for Cd doping).

 0021-8979/96/79(8)/5236/2/$10.00 © 1996 American Institute of Physics

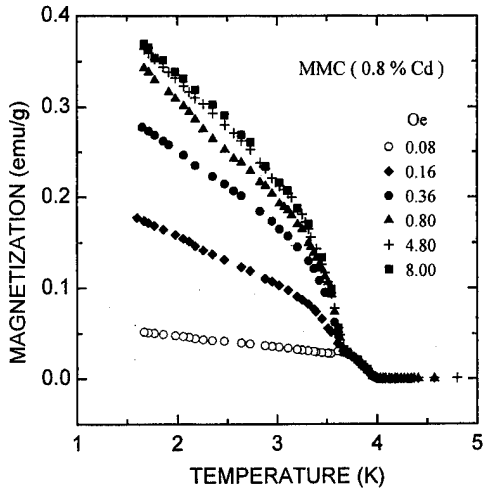


FIG. 2. Temperature dependence of the magnetization along the easy axis of antiferromagnetic alignment of a crystal of MMC with 0.8% of Cd substitution.

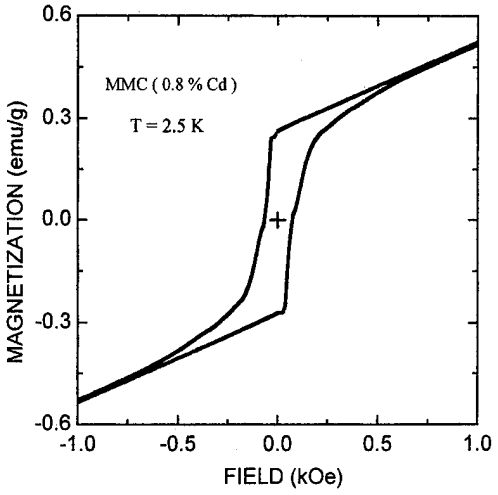


FIG. 3. Hysteresis cycle of the Cd-substituted crystal at $T=2.5$ K after cooling the sample in an axial field of 4 Oe.

sublattice magnetization of pure MMC. This value is also roughly higher by a factor of 3 than that measured in the corresponding powder sample. No thermal hysteresis were observed in the measurements, e.g., for a given axial field the experimental points obtained during the cooling process and those obtained in the heating process fall into the same M vs T curve.

We observed that once a value of the remanent magnetization is established below T_N the removal of the small axial field has no effects on the value of M_r, e.g., no relaxation effects were detected at these low fields. This behavior was also observed in the measurements made with the powder samples of Cu and Cd doped compounds. The influence of an applied axial field at temperatures below T_N was also investigated. Figure 3 shows the hysteresis cycle obtained at $T=2.5$ K after the sample being cooled in an axial field of 4.0 Oe. Here the external field was provided by a small superconducting coil. Cycles at different temperatures where obtained and the observed behavior for these cycles indicate that at $T=1.5$ K a field of the order of 200 Oe suffices to reverse the remanent magnetization of the sample. This "coercive" field decreases approaching T_N and from the data obtained at 3.77 K we found that a field of ~20 Oe is needed in order to reverse the magnetization.

Similar behavior was recently reported in other diluted antiferromagnets.[3–6] In particular, the general features here observed are analogous to those found in the diluted systems $A_2Fe_{1-x}In_xCl_5\cdot H_2O$ (A=K, Rb)[3,4] and $Mn_{1-x}Zn_xF_2$.[5] These are also low-anisotropy antiferromagnets but with a three-dimensional character. The overall shape of the M vs T curve and the saturation behavior are very similar except for the region near T_N were, as pointed out in the present case, the saturation seems to occur at very low fields. It was shown[7] that the behavior of the remanent magnetization follows a universal law with a quasilinear behavior in the range $0.25\ T_N<T<0.75\ T_N$. Our data seem also to follow this last tendency. Remanent magnetization was also reported in diluted $Fe_{1-x}Zn_xF_2$ ($x=0.54$).[6] This is a much higher anisotropy system, and the reported data do not show the linearlike trend refered above.

Some previous reports of remanent magnetization in diluted antiferromagnets have been related to an excess magnetization (ΔM) observed between field-cooled (fc) and zero-field-cooled (zfc) procedures, i.e., $\Delta M(T)=M_{fc}(T)-M_{zfc}(T)$.[8] All these studies where performed at much higher fields (>1000 Oe). They were interpreted in terms of an excess magnetization due to random field (RF) induced domains. This RF induced excess magnetization increases with H^α ($\alpha\geq 2$). The effects here reported occurs at much lower fields and saturates at low fields. This saturation indicates that RF are not the origin of this remanent magnetization. It is an intrinsic characteristics of this disordered system.

Our observations seems to agree well with the formation of a structure of domains in the doped samples of MMC. Each of these domains would carry an excess magnetization at their walls. A field of the order of few Oe applied along the easy axis is sufficient to saturate the excess magnetization. The walls of these domains would be stabilized ("pinned") by the presence of the site disorder introduced by doping.

This research was supported by CNPq, FAPESP, CICYT Grant No. MAT94-0043, and the Programa de Cooperation Cientifica com Iberoamerica.

[1] S. Simizu, J. Chen, and S. A. Friedberg, J. Appl. Phys. **55**, 2398 (1984).
[2] A. Paduan-Filho and N. F. Oliveira, Jr., J. Phys. C **17**, L857 (1984).
[3] C. C. Becerra, A. Paduan-Filho, T. Fries, Y. Shapira, and F. Palacio, J. Phys.: Condens. Matter **6**, 5724 (1994).
[4] F. Palacio, M. Gabas, J. Campo, C. C. Becerra, A. Paduan-Filho, T. Fries, and Y. Shapira, Phys. Scripta T **55**, 163 (1994).
[5] Fries, Y. Shapira, A. Paduan-Filho, C. C. Becerra, and F. Palacio, J. Phys.: Condens. Matter **5**, 8083 (1993).
[6] M. Lederman, J. Hammann and R. Orbach, Physica B **165–166**, 179 (1990).
[7] C. C. Becerra, A. Paduan-Filho, T. Fries, Y. Shapira, and F. Palacio, J. Magn. Magn. Mater. **140**, 1475 (1995).
[8] C. Djurberg, J. Mattsson, and P. Nordblad, J. Appl. Phys. **75**, 5541 (1994).

Magnetic properties of Ni_2In type $(Co_{1-x}Mn_x)_{65}Ge_{35}$ compounds

Hiroshi Shiraishi
Natural Science (physics), Shibaura Institute of Technology, Fukasaku 307, Oomiya, Saitama 330, Japan

Tomiei Hori
Department of Electronic Information Systems, Shibaura Institute of Technology, Fukasaku 307, Oomiya, Saitama 330, Japan

Yasuo Iguchi
Natural Science (physics), Shibaura Institute of Technology, Fukasaku 307, Oomiya, Saitama 330, Japan

Yasuo Yamaguchi and Masayoshi Ohashi
Institute of Materials Research, Tohoku University, Sendai 980, Japan

Kazuo Kanematsu
The Physical Science Laboratories, Nihon University at Narashino, Funabashi, Chibaken 274, Japan

The high temperature phase of $(Co_{1-x}Mn_x)_{65}Ge_{35}$ is found to be of the hexagonal Ni_2In type in the range of $0 \leqslant x \leqslant 0.6$. Co_2Ge is Pauli paramagnetic, and ferromagnetism is induced with substitution of Mn for Co. Magnetization measurement and x-ray diffraction experiments for these compounds have been performed. The x dependences of the Curie temperature T_c and magnetization show a maximum near composition $x=0.25$. X-ray studies show that the lattice constants c are minimum at $x=0.25$. The x dependence of the relative intensities of x-ray lines suggests that the Mn and Co atoms at $2(a)$ sites in the compound $x=0.25$ align alternately in the c direction. The Co atoms at $2(d)$ site and the Ge atoms at $2(c)$ site shift along the c direction are found. The neutron diffraction experiment of $x=0.25$ also support such crystal structure. Maximum of Curie temperature and magnetization of compounds near $x=0.25$ are discussed with the ordering of Mn and Co atoms in the crystal lattice. © *1996 American Institute of Physics.* [S0021-8979(96)19008-4]

I. INTRODUCTION

The compound Co_5Ge_3 (Ref. 1) has a hexagonal Ni_2In type structure and shows Pauli paramagnetism. We found that the high temperature phase of the $(Co_{1-x}Mn_x)_{65}Ge_{35}$ system shows a hexagonal structure of the Ni_2In type in the range of $0 \leqslant x \leqslant 0.6$. Magnetization measurements show that ferromagnetism is induced with substitution of Mn for Co. The compound CoMnGe (Ref. 2), which is nearly the same as the $x=0.5$ member of this system, is a ferromagnet with a Curie temperature of 265 K.[3] Mn and Co atoms occupy the $2(a)$ site and $2(d)$ site, respectively in the crystal lattice shown in Fig. 1 and the magnetic structure is of the collinear type with the spins lying in the basal plane.[4] Magnetization measurements of $(Co_{1-x}Mn_x)_{65}Ge_{35}$ samples show that the x dependences of the Curie temperature and magnetization have a maximum near the composition $x=0.25$.

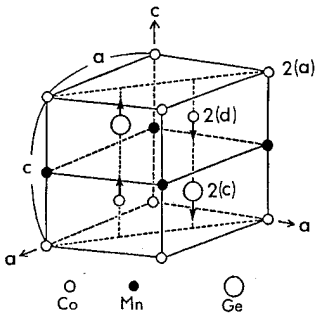


FIG. 1. Determined atomic configulation and shift of Co and Ge atoms in the $2(d)$ and $2(c)$ site, respectively. Mn and Co atoms are ordered in $2(a)$ site. The shift in the c direction was estimated to $0.04c$ from x-ray studies.

In order to investigate the crystal and magnetic properties of the $(Co_{1-x}Mn_x)_{65}Ge_{35}$ system $(0 \leqslant x \leqslant 0.6)$, which is slightly Ge rich from the ideal Ni_2In type, we have made x-ray diffraction experiments, magnetization measurements, and neutron diffraction experiments for $x=0.25$. The maxima of Curie temperature and magnetization of compounds near $x=0.25$ are discussed in terms of the ordering of Mn and Co atoms in the crystal lattice.

II. EXPERIMENTAL PROCEDURE

The polycrystalline $(Co_{1-x}Mn_x)_{65}Ge_{35}$ compounds were prepared from cobalt (99.95% pure), electrolytic manganese (99.94% pure) and germanium (99.999% pure) by arc furnace melting in an argon atmosphere. The melting was repeated several times for homogeneity. The samples were sealed in an evacuated quartz tube with argon gas of 2.2×10^4 Pa, homogenized for more than 170 ks (2 days) at 1073 K, and quenched into water. The crystal structure of powder samples at room temperature was asertained by x-ray diffraction with Fe K_α radiation. The x-ray diffraction intensity was measured by using the stop count method. Magnetization measurements were made by Faraday type automatic magnetic balance in magnetic fields up to 0.80 MA/m (10 kOe) in the temperature range of 4.2 K and 600 K. Neutron diffraction spectra were taken for $x=0.25$ powder sample at room temperature, using Kinken Powder Neutron Diffractmeter (KPD) of Tohoku University installed in the JRR-3M reactor at Japan Atomic Energy Research Institute. The wave length is 1.767 A. The vacancy concentration of a $x=0.25$ sample was measured by picnometry using CCl_4.

 0021-8979/96/79(8)/5238/3/$10.00 © 1996 American Institute of Physics

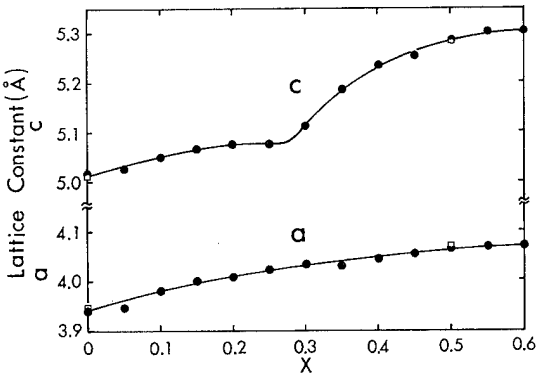


FIG. 2. Composition x dependences of lattice constants a and c at room temperature. □ of $x=0.5$ is data taken from Ref. 3.

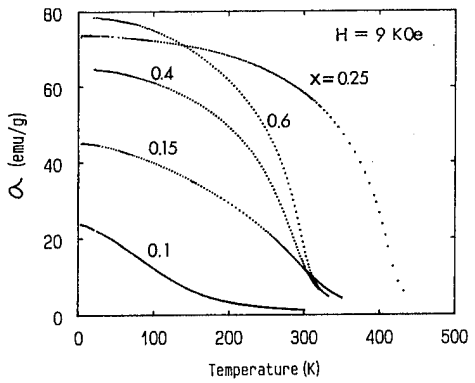


FIG. 4. Temperature dependences of magnetization for the compounds of various composition x in the magnetic field of 9 kOe.

III. RESULTS AND DISCUSSION

The concentration dependences of the lattice constants a and c at room temperature are shown in Fig. 2. Both a and c increase with increasing x. It was found that a contraction of the c axis occurs in the compounds near $x=0.25$ while the a axis changes smoothly with x. The change of unit cell volume with x, calculated from the measured lattice constants a and c is shown in Fig. 3. The contraction of the c axis or unit cell volume may be caused by the ordering of Mn and Co, as is shown later.

The temperature dependence of the magnetization σ for $x=0.1$, $x=0.15$, $x=0.25$, $x=0.4$, $x=0.6$ are shown in Fig. 4. $Co_{65}Ge_{35}$ ($x=0$) is a Pauli paramagnet, and ferromagnetism is induced by substitution of Mn for Co. The magnetization σ of all compounds shows a convex curve against temperature except that of $x=0.1$, which shows a concave curve. They are typical of a ferromagnet. For the composition $x=0.25$, the magnetization has a value of 1.09 μ_B/(Co,Mn) at 77 K, and 0.88 μ_B/(Co,Mn) at 295 K.

Figure 5 shows the x dependence of the Curie temperature T_c. The Curie temperature is determined from the intersection of σ_0^2 vs temperature curve and T axis. σ_0 is spontaneous magnetization. T_c shows a maximum near $x=0.25$, i.e., $T_c=412$ K at $x=0.25$. In the case of Ni_2In type $(Co_{1-x}Fe_x)_{1.67}$ Ge compound,[5] T_c and σ increase monotonically with increasing x. In the paramagnetic region above the Curie temperature, the reciprocal susceptibility χ^{-1} vs T curve shows good linearity. The x dependence of paramagnetic Curie temperature Θ obtained from χ^{-1} vs T curve is almost same as the x dependence of T_c although Θ is slightly (~10 K) high. The effective magnetic moment μ_{eff} of 4.5 μ_B/Mn for the compound of $x=0.5$ is obtained from the χ^{-1} vs T curve. This value is slightly larger than 4.05 μ_B/Mn obtained for CoMnGe by Szytula *et al.*[4] The cause of the maximum observed in the x dependences of T_c and σ are thought to be due to an ordering of the Mn and Co atoms in the $2(a)$ site.

In order to investigate the ordering of Mn and Co atoms in the $2(a)$ site, the x-ray relative intensity $I(001)/I(110)$ was measured. The 001 reflection is a super lattice line that appears due to the ordering of Mn and Co atoms in the $2(a)$ site as shown in Fig. 1, while the 110 reflection is a fundamental line. The 001 reflection is very weak, so we measured the intensity by means of the stop count method. The x dependence of $I(001)/I(110)$ is shown in Fig. 6. The relative intensity shows a maximum just at $x=0.25$. A shift of atoms along the c direction in the $2(d)$ and $2(c)$ sites makes the 001 reflection, but this reflection is small as is obvious from the calculation of x-ray intensity. So the appearance of 001 line is concluded to be the ordering of Mn and Co atoms in the $2(a)$ site.

The shift of Co and Ge atoms along the c direction in the $2(d)$ and $2(c)$ sites is reflected in the remarkable increase of the 104 line intensity and to the decrease of 002, 112, and

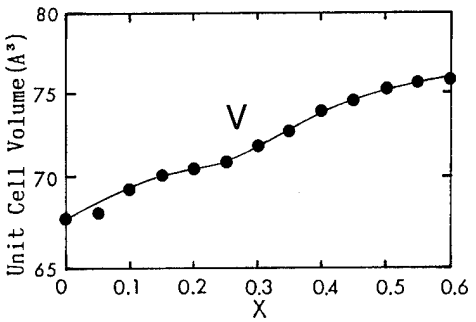


FIG. 3. The composition x dependence of unit cell volume, calculated with the measured lattice constants a and c.

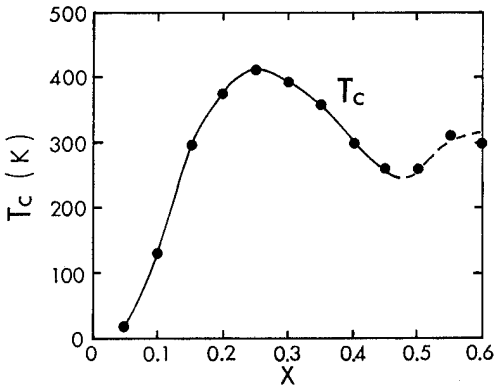


FIG. 5. Composition x dependence of the Curie temperature T_c, determined from σ_0^2-T extraporation.

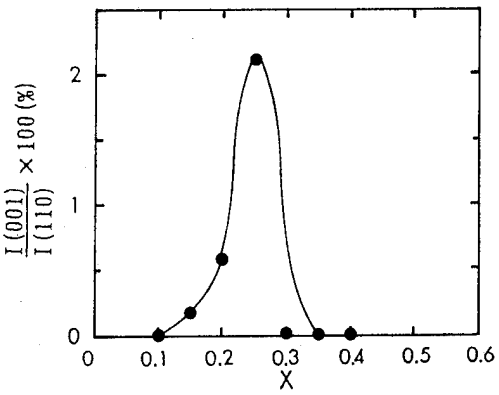


FIG. 6. Composition x dependence of x-ray relative intensity $I(001)/I(110)$, which is measured by stop count method. The 001 line is the superlattice line when Mn and Co atoms are ordered in the $2(a)$ site.

114 line intensities. The observed intensity of 104 line of $0.15 \leqslant x \leqslant 0.25$ are comparably strong. We have measured the line intensities of $x=0.25$ in order to determine the amount of the shift. The shift in the c direction amounts to $0.04c$ in $x=0.25$ from observed and calculated intensities of these lines, where c is lattice constant.

The vacancy concentration in the $2(d)$ of the compound with $x=0.25$ is estimated from the density measurement by picnometry using CCl_4. The vacancy concentration amounts to 8.5%. This value is used to calculate the intensity of neutron scattering.

Neutron diffraction experiment was done for the compound of $x=0.25$ at room temperature to get additional crystallographic and magnetic information. The obtained neutron diffraction intensity vs Bragg angle 2θ is shown in Fig. 7(a). The analyzed intensity of the nuclear and magnetic part vs 2θ is shown together with the observed intensity in Fig. 7(b). The condition of calculation is as follows. The shift of Co atoms in $2(d)$ site and Ge in $2(c)$ site along the c direction is used $0.04c$ as determined by x-ray relative intensity. The vacancy concentration used is 8.5% as determined by picnometry. It is assumed that all of the vacancies exist in $2(d)$ site and that the Co and Mn atoms in $2(a)$ site have perfect order. The Debye temperature is determined by fitting the calculated nuclear intensity data to the observed data at higher Bragg angles where the intensity of the magnetic term can be neglect within the experimental error. The fitting is done in a manner as to minimize the $\Sigma\Delta^2$ where Δ is the difference of calculated intensity and observed one. The determined Debye temperature is 240 K.

The magnetic intensity is calculated with the appropriate Mn and Co moment in the $2(a)$ site and Co moment in the $2(d)$ site but with the total moment to be consistent with the moment obtained from the magnetic measurements. The total intensity (nuclear+magnetic) is also fitted to the observed one so as to minimize the $\Sigma\Delta'^2$. The analyzed result is that Mn and Co moment in the $2(a)$ site is $(2.8\pm0.2)\ \mu_B$ and $(0.77\pm0.2)\ \mu_B$, respectively and Co moment in the $2(d)$ site is $(0.2\pm0.2)\ \mu_B$ and lying in the basal plane.

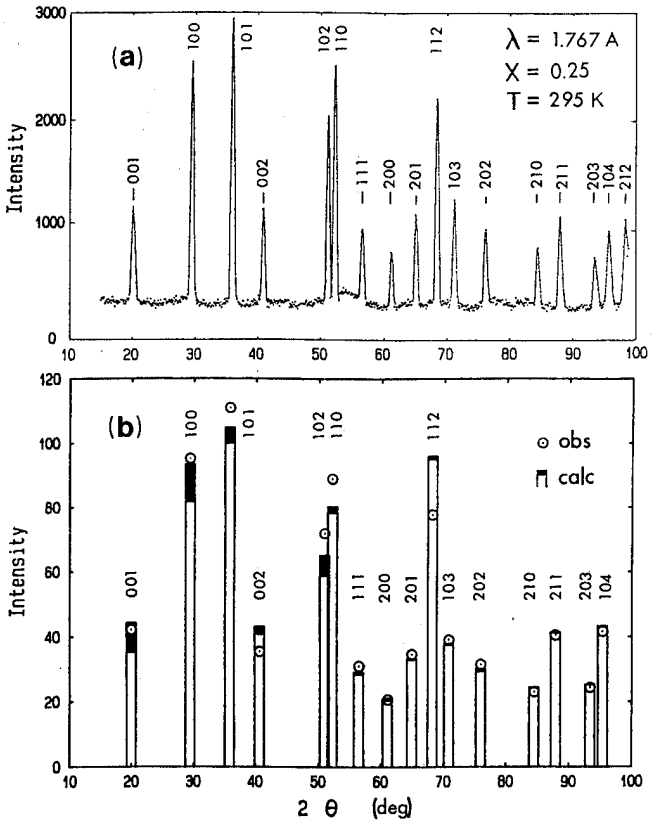


FIG. 7. (a) Powder neutron diffraction spectra for the compound of $x=0.25$ at room temperature. (b) Calculated neutron diffraction intensity for the compound $x=0.25$. The circles are observed intensities and rectangles are calculated ones. See the text for the condition of calculation.

IV. CONCLUSIONS

Ordering of Mn and Co atoms in the $2(a)$ site and a contraction of lattice constant c was found in the compound $(Co_{1-x}Mn_x)_{65}Ge_{35}$ of composition near $x=0.25$ as shown in Fig. 1. Further, the shift of atoms in the $2(d)$ and $2(c)$ sites along the c direction was found.

Maximum of the magnetization and Curie temperature of compound near $x=0.25$ may be caused by contraction of lattice constant c that is induced by the ordering of Mn and Co in the $2(a)$ site, i.e., the shortening of first and second nearest neighbor Co–Mn and third nearest neighbor Co–Co distances is the cause of the maximum. The magnetic interactions J_1, J_2, and J_3 are thought to be ferromagnetic.

ACKNOWLEDGMENT

A part of this work was carried out under the Visiting Researcher's Program of the Institute for Materials Research, Tohoku University.

[1] K. Kanematsu, J. Phys. Soc. Jpn. **17**, 85 (1962).
[2] L. Castelliz, Z. Metallkde, **46**, 198 (1955).
[3] V. Johnson, Inorg. Chem. **14**, 1117 (1975).
[4] A. Szytula, A. T. Pedziwiatr, Z. Tomkowicz, and W. Bazela, J. Magn. Magn. Mater. **25**, 176 (1981).
[5] K. Kanematsu and K. Yasukouchi, J. Phys. Soc. Jpn. **18**, 1429 (1963).

Magnetism of the solid solution $GdGa_{1-x}Ge_x$ (abstract)

A. Leithe-Jasper and K. Hiebl
Institut für Physikalische Chemie, Universität Wien, Währingerstrasse 42, 1090 Wien, Austria

Ternary metal excess rare-earth gallides and germanides have been extensively investigated concerning their interesting physical properties with respect to magnetic and electronic correlations, such as magnetic ordering, intermediate valency, Kondo or heavy fermion behavior. A solid solution of the binary phases GdGa and GdGe was found investigating the phase equilibria in the pseudobinary system Gd-Ga-Ge at $T=800$ °C. Samples with the composition $GdGa_{1-x}Ge_x$ ($x=0$, 0.1, 0.15, 0.25, 0.5) were prepared by arc melting the elements under inert atmosphere and subsequent annealing (350 h) in evacuated silica capsules. The crystal structure and unit-cell dimensions were determined by x-ray powder analyses (Guinier technique, Cu $K\alpha_1$ radiation). Powder patterns were indexed on the basis of a C-centered orthorhombic unit cell. No deviations of the structure type α-ITI (CrB) have been encountered. A monotonic decrease of the unit-cell volume versus Ge concentration is observed. However, a significant decrease of the b and c parameters is thereby compensated by an increase of the a parameter. Magnetic measurements were performed by SQUID and ac techniques over a temperature range $T=5$–300 K and in external fields up to 6 T. All samples exhibit ferromagnetic order with slightly decreasing T_c as well as values of magnetization (at $T=5$ K and $H=0.1$ T) with increasing concentration x. However, metamagnetic transitions are revealed for all samples with $x>0$. The results are discussed within the concept of indirect exchange interaction (RKKY-type interaction). © *1996 American Institute of Physics.*
[S0021-8979(96)42808-3]

Neutron scattering and magnetization clouds in dilute Pd based alloys

R. E. Parra and A. C. González
Centro de Física, Instituto Venezolano de Investigaciones Científicas, Apartado 21827, Caracas 1020-A, Venezuela

Neutron scattering data for dilute PdMn, PdCo, and PdFe alloys show forward peaks at small values of K, which indicate an inhomogeneous distribution of the magnetization in these alloys. These inhomogeneities indicate the existence of magnetization clouds that produce the ferromagnetism in these materials; the shape of the peaks at small K also suggest a quasielastic contribution to the neutron diffuse scattering. We, therefore, calculated the neutron scattering cross sections for these alloys using a local moment model; we also developed an analytic expression for the magnetization clouds that can be compared with experimental results. The calculations were made using Monte Carlo methods in the dilute alloy region of impurity concentration. © *1996 American Institute of Physics.* [S0021-8979(96)19108-0]

The unpolarized neutron scattering of PdCo, PdMn, and PdFe alloys show large peaks at small values of the wave vector K which would indicate magnetization clouds bigger in magnitude than can be obtained by magnetization measurements.[1–3] These results suggest a contribution to the diffuse neutron scattering that cannot be attributed to the magnetization cloud.

Since the pioneering work of Low and Holden,[2] using neutron scattering to study PdCo and PdFe alloys, many authors have attempted to model theoretically their results. Later, several magnetic measurements, including neutron scattering, were also made on PdMn. In this latter case, there was some uncertainty regarding how much of the giant moment was localized on the impurity. In this work, we present an analysis of the neutron scattering for dilute PdCo, PdFe, and PdMn alloys in order to explain the magnetic characteristics mentioned. We used a local moment model[4,5] and Monte Carlo simulation methods for this purpose.

We assume that the impurity moment is not affected by its magnetic environment while the moment of host atoms at site n is

$$\mu_n = p_n \mu_i f_i + (1-p_n) f_h \sum_{m \neq n} \frac{\alpha \mu_i}{\phi_0} \phi_{n-m} p_m , \tag{1}$$

where i refers to an impurity atom and h to a host atom, p_n is a site occupation operator, f is the magnetic form factor, the ϕ's are magnetic moment perturbations, and α is equal to J_{hh}/J_{ih}, with the J's being exchange constants. The Fourier transforms of the moments is given by

$$c(1-c)M(K) = \sum_n e^{iK\cdot n} \langle (p_0 - c)\mu_n \rangle , \tag{2}$$

where $M(K)$ is a magnetic moment-site occupation correlation that can be determined by neutron diffuse scattering. For polycrystals, we perform the spherical averages that appear in Eq. (2), and to make the calculations simpler, we introduce the function m_n defined by

$$m_n = \frac{\alpha \mu_i}{\phi_0} \phi_n , \tag{3}$$

which is equal to μ_n for Pd atoms and to $\alpha\mu_i$ for the impurity atom at site 0. By a Fourier transformation this equation gives

$$m(K) = \sum_n m_n e^{iK\cdot n} , \tag{4}$$

which can be solved obtaining

$$m(K) = \frac{\alpha \mu_i}{\phi_0 [1 - \Gamma F_1(K)]} , \tag{5}$$

where Γ is the susceptibility enhancement factor of palladium and $F_1(K)$ is the first-shell structure factor. Doing this we obtain:

$$M(K) = \mu_i f_i + (1-c) f_h [m(K) - \alpha \mu_i] - c f_h [m(0) - \alpha \mu_i] . \tag{6}$$

This is the general expression that we used to calculate the neutron scattering. In the case of very dilute alloys ($c \to 0$), we obtain a simpler expression

$$M(K) = \mu_i f_i + f_h [m(K) - \alpha \mu_i] . \tag{7}$$

At $K=0$ we are measuring the total size of the magnetization cloud

$$M(0) = \frac{\alpha \mu_i}{\phi_0 [1-\Gamma]} + (1-\alpha)\mu_i , \tag{8}$$

which can be compared with the results obtained by magnetization measurements using the expression

$$M(0) = \frac{d\mu}{dc} , \tag{9}$$

where $\mu = c\mu_i + (1-c)\mu_h$. From Eq. (8) we can then obtain the parameter α, using the value of the susceptibility enhancement factor $\Gamma = 0.947$ as determined by Medina and Parra[4] for Pd.

The values of $M(K)$ were calculated using Eq. (6), and were compared with experimental polarized neutron scattering values for dilute PdMn alloys.[6] The values of μ_{Mn} and of the size of the magnetization cloud, $M(0)$, had to be corrected for antiferromagnetic interactions between Mn pairs.

 0021-8979/96/79(8)/5242/3/$10.00 © 1996 American Institute of Physics

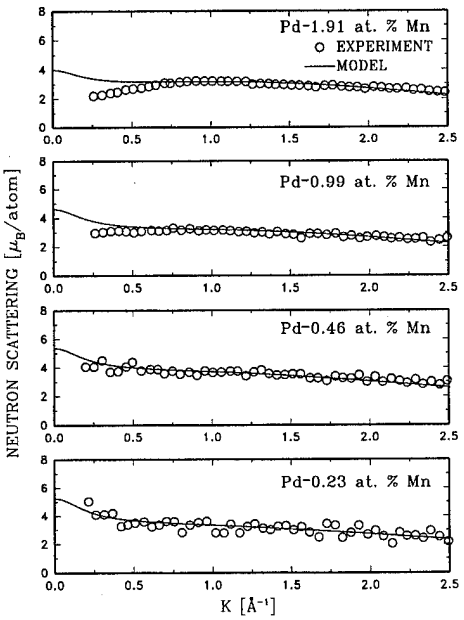


FIG. 1. Comparison of the calculated polarized neutron scattering values with experimental data (Ref. 6) for PdMn dilute alloys.

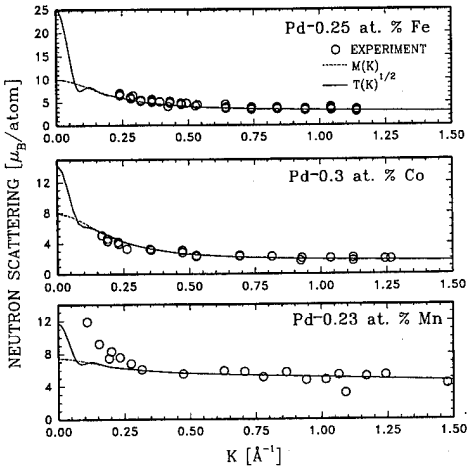


FIG. 2. Calculated unpolarized neutron scattering is compared with experimental data (Refs. 2 and 9) for PdFe, PdCo, and PdMn dilute alloys.

If the alloys were totally ferromagnetic we would have a moment of $\mu_{\mathrm{Mn}}=5\ \mu_B$, in agreement with an $S_{5/2}$ configuration for Mn, and a value of $M(0)\approx 7.5\ \mu_B$ that should agree with Eq. (9). Using the results of Star *et al.*,[7] we interpolated values of $M(0)$, for these concentrations, to determine the parameter α using Eq. (8). This parameter measures the ferromagnetic interaction host impurity, which we assume to be constant. The new corrected values of $M(0)$ were then calculated using the values of μ_{Mn} obtained by Cable and David[6] with polarized neutron scattering. We also corrected for atomic short range order (ASRO), using the values obtained by Morgownik *et al.*[8] for a Pd 9.95 at % Mn alloy since the ASRO parameters have not been measured for the concentrations studied in this work. Therefore, we assumed, that the ASRO parameters were concentration dependent, i.e., that they are proportional to the values obtained by Morgownik *et al.*, and that the factor of proportionality is $(c_i c_h)/(c_{iM} c_{hM})$, where i and h refer to the impurity and host, respectively, and M refer to the Pd 9.95 at % Mn alloy. With these values we then calculated $M(K)$ using Eq. (6) and compared them with the polarized neutron scattering data. The results are shown in Fig. 1. The calculation agrees with experimental data for alloys at the lower concentrations; as the concentration is increased there is a small discrepancy at low K.

We also calculated unpolarized neutron scattering and compared it with the experimental data for dilute PdFe, PdCo, and PdMn alloys.[2,9] We made Monte Carlo calculations using the Hamiltonian

$$H=-\frac{1}{2}\sum_{\substack{i,j\\ i\neq j}} J_{ij}S_i\cdot S_j-\sum_i B\cdot S_i, \tag{10}$$

with a field B along the z axis assumed perpendicular to K and with the conditions that the total magnetic moment keeps its orientation and that the local field is unaffected by the field B.

The quasielastic scattering contribution to the neutron measurements can be calculated using the following formula:

$$T(K)=\frac{1}{(0.27)^2 c(1-c)N}\frac{d\sigma}{d\Omega}=|M(K)|^2\Big\{(\overline{\langle S^{\perp}\rangle})^2 + \frac{1}{c(1-c)N}\sum_{ij} e^{iK\cdot(r_i-r_j)}[\langle S_i^{\perp}\cdot S_j^{\perp}\rangle-(\overline{\langle S^{\perp}\rangle})^2]\Big\}. \tag{11}$$

In this expression, $M(K)$ is given by Eq. (6), $S_i^{\perp}$ is the component of S_i perpendicular to K, the overhead bar indicates spatial averages, and $\langle\rangle$ symbolizes thermal averages.

We then calculated $\langle S_i^z\rangle$, $\langle S_i\cdot S_j\rangle$, and $\langle S_i^z S_j^z\rangle$ from which we obtained the following quantities, needed to calculate $T(K)$ using Eq. (11):

$$\langle S_i^{\perp}\rangle=\langle S_z^{\perp}\rangle\hat{Z}, \tag{12}$$

$$\langle S_i^{\perp}\cdot S_j^{\perp}\rangle=\tfrac{1}{2}\langle S_i^z S_j^z\rangle+\langle S_i\cdot S_j\rangle. \tag{13}$$

The calculations were performed at the temperature of the experiments. The results are shown in Fig. 2. In the case of PdMn, there is a long range contribution that can not be accounted for with this model. On the other hand, the agreement is good for PdFe and PdCo alloys. The calculated scattering shows a strong component of quasielastic scattering due to long range thermal and spatial fluctuations. These long range components of the scattering do not contribute to the magnetization, which is formed by the impurity moment plus all the small moments residing in Pd atoms.

[1] R. M. Bozorth, P. A. Wolff, D. D. Davis, V. B. Compton, and J. H. Wernick, Phys. Rev. **122**, 1157 (1961).
[2] G. G. Low and T. M. Holden, Proc. Phys. Soc. London **89**, 119 (1966).
[3] G. J. Nieuwenhuys and B. H. Verbeek, J. Phys. F **7**, 1497 (1977).
[4] R. Medina and R. E. Parra, Phys. Rev. B **26**, 5187 (1982).

[5]R. Medina, R. E. Parra, G. Mora, and A. C. González, Phys. Rev. B **32**, 1628 (1985).
[6]J. W. Cable and L. David, Phys. Rev. B **16**, 297 (1977).
[7]W. M. Star, S. Foner, and E. McNiff, Phys. Rev. B **12**, 2690 (1975).
[8]A. F. Morgownik, G. J. Nieuwennhuys, J. A. Mydosh, and C. Van Dijk, J. Phys. F **17**, 199 (1987).
[9]C. J. De Pater, C. van Dijk, and G. J. Nieuwenhuys, J. Phys. F **5**, L58 (1975).

Polarization analysis of the electron spin resonance lines in the $S=1$ one-dimensional antiferromagnet $Ni(C_3H_{10}N_2)_2NO_2ClO_4$

M. Hagiwara and K. Katsumata
The Institute of Physical and Chemical Research (RIKEN), Wako, Saitama 351-01, Japan

The results of electron spin resonance (ESR) measurements on the $S=1$ one-dimensional Heisenberg antiferromagnet $Ni(C_3H_{10}N_2)_2NO_2ClO_4$ (NINO) are reported. We have analyzed the polarization dependence of the ESR transition between the singlet ground state and the first excited triplet which is forbidden for an ordinary Hamiltonian. Our results are consistent with the theory by Sakai and Shiba [J. Phys. Soc. Jpn. **63**, 867 (1994)] proposed to explain the forbidden transition.
© *1996 American Institute of Physics.* [S0021-8979(96)19208-7]

One-dimensional Heisenberg antiferromagnets (1DHAFs) have attracted much attention since Haldane conjectured[1] that a 1DHAF with an integer-spin quantum number (S) has an energy gap in the excitation spectrum, while that with a half-odd-integer S has no energy gap. Motivated by this conjecture, a number of experiments have been carried out. The existence of the energy gap in 1DHAFs with $S=1$ was confirmed experimentally by neutron scattering[2] and magnetization[3] measurements. Electron spin resonance (ESR) measurements on 1DHAFs with $S=1$ have unveiled the energy level scheme[4–7] and the ground state properties.[8,9] The first ESR experiment concerning the former topic[4] on the prototypical $S=1$ 1DHAF compound $Ni(C_2H_8N_2)_2NO_2(ClO_4)$, abbreviated as NENP, exhibited a transition within the first excited triplet. Subsequently, ESR transitions between the singlet ground state at wave vector $k=0$ and the first excited triplet at $k=\pi$, which are forbidden for the ordinary Hamiltonian, have been observed.[5–7] A possible mechanism to explain these forbidden transitions has been proposed.[10,11] Namely, the transverse staggered field caused by the staggered inclination of the principle axis of the g-tensor mixes the eigenstate for $k=0$ with that for $k=\pi$, thus making the transitions between the ground state and the first excited one possible. According to the theory, the transitions occur only for the oscillating magnetic field (H_{rf}) parallel to the external magnetic field (H_0). It is important to perform polarization analysis of the ESR lines to test the validity of this mechanism. In the present paper, we describe the results of ESR measurements on the prototypical $S=1$ 1DHAF compound $Ni(C_3H_{10}N_2)_2NO_2(ClO_4)$, abbreviated as NINO.

First, we summarize the crystal and magnetic properties of NINO. This compound crystallizes in the orthorhombic system and belongs to the $Pbn2_1$ space group.[12,13] The lattice constants at room temperature are $a=15.384$ Å, $b=10.590$ Å, and $c=8.507$ Å. A schematic view of the crystal structure of NINO is shown in Fig. 1. The Ni^{2+} ions form the chain structure along the b axis via nitrite groups and the chains are well separated from each other by ClO_4 molecules. Since the local environment around Ni^{2+} in NINO is similar to that of NENP, NINO also has a staggered inclination of the principal axis from the chain direction.[13] The magnetic susceptibilities in a single crystal of NINO along the three crystallographic axes show a hump around 60 K and decrease abruptly when the temperature is decreased further.[14] No long range ordering has been observed down to 1.5 K.

The single crystal of NINO was grown by a slow evaporation method from an aqueous solution containing the stoichiometric amount of $Ni(ClO_4)_2\cdot 6H_2O$, 1,3-propanediamine and $NaNO_2$. The dimensions of the sample used in the measurement are 3 mm×3 mm×1.2 mm. The ESR measurement was performed with a spectrometer using a 20 T superconducting solenoid installed in the Institute of Physical and Chemical Research (RIKEN). In order to analyze precisely the polarization dependence of the ESR lines, we made a specially designed resonant cavity operating at around 50 GHz as shown in Fig. 2. The broken lines in Fig. 2 show the rf magnetic field distributions inside the cavity. We measured the two cases where the sample was located at the position designated as A and that designated as B. The external magnetic field was applied parallel to the b axis of the crystal, which was parallel to the z axis in Fig. 2.

Figure 3 shows the derivative signals of the absorption with respect to the magnetic field. The signal at 1.70 T comes from a crystal of iron alum ($FeNH_4(SO_4)_2\cdot 12H_2O$) and that at 6.45 T from NINO. We used the ESR signal from iron alum to calibrate the signal intensities from NINO. We obtained the ESR intensity by double integration of the spectrum. When the line shape was asymmetric, a half-part of the signal was used. The ratio of an integrated intensity for the ESR signal from NINO at the position A to that at B is about 1.7 ± 0.1.

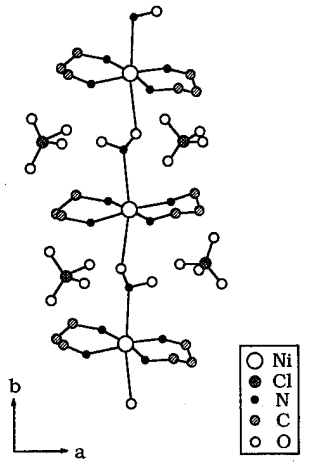


FIG. 1. Schematic view of the crystal structure of NINO.

 0021-8979/96/79(8)/5245/2/$10.00 © 1996 American Institute of Physics

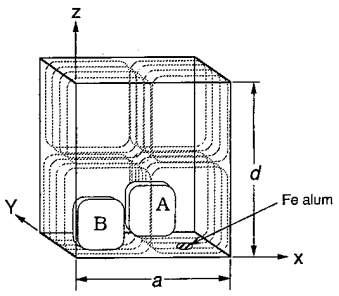


FIG. 2. A cut view of the resonant cavity used in this experiment. Broken lines show the rf magnetic field distributions inside the cavity.

The signal intensity I for the ESR transition between the ground state $|g\rangle$ and the excited one $|e\rangle$ is, apart from the temperature factor, given by

$$I \propto \int \left[\left| \langle e| \sum_j S_j^z |g\rangle \right|^2 \{H_{\mathrm{rf}}^z(x,y,z)\}^2 + \left| \langle e| \sum_j S_j^x |g\rangle \right|^2 \{H_{\mathrm{rf}}^x(x,y,z)\}^2 + \left| \langle e| \sum_j S_j^y |g\rangle \right|^2 \{H_{\mathrm{rf}}^y(x,y,z)\}^2 \right] dv, \tag{1}$$

where H_{rf}^x, H_{rf}^y, and H_{rf}^z are the x, y, and z components of the rf magnetic field, respectively. According to the theory,[10] $|\langle e|\Sigma_j S_j^x|g\rangle| = 0$ and $|\langle e|\Sigma_j S_j^y|g\rangle| = 0$. In this case, the signal intensity is written as

$$I \propto \left| \langle e| \sum_j S_j^z |g\rangle \right|^2 \int \{H_{\mathrm{rf}}^z(x,y,z)\}^2 \, dv. \tag{2}$$

Here, H_{rf}^z is given by

$$H_{\mathrm{rf}}^z = h \cos \frac{2\pi x}{a} \sin \frac{2\pi z}{d}, \tag{3}$$

where a and d are the dimensions of the cavity in the x and z directions, respectively, and h is a constant. We can calculate the signal intensities I_A and I_B from the NINO sample located at the positions A and B in Fig. 2, respectively. From Eq. (2), the ratio I_A/I_B is given by

$$I_A/I_B = \int_A \{H_{\mathrm{rf}}^z(x,y,z)\}^2 \, dv \Big/ \int_B \{H_{\mathrm{rf}}^z(x,y,z)\}^2 \, dv. \tag{4}$$

After performing the integration in Eq. (4) within the sample volume, we get $I_A/I_B = 1.75 \pm 0.1$, in good agreement with the observation (1.7 ± 0.1).

Next, we calculate the absolute intensity for the ESR absorption in NINO. For this purpose, we use the ESR signal from Fe alum to calibrate I_A and I_B. Considering the temperature factor, we get $|\langle e|\Sigma_j S_j^z|g\rangle|^2 \simeq 0.03$, which is proportional to the signal intensity according to the theory.[10] We have tried to compare our results with the theory. Although scatter of the data points in the theory is large at low fields, the theory seems to give the right order of magnitude for $|\langle e|\Sigma_j S_j^z|g\rangle|^2(0.01)$.

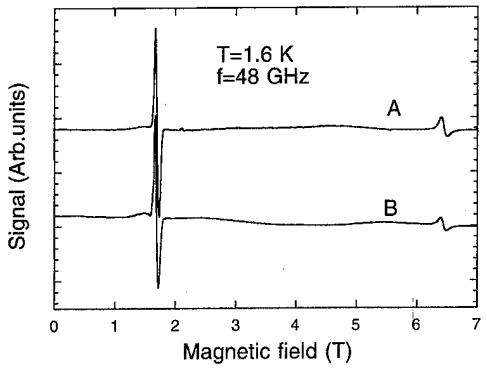


FIG. 3. The ESR signal from Fe alum (left) and that from NINO (right) along the b axis obtained at 1.6 K for the frequency of 48 GHz. Here, A and B label the ESR signal from NINO sample located at the positions A and B in Fig. 2, respectively.

In conclusion, we have made a polarization analysis of the ESR transition between the ground and excited states in NINO. Our results are consistent with the theory by Sakai and Shiba.[10] Clearly, more elaborate calculation of $|\langle e|\Sigma_j S_j^z|g\rangle|^2$ including the single ion anisotropy terms D and E is needed to get a quantitative agreement between theory and experiment.

We would like to thank Professor H. Shiba and Dr. T. Sakai for helpful discussions. This work was partially supported by the "MR Science Research Program" from RIKEN and by a Grand-in-Aid for Science Research from the Japanese Ministry of Education, Science, Sports and Culture.

[1] F. D. M. Haldane, Phys. Rev. Lett. **50**, 1153 (1983).
[2] J. P. Renard, M. Verdaguer, L. P. Regnault, W. A. C. Erkelens, J. Rossat-Mignod, and W. G. Stirling, Europhys. Lett. **3**, 945 (1987).
[3] K. Katsumata, H. Hori, T. Takeuchi, M. Date, A. Yamagishi, and J. P. Renard, Phys. Rev. Lett. **63**, 86 (1989).
[4] M. Date and K. Kindo, Phys. Rev. Lett. **65**, 1659 (1990).
[5] W. Lu, J. Tuchendler, M. von Ortenberg, and J. P. Renard, Phys. Rev. Lett. **67**, 3716 (1991).
[6] L. C. Brunel, T. M. Brill, I. Zaliznyak, J. P. Boucher, and J. P. Renard, Phys. Rev. Lett. **69**, 1699 (1992).
[7] M. Sieling, W. Palme, and B. Lüthi, Z. Phys. B **96**, 297 (1995).
[8] M. Hagiwara, K. Katsumata, I. Affleck, B. I. Halperin, and J. P. Renard, Phys. Rev. Lett. **65**, 3181 (1990).
[9] S. H. Glarum, S. Geschwind, K. M. Lee, M. L. Kaplan, and J. Michel, Phys. Rev. Lett. **67**, 1614 (1991).
[10] T. Sakai and H. Shiba, J. Phys. Soc. Jpn. **63**, 867 (1994).
[11] P. P. Mitra and B. I. Halperin, Phys. Rev. Lett. **72**, 912 (1994).
[12] J. P. Renard, M. Verdaguer, L. P. Regnault, W. A. C. Erkelens, J. Rossat-Mignod, J. Ribas, W. G. Stirling, and C. Vettier, J. Appl. Phys. **63**, 3538 (1988).
[13] T. Yosida and M. Fukui, J. Phys. Soc. Jpn. **61**, 2304 (1992).
[14] T. Takeuchi, M. Ono, H. Hori, T. Yosida, A. Yamagishi, and M. Date, J. Phys. Soc. Jpn. **61**, 3255 (1992).

Highly crystallized (La,Sr)MnO_3 films deposited by facing targets sputtering apparatus

N. Matsushita, K. Noma, S. Nakagawa, and M. Naoe
Department of Physical Electronics, Tokyo Institute of Technology, 2-12-1 O-okayama, Meguro, Tokyo 152, Japan

$La_{1-x}Sr_xMnO_3$ films about 4000 Å thick were deposited on thermally oxidized Si wafers, and then their crystalline orientation and magnetic characteristics were investigated. Orientation of (111) in which large ions such as O^{2-}, La^{3+}, and Sr^{2+} are most closely packed became preferential with increase of total gas pressure P_{total} and partial oxygen pressure P_{O_2}. Although spontaneous magnetization was not detected, even the film deposited at substrate temperature T_s as low as 330 °C revealed obvious orientation of (110) in which metallic ions are most closely packed. The film deposited at T_s of 500 °C, P_{total} of 2.0, and P_{O_2} of 0.1 mTorr, and the film postannealed at 900 °C for 3 h in oxygen atmosphere possessed the saturation magnetization $4\pi M_s$ of 1.2 and 3.5 kG at 77 K and their Curie temperatures were 217 and 313 K, respectively. B–H curves at 77 K revealed that the easy magnetization direction of these films was in-plane. © *1996 American Institute of Physics.* [S0021-8979(96)15108-3]

I. INTRODUCTION

Perovskite oxides such as (La,Sr)MnO_3 and (La,Bi,Sr)MnO_3 are very attractive material because they possess very interesting properties such as electrical conductivity, ferromagnetism, and magneto-optical Kerr effect. Many researchers have investigated the properties of these bulk materials.[1,2] The deposition of perovskite films have also been attempted because they seem to be applicable as magnetic layers in the hybrid devices composed of perovskite oxide layers in which $YBa_2Cu_3O_{7-y}$ and $BaTiO_3$ layers are used as superconductive and ferroelectric components, respectively. However, since these types of oxides exhibit the complicated crystal structure, epitaxial growth substrate such as MgO and $SrTiO_3$ and high substrate temperature T_s, were necessary for depositing the films with good crystallinity. It had been confirmed in a previous study that the facing target sputtering (FTS) apparatus can achieve "plasma-free" deposition and may be very suitable for depositing the oxide films with excellent crystallinity even at low T_s.[3] Therefore, the deposition of $La_{1-x}Sr_xMnO_3$ films were attempted on amorphous substrate by using FTS apparatus and the dependencies of crystallite orientation and magnetic characteristics on the total and partial oxygen pressure P_{total} and P_{O_2}, respectively, were investigated in this study.

II. EXPERIMENT

All specimen films were deposited by using the facing targets sputtering (FTS) apparatus.

A pair of targets with the same composition of $La_{0.76}Sr_{0.24}Mn_{0.78}O_{3-y}$ were prepared by a dry ceramic technique. They were presintered from the starting mixture of La_2O_3, $SrCo_3$, and MnO_2 powder at 1000 °C for 1 h and 1100 °C for 1 h and finally sintered at 1200 °C for 4 h. Sintered targets possessed the saturation magnetization M_s of 38.5 emu/g and it was smaller than 40% of M_s of a perfect single crystal with the same composition (about 100 emu/g).[5]

In this FTS system, the vacuum chamber was evacuated by the diffusion pump and the average background pressure was 8.7×10^{-7} Torr. Total and oxygen gas pressure P_{total} and P_{O_2} were in the range of 1.0–4.0 and 0.0–0.4 mTorr, respectively. The Si plates with thermalized surface layer (SiO_2/Si wafers) were used as substrates. The substrate temperature T_s was in the range of 330–600 °C. Film thickness could be controlled by adjusting deposition conditions and the specimen films about 4000 Å thick were for deposited at T_s of 500 °C and at P_{total} and P_{O_2} of 2.0 and 0.1 mTorr, respectively.

The dc current supply was used for sputtering and it was set at a constant value of 0.2 A. The discharge voltage depended on P_{total} and P_{O_2}, and it was in the range from 240 to 330 V.

Film composition was analyzed by the induced coupled plasma spectroscopy (ICPS). Crystallite orientation was evaluated on the x-ray diffraction (XRD) diagram and saturation magnetization was measured by using the vibrating sample magnetometer (VSM).

III. RESULTS AND DISCUSSIONS

A. Film composition

When the targets with stoichiometric composition of $La_{0.76}Sr_{0.24}Mn_{1.0}O_{3-y}$ were sputtered, Mn content x was higher than 1.0 in the film composition represented as $La_{0.76}Sr_{0.24}Mn_xO_{3-y}$. Therefore, targets with lower x of 0.78, i.e., composition of $La_{0.76}Sr_{0.24}Mn_{0.78}O_{3-y}$ were used and

 0021-8979/96/79(8)/5247/3/$10.00 © 1996 American Institute of Physics

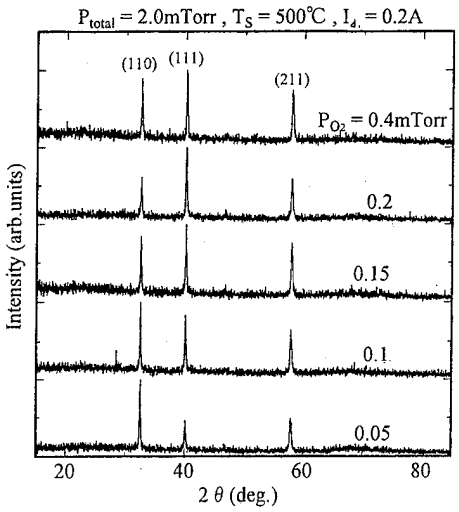


FIG. 1. XRD diagrams of films deposited at various P_{O_2}.

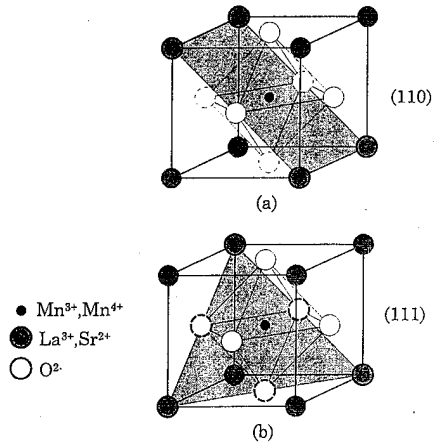


FIG. 3. Schematic illustration of (a) (110) plane and (b) (111) plane in $(La,Sr)MnO_3$ unit cell.

then x in the film composition was 0.97, of which the value seemed to be almost the same as x of 1.0 corresponding to stoichiometric composition.

B. Crystallite orientation

Figure 1 shows the XRD diagrams at various P_{O_2} for the films deposited at T_s of 500 °C and P_{total} of 2.0 mTorr. The ratio in peak height $I_{(111)}/(I_{(110)}+I_{(111)})$ increased with an increase of P_{O_2} as shown in Fig. 2. The (110) peak is the highest in the powder x-ray diffraction diagram and (110) corresponds to the most closely packed plane of metallic ions of La^{3+}, Sr^{2+}, Mn^{3+}, and Mn^{4+} as shown in Fig. 3(a). On the other hand, (111) corresponds to the most closely packed plane of large ions of La^{3+}, Sr^{2+}, and O^{2-} as shown in Fig. 3(b). It seemed to be difficult to deposit the films with sufficient (111) orientation by any conventional sputtering methods, because the oriented plane which is mainly composed of very light O ions would be destroyed by the heavy bombardment of γ-electrons and negative ions. On the other hand, it has been confirmed that FTS system can easily deposit the films with excellent orientation of the most closely packed plane (111) of oxygen ions on the "plasma-free" substrates, when enough amount of oxygen gas exists around the growing film surface.

Figure 4 shows the XRD diagrams for the films deposited at P_{total} of 1.0, 2.0, and 4.0 mTorr. Although the preferential orientation plane was (111) at P_{total} of 1.0 mTorr, it changed to (110) at P_{total} of 4.0 mTorr and the ratio in peak heights were almost the same as that in the x-ray diagram of $(La,Sr)MnO_3$ powder.[4] Since the kinetic energy of sputtered particles decreased with an increase of P_{total} and since the increase of P_{total} correspond to the decrease of mobility of oxygen atoms on the substrate plane, the peak height of (111) seemed to decrease with increase of P_{total}.

Highly crystallized film was deposited even at low T_s of 330 °C and then the preferential orientation plane was (110) as shown in Fig. 5. Since T_s was low enough even for the Sr atom, which has high vapor pressure at 500 °C, the preferential orientation of (110), i.e., the most closely packed plane of metallic ions, was clearly observed. However, since the

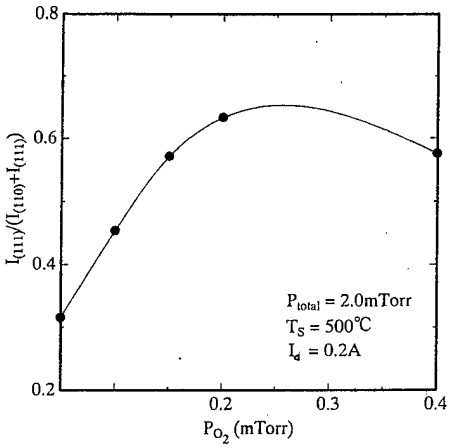


FIG. 2. P_{O_2} dependences of ratio in peak height $I_{(111)}/(I_{(110)}+I_{(111)})$. (The indicated solid curve is intended as a guide to the eye for the reader.)

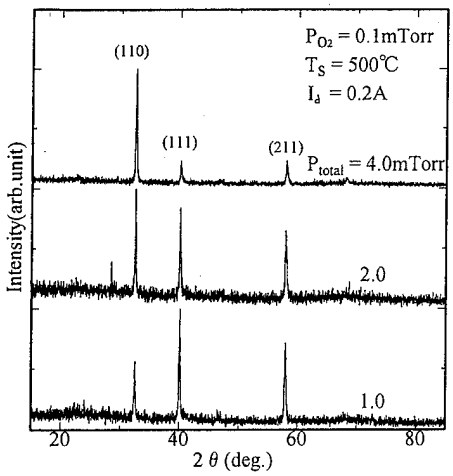


FIG. 4. XRD diagrams of films deposited at various P_{total}.

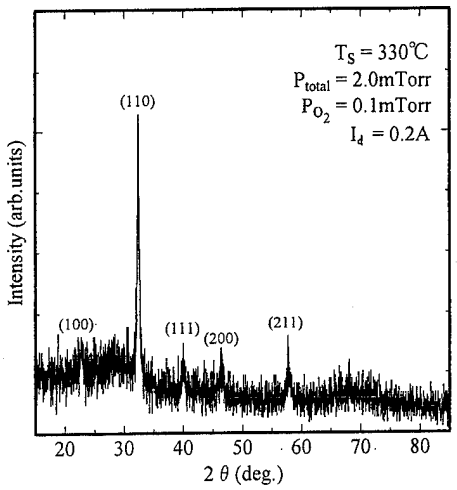


FIG. 5. XRD diagram of film deposited at low T_s of 330 °C.

crystallites did not fully grow at T_s of 330 °C, spontaneous magnetization was not detected even at low measurement temperature of 77 K.

C. Magnetic characteristics

Magnetic characteristics were investigated for the as-deposited films at T_s of 500 °C, P_{total} of 2.0 mTorr and

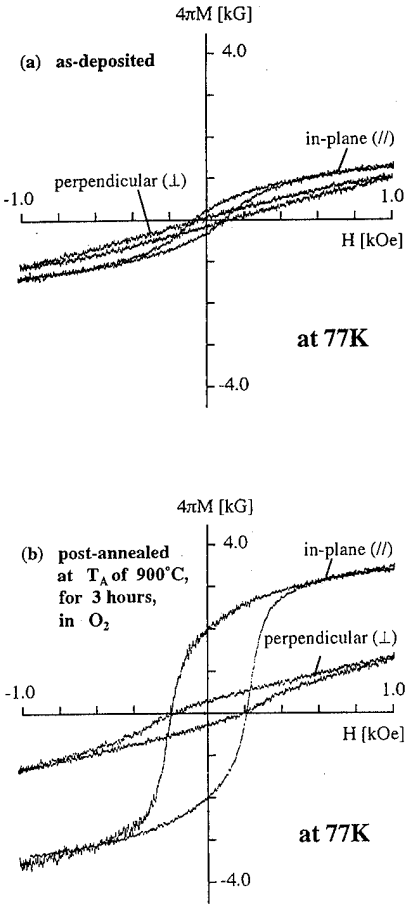


FIG. 6. In-plane(∥) and perpendicular(⊥) B–H loops of as-deposited and postannealed films at 77 K.

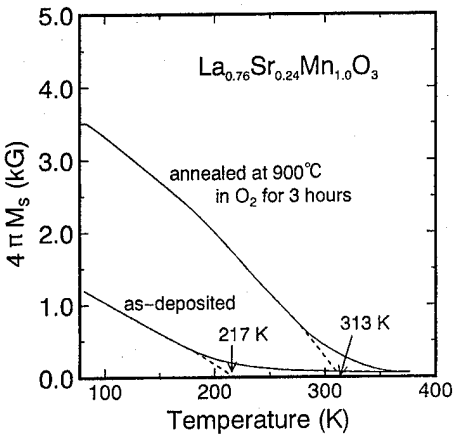


FIG. 7. Temperature dependences of saturation magnetization $4\pi M_s$ of as-deposited and postannealed films.

P_{O_2} of 0.05–0.4 mTorr and for the films postheated at the annealing temperature T_A of 900 °C for 3 h in oxygen gas. The as-deposited films possessed very small saturation magnetization $4\pi M_s$ at room temperature and the maximum value of $4\pi M_s$ was 0.24 kG at P_{O_2} of 0.1 mTorr. The annealing treatment increased $4\pi M_s$ for all films deposited at any P_{O_2}. Although the films deposited at P_{O_2} of 0.1 mTorr took the maximum value of 0.47 kG, it was fairly smaller than that of the bulk with same composition (about 5.0 kG).

Therefore, B–H loops of the as-deposited and the postannealed films were measured at 77 K in in-plane(∥) and perpendicular(⊥) direction, respectively, as shown in Figs. 6(a) and 6(b). Since B–H(∥) was saturated and B–H(⊥) was not saturated at the applied field of 1 kOe, it was clear that their easy magnetization direction was in-plane, while the coercivities $H_{c_\parallel}$ and $H_{c_\perp}$ were not so different. It seemed that, since the crystallinity was improved by annealing the films in oxygen atmosphere, larger $4\pi M_s$ and higher H_c were obtained. Since the lack of oxygen ions causes the change of spin arrangement from parallel to antiparallel, the as-deposited film possessed smaller $4\pi M_s$ than the postannealed one. However, the $4\pi M_s$ of the postannealed film took the maximum value of 3.5 kG, which was smaller than that of the bulk. Figure 7 shows the temperature dependencies of $4\pi M_s$ of as-deposited and the postannealed films. They seemed to possess larger $4\pi M_s$ at a temperature below 77 K. The Curie temperatures T_C were 217 and 313 K, respectively, while T_C of the bulk $La_{0.67}Sr_{0.33}Mn_{1.0}O_3$ was about 360 K. It seemed that, since crystallites did not fully grow up and the oxygen content was insufficient even in the postannealed film, it exhibited lower T_C and smaller $4\pi M_s$ than the bulk.

[1] J. H. van Santen and G. H. Jonker, Physica **165**, 599 (1950).
[2] T. J. A. Popma and M. G. J. Kamminga, Solid State Commun. **17**, 1073 (1975).
[3] N. Matsushita, K. Noma, S. Nakagawa, and M. Naoe, J. Appl. Phys. **75**, 5975 (1994).
[4] M. Imura, M. Kawata, T. Tanaka, S. Sugimoto, M. Homma, and M. Okada, J. Magn. Soc. Jpn. **19**, 245 (1995).

α''-$Fe_{16}N_2$ phase epitaxially grown by sputter beam method

Satoshi Okamoto, Osamu Kitakami, and Yutaka Shimada
Research Institute for Scientific Measurements, Tohoku University, Sendai 980-77, Japan

Epitaxial Fe-N films have been grown on Fe or Ag (001) single-crystal underlayers by the sputter beam method. The Fe-N films on both underlayers have a bct structure (α'-martensite), whose lattice is elongated along the [001] direction by nitrogen atoms located in octahedral interstices of α-Fe. These films possess well-defined crystal orientation and exhibit a higher saturation magnetization ($4\pi M_s$) than that of α-Fe for a certain range of various nitrogen content. Postannealing promotes ordering of nitrogen atoms in the bct lattice, resulting in precipitation of a metastable α''-$Fe_{16}N_2$ phase in Fe-N films. The $4\pi M_s$ of the annealed samples tends to increase with the increase of the α'' volume fraction, and the Fe-N film with $4\pi M_s$ of about 25 kG contains 26–33 vol% α'' phase. While both Fe and Ag underlayers can promote epitaxial growth of the Fe-N films, very fast ordering of nitrogen atoms and easily decomposed α''-$Fe_{16}N_2$ have been observed in the sample on a Ag underlayer. This fact leads to the fact that the ordering rate and the stability of α''-$Fe_{16}N_2$ are very sensitive to its crystal quality. © *1996 American Institute of Physics.* [S0021-8979(96)41308-X]

I. INTRODUCTION

Since the discovery of an abnormally high magnetization (28.3 kG) in α''-$Fe_{16}N_2$ by Kim and Takahashi,[1] a lot of intensive work has been done to clarify the physical properties of α''-$Fe_{16}N_2$. However there have been many controversial results on the magnetic properties of the α''-$Fe_{16}N_2$. The reported values of the saturation magnetization ($4\pi M_s$) range from about 30 kG[2,3] or 25–28 kG[4–7] to almost the same for α-Fe.[8] A crucial discrepancy has also been seen in the Mössbauer spectra of the α''-$Fe_{16}N_2$. Most reports insist that the three different hyperfine fields correspond to three Fe sites in the α''-$Fe_{16}N_2$.[4,8,9] In contrast, Sugita *et al.* have recently confirmed that there is only one hyperfine field in the α''-$Fe_{16}N_2$ single-crystal film.[2]

We consider that such a contradiction was mainly caused by inappropriate structural characterization of the Fe-N samples. Usually, the structural analysis of Fe-N samples is performed by the conventional x-ray diffraction (XRD) method. As was pointed out in the previous paper,[10] improper conclusions will be derived unless very careful corrections are performed.

In the present study, Fe-N films are epitaxially grown on Fe or Ag (001) underlayers by the sputter beam (SB) method by which high quality single-crystal films have been fabricated,[11] and their structures are carefully determined. We will show the relationship between the magnetization and some structural factors of the Fe-N films on Fe and Ag underlayers.

II. EXPERIMENT

Figure 1 shows a schematic diagram of the SB system. This system consists of a discharge chamber and a film deposition chamber.[11] GaAs (001) single-crystal wafers were used as substrates. Prior to film deposition, the SB system was evacuated to 3×10^{-7} Torr for the discharge chamber and 3×10^{-8} Torr for the deposition chamber.

Fe underlayers were deposited directly onto GaAs substrates, while Ag underlayers were deposited on 30-Å-thick Fe seed layers. The substrate temperature (T_s) was 250 °C with an Ar gas pressure (P_{Ar}) of 4 mTorr in the discharge chamber and 0.1 mTorr in the deposition chamber. Fe-N films were deposited at T_s=room temperature (rt) with P_{Ar}=4 mTorr in the discharge chamber and N_2 partial pressure (P_N)=0.1–0.35 mTorr in the deposition chamber. The final forms of the prepared samples are Fe-N (800 Å)/Fe (400 Å)/GaAs (001) and Fe-N (1200 Å)/Ag (500 Å)/Fe (30 Å)/GaAs (001). The deposition rate was controlled to be 4–4.2 Å/min throughout the experiments. Bias voltage (V_b) of −20 V was applied to the substrate during the deposition of the Fe-N films in order to enhance epitaxial growth of the films by Ar ion bombardment.[12] In the present experimental conditions, the kinetic energy of the ions is about −17 eV which is an optimum value for epitaxial growth of

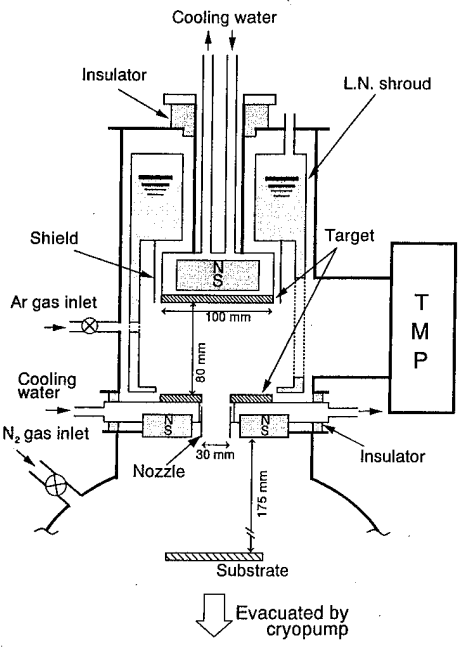


FIG. 1. The schematic of the sputter beam system.

 0021-8979/96/79(8)/5250/3/$10.00 © 1996 American Institute of Physics

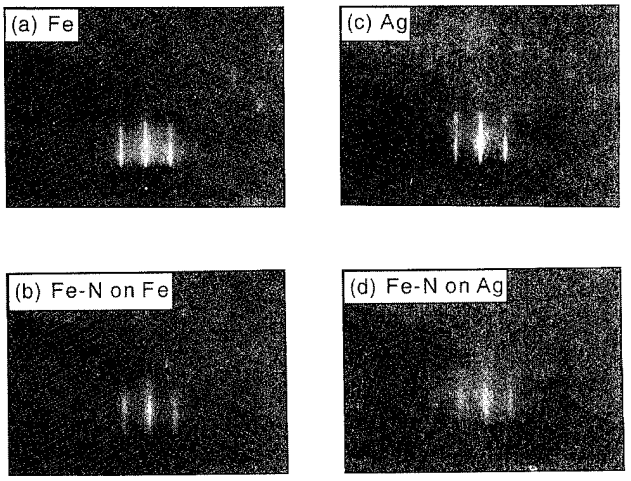


FIG. 2. RHEED patterns from [110] direction of the (a) Fe underlayer, (b) Fe-N film on Fe underlayer, (c) Ag underlayer, and (d)Fe-N film on Ag underlayer.

Fe-N film.[10] Annealing of the films was sequentially carried out at a temperature (T_a) of 200 °C for 10–100 h. The crystal structures of the films were investigated by an x-ray diffractometer (using Cu Kα line) which has a focusing length of 185 mm, and their surface structures were investigated by the reflection high-energy electron diffraction (RHEED). The value of $4\pi M_s$ was measured by a vibrating sample magnetometer (VSM) with an applied field of 15 kOe. The $4\pi M_s$ of our α-Fe single-crystal films was within 21.5±0.5 kG.

III. RESULTS AND DISCUSSION

Figure 2 shows the RHEED patterns of the Fe-N films grown on Fe and Ag underlayers. The diffraction from the two underlayers shows very sharp streaks, indicating that they are epitaxially grown and possess very flat surfaces. We note that the Fe-N films on those underlayers also exhibit continuous streaks reflecting the symmetry of the underlayers although the streaks become a little obscure. The crystal quality of the Fe-N film on the Ag underlayer is found to be somewhat inferior to that on the Fe underlayer. From the RHEED and XRD measurements, the crystal structure of those Fe-N films is obviously the disordered phase (α'-martensite). According to the rocking curve measurements, the dispersion angle of the Fe and Ag (002) peak is smaller than 1° and that of α'-Fe-N (002) peak is less than 2°.

The RHEED patterns of the annealed Fe-N films are shown in Fig. 3. The streaks with a half period of the original ones appear and become clearer as the annealing time increases. These streaks indicate formation of the ordered phase (α''-$Fe_{16}N_2$). For the sample annealed for 100 h, the streaks with the half period are very strong but with rather spotty diffraction, indicating that clusterlike α'' phase precipitates in the Fe-N film. As is clear in the RHEED pattern of the sample annealed for 30 h, more rapid ordering of N sites is found in the sample on the Ag underlayer. Too prolonged annealing, however, reduces the diffraction intensity of the ordered phase. From this result, it is clear that the ordering of N atoms is related to the morphology of Fe-N

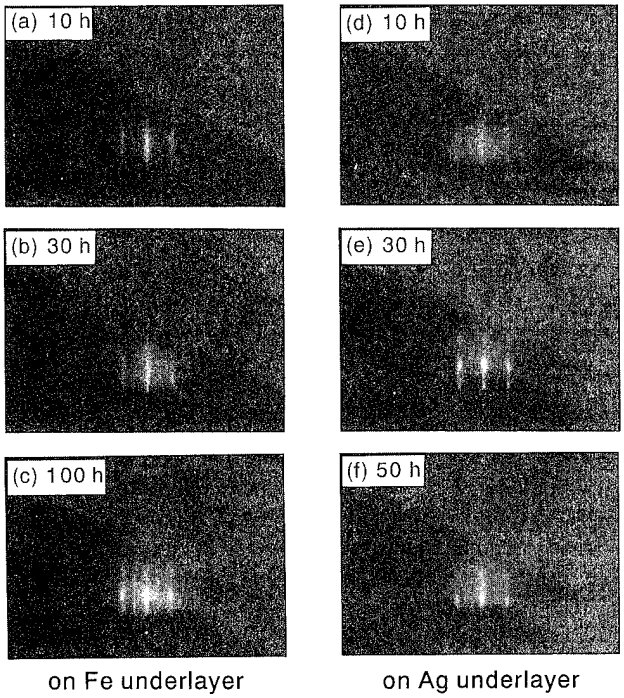


FIG. 3. Change of RHEED patterns of Fe-N films with the annealing time. (a)–(c) are those on Fe underlayer and (d)–(f) are those on Ag underlayer.

films. Since surface energy of Ag is extremely small compared with that of Fe, the Fe-N film on the Ag underlayer may take the form of the so-called island structure, resulting in a higher density of defects and grain boundaries. Hence, the N atoms in the Fe-N film will easily move to the ordered sites of α''-$Fe_{16}N_2$ through diffusion through the lattice defect or grain boundary.

Figure 4 shows the XRD profiles of the annealed Fe-N

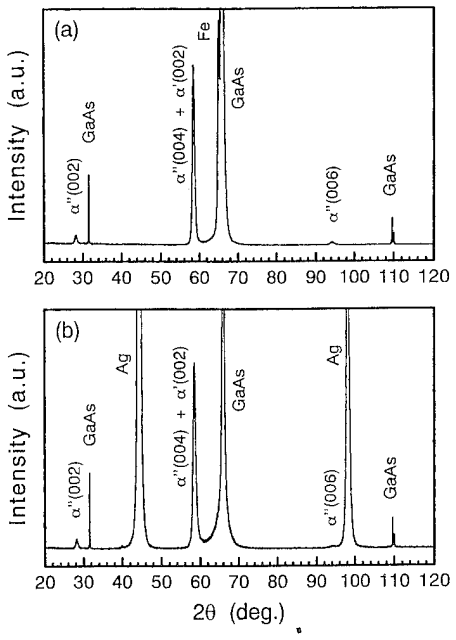


FIG. 4. Typical XRD profiles of annealed Fe-N films on (a) Fe underlayer and (b) Ag underlayer.

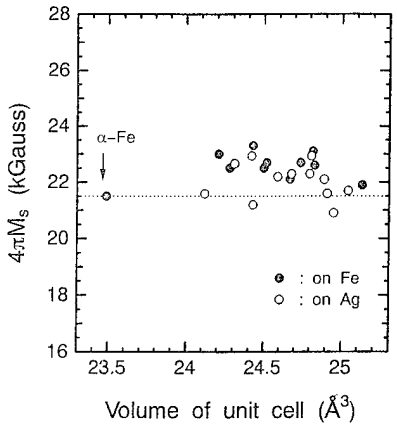


FIG. 5. Saturation magnetization $4\pi M_s$ of Fe-N films on Fe and Ag underlayers as a function of the unit cell volume of α'-martensite.

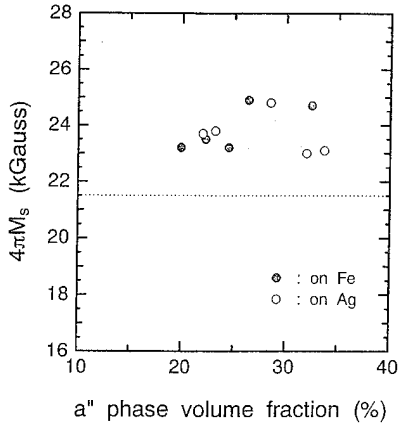


FIG. 6. Saturation magnetization $4\pi M_s$ of Fe-N films on Fe and Ag underlayers as a function of the volume fraction of α''-$Fe_{16}N_2$.

films. Both the Fe-N films on Fe and Ag underlayers exhibit the distinct diffraction peaks from $\alpha''(002)$ and $\alpha''(006)$, and these peaks are evidence of the existence of α''-$Fe_{16}N_2$. In addition to (002) and (006) peaks, we have observed the peculiar peaks of (103), (105), (204), and (114) from α''-$Fe_{16}N_2$ by asymmetric XRD measurements.[10] For both Fe and Ag underlayers, the lattice constants a and c of α''-$Fe_{16}N_2$, respectively, are 5.70–5.71 and 6.30–6.31 Å, which are very close to the values reported by Jack (a=5.72 Å and c=6.29 Å)[13] and so the bct structure of our α''-$Fe_{16}N_2$ is slightly expanded to the c-axis direction.

Figure 5 shows the dependence of $4\pi M_s$ on the unit cell volume of α' phase. It has been found to be proportional to the nitrogen content in the Fe-N film.[12] $4\pi M_s$ of α' phase on both Fe and Ag underlayers are obviously larger than that of Fe for all N content range examined in this experiment. The maximum value of $4\pi M_s$ of α' phase is 23.3 kG. However, $4\pi M_s$ tends to decrease to the value of α-Fe as α' unit cell expands further in the high N content region. This decrease may be attributed to existence of nonmagnetic phase (γ-austenite) or the other unknown reason. The Mössbauer measurement is in preparation in order to explain this change.

In Fig. 6, $4\pi M_s$ of Fe-N films are shown as a function of the α'' phase volume fraction. The α'' volume fraction was determined from x-ray diffraction intensity ratio $I_{\alpha''(002)}/I_{[\alpha''(004)+\alpha'(002)]}$ with the theoretical intensity ratio $I_{\alpha''(002)}/I_{\alpha''(004)}$ of α''-$Fe_{16}N_2$. The theoretical ratio was determined with exact evaluation of the line absorption factor and irradiation area of the x-ray beam. As seen in this figure, $4\pi M_s$ of the annealed films tends to increase from 23 kG to about 25 kG with increasing the fraction of the α''-$Fe_{16}N_2$. This result demonstrates that α''-$Fe_{16}N_2$ obviously has a very high magnetization. It is, however, difficult to accurately determine the $4\pi M_s$ of α''-$Fe_{16}N_2$ because of the limited α'' volume fraction, and as is noted in Fig. 5, $4\pi M_s$ of α'-martensite cannot be fixed.

IV. CONCLUSIONS

Fe-N (001) epitaxial films were grown on Fe and Ag (001) single-crystal underlayers by the SB method, and α''-$Fe_{16}N_2$ phase was precipitated in the films by post annealing. The epitaxially grown Fe-N (001) film, whose structure is bct α'-martensite, possesses a saturation magnetization larger than that of α-Fe. Formation of α''-$Fe_{16}N_2$ was clearly observed in the films annealed at 200 °C. The magnetization of the annealed Fe-N films tends to increase with increasing the volume fraction of the α''-$Fe_{16}N_2$. This result indicates that the α''-$Fe_{16}N_2$ has a magnetization much larger than α-Fe. But the magnetization of α''-$Fe_{16}N_2$ cannot be accurately determined in this study. We are now preparing Mössbauer measurements in order to determine the magnetization of α''-$Fe_{16}N_2$ and α'-martensite in our Fe-N film.

We did not find out any distinct differences in the magnetic properties and the crystal structures of the Fe-N films on Fe and Ag underlayers. However, the ordering of N atoms is more rapid in the α'-martensite on the Ag underlayer than that on the Fe underlayer, moreover, too long annealing made α''-$Fe_{16}N_2$ easily decompose in the samples on the Ag underlayer. That the morphology of the Fe-N films may affect the ordering rate and the stability of α''-$Fe_{16}N_2$. The lattice defect or grain boundary may accelerate ordering of N atoms in the α'-martensite, but may also impede the thermal stability of ordered N atoms in α''-$Fe_{16}N_2$.

[1] T. K. Kim and M. Takahashi, Appl. Phys. Lett. **20**, 492 (1972).
[2] Y. Sugita, H. Takahashi, M. Komuro, K. Mitsuoka, and A. Sakuma, J. Appl. Phys. **76**, 6637 (1994).
[3] C.Gao and W. D. Doyle, J. Appl. Phys. **73**, 6579 (1993).
[4] K. Nakajima, S. Okamoto, and T. Okada, J. Appl. Phys. **65**, 4357 (1989).
[5] C. Ortiz, G. Dumpich, and A. H. Morrish, Appl. Phys. Lett. **65**, 2737 (1994).
[6] H. Jiang, K. Tao, and H. Li, J. Phys. Condens. Matter **6**, L279 (1994).
[7] W. E. Wallace and M. Q. Huang, J. Appl. Phys. **76**, 6648 (1994).
[8] M. Takahashi, H. Shoji, H. Nashi, T. Wakiyama, M. Doi, and M. Matsui, J. Appl. Phys. **76**, 6642 (1994).
[9] T. Moriya, Y. Sumitomo, H. Ino, E. Fujita, and Y. Maeda, J. Phys. Soc. Jpn. **35**, 1378 (1973).
[10] S. Okamoto, O. Kitakami,and Y. Shimada, J. Appl. Phys. (to be published).
[11] S. Okamoto, O. Kitakami, and Y. Shimada, Jpn. J. Appl. Phys. **33**, 6164 (1994).
[12] T. Ohmi, T. Ichikawa, T. Shibata, K. Matsudo, and H. Iwabuchi, Appl. Phys. Lett. **53**, 45 (1988).
[13] K. H. Jack, Proc. R. Soc. London Ser. A **208**, 216 (1951).

The formation of stable Co/Co_2MnSn two phase magnets

T. W. Kim and R. J. Gambino
Department of Materials Science and Engineering, SUNY at Stony Brook, New York 11794

The phase equilibria in the system Co–Mn–Sn have been studied with compositions along the join Co–CoMnSn. This is part of an effort to form a macroscopic ferrimagnet with two metallic ferromagnetic phases, Co and Co_2MnSn. As-cast arc melted alloys have been made with Co compositions from 33 to 78 at. %. Three different phase and magnetization regions are observed with increasing Co composition. Cobalt becomes the primary phase at more than 71 at. % Co and crystallizes out of a Co_2MnSn rich matrix. It is shown from x-ray diffraction analysis and the T_c change with Co compositions that the Co phase in Co_2MnSn matrix is probably a Co–Mn solid solution. From the break in the magnetization vs temperature curves of two phase magnets with two different compositions, Curie temperatures are determined as approximately 160 °C and 175 °C for the Co–Mn solid solution phase. The exchange coupling at phase boundary is proposed by the analysis of coercivity vs temperature data. © *1996 American Institute of Physics.* [S0021-8979(96)27908-1]

INTRODUCTION

Macroscopic ferrimagnets consist of two phases in intimate contact which exchange couple ferrimagnetically. Previous work on Co–EuS films which consist of about 10 nm particles of EuS have shown that macroscopic ferrimagnets can have unusual magneto-optical[1] and magneto-transport[2] properties. The EuS is exchange coupled antiferromagnetically to the cobalt at least at the Co/EuS interface. In the Co–EuS system, the Co matrix is a conductor but the EuS in the precipitate particles is a semiconductor. Even though the resistivity change of this system is large, the magnetoresistance is small because of the high resistivity of a large volume fraction of semiconducting phase.[3]

For this reason, we are investigating phase equilibria in a system containing two metallic ferromagnetic phases, Co and Co_2MnSn. We have found that in the Co/Co_2MnSn system the two metallic phases are a low T_c and low magnetization phase, hexagonal Co solid solution, and a high T_c and high magnetization phase, Co_2MnSn. Microstructure shows a Co solid solution precipitates in the Co_2MnSn Heusler alloy matrix, which may be crystallographically coherent with the matrix.

EXPERIMENTAL METHODS

Ingots were prepared by arc melting in a commercial arc furnace with a water cooled hearth and a water cooled tungsten electrode. The chamber was evacuated by a mechanical pump and back filled with argon several times. The high purity argon gas (99.999%) flowed through the chamber continuously during arc melting. The analysis of microstructures was made with backscattered electron image on a scanning electron microscope (SEM) because optical microscope did not provide enough contrast to analyze the Co precipitates in Co_2MnSn Heusler alloy. The composition analysis of the phases was carried out with energy-dispersive analysis of x rays (EDAX). The samples with two phases were characterized by x-ray diffraction analysis. Magnetization loops and magnetization vs temperature were made using a vibrating sample magnetometer (VSM) with a temperature controlling system.

RESULTS AND DISCUSSION

There are three different phases, Fig. 1, and three magnetization regions, Fig. 2, with composition along the join Co–CoMnSn. At 33–50 at. % Co, Co–Mn–Sn phase is surrounded by paramagnetic Sn-rich phase, Fig. 1(a). The magnetizations in this region are relatively small compared to other two phase regions. Figure 1(b) shows that Co_2MnSn Heusler alloy with 50 at. % of Co is formed as a single phase. At 50–71 at. % Co, Co particles precipitate along the columnar boundary which surround Co_2MnSn [Co_3MnSn; Fig. 1(c)], and with increasing Co, Co particles start to precipitate in Co_2MnSn matrix [Co_4MnSn; Fig. 1(d)]. The magnetization of Co_2MnSn is large and increases with Co con-

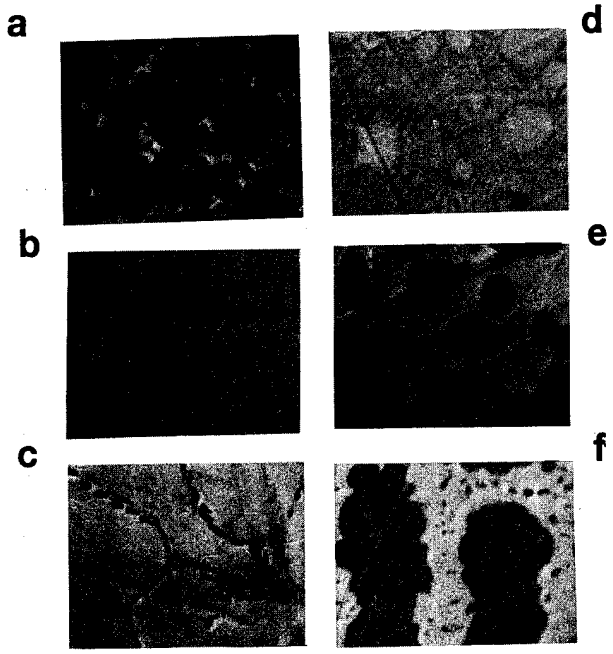


FIG. 1. SEM backscattered electron images of polished sections of ingots; (a) CoMnSn (33 at. % Co), (b) Co_2MnSn (50 at. % Co), (c) Co_3MnSn (60 at. % Co), (d) Co_4MnSn (67 at. % Co), (e) Co_5MnSn (71 at. % Co), (f) Co_7MnSn (78 at. % Co).

 0021-8979/96/79(8)/5253/3/$10.00 © 1996 American Institute of Physics

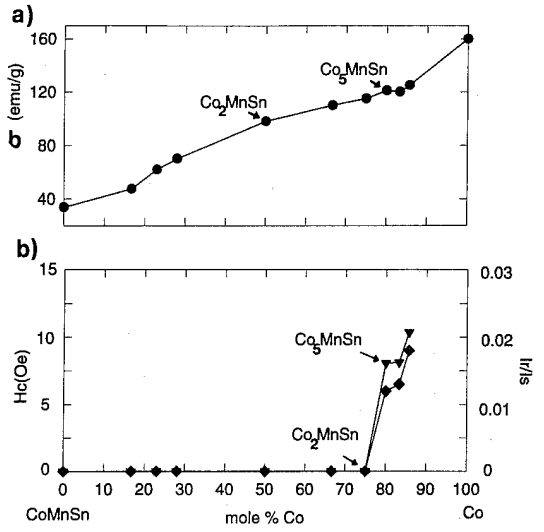


FIG. 2. (a) Magnetization, (b) coercivity and l_r/l_s as a function of Co composition along the join Co–CoMnSn.

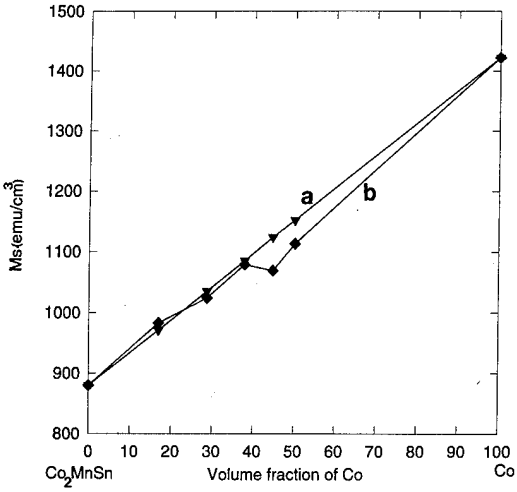


FIG. 3. Saturation magnetization, M_s(emu/cm^3), as a functuation of volume fraction of Co to Co_2MnSn; (a) theoretical magnetization, (b) experimental magnetization.

centration. Cobalt becomes the primary phase at more than 71 at. % Co [Co_5MnSn; Fig. 1(e)] and crystallizes out of a Co_2MnSn rich matrix. The remanence and coercivity suddenly increase at this composition [Fig. 2(b)]. Even though Co concentration increases, magnetization decreases, then increases again in this Co composition range but the change of magnetization is small. The change of remanence is also small. The volume fraction of Co phase increases with Co composition [Co_7MnSn; Fig. 1(f)]. The x-ray diffraction pattern from the Co_7MnSn composition shows two phases. Comparing with the peaks from arc-melted pure Co and single phase Co_2MnSn Heusler alloy, the diffraction peaks of Co_7MnSn match with those of hexagonal Co and Co_2MnSn Heusler alloy. All peaks from hexagonal Co are shifted in this sample. The peaks from Co_2MnSn with typical Heusler alloy structure are not shifted. New lattice parameters were calculated using the diffraction angles of (100) and (002) peaks of hexagonal Co. The c axis increases 2.2% to 4.17 Å and the a axis decreases 2.3% to 2.45 Å. On the basis of these new lattice parameters, the diffraction angles of other hexagonal Co peaks were calculated. These calculated angles are compatible with the observed hexagonal Co peaks in the two phase magnet. From the overlap of hexagonal Co and Co_2MnSn peaks and the shift of the hexagonal Co peaks, it is possible that the Co phase and Co_2MnSn Heusler alloy phase are crystallographically coherent. The intensities of (200), (222), (420) reflections of Co_2MnSn Heusler alloy are significantly small, indicating that Mn and Sn in the structure of Co_2MnSn phase are disordered.[4]

The saturation magnetization, M(emu/cm^3), vs volume fraction of Co to Co_2MnSn is shown in Fig. 3. Line a is the calculated magnetization based on volume fractions of Co and Co_2MnSn and the magnetization in line b comes from experimental data. The volume fraction was calculated assuming that Co and Co_2MnSn have their normal crystalline densities.

The magnetization and coercivity vs temperature on Co_6MnSn and Co_7MnSn compositions which have more volume fraction of Co are shown in Fig. 4(a) and Fig. 4(b), respectively. The phase transformation from hexagonal Co to fcc Co takes place at around 430 °C.[5] Therefore, this experiment was carried out at −150–400 °C temperature range. By extrapolating high-temperature data, T_c of the lower T_c phase can be estimated. Figure 4(a) shows that these samples contain two phases: one with low T_c and low magnetization and the other with high T_c and higher magnetization. By extrapolating the two curves of Co_6MnSn and Co_7MnSn to

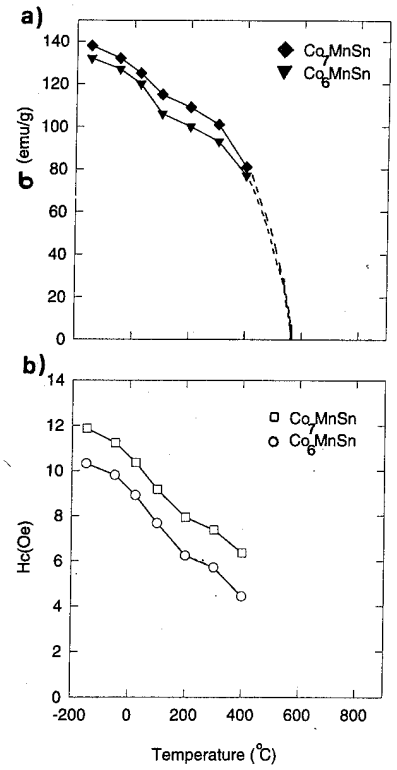


FIG. 4. (a) Magnetization vs temperature, and (b) coercivity vs temperature curves of the Co_6MnSn and Co_7MnSn samples with stable Co/Co_2MnSn two phases.

high temperature, the curves merge on the temperature axis. The temperature at this point is approximately 570 °C consistant with T_c, 556 °C, of Co_2MnSn of Heusler alloy. The T_c of the hexagonal Co solid solution can be estimated by extrapolating from the break in the magnetization curve [Fig. 4(a)]. The Curie temperatures of the Co–Mn solid solution in the Co_6MnSn and Co_7MnSn samples are approximately 160 °C and 175 °C, respectively. The increase of Mn concentration lower T_c, which is evidence of Co–Mn solid solution.

Figure 4(b) shows the coercivity in Co_6MnSn and Co_7MnSn samples as a function of temperature. The coercivity change with temperature can be divided as two regions with about 150 °C in the center as the case of magnetization vs temperature. The coercivity at $T<150$ °C is that of the Co phase. The Curie temperatures determined from the temperature at which $H_c(T)$ changes slope is about 180 °C in approximate agreement with the T_c from magnetization vs temperature [Fig. 4(a)]. The single phase Co_2MnSn Heusler alloy shows a closed loop without coercivity or remanence. In Fig. 4(a), however, there is extra coercivity at $T>150$ °C where the Co_2MnSn phase is the only magnetic phase. This suggests that the extra coercivity at $T>150$ °C is associated with exchange coupling of Co and Co_2MnSn Heusler phase at the phase boundary.

CONCLUSIONS

Stable Co/Co_2MnSn two phase magnet consisting of metastable Co precipitates in Co_2MnSn Heusler alloy matrix is formed at composition >71 at. % of Co. Both phases may be crystallographically coherent. The extra coercivity at $T>150$ °C and the Co composition dependence of Curie temperature probably indicate that there is the exchange coupling at phase boundary. It can be expected that the exchange coupling will be increased by forming the very small particles through rapid quenching methods or thin film technology because of the increased surface to volume ratio.

[1] R. J. Gambino and P. Fumagalli, IEEE Trans. Magn. **30**, 4461 (1994).
[2] R. J. Gambino and J. Wang, Scr. Metall. Mater. **33**, 1877 (1995).
[3] R. J. Gambino, T. R. McGuire, and J. Wang, IEEE Trans. Magn. **31**, 3915 (1995).
[4] H. Ido, J. Magn. Magn. Mater. **54–57**, 937 (1986).
[5] T. Nishizawa and K. Ishida, Bull. Alloy Phase Diagrams **4**, 388 (1983).

Magnetic phase transitions in $RENi_2B_2C$ (RE=Ho,Dy,Tb) studied by ^{57}Fe Mössbauer spectroscopy (abstract)

D. Sánchez, H. Micklitz,[a] M. B. Fontes, S. L. Bud'ko, and E. Baggio-Saitovitch
Centro Brasileiro de Pesquisas Físicas, Rua Xavier Sigaud 150, Urca, Rio de Janeiro, Brazil

The rare earth (RE) nickel borocarbides are intermetallic layered compounds which offer the possibility to study the interplay between superconductivity and magnetism. We have doped $RENi_2B_2C$ (RE=Ho,Dy,Tb) with ~1 at. % ^{57}Fe in order to study the magnetic phase transitions occurring in these systems by a local probe, i.e., by ^{57}Fe Mössbauer spectroscopy. Sample characterization by x-ray diffraction as well as ac susceptibility measurements showed mainly single phase. The room temperature and 4.2 K ^{57}Fe ME spectra essentially show one quadrupole doublet ($\Delta \sim 0.20$ mm/s) for all compounds, except for RE=Tb.[1] A magnetic hyperfine (hf) field appears in the case of RE=Tb and Ho at $T_N \sim 15$ and 8 K, respectively. The magnetic hf field for Tb at 4.2 K is $B_{hf}=0.86$ T, while it is quite smaller for Ho [$B_{hf}(5\ K) \sim 0.30$ T]. Since ^{57}Fe at the Ni sites in $RENi_2B_2C$ does not have its own magnetic moment, all magnetic hf fields are resulting from the neighboring RE moments.[1] The absence of a hf field in $DyNi_2B_2C$ at 4.2 K confirms the results from neutrons diffraction experiments:[2] the magnetically ordered state in these two compounds is a simple collinear antiferromagnet. For Tb and Ho, however, the spin structure in the magnetically ordered state is not collinear, resulting in a transferred magnetic hf field at the ^{57}Fe nucleus. © *1996 American Institute of Physics.* [S0021-8979(96)473608-1]

---

[a]Visitor from II. Phys. Inst., Universität zu Köln, Germany.

[1]E. Baggio-Saitovitch, M. B. Fontes, and S. L. Bud'ko, LACAME'94 (to be published).
[2]P. Devernagas, J. Zarestky, C. Stassis, A. I. Goldmank, P. C. Canfield, and B. K. Cho (to be published).

 0021-8979/96/79(8)/5256/1/$10.00 © 1996 American Institute of Physics

Morin-like spin reorientation in BiPb-2201 ferrates with iron in octahedral oxygen coordination

M. Rosenberg and Th. Sinnemann
Experimentalphysik VI, Ruhr-Universität Bochum, 44780 Bochum, Germany

G. Filoti
Institute of Physics & Technology of Materials, P.O. Box MG 76900 Bucharest, Romania

S. Kemmler-Sack
Institut für Anorganische Chemie, Universität Tübingen, 72076 Tübingen, Germany

From a Mössbauer spectroscopy study of the $BiPbSrCaFe_{6+z}$ ferrate, prepared under different conditions, strong evidence for a variety of Morin-like spin-reorientation processes similar to the ones occuring in hematite was found. The phase evolution, their energetical and dynamical Mössbauer parameters as well as the spin-rotational process are described in detail and finally correlated with a proposed mechanism. © *1996 American Institute of Physics.* [S0021-8979(96)09008-0]

The mechanism of the Morin spin reorientation occurring in hematite is based on the interplay of the two types of anisotropies of the iron ions, i.e., the single-ion anisotropy which gives rise to a preference for an axial orientation of the Fe magnetic moments and the anisotropy of the magnetic dipole-dipole interaction which makes a planar spin orientation more favorable. It is worth mentioning that according to the theoretical study of Artman *et al.*[1] the two opposite contributions to the anisotropy energy differ only slightly in magnitude (about 2%), but the single-ion component predominating at low temperature gives rise to the orientation of the iron spins along the trigonal axis. Because of the slight difference in the temperature dependence of the two types of anisotropy energies, the dipolar magnetic energy becomes larger around 260 K giving rise to the Morin spin reorientation and therefore to the arrangement with the spins lying in the basal plane. Recently strong evidence for a spin reorientation of a type similar to the one observed in hematite was found in a Mössbauer spectroscopy (MS) study of the new 2201 type ferrate $BiPbSr_2FeO_{6+z}$.[2]

In the present paper we extended our study to the isostructural ferrate $BiPbSrCaFeO_{6+z}$ prepared as described in Ref. 3, hereafter denoted as sample B and to two other samples obtained after annealing sample B first for 30 h at 700 °C and subsequently 17 h (sample B5) or 24 h at 850 °C (sample B8).

We start with the set of Mössbauer spectra of sample B, taken over a large temperature range, some of them shown in Fig. 1. Between 4.2 and 60 K there is no significant change in the shape of the spectra. Above 60 K the Mössbauer spectra become more complex and an increasing amount of a new phase with different hyperfine parameters appears. At 130 K, i.e., sensibly below the Néel temperature of 245 K the only magnetically split spectrum present belongs to the new phase. A similar behavior was previously observed in the case of $BiPbSr_2FeO_{6+z}$.[2] We have therefore to consider a low-temperature and a high-temperature modification of the same magnetic compound, hereafter denoted as a LT phase and a HT phase.

About 90% of Fe is in the Fe^{3+} state as derived from the values of the hyperfine field (HF) and isomer shift (IS) at 4.2 K. Two more aspects are worth mentioning: (1) the presence of an amount of 10%–12% Fe^{4+} and (2) the occurrence of a paramagnetic phase, appearing at 60 K and increasing steadily to 20% at a temperature of 20 K below the Néel point.

A comparison between the value of the quadrupole splitting (QS) in the paramagnetic regime above T_N and the double of the quadrupole shift qs in the magnetically ordered range usually allows one to get valuable information about the orientation of the Fe spins in the spin frozen state. In this respect the most important finding is that for the LT phase 2 qs is positive and practically equal to the QS value in the paramagnetic range. This result in conjunction with the sym-

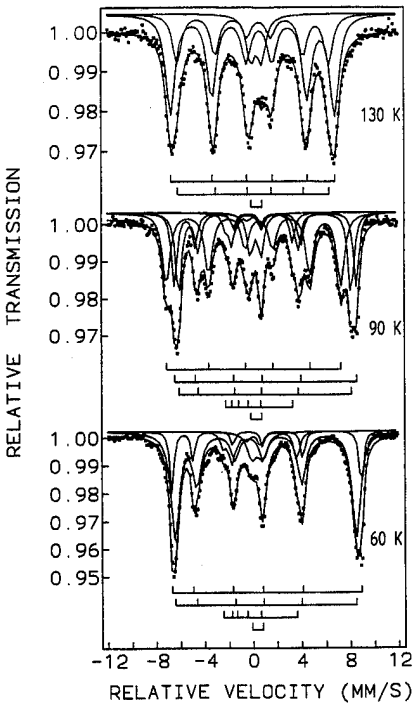


FIG. 1. Mössbauer spectra of $BiPbSrCaFeO_{6+z}$ (sample B) taken at several temperatures.

 0021-8979/96/79(8)/5257/3/$10.00 © 1996 American Institute of Physics

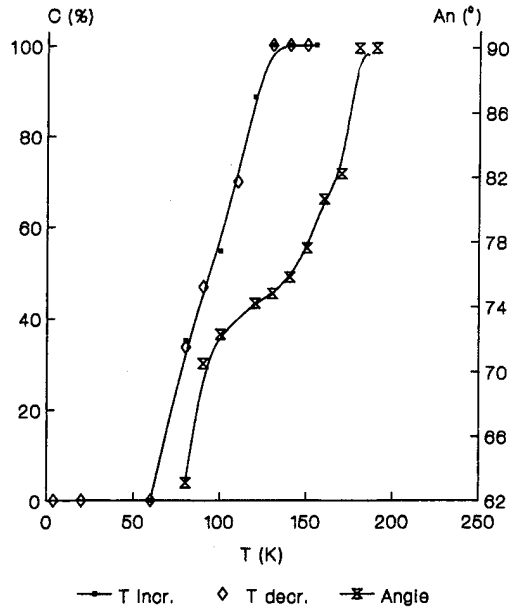


FIG. 2. Concentration c of the HT phase measured in increasing (■) and decreasing (◇) temperature regimes and the angle (An) between Fe spins and c axis vs T for sample B.

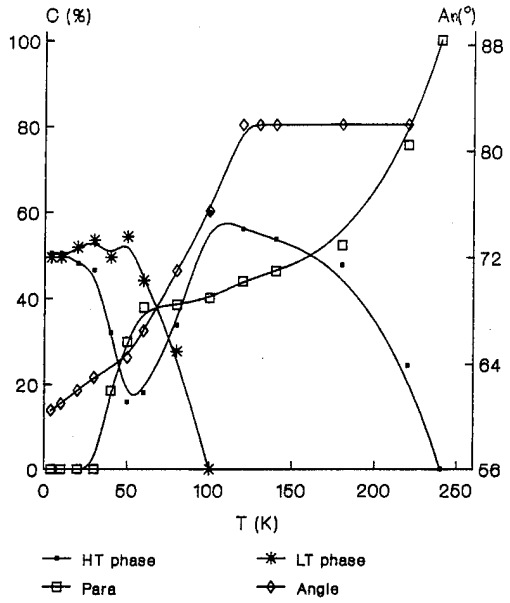


FIG. 3. Concentration c of the HT phase (■) and LT phase (*) of the paramagnetic component (□) and the angle (An) between Fe spins and c axis vs T for the sample B5.

metry of the octahedral environment of the Fe ions allowed us to assume a local axial symmetry of the crystalline field at the Fe site and therefore to use for QS and 2qs the equations:

$$\mathrm{QS}=(1/4)eQV_{zz} \tag{1}$$

and

$$2\mathrm{qs}=(1/2)\mathrm{QS}\ \mathrm{sgn}(V_{zz})(3\cos^2\vartheta-1). \tag{2}$$

Here Q is the ^{57}Fe nuclear quadrupole moment, V_{zz} the axial component of the electrical field gradient (EFG), in our case the projection along the c axis.

For the LT phase we have 2qs=QS=+1.46 mm/s (mean value), leading therefore to the result $\vartheta=0$, i.e., the Fe spins are oriented along the c axis as in the low-temperature phase of hematite below the Morin point. Using Eq. (2) one finds for the HT phase to which belong all the magnetically ordered Fe spins above 130 K, the value $\vartheta=90°$, i.e., a spin orientation in the $a-b$ plane, this time similar to a purely antiferromagnetic hematite above the Morin point.

A first remarkable aspect is the coexistence of both phases over a rather broad temperature interval of about 60 K. A second point is the continuous variation of the relative concentrations of the LT phase with $\vartheta=0$ and of the HT phase with temperature dependent ϑ.

The first point is not the consequence of a thermal hysteresis as can be seen from Fig. 2 where the concentration of the HT phase measured in both increasing and decreasing temperature regimes lies on the same curve. Concerning the second point it is worth mentioning that subsequent heat treatments gave rise to more complex behaviors as was the case with the samples B5 and B8 for instance. In the former case even at 4.2 K about half of the iron still belonged to the HT phase (Fig. 3). A scrutiny of Figs. 2 and 3 shows that at variance with the way the Morin transition occurs in good hematite crystals as evidenced in the MS study of Van der Woude[4] the spin reorientation in $BiPbSrCaFeO_{6+z}$ despite the gradual and anhysteretic character of the transition cannot be designed as a pure second-order phase transition.

In fact, taking the angle ϑ as order parameter for instance, we see that it changes continuously for the HT phase with decreasing temperature, the spins making larger and larger angles with the basal plane. In the same time the amount of the LT phase with the spins only along the c axis increases, involving below 60 K all the Fe atoms in the probably most favorable case of sample B.

Typical dependencies on temperature of the average hyperfine fields of both LT and HT phases, as well as the variation of the concentration of the paramagnetic phase with temperature are shown for the sample B in Fig. 4.

In order to better fit the 4.2 K spectra of sample B, for instance, one needed two sextets with higher HF values of 49.7 and 47.7 T and one with HF=18.6 T for about 11% of the total iron. The latter HF value can be ascribed to Fe^{4+} ions anyway expected because of a slight overoxidation corresponding to 6.13 oxygen atoms per formula unit. Even at 4.2 K the linewidths of the fitting sextets are rather large and the need for the two sextets with the higher HF values has probably to be correlated to a distribution of Bi and Sr around the apical oxygen ions in the FeO_6 layers, leading to slightly different distortions of the Fe–O distances.

At this point one has to envisage the quasi-two-dimensional character of the layers of FeO_6 octahedrons in the compounds we studied. Two layers of a Bi and Pb oxide with rocksalt structure separate along the c axis two layers of FeO_6 octahedrons. For this reason whereas the distance between two Fe containing planes reaches about 1.3 nm, the distance between two Fe atoms in the basal plane is only 0.4 nm giving rise to a strong structural anisotropy favorable to

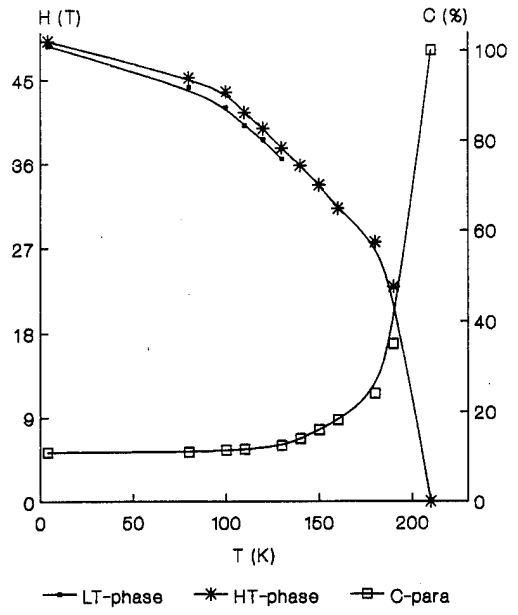


FIG. 4. Average hyperfine field H for the HT phase (*) and LT phase (■) and the concentration c of the paramagnetic component (□) vs T for the sample B8.

the single-ion anisotropy of the iron ions and the two-dimensional character of the superexchange interactions. The quasi two dimensionality can explain the relatively low Néel temperature of the compounds studied here (200–250 K) when compared with the Néel temperature of 512 K for $(Bi,Pb)_2Sr_2BiFe_2O_{9+z}$ with double layers of apically connected FeO_6 octahedrons. The lower dimensionality could also be the reason for the HF values at 4.2 K which are 3–5 T lower than the ones found for the FeO_6 multilayer compounds[5] and makes the spin-reorientation transition more sensitive to local changes of chemical or/and structural nature.

It is worth mentioning that versions of the Morin transition reminiscent of the features we found in our study were also reported in several studies of the influence of crystallinity and impurities on this phase transition. The explanation proposed by de Grave *et al.*[6] based on the combined influence of porosity, particle size, impurities, and local variations in the strength of the exchange interactions is probably also true for the compounds we studied here. But in order to be more specific we have to try to better define the similar factors which can be dominant in our case. An irregular distribution of the Sr and Ca atoms as important factor can be eliminated because we find the same complex behavior in the case of $BiPbSr_2FeO_{6+z}$.[2] But common to both compounds is the presence of about 10% Fe^{4+}. We believe that the tetravalent Fe ions play the role of the impurities known for their strong influence on the Morin transition of hematite. Because of their smaller radius the Fe^{4+} ions can give rise to local distortions of the Fe–O distances and therefore to local changes in the single ion anisotropy and superexchange. Together with the occurence of Fe^{4+} ions some regions of the crystals have to accommodate the extra oxygen, most probably in the (Bi,Pb)O bilayers, giving rise again to local changes in the single-ion anisotropy of Fe^{3+}.

We want to express our thanks to Dr. A. Wieck from the Ruhr University Bochum for allowing us to use the experimental facilities of his Institute and to the Bundesministerium für Forschung und Technologie for financial support.

[1] J. O. Artman, J. C. Murphy, and S. Foner, Phys. Rev. A **138**, 192 (1965).
[2] Th. Sinnemann, M. Mittag, M. Rosenberg, A. Ehmann, T. Fries, G. Mayer-von Kürthy, and S. Kenmmler-Sack, J. Magn. Magn. Mater. **95**, 175 (1991); Th. Sinnemann, Ph. D. thesis, Ruhr-University, Bochum, 1993.
[3] G. Filoti, V. Spânu, M. Rosenberg, C. Steudtner, and S. Kemmler-Sack, J. Alloys. Comp. **216**, 141 (1994).
[4] F. Van der Woude, Phys. Status Solidi **17**, 417 (1966).
[5] Th. Sinnemann, L. Ressler, M. Rosenberg, T. Fries, A. Ehmann, and S. Kemmler-Sack, J. Magn. Magn. Mater. **98**, 996 (1991).
[6] E. de Grave, L. H. Bowen, R. Vochten, and R. E. Vanderberghe, J. Magn. Magn. Mater. **72**, 141 (1988).

Magnetization behavior of $(NBu_4)_2Mn_2[Cu(opba)]_3$ and related solvated ferromagnets

S. A. Chavan, R. Ganguly, V. K. Jain, and J. V. Yakhmi[a)]
Chemistry Division, Bhabha Atomic Research Centre, Bombay 400 085, India

Direct current magnetization studies are reported for the organic ferromagnet $(NBu_4)_2Mn_2[Cu(opba)]_3$ (T_C=22 K), where opba stands for *o*-phenylenebis (oxamato), and related compounds obtained by solvating it with dimethylsulphoxide, methanol, and acetonitrile, which have T_C values of 15, 12, and 14.5 K, respectively. $M(H)$ plots for the first two compounds show very little width and criss-cross at low applied field values (<50 Oe). Zero field-cooled magnetization and field-cooled magnetization curves for $(NBu_4)_2Mn_2[Cu(opba)]_3$ nearly overlap and its remanence plot changes sign at 11.5 K, exhibiting a compensation behavior. Negative remanent magnetization has also been observed for the other three compounds. The results are discussed in terms of the ferrimagnetic nature of the building blocks. © *1996 American Institute of Physics.* [S0021-8979(96)09108-7]

The occurrence of spontaneous magnetization in molecular organic materials was first reported in 1986.[1] Since then different categories of molecular ferromagnets have been synthesized depending on whether the unpaired electrons reside (i) in *p* orbitals only; (ii) in both *p* and *d* orbitals; and (iii) in *d* orbitals only. Kahn's group has synthesized a number of organic ferromagnets belonging to the last category by using bimetallic quasi-one-dimensional chains comprising antiparallel alignment of alternating uncompensated spins as building blocks.[2–5] A typical example of such a bimetallic chain is $Mn^{II}Cu^{II}(obbz)\cdot nH_2O$ [obbz=oxamido bis benzoato] with an antiferromagnetic interaction between the adjacent local spins S_{Mn}=5/2 and S_{Cu}=1/2 separated by oxamido and carboxylato bridging groups which transmit the magnetic effects. When these ferrimagnetic chains are assembled appropriately in a three-dimensional lattice, interchain interactions may, under suitable conditions, lead to ferromagnetic order as happens in the case of $MnCu(obbz)\cdot 1H_2O$ (T_C=14 K).[5] Attempts have been made to raise the Curie temperature (T_C) by increasing the dimensionality of the bimetallic assemblies so as to strengthen the interchain interactions.[6] For instance, cross-linking the one-dimensional ferrimagnetic $Mn^{II}Cu^{II}$ chains in the compound $MnCu(opba)(DMSO)_3$ [where opba stands for *o*-phenylenebis(oxamato) and DMSO for dimethylsulphoxide] results in a two-dimensional $Mn^{II}_2Cu^{II}_3$ network, where Mn atoms are surrounded by three Cu (opba) groups, instead of two, and yields ferromagnetism at 15 K in $(NBu_4)_2Mn_2[Cu(opba)]_3\cdot 6DMSO\cdot H_2O$ and at 22.5 K in its desolvated analog $(NBu_4)_2Mn_2[Cu(opba)]_3$.[7,8] These compounds are soft magnets with $M(H)$ curves exhibiting very narrow hysteresis loops, with coercive fields of 10 Oe or lower at 4.2 K.[9] In this article, we report the results of our dc magnetization studies on the series of ferromagnetic compounds $(NBu_4)_2Mn_2[Cu(opba)]_3\cdot S$, where S stands for solvent molecule, including the above-mentioned $(NBu_4)_2Mn_2[Cu(opba)]_3\cdot 6DMSO\cdot 1H_2O$ and the $(NBu_4)_2Mn_2[Cu(opba)]_3$, hereafter called **A** and **B**, respectively, and two other related ferromagnetic compounds **C** (T_C=12 K) and **D** (T_C=14.5 K) obtained by solvating **B** with methanol (CH_3OH) and acetonitrile (CH_3CN), respectively. We report negative thermoremanent magnetization for all these compounds, a novel phenomenon observed for the first time, and a compensation behavior leading to valleylike remanence plots for samples **B** and **C**.

The sample **A** was synthesized following the procedure given by Stumpf *et al.*[7] A part of the sample **A** was heated at 175 °C for ~3 h under vacuum to remove the solvent molecules $6DMSO\cdot 1H_2O$ and was called **B**. The samples **C** and **D** were obtained by solvating **B** with methanol and acetonitrile, respectively. ac susceptibility measurements made on samples **A**, **B**, **C**, and **D** using an Air Products Division susceptometer with EG & G Model 5208 lock-in amplifier exhibited a sudden divergence at 16, 22, 12, and 14.5 K, respectively. The dc magnetization measurements were made using EG & G P.A.R. Model 4500 Vibrating Sample Magnetometer fitted with an 8 kOe Walker electromagnet and Tidewater bipolar power supply both as a function of temperature, $M(T)$, and applied field, $M(H)$. A Hall-probe Guassmeter was used to check the absence of residual field between the poles down to <1 Oe.

Zero field-cooled magnetization (ZFCM) data was recorded by cooling the sample down to 5 K in zero applied field, switching the applied field (10 Oe) on at this temperature and recording the magnetization while warming the sample up. Field-cooled magnetization (FCM) data was collected after cooling the sample in 10 Oe field and recording the data while warming up, keeping the field on. Next, remanent magnetization (REM) data was taken after cooling the sample in 10 Oe field to 5 K, and recording the data while warming up after reducing the field to zero (which is accomplished via the software command to the bipolar power supply). It was ensured that the applied field as measured by the Hall probe was indeed zero before taking remanence measurements.

Figure 1 shows the ZFCM, FCM, and REM data as function of temperature for the sample **A**. The ZFCM and FCM

a)Author to whom correspondence should be addressed. Electronic mail: yakhmi@magnum.barct1.ernet.in

 0021-8979/96/79(8)/5260/3/$10.00 © 1996 American Institute of Physics

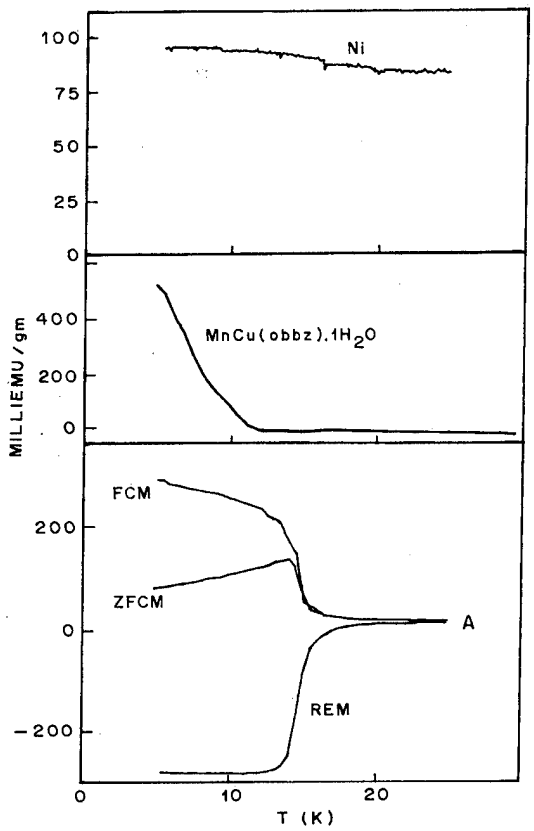


FIG. 1. ZFCM, FCM, and REM data for the sample **A**. REM data for a standard Ni sample and an organic ferromagnet, MnCu(obbz)·$1H_2O$ are also shown for comparison.

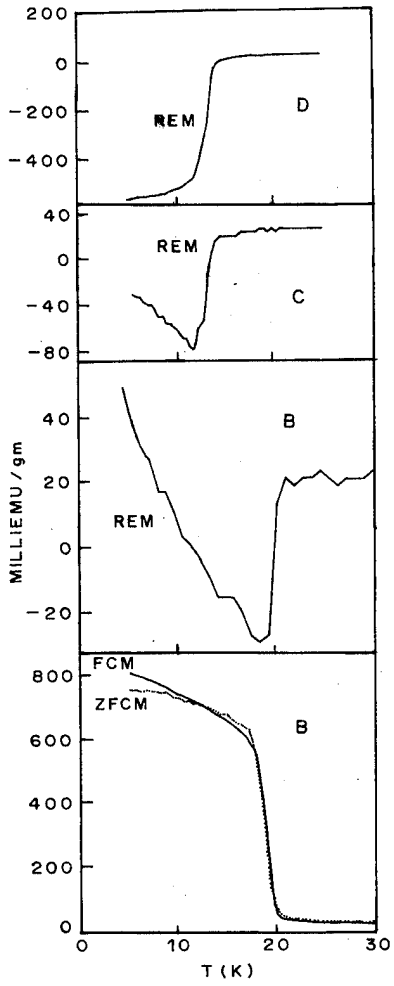


FIG. 2. ZFCM, FCM, and REM data for the sample **B**. REM plots for the samples **C** and **D** are also shown.

magnetization plots for the sample **A** showed conventional behavior with a hump below T_c in the ZFCM as reported by Stumpf *et al.*,[7] except that the magnitudes of ZFCM and FCM were 80 and 285 memu/g in our case. The published work in literature on different ferromagnetic materials reports positive values for remanence. The remanence for the sample **A**, however, showed negative values remaining nearly constant (−285 memu/g) between 5 and 13 K, becoming zero at ~16 K upon warming. The observation of negative remanence is a novel and intriguing observation. One obvious question that comes to mind is whether it has been caused by any residual negative field present between the pole pieces of the electromagnet. As mentioned earlier, we ensured before making any remanence measurements that the residual field is brought to zero (within ±1 Oe). The sample **A** showed negative REM behavior even when it was cooled under a higher applied field of 50 Oe before recording the data. In order to give further credibility to our data, we also present REM data taken on a standard Ni sample and another organic ferromagnet MnCu(obbz)·$1H_2O$ (T_C=14 K),[10] which show positive values of REM, as expected.

Figure 2 shows the ZFCM, FCM, and REM data for **B**. The ZFCM curve for ferromagnets, including those belonging to the category of bimetallic organic ferromagnets reported thus far, always lie much lower than the FCM because the domain walls do not move freely. However, the ZFCM plot for the sample **B** is only marginally lower than the FCM for $5<T\leq 13$ K. Both ZFCM and FCM overlap for $T>13$ K and even criss-cross a number of times, which is quite rare and implies that the domain walls are able to move rather freely. The remanence value for **B** which was about +50 memu/g at 5 K, dropped sharply upon warming becoming zero at 11.5 K and attained negative values between 11.5 and 19 K, becoming positive again for temperatures above 20 K, a valleylike feature.

ZFCM and FCM curves for the sample **D** nearly overlapped (like for **B**). The REM plot for **D** (Fig. 2) is similar in shape to that of sample **A**. REM plot for the methanol-solvated compound **C**, on the other hand, showed a valleylike feature (Fig. 2) but the values remain negative between 5 and 12 K.

The negative values of remanence as well as the valleylike feature have never been observed or reported for ferromagnetic samples. In fact, in most cases the values of Curie temperature is identified as the temperature where the value of REM falls exactly to zero. It should be noted that the magnitude of REM may vary among different polycrystalline samples of a particular ferromagnet because it is generally recognized that it is influenced by sample dependent factors like the grain size and shape. The valleylike feature in the

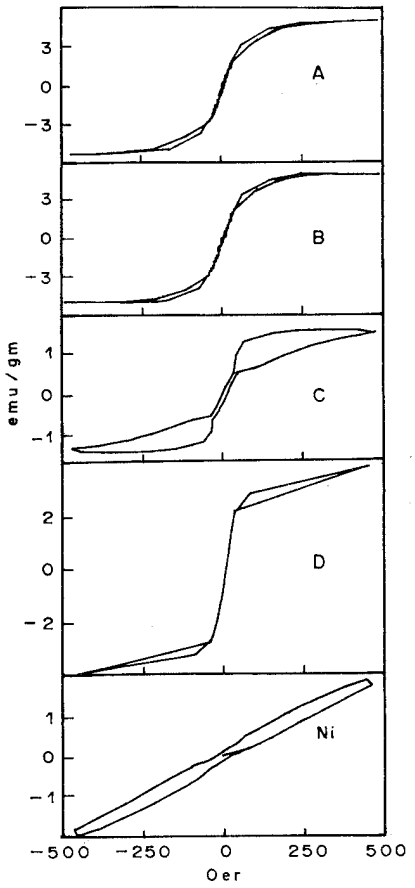


FIG. 3. $M(H)$ plots for the samples **A**, **B**, **C**, **D**, and Ni recorded at 5 K under applied field of ±500 Oe.

REM plot indicates a compensation behavior which can possibly arise from the ferrimagnetic nature of samples, the basic building blocks for our samples being the ferrimagnetic $Mn^{II}_2Cu^{II}_3$ planar units.[7] A compensation behavior can be explained if one considers the two individual sublattices separately as ferromagnetic, each with its own critical temperature and $M(T)$ curve. When combined antiferromagnetically, the net magnetization could take a variety of shapes, including negative values and a compensation point at a temperature where a complete cancellation occurs.

Figure 3 shows M vs H plots at 5 K for the samples **A**, **B**, **C**, **D**, and Ni (standard, for comparison) all recorded under the application of ±500 Oe field and identical conditions. The plots for **A** and **B** are nearly S-shaped curves with very little width (hysteresis), the low-field (−40–+40 Oe) portion, in particular, exhibiting a criss-crossing between the curves corresponding to increasing or decreasing field. The M vs H plot for the sample **D**, too, showed little width with absence of hysteresis at low applied fields. The $M(H)$ plot for the sample **C**, on the other hand, showed comparatively a substantial width, apparently an influence of the solvent molecules, but no criss-crossing. Samples **A** and **B** undergo saturation at ~300 Oe. The sample **C** saturates at ~400 Oe whereas the saturation field for **D** appears to be >500 Oe.

In summary, we observe three different kinds of remanence behavior for the four samples studies, whose T_C values range between 12 and 20 K: (i) sharp transition to negative values of remanence for the samples **A** and **D**; (ii) a valleylike feature for **B**, with a compensation feature resulting in a change of sign at 12 K; and (iii) a valleylike feature for **C** but the remanence keeping negative at all temperatures below T_C, indicating that the compensation point may be lying much below our lowest temperature of measurement, viz., 5 K. These observations indicate that the unusual magnetization behavior is inherent in the $(NBu_4)_2Mn_2[Cu(opba)]_3$ assembly. The compounds **A**, **B**, and **D** exhibited S-shaped $M(H)$ hysteresis plot with hardly any measurable width, indicating soft ferromagnetic behavior whereas the $M(H)$ loop ($H_{app}=\pm 500$ Oe) for **C** showed a substantial width.

The only other reports of unusual magnetic behavior are the observation of (i) a strong negative magnetization below 30 K for a molecular ferromagnet $(NBu_4)Fe^{II}Fe^{III}(C_2O_4)_3$ by Peter Day and co-workers[11] and (ii) a negative, valleylike, rotational remanent magnetization for lithium chromium ferrite.[12] At this stage, the mechanism giving rise to the observation of negative remanence in our samples is not clear and is at best speculative. In general, a negative remanent magnetization could imply a field-induced magnetization effect in which a sample, which is magnetic in the presence of a field, becomes diamagnetic in the absence of a field. However, these bimetallic organic magnets are known to exhibit spontaneous magnetization below T_C even in the absence of an applied field. It is possible that the anomalous solvent-sensitive thermoremanent magnetization data, including a compensation behavior for the samples **B** and **C** and the criss-crossing of $M(H)$ plot in some cases, arise due to an antiferromagnetic coupling of hard and soft regions.

The authors acknowledge useful comments by Professor A. J. Epstein, Dr. W. B. Brinckerhoff, and Dr. I. A. Campbell. Thanks are also due to Dr. I. K. Gopalakrishnan for help during measurements.

[1] J. S. Miller, J. C. Calabrese, R. W. Bigelow, A. J. Epstein, J. H. Zhang, and W. M. Reiff, J. Chem. Soc. Chem. Commun. 1026 (1986).
[2] O. Kahn, Y. Pei, K. Nakatani, and Y. Journaux, New J. Chem. **16**, 269 (1992).
[3] O. Kahn, Y. Pei, M. Verdaguer, J. P. Renard, and J. Sletten, J. Am. Chem. Soc. **110**, 782 (1988).
[4] K. Nakatani, P. Bergerat, E. Codjove, C. Mathoniere, Y. Pei, and O. Kahn, Inorg. Chem. **30**, 3978 (1991).
[5] K. Nakatani, J. Y. Carriat, Y. Journax, O. Kahn, F. Lloret, J. P. Renard, Y. Pei, J. Sletten, and M. Verdaguer, J. Am. Chem. Soc. **111**, 5739 (1989).
[6] H. Okawa, M. Mitsumi, M. Ohba, M. Kodera, and N. Matsumoto, Bull. Chem. Soc. Jpn. **67**, 2139 (1994).
[7] H. O. Stumpf, Y. Pei, O. Kahn, J. Sletten, and J. P. Renard, J. Am. Chem. Soc. **115**, 6738 (1993).
[8] H. O. Stumpf, L. Ouahab, Y. Pei, P. Bergerat, and O. Kahn, J. Am. Chem. Soc. **116**, 3866 (1994).
[9] H. O. Stumpf, Y. Pei, C. Michaut, O. Kahn, J. P. Renard, and L. Ouahab, Chem. Mater. **6**, 257 (1994).
[10] S. A. Chavan, J. V. Yakhmi, and I. K. Gopalakrishnan, Mol. Cryst. Liq. Cryst. **274**, 11 (1995).
[11] C. Mathoniere, S. G. Carling, D. Y. Sheng, and P. Day, J. Chem. Soc. Chem. Commun. **1994**, 1551.
[12] A. Stephenson, Philos. Mag. B **58**, 91 (1988).

Magnetic properties and grain growth stability of nanocomposite Fe–ZrO_2 granular solids prepared by mechanical milling

S. C. Axtell and R. Schalek
Department of Mechanical Engineering and Center for Materials Research and Analysis, University of Nebraska, Lincoln, Nebraska 68588-0656

Correlations between the grain size [or the diffracting particle size (DPS)] and the magnetic properties of mechanically milled Fe–ZrO_2 nanocomposite powders are reported. Nanocomposite powders with iron volume fractions below, near, and above the percolation value were annealed at temperatures between 573 and 1083 K and investigated. The composite as-milled powders exhibited enhanced coercivities (>300 Oe) compared to similar mechanically milled iron powders. The iron diffracting particle size (grain size) as a function of annealing temperature showed two regimes. The first regime, corresponding to temperatures at and below 773 K, consisted of enhanced coercivities and remanence ratios with a relatively stable iron diffracting particle size of ~25 nm. In the second temperature regime, above 773 K, the DPS increased, but remained well below the value for pure iron. Concomitant with this increase, large reductions in the coercivities were observed in the second regime. © *1996 American Institute of Physics.* [S0021-8979(96)09208-3]

I. INTRODUCTION

Granular metals consist of nanometer-size metal granules homogeneously distributed in a matrix. The unique microstructure results in a large variety of interesting properties.[1] Granular metal systems have been successfully fabricated by various deposition[2] and milling techniques[3] with metals Fe, Ni, Co, and Au, in various matrices (e.g., SiO_2, Al_2O_3, and MgO). In granular materials, the critical parameters affecting the magnetic properties include the metallic particle size, and the metal volume fraction (x_v) relative to the percolation volume fraction (x_p). For many granular systems $x_p \approx 0.5$.[4,5] Granular solids with $x_v > 0.5$ consist of metal regions forming a continuous matrix, while for $x_v < 0.5$ the metal forms isolated particles.

In recent years mechanical milling has demonstrated the ability to produce nanocomposite granular powders.[3,6] This technique has some advantages over thin film deposition techniques since large quantities of material may be produced quickly and cheaply. Furthermore, the grain size (diffracting crystallite size) of the constituent materials can be easily controlled by varying the milling parameters. This study attempts to correlate the magnetic properties of mechanically milled Fe–ZrO_2 nanocomposites with the iron diffracting particle size as a function of annealing temperature. A monodisperse, amorphous ZrO_2 powder that crystallizes with a diffracting particle size of 5.5 nm was chosen as the matrix. Iron volume fractions above, near, and below x_p were investigated.

II. EXPERIMENTAL PROCEDURES

The starting powders consisted of −100 mesh Fe (Cerac) and amorphous ZrO_2 powders. The Fe and the ZrO_2 powders were combined at compositions of $Fe_x(ZrO_2)_{1-x}$ where $x=0.32$, 0.52, and 0.70, where x is reported in volume percent. Using a ball-to-powder mass ratio of two, the powders were milled in a Spex 8000 Mixer/Mill under an argon atmosphere using three 12 g tungsten carbide (WC) balls in a WC lined grinding chamber. X-ray diffraction (XRD) patterns were acquired using a Philips 3100 x-ray diffractometer outfitted with a copper x-ray tube and graphite monochromator. The XRD patterns were collected using a 0.2° receiving slit and a 1°–4° variable divergent slit. The single-peak profile Fourier analysis technique described by Ganesan *et al.*[7] was used to calculate the average diffracting particle size (DPS) from the (110) iron x-ray peak. The powders were annealed for 1 h in flowing argon at temperatures from 573 to 1073 K. Milled powders were mixed with paraffin to prevent magnetization reversal via particle rotation when measuring hysteresis loops.

III. RESULTS AND DISCUSSION

Figure 1 shows the average iron DPS as a function of composition and annealing temperature. The as-milled DPS (represented by the 300 K value) ranges from a steady state 6.5 nm [below the single domain size of ~10 nm (Ref. 8)] for pure iron to 19.6 nm for the $x=0.70$ powder. The dependence of the DPS on the composition is a complicated function of co-deformation processes occurring during milling. These results indicate that, though the milling times were held constant, the conditions for obtaining the steady state iron DPS for the composite powders were not realized and, hence, the defect structure of the powders is slightly different.

The DPSs of the $x=0$, 0.32, and 0.52 nanocomposites are relatively stable (<25 nm) for temperatures of 773 K and below. The rapid grain growth observed above 773 K is consistent with other reports of where accelerated grain growth in single and two-phase nanocrystalline materials occurred above a critical temperature.[9,10] At 873 K and above, larger changes in the DPS are seen, with the pure iron powders showing a tremendous increase relative to $x=0.32$ and 0.52. Two temperature regimes can be identified from the data in Fig. 1 for $x=0$, 0.32, and 0.52: (1) for $T \leqslant 773$ K, the DPS remains near 25 nm and (2) for $T > 773$ K, where significant increases in the DPS are seen. Interestingly, the annealing temperature corresponding to this division coincides not only

 0021-8979/96/79(8)/5263/3/$10.00 © 1996 American Institute of Physics

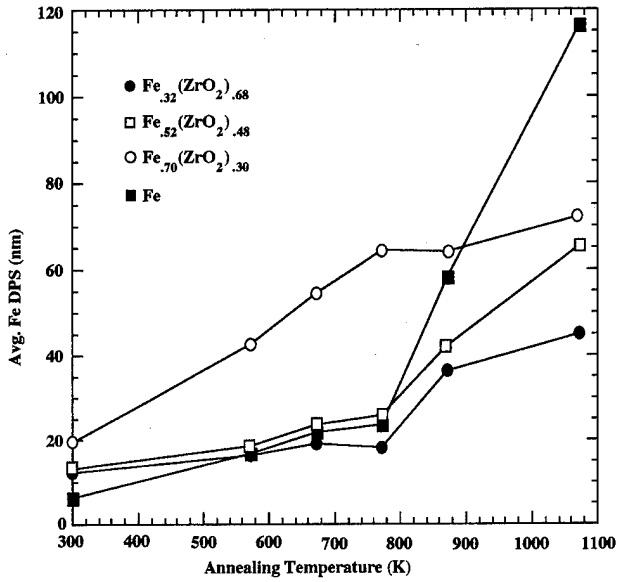


FIG. 1. The average diffracting particle size as a function of powder composition and annealing temperature. The large increase in iron DPS at 873 K indicates a demarcation point for grain growth stability. (Note: compositions are reported in volume percent.)

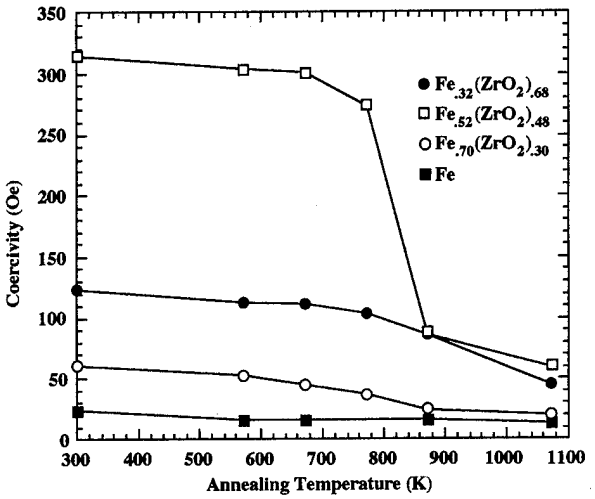


FIG. 2. The dependence of the coercivity on the powder composition and on the annealing temperature. Significant decreases in the coercivity are observed for $T>773$ K. (Note: compositions are reported in volume percent.)

with large increases in the DPS, but also with the crystallization temperature of the ZrO_2 powder.

The behavior of the $x=0.70$ powders provides further evidence of poor thermal stability of the iron regions for DPSs$\geqslant\sim$20 nm. In this case, the DPS increases substantially from the as-milled value of 19.6 nm upon annealing at low temperatures, but tends to stabilize at higher temperatures. This behavior suggests that short-range iron diffusion and defect removal increases the DPS. At higher temperatures, the DPS of the composited powders (including the $x=0.70$) is suppressed by the ZrO_2 particles when compared to the pure iron powder.

Hysteresis loops of the milled powders were studied as a function of iron volume fraction and annealing temperature to facilitate understanding of the effects of the nanoscaled iron structure with respect to the separation distance of the iron particles. The coercivity, H_c, as a function of annealing temperature is shown in Fig. 2 for each concentration. Error bars (omitted for clarity) are smaller than the symbol size. H_c is enhanced in the as-milled condition ($T=300$ K) for all composites. H_c is a maximum for $x=0.52$ (a value near x_p) with a value of 314 Oe. The $x=0.32$ and 0.70 powders show H_c values intermediate to the pure iron and $x=0.52$ powders. This trend is consistent with that reported by Xiao and Chien[11] for Fe–SiO_2 films, but disagrees with the results reported by Ambrose *et al.*[6] and Linderoth and Pedersen[3] for ball-milled Fe–Al_2O_3. The ball-milled Fe–Al_2O_3 powders exhibit peak coercivity enhancements at volume fractions of 0.4 and 0.3, respectively. Comparing the coercivity measurements with the DPS values indicates that, though significantly different H_c were measured for the $x=0.32$ and 0.52 powders, the DPS values are very similar. This result is most likely due to a combination of the milling conditions and composition. For instance, the $x=0.52$ powders possibly have a large fraction of single-domain regions, while the $x=0.32$ powders have a large fraction of superparamagnetic regions, although the average DPS in both cases is similar.

Slight decreases in H_c are observed for annealed powders. In particular, gradual decreases in the coercivity are seen for the $x=0.32$ and 0.70 powders, while the $x=0.52$ powder shows a gradual decrease followed by a large decrease (a change of 187 Oe) for $T>773$ K. This temperature correlates well with the demarcation of the DPS regimes identified by Fig. 1. In addition, the heat treatments cause the DPS to double in size for all the powders except the $x=0.70$ sample. To eliminate iron oxide formation as a possible cause to the decrease in coercivity, x-ray diffraction analysis was performed on the annealed powders. No oxide peaks were observed; however, thin interfacial oxides between particles may be undetectable and possibly contribute to de-

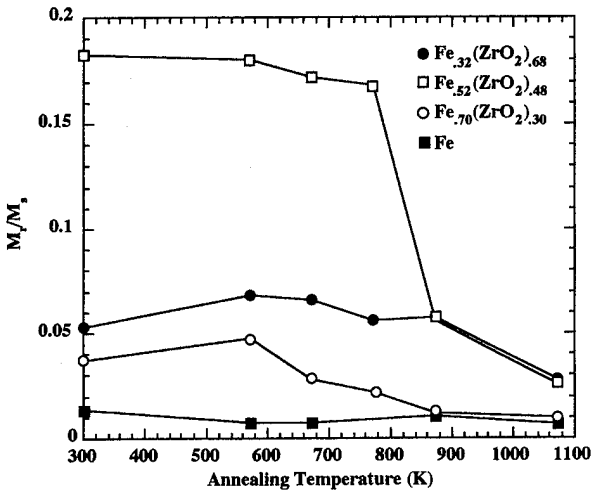


FIG. 3. The dependence of the remanence ratio on the annealing temperature and particle composition. (Note: compositions are reported in volume percent.)

creases in H_c.[12] In the second temperature regime, the powders with x above or near x_p (x=0.32 and 0.52) retain an increased coercivity, while the powder with iron concentration below x_p (DPS=72 nm) has a coercivity approximately equal to the pure iron case (DPS=116 nm).

As shown in Fig. 3, a larger remenance ratio is also observed for the composite powders in the first temperature regime. Again, the demarcation temperature corresponds to 773 K and a DPS of ~25 nm. These results indicate that the H_c and the remenance ratio are rather weakly dependent on the DPS for values <~25 nm, but increase in sensitivity for larger DPSs.

IV. CONCLUSIONS

The diffracting particle size and the magnetic properties of mechanically alloyed Fe–ZrO_2 nanocomposite powders annealed at temperatures between 573 and 1083 K were investigated. Two temperatures regimes were identified. In the first regime, ($T \leqslant 773$ K) the composites displayed enhanced coercivities and remenance ratios, with the iron DPS remaining relatively stable at ⩽25 nm (for the x=0.32 and 0.52 samples). For T>773 K, the DPSs increase and concomitant reductions in the magnetic properties are observed.

ACKNOWLEDGMENTS

Support for this article was provided by the NSF. Thanks also to Dr. Burton Davis at the University of Kentucky for providing the ZrO_2 particles and Dr. D. J. Sellmyer for use of the AGFM.

[1] C. L. Chien, J. Appl. Phys. **69**, 5267 (1986).
[2] R. W. Cohen and B. Abeles, Phys. Rev. **168**, 444 (1967).
[3] S. Linderoth and M. S. Pedersen, J. Appl. Phys. **75**, 5867 (1994).
[4] P. Sheng, Phys. Rev. Lett. **45**, 60 (1980).
[5] B. Abeles, P. Sheng, M. D. Couts, and Y. Arie, Adv. Phys. **24**, 407 (1975).
[6] T. Ambrose, A. Garvin, and C. L. Chien, J. Magn. Magn. Mater. **116**, L311 (1992).
[7] P. Ganesan, H. K. Kuo, A. Saavedra, and R. J. De Angelis, J. Catal. **52**, 310 (1978).
[8] F. E. Lurborsky, J. Appl. Phys. **32**, 171 (1963).
[9] U. Klement, U. Erb, and K. T. Aust, Nanostruct. Mater. **6**, 581 (1995).
[10] C. Rock and K. Okazaki, Nanostruct. Mater. **6**, 657 (1995).
[11] G. Xiao and C. L. Chien, Appl. Phys. Lett. **51**, 1280 (1987).
[12] G. C. Hadjipanayis, S. Gangopadhyay, L. Yiping, C. M. Sorensen, and K. J. Klabunde, in *Science and Technology of Nanostructured Magnetic Materials*, edited by G. C. Hadjipanayis and G. A. Prinz (Plenum, New York, 1991), p. 497.

The macroscopic ferri-ferromagnetic transition in amorphous Y–Co/Gd–Co bilayers

T. Yonamine
Instituto de Física, Universidade de São Paulo, CP 66318, 05389-970, São Paulo, Brazil

Y. Souche
Laboratoire de Magnétisme Louis Néel-CNRS, 38042 Grenoble Cedex, France

A. D. Santos
Instituto de Física, Universidade de São Paulo, CP 66318, 05389-970, São Paulo, Brazil

We developed a model to completely explain the domain wall existing at the interface of an amorphous Y–Co/Gd–Co bilayer. Samples produced by sputtering, were characterized by Rutherford backscattering spectrometry and transverse magneto-optical Kerr effect. From the experimental parameters we determined the thickness (δ) and relative position (Δ) of the domain wall, and also the exchange constant (A) for the Co–Co atom pair. The room temperature value of A was found to be $(4.8\pm1.4)\times10^{-8}$ erg/cm. © *1996 American Institute of Physics.* [S0021-8979(96)15208-X]

I. INTRODUCTION

A macroscopic ferri-ferromagnetic transition was reported[1,2] for the sandwich system composed of amorphous RE–Co layers, where RE=Y and Gd. The Gd and Co atoms are antiferromagnetically coupled, while the Y–Co amorphous alloys only the Co atoms contributes magnetically. Due to the exchange interaction, all the Co magnetic moments are aligned. When an in-plane magnetic field, larger than the magnetic transition field (H_t) is applied parallel to the easy axis direction, a reversion on the Gd–Co magnetic moment occurs. As a consequence, a domain wall (DW) is created at the interface region. This DW is large and parallel to the interface and minimizes the exchange interactions between the cobalt atoms. Our intention here, is completely characterize this DW. We produced amorphous $YCo_2/GdCo_2$ bilayers on glass substrates. Using transverse magneto-optical Kerr effect (TMOKE) magnetometry we can determine the magnetic properties for each layer in each sample.

II. EXPERIMENT

The samples are composed of magnetic layers of nominal composition YCo_2 and $GdCo_2$ deposited on a glass substrate. Layers of Si_3N_4 are used under and over the magnetic layers, to protect the samples. The thickness of the magnetic layers ranges from 400 to 1200 Å. To produce the amorphous films, we used dc triode sputtering, with the substrate cooled to liquid N_2 temperature. A magnetic field of 300 Oe was applied during the deposition, to induce an in-plane anisotropy. Film thickness and composition were determined by Rutherford backscattering analysis (RBS). We used a TMOKE to characterize the magnetization of the films. It is based on a laser-diode (λ=670 nm), giving a 60° incident p-polarized wave. A Helmholtz coil produced a 180 Oe maximum magnetic field H_{dc} and frequency 30 mHz. The TMOKE was used to determine the hysteresis loops and the magneto-optical transversal susceptibility (χ_t).[3] In the latter case a second coil, perpendicular to the first one, produced an in-plane oscillating magnetic field H_{ac} of ~1 Oe at a frequency of 5 kHz. The lock-in amplifier was synchronized to this frequency. From the magnetic field dependence of χ_t, we determined the anisotropy field (H_k) as the magnetic field corresponding to the peak signal. As H_{dc}, in this case, is applied parallel to the hard axis of the sample, there is neither coercive nor transition effects on this measurement. As the penetration depth of the light is less than each layer thickness, the magneto-optical (MO) signal comes independently from each layer of the sample. The red light (1.85 eV) of the laser can induce an optical process only for the magnetic electrons of the Co atoms, meaning the MO hysteresis loops corresponds only to the magnetic contribution of the Co atoms. To complete the magnetic characterization of the samples, we also used a vibrating sample magnetometer (VSM) and a hysteresis loop tracer.

III. THEORETICAL MODEL

Ndjaka[4] and Dieny[5] presented for the sandwich system, a theoretical model for the Bloch wall. It was based on the exchange and Zeeman energies. The measurements on our bilayers give us comparable values of H_t and H_k. Thus we needed to add the effective anisotropy term in our model.

In the model, a and b represent, respectively, the YCo_2 and $GdCo_2$ materials: $M_{a,b}$ are their saturation magnetizations; $e_{a,b}$ the layer thicknesses and $\delta=\delta_a+\delta_b$ is the total thickness of the DW. $\delta_{a,b}$ is the portion of the DW in each layer. $K_{a,b}=M_{a,b}\times H_{ka,b}/2$ is the effective anisotropy constant, supposed to be uniaxial and in-plane. It is also necessary to define the relative position of the DW, $\Delta=\delta_a/\delta$. The values of Δ range from 0 to 1, corresponding, respectively, to the DW passing from inside layer b to a. The direction of the magnetization inside the DW is supposed to change linearly with position. Our theoretical model describing the DW at the interface of the amorphous bilayer considers the exchange (E_{ex}), the effective anisotropy (E_k) and the Zeeman (E_z) energies. From Chikazumi[6] we can write each of these terms as:

(1) For $|H|<H_t$ (without DW)

$$E_{z,i}=-M_aHe_a+M_bHe_b, \qquad (1)$$

$$E_{ex,i}=E_{k,i}=0.$$

 0021-8979/96/79(8)/5266/3/$10.00 © 1996 American Institute of Physics

(2) For $|H| \geqslant H_t$ (with DW)

$$E_{z,f} = -\frac{M_a H}{2}\left[e_a - \delta\Delta + \frac{\delta \sin(\pi\Delta)}{\pi}\right] \pm \frac{M_b H}{2} \times \left[e_b - \delta(1-\Delta) - \frac{\delta \sin(\pi\Delta)}{\pi}\right], \quad (2)$$

$$E_{k,f} = \frac{M_a H_{ka}}{2}\left[\frac{\delta\Delta}{2} - \frac{\delta}{4\pi}\sin(2\pi\Delta)\right] + \frac{M_b H_{kb}}{2}\left[\frac{\delta(1-\Delta)}{2} + \frac{\delta}{4\pi}\sin(2\pi\Delta)\right], \quad (3)$$

and

$$E_{\mathrm{ex},f} = A\pi^2/\delta, \quad (4)$$

where A is the Co–Co atomic pair exchange constant.

Minimizing the total energy, $E_{\mathrm{tot},f} = E_{z,f} + E_{k,f} + E_{\mathrm{ex},f}$, in relation to Δ, we get

$$-\frac{(M_a - M_b)H}{(M_a H_{ka} - M_b H_{kb})} = \frac{\sin^2(\pi\Delta)}{1-\cos(\pi\Delta)}, \quad (5)$$

The right-hand side of Eq. (5) is in the range from 0 ($\Delta=1$) to 2 ($\Delta=0$), while the left-hand side is not limited. If its value is negative or larger than 2, this means the DW would be far from the interface. Under these conditions, the energy minimum would not be attained, due to the portion of the layer between the DW and the interface that would have its magnetization inverted relative to the magnetic field. Now, minimizing $E_{\mathrm{tot},f}$ in relation to δ, we can determine the total thickness of the DW,

$$\delta = \pi(2A)^{1/2}\left[M_a H\left(\Delta - \frac{\sin(\pi\Delta)}{\pi}\right) + K_a\left(\Delta - \frac{\sin(2\pi\Delta)}{2\pi}\right) + M_b H\left(1-\Delta+\frac{\sin(\pi\Delta)}{\pi}\right) + K_b\left(1-\Delta+\frac{\sin(2\pi\Delta)}{2\pi}\right)\right]^{-1/2}. \quad (6)$$

And, finally, from the equilibrium between $E_{\mathrm{tot},i}$ and $E_{\mathrm{tot},f}$, at $H = H_t$, we have

$$A\pi^2/\delta_t - H_t(M_b e_b)/2 = 0, \quad (7)$$

where δ_t corresponds to the DW thickness at $H = H_t$.

Equations (5)–(7) are interdependent and their solution is different for each sample, depending upon its specific magnetic properties. Then, from the values of the $M_{a,b}$, $H_{ka,b}$, $e_{a,b}$, and H_t of the sample, we can determine the magnetic field dependence on δ and Δ, and also the value of A for the Co–Co atomic pair.

TABLE I. Experimental parameters from RBS and VSM measurements.

Composition	Thickness (Å)	m_s (emu)	Area (cm^2)	M_s (emu/cm^3)
$Y_{0.33}Co_{0.67}$	3450	0.0130	1.3±0.2	279±46
$Gd_{0.29}Co_{0.71}$	3550	0.0193	2.4±0.3	223±30
$Y_{0.32}Co_{0.68}/Gd_{0.31}Co_{0.69}$	1180/1150	0.023	3.3±0.4	···

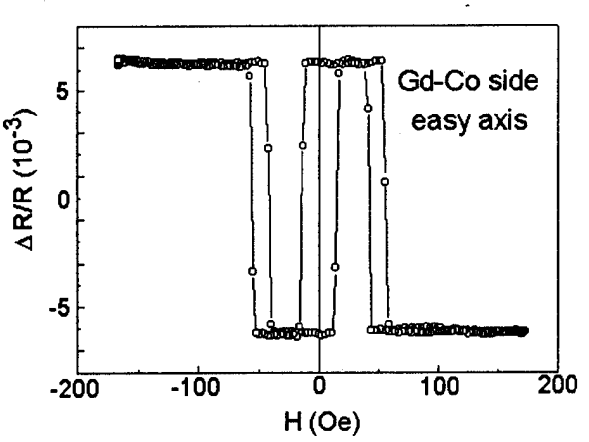


FIG. 1. TMOKE hysteresis loop from the Gd–Co side of the bilayer. The vertical axis is the relative variation of the reflectivity.

IV. EXPERIMENTAL RESULTS AND DISCUSSION

The samples were produced with thicknesses of each layer in the range from 400 to 1200 Å. Depending on the sample, the H_t and H_k values were 40–350 Oe and 30–150 Oe, respectively. Here we will present results of one bilayer that represents quite well the utilization of the model. Single-layer films were prepared to determine the saturation magnetization of the Y–Co and Gd–Co layers. In Table I we have the results of the characterization of these three samples, using RBS and VSM.

In Figs. 1 and 2, we have the TMOKE hysteresis loops, respectively, for the Gd–Co and Y–Co sides of the bilayer. These easy axis loops represent only the contribution of the Co atoms, as explained before. It is possible to see for low magnetic fields (<30 Oe), that the Co atoms of both layers are ferromagnetically aligned. At $H \sim 50$ Oe there is the ferri-ferromagnetic transition, with the inversion of the magnetization of the Gd–Co layer. For large values of H, this con-

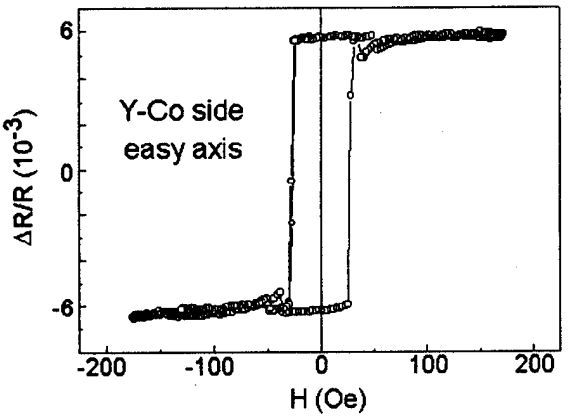


FIG. 2. TMOKE hysteresis loop from the Y–Co side of the bilayer.

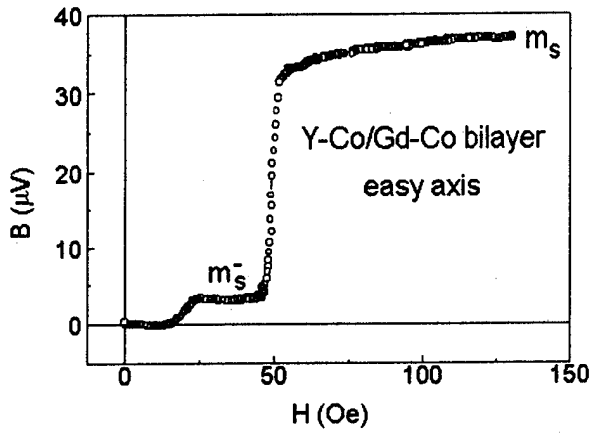


FIG. 3. B vs H curve of the Y–Co/Gd–Co bilayer. At $H\sim 50$ Oe there is a ferri-ferromagnetic transition.

figuration remains stable. The small perturbation visible on the Y–Co side for a magnetic field of about $H=50$ Oe will be explained later. In Fig. 3 we have the B vs H curve obtained using the hysteresis loop tracer, where B is in mV due the difficulty of defining the cross-sectional area of the sample. Anyway, the vertical axis can be calibrated using the value of $m_s=0.023$ emu from Table I. At $H\sim 20$ Oe the coercive field is visible, in agreement with Figs. 1 and 2. From Fig. 3 we can determine the transition field as $H_t=49$ Oe. Just below the transition we have the magnetic moment of the Co atoms in both layers aligned with the magnetic field, while the Gd moment is in the inverse sense. We will define the magnetic moment of this point as m_s^-, and its value is $\sim 10\%$ of m_s, for this sample. Next, we present in Fig. 4, the TMOKE susceptibility (χ_t) vs H of the Y–Co side of the bilayer. The shape of this curve is typical; it is obtained applying H_{dc} parallel to the hard axis and gives us, from the peak, $H_{ka}=33$ Oe. In the insert we have the hysteresis loops to the same condition, showing no transition on the hard axis. The measurement on the other side of the same sample (Gd–Co) gives $H_{kb}=126$ Oe.

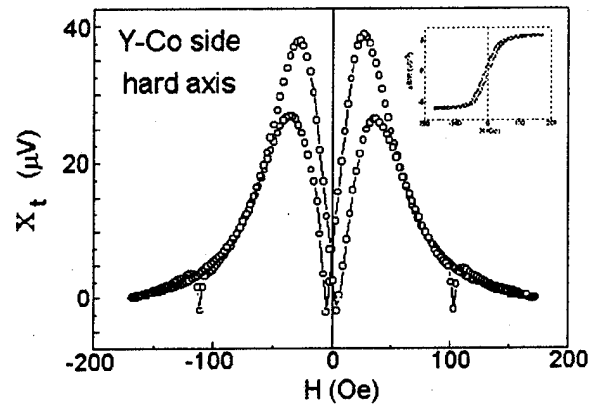


FIG. 4. TMOKE transverse susceptibility χ_t vs H for the Y–Co side of the bilayer. From the peak, we determine $H_{ka}=33$ Oe. Insert: hard axis TMOKE hysteresis loops.

Now, applying these experimental results to the theoretical model, we got from Eq. (5), $\Delta=0.83$ when $H=49$ Oe. This means 83% of the DW is in the Y–Co layer. Increasing H leads to a reduction in Δ, indicating a displacement of the DW in the direction of the Gd–Co layer. In order to determine simultaneously the value of δ_t and A, we used Eqs. (6) and (7) together with $H_t=49$ Oe and $\Delta=0.83$. Then, we obtained $\delta_t=(730\pm 140)$ Å and $A=(4.8\pm 1.4)\times 10^{-8}$ erg/cm.

At the transition, 83% of the DW (607 Å) is in the Y–Co layer. This means the DW is at ~500 Å from the surface and, since the light penetration depth is of the order of hundreds of Å, we can explain the small signal around H_t in Fig. 2. Before the transition, the magnetization of the Gd–Co layer is in the opposite sense to that of the Y–Co layer. Then we can calculate m_s^- as, $m_s^-=[M_a e_a - M_b e_b]S$, where S is the surface area of the sample, as presented in Table I. This give us $m_s^-=(2\pm 2)\times 10^{-3}$ emu. After the transition, both the magnetizations are in the same sense, so that $m_s^+=[M_a e_a + M_b e_b]S$. We found $m_s^+=(19\pm 3)\times 10^{-3}$ emu. This value agrees quite well with the saturation magnetic moment measured in the VSM. It is also ten times larger than the m_s^- value, in agreement with Fig. 3.

V. CONCLUSIONS

We developed a model to completely explain the DW existing at the interface of an amorphous bilayer of Y–Co/Gd–Co. Using parameters measured in our samples, we can calculate the magnetic field dependence of δ and Δ. Both are qualitatively reasonable and consistent with the magneto-optical hysteresis loops. For $H=H_t$, the DW was almost completely in the Y–Co layer. For the $Y_{0.32}Co_{0.68}$/$Gd_{0.31}Co_{0.69}$ amorphous bilayer analyzed here, $\delta=730$ Å. The room temperature value of A for the Co–Co atomic pairs was found to be $(4.8\pm 1.4)\times 10^{-8}$ erg/cm, one order lower than that determined using estimated parameters, in Ref. 5. Our result better agrees to that presented by Raasch,[7] $A=2\times 10^{-7}$ erg/cm, for a $Gd_{21.2}Co_{78.8}$ amorphous film. The Co concentration may be responsible by the difference in these values.

ACKNOWLEDGMENTS

This work was supported by FAPESP, CNPq, and FINEP.

[1] D. Givord, A. D. Santos, Y. Souche, J. Voiron, and S. Wüchner, J. Magn. Magn. Mater. **121**, 216 (1993).
[2] S. Wüchner, J. Betz, D. Givord, K. Mackay, A. D. Santos, Y. Souche, and J. Voiron, J. Magn. Magn. Mater. **126**, 352 (1993).
[3] T. Yonamine, M.Sc. thesis, Universidade de São Paulo, Brazil, 1995.
[4] J. M. B. Ndjaka, Ph.D. thesis, Université Joseph Fourier, Grenoble, France, 1990.
[5] B. Dieny, D. Givord, J. M. B. Ndjaka, and J. M. Alameda, J. Appl. Phys. **67**, 5677 (1990).
[6] S. Chikazumi, *Physics of Magnetism* (Wiley, New York, 1964), p. 186.
[7] D. Raasch, J. Reck, C. Mathieu, and B. Hillebrands, J. Appl. Phys. **76** 1145 (1994).

Published without author corrections

Weak ferromagnetic resonance of Gd_2CuO_4 small particles (abstract)

J. Mira and J. Rivas
Departamento Física Aplicada, Universidade de Santiago, E-15706 Santiago, Spain

A. Butera and M. Tovar
CAB-IB, 8400 S.C. de Bariloche, Argentina

C. Vázquez-Vázquez, J. Mahía, and M. A. López-Quintela
Departamento Química-Física, Universidade de Santiago, E-15706 Santiago, Spain

S. B. Oseroff
San Diego State University, San Diego, California 92182

RE_2CuO_4 (RE=rare earth) compounds constitute an interesting family of materials because of their magnetic complexity as well as for their relationship with high T_c superconductors. For R=Gd and heavier rare earths, a weak ferromagnetic component (WF) is observed below ~280 K. This component has its origin in a canting of the Cu antiferromagnetic (AF) structure due to a distortion of the oxygen ions between the copper atoms. In this contribution we center our work in Gd_2CuO_4, which is the only WF compound in the series that can be synthesized at normal pressures. WF can be easily detected by microwave absorption, due to the presence of an associated low field absorption signal.[1] We have synthesized the material by sol-gel methods, allowing a control of grain size, dependent on time and the final calcination temperature. The microwave absorption results show that the onset point for the WF component shifts from 290 K for the bulk material, to 210 K for particles with an average size of 120 nm. For particles less than 90 nm the WF resonance line is not observed, suggesting the absence of weak ferromagnetism. As the WF component is associated to the AF ordering, we interpret our results as the elimination of the long range order motivated by the particle size reduction. © *1996 American Institute of Physics.* [S0021-8979(96)47408-7]

[1] S. B. Oseroff *et al.*, Phys. Rev. B **41**, 1934 (1990).

Inverse giant magnetoresistance (invited)

J.-P. Renard, P. Bruno, R. Mégy, B. Bartenlian, P. Beauvillain, C. Chappert, C. Dupas, E. Kolb, M. Mulloy, J. Prieur, P. Veillet, and E. Vélu
Institut d'Electronique Fondamentale, CNRS URA 022, Bâtiment 220, Université Paris-Sud, 91405 Orsay Cedex, France

Inverse giant magnetoresistance (GMR) is obtained in multilayers alternating two ferromagnetic layers F_1 and F_2 with different asymmetry of spin scattering, $\alpha_1>1$ and $\alpha_2<1$. This is clearly demonstrated in the simple spin-valve system with perpendicular magnetization $Fe_{1-x}V_x$/Au/Co. With respect to Fe, the FeV alloys with $x=0.18$ and 0.29 exhibit an inversion of the spin scattering coefficients ($\alpha_{Fe}>1$, $\alpha_{FeV}<1$) due to the change of the densities of states at the Fermi level. The inverse MR of FeV/Au/Co is studied as a function of FeV layer thickness and temperature and compared to calculations based on the Camley–Barnas model. The data show that the inverse GMR is due to the bulk scattering within the FeV layer, which coexists with a substantial interface scattering favoring normal GMR. © *1996 American Institute of Physics.*
[S0021-8979(96)53308-7]

I. INTRODUCTION

Giant magnetoresistance (GMR)[1–3] has been widely studied in a large number of magnetic multilayers. It is now well established that GMR is due to spin-dependent scattering of the conduction electrons in the bulk or at the interface of the ferromagnetic (F) layers.[4,5] More precisely, the scattering probability, D, for a conduction electron crossing a ferromagnetic layer depends on its spin orientation with respect to that of the majority band so that $D\uparrow \neq D\downarrow$, where $D\uparrow(D\downarrow)$ refers to electrons with spin parallel (antiparallel) to majority spin band. The spin asymmetry of scattering is usually defined by $\alpha=D\downarrow/D\uparrow$.[6] In a simple system with two ferromagnetic layers F_1 and F_2, the magnetoresistance ratio, $\Delta R/R$, is given in first approximation by

$$\Delta R/R=(R_{AP}-R_P)/R_P \propto (D_1^{\downarrow}-D_1^{\uparrow})(D_2^{\downarrow}-D_2^{\uparrow}), \quad (1)$$

where R_{AP} and R_P are, respectively, the resistances for an antiparallel and parallel arrangement of the magnetization directions of F_1 and F_2. For equivalent ferromagnetic layers, the resistance is larger for an antiparallel arrangement than for a parallel one ($\Delta R/R>0$), which is the normal GMR, independently of whether $\alpha>1$ or $\alpha<1$. On the other hand, if F_1 and F_2 are different and such that $\alpha_1>1$ ($D_1^{\downarrow}>D_1^{\uparrow}$) and $\alpha_2<1$ ($D_2^{\downarrow}<D_2^{\uparrow}$), one would expect an *inverse* GMR ($\Delta R/R<0$). These mechanisms are sketched in Fig. 1. A more detailed theoretical analysis has been given recently by Hasegawa.[7]

The inverse GMR has been checked by George *et al.*[8] on a Cu based multilayer in which F_1 is a Fe film and F_2 a 0.4-nm-thick Cr film intercalated between two 1.6-nm-thick Fe films. This structure exhibits the expected inverse MR at low field but also a normal MR, i.e., $dR/dH<0$ at high field. This relatively complex behavior attributed to the misalignment of the magnetizations of the two Fe layers separated by Cr "makes the inverse MR effect less clear than might have been expected".[8]

A clearer demonstration of inverse GMR is brought by the simple spin-valve system $Fe_{1-x}V_x$/Au/Co.[9] This system was chosen for the following reasons. The scattering rates, $D^{\uparrow,\downarrow}$, are expected to be proportional to the densities of states at the Fermi energy $n^{\uparrow,\downarrow}(E_F)$. For Co, which is a strong ferromagnet, one has $n^{\uparrow}(E_F)<n^{\downarrow}(E_F)$, i.e., $\alpha(\text{Co})>1$. On the other hand, due to its bcc structure, Fe exhibits a pronounced valley in the density of states with $n^{\uparrow}(E_F)>n^{\downarrow}(E_F)$ because the Fermi level lies in the bottom of this valley for the minority spins. The position of the Fermi level for the

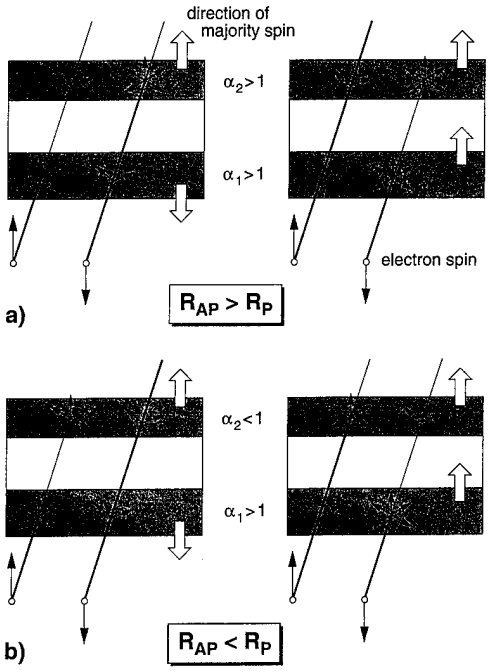


FIG. 1. Schematic picture of the normal (a) and inverse (b) giant magnetoresistance mechanism for a simple structure with two ferromagnetic layers.

 0021-8979/96/79(8)/5270/6/$10.00 © 1996 American Institute of Physics

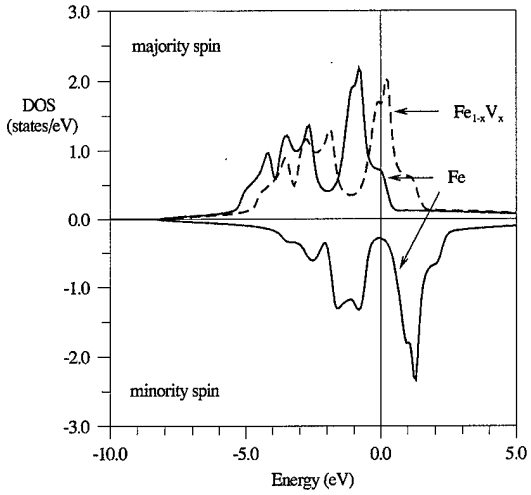


FIG. 2. Density of states of Fe (solid line); upper panel: majority spin; lower panel: minority spin. The zero of energy is taken at the Fermi level. Broken line: sketch of the majority spin density of states for a $Fe_{1-x}V_x$ alloy, with $x \approx 30\%$.

majority spins, near the upper edge of the $3d$ band is however such that the spin asymmetry is rather weak, as seen in Fig. 2. The asymmetry can be considerably enhanced by alloying the Fe with a $3d$ metal of lower valence such as V, as sketched in Fig. 2. Fe and V form solid solutions with a bcc structure over the whole concentration range $0<x<1$.[10] The $Fe_{1-x}V_x$ alloy is ferromagnetic up to $x=0.5$[11] and follows nicely the Slater–Pauling curve.[12] The latter means that upon alloying with V, the majority spin $3d$ band moves towards higher energy whereas the minority spin $3d$ band remains essentially unchanged, as sketched in Fig. 2. The maximum asymmetry, and hence maximum inverse MR, is expected for a valence reduction of about one electron, i.e., for a V concentration around 30 at. %. In fact, this band model is rather crude and should be considered as a guide for intuition. First-principles calculations of the electronic structure of $Fe_{1-x}V_x$ using a coherent potential approximation (CPA) show little change, with respect to Fe, in the minority band and in the position of the Fermi level in its valley, whereas the majority band is strongly broadened and disordered.[13]

II. SAMPLES AND EXPERIMENTAL TECHNIQUES

The samples are composed of two ferromagnetic layers separated by a Au spacer layer with either a variable Au thickness, t_{Au}, or a fixed Au thickness of 2.35 nm. They are grown at room temperature by evaporation in ultrahigh vacuum with a base pressure of about 10^{-10} mbar on a 28-nm-thick Au buffer layer deposited on a float glass substrate. The protection against oxidation is ensured by a Au cap layer 5 nm thick. The Au buffer layer is deposited at $T \approx 210$ K, at a rate of about 0.06 nm/s. After a 1 h annealing at 450 K controlled by reflection high energy electron diffraction (RHEED), the surface becomes atomically flat, oriented as a (111) plane and made of compact (111) terraces with a few 10 nm lateral size separated by monoatomic steps.[14] The 3-monolayer-thick (3 ML=0.6 nm) Co film was deposited directly on the Au buffer layer. The FeV alloy was prepared

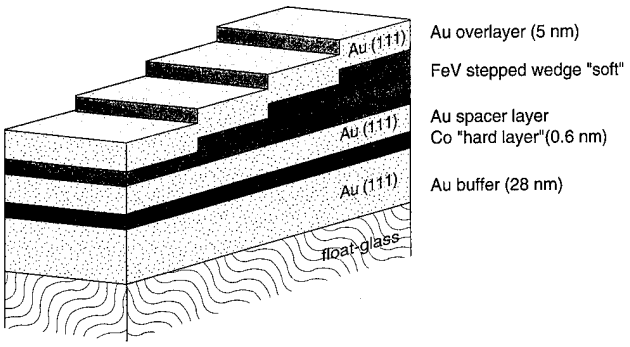


FIG. 3. Schematic view of the structure of samples 4 and 5, with variable FeV thickness.

by evaporating simultaneously Fe from an alumina crucible and V using an electron gun. Precise determination of the alloy concentration was obtained by measuring separately the Fe and V deposition rates with a quartz microbalance, immediately before and after deposition of the alloy layer. Both measurements gave the same value to within a few percent, which gives confidence that the alloy concentration is constant within the layer. The Co and FeV layers were deposited at a rate of about 1 ML (0.2 nm)/mn. The growth of Co, Fe, and FeV on Au (111) does not follow a layer by layer mode but rather the surface spreads on 2–3 ML for low thickness films. The orientation of hcp Co on Au (111) is (0001)[14,15] and that of Fe and FeV is (110).[16] Due to the large misfit between Au and the $3d$ transition metals in these orientations, the lateral coherence of the ferromagnetic films is not very large.[14]

Five different samples, (1) Fe(0.5)/Au(t)/Co(0.6), (2) $Fe_{0.82}V_{0.18}$(0.8)/Au(t)/Co(0.6), (3) $Fe_{0.82}V_{0.18}$(0.8)/Au(t)/$Fe_{0.82}V_{0.18}$(0.8), (4) $Fe_{0.82}V_{0.18}$(t)/Au(2.35)/Co(0.6), and (5) $Fe_{0.71}V_{0.29}$(t)/Au(2.35)/Co(0.6), in which the layer thicknesses are given in nm, have been made following the preparation technique described above. The Au spacer layer of the first three samples and the FeV layer of the last two have a stepped wedge shape with ten different thicknesses ranging from 2 to 11 ML.[17] A schematic view of a sample with variable t_{FeV} is shown in Fig. 3.

The hysteresis loops of the samples were recorded at room temperature by a perpendicular magneto-optical Kerr effect (PMOKE). As discussed later, they exhibit perpendicular magnetic anisotropy and square hysteresis loops except for the largest $Fe_{0.82}V_{0.18}$ thickness values. For performing resistivity and magnetoresistance measurements, well separated 1-mm-wide strips were obtained on each step by scribing the metal film with a diamond stylus along the step direction. Electrical contacts were made by sticking gold leads with silver paint on the Au cap layer. Four points measurements were performed with an ac bridge operating at low frequency in the temperature range 1.4–300 K. Perpendicular magnetic fields up to 100 kOe could be applied.

III. EXPERIMENTAL DATA

The hcp Co(0001) and bcc Fe(110) ultrathin films sandwiched in Au(111) have a strong perpendicular interface

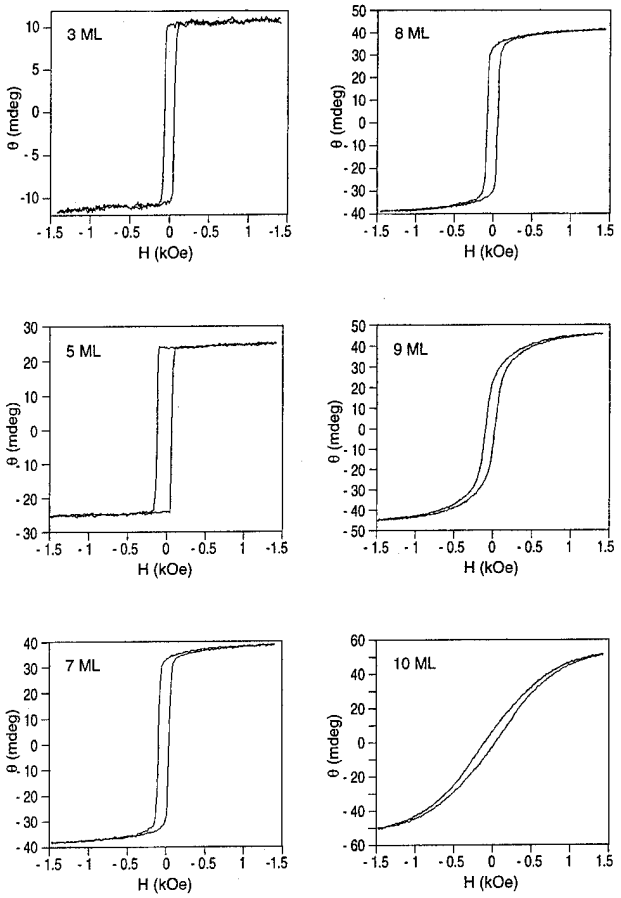


FIG. 4. PMOKE hysteresis loops at room temperature of $Au/Fe_{0.82}V_{0.18}/Au(111)$ for six different FeV layer thicknesses, 3, 5, 7, 8, 9, and 10 monolayers. Notice the change from perpendicular to parallel magnetization around $t_{FeV}=8-9$ ML.

magnetic anisotropy.[18,19] The crossover thickness, t^*, below which the magnetization is perpendicular to the film plane is $t^* \approx 9$ ML (≈ 1.8 nm) for Co and $t^* \approx 3$ ML for Fe at room temperature. The PMOKE measurements performed on the FeV alloy ultrathin films also reveal a strong perpendicular anisotropy. This is exemplified by the PMOKE data on $Fe_{0.82}V_{0.18}$ in Fig. 4. Square hysteresis loops are obtained at thicknesses below 8 ML and t^* likely lies between 8 and 9 ML. For $Fe_{0.71}V_{0.29}$, perpendicular magnetization is observed in the whole investigated thickness range which means that $t^* > 11$ ML. Assuming that the interface magnetic anisotropy remains unchanged when alloying Fe with V and neglecting volume anisotropy, t^* should be inversely proportional to the square magnetization of the FeV alloy. In this frame, with respect to the pure Fe film, t^* should increase by a factor 1.8 for $x=18\%$ and by 3 for $x=29\%$, leading, respectively, to $t^* \approx 5.5$ and 9.2 ML. These values are clearly much smaller than the experimental ones which means that the perpendicular magnetic anisotropy is reinforced by alloying Fe with V. Among different possible mechanisms, a bond anisotropy induced by antiparallel alignment of the magnetic moments of Fe and V could be at the origin of this effect.[20]

For the present experiments, a crucial point is that both ferromagnetic layers have their easy magnetization axis perpendicular to the film plane. In addition, the coercive field of

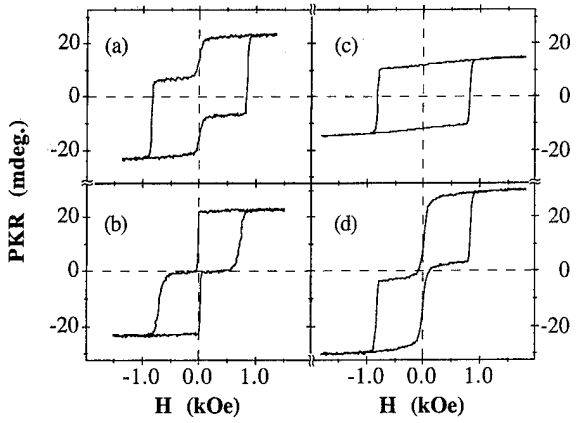


FIG. 5. PMOKE hysteresis loops of Fe/Au/Co and $Fe_{1-x}V_x/Au/Co$ trilayers at room temperature for films with a Au interlayer thickness $t=2.35$ nm (10 ML) and Co thickness $t=0.6$ nm (3 ML): (a) Fe(0.5 nm); (b) $Fe_{0.82}V_{0.18}$(0.8 nm); (c) $Fe_{0.71}V_{0.29}$(0.8 nm); (d) $Fe_{0.71}V_{0.29}$(2 nm). The higher coercive field is the one of the Co layer. Notice the squareness of the FeV layer magnetization in (b) and (d). In (c), the FeV layer is still paramagnetic ($T_c<300$ K).

the Co layer, H_1, is much larger than the coercive field of the Fe or FeV layer, H_2, and thus a perfect antiparallel alignment of the magnetization directions of the two F films can be achieved over a wide field range, $H_1 > H > H_2$. Moreover, this allows an easy determination of the interlayer coupling from the shift of the minor hysteresis loop as previously reported.[17] Hysteresis curves for Fe/Au/Co (sample 1), $Fe_{0.82}V_{0.18}/Au/Co$ (*s.* 2), and $Fe_{0.71}V_{0.29}/Au/Co$ (*s.* 5), trilayers with a Au interlayer thickness of 10 AL, measured by polar Kerr rotation at room temperature, are shown in Fig. 5. One notices the fairly rectangular shape of the magnetization curve of the FeV layer, Figs. 5(b) and 5(d), compared to that of the pure Fe layer, Fig. 5(a). The 4-ML-thick $Fe_{0.71}V_{0.29}$ layer in Fig. 5(c) is paramagnetic at 300 K.

The MR curves of the same trilayers under perpendicular magnetic field are shown in Fig. 6. The MR curves have the plateau shape usual for two *F* films with rectangular magnetization loops and different coercivities.[21,22] While the GMR of Fe/Au/Co, Fig. 6(a), is normal (i.e., the largest resistance

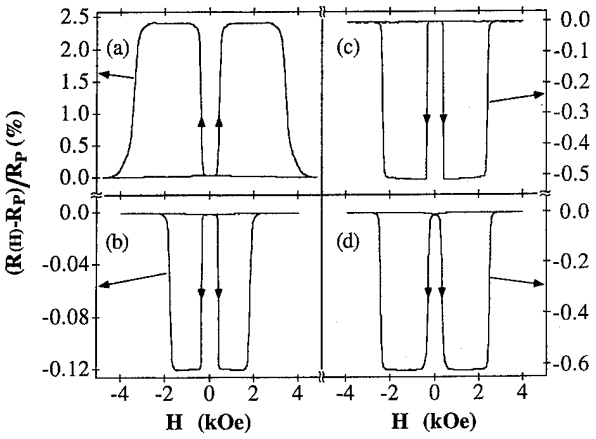


FIG. 6. Magnetoresistance curves of Fe/Au/Co and $Fe_{1-x}V_x/Au/Co$ trilayers with $t_{Au}=10$ ML and $t_{Co}=3$ ML measured at $T=60$ K. (a) Fe(0.5 nm); (b) $Fe_{0.82}V_{0.18}$(0.8 nm); (c) $Fe_{0.71}V_{0.29}$(0.8 nm); (d) $Fe_{0.71}V_{0.29}$(2 nm).

corresponds to the antiparallel arrangement of the magnetization directions), the GMR of $Fe_{1-x}V_x$/Au/Co is inverse, Figs. 6(b), 6(c), and 6(d). This effect cannot be due to anisotropic magnetoresistance, since the magnetizations of the F layers remain perpendicular to the film plane, only the mutual direction of the magnetizations changes. This is the ideal situation for isolating the spin-valve effect. Although very clear, the observed inverse GMR is small. At low temperature, in similar Au/M/Au/Co/Au structures, the maximum value of the GMR, $\Delta R/R$, is about 8% for M=Co, 3% for M=Fe and -0.8% in the best case for M=$Fe_{1-x}V_x$. One may point out that the strong reduction of GMR from Co to Fe reflects a decrease in $(D\downarrow - D\uparrow)$ that we attribute crudely to the fact that $n^{\uparrow}(E_F)$ and $n^{\downarrow}(E_F)$ become closer together. Such a MR reduction has also been observed from Co/Cu to Fe/Cu multilayers.[23]

It should be pointed out that, if inverse MR has been observed at low temperature in all the investigated FeV/Au/Co samples, rather different values were obtained in two samples with identical structure and composition ($x=0.18$), prepared in two different deposition runs. For the sample 2 with $t_{Au}=2.35$ nm, the MR was found to be slightly positive at 300 K and amounts to -0.2% at 60 K. For sample 4 with $t_{FeV}=4$ ML, the MR amounts to -0.13% and -0.69%, respectively, at 300 and 60 K. These two samples only differ by the quality of the Au buffer on which they were grown. For sample 2, the RHEED pattern revealed a larger roughness of the buffer than for sample 4. Since the interface roughness strongly influences the scattering of the conduction electrons and thus, the MR,[24,25] one can anticipate that interface scattering cannot be neglected in the FeV/Au/Co samples.

A confirmation that the inverse GMR is due to a difference in sign of $(D\downarrow - D\uparrow)$ for FeV with respect to Co is given by the MR of sample 3, FeV/Au(t)/FeV. Its MR is barely measurable, except for Au thicknesses corresponding to the first peak, $t=5$ ML, and to the second peak, $t=10$ and 11 ML of antiferromagnetic coupling.[26] A normal (i.e., always positive) MR is observed in agreement with Eq. (1), $\Delta R/R=+0.024$ and $+0.16\%$ for $t=5$ and 10 AL, respectively, at 1.4 K.

The rectangular shape of the curves of resistivity versus magnetic field allows a reliable measurement of $\Delta R/R$. The MR dependence with the FeV layer thickness has been studied on samples 4 and 5. The temperature dependence has been investigated on all samples; preliminary measurements on samples 2 and 5 have been reported previously.[9] In addition, the exchange coupling between the Co and FeV layers has been measured by the technique of minor hysteresis loops, previously initiated in MOKE studies of Co/Au/Co.[17] An oscillatory behavior versus the Au spacer thickness, quite similar to that reported in Fe/Au/Co,[27] is observed.

The experimental data for $\Delta R/R$ vs t_{FeV} are shown in Fig. 7, for two temperatures, $T=60$ K and $T=300$ K. The magnitude of inverse MR in the two studied samples, with $x=0.18$ and $x=0.29$, increases with t_{FeV}. This clearly establishes that the inverse MR is mainly due to a bulk scattering process. Indeed, for predominant interface scattering, the magnitude of MR should decrease with increasing t_{FeV}.

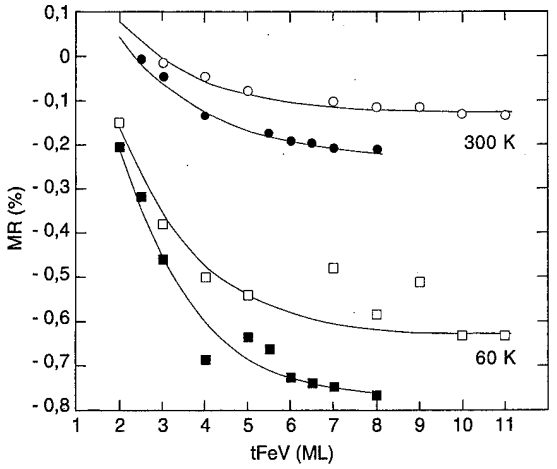


FIG. 7. Magnetoresistance vs FeV thickness, t_{FeV}, in two $Fe_{1-x}V_x$/Au/Co samples, 4 and 5, with variable t_{FeV} at $T=60$ K and $T=300$ K. The full squares and circles are the experimental data for sample 4 ($x=0.18$), respectively, for $T=60$ and 300 K. The open squares and circles correspond to sample 5 ($x=0.29$). The full lines are the results of calculations based on the Camley–Barnas model, with the parameters given in Table I (see Sec. IV).

However, the relatively fast MR variation at low FeV thicknesses suggests that interface scattering is superimposed to bulk scattering. This point will be discussed in detail in Sec. IV.

The temperature dependence of MR for sample 4 at different FeV thicknesses is shown in Fig. 8. A relatively strong temperature dependence is observed for all FeV thickness, especially for the lowest ones, 2 and 2.5 ML, for which the MR tends to become positive near 300 K.

IV. DISCUSSION

In order to interpret the experimental MR data in FeV/Au/Co, MR calculations based on the Camley–Barnas model,[3] have been developed. In contrast to previous calculations on (Au/Co) multilayers with very small Co thicknesses,[28] we have taken into account in addition to the interface scattering, the bulk scattering processes in the FeV

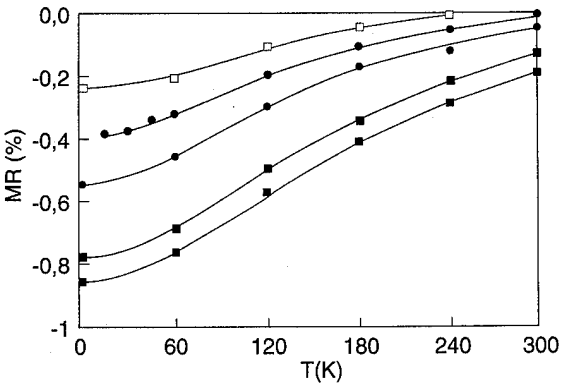


FIG. 8. Magnetoresistance vs temperature for sample 4 ($x=0.18$) at different FeV layer thicknesses. From the top to the bottom, $t_{FeV}=2$ ML (open squares), 2.5 ML (grey circles), 3 ML (black circles), 4 ML (grey squares), and 8 ML (black squares). The full lines are guides for the eye.

TABLE I. Spin-dependent mean free paths $\lambda\uparrow$, $\lambda\downarrow$ and spin-dependent interface scattering coefficients $D\uparrow$ and $D\downarrow$ for $Fe_{1-x}V_x$ ($x=0.18$ and $x=0.29$) at $T=60$ and 300 K.

		$\lambda\uparrow$ (nm)	$\lambda\downarrow$ (nm)	$D\uparrow$	$D\downarrow$
$Fe_{0.82}V_{0.18}$	60 K	2.2	4.3	0.27	0.33
"	300 K	1.8	2.7	0.27	0.33
$Fe_{0.71}V_{0.29}$	60 K	1.5	5.0	0.45	0.55
"	300 K	1.2	2.2	0.45	0.55

layer by means of two different mean free paths, $\lambda\uparrow$ and $\lambda\downarrow$, for conduction electrons, respectively, with spin parallel and antiparallel to the FeV majority spin. The spin-dependent scattering at FeV/Au interfaces is taken into account by means of two scattering coefficients $D\uparrow$ and $D\downarrow$. The other parameters in the calculation are the coefficients of specular reflection at the Au surfaces, R_1 at the bottom of the Au buffer, and R_2 at the top of the Au cap layer, the spin-dependent transmission coefficients $T\uparrow$ and $T\downarrow$ across the Co film supposed of negligible thickness and the electron mean free path in Au, λ. These latter parameters are well known from previous resistivity measurements on single Au films[29] and from our MR studies of (Au/Co) multilayers.[30] The following fixed values were used: $R_1=0.85$, $R_2=0.5$, $T\uparrow=0.7$, $T\downarrow=0.1$, $\lambda(60\text{ K})=120$ nm and $\lambda(300\text{ K})=32$ nm. In addition, in order to reduce the number of fit parameters of FeV layers, the mean interface scattering at FeV/Au interface has been fixed to a value close to that of Co/Au interface, i.e., $(D\uparrow+D\downarrow)/2\approx 0.3-0.5$. Finally, three parameters characteristic of the FeV layer, $\lambda\uparrow$, $\lambda\downarrow$, and $(D\downarrow-D\uparrow)$, were varied for minimizing the fit variance.

For both samples investigated, reliable values of these parameters, given in Table I, have been obtained at 60 and 300 K. A comparison between the experimental data and the calculated MR vs t_{FeV} curves is shown in Fig. 7. The fit between experiment and calculation is fairly good for $x=0.18$ (sample 4) but not so satisfactory for $x=0.29$, due to some dispersion in the experimental data and to the fact that T_c is low at the smallest FeV thicknesses. An interesting feature is that both interface and bulk spin-dependent scattering by FeV films are needed to fit the experimental data and that these scattering processes are competing; the interface scattering favors normal GMR, $D\downarrow>D\uparrow(D\downarrow/D\uparrow\approx 1.2)$, whereas the bulk scattering leads to inverse GMR, $\lambda\uparrow<\lambda\downarrow$. The fit values for $\lambda\uparrow$, $\lambda\downarrow$, $D\uparrow$, and $D\downarrow$ are reported in Table I. The α values ($\alpha=\lambda\uparrow/\lambda\downarrow$) obtained for bulk FeV at 60 K, $\alpha(x=0.18)=0.5$ and $\alpha(x=0.29)=0.3$ are in qualitative agreement with α for dilute V impurities in Fe ($\alpha\approx 0.13$).[31] Furthermore, the average mean free path for $x=0.18$ is consistent with the resistivity data on FeV alloys.[32] The observed decrease of $\lambda\uparrow$ and $\lambda\downarrow$ at 300 K can be attributed to the phonons. On the other hand, $(D\downarrow-D\uparrow)$ does not change between 60 and 300 K. One could expect to increase the magnitude of inverse MR with increasing x. Nevertheless, samples 4 and 5 have about the same MR. In fact, sample 5 ($x=0.29$) exhibits a larger interface scattering than that of sample 4 ($x=0.18$), which reduces the magnitude of its inverse MR.

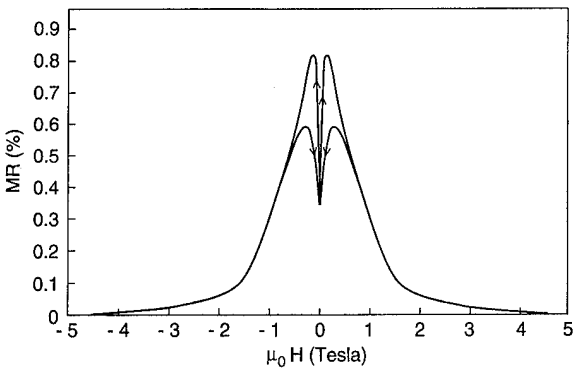


FIG. 9. Magnetoresistance of Co (2 nm)/Au (1.65 nm)/Co (0.6 nm) in field parallel to the film plane. An apparent inverse GMR is observed at low field, due to an initial increase with field of the angle between the magnetizations of the Co layers.

The qualitative difference between bulk and interface scattering could be explained in the frame of the simple band model of Sec. I. At the interface between Au and Ag and $3d$ metals, it is well known that the $3d$ band is strongly narrowed, leading to enhanced interface magnetic moments.[33] This narrowing gives rise to a better filling of the majority band and thus, to a decrease of the density of states for majority spin with respect to the bulk. The normal spin-dependent interface scattering is likely the major difficulty to produce inverse GMR.

Finally, we would like to emphasize that nonintrinsic inverse GMR can occur in multilayers where the magnetizations of successive layers are not colinear. This is exemplified Fig. 9 showing the GMR of Au/Co(2)/Au(1.6)/Co(0.6)/Au in field parallel to the film plane. In a high magnetic field, the magnetizations of the Co films are aligned parallel to the field leading to a low resistance state. Then, in decreasing field the magnetization of the thinner Co film, 0.6 nm thick, becomes progressively perpendicular, due to its strong perpendicular magnetic anisotropy, leading to a resistance increase. At low field values, the magnetization of the thicker film tends to become perpendicular to the film plane and parallel to the magnetization of the thinnest Co film under the combined effect of small perpendicular anisotropy and ferromagnetic interlayer coupling. An additional complexity is brought by a small perpendicular field component and the large coercivity of the thinnest Co film which gives rise to the MR hysteresis. The MR versus field curve of Fig. 9 is strikingly similar to that observed by George *et al.* on (Fe/Cr/Fe)/Cu/Fe multilayers in which intrinsic inverse GMR at low fields is superimposed to normal GMR at higher fields.[8]

In conclusion, inverse GMR has been clearly observed in simple trilayers, FeV/Au/Co grown on Au(111). Alloying Fe with V has a qualitative effect on the spin scattering process, leading to a change of the asymmetry parameter from $\alpha>1$ to $\alpha<1$. The detailed MR dependence on the FeV layer thickness reveals a competition between interface scattering which gives normal GMR and bulk scattering responsible for the observed inverse GMR. It should be interesting to improve the knowledge of the thin FeV layers by microscopic

techniques such as x-ray magnetic circular dichroism and to investigate MR in multilayers including other Fe alloys such as FeCr and FeTi.

ACKNOWLEDGMENTS

The authors wish to thank N. Bardou and A. Bounouh for their help in magneto-optical experiments and A. Charrier for help in preparation of the artwork. This work was supported by the European Community HCM program in the frame of the network "EuroGMR"; one of us (M. M.) was funded by this program. Institut d'Electronique Fondamentale is Unité de Recherche Associée au Centre National de la Recherche Scientifique (URA 22).

[1] For a recent review, A. Fert and P. Bruno, in *Ultrathin Magnetic Structures II,* edited by B. Heinrich and J. A. C. Bland (Springer, Berlin, 1994), p. 82; S. S. P. Parkin, *ibid.* p. 148.
[2] M. N. Baibich, J. M. Broto, A. Fert, F. Nguyen Van Dau, F. Petroff, P. Etienne, A. Friederich, and J. Chazelas, Phys. Rev. Lett. **61**, 2472 (1988).
[3] P. E. Camley and J. Barnas, Phys. Rev. Lett. **63**, 664 (1989).
[4] S. S. P. Parkin, Phys. Rev. Lett. **71**, 1641 (1993).
[5] B. A. Gurney, V. S. Speriosu, J. P. Nozières, H. Lefakis, D. R. Wilhoit, and O. U. Need, Phys. Rev. Lett. **71**, 4023 (1993).
[6] A. Fert and I. A. Campbell, J. Phys. F **6**, 849 (1976).
[7] H. Hasegawa, Phys. Rev. B **51**, 3655 (1995); Mater. Sci. Eng. B **31**, 31 (1995).
[8] J. M. George, L. G. Pereira, A. Barthélémy, F. Pétroff, L. Steren, J. L. Duvail, A. Fert, R. Loloee, P. Holody, and P. A. Schroeder, Phys. Rev. Lett. **72**, 408 (1994).
[9] J. P. Renard, P. Bruno, R. Mégy, B. Bartenlian, P. Beauvillain, C. Chappert, C. Dupas, E. Kolb, M. Mulloy, P. Veillet, and E. Vélu, Phys. Rev. B **51**, 12821 (1995).
[10] M. V. Nevitt, in *Electronic Structure and Alloy Chemistry of the Transition Elements,* edited by P. A. Beck (Interscience, New York, 1962).
[11] N. Môri and T. Mitsui, J. Phys. Soc. Jpn. **26**, 1087 (1969).
[12] F. Gautier, in *Magnetism of Metals and Alloys,* edited by M. Cyrot (North-Holland, Amsterdam, 1982).
[13] D. D. Johnson, F. J. Pinski, and J. B. Staunton, J. Appl. Phys. **61**, 3715 (1987).
[14] D. Renard and G. Nihoul, Philos. Mag. B **55**, 75 (1987).
[15] C. Cesari, J. P. Faure, G. Nihoul, K. Le Dang, P. Veillet, and D. Renard, J. Magn. Magn. Mater. **78**, 296 (1989).
[16] C. Marlière, J. P. Chauvineau, and D. Renard, Thin Solid Films **189**, 359 (1990).
[17] V. Grolier, D. Renard, B. Bartenlian, P. Beauvillain, C. Chappert, C. Dupas, J. Ferré, E. Kolb, M. Mulloy, J. P. Renard, and P. Veillet, Phys. Rev. Lett. **71**, 3023 (1993).
[18] C. Chappert, K. Le Dang, P. Beauvillain, H. Hurdequint, and D. Renard, Phys. Rev. B **34**, 3192 (1986).
[19] G. Lugert and G. Bayreuther, Thin Solid Films **175**, 311 (1989).
[20] H. Fu, M. Mansuripur, and P. Meystre, Phys. Rev. Lett. **66**, 1086 (1991).
[21] C. Dupas, P. Beauvillain, C. Chappert, J. P. Renard, F. Trigui, P. Veillet, E. Vélu, and D. Renard, J. Appl. Phys. **67**, 5680 (1990).
[22] J. Barnas, A. Fuss, R. E. Camley, P. Grünberg, and W. Zinn, Phys. Rev. B **42**, 8110 (1990).
[23] B. Dieny, V. S. Speriosu, J. P. Nozières, B. A. Gurney, A. Vedyayev, and N. Ryzhanova, in *Magnetism and Structure in Systems of Reduced Dimension,* edited by R. F. C. Farrow *et al.* (Plenum, New York, 1993), p. 279.
[24] F. Petroff, A. Barthélémy, A. Hamzic, A. Fert, P. Etienne, and G. Creuzet, J. Magn. Magn. Mater. **93**, 95 (1991).
[25] E. E. Fullerton, D. M. Kelly, J. Guimpel, I. K. Schuller, and Y. Bruynseraede, Phys. Rev. Lett. **68**, 859 (1992).
[26] The oscillatory interlayer exchange coupling between FeV and Co through Au (111) is very similar to that recently studied in Au/Fe/Au/Co/Au(111) in Ref. 27. The first and second maxima of AF coupling occur at t_{Au}=5 and 10 AL.
[27] C. Chappert, P. Bruno, B. Bartenlian, P. Beauvillain, A. Bounouh, R. Mégy, and P. Veillet, J. Magn. Magn. Mater. **148**, 165 (1995).
[28] F. Trigui, E. Vélu, and C. Dupas, J. Magn. Magn. Mater. **93**, 421 (1991).
[29] J. P. Chauvineau and C. Pariset, Surf. Sci. **36**, 155 (1973).
[30] M. Mulloy, E. Vélu, C. Dupas, M. Galtier, E. Kolb, D. Renard, and J. P. Renard, J. Magn. Magn. Mater. **147**, 177 (1995).
[31] J. W. F. Dorleijn, Philips Res. Rep. **31**, 287 (1976).
[32] H. Fujiwara, N. Sueda, and Y. Fujiwara, J. Phys. Soc. Jpn. **28**, 527 (1970).
[33] S. Onishi, M. Weinert, and A. J. Freeman, Phys. Rev. B **30**, 36 (1984).

Ab initio calculations of spin-dependent transport properties (invited) (abstract)

I. Mertig
TU Dresden, Institut für Theoretische Physik, D-01062 Dresden, Germany

Ab initio calculations of transport properties for ferromagnetic dilute alloys and magnetic multilayers are reported. The electronic structure of the considered system is calculated within the frame of density functional theory using local spin density approximation. The scattering of the electrons by impurities is described self-consistently by means of the Green function of the perturbed system. As a result the spin anisotropy of the scattering can be discussed without any free parameter. The transport is described quasiclassically, that is, the linearized Boltzmann equation is solved taking into account the anisotropy of the Fermi surface and the anisotropy of electron-impurity scattering. The method is applied to calculate the residual resistivity of dilute ferromagnetic Fe and Co alloys which are in very good agreement with experiment. Giant magnetoresistance (GMR) was computed for Fe/Cr multilayers for CIP (current in plane) and CPP (current perpendicular to plane) geometry. It can be shown that GMR exists for spin-independent scattering (Fe impurities in Cr layers) determined by the electronic structure of multilayers in ferro- and antiferromagnetic configuration. The consideration of spin-dependent scattering (say Cr impurities in Fe layers) enhances or reduces the GMR effect in dependence of the spin-anisotropy. It can be shown especially that combination of defects with different spin-anisotropy can produce inverse GMR. Finally, calculations are presented for GMR in granular Cu(Co) systems. From the investigation becomes obvious, that the effect is strongly influenced by the spin anisotropy of scattering. © *1996 American Institute of Physics.* [S0021-8979(96)60508-4]

 0021-8979/96/79(8)/5276/1/$10.00 © 1996 American Institute of Physics

Optimizing the giant magnetoresistance of symmetric and bottom spin valves (invited)

W. F. Egelhoff, Jr., P. J. Chen, C. J. Powell, M. D. Stiles, and R. D. McMichael
National Institute of Standards and Technology, Gaithersburg, Maryland 20899

C.-L. Lin,[a] J. M. Sivertsen,[a] and J. H. Judy[b]
Center for Micromagnetics and Information Technology, University of Minnesota, Minneapolis, Minnesota 54455

K. Takano and A. E. Berkowitz
Department of Physics, University of California at San Diego, LaJolla, California 92093

T. C. Anthony and J. A. Brug
Hewlett-Packard Laboratories, 1501 Page Mill Road, Palo Alto, California 94304

We have attempted to optimize the values of the giant magnetoresistance in symmetric spin valves of the type NiO/Co/Cu/Co/Cu/Co/NiO (achieving 23.4%) and in bottom spin valves of the type Co/Cu/Co/NiO (achieving 17.0%), the largest values ever reported for such structures. The key elements in this achievement are improved vacuum conditions and careful attention to the film thicknesses. © *1996 American Institute of Physics.* [S0021-8979(96)53408-3]

I. INTRODUCTION

Symmetric[1] (or dual[2]) spin valves are important in the field of giant magnetoresistance (GMR) because they offer the possibility of achieving large GMR values in magnetic multilayers which exhibit relatively low saturation fields. To put the issues in context, it is helpful to note that GMR values as large as 80% have been achieved in Co/Cu superlattices but at the cost of very large saturation fields, e.g., ~1 T, or 10^4 Oe.[3] Saturation fields as low as 0.2 mT, or 2 Oe, have been reported for simple spin valves (containing only one Cu film), but the GMR of such structures is only 3%.[4] Symmetric or dual spin valves represent an intermediate case (with two Cu films). Figure 1 illustrates a symmetric spin valve typical of those investigated in the present work. Also illustrated is one type of simple spin valve, a so-called bottom spin valve,[1] which may be viewed as the lower part of a symmetric spin valve.

The term bottom spin valve refers to the location of the pinning film, here NiO, which is at the bottom of the spin valve. In more conventional spin valves, the pinning film of FeMn is at the top.[5] The NiO in the structures of Fig. 1 pins the adjacent magnetic films in a different manner than does FeMn. The FeMn acts by providing an exchange bias, whereas the NiO acts by inducing a very large coercivity in the adjacent Co film. In the bottom spin valve, the top Co film is unpinned and free to switch magnetically at relatively low fields. In the symmetric spin valve the top and bottom Co films are pinned and the central Co film is free.

Symmetric spin valves might be expected to have substantially larger GMR values than simple spin valves because significantly longer electron mean free paths (MFPs) should be possible (perhaps through the entire five-film structure) for spin-allowed conduction paths when the Co films are magnetically in a parallel alignment state. However, in the anitparallel alignment state, symmetric spin valves should exhibit short MFPs just as simple spin valves or superlattices do.

The goal of the present work is to achieve the largest GMR values possible in symmetric spin valves and bottom spin valves. A comparison of the resulting values should help to put on a quantitative basis the magnitude of the advantage that can be gained by the symmetric spin valve concept.

II. EXPERIMENT

The NiO substrates used in this work were polycrystalline films ~50 nm thick, deposited on 3 in. Si wafers by reactive magnetron sputtering at the University of California at San Diego and the University of Minnesota.[6] At the National Institute of Standards and Technology, the wafers were cleaved into ~1 cm^2 squares, cleaned ultrasonically, rinsed, dried, and installed in the deposition chamber. The base pressure before depositing a spin valve was typically 2×10^{-8} Torr ($\sim2\times10^{-6}$ Pa) of which ~95% was H_2 and the remainder primarily H_2O (as indicated by a mass spectrometer). The presence of H_2 during deposition has no apparent effect on spin valve properties unless the partial pressure exceeds $\sim10^{-6}$ Torr. The base pressure is achieved partly by depos-

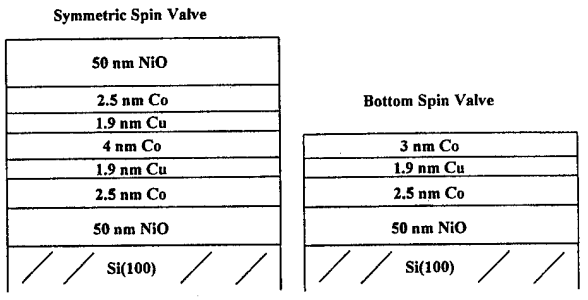


FIG. 1. An illustration of the symmetric spin valve and bottom spin valve structures typical of those investigated in the present work.

[a]Dept. of Chemical Engineering and Materials Science.
[b]Dept. of Electrical Engineering.

 0021-8979/96/79(8)/5277/5/$10.00 © 1996 American Institute of Physics

iting a ~1.5 nm Ti film on the inside of the deposition chamber from a centrally mounted Ti filament just prior to deposition of each spin valve.

A base pressure of 3×10^{-10} Torr was achieved after baking the chamber overnight at 150 °C, but this base pressure was degraded sharply when films were deposited by magnetron sputtering. During magnetron sputtering the walls of the chamber are bombarded by energetic electrons, atoms, and ions which desorb gases from the walls and degrade the vacuum. The best base pressure achievable within an hour after deposition of a symmetric spin valve was typically in the high 10^{-9} Torr region, even in a baked chamber. Thus, with the passage of time and with the deposition of many symmetric spin valves both a baked and an unbaked chamber converge on a base pressure of $\sim10^{-8}$ Torr. Part of the problem is that some H_2O is formed from H_2 and O_2 during the deposition of the top 50 nm of NiO in a symmetric spin valve. However, even after repeated deposition of bottom spin valves (no NiO deposited) the base pressure was still no better than the low 10^{-9} Torr range.

The magnetoresistance (MR) measurements were made *in situ* at room temperature (RT) using the four-point probe dc mode. Several symmetric spin valves were checked *ex situ* in two separate facilities and were found to have the same MR values. The bottom spin valves did not appear to be affected by exposure to background gases during the MR measurements. However, exposure to O_2 did produce significant effects, as discussed below.

It is very important to remove the hydrocarbon contamination (several tenths of a nanometer, which accumulates on the NiO from exposure to the laboratory air) prior to the deposition of each spin valve in order to achieve strong pinning and the largest GMR values. Samples were sputtered with a neutralized-beam Ar-ion gun at a beam energy of 100 eV until the carbon was removed (as judged by *in situ* x-ray photoelectron spectroscopy). Ion beam energies of several hundred eV gave reduced pinning and GMR values, probably due to damage of the NiO surface. The metal films were deposited at RT by dc-magnetron sputtering in 2 mTorr Ar at a rate of ~0.1 nm/s. The top NiO film was deposited by sputtering a Ni target with an 85/15 mixture of Ar/O_2.

III. RESULTS AND DISCUSSION

A. Symmetric spin valves

In a previous publication,[7] we presented our initial studies of symmetric spin valves. We found that the largest GMR values occurred in samples with film thickness values typical of those illustrated in Fig. 1. We also reported the dependence of GMR on the thickness of the Co films and on the sample temperature.

Subsequently, the most interesting result we have obtained on symmetric spin valves is the dependence of the GMR on the partial pressure of H_2O in the chamber just prior to deposition of the structure. The results are presented in Fig. 2 and indicate that the largest GMR values are obtained for the lowest H_2O partial pressures. Moreover, we find no indication that the GMR values are saturating at the lowest H_2O partial pressures we can reach.

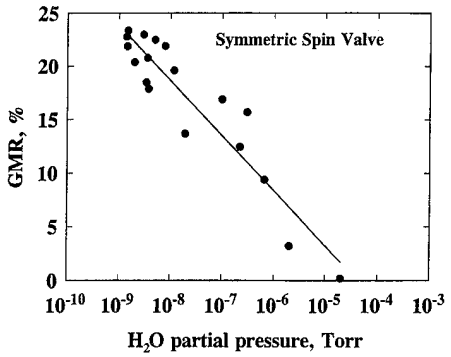


FIG. 2. A plot of the GMR values obtained for symmetric spin valves of the type illustrated in Fig. 1 as a function of the partial pressure of H_2O in the chamber just prior to deposition.

It should be emphasized that the H_2O partial pressures just prior to spin valve deposition in Fig. 2 are probably somewhat lower than the partial pressures during spin valve deposition. The presence of the sputtering gas (2 mTorr of Ar) prevents such a measurement during deposition. Nevertheless, during spin valve deposition, the partial pressure of H_2O and other contaminant gases is probably higher than just prior to deposition. This likely increase is due to the desorption of atoms and molecules from walls of the chamber by the impact of the energetic electrons, atoms, and ions produced by the magnetron sputtering process. In general, we find that immediately after the Ar has been pumped out following the deposition of a spin valve, the H_2O partial pressure is higher than just before deposition. (Note here that H_2O pumps away more slowly than Ar due to its tendency to stick to the walls.) This increase is about a factor of 2 for bottom spin valves and about a factor of 5 for symmetric spin valves (deposition of the final NiO film by reactive sputtering apparently synthesizes some H_2O). Therefore, although the values of H_2O partial pressure plotted in Fig. 2 are not the actual pressures during spin valve deposition, they are probably a reasonable indication of the relative H_2O partial pressures during deposition.

The results of Fig. 2 are important because most laboratories make GMR spin valves in deposition systems for which the base partial pressure of H_2O is considerably higher than the best we can achieve. Typically, base pressures are $\sim10^{-7}$ Torr, and H_2O is the primary component. The implications of Fig. 2 are that lower partial pressures of H_2O in the system should lead to significant increases in the GMR and that efforts to improve base pressures would be worthwhile for most laboratories.

It is possible that H_2O is not the contaminant responsible for the loss of GMR in Fig. 2, but it is the most likely candidate. As discussed in Sec. II, the chamber contains predominantly H_2 at the base pressure. However, the H_2 partial pressure is then typically around $\sim10^{-8}$ Torr and one must introduce $\sim10^{-6}$ Torr of H_2 into the chamber during deposition to produce a noticeable reduction of GMR in these samples (i.e., more than the usual $\pm10\%$ scatter in the data). Another contaminant in the chamber is CO, which typically has a partial pressure a factor of ten lower than that of H_2O,

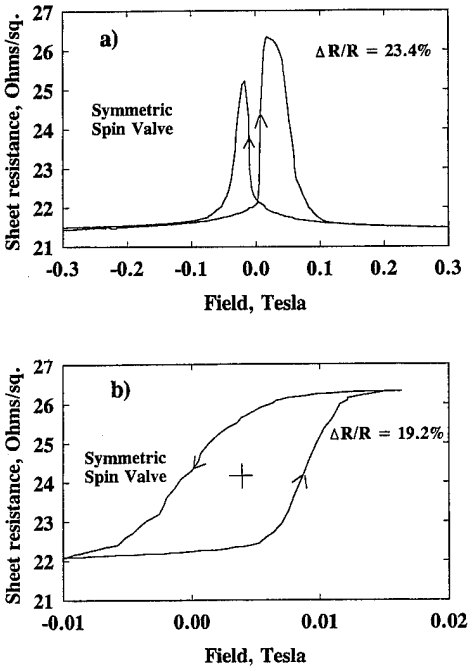


FIG. 3. Magnetoresistance loops for the symmetric spin valve with the largest GMR ($\Delta R/R$) for (a) high fields and (b) low fields, recorded after saturation in a negative field (see arrows). The cross in (b) marks the center of the loop, which is shifted from zero field due to the coupling between the center Co film and the top and bottom Co films. (Note: 0.01 T=100 Oe.)

and could possibly make a contribution to the GMR reduction. The ratio of CO and H_2O partial pressures does not change much because our primary method of varying the H_2O partial pressure is the length of the pumpdown time since the last exposure of the chamber to air. The H_2O partial pressure is also modified by the deposition of spin valves and by the deposition of Ti films, but the ratio of CO and H_2O partial pressures is approximately constant. Other contaminants in the chamber typically have partial pressures at least a factor of five less than CO and are probably unimportant.

The mechanism for the reduction in GMR in Fig. 2 is not known, but one possibility is impurity scattering of conduction electrons by oxygen-atom impurities. The sheet resistance (in a saturation field) of the samples used for the data in Fig. 2 increases from 21.5 Ω/sq. to 28 Ω/sq. as the GMR drops from 23.4% to 3.1%.

Another possible contribution to the drop in GMR is a weakening observed in the strength of the pinning of the top Co film by the top NiO. This weakness indicates that the magnetization of the top and center Co films are never completely antiparallel.

Figure 3 presents the high-field and low-field GMR loops for the sample with a GMR of 23.4%, the largest value we achieved. The shape of the high-field loop in the Fig. 3(a) is explained by the top and bottom Co films being pinned by the adjacent NiO so that they exhibit large coercivities. The center Co film has a small coercivity and switches from parallel to antiparallel to produce the increase in resistance found in the center of the high-field loop (see arrows). The general shape of this loop is typical for simple spin valves which employ magnetic films of differing coercivity.[8]

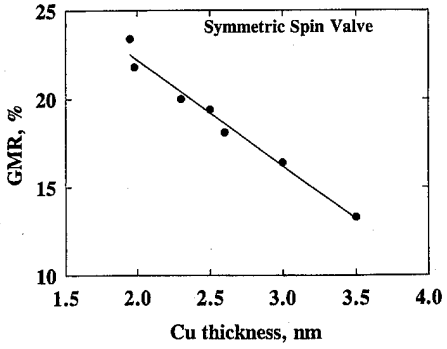


FIG. 4. A plot of the GMR vs the thickness of the Cu films for symmetric spin valves of the type illustrated in Fig. 1.

In the low-field loop in Fig. 3(b), little change occurs in the magnetization of the top and bottom Co, and only the center Co film is switched. Note that the high-field loop exhibits a weak tail extending out beyond 0.1 T (1000 Oe) so that the GMR of the low-field loop is only 19.2%. The weak tail is likely due to some grains in the polycrystalline NiO strongly pinning small patches of Co in random directions so that a large field is required for complete parallel alignment.

Figure 4 shows the strong dependence of the GMR on the thickness of the Cu films (the dependence on the Co film thicknesses was published in Ref. 7). The steep increase in GMR with decreasing Cu thickness is a strong motivation to investigate novel methods of deposition that will permit the use of thinner Cu films in these structures. The impediment to thinner Cu films is that the ferromagnetic coupling of the center Co film to the top and bottom Co films rises very sharply for Cu thickness less than about 1.8 nm so that complete antiparallel alignment cannot be attained and the GMR drops. This coupling is attributable partly to magnetostatic "orange peal" coupling caused by interfacial roughness,[9] and partly to the well-known oscillatory exchange coupling.[10] In recent work, we have investigated the correlation between the surface roughness during spin valve deposition, as observed by *in situ* scanning tunneling microscopy, and the coupling strength.[11] Although that work was primarily based on glass and aluminum oxide substrates, a brief examination of spin valves deposited on NiO substrates found general similarities in grain size (~10 nm) and roughness (0.5–0.9 nm).[11]

We are presently investigating various approaches to reducing the ferromagnetic coupling, including deposition at low substrate temperatures to suppress interdiffusion at the Co/Cu interfaces and the use of surfactants such as In, Pb, and Au to smooth the Co and Cu surfaces during deposition. These studies will be the subject of future publications.

The thermal degradation of our spin valves by prolonged annealing at 250 °C is the subject of other publications. See Ref. 12.

B. Bottom spin valves

Bottom spin valves do not appear to have any important performance advantages over symmetric spin valves. Nevertheless, it was useful to investigate their properties since some interesting insights have emerged.

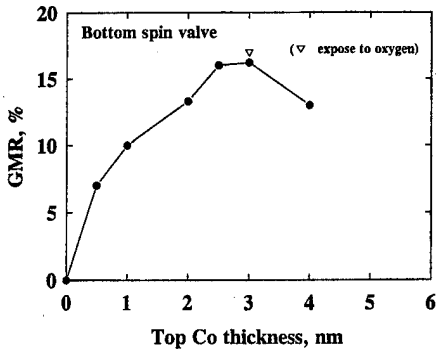


FIG. 5. A plot of the GMR (in vacuum) vs the top Co film thickness for bottom spin valves of the type illustrated in Fig. 1 (the bottom Co film thickness is 2.5 nm). The effect of exposing the 3 nm Co sample to $\sim 10^{-2}$ Torr s of O_2 is also plotted.

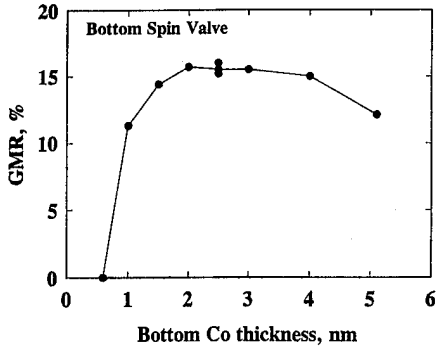


FIG. 6. A plot of the GMR (in vacuum) vs the bottom Co thickness for bottom spin valves of the type illustrated in Fig. 1 (the top Co film thickness was 3 nm).

The GMR loops of bottom spin valves generally have a very similar appearance to those of symmetric spin valves, e.g., Fig. 3. The principal difference is that the GMR is significantly smaller for bottom spin valves. Minor differences are often noted in the coercivity and coupling exhibited by the unpinned Co film, and they are generally slightly smaller for the bottom spin valves.

Figure 5 presents the dependence of the GMR on the thickness of the top Co film. The GMR is a maximum for a Co thickness of about 2.5–3.0 nm of Co. The results here are quite different from those for the center Co film of a symmetric spin valve (see Ref. 7), where the GMR exhibited a maximum for a center Co film thickness of about 3.0–5.0 nm of Co. One possible explanation for the bottom spin valve requiring less Co in the unpinned or "valve" film would be that some conduction electrons reflect specularly at the Co/vacuum interface. Note that specular reflection at this interface would increase the effective thickness of the Co.[13]

Also of interest in Fig. 5 is the effect of exposure to O_2. We have consistently found that when the thickness of the top Co is close to its optimum value, a small additional increase in GMR can always be obtained by exposure of the sample to O_2. It was found by x-ray photoelectron spectroscopy that the top two or three atomic layers of Co are readily oxidized, but as the surface oxidizes it becomes passivated, and O_2 exposures larger than $\sim 10^{-2}$ Torr s have little additional effect. The mechanism for the increase in GMR is not known, but one possibility is that an increase occurs in the amount of specular scattering (i.e., Co/CoO interface might scatter a larger fraction of the incident electrons specularly than does the Co/vacuum interface). Note here that specular scattering (as opposed to diffuse scattering) has the effect of allowing an electron to travel farther (in the direction of the current).

The GMR of 17.0% found after the exposure to O_2 (Fig. 5) is the largest value ever reported for a simple (one Cu film) spin valve. However, a disadvantage of this treatment is that the coercivity of the unpinned Co film increases from 3.5 to 5.4 mT (35 to 54 Oe).

This increase in coercivity represents the initial stage of the pinning process that occurs when a NiO film is deposited on Co (as in a symmetric spin valve). The NiO film is deposited after 2 mTorr of an 85/15 Ar/O_2 mixture is introduced into the chamber and the Ni magnetron gun is turned on. Two or three atomic layers of Co will oxidize under these conditions before any NiO is deposited. Thus, CoO is actually in contact with the top Co film in a symmetric spin valve. We have attempted to increase the pinning of the top Co film in symmetric spin valves by depositing a few atomic layers of Ni on the Co prior to NiO deposition to prevent formation of the CoO, but so far no increases in the pinning have been achieved. The rationale for these attempts was that NiO has a much higher Néel temperature than CoO.

The maximum GMR without the use of O_2 is 16.2% (in Fig. 5). This value should be compared with the maximum GMR of 23.4% achieved for symmetric spin valves. The increase from 16.2% to 23.4% appears to be representative of the degree of improvement that can be expected in going from a simple spin valve to a symmetric spin valve.

The dependence of the GMR on the thickness of the bottom Co film, shown in Fig. 6, is quite different from that of the top Co film (in Fig. 5). Perhaps the most surprising result is that a mere 1 nm of Co gives a respectable 11.3% GMR. This result is surprising because conductivity measurements indicate that 1 nm Co is near the percolation threshold, and a very patchy film is likely.

Figure 7 presents the coercivity of the bottom (pinned) Co film as a function of its thickness. If the pinning is purely due to the underlying NiO, i.e., if there is no contribution from the Co itself, a $1/t$ dependence would be expected as thicker Co provides a larger lever arm, as it were, to rotate the magnetization. The solid line in Fig. 7 is a $1/t$ extrapolation from the largest Co thickness backwards to smaller values. The fit is quite good down to 2 nm. Below 2 nm it appears that a different effect is occurring. The coercivity appears to be dropping sharply, as illustrated by the dashed line. This drop is presumably associated with the Co film becoming discontinuous.

Figure 8 presents the dependence of the coercivity and the coupling of the top Co film on its thickness. The scatter in the data prevents identification of the functional dependence but the coupling decreases roughly as $1/t$ (the solid

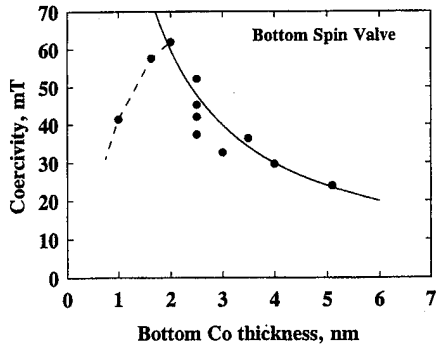


FIG. 7. A plot of the coercivity of the bottom Co film vs its thickness for bottom spin valves. See the text for explanations of the solid and dashed curves. (Note: 10 mT=100 Oe.)

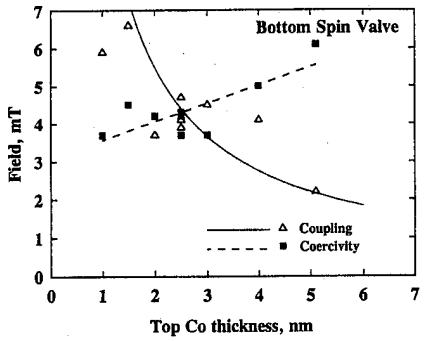


FIG. 8. A plot of the coercivity and the coupling of the top Co film vs its thickness for bottom spin valves. See the text for explanations of the solid and dashed curves. (Note: 1 mT=10 Oe.)

curve), and the coercivity increases roughly linearly (the dashed curve) with Co thickness. From all points of view, the bottom spin valve properties are clearly optimized with a top Co thickness of 2.5–3 nm.

IV. CONCLUSIONS

The major conclusions of this work may be summarized as follows:

(1) The GMR of symmetric spin valves increases strongly as the partial pressure of H_2O in the chamber prior to film deposition decreases.
(2) The GMR increase in symmetric spin valves shows no sign of saturating at the lowest H_2O partial pressures obtainable in the present work, $\sim 10^{-9}$ Torr.
(3) The largest GMR value obtained for a symmetric spin valve in this work is 23.4% at RT.
(4) The largest GMR value obtained for a bottom spin valve is 17.0% at RT.
(5) There are some indications that specular scattering of conduction electrons may occur at Co/vacuum and Co/CoO interfaces and may increase the GMR slightly.

ACKNOWLEDGMENTS

This work has been supported in part (W.F.E. and R.D.McM.) by the NIST Advanced Technology Program and in part (A.E.B.) by NSF Program No. DMR-9400439.

[1] T. C. Anthony, J. A. Brug, and S. Zhang, IEEE Trans. Magn. **30**, 3819 (1994).
[2] P. M. Baumgart, B. Dieny, B. A. Gurney, J.-P. Nozieres, V. S. Speriosu, and D. R. Wilhoit, U. S. Patent 5,287,238; Feb. 15, 1994.
[3] H. Kano, K. Kagawa, A. Suzuki, A. Okabe, K. Hayashi, and K. Aso, Appl. Phys. Lett. **63**, 2839 (1993).
[4] Th. G. S. M. Rijks, W. Folkerts, J. C. S. Kools, W. J. M. de Jonge, and R. Coehoorn, in Colloquium Digest, 14th Int. Coll. on Mag. Films and Surf., Dusseldorf, 1994, p. 29.
[5] V. S. Speriosu, B. Dieny, P. Humbert, B. A. Gurney, and H. Lefakis, Phys. Rev. B **44**, 5358 (1991); B. Dieny, V. S. Speriosu, S. S. P. Parkin, B. A. Gurney, D. R. Wilhoit, and D. Mauri, *ibid.* **43**, 1297 (1991); C. Meny, J. P. Jay, P. Panissod, P. Humbert, V. S. Speriosu, H. Lefakis, J. P. Nozieres, and B. A. Gurney, Mater. Res. Soc. Symp. Proc. **313**, 289 (1993); B. Dieny, J. Magn. Magn. Mater. **136**, 335 (1994).
[6] M. J. Carey, F. E. Spada, A. E. Berkowitz, W. Cao, and G. Thomas, J. Mater. Res. **6**, 2680 (1991); M. J. Carey and A. E. Berkowitz, Appl. Phys. Lett. **60**, 3060 (1992); M. J. Carey and A. E. Berkowitz, J. Appl. Phys. **73**, 6892 (1993).
[7] W. F. Egelhoff, Jr., T. Ha, R. D. K. Misra, Y. Kadmon, J. Nir, C. J. Powell, M. D. Stiles, R. D. McMichael, C.-L. Lin, J. M. Sivertsen, J. H. Judy, K. Takano, A. E. Berkowitz, T. C. Anthony, and J. A. Brug, J. Appl. Phys. **78**, 273 (1995).
[8] A. Chaiken, P. Lubitz, J. J. Krebs, G. A. Prinz, and M. Z. Harford, J. Appl. Phys. **70**, 5864 (1991).
[9] L. Néel, Comp. Rend. Acad. Sci. (France) **255**, 1545 (1962); **255**, 1676 (1962).
[10] S. S. P. Parkin, R. Bhadra, and K. P. Roche, Phys. Rev. Lett. **66**, 2152 (1991).
[11] R. D. K. Misra, T. Ha, Y. Kadmon, C. J. Powell, M. D. Stiles, R. D. McMichael, and W. F. Egelhoff, Jr., Mater. Res. Soc. Symp. Proc. **384**, 373 (1995).
[12] R. D. McMichael, W. F. Egelhoff, Jr., and M. Ha, Mater.Res. Soc. Symp. Proc. **384**, 397 (1995); R. D. McMichael, W. F. Egelhoff, Jr., and L. H. Bennett, IEEE Trans. Magn. **31**, 3930 (1995).
[13] K. Fuchs, Proc. Camb. Philos. Soc. **34**, 100 (1938); E. H. Sondheimer, Adv. Phys. **1**, 1 (1952); A. E. Ennos, Brit. J. Appl. Phys. **8**, 113 (1957); N. S. P. Lucas, Appl. Phys. Lett. **4**, 73 (1964); J. P. Chauvineau and C. Pariset, Surf. Sci. **36**, 155 (1973); J. R. Sambles, K. C. Elsom, and D. J. Jarvis, Philos. Trans. R. Soc. A **304**, 365 (1982); J. R. Shambles, Thin Solid Films **106**, 321 (1983); M. Jałochowski and E. Bauer, Phys. Rev. B **37**, 8627 (1988); M. Jałochowski and E. Bauer, Phys. Rev. B **38**, 5272 (1988).

First principles calculations of electrical conductivity and giant magnetoresistance of periodic multilayers and spin valves (invited)

W. H. Butler, X.-G. Zhang, and D. M. C. Nicholson
Oak Ridge National Laboratory, Oak Ridge, Tennessee 37831-6114

T. C. Schulthess
Lawrence Livermore National Laboratory, Livermore, California 94551

J. M. MacLaren
Department of Physics, Tulane University, New Orleans, Louisiana 70118

We used the Layer Korringa Kohn Rostoker technique to calculate the electronic structure of cobalt-copper multilayers and spin valves from first principles within the local spin density approximation. Using this electronic structure together with a phenomenological self-energy which may vary from layer to layer, we calculated the non-local layer-dependent conductivity by means of the Kubo linear response formalism. By calculating the majority and minority conductivities for parallel and anti-parallel alignment of the moments in the cobalt layers we determined the giant magnetoresistance (GMR). Several interesting features emerge from the calculations. When the scattering rates are relatively high, we find that the contributions to the GMR are largely non-local, with the largest contributions arising from changes in the currents carried in a cobalt plane next to copper due to fields sensed in the cobalt layer on the other side of copper. When scattering rates are relatively low (comparable to that of cobalt and copper at room temperature), there are important contributions to the GMR from local conduction in the copper layers. This effect arises from the fact that when the component of the majority spin electron momentum parallel to the layers exceeds a certain value, it gets trapped in the copper layers. If the scattering rate is lower in the copper than in the cobalt there is a significant enhancement in the majority spin conductivity and in the GMR. This effect is analogous to the channeling of light by an optical waveguide. © *1996 American Institute of Physics.* [S0021-8979(96)79508-1]

I. INTRODUCTION

A new form of magnetoresistance called "giant" magnetoresistance (GMR) was discovered in 1988.[1,2] GMR is a change in the electrical resistance of an inhomogeneous system that is observed when an applied magnetic field causes an alignment of the magnetic moments in different parts of a material. This phenomenon has aroused considerable interest because it can be used to make magnetic field sensors and because it gives valuable insight into spin dependent transport.

GMR has been observed in several geometries, but the GMR systems that have aroused the greatest interest for magnetic sensor applications are composed of extremely thin layers of ferromagnetic material separated by non-magnetic or very weakly magnetic spacer layers. Two geometries are particularly attractive. One is the "spin valve" geometry which consists of two ferromagnetic layers separated by a non-magnetic spacer layer.[3] The magnetic moment of one of the ferromagnetic layers is pinned by exchange coupling to a hard anti-ferromagnet while the other is relatively free to rotate with an applied field. The other geometry is a (more or less) periodic multilayer consisting of alternating ferromagnetic and non-magnetic spacer layers. For the multilayer geometry, one depends on the moments in alternate ferromagnetic layers having an anti-parallel alignment in the absence of an applied field.

The transport properties of layered materials have been the subject of previous theoretical investigations, most of which have used the model of free electrons with random point scatterers (FERPS). References to most of this work may be found in a recent review.[4]

In this paper we report on first-principles calculations of the transport properties of Co|Cu multilayers and Co|Cu|Co spin valves. The electronic structure of these systems is calculated self-consistently using the local spin density approximation to density functional theory. We then use this electronic structure to calculate the conductivity by evaluating the Kubo-Greenwood linear response formula. Our calculations reveal two new effects that are important for GMR, a "resonance" effect and an electron channeling effect. The latter effect is analogous to the channeling of light by an optical waveguide.

II. NON-LOCAL CONDUCTIVITY OF FREE ELECTRONS, COPPER, AND COBALT

When an electromotive force is applied to a material, a local applied electric field, $E_\nu(\mathbf{r})$, is created which induces currents, $J_\mu(\mathbf{r})$. The linear, non-local coefficient relating the current to the applied field is the conductivity $\sigma_{\mu\nu}(\mathbf{r},\mathbf{r}')$,

$$J_\mu(\mathbf{r}) = \int d\mathbf{r}' \sum_\nu \sigma_{\mu\nu}(\mathbf{r},\mathbf{r}') E_\nu(\mathbf{r}'). \tag{1}$$

Thus, $\sigma_{\mu\nu}(\mathbf{r},\mathbf{r}')$ is the current in direction μ at point $\mathbf{r}$ induced by an applied field of unit magnitude applied at the point $\mathbf{r}'$. This non-local conductivity is given by[5,6]

$$\sigma_{\mu\nu}(\mathbf{r},\mathbf{r}') = \pi\hbar \langle j_\mu \ \mathrm{Im}\ G(E_F;\mathbf{r},\mathbf{r}') j'_\nu \ \mathrm{Im} G(E_F;\mathbf{r}',\mathbf{r}) \rangle, \tag{2}$$

 0021-8979/96/79(8)/5282/6/$10.00 © 1996 American Institute of Physics

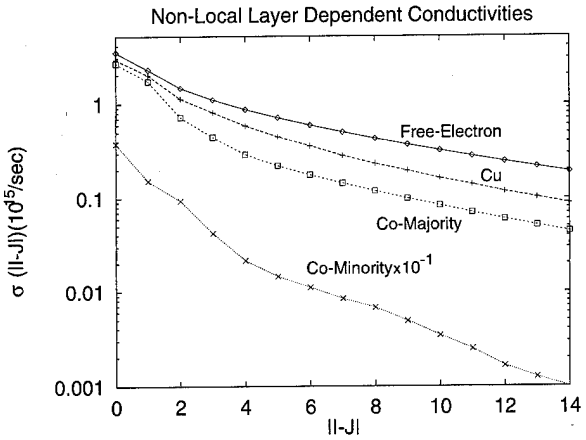


FIG. 1. Non-local layer dependent conductivity parallel to the planes for free electrons, copper, cobalt majority and cobalt minority. For free electrons and for copper, the Fermi energy is chosen so that the Fermi surface contains 0.5 electrons/atom-spin.

where j_μ is the current operator $(-ie\hbar/m)\partial/\partial r_\mu$, and the imaginary part of the Green function arises from a sum over the exact eigenstates of the system. The angular brackets in Eq. (2) indicate a configurational average.

In this paper we consider systems which consist of stacks of atomic planes. Although these planes may differ, we assume that they have a common underlying two-dimensional periodicity. We find it convenient and instructive to calculate the non-local layer conductivity, $\sigma_{\mu\nu}(I,J)$ which is the current in direction μ in atomic plane I due to an applied electric field of unit magnitude in direction ν applied in atomic plane J. $\sigma_{\mu\nu}(I,J)$ is given in terms of the non-local conductivity $\sigma_{\mu\nu}(\mathbf{r},\mathbf{r}')$ by integrating over the atomic cells in plane J and averaging over the atomic cells in plane I,

$$\sigma_{\mu\nu}(I,J)=N_I^{-1}\sum_i \sum_j \Omega_i^{-1}\int_{\Omega_i} d\mathbf{r}\int_{\Omega_j} d\mathbf{r}'\,\sigma_{\mu\nu}(\mathbf{r},\mathbf{r}'). \tag{3}$$

Here N_I is the number of cells in plane I and Ω_j is the volume of an atomic cell in plane J. The sums run over the cells in planes I and J, respectively.

For the FERPS model of a *homogeneous* system, the non-local *layer dependent* conductivity obtained by dividing space into artificial atomic planes can be obtained analytically.[7] The conductivity is determined by the Fermi energy and by the imaginary part of the self-energy which is the scattering rate, $\mathrm{Im}\,\Sigma/\hbar = 1/(2\tau)$. The non-local layer dependent conductivity parallel to the layers for free electrons with one electron per atom and a density corresponding to copper is shown in Figure 1. The scattering rate, $\mathrm{Im}\,\Sigma$, is taken to be 0.005 Hartree (= 0.136 eV). The non-local conductivity shown in the figure is the contribution to the current in layer I parallel to this layer due to a field applied in the same direction in layer J. The layers are slabs, 0.208 nm in thickness corresponding to the thickness of {111} atomic planes in copper. The Fermi Energy is 7.058 eV correspond-

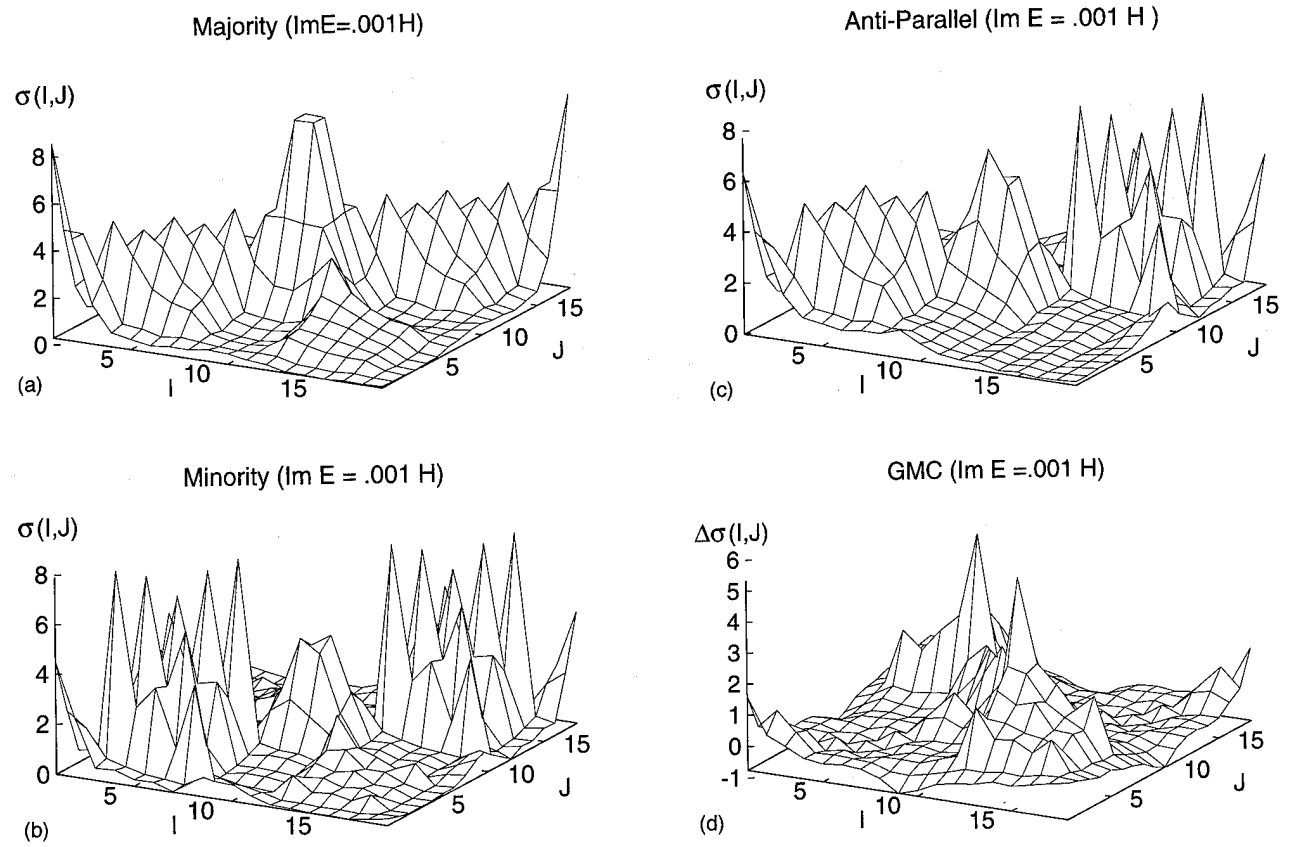


FIG. 2. Non-local depenent conductivity for a perioic Co_5Cu_4 multilayer: (a) majority spin conuctivity for moments aligne, (b) minority spin conuctivity for moments aligned, (c) majority spin conductivity for moments anti-aligned, an (d) change in conductivity of both spin channels between aligned and anti-aligned configurations of moments.

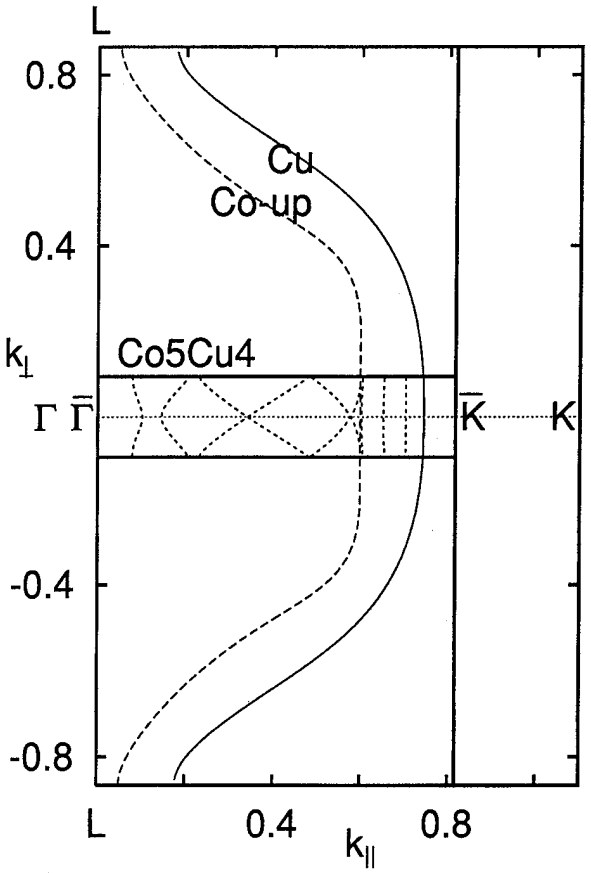


FIG. 3. Cuts through Fermi surfaces of bulk copper, majority bulk cobalt, and majority Fermi surface of a periodic Co_5Cu_4 (111) multilayer. The labels $\bar{\Gamma}$ and $\bar{K}$ refer to points at the center and corners, respectively, of the hexagonal two dimensional Brillouin zone. The points labeled Γ, L, and K refer to symmetry points in the three dimensional Brillouin zone. $k_{\|}$ and $k_{\perp}$ are expressed in units of $2\pi/a$, where a is the fcc lattice constant.

ing to 0.5 electrons/spin. The conductivity is given in units of 10^{15}/s. This conductivity can be converted to a resistivity in $\mu\Omega$ cm by dividing it into 898.8. The sum of $\sigma(I,J)$ over I or J gives the total conductivity for this homogeneous system.

These non-local layer dependent conductivities for free electrons can be compared with similar quantities which we calculated for copper and cobalt. The techniques which we have developed for calculating non-local layer dependent conductivities from the Kubo formula have been described previously.[8–11] Figure 1 also shows the calculated values of the non-local layer dependent conductivity, $\sigma_{xx}(I,J)$, for copper and for cobalt at their respective Fermi energies using the same scattering rate of 0.005 Hartree (0.136 eV). The atomic planes were again taken to be perpendicular to the {111} direction.

It can be seen from Figure 1 that the non-local conductivity of coper perpendicular to the {111} direction resembles that of free electrons although the overall conductivity is less and the mean free path (roughly the inverse of the slope of the non-local conductivity curve) is less than for free electrons with the same scattering rate. The non-local conductivity of majority cobalt also resembles that of free electrons although the differences are greater. It appears that there are fewer carriers in majority cobalt and that they have more than one mean free path. These results are consistent with our knowledge of the electronic structure of copper and cobalt. The copper Fermi surface contains 0.5 electrons/spin channel but its conductivity is reduced from that of free electrons with the same scattering rate because the Fermi velocities are lower. The conductivity of majority cobalt is lower still because its volume is smaller and its velocities are lower due to a larger admixture of d-character.

The Fermi energy for the minority spins lies within the d-bands and is quite complicated with multiple sheets. The band velocities are low over most of the cobalt minority Fermi surface but the surface area is sufficiently large that that the total minority conductivity is approximately the same as the majority conductivity if the scattering rates are the same. The character of the conductivity is different, however, it is much more localized in space, hence the more rapid decay of the non-local conductivity of minority cobalt in Figure 1.

III. NON-LOCAL CONDUCTIVITIES OF PERIODIC MULTILAYERS AND SPIN VALVES

We have calculated the electronic structure and the non-local conductivity of periodic multilayers consisting of 5 {111} atomic planes of cobalt alternating with 4 {111} atomic planes of copper. This system was chosen becaused it is similar to the one for which a very large GMR, $\Delta\rho/\rho > 0.35$, was observed[12] at room temperature. The stacking was assumed to be fcc for all of the layers. A uniform scattering rate, $\mathrm{Im}\,\Sigma = 0.001$ Ha, was assumed for all layers and for both spin channels. Figures 2(a) and 2(b) show results of these calculations for the majority and minority channels respectively for the case in which all of the cobalt moments are aligned. Figure 2(c) shows the non-local conductivity for one of the channels for the case in which alternate layers of cobalt have their moments anti-aligned. Figure 2(d) shows the difference for the total non-local layer conductivity in both channels between the aligned and anti-aligned cases. The figures show $\sigma_{xx}(I,J)$ where x is a direction parallel to the {111} planes. The arrangement of the atomic planes as shown in the figures is $Cu_2|Co_5|Cu_4|Co_5|Cu_2$, periodically repeated. Thus atomic planes, I or J= 1,2, 8-11, 17 and 18 are copper, while atomic planes 3-7 and 12-16 are cobalt.

The majority channel conductivity for aligned moments, Figure 2(a), shows several interesting effects. The non-local conductivity in the cobalt layers is largest for $|I-J|=0$ and falls off similarly to its behavior in bulk cobalt if both I and J are cobalt layers. $\sigma(I,J)$ for I a cobalt layer drops when J enters the copper region, but it then *increases* when J enters the second cobalt region. This surprising effect lies outside a simple FERPS model and is a major contributor to the GMR. For brevity, we shall refer to this effect as the "resonance" effect since we suspect that it is caused by the similarity of the wave functions and energy levels on different cobalt layers. A similar but smaller effect can be seen between copper layers and between cobalt layers in the minority channel.

The most striking feature of Figure 2(a) is the large conductivity localized on the copper layers. The values of non-

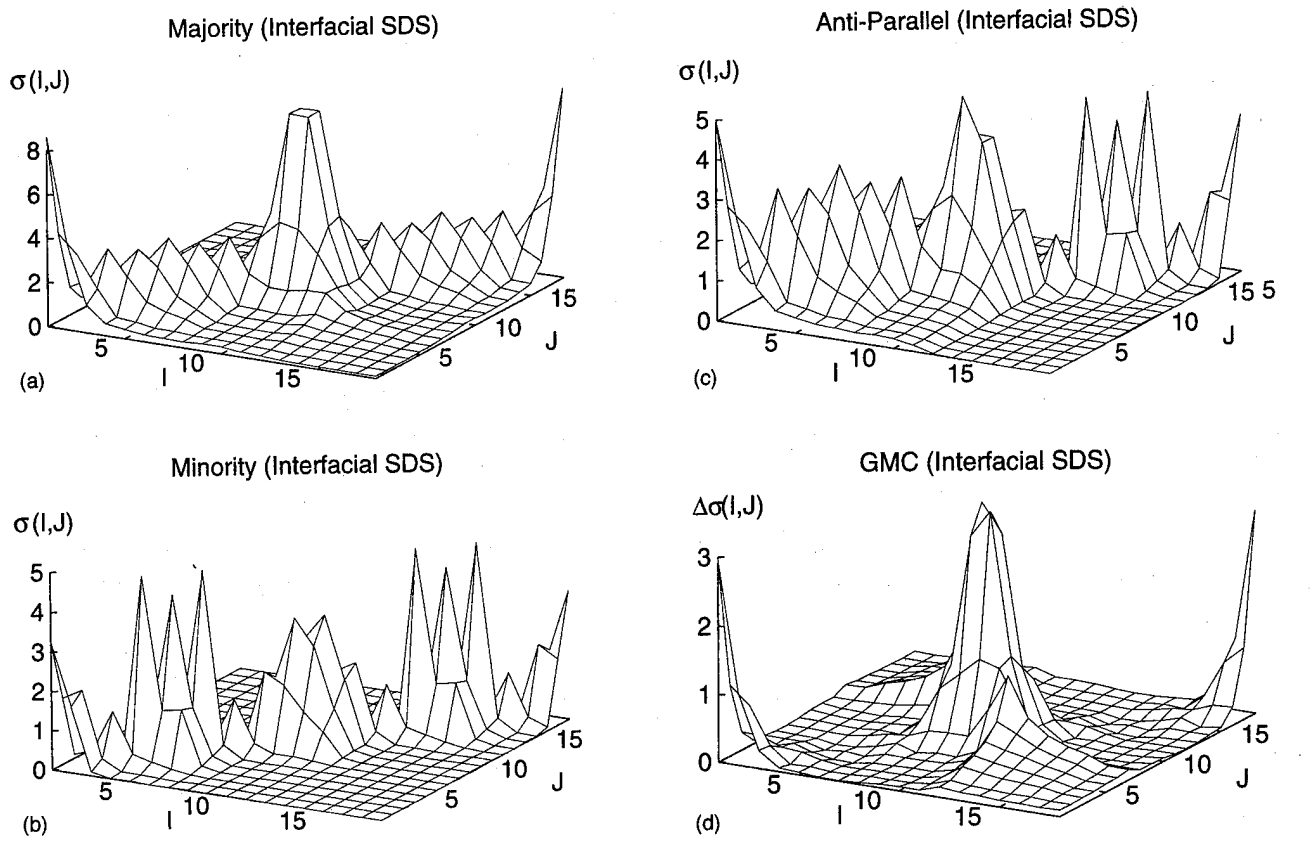


FIG. 4. Non-local layer dependent conductivities assuming different scattering rates in the copper and cobalt layers and different scattering rates for majority and minority spin cobalt: (a) majority spin conductivity for parallel alignment of cobalt moments, (b) minority spin conductivity for parallel alignment of cobalt moments, (c) conductivity for anti-parallel alignment, (d) giant magnetoconductance.

local conductivity $\sigma(I,J)$ when I and J are both in the same copper layer are larger than they would be in bulk copper. This surprising enhancement of the local conductivity in the copper is due to an electron channeling effect. Figure 3 shows cuts through the Fermi surfaces of copper, majority cobalt, and majority Co_5Cu_4 along the direction $\bar{\Gamma}\rightarrow\bar{K}$ in the two dimensional Brillouin zone. This cut also includes the points Γ, K, and L of the three dimensional zone. We can see that for values of $k_\parallel$ between approximately 0.6 and 0.74, there is a valid value of $k_\perp$ for copper but not for majority cobalt. For most directions in the two dimensional zone, there is a similar region where $k_\perp$ is allowed for copper but not for majority cobalt. Thus, when Co and Cu are combined to make the multilayer, Co_5Cu_4, one or more majority bands will split off that are relatively dispersionless in k_z when viewed as a function of $k_\parallel$. The majority Fermi surface of Co_5Cu_4 is also shown in Fig. 3. The bands responsible for the electron channeling are the essentially vertical lines near $k_\parallel=0.65$ and 0.705. The fact that a single value of $k_\parallel$ corresponds to all values of $k_\perp$ indicates that the electrons corresponding to this band are localized perpendicular to the layers. Examination of the wave functions indicates that they are localized on the copper layers. The complicated cobalt minority Fermi surface provides valid values of $k_\perp$ for essentially all values of $k_\parallel$ for which there are valid values of $k_\perp$ in copper. Thus, there is no channeling of minority electrons in copper.

Electrons can also be channeled within the cobalt layers. From Figure 3 it is clear that there is a region near $k_\parallel=0$ for which there are allowed values of $k_\perp$ in majority cobalt but not in copper. This leads to electrons being "trapped" in the cobalt, but the effect is much smaller than channeling within the copper layers because only a small portion of the Fermi surface is involved.

Figure 2(d) shows the contributions to the giant magnetoconductance, i.e., the difference between the conductivity of both channels for the moments aligned and the conductivity of both channels with the moments anti-aligned. For this case in which the scattering rate is the same on all layers and for both spins, we see that the resonance effect makes the primary contribution to the GMR. The GMR obtained by summing over the contributions shown in Figure 2(d) is $\Delta\sigma/\sigma_{AP}=0.13$.

The calculations represented by Figures 2(a)–2(d) assumed a constant scattering rate for all atomic planes and both spins. We have performed an analogous set of calculations assuming a scattering rate in the copper that is appropriate to room temperature copper, and which assumes differing scattering rates for the majority and minority cobalt spins. The cobalt scattering rates were fixed by the known room temperature resistivity of cobalt and the assumption that the majority and minority scattering rates in the cobalt are proportional to their Fermi energy state densities. The results of these calculations are shown in Figures 4(a)–4(d).

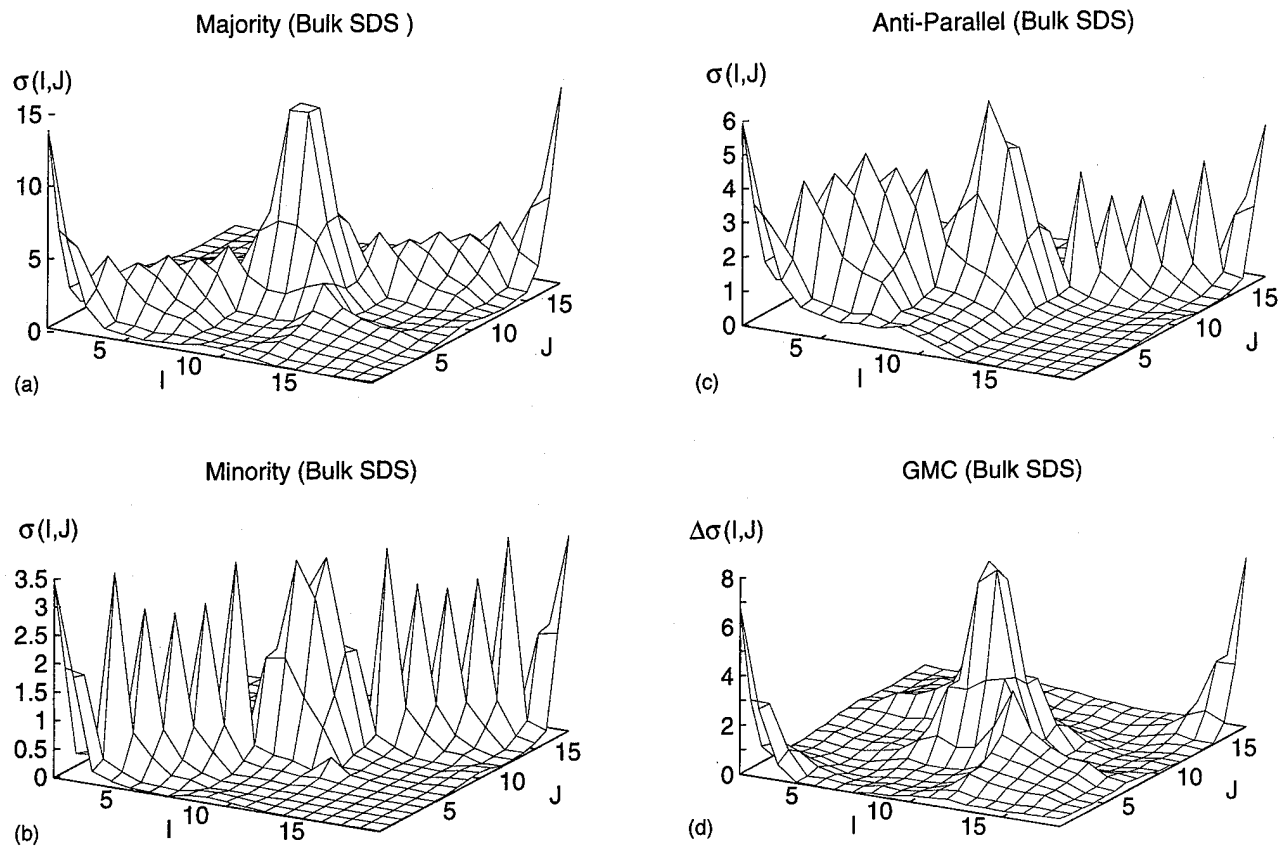


FIG. 5. Calculated non-local layer dependent conductivities for the case of strong interfacial scattering: (a) majority spin conductivity for parallel alignment, (b) minority spin conductivity for parallel alignment, (c) majority spin conductivity for anti-parallel alignment, (d) giant magnetoconductance.

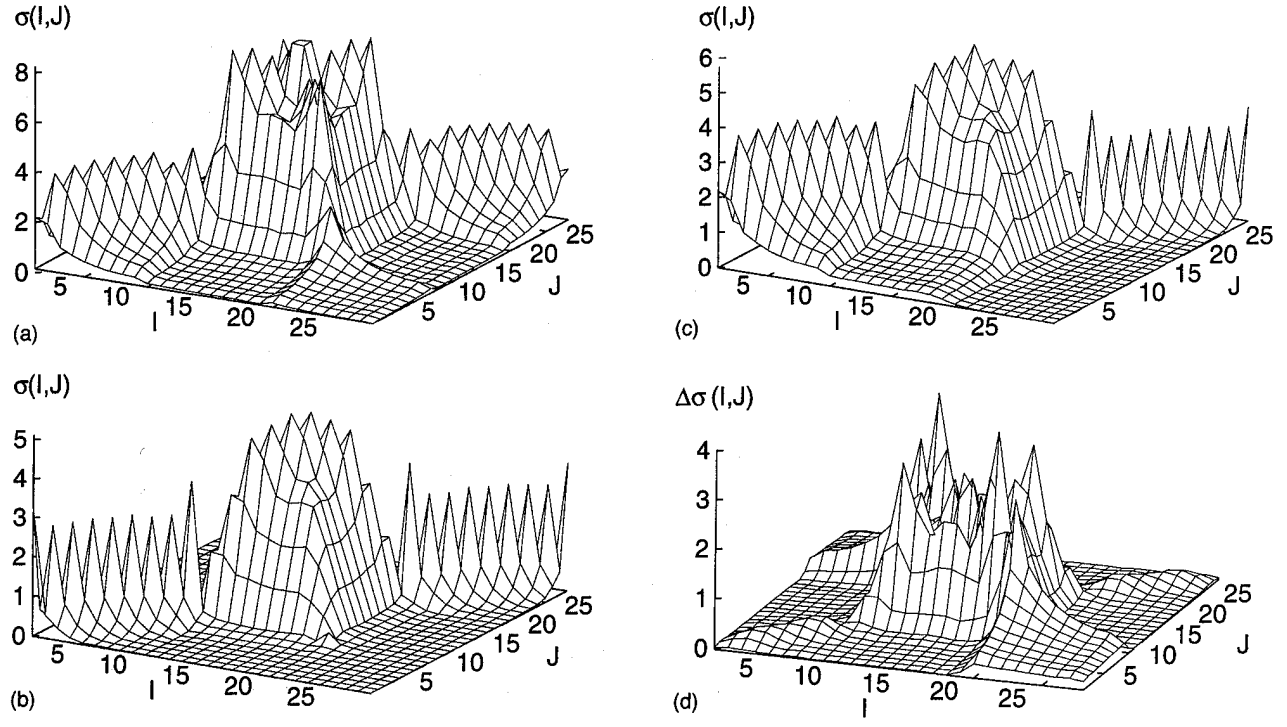


FIG. 6. Non-local layer dependent conductivities for a spin valve: (a) majority spin conductivity, (b) minority spin conductivity for parallel alignment, (c) majority spin conductivity for anti-parallel alignment, (d) giant magnetoconductance.

An enhancement of the local conductivity in the copper for the majority electrons due to electron channeling is seen similarly to the case of uniform scattering rates. In this case, the form of the giant magnetoconductance is quite different. There are large contributions involving a single copper layer. Thus electron channeling greatly increases the majority conductivity even when the scattering is spin and species independent, but when the scattering is stronger in the cobalt than in the copper it can have a large effect on the GMR as well. The GMR obtained by summing over the contributions shown in Figure 4(d) is $\Delta\sigma/\sigma_{AP}=0.43$.

In addition to assuming a constant scattering rate and one in which the bulk scattering rates in the cobalt differ, we also considered the possibility that the scattering rates on the cobalt planes are the same for majority and minority spin channels and that there is strong spin-dependent scattering near the interfaces. Such strong spin dependent scattering is quite plausible if there is intermixing between the cobalt and copper in the interfacial layers. Specifically, we assumed that the scattering rate in the cobalt was $\mathrm{Im}\,\Sigma=.0025$ Ha for both majority and minority cobalt and that the scattering rate in the copper was $\mathrm{Im}\,\Sigma=.0006$ Ha. On the interfacial cobalt planes we assumed scattering rates of .005 Ha for the majority channel and .06 Ha for the minority channel. The factor of 12 difference in scattering rates is based on CPA calculations for cobalt with copper impurities. On the interfacial copper planes scattering rates of .002 Ha and .005 Ha were assumed for the majority and minority channels, respectively. The calculated non-local conductivities are shown in Figures 5(a)–5(d). The increased conductivity in the copper layers due to electron channeling is evident. The GMR obtained by summing over the contributions shown in Figure 6(d) is $\Delta\sigma/\sigma_{AP}=0.22$.

We have also calculated the electronic structure and non-local conductivity of cobalt-copper spin valves. The electronic structure of these spin-valves has been described previously.[11] Figure 6 shows the calculated non-local conductivity of a spin valve consisting of 10 atomic {111} copper planes with 10 {111} cobalt planes (with fcc stacking) on either side. We assume the same scattering rates as for the periodic multilayer of Figure 4. A strong enhancement of the conductivity in the copper layers is evident for the majority electrons and parallel configuration. Figure 6(d) shows that there are strong contributions to the GMR from both the resonance effect evidenced by the peak when I and J are in different cobalt layers and from the channeling effect evidenced by the peak when both I and J are in the copper layer. The GMR obtained for this spin valve was $\Delta\sigma/\sigma_{AP}=0.26$.

IV. ORIGINS OF GMR IN COBALT-COPPER MULTILAYERS AND SPIN VALVES

Our first principles calculations illustrate two quite different effects which may be important sources of the large giant magnetoresistance that is seen in cobalt-copper multilayers and spin valves. The first of these mechanisms may be described as a tunneling or resonance effect and is characterized by a surprising peak in the non-local conductivity between two neighboring ferromagnetic layers compared to the conductivity between one of the ferromagnetic layers and the neighboring spacer layer.

The second mechanism is electron channeling which is quite analogous to the channeling of light by an optical waveguide. The channeled electrons have an interesting mode structure which we hope to describe elsewhere. The channeling effect does not seem to lead to a dramatic increase in the GMR if all scattering rates are the same. However, if there are different scattering rates in the cobalt and in the copper, the effects of channeling on the GMR can be quite spectacular. This suggests strategies for increasing the GMR which we shall discuss elsewhere. It also raises the question of whether or not interfaces in current GMR systems are so rough that the channeling effect is killed by diffuse scattering at the interface.

The possibility of electron channeling has been noted previously by Hood and Falicov[13] who treated the semiclassical FERPS model and by Vedyaev *et al.*[14] who used the quantum FERPS model.

ACKNOWLEDGMENTS

Work at Oak Ridge was sponsored by DOE Assistant Secretary of Defense Programs, Technology Management Group, Technology Transfer Initiative, by the High Performance Computing and Communication Initiative, and by the Division of Materials Sciences Office of Basic Energy Sciences under contract DEAC05-84OR21400 with Lockheed Marietta Energy Systems. Work at Livermore was performed under the auspices of the U.S. Department of Energy by Lawrence Livermore National Laboratory under contract W-7405-ENG-48. Work at Tulane University was partially supported by the Louisiana Quality Education Support Fund under grant number LEQSF (1991-1994)-RD-A-30. Some of the computations were performed at the ORNL Center for Computational Sciences.

[1] M. N. Baibich, J. M. Broto, A. Fert, F. Nguyen Van Dau, F. Petroff, P. Etienne, G. Creuzet, A. Friederich, and J. Chaezelas, Phys. Rev. Lett. **61**, 2472 (1988).
[2] G. Binasch, P. Grünberg, F. Sauerbach, and W. Zinn, Phys. Rev. B **39**, 4828 (1989).
[3] B. Dieny, V. S. Speriosu, S. S. P. Parkin, B. A. Gurney, D. R. Wilhoit, and D. Mauri, Phys. Rev. B **43**, 1297 (1991).
[4] P. M. Levy, *Solid State Physics* (Academic, New York 1994), Vol. 47, p. 367.
[5] R. Kubo, J. Phys. Soc. Jpn. **12**, 570 (1957).
[6] D. A. Greenwood, Proc. Phys. Soc. London **71**, 585 (1958).
[7] X.-G. Zhang and W. H. Butler, Phys. Rev. B **51**, 10085 (1995).
[8] W. H. Butler, Phys. Rev. **31**, 3260 (1985).
[9] W. H. Butler, X.-G. Zhang, D. M. C. Nicholson, and J. M. MacLaren, J. Appl. Phys. **76**, 6808 (1994).
[10] J. M. MacLaren, S. Crampin, D. D. Vvednsky, R. C. Albers, and J. B. Pendry, Computer Physics Communications **60**, 365 (1990).
[11] W. H. Butler, X.-G. Zhang, D. M. C. Nicholson, and J. M. MacLaren, Phys. Rev. B (in press).
[12] S. S. P. Parkin, R. Bhadra, and K. P. Roche, Phys. Rev. Lett. **66**, 21512 (1991).
[13] R. Q. Hood and L. M. Falicov, Phys. Rev. B **46**, 8287 (1992).
[14] A. Vedyayev, C. Cowache, N. Ryzhanova, and B. Dieny, J. Phys: Condens. Matter **5**, 8289 (1993).

Origins of colossal magnetoresistance in perovskite-type manganese oxides (invited)

Y. Tokura
Joint Research Center for Atom Technology (JRCAT), Tsukuba 305, Japan and Department of Applied Physics, University of Tokyo, Tokyo 113, Japan

Y. Tomioka, H. Kuwahara, A. Asamitsu, Y. Moritomo, and M. Kasai
Joint Research Center for Atom Technology (JRCAT), Tsukuba 305, Japan

Phenomena of colossal magnetoresistance (MR) or magnetic field induced insulator–metal ($I-M$) transitions have been investigated for single crystals of perovskite-type manganese oxides with controlled carrier density and one-electron bandwidth. In addition to the canonical MR behavior near the Curie temperature, the first-order phase transition accompanying several orders of magnitude change in resistivity has been observed under an external magnetic field for many of the composition-controlled crystals as an intrinsic bulk phenomenon. It was proved by the systematic experimental investigations that the field-induced destruction of the charge-ordered state accompanying the lattice structural as well as metamagnetic transition is a major origin of such a colossal MR. Versatile MR phenomena and $I-M$ phase diagrams in the $T-H$ plane are presented with their interpretation. © *1996 American Institute of Physics.* [S0021-8979(96)53508-X]

I. INTRODUCTION

Large magnetoresistance (MR) near the Curie temperature in perovskite-type manganese oxides is of current interest, but was readily reported in 1969 by Searle and Wang[1] for a flux-grown crystal of $La_{1-x}Pb_xMnO_3$. Soon after, Kubo and Ohata[2] presented the theoretical calculation based on the Kondo-lattice model with ferromagnetic coupling, which could give an essential account for the large MR observed near the Curie temperature T_c. More recently, however, unusually large MR was found in thin films[3,4] and single crystals[5–9] of various perovskite-type manganese oxides $RE_{1-x}AE_xMnO_3$ (RE and AE being trivalent rare earth and divalent alkaline earth ions, respectively), which cannot be accounted for in terms of the simple double-exchange mechanism. On the basis of the experimental investigations on the high-quality single crystals with accurately controlled compositions, we propose here that the charge-ordering phenomenon as well as its collapse under an external field is a key to understanding of such a colossal magnetoresistance (CMR).

The charge ordering in pseudocubic and layered perovskite manganites[5,10–15] has been assigned to the real space ordering of e_g electrons with the $(\pi,\pi,0)$ pattern, i.e., the alternating Mn^{3+}/Mn^{4+} sites on the (001) plane and hence tends to be most stabilized at the nominal hole concentration $x=0.5$. The charge-ordering accompanies, in general, a change (0.04%–2%) in lattice parameters, yet the transition temperature T_{CO} does not always coincide with the spin-ordering (or orbital-ordering) critical temperature: in some cases T_{CO} is higher than the Néel temperature T_N but in other cases lower than the Curie temperature T_c, as shown later in detail. The relative stability of the charge-ordered (CO) state to the ferromagnetic state mediated by the double-exchange interaction critically depends on the lattice form (or the tolerance factor of the crystal) as well as on the nominal hole concentration x.

II. ELECTRONIC PHASE DIAGRAM

We show in Fig. 1 electronic phase diagrams in the temperature (T)–hole concentration (x) plane for prototypical compounds: $La_{1-x}Sr_xMnO_3$ (left), $Pr_{1-x}Sr_xMnO_3$ (middle), and $Pr_{1-x}Ca_xMnO_3$ (right). As the tolerance factor or equivalently the average ionic radius of the perovskite A site decreases from (La,Sr) to (Pr,Ca) through (Pa,Sr), the orthorhombic distortion of the $GdFeO_3$-type increases, resulting in the bending of the Mn—O—Mn bond and hence in the decrease of the one-electron bandwidth of the e_g-state carriers.[16] This means that other electronic instabilities, such as the charge-ordering and superexchange interactions, which compete with the double-exchange interaction may become dominant in specific x and temperature regions.

The phase diagram for $La_{1-x}Sr_xMnO_3$[17–19] is canonical as the double-exchange system. The Jahn–Teller distorted end compound $LaMnO_3$ undergoes the phase transition to the spin-cant phase below $x=0.1$.[20] With further doping, the fer-

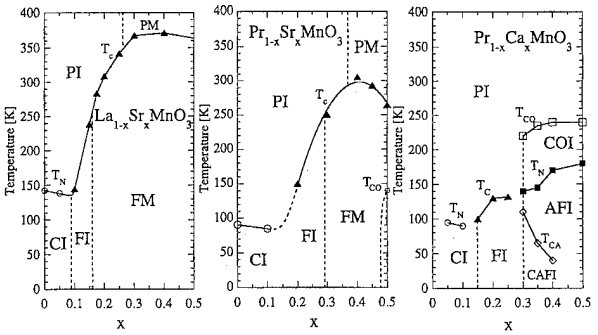


FIG. 1. The magnetic as well as electronic phase diagrams for $La_{1-x}Sr_xMnO_3$ (left) (Refs. 17–19), $Pr_{1-x}Sr_xMnO_3$ (middle) (Ref. 5), and $Pr_{1-x}Ca_xMnO_3$ (right) (Refs. 6 and 8). PI, PM, and CI denote the paramagnetic insulating, paramagnetic metallic, and spin-canted insulating states, respectively. FI and FM denote the ferromagnetic insulating and ferromagnetic metallic states, respectively. For $0.3\leqslant x\leqslant 0.5$ in $Pr_{1-x}Ca_xMnO_3$, the antiferromagnetic insulating (AFI) and canted antiferromagnetic insulating (CAFI) states exist in the charge-ordered insulating (COI) state.

 0021-8979/96/79(8)/5288/4/$10.00 © 1996 American Institute of Physics

romagnetic metallic phase appears below T_c which steeply increases with x up to 0.3 and then saturates. The temperature dependence of resistivity above T_c is insulating or semiconductive for $x<0.3$, which may be interpreted in terms of the carrier localization arising from some random potential or electron–phonon coupling (e.g., dynamic Jahn–Teller effect[21]). The ferromagnetic insulating (FI) phase is present in a fairly narrow x region ($x=0.10-0.17$), in which the double-exchange carrier is subject to localization (Anderson localization) but can still mediate the ferromagnetic interaction between the neighboring sites and realize the ferromagnetic state in a bond-percolation manner.

Such a ferromagnetic but insulating region becomes expanded as the tolerance factor is decreased: The low-temperature ferromagnetic phase is insulating up to $x=0.3$ for $Pr_{1-x}Sr_xMnO_3$ (Ref. 5) and $Pr_{1-x}Ca_xMnO_3$ (Refs. 6 and 8) as seen in Fig. 1. For the former compound, the ferromagnetic metallic (FM) phase shows up for $x\geq 0.3$, yet in the immediate vicinity of $x=0.5$ the insulating CO phase sets in below $T_{CO}=140$ K. For $Pr_{1-x}Ca_xMnO_3$ with a further reduced tolerance factor, the CO phase is present below 220–240 K for $x\geq 0.3$ and no FM phase shows up in any x region at zero field. In the CO phase of this compound, there are successive magnetic transitions to the charge-ordered antiferromagnetic insulating (AFI) phase and to the charge-ordered spin-canted insulating (CAFI) phase.[10–13] An observed variation of the transition temperatures T_N and T_{CA} with x can be interpreted in terms of the partial revival of the double-exchange carriers in the CO phase: The CO pattern is always $(\pi,\pi,0)$ in the pseudocubic setting irrespective of x and hence the deviation of x from $x=0.5$ may produce extra carriers which play a role of modifying the spin structure as observed. Such a discommensuration of the nominal hole concentration seems to affect not only the temperature-dependent spin structure but also magnetoresistance and metal-insulator phase diagram in the $T-H$ plane as discussed below.

III. FIELD-INDUCED MELTING OF CHARGE-ORDERED STATE

In the perovskite-type manganites the resistivity near T_c is much reduced by applying an external field, since the field forcedly aligns the t_{2g} local spins and hence the double-exchange carriers gain a mobility due to a reduced spin scattering. This is typically seen in temperature dependence of resistivity for $La_{1-x}Sr_xMnO_3$ ($x=0.175$, $T_c=284$ K)[18] shown in Fig. 2 (left). Incidentally, the resistivity anomaly around 220 K is due to the rhombohedral–orthorhombic structural transition and its transition temperature is also affected by an external field (see Ref. 22 for details of this novel phenomenon).

Such a resistivity change near T_c is also observed for $Pr_{1-x}Sr_xMnO_3$ ($x=0.5$, $T_c=250$ K) as shown in Fig. 2 (middle). However, a more remarkable field effect for this compound is seen upon the CO phase transition associated with a large resistivity change:[5] At zero field, the metallic resistivity shows an abrupt jump at $T_{CO}=150$ K due to the onset of the CO phase (see also Fig. 1). The CO transition temperature appears to be decreased with increasing field and

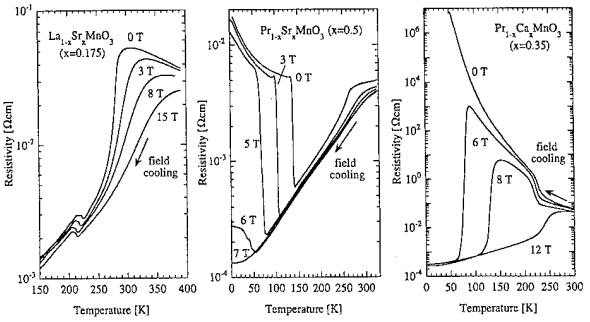


FIG. 2. Temperature dependence of resistivity under magnetic fields for $La_{1-x}Sr_xMnO_3$ ($x=0.175$, left) (Ref. 18), $Pr_{1-x}Sr_xMnO_3$ ($x=0.5$, middle) (Ref. 5), and $Pr_{1-x}Ca_xMnO_3$ ($x=0.35$, right) (Ref. 8).

above 7 T the insulating CO phase is totally extinguished over the whole temperature region. The phenomena may be viewed as a field-induced melting of the generalized Wigner crystal.

For $Pr_{1-x}Ca_xMnO_3$ where the CO state dominates over the double-exchange FM state in the fairly wide x region, a much higher field (about 30 T at 4.2 K) is needed for destruction of the CO state at $x=0.5$.[23] However, the deviation of x from 0.5 (discommensuration) brings about a drastic modification in the field-induced $I-M$ transitions. We show in Fig. 2 (right) the temperature dependence of the resistivity for the $x=0.35$ crystal under various fields.[8] The CO transition manifests itself as a steep rise of the resistivity at $T_{CO}=230$ K. Contrary to the case of $Pr_{1-x}Sr_xMnO_3$ ($x=0.5$), the field-induced $I-M$ transition takes place from a low-temperature side with increase of field. In other words, under a magnetic field (e.g., below 10 T) the FM state positions at lower temperature than the CO state while vice versa for $Pr_{1-x}Sr_xMnO_3$. The measurement of the magnetization[6] as well as the neutron scattering study[13] under a field proved that the field-induced insulator–metal ($I-M$) transition is accompanied by the metamagnetic (spin-canted antiferromagnetic to ferromagnetic) transition as well as the collapse of the CO state.

The isothermal magnetoresistance (MR) shown in Fig. 3 also clearly indicates the collapse of the CO state under a field, showing a field-induced $I-M$ transition or the so-

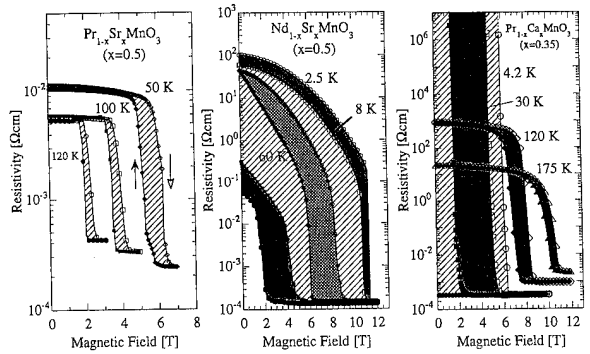


FIG. 3. Isothermal magnetoresistance for $Pr_{1-x}Sr_xMnO_3$ ($x=0.5$, left), $Nd_{1-x}Sr_xMnO_3$ ($x=0.5$, middle) (Ref. 7) and $Pr_{1-x}Ca_xMnO_3$ ($x=0.35$, right) (Ref. 8). Hatches indicate the hysteretic field regions.

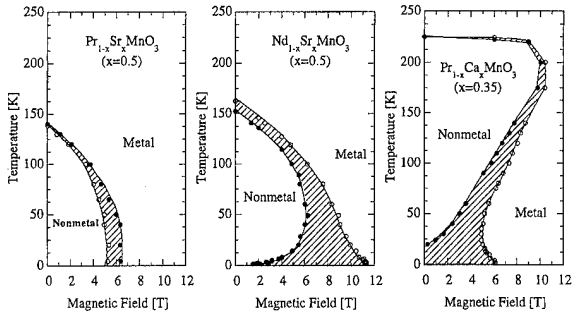


FIG. 4. The electronic phase diagrams in the $T-H$ plane for $Pr_{1-x}Sr_xMnO_3$ ($x=0.5$, left) (Ref. 5), $Nd_{1-x}Sr_xMnO_3$ ($x=0.5$, middle) (Ref. 7) and $Pr_{1-x}Ca_xMnO_3$ ($x=0.35$, right) (Ref. 8).

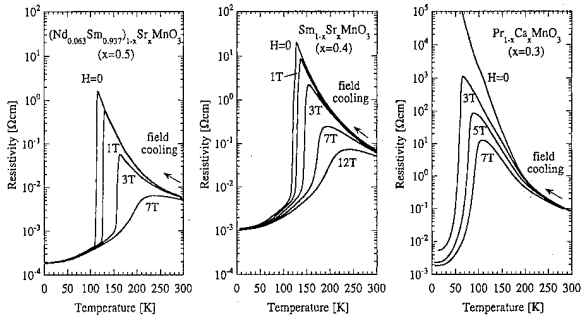


FIG. 5. Temperature dependence of resistivity under magnetic fields for $(Nd_{0.063}Sm_{0.937})_{1-x}Sr_xMnO_3$ ($x=0.5$, left) (Ref. 9). $Sm_{1-x}Sr_xMnO_3$ ($x=0.4$, middle) (Ref. 24) and $Pr_{1-x}Ca_xMnO_3$ ($x=0.3$, right) (Ref. 5) as examples of the striction-coupled first-order phase change to the ferromagnetic metallic state.

called CMR. Reflecting the first-order nature of the CO transition (associated with a change in lattice parameters), the isothermal MR for $Pr_{1-x}Sr_xMnO_3$ ($x=0.5$) in Fig. 3 (left) shows a temperature-dependent hysteresis against the field. The hysteretic field region seems to be gradually expanded with decrease of temperature. Such a first-order nature is more clearly seen for $Nd_{1-x}Sr_xMnO_3$ ($x=0.5$)[7] with a smaller tolerance factor: the hysteretic field region at lower temperature is expanded and even covers those at higher temperatures as indicated by different hatches in Fig. 3 (middle).

The isothermal MR for $Pr_{1-x}Ca_xMnO_3$ ($x=0.35$) is shown in Fig. 3 (right).[8] The resistivity at relatively low temperatures (say, below 40 K) shows a conspicuous change from an insulating value above 10^7 Ω cm to a typical metallic value (3×10^{-4} Ω cm) exceeding ten orders of magnitude. The hysteretic field region is expanded with lowering temperature and the field-induced $I-M$ transition becomes even irreversible below 15 K, as exemplified by the MR curve at 4.2 K in Fig. 3 (right).

On the basis of the isothermal MR data, we have obtained the $I-M$ phase diagram in the $T-H$ plane (Fig. 4) for these prototypical compounds; $Pr_{1-x}Sr_xMnO_3$ ($x=0.5$, left), $Nd_{1-x}Sr_xMnO_3$ ($x=0.5$, middle), and $Pr_{1-x}Ca_xMnO_3$ ($x=0.35$, right). The respective $I-M$ phase boundaries show the temperature-dependent hysteresis against field. The hysteretic field region (indicted by hatches in Fig. 4) is expanded with decrease of temperature, which gives rise to a peculiar shape of phase boundary for $Nd_{1-x}Sr_xMnO_3$ and $Pr_{1-x}Ca_xMnO_3$. This can be interpreted in terms of the suppression of thermal fluctuation effect for the first-order transition.[7,8] The transition of a metastable state is essentially prohibited when thermal energy is much lower than the potential barrier height. The low-temperature metallic phase ("charge liquid" phase) in the $T-H$ plane is thus a sort of supercooled state which is present even at lower temperatures below the "charge crystal" (CO) phase in the $T-H$ plane. In particular, the metallic phase appears to invade toward the low-field region for $Pr_{1-x}Ca_xMnO_3$ ($x=0.35$). This seems to be closely correlated with the discommensuration of the CO state and the resultant change of the spin structure to the canted antiferromagnetic state which is more amenable to an external field than the antiferromagnetic state.

IV. STRICTION-COUPLED MAGNETORESISTANCE

The CO state is located above the FM state at a external field (<10 T) in the case of $Pr_{1-x}Ca_xMnO_3$ ($x=3.5$) as shown in Figs. 3 and 4. The CO transition is always accompanied more or less by a structural change and hence the CO-to-FM transition is of the first order in nature. For $Pr_{1-x}Ca_xMnO_3$ systems, such a phase transition is also seen for the $x=0.3$ crystal[6] (left panel of Fig. 5) in which the CO transition is not so clearly discernible in the temperature dependence of resistivity but of magnetization and can be detected as a structural transition around 200 K.[13] Due to the enhanced discommensuration from $x=0.5$, the low-temperature FM state is produced with a relatively low field, e.g., at 3 T for $Pr_{1-x}Ca_xMnO_3$ ($x=0.3$).

With fine tuning of the discommensuration and/or the tolerance factor, we can realize the first-order CO-to-FM transition with decrease of temperature even at zero field as exemplified in Fig. 5 (left and middle) for $(Nd_{0.063}Sm_{0.937})_{1-x}Sr_xMnO_3$ ($x=0.5$)[9] and $Sm_{1-x}Sr_xMnO_3$ ($x=0.4$),[24] respectively. The former system is derived by further decreasing the tolerance factor (or the one-electron bandwidth) from $Nd_{1-x}Sr_xMnO_3$ while keeping the nominal hole concentration at a commensurate value ($x=0.5$). On the other hand, the latter system may be viewed as derived by increasing the tolerance factor from $Pr_{1-x}Ca_xMnO_3$ while maintaining the discommensuration from $x=0.5$. The inverse magnetization of these compounds shows a Curie–Weiss-like behavior above 250 K but a clear deviation with a slight upturn or plateau below 230–240 K down to T_c.[9] Upon the transition to the FM state, a lattice structural change occurs and the resistivity shows a sharp drop by several orders of magnitude. These are reminiscent of the presence of the CO state above T_c but below 240 K as in the case of $Pr_{1-x}Ca_xMnO_3$ ($x=0.3$)[6,13] under a magnetic field. The first-order transition from such a CO-like state to the FM state is quite sensitive to an external field as shown in Fig. 5 (left and middle). It was confirmed by magnetostriction measurements[9] that the FM transition under a field is also accompanied by a structural change perhaps arising from the field-induced collapse of the CO state. Judging from the phase diagram for $Pr_{1-x}Ca_xMnO_3$ (left panel of Fig. 4), the FM state at low temperatures is mostly the metastable state

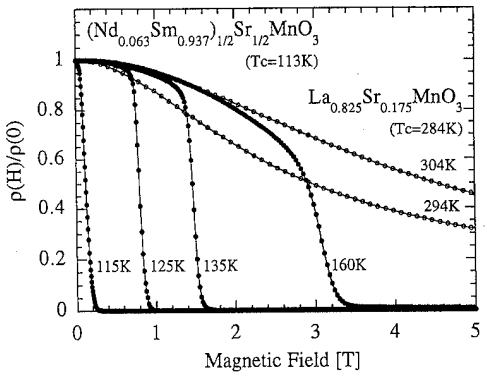


FIG. 6. Isothermal magnetoresistance for a $(Nd_{0.063}Sm_{0.937})_{1-x}Sr_xMnO_3$ ($x=0.5$) (Ref. 9) crystal in comparison with that for a $La_{1-x}Sr_xMnO_3$ ($x=0.17$) crystal near above the respective Curie temperature T_c.

which cannot decay to the thermodynamically stable state (perhaps the antiferromagnetic CO state) due to the aforementioned suppression of the thermal fluctuation at low temperatures.

Reflecting the first-order nature of the CO–FM transition at T_c, the striction-coupled MR shows a switching-like behavior near above T_c (113 K), as exemplified for $(Nd_{0.063}Sm_{0.937})_{1-x}Sr_xMnO_3$ ($x=0.5$) in Fig. 6. For comparison, the isothermal MR is also plotted for $La_{1-x}Sr_xMnO_3$ ($x=0.175$) near T_c. As compared with the conventional MR for this compound, the striction-coupled MR change for $(Nd_{0.063}Sm_{0.937})_{1-x}Sr_xMnO_3$ ($x=0.5$) is quite remarkable: The resistivity drop associated with the phase change is more than three orders of magnitude as seen in Fig. 5 and hence appears to reach nearly zero level in such a linear-scale plot as Fig. 6. The switching-like CMR is observed, though accompanied by the hysteresis (not shown in Fig. 6), even at a low field as far as the temperature is close to T_c. The phenomena may have potential for some application to magnetoswitching materials and devices.

V. CONCLUSION

We have briefly reviewed our recent studies on the CMR phenomena of perovskite-type manganese oxides with use of single crystals in which the tolerance factor and the nominal hole concentration are finely controlled. It was proved by the systematic investigation on the magnetotransport and related magnetic and structural properties that the collapse of the charge-ordered insulating state under an external field is closely correlated with the field-induced colossal change of resistivity accompanying a release of the striction. Both the tolerance factor (or equivalently the one-electron bandwidth of the e_g carriers) and the nominal hole concentration x affect crucially the metal-insulator phase diagram in the $T-H$ plane which is modified as a result of the competition between the double-exchange and charge-ordering interactions.

ACKNOWLEDGMENTS

We would like to thank H. Yoshizawa and H. Kawano for enlighting discussions. This work was supported by the New Energy and Industrial Technology Development Organization (NEDO) of Japan and by a Grant-In-Aid for Scientific Research from the Ministry of Education, Science and Culture, Japan.

[1] C. W. Searle and S. T. Wang, Can. J. Phys. **47**, 2703 (1969).
[2] K. Kubo and N. Ohata, J. Phys. Soc. Jpn. **33**, 21 (1972).
[3] S. Jin, T. H. Tiefel, M. McCormack, R. A. Fastnacht, R. Ramesh, and L. H. Chen, Science **264**, 413 (1994).
[4] G. C. Xiong, Q. Li, H. L. Ju, S. N. Moo, L. Senapati, X. X. Xi, R. L. Greene, and T. Venkatesan, Appl. Phys. Lett. **66**, 1427 (1995).
[5] Y. Tomioka, A. Asamitsu, Y. Moritomo, H. Kuwahara, and Y. Tokura, Phys. Rev. Lett. **74**, 5108 (1995).
[6] Y. Tomioka, A. Asamitsu, Y. Moritomo, and Y. Tokura, J. Phys. Soc. Jpn. **64**, 3626 (1995).
[7] H. Kuwahara, Y. Tomioka, A. Asamitsu, Y. Moritomo, and Y. Tokura, Science, **270**, 961 (1995).
[8] Y. Tomioka, A. Asamitsu, H. Kuwahara, Y. Moritomo, and Y. Tokura, Phys. Rev. B **53**, R1689 (1996).
[9] H. Kuwahara, Y. Tomioka, Y. Moritomo, A. Asamitsu, M. Kasai, R. Kumai, and Y. Tokura, (to be published).
[10] Z. Jirak, S. Krupicka, V. Nekvasil, E. Pollert, G. Villeneuve, and F. Zounova, J. Magn. Magn. Mater. **15–18**, 519 (1980).
[11] Z. Jirak, S. Krupicka, Z. Simsa, M. Dlouha, and Z. Vratislav, J. Magn. Magn. Mater. **53**, 153 (1985)
[12] K. Knizek, Z. Jirak, E. Pollert, F. Zounova, and S. Vratislav, J. Solid State Chem. **100**, 292 (1992).
[13] H. Yoshizawa, H. Kawano, Y. Tomioka, and Y. Tokura (to be published).
[14] Y. Moritomo, Y. Tomioka, A. Asamitsu, and Y. Tokura, Phys. Rev. B **51**, 3297 (1995).
[15] B. J. Sternlieb, J. P. Hill, U. C. Wildgruber, G. M. Luke, B. Nachumi, Y. Moritomo, and Y. Tokura (to be published).
[16] H. Y. Hwang, S.-W. Cheong, P. G. Radaelli, and B. Batlogg, Phys. Rev. Lett. **75**, 914 (1995).
[17] G. H. Jonker, Physica **16**, 337 (1950).
[18] Y. Tokura, A. Urushihara, Y. Moritomo, T. Arima, A. Asamitsu, G. Kido and N. Furukawa, J. Phys. Soc. Jpn. **63**, 3931 (1994).
[19] A. Urushihara, Y. Moritomo, T. Arima, A. Asamitsu, G. Kido, and Y. Tokura, Phys. Rev. B **51**, 14103 (1995).
[20] E. O. Wollan and W. C. Koehler, Phys. Rev. **100**, 545 (1955).
[21] A. J. Millis, P. B. Littlewood, and Boris I. Shraiman, Phys. Rev. Lett. **74**, 5144 (1995); A. J. Millis, Boris I. Shraiman, and R. Mueller (to be published).
[22] A. Asamitsu, Y. Moritomo, Y. Tomioka, T. Arima, and Y. Tokura, Nature **373**, 407 (1995).
[23] M. Tokunaga, N. Miura, Y. Tomioka, and Y. Tokura (unpublished).
[24] Y. Tomioka and Y. Tokura (unpublished).

Colossal magnetoresistivity in manganese-based perovskites (invited) (abstract)

R. Ramesh, T. Venkatesan, S. B. Ogale, R. L. Greene, and S. M. Bhagat
Center for Superconductivity Research, University of Maryland, College Park, Maryland 20742

Magnetoresistivity values of the order of 10^6% (and in some cases even higher) have been obtained in epitaxial $A_xB_{1-x}MnO_{3-y}$ (A=La,Nd; B=Ca,Sr,Ba) thin films grown by pulsed laser deposition. Ferromagnetic resonance experiments suggest a granular-type behavior with conducting ferromagnetic regions (R_{cond}<10 mΩ cm) in a less conducting matrix ($R_{insulazting}$>100.R_{cond}). Ion channeling experiments over a range of temperatures clearly reveal the existence of structural distortion at the peak resistivity temperature T_P. Systematic studies of samples prepared under a variety of oxygenation conditions show that the resistivity above T_P can be modeled with a single functional form: $R_{cond}\approx e^{\Delta/kT}$, where Δ, the activation energy, is of the order of 50–200 meV. This suggests that these different samples represent the same basic material in a semiconducting matrix, with differing volume fractions of the two components which depends on the processing conditions. These "colossal" values of MR have been obtained at temperatures lower than room temperature and at fields of the order of a few Teslas, both of which are impediments to the development of viable MR sensor and nonvolatile storage technologies. We are therefore addressing the critical scientific and technological issues through a variety of materials integration approaches. Using structural chemistry and lattice matching as fundamental guiding principles, we are growing epitaxial heterostructure superlattices consisting of the CMR oxides interleaved with magnetic perovskites such as La–Sr–Co–O (metallic ferromagnet), rare earth–Fe–O (ferromagnetic insulator). We are also exploring the possibility of using the semiconducting properties of these materials in an all-perovskite field effect transistor device. In this presentation, we will describe our progress to date on these studies to enhance the field and temperature dependence of the MR properties and explore new device architectures that utilize the inherently novel properties of these materials. © *1996 American Institute of Physics.* [S0021-8979(96)60608-4]

 0021-8979/96/79(8)/5292/1/$10.00 © 1996 American Institute of Physics

Magnetic properties of monodomain Nd-Fe-B-C nanoparticles

E. M. Brunsman, J. H. Scott, and S. A. Majetich[a)]
Department of Physics, Carnegie Mellon University, Pittsburgh, Pennsylvania 15213-3890

M. E. McHenry and M.-Q. Huang
Department of Materials Science and Engineering, Carnegie Mellon University, Pittsburgh, Pennsylvania 15213-3890

Nanoparticles of Nd-Fe-B-C with their crystal structure similar to the $Nd_2Fe_{14}B$ phase were generated in a carbon arc. With an average diameter of less than 40 nm, they are monodomain. They have a smaller room-temperature coercivity than would be predicted from the bulk magnetocrystalline anisotropy. However, their coercivity is greater than was previously observed in particles <5 μm prepared by spark erosion. While the carbon arc process is useful for making small carbon-coated particles which resist oxidation, here dispersion of excess Nd in the carbon matrix results in a significant paramagnetic signal. The dc demagnetization curves enable the paramagnetic and ferromagnetic contributions to be distinguished. © *1996 American Institute of Physics.* [S0021-8979(96)40308-8]

I. INTRODUCTION

Fine particle magnetism has been an active field for many years.[1–3] Experimental support for this theory has been obtained for a variety of ferromagnetic fine particles.[4] However, since this time there have been significant developments both in permanent magnet materials and in fine particle synthesis. Here we combine two of these breakthroughs, the high magnetocrystalline anisotropy alloy neodymium iron boron and the carbon arc process[5] for preparing nanocrystals,[6] and analyze the magnetic properties of the resulting monodomain particles.

Bulk neodymium iron boron magnets have the highest known energy product of any permanent magnet material.[7] This ternary alloy is quite complex. Boron is present to stabilize the hard magnetic phase, tetragonal $Nd_2Fe_{14}B$.[8] Sintered magnets frequently have a secondary α-Fe phase of approximately 10 nm thickness at the grain boundaries,[9] which may be significant in the oxidation which plagues these materials. At low temperatures, bulk $Nd_2Fe_{14}B$ also undergoes a spin reorientation transition at 135 K.[10] The magnetic properties of the related materials, $Nd_2Fe_{14}B_{.5}C_{.5}$ and $Nd_2Fe_{14}C$, have also been reported.[11]

Several groups have prepared micron-sized particles of Nd-Fe-B alloys, by spark erosion in liquid argon,[12] by ball milling,[13] and by heat treatment of metal and oxide powders.[14] In all of these materials the particle sizes were on the order of microns, and they therefore contained multiple magnetic domains. The coercivities measured were significantly smaller than in the bulk material.

Monodomain particles of Nd-Fe-B-C are of interest to test the model of size-dependent coercivity.[15] The maximum size for a single magnetic domain has been estimated at ~200 nm for $Nd_2Fe_{14}B$.[16] The carbon arc process has been applied to a variety of metals and alloys to prepare nanoparticles in the 5–50 nm size range, well below the single domain threshold. The carbon coating of the nanoparticles is also an advantage in preventing oxidation. Cobalt particles made by this method have been boiled in sulfuric acid without reaction.[17] We have recently demonstrated the use of electron spectroscopic imaging to obtain elemental maps on a nanometer scale,[18] which could enable us to detect nanometer-scale phase separation in this alloy. With this new approach to synthesis and and a new tool to characterize chemical inhomogeneity, we sought to understand the behavior of these monodomain magnets.

II. EXPERIMENT

Nanoparticles embedded in a carbon matrix were prepared by a variation of the Huffman–Krätschmer carbon arc process.[5] To make the nanoparticles, a composite anode was made from graphite and 30 wt % Nd-Fe-B (Crucible, Inc.), with dextrin as a binder. Though this method has been used to prepare other materials with up to 70 wt % metal,[19] a 30 wt % metal fraction was studied here. The composite anode was combined with a graphite cathode in a carbon arc (30 V dc, 100 A, 500 Torr He), and vaporized. The nanoparticles were collected as a powder from the reactor walls.

The nanoparticle morphology was determined through a combination of transmission electron microscopy (TEM) and x-ray diffraction (XRD) measurements on as-prepared and annealed powder samples. Electron spectroscopic imaging (ESI) of an annealed sample was done with a Gatan Imaging Filter attachment to a JEOL 4000 EX electron microscope. In this technique a combination of high-resolution imaging and electron energy loss spectrometry is used to generate elemental maps.

For magnetic measurements, the powders were dispersed in epoxy and placed in a Quantum Design SQUID magnetometer at fields between ± 5 kOe for temperatures ranging

a)Author to whom correspondence should be addressed.

 0021-8979/96/79(8)/5293/3/$10.00 © 1996 American Institute of Physics

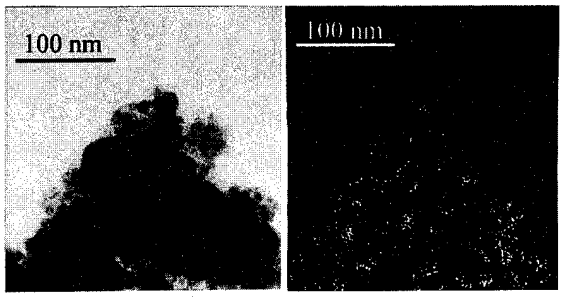


FIG. 1. Left: TEM of carbon-coated Nd-Fe-B-C nanoparticles. Dark spheroidal regions are the nanoparticles and smaller spheres are part of the amorphous carbon matrix. Right: electron spectroscopic imaging of the same sample, showing the distribution of Nd. The corresponding Fe map shows that only the nanoparticles contain iron.

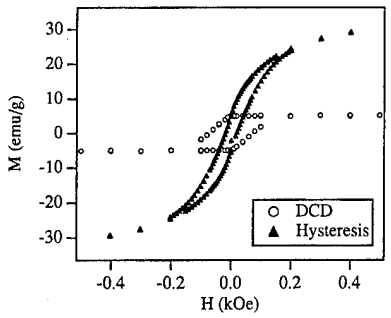


FIG. 2. Ordinary hysteresis loop for Nd-Fe-B-C nanoparticles, and dc demagnetization curve for the same sample.

from 2 to 300 K. The diamagnetic contributions of the epoxy and carbon matrix were measured separately and subtracted from the magnetization data. Due to the possibility of additional paramagnetic contributions from Nd carbides, the dc demagnetization (DCD) curves[20] were also measured. Here the sample was first saturated and then subjected to an increasingly negative field. The remanent magnetization, M_r, is measured after the field is removed.

III. RESULTS AND DISCUSSION

The carbon arc process generated gram quantities of spherical nanoparticles well below the monodomain threshold. The particles were embedded in an amorphous carbon matrix, and followed a log-normal size distribution, with an average radius of 18.2 nm and a standard deviation of 1.9 nm.

The sample was annealed in argon for 12 h at 900 °C, without increasing the average particle size determined by TEM. Several x-ray diffraction peaks similar to those in the $Nd_2Fe_{14}B$ phase emerged: (410), 100%, 2θ=42.4°; (411), 64%, 43.5°; (314), 77%, 44.6°, though not all of the prominent features were detected. No evidence of α-Fe, NdC_2, or $Nd_3Fe_{20}C_x$ (Ref. 21) was observed. Nominal $Nd_2Fe_{14}C$ is actually a mixture of rhombohedral $Nd_2Fe_{17}C_x$ and α-Fe,[11] and is inconsistent with our data. The most likely structure is an alloy similar to $Nd_2Fe_{14}B$, but containing a mixture of B and C.

Electron spectroscopic imaging was used to obtain Nd (Fig. 1) and Fe maps in an annealed sample. While the iron was localized within the nanoparticles, we found that Nd was distributed throughout both the particles and the matrix. In the matrix, it presumably took the form of NdC_2 or Nd_2C_3 clusters too small to be detectable by XRD. These species are paramagnetic and therefore contribute to the overall magnetization, but not to the remanence or coercivity. We saw no evidence of a Nd-deficient layer near the nanoparticle surface as found in the bulk material, or for a mixture of Nd-Fe and α-Fe phases. No oxygen was detected in these samples, verifying that the carbon coating protects the nanoparticles from oxidation. While this technique is extremely useful for measuring elemental abundances on a nanometer scale, this is not yet a quantitative technique. It could not be used to determine the exact stoichiometry, because the carbon signal could arise from either dissolved carbon in the nanoparticles or from the carbon coating which surrounds them.

The hysteresis loops for the Nd-Fe-B-C nanoparticles show coercivity even at room temperature (Fig. 2), but H_c is considerably smaller than would be predicted from the particle size and the room-temperature anisotropy of the bulk material. For a sample prepared from 30 wt % Nd-Fe-B starting material, M_s=49.5 emu/g, M_r=14.2 emu/g, and H_c=830 Oe at 5 K. The switching field distribution showed no indication of multiple phases with widely differing coercivities. The remanent magnetization dropped sharply with temperature up to approximately 45 K, and continued to drop more slowly up to room temperature. This contrasts with a maximum in the magnetization at ~100 K in bulk $Nd_2Fe_{14}B_{0.5}C_{0.5}$, which has a spin reorientation temperature of 128 K.[11]

The difference between the saturation and remanent magnetizations is greater than the factor of two expected for random ordering, but consistent with a large paramagnetic contribution from the neodymium carbide clusters. DCD measurements (Fig. 2) showed similar values for M_r, but smaller values of M_s and larger values of H_c (1500 Oe at 5 K) because the paramagnetic contributions were absent. The magnetization reversal of the paramagnetic fraction before that of the ferromagnetic particles reduces the overall magnetization and shifts the field for which M=0, thereby reducing the measured coercivity. Efforts to model the DCD curves are underway.

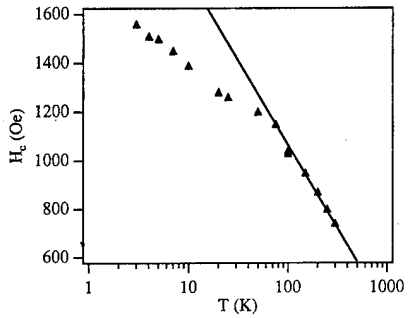


FIG. 3. The dc demagnetization curve coercive field as a function of temperature. Fit to high-temperature data indicates an (A-$BT^{0.28}$) dependence, where A and B are constants.

In spherical particles of $Nd_2Fe_{14}B$, magnetocrystalline anisotropy is expected to dominate the shape anisotropy in determining the field required for magnetization reversal. Stoner–Wohlfarth theory[2] predicts that below the blocking temperature, T_B, the lowest temperature at which the coercivity equals zero, H_c will obey at $T^{1/2}$ power law. Experimentally we observe a $T^{0.28}$ dependence of the measured coercivity (Fig. 3) above 75 K and a $T^{0.17}$ dependence below it. Because the anisotropy energy density of bulk $Nd_2Fe_{14}B_{0.5}C_{0.5}$ changes sign at low temperature,[11] the Stoner–Wohlfarth model cannot be used to quantitatively interpret the results. A temperature dependence T^x with $x<0.5$ has been observed in nanocrystalline materials with interacting grains, and here we may have some interactions between nanoparticles. Studies in lower abundance samples are underway.

IV. CONCLUSIONS

High coercivity monodomain nanoparticles of Nd-Fe-B-C in a carbon matrix have been prepared by the carbon arc process. Structural and chemical characterization indicates the presence of a phase similar to that of $Nd_2Fe_{14}B$, probably containing carbon. Neodymium was found to be dispersed throughout the carbon matrix, leading to a significant paramagnetic contribution to the magnetic results, and making dc demagnetization measurements essential for measuring the magnetic behavior of the nanoparticles. While the measured coercivity is greater than previously reported for micron-sized particles, it is still far below the value predicted from the bulk anisotropy energy density.

ACKNOWLEDGMENTS

The NSF has supported this research through Grants No. DMR-9258450 (S.A.M.), No. DMR-9258308 (M.E.M.), and No. DMR-95000313 (S.A.M. and M.E.M). This work is also based (in part) upon work supported by the NSF under Grants No. ECD-8907068 and No. DMR-9403621. We would like to thank Dr. A. Kim of Crucible, Inc. for providing Nd-Fe-B powder starting material. The participation of the CMU Buckyball Project members have been extremely helpful.

[1] L. Néel, Ann. Geophys. **5**, 99 (1949); C. R. Acad. Sci. **228**, 664 (1949).
[2] E. C. Stoner and E. P. Wohlfarth, Philos. Trans. R. Soc. London **240**, 599 (1948).
[3] W. F. Brown, Jr., J. Appl. Phys. **29**, 470 (1958); **30**, Suppl. 130S (1959).
[4] F. E. Luborsky, J. Appl. Phys. **32**, Suppl. 171S (1961).
[5] W. Krätschmer, L. D. Lamb, K. Fostiropoulos, and D. R. Huffman, Nature **347**, 354, (1990).
[6] S. A. Majetich, J. O. Artman, M. E. McHenry, N. T. Nuhfer, and S. W. Staley, Phys. Rev. B **48**, 16845 (1993).
[7] R. A. McCurrie, *Ferromagnetic Materials: Structure and Properties* (Academic, New York 1994), Chap. 5, p. 278.
[8] R. A. McCurrie, Ferromagnetic Materials: Structure and Properties (Academic, New York, 1994), Chap. 5, p. 271.
[9] S. Hirosawa, K. Tokuhara, Y. Matsuura, H. Yamamoto, S. Fujimura, and M. Sagawa, J. Magn. Magn. Mater. **61**, 363 (1986).
[10] J. Hu, X. C. Kou, and H. Kronmüller, Phys. Status Solidi A **138**, K41 (1993).
[11] X. C. Kou, X. K. Sun, Y. C. Chuang, R. Grössinger, and H. R. Kirchmayr, J. Magn. Magn. Mater. **80**, 31 (1989).
[12] H. Wan and A. E. Berkowitz, Scr. Metall. Mater. **32**, 1827 (1995).
[13] S. Ram and J. C. Joubert, J. Appl. Phys. **72**, 1164 (1992).
[14] A. Ahmad, P. J. McGuiness, and I. R. Harris, IEEE Trans. Magn. **26**, 2625 (1990).
[15] G. Herzer, IEEE Trans. Magn. **26**, 1397 (1990); J. Magn. Magn. Mater. **112**, 258 (1992).
[16] K. D. Durst and H. Kronmüller, J. Magn. Magn. Mater. **59**, 86 (1986); **68**, 63 (1987).
[17] S. A. Majetich, J. H. Scott, E. M. Brunsman, M. E. McHenry, and D. C. Winkler, *Fullerenes: Physics, Chemistry, and New Directions VII*, edited by R. S. Ruoff and K. M. Kadish (The Electrochemical Society, Pennington, NJ, 1995), p. 584.
[18] J. H. J. Scott and S. A. Majetich, Appl. Phys. Lett. (unpublished)
[19] J. H. Scott and S. A. Majetich, Phys. Rev. B **52**, 12564 (1995).
[20] S. Gangopadhyay, G. C. Hadjipanayis, C. M. Sorensen, and K. J. Klabunde, IEEE Trans. Magn. **29**, 2619 (1993).
[21] L. Sheng, Z. Lui, Z. Guowei, P. Xiedi, J. Wei, and H. Wenwang, IEEE Trans. Magn. **23**, 3095 (1987).

Magnetic properties and imaging of Mn-implanted GaAs semiconductors

Jing Shi, J. M. Kikkawa, and D. D. Awschalom
Department of Physics, University of California at Santa Barbara, Santa Barbara, California 93106

G. Medeiros-Ribeiro and P. M. Petroff
Department of Materials, University of California at Santa Barbara, Santa Barbara, California 93106

K. Babcock
Digital Instruments, Santa Barbara, California 93111

Submicron ferromagnets have been successfully incorporated into GaAs semiconductors by Mn^+ ion implantation and subsequent heat treatment. Transmission electron microscopy, x-ray fluorescence spectrum analysis, and atomic force microscopy are used to structurally characterize the GaMn precipitates which form within the GaAs matrix. These crystallites are room-temperature ferromagnets with controllable magnetic properties. Magnetic force microscopy images reveal that unmagnetized samples contain both magnetic dipoles and quadrupoles, but that after magnetization the single-domain state predominates. © *1996 American Institute of Physics.*
[S0021-8979(96)04708-6]

Spin-dependent phenomena seen in metallic multilayers and granular systems have raised basic questions about carrier magnetism and are currently finding technological applications.[1,2] Effects such as giant magnetoresistance are highly desirable in semiconducting hosts, as such materials would offer great potential for exploring carrier spin scattering because the carrier densities are tunable through a wide range and their spatial confinement is easily controlled. These systems may then enable new magnetoelectronic and magneto-optical devices.[3] To this end, we have successfully incorporated submicron room temperature ferromagnets into semiconductor materials by a simple process of ion implantation and subsequent heat treatment.[4] Herein we present structural and magnetic characterizations of this new system.

The semiconductor samples are grown by molecular beam epitaxy (MBE) on semi-insulating GaAs substrates and consist of 500 nm undoped GaAs epilayers grown atop 50 nm AlAs and a 500 nm GaAs buffer. These structures are then uniformly implanted to depths of several hundred nanometers with Mn^+ ions at energies of 50 and 200 keV and doses ranging from 1×10^{14} to 5×10^{16} Mn^+/cm^2. For comparison with MBE-grown materials, semi-insulating GaAs substrates are also implanted with comparable doses. To magnetically activate the implanted ions, the samples are covered with Si substrates and annealed in a forming gas (90% N_2, 10% H_2) at temperatures from 600 to 920 °C for durations ranging from 5 s to 20 min. Both annealed and unannealed samples are thinned chemically and by ion milling for transmission electron microscopy (TEM) study. Electron microdiffraction and electron-beam-induced x-ray fluorescence spectroscopy are also employed for structural and compositional analysis. For magnetization measurements only, the GaAs substrate is removed to reduce the diamagnetic background. Etching the thin AlAs slab in diluted hydrofluoric acid[5] releases the 500-nm-thick implanted surfaces from the substrate, and magnetization measurements of the resulting films are obtained from a rf SQUID magnetometer in fields up to 5 T and temperatures ranging from 5 to 400 K. Atomic force microscopy (AFM) and magnetic force microscopy (MFM) are employed at room temperature to spatially probe both topography of the sample surfaces and the local magnetic fields generated by the submicron magnetic structures. Both unmagnetized and magnetized samples are studied by MFM in zero applied magnetic field. Furthermore, an electromagnet with fields up to 8 kOe enables MFM imaging in a variable magnetic field. Micromagnetic behavior of the submicron ferromagnets has been studied in applied magnetic fields and the results will be reported elsewhere.[6]

Figure 1(a) is a plan-view TEM micrograph taken on an

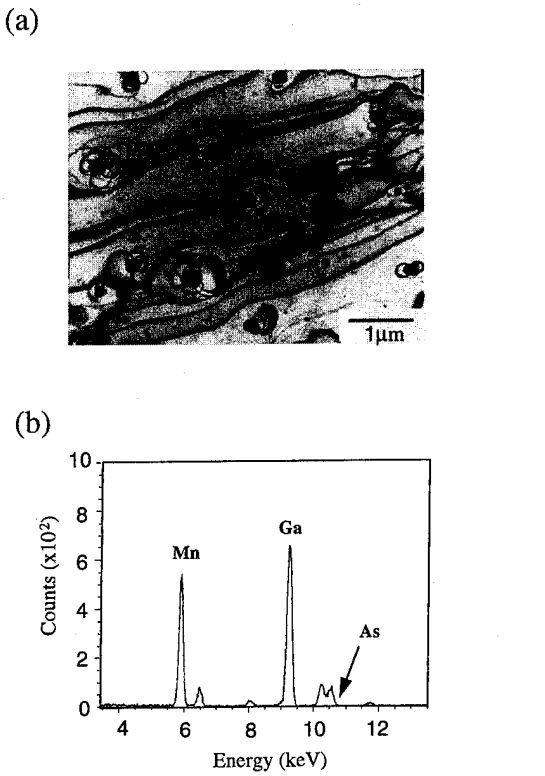


FIG. 1. (a) Plan-view TEM micrograph for a 1×10^{16} Mn^+/cm^2 sample implanted at 200 keV and annealed at 920 °C for 60 s. (b) Electron-induced x-ray fluorescence spectrum taken on a single precipitate in (a). Semiquantitative analysis indicates that it contains 60% Ga and 40% Mn. The small As signal is from the GaAs substrate.

 0021-8979/96/79(8)/5296/3/$10.00 © 1996 American Institute of Physics

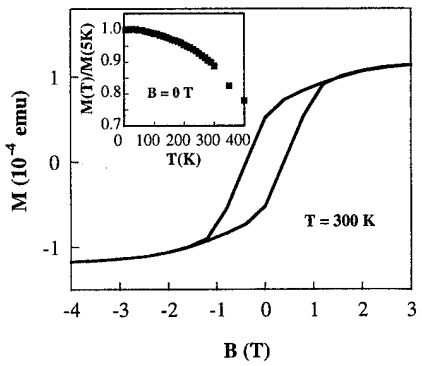


FIG. 2. SQUID magnetization data (300 K) of a 5×10^{16} Mn^+/cm^2 sample annealed at 920 °C for 60 s (the diamagnetic background has been removed). The inset shows the normalized remanent magnetization, $M(T)/M(5\ K)$, as a function of temperature.

Mn^+-implanted (10^{16} ions/cm^2) and annealed (920 °C for 60 s) GaAs sample. The dark spots seen in the picture are second phase precipitates which only appear in the annealed samples, whereas the dark streaks appearing elsewhere are strain-induced bend contours within the GaAs substrate. The precipitates are about 200 nm in diameter with an average separation of about 1.5 μm. An x-ray fluorescence spectrum taken on one of these precipitates is shown in Fig. 1(b). Although a small As peak is present in this plan-view spectrum, similar spectra taken on precipitates in cross-sectional TEM samples show no As contribution, indicating that the As signal comes from the GaAs substrate only. Semiquantitative compositional analysis indicates that the Ga:Mn atomic ratio is about 60:40. Cross-sectional TEM study[4] of annealed samples reveals that GaMn precipitates pierce the implanted surface, enabling monitoring of precipitate formation by AFM.

Bulk magnetization measurements of the 500 nm implanted GaAs epilayers reveals room-temperature ferromagnetism. Figure 2 shows a magnetic hysteresis loop at 300 K arising from a sample implanted at 5×10^{16} Mn^+ and annealed at 920 °C for 60 s. The coercivity H_c is about 5 kOe at 300 K and is relatively insensitive to temperature. The inset shows remanent magnetization M_R (normalized at 5 K) as a function of temperature from 5 to 400 K. At 400 K, M_R drops to about 77% of its low-temperature value, implying that the Curie temperature is significantly higher than room temperature. In contrast, both (1) unimplanted and annealed and (2) implanted and unannealed controls are nonferromagnetic.

To study how this ferromagnetism develops throughout the annealing process, a series of implanted samples (1×10^{16} Mn^+/cm^2) is prepared under different annealing conditions. The resulting coercivities appear in Table I and show a peculiar trend. At the highest temperature of 920 °C, longer annealing times result in lower coercive fields. Yet at an intermediate temperature of 800 °C, longer annealing produces *higher* coercivities. Finally, at 600 °C for 60 s, the hysteresis loop vanishes and the magnetization data can be fit to a Brillouin function. Results obtained from the Brillouin fit indicate that single or few spin complexes contribute to the paramagnetic behavior. The dependence of H_c on annealing conditions is not presently known, and may arise from changing crystalline structures (crystalline anisotropy) or from differences in interfacial strain between the GaMn precipitates and the GaAs substrate (strain anisotropy).

TABLE I. Coercive field H_c vs annealing condition for GaAs samples implanted with 10^{16} Mn^+/cm^2.

Annnealing	H_c (kOe)	Annealing	H_c (kOe)
920 °C, 5 min	<0.5	800 °C, 20 min	5
920 °C, 1 min	0.5	800 °C, 60 s	1
920 °C, 5 s	7	800 °C, 5 s	1

Room-temperature MFM measurements directly confirm that the ferromagnetism originates from the GaMn precipitates. Figure 3(a) is a topographic image of an area in a sample receiving 10^{15} Mn^+/cm^2, and Fig. 3(b) is a magnetic force image of the same area. The sample used for this imaging is unmagnetized and images are taken at zero applied magnetic field with a vertically magnetized Co-Cr coated tip. The bright and dark areas in Fig. 3(b) correspond to regions where the magnetic force acting on the MFM tip is repulsive and attractive, respectively. Although a one-to-one correspondence can be found between the two images, there are apparently three types of patterns in the magnetic force im-

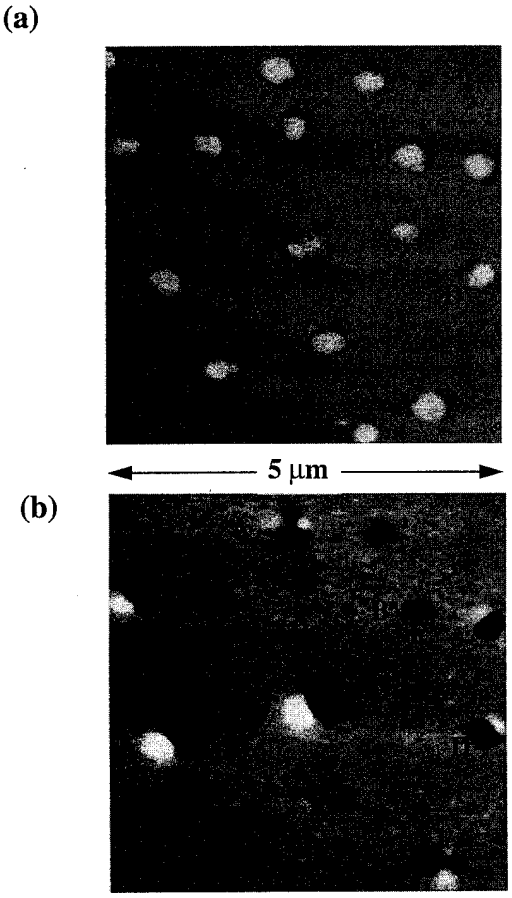


FIG. 3. (a) Zero-field topographic and (b) magnetic force images of the same area on an unmagnetized 1×10^{15} Mn^+/cm^2 sample annealed at 920 °C for 60 s.

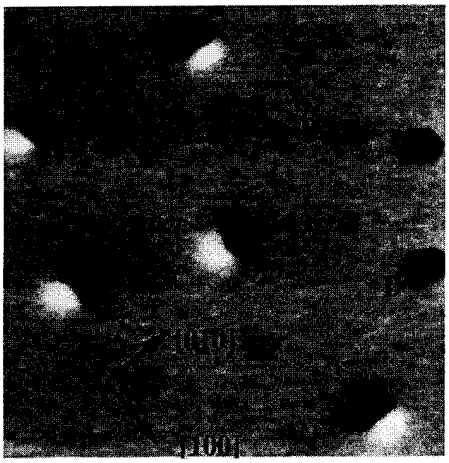


FIG. 4. Zero-field magnetic force image of the same area after the sample used in Fig. 3 is magnetized in a 2 kOe field outside of the MFM. The field applied is perpendicular to the sample surface.

age, indicative of different micromagnetic states. One type of pattern, appearing at particle "A" of Fig. 3(b), contains two bright-dark pairs. With a vertically magnetized MFM tip as used in this image, simulations of dipole-dipole interactions between tip and sample indicate that this type of pattern can only arise from a magnetic quadrupole. Another type of pattern, at "B," shows a relatively weak contrast. The sensitivity of our apparatus ensures that this signal is magnetic in nature, and the attractive interaction between the tip and these precipitates suggests a paramagnetic or superparamagnetic response to the stray field (~500 Oe) of the MFM tip. The third type of pattern, at "C" and "D," consists of two opposite magnetic poles and represents a magnetic dipole whose magnetic moment is not parallel to that of the MFM tip. Since the tip used for this imaging has been magnetized normal to the sample surface, symmetric bright-dark patterns as seen in "C" correspond to single-domain particles whose magnetic moment lies in the surface plane. Asymmetric patterns such as that in "D" correspond to single-domain precipitates with moments tilted out-of-plane.

A magnetic force image is obtained in the same area shown in Fig. 3 after removing the sample from the microscope, magnetizing it with the ~2 kOe stray field of a permanent magnet, and subsequently replacing it. Distinct differences can be found between the images of the unmagnetized and magnetized samples (Fig. 4). First, magnetic quadrupoles such as that previously seen at "A" have been converted to dipoles. The quadrupole-to-dipole conversion indicates that the single-domain state is a magnetically stable state for the submicron GaMn structures. Furthermore, this conclusion also holds for samples implanted with other doses. Second, the dipoles whose magnetic moments are initially at angles to the surface have switched to the field direction and appear as dark spots (e.g., "D"), while magnetic moments of the planar dipoles remain unchanged (e.g., "C").

Upon the application and removal of a magnetizing field, the moments of single-domain particles align with the field and relax into locally stable energy minima; they remain locked along easy axes after the field is removed. As described by the Stoner–Wohlfarth coherent rotation model,[7] there is no hysteretic behavior for the particles with their easy axes perpendicular to the applied field, and thus, their moments will rotate back to the initial state after the vertical field is removed. Accordingly, we do not observe any change in contrast for planar magnetic moments, such as particle "C," after the sample is magnetized. A survey of larger areas in the magnetized sample shows that the easy axes of 80% of the GaMn particles align preferentially along three equivalent ⟨001⟩ directions of the GaAs substrate, as demonstrated in Fig. 4. However, we do not observe such preferential orientations in samples implanted with the highest dose. To study how a magnetic moment dynamically responds to a field for various easy axis orientations, we have constructed an electromagnet which can provide lateral magnetic fields up to 8 kOe while magnetic force imaging is performed *in situ*. Since the magnetic state of MFM tips also changes in lateral fields, it is impossible to interpret the actual images without knowing the response of the tip magnetization. We have used fine current strips as a magnetic field standard and obtained three components of the MFM tip magnetization vector vs. an applied magnetic field. The detailed micromagnetic study of MFM tips will be reported separately.[6,8]

In summary, annealing crystallizes submicron GaMn ferromagnets within Mn^+-implanted GaAs. Bulk magnetization measurements indicate that the Curie temperature of the GaMn precipitates exceeds room temperature. The coercivity of GaMn ferromagnets can be tuned over a wide range by varying annealing conditions. MFM measurements demonstrate that these magnetically stable submicron ferromagnets are single-domain particles with easy axes aligned preferentially along the ⟨001⟩ directions in magnetized lower dose samples.

This work was supported in part by grants from the Air Force Office of Scientific Research, the National Science Foundation Division of Materials Research, the NSF Materials Research Laboratory, and the QUEST NSF Center for Quantized Electronic Structures. J. M. Kikkawa acknowledges support of a Parsons Foundation Fellowship.

[1] S. S. P. Parkin, R. Bhadra, and K. P. Roche, Phys. Rev. Lett. **66**, 2152 (1991); A. E. Berkowitz, J. R. Mitchell, M. J. Carey, and A. P. Young, *ibid.* **68**, 3745 (1992); J. Q. Xiao, J. S. Jiang, and C. L. Chien, *ibid.* **68**, 3749 (1992).
[2] J. Daughton and Y. J. Chen, IEEE Trans. Magn. **29**, 6 (1993).
[3] G. Prinz, Science **250**, 1092 (1990).
[4] J. Shi, J. M. Kikkawa, R. Proksch, T. Schaeffer, D. D. Awschalom, G. Medeiros-Riberio, and P. M. Petroff, Nature **377**, 707 (1995).
[5] E. Yablonovitch, T. Gmitter, J. P. Harbison, and R. Bhat, Appl. Phys. Lett. **51**, 2222 (1987).
[6] J. Shi, K. Babcock, and D. D. Awschalom (in preparation).
[7] E. C. Stoner and E. P. Wohlfarth, Philos. Trans. R. Soc. London, Ser. A **240**, 599 (1948).
[8] K. Babcock, J. Shi, D. D. Awschalom, and P. M. Petroff (in preparation).

Finite size effects in nanoscale Tb particles

D. Johnson, P. Perera, and M. J. O'Shea
Cardwell Hall, Department of Physics, Kansas State University, Manhattan, Kansas 66506-2601

Tb nanoscale particles are prepared in a matrix of Ti by sputtering. A range of samples are made with average particle diameter ranging from 1.5 to 21 nm. The magnetic transition temperature is depressed for smaller particles due to finite size effects. The coercivity at 4.5 K shows a maximum of 22 kOe at approximately 7 nm being a factor of 2.4 larger than a thick film of Tb. We compare the coercivity of our particle samples to multilayers of the form Tb/Mo and find larger coercivity in the particle systems due to the more confined geometry of the particles. © *1996 American Institute of Physics.* [S0021-8979(96)04808-2]

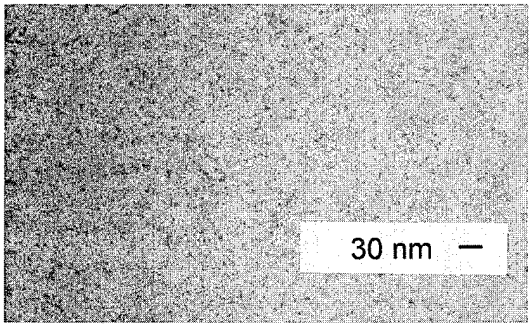
We report a systematic study of the magnetic properties of nanoscale particles of the rare-earth Tb prepared in a matrix of Ti as a function of particle diameter. It has been known for some time that the magnetism of nanoscale particles is influenced by the presence of a large amount of interface and by their small (finite) size.[1–3] Our purpose here is to look at the influence of finite size and of a large amount of interface on magnetic properties of rare-earth systems where the intrinsic anisotropy is large. The intrinsic anisotropy of the rare earths is a single-ion anisotropy and derives from the large orbital angular momentum of the rare-earth ion. In bulk rare earths this large intrinsic anisotropy leads to a large hysteresis and a large coercivity.[4]

Tb is selected as the rare earth since it has one of the highest anisotropies of the rare earths[4] and because its alloys tend to have the largest values of the magnetic transition temperature among the rare earths due to the large Tb spin ($S=3$) in the trivalent state.[4,5] Ti is selected as the matrix since it has low solubility in Tb.[6]

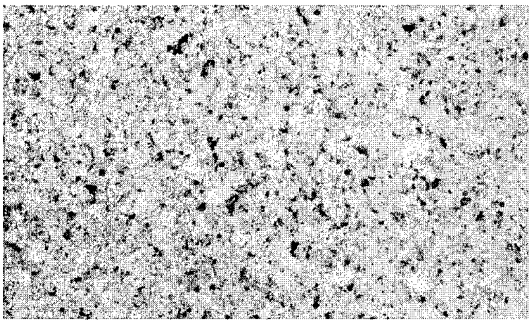
The Tb particles are prepared in a matrix of Ti by dc Ar ion sputtering at a pressure of 5 mTorr on a Kapton substrate. Ti and Tb are alternately deposited. The Ti layers are 10 nm thick and the amount of Tb deposited is varied over an equivalent thicknesses t ranging from 0.4 to 8 nm. We find that for thinner equivalent thickness the Tb does not form a layer, rather it forms particles on the Ti layer. Two types of sample are prepared. The first samples are for electron microscopy studies and are trilayers of the form Ti(10 nm)/Tb(t nm)/Ti(10 nm), where t is the equivalent layer thickness of Tb deposited. The second samples are for magnetization studies and are of the form [Ti(10 nm)/Tb(t nm)]×20. Generally we find that the average particle diameter is a factor of 4 or 5 large than the equivalent layer thickness t and in the discussion below we only give the average particles diameter as measured by electron microscopy. Electron microscopy and magnetization samples are prepared in pairs one after the other during the same sputter run with the same value of equivalent Tb thickness t.

Transmission electron microscopy studies of the particle systems were done with a Philips 201 100 kV electron microscope. The Ti layer was thin enough at 10 nm that we were able to obtain reasonable contrast between the Tb particles and the background Ti matrix. The Tb particles show up as dark spots since they are more absorbing than the Ti background and they grow as more Tb is deposited. Figure 1 shows electron micrographs for two Ti/Tb/Ti samples and the dark Tb spots grow significantly when the amount of the Tb deposited is increased from 1.2 to 4.4 nm. The average particle diameters for these equivalent layer thickness are 5 and 13 nm, respectively. Figure 2 shows electron diffraction from a Ti/Tb/Ti sample and all the rings seen can be associated with either bulk hexagonal Tb or bulk hexagonal Ti lattice plane spacings. We have also done element specific real space imaging (through McCrone Associates) of Tb crystallites by selecting electron intensity from two Tb diffraction rings (within the ring shown in Fig. 2) and confirm the presence of particles and will report these results in more detail elsewhere. From electron microscopy measurements we find a range of particle sizes in each sample characterized by a standard deviation in particle diameter of about 30% of the mean particle diameter.

A thick homogeneous Tb film was also prepared on a



(a)



(b)

FIG. 1. Electron micrographs for Tb particle systems with average particle diameter of: (a) 5 nm, and (b) 13 nm. The equivalent layer thickness t deposited are 1.2 and 4.4 nm, respectively.

 0021-8979/96/79(8)/5299/3/$10.00 © 1996 American Institute of Physics

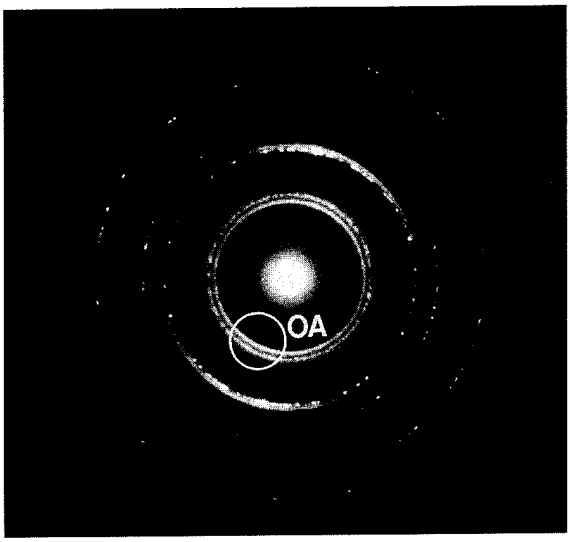


FIG. 2. Electron diffraction pattern for a Tb particle system with average particle diameter 13 nm.

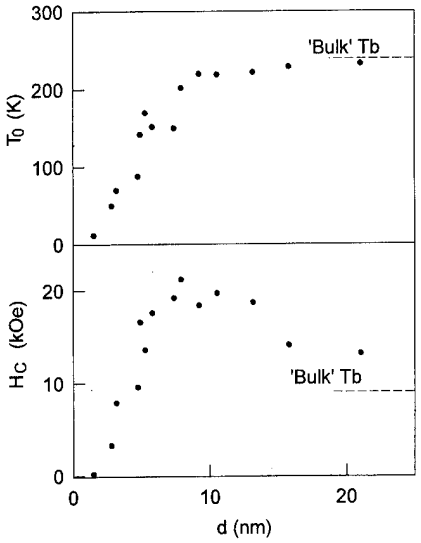


FIG. 4. Variation of transition temperature T_0 (upper panel) and coercivity at 4.5 K (lower panel) as a function of average particle diameter d.

Kapton substrate so that bulk properties (Curie–Weiss temperature T_0, coercivity H_c) of sputtered Tb could be compared to properties of the particle samples. The Tb film thickness is 360 nm and it is coated with 20 nm of Ti to provide protection from oxidation. X-ray diffraction indicates that this film has the hexagonal structure of bulk Tb and is polycrystalline.

Figure 3 shows magnetization versus temperature for three particle samples. There are two curves for each sample corresponding to field-cooled magnetization (upper curve in each case) and zero-field-cooled magnetization (lower curve in each case). The largest particle systems show a magnetic transition temperature close to that of bulk Tb which is 230 K. As can be seen the particle samples have a depressed transition. Curie–Weiss plots ($1/\chi$ vs T) are done to determine the Curie–Weiss temperature T_0 and this is taken as a measure of the transition temperature. Figure 4 summarizes the variation of T_0 with average particle diameter. Below 10 nm T_0 decreases rapidly while above 10 nm it is close to the bulk value. Such a decrease is expected from the effects of finite size[7,8] and has been seen in a number of transition metal multilayers,[9,10] a rare-earth multilayer,[11] and in fine particle CuMn systems.[3]

All of the particle samples of this work show large hysteresis at low temperatures. Figure 5 shows magnetization curves for selected Tb particle samples. Figure 4 summarizes the coercivities of all the particle samples of this work and the coercivity shows a maximum for a particle diameter of about 7 nm. At large values of d, H_c approaches the bulk value (indicated in Fig. 4.) Such a maximum has been seen in coercivity versus particle diameter in other particle systems, e.g., Fe[3], Fe_3O_4,[12,13] and Fe-C,[14] but with a lower maximum coercivity.

It is expected that in isolated fine particle systems the coercivity H_c should depend on temperature as[15]

$$H_c = H_0(1 - \sqrt{(T/T_B)}), \tag{1}$$

where T_B is a blocking temperature to be determined and H_0 is a constant. We have measured H_c as a function of temperature in a number of our particle systems and an example is shown in Fig. 6 for a sample with average particle size 7 nm. The straight line represents a least squares fit of Eq. (1)

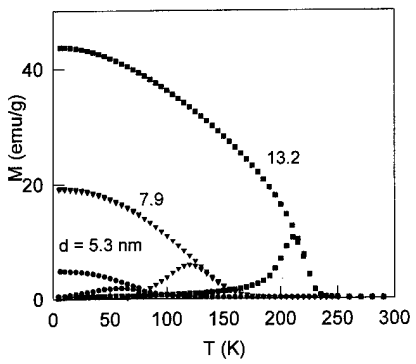


FIG. 3. Field-cooled and zero-field-cooled (upper and lower curves for each sample) magnetization at 200 Oe vs temperature for selected samples. Average particle diameter is given in nanometers. The lines are guides to the eye.

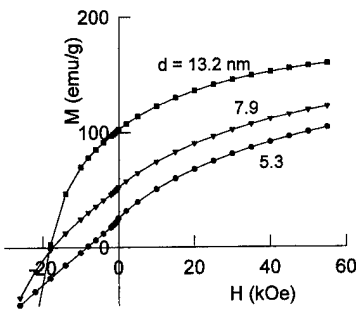


FIG. 5. Magnetization curves for selected Tb particle samples.

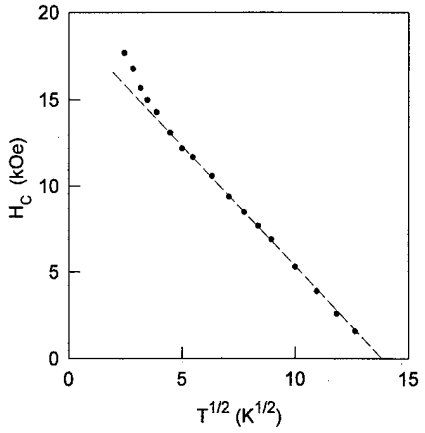


FIG. 6. Variation of coercivity with temperature for the particle sample with average particle diameter 7 nm.

to the data above 20 K and H_c follows the dependence of Eq. (1) in this regime. The fitted blocking temperature T_B is 190 K.

We have also looked at multilayers of Tb of the form Tb(t nm)/Mo(18 nm) prepared by sputtering and find that these systems show a maximum in the magnitude of the coercivity as a function of layer thickness.[16] This maximum value is 11 kOe and occurs at a value of t (Tb layer thickness) of 9 nm. Thus both systems show a maximum in coercivity at approximately the same size scale, 9 nm layer thickness for Tb multilayers as compared to 7 nm particle diameter for Tb particles. Also the nanoscale particles show a larger maximum coercivity than the multilayers.

We attribute the larger coercivity in the particles to the fact that the particles have a more confined geometry. This more confined geometry can contribute to a larger coercivity in two ways. Particles will have more surface area per unit volume than multilayers whose layer thickness is the same as the particle diameter. This interface will contribute an anisotropy[1–3,17] and the total interfacial anisotropy present will be larger in particles than multilayers. Single magnetic domain reversal could also be important here and we are doing more detailed magnetic measurements to determine how each of these effects contribute to the large coercivity in these particles.

In summary, we have prepared a series of nanoscale particle samples of Tb and find that the finite size and large amount of interfacial area strongly modify the properties of these strong anisotropy magnetic systems.

This work was supported by NSF OSR92-55223.

[1] R. P. Andres *et al.*, J. Mater. Res. **4**, 704 (1989).
[2] *Magnetic Properties of Fine Particles*, edited by J. L. Dorman and D. Fiorani (North-Holland, Amsterdam, 1992).
[3] C. L. Chien, J. Appl. Phys. **69**, 5267 (1991).
[4] K. Moorjani and J. M. D. Coey, *Magnetic Glasses* (Elsevier, Amsterdam, 1984), Chap. VI.
[5] M. J. O'Shea and K. M. Lee, J. Magn. Magn. Mater. **99**, 103 (1991).
[6] W. Moffatt, *The Handbook of Binary Phase Diagrams* (Genium, New York, 1986).
[7] K. Binder and P. C. Hohenberg, Phys. Rev. B **9**, 2194 (1974).
[8] P. V. Hendriksen, S. Linderoth, and P.-A. Lindgard, J. Magn. Magn. Mater. **104**, 1577 (1992).
[9] C. M. Schneider *et al.*, Phys. Rev. Lett. **64**, 1059 (1990).
[10] F. Huang *et al.*, J. Appl. Phys. **73**, 6760 (1993).
[11] P. Perera and M. J. O'Shea, J. Appl. Phys. **75**, 6672 (1994).
[12] A. E. Berkowitz, F. T. Parker, S. B. Slade, and G. Podolsky, J. Appl. Phys. **67**, 5155 (1990).
[13] S. U. Jen *et al.*, J. Magn. Magn. Mater. **96**, 82 (1991).
[14] S. Linderoth *et al.*, J. Magn. Magn. Mater. **124**, 269 (1993).
[15] E. F. Kneller and F. E. Luborsky, J. Appl. Phys. **34**, 656 (1963).
[16] P. Perera and M. J. O'Shea, J. Magn. Magn. Mater. (1996) (to be published).
[17] P. Perera and M. J. O'Shea, J. Appl. Phys. **69**, 5292 (1991); **70**, 6212 (1991).

Effect of preparation technique on the structural and magnetic properties of granular Fe-SiO_2 (abstract)

J. A. Christodoulides, N. B. Shevchenko, A. S. Murthy, and G. C. Hadjipanayis
Department of Physics and Astronomy, University of Delaware, Newark, Delaware 19716

Previous studies have shown that large coercivities, exceeding 2 kOe,[1] can be obtained in Fe-based ceramic granular films. The coercivities were also found to be sensitive to the type of matrix material used, being higher in the SiO_2 matrix.[2] In this study the hysteresis behavior of $Fe_x(SiO_2)_{1-x}$ granular films was studied as a function of the preparation technique. The films were prepared by dc magnetron sputtering over the composition range of x_v=0.1–0.9 volume fraction of Fe. Tandem deposition both with and without titanium sublimation, and deposition from a composite target were used in preparing the films, which resulted in different oxygen environments. Coercivity measurements were found to be strongly composition dependent, with maximum values up to 700 Oe at $x_v \approx 0.5$ of Fe, for all sets of samples. Typical granular structure was observed, with grain size in the range of 5–20 nm, with the smaller size obtained from composite targets. X-ray diffraction and selected area diffraction showed a structure of a-Fe (bcc). Thermomagnetic curves showed a peak which can be associated with the onset of superparamagnetism. By varying the deposition method and the oxygen environment, we were able to switch from a relatively magnetically hard sample ($H_c \sim 500$ Oe) to a soft sample ($H_c \sim 20$ Oe). Mossbauer data are being analyzed to determine the presence of any oxides, their magnetic state and their effect on hysteresis. © *1996 American Institute of Physics.* [S0021-8979(96)80708-8]

Work supported by the National Science Foundation under Contract No. NSF DMR-9307676.

[1] C. L. Chien *et al.*, J. Appl. Phys. **63**, 4252 (1988).
[2] A. Tsoukatos *et al.*, J. Appl. Phys. **72**, 6967 (1993).

 0021-8979/96/79(8)/5302/1/$10.00 © 1996 American Institute of Physics

Preparation and quantitative magnetic studies of single-domain nickel cylinders

R. O'Barr, M. Lederman,[a] and S. Schultz
Department of Physics and Center for Magnetic Recording Research, University of California, San Diego, 9500 Gilman Drive, La Jolla, California 92093-0319

Weihua Xu and A. Scherer
Department of Electrical Engineering, California Institute of Technology, Pasadena, California 91125

R. J. Tonucci
Optical Sciences Division, Naval Research Laboratories, Washington DC 20375

For a complete experimental and theoretical explanation of the magnetic processes in an interacting collection of submicron magnetic particles, a fundamental understanding of the magnetic properties of individual single-domain particles must first be achieved. We have prepared elongated Ni columns ranging in diameter from 0.15 to 1.0 μm by electroplating into specially prepared Al_2O_3 and glass channeled pore membranes. We have also prepared controlled arrays of Ni columns using e-beam lithography, subsequently electroplating into the written patterns. Using transmission electron microscopy, we have characterized the shape, size, morphology, and crystal structure of the columns. Magnetic force microscopy has been used to determine the switching field H_s versus the applied field angle of the columns. Although the switching field data can be fit to the functional form for nucleation by curling in an infinite cylinder, the observed weak dependence of H_s on column diameter is inconsistent with that expected for curling, particularly for columns of diameter >0.3 μm. © *1996 American Institute of Physics.* [S0021-8979(96)40408-4]

I. INTRODUCTION

The magnetization state of a collection of magnetic particles is generally a complicated function of the applied field history and is a problem still lacking a complete theoretical description. The complexity is due mostly to the long range magnetostatic interactions between every pair of particles. Before a fundamental theory for the magnetization reversal of an interacting collection of particles can be formulated, one must first understand the reversal properties of the individual constituents, single-domain particles.

Our approach to this problem is to gather experimental data for the behavior of model single-domain particles specifically prepared for this purpose. Over the past few years, studies of the switching field versus applied field angle have been made on single-domain rectangular permalloy platelets,[1] barium-ferrite platelets,[2] γ-Fe_2O_3 particles,[3] Fe particles,[4] rectangular Ni platelets,[5] and long Ni cylinders.[6] In this article, we describe the preparation, characterization, and magnetic measurements of single-domain elongated Ni columns, and a method used to prepare controlled assemblies of Ni columns in designed configurations.

II. SAMPLE PREPARATION

The method we have used to prepare samples consists of electroplating Ni into channel pore membranes prepared by three different techniques:

A. Anodized aluminum

One type of porous membrane which we have filled by electroplating are Al_2O_3 filters commercially available from Whatman Inc.[7] Details of the set up and the plating conditions used have been previously reported.[6] The standard Whatman Al_2O_3 filters have diameters ranging from ~0.25–0.45 μm and we can vary the length of the columns prepared by changing the duration or the current density used in the plating process. We have also utilized a series of custom made filters for which the anodization conditions have been adjusted to produce pores with smaller hole sizes.

B. Nanochannel glass arrays

A second type of porous membranes are nanochannel glass arrays developed by Tonucci *et al.*,[8] with pore diameters of 1 μm. Nanochannel glass membranes contain highly uniform parallel pores or channels in large arrays. Samples are prepared by polishing a channel glass wafer to a thickness appropriate for the desired column length. The wafer is then etched with a weak acetic acid solution exposing the channels in the array. The channel glass wafer is then sealed over a hole in a glass cover slip in preparation for electrodeposition. Details of the plating conditions were similar to that used for the anodized aluminum samples discussed above.

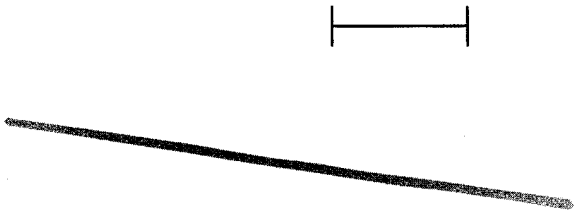


FIG. 1. Bright field TEM image of column α which has an aspect ratio of 63:1...Scale bar is 4 μm.

[a]Currently at Read-Rite Corp.

 0021-8979/96/79(8)/5303/3/$10.00 © 1996 American Institute of Physics

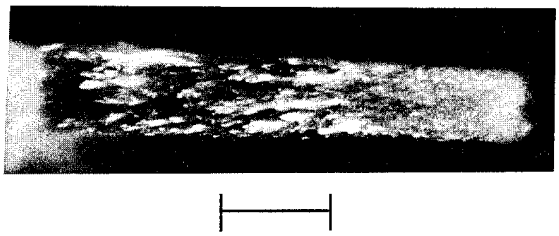


FIG. 2. Dark field TEM image of a particle written by e-beam lithography. The scale bar is 0.2 μm.

C. Electron-beam lithography

A third method for preparing columnar pores utilizes electron-beam lithography as reported by Chou *et al.*[9] The details of our lithography will be included in Ref. 10. In brief, a thin gold layer is evaporated onto a semiconducting or insulating substrate in a pattern that consists of a beam-writing pad and two electrically connected probe contact pads. We then spin-coat a single, high molecular weight polymethyl methacrylate (950k PMMA) resist layer. The resist is then patterned using a Phillips EM-430 scanning transmission electron microscope (STEM) with an acceleration voltage of 250 kV. Following the lithographic exposure, the exposed patterns are developed in a 3:7 cellulose-methanol mixture. Electrodeposition at constant current is then carried out using a nickel sulfamate electrolyte. Using this technique, we have prepared columns ranging from 0.02 to 0.2 μm in diameter, and exceeding 1 μm in length.

III. SAMPLE CHARACTERIZATION

To determine the size, shape, morphology, and crystal structure of the Ni columns, we first remove the surrounding membrane. The Al_2O_3 filters and nanochannel glass membranes are removed by etching in 1 M NaOH. The PMMA is removed by an oxygen plasma etch. The columns can then be observed directly in a SEM or placed in water, ultrasonicated, and evaporated onto a transmission electron microscopic (TEM) grid. Figure 1 shows a bright field image of a column previously designated as α,[6] prepared using an Al_2O_3 filter. This column has a diameter $d=0.27$ μm, length $L=17$ μm, and an aspect ratio of 63:1.

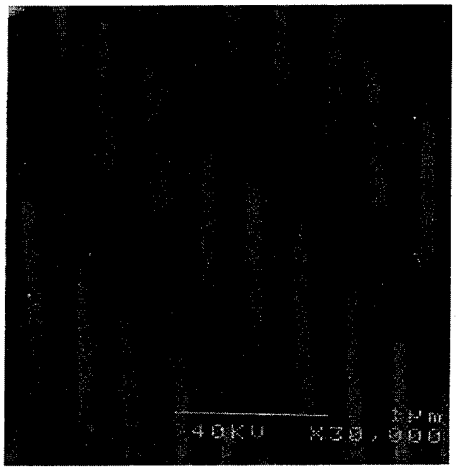


FIG. 3. SEM micrograph of an array of columns written by e-beam lithography after removal of the PMMA layer. Column height is >1 μm, $d=0.1$ μm, and the spacing between columns ~ 1 μm.

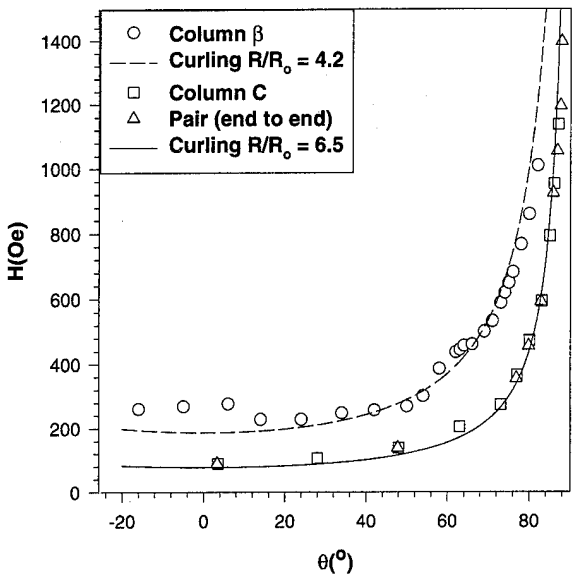


FIG. 4. Switching field vs angle between external field and the long axis, $H_s(\theta)$ of column C, and a pair of similar columns aligned end-to-end ($d=1$ μm, and $L=44$ μm), and for column β ($d=.15$ μm, $L=1.65$ μm). The solid and dashed curves correspond to $H_s(\theta)$ for nucleation by curling in an infinite cylinder. For Ni, $R_0=\sqrt{A}/M_S$ is 206 Å, where A is the exchange constant, and M_s is the saturation magnetization.

Figure 2 is a dark field image of a particle written by e-beam lithography. As can be seen in this image, the crystal structure is polycrystalline with a decrease in the grain size as the plating progresses. We intend to improve the crystallinity by varying and optimizing the plating parameters. An illustration of an array of columns written by e-beam lithography as visualized by SEM after the removal of the PMMA, is shown in Fig. 3.

IV. MEASUREMENT OF MAGNETIC PROPERTIES

Using a magnetic force microscope (MFM)[11] with an *in situ* electromagnet, we have measured the switching field versus applied field angle for several different columns. Columns are first located and characterized by TEM on a grid, and then relocated by correlation of various marking features in the MFM. The measurement sequence is as follows. A reverse field of 1650 Oe is pulsed in a direction making an angle θ with the long axis of the column for 1 s. This field is verified to be sufficient to reverse saturate the column's magnetization. A forward field H, is then applied for 2 s. Before the fields are applied, the MFM tip is backed away to a distance of 12 μm. After the application of the field pulses, the column is then imaged in the **remanent state** to see if the forward field H was sufficient to reverse the direction of magnetization. The lowest H necessary to switch the direction of the magnetization of the column is defined as the switching field H_s for that angle.

The results for an isolated column, prepared with nanochannel glass membranes (designated as C) and for two

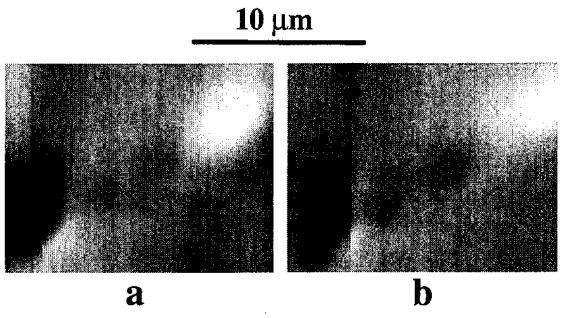


FIG. 5. MFM images of column A (d=.45 μm, L=12.7 μm) scanned in remanence after applying a field of (a) H=0 and (b) H=475 Oe. For this particular case, H_s=480 Oe.

similar columns aligned end-to-end, each with d=1 μm and L=44 μm, and for an isolated column prepared with an Al_2O_3 filter (designated β) are presented in Fig. 4. The solid and dashed curves correspond to the analytical micromagnetic solution of $H_s(\theta)$ for curling[12] in an infinite cylinder where we have adjusted R/R_0 to get a best fit, where R is the cylinder radius and R_0 is the critical radius for curling. Even though we don't expect curling to be valid over the entire range, in Fig. 4 we plot the relationships for comparison. MFM images, such as those in Fig. 5, show that magnetic charge is concentrated only at the ends of the columns, with negative charge at one end and positive at the other, with the polarity (of the magnetization) dependent on whether the previously applied field $H>H_s$. At **remanence**, a multidomain state has never been observed, even if the previously applied field was near H_s (see Fig. 5). It is surprising that even the columns with d=1 μm are single-domain which may be due to the large aspect ratio which should help to stabilize the single-domain state. The angular dependence for column C is similar to that of columns 1,2 (d=0.3 μm, L=5.5 μm), A,B(d=0.45 μm, L=12.7 μm), and α (d=0.27 μm, L=17 μm) given in Fig. 2 of Ref. 6. The angular dependence for column β (d=0.15 μm, L=1.65 μm) is different in that H_s increases slightly as θ approaches 0^0. The switching field at zero degrees $H_s(\theta=0^0)$ versus column radius R is plotted in Fig. 6. The solid line is the solution for the nucleation field via curling in an infinite Ni cylinder. Column β has a zero angle switching field of 276 Oe, a value close to the theoretical curve.

V. CONCLUSION

We have prepared columns by electroplating into porous membranes ranging in diameter from 0.15 to 1.0 μm and have measured the switching field versus applied field angle. We have also demonstrated the capability to prepare arrays of columns with diameters as small as.02 μm using e-beam lithography. In general, the observed angular dependence of the switching field (Fig. 4) agrees with the **functional form**

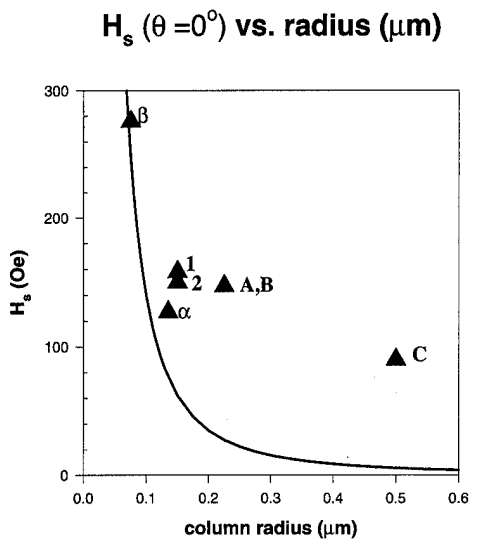


FIG. 6. Switching field when the external field is aligned with the column long axis vs column radius. Solid line is the solution given for nucleation by curling in an infinite cylinder.

corresponding to curling in an infinite cylinder, although at the expense of reassigning the R/R_0 value to get a best fit. For Fig. 4 that adjustment is from 24.3 to 6.5 for column C and from 3.64 to 4.2 for column β. For d>0.3 μm, the dependence of H_s on diameter is weak which is not consistent with curling and may indicate another mode for initiating reversal such as nucleation at the particle ends.

ACKNOWLEDGMENTS

Work was sponsored by the Center for Magnetic Recording Research, NSF Grant No. DMR-94-00439 (MRSEC), and ARPA/ETP.

[1] M. Lederman, G. A. Gibson, and S. Schultz, J. Appl. Phys. **73**, 6961 (1993).
[2] T. Chang and J. Zhu, J. Appl. Phys. **75**, 5553 (1994).
[3] M. Lederman, D. R. Fredkin, R. O'Barr, S. Schultz, and M. Ozaki, J. Appl. Phys., **75**, 6217 (1994); C. Salling, R. O'Barr, S. Schultz, I. McFadyen, and M. Ozaki, *ibid.* **75**, 7989 (1994).
[4] Y. Luo and J. Zhu, IEEE Trans. Magn. **30**, 4080 (1994).
[5] S. Chou, P. Krauss, W. Wei, and P. Fischer, Scr. Metall. Mater. **33**, 1537 (1995).
[6] M. Lederman, R. O'Barr, and S. Schultz, IEEE Trans. Magn. **32**, 3793 (1995).
[7] Whatman Corp. Catalog Number 20046S50.
[8] R. J. Tonucci, B. L. Justus, A. J. Campillo, and C. E. Ford, Science **258**, 783 (1992).
[9] S. Y. Chou, M. S. Wei, P. R. Krauss, and P. B. Fischer, J. Appl. Phys. **76**, 6673 (1994).
[10] H. Xu, J. Wong, C. C. Cheng, R. Johnson, and A. Scherer, J. Vac. Sci. Technol. B **13**, 2372 (1995).
[11] G. A. Gibson, J. F. Smyth, S. Schultz, and D. P. Kern, IEEE Trans. Magn. **27**, 5187 (1991).
[12] E. H. Frei, S. Shtrikman, and D. Treves, Phys. Rev. **106**, 446 (1957); S. Shtrikman and D. Treves, J. Physique (Paris) **20**, 286 (1959).

Magnetic domain percolation in granular Co-Ag

A. Gavrin[a] and M. H. Kelley
National Institute of Standards and Technology, Gaithersburg, Maryland 20899

J. Q. Xiao[b] and C. L. Chien
Department of Physics and Astronomy, The Johns Hopkins University, Baltimore, Maryland 21218

The most dramatic changes in the properties of granular metals occur near the percolation threshold x_c, which generally occurs at a volume fraction of approximately 0.50. There has been much speculation concerning the evolution of magnetic domains at x_c, however, no direct observations have been produced. Using scanning electron microscopy with polarization analysis, we investigate the formation of domains in a series of granular Co-Ag samples. We find x_c to lie in the range [0.50, 0.55], and we report on the size and morphology of the observed domains. Below x_c, a domain pattern appears which may be due either to interparticle correlations or to residual Co in the silver matrix; we have previously discussed the ramifications of this observation on an understanding of GMR. In this paper, we place limits on the latter of these two models. Above x_c, the domains resemble "stripe domains" which have been observed in amorphous materials. This observation suggests the presence of anisotropy perpendicular to the film plane. © *1996 American Institute of Physics.* [S0021-8979(96)04908-9]

Granular ferromagnets are nanocomposite materials with one ferromagnetic and at least one nonmagnetic component. The ferromagnet may be either a pure metal or an alloy; the remaining material or materials may vary widely, so long as they are immiscible with the ferromagnet. In this paper, we will consider samples in which the ferromagnetic component is pure cobalt, and the nonmagnetic component is silver. Because the components (often called phases) are largely segregated from one another, we give the composition of the samples in terms of the volume fractions of the phases. Thus, we denote our samples Co_xAg_{1-x}: a sample with $x=0.40$ contains 40% cobalt by volume, with the balance silver. We selected the cobalt-silver system because the mutual solubility of this pair is minimal, and because of the great recent interest in the magnetoresistance of this system.[1] However, we must state at the outset that the microstructure of our Co_xAg_{1-x} samples may be more complex than the simple picture of granular materials presented here. In particular, there is evidence that the two components are not simply segregated: the samples may have a Co-Ag alloy phase in addition to pure cobalt and pure silver.

Granular ferromagnets have been investigated since the early 1970's, and continue to provide important fundamental results and potential applications.[2] Many of these are associated with the microstructural transition (often described as a percolation transition) which occurs at a critical volume fraction near to 50%, i.e., $x_c=0.50$. For reasons that we outline below, granular ferromagnets are not expected to have a macroscopic domain structure below x_c, whereas above x_c such a domain structure will develop. There is little doubt that this occurs, and the formation of a domain structure above x_c is an integral part of our understanding of these materials. However, the development of the domain structure has not, to our knowledge, ever been investigated directly. This paper provides a first investigation of this kind.

The microstructure of a granular ferromagnet affects its magnetic properties primarily though the suppression of domain walls at low volume fractions. Below x_c, the ferromagnetic phase exists in the form of isolated, roughly spherical particles a few nanometers in size. Particles of this size behave as single magnetic domains, thus, we may understand the magnetic properties of the material by considering an ensemble of such particles, possibly including some interparticle interactions. A number of phenomena of theoretical and practical importance have been understood in this way, including superparamagnetism, enhanced coercivity, and giant magnetoresistance (GMR).[3] In each case, a crucial feature is the lack of domain walls when the ferromagnetic particles are small and isolated from one another. The magnetic response of such a material does not include a component due to the motion of domain walls—the dominant component in most magnetic materials. Above the critical volume fraction the ferromagnetic material "percolates" through the material; thus, magnetic domains may form, and the response of the material to an external field will include domain wall motion.

We have used high-resolution scanning electron microscopy with polarization analysis (SEMPA) to image the magnetic domain structure of our Co_xAg_{1-x} samples over a range of volume fractions including x_c. We have previously reported the (somewhat surprising) existence of a domain structure below x_c, and we have discussed possible origins of these domains.[4] In particular, we have considered domain formation due to interparticle interactions and due to residual cobalt in the silver matrix. In this paper, we extend the range of our investigation to compositions well beyond the critical volume fraction. Between $x=0.50$ and $x=0.55$ the domain structure changes dramatically, suggesting the onset of percolation. Thus, we identify the critical volume fraction $0.50 \leq x_c \leq 0.55$.

We produced the materials described herein by dc mag-

[a]Present address: Department of Physics, Indiana Univ.-Purdue Univ. Indianapolis, 402 N. Blackford St., Indianapolis, IN 46202-3274.
[b]Present address: Department of Physics and Astronomy, University of Delaware, Newark, DE 19716.

 0021-8979/96/79(8)/5306/3/$10.00 © 1996 American Institute of Physics

netron sputtering from composite targets, the details may be found elsewhere.[5] The samples cover the composition range $0.35 \leq x \leq 0.65$, and have been vacuum annealed at temperatures up to 600 °C. For comparison, we have also produced a pure cobalt film under identical conditions. The annealing temperatures are known to ±25 °C and the sample compositions are known to ±0.005.[6] Annealing was performed under vacuum, at pressure $p \leq 7.0 \times 10^{-5}$ Pa.

The magnetic images were acquired by using SEMPA. The principles of this technique have been described previously.[7] In brief, the SEMPA microscope independently records two orthogonal components of the magnetization in the plane of the sample. Subsequently, we employ digital image processing to determine the direction and magnitude of the in-plane magnetization vector. Near the surface, the in-plane component accounts for nearly all of the magnetization, because moments that are perpendicular to the surface are energetically costly. We recorded all of the images at room temperature.

The magnetic information recorded by the SEMPA system is carried by low-energy secondary electrons (≤10 eV). The mean-free path of these electrons is exceedingly short, only a few nanometers. Thus, the domain structures recorded by the SEMPA are those present in the first few monolayers at the sample surface. This has two important ramifications: the sample must be free of surface contamination, and the domain pattern in the bulk of the sample must be inferred from the surface domains and micromagnetic principles. We clean the sample surface under UHV conditions using ion bombardment with 1.15 keV Ar^+ ions. A discussion of the extension from surface to bulk will be included later in this paper.

Many aspects of our results are evident in Figs. 1(a)–1(d), in which we present the domains in four Co_xAg_{1-x} samples. These images were recorded at moderate magnification (10 k×) in order to illustrate the typical domain sizes and morphologies at several compositions. In these images, we display the direction of the magnetization vector for four samples: $x=[0.40,0.50,0.55,0.65]$. All of the samples are as-deposited. The "grey wheel" in the upper left corner of Fig. 1(a) shows the correspondence between angle and grey level. Pure black and pure white correspond to magnetization in the $+x$ direction, 75% grey to $+y$, etc. The artificial discontinuity between black and white is unfortunate, but does not significantly affect the issues we wish to discuss here.

The differences between Figs. 1(a),1(b) and Figs. 1(c),1(d) are striking. The former show domains that are typically 300–600 nm in extent, and are fairly isotropic. In contrast, the latter show domains that are highly anisotropic, extending for tens of microns along one direction and approximately 1 μm in the orthogonal direction. Furthermore, the domains in 1(a) and 1(b) have previously been shown to lack any substructure down to length scale of about 20 nm,[4] whereas Fig. 2(b) reveals a complex substructure to the domains shown in Fig. 1(d).

In Fig. 2, we present low (2 k×) and high (100 k×) magnification images of a sample with $x=0.65$—the same as that imaged in Fig. 1(d). The low magnification image, Fig. 2(b), illustrates the full extent of the domain pattern over

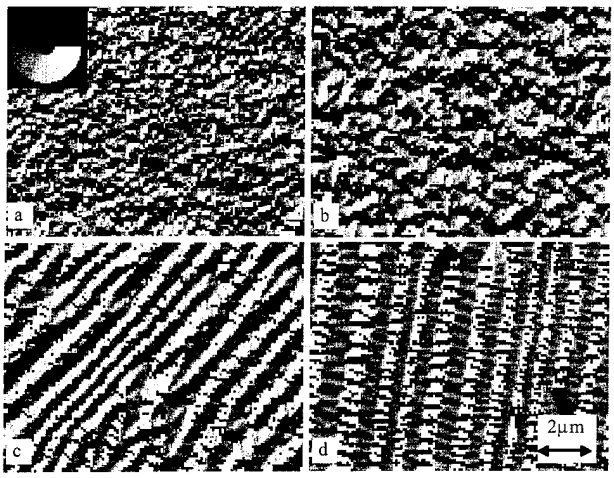


FIG. 1. Domain images of Co_xAg_{1-x} at a magnification of 10 $k\times$. The compositions are (a) $x=0.45$, (b) $x=0.50$, (c) $x=0.55$, and (d) $x=0.65$. The greywheel in (a) illustrates the correspondence between direction and grey value. In each of these images, the physical size of one pixel is 89.3 nm. The micron marker in (d) applies to each image.

long distances; the high magnification image, Fig. 2(b), shows the complex substructure of the domains. Figure 2(c) is a vector map derived from the data shown in Fig. 2(b). This representation reveals the presence of several surface magnetic singularities. Structures such as these are indicative of magnetization perpendicular to the sample plane, and were also observed at lower volume fractions.[4]

We must consider what bulk domain-pattern could give rise to these surface domains. The alternating dark and light bands observed in Fig. 2(a) represent domains that are head-to-head and tail-to-tail. We illustrate this situation schematically in Fig. 3(a). Such a situation is extremely unlikely to persist in the bulk, because a discontinuity in the perpendicular component of M across an interface is equivalent to a sheet of magnetic charge: a very high-energy situation. In Fig. 3(b), we illustrate the possibility that the observed domains are closure domains at the surface of a bulk domain

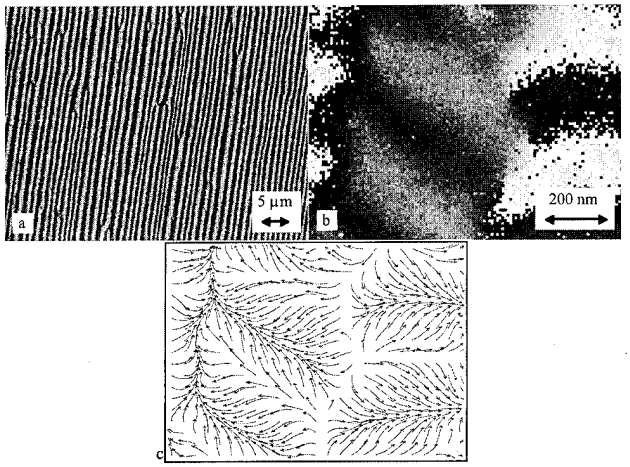


FIG. 2. SEMPA images of $Co_{0.65}Ag_{0.35}$. (a) Magnification of 2 k×, the physical size of each pixel is 112 nm. (b) Magnification of 100 k×, physical size of each pixel is 8.93 nm. (c) Vector map representation of the domains shown in (b).

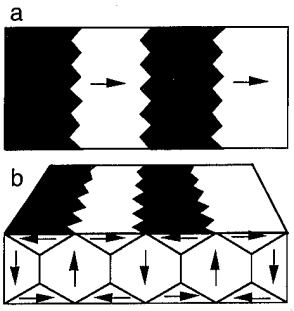


FIG. 3. Schematic representation of the domains observed in $Co_{0.65}Ag_{0.35}$. (a) Plan view, and (b) simple closure domain construction.

pattern perpendicular to the film plane. This model is supported by hysteresis measurements that we present in a separate paper.[8] We note the similarity between these domains and "stripe domains" which have been observed in amorphous metal films,[9] and wires,[10] and which have also been attributed to closure domains.

A more vexing question is the degree of segregation between the cobalt and silver; previous results provide a mixed picture. The magnetic properties of the samples suggest that there is substantial segregation. Samples with $x \leqslant 0.30$ show superparamagnetic relaxation with blocking temperatures below room temperature.[11] Furthermore, it is widely accepted that giant magnetoresistance can only occur in the presence of short range magnetic disorder. In Co-Ag this disorder is usually assumed to result from the random orientations of the moments of individual magnetic particles.[3] In opposition, our observation of magnetic domains at low x can be readily understood if enough cobalt remains dissolved in the silver to maintain ferromagnetism of the alloy. There are also preliminary microanalytic results indicating that the samples may contain pure silver particles in a Co-Ag alloy matrix.[12]

We have previously demonstrated that some fraction of the cobalt in our samples does not participate in the GMR. In particular, we have considered the possibility that some of the cobalt remains dissolved in the alloy matrix while the remainder resides in single-domain particles that are responsible for the GMR. In this case, the matrix material remains ferromagnetic and supports the domains that we observe at $x \leqslant 0.50$. In Ref. 4 we argued that this model is subject to two constraints: the concentration of cobalt in the matrix (α) must be high enough to support ferromagnetism at room temperature, and the volume fraction of the matrix (y) must be great enough for the matrix to percolate. We considered $\alpha \geqslant 0.30$ and $y \geqslant 0.27$ or $y \geqslant 0.55$. Using these conditions, we discussed the sample with $x=0.35$ and calculated the maximum volume fraction of cobalt in the small particle phase to be $x_{max}=0.22-0.29\pm0.01$ (depending on the requirement for percolation of the matrix). In essence, this argument sets a lower limit on the degree of segregation of the sample.

If we assume that the change in the domain structure above $x=0.55$ represents percolation of the pure cobalt phase, then the present result sets an upper limit on segregation. Taking the matrix phase to contain the same minimum cobalt content (30 at. %), the range of possible volume fractions for pure cobalt becomes $x_{segregated}=0.40-0.55\pm0.01$. That is, minimum segregation corresponds to a percolation threshold of $x_c=0.40$ and maximum segregation gives $x_c=0.55$. Taking percolation to occur at 0.45, and applying the same degree of segregation to the example above yields $x_{max}=0.20\pm0.01$, near the lower given above. Thus, only $20/35\approx57\%$ of the cobalt participates in the GMR.

This result in no way rules out the other model suggested in Ref. 4. If the domains observed at $x \leqslant 0.50$ result from correlations among single-particle moments in a well-segregated sample, then the transition observed here may be simply understood. The small domains at low x are the result of dipole-dipole and exchange interactions through a nonmagnetic matrix phase; the large domains occur above percolation as a result of direct exchange.

This work was supported by NSF Grant No. DMR-9200280 and ONR Grant No. N00014-91-J-1633 at The Johns Hopkins University, and by the Technology Administration of the U.S. Department of Commerce and the Office of Naval Research for work at NIST.

[1] H. Wan, A. Tsoukatous, G. C. Hadjipanayis, Z. G. Li, and J. Liu, Phys. Rev. B **49**, 1524 (1994); Y. Lee, V. R. Deline, G. Gorman, A. Kellock, D. Miller, D. Neiman, R. Savoy, J. Vazquez, and R. Beyers, J. Appl. Phys. **74**, 5871 (1993).
[2] B. Abeles, in *Applied Solid State Science: Advances in Materials and Device Research*, edited by R. Wolfe (Academic, New York, 1976), p. 1; C. L. Chien, J. Appl. Phys. **69**, 5267 (1991).
[3] S. Zhang, Appl. Phys. Lett. **61**, 1855 (1992); J. H. Kim, J. Q. Xiao, C. L. Chien, Z. Tesanovic, and L. Xing, Solid State Commun. **89**, 157 (1994).
[4] A. Gavrin, M. H. Kelley, John Q. Xiao, and C. L. Chien, Appl. Phys. Lett. **66**, 1683 (1995).
[5] J. Q. Xiao, J. S. Jiang, and C. L. Chien, Phys. Rev. Lett. **68**, 3749 (1993).
[6] Error estimates quoted in this paper are to be interpreted as one standard deviation combined random and systematic errors unless otherwise indicated.
[7] M. R. Scheinfein, J. Unguris, M. H. Kelley, D. T. Pierce, and R. J. Celotta, Rev. Sci. Instrum. **61**, 2501 (1990).
[8] J. Q. Xiao, A. Gavrin, and C. L. Chien, these proceedings.
[9] A. P. Malozemoff, W. Fernengel, and A. Brunsch, J. Magn. Magn. Mater. **12**, 201 (1979).
[10] J. Yamasaki, F. B. Humphrey, K. Mohri, H. Kawamura, H. Takamura, and R. Mälmhäll, J. Appl. Phys. **63**, 3949 (1988).
[11] J. Q. Xiao, Ph.D thesis, The Johns Hopkins University, 1993.
[12] S. Majetich (private communication).

Observation of perpendicular anisotropy in granular magnetic solids

John Q. Xiao[a] and C. L. Chien
Department of Physics and Astronomy, The Johns Hopkins University, Baltimore, Maryland 21218

A. Gavrin
Department of Physics, Indiana University-Purdue University at Indianapolis, Indianapolis, Indiana 46202-3273

Granular Co-Ag materials with low Co contents exhibit giant magnetoresistance and single-domain magnetic properties. In this paper, we discuss unusual hysteresis behavior that we have observed in Co-rich samples, where the magnetization is approximately linear with the applied field up to saturation, and the coercivity and remnant magnetization are both nearly zero. We attribute this unusual behavior to a perpendicular anisotropy that depends on the nanostructure in the phase-segregated materials. These results are corroborated by magnetic domain imaging using scanning electron microscopy with polarization analysis. © *1996 American Institute of Physics.* [S0021-8979(96)01808-7]

Recently, granular metallic solids have been extensively studied due to the discovery of giant magnetoresistance (GMR),[1,2] enhanced coercivity (H_c),[3] extraordinary Hall effect,[4] giant magnetothermal properties,[5] and other enhanced properties. Granular metallic solids can be conveniently produced by cosputtering of two immiscible metals.[6] Using low substrate temperatures, the as-prepared samples may be metastable crystalline alloys. Post-deposition annealing or the use of elevated substrate temperatures result in the formation of granular solids; the size of the ultrafine particles can be adjusted by varying the substrate or annealing temperature.

Numerous studies of granular solids have established that isolated granules are found in samples with low volume fractions. For samples with volume fraction (x) above the percolation volume fraction (x_p), the granules form a continuous network. For a wide variety of magnetic granular solids, the values of x_p have been near 0.5.[3] High coercivity and GMR are realized for samples with $x<x_p$. Above x_p, the coercivity reverts to small values and there is no GMR. Consequently, the magnetic properties of granular solids with $x>x_p$ are usually considered uninteresting.

Very recently, we have imaged the domain structures in the demagnetized state of granular Co_xAg_{1-x} by using scanning electron microscopy with polarization analysis (SEMPA).[7,8] The results suggest that the magnetization may have an out-of-plane component, a prospect generally not expected in thin magnetic films. In this work we report the observation of perpendicular anisotropy in granular magnetic materials. This perpendicular anisotropy is most pronounced near the percolation threshold ($x\approx0.5$), and occurs only in-phase separated magnetic systems. The phenomenon is not material specific, and has been observed in a number of granular magnetic systems. In this paper we confine ourselves to the results in Co_xAg_{1-x}, and other results will be discussed elsewhere.

Thin-film samples, several μm thick, of Co_xAg_{1-x} with Co volume fraction $0.35\leqslant x\leqslant0.75$, were fabricated using dc magnetron sputtering onto room-temperature Si(100) substrates.[3] Some of the samples have been annealed in a vacuum at temperatures of $T_A=300$ and 600 °C. We have analyzed the sample structures using x-ray diffraction; the magnetic properties have been measured using a vibrating sample magnetometer (VSM).

Figure 1 shows x-ray diffraction results of the as-prepared Co_xAg_{1-x} samples with $x=0.55$, 0.65, and 0.75. Despite larger contents of Co, the diffraction peaks due to Ag [Ag(111) and Ag(200)] are more prominent than those of Co [Co(100) and Co(002)] because of the larger scattering factor of Ag. The Co(002) peak is not resolvable because it is practically at the same position as that of Ag(200). The appearance of both Co and Ag peaks in Fig. 1 shows that phase separation has occurred in the sample with $x=0.75$, although less obvious in the samples with $x=0.55$ and 0.65, because the Co(100) peak is barely observable. Some Co-Ag alloys may also be present. After annealing at $T_A=300$ and 600 °C, we clearly observe diffraction patterns of Co and Ag with narrower lines due to larger grain sizes.

In Fig. 2 we show the magnetic hysteresis loops at room temperature for the as-prepared ($T_A=27$ °C) and the annealed samples ($T_A=300$ and 600 °C) of $Co_{0.65}Ag_{0.35}$. In

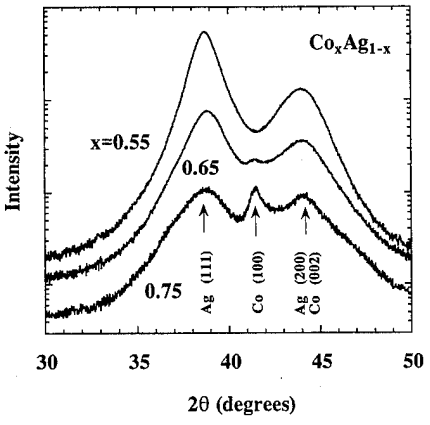


FIG. 1. X-ray diffraction result of as-prepared Co_xAg_{1-x} samples with $x=0.55$, 0.65, and 0.75.

[a]Present address: Department of Physics and Astronomy, University of Delaware, Newark, DE 19716.

 0021-8979/96/79(8)/5309/3/$10.00 © 1996 American Institute of Physics

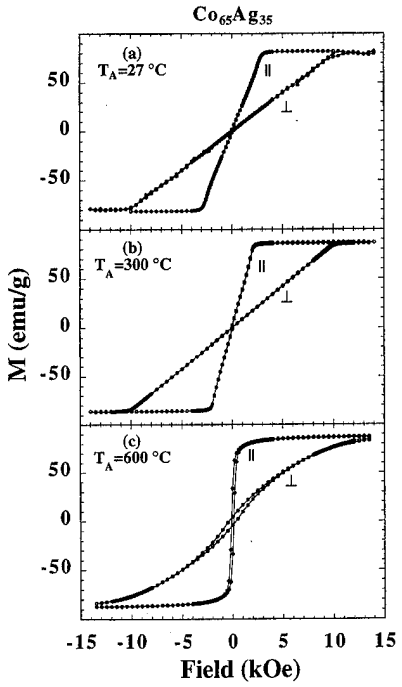


FIG. 2. Magnetic hysteresis loops with an in-plane (||, open symbols) and out-of-plane (⊥, solid symbols) external fields of $Co_{0.65}Ag_{0.35}$ annealed at (a) 27 °C, (b) 300 °C, and (c) 600 °C.

each case, solid and open symbols denote results of measurements with the external field applied parallel and perpendicular to the film plane, respectively. Beginning with the results shown in Fig. 2(a) for parallel field ($H_{\|}$), we note several unexpected features. A much larger than expected saturation field ($H_{s\|}$), of about 3 kOe, is required to align the magnetization in the film plane. The hysteresis loop with parallel field is linear in $H_{\|}$, exhibiting practically *zero* remanence and coercivity. The hysteresis should exhibit a large remanence and a coercivity of a few tens of Oe. The results obtained under a perpendicular field ($H_{\perp}$) are similar, except that the saturation field ($H_{S\perp}$) is even larger, about 10 kOe. The magnetization is also linear in $H_{\perp}$. These features, totally different from those of homogeneous and polycrystalline Co films, suggest the existence of a strong perpendicular anisotropy, in addition to the usual shape anisotropy. In Table I, we list the values of $H_{s\|}$, $H_{s\perp}$, and the saturation magnetization ($4\pi M_s$) for various samples of Co_xAg_{1-x} with $0.35 \leqslant x \leqslant 0.75$. Here the value of M_s is in emu/cm^3, that is, per volume of the Co_xAg_{1-x} sample.

TABLE I. Saturation fields in parallel field ($H_{S\|}$) and perpendicular field ($H_{S\perp}$), saturation magnetization ($4\pi M_S$), anisotropy constant (K) of granular Co_xAg_{1-x} with Co volume fraction x, and θ is the angle between the anisotropy axis and the film normal.

x	$H_{S\|}$ (Oe)	$H_{s\perp}$ (Oe)	$4\pi M_s$ (G)	K (10^6 ergs/cm^3)	θ (degree)
0.35	2630	4130	4273	0.42	0
0.40	3400	5670	5579	0.77	5
0.45	3670	6530	6672	0.94	0
0.50	3750	6250	6208	0.94	6
0.55	3600	7700	8004	1.05	0
0.65	3250	10200	9550	1.48	24
0.75	2600	12400	11008	1.75	36

To facilitate further discussion of this unexpected anisotropy, we first review the consequence of an additional magnetic anisotropy of energy K with an angle θ with respect to the film normal.[9] For the moment, we will neglect the magnetocrystalline energy for simplicity. When the magnetization is aligned in the film plane at $H=H_{s\|}$, we have

$$-\frac{1}{2}M_sH_{s\|}+K\cos^2\theta=0 \tag{1}$$

or

$$H_{\|}=\frac{2K\cos^2\theta}{M_s}. \tag{2}$$

Similarly, when the magnetization is aligned perpendicular to the film at $H=H_{s\perp}$, we have

$$2\pi M_s^2-\frac{1}{2}M_sH_{s\perp}+K\sin^2\theta=0 \tag{3}$$

or

$$H_{s\perp}=4\pi M_s+\frac{2K\sin^2\theta}{M_s}, \tag{4}$$

where the first term in Eq. (3) is the contribution of the demagnetization field. It may be noted that

$$H_{s\|}+H_{s\perp}=4\pi M_s+\frac{2K}{M_s}. \tag{5}$$

According to this simple analysis, from the experimentally measured values of $H_{s\|}$, $H_{s\perp}$, and M_s, one can determine the value of K using Eq. (5). The angle θ can be consistently determined using Eq. (2) or Eq. (4). We summarize these results in Table I. First, the unexpected hysteresis loops shown in Fig. 2, and the large values of $H_{s\|}$ and $H_{s\perp}$ can be well accounted for by using this simple model that includes an additional *uniaxial* anisotropy. This anisotropy is essentially *perpendicular* ($\theta \approx 0$) for granular samples with low volume fractions as well as those near the percolation threshold (e.g., $x \approx 0.5$). Only above the percolation threshold, does the angle θ increase with increasing Co concentration. We also note that the largely perpendicular anisotropy is not strong enough to overcome the demagnetization field: the magnetization axis does not spontaneously point in the normal direction of the film plane.

The deduced values of K, as listed in Table I, indicate that the perpendicular anisotropy is related to the volume fraction and hence to interparticle interactions. Its magnitude is minimum for samples with low values of x, becomes larger at larger x and surely becomes in-plane ($\theta=90°$) at $x=1$. Similar results have also been observed in other granular systems. We would also like to emphasize that the magnetic anisotropy with constant K here is different, in both magnitude and characteristics, from the magnetic surface anisotropy constant with K_s observed in certain magnetic multilayers. The value of $K \approx 1\times10^6$ ergs/cm^3 for granular Co-Ag is much smaller than $K_s=3$–7×10^6 ergs/cm^3 ob-

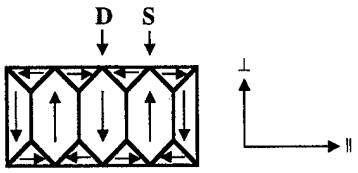


FIG. 3. Proposed domain structure of granular solids with perpendicular anisotropy, where "D" and "S" represent the "drain" and "source" points, respectively, observed in surface domain structure.

served in Co/Pd multilayers. Furthermore, in Co/Pd multilayers, the easy magnetic axis is perpendicular to the plane.[10]

As shown in Fig. 2(b), after annealing at $T_A=300$ °C, the results do not change appreciably. However, for the sample annealed at $T_A=600$ °C, the unusual hysteresis loop has reverted to the anticipated and normal shape, as shown in Fig. 2(c), having a square loop for the $H_{\|}$ measurement, and the $H_{\perp}$ loop extends to $4\pi M_s$. Furthermore, both loops exhibit a coercivity and a sizable remanence as homogeneous Co films would. Evidently, the subtle nanostructure that causes the perpendicular anisotropy has been altered by the $T_A=600$ °C annealing.

The highly unusual and certainly unexpected results from the magnetic measurements corroborate the domain structures recently imaged by SEMPA.[7,8] We would like to point out that the SEMPA technique is highly surface sensitive, whereas hysteresis loops are bulk magnetization measurements. At the sample surface, SEMPA measurements show stripe domains with alternating "sources" and "drains." Together with the results of the magnetic measurements, a model for the domains within the thickness of the sample is shown in Fig. 3. While most of the domains within the thin films are perpendicular to the film plane, the surface domain structures consist of stripes with alternating source and drain, which are indicated by the letters "S" and "D," respectively.

The key question is the source of this elusive anisotropy, which is largely perpendicular to the film plane, as shown in Fig. 3. All the results indicate that the perpendicular anisotropy is related to the nanostructure and not the materials. It may be emphasized again that the unexpected hysteresis loops occur only in phase-separated materials. In metastable alloys with no phase separation, using low substrate temperatures for example, one does not observe the unusual hysteresis loops. This rules out any deposition-related mechanisms. Since phase separation is a prerequisite, the nanostructure must contain unusual arrangements of the Co phase. While direct experimental verifications are underway, we suggest two possibilities. The Co phase may have a preferential crystalline orientation; then in the simple model outlined above, the anisotropy constant K is in fact the magnetocrystalline anisotropy constant, perhaps modified to reflect the far from ideal orientation. The value of $K\approx 10^6$ ergs/cm^3 is within an order of magnitude of the magnetocrystalline anisotropy constant for bulk Co.[9] The other possibility involves preferential arrangement of the Co particles in the direction perpendicular to the film plane. These scenarios can in principle be resolved using high-resolution characterizations.

In summary, we have found unusual hysteresis loops in magnetic granular solids. The hysteresis loops are characterized by large saturation fields and a linear dependence of the applied field with zero remanence and coercivity. These unusual results are due to the perpendicular anisotropy present in the phase-separated materials with certain nanostructure.

This work has been supported by ONR Grant No. N00014-91-J-1633. One of the authors (A.G.) was supported by the Technology Administration of the U.S. Department of Commerce and ONR.

[1] A. E. Berkowitz, J. R. Mitchell, M. Carey, A. P. Young, S. Zhang, F. E. Spada, F. T. Parker, A. Hutten, and G. Thomas, Phys. Rev. Lett. **68**, 3745 (1992).
[2] John Q. Xiao, J. S. Jiang, and C. L. Chien, Phys. Rev. Lett. **68**, 3749 (1992).
[3] See, e.g., C. L. Chien, J. Appl. Phys. **69**, 5267 (1991).
[4] P. Xiong, G. Xiao, J. Q. Wang, J. Q. Xiao, J. S. Jiang, and C. L. Chien, Phys. Rev. Lett. **69**, 3220 (1992).
[5] L. Piraux, M. Cassart, E. Grivei, M. Kinany-Alaoui, V. Bayot, J. S. Jiang, J. Q. Xiao, and C. L. Chien, J. Magn. Magn. Mater. **136**, 221 (1994).
[6] J. R. Childress and C. L. Chien, J. Appl. Phys. **70**, 5885 (1991).
[7] A. Gavrin, M. H. Kelly, J. Q. Xiao, and C. L. Chien, Appl. Phys. Lett. **66**, 1683 (1995).
[8] A. Gavrin, J. Q. Xiao, and C. L. Chien, these proceedings.
[9] See, e.g., A. H. Morrish, *The Physical Principles of Magnetism* (Wiley, New York, 1965).
[10] B. N. Engel, C. D. England, R. A. van Leeuwen, M. Nakada, and C. M. Falco, J. Appl. Phys. **69**, 5643 (1991); **70**, 5873 (1991).

Self-stabilized magnetic colloids: Ultrafine Co particles in polymers

Diandra L. Leslie-Pelecky,[a] X. Q. Zhang,[b] and Reuben D. Rieke[b]
Center for Materials Research & Analysis, University of Nebraska, Lincoln, Nebraska 68588

Self-stabilized magnetic colloids consist of magnetic particles dispersed in an appropriate matrix. Fixing the particles in a stabilizing matrix has the advantage of preventing particle agglomeration, increasing resistance to oxidation, and allowing control over the interparticle spacing and particle size. We describe the chemical synthesis of cobalt nanoparticles in a polystyrene/triphenylphosphine polymer matrix. Depending on the synthesis parameters, magnetic properties of the as-synthesized nanocomposites range from superparamagnetic to ferromagnetic with coercivities on the order of 130 Oe. Solvent choice and polymer crosslinking significantly affect the magnetic properties. Annealing in vacuum produces coercivities of up to 600 Oe and remanence ratios of up to 0.4. Measurement of the isothermal remanence magnetization and dc demagnetization indicate the presence of both magnetizing and demagnetizing interactions, in contrast to particles synthesized without the polymer, which show no evidence for magnetizing interactions. The zero-field-cooled temperature-dependent magnetization displays a cusp, while the field-cooled magnetization increases monotonically below the cusp temperature. Glassy behavior is observed for temperatures below the cusp, although the mechanism producing this behavior is not yet understood. © *1996 American Institute of Physics.* [S0021-8979(96)01908-3]

Nanoscale particles have unique electrical, chemical, structural, and magnetic properties, with potential applications in information storage, color imaging, catalysis, bioprocessing, magnetic refrigeration, and ferrofluids.[1] Fabrication techniques for the production of ultrafine particles include: gas condensation,[2] inverse micelle synthesis,[3] arc techniques,[4] sputtering,[5,6] self-assembled phospholipids,[7] chemical reduction,[8–10] and microemulsion synthesis[11] among others. Studies of these systems are often hampered by two problems. First, the large ratio of surface-to-bulk atoms results in high reactivity. While desirable for catalysis, reaction with oxygen can adversely affect magnetic properties. Controlled passivation can deactivate the particle surface; however, this may form additional magnetic phases that complicate analysis. The second problem is the spontaneous production of macroscopic-sized agglomerates that lack the unique properties of nanoscale particles.

The fabrication of highly reactive particles by the reduction of metal halides was pioneered by Rieke and collaborators.[9] In this technique, a metal salt is reduced using a hydrocarbon or ethereal solvent in the presence of lithium and naphthalene. We have extended this technique to fabricate cobalt particles in a polymer matrix, which decreases agglomeration and improves oxidation resistance.

Self-stabilized colloids have been fabricated using other techniques, including ion exchange[1,12] and sputtering;[6] however, in most cases the particle size is small and cannot be conveniently varied. These systems tend to be superparamagnetic unless the metal volume concentration is above the percolation point. On the other end of the size scale, macroscopic composites of 10–100 μm transition metal[13] and ferrite[14] powders in polymers have been fabricated to study modifications of electrical and magnetic properties.

We have synthesized Co nanocomposites using a polystyrene backbone and triphenylphospine sidechains. Samples have been synthesized using both a commercially available crosslinked polymer and a linear polymer. Different solvents were chosen to assist in the synthesis: solvent choice has been shown to affect particle size during standard syntheses[9] (i.e., without the polymeric matrix). The cobalt loading was determined to be 70% through chemical assaying. X-ray diffraction of the as-synthesized samples shows no evidence of crystalline cobalt; however, the volume fraction of the cobalt compared to the polymer is very small.

Samples were sealed in Pyrex tubes under vacuum and annealed at temperatures up 350 °C for the crosslinked samples and 160 °C for the linear samples. Magnetic measurements were made using an alternating gradient force magnetometer and a SQUID susceptometer. In both cases, powders were loaded into a paraffin-filled polyethylene bag in an argon atmosphere. The samples were sealed into the bags and the paraffin melted to prevent magnetization rotation due to physical rotation of an entire particle. All bagged samples were stored in a vacuum dessicator.

All of the samples were ferromagnetic in their as-synthesized state, except for the linear polymer synthesized with THF, which was superparamagnetic. Table I summarizes the magnetic parameters for each of the different syntheses. The choice of polymer type and solvent produce significant variations in the magnetic properties of the four runs. Solvent selection has been shown to affect particle size in similar syntheses,[15] as has the degree of crosslinking.

TABLE I. Summary of magnetic properties of as-synthesized nanocomposites.

Run #	Crosslinking	Solvent	H_c (Oe)	M_r/M_s
33	Crosslinked	Ether	56	0.083
34	Crosslinked	Toluene	133	0.151
57	Linear	Toluene	49	0.021
58	Linear	Tetrahydrofuran (THF)	8	0.004

[a]Department of Physics and Astronomy.
[b]Department of Chemistry.

 0021-8979/96/79(8)/5312/3/$10.00 © 1996 American Institute of Physics

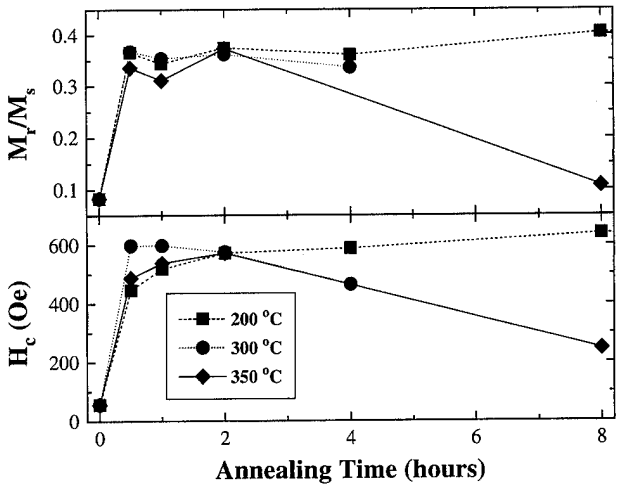


FIG. 1. The dependence of the coercivity H_c and the remanence ratio M_r/M_s on annealing time at different temperatures for Run 33 (crosslinked polymer, ether solvent).

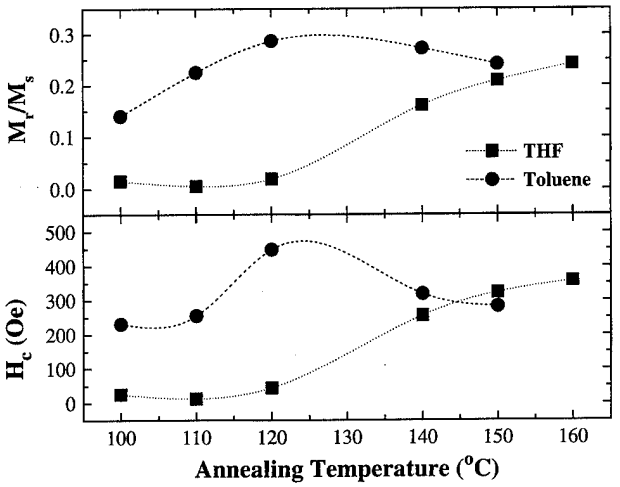


FIG. 2. The dependence of the coercivity H_c and the remanence ratio M_r/M_s on annealing temperature for samples made with initially linear polymer. Samples made with THF are shown as squares and those made with toluene are shown as circles.

Figure 1 shows the dependence of the coercivity H_c and remanence ratio M_r/M_s on annealing time for Run 33 (crosslinked polymer, ether solvent). H_c rises rapidly from 56 to 450–600 Oe after short (<1 h) annealing times. Samples annealed at $T>300$ °C experience a significant decrease in coercivity after 2 h of annealing. Longer annealing times at lower temperatures result in a slight continued increase in both H_c and M_r/M_s, with values plateauing after about 10 h. Samples annealed at $T<200$ °C (not shown in Fig. 1) follow the same qualitative behavior as the data shown for annealing at 200 °C, but plateau at lower values. Similar behavior is observed for Run 34 (initially crosslinked polymer, toluene solvent). This run has a higher initial H_c, but annealing produces less of an increase in the coercivity and the remanence ratio. H_c never rises above 225 Oe and M_r/M_s is $\leqslant 0.2$ for all annealing conditions.

The effect of solvent choice on particle size and crystallinity is not well understood. One possibility is that the solvents form protective coatings around the particles, limiting particle size. Our studies of particles synthesized without the polymer matrix suggest that the metal particles are initially crystalline on the scale of 2–5 nm, with amorphous material surrounding the crystallites. Short-time annealing slightly increases the size of the crystallites without allowing significant agglomeration. Transmission electron microscopy and mass calculations of particle syntheses without a matrix indicate that lithium, naphthalene and/or some of the solvent is retained within the particles. Annealing may vaporize trapped organics, allowing crystallite growth.

In the initially linear polymers, annealing was performed at temperatures up to 160 °C (20 °C above the glass transition temperature of the undoped polymer). H_c and M_r/M_s both initially rise with increasing annealing time, then plateau around 2–4 h, regardless of the annealing temperature. Figure 2 shows H_c and M_r/M_s as a function of annealing temperature for samples annealed for 1 h. The toluene-based samples (shown as circles) achieve maximum coercivity and remanence ratio for annealing temperatures of 125–130 °C, while the THF-based samples (shown as squares) display monotonically increasing values of these parameters with increasing annealing temperature.

The isothermal remanent magnetization (IRM) and dc demagnetization (DCD) have been measured to investigate the nature of the magnetic interactions. The IRM is measured from a field demagnetized state in which the initial moment is <0.1% M_s. Kelly *et al.*,[16] following Wohlfarth,[17] suggested that deviations from the ideal system of single-domain, noninteracting uniaxial particles will have a nonzero value of ΔM, where ΔM is defined by

$$\Delta M(H)=\frac{M^{\mathrm{DCD}}(H)}{M^{\mathrm{IRM}}(\infty)}-\left(1-2\frac{M^{\mathrm{IRM}}(H)}{M^{\mathrm{IRM}}(\infty)}\right). \tag{1}$$

Positive values of $\Delta M(H)$ are due to stabilizing (ferromagnetic) interactions, while negative values can be attributed to demagnetizing (antiferromagnetic) interactions. Fig-

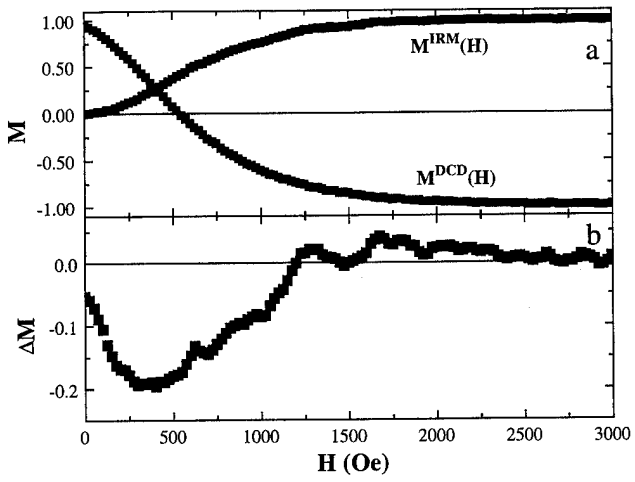


FIG. 3. (a) The isothermal remanence magnetization $M^{\mathrm{IRM}}(H)$ and the dc demagnetization remanence $M^{\mathrm{DCD}}(H)$. (b) The quantity ΔM, as defined by Eq. (1).

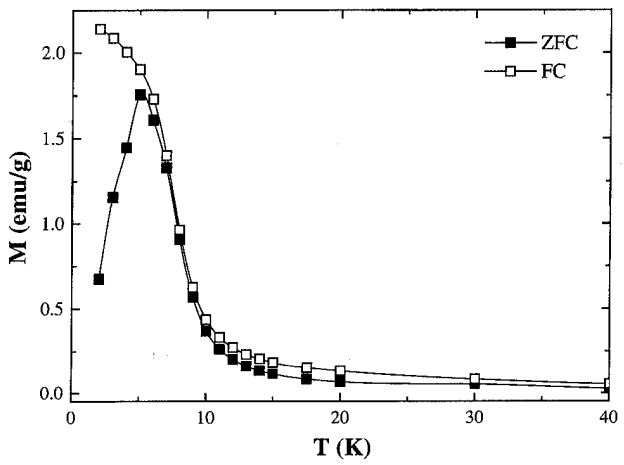


FIG. 4. The zero-field-cooled (ZFC) and field-cooled (FC) magnetization. The magnetization is normalized to the density of the nanocomposite.

ure 3(a) shows $M^{\mathrm{DCD}}(H)$ and $M^{\mathrm{IRM}}(H)$ (both normalized) for a sample from Run 34 (crosslinked polymer, toluene solvent) annealed at 200 °C for 8 h. Figure 3(b), which shows $\Delta M(H)$, indicates the presence of both magnetizing and demagnetizing interactions. The predominantly demagnetizing interactions seen in Fig. 3(b) are consistent with the remanence ratio of 0.33 for this sample. The presence of both types of interactions in the same sample has been previously observed.[18,19] Contrary to the nanocomposites, particles without the polymer matrix do not exhibit evidence of any magnetizing interactions. The data shown in Fig. 3 are qualitatively representative of both crosslinked and linear polymer samples, although the ratio of magnetizing to demagnetizing interactions varies with annealing time and solvent choice.

$M(T,H=100$ Oe) is shown in Fig. 4 for field-cooled (FC) and zero-field-cooled (ZFC) measurements of an unannealed sample from Run 57 (linear polymer, toluene solvent). The undoped polymer exhibits a diamagnetic plus a Curie–Weiss magnetization with no dependence on the presence of a cooling field. The ZFC magnetization exhibits a cusp at about 5 K, with the temperature of the cusp decreasing as the interactions—measured by the remanence ratio—decrease. The width of the cusp increases in more strongly interacting systems. The FC magnetization follows the ZFC curve until a temperature of about 10 K, at which point the two curves depart and the FC curve continues to rise. As the measuring field increases, the cusp temperature decreases, and the cusp broadens and flattens. Measurements below the cusp temperature show behavior similar to that seen in glassy systems, such as spin glasses and frozen ferrofluids with random anisotropy;[20] however, more detailed, systematic measurements are required to determine the nature of the phenomena producing the cusp.

In conclusion, we have demonstrated a synthesis technique for fabricating self-stabilized magnetic colloids consisting of cobalt nanoparticles embedded in a polymer matrix. Variation of solvent type, degree of polymer crosslinking, and annealing parameters can all significantly affect the magnetic properties. Determination of structural properties, which is complicated by the small volume fraction of cobalt to polymer, is necessary to better understand the magnetic properties. Each of the fabricated systems exhibits a cusp in the zero-field-cooled magnetization, and differences between the field-cooled and zero-field-cooled behavior. Data taken below the cusp is indicative of glassy behavior. Much work remains to better understand the properties of this novel system.

We acknowledge financial support from the National Science Foundation and the Center for Materials Research and Analysis at UNL.

[1] R. F. Ziolo, E. P. Giannelis, B. Weinstein, M. P. O'Horo, B. N. Ganguly, V. Mehrotra, M. W. Russell, and D. R. Huffman, Science **257**, 219 (1992), and references therein.
[2] J. Eastman and R. W. Siegel, Research and Development, January, 56 (1989); R. W. Siegel, Nanostructured Mater. **4**, 121 (1994); H. Gleiter, Prog. Mater. Sci. **33**, 223 (1989).
[3] J. P. Chen, K. M. Lee, C. M. Sorenson, K. J. Klabunde, and G. C. Hadjipanayis, J. Appl. Phys. **75**, 5876 (1994).
[4] M. E. McHenry, S. A. Majetich, M. DeGraef, J. O. Artman, and S. W. Staley, Phys. Rev. B **49**, 11358 (1994); M. E. McHenry, Y. Nakamura, S. Kirkpatrick, F. Johnson, S. A. Majectich, and E. M. Brunsman, in *Fullerenes: Physics, Chemistry, and New Directions VI*, edited by R. S. Ruoff and K. M. Kadish (The Electrochemical Society, Pennington, NJ, 1994), p. 1463.
[5] T. Ambrose, A. Gavrin, and C. AL. Chien, J. Magn. Magn. Mater. **116**, L311 (1992).
[6] C. Laurent, D. Mauri, E. Kay, and S. S. P. Parkin, J. Appl. Phys. **65**, 2017 (1989).
[7] A. Singh, M. Markowitz, and G. M. Chow, Nanostructured Mater. **5**, 141 (1995).
[8] L. Yiping, G. C. Hadjipanyayis, C. M. Sorenson, and K. J. Klabunde, J. Appl. Phys. **69**, 5141 (1991).
[9] R. D. Rieke, Crit. Rev. Surf. Chem. **1**, 131 (1991), and references therein.
[10] D. L. Leslie-Pelecky, X. Q. Zhang, G. L. Krichau, and R. D. Rieke, Proc. Chem. Soc. Div. Polym. Mater. Sci. Eng. **73**, 66 (1995).
[11] J. P. Chen, K. M. Lee, C. M.Sorenson, K. J. Klabunde, and G. C. Hadjipanayis, J. Appl. Phys. **75**, 5876 (1994).
[12] R. F. Ziolo, E. P. Giannelis, and R. D. Shull, Nanostructured Mater. **3**, 85 (1993).
[13] A. Etawansi, N. Kinawy, and M. Emitwally, J. Mater. Sci. **24**, 2497 (1989).
[14] J. Yacubowicz and M. Narkis, Poly. Eng. Sci. **30**, 469 (1990).
[15] S. S. Kher and R. Wells, Chem. Mater. **6**, 2056 (1994).
[16] P. E. Kelly, K. O'Grady, P. I. Mayo, and R. W. Chantrell, IEEE Trans. Magn. **MAG-25**, 3881 (1989).
[17] E. P. Wohlfarth, J. Appl. Phys. **29**, 595 (1958).
[18] P. I. Mayo, A. Bradbury, R. W. Chantrell, P. E. Kelly, H. E. Jones, and P. R. Bissell, IEEE Trans. Magn. **MAG-26**, 229 (1991).
[19] P. I. Mayo, R. M. Erkkila, A. Bradbury, and R. W. Chantrell, IEEE Trans. Magn. **MAG-26**, 1894 (1991).
[20] W. Luo, S. R. Nagel, R. F. Rosenbaum, and R. E. Rosenzweig, Phys. Rev. Lett. **67**, 2721 (1991).

Complementary imaging of granular Co-Ag films with magneto-optical indicator film technique and magnetic force microscopy

M. J. Donahue, L. H. Bennett, R. D. McMichael, L. J. Swartzendruber, and A. J. Shapiro
National Institute of Standards and Technology, Gaithersburg, Maryland 20899

V. I. Nikitenko, V. S. Gornakov, L. M. Dedukh, and A. F. Khapikov
Institute of Solid State Physics RAS, Chernogolovka, Moscow District, 142432, Russia

V. N. Matveev and V. I. Levashov
Institute of Microelectronics Technology and High Purity Materials RAS, Chernogolovka, Moscow District 142432, Russia

A magneto-optical indicator film (MOIF) technique and magnetic force microscopy were used for visualization and direct real-time experimental study of the magnetization processes of magnetic $Co_{90}Ag_{10}$ granular films. It is shown that the magnetization reversal of the as-deposited films follows a specific two-step course. The first stage is characterized by gradual spin rotation to large angles up to 90° without domain formation. Further magnetization reversal proceeds by the nucleation and motion of zigzag-shaped domain walls. The dendritic structure of the domain walls was observed using both techniques. Also tracks of magnetic inhomogeneities remaining behind moving zigzag-shaped domain walls was revealed by MOIF. © *1996 American Institute of Physics.* [S0021-8979(96)05008-3]

In the last few years nanostructured materials consisting of magnetic and nonmagnetic components have attracted a great deal of attention.[1,2] It has been discovered that such materials exhibit peculiar properties, in particular giant magneto resistance. These materials are very attractive for use in the next generation of magnetic field sensors and computer disk drive reading elements. As a result, the development of experimental techniques for the investigation of real-time magnetization dynamics and nondestructive characterization of magnetic multilayered and clustered systems is of great interest.[3–6]

In this paper we demonstrate the use of a novel magneto-optical indicator film (MOIF) technique for the study of ferromagnetic granular films. The MOIF technique was initially developed for investigation of magnetization processes and quality characterization of high-temperature superconductors,[7] and has more recently been used to study magnetic multilayers.[8] We also illustrate the use of magnetic force microscopy (MFM) as a complementary method to MOIF. With MFM one can study magnetic structures smaller than can be resolved via MOIF. Magnetic features as small as 10 nm have been reported using MFM,[9] but such resolution is sample dependent, and the sample studied here revealed no significant features smaller than about 250 nm.

The Co-Ag granular films were prepared at room temperature by laser sputtering on glass substrates in a vacuum chamber at a pressure of approximately 10^{-4} Pa. A 1.06 μm wavelength pulse laser was used with 10 ns pulses at a rate of 25 s^{-1}. The target was pressed from Co and Ag powders and annealed in a vacuum at 800 °C for 4 h. The nominal composition of the 1000-Å-thick films was 90% Co and 10% Ag (atomic fractions). The grain size was shown by scanning electron microscopy to be $\approx$0.2 μm.

The MOIF technique[7,8] places on top of the sample a transparent Bi-substituted iron garnet indicator film with in-plane anisotropy. Polarized light is passed through the indicator film and is reflected by an Al underlayer. The normal component of the magnetic stray field (B_z) is detected in a polarized microscope by the magneto-optic Faraday effect.

The magnetic force microscopy (MFM) investigations employed a standard commercial microscope utilizing a dual scan technique. In the first pass a cantilever with an integral magnetized tip is tapped along the surface to determine the sample's topography. A second scan is then performed that tracks at a constant height (typically $\approx$75 nm) above the surface while vibrating the cantilever. In contrast to the MOIF technique which responds to B_z, the MFM is sensitive to $\partial B_z/\partial z$ or $\partial^2 B_z/\partial z^2$.[10,11]

A typical granular film magnetization reversal is illustrated in Figs. 1(a)–1(f). Figure 1(a) shows the MOIF image resulting from a saturating in-plane magnetic field of 150 mT

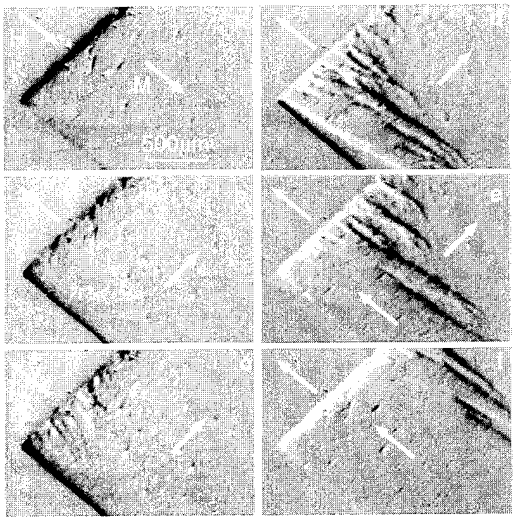


FIG. 1. MOIF patterns demonstrating a two-step magnetization of a ferromagnetic granular $Co_{90}Ag_{10}$ film. Direction of magnetic field H and approximate magnetization vectors are indicated. (a) H=150 mT, (b) −2.4 mT, (c) −2.65 mT, (d),(e) −3.05 mT, (f) −3.4 mT. (e) is obtained within 30 s of (d).

 0021-8979/96/79(8)/5315/3/$10.00 © 1996 American Institute of Physics

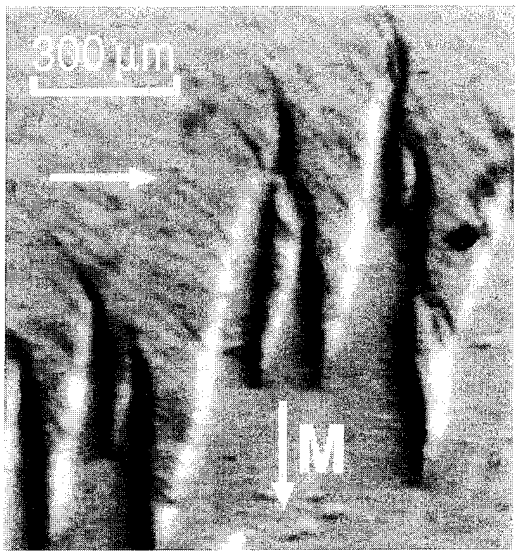


FIG. 2. MOIF image of tree-like domain walls.

directed parallel to the lower left edge of the film. The dark thin stripe indicates magnetic flux entering the sample through the edge perpendicular to the external field. The gray tone of the edge parallel to the field indicates that the magnetization is directed along this edge. This image changes only slightly as the applied field is reduced to zero, but when a field in the opposite direction is applied and is slowly increased, the MOIF pattern changes. Figure 1(b) was obtained after the field was brought to -2.4 mT. The edge parallel to the applied field becomes dark, whereas the perpendicular edge is seen to be gray, indicating that the magnetization has rotated to the direction approximately perpendicular to the magnetic field. The magnetization rotation proceeds gradually and somewhat nonuniformly as the magnetic field is increased. A further increase in the applied field causes the nucleation and growth of domains with magnetization parallel to the external field [Figs. 1(c)–1(f)]. The direction of the magnetization in the domains is established by analysis of the stray fields at the sample edges [compare, for example, the tone of the sample edges in Figs. 1(e) and 1(f)], and has been independently verified via vector vibrating sample magnetometer (VSM) measurements.

An important feature of the motion of the nucleated 90° domain walls is their creep. This phenomenon is apparent from a comparison of Figs. 1(d) and 1(e) which are at the same field value, but Fig. 1(e) was obtained within 30 s of Fig. 1(d). Although the applied field is not changed, a considerable displacement of the domain walls is observed. Time dependence of magnetization is often found to follow the form $M=M_0-S\ln(t/\tau)$. The magnetic viscosity coefficient S has been shown to be related to the irreversible susceptibility, $\chi_{\rm irr}$ by $S=kT\chi_{\rm irr}/vM$, where v is the activation volume, roughly the inverse of the pinning site density.[12] Because $\chi_{\rm irr}$ is large and we expect a high density of pinning sites at Ag inclusions in the predominantly Co film, significant time-dependent effects are not surprising.

The two-step magnetization process (gradual rotation of the magnetization up to a large angle followed by nucleation and growth of domains) is observed when the the external magnetic is applied in any direction in the film plane, although the details may differ. In particular, the critical magnetization angle and the form and size of the domain walls will vary with the field direction, though they are always arranged along the magnetic field direction. VSM measurements have confirmed a uniaxial anisotropy much smaller than the magnetocrystalline anisotropy of pure Co granules, so it is reasonable to suspect that these films are comprised of randomly oriented uniaxial Co clusters coupled by strong exchange interactions.

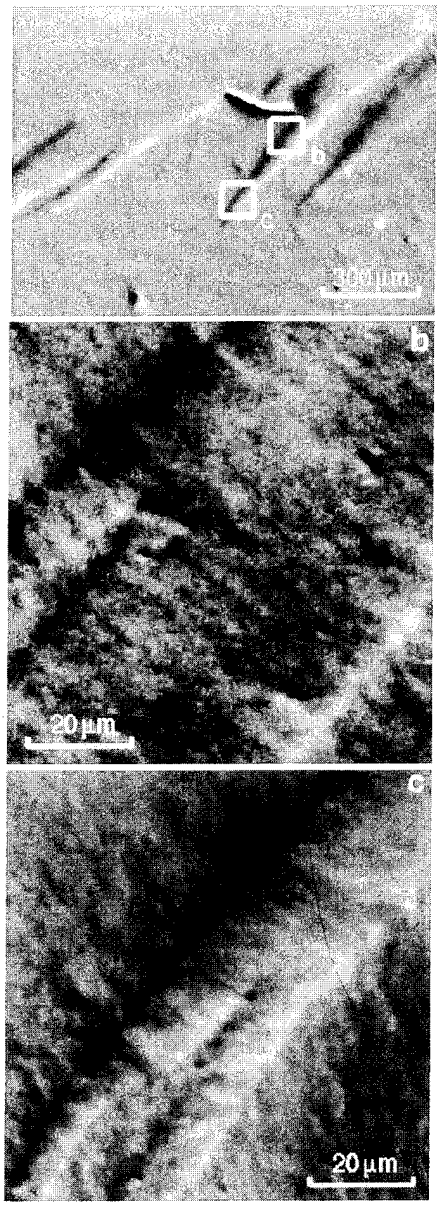


FIG. 3. Domain structures in a Co-Ag granular film, imaged by (a) MOIF, and (b),(c) higher-resolution MFM as indicated.

The large-scale domain walls shown in Fig. 2 have a zigzag form typical for charged walls, but a more fine tree-like structure can also be discerned. A similar structure is studied in Fig. 3, where one section of the film is imaged using both MOIF and MFM, in zero applied field. Figure 3(a) is the MOIF image, with two rectangles indicating the

regions where higher resolution MFM scans were performed [Figs. 3(b) and 3(c)]. It is clear from the first MFM image that the black line has a complicated structure with multiple sections. This can just be discerned in the MOIF image, but the fine cross-tie pattern revealed by the MFM scans is not evident in Fig. 3(a). Figure 3(c) shows that the tip of the sawtooth has a more complicated dendritic structure than is apparent from the MOIF image. Just outside and below this image is a micron-scale pit in the film surface that was detected by the topographical portion of the MFM scan. This imperfection is most likely responsible for the pinning of the domain wall and some of the features observed in Fig. 3(c).

The tree-like domain wall dynamics are found to be irreversible in the following sense: if the magnetic field sweep is stopped and reversed, existing domain walls remain at rest, and new domain walls nucleate at the edge of the sample and move toward and eventually annihilate the old domain walls. Figure 4 illustrates light "ghost" tracks that occur immediately following the passage of zigzag-shaped domain walls. These tracks require from 5 to 30 min to disappear, even without an applied field.

To summarize, we have shown the Co-Ag granular film magnetization sequence to be comprised of a large-angle magnetization rotation followed by domain wall nucleation and motion. Although a uniaxial in-plane anisotropy was detected by vector VSM measurements, a simple model including the uniaxial anisotropy would not explain the high remanence and the near 90° magnetization rotation observed for most directions of the applied field.

The domain wall pattern was observed through a complementary combination of MOIF and MFM techniques to have a fractal-like structure. The domain walls exhibited time-dependent creep in constant field, and moving domain walls were observed to leave magnetic "tracks" in the magnetization.

We thank H. J. Brown for assistance with measurements. Russian co-workers from the Institute of Solid State Physics acknowledge partial support from the International Science Foundation under Grant No. REO000.



FIG. 4. MOIF image of magnetic tracks (light stripes) remaining after passage of zigzag-shaped domain walls.

[1] *Magnetic Multilayers*, edited by L. H. Bennett and R. E. Watson (World Scientific, River Edge, NJ, 1994).

[2] J.-Q. Wang and G. Xiao, Phys. Rev. B **49**, 3982 (1994).

[3] M. Rührig, R. Schäfer, A. Hubert, R. Mosler, J. A. Wolf, S. Demokritov, and P. Grünberg. Phys. Status Solidi A **125**, 635 (1991).

[4] A. Gavrin, M. H. Kelley, J. Q. Xiao, and C. L. Chien, Appl. Phys. Lett. **66**, 1683 (1995).

[5] L. J. Heyderman, J. N. Chapman, and S. S. Parkin, J. Phys. D **27**, 881 (1994).

[6] G. Bochi, C. A. Ballentine, H. E. Inglefield, C. V. Thompson, R. C. O'Handley, H. J. Hug, B. Stiefel, A. Moser, and H.-J. Güntherodt, Phys. Rev. B **52**, 7311 (1995).

[7] L. A. Dorosinskii, M. V. Indenbom, V. I. Nikitenko, Yu. A. Ossip'yan, A. A. Polyanskii, and V. K. Vlasko-Vlasov, Physica C **203**, 149 (1992).

[8] L. H. Bennett, R. D. McMichael, L. J. Swartzendruber, S. Hua, D. S. Lashmore, A. J. Shapiro, V. S. Gornakov, L. M. Dedukh, and V. I. Nikitenko, Appl. Phys. Lett. **66**, 888 (1995).

[9] P. Grütter, A. Wadas, E. Meyer, H. Heinzelmann, H.-R. Hidber, and H.-J. Güntherodt, J. Vac. Sci. Technol. A **8**, 406 (1990).

[10] C. Schönenberger and S. F. Alvarado, Z. Phys. B **80**, 373 (1990).

[11] T. Chang, M. Lagerquist, J.-G. Zhu, and J. H. Judy, IEEE Trans. Magn. **MAG-28**, 3138 (1992).

[12] P. Gaunt, J. Appl. Phys. **59**, 4129 (1986).

Perpendicular spin valve behavior in a microstructured Co/Cu-Cu oxide/Co trilayer

K. Matsuyama, H. Asada, I. Matsuguma, T. Saeki, and K. Taniguchi
Department of Electrical Engineering, Kyushu University 36, Fukuoka 812, Japan

In this article we report a perpendicular spin valve behavior in a microstructured noncoupling magnetic trilayer system of Co/Cu-Cu oxide/Co. The Co thin films having markedly different coercivity H_c were prepared with a vacuum evaporation with electron beam (H_c= 20–30 Oe) and rf sputtering (H_c= 90–260 Oe), which enables the selective switching of the magnetization in the base and counter Co layers. The film surface of the Cu was oxidized by the rf sputter etching, which results in the increase of the resistance for the perpendicular current and enables measurements of the perpendicular spin valve behavior at room temperature. The additional spacer layer of sputtered SiO_2 with a contact hole of 5 μm diameter was fabricated with photolithographic method between the bottom Co and the intermediate Cu layer, which defined the current path perpendicular to the film plane. The measured magnetoresistance ratio was 0.85% (dR=7.6 mΩ, R=0.89 Ω) at room temperature. © *1996 American Institute of Physics.* [S0021-8979(96)40508-0]

I. INTRODUCTION

Studies on the magnetoresistance (MR) in a current perpendicular to the film plane (CPP) are believed to provide a fundamental insight into spin polarized electron transport. One of the difficulties in the experiments on CPP MR is to detect a very small resistance due to the particular current path geometry. The use of superconducting electrodes[1] or the microfabrication techniques[2,3] have enabled the experiments on CPP MR. The other promising device structure is that it consists of ferromagneto–insulator–ferromagneto (FIF) multilayer, where the resistance for the CPP current is expected to be large due to a potential barrier at the insulating layer. The magnetic tunneling valve (MTV) effects have been observed in various FIF systems,[4–6] where the tunneling conductance depends on the relative spin orientation in the two magnetic layers. In the previous work,[7] we observed the MTV effect in a microfabricated FIF junction consisting of a NiFe/Al-Al_2O_3/Co system. In the present study, the Co films were used for both magnetic layers to increase the MR ratio, considering an enhanced spin polarization in the Co.[8] The dependence of the coercivity on a substrate temperature in the rf sputtering has been studied to realize an antiparallel spin orientation for the two Co layers. The surface oxidation layer on the intermediate Cu, produced with the rf sputter oxidation,[9] was used as an insulating layer in this study. A CPP spin valve behavior has been studied for a microfabricated perpendicular current path with a dc four-terminal method.

II. DEVICE FABRICATION

Schematic figures for the top and cross-section view for a fabricated device are shown in Fig. 1. The designed electrode configuration allows limited components of the current contribute the voltage drop, that is, the perpendicular component to the film plane and the in-plane component parallel to the applied field H. Test chips containing six junctions were fabricated on a 1.0×1.0×0.04 cm glass substrate. The multilayer system of Co/Cu-Cu oxide/Co was studied in this work. The two different deposition methods of vacuum evaporation with electron beam and rf sputtering were adopted for the fabrication of the base and counter Co layer. Representative values for the thicknesses of base Co, Cu, and counter Co layers were 0.1, 0.03, and 0.1 μm, respectively. The sputter deposited SiO_2 layer of 0.4 μm thickness was used as a spacing layer between the electrodes. The perpendicular current path was confined with a fine contact hole of 5 μm diameter in the SiO_2 insulating layer.

Microfabrication techniques used in this study are as follows. Lithography for electrodes and the contact hole was performed by the ion milling, with 600 V Ar of 0.6 mA/cm^2 current density, using a photoresist mask. A leak free insulation by the SiO_2 spacing layer was confirmed by a process test chip with no contact hole. A dummy substrate was also used to detect the milling end point to produce a contact hole

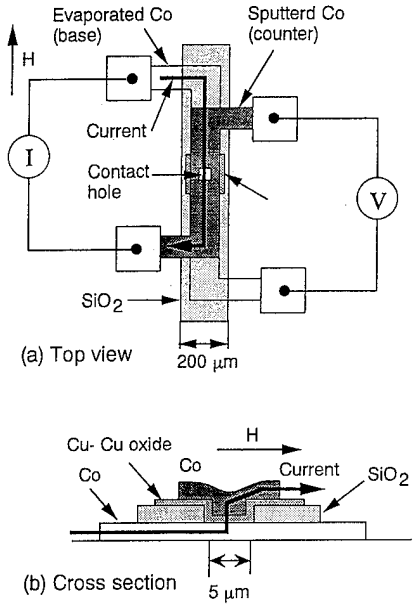


FIG. 1. Configuration of a microstructured device for measurement of CPP MR behavior. (a) Top view of device and experimental setup. (b) Schematic cross-section view.

 0021-8979/96/79(8)/5318/3/$10.00 © 1996 American Institute of Physics

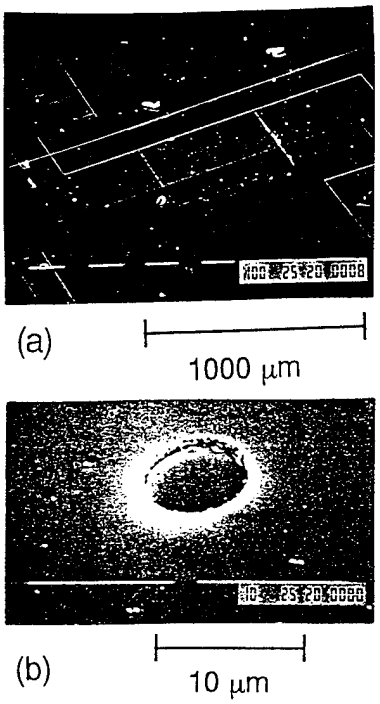


FIG. 2. SEM photographs of a fabricated device. (a) Whole view of device. (b) Contact hole produced in a SiO_2 spacing layer.

with the designed thickness. The spacer layer SiO_2 was deposited on the dummy substrate, with a predeposited thin metal film of 0.01 μm. The milling end was detected by observing the disappearance of under coated metal film in the dummy one. There is no significant influence on the MR behavior due to the overmilling of 0.01 μm on the bottom electrode of the Co layer. The rf sputter etching in oxygen plasma was adopted for producing the Cu oxidation layer; typical oxidation parameters used were oxygen pressure of 50 mTorr and rf power density of 0.4 W/cm^2. Immediately after the oxidation, the rf power was switched from the substrate holder to the cathode with Co target for the counter layer deposition. A 10 min backsputter was performed for the surface cleaning with 0.8 W/cm^2 rf power and 40 mTorr Ar pressure, before the deposition of Cu layer and the sputter oxidation of the Cu layer. SEM photographs of whole view and the contact hole of the fabricated device are shown in Fig. 2. The fine contact hole with the flatly shaped bottom surface was successfully produced by the Ar ion milling. Protublences at the contact hole edge would be formed by the redeposition of the sputtered SiO_2.

The Co films with lower coercive field of 20–30 Oe were deposited by an *e*-gun type vacuum evaporation system with the following parameters: base pressure $<3\times10^{-6}$ Torr, deposition rate 0.4 Å/s at an ambient temperature. Relatively hard Co films were deposited with a rf diode sputtering system. The dependence of the coercive field and the remanence ratio on the substrate temperature have been studied, as shown in Fig. 3. All of these samples were deposited with a rf power of 2.1 W/cm^2 and an Ar pressure of 20 mTorr, whose thickness was around 0.1 μm. The prominent tem-

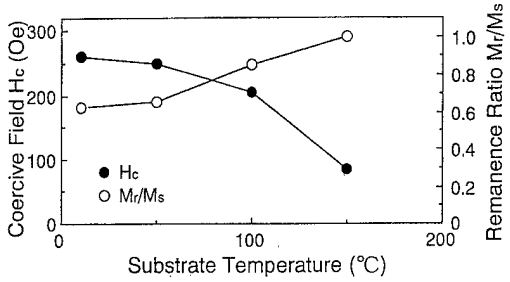


FIG. 3. Dependence of magnetic properties on substrate temperature for rf sputter deposition.

perature dependence of the magnetic properties would be associated with the different film structure (grain size). The substrate temperature of 150 °C was adopted for the device fabrication, considering a high remanence ratio, which leads to a well defined antiparallel magnetization configuration in the remanent state. Saturation induction $4\pi M_s$ for the evaporated and the sputtered Co were 14–15 kG and 11–13 kG, respectively. The lower saturation induction in the sputtered Co would be due to the inclusion of Ar during the deposition.

III. RESULTS AND DISCUSSIONS

Figure 4 shows a *M-H* hysteresis for a trilayer sample prepared simultaneously with the device, except that no photolithographic process was performed on it. The asymmetry in the hysteresis could be ascribed to the oxidation of Co at the surface or the interface between the oxidized Cu layer. The difference of the coercive field between the single layer (Fig. 3) and trilayer sample can be ascribed to the difference of under layer, that is, the former is sputtered on the glass substrate, while the latter on the oxidized Cu layer. The appearance of the intermediate shoulder in the *M-H* hysteresis confirms the selective switching in the two Co layers. However, a not so sharp intermediate shoulder suggests an occurrence of cooperative magnetization switching in the two layers, which would be caused by a local ferromagnetic exchange coupling or a magnetostatic interaction between them.

A measured MR hysteresis for the fabricated device is shown in Fig. 5. A comparison between the *M-H* and MR hysteresis confirms the dependence of the resistance on the relative angle between the magnetization direction in the two

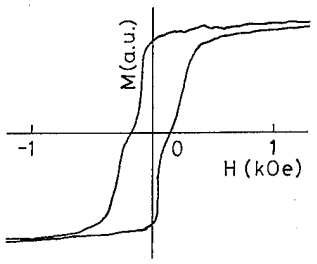


FIG. 4. *M-H* hysteresis curve for a Co (evaporated)/Cu-Cu oxide/Co (sputtered) trilayer film.

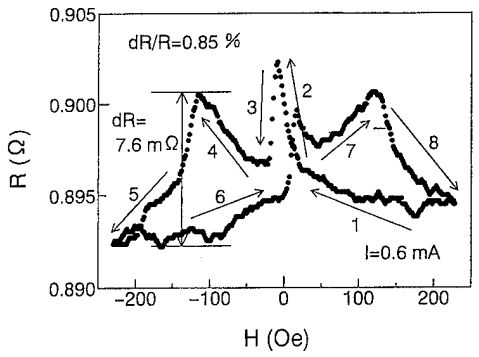


FIG. 5. Magnetoresistance hysteresis measured at room temperature for a perpendicular current confined with a 5-μm-diam contact hole.

Co layers. However, the complicated magnetization switching behavior suggested in the MR hysteresis was not observed in the *M-H* hysteresis. We suspect that the MR hysteresis is related to the switching of the magnetization direction in the local region where the thickness of the CuO insulating layer is relatively thin, while the *M-H* hysteresis presents the averaged magnetization. Another probable cause for the difference is the change of the magnetic properties due to the fabrication process.

The anisotropic MR (AMR) caused by in-plane components of the current is expected to decrease the resistance from the saturation value in our electrode design, where the saturated magnetization direction is parallel to the in-plane current direction. Thus, the increase of the resistance from the saturation value, observed in the MR hysteresis, can be ascribed by assuming that the CPP MR is caused by a development of an antiparallel spin orientation in the two Co layers. Meanwhile, the AMR term appears to be negligible, since no significant decrease of the resistance from the saturation value is observed. The prominent dip of resistance (arrow 3) at around 50 Oe can be ascribed to the local switching of the sputtered (hard) Co layer. When the absolute value of the external field exceeds 100 Oe, the resistance decreases by the magnetization switching in the hard Co layer (arrows 5, 8). The MR ratio of 0.85% has been observed at room temperature.

IV. CONCLUSION

A perpendicular spin valve behavior in a microfabricated magnetic trilayer system of Co/Cu-Cu oxide/Co has been studied using microfabrication technique. The Co thin films having markedly different coercive fields H_c were prepared by the different deposition methods of *e*-gun vacuum evaporation (H_c=20–30 Oe) and rf sputtering (H_c=90–260 Oe), which resulted in the selective switching of the magnetization in the multilayer Co film. The film surface of the Cu was oxidized by the rf sputter etching, which results in the increase of the junction resistance and enables measurements of the perpendicular spin valve behavior at room temperature. The microstructured current pass perpendicular to the film plane was confined with a contact hole of 5 μm diameter produced in the SiO_2 spacer layer with an Ar ion milling. The magnetoresistive hysteresis measured by a dc four-terminal method confirms the spin valve properties in the perpendicular current through the contact hole. The measured magnetoresistance ratio was 0.85% (dR=7.5 mΩ, R=0.89 Ω) at room temperature.

[1] W. P. Pratt, S. F. Lee, J. M. Slaughter, R. Loloee, P. A. Schroeder, and J. Bass, Phys. Rev. Lett. **66**, 3060 (1991).
[2] M. A. M. Gijs, S. K. J. Lenczowski, and J. B. Giesbers, Phys. Rev. Lett. **70**, 3343 (1993).
[3] W. Vavra, S. F. Cheng, A. Fink, J. J. Krebs, and G. A. Prinz, Appl. Phys. Lett. **66**, 2579 (1995).
[4] M. Jullier, Phys. Lett. A **54**, 225 (1975).
[5] S. Maekawa and U. Gafvert, IEEE Trans. Magn. **MAG-18**, 707 (1982).
[6] J. C. Slonczewski, Phys. Rev. B **39**, 6995 (1989).
[7] K. Matsuyama, H. Asada, H. Miyoshi, and K. Taniguchi, Digests of INTERMAG'95, CD-03 (1995).
[8] P. M. Tedrow and R. Meservey, Phys. Rev. B **7**, 318 (1973).
[9] J. H. Greiner, J. Appl. Phys. **42**, 5151 (1971).

Epitaxial $Fe_{16}N_2$ films grown on Si(001) by reactive sputtering

M. A. Brewer[a] and Kannan M. Krishnan
Materials Sciences Division, Lawrence Berkeley National Laboratory, Berkeley, California 94720

C. Ortiz
IBM Research Division, Almaden Research Center, San Jose, California 95120

We present a crystallographic template for the growth of the range of Fe-N phases on Si(001) by lattice matching on selected underlayers. Epitaxial films of pure α-Fe, γ'-Fe_4N, and α'-Fe_8N (N martensite) were grown individually by the optimization of reactive N_2 sputtering parameters. The orientation relation of the Fe-N phases was Fe-N(001)‖Ag(001)‖Si(001) and Fe-N[100]‖Ag[110]‖Si[100]. Annealing the α'-Fe_8N films resulted in the formation of α'-Fe_8N/α''-$Fe_{16}N_2$ mixtures. In addition to the crystallographic and structural analysis, quantification of x-ray diffraction peak intensities confirmed that the α'/α'' mixtures contained as much as 46 vol % α'' (remaining α'). Vibrating sample magnetometry and SQUID magnetometry measurements of the α' and α'(54%)/α''(46%) mixture, respectively, indicate enhanced magnetic moments for both the α' and α'' phases with respect to pure Fe. © *1996 American Institute of Physics.* [S0021-8979(96)05108-X]

I. INTRODUCTION

It has been claimed that α''-$Fe_{16}N_2$ possesses a giant magnetic moment.[1] After two decades, this claim is still under considerable scrutiny. The controversy is fueled by the widely varying magnetization values observed by different workers, and by the lack of reproducible single-phase α''. In 1972 Kim and Takahashi produced thin films by evaporating iron in nitrogen which had a magnetization as high as 2.64 T.[1] The films were predominately α-Fe, and the magnetization of α''-$Fe_{16}N_2$ was inferred to be 2.76 T (295 emu/g). Unfortunately, they were not able to reproduce their results,[2] and $Fe_{16}N_2$ was forgotten for nearly twenty years until pure α'' films on $In_{0.2}Ga_{0.8}As$(001) and Fe/GaAs(001) with giant moments of 2.9 T (310 emu/g) were reported by Sugita and co-workers.[3,4] Attempts at growth on simpler substrates have resulted in only a modest enhancement in moment and often in multiphase mixtures. While the giant moment has been claimed in bulk α'' as well,[5] the moment was extracted from mixed-phase samples in which volumetric analysis is problematic. Mixed phases are commonly observed in the complicated Fe-N phase diagram and, consequently, γ'-Fe_4N and/or α-Fe either accompany or are formed preferentially to the metastable α''-$Fe_{16}N_2$ phase. Theoretical calculations based on the band structure of $Fe_{16}N_2$ predict values for the magnetization around 2.4 T (~260 emu/g),[6–9] well below Sugita's claims, but consistent with the magnetizations reported by several other workers.[10–12]

Jack first proposed the structure of $Fe_{16}N_2$ in 1951.[13] The iron structure is body-centered tetragonal (a=5.72 Å, c=6.29 Å) with nitrogen atoms occupying every other octahedral site. It is formed by annealing the metastable nitrogen martensite, α'-Fe_8N, in which the nitrogen occupation is randomly distributed in the octahedral sites of a similar bct structure (a=2.84 Å, c=3.14 Å). Magnetic property measurements of single-phase $Fe_{16}N_2$ are needed to confirm the giant moment in α''. Therefore, we attempted deposition of α'' using a commercially relevant substrate with an uncomplicated template and process. We report the structural and magnetic characterization of systematically grown Fe-N phases on Si(001).

II. EXPERIMENT

Epitaxial iron nitride films were deposited by conventional reactive (N_2) dc magnetron sputtering on Si(001). The substrates were cleaned in a standard sulfuric acid process, followed by hf etching of the native oxide layer and hydrogen passivation of the surface. Substrates were loaded immediately into the vacuum chamber and were not heat treated. Base vacuum was at least 1.2×10^{-7} Torr. The crystal structures were characterized using a Siemens D5000 x-ray diffractometer with Cu $K\alpha$ radiation. Magnetization data for α-Fe, γ'-Fe_4N, and α'-Fe_8N were acquired at room temperature for fields up to 10 kOe applied parallel to the film plane using a 2 T EG&G PARC vibrating sample magnetometer. Magnetization data for α'-Fe_8N/α''-$Fe_{16}N_2$ mixtures were acquired at 15 K for fields up to 15 kOe using a 5.5 T Quantum Design SQUID magnetometer. Orientation relationships were determined by selected-area electron diffraction in a JEOL 200CX transmission electron microscope.

III. RESULTS AND DISCUSSION

Growth of $Fe_{16}N_2$ on MgO(001) using an Fe seed layer and Ag underlayer has been reported recently.[12] Ag(001) has a 1% lattice mismatch with α''-$Fe_{16}N_2$(001) when it acquires an in-plane rotation of 45°, i.e., when $Fe_{16}N_2$[100]‖Ag[110]. A similar epitaxy can be achieved with Si(001), i.e., Ag[100]‖Si[100], but with a somewhat larger lattice mismatch of 6.4%. These orientation relationships were used sequentially to generate a template [Fig. 1(a)] for the epitaxial growth of the Fe-N phases with a c-axis normal. Further, the growth of individual Fe-N phases (α-Fe, γ'-Fe_4N, and α'-Fe_8N) was accomplished by the optimization of substrate temperature, sputtering rates and gas flow rates. Silver was deposited directly on Si(001) at 100 °C by rf magnetron

[a]Also at Materials Department, University of California, Santa Barbara, CA 93106.

 0021-8979/96/79(8)/5321/3/$10.00 © 1996 American Institute of Physics

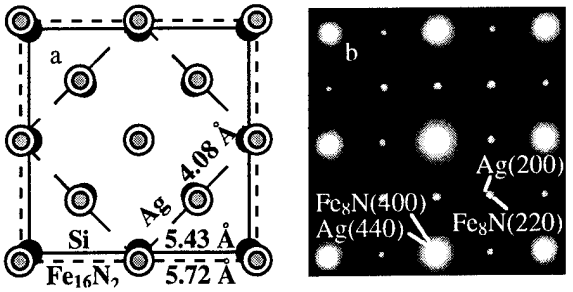


FIG. 1. (a) Epitaxial template for $Fe_{16}N_2(001)$ growth on Ag(001) underlayers on Si(001) substrates. $Fe_{16}N_2[100]\|Ag[110]\|Si[100]$, and (b) plan-view TEM diffraction pattern of an Fe_8N/Ag free-standing film.

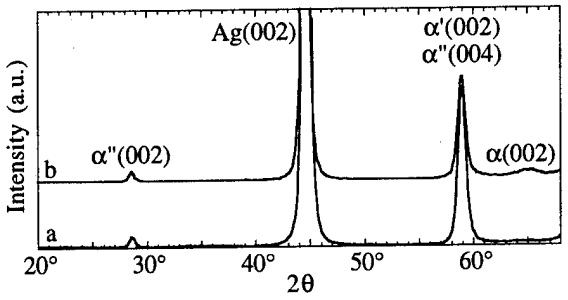


FIG. 3. XRD pattern of α'-Fe_8N deposited and annealed as in Fig. 2(d); (a) Ag deposited at 5.2 Å/s and (b) Ag deposited at 1.9 Å/s.

sputtering in argon (3 mTorr), with a thickness of 1000 Å and growth rates ranging from 0.3 to 5.0 Å/s. All Fe-N films were deposited by dc magnetron sputtering at a growth rate of 0.5 Å/s within a thickness range of 600–1000 Å. Pure α-Fe was grown at 25 °C in argon. γ'-Fe_4N was grown at 100 °C in a mixture of Ar and N_2 with a ratio of 46/5 sccm. α'-Fe_8N was grown at 45 °C with an Ar/N_2 ratio of 46/4 sccm. α' films were annealed at 150 °C for 2 h in vacuum (at least 10^{-6} Torr) to produce an α'/α'' mixture. The growth configuration of α'-Fe_8N was confirmed by electron diffraction of plan-view samples in a transmission electron microscope (TEM). The diffraction pattern shown in Fig. 1(b) is a superposition of patterns from individual Fe_8N and Ag layers. We deduced the orientation relationship to be $Fe_8N[100]\|Ag[110]$.

X-ray diffraction spectra of α, γ', α', and α'/α'' films are shown in Fig. 2. The Ag underlayers, deposited at growth rates around 5 Å/s, are of good quality with strong (001) epitaxy. Fe-N films are also epitaxial but have broader peaks. The integrated intensity in x-ray scattering is given by $I_{hkl}=A|F_{hkl}|^2L_pP$,[14] in which A is a constant, L_p the combined Lorentz and polarization factor, and P the multiplicity factor. The Lorentz factor, $\cos\theta(1/\sin 2\theta)^2$, is modified to

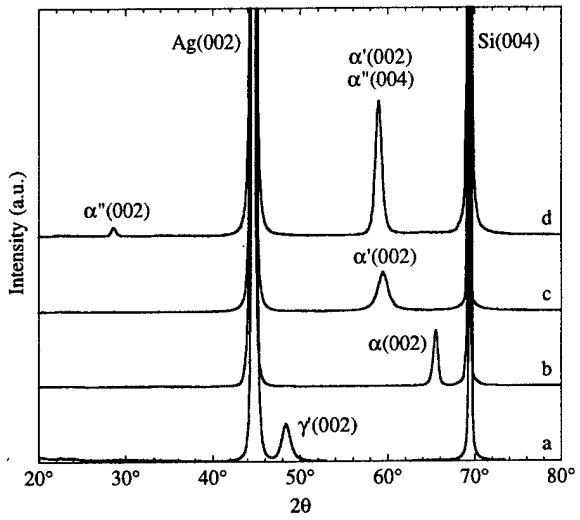


FIG. 2. XRD patterns of Fe-N films grown on Ag/Si(001); (a) γ'-Fe_4N, (b) α-Fe, (c) α'-Fe_8N, and (d) α'-Fe_8N/α''-$Fe_{16}N_2$.

$(1/\sin 2\theta)^2$ since the $\cos\theta$ term is only included for randomly oriented specimens. The polarization factor is unity for monochromatic radiation, and the multiplicity is unity for an oriented specimen. The structure factors were calculated using formulas derived by Nakajima and Okamoto,[15] and atomic scattering factors for Fe and N were those reported by Cullity.[14] Calculations were based on an ideal structure in which the Bragg angles (θ_B) are 14.2° and 29.4° for $\alpha''(002)$ and $\alpha''(004)$, respectively. The sample area was large compared to the beam size, but the thickness was smaller than the effective x-ray penetration depth. Therefore, the integrated intensity was multiplied by the factor $G=1-\exp(-2\mu t/\sin\theta_B)$,[14] in which μ denotes the line absorption coefficient. We calculated the ideal integrated intensity ratio, $I_{\alpha''(004)}/I_{\alpha''(002)}$, to be 5.8 for a single-crystal α'' film. In addition, to determine the volume fractions of α' and α'', we obtain the ideal $I_{\alpha'(002)}/I_{\alpha''(002)}$ integrated intensity ratio for a 50/50 wt % mixture of α' and α'', since α' and α'' have different scattering intensities for the same mass. Using similar parameters and values the intensity ratio was calculated to be 9.3. It can be shown that the x-ray intensities of α'/α'' mixtures satisfy the relationship

$$\frac{I_{\alpha''(004)}}{I_{\alpha''(002)}}+\left(\frac{1-x}{x}\right)\frac{I_{\alpha'(002)}}{I_{\alpha''(002)}}=\left(\frac{I_{\alpha'(002)}+I_{\alpha''(004)}}{I_{\alpha''(002)}}\right)_{\text{expt}}$$

in which x is the mass fraction (and volume fraction if one assumes similar densities for α' and α'') of α''. The left side of the equation contains the calculated ratios while the right side contains the measured ratio. Using the above formula and the experimental data, the α'/α'' mixtures were estimated to be 46 vol % α''.

The nature of annealed α' films is affected by the silver morphology as well as the annealing temperature and duration. In Fig. 2(c), the data represent an α' film grown on Ag deposited at 5.2 Å/s. An α' film grown under the same conditions except for the Ag deposition rate (1.9 Å/s), showed similar x-ray characteristics. Upon annealing at 150 °C for 2 h, however, the resulting α'/α'' mixtures varied in quality and purity. Compared to the spectra in Fig. 2(d) [reproduced in Fig. 3(a)], the x-ray diffraction (XRD) spectra in Fig. 3(b) indicates a film containing a similar α'/α'' ratio mixed with a small amount of α-Fe. Work is in progress to better understand the effect of silver morphology and texture on nitrogen

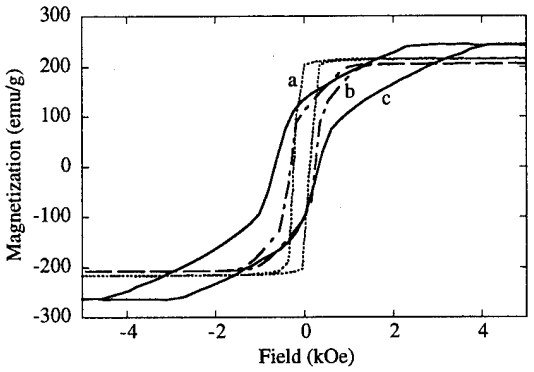


FIG. 4. VSM hysteresis loops of (a) α-Fe, (b) γ'-Fe_4N, and (c) α'-Fe_8N, normalized with sample mass.

ordering and phase separation. In general, annealing temperatures above 150 °C resulted in phase separation of α' into γ'-Fe_4N and α-Fe.

Vibrating sample magnetometry (VSM) data acquired at room temperature and normalized with sample mass are shown in Fig. 4. Assuming a magnetization of 217 emu/g for α-Fe [Fig. 4(a)], the film mass was estimated. The film thickness was then calculated from the estimated mass, area and density, and was used as a calibration for γ'-Fe_4N (including volume expansion), since the α and γ' films were grown under identical sputtering conditions. The γ' magnetization was then estimated to be 205 emu/g [Fig. 4(b)]. These moments are based on ideal structures and densities, which have not been confirmed beyond the x-ray analysis. The thickness of α'-Fe_8N was measured with a profilometer and α' was estimated to have a moment of 240 emu/g [Fig. 4(c)]. The film thickness after annealing was assumed to be approximately the same as the single-phase α'. Figure 5 shows normalized SQUID magnetometry data taken at 15 K for the α'/α'' film shown in Fig. 2(d). We estimate that the moment of the α'/α'' film is also around 240 emu/g. These magnetic moments vary widely ($\pm$20 emu/g) depending on the mass estimates used for each film. More accurate mass and density measurements are underway. In addition, nitrogen contents of the films are still to be determined.

IV. CONCLUSION

We have successfully grown several phases (α, γ', α', and α'') of the Fe-N system epitaxially on a technologically relevant substrate using a reactive sputtering process. Growth conditions were optimized and the orientation relationships were confirmed. The growth of the α''-$Fe_{16}N_2$ phase was accomplished only as a mixture with α'-Fe_8N; however, the exact ratio of the two phases was determined (46% α'', remaining α') by a refinement of x-ray diffraction intensities. Our preliminary results indicate an enhancement in the moment with respect to pure α-Fe. Further characterization of the magnetic structure of these films by Mössbauer spectroscopy will be reported in the near future.

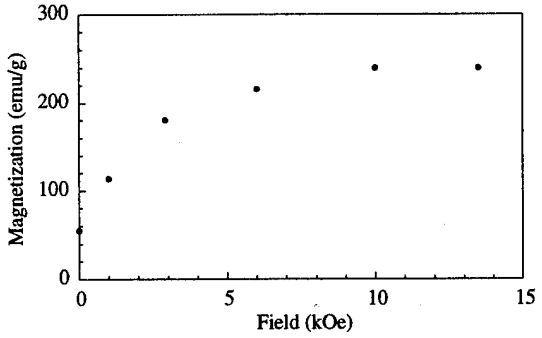


FIG. 5. SQUID magnetization data for an α'-Fe_8N/α''-$Fe_{16}N_2$ mixture, normalized with sample mass.

ACKNOWLEDGMENTS

The authors would like to thank Jesse Salem (IBM Almaden Research Center) for his technical assistance with the sputtering equipment. This work was partially supported by the Office of Basic Energy Sciences of the U.S. Department of Energy under Contract No. DE-AC03-76SF00098. M. A. B. was partially supported by a National Science Foundation Graduate Research Fellowship.

[1] T. K. Kim and M. Takahashi, Appl. Phys. Lett. **20**, 492 (1972).
[2] M. Takahashi, IEEE Trans. J. Magn. Jpn. **6**, 1024 (1991).
[3] Y. Sugita, K. Mitsouka, M. Momuro, H. Hoshiya, Y. Kozono, and M. Hanazono, J. Appl. Phys. **90**, 5977 (1991).
[4] M. Komuro, Y. Kozono, M. Hanazono, and Y. Sugita, J. Appl. Phys. **67**, 5126 (1990).
[5] M. Q. Huang, W. E. Wallace, S. Simizu, and S. G. Sankar, J. Appl. Phys. **75**, 6574 (1994); J. Magn. Magn. Mater. **135**, 226 (1994).
[6] B. I. Min, Phys. Rev. B **46**, 8232 (1992).
[7] R. Coehoorn, G. H. O. Daalderop, and H. J. F. Jansen, Phys. Rev. B **48**, 3830 (1993).
[8] J. M. D. Coey, K. O'Donnell, Q. Qinian, and others, J. Phys.: Condens. Matter **6**, L23 (1994).
[9] A. Sakuma and Y. Sugita, Mater. Res. Soc. Symp. Proc. **313**, 257 (1993).
[10] K. Nakajima and S. Okamoto, Appl. Phys. Lett. **56**, 92 (1990).
[11] M. Takahashi, H. Shoji, H. Takahashi, T. Wakiyama, M. Kinoshita, and W. Ohta, IEEE Trans. Magn. **29**, 3040 (1993).
[12] C. Ortiz, G. Dumpich, and A. H. Morrish, Appl. Phys. Lett. **65**, 2737 (1994).
[13] K. H. Jack, Proc. R. Soc. London Ser. A **208**, 216 (1951).
[14] B. D. Cullity, *Elements of X-Ray Diffraction* (Addison–Wesley, Reading, MA, 1978), pp. 126–139.
[15] K. Nakajima and S. Okamoto, Appl. Phys. Lett. **54**, 2536 (1989).

Classical and quantum magnetism in synthetic ferritin proteins

S. Gider and D. D. Awschalom
Department of Physics, University of California, Santa Barbara, California 93106

T. Douglas, K. Wong, and S. Mann
School of Chemistry, University of Bath, Bath BA2 7AY, United Kingdom

G. Cain
Department of Physics, Santa Barbara City College, 721 Cliff Drive, Santa Barbara, California 93109

The magnetic properties of nanometer-scale particles are studied using the protein-complex ferritin as a vesicle for either an antiferromagnet or a ferrimagnet. For antiferromagnetic ferritin particles, the anisotropy energy is found to depend linearly on the particle volume, suggesting that bulk anisotropy dominates over surface anisotropy. Effects due to the bulk and surface spins are discerned at high magnetic fields (27 T). At very low magnetic fields (1 nT) and temperatures (20 mK), the tunneling frequency of the Néel vector is observed to scale exponentially with the particle volume, consistent with the linear dependence of the anisotropy barrier on volume and with theories of macroscopic quantum coherence. In the ferrimagnetic particles, the anisotropy barrier decreases for smaller particles while simultaneously displaying a slight increase in coercivity and a dramatic decrease in the remanence over three orders of magnitude. © *1996 American Institute of Physics.*
[S0021-8979(96)05208-6]

Ferritin is a versatile system in which to study magnetism on the nanometer length scale. The globular apoferritin protein shell has an ~8-nm-diam cavity which can serve has a host for a variety of materials. In natural ferritin, the core is composed of an antiferromagnetic iron oxide hydroxide similar to the mineral ferrihydrite.[1,2] The cores can also be artificially reconstituted within the intact apoferritin with control of the particle volume from 100 to 3000 iron ions per core.[3] Alternatively, the cores can be synthesized with a ferrimagnetic compound such as magnetite or maghemite to produce "magnetoferritin."[4] Thus we control both the magnetic state and the particle size.

For the present study, a series of antiferromagnetic and ferrimagnetic samples are prepared with iron loading per core ranging from 100 to 3000 ions. The loading is determined by measurements of the iron content using atomic absorption analysis and by measurements of the protein concentration using the Lowry method.[3] Designations of the samples by iron loading therefore represent an average number of iron ions per protein. The core diameters are also measured by transmission electron microscopy (TEM). Prior to any magnetic measurements, all samples are dried in air at temperatures not exceeding 40 °C. A sample of natural horse spleen ferritin is also studied for comparison with the artificial samples. Initial characterization is performed with an rf SQUID magnetometer at temperatures from 2 to 300 K and fields up to 5 T. Measurements at higher fields to 27 T utilize a microfabricated cantilever magnetometer.[5] To study the dynamics of tunneling at temperatures as low as 20 mK and fields of ~1 nT, an integrated dc SQUID susceptometer is employed.[6]

All the antiferromagnetic and ferrimagnetic samples are superparamagnetic at temperatures above 100 K. A comparison of the magnetization of the two types of samples is shown in Fig. 1 at 5 K, a temperature below the blocking temperatures T_B at 50 mT of both the antiferromagnet and ferrimagnet samples (10.5 and 40 K, respectively). The antiferromagnetic ferritin has a weaker moment but a larger coercive field. The shape of the two curves is also significant: the antiferromagnet does not saturate even in a field of 27 T (Fig. 2), whereas the ferrimagnet saturates at rather modest fields (<0.5 T). This is due to the fact that the magnetization measured in the former is a sum of different contributions from the antiferromagnetic core (the bulk spins) and an uncompensated surface moment,[7–9] whereas in the ferrimag-

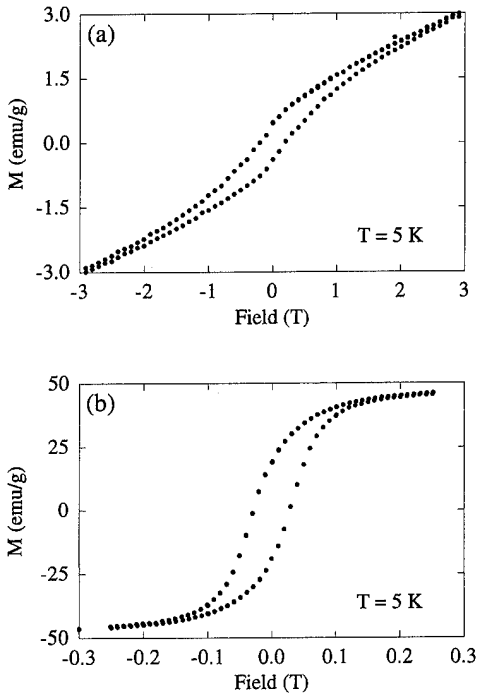


FIG. 1. Magnetization vs field for (a) the natural horse spleen ferritin (~2000 iron ions/particle) and (b) the ferrimagnetic artificial ferritin-"magnetoferritin" (3100 iron ions/particle). Note the difference of an order of magnitude in both the x and y scales. The sample quantities are on the order of 250 μg.

 0021-8979/96/79(8)/5324/3/$10.00 © 1996 American Institute of Physics

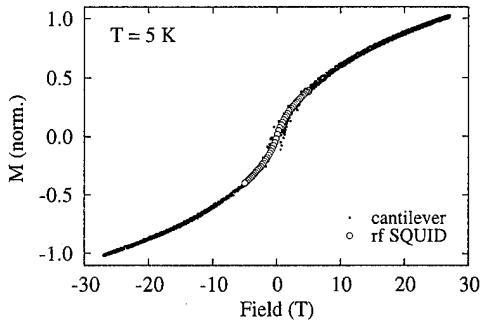


FIG. 2. Magnetization of the natural horse spleen ferritin using a cantilever magnetometer compared with the scaled measurement from the rf SQUID. The magnetization is normalized by the value at 27 T. The hysteresis is not visible on this scale.

netic sample the bulk and surface spins appear to contribute in the same manner to the magnetization. Previous high-field measurements suggested a saturation of the moment followed by a discontinuity interpreted as a spin-flop transition.[10] When the high-field data are properly normalized, however, the moment does not saturate by 27 T, and there is no discernible discontinuity in the magnetization curves. Nevertheless, the magnetization at high fields still does not linearly extrapolate to zero, implying that the susceptibility of the surface remains substantial compared to that of the bulk at all fields examined.

Below the blocking temperature, while the magnetization may be classically forbidden from crossing over the anisotropy energy barrier, it may coherently tunnel through the barrier, producing a resonance in the magnetic susceptibility or noise.[11] This quantum reversal mechanism is favored for antiferromagnets over ferrimagnets, and furthermore, the resonance frequency depends exponentially on the magnitude of the energy barrier.[12,13] In turn, the energy barrier depends on the volume of the particles, and if the latter dependence could be established by independent means, then one could test the theories of macroscopic quantum coherence. Through measurements of the blocking temperature with an rf SQUID magnetometer, we have inferred a linear dependence of the anisotropy energy barrier on the volume of the antiferromagnetic particles, which suggests that bulk and surface spins experience the same anisotropy.[10] Measurements of the resonant tunneling frequency with the dc SQUID susceptometer then reveal an exponential dependence as seen in Fig. 3(a).

It is interesting to draw a comparison between the observation of blocking in the regime of a few K and the appearance of coherence in the mK regime. Note that the blocking temperatures are obtained in the presence of a magnetic field on the order of 10 mT. As seen in Fig. 3(b), the blocking temperature can be reduced by decreasing the applied field. (The blocking temperature can also be reduced by increasing the field above the coercive field.) In contrast, the frequency dependent susceptibility measurements are performed with a field on the order of nT and at temperatures as low as 20 mK, a difference of seven orders of magnitude in field and three orders of magnitude in temperature. An attempt to extrapolate from 10 mT to 1 nT and from 10 K to 20 mK would

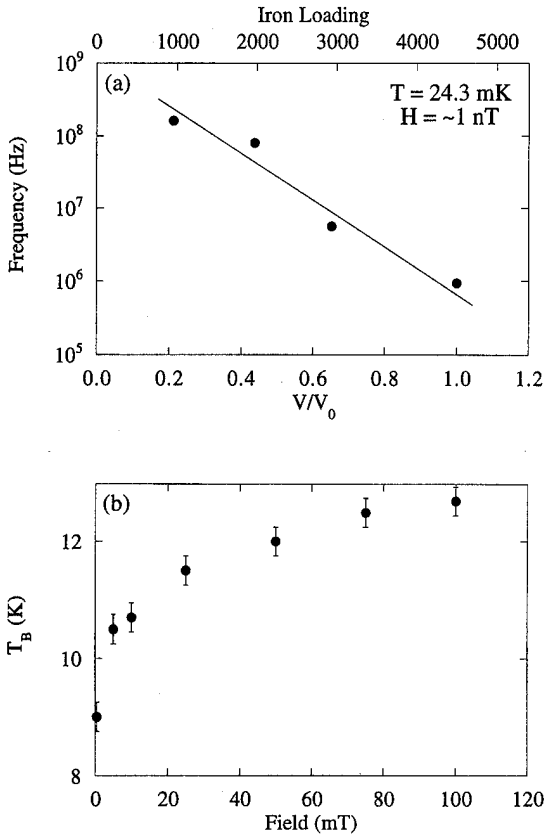


FIG. 3. (a) Dependence of the resonance frequency in the magnetic noise on the size of antiferromagnetic particles, as obtained with an integrated dc SQUID susceptometer. The volume has been normalized by V_0, the volume of the largest particles studied (~4500 iron ions/particle). The line is a guide to the eye. (b) The variation of the blocking temperature in the (antiferromagnetic) natural horse spleen ferritin vs applied field.

obviously be questionable. Although the dynamics would most likely change over such a large range, it is not possible to conclude from measurements at 10 mT and 10 K whether the particles are blocked in the classical sense at 1 nT and 20 mK.

Moreover, the measurements of the amplitude of the ac susceptibility[14] demonstrate that coherence vanishes for fields exceeding ~100 nT. Similarly, if the sample is not diluted at least by a factor of 1000, the dipolar couplings completely suppress the coherence.[15] Thus the experimental condition under which the blocking temperature is measured (high fields and low dilution) is such that the quantum two-level system is detuned and no coherence can develop under these conditions, even if the observation temperature is lowered far below the blocking temperature. The fact that the blocking temperature is much higher than the cross-over temperature which is observed in the ac susceptibility data (low fields and high dilution) is indeed compatible with the interpretation of the resonance as macroscopic quantum coherence.

Most of the work thus far has focussed on the antiferromagnetic ferritin. More recent work has sought to elucidate the size dependence of the magnetic properties of the ferrimagnetic ferritin (magnetoferritin) to complement the initial measurements of the fully loaded particles.[10,16] Anisotropy

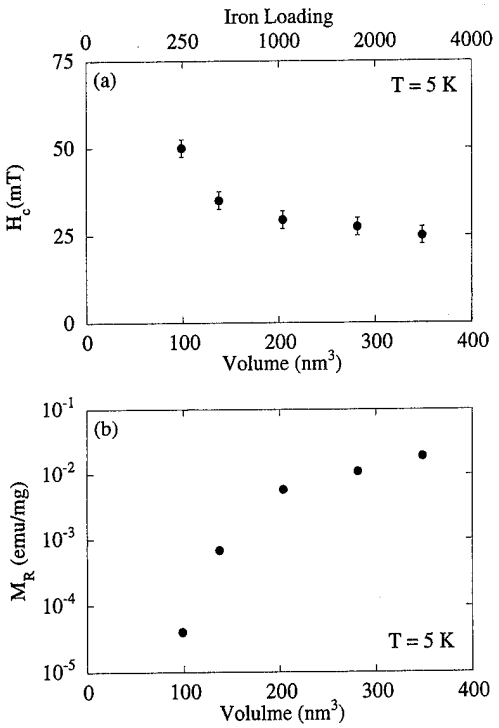


FIG. 4. The (a) coercivity and (b) remanence of the magnetoferritin samples at low temperatures.

was previously observed in magnetoferritin in the difference between field-cooled and zero-field-cooled temperature sweeps but not resolved in the field sweeps.[10] In Fig. 1(b), the anisotropy results in hysteretic field sweeps when observing on a field scale ten times finer than for the antiferromagnetic sample. There is no anomaly in the remanence up to 150 K implying there is no Verwey transition.[17] This observation, together with Mössbauer data,[18] suggests that the mineral in the magnetoferritin is maghemite instead of magnetite, which could not be formerly distinguished by x-ray diffraction. Like the natural ferritin, the magnetoferritin also displays an increase in the blocking temperature with decreasing volume from almost 10 to 100 K for iron loading from 100 to 3100 ions, respectively.

The larger moment of the magnetoferritin as compared to the antiferromagnetic ferritin allows for a more complete study of hysteresis over the entire range of samples. First, the field required to saturate the moment is found to increase as the particle volume decreases. This is consistent with a decrease in the moment per particle for superparamagnetic particles whose magnetization is well described by a Langevin function. Second, the coercive field is observed to increase as the volume decreases [Fig. 4(a)]. There are two possible explanations for this effect: (1) the likelihood of forming magnetic domains becomes less favorable as the volume decreases, or (2) if the anisotropy constant K does not change, the decrease in the moment M implies an increase in the coercive field $H_c = 2K/M$ for coherent reversal of magnetization within the Stoner–Wohlfarth model. Finally, the remanence is found to decrease by three orders of magnitude while the volume changes by less than one order of magnitude. Thus the stability of the particles is extremely sensitive to the size of the particles.

While the present work has involved iron oxides, ferritin can also serve as a host for iron sulfide[19,20] or even manganese and uranium oxides.[19,21] The magnetic properties of the latter are as yet unexplored. Ferritin also has potential in biological applications since the protein shell makes the mineral cores compatible with living organisms. One example is as a site-specific contrast agent for magnetic resonance imaging.[16] Thus ferritin will likely continue to be of interest to basic and applied studies of magnetism on the nanometer scale.

This work is supported by the AFOSR, the UCSB Materials Research Laboratory, and the National High Magnetic Field Laboratory (NHMFL). We thank M. Chaparala for assistance with the high-field measurements, and D. P. DiVincenzo and D. Loss for helpful discussions.

[1] P. M. Harrison and T. H. Lilley, in *Iron Carriers and Iron Proteins*, edited by T. M. Loehr (VCH, New York, 1989).
[2] T. G. St. Pierre, J. Webb, and S. Mann, in *Biomineralization: Chemical and Biochemical Perspectives*, edited by S. Mann, J. Webb, and R. J. P. Williams (VCH, New York, 1989).
[3] I. G. Macara, T. G. Hoy, and P. M. Harrison, Biochem. J. **126**, 151 (1972).
[4] F. C. Meldrum, B. R. Heywood, and S. Mann, Science **257**, 522 (1992).
[5] M. Chaparala, O. H. Chung, and M. J. Naughton, in *Superconductivity and Its Applications*, edited by H. S. Kwok, D. T. Shaw, and M. J. Naughton, AIP Conf. Proc. 273 (AIP, New York, 1992), p. 407.
[6] M. B. Ketchen *et al.*, IEEE Trans. Magn. **MAG-25**, 1212 (1989).
[7] L. Néel, C. R. Acad. Sci. **253**, 9 (1961).
[8] A. Blaise, J. Féron, J.-L. Girardet, and J.-J. Lawrence, C. R. Acad. Sci. B **265**, 1077 (1967).
[9] S. H. Kilcoyne and R. Cywinski, J. Magn. Magn. Mater. **140-144**, 1466 (1995).
[10] S. Gider, D. D. Awschalom, T. Douglas, S. Mann, and M. Chaparala, Science **268**, 77 (1995).
[11] D. D. Awschalom, D. P. DiVincenzo, and J. F. Smyth, Science **258**, 414 (1992).
[12] B. Barbara and E. M. Chudnovsky, Phys. Lett. A **145**, 205 (1990).
[13] I. V. Krive and O. B. Zaslavskii, J. Phys.: Condens. Matter **2**, 9457 (1990).
[14] D. D. Awschalom, J. F. Smyth, G. Grinstein, D. P. DiVincenzo, and D. Loss, Phys. Rev. Lett. **70**, 2199 (1993).
[15] S. Gider and D. D. Awschalom, in *Proceedings of the NATO ASI on Quantum Tunneling of Magnetization, Grenoble, 1994*, edited by B. Barbara and L. Gunther (Kluwer, Dordrecht, 1995).
[16] J. W. M. Bulte *et al.*, J. Magn. Res. Imag. **4**, 497 (1994).
[17] S. Chikazumi, *Physics of Magnetism* (Wiley, New York, 1964). There exists the possibility that the Verwey transition is not well pronounced in small particles. See P. J. Flanders, J. Appl. Phys. **75**, 5931 (1994).
[18] Q. A. Pankhurst *et al.*, Hyp. Int. **91**, 847 (1994).
[19] F. C. Meldrum, V. J. Wade, D. L. Nimmo, B. R. Heywood, and S. Mann, Nature **349**, 684 (1991).
[20] T. Douglas *et al.*, Science **269**, 54 (1995).
[21] F. C. Meldrum, T. Douglas, S. Levi, P. Arosio, and S. Mann, J. Inorg. Biochem. **58**, 59 (1995).

Magnetic recording measurements of high coercivity longitudinal media using magnetic force microscopy (MFM)

P. Giljer
Information Storage Materials Laboratory, Toyota Technological Institute, Nagoya 468, Japan

J. M. Sivertsen and J. H. Judy
The Center for Micromagnetics and Information Technologies (MINT), University of Minnesota, Minneapolis, Minnesota 55455

C. S. Bhatia and M. F. Doerner
IBM-SSD, San Jose, California 95193

T. Suzuki
Information Storage Materials Laboratory, Toyota Technological Institute, Nagoya 468, Japan

Longitudinal magnetic recordings written on high coercivity medium ($Hc=2500$ Oe) were investigated using magnetic force microscopy (MFM). Recorded tracks with bit density up to 6000 fr/mm were investigated. A variety of qualitative information about the recorded tracks and domain structure in the medium was obtained. It was determined that the recorded bits strongly interacted with domains in the medium at the track edges, causing severe jitter. Also bit bending due to the head field was observed. A new method for the quantitative analysis of recorded tracks was used. Using this method, recording signal and medium signal-to-noise ratio were calculated from MFM data. Parameters obtained in this way showed excellent agreement with signal and signal-to-noise ratio obtained from the recording measurement using a MR head. © *1996 American Institute of Physics.* [S0021-8979(96)09308-X]

I. INTRODUCTION

Ultra-high density magnetic recording at recording densities of 10 Gbits/in.^{2} and higher will be achieved only if basic understanding of media noise is achieved. Media noise is a material property that depends strongly on the magnetic microstructure of the medium. Newly developed magnetic force microscopy (MFM)[1] provides a unique opportunity to study both qualitatively and quantitatively the micromagnetic structure of the material as well as magnetic bits recorded on such a medium.[2,3]

There have been a number of reported qualitative studies of magnetic recording using MFM.[2] Quantitative description of MFM images was usually limited to the estimation of bit and domain sizes. However virtually no attempts were made to obtain signal, noise, or any other quantitative recording information using MFM scans.

The purpose of this article is to present the results of the qualitative and quantitative MFM investigations of recording properties of high coercivity longitudinal media.

II. EXPERIMENTAL PROCEDURE

The magnetic recording patterns (all-ones) were recorded on commercially supplied, prototype, high coercivity, planar isotropic longitudinal media in the as-deposited, demagnetized state. The medium had coercivity $H_c=2500$ Oe and remanent magnetization-thickness product $M_r\delta=0.65$ memu/cm^2. Carbon overcoat thickness was 7.5 nm. The standard noise measurements were performed, using a MR-read head. The head gap width was 0.2 μm and the flight height was 49 nm. The recorded patterns were observed in MFM with an ac detection scheme[2] using a tip lift of 80 nm. The MFM tip was coated with thin CoCrPt/Cr and magnetized in the transverse (perpendicular to the sample plane) direction. Thus the contrast in the MFM scans arose mainly due to the z component of the stray magnetic field from the medium.[2–5] Therefore the highest MFM signal from recorded track was detected at the magnetic transitions. This contrast was used

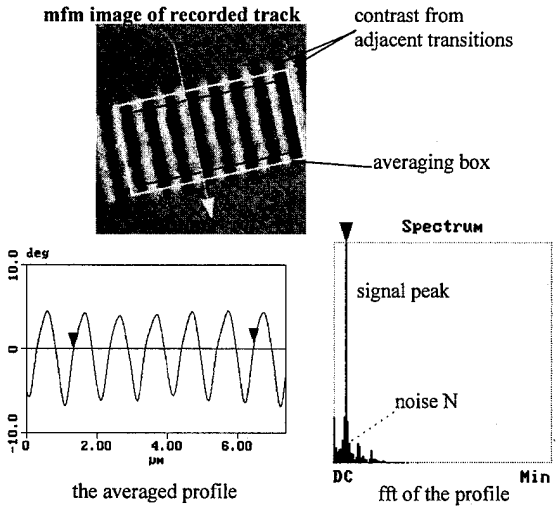


FIG. 1. A method for measuring recording signal and signal-to-noise ratio using MFM.

 0021-8979/96/79(8)/5327/3/$10.00 © 1996 American Institute of Physics

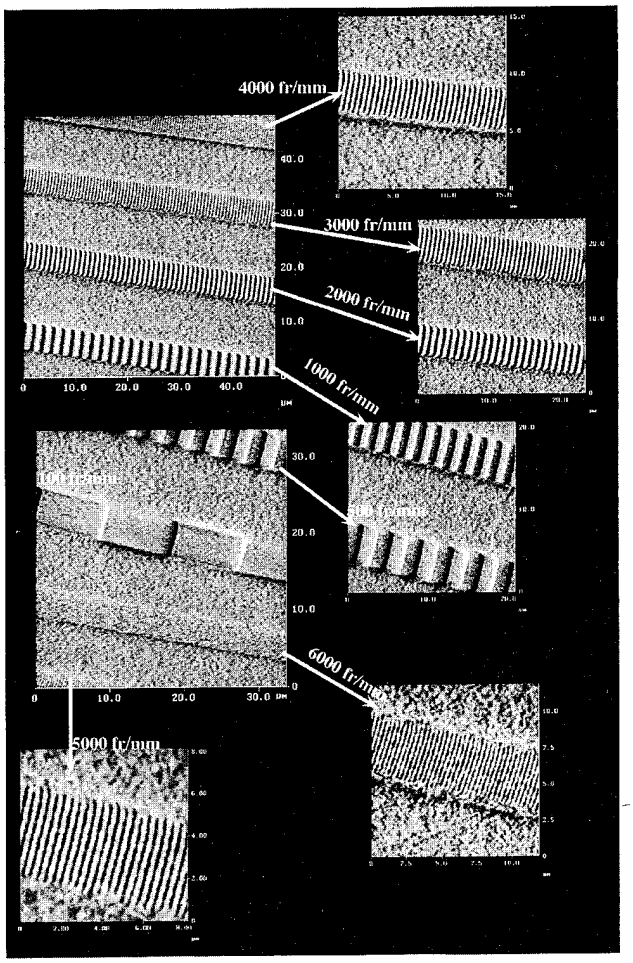


FIG. 2. MFM images of the examined tracks. Linear recording densities are given in the figure.

to measure the "MFM-recording" signal, media noise and signal-to-noise ratio. The method of signal and signal-to-noise calculation is explained in Fig. 1. The profile of the magnetic signal was averaged across the recording track. The averaging box was 2.9 μm across the track and included ~15 transitions along the track. The recording tracks with densities >1000 fr/mm were quantified. The recording signal amplitude (MFM signal) was calculated as R_z of such a profile. The R_z parameter is defined as the average peak to peak value for five highest peaks and five lowest valleys. The medium noise was estimated from the fast Fourier transform (FFT) of the averaged profile. The noise N was calculated by integrating the noise spectrum from FFT, discarding the signal peaks, and dividing it by the band width. The MFM signal-to-noise ratio was calculated as

$$S_0/N = 20 \log(R_z'/2N), \tag{1}$$

where R_z' was the MFM signal for the isolated transitions.

Thus calculated recording parameters were compared with corresponding parameters from recording experiments using a recording head.

It should be noted the noncontact mode in the scanning probe microscope, using a magnetic tip may sense both magnetic (MFM) and height information (AFM). The comparison between AFM and MFM data from the same area of the sample showed complete separation of magnetic and height signal for the microscope settings used in the experiments.

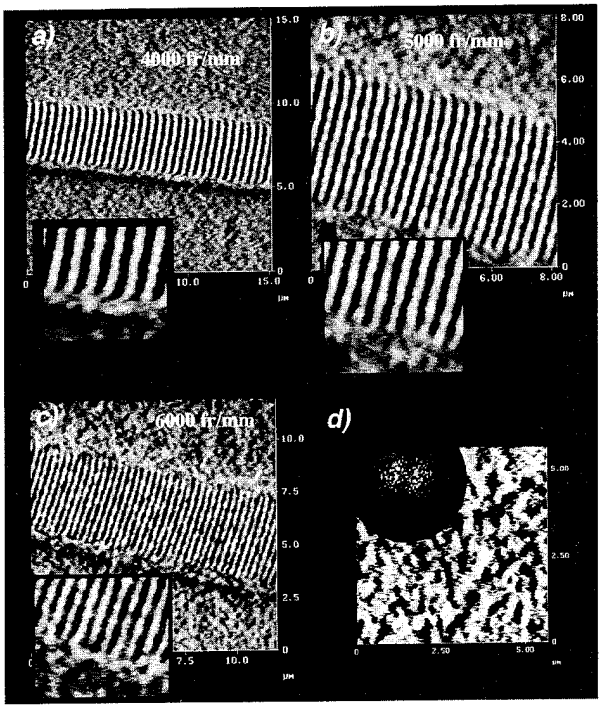


FIG. 3. MFM images of high density patterns with enlarged track edge images; (d) MFM image and corresponding FFT pattern (upper left corner) from the unrecorded part of the disk.

III. RESULTS AND DISCUSSION

Tracks with longitudinal patterns recorded with densities from 100 to 6000 fr/mm are shown in Figs. 2 and 3. The bright and dark lines are clearly visible inside all the tracks. These lines correspond to the magnetic flux coming up from the transition or going down to the transition.[2] Also, a fine magnetic contrast in the unrecorded background and in the magnetic bits area is quite visible.

A. Qualitative MFM analysis

The recorded tracks had a width of ~3.9 μm. The transitions recorded at low densities were clearly curved at the track edges. The curvature was observed also at higher recording densities (>3000 fr/mm) but it appeared to be smaller. The curving bits and an asymmetry in the magnetic contrast at the track edge (one side clearly darker) were probably due to the geometry of the head resulting in a specific writing field gradient.[6] The bits (magnetic transitions) interacted with the magnetic domain walls in the background. This effect was most visible at the track edges of high density tracks (Fig. 3). It was observed that the bits at track edges were bent towards the magnetic transitions with the same sign present in the unrecorded background and vice-versa. This caused a severe jitter at the track edges. All the observed track-edge effects suggest that the track width used for reading should be smaller than the total track width to avoid reading errors.

Some degree of percolations was observed in between the recording transitions written with densities ≥4000 fr/

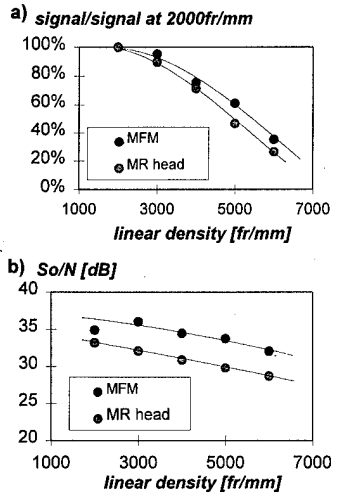


FIG. 4. Results of recording measurements using MFM compared to the results of measurements using MR-head: (a) normalized signal; (b) medium signal-to-noise ratio.

mm. The number of percolations increased with the recording densities. At 6000 fr/mm recording density "bridges" between transitions with the same sign were clearly visible. Such bridges resulted from the interactions between parts of the transitions.

Also a MFM image was scanned from the unrecorded part of the disk in between the tracks [Fig. 3(d)]. The image consisted of elongated bright and dark features of ~0.5 μm×2 μm. Also some smaller features can be observed in the MFM scan. The smallest magnetic contrast features observed in the image were ~150–200 nm and were estimated from the FFT pattern. Slight directionality observed in the FFT pattern [Fig. 3(d)] could be a result of the interaction between written tracks and intrinsic media domains.

B. Quantitative analysis: MFM "recording measurements"

The recording parameters such as read-out signal and signal-to-noise ratio were measured using MFM, as described in Sec. II. Figure 4 shows results of the MFM analysis compared with the magnetic recording data using a recording head. The change of the MFM read-back signal with recording density shows excellent qualitative agreement with the magnetic recording data. Also the signal-to-noise ratio changes in a similar way in both MFM and magnetic recording measurement. A consistently higher S_0/N ratio (by 2–4 dB) in the MFM case was due to better sensitivity and resolution of the MFM measurement as compared to a standard reading result in a recording tester.

IV. CONCLUSIONS

Recording patterns written on high coercivity, low noise media were studied using MFM. Various track edge effects were observed, such as bending of the bits and interaction of the bits with the magnetic domains in the unrecorded background. This result suggests a need for using narrower track width for reading as compared to total track width.

A method for measuring recording parameters such as signal and signal-to-noise ratio using MFM was proposed and tested on the recorded medium. Measured parameters show that both the MFM signal and MFM signal-to-noise ratio decreased with recording density. The significant drop in signal-to-noise ratio at high densities was due to signal loss and increased noise due to percolations observed inside the track in the MFM scans. The change of MFM signal and MFM signal-to-noise ratio were in excellent agreement with the magnetic recording data obtained with MR read head. This result shows that the proposed MFM magnetic recording read-out may be used for testing the media for which a suitable read-head has not yet been developed.

[1] J. J. Saenz and N. Garcia, J. Appl. Phys. **62**, 4293 (1987).
[2] D. Rugar, H. J. Mamin, P. Guethner, S. E. Lambert, J. E. Stern, I. McFayden, and T. Yogi, J. Appl. Phys. **68**, 1169 (1990).
[3] P. Grutter, D. Rugar, and H. J. Mamin, Ultramicroscopy **47**, 393 (1992).
[4] U. Hartman, J. Vac. Sci. Technol. A **8**, 411 (1990).
[5] D. W. Abraham and F. A. McDonald, Appl. Phys. Lett. **56**, 1181 (1990).
[6] R. M. White, *Introduction to Magnetic Recording* (IEEE, New York, 1985), Chap. 4.

Grain growth and ordering kinetics in CoPt thin films

K. Barmak and R. A. Ristau
Department of Materials Science and Engineering, Lehigh University, Bethlehem, Pennsylvania 18015

K. R. Coffey, M. A. Parker, and J. K. Howard
IBM, Storage Systems Division, San Jose, California 95193

Grain growth and ordering kinetics have been studied in a 10-nm-thick CoPt alloy film of equiatomic composition annealed in the temperature range 550–700 °C by quantifying the grain size, grain size distribution, ordered fraction and ordered domain size. The mean grain size of the as-deposited films is 5 nm and the film is fully face-centered cubic. Upon annealing in the temperature range 550–600 °C, the mean grain size reaches a stagnation limit of 27 nm and the grain size distribution is lognormal. Grain growth resumes beyond 600 °C and the mean grain size reaches as high as 55 nm at 700 °C. Ordering occurs by nucleation and growth of $L1_0$ ordered domains, with a mean size of 3 nm at 550 °C and 19 nm at 700 °C. The ordered fraction shows a dramatic increase from 1% to ~28% between the two extremes of annealing temperature. The increase in the coercivity of the annealed films follows the increase in the ordered fraction more closely than the increase in grain size. The shape of the $M-H$ loop shows evidence of coupling between the magnetically hard (ordered) and soft (disordered) regions. © *1996 American Institute of Physics.* [S0021-8979(96)09408-6]

Interest in thin film media which show high coercivity and low media noise for high density longitudinal magnetic recording is increasing. One promising material is equiatomic CoPt which has a face-centered-cubic (fcc) crystal structure in the as-deposited state, but undergoes an ordering transformation to the tetragonal $L1_0$ structure upon annealing. Recently, Coffey *et al.*[1] reported the preparation, magnetic properties and recording performance of partially ordered $M_{1-x}Pt_x$ (where M is Co or Fe, and x is 0.5) thin films with thicknesses in the range 2.5–20 nm. The samples used in the present study were 10-nm-thick CoPt films that were deposited by dc magnetron sputtering and annealed in the range 550–700 °C.

Specimens were prepared for transmission electron microscopy (TEM) by chemically back-etching the substrate and studied in a Philips EM 400T TEM/STEM. For grain size measurements, successive bright field images of the same area were taken with the specimen holder tilt angle varying by 1° or 2°. A single, high-contrast composite tracing of the grain boundaries was made from the image series for each specimen and was entered into the LECO 2001 Image Analyzer via a video camera for grain size measurements. Several areas of each specimen were sampled in this manner until between 1100 and 1700 grains were measured. By varying the magnification of the images and/or enlargements, grains below 1 nm diameter could be reliably measured.

The ordered fraction was determined by taking the ratio of the illuminated area in a dark field image using the (110) ring, allowed only in $L1_0$ structure, to the illuminated area in a dark-field image using the (220) ring, allowed in both fcc and $L1_0$. It should be noted that in the ordered phase the latter ring is split due to a difference in lattice parameter

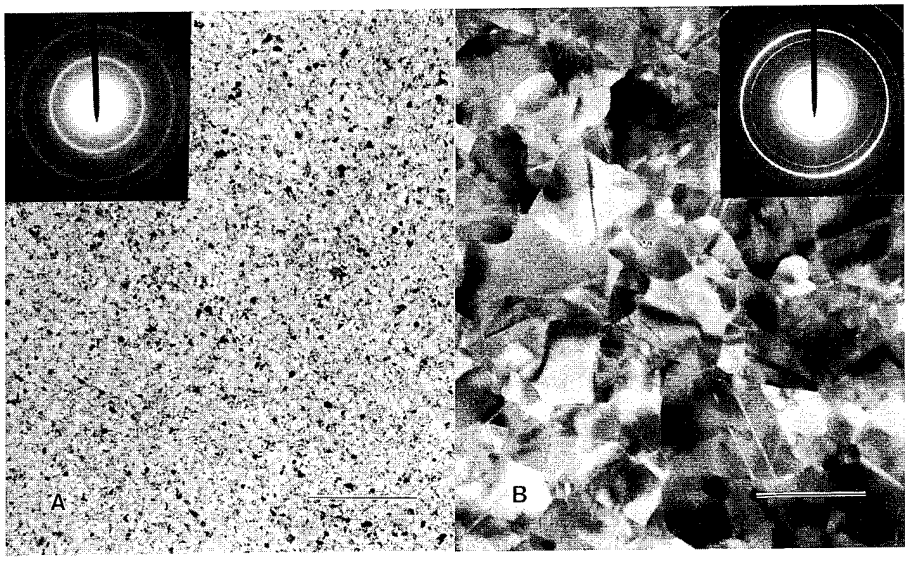


FIG. 1. Bright field TEM micrograph and diffraction pattern of CoPt thin film as-deposited (A) and annealed 700 °C (B). 100 nm bar.

 0021-8979/96/79(8)/5330/3/$10.00 © 1996 American Institute of Physics

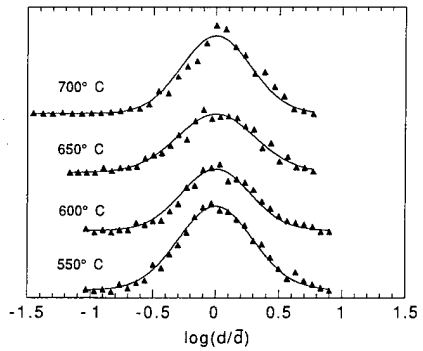


FIG. 2. Grain size distribution plotted as $\log(d/\bar{d})$, where d is the grain size and $\bar{d}$ the mean grain size, for anneal temperatures indicated.

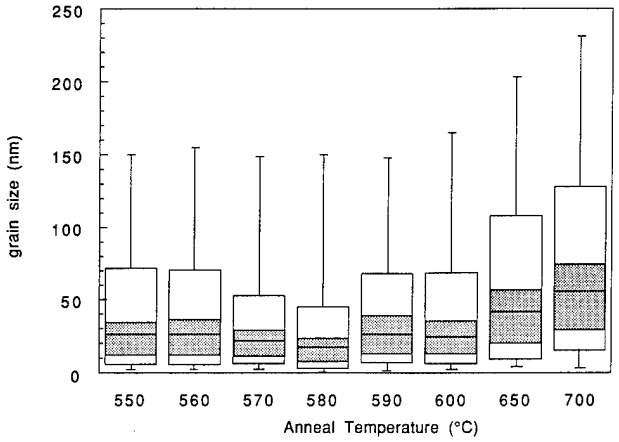


FIG. 3. Grain size distribution for all anneal temperatures. Horizontal line is mean size; shaded box contains 50% of population; large box 90%; bars extend to maximum and minimum values.

between ordered and disordered phases and therefore both rings should be included. In order to compare related areas, a single dark field image was made of the entire diffraction ring at zero tilt angle using a conical scanning hybrid-diffraction unit in a Philips CM200 FEG TEM/STEM. The areas of the illuminated regions in the dark-field images were again measured by the LECO 2001. The size of the individual ordered regions was measured from the dark field images using the (110) ring.

TEM and selected area electron diffraction analysis of the as-deposited film, presented in Fig. 1(A), reveal that the film has the fcc crystal structure and is polycrystalline. After the *ex situ* anneals the grains are larger, as can be seen for the 700 °C annealed sample in Fig. 1(B), and superlattice reflections in the diffraction pattern indicate the formation of $L1_0$ ordered phase. A plot of the number of grains versus $\log(d/\bar{d})$, where d is the grain size and $\bar{d}$ the mean grain size, reveals the distribution of grain size to be lognormal. This plot is presented in Fig. 2, which also includes the data for other samples annealed at 50 °C intervals.

The mean grain size for the as-deposited film was 5 nm with a narrow distribution between a minimum of 0.8 nm and a maximum of 12 nm. Figure 3 shows the mean grain size and grain size distribution of the annealed films. The minimum to maximum range was 2–150 nm for 550 °C and 2–230 nm for 700 °C. From Fig. 3 it also appears that between 550 and 600 °C the mean grain size reaches a limit of 27 nm, suggesting grain growth stagnation. Grain growth resumes again beyond 600 °C. The smaller grain size of 570 and 580 °C annealed samples are believed to be a result of the presence of impurities in the annealing furnace and not a result of variations in the furnace temperature. In metals, impurities typically reduce grain boundary mobility, and thus inhibit grain growth.

Conical dark field TEM images using the ordered reflection (110) showed numerous small regions of the $L1_0$ phase for the lower annealing temperatures. The ordered domains increased in size, while their number decreased as annealing temperature was increased, consistent with a first order transformation that proceeds by a nucleation and growth mechanism. Figures 4(A) and 4(B) show the dark field images for the 600 and 700 °C annealed samples, respectively. From the

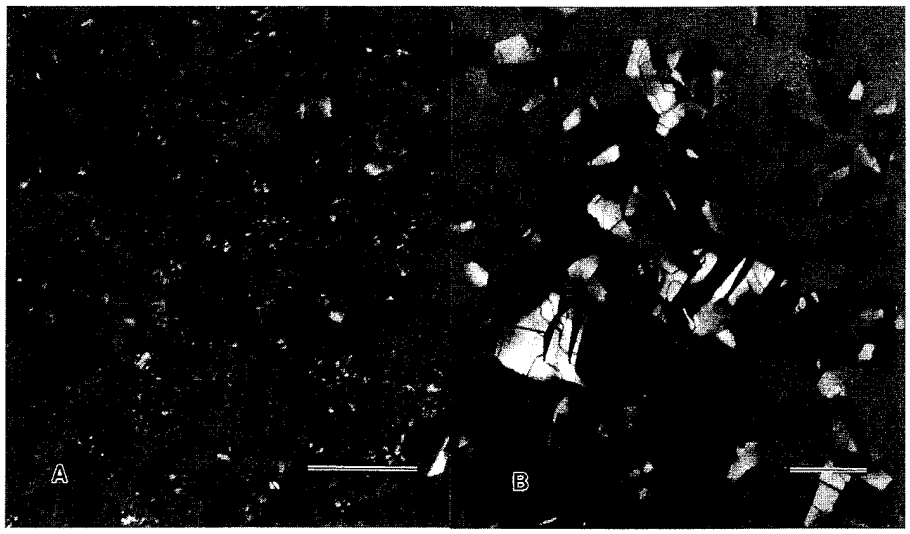


FIG. 4. Dark field TEM micrographs of $L1_0$ ordered phase for 600 °C (A) and 700 °C (B). 100 nm bar.

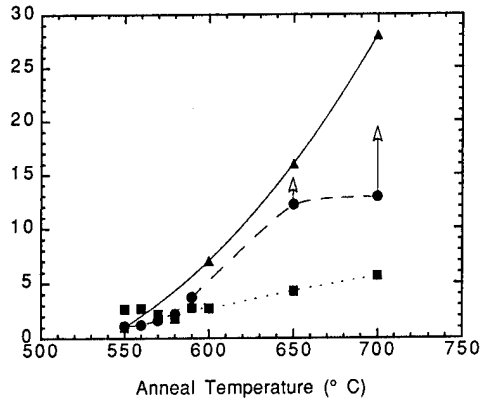


FIG. 5. Ordered fraction per cent (solid line), H_c in kOe (broken line) and mean grain size divided by film thickness of 10 nm (dotted line) as functions of anneal temperature. Arrows indicate expected actual H_c is higher than measured.

profusion of ordered domains at the lower temperatures we expect that each grain will have at least one ordered domain, whereas at 700 °C we observe evidence for grains which are free of ordered domains. The large scale inhomogeneity in the latter films may result in higher media noise for magnetic recording applications. Mean domain size increased from 3 nm for 550 °C to 19 nm for 700 °C anneals, as compared to mean grain size of 27 and 55 nm, respectively. The ordered fraction, plotted in Fig. 5, showed a dramatic increase from 1% for 550 °C to 28% for 700 °C.

Figure 6 presents three $M-H$ plots for the annealed films. The as-deposited film has a very low coercivity, H_c, near 20 Oe. From these $M-H$ plots it is not possible to tell whether the reduction in saturation magnetization, M_s, of the annealed films is due to a minor loop being traced at the maximum measurement field (22 kOe) of our equipment, or due to an increase in the fraction of the ordered phase which has a lower M_s than the disordered phase. When annealed

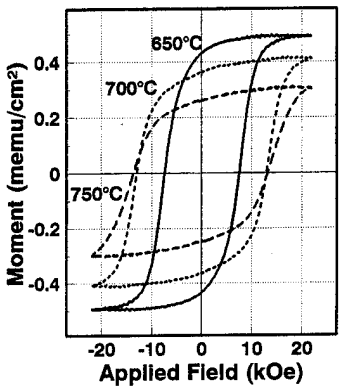


FIG. 6. $M-H$ loops at ±22 kOe of CoPt films annealed at temperatures indicated.

above the order/disorder transition temperature of 825 °C, a recovery of sample moment can be observed, thus verifying that the reduction of M_s for 550–700 °C annealed samples is not due to film oxidation. The coercivities of the annealed samples are plotted as a function of temperature in Fig. 5 and range from near 1000 to over 12 000 Oe. We expect the actual coercivity of the 650 and 700 °C annealed films to be significantly higher.

From the data we observe that the mean grain size grows to 2.7 times the film thickness at which point growth stagnates. This stagnation of grain growth at mean grain sizes between two and three times the film thickness has been found in many studies of thin film systems[2] and is believed to be a result of grain boundary grooving and thus pinning of the boundaries.[3] Previous studies also find that at the point of stagnation the grain size has a lognormal distribution, which agrees well with our findings. Annealing at successively higher temperatures will eventually allow the grains (or at least some of them) to become unpinned and to resume their growth. Although we find that this is indeed the case, we do not find clear evidence for secondary grain growth that has been observed in other studies.[4] The distributions of our grain size remains lognormal with no deviation from this distribution evident at the high end. On the other hand, we find that a significant portion of the grains resist growth. The determination of mechanisms of grain growth will require extensive studies as a function of time at each annealing temperature and will be reported in future publications.

While the mean grain size grows by only a factor of 2 (27–55 nm) in the temperature range of 550–700 °C, the ordered domain size increases by a factor of 6 (3–19 nm) and the ordered fraction shows a remarkable increase from 1% to 28%. A comparison with the increase in coercivity in the same temperature range, presented in Fig. 5, shows that coercivity follows more closely the increase in the ordered fraction than the increase in grain size. The relationship between ordered fraction and coercivity has also been observed in bulk studies of CoPt.[5] In addition, we find that even though the films are two-phased, the $M-H$ plots appear to be a single loop and not the superposition of two separate loops for a soft and hard phase. This indicates that the ordered (hard) and disordered (soft) regions are magnetically coupled (i.e., these materials are "exchange spring" magnets).[6]

Two of the authors (R. R. and K. B.) acknowledge NSF DMR-9256332 and DMR-9458000, Philips for the use of the CM200 TEM/STEM and Y. Feng for his assistance.

[1] K. R. Coffey, M. A. Parker, and J. K. Howard, IEEE Trans. Magn. **31**, 2737 (1995).
[2] J. E. Palmer, C. V. Thompson, and H. I. Smith, J. Appl. Phys. **62**, 2492 (1987).
[3] C. V. Thompson, Mater. Res. Soc. Symp. Proc. **343**, 3 (1994).
[4] H.-J. Kim and C. V. Thompson, J. Appl. Phys. **67**, 757 (1990).
[5] R. A. McCurrie and P. Gaunt, Philos. Mag. **13**, 579 (1966).
[6] E. F. Kneller, IEEE Trans. Magn. **27**, 3588 (1991).

Co-Sm ($\bar{1}100$)[0001]//Cr ($\bar{1}2\bar{1}$)[$\bar{1}01$] epitaxy and its effects on magnetic properties of Co-Sm//Cr films

Y. Liu
Center for Materials Research and Analysis, and Department of Mechanical Engineering, University of Nebraska, Lincoln, Nebraska 68588-0656

D. J. Sellmyer
Center for Materials Research and Analysis, and Behlen Laboratory of Physics, University of Nebraska, Lincoln, Nebraska 68588-0113

B. W. Robertson
Center for Materials Research and Analysis, and Department of Mechanical Engineering, University of Nebraska, Lincoln, Nebraska 68588-0656

It is well known that the Cr underlayer plays a critical role in generating large in-plane coercivity in Co-based magnetic thin films. In this paper we report in detail the Co-Sm ($\bar{1}100$)[0001]//Cr ($\bar{1}2\bar{1}$)[$\bar{1}01$] epitaxy revealed by high resolution electron microscopy. The lattice mismatch between Co-Sm ($\bar{1}100$) and Cr ($\bar{1}2\bar{1}$) is less than 2%, suggesting an energetically favorable configuration. The high anisotropy observed in Co-Sm films is discussed by this epitaxial relation. © *1996 American Institute of Physics.* [S0021-8979(96)15308-6]

I. INTRODUCTION

In pursuing Co-based magnetic thin films for high density recording, it is well known that the Cr underlayer plays a critical role in generating large in-plane coercivity in Co-based magnetic thin films. The Co-based thin films have the hexagonal close-packed (HCP) structure which can grow on Cr underlayer epitaxially. Three kinds of microstructures in Co-based magnetic thin films with large in-plane anisotropy have been reported, which are all based on the epitaxial relation Co-alloy ($11\bar{2}0$)[0001]//Cr (001)[110]. The first kind has (001) texture of the Cr underlayer with the [010] direction randomly distributed in the film plane. Consequently the easy axes of the crystallites in the Co alloy magnetic thin films are randomly distributed in the film plane.[1,2] The second kind has a single crystalline Cr underlayer with the (100) in film plane. The c axes of the hexagonal crystallites in the magnetic film are epitaxially grown in two perpendicular directions [110] and [$\bar{1}$10] of the Cr underlayer. Such structure has been named bicrystal.[3,4] The third kind of microstructure is produced by depositing the Co alloy on a scratched (100) Cr single crystal. As a result, the c axis of the crystallites are aligned in one [110] direction only and the film has uniaxial anisotropy.[5]

Recently it has been shown that Co-Sm films with a nominal composition from Co_4Sm to Co_7Sm_2 exhibit high coercivity and in-plane anisotropy.[6,7] Transmission electron microscopy studies of Co-Sm films have shown that the microstructure of a Co-Sm thin film is composed of the amorphous matrix and crystallites with a grain size of about 5 nm.[8] The crystallites in the as-deposited Co-Sm films have a close-packed structure.[9] Each crystallite has a particular stacking mode which consists of local random stacking, occasionally a few unit cells of two layer stacking AB, three layer stacking ABC, and four layer stacking $ABAC$. However, the epitaxy relation between the Co-Sm crystallites and the Cr, if any, remains a mystery. In this paper we report our discovery of a new epitaxial relation between the Co-Sm crystallites and the Cr underlayer, that is, Co-Sm ($\bar{1}100$)//Cr ($\bar{1}2\bar{1}$) and Co-Sm [$11\bar{2}0$]//Cr [111] (equivalent to Co-Sm [0001]//Cr [$\bar{1}01$]. This epitaxy relation is responsible for the high in-plane coercivity of Co-Sm films grown on Cr underlayer with {110} texture. We think the discovery of this epitaxy relation is important also because it will now be possible to grow uniaxial anisotropic Co-Sm films (true for Co-based alloy with hexagonal close-packed structure) on single crystalline Cr of (121) surface. The resultant film will have the magnetic easy axis aligned in one direction and will have the highest anisotropy. Much higher coercivity, and coercive squareness can be expected from the uniaxial anisotropic Co-Sm films compared to current Co-Sm films.

II. EXPERIMENTAL PROCEDURE

The Co-Sm target used for deposition has a nominal composition of Co_7Sm_2. The films were deposited by dc magnetron sputtering under an Ar pressure of 5 mTorr at room temperature. The film configuration from substrate to film is 220 μm glass, 80 nm Cr, 30 nm Co-Sm and 10 nm Cr. Cross sectional transmission electron microscope (TEM) samples were prepared by embedding the strips of the films into a 3-mm-diam Cu tube with EMbed 812 (supplied by Electron Microscopy Sciences, P.O. Box 251, Ft. Washington, Pa 19034). The Cu tube with the films was cross-sectioned into about 0.3 mm slices. The slices were dimpled to 50 μm at the center and then ion milled until perforation. The high resolution electron microscopy (HREM) and diffraction work was performed using a JEOL 2010 transmission electron microscope operating at 200 kV.

III. RESULTS

Figure 1 shows the cross sectional HREM image of a Co-Sm film on Cr. Two Cr grains are observed. The Cr grain on the left side (marked G1) is on a random orientation and no lattice fringes are observed. The orientations of the Co-Sm crystallites with a grain size of about 5 nm grown on

 0021-8979/96/79(8)/5333/3/$10.00 © 1996 American Institute of Physics

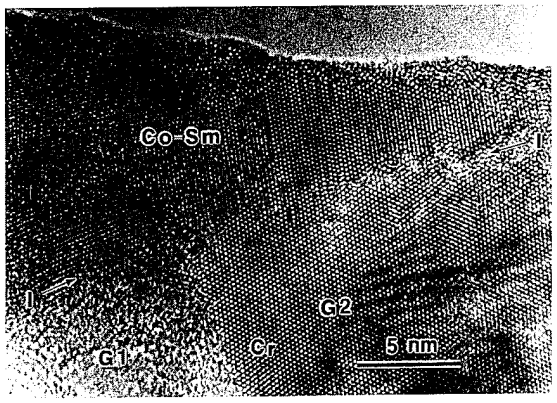


FIG. 1. HREM image of a cross-sectional Co-Sm film. A Cr grain is aligned on [111] zone axis while the Co-Sm crystallite is aligned on [11$\bar{2}$0] zone axis. The epitaxy is Cr ($\bar{1}2\bar{1}$)//Co-Sm ($\bar{1}$100) and Cr [111]//[11$\bar{2}$0]. The interface is indicated by letter *I*.

this Cr grain are not identified. The Cr grain on the right side (marked G2) is aligned on the [111] zone axis. The Co-Sm film grown on this Cr grain is on the [11$\bar{2}$0] zone axis. The epitaxy is Cr ($\bar{1}2\bar{1}$)//Co-Sm ($\bar{1}$100) and Cr [111]//Co-Sm [11$\bar{2}$0]. The interface between the Cr underlayer and the Co-Sm film is indicated by letter I. Figure 2 is the magnified interface region shown in Fig. 1. The crystal structures of the Cr underlayer and the Co-Sm crystallite are well revealed by the optical diffraction patterns, which are attached to the corresponding regions. The optical diffraction patterns clearly show that the Co-Sm has the close-packed structure and the Cr the *BCC* structure. The Co-Sm layer is basically a two-

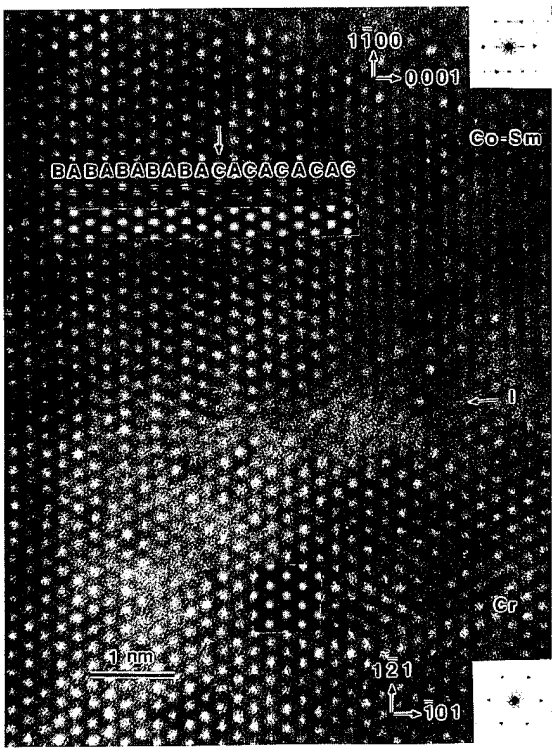


FIG. 2. Magnified interface region of Co-Sm on Cr underlayer. The stacking sequence in the Co-Sm film is well identified by the HREM image.

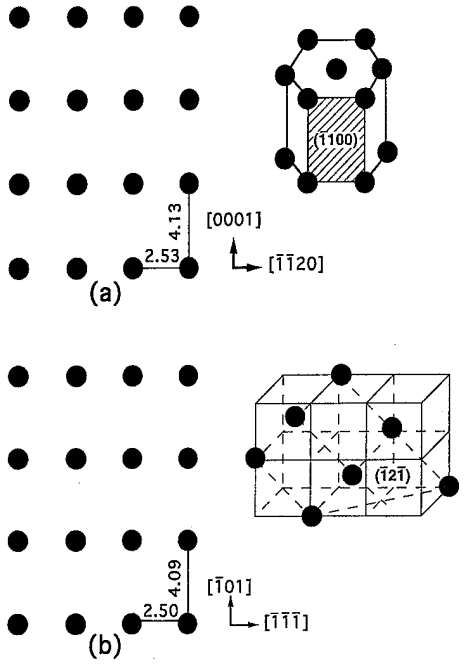


FIG. 3. Schematic illustration of atomic planes of (a) ($\bar{1}$100) in Co-Sm of hexagonal unit cell with lattice parameters $a=0.253$ nm, $c=0.413$ nm. (b) ($\bar{1}2\bar{1}$) in BCC Cr with lattice parameter $a=0.289$ nm.

layer stacking, *ABAB*, with a stacking fault. The stacking sequence is well defined by drawing three lines corresponding to *A* layers, *B* layers, and *C* layers. The stacking sequence is *BABA* on the left side and then switched to *CACA* as indicated by the arrows. Simulated images based on the above stacking sequence for the Co-Sm crystallite and the *BCC* structure for the Cr underlayer show excellent match to the HREM image.

Figure 3 schematically illustrates the atomic planes of Co-Sm ($\bar{1}$100) and Cr ($\bar{1}2\bar{1}$). The distances between atoms were deduced according to the lattice parameters $a=0.253$ nm, $c=0.413$ nm for the Co-Sm crystallite, and $a=0.289$ nm for Cr. Note that the lattice mismatch between the Co-Sm phase and the Cr is very small (~1%). Therefore such epitaxy is energetically favorable.

IV. DISCUSSION

The magnetic films fabricated using Co-based alloys have been available for magnetic recording for many years. The films also have the hexagonal close packed structure grown on the Cr underlayer. The epitaxy reported for the Co-alloy film on Cr underlayer is limited to Co-alloy (11$\bar{2}$0)[0001]//Cr (001)[110]. The reason that Co-alloy ($\bar{1}$100)[0001]//Cr ($\bar{1}2\bar{1}$)[$\bar{1}$01] epitaxy was not discovered by earlier researchers, if it existed in Co alloy films, is that when a ⟨111⟩ direction of Cr is aligned parallel to the electron beam, the Co-Sm ($\bar{1}$100)[0001]//Cr ($\bar{1}2\bar{1}$)[$\bar{1}$01] epitaxy is not necessarily to be seen. This is because HREM images are only obtainable for certain directions of Cr and Co-Sm crystallites. HREM images contain structural information only when the projections of the atoms are within the microscope resolution limit which is 0.14 nm for the JEOL

2010. If the projection of the atomic columns in a zone axis has a smaller spacing than 0.14 nm, no clear HREM images can be obtained. Therefore, for the Co-Sm $(\bar{1}100)[11\bar{2}0]$// Cr $(\bar{1}2\bar{1})[111]$ epitaxy, if the [111] zone axis of the Cr grain is aligned parallel to the electron beam, both the Cr [111] zone axis HREM image and the Co-Sm $[11\bar{2}0]$ zone axis image will be a projection of the structure and the epitaxy will be observed. However, for the same Co-Sm $(\bar{1}100)[11\bar{2}0]$//Cr $(\bar{1}2\bar{1})[111]$ epitaxy, if any of the other three $\langle 111\rangle$ zone axis of the same Cr grain ($[\bar{1}11]$, $[1\bar{1}1]$ or $[111\bar{1}]$) is aligned parallel to the electron beam, the corresponding zone axis of Co-Sm crystallite is a high index zone axis but not a $[11\bar{2}0]$ type zone axis. In this case, high resolution image will be obtained for the Cr grain but not for the Co-Sm crystallite and the epitaxy will not be revealed. Therefore, if an arbitrary $\langle 111\rangle$ type direction of Cr is chosen for high resolution imaging, the chance of seeing Co-Sm $(\bar{1}100)[11\bar{2}0]$//Cr $(\bar{1}2\bar{1})[111]$ epitaxy is one out of four.

In the x-ray diffraction spectrum of the Cr underlayer in the Co-Sm films, only strong {110} peak is observed, suggesting an {110} texture. The in-plane anisotropy of Co-Sm films on {110} textured Cr underlayers can also be explained by this epitaxy relation. Figure 4 depicts the Co-Sm hexagonal structure grown on Cr underlayer with {110} texture. The growth direction of the Cr underlayer is $[\bar{1}10]$. The two {112} planes have a 30° angle with the $(\bar{1}10)$. Such a structure is a close approximation for the Cr underlayer morphology grown by sputtering as revealed by atomic force microscopy [10]. The Co-Sm crystallites lie on the two {112} planes with the c easy axis 30° from the $(\bar{1}10)$ plane. However, even larger anisotropy of Co-Sm films will be expected if the [0001] easy axis of Co-Sm crystallites lie in the film plane which could be achieved by depositing Co-Sm films on Cr single crystal with a (121) surface.

V. CONCLUSIONS

HREM study has clearly shown the existence of Co-Sm $(\bar{1}100)[11\bar{2}0]$//Cr $(\bar{1}2\bar{1})[111]$ epitaxy with a lattice mismatch of less than 2%. Such epitaxy makes it possible to grow uniaxial anisotropy Co-Sm//Cr films.

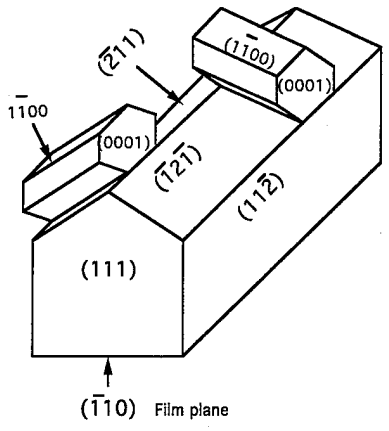


FIG. 4. Co-Sm $(\bar{1}100)[11\bar{2}0]$//Cr $(\bar{1}2\bar{1})[111]$ epitaxy shown on a Cr grain.

ACKNOWLEDGMENTS

The authors thank Professor Z. S. Shan, S. H. Liou for film deposition and discussions, T. Voiles and X. Zhao for TEM specimen preparations. Research was supported by ARPA/NSIC under Grant MDA 972-93-1-0009, and NSF under grants DMP 9222976 and OSR 9255225.

[1] B. Y. Wong, D. E. Laughlin, and D. N. Lambeth, IEEE Trans. Mag. **27**, 4733 (1991).
[2] S. L. Duan, J. O. Artman, B. Wong, and D. E. Laughlin, IEEE Trans. Mag. **26**, 1587 (1990).
[3] M. Mirzamaani, C. V. Jahnes, and M. A. Russak, J. Appl. Phys. **69**, 5169 (1991).
[4] T. Min and J. G. Zhu, J. Appl. Phys. **75**, 6129 (1994).
[5] M. Mirzamaani, K. Johnson, D. Edmonson, P. Evett, and M. Russak, J. Appl. Phys. **67**, 4695 (1990).
[6] E. M. T. Velu and D. N. Lambeth, IEEE Trans. Magn. **28**, 3249 (1992).
[7] D. J. Sellmyer, Z. S. Shan, Yi Liu, S. H. Liou, S. Malhotra, and B. W. Robertson, Scr. Metall. Mater. **33**, 1545 (1995).
[8] Y. Liu, B. Robertson, Z. S. Shan, S. Malhotra, M. J. Yu, S. K. Renukunta, S. H. Liou, and D. J. Sellmyer, IEEE Trans. Magn. **6**, 4035 (1994).
[9] Y. Liu, D. J. Sellmyer, B. Robertson, Z. S. Shan, and S. H. Liou, IEEE Trans. Magn. **31**, 2740 (1995).
[10] E. M. T. Velu, D. N. Lambeth, J. T. Thonton, and P. E. Russell, J. Appl. Phys. **69**, 6132 (1991).

Magnetic and recording properties of monolayer and multilayer thin-film media by using composite targets

Brij B. Lal, A. Bourez, and Michael A. Russak
HMT Technology, Fremont, California 94538

A single chamber deposition process (N-process) to produce multilayer media was developed using a newly designed magnetron cathode. The key feature of this cathode is its use of a composite target and magnetron design which permits specific areas of the target to be independently activated. Magnetic properties, read/write performance, and media-noise of single-layer (SL) and multilayer (ML) media produced with this cathode were compared to media fabricated using a standard two chamber process (S-process). CoCrTa:SL-media sputtered using the N-process produced ~400–600 Oe higher H_c, ~24% lower noise, and ~3 dB higher SNR at 136.4 KFCI recording density in comparison to SL media sputtered by S-process. X-ray diffraction analysis indicated a higher degree of in-plane c-axis orientation in N-process SL media. Sputtering the magnetic layer at elevated temperature due to zero dwell time between Cr and magnetic layer deposition and the formation of preferred in-plane orientation in the magnetic layer contributed to the increase in H_c of N-process media. ML-media fabricated by two different sputtering processes with Cr-interlayer (Cr-IL) of 5–15 Å (1-chamber and 2-chamber) showed similar noise reduction: ~30% at 153.4 KFCI recording density. In addition, for the comparable H_c and M_rt, the ML media sputtered by N process produced lower pulse width (PW-50), better overwrite (OW), and lower bit shift (BS). © *1996 American Institute of Physics.* [S0021-8979(96)09508-2]

I. INTRODUCTION

It is well known that the temperature at which the magnetic layer is deposited during the fabrication of Co based thin-film recording media has a strong effect on the resultant H_c and recording characteristics.[1,2] Also, during fabrication of multilayer (ML) media the heat loss due to dwell time between each layer can affect the same parameters.[3–5] In addition, production of ML media in a single disk system such as an Intevac MDP-350 requires several chambers to deposit the films. This contributes significantly to heat loss from the substrate. In this article we report results on media fabricated using a new cathode capable of depositing several layers of two different materials in a single sputtering chamber in an MDP-350 machine (N-process). This dc-magnetron cathode was used to deposit CoCrTa: single-layer(SL)- and ML media. The cathode uses concentric annular shaped targets and has the means to alternately address each portion of the target to deposit specific materials independently. Magnetic and recording properties of these SL and ML media will be presented.

II. EXPERIMENTAL DETAILS

Samples of $Co_{84.5}Cr_{12.5}Ta_3$/Cr:SL and $Co_{84.5}Cr_{12.5}Ta_3$/Cr/$Co_{84.5}Cr_{12.5}Ta_3$/Cr:ML media were sputtered on NiP/Al substrates in one chamber at 260 °C with varying thickness of Cr underlayer, magnetic layer, and Cr interlayer (IL). The new cathode assembly consisted of inner (Cr) and outer (magnetic) concentric targets (Fig. 1) for depositing thin-film layers of Cr and the magnetic alloy. For the N and S processes, the dwell time between the Cr and the magnetic-layer deposition was zero and 12 s, respectively. For comparison SL media were sputtered by using the conventional S process. The thickness of Cr and Co-alloy films were measured by x-ray fluorescence technique and bulk magnetic properties were measured by a vibrating-sample magnetometer (VSM). X-ray diffractometry was used to characterize film's texture. The recording characteristics were evaluated by using an inductive write head and a magnetoresistive playback head (shield-to-shield gap=0.7 μm, track width=3.5 μm). The flying height was 2.2 microinch with a linear disk speed of 8 m/s.

III. RESULTS AND DISCUSSION

A. CoCrTa/Cr:SL media

To demonstrate the effects of N versus S processes for SL media, typical magnetic properties of two groups of disks fabricated under similar sputtering conditions are summarized in Table I. These data show that for the N-process SL media, the increase in H_c is ~20% with no significant difference in squareness ratio (SR), coercive squareness (S^*),

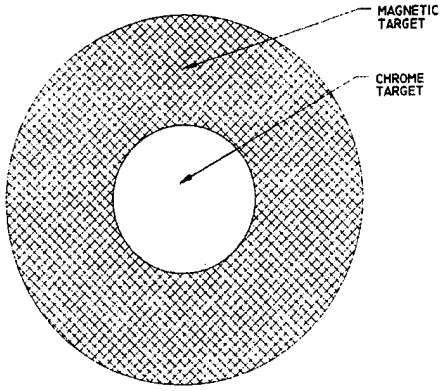


FIG. 1. Concentric annular shaped composite targets of Cr and magnetic materials.

 0021-8979/96/79(8)/5336/3/$10.00 © 1996 American Institute of Physics

TABLE I. Comparison of magnetic properties for CoCrTa:SL media (magnetic film thickness: 160 Å) sputtered by N vs S processes.

Sputtering Process	VSM Data H_c (Oe)	SR	S^*	OR (Mr:cir/Mr:rad)	M_rt (memu/cm^2)
S process (conventional)	2326	0.85	0.82	1.4	0.97
N process (new)	2785	0.91	0.78	1.4	0.95

and orientation ratio (OR). The change in the H_c with M_rt for SL media sputtered by N versus S processes is shown in Fig. 2. For both type of media, as M_rt decreases, H_c increases monotonically reaching a maximum at 2338 Oe with M_rt:1.2 memu/cm^2 for the S-process SL media. Whereas, for the N-process SL media a peak in the M_rt versus H_c curve was not observed within the range measured, however, a maximum value of $H_c \sim 2800$ Oe at a M_rt of 0.92 memu/cm^2 was obtained. This means that the SL-magnetic films sputtered by N process approach the superparamagnetic state at a lower M_rt (thinner magnetic film) than the SL-magnetic film sputtered by S process. In addition, for SL-media sputtered in a single chamber, we found that for a small increase in Cr-underlayer thickness from 50–100 Å, H_c increased from 1750 to 2201 Oe for media with M_rt:1.2 memu/cm^2 (Fig. 3). It should be noted that in N process, the magnetic layer is deposited on the Cr underlayer at a higher temperature, and also, due to zero dwell time, the Cr-underlayer film surface is not exposed to the residual gases present in the main vacuum chamber which affects the interfacial structure and chemistry for the epitaxial growth of Co-alloy film. Furthermore, higher deposition temperature produces more in-plane c-axis grains and promotes decoupling of the grains due to Cr segregation at grain boundaries. These observations are consistent with the earlier work reported on CoCrTa/Cr media[6,7] where high deposition temperature and ultraclean process conditions produced high H_c due to high magnetocrystalline anisotropy and enhanced Cr-segregated grain boundary for reduced intergranular exchange coupling. Also, it was found that for comparable high-frequency (HF) amplitude, N-process SL media produced ~24% lower media noise and ~3 dB higher SNR

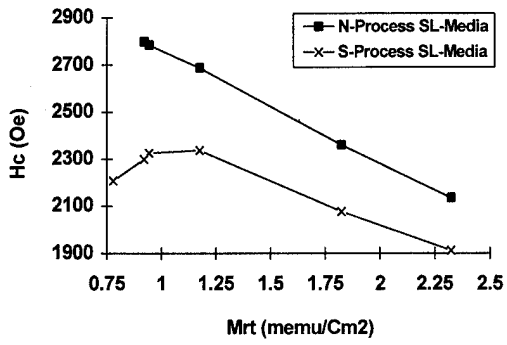


FIG. 2. Coercivity vs M_rt for CoCrTa/Cr:SL media sputtered by N and S processes.

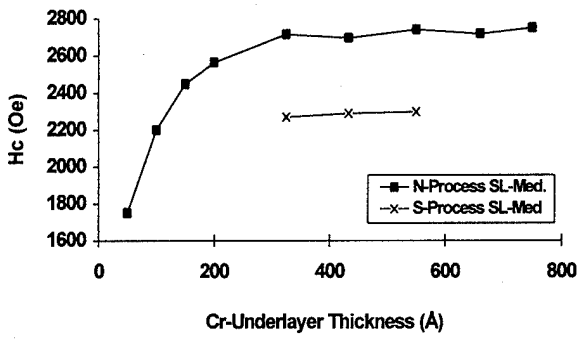


FIG. 3. Coercivity as a function of Cr-underlayer thickness for CoCrTa/Cr:SL media sputtered by N vs S processes.

(Fig. 4) in comparison to standard S-process SL media at 136.4 KFCI recording density. Figure 5 depicts x-ray diffraction (XRD) spectra of SL media sputtered by N and S processes. The Co(11.0) peak was not recorded in wider angle scans (θ-2θ:20°–80°) of these samples. Also, for both samples data taken at a shallow grazing angle of 0.3° indicated the presence of only two peaks: Co(10.0) and Co(10.1) and did not show Co(002) plane which means that the texture of these samples near 44° is due to Cr(110), not the Co(002). Among the CoCrTa/Cr peaks, the Co(10.0) and Co(10.1) peaks are stronger in N media when compared to S media, indicating a higher degree of preference for the c axis of CoCrTa to lie in or near the plane of the film and producing higher in-plane H_c. In addition, Co(10.1)/Cr(110) epitaxy of CoCrTa/Cr is more noticeable in the N-process media. This may be due to the higher deposition temperature for the magnetic layer during the N process. It has also been noted that the Co(10.1)/Cr(110) epitaxy is preferable to the Co(11.0)/Cr(200) epitaxy for reduction of intergranular exchange coupling.[1]

B. CoCrTa/Cr/CoCrTa:ML media

Magnetic and recording properties of CoCrTa SL and ML media sputtered by N process are summarized in Table II. These data show that the H_c decreases slightly with no change in M_rt and S^* for ML media with Cr-IL:10 Å in

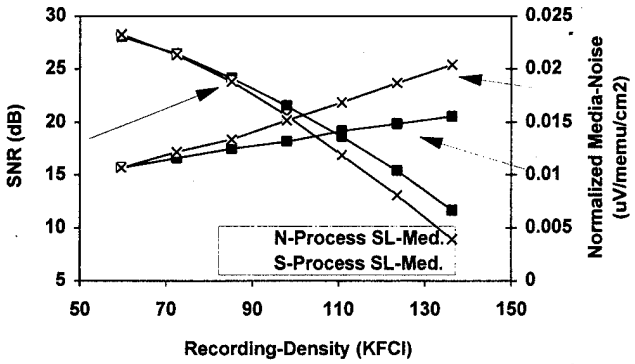


FIG. 4. Normalized media noise and SNR as a function of linear recording density for CoCrTa/Cr:SL media (magnetic film thickness: 190 Å) sputtered by N vs S processes.

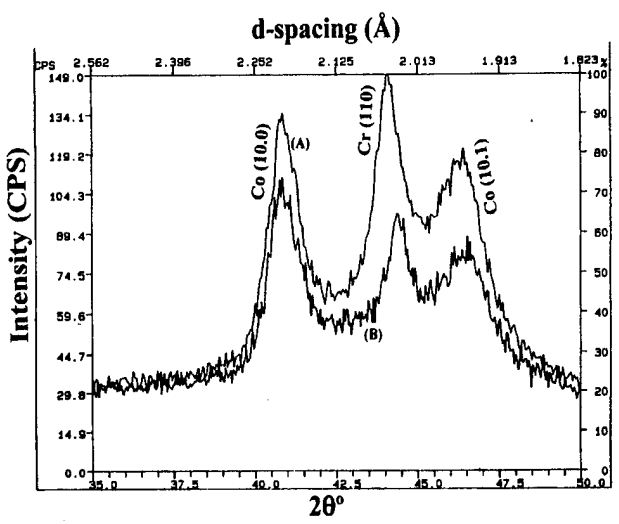


FIG. 5. X-ray diffraction patterns of CoCrTa/Cr:SL media (magnetic film thickness: 190 Å) sputtered by (A) *N* and (B) *S* processes.

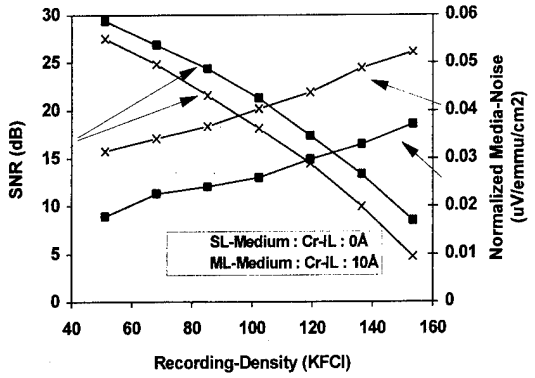


FIG. 6. Normalized media noise and SNR as a function of linear recording density for CoCrTa:SL vs ML media (magnetic film thickness: 190 Å) sputtered by *N* process.

comparison to SL media. Comparison of recording characteristics: HF amplitude, pulse width (PW-50), overwrite (OW), bit shift (BS), and SNR at 68.2 KFCI recording density for SL and ML media with comparable H_c and M_rt showed superior performance for ML media. ML-media sputtered in single chamber produced higher HF amplitude, lower PW-50, better OW, lower BS. In the case of conventional ML media, the OW degrades due to higher write field needed to satisfy the mean switching field of the media with the lower S^*.[8] Further, to compare the noise characteristics of these SL and ML media, normalized media noise and SNR as a function of recording density were measured and are illustrated in Fig. 6. It was observed that the ML media with Cr-IL:10 Å produced ~29% lower media noise and ~4 dB higher SNR at 153.4 KFCI recording density in comparison to SL media. It has been shown that the Cr-enriched grain boundaries with Cr-IL:5–15 Å thickness might be enough to reduce the exchange coupling between the upper and lower magnetic layers.[4,5,9] Also, a thinner Cr interlayer is helpful in reducing the head-media spacing loss which affects the recording performance.

IV. CONCLUSIONS

SL media fabricated by *N*-process produced ~400–600 Oe higher H_c, ~24% lower media noise and ~3 dB higher SNR at 136.4 KFIC recording density in comparison to *S*-process SL media. XRD of *N*-process SL media showed strong preferred orientation indicating high number of grains with their *c* axis in or near the film plane producing high in-plane H_c. Due to zero dwell time, the interfacial structure and chemistry for the epitaxial growth of Co-alloy film produced lower transition noise, possibly due to enhancement in Cr segregation at grain boundaries. ML media fabricated by *N*-process showed no reduction in M_rt and S^*, and exhibited superior read/write characteristics in comparison to SL media. In summary, the new composite-target cathode process eliminates the heat loss in between the deposition layers, improves the magnetic and recording performance, approaches superparamagnetic state at a maximum H_c with lower M_rt for high density recording, and reduces the number of sputtering chambers and targets required to fabricate SL and ML media in production.

TABLE II. Comparison of magnetic and recording properties of CoCrTa:SL vs ML media (magnetic film thickness: 190 Å) sputtered by *N* process.

Media type	Cr IL	H_c (Oe)	M_rt (memu/cm^2)	S^*	HF (uV)	PW-50 (nS)	OW (-dB)	BS (nS)	SNR (dB) at 68.2 KFCI
SL media	0	2210	1.1	0.77	1177	33.6	41.2	4.8	24.1
ML media	10 Å	2075	1.1	0.76	1213	31.6	41.8	4.2	26.9

ACKNOWLEDGMENTS

Authors would like to thank T. Shinohara (HMRL, Japan) and M. Alex for helpful discussions, C. Sordello for electrical measurements, Steve Robie (Scintag, Inc.) for x-ray diffraction analysis, and V. Patel for magnetic measurements and data collection.

[1] Y. Shen, D. E. Laughlin, and D. Lambeth, IEEE Trans. Magn. **28**, 3261 (1992).
[2] J. Judy, IEEE Trans. **29**, 209 (1993).
[3] B. Cord, K. H. Schuller, H. Zahel, G. Chaput, and S. Duan, IEEE Trans. Magn. **29**, 3694 (1993).
[4] B. Lal and T. Shinohara, IEEE Trans. Magn. **30**, 3981 (1994).
[5] E. Teng and A. Eltoukhy, IEEE Trans. Magn. **29**, 3679 (1993).
[6] J. Nakai, A. Kikuchi, M. Kuwabara, T. Sakurai, T. Shimatsu, and M. Takahashi, INTERMAG-95, Digest #JA-05, San Antonio, TX, April 18–21, 1995.
[7] S. Kojima, S. Fukaya, Y. Yahisa, Y. Hosoe, and N. Kodama, INTERMAG-95, Digest #JA-04, San Antonio, TX, April 18–21, 1995.
[8] T. Yogi, C. Tsang, T. A. Nguyen, K. Ju, G. I. Gorman, and G. Castillo, IEEE Trans. Magn. **26**, 2271 (1990).
[9] A. Murayama, M. Miyamura, K. Miyata, and Y. Oka, IEEE Trans. Magn. **27**, 5064 (1991).

Dependence of media noise on grain size and intergranular coupling in thin-film media

Akira Kikuchi
Fujitsu Limited, Nagano, 381 Japan

Shinya Kawakita
Nippon Sheet Glass Co., Ltd., Mie, 510 Japan

Junichi Nakai
Kobe Steel, Ltd., Kobe, 651-22 Japan

Takehito Shimatsu and Migaku Takahashi
Department of Electronic Engineering, Tohoku University, Sendai, 980-77 Japan

The media noise performance is discussed in connection with grain size and intergranular coupling for the $Co_{85.5}Cr_{10.5}Ta_4$, $Co_{78}Cr_{17}Ta_5$, and $Co_{62.5}Ni_{30}Cr_{7.5}$ thin-film media fabricated under the ultraclean sputtering process (UC process). It is clarified that the value of S/N_m is quantitatively represented as functions of the value of H_c/H_k^{grain} and the grain size in every kind of media. The value of signal-to-media noise ratio (S/N_m) increases with the increment in H_c/H_k^{grain} and also with the decrement in grain size. In the media with grains adequately separated by segregated grain boundaries fabricated by the UC process, grain-size reduction, taking account of the decrease in intergranular magnetostatic coupling, is required to obtain even higher S/N_m values. © *1996 American Institute of Physics.* [S0021-8979(96)09608-9]

I. INTRODUCTION

Low media noise is essentially required for thin-film media to achieve high-density magnetic recording. The decrement of intergranular exchange coupling and grain-size reduction are generally suggested to be essential factors to decrease media noise,[1] but quantitative evaluation concerning the effects of grain size and intergranular coupling on media noise has not been experimentally clarified.

An ultraclean sputtering process (UC process) is proposed to be a key technology to enable the enhancement of Cr segregation at grain boundary resulting in low intergranular exchange coupling.[2,3] Furthermore, by decreasing underlayered Cr thickness, the UC process realizes the reduction of ferromagnetic grain size without the increment of intergranular exchange coupling.

In the present study, dependence of recording properties on Cr thickness was examined for thin-film media fabricated under the UC process. The media noise performance is discussed in connection with grain size and intergranular coupling.

II. EXPERIMENTAL PROCEDURE

The thin-film media were fabricated under the UC process with a specialized production-type sputtering machine (ILC3013 ANELVA) and ultraclean Ar gas (UC-Ar). The base pressure of each process chamber is less than 3×10^{-9} Torr and the buildup rate is less than 5×10^{-7} Torr ℓ/s. The impurity level of UC-Ar is about 1 ppb (H_2O level) at the point of use.

In this study, $Co_{85.5}Cr_{10.5}Ta_4$, $Co_{78}Cr_{17}Ta_5$, and $Co_{62.5}Ni_{30}Cr_{7.5}$ targets with low impurities were used for the magnetic alloys. The films were deposited on extremely smooth nontextured (Ra below 1 nm) NiP/Al substrates with underlayered Cr films. The value of tB_r (the product of film thickness and remanence) was fixed at 100–120 G μm, which corresponds to thicknesses of about 16 nm in $Co_{85.5}Cr_{10.5}Ta_4$, 28 nm in $Co_{78}Cr_{17}Ta_5$, and 13.5 nm in $Co_{62.5}Ni_{30}Cr_{7.5}$. The underlayered Cr thickness was varied from 2.5 to 100 nm. The substrate temperature was kept at 250 °C during the film deposition. The dry-etching time of substrate surface just prior to film deposition[4] was fixed at 0 or 10 s, which corresponds to 0 or about 0.2 nm in etched depth.

The recording characteristics were evaluated by using a magnetoresistive head. The thin-film media were dc erased prior to the evaluation of the recording characteristics. The signal frequency was 16.8 MHz. The linear velocity was 12.2 m/s. The spacing between the head and the media was 0.08–0.10 μm. The media noise was measured using a spectrum analyzer and calculated by integrating the readback noise spectrum from 0 to 33.6 MHz.

III. RESULTS AND DISCUSSION

In Fig. 1, the values of readback S/N_m at 69.7 k FCI in $Co_{85.5}Cr_{10.5}Ta_4$, $Co_{78}Cr_{17}Ta_5$, and $Co_{62.5}Ni_{30}Cr_{7.5}$ media are plotted against the thickness of Cr underlayer. These media were fabricated onto the substrate surface with dry-etching treatment.

In the $Co_{85.5}Cr_{10.5}Ta_4$ and $Co_{78}Cr_{17}Ta_5$ media, S/N_m gradually increases with decreasing Cr thickness, and shows highest values at extremely thin Cr thicknesses of about 2.5–5 nm. This increase in S/N_m with decreasing Cr thickness was mainly caused by the decrement in media noise. On the other hand, even in the $Co_{62.5}Ni_{30}Cr_{7.5}$ media, high S/N_m is realized by applying the UC process due to the remarkable decrement in media noise.[3] However, S/N_m in this media gradually decreases with decreasing Cr thickness especially from about 10 nm in thickness.

 0021-8979/96/79(8)/5339/3/$10.00 © 1996 American Institute of Physics

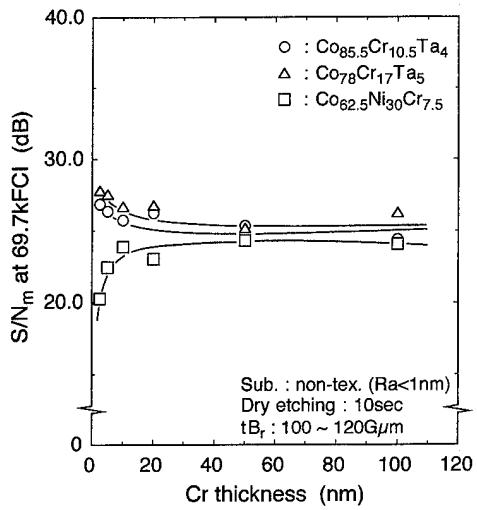


FIG. 1. The values of S/N_m at 69.7 k FCI in $Co_{85.5}Cr_{10.5}Ta_4$, $Co_{78}Cr_{17}Ta_5$, and $Co_{62.5}Ni_{30}Cr_{7.5}$ media (fabricated onto the substrate surface with dry-etching treatment) plotted against the thickness of Cr underlayer.

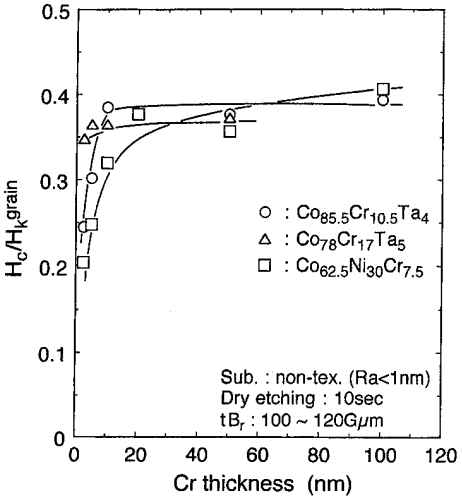


FIG. 3. The values of H_c normalized by H_k^{grain} in the $Co_{85.5}Cr_{10.5}Ta_4$, $Co_{78}Cr_{17}Ta_5$, and $Co_{62.5}Ni_{30}Cr_{7.5}$ media (fabricated onto the substrate surface with dry-etching treatment) plotted against the thickness of Cr underlayer.

In Fig. 2, the values of coercive force H_c in these media are plotted in the similar way. Here, H_c of these media is isotropic in the film plane.

H_c in both the $Co_{85.5}Cr_{10.5}Ta_4$ and $Co_{78}Cr_{17}Ta_5$ media shows almost a constant value of about 2.3 kOe through 10 nm in Cr thickness. With further decreasing Cr thickness, H_c in both media drastically decreases. However, H_c in the $Co_{78}Cr_{17}Ta_5$ media maintains its large value of about 2.1 kOe at even 2.5 nm in Cr thickness. On the contrary, H_c in the $Co_{62.5}Ni_{30}Cr_{7.5}$ media decreases gradually from 2.6 to 0.8 kOe with decreasing Cr thickness from 100 to 2.5 nm. Cr thickness dependences of S/N_m in Fig. 1 are found not to correspond simply to those of H_c, especially in the $Co_{85.5}Cr_{10.5}Ta_4$ and $Co_{78}Cr_{17}Ta_5$ media.

In order to discuss the effect of the degree of intergranular coupling on media noise, in Fig. 3, the values of H_c normalized by H_k^{grain} in these media are plotted in the similar way. Here, H_k^{grain} was evaluated from the magnetic field where rotational hysteresis loss just vanishes.[5] The value of H_c/H_k^{grain} means the degree of intergranular coupling of magnetization, and takes the ideal maximum of about 0.5 in the case of isotropic media with no intergranular coupling.

In both the $Co_{85.5}Cr_{10.5}Ta_4$ and $Co_{78}Cr_{17}Ta_5$ media, H_c/H_k^{grain} maintains its large value more than 0.37 through 10 nm in Cr thickness. With further decreasing Cr thickness, the value of H_c/H_k^{grain} in the $Co_{85.5}Cr_{10.5}Ta_4$ media drastically decreases. However, in the $Co_{78}Cr_{17}Ta_5$ media, a large value of about 0.35 is retained even at 2.5 nm in Cr thickness. This result implies that, in the $Co_{78}Cr_{17}Ta_5$ media, extremely low intergranular coupling is realized with an extremely thin Cr underlayer. On the other hand, large H_c/H_k^{grain} values are realized even in $Co_{62.5}Ni_{30}Cr_{7.5}$ media, which means the realization of low intergranular exchange coupling due to the enhancement of Cr segregation at grain boundaries.[3] However, the value of H_c/H_k^{grain} in the $Co_{62.5}Ni_{30}Cr_{7.5}$ media gradually decreases with decreasing Cr thickness. In the thinner Cr region, the values of H_c/H_k^{grain} in the $Co_{62.5}Ni_{30}Cr_{7.5}$ media are adequately smaller than those in both the $Co_{85.5}Cr_{10.5}Ta_4$ and $Co_{78}Cr_{17}Ta_5$ media.

In the $Co_{62.5}Ni_{30}Cr_{7.5}$ media, the decrease in S/N_m with decreasing Cr thickness is found to correspond qualitatively to the increase in intergranular exchange coupling. However, S/N_m in both the $Co_{85.5}Cr_{10.5}Ta_4$ and $Co_{78}Cr_{17}Ta_5$ media gradually increases in spite of the decreasing in H_c/H_k^{grain} with decreasing Cr thickness.

It should be noted here that, even in the media with grains sufficiently separated by the segregated grain boundaries, grain-size reduction is suggested to increase the intergranular magnetostatic coupling due to the increment in the number of magnetically coupled grains. In every media presently examined, grain size strongly depends on Cr thickness. In both the $Co_{85.5}Cr_{10.5}Ta_4$ and $Co_{78}Cr_{17}Ta_5$ media, the grain size markedly decreases from about 25 nm to about 11 nm with decreasing Cr thickness from 50 to 2.5 nm. Therefore, in present media, precise discussion is possible for the cor-

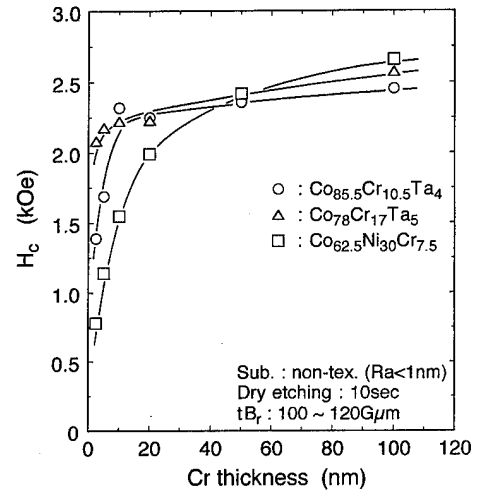


FIG. 2. The values of coercive force H_c in the $Co_{85.5}Cr_{10.5}Ta_4$, $Co_{78}Cr_{17}Ta_5$, and $Co_{62.5}Ni_{30}Cr_{7.5}$ media (fabricated onto the substrate surface with dry-etching treatment) plotted against the thickness of Cr underlayer.

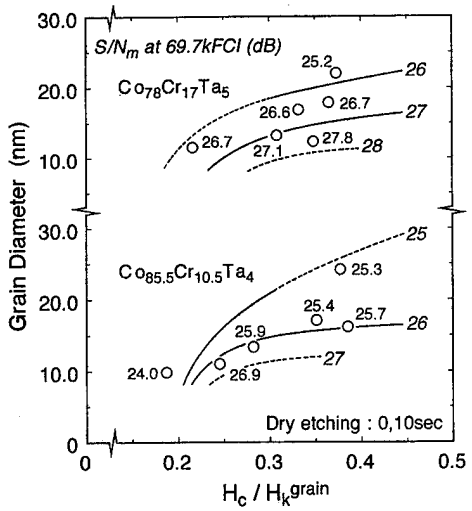


FIG. 4. The values of S/N_m at 69.7 k FCI in $Co_{85.5}Cr_{10.5}Ta_4$ and $Co_{78}Cr_{17}Ta_5$ media plotted as functions of H_c/H_k^{grain} and grain diameter.

relation between intergranular coupling and S/N_m from the viewpoint not only of the degree of grain separation at grain boundaries but also of the grain size.

In Fig. 4, the values of S/N_m in both the $Co_{85.5}Cr_{10.5}Ta_4$ and $Co_{78}Cr_{17}Ta_5$ media fabricated under several fabrication conditions (with and without dry-etching treatment) plotted as functions of H_c/H_k^{grain} and grain diameter.

As seen, it is clearly found that S/N_m increases with the increasing in H_c/H_k^{grain}. Furthermore, with the reduction of the grain diameter, S/N_m remarkably increases in both media. That is to say, S/N_m increases not only with the decrease in intergranular coupling but also with the reduction in the grain size.

In Fig. 5, the values of S/N_m in the $Co_{62.5}Ni_{30}Cr_{7.5}$ media

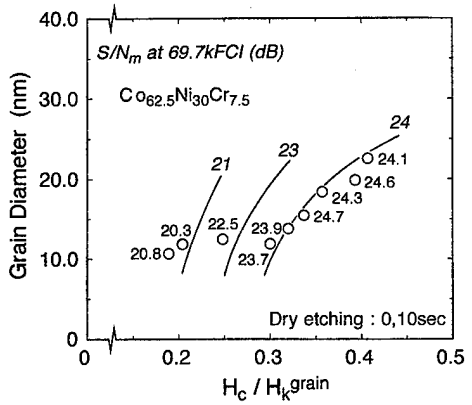


FIG. 5. The values of S/N_m at 69.7 k FCI in $Co_{62.5}Ni_{30}Cr_{7.5}$ media plotted as functions of H_c/H_k^{grain} and grain diameter.

fabricated under several fabrication conditions (with and without dry-etching treatment) are plotted as functions of H_c/H_k^{grain} and grain diameter.

The S/N_m of the $Co_{62.5}Ni_{30}Cr_{7.5}$ media shows similar dependence on the H_c/H_k^{grain} and grain diameter as those in both the $Co_{85.5}Cr_{10.5}Ta_4$ and $Co_{78}Cr_{17}Ta_5$ media.

These experimental results shown in Figs. 4 and 5 mean that S/N_m of thin-film media can be quantitatively discussed as functions of the intergranular coupling and the grain size. In the media with grains adequately separated by segregated grain boundaries, the reduction of the grain size is effective for the improvement of S/N_m. Furthermore, the increase in H_c/H_k^{grain} value through the decrease in intergranular magnetostatic coupling is found to be essential in order to realize even higher S/N_m values in these media. For the decrement in intergranular magnetostatic coupling in these media, the selection of alloy composition, which gives a small ratio of saturation flux density $4\pi M_s$ to H_k^{grain}, is suggested to be the most important factor.[6]

IV. CONCLUSIONS

The media noise performance is discussed in connection with grain size and intergranular coupling for the $Co_{85.5}Cr_{10.5}Ta_4$, $Co_{78}Cr_{17}Ta_5$, and $Co_{62.5}Ni_{30}Cr_{7.5}$ thin-film media fabricated under the UC process.

As a result,

(1) The value of S/N_m is quantitatively represented as functions of the value of H_c/H_k^{grain} and the grain size in every kind of media. The value of S/N_m increases with the increment in H_c/H_k^{grain} and also with the decrement in grain size.

(2) In the media with grains adequately separated by segregated grain boundaries fabricated by the UC process, grain-size reduction, taking account of the decrease in intergranular magnetostatic coupling, is required to obtain even higher S/N_m values.

ACKNOWLEDGMENTS

This study has been made by Tohoku University in cooperation with 13 companies in Japan (Fujitsu, Nippon Sheet Glass, Kobe Steel, Fuji Electric, Kao, Anelva, Asahi Komag, Hitachi Metals, Hoya, Japan Energy, Teijin, Mitsubishi Materials, and Alps Electric).

[1] For example, H. Neal Bertram and R. Arias, J. Appl. Phys. **71**, 3439 (1992).
[2] M. Imakawa, S. Ishibashi, A. Hatashita, T. Shimatsu, and M. Takahashi, Proceedings of 14th ICMFS and E-MRS Joint Colloquium, Germany, 1994 (unpublished), p. 247.
[3] T. Shimatsu and M. Takahashi, J. Mater. Chem. Phys. **41**, 134 (1995).
[4] S. Kawakita, T. Sakurai, A. Kikuchi, T. Shimatsu, and M. Takahashi (in press).
[5] M. Takahashi, T. Shimatsu, M. Suekane, M. Miyamura, K. Yamaguchi, and H. Yamasaki, IEEE Trans. Magn. **28**, 3285 (1992).
[6] T. Shimatsu and M. Takahashi (in press).

The role of stress-induced anisotropy in longitudinal thin film magnetic recording media

C. A. Ross, M. E. Schabes, R. Ranjan, G. Bertero, and T. Chen
Komag Inc., 275 S. Hillview Drive, Milpitas, California 95035

Measurements of stress and magnetostriction have been made in longitudinal CoCrTa magnetic recording media. The stress in Cr and CoCrTa/Cr films deposited onto grooved substrates is higher parallel to the grooves compared to perpendicular to the grooves by up to a few hundred MPa. Combined with a magnetostriction coefficient of -3×10^{-5} in $CoCr_{10}Ta_6$/Cr, magnetostriction makes a contribution to the in-plane anisotropy observed in such media. © *1996 American Institute of Physics.* [S0021-8979(96)15408-2]

I. INTRODUCTION

Longitudinal magnetic recording media are typically made by sputtering a Cr underlayer, Co alloy magnetic layer and C overcoat sequentially onto a heated nickel phosphorus-coated aluminum substrate which has been circumferentially textured or grooved. It is commonly observed that the magnetic film has higher coercivity, remanence and squareness in the in-plane circumferential direction compared to the radial direction. The ratio of circumferential to radial coercivity is known as the coercivity orientation ratio, OR_{Hc}. Several explanations have been proposed for this in-plane anisotropy, including magnetostrictive effects caused by in-plane stress differences.[1–4] Despite some modeling,[5] the theory for texture-induced magnetic anisotropy remains incomplete. In this article we explore the importance of stress-induced anisotropy by measuring stress and magnetostrictive effects in CoCrTa/Cr media.

II. EXPERIMENTAL METHODS

Samples were made by dc magnetron sputtering of Cr and Co alloy films in an Intevac 250 A system onto 3 cm ×3 cm×0.8 mm coupons of smooth and textured nickel–phosphorus coated aluminum substrate. The coupons were preannealed at 250 °C for 2 h in air to stabilize them against warping during high temperature processing. The curvature of the coupons was measured in two perpendicular directions, parallel and perpendicular to the grooves, using a profilometer, both before and after film deposition. The stress in the films was calculated from the change in curvature of the coupons, taking account of the nonuniform biaxial stress state. Changes in curvature due to 100 nm thick films were typically 100–200 nm over a 20 mm scan length. The aim of the experiment was to use real disk substrates, rather than glass or silicon substrates, so that the microstructure of the films would be the same as found in recording media. However, the relatively high thickness of the substrates necessitated deposition of 75–100 nm thick films to obtain adequate sensitivity in the stress measurement.

Magnetostriction was measured in a torque magnetometer using a fixture similar to that of Mauri *et al.*[6] Samples of size 8 mm×5 mm were cut from sputtered disks and the pieces were thinned to 0.5 mm from the back by milling. The film was removed from the ends of the sample so that a 4 mm×5 mm area of Cr/Co alloy film was left at the center of the sample. The fixture applied a variable biaxial stress to the film by a three point bending of the sample. The actual stress applied during each measurement was deduced by measuring the curvature of the 4 mm×5 mm area of film using a profilometer. The fixture applied a plane biaxial stress to the sample which was much higher along the direction of bending compared to the perpendicular direction. The applied stress $\Delta\sigma$ was taken as the difference between the two in-plane stress components. In-plane anisotropy K was measured as a function of applied stress, and magnetostriction λ was calculated from the change in anisotropy, ΔK with stress from the relation $\Delta K=-3/2\lambda\Delta\sigma$. Magnetostriction was measured at low applied stress where deformation was still elastic.

III. RESULTS

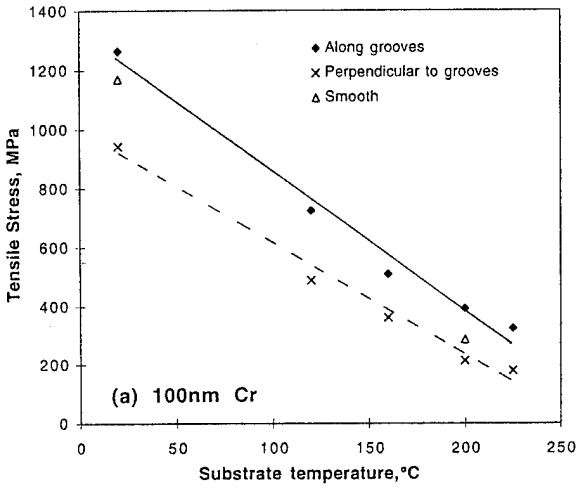
A. Stress in Cr and CoCrTa films

Stress was measured in 100 nm thick Cr films sputtered at 20–200 °C onto smooth and textured substrates. Figure 1(a) shows clearly the effect of the substrate grooving in Cr films. The stress is 1.4 times smaller perpendicular to the grooves compared to the stress parallel to the grooves. In contrast, the stress in films on mirror polished substrates was always isotropic and similar to the stress parallel to the grooves in the textured samples.

The sputter system has circular symmetry and the substrates were not moved during deposition, so stress anisotropy might be caused by the geometry of the sputter system. However, orienting the grooves in different directions had no effect on the stress, showing that the stress difference originates from the substrate texture. Figure 1(a) shows that the film stress decreases as the substrate temperature increases. As the sample cools from the sputter temperature, a compressive thermal mismatch stress is added to the intrinsic stress in the film.

Stress in CoCrTa films on a chromium underlayer were estimated by depositing bilayer samples with a 25 nm chromium layer and 75–100 nm CoCrTa and subtracting the contribution of the Cr stress to the curvature, calculated from the results on the 100 nm Cr films. This assumes that the stress in the Cr layer is independent of thickness, and more importantly, it neglects changes in the stress in the Cr caused by epitaxial growth of the Co overlayer. As a result of the Cr subtraction, the results for stress in CoCrTa on Cr show

 0021-8979/96/79(8)/5342/3/$10.00 © 1996 American Institute of Physics



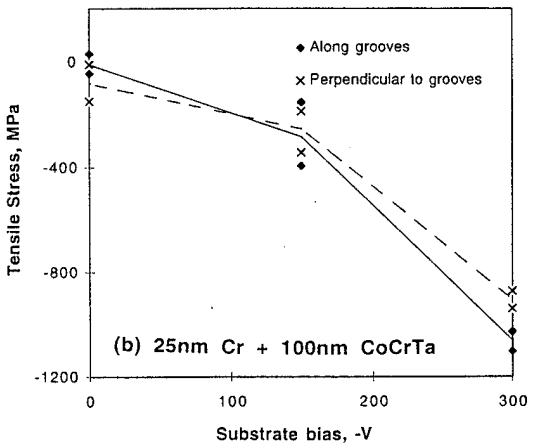


FIG. 1. Stress in films measured parallel and perpendicular to the texture lines. (a) Cr on smooth and textured substrates; (b) CoCrTa on a Cr underlayer, in which the Cr contribution has been subtracted. Points are joined for clarity.

greater scatter than results for a single Cr layer. Figure 1(b) shows that the stress in the CoCrTa layer becomes compressive as substrate bias is applied, due to greater bombardment of the film during growth. Stress was generally smaller perpendicular to the grooves, an effect similar to that found in the single Cr films. The maximum in-plane stress difference measured in the CoCrTa was 300 MPa over a range of deposition conditions.

The total stress consists of a thermal component, which becomes more compressive as deposition temperature increases, and an intrinsic component. The temperature dependence of total stress in the CoCrTa was found to be small, indicating that the intrinsic stress in the CoCrTa becomes more tensile at higher deposition temperature, due to changes in grain size, crystal orientation, and segregation of the alloying elements.

B. Effect of applied stress on in-plane magnetic anisotropy

Figure 2 shows the in plane anisotropy as a function of applied tensile stress for CoCrTa/Cr samples deposited at different substrate temperatures. In these samples the

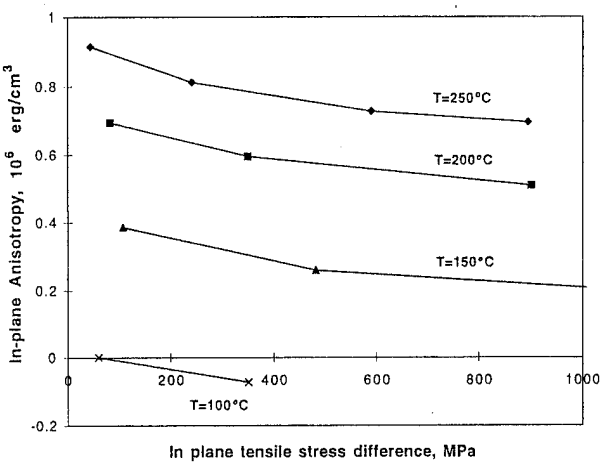


FIG. 2. Effect of applied stress on in-plane anisotropy of CoCrTa/Cr films deposited at different temperatures.

CoCrTa and Cr films were 40 nm thick, typical of hard disk media, and thinner than the samples used for stress measurements. Tension was applied parallel to the texture lines. The abscissa shows the tensile stress difference between the two principal directions of stress in the film plane. Hysteresis loops were also measured for these samples and showed that tensile stress lowered the coercivity parallel to the tensile axis and raised it in the perpendicular direction. This is characteristic of a negative magnetostriction coefficient.

Applying a tensile stress parallel to the grooves made the textured samples less anisotropic. In comparison, films on smooth substrates developed in-plane magnetic anisotropy as the applied stress increased. The magnetostriction coefficient λ was measured from the data taken at low applied stress. In $CoCr_{10}Ta_6$/Cr deposited on a textured substrate, magnetostriction increased with deposition temperature, from -4×10^{-6} at 20 °C to -26×10^{-6} at 200 °C and -34×10^{-6} at 250 °C. For the same samples, OR_{Hc} increases from 1.0 to 1.6 with increasing substrate temperature. The difference in λ between films made on heated versus unheated substrates reflects differences in crystal orientation and microstructure. The Cr has a (110) orientation when sputtered onto an unheated substrate so the Co grows with a significant c-axis out of plane component. This is expected to change the measured λ,[7] as will composition differences in the Co due to differences in grain boundary segregation. $CoCr_{17}Pt_{12}$/Cr deposited onto a textured substrate at 200 °C had $OR_{Hc}=1.3$ and $\lambda=-8\times10^{-6}$.

IV. DISCUSSION

Our stress measurements showed that stresses were higher parallel to the grooves in films on textured substrates. The torque experiments demonstrate that a stress applied to a magnetic film leads to an in-plane anisotropy in which the more compressive (or less tensile) direction becomes the direction of higher coercivity in a material with negative magnetostriction. This mechanism, combined with the observed

stress differences in textured samples, leads to a stress-induced contribution to the magnetic anisotropy of oriented media.

The magnitude of the anisotropy is proportional to both the magnetostriction coefficient and the in-plane stress difference between directions parallel and perpendicular to the texture lines. Samples with low magnetostriction, such as those sputtered on unheated substrates, will have low stress-induced magnetic anisotropy even if the in-plane stress is anisotropic. The commonly observed increase in magnetic anisotropy with deposition temperature may be partly related to the measured increase in magnetostriction, and increases in magnetic anisotropy[8] with substrate bias to changes in in-plane stress difference.

These measurements show that stress parallel to the texture lines exceeds stress perpendicular to the texture lines by up to 300 MPa in thick films of CoCrTa on Cr. The CoCrTa films in this study were in compression. A stress difference $\Delta\sigma$ of 300 MPa, coupled with a magnetostriction coefficient of -26×10^{-6} for the 200 °C sample leads to stress-induced magnetic anisotropy $K_\sigma=(3/2)\lambda\Delta\sigma$ of 1.2×10^5 ergs/cm^3. The total anisotropy K_{tot} was 8×10^5 ergs/cm^3, a value similar to one reported elsewhere for CoCrTa/Cr media with a textured substrate.[2]

These calculations show that if $\lambda=-26\times10^{-6}$, stress-induced magnetic anisotropy can account entirely for total in-plane anisotropy only if an in-plane stress difference much greater than 1000 MPa exists in the film. X-ray measurements by Kawamoto and Hikami[2] gave an in-plane strain corresponding to a stress difference of up to 1200 MPa, taking Young's modulus of 200 GPa, but other measurements by x-ray diffraction indicate smaller in-plane stress differences of 300 MPa (Ref. 1) or 200–400 MPa (Ref. 9). Of these, only Kawamoto's samples[2] have sufficient in-plane stress difference to account entirely for K_{tot}. The curvature method used here in its present form is insufficiently accurate to measure stress in the thinner 20–40 nm films used in current media, and it is also limited by the need to subtract the effect of the Cr layer. The method gives an average stress, and does not indicate small scale stress fluctuations near features such as texture lines. Additional measurements indicate that the stress, and presumably the in-plane stress difference, in thinner films is greater than the stress in the thick films reported here.

The nonuniform biaxial stress observed in the films on grooved substrates originates during topographically induced anisotropic growth of the crystals or by relaxation at structural discontinuities within the film, caused for instance by shadowing at texture valleys. A finite element calculation of stress in strips of film separated by discontinuities, Fig. 3, shows that as the aspect ratio (the ratio of distance between discontinuities to film thickness) decreases, the stress perpendicular to the grooves decreases.[10] With an aspect ratio of 9, the stress parallel to the grooves exceeds that perpendicular to the grooves by a factor of 1.4 as seen in the Cr. Differential stresses can exist even if the film discontinuities are very narrow. Stress relaxation at the tops of texture ridges [11] is of minor importance since in a typical texture the surface

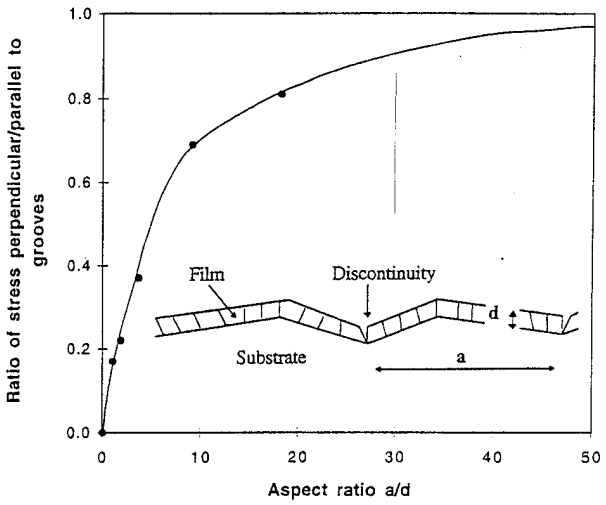


FIG. 3. Calculated stress ratio in a discontinuous film on a textured substrate for different a/d ratios, where d represents film thickness and a represents the distance between film discontinuities.

angles are generally no more than a few degrees, and finite element calculation of stress in a continuous film deposited on such a substrate shows negligible stress relaxation over the relatively smooth topography.

V. CONCLUSIONS

Measurements of stress in 75–100 nm Cr and CoCrTa films deposited over grooved substrates show a greater stress parallel to the grooves compared to the stress perpendicular to the grooves. The stress is compressive in films made at high substrate biases and substrate temperatures, and the in-plane stress difference can reach a few hundred MPa. The magnetostriction coefficient of 40 nm $CoCr_{10}Ta_6$/Cr films deposited at 200 °C was measured as -26×10^{-6}. Combined with the in-plane stress difference, stress-induced anisotropy provides a contribution to the in-plane anisotropy of films deposited onto textured media. Anisotropy is low in films with low magnetostriction, such as CoCrTa/Cr on a cold substrate. Further measurements are underway to resolve the differences reported in the x-ray strain data from the literature.

[1] J. A. Bain, B. M. Clemens, S. M. Brennan, and H. Kataoka, IEEE Trans. Magn. **29**, 300 (1993).
[2] A. Kawamoto and F. Hikami, J. Appl. Phys. **69**, 5151 (1991).
[3] M. F. Doerner, P. W. Wang, S. M. Mirzamaani, D. S. Parker, and A. C. Wall, Mater. Res. Soc. Symp. Proc. **232**, 27 (1991).
[4] Y. Yahisa, Y. Matsuda, J. Inagaki, M. Shoda, A. Katou, and Y. Hosoe, J. Magn. Soc. Jpn. **19**, 77 (1995).
[5] Y. Zhao and H. N. Bertram, J. Appl. Phys. **77**, 6411 (1995).
[6] D. Mauri, V. S. Speriosu, T. Yogi, G. Castillo, and D. T. Peterson, IEEE Trans. Magn. **26**, 1584 (1990).
[7] R. M. Bozorth, *Ferromagnetism* (IEEE, New York, 1951).
[8] S. Duan, M. R. Khan, J. E. Haefele, L. Tang, and G. Thomas, IEEE Trans. Magn. **28**, 3258 (1992).
[9] T. P. Nolan, Ph.D. thesis, Stanford University, 1994.
[10] C. A. Ross, IEEE Trans. Magn. **29**, 2266 (1993).
[11] T. Chen, R. Ranjan, D. Wachenschwanz, C. A. Ross, T. Yamashita, and D. Bartholomew, presented at the 1995 Intermag Conference, San Antonio, Texas, April 1995 (unpublished).

The role of Ta and Pt in segregation within Co-Cr-Ta and Co-Cr-Pt thin film magnetic recording media

K. M. Kemner, V. G. Harris, V. Chakarian, Y. U. Idzerda, and W. T. Elam
U.S. Naval Research Laboratory, Washington, DC 20375

C.-C. Kao
Brookhaven National Laboratory, Upton, New York 11973

Y. C. Feng and D. E. Laughlin
Department of Materials Science and Engineering, Carnegie Mellon University, Pittsburgh, Pennsylvania 15213

J. C. Woicik
National Institute of Standards and Technology, Gaithersburg, Maryland 20899

Polarization dependent extended x-ray absorption fine structure (PD-EXAFS) and magnetic circular dichroism (MCD) measurements of CoCrTa and CoCrPt films, sputter deposited at varying substrate temperatures, were performed to investigate the average local structure and chemistry about the Ta, Pt, and Co atoms and the average magnetic moment of the Co and Cr atoms within these films. Results from the MCD measurements indicate the average net magnetic moment of the Cr atoms is opposite in direction and five percent in amplitude relative to the Co moments. Inspection of the Fourier transforms of the XAFS data from these samples shows an increase in structural disorder around the Ta and Pt atoms with increasing substrate deposition temperature. A further comparison between the Ta and Pt edge EXAFS results show that the temperature-dependent increase in structural disorder is greater around the Ta atoms in the CoCrTa system than it is around the Pt atoms in the CoCrPt system. © *1996 American Institute of Physics.* [S0021-8979(96)09708-5]

I. INTRODUCTION

Compositional inhomogeneities have long been thought to play an important role in determining the magnetic properties of Co-Cr based magnetic thin films. Previous studies of CoCr-based thin films deposited at elevated temperatures indicated the presence of fine, periodic compositional variations within grains.[1] The addition of Ta has been shown to decrease the size of the Co enriched regions within these films, demonstrating the importance of the addition of Ta. Similarly, the addition of Pt has been shown to increase these films' coercivities. Previous studies have also proposed that nonmagnetic or paramagnetic Cr enriched regions[2,3] between the magnetic Co enriched regions aid in decoupling the magnetic domains within these films thus leading to higher storage density and lower noise media.

The films investigated in this study were sputter deposited on glass substrates at temperatures (T_s) of room temperature and 260 °C. The nominal composition of the films studied were $Co_{86}Cr_{12}Ta_2$, and $Co_{86}Cr_{12}Pt_2$. The thickness of the films was 300 Å. All films were capped with a 50 Å layer of Al to prevent any oxidation effects, and had a 1000-Å-Cr underlayer.

The average local structure around the Co, Ta, and Pt atoms in these films was investigated by using polarization-dependent extended x-ray absorption fine structure (PD-EXAFS), a local structural probe having both elemental and directional sensitivity. Analysis of this data shows a greater amount of structural disorder around the Ta and Pt atoms with increasing substrate deposition temperature. A further comparison between the Ta and Pt edge PD-EXAFS results shows that the temperature-dependent increase in structural disorder is greater around the Ta atoms in the CoCrTa system than it is around the Pt atoms in the CoCrPt system. Chemical segregation of Co-enriched regions within the films was confirmed also via PD-EXAFS at the Co absorption edge.

Magnetic circular dichroism (MCD) measurements were also made on these samples. MCD is an element-specific magnetic spectroscopic tool in which the difference in the absorption of left- and right-circularly polarized photons are measured at the absorption edges of the constituent elements. This difference in absorption cross sections, appropriately normalized, is a measure of the average magnetic moment of an atomic species at a given atomic site.[4,5] Results from this study show the existence of a small average net magnetic moment associated with the Cr atoms that is opposite in direction relative to the average net magnetic moment of the Co atoms. MCD therefore enables measurement of direction and magnitude of the average magnetic moment for each constituent atomic species within a sample. Thus, it is a very good technique to use to determine if there is a magnetic moment associated with the Cr atoms within these films.

II. DATA COLLECTION AND ANALYSIS

PD-EXAFS and MCD measurements were performed on four films deposited on glass with nominal compositions $Co_{86}Cr_{12}Ta_2$, and $Co_{86}Cr_{12}Pt_2$ and T_s equal to room temperature and 260 °C.

X-ray absorption spectra were collected on the Naval Research Laboratory's materials analysis beam line, X23B, and the National Institute of Standards and Technology XAFS beamline X23A2, at the National Synchrotron Light Source (Brookhaven National Laboratory, Upton, NY). The fine structure appearing above the Co K edge (7709 eV), the Ta LIII-edge (9881 eV) and the Pt LII edge (13273 eV) were

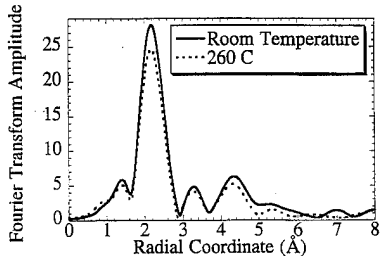


FIG. 1. Fourier transform of Ta EXAFS data on $Co_{86}Cr_{12}Ta_2$ films grown at substrate deposition temperatures of room temperature (solid line) and 260 °C (dotted line).

collected in electron yield mode[6] using normal and glancing angle (10° with respect to the film plane) incident radiation. Because the EXAFS signal originates with a $\cos^2$ angular dependence with respect to the electric-field vector of the incident radiation and the bond between the absorbing and backscattering atom, these orientations allow preferential sampling of the in-plane and out-of-plane structure, respectively. The EXAFS data were subjected to standard analysis procedures,[7] leading to the Fourier transformation of the data to radial coordinates. To obtain quantitative measurement of the average near neighbor environment around the Co atoms, Fourier transformed data of the first Fourier peak from the Co K-edge PD-EXAFS data were back-Fourier transformed to wave vector space and fitted using parameterized theoretical EXAFS spectra. The theoretical EXAFS spectra were generated using the FEFF codes developed by Rehr and co-workers.[8] This analysis allows the calculation of the average coordination number, radial distance, and Debye–Waller factors of atomic shells around each atomic species in both the parallel and perpendicular directions relative to the film surface.

MCD measurements were performed on these samples at beamline U4B and X13 at the National Synchrotron Light Source (Brookhaven National Laboratory, Upton, NY). MCD enables measurement of direction and magnitude of the average magnetic moment for each constituent atomic species within a sample. Thus, it is a very good technique to use to determine if there is a magnetic moment associated with the Cr atoms within these films. Measurements of the CoCrTa and CoCrPt films were made in the plane of the films while alternating the direction of the applied magnetic field (10 kOe) between parallel and antiparallel orientations at each energy throughout the scan. The thickness of the glass substrate prohibited absorption measurements by transmission, therefore absorption was determined from the x-ray fluorescence signal[9] as a function of incident energy and applied magnetic field. Since this study is only qualitatively addressing the existence of a magnetic moment associated with Cr, no fluorescence amplitude correction[10] was included in the analysis.

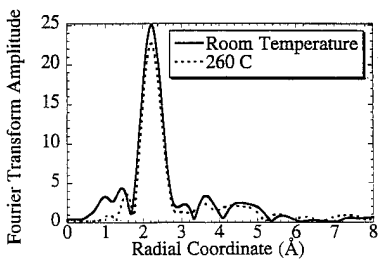


FIG. 2. Fourier transform of Pt EXAFS data on $Co_{86}Cr_{12}Pt_2$ films grown at substrate deposition temperatures of room temperature (solid line) and 260 °C (dotted line).

III. RESULTS AND DISCUSSION

For all films, qualitative analysis of the Fourier Transformed PD-EXAFS data from the Co K edge show that the Co atoms are incorporated into the films in a close-packed structure.[11,12] Results from a quantitative analysis of the filtered first shell data from the Co K-edge PD-EXAFS data indicate at least 95% of all the atoms surrounding the Co absorbing atoms are Co atoms. This is significantly larger than the 86% value expected had a solid solution of $Co_{86}Cr_{12}Ta_2$ or $Co_{86}Cr_{12}Pt_2$ had been formed. This illustrates the presence of Co-enriched regions within the films, and thus indirectly illustrates the presence of Cr-enriched regions.

Figures 1 and 2 are plots of the Fourier transformed Ta and Pt EXAFS data for T_s of room temperature (solid line) and 260 C (dotted line). The general characteristic shapes of these data suggests that, for both substrate deposition temperatures, both the Ta and Pt atoms are incorporated within the films' close-packed structure with a large amount of local structural disorder. Furthermore, the local environment of the Ta and Pt atoms is not bcc or fcc clusters as one might expect if the Ta or Pt atoms had phase separated. Further analysis of the first Fourier transform peaks for the Ta and Pt data shows that for an increasing T_s, the average total number of atoms surrounding Ta and Pt decreases while the EXAFS Debye–Waller term increases. (An increase in the EXAFS Debye–Waller term corresponds to a broader distribution of radial distances about their average distance.) This temperature-dependent trend however, is not seen around the Co atoms in the CoCrTa or CoCrPt films. These two trends are consistent with vacancies preferentially segregating to the Ta or Pt atoms thereby decreasing the diffusion of the Co or Cr atoms, and thereby refining the length scale of the Co-enriched regions. A further comparison between the Ta and Pt edge PD-EXAFS results shows that the temperature-dependent increase in structural disorder is greater around the Ta atoms in the CoCrTa system than it is around the Pt atoms in the CoCrPt system.

Figures 3 and 4 are the MCD spectra for the Co and Cr atoms in a 2000-Å-thick $Co_{86}Cr_{12}Ta_2$ film with T_s at room temperature. MCD measurements were made on this sample instead of the 300 Å film because it did not have a 1000-Å-Cr underlayer which would contaminated the Cr MCD signal. These figures represent the difference in absorption of circularly polarized photons parallel and anti-parallel to an external magnetic field (10 kOe) applied in the plane of the films. The amplitude of these signals are normalized to the relative numbers of Co and Cr atoms in the film. The figure depicting the Co MCD spectra (Fig. 3) shows a negative

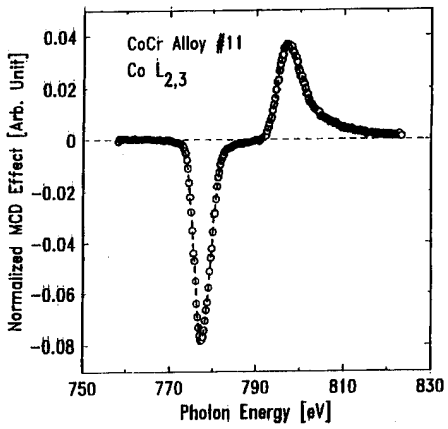


FIG. 3. MCD spectrum of the Co LIII and LII edges on the $Co_{86}Cr_{12}Ta_2$ film grown at room temperature.

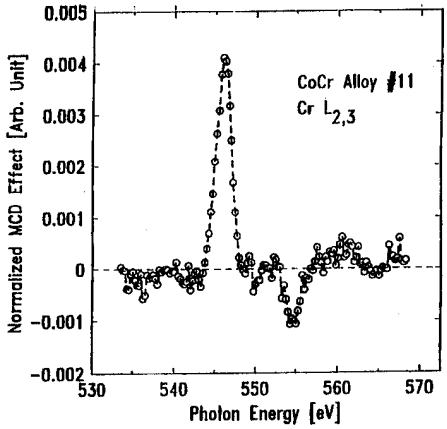


FIG. 4. MCD spectrum of the Cr LIII and LII edges on the $Co_{86}Cr_{12}Ta_2$ film grown at room temperature.

difference signal at the LIII edge step and a positive difference signal at the LII edge step. Conversely, the figure depicting the Cr MCD spectra (Fig. 4) shows a positive signal at the LIII edge step and a negative signal at the LII edge step. The ratio of the magnitudes of the MCD effect for the Co and Cr atoms is approximately 20:1. A similar ratio exists for the 2000-Å-CoCrTa film grown with a 260 C T_s. This ratio does not exhibit any substrate deposition temperature dependence. In all cases, the absolute magnitude of this effect has not been corrected for self-absorption effects. However, although self-absorption effects may cause the amplitude of the MCD effect to change, the existence of the effect and its direction will not change. Therefore, this demonstrates that

(1) there is a small net magnetic moment associated with the Cr atoms in the CoCrTa system,
(2) the moment associated with the Cr atoms is anti aligned relative to the Co atoms, and
(3) the ratio of the net Cr/Co magnetic moments is not temperature dependent.

IV. SUMMARY

In summary, we have used PD-EXAFS to verify that the local environments about the Co, Ta, and Pt atoms in $Co_{86}Cr_{12}Ta_2$, and $Co_{86}Cr_{12}Pt_2$ thin films are a close-packed structure. Results from analysis of the Co atoms' average first shell environments show Co-Co coordination numbers greater than that expected in a totally random case. This illustrates chemical segregation, within these films, into Co-enriched regions. Inspection of the Fourier transformed Ta edge and Pt edge PD-EXAFS data shows a change in the average local structure surrounding the Pt and Ta atoms in that there is a greater amount of structural disorder around these atoms with increasing substrate deposition temperature. A further comparison shows that the temperature-dependent increase in structural disorder is greater around the Ta atoms in the CoCrTa system than it is around the Pt atoms in the CoCrPt system. Results from the MCD measurements of these films at the Co and Cr LIII and LII edges show that the average net magnetic moment of the Cr atoms is opposite in direction and five percent in amplitude relative to the Co moments. The amplitude and direction of the net magnetic moment of Cr exhibits no dependence on substrate deposition temperature.

ACKNOWLEDGMENTS

This research was carried out, in part, at the National Synchrotron Light Source (Brookhaven National Laboratories, Upton, NY), which is sponsored by the U.S. Department of Energy (Division of Material Science and Division of Chemical Sciences of the Office of Basic Energy Sciences). The research at CMU was sponsored by the Department of Energy, Grant No. DE-FG02-90ER45423. This research was performed while K.M.K. held a National Research Council-Naval Research Laboratory Research Associateship.

[1] Yasushi Maeda and Koji Takei, IEEE Trans. Magn. **27-6**, 4721 (1991).
[2] J. Nakai, E. Kusumoto, M. Kuwabara, T. Miyamoto, M. R. Visokay, K. Yoshikawa, and K. Itayama, IEEE Trans. Magn. **30-6**, 3969 (1994).
[3] For multiple references see: J. C. Lodder, in *High Density Digital Recording*, edited by K. H. J. Buschow, Gary J. Long, and Fernande Grandjean (Kluwer, Worwell, MA, 1993).
[4] B. T. Thole, P. Carra, F. Sette, and G. van der Laan, Phys. Rev. Lett. **68**, 1943 (1992).
[5] P. Carra, B. T. Thole, M. Altarelli, and X. Wang, Phys. Rev. Lett. **70**, 694 (1993).
[6] W. T. Elam, J. P. Kirkland, R. A. Neiser, and P. D. Wolf, Phys. Rev. B **38**, 26 (1988).
[7] D. E. Sayers and B. A. Bunker, in *X-Ray Absorption: Basic Principles of EXAFS, SEXAFS, and XANES*, edited by D. C. Koningsberger and R. Prins (Wiley, New York, 1988).
[8] J. J. Rehr, J. Mustre de Leon, S. I. Zabinski, and R. C. Albers, J. Am. Chem. Soc. **113**, 5135 (1991).
[9] *X-Ray Absorption: Basic Principles of EXAFS, SEXAFS, and XANES*, edited by D. C. Koningsberger and R. Prins (Wiley, New York, 1988).
[10] Y. U. Idzerda, C. T. Chen, H.-J. Lin, G. Meigs, G. H. Ho, and C.-C. Kao, Nucl. Instrum. Methods Phys. Res. A **347**, 134 (1994).
[11] K. M. Kemner, V. G. Harris, W. T. Elam, and J. C. Lodder, IEEE Trans. Magn. **30-6**, 4017 (1994).
[12] K. M. Kemner, V. G. Harris, W. T. Elam, and J. C. Lodder, Mater. Res. Soc. Symp. Proc. **375**, 21 (1995).

Microstructure and magnetic properties of CoCrPt/Cr films on ultrasmooth NiP/AlMg substrates

Li Tang, David E. Laughlin, and David N. Lambeth
Data Storage Systems Center, Carnegie Mellon University, Pittsburgh, Pennsylvania 15213

Mary F. Doerner
IBM Storage Systems Division, 5600 Cottle Road, San Jose, California 95193

Investigation of the correlation between the microstructure and magnetic properties of $Co_{68}Cr_{20}Pt_{12}$/Cr thin films which were sputter deposited under different conditions onto 95 mm ultrasmooth NiP/AlMg disk substrates (R_a~2 Å) has been carried out. Grain morphology characteristics of the films and disk surface roughness were studied by transmission electron microscopy (TEM) and by atomic force microscopy. Tilted-specimen electron diffraction patterns were used to determine the crystallographic texture of the films. The low coercivity of the disks deposited at 100 °C preheated substrates is attributed to the randomly oriented grains of the CoCrPt/Cr layers. Enhancement of the coercivity of the disks deposited on 220 °C preheated substrates is thought to be mainly due to the $(11\bar{2}0)$CoCrPt/(002)Cr crystallographic texture and uniformly distributed grains which are equiaxed in shape. The strength of the $(11\bar{2}0)$CoCrPt/(002)Cr texture can be modified by the Ar gas pressure during the deposition of the Cr underlayer. © *1996 American Institute of Physics.* [S0021-8979(96)09808-1]

For magnetic recording thin film media, structural characteristics such as grain size, shape, and separation, as well as composition inhomogeneity are believed to be closely related to the media magnetic and recording properties.[1,2] Another important feature is the crystallographic texture of the films. This is difficult to measure by x-ray diffraction techniques for Co–alloy/Cr thin films deposited on NiP/AlMg substrates since the substrates are much thicker than the Co–alloy/Cr layers and usually contribute a strong background signal to the x-ray diffraction spectra of Co–alloy/Cr/NiP/AlMg disks.[3,4] On the other hand, tilted electron diffraction patterns of both the Cr underlayer and Co–alloy film can be obtained separately from the same transmission electron microscopy (TEM) specimen in which thin areas of both the layers exist and the NiP/A1Mg substrates are removed.[5] From these diffraction patterns the texture axis and the distribution angle about the axis of the layers can be determined. Furthermore, information of grain morphology of the films including grain size, shape, and separation can also be obtained from TEM images. In this article, we present results of TEM and atomic force microscopy (AFM) studies of the microstructures of $Co_{68}Cr_{20}Pt_{12}$/Cr films sputter deposited under different conditions onto ultrasmooth NiP/AlMg substrates. Correlation between the microstructure and magnetic properties of the films is also discussed.

$Co_{68}Cr_{20}Pt_{12}$ (220 Å)/Cr (750 Å) films were dc-magnetron sputter deposited onto 95 mm ultrasmooth NiP/AlMg disk substrates (R_a~2 Å) at varying substrate temperatures and Ar gas pressures (Table I). In-plane magnetic properties of the disks were measured using a vibrating sample magnetometer (VSM). Microstructural studies of the CoCrPt/Cr films were carried out using a Philips 420T transmission electron microscope. Specimen-tilted electron diffraction patterns were used to determine the crystallographic texture of the magnetic and underlayer films. This method has been described in detail elsewhere.[5,6] Surface roughness of the disks was measured using an atomic force microscope.

In-plane magnetic properties of the CoCrPt/Cr/NiP/AlMg disks prepared under different conditions are listed in Table I. It can be noted that when the Ar gas pressure during the sputtering of Cr (15 mTorr) and of CoCrPt (5 mTorr) films is kept the same, raising the substrate temperature from 100 °C (sample no. 1) to 220 °C (sample no. 2) increases the coercivity of the CoCrPt film significantly. Reducing the Ar gas pressure from 15 to 5 mTorr during the deposition of the Cr underlayer on 220 °C heated substrates, however, reduces the coercivity (sample no. 3) of the magnetic layer.

The bright field TEM images of the Cr underlayer and CoCrPt film at 0° tilt for sample no. 1 are shown in Figs. 1(a) and 2(a), respectively. The Cr grains in Fig. 1(a) (grains in dark contrast in this figure are residual CoCrPt grains which have not been totally removed) are well separated and elongated with a length to width (~100 Å) ratio of 4:1. The CoCrPt grains in Fig. 2(a) are not obviously elongated in shape as are the grains of its Cr underlayer, and furthermore the grain size seems to have a wide distribution. Grain sepa-

TABLE I. Processing parameters and magnetic properties of CoCrPt/Cr thin films.

Sample no.	Substrate temperature (°C)	Ar pressure CoCrPt/Cr (mTorr)	H_c (Oe)	M_rT (memu/cm^2)	S^*
1	100	5/15	1360	0.68	0.91
2	220	5/15	2400	0.75	0.84
3	220	5/5	2000	0.75	0.91

 0021-8979/96/79(8)/5348/3/$10.00 © 1996 American Institute of Physics

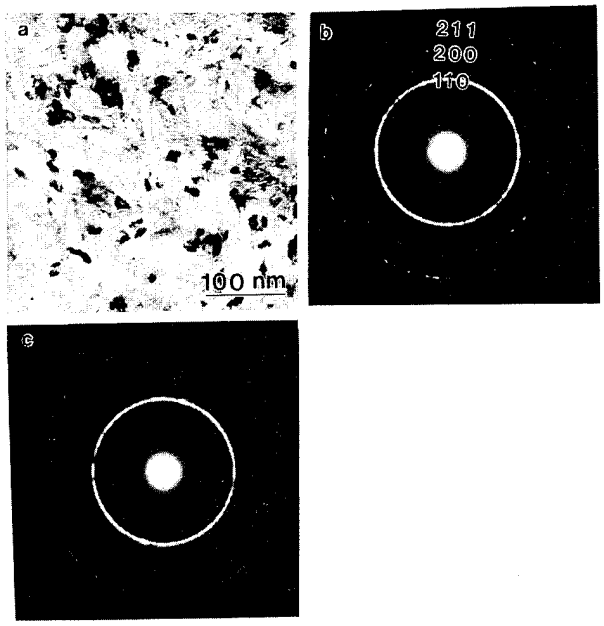


FIG. 1. (a) Bright field TEM image at 0° tilt. Electron diffraction patterns at (b) 0° tilt and (c) 40° tilt of the Cr underlayer of sample no. 1.

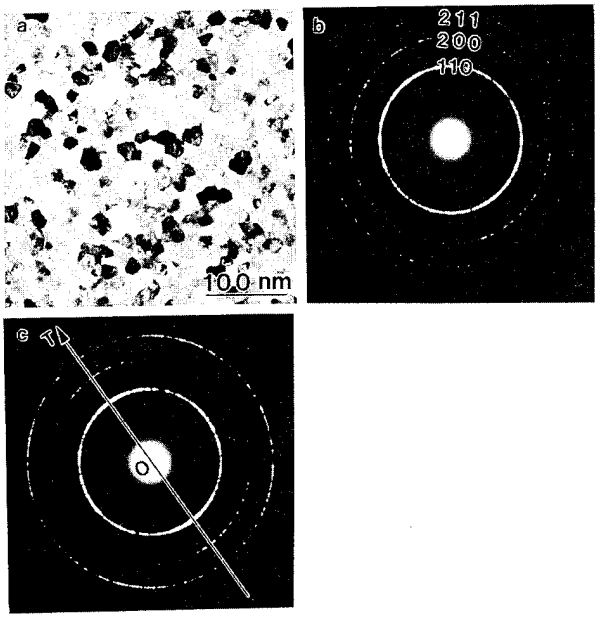


FIG. 3. (a) Bright field TEM image at 0° tilt. Electron diffraction patterns at (b) 0° tilt and (c) 50° tilt of the Cr underlayer of sample no. 2.

ration is also noted between some of the grains. AFM measurement indicates that the surface of the disk after the media is deposited is much rougher (R_a~13 Å) than the NiP/AlMg substrate. Electron diffraction patterns at 0° tilt and 40° tilt from the bcc Cr underlayer and from the hcp CoCrPt film of sample no. 1 are shown in Figs. 1(b) and 1(c) Figs. 2(b) and 2(c), respectively. No distinction can be made between the diffraction patterns at 0° and 40° tilt of the layers, indicating that grains in the Cr underlayer and CoCrPt film are randomly oriented three dimensionally. This may contribute to the low coercivity of this disk.

For sample no. 2, which was deposited at higher substrate temperature, the surface roughness (6 Å) is much smaller than that of sample no. 1. The grains of the Cr underlayer [Fig. 3(a)] are no longer elongated but are equiaxed in shape and uniformly distributed with a grain size of about 230 Å. This change of grain shape is believed to be due to the higher adatom mobility on the higher temperature substrate. Also, separation between some of the grains can be observed from Fig. 3(a). The Cr underlayer has a small amount of (002) texture, as can be seen from the change of the diffraction patterns when the specimen is tilted from 0° position [Fig. 3(b)] to 50° [Fig. 3(c), **OT** is the tilt axis

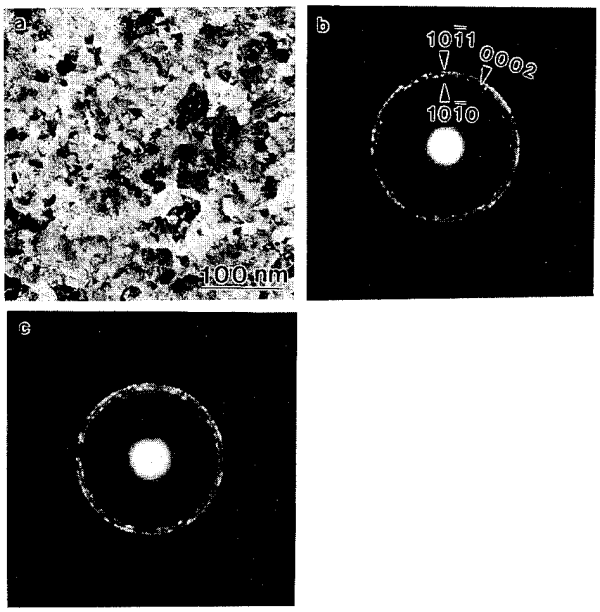


FIG. 2. (a) Bright field TEM image at 0° tilt. Electron diffraction patterns at (b) 0° tilt and (c) 40° tilt of the CoCrPt film of sample no. 1.

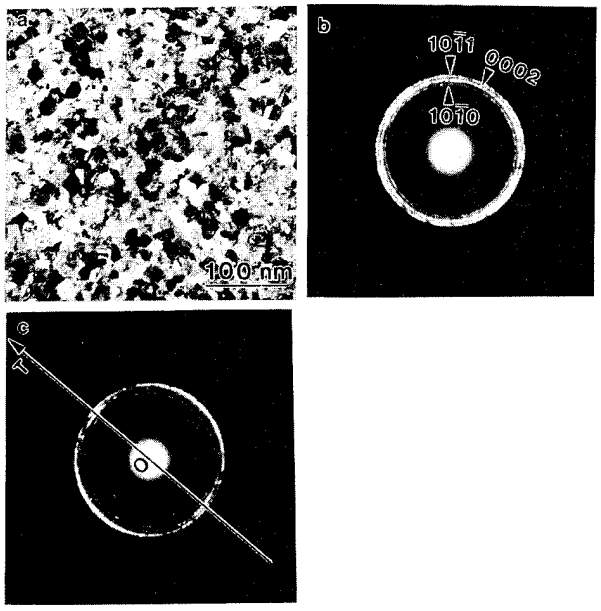


FIG. 4. (a) Bright field TEM image at 0° tilt. Electron diffraction patterns at (b) 0° tilt and (c) 50° tilt of the CoCrPt film of sample no. 2.

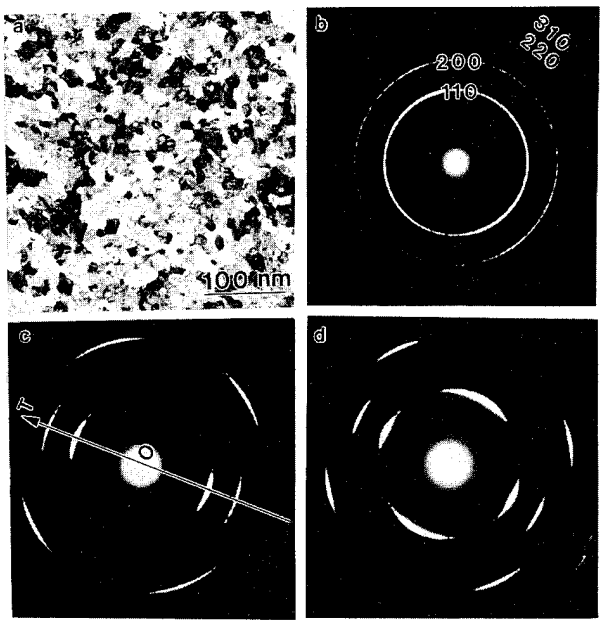


FIG. 5. (a) Bright field TEM image at 0° tilt. Electron diffraction patterns at (b) 0° tilt, (c) 30° tilt, and (d) 42° tilt of the Cr underlayer of sample no. 3.

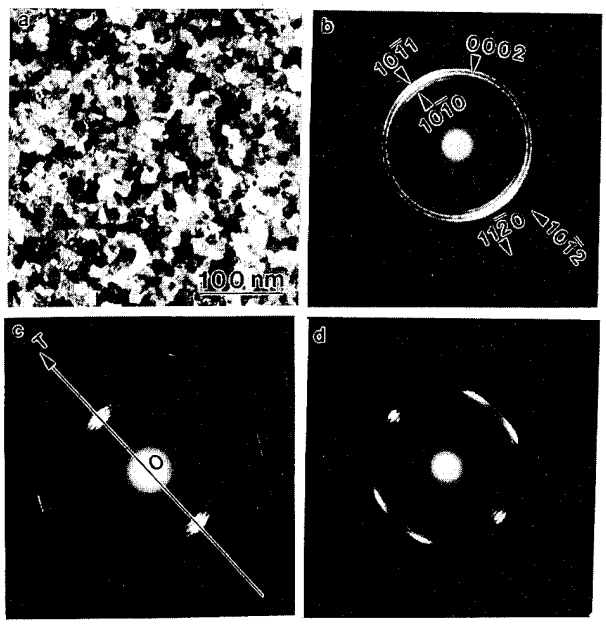


FIG. 6. (a) Bright field TEM image at 0° tilt. Electron diffraction patterns at (b) 0° tilt, (c) 36° tilt, and (d) 56° tilt of the CoCrPt film of sample no. 3.

direction]. Correspondingly, grains of the CoCrPt film are also equiaxed in shape but without separation [Fig. 4(a)] and there is a tendency for $(11\bar{2}0)$ texture, as can be seen from the diffraction patterns at 0° [Fig. 4(b)] and 50° tilt [Fig. 4(c)]. It is well known that $(11\bar{2}0)$ textured CoCrPt bicrystals with the c axis 90° relative to each other grow on (002) textured Cr grains.[7] Micromagnetic modeling studies show that exchange coupling between the bicrystals reduces the coercivity of the magnetic layer significantly.[8] Since the CoCrPt(1120)/Cr(002) texture is weak in this disk, the above mentioned effect is also weak which allows a high in-plane anisotropy and therefore high in-plane coercivity and small S^*. It seems that equiaxed grain shape is also important for the coercivity enhancement of this disk.

The grain shape of the Cr underlayer [Fig. 5(a)] and CoCrPt film [Fig. 6(a)] for sample no. 3 is similar to that of sample no. 2. But the grain size is a slightly smaller (~200 Å) and the disk surface roughness is further reduced to 3.5 Å as measured by AFM. No grain separation is observed in either of the layers. The (002) Cr and $(11\bar{2}0)$ CoCrPt textures of this disk are much stronger than that observed in sample no. 2. This can be seen from the diffraction patterns of the Cr underlayer at 0°, 30°, and 42° tilt [Figs. 5(b)–5(d)] and the CoCrPt film at 0°, 36°, and 56° tilt [Figs. 6(b)–6(d)]. The distribution angles of the Cr [002] and CoCrPt $[11\bar{2}0]$ texture axis are determined to be 10° and 6°, respectively.[5] The coercivity (2000 Oe) of this disk, however, is lower than that of sample no. 2. This is believed to be due to the lower effective anisotropy of the strongly exchange coupled CoCrPt bicrystals arising from the strong CoCrPt $(11\bar{2}0)$/Cr (002) texture.[8] The slightly smaller grain size may also play a role here.

In summary, the grains of both the Cr underlayer and CoCrPt films deposited at 100 °C preheated substrates are randomly oriented and result in the low in-plane coercivity. For films deposited on substrates which were preheated to 220 °C, the enhancement of in-plane coercivity is believed to be mainly due to the $(11\bar{2}0)$ CoCrPt/(002)Cr texture. In order to achieve the highest in-plane coercivity the strength of the $(11\bar{2}0)$CoCrPt/(002)Cr texture seems to be of critical importance. The surface roughness (3.5–6 Å) of the disks deposited on higher temperature substrates is much lower than that (13 Å) of the disks deposited on low temperature substrates. The correlation between the surface roughness and the magnetic properties, however, needs further study.

This work is supported by the DSSC of Carnegie Mellon University under National Science Foundation Grant No. ECD-8907068. The government has certain rights to this material.

[1] D. E. Laughlin, Y. C. Feng, L. L. Lee, D. N. Lambeth, and L. Tang, these proceedings.
[2] T. Lin, J. Magn. Magn. Mater. **86**, 159 (1990).
[3] M. F. Doerner, P.-W. Wang, S. M. Mirzamaani, and D. S. Parker, Mater. Sci. Symp. Proc. **232**, 27 (1991).
[4] H.-C. Tsai, B. B. Lal, and A. Eltoukhy, J. Appl. Phys. **71**, 3579 (1992).
[5] L. Tang, D. Lu, and G. Thomas, J. Appl. Phys. **77**, 47 (1995).
[6] L. Tang and D. E. Laughlin, J. Appl. Crystallogr. (to be published).
[7] B. Y. Wong, D. E. Laughlin, and D. N. Lambeth, IEEE Trans. Magn. **27**, 4733 (1991).
[8] Q. Peng, H. N. Bertram, N. Fussing, M. Doerner, M. Mirzamaani, D. Margulies, R. Sinclair, and S. Lambert, IEEE Trans. Magn. **31**, 2821 (1995).

Reduction of Co–Cr–Pt media noise by addition of Ti to Cr underlayer

Y. Matsuda, Y. Yahisa, J. Inagaki, E. Fujita, and A. Ishikawa
Data Storage and Retrieval Systems Division, Hitachi, Ltd., Odawara, Kanagawa 256, Japan

Y. Hosoe
Central Research Laboratory, Hitachi, Ltd., Kokubunji, Tokyo 185, Japan

Effects of Ti addition to a Cr underlayer on the magnetic and crystallographic properties of Co–Cr–Pt media were investigated. C/Co–Cr_{20}–Pt (Pt: 8 and 12 at. %)/Cr–Ti (Ti: 0–30 at. %) films were deposited on textured Ni–P/Al–Mg substrates by dc magnetron sputtering. In-plane H_c and S^* increased as Ti was added to the Cr underlayer. The media noise at 167 kFCI decreased with an increase of the Ti content from 0 to 20 at. %. The normalized media noise of $Co_{72}Cr_{20}Pt_8/Cr_{75}Ti_{25}$ media was 20% lower than that of $Co_{68}Cr_{20}Pt_{12}/Cr_{90}Ti_{10}$ media where their coercivity and S^* were almost the same. Further increase of the Ti caused the increase of the media noise. Transmission electron microscopy studies showed that average grain size of Cr–Ti films decreased from 30 to 20 nm with the increase of the Ti content from 0 to 20 at. %. The activation volume of $Co_{68}Cr_{20}Pt_{12}$ films measured from the time dependences of remanence coercivity decreased by 30% as the Ti content increased from 0 to 20 at. %. The reduction of media noise is probably due to the decrease of the magnetic switching volume which is caused by the reduction of the grain size of Cr–Ti underlayers. © *1996 American Institute of Physics.* [S0021-8979(96)09908-8]

I. INTRODUCTION

Magnetic recording media are required to have high coercivity, high S^*, and low media noise to achieve higher areal density of rigid disk drives. Co–Cr–Pt/Cr thin film media have been developed as the candidate for gigabit density recording.[1,2] Coercivity of the Co–Cr–Pt films increased as Ti was added to Cr underlayers.[3] A possible mechanism for the coercivity increase is the decrease of lattice mismatch between the underlayers and the Co–Cr–Pt films.[3]

It is also suggested that the magnitude of the intergranular exchange interactions in the Co–Cr–Pt films is large for the film with high Pt content.[4] The large exchange interaction causes the increase of the media noise. The physical separation of crystal grains or Cr segregation in the Co–Cr–Pt films is effective in reducing the media noise.[5] This article reports the reduction of media noise of the Co–Cr–Pt media by the addition of Ti to the Cr underlayers. The mechanism of the noise reduction is discussed using the results of magnetic viscosity measurements and microstructure analyses.

II. EXPERIMENT

A Cr–Ti alloy underlayer (30-nm-thick), a Co–Cr–Pt alloy magnetic layer (23-nm-thick), and a C protective layer (10-nm-thick) were successively deposited on textured Ni–P-plated Al–Mg-alloy substrates (R_a=3 nm) using a dc magnetron sputtering system. The substrate temperature was 270 °C and the Ar pressure was 5 mTorr. The Ti content of the Cr–Ti underlayers was changed from 0 to 30 at. % by changing the composition of the Cr–Ti-alloy targets. The compositions of magnetic films studied were $Co_{72}Cr_{20}Pt_8$ and $Co_{68}Cr_{20}Pt_{12}$. The remanence thickness product ($B_r t_{mag}$) was adjusted by 100 G μm for both magnetic film compositions. Magnetic properties were measured by a vibrating sample magnetometer with a maximum applied field of 10 kOe. The product of activation volume and saturation magnetization (vI_s) was evaluated by measuring a time dependence of remanence coercivity (H_r).[6] vI_s is given by the following equations:

$$vI_s = kT/H_f, \tag{1}$$

$$H_r(t) = -H_f \ln t + \text{const}, \tag{2}$$

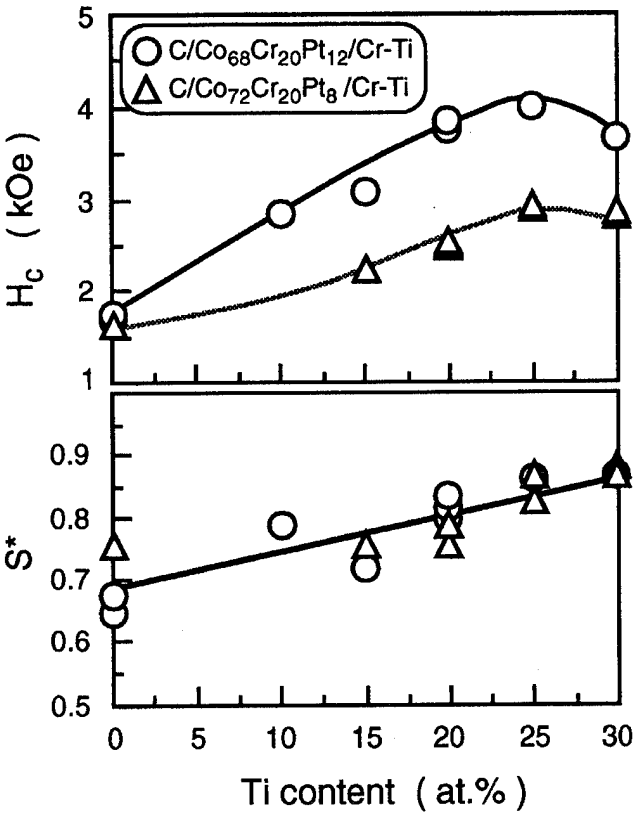


FIG. 1. Dependence of magnetic properties of Co–Cr–Pt/Cr–Ti media on Ti content.

 0021-8979/96/79(8)/5351/3/$10.00 © 1996 American Institute of Physics

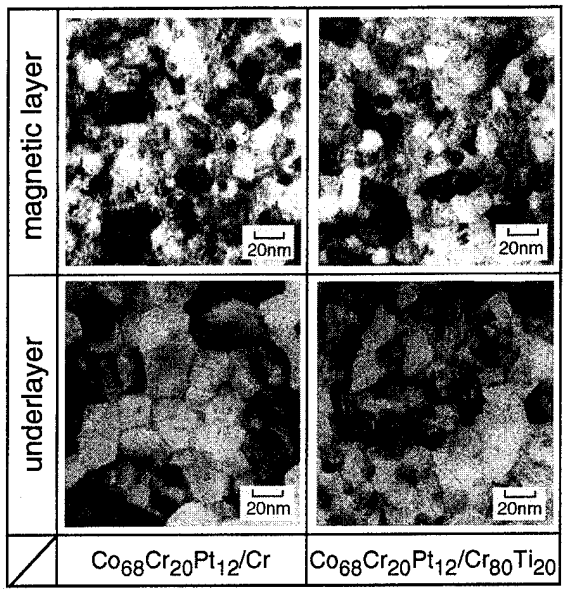


FIG. 2. Plan-view TEM images of the magnetic layer and underlayer of $Co_{68}Cr_{20}Pt_{12}$/Cr and $Co_{68}Cr_{20}Pt_{12}/Cr_{80}Ti_{20}$.

where I_s is the saturation magnetization in the activation volume (v), k is Boltzmann's constant, and H_f is the fluctuation field. The crystallographic texture of the films was analyzed by x-ray diffractometry with Cu $K\alpha$ radiation. Transmission electron microscopy (TEM) was used to measure the average grain sizes of the Co–Cr–Pt magnetic layers and the Cr–Ti underlayers. Media noises were measured using a magnetoresistive (MR) head with a read track width of 2.6 μm at a magnetic spacing of 70 nm. We defined a normalized media noise using the media noise (N_d) that was integrated in a noise spectrum, isolated output ($V_{p\text{-}p}$ where the subscript means peak-to-peak), and the read track width (T_w) as the following equation:

$$\text{Normalized } N_d = N_d\sqrt{T_w}/V_{p\text{-}p}. \tag{3}$$

III. RESULTS AND DISCUSSION

A. Magnetic and crystallographic properties

Figure 1 shows the H_c and S^* as a function of Ti content. H_c increased as Ti was added, and showed a maximum value at 25 at. % Ti. S^* monotonously increased with the addition of Ti. The crystallographic texture of Co–Cr–Pt(11.0)/Cr–Ti(100) was observed in all specimens. The enhancement of H_c and S^* is probably due to the lattice matching between Co–Cr–Pt and Cr–Ti films by expanding the Cr lattice with the addition of Ti.[3]

Figure 2 shows the plan-view TEM images of the magnetic layers and the underlayers of $Co_{68}Cr_{20}Pt_{12}$/Cr and $Co_{68}Cr_{20}Pt_{12}/Cr_{80}Ti_{20}$ films. The grain size of Cr–Ti film is significantly smaller than that of the pure Cr. Figure 3 shows the average grain size of Cr–Ti films. The grain sizes decreased from 30 to 20 nm with the increase of the Ti content from 0 to 20 at. %. The decrease of grain size seems to correlate to the nucleation density of the Cr–Ti films. Further study is necessary to learn more about the change of grain sizes.

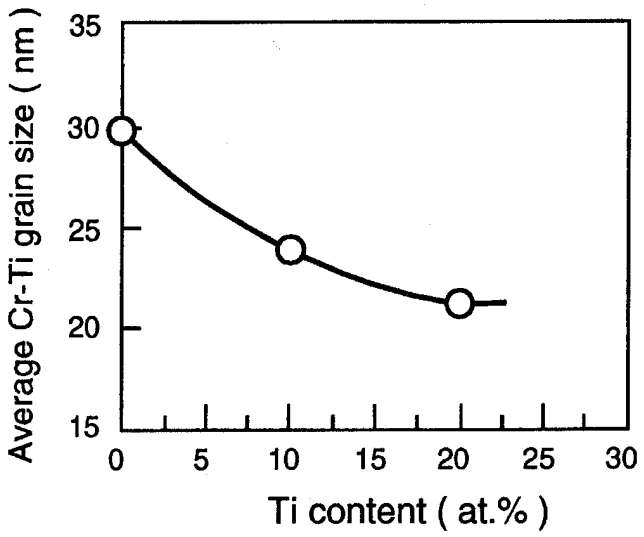


FIG. 3. Dependence of the average Cr–Ti grain size on Ti content.

On the other hand, the change of Co–Cr–Pt grain size is not accurately calculated because of the relatively diffused grain boundaries as shown in Fig. 2.

B. Activation volume

The activation volume (v) is recognized as the size of the magnetic reversal unit of magnetic films.[7–9] Figure 4 shows the dependence of vI_s on the Ti content for $Co_{72}Cr_{20}Pt_8$/Cr–Ti and $Co_{68}Cr_{20}Pt_{12}$/Cr–Ti films. vI_s decreased by about 30% with an increase of the Ti content from 0 to 20 at. %. Assuming that the I_s is the average value for the total quantity of the Co–Cr–Pt film, the reduction of vI_s corresponds to the decrease of the activation volume (v) from 3.8×10^{-18} to 2.3×10^{-18} cm^3 in the case of $Co_{68}Cr_{20}Pt_{12}$/Cr–Ti films. If the magnetic reversal unit is assumed as columnar shape with a height of magnetic film thickness, the diameter of the column is estimated as 15 and 11 nm with the Ti content of 0 and 20 at. %. The calculated

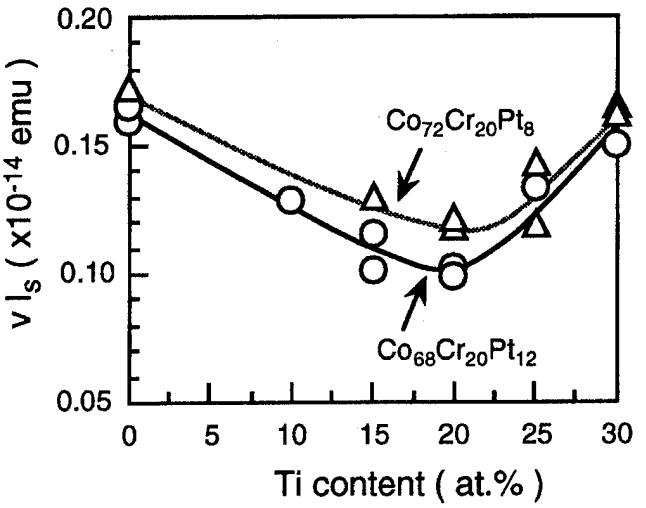


FIG. 4. Dependence of vI_s ($=kT/H_f$) of Co–Cr–Pt/Cr–Ti media on Ti content.

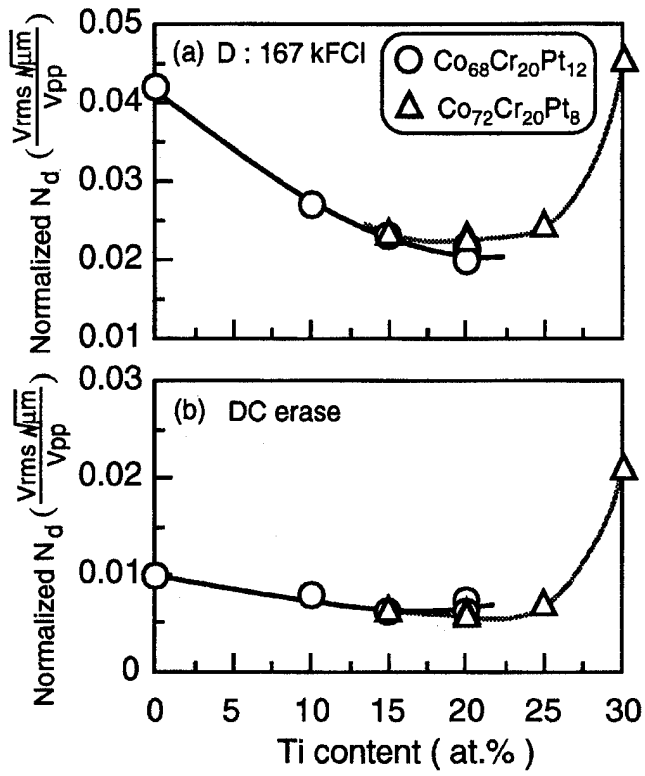


FIG. 5. Normalized media noise of Co–Cr–Pt/Cr–Ti media on Ti content for (a) recording density of 167 kFCI, and (b) dc erased state.

diameter is similar to the observed value in TEM image as shown in Fig. 2. The decrease of magnetic switching volume is probably caused by the reduction of grain size of Cr–Ti underlayer. This is because the reduction ratio of vI_s is almost equal to the decrease of the Cr–Ti grain size with the addition of Ti as shown in Fig. 3.

On the other hand, vI_s increased at the Ti content larger than 20 at. %. The reason for the increase of vI_s at high Ti content is discussed in the following section.

C. Media noise characteristics

Figure 5 shows the normalized media noise (N_d) of Co–Cr–Pt/Cr–Ti media as the function of the Ti content. At a recording density of 167 kilo flux change per inch (kFCI) [Fig. 5(a)] the normalized N_d decreased with an increase of the Ti content from 0 to 20 at. %. The normalized N_d of $Co_{72}Cr_{20}Pt_8/Cr_{75}Ti_{25}$ media was about 20% lower than that of $Co_{68}Cr_{20}Pt_{12}/Cr_{90}Ti_{10}$ media, where coercivity and S^* of the media are almost the same. As the change of activation volume with Pt content was small compared to the change by the Ti content, it is considered that the reduction of normalized N_d is due to the decrease of magnetic switching volume which is caused by the reduction of the grain size of Cr–Ti underlayers.

It has been proposed that the media noise is reduced by the decreasing exchange interaction between the crystal grains, which leads to a decrease of S^*.[5] However, the decrease of S^* causes the decrease of the read output. Accordingly, the addition of Ti to Cr underlayer is advantageous since the noise is reduced without the decrease of S^*.

The normalized N_d, especially the dc erase noise, increases with the increase of the Ti content from 25 to 30 at. %. No significant change was observed in the crystallographic texture of Co–Cr–Pt(11.0)/Cr–Ti(100) films at this composition. From the structural analyses it seemed that the increase of N_d was caused by the increase and a wider distribution of grain size of Cr–Ti films at the high Ti content.

IV. CONCLUSIONS

Effects of Ti addition to a Cr underlayer on the magnetic and crystallographic properties were investigated. An increase of the Ti content resulted in an increase of H_c and S^* and a decrease of media noise. The grain sizes of Cr–Ti films decreased from 30 to 20 nm with the increase of the Ti content from 0 to 20 at. %. The reduction of media noise is assumed to be due to the decrease of magnetic switching volume which is caused by the reduction of the grain size of the Cr–Ti underlayer. Ti addition to Cr underlayers is advantageous to improve the recording properties since the media noise is remarkably reduced without a decrease of S^*.

ACKNOWLEDGMENTS

The authors are grateful to Dr. K. Yamanaka for the measurement of the magnetic viscosity. The authors would also like to thank Dr. S. Narishige and Mr. S. Kojima for helpful discussions about the structure and magnetic properties of Co–Cr–Pt/Cr–Ti media.

[1] T. Yogi, C. Tsang, T. Nguyen, K. Ju, G. Gorman, and G. Castillo, IEEE Trans. Magn. **26**, 2271 (1990).
[2] Y. Futamoto, F. Kugiya, M. Suzuki, H. Takano, Y. Matsuda, N. Inaba, Y. Miyamura, K. Akagi, T. Nakao, H. Sawaguchi, H. Fukuoka, T. Munemoto, and T. Takagaki, IEEE Trans. Magn. **27**, 5280 (1991).
[3] Y. Shiroishi, Y. Hosoe, A. Ishikawa, Y. Sugita, H. Suzuki, T. Ohno, and M. Ohura, J. Appl. Phys. **73**, 5569 (1993).
[4] P. Glijer, J. M. Sivertsen, and J. H. Judy, J. Appl. Phys. **75**, 6141 (1994).
[5] K. E. Johnson, K. J. Schulz, and J. M. Severson, IEEE Trans. Magn. **29**, 3670 (1993).
[6] K. Yamanaka, T. Takayama, Y. Ogawa, A. Yano, and T. Okuwaki, J. Magn. Magn. Mater. **145**, 255 (1995).
[7] E. P. Wohlfarth, J. Phys. F **14**, L155 (1984).
[8] P. Gaunt, J. Appl. Phys. **59**, 4129 (1986).
[9] R. W. Chantrell, J. Magn. Magn. Mater. **95**, 365 (1991).

Magnetic and crystallographic properties of CoCrPt thin films formed on Cr–Ti single crystalline underlayers

N. Inaba, A. Nakamura, T. Yamamoto, Y. Hosoe, and M. Futamoto
Central Research Laboratory, Hitachi Ltd., Kokubunji, Tokyo 185, Japan

By using an epitaxial growth technique, $Co_{73}Cr_{15}Pt_{12}(11\bar{2}0)$ bi-crystalline thin films formed on Cr–Ti_x(001)[x=0–15 at. %] single crystalline underlayers were prepared to investigate the relationship between the magnetic properties and the lattice distortion in the magnetic layer. X-ray diffraction measurement shows that the best lattice matching between the c axis of the CoCrPt and the [110] direction of the Cr–Ti underlayer is realized and the CoCrPt layer shows an ideal symmetrical hcp. structure when the Ti concentration is 10 at. %, where the maximum magneto-crystalline anisotropy energy and coercivity values are observed. Distortion in the hcp. CoCrPt magnetic crystal grains decreases the uniaxial magneto-crystalline anisotropy energy, thus lowering the attainable medium coercivity. © *1996 American Institute of Physics.*
[S0021-8979(96)06408-0]

I. INTRODUCTION

Magnetic properties of longitudinal magnetic recording media depend on the crystalline orientation relationship between the magnetic layer and the underlayer.[1,2] The crystal lattice distortion is caused by the lattice misfit between the magnetic layer and the underlayer. However, the interrelationship among these properties has not yet been precisely made clear for practical media, since they consist of very small polycrystalline grains.

In our previous works,[3,4] Co/Cr and CoCrPt/Cr bilayer thin films are epitaxially grown on MgO(001) single crystal substrates with the crystallographic orientation relationship of MgO(001)[100]‖Cr(001)⟨110⟩‖Co or CoCrPt(11$\bar{2}$0)[0001]. The Cr layer has a (001)-oriented single-crystalline structure, while the magnetic layer shows a bi-crystalline structure consisting of two different domains with their c axes lying in-plane and aligned perpendicular to each other. By using well defined specimens, the magnetocrystalline anisotropy of the magnetic layer as well as the lattice spacings of both the layers can be precisely determined.[5]

In the present research, by using the epitaxial growth technique, we prepared CoCrPt bi-crystalline thin films grown on Cr–Ti single crystalline underlayers while changing the Ti concentration in the underlayer to vary the lattice constant of the underlayer. The relationship between the fundamental magnetic and crystallographic properties for the CoCrPt/Cr–Ti bi-layer film system is investigated.

II. EXPERIMENTAL PROCEDURE

Thin films were deposited by using a dc magnetron sputtering system on MgO(001) single crystal substrates kept at 300 °C under an Ar pressure of 3 m Torr. A Cr–Ti underlayer (50 nm), $Co_{73}Cr_{15}Pt_{12}$ magnetic layer (25 nm) and a carbon overcoat layer (10 nm) were sequentially formed on MgO substrates. Ti concentration in the Cr–Ti underlayer was changed from 0 to 15 at. %.

The crystal lattice parameters were determined by x-ray diffraction analysis. Plan-view microstructures of the magnetic layer were observed using a transmission electron microscope (TEM). Magnetic torque curves and magnetization curves were measured by using a torque magnetometer and a vibrating sample magnetometer, respectively.

III. RESULTS AND DISCUSSIONS

A. Lattice structure of CoCrPt thin films

All the specimens showed only the Cr–Ti(002), the CoCrPt(11$\bar{2}$0) and the MgO(002) sharp peaks in the θ–2θ scan x-ray diffraction, which indicated epitaxial growth of these films. Figure 1 shows the variation of lattice spacing and the full width at half maximum ($\Delta\theta_{50}$) of an x-ray reflection rocking curve measured for the Cr–Ti(002) and the CoCrPt(11$\bar{2}$0) layers when Ti concentration in the Cr–Ti underlayers is changed. The lattice spacing of Cr–Ti(002) increases linearly by increasing the Ti concentration. The $\Delta\theta_{50}$ of the Cr–Ti layer is almost constant at 0.4°–0.5°. On the contrary, by increasing the Ti concentration, the lattice spacing of CoCrPt(11$\bar{2}$0) decreases taking the minimum value of 1.286 Å at 10 at. % Ti. The $\Delta\theta_{50}$ of CoCrPt(11$\bar{2}$0) decreases monotonically down to 0.9° by increasing the Ti concentration to 15 at. %. This result suggests that the crystallographic orientation of the CoCrPt layer is more aligned with increasing the lattice constant of the underlayer.

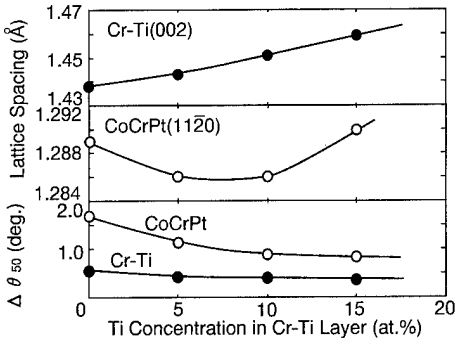


FIG. 1. Lattice spacings and full width at half maximum ($\Delta\theta_{50}$) of x-ray reflection rocking curves for Cr–Ti(002) and CoCrPt(11$\bar{2}$0) when Ti concentration in the Cr–Ti underlayer is changed.

 0021-8979/96/79(8)/5354/3/$10.00 © 1996 American Institute of Physics

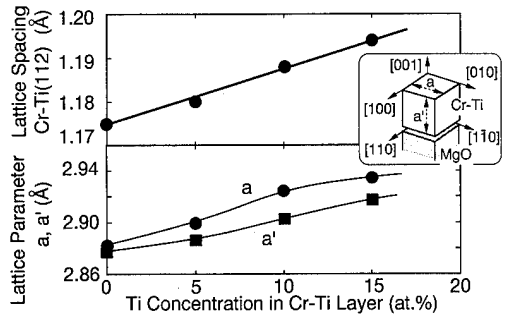


FIG. 2. Variations of lattice spacing for Cr–Ti(112) and lattice parameters, a and a′, when Ti concentration is changed.

We measured the lattice parameters of the films that were parallel and not parallel to the substrate plane by θ–2θ scan x-ray diffraction measurements for the samples set with offset angles in order to determine accurately the crystal structures of the CoCrPt/CrTi bi-layer films. The lattice parameters of the Cr–Ti underlayer parallel and perpendicular to the film plane, a and a′, are estimated by the lattice spacings of the Cr–Ti(002) and (112) planes shown in Figs. 1 and 2. The [100] and [010] axes of the Cr–Ti crystal are equivalent. Both a and a′ parameters increase by increasing the Ti concentration. However, the a′ parameter is about 0.5% smaller than a parameter, which shows that the bcc. lattice of Cr–Ti crystals formed on the MgO(001) substrates is deformed about 0.5% from an ideal symmetrical bcc. structure.

The lattice parameters of the CoCrPt hexagonal closed-packed structure, a, a′, and c, were estimated by the lattice spacings of CoCrPt(11$\bar{2}$0), (20$\bar{2}$0), and (11$\bar{2}$2) planes, as shown in Fig. 3. The dotted line in Fig. 3 is the variation of the two times of the Cr–Ti(110) lattice spacing, which coincide with the lattice spacing of CoCrPt(0001), or the c parameter, under an epitaxial growth condition. The a parameter remains almost unchanged regardless of the Ti concentration in the underlayer. On the other hand, the a′ and c parameters increase by increasing the Ti concentration in the underlayer and shows the maximum value at the Ti concentration of 10 at. %, where the lattice mismatch between the c axis of the CoCrPt and the [110] direction of the Cr–Ti underlayer is minimized. The ratio of a′/a also increases by increasing the Ti concentration and approaches to 1.0 for the same underlayer composition. Since the CoCrPt layer is epitaxially grown on the underlayer, the crystal lattice distortion is introduced to the CoCrPt magnetic crystals by increasing of the lattice misfit between the magnetic layer and the underlayer.

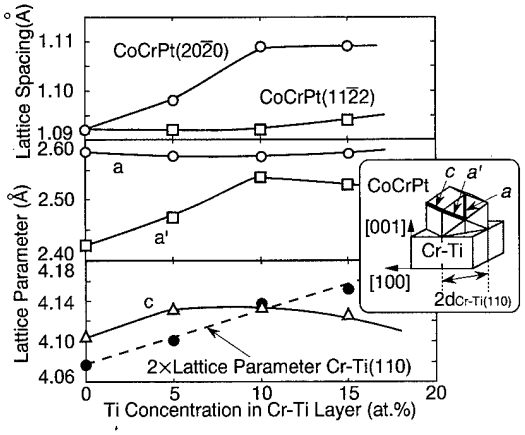


FIG. 3. Variations of lattice spacing measured for CoCrPt(20$\bar{2}$0), CoCrPt(11$\bar{2}$2), and lattice parameters, a, a′, and c when Ti concentration in the underlayer is changed.

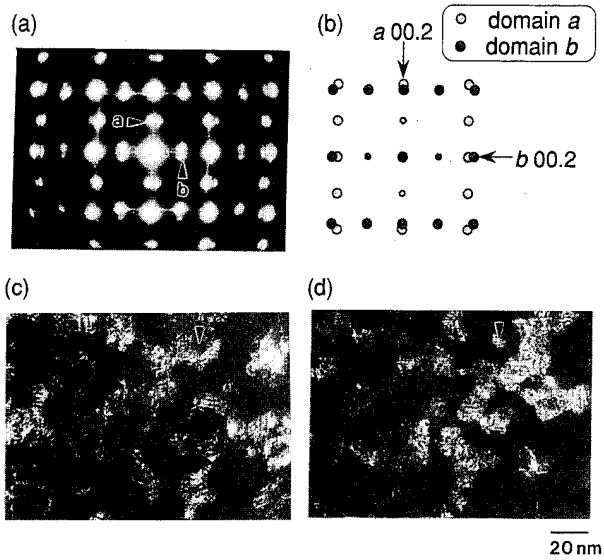


FIG. 4. Plan-view microstructure of epitaxially grown CoCrPt, (a) selected-area electron diffraction pattern, (b) indexed electron diffraction pattern, (c) and (d) show the dark field images for the same area which are observed by using the diffraction spots a and b indicated in (a), respectively.

Plan-view microstructure of the CoCrPt layer was observed by using a TEM. Figures 4(a) and 4(b) show the selected-area electron diffraction pattern and the diffraction index, respectively. The result indicates the CoCrPt layer has (11$\bar{2}$0) orientation and consists of two different types of domains with the c axes perpendicular to each other. Figures 4(c) and 4(d) show the dark field TEM images observed from a same area of the CoCrPt layer by using the diffraction spots of a and b indicated in Fig. 4(a). The magnetic grain size is about 20 nm in diameter. Several grains that have a same crystal orientation tend to form a continuous larger size grain.

B. Magnetocrystalline anisotropy of CoCrPt

The magneto-crystalline anisotropy of the CoCrPt thin films was determined by magnetic torque measurements. The magnetic field, H_{ex}, is applied in the (001) plane of the MgO substrates, or the CoCrPt(11$\bar{2}$0) plane. Since the CoCrPt layer shows bi-crystalline structure consisting of two types of domains with the c axes perpendicular to each other, the magnetic anisotropy energy per unit volume, E_{in}, is given by the following equation:

$$E_{\text{in}}=K_{\text{u1}}/2+K_{\text{u2}}(\sin^4\theta_{\text{in}}+\cos^4\theta_{\text{in}})/2. \quad (1)$$

Where K_{u1} and K_{u2} are the magneto-crystalline anisotropy constants, θ_{in} is an angle between the direction of magneti-

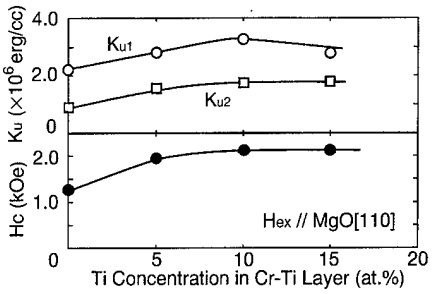


FIG. 5. Variations of K_{u1}, K_{u2}, and H_c measured for CoCrPt layer when Ti concentration in the underlayer is changed.

zation and the MgO[100] axis, and the two types of bi-crystalline domains have the same volume. The magnetic torque, L_{in}, is given by

$$L_{in} = -\partial E_{in}/\partial \theta_{in} = (K_{u2}/4)\sin 4\theta_{in}. \quad (2)$$

The direction of H_{ex} was varied out of the CoCrPt film plane around the MgO[010] axis. In this case, the magnetic anisotropy of the magnetic domains, whose c axes are parallel to the MgO[010] direction, can be ignored. The magnetic anisotropy energy per unit volume, E_{out}, and the magnetic torque, L_{out}, are given by

$$E_{out} = (K_{u1}\sin^2 \theta_{out} + K_{u2} \sin^4 \theta_{out})/2 + 2\pi M_s^2 \sin^2 \theta_{out}, \quad (3)$$

$$L_{out} = (K_{u1}/2 + K_{u2}/2 + 2\pi M_s^2)\sin 2\theta_{out} - (K_{u2}/4)\sin 4\theta_{out}, \quad (4)$$

where $2\pi M_s^2$ is the shape anisotropy energy, and θ_{out} is the angle between the direction of the magnetization and the MgO[100] axis. Therefore, K_{u1} and K_{u2} can be obtained by Fourier analysis of the torque curves.

The magnetic torque curves of the CoCrPt thin films measured in the MgO(001) plane had fourfold symmetry. The directions of the c axes in the CoCrPt bi-crystal films, which are parallel either to MgO[100] or [010] directions, are the effective magnetic hard axes. Since the components proportional to $\sin 2\theta_{in}$ in the curves are less than one tenth of that of $\sin 4\theta_{in}$, two types of bi-crystalline domains have the same volume. Figure 5 shows the variations of K_{u1} and K_{u2} of the CoCrPt thin films determined by using the above mentioned technique. By increasing the Ti concentration in the Cr–Ti underlayer, both K_{u1} and K_{u2} increase and show the maximum values of 3.4×10^6 erg/cc (K_{u1}) and 1.8×10^6 erg/cc (K_{u2}) at the Ti concentration of 10 at. %, where the best lattice matching between the magnetic layer and underlayer is realized. The coercivity of the CoCrPt specimen, H_c, also shows the maximum value at the same underlayer composition. The variation of coercivity corresponds to that of the magneto-crystalline anisotropy energy. These results clearly indicate that the K_{u1} and the K_{u2} of the film show the maximum values when the crystallographic distortion of the CoCrPt magnetic crystals formed on the underlayer is minimized. Therefore, it is very important to realize a good lattice matching between the magnetic layer and the underlayer in order to increase the coercivity of longitudinal magnetic recording media.

IV. CONCLUSIONS

We investigated the relationship between the crystalline distortion and the magneto-crystalline anisotropy for the CoCrPt/Cr–Ti[Ti:0–15 at. %] bi-layer film system prepared by using the epitaxial growth technique. The lattice constant of the Cr–Ti underlayer increases from 2.88 to 2.94 Å by increasing the Ti concentration from 0 to 15 at. %. When the CoCrPt bi-crystalline thin film is formed on the Cr-10 at. % Ti underlayer, the best lattice matching between the c axis of the CoCrPt and the [110] direction of the Cr–Ti underlayer is realized and the CoCrPt layer shows an ideal symmetrical hcp. structure. This CoCrPt layer possesses the maximum values of K_u (3.4×10^6 erg/cc) and H_c (2.2 kOe). The distortion in the hcp. crystal structure decreases the uniaxial magneto-crystalline anisotropy energy of the CoCrPt material, thus lowering the attainable medium coercivity.

ACKNOWLEDGMENTS

The authors would like to thank emeritus Professor S. Chikazumi of Tokyo University and Dr. Y. Sugita of Hitachi Central Research Laboratory for their encouragement and helpful discussions. They also thank E. Mangyou for the specimen preparation.

[1] Y. Shiroishi, Y. Hosoe, A. Ishikawa, Y. Yahisa, and Y. Sugita, J. Appl. Phys. **73**, 5569 (1993).
[2] M. A. Parker, J. K. Howard, R. Ahlert, and K. R. Coffey, J. Appl. Phys. **73**, 5560 (1993).
[3] A. Nakamura and M. Futamoto, Jpn. J. Appl. Phys. **32**, L1410 (1993).
[4] M. Futamoto, M. Suzuki, N. Inaba, A. Nakamura, and Y. Honda, IEEE Trans. Magn. **MAG-30**, 3975 (1994).
[5] N. Inaba, Y. Matsuda, M. Suzuki, A. Nakamura, and M. Futamoto, J. Appl. Phys. **75**, 6126 (1994).

Magnetic and microstructural properties of CoCrTa/Cr/Al thin films (abstract)

H. S. Chang, T. D. Lee, and J. K. Park
Department of Material Science and Engineering, Korea Advanced Institute of Science and Technology, Taejon, Korea

K. H. Shin and K. Park
Division of Metals, Korea Institute of Science and Technology, Seoul, Korea

CoCrTa/Cr/Al and CoCrTa/Cr thin films were deposited on glass substrate at 280 °C using dc magnetron sputtering. The coercivity of CoCrTa/Cr films increased by introducing an Al underlayer. In 500 Å CoCrTa/Cr films, the coercivity increased with increasing Cr thickness and saturated above 700 Å Cr thickness (Hc=1050 Oe). On the other hand, in 500 Å CoCrTa/Cr/700 Å Al films, the coercivity increased sharply with increasing Cr thickness and showed a maximum value at 700 Å Cr thickness (Hc=1380 Oe). The coercivity squareness of the CoCrTa/Cr/Al and CoCrTa/Cr films was increased with increasing Cr thickness. The coercivity squareness of CoCrTa/Cr/Al films was lower than that of CoCrTa/Cr films. To study the origin of coercivity enhancement in CoCrTa/Cr films when deposited on an Al underlayer, microstructures of the two films were investigated using transmission electron microscopy (TEM). We controlled grain sizes of CoCrTa films by changing the thickness of the Cr layer. The grain size of CoCrTa films increased with increasing Cr thickness. The coercivity of CoCrTa/Cr/Al films showed a maximum value at a grain size of 430 Å. These results suggest that the transition from single domain to multidomain could occur at a grain size of ~400 Å. To understand the coercivity squareness changes by the introduction of an Al underlayer, the angular variation of coercivity was measured. The magnetization of CoCrTa/Cr films was reversed by domain wall motion. On the other hand, by the incorporation of an Al underlayer, the angular variation of coercivity deviated from the domain wall motion mode. Cross-sectional TEM studies of CoCrTa/Cr/Al films showed that Cr atoms in Cr layers diffused into an Al underlayer and Al atoms were detected in both Cr and CoCrTa layers, but magnetization of the magnetic layer was not decreased. The decrease in coercivity squareness of CoCrTa/Cr/Al films would be attributed to magnetic decoupling by segregation of Al atoms in grain boundaries of CoCrTa films. © *1996 American Institute of Physics.* [S0021-8979(96)45908-1]

Influence of sputter gas and sputter pressure on the structure and magnetic properties of Co–Pt–Cr thin films (abstract)

A. Roshko and L. L. Dulcie
Electromagnetic Technology Division, NIST, Boulder, Colorado 80303

T. Nguyen and T. Yogi
IBM Research Division IBM, San Jose, California 95120

The magnetic properties of high density recording media have been shown to be very sensitive to the film microstructure. We have investigated the influences of different sputter gases (Ar, Xe, Kr) and different sputter pressures (3 to 24 mTorr) on the microstructures and magnetic properties of CoPtCr/Cr thin films. The magnetic properties of the films (coercive field, H_c, coercive squareness, S^*, and remanant moment, M_r) were determined using a vibrating sample magnetometer. The microstructures were examined by transmission electron microscopy and x-ray diffraction. For all three gases studied the microstructures and properties of the CoPtCr films were found to change with sputter pressure in similar manners. Films deposited at the lowest pressure consisted of well connected, equiaxed grains. With only a slight increase in pressure, the grains formed chains separated by small gaps. As the gas pressure increased further, the chains became better defined and the gaps between them widened. The coercive squareness and coercive field correlate with the film microstructures. S^* decreased with increasing sputter gas pressure, and H_c first increased and then decreased. For all three sputter gases, H_c reached a maximum around 12 mTorr. Likewise, S^* decreased quite slowly with increasing pressure up to 12 mTorr and then exhibited a sharp drop between 12 and 18 mTorr. From these results it appears that the sputter pressure, rather than the mass of the sputter gas, is most important for the microstructural development of the film. Likewise, the values of S^* were found to be independent of the sputter gas. However, in spite of the similar microstructures, films deposited with Ar had higher values of H_c than films deposited with Xe or Kr, for all sputter pressures examined. The role of the sputter gas mass will be discussed. © *1996 American Institute of Physics.* [S0021-8979(96)46008-X]

 0021-8979/96/79(8)/5358/1/$10.00 © 1996 American Institute of Physics

Improvement of $Co_{71}Cr_{19}Pt_{10}/Ti_{90}Cr_{10}$ perpendicular recording media by independent optimization of film nucleation and growth processes

T. P. Nolan, Y. Hirayama, and M. Futamoto
Central Research Laboratory, Hitachi, Ltd., Kokubunji, Tokyo 185, Japan

CoCrPt/TiCr perpendicular recording media having independently optimized nucleation and growth conditions have been prepared by changing the argon pressure during sputter deposition of each film. A low argon pressure CoCrPt nucleation layer produces strong c-axis perpendicular orientation that can be maintained during continued CoCrPt deposition at high argon pressure. The two-layer media combines increased particle separation from high pressure growth and strong orientation to produce higher signal to noise ratio than either high pressure or low pressure single layer CoCrPt media. TiCr underlayers, despite poor orientation and a noncolumnar structure, improve CoCrPt c-axis perpendicular orientation. Low argon pressure during TiCr deposition maximizes CoCrPt orientation. A TiCr bilayer having a low pressure nucleation layer followed by a high pressure growth layer improves performance of the subsequent CoCrPt layer. A TiCr bilayer having a high pressure growth layer followed by a thin low pressure template produces even greater recording performance enhancement. This media has H_c=2560 Oe, D_{50}=90 kfci and S_0/N_d at 240 kfci=4.0. An identical CoCrPt layer deposited on the low pressure TiCr underlayer has H_c=1850 Oe, D_{50}=80 kfci and S_0/N_d at 240 kfci=2.4. © *1996 American Institute of Physics.* [S0021-8979(96)28008-6]

I. INTRODUCTION

The ultimate density limit of perpendicular recording may be higher than that of longitudinal recording.[1,2] Perpendicular media combined with new technology for in contact recording systems using integrated circuit (IC) process fabricated giant magnetoresistance microflex-heads is promising.[3]

Hexagonal, sputtered CoCrPt alloys similar to those used in longitudinal recording have sufficient magnetocrystalline anisotropy to counteract the demagnetization and shape anisotropy of the perpendicular geometry, and microstructural features desirable for perpendicular magnetic recording.[4] They naturally grow with the required c-axis vertical orientation on many materials.[5–9]

Seed layers are used to improve CoCrPt microstructural, crystallographic and magnetic properties.[6–9] $Ti_{90}Cr_{10}$ underlayers have been demonstrated to improve CoCrPt microstructure and c-axis vertical orientation on SiO_2/Si substrates. Promising media having higher signal-to-noise ratio (SNR) at >200 kfci than comparable longitudinal media, at recording densities above 200 kfci, have already been demonstrated.[6] However, optimization of the microstructure to further increase SNR and D_{50} is required.

This is difficult because microstructure varies with each deposition parameter of both the TiCr and CoCrPt layer depositions. Ideal deposition conditions for film nucleation and film growth also differ. Furthermore, optimal CoCrPt nucleation may require a template layer, giving the five separate growth steps shown schematically in Fig. 1.

This paper demonstrates a method for independently tailoring the microstructure of these five stages of magnetic recording media film growth. Argon pressure (P_{Ar}) is changed during deposition from one target, to change the adatom mobility during the different growth stages. Control of mobility by adjustment of argon pressure is chosen for its feasibility in production applications.

Small separated grain structures are produced with reduced loss of preferred orientation, giving rise to improved CoCrPt magnetic properties.

II. MEDIA PREPARATION AND ANALYSIS

100 nm $Co_{71}Cr_{19}Pt_{10}$ magnetic layers and 30 nm $Ti_{90}Cr_{10}$ underlayers were dc magnetron sputter deposited onto rf sputter cleaned, oxidized silicon wafers. Substrates were heated to 230 °C with base pressure maintained below 10^{-8} Torr. Samples are separated into two groups.

Group A samples have identical TiCr underlayers deposited with P_{Ar}=2 mTorr. Sample A1 has $P_{Ar(CoCrPt)}$=2 mTorr. Sample A2 has $P_{Ar(CoCrPt)}$=15 mTorr. Sample A3 was prepared by depositing 10 nm of CoCrPt under conditions identical to A1, followed by 90 nm deposited under the conditions for A2.

Group B samples all have $P_{Ar(CoCrPt)}$=2 mTorr. Sample B1 has $P_{Ar(TiCr)}$=2 mTorr. Sample B2 has a 5 nm nucleation layer with $P_{Ar(TiCr)}$=2 mTorr followed by a 25 nm growth layer with $P_{Ar(TiCr)}$=35 mTorr. Samples were also deposited

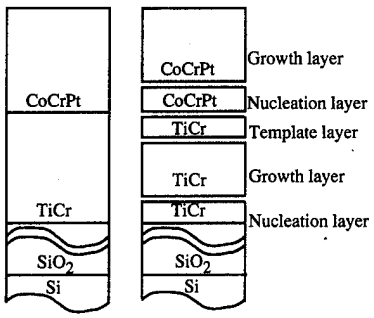


FIG. 1. Model of microstructure development stages for deposition optimization.

 0021-8979/96/79(8)/5359/3/$10.00 © 1996 American Institute of Physics

TABLE I. Group A data.

Sample	CoCrPt θ_{50} (deg)	Particle size (nm)	$H_{c\perp}$ (Oe)	$H_{c\parallel}$ (Oe)
A1	2.2	43	1850	220
A2	4.8	74	1060	350
A3	3.7	39	1840	220

with 15 nm and 45 nm growth layers. Sample B3 has a 25 nm, $P_{\mathrm{Ar(TiCr)}}$=35 mTorr growth layer followed by a 5 nm, $P_{\mathrm{Ar(TiCr)}}$=2 mTorr template layer.

Preferred orientation strength was measured from x-ray rocking curves of the TiCr and CoCrPt {0002} peaks. Surface morphology was analyzed using a Hitachi S5000 FESEM with samples heated to 150 °C to reduce contamination. Hysteresis loops were measured perpendicular and parallel to the thin-film plane by vibrating-sample magnetometry (VSM).

Recording measurements employed a composite head having a permalloy inductive write head with track width, T_w=10.3 μm, and gap length, G_l=0.6 μm; and a magnetoresistance (MR) read head with T_w=3.4 μm and G_l=0.5 μm. Write and read head flying heights were 65 nm and 60 nm respectively, head velocity was 4.0 m/s and the writing current was 35 mA. Low frequency output signal (S_0), recording density giving output voltage=$S_0/2$ (D_{50}), media noise at 240 kfci (N_d), and S_0/N_d were measured.

III. CoCrPt NUCLEATION AND GROWTH

Low P_{Ar} (A1) provides stronger c-axis vertical preferred orientation than high P_{Ar} (A2), as demonstrated by the rocking curve data in Table I. This is expected owing to the lower adatom energy at high P_{Ar} that makes surface transport to the lowest energy position more difficult. A low P_{Ar} nucleation layer followed by high P_{Ar} deposition (A3) produces significantly better orientation than a single high P_{Ar} layer, despite identical conditions for 90% of the deposition.

The small separations between the particles are near the detection limit of high-resolution scanning electron microscopy (HRSEM) under the experimental conditions, but clear differences between samples are nevertheless observable in Fig. 2.

High P_{Ar} CoCrPt deposition (A2) produced a very large (74 nm) feature size (Table I) that may have resulted from the high pressure nucleation process or orientation dependent

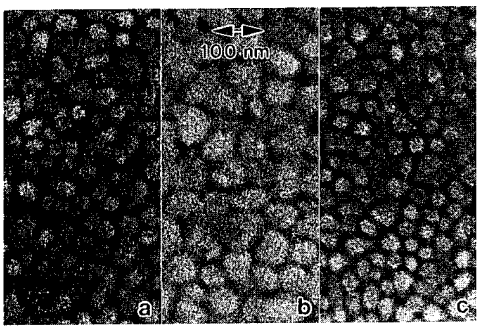


FIG. 2. HRSEM images of (a) sample A1 (b) sample A2, and (c) sample A3.

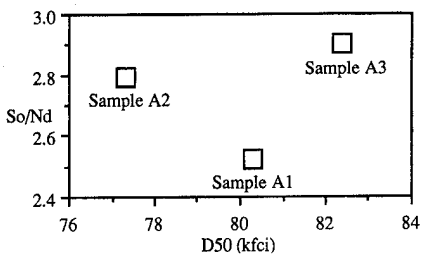


FIG. 3. S_0/N_d and D_{50} of CoCrPt/TiCr media samples.

grain growth. The low pressure (A1) and two-layer (A3) structures have similar particle sizes (43 and 39 nm), owing to their identical nucleation layers.

Magnetically, low $H_{c\perp}$ and relatively high $H_{c\parallel}$ in A2 result from large particles and poorer orientation (Table I). High H_c in A1 and A3 is consistent with a better oriented, small grain structure.

Despite the large particle size, shadowing induced separation at high pressure decreases S_0/N_d of A2 compared to A1, but high density recording performance, as measured by D_{50} reduces (Fig. 3), probably owing to poor orientation and large particles that reduce perpendicular anisotropy H_k. The two-layer sample has higher S_0/N_d and D_{50} than the single layer samples, attributable to small separated particles and only a small loss of preferred orientation with respect to the low P_{Ar} sample.

IV. TiCr NUCLEATION AND GROWTH

Cross-section high-resolution transmission electron microscopy showed multiple renucleation of misoriented ~5 nm TiCr grains during 2 m Torr film growth.[6] Correspondingly, the TiCr {0002} x-ray diffraction peaks are weak and TiCr rocking curves are noisy and quite broad, confirming weak c-axis vertical orientation (Table II). CoCrPt {0002} diffraction is much stronger and the rocking curves are much sharper, suggesting that the primary CoCrPt orientation mechanism is not epitaxy. Nevertheless, a low P_{Ar} underlayer (B1) produces better CoCrPt orientation (θ_{50}=2.2°) than a high pressure underlayer (θ_{50}~9°).

For two-layer underlayers, good orientation of the CoCrPt layer is maintained despite brief 35 mTorr growth [θ_{50}=2.5° for 15 nm and 2.7° for 25 nm (B2)], but is lost after further deposition (θ_{50}~9° for 45 nm).[10] Some crystallographic information is apparently transferred from the underlayer to the CoCrPt layer and the orientation mechanism, although not determined, seems to be related to both the crystallography of the underlayer and the details of the surface structure.

TABLE II. Group B data.

Sample	CoCrPt θ_{50} (deg)	TiCr θ_{50} (deg)	Particle size (nm)	$H_{c\perp}$ (Oe)	$H_{c\parallel}$ (Oe)
B1	2.2	8.4	43	1850	220
B2	2.7	7.6	61	2040	300
B3	3.5	8.4	38	2560	330

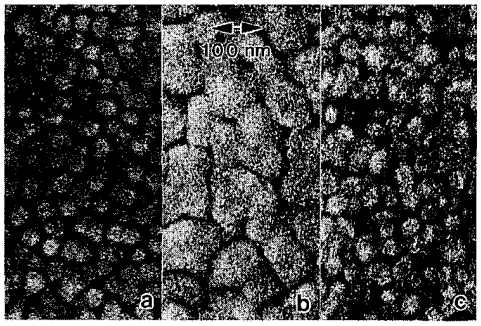


FIG. 4. HRSEM images of (a) sample B1 (b) sample B2, and (c) sample B3.

B2 shows the affect of the nucleation layer upon CoCrPt orientation. B3 shows the effect of changing surface structure. Renucleation in 2 mTorr TiCr occurs every 5 nm (Ref. 6) so B3 should have TiCr surface properties resembling those of the standard film (B1) despite increased particle separation induced by the high pressure underlayer growth.

The B2 and B3 CoCrPt rocking curves ($\theta_{50(B2)}$=2.7°) and ($\theta_{50(B3)}$=3.5°), although broader than the 2 mTorr B1 curve, are both significantly reduced from the ~9°, value for continued growth at 35 mTorr.

The CoCrPt particle size of B2 is much larger than that for nucleation on the 2 mTorr B1 underlayer (Fig. 4). The particle size of sample B3 is nearly the same as B1, suggesting that the nucleation condition was indeed controlled in large by the template surface.

Magnetically, high $H_{c\perp}$ and low $H_{c\parallel}$ in B2 suggest separated, well oriented particles. Consistently, the large particles reduce D_{50} (Fig. 5), but S_0/N_d is larger than that of B1, as expected for improved particle separation.

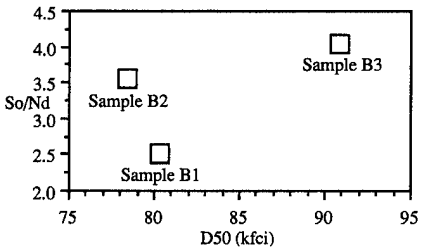


FIG. 5. S_0/N_d and D_{50} of CoCrPt/TiCr media samples.

The combination of small separated particles and strong c-axis orientation in B3 significantly increase $H_{c\perp}$ while maintaining low $H_{c\parallel}$. Correspondingly, there is a large D_{50} and S_0/N_d increase.

V. CONCLUSIONS

Magnetic recording performance of CoCrPt/TiCr sputter deposited perpendicular recording media can be enhanced by independently optimizing the nucleation, growth, and interface microstructures during film growth.

CoCrPt magnetic layers grow columnarly, and can be improved by (a) nucleating oriented grains at low P_{Ar}, and (b) growing oriented, separated columns at high P_{Ar}. Improved orientation was maintained despite 90% of the film thickness being grown at high pressure.

TiCr underlayers do not grow columnarly, but CoCrPt orientation is better for growth on a TiCr surface deposited at low P_{Ar}. An improved underlayer was formed by (a) growing a separated structure at high P_{Ar} and (b) forming a thin low P_{Ar} surface layer for oriented CoCrPt growth.

This preliminary experiment suggests a method to enhance performance of a wide variety of perpendicular and longitudinal recording media.

[1] Y. Nakamura and K. Ise, J. Magn. Soc. Jpn. **15** (S2), 185 (1991)
[2] D. J. Mapps, G. Pan, M. A. Akher, S. Onodera, and A. Okabe, J. Magn. Magn. Mater. **120**, 305 (1993).
[3] H. Hamilton, J. Mag. Soc. Jpn. **18** (S1), 171 (1994).
[4] S. I. Iwasaki and Y. Nakamura, IEEE Trans. Magn. **13**, 1272 (1977).
[5] P. Glijer, J. M. Sivertsen, and J. H. Judy, J. Mag. Soc. Jpn. **18** (S1), 107 (1994).
[6] Y. Matsuda, M. Suzuki, Y. Hirayama, Y. Honda, and M. Futamoto, J. Mag. Soc. Jpn. **18** (S1), 99 (1994).
[7] M. Futamoto, Y. Honda, H. Kakibayashi, and K. Yoshida, IEEE Trans. Magn. **21**, 1426 (1985).
[8] G. Pan, D. J. Mapps, M. A. Akhter, J. C. Lodder, P. Berge, H. Y. Wong, and J. N. Chapman, J. Magn. Magn. Mater. **113**, 21 (1992).
[9] Y. Matsuda, Y. Shiroishi, T. Shimotsu, and K. Takagi, J. Mag. Soc. Jpn. **13** (S1), 391 (1989).
[10] T. P. Nolan, Y. Hirayama, and M. Futamoto, Mater. Res. Soc. Symp. Proc. (in press).

High recording performance of Co–Cr medium sputter-deposited at high Ar pressure and high substrate temperature

Naoki Honda, Satoshi Yanase, and Kazuhiro Ouchi
AIT (Akita Research Institute of Advanced Technology), Akita 010-16, Japan

Shun-ichi Iwasaki
Tohoku Institute of Technology, Sendai 982, Japan

Co–Cr films were prepared by sputter deposition at a high Ar pressure of 70 Pa with elevated substrate temperatures up to 400 °C. Films of 100 nm thickness were deposited using a 19 at. % Cr–Co target onto a well c-axis oriented Ti underlayer prepared on glass disk substrates. The perpendicular coercivity, $H_{c_\perp}$, of the films increased from 660 to 1940 Oe with increasing temperature. The films with high $H_{c_\perp}$ exhibited a dense fine microstructure with distinct grain boundaries. The recording performance of the disk samples were measured by using a metal in gap type ring head, comparing with that of conventional Co–Cr films deposited at a low Ar pressure of 0.2 Pa. It was found that the high pressure deposited Co–Cr film exhibited higher output by more than 2 dB at the densities below 320 kFRPI (flux reversals per inch) compared with the conventional film with the same high coercivity. The D^*_{50} of as high as 250 kFRPI and the highest recordable density of over 600 kFRPI were confirmed for the new type of Co–Cr film deposited at 70 Pa and at 400 °C. The noise level of the film, however, was slightly higher than that of conventional method films, disagreeing with the suggestion of the microstructure. © *1996 American Institute of Physics.* [S0021-8979(96)10008-8]

I. INTRODUCTION

Co–Cr films have been intensively studied as one of the most preferable candidates for ultrahigh density recording media.[1–3] Recent our work showed that the Co–Cr films deposited at a high Ar pressure with an elevated substrate temperature could have a fine grained dense microstructure with distinct grain boundaries accompanied by a high perpendicular coercivity.[4] These properties of the films are expected to exhibit a high recording performance with a low noise property when the films are used as perpendicular recording media. In the present article, the effect of the substrate temperature on the magnetic properties and the microstructure of the Co–Cr films deposited at high Ar pressures were studied and the recording properties of the disk samples of such films were measured. A high recording performance of the medium will be discussed.

II. EXPERIMENT

Disk samples were prepared by dc magnetron sputter deposition using 2.5 in. ϕ glass disk substrate. The preparation conditions are listed in Table I. A well c-axis oriented Ti underlayer ($\Delta\theta_{50}<6°$) was first applied onto the glass substrate to obtain a high crystal orientation for the Co–Cr layer. The Co–Cr films of 100 nm thickness were deposited onto the Ti underlayer with substrate temperatures ranging from room temperature up to 400 °C under both high (70 Pa) and low (0.2 Pa) Ar pressures, using a Co–19 at. % Cr target. The sputtering input power was 200 W for the target size of 75 mm in diameter and the target–substrate distance of 55 mm. After the surface was sputter-overcoated with a SiO_2 layer of 10 nm thickness, the recording performances of the disk samples were measured by using a commercial 8 mm VCR's metal in gap type ring head with a gap length of 0.22 μm. A self-weighted contact head interface[5] was adopted using relative head velocities of 1 and 2 m/s for recording and noise measurements, respectively. The magnetic properties were measured by a vibrating sample magnetometer (VSM). A scanning electron microscope (SEM) with a field emission electron gun was used to observe microstructures of the films.

III. RESULTS AND DISCUSSIONS

A. Magnetic properties

Figure 1 shows substrate temperature dependence of the perpendicular coercivity, $H_{c_\perp}$, and the in-plane coercivity, $H_{c_\parallel}$, for Co–Cr films sputter-deposited at high (70 Pa) and low (0.2 Pa) Ar pressures. When the films were deposited at room temperature, deposition at high Ar pressure resulted in a film with a much higher $H_{c_\perp}$ than that of low Ar pressure depositions, as we have reported.[6] The $H_{c_\perp}$ drastically increased with increasing substrate temperature and saturated at high temperatures, yielding a high $H_{c_\perp}$ larger than 1800 Oe for both Ar pressure depositions, but the increase in $H_{c_\perp}$ for the 70 Pa deposition took place at higher temperatures than for the 0.2 Pa deposition. This may be attributed to reduced kinetic energy of the depositing atoms due to increased number of collisions with Ar atoms at such an extremely high Ar pressure. The in-plane coercivity $H_{c_\parallel}$ exhib-

TABLE I. Sputter-deposition conditions for Ti underlayer and Co–Cr layer.

Conditions	Ti layer	Co–Cr layer
Target	99.9% pure	19 at. % Cr–Co
Ar pressure	0.2 Pa	0.2 and 70 Pa
Temperature	Room temp.	Room temp. −400 °C
Film thickness	70 nm	100 nm

 0021-8979/96/79(8)/5362/3/$10.00 © 1996 American Institute of Physics

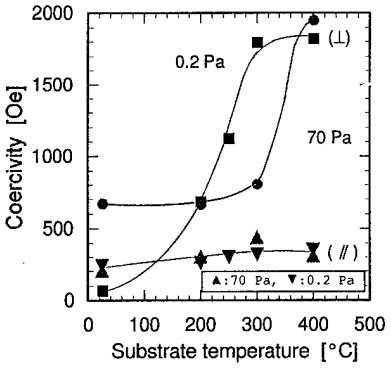


FIG. 1. Substrate temperature dependence of perpendicular (⊥) and in-plane (∥) coercivities for Co–Cr films deposited at high (70 Pa) and low (0.2 Pa) Ar pressures.

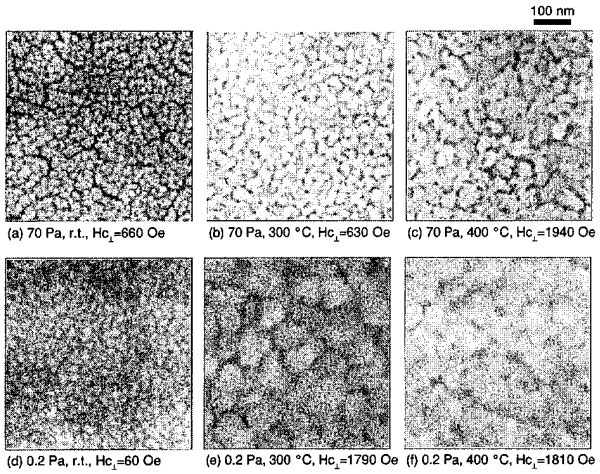


FIG. 3. SEM images of film surfaces for Co–Cr films deposited at high (70 Pa) and low (0.2 Pa) Ar pressures with different substrate temperatures.

ited only a small increase with the temperature; this may be attributed to high crystal orientations of Co–Cr layers ($\Delta\theta_{50}<5°$) which were maintained by the Ti underlayer.

A substantial increase in the saturation magnetization M_s with increasing temperature was observed for the films deposited at 70 Pa, as shown in Fig. 2. The increase of M_s is larger than that of the films deposited at 0.2 Pa. This suggests development of some Cr microsegregation in the films with the elevated temperature, although our previous study on the microsegregation in the films by using chemical etching suggested that Cr microsegregation is less in the grains.[4]

B. Microstructure

An SEM observation of the film surface, shown in Fig. 3, revealed that when the films were deposited at a high Ar pressure of 70 Pa, a channeled structure of the film deposited at room temperature [Fig. 3(a)] changed to a dense structure with distinct grain boundaries with increasing substrate temperature [Fig. 3(b)]. Further elevation of the temperature resulted in small increase in the grain size, suggesting coalescing of the grains [Fig. 3(c)]. The growth of the grains may be caused by increased mobilities of adatoms on the surface by the elevated temperature. On the other hand, films deposited at 0.2 Pa exhibited much larger grain growth with increasing temperature, but showed minute change in grain boundary structure, which still remained dense and faint [Figs. 3(d) to 3(f)].

C. Recording performances

Figure 4 shows recording density response for the Co–Cr disk samples deposited at a Ar pressure of 70 or 0.2 Pa and at the highest substrate temperature of 400 °C. Both disks exhibited the highest perpendicular coercivities at each Ar pressure. Reproduced output for the disk medium deposited at 70 Pa was higher by about 2 dB than that of the medium deposited at 0.2 Pa at the recording densities below 320 kFRPI, which corresponds to the second peak density in the response. Although the medium deposited at 70 Pa exhibited reduced output at higher densities over 400 kFRPI, the half output density for the envelope response D_{50}^{*} of as high as 250 kFRPI and the highest recordable density of over 600 kFRPI were obtained.

A small degradation in the perpendicular anisotropy of the present film may be one of the causes for the above high recording performance. The same improvement in recording

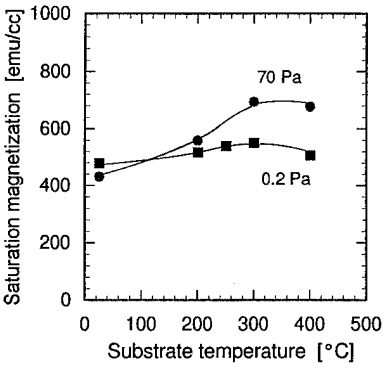


FIG. 2. Substrate temperature dependence of saturation magnetization M_s for Co–Cr films deposited at high (70 Pa) and low (0.2 Pa) Ar pressures.

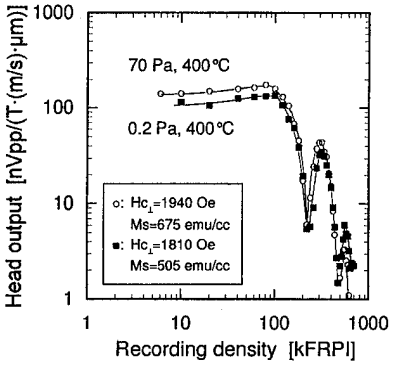


FIG. 4. Recording density dependence of normalized output for Co–Cr films deposited at high (70 Pa) and low (0.2 Pa) Ar pressures.

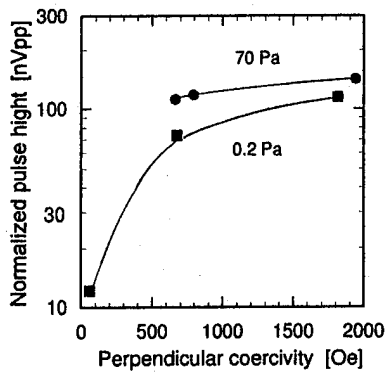


FIG. 5. Perpendicular coercivity dependence of normalized pulse height for Co–Cr films deposited at high (70 Pa) and low (0.2 Pa) Ar pressures.

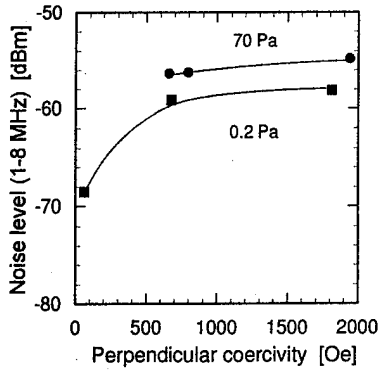


FIG. 6. Perpendicular coercivity dependence of dc erase noise level for Co–Cr films deposited at high (70 Pa) and low (0.2 Pa) Ar pressures.

performance is reported for recording on evaporated Co–Cr films with a ring head,[7] in which the increase in output is explained in terms of a small increase in in-plane anisotropy.

The isolated pulse height increased with the coercivity increase for both media deposited at the high and low Ar pressures, as shown in Fig. 5. It is also indicated that the high pressure deposited media exhibit higher output by 1–2 dB than the low pressure deposited media at the same coercivity. However, the high output property of the medium would be diminished by the higher noise level of the film, which is shown in Fig. 6 as the coercivity dependence of the dc erased noise level integrated for 1 to 8 MHz (which corresponds to the wavelength of 0.25 to 2 μm). The SEM image seen in Fig. 3 indicates smaller grain size for the film deposited at 70 Pa [Fig. 3(c)] than the film deposited at 0.2 Pa [Fig. 3(f)], suggesting lower noise level for the medium deposited at the high Ar pressure. The higher saturation magnetization M_s seen in Fig. 2 could be the cause of the increased noise level. The exact reason of the higher noise level for the media is not clear at present. Further investigation is required.

IV. SUMMARY

Co–Cr disk samples were prepared by sputter deposition at a high Ar pressure of 70 Pa with elevated substrate temperatures.

The perpendicular coercivity of the films increased from 660 to 1940 Oe with increased temperature. The high coercivity films exhibited a dense fine microstructure with distinct grain boundaries. The evaluation of the recording performance by using a ring head revealed that the high pressure deposited Co–Cr film provides a higher output by about 2 dB at densities below 320 kFRPI than the low pressure deposited film with the same high coercivity and the thickness. Although the noise level of the film could not be improved, the D_{50}^{*} of as high as 250 kFRPI and the highest recordable density of over 600 kFRPI were obtained for the film deposited at 70 Pa and at 400 °C.

ACKNOWLEDGMENTS

The authors would like to thank S. Okamoto and M. Uchida for their help in the experiment.

[1] S. Yamamoto, Y. Nakamura, and S. Iwasaki, IEEE Trans. Magn. **23**, 2070 (1987).
[2] H. Uchiyama, E. Oyanagi, and N. Honda, J. Magn. Soc. Jpn. **15-S2**, 863 (1991).
[3] H. Wakamatsu, K. Kiuchi, M. Shinohara, and Y. Miura, J. Magn. Soc. Jpn. **15-S2**, 875 (1991).
[4] N. Honda, J. Ariake, K. Ouchi, and S. Iwasaki, *Abstracts of the 6th International Conference on Magnetic Recording Media* (IOP, Oxford, 1995), Abstract BA-04.
[5] Y. Nakamura, K. Ouchi, S. Yamamoto, and I. Watanabe, IEEE Trans. Magn. **26**, 2436 (1990).
[6] N. Honda, K. Ouchi, and S. Iwasaki, J. Appl. Phys. **75**, 5984 (1994).
[7] S. Yamagata, Y. Ogawa, and O. Kitakami, J. Magn. Soc. Jpn. **15-S2**, 365 (1991).

Microwave solitons in magnetic films (invited) (abstract)

A. D. Boardman, K. Xie, and H. Mehta
Joule Laboratory, Department of Physics, University of Salford, Salford, M5 4WT, England

S. A. Nikitov
Institute of Radio Engineering and Electronics, Russian Academy of Sciences, 11 Mokhovaya St., 103907, Moscow, Russia

Nonlinear waves in the form of solitons in magnetic films are attracting attention because of the interesting possibility of making novel spatial, and temporal, soliton devices that will operate in the technologically important microwave (GHz) frequency window. Some fascinating pioneering experimental work has been performed in this area and there is now every possibility that manipulation of solitonlike microwave pulses will be the basis of an entirely new range of devices.[1] Both theory and experiment show that solitons are extremely robust and behave rather like particles. Magnetic films look set to become as successful as optical fibers in supporting bright envelope solitons; yet soliton behavior can often seem hard to comprehend. While they are subtle in their behavior they can be understood from many points of view that are physically, or mathematically, based. This presentation will explain what bright microwave envelope solitons are, drawing upon as much physical insight and analogy as possible. The necessary and sufficient conditions for soliton existence will be carefully set out, especially with respect to their relationship to the input conditions of a device. A substantial number of numerical examples will be used and the prospects for major expansion in the experimental area will be assessed. In the latter part of the presentation some important applications for solitons will be addressed. These will include the analysis of a switching device but logic devices, and various forms of pump–probe arrangements, will also be retrieved. Finally, the optimistic view that solitons in magnetic materials are now realistic tools will be expressed and the opportunities provided by dark and higher-dimensional solitons will be discussed. © *1996 American Institute of Physics.* [S0021-8979(96)68508-2]

[1] A. D. Boardman, S. A. Nikitov, K. Xie, and H. Mehta, J. Magn. Magn. Mater. **145**, 357 (1995).

Thresholds of spin wave envelope soliton formation in magnetic films with dissipation (abstract)

A. N. Slavin[a)]
Oakland University, Rochester, Michigan 48309

The nonlinear mechanism responsible for the spin wave envelope soliton formation in magnetic films from input pulses of finite duration is the four-wave process with conservation law $\omega(k_0) + \omega(k_0) = \omega(k_0 + \kappa) + \omega(k_0 - \kappa)$, $\kappa \ll k_0$. This process is also responsible for modulation instability of CW wave in a nonlinear dispersive medium and can only take place if the nonlinearity N and the dispersion D in the medium have opposite signs. In a dissipative medium this process has a finite amplitude threshold determined by the dissipation parameter γ and the effective "detuning" $\Delta\omega$ proportional to the dispersion D and the square of the modulation wave number κ,[1,2] $|\varphi|^2_{\text{th}} = [\gamma^2 + (\Delta\omega)^2/4]/|N\Delta\omega|$, hereafter referred to as Eq. (1), where $|\varphi|$ is the dimensionless wave amplitude. For the process of modulational instability of a CW wave $\Delta\omega = D\kappa^2$. For the process of soliton formation from a finite input pulse (of the duration T) $\Delta\omega = D\kappa_n^2$, where $\kappa_n = (2n-1)\pi/vT$, n is the number of solitons formed, and v is the group velocity of spin waves. Equation (1) gives a good description of the recent measurements of thresholds of spin wave envelope soliton formation in YIG films presented in Ref. 3. In particular, describes correctly the shape of the threshold curve, positions of threshold minima for the formation of one and two solitons, and explains the finite intercept on the threshold power dependence on the inverse square of the input pulse duration that was not explained in Ref. 3. © *1996 American Institute of Physics.* [S0021-8979(96)68608-9]

[a)]Supported by the NSERC of Canada and the Research Corporation.

[1] V. E. Zakharov, Zh. Prikl. Mech. Tech. Fiz. **2**, 86 (1968).
[2] V. E. Zakharov *et al.*, *Theory of Solitons* (Plenum, New York, 1984).
[3] J. M. Nash *et al.*, J. Appl. Phys. **75**, 5629 (1994).

 0021-8979/96/79(8)/5366/1/$10.00 © 1996 American Institute of Physics

Phase properties of microwave magnetic envelope dark solitons in yttrium iron garnet thin films (abstract)

J. M. Nash, P. Kabos, C. E. Patton, and R. Staudinger
Department of Physics, Colorado State University, Fort Collins, Colorado 80523

Although microwave magnetic envelope (MME) solitons in thin yttrium iron garnet (YIG) films have been studied extensively, only recently have dark MME solitons been observed.[1] For a single dark soliton, one has a carrier phase change of 180°. Reference 1 indicated such a change. However, the overall phase change for a given dark pulse experiment should be 0°. The objective of this work was to examine phase profiles in detail for the dark soliton experiment. The results show that both of the above expectations are, in fact, satisfied. The 5 GHz measurements were done with a magnetostatic wave delay line structure with a long and narrow 7.2 μm thick single crystal YIG film oriented in the surface wave configuration. A GaAs microwave switch produced 300 ns long bright pulses separated by a dark pulse with a width in the 15 ns range. The input power was 0.002–1.0 W. The output signal showed two main dark pulse features, independent of power level. At low powers, the changes in phase across both features were small. With increasing power, the phase change across the first feature showed a rapid increase while the phase change for the second feature remained small. The phase change for the first feature saturated at a large value, on the order of 200°, relative to the phase change at low power. The phase change over the entire profile was always 0°. These results show: (1) There are significant phase changes at both low and high powers in the dark pulse experiment. (2) The phase change for a dark soliton must take into account the background phase change at lower powers. (3) Only the main dark pulse feature in the output profile exhibits single dark soliton characteristics through a clearly resolved phase saturation at 180°. (4) These thresholds are on the order of 10 mW for typical strip line transducer structures, compared to 100 mW or so for bright solitons. © *1996 American Institute of Physics.* [S0021-8979(96)68708-5]

This work was supported in part by NSF Grant No. DMR-9400276 and by the U.S. Army Research Office under Grant No. DAAL03-31-G327.

[1] M. Chen, M. A. Tsankov, J. M. Nash, and C. E. Patton, Phys. Rev. Lett. **70**, 1707 (1993).
[2] A. Slavin, Digests of the INTERMAG '95 Conference, FD-10, San Antonio, April 1995.

Two-dimensional solitons in the classical Heisenberg antiferromagnet with nonmagnetic impurities

Kala Subbaraman, Craig E. Zaspel, and John E. Drumheller
Department of Physics, Montana State University, Bozeman, Montana 59717

Experimental evidence is presented for the existence of nonlinear localized spin excitations (solitons) in the classical two-dimensional Heisenberg magnet doped with nonmagnetic impurities. These solitons are shown to provide the dominant mechanism for spin relaxation in electron paramagnetic resonance linewidths immediately above the ordering temperature for layered Mn compounds with a small impurity concentration. The new gapless excitations are pinned by the nonmagnetic impurities thereby becoming topologically unstable and lower in energy than the nonlinear excitations (skyrmions) that may exist in the pure material. Concentration-dependent results preclude a spin-wave mechanism for this effect. © *1996 American Institute of Physics.* [S0021-8979(96)72308-2]

INTRODUCTION

It has been assumed that the thermodynamic quantities, such as the spin correlation functions, of lower dimensional magnets are determined by the spin wave spectrum. Recent work, however, on nonlinear excitations has shown that they have a much different effect on correlation functions than the spin waves. These effects lead to possible methods of experimentally detecting nonlinear excitations. For example, Mertens *et al.*[1] have shown that mobile vortices give rise to a central peak in the dynamic spin correlation function, and similarly, we have shown that a central peak will result from moving solitons.[2] Waldner[3,4] was the first to suggest that solitons were indirectly observed in the Arrhenius behavior, $\exp(E_s/T)$, of the temperature-dependent electron paramagnetic resonance (EPR) linewidth in layered antiferromagnets, (AFMs). It was assumed that E_s was the soliton excitation energy, but at that time there was no linewidth calculation showing that this temperature dependence should be expected.

More recently[5] we have calculated the temperature-dependent EPR linewidth due to solitons, with the result that solitons indeed dominate the dynamic spin correlation function in the classical two-dimensional (2D) AFM. This dominance is seen as an Arrhenius temperature dependence. The solitons are of the static type first predicted by Skyrme[6] and applied to the 2D magnet by Belavin and Polyakov.[7] Structurally, these excitations correspond to a mapping of the spin sphere onto the lattice sphere with a constant magnetization far from the soliton center. In this article we will report the experimental results of the effect of doping (n-propylammonium)$_2$ tetrachloro-manganese(II) (PAMC) with nonmagnetic impurities on the EPR linewidth. It is shown that owing to the lower energy, solitons pinned by the very small impurity concentrations (less than 1%) will significantly affect the temperature-dependent EPR linewidth.

EXPERIMENTAL DETAILS

EPR experiments were performed with PAMC because it is a good example of a classical isotropic 2D Heisenberg AFM.[8] This is a layered compound with $MnCl_4^{2-}$ layers well separated by a bilayer of the hydrocarbon chains, resulting in a very small interlayer to intralayer coupling ratio $J'/J \approx 10^{-5}$. The doped samples were grown by slow evaporation of a solution of propylammoniumchloride and manganese chloride and cadmium or zinc chloride in ethanol. It was noted that the Zn concentrations present in the single crystals were roughly an order of magnitude lower than the amount that went into the solution while the opposite effect was observed in the case of cadmium. Faint pink platelets were obtained with masses varying from 2 to 5 mg. The dimensions of these crystals were roughly $5\times5\times0.2$ mm^3 with the smaller dimension corresponding to the b axis. From the powder susceptibility data on pure PAMC[9] it was estimated that about 0.1% of Mn^{2+} ions are present as paramagnetic impurities. Extreme care was taken in growing the crystals since the paramagnetic impurities present were comparable to the dilution strengths. Cd concentrations were determined using atomic absorption spectroscopy while Zn concentrations were measured using gravimetric analysis. The uncertainty in the chemical analysis varies from 5% at $x=0.001$ to 25% at $x=0.01$.

RESULTS AND DISCUSSION

EPR data were obtained with an X-band spectrometer for the pure Mn compound, as well as for $(nPA)_2Mn_{1-x}Zn_xCl_4$ with $0.001<x<0.01$ and $(nPA)_2Mn_{1-x}Cd_xCl_4$ with $0.001<x<0.08$. At room temperature the compounds exhibited similar angular- and temperature-dependent ERP linewidths, with characteristics of 2D spin diffusion.[10] Lowering T from room temperature toward the AF transition the linewidth initially decreases until a minimum is reached at approximately 70 K. At temperatures near T_N ($T_N=39.2$ K) a rapid increase in linewidth ΔH is observed for all concentrations.[11] The exponential rise of ΔH as T_N is approached is the part of the data illustrating 2D soliton behavior. Figure 1 shows a plot of $\ln(\Delta H)$ vs T_N/T for the temperature range $1.2T_N \leqslant T \leqslant 1.5T_N$ for $x=0$, $x=0.004$, and $x=0.0106$ for the Zn-doped crystals. Figure 2 shows a similar plot for the Cd-doped crystals. Below $T_N/T=0.9$ the linewidths continue to broaden so severely that the measurement of ΔH becomes less certain. Linewidth measurements were made on three crystals with similar concentrations and the average E_s cal-

 0021-8979/96/79(8)/5368/3/$10.00 © 1996 American Institute of Physics

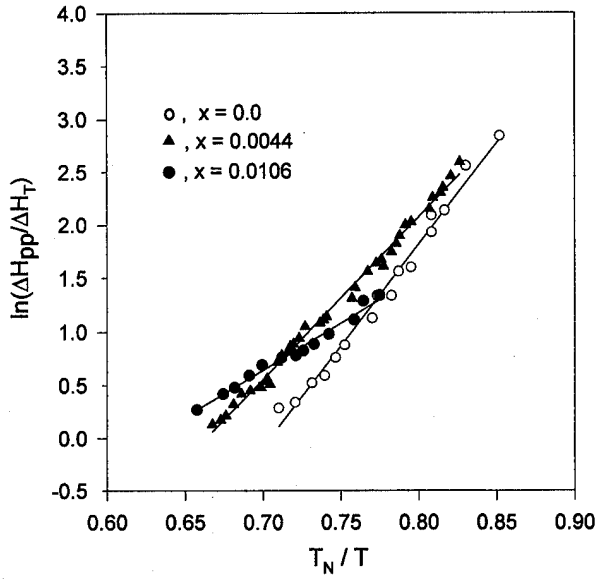


FIG. 1. Straight-line fits to the log of the linewidth vs T_N/T curves for three Zn diluted compounds yielding the soliton excitation energies as slopes. The solid line is a spline interpretation to be used as a guide for the eye. $\Delta H_T = 21$ G is the linewidth at room temperature.

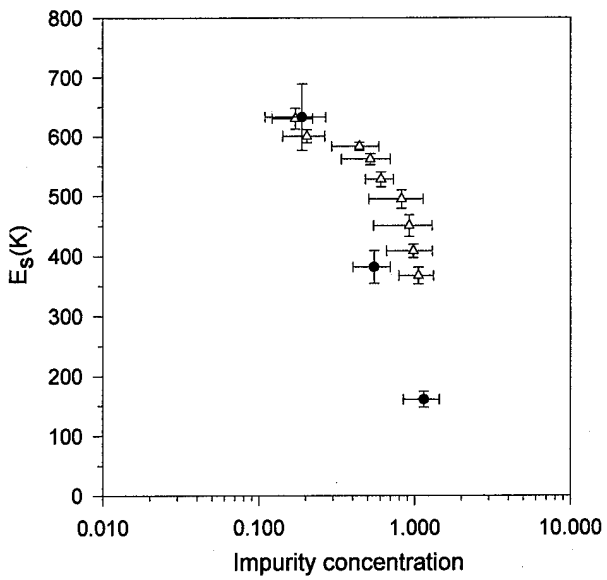


FIG. 3. The decrease of the soliton excitation energy as the percentage of impurity concentrations is increased. ○—data for Zn-doped samples, ●—data for Cd-doped samples.

culated in each case. Figure 3 is a plot of E_s vs x and shows a steady decrease in soliton excitation energy with an increase in the impurity concentration.

The ac susceptibility measurements were made on a few larger single crystals with $0.001<x<0.05$. For such low dilution strengths there was no change observed in T_N or the exchange constant J as a function of Zn or Cd concentration. This precludes the possibility of a variation in T_N causing the observed effect.

The data were compared with theoretical calculations of the excitation energy in Ref. 11. The comparison indicated a discrepancy of an order of magnitude. This disagreement is not surprising in view of the limitations of the theory presented in that article. In the magnetic vortex problem[12] it is found that the vortex structure is strongly affected by the discreteness of the lattice, especially near the core. Large solitons, in general, can be described by a continuum field, as was done in Ref. 11. For small solitons, the discreteness of the solitons becomes important at small distances from the core, and have to be taken into consideration when determining the spin dynamics.

It was also observed that the discrepancy between theory and the data is more pronounced in the case of Zn-doped crystals than the Cd-doped ones. This seems to indicate clustering effects, which will result in a larger measured x. Clustering lowers the effective concentration since a cluster may be taken to be a single site for a static excitation, and so this would enhance the observed effect if it is present in any large degree. The chemistry of the crystals, which appears to depend on the type of dopant used, is not clearly understood. Errors in the chemical procedures used to produce the dilutions are the most likely source of error, though great care was taken to avoid this situation.

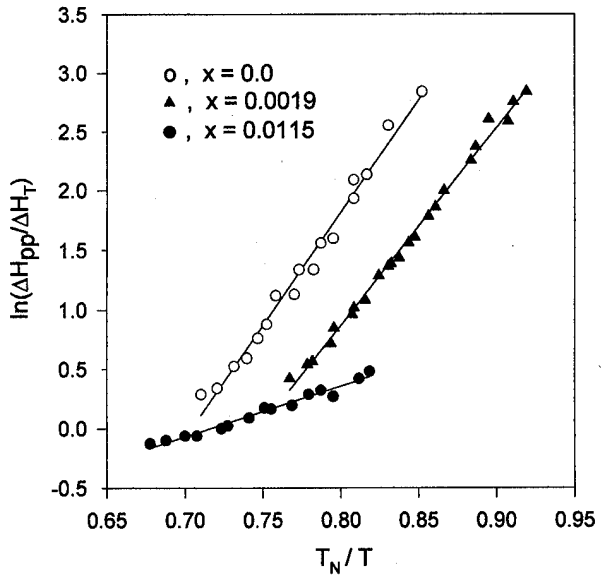


FIG. 2. Straight-line fits to the log of the linewidth vs T_N/T curves for three Cd diluted compounds yielding the soliton excitation energies as slopes. The solid line is a spline interpretation to be used as a guide for the eye. $\Delta H_T = 21$ G is the linewidth at room temperature.

CONCLUSION

Both experimental and theoretical investigations of the EPR strongly indicate the dominating role of nonlinear localized excitations in the thermodynamics of the 2D isotropic Heisenberg magnet PAMC. While the introduction of nonmagnetic impurities into such a sample has rendered the nonlinear solutions observable by creating a gapless energy spectrum,[11] there also exists a strong concentration dependence which has been used to distinguish the nonlinear effect from that of spin waves. However it is not clear how the presence of nonmagnetic impurities will affect the spin dynamics of the solitons in detail. Further theoretical work,

which includes the discrete nature of the lattice near the core, is necessary for a better understanding of the critical dynamics of the 2D magnets.

ACKNOWLEDGMENTS

This work was made possible by the financial support under NSF Grant No. DMR 93-10967. One of us, K.S. wishes to thank Dr. Ken Emerson for helpful discussions and for use of his chemistry laboratory.

[1] F. G. Mertens, A. R. Bishop, G. M. Wysin, and C. Kawabata, Phys. Rev. B **39**, 591 (1989).
[2] C. E. Zaspel, Phys. Rev. B **48**, 926 (1993).
[3] F. Waldner, J. Magn. Magn. Mater. **31–34**, 1203 (1983).
[4] F. Waldner, J. Magn. Magn. Mater. **54–57**, 873 (1986).
[5] C. E. Zaspel, T. E. Grigereit, and J. E. Drumheller, Phys. Rev. Lett. **74**, 4539 (1995).
[6] T. H. R. Skyrme, Proc. R. Soc. London **262**, 237 (1961).
[7] A. A. Belavin and A. M. Polyakov, JETP Lett. **22**, 245 (1975).
[8] L. J. De Jongh and A. R. Miedema, Adv. Phys. **23**, 1 (1974).
[9] H. A. Groenendijk, A. J. van Duyneveldt, and R. D. Willett, Physica B **98**, 53 (1979).
[10] P. M. Richards and M. B. Salamon, Phys. Rev. B **9**, 32 (1974).
[11] T. E. Grigereit, C. E. Zaspel, and J. E. Drumheller, J. Appl. Phys. **73**, 7010 (1993).
[12] G. M. Wysin, Phys. Rev. B **49**, 49 (1994).

Interaction of light with a nonlinear spin wave in a normally magnetized ferromagnetic film

A. A. Stashkevich and M. G. Cottam
Centre for Chemical Physics, University of Western Ontario, London, Ontario N6A 3K7, Canada

A. N. Slavin
Physics Department, Oakland University, Rochester, Michigan 48309-4401

A strong collinear magneto-optical interaction of guided light with an intensive forward volume spin wave (SW) has been studied in a normally magnetized film. A numerical perturbation technique has been developed to quantify the effects, which accompany the optical diffraction. Extensive numerical simulations of the magneto-optical diffraction by the SW affected by nonlinear automodulation were carried out. The parameters of interaction related to automodulation mechanisms were varied within a wide range of values, covering most practical situations. Specifically, the automodulation frequency assumed values of 1 MHz$<F<$100 MHz, and the index of phase modulation, linear in modulation instability threshold, the values of $1<v<4$. © *1996 American Institute of Physics.* [S0021-8979(96)72408-9]

INTRODUCTION

In the last decade it has been demonstrated that high efficiency can be achieved in the light–spin wave (SW) magneto-optic interactions.[1–3] Intensive SWs used in the experiments manifest strong nonlinearity,[4–6] including amplitude instability.[4] This transforms the spectrum of an initially sinusoidal SW into a multifrequency one. However, thus far theoretical work has been restricted to diffraction of light by a *linear purely sinusoidal SW.* This article addresses the analytical and numerical theory of the interaction of light with a *nonlinear multifrequency SW* in a normally magnetized film.

THEORY

First, a purely sinusoidal intensive SW is excited in a ferromagnetic film and, due to the nonlinearity, it is transformed into a multifrequency one. At the second stage, an optical waveguide mode traveling in the same film is diffracted by a phase grating induced by the now multifrequency SW medium through magneto-optical effects. These stages take place sequentially. We consider below a case when a finite amplitude sinusoidal forward volume spin wave (FVSW) is initially excited in a perpendicularly magnetized film.

We restrict attention to the case when only the four-wave interaction processes determine the nonlinear properties. Further we use the theory of four-wave SW instability developed in Ref. 7 and later applied to a ferromagnetic film.[8] As shown in Ref. 9, in the case of continuous excitation the nonlinear equation describing the SW behavior leads to the modulational instability of a monochromatic SW propagating in a film. Assuming a narrow packet of SWs (central in-plane wave vector $\mathbf{Q}_0$, central frequency ω_0, and amplitude b_0) linearly excited in a film, the conservation laws for the four-wave interaction process take the form $2\omega_0=\omega_1+\omega_2$, $2\mathbf{Q}_0=\mathbf{Q}_1+\mathbf{Q}_2$.

The instability increment ν for the above process, described by an equation of motion for the SW amplitudes of the two nonlinearly generated harmonics, is given by Refs. 7 and 10: $\nu^2=-D\kappa^2(D\kappa^2+4N|b_0|^2)/4$, where N is a coefficient of the four-wave Hamiltonian, describing nonlinear coupling between SWs. We denoted $\mathbf{Q}_1=\mathbf{Q}_0+\boldsymbol{\kappa}$ and $\mathbf{Q}_2=\mathbf{Q}_0-\boldsymbol{\kappa}$, assuming without loss of generality that $\kappa\ll Q_0$ and $\boldsymbol{\kappa}$ is collinear to $\mathbf{Q}_0$. Also a Taylor series expansion for the SW dispersion characteristic was utilized, defining $v_g=(\partial\omega_Q/\partial Q)_{Q=Q_0}$ and $D=(\partial^2\omega_Q/\partial Q^2)_{Q=Q_0}$. For a medium with dissipative parameter ω_r the squared instability increment must be larger than the square of the dissipation parameter $\nu^2\geqslant\omega_r^2$, which leads to the threshold formula:

$$|b_{n0}|^2_{\rm th}\geqslant\frac{\omega_r^2+(D\kappa^2)^2/4}{|ND|\kappa^2}. \tag{1}$$

The threshold calculated from Eq. (1) is shown in Fig. 1 by a solid line, while the broken line shows the threshold in a lossless medium. It follows that the threshold of modulational instability has a minimum value $|b_0|^2_{\rm th_{min}}=\omega_r|N|$ for the instability having the characteristic wave number $\kappa_m=(2\omega_r/|D|)^{1/2}$ and frequency $F_m=v_g\kappa_m/2\pi$.

When the minimum threshold is exceeded by the factor $\zeta=|b_0|^2/|b_0|^2_{\rm th_{min}}$, the range of possible modulation frequencies is $\zeta-(\zeta^2-1)^{1/2}<(F/F_m)^2<\zeta+(\zeta^2-1)^{1/2}$. The modulation frequency at the threshold can be easily estimated using the data[11] for a typical experiment on FVMSW in a YIG film (thickness $h=7.2$ μm), yielding $F_m=49.5$ MHz. When the supercriticality is $\zeta=2$, which corresponds to a SW power of

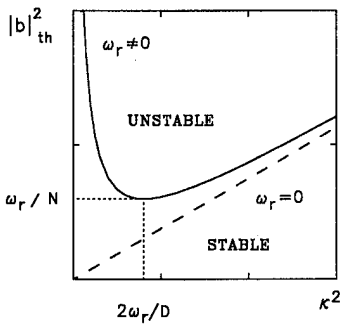


FIG. 1. Threshold of modulational instability in a dissipative medium.

 0021-8979/96/79(8)/5371/3/$10.00 © 1996 American Institute of Physics

approximately 50 mW, the possible modulation frequencies satisfy 25 MHz$<F_m<$95.5 MHz. However, the value of D can change considerably. For example, in the vicinity of a dipole-exchange gap it increases by at least one order of magnitude.[12] In our numerical simulations we therefore vary the SW automodulation frequency from 1 to 100 MHz to cover typical situations.

The optical part of the problem is as follows. A monochromatic optical waveguide mode (incident wave or zero diffraction order) is excited in the ferromagnetic film in a direction parallel to that of an intensive multifrequency SW. Due to the magneto-optic interaction the incident light wave is partially converted into an optical mode of orthogonal polarization (diffracted wave or first diffraction order). We restrict our attention to the collinear geometry which is most promising for optical frequency shifters. Such devices require high diffraction efficiency and SWs of elevated intensity.

To solve the diffraction problem we have selected the perturbation approach described in detail in Ref. 13. The amplitude in the first diffraction order is expanded as

$$A_s(\omega)=\sum_{m=0}^{\infty}(v)^m A_s^m(\omega), \tag{2}$$

where $v=\beta\Delta nL$ is the index of phase modulation. The convergence of the series (2) is discussed in detail in the next section. Here β is the light wave number *in vacuo*, Δn is the perturbation of refractive index of the film induced by the SW, and L is the interaction length.

NUMERICAL RESULTS

Our numerical simulations are consistent with a real magneto-optical experiment.[1–7] In particular, the interaction length is 5 mm. The spectral transformations resulting from our simulations are illustrated in Fig. 2. An initially excited SW is represented by just one harmonic [Fig. 2(a)]. Due to the nonlinearity of the SW, two additional harmonics are generated which describe the process of amplitude modulation. We assume that the rate of modulation, i.e., the ratio of the sideband and central frequencies, $a=0.5$ [Fig. 2(b)].

As $F\to 0$ the optical Bragg condition has no effect on the diffraction process. The perturbation approach allows us to consider the magneto-optical diffraction as a multiple-scattering process. For weak interaction (such that $v\ll 1$), the onefold scattering is predominant. In this case the optical spectrum duplicates that of a nonlinear SW without distortion. However, for $v>1$ scattering of higher multiplicity has to be taken into account. Mathematically n-fold scattering corresponds to a nonlinear operation of n-fold autoconvolution of the SW spectrum. In particular, additional harmonic multiples of F are generated. Such nonlinear spectral distortions, with the increase of v, are illustrated in Fig. 2(c)–2(f). The results in Fig. 2 are graphically indistinguishable from those for the case $F=1$ MHz. In our calculations we retained nine terms in series (2), ensuring an accuracy exceeding the graphic resolution.

With increasing F many scattering mechanisms are prohibited because of the optical Bragg condition. The effect on

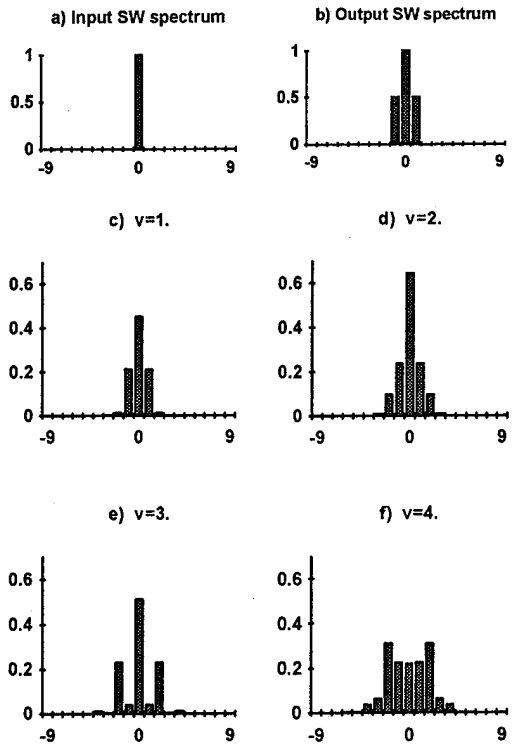


FIG. 2. Spectral transformations in the course of (a), (b) nonlinear SW automodulation; (c)–(f) magneto-optical interaction (in the $F\to 0$ limit).

the diffracted light spectrum is illustrated in Figs. 3(a), 3(b), 3(d), 3(e), 3(g), and 3(h). The horizontal scale is the multiplicity number of an optical harmonic. Figures 3(c), 3(f), and 3(i) show the amplitudes of the main optical spectral components as functions of v. Curve 0 corresponds to the zero-harmonic amplitude $A(f)$ (due to the initial monochromatic SW), curve 1 corresponds to the first-harmonic amplitude $A(f+F)$ (due to the nonlinearity of the SW system), curve

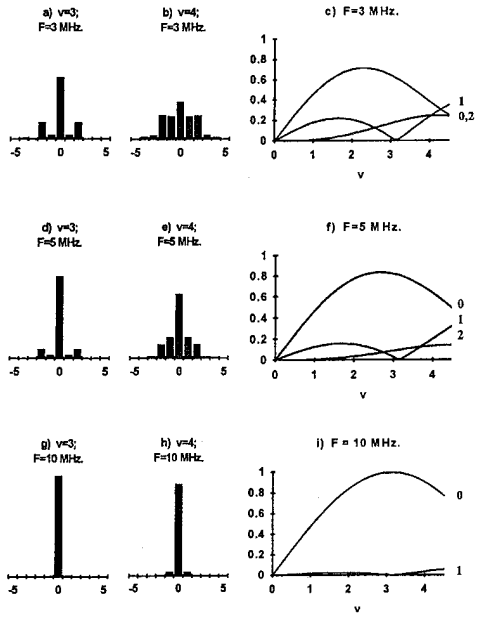


FIG. 3. Optical spectra for different values of automodulation frequency: (a)–(c) $F=3$ MHz; (d)–(f) $F=5$ MHz; (g)–(i) $F=10$ MHz.

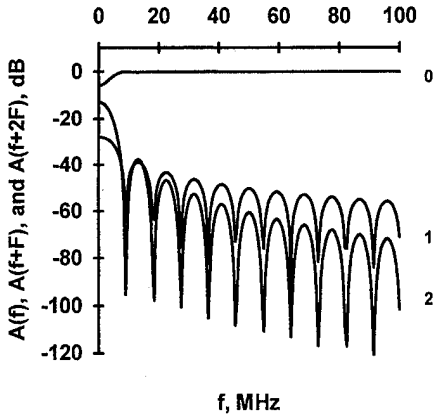


FIG. 4. Frequency performance of optical spectral components $A(0)$ (curve 0), $A(1)$ (curve 1), and $A(2)$ (curve 2).

2 corresponds to the second-harmonic amplitude $A(f+2F)$ (the first additional harmonic which is due to the nonlinear character of the diffraction distortion). With the growth of F one can concentrate almost all optical power (up to 99%) in the zero harmonic which is very important for potential applications. Also, for large values of v the additional "spurious" harmonics are still noticeable, which is equally important for optical devices. The corresponding amplitudes as a function of the nonlinear modulation frequency F are presented in Fig. 4. The value of v is chosen to be 3, i.e., in the vicinity of the point of maximum diffraction efficiency [see Figs. 3(c), 3(f), and 3(i)]. The amplitude $A(f+2F)$, which is due mainly to higher order scattering, declines more rapidly than $A(f+F)$. By adjusting v to be close to π we can minimize $A(f+F)$. However, this will have no noticeable effect on $A(f+F)$, which means that to keep the level of spurious harmonics below 60 dB we must ensure $F>60$ MHz.

The above results are presented in terms of v, which is implicitly related to the SW amplitude through the quantity Δn. With the development of new materials with elevated values of magneto-optical constants[2–4] Δn can vary significantly for identical SW amplitudes. Numerical estimates show that SW amplitude automodulation threshold levels (tens to hundreds of mW) induce Δn values in a film consistent with $1<v<4$.

CONCLUSION

When considering the interaction of guided light with an intensive SW, one should take into account the effect of the nonlinear SW automodulation and multifrequency aspects of the subsequent optical diffraction. In a normally magnetized film this can cause the generation of two spurious harmonics, which corresponds to an amplitude modulation of a FVSW with a frequency of 1 MHz $<F<100$ MHz. The perturbation approach proved to be effective in numerical simulations of the optical spectrum of the diffracted light. High accuracy is ensured, even for very strong interactions ($v\cong 3-4$), by retaining nine terms in the expansion. An increase in F minimizes the diffraction-related distortions of the optical spectrum. For a typical situation, when the rate of SW amplitude modulation $a=0.5$ the condition $F>10$ MHz ensures that over 99% of the energy will be concentrated in the zero harmonic. However, it is not easy to entirely suppress higher order harmonics. For example, it is only for $F>60$ MHz that the level of the second harmonic falls below 60 dB.

[1] H. Tamada, M. Kaneko, and T. Okamoto, J. Appl. Phys. **64**, 554 (1988).
[2] D. Young and C. S. Tsai, Appl. Phys. Lett. **55**, 2242 (1989).
[3] V. V. Matyushev, A. A. Stashkevich, and J. M. Desvignes, J. Appl. Phys. **69**, 5972 (1991).
[4] A. A. Stashkevich, B. A. Kalinikos, N. G. Kovshikov, O. G. Rutkin, A. N. Sigaev, and A. N. Ageev, Sov. Tech. Phys. Lett. **11**, 20 (1987).
[5] S. Jun, R. Marcelli, and P. De Gasperis, these proceedings.
[6] A. Probhakar and D. Stancil, these proceedings.
[7] V. S. L'vov, *Wave Turbulence under Parametric Excitation* (Springer, Berlin, 1993).
[8] A. N. Slavin and B. A. Kalinikos, Sov. Phys. Tech. Phys. **32**, 1446 (1987).
[9] B. A. Kalinikos, N. G. Kovshikov, and A. N. Slavin, Sov. Tech. Phys. Lett. **10**, 392 (1984).
[10] V. E. Zakharov, V. S. L'vov, and S. S. Starobinets, Sov. Phys. Usp. **17**, 896 (1975).
[11] M. A. Tsankov, M. Chen, and C. E. Patton, J. Appl. Phys. **76**, 4274 (1994).
[12] B. A. Kalinikos, N. G. Kovshikov, and A. N. Slavin, J. Appl. Phys. **69**, 5712 (1991).
[13] A. A. Stashkevich, in *High Frequency Processes in Magnetic Materials*, edited by G. Srinivasan and A. N. Slavin (World Scientific, Singapore, 1995).

Variations in auto-oscillation frequency at the main resonance in rectangular yttrium–iron–garnet films

A. Prabhakar
Department of Physics, Carnegie Mellon University, Pittsburgh, Pennsylvania 15213

D. D. Stancil
Electrical and Computer Engineering, Carnegie Mellon University, Pittsburgh, Pennsylvania 15213

High power microwave experiments conducted on a rectangular yttrium-iron-garnet (YIG) film indicate a parabolic dependence of the square of the frequency of auto-oscillations on microwave signal amplitudes, an observation that is qualitatively consistent with prior theoretical predictions. Forward volume magnetostatic waves were excited using a microstrip transducer kept in contact with a YIG film placed in a constant external magnetic field (H_{dc}=3.48 kG). Variations in the input microwave power (10 dBm$<P<$25 dBm) and frequency (5.1 GHz$<f<$5.7 GHz) were used to locate and study auto-oscillations close to the Suhl instability at the main resonance. A novel method of viewing changes in the microwave passband using density plots enables us to study variations in the dipole gaps in the passband near the Suhl instability. A broadening of dipole gaps into fingerlike regions of weak transmission marks the onset of auto-oscillations beyond the instability threshold. These regions are associated with a variety of spin-wave dynamics ranging from simple auto-oscillations to auto-oscillations with period doubling and in some cases an abrupt transition to a turbulent wide-band power spectrum. The parabolic dependence of the auto-oscillation frequency persists despite a period-doubling bifurcation. © *1996 American Institute of Physics.* [S0021-8979(96)72508-5]

I. INTRODUCTION

Modulational instabilities at high microwave power levels have been previously studied in thin yttrium-iron-garnet (YIG) films[1] and in YIG spheres.[2,3] These studies indicate that the frequency of auto-oscillation (AO) increases monotonically with an increase in the amplitude of the microwave signal. Using the center-manifold theory on the entire degenerate spin-wave manifold, Zhang and Suhl[4] calculated the frequency of the limit cycle associated with the AO and predicted that the square of the frequency would vary in a parabolic manner with an increase in the microwave signal amplitude. Our experimental observations on a rectangular YIG film are qualitatively consistent with these predictions. Careful measurements taken at the main resonance, close to the second Suhl instability (SI) threshold, reveal that the parabolic behavior persists even when the system undergoes a period-doubling bifurcation. However, as also noted by various authors,[2–5] depending on the exact input parameters it is possible to follow a route to chaos where the frequency of AO appears to merely increase monotonically and the spin-wave manifold undergoes an abrupt transition to turbulence without observing the parabolic behavior predicted theoretically.

The ferromagnetic resonance (FMR) measurements by McMichael and Wigen on circular YIG films[6] indicate the existence of fingerlike regions of AO associated with the standing wave magnetostatic modes in low-power FMR spectra. In our experiments on propagating waves in rectangular YIG films at high power, we observed the emergence of similarly shaped fingers that corresponded to regions of weak transmission. A wide variety of chaotic dynamics, including AO, were visible in the fingerlike regions. By monitoring the changes in the microwave passband with increases in microwave power, we note that the fingers are associated with the broadening and shifting of the dipole gaps in the passband. The use of density plots to display the data enables us to map the regions of weak transmission over a wide range of input parameters (10 dBm$<P<$25 dBm and 5.1 GHz$<f<$5.7 GHz).

II. EXPERIMENTAL RESULTS

Our experiments were carried out on a rectangular YIG film (5 mm×10 mm×7.4 μm). Separate low power FMR measurements on the film indicate a linewidth of 0.9 Oe at 9.2 GHz suggesting a decay rate of 1.27 cm^{-1}. A constant magnetic field, H_{dc}=3.48 kG, was applied perpendicular to the film plane and spin-waves were excited using a microstrip transducer in contact with the film. A second transducer, 3 mm from the first, picks up the output signal from the device and feeds it to a spectrum analyzer where the AO appear as secondary peaks surrounding the primary input frequency. The frequency of AO is calculated as the average separation between adjacent peaks in the output spectrum. Figure 1 shows the variation of the AO frequency as a function of input signal amplitude both with and without a period doubling bifurcation. The signal amplitude was calculated at the input terminals of the device after accounting for cable losses and the reflected power. The parabolic nature of the variation in frequency is qualitatively consistent with the theoretical predictions by Zhang and Suhl.[4,7] A quantitative comparison of the experimental and theoretical results would involve (a) estimating the decay constants and coupling coefficients associated with interacting modes, (b) modeling the microstrip geometry to calculate the amplitude of the rf field and (c) reformulating the center-manifold theory to in-

 0021-8979/96/79(8)/5374/3/$10.00 © 1996 American Institute of Physics

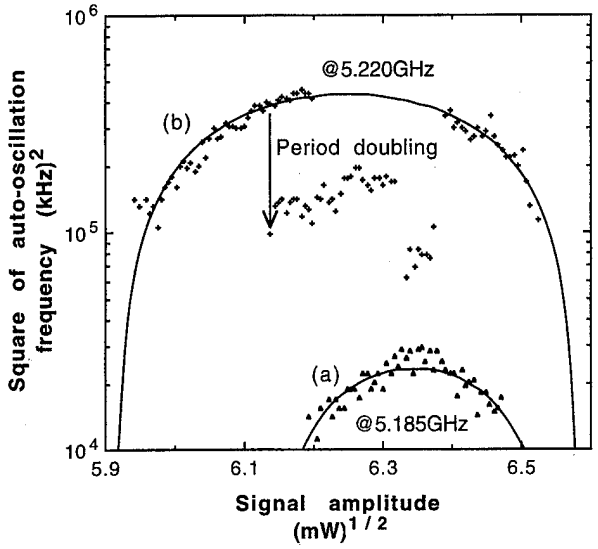


FIG. 1. Variations in the square of AO frequency with increasing microwave signal amplitudes. (a) Simple parabolic dependence and (b) parabolic dependence with a period doubling bifurcation. Both sets of data have been fit to binomial expressions to facilitate comparisons.

clude the dependence of the coupling coefficients and decay constants on the mode number, tasks that are beyond the scope of this article.

We observe a wide range of AO frequencies depending on the location of the input signal frequency in the microwave passband. As one approaches the top of the parabola, the spin-wave system attempts to follow one of various competing routes to chaos. While this attempt manifests itself as a small deviation from the parabolic behavior in the curve of Fig. 1(a), the curve of Fig. 1(b) demonstrates a case of period doubling with the formation of a limit-two cycle, where the system returns to its original limit cycle after further increases in signal amplitude. Very often, as we increase the input power, we see an abrupt transition to turbulence near the top of the parabola. Such behavior is reminiscent of attractor destruction when, as the power reaches a critical value P_c, the attractor collides with the stable manifold of an unstable periodic orbit (boundary crisis). Carroll, Pecora and Rachford[5] have reported similar observations in their experiments on YIG spheres near the first Suhl instability. They also provide a description of the overlapping basins of attraction for chaotic and nonchaotic attractors in the spin-wave system that can explain the deviations from the parabolic dependence that we sometimes observe.

A typical microwave passband measurement using a network analyzer with a device input power of −24 dBm is shown in Fig. 2. The dipole gaps in the passband are due to the pinning of spin-waves on the surfaces of the film.[8,9] Figure 2 also shows the location in the passband where the measurements in Fig. 1 were made. By replacing the network

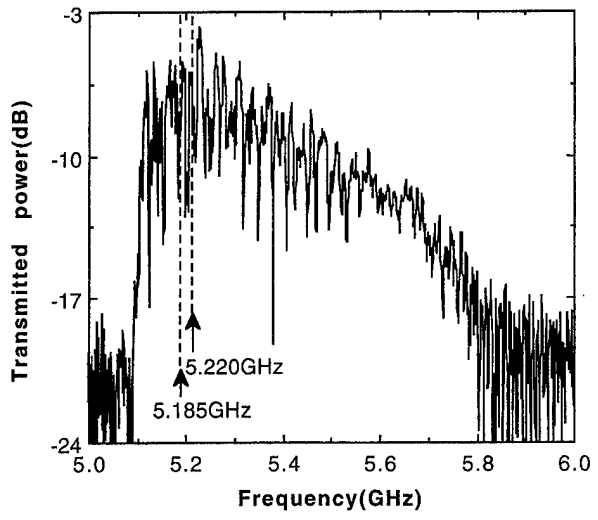


FIG. 2. Transmission characteristics of the YIG film. The passband was obtained with a device input power of −24 dBm in the presence of an external field H_{dc}=3.48 kG. The arrows mark the frequencies at which the two sets of data in Fig. 1 were taken.

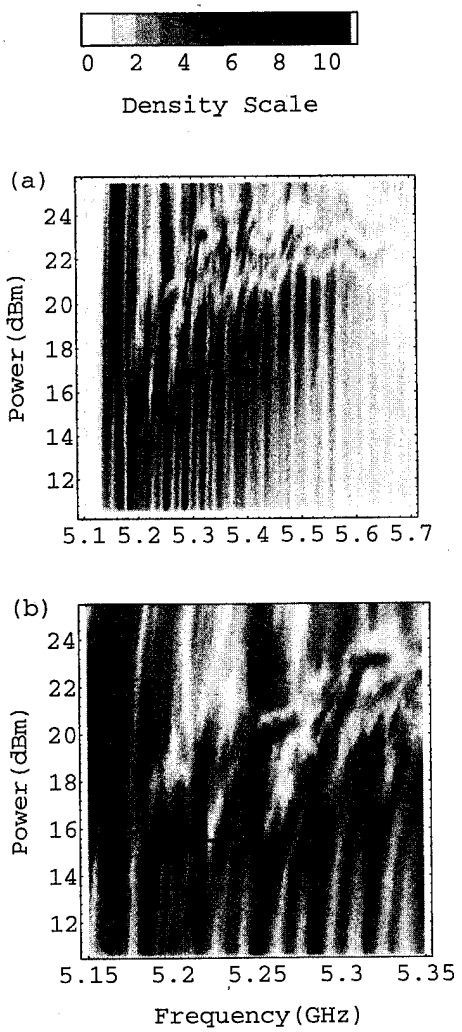


FIG. 3. (a) Density plot of the passband obtained by stepping the input power between 10 and 25 dBm in steps of 0.2 dBm. The frequency scale is accurate to within 1.2 MHz. The white areas correspond to regions of weak transmission. The density is proportional to $P_{\text{transmitted}}/P_{\text{incident}}$, normalized on a scale of 0 to 10. (b) An inset that shows the emergence of global patterns associated with weak transmission (patterns similar to the fingers of AO). The cross-hairs mark the regions where the data in Fig. 1 were obtained.

analyzer with an amplifier and a diode detector, and sending the output to a digital oscilloscope, we observe changes in the passband at much higher power levels (10 dBm $>P>$25 dBm). Figure 3 is a density plot of the passband over a region of frequency-power phase space. The density is linearly proportional to transmitted power divided by power incident on the device, with black corresponding to maximum transmission. The y-scale shows the raw incident power at the device and has not been corrected for any reflections from the input port. The dipole gaps in the passband, which at low power appear as thin white lines, eventually broaden into wider regions with weak transmission characteristics. These broad white regions reveal very complex routes to chaos while their edges approximately mark the onset of AO. Similar contiguous regions of AO have previously been referred to in the literature as fingers of AO.[6] Although the orientation of the regions of weak transmission in Fig. 3 appears to be different from that of the fingers of AO reported by McMichael and Wigen,[6] when we keep H_{dc} constant and sweep the frequency, we are actually mapping regions in phase space similar to theirs. The measurements of the AO frequency were made at the edges of the white regions, presumably in areas having fewer interacting spin-wave modes. The cross-hairs in Fig. 3(b) reveal the exact locations in phase space where the AO measurements were taken. The marked difference in the parabolic dependence seen in Fig. 1 appears to be a result of experiments conducted at different locations in parameter space, possibly in different fingers of AO. There is a shift in the bottom of the passband ($\approx$10 MHz) similar to the frequency shift observed in experiments on magnetostatic wave delay lines.[10,11] Measurements of the reflected power indicate that the waviness in the white pattern visible at high frequencies is due to reflections from the input port of the device. These reflections cause variations in the actual power coupled into the spin system. However, the broadening of dipole gaps that leads to the formation of regions of instability is a nonlinear phenomenon that does not appear in a density plot of the reflected power. The various features that appear in the density plots for transmitted power (Fig. 3) and reflected power are currently under investigation.

III. CONCLUSIONS

The onset of AO at the main resonance was observed experimentally. The square of the frequency of AO followed a parabolic dependence on the input signal amplitude in a manner consistent with theoretical predictions. The exact location in frequency-power phase space where the measurements were possible was determined using density plots of the microwave passband. It was found that the dipole gaps in the passband broaden out and shift toward higher frequencies, eventually forming wide regions of weak transmission. Since these regions are fairly rich in a variety of routes to chaos, the measurements on AO frequency were made at their edges. The parabolic dependence is observed even when the spin-wave system undergoes a period doubling bifurcation. The exact nature of the dependence varies with the location in parameter space.

The density plots of the transmitted power have revealed a global absorption pattern similar to the fingers of AO. There is also a frequency shift in the entire passband that could be a combination of thermal and nonlinear effects.

ACKNOWLEDGMENTS

We would like to express our gratitude to Dr. J. D. Adam for supplying the YIG film used in these experiments. This research was supported in part by the National Science Foundation under Grant No. ECS-9206817.

[1] B. A. Kalinikos, N. G. Kovshikov, and N. Slavin, JETP Lett. **10**, 392 (1984).
[2] P. H. Bryant and C. D. Jefferies, Phys. Rev. A **38**, 4223 (1988).
[3] F. M. Aguiar, A. Azevedo, and S. M. Rezende, J. Appl. Phys. **73**, 6825 (1993).
[4] X. Y. Zhang and H. Suhl, Phys. Rev. B **38**, 4893 (1988).
[5] T. L. Carroll, L. M. Pecora, and F. J. Rachford, Phys. Rev. Lett. **59**, 2891 (1987).
[6] R. D. McMichael and P. E. Wigen, Phys. Rev. Lett. **64**, 64 (1990).
[7] H. Suhl and X. Y. Zhang, Phys. Rev. Lett. **57**, 1480 (1986).
[8] J. D. Adam, T. W. O'Keefe, and R. W. Patterson, J. Appl. Phys. **50**, 2446 (1979).
[9] B. A. Kalinikos, N. G. Kovshikov, and A. N. Slavin, JETP **38**, 413 (1983).
[10] M. A. Tsankov, M. Chen, and C. E. Patton, HE-10, Sixth Joint MMM-Intermag Conference, Alberquerque, NM (June 1994).
[11] A. F. Cash and D. D. Stancil, HE-11, Sixth Joint MMM-Intermag Conference, Alberquerque, NM, June 1994 [IEEE Trans. Magn. (to be published)].

Driven spin-wave dynamics in yttrium–iron–garnet films (abstract)

D. J. Mar, T. L. Carroll, L. M. Pecora, J. F. Heagy, and F. J. Rachford
Naval Research Laboratory, Washington, DC 20375

Yttrium–iron–garnet (YIG) is an important component used in filters and other microwave devices. In this work we investigate the behavior of driven magnetostatic wave modes in rectangular YIG films subject to an in-plane magnetic field. Patterned slotlines and coplanar waveguides are used to drive the film at separate spatial locations with microwave (2–4 GHz) excitations corresponding to the magnetostatic wave modes. For a single excitation with sufficient power above the Suhl instability, the transmitted power through the film displays periodic low-frequency (10 kHz) auto-oscillations. As the drive amplitude is increased, these oscillations may display period-doubling, intermittency, and high-dimensional behavior, including chaos. A second microwave drive applied to the sample excites additional spin-wave modes that interact with those arising from the original excitation. These interactions result in additional low-frequency components in the observed auto-oscillations. © *1996 American Institute of Physics.*
[S0021-8979(96)68808-1]

 0021-8979/96/79(8)/5377/1/$10.00 © 1996 American Institute of Physics

Synchronization of chaos in circular yttrium iron garnet films

D. W. Peterman, M. Ye,[a] and P. E. Wigen
Department of Physics, The Ohio State University, Columbus, Ohio 43210

The results of the synchronization of two ferromagnetic resonance signals are presented. In the experiment, a thin yttrium iron garnet (YIG) film was placed in the perpendicular resonance configuration and the bias field, rf power, and frequency were chosen so that the rf absorption of the YIG sample was chaotic. A segment of this chaotic signal was stored into memory. The goal was to induce the sample to synchronize to its prerecorded output through a perturbation applied to a system parameter. The results of these synchronization experiments were predicted by a numerical model. © *1996 American Institute of Physics.* [S0021-8979(96)72608-1]

INTRODUCTION

To synchronize two chaotic signals appears to be a daunting task, since any small discrepancies in the signals are predicted to diverge rapidly. However, it has been shown theoretically that chaotic signals can be synchronized with the appropriate coupling[1–3] and chaotic synchronization has been realized in several experiments.[1,4–9] Secure communications are a possible application of the phenomenon. This report will present results of synchronization in ferromagnetic resonance (FMR) involving thin yttrium iron garnet (YIG) disks.

High power FMR studies involving YIG have a long history of experimental[10–12] and theoretical[13,14] activity in nonlinear and chaotic dynamics. For the results presented here, a YIG disk 2 mm in diameter and 1 μm was immersed in a magnetic field oriented perpendicular to the film plane. A perpendicular uniform rf pumping field at 1.2 GHz generated by a slot line structure[15] excited the magnetostatic modes in the sample. A diode detected the reflected rf fields, which allowed for the rf absorption of the sample to be determined. At low rf powers, smooth, well-defined peaks in the magnetostatic mode spectrum are observed. In circular YIG films, the magnetostatic modes take the form of Bessel functions. As the rf power is increased, certain regions of the magnetostatic spectrum develop a periodic ac absorption component (auto-oscillation) superimposed upon the dc absorption component. This ac component is due to the nonlinear dipole interactions between the magnetostatic modes in the sample. Further increasing the rf power above the auto-oscillation threshold often leads to an ac absorption displaying a bifurcation route to chaos.[10,11,13] The frequencies associated with the auto-oscillations and chaos are in the range of 0.5–10 MHz.

EXPERIMENT

In the experiment, the magnetic field and rf frequencies were chosen so that the sample absorption possessed a chaotic ac component. A segment of the chaotic FMR signal was recorded into memory. A small 20 turn coil 1.5 cm in diameter oriented parallel to the film plane was suspended 2 mm above the sample to perturb the bias magnetic field. In a previous experiment, it was found that time-delayed perturbations to the sample bias field were able to control the chaotic behavior of the YIG sample.[16] The goal of this experiment was to perturb the bias magnetic field to induce the real time signal to follow its prerecorded output.

In synchronizing FMR signals, some of the previously proposed synchronization techniques cannot be implemented due to the nature of the FMR experiment. For example, Carroll and Pecora (CP),[1] in theory and experiment, demonstrated that the decomposition of a chaotic system into coupled drive and response subsystems will synchronize if the response system has only negative Lyapunov exponents. Another method of chaotic synchronization has been proposed by Lai and Grebogi (LG).[2] Their method does not require decomposition of the system, but involves a continual complex calculation of the coupling parameter. In our FMR experiment, a uniform rf driving field couples to all the magnetostatic modes, and therefore the FMR dynamical system cannot be decomposed, as required by CP. In addition, the submicrosecond time scales in the FMR dynamics do not allow a computationally intensive parameter perturbation such as the one proposed by LG.

For these reasons, the perturbation to the bias field required to synchronize the FMR signal to its prerecorded output was proportional to the difference between the prerecorded FMR signal and real-time FMR signal,

$$\delta H_{\text{bias}} = K(V_{\text{master}} - V_{\text{slave}}). \tag{1}$$

In the above equation, V_{master} refers to the prerecorded FMR signal, V_{slave} refers to the real-time FMR signal, and K is an experimentally determined proportionality constant. This synchronization scheme is similar to the one proposed by Pyragas,[3] and has been proven successful in previous experiments.[6–9]

When the sample bias field was perturbed in accordance with Eq. (1), the difference between the master and slave signal was reduced by more than an order of magnitude. The difference between the master and slave signal was reduced to approximately the noise level in the experiment within about 10 μs. This transient behavior when the control is applied is shown in Fig. 1. In Fig. 2, a delay coordinate plot of the FMR slave signal during synchronization is presented, indicating the chaotic nature of the dynamics during synchronization. The perturbation fields required to achieve synchronization are small. In the initial transient, the perturba-

[a]Current address: Supply Tech, Inc., 1000 Campus Drive, Ann Arbor, MI 46104.

 0021-8979/96/79(8)/5378/3/$10.00 © 1996 American Institute of Physics

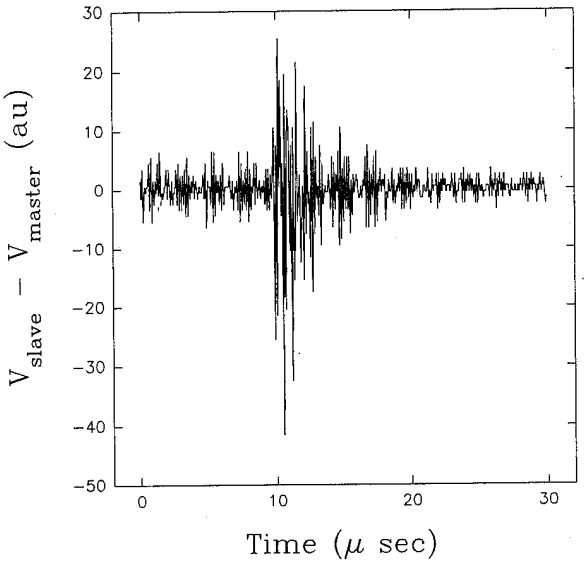


FIG. 1. The difference between the master and slave in the experiment. At $t=0$, the two signals are synchronized by the parameter perturbations. At approximately 10 μs, the stored signal loop restarts, creating a discontinuity time master signal, resulting in a divergence of the two signals. The parameter perturbation cause the signals to reconverge in about 10 μs.

tion is no greater than 1 Oe. After the initial transient, fields in the 0.01–0.1 Oe range are required to maintain the synchronization. When the synchronization control was removed, the sample dynamics instantly began to diverge from the prerecorded signal. This synchronization effect has been observed in several chaotic regions of this and other samples.

The effectiveness of the synchronization appeared to be somewhat insensitive to the proportionality constant K. While there indeed existed a window of K values in which synchronization was achievable, the upper limit of this window was often 2–4 times the value of the lower limit. Below this window, the two signals were observed to follow a pattern of nearly similar trajectories for a few microseconds interspersed by periods of divergence in the two signals. As K was increased and approached the lower bound of the synchronization window, the divergences reduced in severity

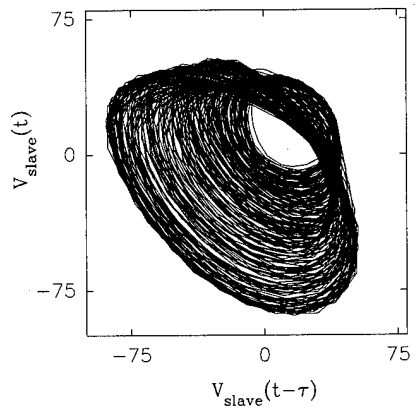


FIG. 2. Delay coordinate plot in arbitrary units of the FMR slave signal's attractor during synchronization ($\tau=50$ ns).

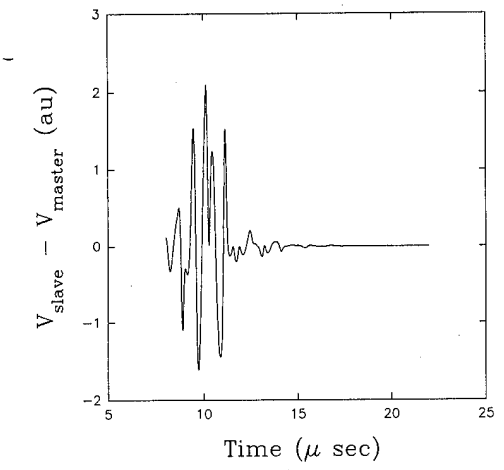


FIG. 3. Difference between the master and slave in the numerical model. The synchronization perturbations are switched on at $t=10$ μs.

and in duration. When K was increased above the upper limit of the synchronization window, the master signal was over corrected and was consistently divergent from the slave signal.

While a wide range of K values were able to maintain synchronization, the ability to synchronize the two signals was quite sensitive to differences in the experimental conditions responsible for the master and slave signals. This suggests that when the prerecorded signal and YIG sample dynamics arise from the same underlying attractor, the YIG sample is easily induced to follow its precorded output. However, when the prerecorded output and YIG sample dynamics have slightly different underlying attractors, i.e., changes in the magnetic bias field, the sample is resistant to follow the dynamics of a different attractor, even if this difference is slight.

NUMERICAL MODELING

A theoretical model of FMR developed by McMichael and Wigen[12] was used for numerical simulations of the observed synchronization. The complex magnetostatic mode amplitudes were determined by integrating the coupled nonlinear equations of motion in this model. The FMR signal in the model was proportional to the sum of the imaginary parts of the mode amplitudes, which corresponds to the rf absorption in the experiment.

To model the experimental results, the numerical parameters were chosen to lie in a chaotic regime and a chaotic time series segment of the FMR signal was captured. This stored signal corresponds to the master signal in the experiment. The simulation was run again. The FMR signal was continuously compared with a random segment of the stored chaotic time series, and the static magnetic field was perturbed proportional to this difference between the signals, as in Eq. (1). Figure 3 shows the two signals synchronize in 5–10 μs, and the difference of the signals approaches zero, in agreement with the experimental results. However, different random master segments require different transient times,

with 5–10 μs being typical. Transient times as long as 30 μs have been observed.

The numerical modeling displays a similar insensitivity to the K observed in the experiment. In addition, changes in the numerical parameters of a few percent reduce the synchronization effect by at least a factor of 10. This roughly corresponds to the high sensitivity of the synchronization scheme to differences in the underlying experimental conditions of the master and slave signals observed in the experiment.

CONCLUSION

Two chaotic FMR signals have been synchronized through a perturbation applied to a system parameter, the static bias field of the YIG sample. The perturbation is proportional to the difference between the real-time FMR signal and a prerecorded signal. The FMR signals that are synchronized possess frequency components in the 0.5–10 MHz range, making these chaotic dynamics the fastest ever synchronized to the authors' knowledge. While the dynamics of the system are well modeled, the underlying equations of motion can remain unknown in this synchronization scheme. A more quantitative and physical understanding of the dependence of the synchronization to K and to differences in the underlying master and slave attractors appears to be a promising future direction of this research.

ACKNOWLEDGMENT

The authors wish to acknowledge funding from the National Science Foundation, Grant No. DMR-9017223.

[1] L. M. Pecora and T. L. Carroll, Phys. Rev. Lett. **64**, 1196 (1990).
[2] Y. Lai and C. Grebogi, Phys. Rev. E **47**, 2357 (1993).
[3] K. Pyragas, Phys. Lett. A **181**, 201 (1993).
[4] K. M. Cuomo and A. V. Oppenheim, Phys. Rev. Lett. **71**, 65 (1993).
[5] R. Roy and K. S. Thornburg, Phys. Rev. Lett. **72**, 2009 (1994).
[6] T. C. Newell, P. M. Alsing, A. Gaurielides, and V. Kovanis, Phys. Rev. E **49**, 313 (1994).
[7] A. Kittel, K. Pyragas, and R. Richter, Phys. Rev. E **50**, 262 (1994).
[8] Y. H. Yu, K. Kwak, and T. K. Lim, Phys. Lett. A **191**, 233 (1994).
[9] D. W. Peterman, M. Ye, and P. E. Wigen, Phys. Rev. Lett. **74**, 1740 (1995).
[10] G. Gibson and C. Jeffries, Phys. Rev. A **29**, 811 (1984).
[11] F. M. de Aguiar, A. Azevedo, and S. M. Rezende, Phys. Rev. B **39**, 9448 (1989).
[12] R. McMichael and P. Wigen, Phys. Rev. Lett. **64**, 64 (1990).
[13] X. Y. Zhang and H. Suhl, Phys. Rev. B **38**, 4893 (1988).
[14] V. E. Zakharov, V. S. L'vov, and S. S. Starobinets, Sov. Phys. Usp. **17**, 896 (1975).
[15] B. Lührmann, M. Ye, H. Dötsch, and A. Gerspach, J. Magn. Magn. Mater. **96**, 237 (1991).
[16] M. Ye, D. W. Peterman, and P. E. Wigen, Phys. Lett. A **203**, 23 (1995).

Experimental observation of the longitudinal resonance mode in ferromagnets with random anisotropy

G. Suran and E. Boumaiz
Laboratoire de Magnetisme et Optique de Versailles, CNRS, Meudon 92195, France

J. Ben Youssef
LMIMS, CNRS, Meudon 92195, France

We report here the first experimental observation of the longitudinal resonance mode in ferromagnets with a wandering axis (FWA). The mode is detected in amorphous $Co_{93-x}Zr_7(RE)_x$ thin films with RE=Pr,Nd,Tb, and Dy, $0 \leqslant x \leqslant 4$, but only if the film exhibits a very well defined in-plane uniaxial anisotropy field H_k. The experimental identification and some of the main properties of the longitudinal mode are reported and compared with theoretical predictions.
© *1996 American Institute of Physics.* [S0021-8979(96)72708-8]

I. INTRODUCTION

A considerable amount of experimental and theoretical work has been performed on ferromagnets which possess a random anisotropy (FRA). One of the main questions raised was if these systems will exhibit dynamical properties the behavior of which is essentially controlled by the random anisotropy. Several theoretical suggestions were advanced,[1–3] but were not followed by experimental observations.

Here we report a completely new resonance phenomenon which can be observed only in FRA: We detected experimentally for the first time the so-called longitudinal resonance (LR) mode and for the transverse configuration, the localized transverse resonance (TR) mode. One of the chief reasons which previously prevented this experimental discovery is that these modes can be discerned only on compounds having specific properties. The structure of the article is the following: First we expound a brief theoretical review of the physics of magnetic resonance. Then the experimental data are reported and discussed. To begin we expose the properties of compounds in which the LR and TR modes could be detected, followed by the main magnetic properties of the LR mode.[4] Some of the main features of the LR and that of the uniform resonance obtained on the same sample will be compared directly. It is a highly instructive way to illustrate the peculiarities of the LR mode.

II. THEORETICAL REVIEW

The magnetic properties of an amorphous solid—which is by definition a FRA—are determined by the same two main magnetic parameters as those of crystalline solids: Exchange A and magnetic anisotropy energy. The properties reported hereafter are essentially determined by the local anisotropy constant K_l.[5] The effect of randomness upon A will be neglected. Such approximations are fairly usual in this area.

The new resonance modes have been detected on thin films which are ferromagnets with weak random anisotropy (FWRA), i.e., $H_r < H_{ex}$, $H_r = 2K_l/M_s$, $H_{ex} = 2A/M_s R_a^2$, and $R_a \approx 10$ Å is the structural correlation length. In conformity with theoretical analysis[6] a FWRA presents several magnetic regimes according to the strength of the external field H. If H is smaller than a critical field H_s, the long-range magnetic regime is destroyed and the material exhibits a correlated spin glass (CSG) regime. If $H > H_s$, the system has a significant moment with a slightly noncollinear structure, the so-called ferromagnet with wandering axis (FWA). A FWA regime is attained if the system also possesses a coherent uniaxial anisotropy.

Ferromagnetic resonance (FMR) is a well understood phenomenon in crystalline compounds. As a result of the strong exchange force the spins forming the magnetization M_s maintain a perfect parallelism when a steady field H is applied. The static equilibrium direction of M_s, M_s^{eq}, is oriented along the effective field determined by the various magnetic energies of the system, and M_s precesses coherently around M_s^{eq}. However because of the existing damping, the precession motion has to be maintained by applying a high frequency rf field $\mathbf{h}_{rf}$ perpendicular to $\mathbf{M}_s^{eq}$ with $|h_{rf}| \ll |H|$. A so-called collective (or uniform) resonance occurs when the frequency of this transverse h_{rf} is equal to the precession frequency of the system, the field for resonance being determined by the classical Kittel formula. Until now only this collective mode has been detected in amorphous systems.

Now let us consider the physics of FMR in a FRA.[2] If K_l is neglected, using the proposed approximation one finds a perfect ferromagnetic alignment of the spins along H. If K_l is considered, as this anisotropy energy does not have any preferred direction, the neighboring spins will slightly reorient themselves and will not be exactly collinear anymore. Consequently the equilibrium direction varies from site to site, so the rotation of the spin system about any axis leads to a restoring torque. One way to take into account this effect in the computation is to include a spin–space rotation angle about the magnetization vector as a dynamical variable. This hypothesis is extremely important from a conceptual point of view, because it assumes that the random anisotropy is metastable so it can change direction during the precession. It follows from the overall computation that one finds a LR[2] and a TR mode.[2]

In the LR mode the equilibrium state of M_s (M_s^{eq}) is parallel to the h_{rf} field. The condition for resonance can be expressed in terms of the longitudinal macroscopic anisotropy strength, i.e., the anisotropy associated with a uniform

rotation of the system around the axis parallel ($K_{\parallel}$) to the average magnetization. The mode is a dissipative one so it presents a peculiar relaxation mechanism.

III. EXPERIMENTAL RESULTS

A. Properties of the compounds

Among the highly different amorphous compounds which we studied by FMR until now, the LR and TR modes could be detected on amorphous $Co_{93-x}Zr_7(RE)_x$ thin films where RE=Nd,Pr,Dy,Tb and for the concentration range $0<x<4$.[7,8] The films were prepared by rf cosputtering. The Zr is incorporated in order to obtain a well-defined amorphous state even for such low RE concentration. The structure was controlled experimentally.

Moreover a necessary condition to be satisfied is that the films exhibit an in-plane anisotropy field $H_k=2K_u/M_s$. On magnetically isotropic thin films or films which display perpendicular anisotropy, the LR and TR modes could not be detected. H_k was formed by applying a dc magnetic field $H_d=700$ Oe in the film plane during deposition. The full mechanism is described elsewhere.[8]

B. LR mode: Experiments and discussion

The magnetic properties were determined by B–H loop tracer and transverse biased initial susceptibility (TBIS) measurements.[9] Whatever the RE was substituted for, the whole concentration range is 10^4 Oe$\leqslant 4\pi M_s \leqslant 1.2\times10^4$ Oe, where $4\pi M_s$ decreases for higher RE contents. These compounds are soft ferromagnets as confirmed by the small coercive field H_c, typically in the range of 0.5 Oe$\leqslant H_c \leqslant$3 Oe.[6–8]

FMR investigations were performed using a commercial 9.8 GHz spectrometer with a TE_{011} cavity. The spectra were obtained by changing the orientation of H with respect to the film plane, and also by varying the angle between h_{rf} and the easy axis. Here we report results obtained when the mode exhibits a pure longitudinal character—the case where $\theta\leqslant 10^0$. The properties of the LR mode are practically the same for the various RE substituted. The results will be illustrated by those obtained for RE=Tb.

Let us consider the case $\theta=0°$, i.e., H is applied perpendicular to the film plane (Fig. 1). On all samples one detects the collective resonance, the main properties of which were reported previously:[6] The field for resonance is typically in the range $1.4\times10^4\leqslant H_\perp \leqslant 1.6\times10^4$ Oe with $H_\perp$ decreasing with increasing RE content. The variations of the resonance linewidth $\Delta H_\perp$ are also characteristics: $\Delta H_\perp$ increases linearly as a function of increasing RE concentration and its magnitude is determined by the particular RE substituted. The properties of the collective mode are independent of the existence and/or the definition of H_k.

Apart from the collective mode another mode has been detected on a large number of samples, which can be formally identified as the LR mode. An extremely strict condition that the LR mode could observe is that the in-plane uniaxial anisotropy field H_k is very well defined. One can easily show both by computation and by experimental investigations, using TBIS or observation of the domain structure,

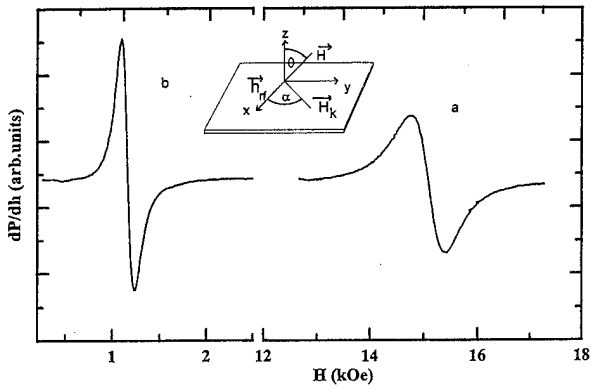


FIG. 1. Typical derivative absorption spectra with the applied dc field being perpendicular to the film plane ($H_\perp$): (a) Collective (uniform) resonance, (b) LR mode. The modes were detected with the same sensitivity. h_{rf} is parallel to the easy axis.

that the H_k imposes a FWA magnetic regime. So a necessary condition which must be satisfied so that the LR can be detectable is that the samples exhibit a FWA regime. The properties of the LR are determined by the definition of H_k which can be studied by two different techniques: Visual inspection of the $B-H$ loop along the hard axis, and quantitatively by TBIS[9] measurements: TBIS allows one to separate without any ambiguity the intrinsic fluctuations of M_s related to K_l, the so-called ripples, from the long-range dispersion of H_k, the skew.[9]

First we review the characteristics of the LR mode obtained on films where the skew as negligible. The field for resonance is $H_\perp^{LR}=1100\pm150$ Oe. $H_\perp^{LR}$ is independent of the nature, or the concentration of the RE and apparently fluctuates randomly. One has $H_\perp^{LR}\ll 4\pi M_s$, consequently the magnetization of the film lies practically in its plane (M_s comes out from the film plane with an angle of about 3°–5°), so the demagnetizing field can be considered as negligible. In these conditions one can be tempted to compare the experimental results with the theoretical formula established for a FWA with negligible demagnetizing field,[3]

$$\omega=2\gamma(H^3H_{ex})^{1/4}. \tag{1}$$

If one takes, for $H_{ex}=2.5\times10^5$ Oe, the value obtained with $A=10^{-6}$ ergs/cm^3 and $M_s=800$ emu/cm^3, the computation gives $H\approx300$ Oe. The difference between this H and $H_\perp^{LR}$ could be related to several factors: Equation (1) was not established for a thin film which possesses a H_k and the particular configuration of the experiment ($H_\perp$) could also affect the results.

Equation (1) predicts a rather unusual $H^{3/4}$ dependence of the longitudinal resonance frequency. We tried to verify it by performing measurements using a variable-frequency spectrometer. In Fig. 2 we present the magnetic field at resonance as a function of spectrometer frequency f. The observed variations are effectively extremely regular, but these data do not allow us to determine definitely if f follows a $H^{3/4}$ or a linear law versus H. H_{ex} deduced from the fitting of the $H^{3/4}$ curve is $H_{ex}=2\times10^3$ Oe, a value which is much

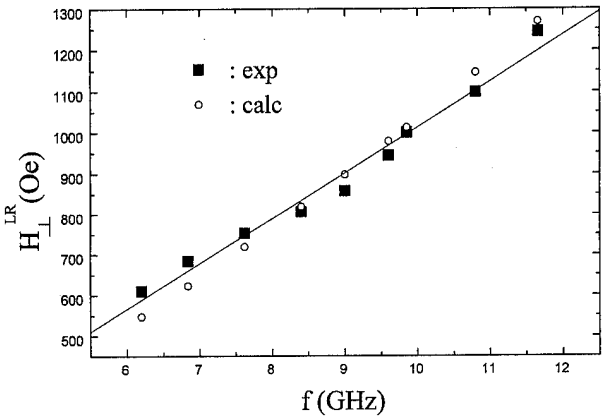


FIG. 2. Variations of the resonance field, $H_\perp$ of the LR mode vs frequency f in a typical sample. The data are compared with a linear and a $H^{3/4}$ fitting.

smaller than the expected one. $\Delta H_\perp^{LR}$ was found to be independent of f and for the reported sample it is $\Delta H_\perp^{LR}=160\pm10$ Oe.

The longitudinal nature of the mode could be proven formally by studying its variation as a function of α. While the values of the field for resonance $H_\perp^{LR}$ and that of the linewidth $\Delta H_\perp^{LR}$ are effectively strictly independent of α, the microwave power absorbed at resonance, contrary to the collective resonance, varies extremely strongly with α and follows closely the law (Fig. 3)

$$P(\alpha)=P(0)\cos^2\alpha, \tag{2}$$

where P is the absorbed microwave power and $P(0)$ corresponds to $h_{rf}\|H_k$. The magnitude of h_{rf} is fairly small. Consequently whatever the orientation of h_{rf}, M_s is practically aligned along H_k which is its equilibrium direction. One can conclude that P is maximum for $\alpha=0°$ or when $\vec{h}_{rf}\|\vec{M}^{eq}$. Therefore the mode is longitudinal. Consequently, in agreement with a computation reported elsewhere, for a linearly polarized microwave field the variations of $P(\alpha)$ vs α are given by Eq. (2). The residual value of P for $\alpha=90°$ could be related to the fact that the experiments are performed with a field applied perpendicular to the film plane.

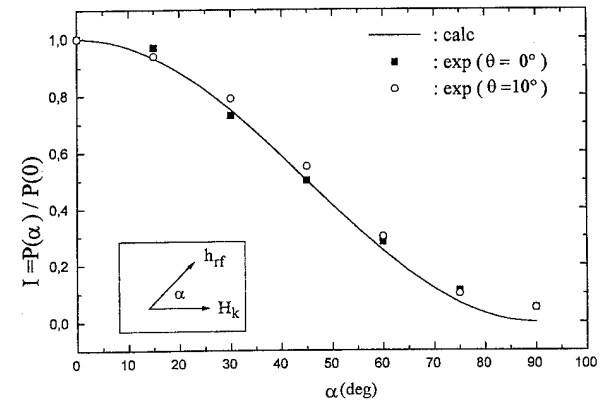


FIG. 3. Variations for $\theta=0°$ and $\theta=10°$ of the localized resonance mode intensity as a function of α. The solid line is a curve computed using the expression $I=P(\alpha)/P(0)=\cos^2\alpha$. (■,○): experimental data.

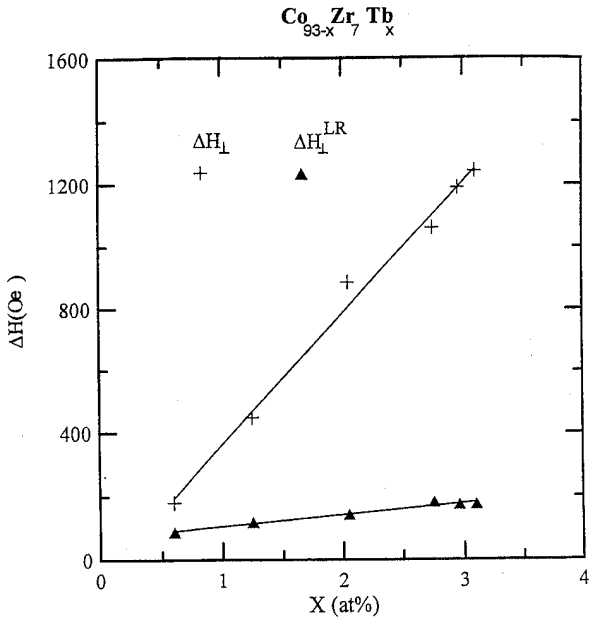


FIG. 4. Variations of the derivative resonance linewidth corresponding to the collective ($\Delta H_\perp$) and LR ($\Delta H_\perp^{LR}$) mode, respectively, as a function of Tb content.

The particular nature of the mode is also confirmed by the unusual properties of the corresponding resonance linewidth $\Delta H_\perp^{LR}$ (Fig. 4). $\Delta H_\perp^{LR}$ seems to be independent of the nature and/or the amount of the substituted RE and fluctuates in the range of 80–200 Oe. Its value appears to be essentially related to the determination of H_k, but one cannot exclude the contribution of other actually unidentified parameters. This independence of $\Delta H_\perp^{LR}$ from the magnetic properties and the concentration of the RE is a highly unusual behavior and could be related to the dissipative nature of the mode: It could be explained by the rotatable precession of the random anisotropy.

A comparison of the absorbed microwave power corresponding to the collective and LR modes, respectively, shows that, contrary to the collective mode to which all magnetic spins contribute, only a limited number of spins participate in the LR. This amount can be estimated from $N\sim I_1\Delta H_1^2/I_2\Delta H_2^2$ where I is the intensity and the suffix 1 corresponds to the LR mode. N fluctuates randomly in the range $1/20<N<1/7$. A possible hypothesis to explain this result is that only those spins contribute to the LR mode that have an easy axis oriented closely to H_K.

[1] R. Alben, J. J. Becker, and M. C. Chi, J. Appl. Phys. **49**, 1653 (1978).
[2] W. M. Saslow, Phys. Rev. Lett. **50**, 1320 (1983).
[3] W. M. Saslow, Phys. Rev. B **35**, 3454 (1987).
[4] Due to the lack of space the observations of the TR mode will be reported in a forthcoming work.
[5] For the definition of K_l see, i.e., Ref. 6.
[6] E. M. Chudnovsky, W. M. Saslow, and R. A. Serota, Phys. Rev. B **33**, 251 (1986).
[7] G. Suran, H. Ouahmane, M. Rivoire, and J. Sztern, J. Appl. Phys. **73**, 5721 (1993).
[8] G. Suran, K. Roky, J. Sztern, F. Machizaud, and J. M. Mackowski, IEEE Trans. Magn. **30**, 4770 (1994).
[9] G. Suran, H. Ouahmane, I. Iglesias, R. Rivas, J. A. Corrales, and C. Contreras, J. Appl. Phys. **76**, 1749 (1994).

Investigation of the spin-Peierls phase diagram of $CuGeO_3$: Far-infrared electron spin resonance in high field

W. Palme, G. Ambert, and J. P. Boucher
Laboratoire des Champs Magnétiques Intenses, Centre National de la Recherche Scientifique and Max-Planck Institut für Festkörperforschung, 25 Avenue des Martyrs, B 166, F-38042 Grenoble Cedex 9, France

G. Dhalenne and A. Revcolevschi
Laboratoire de Chimie des Solides, Université de Paris-Sud, batiment 414, F-91405 Orsay, France

Electron spin resonance on single crystals of the spin-Peierls compound $CuGeO_3$ has been performed in magnetic fields up to 17 T in the temperature range 1.8–20 K. Using far-infrared laser frequencies of 245 and 525 GHz we could observe resonance conditions in the three different magnetic phases, i.e., the uniform, the dimerized, and the incommensurate phases for a magnetic field applied parallel to the a axis of the crystal. So for the first time data on electron spin dynamics in the incommensurate phase are reported for fields far from the transition to the dimerised phase. Striking effects concerning the g factor, linewidth, and hysteresis are observed. © *1996 American Institute of Physics.* [S0021-8979(96)72808-4]

The phase diagram of the inorganic compound $CuGeO_3$ has recently been shown to follow rather well the predictions for a "spin-Peierls" system.[1] In such a model, three magnetic phases can be defined.[2] There is the uniform (U) phase which essentially describes the behavior of $s=1/2$ isotropic Heisenberg antiferromagnetic (AF) chains, the dimerized (D) phase observed at low temperatures, and an incommensurate (I) phase which can only be achieved in the presence of a strong magnetic field. Applying the far-infrared electron spin resonance (ESR) technique to $CuGeO_3$, we have been able to probe elementary excitations in these three different phases.

$CuGeO_3$ has an orthorhombic structure with a space group *Pbmm*. The AF chains are formed by the $S=1/2$ Cu^{2+} ions running along the c axis of the crystal. In the U phase, the exchange interaction along the chains has been assumed to be of the isotropic Heisenberg type $\mathbf{H}=J_c\ \Sigma_i \mathbf{S}_i\mathbf{S}_{i+1}$ with $J_c\sim 100$ K.[1] In the D phase, interchain couplings along the b and a axes have also been evaluated, yielding $J_b\sim 10$ K and $J_a\sim -1$ K, respectively.[3] Concerning its magnetic properties, $CuGeO_3$ can be regarded as a quasi-one-dimensional spin system. Samples used in the present study were grown from the melt by a floating zone technique.[4] The phase diagram for such a crystal is shown in Fig. 1 for a magnetic field (H) applied along the a direction. This diagram has been determined from magnetization (M) measurements, the points corresponding to maxima in the susceptibility $\chi\sim\partial M/\partial H$.[5] In zero field, the lattice dimerization is seen to occur at $T_{sp}\sim 14$ K and the critical field H_c, which determines the first-order transition between the D and I phases, is $H_c\sim 12.5$ T. All these results agree well with the determination made initially by Hase *et al.*[6] The electron spin resonance (ESR) measurements to be discussed below were obtained also for H applied parallel to the a axis. The resonance conditions were achieved by transmitting electromagnetic waves—provided by an infrared laser—through the sample in Faraday geometry and by sweeping the magnetic field. In the present work, very thin crystals (about 0.2 mm in the a direction) have been used in order to avoid possible artefacts due to interference effects which can occur when the wavelength of the transmitted light becomes smaller than the thickness of the sample. This could well explain the differences we observed with previous results. In particular, unlike what was reported in Ref. 7 for the D phase, no additional structure in the ESR line—see Figs. 1 and 2 in Ref. 7—is now observed when the temperature is increased. With such a thin crystal, we always found a single resonance line in the temperature range 4.2–20 K, and for fields up to 17 T.

The temperature dependence of the integrated intensity (I) of the ESR absorption allows one to distinguish ground state excitations from transitions between excited states. In the latter case, the observed behavior has to be compared with the temperature dependence calculated for a population difference between the initial and final states governed by Boltzmann statistics for instance. Finally, a fitting procedure of such a model with the data can provide an evaluation of the gap value between the ground state and the initial state of the transition. For the ESR absorption observed at 245 GHz/8.1 T, we extended the previous investigation presented in Ref. 7 down to 1.8 K. Figure 2 shows the experimental values of I and the result of the fitting procedure (the solid line). With this procedure the gap in zero field is evaluated to be $\Delta=23.5$ K in excellent agreement with neutron data.[3] In Fig. 2, the deviation observed between the data and the curve above 7 K can be attributed to the renormalization of the energy gap as $T\rightarrow T_{sp}$, which for this field value is $T_{sp}\sim 13$ K. Above T_{sp}, i.e., in the U phase, the ESR line is expected to have a different origin. It results from transitions from the ground state and can be considered as describing the "uniform" mode of the continuum of excitations known to characterize Heisenberg AF chains. Remarkably, no drastic change in shape and position of the ESR line is observed at the transition between the D and U phases. This is clearly seen in Figs. 3(a) and 3(b), where the ESR linewidth (ΔH) and the g factor of the 245 GHz/8.1 T resonance are given as a function of temperature. For ΔH (full width at half-maximum) a minimum is observed at about 7 K, as already reported in Ref. 8 for the neighboring frequency of 232.3 K. However, compared to that work, the values that we obtained for ΔH are appreciably smaller, $\Delta H\sim 22.5$ mT at 20 K, against $\Delta H\sim 50$ mT in Ref. 8. Similarly, important differ-

 0021-8979/96/79(8)/5384/3/$10.00 © 1996 American Institute of Physics

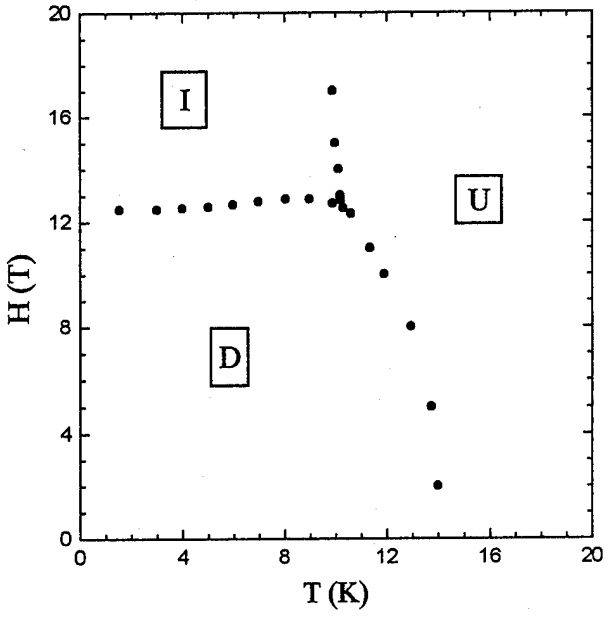


FIG. 1. Phase diagram of $CuGeO_3$, for H parallel to the a axis of the crystal, defining the uniform (U), the dimerized (D), and the incommensurate (I) phases.

ences are also obtained for the g factor. Between 20 and 5 K, the observed decrease of g is of the order 0.2% five times less than in Ref. 8. These important differences might be due to the fact that all the measurements reported in the present work have been performed on very thin crystals. Finally it is worth mentioning the change in the variation of g which occurs at low temperature: below 5 K, surprisingly g starts to increase again.

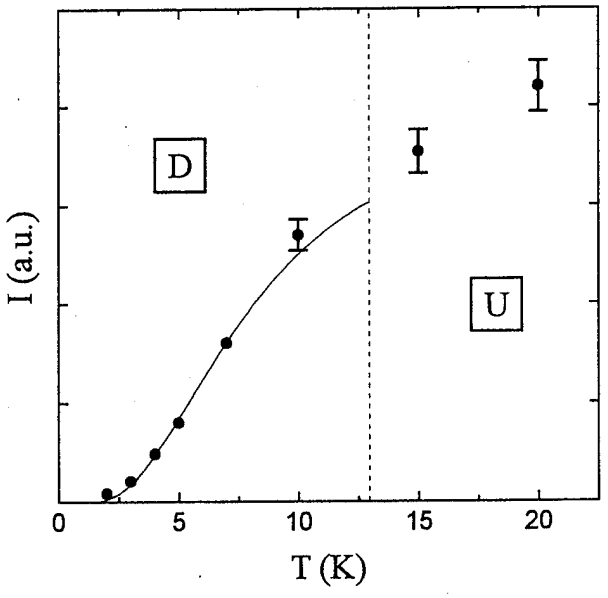


FIG. 2. Integrated intensity (I) of the ESR absorption spectra for the 245 GHz/8.1 T resonance as a function of temperature. The solid line is a theoretical curve according to Boltzmann statistics (see the text).

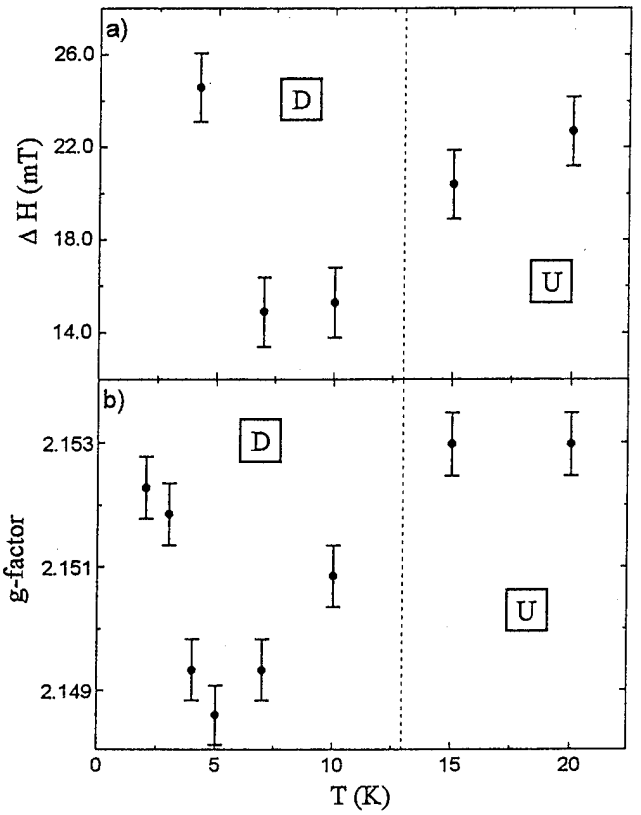


FIG. 3. The linewidth ΔH and g factor of the 245 GHz/8.1 T resonance as a function of temperature.

In the U phase, the application of a strong magnetic field results essentially in a broadening of the linewidth. This is easily seen by comparing the two resonances—245 GHz/8.1 T and 525 GHz/17.4 T. At 8.1 T, between 15 and 20 K, the g factor and the linewidth stay almost constant [see Figs. 3(a) and 3(b)]. For 17.4 T the g factor is the same as for 8.1 T, but the linewidth is strongly increased: $\Delta H \sim 58$ mT at 17.4 T, compared to $\Delta H \sim 20$ mT at 8.1 T. The interesting point now is to follow the ESR line through the transition between the U and I phases, and to explore the I phase. Figure 4 shows the ESR spectra obtained at $H \sim 17$ T. Due to a field modulation technique, the recorded signals correspond to derivatives of transmission spectra. Signal 4(a) was obtained at 16 K, i.e., in the U phase, signal 4(b) at 10 K which is practically the spin-Peierls temperature for that field value, and signal 4(c) at 8 K, i.e., in the I phase. Except for a small narrowing, no drastic change is seen on the ESR line when one goes from the U phase to the I phase. However, lowering the temperature below ~7 K, i.e., going further in the I phase, a remarkable hysteresis effect is observed. As shown in 4(d), the ESR line now depends drastically on whether the transmission spectrum (the frequency of the electromagnetic wave is constant) is taken with increasing or decreasing field.

The changes concern the line shape, the linewidth, and the line position. For the 525 GHz/17.4 T resonance at $T=4.2$ K, the linewidths are $\Delta H \sim 62$ mT for fields going up (solid line) and $\Delta H \sim 55$ mT for fields going down (broken line). The hysteresis effect is also seen on the center of the

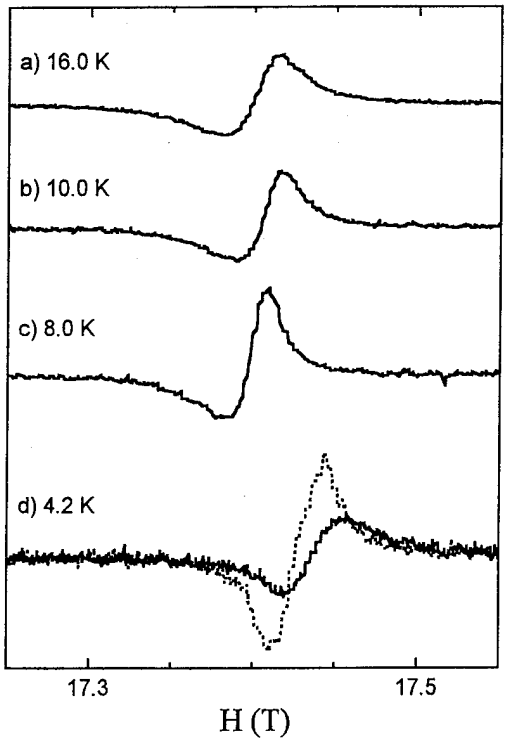


FIG. 4. Derivatives of transmission spectra recorded at the fixed frequency of 525 GHz, for different temperatures. At 4.2 K, the hysteresis effect is clearly observed: the solid and broken lines correspond to increasing and decreasing fields, respectively.

line which is shifted by about 100 G ($\Delta g/g \sim 0.06\%$). Finally, at such high fields, we observed that the integrated intensity increases when the temperature is lowered. This result suggests that, in the I phase, the ESR line corresponds to transitions induced from the ground state.

As shown in the present work, the high field far-infrared (ESR) technique allows us to probe the spin dynamics in the different phases of the spin-Peierls system $CuGeO_3$. We have shown that at such high frequencies, the size of the sample might be a crucial point. The features described here are certainly more reliable, in particular with respect to their quantitative evaluation. In the D phase, two types of transitions can be observed, from the ground state and between excited states associated with the triplet of the spin-Peierls gap.[7] For that case, the variation observed in the g factor is worth noting. It can be attributed to slight changes in the lattice structure. This can be well understood at T_{sp} where the lattice is known to dimerize. However, the new increase observed at low T is more surprising: it shows that the lattice of $CuGeO_3$ is very sensitive to thermal effects even in the D phase. In the U phase, the ESR signal is attributed to an elementary excitation of the spin system. The linewidth is strongly field dependent. Is this effect related to the magnetic incommensurability which is predicted to develop in Heisenberg AF chains in a field?[9] In the I phase, we have shown for the first time that, even far from the $D-I$ transition, hysteretic behaviors can be observed. A more complete analysis of this remarkable effect has to be done. Anyhow, it shows that, in the I phase, the crystallographic structure of $CuGeO_3$ is also very sensitive to the applied magnetic field.

Partial financial support by the New Energy Development Organization is gratefully acknowledged.

[1] M. Hase, I. Terasaki, and K. Uchinokura, Phys. Rev. Lett. **70**, 3651 (1993).
[2] D. Bloch, J. Voiron, and L. J. De Jongh, Proceedings of the International Symposium on High Magnetism, edited by M. Date (unpublished), p. 19.
[3] M. Nishi, O. Fujita, and J. Akimitsu, Phys. Rev. B **50**, 6508 (1994); L. P. Regnault, M. Aïn, B. Hennion, G. Dhalenne, and A. Revcolevschi, Phys. Rev. B (to appear).
[4] A. Revcolevschi and R. Collonges, C. R. Acad. Sci. **366**, 1767 (1969).
[5] Hans van Tol, T. Brill, J. Voiron, J. P. Boucher, G. Dhalenne, and A. Revcolevschi (unpublished).
[6] M. Hase, I. Terasaki, K. Uchinokara, M. Togunaka, N. Miura, and H. Obara, Phys. Rev. B **48**, 9616 (1993).
[7] T. M. Brill, J. P. Boucher, J. Voiron, G. Dhalenne, A. Revcolevschi, and J. P. Renard, Phys. Rev. Lett. **73**, 1545 (1995).
[8] H. Otha, S. Imagawa, H. Ushiromaya, M. Motokawa, O. Fujita, and J. Akimitsu, J. Phys. Soc. Jpn. **63**, 2870 (1994); H. Otha, S. Imagawa, Y. Yamamoto, M. Motokawa, O. Fujita, and J. Akimitsu, J. Magn. Mater. **140–144**, 1685 (1995).
[9] G. Müller, H. Thomas, H. Beck, and J. C. Bonner, Phys. Rev. B **24**, 1429 (1981).

Magnetic anisotropies in thick body centered cubic Co

X. Liu, R. L. Stamps, and R. Sooryakumar
Department of Physics, The Ohio State University, Columbus, Ohio 43210

G. A. Prinz
Naval Research Laboratory, Washington, D. C. 20375

Magnetic anisotropies of a 357-Å-thick Co film in the bcc phase were examined using Brillouin light scattering. This film, one of the thickest known bcc Co structures, is found to have a fourfold magnetic anisotropy that is markedly different from those of thinner films. A large possibly strain-induced uniaxial anisotropy is also found. The film is thick enough so that the surface and $n=1$ bulk magnon are within a few GHz of each other and strongly hybridize. Unusual behavior of the scattering intensities suggest the possible presence of surface anisotropies and/or inhomogeneous internal fields. © *1996 American Institute of Physics.* [S0021-8979(96)72908-0]

Stabilization of fcc and bcc phases of Co can be accomplished by epitaxial growth on suitably chosen substrates.[1,2] The bcc structure is interesting because it is predicted to be a true metastable state having a large exchange splitting between majority and minority spin bands.[3] Experimental determination of magnetic properties in bcc Co films therefore provide useful data for comparison to theoretical models. Also, in a true metastable phase the lattice constant should be independent of film thickness with no distortions of the crystal due to competition between the bulk and interfacial strain energies. The magnetic properties should then be uniform throughout the film, although they may differ from those of the bulk material. In this article we present measurements of anisotropies in a thick bcc Co (357 Å) film, one of the thickest known bcc Co structures, and discuss possibilities for inhomogeneities in the internal effective fields.

At present, theoretical work on magnetic properties has concentrated on exchange splittings and magnetic moments[4,5] with calculations of magnetic anisotropies reviewed in Ref. 6. From the experimental side, large uniaxial anisotropies have been observed in a 202-Å-thick bcc Co (110) film.[7] This is surprising in that the cubic symmetry of the bcc lattice suggests that the lowest order magnetocrystalline anisotropies should have fourfold symmetry. In a previous paper[7] we used measured values for elastic constants to argue for a magnetoelastic origin of the uniaxial anisotropies in this 202-Å-thick bcc Co film. A fourfold anisotropy was not observed in this film although a small negative fourfold anisotropy was found in a (100) grown bcc Co film.[7] Our present results for the 357 Å bcc film indicate a larger negative fourfold anisotropy in addition to a large uniaxial anisotropy.

The sample was a single-crystal 357 Å film of bcc Co grown on GaAs (110) by molecular beam epitaxy.[1] The bcc structure was confirmed by x-ray diffraction and extended x-ray-absorption fine structure studies.[8] Brillouin spectra were taken in backscattering with 5145 Å laser light using the same setup as described in Ref. 7. The angle of incidence was 30°. The specimen was rotated in order to change the orientation of the applied field (H_0) relative to the crystal axes so that the plane of incidence was always normal to the direction of H_0. The magnetization of the film was determined with a superconducting quantum interference device magnetometer.

The theory used to fit the Brillouin data is discussed in detail in Refs. 9–11 and is a generalization of the work by Camley and Mills[9] to include anisotropies and arbitrary in-plane orientations of the magnetization with respect to H_0. In brief, a free energy containing the Zeeman energy of the static magnetization M_s in field H_0, a uniaxial in-plane anisotropy energy K_u, a uniaxial out-of-plane anisotropy energy K_p, and a fourfold anisotropy energy K_1 is minimized to determine the equilibrium orientation of M_s. For the (110) film, the free energy has the form[12]

$$E^{(110)} = -H_0 M_s \sin\theta \cos(\phi_H - \phi) + \frac{K_1}{4}\left\{\cos^4\theta + \sin^4\theta[\sin^4\phi + \sin^2(2\phi)] + \sin^2(2\theta) \times\left(\cos^2\phi - \frac{1}{2}\sin^2\phi\right)\right\} - K_u \sin^2\theta\cos^2\phi + K_p\cos^2\theta + 2\pi M_s\cos^2\theta,$$

where θ and ϕ are equilibrium angles of M_s measured with respect to the film normal and the [001] axis, respectively. ϕ_H is the angle of H_0 measured with respect to [001]. The frequencies for the spin waves are found in the long wavelength limit from torque equations[9] constructed using the above energy and linearized with respect to small fluctuations about the equilibrium orientation. The magnetostatic limit is assumed and exchange interactions are accounted for via an effective field $(2A/M_s^2)\nabla^2\mathbf{m}$ where A is the exchange constant. Plane wave solutions are assumed with an in-plane wave vector $k_\parallel$. The perpendicular wave vectors are determined from the equation of motion together with exchange and electromagnetic boundary conditions.

Spin wave frequencies and scattering intensities were measured in three different series of experiments: as a function of field along an easy direction [001]; as a function of field along a hard direction [$\bar{1}$10]; and as a function of orientation angle ϕ_H at fixed applied magnetic field strength. The surface and two lowest order bulk modes referred to as "S", "B_1", and "B_2" were visible for this film thickness. Magnetization measurements gave the value 14.3 kG for

 0021-8979/96/79(8)/5387/3/$10.00 © 1996 American Institute of Physics

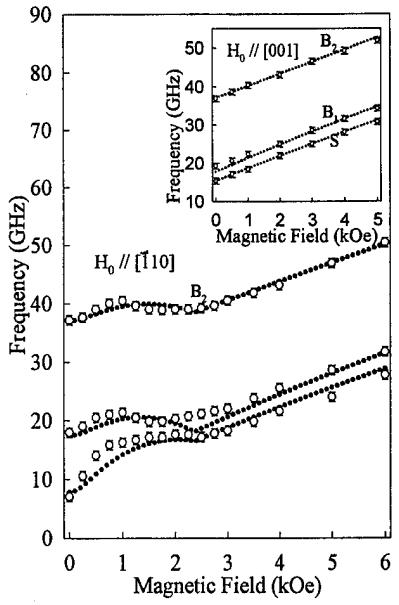


FIG. 1. Magnetic field (H_0) dependence of spin wave frequencies (S, B_1, and B_2). The frequencies of modes when H_0 is along the hard axis [$\bar{1}$10] are shown and the inset shows when H_0 is parallel to the easy axis [100]. The 5145 Å radiation was backscattered at an angle of incidence of 30° in both cases. The dotted lines are fits to the data.

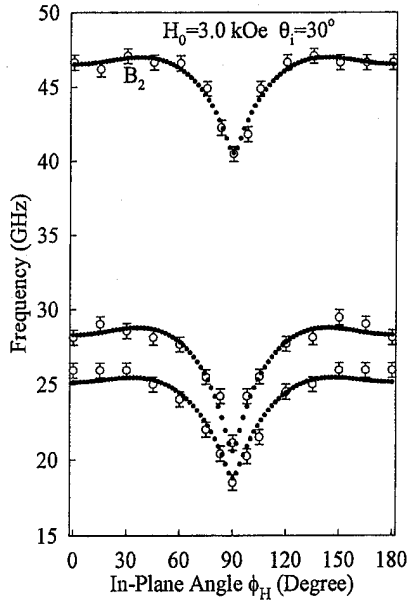


FIG. 2. In-plane angular dependence ϕ_H of the surface and two lowest bulk spin waves. The applied magnetic field is 3.0 kOe and the angle of incidence is 30°. The dotted lines are fits to the data using $K_1=-4.5\times10^5$ ergs/cm^3, $K_u=9.0\times10^5$ ergs/cm^3, $K_p=-22\times10^5$ ergs/cm^3, $g=2.1$, and $A=1.4\times10^{-6}$ ergs/cm.

$4\pi M_S$, and was used in our fits. The exchange constant A, gyromagnetic ratio g, and anisotropies K_u, K_p, and K_1 were chosen to provide the best fits to all the data. Each parameter controls a different aspect of the spin wave frequencies and the individual effect of each parameter can to a large extent be identified in the experiments. For example, the quantity A controls the frequency difference between the B_1 and B_2 modes. For this M_S, A was found to be 1.4×10^{-6} ergs/cm.

Spin wave (S, B_1, B_2) frequencies as a function of H_0 applied in the [001] direction are shown in the inset of Fig. 1. The frequencies increase approximately linearly with field. The dotted lines are calculated fits using the analysis described above. The slope is controlled by the gyromagnetic ratio g. We used the value 2.1 which also reproduces the slope at high fields for the data shown in the main Fig. 1 where H_0 is now along [$\bar{1}$10]. The low field structure in Fig. 1 is due to the rotation of the magnetization away from the easy direction [001]. The magnetization is entirely along the hard direction for field strengths greater than 2.4 kOe. This is also consistent with the saturation field found from hysterisis loop measurements.[1] The saturation field coincides with a slight dip in the spin wave frequencies in Fig. 1. The magnitude of this field equals $2(K_u-K_1)/M_s$.

In Fig. 2, the spin wave frequencies are shown as a function of ϕ_H with an applied field of 3.0 kOe which is sufficient to yield saturation in the hard direction at $\phi_H=90°$. The appearance of the crystalline anisotropy is evident in the structure of the data near 90°. The best fit to Figs. 1 and 2 (solid dots) obtained with simultaneous adjustment of parameters K_1, K_p, K_u, g, and A gave $K_1=-4.5\times10^5$ ergs/cm^3 while the value for the uniaxial anisotropy K_u is 9.0×10^5 ergs/cm^3. A negative K_1 places its easy axes along [$\bar{1}$11]. For the (110) surface, a [$\bar{1}$11] direction is at $\phi_H=55°$. Since K_1 is a fourth-order anisotropy, M_s would prefer to stay near the [$\bar{1}$11] direction even for ϕ_H fairly far from 55°. This leads to the sharp narrow dip at $\phi_H=90°$ as M_s finally moves closer toward the field direction when H_0 is within about 15° of the [$\bar{1}$10] axis. With these two anisotropy constants (K_1,K_u), the calculated saturation field $2(K_u-K_1)/M_s$ is 2.37 kOe, which agrees well with the dip in Fig. 1 and hysterisis measurements.[1] Once A, K_1, and K_u were determined, we found that $K_p=-22\times10^5$ ergs/cm^3 gave good agreement for all experiments.

Inspection of Figs. 1 and 2 show that there is good agreement between the frequency data and theory using the values for the anisotropies and exchange given above. The values determined for the uniaxial anisotropies are consistent with those measured in thinner bcc Co films and with estimates based on magnetoelastic effects.[7] The fourfold K_1 anisotropy is roughly twice that found in a 216 Å (100) film.[7] A fourfold anisotropy is consistent with the cubic symmetry of the bcc crystal and may therefore be magnetocrystalline in origin.

A problem however appears when we examine the measured light scattering intensities. Intensities for the magnons vs ϕ_H measurements are shown in Fig. 3. The strongest intensity peaks are labeled by S and are normally due to scattering from surface magnons. Therefore the peak B_1 is assigned to the lowest order bulk mode. Note that frequencies of S and B_1 peaks are very close for this film thickness, which means that hybridization between them may be significant.

The problem mentioned above is that based on the observed intensities modes S and B_1 appear to cross between

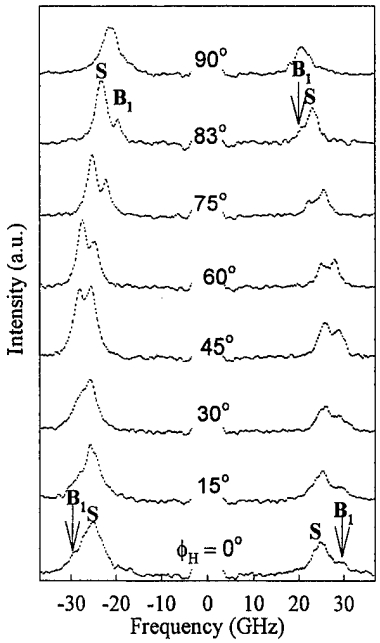


FIG. 3. Brillouin spectra showing the in-plane angular (ϕ_H) dependence at a fixed field of 3.0 kOe. The strong features are labeled as "S" for surface spin wave and the weak features as "$B1$" for the lowest order bulk mode. The incident power was about 100 mW with total accumulation time per spectrum of about 1 h.

ϕ_H=50° and ϕ_H=80° in Fig. 3. A possible mode crossing is also suggested by experimental data in Fig. 1 at 1.9 kOe. However the calculated mode profiles using the parameters determined above do not show such a crossing.[13] Instead the mode profile calculations predict that the surface mode remains the lowest frequency peak for all ϕ_H as shown by the fits in Fig. 2. If mode crossing is present, then a gap (small but not significantly smaller than 2 GHz) in the frequencies as the modes cross should exist.[14] In addition if there is crossing, from the data in Fig. 2, it would follow that the surface mode must be less strongly influenced by the anisotropies than the bulk modes. This could happen when surface anisotropies are introduced to "pin" the bulk modes.[13] However, including a single simple surface anisotropy still could not reproduce the mode behavior shown in Fig. 2 since the data require that the repulsion take place over a large range of orientation angles $50° \leqslant \phi_H \leqslant 80°$. The surface anisotropy represents differences between effective internal fields at the very surface and the bulk fields; a distribution of surface anisotropies would be required to produce a repulsion similar to that suggested by the data. This would mean the existence of a distribution of inhomogeneities in the internal effective magnetic fields that may extend over several atomic layers near the film surface. Evidence for variation of M_s with depth has, in fact, been reported in a thin bcc Co film grown on GaAs.[15] It is noted however that in this particular bcc Co film where S and B_1 are strongly hybridized it is important that, in addition to the mode profiles considered here, the scattering cross sections of the spin waves be considered in making the assignment of the magnon peaks. This is underway and will be published elsewhere.[13]

In summary, we have examined in detail the magnetic anisotropies of a 357-Å-thick bcc Co film using Brillouin light scattering. An in-plane uniaxial anisotropies (K_u) with the easy axis along the [001] direction and an out-of-plane uniaxial anisotropy (K_p) were found with magnitudes and signs in agreement with those of thinner bcc Co films. An additional fourfold anisotropy (K_1) was determined by measuring spin wave frequencies with H_0 noncollinear with M_s. This anisotropy was much larger than that measured in thinner bcc Co films. Finally, examination of the spin wave frequencies and measured relative light scattering intensities suggest the existence of surface anisotropies and/or nonuniform internal fields.

Work at OSU was supported by the NSF and that at NRL by the Office of Naval Research.

[1] G. A. Prinz, Phys. Rev. Lett. **54**, 1051 (1985).
[2] G. R. Harp, R. F. C. Farrow, D. Weller, T. A. Rabedeau, and R. F. Marks, Phys. Rev. B **48**, 17538 (1993).
[3] Y. U. Idzerda, D. M. Lind, D. A. Papaconstantopoulos, G. A. Prinz, B. T. Jonker, and J. J. Kerbs, Phys. Rev. Lett. **61**, 1222 (1988).
[4] D. Bagayoko, A. Ziegler, and J. Callaway, Phys. Rev. B **27**, 7046 (1983).
[5] B. I. Min, T. Oguchi, and A. J. Freeman, Phys. Rev. B **33**, 7852 (1986).
[6] J. G. Gay and R. Richter, in *Ultrathin Magnetic Structures I,* edited by J. A. C. Bland and Heinrich, (Springer, Berlin, 1994), p. 21.
[7] S. Subramanian, X. Liu, R. L. Stamps, R. Sooryakumar, and G. A. Prinz, Phys. Rev. B **52**, 10194 (1995).
[8] S. Subramanian, R. Sooryakumar, G. A. Prinz, B. T. Jonker, and Y. U. Idzerda, Phys. Rev. B **49**, 17319 (1994).
[9] R. E. Camley and D. L. Mills, Phys. Rev. B **18**, 4821 (1979).
[10] R. L. Stamps, Phys. Rev. B **49**, 339 (1994).
[11] G. Rupp, W. Wettling, R. S. Smith, and W. Jantz, J. Magn. Magn. Mater. **45**, 404 (1984).
[12] B. Hillebrands, P. Baumgart, and G. Güntherodt, Phys. Rev. B **36**, 2450 (1987).
[13] X. Liu, R. L. Stamps, R. Sooryakumar, and G. A. Prinz (unpublished).
[14] P. Kabos, W. D. Wilber, C. E. Patton, and P. Grünberg, Phys. Rev. B **29**, 6396 (1984).
[15] J. A. C. Bland, R. C. Bateson, P. C. Riedi, R. G. Graham, H. J. Lauter, J. Penfold, and C. Shackleton, J. Appl. Phys. **69**, 4989 (1991).

Two magnon ferromagnetic resonance linewidths in uniaxial and planar single crystal hexagonal ferrites (abstract)

D. R. Franklin, M. J. Hurben, and C. E. Patton
Department of Physics, Colorado State University, Fort Colins, Colorado 80523

Hexagonal ferrites are ideally suited for millimeter-wave applications but have seen limited use because of large losses. High field effective linewidth and ferromagnetic resonance (FMR) linewidth measurements for single crystal barium ferrite indicate that these losses may be due to an inhomogeneity related two magnon scattering contribution to the relaxation.[1] Calculations of the linewidth as a function of the external magnetic field orientation in films and thin disks give characteristic dependencies if two magnon scattering relaxation is present.[2] The objective of this work was to measure the angle dependence of the FMR linewidth in single crystal Zn–Y and Ba–M hexagonal ferrite disks and compare the results to the theoretical predictions. The materials were flux grown Mn doped Ba–M and Zn–Y single crystals. The Ba–M and Zn–Y disks were 1.0 mm in diameter and 0.13 and 0.4 mm thick, respectively. Measurements were made at 53 GHz for the Ba–M and 9.5 GHz for the Zn_2–Y. The FMR was measured by a shorted waveguide technique as a function of the field angle relative to the out-of-plane direction. The linewidth for the Ba–M increased from minimum value of 35 Oe at 0°, to a maximum of 330 Oe at 68°, followed by a small decrease out to the maximum angle of 75° for which FMR could be observed. For the Zn_2–Y, the linewidth increased from 95 Oe at 0° to 420 Oe at 5°, followed by a decrease to 37 Oe at 90°. The two-magnon model gives large peaks in the linewidth as a function of angle, the sizes and positions of which depend upon the anisotropy and the size of the scattering inhomogeneities. The experimental results for both materials are in good agreement with model two-magnon calculations based on an inhomogeneity size on the order of 0.5 μm.

This work was supported, in part, by the United States Office of Naval Research, Grants No. N00014-94-1-0096 and No. N00014-90-J-4078. The samples were provided by Dr. M. A. Wittenauer of Purdue University.

[1] R. Karim, S. D. Ball, J. R. Truedson, and C. E. Patton, J. Appl. Phys. **73**, 4512 (1993).
[2] M. J. Hurben and C. E. Patton, Digests of the INTERMAG '95 Conference, JC-03, San Antonio, April 1995.

 0021-8979/96/79(8)/5390/1/$10.00 © 1996 American Institute of Physics

Finite temperature effects in the $S=1/2$ Heisenberg chain $Cu(C_6D_5COO)_2\cdot 3D_2O$ (abstract)

D. Dender, D. H. Reich, and C. Broholm
Department of Physics and Astronomy, The Johns Hopkins University, Baltimore, Maryland 21218

K. Lefmann
Department of Solid State Physics, Risø National Laboratory, DK-4000 Roskilde, Denmark

G. Aeppli
AT&T Bell Laboratories, Murray Hill, New Jersey 07974

Quasi-one-dimensional magnetic materials provide important test beds for rigorous models of interacting many-body systems. Nevertheless, there have been few studies of finite temperature effects on spin correlations in low-spin systems, though these are most likely to exhibit quantum effects. Copper benzoate, $Cu(C_6D_5COO)_2\cdot 3D_2O$, is a good realization of the $S=1/2$ Heisenberg antiferromagnetic chain (HAFC).[1] We have performed ac susceptibility and inelastic neutron scattering experiments on this material which establish the Hamiltonian and an excitation spectrum which is consistent with the spinon continuum ansatz of Müller *et al.* We present inelastic neutron scattering measurements of the temperature evolution of the dynamic spin–spin correlation function $S^{zz}(\pi,\omega)$. Comparison will be made to the classical prediction and to a finite temperature field theory of Schulz as applied to this $S=1/2$ HAFC.[2] © *1996 American Institute of Physics.* [S0021-8979(96)69008-8]

[1] K. Oshima, K. Okuda, and M. Date, J. Phys. Soc. Jpn. **44**, 757 (1978).
[2] H. J. Schulz, Phys. Rev. B **34**, 6372 (1986).

Cu_2(1,4-diazacycloheptane)$_2Cl_4$: A quasi-one-dimensional $S=1/2$ spin liquid system

Philip R. Hammar and Daniel H. Reich
Department of Physics and Astronomy, The Johns Hopkins University, Baltimore, Maryland 21218

The structure of Cu_2(1,4-diazacycloheptane)$_2Cl_4$ consists of well-separated zig-zag chains of Cu atoms, suggesting the possibility of significant antiferromagnetic near-neighbor and next-nearest-neighbor interactions. We report on measurements of magnetic susceptibility $\chi(H,T)$ and heat capacity $C_p(T)$ that show that this material does not behave as a simple linear antiferromagnetic chain with spin $S=1/2$. $\chi(H=0,T)$ shows a broad peak at 8 K indicative of one-dimensional antiferromagnetic correlations, but below the peak, χ drops dramatically toward zero instead of remaining finite as $T\rightarrow 0$. For $T\ll T_{\rm peak}$, $\chi(H)$ is independent of field below a critical field $H_c\approx 6.6$ T, and rises sharply above H_c to a plateau at 8 T. Below $T_{\rm peak}$, $C_p(T)\propto\exp(-\Delta/T)$ with an activation energy $\Delta=6.8$ K. These data indicate the presence of a gap between the ground state and the lowest-lying excited states. This material is thus a candidate for a model quasi-one-dimensional $S=1/2$ system with a disordered ground state that is significantly affected by competing interactions. © *1996 American Institute of Physics.* [S0021-8979(96)73008-1]

I. INTRODUCTION

The simplest way to introduce geometrical frustration in a one-dimensional (1D) antiferromagnet (AFM) is to include next-nearest-neighbor (NNN) interactions, as in the model Hamiltonian

$$\mathcal{H}_1=J_1\sum_i \mathbf{S}_i\cdot\mathbf{S}_{i+1}+J_2\sum_i \mathbf{S}_i\cdot\mathbf{S}_{i+2}. \quad (1)$$

A potential physical realization of $\mathcal{H}_1$ is the zig-zag chain shown in Fig. 1(a), where the inside bonds are between near neighbors, and the outside ones between next-near neighbors. This model has received considerable theoretical attention, largely because for the particular value $J_2/J_1=1/2$ the ground state is known exactly.[1] At this point, there is a gap to excitations, and the two-spin correlation function is extremely short ranged,[2] both signatures of a spin liquid ground state. Despite these unusual features, however, there has been very little experimental work on NNN chain systems, due principally to the lack of good model systems. One of the only candidate materials known is Cu_2(1,4-diazacyclo heptane)$_2Cl_4$(CHpC). It was first synthesized by Chiari *et al.*[3] who, based on its structure and high temperature susceptibility measurements, suggested that NNN interactions may be important in determining its behavior. In this article, we present a detailed exploration of the low-temperature magnetic and thermal properties of CHpC. Our results demonstrate the presence of a collective singlet ground state with a gap to magnetic excitations, and provide strong evidence that NNN interactions play a significant role in this material.

II. DATA

In the crystal structure of CHpC, the Cu_2(1,4-diazacycloheptane)$_2Cl_4$ molecules stack in a canted fashion, forming chains as sketched in Fig. 1(b).[3] Small crystals may be grown by slow cooling of saturated methanol solutions. We produced clean powder samples for susceptibility and heat capacity measurements by grinding up such crystals. The dc susceptibility and magnetization for $T>2$ K and magnetic fields $H\leq 5$ T were measured in a commercial (Quantum Design) superconductor, quantum interference device magnetometer. For $0.1\leq T\leq 8$ K, and in dc fields up to 9 T, the ac susceptibility was measured with a home-built susceptometer mounted in a dilution refrigerator. Zero-field heat capacity measurements were also made in the dilution refrigerator using the relaxation method.[4]

Figure 2 shows the dc susceptibility $\chi_{\rm dc}=M/H$ for CHpC, measured in an applied field $H=20$ G. The characteristic rounded peak of a 1D AFM appears at $T_p=8$ K. Fitting a Curie–Weiss law to the high temperature tail ($T>30$ K) gives a Curie–Weiss temperature $\Theta_{\rm CW}=-6.05(1)$ K, confirming the antiferromagnetic nature of the interactions. Below the peak, however, χ drops much more rapidly than for the linear $S=1/2$ chain with only NN interactions.[5] The field dependence of the dc response M/H is shown in the inset of Fig. 2 at fields of $H=0.1$ and 5.0 T. These data are largely field independent for $T>T_p$, but significant field dependence develops for $T<T_p$.

The field dependence of the ac susceptibility χ is shown in Fig. 3. At $T=0.2$ K, $\chi(H)$ is essentially zero for $H<4$ T. Between 5 and 7.5 T, however, $\chi(H)$ grows dramatically before saturating at a constant, nonzero value at high field. The fact that $\chi(H)$ remains zero over a large range of fields is an explicit demonstration that CHpC has a nonmagnetiz-

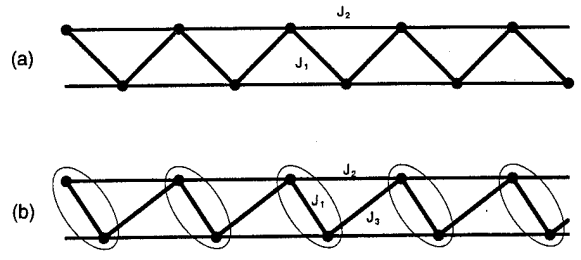


FIG. 1. (a) The ideal next-near-neighbor chain. The inner bonds (J_1) couple near neighbors, and the outer bonds (J_2) couple next-near neighbors. (b) Schematic of the chain structure of CHpC, indicating possible near-neighbor bond alternation (J_3). The ellipses show how the dimer units stack.

 0021-8979/96/79(8)/5392/3/$10.00 © 1996 American Institute of Physics

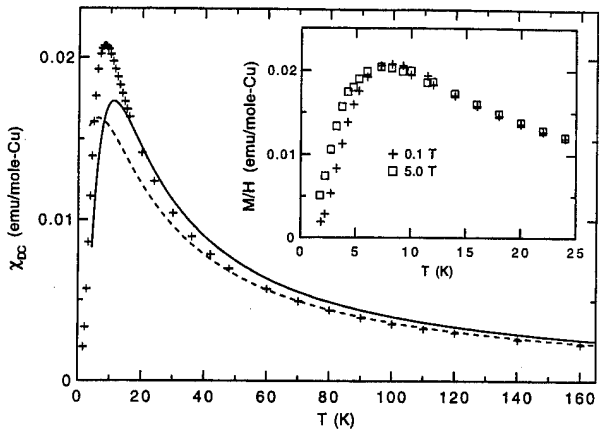


FIG. 2. dc susceptibility of CHpC. The dashed (solid) line is a fit derived from the NNN (alternating) chain model. Inset: dc response M/H at $H=0.1$ and 5 T.

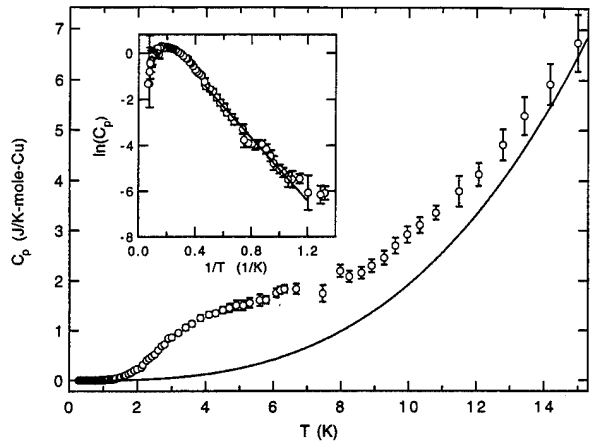


FIG. 4. Specific heat of CHpC. The solid line is the lattice contribution. Inset: In C_p vs $1/T$ showing activated dependence of C_p at low T.

able, singlet ground state with a gap that prevents the excitation of spin-carrying excitations at low T. The gap is closed when the Zeeman splitting of these higher levels drives states with nonzero spin below the low-field ground state level. This leads to an increase in both χ and M. $M(H)$, as determined by integrating χ, is shown in the inset to Fig. 3. It is essentially zero up to a critical field H_c and rises linearly at high field. A linear extrapolation to $M=0$ yields $H_c=6.6(1)$ T. Figure 3 also shows the evolution of $\chi(H)$ with T. At $T=1.7$ K the gap is still well developed at low field, but thermal excitations cause χ to increase before H reaches H_c. At $T=3$ K and $T=6$ K, there are significant thermal excitations above the gap even at low field, and the field dependence for the higher temperatures shown in Fig. 2 is recovered.

Additional evidence for a gap can be found in the specific heat, C_p, of CHpC shown in Fig. 4. The lattice component of C_p (the solid line in Fig. 4) was determined by fitting the data for $T>10$ K to $C_p=AT^{-2}+BT^3$ to extract the phonon piece from the Shottky-like tail of the magnetic peak.[6] The magnetic contribution to C_p appears as a bump superimposed on the phonon contribution. Below the maximum in the magnetic contribution, C_p is activated, as can be seen in the inset to Fig. 4, which shows ln C_p vs $1/T$. The excellent linear fit shown indicates that $C_p \propto \exp(-\Delta/T)$, with $\Delta=6.8(2)$ K.

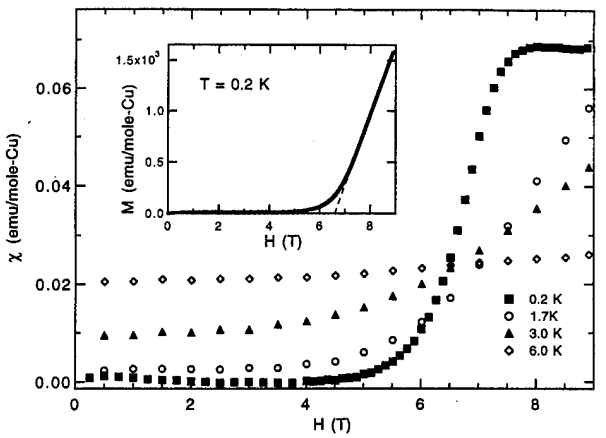


FIG. 3. Field dependence of ac susceptibility in CHpC at fixed T, showing development of the gap at low T. Inset: Magnetization obtained from integrating $\chi(H,T=0.2$ K) data.

III. DISCUSSION

In their pioneering work on CHpC,[3] Chiari *et al.* pointed out that this material may differ from the Hamiltonian $\mathscr{H}_1$ through the presence of more than two Cu–Cu exchange couplings. On the basis of high temperature susceptibility data alone, they were not able to place strong constraints on the possible models, but they concluded that the most likely situation is that the intradimer and interdimer NN interactions are different as indicated in Fig. 1(b). In a material where there are several exchange constants present, it is difficult to determine them individually from bulk measurements. One is therefore forced to consider a variety of possible models to determine which best describes the system at hand.

The simplest system with a singlet ground state and a gap consists of isolated dimers with an AFM intradimer interaction. At high temperatures $\chi(T)$ in this model is described by a Curie–Weiss law with $\Theta_{CW}=-S(S+1)J/3$, where J is the strength of the intradimer exchange. With $S=1/2$ and $\Theta_{CW}=-6.05$ K, this implies $J=24.2$ K. The heat capacity in this model, however, shows activated behavior with $\Delta=J$. This is inconsistent with our measured value $\Delta=6.8$ K.

We note that the linear rise of $M(H)$ at low temperatures and high fields rules out not only the dimer model, but any collection of isolated groups of spins with a spectrum of discrete levels. $M(H)$ in such a system at low T will have a set of steps as a series of discrete levels with increasing spin successively becoming the ground state with increasing field. A linear $M(H)$ response can only arise if there is a band of finite-spin excitations above the gap that is continuously populated for $H>H_c$. Such behavior is well documented in the case of the Haldane gap in $S=1$ AFM chains.[7] This fea-

ture of our data suggests that the ground state is cooperative in this material, and the excitations are extended.

We now consider several possible extended linear chain models. The uniform near-neighbor chain is easily ruled out by the presence of the gap, as discussed above. Alternation of the near-neighbor interaction

$$\mathscr{H}_2=\sum_{i=1}^{N/2}\left[J_1\mathbf{S}_{2i}\cdot\mathbf{S}_{2i+1}+J_3\mathbf{S}_{2i+1}\cdot\mathbf{S}_{2i+2}\right] \tag{2}$$

introduces a gap between the singlet ground state and the lowest $S=1$ excited state.[18] This model could be appropriate for CHpC if the NNN coupling were very weak [$J_2\simeq 0$, $J_1\neq=J_3$ in Fig. 1(b)]. Hatfield has described a method for fitting $\chi(T)$ in this model to determine J_1 and J_3.[9] In this method, χ is fit by the ratio of a quadratic and a cubic equation in J_1/T whose coefficients are polynomials of the ratio $\alpha=J_3/J_1$, found by fitting to exact diagonalization solutions to the alternating chain Hamiltonian of 10 spins. For the alternating chain, one expects $\Theta_{CW}=-S(S+1)(J_1+J_3)/3=S(S+1)J_1(1+\alpha)/3$, which for our results implies $J_1=24.18/(1+\alpha)$ K. Fitting $\chi(T)$ using Hatfield's prescription with the addition of this constraint gives $\alpha=0.58(1)$ and thus $J_1=15.3(1)$ K. This fit is shown as a solid in Fig. 2. From numerical work on this model,[10] we find that for $\alpha=0.58$, $\Delta=0.34(1)\ J_1$. This gives $\Delta=5.2(1)$ K, which is inconsistent with the value of 6.8 K determined from our $C_p(T)$ data. Thus the simple alternating chain also fails to describe adequately this material.

The final model that we consider is the NNN chain without alternation, given by Eq. (1). We have calculated $\chi(T)$ for a range of J_2/J_1 from exact diagonalization of chains of up to 14 spins. Based on finite-size scaling, we expect this calculation to be accurate to 1% for $T>0.21J_1$. The best fit is obtained for $J_2/J_1=0.30(1)$, but as shown by the dashed line in Fig. 2, it is not satisfactory, and it is therefore unlikely that this model is sufficient.

Having exhausted these simpler possibilities, we are forced to the conclusion that at least three different exchange constants are important in this system, and that bond alternation as well as competing NNN interactions are necessary to describe the behavior of this material. We note that we have found no evidence for three-dimensional ordering down to $T=0.2$ K in either the susceptibility or the heat capacity, and thus the singlet ground state of the 1D system appears to be robust, a rarity for $S=1/2$. Despite its complexity, therefore, CHpC is deserving of further exploration as a model 1D system with competing interactions.

ACKNOWLEDGMENTS

This work was supported by the NSF under Grant N.S. DMR-9357518 and DMR-9302065, and by the David and Lucile Packard Foundation.

[1] C. K. Majumdar and D. K. Ghosh, J. Phys. C **3**, 911 (1969).
[2] B. S. Shastry and B. Sutherland, Phys. Rev. Lett. **47**, 964 (1981).
[3] B. Chiari, O. Piovesana, T. Tarantelli, and P. F. Zanazzi, Inorg. Chem. **29**, 1172 (1990).
[4] R. Bachmann, F. J. DiSalvo, Jr. T. H. Geballe, R. L. Greene, R. E. Howard, C. N. King, H. C. Kirsch, K. N. Lee, R. E. Schwall, H. U. Thomas, and R. B. Zubeck. Rev. Sci. Instrum. **42**, 205 (1972).
[5] J. C. Bonner and M. E. Fisher, Phys. Rev. **135**, A640 (1964).
[6] S. A. Friedberg and C. A. Raquet, J. Appl. Phys. **39**, 1132 (1968).
[7] K. Katsumata, H. Hori, T. Takeuchi, M. Date, A. Yamagishi, and J. P. Renard, Phys. Rev. Lett. **63**, 86 (1989); Y. Ajiro, T. Goto, H. Kikuchi, T. Sakakibara, and T. Inami, *ibid.* **63**, 1424 (1989).
[8] J. C. Bonner, H. W. Blöte, J. W. Bray, and I. S. Jacobs, J. Appl. Phys. **50**, 1810 (1979).
[9] W. Hatfield, J. Appl. Phys. **52**, 1985 (1981).
[10] J. C. Bonner, S. A. Friedberg, H. Kobayashi, D. L. Meier, and H. J. Blöte, Phys. Rev. B **27**, 248 (1983).

Published without author corrections

Magnetic fluctuation spectrum of $CuGeO_3$: Raman scattering

P. H. M. van Loosdrecht, J. P. Boucher, and G. Martinez
Grenoble High Magnetic Field Laboratory, Max-Planck-Institut für Festkörperforschung and Centre National de la Recherche Scientifique, 25 Avenue des Martyrs, BP 166, F-38042 Grenoble Cedex 9, France

G. Dhalenne and A. Revcolevschi
Laboratoire de Chimie des Solides, Univerité de Paris-Sud, bâtiment 414, F-91405 Orsay, France

Raman spectra of the magnetic fluctuation spectrum of $CuGeO_3$ are presented for $4<T<300$ K and $B\leqslant 20$ T. For $B=0$ the results show good agreement with theoretical expectations for a one-dimensional isotropic Heisenberg antiferromagnet which exhibits a spin–Peierls transition. In the presence of a magnetic field the phase transition to the incommensurately modulated phase is observed around $B=12.8$ T at $T=4.2$ K. The spectra obtained in the high field phase clearly show evidence for a well-defined spin fluctuation spectrum, which appears to present an intermediate case between the dimerized phase and the short-range order regime of the uniform phase. © *1996 American Institute of Physics.* [S0021-8979(96)73108-8]

I. INTRODUCTION

Recently it has been shown that $CuGeO_3$, an inorganic compound, undergoes a spin–Peierls distortion below 14 K.[1] The magnetic interactions above this second-order transition are well described as a nearly one-dimensional isotropic $S=1/2$ Heisenberg antiferromagnet. The magnetic fluctuations in such a quantum system are of special interest due to the lack of long-range order, and differ substantially from what one expects for a classical system. In the dimerized (D) phase, one expects a gap in the fluctuation spectrum. The occurrence of this gap in $CuGeO_3$ has been confirmed by various experimental techniques.[2–4] Applying a magnetic field in the D phase induces a second phase transition, of first order, to a presumably incommensurate (IC) phase around $B=13$ T.[3,5]

$CuGeO_3$ has an orthorhombic structure with a space group $Pbmm$.[6] The magnetic chains are formed by the $S=1/2$ Cu^{2+} ions running along the c axis of the crystal. The magnetic interaction is described by the isotropic Heisenberg Hamiltonian $H=\Sigma_i 2J_i\mathbf{S}_i\mathbf{S}_{i+1}$, with an intrachain exchange coupling $J=J_c\approx 60$ K. In the dimerized phase small interchain couplings $J_b\approx 0.1J_c$ and $J_a\approx -0.01J_c$ have been found.[2]

The present article is concerned with the magnetic fluctuation spectrum of $CuGeO_3$ in the uniform (U), the D, and the IC phase as probed by polarized Raman scattering experiments. Generally the most important contribution to magnetic inelastic scattering in antiferromagnets is the exchange scattering mechanism. In $CuGeO_3$ the scattered intensity can be expressed as $I(\omega)\propto\Sigma_{\mathbf{q}} f_{\mathbf{q}}\langle S^{\alpha}_{\mathbf{q}}(t)S^{\alpha}_{-\mathbf{q}}(t) \times S^{\alpha}_{\mathbf{q}}(0)S^{\alpha}_{-\mathbf{q}}(0)\rangle_{\omega}$, where $f_{\mathbf{q}}=\cos^2(q_c)$ is the weighing function which arises from the matrix elements for the exchange interaction.[7] The magnetic scattering is thus mainly due to the density of states (DOS), and the structure therein, in the first-half of the Brillouin zone.

II. EXPERIMENT

The samples used in this study were grown from the melt by a floating zone technique.[8] They were cleaved perpendicular to the (100) direction and mounted in a cold finger flow cryostat (temperature accuracy ~1 K). Raman spectra have been recorded in a backscattering geometry using a charge-coupled device equipped spectrometer (DILOR XY). The 514 nm line of an Ar-ion laser was used for excitation, keeping the intensity below 200 W/cm^2 to minimize local heating. Polarized experiments have been performed in a $(\mu\nu)$ scattering geometry, where μ,ν denote the polarization of the incident and scattered light, respectively. Magnetic scattering is only observed in the (cc) geometry, where c is along the chain direction. The results obtained in other geometries, as well as the results on vibrational scattering and wavelength dependence will be presented elsewhere.[9]

III. RESULTS FOR $B=0$ T

The magnetic scattering in $CuGeO_3$ is found to be strongly temperature dependent. As shown in Fig. 1, three types of behavior can be distinguished. In the uniform phase a well-defined broad scattering band is observed centered around 230 cm^{-1} for temperatures below 60 K [Fig. 1(b)]. This is also the temperature where the maximum in the susceptibility curve is observed. Above this temperature the scattered intensity is observed to be transferred to a quasi-elastic central peak which gains intensity as the temperature increases [Fig. 1(c)]. In the D phase [$T<14$ K, Fig. 1(a)], the broad maximum becomes sharp, and several new, sharp features appear in the spectrum at 32, 105, 370, and 820 cm^{-1}.

A detailed discussion of the results obtained for $B=0$ has been given elsewhere.[7] Here only the key points are discussed. The observed spectra in the U phase can be understood in terms of the magnetic fluctuation spectrum expected for a one-dimensional $S=1/2$ Heisenberg antiferromagnet.[10] Although such a system does not order, not even at $T=0$, short-range correlations do develop at low temperatures. In this short-range order (SRO) regime the fluctuation spectrum is expected to form a continuum in $(\omega,\mathbf{q})$ space, bounded by $\omega_1(q_c)=\pi J|\sin(q_c)|$ and $\omega_2(q_c)=2\pi J|\sin(q_c/2)|$. The intensity of the fluctuations in this spin wave continuum (SWC) diverges at the lower limit $\omega_1(q_c)$, and rapidly decreases for increasing frequency. Using this description one can now understand the observed spectrum in the SRO regime [Fig. 1(b)]. The maximum in intensity around 230 cm^{-1} arises due

 0021-8979/96/79(8)/5395/3/$10.00 © 1996 American Institute of Physics

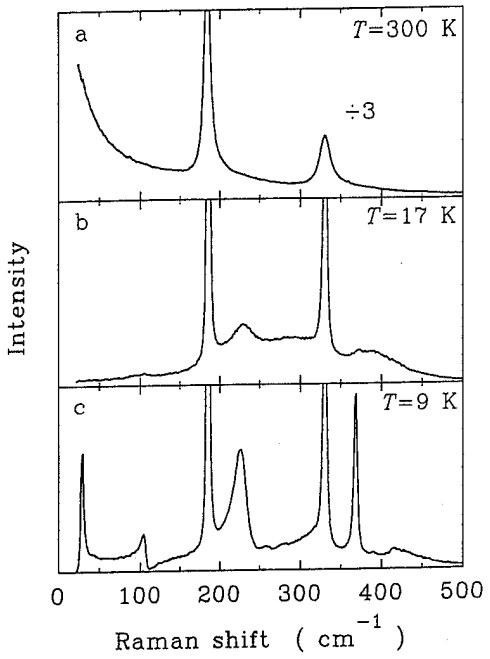


FIG. 1. Polarized (cc) Raman spectra of $CuGeO_3$ in the uniform and dimerized phases. (a) Uniform phase, high temperature regime. (b) Uniform phase, short-range order regime. (c) Dimerized phase. Spectrum (a) has been scaled down by a factor of 3.

to fluctuations around $q_c=\pi/2$, where the flatness of $\omega_1(q_c)$ yields a strongly peaked DOS. Model calculations including only the SWC show a good agreement with the observed spectrum for $\omega<250$ cm^{-1}, using $J=60$ K. The intensity at higher energies, however, cannot be due to the SWC. The origin of this high energy scattering is not fully understood at present, but preliminary results on the pressure dependence of the spectrum indicate that it is due to spin–phonon interactions.[9]

As the temperature increases the magnetic correlation length becomes shorter and the above picture breaks down. In the absence of correlations the magnetic fluctuations become diffusive, and the intensity of the fluctuation spectrum is transferred toward $(\omega,\mathbf{q})=(0,\mathbf{0})$. Since the magnetic system of $CuGeO_3$ is nearly one dimensional this leads to a divergent DOS at $\omega=0$. The Raman spectrum at high temperatures [$T>60$ K, Fig. 1(a)] indeed shows a quasidiverging central peak with a tail extending up to 400 cm^{-1}.

The magnetic fluctuation spectrum in the D phase [Fig. 1(c)] shows two peaks which can be assigned to two-spin scattering processes. The first peak at 32 cm^{-1} is due to the spin–Peierls gap at $(q_b,q_c)=(0,\pi)$, and shifts to lower frequency as the temperature approaches the spin–Peierls transition. The peak around 230 cm^{-1} is due to the maximum in the DOS for $q_c=\pi/2$. In addition to this purely magnetic scattering there are several other peaks observed in the D phase, which disappear in the U phase. The asymmetric peak at 105 cm^{-1} could be due to the gap in the fluctuation spectrum at $(q_b,q_c)=(0,0)$. However, the position of the peak is independent of temperature and no splitting of this peak has been observed in a magnetic field. Therefore this peak cannot be due to a spin–Peierls gap. It is more likely that this peak

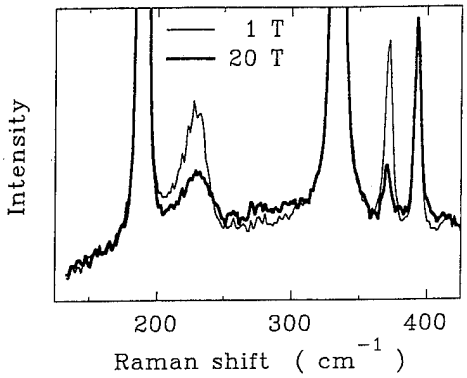


FIG. 2. Unpolarized Raman spectra of $CuGeO_3$ in the D and IC phase at $T=4.2$ K. (a) D phase, $B=1$ T, (b) IC phase, $B=20$ T.

is in fact due to a phonon which is activated by the cell doubling in the D phase, where its asymmetry is due to a coupling to the spin system. Also the peak at 370 cm^{-1} cannot be due to purely magnetic excitations, given its relatively high energy, and again the cell doubling in the D phase may be responsible for the appearance of this peak in the Raman spectrum.

IV. RESULTS FOR $B\neq0$ T

Figure 2 shows representative unpolarized Raman spectra for the D phase ($B=1$ T) and the IC phase ($B=20$ T) at $T=4.2$ K. In order to clarify the magnetic contribution, the B_{1g} phonon at 228 cm^{-1} has been suppressed by subtracting the same Lorentzian peak from both spectra. It is interesting to compare the spectrum observed in the IC phase to those obtained in the D phase and in the SRO regime, since the spectrum observed in the IC phase appears to present an intermediate case between those in the D phase and in the SRO regime. It is clear that, like in the SRO regime, in the

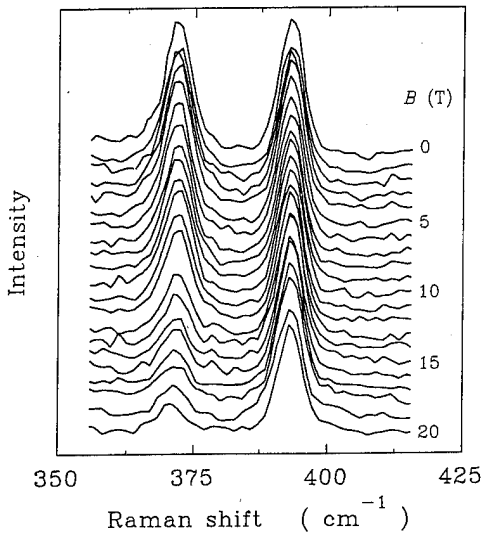


FIG. 3. Field dependence of the 370 cm^{-1} mode showing the discontinuous decrease at the D–IC phase transition around 12.8 T. The mode at 394 cm^{-1} is assigned to a B_{1g} phonon.

IC phase the maximum around 230 cm^{-1} broadens and loses some intensity as compared to the D phase, but the changes are found to be less drastic. Also the increase in intensity for energies above 230 cm^{-1} found in the SRO regime is observed in the IC phase, but again is less pronounced. Hence, many of the characteristics of the D phase are retained in the IC phase. This also holds for the mode observed at 370 cm^{-1} in the D phase, which is absent in the SRO regime. In fact the intensity of this mode provides a convenient means to study the phase transitions in $CuGeO_3$. Upon increasing the temperature from either the IC or the D phase the intensity of this mode continuously decreases until it has completely disappeared at the second-order phase transition to the U phase. The magnetic field dependence at 4.2 K of this mode is shown in Fig. 3, which also shows the B_{1g} phonon at 390 cm^{-1}. This phonon structure is found to be field independent, and is used as a reference for comparison to the 370 cm^{-1} feature. Upon increasing magnetic field, starting from the D phase the intensity of the 370 cm^{-1} mode slowly decreases. At the first-order D–IC phase transition the intensity drops sharply by about 20% over 0.2 T, after which it continues to decrease slowly until it reaches a more or less stable value around 17 T. Clearly this mode is intrinsic not only to the D phase, but also to the IC phase.

The observation that the Raman spectra in the IC phase shows characteristics of both the D phase and the SRO regime might not be so surprising since one can anticipate that the *average* structure of the high field phase is the same as the structure of the U phase, whereas the *actual* structure is likely to be close to the dimerized structure of the D phase. In other words, it seems likely that the D phase is the lock-in phase of the IC phase, which itself is obtained by an incommensurate modulation of the U phase with a modulation wave vector close to 1/2 (the commensurate modulation of the D phase). Whether this picture holds, however, remains to be proven and has to await theoretical results for the IC phase which are not available at present.

V. CONCLUSIONS

The results obtained on the fluctuation spectrum of $CuGeO_3$ in the U phase clearly show the importance of quantum spin fluctuations in this system. In the first place the observed maximum around 230 cm^{-1} can only be understood from a quantum description, classically this energy is scaled down by a factor $\pi/2$. In the second place, the spectrum in the SRO regime of the U phase has no classical interpretation and is due to SWC excitations. In the third place the observed diffusive scattering at low energies which start to develop already at low temperatures, and dominates the high temperature spectra is in good agreement with the $T>0$ finite quantum spin chain calculations of Müller *et al.*[10]

The results obtained in the IC phase clearly show the existence of a continuum of spin excitations, whose spectrum appears to present an intermediate spectrum between the D phase and the SRO regime of the U phase.

It is clear from the discussions in the present article that many aspects of the spin fluctuation spectrum are only qualitatively understood. This is mainly due to the lack of theoretical results for B and/or $T\neq 0$ for this magnetoelastic compound. We hope therefore that the present results stimulate further theoretical and experimental work on this fascinating system.

ACKNOWLEDGMENT

Partial financial support by the New Energy Development Organisation is gratefully acknowledged.

[1] M. Hase, I. Terasaki, and K. Uchinokura, Phys. Rev. Lett. **70**, 3651 (1993).
[2] M. Nishi, O. Fujita, and J. Akimitsu, Phys. Rev. B **50**, 6508 (1994).
[3] T. M. Brill, J. P. Boucher, J. Voiron, G. Dhalenne, and A. Revcolevschi, Phys. Rev. Lett. **73**, 1545 (1994).
[4] H. Kuroe, T. Sekine, M. Mase, Y. Sasago, K. Uchinokura, M. Kojima, I. Tanaka, and Y. Shibura, Phys. Rev. B **50**, 16468 (1994).
[5] M. Hase, I. Terasaki, M. Tokunaga, N. Miura, and H. Obara, Phys. Rev. B **48**, 9616 (1993).
[6] H. Völlenkle, A. Wittman, and N. Nowotny, Monatsh. Chem. **98**, 1352 (1967).
[7] P. H. M. van Loosdrecht, J. P. Boucher, G. Martinez, G. Dhalenne, and A. Revcolevschi, Phys. Rev. Lett. **76**, 311 (1996).
[8] A. Revcolevschi and R. Collongues, C. R. Acad. Sci. **266**, 1767 (1969).
[9] P. H. M. Van Loosdrecht (unpublished).
[10] G. Müller, H. Thomas, H. Beck, and J. C. Bonner, Phys. Rev. B **24**, 1429 (1981).

Neutron diffraction study of the magnetic structures of $CeMn_2Ge_2$ and $CeMn_2Si_2$

J. A. Fernandez-Baca
Solid State Division, Oak Ridge National Laboratory, Oak Ridge, Tennessee 37831-6393

Peggy Hill
Department of Physics, Southern Illinois University, Carbondale, Illinois 62901

B. C. Chakoumakos
Solid State Division, Oak Ridge National Laboratory, Oak Ridge, Tennessee 37831-6393

Naushad Ali
Department of Physics, Southern Illinois University, Carbondale, Illinois 62901

We have performed high-resolution neutron powder diffraction measurements on $CeMn_2Si_2$ and $CeMn_2Ge_2$ at temperatures between 12 and 550 K. Our measurements indicate that at high temperatures both compounds are paramagnetic. Below T_N=380 K $CeMn_2Si_2$ becomes a collinear AF, with a structure similar to that reported by Siek *et al.* in which the magnetic propagation vector is τ=(0 0 1). $CeMn_2Ge_2$, on the other hand, exhibits two different magnetic transitions. At $T_N\approx$415 K there is a transition to a collinear AF phase characterized by the commensurate propagation wave vector τ=(1 0 1). At $T_C\approx$318 K there is a transition to a conical structure with a ferromagnetic component along the *c* axis and a helical component in the *ab* plane. The helical component is characterized by the incommensurate propagation vector $\tau=(1\ 0\ 1-q_z)$, where q_z is temperature dependent. © *1996 American Institute of Physics.* [S0021-8979(96)73208-8]

INTRODUCTION

The family of layered compounds of the form RM_2X_2 (R=rare earth, M=transition metal, X=Si, Ge) crystallizes with the $ThCr_2Si_2$ (*I4/mmm*) structure and exhibits a rich variety of interesting physical phenomena that include superconductivity, magnetism, mixed valence, heavy fermion or Kondo behavior. Of particular interest is the system $CeMn_2X_2$, which exhibits magnetic moments only at the Mn sites. In this system the Mn atoms form a simple tetragonal lattice and are coupled with an exchange interaction that has been thought to be sensitive to the Mn-Mn distances within (0 0 1) planes (intralayer exchange) and relatively insensitive to the Mn-Mn distances along the *c* axis (interlayer exchange). It has been reported that the Mn moments in $CeMn_2Si_2$ are aligned ferromagnetically within the (0 0 1) planes, and that these planes are coupled antiferromagnetically below T_N=379 K.[1] The $CeMn_2Ge_2$ system, on the other hand, has been reported to be ferromagnetic (FM) below T_C=316 K.[2,3] Recently Venturini *et al.*[4] have reported that in the related compounds $LaMn_2Si_2$ and $LaMn_2Ge_2$ there is strong evidence of dominant intralayer antiferromagnetic interactions, which give rise to conical incommensurate phases at low temperatures. These results suggest that the nature of the magnetic interactions in this family of compounds is more complex than originally thought, and that the magnetic structures of $CeMn_2Si_2$ and $CeMn_2Ge_2$ should be reexamined. We have performed high-resolution neutron powder diffraction measurements on these compounds to resolve the magnetic structures and the nature of the magnetic interactions in these systems. In this article we report the findings of our preliminary analysis of these measurements. We found that at high temperatures both compounds are paramagnetic. $CeMn_2Si_2$ becomes a collinear antiferromagnet below $T_N\approx$380 K, with a structure similar to that reported by Siek *et al.*,[1] in which the magnetic propagation vector is τ=(0 0 1). Below $T_N\approx$415 K $CeMn_2Ge_2$ is a collinear antiferromagnet with a commensurate propagation wave vector τ=(1 0 1). Below $T_C\approx$318 K the Mn moments in this system exhibit a conical structure with a ferromagnetic component along the *c* axis and a helical component in the *ab* plane, similar to that of $LaMn_2Ge_2$ reported by Venturini *et al.*[4] This helical component is characterized by the incommensurate propagation vector $\tau=(1\ 0\ 1-q_z)$, where q_z is temperature dependent and varies from 0 (at T_C) to 0.32 reciprocal lattice units (at T= 12 K). These findings are consistent with the recent results reported by Welter *et al.*[5]

EXPERIMENT

About 10 g of $CeMn_2Ge_2$ and $CeMn_2Si_2$ were prepared by arc melting stoichiometric amounts of the constituents in an argon atmosphere. X-ray diffraction analysis showed that these specimens had no significant amounts of impurity phases. The samples were powdered and loaded in thin-walled aluminum or vanadium cells for the neutron diffraction measurements. For the measurements between 12 and 330 K the cells were sealed in a He gas environment, and then placed in a closed cycle He refrigerator. For the high temperature measurements (330 K<T<550 K) the cells were placed in a furnace. The neutron diffraction measurements were performed at the HB4 high-resolution powder diffractometer at the High Flux Isotope Reactor at Oak Ridge National Laboratory using neutron wavelengths of 1.417 and 2.222 Å.

$CeMn_2Si_2$

Powder diffraction patterns of $CeMn_2Si_2$ were collected between 12 and 430 K. At 430 K there was no evidence of any magnetic contribution to the diffraction pattern, and the crystal structure at this temperature was refined using the computer program RIETAN.[6] The refined structural param-

 0021-8979/96/79(8)/5398/3/$10.00 © 1996 American Institute of Physics

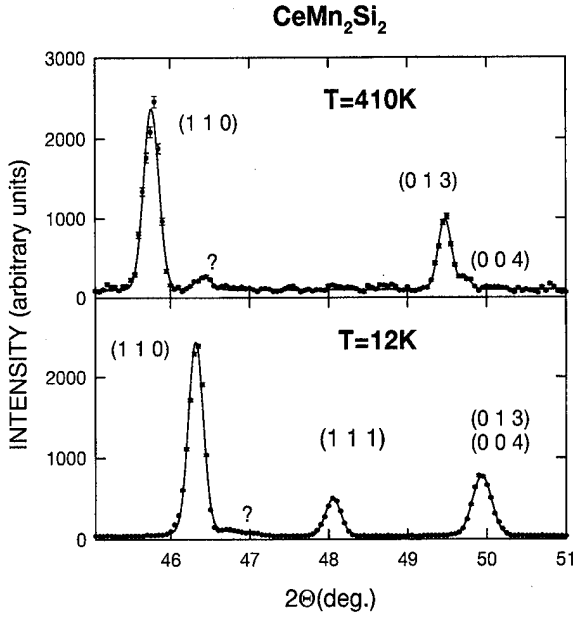


FIG. 1. Partial neutron powder diffraction pattern for $CeMn_2Si_2$ at $T=410$ K and 12 K. The low temperature (1 1 1) peak is of magnetic origin and is indicative of an antiferromagnetic structure with a characteristic propagation wavevector $\tau=(0\ 0\ 1)$ (see text). The solid lines are the result of fits to Gaussian lineshapes. The peak labeled with a question mark corresponds to an unidentified impurity phase. The neutron wavelength for this measurement was $\lambda=2.22$ Å.

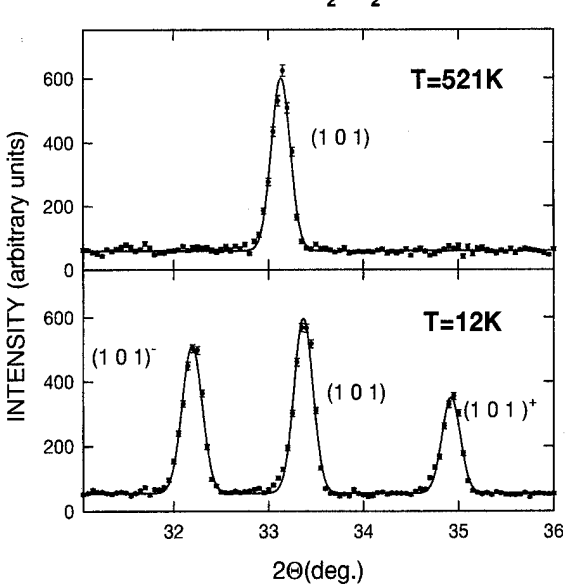


FIG. 2. Partial neutron powder diffraction pattern for $CeMn_2Ge_2$ at $T=521$ K and 12 K. The low temperature magnetic satellites in the vicinity of the (1 0 1) peak are of magnetic origin and are indicative of a helical component of the Mn magnetic moments with characteristic propagation wavevector $\tau=(1\ 0\ 1-q_z)$. The neutron wavelength for this measurement was $\lambda=2.22$ Å.

eters are consistent with the published values for this material with the Ce, Mn, and Si atoms at the 2(*a*), 4(*d*) and 4(*e*) sites of the space group *I*4/*mmm*, $a=4.0417(6)$ Å, $c=10.5546(19)$ Å, and $z=0.382(1)$ (where z is the variable fractional coordinate of the Si atoms). In this space group the nuclear reflection conditions for (hkl) are $h+k+l=2n$. An extra reflection condition, $l=2n$, exists for the scattering contribution from the Mn sites. As the temperature was lowered two superlattice peaks were observed. These could be indexed as the (1 1 1) (see Fig. 1) and the (1 1 3) reflections. These superlattice peaks appeared below $T_N\approx380$ K and persisted all the way down to 12 K. These findings are similar to those reported by Siek *et al.*[1] and correspond to an antiferromagnetic structure with a propagation vector $\tau=(0\ 0\ 1)$. The absence of reflections of the form $(0\ 0\ 2n\pm1)$ indicates that the magnetic moments are parallel to the c axis. In this collinear antiferromagnetic structure the magnetic moment M_z at the Mn site $\mathbf{r}_1$ is

$$M_z(\mathbf{r}_1)=M_0\cos(\mathbf{r}_1\cdot\tau), \tag{1}$$

where τ is the propagation vector characteristic of the magnetic structure in reciprocal lattice units, and M_0 is the magnitude of the magnetic moment. Thus in this structure all the Mn moments in the (0 0 1) planes are coupled ferromagnetically, while the moments in adjacent (0 0 1) planes are coupled antiferromagnetically. The magnetic moment per Mn atom at 12 K was calculated from the integrated intensities of the (1 1 1) magnetic peak and the (1 1 0) nuclear peak shown in Fig. 1. In this calculation a small correction (<5%) was made to account for the preferred orientation present in the powder. The calculated moment was of 1.9(2) μ_B per Mn atom. This value is lower than the value 2.30(5) μ_B reported by Siek *et al.*[1] and lower than the paramagnetic moment of 3.3 μ_B reported by Liang *et al.*[7] At $T=12$ K the refined structural parameters were $a=3.9913(4)$ Å, $c=10.4935(13)$ Å, and $z=0.3805(8)$.

$CeMn_2Ge_2$

Powder diffraction patterns of $CeMn_2Ge_2$ were collected between 12 and 550 K. At 550 K there was no evidence of any magnetic contribution to the diffraction pattern, and the crystal structure at this temperature was refined using the computer program RIETAN.[6] This structure is similar to that of $CeMn_2Si_2$, with the Ce, Mn, and Ge atoms at the 2(*a*), 4(*d*) and 4(*e*) sites of the space group *I*4/*mmm*, the refined structural parameter at 521 K were $a=4.1623(3)$ Å, $c=11.0081(9)$ Å, and $z=0.3832(5)$ (where z is the variable fractional coordinate of the Ge atoms). As the temperature was lowered we found evidence of two magnetic transitions. Below $T_N\approx415$ K the intensity of the (1 0 1) reflection increased, reaching a maximum at about $T=320$ K and then dropped rapidly to the same level of the high temperature patterns. Below $T_C\approx318$ K magnetic satellites appeared in the vicinity of the (1 0 1) (see Fig. 2), (1 0 3), (1 0 5), (2 1 1), and (2 1 3) reflections, at the same time that the intensity of the (1 1 0), (1 1 2), (1 1 4) and (2 0 2) peaks increased. The intensities of the reflections (0 0 2*n*) remained unchanged in the whole temperature range studied. These observations are consistent with the existence of two different magnetic phases in $CeMn_2Ge_2$.

The enhancement of the (1 0 1) reflection below T_N could originate either by the appearance of ferromagnetic

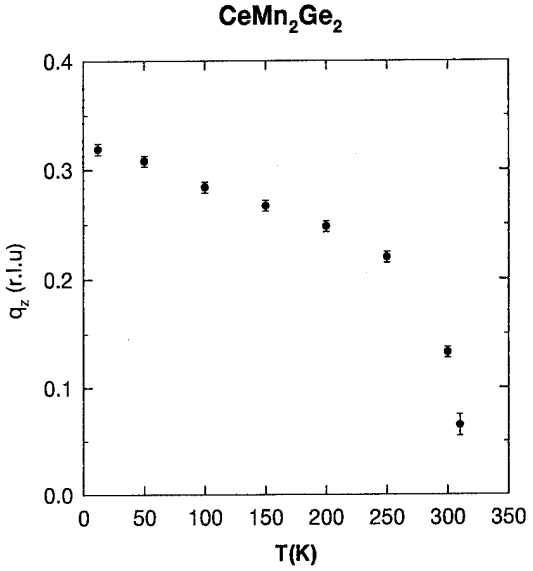


FIG. 3. Temperature dependence of q_z for $CeMn_2Ge_2$. q_z is given in reciprocal lattice units (r.l.u).

ordering of the Ce atoms, or by the appearance of antiferromagnetic ordering of the Mn atoms (i.e., by the formation of a superlattice of Mn atoms). The magnetic ordering of the Ce atoms, however, would also increase the intensity of most of the allowed nuclear reflections. This intensity enhancement has not been observed, indicating that no magnetic ordering is associated with the Ce atoms. This observation is consistent with earlier reports that Ce is nonmagnetic in this family of compounds.[8,9] Other Lanthanides in RMn_2X_2 systems exhibit magnetic order but at much lower temperatures.[8] The enhancement of the (1 0 1) reflection can then be attributed to the antiferromagnetic ordering of the Mn atoms with a characteristic propagation wave vector $\tau=(1\ 0\ 1)$. As in the case of $CeMn_2Si_2$ the direction of the magnetic moments is parallel to the c axis. Unlike the $CeMn_2Si_2$ system both the intralayer and interlayer couplings of the Mn moments are antiferromagnetic, their directions given by Eq. (1).

The enhancement of the (1 1 0), (1 1 2), (1 1 4) and (2 0 2) peaks below $T_C \approx 318$ K can be attributed to the development of a ferromagnetic alignment of the Mn moments. The appearance of magnetic satellites at the same temperature can be attributed to the simultaneous appearance of a helical component of the Mn moments in the ab plane, with a characteristic wave vector $\tau=(1\ 0\ 1-q_z)$. The value of q_z is incommensurate with the lattice and is temperature dependent (see Fig. 3), varying from 0 (at T_c) to ≈ 0.32 (at 12 K). In this structure the M_x, M_y, and M_z components of the magnetic moment $\mathbf{M}(\mathbf{r}_1)$ are given by

$$M_x(\mathbf{r}_1)=M_0\cos(\mathbf{r}_1\cdot\tau+\phi),$$
$$M_y(\mathbf{r}_1)=M_0\sin(\mathbf{r}_1\cdot\tau+\phi),\quad M_z(\mathbf{r}_1)=M_1. \tag{2}$$

These components result in a conical structure similar to that described by Venturini *et al.* for $LaMn_2Ge_2$.[4] The refined ferromagnetic component M_z for Mn at $T=12$ K was $2.4(2)\mu_B$. The refined structural parameters at this temperature were $a=4.1291(2)$ Å, $c=10.9016(7)$ Å, and $z=0.3820(4)$.

DISCUSSION

The nature of the magnetic interactions in the systems under study is more complex than originally thought. The short distance between the Mn nearest neighbors ($a\sqrt{2}/2$) is suggestive of strong direct exchange interactions between the magnetic ions. The relatively large distance ($c/2$) between the Mn (0 0 1) planes suggests indirect exchange interactions mediated by the Ge/Si and Ce atoms. For $CeMn_2Si_2$ the intralayer exchange interaction between Mn moments is ferromagnetic, while the interlayer is antiferromagnetic. For $CeMn_2Ge_2$ on the other hand, the intralayer exchange is antiferromagnetic, while the interlayer is such that gives rise to a transition from a commensurate antiferromagnetic phase to an incommensurate conical structure. The nature of this commensurate-to-incommensurate phase transition, which takes place with a magnetic moment reorientation is of special interest and should be studied further. Recent bulk magnetization measurements on a specimen of $CeMn_2Ge_2$ (from the same batch as our sample) revealed an anomaly in the magnetization at the same temperature where this spin reorientation takes place.[10] When this work was in progress we learned of the recent published results of Welter *et al.*[5] on $CeMn_2Ge_2$; our results on this system are in general agreement with theirs. Our results are also in general agreement with the recent Mössbauer experiments by Nowick *et al.*[11]

ACKNOWLEDGMENTS

The work at ORNL supported by the US DOE, under Contract No. DE-AC05-84OR21400 with Lockheed Martin Energy Systems. One of the authors (P.H.) acknowledges partial support from the SDE/Graduate Women in Science Adele Lewis Fellowship and from a Research Travel Grant from the Oak Ridge Institute for Science and Education.

[1] S. Siek, A. Szytula, and J. Leciejewicz, Phys. Status Solidi A **46**, K101 (1978).
[2] K. S. V. Narasimhan *et al.*, AIP Conf. Proc. **29**, 594 (1979).
[3] J. Leciejewicz, A. Szytula, W. Bazela, and S. Siek, J. Magn. Magn. Mater. **89**, 29 (1990).
[4] G. Venturini, R. Welter, E. Ressouche, and B. Malaman, J. Alloys Comp. **210**, 213 (1994).
[5] R. Welter, G. Venturini, E. Ressouche, and B. Malaman, J. Alloys Comp. **218**, 204 (1995).
[6] RIETAN is a full profile Rietveld refinement code developed by F. Izumi. Y. Morii, H. R. Child, S. Funahashi, and F. Izumi, JAERI-M 91-162 (translation from Japanese).
[7] G. Liang and M. Croft, Phys. Rev. B **40**, 361 (1989).
[8] A. Szytula and J. Leciejewicz, in *Handbook on the Physics and Chemistry of the Rare Earths*, edited by K. A. Gschneider, Jr. and L. Eyring (1989), pp. 12,123; A. Szytula, J. Alloys and Comp. **181**, 123 (1992).
[9] M. P. Hill, Ph.D. thesis, Southern Illinois University at Carbondale, 1994 (unpublished).
[10] M. P. Hill (unpublished).
[11] I. Nowick, Y. Levi, I. Felner, and E. R. Bauminger, J. Magn. Magn. Mater. **147**, 373 (1995).

Magnetic studies of the metal–insulator transition in $CuIr_2S_{4-x}Se_x$ (x=0, 0.1, and 4)

P. Somasundaram and J. M. Honig
Department of Chemistry, Purdue University, West Lafayette, Indiana 47907

T. M. Pekarek and B. C. Crooker
Department of Physics, Purdue University, West Lafayette, Indiana 47907

Magnetic properties and the metal–insulator transition in $CuIr_2S_{4-x}Se_x$ with x=0.0, 0.1, and 4.0 were investigated. $CuIr_2S_{3.9}Se_{0.1}$ exhibits a transition from paramagnetism ($M/H=+1.3\times10^{-7}$ emu/g G) at higher temperatures to diamagnetism ($M/H=-1.5\times10^{-7}$ emu/g G) at lower temperatures and exhibits hysteresis on heating and cooling. The transition on warming in $CuIr_2S_{3.9}Se_{0.1}$ occurs at a lower temperature (200 K) than in $CuIr_2S_4$ (218 K) and is not observed in $CuIr_2Se_4$. © *1996 American Institute of Physics.* [S0021-8979(96)73308-0]

I. INTRODUCTION

Among the chalcogenide spinel compounds, $CuRh_2S_4$ exhibits superconductivity with a transition temperature of 4.7 K.[1–3] Recently a new thiospinel compound, $CuIr_2S_4$, with the same structure was synthesized.[4] This compound exhibits a metal–insulator transition with a transition temperature T_t=230 K. The resistivity increases by more than two orders of magnitude below T_t. This metal–insulator transition is also accompanied by a first-order structural transition from cubic spinel above T_t to tetragonal below as well as a paramagnetic to diamagnetic transition. We have investigated the effects of Se substitution in the $CuIr_2S_{4-x}Se_x$ system using x-ray diffraction, conductivity, magnetization, and heat capacity measurements. The results of magnetic studies are presented below for samples with Se concentrations x=0.0, 0.1, and 4.0.

II. EXPERIMENT

Stoichiometrically mixed powders of Cu, Ir, S, and Se were calcined at 850 °C in sealed quartz ampoules for 8 days. After regrinding, the powders were pelletized and sintered at 850 °C for 4 days. During sintering the ampoules were enclosed with additional powder of the same composition to minimize the escape of S and Se from the pellet. Powder x-ray diffraction was performed on a Siemens D500 diffractometer with Cu $K\alpha$ radiation. Sintered samples were used for magnetization studies using a Cryogenic Consultants Limited superconducting quantum interference device magnetometer. Magnetization data were taken at 5–324 K in fields up to 6 T.

III. RESULTS AND DISCUSSION

The x-ray diffraction results at 300 K confirmed that the x=0.0, 0.1, and 4.0 compositions of $CuIr_2S_{4-x}Se_x$ were monophasic at the limit of detection. Magnetization versus temperature measurements in a 0.1 T field for the x=0 and 0.1 samples are shown in Figs. 1(a) and 1(b). For the x=0 sample there is a sharp increase in magnetization on heating above T_t=218 K, and a sharp decrease below T_t=206 K. Here the transition temperature is defined as the temperature corresponding to half the change in magnetization. Resistance measurements were done on the $CuIr_2S_4$ sample using a four-probe technique. The variation of resistance as a function of temperature is given as an inset of Fig. 1(a). As can be seen, there is a sharp change in resistance of approximately two orders of magnitude at the metal–insulator transition. Our transition temperatures T_t differ from those reported by Takao *et al.*[4] who reported a T_t for $CuIr_2S_4$ of 238 K on heating and 226 K on a cooling. A detailed study of the dependence of the transition temperatures on the sulfur/metal ratio has to be carried out to understand this discrepancy. From Fig. 1(b) it is clear that the transition for the x=0.1 sample is shifted to lower temperatures, i.e., 200 K on warming and 188 K on cooling. The magnetization is almost tem-

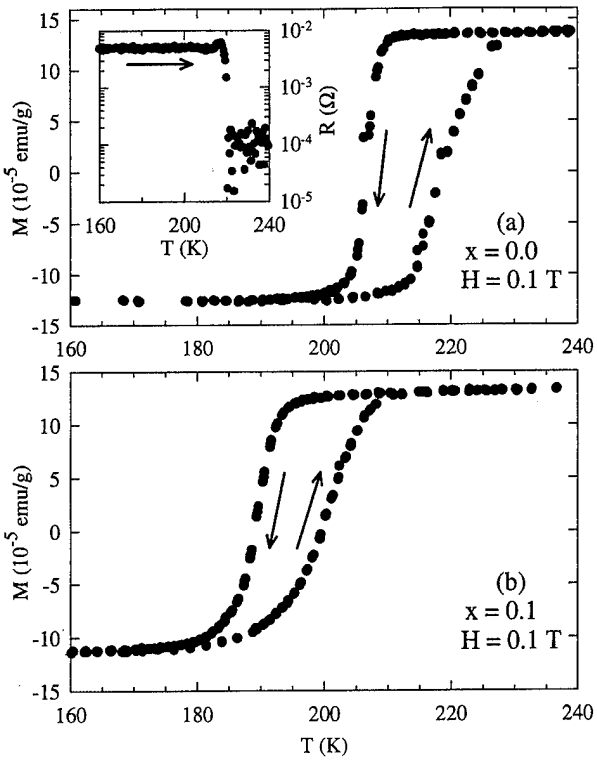


FIG. 1. Figures (a) and (b) show warming and cooling magnetization vs temperature data indicating a shift in the metal to insulator transition of $CuIr_2S_{4-x}Se_x$ for x=0.0 and 0.1, respectively. The inset of (a) shows resistance vs temperature data taken on warming in zero field.

 0021-8979/96/79(8)/5401/2/$10.00 © 1996 American Institute of Physics

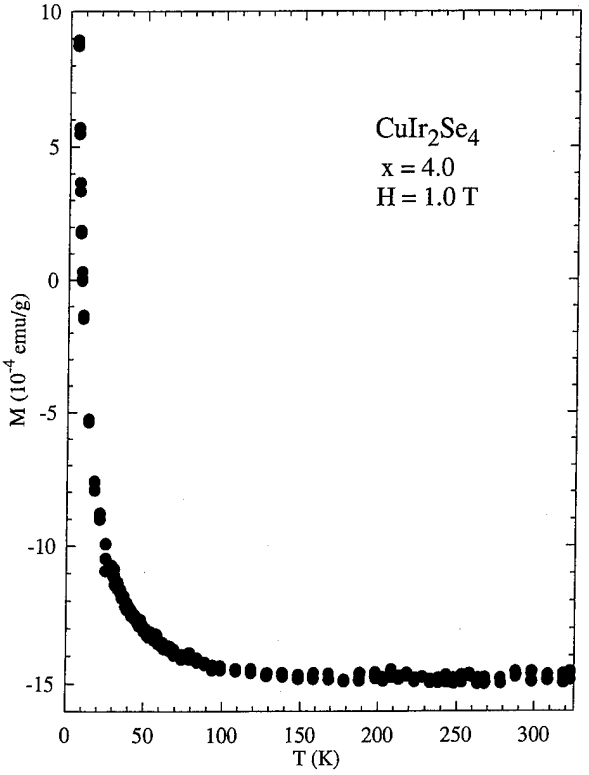


FIG. 2. Magnetization vs temperature for $CuIr_2Se_4$. The magnetization consists of a diamagnetic and a Curie contribution. No metal–insulator transition is present.

perature independent both above and below the transitions, suggesting a relatively constant carrier concentration at all temperatures in these regions. The magnetization is linearly proportional to the applied field at high (270 K) and low (150 K) temperatures. The values of M/H at 270 and 150 K for $CuIr_2S_{3.9}Se_{0.1}$ are $+1.3$ and -1.5×10^{-7} emu/g G, respectively. The change in magnetization at the metal–insulator transition is 2.7×10^{-4} emu/g for $CuIr_2S_4$ while for $CuIr_2S_{3.9}Se_{0.1}$ it is 2.5×10^{-4} emu/g. There is also a small Curie-like ($1/T$) variation at low temperature (<50 K) which is likely due to the presence of residual iridium.

Unlike the previous two samples, the $CuIr_2Se_4$ sample does not exhibit a metal–insulator transition. As can be seen in Fig. 2 the magnetization is composed of diamagnetic and Curie ($1/T$) terms. The variation of resistance as a function of temperature indicated that $CuIr_2Se_4$ is metallic from room temperature to 20 K.

Studies are underway to determine the variation of the metal–insulator transition temperature with Se concentration, x, and the point at which the metal–insulator transition disappears. Room temperature x-ray diffraction studies indicate that the spinel structure is maintained from $x=0.0$ to 4.0 in the $CuIr_2S_{4-x}Se_x$ series even past the metal–insulator transition. Takao *et al.*,[4] using magnetic susceptibility measurements, detected an increase in the metal–insulator transition temperature at higher pressures. This is contrary to the effect of pressure in most oxides that exhibit metal–insulator transition, including V_2O_3, VO_2, and Fe_3O_4.[5,6] Selenium substitution expands the lattice and reduces the chemical pressure, which should decrease the transition temperature of the metal–insulator transition, as observed in the present study.

IV. CONCLUSIONS

We have presented magnetic measurements on $CuIr_2S_{4-x}Se_x$ with $x=0.0$, 0.1, and 4.0. We found that the metal–insulator transition on warming in $CuIr_2S_{3.9}Se_{0.1}$ occurs at a lower temperature (200 K) than $CuIr_2S_4$ (218 K) and is not observed at all in $CuIr_2Se_4$.

ACKNOWLEDGMENTS

This research was supported in part by a grant from the Eppley Foundation. P.S. and J.M.H. were supported by DOE Grant No. DE-FG-90ER-45427. T.M.P. was supported by NSF Grant No. DMR-92-21390 and the Purdue Research Foundation. B.C.C. was supported by NSF Grant No. DMR-92-21390.

[1] N. H. VanMaaren, G. M. Schaeffer, and F. K. Lotgering, Phys. Lett. **25A**, 238 (1967).
[2] M. Robbins, R. H. Williams, and R. C. Miller, Solid State Commun. **16**, 933 (1967).
[3] T. Bitoh, T. Hagino, Y. Seki, S. Chikazava, and S. Nagata, J. Phys. Soc. Jpn. **61**, 3011 (1992).
[4] T. Furubayashi, T. Matsumoto, T. Hagino, and S. Nagata, J. Phys. Soc. Jpn. **63**, 3333 (1994).
[5] L. L. Van Zandt and J. M. Honig, in *Annual Review Materials Sciences*, edited by R. A. Huggins, R. H. Bube, and R. W. Roberts (Annual Reviews, Inc., Palo Alto, CA, 1974), Vol. 4.
[6] N. F. Mott, in *Metal–Insulation Transitions*, 2nd ed. (Taylor and Francis, London, 1990).

Magnetization and specific heat studies of Gd_2In

Chan-Soo Jee
Department of Science Education, Kangwon National University, Chun-Cheon 200-701, Korea

C. L. Lin and T. Mihalisin
Department of Physics, Temple University, Philadelphia, Pennsylvania 19122

Xue-Qin Wang
Department of Materials Science and Engineering, University of Pennsylvania, Philadelphia, Pennsylvania 19104

We have measured the temperature and magnetic field dependence of the magnetization for Gd_2In. The results show that Gd_2In exhibits a helical ferromagnetic transition at 190 K and an antiferromagnetic transition at 100 K in zero and low applied fields. Both the helical ferromagnetic state at temperatures between 100 and 190 K and the antiferromagnetic state at low temperatures are transformed to a simple ferromagnetic state by high applied fields. The antiferromagnetic transition temperature decreases with increasing applied field and approaches zero at $H=25$ kOe. We have also measured the temperature dependence of the specific heat for Gd_2In. The data show two distinct specific heat anomalies which are associated with the two magnetic transitions. © *1996 American Institute of Physics.* [S0021-8979(96)73408-7]

Several rare-earth-based intermetallic compounds R_2In, where R=rare earths, undergo a magnetic phase transition below room temperature and exhibit magnetization that has an unusual temperature dependence at low temperatures.[1–5] Gamari-Seale *et al.*[1] and McAlister *et al.*[6] have reported from measurements of the magnetization and electrical resistivity that Gd_2In orders ferromagnetically at $T_c=190$ K and orders as a metamagnetic antiferromagnet below $T_N=99.5$ K. McAlister *et al.* have also suggested that below 99.5 K Gd_2In has a spiral antiferromagnetic structure. However, Delyagin *et al.*[7] have concluded from ^{119}Sn Mössbauer measurements for Gd_2In that the magnetic structure remains ferromagnetic over the entire temperature interval from 5 K to $T_c=190$ K. We have extended measurements of the temperature and magnetic field dependence of the magnetization in several respects. From measurements of the field dependence of the magnetization at several temperatures between 100 and 190 K, we infer that Gd_2In exhibits a helical ferromagnetic state between 100 and 190 K in both zero field and low applied fields. In high applied fields the helical ferromagnetic state is transformed to a simple ferromagnetic state. This behavior is similar to that previously observed from the magnetization measurements for MnSi,[8] $Fe_{1-x}Co_xSi$,[9] and Co_2ScSn.[10] The helical magnetic state of MnSi and $Fe_{1-x}Co_xSi$ has been confirmed by neutron diffraction studies.[9,11] We have also measured the temperature and field dependence of the magnetization of Gd_2In below 100 K. The results show that Gd_2In is a metamagnetic antiferromagnetic at low temperatures and low applied fields. The antiferromagnetic state is induced to the ferromagnetic state by high applied fields, and T_N decreases monotonically with an increasing applied field approaching zero for a field of 25 kOe. In addition, we have measured the temperature dependence of the specific heat for Gd_2In and La_2In. To the best of our knowledge this is the first specific heat study for Gd_2In. The data for Gd_2In show two distinct specific heat anomalies at temperatures which are consistent with those obtained from magnetization measurements.

Polycrystalline Gd_2In and La_2In samples were prepared in an inert atmosphere arc furnace with appropriate care taken to compensate for the weight loss of the more volatile In. The samples were wrapped in Ta foils and were annealed under high vacuum at 800 °C for 7 days. Powder x-ray diffraction measurements at room temperature indicated that both the small magnetization sample (50 mg) and the larger specific heat sample (2 g) were single phase and crystallized with the Ni_2In structure. The lattice parameters $a=5.41$ A and $c=6.76$ A for Gd_2In are in good agreement with those previously published.[12] The magnetization was measured from 5 to 400 K in magnetic fields up to 5 T using a commercial superconducting quantum interference device magnetometer. The specific heat was measured from 15 to 300 K using a semiadiabatic heat pulse technique.

Shown in Fig. 1 is the temperature dependence of the magnetization of Gd_2In measured in applied fields of 200 Oe and 2 kOe. It can be seen from the data for $H=200$ Oe that the magnetization increases rapidly as the sample is cooled below 210 K and saturates at about 190 K, which is the magnetic phase transition temperature. The magnetization is essentially temperature independent from 190 down to 110 K. Below 110 K the magnetization decreases dramatically indicating a second magnetic transition. At lower temperatures the magnetization becomes temperature independent again. This behavior is the same as that previously reported by McAlister *et al.*[6] The data measured at 2 kOe show a qualitatively similar behavior except that M decreases more gradually from 150 to 190 K and thus has a more "rounded" shape. Later we will show that the temperature independent behavior above 110 K completely disappears for higher fields. Shown in the inset of Fig. 1 is $1/M$ vs T measured at 2 kOe. It can be seen that the high temperature data, i.e., $T>240$ K, follow the Curie law. From the slope we can calculate the Curie constant and thus the paramagnetic effective moment. We find a value of 7.5 u_B which is reasonably close to the 7.94 u_B predicted theoretically for the trivalent Gd ion.[13]

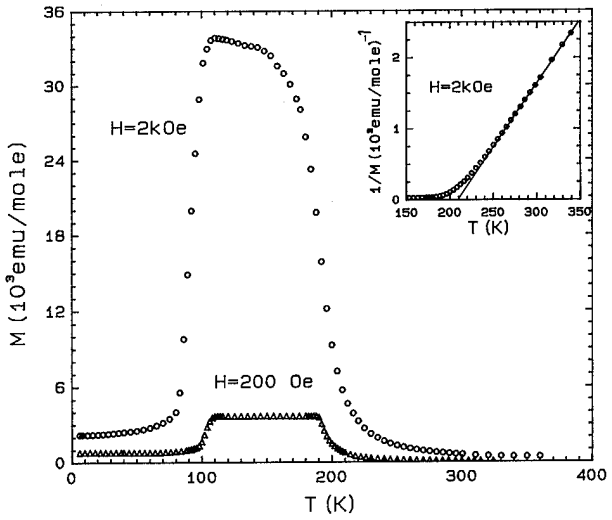


FIG. 1. M vs T for Gd_2In measured at $H=200$ Oe and $H=2$ kOe.

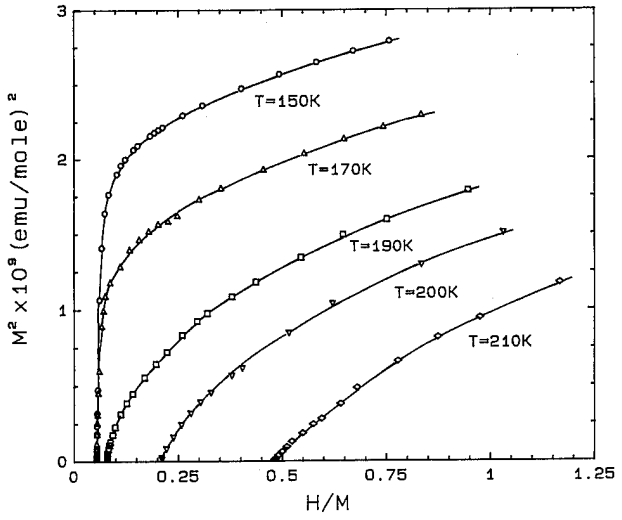


FIG. 3. Arrott Plots (M^2 vs H/M) for Gd_2In at $T=150$, 170, 190, 200, and 210 K.

In order to understand the temperature independent behavior of the magnetization between 110 and 190 K, we have measured the field dependence of the magnetization at several temperatures in this interval. Shown in Fig. 2 are the $M(H)$ curves measured at $T=110$, 150, 170, 190, and 200 K. Note that at $T=110$ K $M(H)$ increases linearly with increasing applied field up to a critical field H_c of about 2 kOe, then it starts to saturate when the applied field is increased further. This linear behavior of $M(H)$ at low fields is different from that of simple ferromagnets. For higher temperatures, e.g., $T=150$, 170, and 190 K, $M(H)$ shows the same type of behavior except the critical field H_c decreases. At $T=200$ K, the linear behavior disappears and $M(H)$ shows a negative curvature over the entire applied field range as one would expect for $T>T_{\text{Curie}}$. The $M(H)$ behavior described above has been observed for other magnets, e.g., MnSi,[8] $Fe_{1-x}Co_xSi$,[9] and Co_2ScSn.[10] This behavior has been explained in terms of a helical magnetic structure below T_c for zero and low applied fields. This interpretation has been confirmed by neutron diffraction and electron spin resonance measurements for the MnSi and $Fe_{1-x}Co_xSi$ systems.[9,11] Moreover, theoretical calculations[14,15] for helical magnets have predicted the same behavior. . Mössbauer and spin resonance experiments to confirm the helical ferromagnetic structure of Gd_2In between 190 and 110 K would be useful.

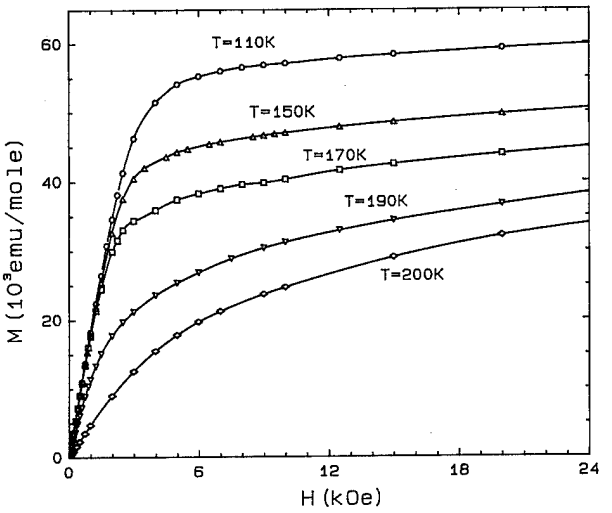


FIG. 2. M vs H for Gd_2In measured at $T=110$, 150, 170, 190, and 200 K.

To obtain the helical ferromagnetic transition temperature T_c, we have plotted M^2 vs H/M (Arrott plots) for Gd_2In at various temperatures. It can be seen from Fig. 3 that these plots do not show the linear behavior which is characteristic of simple ferromagnets. But these plots are similar to those obtained for the helical systems mentioned above. For simple ferromagnets the transition temperature is defined as the temperature for which a linearly extrapolated curve on the Arrott plot goes through the origin. However, for the helical systems T_c is obtained from low field M^2 vs H/M plots by selecting the isotherm for which the H/M axis intercept first deviates from the $T<T_c$ value. In Fig. 3 this is the $T=190$ K isotherm. This T_c value is the same as that determined by other groups[6,16] from magnetization and electrical resistivity measurements.

It was mentioned earlier that the magnetization measured at $H=2$ kOe exhibits a rounded behavior for $T>150$ K as shown in Fig. 1. This rounded behavior indicates that the helical ferromagnetic state is suppressed and a simple ferromagnetic state occurs for $T>150$ K and $H=2$ kOe. It was also mentioned that the critical field H_c increases with decreasing temperature indicating that at lower temperatures, i.e., T near 110 K, the helical ferromagnetic state can only be suppressed by a much larger field. Shown in the main portion of Fig. 4 is the temperature dependence of the magnetization measured at higher fields, i.e., 10, 15, 20, and 25 kOe. It can be seen that the helical ferromagnetic state is completely suppressed and only a simple ferromagnetic state occurs for these fields.

Returning to Fig. 1, the temperature dependence of the low field magnetization shows that Gd_2In undergoes a second magnetic phase transition at a lower temperature. The

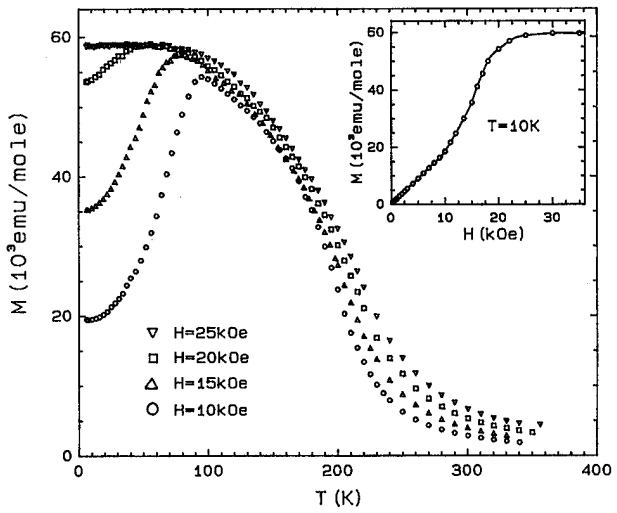


FIG. 4. M vs T for Gd_2In measured at $H=10$, 15, 20, and 25 kOe. Inset: M vs H for Gd_2In measured at $T=10$ K.

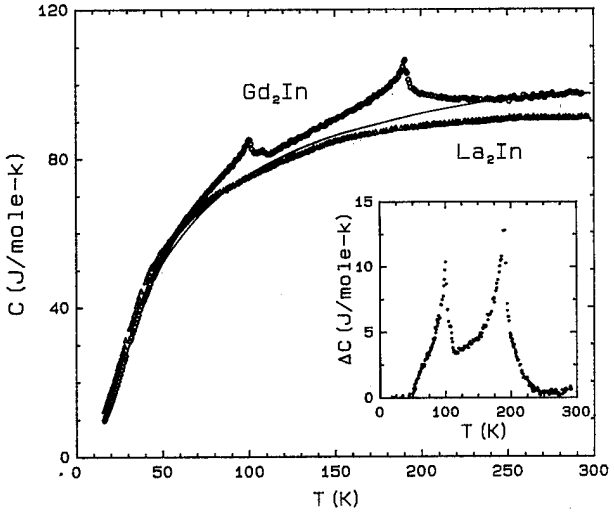


FIG. 5. C vs T for Gd_2In and La_2In. The solid curve is the theoretical fit to the experimental data of Gd_2In. Inset: The magnetic specific heat of Gd_2In.

transition temperature which can be determined as the maximum slope of the magnetization has a value of 100 K for the data measured at 200 Oe. We have measured the field dependence of the magnetization at various temperatures below 100 K. Shown in the inset of Fig. 4 is $M(H)$ at $T=10$ K. For $H<10$ kOe $M(H)$ increases linearly with increasing applied field. This linear field dependence together with the sharp decrease in magnetization with decreasing temperature in the vicinity of 100 K (see the data measured at $H=200$ Oe and 2 kOe shown in Fig. 1.) indicate that below 100 K Gd_2In has an antiferromagnetic state. The temperature independent magnetization below 100 K measured for low fields (e.g., 200 Oe shown in Fig. 1) could be due to a helical antiferromagnetic structure. McAlister *et al.*[6] have proposed a spiral magnetic structure below 100 K by comparing the behavior of Gd_2In with that of other compounds.

The inset of Fig. 4 shows that for $H>10$ kOe the magnetization measured at 10 K increases significantly (about a factor of 3) and finally saturates at the higher fields. This indicates that Gd_2In is a metamagnetic antiferromagnet at low temperatures and that the antiferromagnetic state is induced to the ferromagnetic state by high applied fields.

We have also measured the temperature dependence of the specific heat of Gd_2In and La_2In, which has not been reported in the literature. The results are shown in Fig. 5. It can be seen that two specific heat anomalies occur at 100 and 190 K for Gd_2In which are associated with the antiferromagnetic and helical ferromagnetic transitions, respectively.

To obtain the magnetic specific heat and calculate the entropy for Gd_2In, we need to subtract the phonon contribution from the total specific heat. However, the specific heat of La_2In cannot be used as the nonmagnetic specific heat contribution for Gd_2In since it is greater than the specific heat of Gd_2In below 50 K. In order to obtain the phonon contribution to the specific heat of Gd_2In, we have used the theoretical Debye model to fit the low temperature (below 50 K) and the high temperature (above 220 K) data of Gd_2In. Note that we have assumed that above 220 K the specific heat is only due to the phonon contribution. The fit is shown by the solid curve in Fig. 5. The magnetic specific heat can be extracted from subtracting the theoretical Debye curve from the total specific heat. The result is shown in the inset of Fig. 5. The magnetic entropy of Gd_2In below 200 K is estimated by the above procedure to be about 6 J/mol K. This value is much smaller than $2R[\ln(2J+1)]=34$ J/mol K with $J=7/2$ for the disordered Gd moment. This small value could be due to the helical ferromagnetic state between 100 and 190 K and the helical antiferromagnetic state below 100 K.

[1] H. Gamari-Seale, T. Anagnostopoulos, and J. K. Yakinthos, J. Appl. Phys. **50**, 434 (1979).
[2] S. Parviainen and S. Penttila, Phys. Status Solidi a **60**, K119 (1980).
[3] R. D. Hutchens, W. E. Wallace, and N. Nereson, J. Solid State Chem. **9**, 152 (1974).
[4] S. Kawano, H. Umezaki, and T. Shibata, Annu. Rep. Res. Reactor Inst. Kyoto Univ. **7**, 99 (1974).
[5] H. Umezaki, S. Kawano, N. Achiwa, and T. Shibata, Annu. Rep. Res. Reactor Inst. Kyoto Univ. **7**, 94 (1974).
[6] S. P. McAlister, J. Phys. F **14**, 2167 (1984).
[7] N. N. Delyagin, G. T. Mudzhiri, V. I. Nesterov, and S. I. Reiman, Sov. Phys. JETP **59**, 592 (1984).
[8] K. Motoya, H. Yasuoka, Y. Nakamura, and J. H. Wernick, J. Phys. Soc. Jpn. **44**, 1525 (1978).
[9] J. Beille, J. Voiron, F. Towfiq, M. Roth, and Z. Y. Zhang, J. Phys. F **11**, 2153 (1981).
[10] C. L. Lin, T. Mihalisin, and N. Bykovetz, J. Magn. Magn. Mater. **116**, 355 (1992).
[11] M. Ishida, Y. Endoh, S. Mitsuda, Y. Ishikawa, and M. Tanaka, J. Phys. Soc. Jpn. **54**, 2975 (1985).
[12] A. Palenzona, J. Less-Common Metals **16**, 379 (1968).
[13] See, for example, C. Kittel, *Introduction to Solid State Physics* (Wiley, New York, 1971).
[14] O. Nakanishi, A. Yanase, and A. Hasegawa, J. Magn. Magn. Mater. **15–18**, 879 (1980).
[15] P. Bak and M. H. Jensen, J. Phys. C **13**, L881 (1981).
[16] W. L. Liu, M. Yamashita, M. Kurisu, H. Kadomatsu, and H. Fujiwara, J. Phys. Soc. Jpn. **56**, 421 (1987).

Magnetic viscosity far and close to equilibrium in the superparamagnetic alloy

A. Maraner
Centro di Fisica degli stati Aggregati ITC-CNR, I-38050, Povo, Trento, Italy

X. Zhang
Department of Fundamental Physics, University of Barcelona, E-08028 Barcelona, Spain

A. Cavalleri
Centro di Fisica degli Stati Aggregati ITC-CNR, I-38050, Povo, Trento, Italy

J. Tejada
Department of Fundamental Physics, University of Barcelona, E-08028 Barcelona, Spain

S. Vitale
Department of Physics, University of Trento, I-38050, Povo, Trento, Italy

We report on the simultaneous measurements of the magnetic viscosity and of the ac linear magnetic susceptibility for a sample of $Cu_{90}Co_{10}$. The magnetic viscosity $S=(1/M_0)\ [dM/d\ \ln(t)]$, with M the sample magnetization and M_0 the magnetization value at the beginning of the logarithmic relaxation, is measured by a standard method that involves the application to the sample of a large field step after saturation. The ac susceptibility is measured both directly at very low (≈microoersteds) ac field amplitudes and from the thermal magnetization noise in the sample, the two values always being found in quantitative agreement. The imaginary susceptibility is found to be a frequency independent value $\chi_0''(T)$ at low frequencies, a behavior that translates, when expressed in the time domain, to logarithmic relaxation $(dM/d\ \ln t) = (2/\pi)\chi_0''(T)H_0$, of the magnetization after a step excitation H_0. Both S and $\chi_0''(T)$ are found to be proportional to the temperature for temperatures ≤4.2 K. In addition, S and $\chi_0''(T)$ are found to be of the same order of magnitude. We discuss how these results are in agreement with the idea that in both kinds of experiments one is probing an energy barrier height distribution and that, in addition, the size of the distribution involved in the "critical state," prepared by relaxation experiments, is of the same order of magnitude as that involved in the quasiequilibrium state probed by the ac susceptibility measurements. © *1996 American Institute of Physics.* [S0021-8979(96)73508-3]

I. INTRODUCTION

Magnetic viscosity experiments have proven to be a very valuable means to explore the dynamics of spin systems in magnetic materials. The standard way to perform a measurement of magnetic viscosity is by means of relaxation experiments.[1,2] In a relaxation experiment, the decay of the magnetization of a system after a stepwise change of the applied magnetic field is measured. The typical step–field amplitude is large, comparable to or greater than the coercive field. In the appropriate time window the relaxation is at least approximately logarithmic with time. The proportionality factor $S(T)$ between the magnetization and the logarithm of the time is called magnetic viscosity:

$$M(t)/M_0=1-S(T)\ln(t/t_0), \tag{1}$$

where M_0 is the value of the magnetization at the beginning of the logarithmic relaxation.

The phenomenon is usually attributed to the existence of a collection of simple exponential relaxations with distributed time constants.[3] Magnetic systems exhibiting hysteresis are characterized by a distribution of energy barriers. The sudden magnetization reversal used in the relaxation experiments brings the system into a new configuration far from its equilibrium state. Each portion of the system which is trapped in a metastable state relaxes toward a stable state either by thermal activation or by any nonthermal process like quantum tunneling. The lifetime of the metastable state is related to the barrier energy parameters. Thus magnetic viscosity experiments probe the energy barriers distribution features.

In addition linear ac susceptibility and thermal equilibrium noise experiments have been shown[4–7] to give a means to perform magnetic relaxation measurements. In many magnetic systems the equilibrium magnetization noise shows, in the low frequency range, a $1/f$ power spectrum. This originates, via the standard fluctuation–dissipation formula, from a frequency independent imaginary part $\chi_0''(T)$ in the ac susceptibility. This is measured in the linear response regime where the typical amplitude of the field applied to the sample is much lower than the coercive field. The frequency independent imaginary susceptibility $\chi_0''(T)$ translates, in the time domain, into a logarithmic relaxation[6,7] with velocity:

$$dM/d\ \ln(t)=(2/\pi)\chi_0''(T)H_0. \tag{2}$$

Thus the measurement of the ac linear imaginary susceptibility $\chi_0''(T)$ is the thermal equilibrium analogous to the measurement of the magnetic viscosity $S(T)$.

At thermal equilibrium the picture of magnetic subsystems relaxing outside a metastable state should be rephrased in terms of subsystems whose magnetization is hopping between nearby free energy minima.[8] Both the barrier features and the energy splitting between the minima now

 0021-8979/96/79(8)/5406/3/$10.00 © 1996 American Institute of Physics

affect the dynamics of the systems and thus both the susceptibility and the related thermal magnetic noise.[8]

The two experimental methods operate at scales of field and magnetization variations that differ by orders of magnitude. Thus it is worth asking whether the involved energy distributions can be the same.

The question has become more puzzling in connection with the problem of the macroscopic quantum tunneling of magnetic systems. Indeed both kinds of experiments have observed dependencies of $S(T)$ or $\chi_0''(T)$ on the temperature which could possibly be explained by assuming an underlying quantum tunneling mechanism.

In the present article we give for the first time the results of the simultaneous measurement of the magnetic viscosity, the linear susceptibility, and the equilibrium thermal noise on a sample of the superparamagnetic alloy $Cu_{90}Co_{10}$. The comparison between the two sets of data shows that the barrier energy height distributions involved in the two experiments are of the same order of magnitude.

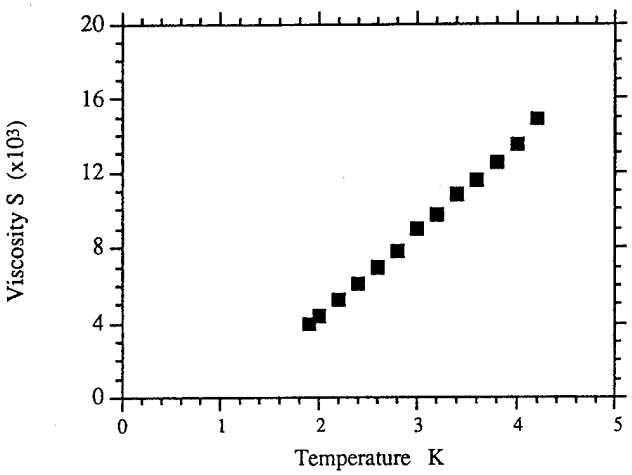


FIG. 1. The magnetic viscosity $S(T)$ as a function of the temperature.

II. EXPERIMENTAL METHODS AND RESULTS

The sample studied is a $Cu_{90}Co_{10}$, 60-μm-thick, 5-mm wide rapidly quenched ribbon, prepared by planar flow casting. As shown by x-ray diffractometry,[9] the Cu and Co phases are immiscible and the Co forms very small clusters of fcc ordered phase.

Both the dc magnetic measurements and the relaxation measurements have been carried out using a commercial rf superconducting quantum interference device (SQUID) magnetometer in the temperature range of 2–300 K. The magnetization versus applied field at room temperature, has been measured and the data fitted to the Langevin law. Thus an estimation of the average diameter $\langle d\rangle$ of the Co magnetic clusters with a value of $\langle d\rangle = 4.2$ nm has been obtained.

The magnetization has been measured both with the zero-field cooling (ZFC) and the field cooling (FC) procedures.[1] A blocking temperature[1] $T_B = 16$ K has been found. Below this temperature the sample exhibits hysteresis.

For the measurement of the magnetic viscosity versus temperature, the magnetization decay at each temperature has been measured in a time window of 2 h. The sample is cooled down to the desired temperature in an applied field $H_1 = 8\times10^3$ A/m and then the magnetization is reversed by suddenly switching the field to the new value of $H_2 = -8\times10^3$ A/m. The magnetization has been found to follow a logarithmic decrease with time. The magnetic viscosity values $S(T)$ reported in Fig. 1 are obtained by fitting Eq. (1) to the data. The figure shows that the viscosity depends linearly on the temperature. A best fit to the data gives a slope $dS/dT = (4.8\pm0.2)\times10^{-3}$ K^{-1}. The data do not extrapolate to zero at $T = 0$ K.

The complex susceptibility and magnetic noise measurements have been performed in the temperature range of 1.1–4.2 K. The experimental setup has already been described.[10] Here we only recall that the method basically consists of measuring the complex self-unductance $L(\omega) = L'(\omega) + iL''(\omega)$ of a superconducting transformer coupled to the SQUID on one side and to the sample on the other. At each temperature, the self-inductance is measured as a function of the frequency. During the measurement the ac field variation applied to the sample has been $H_0 \approx 8\times10^{-4}$ A/m.

The data for $L(\omega)$ are converted to the complex susceptibility using standard formulas for coils. The inaccuracy due to geometrical factors affects the calculated value of the susceptibility, the error being larger for samples with a real susceptibility of less than unity, like the present one. However this does not affect the comparison with the noise data. In fact the Nyquist formula only contains the imaginary part $L''(\omega)$ of the inductance,

$$S_\phi(\omega) = 2k_BT(M_{SQ}^2/|L(\omega)|^2)[L''(\omega)/\omega] + S_0, \qquad (3)$$

where $S_\phi(\omega)$ is the noise spectral density at the SQUID output, M_{SQ} is the mutual inductance between the transformer and the SQUID, and S_0 is the noise of the SQUID in the absence of the sample.

The measured values of $S_\phi(\omega)$ have been found to show a $1/f$ shape and to agree without any adjustable parameter with the spectra calculated from the measured inductance data through formula (3). The consistency of the two sets of data demonstrates the thermal equilibrium of the sample at the measured temperature T.

The imaginary susceptibility has been found to be frequency independent at each temperature in the frequency range of 0.01–10 Hz. The frequency independent imaginary susceptibility $\chi_0''(T)$, both the data directly observed and those derived from the noise via Eq. (3), are shown in Fig. 2 as a function of the temperature. The figure shows that $\chi_0''(T)$ depends linearly on the temperature. A best fit of the data gives a slope $d\chi_0''/dT = (3.2 \pm 0.3)\ 10^{-3}\ \mathrm{K}^{-1}$.

III. DISCUSSION

It is natural to compare, through Eqs. (1) and (2), the rates of logarithmic relaxation obtained by the two experimental methods: $(1/H_0)[dM/d\ \ln(t)] = (2/\pi)\chi_0''(T) \approx 1.2 \times 10^{-2}$ ($T = 4.2$ K) and $S(4.2\ \mathrm{K}) \approx 1.5\times10^{-2}$. As the two quantities are found at least to be in an order of magnitude

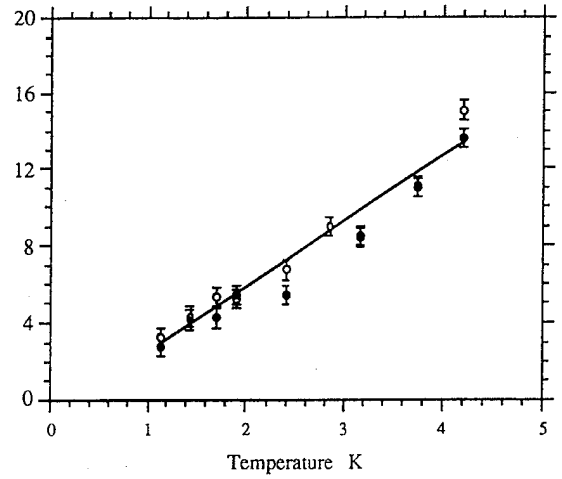


FIG. 2. The imaginary susceptibility $\chi_0''(T)$ as a function of temperature. Open symbols represent the as-measured data. Closed symbols represent the data calculated from noise via Eq. (3). The continuous line represents the linear best fit to the data.

agreement let us discuss if this agreement is coincidental or if instead it can be explained by looking at the underlying physical picture.

The escape of the magnetization from a metastable state occurs as an exponential relaxation, $dM/dt \propto e^{-\Gamma t}$, where Γ is the decay rate. If the escape is thermally activated, the decay rate follows the Arrhenius law $\Gamma=\Gamma_0 \exp(-U/k_BT)$, with U the energy barrier height and Γ_0 the attempt frequency. It is known that by invoking the collective contribution of many exponentially relaxing subsystems with suitably distributed rates Γ one can explain the observed logarithmic time law.[3] To be specific, it has been shown that by integrating over a wide and smooth enough distribution of U, the magnetic viscosity becomes[1,11]

$$S(T)=k_BT/\langle U\rangle \tag{4}$$

where, $\langle U\rangle$ is the average activation energy. As $S(T)$ does not extrapolate to zero at $T=0$, the model describes the experiment only qualitatively. However to get a broad estimate of $\langle U\rangle/k_B$ one can use the highest available temperature data, $T=4.2$ K, to get $\langle U\rangle/k_B \approx 300$ K.

$\langle U\rangle$ also determines the temperature at which the magnetization reaches a maximum in the ZFC magnetization process[1,11] and is then related to the blocking temperature by $\langle U\rangle \approx 30 k_B T_B$. This gives $\langle U\rangle/k_B \approx 500$ K. Notice that this value is not far off the upper limits one gets when estimating the overall anisotropy energy of a grain, $U \approx KV_g$, with V_g indicating some average value of the volume of a single grain and K the anisotropy constant. Taking[9] $K \approx 3\times 10^5$ J/m^3 and V_g from the figure quoted in the previous section, one gets $U/k_B \approx 1000$ K.

As already stated, the description of the system behavior at thermal equilibrium is based on a collection of two-level systems. The local magnetization overcomes the barrier between two nearby free energy minima, which are in general nondegenerate. The escape rate is then the sum of the rates of the two minima, the ratio of which has to agree with thermal equilibrium requirements.[7,8] If the escape is due to thermal activation, if the energy barrier heights are distributed, and if the energy Δ of separation between the minima is also distributed up to a maximum value $\Delta_{\max}$ and $\Delta_{\max} \gg k_BT$, then the frequency independent imaginary susceptibility is linear with the temperature:

$$\chi_0'' \approx (N_gV_g/V_s)(\mu_0 M_g^2 V_g/\Delta_{\max})(k_BT/\langle U\rangle), \tag{5}$$

where N_g and M_g are the total grain number and the grain magnetization, respectively, and V_S is the sample volume. Equation (5) is taken from Ref. 8 with the additional factor N_gV_g/V_s due to the dilution of the clusters within the sample. By comparison with Eqs. (4) and (5) this gives

$$\chi_0'' \approx (N_gV_g/V_s)(\mu_0 M_g^2 V_g/\Delta_{\max})S(T). \tag{6}$$

The first factor, the dilution, can be estimated to be $(N_gV_g/V_s) \approx 0.1$. Thus in order to explain the observed agreement one should have $(\mu_0 M_g^2 V_g/\Delta_{\max}) \approx 10$.

If the energy splitting Δ of the two-level system is of dipolar origin, then $\Delta=\mu_0 \mathbf{m}\cdot\mathbf{H}$ with $\mathbf{m}$ the total cluster magnetic moment and $\mathbf{H}$ the local value of the magnetic field. The maximum $\Delta_{\max}$ is attained for antiparallel vectors and is $\Delta_{\max}=\mu_0 M_g V_g H_{\max}$, with $H_{\max}$ the maximum value of the field experienced by the grain so that $(\mu_0 M_g^2 V_g/\Delta_{\max}) \approx M_g/H_{\max}$. To quantitatively evaluate $H_{\max}$ is difficult. Estimating $H_{\max}$ as the mean magnetization of the sample and taking M_g in the range of values observed for cobalt and cobalt alloys, one gets $1 \leqslant (\mu_0 M_g^2 V_g/\Delta_{\max}) \leqslant 100$ which is in the right range to explain the observed agreement.

The data so far presented and discussed are consistent with the thermal activation regime as no crossover to a nonthermal behavior has been detected yet with either technique. The above discussion predicts that if a crossover exists to a quantum regime, both methods should detect it at the same temperature T_c. Quantum tunneling theories predict[1,11] for the present sample $T_c \approx 0.1$ K. Experiments are in progress to verify this prediction.

ACKNOWLEDGMENTS

Work supported in part by UE Grant No. ERB4050PL930639 and Consoraio Criospario Ricerche.

[1] J. Tejada, X. X. Zhang, and E. M. Chudnovsky, Phys. Rev. B **47**, 14977 (1993); J. Tejada, X. X. Zhang, and L. L. Balcells, J. Appl. Phys. **73**, 6709 (1993), and refences therein.

[2] B. Barbara *et al.* J. Magn. Magn. Mater. **140–144**, 1825 (1995); B. Barbara, *et al.*, J. Appl. Phys. **73**, (1993) and references therein.

[3] R. Street and J. C. Wolley, Proc. Phys. Soc. London Sect. A **62**, 562, (1949).

[4] M. Ocio, H. Bouchiat and P. Monod, J. Phys. Lett. **46**, L647 (1985).

[5] G. A. Prodi, S. Vitale, M. Cerdonio, and P. Falferi, J. Appl. Phys. **66**, 5984 (1989); G. Durin, P. Falferi, M. Cerdonio, G. A. Prodi, and S. Vitale, *ibid.* **73**, 5363 (1993).

[6] M. Cerdonio, P. Falferi, G. Durin, A. Maraner, G. A. Prodi, R. Tommasini, and S. Vitale, Physica B **165&166**, 65, (1990).

[7] S. Vitale, A. Cavalleri, M. Cerdonio, A. Maraner, and G. A. Prodi, J. Appl. Phys. **76**, 6332 (1994).

[8] S. Vitale, M. Cerdonio, G. A. Prodi, A. Cavalleri, P. Falferi, and A. Maraner, in *Quantum Tunnelling in Magnetic Systems*, edited by B. Barbara and L. Ghunter, Nato Series in Physics (in press).

[9] R. H. Yu, X. X. Zhang, J. Tejada, M Knobel, P. Tiberto, and P. Allia, J. Appl. Phys. (in press).

[10] S. Vitale, G. A. Prodi, and M. Cerdonio, J. Appl. Phys, **65**, 2130 (1989).

[11] J. Tejada and X. X. Zhang, in Ref. 8.

Simultaneous molecular and spin dynamics: Quasiclassical approximation and quantum effects

V. P. Antropov and B. N. Harmon
Ames Laboratory and Department of Physics & Astronomy, Iowa State University, Ames, Iowa 50011

We sketch the derivation of a set of equations of motion for the simultaneous treatment of both molecular and spin dynamics. The equations can be extended through the concept of imaginary time density functional theory, to describe the penetration of classically forbidden regions. © *1996 American Institute of Physics.* [S0021-8979(96)73608-3]

First principles calculations of spin dependent electronic structures have been restricted to $T=0$ K, static magnetic moment (MM) configurations. To overcome these limitations we have recently proposed a method[1] which allows the torque on individual MM to be obtained and their dynamics evaluated, much in the way *ab initio* temperature dependent molecular dynamics is presently performed. Here we give more details about the description of simultaneous spin and molecular dynamics announced in Ref. 1, and discuss how several quantum effects can be included within the present formalism. An application for fcc Fe can be found in Ref. 1.

There are several ways at arriving at the final equations. Here we follow a quite general approach involving the time dependent WKB method for the adiabatic and quasiclassical approximations. In the former one obtains the adiabatic limit when there is a large difference in characteristic time scales between various degrees of freedom (e.g., nuclei and electrons), while in the latter one obtains the quasiclassical limit when the length over which the potential changes is much larger than the electron wavelength.[2]

We start from the basic time-dependent Schrödinger equation

$$i\frac{d}{dt}\Psi=\hat{H}\Psi, \tag{1}$$

where $\hat{H}$ is the total Hamiltonian,

$$\hat{H}=-\sum\frac{\nabla_{\mathbf{R}}^2}{2M}+V_{II}-\sum\frac{\nabla_{\mathbf{r}}^2}{2m}+V_{ee}+V_{Ie} \tag{2}$$

(for simplicity we will omit electron spin indices for the time being). Here indices I and e are ionic and electronic indices, respectively. We can separate the wave function in a manner convenient for applying subsequent approximations

$$\Psi=C(t)U_sU_{\mathbf{R}}\Phi(\mathbf{R},t)\psi(\mathbf{R},\mathbf{r},t), \tag{3}$$

where $C(t)$ is the semiclassical caustic,

$$U_{\mathbf{R}}=\exp\{iS(\mathbf{R},t)\} \tag{4}$$

and

$$U_s=\exp\{S_s(\mathbf{r},t)\}=\exp\{\lambda\sigma_- -\lambda^*\sigma_+\}. \tag{5}$$

In Eq. (5) λ chosen to diagonalize the Hamiltonian in spin space, is some function of angles related to the direction of the internal magnetic field **B** and, in general, is a function of electronic coordinates.

We first assume that the S function changes slowly in time and in space, then the time-dependent WKB approach starts from the expansion

$$S(\mathbf{R},t)=S(\mathbf{R}_0,t_0)+\int_{\mathbf{R}_0}^{\mathbf{R}}\nabla_{\mathbf{R}}S\,d\mathbf{R}+\int_{t_0}^{t}\nabla_tS\,dt. \tag{6}$$

To find possible trajectories we have to optimize the quantum mechanical action

$$L=\int_{t_0}^{t}dt\left\langle\Psi\left|\left[i\hbar\frac{\partial}{\partial t}-\hat{H}\right]\right|\Psi\right\rangle \tag{7}$$

using the set of wave functions from Eqs. (3)–(5). Simple but tedious variational calculations (relative to ψ) lead us to the next electronic equation

$$i\frac{\partial\psi}{\partial t}=H\psi+\gamma_I\psi+\gamma_s\psi, \tag{8}$$

where the electronic Hamiltonian is written as

$$H=\left(-\sum\nabla_{\mathbf{r}}^2+V_{ee}(\mathbf{r})+V_{eI}(\mathbf{r},\mathbf{R})+\frac{1}{2}\sum\sigma_{z_i}B_{z_i}\right)\psi, \tag{9}$$

with site-dependent spin coordinate systems. The additional terms in Eq. (8) are

$$\gamma_I=\sum\int_{t_0}^{t}(\mathbf{P}\,d\mathbf{R}+\mathbf{R}\,d\mathbf{P}), \tag{10}$$

a molecular phase factor,[3] and the factor

$$\gamma_s=\sum(\alpha\dot{\alpha}^*-\alpha^*\dot{\alpha})\frac{\sigma_z}{2}=\sum\frac{\sigma_z}{2}\int dt\dot{\varphi}(1-\cos\theta), \tag{11}$$

where $\alpha=\xi/(1+|\xi|^2)^{1/2}$ and $\xi=\exp(-i\varphi)\tan\theta/2$, is directly connected with the spin geometric phase.[3] It is worthwhile to note that these additional terms in the Hamiltonian are not kinetic or potential energy terms. Their appearance is associated with the reduction of some of the degrees of freedom in the original wave equation.

To install the connection with the well known adiabatic approach we note that in this derivation the following terms have been dropped in the above equations:

$$H_{Ie}^{\text{off}}=\Phi^2\psi^*\nabla_{\mathbf{R}}^2\psi+2\Phi\psi^*\nabla_{\mathbf{R}}\Phi\nabla_{\mathbf{R}}\psi \tag{12}$$

and

$$H_{wp}=\psi^*\psi\Phi\nabla_{\mathbf{R}}^2\Phi \tag{13}$$

 0021-8979/96/79(8)/5409/3/$10.00 © 1996 American Institute of Physics

in order to remove non-adiabatic ion–electron interactions and the wavepacket motion explicitly. At the same time we have dropped a spin flip term $H_{es}^{\text{off}} \sim A\sigma_- + A^*\sigma_+$ which would otherwise appear in Eq. (8).

The terms (12) which arise from the time-dependent WKB and adiabatic approximation are exactly the terms dropped in the adiabatic molecular dynamics (Born-Oppenheimer) equations of motion. The term (13) is a separate term arising in the WKB approach and is associated with the motion of the ionic wavepacket. The extraction of the analogous terms for the spin motion is more complicated because in general the angles of the MM are functions of the electronic coordinates. In order to arrive at a set of computationally feasible dynamical equations in which the spin term γ_s can be treated as a pure phase factor we need to remove the dependence on electronic coordinates. This may be accomplished by assuming about each site (e.g., within a muffin-tin sphere or an atomic polyhedra) that the spin or moment density direction is independent of the spatial coordinates. The dynamics of the local moment will then correspond to a "rigid" spin approximation (RSA).

Finally the total wave function can be written as

$$\Psi(\mathbf{R},\mathbf{r},t)=\sum C(t)\Phi(\mathbf{R}_0,t_0) \times\exp[\gamma_I+\gamma_s+\boldsymbol{\delta}\boldsymbol{\omega}/4]\psi(\mathbf{R},\mathbf{r},t), \tag{14}$$

where $\boldsymbol{\omega}$ is a vector of fundamental frequencies of the trajectory and $\boldsymbol{\delta}$ is a vector of Maslov indices, associated with the quantum effects of zero point motion.[4] Then we obtain for the equations of the slow degrees of freedom (obtained by extremizing the corresponding classical trajectories)

$$\dot{\mathbf{P}}=-\nabla_{\mathbf{R}}V_{II}-\langle\psi|\nabla_{\mathbf{R}}V_{eI}|\psi\rangle; \quad M\dot{\mathbf{R}}=\mathbf{P}, \tag{15}$$

for the ionic coordinates, and for each site we have

$$\begin{aligned}\dot{\alpha}&=\frac{\partial V_{ss}}{\partial\alpha^*}+\langle\psi|\frac{\partial V_{es}}{\partial\alpha^*}|\psi\rangle;\\ \dot{\alpha}^*&=-\frac{\partial V_{ss}}{\partial\alpha}-\langle\psi|\frac{\partial V_{es}}{\partial\alpha}|\psi\rangle\end{aligned} \tag{16}$$

for the MM orientation. The corresponding EOM for the fast electronic degrees of freedom has the form

$$i\frac{\partial\psi}{\partial t}=H\psi, \tag{17}$$

where H is given in Eq. (9). In Eq. (16) we have separated the spin dependent potential into a term V_{ss}, which gives the torque due to the interaction among the rigid moments, and a second term which involves the coupling to the electronic degrees of freedom and contains non-classical corrections such as orbital and coordinate dependence. This whole set of equations is suitable for the description of time dependent processes in chemical reactions and solids where magnetic or spin effects play a role. The forces in (15) became the usual Hellmann-Feynman forces in the adiabatic limit.

Now we would like to discuss the opportunity to add some stationary quantum corrections to this dynamics (the semiclassical quantization of levels and tunneling effects). A

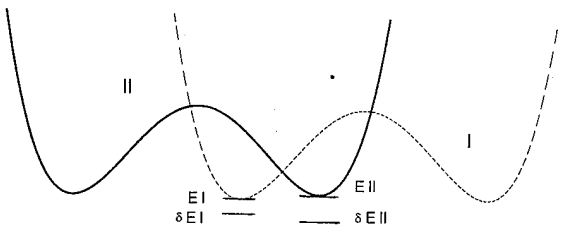


FIG. 1. Tunneling splitting as function of the potential well.

first approach to quantization using these dynamical equations is to solve Eq. (15) in the classical region and use the semiclassical Einstein-Brillouin-Keller quantization rules (see, for instance, Ref. 5). For tunneling effects one must consider motion in the non-classical region. This can be done using the formalism of the classical EOM with an imaginary time ($t\rightarrow i\tau$), which allows a description of motion in the classically forbidden region. Such modified EOM can be written in simplest form as

$$M\frac{\partial^2}{\partial\tau^2}\mathbf{R}=\nabla_{\mathbf{R}}V, \quad i\frac{\partial}{\partial\tau}\alpha=\frac{\partial V_{ss}}{\partial\alpha^*} \tag{18}$$

$$\frac{\partial\psi}{\partial\tau}=H\psi. \tag{19}$$

The discussion of the imaginary time dynamics itself can be found in Refs. 2,6,7,8. The set of coupled equations (15)–(19) should be solved simultaneously with the real time and nuclear coordinates treated in Eq. (19) for the $\psi\equiv\psi(\mathbf{r},\tau;\mathbf{R},t)$ as parameters. The quantity to be estimated is

$$\gamma=\int_{-T/2}^{T/2}d\tau\left\langle\psi(-\tau)\left|\frac{\partial}{\partial\tau}\right|\psi(\tau)\right\rangle, \tag{20}$$

which can be considered as an alternative to Eq. (10)–(11) and represents the exponential factor in the expression for the shift in energy levels of oscillator due to quantum tunneling[9]

$$\delta E_n=K^{2n+1}\exp\{-\gamma\}/2^n\omega^{n-1/2}n!, \tag{21}$$

where K is the exponential prefactor, n is a quantum level, and ω is a frequency related to the potential minimum. In general the question of how to search for the optimal path of such dynamics is very complicated. For imaginary time dynamics of the ground state (instanton dynamics) and symmetrical systems, such paths can be found fairly easily.[8] It is worthwhile to note that an alternative approach is to solve the classical Eq. (15) in the forbidden region using complex coordinates (or angles).[2] It is unclear at the moment which technique will be more suitable for real systems.

Let us illustrate the quantum dynamics described above by using a simple potential curve shown in Fig. 1. The regions I and II represent locally two well potential situations, which can be reached independently at the real time moments t_I and t_{II} by solving Eq. (15), with the corresponding classical (for the nuclei) total energy minima E_{I} and E_{II} ($E_{\text{I}}<E_{\text{II}}$). The tunneling (exchange) taking place at t_{I} and t_{II} gives an additional energy (21). The quantum corrections

change the classical ground state from $E_{\mathrm{I}}'=E_{\mathrm{I}}+\delta E_{\mathrm{I}}$ to $E_{\mathrm{II}}'=E_{\mathrm{II}}+\delta E_{\mathrm{II}}$ and stabilize the geometry of region II more strongly than that of region I. Also the double well potential having in the classical description two degenerate states (with the system classically choosing only one well in the ground state and breaking symmetry), with the addition of imaginary time dynamics, has a unique symmetric ground state.

The above discussions concerning spin dynamics are based on the adiabatic use of the stationary Schrödinger equation to evaluate the system's path. The effects of temperature can be incorporated in the SD equations in a manner analogous to the adding of a thermal bath to MD simulations,[1] however, for spin systems the implementation of a thermal reservoir is less evident than for a MD simulation of ions governed by classical EOM. The result of the thermalization should be the introduction of fluctuations so that the local spin relative to the local exchange field direction has an average alignment given by the Brillouin function. Spin systems may also be generalized to include nonclassical, or quantum, effects. Already the EOM for SD, Eq. (16), contain the quantum terms V_{es}. It may also be possible to introduce temperature at the quantum level. For instance, in Ref. 10 it has been shown how to introduce thermal effects at the quantum level so that the generated wave functions are ergodic. The generalization of this technique to *ab initio* molecular or spin dynamics (in a sort of classical-quantum hybrid) looks like a promising way to obtain quantum statistical effects (e.g., the Bloch law for the low temperature magnetization and the Debye law for specific heat in MD).

The application of the classical SD described above has been shown to be quite successful in finding many new magnetic phases in fcc Fe,[1] and looks promising as a method for classical temperature simulations. The description of quantum effects is possible and can be implemented as a natural extension of the methods described above.

We would like to thank M. I. Katsnelson and M. van Schilfgaarde for many discussions. This work was carried out at the Ames Laboratory, which is operated for the U. S. Department of Energy by Iowa State University under Contract No. W-7405-82. This work was supported by the Director for Energy Research, Office of Basic Energy Sciences of the U. S. Department of Energy.

[1] V. P. Antropov, M. I. Katsnelson, M. van Schilfgaarde, and B. N. Harmon, Phys. Rev. Lett. **75**, 729 (1995).
[2] L. D. Landau and E. M. Lifshitz, *Quantum Mechanics* (Pergamon, Oxford, 1975), Sec. 53.
[3] A. Shapire and F. Wilczhek, *Geometric Phases in Physics* (World Scientific, Singapore, 1989).
[4] V. P. Maslov, *The Complex WKB Method for Non-Linear Equations I* (Birkhauser, Berlin, 1994).
[5] N. De Leon and J. Heller, J. Chem. Phys. **78**, 4005 (1983).
[6] W. H. Miller, J. Chem. Phys. **62**, 1899 (1975).
[7] S. Coleman, in *The Whys of Subnuclear Physics,* edited by A. Zichichi (Plenum, New York, 1977).
[8] M. I. Katsnelson, V. P. Antropov, M. van Schilfgaarde, and B. N. Harmon JETP Lett. **62**, 439 (1995).
[9] U. Weiss and W. Haeffner, Phys. Rev. D **27**, 2916 (1983); U. Weiss, *Quantum Disspative Systems* (World Scientific, Singapore, 1993).
[10] D. Kuznezov, Phys. Lett. A **184**, 50 (1993).

Magnetic exchange coupling mediated by bound states

C. A. R. Sá de Melo
Argonne National Laboratory, Materials Science Division, Argonne, Illinois 60439

Usually indirect exchange coupling is mediated by unbound, noncorrelated intermediate states (RKKY-like mechanisms) or by unbound, correlated intermediate states (superexchange-like mechanisms). Here we investigate the possibility of indirect magnetic exchange coupling mediated by bound, correlated intermediate states. As a concrete example we study the magnetic coupling between two magnetic impurities embedded in a semiconductor matrix. The importance of long ranged attractive Coulomb interactions between electrons and holes is emphasized. This attraction leads to exciton bound states which act as mediators of the effective exchange interaction between the two impurities. The resulting exchange interaction presents strong temperature dependence and can be analyzed in terms of the symmetry of the internal wavefunction of the exciton bound states. Possible applications of these results may include recent experimental results on ferromagnetic metal-semiconductor multilayers. © *1996 American Institute of Physics.*
[S0021-8979(96)73708-X]

Typically, indirect magnetic exchange interactions are thought of as being mediated by unbound, non-correlated intermediate states as it is the case for RKKY-like mechanisms when applied to metals[1] or to semiconductors.[2] In addition, the indirect magnetic exchange interaction is also thought as being mediated by unbound, correlated intermediate states as it is the case for the superexchange-like mechanisms when applied to insulating transition metal oxides.[3] Our main aim in this paper is to describe a situation which is completely different from the two described above. Namely a case where the indirect magnetic exchange coupling is mediated by a bound, correlated intermediate state. The choice of a system to study the proposed effect is very important. We choose to study the concrete example of the indirect magnetic exchange between two magnetic impurities embedded in a semiconductor matrix, which may be extended to the case of a magnetic impurity lattice. Our analysis is not only of academic interest but also may be relevant to recent experiments on ferromagnetic metal-semiconductor multilayers like Fe/FeSi,[4] Fe/Si,[5] MnTe/CdTe, and EuTe/PdTe[6] and possibly to other systems like Fe/GaAs yet to be synthesized.

Now let us briefly discuss the central physical picture of the mechanism. Consider two magnetic impurities inside of a direct gap semiconductor and allow an attractive Coulomb interaction between an electron in the conduction band and a hole in the valence band. The Coulomb interaction binds electron-hole pairs into excitons, which exist in the gap of the semiconductor (excitons are stable bound states with relatively long lifetimes). As a result, these bound states provide intermediate states inside the gap which can mediate the exchange of spin information between the two magnetic impurities. This mediation is possible since excitons, although chargeless, can carry spin information, i.e., can be singlet or triplet. It is also important to emphasize that these bound states inside the gap can mediate the indirect magnetic coupling more effectively than the unbound electron-hole pairs, which have energies greater than the gap size.

As a result of the existence of these bound states inside the gap of the semiconductor, the magnetic exchange coupling increases with temperature. This increase in the indirect coupling with increasing temperature is a natural consequence of the population increase of these bound states caused by thermal excitations. In addition to this thermal effect, we shall see that the finite extension of the excitons internal wavefunctions and their symmetries play an important role in the determination of the *magnitude* and *sign* of the effective exchange coupling $J_{\rm eff}$.

Let us begin our analysis with the choice of the model and the geometry. First, let us study the situation of two magnetic impurities embedded in an isotropic and direct gap semiconductor matrix in order to establish the basic mechanism of the effective magnetic exchange. The starting Hamiltonian is of the following form

$$H=H_a+H_c+H_v+H_{cv}+H_{acv}, \tag{1}$$

where $H_a=\Sigma_{i,\sigma}\epsilon_\sigma C^\dagger_\sigma(R_i)C_\sigma(R_i)$ is the kinetic energy term of the magnetic impurities located at positions R_i, with $i=1,2$; $H_c=\Sigma_{k_e,\sigma_e}\epsilon_c(k_e)f^\dagger_{c,\sigma_e}(k_e)f_{c,\sigma_e}(k_e)$ is the kinetic energy for the conduction electrons in the semiconductor matrix, with $\epsilon_c(k_e)=E_c+k_e^2/2m_e-\mu$; the term $H_v=\Sigma_{k_h,\sigma_h}\epsilon_v(k_h)f^\dagger_{v,\sigma_h}(k_h)f_{v,\sigma_h}(k_h)$ is the kinetic energy of the valence electrons with dispersion $\epsilon_v(k_h)=E_v-k_h^2/2m_h-\mu$. Here the gap of the semiconductor is $E_g=E_c-E_v$. The Coulomb interaction between an electron in the conduction band and a hole in the valence band is

$$H_{cv}=\sum{}' V_{\sigma_e,\sigma_h}(q)f^\dagger_{c,\sigma_e}(k_e+q)f_{c,\sigma_e}(k_e)\times f^\dagger_{v,\sigma_h}(k_h-q)f_{v,\sigma_h}(k_h)$$

with the summation ($'$)being over $(k_e,k_h,q,\sigma_e,\sigma_h)$, and $V_{\sigma_e,\sigma_h}=4\pi e^2/(\epsilon q^2)$, where ϵ is the dielectric constant of the semiconductor. Finally,

$$H_{acv}=-\sum{}'' \tilde{J}\tilde{\delta}f^\dagger_{c,\sigma_e}(k_e)f_{v,\sigma_h}(k_h)C^\dagger_{\sigma'}(R_i)C_\sigma(R_i)+h.c.$$

is the *exchange* interaction between the local magnetic impurity and an electron in the conduction band and a hole in the valence band. Here, the summation ($''$) is over

 0021-8979/96/79(8)/5412/3/$10.00 © 1996 American Institute of Physics

$(k_e,k_h,\sigma,\sigma',\sigma_e,\sigma_h)$; $\tilde{J}=J^{\sigma,\sigma'}_{\sigma_e,\sigma_h}(k_e,k_h)\exp[i(k_h-k_e)\cdot R_i]$is the *exchange* coupling and the spin conservation function $\tilde{\delta}=\delta_{\sigma_e,\sigma}\cdot\delta_{\sigma_h,\sigma'}$.

We continue our approach by constructing the action of the system

$$S=\int_0^\beta d\tau[K(\tau)-H(\tau)]$$

where $K(\tau)=K_a+K_c+K_v$, with the first term being $K_a=\Sigma_{i,\sigma}C^\dagger_\sigma(R_i,\tau)\partial_\tau C_\sigma(R_i,\tau)$, the second being $K_c=\Sigma_{k_e,\sigma_e}f^\dagger_{c,\sigma_e}(k_e,\tau)\partial_\tau f_{c,\sigma_e}(k_e,\tau)$ and the last being $K_v=\Sigma_{k_h,\sigma_h}f^\dagger_{v,\sigma_h}(k_h,\tau)\partial_\tau f_{v,\sigma_h}(k_h,\tau)$. Now we use the functional integral formalism to derive the effective action which involves only the fermion variables of the magnetic atoms. Upon functional integration of the valence and conduction fermions with actions $S_c=\int_0^\beta d\tau[K_c-H_c]$, $S_v=\int_0^\beta d\tau[K_v-H_v]$ and interaction actions $S_{cv}=-\int_0^\beta d\tau H_{cv}(\tau)$ and $S_{\ell cv}=-\int_0^\beta d\tau H_{\ell cv}(\tau)$ we obtain

$$\int Df^\dagger Df\exp[S_c+S_v+S_{cv}+S_{acv}]\approx\exp[S_{\rm eff}]$$

and arrive at the effective action $S_{\rm eff}=-H_{\rm eff}$.[7]

When $\tilde{J}=J$, i.e., $\tilde{J}$ is spin and momentum independent, the *magnetic* part $H_{\rm mag}$ of $H_{\rm eff}$ takes the Heisenberg form

$$H_{\rm mag}(\mathbf{R}_{12})=-\sum_{i\omega}\bar{J}_{\rm eff}(\mathbf{R}_{12},i\omega)\mathbf{S}_1(i\omega)\cdot\mathbf{S}_2(-i\omega). \quad (2)$$

The effective exchange $\bar{J}_{\rm eff}$ can be calculated in the limit of low density of electrons and holes by solving the Bethe–Salpeter equation.[8–10] The usual procedure in the evaluation of the interaction Hamiltonian $H_{\rm mag}$ as defined in (2) is to analyze the static limit $i\omega=0$ and thus obtain the interaction $\bar{J}_{\rm eff}(\mathbf{R}_{12},i\omega=0)$. In the approximation considered here this limit would mean the complete absence of temperature dependence in $\bar{J}_{\rm eff}(\mathbf{R}_{12},i\omega=0)$, which would be uninteresting from our point of view. Thus, we do not discuss this limit here. Here, we will be concerned only with the *instantaneous* part of $H_{\rm mag}$,

$$\bar{J}_{\rm eff}(q,\tau=0)=\frac{|J|^2}{T}\sum_\lambda N_B[\omega_\lambda(q)]R_\lambda(q), \quad (3)$$

with N_B being the Bose function. Here, $R_\lambda(q)=\Sigma_k\phi^*_\lambda(k;q)\phi_\lambda(k;q)$, where the auxiliary functions $\phi_\lambda(k;q)=\int d\mathbf{r}\exp[i\mathbf{k}\cdot\mathbf{r}]\exp[i\gamma\mathbf{q}\cdot\mathbf{r}]\xi_\lambda(\mathbf{r})$ are expressed in terms of the hydrogenic wave functions $\xi_\lambda(\mathbf{r})$ for the relative coordinate of the electron-hole bound state (exciton) with quantum numbers $\lambda\equiv(n,\ell,m)$. The corresponding eigenenergies are $\omega_\lambda(q)=E_g-\mathscr{R}/n^2+\hbar^2q^2/2M$, where $M=m_e+m_h$, $\mathscr{R}=\mu R_y/(m_e\epsilon^2)$ with μ being the reduced mass of the bound electron-hole pair and $R_y=13.6$ eV being the Rydberg. The characteristic size of the bound electron-hole pair in the state $\lambda\equiv(n,\ell,m)$ is $r_{eh}=n^2a_0$ where $a_0=\epsilon(m/\mu)a_B$ is the Bohr radius of the electron-hole problem, while $a_B=0.529$ Å is just the Bohr radius for the hydrogen atom. In addition, the parameter $\gamma=\Delta m/2M$, where $\Delta m=m_e-m_h$.

In the Boltzmann limit $(min[\omega_\lambda(q)]\gg T)$ the integration over momentum $\mathbf{q}$ in (3) is performed to obtain

$$\bar{J}_{\rm eff}(\mathbf{R}_{12},\tau=0)=\sum_\lambda J_\lambda(\mathbf{R}_{12}), \quad (4)$$

where

$$J_\lambda(\mathbf{R}_{12})=\frac{|J|^2}{T}\exp[-E_\lambda/T]M_\lambda(T) \quad (5)$$

is an effective coupling that depends on the internal quantum numbers $\lambda\equiv(n,\ell,m)$ of the bound state via the dimensionless matrix element

$$M_\lambda(T)=\int d\tilde{\mathbf{r}}_1\,d\tilde{\mathbf{r}}_2\,\tilde{\xi}_\lambda(\tilde{\mathbf{r}}_1)\tilde{U}(\tilde{\mathbf{R}}_{12},\tilde{\mathbf{r}}_{12},\alpha)\tilde{\xi}^*_\lambda(\tilde{r}_2), \quad (6)$$

with the effective dimensionless potential being

$$\tilde{U}(\tilde{\mathbf{R}}_{12},\tilde{\mathbf{r}}_{12};\alpha)=\frac{2^{3/2}}{\alpha^3}\exp[-(\gamma\tilde{x}_{12})^2/\alpha^2]\times\exp[-(\gamma\tilde{y}_{12})^2/\alpha^2]\times\exp[-(\tilde{Z}_{12}-\gamma\tilde{z}_{12})^2/\alpha^2] \quad (7)$$

and the dimensionless wavefunctions being $\tilde{\xi}_\lambda(\tilde{\mathbf{r}})=a_0^{3/2}\xi_\lambda(\mathbf{r})$. Here, $\alpha=a_T/a_0$, where $\alpha_T=\hbar\sqrt{2/MT}$ is the characteristic thermal length and a_0 is the characteristic Bohr radius of the electron-hole bound state. In (7), without loss of generality, we have chosen the z axis of our system to be along the line that connects the two impurities, thus we defined $\mathbf{R}_{12}\equiv Z_{12}$, i.e., $X_{12}=Y_{12}=0$. It is very important to notice in (4) that the coupling J_λ changes *sign* depending on the *sign* of M_λ.

The dimensionless effective potential $\tilde{U}$ is of crucial importance in establishing the strength of the matrix element M_λ and thus determining $\bar{J}_{\rm eff}$. The most interesting case occurs when $\alpha\ll1$, i.e, when the thermal length a_T is much smaller than the characteristic Bohr radius a_0. In this case the potential $\tilde{U}\gg1$ and the coupling J_λ can be appreciable. The most interesting limit occurs when $\alpha\to0$, in which case

$$\tilde{U}=(2\pi)^{3/2}\delta(\gamma\tilde{x}_{12})\,\delta(\gamma\tilde{y}_{12})\,\delta(\tilde{Z}_{12}-\gamma\tilde{z}_{12}) \quad (8)$$

and the matrix element

$$M_\lambda=\frac{(2\pi)^{3/2}}{|\gamma|^3}\int d\tilde{\mathbf{r}}_1\tilde{\xi}_\lambda(\tilde{x}_1,\tilde{y}_1,\tilde{z}_1)\tilde{\xi}^*_\lambda(\tilde{x}_1,\tilde{y}_1,\tilde{z}_1-\tilde{Z}_{12}/\gamma) \quad (9)$$

is now just a simple overlap integral between the internal bound state wave functions separated by the distance $\tilde{Z}_{12}/\gamma$. The final expression for $\bar{J}_{\rm eff}$ is valid under two conditions. The first corresponds to the Boltzmann approximation, which is valid when $T_0\equiv\min[\omega_\lambda(q)]\gg T$ is satisfied, i.e., $T_0\gg T$, with $T_0=E_g-\mathscr{R}$. It is required that T_0 be positive, otherwise there is no bound state inside the gap. The second condition corresponds to $\alpha\ll1$, which implies $T\gg T_u$, where $T_u=4(\mu/M)\mathscr{R}$. As a result, the approximation used so far is valid in the temperature range $T_u\ll T\ll T_0$.

We shall now turn our attention to some qualitative aspects of the magnetic coupling J_λ. The first important qualitative aspect is the determination of the *sign* of the magnetic coupling J_λ which is in turn governed by the *sign* of M_λ in the temperature range $T_u\ll T\ll T_0$. It is not difficult to convince ourselves that for the $1s$ bound state $(n=1,\ \ell=0,$

$m=0$) M_{1s} is always positive, thus J_{1s} has always the *ferromagnetic* sign. In the case $n=2$, the $2s$ ($\ell=0$) bound state also produces $M_{2s}>0$ and $J_{2s}>0$. A similar situation also occurs for the $2p_x$ and $2p_y$ ($\ell=1$) bound states. In contrast, a more interesting situation occurs for the $2p_z$ state ($\ell=1$): for small separations $\tilde{Z}_{12}/\gamma \ll 4$, the overlap M_{2p_z} is positive and thus J_{2p_z} has the *ferromagnetic* sign; for large separations $\tilde{Z}_{12}/\gamma \gg 4$, the overlap $M_{2p_z}<0$ and J_{2p_z} has the *antiferromagnetic* sign. Similar analysis can be also performed for the higher n states, from which the qualitative behavior of M_λ for different orbital ℓ and azimuthal m quantum numbers can be easily extracted from the knowledge of the shapes of the bound state wave functions.

The second important qualitative aspect of J_λ is that in the temperature range of interest ($T_u \ll T \ll T_0$) the matrix element M_λ is temperature independent and thus the magnetic exchange coupling has a simple activated form that can be read off from (5). The exact form of the activated behavior in (5) follows from the Boltzmann approximation used here, but physically it reflects the fact that when the temperature is increased more bound states (inside the gap) are populated and thus they can more effectively mediate the exchange interaction between the impurities. Conversely, when the temperature is lowered there are less bound states thermally populated and as a result the *magnitude* of the magnetic exchange J_λ is reduced.

Our results should be compared with the RKKY-like mechanisms (which neglect long ranged Coulomb interactions) applied to metals[1] and semiconductors.[2] In the case of metals, where there is good screening, RKKY-like mechanisms have been quite successful in predicting the indirect exchange coupling between two magnetic impurities mediated by unbound particle-hole states, where the coupling oscillates (for large distances) between *ferromagnetic* and *antiferromagnetic* as a function of separation of the impurities.[1] In the case of semiconductors, where the screening is not so good, RKKY-like mechanisms (mediation via unbound electron-hole states) predict for a direct gap semiconductor that the indirect exchange coupling (at large separations) decays exponentially with decay length $\ell_d=[2E_gM]^{-1/2}$ where the *sign* of the coupling is always *ferromagnetic*.[2] The inclusion of long range attractive Coulomb interaction between conduction electrons and valence holes allows the formation of exciton bound states, which in turn act as mediators of the indirect exchange interaction. As can be inferred from Eq. (5), the decay of J_λ is still exponential at large distances, but its *sign* depends on the *symmetry* of the intermediate (correlated) bound state. This should be compared with the strong dependence of the superexchange interaction[3] on the *symmetry* of the intermediate (correlated) unbound states in the context of transition metal oxides.[11]

To compare our predictions qualitatively with experiments one must first consider the boundary conditions on ferromagnetic-metal/semiconductor multilayers and establish the existence of stable excitons in the semiconductor spacer. Secondly, one needs to identify the dominant *symmetry* of these stable intermediate states. At this stage our results would suggest that for semiconductor spacers with dominant $2s$-excitons the indirect exchange coupling is *ferromagnetic* for all spacer thicknesses, while for spacers with dominant $2p_z$-excitons the indirect exchange coupling is ferromagnetic at small thicknesses but *antiferromagnetic* at intermediate and larger thicknesses.

We would like to thank A. A. Abrikosov for encouragement. We would like to thank J. E. Mattson, E. E. Fullerton and S. Bader for useful discussions. This work has been supported by the U.S. Department of Energy, Basic Energy Sciences-Materials Sciences, under contract No. W-31-109-ENG-38.

[1] M. A. Ruderman and C. Kittel, Phys. Rev. **96**, 99 (1954); T. Kasuya, Progr. Theor. Phys. **16**, 45, 58 (1956); K. Yosida, Phys. Rev. **106**, 893 (1957).

[2] N. Bloembergen and T. J. Rowland, Phys. Rev. **97**, 1679 (1955); R. Sokel and W. A. Harrison, Phys. Rev. Lett. **36**, 61 (1976); A. A. Abrikosov, Adv. Phys. **29**, 869 (1980).

[3] H. Kramers, Physica (Utrecht) **1**, 182 (1934); P. W. Anderson, Phys. Rev. **79**, 350 (1950).

[4] J. E. Mattson, S. Kumar, E. E. Fullerton, S. R. Lee, C. H. Sowers, M. Grimsditch, S. D. Bader, and F. T. Parker, Phys. Rev. Lett. **71**, 185 (1993); S. Toscano, B. Briner, H. Hopster, and M. Landolt, J. Magn. Magn. Mater. **114**, L6 (1992).

[5] B. Brinner and M. Landolt, Z. Phys. B **92**, 135 (1993); B. Brinner and M. Landolt, Phys. Rev. Lett. **73**, 340 (1994).

[6] T. M. Giebultowicz, W. Faschinger, V. Nunez, P. Klosowski, G. Bauer, H. Sitter, and J. K. Furdyna, J. Cryst. Growth **138**, 877 (1994); T. M. Giebultowicz, V. Nunez, G. Springholz, G. Bauer, J. Chen, M. S. Dresselhaus, and J. K. Furdyna, The 6th Joint MMM-Intermag Conference Abstracts, 1994, p. 163.

[7] For useful tricks used to obtain effective actions see, e.g., V. N. Popov, *Functional Integrals and Collective Excitations* (Cambridge University Press, Cambridge, 1987).

[8] C. A. R. Sá de Melo, Phys. Rev. B **51**, 8922 (1995).

[9] See for instance, J. W. Negele and H. Orland, *Quantum Many-Particle Systems* (Addison-Wesley, Reading, MA, 1987), Ch. 2, 5, and 6.

[10] See for instance, P. Nozières, *Theory of Interacting Fermi Systems* (W. A. Benjamin, Inc., New York, 1964).

[11] J. B. Goodenough, Phys. Rev. **100**, 564 (1955); J. Kanamori, Phys. Chem. Solids **10**, 87 (1959).

Phenomenological description of the magnetization relaxation (abstract)

V. L. Sobolev and Huei Li Huang
Department of Physics, National Taiwan University, Taipei, Taiwan, Republic of China

The dynamics and relaxation of magnetization $\mathbf{M}(\mathbf{r},t)$ is usually described phenomenologically by the Landau–Lifshitz (LL) equation with relaxation term $\mathbf{M} = -\gamma[\mathbf{M}\times\mathbf{F}]+\mathbf{R}$, where γ is the gyromagnetic ratio ($\gamma>0$), $\mathbf{F}$ is the effective field, and $\mathbf{R}$ describes the relaxation of the magnetization toward its equilibrium value. It is already well known that the relaxation term of either the LL or Gilbert form does not give a correct description of the dependence of spin-wave damping on the wave vector at small wave vectors for the models of an isotropic and easy plane ferromagnet. The correct behavior of the spin wave damping may be obtained by taking into account the spatial dispersion of the relaxation caused by the exchange interaction and correct symmetry structure of the relativistic part of the relaxation term[1] which now has to be represented as a sum of the exchange and relativistic parts by $\mathbf{R}=\mathbf{R}_{ex}+\mathbf{R}_{\tau}$. A review of the recent results on the relaxation obtained in the frames of the LL equation with the relaxation term suggested by Bar'yakhtar is presented. Comparison of the spin wave damping calculated in the frames of the phenomenological and microscopic approaches has been carried out. In particular it is shown that, in the case of yttrium iron garnet or substituted garnets, the estimation of the value of phenomenological constant of the exchange relaxation has to be carried out by properly taking into account the many sublattice magnetic structure of these magnets. Numerical estimations of the phenomenological relaxation constants for the yttrium iron garnet are given. © *1996 American Institute of Physics.* [S0021-8979(96)69108-7]

Supported in part by NSC-85-2216-E-002-014.

[1] V. Bar'yakhtar, Sov. Phys. JETP **60**, 863 (1984); Physica B **159**, 20 (1989).

 0021-8979/96/79(8)/5415/1/$10.00 © 1996 American Institute of Physics

Atomic magnetic moments and spin notion

Xavier Oudet
Laboratoire de Magnétisme et d'Optique de l'Université de Versailles, C.N.R.S., 45 Avenue des Etats-Unis, 78000 Versailles, France

It is shown that there is an energy associated with the spin. Then the electron is considered as a fluid mass and the wave function as a quantification of the mechanical action. This approach enables us to understand why in Dirac's theory just the total angular momentum is a constant of the motion and allows an explanation of the g factor. Then an interpretation of Dirac's equation is proposed putting in view the trajectory of the electron. © *1996 American Institute of Physics.*
[S0021-8979(96)73808-6]

I. INTRODUCTION

The spin hypothesis has been proposed to explain the doublet structure of several spectral series. This hypothesis was a real success and it appeared natural that the two lines of a doublet correspond to the two spin states as expressed today by $j=l+1/2$ and $j=l-1/2$. The study of Dirac's theory shows that it is not in this way that one has to understand the properties associated with a doublet and its application to the calculation of the magnetic moments has also brought new evidence of this difficulty. To clarify this difficulty we have revisited some properties characterizing the two lines of a doublet. This study suggests that the electron has to be thought of as a fluid with a volume and that the wave function stands for the mechanical action which leads the electron upon its trajectory. The doublet then corresponds to two different ways to receive the action giving its own rotation to the electron. This model allows an explanation of the Landé factor g as a property of the action with respect to the total angular momentum.

This work is strongly suggested by the previous results obtained with the calculation of the magnetic moment that we wish now to recall shortly. Indeed with the spin hypothesis the electron has been thought as a small rigid mass having an additional angular momentum which is supposed to be added to or subtracted from the orbital angular momentum. But with such a conception the orbital and the spin contribution appear separately as constants of motion. There is a difficulty in the understanding of the magnetic properties because, on the contrary Dirac's theory of the hydrogen atom,[1] implies that only the total angular momentum is a constant of motion. Furthermore we have shown that, in a solid, this property is still that of individual electrons which bring their magnetic contribution whatever be the interactions acting on the electron.[2,3] In this approach the g or Landé factor appears to play a fundamental role, characteristic of the two types of spin states in the same shell. Indeed $g=k/(k+1/2)$ and takes two values in the same shell corresponding to the two types of spin: $g=0.8$ with $k=2$ and $g=1.2$ with $k=-3$ in the $3d$ shell. For example, the experimental magnetic moment of iron is $2.22\mu_B$ where μ_B is the Bohr magneton. In Dirac's model it can arise from the sum of the magnetic contributions of two electrons belonging to the two different types of spin $0.4\mu_B=0.8(1/2)\mu_B$ and $1.80\mu_B=1.2(3/2)\mu_B$ where 0.8 and 1.2 are the corresponding g factors of the two kinds of spin of the $3d$ shell and 1/2 and 3/2 are two projections of the total angular momentum. Similar results are obtained for cobalt, nickel, rare earth metals and chromium compounds and with paramagnetic compounds.[2,3]

II. THE QUANTUM NUMBERS, THE SPIN AND THE ENERGY

In the first quantum theory the angular and radial motions are characterized respectively by the quantum numbers k and r. The total energy is $E_n=1/2nh\nu$ where ν is the frequency of the periodic motion and n is the total quantum number $n=k+r$ This is obtained from the quantification of the mechanical action with $E_k=1/2kh\nu$ and $E_r=1/2rh\nu$ for the corresponding motions. In Schrödinger's approach we have $n=l+r+1$. The number l replaces k and characterizes the angular momentum, r is still the radial quantum number with the corresponding energy for these two numbers. As a result, the unity in $n=l+r+1$, appears as a special unit of quantification to which corresponds the energy $E_s=1/2h\nu$, but which is not associated to a well defined degree of freedom. We will show that this energy corresponds to the spin motion. In this view let us recall how the doublet energy levels appear in Dirac's theory with $E_{n,k}$ level:

$$\frac{E_{n,k}}{m_0c^2}=\left(1+\frac{\alpha^2Z^2}{[p+\sqrt{k^2-\alpha^2Z^2}]^2}\right)^{-1/2}-1. \tag{1}$$

In this expression p and k are two quantum numbers with $n=|k|+p$, the other symbols have their classical meaning. The doublet energy levels characterize two types of solutions:

$$\text{Type I:}\quad k=-l-1 \quad\text{and}\quad p=r;$$
$$\text{Type II:}\quad k=l \quad\text{and}\quad p=r+1. \tag{2}$$

For the two types the energy is almost the same, p characterizes in the wave function $\Psi_{n,k}$ the amount of energy associated with the radial part and $|k|$ the one associated with the angular part. From the study of the solutions the two values $k=-l-1$ and $k=l$ give the same value $l(l+1)$ to the product $k(k+1)$ and form a spin doublet.[1,4] The relations between p and r result from the study of the correspondence between Dirac's and Schrödinger's solutions. This study shows that the radial functions which enter in the expression of $\Psi_{n,k}$ are very close to each other and they both tend to the Schrödinger wave function.[1,5]

 0021-8979/96/79(8)/5416/3/$10.00 © 1996 American Institute of Physics

Thus in Dirac's solutions the energy is characterized by the total quantum number n with the relations $n=|k|+p$ and $n=l+r+1$. The number l characterizes the orbital angular momentum and the corresponding energy. On the other hand r characterizes the radial motion and its corresponding energy. Furthermore there is still one special unit of quantification apparently not associated with a degree of freedom. But in this approach this special unit comes either from the angular part for type I or from the radial part for type II of $\Psi_{n,k}$ wave function. Now we know that for the two types the spin is an additional angular momentum $s=1/2h$. As a result it seems reasonable to suppose that this special unit of quantification characterizes the spin and that the energy associated with it is that of the spin motion.

III. THE WAVE FUNCTION, THE ACTION AND THE *g* FACTOR

To understand this hypothesis we will consider the electron as a fluid mass[5,6] and suppose that this fluid is composed of small particles that we call "grains." We also suppose that the electromagnetic field is made of the same "grains." Thus along its trajectory the electron receives energy which could be formed of these "grains" from the field but as it cannot continuously accumulate energy it also emits the same amount to keep the balance and in order to have a stable state. This is a possible explanation of the principle of the least action. This picture allows, to understand the wave function as a quantification of the mechanical action.[7] Indeed, when we search for the solutions of Dirac's equation we try a function which has the spherical symmetry of the electrical field but which is not the one of the trajectory. Now when the field acts on the electron, as a result of its fluidity, there is dispersion which continuously modifies the momenta. As a result the law of conservation of these momenta is deeply modified and indeed we know from Dirac's theory that just the total angular momentum is a constant of motion. In the Sommerfeld approach we have the indication that the wave function is the quantification of the action. We know that before Dirac, he has found the formula of the energy (1) by introducing the relativistic change of the mass along the orbital motion. In doing so one quantifies the action along the trajectory.[8–10] But Sommerfeld worked with an electron as a material point before the discovery of the spin property. As a result there was no way to recognize that one unit of quantification has to be attributed to the own rotation and that this unit can be taken either from angular or radial part of the action. With this hypothesis we can understand that Sommerfeld finds the same relation as Dirac for the energy of the state.

There is another support to this approach in the magnetic contribution of a given quantum state. Let us first consider the spin contribution to the total angular momentum. When the energy associated with the spin is taken from the angular action, the spin contribution reduces the possible angular momentum $|k|\hbar$ and this is the reason for the negative sign of k. On the contrary, when this energy is taken from the radial action the spin contribution is added to the possible angular momentum $k\hbar$. As a result, the total angular momentum for the two types is $M=|k+1/2|\hbar$ taking into account the algebraic sign of k. This is different from the hypothesis that the spin contribution must be added to l in $\hbar$ units giving $j=l+1/2$ or $j=l-1/2$. In fact they are the highest values of the magnetic quantum number of the type I and II, respectively. This can be obtained in calculating the magnetic contribution of an electron in a given quantum state. Let u be the projection in $\hbar$ unit of the angular momentum of the state. In a classical approach its magnetic contribution is: $u_e=u\mu_B$ where μ_B is the Bohr magneton. To establish this relation one has to use the classical expression $\mu_e=IS/c$ giving the magnetic moment of a circular current. In this expression I is the intensity of the current and S the surface of the circle. For the electron with an orbital motion having a period T, one has $I=e/T$. On the other hand the area law satisfied in classical as well in relativistic mechanics expressed upon one period gives the relation $2mS=T_M M$. With $u\hbar$ for the projection of M this leads to $\mu_e=u\mu_B$ if $T=T_M$. But the corresponding action of the total angular momentum $M=|k+1/2|\hbar$ is equal to $|k|\hbar$. As a result the periods T and T_M are different. The period T_M is indeed fictitious and there are the relations:

$$2mS=T|k|\hbar=T_M|k+1/2|\hbar$$

so that

$$T_M=gT \quad \text{with} \quad g=k(k+1/2). \tag{3}$$

As a result, the magnetic moment corresponding to u the projection of $M=|k+1/2|\hbar$ must be multiplied by g, that is $\mu_e=gu\mu_B$ where the Landé factor g is given by 3. This factor as a function of k was first calculated by Dirac[4] and its role in the magnetic contribution of the electrons is well established in the calculation of the magnetic moment of the atoms[2,3] and in the interpretation of the Zeeman effect through Runge's law.[9]

IV. WAVE FUNCTION AND TRAJECTORY

The interpretation of the g factor is based upon the hypothesis of a trajectory for the electron. Let us show that with a fluid electron it is possible to describe Dirac's equation as the exchanges of grains between the electron and the field along the trajectory. These exchanges of grains correspond to an amount of energy, mass, momenta and displacement. To satisfy the quantification we suppose that the exchanges of grains are such that: "the characteristic energy of a state must be exchanged on a section of trajectory having a length λ of the wave during the time T of the period associated to λ in such a way that at each time if p is the momentum one has $ET=p\lambda=h$."

Starting with the momentum parallel to the x axis, the exchanges of grains transform a part p_x of this momentum in $\pm p_y$ and $\pm p_z$. The amount of these exchanges is proportional to the cross section σ of the electron, to the velocity c of the light and to the interval of time dt; that is: $dv=\sigma c\ dt$. It can be described with $h\Psi_a\sigma c\ dt$ and Ψ_a can be divided into two components Ψ_3 and Ψ_4. Let us consider that this exchange of grains leading to a modification of the position of the electron is an absorption. To counterbalance this absorption it must have an emission $h\Psi_e\sigma c\ dt$ and Ψ_e can be divided into two components Ψ_1 and Ψ_2.

Let us then consider Dirac's equation:

$$i[(W+eV)/c+m_0c]\Psi_1\,dv = (P_x+iP_y)h\Psi_4 dv + P_z h\Psi_3\,dv, \quad \text{(D1)}$$

$$i[(W+eV)/c+m_0c]\Psi_2\,dv = (P_x-iP_y)h\Psi_3 dv - P_z h\Psi_4\,dv, \quad \text{(D2)}$$

$$i[(W+eV)/c+m_0c]\Psi_3\,dv = (P_x+iP_y)h\Psi_2 dv + P_z h\Psi_1\,dv, \quad \text{(D3)}$$

$$i[(W+eV)/c+m_0c]\Psi_4\,dv = (P_x+iP_y)h\Psi_1 dv - P_z h\Psi_2\,dv, \quad \text{(D4)}$$

according to de Broglie presentation.[10] In this equation P_x stands for $\partial/\partial x$ and so on.

To put in view the amount of emitted or absorbed grains we have multiplied the wave components by $dv=\sigma c\,dt$. In the equations (D1) and (D2) $(P_x+iP_y)\Psi_4\,dv$ and $(P_x-iP_y)\Psi_3\,dv$ represent two opposite rotations parallel to the x,y plane. With these two rotations one will recognize a part of the Pauli hypothesis: a wave component for each spin state, but it is the difference of these two rotations which gives the real rotation of the electron. On the other hand $P_z\Psi_3\,dv$ and $-P_z\Psi_4\,dv$ represent two opposite translations parallel to the z axis. The trajectory is the result of these opposite motion. Let us remark that in the equation (D1):

$$i[(W+eV)/c+m_0c]\Psi_1\,dv = i[(W+eV)+m_0c^2]\Psi_1\sigma\,dt,$$

where $(W+eV)\Psi_1\sigma\,dt$ represents an emission of energy proportional to the difference of density of grains between the electron and the field. On the other hand $m_0c^2\Psi_1\,\sigma\,dt$ represents an emission proportional to the energy of the rest mass of the electron that is the condition to keep the rest mass constant. As a result the first equation appears as an equilibrium between the absorption for one way of variation of momentum and on the other hand the corresponding emission to keep the energy and mass constant. The second equation corresponds to opposite way of variation of momentum.

Finally variations of momentum induce variations of energy of motion. Reciprocally, variation of energy of motion induce variations of momentum. The role of the third and fourth equations is to satisfy this aspect of the motion.

V. CONCLUSION

When we undertook this work our purpose was to get the core of the notion of "spin." For this purpose we have introduced the hypothesis of an electron as a fluid mass made of grains as the electric field and the photon. With this hypothesis it appears then possible to find the equation of Dirac starting from the motion of the electron and as a result to propose a new perception of the wave corpuscle duality. In this view it was essential to recognize the reality of the electronic trajectories as one can do it with the chemical bond or as a consequence of the magnetic properties of the electron. To conduct this work we have used a law of quantification that we can express like this: "the characteristic energy of a state must be exchanged on a section of trajectory having a length λ of the wave during the time T of the period associated to λ in such a way that at each time if p is the momentum one has $ET=p\lambda=h$." Thus this characteristic energy of the occupied quantum state is nothing other than Planck's constant along a wave length and during the associated period. This property arises from the fact that there is no exchange of energy without duration and length. But this constant of action h does not vary with the medium that is of the complexity of the atom, of the molecule or still of the solid, liquid or gas state of the matter in which the electron moves. Thus we understand that the quantum numbers which characterize the quantum state subsist whatever be the situation of the atom. It is that which allows to understand the structure of the periodic table which synthesizes so many chemical and physical properties of the matter. We also understand that the total angular momentum is always the same whatever be the complexity of the atom to which belongs the electron and the medium to which belongs the atom, a property which had remained mysterious.[1,2]

[1] P. A. M. Dirac, Proc. Roy. Soc. A **117**, 610 (1928).
[2] X. Oudet and G. Lochak, J. Magn. Magn. Mater. **65**, 99 (1987).
[3] X. Oudet, J. Magn. Magn. Mater. **98**, 298,307 (1991).
[4] P. A. M. Dirac, Proc. Roy. Soc. A **118**, 351 (1928).
[5] X. Oudet, Ann. Fondation Louis de Broglie **6**, 127 (1981).
[6] X. Oudet, Ref. 3, see the conclusion p. 324.
[7] X. Oudet, Ann. Fondation Louis de Broglie **20** (in press).
[8] A. Sommerfeld, Ann. Phys. **51**, 1 (1916).
[9] H. E. White, *Introduction to Atomic Spectra* (McGraw-Hill, New York, 1934).
[10] L. de Broglie, *L'Electron Magnétique (théorie de Dirac)* (Hermann, Paris, 1934).

Published without author corrections

Aharonov–Bohm oscillations at finite temperature

P. Schlottmann
Department of Physics, Florida State University, Tallahassee, Florida 32306

A. A. Zvyagin
B. I. Verkin Institute for Low Temperature Physics and Engineering of the Ukrainian Academy of Sciences, 47 Lenin Avenue, Kharkov 310164, Ukraine

The Aharonov–Bohm effect is the quantum interference of charged particles in mesoscopic rings enclosing a magnetic field. The wavefunction acquires a phase due to the field flux ϕ and gives rise to flux-dependent oscillations in persistent charge currents. The period and amplitude of the oscillations are associated with the properties of the Fermi surface of the elementary excitations. For systems with one Fermi surface the groundstate persistent current has the form of a saw-tooth. The temperature reduces the amplitudes of oscillation by smearing the Fermi surface. The amplitude of higher harmonics decreases faster with T than the fundamental one, changing the saw-tooth to a more sinusoidal form with much smaller amplitude. The controlling parameter is LT/zv_F, where L is the length of the ring, v_F is the Fermi velocity and z the dressed generalized charge. Our calculations are performed within the framework of Bethe's ansatz. © *1996 American Institute of Physics.* [S0021-8979(96)73908-2]

The exact solution of numerous 1D models by means of Bethe's ansatz and the quantum inverse scattering method in conjunction with field-theoretical treatments provided deep insight into the ground state properties, classification of states, thermodynamics, and the asymptotic behavior of correlation functions.

Finite size effects, i.e., the finite length of a conducting or magnetic ring, can manifest itself in several ways: (i) The contribution of impurities to extensive quantities (e.g., the energy) can become large and observable in mesoscopic systems. (ii) The finite length of a ring gives rise to quantum topological effects, i.e., to persistent currents with oscillation periods given by interference patterns of the Aharonov–Bohm (AB)[1] and Aharonov–Casher (AC)[2] type. (iii) Finite size corrections to the energy determine the critical exponents of the asymptotic dependence at long-distances of correlation functions via conformal field theory.[3–5]

In the AB effect[1] the wave function of charged particles along a ring picks up a phase proportional to the enclosed magnetic field flux. Dual to the AB effect is the AC[2] in which the wave function of particles with a magnetic moment acquires a phase due to a radial electric field caused by a straight charged line enclosed by the ring. The quantization of the flux or the phase (modulo 2π) leads to periodic oscillations of the current.[6] Persistent currents have been observed experimentally in small metal and semiconductor rings.[7]

Persistent currents in interacting systems were studied theoretically with the exact Bethe ansatz method[8] and the bosonization technique.[9] The system responds to a magnetic flux by virtually creating and annihilating states at the left and right Fermi points of the Dirac sea. The change of the energy with the flux is on a mesoscopic scale, L^{-1}, if the states are gapless, where L is the length of the ring.

In this paper we present a theoretical study of the AB oscillations in a ring of interacting charged spinless particles. We first state the Bethe ansatz solution for a general integrable model and the finite size corrections to the ground-state energy. Then we formulate the persistent currents for finite temperatures. The oscillations are strongly suppressed with temperature due to the incoherence introduced by the smearing of the Fermi surface. AB oscillations at finite T were studied previously by bosonizing spinless fermions.[9] We discuss the limitations of this procedure and the differences with our exact formulation. Finally, we present examples and a brief summary of our results.

We consider N spinless bosons or fermions in 1D interacting via a potential $V(x)$

$$H=-\sum_{j=1}^{N}\frac{\partial^2}{\partial x_j^2}+\sum_{i<j}V(|x_i-x_j|). \tag{1}$$

We restrict ourselves to potentials that do not lead to bound-states and systems that are integrable. The model can then be solved by means of the asymptotic Bethe ansatz,[10] which expresses the many-body energy eigenvalues in terms of the two-particle phase-shift without explicit knowledge of the manybody wave functions. The application of the asymptotic Bethe ansatz requires an independent proof that the model is integrable. If the model is integrable it suffices to know the asymptotic behavior of the incoming and outgoing wave-function at long distances, i.e., the scattering phase shift.

The asymptotic two-body wave function for $x_1 \ll x_2$ is

$$\psi(x_1,x_2)=\exp[i(k_1x_1+k_2x_2)] \pm\exp[i(k_2x_1+k_1x_2)+i\theta(k_1-k_2)], \tag{2}$$

while for $x_1 \gg x_2$ we have $\psi(x_1 \gg x_2)=\pm\psi(x_1 \ll x_2)$ for bosons and fermions, respectively. With $k=k_1-k_2$, k_j being the wave numbers, the scattering matrix is $S(k)=-\exp[-i\theta(k)]$ and $\theta(k)$ is twice the two-body phase-shift. $\theta(k)$ is an odd function of k and the energy is $E=k_1^2+k_2^2$.

For an integrable model the N-particle scattering matrix asymptotically for large distances between the particles factorizes into a product of $(N-1)$ two-particle scattering matrices. Imposing twisted boundary conditions we obtain[10]

 0021-8979/96/79(8)/5419/3/$10.00 © 1996 American Institute of Physics

$$e^{-i(kL-2\pi\alpha)}=\prod_{q\neq k} S^{-1}(k,q)=(-1)^{N-1}$$

$$\times\exp\left[i\sum_{q\neq k}\theta(q-k)\right], \tag{3}$$

and after taking the logarithm we have

$$kL=2\pi(I_k+\alpha)+\sum_{q\neq k}\theta(k-q), \tag{4}$$

where $\alpha=\phi/\phi_0$ with ϕ being the magnetic flux through the ring and $\phi_0=hc/e$ the elemental magnetic flux quantum. The wave functions are only linearly independent if all rapidities k are different (the rapidities obey Fermi statistics). In the ground state the I_k are different consecutive integers (half-integers) if N is odd (even), $I_{\min}\leq I_k\leq I_{\max}$. The energy is given by $E=\Sigma_{j=1}^{N}k_j^2$. Note that Eq. (4) is invariant under the replacement of α by its fractional part to the nearest I_k, $\{\alpha\}$.

In the thermodynamic limit we introduce distribution densities for the rapidities $\rho(k)$ and "holes" $\rho_h(k)$. For the ground state Eq. (4) reduces to the following integral equation

$$\rho_h(k)+\rho(k)+\int_{-Q}^{Q}(dq/2\pi)\rho(q)\theta'(k-q)=1/(2\pi) \tag{5}$$

with $\theta'(k)=d\theta(k)/dk$. The ground state energy and the number of particles are

$$E_\infty=L\int_{-Q}^{Q}dkk^2\rho(k), \quad N/L=\int_{-Q}^{Q}dk\rho(k). \tag{6}$$

We define an energy band as $\epsilon(k)=\lim_{T\to 0}T\ln[\rho_h(k)/\rho(k)]$, which satisfies

$$\epsilon(k)=k^2-\mu+\int_{-Q}^{Q}dq\epsilon(q)\theta'(k-q), \tag{7}$$

where μ is the chemical potential. According to the Fermi statistics obeyed by the rapidities, states with negative ϵ are occupied (particles), while states with positive energy potential are empty (holes). The zeroes of ϵ, i.e., $\epsilon(\pm Q)=0$ define the Fermi surface and also relate the integration limit Q to μ.

A particle (hole) excitation is introduced into the Fermi sea by adding (removing) a rapidity to (from) the set $\{k\}$. The energy and momentum of the excitations is given by

$$\mathscr{E}_{\rm exc}(k)=|\epsilon(k)|, \quad p(k)=2\pi\int_0^k dq[\rho_h(q)+\rho(q)]. \tag{8}$$

Excitations with $|k|<Q$ correspond to holes, while $|k|>Q$ parametrizes particles. The excitation energy vanishes at the Fermi level, $k=\pm Q$. The Fermi momentum is then $p_F=\pi N/L$. The linear superposition principle holds for any finite number of excitations.

Close to the Fermi points the energy dispersion (8) is proportional to the momentum, $\mathscr{E}_{\rm exc}(p)=v_F(||p|-p_F|)$, with the Fermi velocity given by

$$v_F=|\partial\epsilon(k)/\partial k|_{k=Q}[2\pi\rho(Q)]^{-1}. \tag{9}$$

The corrections to the energy due to the finite length of the ring can be calculated following the procedure developed in Refs. 3 and 11. The change of the energy, $\Delta E(\alpha)$, associated with the magnetic field flux is

$$\Delta E(\alpha)=(2\pi v_F/L)([z(D+\{\alpha\})]^2-1/12), \tag{10}$$

where $2D=I_{\max}+I_{\min}$ is a number determined mod(1) that gives the initial phase shifts or parity of the level crossing. The quantity z is the dressed generalized charge at the Fermi points, $z=\xi(k=Q)$, determined by

$$\xi(k)=1-\int_{-Q}^{Q}dq\xi(q)\theta'(k-q). \tag{11}$$

Note that for particles with parabolic dispersion, as in Eq. (1), $\xi(k)=2\pi(\rho_h(k)+\rho(k))$. According to Eq. (10) the ground state energy is a parabolic periodic function of the magnetic flux.

To study the temperature dependence of the oscillations we write the free energy as

$$F=E_\infty+\Delta E(\alpha)+\Delta F(T),$$

$$\Delta F(T)=-(TL/2\pi)$$

$$\times\int dp\ln\{1+\exp[-\mathscr{E}_{\rm exc}(p,\alpha)/T]\}, \tag{12}$$

where $\Delta F(T)$ is the thermal population of the particle and hole excitations according to the Fermi statistics of the rapidities. $\Delta F(T)$ vanishes as $T\to 0$. The expression for $\Delta F(T)$ is valid only for low temperatures, since we neglect the change of the spectrum with T.

We are interested in the finite size corrections associated with the magnetic flux contained in $\Delta F(T)$. The dimensionless parameter controlling the amplitude is zv_F/LT, i.e., the range of T over which the oscillations are observable decreases with L. For low-energy excitations we use the linearized dispersion about the Fermi points at $\pm p_F$. Both Fermi points contribute equally. For excitations about the Fermi point at $+p_F$ we have

$$p-p_F=2\pi\rho(Q)(k-Q)=2\pi z(I-I_{\max}+D+\{\alpha\})/L, \tag{13}$$

where $(I-I_{\max})$ is an integer, D is zero (1/2) if N is odd (even), and we introduced the phase-shift α due to the magnetic flux. The integral over the physical momentum is now replaced by a sum over integers I

$$\Delta F(T)=-2Tz\sum_{I=-\infty}^{\infty}\ln[1+\exp(-zv_F2\pi|I+\{\alpha\}|/LT)], \tag{14}$$

where D has been absorbed into α and the sum has been extended to infinity since the exponential converges fast. Using Poisson's formula we obtain

$$\Delta F(T)=-(zTL/\pi)\int_{-\infty}^{\infty}dx\ln[1+\exp(-zv_F|x|/T)]$$

$$-(2zTL/\pi)\sum_{s=1}^{\infty}(-1)^s\cos(2\pi\alpha s)$$

$$\times\int_{-\infty}^{\infty}dx\cos(Lxs)\ln[1+\exp(-zv_F|x|/T)], \tag{15}$$

where the symmetry of the excitation spectrum about p_F has been used. The first term is extensive and nonoscillatory; it gives rise, e.g., to the low-T specific heat $C/L=(\pi T/3v_F)$.

Two partial integrations of the oscillatory terms yield

$$\Delta F_{\rm osc}(T)=-(2z^2v_F/\pi L)\sum_{s=1}^{\infty}(-1)^s s^{-2}\cos(2\pi\alpha s)\times\left(1-(zv_F/4T)\int_{-\infty}^{\infty}dx\,\cos(Lxs)\times\cosh^{-2}(zv_F|x|/2T)\right). \tag{16}$$

The sum of the first term and the integral in the second term can be evaluated yielding

$$\Delta F_{\rm osc}(T)=-(2\pi z^2v_F/L)[\{\alpha\}^2-1/12]+2zT\times\sum_{s=1}^{\infty}(-1)^s s^{-1}\cos(2\pi\alpha s)\sinh^{-1}(\pi LsT/zv_F). \tag{17}$$

As $T\to 0$ the two terms in Eq. (17) cancel each other. The effect of parity is incorporated by replacing $\{\alpha\}$ by $(\{\alpha\}+D)$.

Collecting all finite size effects from (10), (12), and (17) we obtain

$$F_{\rm osc}=\frac{\pi v_F}{6L}[z^2-1]+2zT\sum_{s=1}^{\infty}\frac{(-1)^{Ns}}{s}\frac{\cos(2\pi\alpha s)}{\sinh(\pi LsT/zv_F)}. \tag{18}$$

The first term is a constant finite size correction and not relevant to the persistent current. The parity effect is now explicitly contained. The persistent current is the derivative of F with respect to the flux.

We have calculated the finite size corrections for a gas of spinless interacting particles at finite T. Charged particles couple to the magnetic field flux enclosed by the ring, giving rise to an AB quantum interference and persistent current. As a function of the magnetic field the persistent current oscillates with the periodicity of the elemental flux quantum. At $T=0$ the current has a saw-tooth shape, which is changed to a more sinusoidal pattern (with the same periodicity but strongly reduced amplitude) at finite T. The controlling dimensionless parameter is (LT/zv_F). T suppresses the higher harmonic content, as a consequence of the smearing of the Fermi surface. The physical picture is the same as in the de Haas–van Alphen effect, where T introduces incoherence in the wave function while a particle completes its closed orbit.

We have restricted our calculation to integrable systems with only one Fermi surface and to potentials that do not lead to boundstates (no string solutions of the Bethe ansatz equations). We believe that our results are a generic feature of 1D systems valid independently of the integrability. In particular, any one-component Luttinger liquid should exhibit this behavior. Using the bosonization of fermions Loss[9] calculated the T-dependence of the persistent AB current for spinless charged fermions with nearest neighbor interaction

$$H=-\sum_i (c_i^\dagger c_{i+1}+c_{i+1}^\dagger c_i)+U\sum_i c_i^\dagger c_i c_{i+1}^\dagger c_{i+1}. \tag{19}$$

The bosonization neglects the natural cutoffs of the model, i.e., of the tight-binding band and the interaction. Results are therefore restricted to small coupling strengths. The bosonization is strictly valid only in the thermodynamic limit; this may cause some ambiguities in the extraction of finite size effects. Expectedly Loss' results[9] differ from our exact ones in the dressing of the quantities (selfenergy effects).[12]

A few integrable models for which our results are exact are the following (listed are the potentials and the function θ): (i) For charged bosons interacting via the potential $V(x)=2c\,\delta(x)$ the phase-shift is $\theta(k)=-2\tan^{-1}(k/c)$,[13] (ii) for spinless particles interacting via the potential $V(x)=g(\pi/L)^2\sin^{-2}(\pi x/L)$ we have $\theta(k)=(\pi/2)\mathrm{sgn}(k)[(1+2g)^{1/2}-1]$,[10] (iii) for particles interacting via $V(x)=2\lambda(\lambda+1)\sinh^{-2}(x)$ the $\theta(k)$ is[10]

$$\theta(k)=2iIm\,\ln[\Gamma(1+ik)/\Gamma(1+\lambda+ik)], \tag{20}$$

and (iv) for a potential of the Toda-type $V(x)=(\omega^2/2\gamma^2)\{\exp[-\gamma(|x|-x_0)]+\gamma(|x|-x_0)-1\}$, where γ controls the anharmonicity and x_0 is a hard-sphere radius,[14]

$$\theta(k)=k(x_0+(2/\gamma)\ln(\omega/2\gamma^2)+2iIm\,\ln[\Gamma(1+ik/\gamma)]. \tag{21}$$

With minor modifications to Eqs. (5)–(7) our results are also valid for lattice models, for example (v) the model (19), which can be mapped onto the XXZ-Heisenberg chain via a Wigner–Jordan transformation,[15] and (vi) the Hubbard model with attractive U.[16] In the Hubbard model the electrons form singlet boundstates of the Cooper-pair-type which have a Fermi surface and are the particles displaying the persistent current. Gaps prevent the population of all other excitations at low T.

The support of the U.S. Department of Energy under Grant No. DE-FG05-91ER45443 is acknowledged.

[1] Y. Aharonov and D. Bohm, Phys. Rev. **115**, 485 (1959).
[2] Y. Aharonov and A. Casher, Phys. Rev. Lett. **53**, 319 (1984).
[3] H. J. de Vega and F. Woynarovich, Nucl. Phys. B **251**, 439 (1985).
[4] H. Frahm and V. E. Korepin, Phys. Rev. B **42**, 10 553 (1990).
[5] I. Affleck and A. W. W. Ludwig, Nucl. Phys. B **360**, 641 (1991).
[6] A. D. Stone and Y. Imry, Phys. Rev. Lett. **56**, 189 (1986); V. Ambegaokar and U. Eckern, *ibid.* **65**, 381 (1990); B. L. Al'tshuler, Y. Gefen, and Y. Imry, *ibid.* **66**, 88 (1991).
[7] L. P. Levy *et al.*, Phys. Rev. Lett. **64**, 2074 (1990); V. Chandrasekhar *et al.*, *ibid.* **67**, 3578 (1991); D. Mailly *et al.*, *ibid.* **70**, 2020 (1993); W. J. Elion *et al.*, *ibid.* **71**, 2311 (1993).
[8] A. A. Zvyagin, Sov. Phys. Solid State **32**, 905 (1990); Sov. Phys. JETP **76**, 167 (1993); B. S. Shastry and B. Sutherland, Phys. Rev. Lett. **65**, 243 (1990); C. A. Stafford, A. J. Millis, and B. S. Shastry, Phys. Rev. B **43**, 13 660 (1991); N. Yu and M. Fowler, *ibid.* B **45**, 11 795 (1992).
[9] D. Loss, Phys. Rev. Lett. **69**, 343 (1992).
[10] B. Sutherland, J. Math. Phys. **12**, 251 (1971); Phys. Rev. A **4**, 2019 (1971); Rocky Mountain J. Math. **8**, 413 (1978).
[11] F. Woynarovich, H. Eckle, and T. Truong, J. Phys. A **22**, 4027 (1989).
[12] In addition the result of Ref. 9 differs from (17) by factors of two, thus not reproducing the free fermion case.
[13] E. Lieb and W. Liniger, Phys. Rev. **130**, 1605 (1963).
[14] F. G. Mertens, Z. Phys. B **55**, 353 (1984).
[15] C. N. Yang and C. P. Yang, Phys. Rev. **150**, 321, 327 (1966).
[16] T. B. Bahder and F. Woynarovich, Phys. Rev. B **33**, 2114 (1986); K. Lee and P. Schlottmann, *ibid.* **40**, 9104 (1989).

Study of the frequency dependence of the ferromagnetic resonance linewidths of nickel ferrites from 8–60 GHz

L. Torres, M. Zazo, A. G. Flores, V. Raposo, and J. Iñiguez
Departamento de Física Aplicada, Universidad de Salamanca, E-37071 Salamanca, Spain

In this communication we present in a systematic way experimental data on ferromagnetic resonance (FMR) linewidths of polycrystalline nickel ferrites ($Ni_xFe_{3-x}O_4$ with $0.8<\times<1.5$) from 8 to 12.4 GHz and from 26.5 to 60 GHz. Data from 26.5 to 60 GHz were taken at room temperature while measurements at X band have been carried out from 77 to 400 K. Neither in X band nor from 26.5 to 60 GHz was a clear frequency dependence found. Classical contributions to the FMR linewidth according to Sparks' outline are analyzed in the whole range of frequencies from 8 to 60 GHz. Contributions of the porosity, anisotropy, slowly and rapidly relaxing impurities, valence exchange and eddy current mechanisms are considered. © *1996 American Institute of Physics.* [S0021-8979(96)29708-2]

I. INTRODUCTION

Part of our work in the last years has been devoted to the study of nickel ferrites. Our research has mainly dealt with magnetic disaccommodation and ferromagnetic resonance (FMR) processes. In magnetic disaccommodation, experiments have always been performed at 1 kHz[1] while in FMR we have worked in X band,[2] $K\alpha$ (26.5–40 GHz) and U (40–60 GHz) bands.[3] We have handled both single and polycrystalline nickel ferrites and lately we have also found new relationships between disaccommodation and FMR measurements[4] using an induced anisotropy formalism.

In this article we present a study of the frequency dependence of the linewidth joining our results from 8 to 60 GHz. As is well known, nickel ferrites are used by technology in several fields and together with Mn and Zn ferrites they are the basis for more complicated compositions. For instance, nickel ferrites partially substituted by zinc are one of the most used compositions in commercial microwave materials.[5] Therefore, our study of the dependence of the linewidth with frequency and temperature for nickel ferrites in such a wide range offers interesting information about relaxation processes in FMR which could be very useful in order to minimize the losses in technical applications.

II. EXPERIMENT

Nickel ferrite samples $Ni_xFe_{3-x}O_4$ with $0.8<x<1.5$ were prepared following the ceramic method by sintering intimate mixtures of the appropriate high-purity oxides. Sintering was performed at 1400 °C during 24 h in oxygen atmosphere. As is usual, at the end of the process the samples were rapidly quenched in liquid nitrogen. In order to carry out FMR measurements, the samples were spherically shaped with a diameter between 0.6 and 0.7 mm. The surface was polished with diamond paste of 6 μm so that the diameter of the pits is of this magnitude.[6]

Two different experimental techniques have been used for measuring FMR. At X band a standard SMA coaxial transmission line has been chosen in order to facilitate the implementation of the system in a conventional cryostat. From 26.5 to 60 GHz a waveguide setup was required because at these frequencies the losses in transmission lines are too large.

In both cases the measurement was accomplished by monitoring the reflected wave in a short circuit. The linewidth is obtained by sweeping the static magnetic field around the resonance situation for each temperature and storing in the computer the relative reflected power. As is well known, this microwave absorption is proportional to the imaginary part χ_e'' of the diagonal component χ_e of the external susceptibility tensor $\underline{\chi}_e$ (Ref. 6) and the linewidth ΔH is defined as the mid-height width of the curve χ_e'' vs H (static magnetic field). The linewidths ΔH presented here are calculated, according to this classical definition, fitting the experimental points by means of a nonlinear computational technique.

At X band, the temperature of the cryostat chamber is controlled by an intelligent temperature controller with a stability better than 0.1 K. An additional platinum resistance located outside the short circuit at a distance of 2 mm from the sample registers its temperature. The whole process is automated so that the dependence with the temperature of FMR linewidth can be obtained in a few hours.[2]

At $K\alpha$ and U bands, most of measurements were performed at room temperature although some measurements at liquid nitrogen temperature could be done at $K\alpha$ band.[3]

III. RESULTS

Measurements at room temperature were carried out for all compositions from 8 to 12.4 GHz but no clear dependence of the linewidth appears in this range for most of the samples. In Fig. 1 measurements from 77 to 350 K for $Ni_{0.8}Fe_{2.2}O_4$ at several frequencies can be observed. It seems that there is a slight increase in the linewidth with frequency but we should take into account that the experimental error is

 0021-8979/96/79(8)/5422/3/$10.00 © 1996 American Institute of Physics

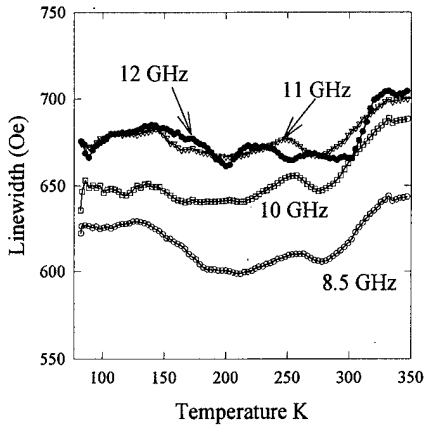


FIG. 1. FMR linewidths from 77 to 350 K for $Ni_{0.8}Fe_{2.2}O_4$ at 8.5, 10, 11, and 12 GHz.

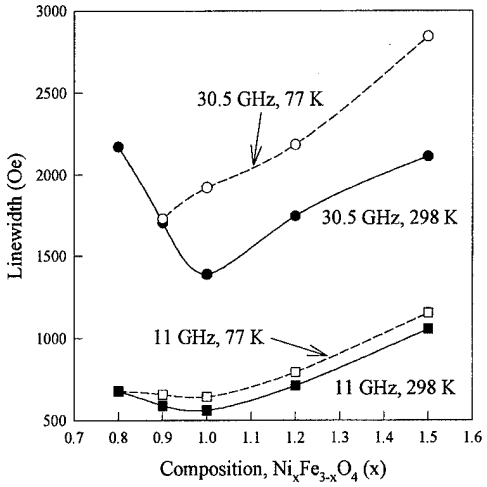


FIG. 3. FMR linewidths for $Ni_xFe_{3-x}O_4$ with $0.8<X<1.5$ measured at 11 and 30.5 GHz at 77 and 298 K.

around 7% (as is typical for FMR experiments[2,3,6]) and that the maximum change in the linewidth with frequency is of 10%. Then we cannot affirm that there is a clear increase in the linewidth with frequency.

In Fig. 2 we show the linewidths for the different compositions measured at 11 GHz from 77 to 350 K. The dependence of the linewidths with temperature provides information about the relaxation processes present in the samples and it will be useful for the study of the frequency dependence, as will be shown in the Discussion.

FMR from 26.5 to 60 GHz was measured in detail at room temperature and no clear dependence in the linewidth came into view.[3] The value of the average linewidth for all the samples at these frequencies was clearly larger than the one found at X band. In Fig. 3, the linewidth for the different compositions measured at 11 and 30.5 GHz can be seen. In the same graph we present the data for liquid nitrogen and room temperature.

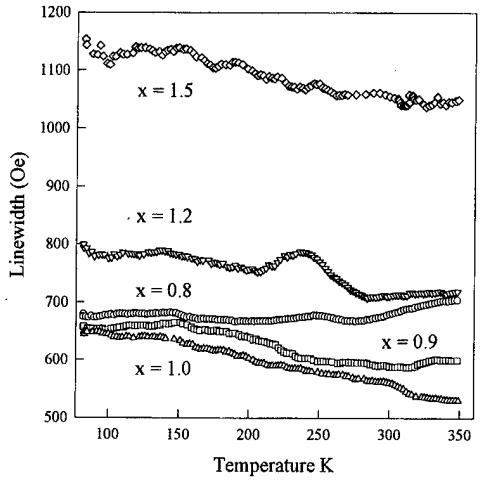


FIG. 2. FMR linewidths from 77 to 350 K at 11 GHz for $Ni_xFe_{3-x}O_4$ with $0.8<X<1.5$.

IV. DISCUSSION

From measurements carried out in such a wide range of frequencies some aspects are worth noting:

(1) For all the compositions linewidths are not clearly frequency dependent either in the X band or from 26.5 to 60 GHz. On the other hand, there is a clear difference between the average values of the linewidths in the X band and the average values from 26.5 to 60 GHz.

(2) The variation of the linewidth with composition is similar for the X band and $K\alpha$ and U bands with the lowest linewidths being always found for $Ni_1Fe_2O_4$. However, at room temperature, in X band the largest linewidths are found for $Ni_xFe_{3-x}O_4$ with $x>1$ while at $K\alpha$ and U bands the largest ones are found for $Ni_xFe_{3-x}O_4$ with $x<1$.

In order to understand these aspects, the contributions to the linewidth in polycrystalline samples have to be analyzed. The total linewidth for a polycrystalline ferrite is[6]

$$\Delta H=\Delta H_p+\Delta H_a+\Delta H_s, \tag{1}$$

where ΔH_p is the contribution induced by the porosity, ΔH_a is the broadening due to the random orientation of the anisotropy axes of the different crystallites of the polycrystal, and ΔH_s is the linewidth of the single crystal.

ΔH_s should include the following contributions: intrinsic contribution of Kasuya–Le Craw type,[6] surface roughness, valence exchange, slowly relaxing impurities, and rapidly relaxing impurities.[6] From these contributions we will not consider the intrinsic and the surface ones because their magnitude is negligible when we are dealing with polycrystalline linewidths of some hundred of oersted. Besides, we will not consider the rapidly relaxing impurities contribution because it should exhibit a linear dependence with frequency which has not been observed in our measurements.

In this way, ΔH_s will include valence exchange and slowly relaxing impurity mechanisms. The latter will be present for compositions with $x>1$[2] while the former will

contribute in compositions with $x<1$ in which the presence of Fe^{2+} ions gives rise to a valence exchange mechanism between Fe^{2+}–Fe^{3+}.

The contribution of porosity takes the form[6]

$$\Delta H_p=\frac{8\pi}{45}4\pi M_s\frac{1}{\cos\theta_u}\frac{V_{\text{pits}}}{V}\left(1-\frac{V_{\text{pits}}}{V}\right), \tag{2}$$

where V_{pits} is the volume of the pores in the sample, V the total volume of the sample, M_s is the saturation magnetization, and θ_u is the angle between the internal magnetic field and the wave vector k of the spin waves. For $k=0$, $\omega_\kappa=\omega_u=\omega_0=\gamma H_0$ we find[6]

$$\cos^2\theta_u=\frac{1}{3}\left(\frac{3-2\alpha}{3-\alpha}\right);\quad \alpha=\frac{4\pi M_s}{H_0}, \tag{3}$$

where H_0 is the resonance field.

According to Schlöman's calculations,[7] the anisotropy contribution can be written as

$$\Delta H_a=2.07\frac{H_a^2}{4\pi M_s}\left[\frac{\Omega+\frac{1}{3}+19\Omega/360}{\sqrt{\Omega(\Omega-\frac{1}{5})}}\right], \tag{4}$$

with

$$\Omega=\frac{f}{\gamma 4\pi M_s}-\frac{1}{3},\quad H_a=-\frac{2k_1}{M_s}, \tag{5}$$

where γ is the gyromagnetic ratio and k_1 is the first-order anisotropy constant, H_a being the anisotropy field.

The peak processes contribution (valence exchange or slowly relaxing) can be expressed as[6]

$$\Delta H=C\frac{\omega\tau_r}{1+(\omega\tau_r)^2}, \tag{6}$$

where C is a constant and τ_r is the relaxation time of the corresponding process which can be expressed as[6]

$$\tau_r=\tau_0\exp\frac{Q}{kT}, \tag{7}$$

where Q is the activation energy and τ_0 is a pre-exponential time factor.

For the composition $Ni_1Fe_2O_4$, at room temperature, a study of the frequency dependence of the different contributions to the linewidth has been carried out. The contributions given by Eqs. (2), (4), and (6) have been computed considering the theoretical values of $M_s=270$ Oe,[8] $k_1=-620\,00$ erg/cm^3[8] and the effective Lande factor, $g_{ef}=2.19$.[8] We have also considered the experimental values of porosity ($V_{\text{pits}}/V=0.06$)[9] and the resonance field. Besides we have taken $\tau_0=3\times10^{-13}$ s and $Q=0.06$ eV, as measured in hopping processes.[10]

The best fitting for X band is obtained for $C=1000$ Oe [see Eq. (6)]. With this value of C, X band data are correctly fitted but some deviations appear in $K\alpha$ and U bands where theoretical linewidths are lower than the experimental ones. Although this kind of analysis is not very accurate, mainly in our ferrites where porosity contribution is important, it is very useful in order to know which relaxation processes are taking place in these ferrites.

From the study of the results of the fitting it could be thought that the lower theoretical values obtained in $K\alpha$ and U bands are related to an eddy current contribution. The eddy current linewidth was studied by Sparks in the case of infinite skin depth.[6] He found that this contribution was linear versus the conductivity, increases as the square of frequency and also as the square of sample diameter. Then the eddy current contribution could justify the linewidth at high frequencies where this contribution is more important. However, this elementary assumption would imply an eddy current linewidth which should be proportional to the square of frequency[6] but this dependence is not observed experimentally.[3]

Nevertheless, the largest linewidths at high frequencies are found for $Ni_xFe_{3-x}O_4$ with $x<1$. For compositions with $x<1$ hopping between Fe^{2+}–Fe^{3+} produces valence exchange and then eddy current losses can be larger. The fact that at high frequencies samples with $x<1$ present larger linewidths indicates that there is some kind of eddy current contribution. In spite of that this contribution cannot be proportional to the square of frequency because it has not been observed.

We think that in our samples the eddy current losses are also affected by the decrease of the skin depth, δ, with the increasing frequency, i.e., for $Ni_{0.8}Fe_{2.2}O_4$ $\delta=1.03$ mm for $f=8$ GHz and $\delta=0.37$ mm for $f=60$ GHz.[11] The competition in the eddy current contribution between the increasing frequency and the decreasing skin depth could give rise to the observed experimental linewidths. The eddy current contribution for finite spherical samples in which the skin depth cannot be considered infinite has not been reported. It does not seem easy to calculate mainly because if the skin depth is not infinite a broad spectrum of spin waves could be excited.

ACKNOWLEDGMENT

This work was partially supported by the Consejería de Fomento de la Junta de Castilla y León under Project No. VA 25/94.

[1] L. Torres, M. Zazo, J. Iñiguez, C. de Francisco, and J. M. Muñoz, J. Magn. Magn. Mater. **40**, 1919 (1995).
[2] L. Torres, M. Zazo, J. Iñiguez, C. de Francisco, and J. M. Muñoz, IEEE Trans. Magn. **29**, 3434 (1993).
[3] L. Torres, M. Zazo, J. Iñiguez, and M. Quintillan, Appl. Phys. A **55**, 154 (1992).
[4] L. Torres, M. Zazo, J. Iñiguez, C. de Francisco, and J. M. Muñoz, Appl. Phys. A **60**, 303 (1995).
[5] J. Nicolas, *Microwave Ferrites* (North-Holland, Amsterdam, 1980), Vol. 2.
[6] M. Sparks, *Ferromagnetic Relaxation Theory* (McGraw-Hill, New York, 1965).
[7] E. Schlöman, J. Phys. Chem. Solids **6**, 242 (1958).
[8] J. Smit and H. P. J. Wijn, *Ferritas* (Biblioteca técnica de Philips, Madrid 1965).
[9] J. Iñiguez, C. Pereira, and J. Rivas, Appl. Phys. **36**, 159 (1985).
[10] F. Walz, V. A. M. Brabers, S. Chicazumi, H. Kronmüller, and M. O. Rigo, Phys. Status Solidi A **110**, 471 (1982).
[11] J. Iñiguez, C. de Francisco, J. M. Muñoz, and J. Rivas, Ann. Fis. B **82**, 177 (1986).

Variable texture $NiOFe_2O_3$ ferrite films prepared by pulsed laser deposition

P. Samarasekara,[a] R. Rani,[a] and F. J. Cadieu[a]
Center for Materials Research and Technology (MARTECH), Department of Physics, Florida State University, Tallahassee, Florida 32306

S. A. Shaheen
Center for Materials Research and Technology (MARTECH), Department of Physics, Florida State University, Tallahassee, Florida 32306

Pulsed laser deposition using bulk $NiOFe_2O_3$ targets onto heated substrates has been used to synthesize single phase Ni spinel ferrite films onto various substrates. Flowing oxygen has been used during the deposition to maintain the oxygen stoichiometry. Ni ferrite films have been deposited onto *C*-, *R*-, and *A*-plane sapphire, polycrystalline Al_2O_3, and fused silica. Single-crystal (111) oriented $NiOFe_2O_3$ films have been made onto *C*-plane sapphire for substrate temperatures of greater than 900 °C. Polycrystalline highly (400) textured Ni ferrite films have been made onto *R*-plane sapphire with $I(400)/I(311)=6.15$. Films made onto *A*-plane sapphire, polycrystalline alumina, and fused silica showed only moderate texturing. The coercive force of the (111) oriented $NiOFe_2O_3$ was 120 Oe perpendicular to the film plane and 95 Oe in plane. © *1996 American Institute of Physics.* [S0021-8979(96)29808-9]

I. INTRODUCTION

The development of ferrite films for use in monolithic microwave integrated circuits is an area of active research.[1] Generally most methods of ferrite film preparation require multiple step processing. Pulsed laser deposition is an exception to this since deposition with flowing oxygen onto heated substrates can produce spinel ferrite films without any subsequent heat treatments as first shown for Zn ferrite.[2] Polycrystalline Ni–Zn–ferrite films were also made onto glass substrates by pulsed laser deposition at relatively low substrate temperatures.[3] Pulsed laser deposition oriented Ni ferrite films with certain orientations have been reported for some substrates.[4] The synthesis of certain ferrite films has been reviewed recently.[5] Sputtered film growth usually requires a postdeposition heat treatment to develop the spinel ferrite structure.[6] Preferential (*hhh*) textured spinel films were obtained following postdeposition annealing for ion-beam sputtered films.[6] In this article we report the synthesis of single step, single phase $NiOFe_2O_3$ ferrite films prepared by pulsed laser deposition from bulk nickel ferrite targets. Distinctly different crystal textured films have been grown by using different substrates. Single-crystal (111) oriented $NiOFe_2O_3$ films were grown onto *C*-plane sapphire substrates as verified by Kikuchi backscattered electron diffraction. Polycrystalline highly (400) textured $NiOFe_2O_3$ films were grown onto *R*-plane sapphire substrates. To the best of our knowledge, no other reporting of such fully textured Ni–ferrite films has been found in the literature. It is especially important for optimal applications to utilize films such that the easy direction of magnetization is perpendicular to the film plane. For $NiOFe_2O_3$ the easy direction of magnetization is along the (111) direction.[7]

[a]Physics Department, Queens College of CUNY, Flushing, New York 11367.

II. EXPERIMENT

A Nd–yttrium aluminum garnet (YAG) pulsed laser deposition system located at MARTECH, FSU, has been used to deposit nickel ferrite films onto various heated substrates. The laser wavelength was 1064 nm with 30, 8 ns wide, pulses/s. The pulse energy was 700 mJ with a peak power of 85 MW. The laser beam was directed at 20° from the target normal with a target to substrate distance of 1.5 cm. The laser beam was rastered over the target surface by a computer controlled movable mirror. Different polished substrates have been used including *C*-plane sapphire, *A*-plane sapphire, *R*-plane sapphire, polycrystalline Al_2O_3, and fused silica. The substrate size was 5 mm×5 mm for sapphire and fused silica, and 50 mm×12.5 mm for the polycrystalline alumina substrates. A flowing O_2 gas pressure of 200 m Torr was used during the deposition for the data presented here. The films were deposited at an average rate of 5 Å/s for 2 h. This allowed relatively thick films to be produced and steady-state deposition conditions to be established. Lower O_2 pressures resulted in films exhibiting α-Fe and impurity phases. Except as noted the samples have not been subjected to any postdeposition heat treatments. X-ray diffraction data have been collected using a diffractometer with Cu $K\alpha$ radiation. The film thicknesses were measured by profoilometer with 5 Å resolution. Magnetic measurements have been made using a vibrating-sample magnetometer located at Queens College of CUNY.

III. RESULTS AND DISCUSSION

Single-crystal nickel ferrite, $NiOFe_2O_3$, films oriented to have the cubic cell diagonal perpendicular to the substrate plane have been grown by using pulsed laser deposition to deposit the films at relatively high temperatures onto *C*-plane sapphire substrates. An x-ray diffraction trace of such a fully oriented film grown onto a *C*-plane sapphire substrate at 930 °C is shown in Fig. 1. Only the $NiOFe_2O_3$ (111), (222), and (333) family of reflections was evident for the higher

 0021-8979/96/79(8)/5425/3/$10.00 © 1996 American Institute of Physics

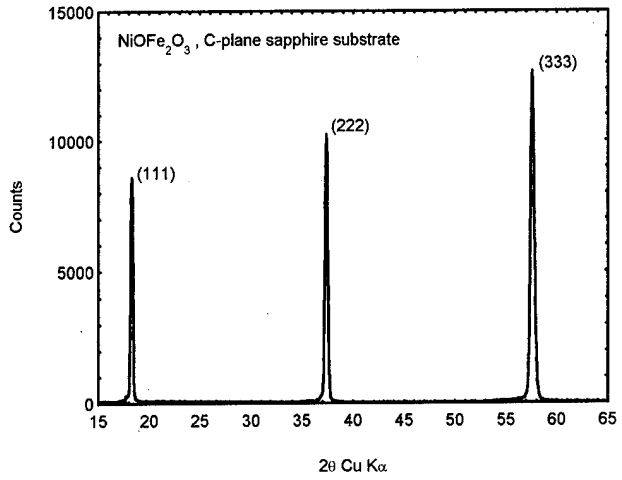


FIG. 1. A x-ray diffractometer trace, Cu $K\alpha$ radiation, for a $NiOFe_2O_3$ film made onto a 930 °C C-plane sapphire substrate is shown. The oxygen pressure during deposition was 200 m Torr. Kikuchi backscattered electron diffraction has been used to show this is a single-crystal film.

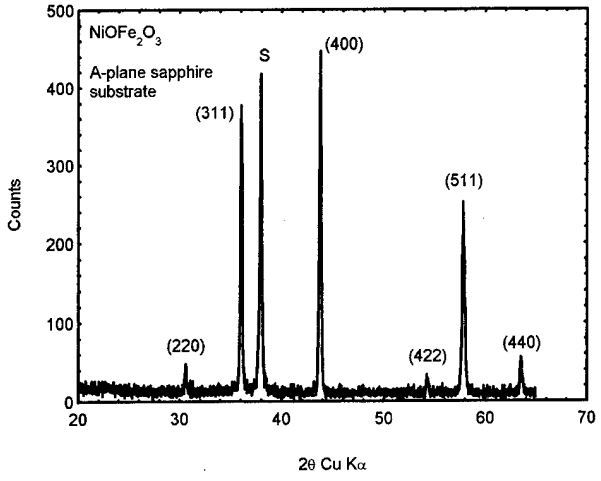


FIG. 3. An x-ray diffractometer trace, Cu $K\alpha$ radiation, for a $NiOFe_2O_3$ film made onto a 910 °C A-plane sapphire substrate is shown. The oxygen pressure during deposition was 200 m Torr. The (110) sapphire line is indicated by the letter S.

substrate temperatures of $\geqslant$830 °C. The (006) C-plane sapphire line at 41.68° is very weak so that there are no competing substrate lines. It was determined that the film of Fig. 1 was single crystal by Kikuchi backscattered electron diffraction.[8] No rotation of the Kikuchi pattern was observed for this film as the electron beam was scanned across the film. This verified that the film was single crystal. The films on C-plane sapphire were $\approx$3.6 μm thick. For lower substrate temperatures the (311) and (400) reflections began to become evident first. For a C-plane sapphire substrate temperature during deposition of 625 °C, the (222) reflection was still enhanced but the (311) dominant reflection of the powder pattern dominated.

Nickel ferrite films similarly deposited onto R-plane sapphire substrates exhibited predominantly (400) textured growth for the higher substrate temperatures during the deposition. An x-ray diffractometer trace for a $NiOFe_2O_3$ film deposited onto R-plane sapphire is shown in Fig. 2. Kikuchi backscattered electron diffraction measurements gave no pattern in this case indicating that the films consisted of oriented crystallites with a diameter of less than 1 μm.

In contrast to the extreme textures grown on C-plane and R-plane sapphire, films grown onto A-plane sapphire were not fully textured even at the higher substrate temperatures. An x-ray trace for a $NiOFe_2O_3$ film grown onto A-plane sapphire is shown in Fig. 3. In this the (400) reflection exceeded the (311) intensity which is in contrast to the powder pattern where the (311) dominates the (400) intensity by a factor of 4.

The x-ray lines of the nickel ferrite films grown onto all three sapphire cuts were sharp and distinct for the as-deposited films.

Similar films grown onto fused silica substrates also produced sharp diffraction lines, but strong preferential textur-

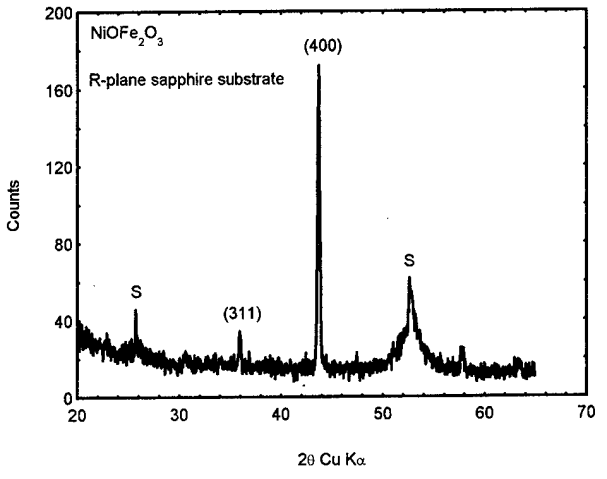


FIG. 2. An x-ray diffractometer trace, Cu $K\alpha$ radiation, for a $NiOFe_2O_3$ film made onto a 910 °C R-plane sapphire substrate is shown. The oxygen pressure during deposition was 200 m Torr. Substrate lines are indicated by the letter S.

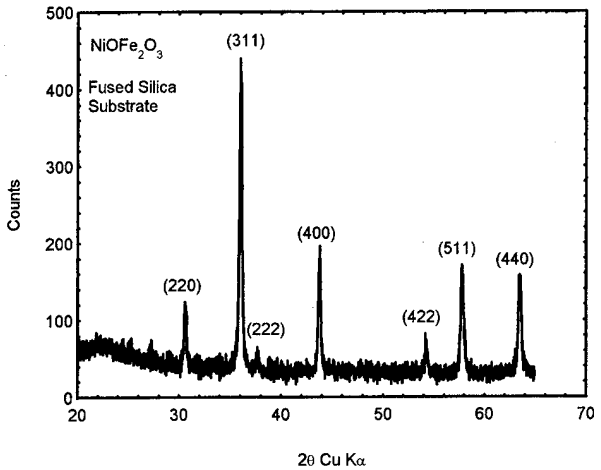


FIG. 4. An x-ray diffractometer trace, Cu $K\alpha$ radiation, for a $NiOFe_2O_3$ film made onto a 650 °C fused silica substrate is shown. The oxygen pressure during deposition was 200 m Torr.

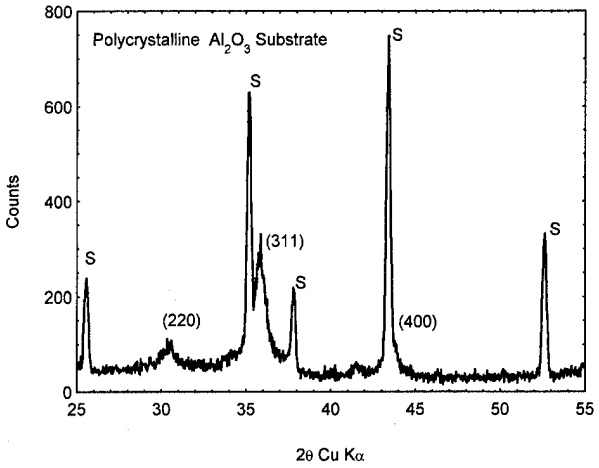


FIG. 5. An x-ray diffractometer trace, Cu $K\alpha$ radiation, for a $NiOFe_2O_3$ film made onto a 750 °C polycrystalline alumina, Al_2O_3, substrate is shown. The oxygen pressure during deposition was 200 m Torr. The substrate lines are indicated by the letter *S*.

ing was not evident. In this case the relative x-ray intensities approached those observed in the powder pattern. An x ray for a $NiOFe_2O_3$ film grown onto a fused silica substrate is shown in Fig. 4. In this case the background has an amorphous hump near 22° from the substrate.

Similarly synthesized nickel ferrite films made onto heated polycrystalline Al_2O_3 substrates exhibited broadened diffraction lines which could only be sharpened to a certain extent by subsequent heat treatments of the films. An x-ray trace showing the broadened lines of $NiOFe_2O_3$ (311) dominant reflection is shown in Fig. 5. In this case the diffraction lines of the polycrystalline Al_2O_3 substrate dominate the pattern and some impurity phases are present.

Room-temperature magnetic hysteresis loops were measured for the as-deposited films. The (222) $NiOFe_2O_3$ textured film of Fig. 1 grown onto *C*-plane sapphire indicated a coercive field of 120 Oe measured perpendicular to the film plane and 95 Oe measured in the plane of the film. The saturation flux density, $4\pi M_s$, was 1.9 kG as deduced from the approach to saturation of the perpendicular magnetization. This method can be used since the demagnetization factor for the perpendicular to the film plane measurements is very close to $N_d = 4\pi$. The easy direction of magnetization is shown to be in the (222) direction as expected. The sample of Fig. 5 grown onto polycrystalline alumina exhibited a coercivity of 150 Oe both perpendicular and parallel to the film plane.

The texture modes grown by using the different substrates are summarized in Table I. The most important results

TABLE I. The dominant $NiOFe_2O_3$ x-ray texture for different substrates is shown for pulsed laser deposition with 200 m Torr O_2 and high substrate temperatures.

Substrate	Ni–ferrite Dominant texture	$I(400)/I(311)$ Intensity ratio
C-Plane sapphire (006)	(111), (222), (333) only single-crystal films	Neither detected
A-Plane sapphire (110)	(311)	1.20
R-Plane sapphire (012)	(400)	6.15
Fused silica	Random, (311)	0.400
Polycrystalline Al_2O_3	(311) as deposited,	$I(220)/I(311) = 0.544$[a]
	after flash heating in air	$I(220)/I(311) = 0.433$[a]

[a]For the polycrystalline Al_2O_3 substrates the intensity ratio for the $I(220)$ reflection is used because of the strong Al_2O_3 (113) peak which is nearly coincident with the $NiOFe_2O_3$ (400) peak.

of this article are that single-crystal $NiOFe_2O_3$ films can be grown by pulsed laser deposition with (111) orientation onto *C*-plane sapphire, and that highly (400) textured polycrystalline $NiOFe_2O_3$ films can be grown onto *R*-plane sapphire substrates. Single-crystal (111) oriented $NiOFe_2O_3$ films exhibit threefold symmetry in the substrate plane and d_{111} exceeds the *a* lattice parameter of Al_2O_3 by only 1.18%. These conditions allow the growth of single-crystal (111) oriented $NiOFe_2O_3$ films onto *C*-plane sapphire. Relatively high substrate temperatures of $\geqslant$900 °C have been required to grow completely oriented and/or textured films. The single-crystal (111) oriented films are of special interest since the easy direction of magnetization for $NiOFe_2O_3$ is along that direction.

ACKNOWLEDGMENT

This work was in part supported by a grant to one of the authors (F.J.C.) at Queens College from the Air Force Office of Scientific Research.

[1] J. D. Adam, S. V. Krishnaswamy, S. H. Talisa, and K. C. Yoo, J. Magn. Magn. Mater. **83**, 419 (1990).
[2] Sushama Joshi, Rashmi Nawathey, V. N. Koinkar, V. P. Godbole, S. M. Chaudhari, S. B. Ogale, and S. K. Date, J. Appl. Phys. **64**, 5647 (1988).
[3] K. Tanaka, Y. Omata, Y. Nishikawa, Y. Yoshida, and K. Nakamura, IEEE Trans. J. Magn. Jpn. **6**, 1001 (1991).
[4] R. B. van Dover, E. M. Gyorgy, J. M. Phillips, J. H. Marshall, R. J. Felder, R. M. Fleming, and H. O'Bryan, Jr., J. Appl. Phys. **75**, 6124 (1994).
[5] Carmine A. Carosella and Douglas B. Chrisey, *Pulsed Laser Deposition of Ferrite Thin Films, in Pulsed Laser Deposition of Thin Films*, edited by Douglas B. Chrisey and Graham K. Hubler (Wiley, New York, 1994).
[6] Hae Seok Cho, Sang Ki Ha, Min Hong Kim, and Hyeong Joon Kim, J. Mater. Res. **10**, 274 (1995).
[7] Raul Valenzuela, *Magnetic Ceramics* (Cambridge University Press, Cambridge, 1994), p. 140.
[8] The Kikuchi backscattered electron measurements were done by H. Garmestani at the National High Magnetic Field Laboratory, Florida State University.

Atomic migration in Ni–Co ferrite

Chul Sung Kim, Seung Wha Lee, and Seung Iel Park
Department of Physics, Kookmin University, Seoul 136-702, Korea

Jae Yun Park
Department of Materials Science and Engineering, University of Inchon, Inchon 402-749, Korea

Young Jei Oh
Division of Ceramics, Korea Institute of Science and Technology, Seoul 130-650, Korea

Ni–Co ferrite has been studied with Mössbauer spectroscopy and x-ray diffraction. The crystal structure for this system is spinel, and the lattice constant is in accord with Vegard's law. The Mössbauer spectra consist of two six-line patterns corresponding to Fe^{3+} at the tetrahedral (A) and octahedral (B) sites. The Néel temperature increases linearly with Ni concentration, suggesting the superexchange interacion for the Ni–O–Fe link is stronger than that for the Co–O–Fe link. It is found that Debye temperatures for the A and B sites of $CoFe_2O_4$ and $NiFe_2O_4$ are found to be $\theta_A=734$ K, $\theta_B=248$ K, and $\theta_A=378$ K, $\theta_B=357$ K, respectively. The intensity ratio of the A to B patterns is found to increase at low temperatures with increasing temperature due to the large difference of Debye temperatures of the two sites and to decrease at high temperatures due to migration of Fe^{3+} ions from A to B sites. Atomic migration of $CoFe_2O_4$ starts near 400 K and increases rapidly with increasing temperature to such a degree that 69% of the ferric ions as the A sites have moved over to the B sites by 780 K. It is noted that, as the Ni concentration in cobalt ferrite increases, the Debye temperatures tend to decrease the migration at the A and B sites is slow.
© *1996 American Institute of Physics.* [S0021-8979(96)29908-5]

I. INTRODUCTION

A ferrimagnetic spinel can be represented by the formula AB_2O_4, the $A-B$ magnetic interactions between the magnetifc atoms on the A (tetrahedral) sites and the magnetic atoms on the B (octahedral) sites are stronger than the $A-A$ and $B-B$ interactions.[1] Metallic atoms of a ferrimagnetic spinel are in an inverse distribution; half the atoms of iron are in the A sites and the other half plus magnetic atoms in the B sites. However, $CoFe_2O_4$[2,3] is not completely inverse, and the degree of inversion depends on the heat treatment. The area ratio, $Fe(A)/Fe(B)$, has been found to vary from 0.61 ± 0.04 to 0.87 ± 0.04 for two extreme quenched and slowly cooled $CoFe_2O_4$ samples, respectively. $NiFe_2O_4$ is an inverse spinel. Chappert and Frankel[4] have shown that the spin arrangement in $NiFe_2O_4$ is of the Neél collinear type. The ferrimagnetic Neél temperature was found to be 868 K by the thermal scanning technique.[5]

In this article, we present our Mössbauer and x-ray results on slowly cooled $Ni_xCo_{1-x}Fe_2O_4$ with special emphasis on atomic migration as a function of temperature and on the Debye temperature for A and B sites.

II. EXPERIMENT

The slowly cooled $Ni_xCo_{1-x}Fe_2O_4$ samples were prepared by direct reaction of elements in an evacuated quartz tube. The starting materials were high-purity Fe_2O_3 (99.995%), NiO (99.999%), and CoO (99.999%). Mixtures of the elements in the proper proportions were sealed in evacuated quartz ampoules, heated at 1000 °C for two days, and then slowly cooled to room temperature at a rate of 10 °C/h. In order to obtain a homogeneous mateial, it was necessary to grin the samples after the first firing and to press the powders into pellets before annealing then for a second time in evacuated and sealed quartz ampoules. The Mössbauer spectra were recorded using a conventional Mössbauer spectrometer of the electromechanical type[6] with a 10 mCi ^{57}Co source in a Rh matrix.

III. RESULTS

X-ray diffraction patterns of the $Ni_xCo_{1-x}Fe_2O_4$ were obtained in the $\theta-2\theta$ geometry with Cu K_α radiation. The lattice constant a_0 for each composition was found by plotting a (θ) against the Nelson–Riley function[7] and extrapolating to $\theta=90°$. The results are shown in Table I. The unit cell

TABLE I. Lattice parameter (a_0) at room temperature, magnetic hyperfine field (H_{hf}), quadrupole shift (ΔE_Q), and isomer shift (δ) at 13 K for $Ni_xCo_{1-x}Fe_2O_4$. δ is relative to the iron metal.

		H_{hf} (kOe)		ΔE_Q (mm/s)		δ (mm/s)	
x	a_0 (Å)	B	A	B	A	B	A
0.0	8.381	553	516	−0.02	−0.01	0.38	0.25
0.1	8.370	554	515	−0.02	−0.01	0.37	0.25
0.3	8.361	555	515	−0.01	−0.01	0.38	0.25
0.5	8.346	555	513	−0.01	0.00	0.36	0.24
0.7	8.336	556	513	−0.01	0.00	0.36	0.24
1.0	8.326	557	511	0.01	0.00	0.39	0.26

 0021-8979/96/79(8)/5428/3/$10.00 © 1996 American Institute of Physics

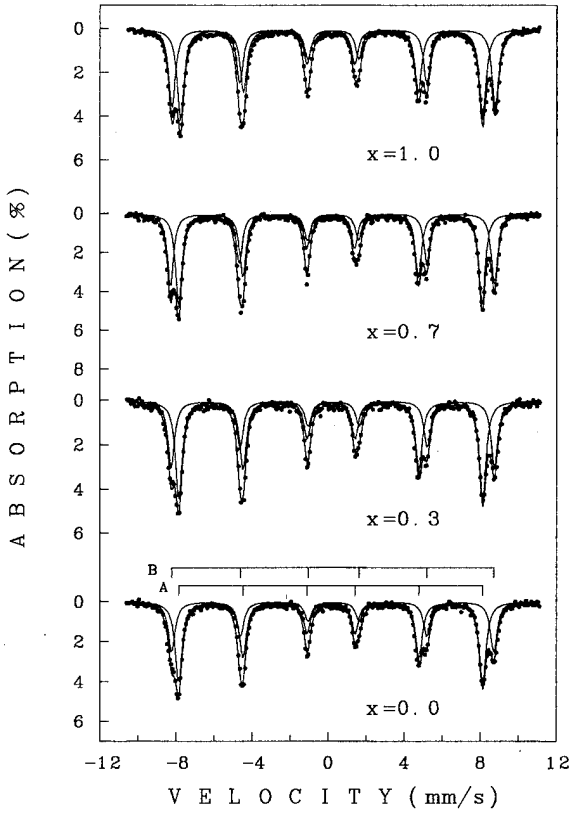


FIG. 1. Mössbauer spectra of $Ni_xCo_{1-x}Fe_2O_4$ at room temperature.

parameter (a_0) decreases linearly with increasing nickel concentration (x) and follows Vegard's law approximately. This can be expected in view of the fact that the ionic radius of 0.69 Å for Ni^{2+} ions is smaller than that of 0.78 Å for Co^{2+} ions. Mössbauer spectra of $Ni_xCo_{1-x}Fe_2O_4$ were measured at various absorber temperatures from 13 to 800 K. The Mössbauer spectra are composed of two six-line hyperfine pattern A and B sites. Using a least-squares computer program, two sets of six Lorentzians lines were fitted to the Mössbauer spectra under the usual constraints,[8] which are valid when the quadrupole interaction is much weaker than the magnetic

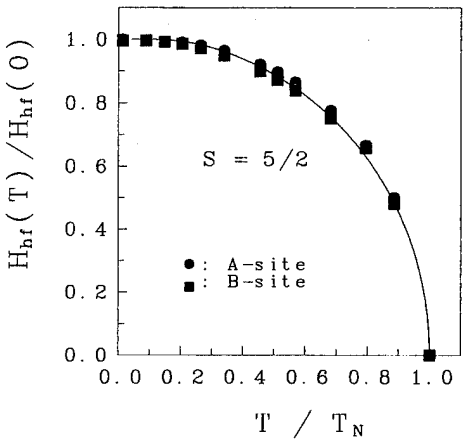


FIG. 2. Reduced magnetic hyperfine field $H_{hf}(T)/H_{hf}(0)$ against reduced temperature T/T_N for the A and B sites of $Ni_{0.1}Co_{0.9}Fe_2O_4$. Points marked are the experimental values. The full curve is the Brillouin curve for $S=5/2$.

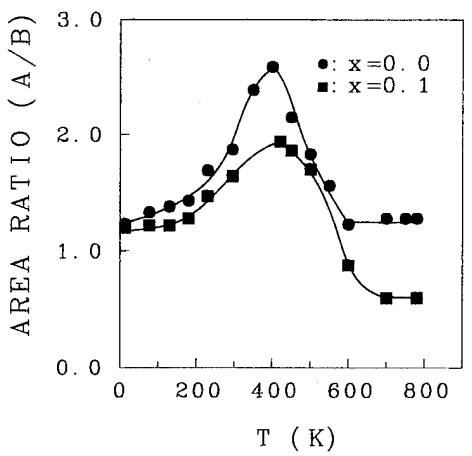


FIG. 3. Temperature dependence of the ratio of A to B sites for $Ni_xCo_{1-x}Fe_2O_4$.

hyperfine interaction. Some of them are shown in Fig. 1. The results of the computer analysis are presented in Table I.

The isomer-shift values at room temperate for A and B patterns are found tot be (0.13–0.16)±0.01 and (0.25–0.28) ±0.01 mm/s relative to the Fe metal, respectively, which are consistent with the high-spin Fe^{3+} charge states.[9] The smaller value of A-site isomer shift is due to a large convalency at the A site.

It is worth noting that in Fig. 1 and Table I the quadrupole shifts for both the A and B patterns vanish in accord with the cubic crystal structure of $Ni_xCo_{1-x}Fe_2O_4$. Plots of the reduced magnetic hyperfine field $H_{hf}(T)/H_{hf}(0)$ against reduced temperature T/T_N for the A and B sites of $Ni_{0.1}Co_{0.9}Fe_2O_4$ are given in Fig. 2 along with the Brillouin curve[10] $B(S)$ for $S=5/2$.

Figure 3 shows the temperature dependence of the absorption area ratio of A site to B site. It is worth noting in Fig. 3 that at low temperature the area ratio increases with increasing temperature and then decreases at high temperature. The cation distribution of $Ni_xCo_{1-x}Fe_2O_4$ is $(Co_yFe_{1-y})^A[Ni_xCo_{1-x-y}Fe_{1+y}]^BO_4$, indicating the y of the tetrahedral site Fe^{3+} ions have migrated from A to B sites

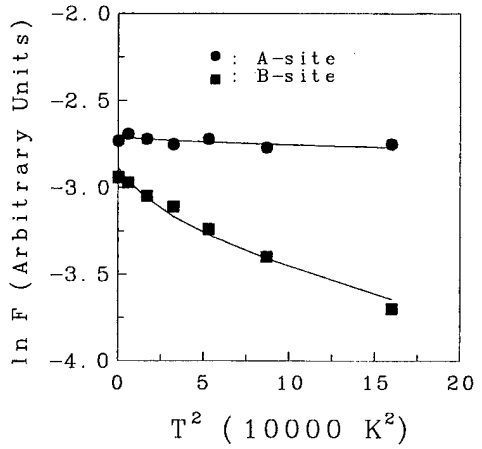


FIG. 4. Natural logarithm of the absorption area, F, vs T^2 for the A and B subspectra of $Ni_{0.1}Co_{0.9}Fe_2O_4$.

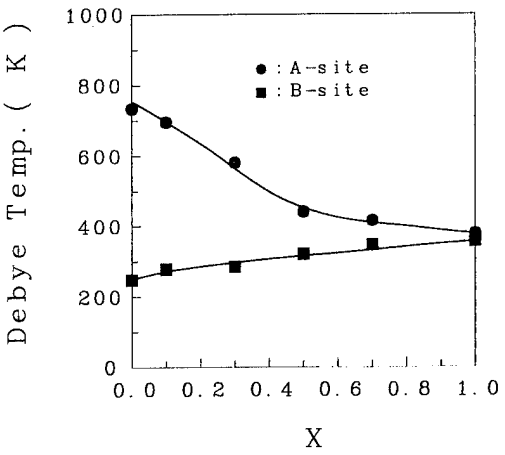


FIG. 5. Debye temperatures for $Ni_xCo_{1-x}Fe_2O_4$.

(the same number of Co ions have moved from B to A sites). The area ratio of A and B subspectra for the above distribution[11] is

$$\frac{I_A}{I_B}=\frac{(1-y)f_A}{(1+y)f_B}, \tag{1}$$

where f_A and f_B represent the recoil-free fractions of A and B site Fe ions, respectively. The Debye model gives the following expression for the recoil-free fraction:[12]

$$f=\exp\left[-\frac{3E_R}{2k_B\theta}\left(1+\frac{4T^2}{\theta^2}\int_0^{\theta/T}\frac{x\,dx}{e^x-1}\right)\right], \tag{2}$$

where E_R is the recoil energy of ^{57}Fe for the 14.4 keV gamma ray. θ and k_B represent the Debye temperature and the Boltzmann constant, respectively. The Debye temperature for each site can be calculated from the temperature dependence of the resonant absorption area of each subspectra at low temperatures.

Figure 4 shows ln F vs T^2 for $Ni_{0.1}Co_{0.9}Fe_2O_4$, where F stands for the total resonance absorption areas of A and B sites a Mössbauer spectrum at T. F is proportional to the recoil-free fraction f. The curves are close to straight lines, and the results are $\theta_A=679\pm5$ K and $\theta_B=278\pm5$ K. Figure

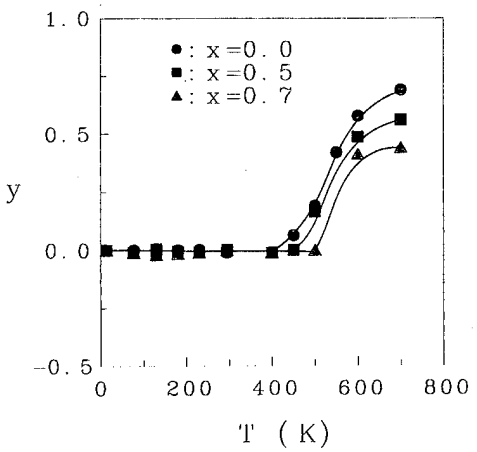


FIG. 6. Temperature dependence of the fraction y of the tetrahedral site Fe^{3+} ions that migrate to B sites.

TABLE II. Atomic migration temperature, T_m and ratio of atomic migration, R_m at 700 K for $Ni_xCo_{1-x}Fe_2O_4$.

x	0.0	0.1	0.3	0.5	0.7
T_m (K)	400	420	450	470	520
R_m (%)	69	67	61	56	44

5 and Table II show the Debye temperature as a function of the nickel concentration x, for $Ni_xCo_{1-x}Fe_2O_4$. Since θ_B is much less than θ_A, it is evident from Eq. (1) that f_B decreases much more rapidly with increasing temperature than f_A; f_A/f_B in turn increases with increasing temperature, thus explaining the tendency of the area ratio to increase with increasing temperature at low temperatures, as shown in Fig. 3. The tendency of the area ratio to decrease at high temperature in Fig. 3 can be explained in terms of the migration of Fe ions from the A sites to the B sites: in other words, an increase in the y value in Eq. (1) will result in a decrease in the area ratio.

Substituting the experimental area ratios from Fig. 3 and the f values from Eq. (2) into Eq. (1) we obtained the y values as a function of temperature, as shown in Fig. 6. It can be seen in Table II that the Debye temperature decreases with increasing nickel concentration x. Ni ions replacing Co ions seem to weaken the interatomic binding force between Co and O ions. Figure 6 shows that atomic migration of $Ni_{0.7}Co_{0.3}Fe_2O_4$ starts near 520 K and increases rapidly with increasing temperature to such a degree that 44% of the iron ions at the A sites move over to the B sites at 700 K. This onset temperature is higher by about 100 K than the for $CoFe_2O_4$. An implication of this result is that increased Ni concentration enervates atomic migration.

ACKNOWLEDGMENTS

The present studies were supported by the Basic Science Research Institute Program, the Ministry of Education, 1996 (No. 2424) and the Korea Science and Engineering Foundation.

[1] C. M. Srivastava, G. Srinivasan, and N. G. Nanadikar, Phys. Rev. B **19**, 499 (1979); C. S. Kim, H. M. Ko, W. H. Lee, and C. S. Lee, J. Appl. Phys. **73**, 6298 (1993).
[2] M. R. De Guire, R. C. O'Handley, and G. Kalonji, J. Appl. Phys. **65**, 3167 (1989).
[3] G. A. Sawatzky, F. van der Woude, and A. H. Morrish, J. Appl. Phys. **39**, 1204 (1968); C. S. Kim, S. I. Park, Y. L. Um, Y. J. Lee, S. W. Lee, and S. R. Hong, J. Korean Phys. Soc. **27**, 323 (1994).
[4] J. Chappent and R. B. Frankel, Phys. Rev. Lett. **19**, 570 (1967).
[5] F. van der Woude, G. A. Sawatzky, and A. H. Morrish, Phys. Rev. **167**, 533 (1968).
[6] H. N. Ok, K. S. Baek, E. C. Kim, and C. S. Kim, Phys. Rev. B **48**, 3212 (1993).
[7] J. B. Nelson and D. P. Riley, Proc. Phys. Soc. **57**, 160 (1945).
[8] H. N. Ok and J. G. Mullen, Phys. Rev. **168**, 563 (1968).
[9] C. S. Kim, D. Y. Kim, H. M. Ko, J. K. Kim, and J. Y. Park, J. Appl. Phys. **73**, 6986 (1993).
[10] P. Muthukumarasamy, T. Nagarajan, and A. Narayanasamy, J. Phys. C **15**, 2519 (1982).
[11] K. S. Baek, S. W. Nam, H. Choi, H. L. Park, H. N. Ok, and C. S. Kim, J. Korean Phys. Soc. **24**, 155 (1991).
[12] R. L. Mössbauer and W. H. Wiedermann, Z. Phys. **159**, 33 (1960).

EXAFS and magnetic characterization of inverted ball milled zinc ferrite powders (abstract)

S. A. Oliver
Center for Electromagnetics Research, Northeastern University, Boston, Massachusetts 02115

V. G. Harris
Code 6342, Naval Research Laboratory, Washington, DC 20375

H. H. Hamdeh and J. C. Ho
Physics Department, Wichita State University, Wichita, Kansas 67260

Divalent zinc is commonly used as a replacement cation in ferrites, as it increases the material magnetization when substituted in moderate amounts. However, pure zinc ferrite ($ZnFe_2O_4$) is a normal spinel, as zinc has a strong preference for the tetrahedral (A) site in the spinel structure, with Fe occupying the octahedral (B) sites. Then antiferromagnetic B–B coupling dominates the magnetic behavior yielding a material with a Neel temperature near 10 K. It is typically difficult to produce inverted zinc ferrite due to this strong site preference, but recently we produced fine zinc ferrite powders having an inversion parameter of 0.20 using an aerogel process.[1] Ball milling these powders increased the inversion parameter to 0.55, and the median particle size from 14 to 40 nm. To confirm the x-ray diffraction inversion parameters, extended x-ray absorption fine structure (EXAFS) measurements were taken on these powders and $ZnFe_2O_4$ standards for both the Fe K_α and Zn K_α absorption edges. Fourier transformed results were fingerprinted against theroretical radial distrubtion functions generated from multiple-scattering FEFF codes for scattering atoms located on the tetrahedral and octahedral sites. Qualitatively, the zinc ferrite standard appears as a normal spinel, while both the iron and zinc radial distributions for the ball milled sample showed large site occupation of both A and B sites. This sample shows superparamagnetic behavior at room temperature, with some ferrimagnetic particles exceeding the critical volume, as indicated by a 15 Oe coercive field. The saturation magnetization of the metastable ball milled powder exceeds 2100 G. © *1996 American Institute of Physics.* [S0021-8979(96)64508-5]

[1] H. H. Hamdeh *et al.*, IEEE Trans. Magn. **31**, 3808 (1995).

High-power-use Mn–Zn ferrites with monodomain structure prepared by low-temperature sintering

C. S. Liu and J. M. Wu
Department of Material Science and Engineering, National Tsing Hua University, Hsinchu, Taiwan, Republic of China

I. Nan Lin
Materials Science Center, National Tsing Hua University, Hsinchu, Taiwan, Republic of China

C. J. Chen
Materials Research Laboratories, Industrial Technology Research Institute, Hsinchu Taiwan, Republic of China

Densely sintered Mn–Zn ferrites with grain size varying between 1 and 6 μm were obtained. Then the effect of grain size was investigated in detail by power loss analysis and scanning electron microscopy examination of microstructure. It is found that the power loss is seen to be lowered from 260 to 120 kW/m^3 at 500 kHz, 50 m T and 90 °C with grain size decreased in the order of 3 μm. It is assumed that the residual loss from domain wall resonance is a dominant factor of power loss from 500 kHz to 1 MHz. Therefore we conclude that Mn–Zn ferrite display a grain size dependent power loss with transition at grain size about 3 μm due to the absence of intragranular domain wall and these fine core materials can be prepared by low sintering temperature and the optimum control of atmosphere containing 0.5% O_2. © *1996 American Institute of Physics.* [S0021-8979(96)30008-5]

I. INTRODUCTION

Because the driving frequency of switching power supplies has been raised from several kHz to around 1 MHz, there is an urgent need for the reduction of power loss of core material at high frequency. Mn–Zn ferrites, usually used as core materials in the switching power supplies, exhibit a high power loss at high frequencies. Therefore, many efforts have been made to reduce the power loss of Mn–Zn ferrites. Theoretically, power loss P_b is divided into three parts, hysteresis loss P_h, eddy current loss P_e, and residual loss P_r.[1] As P_e and P_r could not be measured experimently, they are obtained by subtracting hysteresis loss. Besides, the magnetic domain configurations of polycrystalline Mn–Zn ferrites are not clear today. The wall-related loss P_r was generally ignored below MHz. Recently, several studies mentioned that P_r becomes dominant at this frequency range and at high temperature.[2] Moreover, the relation between grain size and domain size in Mn–Zn ferrite was also studied by neutron depolarization.[3] It is found that the domain size is identical to the grain size for Mn–Zn ferrites for grain size between 0.3 and 3 μm. In this article, the present authors examined the effect of various grain sizes in low-loss Mn–Zn ferrites in order to resolve the above-mentioned problem. Power loss has been analyzed as a function of grain size in order to study wall-related power loss.

II. EXPERIMENT

Mn–Zn ferrite samples with the chemical composition $Mn_{0.72}Zn_{0.22}Fe_{2.06}O_4$, plus optimum $CaO–SiO_2$ content of 0.07 wt%, were prepared by conventional powder ceramic process. The samples with various grain size from 1 to 6 μm were sintered at 1170 °C in $N_2–O_2$ atmosphere of 0.5% O_2 and obtained by adjusting the sintering time between 1 and 8 h.

Final dimensions of toroidal samples were 17 mm outside diameter (o.d.), 8 mm inside diameter (i.d.), and 5 mm height. For electrical measurements, the specimen was 9 mm in diameter and 4 mm long, and both ends were indium gallium coated as an electrode.

Permeability was measured on toroidal samples by a LCR meter HP4284A. The power loss, P_b, was measured by an apparatus made by Ryowa Company. The hysteresis losses, P_h, were obtained by DC–BH tracer made by Walker company. Then, scanning electron microscopy (SEM) was used to observe the grain size.

III. RESULTS AND DISCUSSION

Table I shows that when samples were sintered at 1170 °C, densely sintered Mn–Zn ferrites with grain size varying between 1 and 6 μm were obtained. It is shown that with grain size around 3 μm, the optimum initial permeability is obtained, however the initial permeability decreases with further increase of grain size. This would be attributed to the effect of grain boundaries, because each grain of Mn–Zn ferrite is covered by a high-electrical-resistivity layer made of SiO_2 and CaO in order to prevent eddy current circulation. The thickness of high-electrical-resistivity boundary layer is believed to be influenced by the reduction of grain boundary thickness accompanying the increase of grain size. This phenomena causes the increase of dc resistivity and hysteresis loss for the samples with larger grain size. However, this layer also increases the apparent permit-

TABLE I. Static characteristics for samples with various grain sizes.

Grain size	1 μm	3 μm	5 μm	6 μm
Permeability	1070	1440	1330	1240
Sintered density (g/cm^3)	4.88	4.90	4.90	4.90
dc ρ (Ωm)	13	22	20	27
[a]P_h/f(J/m^3)	0.22	0.15	0.15	0.23

[a]At 50 m T and RT.

 0021-8979/96/79(8)/5432/3/$10.00 © 1996 American Institute of Physics

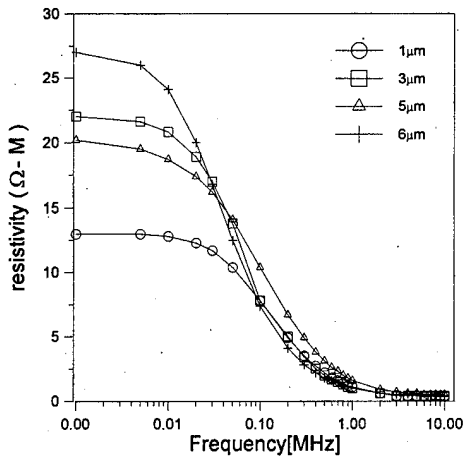


FIG. 1. Frequency dependence of resistivity for samples with various grain sizes.

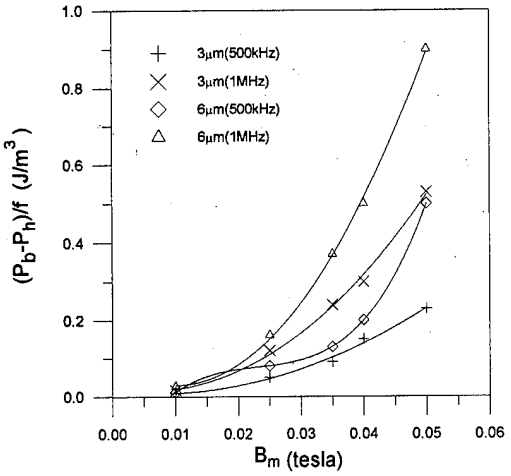


FIG. 3. Dependence of $(P_b-P_h)/f$ on maximum flux density for samples with grain size 3 and 6 μm.

tivity, so that at high frequency, these layers are short circuited by their capacitive properties. Figure 1 shows the frequency dependence of resistivity for samples with various grain sizes. It is found that although different dc resistivity is observed, the values of resistivity have similar frequency dependence above 500 kHz. According to a report,[4] if the frequency dependence of resistivity is taken into account, a model can only approach the measured results in MHz region but can be quite different in the lower frequency range (500 kHz $<f<1$ MHz). The magnetic domain configuration of polycrystalline Mn–Zn ferrites was not clear until now. P_b/f is expressed by the following equation:[1]

$$P_b/f=kB^3+\alpha\pi^2SB^2f/C\cdot\rho+P_r/f,$$

where k is a constant, B is the magnetic flux density, α is anomaly factor, S is the cross-section area, ρ is the microscopic electric resistivity, and C is the sample constant. P_b per cycle is plotted against frequency and shown in Fig. 2. Linear relationships were obtained for the sample with grain size $D=3$ μm, but deviation from the linear behavior was found for samples with larger grain size (6 μm). The deviation from the linear behavior corresponds to residual loss[1] according the equation described above. The residual loss is close related to the number of domain wall. The reason is that resonance of ferrites arises from domain wall, dimensional, or natural resonance. We assume the observed residual loss was caused by domain wall movement, because the resonance frequency is considerably lower than the calculated natural resonance frequency and because P_r is independent of the sample dimensions. Besides, in Fig. 2 it is found that the residual loss tends to increase with frequency at higher magnetic flux density (50 m T) for the sample with grain size $D=6$ μm. In other words, P_r cannot be ignored at this induction level.

On the other hand, we try to explain the domain configuration effect in terms of the empirical relation $W_e\alpha B_m^y$.[5] W_e and B_m represent $[(P_b-P_h)/f]$ and maximum flux density, respectively. Compared with the value of $y=2$ for the Mn–Zn ferrite with grain size $D=3$ μm, we find that $y>2$ is observed for the sample measured at 500 kHz with grain size $D=6$ μm in Fig. 3. This finding correspond to the

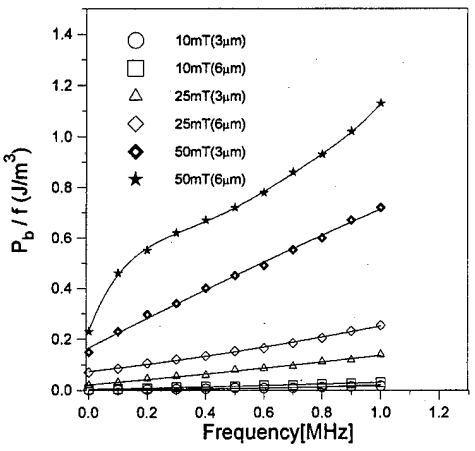


FIG. 2. Relationship between power loss per cycle and frequency at different induction levels.

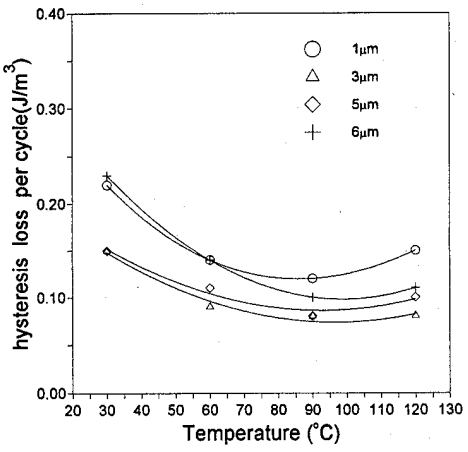


FIG. 4. Temperature dependence of hysteresis loss per cycle for samples measured at d.c., 50 m T with various grain sizes.

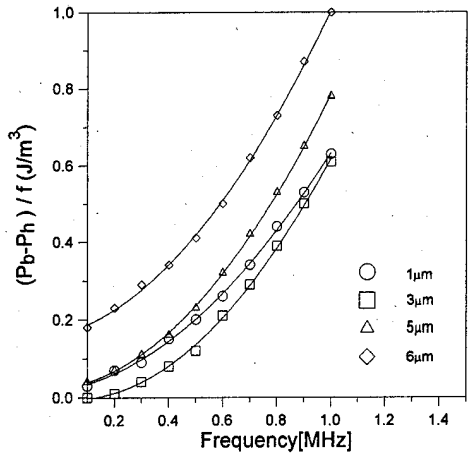


FIG. 5. Relationship between $(P_b-P_h)/f$ and frequency for samples measured at 50 m T, 90 °C with various grain sizes.

model mentioned by Sato and Sakaki,[5] which indicates that when $y>2$ domain walls within the crystal are annihilated and generated repeatedly but there is no evidence of domain wall annihilation when $y=2$.

As discussed above, we assume that with grain size on the order 3 μm, residual loss from domain wall resonance will be improved due to the absence of intragranular domain wall. The results also correspond to the findings that a transition in the intragranular domain structure from mono to two domains is observed by neutron depolarization at grain size $D=3$ μm.[3]

In order to investigate the high-power performance of Mn–Zn ferrites, samples measured at high induction level 50 m T were studied further. Figure 4 shows the dependences of the hysteresis losses per cycle, $W_h(W_h=P_h/f,\ \mathrm{J/m^3})$ on the temperature for samples with various grain sizes. It is shown that the variation of hysteresis loss with temperature is alike for the samples with grain size above 3 μm. Meanwhile, it is also noticeable that the values of hysteresis loss are identical for samples of 3 and 5 μm at 90 °C, however the difference of $(P_b-P_h)/f$ with frequency are remarkable for the two samples as shown in Fig. 5. It is proved that the hysteresis

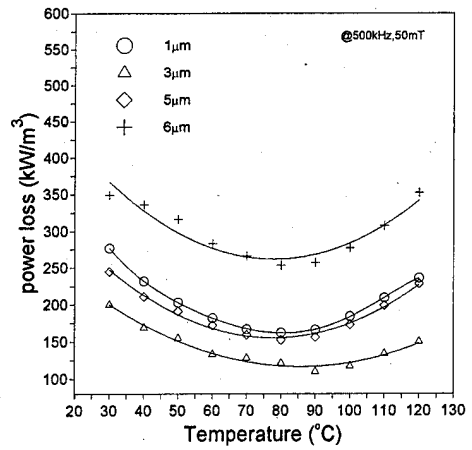


FIG. 6. Temperature dependence of power loss for samples measured at 500 kHz, 50 m T with various grain sizes.

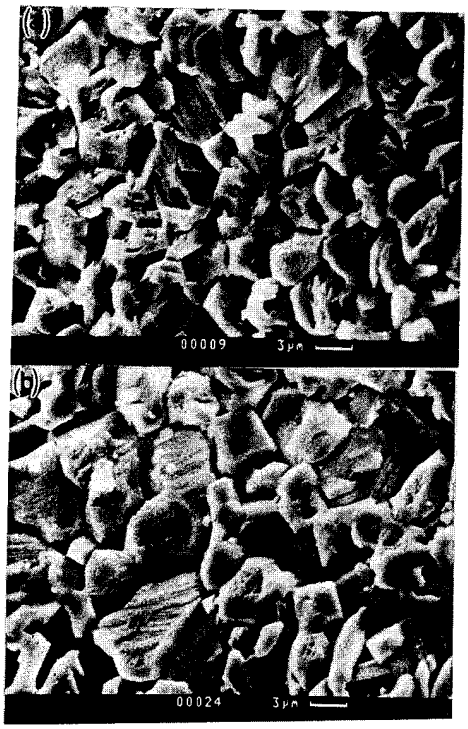


FIG. 7. SEM micrographs for samples with grain size (a) 3 μm and (b) 6 μm.

loss comprises a small part of P_b. Therefore, the power loss in the frequency range is mainly dominated by eddy current loss or residual loss. However, if the frequency variation of resistivity given in Fig. 1 is taken into consideration, it is believed the power loss is dominated by residual loss within the frequency range of 500 kHz–1 MHz. Although the residual loss will increase with increase of temperature, the sample with grain size $D=3$ μm still exhibits optimum power loss at 90 °C, as shown in Fig. 5. It is seen in Fig. 6 that the power loss is lowered dramatically from 260 to 120 $\mathrm{kW/m^3}$ at 500 kHz 50 m T and 90 °C with grain size decreased in the order of 3 μm. Therefore, we conclude that a high-power-use Mn–Zn ferrites added with optimum $CaO–SiO_2$ content are improved by controlling the grain size around 3 μm and this fine material can be obtained by low temperature sintering. The SEM examination of microstructure is shown in Fig. 7 for two representative samples of this study.

ACKNOWLEDGMENTS

The authors would like to thank the Ministry of Economics Affairs, Republic of China, for financial support under Contract No. 3KF2200 to the Industrial Technology Research Institute.

[1] O. Inoue, N. Matsutani, and K. Kugimiya IEEE Trans. Magn. **29**, 3532 (1993).
[2] S. Yamada and E. Otsuki (in press).
[3] P. J. Van der Zaag, M. T. Johnson, A. Noor dermeer, J. Magn. Magn. Mater. **99**, L1–L6 (1991).
[4] Yo Sakaki, Mitsunobu Yoshida, and Toshiro Sato, IEEE Trans. Magn. **29**, 3517 (1993).
[5] T. Sato and Y. Sakaki, IEEE Trans. J. Magn. Jpn. **3**, 531 (1988).

Magnetic properties of Zn–Mg ferrite fine powders (abstract)

H. H. Hamdeh and J. C. Ho
Department of Physics, Wichita State University, Wichita, Kansas 67260

S. A. Oliver
Center for Electromagnetics Research, Northeastern University, Boston, Massachusetts 02115

R. J. Willey
Department of Chemical Engineering, Northeastern University, Boston, Massachusetts 02115

M. J. O'Shea
Department of Physics, Kansas State University, Manhattan, Kansas 66506

Several fine powder samples of $Zn_xMg_{1-x}Fe_2O_4$, $0 \leqslant x \leqslant 1$, were prepared by the supercritical sol-gel (aerogel) process, and were annealed at 500 °C for 2 h. The structure, crystallite size and inversion parameter were determined by x-ray diffraction. The crystallite diameter of the as-prepared powders ranged from 6.5 to 8.5 nm. The minimum size was achieved for the samples with $0.25 \leqslant x \leqslant 0.50$. After annealing the crystallite size increased by an average of 3 nm. The values of the inversion parameters, before and after annealing, reflect roughly the chemical preference of Zn cations to the tetrahedral sites and Mg cations to the octahedral sites of the spinel structure. However, these values indicate that the as-prepared materials were not in the equilibrium state. The magnetic properties were studied by ^{57}Fe Mössbauer spectroscopy over a temperature range of 25 K to room temperature. Taking advantage of their sensitivity to the superparamagnetic behavior induced by the size effects, the Mössbauer spectra were used to determine the blocking temperatures. The calculated values peaked at $x=0.50$ for both the as-prepared and annealed powders. SQUID magnetometry measurements are currently underway. © *1996 American Institute of Physics.* [S0021-8979(96)64608-5]

Comparison between disaccommodation and ferromagnetic resonance measurements in polycrystalline yttrium–iron–garnet samples

L. Torres, M. Zazo, and J. Iñiguez
Departamento de Física Aplicada, Universidad de Salamanca, E-37071 Salamanca, Spain

C. de Francisco, J. M. Muñoz, and P. Hernandez
Departamento de Electricidad y Electronica, Universidad de Valladolid, E-47071 Valladolid, Spain

Polycrystalline yttrium–iron–garnet (YIG) samples were sintered in air at temperatures ranging from 1350 to 1450 °C. Ferromagnetic resonance measurements have been accomplished at 11 GHz from 77 to 350 K. The different contributions to the linewidth have been analyzed. These results are compared with previous measurements of magnetic disaccommodation in the same samples. A qualitative relationship between both kind of measurements for polycrystalline YIG samples by means of an induced anisotropy formalism is provided. © *1996 American Institute of Physics.* [S0021-8979(96)30108-1]

I. INTRODUCTION

Magnetic relaxation processes have been thoroughly studied in yttrium iron garnet (YIG), mainly in the initial stages of ferromagnetic resonance (FMR) research, due to the technological applications of this material because of its very low FMR linewidth.[1,2] On the other hand in the past few years several works about new aspects in magnetic relaxation in YIG at low frequencies have appeared. These papers are mainly devoted to the aftereffect processes in single-crystal samples,[3–5] which in some cases are illuminated or gamma-ray irradiated.[6,7]

Our group has performed experiments both in low frequency (1 kHz) and FMR frequencies (11 GHz). At 1 kHz, magnetic disaccommodation (DA) has been measured for several series of polycrystalline YIG,[8,9] FMR measurements are the purpose of the present article. Besides, in the last months our group has published results on nickel and lithium ferrites[10,11] for which relations between DA and FMR measurements have been found. The comparison is attained by comparing the normalized value of the induced anisotropy constants calculated from DA and FMR experiments.[10,11] In this article we present the relationships between DA and FMR found for YIG samples by means of an induced anisotropy formalism.

II. EXPERIMENT

A series of polycrystalline samples with nominal composition $Y_3Fe_5O_{12}$ has been prepared from stoichiometrically mixed high-purity powders of Fe_2O_3 and Y_2O_3. The mixtures were ball milled in an agate mortar, pressed in a cylindrical die, and sintered for 8 h in air atmosphere at temperatures ranging from 1350 to 1450 °C according to the phase diagrams of the system Y–Fe–O.[12] Finally, vacancy annealing was avoided by rapid quenching in an air stream.

Disaccommodation was measured recording the variation of the initial permeability with time after the sample demagnetization.[13] In this way isothermal curves are obtained but, as is usual in the literature, we have chosen a representation in terms of the isochronal relaxation curves which show the relative variation of permeability at different rate windows:

$$\frac{\Delta\mu(t_1,t_2,T)}{\mu(t_1,T)}=\frac{\mu(t_1,T)-\mu(t_2,T)}{\mu(t_1,T)}, \tag{1}$$

where in our experiences $t_1=2$ s and t_2 varies between 4 and 256 s. The experimental results are processed by using the analysis techniques described in Ref. 14.

FMR linewidth measurements were basically accomplished by monitoring the reflected wave in a short-circuited standard subminiature A (SMA) coaxial transmission line. The reduced size of this line facilitates the implementation of the system in a conventional cryostat. The temperature of the cryostat chamber is controlled by an intelligent temperature controller with a stability better than 0.1 K. An additional platinum resistance located outside the short-circuit at 2 mm from the sample registers its temperature.

The linewidth is obtained by sweeping the static magnetic field around the resonance situation for each temperature and storing in the computer the relative reflected power. As is well known, this microwave absorption is proportional to the imaginary part χ_e'' of the diagonal component χ_e of the external susceptibility tensor $\overline{\chi_e}$ (Ref. 1) and the linewidth ΔH is defined as the midheight width of the curve χ_e'' vs H (static magnetic field). The linewidths ΔH presented here are calculated, according to this classical definition, fitting the experimental points by means of a nonlinear computational technique. The whole process is automatized so that the dependence with temperature of the FMR linewidth can be obtained in a few hours.[10]

III. RESULTS AND DISCUSSION

DA measurements were performed previously and the results can be found in detail in Ref. 9. As can be seen in Fig. 1 for the YIG sample sintered at 1350 °C, a relaxation peak process appears in the isochronal spectrum around 130 K. A similar peak appears for all the samples but its amplitude depends on the sintering temperature. Besides, for the samples sintered at 1420 and 1450 °C there is a shift in the maximum to higher temperatures.[9]

FMR linewidths measured at 11 GHz from 77 to 350 K can be observed in Fig. 2. The lowest linewidths are obtained

 0021-8979/96/79(8)/5436/3/$10.00 © 1996 American Institute of Physics

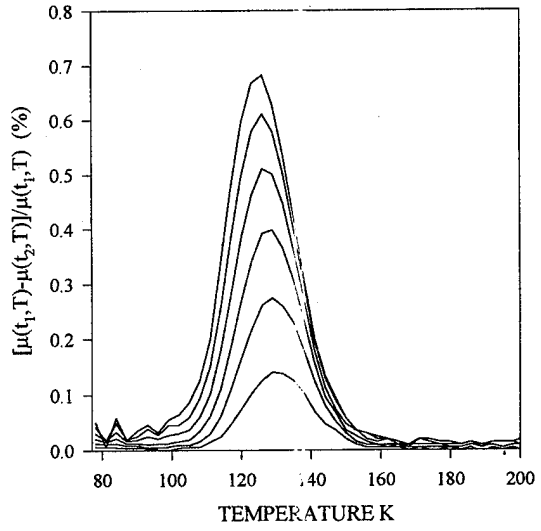


FIG. 1. Disaccommodation isochronal spectrum for YIG sintered at 1350 °C (t_1=2 s and t_2=4, 8, 16, 32, 64, and 128 s).

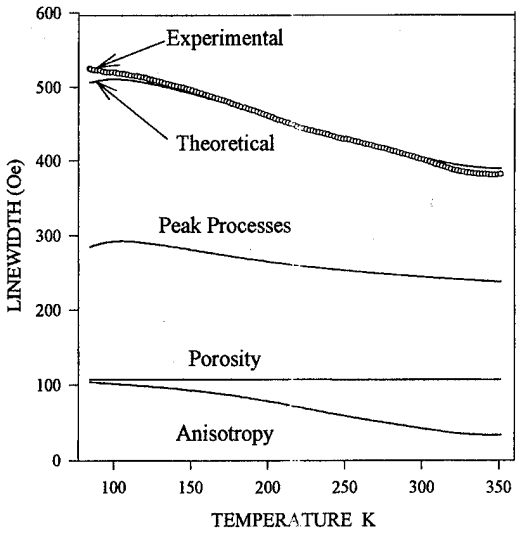


FIG. 3. Theoretical fitting together with the experimental linewidths for the YIG sample sintered at 1420 °C.

for the YIG samples sintered at 1415 °C, for this sample the DA isochronal spectrum also showed the peak with least amplitude (see Fig. 4).

In order to achieve a comparison between DA and FMR we have to look for the effect of induced anisotropy in FMR measurements. According to Krupicka *et al.*[15] this effect underlies the peak processes whose maximum with temperature is frequency dependent. The relaxation mechanisms involved in these peak processes are valence-exchange and slowly relaxing impurities.[1] So the first step to take is to separate the different contributions to the linewidth. We have considered the typical contributions to the polycrystalline linewidth ΔH,[10]

$$\Delta H=\Delta H_p+\Delta H_a+\Delta H_s, \tag{2}$$

where ΔH_p is the contribution induced by the porosity, ΔH_a is the broadening due to the random orientation of the anisotropy axes of the different crystallites of the polycrystal, and ΔH_S is the linewidth of the single crystal.

ΔH_S should include the following contributions: intrinsic contribution of the Kasuya–Le Craw type,[1] surface roughness, valence exchange, slowly relaxing impurities, and rapidly relaxing impurities.[1] Here we will not consider the intrinsic and surface contributions because their magnitude is negligible when we are dealing with polycrystalline linewidths of some hundred of oersted. We will also not consider the rapidly relaxing impurities contribution because it should exhibit a linear dependence with frequency which has not been observed. After these considerations ΔH_S will include just valence exchange and slowly relaxing impurities. These temperature peak processes are the ones mechanisms. related to the induced anisotropy.

According to DA measurements[9] some Fe^{2+} ions are present in our samples so that valence exchange is possible there could also be some impurities acting as slow relaxers. We have then supposed a general temperature peak process contribution which would have the form,[1]

$$\Delta H=C\,\frac{\omega\tau_r}{1+(\omega\tau_r)^2}. \tag{3}$$

where C is a constant, with τ_r being

$$\tau_r=\tau_0\exp\frac{Q}{kT}, \tag{4}$$

where τ_0 is the preexponential relaxation time and Q the activation energy. Taking $\tau_0=10^{-13}$ s and $Q=10^{-2}$ eV, typical for electronic processes,[1] we have fitted the linewidths of Fig. 2 obtaining the best value for the constant C of Eq. (3). The contributions of porosity and anisotropy have been computed using the expressions of Sparks[1] as in our previous work.[10] The fitting obtained for the sample sintered at 1420 °C is shown in Fig. 3.

In order to compare DA and FMR measurements we have shown in Ref. 10 that a qualitative relation can be

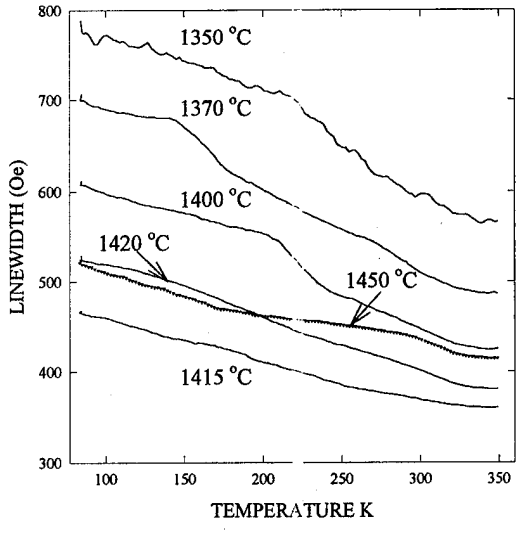


FIG. 2. FMR linewidth from 77 to 350 K for the YIG samples sintered at different temperatures.

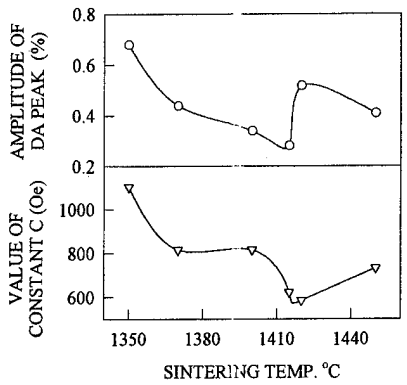


FIG. 4. Dependence with the sintering temperature of the amplitude of the DA peak and the value of the constant C from the FMR peak process.

achieved through the induced anisotropy constants. These constants are proportional both to the amplitude of the DA peaks and to the value of C of expression (3). A quantitative comparison is not possible mainly because in DA measurements just the temporal variations of the permeability after demagnetization are computed, so that absolute values of permeability are not obtained. Anyway a qualitative study of the effect of induced anisotropy in DA and FMR can be accomplished comparing the DA peak amplitude and the C constant [Eq. (3)] for the different samples. In Fig. 4 results of the DA peak and C for the YIG samples sintered at different temperatures can be observed. It can be noted how the effect of the induced anisotropy is similar in the two kinds of measurements—it decreases with sintering temperature until 1415 °C. For sintering temperatures higher than 1415 °C an increase in the effect of induced anisotropy is found although this increase is larger in DA than in FMR. These deviations could be related to the presence of diffusants similar to those found by Guyot *et al.* in their works about polycrystalline YIG.[16–19]

IV. CONCLUSIONS

As a summary we could conclude that DA and FMR measurements have been qualitatively compared for polycrystalline YIG sintered at different temperatures. This comparison has been carried out by means of an induced anisotropy formalism. The effect of the induced anisotropy is similar in both kinds of experiments but for samples sintered at temperatures higher than 1415 °C some deviations appear. These deviations are related to the presence of diffusants, previously found in other studies,[16–19] which mainly affect DA processes.

ACKNOWLEDGMENT

This work was partially supported by the Consejeria de Fomento de la Junta de Castilla y León under Project No. VA 25/94.

[1] M. Sparks, *Ferromagnetic Relaxation Theory* (Mc Graw-Hill, New York, 1965).
[2] S. Geller, H. J. Williams, G. P. Espinosa, and R. C. Sherwood, Bell. Syst. Tech. J. **XLIII**, 565 (1964).
[3] V. S. Gornakov and V. T. Synogach, J. Magn. Magn. Mater. **133**, 24, (1994).
[4] V. T. Synogach and V. S. Gornakov, IEEE Trans. Magn. **30**, 4021 (1994).
[5] L. Torres, M. Zazo, J. Iñiguez, C. de Francisco, J. M. Muñoz, and P. Hernandez, Appl. Phys. Lett. **68**, 564 (1996).
[6] K. Hisatake, I. Matsubara, K. Maeda, Y. Kawai, and S. N. Lyakhimets, IEEE Trans. Magn. **30**, 975 (1994).
[7] K. Hisatake, I. Matsubara, K. Maeda, H. Wakao, T. Fujihara, Y. Kawai, and K. Uematsu, J. Magn. Magn. Mater. **112**, 387 (1992).
[8] L. Torres, C. de Francisco, J. M. Muñoz, M. Zazo, and J. I. Iñiguez, J. Appl. Phys. **73**, 6301 (1993).
[9] L. Torres, M. Zazo, J. Iñiguez, C. de Francisco, and J. M. Muñoz, IEEE Trans. Magn. **30**, 4903 (1994).
[10] L. Torres, M. Zazo, J. Iñiguez, C. de Francisco, and J. M. Muñoz, Appl. Phys. A **60**, 303, (1995).
[11] A. G. Flores, L. Torres, M. Zazo, V. Raposo, and J. Iñiguez, Appl. Phys. Lett. **67**, 427 (1995).
[12] H. J. Van Hook, J. Am. Ceram. Soc. **44**, 208 (1961).
[13] C. de Francisco, J. Iñiguez, and J. M. Muñoz, IEEE Trans. Magn. **MAG-23**, 1866 (1987).
[14] C. de Francisco, J. Iñiguez, and J. M. Muñoz, IEEE Trans. Magn. **MAG-25**, 4413 (1989).
[15] S. Krupicka and K. Zaveta, in *Magnetic Oxides*, edited by D. J. Craik (Wiley, New York, 1975).
[16] M. Guyot and V. Cagan, J. Magn. Magn. Mater. **27**, 202 (1982).
[17] T. Merceron, M. Guyot, and V. Cagan, Phys. Lett. **95A**, 388 (1983).
[18] M. Guyot, T. Merceron, and V. Cagan, Phys. D. Appl. Phys. **16**, L93 (1983).
[19] M. Guyot, V. Cagan, and T. Merceron, IEEE Trans. Magn. **MAG-20**, 2157 (1984).

Magnetic properties of $BaFe_{12-(x+y)}Sn_xCo_yO_{19}$ single crystals (abstract)

R. Solé
Labs. Física Aplicada i Cristal.lografia Univ. Rovira i Virgili, Plaza Imperial Tarraco 1, 43005 Tarragona, Spain

X. X. Zhang
Fac. Física, Universitat de Barcelona, Diagonal 647, 08028 Barcelona, Spain

X. Ruiz, M. Aguiló, and F. Díaz
Labs Física Aplicada i Cristal.lografia, Univ. Rovira i Virgili, Plaza Imperial Tarraco 1, 43005 Tarragona, Spain

J. Tejada
Fac. Física, Universitat de Barcelona, Diagonal 647, 08028 Barcelona, Spain

$BaFe_{12-(x+y)}Sn_xCo_yO_{19}$ single crystals, with $0 \leqslant x \leqslant 2$ and $0 \leqslant y \leqslant 2$, have been grown from high temperature solution by slow cooling using the TSSG method. Magnetic properties of these single crystals have been investigated using a commercial quantum design SQUID magnetometer in the temperature range 6 to 320 K and with a varying field from -5 to $+5$ T applied parallel and perpendicular to their c axis. It is found that the replacement of part of the Fe^{3+} ions by Co^{2+} and Sn^{4+} ones reduces the anisotropy as well as the saturation magnetization of the materials. For a small amount of substitution, the magnetization as a function of applied fields, which were oriented in the c axis, exhibits a hysteresis loop indicating that the magnetic domain wall moving was pinned by the imperfections of magnetic structures. When the substitution was increased to $x + y = 2.5$, long distance magnetic coupling was destroyed, and the sample behaved as a magnetic granular material consisting of randomly distributed magnetic clusters. © *1996 American Institute of Physics.* [S0021-8979(96)64708-4]

Epitaxial single crystal $Fe_{16}N_2$ films grown by facing targets sputtering

D. C. Sun
Department of Applied Physics, Tianjin University, Tianjin 300072, People's Republic of China and Department of Materials Science & Engineering, Tsinghua University, Beijing, People's Republic of China

E. Y. Jiang
Department of Applied Physics, Tianjin University, Tianjin 300072, People's Republic of China

M. B. Tian
Department of Materials Science & Engineering, Tsinghua University, Beijing, People's Republic of China

C. Lin and X. X. Zhang
Department of Applied Physics, Tianjin University, Tianjin 300072, People's Republic of China

α''-$Fe_{16}N_2$ single crystal films can be prepared successfully by facing targets sputtering directly onto NaCl(100) substrates in a mixture of argon and nitrogen gases. Both x-ray diffractometer and transmission electron microscope are employed to characterize the crystal structure of the films. The perfect electron diffraction patterns of α''-$Fe_{16}N_2$ single crystal in $[\bar{1}11]$, [011], and [001] directions can be distinctly observed by double tilting. These patterns confirm that the crystal structure of the films corresponds to a body-centered tetragonal (bct) lattice with the parameters of $a=b=5.72$ Å and $c=6.29$ Å . The x-ray diffraction patterns show that α''-$Fe_{16}N_2$ epitaxially grows on the NaCl(100) substrate with an orientation relationship α''-$Fe_{16}N_2(001)\|$NaCl(001) and α''-$Fe_{16}N_2[100]\|$NaCl[100]. The saturation magnetization of the $Fe_{16}N_2$ films is around 2100−2300 emu/cc, which agrees well with the value reported by Sugita *et al.*. © *1996 American Institute of Physics.* [S0021-8979(96)30208-8]

I. INTRODUCTION

The Fe-N binary system was thoroughly investigated by Jack[1,2] in the early 1950s. In the iron nitride diagram, α''-$Fe_{16}N_2$ phase with a deformed body-centered tetragonal (bct) structure is of great importance. It is reported by Kim and Takahashi[3] that α''-$Fe_{16}N_2$ has a giant saturation magnetic flux density (B_s=2.58 T) which was 17% larger than that of pure iron. The deduced B_s of α''-$Fe_{16}N_2$ would be 2.83 T from the volume ratio of α''-$Fe_{16}N_2$ in the film. Many researchers have been trying hard to synthesize pure α''-$Fe_{16}N_2$ into both bulk[4–6] and thin film[7–19] forms by various methods. However, only a few have succeeded in fabricating single phase $Fe_{16}N_2$; most deposition techniques tend to obtain multiphase products.

Inspiring progress has been made by Sugita and his co-workers.[13,14] They succeeded in growing single crystal α''-$Fe_{16}N_2$ film on Fe(100)/$In_{0.2}Ga_{0.8}As$(100) substrates using molecular beam epitaxy (MBE). They reported that the B_s of α''-$Fe_{16}N_2$ would be 2.8 T at room temperature. In their subsequent papers,[14] the B_s of α''-$Fe_{16}N_2$ is determined to be 3.2 T at liquid helium temperature, which corresponds to the average magnetic moment of 3.5 μ_B per Fe atom, and therefore, is far beyond the Slater–Pauling curves. Very recently, Ortiz *et al.*[18] claimed their success in epitaxially growing single crystal α''-$Fe_{16}N_2$ films on single crystal MgO substrates by reactive sputtering. But the average magnetic moment is only 250 emu/g (1853 emu/cc) in the experiment.

The saturation magnetization of α''-$Fe_{16}N_2$ estimated from different experiments was considerably diverse especially between bulk and film forms,[6,14] ranging from 226 emu/g[15] which is close to that of bcc iron to the very giant value of 310 emu/g.[14] Moreover, there have been several theoretical studies[20–22] to expound the high saturation magnetization. However, no calculations based on band structure can successfully explain the giant magnetization and its origin is still mysterious in theory.

In this paper, we have been able to obtain single crystal α''-$Fe_{16}N_2$ films on NaCl(100) substrates. We also distinctly observed a series of electron diffraction patterns with perfect symmetry in the directions of $[\bar{1}11]$, [011], and [001]. The vibrating sample magnetometer (VSM) measurement shows that the α''-$Fe_{16}N_2$ film has saturation magnetization as large as ~2200 emu/cc, which gives strong support to that reported by Sugita *et al.*[13,14]

II. EXPERIMENTAL PROCEDURES

The Fe-N films were prepared by facing targets sputtering (FTS) onto NaCl(100) single crystals with freshly cloven surface. The lattice constant of NaCl is 5.63 Å, which is smaller by only 1.6% than that of a-axis of $Fe_{16}N_2$ (5.72 Å). This provides the possibility of epitaxial growth. The base pressure was 6×10^{-5} Pa. The working gas is a mixture of argon and nitrogen. During sputtering, the partial pressures of Ar and N_2 gases were held constant at 0.3 Pa and 0.05 Pa, respectively. The deposition rate was 2.0 Å /s, and the substrate temperature was about 150 °C.

The crystal structure was examined with a Rigaku x-ray diffractometer (XRD) with Cu $K\alpha$ radiation and a JEM-200CX transmission electron microscope (TEM) operating at 200 keV. The saturation magnetization was measured at room temperature by VSM with a resolution of 2×10^{-6} emu in an external magnetic field of 8 kOe which was applied parallel to the sample plane. The hysteresis loop of the

 0021-8979/96/79(8)/5440/3/$10.00 © 1996 American Institute of Physics

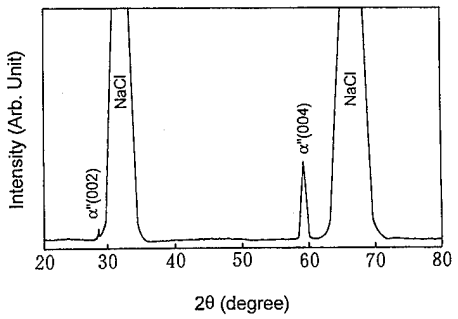


FIG. 1. The XRD patterns of $Fe_{16}N_2$ (400 Å) on NaCl(001) substrate.

NaCl substrate and the holder was measured and the magnetic moment was about 1–2 orders of magnitude lower than that of the samples. The hysteresis loops of the samples were then measured and the magnetization of the holder and substrates was subtracted automatically by a computer during measuring. The thickness of the films was monitored by an *in situ* quartz oscillator in the system. The total error involved in the measurement of the magnetization was safely estimated to be no more than 6%.

III. RESULTS AND DISCUSSION

Figure 1 shows the XRD patterns of the $Fe_{16}N_2$ film deposited directly onto NaCl(100) substrate. There is an intense α''-$Fe_{16}N_2$(004) peak and a weak α''-$Fe_{16}N_2$(002) peak in the pattern. This reveals that $Fe_{16}N_2$ has the same crystallographic orientation as the NaCl substrate. From the point of view of x-ray diffractometry, it is regarded that α''-$Fe_{16}N_2$ grows epitaxially on the NaCl substrates with the following orientation relationships:

$$\alpha''\text{-}Fe_{16}N_2(001)\|NaCl(001),$$

$$\alpha''\text{-}Fe_{16}N_2[001]\|NaCl[001],$$

i.e., the growth plane is (001) with c-axis perpendicular to the film plane, which is quite different from the case of (110) growth on InGaAs substrate.[14] The interplanar spacing of α''-$Fe_{16}N_2$(200) is 2.86 Å , while that of NaCl(200) is 2.815 Å . The unit cell of α''-$Fe_{16}N_2$ grows on one single unit cell of NaCl, and the mismatch between $Fe_{16}N_2$ and NaCl is only 1.6%. This guarantees the epitaxial growth with the above-mentioned orientation relationships. By the Scherrer formula, the calculated mean crystalline size of single crystal α''-$Fe_{16}N_2$ is about 500 Å from the full width at half maximum of the peak in the XRD pattern.

TEM was employed to further characterize the crystal structure of $Fe_{16}N_2$. Figure 2 shows the selected area electron diffraction (SAED) patterns. A series of SAED patterns are obtained by means of double tilting. Figure 2(a) is the SAED pattern with $[\bar{1}11]$ incidence of α''-$Fe_{16}N_2$ single crystal. The spots displaying a quasi-sixfold symmetry (caused by the difference between a and c parameters) are denoted as tetragonal body-centered lattice. Figure 2(b) is the illustration of SAED pattern with $[\bar{1}11]$ incidence of α''-$Fe_{16}N_2$ single-crystal corresponding to Fig. 2(a). The representative indexing results are listed in Table I. Figure 2(c)

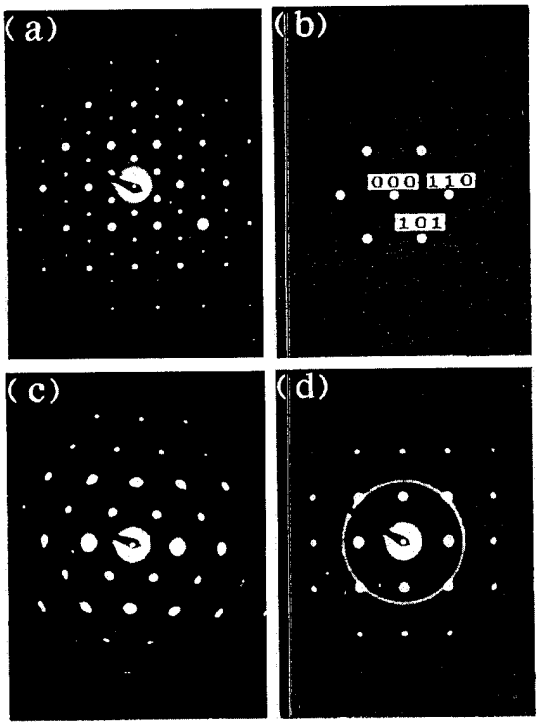


FIG. 2. The selected area electron diffraction (SAED) patterns of $Fe_{16}N_2$ (400 Å) film: (a) with the incidence of $[\bar{1}11]$; (b) the schematic illustrations of SAED patterns corresponding to (a); (c) with the incidence of [011] by means of double tilting; (d) with the incidence of [001].

shows the SAED pattern in [011] direction at an angle of 37.8° to $[\bar{1}11]$ direction while Fig. 2(d) is the pattern at an angle of 52° to $[\bar{1}11]$ which is the incidence direction of [001]. The representative indexing results are also listed in Table I. One can see that all three patterns display a perfect symmetry. By the way, in Figs. 2(c) and 2(d) the presence of rings may be due to the damage on the crystal structure by electron irradiation. It may take some time to seek the zone-axis by double tilting.

Previously, the Hitachi group gave the SAED pattern of $Fe_{16}N_2$ single crystal in [001] direction by a cross sectional TEM.[14] However, the spatial distribution of the diffraction spots didn't exhibit perfect symmetry. This paper gives the perfect electron diffraction patterns of α''-$Fe_{16}N_2$ single crystal in the three directions of $[\bar{1}11]$, [011], and [001] simultaneously for the first time. Moreover, the pattern in $[\bar{1}11]$ direction instead of [001] represents the characteristic

TABLE I. The interplanar spacing of the representative (*hkl*) in Fig. 2.

(*hkl*)	d_{exp} (Å)	d_{calc} (Å)
110	4.08	4.04
011	4.29	4.23
121	2.43	2.37
112	2.53	2.48
111	3.36	3.40
022	1.99	2.02
311	1.70	1.74
200	2.79	2.86
220	1.97	2.02

TABLE II. The saturation magnetization from VSM measurements.

Sample No.	1	2	3	4	5
Thickness (Å)	280	300	400	510	720
M_s (emu/cc)	2289	2270	2210	2125	2182

of bct $Fe_{16}N_2$, for the large interplanar distances of (011) (4.23 Å), and (110) (4.045 Å) are unlikely to be confused with those of other Fe-N phases. It is of interest to note that the behaviors of the three SAED patterns are different, i.e., showing different zero rules. In the [011] and [001] directions, the spot intensity obeys the zero rule of fcc lattice, i.e., (*hkl*) spots disappear if *h, k, l* are odd-even mixed. On the contrary, in $[\bar{1}11]$ direction, the spot intensity shows the bcc lattice zero rule, i.e., the spots vanish if $(h+k+l)$ is an odd integer. It is well known that the observed diffraction pattern is equivalent to the points of intersection of the Ewald sphere of radius $1/\lambda$ with the reciprocal-lattice nodes. When Bragg condition is satisfied, by neglecting the lattice amplitude which depends only on the external shape of the crystal, the structure amplitude which depends only on the position of the atoms inside the unit cell is decisive to the spot intensity. And consequently, it is rather difficult to understand our present experimental results.

It is worth mentioning that the substrate temperature is crucial in preparing single crystal $Fe_{16}N_2$ film. Substrate temperature may influence the diffusion process of the atoms on the substrate. When the substrate temperature is higher than 180 °C, the nitrogen atoms become more active and then it is more likely to form γ'-Fe_4N with a high nitrogen concentration. When the substrate temperature is lower than 100 °C, it tends to form α'-martensite instead of α''-$Fe_{16}N_2$.[19]

In order to clarify the saturation magnetization of $Fe_{16}N_2$ single crystal films, the VSM measurement is employed and the results are listed in Table II. The values are distributed around ~2200 emu/cc. Considering the errors involved in the VSM measurement and the volume estimation, the M_s of $Fe_{16}N_2$ single crystal is reasonably expected to be 2200 emu/cc, which is in good agreement with the results of Kim *et al.*[3] and of Sugita *et al.*[14] It is quite different from the theoretical calculated values by Sakuma,[20] Min,[21] and Coehoorn *et al.*[22] Thus the origin of the giant saturation magnetization is still confusing. It is regarded[11,14] that the volume expansion and charge transfer effects are responsible for the high saturation magnetization of $Fe_{16}N_2$. Recent theoretical work by Papanikolaou *et al.*[23] indicates that nitrogen, as either a substitutional or interstitial impurity in alkali metals, may have quite a sizable magnetic moment of between 1.5–3.0 μ_B. However, the band calculated moment value of nitrogen is only 0.05 μ_B by Min[21] and −0.03 μ_B by Coehoorn *et al.*[22] This reminds the authors that it is desirable to treat the moment of nitrogen atoms in a more satisfactory manner in theoretical calculation rather than accept the previous results.

IV. CONCLUSION

In summary, α''-$Fe_{16}N_2$ single crystal films can be successfully prepared by the FTS method directly onto single crystal NaCl(001) substrates, at a deposition rate as high as 2.0 Å/s. The epitaxial growth relationships can be figured out as α''-$Fe_{16}N_2(001)\|NaCl(001)$, α''-$Fe_{16}N_2[001]\|NaCl[001]$. The perfect electron diffraction patterns of α''-$Fe_{16}N_2$ single crystal in the directions of $[\bar{1}11]$, [011], and [001] were distinctly observed. The saturation magnetization of α''-$Fe_{16}N_2$ is measured to be around 2200 emu/cc, which agrees well with that reported by Sugita *et al.*[14] within experimental errors. The origin of such an ultra-high M_s is still unclear.

ACKNOWLEDGMENTS

This work is financially supported by the National Natural Science Foundation of China and Beijing Zhongguancun Associated Center of Analysis and Measurement. X. X. Zhang thanks National Natural Science Foundation of China for financial support (No. 59510710326).

[1] K. H. Jack, Proc. R. Soc. London Ser. A **208**, 216 (1951).
[2] K. H. Jack, Proc. R. Soc. London Ser. A **208**, 200 (1951).
[3] T. K. Kim and M. Takahashi, Appl. Phys. Lett. **20**, 492 (1972).
[4] X. H. Bao, R. M. Metzger, and M. Carbucicchio, J. Appl. Phys. **75**, 5870 (1994).
[5] M. Q. Huang, W. E. Wallace, S. Simizu, A. T. Pedziwiatr, R. T. Obermyer, and S. G. Sankar, J. Appl. Phys. **75**, 6574 (1994).
[6] J. M. D. Coey, K. O. Donnell, Q. N. Qi, E. Touchais, and K. H. Jack, J. Phys. Condens. Matter **6**, L23 (1994).
[7] A. Kano, N. S. Kazama, H. Fujimori, and T. Takahashi, J. Appl. Phys. **53**, 8332 (1988).
[8] A. Morisako, K. Takahashi, M. Matsumoto, and M. Naoe, J. Appl. Phys. **63**, 3230 (1982).
[9] K. Nakajima, S. Okamoto, and T. Okada, J. Appl. Phys. **65**, 4357 (1989).
[10] K. Nakajima and S. Okamoto, Appl. Phys. Lett. **56**, 92 (1990).
[11] K. Nakajima, T. Yamashita, M. Takata, and S. Okamoto, J. Appl. Phys. **70**, 6033 (1991).
[12] C. Gao, W. D. Doyle, and M. Shamsuzzoha, J. Appl. Phys. **73**, 6579 (1993).
[13] M. Komuro, Y. Kozono, M. Hanazono, and Y. Sugita, J. Appl. Phys. **67**, 5126 (1990).
[14] Y. Sugita, K. Mitsuoka, M. Komuro, H. Hoshiya, Y. Kozono, and M. Hanazono, J. Appl. Phys. **70**, 5977 (1991).
[15] M. Takahashi, H. Shoji, H. Takahashi, T. Wakiyama, M. Kinoshita, and W. Ohta, IEEE. Trans. Magn. **29**, 3040 (1993).
[16] M. A. Russak, C. V. Jahnes, E. Klokholm, J. W. Lee, M. E. Re, and B. C. Webb, J. Appl. Phys. **70**, 6427 (1991).
[17] M. Kopcewicz, J. Jagielski, A. Turos, and D. L. Williamson, J. Appl. Phys. **71**, 4217 (1992).
[18] C. Ortiz, G. Dumpich, and A. H. Morrish, Appl. Phys. Lett. **65**, 2737 (1994).
[19] D. C. Sun, C. Lin, and E. Y. Jiang, J. Phys. Condens. Matter **7**, 3667 (1995).
[20] A. Sakuma, J. Magn. Magn. Mater. **102**, 127 (1991).
[21] B. I. Min, Phys. Rev. B **46**, 8232 (1992).
[22] R. Coehoorn, G. H. O. Daalderop, and H. J. F. Jansen, Phys. Rev. B **48**, 3830 (1993).
[23] N. Papanikolaou, N. Stefanou, R. Zeller, and P. H. Dederichs, Phys. Rev. Lett. **71**, 629 (1993).

(100)-textured 3% silicon steel sheets by manganese removal and decarburization

Toshiro Tomida
Corporate Research and Development Laboratories, Sumitomo Metal Industries, Ltd., 1-8 Fuso-cho, Amagasaki 660, Japan

Texture development in 3% Si steel sheets by the manganese removal and decarburization process has been investigated. The 3% Si steel sheets that contain Mn and C were first annealed in vacuum at α-ferrite (α)/austenite (γ) duplex or γ phase temperatures, and then decarburized. During the vacuum annealing a manganese removal induced phase transformation to α occurs in a thin layer near the sheet surface. Pronounced (100) textures with a variety of in-plane anisotropies develop in the layer. The subsequent decarburization promotes the growth of the surface grains into the interior, providing the entire sheet with the same texture. The resultant materials exhibit excellent soft-magnetic properties. © *1996 American Institute of Physics.* [S0021-8979(96)30308-4]

I. INTRODUCTION

Although the (100) texture development in silicon steel sheets was the subject of extensive studies in the late 1950s and 1960s,[1–4] the subsequent 30 years have seen little progress. The texture for which (100) is parallel to the sheet surface maximizes the number of easy magnetization directions of the steel in the sheet plane and is therefore ideal for the magnetic core of rotating machines and transformers in which magnetic flux travels along multiple directions in the plane. Nevertheless, no current commercial steel closely approaches this texture.

Recently an enticing process for the (100) texture development by manganese removal and decarburization (MRD process)[5] has been discovered. This process is a two-stage annealing of Si steel sheets that contain Mn and C. During the first annealing a manganese removal occurs, and decarburization takes place in the second. A pronounced (100) texture has been reported to form in 2% Si steel sheets of 0.5 mm in thickness. However, the applicability of the MRD process to steel with higher silicon concentrations is unclear, although the increase in Si concentration will lower core loss because of the reduction in eddy current loss. The purpose of this research is, therefore, to examine whether the (100) texture develops in 3% Si steels by the MRD process and to investigate the effects of the texture development on magnetic properties.

II. EXPERIMENTAL PROCEDURE

Vacuum melted steels of the composition listed in Table I were made at the research laboratory. The resulting ingots from A to D were hot rolled to 5.0-mm-thick plates, machined to remove oxidized surface layers to 3.0- (A and B) and 1.5-mm- (C and D) thick plates, and then cold rolled to the final gauge of 0.35 mm in thickness. The ingot E was hot rolled to 4.0-mm-thick plates, pickled, and cold rolled to the same final gauge. They were then subjected to the MRD process as follows. The specimens were first annealed in a vacuum of 10^{-3} Pa at α-ferrite (α)/austenite (γ) duplex or γ phase temperatures of around 1000 °C for periods up to 12 h (the annealing for removal of manganese).[5] They were then decarburized at 1000 °C in a dry hydrogen gas or at 850 °C in a wet 20% hydrogen–argon gas mixture of 10 °C of the dew point.

The chemical composition, microstructure, texture, and magnetic properties of the specimens were investigated. The texture was measured by using pole figure and inverse pole figure techniques. These methods were used to measure the pole densities, $(I/I_R)_{hkl}$, where $(I/I_R)_{hkl}$ refers to the ratio of the x-ray integrated intensity of a particular plane for a given sample to the integrated intensity of the same plane for a "random" powder sample. Magnetic properties were measured by a single strip tester with 30×100 mm strips or by using ring-shaped specimens of which the inside and outside diameters are 33 and 45 mm, respectively. The strips and rings for the measurement were cut from the specimens and stress relieved by annealing at 800 °C for 1 h in an argon atmosphere. To investigate the effects of sheet thickness and stress on magnetic properties, some strip samples were thinned by chemical etching and magnetic properties were measured applying tensile stresses of up to 8×10^6 Pa in the magnetizing direction.

TABLE I. Chemical compositions of steels used (wt %).

Steels	C	Mn	Si	Al
A	0.096	1.82	2.77	0.002
B	0.097	2.53	2.81	0.002
C	0.050	1.02	2.81	0.002
D		The same as steel A		
E	0.051	1.11	3.03	0.001



FIG. 1. Optical micrographs of the cross sections near the sheet surface of the steels A (a) and B (b) vacuum annealed at 950 °C for 9 h.

 0021-8979/96/79(8)/5443/3/$10.00 © 1996 American Institute of Physics

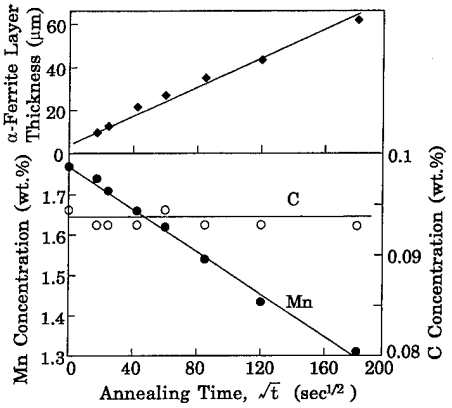


FIG. 2. Variation of the thickness of the surface α layer and Mn and C concentrations for steel A vacuum annealed at 1000 °C with annealing time.

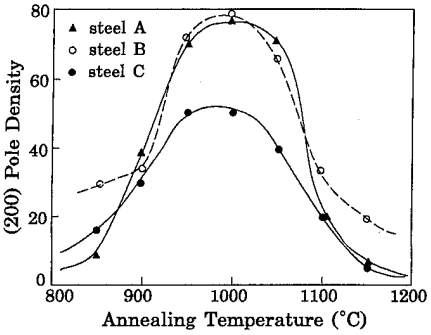


FIG. 3. Effect of vacuum-annealing temperature on the texture of the surface α layer. The annealing time is 9 h.

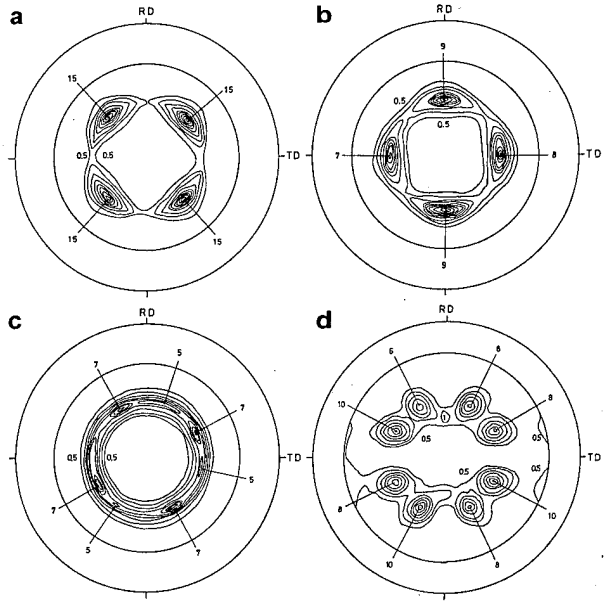


FIG. 4. The (110) pole figures showing variation of the in-plane anisotropy of the (100) texture. The textures of steels A (a), C (b), D (c), and E (d) are approximated as (100) [011], (100) [001], (100) [0vw], and (100) [021], respectively. The steels A–D and E were vacuum annealed at 950 °C for 9 and 12 h, respectively.

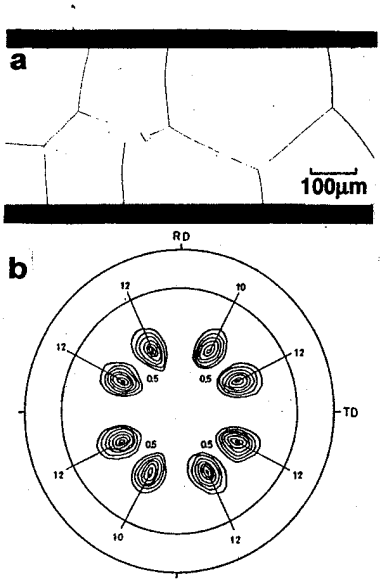


FIG. 5. Optical photograph of the cross section (a) and (110) pole figure (b) for steel E vacuum annealed at 950 °C for 12 h and decarburized at 1000 °C for 1 h in a dry hydrogen.

III. RESULTS AND DISCUSSION

The microstructure typical of the vacuum-annealed specimen is shown in Fig. 1. The annealing temperature in this case, 950 °C, is α/γ duplex and γ phase temperatures for steels A and B, respectively. The microstructures of the inner portions of the specimens, the fine equiaxial grain structure (for steel A), and coarse grains (for steel B) with carbide precipitates (dark particles), correspond to the above phase states at the annealing temperature. On the other hand, just below the sheet surface exist thin layers of about 50 μm in thickness without carbide precipitates. These surface layers without carbides indicate that an isothermal phase transformation to α occurs near the surface during this stage of annealing. We will refer to this layer without carbides as the "surface α layer."

As shown in Fig. 2, the thickness of the surface α layer increases (with increasing annealing time, t) linearly with the square root of t. Correspondingly, the concentration of Mn also decreases linearly with $\sqrt{t}$, whereas the C concentration scarcely changes. Note that this compositional analysis is not for the surface α layer but for the entire sheet. The "averaged" Mn concentration decreases by 30%, when annealing steel A at 1000 °C for 9 h. Therefore, the removal of Mn occurs at this stage of annealing, and causes the formation of the surface α layer. It is believed that the significant Mn depletion near the surface increases the chemical potential of

TABLE II. Magnetic properties measured with ring specimens for the specimen shown in Fig. 5.

Coercivity (A/m)	Relative permeability at 1.5 T	Flux density (T)		Core loss (W/kg)	
		B_{10}	B_{50}	$W_{10/50}$	$W_{15/50}$
7.5	4506	1.601	1.764	0.54	1.37

TABLE III. Magnetic properties in easy magnetizing direction for the steel A with (100) [011] texture. The specimen was vacuum annealed at 950 °C, for 9 h and decarburized at 850 °C for 30 min in a wet hydrogen–argon gas atmosphere.

Sheet thickness (mm)	Stress (10^6 Pa)	Flux density B_{10} (T)	Core loss (W/kg)		Hysteresis loss in $W_{15/50}$ (W/kg)
			$W_{15/50}$	$W_{17/50}$	
0.3	0	1.818	1.05	1.40	0.69
0.3	6.1	1.820	0.79	1.13	0.42
0.2	0	1.810	0.79	1.03	0.57
0.2	7.6	1.805	0.55	0.78	0.37

carbon and that, as a consequence, the carbon atoms near the surface diffuse into the interior, resulting in a significant reduction in C concentration near the surface. This causes the transformation to the single α phase.[5] The Mn removal is thought to be due to the evaporation of Mn, of which the equilibrium vapor pressure is as high as 0.4 Pa at 950 °C.[6] Moreover the $\sqrt{t}$ dependence of the surface α layer thickness and Mn concentration suggests that the growth of the surface α layer is mainly controlled by the diffusion of Mn.

The (100) texture has been observed to markedly develop within the surface α layer during the vacuum annealing. As shown in Fig. 3, the (200) pole density has increased over 50, in expense of other pole densities, by vacuum annealing at the temperatures ranging from 950 to 1050 °C for 9 h for all steels under investigation. This insensitivity of the (100) texture development to the chemical compositions and preannealing processing conditions supports the hypothesis that the selective driving force for the texture development is the anisotropy of surface energy.[5]

The in-plane anisotropy of the (100) texture, however, varies depending upon the chemical compositions and the preannealing processing conditions. Figure 4 shows such a variation of the in-plane anisotropy. The textures with some spread around (100) [001], (100) [011], and (100) [021] and an approximately random cube texture have been observed. An investigation is underway on the mechanism that determines the in-plane anisotropy.

The subsequent decarburizing annealing at α/γ duplex or γ phase temperatures results in a structure consisting of grains of several hundred μm in diameter without carbide precipitates, as seen in Fig. 5(a). Interestingly enough, the texture of the decarburized sheet is almost the same as that of the surface α layer formed by the preceding vacuum annealing [compare Figs. 5(b) and 4(d)]. This clearly suggests that, under proper decarburizing conditions, the grains in the surface α layer preferentially grow inward and this grain growth dominates the structure change at this stage of annealing.

As expected by the highly developed (100) texture and relatively fine grain structure, the MRD-processed sheets exhibit excellent magnetic properties. The typical magnetic properties measured with ring specimens are listed in Table II. For example, the relative permeability at 1.5 T is 4500, and the core loss at 1.5 T and 50 Hz, $W_{15/50}$ is 1.4 W/kg. That is, the MRD-processed 3% Si steel sheets have approximately twice the permeability at 1.5 T as conventional 3% Si nonoriented electrical steel sheets,[7] and the core loss is about two-thirds. Moreover a small in-plane magnetic anisotropy, which is desired for the magnetic core of rotating machines, can be attained not only by the approximately random cube texture but also the (100) [021] texture shown in Fig. 5. Since the (100) [021] texture consists of two inclined cube components that are rotated by about $\pm 26°$ from (100) [001] around [100], the magnetic anisotropies of the two components nearly cancel each other. The change in the magnetic flux density at 5000 A/m, B_{50}, in the sheet plane is 0.1 T for the specimen shown in Fig. 5 and Table II, which is only 5.7% of the averaged B_{50}.

An increased in-plane anisotropy leads to a higher magnetic flux density and a lower core loss in two directions perpendicular to each other. In Table III are listed the magnetic properties of the specimen with the (100) [011] texture; the magnetizing direction is inclined by 45° from the rolling direction in the sheet plane, i.e., easy magnetizing direction. The magnetic flux density at 1000 A/m, B_{10} is about 1.81 T. The core loss at 1.7 T and 50 Hz, $W_{17/50}$ is 1.40 and 1.03 W/kg for the 0.3- and 0.2-mm-thick sheets, respectively, and it deceases markedly when a tensile stress is applied. This decrease in core loss by the stress is primarily due to the decrease in hysteresis loss (see Table III). It is also worth noting that, although the B_{10} of the specimen is not as large as that of today's grain-oriented 3% Si steel sheets (GO),[7] the core loss is comparable to that of GO. The mechanism of this reduced core loss, which must relate to the fine grain structure, and modifications of the process to maximize the magnetic anisotropy obviously deserve further investigation.

[1] F. Assmus, K. Detert, and G. Ibe, Z. Metallk. **48**, 341 (1957).
[2] K. Detert, Acta Met. **7**, 589 (1959).
[3] J. L. Walter, Acta Met. **7**, 424 (1959).
[4] S. Taguchi and A. Sakakura, Kinzoku Butsuri **7**, 221 (1968).
[5] T. Tomida and T. Tanaka, Tetsu to Hagane **79**, 1350 (1993); Iron Steel Inst. Jpn. Int. **35**, 548 (1995).
[6] O. Kubaschewski, E. L1, Evans, and C. B. Alcock, in *Metallurgical Thermochemistry* (Pergamon, New York, 1967).
[7] H. Honma, T. Nozawa, H. Kobayashi, Y. shimoyama, T. Tachina, and K. Miyoshi, IEEE Trans. Magn. **MAG-21**, 1903 (1985).

Deposition condition and thickness dependence on magnetic properties of sputtered NiFeCo thin films

A. Tsoukatos and S. Gupta
Materials Research Corporation, Orangeburg, New York 10962

Y. K. Kim
Quantum Peripherals Colorado Inc., Louisville, Colorado 80028

The soft magnetic properties of polycrystalline NiFeCo films have been investigated in the thickness range of 20–2400 Å. The films were deposited by dc magnetron sputtering, at 5 Å/s, from a $Ni_{66}Fe_{16}Co_{18}$ high purity target, and under an applied magnetic field of 85 Oe. The effects of deposition pressure on the film crystal structure and magnetic properties have been investigated via x-ray diffraction and magnetic measurements. Both easy and hard axis coercivity values decrease significantly as the deposition pressure was changed from 7 to 3 mTorr, with the corresponding effects observed in the magnetoresistance and anisotropy field values, respectively. The magnetic data at 3 mTorr showed a nonlinear behavior at thicknesses below 1000 Å, while at 7 mTorr the nonlinearity is present in both the low and high end thicknesses. © *1996 American Institute of Physics.* [S0021-8979(96)30408-0]

I. INTRODUCTION

Complex thin film structures of NiFe/Ag[1,2] and NiFeCo/Ag, Cu[3–6] have been used for the development of magnetoresistive elements of considerable sensitivity at room temperature. However, unlike the Fe[7] and the NiFe[8,9] soft magnetic films, the properties of the soft magnetic component in these structures, the ternary NiFeCo alloy, have not been investigated under similar deposition conditions. It is the objective of this work to investigate the crystal structure and the magnetic properties of this NiFeCo alloy over a wide range of thicknesses.

The deposition conditions were chosen in order to ensure single layer integrity and repeatability in the thinner layer regime, although at lower deposition rates the grain growth caused the coercivity values to increase. However, the importance of high quality multilayer structures, for subsequent thermal processing for giant magnetoresistance (GMR) optimization, dictates the range of deposition rates[3] and the relevant magnetic properties and crystal structures of the single layer were therefore addressed at identical deposition conditions.

II. EXPERIMENTAL PROCEDURES

Single layer NiFeCo samples were deposited over the thickness range of 20–2400 Å. The films were grown on 3 in. thermally oxidized silicon (100) substrates, with base deposition pressures of the order of 10^{-8} Torr. The films were dc magnetron sputtered at dynamic argon pressures of 3 and 7 mTorr, with corresponding deposition rates of 5 Å/s. A magnetic field of 85 Oe was applied to the substrate during the film growth, so that magnetically oriented films were obtained.

Film thickness was determined using a Tencor P1 profilometer. For the thinner NiFeCo films, thickness uniformity data were obtained from four point probe measurements, which in correlation with the low angle diffraction data were used to evaluate these films. The crystal structure of the films was determined via x-ray diffraction (XRD), from high and low angle spectra. Low angle diffraction was used to quantify the repeatability of the thin NiFeCo layers and it was obtained from stacks of ten (Ag/NiFeCO) bilayers. The latter work was also done in correlation to Ref. 3, where good quality layered structures are important for the subsequent GMR performance of these films. The upper NiFeCo layer was protected from oxidation by the deposition of a 100 Å silver layer.

Magnetic measurements were done on a SHB-109 BH loop tracer at applied fields of 50 Oe. Four point probe measurements were used for the determination of the magnetoresistance (MR) change in the films as a function of film thickness. A vibrating sample magnetometer (VSM) was also used to identify the saturation magnetization values of these single layer films.

III. RESULTS AND DISCUSSION

A. Crystal structure

XRD studies were used for the crystal structure identification of the single layer NiFeCo films. Figure 1 shows the XRD spectra of two 2400 Å films as deposited at 3 and 7 mTorr. The characteristic (111), (200), and (211) fcc lines are present for both film structures. The overall crystal structure present in these films is polycrystalline face centered cubic. The effect of higher deposition pressure results in a less pronounced spectrum intensity, possibly due to excess scattering of the incident beam, at surface inhomogeneities induced by the film porosity.

Verification of the integrity and repeatability of the thinner films studied (i.e., 20, 50 Å in thickness) required the use of low angle XRD along with the regular high angle scans. These samples were evaluated in stacks of ten bilayer structures, which consisted of NiFeCo and Ag layers. The Ag layer thickness was kept constant at 100 Å, while the NiFeCo layer thickness was varied from 20 to 100 Å. The insert of Fig. 2 shows the low angle XRD spectrum for a [Ag-100/NiFeCo-20] multilayer, as obtained at normal incidence, with the corresponding bilayer thickness calculated at

 0021-8979/96/79(8)/5446/3/$10.00 © 1996 American Institute of Physics

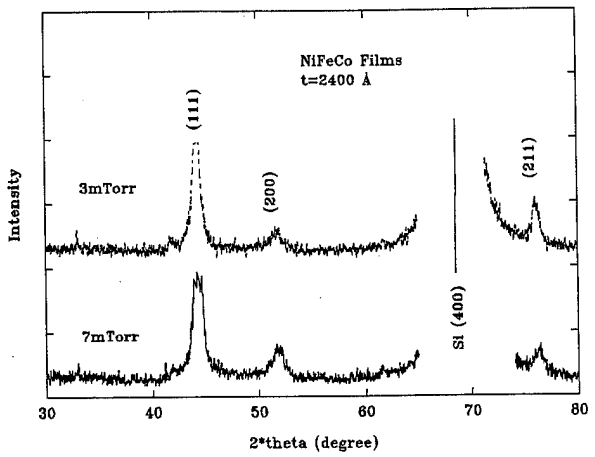


FIG. 1. XRD spectra of single-layers, 2400 Å thick, NiFeCo films deposited at 3 and 7 mTorr—single phase fcc structures.

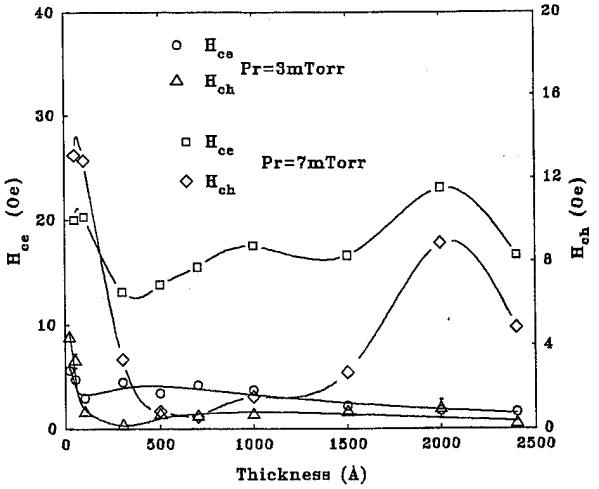


FIG. 3. Easy and hard axis coercivity data for the NiFeCo films, as deposited at 3 and 7 mTorr, plotted as a function of film thickness.

(115±5) Å. High angle scans of these samples were used to indirectly verify the repeatability of the thin NiFeCo layers. In Fig. 2 the corresponding high angle scan of the same sample is shown, in which the (111) line of the silver layer is observed along with its corresponding satellite peaks. A rather broad amorphouslike peak is observed over the (111) line region for NiFeCo, as would be expected from a 20 Å thin layer.

B. Magnetic data

The easy and hard axis H_c values were measured at an applied field of 50 Oe, with nominal values of 2 and 0.5 Oe, respectively, at thicknesses of 500 Å. Significantly lower values can be obtained at deposition rates higher than 15 Å/s; however, the nominal deposition rates for the films in this study are at a fraction of that, at 5 Å/s. A summary of the easy and hard axis coercivities evaluated over the entire deposition range are shown in Fig. 3. The magnetic properties of the low end thickness films (i.e., 20 and 50 Å of NiFeCo) were determined from the same bilayer stacks used for the low angle XRD measurements. This allowed for noise elimination and more accurate determination of the particular magnetic properties. Interaction of the individual magnetic layers was prevented by the Ag interlayers, which were grown to adequate thicknesses for this purpose. However, the presence of silver interfaces may be the cause of the modified magnetic behavior in these films, which in this configuration lack the free surface of a single-layer film. Nevertheless, the choice was made so that the thinner layers could be evaluated with the available instrumentation. The coercivity response curve is highly nonlinear with thickness, in the range below 500 Å, for both 3 and 7 mTorr pressures. This behavior may be attributed to varying stages of growth dynamics that are characteristic for each of the thicknesses. However, in the high thickness range the properties were found in the same range as that expected for the bulk alloy. The values of the MR and anisotropy fields are following the same pattern as that of the coercivity curves (Fig. 4). That is, the higher anisotropy fields correspond to the lower MR values. Similar oscillatorylike behavior as a function of thickness, in the magnetic hysteresis and MR properties has been observed for NiFe films, with its origin attributed to quantum size effects.[10,11] The magnetic data of the samples deposited at 7 mTorr are highly differentiated as compared with the results at 3 mTorr. The differences may be attributed to structural variations of the grains in the two pressure regimes. Although the deposition rate is not affected at the two different pressures for the same deposition power, it is the grain formation and gas adsorption that may be significantly changed as the pressure increases. The films grown at lower deposition pressure are denser with substantially lower coercivities.[12] At 7 mTorr the easy axis coercivities are much higher, as expected, with the higher corresponding anisotropy fields. The hard axis coercivities were found to deviate significantly at thicknesses above 1500 Å for the 7 mTorr films, with the deviation well above the experimental error

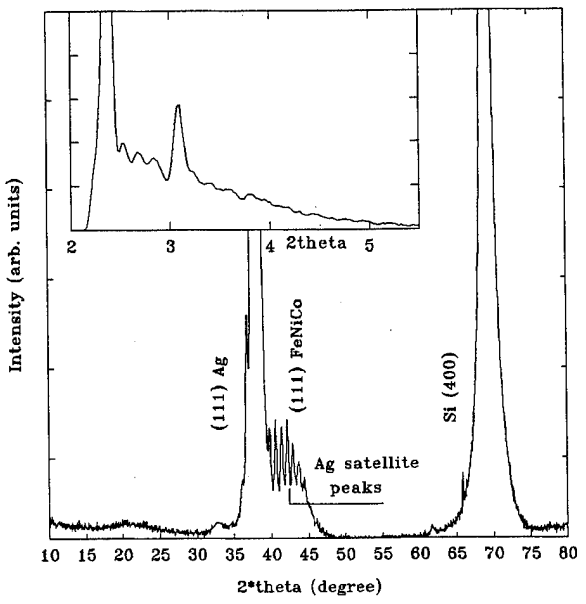


FIG. 2. Low angle and high angle XRD spectra of an [Ag-100/NiFeCo-20] multilayer signifying the periodicity of the constituent layers.

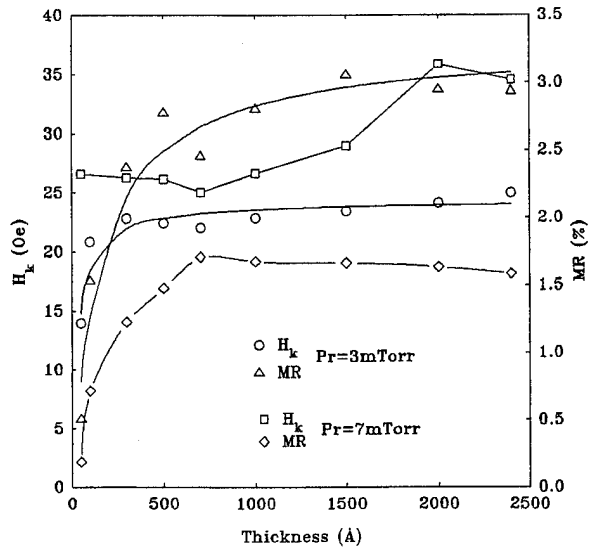


FIG. 4. The corresponding MR and H_k values for the NiFeCo samples of Fig. 3.

(better than 5%). The in-plane dispersion of the magnetic moments becomes significantly large for these highly anisotropic films, as shown in Fig. 6. The angle of dispersion at 90% saturation increases dramatically above 1500 Å, while it is $\leqslant 2°$ for the thicknesses below 1500 Å. At 3 mTorr, α_{90} is $\leqslant 1°$ as long as the film thickness remains below 2000 Å, and $\leqslant 2°$ above that thickness range, as determined from the BH loop tracer measurements.

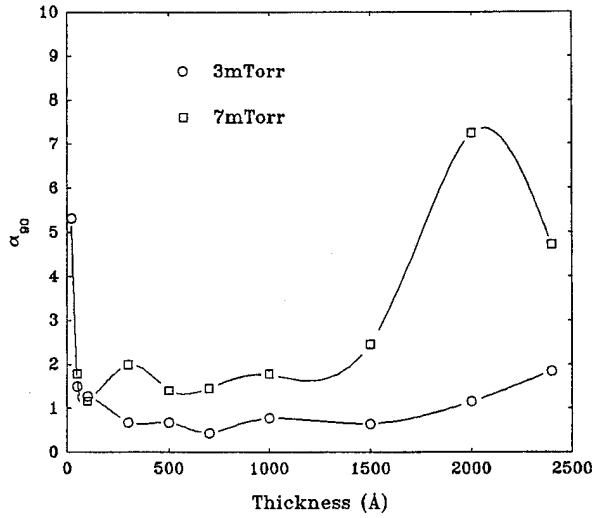


FIG. 5. Angle of dispersion at 90% saturation for the NiFeCo range of thicknesses studied.

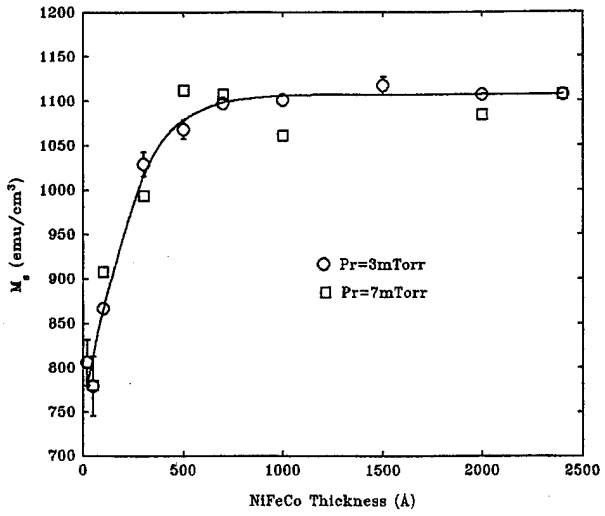


FIG. 6. Saturation magnetization data as obtained at 500 Oe applied magnetic field, as a function of film thickness.

The saturation magnetization values were determined from VSM measurements and are shown in Fig. 6. The values of M_s for films thicker than 300 Å are essentially constant at about 1050 ± 50 emu/cm^3. For the thinner films, instrumental sensitivity limitations and experimental error (in addition to the possibility of modified magnetic behavior due to the multilayer configuration) may account for the deviation, since the XRD data did not indicate the presence of oxide peaks.

ACKNOWLEDGMENTS

The authors would like to thank Dr. L. Withanawasam and I. Werasekera for their helpful contribution in the development of this manuscript.

[1] T. L. Hylton, K. R. Coffey, M. A. Parker, and J. K. Howard, Science **261**, 1021 (1993).
[2] Y. K. Kim and S. C. Sanders, Appl. Phys. Lett. **66**, 1009 (1995).
[3] J. W. Dykes, Y. K. Kim, A. Tsoukatos, S. Gupta, and S. C. Sanders, J. Appl. Phys. **79** (1996).
[4] S. Tsunashima, M. Jimbo, T. Kanda, S. Goto, and S. Uchiyama, Mater. Res. Soc. Symp. Proc. **313**, 271 (1993).
[5] M. Jimbo, T. Kanda, S. Goto, S. Tsumashima, and S. Uchiyama, J. Appl. Phys. **31**, L1348 (1992).
[6] H. Sakakima, M. Satomi, K. Onaka, and S. Yamamoto, J. Magn. Magn. Mater. **145**, L268 (1995).
[7] Y. K. Kim and M. Oliveria, J. Appl. Phys. **74**, 1233 (1993).
[8] J. Lo, C. Hwang, T. C. Huang, and R. Cambell, J. Appl. Phys. **61**, 3520 (1987).
[9] R. M. Valletta, G. Guthmiller, and G. Gorman, J. Vac. Sci. Technol. A **9**, 2093 (1991).
[10] T. Yeh, J. M. Sivertsen, and J. H. Judy, IEEE Trans. Magn. **23**, 2215 (1987).
[11] D. C. Larson, Phys. Thin Films **6**, 81 (1971).
[12] J. C. Brice, J. A. Cundall, and A. P. King, J. Mater. Sci. **1**, 170 (1966).

Ferromagnetism of $Y_2(Fe_{1-y}Co_y)_{17-x}Al_x$

N. Ohkubo and K. Kanematsu
The Physical Science Laboratories, Nihon University at Narashino, Funabashi, Chiba 274, Japan

Magnetization and x-ray measurements of alloy systems, $Y_2(Fe_{1-y}Co_y)_{17-x}Al_x$ ($y=1/3,2/3$), were performed and the magnetic and crystallographic data are shown with the results of the systems where $y=0$ and 1.0. The crystal structure of all alloys changes from hexagonal Th_2Ni_{17} type to rhombohedral Th_2Zn_{17} type with increasing aluminum concentration. The average magnetic moments of the $3d$ metal atom of all alloy systems decrease with increasing aluminum concentration. The Curie temperatures of the alloy systems where $y=1/3$, 2/3, and 1.0 decrease smoothly with increasing aluminum concentration. On the other hand, the system where $y=0$ at first increases and then decreases. These magnetic properties are discussed by Stoner's model. © *1996 American Institute of Physics.* [S0021-8979(96)30508-7]

I. INTRODUCTION

The magnetization and Curie temperature of $Y_2Co_{17-x}Al_x$ decrease with increasing aluminum concentration. The Curie temperature as a function of the magnetic moment of cobalt qualitatively agrees with a relation predicted by Stoner's theory.[1,2] The magnetization of $Y_2Fe_{17-x}Al_x$ similarly decreases with increasing aluminum concentration; however the Curie temperature increases with increasing aluminum concentration and turns to decrease.[3–5] The aluminum concentration dependence of the Curie temperature is qualitatively explained by a localized moment model. Thus the magnetic properties of $Y_2Co_{17-x}Al_x$ and $Y_2Fe_{17-x}Al_x$ are explained by two extreme models. The purpose of this paper is to report the magnetic properties of alloys with an intermediate composition.

II. EXPERIMENTAL PROCEDURE

The alloys were prepared by arc melting a mixture of Y (99.9% pure), Fe (99.9% pure), Co (99.9% pure), and Al (99.9% pure), with each composition in an argon atmosphere. Arc melting was repeated several times. Then the alloys were sealed in an evacuated silica tube and annealed at 1200 K for 0.6 Ms (7 days). Magnetization measurements were carried out by a vibrating sample magnetometer in a magnetic field of 0.84 MA/m (10.6 kOe).

III. X-RAY AND MAGNETIZATION MEASUREMENTS

In the crystal structure of R_2T_{17} alloys, there are two types of structure: (1) a hexagonal Th_2Ni_{17} structure, which consists of two layers stacked in a hexagonal block with a composition of R_2T_{17}; and (2) a rhombohedral Th_2Zn_{17} structure, which consists of three layers stacked in a hexagonal representation. There are four sites for T atoms in the hexagonal block; $T_1=6g$, $T_2=12j$, $T_3=12k$, $T_4=4f$ in the Th_2Ni_{17} structure and $T_1=9d$, $T_2=18f$, $T_3=18h$, and $T_4=6c$ in the Th_2Zn_{17} structure.

X-ray diffraction with Cu-$K\alpha$ radiation shows that all alloys without aluminum have a Th_2Ni_{17} structure. Substitution of aluminum for the transition metals weakens and ultimately leads to the disappearance of the characteristic line (221) of the Th_2Ni_{17} structure. Further substitution of alumi-

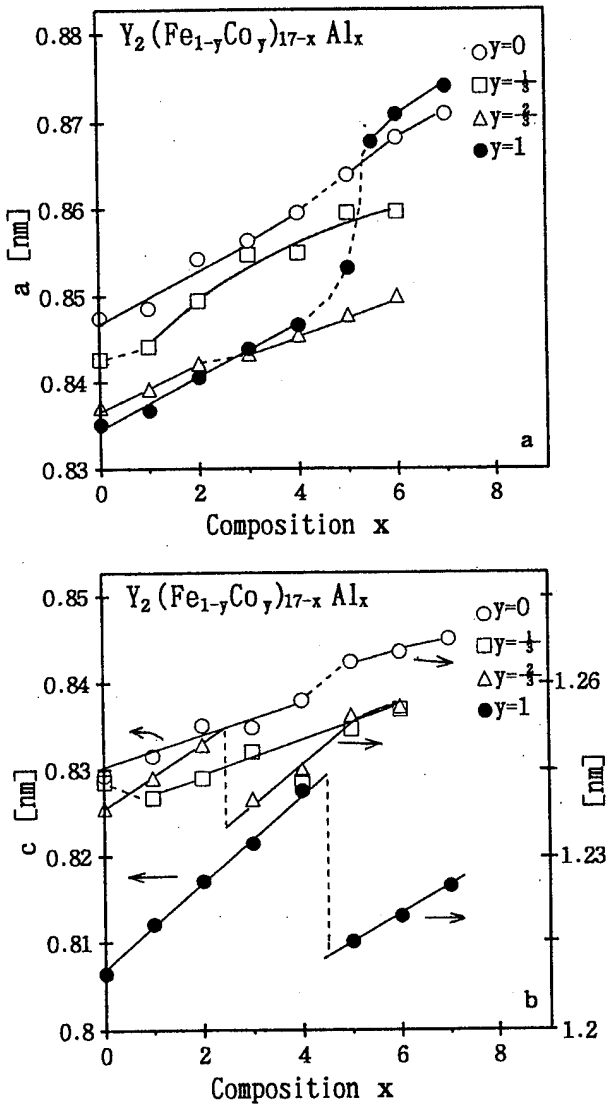


FIG. 1. Lattice constants of $Y_2(Fe_{1-y}Co_y)_{17-x}Al_x$ ($y=0$, 1/3, 2/3, 1.0) are plotted for the aluminum concentration x. Structural changes from hexagonal Th_2Ni_{17} type to rhombohedral Th_2Zn_{17} type (represented hexagonal structure) occur at $4<x<5$ for $y=0$, $0<x<1$ for $y=1/3$, $2<x<3$ for $y=2/3$, and $4<x<5$ for $y=1.0$: (a) Lattice constants a; (b) lattice constants c.

 0021-8979/96/79(8)/5449/3/$10.00 © 1996 American Institute of Physics

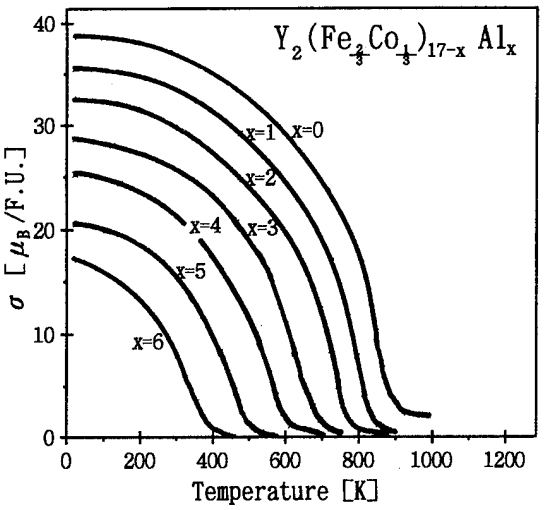


FIG. 2. Thermomagnetic curves of $Y_2(Fe_{2/3}Co_{1/3})_{17-x}Al_x$ measured in a magnetic field of 10.6 kOe.

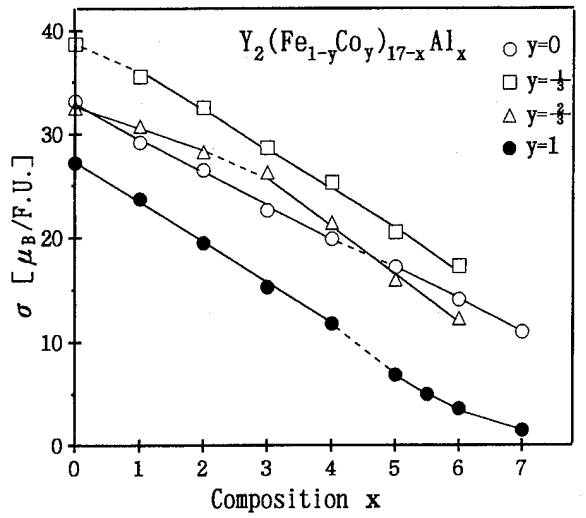


FIG. 4. Magnetizations σ of $Y_2(Fe_{1-x}Co_y)_{17-x}Al_x$ ($y=0$, 1/3, 2/3, 1.0) at 0 K, expressed in terms of Bohr magneton per formula unit $[Y_2(Fe_{1-y}Co_y)_{17-x}Al_x]$, are plotted for aluminum concentration x. The dotted lines show the composition of structural change from Th_2Ni_{17} type to Th_2Zn_{17} type.

num leads to the appearance of and subsequently strengthens the characteristic line (104) of the Th_2Zn_{17} structure. The structural change from Th_2Ni_{17} to Th_2Zn_{17} occurs at $4<x<5$ in the alloy system where $y=0$, at $0<x<1$ in the system where $y=1/3$, at $2<x<3$ in the system where $y=2/3$, and at $4<x<5$ in the system where $y=1$. The lattice constants of the alloys are shown in Fig. 1.

The thermomagnetic curves of alloys in two alloy systems, where $y=1/3$ and 2/3, are shown in Figs. 2 and 3, respectively. The compositional dependencies on magnetization and Curie temperature of both alloy systems are shown with the results of the $Y_2Co_{17-x}Al_x$ and $Y_2Fe_{17-x}Al_x$ systems in Figs. 4 and 5, respectively. The structural change induces the changes in the compositional dependencies on magnetization and Curie temperature of each alloy system.

IV. ANALYSIS BY STONER'S MODEL

The decreasing rates of magnetization per formula unit $Y_2(Fe_{1-y}Co_y)_{17-x}Al_x$ ($y=1/3,2/3$) due to the substitution of aluminum for the transition element (Fe, Co) are 3.5 μ_B/f.u. ($y=0$), 3.6 μ_B/f.u. ($y=1/3$), and 2.1 μ_B/f.u. ($y=2/3$) at $0<x<3$, 4.5 μ_B/f.u. ($y=2/3$) at $3<x$, and 3.9 μ_B/f.u. ($y=1$). According to the band model, the energies of the 3*d* upspin subband and 3*d* downspin subband are separated by an exchange interaction, and the net magnetic moment of the 3*d* metal arises from the excess population. A simple band theory tells us that the valence electrons of aluminum transfer to the unfilled 3*d* and 4*s* band of the 3*d* metal atom and

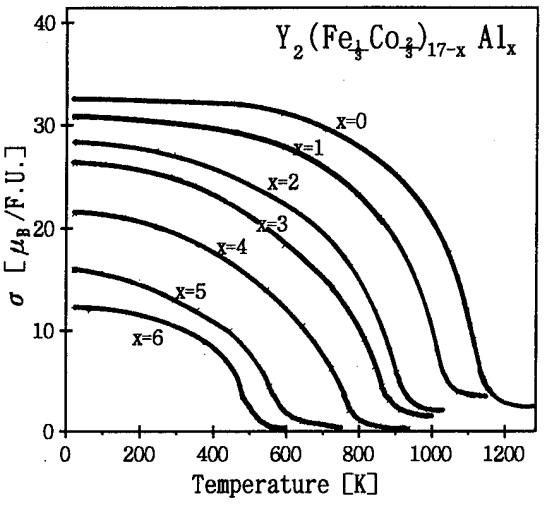


FIG. 3. Thermomagnetic curves of $Y_2(Fe_{1/3}Co_{2/3})_{17-x}Al_x$ measured in a magnetic field of 10.6 kOe.

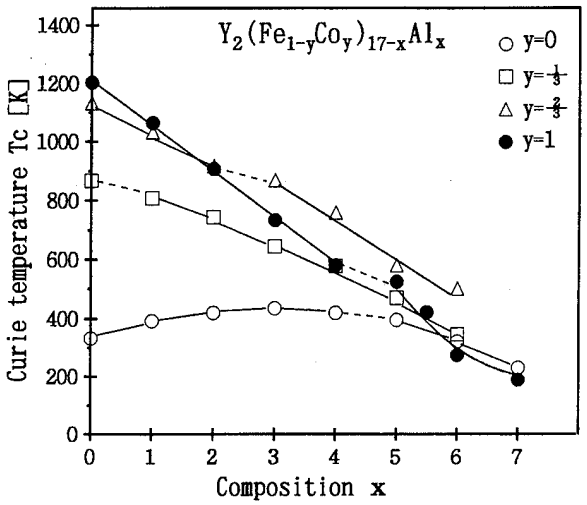


FIG. 5. Curie temperatures T_C of $Y_2(Fe_{1-y}Co_y)_{17-x}Al_x$ ($y=0$, 1/3, 2/3, 1.0) are plotted for the aluminum concentration x. The dotted lines show the composition of structural change from Th_2Ni_{17} type to Th_2Zn_{17} type.

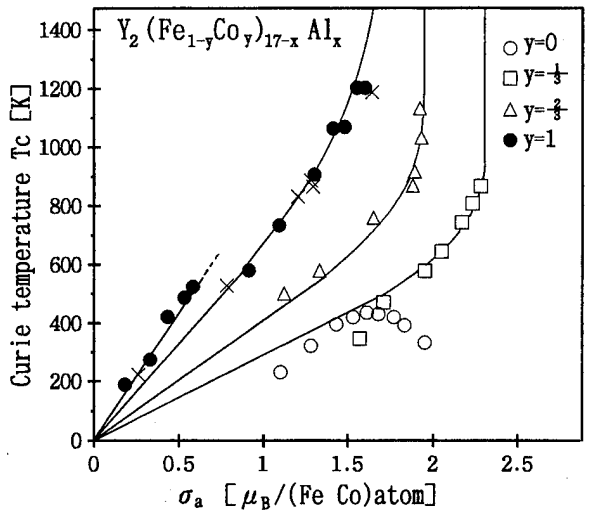


FIG. 6. Average magnetic moments of the $3d$ metal atom, $\sigma_a=\sigma/(17-x)$, are plotted for Curie temperature T_C. Solid lines are theoretical curves obtained by the Stoner model with a parabolic band.

that the decreasing rate of magnetization due to the substitution is equal to or less than 3.0 μ_B. However, most of the experimental data are larger.

A second interpretation is that the aluminum atoms surrounding the $3d$ metal atom weaken the exchange interaction and make the net magnetic moment decrease. According to this model, the spontaneous magnetization of alloys occurs in incomplete saturation. This is discussed in Stoner's theory.[6] This theory suggests that the ferromagnetism of $Y_2(Fe_{1-y}Co_y)_{17-x}Al_x$ ($y=1/3,2/3,1.0$) is in incomplete saturation and that an increase of the interaction energy $k\theta'$ leads to an increase of the magnetization and Curie temperature. Figure 6 shows the Curie temperature curves of every alloy system plotted as functions of the average magnetic moments of the $3d$ metal atom (Fe and Co) σ_a with the aluminum concentration as the implicit parameter. The average magnetic moments σ_0 are obtained from the magnetizations σ by assuming that the yttrium and aluminum have no magnetic moment. The solid lines are curves calculated from Stoner's theoretical curves of kT_C/ϵ_0 vs σ_0/σ_{a0},[6] where T_C is the Curie temperature and σ_{a0} is the average magnetic moment in complete saturation. The values of ϵ_0 and σ_{a0} used in the theoretical curves are $\sigma_{a0}=2.30$ μ_B and $\epsilon_0=2210$ K for the alloy system of $Y_2(Fe_{1-y}Co_y)_{17-x}Al_x$ where $y=1/3$, $\sigma_{a0}=1.94$ μ_B and $\epsilon_0=2570$ K for the system where $y=2/3$, $\sigma_{a0}=1.68$ μ_B and $\epsilon_0=3870$ K for the system where $y=1.0$ with a Th_2Ni_{17} structure and $\sigma_{a0}=1.68$ μ_B and $\epsilon_0=5150$ K for the system where $y=1.0$ with a Th_2Zn_{17} structure. Assuming that the net magnetic moment comes from the hole of the $3d$ band, the values of σ_{a0} and the magnitude of ϵ_0 are reasonable. The agreement between the experimental values and theoretical curves is very good even though the Stoner model is a simple theory that neglects the band structure and other important factors. The effect of aluminum on the interaction energy is estimated from the theoretical curve of $k\theta'/\epsilon_0$ vs σ_0/σ_{a0}, and the rate of decrease of $k\theta'/\epsilon_0$ with the addition of one aluminum atom is 0.014–0.018.

The decrease of the average magnetic moment of iron with increasing aluminum concentration in $Y_2Fe_{17-x}Al_x$ suggests that the magnetism of this system is an itinerant electron magnetism, but it is not easy to interpret the aluminum concentration dependence on Curie temperature by an itinerant electron model like Stoner's theory.

[1]N. Ohkubo and K. Kanematsu, J. Magn. Soc. Jpn. **19**, 233 (1995) (in Japanese).
[2]M. Hamano and S. Yajima, Trans. Jpn. Inst. Met. **18**, 185 (1977).
[3]K. Itoh, N. Ohkubo, and K. Kanematsu, Jpn. J. Appl. Phys. **32**, 322 (1993).
[4]D. Plusa, R. Pfranger, B. WycLocki, and T. Mydlarz, J. Less-Common Met. **120**, 1 (1986).
[5]T. H. Jacobs, K. H. J. Buschow, G. F. Zhou, X. Li, and F. R. Boer, J. Magn. Magn. Mater. **116**, 220 (1992).
[6]E. C. Stoner, Proc. R. Soc. London Ser. A **165**, 372 (1938).

Ferromagnetism of deuterides YFe_2D_x (abstract)

K. Kanematsu, N. Ohkubo, K. Itoh, and S. Ban
The Physical Science Laboratories, Nihon University at Narashino, Funabashi, Chiba, Japan

T. Miyajima
Department of Electrical Engineering, College of Industrial Engineering, Nihon University, Narashino, Chiba, Japan

Y. Yamaguchi
Institute for Materials Research, Tohoku University, Sendai, Japan

Cubic Laves phase alloy YFe_2 forms four types of hydrides, YFe_2Hx: β_1, β_2 (hexagonal) of $1.2<x<1.6$, γ (hexagonal) of $2.8<x<3.45$, and δ (orthorhombic) of $3.7<x$. The β_1 and β_2 hydrides are formed in the hydrogen absorption below and above 500 K.[1] The deuterides YFe_2D_x have been prepared by deuterium absorption at various temperatures for YFe_2 powders of diameters less than 0.3 mm. The formed samples are mixtures of main and extra deuteride phases. The x-ray and magnetization measurements in a magnetic field of 10.6 kOe showed five types of ferromagnetic deuterides with Curie temperatures of about 100 K (δ_1), 300 K (δ_2), 380 K (γ), 300–380 K (β_1), and 540 K (amorphous). The extrapolated values of magnetization at 0 K are $3.5\mu_B/YFe_2D_x$. The crystal structures are as follows: δ_1, hexagonal, $a=0.57$ nm, $c=2.74$ nm; δ_2, cubic, $a=0.79$ nm; γ, hexagonal, $a=0.56$ nm, $c=2.63$ nm; and β, hexagonal ($a=0.53$ nm, $c=0.87$ nm)–($a=0.51$ nm, $c=0.82$ nm). © *1996 American Institute of Physics.*
[S0021-8979(96)64808-4]

[1] K. Kanematsu, J. Appl. Phys. **75**, 7105 (1994).

 0021-8979/96/79(8)/5452/1/$10.00 © 1996 American Institute of Physics

Hydrogen charging in nickel and iron and its effect on their magnetic properties

A. Ramesh, M. R. Govindaraju, D. C. Jiles, S. B. Biner, and J. M. Roderick
Department of Materials Science and Engineering, Iowa State University, Ames, Iowa 50011

The current study was undertaken to explore the possibility of detecting hydrogen cavitation in magnetic materials through magnetic property measurements. It is known that dissolved hydrogen in a material causes microvoids. These voids may affect the structure-sensitive magnetic properties such as coercivity and remanence. In this study, hydrogen was introduced into nickel and iron by two processes, namely thermal charging and cathodic charging. The effect on the magnetic properties was measured. In addition, the variation of the magnetic properties with porosity was studied. © *1996 American Institute of Physics.* [S0021-8979(96)30608-3]

I. INTRODUCTION

The presence of hydrogen in metals is known to have a significant impact on the mechanical properties.[1] Generally, hydrogen is taken up in interstitial sites, but at higher concentrations it can lead to the formation of voids. Oriani[2] has confirmed that the exact nature of hydrogen dissolved in a metal is that of a proton which has given up its electron to the electron gas of the metal. The solubility of hydrogen in nickel and iron is proportional to the square root of the external hydrogen pressure, at least for small concentrations according to Sieverts.[3] Also the diffusion of hydrogen through a metal follows the Arhennius equation and is therefore much faster at higher temperatures. Lord[4] has suggested that hydrogen is more likely to reside in octahedral rather than the tetrahedral sites in iron.

When hydrogen is introduced into a lattice at high temperature and pressure and the material is then quenched back to ambient conditions, the lattice is no longer capable of retaining all of the hydrogen. The excess hydrogen is taken up by internal traps such as dislocations, grain boundaries, and vacancies. Thus the physical picture is that of hydrogen dissolved in the lattice with the excess amount residing in internal voids. The presence of dissolved hydrogen in a metal causes an expansion of its lattice. Smialowski[5] concluded that the irreversible external dimensional changes of iron samples caused when they are charged with hydrogen, are due to molecular hydrogen gas at very large pressures. However, detection of hydrogen in a material is very difficult due to its extremely small equilibrium lattice solubility of only 5×10^{-10} at normal temperature and pressure.

In a ferromagnetic material, the process of magnetization occurs by the movement of the domain walls. This motion can be hindered by the presence of pinning sites such as second phase particles and inclusions resulting in hysteresis. According to the model of Kersten and Neel,[6,7] the presence of nonmagnetic inclusions or voids causes pinning of magnetic domain walls and leads to an increase in the coercivity and a decrease in permeability. Baum[8] noted that the structure-sensitive properties such as coercivity and permeability appear to be dependent on the porosity of iron. More recently, Jiles *et al.*[9] have reported that the coercivity of iron is at maximum when the pores have a diameter of about 8–11 μm.

Oriani and Josephic[10] studied the effect of hydrogen on the plastic deformation of steel and reported that the basic effect is an increase in the population of the microvoids at a given strain. Hydrogen of very high fugacity nearly doubles the microvoid population. This causes an increase in the number of voids present in the material which acts as pinning sites, thus leading to changes in its magnetic properties. In addition, the presence of hydrogen causes local strain in the material, which also impedes the motion of the domain walls as suggested by Becker.[11] In view of these effects, an attempt has been made in the present work to study the effect of hydrogen on the magnetic properties of materials based on iron and nickel.

II. EXPERIMENTAL PROCEDURE

Hydrogen can be introduced into the metal in several ways. These include thermal charging, cathodic charging, and acid corrosion.[12] Of these methods the first two were used in the present work and the change in the magnetic properties was studied.

A. Thermal charging

Pure nickel rods of 10 mm diameter and 100 mm length were put in a chamber which was evacuated and then subjected to a pressure of 100 atm of hydrogen at 500 °C. The maximum solubility of hydrogen under these conditions was calculated as 0.0015 atoms of H_2/atom of nickel. The time taken for saturation of hydrogen was 2.5 h. During charging, the samples were subjected to hydrogen charging for different periods of time, causing varying uptakes of hydrogen. Baseline magnetic measurements were taken after annealing the sample at 500 °C for 12 h. Magnetization measurements were made using a magnetic hysteresisgraph. Results were analyzed using a software package written exclusively for the experimental system.

B. Cathodic charging

Cathodic charging has often been used to introduce hydrogen into metals because of its convenience and its ability to produce high fugacity of hydrogen. This is an electrolytic process in which hydrogen is charged into the metal cathodically using platinum wire as the anode. Boniszweski and Smith[13] have used this method to study the effect of hydro-

 0021-8979/96/79(8)/5453/3/$10.00 © 1996 American Institute of Physics

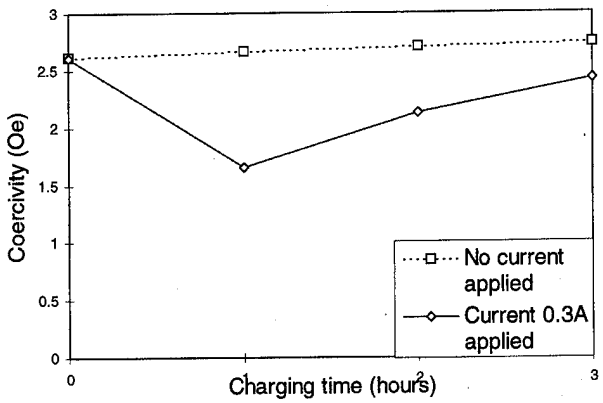


FIG. 1. Variation of coercivity of iron as a result of cathodic charging.

gen in the plastic deformation of nickel. In the current study charging was done in a 1 N sulfuric acid bath at room temperature with a current density of about 500 A/m^2 for different times. Thiourea was used as the catalyst, causing a hydrogen input fugacity of 10^7 MN/m^2. The magnetic properties were measured as a function of the amount of hydrogen in the sample. These are shown in Fig. 1.

III. RESULTS AND DISCUSSION

A. Thermal charging

The results of thermal charging are shown in Fig. 2. Initially, the coercivity and remanence decreased as expected,since a large number of dislocations and stress fields which act as pinning sites for the domain walls are removed as a result of annealing. Upon charging to 100 atm of hydrogen at 500 °C, the magnetic properties varied due to both the addition of hydrogen and exposure to high temperature which further relieved the residual stress. During the initial stages of charging, the main effect was simply the annealing of residual stress, thus the coercivity decreased. However, as the hydrogen content increased, it caused an increase in the density of voids and resulting internal stress and led to an increase in the coercivity. Quantitatively, the changes due to hydrogen charging were small, amounting to a maximum of 0.5 Oe. The small changes in the magnetic properties resulted from a low hydrogen intake which resulted in a small number of additional voids formed. Also, the excess hydrogen was preferentially chemically adsorbed on to inclusions and grain boundaries which acted as pinning sites even in the absence of hydrogen.[1] In these cases, the number of new pinning sites introduced by the hydrogen absorption would be small, leading to only a small increase in coercivity.

B. Cathodic charging

Hydrogen introduced by charging may affect the magnetic properties of iron-based alloys either by the formation of hydrides or by the formation of voids. Kimura and Birnbaum[14] have reported observations using transmission electron microscopy of small gas bubbles in iron cathodically charged at 20 A/m^2 which caused blisters to form due to the high pressure of hydrogen. According to Boniszweski and Smith,[13] hydrides could be formed on the surface layers of the material under certain charging conditions. It has also been reported in the literature that the thickness of the hydride layer formed on the surface by cathodic charging at room temperature for 48 h was as small as 10 μm. The high fugacity of hydrogen, and the corresponding high hydrogen concentration gradients, may therefore affect only the surface layers of the specimen. This has also been confirmed by Kimura and Birnbaum.[14] While cathodic charging of relatively thick specimens had relatively little effect on their measured flow stress, large effects were observed for smaller specimens with diameters of 0.1 mm or less. Thus it is established that the effect of hydrogen on the magnetic properties is entirely a surface phenomena. The measured hysteresis properties were however averaged values over the bulk sample and therefore these magnetic properties do not exhibit significant changes due to the addition of hydrogen.

IV. EFFECT OF POROSITY

In order to confirm these conclusions concerning the effect of hydrogen on the magnetic properties, it was decided to study the effect of uniformly distributed pores on the mag-

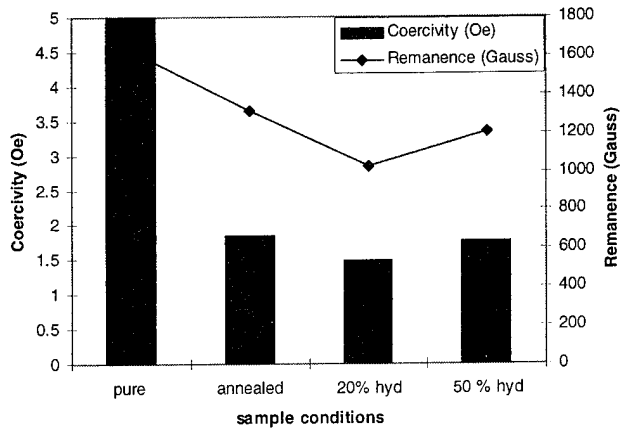


FIG. 2. Variation of coercivity and remanence of nickel as a result of thermal charging.

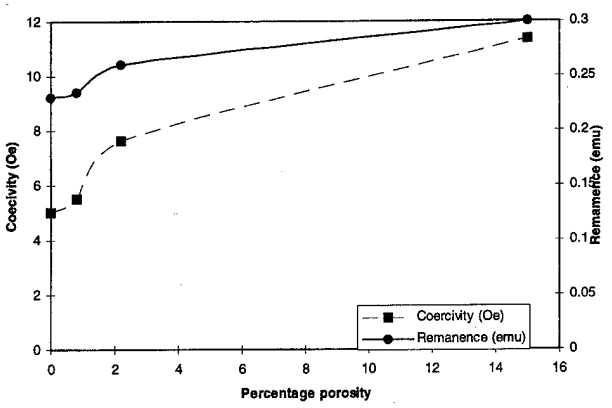


FIG. 3. Variation of coercivity and remanence with the density of nickel specimens with controlled amounts of porosity.

netic properties of pure nickel. For this purpose, pure nickel rods with different levels of porosity were prepared and their magnetic properties were studied. Compacts were made using nickel powder mainly composed of individual particles that were typically a few microns in diameter. The compacts were cold isostatically pressed by applying a pressure of 4400 atm and sintered under different conditions to obtain different densities. The four compacts thus obtained were tested for their magnetic properties at room temperature. From the data plotted in Fig. 3, it can be seen that there was a regular decrease in some of the magnetic properties such as the coercivity and remanence, as the density increased. This is because the number of pores decreases as the density increases and these act as the pinning sites for the motion of the domain walls. As a result, the irreversible nature of the magnetization was enhanced and therefore the coercivity, remanence, and hysteresis loss increased at low densities.

V. CONCLUSIONS

Hydrogen absorption in nickel under extreme conditions of high temperature and pressure had a small effect on the bulk magnetic properties, since the hydrogen does not form new pinning sites, but is adsorbed on those that already exist. The largest measured change in coercivity was from 2.0 to 1.5 Oe. Cathodic charging of nickel or iron resulted only in changes to the surface from the formation of hydrides or voids and this did not greatly affect the bulk magnetic properties. In this case the largest change in coercivity was from 2.6 to 1.6 Oe. The presence of voids in the bulk of the material affected the magnetic properties and can be related directly to the density of the material. These results led to the conclusion that the detection of hydrogen by bulk magnetic measurements is problematic unless the amount of hydrogen is very high, the hydrides can be formed in the bulk material, or the resolution of the magnetic measurements is sufficiently high.

ACKNOWLEDGMENT

This work was supported by Division of Materials Research, National Science Foundation under Grant No. DMR-93-10273.

[1] I. M. Bernstein, Mater. Sci. Eng. **6**, 1 (1970).
[2] R. A. Oriani, Proceedings of the Symposium on Stress Corrosion Cracking, 1967 (unpublished), p. 32.
[3] A. Sieverts, Z. Metallk. **21**, 37 (1929).
[4] A. E. Lord, Acta Metall. **15**, 1241 (1967).
[5] M. Smialowski, *Hydrogen in Steel* (Pergamon, Oxford, 1962), p. 452.
[6] M. Kertsen, Phys. Z. **44**, 63 (1943).
[7] L. Neel, Ann. Univ. Grenoble **22**, 299 (1946).
[8] L. W. Baum, Precision Met. **32**, 47 (1974).
[9] D. C. Jiles, C. V. Owen, and W. A. Spitzig, J. Non-destruct. Eval. **6**, 3 (1987).
[10] R. A. Oriani and P. H. Josephic, Scripta Metall. **13**, 469 (1979).
[11] R. Becker, Phys. Zeits **33**, 905 (1932).
[12] L. S. Darken and R. P. Smith, Corrosion **5**, 1 (1949).
[13] T. Boniszweski and G. C. Smith, Acta Metall. **11**, 165 (1963).
[14] A. Kimura and H. K. Birnbaum, Acta Metall. **35**, 1077 (1987).

Magnetic viscosity investigations of nanograin iron powder

U. Atzmony,[a] Z. Livne,[a] R. D. McMichael, and L. H. Bennett
National Institute of Standards and Technology, Gaithersburg, Maryland 20899

Magnetic properties of three kinds of nanograin Fe powder were studied. The first two, designated as NM(Ar) and NM(N), were obtained by ball milling the iron powder under an argon or nitrogen atmosphere. The third, designated NN, was obtained by evaporation and condensation. They have grain sizes of 20, 7, and 60 nm, respectively. The particle sizes of the first two were in the micrometer range, whereas those of the NN were in the nanometer range. The NN powder exhibited a coercivity of 79 mT; its magnetic moment at saturation was lower than that of bulk iron. The coercivities of the NM(N) and NM(Ar) were much smaller and their magnetic moment values at high fields were closer to that of bulk iron (210 $A \cdot m^2/kg$). The NM(N) and NN samples exhibited marked time dependences of the magnetic moments following a relatively abrupt change of the applied field. The moment changes by more than 0.5% of the saturation moment within 50 min and continues to change for many hours. Much smaller effects were detected in the NM(Ar) sample. The viscosities were investigated as a function of temperature and jump field. The results showed differences in the behavior of the three samples. The powders were consolidated by cold isostatic pressing followed by sintering at around 600 °C for several hours. The magnetic behavior of the sintered samples approach that of bulk iron. © *1996 American Institute of Physics.*
[S0021-8979(96)30708-X]

I. INTRODUCTION

Ultrafine ferromagnetic particles are of technological interest for magnetic fluids, magnetic recording media, permanent magnets, and catalysts. Viscosity effects were always detected in either alloys or layered samples. This article represents the first time that this effect was detected and investigated in elemental samples.

The magnetization, M, of a hysteretic magnetic material in a steady applied field is often well described by a logarithmic time dependence,

$$M = M_0 - S \cdot \ln(t/\tau). \tag{1}$$

The magnetic viscosity, S, is a consequence of thermally exited irreversible processes, and has been shown to be related to the irreversible susceptibility, χ_{irr}, by

$$S = k_B T \frac{\chi_{\text{irr}}}{(\partial E_b / \partial H)}, \tag{2}$$

where E_b is the height of the energy barrier.[1]

II. EXPERIMENT

Three iron powder samples, designated as NM(N), NM(Ar), and NN, were investigated. The first letter in the name symbolizes the grain size (N suggests nanometer size and M, micrometer) and the second letter, the particle size. Sizes were provided by the producers[2,3] and checked by us: grain sizes were derived from x-ray analysis and particle sizes from SEM (see Table I). The NM powders were made by ball milling iron under N or Ar atmospheres, respectively,[2] while the NN was prepared by evaporation and condensation.[3] Room temperature Mössbauer studies revealed the existence of ≈5% oxidized phase (apparently Fe_3O_4) in the NN powder samples. Because this powder is not pyrophoric, we believe that this oxide phase forms a coating on the particles. No oxide was observed by Mössbauer in the NM powder samples.

In addition to these "as received" powders, magnetic measurements were made on powders consolidated by cold isostatic pressing (CIP) followed by sintering at 580 and 850 °C for several hours. Mössbauer measurements showed that the amount of oxidized phase increased to ≈20% during the consolidation and heat treatment.

Magnetic properties were studied mainly using a DC extraction magnetometer. In this technique, the flux change is detected as the sample is removed from a sensing coil within a superconducting magnet. In several instances, measurements were also taken with a SQUID magnetometer.

The time dependence was measured using the following protocol: After reaching the desired temperature under zero field, the field was set to 0.8 T. Then, under computer control, the field was reset to a value H_2, $H_2 < 0.8$ T. It took ≈50 s for the field to stabilize. After the reset value of the field was stabilized, the magnetization was recorded as a function of time for up to 4 days. The time behavior was linearly best fitted to $M = M_0 + S \cdot \ln(t)$, where the slope, S, was defined as the magnetic viscosity or after effect.

[a]Permanent address: NRCN, P.O. Box 9001, Beer-Sheva, Israel 84190.

 0021-8979/96/79(8)/5456/3/$10.00 © 1996 American Institute of Physics

TABLE I. Sizes and impurities in powder samples.

Powder	Grain size nm from Refs. 2 and 3	X-ray	Particle size μm from Refs. 2 and 3	SEM	[O] weight %	[N] weight %
NM(N)	5–6.5	7.8	4–27	1–10	2.45±0.25	1.15±0.05
NM(Ar)	11–13.5	23	4–27	1–10	2.46±0.05	0.11
NN	···	60	0.1–0.2	0.06	5.7	0.005

III. RESULTS AND DISCUSSION

Major and minor hysteresis loops of the three powder samples and that of consolidated NM(N) and NN were recorded at various temperatures between 5 and 300 K. Examples of major loops are shown in Fig. 1. The loops exhibited striking differences between one another and between bulk metallic iron. The powder NN sample has the widest loop (coercivity, $H_c = 79$ mT at 5 K) and the smallest saturation magnetization, M_s. The value of M_s at 5 K (205 $A \cdot m^2/kg$) for the NM(Ar) powder sample was very near to that of metallic iron (210 $A \cdot m^2/kg$). These results do not agree in detail with some published data.[4] Consolidation of the powders shifts the hysteresis loops towards that of metallic iron; namely, the coercivity is reduced and the value of M_s increases for the consolidated sample compared to the relevant powder ones.

The temperature behaviors of the NM(N) and NN powder samples were derived both from the different hysteresis loops, and from direct measurements of M versus T at various fields. The coercivity of the NM(N) powder sample showed a maximum (≈8 mT) near 30 K. It then decreased with increasing temperature to ≈6 mT and remained at this value up to 300 K. The coercivity of the NN powder monotonically decreased with concave behavior from 79 mT at 5 K to 60 mT at 300 K.

Magnetic after effects were measured for different jump fields H_2, for the three powder samples at different temperatures. An example is given in Fig. 2, where the results for a bulk Fe alloy is shown for comparison. Following the protocol described in the experimental section, the field was abruptly changed from 0.8 T to a smaller value H_2. The value of the magnetic moment thus decreases, and when H is stabilized, the moment is near the value obtained directly from the hysteresis loop. With time, this value continues to decrease and the change continues for many days. The NM(N) and NN samples exhibited distinctive time effects with the slopes reaching values of ≈−0.1 $(A \cdot m^2/kg)/\ln(s)$, i.e., changes of around 1 $A \cdot m^2/kg$ in 3000 s. The maximum total changes due to time effects are ≈0.5% to 1% of the value of the magnetic moment at high fields. In the NM(Ar) sample, the effect was very small, less than 0.05% of the value of the magnetic moment, and thus, detailed investigations of time effects were limited to the NM(N) and NN samples. No changes were detected for the bulk iron sample. This excludes an assumption that the drifts reflect a drift of the superconducting magnet.

When we previously explored the time effect phenomenon in multilayer systems,[5] we found that the magnitude of the effect reached a maximum for jump field values near the reverse coercivity, and decreased in magnitude to both sides in an approximately Lorentzian shape. Similar behavior was observed here with the NN sample. At 5 K, the maximum was obtained around −79 mT, the negative coercive force, with a Lorentzian width of ≈50 mT. But the slope values, for fields which were more than twice the width from the center, departed from the Lorentzian behavior by decreasing more slowly. Better agreement with a Lorentzian behavior was obtained for 80 K (Fig. 3). At 80 K, the coercivity was ≈70 mT, but the maximum value of $|S|$ was obtained at −110 mT, with a width of ≈80 mT. The maximum thus appears to be closer to the maximum of dM/dH, which occurs at ≈−100 mT, than to the coercivity.

The behavior of the H_2 dependence of S in the NM(N) sample is quite different. Both the NN and the NM(M) samples showed increases of $|S|$ between 5 and 30 K, but for the NN sample, the slope was almost insensitive to tempera-

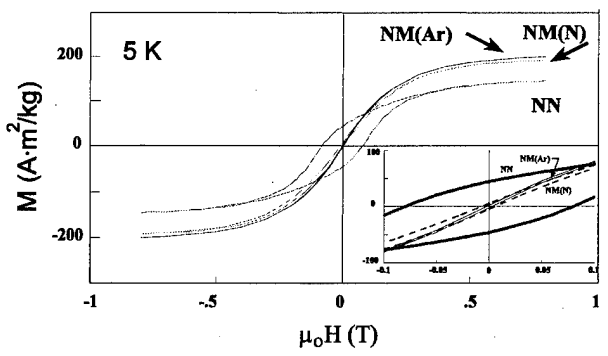


FIG. 1. Hysteresis loops of the three nanograin powders at 5 K.

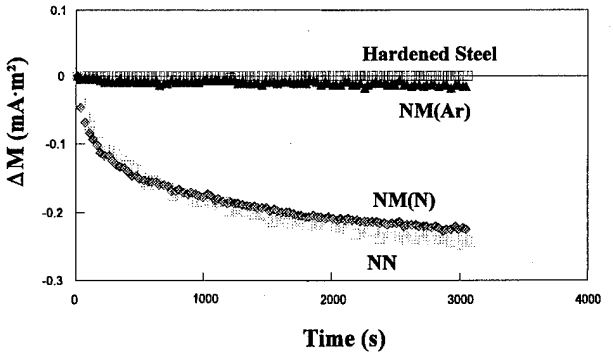


FIG. 2. Magnetic after effect in three nanograin Fe powders, and in bulk steel. The magnetization decay after a field jump from 0.8 T to −30 mT at 5 K is shown as a function of the time after the jump.

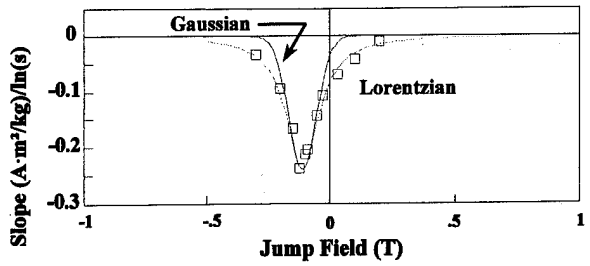


FIG. 3. Slopes of the decay of the magnetization for the NN Fe powder at 80 K after a jump from 0.8 T to the jump fields shown. Each data point represents a best linear fit to a magnetization vs ln time after the jump.

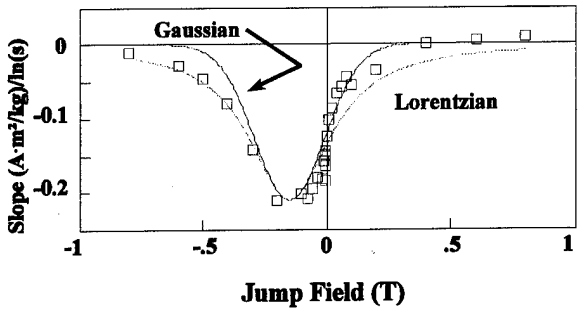


FIG. 5. Slopes of the decay of the magnetization for the NM(N) Fe powder at 30 K after a jump from 0.8 T to the jump fields shown.

tures above 30 K. In contrast, the NM(N) slope values reached a maximum at this temperature, and then decreased as the temperature was raised to 300 K (Fig. 4). A similar decrease is seen for the value of S at differing values of H_2, two of which are shown in Fig. 4. The decrease from the maximum value is more rapid for jump fields which are greater than H_c, which is $\approx$8.5 mT. The maximum of dM/dH is near zero.

At 30 K (see Fig. 5), the NM(N) sample exhibited a "square"-like maximum for H_2 between -50 and -200 mT, with the negative field side decreasing in a Lorentzian behavior, and the positive field side fitting a Gaussian function. More detailed examination of the effects of demagnetizing factor and of the irreversible susceptibility are underway.

In many discussions of magnetic viscosity, it was found that the time behavior of the magnetic moments best described as a linear dependence on the logarithm of the time,[5] and the slope for a best fit to such behavior was the measure for our reported time effects. To check this statement more thoroughly, several time dependence measurements, at values for which relative high slopes were obtained, were carried for a longer period of time up to 14 h. The lines were then fitted to the logarithmic behavior. The agreement between the fit for this longer time and the results for a duration of 3000 s was very good; the NM(N) was exceptionally good. For longer times with the NN sample, the change of magnetic moment was faster than the logarithmic behavior; i.e., the slopes at the longest times are larger. For even longer times, the fit was quite good again; i.e., the real behavior "rotated" around the best fit.

For both samples, the slopes were drastically decreased after consolidation. As an example, Fig. 4 shows two consolidated NM(N) samples, one at 580 °C for 3 h and one at 850 °C for 3 h. Both samples exhibited similar jump field and temperature dependencies, with a minimum at 30 K and with a wide jump field dependence between -100 and 100 mT.

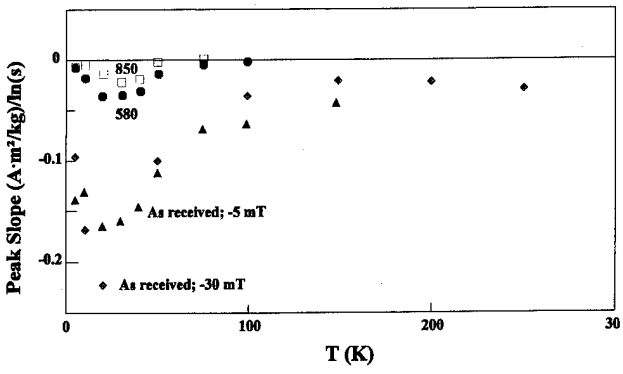


FIG. 4. Slopes of magnetization vs ln time for the NM(N) Fe powder plotted vs temperature. Two of the curves are for the untreated powder, with jump fields of -30 and -5 mT. The other two curves are for the same powder after sintering at 580 and 850 °C, with jump fields of -5 mT.

IV. SUMMARY

The magnetic viscosity was measured in three types of nanograin powders of iron. The low values of S in the NM(Ar) powder, along with its low coercivity, suggest that irreversible processes are weak in this sample. The NM(N) sample showed a maximum in $|S|$ near 30 K; the NN had an approximately flat behavior from 300 to 30 K. These results need to be discussed in terms of particle switching, particularly for the NN, and weak domain wall pinning,[6] particularly for the NM(N). The broad distribution of S versus H_2 (Fig. 5) remains a mystery.

ACKNOWLEDGMENTS

We thank H. Brown and R. Drew for assistance with the measurements and the data reduction.

[1] R. Street and J. C. Wooley, Proc. Phys. Soc. A **62**, 562 (1949); P. Gaunt, J. Appl. Phys. **59**, 4129 (1986).
[2] C. P. Dogan, J. C. Rawers, R. D. Govier, and G. Korth, Nanostructured Mater. **4**, 631 (1994).
[3] V. G. Gryaznov, M. Yu. Gutkin, A. E. Romanov, and L. I. Trusov, J. Mater. Sci. **28**, 4359 (1993).
[4] W. Gong, H. Li, Z. Zhao, and J. Chen, J. Appl. Phys. **69**, 5119 (1991).
[5] For example, K. O'Grady and R. W. Chantrel, J. Magn. Magn. Mater. **54-57**, 755 (1986).
[6] For example, J. Liu, H. Luo, and S. Pan, J. Appl. Phys. **69**, 5557 (1991).

Magnetic properties and the crystallization of amorphous $Fe_{83}B_9Nb_7Cu_1$

Chul Sung Kim and Sung Baek Kim
Department of Physics, Kookmin University, Seoul 136-702, Korea

J. S. Lee and T. H. Noh
Division of Metals, Korea Institute of Science and Technology, Seoul 130-650, Korea

The amorphous state of ferromagnetic $Fe_{83}B_9Nb_7Cu_1$ and its nanocrystallization have been studied by x-ray, Mössbauer spectroscopy, and magnetic moment measurements. In the amorphous state at 13 K, the Mössbauer spectrum exhibits an essentially symmetric hyperfine field distribution with a half-width of 72 kOe. The average hyperfine field $H_{hf}(T)$ of the amorphous state shows a temperature dependence of $[H_{hf}(T)-H_{hf}(O)]/H_{hf}(O)=-0.48(T/T_C)^{3/2}-0.22(T/T_C)^{5/2}$ for $T/T_C<0.7$, indicative of spin-wave excitation. The quadrupole splitting just above the Curie temperature T_C is 0.43 mm/s, whereas the average quadrupole shift below T_C is zero. The Curie and crystallization temperatures are determined to be $T_C=393$ K and $T_x=775$ K, respectively, for a heating rate of 5 K/min. The occupied area of the nanocrystalline phase at the optimum annealing temperature is about 33%–71%. It is notable that the magnetization of the amorphous phase decreases more rapidly with reduced temperature than those of nanocrystalline ferromagnets, suggesting the presence of the distribution of exchange interactions in the amorphous phase or high metalloid contents. © *1996 American Institute of Physics.* [S0021-8979(96)30808-6]

I. INTRODUCTION

Fe-based amorphous ferromagnets like Fe–Si–B–Cu–Nb[1] and Fe–B–Cu–(Zr,Hf,Nb)[2,3] are improved by annealing above the crystallization temperature T_x. This improvement is caused by the precipitation of α-Fe in the amorphous matrix. Ferromagnetic nanocrystalline phases, produced by the crystallization of an amorphous phase, display a high initial magnetic permeability and a low coercivity.[4] The average magnetic hyperfine field measured at the Fe sites of a number of glassy ferromagnets has been reported to decrease more rapidly with increasing temperature than that that of crystalline Fe. In particular, the glassy $Fe_{83}B_9Nb_7Cu_1$ has been researched and it exhibits a combination of remarkable soft magnetic properties.[2] After properly annealing at 830 K the material becomes an ultrafine grain structure (10 nm) of α-Fe embedded in a residual amorphous phase.

In this work, a study of the development of the nanocrystalline phase in the $Fe_{83}B_9Nb_7Cu_1$ alloy using Mössbauer spectroscopy is presented. When properly analyzed, Mössbauer spectra can yield magnetic information not easily obtained by other methods. The amorphous and crystalline volume fractions have also been determined. The magnetic and crystallographic properties are studied using Mössbauer spectroscopy, x-ray, and vibrating sample magnetometer techniques.

II. EXPERIMENT

Ultrathin $Fe_{83}B_9Nb_7Cu_1$ amorphous ribbons were fabricated by a single-roll melt-spinning method at pressures of 10^{-3}–10^{-5} Torr. The conditions for producing ultrathin ribbons were a roll speed of 40–60 m/s, an ejection pressure of 0.005–0.02 kg/cm^2, and a rectangular slit of 0.15×4 mm. The ribbons obtained were 7–12 μm in thickness and 2–4 mm in width. The ribbons were wound into a toroidal core with a 21 mm inner diameter and subsequently annealed at 530 °C for 1 h. The Mössbauer spectra were recorded using a conventional spectrometer of the electromechanical type[5] with a ^{57}Co source in a rhodium matrix. The low temperature was obtained using an APD CS-202 displex closed-cycle refrigeration system with a DMX-20 Mössbauer vacuum shroud interface, and the temperature controller was a model DRC-91 C manufactured by Lake Shore Cryotronics, Inc.

III. RESULTS AND DISCUSSION

Mössbauer spectra of the as-quenched amorphous $Fe_{83}B_9Nb_7Cu_1$ below the Curie temperature T_C exhibit broadened six-line patterns as shown in Fig. 1. The broad

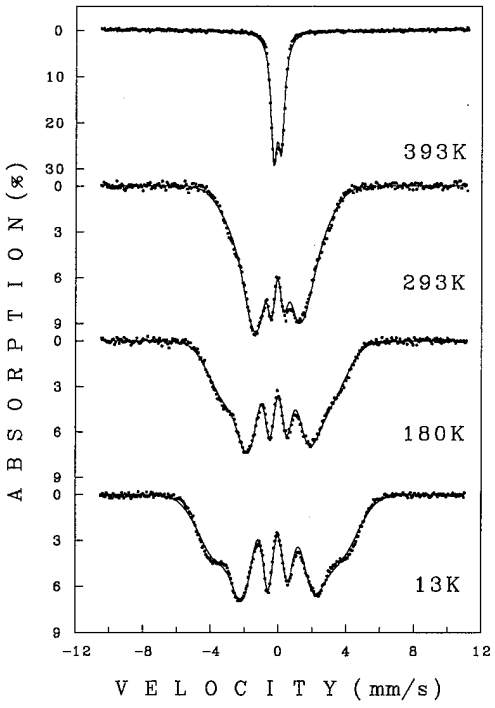


FIG. 1. Mössbauer spectra of amorphous $Fe_{83}B_9Nb_7Cu_1$ at various temperatures.

 0021-8979/96/79(8)/5459/3/$10.00 © 1996 American Institute of Physics

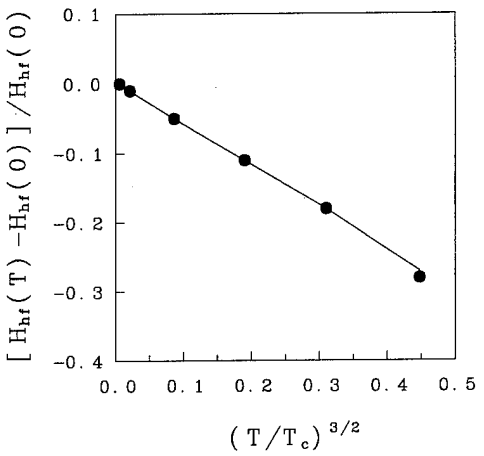


FIG. 2. Fractional change of the magnetic hyperfine field, H_{hf}, as a function of $(T/T_C)^{3/2}$.

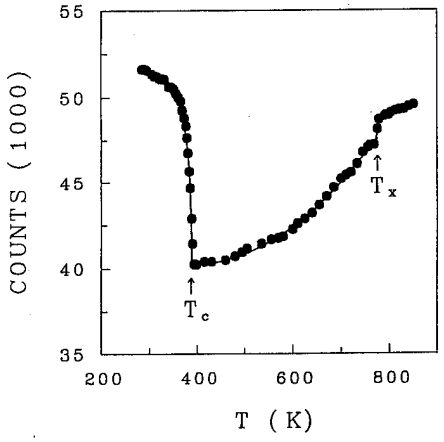


FIG. 3. Counts measured for 10 s at zero Doppler velocity as a function of temperature for $Fe_{83}B_9Nb_7Cu_1$.

lines are to be expected in view of the disordered atomic arrangements, in which the strength of the hyperfine interactions changes from site to site due to the structurally inequivalent Fe environments. In the amorphous $Fe_{83}B_9Nb_7Cu_1$ at 13 K, the Mössbauer spectrum exhibits an essentially symmetric hyperfine field distribution with a half-width of 72 kOe by the Vincze[6] model.

Figure 2 shows the fractional change of the magnetic hyperfine field, $[H_{hf}(T)-H_{hf}(0)]/H_{hf}(0)$, as a function of T. For most amorphous ferromagnets investigated so far, the magnetic hyperfine field decreases with increasing temperature as defined below,[7]

$$\frac{H_{hf}(T)-H_{hf}(0)}{H_{hf}(0)}=-B_{3/2}\left(\frac{T}{T_C}\right)^{3/2}-C_{5/2}\left(\frac{T}{T_C}\right)^{5/2}. \qquad (1)$$

A least-squares fit of Eq. (1) to the magnetic hyperfine field data gave $B_{3/2}=0.48\pm0.05$ and $C_{5/2}=0.22\pm0.05$. This value of $B_{3/2}$ for the amorphous ferromagnet $Fe_{83}B_9Nb_7Cu_1$ is much larger than those of crystalline ferromagnets[8,9] such as α-Fe and Ni; $B_{3/2}=0.12$ for Ni and $B_{3/2}=0.11$ for α-Fe. At low temperatures the values of the magnetic hyperfine field $H_{hf}(T)$ show a $T^{3/2}$ dependence that is related to the preferential excitation of long wavelength spin waves. The $T^{3/2}$ coefficient is about four times as large as those of crystalline Fe or Ni. So, more spin waves having long wavelengths are excited in amorphous ferromagnets than in crystalline ferromagnets. The quadrupole splitting just above the Curie temperature T_C is 0.43 mm/s, whereas the average quadrupole shift below T_C is zero.

In order to determine the Curie temperature T_C and the crystallization temperature T_x, the velocity transducer of the Mössbauer spectrometer was set at zero velocity and counts were recorded for a fixed counting time, 10 s, while the temperature was raised at a rate of 5 K/min from 293 to 850 K. The results are shown in Fig. 3. From the graph the Curie temperature is determined to be 393 K. As the temperature was further increased, the count rate increased slowly due to the second-order Doppler effect, and then increased suddenly at 775 K. After the amorphous $Fe_{83}B_9Nb_7Cu_1$ has reached the crystallization temperature $T_x=775$ K, the amorphous state gradually transformed into the microstructure of the nanocrystalline phases.

Figure 4 shows Mössbauer spectra of the amorphous $Fe_{83}B_9Nb_7Cu_1$ taken above the crystallization temperature. In contrast to Fig. 1 for the amorphous phase, the Mössbauer spectra consists of six absorption lines (α-Fe phase) and a quadrupole doublet (amorphous phase). The occupied area ratio of the α-Fe phase at 780 K is 33%. Mössbauer spectra of an amorphous $Fe_{83}B_9Nb_7Cu_1$ furnace annealed at 830 K for 1 h are shown in Fig. 5. The analysis of the Mössbauer spectra shows that nanocrystalline $Fe_{83}B_9Nb_7Cu_1$ yields two phases. The corresponding hyperfine parameters are given in Table I. The nanocrystalline $Fe_{83}B_9Nb_7Cu_1$ showed 49%

TABLE I. Mössbauer parameters for amorphous $Fe_{83}B_9Nb_7Cu_1$ after annealing at 830 K for 1 h. H_{hf} is the magnetic hyperfine field, ΔE_Q is the quadrupole splitting, δ is the isomer shift and area ratio of α-Fe at various temperatures.

T (K)	Phase	H_{hf} (kOe)	ΔE_Q (mm/s)	δ (mm/s)	Area ratio (%)
13	α-Fe	342	0.00	0.01	48
	Amorphous	233	0.00	0.01	52
77	α-Fe	340	0.00	0.00	47
	Amorphous	225	0.00	0.01	53
293	α-Fe	329	0.00	−0.01	49
	Amorphous	150	0.01	−0.01	51

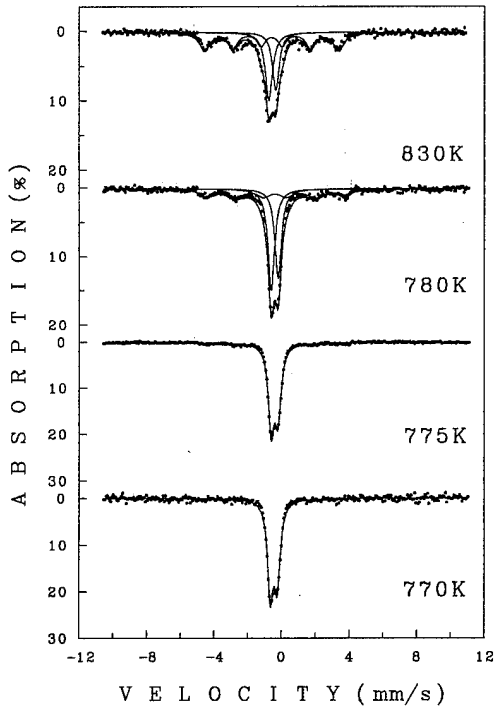


FIG. 4. Mössbauer spectra of $Fe_{83}B_9Nb_7Cu_1$ above the crystallization temperature.

α-Fe and 51% amorphous at room temperature. The occupied area of the α-Fe phase at the optimum annealing temperature at around 900 K is about 71%.

The magnetic moment of the amorphous $Fe_{83}B_9Nb_7Cu_1$ has been measured at H_{app}=8 kOe at various temperatures from the liquid–nitrogen temperature to the Curie temperature of the sample. The results are shown in Fig. 6 in reduced units along with the magnetic hyperfine fields obtained from the Mössbauer specta. From Fig. 6, it is evident that the magnetic moment is proportional to the magnetic hyperfine field in the amorphous $Fe_{83}B_9Nb_7Cu_1$. The saturation magnetization of the as-quenched amorphous material extrapolated to 0 K is found to be 2.01 μ_B/Fe atom. This value is smaller than the 2.22 μ_B of bcc Fe,[11] suggesting electron transfer from the metalloid atoms to the d band of the Fe atoms.

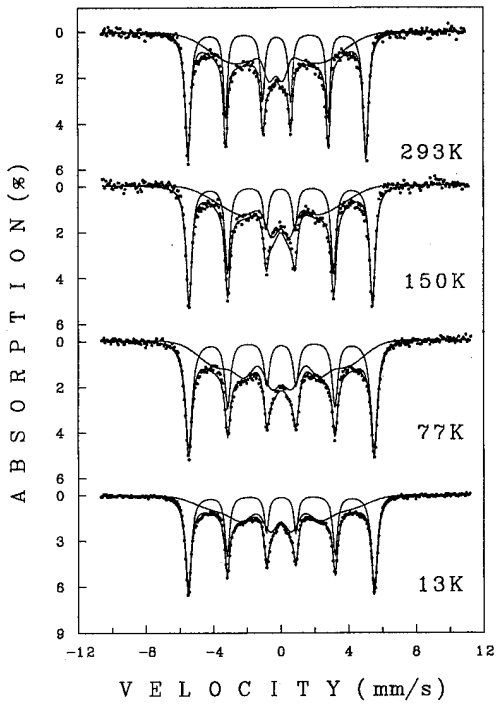


FIG. 5. Mössbauer spectra of annealed $Fe_{83}B_9Nb_7Cu_1$ at low temperatures.

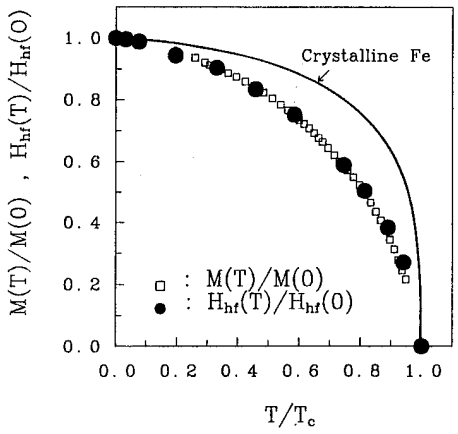


FIG. 6. Reduced magnetization and hyperfine field vs reduced temperature of the amorphous $Fe_{83}B_9Nb_7Cu_1$ and the crystalline phases after crystallization.

The reduced hyperfine field $H_{hf}(T)/H_{hf}(0)$ or equivalently the reduced magnetization $M(T)/M(0)$ of the amor phous phase decreases more rapidly with reduced temperature T/T_C rather than those of crystalline ferromagnets as shown in Fig. 6. This kind of rapid decrease can be explained in terms of either a distribution of exchange interactions in the amorphous phase or high metalloid contents.

ACKNOWLEDGMENTS

This work was supported by the Special Fund for University Research Institute, Korea Research Foundation, and KIST-2000 Research Program.

[1] M. Baricco, C. Antonione, P. Allia, P. Tiberto, and F. Vinai, Mater. Sci. Eng. A **179**, 572 (1994).
[2] J. S. Lee, K. Y. Kim, T. H. Noh, I. K. Kang, and Y. C. Yoo, IEEE Trans. Magn. **30**, 4845 (1994).
[3] K. Suzuki, M. Kikuchi, A. Makino, A. Inoue, and T. Masumoto, Mater. Trans. Jpn. Inst. Met. **32**, 961 (1991).
[4] G. Herzer and H. Warlimount, Nanostruct. Matter. **1**, 243 (1992).
[5] H. N. Ok, K. S. Baek, E. C. Kim, and C. S. Kim, Phys. Rev. B **48**, 3212 (1993).
[6] I. Vincze, Solid State Commun. **25**, 689 (1978).
[7] C. L. Chien and R. Hasegawa, Phys. Rev. B **16**, 2115 (1977).
[8] B. E. Argyle, S. H. Charap, and E. W. Pugh, Phys. Rev. **132**, 2051 (1963).
[9] H. N. Ok, K. S. Baek, and C. S. Kim, Phys. Rev. B **24**, 6600 (1981).
[10] R. S. Tebble and D. J. Craik, *Magnetic Materials* (Wiley-Interscience, New York, 1969), p. 51.

Resonant microwave cavity response of amorphous ribbons

A. N. Medina, M. Knobel, S. Salem-Sugui, and F. G. Gandra
Universidade Estadual de Campinas, Instituto de Fisica, Cidade Universitaria, Campinas, SP, 13083-970, Brazil

In this study we report microwave experiments on the amorphous ribbon $Fe_{4.6}Co_{70.4}Si_{15}B_{10}$ using the usual setup for magnetic resonance experiments at 9.4 GHz to observe the cavity response. Several samples cut from the same tape were annealed, either in the presence or in the absence of a magnetic field. For each sample the magnetization and magnetoimpedance (MI) curves were obtained, with MI ratios between 1% and 40%. The magnetic resonance spectrum consists of the usual ferromagnetic line and an anomalous low field cavity response for $H<100$ Oe. The shape of this low field signal depends on the thermal treatment and on the orientation of the external field. We believe that this signal is in part a ferromagnetic peak but it also carries information of the skin-depth changes with a sweeping magnetic field. © *1996 American Institute of Physics.* [S0021-8979(96)30908-2]

I. INTRODUCTION

Since the discovery of amorphous metals, their magnetic properties have been extensively studied due to their enormous potential in technological applications. In recent years these investigations have taken a strong impulse with the development of nanocrystalline materials,[1] and more recently, with the observation of the so-called giant magnetoimpedance (GMI) effect.[2–4] GMI consists of large (up to 360%)[5] and sensitive (up to 1700%/Oe)[6] variations in the impedance (Z) of soft magnetic wires or ribbons upon the application of an external magnetic field (H). The field and frequency response of the impedance reflects, in a complex way, the behavior of the magnetic permeability, and can be roughly modeled using the classical Maxwell equations of electrodynamics. There are, however, several points that remain unclear, such as the effect of induced anisotropies and the contribution of the different magnetization processes to the whole phenomenon. In particular, samples submitted to peculiar thermal treatments[6,7] or tensile stresses display clear maxima in the $Z(H)$ curves, generally located at the materials' effective anisotropy field H_k.

In the present work, we study the GMI effect for a nearly zero magnetostriction amorphous ribbon subjected to different thermal treatments. The induced anisotropies are analyzed by ferromagnetic resonance (FMR) measurements, which also allows one to obtain valuable information about the overall magnetization process. We observed an interesting peak in the low-field side of the derivative resonance spectra that is similar to the one recently observed in amorphous thin films by Rivoire and Suran.[8] According to these authors, this peak is directly related to the magnetization process that occurs along the hard axis, in the case of films with in-plane uniaxial anisotropy. Besides the fact that our samples are amorphous ribbons (thickness 22 μm), a major difference in the spectra is that the observed peak displays some differences in shape. These differences depend on the thermal treatment and magnetic field orientation and we believe that they can be related to the same mechanism that is responsible for the MI effect.

II. EXPERIMENTAL PROCEDURES AND RESULTS

An amorphous ribbon of nominal composition $Co_{70.4}Fe_{4.6}Si_{15}B_{10}$, 4 mm width and 22 μm thick, was produced by melt–spinning in air. This sample is characterized by a slightly negative magnetostriction constant ($\lambda_s=-1\times10^{-7}$), which is responsible for its very soft magnetic behavior. Four adjacent sections 1.5 cm long of the same amorphous ribbon were subjected to different magnetic annealing conditions. Sample a was kept in the as-quenched state while the remaining samples were annealed at 250 °C for 15 min in argon. Sample b was heated and cooled in zero field (ZFT) while for samples c and d an external field of 2 kOe was applied transversely or longitudinally to the ribbon axis. The field was maintained until the sample was cooled to room temperature.

The field dependence of the impedance in the 1.5-cm-long ribbons was measured at a fixed frequency (100 kHz) using a vector lock-in amplifier with a driving current intensity of 20 mA parallel to the ribbon axis and with dc applied fields up to 30 Oe generated by a Helmholtz coil. The contacts were made with silver paint and have typically 1 Ω resistance. Figure 1 shows the MI ratio, defined as $[Z(H)-Z(H=0)]/Z(H=0)$, obtained for H parallel to the ribbon axis for all samples. For H perpendicular to both of them, the ribbon axis and current direction—as well as for dc driving currents—the MI ratio was always less than the experimental error. The curves obtained for samples a and d show a similar MI behavior while for the ZFT sample less than 1% MI ratio was observed. This suggests that, in our case, even after annealing with a longitudinal field, there is a remaining contribution to the transverse permeability. On the other hand, ZFT promoted a strong internal stress relief, drastically reducing the magnetoelastic anisotropy and the MI ratio, in agreement with recent data.[7] A rather strong peak close to 40% is observed for sample c, which is also in good agreement with previous measurements.[2,7]

The microwave experiments were carried out at room temperature in a conventional X band magnetic resonance spectrometer using a commercial Varian TE_{102} cavity with 100 kHz modulation field and 0.2 mW power. The sample was positioned at the center of the cavity such that the ex-

 0021-8979/96/79(8)/5462/3/$10.00 © 1996 American Institute of Physics

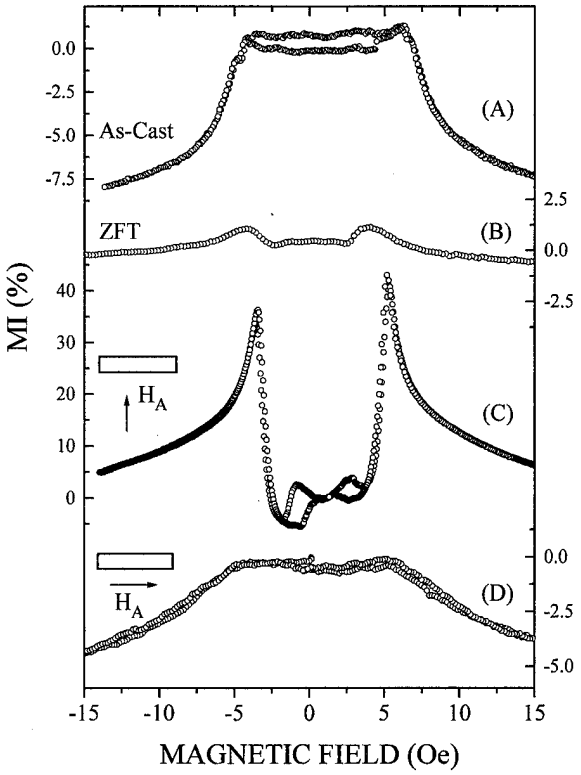


FIG. 1. Magnetoimpedance ratio for the different magnetic annealing conditions as described in the text. The magnetic field was applied parallel to the direction of the ac electrical current.

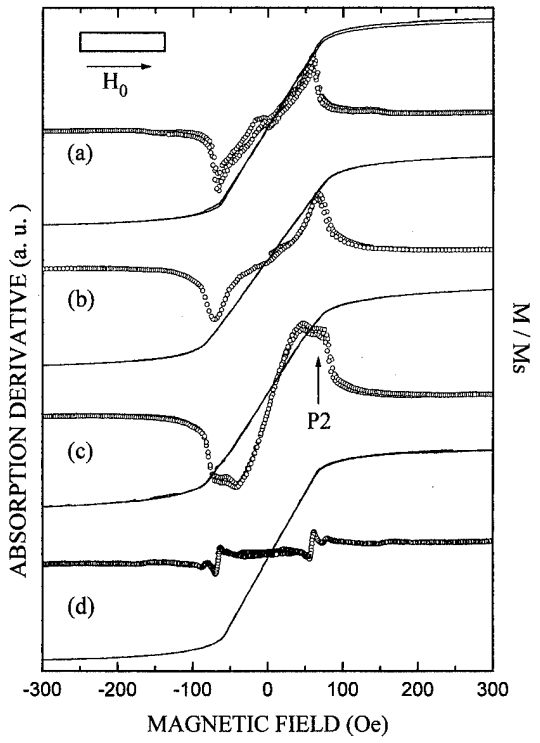


FIG. 3. Magnetic resonance spectra and normalized magnetization for the external field oriented along the ribbon axis.

ternal magnetic field was in plane with the sample and directed either along or transverse to the ribbon axis. For these measurements, 2×2 mm samples were cut from the annealed ribbons. Since the dimensions of these samples are very different from those of MI measurements, a different demagnetization factor must be considered. In this setup the magnetic field can sweep from positive to negative values continuously.

Figure 2 shows the resonance spectrum obtained for sample c where one can clearly see the normal FMR mode

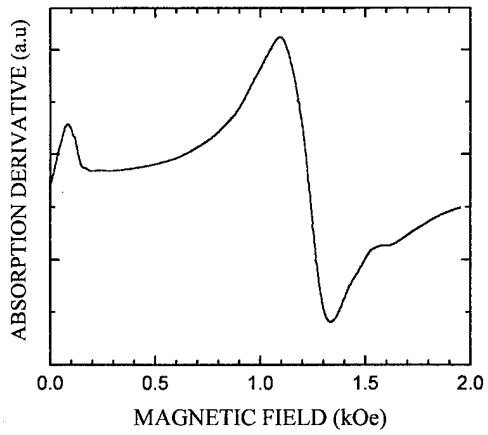


FIG. 2. Magnetic resonance spectrum for sample c obtained with external field along the ribbon axis. A peak below 100 Oe and the normal mode of the FMR at 1.25 kOe are clearly observed.

and a low field peak. Low field structures have been observed for a long time in FMR studies in metals.[9,10] Recently Rivoire and Suran[8] described experimental results in amorphous thin films, which are very similar to our results. They calculated the resonance spectra for an amorphous thin film with uniaxial in-plane anisotropy, considering the movement of magnetization for H oriented along the hard axis. For this configuration two resonance modes can be calculated, for $H<H_k$ and $H>H_k$, respectively. For such low anisotropy materials, the solution for $H<H_k$ requires that the working frequency be smaller than the natural frequency, which we estimated to be close to $\nu_0=1$ GHz in our case. If $\nu>\nu_0$, they show that the low field peak can be described by a complicated function centered at H_k. This peak is obtained for H along the hard axis and the rf microwave field along the easy axis.

Figures 3 and 4 show the low field part of the resonance spectra (absorption derivative) together with the normalized magnetization for each orientation of the external field relative to the ribbon. The spectra for the ZFT sample are essentially the same for both field orientations owing to the negligible magnetic anisotropy. However, there are significant differences in the magnetic resonance spectra for the remaining samples, which depend on the induced anisotropy. For these samples the spectra are quite different for each field orientation and a second peak (hereafter called P2) is clearly visible superposed on the expected one. Assuming that the usual FMR theory explains the main low field peak,[8] it is interesting to check if peak P2 can be associated with the same mechanism that drives the MI effect, that is, field induced changes in the sample's magnetic penetration depth. In

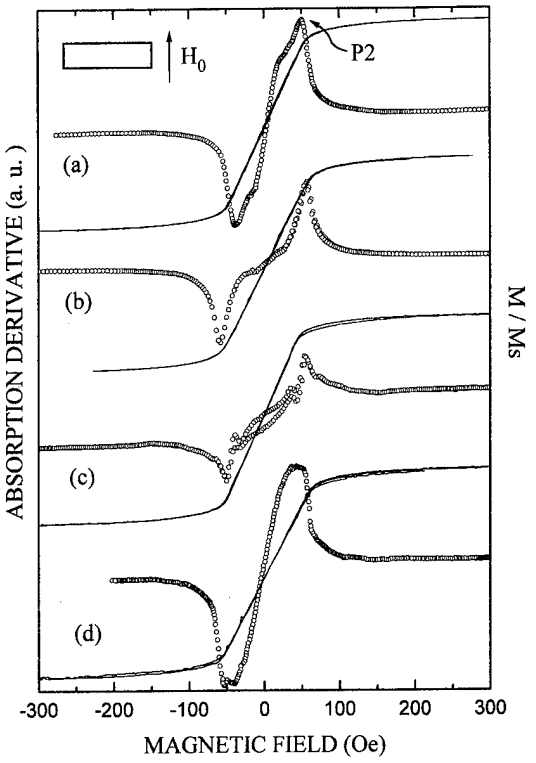


FIG. 4. Magnetic resonance spectra and normalized magnetization for the external field oriented transversely to the ribbon axis.

the same way as the microwave power was absorbed in the FMR, these impedance changes would induce a slight decoupling of the microwave cavity that would be detected by the reflected microwave power.

For sample d the FMR peak [Fig. 3(a)] is practically absent for H parallel to the easy axis (which is now along the ribbon axis), but is quite large when H is along the hard axis [Fig. 4(d)]. Since the MI is very low for H parallel to the ribbon's axis and negligible for H transverse to the ribbon, we can infer that the peak observed in Fig. 4(d) corresponds basically to the expected FMR signal, which is strongly reduced when the field is applied along the easy axis [Fig. 3(d)].

The resonance results indicate that there is a net orientation of the domains along the ribbon axis already in the as-quenched ribbon (sample a), which is probably a consequence of the quenching process. In Fig. 4(a) it is possible to see the FMR peak and peak P2 centered at 50 Oe. For H parallel to the easy axis [Fig. 3(a)] only the contribution to peak P2 is left.

The resonance spectra for samples c and a are very similar, if one considers the different anisotropy. Sample c was treated with H transverse to the ribbon and therefore, the hard and easy axis directions are inverted relative to samples a and d. Although the 40% MI ratio was observed in sample c, the resonance peak P2 observed for the longitudinal field [Fig. 3(c)] was of the same magnitude of the FMR peak.

P2 is displaced toward larger H values in comparison to the peak observed in the GMI. Notice, however, that the reduced dimension of the sample increases the demagnetization field. Also, additional stresses introduced when the sample was cut from the ribbon can induce non-negligible anisotropies.

In conclusion, we have found that the MI effect is strongly dependent on the magnetic anisotropies induced by the different thermal treatments. In order to obtain large MI ratios, it is important to have not only large permeabilities, but also tailored anisotropies. It was also shown that FMR is a suitable technique to study the anisotropies in these ribbons. Two superposed peaks were observed in the low field part of the magnetic resonance spectrum for H along the hard axis. One peak is explained by the FMR theory and the second peak is possibly associated with the same skin-depth effect that promotes the observed MI. However, FMR experiments and calculations must be extended for H parallel to the easy axis and rf along the hard axis in order to obtain detailed information from peak P2. Also, further investigations on the normal FMR mode can provide important information about the anisotropy field.

ACKNOWLEDGMENTS

This work was partially financed by FAPESP and CNPq, Brazilian agencies.

[1] Y. Yoshizawa, S. Oguma, and K. Yamauchi, J. Appl. Phys. **64**, 6044 (1988).
[2] F. L. A. Machado, C. S. Martins, and S. M. Rezende, Phys. Rev. B **51**, 3926 (1995).
[3] R. S. Beach and A. M. Berkowitz, Appl. Phys. Lett. **64**, 3652 (1994).
[4] L. V. Panina and K. Mohri, Appl. Phys. Lett. **65**, 1189 (1994); L. V. Panina, K. Mohn, T. Uchiyama, M. Nota, and K. Bushida, IEEE Trans. Magn. **31**, 1249 (1995).
[5] M. Knobel, M. L. Sánchez, J. Velazquez, and M. Vázquez, J. Phys. Condens. Matter **7**, L115 (1995).
[6] J. L. Costa-Krämer and K. V. Rao, IEEE Trans. Magn. **31**, 1261 (1995).
[7] R. Sommer and C. L. Chien, Appl. Phys. Lett. **67**, 857 (1995).
[8] M. Rivoire and G. Suran, J. Appl. Phys. **78**, 3, 1899 (1995).
[9] S. Haraldson, L. Pettersson, and S. M. Bhagat, J. Magn. Reson. **32**, 115 (1978).
[10] D. O. Smith, J. Appl. Phys. **29**, 264 (1958).

Coercivity and remanence of amorphous and nanocrystalline Fe–(Cu,Ta)–SiB ribbons

N. Murillo and J. González
Departamento de Física de Materiales, Facultad de Químicas, 20080 San Sebastian, Spain

J. M. Blanco
Departamento de Física Aplicada I, Escuela Universitaria de Ingenieria Técnica Industrial, 20010 San Sebastian, Spain

J. M. González
Departamento de Propiedades Opticas, Magnéticas y de Transporte, Instituto de Ciencia de Materiales de Madrid—CSIC, Serrano 144, 28006 Madrid, Spain

We report on the evolution, with the thermal treatment parameters, of the remanence and coercive force of amorphous melt spun ribbons having compositions of $Fe_{77.5}Si_{13.5}B_9$, $Fe_{76.5}Cu_1Si_{13.5}B_9$, and $Fe_{74.5}Ta_3Si_{13.5}B_9$. The thermal treatments were carried out by using the current annealing technique with and without the simultaneous application of a tensile stress along the axis of the samples. Our results show that upon low temperature (low current), short time treatments both the remanence and the coercive force are basically determined by the characteristics of the effective anisotropy induced during the treatment. In contrast, high temperature (high current) treatments result in values of both quantities that are linked to the (partial or total) accomplishment of the first stage of the crystallization process of the samples. © *1996 American Institute of Physics.*
[S0021-8979(96)31008-7]

I. INTRODUCTION

The elevated atomic mobility characteristic of the amorphous state allows, through appropriate thermal treatments, control of both the effective magnetic anisotropy and the hysteresis in melt spun transition metal–metalloid amorphous alloys.[1] That elevated mobility is a direct consequence of the metastable nature of the amorphous phases which upon suitable anneals decay in one or more stages toward stable distributions of crystalline phases. As was shown by Yoshizawa *et al.*[2] the crystallization process can also result in very interesting soft magnetic properties. The crystallization-induced softening of some Fe-based amorphous materials[3] is linked to the appearance, of a nanostructure characterized by grain sizes of the order of 10 nm which are strongly coupled to an amorphous matrix in which they are embedded. That coupling allows the average down to small values of the interactions of the magnetic moments with their randomly oriented local easy axes[3] and the consequential observation of high permeabilities and small coercive forces (a reduced effective magnetostriction resulting from the two-phase nature of the samples is also observed in the prototypical FeCuNbSiB system). Since it must be adequately scaled to the effective exchange correlation length the critical microstructural parameter to be controlled during the crystallization process is the grain size. There are two basic strategies to achieve that control: to take advantage of the kinetics of the crystallization process[4] and to use adequate additives to limit the grain growth and or enhance the occurrence of nucleation.[5]

The authors have recently presented results[6] about the induction of magnetic anisotropy in different FeSiB-based amorphous systems characterized by the partial substitution of Fe by Cu and Ta. In the present work we will report on the evolution, after different thermal treatments, of the hysteretic parameters of the samples of those systems.

II. PREPARATION OF SAMPLES AND EXPERIMENTAL TECHNIQUES USED

Ribbon-shapped samples of nominal compositions $Fe_{77.5}Si_{13.5}B_9$ (FeSiB), $Fe_{76.5}Cu_1Si_{13.5}B_9$ (FeCuSiB), and $Fe_{74.5}Ta_3Si_{13.5}B_9$ (FeTaSiB) and having a width of 4 mm and an average thickness of 20 μm were prepared by means of a single roller melt spinning device. The annealing treatments were performed by using the so-called current annealing technique. Such current anneals were carried out with and without the simultaneous application of a longitudinal tensile stress in the range from 150 to 200 MPa (applied stress and stress free anneals, respectively).

The phase distribution of both the as-quenched and thermally treated samples was examined by means of x-ray diffraction. The hysteretic measurements (obtained in 10-cm-long samples) were performed by means of a computer controlled dc (2–10 Hz) induction setup described in Ref. 7. Both the remanence and coercive force of the samples were evaluated from the loops measured under a maximum applied magnetic field of 2000 A/m.

III. RESULTS AND DISCUSSION

According to the x-ray diffractograms taken in the as-quenched ribbons these samples were amorphous down to the resolution of the technique. In Fig. 1(a) we present the results obtained in the FeSiB samples for the evolution with the annealing time, t_{ann}, of the remanence, M_r. We must note that after all the treatments the maximum applied field was clearly sufficient to achieve technical saturation of the samples and that there were no indications concerning the shape of the measured hysteresis loops after the occurrence

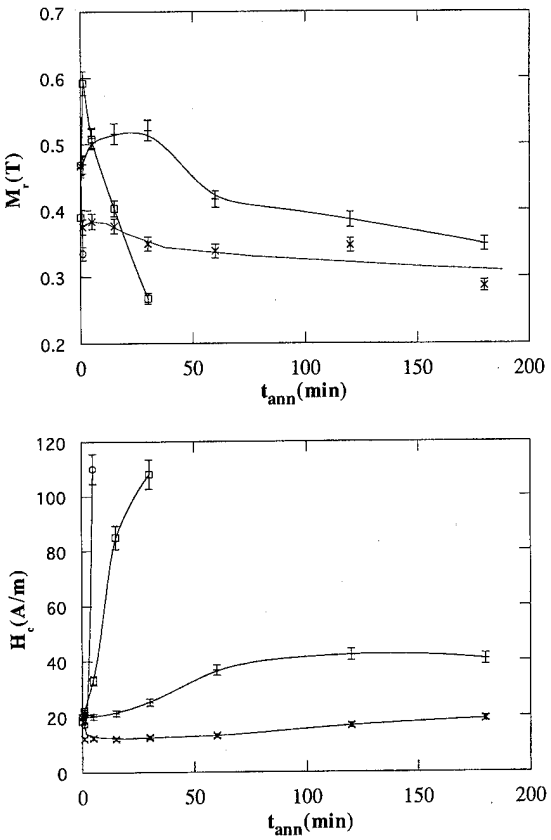


FIG. 1. (a) Annealing time dependence of the remanence measured in samples of the FeSiB system: (+) 2.1 A; (×) 2.1 A and 200 MPa; (□) 2.35 A and (○) 2.35 A and 200 MPa. (b) Annealing time dependence of the coercive force measured in samples of the FeSiB system: (+) 2.1 A; (×) 2.1 A and 200 MPa; (□) 2.35 A; and (○) 2.35 A and 200 MPa.

of phase separation. In the particular case of the samples treated with a current of 2.1 A, the stress free anneals were associated with an initial increase of M_r with t_{ann}. That increase led to a maximum being achieved after 25 min. For longer treatment times a steady decrease of M_r was observed. In the case of the applied stress annealed sample treated by using the same current, the measured evolution of M_r with t_{ann} was characterized by a rapid decrease of the remanence with an increase of the treatment time, down to a more or less annealing time-independent value. A clearly different behavior was observed in the sample treated using higher currents: For annealing times longer than a few minutes the remanence measured in both the applied stress and stress free annealed samples decreased markedly. Results corresponding to the variation with t_{ann} of the coercive force, H_c, measured in the FeSiB samples are shown in Fig. 1(b). Clear corresponding with the remanence results, a remarkable difference was observed between the samples treated at low and high current intensities: Whereas in the case of the samples treated at 1.8 A the coercive force was weakly dependent on the treatment time, it increased rapidly with t_{ann} in the samples treated at 2.1 A. It is interesting to remark that short time stress free anneals allowed us to obtain a coercive force of the order of 12 A/m, that is, 55% of the measured (22 A/m) as-quenched value.

According to the results reported in Ref. 6, low intensity treatments carried out in samples of the FeSiB system (both with and without applied stress) resulted in a tendency to shift the effective easy axis of the samples toward the direction transverse to the ribbon axis. This result can clearly account for the origin of the observed behavior of both the M_r vs t_{ann} and H_c vs t_{ann} low current curves. Regarding the occurrence of a maximum in the stress free anneals of 2.1 A curves, we suggest that it could be linked to inhomogeneities in the anisotropy distribution resulting either from the partial elimination of the as-quenched anisotropies (of magnetoelastic origin and therefore linked to the stresses built-in during the quenching process) or from the occurrence of temperature gradients across the ribbon thickness associated with the use of the current annealing technique. The rapidly growing transverse anisotropy measured[6] in the case of the high current treatments underlies the annealing behavior of the hysteretic parameters of these samples and, according to the corresponding x-ray diffractograms, is linked to the onset of the first stage (FeSi precipitation) of the crystallization process.

Figure 2(a) shows data corresponding to the treatment time evolution of the remanence measured in the FeCuSiB annealed samples. From Fig. 2(a) it is possible to conclude that M_r is only slightly changed by the stress free characteristic of the applied stress anneals if they are carried out by using low current intensity. In contrast, if the treatments are carried out by applying higher currents during long annealing times they result in a remarkable increase of the reduced remanence values.

A similar dependence on t_{ann} was observed for the H_c values measured in the FeCuSiB annealed samples: They were not remarkably changed by the low current treatments and increased steadily with treatment time in the case of higher current treatments.

Again the results obtained in this system for the annealing evolution of the induced anisotropy[6] seem to explain the evolution of the remanence and coercivity: The induced easy axis was, for the low current treatments, parallel to the ribbon axis and its intensity was independent of the treatment time for t_{ann} longer than a few minutes. As in the FeSiB system the samples treated using the high current intensity value were partly crystallized (an average grain size of 100 nm was estimated from x-ray diffraction results).

Data corresponding to the annealing time dependence of both the remanence and coercive force measured in FeTaSiB are presented in Figs. 3(a) and 3(b), respectively. Different from the previous systems, for short treatment times the remanence increased in a similar way after low and high current stress free anneals. After this initial increase maxima taking place at t_{ann}=20 min (stress free annealed samples) and at 60 min (applied stress annealed samples) were observed (a further increase of the remanence with that of the treatment time was measured in the case of the low annealing current samples). The evolution of the remanence corresponding to the applied stress treatments was qualitatively similar to that observed in the stress free ones with the only remarkable difference of the observation being the less pronounced maxima. Regarding the coercive force results, the

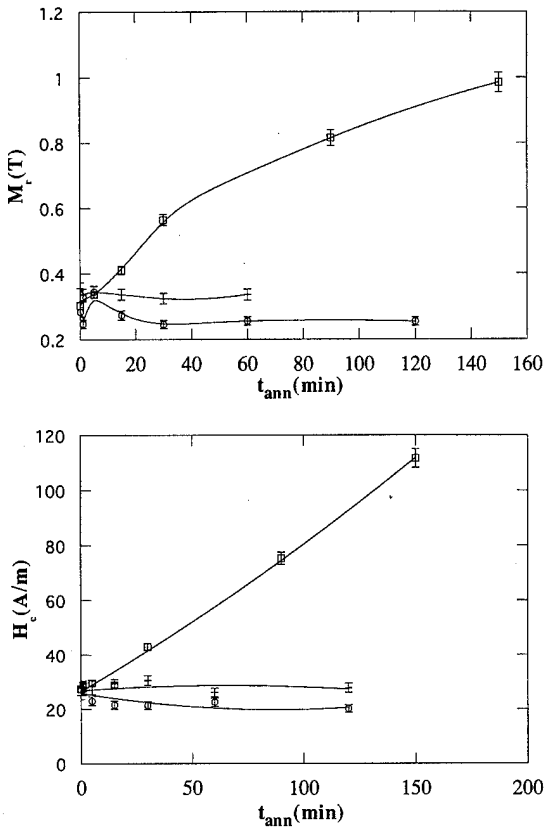


FIG. 2. (a) Annealing time dependence of the remanence measured in samples of the FeCuSiB system: (+) 1.8 A; (○) 1.8 A and 150 MPa; and (□) 2.2 A. (b) Annealing time dependence of the coercive force measured in samples of the FeCuSiB system: (+) 1.8 A; (○) 1.8 A and 150 MPa; and (□) 2.2 A.

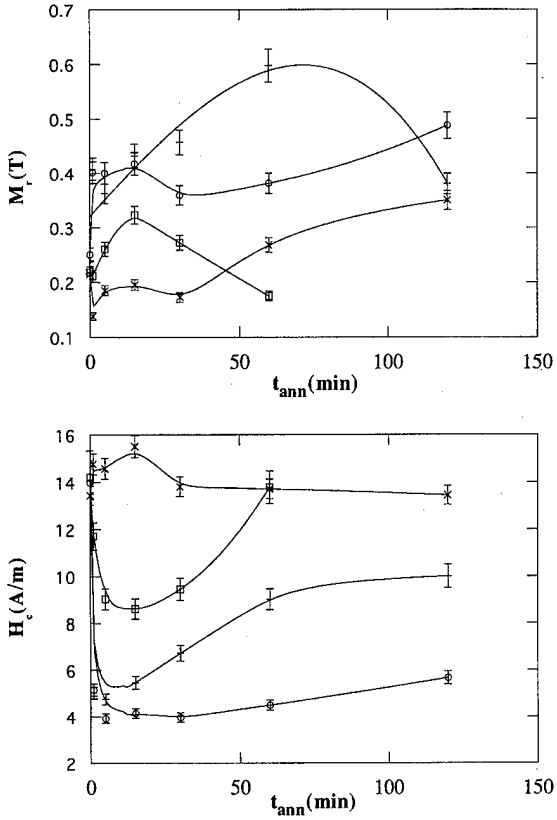


FIG. 3. (a) Annealing time dependence of the remanence measured in samples of the FeTaSiB system: (○) 1.8 A; (×) 1.8 A and 200 MPa; (+) 2.0 A, and (□) 2.2 A and 200 MPa. (b) Annealing time dependence of the coercive force measured in samples of the FeTaSiB system: (○) 1.8 A; (×) 1.8 A and 200 MPa; (+) 2.0 A, and (□) 2.2 A and 200 MPa.

stress free and applied stress anneals led to a very different evolution: whereas the treatments carried out under applied stress produced a slight increase of the coercivity, in the case of the stress free treatments a noticeable softening of the material (down to H_c values of the order of 4 A/m comparable to the best values obtained in the FeCuNbSiB system) was detected after anneals carried out during times in the range from 5 to 30 min. As for the high current anneals, it was possible to show how, after originating a decrease of H_c for short treatment times, they resulted, both for the stress free and the applied stress cases, in a clear tendency to increase of coercivity. We must remark that, in the particular case of the applied stress samples treated for times longer than 60 min and using 2.0 A, the hysteresis loop clearly evidenced the occurrence in the samples of two weakly coupled magnetic phases (and therefore the partial accomplishment of crystallization).

From the correlation of these results with those corresponding to the induced anisotropy[6] and phase distribution of the FeTaSiB annealed samples, it is possible to conclude that the maxima observed in the M_r vs t_{ann} curves corresponding to the samples treated using a current of 2.0 A were related to the onset of crystallization (this onset was also related to the increase of the remanence observed in the low current long treatment time anneals). Again from the induced anisotropy results, the increase of the remanence observed in the stress free, low current short time anneals should be ascribed to the induction of a large longitudinal anisotropy. Finally, let us point out that the very different evolution with t_{ann} of the coercive force of the low current stress free and applied stress annealed samples was not correlated to that of the anisotropy resulting from the treatments since both types led to the induction of a longitudinal anisotropy of a similar value. We then conjecture about the presence in the applied stress annealed sample of a larger amount of anisotropy inhomogeneities, which could be linked either to the partial elimination of the as-quenched anisotropies or to the induction during the current anneal of an inhomogeneous anisotropy.

[1] O. V. Nielsen, A. Hernando V. Madurga, and J. M. Gonzalez, J. Magn. Magn. Mater. **46**, 341 (1985).
[2] Y. Yoshizawa, S. Oguma, and K. Yamauchi, J. Appl. Phys. **64**, 6044 (1988).
[3] G. Herzer, IEE Trans. Magn. **MAG-26**, 1397 (1990).
[4] V. E. Martin, J. Bernardi, J. Fidler, F. Cebollada, and J. M. Gonzalez, J. Alloys Comp. **191**, 127 (1993).
[5] Y. Yoshizawa and K. Yamauchi, J. Jpn. Inst. Met. **63**, 241 (1989).
[6] J. Gonzalez, N. Murillo, J. M. Blanco, T. Kulik, J. M. Gonzalez, and J. Echevarria, IEEE Trans. Magn. (in press).
[7] T. Kulik, H. T. Savage, and A. Hernando, J. Appl. Phys. **73**, 6855 (1993).

NMR study of the local inhomogeneities in the soft magnetic alloy $Co_{74.26}Fe_{4.74}Si_{2.1}B_{18.9}$ (abstract)

L. Iannarella
Centro Brasileiro de Pesquisas Físicas, 22290-180 Rio de Janeiro, Brazil
and Facultad de Ciencias, Universidad Nacional de Ingenieria, P.O. Box 31-139, Lima, Peru

C. Kim and R. C. O'Handley
Facultad de Ciencias, Universidad Nacional de Ingenieria, P.O. Box 31-139, Lima, Peru

A. P. Guimarães
Centro Brasileiro de de Pesquisas Físicas, 22290-180 Rio de Janeiro, Brazil

Results of a pulsed NMR study of the soft ferromagnetic amorphous alloy $Co_{74.26}Fe_{4.74}Si_{2.1}B_{18.9}$ in the as-cast and the heat treated (at 410 °C for 12 minutes) states re reported. The measurements were performed at 4.2 K. Very intense resonances lines are observed in the frequency region 10–110 MHz (range of the present study), for both as-cast and heat treated samples. The NMR signal intensity depends on the rf power level; this suggests the existence of several magnetic regions with different local anisotropies. We identify NMR lines in two frequency ranges: (a) 10–50 MHz, which probably come from ^{57}Fe, ^{11}B, and ^{29}Si nuclei in Fe–Si-like regions and ^{57}Fe in Co(Fe) solid solutions; and (b) for frequencies above 50 MHz, lines from ^{59}Co (and probably ^{11}B) in Co-rich crystalline-like environments with short-range order as in Co_2B, in the range 70–110 MHz. In the higher frequency region, the NMR spectra suggest that the environments are similar to Co_3B and to Co(B) solid solutions. For the heat treated sample, lines above 95 MHz disappear for lower rf power levels; also, this sample shows lines around 75 MHz narrower than those for the amorphous alloy. These results give evidence of the concentration inhomogeneity of the samples, both in the as-cast and heat-treated forms. © *1996 American Institute of Physics.* [S0021-8979(96)64908-0]

 0021-8979/96/79(8)/5468/1/$10.00 © 1996 American Institute of Physics

Evolution from soft to hard magnetic behavior in Co-based devitrified glassy alloy

G. Bottoni, D. Candolfo, and A. Cecchetti
INFM—Dipartimento di Fisica, Università di Ferrara, 44100 Ferrara, Italy

From the amorphous alloy 6030V having the composition $Co_{71.5}Fe_{1.5}Mo_1Mn_4Si_{13}B_9$, a series of devitrified specimens with increasingly coarser microstructure and magnetic hardening is produced by annealing. From the features of the coercivity, the squareness ratio, the rotational hysteresis integral, and the magnetic interactions we infer that the magnetic hardening is due initially (T_a<600 °C) to a strengthening of the pinning effect of the precipitates on the domain walls, and then (T_a>600 °C) to the formation of single-domain Co crystallites where the magnetization reversal mode is of incoherent type. © *1996 American Institute of Physics.* [S0021-8979(96)31108-3]

I. INTRODUCTION

The devitrification process in glassy alloys may produce a magnetic softening or a magnetic hardening of the material, depending on the microstructure formed during the annealing treatment. In the commercial amorphous alloy 6030 Vitrovac (Vacuumschmelze-D) of nominal composition $Co_{71.5}Fe_{1.5}Mo_1Mn_4Si_{13}B_9$, the thermal treatment, performed in the temperature range of 500–750 °C, gives rise to a magnetic hardening which depends on the annealing temperature T_a.

The purpose of this work is to analyze the magnetization process occurring at various stages of the magnetic hardening as deducible from the feature of some magnetic properties, i.e., the coercivity H_c, the squareness ratio M_r/M_s, the rotational hysteresis integral R, and the magnetic interactions among the crystallites.

II. EXPERIMENTAL RESULTS AND DISCUSSION

A. Influence of the annealing treatments on the magnetic properties

In the amorphous state (or the as-received state: ar.) the 6030V alloy is furnished in the form of a ribbon, 23 μm thick, having the following physical properties: saturation magnetization M_s=652 emu/cm^3, coercivity H_c=0.01 Oe, Curie temperature T_C=365 °C, crystallization temperature T_{cr}=480 °C. Disk specimens, 3 mm in diameter [suitable for magnetic measurements by a vibrating sample magnetometer (VSM)], cut from the ribbon, are annealed in vacuum at various temperatures (500–750 °C) and times so as to obtain a set of samples with increasing granularity (Fig. 1) and coercivity (Fig. 2). This treatment gives rise to an increase of coercivity up to 400 Oe (Fig. 2), while M_s decreases with T_a and tends to a limit value of 600 emu/cm^3.

The crystalline phase is principally constituted of fcc crystallites having a Curie temperature of 750 °C which is lower than that of the pure Co due to the formation of compounds or impurities in the Co lattice.[1]

The behavior of the squareness ratio against the annealing temperature T_a (Fig. 2) is a useful parameter for understanding the magnetization processes in the various stages of magnetic hardening. In the ar. state $M_r/M_s \cong 1$ in a core wound ribbon, but it decreases to 0.025 in the disk samples due to the demagnetizing effect. Owing to the magnetic hardening, M_r/M_s increases in the disk samples against the demagnetizing field and reaches a peak value of 0.7 (Fig. 2), then it tends to a limit value of 0.5 which corresponds to the value of the squareness ratio of an assembly of randomly oriented particles.

Noting that in the amorphous state the dominant magnetization process is the domain wall (dw) motion, the initial increase of M_r/M_s and H_c, when the crystallite formation starts, is ascribed to a strengthening of the pinning effect that the small crystallites, dispersed in the amorphous matrix, exert on the dw.[2] No evidence for attributing the magnetic hardening to exchange coupling between precipitates and the soft magnetic phase[3] was found in the present system. There-

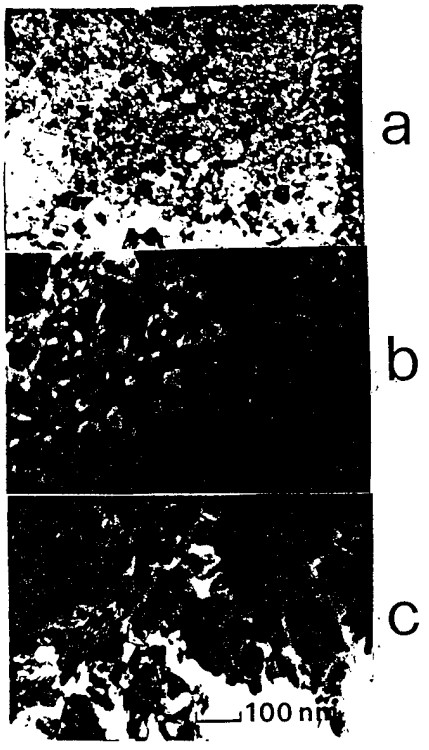


FIG. 1. Transmission electron microscopy micrographs of the devitrified samples after annealing for 1 h at T_a=550 °C (a), 650 °C (b), and 750 °C (c).

 0021-8979/96/79(8)/5469/3/$10.00 © 1996 American Institute of Physics

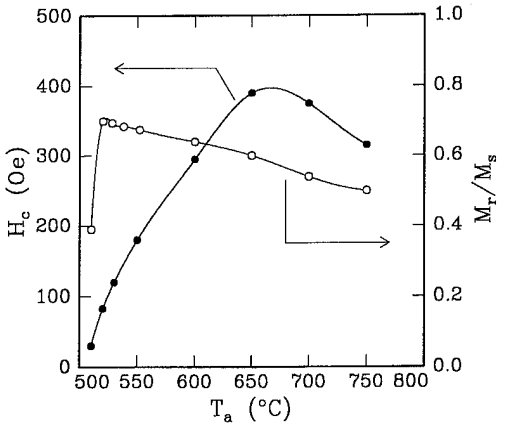


FIG. 2. The coercivity and the squareness ratio vs annealing temperature.

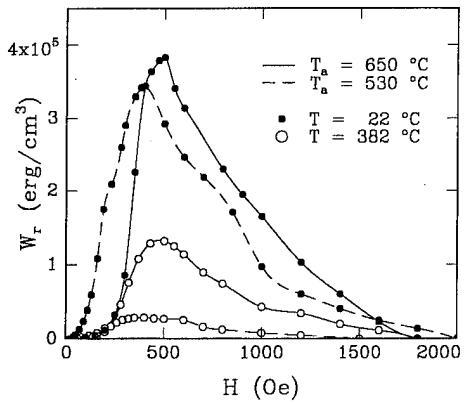


FIG. 3. Rotational hysteresis loss vs amplitude H of the rotating field, measured at two different temperatures, for the sample annealed for 1 h at 530 °C and the sample annealed for 1 h at 650 °C.

fore, we assume that the increase of the pinning strength on the dw, due to the formation of precipitates, is the main cause of the initial magnetic hardening of the material. This assumption is supported by the evolution of the rotational hysteresis integral R which indicates that at this stage the dominant magnetization process is still the dw motion (Table I). We remember that R is a number defined by $R=\int W_r/M_s d(1/H)$, where W_r is the rotational loss, and the values of R depend on the magnetization reversal mechanism.[4] For the ar. sample $R\cong 0$ because the rotational hysteresis losses are very small; but, as the magnetic hardening increases, R goes up to about 3.5, which approaches the typical value for the magnetization reversal model by dw motion.[5] High values of R are also typical of the curling model in elongated single-domain particles[4] or of the fanning model for particles behaving as chains of spheres touching each other by a surface area.[6,7] However, these latter models do not fit the current case since they involve the presence of elongated particles, while at this stage the sample is still composed of an amorphous phase containing crystallites of irregular shape (Fig. 1).

As the devitrification proceeds for higher annealing temperatures, the coercivity increases, while the rotational hysteresis integral decreases and tends to values between 1.5 and 1, and the squareness ratio converges to 0.5 (Fig. 2). These values coincide with those of the incoherent reversal model for an assembly of randomly oriented single-domain particles.[4]

The successive decrease of H_c for $T_a>700$ °C (Fig. 2), when the sample is fully crystallized and the material is rather brittle, is ascribed to the formation of dw in the biggest crystallites.

B. Magnetic measurements at various temperatures

It is interesting to note the magnetic behavior of the partially devitrified samples at temperatures higher than the Curie temperature of the amorphous phase, i.e., $T>365$ °C. In this paper we report the data obtained on two samples: the former sample is one where the dominant magnetization process at room temperature is still the dw motion (the sample annealed for 1 h at 530 °C), the latter is a sample where the dominant magnetization process is the incoherent reversal mode, similar to the systems of single-domain particles (the sample for annealed 1 h at 650 °C).

Table I shows some magnetic parameters detected on these samples at room temperature (22 °C) and at $T=382$ °C. The squareness ratio of the sample annealed at 530 °C, which is 0.7 at $T=22$ °C, drops to 0.28 at $T=382$ °C while the coercivity increases. This is due to the disappearance of the soft ferromagnetic amorphous phase whose amount is about 60% as deducible by comparing M_r/M_s at room temperature and at $T=382$ °C. For the sample annealed at 650 °C, where the fraction of the soft phase is about 25%, the variation of M_r/M_s is smaller than in the previous case and H_c does not increase at $T=382$ °C (Table I).

Figure 3 shows the rotational hysteresis loss W_r vs amplitude H of the rotating field for the two samples of Table I measured at two different temperatures. The losses are larger at $T=22$ °C owing to the greater values of anisotropy at room temperature. At this temperature, the rotational hysteresis integral R is 2.95 for the sample containing the highest fraction of amorphous phase where the reversal magnetization is principally governed by the dw motion, while R becomes equal to 1.36 for the sample containing the lowest

TABLE I. Magnetic parameters monitored at two different temperatures on two samples annealed for 1 h at different T_a.

Sample annealed at $T_a=530$ °C				Sample annealed at $T_a=650$ °C		
T (°C)	M_r/M_s	H_c (Oe)	R	M_r/M_s	H_c (Oe)	R
22	0.68	129	2.95	0.60	390	1.36
382	0.28	145	1.56	0.45	265	1.21

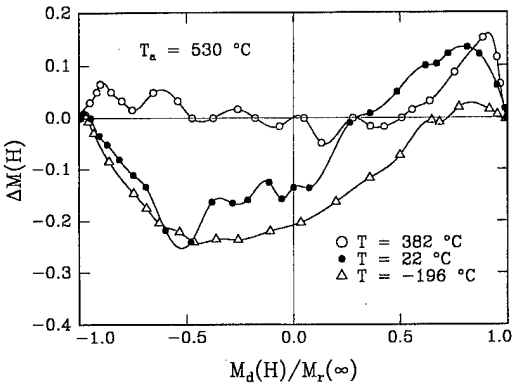


FIG. 4. Deviation ΔM from the noninteracting particle equation for the sample annealed for 1 h at 530 °C. The measurements are made at three different temperatures.

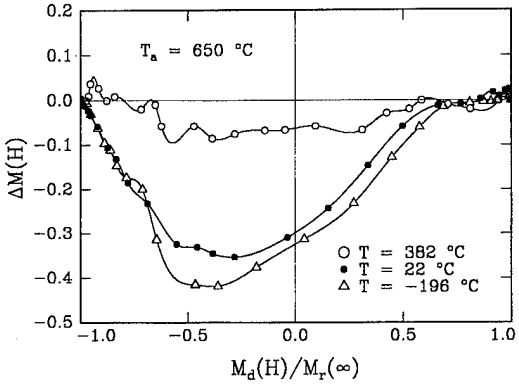


FIG. 5. Deviation ΔM from the noninteracting particle equation for the sample annealed for 1 h at 650 °C. The measurements are made at three different temperatures.

fraction of the amorphous phase which behaves similarly to a system of single-domain particles following a fanning reversal model. For $T=382$ °C a more drastic reduction of W_r occurs in the former sample because of the disappearance of the amorphous phase, and R drops to 1.56 because only the crystallites present in the specimen remain magnetically effective. This value of R is close to that of the sample annealed at 650 °C containing the highest fraction of crystallites and where the dominant magnetization mechanism is the incoherent reversal mode.

C. Magnetic interactions

In the fine particle systems the magnetic interactions are of interest because of applications in the field of magnetic recording. These interactions are often studied by the method of the two remanence curves.[8] According to this method the particle interactions are evaluated by the deviation ΔM from the Wohlfarth equation valid for a system of noninteracting particles: $\Delta M = M_d(H) - [1 - 2M_r(H)]$ where $M_d(H)$ and $M_r(H)$ are the demagnetizing and remagnetizing remanence curves in reduced units.[8]

Figures 4 and 5 show these curves measured (using a VSM) at three different temperatures ($T=-196$ °C, $T=22$ °C, and $T=382$ °C) for the two samples annealed at 530 and 650 °C. The strongest interactions are present in the sample annealed at 650 °C which contains the highest fraction of crystalline phase. No large difference occurs between the curves at $T=-196$ °C and $T=22$ °C for this sample. This indicates that the fraction of superparamagnetic crystallites at room temperature is low, the particle interactions possibly preventing the superparamagnetic relaxation. We note that an evaluation of the overall effect of the interactions may also be deduced from the area between the curve ΔM and the axis $\Delta M=0$ of the plot of Fig. 5, i.e., the so-called Δ plot area.[9] A large reduction of the interactions is observed at $T=382$ °C, which is ascribed to various effects: a decrease of the magnetic moment of the crystallites, an increase of the fraction of superparamagnetic particles, and the disappearance of the amorphous phase which may favor the flux conduction. In the sample annealed at 530 °C, which contains the lowest fraction of crystals dispersed in the amorphous matrix, the interactions are weaker than in the previous case and the difference between the curve at $T=22$ °C and $T=-196$ °C is more pronounced indicating the presence of a higher fraction of superparamagnetic crystallites at room temperature. Particularly, the positive ΔM deviation which appears in correspondence with $M_d(H)/M_r(\infty)=0.7$ at room temperature, is ascribed to a resistance to remagnetization.[8] At $T=382$ °C the interactions practically disappear (ΔM fluctuates around zero: Fig. 4) since in this sample the crystallites are well diluted in a nonferromagnetic matrix.

As a conclusion, we have shown that the thermal treatments of the present amorphous alloy give rise to a system of magnetic particles (or crystallites) which, unlike the particulate media, are embedded in a magnetic matrix. Consequently, the magnetic behavior of this system (i.e., occurrence of domain wall motion, magnetization reversal model, interactions between crystallites, etc.) may be controlled by regulating, through suitable thermal treatments, both the fraction of the magnetic matrix and the crystallite size.

[1] E. Vogt, in *Magnetism and Metallurgy*, edited by A. I. Berkowitz and E. Kneller (Academic, New York, 1969), Vol. 1, Chap. VI, p. 295.
[2] R. C. O'Handley, J. Megusar, S.-W. Sun, Y. Hara, and N. G. Grant, J. Appl. Phys. **57**, 3563 (1985).
[3] I. Navarro, E. Pulido, P. Crespo, and A. Hernando, J. Appl. Phys. **73**, 6525 (1993).
[4] F. E. Luborsky, J. Appl. Phys. **32**, 171S (1961).
[5] M. Prutton, *Thin Ferromagnetic Films* (Butterworths, London, 1964), p. 116.
[6] Y. Ishii and M. Sato, J. Appl. Phys. **59**, 880 (1986).
[7] Y. Ishii and M. Sato, J. Appl. Phys. **61**, 311 (1987).
[8] P. I. Mayo, A. Bradbury, R. W. Chantrell, P. E. Kelly, H. E. Jones, and P. R. Bissel, IEEE Trans. Magn. **26**, 228 (1990).
[9] G. Bottoni, D. Candolfo, A. Cecchetti, and F. Masoli, J. Magn. Magn. Mater. **116**, 285 (1992).

Nanocrystalline Fe-M-B-Cu (M=Zr, Nb) alloys with improved soft magnetic properties (abstract)

A. Makino and T. Bitoh
Central Research Laboratory, Alps Electric Co. Ltd, Nagaoka 940, Japan

A. Inoue and T. Masumoto
Institute for Materials Research, Tohoku University, Sendai 980, Japan

We have recently succeeded in producing good soft magnetic properties and high saturation magnetic density (B_s) for nanocrystalline Fe-M-B (M=Zr, Hf, or Nb) ternary alloys prepared by melt spun[1] and sputtered technic.[2] The alloys have the mixed structure consisting of α-Fe particles with 10–20 nm in size embedded in a remaining amorphous phase. The nanocrystalline bcc $Fe_{90}Zr_7B_3$, $Fe_{89}Hf_7B_4$ and $Fe_{84}Nb_7B_9$ alloy ribbons subjected to the optimum annealing exhibit high B_s of 1.5–1.7 T as well as high effective permeability (μ_e) of 22 000–32 000 at 1 kHz.[3] The soft magnetic properties of the nanocrystalline Fe-M-B alloys were found to be improved by adding small amounts of Cu and by optimizing the chemical composition. The addition of Cu to the alloys decreases the bcc grain size. The excellent soft magnetic properties (high μ_e of 100 000 at 1 kHz combined with high B_s of 1.53 T) can be achieved in the region where small grain size as well as nearly zero magnetostriction are obtained, which is attained in the compositional range around $Fe_{84}Nb_{3.5}Zr_{3.5}B_8Cu_1$. The soft magnetic properties can be further improved by preannealing before crystallization treatment, probably resulting from the decrease in the distribution of the grain size at the crystallized state. Consequently, the μ_e reaches the maximum value of 120 000 for the nanocrystalline $Fe_{84}Nb_{3.5}Zr_{3.5}B_8Cu_1$ alloy. © *1996 American Institute of Physics.*
[S0021-8979(96)82308-3]

[1] K. Suzuki, N. Kataoka, A. Inoue, A. Makino, and T. Masumoto, Mater. Trans. JIM **31**, 743 (1990).
[2] A. Makino, Y. Yamamoto, Y. Hirotsu, A. Inoue, and T. Masumoto, Mater. Sci. Eng. **A179/A180**, 495 (1994).
[3] A. Makino, K. Suzuki, A. Inoue, and T. Masumoto, Mater. Sci. Eng. **A179/A180**, 127 (1994).

Comparison of experimental and theoretical initial permeability taking into account anistropy dispersion in CoNbZr thin films (abstract)

M. C. Contreras, M. Rivas, J. F. Calleja, and I. Iglesias
Departamento de Fisica, Universidad de Oviedo, Spain

M. Guyot, V. Cagan, and R. Krishnan
Laboratoire de Magnétisme et d'Optique de Versailles, C.N.R.S., France

For thin films with very well defined uniaxial anisotropy, initial permeability spectra in the hard direction may be well described by Landau–Lifshitz theory that, in the low frequency range, is reduced to $\mu_i = 4\pi M_s/H_k$. But the switching process of the magnetization becomes more complex when it is dominated by local variations of the anisotropy, what is known as magnetization ripple. Then, initial permeability at low frequency may be expressed as $\mu_i = 4\pi M_s/H_{\text{eff}}$. Here, effective field H_{eff} is, from ripple theory: $H_{\text{eff}} = H_k(1+b+c)$, the terms b and c being additional anisotropy fields due to short and long range magnetization fluctuations. Measurements of H_k, b, and c can be obtained from the transverse bias permeability that has been measured along easy and hard axis by transverse Kerr effect. We obtain values of $b+c$ between 0.04 and 0.30, what imply a reduction of permeability between 4% and 30% due to the dispersion of the anisotropy. Saturation magnetization was measured using a VSM and also with a computer aided hysteresismeter. Then, initial permeability was measured along hard axis using an inductive system previously described. © *1996 American Institute of Physics.* [S0021-8979(96)65008-6]

 0021-8979/96/79(8)/5472/2/$10.00 © 1996 American Institute of Physics

Crystallization behavior of a mechanically alloyed amorphous $Fe_{80}Zr_8B_{11}Cu_1$ alloy

Jianqiang Zhang and Bingyao Wu
Department of Mechanical Engineering, Southeast University, Nanjing 210096, People's Republic of China

Xiaohua Wu, Guiqin Wang, and Jiwan Zhao
Department of Physics, Nanjing University, Nanjing 210008, People's Republic of China

An amorphous alloy of $Fe_{80}Zr_8B_{11}Cu_1$ has been prepared by mechanical alloying, milled for 72 h, and annealed in the temperature range from 673 to 1173 K. The crystallization behavior of this sample at different annealing temperatures has been investigated by x-ray diffractometry, electron microscopy, and Mössbauer spectroscopy. With the increase of annealing temperature, about a 15 nm bcc phase is formed in the amorphous base. Upon further increasing the annealing temperature to 1173 K, in addition to the metastable α -Fe (Zr,B) phase, a ZrB_2 phase appears. Furthermore, the results from Mössbauer spectroscopy reveal that there are two different magnetic areas in these amorphous phases at different annealing temperatures. © *1996 American Institute of Physics.* [S0021-8979(96)31208-X]

I. INTRODUCTION

Recently, excellent soft magnetic properties and high saturation magnetization B_S have been confirmed for some nanocrystalline alloys in the FeCuNbSiB,[1,2] Fe–M–B (M =Zr,Hf, or Nb),[3] and Fe–P–C–Ge–Cu systems,[4] etc. Of these alloys, the highest B_S with good soft magnetic properties has been achieved for the Fe–M–B ternary alloys, because an amorphous phase with Fe concentrations higher than those in the other systems is obtained owing to the high glass-forming ability of M elements and the formation of a nanocrystalline bcc phase.

Usually, Fe–M–B nanocrystalline alloys are prepared by annealing melt–spun amorphous ribbons at a temperature above the crystallization temperature. But in some cases such as magnetic cores used in inductors or irregular shape samples which ribbons could not perform, we need a bulk specimen. In order to produce Fe–M–B bulk alloys, we must prepare amorphous alloy powders first. Then we consolidate amorphous alloy powders to bulky forms.

Mechanical alloying (MA) is an effective way to synthesize amorphous alloy powders in mass production.[5] However, the amorphous forming composition range of MA is different from rapid quenching. From our previous work,[6] we obtained an almost completely amorphous phase when the value of Fe atoms is less than 77 at. %. If the percentage of Fe exceeds 85 at. %, there would be no completely amorphous phase.

Here, we report on the microstructure changes of mechanically alloyed amorphous $Fe_{80}Zr_8B_{11}Cu_1$ samples during annealing.

II. EXPERIMENTAL PROCEDURE

Besides elemental powders of Fe (>98%) and Cu (99.5%,~200 mesh), ingots of Fe–Zr (Zr 75%) and Fe–B (B 20%) binary systems were used as starting materials. Ingots of Fe–Zr and Fe–B were crushed with a pulverizer and the resulting powders were sifted out. Then, the powders were mixed to give the desired composition as $Fe_{80}Zr_8B_{11}Cu_1$ and sealed in a cylindrical stainless steel container under an Ar atmosphere. The MA was performed in a planetary ball mill with a ball to powder weight ratio of 40:1 and a speed of 160 rev min^{-1}. The diameter of the hardening balls was 9.6 mm. A little methanol was used to prevent excessive welding in the chamber thus allowing a high degree of mixing.

The mechanically alloyed powders were annealed for 1 h at various temperatures ranging from 673 to 1173 K inside a sealed vacuum tube below 10^{-4} Torr.

The x-ray diffraction patterns were obtained using Cu $K\alpha$ radiation of a Dmax-rA diffractometer equipped with a graphite monochromator. The microstructure of the samples was characterized by transmission electron microscopy (TEM) using JEOL 2000. The Mössbauer spectra of the studied samples were performed at room temperature in the transmission geometry using a conventional constant acceleration spectrometer and a ^{57}Co–Pd source of 50 mCi. Saturation magnetization was measured in a vibrating sample magnetometer (model 155-1).

III. RESULTS AND DISCUSSION

Figure 1 shows the change of x-ray diffraction patterns as a function of annealing temperature for a 72 h mechani-

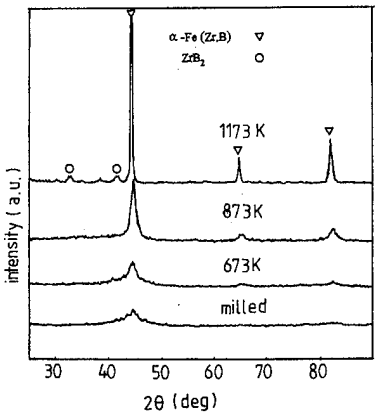


FIG. 1. X-ray diffraction patterns of a mechanically alloyed $Fe_{80}Zr_8B_{11}Cu_1$ alloy at different annealing temperatures.

 0021-8979/96/79(8)/5473/3/$10.00 © 1996 American Institute of Physics

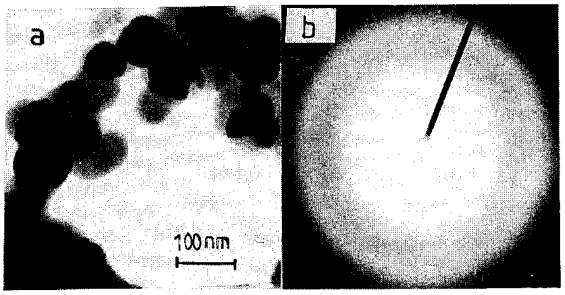


FIG. 2. TEM micrograph (a) and diffraction pattern (b) of a mechanically alloyed $Fe_{80}Zr_8B_{11}Cu_1$ sample.

cally alloyed $Fe_{80}Zr_8B_{11}Cu_1$ alloy. The sample milled for 72 h consists only of a diffuse peak. In Fig. 2, the TEM micrography and diffraction pattern of milled powder reveal the formation of an amorphous phase. When annealed at 673 K, this diffuse peak becomes sharp. Upon annealing at 873 K,the α-Fe phase becomes significant, and no other crystalline states exist. When the annealing temperature reaches 1173 K, a few newly precipitated phases as well as a bcc phase are observed. This phenomenon is similar to other quenched samples.[7,8]

The lattice parameter of the bcc phase is measured to be 0.2868 nm at 873 K and 0.2884 nm at 1173 K and there is a tendency to increase with increasing annealing temperature. The lattice parameter at 1173 K is larger than 0.2866 nm for pure α-Fe, indicating that some solute elements are dissolved into the α-Fe phase. It could be concluded that when the annealing temperature reaches 1173 K, in addition to some Zr and B elements precipitating in the form of ZrB_2, the rest have been dissolved into the bcc phase. This result is different from the report[8] that the increase of annealing temperature results in a mixed structure of α-Fe and $Fe_3(Zr,B)$ phase for an as-quenched amorphous $Fe_{91}Zr_7B_2$ alloy.

Figure 3 shows the TEM microstructure of a $Fe_{80}Zr_8B_{11}Cu_1$ alloy annealed at 673 K. It is clear that there is a new phase well distributed in an amorphous base. Combined with the x-ray diffraction result, we know that this new phase must be an α-Fe (Zr, B) bcc phase. Further raising the temperature to 873 K causes a bcc phase increase. It could be



FIG. 3. TEM micrograph of a mechanically alloyed $Fe_{80}Zr_8B_{11}Cu_1$ sample after annealing at 673 K.

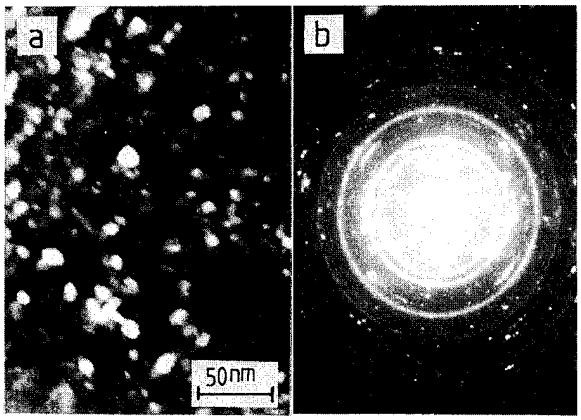


FIG. 4. Dark-field electron micrograph (a) and diffraction pattern (b) of a mechanically alloyed $Fe_{80}Zr_8B_{11}Cu_1$ sample after annealing at 873 K.

seen from the dark-field electron micrograph in Fig. 4(a). The dimension of this phase is about 15 nm. The selected area diffraction pattern corresponding to Fig. 4(a) is shown in Fig. 4(b).

In Fig. 5, we present saturation magnetization as a function of annealing temperature. It is apparent that the saturation magnetization increases with the annealing temperature, corresponding to the increase of α-Fe (Zr, B) during annealing.

In Fig. 6, we present the fitted Mössbauer spectra at room temperature milled for 72 h and all the annealed samples of $Fe_{80}Zr_8B_{11}Cu_1$. From x-ray diffraction patterns, there seems to be few crystalline phases in the $Fe_{80}Zr_8B_{11}Cu_1$ sample milled for 72 h. But we could see from Fig. 6 that there is clearly part of a crystalline phase in this sample. With the increase of annealing temperature, the crystallization part also increases. Upon annealing at 1173 K, the amorphous phase no longer exists, as shown in Fig. 6.

Figure 7 is the hyperfine field distributions of the amorphous phase corresponding to the Mössbauer spectra shown in Fig. 6. In hyperfine field distribution patterns, there are two clear peaks, representing two different sites of the iron atoms with different short range orders.[9,10] In Table I, we present the results of the average magnetic hyperfine field, corresponding to the two different amorphous phases, $\bar{H}_1$ and

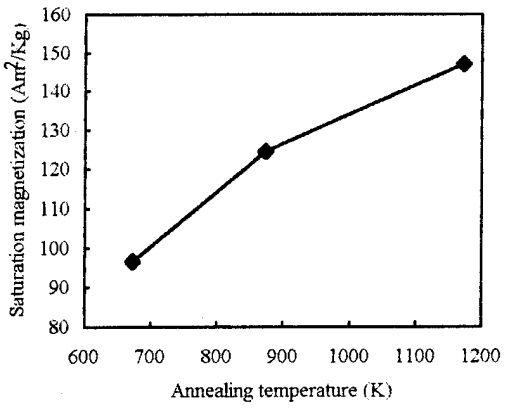


FIG. 5. Saturation magnetization as a function of annealing temperature.

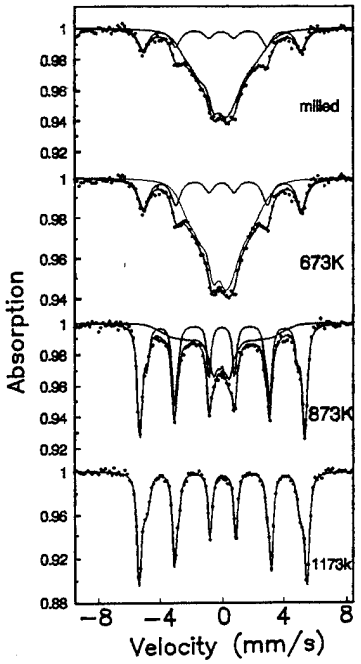


FIG. 6. Mössbauer spectra and fittings of mechanically alloyed samples annealed at different temperatures.

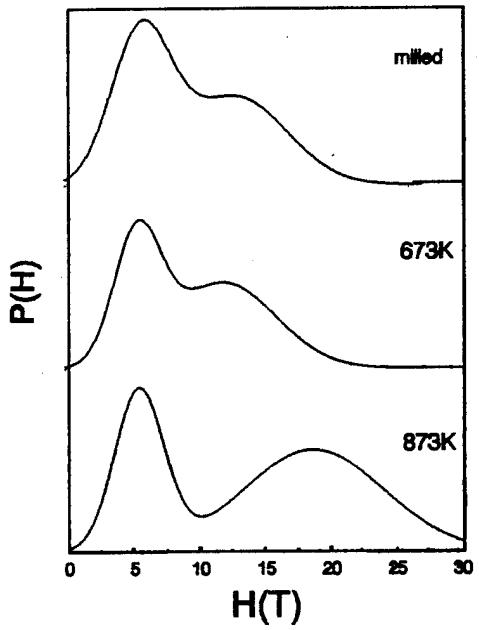


FIG. 7. Hyperfine field distribution of the amorphous phase corresponding to the Mössbauer spectra shown in Fig. 6.

TABLE I. Average magnetic hyperfine field, $\bar{H}_1$, $\bar{H}_2$, and $\bar{H}$, σ_1/σ_2 of two different amorphous phases and percentages of α-Fe(Zr,B) at different annealing temperatures.

Annealing temperature (K)	$\bar{H}_1$ (T)	$\bar{H}_2$ (T)	σ_1/σ_2	$\bar{H}$ (T)	% α-Fe (Zr,B)
Milled	6.0	13	1.3	9.0	23
673	5.4	12	0.8	9.1	25
873	5.3	18	0.6	13.2	61

$\bar{H}_2$, and the total amorphous phases, $\bar{H}$. We also present the calculated ratios of Fe atoms in two amorphous phases, σ_1/σ_2, as well as percentages of α-Fe (Zr,B) for the samples milled for 72 h and annealed at 673 and 873 K. It reveals that, with the increase of annealing temperature, the relative value of amorphous phase 2 and the average magnetic hyperfine field for the total amorphous phase increase, but the average magnetic hyperfine field for amorphous phase 1 decreases slightly. Further, the percentage of bcc phase increases with increasing annealing temperature.

IV. SUMMARY

An amorphous $Fe_{80}Zr_8B_{11}Cu_1$ sample has been formed by mechanical alloying after 72 h milling and then annealed at a different temperature. With the increase of temperature, the bcc phase precipitates from the amorphous base. Upon annealing at 873 K, the percentage of the bcc part will be 61%. When annealed at 1173 K, the amorphous phase completely converts into an α-Fe solution and a small ZrB_2 phase. Furthermore, Mössbauer spectroscopy reveals that there are two short range orders in the amorphous phase at different temperatures.

ACKNOWLEDGMENT

The authors wish to express their gratitude to the Science and Technology Council, Jiangsu Province, China, for funding this work.

[1] Y. Yoshizawa and K. Yamauchi, J. Jpn. Inst. Met. **63**, 241 (1989).
[2] Y. Yoshizawa, S. Oguma, and K. Yamauchi, J. Appl. Phys. **64**, 6044 (1989).
[3] K. Suzuki, N. Kataoka, A. Inoue, A. Makino, and T. Masumoto, Mater. Trans. Jpn. Inst. Met. **31**, 743 (1990).
[4] Y. Fujii, H. Fujita, A. Seki, and T. Tomida, J. Appl. Phys. **70**, 6241 (1991).
[5] A. W. Weeber and H. Bakker, Physica B **153**, 93 (1988).
[6] J. Q. Zhang, B. Y. Wu, X. H. Wu, G. Q. Wang, and J. W. Zhao, Acta Metall. Sin. **8**, 215 (1995).
[7] A. Kojina, H. Horikiri, Y. Kaqamura, A. Makino, A. Inoue, and T. Masumoto, Mater. Sci. Eng. A **179**, 511 (1994).
[8] K. Suzuki, A. Makino, N. Kataoka, A. Inoue, and T. Masumoto, Mater. Trans. Jpn. Inst. Met. **32**, 93 (1991).
[9] P. Gorria, I. Orue, F. Plazaola, M. L. Fernandez-Gubieda, and J. M. Barandiaran, IEEE Trans. Magn. **29**, 2682 (1993).
[10] S. N. Kaul, V. Siruguri, and G. Chandra, Phys. Rev. B **45**, 12 343 (1992).

Microstructure and magnetic properties of $Cu_{0.8}(Fe_{1-x}Co_x)_{0.2}$ alloy powders manufactured by a mechanical alloying process

Yong Goo Yoo and Seong Cho Yu
Department of Physics, Chungbuk National University, Cheongju 360-763, Korea

Won Tae Kim
Rapidly Solidified Materials Engineering Research Center, Department of Physics, Chongju University, Chongju 360-764, Korea

Changes in structural and magnetic properties during mechanical alloying and heat treatment were studied in $Cu_{0.8}(Fe_{1-x}Co_x)_{0.2}$ (x=0, 0.1, 0.2, 0.3, 0.4, 0.5, 0.6) alloys using x-ray diffractometry, transmission electron microscopy, and magnetometry. Supersaturated solid solutions with a fcc crystal structure were obtained in all alloys by mechanical alloying. The grain sizes of the solid solutions were about 20 nm. Magnetization of the supersaturated solid solutions could be explained by a mixture of two types of particles showing paramagnetism and ferromagnetism. The variation in magnetization with Co content in the solutions was similar to the Slater–Pauling curve. Fe–Co with a bcc structure precipitates during annealing of the $Cu_{0.8}Fe_{0.1}Co_{0.1}$ alloy. With increasing annealing temperature ferromagnetic behavior becomes dominant due to a coarsening of the precipitates. © *1996 American Institute of Physics.* [S0021-8979(96)31308-6]

I. INTRODUCTION

Mechanical alloying at low temperatures has been used to prepare metastable phase alloys, such as supersaturated solid solutions or amorphous phase powders from elemental or intermetallic powders in many alloy systems.[1–5] Much work has been done to produce a metastable solid solution in immiscible alloy systems such as Fe–Cu,[1–4] Cu–Co,[5] and Cu–Fe–Co.[6] Structural evolution and magnetic property changes during mechanical alloying have been studied.

In this study, $Cu_{0.8}(Fe_{1-x}Co_x)_{0.2}$ (x=0.0, 0.1, 0.2, 0.3, 0.4, 0.5, 0.6) alloys were selected to produce a supersaturated solid solution and then precipitate ferromagnetic particles in a nonmagnetic Cu matrix by subsequent heat treatment. The content of the ferromagnetic components was fixed at 0.2 to prevent the rapid growth of precipitates and prevent contact between particles during heat treatment. The alloy system was also selected because Fe–Cu and Co–Cu are immiscible systems whereas Fe–Co is miscible. Changes in microstructure and magnetic properties during mechanical alloying and postheat treatment were studied using x-ray diffractometry, transmission electron microscopy, and magnetometry.

II. EXPERIMENT

The chosen compositions were $Cu_{0.8}(Fe_{1-x}Co_x)_{0.2}$ (x =0.0, 0.1, 0.2, 0.3, 0.4, 0.5, 0.6). Mixtures of the appropriate amounts of Fe, Cu, and Co (−80 mesh, 99.9%) powders were mechanically alloyed using a SPEX 8000 mixer and mill with stainless steel balls and vial. Mechanical alloying was performed under an Ar atmosphere with a ball-to-powder ratio of 6:1. The processing time varied from 1 to 24 h to observe structural changes during the process. Heat treatment was performed in a vacuum of 10^{-3} Torr for 1 h at various temperatures between 573 and 673 K. The progress of structural change during mechanical alloying was studied by using x-ray diffraction (XRD) with Mo K_α radiation. Grain size in mechanically alloyed powders was estimated from the XRD profiles by using a Williams–Hall plot. The microstructure was observed in a CM 30 transmission electron microscope operating at 200 kV. Variation of magnetization with processing time was measured at room temperature and at 77 K using a vibrating-sample magnetometer with a maximum applied field (H) of 10 kOe. Also a superconducting quantum interference device (SQUID) magnetometer was used to measure magnetization at 5 K with a maximum magnetic field of 20 kOe.

III. RESULTS AND DISCUSSION

A. Structural change

Figure 1(a) shows XRD patterns obtained from $Cu_{0.8}Fe_{0.1}Co_{0.1}$ alloys for various processing times. An XRD pattern from as-mixed powders could be separated into a mixture of diffraction peaks from bcc Fe, fcc Cu, hcp Co, and fcc Co. The elemental Co powders used here were a mixture of fcc and hcp Co crystals. With increasing processing time, the diffraction peaks from Co disappeared first, peaks from Cu and Fe became weak and broad, and peaks from bcc Fe finally disappeared. All the XRD peaks from powders mechanically alloyed for 24 h had a fcc structure, indicating the formation of a supersaturated solid solution. A supersaturated fcc solid solution was obtained in all alloys after mechanical alloying for 24 h. The grain size of the supersaturated solid solution, calculated from the XRD patterns of the Williams–Hall plot,[7] was about 20 nm and independent of Co content. With increasing Co content, the lattice parameter of the solid solutions decreased due to the substitution of smaller Co atoms for larger Fe atoms, again indicating the formation of solid solution.

Figure 1(b) shows XRD patterns obtained from $Cu_{0.8}Fe_{0.1}Co_{0.1}$ powders heat treated for 1 h at 573 and 623 K. When compared with XRD patterns from the as-mechanically-alloyed sample shown in Fig. 1(a), it can be seen that extra peaks appeared due to the decomposition of the metastable supersaturated solid solution. All of the additional peaks could be analyzed as a bcc Fe–Co solid solu-

 0021-8979/96/79(8)/5476/3/$10.00 © 1996 American Institute of Physics

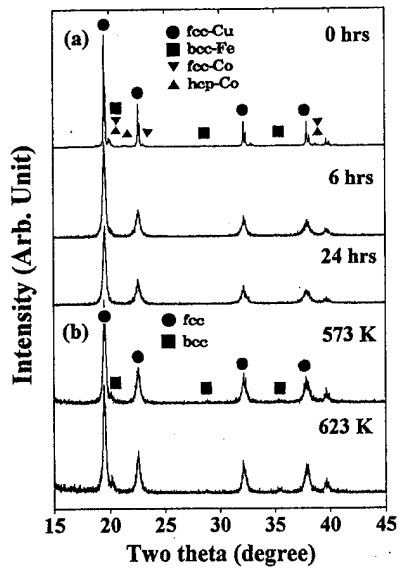


FIG. 1. X-ray diffraction profiles from $Cu_{0.8}Fe_{0.1}Co_{0.1}$ powders; (a) processed for 0, 6, 24 h, (b) and then annealed for 1 h at 573 and 623 K.

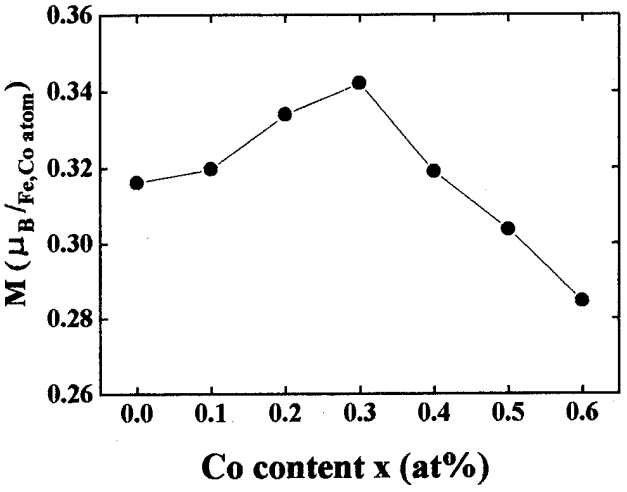


FIG. 3. Variation in magnetization of $Cu_{0.8}(Fe_{1-x}Co_x)_{0.2}$, mechanically alloyed for 24 h as a function of Co content.

tion. In melt–spun $Cu_{0.8}Co_{0.15}Fe_{0.05}$ alloys, fcc Co has been reported to precipitate during heat treatment at low temperatures while the bcc Fe–Co solid solution precipitates at higher temperatures. The precipitation of the Fe–Co phase in the mechanically alloyed sample, as opposed to the separate precipitation of Co and Fe, may result from accumulated strain and high dislocation densities in the mechanically alloyed powders, which are typically about 0.5% and $10^{16}/m^2$, respectively.[4] The driving force for precipitation of bcc Fe–Co is larger than that for separate precipitation due to a negative heat of mixing in the Fe–Co system.

Figures 2(a) and 2(b) show the bright field and selected area diffraction patterns (SADP), respectively, from $Cu_{0.8}Fe_{0.1}Co_{0.1}$ powders processed for 24 h. Figures 2(c) and 2(d) show a corresponding micrograph and SADP, respectively, from $Cu_{0.8}Fe_{0.1}Co_{0.1}$ processed for 24 h and then heat treated for 1 h at 593 K. The grain size of the as-mechanically alloyed specimen was measured from the bright-field image to be about 20 nm. Due to the small grain size and high dislocation density, the grain boundary in the bright-field image is not clear. The SADP from the as-mechanically alloyed sample shows only a sharp fcc ring pattern, in agreement with the XRD. The bright-field image of the heat-treated sample shows 5 nm precipitates, as marked by arrows, in a Cu matrix. The Cu grain size is slightly larger than that in the as-mechanically alloyed sample. The SADP from the heat-treated specimen shows not only a sharp fcc ring pattern but also extra dim rings. These extra rings (marked by arrows) can be analyzed as being from a bcc crystal structure. No rings appeared from fcc Co particles, indicating that the bcc phase is a solid solution of Fe–Co, again in agreement with the XRD diffraction study. Thus, the small precipitates seem to be a bcc Fe–Co phase.

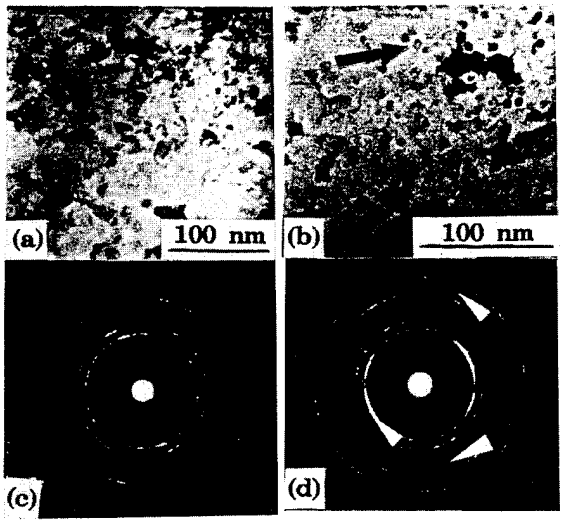


FIG. 2. Bright-field image and selected area diffraction pattern from $Cu_{0.8}Fe_{0.1}Co_{0.1}$ powders, (a) and (b): as-mechanically alloyed for 24 h, (c) and (d): mechanically alloyed for 24 h and heat treated for 1 h at 593 K.

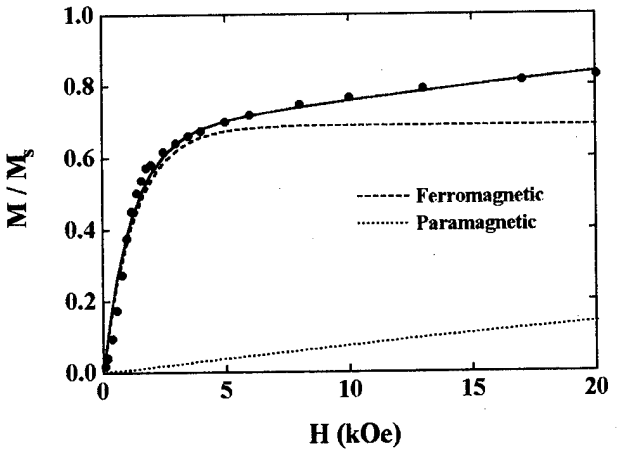


FIG. 4. Variation in magnetization of $Cu_{0.8}Fe_{0.1}Co_{0.1}$ powders, mechanically alloyed for 24 h, at 5 K. The solid line represents the fits of Eq. (1).

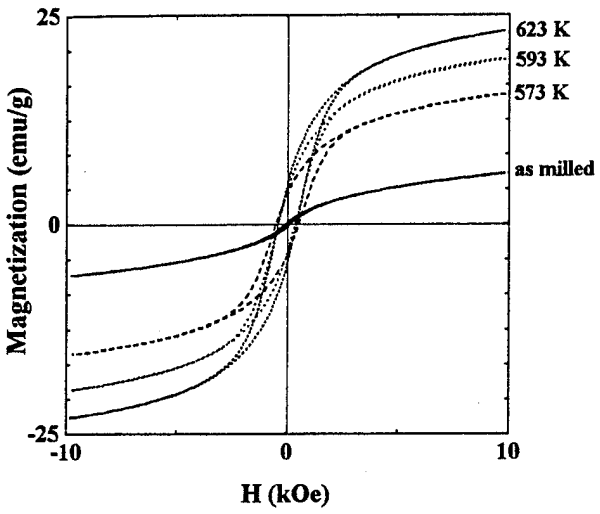


FIG. 5. Hysteresis loops measured from $Cu_{0.8}Fe_{0.1}Co_{0.1}$ alloys, mechanically alloyed for 24 h and heat treated for 1 h at different temperatures.

B. Magnetic properties

Figure 3 shows the variation of magnetization, measured at room temperature with an external field of 1 T, of $Cu_{0.8}(Fe_{1-x}Co_x)_{0.2}$ mechanically alloyed for 24 h, as a function of Co content. Magnetization of the alloys increases with Co content and reaches a maximum at about $x=0.3$ of Co fraction, and then decreases with a further increase of Co content. The variation of magnetization with Co content is in agreement with the Slater–Pauling curve.[8]

Figure 4 shows the magnetization curve for the mechanically alloyed $Cu_{0.8}Fe_{0.1}Co_{0.1}$ alloy, measured at 5 K by using a SQUID magnetometer. The magnetization does not saturate under the maximum field of 20 kOe. The curve was fit with a two component function representing the sum of the ferromagnetic component and a paramagnetic component, which is used by Rubinstein *et al.*[9]

$$\frac{M(H)}{M_s}=(1-\alpha)\left[1-\exp\left(-\frac{H}{H_s}\right)\right]+\alpha\tanh\left(\frac{BH}{T}\right). \quad (1)$$

The first and second components of the equation represent ferromagnetic and paramagnetic contributions, respectively, where α is the fraction of paramagnetic contribution and H_s and M_s are the saturation field and saturation magnetization, respectively. B is an adjustable parameter. The solid line in Fig. 4 is the plot of Eq. (1) with $\alpha=0.33$ and $H_s=1200$ Oe, and the ferromagnetic and paramagnetic components are also included in Fig. 4 for comparison. The analysis indicates that about 33% of the magnetization results from paramagnetic components. Therefore, the magnetization behavior of the mechanically alloyed powders can be explained by a mixture of ferromagnetism and paramagnetism.

Figure 5 shows the hysteresis loops measured at room temperature from $Cu_{0.8}Fe_{0.1}Cu_{0.1}$ specimens, annealed for 1 h at different temperatures. With increasing annealing temperature, magnetization increased due to coarsening of the magnetic particles. However, magnetic saturation was still not obtained. The increases in magnetization and coercivity in heat-treated samples indicate that the ferromagnetic component becomes increasingly dominant due to the coarsening of the magnetic particles.

IV. CONCLUSION

Supersaturated fcc solid solutions, with grain sizes of about 20 nm, were prepared by mechanical alloying $Cu_{0.8}(Fe_xCo_{1-x})_{0.2}$ ($x=0.0$, 0.1, 0.2, 0.3, 0.4, 0.5, 0.6) powders. The variation in magnetization with Co content in these supersaturated ternary solid solutions was similar to the Slater–Pauling curve. The magnetization behavior of the supersaturated solid solutions showed a mixture of ferromagnetic and paramagnetic behavior. Heat treatment of the supersaturated solid solutions resulted in the precipitation of the bcc Fe–Co phase and the ferromagnetic behavior becoming increasingly dominant as the annealing temperature was increased.

ACKNOWLEDGMENT

This research was supported by the Korean Ministry of Education Research Fund for Advanced Materials in 1995.

[1] A. R. Yavari, P. J. Dere, and T. Benameur, Phys. Rev. Lett. **68**, 2335 (1992).
[2] K. Uenishi, J. C. Holzer, C. E. Krill, and W. L. Johnson, Z. Metallk. **83**, 2 (1992).
[3] T. Ambrose, A. Gavrin, and C. L. Chin, J. Magn. Magn. Mater. **124**, 15 (1993).
[4] J. Eckert, K. F. Kobayashi, S. Nasu, H. Hatano, K. N. Ishihara, and P. H. Shingu, J. Appl. Phys. **73**, 2794 (1993).
[5] C. Kuhrt and L. Schultz, J. Appl. Phys. **71**, 1896 (1992).
[6] Y. G. Yoo, W. T. Kim, and S. C. Yu, IEEE Trans. Magn. (in press).
[7] H. P. Klug and L. E. Alexander, *X-Ray Diffraction Procedures for Polycrystalline and Amorphous Materials* (Wiley, New York, 1974), p. 637.
[8] G. Couderchon and J. F. Thiers, J. Magn. Magn. Mater. **26**, 196 (1982).
[9] M. Rubinstein, V. G. Harris, B. N. Das, and N. C. Koon, Phys. Rev. B **50**, 12550 (1994).

Mechanically ground $Fe_{73.5}Cu_1Nb_3Si_{13.5}B_9$: A soft magnetic material in powdered form

Anit K. Giri, P. García Tello, J. González,[a] and J. M. González
Departamento de Propiedades Ópticas, Magnéticas y de Transporte, Instituto de Ciencia de Materiales de Madrid—CSIC, Cantoblanco, 28049 Madrid, Spain

We report on the preparation, by high energy ball milling and starting from an amorphous melt–spun material, of powdered samples exhibiting, after suitable thermal treatments, saturation coercive forces of the order of a few tens of mOe. © *1996 American Institute of Physics.* [S0021-8979(96)31408-2]

I. INTRODUCTION

Soft magnetic behavior, i.e., the simultaneous occurrence of high initial susceptibility and reduced coercive force, is linked to the occurrence, in a specific material, of particular structural and microstructural characteristics. Among these characteristics, the most relevant ones are a low value of the effective magnetic anisotropy (including magnetoelastic contributions) and the absence of large fluctuations of both the intrinsic (magnetization, exchange) and extrinsic (defects in a generalized sense and some morphological features such as grain size, and shape) properties. The low anisotropy values favor both magnetization rotation and the nucleation processes, and the homogeneity is linked to the absence of hindrances to domain wall displacement.

The reduction of the effective magnetic anisotropy is achieved either by the combination of a low structural (magnetocrystalline) anisotropy with a large degree of texture (electrical steels)[1] or through the exchange induced average over long distances of the coupling of the magnetization with the local structure (the atomic short range order crystalline field and local easy axes in the particular cases of the transition metal–metalloid amorphous alloys[2] and the so-called nanocrystalline materials,[3] respectively).

There exist a variety of techniques to obtain soft magnetic materials, but most of the research effort and industrial interest are centered on the different implementations of the melt spinning and the in-rotating-water quenching methods since both allow the production of soft materials (ribbon and wire, respectively) in a continuous way and with highly controlled and perfect morphologies. The ribbon and wire geometries are very satisfactory for a range of applications, such as sensors and pulse generators, but are not the best (the actually achieved thicknesses and diameters are lower than 200 μm) for those in which large mass or volume of soft material or complexly shaped soft parts are required.

In this context, the solid state reaction techniques in which the possibility of amorphization is not limited by the relationship between the cooling rate and the transverse dimensions, represent a relevant alternative. Among these techniques those having a greater potential for use are mechanical alloying (MA) and mechanical grinding (MG) since they combine the possibility of phase formation (in MA) or phase transformation (in MG) with a product material which is in powdered form, and therefore is suitable for compaction and densification in a variety of shapes.

In the present work we will present results about the nanocrystallization by MG of an amorphous melt–spun alloy and report on the development, through relaxation-type thermal treatments, of magnetic softness in the ground material.

II. PREPARATION OF SAMPLES AND EXPERIMENTAL TECHNIQUES

The samples were prepared by mechanical grinding of a precursor melt–spun material having a nominal composition of $Fe_{73.5}Cu_1Nb_3Si_{13.5}B_9$. The ribbons were cut into small pieces of ~5 mm transverse dimension. These pieces were sealed, under an Ar atmosphere, in a hard stainless steel jar (having an inner diameter of 50 mm) together with four hard stainless steel balls (each having an 8 mm diam and in a mass of precursor material to mass of the balls ratio of 1:10) and milled in a Fritsch Pulverisette 7 mill for 1–3 h. The phase distribution of both the precursor material and the milled product was examined by means of x-ray diffraction (XRD, CuK_α) and their thermal stability and crystallization processes were investigated by differential scanning calorimetry (DSC—all the thermograms were taken in a continuous heating mode at a constant rate of 40 K min^{-1}). The DSC unit was also used to thermally treat the samples after which their coercivity was measured in a low field extraction magnetometer. Considering the shape of the samples used for the magnetic measurements (pressed powder pellets 3 mm in diameter and 3 mm in height), their coercivity was measured by means of a zero drift integrating unit after saturating the samples in 20 kOe field.

III. RESULTS AND DISCUSSION

The milling process reduced the starting melt–spun material pieces to powder form. The compromise, typical of ball milling, between particle fracture and particle welding led in our particular case to the attainment, after 1 h of milling, of particles having an average transverse dimension of 35 μm. This should be an equilibrium particle size since, in the milling time range we explored, we were not able to detect any variation of this average dimension.

Figure 1 presents the XRD diffractograms measured in the precursor material [Fig. 1(a)] as well as in the as-milled samples [for 1, 2, and 3 h of milling; see Figs. 1(b), 1(c), and 1(d), respectively]. Figure 1 shows that the precursor mate-

[a]Also at Facultad de Química. Universidad del País Vasco. Apdo. 1072, 20080 San Sebastián, Spain.

 0021-8979/96/79(8)/5479/3/$10.00 © 1996 American Institute of Physics

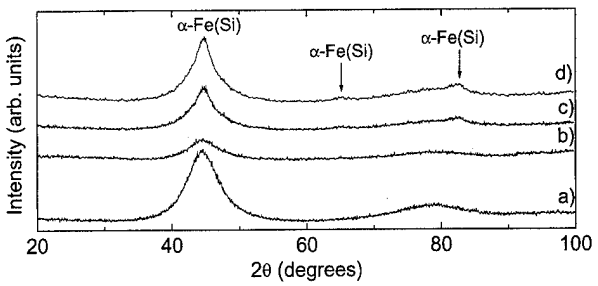


FIG. 1. XRD patterns obtained in the (a) amorphous precursor, (b) 1 h milled sample, (c) 2 h milled sample, and (d) the 3 h milled sample.

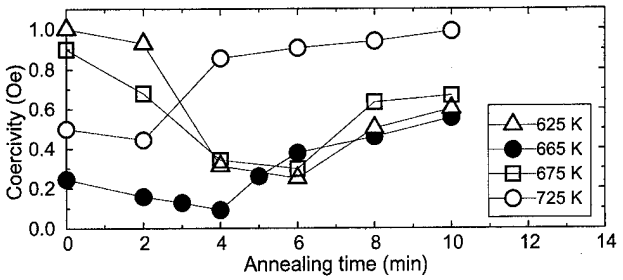


FIG. 3. Treatment time dependence of the coercivity of the 1 h milled samples annealed at different temperatures.

rial has an amorphous structure and that, as the milling time increases, the corresponding as-milled samples develop some crystalline reflections at positions indistinguishable from those corresponding to α-Fe, indicating the occurrence of partial crystallization and an increase of the average grain size associated with the increase of the milling time. The average grain sizes, evaluated using the method of Scherrer after subtracting from the diffractograms the precursor material halo and carrying out corrections for the instrumental broadening, were 5, 9, and 12 nm in the samples milled for 1, 2, and 3 h, respectively.

The DSC thermograms obtained both in the precursor material and in the as-milled samples are shown in Fig. 2. Similar to previous reports,[4] the crystallization of the starting amorphous material proceeds through two distinguishable exothermic processes: one at 843 K, identified as a primary crystallization (yielding nanograins of a solid solution of Si in Fe) and one at 973 K, a pseudoeutectic crystallization associated with the precipitation of Fe_2B (this second stage was not completely developed in our thermograms). The accomplishment of partial crystallization during the milling process is evidenced by the measurement of the enthalpy per unit mass associated with the first crystallization stage: 1.3×10^9, 5.3×10^8, 4.8×10^8, and 4.6×10^8 ergs/g in the case of the amorphous precursor, 1, 2, and 3 h milled samples, respectively.

Despite the presumably large percentage of amorphous phase present in the milled samples, their coercive forces were of the order of several Oe, i.e., clearly higher than those measured in the unmilled amorphous samples. We attribute this to the combination of two different mechanisms: (1) the induction of magnetoelastic anisotropies linked to the stresses built-in during the grinding process, and (2) the presence of hindrances to the domain wall motion, which could be related to the weak coupling of the crystallites to the amorphous phase. To relax these large as-milled coercivities we submitted the samples to thermal treatments carried out, in all the cases, by continuously heating the samples at a rate of 40 K min^{-1} up to a given temperature, T_{ann} (T_{ann} = 625, 665, 675, and 725 K, i.e., always well below the peak temperature of the first crystallization stage), keeping the samples at that temperature for a time t_{ann} (in the range from 0 to 12 min) and then quenching them at a rate of 200 K min^{-1}. The coercive force values measured after these anneals in the 1 h milled sample are plotted in Fig. 3. The best treatment parameters corresponded to T_{ann} = 665 K and t_{ann} = 4 min, which reduced the coercive force to a value of 0.091 ± 0.004 Oe. The results corresponding to the relaxation of the 2 h milled sample are presented in Fig. 4. These results have a similar evolution with t_{ann} to those presented for the 1 h milled sample. The only remarkable difference of the occurrence was a broad minimum in the curve corresponding to annealing at 675 K. Particularly, by annealing the sample at this temperature for 6 min we got a coercivity value of 0.055 ± 0.004 Oe. Relaxation did not proceed to that extent in the 3 h milled sample (Fig. 5) where, almost independent of T_{ann}, a minimum coercive force value of the order of 0.3 Oe was reached after 6–8 min of annealing.

The evolution with the treatment parameters of the phase distribution of the ground samples is illustrated in Fig. 6, where the XRD results obtained in the 2 h milled, 675 K, 6 and 12 min annealed samples are compared to the diffractograms corresponding to the as-milled materials. According to these results, the short time treatments (those leading to co-

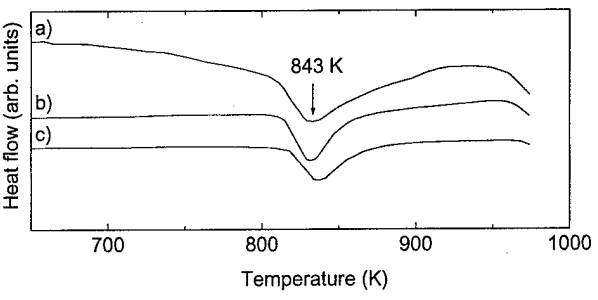


FIG. 2. DSC thermograms measured in the (a) amorphous precursor, (b) 1 h milled sample, and (c) the 2 h milled sample.

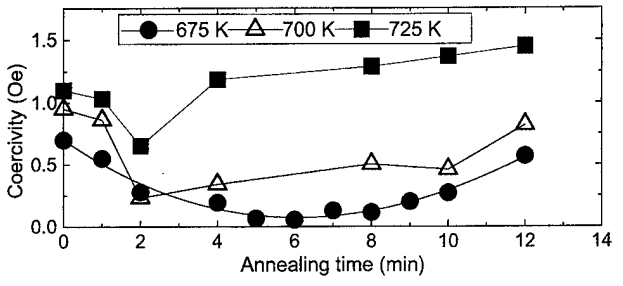


FIG. 4. Treatment time dependence of the coercivity of the 2 h milled samples annealed at different temperatures.

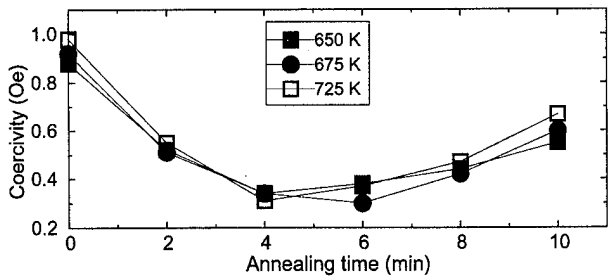


FIG. 5. Treatment time dependence of the coercivity of the 3 h milled samples annealed at different temperatures.

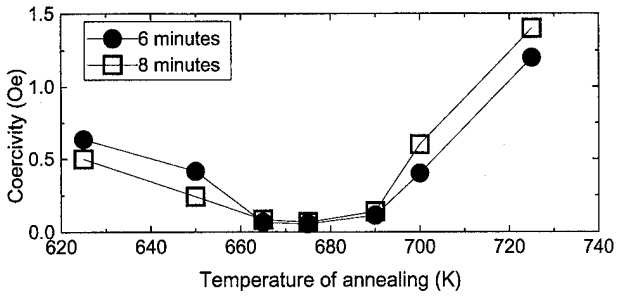


FIG. 7. Treatment temperature dependence of the coercivity of the 2 h milled samples annealed for 6 and 8 min.

ercivity decrease) do not produce any observable change in the diffractograms whereas anneals carried out at times longer than that corresponding to the minimum resulted in clear grain growth. This was confirmed by the measurement in the 675 K, 6 min annealed sample of an enthalpy per unit mass associated to the first crystallization stage of 4.4×10^8 ergs/g, which is almost identical to the as-milled sample value.

IV. CONCLUSIONS

Ball milling of the melt–spun ribbon-shaped material resulted in micron-sized powders in which the first crystallization stage was partially accomplished and which exhibited high coercivities. Thermal treatments of the as-milled samples produced a remarkable coercivity relaxation which (as shown in Fig. 7) led to optimum values for temperatures in the range from 665 up to 675 K and short time treatments of the order of 6–8 min. Considering the fact that there was no detectable difference between the phase distributions of the as-milled and the optimum treated material we suggest that coercivity relaxation was related to stress relaxation in the amorphous part of the samples and to a (chemical) homogenization process taking place at the grain boundaries. These resulted in a better coupling of the crystalline nanograins with the amorphous matrix. Under these conditions, and considering the differences between the average grain size and the domain wall thickness, uniformly distributed nanosized grains weakly interact with thick domain walls. Our suggestion about the role of weakly coupled crystallites as pinning centers is supported by the fact that the minimum coercivity we were able to achieve was obtained in the 2 h milled sample despite the presumably larger value of the stresses residual to the preparation process compared to the 1 h milled sample. We identify grain growth (up to dimensions at which the grain size is comparable to the domain wall thickness) as the origin of the coercivity increase associated with the long time anneals.

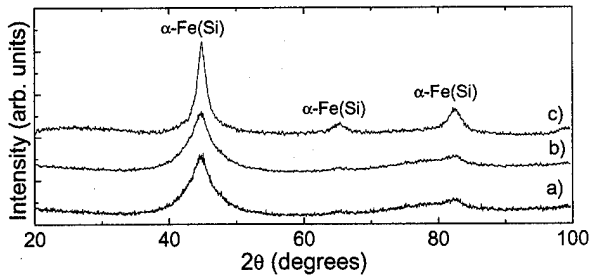


FIG. 6. XRD patterns obtained in the (a) as-milled 2 h milled sample, (b) 2 h milled sample after a 675 K, 6 min anneal, and (c) the 2 h milled sample after a 675 K, 12 min anneal.

ACKNOWLEDGMENT

We thank Dr. G. Herzer from Vacuumschmelze (Hanau, Germany) for providing the precursor melt–spun material.

[1] M. Mager and J. Wieting, J. Magn. Magn. Mater. **133**, 170 (1994).
[2] G. Herzer, IEEE Trans. Magn. **26**, 1397 (1990).
[3] R. Alben, J. J. Becker, and M. C. Chi, J. Appl. Phys. **43**, 1653 (1978).
[4] Y. Yoshizawa, S. Oguma, and K. Yamauchi, J. Appl. Phys. **64**, 6044 (1988).

Correlation of magnetic and mechanical properties of hydrogenated, compositionally modulated, amorphous $Fe_{80}Zr_{20}$ films (abstract)

S. Rengarajan, E. J. Yun, B. H. Lee,[a] B. I. Cho,[b] and R. M. Walser
I/UCR Center for Magnetics, University of Texas at Austin, Austin, Texas 78712

Recent research has demonstrated that large amounts of hydrogen can be electrolytically incorporated in amorphous, compositionally modulated (CM) FeZr films.[1] The first irreversible changes in the magnetic state of an electrolytically hydrogenated iron-rich amorphous alloy were observed. The hydrogen-induced changes in the magnetization were interpreted in terms of specific structural rearrangements. In this work, simultaneous measurements of the variations in the magnetization and mechanical properties of these films were measured as a function of hydrogen charging to further clarify the hydrogen-induced structure changes. The Young's moduli E and internal friction d of as-deposited, and as-hydrogenated CM $Fe_{80}Zr_{20}$ thin films were calculated from the displacements of a vibrating composite cantilever, measured using a laser heterodyne interferometer (LHI) having a displacement sensitivity of ~0.01 Å.[2] E and d were measured using the resonant frequency method.[3] CM films with thickness 1390 Å and modulation wavelength ~10 Å were deposited on glass cantilevers (5 mm long, 2 mm wide, and 150 μm thick) by sequentially sputtering (rf diode) elemental Fe and Zr targets. The samples were electrolytically hydrogenated for various times in 2 N phosphoric acid with a current density of 26.3 mA/cm^2. The maximum change in magnetization of the film (from 71.5 to 551 emu/cm^3) was observed after 5 min. During this time, E increased 18-fold from 535 GPa to 9.63 TPa. The unusually high Young's modulus of the as-deposited CM film is comparable to those previously observed in other CM films.[4] The change is three times larger than the change in the E of carbon steel at the martensitic transformation, and nine times larger than the hydrogen induced increase in E of pure single crystals of iron. The d of the cantilever resonance decreased with hydrogenation, indicating that the incorporated H reduced the internal friction of the CM film. Preliminary analysis of the results indicates that the mechanical and magnetic changes can be interpreted in terms of similar atomic scale changes. Measurements on films with different CM wavelengths are in progress. © *1996 American Institute of Physics.* [S0021-8979(96)82408-2]

[a]Samsung Display Devices Co., Ltd., Suwon, Korea.
[b]Optical Storage Media Lab., Materials Devices Research Center, Samsung Advanced Institute of Technology, P.O. Box 111, Suwon 440-600, Korea.

[1]B. I. Cho, W. Win, E. J. Yun, and R. M. Walser, IEEE Trans. Magn. **31**, 3859 (1995).
[2]S. Rengarajan, B. H. Lee, G. Choe, and R. M. Walser, IEEE Trans. Magn. **31**, 3391 (1995).
[3]K. E. Petersen and C. R. Guarnieri, J. Appl. Phys. **50**, 6761 (1979).
[4]T. Tsakalakos and J. E. Hilliard, J. Appl. Phys. **54**, 734 (1983).

 0021-8979/96/79(8)/5482/1/$10.00 © 1996 American Institute of Physics

Application of Co-based amorphous ribbon to a noise filter and a shielded cable

Osamu Ishii, Masakatsu Senda, Koji Takei, Yasuhiro Koshimoto, and Toshinori Mori[a)]
NTT Interdisciplinary Research Laboratories, Tokai, Ibaraki 319-11, Japan

This paper describes the application of a Co-based amorphous alloy ribbon to a common-mode noise filter in the 1 MHz–1 GHz frequency range. Its saturation magnetization, and relative permeability were 6000 G and 1450, respectively. The 10-μm-thick amorphous ribbon exhibits high loss characteristics. The resistance of a 2-mm-diam roll of amorphous ribbon (12.5 mm wide and 30 cm long) increases from 3 Ω at 1 MHz to 50 Ω at 350 MHz. It is confirmed that a filter 1/17th the volume of a conventional (ferrite core) filter exhibits the same noise attenuation. Moreover, the noise emission from a twisted pair cable is greatly reduced without any increase in the cable volume by employing the amorphous ribbon as a shielding material. © *1996 American Institute of Physics.* [S0021-8979(96)74008-7]

INTRODUCTION

Electromagnetic interference (EMI) is a growing problem with electronic equipment.[1] A large amount of EMI is caused by radiated emission which is due to the common-mode noise current in the cables used to connect digital equipment. Noise emissions from cables are prevented by using common-mode noise filters. A conventional noise filter consists of a cylindrical ferrite core through which a cable is passed. In this configuration, the ferrite core absorbs the magnetic field caused by common-mode noise current in the MHz–GHz frequency range. The ferrite cores, however, are too large to allow circuit boards or circuit units to be housed compactly.

Several investigations have been undertaken on magnetic thin films[2] and magnetic amorphous flake[3] in order to realize high loss characteristics and a large attenuation for common-mode noise in this frequency range. Senda *et al.*, reported that the thickness and magnetic anisotropy of soft magnetic films can be designed so that the film exhibits a large eddy-current loss.[4] This paper describes the application of Co-based amorphous alloy ribbon to an EMI noise filter which is much smaller than a ferrite core. The ribbon is also applied as the shielding material for a shielded twisted pair cable thus reducing the noise emission.

EXPERIMENT

The 10-μ-thick and 12.5-mm-wide amorphous ribbon (ACO-5, Hitachi Metals, Ltd.) was prepared by the roll cooling method. The ribbon was designed to have zero magnetostriction (nominal composition: $Co_{68.59}Fe_{1.28}Mo_{2.57}Mn_{3.7}Si_{4.66}B_{9.2}$) in order to maintain its high permeability when wound around cables. The magnetic properties of the ribbon, which were measured with a B-H loop tracer, are listed in Table I. The specific resistance was 120 $\mu\Omega$ cm.

Its impedance was measured from 1 MHz to 1 GHz with an impedance meter. The sample consisted of a 30-cm-long amorphous ribbon wound around a 16-mm-long current lead, with a sheath diameter of 2 mm.

Figure 1 shows the noise current measurement setup. The transmission characteristics of the cables were measured from 1 MHz to 1 GHz with a network analyzer. We used 130-cm and 210-cm-long twisted pair cables with a characteristic impedance of 110 Ω. One end of the cable was connected to port 1 of a network analyzer via an impedance matching circuit and the other end was terminated with a resistance of 110 Ω. A section of cable at the input end was wrapped with the amorphous ribbon which was attached with organic paste. The total volume of the amorphous ribbon was 0.225 cc (ribbon length: 180 cm). A commercially available ferrite core (inner diameter: 9 mm, outer diameter: 16 mm, length: 28 mm, volume: 4 cc) was also used for comparison. Common-mode noise current, which is equivalent to the transmitted power, S_{21}, was detected with a current probe.

Figure 2 shows the radiated noise field measurement setup. A digital signal generator whose clock frequency was 4 MHz and a receiver were housed in a shield case and connected with 3-m-long shielded twisted pair cable. This was all placed on a turntable. The radiated noise power was received by a biconical antenna (30–300 MHz) or a log-

TABLE I. Magnetic properties of the amorphous ribbon.

Saturation magnetization	6000 G
Relative permeability	1450
Coercivity	<0.3 Oe

[a)]Also with NTT Network Service Systems Laboratories, Musashino, Tokyo, 180, Japan.

 0021-8979/96/79(8)/5483/3/$10.00 © 1996 American Institute of Physics

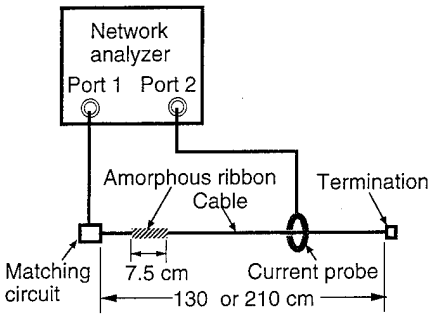


FIG. 1. Schematic diagram of the noise current measurement setup.

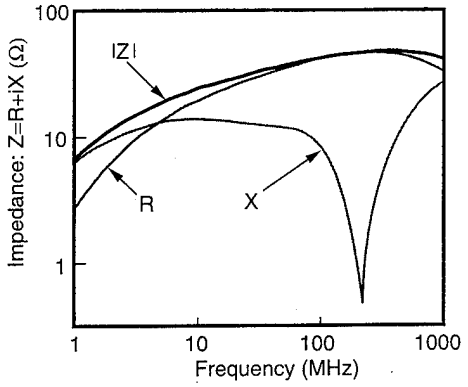


FIG. 3. Frequency dependence of the impedance ($Z=R+iX$) for a 30-cm-long amorphous ribbon.

periodic antenna (300–1000 MHz) which was placed 3 m away from the shield case at a predetermined height of 1 m or 4 m. The horizontal and vertical electromagnetic polarization spectra were measured with a spectrum analyzer at both heights for all azimuth angles. In the spectrum where the strongest radiation peak was obtained, the 20 strongest peaks (harmonics of the clock signal) were averaged to obtain the noise intensity. This measurement was carried out in a radio wave anechoic chamber.

RESULTS AND DISCUSSION

Figure 3 shows the frequency dependence of the impedance ($Z=R+iX$) for a 30-cm-long amorphous ribbon. The reactance, X, has a broad peak of ~10 Ω at around 5 MHz and then drops to 0 Ω at 200 MHz. The resistance, R, increases from 3 Ω at 1 MHz to 50 Ω at 350 MHz with increasing frequency. R is larger than X above 5 MHz. The impedance, Z, of a magnetic cylinder (l: length, t: thickness, r: inner diameter) is

$$Z=(2\pi f\cdot \mu r\cdot \mu o\cdot l\cdot t)/(2\pi r),$$

where f, μo, and μr are the frequency, the permeability of a vacuum, and the relative permeability ($\mu r=\mu r'-i\mu r''$) of the cylinder, respectively.[2] As the imaginary part of the relative permeability, $\mu r''$, increases, the R value also increases. According to the eddy-current loss theory, $\mu r''$ approaches $\mu r'$ at a thickness of 2–3δ, where δ is the skin depth.[5] This means that R approaches X at a thickness of 2–3δ. The fact that R is larger than X above 5 MHz is qualitatively consistent with the eddy-current loss theory, because the thickness of the amorphous ribbon is calculated to be about 2δ at 5 MHz. Hence, the amorphous ribbon is expected to exhibit a large noise attenuation above 5 MHz. In fact, the tendency of R to increase with frequency is very similar to that of a conventional ferrite core, whose R value ranges from several tens of Ω in the MHz region to several hundred Ω in the GHz region. The maximum R value estimated for six rolls (180 cm long) of amorphous ribbon is about 300 Ω above 350 MHz, which is almost the same as that of the ferrite core. Consequently, the six rolls of amorphous ribbon were considered to have the same noise attenuation potential as the ferrite core.

Figure 4 shows the frequency dependence of S_{21} for the 130 cm long cables on which the six rolls of amorphous ribbon or the ferrite core were attached. Since the cable operates as an antenna for common-mode noise current, both the noise emission and noise attenuation are enhanced at the resonant frequency (50 MHz) and at higher harmonic frequencies. The noise attenuation of the amorphous ribbon rolls was 15 dB at 50 MHz which is almost the same as the ferrite core.

Figure 5 shows the frequency dependence of s_{21} for the 210-cm-long cables with either the six rolls of amorphous ribbon or the ferrite core attached. Also in this configuration,

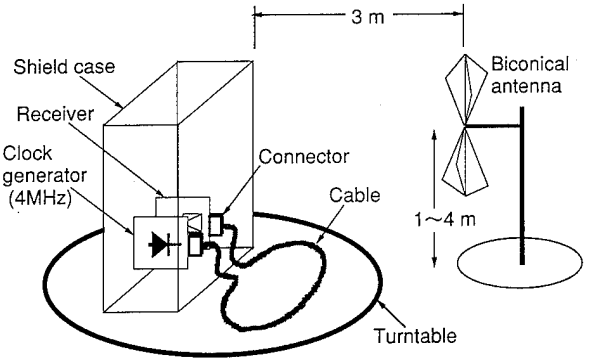


FIG. 2. Schematic diagram of the radiated noise field measurement setup.

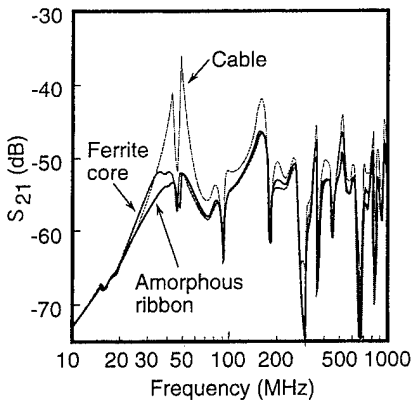


FIG. 4. Frequency dependence of S_{21} for 130-cm-long cable.

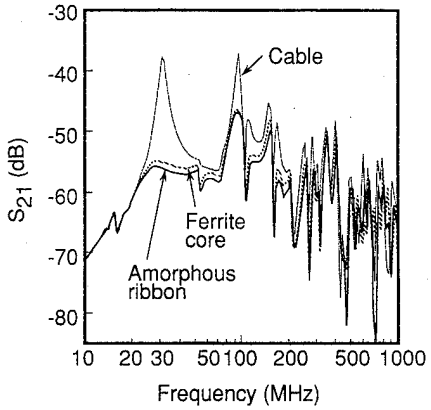


FIG. 5. Frequency dependence of S_{21} for 210-cm-long cable.

both the noise emission and noise attenuation are enhanced at the resonant frequency (30 MHz) and at higher harmonic frequencies. The noise attenuation of the amorphous ribbon rolls (~16 dB at 30 MHz) is almost the same as that of the ferrite core. Since the noise attenuation values of the six amorphous ribbon rolls for the 130-cm and 210-cm-long cables are the same as that of the ferrite core, the amorphous ribbons enable the volume of an EMI noise filter to be reduced to 1/17th that of a ferrite core.

Another advantage of the amorphous ribbon is that it can be used as cable shielding material because of its flexibility. Figure 6 shows the radiated noise spectra from twisted pair cables;

(a) shielded with Al foil and

(b) shielded with amorphous ribbon.

The cable was wrapped with an average of three layers of amorphous ribbon. The radiation produced by the common-mode noise current along the cables was reduced by an average of 8 dB in the 30–1000 MHz frequency range by using amorphous ribbon rather than Al foil as the shielding material. This noise attenuation is the same as that obtained with a series of six ferrite cores. Since the total volume of the amorphous ribbon used for the shielding was 2.5 cc (~20 m long) which is 60% that of the ferrite core, the noise attenuation of the former is ten times larger than that of the latter. Because the noise current is distributed along a cable, the optimum loading position for the amorphous ribbon is the point at which the current is maximum. However, the noise current is reduced uniformly in the amorphous ribbon shielded cable so that the size is reduced to 1/10th that of a ferrite core. Although this improvement is not as great as that achieved with the six amorphous ribbon rolls, it should be noted that there is no change in the practical volume of the cables because the shielding was covered with plastic sheath with the same diameter. The amorphous ribbon shielded cable has a large potential for suppressing EMI

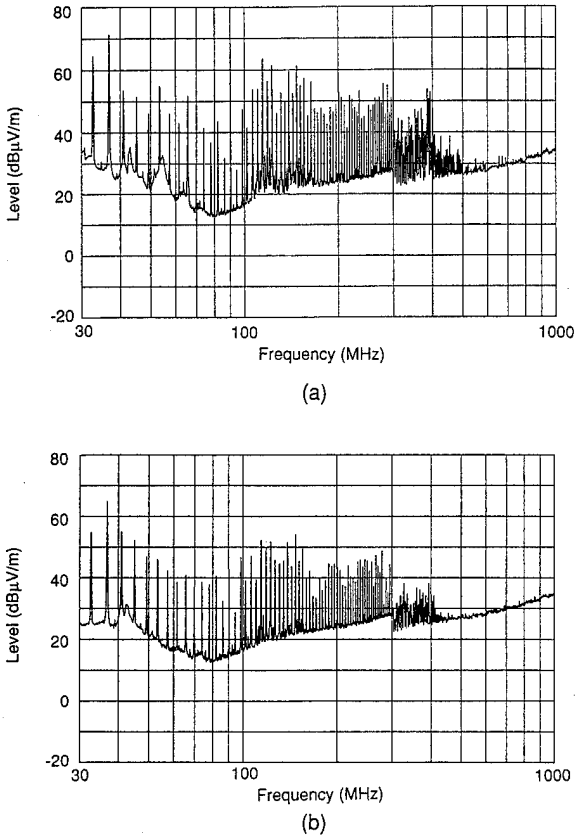


FIG. 6. Radiated noise spectra for Al foil shielded cable (a) and amorphous ribbon shielded cable (b).

noise and realizing the high density housing of digital circuit boards and units.

CONCLUSION

10-μm-thick Co-based amorphous alloy ribbon was confirmed to be a promising candidate for use in common-mode noise filters and as shielding material for shielded twisted pair cable. The amorphous ribbon exhibits high loss characteristics and can provide the same noise attenuation as a ferrite core with 1/17th in the volume. Moreover, the noise emission from the twisted pair cable is greatly reduced without any increase in the cable volume by employing the amorphous ribbon as a shielding material.

ACKNOWLEDGMENTS

The authors would like to thank Dr. Yutaka Ichinose and Dr. Ken-ichi Nakano for their continuous encouragement.

[1] Y. Kami, IEICE Trans. Commun. **E75-B**, 115 (1992).
[2] M. Senda, O. Ishii, and T. Mori, J. Magn. Soc. Jpn. **18**, 511 (1994).
[3] O. Ishii, M. Senda, K. Takei, and T. Mori, Jpn. J. Appl. Phys. **34**, L359 (1995).
[4] M. Senda and O. Ishii, J. Magn. Soc. Jpn. **17**, 489 (1993).
[5] R. M. Bozorth, *Ferromagnetism* (IEEE Press, New York, 1993), p. 775.

A gigahertz-range electromagnetic wave absorber with wide bandwidth made of hexagonal ferrite

Morihiko Matsumoto and Yoshimori Miyata
Nippon Telegraph and Telephone Corporation, NTT Technical Assistance & Support Center, 3-9-11, Midori-cho, Musashino-shi, Tokyo 180, Japan

A thin electromagnetic wave absorber has been investigated; it is composed of hexagonal ferrite and retains high permeability even in the gigahertz-range. The grid-type wave absorber composed of the hexagonal ferrite was examined to broaden the bandwidth in a gigahertz-range by introducing free space in the direction perpendicular to the electric field, which decreased total permittivity. Absorbers made of $Ba_3Co_2Fe_{24}O_{41}$ (Co_2Z) and $Ba_2(Zn_{0.8}Mn_{0.2})_2Fe_{12}O_{22}$ [$(Zn_{0.8}Mn_{0.2})_2Y$] showed wide bandwidths of 1.8–5 GHz and 1.5–4.5 GHz (>15 dB), respectively, when the free space was 37% (v/v) and the thickness of the ferrite was about 5 mm. Increasing the free space led to a wider bandwidth: 1.7–9 GHz was achieved with a 50% (v/v) of free space when the thickness of the $(Zn_{0.8}Mn_{0.2})_2Y$ was 7 mm. © *1996 American Institute of Physics.* [S0021-8979(96)74108-3]

I. INTRODUCTION

Soft ferrite materials are extensively used as electromagnetic-wave absorbers. A gigahertz-range wave absorber has attracted much attention because this frequency region has recently become widely used. Two types of gigahertz-range absorbers using ferrite are commercially available: the cubic ferrite/rubber composite type and the pyramidal structure type. The former is thin (≃7 mm) but has a narrow bandwidth, while the latter is thick (>100 mm) but has a wide bandwidth. The narrow bandwidth could be due to the impedance mismatch that results from ferrite possessing greater permittivity than the permeability in the gigahertz region. A grid-type wave absorber composed of cubic ferrite was developed to broaden the bandwidth by introducing free space into the ferrite in the direction perpendicular to the electric field so as to decrease the total permittivity.[1] However, this type of absorber is thick for various applications with frequencies above 1 GHz because the permeability of the cubic ferrite dramatically decreases in the gigahertz range.

We have investigated a new grid-type absorber for the gigahertz range that uses Co_2Z or $(Zn_{0.8}Mn_{0.2})_2Y$ ferrite with a hexagonal crystal structure. This type of ferrite has a higher permeability in the gigahertz range than the cubic ferrite,[2] and is thus expected to lead to thinner wave absorbers in the gigahertz range.

We first measured the relative complex permeability ($\dot{\mu}=\mu'-i\mu''$) and permittivity ($\dot{\epsilon}=\epsilon'-i\epsilon''$) in the range from 1 MHz to 10 GHz to clarify the electromagnetic material properties of the hexagonal ferrite in the high-frequency region. We then used these $\dot{\mu}$ and $\dot{\epsilon}$ data to estimate the absorption characteristics of the grid-type wave absorber by numerical simulation based on the distributed-constant circuit model. We also directly measured the reflection loss of the absorbers to evaluate their absorption characteristics.

II. EXPERIMENT

We pressed Co_2Z and $(Zn_{0.8}Mn_{0.2})_2Y$ powders into toroidal shapes and sintered them in air at 1300 °C and 1250 °C, respectively.

The $\dot{\mu}$ and $\dot{\epsilon}$ were evaluated by measuring the S_{11} and S_{21} parameters in the frequency range of 50 MHz to 10 GHz by using an HP 8720C network analyzer. We also used another HP 4291A rf impedance/material analyzer to determine $\dot{\mu}$ and $\dot{\epsilon}$ in the frequency range between 1 MHz and 1 GHz. Data from both methods were almost identical. The absorption characteristics were evaluated by measuring the S_{11} (reflection loss) of the ferrite sample backed by a metal plate. A schematic diagram of the grid-type ferrite absorber mounted in a coaxial holder is illustrated in Fig. 1. Numerical simulation was carried out from the measured values of $\dot{\mu}$ and $\dot{\epsilon}$, using 100 data points between 1 MHz and 10 GHz.

III. RESULTS AND DISCUSSION

Figure 2(a) and (b), respectively, show the frequency dependence of the real part (μ') and the imaginary part (μ'') of the relative complex permeability for a commercially available cubic ferrite/rubber composite,[3] and hexagonal ferrites Co_2Z and $(Zn_{0.8}Mn_{0.2})_2Y$. The hexagonal ferrites clearly have a higher permeability than that of the cubic ferrite in the range above 1 GHz, suggesting that hexagonal ferrite may lead to a thinner wave absorber for use in the gigahertz region.

Table I lists some properties of ferrite, obtained by measuring the reflection loss of a sample fully occupying the coaxial holder. A smaller matching thickness was obtained

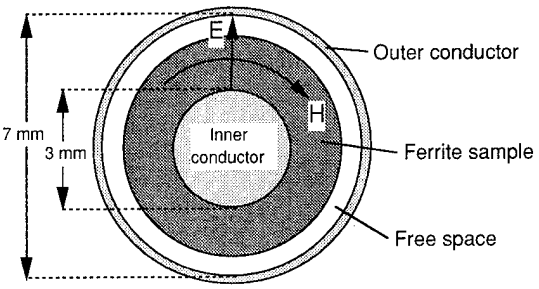
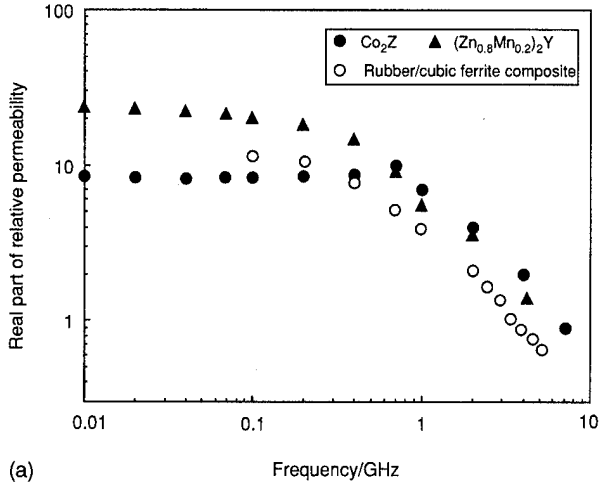


FIG. 1. Schematic design of grid-type wave absorber mounted in a coaxial sample holder.

 0021-8979/96/79(8)/5486/3/$10.00 © 1996 American Institute of Physics



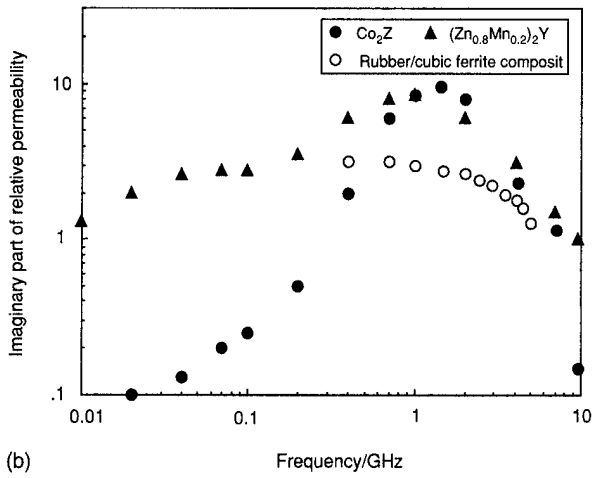


FIG. 2. Frequency dependence of real part (a) and imaginary part (b) of relative permeability for various ferrite-based systems.

for the hexagonal ferrite system (4.5 mm) than for the cubic ferrite system (6.7 mm), although all these systems have a similar matching-frequency region, because the hexagonal ferrite has superior high-frequency characteristics for μ' compared to the cubic ferrite (see Fig. 2). However, it should be noted that the bandwidth for all systems is narrow for many applications. This may result from the impedance mismatch due to the differences between $\dot{\mu}$ and $\dot{\epsilon}$.

The relative μ' and ϵ' are plotted against frequency for Co_2Z and $(Zn_{0.8}Mn_{0.2})_2Y$ systems in Fig. 3. Both systems have a constant μ' up to the dispersion frequency; then it drops drastically. In contrast, ϵ' remains nearly constant and is higher than μ' in all frequency regions. In particular, in the

TABLE I. Some properties of ferrite-based wave absorbers.

	Matching frequency (GHz)	Matching thickness (mm)	Frequency range (>15 dB) (GHz)
Co_2Z	1.8	4.5	1.3–2.3
$(Zn_{0.8}Mn_{0.2})_2Y$	1.2	4.5	0.9–1.5
Rubber/cubic ferrite composite	0.9	6.7	0.7–1.1

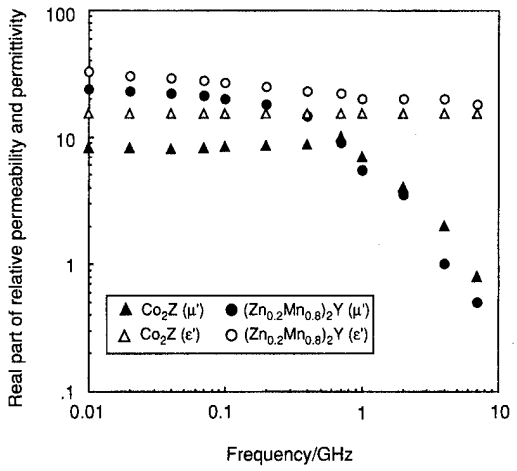


FIG. 3. Frequency dependence of the real part of relative permeability and permittivity for various ferrite systems.

range above 1 GHz, the difference between ϵ' and μ' is considerably large, resulting in a large reflection in the gigahertz region. Therefore, ϵ' must be decreased to obtain a wave absorber with a wide bandwidth in the gigahertz region. Using the grid-type ferrite absorber is a way to reduce ϵ' and broaden the absorption bandwidth.

We first numerically simulated the reflection loss of the grid-type ferrite absorber on the basis of the measured complex permeability and permittivity of the ferrite, i.e., $\dot{\mu}_{\text{fer.}}$ and $\dot{\epsilon}_{\text{fer.}}$, so as to predict the matching thickness and the band contour of the reflection loss. Since free space is introduced in the direction perpendicular to the electric field and thus the direction parallel to the magnetic field, the total complex permeability, $\dot{\mu}_{\text{total}}$, and permittivity, $\dot{\epsilon}_{\text{total}}$, of the grid-type ferrite absorber can be calculated as follows:

$$\dot{\mu}_{\text{total}} = \dot{\mu}_{\text{fer.}} v_{\text{fer.}} + \dot{\mu}_{\text{air}} v_{\text{air}}, \tag{1}$$

$$\dot{\epsilon}_{\text{total}} = \dot{\epsilon}_{\text{fer.}} \dot{\epsilon}_{\text{air}} / (\dot{\epsilon}_{\text{fer.}} v_{\text{air}} + \dot{\epsilon}_{\text{air}} v_{\text{fer.}}), \tag{2}$$

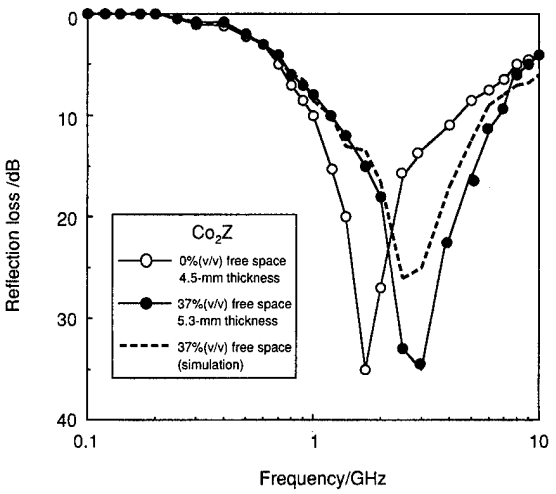


FIG. 4. Frequency dependence of reflection loss of Co_2Z-based grid-type wave absorber [free space 37% (v/v)].

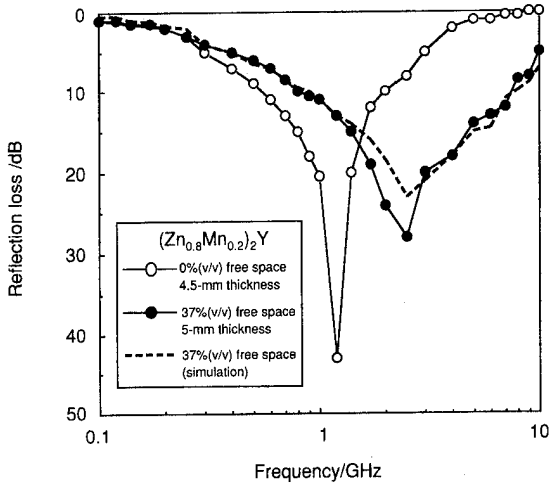


FIG. 5. Frequency dependence of reflection loss for $(Zn_{0.8}Mn_{0.2})_2Y$-based grid-type wave absorber [free space 37% (v/v)].

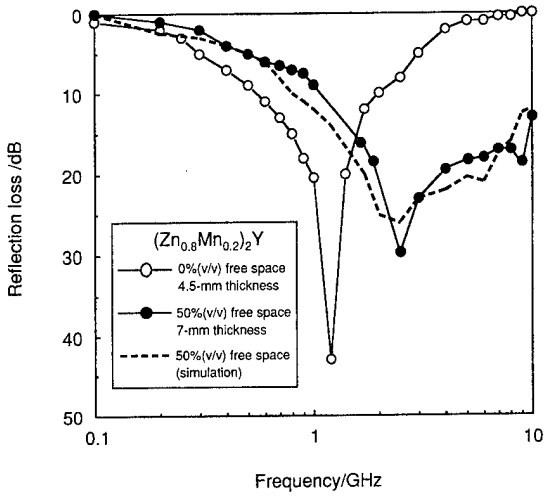


FIG. 6. Frequency dependence of reflection loss for $(Zn_{0.8}Mn_{0.2})_2Y$-based grid-type wave absorber [free space 50% (v/v)].

where $v_{\text{fer.}}$ and v_{air} are the normalized volume of ferrite and air, respectively, in which magnetic and electric fields can pass and $v_{\text{fer.}}+v_{\text{air}}=1$.

Equation (2) shows that introducing free space in the direction perpendicular to the electric field effectively reduces ϵ'_{total}. For example, if the relative $\epsilon''_{\text{fer.}}$ is very small (<0.1), the relative ϵ'_{total} is at its highest, about 3.5 and 2, for arbitrary values of $\epsilon'_{\text{fer.}}$ when the free space occupies 37% (v/v) and 50% (v/v), respectively, in the coaxial holder.

In Figures 4 to 6, the reflection loss of the hexagonal ferrite absorber estimated by numerical simulation is shown by the dashed line together with the measurement value (solid line) as a function of frequency. The band profile obtained by the simulation is almost consistent with that obtained by measurement. For both the Co_2Z and $(Zn_{0.8}Mn_{0.2})_2Y$ systems, the peak position (matching frequency) shifted to a higher frequency when free space was introduced into the ferrite. This is probably because the large decrease in ϵ'_{total} relative to μ'_{total} leads to an impedance mismatch, shifting the matching frequency to a higher frequency. For the grid-type absorbers with 37% (v/v) free space, both the Co_2Z and $(Zn_{0.8}Mn_{0.2})_2Y$ systems had wide bandwidths: 1.8–5 GHz and 1.5–4.5 GHz (>15 dB), respectively, at a matching thickness of about 5 mm. These bandwidths are appreciably wider than those obtained for the 0% (v/v) free-space systems; 1.3–2.3 GHz for the Co_2Z system and 0.9–1.5 GHz for the $(Zn_{0.8}Mn_{0.2})_2Y$ system (see Table I). The matching thickness of these two systems without free space is the same (4.5 mm). The more free space, the wider the bandwidth, but the larger ferrite thickness is required. Increasing the free space led to a wider bandwidth: 1.7–9 GHz was achieved with a free space of 50% (v/v) when the thickness of the $(Zn_{0.8}Mn_{0.2})_2Y$ was 7 mm (see Fig. 6).

IV. CONCLUSION

Grid-type wave absorbers composed of hexagonal ferrite showed wide bandwidths: 1.5–4.5 GHz and 1.8–5 GHz (>15 dB) for $(Zn_{0.8}Mn_{0.2})_2Y$ and Co_2Z systems, respectively, when the free space occupied 37% (v/v) and the thickness of the ferrite was about 5 mm. An increase in the free space led to a wider bandwidth: 1.7–9 GHz could be achieved with a free-space of 50% (v/v) when the thickness of the $(Zn_{0.8}Mn_{0.2})_2Y$ was 7 mm.

[1] Y. Naito, M. Takahashi, T. Mizumoto, and H. Nose, The Transactions of the Institute of Electronics, Information and Communication Engineers, Paper J76-B-II, pp. 7, 641 (1993) (in Japanese).
[2] *Ferrites*, edited by J. Smith and H. P. J. Wijn (Philips Technical Library, The Netherlands, 1959).
[3] "Fuji Electrochemical Co., Ltd., Technical Report on Electromagnetic Wave Absorbers," 1994.

Rapidly solidified Fe–6.5%Si alloy powders for high frequency use (abstract)

Seung Duk Choi and Choong Jin Yang
Electromagnetic Materials Laboratory, Research Institute of Industrial Science & Technology (RIST), P.O. Box 135, 790-600 Pohang, Korea

Fe–(3~6.5%) Si alloy powders having a high magnetic induction (B_s) and a low core loss value for high frequency use were obtained by an extractive melt spinning as well as a centrifugal atomization technique. Sintered core rings made by the rapidly solidified Fe–6.5% Si powders exhibited the high frequency electromagnetic properties: saturated induction (B_8) of 1.23 T, coercivity (H_c) of 9.5 A/m, relative permeability (μ_a) of 6321, and core loss ($W_{10/50}$) of 1.27 W/kg from the rings of 1.1 mm thick. The saturated induction values were found to be almost identical to those of nonoriented Fe–3% Si steel sheet and 6.5% Si sheet prepared by the CVD technique. The high frequency core loss values were measured not to be changed much up to 10 kHz ($W_{1/10k}$=55 W/kg) in applied ac frequency. © *1996 American Institute of Physics.* [S0021-8979(96)69208-5]

Large shielding factor obtained by a multiple-shell magnetic shield having separate magnetic shaking

I. Sasada, T. Yamamoto, and T. Yamauchi
Department of Electronics, Kyushu University 36, Fukuoka 812, Japan

Large shielding factors obtained by magnetic shaking techniques are reported. A cylindrical magnetic shield with both ends open (length=120 cm, inner diameter=52 cm) was constructed as a one-half model of an actual size. Metglas 2705M amorphous tapes of 5 cm in width and about 22 μm in thickness were wound helically on the outer surface of a tube (outer diameter=52 cm) to form a thin multiple-shell structure of five shells. The outer three shells, each made of 4 layers of tapes, were subjected to a common magnetic shaking (200 Hz). The fourth shell made of 8 layers was subjected to a different magnetic shaking (536 Hz). The innermost one was a passive shell. The shielding factor in the center of the shield measured for a transversely applied magnetic field (100 mG) showed 1/*f*-like behavior and extremely large values of 90 900 at 1 Hz and 21 000 at 10 Hz when the opening compensation was on. The shielding factor was much lower and constant at the level of 7000 at frequencies of less than 10 Hz when opening compensation was off. The residual dc magnetic field at the center was as small as 5 μG. It is shown by the experiments that a multiple-shell structure with even narrow spacings exhibits large shielding factors when a magnetic shaking technique is applied. It is also shown that the opening compensation technique is a key to building an open-structure magnetic shield with a large shielding factor. © *1996 American Institute of Physics.* [S0021-8979(96)74208-X]

I. INTRODUCTION

For extremely weak and low-frequency magnetic field measurements, the use of magnetic shielding as well as the use of superconducting quantum interference device (SQUID) magnetic sensors is inevitable. Current magnetic shielding systems are based on the classical approach such as the one in Ref. 1. There is, however, a big technological gap between the SQUID sensor systems and the magnetic shielding system used today. Hence, the development of a new and effective method of magnetic shielding is a key for extremely weak magnetic field measurement techniques. The magnetic shielding system should have large shielding factor at low-frequency to attenuate ambient disturbing magnetic fields of the 1/*f* nature,[2,3] and should be low-cost and lightweight. Furthermore, open structure is strongly recommended for easy access and for preventing claustrophobia when it is used for magnetic field measurements of the human brain in the hospital. We have been working on this issue and proposed magnetic shaking techniques applied to square *BH*-loop materials[4,5] and opening compensation technique to allow an open structure.[6]

In this paper, we report on large shielding factors obtained by a cylindrical magnetic shield with a thin multiple-shell structure subjected to magnetic shaking enhancement and with a compensation system at the open ends of the shield. We emphasize the merit of the use of multiple-shell structures even with narrow spacings when the material permeability is as high as $4-6\times10^5$, and the effectiveness of our shield and compensation technique to get a large shielding factor on open ended shields.

II. EXPERIMENT

A cylindrical magnetic shield with both ends open (length=120 cm, inner diameter=52 cm) was constructed as a one-half model of an actual size. Metglas 2705M amorphous tapes of 5 cm in width and about 22 μm in thickness were wound around a tube (outer diameter=52 cm) to form five separate magnetic shells as shown in Fig. 1. Shells #1–#3 carry a common toroidal shaking coil (shaking coil #1 in the figure) and shell #4 carries its own toroidal shaking coil (shaking coil #2 in the figure). The shell #5 was not subjected to magnetic shaking but used to attenuate the shaking magnetic field leaking from shells #1–#4. The total weight of the tapes used was 15 kg. Nominal diameters of the shells are 56 cm for #1, 55.3 cm for #2, 54.6 cm for #3, 52.6 cm for #4, and 52 cm for #5. Numbers of turns were 50 for shaking coils #1 and #2 and 20 for the demagnetizing coil

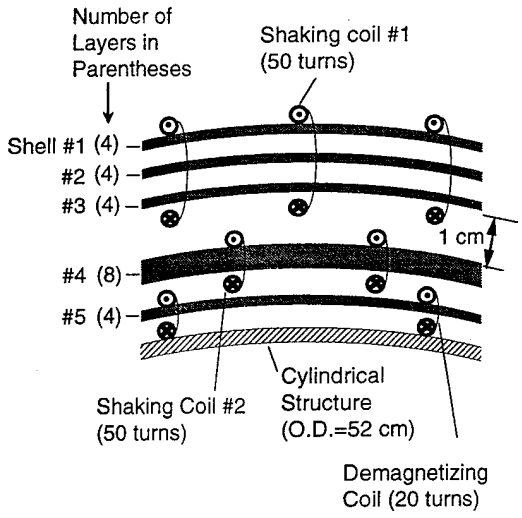


FIG. 1. Cross sectional view of thin multiple-structure. Spacings between shells are about 3.5 mm, unless otherwise indicated.

 0021-8979/96/79(8)/5490/3/$10.00 © 1996 American Institute of Physics

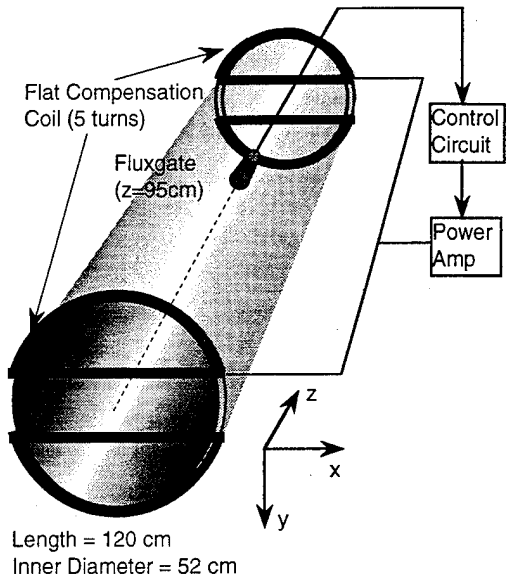


FIG. 2. Schematic view of opening compensation system. The system is shown only for y component of disturbing magnetic field.

on the shell #5. Excitations to the shaking coils #1 and #2 were given separately. In this case, the frequency Fs_1 of excitation #1 and the frequency Fs_2 of excitation #2 should be chosen carefully to avoid a modulation effect, in which $|2nFs_2-mFs_1|$ Hz components, where $2nFs_2$ is even harmonics of Fs_2 and mFs_1 is harmonics of Fs_1, appear inside shell #4, see also Ref. 7. In order to avoid $|2nFs_2-mFs_1|$ being a low-frequency component, one can set $Fs_1=Fs_2$, however, we chose 200 Hz for Fs_1 and 536 Hz for Fs_2 experimentally. In this combination, a 16 Hz component should appear for $n=3$ and $m=16$, but it was too small to be detected by a fluxgate magnetometer. Lower sidebands of the modulation effect become small when n and m tend to be large numbers. Figure 2 shows a schematic view of the opening compensation.[6] Only one coil set for compensating the y-component of the disturbing magnetic field was installed for the experiments. When the sources of the disturbing magnetic fields are far from the magnetic shield, those fields can be almost the same at both ends. In this case, one can compensate magnetic disturbances at both ends by using a single magnetometer as shown.

The magnetic shield under investigation was positioned horizontally and exposed transversely to the earth's magnetic field. Shell #5 was demagnetized at the beginning of experiments with the two magnetic shaking coils excited to reduce remanent magnetization of the shell. A transverse magnetic field (100 mG) was applied to the magnetic shield by a large rectangular Helmholtz coil set[6] and the magnetic field inside the shield was detected by a fluxgate magnetometer situated on the axis of the cylinder with a lock-in amplifier to enhance SN ratio. The distribution of the residual dc magnetic field was also measured down to 5 μG. In these measurements, the dc magnetic field was measured more than twice at a place by reversing the direction of the magnetometer to separate offsets.

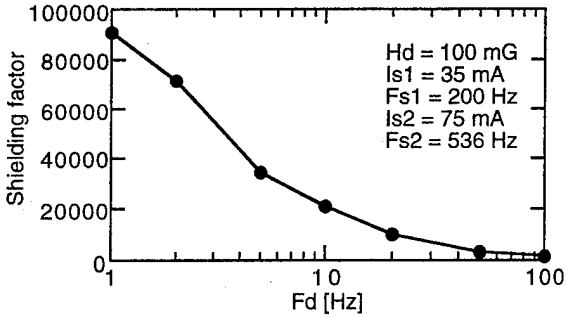


FIG. 3. Shielding factor in the center with end compensation on.

III. RESULTS AND DISCUSSION

The shielding factor (ratio of magnetic field applied to magnetic field inside) with the opening compensation on is shown in Fig. 3 for the frequencies of the transversely applied magnetic field. The shaking conditions are given in the figure. The shielding factor becomes larger toward low frequency and reaches 90 900 at 1 Hz. This is extremely high compared to the typical value of conventional magnetic shields which have normally factors of only 10–100. Incremental permeability shows a frequency dependence even at low frequencies when it is enhanced by magnetic shaking.[5] In the present case, however, the strong frequency dependence of shielding comes not only from the frequency dependence of the permeability but also from the thin multiple-shell structure with end compensation. As shown by Thomas[8] for an infinitely long cylindrical shield of multiple-shell structure, shielding factor is a nth order polynomial function of the relative permeability μ_r when a shield consists of n magnetic shells. In our case, the order of the polynomial function is 4 because shells #1–#4 are subjected to magnetic shaking. The permeability of shell #5 is treated as a constant equal to 2000. When the distances between the neighboring shells are small, coefficients of higher order terms become small. Therefore, when the permeability is low, higher order terms do not affect a resulting shielding factor. In other words, a thin multiple-shell structure behaves as a single shell with the same total thickness when the permeability is low. On the other hand, when the permeability is sufficiently large, higher order terms with small coefficients become substantial, so a thin multiple-shell does work to increase shielding factor.

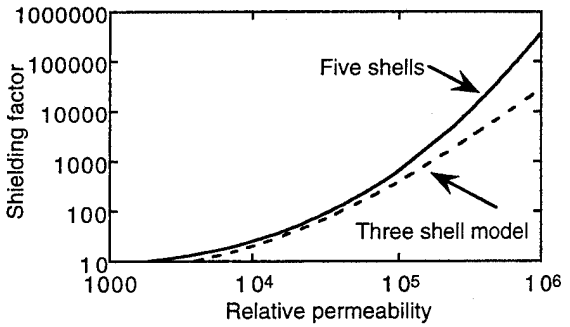


FIG. 4. Relationship between shielding factors and relative permeability.

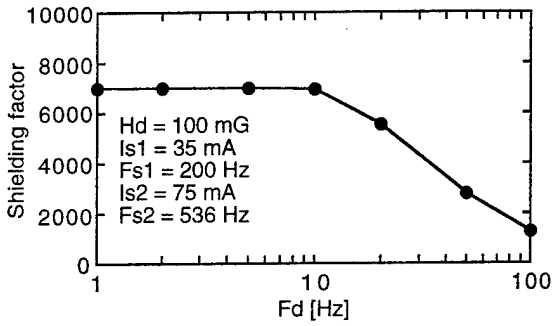


FIG. 5. Shielding factor in the center with end compensation off.

The shielding factors were calculated as a function of relative permeability assuming infinitely long cylindrical shields[8] for the exact cross sectional structure and for a three shell model in which shells #1–#3 are treated as a single shell with the same total thickness and the mean diameter of the three. It is obvious that even narrow spacings (3.5 mm) between shells yield much higher shielding factor when the relative permeability is higher than 10^5. The steep gradient of the solid line in Fig. 4 explains the strong frequency dependence in Fig. 3, that is, frequency dependence of the permeability itself is enhanced through this steep gradient. The value of shielding factor at 1 Hz, 90 900 is obtained at $\mu_r=6.5\times10^5$ in Fig. 4 and the factor 21 000 at 10 Hz with $\mu_r=4.0\times10^5$. These values are obtained by magnetic shaking.[4]

Figure 5 shows the shielding factors under the same shaking condition when the end compensation was off. The shielding factors were low and constant at the level of 7000 at the frequencies of less than 10 Hz due to overwhelming leaks from the openings. Figure 6 shows the flux density profile along the cylinder axis for the transversely applied magnetic field of 100 mG when the opening compensation is on. Obtaining a larger shielding factor and obtaining a wider uniform area of magnetic field is in trade-off relationship in the magnetic shield with open ends. The residual dc magnetic field profile on the same axis is shown in Fig. 7 for two cases: opening compensation on and off. When the opening compensation is on, the residual magnetic field is as small as 5 μG.

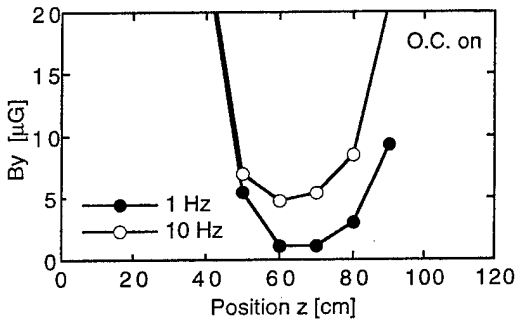


FIG. 6. Flux density profile along the cylinder axis for the transversely applied ac magnetic fields.

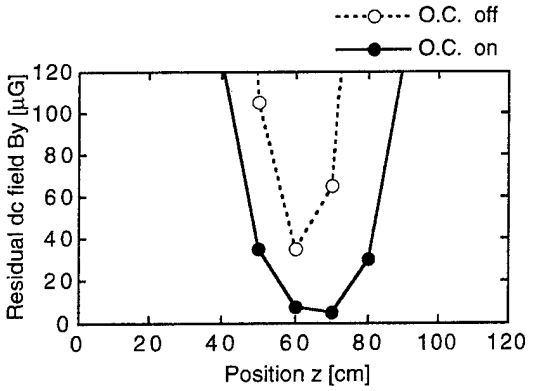


FIG. 7. Residual dc magnetic field profile along the cylinder axis.

One can build a magnetic shield large enough for the human body by scaling to twice the size as the one discussed with amorphous tapes weighing 120 kg. The total weight would be one tenth and the performance far better compared to conventional magnetic shields using Permalloy.

In this paper, we focused only on the shielding factor, however, leakage magnetic fields consisting of higher harmonics of the magnetic shaking field are also an important issue. To reduce these leakage fields, the shaking coils should be wound symmetrically with many turns. The use of inner shells made of magnetic materials with fairly high permeability without magnetic shaking is also effective to attenuate these shaking fields. This issue will be addressed later time.

IV. CONCLUSIONS

We demonstrated that a large shielding factor (90 900 at 1 Hz) was obtained by a cylindrical magnetic shield with magnetic shaking. We showed that a thin multiple-shell structure with even narrow spacings between the shells does increase the shielding factor when the permeability is enhanced by magnetic shaking. We also showed the effectiveness of our shield end compensation technique to get a large shielding factor on open ended shields.

ACKNOWLEDGMENT

This work is supported by the Grant-in-Aid for Development Scientific Research from The Ministry of Education, Science, Culture and Sport.

[1] A. Mager, IEEE Trans. Magn. **6**, 67 (1970).
[2] V. O. Kelha, J. M. Pukki, R. S. Peltonen, A. J. Penttinen, R. J. Ilmonemi, and J. J. Heino, IEEE Trans. Magn **18**, 260 (1982).
[3] S. N. Erne, H.-D. Hahlbohm, H. Scheer, and Z. Trontelj, *Biomagnetism*, edited by S. N. Erne (Walter de Gruyter, Berlin, 1981), p. 79.
[4] I. Sasada, S. Kubo, and K. Harada, J. Appl. Phys. **64**, 5969 (1988).
[5] I. Sasada, S. Kubo, R. C. O'Handley, and K. Harada, J. Appl. Phys. **67**, 5583 (1990).
[6] I. Sasada and Y. Oonaka, J. Appl. Phys. **75**, 6984 (1994).
[7] I. Sasada, IEEE Trans. Magn. **30**, 4638 (1994).
[8] A. L. Thomas, IEEE Trans. Electromagnetic Compatibility **EMC-10**, 142 (1968).

Published without author corrections

The magnetomechanical effect in electrolytic iron

M. K. Devine and D. C. Jiles
Ames Laboratory, Ames, Iowa 50011

The effect of stress on the magnetization of high purity iron has been studied systematically at different locations on the M,H plane corresponding to a variety of magnetic states of the material. The results confirm earlier studies that show the sign of the derivative $dM/d\sigma$ changes at different locations on the M,H plane, and can even change as a result of a monotonic increase of stress either in compression or tension. The observed behavior can be explained on the basis of a recent theory which predicts that the irreversible changes in magnetization resulting from changes in applied stress cause the magnetization to approach the anhysteretic magnetization curve at the given applied field strength. © *1996 American Institute of Physics.* [S0021-8979(96)74308-6]

INTRODUCTION

The behavior of ferromagnetic materials subjected to a time dependent applied stress has been difficult to explain theoretically. Recent work[1–4] has shown the effect can be asymmetric with respect to tensile and compressive stress, depending where on the hysteresis loop measurements were taken.

Magnetization changes occur as a result of a change in the energy of the system. The derivative of the Helmholtz free energy with respect to magnetization leads to an equation for the effective field,[5]

$$\frac{dA}{dM}=\mu_0 H+\mu_0\alpha M+\left(\frac{3}{2}\right)\sigma\left(\frac{d\lambda}{dM}\right) \tag{1}$$

so that

$$H_{\text{eff}}=\left(\frac{1}{\mu_0}\right)\left(\frac{dA}{dM}\right)=H+\alpha M+\left(\frac{3}{2}\right)\left(\frac{\sigma}{\mu_0}\right)\left(\frac{d\lambda}{dM}\right). \tag{2}$$

Here, the effect of stress occurs in the third term. The factor $d\lambda/dM$, the dependence of magnetostriction on magnetization, determines the magnitude of the effective field under a given stress. These two factors, the stress and $d\lambda/dM$ combined, produced the magnetomechanical effect.

EXPERIMENTAL PROCEDURE

Previous research has dealt with rather complex alloys of iron, usually low to medium carbon steel. To simplify the investigation, samples of iron without carbon or other solutes were measured here. Measurements reported were made on a normalized sample of electrolytic iron (99.99% pure Fe) in the shape of a short cylindrical tensile sample, of dimensions 95 mm length, and 12 mm gauge diameter. A flux coil, strain gauge and Hall-element sensor were attached. The sample was magnetized using a solenoid. Four measurements were taken at constant field strengths, with magnetizations along the upper branch of the hysteresis loop (i.e., decreasing from saturation magnetization): these included measurements at remanence, positive and negative saturation as shown in Fig. 1. The sample was cycled through two complete hysteresis loops before setting the magnetic field H at the desired level prior to measurement. Tension and compression were applied via a mechanical tensile tester and the stress axis was coaxial with the magnetization. Stress was applied in a series of stress/release cycles, with the amplitude increasing slightly with each cycle. The variation of flux density with strain was then recorded.

RESULTS

The magnetomechanical effect measured near saturation induction is shown in Fig. 2. At this location the derivative $d\lambda/dM$ was negative. Under tensile stresses the magnetic induction B decreased while under compression it increased. There was a small amount of irreversibility after each cycle amounting to less than 0.5×10^{-4} T per cycle.

The magnetomechanical response at a magnetic induction of 1.64 T ($H=6600$ A/m) is shown in Fig. 3. At this location the derivative $d\lambda/dM$ was positive. Tension produced a positive change in magnetic induction while compression induced a decrease. There was greater irreversibility present after compression than after tension. Also, a significant amount of the decrease in induction occurred just after the stress for a given cycle exceeded the maximum of the previous cycle. The incremental amount of irreversibility after each cycle decreased as the number of cycles increased.

The behavior at remanence ($B=0.34$ T, $H=0$) is shown in Fig. 4. Here there was a decrease in induction, regardless

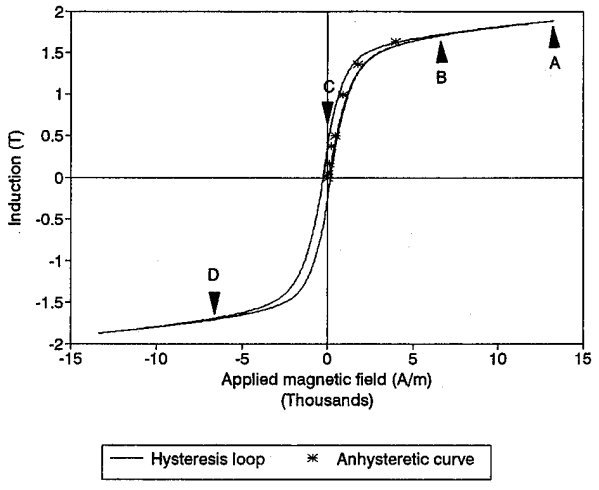


FIG. 1. Hysteretic (line) and anhysteretic curves (points) for the iron specimen, zero stress.

 0021-8979/96/79(8)/5493/3/$10.00 © 1996 American Institute of Physics

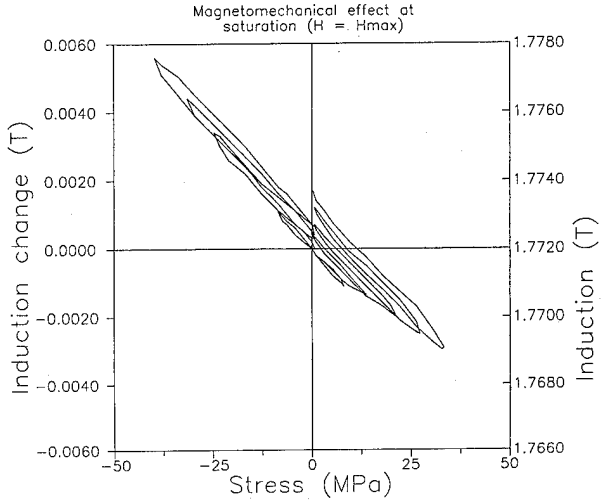


FIG. 2. Magnetomechanical effect near positive saturation induction (point A in Fig. 1).

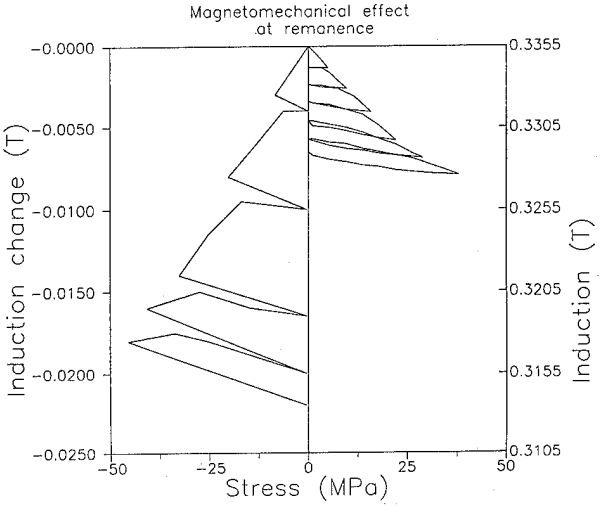


FIG. 4. Magnetomechanical effect at positive remanence (point C in Fig. 1).

of whether the applied stress was positive or negative. Under tensile stress there was less change than under compressive stress. The behavior under compression was similar to that seen in Fig. 3, that is much of the induction change occurred after the maximum stress of the previous cycle has been exceeded. In addition, the direction of the induction change upon application (but not release) of the stress changed direction. During the first two stress/release cycles the induction increased with stress, but afterwards the induction decreased with stress.

Figure 5 shows the behavior at $H=-6600$ A/m, and an induction of -1.55 T. The behavior here was similar to those seen in Fig. 3 except the sign of the stress response was reversed. Tension produced a decrease in induction while compression produced an increase, and there was significant hysteresis on the tensile side.

DISCUSSION

The observed magnetomechanical effect near saturation induction (Fig. 2) was a reversible response to stress. Near saturation, the derivative of magnetostriction was negative[6] so the change in magnetization was negative for tensile stresses and positive for compressive stresses. Since domain magnetization rotation is a reversible process, the curves in Fig. 2 are similarly reversible. The effective field H_σ at saturation was calculated to be -192 A/m at maximum tensile stress and $+312$ A/m at maximum compressive stress. These fields are of the magnitude required to produce the small observed change in induction.

Far from saturation, different magnetization mechanisms dominated the process. After domain rotation, the first mechanism to be activated upon decrease from saturation is

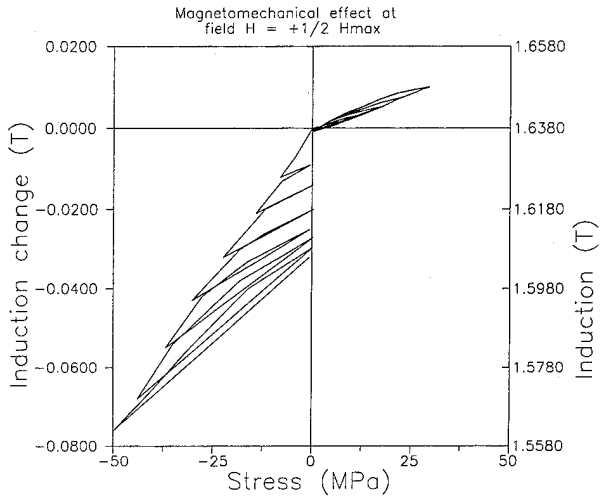


FIG. 3. Magnetomechanical effect at applied magnetic field $H=+1/2H_{\max}$ (point B in Fig. 1).

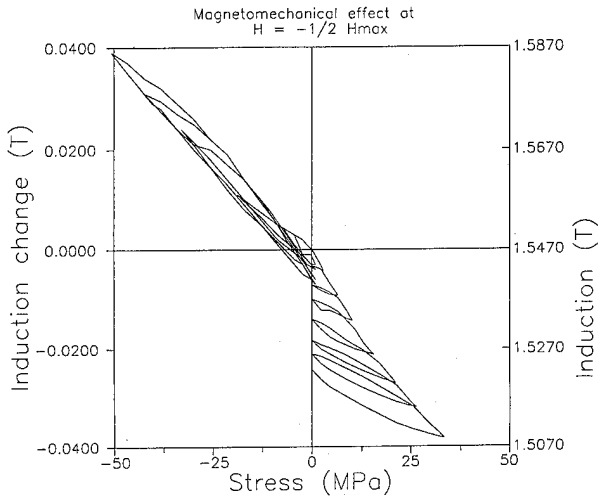


FIG. 5. Magnetomechanical effect at applied magnetic field $H=-1/2H_{\max}$ (point D in Fig. 1).

domain wall translation. At $H=6600$ A/m, reverse domains were created and grew (via wall movement), which reduced the magnetization. Since the magnetostriction is positive in this region,[6] the effective magnetic field due to the stress tends to increase the magnetization. Thus the applied field (from the solenoid) H_{app} and the effective magnetic field (from the stress) H_σ oppose each other in the tensile regime and reinforce each other in the compressive regime. At this point, the effective field H_σ was calculated to be 480 A/m from the tensile stress and -780 A/m from the compressive stress.

At remanence there is no applied field but the induction decreased with stress both in the tensile and compressive regime. This is because at this point the magnetization is above the anhysteretic and stress cycling will tend to reduce the total energy by decreasing its magnetization. The tendency for larger changes in magnetization to occur in the compressive regime is because compressive stress favors the formation of domains orientated at 90° to the applied stress axis (usually in the form of closure domains).[2] Since more 90° domains are formed in compression than in tension, the magnetization decrease more under compression.

CONCLUSIONS

The magnetomechanical effect is known to produce apparently complicated behavior in iron. The response of the material has been shown to be asymmetrical, contrary to earlier theories. The behavior of the magnetization as a function of stress depends on which magnetization mechanism is dominant at a particular point on the hysteresis loop and also on the sign of the derivative $(d\lambda/dM)$. The observed results have been explained in terms of a recent theory of the magnetomechanical effect.[7]

[1] K. C. Pitman, IEEE Trans. Magn. **26**, 1978 (1990).
[2] M. G. Maylin and P. T. Squire, J. Appl. Phys. **73**, 2948 (1993).
[3] M. G. Maylin and P. T. Squire, IEEE Trans. Magn. **29**, 3499 (1993).
[4] I. M. Robertson, Acta Metall. Mater. **42**, 661 (1994).
[5] M. J. Sablik, G. L. Burkhardt, H. Kwun, and D. C. Jiles, J. Appl. Phys. **63**, 3930 (1988).
[6] R. M. Bozorth, *Ferromagnetism* (IEEE, New York, 1993), p. 633.
[7] D. C. Jiles, J. Phys. D **28**, 1 (1995).

Effect of cutting techniques on local magnetic characteristics of SIFE (abstract)

D. A. Philips, L. R. Dupre, K. Eloot, and J. A. Melkebeek
Laboratory for Electrical Machines and Power Electronics, Department of Electrical Power Engineering, University of Gent, Belgium

In this article the effect of cutting techniques on the local magnetic characterization of nonoriented motor lamination iron is presented. Starting from the same material (0.3% Si, 0.3% Al, finally annealed condition), rings have been cut using three different techniques: spark erosion, laser cutting, and punching. First a classical[1] measurement has been performed on stacks of ten identical rings, using a measurement winding applied uniformly along the circumference of the ring. In this way, the *average BH* loops under quasistatic conditions have been obtained, and are used as a *reference* further on. It is found that the cutting techniques have a considerable impact on these average magnetic characteristics. In a second step, local measurement windings have been wound on single rings. The quasistatic *BH* loops have then been measured as a function of the position along the circumference of the ring, with *B* still the average induction over the entire magnetic cross section. A systematic fluctuation of typically 5% around the reference loop has been observed for all three materials, which cannot be attributed to measurement errors. In a third step, quastistatic *local BH*-loops have been measured at different radial positions. A dedicated measurement technique[2] has been used, allowing the measurement of the local flux between two points 1 mm apart. No variation of the *BH* loops with the radial position has been observed in case of the material cut using spark erosion. This result is in agreement with the very low mechanical impact of the cutting technique. In case of the material cut with a laser, a considerable variation of the *BH*-loops with the radial position has been observed. This proves that the heat affected zone extends several mm inside the material. For the punched material again no variation with the radial position could be observed. This shows that the impact of the punching is confined to a region <1 mm wide, close to the edge. © *1996 American Institute of Physics.* [S0021-8979(96)69308-1]

[1] IEC404-4 norm.
[2] D. Philips (unpublished).

 0021-8979/96/79(8)/5496/1/$10.00 © 1996 American Institute of Physics

The soft magnetic properties of stripes fabricated using laser ablation of multilayer thin films

Craig A. Grimes and Janet K. Lumpp
Department of Electrical Engineering, The University of Kentucky, Lexington, Kentucky 40506

We examine the low frequency *BH* loop and complex permeability spectra of multilayer permalloy films laser processed to define samples consisting of stripes parallel to the as-deposited hard axis. We begin by examining different laser energy densities for groove definition in films of different thickness. We observe that for well coupled multilayer films with thin, 15 nm, spacer layers the demagnetizing field, which is a function of groove depth, is able to reorient the easy and hard axes from the initial orientation. As the groove becomes more clearly defined the hard axis permeability increases, while the easy axis permeability decreases. The role of stripe width and ambient processing atmosphere are also investigated. © *1996 American Institute of Physics.* [S0021-8979(96)74408-5]

I. INTRODUCTION

Magnetic structures such as sensors[1,2] and identification markers[3,4] are typically fabricated using photolithographic techniques, in conjunction with etching or ion milling, to define the required geometries from magnetically soft multilayer thin films.[5] The magnetic properties of such devices are process dependent. To see if laser processing could offer a practical alternative to conventional photolithographic techniques we have investigated the use of a KrF excimer laser, with a 100-μm diam spot size and 248 nm wavelength, to define stripe patterns on magnetically soft multilayer thin films by ablation.

The multilayer films consist of four, eight, or twelve 80 nm $Ni_{81}Fe_{19}$ magnetic layers separated by either 15 or 45 nm silicon nitride spacers layers. The original samples were 16 mm squares; the laser beam was rastered across the samples parallel to the hard axis to define stripes separated by the 100-μm-wide laser ablated channel.

Figure 1 shows the experimental setup used for defining stripe geometries upon homogeneous multilayer magnetic thin films by ablation. The setup includes a MPB PSX-100 excimer laser, beam delivery optics, and a vacuum chamber. Excimer lasers do not operate continuously, but deliver pulses of high optical power. The sample holder is in the vacuum chamber which is mounted on a motorized translation stage. Vacuum processing was performed at a base pressure of approximately 10^{-3} Torr. The laser beam was incident normal to the basal plane of the sample. A 100-μm-diam spot size was used throughout this work, with a constant scan speed of 0.635 mm/s. The pulse repetition rate was 25 Hz, producing a constant spacing between pulses of 25.4 μm. Incident energy densities were 3.2, 8, and 18 J/cm^2; the laser pulse was 2.5 ns for power densities of, respectively, 1.3, 3.2, and 7.4 GW/cm^2.

The magnetic thin films examined in this study were fabricated using dc magnetron sputtering. The films were deposited onto 52-μm-thick PET (polyethylene terephthalate).[6] Prior to deposition the substrate was cleaned by sputter etching the substrate web in oxygen at a power level of 3 W/cm^2 for 6 s.[6] Background pressure in the sputtering chamber was 1.8 mTorr, the sputtering gas was argon. The films consisted of 80 nm $Ni_{81}Fe_{19}$ magnetic layers and silicon nitride (Si_3N_4) spacer layers that were either 15 nm or 45 nm thick. A 100 nm Si_3N_4 undercoat separated the substrate and first permalloy layer.[7] The silicon nitride layers were deposited by reactive sputtering from a silicon target in a nitrogen-rich environment.

The samples were cut into 16 mm squares, with the magnetic easy axis (EA) and hard axis (HA) perpendicular to each other along one axis of the square. All stripes were defined parallel to the HA. The lines were scanned 0.5, 1.0, or 2.0 mm center to center, resulting in stripes 0.4 0.9, and 1.9 mm wide with 0.1 mm separating grooves.

The low frequency *BH* loops (10 Hz), anisotropy field and coercive force were measured using a SHB BH-Looper. The complex permeability spectra was measured from 5 to 100 MHz using a thin film permeameter.[8]

II. RESULTS

Six different multilayer films were laser processed in air at the three different energy densities. Table I summarizes the degree to which the laser ablated grooves were defined.

Figure 2 shows the change in the 10 Hz *BH* loop of the film in response to laser rastering 0.9-mm-wide stripes across

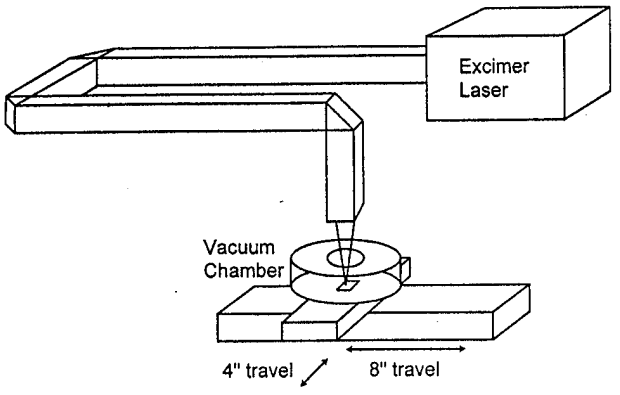


FIG. 1. Experimental setup including laser system, translation stages, and vacuum chamber.

 0021-8979/96/79(8)/5497/3/$10.00 © 1996 American Institute of Physics

TABLE I. Groove definition, in air, per laser energy density and film geometry. 80 nm $Ni_{81}Fe_{19}$ layers with Si_3N_4 spacer layers.

	3.2 J/cm^2	8 J/cm^2	18 J/cm^2
Magnetic layers: 15 nm spacers			
12	≈30%	≈80%	≈100%
8	≈50	100	100
4	100	100	100
Magnetic layers: 45 nm spacers			
12	≈10%	≈25%	≈50%
8	≈15	≈40	≈80
4	≈50	100	100

the sample, parallel to the HA, at the three energy densities. The original films were nearly isotropic, with a measured anisotropy field of approximately 1.4 Oe. Figure 2(a) shows the *BH* loop of the film laser rastered at 3.2 J/cm^2, the general shape of the *BH* loop is essentially unchanged from the as-deposited state, however, the EA and HA have switched directions. Figure 2(b), laser rastered at 8 J/cm^2, shows clearly discernible EA and HA, which are reversed from the as deposited state. Figure 2(c) laser rastered at 18 J/cm^2, has the *BH* loop characteristic of a uniaxial film. The switching of the EA and HA directions from the as deposited orientation can be explained in terms of the demagnetizing field.[9] The stripe is 0.9 mm wide and 1.125 μm thick for a demagnetizing factor of approximately 1.2×10^{-3}. Taking $4\pi Ms$ of the permalloy layer to be 10 400 G, the average $4\pi Ms$ value of the multilayer stack is ≈8875 G. The demagnetizing field of the stripe, which acts to orient the magnetization vector along the length of the stripe (the as-deposited HA), is simply the product of the demagnetizing factor and average $4\pi Ms$ value, approximately 10 Oe. With reference to Fig. 2, this demagnetizing field plays the role of the anisotropy field, which can be determined by extrapolation of the initial, HA linear magnetization curve. The measured *Hk* is 7 Oe, which combined with *Hk* of the as-deposited film indicates a change in the anisotropy field of 8.4 Oe, a value comparable to that calculated for the demagnetizing field.

Figures 3(a) and 3(b) show, respectively, the HA and EA 5–100 MHz complex permeability spectra of the same films measured in Fig. 2. The permeability is measured after application of a saturating dc magnetic field oriented perpendicular to the high frequency measurement field.[8] The HA permeability increases and the EA permeability decreases as the magnetization vector becomes increasingly oriented,

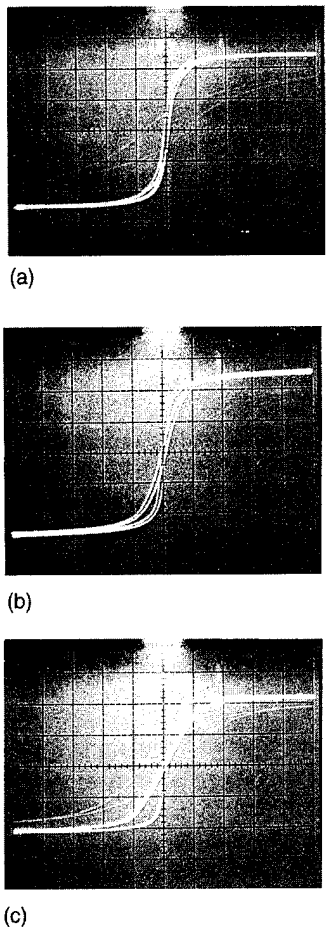
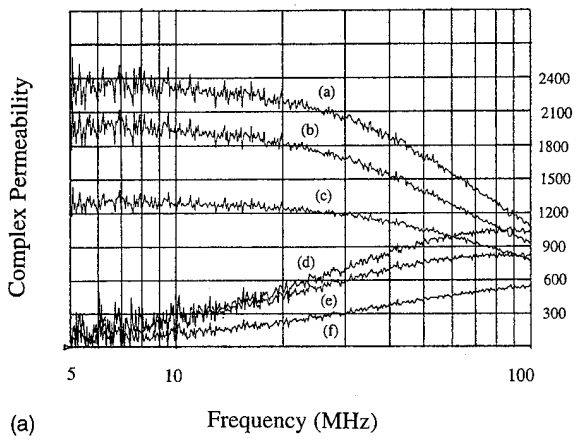


FIG. 2. The 10 Hz *BH* loops of multilayer films consisting of twelve 80 nm $Ni_{81}Fe_{19}$ layers and eleven 15 nm Si_3N_4 spacer layers laser rastered to define 0.9-mm-wide stripes, separated 0.1 mm at energy densities of (a) 3.2 J/cm^2 for partial line definition, (b) 8 J/cm^2 for substantial line definition, and (c) 18 J/cm^2 for complete line definition. X-scale is 5 Oe/div. *Y*-scale is arbitrary units.

which is caused by the geometry becoming more clearly defined through use of higher laser energy densities. Note the scale of Fig. 3 does not take into account the thickness of the spacer layers, or the reduction in material that has been ablated to define the stripes. Figure 4 shows a typical HA complex permeability spectra plot of the as-deposited film; the as-deposited EA trace is similar in shape, but reduced in magnitude by 65% from the HA. As expected, since perme-

TABLE II. Stripe width effect. Multilayer films of four 80 nm $Ni_{81}Fe_{19}$ layers with silicon nitride spacer layers of 15 nm or 45 nm.

	As deposited			Laser processed		
	Hc(Oe)	Hk(Oe)	$\lvert\mu\rvert$	Hc(Oe)	Hk(Oe)	$\lvert\mu\rvert$
Stripe width: 15 nm spacers						
0.4(mm)	0.27	1.4	1800	0.35	5.7	1400
0.9	0.27	1.4	1650	0.30	3.3	1250
Stripe width: 45 nm spacers						
0.4	0.38	5.0	2025	1.0	5.5	1800
0.9	0.38	5.0	2010	0.8	5.5	1800
1.9	0.38	4.8	1950	0.5	5.8	1950



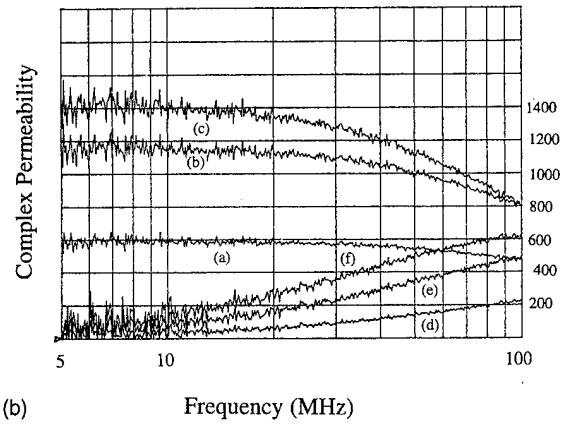


FIG. 3. (a) The hard axis complex permeability spectra of same films shown in Fig. 2: (a) μ' high energy raster, (b) μ' medium energy, (c) μ' low energy, (d) μ'' high energy, (e) μ'' medium energy, (f) μ'' low energy. (b) Corresponding easy axis of (a).

ability magnitude is inversely related to the anisotropy field, the laser processed samples show a dramatic reduction in permeability from the relatively isotropic as-deposited state.

The response of the 45 nm spacer layer films to laser processing is more complicated. In contrast to the 15 nm spacer layer films, the as-deposited 45 nm spacer layer films were fairly well oriented, with an anisotropy field of approximately 5.5 Oe, and, as seen by the *BH* loop, the different magnetic layers tend to act individually. The response of these thicker films to laser processing is still being studied.

The effect of different stripe widths was investigated by defining 1.9, 0.9, and 0.4 mm stripes, separated by 100 μm grooves, by laser rastering at 18 J/cm^2. Generally speaking, for all films smaller stripe widths resulted in higher coercivities; for the 15 nm spacer layer films smaller stripe widths resulted in larger anisotropy field values, while for the 45 nm spacer layer films the anisotropy field stayed generally constant with stripe width. Table II summarizes data obtained on multilayer films consisting of four magnetic layers with either 45 nm or 15 nm spacer layers: $|\mu|$ denotes the 5 MHz permeability magnitude.

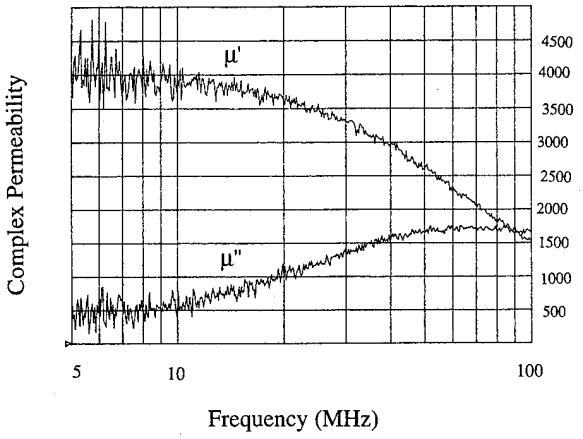


FIG. 4. As deposited, hard axis complex permeability spectra of films laser processed for Fig. 3.

The role of ambient atmosphere was investigated by comparing the magnetic properties of the same six different multilayer films rastered in vacuum at 18 J/cm^2 to define 0.9 mm stripes. Generally speaking, there was little difference in the measured magnetic properties between samples rastered in air or vacuum, although optical inspection showed them to be quite different in appearance. The material laser ablated in air redeposited on the sample in some kind of silicon nitride/permalloy mixture; it appeared that the redeposition plume was approximately 0.5 mm in width. The samples laser processed in vacuum were clean with no sign of redeposition.

ACKNOWLEDGMENT

This work was sponsored in part by the NASA-EPSCOR Office under Contract No. NCCW-60.

[1] T. A. Lafford, M. R. J. Gibbs, and C. Shearwood, J. Magn. Magn. Mater. **132**, 89 (1994).
[2] E. Lindner *et al.*, J. Chem. Soc. Faraday Trans. **89**, 361 (1993).
[3] R. Church and E. Heltemes, U.S. Patent No. 4 825 197.
[4] R. M. Pettigrew *et al.*, U.S. Patent No. 4 940 966.
[5] B. C. Webb *et al.*, J. Appl. Phys. **69**, 5611 (1991).
[6] C. A. Grimes, IEEE Trans. Mag. **31**, 409 (1995).
[7] C. A. Grimes, J. Appl. Phys. **79**, 8 (1996).
[8] C. A. Grimes, P. L. Trouilloud, and R. M. Walser, IEEE Trans. Magn. **MAG-24**, 603 (1988).
[9] J. A. Osborn, Phys. Rev. **67**, 351 (1945).

Magnetic garnet film epitaxy on nonsingular faces (abstract)

S. S. Gorelik, L. M. Letyuk, and A. T. Morchenko
Moscow State Institute of Steel and Alloys, Leninsky Prospect 4, Moscow, 117936 Russia

The single crystal films of magnetic garnets are widely used in various microelectronics devices. The yttrium–iron and bismuth–gallium-substituted magnetic garnet films were grown by liquid phase epitaxy from supercooled solutions on the basis $PbO+B_2O_3$. As substrates for films the gadolinium–gallium garnet wafers crystallographically oriented in the range from (111)- to (110)-directions are used. In experiments such growth process parameters as supercooling temperature and angular velocity of substrate rotation were varied too. The parameters to be examined were thickness, growth rate, crystallografic, magnetic, and magnetooptical characteristics of the as-grown films. To analyze the growth process kinetics it was developed the model, including the terms (supersaturation C_L-C_E) of the first and second orders for description of surface crystallization reaction. The following expression was derived for epitaxial growth rate:

$$f=\frac{D}{\rho\delta}\left[(C_L-C_E)+\frac{k_1\delta+D}{2k_2\delta}-\frac{\sqrt{(k_1\delta+D)^2+4k_2\delta D(C_L-C_E)}}{2k_2\delta}\right],$$

where D is diffusion coefficient, δ is diffusion boundary layer thickness on the solid–liquid interface, ρ is film density, C_L is concentration of garnet phase in the melted solution, C_E is equilibrium concentration, k_m is surface reaction constant (kinetic coefficient) of order m in

$$D\frac{\partial C}{\partial x}(0,t)=k_m[C(0,t)-C_E]^m.$$

A selected parameters are given for $(YBi)_3(FeGa)_5O_{12}$ films grown under the same conditions:

Orientation	0°(110)	30′	2°30′	2°30′	7°30′	90°(111)
Growth rate, μm/min	···	0.1	0.075	0.08	0.16	0.26
Specific Faraday rotation, deg/cm	···	1526	1804	1713	1439	1953

The peculiarities of domain structure and properties of obtained films are discussed.

© *1996 American Institute of Physics.* [S0021-8979(96)69408-8]

 0021-8979/96/79(8)/5500/1/$10.00 © 1996 American Institute of Physics

The effects of average grain size on the magnetic properties and corrosion resistance of NdFeB sintered magnets

D. W. Scott, B. M. Ma, Y. L. Liang, and C. O. Bounds
Rhône-Poulenc, Rare Earths and Gallium, CN 7500, Cranbury, New Jersey 08512

Magnets with a nominal composition of $Nd_{14.5}Fe_{79.5}B_6$ have been prepared by the conventional powder metallurgy technique. Precursor alloy powders with average particle sizes of 2.5, 3.0, 3.5, and 4.2 μm were included in this study. Average particle size and oxygen content were effectively manipulated to control the average grain size in the sintered magnets. Typically, for NdFeB sintered magnets, the corrosion resistance of these magnets was improved with increasing oxygen content. The corrosion resistance of magnets varied significantly with the average particle size of precursor alloy powders. For a fixed oxygen content, magnets made from powders of larger sizes exhibited a higher weight loss (a poor corrosion resistance) when compared to those made from smaller alloy powders. However, the H_{ci} of magnets made from 2.5, 3.0, and 3.5 μm precursor alloy powders was found to decrease drastically with increasing oxygen content while magnets made from the 4.2 μm powder was found to remain relatively constant with increasing oxygen content. To optimize magnetic performance, one needs to compromise the corrosion resistance and the H_{ci} obtained by balancing the average particle size of the precursor alloy powder for magnet fabrication, as well as the oxygen content and the average grain size in the finished magnet. © *1996 American Institute of Physics.* [S0021-8979(96)31508-9]

INTRODUCTION

The average grain size of finished magnets has been found to be a determining factor for the B_r, H_{ci}, and BH_{max} obtained for NdFeB magnets prepared by the powder metallurgy (P/M) and sintering route.[1–3] Using the P/M process, oxygen pick-up has always been a concern for magnet manufacturing. Increasing oxygen content to a certain limit has been found to improve the bulk corrosion resistance and the magnetic properties, namely, B_r, H_{ci}, and BH_{max} of the magnets obtained.[4,5] This raised an interesting idea for producing sintered magnets with both good bulk corrosion resistance and a high H_{ci} and BH_{max}. By balancing the milled powder particle size (or the surface area obtained), powder handling, oxygen pick-up, and sintering conditions: one can actually manipulate the average grain size and the oxygen content in the finished magnets.

In this article, we discuss two different means of controlling the average grain size in sintered NdFeB magnets by (1) varying the average particle size of precursor alloy powder and (2) controlling the oxygen content in finished magnets. It is our intention to relate the B_r, H_{ci}, BH_{max}, and H_k of finished magnets to the average particle size of precursor alloy powders. The relationship of the bulk corrosion rate of the finished magnets to the average grain size and oxygen content will also be discussed.

EXPERIMENT

Magnets included in this study were prepared from a conventionally cast alloy with a nominal composition of $Nd_{14.5}Fe_{79.5}B_6$ using classical powder metallurgy techniques. Four batches of powders with average particle sizes of 2.5, 3.0, 3.5, and 4.2 μm were then prepared by attrition milling. To study the effects of oxygen content on both the magnetic performance and the corrosion resistance, milled powders were deliberately oxidized in a controlled manner. Other than the oxidation step, the magnet fabrications and corrosion testing were identical to regular magnets as reported in previous work.[3]

RESULTS AND DISCUSSION

Table I presents the relationships of the bulk corrosion rate (the weight loss) and the magnetic properties of finished magnets to the average particle size of precursor alloy powders, the average grain size, and the oxygen content in the finished magnets. Magnets made from powders of 2.5 μm powders typically exhibit a higher oxygen content than those made from larger powders exposed to the same amount of air. When processed under the low oxygen condition (i.e., without introducing any excessive air for controlled oxidation), the oxygen contents in finished magnets range from 0.12 to 0.14 wt % for all magnets regardless of the average particle size of powders. When a slight amount of oxygen (150 ml) was introduced, the oxygen content in finished magnets increased sharply from a 0.13 wt % to about 0.47, 0.40, 0.37, and 0.41 wt % for magnets made from precursor alloy powers with the average particle size of 2.5, 3.0, 3.5, and 4.2 μm, respectively. This rapid increase in oxygen content suggests that the precursor alloy powders included in this study exhibit a very high oxygen (or air) affinity.

Shown in Fig. 1 is the relationship between oxygen content of finished magnets and the amount of air injected for controlled oxidation and the average particle size of precursor alloy powders. As mentioned earlier, the oxygen content in finished magnets increased exponentially at low amounts of air injection then become relatively flat when the amount of injected air was increased to more than 300 ml. Because of the smaller particle size and, presumably, the high surface

 0021-8979/96/79(8)/5501/3/$10.00 © 1996 American Institute of Physics

TABLE I. Magnetic properties for $Nd_{14.5}Fe_{80.5}B_6$ sintered magnets for different particle sizes.

Air added (ml)	Oxygen content (wt %)	Weight loss (mg/cm^2)	Grain size (μm)	B_r (kG)	H_c (kOe)	H_{ci} (kOe)	BH_{max} (MGOe)	H_k (kOe)	Density (g/cc)
			2.5 micron powder						
0	0.14	21.2	7.1	13.2	11.2	12.8	41.3	10.9	7.54
150	0.47	0.2	···	12.6	6.9	8.8	29.8	4.1	7.47
300	1.55	−20.1[a]	···	3.4	0.3	0.3	0.3	0.1	5.63
450	1.77	...[b]	···	3.0	0.2	0.2	0.2	0.1	5.56
600	1.75	...,[b]	···	3.1	0.2	0.3	0.3	0.1	5.67
			3.0 micron powder						
0	0.12	30.6	7.5	12.9	11.6	13.4	39.4	11.6	7.55
150	0.40	0.7	7.1	13.2	10.6	12.0	40.6	10.1	7.58
300	0.53	0.1	6.9	12.9	9.2	10.1	38.1	7.2	7.56
450	0.65	0.0	6.2	12.9	8.1	9.0	37.6	6.2	7.56
600	0.52	0.1	7.5	13.0	8.4	9.2	39.2	7.2	7.56
			3.5 micron powder						
0	0.13	54.2	8.8	13.2	11.0	13.4	40.8	10.6	7.56
150	0.37	8.0	···	13.1	11.1	13.1	40.5	10.7	7.57
300	0.47	3.2	···	13.2	10.5	11.7	41.6	10.2	7.54
450	0.49	2.3	···	13.0	10.4	11.6	40.5	10.1	7.54
600	0.49	1.1	···	13.0	10.4	11.5	39.9	10.0	7.54
			4.2 micron powder						
0	0.13	107.8	9.0	13.0	10.3	11.1	39.6	10.1	7.55
150	0.41	52.3	···	13.0	11.3	12.7	40.2	11.2	7.51
300	0.41	43.0	···	12.8	11.1	12.8	38.6	10.9	7.50
450	0.43	38.7	···	12.9	11.3	12.7	39.6	11.2	7.50
600	0.43	32.2	···	13.0	10.9	12.4	40.1	10.7	7.50

[a]Indicates a weight gain.
[b]Sample was destroyed during testing.

area and chemical potential, magnets made from precursor alloy powder of 2.5 μm in size yielded an oxygen content of more than 1.5 wt % when 300 ml of air was injected for controlled oxidation. This value is much higher than magnets made from 3.0, 3.5, and 4.2 μm powders when exposed to the same amount of air. These trends suggest that the average particle size of the precursor alloy powder is a very important factor for magnet processing. Thus, the desired average particle size of precursor alloy powder must be balanced with the oxygen pick-up occurring during processing in order to optimize desired properties.

For a fixed precursor alloy powder, the weight loss of magnets obtained decreased with increasing oxygen content in finished magnets. However, there is an important phenomenon which should be addressed concerning the relationship of the bulk weight loss to the oxygen content of finished magnets. Shown in Fig. 2 is the relationship of weight loss of finished magnets with a 0.1 and 0.4 wt % oxygen content to the average particle size of precursor alloy powders. For a fixed oxygen content, the weight loss increased with increasing size of precursor alloy powder. When the oxygen content of finished magnets was increased from 0.1 to 0.4 wt %, a lower weight loss (i.e., a better corrosion resistance) was obtained as anticipated. This phenomenon may be explained

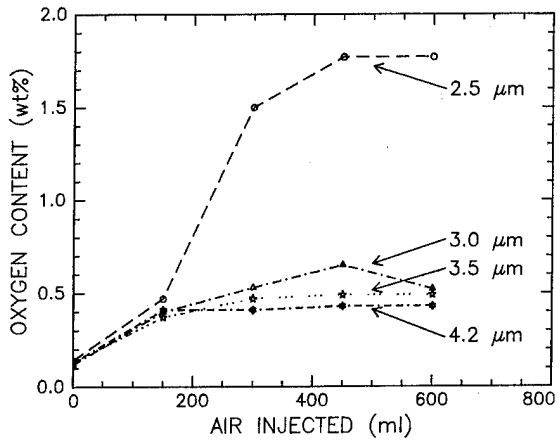


FIG. 1. Relationship of oxygen content in finished magnets to the average particle size of precursor alloy powder and the amount of air injection used for conduction control oxidation.

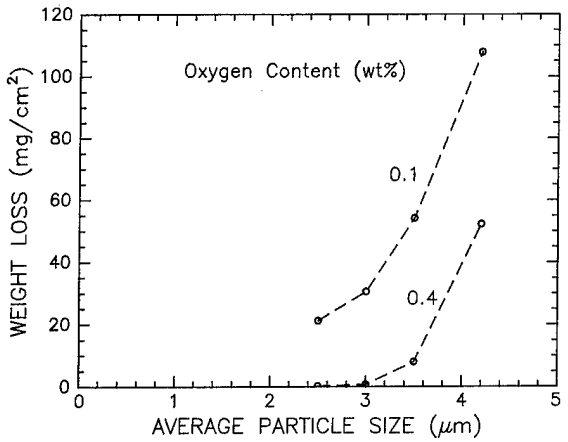


FIG. 2. Relationship of weight loss to the average particle size of precursor alloy powder and the oxygen content in finished magnets.

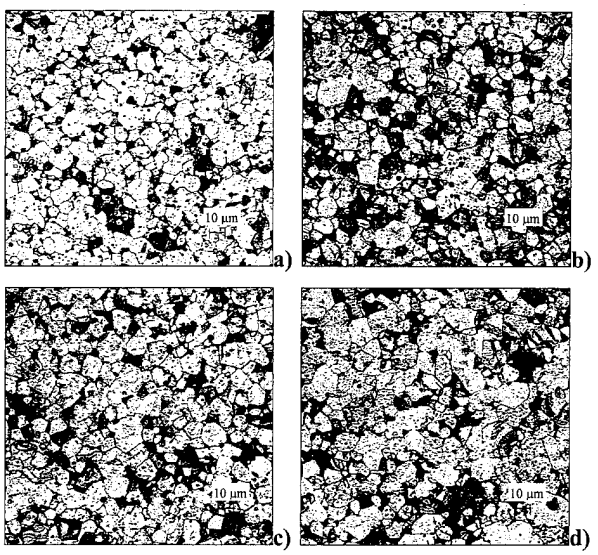


FIG. 3. Optical micrograph of magnets produced from precursor alloy powders with average particle size of (a) 2.5, (b) 3.0, (c) 3.5, and (d) 4.2 μm (FSSS) under low oxygen process. The oxygen content of these magnets were all maintained at about 0.13–0.14 wt %. The average grain size of these magnets are 7.1, 7.5, 8.8, and 9.0 μm, respectively.

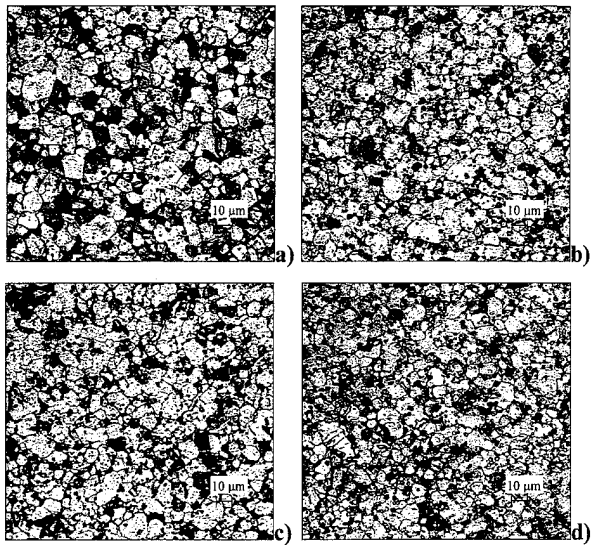


FIG. 4. Optical micrographs of magnets made from precursor alloy powder with average particle size of 3.0 μm with oxygen content of (a) 0.12, (b) 0.40, (c) 0.53, and (d) 0.65 wt % in finished magnets.

by the fact that the Nd-rich phase is more evenly distributed in magnets made from precursor alloy powders of smaller sizes; this issue requires further investigation.

Shown in Figs. 3(a)–3(d) are optical micrographs of magnets made from precursor alloy powders with average particle sizes of 2.5, 3.0, 3.5, and 4.2 μm, respectively, at the lowest oxygen content (0.13–0.14 wt %). As with any P/M process, grain growth occurs during sintering resulting in average grain sizes in the sintered magnets of 7.1, 7.5, 8.8, and 9.0 μm, respectively. Although the average particle size of powder measured by the FSSS cannot be directly translated to the average grain size of finished magnets measured by an image analyzer, it is known that grain growth is more rapid in magnets made from powder of 2.5 μm when compared to those made from 3.5 or 4.2 μm. Besides the difference in average grain sizes of finished magnets, the size of the Nd-rich phase[6] in a magnet made from the 4.2 μm powder appeared to be larger than that made from 2.5 μm. The large size of Nd-rich grain boundary phase may be one cause of the high weight loss of magnets made from powders of large average particle size.

Shown in Figs. 4(a)–4(d) are optical micrographs of magnets made from precursor alloy powder with an average particle size of 3.0 μm with oxygen contents of 0.12, 0.40, 0.53, and 0.65 wt %, respectively. The average grain sizes of these magnets (7.5, 7.1, 6.9, and 6.2, respectively) decreased slightly with increasing oxygen content in finished magnets suggesting that the oxygen (or oxides formed) may act as a grain growth inhibitor during sintering. The size of the Nd-rich grain boundary phase also appeared to be larger and more agglomerated in magnets of low oxygen content (0.12 wt %) than those of higher oxygen contents (0.40, 0.53, and 0.65 wt %). This change in the size and the distribution of the Nd-rich grain boundary phase may contribute to the improvement in weight loss of magnets with oxygen content of more than 0.4 wt %.

Despite the improvement in corrosion resistance (lower weight loss), the H_{ci} of magnets made from 3.0 μm powder decreased from 13.4 to 9.0 kOe (listed in Table I) when the oxygen content was increased from 0.12 to 0.65 wt %. The opposing trends of corrosion resistance and H_{ci} with increasing oxygen content raises an interesting issue: one may need to compromise low weight loss (good corrosion resistance) with high H_{ci} by adjusting the oxygen content in magnets. The decrease of H_{ci} with increasing oxygen content suggests that the Nd-grain boundary phase may have been over oxidized and transforms into nucleation centers during magnetization reversal. The decrease in H_{ci} with increased oxygen content becomes more pronounced when magnets were prepared from the 2.5 μm precursor alloy powder. A similar trend (but less severe) can also be observed on magnets made from 3.5 μm precursor alloy powder. For magnets made from the 4.2 μm precursor alloy powder, this situation is reversed: a slight increase in H_{ci} can be observed when the oxygen content was increased from 0.13 to 0.40 wt %. This opposite trend may be attributed to the fact that the large size of the Nd-rich grain boundary phase is only partially oxidized and still serves as grain insulators for enhancing the H_{ci}.[2] Unlike H_{ci}, both B_r and $BH_{\max}$ seem to be less sensitive to the increasing oxygen content. The variation of H_k with the size of precursor alloy powder or the oxygen content appeared to be very similar to that of H_{ci}.

[1] B. M. Ma and R. F. Krause, in the Proceedings of the 5th International Symposium on Anisotropy and Coercivity in RE Transition Metal Alloys, edited by C. Herget, H. Kronmüller, and R. Poerschke, September 3, 1987, Bad Soden, Germany, Part II, p. 141.
[2] R. Ramish, G. Thomas, and B. M. Ma, J. Appl. Phys. **64**, 6414 (1988).
[3] B. M. Ma, Y. L. Liang, D. W. Scott, W. L. Liu, and C. O. Bounds, in the Proceedings of the 13th International Workshop on RE Magnets & Their Application, Birmingham, U.K., September, 1994, p. 309.
[4] K. Tokuhara and S. Hirosawa, J. Appl. Phys. **69**, 5521 (1991).
[5] A. K. Kim and F. E. Camp, J. Mater. Eng. **13**, 175 (1991).
[6] Y. Matsura, S. Hirosawa, H. Yamamoto, S. Fujimura, M. Sagawa, and K. Osamura, Jpn. J. Appl. Phys. **24**, L635 (1985).

Unusual magnetic behavior in Nd–Fe–B alloy powder compacts

H. Wan,[a] F. T. Parker, F. F. Putris, and A. E. Berkowitz
Center for Magnetic Recording Research, University of California–San Diego, La Jolla, California 92093-0401

We report an unusual magnetic behavior in powders prepared by spark-eroding (in liquid Ar) alloy electrodes containing approximately equal weights of Fe and $Nd_2Fe_{14}B$ in an effort to prepare composite permanent magnets. Magnetization exhibits reproducible thermal hysteresis, peaking in all applied fields near 520 °C when warming, but increasing monotonically when cooling to room temperature from 700 °C and above. Mössbauer spectroscopy was used to show that the behavior is due to the metastability of $Fe_{1-x}O$ produced in the powders by partial oxidation in Ar gas flow. This compound, paramagnetic at room temperature, decomposes only slowly below 570 °C into ferromagnetic Fe and ferrimagnetic Fe_3O_4. The reverse reaction occurs readily at higher temperatures. © *1996 American Institute of Physics.* [S0021-8979(96)31608-5]

I. INTRODUCTION

Materials based on the intermediate compound $Nd_2Fe_{14}B$ offer some of the best permanent magnet properties available.[1] Recently, methods to improve the permanent magnet characteristics have been devised.[2] In the exchange-spring concept, small particles of relatively high magnetization and low magnetocrystalline anisotropy are exchange coupled to small particles of lower magnetization and large magnetocrystalline anisotropy. Particles can be no larger than a few hundred angstroms. One obtains intermediate properties, hopefully with a larger magnetic energy product. Some improvement may be found for randomly aligned particles, with more improvement for aligned particles.[3] Several attempts have made to realize these exchange couples, with the system Fe–$Nd_2Fe_{14}B$ as a typical example. The usual process consists of rapid quenching of the melt to achieve a nearly uniform stoichiometry, often in amorphous structural form, followed by careful annealing to achieve the necessary small grain size. We have previously[4] described preparation by spark erosion of particles of the initial homogeneous alloy mixture of Fe–$Nd_2Fe_{14}B$. In this work, we describe an unusual magnetization thermal hysteresis obtained while annealing spark-eroded particles. This is shown to result from two factors: the ease of oxidation of the elements Nd and B, and the metastability of the compound $Fe_{1-x}O$ which is formed due to partial oxidation of the Fe.

II. EXPERIMENTAL DETAILS

$Nd_2Fe_{14}B$ and Fe were chosen as the high anisotropy and high magnetization phases, respectively. Elements were arc melted to make electrodes. These contained 47 wt % Fe and 53 wt % $Nd_2Fe_{14}B$. Particles of various sizes were produced by spark erosion in liquid Ar, and stored under pentane. Size-cut fine particles (less than 5 μm diam) were obtained by sedimentation in pentane, then dried in Ar and pressed in Ar at about 80 kpsi. X-ray diffraction on the pellets showed an amorphous structure.

Two experimental techniques were primarily used for measurement. Magnetization (M) was measured on a vibrating sample magnetometer (VSM) in applied field (H) to 24 kOe and at temperatures of 296 K and above. Transmission Mössbauer spectroscopy (TMS) measurements were obtained between 79 and 296 K. Velocity calibration and isomer shift reference were obtained with Fe metal at 296 K.

Samples for VSM measurement and TMS were prepared and treated in similar ways. Both were subject to an initial 700 °C crystallization anneal in flowing Ar of 99.99% purity for 20 min. VSM measurements lasted several hours with the sample in a stainless steel furnace in flowing Ar. Several pellets were examined by VSM measurement. The single pellet used in TMS was annealed in flowing Ar in a quartz tube furnace. The Mössbauer pellet had to be somewhat thinner than the VSM pellets (~20 vs ~60 μm).

III. RESULTS AND DISCUSSION

Magnetization versus temperature (T) measurements for freshly pressed, unannealed powder showed a broad magnetic transition near 180 °C, characteristic of amorphous Nd–Fe–B. After the initial crystallization anneal, multiple temperature sweeps of M vs T were obtained. Some ex-

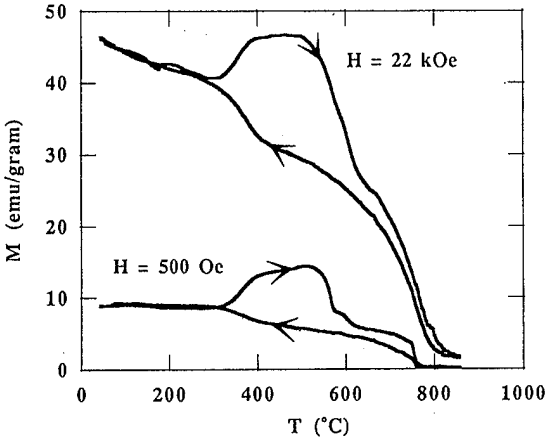


FIG. 1. Magnetization of spark-eroded Nd–Fe–B alloy powder compact vs temperature. The applied fields are shown on the curves. Arrows denote heating and cooling. A complete thermal loop lasted several hours. The sample had been previously annealed at 700 °C (20 min).

[a]Current address: Solid State Electronics Center, Honeywell, Inc., Plymouth, MN 55441.

 0021-8979/96/79(8)/5504/3/$10.00 © 1996 American Institute of Physics

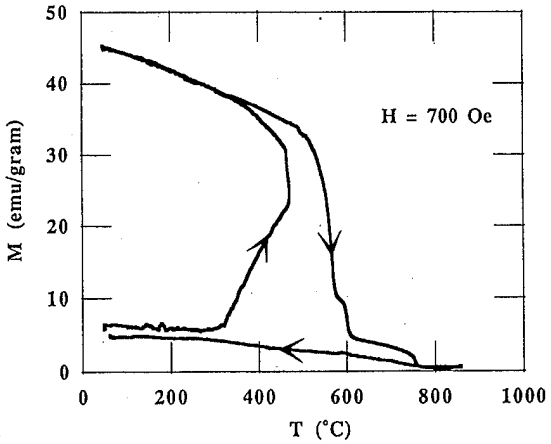


FIG. 2. Magnetization of spark-eroded Nd–Fe–B alloy powder compact vs temperature. The procedure was similar to that shown in Fig. 1, but heating was interrupted at about 465 °C (10 min holding time) and the sample cooled to near room temperature.

amples are shown in Figs. 1 and 2. A large thermal hysteresis is seen in the full-temperature sweep, in both large and small H. Several pellets exhibited similar behavior. On increasing temperature from room temperature (RT), the magnetization shows relatively little change at first, but then increases sharply, reaching a maximum near $T=520$ °C. M then decreases rapidly, and levels off until the Curie temperature (T_C) of α-Fe metal at 770 °C. On then decreasing T, one again finds the α-Fe T_C, but the magnetization then shows a slow monotonic increase to RT. The magnetization at RT is about the same as the initial value. Subsequent thermal loops show similar behavior. If the sample is heated from RT to near 465 °C and then cooled, the larger M is retained at RT (Fig. 2). Subsequent warming retraces the cooling curve, with M dropping sharply above 560 °C as seen in the previous thermal loop (Fig. 1). There is no indication of any $Nd_2Fe_{14}B$ ($T_C=312$ °C).[1] The M vs H curves obtained at various points on the thermal loop show normal ferromagnetic behavior. A sample warmed from RT to 700 °C (the initial crystallization temperature) and then cooled exhibits no peak in M while cooling, with magnetization behavior similar to samples cooled from above the T_C of α-Fe, but with a slightly larger M at all temperatures. The thermal hysteresis seen in all samples seems incompatible with any possible explanation based on purely thermomagnetic arguments.

Mössbauer spectroscopy was used to determine the iron-containing compounds at three positions on the thermal hysteresis curve (Fig. 3). The pellet was first measured after the initial crystallization anneal at 700 °C, which yielded a relatively low magnetization on a small portion of the pellet. This preparation is denoted LM1. The pellet was then heated at 400 °C for 10 min, yielding a larger M, and the preparation is denoted as HM. The pellet was then heated at 850 °C for 10 min, the result denoted as LM2. At this point, the pellet was somewhat reduced in area and in several large pieces. The Mössbauer spectral area is thus reduced relative to the area obtained in the two previous measurements. Warming to and cooling from each treatment temperature

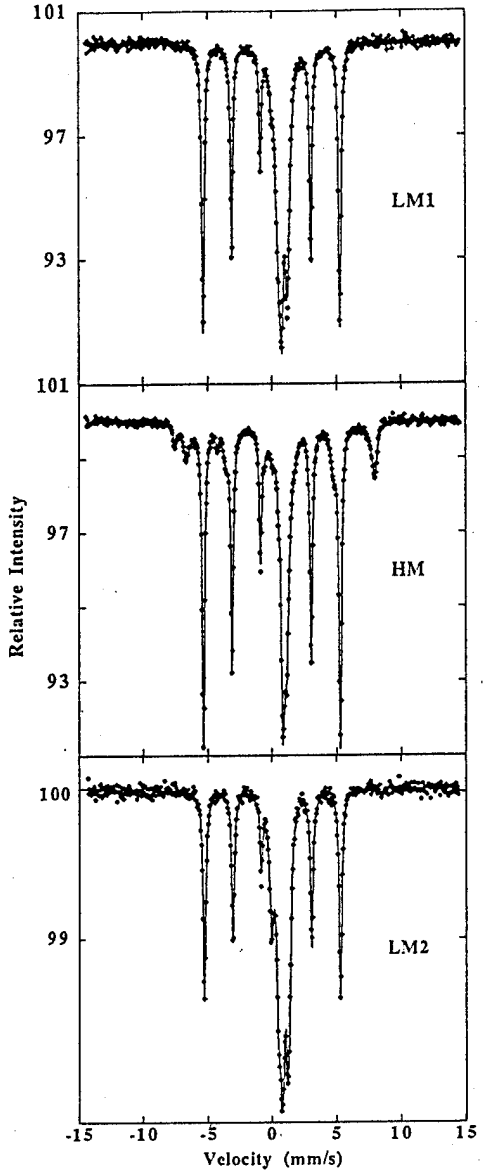


FIG. 3. Mössbauer data obtained for spark-eroded Nd–Fe–B alloy powder compact at 296 K. The measurement denoted as LM1 was obtained after the initial 700 °C (20 min) crystallization anneal, HM after subsequent 400 °C (10 min) anneal, and LM2 after subsequent 850 °C (10 min) anneal. The lines denote least-squares fits.

took only a few minutes, in contrast to the much longer times at elevated temperatures in the VSM furnace.

The Mössbauer spectrum of LM1 can be identified as a combination of subspectra from magnetic α-Fe and paramagnetic $Fe_{1-x}O$ (Table I). The former exhibits a characteristic sextet with a magnetic hyperfine field of 330 kOe and a zero isomer shift. $Fe_{1-x}O$ exhibits a broad quadrupole-split doublet with a large, positive isomer shift characteristic of Fe^{2+} (Table I). There is no evidence of $Nd_2Fe_{14}B$ in the spectrum. By determining the upper limit on the amount of the relatively low-field (287 kOe) $16k_1$ subspectrum of $Nd_2Fe_{14}B$,[5] one finds less than 0.2% of the Fe in $Nd_2Fe_{14}B$, compared to the expected 45%. Similar oxidation characteristics have been seen[6] on the surface of bulk $Nd_2Fe_{14}B$, which was annealed for 1 h at 600 °C in a vacuum with O_2–H_2O partial

TABLE I. Mössbauer parameters for each preparation at 296 K. The first section shows the Fe metal atom fraction for each phase, separated into magnetic and nonmagnetic subsections. Statistical errors are shown in parentheses. The next section shows the fraction of Fe in all of the phases listed in the first section. The final section tabulates the average quadrupole splitting (ΔE) and isomer shift (IS) for $Fe_{1-x}O$.

Metal atom %	LM1	HM	LM2
Magnetic			
% Fe metal	57(1)	55(1)	44(1)
% Fe_3O_4	<1	19(1)	<1
Nonmagnetic			
% Fe^{2+}	39(2)	24(1)	36(3)
% Fe^{3+}	4(1)	2(1)	19(3)
Fe/(Fe+O)	0.69	0.66	0.62
Fe^{2+}			
$\langle \Delta E \rangle$ (mm/s)	0.69(1)	0.26(1)	0.70(1)
$\langle IS \rangle$ (mm/s)	0.93(1)	1.07(1)	0.92(1)

pressures about 5 orders of magnitude lower than for our treatment. Pure Fe metal was found on the surface, the much more electropositive Nd and B preferentially oxidizing into nonmagnetic (at RT) elemental oxides. Oxidation has apparently occurred in our samples due to the water vapor content of the Ar gas used in preparation and VSM measurements.

Several changes are seen in the Mössbauer spectrum of the HM preparation. Most notable is the presence of spinel Fe_3O_4, which can be recognized by the two peaks at the most negative velocity, characteristic of the two subspectra hyperfine field pattern in cubic magnetically ordered Fe_3O_4. The relative subspectral areas, magnetic hyperfine fields of 483 and 450 kOe, and isomer shifts, 0.28 and 0.63 mm/s, respectively, are consistent with Fe_3O_4.[7] The fractional amount of $Fe_{1-x}O$ has decreased from LM1, and the quadrupole splitting decreased, as expected[8] for annealed $Fe_{1-x}O$. The fraction of Fe metal has stayed about the same, even though the oxygen-to-iron ratio has increased from LM1 (Table I). Finally, preparation LM2 shows a spectrum similar to that for LM1, with no Fe_3O_4, but with a small fraction of quadrupole-split nonmagnetic Fe^{3+}. The fraction of Fe metal has decreased sharply from HM, and the amount of $Fe_{1-x}O$ increased. Mössbauer data obtained at lower temperatures (not shown) exhibited the $Fe_{1-x}O$ Néel transition near 200 K, as expected.[8]

The unusual cyclic magnetic behavior is therefore due to the metastable nature of $Fe_{1-x}O$. This material is stable only above 570 °C, but is metastable below about 200 °C.[8] At intermediate temperatures, it decomposes approximately as $4FeO \rightarrow Fe + Fe_3O_4$. Both decomposition products exhibit significant magnetization in the decomposition temperature range, and provide the surge in magnetization as T is raised above 400 °C. Above this T, the Curie point of Fe_3O_4 (585 °C) and reformation of $Fe_{1-x}O$ cause a rapid decrease in M. The T_C of α-Fe provides the highest-T magnetic transition. On cooling, one sees the α-Fe transition, but no surge in M below 570 °C because of the metastability of $Fe_{1-x}O$. The slightly more rapid increase in M seen on cooling below 400 °C is probably due to initial $Fe_{1-x}O$ decomposition. The metastability of $Fe_{1-x}O$ provides another demonstration of the wide variety of magnetic phenomena.

ACKNOWLEDGMENTS

This research was supported by NSF Grants Nos. ECS-9119005 and DMR-9400439.

[1] J. F. Herbst, Rev. Mod. Phys. **63**, 819 (1991).
[2] E. F. Kneller and R. Hawig, IEEE Trans. Magn. **27**, 3588 (1991).
[3] R. Skomski and J. M. D. Coey, Phys. Rev. B **48**, 15812 (1993).
[4] H. Wan and A. E. Berkowitz, Scr. Metall. Mater. **32**, 1827 (1995).
[5] F. Grandjean, G. J. Long, D. E. Tharp, O. A. Pringle, and W. J. James, J. Phys. (Paris) Colloq. **49**, C8-581 (1988).
[6] S. Hirosawa, H. Tanimoto, and S. Nasu, Nucl. Instrum. Methods B **76**, 373 (1993).
[7] E. de Grave, R. M. Persoons, R. E. Vandenberghe, and P. M. A. de Bakker, Phys. Rev. B **47**, 5881 (1993).
[8] H. Schecter, P. Hillman, and M. Ron, J. Appl. Phys. **37**, 3043 (1966).

Magnetocrystalline anisotropy and spin reorientation in $Gd_{1-x}Dy_xCo_4B$

T. Ito, H. Asano, H. Ido, and M. Yamada
Department of Applied Physics, Tohoku Gakuin University, Tagajo 985, Japan

Magnetic measurements at various temperatures have been performed for loose powder and field-oriented samples of $Gd_{1-x}Dy_xCo_4B$ with $x=0$, 0.05, and 0.1. The temperature dependences of spontaneous magnetization in these compounds are determined. It is found that a spin reorientation occurs at around $T=162$ K for $Gd_{0.95}Dy_{0.05}Co_4B$ and at around 225 K for $Gd_{0.9}Dy_{0.1}Co_4B$. The temperature dependences of magnetic anisotropy constants, $K_1(Gd_{1-x}Dy_xCo_4B)$, of $Gd_{1-x}Dy_xCo_4B$ with $x=0$ and 0.1 are determined. The anomalous temperature dependence of K_1 ($GdCo_4B$) is well explained by taking account of the Gd sublattice magnetic anisotropy due to the dipole–dipole interaction and the Co sublattice magnetic anisotropy similar to that in YCo_4B. The temperature dependence of the Dy sublattice magnetic anisotropy constant, $K_1(Dy)$, has also been determined by making use of $K_1(GdCo_4B)$ and $K_1(Gd_{0.9}Dy_{0.1}Co_4B)$. © *1996 American Institute of Physics.* [S0021-8979(96)31708-1]

I. INTRODUCTION

RCo_4B (R=rare earth) compounds have a hexagonal $CeCo_4B$-type structure,[1] which is derived from the $CaCu_5$-type structure by replacing the $2c$-site Co atoms by B atoms. In our previous work, the substitution effect of Dy for the magnetic properties of $GdCo_4B$ were observed to investigate the magnetic state of Dy in the $CeCo_4B$-type structure.[2,3] In this work, to confirm the magnetocrystalline anisotropy of Gd and Co sublattices as well as the very strong anisotropy of the Dy sublattice in the $CeCo_4B$-type structure, the magnetic measurements on $Gd_{1-x}Dy_xCo_4B$ with $x=0$, 0.05, and 0.1 have been extended to the higher temperature region.

II. SPECIMENS AND CRYSTAL STRUCTURE

Ingots of $Gd_{1-x}Dy_xCo_4B$ were prepared by melting raw materials of 99.9% purity for Gd, Dy, and B, and 99.99% for Co in an arc furnace. The ingots were melted eight times to homogenize the composition, and then annealed at 800 °C for three days. The crystal structure has been confirmed by x-ray diffraction to be of the $CeCo_4B$-type structure. Field-oriented samples were prepared by solidifying the mixture of epoxy resin and the powdered specimen (<32 μm) in the magnetic field of 20 kOe at room temperature.

III. EXPERIMENTAL RESULTS AND DISCUSSION

The magnetization curves at various temperatures between 80 and 521 K have been measured in magnetic fields up to 20 kOe for loose powder samples of $Gd_{1-x}Dy_xCo_4B$ with $x=0$, 0.05, and 0.1. Spontaneous magnetizations have been estimated by extrapolating the high field linear part of the magnetization curves to $H=0$, and plotted against temperatures in Fig. 1. The detailed figures above 300 K are also shown separately in the inset. The Curie temperature (T_C) and compensation temperature (T_{comp}) shown in the inset seem to decrease toward the values of 428 and 352 K for $DyCo_4B$,[4] respectively. An anomalous decrease of magnetization of about 0.4 μ_B/f.u. (formula unit) in the temperature regions around 150 and 230 K for the data of $x=0.05$ and $x=0.1$, respectively, is caused by a spin reorientation which will be shown later.

Next, the magnetization curves of field-oriented samples $Gd_{1-x}Dy_xCo_4B$ with $x=0$, 0.05, and 0.1 have been measured at various temperatures between 80 and 300 K. Some examples for $GdCo_4B$ and $Gd_{1-x}Dy_xCo_4B$ with $x=0.05$ and 0.1 are shown in Figs. 2 and 3, respectively. It is seen that $GdCo_4B$ has an axial anisotropy at all temperatures below $T_C=503$ K, while the spin reorientation occurs at around 160 and 230 K for $x=0.05$ and $x=0.1$, respectively.

To estimate the magnetocrystalline anisotropy constant K_1 for $GdCo_4B$ and $Gd_{0.9}Dy_{0.1}Co_4B$, the magnetization curves at various temperatures have been analyzed by the following method. The linear parts of the magnetization curves along with the hard axis in the decreasing field are shifted in parallel so as to go through the origin, and then an anisotropy field H_a is defined as a field at which the shifted straight line reaches the saturation magnetization (M_s). The anisotropy constant K_1 calculated by the equation $K_1=(1/2)M_sH_a$ is plotted against temperature in Fig. 4 for $GdCo_4B$ and in Fig. 5 for $Gd_{0.9}Dy_{0.1}Co_4B$, respectively. The anomalous temperature dependence of K_1 for $GdCo_4B$ is ex-

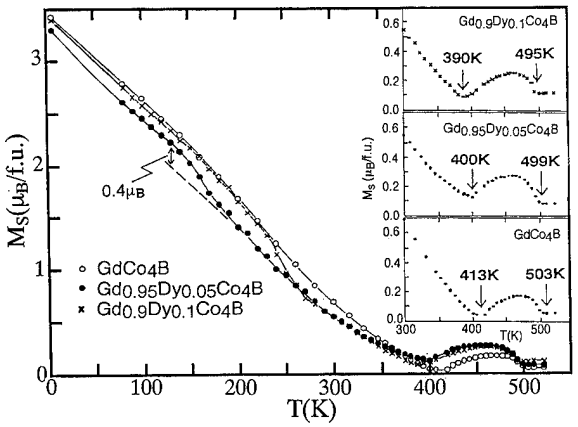


FIG. 1. Spontaneous magnetization vs temperature for $Gd_{1-x}Dy_xCo_4B$ with $x=0$, 0.05, and 0,1. Inset: detailed figures near the Curie and compensation temperatures (see the text).

 0021-8979/96/79(8)/5507/3/$10.00 © 1996 American Institute of Physics

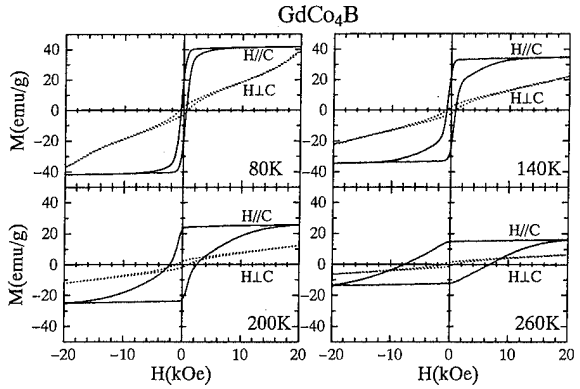


FIG. 2. Some examples for magnetization curves of the field-oriented sample of $GdCo_4B$.

plained by the superposition of the anisotropies of the Gd and Co sublattices. The Gd-sublattice anisotropy of $GdCo_4B$ was calculated by taking account of the Gd–Gd and Gd–Co dipole interactions within a sphere of radius of 1000 Å around the Gd atom in the crystal, and is shown by the dashed line in Fig. 4. By subtracting this Gd-sublattice anisotropy from the experimental data, we can obtain, as shown by the dotted chain line in Fig. 4, the anisotropy constant K_1(Co) for the Co sublattice in $GdCo_4B$. It is found that K_1(Co) changes its sign at $T/T_C=0.2$, which is a little lower than $T/T_C=0.4$ for YCo_4B[5] which is also shown by the double dotted chain line in Fig. 4.

The anisotropy constant of $Gd_{1-x}Dy_xCo_4B$ is approximately expressed by

$$K_1(Gd_{1-x}Dy_xCo_4B)=(1-x)K_1(GdCo_4B) + xK_1(DyCo_4B). \quad (1)$$

Since the left-hand side and the first term on the right-hand side have been obtained as shown in Figs. 5 and 4,

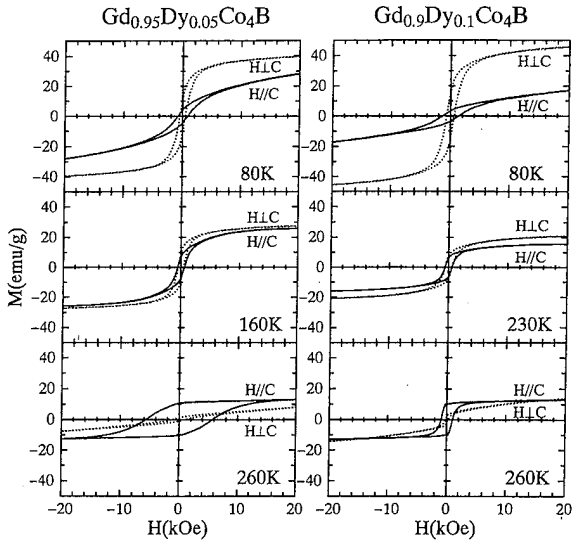


FIG. 3. Some examples for magnetization curves of field-oriented samples of $Gd_{0.95}Dy_{0.05}Co_4B$ and $Gd_{0.9}Dy_{0.1}Co_4B$.

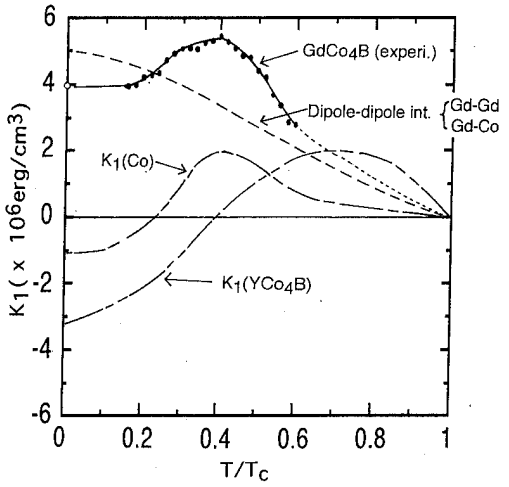


FIG. 4. Temperature dependence of the magnetocrystalline anisotropy constant K_1 for $GdCo_4B$. The dashed, dotted chain, and double dotted chain lines represent the magnetic anisotropy constant K_1(Gd) of the Gd sublattice due to the dipole–dipole interaction, K_1(Co) of the Co sublattice in $GdCo_4B$, and $K_1(YCo_4B)$ of YCo_4B (Ref. 5), respectively (see the text).

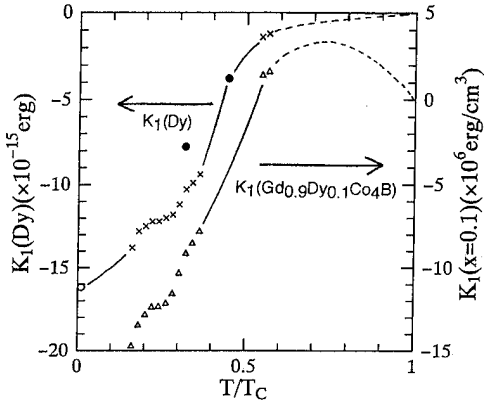


FIG. 5. Temperature dependences of the magnetocrystalline anisotropy constants $K_1(Gd_{0.9}Dy_{0.1}Co_4B)$ and K_1(Dy) per Dy atom. In K_1(Dy), × are the values obtained from the magnetization curves for the field-oriented $Gd_{0.9}Dy_{0.1}Co_4B$ in Fig. 3, ● is determined from the spin reorientation temperatures of $Gd_{0.95}Dy_{0.05}Co_4B$ and $Gd_{0.9}Dy_{0.1}Co_4B$, and ○ is determined from the magnetization curve at $T=5$ K in our previous paper (Ref. 2) (see the text).

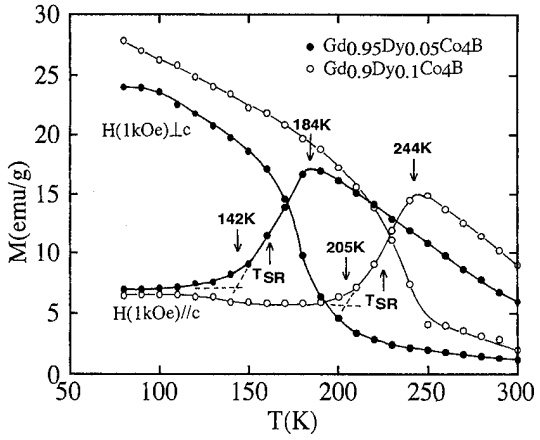


FIG. 6. Temperature dependence of magnetization at $H=1$ kOe for $Gd_{1-x}Dy_xCo_4B$ with $x=0.05$ (●) and 0.1 (○). The temperature regions between the two arrows mean the tilted state regions. T_{SR} represents the spin reorientation temperature defined by the center of the tilted temperature region (see the text).

respectively, $K_1(DyCo_4B)$ can be estimated by Eq. (1). By subtracting $K_1(YCo_4B)$[5] from $K_1(DyCo_4B)$, we can obtain the temperature dependences for $K_1(Dy)$ per Dy atom as shown in Fig. 5. By analyzing the magnetization curve at $T=5$ K in our previous data,[2] we have obtained the value indicated by the open circle (○) in Fig. 5. This value roughly agrees with the value of -21.8×10^{-15} ergs/Dy for $K_1(Dy)$ of $Gd_{0.95}Dy_{0.05}Co_4B$ estimated in our previous work.[3] Since the absolute value of $K_1(Dy)$ in the low temperature region has a very large anisotropy energy compared with $K_1(Gd)$ and $K_1(Co)$ in $GdCo_4B$, it is found that only a small substitution of Dy changes the axial anisotropy of $GdCo_4B$ to the planar one.

To investigate the spin reorientation in $Gd_{1-x}Dy_xCo_4B$ with $x=0.05$ and 0.1, temperature dependences of magnetization at $H=1$ kOe have been observed as shown in Fig. 6. From this figure, $Gd_{1-x}Dy_xCo_4B$ with $x=0.05$ and 0.1 has a tilted state between the temperatures indicated in Fig. 6. They have axial and planar anisotropies in the higher and the lower temperature regions, respectively. Defining the spin reorientation temperature T_{SR} by the center of the tilted temperature region, we get $T_{SR}=162$ and 225 K for $x=0.05$ and 0.1, respectively. At T_{SR}, the left-hand side of Eq. (1) must be zero, so $K_1(Dy)$ can be determined by making use of $K_1(GdCo_4B)$ in Fig. 4. The values determined by this method are shown by the filled circles (●) in Fig. 5.

[1] Y. B. Kuzuma and N. S. Bilonizhko, Sov. Phys. Crystallogr. **18**, 447 (1974).
[2] T. Ito, H. Ogata, H. Ido, and G. Kido, J. Appl. Phys. **73**, 5914 (1993).
[3] T. Ito, H. Asano, H. Ido, M. Yamada, and G. Kido, J. Magn. Magn. Mater. **140–143**, 943 (1995).
[4] H. Ogata, H. Ido, and H. Yamauchi, J. Appl. Phys. **73**, 5911 (1993).
[5] N. M. Hong, N. P. Thuy, T. D. Hien, G. Hilscher, T. S. Zhao, and R. Grossinger, J. Appl. Phys. **73**, 5917 (1993).

Dependence of energy dissipation on annealing temperature of melt–spun NdFeB permanent magnet materials

Z. Gao, D. C. Jiles, D. J. Branagan, and R. W. McCallum
Ames Laboratory, Ames, Iowa 50011

A model of magnetic hysteresis which was developed originally for soft magnetic materials has been applied to melt–spun ribbons of $Nd_2Fe_{14}B$-based material. The crucial ideas in the model description of hysteresis center on a dissipation of energy due to hysteresis which is proportional to the change in magnetization. The $Nd_2Fe_{14}B$ material was melt–spun amorphous and then annealed for a period of 24 h at temperatures ranging from 700 to 950 °C. This resulted in different grain sizes, depending on annealing temperature. Consequently the hysteresis curves represent the properties of the material as a function of both annealing temperature and grain size. It was found that the magnetic properties varied systematically with annealing temperature, and hence grain size, as would be expected. When modeling the magnetic properties it was found that the model parameters also varied systematically, in particular, the energy dissipation parameter k was to a first approximation a simple linear function of the annealing temperature and decreased with increasing annealing temperature as a result of grain growth. Therefore, this study revealed a basic relationship between materials processing conditions, microstructure, model parameters, and magnetic properties. © *1996 American Institute of Physics.* [S0021-8979(96)31808-8]

I. INTRODUCTION

Permanent magnet materials based on $Nd_2Fe_{14}B$, have been the focus of attention of the hard magnet community for the last ten years. A wide range of materials properties has been reported,[1–4] but the overriding property of these materials has been their high maximum energy product, which can exceed 50 MG Oe (~400 kJ/m^3). The latest results reported indicate a maximum energy product of 54 MG Oe (430 kJ/m^3).[5]

While much work has been devoted to the processing and production of these alloys with even greater energy products, remanences, and coercivities, little attention has been paid to the description of these properties in terms of a physical model. Nevertheless, this is important because a model can provide a direct link between microstructure and magnetic properties. In this paper we focus on the application of a model, which was developed originally for soft magnetic materials, in which the crucial idea in the description of hysteresis centers on a dissipation of energy due to hysteresis which is proportional to the change in magnetization. This idea, which was originally developed through a consideration of domain wall displacement, leads to a pair of differential equations for hysteresis which are valid for a wider range of behavior provided that the energy dissipation is proportional to the change in energy.

The hysteresis equations for the model under consideration here have been described in detail elsewhere.[6] They are given here for completeness. The hysteresis-free curve, or anhysteretic curve, is described by

$$M_{\rm an}(H)=M_s\left[\coth\left(\frac{H+\alpha M}{a}\right)-\left(\frac{a}{H+\alpha M}\right)\right],$$

where M_s is saturation magnetization, α is the internal coupling of the domain magnetizations, and $a=k_BT/\mu_0\langle m\rangle$, where k_B is the Boltzmann constant, T is the temperature, μ_0 is the permeability of free space, $\langle m\rangle$ is the mean effective domain size, $M_{\rm an}$ is the anhysteretic magnetization, and H is the magnetic field.

The hysteresis curve is given by

$$\frac{dM(H)}{dH}=\frac{M_{\rm an}(H)-M_{\rm irr}(H)}{k\delta-\alpha[M_{\rm an}(H)-M_{\rm irr}(H)]}+c\left(\frac{dM_{\rm an}(H)}{dH}-\frac{M_{\rm an}(H)-M_{\rm irr}(H)}{k\delta-\alpha[M_{\rm an}(H)-M_{\rm irr}(H)]}\right).$$

These equations can then be solved to give the hysteresis curves of the material. Here k is the energy loss per unit change in magnetization and c, which gives a measure of the amount of the reversible domain wall motion, can be related directly to the domain wall surface energy.

It should be noted that the anhysteretic curve used in the model calculation here is for isotropic materials. Therefore the model cannot be expected to exactly fit the part of the experimental curve where the change of magnetization is due to the reversible rotation of the magnetic moments with respect to the randomly oriented crystallographic easy axis.

II. EXPERIMENT

Amorphous $Nd_2Fe_{14}B$ was prepared by melt spinning with a wheel speed of 45 m/s. The resulting samples were annealed at temperatures ranging from 750 to 950 °C for a period of 24 h. The hysteresis data were taken using a Quantum Design dc SQUID. In order to make the measurements, about 40 ribbons were laid parallel in two layers on double-sided adhesive tape. Then the tape was wrapped onto a quartz rod. To minimize demagnetizing effects, the long axis of the ribbons was situated parallel to the applied magnetic field. No corrections due to demagnetization effects were made.

 0021-8979/96/79(8)/5510/3/$10.00 © 1996 American Institute of Physics

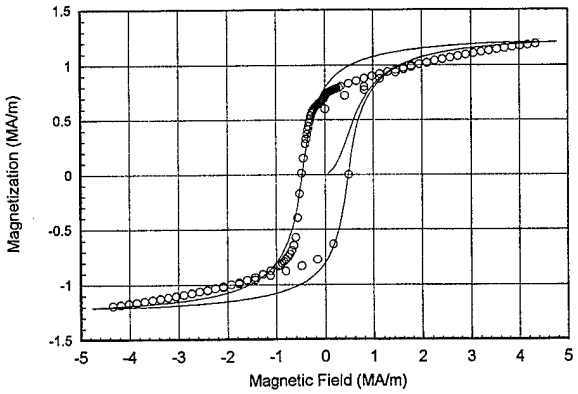


FIG. 1. Measured and modeled hysteresis curves for specimen 1. The measured data are the circles, the model calculation is the curve.

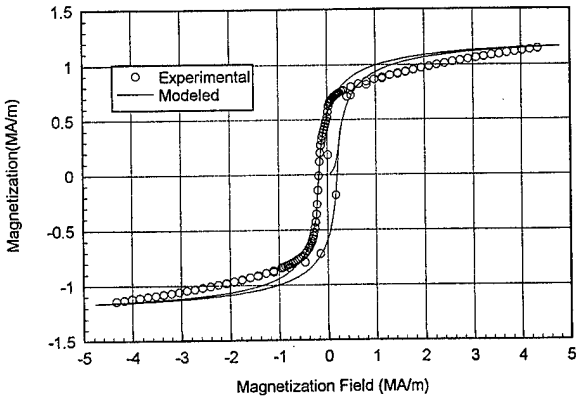


FIG. 3. Measured and modeled hysteresis curves for specimen 6. The measured data are the circles, the model calculation is the curve.

III. RESULTS

The hysteresis curves for seven specimens of NdFeB were measured and representative samples of these measurements are shown in Figs. 1–3. The magnetic properties changed progressively from one specimen to the next as the annealing temperature increased from 700 to 950 °C. For example, the coercivity in the specimen annealed at 700 °C was 487 kA/m while in the specimen annealed at 950 °C it was found to be 97 kA/m. In addition the differential permeability was greater at all points on the hysteresis loop in the materials annealed to higher temperatures, and there was a general decrease in remanence as the annealing temperature increased. A summary of the measured magnetic properties is given in Table I.

The grain sizes in specimens 2 and 7 were measured. These were 20–156 nm (with a mean of 75 nm) in specimen 2; and 154–740 nm (with a mean of 361 nm) in specimen 7.

IV. MODELING OF MAGNETIC PROPERTIES

The magnetic properties were used to determine the hysteresis model parameters. The values of the model parameters are shown in Table II for each of the materials investigated. From this it is clear that there was a progressive change in the hysteresis parameters such as k, the energy dissipation, and a, the effective domain density, as the annealing temperature was changed.

A comparison of the measured and modeled hysteresis curves is shown in Figs. 1–3. In the region near the coercive field, the model fits the data reasonably well. The model cannot, however, be expected to fit the part of the experimental curve where the change of magnetization is due to the reversible rotation of the magnetic moments with respect to the randomly oriented crystallographic easy axis, and in fact there are systematic differences between the measured and modeled curves in this region. If the anhysteretic curve of Eq. (1) is replaced by the minimum energy curves calculated by the Stoner–Wohlfarth model,[7] it would appear that the theory will fit the data rather well. Nevertheless, the present modeled values of magnetization are within 10% of the measured values along most of the curve, with some deviations of up to 20% in limited regions close to the knee of the demagnetization curve.

The variation of the energy dissipation parameter with annealing temperature is shown in Fig. 4. To a first approximation this appears to be linear with the relationship

$$k = k_0 - k_1 T_{\text{ann}},$$

where $k_0 = 2\times10^6$ A m^{-1}, and $k_1 = 2\times10^3$ A m^{-1} C^{-1}.

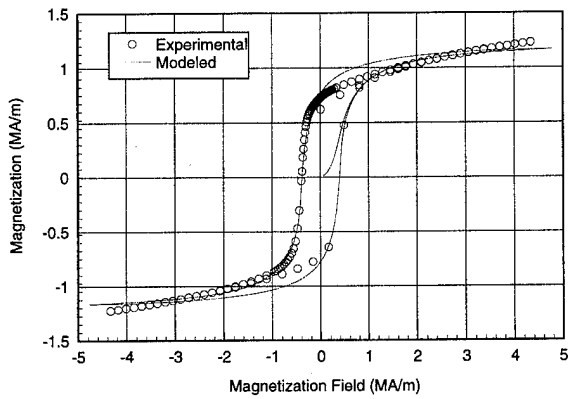


FIG. 2. Measured and modeled hysteresis curves for specimen 3. The measured data are the circles, the model calculation is the curve.

TABLE I. Measured magnetic properties of annealed NdFeB permanent magnet materials.

Specimen	Annealing temperature (0 °C)	M_s (T)	H_c (kA/m)	M_r (T)
1	700	1.19	487	0.72
2	750	1.19	466	0.71
3	800	1.23	397	0.73
4	825	1.17	409	0.67
5	850	1.15	264	0.65
6	900	1.14	192	0.57
7	950	1.17	97	0.58

TABLE II. Model parameters used to generate the modeled hysteresis curves.

	Model parameters					
Specimen	M_s (kA/m)	a (kA/m)	k (kA/m)	α	c	$3a-\alpha M_s$ (kA/m)
1	1300	358	545	0.685	0.18	183.5
2	1300	358	505	0.765	0.18	79.5
3	1250	373	439	0.845	0.18	62.75
4	1250	373	439	0.845	0.18	62.75
5	1250	386	248	0.845	0.18	101.75
6	1250	399	191	0.824	0.18	167
7	1150	400	81	0.960	0.18	96

V. CONCLUSIONS

The effects of different annealing temperatures on the magnetic properties of melt–spun NdFeB permanent magnet material have been studied. The measured hysteresis curves of these specimens have been used to calculate the model parameters for an established hysteresis model developed originally for soft magnetic materials. A comparison has been made between the measured and modeled hysteresis curves, showing good agreement, although indicating that the model could be made more appropriate for these materials by the introduction of anisotropy. It was found that the model energy dissipation parameter, k, which represents the rate of energy loss per unit change in magnetization, decreased linearly with annealing temperature.

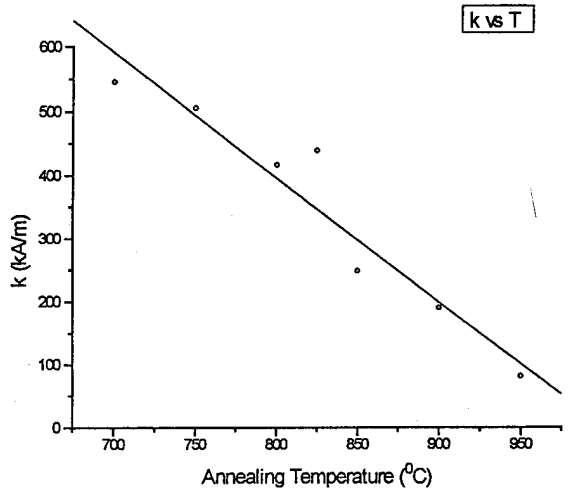


FIG. 4. Dependence of the model parameter k on the annealing temperature T_{ann}. This reveals that k decreases with grain size.

ACKNOWLEDGMENT

This work was supported by the U.S. Department of Energy, Office of Basic Energy Sciences, Division of Materials Sciences through the Center for Excellence in Synthesis and Processing, Program on Tailored Microstructures in Hard Magnets.

[1] J. J. Croat, J. F. Herbst, R. W. Lee, and F. E. Pinkerton, J. Appl. Phys. **55**, 2078 (1984).
[2] M. Sagawa, S. Fujimura, N. Togawa, H. Yamamoto, and Y. Matsuura, J. Appl. Phys. **55**, 2083 (1984).
[3] J. M. D. Coey and H. Sun, J. Magn. Magn. Mater. **87**, L251 (1990).
[4] R. J. Parker, *Advances in Permanent Magnetism* (Wiley, New York, 1990).
[5] M. S. Walmer and C. H. Chen, these proceedings.
[6] D. C. Jiles, J. B. Thoelke, and M. K. Devine, IEEE Trans. Magn. **28**, 27 (1992).
[7] R. W. McCallum, A. M. Kadin, G. B. Clemente, and J. E. Keem, J. Appl. Phys. **61**, 3577 (1987).

Quantitative characterization of additional ferromagnetic phase in melt-quenched and sintered Nd–Fe–B-based magnets

L. H. Lewis and D. O. Welch
Department of Applied Science, Brookhaven National Laboratory, Upton, New York 11973

F. Pourarian
Carnegie Mellon Research Institute, Carnegie Mellon University, Pittsburgh, Pennsylvania 15230-2950

Quantitative evidence of a ferromagnetic Fe-rich minor phase present in both melt-quenched/die-upset and sintered magnets based on the $Nd_2Fe_{14}B$ composition is presented. Full hysteresis loops were obtained at elevated temperatures (650 K$\leqslant T\leqslant$800 K) and were subsequently decomposed to obtain the saturation magnetization M_s of the minor phase as well as the paramagnetic slope of the 2-14-1 major phase as a function of temperature. Assuming a composition of pure iron, the calculated volume % of the impurity phase in the die-upset magnets is consistent with that obtained from previous observations of the widths and geometry of the intergranular phase found in the same magnets. The magnetization of the ferromagnetic impurity phase in the melt-quenched magnets decreases more rapidly than that of pure iron; extrapolation indicates a Curie temperature in the range 925 K$<T<$975 K. The paramagnetic susceptibility of the $Nd_2Fe_{14}B$ main phases exhibits Curie–Weiss behavior with the same paramagnetic Curie temperature for both sintered and die-upset samples. The Curie constants differ, however, probably due to the different degrees of crystallographic alignment. © *1996 American Institute of Physics.*
[S0021-8979(96)42108-9]

INTRODUCTION

The identification of dominant reversal mechanisms of magnets based on the $Nd_2Fe_{14}B$ composition is important to both the fundamental understanding of the physics governing their magnetic behavior as well as to the engineering of increasingly economical and effective magnets for the world market. It is generally agreed upon in the literature that 2-14-1-based magnets made by the sintering process achieve their coercivity by the nucleation of reversed domains.[1,2] In contrast, the limiting mechanism which controls magnetic reversal in the $RE_2Fe_{14}B$ die-upset magnets produced by melt-quenching methods remains an unsettled question in the literature.[3] In particular, the role that intergranular interactions, both magnetostatic and exchange, play in aiding or hindering magnetic reversal is attracting attention in both the theoretical[4,5] and the experimental[6,7] arenas. Characteristics such as relative grain orientation, size, and what consequences the existence and nature of intergranular phases have upon the global reversal mechanism is presently being questioned.

While it is a known fact that bcc iron does occur in sintered magnets,[8] recent work has demonstrated the existence of a previously unknown iron-rich grain-boundary phase in melt-quenched, thermomechanically processed magnets fabricated by General Motors Research and Development (R&D) Center. This iron-rich grain-boundary phase was identified and characterized by two independent transmission electron microscopy (TEM) methods: high-resolution analytical electron microscopy, using a nominal 5 Å probe[7] and low-angle dark-field imaging based on inner-potential differences at the grain boundaries.[9] Characterization of the hysteretic properties of the same die-upset samples at elevated temperatures has yielded data that suggests nucleation-controlled magnetization,[7] as well as the presence of an unknown ferromagnetic phase.[10] In this paper we present further characterization of the unknown ferromagnetic phase in a selection of compositionally related magnets produced by both melt-quenched and sintering methods.

EXPERIMENTAL METHODS

Hysteresis loops of 2-14-1-based magnets fabricated by both melt-quenching and sintering methods were measured with SQUID magnetometry at temperatures in the range 650 K$\leqslant T\leqslant$800 K. The bulk compositions, processing conditions and the dimensions of the magnets studied are given in Table I. Die-upset, melt-quenched magnets made by standard hot deformation processing methods[11] were obtained from General Motors R&D Center. Sintered magnets were fabricated by vacuum-sintering at 1080 °C for 1 h and then post-sintered for 4 h at temperatures ranging from 600 °C to 950 °C. Magnetic measurements were made on samples ma-

TABLE I. Description of samples.

Processing	Name	Bulk composition	Dimensions
Die-upset (MQ-3)	DU1418	$Nd_{13.75}Fe_{80.25}B_6$	1.423 mm×1.217 mm×1.933 mm
Die-upset (MQ-3)	DU1929	$Pr_{13.75}Fe_{80.25}B_6$	1.264 mm×1.255 mm×2.008 mm
Sintered	sint. NdFeB	$Nd_{15}Fe_{78.5}B_{6.5}$	1.254 mm×1.157 mm×2.181 mm
Sintered	sint. PrFeB	$Pr_{15}Fe_{78.5}B_{6.5}$	1.146 mm×1.190 mm×2.134 mm

 0021-8979/96/79(8)/5513/3/$10.00 © 1996 American Institute of Physics

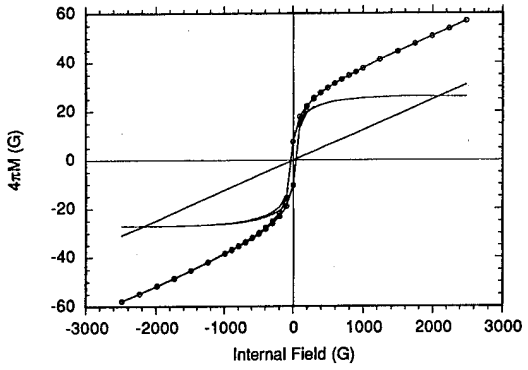


FIG. 1. Measured hysteresis loop of sample DU1929 measured $T=800$ K, decomposed into the paramagnetic contribution from the 2-14-1 phase and the ferromagnetic contribution from the additional Fe-rich phase.

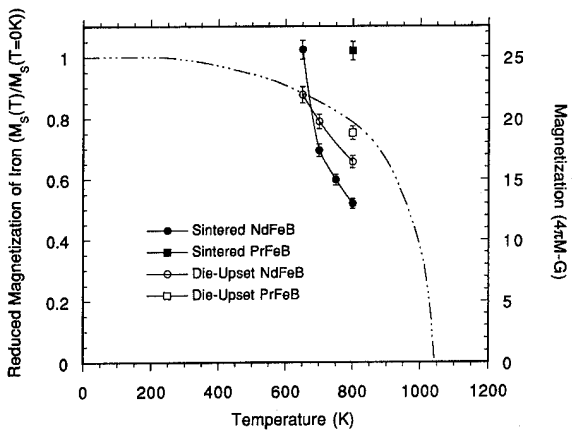


FIG. 2. Saturation magnetizations as a function of temperature for the unknown ferromagnetic phases. The magnetization curve of pure iron, dashed line, is included for reference.

chined down to the appropriate dimensions to fit inside quartz capillary tubes that were evacuated to a base pressure of 5.6×10^{-5} Torr and sealed with Zr turnings to avoid oxidation during measurement. Prior to each hysteresis loop measurement the magnets were brought to temperature and then saturated in an applied field of +5.5 T.

The resultant hysteresis loops were corrected for demagnetization using a method previously described,[7] and the magnetic signals from the 2-14-1 matrix phase and the unknown phase were separated as follows: The hysteresis loop is the superposition of the main-phase paramagnetic signal and the unknown phase ferromagnetic signal.[12] At relatively large fields ($H_{\text{int}}>1000$ G) the signal consists almost entirely of the paramagnetic contribution, displaced from the origin by an amount equal to the saturation magnetization of the unknown phase. Thus a linear fit to the high-field portion of the total signal yields both the paramagnetic slope and the saturation magnetization of the ferromagnetic phase. The paramagnetic contribution is then subtracted from the total signal to yield the ferromagnetic signal. Figure 1 shows a corrected hysteresis loop measured at 800 K for the Pr-based die-upset sample DU1929 that has been decomposed into the 2-14-1 paramagnetic contribution and the additional phase ferromagnetic contribution. During the course of this work it was found that the M_s(y-intercept) determination was very sensitive to the points selected for the linear fit, so care was taken to only involve those measurements of the loop for $H_{\text{int}}\geqslant1500$ G. In contrast, the determination of the paramagnetic slope of the 2-14-1 main phase was found to be quite insensitive to the choice of points to fit. From multiple measurements performed on the same sample the error in M_s is estimated to be on the order of 3%.

In order to obtain a quantitative estimation of the amount of ferromagnetic phase present within the volume of the samples at $T>T_c$(2-14-1), it was necessary to assume that the phase consisted of pure iron, with a saturation magnetization of approximately 1370 emu/cc at 800 K. It is also important to consider the contribution to the total magnetic signal due to the probable surface disproportionation and the limited oxidation of the 2-14-1 main phase into such possible products as α-Fe, Nd_2O_3, Fe_2O_3, and BO_x. Using results of the depth of the disproportion layer obtained on similar samples subjected to similar atmospheric and temperature conditions by Hirosawa *et al.*,[13] an upper-bound estimate of the contribution from the corroded surface to the total signal was computed and subtracted from the unknown $M_s(T)$ signal. By assuming the existence of layer of α-Fe that covers the entire surface of each sample and possess a thickness of 100 nm (the upper limit to the thickness as reported by Hirosawa), 7–8 G, depending upon the temperature, was subtracted from the measured saturation magnetization M_s of each sample.

RESULTS AND DISCUSSION

The saturation magnetization of the unknown ferromagnetic phase and the paramagnetic slopes of the 2-14-1 matrix phase that result from the decomposition of the hysteresis loops are shown in Figs. 2 and 3 and in Table II. For reference, the reduced magnetization curve as a function of temperature for pure iron is included in Fig. 2.[14] The M_s vs temperature trend of the die-upset FeNdB resembles that for pure iron but falls faster, implying that the unknown ferromagnetic phase has lower Curie temperature than iron. Extrapolation of the magnetization curve of DU1418 yields a

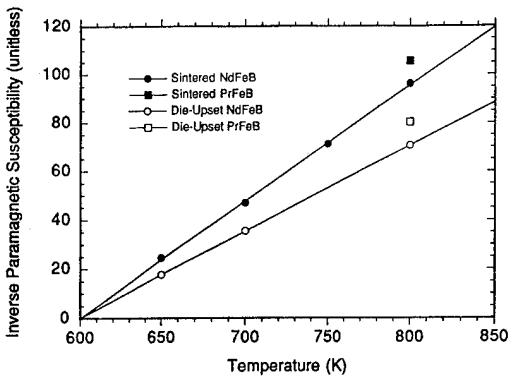


FIG. 3. Reciprocal paramagnetic susceptibilities of the 2-14-1 matrix phases a functions of temperature.

TABLE II. Comparison of volume percentages of grain boundary phase and unknown phase.

Sample	Bulk composition	Vol % of grain boundary phase calculated from microstructural characterization	Vol % of unknown phase calculated from magnetic measurements $T=800$ K
DU1418	$Nd_{13.75}Fe_{80.25}B_6$	0.33	0.095
DU1929	$Pr_{13.75}Fe_{80.25}B_6$	0.58	0.109

Curie temperature in the range 925 K$<T<$975 K for the unknown ferromagnetic phase. This result underscores the expectation that the grain boundary phase does not consist of pure iron. The magnetization trend for the unknown ferromagnetic phase present in the sintered FeNdB does not look at all like that for pure iron, though other researchers have verified the presence of α-Fe in sintered magnets.

Earlier detailed studies on the microstructures of DU1418 and DU1929 (Refs. 7 and 9) have indicated the presence of an Fe-rich intergranular phase. This phase was found to be amorphous, and its presence is dependent upon the nature of the grain boundary in question; for example, there appears to be no intergranular phase in (001) twist boundaries parallel to the tetragonal basal plane. The average width of the intergranular phase was found to be 8–12 Å in the Nd-based magnet and 15–20 Å in the Pr-based magnet. The average dimensions of the deformed grains are 600 nm $\pm$150 nm in length by 150 nm$\pm$75 nm in width. Using these characterizations, and making the assumption that the microstructure of the melt-quenched samples is completely comprised of uniformly deformed square platelets, Table II gives the results for the expected vol % of Fe-rich grain-boundary phase. Quantitative determinations of the vol % of grain-boundary phase calculated from magnetic measurements made on the other samples whose microstructures have not been carefully examined with HRTEM methods are included in Table III. Previous determinations indicate that the vol % of pure iron in sintered magnets is on the order of 2–10 vol %;[12] the results presented in Table III for the sintered magnets show significantly less excess iron.

The determination of the vol % of grain boundary phase of the die-upset magnets calculated from the microstructural characterizations exceeds that calculated from the magnetic measurements by a factor of roughly 3.5 for the Nd-based sample and 5 for the Pr-based sample. However, this is actually an encouraging agreement when one considers the extreme inhomogeneity in both composition and structure of the melt-quenched and die-upset samples.[15] Additionally, previous determinations of the composition of the grain boundary phase[7] confirm that it does not consist of pure iron, and thus the vol % determined from microstructural considerations is inherently overestimated. It is thus very likely that the source of the ferromagnetic signal at elevated temperatures is, at least in part, due to the Fe-rich intergranular phase.

TABLE III. Calculated magnetic properties of unknown and 2-14-1 matrix phases.

Sample	Measured temperature (K)	Unknown phase M_s ($4\pi M$-G)	2-14-1 Paramagnetic susceptibility (unitless)	Vol % of unknown phase
DU1418	650	21.9	0.0566	0.114
	700	19.7	0.0282	0.106
	800	16.4	0.0142	0.095
DU1929	800	18.8	0.0128	0.109
sint. NdFeB	650	25.6	0.0407	0.133
	700	17.4	0.0213	0.093
	750	15.0	0.0141	0.083
	800	13.0	0.0104	0.075
sint. PrFeB	800	25.5	0.0095	0.148

The reciprocal paramagnetic susceptibilities of the 2-14-1 matrices of both types of magnets as a function of temperature are presented graphically in Fig. 3. In both cases a Curie–Weiss dependence is observed, extrapolating to the same value, approximately 600 K, of the paramagnetic Curie temperature. This temperature is slightly higher than the actual Curie temperature of 585 K,[16] as is generally observed to be the case for ferromagnets.[17] The differences between the Curie constants (slopes) of the two materials may reflect intrinsic differences between the 2-14-1 matrices found in the die-upset magnet versus the sintered magnet, such as compositional or crystallinity differences. However, since the paramagnetic Curie temperatures are the same, this behavior probably reflects a difference in the bulk texture of the two types of magnets.

ACKNOWLEDGMENTS

We are grateful to C. D. Fuerst for providing us with samples and for helpful discussions. This research was sponsored by US DOE, Laboratory Directed Research and Development Program, Contract No. DE-AC02-76CH00016.

[1] H. Kronmuller, K. D. Durst, and M. Sagawa, J. Magn. Magn. Mater. **74**, 241 (1988).
[2] D. Givord, P. Teneaud, and T. Viadieu, IEEE Trans. Magn. **MAG-24**, 291 (1988).
[3] M. Gronefeld and H. Kronmuller, J. Magn. Magn. Mater. **88**, L267 (1990).
[4] T. Schrefl, H. Kronmüller, and J. Fidler, J. Magn. Magn. Mater. **127**, L273 (1993).
[5] R. Skomski, K. -H. Müller, P. A. P. Wendhanson, and J. M. D. Coey, J. Appl. Phys. **73**, 6047 (1993).
[6] L. Folks, R. Street, and R. Woodward, J. Appl. Phys. **75**, 6271 (1994).
[7] L. Henderson Lewis, Y. Zhu, and D. O. Welch, J. Appl. Phys. **76**, 6235 (1994).
[8] G. Schneider, E. Henig, G. Petzow, and H. H. Stadelmaier, Z. Metllkd. **77**, 755 (1986).
[9] Yimei Zhu, J. Tafto, L. H. Lewis, and D. O. Welch, Philos. Mag. Lett. **71**, 297 (1995).
[10] L. H. Lewis, Yimei Zhu, and D. O. Welch, Scr. Metall. Mater. **33** (10/11), 1774 (1995).
[11] R. W. Lee, Appl. Phys. Lett. **46**, 790 (1985).
[12] W. L. Liu, Y. L. Liang, L. Peeters, B. M. Ma, and C. O. Bounds, Proceedings of the Second Int. Workshop on RE Magnets and their Applications, Canberra, Australia, 1992, p. 168.
[13] S. Hirosawa, H. Tanimoto, S. Nasu, and K. Tokuhara, J. Appl. Phys. **70**, 6369 (1991).
[14] Sushin Chikazumi and Stanley H. Charap, *Physics of Magnetism* (Krieger, Florida, 1984), p. 69.
[15] Raja K. Mishra, J. Appl. Phys. **62**, 967 (1987).
[16] J. F. Herbst, Rev. Mod. Phys. **63**, 819 (1991).
[17] J. S. Smart, *Effective Theories of Magnetism* (Saunders, Philadelphia, 1966), p. 40.

Crystallographic and magnetic properties of $NdFe_{10.7}TiM_{0.3}$(M=B, Ti)

Chul Sung Kim, Young Jong Lee, and Seung Wha Lee
Department of Physics, Kookmin University, Seoul 136-702, Korea

Y. B. Kim and C. S. Kim
Korea Research Institute of Standards and Science, Taejon 305-606, Korea

$NdFe_{10.7}TiM_{0.3}$(M=B, Ti) has been studied with x-ray diffraction, Mössbauer spectroscopy, and a vibrating sample magnetometer. The alloys were prepared by arc-melting under an argon atmosphere. The $NdFe_{10.7}TiB_{0.3}$ exhibits a pure single phase, whereas the $NdFe_{10.7}Ti_{1.3}$ contains some α-Fe, from x-ray and Mössbauer measurements. The $NdFe_{10.7}TiB_{0.3}$ has the $ThMn_{12}$-type tetragonal structure with a_0=8.587 Å and c_0=4.788 Å. The Curie temperature (T_C) is 570 K from Mössbauer spectroscopy performed at various temperatures ranging from 13 to 770 K. Each spectrum below T_C was fitted with five subspectra of Fe sites in the structure ($8i_1$, $8i_2$, $8j_1$, $8j_2$, and $8f$). The area fraction of the subspectra at room temperature are 16.4%, 8.2%, 14.8%, 21.3%, and 39.3%, respectively. Magnetic hyperfine fields for the Fe sites decrease on the order of $H_{hf}(8i)>H_{hf}(8j)>H_{hf}(8f)$. The average hyperfine field $H_{hf}(T)$ of the $NdFe_{10.7}TiB_{0.3}$ shows a temperature dependence of $[H_{hf}(T)-H_{hf}(O)]/H_{hf}(O)=-0.39(T/T_C)^{3/2}-0.17(T/T_C)^{5/2}$ for $T/T_C<0.7$, indicative of spin-wave excitation. Annealing the alloy at around T_C for 60 min resulted in a two phase microstructure consisting of a $ThMn_{12}$-type structure and α-Fe. © *1996 American Institute of Physics.* [S0021-8979(96)31908-4]

I. INTRODUCTION

The $Nd_2Fe_{14}B$ and related Fe-rich Fe–R–B permanent magnets have large coercivities and high energy products $(BH)_{max}$ in excess of 45 MG Oe.[1,2] The shortcomings of the Fe–R–B magnets and their derivatives have led to the search for novel Fe-rich compounds that might serve as alternatives for starting materials in permanent magnets. The R(Fe, M)$_{12}$ (R=Sm, Nd, Pr, Gd; M=Ti, V, Mo, Cr) compounds with the tetragonal $ThMn_{12}$-type structure have been reported for the potential candidates for permanent magnet development. We concentrate on the Nd(Fe, M)$_{12}$ compounds, where the cost of Nd is much lower than that of Sm. The substitution effects of Ti for Fe in Nd(Fe, Ti)$_{12}$ have been investigated by several researchers,[3,4] and the Curie temperature, anisotropy field, and the saturation magnetization were found to increase with Ti substitution. Neutron diffraction experiments[5] for a $ThMn_{12}$-type R(Fe,M)$_{12}$ structure have shown that the iron atoms occupy the $8j$ and $8f$ sites preferentially, and the M atoms occupy $8f$ sites with the rest on $8i$ sites.

In this study, we have to tried to prepare $NdFe_{10.7}TiM_{0.3}$(M=B, Ti) compounds by substituting B for Ti in order to enhance the intrinsic magnetic properties of the $NdFe_{11}Ti$-type compound. The magnetic and crystallographic properties are studied using Mössbauer spectroscopy, a vibrating sample magnetometer (VSM), and x-ray diffraction techniques.

II. EXPERIMENTAL TECHNIQUE

Alloys of $NdFe_{10.7}TiM_{0.3}$(M=B, Ti) were prepared by arc-melting under an argon gas atmosphere. The buttons of $NdFe_{10.7}TiM_{0.3}$(M=B, Ti) alloys were ground into powders under 45 μm in size for Mössbauer measurements. A Mössbauer spectrometer of the electromechanical type[6] was used in the constant-acceleration mode. A ^{57}Co single-line source in a rhodium matrix was used at room temperature. To produce a uniform thickness over the area of the Mössbauer absorber, each sample was mixed with boron nitride powder and clamped between two beryllium disks 0.005 in. thick and 1 in. diam. The low temperature data were obtained using an APD CS-202 displex closed-cycle refrigeration system with a DMX-20 Mössbauer vacuum shroud interface.

X-ray-diffraction patterns of the samples were obtained with Cu K_α radiation. A slow scanning speed of 0.25° advance in 2 θ/min was used in order to optimize resolution of the closely spaced reflections.

III. RESULTS AND DISCUSSION

X-ray diffraction patterns for $NdFe_{10.7}Ti_{1.3}$ and $NdFe_{10.7}TiB_{0.3}$ obtained at room temperature. Every peak in the patterns for $NdFe_{10.7}TiM_{0.3}$(M=B, Ti) can be indexed on the basis of the tetragonal $ThMn_{12}$-type unit cell. The lattice constants and Curie temperatures of $NdFe_{10.7}TiM_{0.3}$(M=B, Ti) are listed in Table I. The $NdFe_{10.7}TiB_{0.3}$ alloy, by substituting B for Ti, exhibits a pure single phase of $ThMn_{12}$-type structure with the following unit cell constants: a_0=8.587 Å and c_0=4.788 Å. However, $NdFe_{10.7}Ti_{1.3}$ has a nearly single $ThMn_{12}$-type phase except for a small amount of the α-Fe phase.

Figures 1 and 2 show some of the Mössbauer spectra of $NdFe_{10.7}TiB_{0.3}$ measured at various absorber temperatures from 13 to 770 K. Using a least-squares computer program, five sets of six Lorentzian lines corresponding to the $8i_1$, $8i_2$, $8j_1$, $8j_2$, and $8f$ sites were fitted to the Mössbauer spectra below Curie temperature, T_C under the well-known restraints,[7] which are valid when the quadrupole interaction is much weaker than the magnetic hyperfine interaction.

In Nd(Fe, M)$_{12}$ structure, the distribution of M atoms may cause a distribution of Fe nearest neighbors in each Fe site, which results in quite broad outer lines in the Mössbauer spectra due to a distribution of hyperfine fields. By the neutron diffraction studies, an acceptable fit of the Mössbauer

 0021-8979/96/79(8)/5516/3/$10.00 © 1996 American Institute of Physics

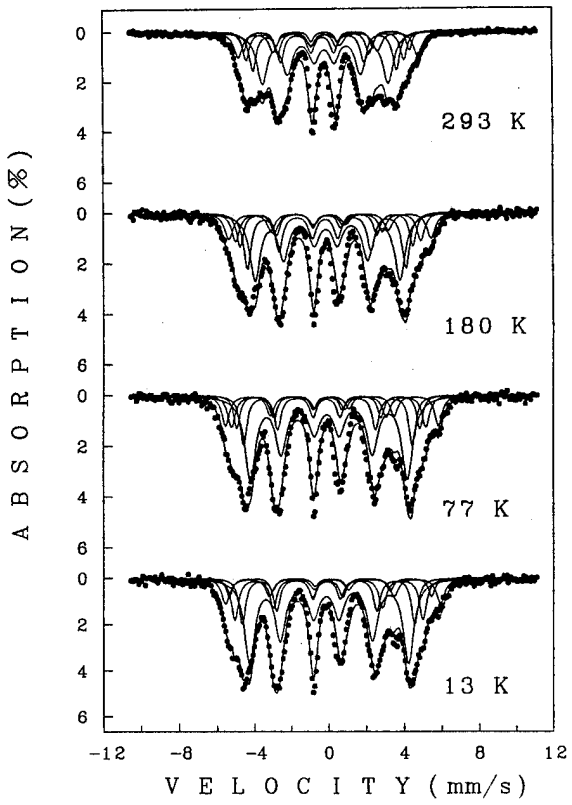


FIG. 1. Mössbauer spectra of $NdFe_{10.7}TiB_{0.3}$ at low temperature.

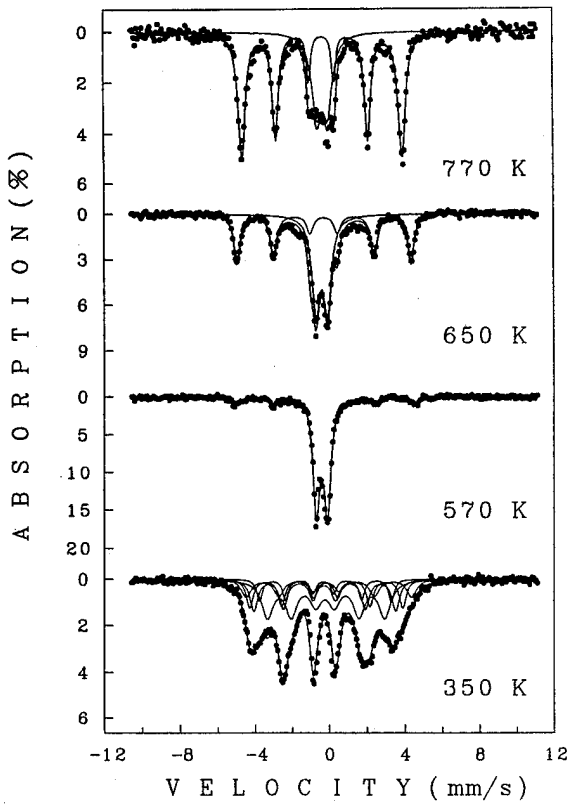


FIG. 2. Mössbauer spectra of $NdFe_{10.7}TiB_{0.3}$ near the Curie temperature.

spectra of the $NdFe_{10.7}TiB_{0.3}$ was performed using five sites ($8i_1$, $8i_2$, $8j_1$, $8j_2$, and $8f$).[8] The resulting area of the subspectra $8i_1$, $8i_2$, $8j_1$, $8j_2$, and $8f$ at room temperature are 16.4%, 8.2%, 14.8%, 21.3%, and 39.3%, respectively.

The temperature dependence of the isomer shifts, relative to α-Fe at room temperature, is shown in Fig. 3. The shifts for each site increase with decreasing temperature, consistent with the second-order Doppler shift.[9]

Figure 4 shows the temperature dependence of magnetic hyperfine field for $NdFe_{10.7}TiB_{0.3}$. The magnetic hyperfine fields for the Fe sites then decrease in the order, $H_{hf}(8i)>H_{hf}(8j)>H_{hf}(8f)$.

Figure 5 shows the fractional change of the average magnetic hyperfine field, $[H_{hf}(T)-H_{hf}(0)]/H_{hf}(0)$, as a function of T. The magnetic hyperfine field decrease with increasing temperature according to[10]

$$\frac{H_{hf}(T)-H_{hf}(0)}{H_{hf}(0)}=-B_{3/2}\left(\frac{T}{T_C}\right)^{3/2}-C_{5/2}\left(\frac{T}{T_C}\right)^{5/2}. \quad (1)$$

A least-squares fit of Eq. (1) to the magnetic hyperfine field data gave $B_{3/2}=0.39\pm0.05$ and $C_{5/2}=0.17\pm0.05$. This value of $B_{3/2}$ for $NdFe_{10.7}TiB_{0.3}$ is much larger than those of α-Fe and Ni: $B_{3/2}=0.12$ for Ni and $B_{3/2}=0.11$ for α-Fe.[11] So, spin waves having long wavelengths are excited in the alloys rather than in α-Fe and Ni.

Annealing the $NdFe_{10.7}TiB_{0.3}$ alloys at around Curie temperature, $T_C=570$ K,[12] for 60 min resulted in a two phase microstructure consisting of $ThMn_{12}$ and α-Fe and according to the percentage of $ThMn_{12}$ and α-Fe phases present: 93 wt %$ThMn_{12}$/7 wt % α-Fe. When the alloys are annealed above the Curie temperature the α-Fe phases increased linearly as a function of the temperatures. Mössbauer results on the alloy showed 20 wt % $ThMn_{12}$ and 80 wt % α-Fe at

TABLE I. Lattice constants, a_0 and c_0, and the Curie temperature, T_C for $NdFe_{10.7}TiM_{0.3}$(M=B, Ti).

Sample	a_0 (Å)	c_0 (Å)	T_C (K)
$NdFe_{10.7}Ti_{1.3}$	8.607	4.790	553
$NdFe_{10.7}TiB_{0.3}$	8.587	4.788	570

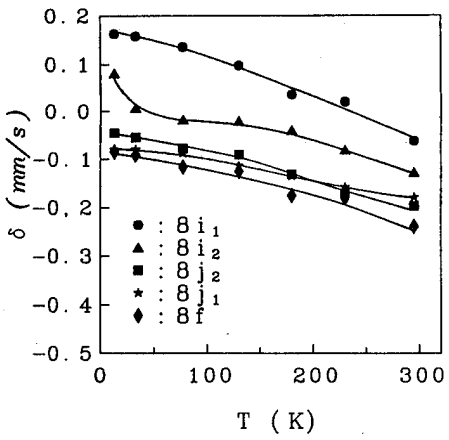


FIG. 3. Dependence of isomer shifts, δ, on the temperature in $NdFe_{10.7}TiB_{0.3}$.

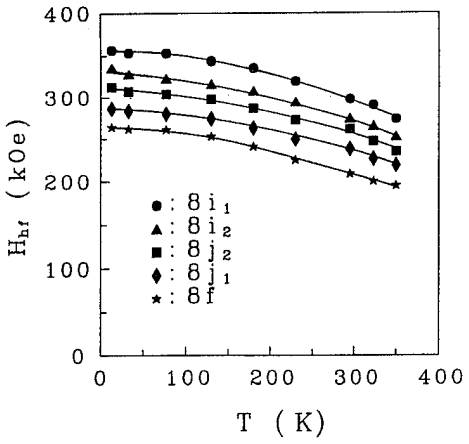


FIG. 4. Dependence of magnetic hyperfine fields, H_{hf}, on the temperature in $NdFe_{10.7}TiB_{0.3}$.

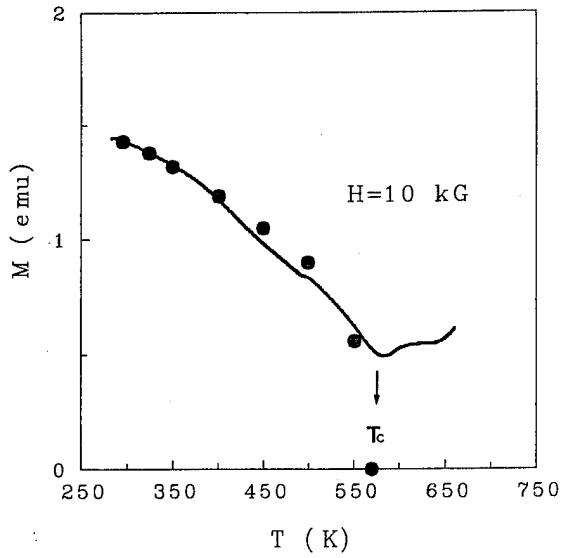


FIG. 6. Temperature dependence of the magnetic moment under an applied field of 10 kG for $NdFe_{10.7}TiB_{0.3}$. The solid circles are average normalized magnetic hyperfine fields taken from Mössbauer spectra.

around 770 K for 60 min. Since the $NdFe_{10.7}TiB_{0.3}$ alloy above the Curie temperature contains the α-Fe phase, the remanent magnetization changed to a low but nonzero value.

The temperature dependence of the magnetic moment of $NdFe_{10.7}TiB_{0.3}$ under an applied field $H=10$ kG is shown in Fig. 6. The solid circle indicates the normalized magnetic hyperfine field taken from the Mössbauer spectra. The magnetic moment measured as a function of temperatures with a VSM are marked with a solid line. These data show the magnetic moments measured with Mössbauer spectroscopy and VSM agree with each other very well below the Curie temperature (570 K). Above the Curie temperature, VSM data show that the magnetic moments increase again. The formation of α-iron is the main reason for the increasing moment that is conformed with the Mössbauer experiment as shown in Fig. 2. By substituting Ti by B, it is concluded that B strongly affects the increase of both the Curie temperature and the magnetization.

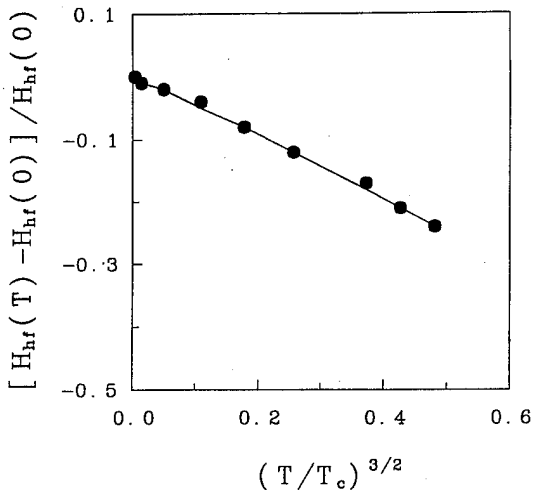


FIG. 5. Fractional change of the average magnetic hyperfine field; H_{hf}, as a function of $(T/T_C)^{3/2}$.

ACKNOWLEDGMENTS

This work was supported by Special Fund for University Research Institute, Korea Research Foundation, and Korea Science and Engineering Foundation.

[1] M. Sagawa, S. Fujimura, H. Yamamoto, and Y. Matsuura, J. Appl. Phys. **55**, 2083 (1984).
[2] K. S. V. L. Narasimhan, J. Appl. Phys. **57**, 4081 (1985).
[3] Y. Yang, X. Zhang, S. Ge, Q. Pan, L. Kong, H. Li, J. Yang, B. Zhang, Y. Ding, and C. Ye, J. Appl. Phys. **70**, 6001 (1991).
[4] Y. Z. Wang and G. C. Hadjipanayis, J. Appl. Phys. **70**, 6009 (1991).
[5] H. Sun, Y. Morri, H. Fujii, M. Akayama, and Funahashi, Phys. Rev. B **48**, 13333 (1993).
[6] H. N. Ok, K. S. Baek, E. C. Kim, and C. S. Kim, Phys. Rev. B **48**, 3212 (1993).
[7] C. S. Kim, Y. R. Um, S. I. Park, S. H. Ji, Y. J. Oh, J. Y. Park, S. J. Lee, and C. H. Yo, IEEE Trans. Magn. **30**, 4918 (1994).
[8] Q. Qi, B. Hu, and J. M. D. Coey, J. Appl. Phys. **75**, 6235 (1994).
[9] Z. W. Li, X. Z. Zhou, and A. H. Morrish, Phys. Rev. B **41**, 8617 (1990).
[10] C. L. Chien and R. Hasegawa, Phys. Rev. B **16**, 2115 (1977).
[11] H. N. Ok, K. S. Baek, and C. S. Kim, Phys. Rev. B **24**, 6600 (1981).
[12] L. Withanawwasam, G. C. Hadjipanayis, and R. F. Krause, J. Appl. Phys. **75**, 6646 (1994).

Structure and magnetic properties of mechanically alloyed $Nd(Fe,V)_{12}N_x$ compounds

Jun Yang, Ou Mao, and Z. Altounian
Center for the Physics of Materials, Department of Physics, McGill University, 3600 University Street, Montréal, Québec H3A 2T8, Canada

The structure and magnetic properties of $Nd(Fe,M)_{12}N_x$ (M=Ti,Mo,V) compounds prepared by mechanical alloying (MA) have been studied using x-ray diffraction and magnetic measurements. It is found that after annealing, single-phase $Nd(Fe,V)_{12}$ compounds can be obtained over a large composition range, but can only be obtained in $Nd(Fe,V)_{11}$ after MA. The crystallization of stoichiometric compounds at 750–950 °C always produces a small amount of α-Fe(V) in addition to the 1:12 phase. Below 750 °C, the crystallization is not complete and large amounts of α-Fe(V) are present. When nitriding at 450 °C, the α-Fe(V) phase disappears accompanied by the formation of an amorphous phase and a 1:7 nitride phase. The crystallized phase retains the 1:12 structure when nitriding at 480 °C. The highest coercivity of 8.8 kOe has been obtained for the $NdFe_{10.5}V_{1.5}N_x$ compound. The difference between the coercivities of MA $Nd(Fe,V)_{12}N_x$, $Nd(Fe,Mo)_{12}N_x$, $NdFe_{11}TiN_x$, and $Sm_2Fe_{17}N_x$ compounds is attributed to their different crystallization behavior and phase stability during nitrogenation. © *1996 American Institute of Physics.* [S0021-8979(96)32008-9]

I. INTRODUCTION

$Nd(Fe,M)_{12}N_x$ compounds (M=Ti,Mo,V), which have high Curie temperature, high saturation magnetization, and large (easy c-axis) anisotropy field, are promising candidates for permanent magnet applications.[1–4] $Nd(Fe,V)_{12}N_x$ compounds show better intrinsic magnetic properties than $Nd(Fe,Mo)_{12}N_x$ compounds with similar coercivities. They also have much higher coercivities compared to $NdFe_{11}TiN_x$ compounds. This indicates that $Nd(Fe,V)_{12}N_x$ compounds are more attractive as permanent magnets. As mechanical alloying (MA) can produce high coercivity in permanent magnets due to the nanometer sized grains, we have investigated the structural and magnetic properties of $Nd(Fe,M)_{12}N_x$ compounds prepared by mechanical alloying.

II. EXPERIMENTAL METHODS

Alloys of $Nd(Fe,M)_{12}$ compounds with M=Ti,V,Mo were prepared by induction melting of 99.9 wt % pure materials in a purified argon atmosphere in a cold crucible. An additional amount of Nd (3 wt %) was added to compensate for its loss in the preparation process. The ingots were wrapped in a tantulum foil and sealed into a vacuum silica tube, then annealed at 900–1100 °C for 1 week. For MA, the annealed compounds were crushed into particles of diameter less than 10 μm and sealed into a steel vial with two stainless steel balls in the ratio of powder to ball of 1 to 10 in an argon atmosphere. MA was done in a high energy Spex 8000 mixer/mill for 10–20 h. Crystallization was carried out in the temperature range from 600 to 950 °C for 0.5–3 h in an argon atmosphere. The recrystallized compounds were nitrided at 400–600 °C for 3 h in a thermopiezic analyzer (TPA). Structural and phase analysis studies were done with an automatic Nicolet–Stöe powder diffractometer with Cu K_α radiation and from thermomagnetic scans using a Perkin–Elmer thermogravimetric analyzer (TGA) in a small field gradient. Magnetic hysteresis loops were measured on a vibrating sample magnetometer operating in a field of up to 1.5 T and in a pulsed field magnet in a field of up to 17 T at 300 K.

III. RESULTS AND DISCUSSION

A. Phase transformation during MA and crystallization

Single-phase $Nd(Fe_{1-x}V_x)_y$ compounds can be obtained for $x=0.125$–0.17 and $y=11$–13 after annealing at 950 °C for 1 week. After MA, a mixture of α-Fe(V) and an amorphous phase is formed. The phase composition after crystallization depends on the composition of the compounds and annealing temperature. Crystallizing the stoichiometric or slightly Fe(V) rich compounds at 750–950 °C always produces a small amount of α-Fe(V) in addition to the 1:12 phase. Below 750 °C, the crystallization is not complete and large amounts of α-Fe(V) are present. Single phase 1:12 compounds can be obtained by crystallizing a MA Nd-rich $Nd(Fe_{0.83}V_{0.17})_{11}$ compound. As an example, Fig. 1 shows the x-ray diffraction patterns of a $NdFe_{10.5}V_{1.5}$ compound after annealing (a), after MA (b), after crystallizing at 750 °C for 3 h (c), at 850 °C for 3 h (d), and a $Nd(Fe_{0.83}V_{0.17})_{11}$ compound after crystallizing at 850 °C for 3 h (e). Rare earth transition metal intermetallic compounds are brittle in nature because of the lack of slip systems available. This is a consequence of the large unit cell and noncubic symmetry of the structure. During the MA process, mechanical forces induce lattice distortions and defects thus increasing the free energy of the compounds. Eventually, the so-called mechanically driven disorder and phase transformation takes place. If the amount of one element is too large, it does not mix fully with other elements, and a homogeneous amorphous phase, similar to the melt–spun case, cannot be obtained. Instead, a mixture of an amorphous phase and a metal phase with small grains will be formed, which can be observed directly from the broadening of the α-Fe(V) peak in Fig. 1(b).

 0021-8979/96/79(8)/5519/3/$10.00 © 1996 American Institute of Physics

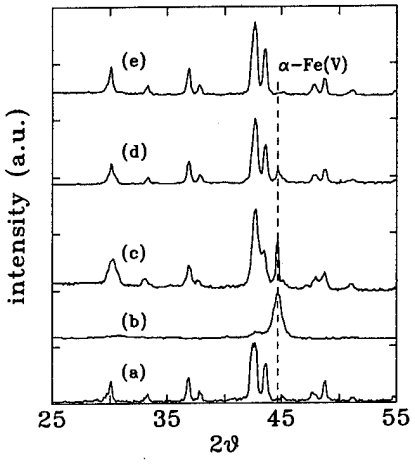


FIG. 1. X-ray diffraction patterns of $NdFe_{10.5}V_{1.5}$ in annealed state (a), MA state (b), after crystallizing at 750 °C for 3 h (c), after crystallizing at 850 °C for 3 h (d), and $Nd(Fe_{0.83}V_{0.17})_{11}$ after crystallizing at 850 °C for 3 h (e).

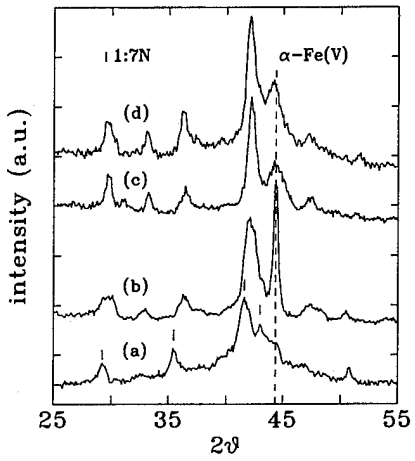


FIG. 2. X-ray diffraction patterns of (a) $NdFe_{10.5}V_{1.5}$ (crystallized at 750 °C, nitrided at 450 °C), (b) $NdFe_{10.5}V_{1.5}$ (crystallized at 750 °C, nitrided at 480 °C), (c) $NdFe_{10.5}V_{1.5}$ (crystallized at 850 °C, nitrided at 480 °C), (d) $Nd(Fe_{0.83}V_{0.17})_{11}$ (crystallized at 850 °C, nitrided at 480 °C).

Upon annealing, the amorphous phase will either react directly with Fe(V) to form the $ThMn_{12}$ structure or it will first crystallize into small grain-sized crystals followed by the reaction. Therefore, the crystallizing temperature and time will affect the phase composition and the final grain size of the product as shown in Figs. 1(c) and 1(d). In addition, as it is necessary to add a third element to stabilize the 1:12 phase, the recrystallized phases will also depend, for a given temperature, on the composition of alloying elements M. The composition and temperature range for the formation of $NdFe_{12-x}M_x$ are: (i) for Mo, x from 0.8 to 4.5 and below the melting point, (ii) for V, x from 1.2 to 2.5 and below 950 °C, and (iii) for Ti, x from 0.8 to 1.2 and above 1100 °C. This can explain why annealing MA $Nd(Fe,Mo)_{12}$ easily produces a single phase, but for $Nd(Fe,V)_{12}$, it is only achieved in the Nd- and V-rich $Nd(Fe_{0.83}V_{0.17})_{11}$ compound as shown in Fig. 1(e). On the other hand, the $TbCu_7$-type phase and α-Fe(Ti) are formed when crystallizing MA $NdFe_{11}Ti$. Certainly, the solid solubility of V, Ti, and Mo in Fe can also play a critical role as the solubility of V in Fe is much larger than those of Ti and Mo.

B. Phase transformation during nitrogenation

As mentioned above, for the compounds annealed below 750 °C, the crystallization is not complete and large amounts of α-Fe(V) are present together with the 1:12 phase. Upon nitriding these compounds at 450 °C, the α-Fe(V) phase disappears accompanied by the formation of an amorphous phase and a 1:7 nitride as shown in Fig. 2(a). However, when nitriding at 480 °C, the crystallized phase will retain the 1:12 structure but with an obvious increase in the amount of α-Fe(V) [Fig. 2(b)]. When the compounds, crystallized between 750 and 950 °C, are nitrided, they retain the 1:12 structure with only a small amount of precipitated α-Fe(V) [Fig. 2(c)]. This precipitation is unavoidable even if the crystallized phase is a single phase, as in $Nd(Fe_{0.83}V_{0.17})_{11}$ [Fig. 2(d)], which is similar to $NdFe_{11}Ti$ but different from $Nd(Fe,Mo)_{12}$. The crystallized $Nd(Fe,Mo)_{12}$ retains the 1:12 structure even when nitriding at 600 °C without precipitation of α-Fe(Mo). If nitriding at above 600 °C, the $Nd(Fe,M)_{12}$ compounds will decompose into a mixture of RN and α-Fe(M), which is generally explained in view of the minimum of total free energy. Introducing nitrogen atoms into the rare earth transition metal compounds will result in stress or strain buildup in the nitrided particles due to lattice dilation. A stable compound suggests that it can withstand higher stress and/or strain, and it will not decompose during nitriding and the nitrides will be stable at higher temperature. This may explain the different nitriding behaviors of Mo, Ti, and V stabilized 1:12 compounds. When crystallizing MA $Nd(Fe,V)_{12}$ below 750 °C, the 1:12 compound formed is imperfect with many interfaces with the unreacted α-Fe(V). Upon nitriding at 450 °C, stress is induced inside the 1:12 phase, which cannot be relaxed easily, and when combined with the weak lattice constraint, will result in the phase transformation from 1:12 to 1:7. However, when nitriding at 480 °C, the stress is relaxed and can accelerate the decomposition of 1:12 but does not change its crystal structure.

C. Magnetic properties of MA $Nd(Fe,M)_{12}N_x$ compounds

Figure 3 shows the hysteresis loops, for fields of up to 1.5 T (a) and 17 T (b), of $NdFe_{10.5}V_{1.5}N_x$ after crystallizing at 850 °C for 3 h and nitriding at 480 °C for 3 h. The intrinsic coercivity is 8.8 kOe. It can also be seen that the virgin magnetization curve [Fig. 3(a)] is smooth, which implies no pinning sites in the compounds and its coercivity should be determined by the reverse domain nucleation field. However, on the virgin magnetization curves of MA $NdFe_{10.5}Mo_{1.5}N_x$ and $Sm_2Fe_{17}N_x$ (Ref. 5) compounds, there are jumps at magnetization fields equal to their coercivities, which means that domain wall pinning determines the coercivities in these compounds. This difference originates from the precipitated α-Fe(V), which generally is located on the surface of $Nd(Fe,V)_{12}$ particles, and acts as a reverse domain nucleation site reducing the coercivity and the squareness of the demagnetization curve. By controlling the grain size and distribu-

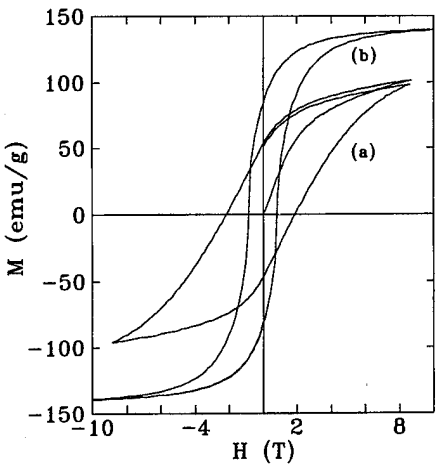


FIG. 3. Hysteresis loops of $NdFe_{10.5}V_{1.5}N_x$ compounds measured in a field of up to 1.5 T (a) and 17 T (b). For (a) the field scale is multiplied by 6 for clarity.

tion of α-Fe(V) and $Nd(Fe,V)_{12}N_x$ compounds, exchanged coupled remanence enhanced composite magnets could be realized.[6]

IV. CONCLUSION

MA has been successfully used in the preparation of $Nd(Fe,M)_{12}N_x$ permanent magnets. Intrinsic coercivity of 8.8 kOe has been obtained for $NdFe_{10.5}V_{1.5}N_x$. The stress introduced by nitrogen atoms and the stability of the original compounds control the phase transformation during nitriding. The difference in coercivities for Ti,V,Mo stabilized $Nd(Fe,M)_{12}N_x$ and $Sm_2Fe_{17}N_x$ compounds originates from the different phase stability range and the morphology of precipitated α-Fe(M). It is also suggested that $Nd(Fe,V)_{12}N_x$ could be used to produce remanence enhanced composite magnets.

ACKNOWLEDGMENTS

This work was supported by grants from the Natural Sciences and Engineering Research Council of Canada, and la Fonds pour la Formation de Chercheurs et l'Aide à la Recherche de la Province du Québec.

[1] Y. C. Yang, X. D. Zhang, S. L. Ge, L. S. Kong, Q. Pan, Y. T. Hou, S. Huang, and L. Yang, *Proceedings of the Sixth International Symposium on Magnetic Anisotropy and Coercivity in RE-TM Alloys*, edited by S. G. Sanker (Carnegie Mellon University, Pittsburgh, 1990), p. 19.
[2] X. Chen, L. X. Liao, Z. Altounian, D. H. Ryan, and J. O. Ström-Olsen, J. Magn. Magn. Mater. **111**, 130 (1992).
[3] Y. Z. Wang, G. C. Hadjipanayis, A. Kim, D. J. Sellymer, and W. B. Yelon, J. Magn. Magn. Mater. **104**, 1132 (1992).
[4] J. Yang, S. Z. Dong, B. P. Cheng, and Y. C. Yang, J. Appl. Phys. **75**, 3013 (1994).
[5] K. Schnitzke, L. Schulz, J. Wecker, and M. Katter, Appl. Phys. Lett. **57**, 57 (1990).
[6] E. Kneller and R. Hawig, IEEE. Trans. Magn. **27**, 3588 (1991).

Neutron diffraction and magnetic studies of $RFe_{12-x}T_xC_y$ (R=Y,Er; T=V,Ti,Mo) alloys

Z. Hu and W. B. Yelon
Research Reactor Center, University of Missouri–Columbia, Columbia, Missouri 65211

X. Zhang and W. J. James
Graduate Center for Materials Research, University of Missouri–Rolla, Rolla, Missouri 65401

$RFe_{12-x}T_xC_y$ (R=Y,Er; T=V,Ti,Mo) alloys were prepared by rf induction melting and analyzed using neutron powder diffraction and superconducting quantum interference device (SQUID) measurements. Rietveld analysis of the neutron diffraction data indicates that V, Ti, and Mo atoms all prefer the $8i$ sites. The refined amount of carbon atoms found in the interstitial sites from neutron diffraction data is significantly less than the nominal carbon content. All samples have the easy direction along the c axis. The Er sublattice couples to the Fe sublattice antiferromagnetically. The average Fe site moments range from 1.3 to 2.8 μ_B. The anisotropies of the crystal structures are found to relate to both the rare earth atoms and the stabilizing transition metal atoms. The SQUID measurements show that all samples have a Curie temperature near 600 K. © *1996 American Institute of Physics.* [S0021-8979(96)32108-5]

INTRODUCTION

It is well accepted that the $RFe_{12-x}T_xC_y$ and $RFe_{12-x}T_xN_y$ (R=rare earths, T=Ti,V,Mo) compounds are among the most promising candidates for permanent magnet applications,[1–8] not only for their excellent magnetic properties, but also for their lower ratio of rare earth to transition metal than those of the 2:17 and 3:29 phases. The nitrogen atoms can only be introduced into the $RFe_{12-x}T_x$ compounds by a gas phase reaction. The carbon atoms can be introduced into the $RFe_{12-x}T_x$ compounds either during melting or by gas phase reaction. Up to the present, better magnetic properties have been observed in nitrides,[1] and thus, the nitrides have attracted much more attention.[1–8] Because of the technical advantage of the melting method, it is very important to study the carbides prepared by melting. Here we report the results of neutron diffraction and magnetic studies of several carbides ($RFe_{12-x}T_xC_y$ with R=Y,Er; T=V,Ti,Mo) prepared by rf-induction melting.

EXPERIMENT

Four samples of $RFe_{12-x}T_xC_y$ (R=Y,Er; T=V,Ti,Mo) were prepared by rf induction melting the constituent elements of purity 99.9%–99.995% in a water-cooled copper boat under flowing argon at the Graduate Center for Materials Research, University of Missouri–Rolla. The ingots were annealed at 980 °C for one week. The ingots were then crushed and ground in an acetone bath. Neutron diffraction data were collected at the University of Missouri Research Reactor using the high resolution linear position sensitive detector diffractometer at room temperature on approximately 2 g samples in about 24 h. The neutron wavelength is 1.4783 Å. The data were measured from 5° to 105° in 2θ. The neutron diffraction powder patterns were analyzed by the Rietveld method using the FULLPROF program for multiphase refinements including magnetic structure refinements. The superconducting quantum interference device (SQUID) measurements were performed with a Quantum Design MPMS system.

RESULTS AND DISCUSSION

The refinement results of the powder neutron diffraction data are given in Table I. Based on the refinements, all samples were confirmed to have the tetragonal $ThMn_{12}$-type structure with space group I4/mmm. No second phase was recognized for any sample. The two possible sites that can be occupied by interstitial C atoms are the octahedral $2b$ (0 0 1/2) sites, with two rare-earth neighbors and four transition metal neighbors, or the tetrahedral $8h$ (~1/4 ~1/4 0) sites, with one rare-earth neighbor and three transition metal neighbors. However, when we refine the C occupancies on those two sites, the C content is found to be much lower than the nominal C content. As shown in Table I, the nominal C content for the Er–V–Fe–C sample is 0.4/formula unit (f.u.), the refined C content on the $2b$ and $8h$ sites is only 0.032/f.u. The nominal C content for the Er–Ti–Fe–C sample is 0.25/f.u., the refined C content on the $2b$ and $8h$ sites is zero. The largest refined C content is obtained for the Y–Mo–Fe–C sample, but the result (0.18/f.u.) is still significantly lower than the nominal value (0.3/f.u.). Because no second phase was observed, this suggests that some or most of the C atoms have possibly been introduced into the structures substitutionally. That is, the C atoms may go into the transition metal sublattice and the doubly substituted compounds form. Because it is not possible to determine the site occupancies of a doubly substituted compound from neutron diffraction data only,[9] it is difficult to determine which site(s) the C atoms occupy. However, because no second phase was found, we assume that the T/Fe ratio in the samples is the same as nominal (1.5T/10.5Fe). By using this and the assumption that the rare-earth site is fully occupied, it is easy to determine the final net compositions of the samples (see the Appendix), which are given in Table I (where C^s stands for the substitutional carbon and C^i represents the interstitial carbon). They are found to be in good agreement with the nominal compositions. A special case is for the sample with the nominal formula $YFe_{10.5}Mo_{1.5}C_{0.3}$ for which only $8i$ sites were observed to contain substituents. Thus it is clear that

 0021-8979/96/79(8)/5522/3/$10.00 © 1996 American Institute of Physics

TABLE I. Refinement results for $RFe_{12-x}T_xC_y$ solid solutions.

Parameter	Compound			
	$ErFe_{10.5}V_{1.5}C_{0.4}$[a]	$ErFe_{10}TiC_{0.25}$	$YFe_{10.5}V_{1.5}C_{0.4}$	$YFe_{10.5}Mo_{1.5}C_{0.3}$
	$ErFe_{10.17}V_{1.45}C^s_{0.38}C^i_{0.03}$[b]	$ErFe_{10.24}Ti_{1.46}C^s_{0.30}C^i_0$	$YFe_{10.33}V_{1.48}C^s_{0.21}C^i_{0.05}$	$YFe_{10.40}Mo_{1.49}C^s_{0.12}C^i_{0.18}$
a (Å)	8.4719(5)	8.5124(7)	8.4948(5)	8.5802(5)
c (Å)	4.7715(3)	4.8028(4)	4.7753(3)	4.8055(3)
c/a	0.5632	0.5642	0.5621	0.5601
V (Å^3)	342.46	348.015	344.59	353.775
x, Fe, 8i	0.2771(3)	0.2814(4)	0.2756(2)	0.2791(2)
x, Fe, 8j	0.3564(3)	0.3519(5)	0.3581(3)	0.3585(2)
b_{eff}/b_{Fe}, 8i	0.61	0.59	0.75	0.89
b_{eff}/b_{Fe}, 8j	0.88	0.91	0.93	1.00
b_{eff}/b_{Fe}, 8k	0.90	0.94	0.95	1.00
C%, 2b	3.2	0.0	4.8	17.6
C%, 8h	0.0	0.0	0.0	0.0
Interstitial C/f.u.	0.03	0	0.05	0.18
u, R, 2a	−2.2(2)	−3.4(3)	0	0
u, Fe, 8i	3.2(2)	1.7(3)	2.8(2)	1.1(2)
u, Fe, 8j	2.8(2)	1.8(3)	2.3(1)	1.6(1)
u, Fe, 8k	2.5(1)	1.5(2)	2.2(1)	1.4(1)
R_p (%)	6.18	6.68	5.81	5.59
R_w (%)	8.06	8.98	7.79	7.34
R_m (%)	7.81	9.54	5.62	4.71
χ^2	3.82	5.06	3.09	3.23
T_c (K)	605	590	592	595

[a]Nominal composition.
[b]Refined composition.

any substitutional C atoms in this sample occupy the 8i sites as Mo atoms do. For the other three samples, multiple site occupancy by C is possible. In fact, because all samples were prepared in a rare-earth rich environment, it is not unreasonable that C atoms occupy some transition metal sites without affecting the phase mix.

Also given in Table I are the ratios of the effective site scattering length/Fe scattering length (b_{eff}/b_{Fe}). Fe has the largest scattering length among the elements involved in this study. Thus, the greater the reduction of b_{eff}/b_{Fe} from 1, the greater the substitution. The biggest reductions of b_{eff}/b_{Fe} are found for the 8i site for all samples, which means the V, Ti, and Mo atoms all show a strong affinity for the 8i sites in the transition metal sublattice. This affinity is determined by coordination effects. The 8i site has only one rare-earth neighbor and 13 transition metal neighbors, indicating that the substituent atoms V, Ti, and Mo avoid bonding to rare earth atoms. The anisotropy of the crystal structures is found to relate to both the rare-earth atoms and the stabilizing transition metal atoms. The substituted Y–Fe–Mo sample is more anisotropic in crystal structure (c/a=0.5601) than the substituted Y–Fe–V sample (c/a=0.5621) which is, in turn, more anisotropic than the Er–Fe–V sample (c/a=0.5632).

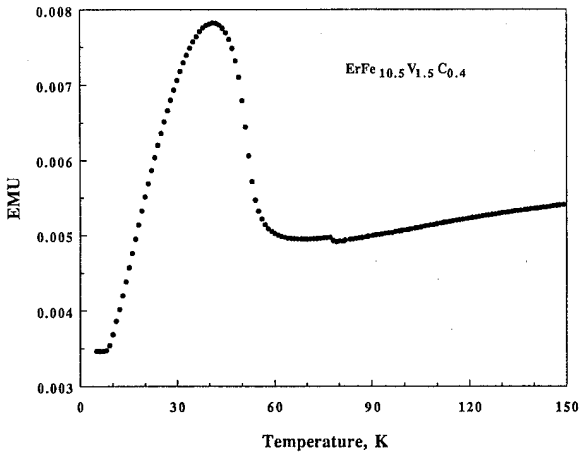


FIG. 1. SQUID magnetization curve for $ErFe_{10.5}V_{1.5}C_{0.4}$.

The refinements show that all samples have the easy direction along the c axis. The average Fe site moments are 1.36 μ_B for the $YFe_{10.5}Mo_{1.5}C_{0.3}$ sample, 1.67 μ_B for the $ErFe_{11}Ti_1C_{0.25}$ sample, 2.43 μ_B for the $YFe_{10.5}V_{1.5}C_{0.4}$ sample, and 2.83 μ_B for the $ErFe_{10.5}V_{1.5}C_{0.3}$ sample. As expected, the Er sublattice was found to couple to the Fe sublattice antiferromagnetically. The Er site moment is smaller in the Er–V–Fe–C sample than in the Er–Ti–Fe–C sample, indicating the antiferromagnetic interaction between the rare earth sublattice and Fe sublattice is weaker in Er–V–Fe–C than in Er–Ti–Fe–C. The heavy rare-earth–Fe compounds usually have Curie temperatures higher than those of the corresponding light rare-earth–Fe compounds, but the antiferromagnetic exchange between the heavy rare earth sublattice and Fe sublattice is a major deficiency of the heavy rare-earth–Fe compounds. This study suggests that the antiferromagnetic exchange in heavy rare-earth–Fe 1:12 compounds can be reduced by changing the composition of the compound. It is also noted that both V-substituted samples have larger site moments than the Ti and Mo samples do. This suggests that more attention should be paid to V-substituted compounds in the future.

It was reported that the easy direction of the $ErFe_{10}V_2N_x$ compound at 10 K is within the ab plane but along the c axis at 300 K.[1] Our SQUID measurement shows that this change of easy direction for $ErFe_{10.5}V_{1.5}C_{0.4}$ happens at around 45 K (Fig. 1). The SQUID measurements also show that all samples have a Curie temperature around 600 K (Table I). The Curie temperatures of the carbides, as expected, are higher than those of the uncarbonated compounds but much lower than those of the corresponding nitrides.[1]

CONCLUSIONS

All the V, Ti, and Mo atoms prefer the $8i$ sites. The interstitial carbon atoms were found in the $2b$ sites. However, the refined amount of carbon atoms found in the interstitial sites from neutron diffraction data is significantly less than the nominal carbon content. Calculation of the net scattering amplitudes on each site supports this assumption. All samples have the easy direction along the c axis. The Er sublattice was found to couple to the Fe sublattice antiferromagnetically. The average Fe site moments range from 1.3 to 2.8 μ_B. The anisotropy of the crystal structures are found to relate to both the rare-earth atoms and the stabilizing transition metal atoms. All samples have a Curie temperature near 600 K.

APPENDIX: DETERMINATION OF THE SUBSTITUENT CONTENTS IN THE T+C DOUBLE SUBSTITUTED 1:12 PHASE, $RFe_{12-x-y}T_xC_y$

For the T+C doubly substituted 1:12 phase, $RFe_{12-x-y}T_xC_y$, the effective scattering lengths of the three iron sites are

$$b_{\text{eff}\,1}=x_1b_T+y_1b_C+(0.25-x_1-y_1)b_{Fe}, \tag{A1}$$

$$b_{\text{eff}\,2}=x_2b_T+y_2b_C+(0.25-x_2-y_2)b_{Fe}, \tag{A2}$$

$$b_{\text{eff}\,3}=x_3b_T+y_3b_C+(0.25-x_3-y_3)b_{Fe}, \tag{A3}$$

where $b_{\text{eff}\,1}$, $b_{\text{eff}\,2}$, and $b_{\text{eff}\,3}$ are refined effective scattering lengths on the three Fe sites, b_T, b_C, and b_{Fe} are the scattering lengths of transition metal, carbon, and Fe, respectively, x_i $(i=1,2,3)$ are transition metal site occupancies, and y_i $(i=1,2,3)$ are C sites occupancies. Taking Eqs. (A1)+(A2)+(A3) we get

$$b_{\text{eff}}=xb_T+yb_C+(0.75-x-y), \tag{A4}$$

where b_{eff} is the total effective scattering length of the three Fe sites, x is the total occupancy of transition metal, y is the total occupancy of carbon, and

$$b_{\text{eff}}=b_{\text{eff}\,1}+b_{\text{eff}\,2}+b_{\text{eff}\,3},$$

$$x=x_1+x_2+x_3,$$

$$y=y_1+y_2+y_3.$$

To determine x and y, we need one more independent equation. Here we assume that the T/Fe ratio in the samples is the nominal one (1.5T/10.5Fe), that is

$$x/(0.75-x-y)=(W_T/M_T)(W_{Fe}/M_{Fe}), \tag{A5}$$

where W_T and W_{Fe} are the starting weights of transition metals and Fe, M_T, and M_{Fe} are the atomic weights of transition metals and Fe, respectively.

By solving the independent Eqs. (A4) and (A5), x and y can be determined.

ACKNOWLEDGMENTS

This work was partially supported by the Division of Materials Research of the National Science Foundation (Grant No. DMR 9305782) and the University of Missouri Research Board.

[1] G. C. Hadjipanayis, Y. Z. Wang, E. W. Singleton, and W. B. Yelon, J. Mater. Eng. Perf. **1**, 193 (1992).
[2] J. M. D. Coey, H. Sun, and D. P. F. Hurley, J. Magn. Magn. Mater. **101**, 310 (1991).
[3] H. Sun, M. Akayama, K. Tatami, and H. Fujii, Physica B **183**, 33 (1993).
[4] W. Gong and G. C. Hajipanayis, J. Appl. Phys. **73**, 6245 (1993).
[5] Y.-C. Yang, L.-S. Kong, S.-H. Sun, D.-M. Gu, and B.-P. Cheng, J. Appl. Phys. **63**, 3702 (1988).
[6] Y.-C. Yang, X. D. Zhang, L. S. Kong, and Q. Pan, Solid State Commun. **78**, 317 (1991).
[7] Y. Z. Wang, B. P. Hu, X. L. Rao, G. C, Liu, L. Yin, and W. Y. Lai, J. Appl. Phys. **73**, 6251 (1993).
[8] Y. Z. Wang and G. C. Hajipanayis, J. Appl. Phys. **70**, 6009 (1991).
[9] Z. Hu and W. B. Yelon, J. Appl. Phys. **76**, 6162 (1994).

Structure and magnetic properties of mechanical alloyed Nd–Fe–Ti compounds and their nitrides

Zhi-qiang Jin, X. K. Sun, W. Liu, X. G. Zhao, Q. F. Xiao, Y. C. Sui, Z. D. Zhang, and Zhigang Wang
Institute of Metal Research, Academia Sinica, Shenyang 110015, People's Republic of China

The Nd–Fe–Ti intermetallic compounds with a $ThMn_{12}$ structure have been successfully prepared by mechanical alloying and then annealed. It has been found that the phase of the hexagonal $TbCu_7$ structure is formed in $Nd_8Fe_{84}Ti_8$ mechanical alloy powders annealed at temperatures ranging from 650 to 850 °C. With an increase in the annealing temperature T_a, the metastable $TbCu_7$ structure transforms into a $ThMn_{12}$ structure at T_a=900 °C. Consequently, the Curie temperature increases from 180 °C of $TbCu_7$ structure at T_a=650 to 300 °C of $ThMn_{12}$ structure at T_a=1050 °C. In the series of $Nd_xFe_{92-x}Ti_8$ annealed at 960 °C for 30 min, it has been observed that the $ThMn_{12}$ structure exists only over the range of compositions of $5 \leqslant x < 11$, and the structure of the type Th_2Zn_{17} is formed for $x \geqslant 11$. All the compounds are nitrited at 400 °C for 15 h, and the Curie temperatures are raised from 400 to 450 °C. The $Nd_9Fe_{83}Ti_8$ powder, annealed at 960 °C for 30 min, and nitrided at 400 °C for 15 h, has a coercivity ${}_iH_c$=2.3 kOe. The low coercivity perhaps mainly results from an excessive growth of α-Fe grains due to the high annealing temperature necessary for forming the hard magnetic phase $Nd(Fe,Ti)_{12}N_\delta$. © *1996 American Institute of Physics.* [S0021-8979(96)32208-1]

I. INTRODUCTION

As far as our knowledge is concerned, the magnets prepared by the mechanical alloying (MA) technique have high coercivity compared with those prepared by traditional methods.[1,2] It is well known that $Nd(Fe,TM)_{12}N_\delta$ compounds (TM=Ti,V,Mo) with a $ThMn_{12}$ structure have excellent intrinsic magnetic properties which are comparable to those of $Nd_2Fe_{14}B$ compounds.[3] In addition, this kind of compound has the lowest relative content of rare earth (without relatively scarce Sm among them) compared to all the other previously discovered rare earth permanent magnet (REPM) compounds. In this regard, they are potentially favorable for the low cost production of REPM. Therefore, the $Nd(Fe,TM)_{12}N_\delta$ compounds with interstitial nitrogen have been thought to be a new perspective candidate of REPM. Unfortunately, no reports concerning MA synthesis of the $Nd(Fe,Ti)_{12}$ compound and its counterpart of nitride (with $ThMn_{12}$ structure) have been found so far, although other rare earth–transition metal compounds such as $SmCo_5$,[4] $Sm_2Fe_{17}N_x$,[1] Sm_5Fe_{17},[2] and $Nd_2Fe_{14}B$[5] have been successfully prepared by MA and subsequent heat treatment. Thus, the facts mentioned above urge us to study the preparation of $Nd(Fe,Ti)_{12}$ compounds and their nitrides by using the MA technique. Primary results of the research are briefly reported here; a somewhat detailed report will be published elsewhere.

II. EXPERIMENT

A series of $Nd_xFe_{92-x}Ti_8$ (x=4–11) specimens was prepared by MA under an argon atmosphere for 5 h of the mixed powders comprising the starting metals with purities of 99.6%, 99%, 99% for Fe, Ti, and Nd elements, respectively. Annealing treatment of the MA powder specimens was carried out at 600–1050 °C for 5–60 min in vacuum of $(2–3)\times10^{-5}$ Torr. Nitrogenation of the annealed powder specimens was performed at 400 °C for 2–40 h in a pure nitrogen atmosphere. X-ray diffraction (XRD) analysis of powder specimens was conducted using Cu K_α radiation with a Rigaku D/Max-rA diffractometer equipped with a graphite crystal monochromater. An initial ac susceptibility measurement was applied to determine the Curie temperature and to make a preliminary estimate of the possible magnetic phases in the specimens under study. The magnetically isotropic magnets made of the powders embedded in epoxy resin were used for the magnetic measurements at room temperature. The magnetic measurements were performed using a pulsed magnetometer in fields up to 8 T.

III. RESULTS AND DISCUSSION

XRD study has been applied to establish the proper milling times of mechanical alloying. It has been found that the characteristic peaks of Nd and Ti have been completely submerged into the background after 5 h, while retaining the prominent characteristic peaks of α-Fe up to milling for 30 h, which implies an extreme difficulty in getting the amorphous structure of iron. Prolonging the time of milling only makes the average particle dimension of the powders approach a stable limit. Thus, the milling time of 5 h has been reasonably selected. Figure 1 represents the XRD patterns of $Nd_8Fe_{84}Ti_8$ powder at different annealing temperatures for 30 min. The magnetic phase identification of the specimens was performed by XRD as shown in Fig. 1, in combination with a thermomagnetic analysis. It has been found that none of the magnetic phases is observed in the specimen annealed at 600 °C and the phase of the $TbCu_7$ structure is formed at T_a=700 °C. Furthermore, it is observed that the transformation of $Nd(Fe,Ti)_7$, of which the Curie temperature T_C increases from 180 °C at T_a=700 to 250 °C at T_a=800 °C, into $Nd(Fe,Ti)_{12}$ (with the $ThMn_{12}$ structure) occurs at 900 °C [cf. Fig. 1(c)]. The Curie temperature of the latter is 270 °C. It may be thought that the transformation is essen-

 0021-8979/96/79(8)/5525/3/$10.00 © 1996 American Institute of Physics

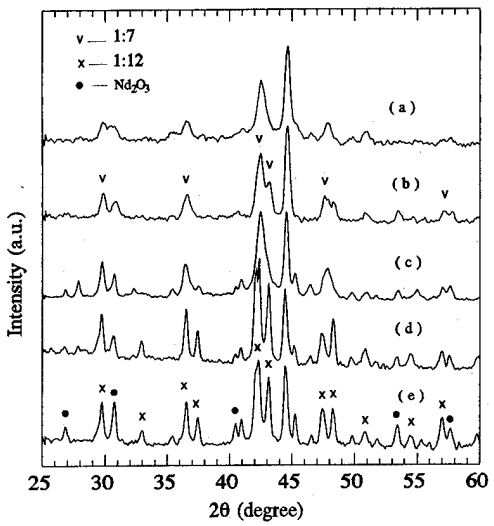


FIG. 1. X-ray diffraction patterns of $Nd_8Fe_{84}Ti_8$ powders of different annealed temperatures for 30 min: (a) 700 °C, (b) 850 °C, (c) 900 °C, (d) 960 °C, and (e) 1050 °C.

tially complete at T_a=960 °C for 30 min [cf. Figs. 1(d) and 1(e)]. The experimental results indicate that the Curie temperature T_C continuously increases with increasing T_a and T_C=300 °C is reached for annealing at T_a=1050 °C. The transformation may result from the high diffusion activity of elements and the evaporation of rare earth elements. In the MA preparation of $Nd(Fe,Ti)_{12}$, a moderately high annealing temperature is needed so that the solid state reaction to form the 1:12 phase can be completed. The experiment of XRD and thermomagnetic analysis show that excessively prolonging annealed time does not essentially influence the transformation between the 1:7 and 1:12 phases. This fact implies that the annealing temperature rather than the time is critical for the transformation from 1:7 to 1:12.

XRD patterns for various contents of Nd in $Nd_xFe_{92-x}Ti_8$ powders prepared by MA and annealed at 960 °C for 30 min are shown in Fig. 2. It can be seen that the alloy composition, to a great extent, determines the phase component of the alloy. The $Nd(Fe,Ti)_{12}$ compound, with a Curie temperature of about 280 °C, and which slightly depends on the composition, is formed for $5 \leqslant x \leqslant 10$, with the existence of α-Fe, Fe_2Ti, and rare earth oxides. A near single phase of $Nd(Fe,Ti)_{12}$ is obtained for $x=10$, where a small amount of rare earth oxides is included. With increasing Nd content, the amounts of α-Fe and Fe_2Ti decrease, and the phase with the Th_2Zn_{17} structure, where the Curie temperature is about 140 °C, is formed for $x \geqslant 11$. Further increasing the Nd content once again results in the formation of Fe_2Ti. Moreover, Nd_2O_3 cannot be avoided in all the compositions of the specimens. Figure 3 shows the dependence of coercivity on nitrided time at 400 °C for $Nd_8Fe_{84}Ti_8$ specimens annealed at 960 °C for 30 min and at 950 °C for 20 min, respectively. It can be seen that the former has a better coercivity than the latter. This result indicates that a properly high temperature and slightly long annealing time are beneficial to the formation of $Nd(Fe,Ti)_{12}N_\delta$. Figure 3 reveals that the coercivity first increases and then decreases with

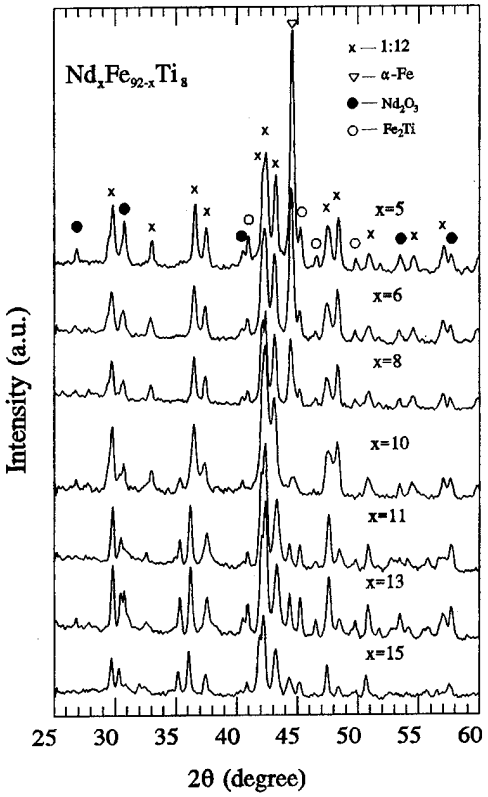


FIG. 2. X-ray diffraction patterns for mechanically alloyed $Nd_xFe_{92-x}Ti_8$ annealed at 960 °C for 30 min.

prolonged nitrided time. Upon annealing at 960 °C for 30 min and nitriding at 400 °C for 18 h, the magnet has a coercivity ${}_iH_c$=2.3 kOe. It should be pointed out that the Curie temperature of $Nd(Fe,Ti)_{12}$ exhibits a notable increase after nitrogenation. It has been found that the Curie temperature is 280 °C for the annealed specimen and 450 °C when the specimen is subsequently nitrided for 15 h. For 2 h nitriding, the two Curie temperatures were found to correspond to two magnetic phases—$Nd(Fe,Ti)_{12}$ and its nitride—and this im-

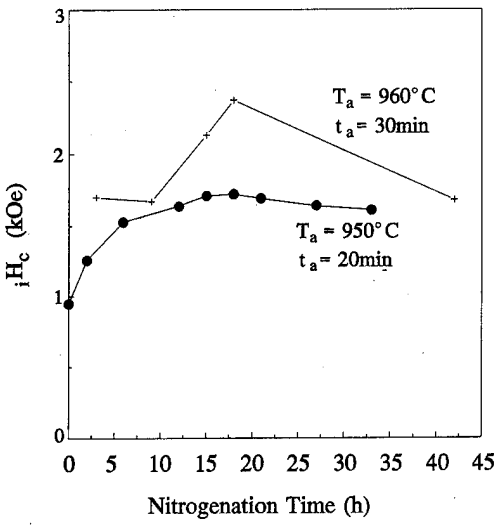


FIG. 3. Dependence of coercivity on nitrided time for $Nd_8Fe_{84}Ti_8N_\delta$ specimens annealed at 960 °C for 30 min and at 950 °C for 20 min, respectively, and nitrided at 400 °C.

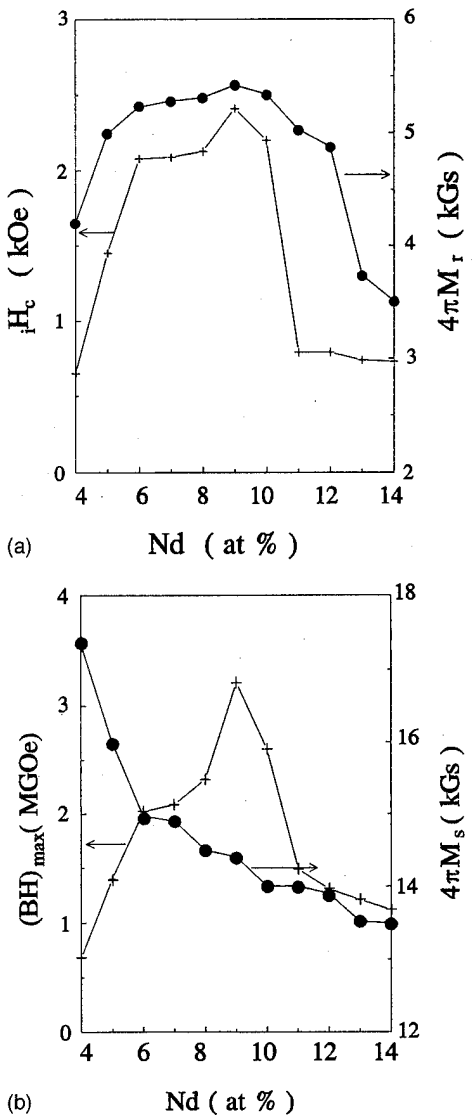


FIG. 4. Dependence of magnetic properties on Nd content for $Nd_xFe_{92-x}Ti_8$ specimens annealed at 960 °C for 30 min and nitrided at 400 °C for 15 h: (a) $_iH_c$ and $4\pi M_r$, (b) $(BH)_{max}$, and $4\pi M_s$.

plies an imperfect nitriding process. Thus, $Nd(Fe,Ti)_{12}$ and $Nd(Fe,Ti)_{12}N_\delta$ coexist. In addition, it should be noted that too high a nitriding temperature (>450 °C) results in a decomposition of the studied compound and thus the magnetic properties are degraded.

The dependence of the magnetic properties in the series of $Nd_xFe_{92-x}Ti_8$ annealed at 960 °C for 30 min and nitrided at 400 °C for 15 h on the composition is shown in Fig. 4. It is observed that the coercivity $_iH_c$, the remanence $4\pi M_r$, and the maximum magnetic energy product $(BH)_{max}$ of the nitrides first increase with increasing Nd content. The maximum values of $_iH_c$=2.3 kOe, $4\pi M_r$=5.8 kG s, and $(BH)_{max}$=3.2 MG Oe, respectively, are obtained at about x=9. It is obvious that the excessive content of neodymium in the specimens with $x>9$, is not favorable for the magnetic hardening of the magnets. A possible reason for this is that the excess of neodymium destroys the perfectness of the structure of the hard magnetic 1:12 phase, which is identified by broadening of the peaks of the XRD pattern for $x=10$, and perhaps, it is a forerunner of the transformation from 1:12 to 2:17, followed by the occurrence of the transformation for $x>10$. In contrast, the saturation magnetization decreases monotonously with increasing x values. Although the incompatible variation of the remanence with the saturation magnetization is very interesting, it is difficult to clearly explain this phenomenon. It should be noted that an unusually low coercivity is attained and this value is expected to be higher due to the high uniaxial magnetocrystalline anisotropy field H_A of $Nd(Fe,Ti)_{12}N_\delta$ ($H_a\approx80$ kOe at room temperature).[3] The low coercivity perhaps mainly results from an excessive growth of α-Fe grains due to the high annealing temperature necessary for forming the hard magnetic phase $Nd(Fe,Ti)_{12}N_\delta$. Therefore, the remanence enhancement could not be achieved by the presence of α-Fe in the magnets.

ACKNOWLEDGMENTS

This work has been supported by the National Natural Foundation of China, the President Foundation of the Chinese Academy of Sciences, the Science and Technology Commission of Shenyang, and the K. C. Wong Education Foundation of Hong Kong.

[1] W. Liu, Q. Wang, X. K. Sun, X. G. Zhao, T. Zhao, Z. D. Zhang, and Y. C. Chuang, J. Magn. Magn. Mater. **131**, 413 (1994).
[2] J. L. Yang, Q. Wang, X. K. Sun, G. Y. Zeng, M. Chen, W. Liu, X. G. Zhao, T. Zhao, and Z. D. Zhang, J. Magn. Magn. Mater. **132**, 197 (1994).
[3] Y. C. Yang, X. D. Zhang, L. S. Kong, Q. Pan. and S. L. Ge, Solid State Commun. **78**, 317 (1991).
[4] J. Wecker, M. Katter, and L. Schlutz, J. Appl. Phys. **69**, 6058 (1991).
[5] L. Schlutz, K. Schnitzke, and J. Wecker, J. Magn. Magn. Mater. **80**, 115 (1989).

High coercivity of melt–spun $Sm_2Fe_{15}Al_2C_{1.5}$ compound

Jun-Xian Zhang, Zhao-Hua Cheng, and Bao-Gen Shen
State Key Laboratory of Magnetism, Institute of Physics, Chinese Academy of Sciences, P.O. Box 603, Beijing 100080, People's Republic of China

The magnetic hardening of melt–spun $Sm_2Fe_{17}C_x$ was studied and the coercivity of 4.6 kOe for $Sm_2Fe_{17}C_{1.5}$ alloys was reported a few years ago. Recently, we have succeeded in preparing single-phase compounds of $Sm_2(Fe, M)_{17}C_x$ (M=Ga, Al, or Si) with high carbon concentration by arc melting. It was found that the substitution of Ga or Al not only facilitated the formation of high carbon concentration rare-earth iron compounds with a 2:17-type structure, but also was very effective in raising the value of the anisotropy field. For example, the sample of $Sm_2Fe_{15}Al_2C_{1.5}$ has a saturation magnetization of 110.2 emu/g, a Curie temperature of 576 K, and an anisotropy field of 111 kOe. It is known that melt spinning is an effective means to obtain high coercivity of magnetically hard materials. In this work, the hard magnetic properties of melt–spun $Sm_2Fe_{15}Al_2C_{1.5}$ alloys were investigated. It was found that the value of coercivity depends strongly on the quenching rates and an optimum coercivity of 9.4 kOe was obtained at the quenching rate of 20 m/s. X-ray diffraction patterns indicate that the as-quenched ribbons have a phase of the Th_2Zn_{17}-type structure. The high coercivity of these as-quenched ribbons originates from the excellent intrinsic magnetic properties of $Sm_2Fe_{15}Al_2C_{1.5}$. It can be concluded that the substitution of Al is very effective in raising the coercivity of melt–spun $Sm_2Fe_{15}Al_2C_{1.5}$ ribbons. © *1996 American Institute of Physics.* [S0021-8979(96)32308-8]

I. INTRODUCTION

The $Sm_2Fe_{17}N_x$ and $Sm_2Fe_{17}C_x$ compounds with higher nitrogen or carbon concentrations are promising candidates for permanent magnets owing to their excellent intrinsic hard magnetic properties.[1,2] However, a serious drawback of the nitrides or carbides prepared by the gas–solid reaction is their poor high-temperature stability. These compounds decompose into the equilibrium phase rare-earth nitrides (carbides) and α-Fe upon heating to 600–700 °C. This restricts the actual application for the sintered permanent magnet. Recently, we have studied the effect of various elemental substitutions for Fe on the formation, structure, and magnetic properties of the $R_2Fe_{17}C_x$ alloys and found that the high-carbon $R_2F_{17}C_x$ compounds containing Ga, Al, or Si, etc., exhibited a high thermal stability. The 2:17-type carbides containing Ga, Al, or Si, etc., can be directly formed by arc melting. It was found that the substitution of Ga, Al, or Si can not only help the formation of 2:17-type rare-earth iron compounds with high carbon concentration, but also is very effective in raising the value of the anisotropy field. We have reported some results of high-carbon $Sm(Fe,M)_{17}C_x$ (M=Ga, Al, or Si) compounds.[3–6] It is known that melt–spinning is an effective means to obtain high coercivity of magnetically hard materials. In this paper, the hard magnetic properties of melt–spun $Sm_2Fe_{15}Al_2C_{1.5}$ alloys were investigated.

II. EXPERIMENT

Fe and C were first melted together into Fe–C alloys and then Fe, Sm, Al, and Fe–C alloys were melted by arc melting in an argon atmosphere of high purity. The elements used were at least 99.9% pure. An excess of 5% Sm was added to compensate for the evaporation during melting and melt–spinning steps. The ingot alloys were melted at least four times to ensure homogeneity. The ingots were melt–spun in a high-purity argon atmosphere using a copper quenching wheel rotating at a surface velocity V_s between 0 and 40 m/s. The ribbons were about 1 mm wide and 20–30 μm thick. The phase composition and structure were investigated with a Cu $K\alpha$ x-ray diffractometer. The hysteresis loops were measured by an extracting sample magnetometer with a magnetic field up to 70 kOe.

III. RESULTS AND DISCUSSION

In our reported work,[6,8] the formation and magnetic properties of $Sm_2Fe_{17-x}Al_xC_y$ compounds were studied. It was found that the sample of $Sm_2Fe_{15}Al_2C_{1.5}$ has excellent intrinsic magnetic properties, such as a saturation magnetization of 110.2 emu/g, Curie temperature of 576 K, and anisotropy field of 110 kOe. Thus, this sample was selected to study the effect of melt–spinning on the coercivity. X-ray diffraction experiments indicate that $Sm_2Fe_{15}Al_2C_{1.5}$ alloys have a rhombohedral Th_2Zn_{17}-type structure. In order to obtain a high coercivity, we prepared ribbons at various quenching rates. For example, Fig. 1 shows the hysteresis loop for as-quenched $Sm_2Fe_{15}Al_2C_{1.5}$ ribbon by direct melt–spinning at 20 m/s. For comparison the hysteresis loop for as-quenched $Sm_2Fe_{15}Ga_2C_{1.5}$ ribbon by optimum melt–spinning at 30 m/s is also shown in Fig. 1. The coercivity of $Sm_2Fe_{15}Al_2C_{1.5}$ ribbons as a function of quenching rates is plotted in Fig. 2. It can be seen that the value of coercivity depends strongly on the quenching rates. The coercivity is found to have a maximum value of 9.4 kOe when the quenching rate is about 20 m/s and is reduced quickly when quenching rate is either slower or faster than optimum, falling to less than 500 Oe at 40 m/s.

The x-ray diffraction patterns of the as-quenched $Sm_2Fe_{15}Al_2C_{1.5}$ ribbons show that the sample for V_s=15, 20, and 25 m/s can be indexed to the Th_2Zn_{17}-type structure, indicating that the ribbons are almost entirely comprised of hard magnetic phase, a few percent of α-Fe was present as

 0021-8979/96/79(8)/5528/2/$10.00 © 1996 American Institute of Physics

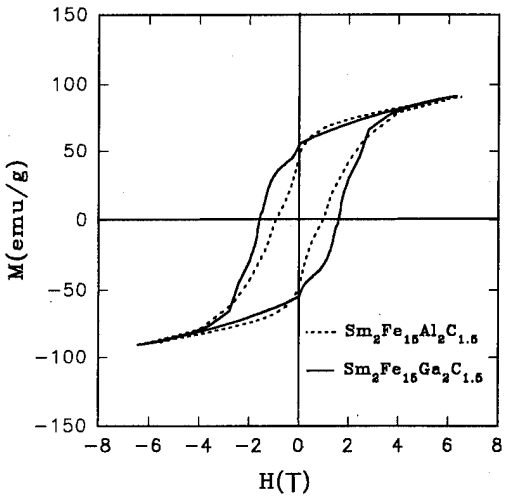


FIG. 1. Hysteresis loops for $Sm_2Fe_{15}Al_2C_{1.5}$ ribbon with a quenching rate of 20 m/s and $Sm_2Fe_{15}Ga_2C_{1.5}$ ribbon with a quenching rate of 30 m/s.

well. Because the magnetization in the grains comprised of the soft magnetic phase is easily reversed under an external small opposite magnetic field, it induces a cascade of demagnetization processes within adjacent grains. For these samples, the value of coercivity is lower. In the

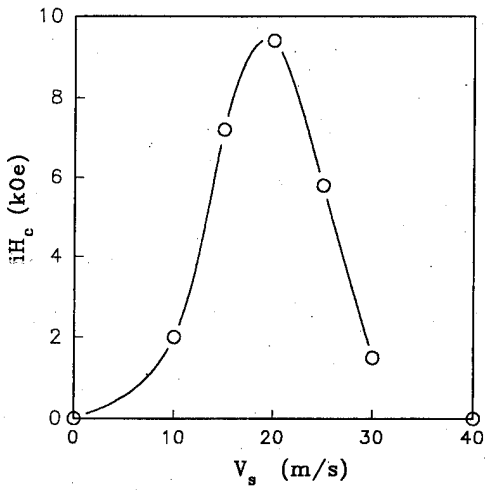


FIG. 2. The coercivity of $Sm_2Fe_{15}Al_2C_{1.5}$ ribbons as a function of quenching rates.

TABLE I. The anisotropy field and coercivity of compounds.

Compounds	H_a (kOe)	H_c (kOe)	$H_c:H_a$
$Sm_2Fe_{17}C_{1.5}$[a]	53	4.6	1:10
$Sm_2Fe_{14}Ga_2C_{1.5}$[b]	120	16	1:10
$Sm_2Fe_{15}Al_2C_{1.5}$	111	9.4	1:10

[a]From Ref. 7.
[b]From Ref. 9.

$Sm_2Fe_{15}Al_2C_{1.5}$ ribbon for V_s=40 m/s an amorphous phase starts to form and only a small amount of the Th_2Zn_{17} phase remains. The formation of the amorphous phase and the very fine grains of the Th_2Zn_{17} phase is consistent with the low coercivity.

Early studies of the $Sm_2Fe_{17}C_x$ alloys showed the anisotropy field is 53 kOe for $Sm_2Fe_{17}C_{1.5}$, and the largest coercivity 4.6 kOe for the quenched sample.[7] For comparison the anisotropy field and the largest coercivity for quenched alloys of $Sm_2Fe_{17}C_{1.5}$, $Sm_2Fe_{15}Ga_2C_{1.5}$,[9] and $Sm_2Fe_{15}Al_2C_{1.5}$ compounds is listed in Table I. The coercivity reaches about 1/10 of the anisotropy field for these compounds. The high coercivity of these as-quenched ribbons originates from the excellent intrinsic magnetic properties of $Sm_2Fe_{17}C_{1.5}$, $Sm_2Fe_{15}Ga_2C_{1.5}$, and $Sm_2Fe_{15}Al_2C_{1.5}$, respectively.

In conclusion, the hard magnetic properties of the $Sm_2Fe_{15}Al_2C_{1.5}$ compounds have been studied by melt–spinning. Coercivity of 9.4 kOe was obtained. It can be conduced that the substitution of Al is very effective in raising the coercivity of melt–spun $Sm_2Fe_{15}Al_2C_{1.5}$ ribbons.

ACKNOWLEDGMENT

This work was supported by the National Natural Sciences Foundation of China.

[1] J. M. D. Coey and H. Sun, J. Magn. Magn. Mater. **87**, L251 (1990).
[2] J. M. D. Coey, H. Sun, Y. Otani, and D. P. F. Hurley, J. Magn. Magn. Mater. **98**, 76 (1991).
[3] B. G. Shen, L. S. Kong, F. W. Wang, and L. Cao, Appl. Phys. Lett. **63**, 2288 (1993).
[4] B. G. Shen, F. W. Wang, L. S. Kong, L. Cao, and H. Q. Guo, J. Magn. Magn. Mater. **127**, L267 (1993).
[5] B. G. Shen, L. S. Kong, F. W. Wang, L. Cao, and W. S. Zhan, Acta Phys. Sin. **43**, 846 (1994).
[6] Z. H. Cheng, B. G. Shen, F. W. Wang, J. X. Zhang, H. Y. Gong, and J. G. Zhao, J. Phys. Condens. Matter 6, L185 (1994).
[7] J. Ding and M. Rosenberg, J. Less-Common Metals **166**, 313 (1990).
[8] Z. H. Cheng, B. G. Shen, J. X. Zhang, F. W. Wang, H. Y. Gong, W. S. Zhan, and J. G. Zhao, J. Appl. Phys. **76**, 6734 (1994).
[9] L. S. Kong, B. G. Shen, F. W. Wang, L. Cai, H. Q. Guo, and T. S. Ning, J. Appl. Phys. **75**, 6251 (1994).

Nuclear magnetic resonance study of R_2Fe_{17} (R=Y, Sm, and Gd) hydrides

N. X. Shen, Y. D. Zhang, J. I. Budnick, and W. A. Hines
Department of Physics and Institute of Material Science, University of Connecticut, Storrs, Connecticut 06269-3046

U. Binninger
Department of Physics, University of Konstanz, P.O. Box 55 68, D-78434 Konstanz, Germany

In order to study the location of hydrogen atoms and the effects of their insertion into R_2Fe_{17}, spin–echo NMR experiments have been carried out on the hexagonal $Y_2Fe_{17}H_x$ (x=0, 3.0, 4.7), rhombohedral $Sm_2Fe_{17}H_x$ (x=0, 1.7, 5.7), and mixed-phase $Gd_2Fe_{17}H_x$ (x=0, 2.3, 5.8) compounds. ^1H and ^{89}Y spectra obtained from $Y_2Fe_{17}H_x$ clearly demonstrate that the hydrogenation process is reversible upon vacuum annealing. For both $Y_2Fe_{17}H_x$ and $Sm_2Fe_{17}H_x$, the ^1H spectra show two broad peaks; the peaks are tentatively assigned to H atoms in the tetrahedral and octahedral interstitial sites, and a hydrogen filling scheme is proposed. For $Gd_2Fe_{17}H_x$, a single broad ^1H peak near 70 MHz is observed; application of an external magnetic field indicates that the hyperfine field has the same direction as the net magnetization. © *1996 American Institute of Physics.* [S0021-8979(96)32408-4]

I. INTRODUCTION

Since the discovery that Sm_2Fe_{17} can absorb a large amount of nitrogen which substantially improves the magnetic properties,[1] much attention has been focused on the R_2Fe_{17} nitrides, carbides, and hydrides, where R is a rare earth atom except lanthanum. In order to understand the nature of the gas phase modification, it is important to determine where these interstitial atoms are located and how they affect the local magnetic properties. So far, several techniques, such as x-ray absorption fine structure (XAFS),[2] neutron diffraction (ND),[3–5] Mössbauer effect (ME),[6,7] as well as nuclear magnetic resonance (NMR),[8–10] have been utilized to study the properties on an atomic scale. Among these techniques, NMR has the advantage of providing a direct measurement for several specific local environments. For example, in the $Y_2Fe_{17}H_x$ hydride system, ^1H and ^{89}Y are excellent NMR probes since they are 100% abundant and have a spin of 1/2. Although it is not as favorable as ^1H and ^{89}Y, the weak ^{57}Fe NMR signal can be observed in this system when it is not overlapped by the stronger ^{89}Y signal. Reviewing previous work, it is generally accepted that nitrogen and carbon occupy principally the octahedral sites ($6h$ and $9e$ for the hexagonal and rhombohedral structures, respectively); hydrogen occupies the octahedral sites exclusively until the H content reaches three H atoms per formula unit, and then goes into the tetrahedral interstitial sites ($12i$ and $18g$ for the hexagonal and rhombohedral structures, respectively).[11] Both nitrogen and carbon have a strong influence on the ^{89}Y hyperfine field,[8,9] whereas it has been reported that hydrogen does not have a significant effect.[8] In this work, spin–echo NMR spectra are presented for the $Y_2Fe_{17}H_x$ (x=0, 3.0, and 4.7), $Sm_2Fe_{17}H_x$ (x=0, 1.7, and 5.7), and $Gd_2Fe_{17}H_x$ (x=0, 2.3, and 5.8) hydride systems. Assignments are made for the ^1H, ^{89}Y, ^{155}Gd, and ^{157}Gd resonance peaks and a filling scheme for the hydrogen occupation is proposed.

II. EXPERIMENTAL PROCEDURE

The Y_2Fe_{17} and Gd_2Fe_{17} parent ingots were fabricated by arc melting, using Fe, Y, and Gd with a purity of 99.95%, followed by annealing at 950 °C in vacuum for seven days. The polycrystalline ingots were ground into powders with the particle sizes ranging from 25 to 32 μm. The Sm_2Fe_{17} parent sample was chemically synthesized with the particle sizes ranging from 3 to 5 μm.[12] The structures of the powders were analyzed by Cu $K\alpha$ x-ray diffraction. R_2Fe_{17} compounds are characterized by either the Th_2Ni_{17}-like hexagonal or Th_2Zn_{17}-like rhombohedral structure, or perhaps, a mixed phase of both structures. Both structures can be indexed on hexagonal cells; the difference between the two structures is the stacking sequence along the c direction. Hydrogen was loaded at temperatures near 200 °C and pressures of 3–5 atm. The H content was determined by measuring the pressure decrease during the hydrogenation.

The spin–echo NMR spectra were obtained at both liquid helium and liquid nitrogen temperatures, in zero external magnetic field, using a phase-coherent pulse spectrometer. More detailed methodology of NMR in magnetically ordered materials is available elsewhere.[13]

III. RESULTS AND DISCUSSION

The x-ray diffraction powder patterns for the Y_2Fe_{17}, Sm_2Fe_{17}, and Gd_2Fe_{17} parent samples are shown in Fig. 1. Since the R_2Fe_{17} compounds may crystallize in a hexagonal, rhombohedral, or mixed-phase structure, it is necessary to estimate the phase composition by looking at the characteristic peaks for each phase, i.e., the (203) hexagonal peak for $2\theta \approx 41°$ and the (024) rhombohedral peak for $2\theta \approx 38°$. It can be seen in Fig. 1 that Y_2Fe_{17} is predominately in the hexagonal phase with a trace amount of the rhombohedral phase; Sm_2Fe_{17} is entirely in the rhombohedral phase; and Gd_2Fe_{17} is in a mixed phase. Also, the x-ray results for all of these parent samples show the absence of bcc α-Fe. The hydrided samples of these compounds retain the same structures as the parent samples, but with a small volume expansion. All of

 0021-8979/96/79(8)/5530/3/$10.00 © 1996 American Institute of Physics

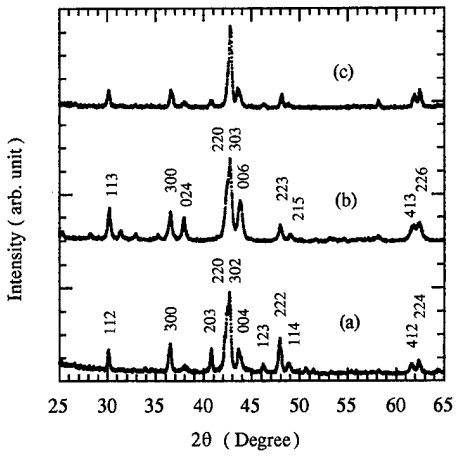


FIG. 1. X-ray diffraction powder patterns for (a) hexagonal Y_2Fe_{17}, (b) rhombohedral Sm_2Fe_{17}, and (c) mixed-phase Gd_2Fe_{17}, which are the parent samples for the corresponding hydrides.

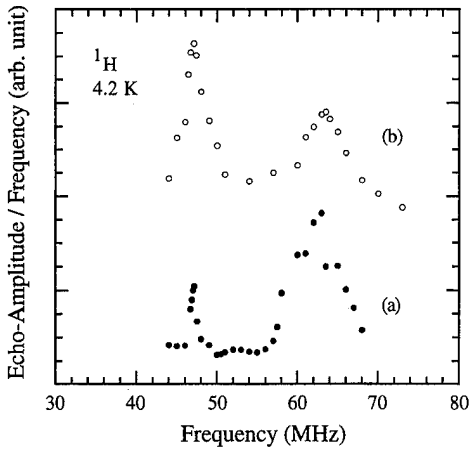


FIG. 3. Spin–echo NMR spectra of ^{1}H at 4.2 K for (a) $Y_2Fe_{17}H_{3.0}$ and (b) $Y_2Fe_{17}H_{4.7}$.

the hydrides show the basal-plane anisotropy.[11] Previous ^{89}Y NMR studies[9,10] on Y_2Fe_{17} and its nitrides show that the hyperfine fields for the hexagonal ($2b$,$2d$) and the rhombohedral ($6c$) Y sites are so similar that phase disordering is not a problem in the analysis of the spectra.

The spin–echo NMR spectra of ^{89}Y and ^{1}H for $Y_2Fe_{17}H_x$ (x=0, 3.0, and 4.7) at 4.2 K are shown in Figs. 2 and 3, respectively. When Y_2Fe_{17} is hydrogenated, the center of gravity of the ^{89}Y peak shifts down by approximately 4 MHz [Figs. 2(b) and 2(c)], which is larger than the shift reported elsewhere.[8] The ^{89}Y peak positions and shape vary somewhat with H content, i.e., the nonsymmetric peak for $Y_2Fe_{17}H_{3.0}$ with a pronounced "shoulder" on the high-frequency side, has its strongest intensity at 38.0 MHz, whereas the peak for $Y_2Fe_{17}H_{4.7}$, with less asymmetry, has its strongest intensity at 38.8 MHz. No ^{89}Y satellite peaks are observed with hydrogenation. This is in contrast to the behavior for $Y_2Fe_{17}N_x$ which shows satellite peaks for Y atoms with one, two, and three N atoms as nearest neighbors.[8,9] In addition, the two new peaks which appear at 47.1 and 63.0 MHz have intensities that depend on the H content (Fig. 3). When the $Y_2Fe_{17}H_{3.0}$ sample was annealed in vacuum at 150 °C for 3 h, the peaks at 47.1 and 63.0 MHz disappeared, and the ^{89}Y peak shifted back to 42.2 MHz with some residual broadening. The NMR results demonstrate that the hydrogenation process is reversible. Based on these observations, it is reasonable to assign the 47.1 and 63.0 MHz peaks to ^{1}H.

In contrast to Y_2Fe_{17}, Sm_2Fe_{17} is magnetically more anisotropic and harder. Consequently, the NMR enhancement factor for this compound is lower and, correspondingly, a larger radio frequency excitation field is required to observe the spin–echo. Figure 4 shows the NMR spectra obtained from $Sm_2Fe_{17}H_x$ (x=1.7, and 5.7) at 1.3 and 77 K. The four vertical bars indicate the hyperfine field values obtained from ME results for the four Fe sites.[6] The NMR spectrum obtained from the parent Sm_2Fe_{17} sample reveals two well-resolved but extremely weak ^{57}Fe peaks at 38.8 and 50.0 MHz. Therefore, in the spectra presented in Fig. 4, the con-

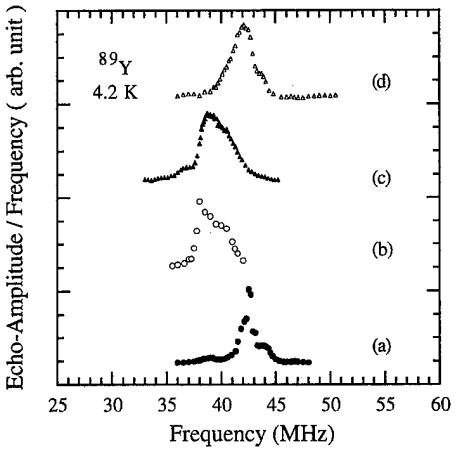


FIG. 2. Spin–echo NMR spectra of ^{89}Y at 4.2 K for (a) Y_2Fe_{17}, (b) $Y_2Fe_{17}H_{3.0}$, (c) $Y_2Fe_{17}H_{4.7}$, and (d) $Y_2Fe_{17}H_{3.0}$ which was annealed at 150 °C for 3 h.

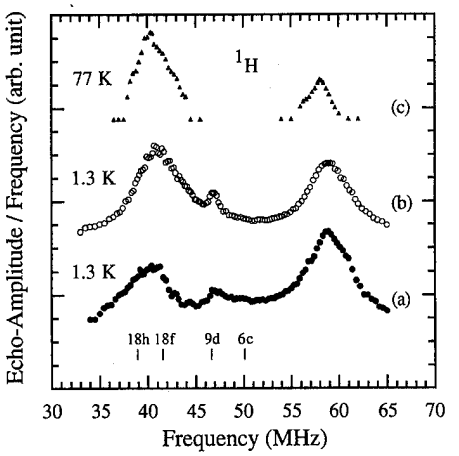


FIG. 4. Spin–echo NMR spectra of ^{1}H at 1.3 K for (a) $Sm_2Fe_{17}H_{1.7}$, (b) $Sm_2Fe_{17}H_{5.7}$, and at 77 K for (c) $Sm_2Fe_{17}H_{5.7}$. The vertical bars indicate the positions of the hyperfine fields for the four Fe sites in Sm_2Fe_{17} (Ref. 6).

tributions from ^{57}Fe in the 2:17 phase are negligible. As shown in Fig. 4, the $Sm_2Fe_{17}H_x$ spectra are characterized by two broad lines at 40.5 and 58.5 MHz, with a small peak at 46.7 MHz. In order to make assignments for these peaks, the corresponding spin–lattice relaxation times were measured. It was found that the spin–lattice relaxation times for the 40.5 and 58.5 MHz peaks were of the same order (1 s); however, that for the 46.7 MHz peak was much shorter (0.01 s). Therefore, the peaks at 40.5 and 58.5 MHz were assigned to ^1H, and the peak at 46.7 MHz was assigned to ^{57}Fe from the small amount of bcc α-Fe precipitation which occurred during hydrogenation, and was not detected by x-ray diffraction. The spectrum obtained from $Sm_2Fe_{17}H_{5.5}$ at 77 K [Fig. 4(c)] confirmed that the 40.5 and 58.5 MHz peaks are only from ^1H since the ^{57}Fe signal is too weak to be seen at liquid nitrogen temperature.

The assignment of the two ^1H peaks for Sm_2Fe_{17} and Y_2Fe_{17} in terms of the hydrogen location is not definite. For the H atoms, a strong dipolar field is indicated from muon spin resonance (μSR).[14] The octahedral site is not a site of unique magnetic symmetry. If it was, the two ^1H peaks that were observed here could arise from the octahedral site H atoms with a splitting caused by the dipolar interaction when the magnetization lies in the basal plane. In this case, the contribution from the tetrahedral sites remains to be observed. Another possible assignment is that the two ^1H peaks are due to the H atoms in these two different sites. A previous ND study reports that both the octahedral and tetrahedral sites are occupied by hydrogen.[7] In terms of the nearest neighbors, a H atom in an octahedral site is surrounded by two rare-earth atoms and four iron atoms, while a H atom in a tetrahedral site is surrounded by two rare-earth atoms and two iron atoms. A simple calculation shows that the volume ratio V_o/V_t for these two sites is 8/3, where V_o is the volume for the octahedral site and V_t is the volume for the tetrahedral site. Therefore, the insertion of a H atom into the octahedral site will be easier since it produces less lattice strain. The NMR results did show the preferential occupancy as indicated by the higher frequency peaks in the ^1H spectra. Based on this assumption, the low frequency peaks (47.1 MHz for $Y_2Fe_{17}H_x$ and 40.5 MHz for $Sm_2Fe_{17}H_x$) were assigned to H atoms in the tetrahedral sites, and the high frequency peaks (63.0 MHz for $Y_2Fe_{17}H_x$ and 58.5 MHz for $Sm_2Fe_{17}H_x$) to H atoms in the octahedral sites. If this assignment is correct, there is clearly a non-negligible occupancy of hydrogen in the tetrahedral sites for $Y_2Fe_{17}H_{3.0}$ [Fig. 3(a)], and even for low H content sample $Sm_2Fe_{17}H_{1.7}$ [Fig. 4(a)]. These results suggest that a filling of both interstitial sites occurs as hydrogen is added to the sample, even though the H atom has the preferential occupancy to the octahedral sites.

The situation for the mixed-phase Gd_2Fe_{17} sample is quite complicated. There are three distinct Gd sites, two for the hexagonal ($2b$ and $2d$) and one for the rhombohedral ($6c$), to take into account. Furthermore, Gd has two isotopes, ^{155}Gd and ^{157}Gd, and a large magnetic moment which interacts strongly with Fe. All of these factors make the analysis of the ^{155}Gd and ^{157}Gd very difficult. Fortunately, the spectra for ^1H are more straightforward. Figure 5 shows NMR spectra observed for $Gd_2Fe_{17}H_x$ (x=0, 2.3, and 5.8) at

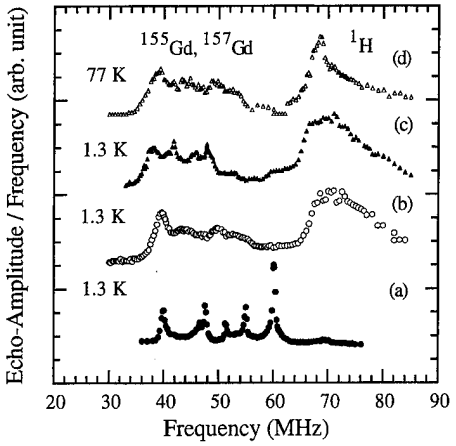


FIG. 5. Spin–echo NMR spectra of ^{155}Gd, ^{157}Gd, and ^1H at 1.3 K for (a) Gd_2Fe_{17}, (b) $Gd_2Fe_{17}H_{2.3}$, (c) $Gd_2Fe_{17}H_{5.8}$, and at 77 K for (d) $Gd_2Fe_{17}H_{2.3}$.

1.3 and 77 K. All the peaks in Fig. 5(a) are certainly from the ^{155}Gd and ^{157}Gd isotopes, and will not be discussed here.[15] It can be seen that hydrogenation makes the ^{155}Gd and ^{157}Gd spectra complicated because of changes in the quadrupolar interactions as well as the hyperfine fields. However, the strong, broad peak occurring near 70 MHz at 1.3 K can clearly attributed to ^1H. At 77 K, this peak shifts to 68.8 MHz and becomes sharper [Fig. 5(d)]. When an external magnetic field of 6.0 kOe was applied, the peak shifted to 85.0 MHz and became broader. This result indicates the hyperfine field of ^1H is in the same direction as the net magnetization.

ACKNOWLEDGMENTS

The authors would like to acknowledge the NSF for financial support (Grant No. DMR 9319367). Also, the authors would like to thank Dr. B. Reinsch of the Max Planck Institute for providing samples of Sm_2Fe_{17} and Dr. T. Manzur for his assistance in the sample preparation.

[1] J. M. D. Coey and H. Sun, J. Magn. Magn. Mater. **87**, L251 (1990).
[2] T. W. Capchart, R. K. Mishra, and F. E. Pinkerton, Appl. Phys. Lett. **58**, 1395 (1991).
[3] R. M. Ibberson, O. Moze, T. H. Jacobs, and K. H. J. Buschow, J. Phys. Condens. Matter **3**, 1219 (1991).
[4] W. B. Yelon and G. C. Hadjipanayis, IEEE Trans. Magn. **28**, 2316 (1992).
[5] O. Isnard, S. Miraglia, J. L. Soubeyroux, and D. Fruchart, Solid State Commun. **81**, 13 (1992).
[6] B. B. Hu, H. S. Li, H. Sun, and J. M. D. Coey, J. Phys. Condens. Matter **3**, 3983 (1991).
[7] O. Isnard, P. Vulliet, A. Blaise, J. P. Sanchez, S. Miraglia, and D. Fruchart, J. Magn. Magn. Mater. **131**, 83 (1994).
[8] Cz. Kapusta, M. Rosenberg, J. Zukrowski, H. Figiel, T. H. Jacobs, and K. H. Buschow, J. Less-Common Metals **171**, 101 (1991).
[9] Y. D. Zhang, J. I. Budnick, N. X. Shen, W. A. Hines, G. W. Fernando, and T. Manzur, J. Magn. Magn. Mater. **140–144**, 987 (1995).
[10] Y. D. Zhang, J. I. Budnick, W. A. Hines, N. X. Shen, T. D. Xiao, and T. Manzur, J. Magn. Magn. Mater. **145**, L11 (1995).
[11] O. Isnard, S. Miraglia, J. L. Soubeyroux, D. Fruchart, and P. l'Heritier, J. Magn. Magn. Mater. **137**, 151 (1994).
[12] B. Reinsch *et al.* (to be published).
[13] Y. D. Zhang, J. I. Budnick, J. C. Ford, and W. A. Hines, J. Magn. Magn. Mater. **100**, 13 (1992).
[14] C. Niedermayer *et al.* (to be published).
[15] R. Sarthour, S. Gama, C. C. Colucci, J. S. Lord, R. C. Reidi, A. P. Guimarães, and J. Magn. Magn. Mater. **140**, 1003 (1995).

Structural and magnetic studies of $Er_2Fe_{17-x}M_xC_y$ (M=Ga and Al) compounds

W. C. Chang, S. L. Lu, S. K. Chen,[a] and Y. D. Yao
Department of Physics, National Chung Cheng University, Ming-Hsiung, Chia-Yi, Taiwan, Republic of China

The effect of Ga and Al substitution for Fe on the structural and magnetic properties of the $Er_2Fe_{17-x}M_xC_y$ (M=Ga, Al; $x=0-4$, $y=0-2$) compounds was investigated. It was found that Ga is superior to Al in stabilizing the single-phase $Er_2Fe_{17-x}M_xC_y$ compounds. The hexagonal Th_2Ni_{17}-type structure persisted in almost all alloys with the exception of $Er_2Fe_{13}Ga_4C$ and $Er_2Fe_{13}Ga_4C_2$. These two compounds exhibited a rhombohedral Th_2Zn_{17} structure. Both the Curie temperature and magnetization can be enhanced with a certain amount of Ga or Al substitution. But they decreased almost monotonically with the increase of Ga or Al content in $Er_2Fe_{17-x}M_xC_y$ ($x>1$, $y>0$). The spin reorientation temperature, T_{sr}, was influenced by both carbon interstitial and Ga or Al substitution for Fe and ascribed to the increase of the c-axis uniaxial anisotropy of the Er^{3+} sublattice by the modification of electron structure around it. The highest T_{sr} of 241 K appears in the compound $Er_2Fe_{14}Ga_3C$. © *1996 American Institute of Physics.* [S0021-8979(96)32508-0]

I. INTRODUCTION

$R_2Fe_{17}C_x$ compounds have been extensively studied because their thermal stability is superior to that of nitrogenated compounds. The addition of Ga and Al was reported to further stabilize the $R_2Fe_{17}C_x$ compounds with high carbon concentration.[1,2] The solubility of Ga and Al in $R_2Fe_{17}C_x$ changes with R elements and consequently determines the magnetic anisotropy of the carbides. Few papers have ever reported their effects in a R=Er system[3,4] and the range of the alloy compounds has not been widely covered. In this study, we first investigate the single-phase region of the $Er_2Fe_{17-x}M_xC_y$ (M=Ga and Al; $x=0-4$, $y=0-2$) compounds, and then the effects of Ga and Al replacement in $R_2Fe_{17}C_x$ compounds on the Curie temperature (T_C), magnetization (M_s), and spin reorientation temperature (T_{sr}). A comparison and discussion of the Ga and Al effect in these $Er_2Fe_{17-x}M_xC_y$ systems will be presented.

II. EXPERIMENT

The studied samples, 2 g for each, with the nominal composition $Er_2Fe_{17-x}M_xC_y$ (M=Ga and Al; $x=0-4$, $y=0-2$) were prepared by arc melting in a high purity argon atmosphere. The alloys were remelted at least three times to ensure homogeneity and then followed with a homogenization treatment at 1100 °C for 24 h. X-ray diffraction with Cu $K\alpha$ radiation was adopted to determine the single-phase and crystallographic structure. The room temperature magnetization of the samples was measured with a vibrating sample magnetometer (VSM). The Curie temperatures were determined from the change of weight with temperature measured by thermal gravimetric analysis (TGA). Finally, the spin reorientation temperatures were determined from the magnetization versus temperature curves measured by a superconducting quantum interference device magnetometer in a magnetic field of 100 Oe.

[a]Also at Department of Materials Science, Feng Chia University, Taichung, Taiwan, Republic of China.

III. RESULTS AND DISCUSSION

From x-ray diffraction studies, it was found that Ga is superior to Al in stabilizing the formation of single-phase $Er_2Fe_{17-x}M_xC_y$ alloys when M=Ga or Al. For the alloy with M=Ga, a single-phase region persisted in the alloy with $x=4$, $y=2$ it mainly exhibited the hexagonal Th_2Ni_{17}-type structure with the exception of the alloy with $x=4$, $y=1-2$ showing the rhombohedral Th_2Zn_{17} structure. However, for alloys with M=Al, a single phase could only persist in the alloy with a $x=4$, $y=1$ hexagonal Th_2Ni_{17}-type structure which appeared in all of the alloys. Table I shows the lattice parameters a, c, V, $\Delta V/V$, and types of structure of the $Er_2Fe_{17-x}M_xC_y$ (M=Ga and Al) compounds with single phase. The different ability in stabilizing the Th_2Ni_{17}-type carbide structure between M=Ga and Al may be due to the fact that the electronegativity difference of Al–C (0.94) is

TABLE I. The lattice parameters, a, c, V, $\Delta V/V$, and types of structure of the $Er_2Fe_{17-x}M_xC_y$ compounds (M=Ga, Al; $x=0-4$, $y=0-2$).

Compound	a (Å)	c (Å)	v (Å^3)	$\Delta V/V$ (%)	Structure
Er_2Fe_{17}	8.433	8.282	510.12	···	Th_2Ni_{17}
$Er_2Fe_{16}GA$	8.472	8.307	516.45	1.2	Th_2Ni_{17}
$Er_2Fe_{15}Ga_2$	8.505	8.335	522.22	2.3	Th_2Ni_{17}
$Er_2Fe_{14}Ga_3$	8.533	8.353	526.80	3.1	Th_2Ni_{17}
$Er_2Fe_{16}GaC$	8.569	8.326	529.52	3.8	Th_2Ni_{17}
$Er_2Fe_{15}Ga_2C$	8.592	8.320	531.96	4.3	Th_2Ni_{17}
$Er_2Fe_{14}Ga_3C$	8.613	8.346	536.18	5.1	Th_2Ni_{17}
$Er_2Fe_{13}Ga_4C$	8.640	12.577	813.17	6.3	**Th_2Zn_{17}**
$Er_2Fe_{15}Ga_2C_2$	8.629	8.361	539.15	5.7	Th_2Ni_{17}
$Er_2Fe_{14}Ga_3C_2$	8.653	8.384	543.64	6.6	Th_2Ni_{17}
$Er_2Fe_{13}Ga_4C_2$	8.670	12.595	819.85	7.1	**Th_2Zn_{17}**
$Er_2Fe_{16}Al$	8.463	8.302	516.61	1.3	Th_2Ni_{17}
$Er_2Fe_{15}Al_2$	8.517	8.313	522.24	2.3	Th_2Ni_{17}
$Er_2Fe_{14}Al_3$	8.540	8.373	529.07	3.7	Th_2Ni_{17}
$Er_2Fe_{13}Al_4$	8.565	8.378	533.14	4.5	Th_2Ni_{17}
$Er_2Fe_{16}AlC$	8.568	8.322	529.18	3.7	Th_2Ni_{17}
$Er_2Fe_{15}Al_2C$	8.576	8.347	531.62	4.2	Th_2Ni_{17}
$Er_2Fe_{14}Al_3C$	8.606	8.351	535.73	5.0	Th_2Ni_{17}
$Er_2Fe_{13}Al_4C$	8.629	8.409	542.28	6.3	Th_2Ni_{17}

 0021-8979/96/79(8)/5533/3/$10.00 © 1996 American Institute of Physics

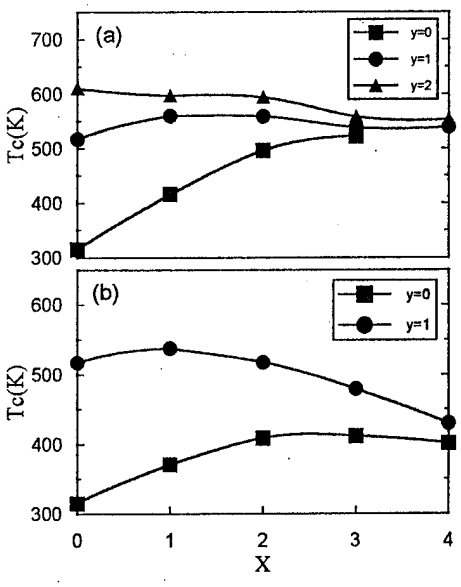


FIG. 1. The Curie temperatures of the $Er_2Fe_{17-x}M_xC_y$ compounds (a) M=Ga and (b) M=Al.

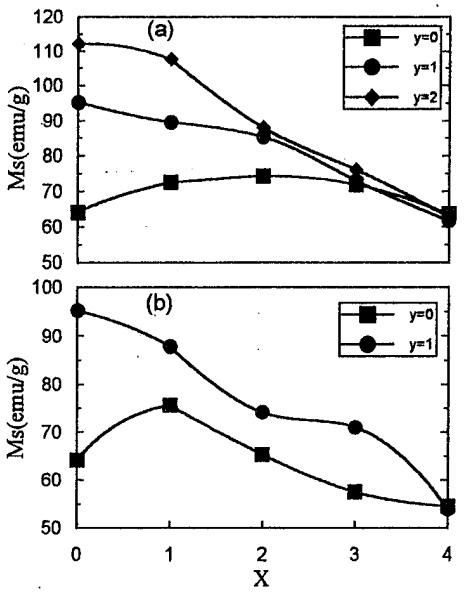


FIG. 2. The room temperature saturation magnetization of the $Er_2Fe_{17-x}M_xC_y$ compounds (a) M=Ga and (b) M=Al.

higher than that of Ga–C (0.74);[5] too much carbon in $Er_2Fe_{17-x}Al_xC_y$ more easily leads to the decomposition of the compound to α-Fe, AlC, and ErC than is the case in $Er_2Fe_{17-x}Ga_xC_y$. On the other hand, the lattice parameters a, c, V, and $\Delta V/V$ all increase with an increase of x and y in both the M=Ga and Al compounds. In comparison with the value of Er_2Fe_{17}, the volume expansion ratio of the unit cell, $\Delta V/V$, for the compound with M=Ga and Al is the same, 6.3%, at the condition of $x=4$, $y=1$. It reaches the highest value, 7.1%, in the $Er_2Fe_{13}Ga_4C_2$ compound.

The Curie temperatures of the $Er_2Fe_{17-x}M_xC_y$ (M=Ga and Al) compounds are shown in Figs. 1(a) and 1(b). It can be seen that T_C increases with increasing carbon content (y) of the compound. For $Er_2Fe_{17-x}Ga_x$, T_C increases monotonically with x, reflecting the fact that the substitution of Ga for Fe enhances the Fe–Fe exchange interaction caused by the expansion of the lattice constant. For $Er_2Fe_{17-x}Ga_xC$, T_C initially increases with x, then decreases. A maximum T_C of 560 K appears at $x=1$. This implies that the Fe–Fe exchange interaction may decrease due to the lattice overexpansion caused by the effect of Ga substitution and C interstitial substitution at the same time. A similar situation is also found for the compound $Er_2Fe_{17-x}Ga_xC_2$ so that T_C again decreases slightly with x. For M=Al, the trend of T_C variation with x in the alloys without carbon and with carbon ($y=1$) is almost the same as for the alloys with M=Ga. However, the value of T_C is lower in the Al substituted compound. A T_C of only 538 K was obtained in the $Er_2Fe_{16}AlC$ compound, which is lower than that of the $Er_2Fe_{16}GaC$ compound (560 K).

Figures 2(a) and 2(b) plot the room temperature saturation magnetization, M_s, of the single-phase $Er_2Fe_{17-x}M_xC_y$ compounds with M=Ga and M=Al, respectively. For the alloys without carbon, M_s reaches a peak value at $x=2$ for M=Ga (74.2 emu/g) and at $x=1$ for M=Al (75.6 emu/g). The occurrence of the M_s peak may be determined by the counterbalance between the increase of the Fe–Fe sublattice exchange interaction due to Ga or Al substitution for Fe and the decrease of the total Fe moment due to the dilution effect by the nonmagnetic elements, i.e., Ga or Al, substitution. However, for the alloys with carbon, M_s decreases almost monotonically with an increase of x in both Ga and Al substituted alloys. The slope of decrease is a little larger for the alloys with M=Al than for that of M=Ga.

Figure 3 shows the temperature dependence, from 5 to 300 K, of the magnetization of the $Er_2Fe_{17-x}Ga_xC$ compounds measured by a superconducting quantum interference device magnetometer in a magnetic field of 100 Oe. It can clearly be found that each curve has a maximum magnetization at certain temperature, called the spin reorientation temperature (T_{sr}), while the spin reorientation temperature of those compounds change with the amount of Ga substitution, x. The same phenomenon is also found in the Al substituted compounds. Figures 4(a) and 4(b) exhibit the summarized composition dependence of the T_{sr} of the $Er_2Fe_{17-x}Ga_xC_y$

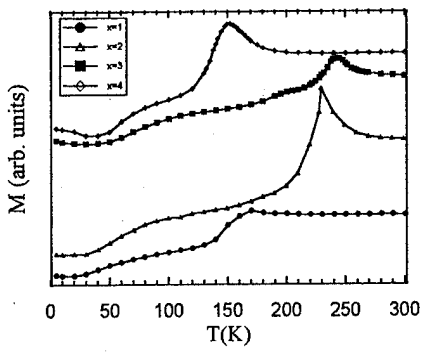


FIG. 3. Temperature dependence of the room temperature magnetization of the $Er_2Fe_{17-x}Ga_xC$ compounds measured in a magnetic field of 100 Oe.

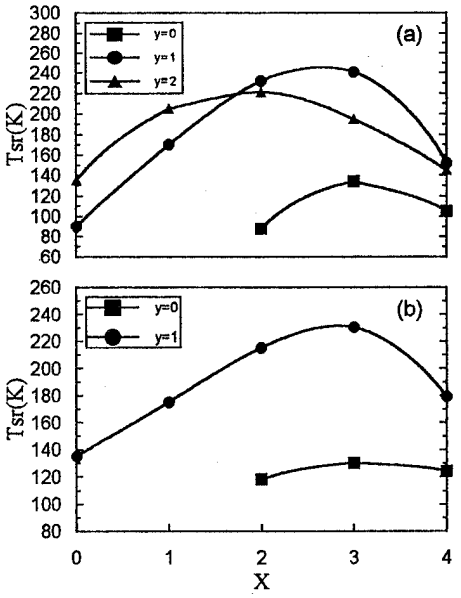


FIG. 4. The spin reorientation temperatures of the $Er_2Fe_{17-x}M_xC_y$ compounds (a) M=Ga and (b) M=Al.

and $Er_2Fe_{17-x}Al_xC_y$ compounds, respectively. Basically, the trend of T_{sr} variation is the same in the above two compounds with $y=0$ and $y=1$. It first increases with x, then decreases again, and their peak values all appear at the alloy with $x=3$. Despite the variation of T_{sr} in $Er_2Fe_{17-x}Ga_xC_2$ compounds being the same as in previous alloys, its peak value is lower and appears at the alloy with $x=2$.

The T_{sr} of the alloys studied is normally determined by the competition between the temperature dependence of the c-axis anisotropy field of the Er^{3+} sublattice $[K_1(Er^{3+})]$ and the planar anisotropy of the Fe sublattice $[K_1(Fe)]$. Any parameter altering the above two factors will somehow change T_{sr}. The rare earth sublattice anisotropy in the crystal field term can be expressed as follows:

$$K_1(R) = -(3/2)\alpha_J\langle r_{4f}^2\rangle\langle 3Jz^2 - J(J+1)\rangle \text{Å}_2,$$

where α_J is the second-order Stevens factor, the quantities in brackets are expectation values, and Å_2 is the second-order crystal field parameter, which is strongly influenced by the rare earth electron charge asphericity.[6] It has been shown that the first-order magnetic anisotropy constant, K_1, of Er^{3+}, is positive,[7] and it is governed by its electron structure around the sublattice, or the value of Å_2. After adding the carbon to the alloy, the electron structure of the Er^{3+} sublattice was modified by the carbon interstitial, and therefore the value of Å_2 becomes more negative, leading to the enhancement of its $K_1(Er^{3+})$ value. In addition, it has been reported that the carbon interstitial also may reduce the degree of planar anisotropy of the Fe sublattice,[8] i.e., $K_1(Fe)$ changes to less negative, as a result, both effects lead to the increment of K_1 (total) $[=K_1(Er^{3+})+K_1(Fe)]$ and the spin reorientation temperature—the temperature at which the anisotropy changes from basal to axial as the temperature decreases—in $Er_2Fe_{17}C_y$ alloys. The increase of T_{sr} with an increasing carbon interstitial up to $y=1$ is therefore ascribed to the above two effects. On the other hand, according to a previous study,[9] the crystal field of the Er^{3+} can also be altered by means of Ga or Al substitution for Fe through the hybridation of the $5d$ and $6f$ valence electrons of Er^{3+} and the valence electrons of the neighboring atoms, such as Ga or Al, which also may result in the variation of magnitude of the Er valence electron asphericity and the value of Å_2. This might explain the increases of T_{sr} with the increase of x up to $x=3$. In the mean time, the value of T_{sr} in the Ga containing alloys is found to be higher than that of Al containing alloys, implying that Ga has a stronger effect in enhancing $K_1(Er^{3+})$ than does Al.

ACKNOWLEDGMENT

The research was supported by National Science Council, Taiwan, under Contract No. NSC-85-2112-M-194-002.

[1] B.-G. Shen, L.-S. Kong, F.-W. Wang, and L. Cao, Appl. Phys. Lett. **63**, 2288 (1993).
[2] B.-G. Shen, F.-W. Wang, L.-S. Kong, L. Cao, B. Zhang, and J.-G. Zhao, J. Appl. Phys. **75**, 6259 (1994).
[3] B.-G. Shen, F.-W. Wang, L.-S. Kong, L. Cao, and H.-Q. Guo, J. Magn. Magn. Mater. **127**, L267 (1993).
[4] S. K. Chen, W. C. Chang, and S. L. Lu, J. Magn. Magn. Mater. **140–144**, 1083 (1995).
[5] L. Pauling, *Nature of the Chemical Bond*, 3rd ed. (Cornell University, Ithaca, NY, 1960).
[6] R. Coehoorn and K. H. J. Buschow, J. Appl. Phys. **69**, 5590 (1991).
[7] B. P. Hu, H. S. Li, H. Sun, and J. M. D. Coey, J. Phys. Condens. Matter. **3**, 3983 (1991).
[8] L.-S. Kong, B.-G. Shen, L. Cao, H.-Y. Gong, and Y.-L. Chen, J. Phys. Condens. Matter. **5**, 2415 (1993).
[9] Z. Hu, W. B. Yelon, S. Mishra, G. J. Long, O. A. Pringle, D. P. Middleton, K. H. J. Buschow, and F. Grandjean, J. Appl. Phys. **76**, 443 (1994).

Thermal stability of nanostructured $Sm_2Fe_{17}C_x$ compounds prepared by ball milling

O. Mao, Z. Altounian, J. Yang, and J. O. Ström-Olsen
Centre for the Physics of Materials, Department of Physics, McGill University, Montréal, Québec H3A 2T8, Canada

The thermal stability of ball-milled nanocrystalline $Sm_2Fe_{17}C_x$ interstitial compounds has been investigated. $Sm_2Fe_{17}C_x$ decomposes into a mixture of phases upon annealing above a certain decomposition temperature, T_{d1}, which depends on the carbon concentration in the compound. Annealing above a certain temperature $T_{d2}(>T_{d1})$, the $Sm_2Fe_{14}C$ phase starts to form. The amount of the $Sm_2Fe_{14}C$ phase increases with increasing annealing temperature at the expense of the Sm_2Fe_{17} carbide until T_{r1}, at which temperature $Sm_2Fe_{14}C$ starts to recombine with other phases to form the Sm_2Fe_{17} carbide. For the starting composition with $x<1.5$, the $Sm_2Fe_{17}C_x$ single phase can be recovered above the recovery temperature $T_{r2}(>T_{r1})$. © *1996 American Institute of Physics.* [S0021-8979(96)32608-7]

I. INTRODUCTION

The presence of interstitial nitrogen and/or carbon atoms in a Sm_2Fe_{17} intermetallic compound of the Th_2Zn_{17} structure type results in useful hard magnetic properties.[1,2] However, the interstitial compound is metastable, and decomposes into a mixture of phases upon annealing. Thermal stability is, therefore, an important consideration in the processing and practical use of these materials. Sm_2Fe_{17} carbides prepared by a gas–solid reaction (GSR) with hydrocarbon gases are unstable upon heating.[3] The decomposition schemes are rather complicated in the case of quaternary systems containing Sm, Fe, C, and H. Meanwhile, it is reported[4] that the $R_2Fe_{14}C$ structure of the $Nd_2Fe_{14}B$ type is more stable than $Sm_2Fe_{17}C_x$ at temperatures lower than a transition temperature T_t (T_t~980 °C for R=Sm). Solid state transformation of $Sm_2Fe_{14}C$ into $Sm_2Fe_{17}C_x$ compound occurs when the annealing temperature is held above T_t and the $Sm_2Fe_{17}C_x$ structure persists even when subjected to subsequential annealing below T_t.[4] In this contribution we report the thermal stability of nanostructured Sm_2Fe_{17} carbides prepared by ball milling (BM).

II. EXPERIMENTAL TECHNIQUES

$Sm_2Fe_{17}C_x$ samples used for this study were synthesized by solid–solid reaction (SSR) of Sm_2Fe_{17}/graphite blends. The blends are mixtures of two pure phases, Sm_2Fe_{17} and graphite, prepared by room temperature BM. SSR was carried out at 450 °C for 10 h. The details of the process are given in Ref. 5. All sample handling procedures were performed in a specially designed glove box with oxygen and humidity levels of less than 1 ppm. For heat treatments, the samples were sealed in a quartz tube under Ar. The annealing time varied with the annealing temperature. Above 700 °C an annealing time of 30 min was adopted, while for lower temperatures, the annealing time was 1 h or longer (up to 10 h for temperatures less than 600 °C). For structural analysis, x-ray diffraction (XRD) was performed in an automated Nicolet–Stöe powder diffractometer with graphite monochromated Cu K_α radiation. Curie temperatures, T_C's, were measured by thermomagnetometry using a Perkin–Elmer thermogravimetric analyzer (TGA-7) in a small magnetic field gradient (TGAM). Differential scanning calorimetry (DSC) was performed using a Perkin–Elmer DSC-2C calorimeter.

III. RESULTS AND DISCUSSION

A. Thermal stability of $Sm_2Fe_{17}C_x$ compounds

The powders prepared by SSR were almost single-phase $Sm_2Fe_{17}C_x$ with a small amount of α-Fe. Upon heating at 800 °C for 30 min, the samples decomposed into mixtures of phases, as shown in Fig. 1. Besides α-Fe two other magnetic phases were detected by TGAM. The phase with the lower T_C(~190 °C) is $Sm_2Fe_{17}C_y$ (y may differ from x) and the phase with T_C~310 °C is identified as $Sm_2Fe_{14}C$[6] (compare XRD patterns 3 and 8 in Fig. 1). The $Sm_2Fe_{17}C_y$ phase coexists with $Sm_2Fe_{14}C$ for $x<1.0$ and vanishes for $x>1$. Due

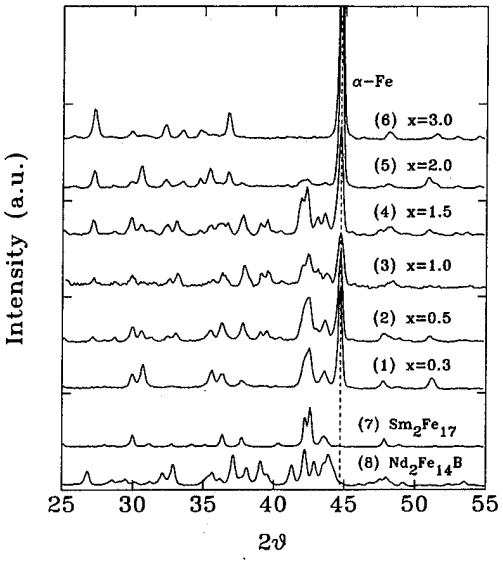


FIG. 1. X-ray diffraction scans of SSR samples (heat treated at 800 °C for 30 min) of (1) $Sm_2Fe_{17}C_{0.3}$; (2) $Sm_2Fe_{17}C_{0.5}$; (3) $Sm_2Fe_{17}C_{1.0}$; (4) $Sm_2Fe_{17}C_{1.5}$; (5) $Sm_2Fe_{17}C_{2.0}$; (6) $Sm_2Fe_{17}C_{3.0}$, and ingots of (7) Sm_2Fe_{17}; and (8) $Nd_2Fe_{14}B$.

 0021-8979/96/79(8)/5536/3/$10.00 © 1996 American Institute of Physics

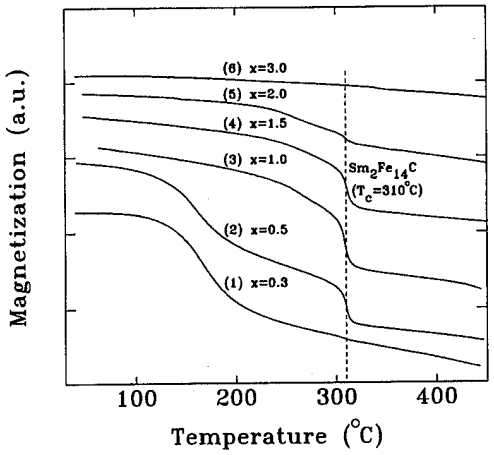


FIG. 2. Thermomagnetic scans of the samples of Fig. 1.

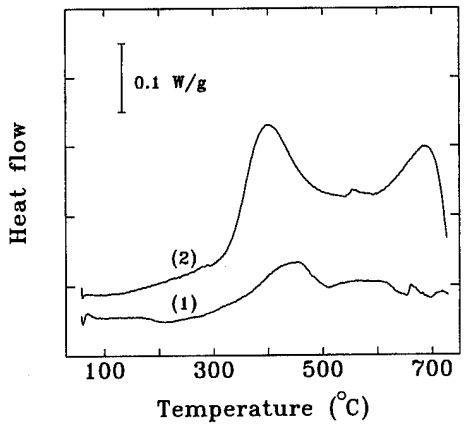


FIG. 4. DSC thermograms for (1) $Sm_2Fe_{17}C_{0.5}$ ball-milled blends; (2) $Sm_2Fe_{17}C_{2.0}$ ball-milled blends.

to the complicated structure of both $Sm_2Fe_{17}C_x$ and $Sm_2Fe_{14}C$, TGAM gives a clearer indication of the presence of these phases as shown in Fig. 2. To understand the nature of the decomposition, $Sm_2Fe_{17}C_{0.5}$ and $Sm_2Fe_{17}C_{1.0}$ single-phase compounds have been prepared for comparison by direct alloying (DA). The 2:17 single-phase structure is formed upon annealing the as-made ingots at 1150 °C for 5 h and persists even under subsequent annealing treatment. This result is in agreement with that reported by Mooij and Buschow.[4] However when the DA ingot was ball milled at the same milling condition as that for preparing the SSR sample, the resulting powder was unstable when annealed at 800 °C. The results of TGAM performed on both DA and SSR samples are given in Fig. 3. Scans 2 and 3 are essentially identical, suggesting that the decomposition is induced by BM. The DA $Sm_2Fe_{17}C_x$ ingot homogenized at 1150 °C for 5 h has grain sizes around 50 μm observed by an optical metallographic microscope. The grain sizes are estimated to be 60 nm in the ball-milled powder from the widths of the Bragg peaks (subtracting out the broadening due to the intrinsic instrumental resolution of the diffractometer and the strain in the lattice). The above results suggest that BM enhances the atomic diffusion as the reduction of grain size leads to an increase in grain boundaries destabilizing the $Sm_2Fe_{17}C_x$ compounds. The enhanced carbon diffusion results in a faster carbiding process in the powders. This is clearly shown in the DSC thermograms (Fig. 4) of the blends where an exothermal reaction occurs at a relatively low temperature region between 300 and 500 °C, indicating the formation of Sm_2Fe_{17} carbides. Integration over this peak area gives the enthalpy of formation of the carbide as ~20 kJ/mol-C atoms. The second exothermal peak on curve 2, at high temperatures, corresponds to the decomposition of the Sm_2Fe_{17} carbide, while the heat evolution associated with the decomposition is insignificant for $x<1.5$ as show in scan 1 in Fig. 4.

B. Decomposition schemes

TGAM results in Fig. 5 show the evolution of $Sm_2Fe_{17}C_{1.0}$ with annealing temperature. Annealing between 600 and 700 °C results in the precipitation of α-Fe and annealing above 740 °C results in the formation of the $Sm_2Fe_{14}C$ phase. Above 1100 °C, the $Sm_2Fe_{17}C_{1.0}$ single phase is recovered. Similar sequential annealings have been

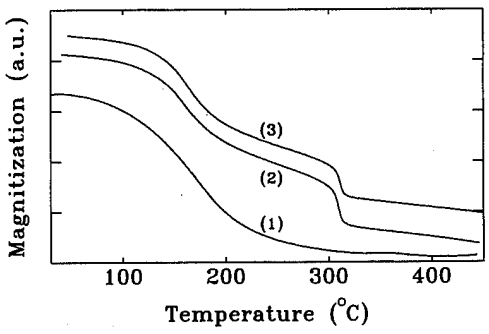


FIG. 3. Thermomagnetic scans of samples annealed at 800 °C: (1) $Sm_2Fe_{17}C_{0.5}$ ingot of direct alloying, DA (1150 °C annealed for 5 h); (2) $Sm_2Fe_{17}C_{0.5}$ ingot of DA after ball milling for 3 h; and (3) $Sm_2Fe_{17}C_{0.5}$ prepared by the SSR technique.

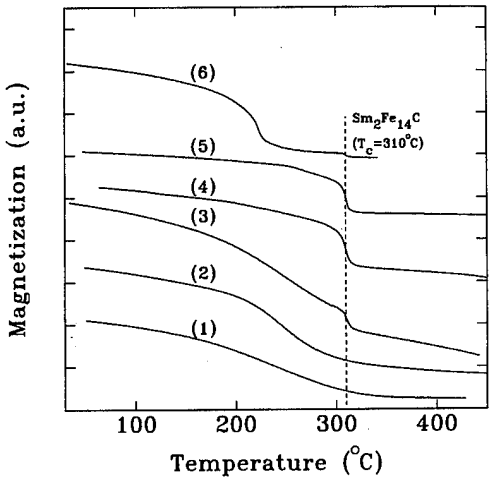


FIG. 5. Thermomagnetic scans of SSR $Sm_2Fe_{17}C_{1.0}$ powders annealed at various temperatures: (1) 480 °C; (2) 700 °C; (3) 740 °C; (4) 800 °C; (5) 1000 °C, and (6) 1100 °C.

TABLE I. Characteristic temperatures (°C) for the various Sm_2Fe_{17} carbides.

Compounds	T_{d1}	T_{d2}	T_{r1}	T_{r2}
$Sm_2Fe_{17}C_{0.5}$	528	···	800	1000
$Sm_2Fe_{17}C_{1.0}$	569	740	1000	1100
$Sm_2Fe_{17}C_{1.5}$	544	···	1100	···
$Sm_2Fe_{17}C_{3.0}$	512	···	···	···
$Sm_2Fe_{17}C_{6.0}$	512	···	···	···

performed for $Sm_2Fe_{17}C_x$ with various x. The evolution of $Sm_2Fe_{17}C_x$ during annealing comprises several stages. (i) At a certain temperature, T_{d1}, α-Fe begins to precipitate and Sm(Fe) carbide may also form to maintain the balance of the reaction equation

$$Sm_2Fe_{17}C_x = Sm_2Fe_{17}C_y + \alpha\text{-Fe} + Sm(Fe) - C. \quad (1)$$

TGAM scans were used to determine T_{d1}, which is defined as the onset of the increase in magnetization. (ii) At a higher temperature, T_{d2}, the $Sm_2Fe_{14}C$ phase begins to form and its amount increases with the annealing temperature at the expense of $Sm_2Fe_{17}C_y$. For starting compositions with $x>1$, the 2:17 phase disappears completely at a certain temperature. (iii) At still higher temperatures, $T_{r1}>T_{d2}$, the $Sm_2Fe_{14}C$ phase starts to recombine with other phases forming the $Sm_2Fe_{17}C_z$ structure. (iv) At a temperature above $T_{r2}(>T_{r1})$, the recovery temperature, the $Sm_2Fe_{17}C_x$ single phase is recovered (only for $x<1.5$). The various reaction temperatures are listed in Table I. For $x>1.5$, the single-phase 2:17 structure cannot be recovered.

IV. CONCLUSIONS

The ball-milled nanocrystalline single-phase $Sm_2Fe_{17}C_x$ compounds are formed, upon heat treatment, with a formation enthalpy of ~20 kJ/mol C. This phase decomposes into a mixture of phases upon annealing above a certain decomposition temperature, T_{d1}, which depends on x, while the $Sm_2Fe_{17}C_x$ ingots prepared by direct alloying are stable after annealing at 1150 °C. Destabilizing of the direct alloyed $Sm_2Fe_{17}C_x$ compound upon BM may result from the fast atomic diffusion enhanced by the reduction of grain sizes. Annealing above a certain temperature $T_{d2}(>T_{d1})$, the $Sm_2Fe_{14}C$ phase starts to form at the expense of the Sm_2Fe_{17} carbide until T_{r1}, where $Sm_2Fe_{14}C$ starts to react with other phases to form the Sm_2Fe_{17} carbide. For starting compositions with $x<1.5$, the $Sm_2Fe_{17}C_x$ single phase is recovered above the recovery temperature $T_{r2}(>T_{r1})$.

ACKNOWLEDGMENTS

This work was supported by grants from the Natural Sciences and Engineering Research Council of Canada (NSERC) and le Fonds pour la Formation de Chercheurs et l'Aide à la Recherche de la Province du Québec.

[1] J. M. D. Coey and H. Sun, J. Magn. Magn. Mater. **87**, L251 (1990).
[2] L. X. Liao, X. Chen, Z. Altounian, and D. H. Ryan, Appl. Phys. Lett. **60**, 129 (1992).
[3] C. N. Christodoulou and T. Takeshita, J. Less-Common Met. **142**, 349 (1988).
[4] D. B. de Mooij and K. H. J. Buschow, J. Less-Common Met. **142**, 349 (1988).
[5] O. Mao, J. O. Ström-Olsen, Z. Altounian, and J. Yang, these proceedings.
[6] C. D. Fuerst and J. F. Herbst, J. Appl. Phys. **69**, 7727 (1991).

Synthesis and magnetic properties of rare earth–iron–chromium phases and their nitrides

O. Kalogirou, V. Psycharis, M. Gjoka, and D. Niarchos
Institute of Materials Science, NCSR "Demokritos," 153 10 Ag. Paraskevi, Attiki, Greece

C. D. Fuerst
Physics Department, General Motors NAO Research and Development Center, 30500 Mound Road, Warren, Michigan 48090-9055

Synthesis, structural, and magnetic properties of $R_3(Fe,Cr)_{29}$ intermetallic compounds (R=Ce,Nd) and their nitrides are reported. The $Ce_3(Fe,Cr)_{29}$ sample was single phase while the R=Nd ingot contained significant contamination by secondary phases. X-ray analysis reveals the monoclinic $Nd_3(Fe,Ti)_{29}$-type structure with space group $A2/m$. The unit cell dimensions for the parent R=Ce compound are $a=10.513(2)$ Å, $b=8.478(1)$ Å, $c=9.657(1)$ Å, $\beta=96.75(1)°$, and $V=854.70$ Å^3. In the case of Ce a relative unit cell expansion of 6.5% is observed upon nitrogenation. The Curie temperature is 326 K for Ce and 432 K for Nd and becomes 612 and 633 K for Ce–nitride and Nd–nitride, respectively. The room temperature magnetization at 5 T is 58.2 A m^2/kg for Ce and 104.1 A m^2/kg for Nd and increases after nitrogenation to 109.8 and 127.2 A m^2/kg for Ce and Nd, respectively. The average hyperfine field of the R=Ce compound at 85 K is 19.2 T. X-ray diffraction measurements on a magnetically aligned powder of $Ce_3(Fe,Cr)_{29}$ indicate that the magnetocrystalline anisotropy of the iron sublattice is most likely an in-plane type. Mössbauer spectrum analysis provided evidence that the Cr enters the dumbbell sites. © *1996 American Institute of Physics.* [S0021-8979(96)32708-3]

The synthesis of the novel ternary compound $R_3(Fe,T)_{29}$, has been reported for R=Y, Ce, Pr, Nd, Sm, Gd, and Tb; and T=Ti, Cr, V, Mn, and Mo.[1–13] The structure is more accurately described in the $A2/m$ space group[11] than in the $P2_1/c$.[12] The arrangement of R, Fe, and T atoms is a combination of the arrangements observed in the well-known rhombohedral Th_2Zn_{17} and tetragonal $ThMn_{12}$ structures, thus affecting the magnetic properties of these compounds in a predictable manner. The Curie temperature T_C values are intermediate between the T_C values of the 1:12 and 2:17 compounds.[4] Point charge calculations[14] have shown that the values of the A_{20}(R) crystal field coefficients for the $4i$ site (2:17 like) and $2a$ site (1:12 like) are of opposite sign, as is also the case for the R sites in the 2:17 and 1:12 structures, and this is probably the reason for the difficulty encountered when describing the magnetic anisotropy for 3:29 compounds with magnetic R ions. For this reason it is important to synthesize and study 3:29 compounds with nonmagnetic R, such as Y or Ce, where only the iron sublattice contributes to the magnetocrystalline anisotropy. The synthesis and the magnetic properties of $Ce_3Fe_{27.5}Ti_{1.5}$ and its nitride have been reported in a previous study.[5] Analysis of ^{57}Fe Mössbauer spectra on magnetically aligned samples of $Ce_3Fe_{27.5}Ti_{1.5}$ has given evidence for an in-plane magnetocrystalline anisotropy of the iron sublattice.[5] X-ray powder diffraction on magnetically aligned powder of $Y_3(Fe,Ti)_{29}$ has led to similar conclusions.[15] Preliminary results on $Ce_3Fe_{24.9}Cr_{4.1}$ are reported in Ref. 3, but that sample was not single phase since an excess in Ce was added in the starting composition. Here, we report the synthesis, and the structural and magnetic properties of higher quality single-phase compounds with stoichiometric starting compositions of $Nd_3Fe_{24.5}Cr_{4.5}$ and $Ce_3Fe_{25}Cr_4$. The existence of single-phase $Ce_3Fe_{25}Cr_4$ and a phase with a composition of $Nd_3Fe_{24.5}Cr_{4.5}$ extends the solubility limit of the T atoms in the Fe sites of the 3:29 compounds.

The $R_3(Fe,Cr)_{29}$ ingots with the nominal starting composition of $Ce_{9.4}Fe_{78.1}Cr_{12.5}$ and $Nd_{9.4}Fe_{76.6}Cr_{14}$ were prepared by induction melting high purity elemental constituents. The ingots were wrapped in tantalum foil, heat treated in vacuum at various temperatures for three days, and water quenched. Fine powder of the annealed alloys (<37 μm) was nitrided in high purity nitrogen gas at 673 K and at 4 atm for 24 h. All samples were characterized by means of x-ray powder diffraction (XRD) using Cu K_α radiation, Rietveld analysis, thermomagnetic analysis (TMA), and electron beam microprobe analysis (energy dispersive x-ray analysis). XRD on magnetically aligned powder samples was carried out to study the magnetocrystalline anisotropy of the compounds. Magnetization measurements on powder samples were performed by a superconducting quantum interference device magnetometer with a maximum field of 5 T at 5 and 300 K. The ^{57}Fe Mössbauer spectra were collected at 85 K on a conventional acceleration spectrometer with a ^{57}Co(Rh) source. The ac-magnetic susceptibility measurements were done in the temperature range of 77–300 K using a homemade ac susceptometer.

The as-cast $Nd_3(Fe,Cr)_{29}$ ingot was split into smaller pieces which were annealed at 1325, 1275, 1225, and 1200 K for three days. At 1325 K the result was a mixture of the 1:12 and 2:17 phases. In the samples annealed at 1275, 1225, and 1200 K, the main phase was $Nd_3(Fe,Cr)_{29}$ but contaminant phases including $Nd(Fe,Cr)_7$ and Fe_3Cr were also detected. For the R=Ce materials single-phase $Ce_3(Fe,Cr)_{29}$ was achieved after annealing at 1175 K for three days. Electron microprobe analysis yielded an average chemical formula $Ce_{2.97}Fe_{24.93}Cr_{4.1}$. In the case of Nd the primary phase had a composition $Nd_3Fe_{24.5}Cr_{4.5}$ and the secondary 1:7 phase

 0021-8979/96/79(8)/5539/3/$10.00 © 1996 American Institute of Physics

TABLE I. Lattice parameters for $Ce_3(Fe,Cr)_{29}$, $Ce_3(Fe,Cr)_{29}N_4$, and $Nd_3(Fe,Cr)_{29}$ determined from powder x-ray diffraction (Cu K_α) using Rietveld analysis.

Sample	a (Å)	b (Å)	c (Å)	β (°)	V (Å^3)
$Ce_3(Fe,Cr)_{29}$	10.513(2)	8.487(1)	9.657(1)	96.75(1)	854.70
$Ce_3(Fe,Cr)_{29}N_4$	10.749(6)	8.664(5)	9.848(7)	96.89(2)	910.59
$Nd_3(Fe,Cr)_{29}$	10.603(3)	8.546(3)	9.699(3)	96.80(2)	872.62

$NdFe_{6.16}Cr_{0.84}$, respectively. Rietveld analysis yielded a phase composition of 71.2% 3:29, 22.3% 1:7, and 6.5% Fe_3Cr. Thus, an overall composition of $Nd_{9.5}Fe_{76.7}Cr_{13.8}$ was calculated very close to the nominal composition of the starting material.

After nitrogenation at 673 K for 12 h both R=Ce and R=Nd showed a mixture of nitrided and non-nitrided phases. After cumulative treatment under the same conditions the non-nitrided compound practically disappeared. The nitrided R=Ce compound showed a lattice expansion of 6.5%. Crystallographic and magnetic data of the parent and the nitrided Ce and Nd compounds are given in Tables I and II. The lattice parameters a, b, c, and β were deduced applying the Rietveld refinement method and using the $A2/m$ space group.

Curie temperature (T_C) values were determined by TMA with a heating rate of 5°/min. The Curie temperatures for $Ce_3Fe_{25}Cr_4$ are very close to the values reported for $Ce_3Fe_{27.5}Ti_{1.5}$.[3,4] In contrast, the magnetization values are lower for the T=Cr group, reflecting the magnetic dilution of the iron sublattice by the large amount of Cr and suggesting that the Cr ion is essentially nonmagnetic. In the ac-susceptibility versus temperature curve of $Nd_3(Fe,Cr)_{29}$ a magnetic transition at about 160 K was observed (Fig. 1). From the shape of the magnetization versus temperature curve it was concluded that this transition most likely corresponds to an ordering temperature of an impurity rather than to spin reorientation.

The XRD patterns of a magnetically aligned powder sample $Ce_3(Fe,Cr)_{29}$ with the magnetic field normal to the sample holder, are shown in Fig. 2. The increase in the intensity of the (4 0 −2) reflection is the most significant change. The intensity of the (2 0 4) reflection decreases slightly. There is not an obvious change in the intensity of the (0 4 0) reflection. The [4 0 −2] crystallographic direction is related to the c axis of the 1:12 structure. On the other hand, the [4 0 −2] and the [0 4 0] directions lie on the $a-b$ plane of the 2:17 structure.[11] The magnetocrystalline anisotropy of Ce–Fe intermetallics is dominated by the iron sublattice which is uniaxial in the case of the 1:12 compounds (along the c axis) and in the basal plane in the case of 2:17. Our results are similar to those observed by Li *et al.*[15] concerning the $Y_3(Fe,Ti)_{29}$ compound. The only difference is that, besides the changes of the (4 0 −2) and (2 0 4) reflections, they have observed a slight increase of the [0 4 0] reflection. From the changes in the intensities of the above-mentioned reflections they have assumed that in 3:29 the iron sublattice should present in-plane anisotropy where the easy plane is determined by the [4 0 −2] and the [0 4 0] directions, the [4 0 −2] direction being dominant. In the case of Cr the fact that there is no significant change in the intensity of the (0 4 0) reflection may be due to a stronger influence of 1:12 leading to an in-plane anisotropy with so strong a preferred direction, [4 0 −2], that no change in the (0 4 0) line can be observed. The presence of uniaxial anisotropy along the [4 0 −2] direction cannot be excluded but in this case the (0 4 0) reflection should decrease. Nevertheless, as concluded from other studies as well[8,11,16] the above-mentioned crystallographic directions play an important role for the anisotropy of the 3:29 system.

In Fig. 3 the ^{57}Fe Mössbauer spectra of the parent R=Ce compound at 85 K is shown. The spectral analysis employed five magnetically split sextets with variable linewidths. In a recent work we analyzed the Mössbauer spectra of the $Pr_3Fe_{27.5}Ti_{1.5}$ compound by using four magnetically split sextets.[17] In that analysis the 11 crystallographic iron sites were divided into four groups according to the number of nearest neighbors (nn) and the average bond lengths taking into account the results of a recent neutron diffraction study

TABLE II. Saturation magnetization (M_s) and Curie temperatures (T_C) for two $R_3(Fe,Cr)_{29}$ phases, R=Ce and Nd, and their respective nitrides, M_s is provided as magnetization per mass (A m^2/kg) and per volume (kG).

Sample	M_s (A m^2/kg)/(kG) T=5 K	M_s (A m^2/kg)/(kG) T=300 K	T_C (K)
$Ce_3(Fe,Cr)_{29}$	104.4/10.36	58.2/5.78	316
$Ce_3(Fe,Cr)_{29}N_4$	126.4/11.86	109.8/10.30	612
$Nd_3(Fe,Cr)_{29}$	128.2/12.47	101.7/9.89	432
$Nd_3(Fe,Cr)_{29}N_4$	137.3/11.69	127.2/12.62	633

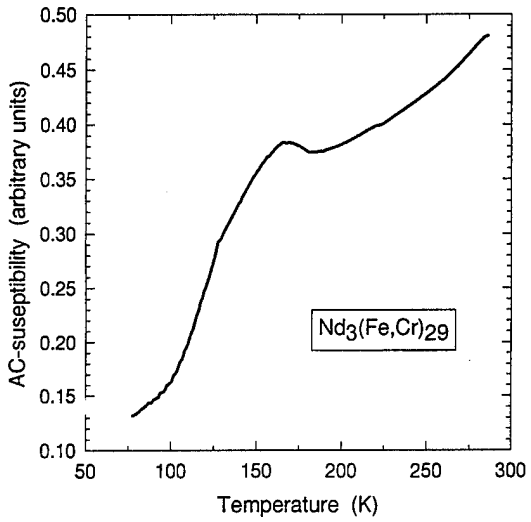


FIG. 1. The ac-susceptibility vs temperature for the annealed $Nd_3(Fe,Cr)_{29}$ ingot.

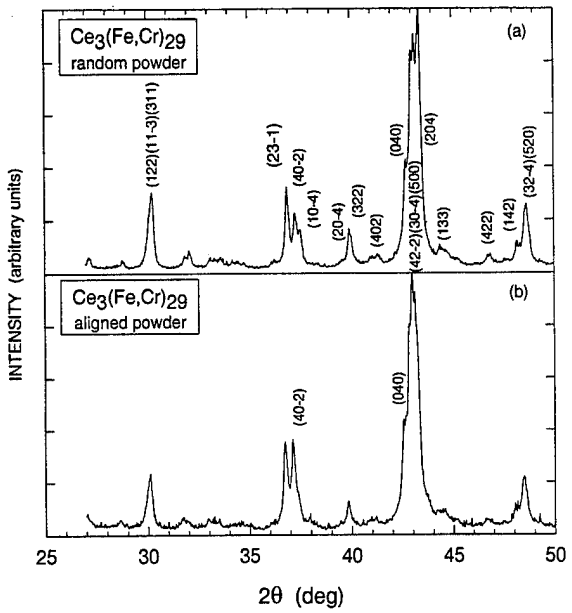


FIG. 2. X-ray diffraction (Cu K_α) data for $Ce_3(Fe,Cr)_{29}$ is presented for (a) a randomly oriented powder, and (b) magnetically aligned powder. The magnetic alignment was performed at room temperature using a field perpendicular to the sample plane.

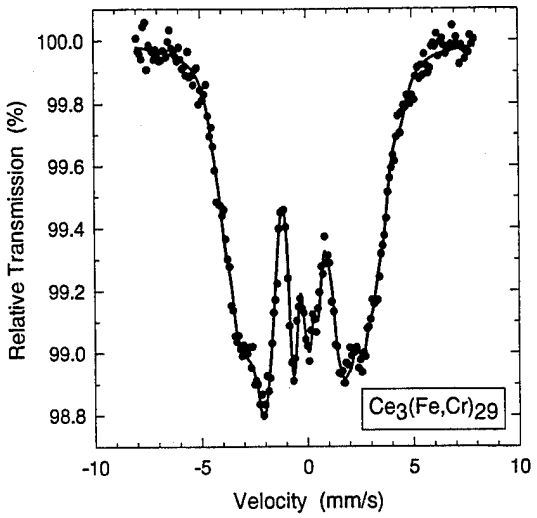


FIG. 3. Low temperature (T=85 K) ^{57}Fe Mössbauer spectrum of the $Ce_3(Fe,Cr)_{29}$ phase is shown along with the corresponding fit.

on $Nd_3(Fe,Ti)_{29}$ that Fe2, Fe3, and Fe6 are partially occupied by Ti, 30%, 20%, and 10%, respectively.[18] That approach has led to an area ratio of $A:B:C:D$=1:2:1.5:1.2 where site A corresponds to the dumbbell sites. The subspectrum with the largest hyperfine field has been assigned to the Fe2, Fe3, and Fe6 (dumbbell sites group) based on the fact that these iron sites present the largest number of nearest neighbors and the largest values of the average bond lengths compared to the other sites. In the case of $Ce_3Fe_{25}Cr_4$ it was assumed that the 4 Cr-substituting atoms are equally distributed on the three dumbbell sites Fe2, Fe3, and Fe6. These iron sites coincide with the 8i site of the related $ThMn_{12}$ structure in the transformation 3:29→1:12 which is preferentially occupied by Ti. Introducing 4 Cr atoms, instead of 1.5 Ti atoms, in the dumbbell sites decreases the number of nn of the rest of the sites rather than of the dumbbell itself and of course the area ratio. Thus, the fit was made with five components according to the number of nn, with variable linewidths and with an area ratio $A:B:C:D:E$=1:4.2:3.2:2.6:2, corresponding to the population of the five iron-site groups. As a matter of fact, the dumbbell site presented the lowest decrease in the hyperfine field compared to $Ce_3Fe_{27.5}Ti_{1.5}$ (Ref. 5) and we believe that this is evidence that Cr indeed enters the dumbbell sites. The average ^{57}Fe Mössbauer field was found to be 19.2 T. This value is much lower compared to that of $Ce_3Fe_{27.5}Ti_{1.5}$, 25.3 T,[5] as expected from the magnetic dilution of the iron sublattice due to the large number of Cr atoms substituting for Fe, with corresponding low magnetization values (Table I).

The authors are very grateful for the support and assistance provided by several researchers at the General Motors Research and Development Center, especially Mike Balogh, Rick Waldo, and Andy Wims of the Analytical Chemistry Department and Earl Brewer, Jan Herbst, Chuck Murphy, and Fred Pinkerton of the Physics Department.

[1] S. J. Collocot, R. K. Day, J. B. Dunlop, and R. L. Davis, Proceedings of the Seventh International Symposium on Magnetic Anisotropy and Coercivity in Rare-Earth Transition Metal Alloys, Canberra, 1992 (unpublished), pp. 437–444.
[2] H. S. Li, D. Courtois, J. M. Cadogan, J. M. Xu, and S. X. Dou, J. Phys. Condens. Matter **6**, L771 (1994).
[3] C. D. Fuerst, F. E. Pinkerton, and J. F. Herbst, J. Appl. Phys. **76**, 6144 (1994).
[4] O. Kalogirou, V. Psycharis, M. Gjoka, and D. Niarchos, J. Magn. Magn. Mater. **147**, L7 (1995).
[5] O. Kalogirou, V. Psycharis, M. Gjoka, E. Devlin, and D. Niarchos, IEEE Trans. Magn. **31**, 3698 (1995).
[6] H. S. Li, Suharyana, J. M. Cadogan, and G. J. Bowden, J. Appl. Phys. **75**, 7120 (1994).
[7] Z. Arnold, J. Kamarad, L. Morellon, P. A. Algarabel, and M. R. Ibarra, Solid State Commun. **92**, 807 (1994).
[8] F. M. Yang, B. Nasunjilegal, H. Y. Pan, J. L. Wang, R. W. Zhao, B. P. Hu, Y. Z. Wang, H. S. Li, and J. M. Cadogan, J. Magn. Magn. Mater. **135**, 298 (1994).
[9] M. R. Ibarra, L. Morellon, J. Blasco, L. Pareti, P. A. Algarabel, J. Garcia, F. Albertini, A. Paoluzi, and G. Turilli, J. Phys. Condens. Matter **6**, L717 (1994).
[10] Ye. V. Schrebakova, G. V. Ivanova, A. S. Yermolenko, Ye. V. Belozerov, and V. S. Gaviko, J. Alloys Compounds **182**, 199 (1992).
[11] O. Kalogirou, V. Psycharis, L. Saettas, and D. N. Niarchos, J. Magn. Magn. Mater. **146**, 335 (1995).
[12] C. D. Fuerst, F. E. Pinkerton, and J. F. Herbst, J. Magn. Magn. Mater. **129**, L115 (1994).
[13] H. S. Li, J. M. Cadogan, R. L. Davis, A. Margarian, and J. B. Dunlop, Solid State Commun. **90**, 487 (1994).
[14] H.-S. Li, J. M. Cadogan, B.-P. Hu, F.-M. Yang, B. Nasunjilegal, A. Margarian, and J. B. Dunlop, J. Magn. Magn. Mater. **140–144**, 1101 (1995).
[15] H.-S. Li (private communication).
[16] F. M. Yang, B. Nasunjilegal, J. L. Wang, H. Y. Pan, W. D. Qing, R. W. Zhao, B. P. Hu, Y. Z. Wang, G. C. Liu, H. S. Li, and J. M. Cadogan, J. Appl. Phys. **76**, 1971 (1994).
[17] V. Psycharis, O. Kalogirou, E. Devlin, M. Gjoka, A. Simopoulos, and D. Niarchos, J. Magn. Magn. Mater. **153**, 75 (1996).
[18] Z. Hu and W. B. Yelon, Solid State Commun. **91**, 223 (1994).

High field magnetization measurements of $SmFe_{11}Ti$ and $SmFe_{11}TiH_{1-\delta}$

O. Isnard, M. Guillot, S. Miraglia, and D. Fruchart
Laboratoire de Cristallographie, CNRS, BP 166, 38042 Grenoble Cedex, France and Laboratoire de Champs Magnétiques Intenses, CNRS/MPI, 38042 Grenoble, France

The magnetic properties of the ferromagnetic compounds, $SmFe_{11}Ti$ and $SmFe_{11}TiH_{1-\delta}$, which are potential candidates for high performance permanent magnets are investigated. At room temperature both compounds exhibit a uniaxial anisotropy, with the easy direction of magnetization parallel to the tetragonal axis. High field magnetization measurements up to 240 kOe in continuous fields are reported. The major changes upon hydrogen insertion are increases of the Curie temperature and of the saturation magnetization. The magnetic anisotropy constants, K_1 and K_2, are determined and the insertion of hydrogen is found to increase K_1. If the external field is applied perpendicular to the alignment direction, anomalous magnetization behaviors are observed in both compounds below about 150 K. The shape of this anomaly is strongly modified by the hydrogen insertion. © *1996 American Institute of Physics.* [S0021-8979(96)32808-X]

INTRODUCTION

The requirements for an effective permanent magnet are good intrinsic magnetic properties, i.e., high Curie temperature, magnetization, and anisotropy field, combined with a suitable microstructure generating a high coercivity.

To fulfill these requirements, research has turned toward alloys composed mainly of the ferromagnetic $3d$ elements, iron or cobalt, thus leading to high magnetization and Curie temperature. Their association with rare earth elements may induce strong uniaxial anisotropy such as in $SmCo_5$ and Sm_2Co_{17}. Since the discovery of $Nd_2Fe_{14}B$, many studies have been devoted to iron-containing materials leading to a new series of intermetallic compounds among which $SmFe_{11}Ti$, $Sm_2Fe_{17}N_3$, and $Sm_2Fe_{17}C_3$ are the most promising in terms of possible permanent magnet applications. Details about the magnetism of these compounds can be found in Refs. 1–3.

In this paper we intend to probe the intrinsic magnetic properties of $SmFe_{11}TiH$ and to quantitatively analyze the effect of hydrogen insertion on the magnetic properties. This paper is organized as follows: First, we describe the sample preparation and the experimental details. Then the crystal structure is presented, the lattice parameters are analyzed, and the location of H in the cell is given. Finally, we present the magnetic characterization and discuss these results in light of earlier publications.

SAMPLE PREPARATION, EXPERIMENTAL DETAILS

The alloys have been obtained by melting the starting elements in a high frequency induction furnace equipped with a water cooled copper crucible. The homogeneity of the ingot was subsequently achieved by annealing at 950 °C for 10 days. The hydrogen insertion has been carried out under 20 bar of H_2 gas and thermal activation was needed to initiate the reaction. The structural parameters were derived from x-ray diffractometry. The x-ray patterns were recorded using a Guinier–Hägg focusing camera operated at Fe K_α radiation, with silicon as an internal standard. The lattice parameters have been refined, taking into account the 22 observed Bragg reflections. Thermomagnetic analysis of the sample being sealed in a silica tube to avoid oxidization or hydrogen release, was performed using a Faraday type balance. Isothermal M vs H curves on magnetically aligned powder were carried out in a field up to 240 kOe at the High Field Facility in Grenoble.[4] The anisotropy constants have been derived as described elsewhere.[5]

RESULTS

The x-ray diffraction pattern shows that $SmFe_{11}TiH$ retains the $I4/mmm$ symmetry of $SmFe_{11}Ti$. This result is in good agreement with earlier measurements by Zhang and Wallace.[6] As shown in Table I the insertion of hydrogen within the crystal lattice induces a significant increase of the unit cell (about 2 $Å^3$/H atom). This feature is quite general when hydrogen goes into intermetallic compounds and has already been observed in other series of magnetic materials such as R_2Fe_{17} (2.5 $Å^3$/H atom) and $R_2Fe_{14}B$ (2.5 $Å^3$/H atom).[7,8]

We now discuss the delicate problem of the precise H content of our compound. The cell increase is found to be larger along the c axis of the structure than along the a basal plane axis. The gravimetric determination of the H concentration indicates that the H concentration is close to 1 atom per formula unit. Hence we will refer to it as $1-\delta$. The unit cell volume is slightly higher than that reported earlier[6] probably because of a higher hydrogen content in our sample. The hydrogenation-induced increase in Curie temperature is also an indirect indication of the hydrogen concentration. Such an increase was already observed by Zhang and Wallace,[6] but their $SmFe_{11}Ti$ hydride exhibited a lower Curie temperature confirming that the hydrogen content in our sample is higher. It may also well be that their hydrogen content was slightly overestimated.

Previous neutron diffraction studies[9] have shown that hydrogen is located in the octahedral $2b$ site with two rare

TABLE I. Relevant structural data for $SmFe_{11}Ti$ and its hydride.

Compound	a (Å)	c (Å)	V (^{3})	T_C (K)
$SmFe_{11}Ti$	8.567	4.798	352	567
$SmFe_{11}TiH_{1-\delta}$	8.574	4.811	354	634

 0021-8979/96/79(8)/5542/3/$10.00 © 1996 American Institute of Physics

TABLE II. Relevant magnetic data for $SmFe_{11}Ti$ and its hydride.

Compound	Temperature (K)	M_S (μ_B/f.u.)	K_1 (MJ/m^3)	K_2 (MJ/m^3)
$SmFe_{11}Ti$	4.2	19.4		
	300	17.5	3.9±0.2	0.11±0.1
$SmFe_{11}TiH_{1-\delta}$	4.2	19.4		
	300	18.2	4.7±0.2	0.11±0.1

earth and four transition metal atoms at the apexes. The complete filling of this interstitial site would lead to a maximum H concentration of one H atom per formula unit, in good agreement with the concentration determined by gravimetric methods. The exclusive filling of this interstitial site has been observed by Tomey[10] in the related $RFe_{10}Mo_2$ series. This interstitial site is close to the rare earth element and hence, changes of the rare earth environment and some magnetic features are expected as will be discussed below. Finally, x-ray analysis performed on magnetically oriented powders of both $SmFe_{11}Ti$ and $SmFe_{11}TiH_{1-\delta}$ shows that, at room temperature, both compounds exhibit uniaxial anisotropy, with the easy magnetization axis parallel to the c axis of the tetragonal structure.

The magnetic features of $SmFe_{11}Ti$ and its hydride are summarized in Tables I and II. The first remarkable effect of H insertion within the lattice is an increase of the Curie temperature from 567 to 634 K. The increase of the Curie temperature is correlated to the increase of the exchange interaction via the increase of the interatomic distances that occurs upon insertion of hydrogen in the lattice. The increase of the ordering temperature upon hydrogenation is larger for the Sm compound than for the Gd compound (T_C=621 K for $GdFe_{11}Ti$ and 652 K for $GdFe_{11}TiH$). The saturation magnetization has been obtained by extrapolation of M vs $1/H^2$. The other major change upon hydrogen insertion is an increase of the saturation magnetization at room temperature as reported in Table II. The iron sublattice magnetization itself is increased as observed on $YFe_{11}Ti$ and $RFe_{10}Mo_2$ (R=Y, Lu).[6,9,10] In Fig. 1, the room temperature magnetization curves of $SmFe_{11}TiH_{1-\delta}$ and $SmFe_{11}Ti$ are shown. The fit of the magnetization curves has been performed between 50 and 240 kOe, the difference in magnetization between the observed and calculated values is lower than 3%. This fit gave the anisotropy constants reported in Table II. The uniaxial anisotropy of $SmFe_{11}Ti$ and its hydride is confirmed by the positive value of K_1 and the K_2 value. The clear increase of the K_1 parameter reflects the strengthening of the uniaxial anisotropy by hydrogen insertion. A similar study on $GdFe_{11}Ti$ and $GdFe_{11}TiH$ where the magnetic anisotropy originates mainly from the iron sublattice shows that the K_1 remains almost unchanged at about 1.4±0.1 kJ/m^3 (at 300 K). These results reveal that most of the anisotropy increase observed in the Sm compound is due to an increase in the Sm sublattice contribution. The rare earth anisotropy is closely related to the electric field gradient (efg) acting on the rare earth site, a change of the efg induced by hydrogen is expected and has been checked by ^{155}Gd Mössbauer spectroscopy.[11] Previous results[12,13] have shown that in the R_2Fe_{17} series hydrogen insertion induces a decrease of the rare earth contribution to anisotropy via a decrease of the efg.[14] The effect of H insertion on the rare earth anisotropy appears to be opposite in the R_2Fe_{17} and $RFe_{11}Ti$ structures

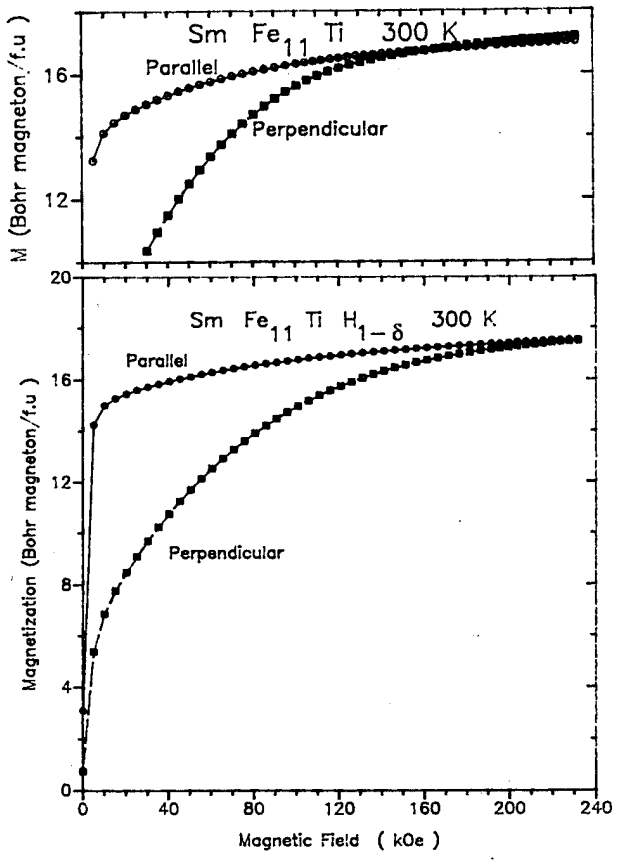


FIG. 1. Isothermal magnetization curves at 300 K on oriented $SmFe_{11}Ti$ and its hydride.

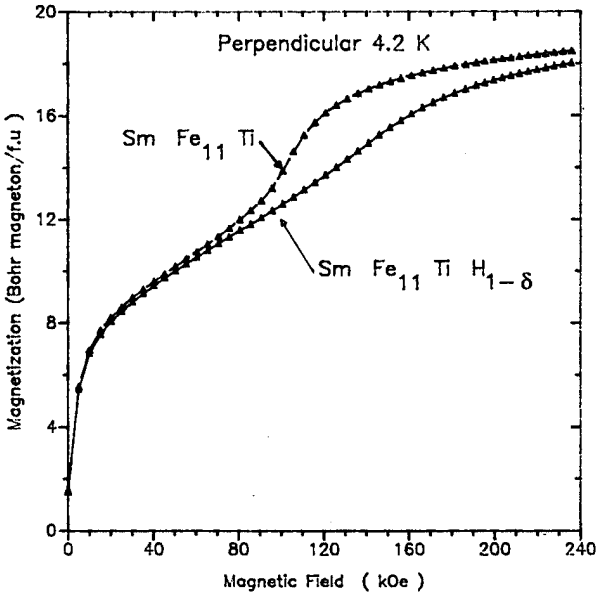


FIG. 2. Isothermal magnetization curves at 4.2 K on $SmFe_{11}Ti$ and its hydride, the field is perpendicular to the alignment direction.

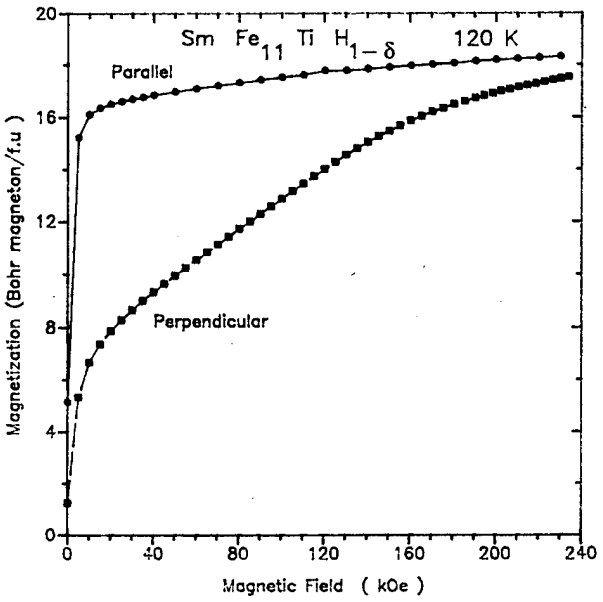


FIG. 3. Isothermal magnetization curves, at 120 K, on oriented $SmFe_{11}TiH_{1-\delta}$.

the reason for this difference may be due to a different location of H in the R neighborhood as discussed elsewhere.[9] Finally it is worthwhile noting that N or C insertion induces a change of magnetocrystalline anisotropy opposite to that due to hydrogen. This difference is related to the nature of the interstitial element itself as already stated in Refs. 12 and 14. The increase in magnetization, ordering temperature, and magnetocrystalline anisotropy observed here make $SmFe_{11}TiH_{1-\delta}$ a potential candidate for permanent magnet applications. However its hysteresis cycle does not show significant coercivity. The magnetization curves of $SmFe_{11}Ti$ with the field applied perpendicular to the alignment direction reveal a surprising steplike behavior, as shown in Fig. 2 in good agreement with data on single crystal obtained by Kaneko *et al.*[15] This agreement with single-crystal data confirms the goodness of the alignment of our powder. As evidenced by the change of slope in Fig. 2, the steplike behavior remains after hydrogen insertion but the shape of the magnetization curve is changed according to the already mentioned increase of the anisotropy. It has been shown that on $SmFe_{11}Ti$, this anomalous magnetization behavior appears below 150 K.[15] We have measured the magnetization curves of $SmFe_{11}TiH_{1-\delta}$ at several temperatures between 4.2 and 300 K, and found that the magnetic transition is already present at 120 K (see Fig. 3). This curvature of the magnetization curve has already been reported by other authors[15,16] for $SmFe_{11}Ti$ and is also present in $SmFe_{12-x}Mo_x$ compounds.[17] However it is not observed[18] in $SmFe_{10}V_2$, probably because of higher than second-order anisotropy terms that are known to play a major role in the $RFe_{12-x}M_x$ series. Kaneko *et al.*[15] proposed that at least three J-multiplets are needed to explain the observed results on $SmFe_{11}Ti$. They have shown that this is not a first-order magnetization process as proposed earlier[16] but a fast continuous rotation of the magnetic moment under the action of the external field. Furthermore, crystal electric field calculations[19] performed for $SmFe_{11}Ti$ show only one minimum energy confirming this interpretation. Studying $SmFe_{12-x}Mo_x$, Kou *et al.* have obtained the same conclusion.[20] The same behavior may be expected for the $SmFe_{11}TiH_{1-\delta}$ compound.

CONCLUSION

Unlike what is observed for $R_2Fe_{14}B$ (Ref. 8) and R_2Fe_{17} (Ref. 14) systems, insertion of hydrogen is found to significantly increase the rare earth magnetic anisotropy of $SmFe_{11}Ti$. Using precise x-ray analysis and high field magnetization measurements, we have given a quantitative analysis of the effect of H on the magnetic anisotropy parameters, magnetization, and Curie temperature of $SmFe_{11}Ti$. For the first time, the effect of hydrogen on the anisotropy parameters K_1 and K_2 has been discussed quantitatively. Besides, we have given results on the $SmFe_{11}TiH_{1-\delta}$ solid solution with the highest reported hydrogen concentration to date. This study has evidenced that $SmFe_{11}TiH_{1-\delta}$ exhibits an anomalous behavior of the magnetization curve at low temperature. This behavior has been compared to results on other $RFe_{12-x}M_x$ compounds.

[1] O. Isnard, S. Miraglia, M. Guillot, and D. Fruchart, J. Appl. Phys. **75**, 5988 (1994).
[2] H. S. Li and J. M. D. Coey, in *Ferromagnetic Materials*, edited by K. H. J. Buschow (Elsevier, New York, 1991), Vol. 6.
[3] D. B. de Mooij and K. H. J. Buschow, J. Less Common Met. **142**, 349 (1988).
[4] J. C. Picoche, M. Guillot, and A. Marchand, Physica B **155**, 407 (1989).
[5] K. D. Durst and H. Kronmüller, J. Magn. Magn. Mater. **59**, 86 (1986).
[6] L. Y. Zhang and W. E. Wallace, J. Less Common Met. **149**, 371 (1989).
[7] O. Isnard, S. Miraglia, D. Fruchart, and J. Deportes, J. Magn. Magn. Mater. **103**, 157 (1991).
[8] O. Isnard, W. B. Yelon, S. Miraglia, and D. Fruchart, J. Appl. Phys. **78**, 1892 (1995).
[9] O. Isnard, Ph.D. thesis, University Grenoble, France, 1993.
[10] E. Tomey, Ph.D. thesis, University Grenoble, France, 1994.
[11] P. Vuillet, D. Isnard, J. P. Sanchez, and D. Fruchart, J. Magn. Magn. Mater. (to be published).
[12] O. Isnard, S. Miraglia, M. Guillot, D. Fruchart, and K. H. J. Buschow, J. Appl. Phys. **76**, 6035 (1994).
[13] O. Isnard, S. Miraglia, M. Guillot, and D. Fruchart, J. Appl. Phys. **75**, 5988 (1994).
[14] O. Isnard, P. Vulliet, A. Blaise, J. P. Sanchez, S. Miraglia, and D. Fruchart, J. Magn. Magn. Mater. **131**, 83 (1993).
[15] T. Kaneko, M. Yamada, K. Ohashi, Y. Tawara, R. Osugi, H. Yoshio, G. Kido, and Y. Nakagawa, in the Tenth International Workshop on Rare Earth Magnets and Applications, Kyoto, Japan, 1989.
[16] H. B. Ping, Ph.D. thesis, University of Dublin, 1990.
[17] X. C. Kou, R. Grössinger, G. Wiesinger, J. P. Liu, F. R. de Boer, I. Kleinsroth, and H. Kronmüller, Phys. Rev. B **51**, 8254 (1995).
[18] R. Grössinger, X. C. Kou, and G. Wiesinger, IEEE Trans. Magn. **30**, 1018 (1994).
[19] X. C. Kou, E. H. C. P. Sinnecker, R. Grössinger, G. Wiesinger, T. Zhao, J. P. Lui, and F. R. de Boer, J. Magn. Magn. Mater. **140**, 1025 (1995).
[20] X. C. Kou, T. S. Zhao, R. Grössinger, H. R. Kirchmayer, and F. R. de Boer, Phys. Rev. B **47**, 3231 (1993).

First-principles calculation of the electronic and magnetic properties of $Nd_2Fe_{17-x}M_x$ (M=Si, Ga) solid solutions

Ming-Zhu Huang and W. Y. Ching
Department of Physics, University of Missouri–Kansas City, Kansas City, Missouri 64110

We have studied the electronic and magnetic properties of the Si and Ga substituted Nd_2Fe_{17} compounds by means of first-principles calculations. The results show that for the $Nd_2Fe_{17-x}Si_x$ (x=1,2,3, and 4) series, the total Fe moments per cell decrease as x increases but the average local Fe moments actually increase up to x=3, except for the 18*h* site which is the most preferable site for substitution. For $Nd_2Fe_{15}Ga_2$, the moments on every Fe site increase. These results are also compared with the earlier calculation on $Nd_2Fe_{17-x}Al_x$ (x=1,2, and 4). From the spin-polarized density of states (DOS) and local DOS for Si, Al, and Ga, it is shown that different substituting elements can change the electronic structure of Nd_2Fe_{17} crystal substantially because of the slightly different interactions with the Fe atoms, and the change in the lattice constants. Estimation of Curie temperatures based on the spin-fluctuation model shows qualitative agreement with experiments. © *1996 American Institute of Physics.* [S0021-8979(96)53608-1]

Study of rare earth iron compounds R_2Fe_{17} (R=rare earth) of the Th_2Zn_{17} type structure (rhombohedral) continues to attract a large number of researchers in the hope of raising the Curie temperature T_c to a sufficiently high level that is required for practical applications.[1–6] Other than the well known approach of doping with N or C, another promising avenue is by elemental substitution by metal or metallic ion such as Al, Si, and Ga.[7–9] The original concept was that introduction of a metalloid atom such as Al with a larger metallic radius than Fe can lead to lattice expansion which is favorable for the ferromagnetic exchange interaction in enhancing T_c. This was the conclusion reached in the case of interstitial doping with N or C. However, in the case of Si-substituted R_2Fe_{17} compounds, it was shown that T_c increases while the unit cell volume decreases.[10–13] Clearly, a simple explanation based on distance-dependent exchange interaction is not sufficient to understand the changes in magnetic properties in these compounds. Systematic calculations of the electronic structure in the substituted R_2Fe_{17}-based compounds are of fundamental importance.

We had previously reported the calculation of the electronic and magnetic properties of the Al-substituted series $Nd_2Fe_{17-x}Al_x$ (x=0, 1, 2, and 4) for different substituted configurations.[14] Our results revealed some microscopic details of the effects of Al substitutions and were in fair agreement with experimental data available. In this article, we present a similar calculation for the $Nd_2Fe_{17-x}Si_x$ (x =1, 2, 3, and 4) series and also $Nd_2Fe_{15}Ga_2$. We study the concentration dependence of the magnetic moments at each site and compare the density of states (DOS) results for $Nd_2Fe_{17-x}Si_x$ (x=1–3), $Nd_2Fe_{15}Al_2$, and $Nd_2Fe_{15}Ga_2$ in order to understand the subtle difference due to different substitution elements. The present results have also been used to test the spin-fluctuation model[15,16] for the calculation of T_c in this class of compounds.[17]

The computational procedure for the present calculation is similar to that for the $Nd_2Fe_{17-x}Al_x$ (Ref. 14) series and will not be repeated here. Basically, the first-principles orthogonalized linear combination of atomic orbitals (OLCAO) method in the local spin density approximation (LSDA) is used to calculate the spin-polarized band structures of these compounds.[14,18] The original rhombohedral cell (19 atoms/cell) with the experimentally measured lattice parameters was used. Experimentally, Long *et al.*[13] and Hu *et al.*[8] have reported neutron diffraction and or Mössbauer spectra for $Nd_2Fe_{17-x}Si_x$ (x=0, 1, 2, 3) and $Nd_2Fe_{15}Ga_2$. For the Si-substituted compounds, they found that Si preferentially occupies the 18*h* site in the Nd_2Fe_{17} structure. The next preferred sites are 9*d* and, for x>2, 18*f*. The 6*c* site is completely avoided. For $Nd_2Fe_{15}Ga_2$, the most preferred substitution site is also 18*h*. In the present calculation, it is necessary to round the number of the substituted atoms to an integer, both for the unit cell and for the substitution site. This is a rather severe approximation and as such, quantitative agreement in the overall moments with experimental data is not expected. However, given the complexity of the system, such calculations can provide useful insights on the electronic and magnetic properties of these compounds. Accordingly, for $Nd_2Fe_{17-x}Si_x$ and for x=1, we replace one Fe (18*h*) site by a Si. For x=2, two cases are studied, one with two Si replacing a Fe(9*d*) and a Fe(18*h*), and the other with two Si replacing two Fe (18*h*). For x=3, we replace one Fe (18*f*) and two Fe (18*h*). And for x=4 Si atoms replace one Fe (18*f*) and three Fe (18*h*). In the $Nd_2Fe_{15}Ga_2$ calculation, two Fe (18*h*) are replaced by Ga and the Ga 3*d* states are treated as core states.

The results of our calculation for the site-decomposed moments are summarized in Table I. As can be seen, the moments at different sites of the same symmetry type as in the Th_2Zn_{17} structure are slightly different as the result of substitution by Si or Ga. Because of the relatively large fraction of substitution, almost every Fe site will have at least one impurity atom as a nearest neighbor, especially for x>2. For all systems calculated we find the total magnetic moments per formula unit (excluded Nd 4*f*) decrease as x increases due to the dilution of the Fe lattice. However, the dependence of the average Fe moment on x for each specific symmetry site is quite different. This is shown in Fig. 1 for the $Nd_2Fe_{17-x}Si_x$ series. For x=0, the average Fe moments are in the decreasing order of (6*c*) (18*f*), (18*h*), and (9*d*). As

 0021-8979/96/79(8)/5545/3/$10.00 © 1996 American Institute of Physics

TABLE I. Calculated magnetic moments (μ_B) for Nd_2Fe_{17}, $Nd_2Fe_{17-x}Si_x$ (x=1, 2, 3, and 4), and $Nd_2Fe_{15}Ga_2$.

	Nd_2Fe_{17}	$Nd_2Fe_{17-x}Si_x$					$Nd_2Fe_{15}Ga_2$
		x=1	x=2		x=3	x=4	
			A	B			
Latt. Cont.							
a(Å)	8.6002	8.5741	8.5524		8.5409	8.5325	8.6281
c(Å)	12.4835	12.4907	12.4988		12.5020	12.4544	12.5531
1 Nd 6(c)	−0.43	−0.37	−0.32	−0.32	−0.28	−0.21	−0.33
2 Nd 6(c)		−0.41	−0.36	−0.36	−0.33	−0.28	−0.36
3 Fe 6(c)	2.00	2.14	2.18	2.20	2.24	2.29	2.15
4 Fe 6(c)		2.05	2.14	2.07	2.12	2.06	2.19
5 Fe 9(d)	1.55	1.67	1.66	1.64	1.61	1.61	1.66
6 Fe 9(d)		1.66	1.74	1.80	1.68	1.69	1.80
7 Fe 9(d)		1.64		1.75	1.81	1.70	1.70
7 Si 9(d)			−0.21				
8 Fe 18 (f)	1.94	1.93	1.84	2.08	1.97	2.01	2.12
9 Fe 18(f)		2.05	1.95	2.18	2.01	1.97	2.15
10 Fe 18(f)		1.99	2.20	2.02	2.08	2.21	2.08
11 Fe 18(f)		1.95	1.86	2.11	2.18	2.18	2.08
12 Fe 18(f)		2.06	1.94	2.07	2.15	2.27	2.10
13 Fe 18(f)		1.94	2.13	2.03			2.08
13 Si 18 (f)					−0.20	−0.18	
14 Fe 18(h)	1.89	1.85	1.95	1.88	1.79	1.86	2.02
15 Fe 18(h)		1.85	1.80	1.79	1.82	1.93	1.93
16 Fe 18(h)		1.93	1.85	2.00	1.83	2.06	2.20
17 Fe 18(h)		1.76	1.86	1.76	1.74		1.93
18 Fe 18(h)		1.76	1.77				
19 Fe 18(h)							
17 Si 18(h)						−0.24	
18 Si(Ga)18(h)				−0.25	−0.22	−0.23	−0.31
19 Si(Ga)18(h)		−0.23	−0.20	−0.22	−0.22	−0.23	−0.27
Total (excl. Nd 4f)	30.79	29.20	27.78	28.24	25.79	24.47	28.92
Average Fe Ms (μ_B)	1.86	1.89	1.92	1.96	1.93	1.99	1.99

x increases, moments for the (6c) and (9d) sites show an initial increase and then saturate between x=2 and 3. For the (18f) site, it starts with a slower increase until it hits x=3 and 4 where the increase becomes more steep. The most erratic dependence is found in the (18h) site which is the preferred site of substitution. It shows some slow decrease from x=0 to x=3 but increases rapidly at x=4. Then at x=4, three of the six (18h) sites are occupied by Si and the statistical error of fluctuation can be quite large. The different Fe moments and their x dependences can be attributed to different local bonding environments of individual atoms. For example, the (6c) site with the largest moment is the so-called dumbbell site. It has one short bond connecting the dumbbells and 12 longer Fe–Fe bonds. In $Nd_2Fe_{15}Si_2$, although the short bond is only 2.38 Å, there are three bonds of 2.63 Å to the (9d) sites, six bonds of 2.77 Å to the (18f) sites, and three bonds of 2.65 Å to the (18h) sites. On the contrary, the (9d) site, which has the smallest Fe moments, has the shortest average bond lengths. It has four bonds of 2.45 Å to Fe (18f), four bonds of 2.46 Å to (18h), and one bond of 2.63 Å to (6c).

Also shown in Fig. 1 are the moments of Si and Nd (6s electrons only) which are negative, indicating slight polarization opposite the Fe moments. The degree of polarization for Si is fairly constant as x varies and that of Nd shows a slight decrease as x increases. This is quite understandable since the polarization of the Nd 6s electrons is basically proportional to the number of Fe atoms in the crystal. For $Nd_2Fe_{15}Ga_2$, the moments on each site are quite close to $Nd_2Fe_{15}Si_2$ for the same site of substitution and show increases in Fe moments for every Fe site.

Figure 1 also shows the average moments at each symmetric site for the $Nd_2Fe_{17-x}Al_x$ series.[14] Unfortunately, these earlier calculations did not include the case for x=3. Still, we can see the x dependence of the Fe moments are somewhat different from the $Nd_2Fe_{17-x}Si_x$ series. This is most pronounced for the (18h) site which is the most preferred site of substitution in both cases. For x from 2 to 4, the moments of the (18h) site and also the (18f) site increase much more rapidly, indicating the influence of the chemical environment on the local Fe moment. On the other hand, the dependence of the negative moments on Nd and Al on x is similar to the Si substitution.

In order to see the differences in the electronic and magnetic structures due to different substitution elements, in Fig. 2 we plot the spin-polarized DOS of Nd_2Fe_{17}, $Nd_2Fe_{15}Al_2$, $Nd_2Fe_{15}Ga_2$, and $Nd_2Fe_{17-1}Si_x$. (x=1–3). The

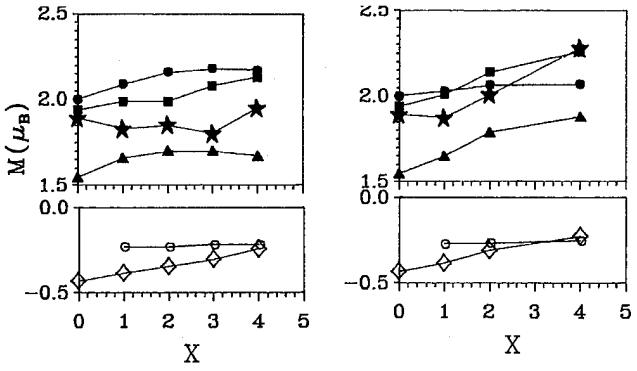


FIG. 1. Calculated local moments at various sites in $Nd_2Fe_{17-x}Si_x$ (left) and $Nd_2Fe_{17-x}Al_x$ (right): for x=0 to 4. (●) (6*c*); (■) (18*f*); (★) (18*h*); (△) (9*d*); (○) Si; (◇) (Nd).

contributions from the Nd 4*f* peaks are substracted out. We can see that substitution by metal or metalloid elements in Nd_2Fe_{17} leads to considerable change in the DOS. First, the total area under the occupied portion decreases due to the reduction of the 3*d* electrons from Fe, which has lead to the reduction of the total Fe moments. Second, the main changes are in the lower part of the DOS where the interaction of the valence *p* electrons of the substituted atom with Fe 4*s* and 4*p* electrons can be significant. Third, there is a reduction in the DOS at the Fermi level E_F, mostly in the majority spin band. These changes are quite subtle and cannot be analyzed in simple terms. In Figs. 2(b)–2(f), the blackened areas correspond to the partial DOS (PDOS) of Al, Ga, and Si, respectively. It can be seen that the three elements affect the Fe 3*d* band differently. For Si, the PDOS is mainly in a region below −4 eV. For Al, it moves up by at least 0.5 eV. In the case of Ga, the distribution of the Ga PDOS is more delocalized and extends toward E_F. These differences reflect the differences in the three atomic species as well as the strong site dependence in the interaction between the substituted atoms and the surrounding Fe. Si has a smaller atomic radius and four valence electrons, its bonding with nearby Fe atoms will be quite different from both Al and Ga, which have larger atomic radii and only three valence electrons. Mulliken population analysis of the calculated wave functions and overlap integrals indicate in all three cases, charge transfer from Fe atoms to the substituted ions occur.

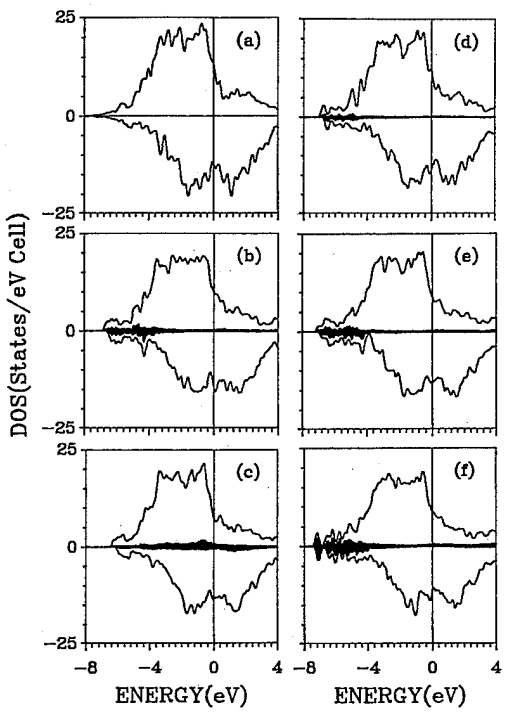


FIG. 2. Calculated total DOS (excluding the Nd 4*f*) for (a) Nd_2Fe_{17}; (b) $Nd_2Fe_{15}Al_2$; (c) $Nd_2Fe_{15}Ga_2$, (d) $Nd_2Fe_{16}Si_1$; (e) $Nd_2Fe_{15}Si_2$; (f) $Nd_2Fe_{14}Si_3$. Positive values correspond to the majority spin band and negative values to the minority pin ban. The shaded areas in (b)–(f) are the partial DOS contributions form Si, Al, and Ga atoms, respectively.

The present results for the electronic structures of the metal-substituted Nd_2Fe_{17} crystals were used to estimate the Curie temperatures in these compounds based on the spin fluctuation model of Mohn and Wohlfarth[16] and the experimentally observed changes in T_c upon substitution were qualitatively accounted for (Refs. 14 and 17). The Curie temperatures for the $Nd_2Fe_{17-x}Si_x$ (x=1,2,3) series show the right enhancement correlation with x even though the cell volume contracts. Apparently, T_c depends more on the DOS at E_F and less on the Fe moments. This is very encouraging and demonstrates the usefulness of electronic structure theory in the study of the magnetic properties of the rare earth-based hard magnets.

This work was supported by U.S. Department of Energy under grant No. DE-FG02-84ER45170.

[1] J. M. D. Coey and H. Sun, J. Magn. Magn. Mater. **87**, L251 (1990).
[2] Y. C. Yang, X. D. Zhang, L. S. Kong, Q. Pan, and S. L. Ge, Appl. Phys. Lett. **58**, 204 (1991).
[3] K. S. V. L. Narasimhan and W. E. Wallace, AIP Conf. Proc. **18**, 1248 (1974); D. McNeely and H. Oesterreicher, J. Less-Common Met. **44**, 183 (1976).
[4] D. Plusa, R. Pfaranger, and B. Wyslocki, J. Less-Common Met. **120**, 1 (1986).
[5] Z. Wang and R. Dunlap, J. Phys. Condens. Matter **5**, 2047 (1993).
[6] B. G. Shen, F. W. Wang, L. S. Kong, and L. Cao, J. Phys. Condens. Matter. **5**, L685 (1993).
[7] W. B. Yelon, H. Xie, G. J. Long, O. A. Pringle, F. Grandjean, and K. H. J. Bischow, J. Appl. Phys. **73**, 6029 (1993).
[8] Z. Hu, W. B. Yelon, S. Misha, G. J. Long, O. A. Pringle, D. P. Middleton, K. H. J. Buschow, and F. Grandjean, J. Appl. Phys. **76**, 443 (1994).
[9] F. Weitzer, K. Hiebl, and P. Rogl, J. Appl. Phys. **65**, 4963 (1989).
[10] R. van Mens, J. Magn. Magn. Mater. **61**, 24 (1986).
[11] E. E. Alp, A. M. Umarji, S. K. Malik, and G. K. Shenoy, J. Magn. Magn. Matter **68**, 305 (1987).
[12] B. P. Hu and S. G. Zhang, Acta Physica Sinica **35**, 352 (1986).
[13] G. J. Long, G. K. Marasinghe, S. Mishra, O. A. Pringle, F. Grandjean, K. H. J. Buschow, D. P. Middleton, W. B. Yelon, F. Pourarian, and O. Isnard, Solid State Commun. **88**, 761 (1993); W. B. Yelon (unpublished).
[14] M. Z. Huang and W. Y. Ching, J. Appl. Phys. **76**, 7046 (1994).
[15] O. Gunnarsson, J. Phys. F **6**, 587 (1976).
[16] P. Mohn and E. P. Wohlfarth, J. Phys. F **17**, 2421 (1987).
[17] W. Y. Ching and M. Z. Huang, these proceedings.
[18] W. Y. Ching, J. Amer. Ceram. Soc. **73**, 3135 (1990).

A novel integrated electric motor/pump for underwater applications

C. Peter Cho
Naval Undersea Warfare Center Division, Newport, Rhode Island 02841

Barry K. Fussell
University of New Hampshire, Durham, New Hampshire 03824

John Y. Hung
Auburn University, Auburn, Alabama 36849

This article presents a novel electric motor/pump system that combines an axial field, permanent magnet motor with a centrifugal pump. This system, unique because the motor permanent magnet rotor and pump impeller vanes are a single unit, provides a compact, reliable, low-noise, and high-power density electrically driven centrifugal pump suitable for underwater applications in which minimizing noise, vibration, and volume are major design objectives. Performance tradeoffs for the electromagnetic analysis were made by three-dimensional finite element analysis models in conjunction with a lumped parameter magnetic circuit model. © *1996 American Institute of Physics.* [S0021-8979(96)40608-7]

I. INTRODUCTION

Because space is severely limited onboard underwater vehicles, the U.S. Navy must streamline components and systems that rob from payload capacity. The traditional electrically driven centrifugal pump set comprises an electric motor, a coupling system, and a pump [Fig. 1(a)].[1] From the perspective of the underwater application, these motor/pump sets have two major disadvantages:

(1) low volumetric power density and

(2) low controllability of noise and vibration.

This paper is about a tradeoff study for a new motor/pump system concept that eliminates these obstacles and promises to improve efficiency for naval underwater vehicles [Fig. 1(b)]. The method used is three-dimensional (3D) finite element analysis (FEA) models in conjunction with the lumped magnetic circuit model.

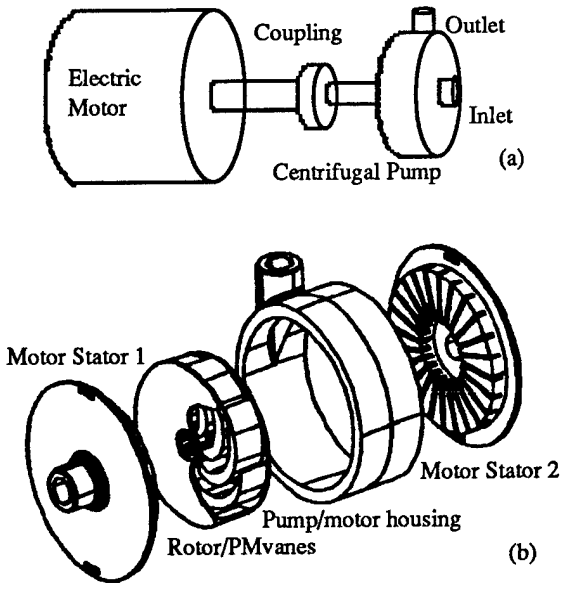


FIG. 1. (a) Traditional motor pump set and (b) exploded view of proposed integrated motor/pump system.

II. INTEGRATED MOTOR/PUMP SYSTEM

The proposed integrated motor/pump system eliminates the inherent disadvantages of the traditional design. Required space is reduced because the motor stators are close to the fluid being pumped and, therefore, no auxiliary motor cooling system is necessary for high power density application. Additionally, the integrated motor/pump concept eliminates the separate coupling element (linkages and bearings), which is a primary source of failure. Vibration isolation of the motor/pump set from other components is simplified. In short, fewer system components reduces production costs, weeds out potential sources of failure, and improves reliability.

A dual air-gap, axial field permanent magnet (PM) motor[2] consists of a double stator with single rotor. A simplified dual air-gap, axial field PM motor is shown in Fig. 2. The rotor structure is a nonmagnetic material such as titanium with PMs; the stators are radial arrays of current-carrying conductors with appropriate end turns and connections fixed in the stator slots.

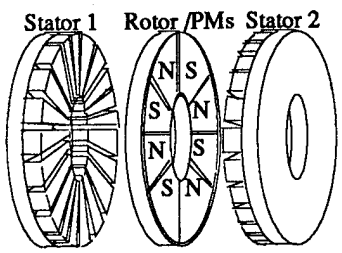


FIG. 2. Simplified dual-airgap, axial field PM motor.

 0021-8979/96/79(8)/5548/3/$10.00 © 1996 American Institute of Physics

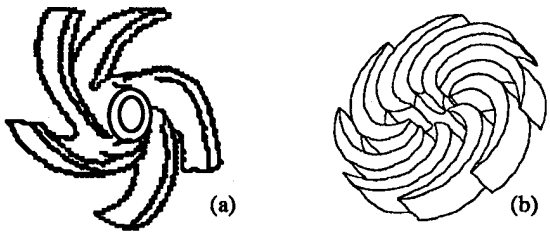


FIG. 3. (a) Typical open impeller and (b) integrated motor/pump impeller.

The motor is configured so that the air gap between the rotor and stators is a plane perpendicular to the axis of rotation. Major PM flux crosses the air gap in the axial direction. Since the PMs must be placed with the pole faces at the air-gap surface, the air-gap flux density is proportional to the PM working flux density. Thus, using high-permanent flux density magnetic materials (such as Nd-B-Fe) is advantageous in generating high torque.

Figure 3 shows a conventional open impeller and the impeller considered in this study, which is a double-suction, radial-flow, closed impeller. Figure 4(a) is a cross section through the plane of the impeller and the stator. The impeller consists of a number of vanes attached to two backing plates. A detailed hydrodynamic analysis is being performed to determine the number and shape of the vanes required to provide a specified capacity and head for a given rotational speed. The exterior radial region of the vanes corresponding to a similar radial region of the motor stator windings is made of PM material.

Each angular sector of the impeller [Fig. 4(b)] is assigned a single magnetic polarization. Polarization alternates between adjacent sectors. The number of alternate sectors depends on the number of phases, number of magnetic poles, and the skewing angle of the impeller vane. The sizing and number of magnetic regions on the impeller are chosen to be compatible with the winding configuration of the motor stators.

III. TRADEOFF STUDY RESULTS

The electromagnetic tradeoff study used FEA 3-D models shown in Figure 5(a) in conjunction with an axial field, brushless, PM motor lumped parameter magnetic circuit model that was developed using the MathCAD spreadsheet program. Figure 5(b) shows the FEA model verification result comparing the calculated vs. measured PM field strength in air and reveals a close correlation.

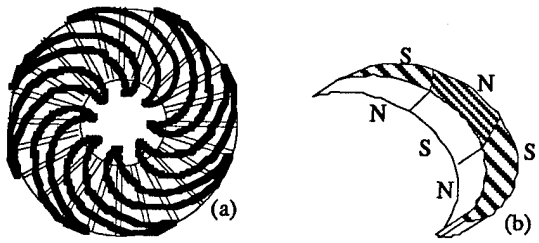


FIG. 4. (a) Cross section through impeller plane and motor stator and (b) impeller vane with angular sectors.

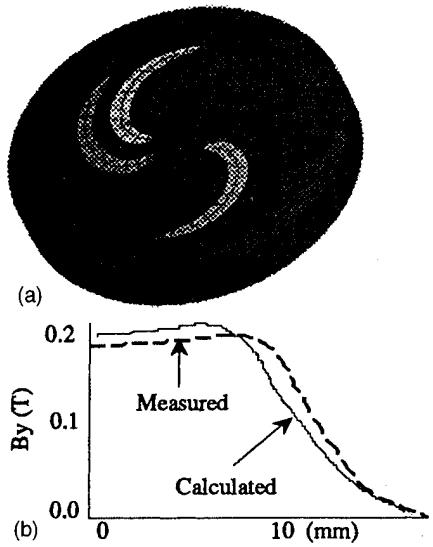


FIG. 5. (a) FEA PM Vanes Model and (b) FEA Model Verification.

The electromagnetic tradeoff study was based on a 15-hp, 1780-rpm motor,[3] for which the base specifications included a 10-inch diameter, 1-inch rotor axial thickness, 5-inch total axial length, 3-phase, 24-slot, 8-pole, and 2 mm-air-gap length.

A. Motor efficiency/SAR/number of poles

Motor efficiency decreases dramatically as the sectional area devoted to PMs decreases. Figure 6(a) shows the effect on efficiency when varying the sectional area ratio (SAR) between the PM and fluid flow area, but keeping the axial length constant (5 inches) at 10-inch diameters. Figure 6(b) shows the influence that the number of PM poles has on motor efficiency for an SAR of 50%. This result shows that there are a optimum number of PM poles in a given geometry with selected materials. In Fig. 6(c), the air-gap magnetic flux density in the axial direction is calculated for the different SARs. These results allow comparison of the magnetic flux density variation as a function of the SAR. Abrupt changes of the flux density will create large cogging force variation, which is a stray force between the stator and rotor. This result also reveals the tradeoff between the smooth operation vs. output torque or power. In Fig. 6(d), the output power (Hp) vs. motor speed was calculated for a different SAR. The result indicates that the high operational condition the losses and leakages are the dominant terms so that there are less SAR effect.

B. Rotor PM/pump vane

The shape of the vane changed as the analyses continued. Initially, wedge-shaped vanes were used, but later the vane evolved into a more hydrodynamic form to reflect the actual shape of typical impeller vanes. The rounded inner edge and sharp outer edge caused problems in modeling accuracy until the FEA model was modified to include fine meshes of elements in both these areas [Fig. 5(a)]. Figure 7 shows the rotor PM vane evolution during the electromagnetic tradeoff study using FEA. A full analysis must be per-

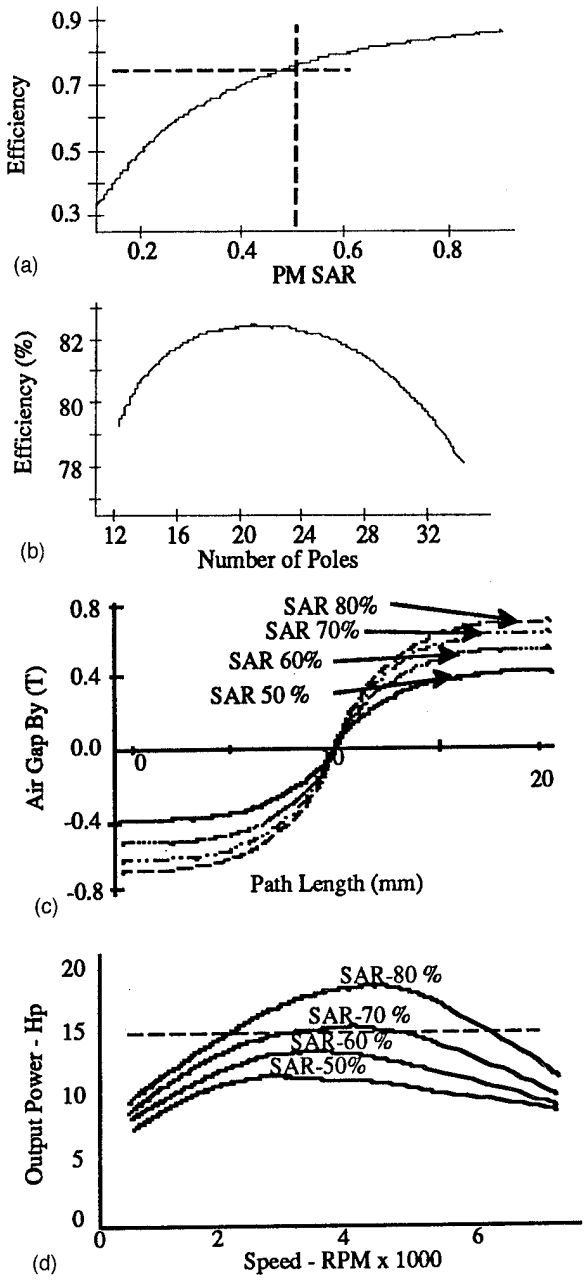


FIG. 6. (a) Motor efficiency vs. SAR, (b) number of poles, (c) Flux density vs. SAR, and (d) Power vs. speed.

formed to determine the most efficient vane shape from the standpoint of hydrodynamics.

C. Manufacturing and material selection

Available magnet materials for good motor electromagnetic performance have serious drawbacks as materials of construction for impeller vanes. Constructing useful and efficient impellers offers challenges. For example, the working fluid, salt water, is corrosive to many materials, and some candidate magnets are very chemically active. The vanes must be strong enough to withstand the fluid dynamic forces and centrifugal force as well as the magnetic forces of the motor.

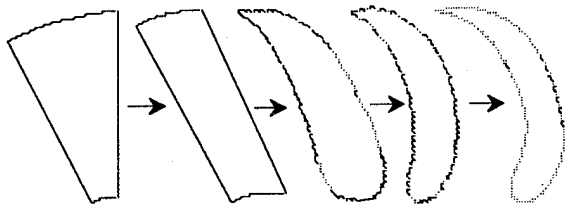


FIG. 7. Rotor/PM vane evolution.

Some candidate magnets, however, are brittle, and some are mechanically weak. Furthermore, optimal magnetic performance dictates the magnetic gap (magnetic flux path through nonpermeable materials and salt water (or air)) be as short as possible. Any structural element (such as a stress-bearing plate) between the magnet and the stator increases the gap. In addition, if the plate is an electrically conductive material, eddy currents that diminish performance may be set up by the changing magnetic fields.

Several impeller design options seem plausible. If stresses in the impeller can be kept low, a plastic impeller, such as carbon-fiber filled PPS, may be possible. The plastic could be injection-molded around the magnets to form a single, chemically sealed unit and serve as the impeller bearing. Another option is that of hollow vanes welded (possibly by electron-beam) between two end plates. Magnet sections, previously coated for corrosion protection, are bonded in the interior of the vanes.

IV. CONCLUSION

This paper presents a novel electric motor/pump system that combines an axial field, permanent magnet motor with a centrifugal pump. Based on the tradeoff study, the authors of this paper have shown the theoretical feasibility of a new, electric motor/pump concept tailored to meet rigid design criteria for underwater systems. The tradeoffs were conducted using 3-D FEA models in conjunction with a lumped parameter magnetic circuit model. The results shows that this new concept will provide sufficient motor efficiency (up to 72% with 50% SAR) with a given geometry. More research to determine the exact vane geometry for high hydrodynamic and overall system efficiencies is planned.

ACKNOWLEDGMENTS

The work described in this article is sponsored by the Naval Undersea Warfare Center's (NUWC's) Independent Research (IR) Program as Project B10303, entitled NOVEL INTEGRATED ELECTRIC MOTOR/PUMP SYSTEM. The IR program is funded by the Office of Naval Research; the NUWC program manager is Dr. S. C. Dickinson (Code 102). An integrated motor/pump system concept described in this paper has been filed with the U.S. Patent Office through the NUWC Office of Council (U.S. Navy Case No. 76609).

[1] R. L. Harrington, *Marine Engineering* (Society of Naval Architects and Marine Engineers Jersey City, NJ, 1992).
[2] C. P. Cho and B. K. Fussell, Proceedings of Incremental Motion Control Systems and Devices , June 1993.
[3] D. M. McGee, MS thesis, Massachusetts Institute of Technology, May, 1993.

Imposition of periodic magnetization patterns on high-energy-product magnetic plates

H. A. Leupold, A. S. Tilak, and E. Potenziani II
U. S. Army Research Laboratory, AMSRL-PS-PC, Fort Monmouth, New Jersey 07703-5601

Periodically magnetized permanent magnet plates with high-energy products are potentially very useful in high-field structures such as free-electron lasers, electrical machinery, and various mechanical applications such as magnetic bearings, for which they are already being used. A major problem is the lack of field sources with sufficient field amplitude to impose such patterns of magnetization on high-coercivity materials. This paper shows how such high amplitudes can be obtained for several patterns by use of modified sources of the augmented "magic ring" and "magic sphere" types. [S0021-8979(96)32908-6]

INTRODUCTION

Permanent magnet structures with a spatially periodic distribution of magnetization are commonly used in a variety of applications. Examples are in electron tubes, free electron lasers, electrical machinery, and mechanical bearings. Often these can be assembled from uniformly magnetized blocks but in some cases such as in circular bearings this is impracticable and the magnetization must be performed on one piece by an externally applied periodic field.

Both methods have drawbacks. The former involves the labor of assembly and bonding, the fragility entailed in multipiece construction, and, in the case of small pieces, wasted space needed to accommodate the binding cement. On the other hand, one-piece magnetization is difficult in high-energy permanent magnet materials because of the difficulty of obtaining sufficiently high periodic magnetizing fields especially in arrays with short periods. This paper describes novel magnetizing structures and methods whereby periodic magnetization can be effected on one-piece magnetic arrays.

ANNULAR PERIODICITY IN DISKS

Magnetic bearings sometimes take the form of pairs of annularly magnetized disks in which the magnetizations in adjacent annulae are opposite in sign. The disks are coaxially mounted so that the annulae facing each other across the air gap between them, are oppositely oriented in magnetization, thereby resulting in mutual repulsion (Fig. 1). The periodicity of magnetization fosters a degree of lateral stability.

Because such structures are exposed to large demagnetizing fields and because strong fields are required by their functions, high-energy-product materials are desirable for their manufacture. But it is the very high coercivities of these materials that militate against their full magnetization and in bearings of this type are typically magnetized to only about one-third the remanence.

To obtain periodic fields of the required peak strengths and amplitudes, we have recourse to a variation of an augmented "magic sphere" structure. Such sources are capable of delivering up to 4 T in structures of reasonable size.[1] For example, a configuration in Fig. 2(a) can produce 4 T in the equatorial slot in its iron core if its outer to inner radius ratio is about 10. If the iron core is cut into coaxial cylindrical shells separated by annular spaces of thickness equal to that of the shells, a periodic field is produced in the equatorial slot where the to-be-magnetized bearing disk is placed [Fig. 2(b)].

Between the iron shells, the disk experiences a substantially larger field than between the spaces separating the shells. If the coercive force of the disk lies between the maximum and minimum fields, corrected for demagnetization (correction typically of the order of 5–10 kOe), it will be fully magnetized where the field is maximum and only partially magnetized at the field minima. The resulting pattern is illustrated by the qualitative sketch of Fig. 3(a).

The disk is then placed into a similar magnetizing fixture in which the pattern of iron cylinders is radially displaced by one-half period with respect to that in the original fixture so that the positions of the maxima and minima are interchanged. Also the disk is oriented opposite to its position during the original magnetization. Then the field minima are applied to where the magnetization of the disk is maximum

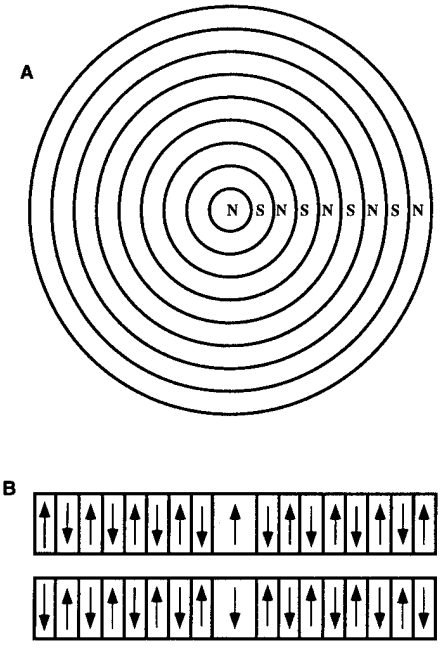


FIG. 1. (A) Top view of the disk with periodic, annular magnetization. (B) Diametric sectional view of disks mounted in opposition to form a levitated bearing.

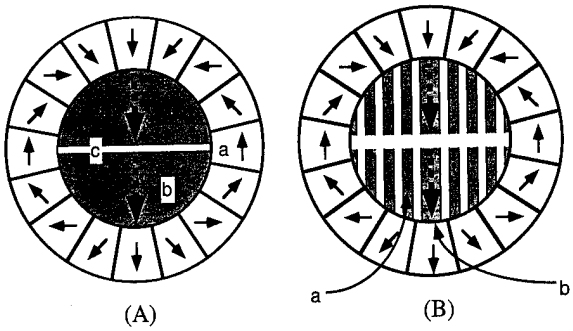


FIG. 2. Cross sections of magic sphere variants. (A) The augmented "magic sphere" consists of magic sphere field sources (a), an iron spherical core (b), and an equatorial slot (c). (B) The augmented magic sphere with an iron core cut into annular cylindrical shells (a) and center rod (b). Solid arrows indicate magnetization of permanent magnets; dotted arrows that of passive materials such as iron.

and the field is insufficient to substantially diminish it. On the other hand, the field maxima are where the magnetization of the sample is much weaker and therefore easily reversed and fully magnetized in the opposite direction. The result is the fully aligned periodic magnetization pattern of Fig. 3(b).

Figure 4 shows the maximum and minimum fields in a seven period iron sphere core as a function of the field applied by the "magic sphere." For convenience, the abscissa of the plot is the outer to inner radius sphere ratio (r_0/r_i) rather than the applied field itself which is given by[2]

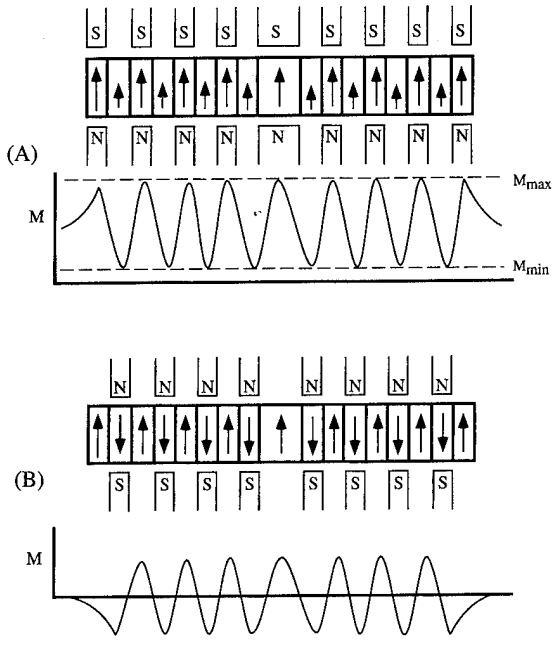


FIG. 3. Magnetization of the disk. (A) The disk is placed in a slot between annular iron shells marked N and S. The resulting magnetization pattern is shown by arrow lengths in disk and by the accompanying qualitative graph. (B) The disk is placed in a second slot with the opposite field sense and with iron shells displaced by one-half period with respect to (A). The graph and arrows show a complete reversal of the weakly magnetized areas of (A) and full magnetization in the new direction while the originally fully magnetized areas of (A) are unaffected.

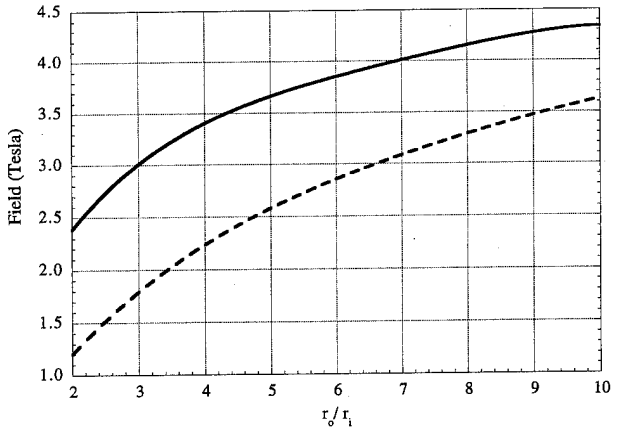


FIG. 4. Fields in equatorial slot of annular periodic magnetizer: — is maximum, --- is minimum. The data are for a slot diameter of 4 cm and a slot width of 0.15 cm. The "magic sphere" material has a remanence of 1.2 T and the seven cylindrical shells in the core are of Hyperco 50.

$$B=(4/3)B_r \ln(r_0/r_i), \tag{1}$$

where B_R is the remanence of the magic sphere material.

Unfortunately, the field amplitude decreases while the magnetizing field grows with increasing applied field. This means that while larger spheres gain accessibility to higher coercive forces, their flexibility with regard to broad coercivities is not as good. Nevertheless, their range of usefulness extends over most of the Sm_2Co_{17} materials, including the frequently used temperature compensated varieties.[3]

Applied fields can be made adjustable by the circumscription of hemispherical shells of increasing radius about the core sphere. Alternatively, adjustable magic spheres such as those described in Ref. 4 could be employed.

To prevent exposure of the disk to erratic magnetization sequences, the magnetization processes should be effected by a jig that contains the upper and lower hemispheres of the magic spheres with their cores. These would be made to converge on the disk in a controlled fashion by a motorized contrivance on the jig. This is necessary because of the large attractive forces that grow between the hemispheres as they approach each other.

RECTILINEAR PERIODICITY ON PARALLELPIPEDS

Similar techniques can be used to impose periodic magnetized striations upon rectangular strips (Fig. 5). In such cases, the magnetization would be accomplished by an augmented magic cylinder.[2] Two such strips facing each other across a gap would constitute a simple free-electron laser or wiggler. Strips of iron covering the outer surfaces of these periodic strips would form a flux return path and augment the periodic field in the gap (Fig. 6).

AXIAL FIELD AZIMUTHAL PERIODICITY

The iron core of an augmented magic sphere can be cut into wedges whose vertices meet on the sphere's polar axis. If alternate wedges are removed, an azimuthally periodic field results in the equatorial slot. This field can then be used to impose an azimuthal pattern on a disk by the successive

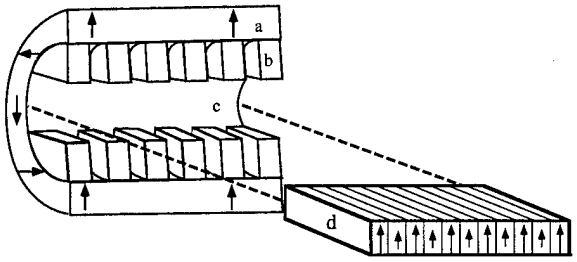


FIG. 5. Half-section of the rectilinear periodic magnetizer; (a) permanent magnet "magic ring:" (b) iron irises, (c) slot for the magnetized bar (d) which emerges with the magnetic pattern shown. As in Fig. 3, the bar must be inverted and moved one-half period along the magic ring axis to obtain the desired pattern.

method of the previous section. The periodic field of the magnetizing structure could also act simultaneously as a wiggler field and as the field confining the charged particles to the desired circular path.

RADIAL FIELD AZIMUTHAL PERIODICITY

The iron core of the magnetizing devices of the previous section can be used to produce an azimuthally periodic radial magnetization pattern on an annular ring rather than an axial one on a disk. Such rings form the stator or rotor in electrical machinery and in circular-trajectory, free-electron lasers where the particle oscillation is in the axial, rather than the radial, direction. This is done by eliminating the equatorial work slot and placing the core in the central cavity of a

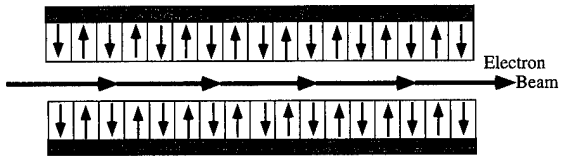


FIG. 6. Wiggler formed from two rectangular strips magnetized in the apparatus of Fig. 5. The shaded outer strips form an iron flux return path.

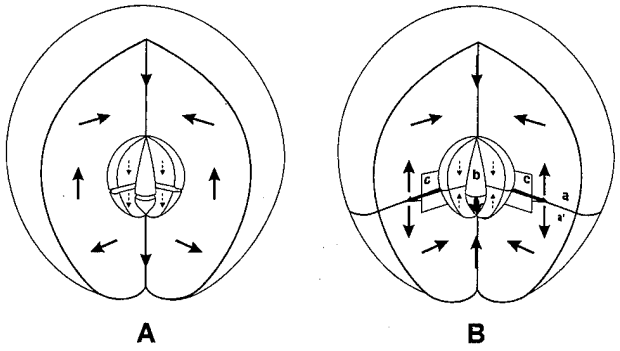


FIG. 7. Structures for the production of azimuthal periodicity of (a) the axial field, (b) the radial field. The latter is indicated by the flat arrows through element c.

sphere formed by two magic hemispheres placed in the opposition. The flux in such a structure would be squeezed radially outward (or inward) in the equatorial plane. The flux density would be greatest in the radial paths in the iron wedges and least in the space between them as in Fig. 7(B). The ring to be magnetized would then be placed in an equatorial annular space in the vicinity of the boundary between the magic sphere and its inner cavity. Other, possibly more efficient iron core structures could also be used in lieu of the spherical wedges described in the preceding paragraphs.

A second magnetization with the ring displaced by one-half period with respect to the magnetizing core would complete the desired magnetic array as in all of the other cases discussed.

[1] H. A. Leupold, E. Potenziani II, and A. S. Tilak, J. Appl. Phys. **73**, 6861 (1993).
[2] H. A. Leupold and E. Potenziani II, IEEE Trans. Magn. **MAG-23**, 3628 (1987).
[3] E. Potenziani II, H. A. Leupold, J. P. Clarke, and A, Tauber, J. Appl. Phys. **57**, 4152 (1985).
[4] H. A. Leupold, A. S. Tilak, and E. Potenziani II, IEEE Trans. Magn. **29**, 2902 (1993).

Effects of slot closure by soft magnetic powder wedge material in axial-field permanent magnet brushless machines

S. Gair
Napier University, 219 Colinton Road, Edinburgh EH14 1DJ, United Kingdom

J. F. Eastham
University of Bath, Claverton Down, Bath BA2 7AY, United Kingdom

A. Canova
Napier University, 219 Colinton Road, Edinburgh EH14 1DJ, United Kingdom

The article reports on a study of the effects of slot closure in axial-field permanent magnet brushless machines by a two-dimensional finite element method (2D FEM) of analysis. The closure of the slots is made by using soft magnetic powder wedge material. Parameter values and machine performance for the open and closed slot configuration are computed. In order to test the 2D FEM model, calculated results are compared with measurements and favorable agreement is shown. © *1995 American Institute of Physics.* [S0021-8979(96)05608-1]

I. INTRODUCTION

The shape of the slot head in electrical machines has an important bearing on the high frequency stator losses which can be induced. Many electrical machines are easier to wind if the slots are open. However, they cause flux pulsations in the air gap of the machine. As a compromise, wedges which saturate are frequently employed. These can be difficult to manufacture because the flux is not unidirectional. A good solution is to use powdered composite slot wedge materials.[1] These effectively close off the slot magnetically and so reduce the perturbation to the flux in the air gap.

The particular machine described in this article is an axial field of permanent magnet disk type. Axial field disk machines[2,3] have important applications in the drive systems of electric vehicles, particularly from the point of view of directly driving the rear wheels of the vehicle. Such machines are difficult to produce with semiclosed slots because there are no individual laminations which can be stamped—the core is formed from a continuous strip (coil) of lamination material, and it is much easier to simply mill a parallel sided slot through the torodial coil. This also makes it much simpler to insert the winding. Hence these machines present a particularly suitable application for powder core wedges.

By employing closed slots in a machine, the ripple flux in the air gap and the pulsating tooth flux can be reduced; also cogging torque and iron losses are diminished, and as a consequence vibration, noise, and efficiency are improved. On the other hand, the closure of the slot produces a decrease in the rotor magnetic field which is linked with the stator winding and an increase of self- and mutual inductances of the phases of the motor.

II. TWO-DIMENSIONAL FINITE ELEMENT METHOD

It is known that the structure of this machine generally requires three-dimensional modeling for accurate analysis—however, the two-dimensional (2D) method adopted here is shown to give good results.

From the symmetry of the magnetic structure, the boundary conditions represented in Fig. 1 are adopted and only one stator and a half of the rotor need to be modeled; moreover, periodic conditions allow us to reduce the problem to a quarter of the machine (one pole pair). The analysis method adopted here has been to introduce a notional radial

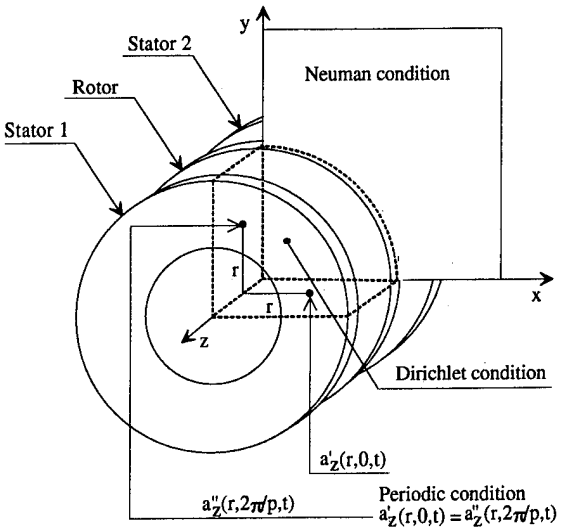


FIG. 1. Boundary conditions (p is the number of pole pairs).

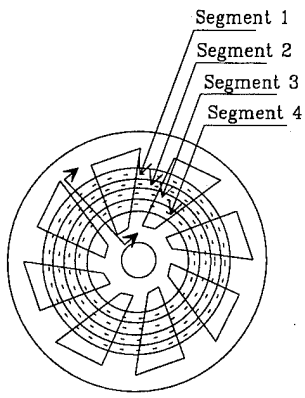


FIG. 2. Front view showing the notional radial cut.

 0021-8979/96/79(8)/5554/3/$10.00 © 1996 American Institute of Physics

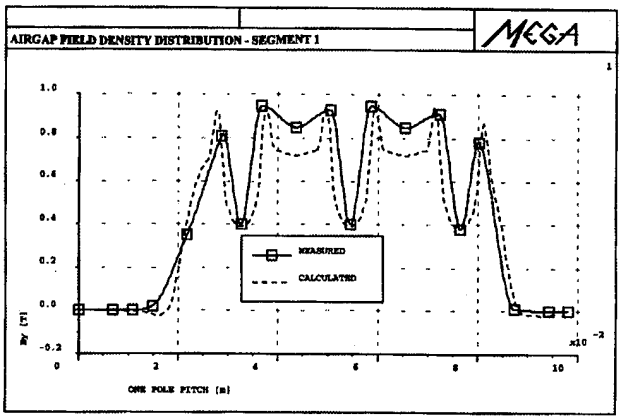


FIG. 3. Air gap flux density distribution.

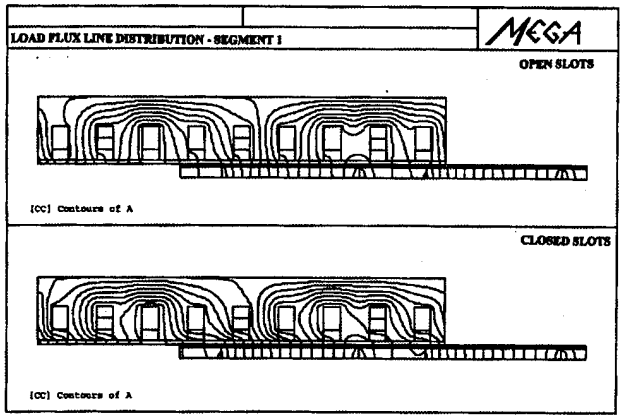


FIG. 6. Load flux line distribution.

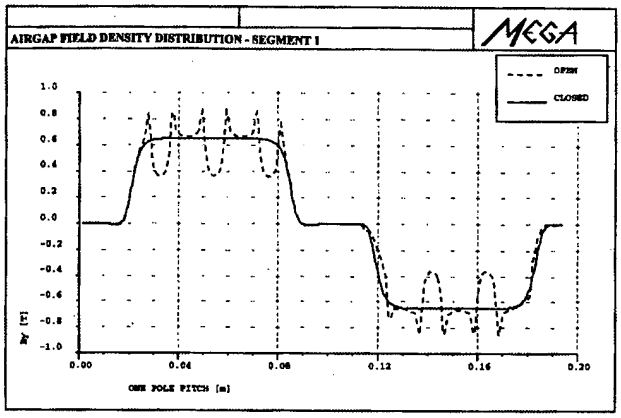


FIG. 4. Air gap flux density distribution along the external segment (segment 1).

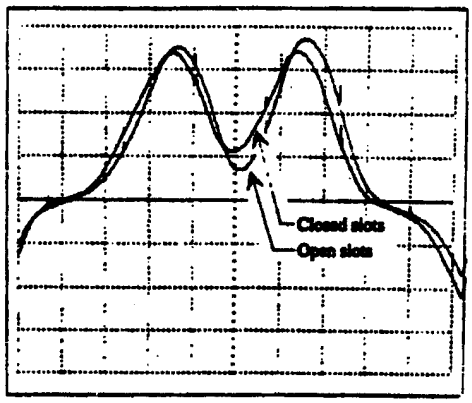


FIG. 7. Tooth-induced emf vs time with open and closed slots.

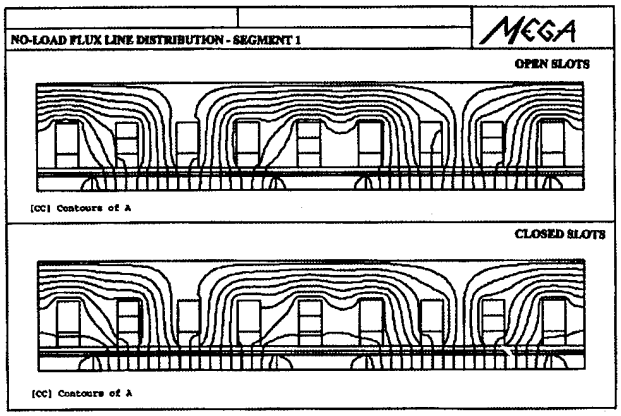


FIG. 5. No-load flux line distribution.

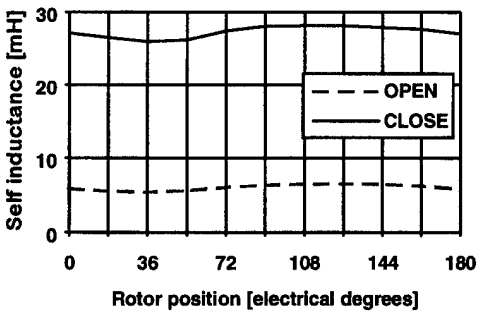


FIG. 8. Phase self-inductance with open and closed slots.

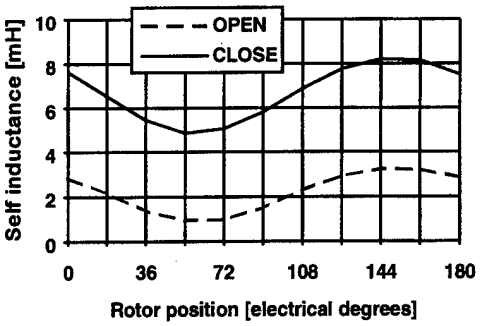


FIG. 9. Phase to phase mutual inductance with open and closed slots.

cut through the stator (Fig. 2) and open the machine out into a linear form. In this article a four-segment model is used.

In order to test the 2D finite element method (FEM) multisegment model, calculated results and measurements are compared for the open slot machine. The computed local quantity—air gap field density distribution around the stator, is found to be very close to the measured value obtained by Gaussmeter measurement (Fig. 3).

III. SLOT CLOSURE BY WEDGE MATERIAL

The use of closed slots results in a reduction of the permeance variations due to the slot openings. This effect can be observed on the wave form of the air gap flux density (Fig. 4) where a very smooth distribution occurs. The contrast in magnetic behavior in the core and air gap between an open and closed slot machine is shown in Figs. 5 and 6, where no-load and load flux line distributions are drawn.

Furthermore, the efficiency improvement in the closed slot design can be tested using a method based on the evaluation of the induced emf per stator tooth due to the rotation of the rotor permanent magnets. This technique has already been used on other types of electrical machines, e.g., asynchronous and radial field brushless motors. This wave form of stator tooth induced emf can be directly related to the teeth and yoke eddy current iron core losses, and for this reason, the tooth-induced emf wave form assumes a very important meaning.

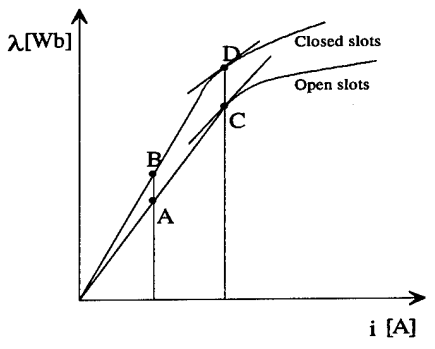


FIG. 10. $\lambda-i$ characteristics for closed and open slot motors.

In Fig. 7, the measured induced emf wave forms are compared for the open and closed slot motor. It should be noted that the closed slot motor has a smaller induced emf ripple and thus smaller iron losses than the motor with open slots.

Unfortunately, the closed slot design results in lower values of phase induced emf since less flux will link the stator conductors, and so result in a slight reduction of the maximum torque provided by the motor.

Furthermore, another important effect due to the closure of the slots can be observed on the self- and mutual inductances. An inspection of these machine parameters reveals that the motor with closed slots possesses greater inductance(s) than the motor with open slots (Figs. 8 and 9).

Moreover, from Figs. 8 and 9 it will be observed that the second-order harmonics of self- and mutual inductances do not change while their average values change markedly, i.e., the percentage values of second-order harmonics of self- and mutual inductances referred to average values are reduced. In the closed slot design, the increase in the inductance values can be attributed to the higher permeance of the magnetic circuit. λ-i profiles shown in Fig. 10. If the saturation level is not high, the magnetic behavior points lie on the linear segment of the magnetic characteristic (point A on the open slot magnetic curve and point B on the closed slot magnetic curve). Moreover, at these points the apparent inductance (λ/i) and incremental inductance ($d\lambda/di$) are equal.[6] Accordingly, the closed slot inductances are greater than the open slot inductances because the closed slot magnetic curve slope is greater than that with open slots. On the contrary, if the saturation level is high and so the behavior point lies on the nonlinear zone of the magnetic characteristic, it is necessary to distinguish between apparent and incremental inductance. In particular, when the open slot magnetic behavior point lies on the nonlinear zone of the magnetic characteristic (point C), the closure of the slots produces a decrement of the slope around the behavior point (point D) and therefore gives rise to incremental self- and mutual inductances.

IV. CONCULSIONS

The article describes the effects of slot closure using soft magnetic powder wedge material in axial-field permanent magnet brushless machines. The analysis has been performed by a 2D FEM procedure. The method adopted here has been to introduce a notional radial cut through the stator and open the machine out into a linear form. A previous test of the model shows a favorable agreement between calculated and measured results. The effect of the closure of the slots on the air gap field distribution and on the tooth-induced emf produce an improvement in the motor behavior. In particular the reduction of the air gap flux density ripple reduces unwanted effects like vibration, noise, and iron losses in the stator teeth.

[1] P. Jasson and M. Persson, PM 94, Paris, June 1994 (unpublished).
[2] J. F. Eastham, M. J. Balchin, T. Betzer, H. C. Lai, and S. Gair, IEEE International Symposium on Industrial Electronics, Athens, Greece, July 1995 (unpublished).
[3] J. F. Eastham, S. Gair, A. Canova, and T. Betzer, Power Electronics, Drives and Energy Systems for Industrial Growth, New Delhi, India, January 1996 (unpublished).

An efficient design to reduce the flux leakage of a spindle motor

T. F. Ying, C. M. Chen, C. P. Liao, M. D. Wu, and D. R. Huang
Opto-Electronics & System Laboratory, ITRI, Chutung, Hsinchu, Taiwan, Republic of China

A small dc brushless spindle motor with small magnetic flux leakage must be used for a CD-ROM drive application because the magnetic flux leakage may affect the magnetic and electric control circuit of the pickup head. This paper presents a motor design that efficiently reduces magnetic flux leakage by using a pair of yokes on the rotor magnet. Using these yokes at a distance of 2.0 mm reduced the magnetic flux leakage from 344 to 29 G along the radial direction and from 117 to 10 G along the axial direction. After shielding for the magnetic flux leakage, the dynamic performance of the motor cannot be affected. The torque of the CD-ROM spindle motor can be controlled at the same range for shielded and unshielded spindle motors. © *1996 American Institute of Physics.* [S0021-8979(96)33008-0]

INTRODUCTION

A CD-ROM drive application requires a spindle motor with a high-rotating torque to reach quick access time. The rotating torque of a spindle motor can be increased by using the rare-earth magnet, which has a high magnetic energy product, but the magnetic flux leakage caused by these magnets is also increased and thus affects the pickup accuracy of the optic head of the CD-ROM drive. The purpose of this research was to develop an efficient shielding design to reduce the flux leakage that is induced by a pair of rare-earth magnets in a CD-ROM spindle motor.

EXPERIMENTS

In an effort to design a compact, efficient motor for a suitable high speed CD-ROM drive application, this laboratory developed a coreless axial spindle motor. The motor has six coils and is driven by a three-phase switching circuit. The rotor magnet, magnetized in the axial direction with eight poles, is made of a ring-shaped NdFeB with $(BH)_{max}=36$ MG Oe. Because the magnetic circuit of this axial spindle motor is formed as a magnetic circuit open loop, the magnetic flux leakage that occurs around the magnets cannot be ignored. The value of flux leakage depends significantly on the different positions of the motor and the distance of measured points from the magnets. Figure 1 shows the structure of a spindle motor without shielding. The x_1, x_2, x_3, and x_4 represent the different positions of the magnet and are used to measure the flux leakage at each fixed distance interval of 0.4 mm along the radial direction. y_1 and y_2 are also used to measure the flux leakage at each distance interval of 0.2 mm along the axial direction. To improve the efficiency of the spindle motor for a CD-ROM drive, a pair of shielding yokes made of carbon steel is used to cover the magnets as shown in Fig. 2. The radial thickness of the yoke, expressed as (l), and the axial thickness, expressed as (m), are 0.8 and 1.0 mm, respectively. The magnetic profiles of the magnets and the leakage of magnetic flux density in both the radial and axial directions from the rotor magnets were measured by using a Hall probe that was connected to a Gauss meter at a different position.[1] The leakage of magnetic flux can be used to evaluate the efficiency for the magnetic shielding design of the spindle motor.

RESULTS AND DISCUSSION

Figure 3 shows the magnetic field profile and flux density of a single rotor magnet. The axial magnetic flux density on the surface of each magnet is about 4400 G. If the gap between the two rotor magnets is 3 mm, the maximum magnetic flux density measured between these two magnets can be increased from 4400 to 5500 G as shown in Fig. 4. The increase of magnetic field strength in this motor with two rotor magnets can also increase the leakage of magnetic flux outside the motor. The measured magnetic flux leakage for an unshielded motor at positions of x_1, x_2, x_3, and x_4 are shown in Fig. 5. The maximum value of the magnetic flux leakage occurred on the surface of the magnet at the x_2 position and is about 2319 G. The testing values of flux leakage at the distance of 2.0 mm from the surface of the magnet at reference positions of x_1, x_2, x_3, and x_4 on the magnet surface are 34, 344, 306, and 19 G, respectively. The measured values for a shield motor are plotted in Fig. 6. The maximum value that occurred at the same position on x_2 is reduced to 412 G. When the distance is 2.0 mm from the magnet, the values of x_1, x_2, x_3, and, x_4 are 7, 29, 5, and 2 G, respectively.

The measured values of the flux leakage along the axial direction for a spindle motor without shielding on y_1 and y_2 are shown in Fig. 7. The maximum value of these data is about 549 G occurred around the position y_2. To reduce the magnetic flux leakage from these two magnets, a plate was

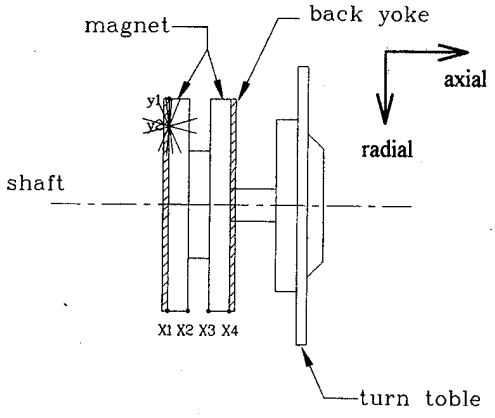


FIG. 1. The structure of the spindle motor without shading yoke.

 0021-8979/96/79(8)/5557/3/$10.00 © 1996 American Institute of Physics

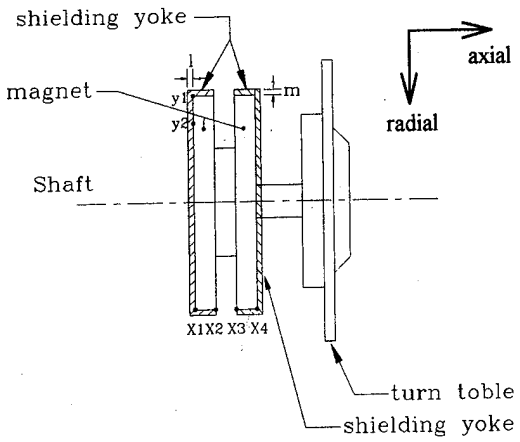


FIG. 2. The structure of the spindle motor with shading yokes.

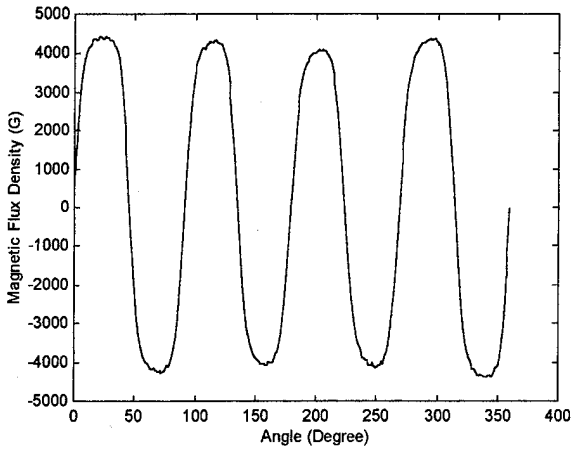


FIG. 3. The magnetic flux density on the magnet surface.

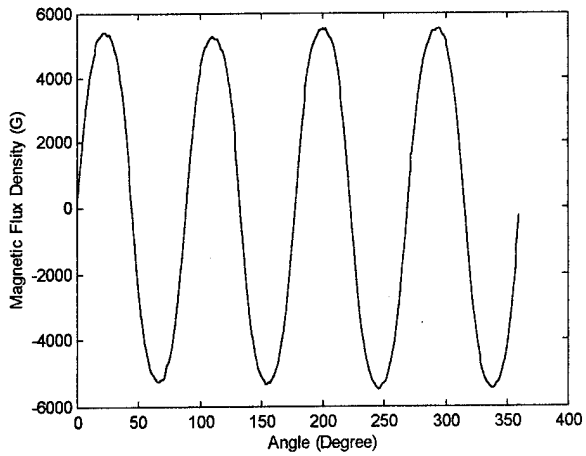


FIG. 4. The magnetic flux density between two magnets.

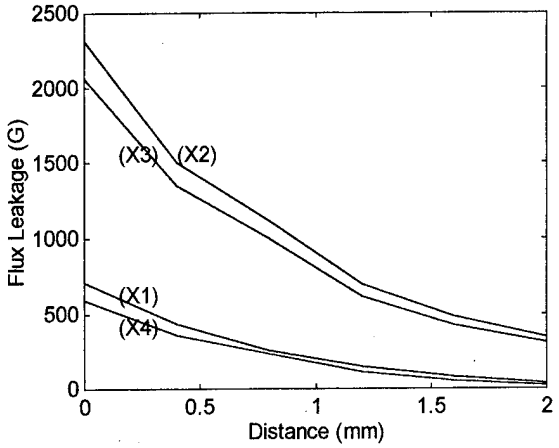


FIG. 5. The magnetic flux leakage distribution along the radial direction with an unshaded condition.

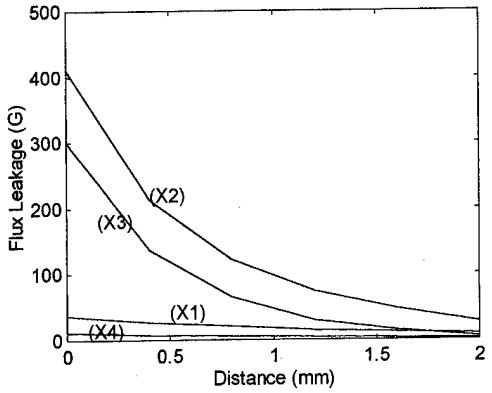


FIG. 6. The magnetic flux leakage distribution along the radial direction with a shaded condition.

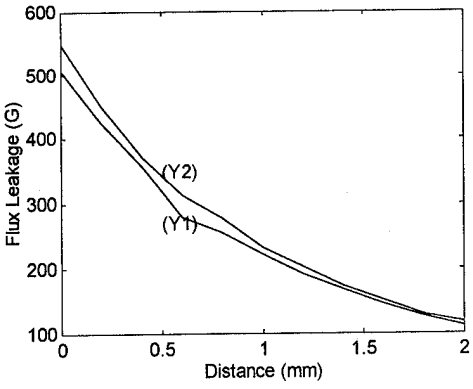


FIG. 7. The magnetic flux leakage distribution along the axial direction with an unshaded condition.

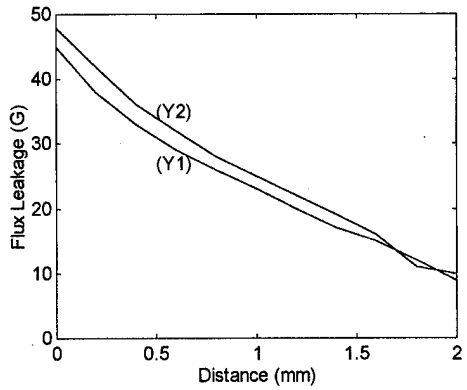


FIG. 8. The magnetic flux leakage distribution along the axial direction with an unshaded condition.

attached to each magnet as a backyoke for the original motor design.[2] Using a backyoke configuration has the same effect as magnetic shielding. The maximum value leaked from each magnet is much less than the 4400 G that was measured on the magnet surface. At the axial distance of 2 mm from the position of y_1 and y_2, the magnetic flux leakage is about 112 and 117 G, respectively. As shown in Fig. 8, the flux leakage is reduced markedly by using the shielding yoke. The leakage values are reduced from 112 and 117 G to 9 and 10 G, respectively.

The magnetic field between the two magnets measured along the radial distance 11 mm extended from the shaft of the motor to the outside of the motor is shown in Fig. 9. The interaction area of coils and magnets is in the area between 6 mm from the shaft and 11 mm from the shaft along the radial direction. Curve 1 shows the magnetic field distribution without shielding. After shielding yokes were added to the magnets, the magnetic field profile changed and is shown as curve 2. The magnetic circuit is changed by using the shielding yoke. When the spindle motor is shielded, the magnetic flux density acting on coils is increased in the inner area between magnetic poles and decrease in the outer area between magnetic poles. It is clear that the magnetic field of the motor with shielding yokes decays markedly compared to the motor without shielding yokes. Good magnetic shielding design for a motor application should not affect the dynamic performance of the motor. The $T-N$ curve expressing the relation between rotation torque and speed is usually used to evaluate the dynamic characteristic of the motor. The testing results of the $T-N$ relation for a shielded and an unshielded condition are shown in Fig. 10. Curve 1 expresses the unshielded condition, and curve 2 expresses the shielded condition. These two curves are almost the same, and the shielding design does not affect the dynamic characteristic of this spindle motor.

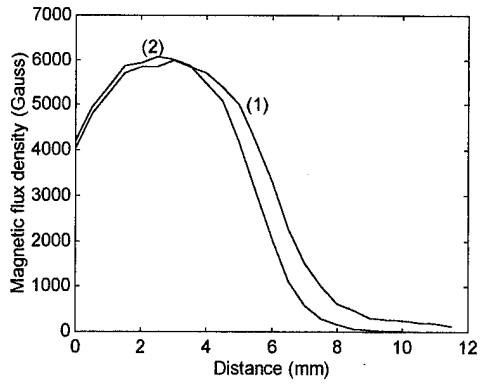


FIG. 9. The magnetic flux density distribution between two magnets.

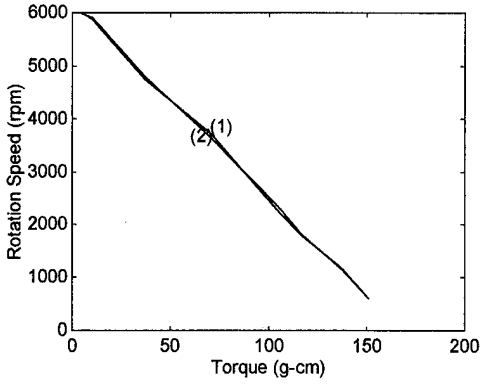


FIG. 10. The $T-N$ curve of the spindle motor.

The mass of these yokes is about 3.9 g and the extra moment inertia caused by these yokes is about 6.1 g cm^2 compared with the nonshielding condition. For a CD-ROM drive application, the inertial moment produced by a disk with a diameter of 12 cm loaded on the spindle motor is about 292.5 g cm^2. The value of 6.1 g cm^2 is much less than 292.5 g cm^2, and obviously it cannot affect the relation of $T-N$. It is another matter why the dynamic performance was not affected by the shielding design. According to the test result shown as Fig. 9, the magnetic flux density of the motor with shielded yokes acting on coils is always more than that of the motor without shielding yokes. Because the stronger magnetic field acting on coils for a shielded condition is eliminated by the extra moment inertia caused by shielding yokes, the $T-N$ relation remains almost the same for these two different conditions (see Figs. 9 and 10).

CONCLUSION

The magnetic flux leakage acting on the pickup head in a CD-ROM drive application can be effectively reduced by using a shielding design of a pair of yokes on the rotor magnets of the spindle motor. The $T-N$ curves of the axial spindle motor show that the dynamic characteristic of rotation is almost not affected by the extra moment inertia produced by the shielding yokes. According to the results of this research, the magnetic flux leakage of a high-torque spindle motor can be reduced efficiently for a CD-ROM drive application.

[1] T. F. Ying, H. J. Tseng, M. D. Wu, and D. R. Huang, 13th International Workshop on Rare-Earth Magnets and Their Applications, 1994 (unpublished), pp. 699–705.

[2] S. J. Wang and D. R. Huang, Proceedings of the Eighth Conference on Magnetism and Magnetic Technologies, 1993 (unpublished), pp. 207–209.

Magnetic profiles of bonded magnets affected by the magnetizing fixtures

Donyau Chiang, Shyh-Jier Wang, and Der-Ray Huang
Opto-Electronics & System Laboratory ITRI, Hsinchu, Taiwan, Republic of China

The four-pole magnetic profiles of the bonded magnets can be obtained by using planar and circular magnetizing fixtures with and without iron backyokes. With the aid of an iron fixture and iron backyoke, the bonded magnets are easily saturated with a shallow saddle profile in each pole. The saturation voltage is about 400 V for a 1600 μF magnetizer. From a practical point of view, it is better to use the planar fixture than to use the circular fixture. © *1996 American Institute of Physics.* [S0021-8979(96)33108-7]

I. INTRODUCTION

The multipole bonded magnet containing Sr–ferrite has been widely used in fan motors as a rotor part. In the design of a fan motor with good performance, a ring magnet with high magnetic strength and optimized magnetic profile to match the stator is one of the dominant components. The magnetic profiles strongly depend on the geometry and material used for the magnetizing fixture. Huang *et al.*[1] used a two-pole fixture to magnetize melt–spun Nd–Fe–B bonded magnets. They found that the magnetic profile is dependent on the fixture geometry. Nakada and Takahashi[2] calculated the effects of magnetic pattern on the torque in a brushless dc motor. They concluded that the magnetic wave forms necessary for high torque are, in increasing order, cosine, trapezoidal, and square wave. In this paper, we demonstrate the effects of planar and circular magnetizing fixtures on the magnetic profile of rubber bonded magnets. Finite element method (FEM) analysis is used to explain the magnetic patterns.

II. EXPERIMENTAL DETAIL

The rubber bonded magnets containing strontium–ferrite were used in this study. The dimensions of the magnets were 57 mm long by 5.1 mm wide by 1.4 mm thick. The magnetic characteristics determined by a vibrating sample magnetometer at 24.6 °C were Br=2336 G, bHc=1965 Oe iHc =2322 Oe, and BH_{max}=1.4 MG Oe, respectively. The geometric features of the magnetizing fixtures and backyokes for the four-pole magnetization are shown in Fig. 1. Two turns of the magnetizing wires with 1.2 mm diam, expressed by the shaded circles in Fig. 1, were wound into each slot for the planar fixture and into the 4.8-mm-diam slot for the circular fixture. Epoxy with high dielectric strength was forced into the space between the slot and wires to prevent wire vibration during the magnetization process. Both magnetizing fixtures and backyokes were made of soft iron and designed to fit the bonded magnet length. The magnetizer was of 1600 μF charge capacity and the applied magnetizing voltages ranged from 300 to 1100 V. The strip magnets were laid on the plate when using the planar fixture and were wound around the fixture when using the circular fixture. We magnetized the bonded magnets with or without the backyokes on them. The peak currents for each magnetization were recorded by a peak current meter. The peak currents for different magnetization conditions are listed in Table I. In general, the currents required for circular fixtures are higher than that for planar fixtures. In each case, there is no significant difference in the current when measured with and without a yoke. After magnetization, the magnet was wound to the shape of a ring and inserted into an iron hollow cylinder. The magnetic profiles of the magnetized magnets were measured by an automatic magnetic measurement system.[3] The distance between the probe sensor and the magnet surface was kept at 0.5 mm. This measuring system was mainly comprised of a gaussmeter, a stepping motor with its controlling unit, and a data acquisition unit. The collected data could be displayed on the screen and printed out immediately. We could also retrieve the data files and do further data operation.

III. FINITE ELEMENT METHOD SIMULATION

Finite element method (FEM) simulation is a useful method for predicting the magnetic profile of the magnetiz-

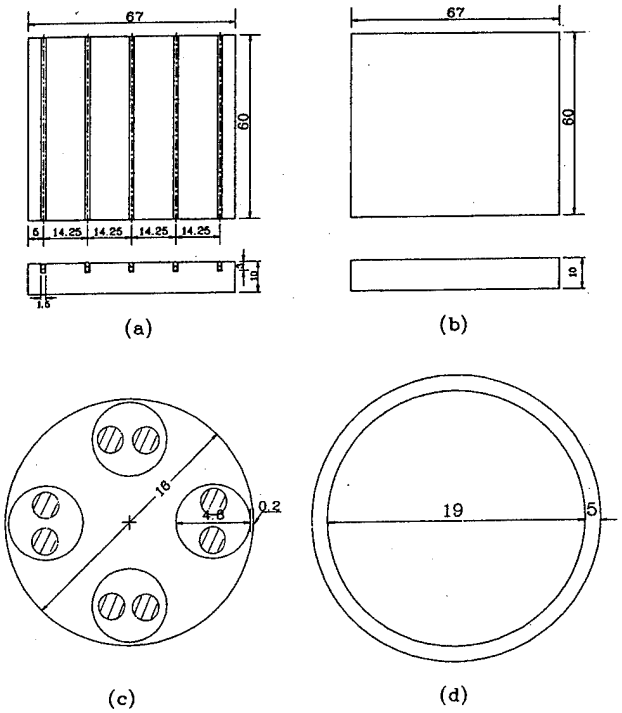


FIG. 1. Geometry and dimensions for top and side view of planar magnetizing fixture (a), top and side view of planar backyoke (b), top view of circular magnetizing fixture (c), and top view of the circular backyoke (d). Dimensions are in millimeters.

 0021-8979/96/79(8)/5560/3/$10.00 © 1996 American Institute of Physics

TABLE I. The peak currents measured from the different magnetization conditions. The unit of the peak current is kA.

Applied voltage (V)	The peak current measured at magnetization conditions (kA)			
	Planar iron fixture		Circular iron fixture	
	With yoke	Without yoke	With yoke	Without yoke
400	3.0	3.1	3.2	3.2
500	3.8	3.7	4.4	4.4
700	5.5	5.4	6.1	6.0
900	6.9	7.1	7.9	7.7
1100	8.5	8.5	9.5	9.4

ing fixture before the fixture design is fabricated. The magnetic patterns calculated by FEM for various geometric features of the fixture are used as a data base which can help reduce the trial and error during the design period. The FEM used in this study was MagNet 5.1 licensed from Inforlytica Co. The magnetic profiles calculated for the circular fixture without a backyoke at applied voltages of 400, 700, and 1100 V are shown in Fig. 2. The geometric features and applied currents are given in Fig. 1(c) and Table I, respectively. The profile in each pole is saddle shaped and the magnetic strengths increase with increasing voltage.

IV. EXPERIMENTAL RESULTS AND DISCUSSIONS

Figure 3 shows the measured profiles when the magnets were magnetized by using a circular iron fixture without a backyoke. The saddle pattern in each pole has a deep valley. The result is comparable to that obtained from the FEM calculation. The coercive force measured for the bonded magnet is 2000 Oe. Empirically, a magnetic strength of three times the coercive force is required to saturate the magnet. From the FEM simulation, a voltage of 700 V is a threshold voltage to bring the magnet saturation in peak position. The maximum peak strengths when magnetized at 700 V are nearly equal to those for 1100 V as depicted in Fig. 3. The

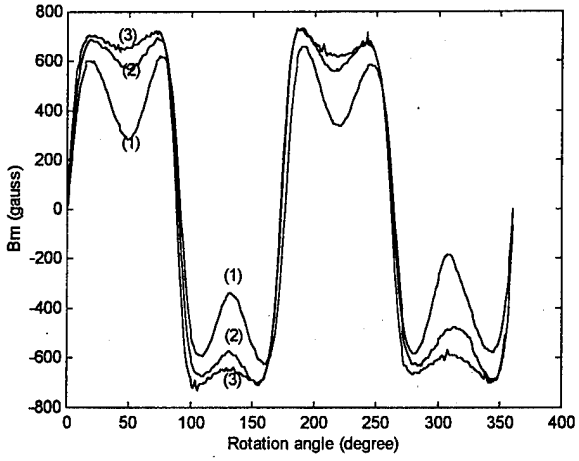


FIG. 3. Magnetic profiles obtained by using the circular iron fixture without an iron backyoke. The applied voltages are 400 V (1), 700 V (2), and 1100 V (3).

magnetic valley strength strongly depends on the magnetizing voltages and the strength increases with increasing applied voltages. The absolute values of magnetic valley strength averaged for 400, 700, and 1100 V are 275, 553, and 628 G, respectively. The peak strengths are 602, 678, and 712 G corresponding to applied voltages of 400, 700, and 1100 V.

The magnetic profiles of the magnets magnetized by a circular fixture with an iron backyoke are depicted in Fig. 4. The saddle shape for each pole is shallow compared to the deep saddle shape obtained by magnetization without the backyoke. The three curves measured for magnetizing voltages of 400, 700, and 900 V, coincide. The bonded magnets approach saturation at 400 V and magnetizing voltages over 400 V have no significant effect on magnetic strengths. The absolute value of magnetic strength in each pole averaged for the three applied voltages is 758 G at the peak position and 626 G at the valley position. The standard deviation is ±40 G for 15 measurements. In Fig. 4, the traces for the three

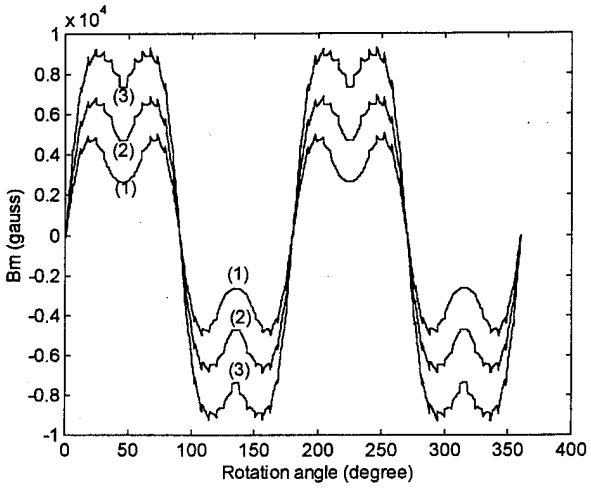


FIG. 2. FEM simulation for a circular iron fixture without backyoke. The applied voltages are 400 V (1), 700 V (2), and 1100 V (3).

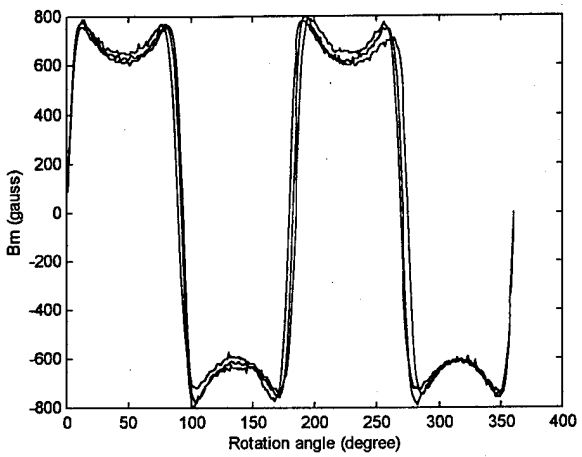


FIG. 4. The magnetic profiles obtained using the circular iron fixture with an iron backyoke. The applied magnetizing voltages are 400, 700, and 900 V.

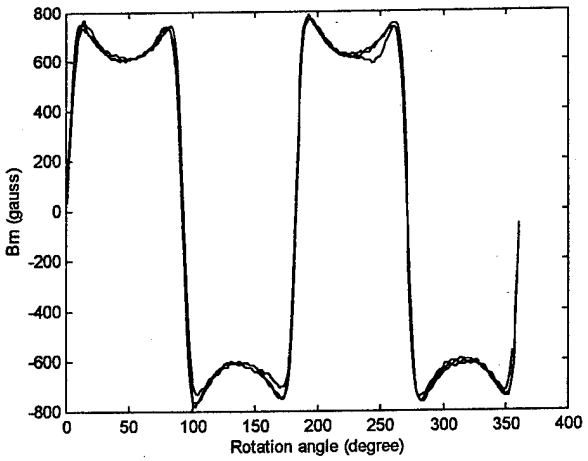


FIG. 5. The magnetic profiles after magnetization by planar fixture with a backyoke. The applied voltages are 400, 700, and 1100 V.

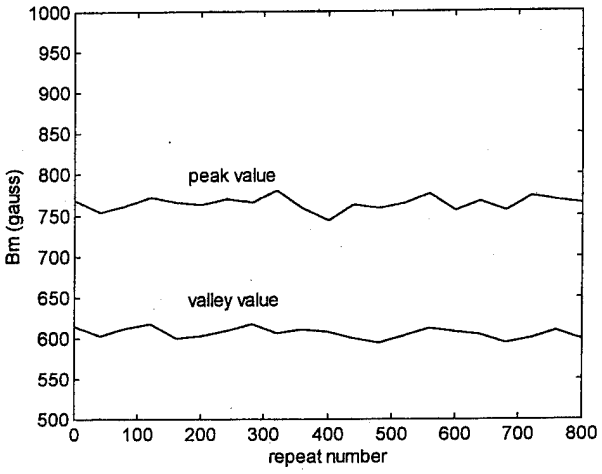


FIG. 7. The magnetic peak strengths and valley strengths vs number of cycles of winding and stretching. No significant difference is observed after 800 winding and stretching cycles.

magnetizing voltages do not coincide exactly. Some portion of the deviation may come from inhomogeneous mixing of the ferrite, and from unequal angular separation of poles. The unequal angular separation results from the limited space available for bending the magnetizing wires and the nonuniform distribution of wires embedded in the fixture slots.

The magnetic profiles of the magnets magnetized by a planar fixture with an iron backyoke are depicted in Fig. 5. The profile shows a shallow saddle shape in each pole, similar that obtained when magnetized by a circular fixture. Because of the intimacy between the magnetizing wires and the fixture slots, the three measured curves for magnets magnetized at 400, 700, and 1100 V are more consistent than those obtained by using the circular fixture. With the help of the backyoke, the bonded magnets saturate at 400 V. The absolute value of magnetic strength averaged for the three applied voltages is 735 G at the peak position and 610 G at the valley position. Again, some portion of the deviation between curves comes from the ferrite inhomogeneity. Typically, the inhomogeneous mixing of ferrite in the bonded magnets can cause ± 27 G deviation from the averaged values measured from 15 measurements. Because the magnets are easily handled when using the planar fixture, there is a practical advantage to use the planar fixture for mass production.

Figure 6 shows the measured profiles when the magnets were magnetized by using the planar iron fixture without an iron backyoke. The saddle pattern, similar to Fig. 3, has a deep valley at each pole in contrast to a shallow valley in Fig. 5. The average absolute values of magnetic strength at the valley position for 400, 700, and 1100 V are 215, 481, and 602 G, respectively. However, the magnetic strengths at the peak positions are approximately equal to each other. The average maximum is 730 G which is close to the 735 G obtained when using a backyoke. Magnetizing voltages of 1100 V or above are needed to saturate the bonded magnet when magnetized using the planar iron fixture without an iron backyoke.

An important point for the practical use of these magnets is that there should be no magnetic degration when winding the magnetized strip into a ring. To examine this point, a magnet magnetized at 900 V was repeatedly wound and stretched and the magnetic profile was recorded. Figure 7 shows the result. Both peak and valley field values are located around their average values within the experimental error of about ± 10 G. The magnets show no magnetic degradation after 800 repeat windings and stretchings.

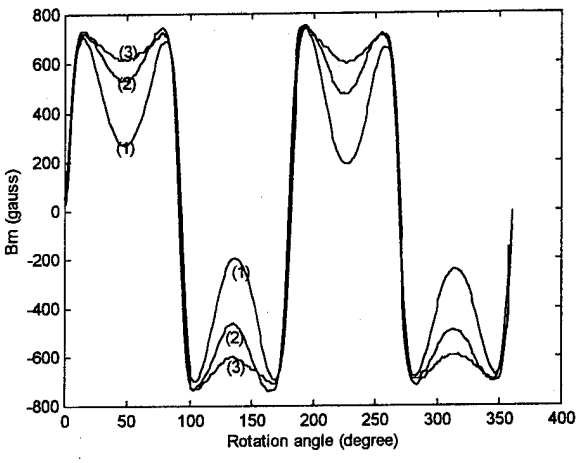


FIG. 6. Magnetization profiles after using a planar fixture without an iron backyoke. The applied voltages shown here are 400 V (1), 700 V (2), and 1100 V (3).

[1] G. X. Huang, W. M. Gau, and S. F. Yu, Proceedings of the Tenth International Workshop on RE Magnets and their Applications, Kyoto, Japan 1989 (unpublished), Part 1, p. 569.
[2] T. Nakada, N. Takahashi, and K. Uehara, IEEE. Trans. Magn. **MAG-22**, 1084 (1986).
[3] T. F. Ying, H. J. Tseng, M. D. Wu, and D. R. Huang, 13th International Workshop on RE Magnets and their Applications, Birmingham, UK 1994 (unpublished), p. 699.

Magnetic multipole cylinders from mould-injection $Nd_2Fe_{14}B$ plastic bonded magnets (abstract)

G. K. Nicolaides[a] and D. Niarchos
IMS, NCSR "Demokritos", Aghia Paraskevi 153 10, Athens, Greece

D. Tsamakis and I. Koubouros
Department of Electrical Engineering, NTUA, Zografou 15773, Athens, Greece

A. Mitsis
Department of Physics–Chemistry, TEI of Pireaus, 122 44, Athens, Greece

Mould injection $Nd_2Fe_{14}B$ magnetic material of density $\rho \sim 4$ g/cc and of an energy product $(BH)_{max} \sim 4$ MGOe, has been pressed into the form of cylindrical segments in order to investigate the possibility of preparing cylindrical magnetic multipoles which could be used as magnetic gears. The obtained cylindrical bonded magnet segments have a length of 3 cm and an angle width of $\varphi = 90°$ or $\varphi = 45°$. These segments are easily magnetized along a radial direction at the angle $\varphi/2$, using a conventional electromagnet at a magnetic field of 2 T. Subsequently, the opposite magnetized segments are combined and bonded together with ultrasonic technique. The final result of the above procedure is the formation of a magnetic multipole cylinder which could be used as a magnetic gear. Here, except the preparation technique, we report the maximum torque applied versus the magnetization M of the poles and the distance between the gears. The dependence of the applied torque on the rotational frequency is also examined. © *1996 American Institute of Physics.*
[S0021-8979(96)65108-1]

This work is supported by PETALPLAST S.A., Kontoni 12, Moshato 18346, Greece and Hellenic General Secretariat for Research and Technology, Pave 92/325.

[a]Also at Department of Physics–Chemistry and Technology of Materials, TEI of Pireaus, Aegaleo 122 44, Athens, Greece.

 0021-8979/96/79(8)/5563/1/$10.00 © 1996 American Institute of Physics

Structure and magnetic moment of α''-$Fe_{16}N_2$ compound films: Effect of Co and H on phase formation (invited)

Migaku Takahashi, H. Takahashi, H. Nashi, H. Shoji, and T. Wakiyama
Electronic Engng., Tohoku University, Sendai 980-77, Japan

M. Kuwabara
Kobe Steel USA Inc., Palo Alto, California 94304

In order to determine the intrinsic value of magnetic moment, σ_s, of α''-$Fe_{16}N_2$ compound, the magnetic moment of $(\alpha''+\alpha')$-$Fe_{16}N_2$ films is discussed in connection with the degree of N site ordering in nitrogen–martensite. To establish the more general relation between Fe–N martensite structure and σ_s, the Fe–N system is expanded to Fe–Co–N and Fe–H–N systems. As a result, it is found that (1) The existence of completely the same structure as bulk α'' phase was reconfirmed even in the film form by the precise structural analysis using x-ray diffraction, transmission electron microscopy and Mössbauer analysis, (2) Fe–H martensite was synthesized by using sputtering under $Ar+H_2$ atmosphere, (3) Stable formation of α''-$(Fe_{100-X}Co_X)_{16}N_2$ ($X=10$–30) phase through N site ordering by postannealing is proposed to be fairly difficult due to the sudden decrement of the phase decomposition temperature, $T_{p.d.}$, of α'-$(Fe_{100-X}Co_X)$–N ($X=0$–30). $T_{p.d.}$ of α'-$(Fe_{100-X}Co_X)$–N ($X=0$–30) phase decreases from 200 °C to RT with increasing Co and N contents, and (4) The intrinsic value of saturation magnetization of the α''-$Fe_{16}N_2$ phase is convinced to be no more than 240 emu/g (≈2.4 μ_B per Fe atom on average) at 300 K. © *1996 American Institute of Physics.* [S0021-8979(96)15508-9]

I. INTRODUCTION

"Giant Moment or Not" in α''-$Fe_{16}N_2$ compound, which is initially proposed by the present authors[1–3] and Coey's group[4,5] against the original report by Kim and Takahashi[6] in 1972, caused a great sensation in magnetism. Some experimentalists still believe the appearance of giant magnetic moment about 2.9T[7–9] in this compound. However, the experimentally proposed values of magnetic moment, σ_s, in α''-$Fe_{16}N_2$ phase by various research groups vary widely from 240 to 315 emu/g.[1–11] Therefore, many magneticians, including theoreticians, have wondered whether one is looking "at revolutionary results or egregious errors."[4]

This physically chaotic situation of σ_s is mainly caused by (1) ambiguity in phase identification of α''-$Fe_{16}N_2$ compound, (2) The unreliable method for fixing the volume fraction of α'' phase in whole films, and (3) lack of exactness in the values of σ_s for other Fe nitrided phases (γ'-Fe_4N and γ-austenite) used in the calculation to determine the σ_s of the α''-$Fe_{16}N_2$phase.

In order to determine the exact σ_s of α'' phase without any ambiguity, Fe nitrided films consisting of α'' single phase are essentially required. From this standing point of view, present authors have developed the precise experiments to synthesize α''-$Fe_{16}N_2$ single phase film (without the α'-$Fe_{16}N_2$ phase).[1–3,12–14] For reliable phase identification, a transmission electron microscopy (TEM) experiment is carried out to ensure the lattice constants and the crystal morphology of the α''-$Fe_{16}N_2$ phase which have been already recognized by former x-ray defraction (XRD) experiment.[1–3] Furthermore, in order to make clear the more precise environment of Fe atoms in body-centered-tetragonal (bct) structure, Mössbauer analysis was also carried out to detect three hyperfine field interactions due to three different Fe sites in bct lattice.

While, for determination of σ_s of α''-$Fe_{16}N_2$ phase by using the net value of σ_s of whole films consisting of a phase mixture, the exact volume fraction of the α'' phase in whole films should be necessary. Up to now, for the estimation of the volume fraction of α'' phase in whole samples, Wallace *et al.*[8] simply adapted the XRD analysis, Gao *et al.* adapted statistical single grain nano probe electron diffraction analysis[9] and the others[1–3,5,10,14] used Mössbauer analysis. However, XRD analysis, which probes the surface region of the powder sample, is considered unsuitable for this purpose. Especially, for films, preferred grain orientation of the films disturb the exact derivation of the volume fraction of α'' phase in the whole films. On the other hand, Mössbauer analysis, which probes all environment of Fe atoms in the films, is more suitable for this estimation. In our study,[3] to determine the exact volume fraction of the $(\alpha'+\alpha'')$-$Fe_{16}N_2$ phase in the whole film, successive experiments of conversion electron Mössbauer analysis was carried out. Through the systematic experimental results mentioned above, we concluded that the intrinsic saturation magnetic moment in α''-$Fe_{16}N_2$ phase should be no more than 240 emu/g.[1–3]

In the present study, in order to see the more general relation between Fe–N martensite structure and σ_s, the Fe–N system is expanded to Fe–Co–N and Fe–H–N systems.

Based on the results for the various nitrogen martensites, the magnetic moment of α''-$Fe_{16}N_2$ films is discussed in connection with the change of unit-cell volume of the bct struc-

 0021-8979/96/79(8)/5564/6/$10.00 © 1996 American Institute of Physics

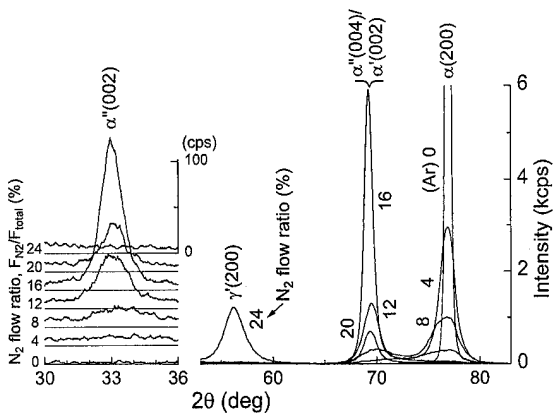


FIG. 1. X-ray diffraction patterns for the Fe–N films fabricated under different N_2 flow ratio (after anneling 150 °C for 2 h.).

ture and the degree of N site ordering in nitrogen martensite.

II. EXPERIMENTAL PROCEDURE

The precise experimental conditions for film fabrication, structure analysis, and magnetization measurement are given in the previously reported articles.[1–3,15]

III. RESULTS AND DISCUSSION

A. Phase formation

1. α', α''-$Fe_{16}N_2$ films

In Fig. 1, typical changes of XRD patterns of the films prepared under $P_{total}=10$ m Torr, deposition rate=240 Å/min after annealing at 150 °C for 2 h are shown. After annealing, the diffracted line from (002) plane of α' phase, $\alpha'(002)$, which had been observed in an as-deposited state, splits into two diffracted lines. One corresponds to $\alpha''(004)$ and/or $\alpha'(002)$ with satisfying stoichiometric N content of α''-$Fe_{16}N_2$ (11 at. %). The other corresponds to $\alpha(002)$ of slightly deformed α-Fe. For the film prepared under N_2 flow ratio of 16%, diffracted intensity from $\alpha(002)$ becomes zero

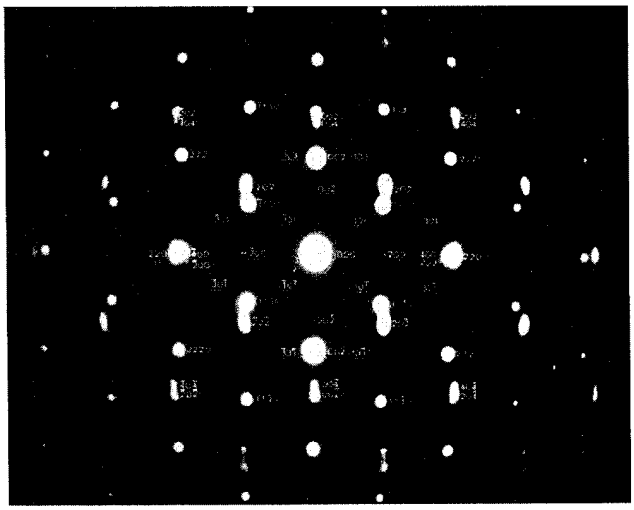


FIG. 2. Electron diffraction pattern of α''-$Fe_{16}N_2$ film annealed at 150 °C for 2 h. M and α correspond to reflections of MgO and α-phase, respectively. Indexes with underline correspond to superlattice reflections of α'' phase.

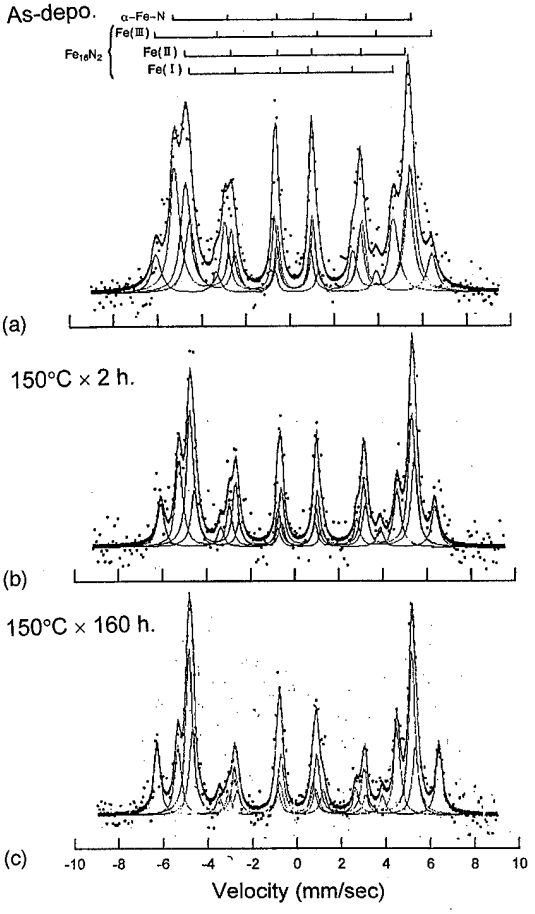


FIG. 3. Mössbauer spectra of $(\alpha''+\alpha')$-$Fe_{16}N_2$ film (non-Cu coated) measured at RT (a) as-deposited, (b) annealed at 150 °C for 2 h, and (c) annealed at 150 °C for 160 h, respectively.

and only diffracted line of $\alpha''(004)$ was found (nearly α'' single phase). Furthermore, simultaneously at around 33° of 2θ, $\alpha''(002)$ which is the unique diffracted line from the α'' phase, comes to be clearly observed. This means that the ordering of N atoms was promoted by annealing while retaining the bct structure and the α'' phase with stoichiometric N content was synthesized.

To confirm the phase formation of α''-$Fe_{16}N_2$ in real films in more detail, x-ray diffraction was made for the lattice plane including a axis of the bct unit cell. The unique diffractions from (103), (105), (112), (114), and (213) planes of the α'' phase, including the a axis for $(\alpha''+\alpha')$-$Fe_{16}N_2$ film, are clearly observed.[1–3] Therefore, the existence of the α'' phase is reconfirmed by these clear unique diffracted lines. The values of the lattice constants a and c of the present films coincided with reported values of the α''-$Fe_{16}N_2$ precipitates in bulk powder.[16]

Figure 2 shows the electron diffraction pattern of the α''-phase film annealed at 150 °C for 2 h. The superlattice reflections from (200), (002), (101), (110), (301), and (103) of α'' phase are clearly observed, accompanied with the extra diffractions from α-Fe. By using these superlattice reflections, determined values of lattice constants a and c of the α'' phase are almost equal to the results obtained by XRD analysis.

Figure 3 shows the changes of Mössbauer spectra of the

TABLE I. Time dependence of the Mössbauer parameters for the $Fe_{16}N_2$ films.

Site	Hi (kOe)	I.S. (mm/s)	e.q.Q. (mm/s)	W_{wid} (kOe)	Area (%)
Fe(I)	289	0.0101	−0.05	7.00	21.3
Fe(II)	316	0.1656	0.04	7.00	31.3
Fe(III)	391	0.1070	−0.05	7.00	11.2
α-Fe–N (As-deposited)	335	0.0197	−0.007	7.00	36.1
Fe(I)	289	0.0101	−0.05	4.00	17.8
Fe(II)	316	0.1656	0.04	4.00	41.8
Fe(III)	391	0.1070	−0.05	4.00	13.1
α-Fe–N (Annealed at 150 °C for 2 h)	335	0.0197	−0.007	4.00	27.3
Fe(I)	290	0.0239	−0.04	2.50	22.4
Fe(II)	316	0.1652	0.03	2.50	42.3
Fe(III)	400	0.1431	−0.06	2.50	17.4
α-Fe–N (Annealed at 150 °C for 160 h)	336	0.0250	−0.002	2.50	17.9

$Fe_{16}N_2$ film with stoichiometric N content by annealing. The fitted Mössbauer parameters are listed in Table I. The spectrum in each film can be fitted into four hyperfine field interactions of H_i. One is H_i of the α-Fe–N phase (I.S. value differs slightly from that of pure α-Fe) and the others are that of Fe(I), Fe(II), and Fe(III) of three different Fe sites for the $(\alpha''+\alpha')$-$Fe_{16}N_2$ phase. The site population of the $(\alpha''+\alpha')$-$Fe_{16}N_2$ phase after annealing 160 h is about 4:7.6:3.2, which is close to the ideal ratio of 4:8:4 determined uniquely from the structure factor of α''-$Fe_{16}N_2$. Half width of the peaks become narrower with increasing annealing time. This result corresponds to the promotion of N site ordering in nitrogen martensite caused by annealing. The volume fraction of the $(\alpha''+\alpha')$-$Fe_{16}N_2$ phase is estimated about 82% after annealing for 160 h.

It is concluded that even in present sputtered films, α'' phase with completely the same structure as precipitates in bulk powder is formed.

2. α', α''-$Fe_{16}(N\text{-}H)_2$ films

Here, turning around the previous experiments concerning Fe nitrided films and powders with giant magnetic moment, we can find experimental conditions in common that in most cases samples were synthesized by using NH_3 gas.[7,8,11] Therefore, it is interesting to know how the nitriding process of Fe atoms was changed by using reactive sputtering under N_2+H_2 mixtured atmosphere. In this section, in order to clarify the role of H atoms for the nitriding process, H_2 gas was introduced into the $Ar+N_2$ atmosphere during film fabrication. The effect of doping of hydrogen on the phase formation of Fe nitrided phase is discussed.

Figure 4 shows the changes of x-ray diffraction patterns for Fe–H films prepared under $Ar+H_2$ atmosphere with different H_2 flow ratio. Only the diffracted lines from (002) plane of α' phase were detected at around 2θ of 74–78°. These diffracted lines shift to low angle of 2θ with increasing H_2 flow ratio. Namely, lattice spacing of (002) plane of α' increases with increasing H_2 flow ratio. Axial ratio, c/a, determined by using the Schultz reflection method, takes constant value about 1.01 up to 60% H_2 flow ratio and increases slightly up to 1.02 around 95% H_2 flow ratio. It is noted here that even in the films prepared under $Ar+H_2$ atmosphere, bct structure with slight deformation from α-Fe was realized in the same way as films sputtered under $Ar+N_2$ atmosphere.

Figure 5 shows x-ray diffraction patterns for films (as-deposited) fabricated under $Ar+N_2$ atmosphere (Ar:1.8 ccm, N_2:0.2 ccm) and under the $Ar+N_2+H_2$ atmosphere (Ar:1.8 ccm, N_2:0.2 ccm; H_2:8.0 ccm), respectively. Here, the same deposition rate was adapted between two different sputtering atmospheres, since the degree of nitriding of Fe strongly depends on the deposition rate. As seen in Fig. 5, for the films prepared under $Ar+N_2$ atmosphere without H_2 gas, the diffracted line from α' phase was detected. On the other hand, contrary to the film prepared under $Ar+N_2$ atmosphere with H_2, the diffracted lines from γ'-Fe_4N and α'-$Fe_{16}N_2$ phase were clearly observed. This fact means that the adding of H_2 gas into $Ar+N_2$ atmosphere during sputtering makes nitriding of Fe atoms accelerate.

3. α', α''-$(Fe_{100-x}Co_x)_{16}N_2$ films

In the Fe–Co binary alloy system, it is known that (1) bcc structure is stably formed up to the composition of 75 at. % Co at RT, that (2) lattice constant a of Fe–Co alloys shows almost constant value up to Co content of 30 at. %,

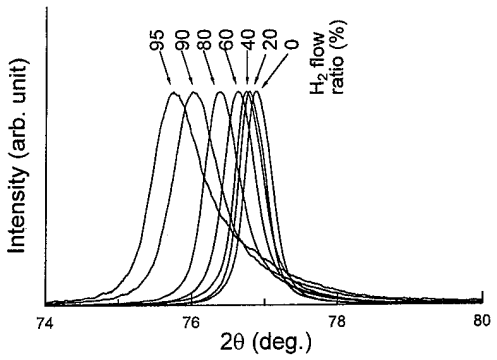


FIG. 4. X-ray diffraction patterns for the Fe–H films fabricated under various H_2 flow ratio.

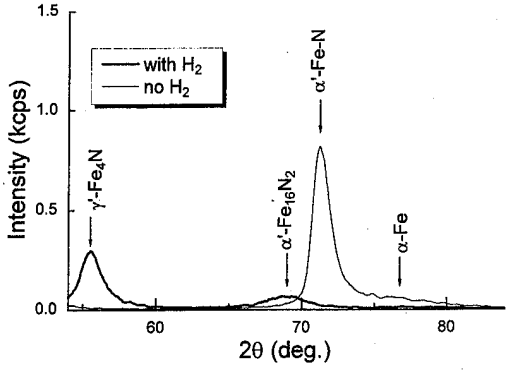


FIG. 5. X-ray diffraction patterns for sputtered films fabricated under $Ar+N_2$ atmosphere (Ar:1.8 ccm, N_2:0.2 ccm) and $Ar+N_2+H_2$ atmosphere (Ar: 1.8 ccm, N_2:0.2 ccm, H_2:8.0 ccm), respectively.

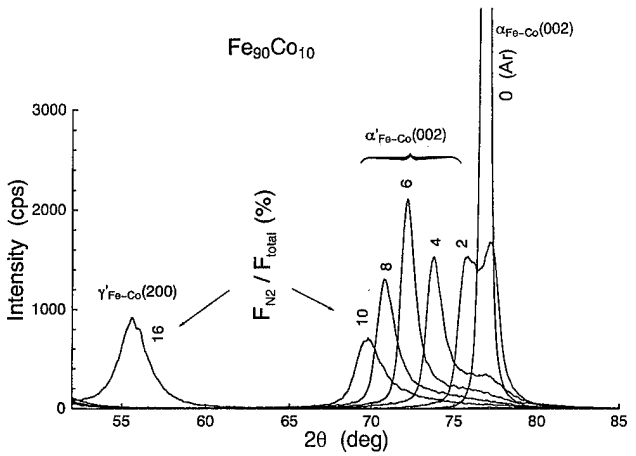


FIG. 6. X-ray diffraction patterns for $Fe_{90}Co_{10}$–N films (as-deposited state) fabricated under different N_2 flow ratio.

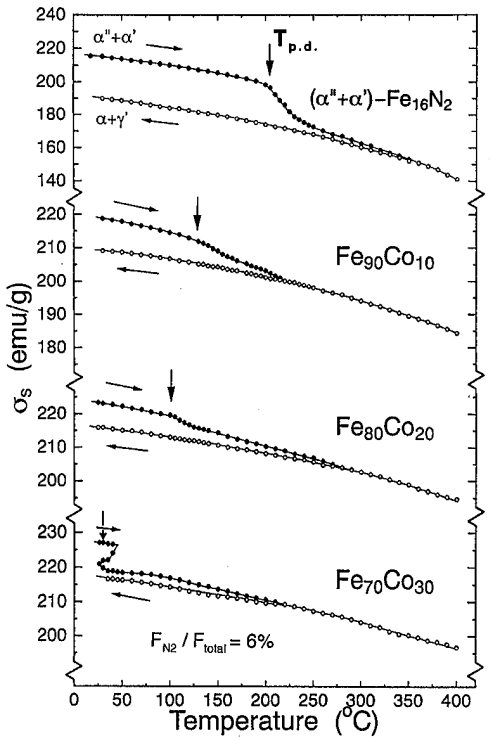


FIG. 7. Temperature dependence of σ_s for the α'-$(Fe_{100-X}Co_X)$–N (X=10–30) films fabricated under N_2 flow ratio of 6%.

and that (3) the magnetic moment of Fe–Co alloys increases with increasing Co content and takes a maximum of 2.46 μ_B at 30 at. % Co.[17] By considering the above physical properties of Fe–Co alloys, it seems to be able to synthesize α''-$(Fe_{100-x}Co_x)_{16}N_2$ in the same way as Fe–N films. From the physical standing point of view, it is interesting to know that (1) change of σ_s as a function of Co content for α''-$(Fe_{100-x}Co_x)_{16}N_2$, and that (2) the giant magnetic moment proposed up to now for α''-$Fe_{16}N_2$ phase is induced or not for α''-$(Fe_{100-X}Co_X)_{16}N_2$ films.

In this section, the possibility of the formation of α' and α''-$(Fe_{100-X}Co_X)_{16}N_2$ (X=0–30) phase with stoichiometric N content is discussed as a function of Co content.

As an example, in Fig. 6, the changes of the x-ray diffraction patterns as a function of N_2 flow ratio, F_{N2}/F_{total}, for $(Fe_{90}Co_{10})$–N films in an as-deposited state was shown. The diffraction line from (002) of α'-$(Fe_{90}Co_{10})$–N phase [$\alpha'_{\text{Fe-Co}}(002)$] with various N content up to stoichiometric N content of 11 at. % were clearly detected. On the other hand, in the case of $(Fe_{70}Co_{30})$–N films, the intensity of diffraction line from $\alpha'_{\text{Fe-Co}}(002)$ becomes to be weak with increasing F_{N2}/F_{total}, and the diffracted line from $\alpha_{\text{Fe-Co}}(002)$ gradually appears. Namely, α'-$(Fe_{70}Co_{30})$–N phase was formed up to 4 at. %, however α'-$(Fe_{70}Co_{30})$–N with stoichiometric N content of 11 at. % was not synthesized.

In Fig. 7, temperature dependencies of σ_s for the α'-$(Fe_{100-X}Co_X)$–N (X=10–30) films fabricated under F_{N2}/F_{total} of 6% are shown. These films consist of nearly α' single phase with various N content of 4–8 at. %. In Fig. 7, the temperature dependence of σ_s for $(\alpha''+\alpha')$-$Fe_{16}N_2$ film (11 at. % N) annealed after 150 °C for 2 h is also shown for comparison.

As reported in previous articles,[2–4] in the case of the $(\alpha''+\alpha')$-$Fe_{16}N_2$ film, the value of σ_s decreases monotonously with increasing measuring temperature. Around 200 °C a sudden discontinuous decrease of σ_s was observed. From XRD analysis this discontinuous change of σ_s corresponds to the phase decomposition from $(\alpha''+\alpha')$-$Fe_{16}N_2$ phase to α-Fe and γ'-Fe_4N phases. While in the case of α'-$(Fe_{100-X}Co_X)$–N (X=10–30) films, similar discontinuous changes of σ_s against measuring temperature were also observed. These discontinuous changes also correspond to the phase change from α'-$(Fe_{100-X}Co_X)$–N to α-$(Fe_{100-X}Co_X)$+γ'-$(Fe_{100-X}Co_X)_4N$. However, it should be noted here that the temperature where the phase decomposition takes place decreases with increasing Co content from 200 °C for $(\alpha''+\alpha')$–Fe–N martensite to 100 °C for α'-$(Fe_{80}Co_{20})$–N film and RT for $(Fe_{70}Co_{30})$–N film, respectively. This means that the phase decomposition temperature of α'-$(Fe_{100-X}Co_X)$–N (X=0–30) phase strongly depends on Co content.

In Fig. 8, the phase decomposition temperature, $T_{\text{p.d.}}$, from α'-$(Fe_{100-X}Co_X)$–N martensite phase to α-$(Fe_{100-X}Co_X)$ and γ'-$(Fe_{100-X}Co_X)_4N$ was replotted against Co content. For the films prepared under the same F_{N2}/F_{total}, $T_{\text{p.d.}}$ decreases with increasing Co content. While for the films with the same Co content, $T_{\text{p.d.}}$ also decreases with increasing F_{N2}/F_{total}. In other words, the phase decomposition temperature, $T_{\text{p.d.}}$ strongly depends not only on Co content but also on N content in α'-(FeCo)–N phase. Therefore it is concluded that stable formation of α''-$(Fe_{100-X}Co_X)_{16}N_2$ (X=10–30) phase through the ordering process of N atoms by postannealing is fairly difficult in the Fe–Co alloy system.

B. Magnetic moment

1. Dependence of magnetic moment on unit-cell volume

Figure 9 shows the changes of σ_s against unit-cell volume of the α' phase with various N contents in an as-deposited state. In Fig. 9, 1/8 of the unit-cell volume of the

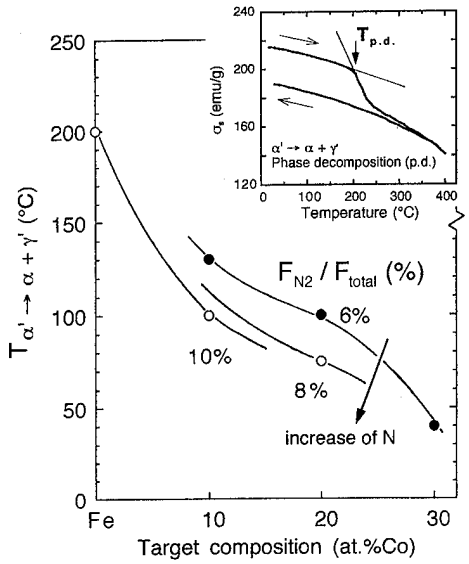


FIG. 8. The changes of phase decomposition temperature, $T_{p.d.}$ (α'-($Fe_{100-X}Co_X$)–N→α-($Fe_{100-X}Co_X$)+γ'-($Fe_{100-X}Co_X$)$_4$N) against Co content.

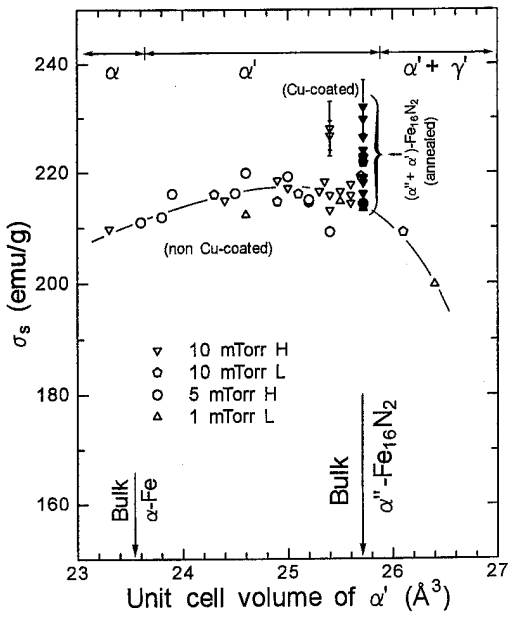


FIG. 9. Changes of σ_s as a function of unit-cell volume: (1) α' phase with various nitrogen contents in an as-deposited state, and (2) annealed ($\alpha''+\alpha'$)-$Fe_{16}N_2$ films with and without Cu coating. *H* and *L* correspond to high (240 Å/min) and low (33 Å/min) deposition rates, respectively.

α''-$Fe_{16}N_2$ phase is indicated. Filled marks correspond to the annealed ($\alpha''+\alpha'$)–$Fe_{16}N_2$ films with stoichiometric N content. In the same figure, σ_s for the Cu-coated films are also shown.

For the films consisting of α' single phase (in an as-deposited state), the values of σ_s increase slightly with the increment of the unit-cell volume. At the unit-cell volume of about 25.5 Å^3 (α' phase with 11 at. % N), σ_s showed 228 emu/g on average (Cu coated) and this value is about 4% higher compared to that of bulk α-Fe.

In the case of annealed ($\alpha''+\alpha'$)-$Fe_{16}N_2$ films (Cu coated), the value of σ_s shows 232 emu/g on average, and are about 2% larger than that of each as-deposited film, while the unit-cell volume of the α'' phase is always constant and coincided with that of the bulk α'' phase. The unit-cell volume of the α'-Fe–N phase with 11 at. % N is equal to that of the α''-$Fe_{16}N_2$ phase within the accuracy of this experiment. Therefore the change of σ_s by annealing in nitrogen–martensite with 11 at. % N content cannot be discussed as a function of the change of unit-cell volume of a bct structure caused by the phase transition from α' to α'' phase.

2. Dependence of magnetic moment on N site ordering

To evaluate the degree of N site ordering in the bct structure of nitrogen–martensite, two factors should be taken into account. One is the change of the integrated intensity of the $\alpha''(002)$ line which is the unique superlattice diffraction from the α'' phase. Another is the integrated intensity ratio of $\alpha''(004)+\alpha'(002)$ to $\alpha''(002)$, R_1, namely

$$R_1 \equiv [I^{\alpha''}{}_{(004)} + I^{\alpha'}{}_{(002)}]/I^{\alpha''}{}_{(002)} \quad (1)$$

The calculated value of R_1 is about 8 for the ideal structure of the α'' phase.

Figure 10 shows the change of XRD profiles against annealing time for the film with stoichiometric N content of the $\alpha''+\alpha'$ phase (11 at. %). From these profiles, any diffraction lines from α and γ' phases are not observed. After annealing for 2 h, $\alpha''(002)$ comes to be observed clearly. With increasing annealing time, the integrated intensity of $\alpha''(002)$ increases. On the other hand, the experimentally determined value of R_1 changes from 50 to about 15 with increasing annealing time.

Therefore, from these experimental results (1) the increase of the integrated intensity of $\alpha''(002)$ and (2) the change of R_1 approaching to the ideal value of 8, the increment of degree of N site ordering in nitrogen–martensite, which directly corresponds to the increase of the volume fraction of the α'' phase in the films, is strongly promoted by annealing.

In Fig. 11, the changes of σ_s in ($\alpha''+\alpha'$)–$Fe_{16}N_2$ films by isothermal annealing at 150 °C are shown against the integrated intensity ratio R_1. The increment of σ_s does not show any drastic changes against R_1 even though R_1 approached to the value of 8. Only σ_s increases slightly about 3% by annealing. However, with further increasing annealing time, in all cases, from these experimental facts, it was found that the degree of N site ordering in nitrogen–martensite does not much affect the increment of σ_s. The expected values of σ_s at R_1=8 (perfect ordered state in α''-$Fe_{16}N_2$) estimated by the simple extrapolation using these data points of σ_s against R_1 are no more than 240 emu/g, which is definitely smaller than the giant magnetic moment of 2.9 T (≈315 emu/g).

On the other hand, as seen in the fitted Mössbauer parameter shown in Table I, for the present films, the average value of H_i was about 325 kOe, which is nearly equal to that of H_i of α-Fe. Therefore, the value of σ_s in ($\alpha''+\alpha'$)-$Fe_{16}N_2$ film of about 232 emu/g determined by vibrating-sample magnetometer (VSM) was consistent with the result of

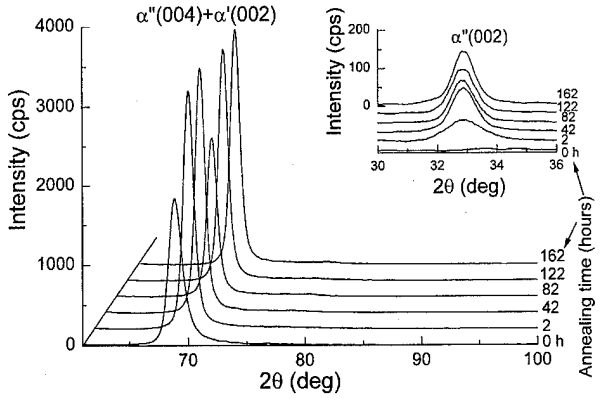


FIG. 10. The change of x-ray diffraction patterns as a function of annealing time for the film with stoichiometric N content of the α'' phase (11 at. % N).

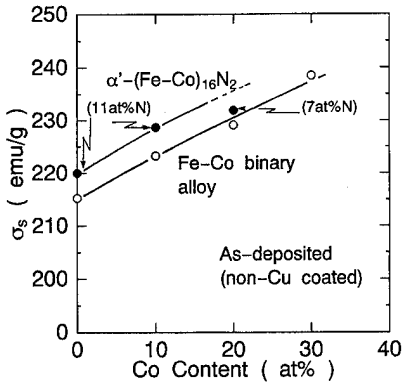


FIG. 12. The changes of σ_s against Co content for α'-$(Fe–Co)_{16}N_2$ films.

Mössbauer spectrum analysis. Based on the fitted Mössbauer parameters, the volume fraction of $(\alpha''+\alpha')$-$Fe_{16}N_2$ in annealed films is estimated to be 82%. Using these experimental values, the value of σ_s in the $(\alpha''+\alpha')$-$Fe_{16}N_2$ phase, σ_{Fe16N2}, is estimated by the following equation:

$$232^{exp}=\sigma_{Fe16N2}\times 0.82+\sigma_{\alpha\text{-}Fe}\times 0.18, \quad (2)$$

where $\sigma_{\alpha\text{-}Fe}$ is 218 emu/g. The obtained value of σ_{Fe16N2} is 235 emu/g.

Considering this calculated result and the result of the dependence of σ_s on R_1, we can conclude that the value of saturation magnetization of the α'' phase (perfect order state) should not be exceed more than 240 emu/g, which agrees well with the result of the recent theoretical band calculation.[18]

3. Dependence of magnetic moment on Co content

Figure 12 shows the change of σ_s for α'-$(Fe–Co)_{16}N_2$ films in an as-deposited state (non-Cu coated) against Co content. In Fig. 12 the change of σ_s for Fe–Co binary alloy film against Co content was also shown for comparison. As mentioned in the previous section of this article, for the films with Co content up to 10 at. %, α'-(Fe–Co)–N with stoichiometric N content of 11 at. % was synthesized. However, for the film with Co content of 20 at. %, α' phase up to about

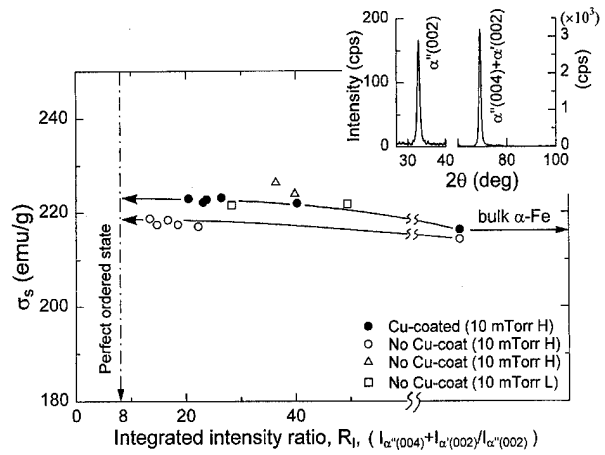


FIG. 11. The changes of σ_s against R_1 for the $Fe_{16}N_2$ films.

7 at. % N was synthesized. However, α' with stoichiometric N content could not be synthesized. Therefore, in Fig. 12, as a reference, the value of σ_s for α'-$Fe_{80}Co_{20}$–N film with N content of 7 at. % was shown.

For the Fe–Co binary alloy films prepared in pure Ar plasma (non-Cu coated), σ_s increases from about 215 to 240 emu/g with increasing Co content. This dependence of σ_s on Co content coincides with the well-known Slater–Pauling curve. While the values of σ_s for α'-$(Fe_{100-x}Co_x)$–N with stoichiometric N content of 11 at. %, films show 220 emu/g for $X=0$ and 228 emu/g for $X=10$. For α'-$(Fe_{80}Co_{20})$-N film with 7 at. % N, σ_s shows 232 emu/g. This dependence of σs on Co content in α'-$(Fe_{100-X}Co_X)$–N with stoichiometric N content of 11 at. % is completely the same as that of Fe–Co binary alloy films. In the increment of σ_s only about 3% is observed.

Judging from the dependence of σ_s for α'-(Fe–Co)–N films with stoichiometric N content of 11 at. % on Co content, we can conclude again that the value of intrinsic saturation magnetization of α''-$Fe_{16}N_2$ phase should be no more than 240 emu/g.

[1] M. Takahashi, H. Shoji, H. Takahashi, T. Wakiyama, M. Kinoshita, and W. Ohta, IEEE Trans. Magn. **MAG-29**, 3040 (1993).
[2] M. Takahashi, H. Shoji, H. Takahashi, and T. Wakiyama, Proceedings of the 3rd IUMRS International Conference on Advanced Materials, Tokyo, 1994 (unpublished), Vol. 15 B, p. 839.
[3] Migaku Takahashi, H. Shoji, H. Takahashi, H. Nashi, T. Wakiyama, M. Doi, and M. Matsui, J. Appl. Phys. **76**, 6642 (1994).
[4] J. M. D. Coey, Phys. World, **6**, 25 (1993).
[5] J. M. D. Coey, J. Appl. Phys. **76**, 6632 (1994).
[6] T. K. Kim and M. Takahashi, Appl. Phys. Lett. **20**, 492 (1972).
[7] Yutaka Sugita, Hiromasa Takahashi, Matahiro Komuro, Katsuya Mitsuoka, and Akimasa Sakuma, J. Appl. Phys. **76**, 6637 (1994).
[8] W. E. Wallace and M. Q. Huang, J. Appl. Phys. **76**, 6648 (1994).
[9] C. Gao, W. D. Doyle, and M. Shamsuzzoha, J. Appl. Phys. **73**, 6579 (1993).
[10] K. Nakajima and S. Okamoto, Appl. Phys. Lett. **56**, 92 (1990).
[11] X. Bao, R. M. Metzger, and M. Carbucicchio, J. Appl. Phys. **75**, 5870 (1994).
[12] T. Tanaka, E. Fujita, M. Takahashi, T. Wakiyama, W. Ohta, and M. Kinoshita, J. Magn. Soc. Jpn. **14**, 265 (1990).
[13] T. Tanaka, E. Fujita, M. Takahashi, T. Wakiyama, W. Ohta, and M. Kinoshita, J. Magn. Soc. Jpn. **15**, 383 (1991).
[14] Migaku Takahashi, H. Shoji, and M. Tsunoda, J. Magn. Magn. Mater. **134**, 403 (1994).
[15] H. Shoji, H. Nashi, K. Eguchi, and M. Takahashi, (to be published).
[16] K. H. Jack, Proc. R. Soc. London Ser. A **208**, 216 (1951).
[17] R. M. Bozorth, *Ferromagnetism* (IEEE, New York, 1993).
[18] A. Sakuma, J. Magn. Magn. Mater. **102**, 127 (1991).

Electronic and magnetic structure of iron nitride, $Fe_{16}N_2$ (invited)

Akimasa Sakuma
Magnetic and Electronic Materials Research Laboratory, Hitachi Metals, Ltd., Mikajiri 5200, Kumagaya 360, Saitama, Japan

The result of spin-polarized band calculation for $Fe_{16}N_2$ is presented. The most distant Fe atoms from N is found to have the largest magnetic moment. The major role of the N atom is to expand the Fe lattice, leading to the enhancement of the magnetic moments. Quantitatively speaking, the calculated moment of $Fe_{16}N_2$ is about 2.4 μ_B which is much smaller than the measured value reported. It is also shown that the correction with the orbital magnetic moment and the generalized gradient approximation (GGA) cannot account for this discrepancy. From the point of view of the many body effects, a possibility of the giant moment is also discussed. An important feature of this model is a generation of hopping sites with the N atoms, which likely promotes a ferromagnetic coupling of Fe atoms keeping their large spin-polarization in the atomic limit. © *1996 American Institute of Physics.* [S0021-8979(96)10108-4]

I. INTRODUCTION

Until the early 1970s, the relationship between ferromagnetism and metal–nonmetal bonding of iron nitrides was the main subject of research for both theory and experiment.[1–9] In 1972, Kim and Takahashi[10] reported a giant magnetic moment in the Fe–N film. Since then, much work has been carried out on the magnetism in the compounds of the transition metals with the elements such as N, C, and B. The interest in such nitrogenated metals was further accelerated through the discovery of new hard magnetic materials, $Sm_2Fe_{17}N_x$ (Ref. 11) and $NdFe_{11}TiN$.[12] The work by Kim and Takahashi showed that their Fe–N film consisted of both Fe and $Fe_{16}N_2$.[13] Much effort has been made to reproduce their result, but there is difficulty because of the uncertainty in estimating accurate moments in multiphase materials. Therefore, some groups tried to prepare the single phase $Fe_{16}N_2$ with several techniques. In 1990, Komuro *et al.*[14] were first able to grow a single crystal $Fe_{16}N_2$ film onto InGaAs epitaxially by molecular beam epitaxy (MBE) technique. They obtained B_S of the $Fe_{16}N_2$ to be 2.8–3.0 T. Concurrently, Nakajima *et al.*[15] also succeeded in fabricating $Fe_{16}N_2$ films by ion implantation and measured the "average" magnetic moment of Fe atom to be about 2.5 μ_B. After all these pioneer works, many experimental studies were initiated to examine if the giant magnetic moment was really present or not.[16–19] Up till now, the data reported by several workers varies from one to another. Among them the moment measured by Takahashi *et al.*[17] was not high at all, but close to that of α–Fe. According to the recent data by Sugita *et al.*,[20,21] the average magnetic moment per Fe atom reaches about 3.5 μ_B at −268 C with help from site ordering of the N atoms in the Fe lattice. The data is apparently projected from one of the other iron nitrides. Therefore, it is very important to theoretically predict such an extremely large moment in $Fe_{16}N_2$ and to discuss how the magnetism of $Fe_{16}N_2$ is related to that of both N-martensite and other iron nitride compounds.

The band calculation for γ'–Fe_4N was carried out by Wei Zhou *et al.*,[22] and the present author[23] based on the local spin density functional theory. Also, the calculations for the $Fe_{16}N_2$ were performed by many workers.[24–33] These results indicate that the theoretical "average" moment per Fe atom is about 2.4–2.5 μ_B, except for one by Lai *et al.*,[32] which will be discussed later. Thus, the result based on the band calculation is at a variance with the experimentally obtained value of $Fe_{16}N_2$. In this paper, the results of the band calculation of $Fe_{16}N_2$ is presented. Further, the magnetism of the $Fe_{16}N_2$ is discussed on the basis not only of the improved band theory, but also of the many body scheme for a highly correlated system.

II. DENSITY OF STATES

First, discussion of the calculated density of states (DOS) of Fe–N in conjunction with the experimental results of the x-ray photoemission spectroscopy (XPS) data[9] is made. The DOS of Fe_4N in paramagnetic (spinless) state is shown in Fig. 1, where the dashed line is for fcc-Fe which leads to Fe_4N with inclusion of the N atom at the body center. The structure around −0.6 to −0.4 Ry in the DOS of

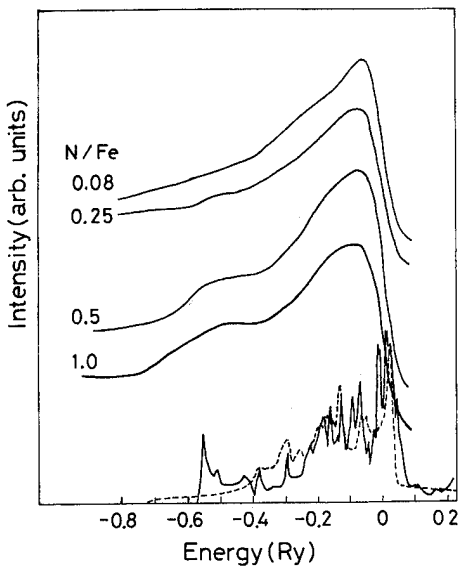


FIG. 1. Comparison of the density of states of paramagnetic Fe_4N (solid line), fcc-Fe (dashed line) and the photoemission data by Ertl *et al.* (Ref. 9). The zero on the energy scale corresponds to the Fermi energy, E_F.

 0021-8979/96/79(8)/5570/6/$10.00 © 1996 American Institute of Physics

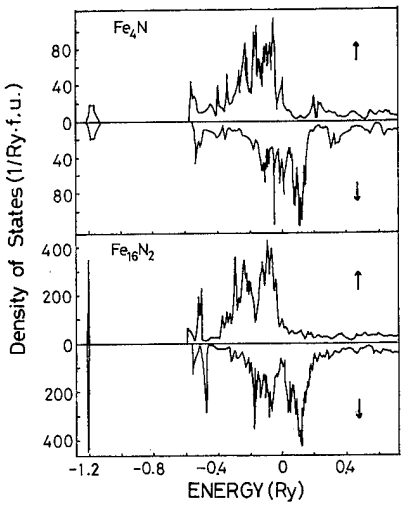


FIG. 2. Total density of states of Fe_4N (up) and $Fe_{16}N_2$ (down). The energy is measured with respect to the E_F.

Fe_4N is attributed to the N atom, which belongs mainly to the $2p$ states. Roughly speaking, both the energy position and the intensity of the N $2p$ state coincide with the observed XPS peak around -0.5 Ry which is enhanced with N concentration. This feature is also agreeable with DOS within accuracy. It should be noted that the peaked feature of DOS of Fe_4N at the Fermi level, E_F, is a consequence of the paramagnetic state, which means that the system is stabilized with a help of spin polarization.

Calculated results of the spin-polarized DOS of Fe_4N and $Fe_{16}N_2$ are shown in Fig. 2. The key features are common for all compounds as follows. The isolated structures located around -1.2 Ry are mainly due to $2s$ states of N. The main structures around the Fermi energy, E_F, are almost composed of $3d$, $4s$, and $4p$ states of Fe. The E_F's are pinned at around the dip position in down spin electron density of states, which makes these states stable with the help of spin polarization. As mentioned previously, the N $2p$ bands are found at about -0.6 Ry to -0.4 Ry below the $3d$ bands, which can be observed in XPS. Furthermore, Ertl's experimental results[9] that no change in the $3d$ bands occurs during nitration can be understood by noting that the features of $3d$ bands are nearly the same for these compounds.

III. MAGNETIC MOMENT

As previously reported,[23] the feature of local densities of states of each Fe in Fe_4N and $Fe_{16}N_2$ is considerably different depending on the site. It should be marked that the most distant Fe atoms from the N atom, FeI for Fe_4N and FeIII for $Fe_{16}N_2$, have the large $3d$ hole in the down spin states just above the E_F, while the up spin states of the sites are almost occupied. Actually, the local magnetic moments of these sites are the largest as shown in Table I which also gives several other calculated results for comparison. The electron numbers of these sites are found to be smaller about 0.3 to 0.6 than that of other sites. So it can be considered that the large moments of these sites are attributed mainly to the shortage of down spin electrons rather than the receipt of the up spin electrons. The variations of these charge distribution on each Fe site can be regarded as an effect of the N atom. Thus, the present result that the moments of FeI and FeII in $Fe_{16}N_2$ are nearly the same is due to the fact that the distances from the N atom are nearly the same for these sites.

Based on the above results, it should be noted that the most distant Fe atoms from the N atom have the largest magnetic moments for Fe_4N and $Fe_{16}N_2$. This is related to the bonding nature between N atom and surrounding Fe atoms. Actually, the variance of the moments on each Fe site has been shown to be brought about by the redistribution of the down spin electrons due to the electronic interference by the interstitial N atoms. This event reflects the relative arrangement of the Fe atoms against the N atoms in these compounds. According to Kanamori,[34] the elements such as B, C, and N enhance the magnetic moments of the next nearest neighboring Fe atoms. That is, the $3d$ levels, especially the down spin state of the nearest neighbor (NN) Fe atoms to the N atoms (Fe_{1st} in Fig. 3) are lowered through the hybridization with a part of the N $2p$ state located around the E_F and in turn the $3d$ down spin state of the next NN Fe atoms (Fe_{2nd} in Fig. 3) are raised conversely. As a result, the electrons mainly of the down spin states transfer from the next NN Fe atoms to the NN Fe atoms (see Fig. 3). This electronic bonding feature is strongly responsible for the variation of the local magnetic moments of each Fe site in the iron nitride system. Actually, the Mössbauer and neutron diffraction measurements for Fe_4N support the above picture

TABLE I. Calculated magnetic moment (in μ_B) on each Fe atom in $Fe_{16}N_2$.

	Present (LMTO)[a]	LMTO[b]	LMTO[c]	ASW[d]	FLAPW[e]	DV-Xα[f]	LMTO[g]	APW[h]	LMTO(LDA+U)[i]	OLCAO[j]
Fe I ($4e$)	2.27	1.96	2.13	2.30	2.04	1.71	2.21	2.00	2.36	2.06
Fe II ($8h$)	2.25	2.41	2.50	2.37	2.33	2.26	2.39	2.295	2.75	2.42
Fe III ($4d$)	2.83	2.91	2.85	2.74	2.82	2.87	2.81	2.757	3.53	2.90
N ($2a$)	-0.07		0.06	-0.01	-0.03			-0.043	-0.01	-0.06
Average/atom	2.39	2.42	2.50	2.42	2.37	2.27	2.45	2.403	2.85	2.44

[a]Reference 24.
[b]Reference 25.
[c]Reference 26.
[d]Reference 27.
[e]Reference 28.
[f]Reference 29.
[g]Reference 30.
[h]Reference 31.
[i]Reference 32.
[j]Reference 33.

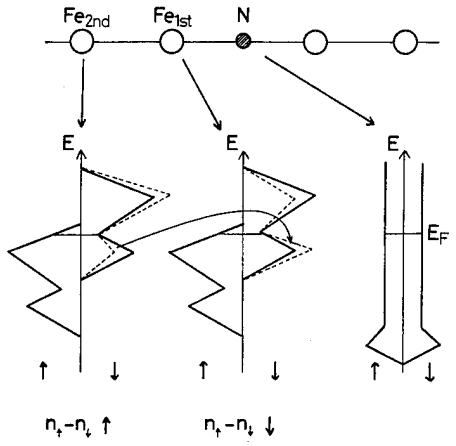


FIG. 3. The local DOS of Fe atoms are changed from solid lines to dashed lines with the inclusion of the N atom and, then the electrons mainly of the down spin states transfer from the Fe_{2nd} to the Fe_{1st}. As a result, the local magnetic moment of Fe_{2nd} is raised while one of Fe_{1st} lowers.

and the magnetic structure can be quantitatively reproduced by the present calculation.

As to the average moments, the present result indicates that the lattice expansion due to N atoms plays a major role in the enhancement of the magnetic moments. In Fig. 4, we give the average magnetic moment of each compound as a function of N concentration. Our calculated result for bcc Fe is also shown in the figure. Though the quantitative agreement with the experiments cannot be reached for $Fe_{16}N_2$, the dependence of the moments on the N concentration can be proved qualitatively. The behavior that the lower concentration of N atoms leads to larger magnetic moment may be understood by the following argument. An interstitial N atom expands the interatomic distance not only of the nearest neighboring Fe atoms but also of the next nearest neighboring and more distant Fe atoms for avoiding the lattice distortion. This certainly enhances the moments of the system even

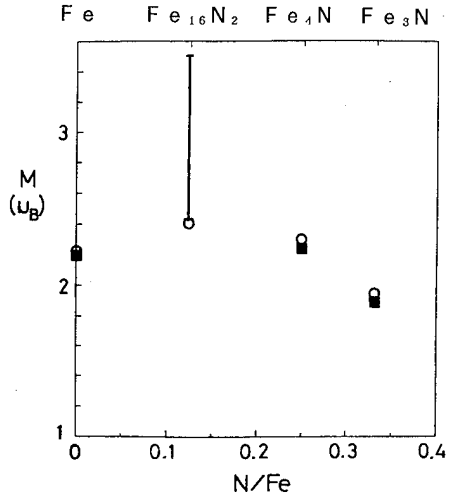


FIG. 4. N concentration dependence of the average magnetic moments of iron nitrides. The open circles indicate the calculated results, and the closed squares and the bar are from the measured values (from the data by Ref. 4 for Fe_3N, Ref. 6 for Fe_4N and Refs. 14–20 for $Fe_{16}N_2$).

TABLE II. Spin and orbital magnetic moments (μ_B) of $Fe_{16}N_2$ and bcc-Fe.

		spin	orbital
	Fe I	2.27	0.082
$Fe_{16}N_2$	Fe II	2.26	0.066
	Fe III	2.82	0.082
bcc-Fe		2.23	0.062

though the concentration of N atom is low. Additionally, as mentioned previously, the N atoms play a role as hopping sites for the electrons, which in turn prevents the exchange splitting concurrently. (Note that this may be inseparable from the charge redistribution which gives the variance of the local magnetic moments.) Eventually, it comes to the conclusion that a lower concentration of N atom is preferable for a larger magnetic moment.

IV. INSPECTION FOR THE MAGNETISM OF $Fe_{16}N_2$

For $Fe_{16}N_2$, the calculated magnetic moment is much smaller than the experimental value. A recent result by Sugita *et al.*[21] of $Fe_{16}N_2$ amounts to 3.5 μ_B at −268 °C. Thus, the magnetic aspect of $Fe_{16}N_2$ seems to be quite outstanding in the series of iron nitrides. In this section, we discuss the magnetism of the $Fe_{16}N_2$.

In Table II, we present the orbital moments of $Fe_{16}N_2$ calculated by introducing the spin–orbit interaction in the linear muffin-tin orbital (LMTO) Hamiltonian. The result for bcc Fe is also shown for comparison. Though the orbital moment of $Fe_{16}N_2$ is slightly larger than that of bcc Fe, it is still smaller, as compared to the case for usual transition metal systems. It is found that the orbital moment to the total cannot account for the discrepancy between theory and experiments. Actually, the g value of this film has been measured to be almost the same as one of bcc Fe.[35,36]

Further we tried a nonlocal correction to the local density approximation with use of generalized gradient approximation (GGA)[37] and obtained an increase of magnetic moment as much as about 0.1 μ_B per Fe atom. Thus, the nonlocal correction is also a minor contribution to the total magnetic moment.

Here let us turn to the foundation of the magnetism, apart from the band theory. The degree of spin polarization in solid is generally dominated mainly by a Coulomb repulsion acting selectively on antiparallel spins drawing near each other especially at around the nuclei. The Coulomb energy consumption for the parallel spins is much less because they are forbidden to draw near each other by the Pauli principle. The energy difference between the parallel and antiparallel spins leads to an exchange energy.

This mechanism can be connected to the Hund's rule in the atomic limit. According to this rule we expect 4 μ_B for an isolated Fe atom. Here, we are led to the question; is there any scenario to give a situation that Fe atoms form solid with keeping their magnetic moment close to 4 μ_B and with having ferromagnetic ordering? In the Hubbard model, an increase of the intra-atomic Coulomb interaction (U) comparing to the hopping integral (t) promotes a spin polarization

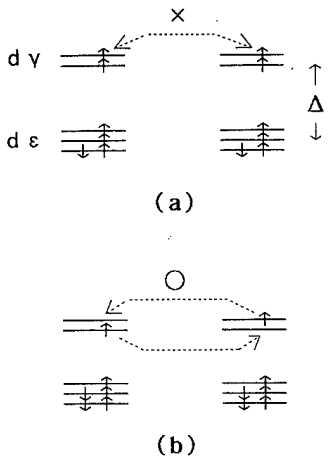


FIG. 5. Schematic representation of the electronic configuration in the d orbitals of Fe atom in the crystalline electric field (CEF) of bcc symmetry. (a) Fully spin-polarized case due to the Hund coupling, which can hardly make a ferromagnetic coupling with neighboring Fe atoms because of the Pauli principle. (b) Partially polarized case which allows ferromagnetic coupling with neighboring Fe atoms through electron hopping between $d\gamma$ orbitals.

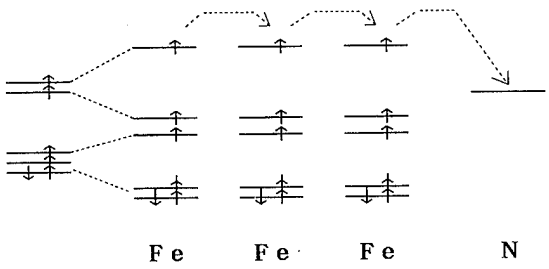


FIG. 6. Model presenting a mechanism for fully polarized ferromagnetic metal. With inclusion of the N atom in the Fe lattice, slight hole is created in one of the $d\gamma$ orbitals split further by the tetragonal distortion. This promotes a hopping of $d\gamma$ electrons and gives rise to the interatomic coupling, without destroying the Hund coupling acting within each Fe atom.

in the three-dimensional metallic system. The basic concept of Lai *et al.*[32] lies in this viewpoint. They postulated that the nitrogen atoms induce U on the Fe atoms.

Here, we try to focus on the other possible role of the nitrogen atom other than the enhancement of the U parameter. Consider a situation where the overlap of the Fe atomic wave functions is small enough in the bcc lattice. In this case, the d orbitals on each Fe atom split into three-fold degenerate $d\epsilon$ orbitals and twofold degenerate $d\gamma$ orbitals by a crystalline electric field (CEF). If six electrons belong to the d orbitals, the electronic configuration is expected to be given as shown in Fig. 5(a). When Fe atoms draw closely to each other, they are to be coupled mainly through an electron hopping between $d\gamma$ orbitals since they extend toward each other, while the $d\epsilon$ orbitals are relatively localized. However, if every Fe atom keeps its electronic configuration as Fig. 5(a), the Pauli principle prevents hopping of electrons of $d\gamma$ orbitals and thus interferes to form solid. One way to realize the interatomic coupling is, contradicting to the Hund coupling, a rearrangement of the electronic configuration as shown in Fig. 5(b) such that a part of electron transfer from up spin state to down spin state in order to make a vacant orbital in the $d\gamma$ orbitals. The atomic energy difference between the electronic configurations of Figs. 5(a) and 5(b) is approximately given by $\Delta E=E(b)-E(a)=3K+U-V-\Delta$ where K is the exchange energy between different orbital, and U and V are direct Coulomb energy within same orbital and different orbital, respectively, Δ is the energy difference between $d\gamma$ and $d\epsilon$ orbitals. If these values are chosen as $U=5$ eV, $V=3$ eV, $K=1$ eV and $\Delta=1$ eV, one obtains $\Delta E=4$ eV. The value is comparable or lower than the cohesive energy per atom which is brought about mainly by the propagation of $d\gamma$ electrons. Thus, the electronic configuration in Fig. 5(b) is more stable with the electron hopping through vacant $d\gamma$ orbitals. The decrease of magnetic moment from 4 μ_B in pure iron can be ascribed mainly to this process. Other possible ways to realize the coupling is to introduce, in the Fe lattice, an additional hopping site having vacant orbitals. This may effectively provide a slight hole in the Fe lattice. If Hund coupling is sufficiently large, down spin electrons which belongs to $d\epsilon$ orbitals have a chance to transfer to a vacant orbital. However, once a lattice distortion is induced with inclusion of the additional atom such as tetragonal distortion, one of the $d\epsilon$ orbitals becomes more localized with its energy lowered (Fig. 6). In this case, it is feasible that the hole is created in the $d\gamma$ orbital shifted to a higher energy level with lattice distortion. When the $d\gamma$ electrons move in the solid, interatomic coupling can be realized without destroying the Hund's rule, and the ferromagnetic ordering can be expected. This is because the itinerant $d\gamma$ electrons align the direction of the total spin of each Fe site through lattice hopping accompanied with Hund coupling with $d\epsilon$ electrons. Under the condition where the hole concentration is not so large and that a sufficient strength of the Hund coupling is held, the Fe atoms can be expected to form ferromagnetic metal, with their moments close to 4 μ_B.

Previous experimental result (electron diffraction measurement[8]) and the band calculations[22,23] for well-established Fe_4N predicted that the N atoms act as an acceptor in the Fe lattice. This supports that the N atoms contribute to the creation of holes in the relevant system. The feature can also be easily anticipated from the fact that the oxygen atoms in the transition metal oxides behave as anion. As to Fe_4N, however, CEF on each Fe atom makes $d\epsilon$ orbitals higher energy than the $d\gamma$ orbitals. In this case, the Hund rule in the atomic limit may be easily destroyed since the highly degenerate $d\epsilon$ orbitals are delocalized and act as a main conduction band. Thus, the present model in which both the Hund coupling and the electron hopping can coexist requires the condition that the inclusion of the nitrogen atoms does not destroy the body center lattice and the long range ordering of the atomic structure. This could provide an interpretation that there exists an optimum N concentration for giving a giant moment, while it does not necessarily require [N]/[Fe]=1/8 to give the largest moment. In addition, the condition of the long range ordering may be consistent with the experimental results that a giant moment requires a site ordering of the N atom in the Fe lattice.[21]

Whereas the essence of the result by Lai *et al.* is an enhancement of the electron correlation energy U, the key feature of the present model is an effect of N atoms as a hopping site in the Fe lattice. This is closely related to the mechanism invented for the metallic ferromagnetism of $La_{1-x}M_xMnO_3$ (M=Ca, Sr, etc.). For $x=0$, this system is an antiferromagnetic insulator and exhibits phase transition to ferromagnetic metal with a partial substitution of La by M element ($x>0$). The magnetic moment on Mn site is about 4 μ_B. The metallic ferromagnetism of this system has been interpreted in terms of the double-exchange interaction[38,39] connected to the Hund coupling.[38,39] Recently, this has been intensively studied with the Kondo lattice model[40,41] in order to understand both the magnetism and the giant magnetoresistance. The distinctive feature of the present model is an introduction of the interstitial site instead of the substitution for the hole creation. Therefore, the Kondo lattice model with a ferromagnetic coupling can also be applied to the present system.

According to our recent study[42] for the Kondo lattice model, the Curie temperature (Tc) is lower than 0.1 D/k_B (K) even for large JS/D limit where D, S, and J are the half width of the conduction band, localized spin and Hund coupling parameter, respectively. The conduction band width we are concerned about may be a few eV. From this, the Tc must be a same level or lower comparing with the iron. This supports the experimental measurement of the Tc of $Fe_{16}N_2$ by Sugita *et al.*[21]

The most serious problem of this model is whether the $d\epsilon$ orbitals can maintain the localized aspect like an atomic state even in the solid. As shown by most studies, band calculations always give negative results to this question. However, once the electron correlation energy or the Hund coupling energy exceeds the energy gain due to a kinetics of the electrons in the lattice, the electrons prefer to be localized on each site and to form atomic state. From the view point of many body theory, this situation is expressed in terms of the band narrowing or the mass enhancement of the electrons. Even with a recent band calculation taking into account the correlation energy through density functional theory, the intra-atomic Coulomb energy is generally underestimated. Therefore, there is always a possibility that the localized picture of the electrons in solids cannot be accounted for properly by the band calculation, as many theoreticians have experienced in most transition metal oxides. The trial by Lai *et al.* is one of the ways to attack this problem, though the other approaches can also improve the band calculation procedure independently. In an actual system of $Fe_{16}N_2$, there may exist a possibility that the effect of tetragonal distortion makes the overlap of $d\epsilon$ orbitals further small with a splitting into twofold and nondegenerate orbitals (see Fig. 6).

Note that the present analysis does not immediately give a direct interpretation to the giant magnetic moment, because in the present model we took into account only the side view of the system which may not be accounted properly in the local density functional approximation. What we should insist here is that there may exist a case where the electron correlation plays a crucial role in the magnetism even in a metallic system. A compromise between the band model and the many body effects in such a critical region is desired.

V. SUMMARY

We have summarized the result of spin-polarized band calculation for $Fe_{16}N_2$. Also given is the result of Fe_4N for comparison. As to the local magnetic moments, the most distant Fe atoms from N have the largest magnetic moment. The major role of the N atom is to expand the Fe lattice to enhance the magnetic moments. It should be noted, however, that the N atoms help a hopping of the electrons and then prevent the exchange splitting. As a consequence, the lower concentration of the N atom gives a larger magnetic moment. Quantitatively, the calculated moment of $Fe_{16}N_2$ is far below the experimental data by Sugita *et al.* which is quite outstanding in the series of other iron nitrides. A possibility of the giant moment has been discussed in view point of the many body effects. Essence is a generation of hopping sites with N atoms, which may promote a ferromagnetic coupling of Fe atoms keeping its large spin polarization in the atomic limit. The model requires the intra-atomic Coulomb interaction such as Hund coupling on each Fe atom, combined with the interatomic propagation of $d\gamma$ electrons with a help of the hole doping in the lattice. Our main emphasis is that the band theory is never a panacea for the magnetism as well as for the cuprate superconductivity. Experimentally, more refined analysis for the crystal structure such as local arrangement of Fe and N atoms and the magnetic data such as neutron diffraction are desired.

ACKNOWLEDGMENTS

The author thanks Dr. Y. Sugita, Dr. M. Komuro, and Mr. H. Takahashi at Hitachi, Ltd. for useful discussions.

[1] A. Wold, R. J. Arnott, and N. Menyuk, J. Phys. Chem. **65**, 1068 (1961).
[2] M. Mekata, H. Yoshimura, and H. Takaki, J. Phys. Soc. Jpn. **33**, 62 (1972).
[3] M. Robbins and J. G. White, J. Phys. Chem. Solids **25**, 717 (1964).
[4] K. H. Eickel and W. Pitsch, Phys. Status Solidi **39**, 121 (1970).
[5] G. W. Wiener and J. A. Berger, J. Met. **7**, 360 (1955).
[6] B. C. Frazer, Phys. Rev. **112**, 751 (1958).
[7] G. Shirane, W. J. Takei, and I. Ruby, Phys. Rev. **126**, 49 (1962).
[8] S. Nagakura, J. Phys. Soc. Jpn. **25**, 488 (1968).
[9] G. Ertl, M. Huber, and N. Thiele, Z. Naturforsch. Teil A **34**, 30 (1970).
[10] T. K. Kim and M. Takahashi, Appl. Phys. Lett. **20A**, 492 (1972).
[11] J. M. Coey and H. Sun, J. Magn. Magn. Mater. **87**, L251 (1990).
[12] Y. C. Yang, X. D. Zhang, L. S. Kong, Q. Pan, S. L. Ge, J. L. Yang, Y. F. Ding, B. S. Zhang, C. T. Ye, and L. Jin, Solid State Commun. **78**, 313 (1991).
[13] K. H. Jack, Proc. R. Soc. London Ser. A **208**, 216 (1951).
[14] M. Komuro, Y. Kozono, M. Hanazono, and Y. Sugita, J. Appl. Phys. **67**, 5126 (1990).
[15] K. Nakajima and S. Okamoto, J. Appl. Phys. **65**, 4357 (1989); Appl. Phys. Lett. **56**, 92 (1990).
[16] M. Takahashi, H. Shoji, H. Takahashi, and T. Wakiyama, IEEE Trans. J. Magn. **29**, 3040 (1993).
[17] Y. Inoue, S. Takebayashi, and T. Mukai, J. Appl. Phys. **76**, 6653 (1994).
[18] W. E. Wallace and M. Q. Huang, J. Appl. Phys. **76**, 6648 (1994).
[19] R. M. Metzger, X. Bao, and M. Carbucicchio, J. Appl. Phys. **76**, 6626 (1994).
[20] Y. Sugita, K. Mitsuoka, M. Komuro, H. Hoshiya, Y. Kozono, and M. Hanazono, J. Appl. Phys. **70**, 5977 (1991).
[21] Y. Sugita, H. Takahashi, M. Komuro, K. Mitsuoka, and A. Sakuma, J. Appl. Phys. **76**, 6637 (1994).
[22] Wei Zhou, Li-jia Qu, and Qi-ming Zhang, Phys. Rev. B **40**, 6393 (1989).
[23] A. Sakuma, J. Phys. Soc. Jpn. **60** 2007, (1991).
[24] A. Sakuma, J. Magn. Magn. Mater. **102**, 127 (1991).

[25] S. Ishida, K. Kitawatase, S. Fujii, and S. Asano, J. Phys. Condens. Matter **4**, 765 (1992).
[26] B. I. Min, Phys. Rev. B **46**, 8232 (1992).
[27] S. Mater, S. Z. Phys. B **87**, 91 (1992).
[28] R. Coehoorn, G. H. O. Daalderop, and H. J. F. Jansen, Phys. Rev. B **48**, 3830 (1993).
[29] K. Miura, S. Imanaga, and Y. Hayafuji, J. Phys. Condens. Matter **5**, 9393 (1993).
[30] J. M. Coey, K. O'Donnell, Qi Qinian, E. Touchais, and K. H. Jack, J. Phys. Condens. Matter **6**, L23 (1994)
[31] H. Sawada, A. Nogami, T. Matsumiya, and T. Oguchi, Phys. Rev. B **50**, 10004 (1994).
[32] W. Y. Lai, Q. Q. Zheng, and W. Y. Hu, J. Phys. Condens. Matter **6**, L259 (1994).
[33] M. Z. Huang and W. Y. Ching, Phys. Rev. B **51**, 3222 (1995).
[34] J. Kanamori, *Proceedings of the 10th International Workshop on Rare-Earth Magnets and Their Applications, Kyoto, Japan, 1989* (The Society of Non-Traditional Technology, Tokyo, 1989), Vol. 1, p. 1.
[35] H. Takahashi, K. Mitsuoka, M. Komuro, and Y. Sugita, J. Appl. Phys. **73**, 6060 (1993).
[36] Y. Sugita, H. Takahashi, M. Komuro, M. Igarashi, R. Imura, and T. Kambe, these proceedings.
[37] J. P. Perdew and Y. Wang, Phys. Rev. B **33**, 8822 (1986); **34**, 7406 (1986).
[38] P. W. Anderson and H. Hasegawa, Phys. Rev. **100**, 675 (1955).
[39] P.-G. de Gennes, Phys. Rev. **118**, 141 (1960).
[40] M. Furukawa, J. Phys. Soc. Jpn. **63**, 3214 (1994).
[41] J. Inoue and S. Maekawa, Phys. Rev. Lett. **74**, 3407 (1995).
[42] A. Sakuma, J. Phy. Soc. Jpn. **64**, 3449 (1995).

Magnetic and electrical properties of single-phase, single-crystal $Fe_{16}N_2$ films epitaxially grown by molecular beam epitaxy (invited)

Yutaka Sugita, Hiromasa Takahashi, Matahiro Komuro, and Masukazu Igarashi
Central Research Laboratory, Hitachi, Ltd. Kokubunji, Tokyo 185, Japan

Ryo Imura
Advanced Research Laboratory, Hitachi, Ltd. Hatoyama, Saitama 350, Japan

Takashi Kambe
Department of Physics, Nihon University, Kanda Surugadai, Tokyo 101, Japan

The average magnetic moment per Fe atom for a single-phase, single-crystal $Fe_{16}N_2(001)$ film epitaxially grown on a GaAs(001) substrate by molecular beam epitaxy has been confirmed to be $3.5\mu_B$ at room temperature by using a vibrating sample magnetometer (VSM) and Rutherford backscattering. The value was in good agreement with that obtained by using a VSM and by measuring the film thickness ($3.3\mu_B$ per Fe atom). The saturation magnetization $4\pi M_s$ has been found to increase with decreasing temperature, obeying $T^{3/2}$ law at lower temperatures. The slope was steeper than that of a pure Fe film, suggesting a lower exchange constant for $Fe_{16}N_2$. The g factor for $Fe_{16}N_2$ has been accurately measured to be 2.17 by using ferromagnetic resonance with changing frequencies of 35.5–115 GHz, which is not unusual compared with the g factor of 2.16 for pure Fe. The resistivity for $Fe_{16}N_2$ has been measured to be around 30 $\mu\Omega$ cm at room temperature compared with 10 $\mu\Omega$ cm for pure Fe and decreases linearly with decreasing temperature. The behavior was that for normal metal and nothing unusual was seen. The anomalous Hall resistivity for $Fe_{16}N_2$ was 4×10^{-7} V cm/A, which is about three times as large as that for pure Fe. The relationship between the giant magnetic moment and the anomalous Hall resistivity has not been clarified yet. © *1996 American Institute of Physics.* [S0021-8979(96)25508-2]

I. INTRODUCTION

Since the pioneering work on high saturation magnetization of Fe–N films including $Fe_{16}N_2$ crystallites was reported by Kim and Takahashi,[1] much attention has been paid to the magnetic properties of Fe–N, especially $Fe_{16}N_2$ films. The $Fe_{16}N_2$ compound itself was discovered earlier by Jack[2] as precipitates formed in Fe–N powders by low temperature annealing.

Quite recently, Komuro *et al.*[3,4] and Sugita *et al.*[5,6] have grown single-phase, single-crystal $Fe_{16}N_2(001)$ films of 300–900 Å thickness epitaxially on $In_{0.2}Ga_{0.8}As(001)$ substrates using molecular beam epitaxy (MBE). They found that the saturation magnetization $4\pi M_s$ of $Fe_{16}N_2$ is around 29 kG at room temperature and around 32 kG at 5 K, respectively. Those values are equivalent to the average magnetic moment of 3.2 and $3.5\mu_B$ per Fe atom at room temperature and 5 K, respectively. These are truly giant magnetic moments, much greater than the Slater–Pauling curves[7] and the average magnetic moments for $Fe_{16}N_2$ calculated based on the conventional band theory of several authors.[8–15]

Also several experiments to prepare $Fe_{16}N_2$ films or powders and foils have been carried out using methods other than MBE, such as sputtering,[16–22] ion implantation,[23–25] and ammonia nitrification.[26–31] In most cases, the samples were not single-phase $Fe_{16}N_2$, but mixtures of several phases such as Fe, $Fe_{16}N_2$, Fe–N martensite, Fe_4N, etc. Therefore, there can be some significant ambiguities in estimated values of $4\pi M_s$ for $Fe_{16}N_2$ and other data such as hyperfine fields.

In this study, the average magnetic moment per Fe atom for a single-phase $Fe_{16}N_2$ film has been measured by using a vibrating sample magnetometer (VSM) and Rutherford backscattering (RBS). Here, the number of Fe atoms included in the film has been obtained without measuring the film thickness. Also the temperature dependence of $4\pi M_s$, the g factor, and the temperature dependence of the resistivity and the anomalous Hall resistivity for $Fe_{16}N_2$ have been investigated in detail.

II. EXPERIMENT

A. Sample preparation

$Fe_{16}N_2$ films were prepared in an atmosphere of mixed gas of N_2 and NH_3 by using a MBE apparatus equipped with electron-beam evaporation sources. $In_{0.2}Ga_{0.8}As$ and GaAs(001) single-crystal wafers were used as substrates. Details of the deposition conditions were described in a previous paper.[6]

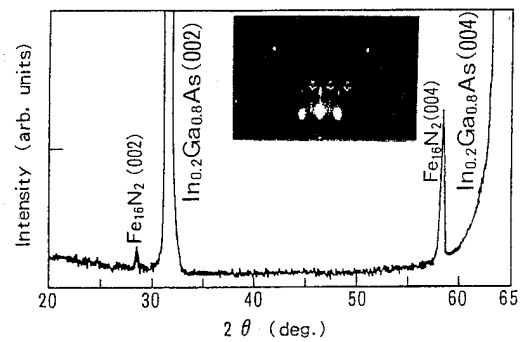


FIG. 1. X-ray diffraction (XRD) and reflection high energy electron diffraction (RHEED) patterns for a sample of $Fe_{16}N_2$.

 0021-8979/96/79(8)/5576/6/$10.00 © 1996 American Institute of Physics

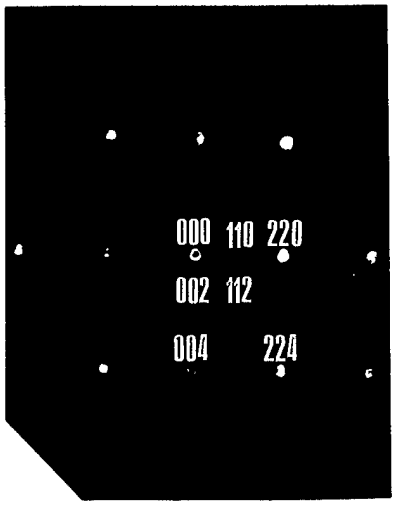


FIG. 2. Transmission electron diffraction spots for a cross section of a sample cleaved along the (110) plane of a GaAs substrate.

Samples were confirmed to be single-phase, single-crystal $Fe_{16}N_2(001)$ films by the x-ray diffraction and reflection high energy electron diffraction (RHEED) patterns as shown in Fig. 1 and also by the transmission electron diffraction as shown in Fig. 2. The photo was taken for a cross-sectional sample cleaved along the (110) substrate plane and thinned down to around 2000 Å by polishing and ion milling. The electron beam spot was around 100 Å in diameter and the acceleration voltage was 200 kV. All diffraction spots were identified as figures of planes of $Fe_{16}N_2$ and spots from other phases were not seen. The ratio of the lattice parameter of the c axis to that of the a axis is determined to be 1.1 from the (004) and (220) spots, which agrees well with the previously reported value.[2] Pure Fe films were also prepared on $In_{0.2}Ga_{0.8}As$ and GaAs(001) substrates in a vacuum of 5×10^{-7} Torr for comparison with $Fe_{16}N_2$ films and reference for measurements.

B. Characterization

1. Rutherford backscattering

The amounts of Fe atoms included in films were measured with Rutherford backscattering (RBS). A sample was bombarded by He ions with 8° inclination and reflected ions were detected with a counter as shown schematically in Fig. 3. The channel of the analyzer was 2.3 keV. The energy of the incident He ions was 2.3 MeV and the diameter of the He ion beam was 1 mm.

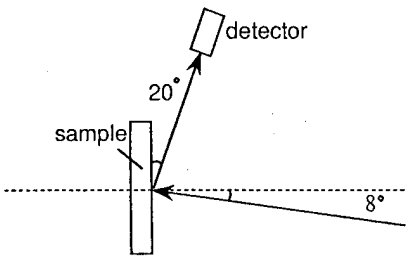


FIG. 3. Schematic view of a RBS experiment.

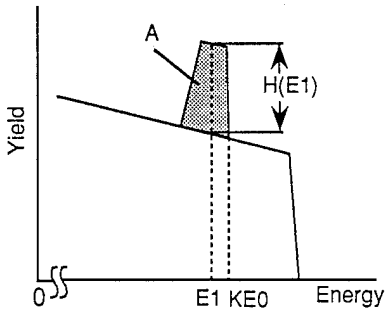


FIG. 4. Schematic RBS spectra.

RBS spectra are schematically shown in Fig. 4. The spectra are composed of two parts, one from the substrate atoms, Ga and As, and the other from the film atoms, Fe. From the intensity $H(E_1)$ and the area of the signal from the film, the total number of Fe atoms can be obtained based on the established method.[32]

2. Ferromagnetic resonance

Ferromagnetic resonance (FMR) measurements were carried out on $Fe_{16}N_2$ films along with pure Fe films using microwave sources with 35.5, 49.5, 90.0, and 115 GHz. Magnetic fields up to 60 kOe were applied parallel and perpendicular to the film plane using a superconducting magnet. The samples were 2-mm-diam circular plates defined by chemical etching. Sample temperature was kept at 77 K. From FMR data, the g factors of $Fe_{16}N_2$ and Fe films were obtained.

3. Measurement of magnetic moment

Magnetic moments of samples were measured by using a superconducting quantum interference device (SQUID) magnetometer at temperatures from 10 to 300 K and also by using a VSM at temperatures from 77 to 700 K.

4. Resistivity and Hall resistivity measurements

Resistivity and Hall resistivity measurements were made on $Fe_{16}N_2$ films along with pure Fe films at temperatures from 10 to 300 K. Samples used for resistivity measurements

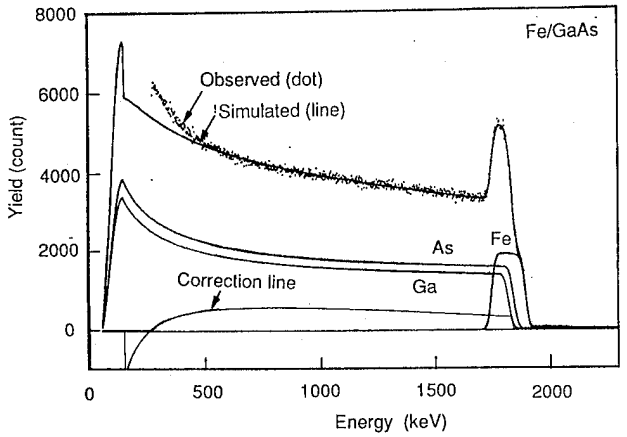


FIG. 5. RBS spectra measured for a Fe film grown on a GaAs substrate.

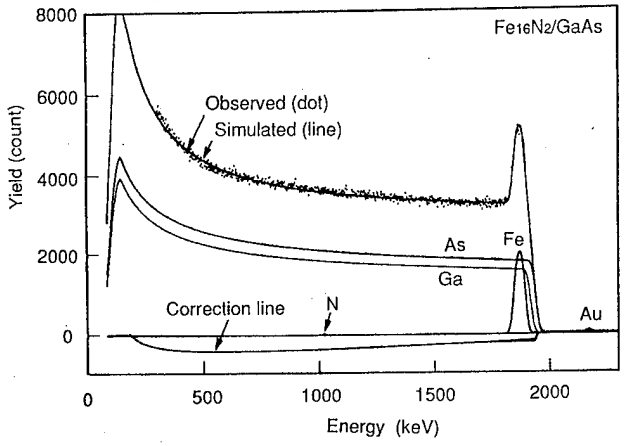


FIG. 6. RBS spectra measured for a $Fe_{16}N_2$ film grown on GaAs.

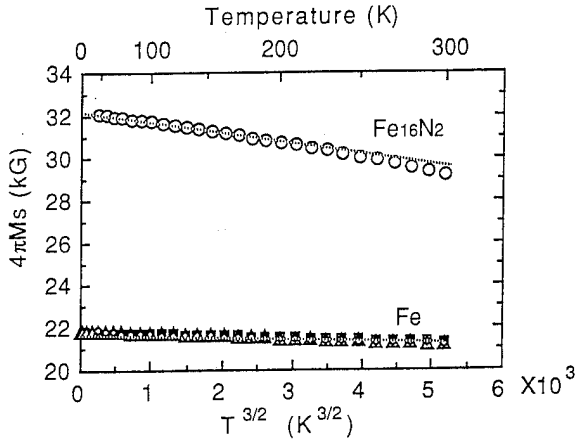


FIG. 7. Temperature dependence of the saturation magnetization $4\pi M_s$ for a $Fe_{16}N_2$ film along with a Fe film.

were 1 mm×4 mm with four terminals made of Au. Samples used for Hall resistivity measurements were 3 mm×3 mm. Hall resistivities were measured by van der Pauw's method.[33] That is, the current was supplied through terminals located at a pair of opposite corners with magnetic field applied perpendicular to the film and the Hall voltage generated between the terminals located at another pair of opposite corners was measured.

III. RESULTS AND DISCUSSION

A. Magnetic moment per Fe atom

Typical RBS spectra measured for Fe and $Fe_{16}N_2$ films are shown in Figs. 5 and 6. Those samples are 6 mm ϕ, 860-Å-thick Fe and 8 mm ϕ, 340-Å-thick $Fe_{16}N_2$ films grown on GaAs(001) substrates. Simulated lines based on previously known data for Ga, As, and Fe are in good agreement with measured data in both cases. Here, the edge energies for As and Ga atoms (around 1800 keV) in Fig. 5 are slightly different from those (around 1900 keV) in Fig. 6. The reason for the difference is due to the difference in film thickness between Fe (~860 Å) in Fig. 5 and $Fe_{16}N_2$ (340 Å) in Fig. 6.

From the intensities and areas of the signals from Fe atoms, the densities (atoms cm^{-2}) of Fe atoms of the films are obtained as shown in Table I. Using the data of magnetic moments measured with a VSM for those samples, the average magnetic moments per Fe atom for Fe and $Fe_{16}N_2$ are obtained to be $2.16\mu_B$ and $3.53\mu_B$ at room temperature, respectively. The value obtained for Fe is very close to that obtained by using the volume of the sample and also to the bulk value.[7] This confirms the accuracy of the data by this method without measuring the film thickness. For $Fe_{16}N_2$, the obtained value is a little higher than that obtained by using the volume of the sample, but the difference is small and this data confirms the giant magnetic moment of $Fe_{16}N_2$.

It should be noticed here that for Fe and $Fe_{16}N_2$ films grown on $In_{0.2}Ga_{0.8}As(001)$ substrates, it is almost impossible to get the accurate values by this method. This is because the signals from Fe and In atoms appear at almost the same positions in RBS spectra, therefore the amount of Fe atoms is hardly obtained accurately.

B. Temperature dependence of $4\pi M_s$

The saturation magnetization $4\pi M_s$ has been measured using a SQUID, changing temperature from 10 to 300 K. The samples used for the measurements were 8-mm-diam circular plates accurately defined by using photolithography and chemical etching. Film thicknesses were measured with a needle contact feeler gauge.

Figure 7 shows the temperature dependence of $4\pi M_s$ for a $Fe_{16}N_2$ film along with that for a pure Fe film. In Fig. 7 $4\pi M_s$ is plotted as a function of $T^{3/2}$. In both cases, $4\pi M_s$ is linearly decreased with increasing temperature at lower temperatures, obeying the $T^{3/2}$ law expressed as[34]

$$4\pi M_s(T)=4\pi M_s(0)(1-CT^{3/2}). \quad (1)$$

Here $4\pi M_s(T)$ and $4\pi M_s(0)$ are the values at a temperature of T and 0 K, respectively. By extrapolating the line to 0 K,

TABLE I. Average magnetic moment for a $Fe_{16}N_2$ film along with that for a Fe film.

Sample	He ion energy E_0 (MeV)	Atomic density t (atoms/cm^2)	Sample shape	Magnetic moment (emu)	Magnetic moment per Fe atom (RBS)	Magnetic moment per Fe atom (thickness and XRD)
Fe/GaAs	2.3	7.17×10^{17}	6 mm ϕ 860 Å	0.00405	$2.16\mu_B$	$2.14\mu_B$
$Fe_{16}N_2$/GaAs	2.3	2.42×10^{17}	8 mm ϕ 340 Å	0.00400	$3.53\mu_B$	$3.28\mu_B$

TABLE II. Experimental data on the temperature dependence of $4\pi M_S$ for a $Fe_{16}N_2$ film along with those for a Fe film.

	$Fe_{16}N_2$	Fe
$4\pi M_S$ (0) (kG)	32.3	21.8
M_B (μ_B)	3.5	2.2
C ($\times 10^{-6}$ kG/K$^{3/2}$)	18	5.5
D (meV Å^2)	70	220
D/T_C	0.08	0.2

$4\pi M_s$'s(0) are obtained to be 32.3 and 21.8 kG for $Fe_{16}N_2$ and Fe, respectively, as shown in Table II. These values of $4\pi M_s$ are equivalent to the average magnetic moments per Fe atom of $3.5\mu_B$ and $2.2\mu_B$ at 0 K for $Fe_{16}N_2$ and Fe, respectively.

The slope of Eq. (1), $C(kG/K^{3/2})$ are 18 and 5.5×10^{-6} for $Fe_{16}N_2$ and Fe, respectively. C is expressed by[35]

$$C=2.612[g\mu_B/4\pi M_s(0)](k_B/4\pi D)^{3/2}. \quad (2)$$

Here g is the g factor, k_B is the Boltzmann constant, and D is the exchange interaction constant between magnetic moments of atoms. The g factors are 2.17 and 2.16 for $Fe_{16}N_2$ and Fe, respectively, as described in Sec. III C. Using those values, D (meV Å^2) is obtained for $Fe_{16}N_2$ to be around 70, which is much smaller than the value for 220 for Fe, as shown in Table II. Even taking into consideration the lower Curie temperature T_C for $Fe_{16}N_2$ (around 810 K),[5] the exchange constant is lower, because D/T_C for $Fe_{16}N_2$ is 0.08, while D/T_C for Fe is 0.2(T_C:1040 K).

In Fig. 8, $4\pi M_s(T)/4\pi M_s(0)$ is shown as a function of T/T_C for $Fe_{16}N_2$ and Fe. It is clear that the decrease of $4\pi M_s$ is much steeper for $Fe_{16}N_2$ than for Fe. The mechanism for this is not clear.

C. The *g* factor

The g factor for $Fe_{16}N_2$ was reported to be around 2.0,[36] but the measurement using FMR was not so accurate. This is because the frequency used in the previous work was fixed at 35.5 GHz and the applied field was 10 kOe at its highest and was not sufficient to saturate the magnetization perpendicular to the film plane.

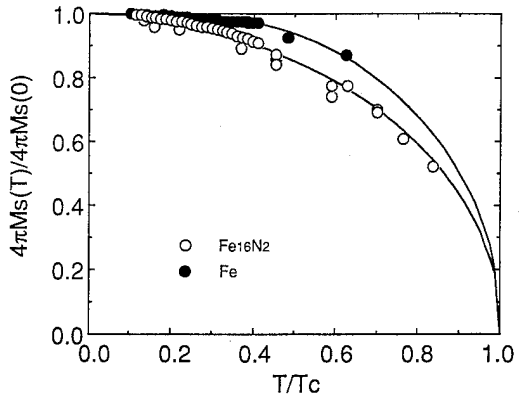


FIG. 8. $4\pi M_s(T)/4\pi M_s(0)$ vs T/T_c for a $Fe_{16}N_2$ film along with that for a Fe film.

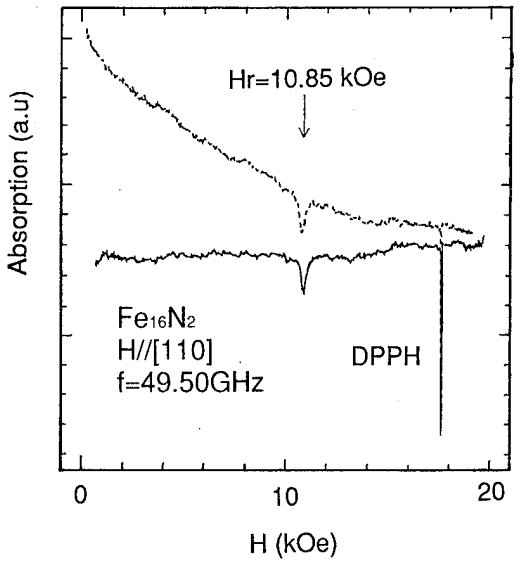


FIG. 9. FMR spectra for a $Fe_{16}N_2$ film measured at 49.50 GHz with magnetic field applied in the [110] direction of the film plane.

In this experiment, the frequency is changed from 35.5 to 115 GHz. The maximum applied field is 60 kOe. Typical FMR data at 49.5 GHz for a $Fe_{16}N_2$ film of 2 mm diam are shown in Figs. 9 and 10. Figure 9 shows the obtained data when the field is applied in the [110] direction of the film plane. There is some drift in absorption between increasing field and decreasing field processes, but the resonance field does not shift at all. Figure 10 shows the data for the case where the field is applied perpendicular to the film plane. In both cases, the magnetic field is calibrated using the FMR field for DPPH (α,α-diphenyl-β-picrylhydrazyl) with g of 2.0 as a standard.

In Fig. 11, the resonance field-frequency diagrams are shown for the three cases. The fields are applied in the [100] and [110] directions of the film plane, and applied in the

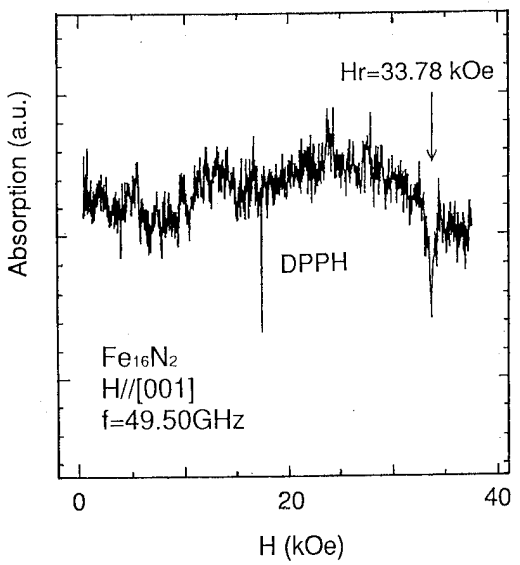


FIG. 10. FMR spectra for a $Fe_{16}N_2$ film measured at 49.50 GHz with magnetic field applied in the [001] direction perpendicular to the film plane.

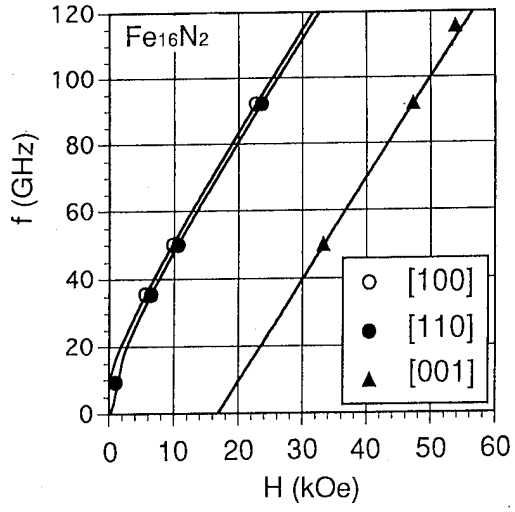


FIG. 11. The relationship between the resonance frequency and the resonance field measured and calculated for the three cases with magnetic field applied in the [100], [110], and [001] axes. The dotted points are measured ones and the solid lines are calculated ones.

[001] perpendicular to the film plane. As previously reported[36] an $Fe_{16}N_2(001)$ film exhibits large uniaxial perpendicular anisotropy with easy axis parallel to the [001] and small anisotropy with easy axes of [100] and [101] in the film plane. The resonance equations for the above three cases as shown in Fig. 11 are expressed as follows:[34]

$$[001] \quad \omega/\gamma = H_r + H_{k\perp} - 4\pi M_s, \tag{3}$$

$$[100] \quad (\omega/\gamma)^2 = (H_r + H_k)(H_r - H_{k\perp} + 4\pi M_s), \tag{4}$$

$$[110] \quad (\omega/\gamma)^2 = (H_r - H_k)(H_r - H_{k\perp} + 4\pi M_s - 1/2H_k). \tag{5}$$

Here $\omega(=2\pi f)$ is the resonance frequency; γ, the gyromagnetic ratio; H_r, the resonance field; $H_{k\perp}$, the uniaxial anisotropy field, and H_k, the in-plane anisotropy field. From the data of Fig. 11, the g factor for $Fe_{16}N_2$ is obtained with least deviation using Eqs. (3)–(5). The value is 2.17.

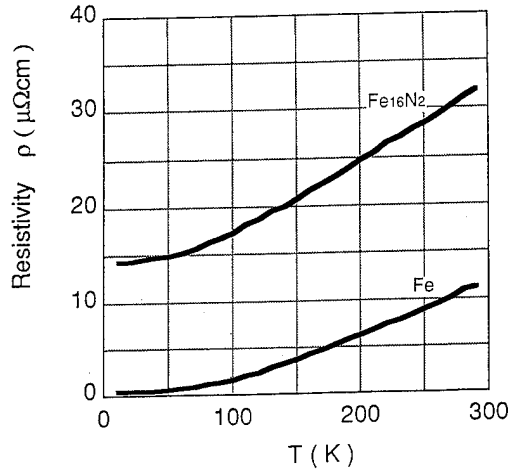


FIG. 12. Temperature dependence of the resistivity ρ for a $Fe_{16}N_2$ film along with a Fe film.

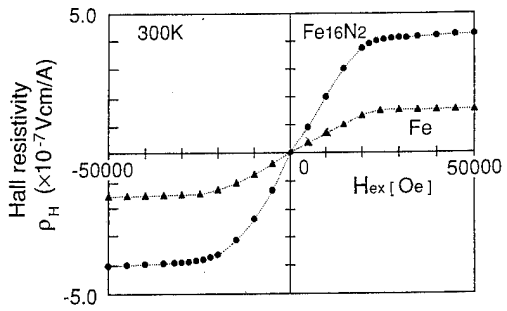


FIG. 13. Hall resistivity ρ_H as a function of magnetic field applied perpendicular to the films plane for an $Fe_{16}N_2$ film along with a Fe film.

In those experiments, H_r is higher than 6 kOe for the case of the in-plane field FMR, which is high enough to saturate the magnetization. Also in the case of perpendicular field FMR, H_r is higher than 40 kOe, which is high enough to saturate the magnetization. Therefore FMR data were taken under the condition that Eqs. (3)–(5) are valid. Consequently the g factor of 2.17 is likely to be accurate. This is supported by the measurement of the g factor for a Fe film. The value obtained by using the same method is 2.16, which agrees well with previously reported data. Details of the FMR data will be reported elsewhere.

The g factor of 2.17 for $Fe_{16}N_2$ is not unusual at all due to its giant and unusual magnetic moment, but this cannot be contradictory.

D. Temperature dependence of resistivity and anomalous Hall resistivity

The temperature dependence of resistivity ρ for a $Fe_{16}N_2$ film is shown along with that for a Fe film in Fig. 12. ρ at room temperature is around 30 $\mu\Omega$ cm, a little higher than the 10 $\mu\Omega$ cm for Fe. ρ is almost linearly decreased with decreasing temperature. The behavior is that for normal metal and nothing unusual is seen.

The Hall resistivity ρ_H versus applied field at room temperature for $Fe_{16}N_2$ is shown along with that for pure Fe in Fig. 13. ρ_H is increased linearly with increasing field and further is almost saturated. From those data, the saturated anomalous Hall resistivity $\rho_{AS}(=R_A 4\pi M_s)$ is obtained based on the following:

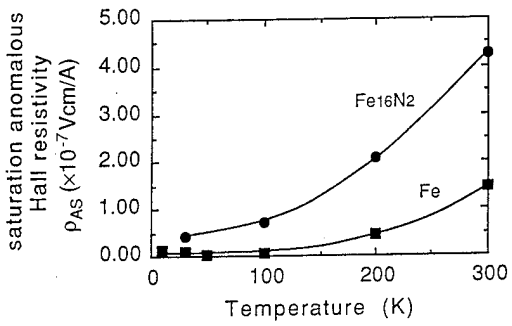


FIG. 14. Temperature dependence of the saturated anomalous Hall resistivity ρ_{AS} for an $Fe_{16}N_2$ film along with a Fe film.

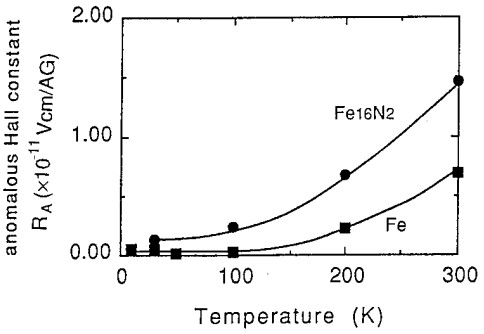


FIG. 15. Temperature dependence of the anomalous Hall constant R_A for a $Fe_{16}N_2$ film along with a Fe film.

$$\rho_H = R_N H + R_A 4\pi M = \rho_N + \rho_A . \quad (6)$$

Here R_N and R_A are normal and anomalous Hall constants, respectively, and ρ_N and ρ_A are normal and anomalous Hall resistivities, respectively. ρ_{AS} for $Fe_{16}N_2$ is 4×10^{-7} V cm/A at room temperature compared with ρ_{AS} of 1.5×10^{-7} V cm/A for pure Fe. It is to be noted here that ρ_{AS} for $Fe_{16}N_2$ is about three times as large as that for Fe. The temperature dependencies of ρ_{AS} and R_A for $Fe_{16}N_2$ are shown along with those for Fe in Figs. 14 and 15, respectively. In both cases, ρ_{AS} and R_A are decreased with decreasing temperature. In the whole temperature range, ρ_{AS} and R_A for $Fe_{16}N_2$ are larger than those for Fe. The reason for those behaviors in ρ_{AS} and R_A and the relationship between anomalous Hall resistivity and the giant magnetic moment are not so clear.

IV. CONCLUSIONS

The average magnetic moment per Fe atom for a single-phase, single-crystal $Fe_{16}N_2$ film epitaxially grown by MBE has been confirmed to be $3.5\mu_B$ at room temperature with VSM and a Rutherford backscattering technique. The value was in good agreement with that of $3.3\mu_B$ obtained with VSM and measuring the film thickness.

The temperature dependence of the saturation magnetization $4\pi M_s$ for $Fe_{16}N_2$ has been found to obey the $T^{3/2}$ law at lower temperatures. The slope was much steeper than that for pure Fe, which suggested lower exchange coupling between magnetic moments of Fe atoms in $Fe_{16}N_2$.

The g factor for $Fe_{16}N_2$ has been measured by FMR changing the frequency from 35.5 to 115 GHz and applying the magnetic field up to 60 kOe. The obtained value was 2.17, which was very close to the g factor of 2.16 for pure Fe.

The resistivity for a $Fe_{16}N_2$ film has been measured at temperatures from 10 to 300 K. The resistivity was around 30 $\mu\Omega$ cm at room temperature and decreased linearly with decreasing temperature. The behavior was that for normal metal and nothing unusual was seen. The saturated anomalous Hall resistivity has been found to be 4×10^{-7} V cm/A, which was about three times as large as that of pure Fe.

Thus the giant magnetic moment for $Fe_{16}N_2$ has been reconfirmed. Further, magnetic and electrical properties for $Fe_{16}N_2$ have been investigated in detail, which will be useful to clarify the origin of the giant magnetic moment in future.

ACKNOWLEDGMENTS

The authors would like to thank Professor E. Kita of Tsukuba University for his collaboration in the measurement of the magnetization with SQUID, Dr. H. Awano and Dr. M. Hiratani, of Hitachi Central Research Laboratory, Dr. Y. Hirai of Hitachi Advanced Research Laboratory, and Dr. A. Sakuma of Hitachi Metals for their valuable discussions on characterization of $Fe_{16}N_2$. They thank also Dr. Y. Shiroishi and Dr. M. Fuyama of Hitachi Central Research Laboratory for their encouragement throughout this study.

[1] T. K. Kim and M. Takahashi, Appl. Phys. Lett. **20**, 492 (1972).
[2] K. H. Jack, Proc. R. Soc. London Ser. A **208**, 216 (1951).
[3] M. Komuro, Y. Kozono, M. Hanazono, and Y. Sugita, J. Appl. Phys. **67**, 5126 (1990).
[4] M. Komuro, H. Hoshiya, K. Mitsuoka, Y. Kozono, M. Hanazono, and Y. Sugita, Mater. Res. Soc. Symp. Proc. **232**, 147 (1991).
[5] Y. Sugita, K. Mitsuoka, M. Komuro, H. Hoshiya, Y. Kozono, and M. Hanazono, J. Appl. Phys. **70**, 597 (1991).
[6] Y. Sugita, H. Takahashi, M. Komuro, K. Mitsuoka, and A. Sakuma, J. Appl. Phys. **76**, 6637 (1994).
[7] R. M. Bozorth, *Ferromagnetism* (Van Nostrand, New York, 1951), p. 441.
[8] A. Sakuma, J. Magn. Magn. Mater. **102**, 127 (1991).
[9] S. Ishida, K. Kitawatase, S. Fujii, and S. Asano, J. Phys. Condens. Matter **4**, 765 (1992).
[10] B. I. Min, Phys. Rev. B **46**, 8232 (1992).
[11] S. Matar, Z. Phys. B **87**, 91 (1992).
[12] R. Coehoorn, G. H. O. Daalderop, and H. J. F. Jansen, Phys. Rev. B **48**, 3830 (1993).
[13] A. Sakuma and Y. Sugita, Mater. Res. Soc. Symp. Proc. **313**, 257 (1993).
[14] W. Y. Lai, Q. Q. Zheng, and W. Y. Hu, J. Phys. Condens. Matter **6**, L 259 (1994).
[15] H. Sawada, A. Nogami, T. Matsumiya, and T. Oguchi, Phys. Rev. B **50**, 100004 (1994).
[16] M. A. Russac, C. V. Jahnes, E. Klokholm, J. Lee, M. E. Re, and B. C. Webb, J. Appl. Phys. **70**, 6427 (1991).
[17] C. Gao and W. D. Doyle, J. Appl. Phys. **73**, 6579 (1993).
[18] C. Gao and M. Shamsuzzoha, IEEE Trans. Magn. **29**, 3046 (1993).
[19] M. Takahashi, H. Shoji, H. Takahashi, T. Wakiyama, M. Kinoshita, and W. Ohta, IEEE Trans. Magn. **29**, 3040 (1993).
[20] M. Takahashi, H. Shoji, H. Takahashi, H. Nashi, T. Wakiyama, M. Doi, and M. Matui, J. Appl. Phys. **76**, 6642 (1994).
[21] C. Ortiz, G. Dumpich, and A. H. Morrish, Appl. Phys. Lett. **65**, 2737 (1994).
[22] S. Okamoto, O. Kitakami, and Y. Shimada, J. Appl. Phys. (submitted).
[23] K. Nakajima and S. Okamoto, Appl. Phys. Lett. **56**, 92 (1990).
[24] K. Nakajima, T. Yamashita, M. Takata, and S. Okamoto, J. Appl. Phys. **70**, 6033 (1991).
[25] E. Deroy, C. Diega-Mariadassou, H. Bernas, O. Kaitasov, R. Krishnan, and M. Tessier, Appl. Phys. Lett. **67**, 560 (1995).
[26] M. Q. Huang, W. E. Wallace, S. Simizu, and S. G. Sankar, J. Magn. Magn. Mater. **135**, 226 (1994).
[27] X. Bao and R. M. Metzger, J. Appl. Phys. **75**, 58 (1994).
[28] J. M. D. Coey, K. O'Donnell, Q. Qinian, E. Touchais, and K. H. Jack, J. Phys. Condens. Matter **6**, L23 (1994).
[29] J. M. D. Coey, J. Appl. Phys. **76**, 6632 (1994).
[30] W. E. Wallace and M. Q. Huang, J. Appl. Phys. **76**, 6648 (1994).
[31] R. M. Metzger, X. Bao, and M. Carbucicchio, J. Appl. Phys. **76**, 6626 (1994).
[32] W. K. Chu, J. W. Mayer, and M. A. Nicolet, *Backscattering* (Academic, New York, 1987), p. 54.
[33] L. J. van der Pauw, Philips Res. Rept. **13**, 1 (1958).
[34] C. Herring and C. Kittel, Phys. Rev. **81**, 869 (1951).
[35] F. Keffer, in *Encyclopedia of Physics* edited by S. Flugge (Springer, Berlin, 1966), Vol. 1, Part I, p. 49.
[36] H. Takahashi, K. Mitsuoka, M. Komuro, and Y. Sugita, J. Appl. Phys. **73**, 6060 (1993).

Mössbauer-effect study of face-centered-cubic-like Fe on Cu(001) (invited) (abstract)

W. Keune, A. Schatz, R. D. Ellerbrock, A. Fuest, K. Wilmers, and R. A. Brand
Laboratory of Applied Physics, University of Duisburg, D-47048 Duisburg, Germany

More than 30 years ago, Weiss[1] has postulated the existence of two different magnetic fcc-Fe states [high-spin (HS)/high atomic volume or low-spin (LS)/low atomic volume] in order to explain the Invar effect in fcc-Fe alloys. Such metastable states may be stabilized by epitaxial growth of ultrathin Fe films on Cu(001) under suitable conditions which depend on film thickness and growth temperature. *In situ* conversion-electron Mössbauer spectroscopy, combined with low-energy electron diffraction, reflection high-energy electron diffraction, and Auger electron spectroscopy, on ~3- and ~7-ML-thick ^{57}Fe films grown in ultrahigh vacuum at 300 K reveals a thickness-dependent transition from a HS ferromagnetic (FM) state with an anisotropically expanded fcc (fct-like) structure ($c/a>1$) to a LS antiferromagnetic (AFM) isotropic fcc state. In contrast, the stability of the HS fct-like phase is extended to at least 7 ML in films grown at low T (90 K) and annealed to 300 K. The HS-FM phase in 7 ML films is rather stable against annealing up to 500 K; annealing at 570 K leads to a HS–LS transformation which is correlated with abrupt surface segregation of Cu. By placing 2-ML-thick isotopically enriched ^{57}Fe-probe layers into a 300 K grown natural Fe film of 7 ML total thickness we could obtain a magnetic depth profile along the film-normal direction: while the LS-AFM state (with T_N~70 K) was found at the film center and a paramagnetic Fe–Cu alloy at the Fe/Cu interface, Fe surface atoms were observed to be in a HS-FM state with a noncubic atomic environment. Only today can we begin to understand the complex behavior of fcc-Fe/Cu(001). © *1996 American Institute of Physics.* [S0021-8979(96)47508-6]

This work was supported by Deutsche Forschungsgemeinschaft (SFB 166).

[1]R. J. Weiss, Proc. R. Soc. London **82**, 281 (1963).

 0021-8979/96/79(8)/5582/1/$10.00 © 1996 American Institute of Physics

Magnetic properties of fcc-Fe multilayer (invited) (abstract)

M. Matsui, M. Doi, A. Kida, and Y. Yamada
Department of Materials Science, Nagoya University, Nagoya 464-01, Japan

Recently, magnetic properties of fcc-Fe ultrathin films have been extensively investigated. The results, however, are complicated and inconsistent with one another. These are antiferromagnetism, ferromagnetism, different Fe magnetic moment for different atomic sites in film or a rearrangement of surface Fe atoms etc. In this article the recent results for fcc-Fe multilayers will be reported and discussed to obtain a unified picture for magnetism of fcc-Fe ultrathin films. Epitaxially grown multilayers of fcc-Fe with Cu or Cu-M (M=Au,Ni) spacer on Cu(001) and Cu(111) substrates were prepared by molecular beam epitaxy method. The Cu-M spacer was adopted to change the mean interatomic distance between Fe atoms at interfaces by changing the composition of M (=Au,Ni), where Au was used to increase the distance and Ni to decrease it. Fe layers on a pure Cu spacer were fcc and the magnetic moment was at most $2.0\mu_B$. Fe layers on a Cu-Au spacer, however, were fct with $c/a<1$ and those on Cu-Ni with $c/a>1$, where a is the in-plane lattice constant and c is the out of plane one. Then a mean magnetic moment of Fe atoms (μ) as a function of Fe atomic volume (V) was obtained. The moment μ continuously increases with increasing V by the so-called magnetovolume effect. The maximum μ value is $2.7\mu_B$ for about $\Delta V=4\%$ (ΔV is a change of V from pure Cu volume). And $\mu=0$ for $\Delta V=-2\%$. The Mössbauer effect and EXAFS were also measured. The measurements revealed that the samples for the $\Delta V\leqslant 0$ region contain two kinds of Fe (mixture state), high spin state with $2.0\mu_B$ and nonmagnetic low spin state. Thus it is concluded that the high to low spin state transition is the first kind as theoretically suggested by Moruzzi *et al.* We also performed band calculations for fcc-Fe/Cu multilayers changing V. Next, the reason for the mixture state is discussed. It is found that a well defined smooth Cu substrate surface promotes a rearrangment of surface Fe atoms due to the surface diffusion, preferring the low spin state and the rough surface obstructs the rearrangement and provides the fcc circumstance by surrounding Cu atoms, which results in the high spin state. Recent inconsistent results for fcc-Fe ultra thin films could be explained by the two spin state model, the surface Fe atomic rearrangement, and the magnetovolume effect. © *1996 American Institute of Physics.* [S0021-8979(96)47608-5]

Giant magnetoresistance and high sensitivity in annealed NiFeCo/Ag multilayers

J. W. Dykes and Y. K. Kim
Quantum Peripherals Colorado, Incorporated, Louisville, Colorado 80028-8188

A. Tsoukatos and S. Gupta
Materials Research Corporation, Orangeburg, New York 10962

S. C. Sanders
Electromagnetic Technology Division, National Institute of Standards and Technology, Boulder, Colorado 80303-3328

We report giant magnetoresistance in annealed NiFeCo (2 nm)/Ag (3.3 nm) multilayers. For all samples, post-deposition annealing was necessary for the observation of GMR analogous to the NiFe/Ag discontinuous multilayer system. The GMR ratio and field sensitivity varied widely as a function of annealing from temperatures between 300 and 400 °C. A high MR ratio of 6.3% and field sensitivity of 11.3%/(kA/m) (0.9%/Oe) were observed for a seven bilayer sample annealed to 350 °C. In general, NiFeCo/Ag multilayers produced greater MR responses and field sensitivities than comparably annealed NiFe/Ag multilayers. NiFeCo/Ag multilayers, however, display more hysteresis than NiFe/Ag multilayers and lack a zero-crossing saturation magnetostriction versus annealing temperature. Multilayer deposition in a magnetic field severely degrades MR performance since it prevents the magnetostatic antiparallel alignment between magnetic grains which occurs in the absence of an applied magnetic field following sample annealing. © *1996 American Institute of Physics.* [S0021-8979(96)53708-2]

I. INTRODUCTION

To prove useful in magnetic recording applications, a magnetoresistive material must display an appreciable magnetoresistive response and sensitivity in small magnetic fields. One material which meets the above criteria in the NiFe/Ag discontinuous multilayer discovered by Hylton *et al.*[1] In this system, post-deposition annealing is required to obtain GMR.[1] A possible mechanism to explain the onset of GMR after annealing is the diffusion of Ag along the columnar grain boundaries. This diffusion effectively breaks up the NiFe layers into grains that interact magnetostatically.[1,2] An antiparallel magnetostatic coupling in the absence of an external magnetic field produces a maximum resistance; the resistance then decreases as a magnetic field is applied and the magnetic moments of the grains become aligned.

In an attempt to exceed the magnetoresistive performance found in NiFe/Ag multilayers, we have synthesized multilayers of NiFeCo/Ag.[3] The addition of cobalt to the magnetic layers should result in an enhanced spin-dependent scattering of bulk origin. NiFeCo/Cu multilayers have been found to have large MR ratios in small saturation fields.[4,5] The $Ni_{66}Fe_{16}Co_{18}$ composition is worthy of consideration since it has zero-magnetostriction and zero-magnetocrystalline anisotropy in single-layered films and shows a large GMR when multilayered with Cu.[4]

Annealed samples which exhibited sizable magnetoresistive responses were subjected to magnetostriction measurements. The saturation magnetostriction λ_s is a critical soft magnetic property which must have a low and tightly controlled value since it frequently induces an undesirable magnetoelastic anisotropy during head fabrication.[6]

II. EXPERIMENT

NiFeCo/Ag multilayer films were deposited onto 76-mm-diam Si wafers maintaining 150 nm of thermal surface oxide using dc magnetron sputtering from $Ni_{66}Fe_{16}Co_{18}$, Ag, and Ta targets. Sputtering occurred at a dynamic argon pressure of 0.93 Pa (7 mTorr) with a deposition rate of 0.5 nm/s for all materials. System base pressures prior to deposition were of the order of 10^{-6} Pa (10^{-8} Torr). When required, a magnetic field of 6.8 kA/m (85 Oe) was applied to the substrate to promote magnetic ordering within the film. The nominal multilayer structures were of the form: Si/SiO_2(150 nm)/Ta(4.5 nm)/Ag(1.6 nm)/NiFeCo(2 nm)/[Ag(3.3 nm)/NiFeCo(2 nm)]$_{N-1}$/Ag(1.6 nm)/Ta(11 nm), where N is the number of bilayers (N=5,7,9). Samples with equal numbers of bilayers were produced with and without a magnetic field present during film growth. Following deposition, the central regions of the wafers were diced into 38 mm×6.4 mm strips and annealed. Annealing was performed in a rapid annealing furnace for 5 min in a 5% H_2-Ar ambient at temperatures of 320, 350, 370, and 400 °C.

The magnetoresistive response of samples was measured at room temperature using a four-point in-line geometry with magnetic fields up to 8 kA/m (100 Oe). The measuring current was applied perpendicular to the in-plane magnetic field. Magnetostriction was likewise measured at room temperature by a high-precision optical tester employing an in-plane rotating magnetic field and laser-beam deflection technique.[7]

 0021-8979/96/79(8)/5584/3/$10.00 © 1996 American Institute of Physics

TABLE I. The magnetoresistive responses and saturation magnetostriction for five, seven, and nine bilayer NiFeCo(2 nm)/Ag(3.3 nm) multilayer samples subjected to 5-min anneals from 340 to 400 °C in a 5% H_2-Ar ambient environment are depicted. The samples were dpeosited in the absence of a magnetic field.

Bilayers	Anneal temp (°C)	$\Delta R/R_s$ (%)	$d(\Delta R/R_s)/dH$ [%/(kA/m)]	λ_s ($\times 10^{-7}$)
5	320	2.8	6.2	10.4
5	350	3.1	3.6	10.4
5	370	3.2	3.0	9.6
5	400	2.4	1.0	5.0
7	320	1.9	5.0	11.5
7	350	6.3	11.3	10.1
7	370	6.5	4.8	6.0
7	400	3.4	1.3	4.4
9	320	1.2	1.3	11.3
9	350	3.9	10.1	12.1
9	370	6.0	5.5	10.5
9	400	3.7	2.5	4.4

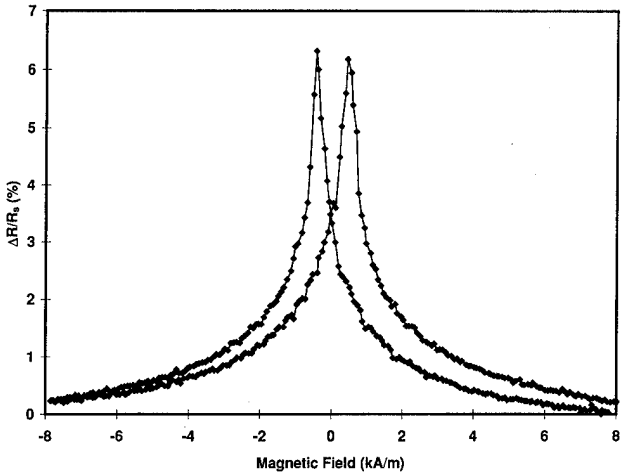


FIG. 1. Magnetoresistive response of a seven bilayer NiFeCo (2 nm)/Ag(3.3 nm) multilayer annealed for 5 min at 350 °C in a 5% H_2-Ar ambient environment. The maximum magnetic field sensitivity $d(\Delta R/R_s)/dH$ is 11.3%/(kA/m) (0.9%/Oe).

III. RESULTS AND DISCUSSION

Similar to NiFe/Ag multilayers,[1,3,8] NiFeCo/Ag multilayers require post-deposition annealing to obtain a GMR response. Data for five, seven, and nine bilayer annealed samples deposited without a magnetic field are listed in Table I. The GMR ratio and field sensitivity vary widely as a function of annealing temperature. The MR response, $\Delta R/R_s$, first increases then decreases as the annealing temperature is increased, regardless of the number of bilayers present in a sample. As Table I shows, a seven bilayer sample yielded the best MR performance with a $\Delta R/R_s = 6.5\%$ for an annealing temperature, T_{an}, of 370 °C. This was also the case for NiFe/Ag discontinuous multilayers where a seven bilayer sample showed $\Delta R/R_s \sim 5\%$ for $T_{an} = 370$ °C.[8] The maximum sensitivity $d(\Delta R/R_s)/dH$ does not correlate with the maximum $\Delta R/R_s$ for five, seven, or nine bilayers. The best $d(\Delta R/R_s)/dH$ is 11.3%/(kA/m) (0.9%/Oe) found in the seven bilayer sample annealed to 350 °C. This sample's MR response is only slightly reduced from the best overall MR response and is illustrated in Fig. 1. As a comparison, a NiFe/Ag multilayer with nominally identical preannealing magnetic and spacer layer thicknesses showed a 2.7% MR ratio and a 5%/(kA/m) (0.4%/Oe) field sensitivity.[8]

The properties of NiFeCo/Ag multilayers are not, however, completely superior to those of NiFe/Ag multilayers. The MR transfer curves for NiFeCo/Ag multilayers tend to be more hysteretic than comparable transfer curves for NiFe/Ag multilayers. For example, the separation between peaks in Fig. 1 is ~1.1 kA/m (~14 Oe). This represents some of the smallest hysteresis present within the sample set listed in Table I. MR transfer curves for NiFe/Ag multilayers, on the other hand, have peak separations less than 0.3 kA/m (~4 Oe).[9] The increased hysteresis present in NiFeCo/Ag multilayers is likely due to an increased coercivity associated with the addition of cobalt. In addition to larger hysteresis, NiFeCo/Ag multilayers yield less-desirable magnetostrictive behaviors. The saturation magnetostriction λ_s of NiFeCo/Ag multilayers does not have a zero-crossing analog like the zero crossing of the curves λ_s versus annealing temperature found systematically in NiFe/Ag.[8,9] Instead, λ_s for NiFeCo/Ag multilayers remains positive for all annealing temperature between 320 and 400 °C. The saturation magnetostriction for NiFeCo/Ag multilayers does, however, decrease as the annealing temperature is increased yielding magnetostriction values of 10^{-6} or lower for materials displaying a large GMR and field sensitivity.

Films which mirrored the number of bilayers and annealing temperature listed in Table I but deposited in a magnetic field were also tested for magnetoresistive response. In all cases, the MR transfer curves revealed extremely poor responses. Among these, the highest $\Delta R/R_s$ value attained was 1.4%. Responses less than 1% were typical. The field sensitivities in all cases were low enough that they were not definable. The inability of these samples to show GMR after annealing is attributed to a magnetic anisotropy produced during deposition which retains sufficient strength during annealing to prevent antiparallel magnetostatic coupling between magnetic grains in the absence of an applied magnetic field.

IV. SUMMARY

In summary, we have observed giant magnetoresistance in annealed NiFeCo (2 nm)/Ag (3.3 nm) multilayers. The resulting MR responses and field sensitivities were highly dependent upon the annealing temperature. A high MR ratio of 6.3% and field sensitivity 11.3%/(kA/m) (0.9%/Oe) were observed for a seven bilayer sample annealed to 350 °C. NiFeCo/Ag multilayers exhibit larger MR responses and field sensitivities than annealed NiFe/Ag multilayers, but with more hysteresis and higher saturation magnetostrictions. The application of a magnetic field during deposition led to a systematic and detrimental reduction in MR response.

[1]T. L. Hylton, K. R. Coffey, M. A. Parker, and J. K. Howard, Science **261**, 1021 (1993).
[2]J. C. Slonczewski, J. Magn. Magn. Mater. **129**, L123 (1994).
[3]J. D. Jarratt and J. A. Barnard, Mater. Res. Soc. Symp. Proc. **343**, 399 (1994).
[4]S. Tsunashima, M. Jimbo, T. Kanda, S. Goto, and S. Uchiyama, Mater. Res. Soc. Symp. Proc. **313**, 271 (1993).
[5]H. Sakakima, M. Satomi, K. Onaka, and S. Yamamoto, J. Magn. Magn. Mater. **145**, L268 (1995).
[6]D. Markham and N. Smith, IEEE Trans. Magn. **24**, 2606 (1988).
[7]A. C. Tam and H. Schroeder, IEEE Trans. Magn. **25**, 2629 (1989).
[8]Y. K. Kim and S. C. Sanders, Appl. Phys. Lett. **66**, 1009 (1995).
[9]Y. K. Kim, S. C. Sanders, and S. E. Russek, IEEE Trans. Magn. **31**, 3964 (1995).

Finite-size effect and its temperature dependence of giant magnetoresistance in magnetic granular materials

Jian-Qing Wang[a] and Gang Xiao
Physics Department, Brown University, Providence, Rhode Island 02912

In magnetic granular alloys such as Co-Ag, a large finite-size effect in giant magnetoresistance (GMR) has been observed as the sample thickness (t) varies. The value of GMR monotonically decreases and eventually vanishes as t approaches zero. The t range, over which the GMR value drops rapidly to zero, has been found to be weakly dependent on temperature. Our results are consistent with a picture that a strong spin-orbit interaction at surfaces is responsible for randomizing spins in different spin channels, thus reducing GMR. © *1996 American Institute of Physics.* [S0021-8979(96)53808-9]

It has been observed that giant magnetoresistance (GMR) in magnetic granular materials depends critically on various dimensional constraints such as magnetic particle size and interparticle distance.[1–3] These dependencies reflect the dominance of the magnetic interface scatterings. Recently, a study[4] on the finite-size effect of GMR has shown that GMR depends strongly on the sample thickness (t). Granular Co-Ag and Fe-Ag thin films, which both show GMR in bulk materials, do not exhibit GMR effect in the two-dimensional (2D) limit. Below a certain length scale which is on the order of the mean free path, GMR monotonically decreases from the bulk value toward zero as t approaches zero.

In heterogeneous magnetic systems, the mechanism responsible for GMR is the spin-dependent scattering of two spin channels. The spin preserving scattering is generally thought to be dominant in controlling the magnetotransport behavior. In magnetic multilayers, there has been a clear demonstration that the spin-flipping scattering influences GMR.[5] Spin-flipping scattering reduces the GMR magnitude by mixing electrons in the two spin channels. There has been no strong evidence that spin-flipping scatterings substantially affect GMR in bulk granular materials. In thin films, however, the existence of surfaces may introduce spin-flipping scattering,[6] and cause GMR to decrease. Our earlier study has indicated[4] that the enhanced spin-orbit interaction at the surfaces causes spin randomization, and hence is responsible for the observed finite-size effect.

There are other interactions that cause spin flipping. One example is the electron-magnon interaction. Our earlier study was carried out at $T=4.2$ K, where electron-magnon interaction can be neglected. At higher temperatures, the strongly T-dependent electron-magnon interaction needs to be considered. It is the subject of the present work to investigate the temperature dependence of the finite-size effect of GMR in granular materials. We have found that although the value of GMR for a particular sample does depend on temperature, the thickness dependence of GMR is nearly independent of temperature. This finding further supports the picture that the surface induced spin-orbit interaction which is T independent is mainly responsible for the finite-size effect.

Our samples were fabricated using a high vacuum magnetron-sputtering system with a base pressure better than 1×10^{-7} Torr during the deposition. To reduce random variation, each series of samples of varying thicknesses was deposited in a single run with a constant sputtering rate and onto a single 2×5 cm^2 glass substrate. A computer controlled stepping shutter was swept across the substrate in steps. The sample thickness at each step was precisely controlled by the duration of exposure time. The step-wedged samples were subsequently patterned into Hall bars by photolithography for magnetotransport measurements. All the samples used in this study were protected by a layer of photoresist immediately after deposition to avoid oxidation. They were not thermally annealed.

The thickness dependence of GMR is presented in Fig. 1 for $Co_{20}Ag_{80}$ granular films measured at $T=4.2$ K. To characterize GMR quantitatively, we use the net change in resistivity ($\Delta\rho$) from zero field to a high field ($H=8$ T). At $H=8$ T, the resistivity [$\rho(H)$] is nearly saturated. The commonly used magnetoresistance ratio, $\Delta\rho/\rho$, is not an appropriate parameter for investigating the finite-size effect, because it is also sensitive to other scatterings, such as disorder, of nonmagnetic origin. We choose $Co_{20}Ag_{80}$, a GMR material whose bulk form has been studied extensively.[2,3] The data in Fig. 1 consist of measurement on two series (denoted by solid dots and triangles) of thin films fabricated under iden-

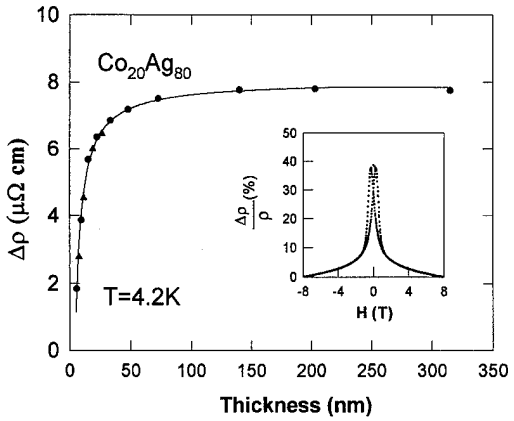


FIG. 1. Net change in resistivity $\Delta\rho=\rho(0)-\rho(8T)$ vs sample thickness t at $T=4.2$ K. The solid dots and triangles are measured points for samples from two different series fabricated identically. Inset: $\Delta\rho/\rho(0)$ vs H for a bulk sample ($t=315$ nm).

[a]Present address: Applied Physics Dept. Yale Univ., New Haven, CT 06520.

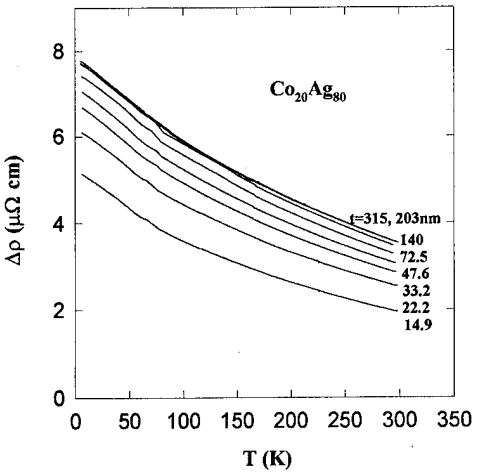


FIG. 2. Measured $\Delta\rho$ vs temperature T for samples of various thicknesses. The numbers by the curves in descending order indicate the sample thicknesses in the same order. Note that the curves of the two thick samples (t=315 and 203 nm) overlap with each other, indicating reaching the bulk limit.

tical conditions. The two sets of data are rather consistent between each other. The inset shows the quantity $\Delta\rho/\rho(0)$ in cycling magnetic field (± 8 T) for a bulk sample with a thickness of 315 nm. It is seen that $\rho(H)$ is almost saturated at 8 T and the bulk sample carries a GMR value of about 40%. At T=4.2 K, the zero field $\rho_{4.2\ \mathrm{K}}$ is about 27 $\mu\Omega$ cm for a bulk sample. The resistivity ratio $\rho_{4.2\ \mathrm{K}}/\rho_{300\ \mathrm{K}}$ is about 1.1. As t reduces to 5 nm, $\rho_{4.2\ \mathrm{K}}$ increases about 40% due to the surface scatterings. Over the whole t range (5–320 nm) studied, the low-T spontaneous magnetization and the size of the magnetic particles remain constant within the experimental uncertainty.[4]

The variation of $\Delta\rho$ with t can be characterized by an initially slow decrease with t in thick samples and a rapid decrease in the thin-film region (t<50 nm). In the 2D limit (t approaching zero), GMR can no longer be sustained. A phenomenological relation $\Delta\rho=\Delta\rho_b(1-e^{-t/t_0})$, where $\Delta\rho_b$ is the bulk value of $\Delta\rho$, gives a reasonable description of the t dependence. The constant t_0 represents a characteristic length scale, that we call the decay length, of the finite-size effect. We believe that the origin of the finite-size effect observed is the enhanced spin-orbit interaction[6] on the surfaces of a thin film. The strong spin-orbit coupling induces spin-flipping scatterings which tend to equalize the different electron mean free paths of the two spin channels. Qualitatively, the larger the surface effect, the longer the decay length t_0.

In addition to the spin-orbit interaction, electron-magnon scattering is also detrimental to GMR, particularly at high T.[7] The study of thermal effect on our samples may provide insight to the mechanism of the observed finite-size effect. For most of our samples we have measured $\Delta\rho$ as a function of T [$\Delta\rho(T)$] from 4.2 to 300 K. The results are presented in Fig. 2 for eight thicknesses. Note that the $\Delta\rho(T)$ curves for the two thick samples (t=203 and 315 nm) coincide with each other, due to the bulk nature of these samples. Figure 2 shows that $\Delta\rho(T)$ shares almost identical T dependence regardless of the film thickness.

In Fig. 3(a), we present $\Delta\rho$ as a function of t at various

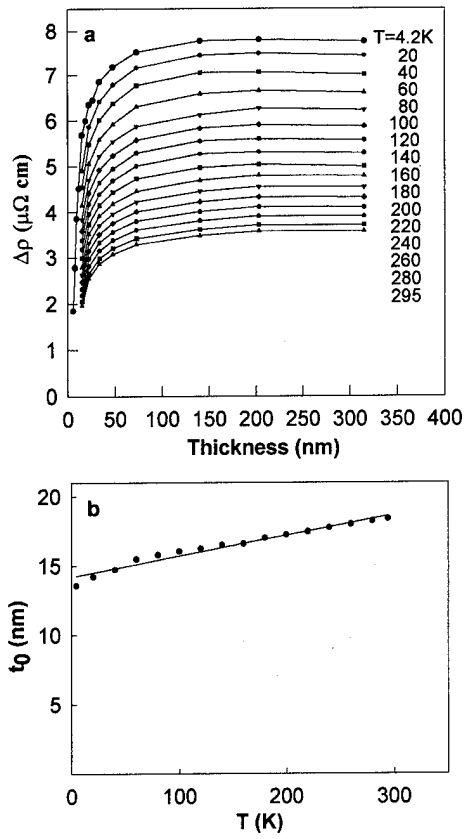


FIG. 3. (a) Net resistivity change $\Delta\rho(T)$ vs t at various temperatures. Solid symbols represent mesaurement data for different sample thicknesses. The thin lines are guides to the eyes. The numbers in descending order give the temperatures for the data curves in the same order. (b) Decay length $t_0(T)$ vs temperature.

temperatures. By fitting the curves with $\Delta\rho(T)=\Delta\rho_b(T)\times[1-e^{-t/t_0(T)}]$, we have obtained the decay length $t_0(T)$ in the T range of our measurement. The derived $t_0(T)$ is shown in Fig. 3(b). Over the tempersature range studied, $t_0(T)$ is weakly dependent on T, increasing only 20% from 4.2 to 295 K. This result further affirms that the dominant mechanism behind the finite-size effect is the surface induced spin-orbit interaction, whose strength is independent of T. A finite T does slightly affect the finite-size effect by increasing $t_0(T)$ albeit by a small amount. There are a few possible causes. Thin films may develop a softening in magnetic structure at finite T, particularly on the surfaces. It is also possible that electron-magnon interaction may be slightly enhanced at the surfaces.

In conclusion, we have studied a finite-size effect of GMR with respect to the sample thickness and its temperature dependence. We found that GMR monotonically decrease with thickness reaching zero as t approaches zero within a decay length of 15 nm. We also found that this decay length is weakly dependent on temperature, which indicates that the main mechanism of finite-size effect is the surface induced spin-orbit interaction.

This work was supported in part by the National Science Foundation (NSF) through the Materials Research Program at Brown University, grant No. DMR-9121747. G.X. is partially supported by the NSF grant No. DMR-9258306.

[1] A. E. Berkowitz, J. R. Mitchell, M. J. Carey, A. P. Young, S. Zhang, F. E. Spada, F. T. Parker, A. Hutten, and G. Thomas, Phys. Rev. Lett. **68**, 3745 (1992); J. Q. Xiao, J. S. Jiang, and C. L. Chien, *ibid.* **68**, 3749 (1992).
[2] J.-Q. Wang and G. Xiao, Phys. Rev. B **49**, 3982 (1994).
[3] P. Xiong, G. Xiao, J.-Q. Wang, J. Q. Xiao, J. S. Jiang, and C. L. Chien, Phys. Rev. Lett. **69**, 3220 (1992).
[4] J.-Q. Wang and G. Xiao, Phys. Rev. B **51**, 5863 (1995).
[5] Q. Yang, P. Holody, S.-F. Lee, L. L. Henry, R. Loloee, P. A. Schroeder, W. P. Pratt, Jr., and J. Bass, Phys. Rev. Lett. **72**, 3274 (1994).
[6] P. E. Lindelof and S. Wang, Phys. Rev. B **33**, 1478 (1986).
[7] J.-Q. Wang and G. Xiao, Phys. Rev. B **50**, 3423 (1994).

Thickness dependence of giant magnetoresistance of AgNiFe heterogeneous alloys films

J. Wiggins, M. L. Watson, and P. A. Gago-Sandoval
Centre for Data Storage Materials, Coventry University, Priority Street, Coventry CV1 5FB, United Kingdom

K. O'Grady
Magnetic Materials Research Group, SEECS, University of Wales, Bangor, Gwynedd LL57 1UT, United Kingdom

We have investigated the thickness dependence of the giant magnetoresistance (GMR) observed in AgNiFe heterogeneous alloy films. The films were sputtered from a mosaic target at the system ambient temperature onto glass substrates. In order to maintain interfacial uniformity, and to control the spin-dependent transmission of electrons at the AgNiFe film interfaces, they were covered by 200-Å-thick NiFe under- and overlayers. The samples have total thicknesses in the range 400–3000 Å. The film resistivity, magnetoresistivity, and magnetization were measured in the temperature range 4–300 K and in fields of up to 1.1 T and the structure examined using both large- and small-angle x-ray diffraction. The results indicate that the observed thickness dependence of the GMR of the AgNiFe films is within the experimental error It is postulated that this is due to coherent spin transmission of conduction electrons across the sandwich interfaces which does not degrade the GMR by mixing of the spin currents. © *1996 American Institute of Physics.* [S0021-8979(96)53908-9]

I. INTRODUCTION

The recent discovery of the giant magnetoresistance (GMR) of magnetic multilayers[1] and heterogeneous alloy films[2] has led to much current worldwide interest in this technologically important effect. Heterogeneous alloys consist of a superparamagnetic nanocrystalline structure in which fine particles of a ferromagnetic material are embedded in a nonmagnetic matrix material. They are formed by the co-deposition of two immiscible metals, one of which is ferromagnetic in bulk. To promote phase segregation the film is either deposited at an elevated temperature or annealed after deposition. When the particles moments are randomly oriented the materials resistivity is higher than when they are aligned by the application of an external magnetic field. It is now generally accepted[3] that GMR is due to spin-dependent scattering of electrons both within and at the interfaces of the ferromagnetic entities (either films or particles).

It has been found that the effect is a sensitive function of both the size of the ferromagnetic particles and the concentration of the ferromagnetic material in the alloy.[4] The former effect has been postulated to be due to the existence of an optimum particle size, determined by the conduction electron mean free path[5] (larger particle sizes result in a reduction of the GMR due to the decrease in particle surface to volume ratio), and the latter effect to the onset of percolation, which acts to couple the particles ferromagnetically.

In multilayers the current flow can be directed either parallel to the plane of the multilayer (CIP GMR) or with more difficulty perpendicular to it (CPP GMR). In CIP-GMR conduction electrons average the properties of the multilayer in the direction perpendicular to the multilayer plane on the length scale of their mean free path, however, it has recently been shown that this is not the case for CPP GMR.[6] For this geometry the key damping parameter in determining the GMR is the spin diffusion length l_{sf}. Analysis of CPP-GMR experiments[7] indicates that l_{sf} is $\approx 10^3$ Å and is therefore very much longer than both the electron mean free path and the thicknesses of the nonmagnetic and ferromagnetic films comprising the multilayer. It is also predicted that when l_{sf} is shorter than the film thicknesses, the CPP GMR will decrease as $\exp(-t_N/2l_{sf})$, where t_N is the thickness of the nonmagnetic film.[6] Such behavior has recently been reported for Co/Ag multilayers in which l_{sf} has been limited by the introduction of Mn impurities to increase spin-orbit scattering.[8] As a typical granular structure contains magnetic particles of mean diameter $\approx$10–40 Å which are separated by $\approx$10–200 Å it is clear that l_{sf} will also be of critical importance in determining the GMR in these materials. Any mechanism, such as spin-dependent interfacial scattering or the jitterbug effect,[9] which acts to mix the spin channels and therefore shorten the spin diffusion length, will therefore degrade the GMR.

GMR in heterogeneous alloys has previously been modeled by considering the self-averaging of the electric-field lines passing through the granular structure.[10] This model predicts that the GMR is quadratic in H and depends strongly on the size of the ferromagnetic particles, the electron mean free paths, and the ratios of the spin-dependent to spin-independent scattering potentials of the particles and interfaces. A second model identifies both the spin-dependent scattering potential and density of states of the d band as being possible origins of the GMR.[11] This model also predicts a quadratic dependence of the GMR on applied field, providing spin-flip scattering is negligible and is supported by measurement of the magnetothermopower of Co–Ag granular alloys.[12] More recently the GMR has been consid-

 0021-8979/96/79(8)/5590/3/$10.00 © 1996 American Institute of Physics

ered within the framework of a modified effective exchange interaction model.[13] This model treats the spin-dependent scattering as arising from an exchange interaction potential between the conduction electrons and magnetic scatterers.

In order to elucidate the effect of spin mixing we have investigated the thickness dependence of the resistivity and GMR. In principle the GMR in heterogeneous alloys should not be thickness dependent provided that the particle size distribution remains constant with thickness. However, this will not be the case if electrons scattered from the film interfaces lose their spin memory, i.e., they are spin flipped, thereby mixing the spin currents and decreasing the spin diffusion length. Such effects have recently been reported for CoAg,[14,15] and FeAg,[16] thin films and discussed in terms of the spin-flip scattering rate.[15]

II. EXPERIMENT

NiFe/Ag–Ni–Fe/NiFe films were rf sputtered onto glass microscope slides at the system ambient temperature. The base pressure was $<2\times10^{-7}$ Torr, the sputtering pressure was 8 mTorr of argon, and the sputtering power was 100 W for both the NiFe and the AgNiFe films. The targets used consisted of a 4 in. Ag (99.999%) disk onto which were placed $Ni_{81}Fe_{19}$ (99.97%) squares arranged in a mosaic pattern and a $Ni_{81}Fe_{19}$ (99.95%) 4 in. target. The film thickness was measured by interferometry and the composition determined using energy-dispersive x-ray analysis (EDAX). The Ag content of the films was fixed at 78±5 at. %.

The resistivity and magnetoresistivity of the films were measured using a computer-controlled four-point dc method in a continuous-flow He cryostat over the temperature range 3.8–300 K in fields of up to 1.1 T. Magnetic measurements were made at 10 K using a PAR 155 vibrating sample magnetometer (VSM) fitted with an Oxford Instruments CF1200 continuous-flow He cryostat.

III. RESULTS

The magnetoresistance measured at 10 K is shown for five representative samples in Fig. 1. As can be seen from this figure the GMR decreases by a factor of ≈2 as the thickness of the AgNiFe film is decreased to 300 Å, however, this may be due to a number of factors other than a thickness dependence (e.g., changes in the film composition or particle size distribution or magnetization). Reduction of the GMR observed in FeAg films due to the second and third effects has already been reported.[16] As the AgNiFe composition was found to be constant for all thicknesses the first effect could be eliminated.

To investigate the second, the GMR was modeled assuming an ensemble of superparamagnetic particles whose diameters are given by a log-normal distribution. This size distribution has previously been found to accurately describe the magnetization of SiO_2/Fe sputtered films.[17] A similar approach has also very recently been found to accurately fit the hysteresis of melt-spun Co–Cu ribbons.[18] Assuming the ensemble of particles is noninteracting and above its blocking temperature, the system can be described by set of Langevin

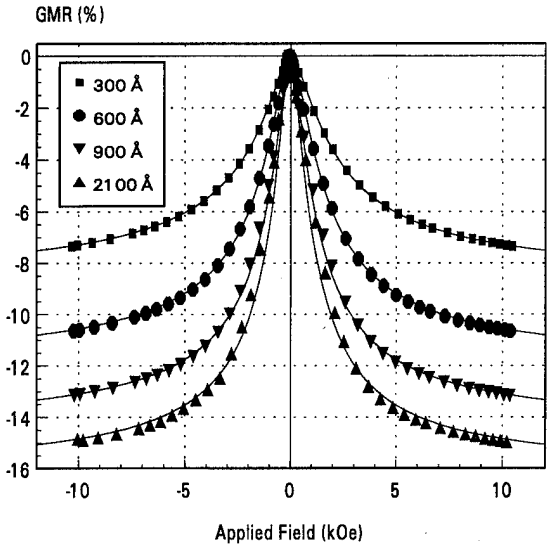


FIG. 1. GMR of five representative NiFe(200 Å)/AgNiFe (× Å)/NiFe(200 Å) films. The solid lines are fits using the model and parameters described.

functions. This is found experimentally to be the case for the films considered here for temperatures above about 20 K. The magnetization is then found from

$$M = pM_s \sum_{D=1}^{300} f(D)\left[\coth\left(\frac{\mu H}{kT}\right) - \left(\frac{kT}{\mu H}\right)\right], \tag{1}$$

where $\mu = (M_s/6)\pi(D^3)$, $f(D)$ is the log-normal function, and p is the concentration of the ferromagnetic material in the film.[17] In heterogeneous alloy systems the GMR is related to the magnetization by the simple relationship

$$\delta R \propto A(M/M_s)^2, \tag{2}$$

where A is a scaling constant related to the spin-dependent scattering efficiency of the particles.[2,4,11,13] Using this relationship and the calculated magnetization the experimental data were fitted assuming a constant particle magnetization (the bulk value for Permalloy). The fits are shown as the solid lines in Fig. 1. The size distribution parameters of the fits indicate that the mean particle diameter increased from 14 to 18 Å and that the deviation of the distribution decreased from 0.26 to 0.22 as the AgNiFe film thickness increased from 300 to 2100 Å. From annealing experiments on single AgNiFe films it has been found that variations of this order do not significantly effect the size of the GMR.[19] Variations in the size of the GMR due to changes in the magnetization of the particles could not be determined due to both the very small volume of Ni and Fe in the AgNiFe films and the masking of its hysteresis by the upper and lower NiFe films. This is demonstrated in Fig. 2 which shows hysteresis loops of three of the set of films measured at 10 K.

To remove the effect of current shunting in the NiFe capping films the sandwich resistance was calculated assuming a parallel resistor model. This has been shown to be a

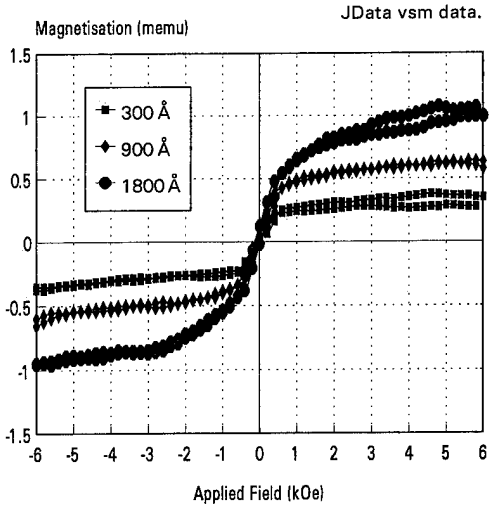


FIG. 2. Hysteresis loops of three representative NiFe(200 Å)/AgNiFe (× Å)/ NiFe(200 Å) films.

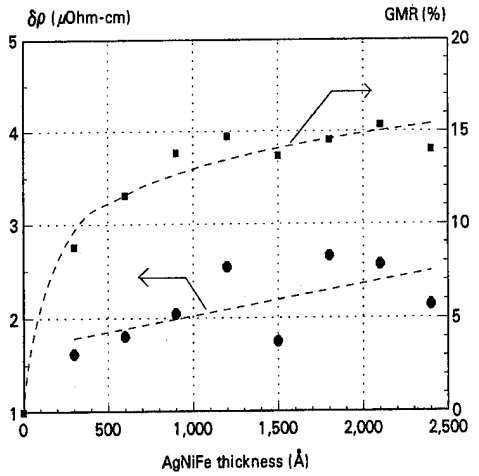


FIG. 3. Variation of the GMR of the AgNiFe after correction for the shunting of the upper and lower NiFe films and the magnetic part of the resistivity with AgNiFe thickness.

reasonable approach, providing the mean free path of the conduction electrons is much less than the thickness of the films.[20] This is clearly the case in these films in which the upper and lower NiFe films are 200 Å thick and the maximum AgNiFe thickness is 300 Å and is supported by the excellent straight line fit obtained for a graph of the inverse of the sandwich resistance plotted against the AgNiFe film thickness. In addition analysis of the resistivity of the NiFe films using a simple free electron approach provides a value for the mean free path much less than the thickness and compares well with the spin-up and spin-down electron mean free paths reported for NiFe (110 and 10 Å, respectively).[21] From this analysis the magnetic contribution to the resistivity was obtained and is shown in Fig. 3. Also shown in this figure is the percentage change of the resistance of the AgNiFe films alone. As can be seen from this figure, the variation of the magnetic part of the scattering with thickness of the AgNiFe films is within the experimental scatter of the results.

IV. CONCLUSION

These results indicate that the thickness dependence of the GMR in AgNiFe heterogeneous alloy films is small when they are placed between two NiFe films. This can be understood by considering the spin-dependent transmission of electrons at the interfaces. Analysis of the GMR of NiFe-based spin valves has shown that electrons are coherently transmitted across NiFe/Cu interfaces.[21] Thus, it is to be expected that there will be very little spin orbit scattering (and hence spin mixing) at the AgNiFe/NiFe interfaces and hence no reduction in the GMR as the thickness of the AgNiFe is decreased.

ACKNOWLEDGMENTS

This work was supported in part by the SERC Magnetism and Magnetic Materials Initiative, and M. L. W. also acknowledges the support of the Nuffield Foundation.

[1] M. N. Baibich, J. M. Broto, A. Fert, F. Nguyen Van Dau, F. Petroff, P. Eitenne, G. Creuzet, A. Freidrich, and J. Chazelas, Phys. Rev. Lett. **61**, 2472 (1988).
[2] A. E. Berkowitz, J. R. Mitchell, M. J. Carey, A. P. Young, S. Zhang, F. E. Spada, F. T. Parker, H. Hutten, and G. Thomas, Phys. Rev. Lett. **68**, 3745 (1992); J. Q. Xiao, J. S. Jiang, and C. L. Chien, *ibid.* **68**, 3749 (1992); J. A. Barnard, A. Waknis, M. Tan, E. Haftek, M. R. Parker, and M. L. Watson, J. Magn. Magn. Mater. **114**, L230 (1992).
[3] R. E. Camley and J. Barnas, Phys. Rev. Lett. **63**, 664 (1989); S. Zhang, Appl. Phys. Lett. **61**, 1855 (1992); S. Zhang and P. M. Levy, J. Appl. Phys. **73**, 5315 (1993); H. E. Camblong and P. M. Levy, Phys. Rev. Lett. **69**, 2835 (1992); H. E. Camblong, S. Zhang, and P. M. Levy, J. Appl. Phys. **75**, 6908 (1994).
[4] J. S. Jiang, J. Q. Xiao, and C. L. Chien, Appl. Phys. Lett. **61**, 2362 (1992); M. L. Watson, J. A. Barnard, S. Hossain, and M. R. Parker, J. Appl. Phys. **73**, 5506 (1993); B. Dieny, S. R. Teixeira, B. Rodmacq, C. Cowache, S. Auffret, O. Redon, and J. Pierre, J. Magn. Magn. Mater. **130**, 197 (1994).
[5] S. Zhang, Appl. Phys. Lett. **61**, 1855 (1992); S. Zhang and P. M. Levy, J. Appl. Phys. **73**, 5315 (1993); P. Xiong, G. Xiao, J.-Q. Wang, J. Q. Xiao, J. S. Jiang, and C. L. Chien, Phys. Rev. Lett. **69**, 3220 (1992).
[6] T. Valet and A. Fert, Phys. Rev. B **48**, 7099 (1993).
[7] W. P. Pratt, Jr., S.-F. Lee, J. M. Slaughter, R. Loloee, P. A. Schroeder, and J. Bass, Phys. Rev. Lett. **66**, 3060 (1991); M. A. M. Gijs, S. K. J. Lenczowski, and J. B. Giesbers, Phys. Rev. Lett. **70**, 3343 (1993).
[8] Q. Yang *et al.*, Ref. 13 of Ref. 6.
[9] G. A. Gehring, J. F. Gregg, S. M. Thompson, and M. L. Watson, J. Magn. Magn. Mater. **140-144**, 501 (1995).
[10] S. Zhang, Appl. Phys. Lett. **61**, 1855 (1992).
[11] L. Xing and Y. C. Chang, Phys. Rev. B **48**, 4156 (1993); L. Xing, Y. C. Chang, M. B. Salamon, D. M. Frankel, J. Shi, and J. P. Lu, *ibid.* **48**, 6728 (1993).
[12] L. Piraux, M. Cassart, J. S. Jiang, J. Q. Xiao, and C. L. Chien, Phys. Rev. B **48**, 638 (1993); J. Shi, E. Kita, L. Xing, and M. B. Salamon, Phys. Rev. B **48**, 16119 (1993).
[13] J.-Q. Wang, P. Xiong, and G. Xiao, Phys. Rev. B **47**, 8341 (1993); J.-Q. Wang, and G. Xiao, *ibid.* **49**, 3982 (1994).
[14] J. R. Mitchell and A. E. Berkowitz, J. Appl. Phys. **75**, 6912 (1994).
[15] J.-Q. Wang and G. Xiao, Phys. Rev. B **51**, 5863 (1995).
[16] C. Yu, Y. Wang, W. Lai, and Z. Wang, J. Magn. Magn. Mater. **145**, 239 (1995).
[17] G. Xiao and C. L. Chien, J. Appl. Phys. **61**, 3308 (1987).
[18] R. H. Yu, X. X. Zhang, J. Tajeda, M. Knobel, P. Tiberto, and P. Allia, J.Phys. Condens. Matter. **7**, 4081 (1995).
[19] M. L. Watson, V. G. Lewis, and K. O'Grady, J. Appl. Phys. **75**, 6927 (1994).
[20] D. M. Edwards, J. Mathon, and R. B. Muniz, IEEE Trans. Magn. **MAG-27**, 3548 (1991).
[21] B. Dieny, V. S. Speriosu, J. P. Nozieres, B. A. Gurney, A. Vedayev, and N. Ryshanova, in *Proceedings of the NATO Advanced Workshop on Structure and Magnetism in Systems of Reduced Dimensions*, edited by R. Farrow *et al.* (Plenum, New York).

Jitterbug spin channel mixing in heterogeneous giant magnetoresistive material

J. F. Gregg and W. Allen
Clarendon Laboratory, Parks Road, Oxford, OX1 3PU, United Kingdom

S. M. Thompson
Physics Department, University of York, York, YO1 5DD, United Kingdom

M. L. Watson
Centre for Data Storage Materials, Coventry University, Priory Street, Conventry, CV1 5FB, United Kingdom

G. A. Gehring
Sheffield Centre for Advanced Magnetic Materials and Devices, University of Sheffield, Hicks Building, Hounsfield Road, Sheffield S3 7RH, United Kingdom

A mechanism is described which considers the effect of small magnetic particles on the spin diffusion length in a granular giant magnetoresistive material. Spin depolarization occurs by precession of the spin orientation of the carrier due to the s–d exchange interaction within a magnetic particle. Numerical simulation of this jitterbug effect is found to generate a temperature and field dependence of the distance a carrier may travel within the sample without losing its spin memory. © *1996 American Institute of Physics.* [S0021-8979(96)54008-2]

INTRODUCTION

In a granular giant magnetoresistive (GMR) material,[1] the magnetic component consists of small, independent, entities embedded in a nonmagnetic, conducting matrix—usually a combination of two or more suitable immiscible metals such as Co and Ag or NiFe and Ag. Such material may be prepared by a variety of methods such as sputtering, coevaporation, or mechanical alloying. During the application of a magnetic field the magnetic orientation of the particles changes from a random configuration at the zero magnetization point (the origin for a superparamagnetic system, otherwise the coercive point) to alignment at magnetic saturation. As for GMR multilayers[2] the spin-dependent scattering at the magnetic particles varies as the degree of alignment of the magnetic regions is altered thereby generating a giant magnetoresistance. The temperature dependence of the magnetoresistance is an important clue in unraveling the dominant scattering mechanisms. In this article we describe a new process of spin depolarization which contributes to the temperature and field dependence of this effect.

THE MODEL

The GMR in these materials can be thought of as resulting from a transfer of magnetic information between adjacent magnetic granules which is mediated by the spin memory of the electrical carriers. By analogy with the concept of spin memory in nuclear magnetic resonance,[3] the information is coded onto the spin population by the first magnetic granule and then subsequently "read" by the second. This spin information is written by the first magnetic cluster in the form of a divergence of the electrochemical potential for up and down spin channels which arises from spin-dependent bulk and interface scattering. In the former case it takes effect over a characteristic length l_f in the ferromagnetic material given by[4]

$$\frac{1}{l_f^2}=\frac{1}{2\tau_{\uparrow\downarrow}}\left(\frac{1}{D_\uparrow}+\frac{1}{D_\downarrow}\right), \tag{1}$$

where $D_\uparrow$ and $D_\downarrow$ are the diffusion coefficients of the respective spin channels in the ferromagnet and $\tau_{\uparrow\downarrow}$ is the spin-flip relaxation length. This expression is therefore dominated by the minority spin diffusion coefficient. For the case of bulk scattering, this would determine a minimum magnetic cluster size for effective spin filtering which contributes to explaining the existence of an optimum magnetic cluster size for maximizing the GMR amplitude.

Magnetic clusters in a granular GMR material thus fall into two classes:

(1) clusters larger than the critical size that can read and write spin information, and

(2) smaller particles which are inefficient spin filters (note that these will also have a lower magnetic polarization for given values of magnetic field and temperature).

The latter do not contribute effectively to modifying the electrochemical potentials. In fact, we argue that their contribution to the GMR is a detrimental one in that they increase the effective longitudinal relaxation rate in the paramagnetic matrix between the large spin filter clusters and hence help decrease the spin diffusion length $l'_{sf}=(D'\tau'_{\uparrow\downarrow})^{1/2}$ in the matrix thereby speeding up the spin memory decay.

The evolution of the spin memory in the interim between read and write operations is evidently crucial to determining the observed GMR amplitude since the spin information must survive for sufficiently long that it can be read by the next magnetic cluster. The spin memory relates directly to the spin flip relaxation time $\tau_{\uparrow\downarrow}$ to which a number of processes contribute. For granular GMR material it arises primarily from spin orbit scattering which is not temperature dependent.[4] The spin diffusion length $l'_{sf}=(D'\tau'_{\uparrow\downarrow})^{1/2}$, which determines the spatial decay of the spin memory, evidently contains the temperature dependence of the diffusion con-

 0021-8979/96/79(8)/5593/3/$10.00 © 1996 American Institute of Physics

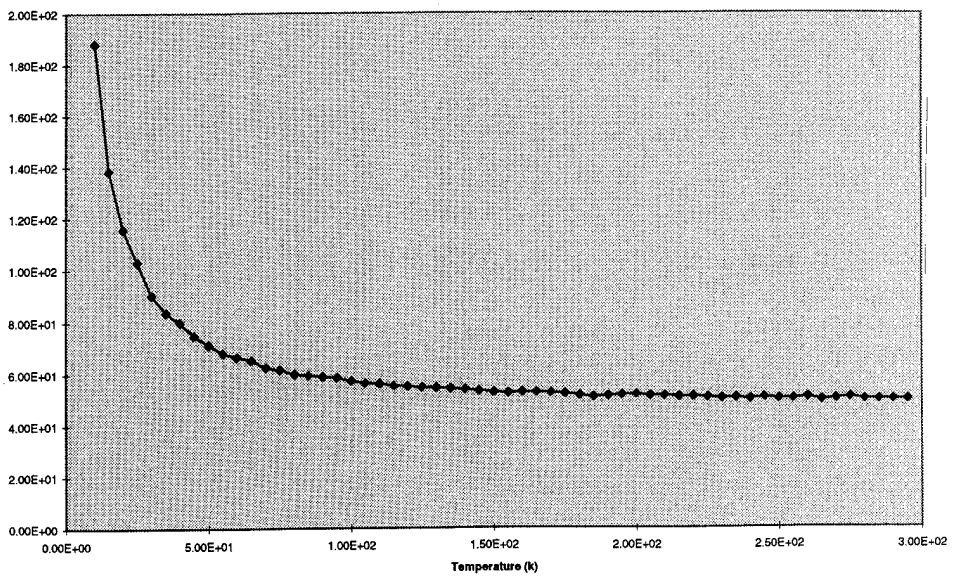


FIG. 1. Variation of l_j (Å) with temperature (K) for a fixed field of 3.1 T and a log normal distribution of particle size with a mean diameter of 15 Å and σ=0.2.

stant D; however, experimentally this is insufficient to model the observed temperature dependence of many granular GMR systems. Given the small magnetic particle sizes, magnon scattering seems to be an unlikely candidate and this leads us to search for a supplementary temperature variation which arises from an additional temperature-dependent contribution to the spin-flip scattering rate.

Accordingly we now postulate a new spin-dependent mechanism which contributes to $\tau_{\uparrow\downarrow}$ by virtue of the pseudo-Larmor precession of the carrier spins owing to the $s-d$ exchange interaction in the magnetic component of the inhomogeneous material. It should be noted that the precession which we describe is termed a pseudo-Larmor precession because it is not associated with the magnetic field within the sample, but involves only the exchange field whose effect is two to three orders of magnitude larger than any imaginable internal magnetic field or indeed any magnetic field that might realistically be externally applied.

The depolarization mechanism that we propose derives from the fact that the exchange fields in the nonmagnetic matrix are small and the situation is thus described by a "sudden" approximation of magnetic resonance in which the spin axis orientation is conserved between magnetic particles.[5] If the magnetic clusters are thermally misaligned from the applied field direction, the spin carrier "jitterbugs" about these successive misaligned quantization directions by

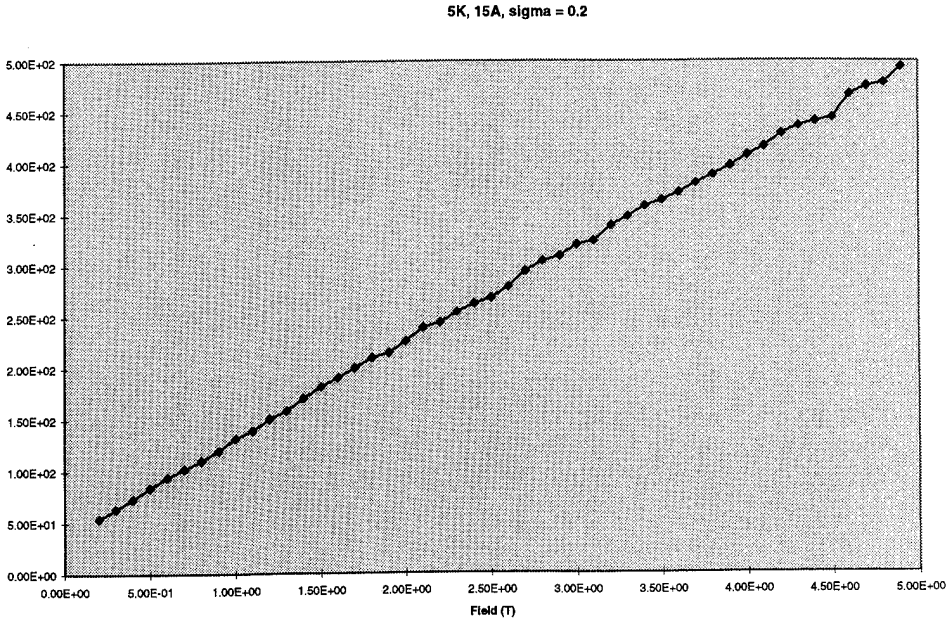


FIG. 2. Variation of l_j (Å) with field (T) at a fixed temperature of 5 K and a log normal distribution of particle size with a mean diameter of 15 Å and σ=0.2.

random angles determined by the exchange precession frequency and the time spent in each magnetic region and hence eventually loses its spin memory. The moment and particle diameter are therefore important parameters determining the degree of precession. Reference 6 elaborates the details of the mechanism. It is found therein that the precession is very sensitive to small deviations of the orientation of two successive clusters. This will therefore be particularly apparent at the approach to saturation where thermal fluctuations result in a small off-axis component of magnetization.

By virtue of its contribution to $\tau'_{\uparrow\downarrow}$ in the paramagnetic matrix, the jitterbug spin channel mixing moderates the GMR observed, particularly in the case of small GMR amplitude where the system is more sensitive to small changes in $l'_{sf}=(D'\tau'_{\uparrow\downarrow})^{1/2}$. Since the polarization of the magnetic clusters responsible for the GMR is a function of B/T (in the absence of anisotropy and interactions), the jitterbug relaxation mechanism affects both the temperature and field dependence of the GMR. Experimentally the mechanism increases the temperature dependence of the GMR. In particular, at fixed temperature the effect of jitterbug mixing may be observed experimentally by its effect on the approach to saturation of the magnetoresistance.

NUMERICAL SIMULATION

The effect on the passage of a spin through an assembly of the smaller class 2 magnetic particles has been modeled to investigate the effect on spin memory of applied field and temperature due to the jitterbug spin depolarization mechanism. The numerical simulation calculated the average spin-flip time for a wide range of fields and temperatures, and for a wide variety of log normal distributions of magnetic particle radii. For each distribution, field, and temperature 10 000 spin trials were made and the average flip time calculated from the resulting flipping distribution. For each trial a random sequence of magnetic particle radii was generated in accordance with the specified particle size distribution. For each of these particle sizes a thermal angular deviation from the applied field direction was randomly generated, the probability distribution of this generation being compatible with the spin phase space and the Boltzmann distribution for the particular particle radius. The particles were assumed to be isotropic and sufficiently well separated that interactions could be neglected. From nucleation and phase separation considerations[7] backed up by transmission electron microscopy evidence[8] their separations were chosen proportional to the sums of radii of successive pairs.

The log normal distribution of particles was normalized to incorporate all the magnetic material present and hence the matrix is by definition free from all paramagnetic impurities and therefore has no effect on the spin memory of the carrier. We consider the incoming coded spins and follow the change in the direction of the spins as they encounter successive particles and undergo jitterbug precession within them.

The spin evolution is tracked by alternately applying precession transform matrices to simulate the behavior of the spin in the local exchange field of one magnetic particle, then rotational vector transformation matrices, to shift the spin to the reference frame of the next particle's exchange field. Each spin trial terminated when the total spin deviation constituted 90° from the start direction.

The average spin-flip time was then converted to the distance l_j traveled by an electron within these magnetic regions before having its spin direction rotated by more than 90° by this pseudo-Larmor precession mechanism. Figure 1 shows the form of the decay of l_j with increasing temperature for an array of particles with a mean particle size of 15 Å, $\sigma=0.2$ and an applied field $H=3.1$ T. The form of this curve is of course directly related to the distribution of particle size and can be scaled with B/T. This is further demonstrated in Fig. 2 in which at a fixed temperature and particle distribution l_j increases linearly with field. The actual value of l_j is highly dependent on the particle size and, hence, the details of the particle size distribution.

DISCUSSION

The jitterbug spin depolarization effect has been shown to be an effective spin channel mixing process which through its dependence on particle size is dependent on both temperature and field. In turn by shortening the spin diffusion length it increases the temperature dependence of the giant magnetoresistance.

ACKNOWLEDGMENTS

The financial support of the EPSRC, Royal Society, EC Human Capital and Mobility program and the British Council are gratefully acknowledged.

[1] J. Q. Xiao, J. S. Jiang, and C. L. Chien, Phys. Rev. Lett. **68**, 3749 (1992); A. E. Berkowitz, J. R. Mitchell, M. J. Carey, A. P. Young, S. Zhang, F. E. Spada, F. T. Parker, A. Hutten, and G. Thomas, *ibid.* **68**, 3745 (1992); J. A. Barnard, A. Waknis, M. Tan, E. Haftek, M. R. Parker, and M. L. Watson, J. Magn. Magn. Mater. **114**, L230 (1992).

[2] M. N. Baibich, J. M. Broto, A. Fert, F. Nguyen Van Dau, F. Petroff, P. Etienne, G. Creuzet, A. Friederich, and J. Chazelas, Phys. Lett. B **61**, 2472 (1988).

[3] Abragam and Goldman, *Nuclear Magnetism, Order and Disorder* (Oxford University Press, Oxford, 1982).

[4] T. Valet and A. Fert, Phys. Rev. B **48**, 7099 (1993).

[5] W. Allen, D. S. Daniel, J. F. Gregg, M. Viret, J. M. D. Coey, S. M. Thompson, and K. Ounadjela (unpublished).

[6] G. A. Gehring, J. F. Gregg, S. M. Thompson, and M. L. Watons, J. Magn. Magn. Mater. **140-144**, 501 (1995).

[7] M. L. Watson (unpublished).

[8] A. K. Petford-Long, R. C. Doole, J. F. Gregg, and C. R. Staddon, Proceedings of ICEM 13, Paris, 17–22 July 1994.

Modeling effects of temperature annealing on giant magnetoresistive response in discontinuous multilayer NiFe/Ag films

J. O. Oti
National Institute of Standards and Technology, Boulder, Colorado 80303

Y. K. Kim
Quantum Peripherals Colorado, Inc., Louisville, Colorado 80028

The giant magnetoresistive (GMR) behaviors of discontinuous double-layer giant magnetoresistive films with different microstructure arising from different annealing conditions, are calculated using a numerical micromagnetic model. The effect of magnetic grain growths in the perpendicular and lateral directions in the magnetic layers, and the formation and growth of grain clusters were studied. The GMR responses of the films are analyzed in terms of magnetostatic interactions between the magnetic layers and the microstructural geometric effects on the transport properties of the samples. © *1996 American Institute of Physics.* [S0021-8979(96)54108-6]

A phenomenological micromagnetic giant magnetoresistance (GMR) model[1] is used to examine the dependence of GMR response on annealing-induced microstructural changes in double-layer NiFe/Ag films having an active area between contact electrodes of 0.42×0.42 μm. Discontinuous multilayer NiFe/Ag films are attractive as GMR magnetic sensors due to their high sensitivity and low saturation fields.[2,3] These films are obtained by subjecting sputtered NiFe/Ag films to moderate thermal annealing. The initial effect of annealing is to partially or completely separate the touching NiFe grain boundaries of the unannealed sample by causing the diffusion of Ag into the grain boundaries. This reduces the surface-free energy of the grain boundaries. Other effects of annealing, such as the formation of grain clusters within the magnetic layers, and bridging of the grains of the magnetic layers through the Ag spacer layer, may occur at high annealing temperatures.[2] These result in further reduction in interfacial and grain boundary energies. Changes in the microstructure of the sample affects the GMR behavior of the films.

In this paper, the effects of the diffusion of Ag into grain boundaries and the formation of grain clusters are modeled separately to isolate the effect of each mechanism. The microstructural dimensions of the sample are chosen in the calculations so that the volume and active area of the sample remain the same or as close as possible to their unannealed values. Two possible mechanisms of cluster formation following an initial Ag diffusion are considered. These are lateral grain growth within a magnetic layer, and the formation and growth of grain clusters. Simulation of clusters in our model by combining grains of a magnetic layer is illustrated in Fig. 1. The grains within a cluster are exchange-coupled to each other, while the remaining grains of the sample are not.

The micromagnetic GMR model[1] calculates the total resistance of a sample from a given magnetization distribution in the sample. The distributions are obtained by using a model[4] in which each magnetic layer is divided into a rectangular array of uniformly magnetized discrete elements having square cross sections of length D in the plane of the sample. The elements simulate the magnetic grains of the sample and in general are not touching. The magnetic layers are characterized by distributions of exchange, anisotropy, and magnetostatic parameters among the grains. The magnetic moment of each grain is allowed to dynamically relax in three dimensions, in the presence of an external field and effective exchange, magnetocrystalline anisotropic, and magnetostatic internal fields. Each grain is characterized by an intrinsic mean resistivity ρ_0 that is modified by an amount $\delta\rho(M)$ due to the magnetization of the medium. This change in resistivity has intralayer and interlayer components representing spin-dependent electron scattering within a magnetic layer and between layers. These components depend on the microstructural and transport properties of the sample, and are proportional to the cosine of the angles between the magnetization of a grain and those of its nearest neighbors.

The magnetic layers considered in this article have the same magnetic properties and linear dimensions, which simplifies the form of the defining equations. In addition, intralayer scattering is assumed to be negligibly small compared to interlayer scattering and is therefore omitted in this treatment. The expression for grain resistivity in this case is given by[1]

$$\rho=\rho_0+\delta\rho(M)=\rho_0[1+\chi\alpha(1-\hat{\mathbf{m}}\cdot\hat{\mathbf{m}}')], \tag{1}$$

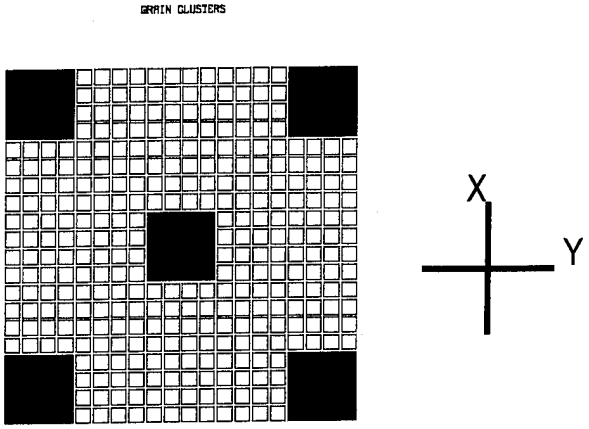


FIG. 1. Plan view of cluster pattern used in calculations. The small squares represent the grains of the sample. The shaded regions represent grains that are combined to form clusters. The clusters in the figure have four grains on the side.

 0021-8979/96/79(8)/5596/3/$10.00 © 1996 American Institute of Physics

where α is an interlayer probability scattering parameter defined as

$$\alpha = \frac{D^2}{(2A-D)^2} e^{-d/\lambda} = Q e^{-d/\lambda}. \quad (2)$$

χ is a material-dependent cofactor, $\hat{\mathbf{m}}$, $\hat{\mathbf{m}}'$ are unit magnetization vectors of a grain and its nearest neighbor in the adjacent magnetic layer, λ is a model-dependent characteristic transport length, A is the distance between the centers of adjacent grains within a magnetic layer, and d is the separation between the magnetic layers. α embodies the dependence of resistivity on the microstructural geometric and transport properties of the sample. Q, which is the geometric term, defines an *incidence cross section*, which represents the fraction of the incidence polarized electron flux in the spacer region that scatters off magnetic grain boundaries. The exponent in Eq. (2) is the transport term and expresses the attenuation of polarized electron flux in the spacer region due to diffusion. λ is in general a tensor, but for simplicity we treat it here as a simple scalar.

In the CIP direction (x direction in Fig. 1), each grain has a resistance of ρ/t. For a given magnetization state of the sample, the resistance of a magnetic layer is obtained by summing the resistances of the grains serially in the direction of current and reciprocally, transverse to the current, in the plane of the sample. The total resistance of the sample is obtained by summing reciprocally the resistances of the magnetic layers.

All the annealed samples studied in this article were assumed to have been derived from an unannealed sample having grain size $D=A=21$ nm, grain thickness $t=2$ nm, and nonmagnetic spacer thickness $d=4$ nm. These dimensions are typical for NiFe/Ag GMR multilayers.[2,3] Each magnetic layer of the unannealed sample was simulated by a 20×20 array of grains for an active sample area of 0.42×0.42 μm. The samples were elongated along the direction of current flow by imposing periodic boundary conditions in this direction. The microstructure and number of grains of the annealed samples were chosen to preserve the size and volume of the active area of the sample at their unannealed values.

The magnetization of the grains was chosen at random from a 80 kA/m interval centered about a mean value of 800 kA/m (10 kG). Each grain was characterized by a uniaxial magnetocrystalline anisotropy strength of 8×10^2 J/m^3, and the orientations of the easy axes were varied randomly in three dimensions from grain to grain. A resistivity of $\rho_0=1$ (in arbitrary units), a cofactor of $\chi=1$, and a transport length of $\lambda=10$ nm (assumed independent of annealing) were used in the simulations. GMR response curves were calculated for uniform in-plane transverse fields (parallel to the y axis in Fig. 1).

The following three cases of the possible effects of annealing were simulated:

(i) Continuous diffusion of Ag into the grain boundaries, which results in a steadily declining grain size $D=21-16$ nm, increasing gap length $G=A-D=0-5$ nm between adjacent grains, increasing grain thickness $t=2-3.4$ nm, and decreasing spacer thickness $d=4-3.5$ nm. Grain growth is therefore normal to the film plane and grain array size is $N=20$.

(ii) Lateral grain growth occurs beginning with a sample of case (i) having grain size $D=18.5$ nm ($G=2.5$ nm, $t=2.6$ nm, $d=4.3$ nm). This sample corresponds to predicted peak GMR response for case I (see below). Microstructural modifications are simulated by uniformly increasing G and D ($D/G=0.135=$const), while keeping t and d fixed. The grain array sizes decrease ($N=20-10$) in order to preserve the area and volume of the sample at their unannealed values. It was not always possible to match areas and volumes of the samples exactly with unannealed ones, since the micromagnetic model is incapable of simulating fractional grains.

(iii) Grain clusters form in the sample starting from the $D=18.5$ nm sample of case (i). Cluster patterns similar to that shown in Fig. 1 are used in the calculations. Clusters of 2 through 6 grains on the side are considered to simulate cluster growth. Two sets of clusters are considered in which intralayer exchange fields[4] per nearest neighbor of 1.3 and 1.6 kA/m are applied inside the clusters.

The maximum of the GMR curve of a sample $[\Delta R/R]_{\max}$ corresponds to the largest misalignment between the magnetization of corresponding grains in the magnetic layers during the magnetization reversal. This misalignment can be quantified by defining an interlayer correlation factor C that is equal to the average scalar product of the unit magnetization vectors of corresponding grains of the magnetic layers. C varies from $+1$ to -1 for complete parallel and antiparallel mutual orientation of the magnetization of the layers.

Calculated $[\Delta R/R]_{\max}$, maximum correlation factor $C_{\max}$, and scattering cross section Q for cases (i) and (ii) are plotted as functions of gap length G in Fig. 2. Inflated $[\Delta R/R]_{\max}$ values arise from the arbitrary choice of ρ_0 and χ. For case (i) $C_{\max}$ and Q decrease monotonically with G, and $C_{\max}$ eventually saturates at -1. $C_{\max}$ decreases as the local magnetostatic coupling between corresponding grains of the layers increases and this has the effect of increasing the GMR response. A decreasing Q, on the other hand, lowers the GMR response, because the flux of spin-polarized electrons that couples the nearest-neighbor grains in the magnetic layers diminishes. $[\Delta R/R]_{\max}$ attains a peak value at around $D=18.5$ nm when these opposing effects combine optimally. After $C_{\max}$ saturates, $[\Delta R/R]_{\max}$ becomes solely dependent on the continually decreasing Q. The exponent in Eq. (2) has a negligible effect during these transformations owing to the small variation in the interlayer separation d. For Case II, Q remains constant for $D>18.5$ nm, so $[\Delta R/R]_{\max}$ again depends on the variation of $C_{\max}$ alone. Increasing G causes $C_{\max}$ to decrease until it eventually saturates at -1. This causes $[\Delta R/R]_{\max}$ to increase until saturation as well.

The presence of clusters in case (iii) complicates the magnetization processes more. Conceptually the clusters may be regarded as larger grains whose internal exchange

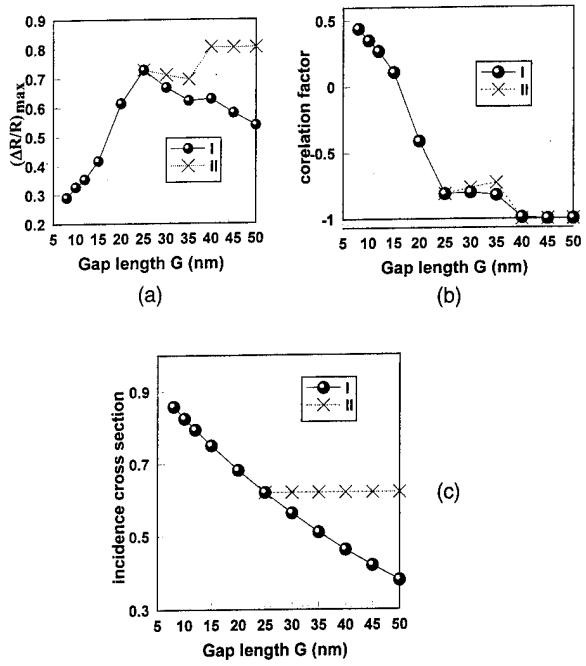


FIG. 2. Dependence of (a) maximum GMR response $[\Delta R/R]_{\max}$, (b) maximum correlation factor $C_{\max}$, and (c) scattering cross section Q on gap length G, for cases (i) and (ii) described in the text. The plotted values of GMR are arbitrary due to the arbitrary choices of resistivity $\rho_0=1$ and cofactor $\chi=1$.

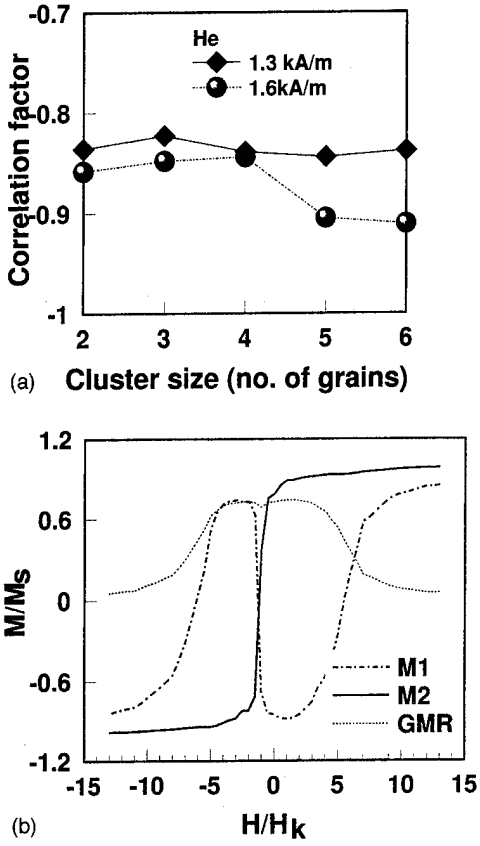


FIG. 3. (a) Maximum correlation factor $C_{\max}$ as a function of cluster size, for two sets of samples with exchange fields in the clusters of 1.3 and 1.6 kA/m; (b) magnetization curves (M1 and M2) of magnetic layers and GMR response curve of a sample with five-grain clusters and cluster exchange coupling fields of 1.3 kA/m.

coupling enables their magnetization to rotate more easily towards an applied field. This tendency increases with exchange coupling. Because of the difference in the properties of the clusters and the surrounding nonexchange-coupled grains, the clusters act as natural nucleation sites for the magnetization reversal of the sample as a whole. At low external fields, interlayer magnetostatic interactions between the clusters promote the misalignment of their magnetization in the layers. This is evident from Fig. 3(a), which compares $C_{\max}$ for the two sets of samples having clusters with internal exchange fields of 1.3 and 1.6 kA/m.

Clusters act as sources of additional domain noise. This is a consequence of jumps in the magnetization reversals of the clusters due to magnetostatic interactions. This behavior can be seen in the calculated magnetization curves of the magnetic layers of a sample with five-grain cluster sizes and exchange field 1.3 kA/m shown in Fig. 3(b). Also plotted in the figure is the GMR response curve of the sample. The magnetic properties of the layers are statistically similar, but not point-to-point identical. Their mutual interactions may thus result in completely different reversal modes in the magnetic layers. As a large positive external field acting on the sample is reduced, the magnetostatic interactions between the layers cause M2 to switch negatively at low fields, so as to attain an antiparallel orientation relative to M1. When the field is increased in the negative direction and M1 is switched negatively, magnetostatic interactions forces M2 to again switch positively.

In this paper we have used a phenomenological GMR model to examine simple models of the microstructural changes brought about by annealing and their effects on the GMR responses of discontinuous NiFe/Ag multilayers. These changes have been considered separately to isolate their various impacts on the GMR responses. A formulation of the model, that assumes that intralayer spin-dependent electron scattering is negligible compared to interlayer scattering, is used. Variations of the considered microstructural features of samples will exist simultaneously in real materials, and their evolutions with annealing temperature will proceed according to a variety of laws other than those considered here. Additional effects due to sample sizes and a greater number of magnetic layers than the two considered here will also be important. However, several important conclusions follow from the simple picture we have presented. Grain-growth mechanisms that increasingly separate grains within a magnetic layer generally promote greater misalignment of the magnetization of the layers due to magnetostatic interactions. This has a tendency to increase the GMR, but may be opposed by other transport properties of the sample such as reduced polarized-electron flux in the sample. Grain clusters act as natural nucleation centers in a sample and generate additional noise.

[1] J. O. Oti, S. E. Russek, S. C. Sanders, and R. W. Cross, IEEE Trans. Magn. (submitted).
[2] T. L. Hylton, K. R. Coffey, M. A. Parker, and J. K. Howard, J. Appl. Phys. **75**, 7058 (1994).
[3] Y. K. Kim and S. C. Sanders, Appl. Phys. Lett. **66**, 1009 (1995).
[4] J. Oti, IEEE Trans. Magn. **29**, 1265 (1993).

Giant magnetoresistance in melt-spun $Cu_{80}Ni_{10}Fe_{10}$ ribbons

L. H. Chen
Department of Materials Engineering, Kaohsiung Polytechnic Institute, Kaohsiung, Taiwan, Republic of China

S. Jin and T. H. Tiefel
AT&T Bell Labs, Murray Hill, New Jersey 07974

S. Y. Liao and Y. D. Yao
Institute of Physics, Academia Sinica, Taipei, Taiwan, Republic of China

Magnetoresistance (MR) behavior in melt-spun ribbons of a $Cu_{80}Ni_{10}Fe_{10}$ alloy has been studied. The rapid solidified ribbon, when properly heat treated for phase decomposition, exhibits giant magnetoresistance behavior with the MR values of 8.5% at room temperature and 29% at 4.2 K. The observed magnetoresistance in the alloy is attributed to spin-dependent scattering at the two-phase interface and in the ferromagnetic phase. The substantial increase in MR, as the temperature decreases from room temperature to 4.2 K, is most likely caused by the reduction of spin-flip scattering of conducting electrons in the paramagnetic regions as a result of magnetic transformation. © *1996 American Institute of Physics.* [S0021-8979(96)54208-2]

I. INTRODUCTION

Cu-Ni-Fe alloys are known to decompose, upon appropriate heat treatment, into Cu-rich and (Ni,Fe)-rich phases.[1,2] We have previously reported the magnetoresistance (MR) behavior of $Cu_{60}Ni_{20}Fe_{20}$ (wt %) alloy spinodally decomposed into an extremely fine scale two-phase microstructure.[3,4] In the present work, a $Cu_{80}Ni_{10}Fe_{10}$ alloy, which is presumably outside the spinodal region, has been rapidly solidified by melt-spinning technique and subsequently heat treated at elevated temperatures in order to obtain a very fine two-phase microstructure. The MR behavior of so-processed Cu-Ni-Fe alloy ribbons is reported.

II. EXPERIMENTAL PROCEDURES

$Cu_{80}Ni_{10}Fe_{10}$ (in wt %) ribbons were prepared by conventional melt spinning and rapid solidification process in an argon atmosphere using a copper wheel rotating at a surface speed of ~50 m/s. The ribbons were 2 mm wide, 20–30 μm thick, and 10–15 cm long. The melt-spun ribbons were sealed in quartz tubes, and annealed at 400 °C for 24 h to modify the microstructure.

X-ray diffraction (XRD) analysis with $K\alpha$ (Cu) radiation was used to characterize the structure of the ribbons. Magnetic measurement was carried out by using a vibrating sample magnetometer (VSM) and superconducting quantum interference device (SQUID) magnetometer with the applied field up to 6 T. The magnetoresistance (MR) of the ribbons was measured by using the four-point technique with a magnetic field of 6 T applied in the ribbon plane.

III. RESULTS AND DISCUSSION

The structure of the melt-spun $Cu_{80}Ni_{10}Fe_{10}$ (in wt %) ribbons was investigated by using XRD. The x-ray diffraction analysis shows essentially single phase like but somewhat broadened Bragg peaks of (111), (200), (220), (311), and (222). This suggests that the as-spun $Cu_{80}Ni_{10}Fe_{10}$ ribbon is polycrystalline, and the compositional inhomogeneity and phase separations in the material are small. After annealing at 400 °C for 24 h, splitting peaks coming from the Cu $K\alpha_2$ diffraction appears at higher diffraction angles, which are related to the improved crystal quality of the ribbon as a result of the aggregation and growth of the extremely fine ferromagnetic (Fe,Ni)-rich phase from the Cu-rich matrix and the stress relief of the microstructure.

Shown in Fig. 1 is the magnetization behavior of the melt-spun ribbon at room temperature and 4.2 K, measured with the maximum field of 6 T. The ribbon exhibits a very small hysteresis and magnetization of only 5 emu/g even at a field as high as 6 T. The observed increase in magnetization by 160% when the field is raised from 1 to 6 T and the presence of a slope at 6 T indicates that the ribbon sample was still not fully saturated at 6 T. This suggests that a very fine-scale, ferromagnetic (Fe,Ni)-rich phase, at least partially separated by a paramagnetic phase around the ferromagnetic phase, could have been formed in the course of the melt-spinning process. The magnetization increases as the temperature is lowered. A substantial ferromagnetism appears for the as-spun ribbon at 4.2 K. The M-H loop shows a hysteresis with a remanence ($M/M_{6\ T}$) of ~0.38, coercivity

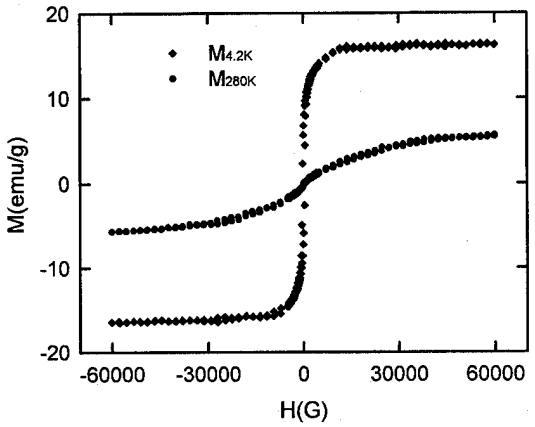


FIG. 1. M-H loops for the as-spun $Cu_{80}Ni_{10}Fe_{10}$ ribbons.

 0021-8979/96/79(8)/5599/3/$10.00 © 1996 American Institute of Physics

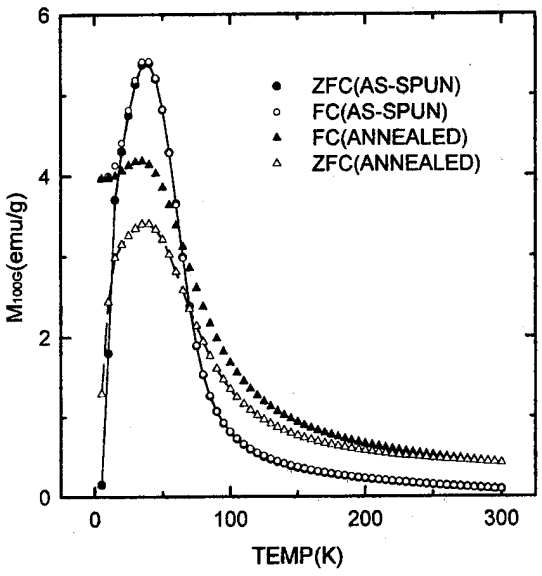


FIG. 2. Temperature dependence of magnetization ($H=100$ Oe) of the as-spun and annealed $Cu_{80}Ni_{10}Fe_{10}$ ribbons.

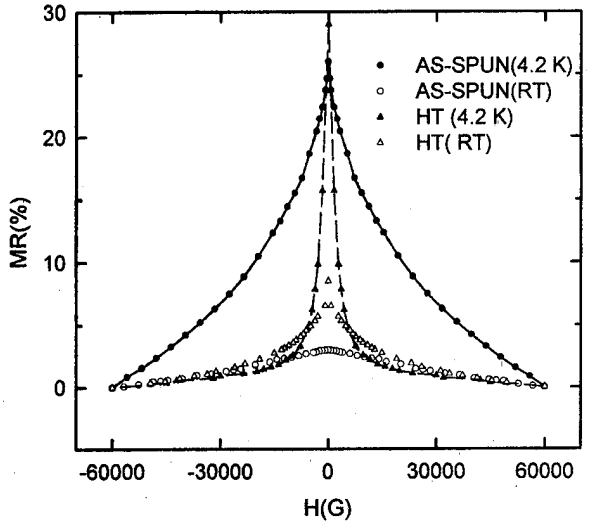


FIG. 3. Field dependence of MR ratio at room temperature and 4.2 K for the as-spun and annealed $Cu_{80}Ni_{10}Fe_{10}$ ribbons.

of ~300 Oe and saturation magnetization of 16 emu/g at 6 T. After annealing, the room-temperature magnetization behavior of the ribbon is quite different from that of the as-spun sample. The annealed ribbon shows a hysteresis with a remanence ($M/M_{6\ T}$) of ~0.05, coercivity of less than 50 Oe, and a higher saturation moment of 14 emu/g at 6 T. A similar magnetization behavior is observed at lower temperatures by the annealed ribbon. The dependence of the magnetization behavior on the annealing process is a consequence of the change of microstructure during an annealing treatment which enhances the phase separation process of the Cu-rich and (Fe,Ni)-rich phases as well as the stress relief process in the melt-spun ribbon.

Figure 2 represents the zero-field-cooled (ZFC) and field-cooled (FC) magnetization curves (at $H=100$ Oe) for the as-spun and annealed $Cu_{80}Ni_{10}Fe_{10}$ ribbons. It can be noticed that no divergence is observed between ZFC and FC plots for the as-spun $Cu_{80}Ni_{10}Fe_{10}$ ribbons until the ZFC peak. A large discrepancy in magnetization between two curves occurs at temperatures below about 50 K. The observation of thermal hysteresis around the peak of the ZFC curve indicates the limited distribution in the size and shape of the magnetic phase. It is also deserved to notice the large increase in the magnetization values at 100 Oe as the temperature decreases from room temperature. Such substantial increase in magnetization is also found in the FC and ZFC curves measured at 1000 Oe. Upon annealing, the higher temperature of thermal hysteresis (~250 K) and broaden maximum peak in ZFC curve reveals the particle growth as well as the increased size distribution of the ferromagnetic phase. From the above results of magnetization behavior measurements, we believed that the magnetic behavior of the $Cu_{80}Ni_{10}Fe_{10}$ ribbons is related with both paramagnetic and superparamagnetic contributions. The superparamagnetic behavior comes from the ferromagnetic (Fe,Ni)-rich phase which are randomly coupled, whereas the paramagnetic behavior is associated with the paramagnetic regions around the ferromagnetic phase, which exhibit Curie temperatures below room temperature.

Shown in Fig. 3 are the magnetoresistance (MR) ratio versus applied field curves of the melt-spun and annealed ribbons. The MR ratio was defined here as $\Delta\rho_m/\rho_s$ or $\Delta R_m/R_s$, where ρ_s (or R_s) is the electrical resistivity or resistance near the saturation field. All the MR effect reported here is negative. In the as-spun ribbon, the resistance at room temperature decreases continuously up to the maximum field of 6 T and gives a MR ratio of 3%. At 4.2 K, the MR ratio drastically increases to 26%. The MR ratio versus applied field curves do not saturate in magnetic fields up to 6 T at both temperatures, indicating that the MR values will be higher if the applied field is increased. The annealing treatment of the melt-spun ribbon at 400 °C for 24 h significantly enhances the room temperature and 4.2 K MR ratios to 8.5% and 29%, respectively. Such dependence of MR ratio on the annealing process is believed to be mostly related to the changes in microstructure. Similarly as in the as-spun ribbon, the MR ratio in the annealed ribbon does not saturate at $H=6$ T, and hence the maximum attainable MR ratio must be higher than the 29% measured at 6 T.

Figure 4 shows the dependencies of MR ratio, resistivity (ρ), and field-induced change in resistivity ($\Delta\rho_m$) on temperature for the as-spun and annealed ribbons. In contrast to the temperature dependence of magnetoresistance of deformed $Cu_{60}Ni_{20}Fe_{20}$ alloys,[4] the ribbon shows a significant increase in the MR ratio of a factor of almost 9 upon cooling from room temperature to 4.2 K [see Fig. 4(a)]. This could be interpreted in terms of relatively strong temperature-dependent increase in $\Delta\rho_m$ by a factor of ~4 combined with a weaker temperature variation of resistivity. As discussed below, the magnetoresistance of the $Cu_{80}Ni_{10}Fe_{10}$ ribbons is likely related to the spin-dependent scattering between neighboring ferromagnetic phases and magnetic fluctuation scattering.

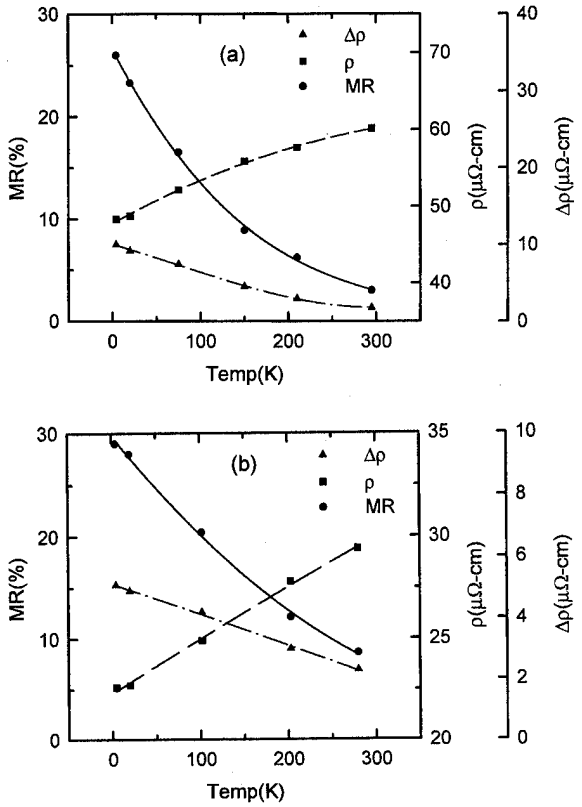


FIG. 4. Temperature dependence of MR, ρ and $\Delta\rho$ for the $Cu_{80}Ni_{10}Fe_{10}$ ribbons, (a) as-spun and (b) after annealing at 400 °C for 24 h.

In our previous report,[4] the MR of a deformed $Cu_{60}Ni_{20}Fe_{20}$ alloy could be mostly attributed to the magnetic excitation in the nearly superparamagnetic alloys, which are suppressed by an applied field and lead to the decreasing MR ratio as the temperature is lowered. The spin-dependent scattering appears to play only a relatively minor role in the magnetoresistance of deformed alloy. However, the MR in the present melt-spun $Cu_{80}Ni_{10}Fe_{10}$ ribbon seems to be dominated by the spin-dependent scattering, as well as the magnetic fluctuation scattering. As shown in Fig. 3, the room-temperature MR curve for the as-spun $Cu_{80}Ni_{10}Fe_{10}$ ribbon consists of gradual and almost linear decrease from zero field to 6 T, which could be caused by the local magnetic fluctuations, such as extremely fine ferromagnetic particles or paramagnetic regions with Curie temperature well below room temperature, which leads to the strong electron scattering. At 4.2 K, a rapid drop in resistance at low fields appears in the MR curve (Fig. 3), which is then followed by a gradual decrease at higher fields. The large initial drop in resistance at low fields is probably related to the spin-dependent scattering at the two-phase interface and in the ferromagnetic phase, similar by as reported for the GMR superlattice structures.[5] As the temperature decreases, more paramagnetic-like regions in the as-spun ribbon become ferromagnetic and make more contribution to the spin-dependent scattering. Such magnetic-transformation related thus leads to an increase in MR for the $Cu_{80}Ni_{10}Fe_{10}$ ribbon as the temperature is lowered.

After annealing, the contribution of spin-dependent scattering to the MR behavior is increased because of the presence of phase separation into the Cu-rich and (Fe,Ni)-rich phases, which creates more ferromagnetic regions in the microstructure, as well as the stress relief of the microstructure. This is evidenced by the obvious drop in room temperature resistivity at low fields (see Fig. 3). The higher $\Delta\rho_m$ combined with lower ρ after annealing thus results in an increase in the room-temperature MR ratio almost by a factor of ~3 (from 3% to 8.5%).

IV. SUMMARY

Melt-spun ribbons of the $Cu_{80}Ni_{10}Fe_{10}$ alloy exhibit giant magnetoresistance behavior when properly heat treated for phase decomposition into Cu-rich and (Fe,Ni)-rich phases. The MR values in annealed $Cu_{80}Ni_{10}Fe_{10}$ ribbons are 8.5% at room temperature and ~29% at 4.2 K at $H=6$ T. The MR behavior in the alloy is mainly attributed to the spin-dependent scattering at the two-phase boundary and in the ferromagnetic phase.

ACKNOWLEDGMENT

This work was partly supported by the National Science Council of Republic of China under Contract No. NSC 84-2216-E-214-002.

[1] E. P. Butler and G. Thomas, Acta Metall. **18**, 347 (1970).
[2] R. J. Livak and G. Thomas, Acta Metall. **19**, 497 (1971).
[3] L. H. Chen, T. H. Tiefel, S. Jin, and S. H. Chang, Phys. Rev. B **49**, 9194 (1994).
[4] L. H. Chen, S. Jin, and T. H. Tiefel, Appl. Phys. Lett. **64**, 1039 (1994).
[5] M. N. Baibich, J. M. Broto, A. Fert, F. Nguyen Van Dau, F. Petroff, P. Etienne, G. Creuzet, A. Friederich, and J. Chazelas, Phys. Rev. Lett. **61**, 2472 (1988).

Giant magnetoresistance properties in multilayered Co-Ag/Cu granular alloys

Makoto Iijima, Yutaka Shimizu, Naomi Kojima, Atsushi Tanaka, and Kazuo Kobayashi
Magnetic Materials & Devices Laboratory, Fujitsu Laboratories, Ltd., 10-1 Morinosato-Wakamiya, Atsugi 243-01, Japan

In this article, we introduce a novel Co-rich Co-Ag/Cu granular alloy structure with increased magnetic sensitivity, and report on our study of the relationship of giant magnetoresistance (GMR) and magnetic properties to annealing temperature and Cu thickness in sputtered Co_{66}-Ag_{34}/Cu multilayered films. We heat treated Co-Ag/Cu films with Cu spacer thickness ranging from 15 to 50 Å up to 500 °C, and found that the MR ratio loosely depends on both the Cu spacer thickness and the annealing temperature, peaking at 7.6% with a 25 Å Cu layer and an annealing temperature of 280 °C. Based on the magnetic properties we observed, as well as x-ray studies, we found that Cu spacers at least 25 Å thick are able to separate the Co-Ag magnetic layers. Our data also indicated that the annealing treatment changed the coupling of magnetic layers from ferromagnetic to antiferromagnetic. The high thermal stability and the high magnetic sensitivity suggest potential use of our novel multilayered structure in applications as magnetic sensors. © *1996 American Institute of Physics.* [S0021-8979(96)54308-9]

I. INTRODUCTION

There has been a great deal of research into granular giant magnetoresistive (GMR) structures because of their high MR ratios and their magnetic behavior.[1–3] Granular GMR structures consist of a matrix of nonmagnetic metals (such as Ag, Cu, or Au) containing small particles of magnetic metals (such as Co, Fe, or Ni). A granular GMR structure has a high MR ratio (up to 50% at room temperature), and has high thermal stability. These properties are important when granular GMR structures are used in applications such as magnetic read heads. However, a granular GMR film needs several kOe of external magnetic field to change its resistivity, making it difficult to apply in practice.

There have been some attempts at enhancing GMR properties by layering or by optimizing of the size of magnetic particles.[4,5] These methods have improved the MR ratio, but the saturation fields are still in the range of several kOe. We tried to use a multilayered Co-Ag granular alloy with Ag spacer layers for magnetic sensor applications. Electron microscopy observation revealed that Ag spacer layers shrank, even in the as-deposited state. This makes the layering structure imperfect. Because of our interest in layer separation, we changed the spacer material to Cu, which does not shrink as much as Ag. In this paper we introduce a novel structure for a Co-rich Co-Ag/Cu film which increases the field sensitivity, and discuss the contributions of Cu thickness and annealing temperature to the MR properties.

II. EXPERIMENTAL METHODS

To determine the appropriate Co content for the Co-Ag granular alloys, we have previously investigated the dependence of MR ratio and the saturation field on the Co content. We found that about 40 at. % Co is appropriate for the Co-Ag granular monolayer to achieve a high MR ratio, while about 66 at. % Co for the multilayered Co-Ag/Cu granular is best for lowering the necessary saturation field strength (Fig. 1). We therefore investigated the GMR properties of a Co-Ag/Cu multilayered film with 66 at. % Co for this article. The 66 at. % Co-Ag (20 Å)/Cu (t=15–20 Å) films were deposited onto a Pyrex substrate by dc magnetron sputtering with an argon pressure of 0.1 Pa. The granular layer was deposited from a $Co_{50}Ag_{50}$ binary alloy target with Co chips. The composition of the granular layer was determined by ICP-AES analysis. The multilayered structure had ten bilayers (pairs of Co-Ag granular layer and Cu spacer). The sputtered sample was split into 8×8 mm chips.

The annealing was performed in a vacuum at less than 5×10^{-8} Torr, and the samples were held at 200–400 °C for 1 h. Throughout the sample fabrication processes magnetic treatment was not carried out.

We measured magnetoresistivities using the conventional dc four-probe method with a maximum magnetic field of 1 kOe. We defined the MR ratio as $(\rho_{Hx}-\rho_{H1k})/\rho_{H1k}$, where ρ_{Hx} is the resistivity of the film to any external mag-

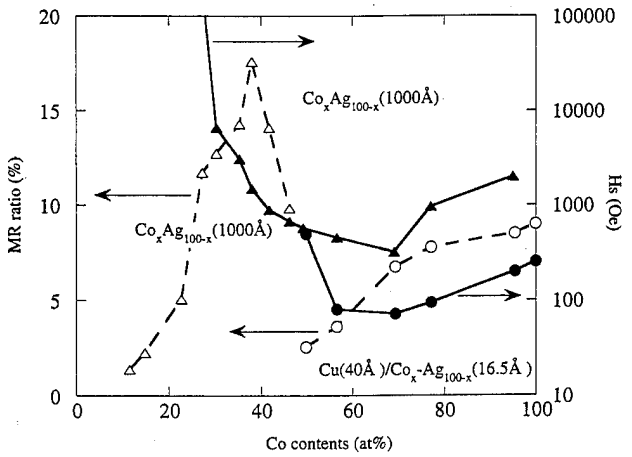


FIG. 1. The MR ratio (dashed line) and saturation field (solid line) dependence on the Co contents of conventional Co-Ag films (triangles) and multilayered Co-Ag/Cu films (circle). Note that scale of H_s is in $\log_{10}$.

 0021-8979/96/79(8)/5602/3/$10.00 © 1996 American Institute of Physics

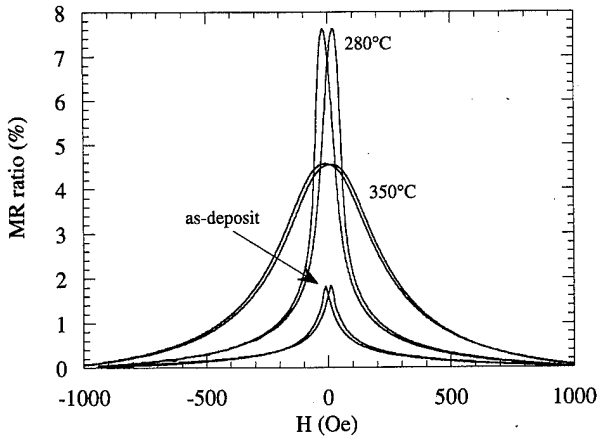


FIG. 2. The MR curves of Co-Ag (20 Å)/Cu (25 Å) films.

netic field, and ρ_{H1k} is the resistivity to an external field of 1 kOe. External magnetic fields were applied parallel to the current.

We measured magnetization curves using a vibrating sample magnetometer with a maximum applied field of 1 kOe. External fields were applied parallel to the plane. We observed interfaces between the granular and spacer layers with low-angle x-ray diffraction (LAXRD). LAXRD measurements were conducted at 2θ angle of up to 4°. All fabrication and measurements were performed at room temperature.

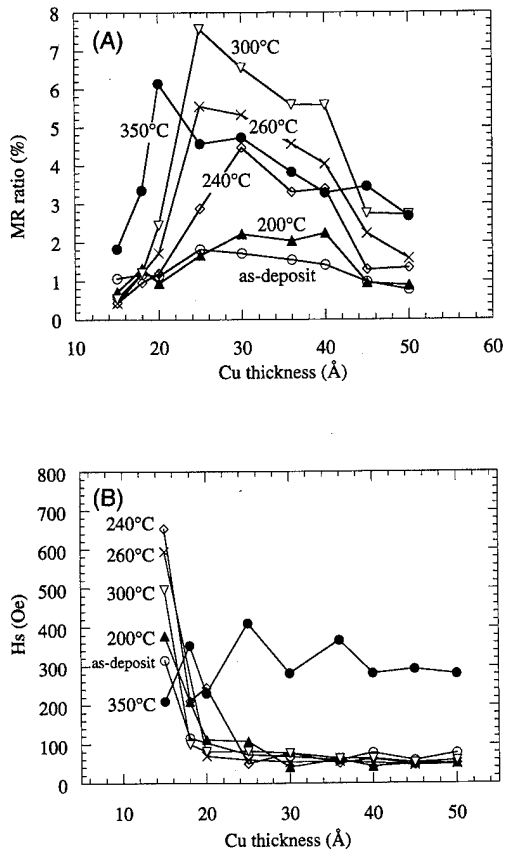


FIG. 3. (a) The dependence of MR ratio of Co-Ag/Cu films on the Cu spacer thickness. (b) The dependence of H_s of Co-Ag/Cu films on the Cu spacer thickness.

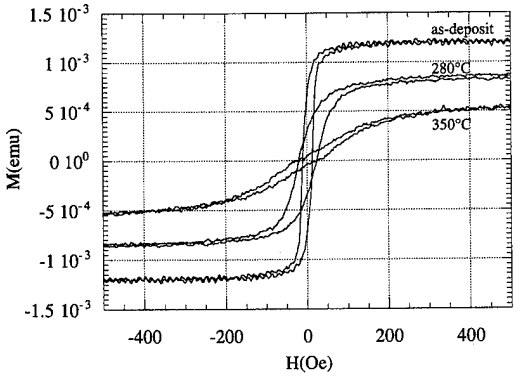


FIG. 4. LAXRD spectrums of Co-Ag (20 Å)/Cu (40 Å) multilayered films. Each spectrum are normalized with maximum peak.

III. EXPERIMENTAL RESULTS

We found that the MR ratio of Co-rich Co-Ag/Cu films depended on both the annealing temperature and the Cu spacer thickness. The MR ratio for the as-deposited film was about 1%, and increased with the annealing temperature up to the maximum of 7.6% at 280 °C, then decreased at 350 °C (Fig. 2). The Cu spacer thickness loosely affected the MR ratio of the film, which peaked in the range from 25 to 40 Å [Fig. 3(a)].

As the Co-Ag as-deposited film was metastable and random mixed state, Ag and Co atoms on the Co-Ag and Cu interface, which results in small MR ratio. The annealing treatment separates Co-Ag alloy into Co and Ag. Separated Co grains in the Ag-rich Co-Ag matrix result in forming the interfaces between Co grain and Cu spacer, which increased the MR ratio. The dependence of MR ratio on Cu thickness suggest that there is some magnetic coupling between the adjacent Co-Ag magnetic layers, but due to the inhomogeneous magnetic layer mentioned above may make the magnetic coupling loose.

Although the saturation field strength (H_s) for the Co-Ag/Cu films varied with the annealing temperature at the films for Cu thickness less than 20 Å, it decreased with the

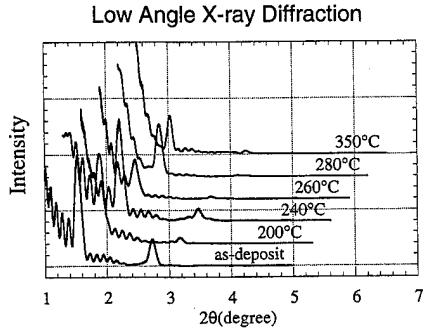


FIG. 5. Magnetization curves of Co-Ag (20 Å)/Cu (40 Å) multilayered films.

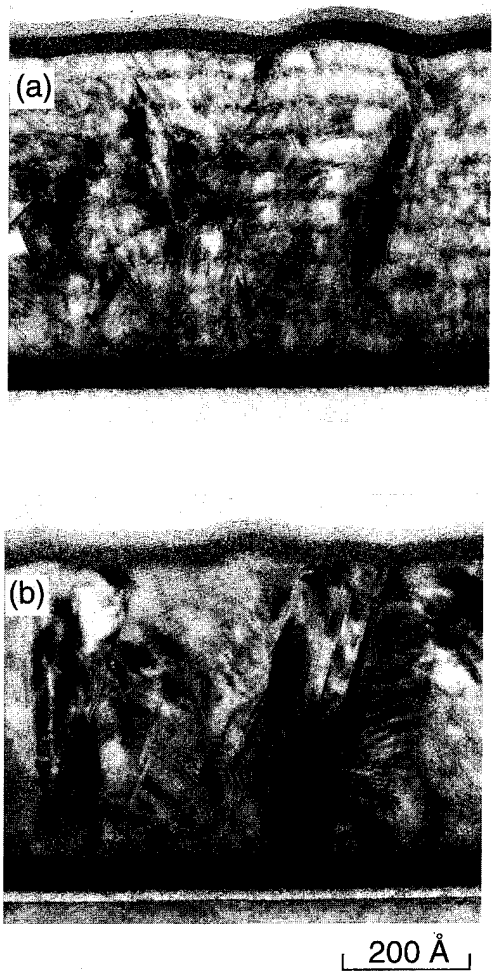


FIG. 6. Cross-sectional TEM images of Co-Ag (20 Å)/Cu (40 Å) multilayered films. (a) As-deposited, (b) annealed at 280 °C.

Cu spacer thickness at Cu thickness over 25 Å, and showed almost the same value around 70 Oe [Fig. 3(b)]. It seems that Cu films less than 20 Å have many pinholes, and therefore Co-Ag magnetic layers connect each other through the pinholes, which result in high H_s like a conventional granular alloys. On the other hand, Cu spacers over 25 Å are able to separate the Co-Ag magnetic layers, which causes weak magnetic coupling. High annealing temperature over 350 °C makes H_s larger. We assumed it is because the roughness of the Co-Ag/Cu interface increased by the interdiffusion of Co atoms into Cu layers, and multilayered film changed to a modulated granular-like structure.

The magnetization curves of Co-Ag/Cu multilayered films changed with the annealing temperature (Fig. 4). The slopes of the magnetization curves show that ferromagnetic coupling is dominant in as-deposit Co-Ag magnetic layers, which changes to weak antiferrocoupling at 280 °C. The magnetization curves also suggested that the coupling became modulated granular-like after the annealing at 350 °C. The saturation magnetization of the films decreased with the annealing temperature because Co atoms diffused into Cu layer and lose their magnetic moments as mentioned above.

The LAXRD spectrum indicated that although the layering structures damaged at the annealing temperature above 260 °C, they were maintained even at annealing temperature up to 350 °C (Fig. 5). The intensity of a maximum peak at 1.5° (first peak) decreased after annealing at above 260 °C, and second peak at 2.8° disappeared at the same annealing temperature, which indicates that roughness of interfaces are increased because of Co grain growth in the Co-Ag magnetic layers. The annealing treatment over 350 °C increase the roughness of magnetic/nonmagnetic interfaces because of diffusion of Co into Cu layers.

The Co-Ag/Cu multilayered structure was clearly observed with the transmission electron microscopy in the as-deposited state, while it almost disappeared after 280 °C annealing although the layered structure was still observed in the LAXRD spectrum [Figs. 6(a) and 6(b)]. These results are the evidence showing that the roughness of the Co-Ag/Cu interfaces increased by the annealing.

IV. CONCLUSION

By layering the Co-Ag granular film with Cu, we have developed the multilayered structure with high sensitivity. The MR of our novel multilayered Co-rich (66 at. % Co) Co-Ag/Cu film structure depends weakly on the Cu spacer thickness and the annealing temperature, which shows MR ratio of 7.8% and H_s of 70 Oe at 25 Å Cu spacer and annealing at 300 °C. In as-deposited Co-Ag magnetic layer which showed small MR ratio around 1%, a ferromagnetic coupling is dominant, and it changed to weak antiferromagnetic coupling after annealing at 280 °C and showed large MR ratio around 7%. However, by annealing at high temperatures over 350 °C MR ratio decreased and H_s increased because of the diffusion of Co atoms into Cu spacers, which result in increased roughness of the interface between Co-Ag magnetic layers and the Cu spacers.

The high thermal stability and the high magnetic sensitivity suggest the potential of our novel multilayered structure for the practical application as magnetic sensors.

[1] J. Q. Xiao, J. S. Jiang, and C. L. Chien, Phys. Rev. Lett. **68**, 3749 (1992).
[2] A. E. Berkowitz, J. R. Mitchell, M. J. Carey, A. P. Young, S. Zhang, F. E. Spada, F. T. Parker, A. Hutton, and G. Thomas, Phys. Rev. Lett. **68**, 3745 (1992).
[3] J. A. Barnard, A. Waknis, M. Tan, E. Haftek, M. R. Parker, and M. L. Watson, J. Magn. Magn. Mater. **114**, L230 (1992).
[4] J. D. Jarratt and J. A. Barnard, J. Appl. Phys. **76**, 6478 (1994).
[5] N. Thangaraj, C. Echer, M. Krishnan, R. F. C. Farrow, R. F. Marks, and S. S. P. Parkin, J. Appl. Phys. **75**, 6900 (1994).
[6] D. H. Mosca, F. Petroff, A. Fert, P. A. Schroeder, W. P. Pratt, Jr., and R. Laloee, J. Magn. Magn. Mater. **94**, L1 (1991).

Modeling giant magnetoresistance and magnetization of $Ag_{1-x}Ni_{x-y}Fe_y$ heterogeneous alloy films (abstract)

J. Wiggins, M. L. Watson, and P. A. Gago-Sandoval
Centre for Data Storage Materials, Coventry University, Priory Street, Coventry CV1 5FB, England

X. Batlle, F. Badia, and A. Labarta
Departament de Fisica Fonamental, Universitat de Barcelona, Av. Diagonal 647, E-08028, Barcelona, Spain

We have investigated the effects of the particle size distribution on the giant magnetoresistance (GMR) and magnetization of $Ag_{1-x}Ni_{x-y}Fe_y$ heterogeneous alloy films both experimentally and through computer simulation. The samples were prepared by sputtering from a mosaic target onto glass substrates at the system ambient temperature. They have thicknesses in the range of 100–300 nm and were rapidly thermally annealed at up to 750 °C to promote phase segregation. The resistivity and magnetoresistivity have been measured in the temperature range 4–300 K in fields of up to 12 kOe and the magnetization by vibrating sample magnetometer at fields of up to 6 T. We have modeled the magnetization and GMR of the system using an ensemble of superparamagnetic particles which have a log normal distribution of diameters. We obtain an excellent fit to the experimental magnetization data at room temperature. This is true for all annealing strategies used. Conversely, we have found a marked difference between the modeled and experimental GMR data for higher temperature annealing strategies. It can be shown that this model accurately fits the magnetoresistance if only particles under a critical diameter are considered. For $Ag_{1-x}Ni_{x-y}Fe_y$ heterogeneous alloy films this critical diameter has been calculated to be 6 nm. Larger particles will contribute only to the magnetization and not the magnetoresistivity. To optimize the magnetoresistance an annealing strategy that favors the creation of particles under this critical diameter is required. © *1996 American Institute of Physics.* [S0021-8979(96)60708-0]

 0021-8979/96/79(8)/5605/1/$10.00 © 1996 American Institute of Physics

Structural evolution in sputtered $Co_{90}Fe_{10}$/Ag giant magnetoresistance multilayers

J. D. Jarratt and J. A. Barnard
The Department of Metallurgical and Materials Engineering and The Center for Materials for Information Technology, The University of Alabama, Tuscaloosa, Alabama 35487-0202

The thermal evolution of structure, giant magnetoresistance (GMR), and magnetic properties in two sequences of sputtered ($Co_{90}Fe_{10}$/Ag) multilayers is presented. Granular-type and "discontinuous" GMR is observed depending on layer thickness. © *1996 American Institute of Physics.* [S0021-8979(96)54408-5]

I. INTRODUCTION

In a previous paper[1] we surveyed giant magnetoresistance (GMR) in $Co_{90}Fe_{10}$/Ag sputtered multilayers as a function of both $Co_{90}Fe_{10}$ and Ag layer thicknesses and annealing conditions. We were able to differentiate the observed GMR behaviors depending on geometry and annealing treatment into different categories: (1) granular-type GMR (GGMR) in ultrathin CoFe layered samples (layered-GGMR), (2) as-deposited GMR in thicker CoFe and Ag layered samples that upon annealing becomes (3) discontinuous GMR [(DGMR), as first described by Hylton *et al.* in NiFe/Ag multilayers[2]], and (4) the absence of GMR originating from antiferromagnetic (AFM) layer coupling. In this paper we focus on two series of multilayers samples with fixed CoFe thicknesses of 12.7 and 7.4 Å and varying Ag thickness. The 12.7 Å CoFe series exhibits DGMR in the thicker Ag range and no GMR when the Ag thickness ranges from ~9 to 30 Å where conventional GMR from oscillating AFM coupling is observed in many other sputtered magnetic/nonmagnetic systems.[3,4] The 7.4 Å CoFe series displays layered-GGMR that oscillates in magnitude with Ag thickness as has been observed in sputtered Co/Ag multilayers with ultrathin Co layers.[5]

II. RESULTS AND DISCUSSION

The films were dc magnetron sputtered in a computer-controlled system onto glass substrates with a permanent magnet positioned behind each substrate providing a 90 Oe field in the film plane. The geometry of the films is [glass/Ta 50 Å/($Co_{90}Fe_{10}$ *X* Å/Ag *Y* Å)×20/Ta 120 Å]. Magnetic properties were measured on a vibrating sample magnetometer (VSM). X-ray diffraction (XRD) was performed using Cu $K\alpha$ radiation. The MR measurements were made in the plane of the films using a four-point in-line probe assembly with the current and easy axis of the film both perpendicular to the applied magnetic field. The MR% is defined as $MR\% = \{[\rho(H) - \rho_{max}]/\rho_{max}\} \times 100$, where $\rho(H)$ is the sample resistivity at a given field value and ρ_{max} is the resistivity at the maximum applied field. The anneals were performed in an argon atmosphere. All measurements were made at room temperature. The reported values for the CoFe and Ag thicknesses are based on thickness measurements made using low-angle XRD (LXRD).

Considering first the 12.7 Å CoFe series, Fig. 1(a) shows the MR% for as-deposited and annealed (15 min at 300 and 400 °C) samples as a function of Ag layer thickness. The maximum MR% consistently occurs in samples with thicker Ag layers. The MR%-*H* profiles for a sequence of annealing temperatures are shown in Fig. 1(b) for separate (CoFe 12.7 Å/Ag 45 Å) samples. Only one half of the full profile is shown for clarity. Notice the sensitive nature of the profile shape to annealing temperature and the profile sharpening upon annealing at the lower temperatures. This MR behavior upon annealing is characteristic of DGMR, a highly field-sensitive GMR arising from negative exchange coupling between ferromagnetic platelets which are formed by CoFe layer breakup due to Ag diffusion through columnar grain boundaries.[2] The source of the as-deposited MR is unclear,

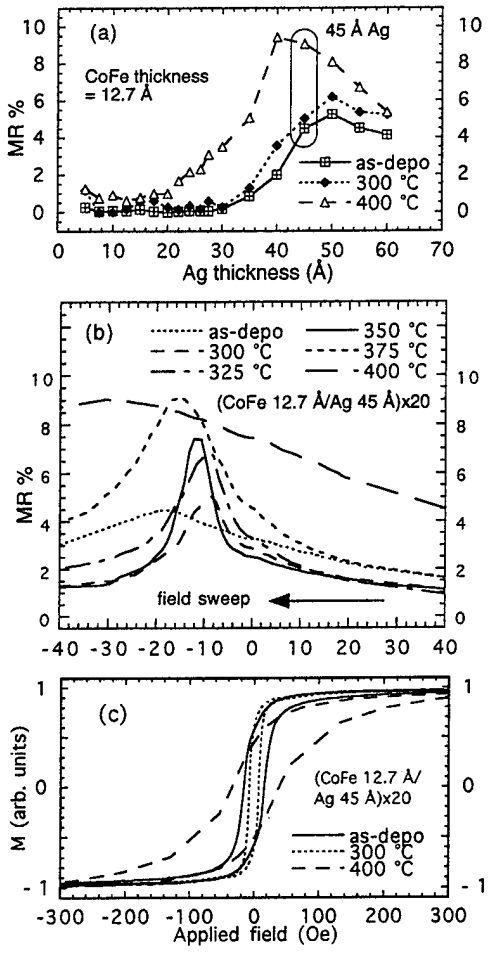


FIG. 1. (a) MR% vs Ag layer thickness in as-deposited and annealed (15 min) samples: [7059 glass/Ta 50 Å/(CoFe 12.7 Å/Ag *X* Å)×20/Ta 120 Å], (b) MR%-*H* profiles [one half of the field sweep (positive to negative) is shown for clarity], and (c) Hard-axis *M*-*H* loops for separate [7059 glass/Ta 50 Å/(CoFe 12.7 Å/Ag 45 Å)×20/Ta 120 Å] samples annealed for 15 min.

 0021-8979/96/79(8)/5606/3/$10.00 © 1996 American Institute of Physics

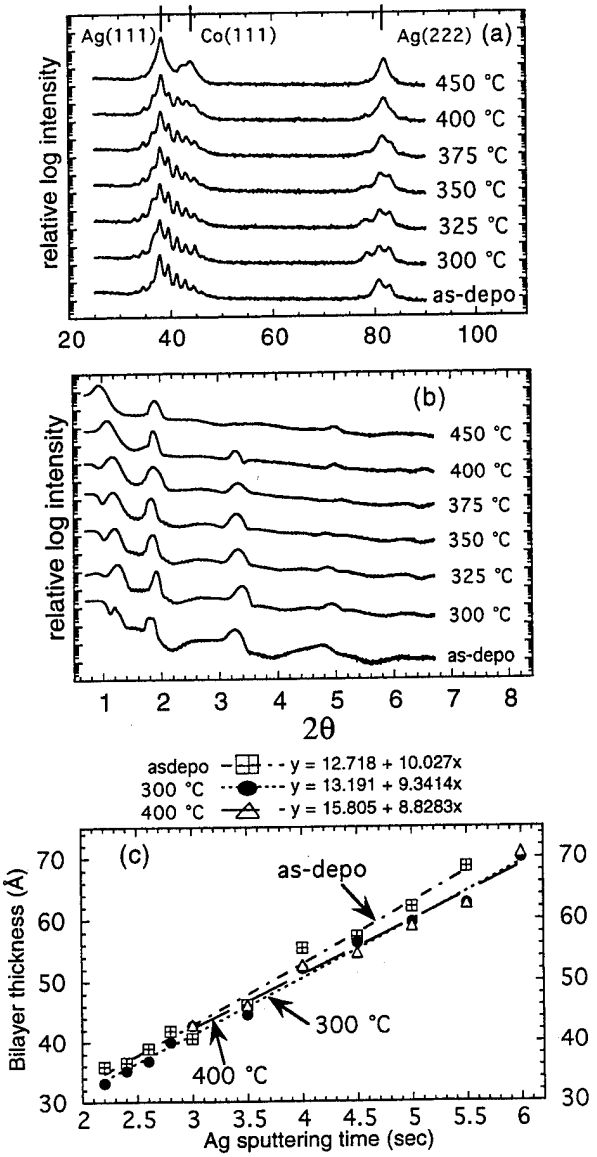


FIG. 2. (a) HXRD scans and (b) LXRD scans vs 15 min anneals on separate [7059 glass/Ta 50 Å/(CoFe 12.7 Å/Ag 45 Å)×20/Ta 120 Å] samples, and (c) plot of measured bilayer thicknesses via LXRD vs Ag deposition time for the CoFe 12.7 Å series.

although it is assumed related to the DGMR. Figure 1(c) shows the hard-axis magnetic hysteresis (M-H) loops for as-deposited and annealed (CoFe 12.7 Å/Ag 45 Å) samples. In-plane uniaxial magnetic anisotropy disappeared in samples annealed at temperatures above 325 °C. Notice the dip in coercivity (H_c) in the 300 °C annealed sample and then the large increase beyond the as-deposited H_c value in the 400 °C annealed sample. This effect is also seen in the MR%-H profiles of Fig. 1(b) where the profile peak position shifts toward zero with low-temperature annealing and then to larger field values beyond the as-deposited value after higher-temperature annealing.

Figures 2(a) and 2(b) are high-angle XRD (HXRD) and LXRD scans, respectively, versus annealing temperature for the (CoFe 12.7 Å/Ag 45 Å) DGMR samples. Satellite peaks around the (111) growth texture are observed in the HXRD scans signifying artificial structural coherency at the interfaces [Fig. 2(b)]. Low-angle Bragg peaks observed in the LXRD scans reveal appreciable film layer flatness and periodicity in the multilayers [Fig. 2(b)]. Low-temperature annealing (300 and 325 °C) reveals a slight smoothing and increased coherency of the interfaces as the GMR starts to increase. This is manifested by the initial formation of additional satellite peaks next to both the Ag(111) and (222) peaks in the HXRD scans, and slightly more intense low-angle Bragg peaks in the LXRD scans. This agrees with the literature on sputtered Co/Ag multilayers where "back diffusion" was observed along with a MR% increase upon annealing.[6] At the "over-annealing" temperatures the artificially layered structure and the interfaces show degradation as only signals from the bulk layers are present in the HXRD scans and the low-angle Bragg peak intensities have decreased in the LXRD scans. There is a slight shift of the low-angle peak positions to higher angles with annealing which corresponds to a decrease in bilayer thickness attributed to film densification from sputtered-in defect elimination and a change in the relative CoFe and Ag layer thicknesses. Figure 2(c) shows a plot of the bilayer thicknesses Λ calculated from LXRD scans for as-deposited and annealed samples. The method used here employs an extrapolation technique described in Ref. 7. The linear fits of Fig. 2(c) allow for the calculation of the average as-deposited CoFe thickness (intercept) of 12.7 Å and the Ag deposition rate (slope) of 10.03 (10.0) Å/s. Annealing results in an apparent increase in the CoFe thickness and an apparent decrease in the measured Ag deposition rate. This is consistent with the idea that Ag diffuses through CoFe grain boundaries resulting in thicker overall CoFe layers (platelets) at the expense of Ag layer thickness, as shown schematically in Fig. 3.

Now we will concentrate on the 7.4 Å CoFe series. Recently, an oscillation in MR% with Ag layer thickness was observed in sputtered (Co 6 Å/Ag X Å) multilayers with the first peak at ~18 Å and the second, much broader peak at ~40 Å Ag.[5] This report also states that Co does not form a continuous layer when deposited on Ag until a thickness of at least ~8 Å is reached, therefore the GMR and the oscillation are not considered to originate strictly from AFM coupling of complete Co layers, but from Co cluster interactions. Figures 4 and 5 show results from the 7.4 Å CoFe series in which the CoFe layers are not considered continuous. These samples are essentially artificially stratified granular films. The GMR observed is characteristic of single-layer phase separating "granular" alloys (broad MR%-H profiles with very low hysteresis).[8–10] The as-deposited MR% values versus Ag thickness in Fig. 4(a) show an oscillation in the 7.4 Å CoFe series with peaks at Ag 17.6 and 39.6 Å, respectively, in agreement with Ref. 5. Annealing results in a loss of this oscillation as the MR% decreases nearly monotonically with Ag thickness above 20 Å. Representative MR%-H profiles and M-H loops for as-deposited and annealed 7.4 Å CoFe samples with Ag thicknesses of 17.6 and 39.6 Å are plotted in Figs. 4(b) and 4(c), respectively. Annealing results in squareness loss that is the most pronounced in the Ag 39.6 Å sample annealed at 400 °C.

XRD of the (7.4 Å CoFe/Ag 17.6 Å) samples shows a similar trend in film structure evolution with annealing to

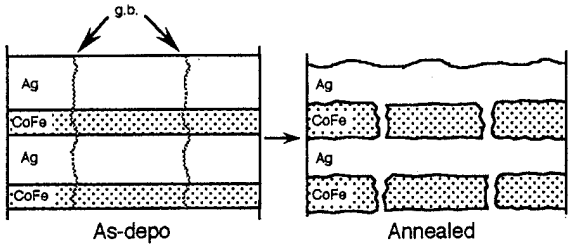


FIG. 3. Schematic of the effect of annealing 12.7 Å CoFe series DGMR films that results in CoFe layer breakup from Ag diffusion through grain boundaries and the subsequent Ag layer thickness decrease and CoFe layer increase.

that observed in the (CoFe 12.7 Å/Ag 45 Å) DGMR samples, where low-temperature annealing (300 °C) results in more distinct satellite shoulder peak formation around the Ag(111) and (222) bulk peaks in the HXRD scan [Fig. 5(a)], and also, the Kiessig fringes from the 20 bilayers are more intense in the LXRD scan [Fig. 5(b)]. Annealing at 400 °C degrades the interfaces and increases the relative intensity of the bulk (111) textured peaks at the expense of the satellite peaks.

The as-deposited magnetization (M_s) in CoFe 12.7 and 7.4 Å samples was ~1320 and ~990 emu/cc, respectively, and independent of Ag thickness for both series (M_s of bulk

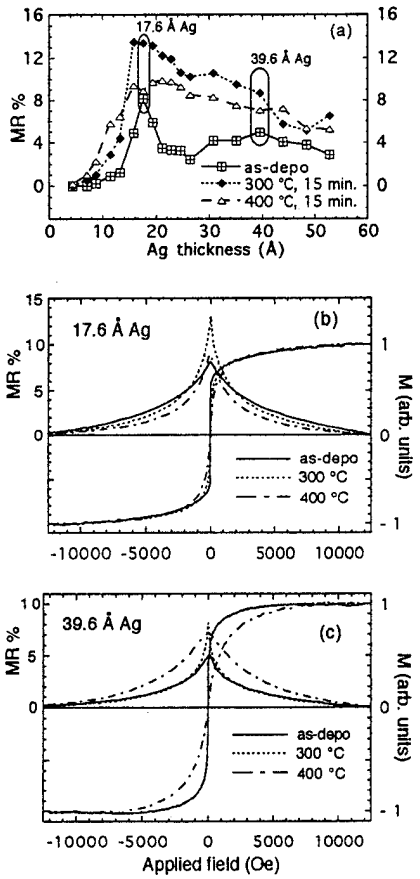


FIG. 4. (a) MR% vs Ag layer thickness in as-deposited and annealed (15 min) samples: [7059 glass/Ta 50 Å/(CoFe 7.4 Å/Ag X Å)×20/Ta 120 Å], (b) MR%-H profiles and M-H loops for as-deposited and annealed [7059 glass/Ta 50 Å/(CoFe 7.4 Å/Ag 17.6 Å)×20/Ta 120 Å] samples, and (c) MR%-H profiles and hard-axis M-H loops for as-deposited and annealed [7059 glass/Ta 50 Å/(CoFe 7.4 Å/Ag 39.6 Å)×20/Ta 120 Å] samples.

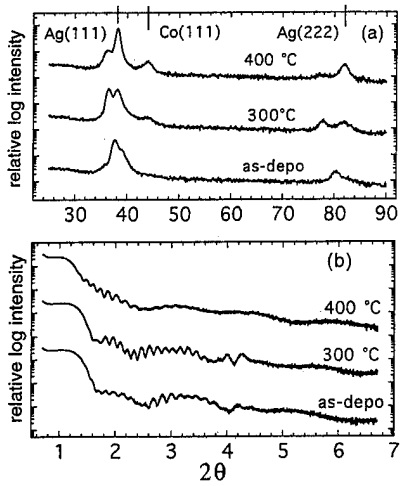


FIG. 5. (a) HXRD scans and (b) LXRD scans vs 15 min anneals on separate [7059 glass/Ta 50 Å/(CoFe 7.4 Å/Ag 17.6 Å)×20/Ta 120 Å] samples.

$Co_{90}Fe_{10}$ is ~1510 emu/cc). The dependence of M_s on CoFe thickness is indicative of the presence of a magnetically "dead" layer (~1.5 Å). Lower-temperature annealing (300–350 °C) resulted in a small increase in M_s (<10%) in both CoFe 12.7 and 7.4 Å samples. Higher-temperature annealing (~400 °C) reduced M_s ~3–19% below the as-deposited value. The rise in M_s could logically be associated with demixing at the interfaces. However, the drop in M_s after 400 °C annealing is not readily explained (oxidation is a potential explanation but no corroborating evidence has been found for this).

Both the aspect ratio (height/width) and spacing of the CoFe platelets (or clusters) are critical in determining the observed MR behavior. The layered clusters formed during growth in the layered-GGMR samples are considered having a higher aspect ratio than the CoFe platelets formed upon annealing in the DGMR samples. The small difference in CoFe layer thickness reveals a dramatic difference in the observed MR behavior with layered-GGMR samples displaying very broad MR%-H profiles and DGMR samples displaying highly field-sensitive MR%-H profiles.

ACKNOWLEDGMENT

This work was supported by NSF-DMR-9301648 and NSF-PYI DMR-9157402.

[1] J. D. Jarratt and J. A. Barnard, IEEE Trans. Magn. **31**, 3952 (1995).
[2] T. L. Hylton, K. R. Coffey, M. A. Parker, and J. K. Howard, Science **261**, 1021 (1993).
[3] S. S. P. Parkin, N. More, and K. P. Roche, Phys. Rev. Lett. **61**, 2304 (1990).
[4] S. S. P. Parkin, Phys. Rev. Lett. **67**, 3598 (1991).
[5] R. Loloee, P. A. Schroeder, W. P. Pratt, Jr., J. Bass, and A. Fert, Physica B **204**, 274 (1995).
[6] L. F. Schelp, G. Tosin, M. Carara, M. N. Baibich, A. A. Gomes, and J. E. Schmidt, Appl. Phys. Lett. **61**, 1858 (1992).
[7] M. Suguwara, M. Kondo, S. Yamazaki, and K. Nakajima, Appl. Phys. Lett. **52**, 742 (1988).
[8] J. A. Barnard, A. Waknis, M. Tan, E. Haftek, M. R. Parker, and M. L. Watson, J. Magn. Magn. Mater. **114**, L230 (1992).
[9] J. C. Xiao, J. S. Jiang, and C. L. Chien, Phys. Rev. Lett. **68**, 3749 (1992).
[10] A. E. Berkowitz, J. R. Mitchell, M. J. Carey, A. P. Young, S. Zhang, F. E. Spada, F. T. Parker, A. Hutten, and G. Thomas, Phys. Rev. Lett. **68**, 3745 (1992).

AUTHOR INDEX

Abadía, C.–(8) 6330
Abarra, E. N.–(8) 5919
Abe, M.–(8) 4561
Abe, S.–(8) 4611
Abele, M. G.–(8) 5199
Achutharaman, V. S.–(8) 4553
Adachi, K.–(8) 4905
Adamashvili, G. T.–(8) 5727
Adenwalla, S.–(8) 4524
Adeyeye, A. O.–(8) 6120
Adly, A. A.–(8) 4675
Aeppli, G.–(8) 5023, 5391
Afonso, S.–(8) 6580, 6593
Aguiló, M.–(8) 5439
Ahern, Brian–(8) 4759
Ahmed, H.–(8) 6120
Ahn, Jong-Guk–(8) 5961
Ahn, Y. M.–(8) 5696
Akagi, K.–(8) 4905
Akeura, K.–(8) 4957
Akhsakhalyan, A. D.–(8) 4625
Akhutkina, A. I.–(8) 6132
Akiba, Etsuo–(8) 5126
Akiyama, J.–(8) 5655
Alba, M.–(8) 6158
Alberts, H. L.–(8) 6519, 6526
Albuquerque, E. L.–(8) 5736
Albuquerque, M. R. M. L.–(8) 5736
Alexandrakis, G. C.–(8) 6586
Algarabel, P.–(8) 5175
Algarabel, P. A.–(8) 4656, 4659, 5178, 6330
Ali, N.–(8) 6007
Ali, Naushad–(8) 5233, 5398, 6154
Allen, W.–(8) 5593
Allenspach, P.–(8) 5869, 5869
Almeida, B. G.–(8) 6246
Al-Omari, I. A.–(8) 4590
Alonso, J.–(8) 5182
Altoé, M. V. P.–(8) 4846, 6555
Altounian, Z.–(8) 4605, 4619, 4769, 4833, 5519, 5536
Amado, M. M.–(8) 6355
Amaral, V. S.–(8) 6246
Ambert, G.–(8) 5384
Ambrose, T.–(8) 5920
Anane, A.–(8) 4554
Anderson, G. W.–(8) 4954, 5641
Andou, T.–(8) 4884
Ang, S.–(8) 6593
Ankner, J. F.–(8) 4762, 4775, 4782
Ansermet, J.-Ph.–(8) 6010, 6090
Anthony, T. C.–(8) 4491, 5277
Anthony, Thomas C.–(8) 6389
Antonov, A. S.–(8) 6532
Antropov, V. P.–(8) 4799, 5409
Appino, C.–(8) 4575
Arabski, J.–(8) 5068
Aragoneses, P.–(8) 6539
Arai, K. I.–(8) 4574
Ardisson, J. D.–(8) 5973
Arnold, Z.–(8) 4656, 5178
Aronson, M. C.–(8) 6432
Arrott, A. S.–(8) 4570, 4635, 4973, 5752, 6051, 6529
Artinian, M.–(8) 5932
Artman, J. O.–(8) 4787
Arvanitis, D.–(8) 4983
Asada, H.–(8) 5318, 6643, 6646
Asamitsu, A.–(8) 5288
Asano, H.–(8) 5507
Asano, S.–(8) 5952
Atherton, D. L.–(8) 6042
Atlan, D.–(8) 4518
Atzmony, U.–(8) 5456
Augustyniak, B.–(8) 6525
Awschalom, D. D.–(8) 5296, 5324, 6095
Axtell, S. C.–(8) 5263
Ayres, A. M.–(8) 5680
Azizi, A.–(8) 6247

Babbar, V. K.–(8) 6515
Babcock, K.–(8) 5296, 5851, 6440
Baberschke, K.–(8) 4983
Back, Young R.–(8) 5788
Bader, S. D.–(8) 4524, 5838
Badia, F.–(8) 5605
Baggio-Saitovitch, E.–(8) 5256
Bahadur, D.–(8) 5995
Bailey, William E.–(8) 6393
Baker, I.–(8) 6028
Bakonyi, Imre–(8) 4811
Baldomir, D.–(8) 4674
Ball, A. R.–(8) 5103
Ballentine, C. A.–(8) 5845
Ban, S.–(8) 5452
Banerjee, R.–(8) 6536
Bao, W.–(8) 4558, 5023
Bao, Xiaohua–(8) 4866, 4869
Barandiarán, J. M.–(8) 5146
Bardou, N.–(8) 5068, 5848
Barmak, K.–(8) 5330
Barnard, J. A.–(8) 5005, 5606, 5904
Barnard, John A.–(8) 5779
Barquín, L. Fernández–(8) 5146
Barry, Walter–(8) 5733
Bartenlian, B.–(8) 5068, 5270, 5848
Basak, A.–(8) 4753
Bass, J.–(8) 5811, 6129, 6151
Basso, V.–(8) 5764
Batlle, X.–(8) 5605
Batlogg, B.–(8) 4541
Bauer, E.–(8) 6423
Bayreuther, G.–(8) 4509
Beauvillain, P.–(8) 5270
Becerra, C. C.–(8) 5236
Beech, R. S.–(8) 5889
Beers, K. L.–(8) 4644
Beitz, James V.–(8) 6512
Bellesis, G. H.–(8) 4496, 5011
Belorisky, E.–(8) 4698
Ben-Dor, L.–(8) 6564
Bennemann, K. H.–(8) 6177
Bennett, B. R.–(8) 5125
Bennett, L. H.–(8) 4712, 5315, 5456, 6073
Bensch, F.–(8) 4509
Berg, H. v.d.–(8) 6181
Berger, A.–(8) 4524, 5619
Bergqvist, A.–(8) 4689, 6476
Berkowitz, A. E.–(8) 5071, 5072, 5277, 5504, 5919
Berkowitz, Ami E.–(8) 4932
Berman, L. E.–(8) 6509
Berry, S. D.–(8) 5102
Bertero, G.–(8) 5342
Bertotti, G.–(8) 4575, 5142, 5764
Bertram, H. N.–(8) 5658
Bertram, H. Neal–(8) 4916, 5661, 5883
Bessho, K.–(8) 5057
Bhagat, S. M.–(8) 5165, 5166, 5292, 5991
Bhatia, C. S.–(8) 5327
Bhatt, R. N.–(8) 5096, 5196
Bhattacharyya, M.–(8) 4491
Bhushan, Bharat–(8) 5791, 5794, 5798, 5799, 5802, 5916
Biagini, Cristiano–(8) 4638
Bian, X.–(8) 4769, 4980
Biner, S. B.–(8) 5453
Binesti, D.–(8) 4575
Binninger, U.–(8) 5530
Biringer, P. P.–(8) 4671
Birsan, M.–(8) 5202, 6042
Bishop, D. J.–(8) 6592
Bissell, P. R.–(8) 4746, 6467
Bitoh, T.–(8) 5472
Blanco, J. A.–(8) 6352
Blanco, J. M.–(8) 5465, 6539
Bland, J. A. C.–(8) 4987, 6120, 6295
Blasco, J.–(8) 5175, 5178
Blondel, A.–(8) 6090
Blundell, S. J.–(8) 6295
Blyakhman, Yuri–(8) 4625
Boardman, A. D.–(8) 5365
Bochi, Gabriel–(8) 5609, 5845
Bohórquez, A.–(8) 6155
Borchers, J. A.–(8) 4762, 5102
Bornfreund, R. E.–(8) 5191
Borsa, F.–(8) 5084
Bottauscio, O.–(8) 4575
Bottoni, G.–(8) 4872, 5469
Bouarab, S.–(8) 5834
Boucher, J. P.–(8) 5384, 5395
Boumaiz, E.–(8) 5381
Bounds, C. O.–(8) 4830, 5501, 6335
Bourez, A.–(8) 5336
Brabers, V. A. M.–(8) 5936
Braga, M. E.–(8) 6246, 6355
Bramwell, S. T.–(8) 4976, 6150
Branagan, D. J.–(8) 4847, 5510
Brand, R. A.–(8) 5582
Brandon, E. J.–(8) 6147
Braun, Hans-Benjamin–(8) 6107
Bresowar, J.–(8) 4766
Brewer, M. A.–(8) 5321
Brinckerhoff, W. B.–(8) 6147
Britel, M.–(8) 5136
Broholm, C.–(8) 5023, 5391
Brown, W. D.–(8) 6593
Brubaker, W. W.–(8) 4644
Brück, E.–(8) 5221, 6321, 6358, 6396
Brucker, C. F.–(8) 5704
Brug, J. A.–(8) 4491, 5277
Brulet, A.–(8) 6158
Bruno, P.–(8) 5270
Brunsman, E. M.–(8) 5293
Brusca, T. E.–(8) 5185
Bucher, J. P.–(8) 5068
Bud'ko, S. L.–(8) 5256
Budnick, J. I.–(8) 4596, 5530
Buehler, C. J.–(8) 5746
Burke, E. R.–(8) 6063
Burke, Edward R.–(8) 6441
Burlet, P.–(8) 6396
Buschow, K. H. J.–(8) 4593, 4599, 4626, 5221, 5945, 6318, 6321
Bush, Gary G.–(8) 6389
Butera, A.–(8) 5269, 6577
Butler, W. H.–(8) 5282
Byers, Jeff M.–(8) 4553

Cabral, F. A. O.–(8) 5973
Cadieu, F. J.–(8) 4614, 5425, 5961
Cadogan, J. M.–(8) 4622, 5149, 5713, 6004, 6161
Cagan, V.–(8) 5472
Cai, Bingchu–(8) 4998, 6048
Cai, M.–(8) 6289
Cain, G.–(8) 5324
Cain, Jason L.–(8) 4860
Caliebe, W. A.–(8) 6509
Calleja, J. F.–(8) 5472, 6545
Camblong, Horacio E.–(8) 6261, 6383
Cambril, E.–(8) 5068
Camp, F. E.–(8) 4840, 5035
Campos, C.–(8) 5973
Candolfo, D.–(8) 4872, 5469
Canedy, C. L.–(8) 4538, 4546, 6126
Canova, A.–(8) 5554
Cao, G.–(8) 4567, 4821, 5876, 6001
Cao, Lei–(8) 5045
Cao, Q. Q.–(8) 6261
Cao, Ruoxin–(8) 6512
Cao, Wei–(8) 4932
Capsoni, D.–(8) 6621
Carbucicchio, Massimo–(8) 4869
Carcenac, F.–(8) 5068
Carl, A.–(8) 4990
Carley, L. R.–(8) 4485
Carling, S. A.–(8) 4644
Carling, S. G.–(8) 6150
Carrera, M.–(8) 6596
Carroll, T. L.–(8) 5377
Castro, S.–(8) 5955
Cava, R. J.–(8) 5856, 5923
Cavalleri, A.–(8) 5406
Cebollada, A.–(8) 5967
Cecchetti, A.–(8) 4872, 5469
Celinski, Z.–(8) 6200
Celotta, R. J.–(8) 6079
Cervantes-Lee, F.–(8) 4715
Chacko, Antony P.–(8) 4863
Chaiken, A.–(8) 4772, 4775
Chakarian, V.–(8) 4558, 5345, 6492, 6493
Chakoumakos, B. C.–(8) 5398
Chakraborty, A.–(8) 5011
Challener, W.–(8) 6440
Challener, W. A.–(8) 5693
Chan, F. T.–(8) 6580, 6593
Chan, K.–(8) 4715
Chandarlapaty, S.–(8) 4644
Chandramouli, M.–(8) 4846
Chang, C. P.–(8) 4790, 6282, 6533
Chang, C. R.–(8) 4919
Chang, Ching-Ray–(8) 4960
Chang, H. S.–(8) 5357
Chang, S. P.–(8) 5699
Chang, T. C.–(8) 6276
Chang, W. C.–(8) 4843, 5159, 5533

Chantrell, R. W.–(8) 4915, 5703, 5767, 6034, 6467
Chao, Y. D.–(8) 6552
Chapman, J. N.–(8) 6452
Chappert, C.–(8) 5068, 5270, 5848
Charap, S.–(8) 5671
Châtel, P. F. de–(8) 4626
Chaussy, J.–(8) 5823, 6370
Chavan, S. A.–(8) 5260
Cheeks, T. L.–(8) 5072
Chen, C. H.–(8) 5923
Chen, C. J.–(8) 5159, 5432
Chen, C. M.–(8) 5557
Chen, C. T.–(8) 4558, 6492, 6493
Chen, E. Y.–(8) 5889
Chen, Ga-Lane–(8) 5782
Chen, K. Y.–(8) 6593
Chen, L. H.–(8) 5599
Chen, L. Y.–(8) 4949
Chen, Liang-Yao–(8) 5193
Chen, Lujun–(8) 4783
Chen, P. J.–(8) 5277
Chen, S. K.–(8) 5533, 5964
Chen, T.–(8) 5342
Chen, T. C.–(8) 6341
Chen, Y. H.–(8) 6512
Chen, Y. J.–(8) 4878
Chen, Yinchao–(8) 5733
Chen, Z. W.–(8) 4812, 6405
Cheng, S. F.–(8) 6084, 6234
Cheng, Y.–(8) 6447
Cheng, Zhao-Hua–(8) 5528, 5709
Cheong, S.-W.–(8) 4558
Cheong, S-W.–(8) 4541
Cherry, H. B.–(8) 5169
Chetkin, M. V.–(8) 6132
Chevalier, B.–(8) 6355
Cheyne, Douglas–(8) 4711
Chiampi, M.–(8) 4575
Chiang, Donyau–(8) 5560
Chiang, W.-C.–(8) 5811, 6129
Chien, C. L.–(8) 5139, 5306, 5309, 5615, 5920, 6117
Chilamakuri, Sameera–(8) 5794
Chin, A.–(8) 6007
Chin, T. S.–(8) 5964
Ching, W. Y.–(8) 4602, 5545
Chmielewski, M.–(8) 6525
Cho, B. I.–(8) 5482, 5696
Cho, C. Peter–(8) 5548
Choe, G.–(8) 4923, 6306, 6536
Choi, G.–(8) 5873
Choi, S. J.–(8) 6299
Chou, C. H.–(8) 5866
Chou, Stephen Y.–(8) 5066, 5066, 5067, 5855, 6101
Chow, Jeff Y.–(8) 6022
Chow, K. H.–(8) 6636
Chowdhury, Ataur R.–(8) 6303
Chrisey, D. B.–(8) 6338
Christianson, A. D.–(8) 6164
Christodoulides, J. A.–(8) 5152, 5302
Chu, C. W.–(8) 6580
Chu, F.–(8) 6405
Chuang, Y. C.–(8) 6324
Chui, S. T.–(8) 4951
Cintolesi, F.–(8) 6624
Ciureanu, P.–(8) 5136
Clark, A. E.–(8) 6213, 6216
Clausen, K. N.–(8) 5078
Clavel, M.–(8) 4571
Clegg, W. W.–(8) 6643
Clemens, B. M.–(8) 6189
Cline, J. P.–(8) 6028
Cochran, J. F.–(8) 4518
Cochrane, R. W.–(8) 6289
Coffey, G. A.–(8) 4644
Coffey, K. R.–(8) 4762, 5330
Cohenca, C. H.–(8) 6564
Coker, G. S.–(8) 4644
Collier, B. F.–(8) 6614
Collins, M. F.–(8) 6614
Colucci, C. C.–(8) 5973
Continentino, Mucio A.–(8) 6345
Continenza, A.–(8) 6423
Conto, C. R.–(8) 4756
Contreras, M. C.–(8) 4936, 5217, 5472, 6545
Cooper, Bernard R.–(8) 6420
Corlett, John–(8) 5733
Cornejo, D. R.–(8) 6312
Corrales, J. A.–(8) 5217
Corti, M.–(8) 5084, 6621, 6624
Cottam, M. G.–(8) 5371, 5724
Courtois, D.–(8) 4622
Coverdale, G. N.–(8) 6034
Cowache, C.–(8) 6370
Cowen, J. A.–(8) 6151
Crooker, B. C.–(8) 5401, 6164, 6436
Cross, R. W.–(8) 5820, 6240, 6386
Crow, J. E.–(8) 4567, 4821, 5876
Cuccoli, Alessandro–(8) 4638
Cullen, J. R.–(8) 6216
Currie, J. F.–(8) 5136

Dabkowska, H.–(8) 5081
Daboo, C.–(8) 4987, 6120
da Cunha, S. F.–(8) 5220
Dahlberg, E. D.–(8) 6447
Dahlberg, E. Dan–(8) 5758
Dail, R.–(8) 5826
Dalton, J. J.–(8) 4753
Das, B. N.–(8) 4890
d'Assunção, A. G.–(8) 5736
Daughton, J. M.–(8) 5889
Dauguet, P.–(8) 5823, 6370
Davidson, R.–(8) 5671
Day, P.–(8) 4644
Daykin, A. C.–(8) 6292
de Aguiar, F. M.–(8) 6309
Dean, C.–(8) 4915, 6467
de Azevedo, M. M. P.–(8) 6246
De Boeck, J.–(8) 4957
de Boer, F. R.–(8) 4626, 5221, 6321, 6324, 6358, 6361, 6396, 6408
de Camargo, P. C.–(8) 6154
Decanini, D.–(8) 5068
Dederichs, P. H.–(8) 5129, 5638
Dedukh, L. M.–(8) 5315, 6073
DeFotis, G. C.–(8) 4644, 4718
Defoug, S.–(8) 6036
de Francisco, C.–(8) 5436, 6545
de Haan, P.–(8) 6243
de Jong, W.–(8) 5632
de Julián, C.–(8) 5955
de Leon Guevarra, A. M.–(8) 4554
Della Torre, Edward–(8) 5773
Delmas, A.–(8) 6485
del Moral, A.–(8) 5175
Demangeat, C.–(8) 5834
de Morais, E.–(8) 5973
Dempsey, N. M.–(8) 5045
Dender, D.–(8) 5391
Deng, Hong–(8) 5779
Denlinger, J. D.–(8) 5626
Dennis, K. W.–(8) 4847
De Raedt, H.–(8) 6110
Despres, J. F.–(8) 6007
Desvignes, J. M.–(8) 5932
De Teresa, J. M.–(8) 5175
Deville, J. P.–(8) 6247
Devine, M. K.–(8) 5493
de Visser, A.–(8) 6358
Dey, Subrata–(8) 5916
de Zhang, Yi–(8) 5709
Dhagat, P.–(8) 4695, 5652
Dhalenne, G.–(8) 5099, 5384, 5395
Dhar, S. K.–(8) 6349, 6367
Díaz, F.–(8) 5439
DiBari, R. C.–(8) 5102
DiBari, Rebecca C.–(8) 5841
Dieny, B.–(8) 6370
Diep, H. T.–(8) 5087
Dimitrov, D. V.–(8) 5106
Ding, Juren–(8) 5892
Dionne, Gerald F.–(8) 5172
Disselnkötter, Rolf–(8) 5208
DiStefano, Sal–(8) 5776
Dittschar, A.–(8) 5618, 6426, 6504
DiTusa, J. F.–(8) 5023
Dmowski, W.–(8) 6253
Dodge, J. S.–(8) 6186
Doerner, M. F.–(8) 5327
Doerner, Mary–(8) 4916
Doerner, Mary F.–(8) 5348
Doi, M.–(8) 5583
Doi, T.–(8) 4699, 4884, 4887, 5214
Domínguez, L.–(8) 6539
Dominguez, M.–(8) 5165, 5991
Donahue, M. J.–(8) 4712, 5315, 6073
Donnet, D. M.–(8) 6243
Dorsey, P. C.–(8) 6338
Doudin, B.–(8) 6010, 6090
Douglas, T.–(8) 5324
Dowben, P. A.–(8) 5838
Doyle, W. D.–(8) 4995, 6489
Dresselhaus, J.–(8) 6508
Dreyssé, H.–(8) 5834
Drouhin, H.-J.–(8) 4734
Drumheller, John E.–(8) 5094, 5368
Du, Tengda–(8) 6034
Duan, Mingqian–(8) 5979
Ducreux, J. P.–(8) 4575
Dugas, M.–(8) 6440
Duk Choi, Seung–(8) 5489
Dulcie, L. L.–(8) 5358
Duncombe, P. R.–(8) 4549
Dunlap, R. A.–(8) 4662, 4679, 5992, 5995
Dunn, J. Hunter–(8) 4983
Dunsiger, S. R.–(8) 6636
Dupas, C.–(8) 4554, 5270
Dupre, L. R.–(8) 5496
Durán, C. A.–(8) 6592
Durin, G.–(8) 5142, 5764
Durlam, M.–(8) 5889
Durst, A. C.–(8) 5196
Dworak, P.–(8) 6203
Dykes, J. W.–(8) 4775, 5584

Earl, J.–(8) 5703
Eastham, J. F.–(8) 4685, 5554
Ebels, U.–(8) 6120
Egami, T.–(8) 6253
Egelhoff, W. F., Jr.–(8) 5277
Elam, W. T.–(8) 5345
El Chahal, L.–(8) 6247
El-Hilo, M.–(8) 6034
Elings, V.–(8) 6440
Ellerbrock, R. D.–(8) 5582
Ellis, D. E.–(8) 6429
Elmers, H. J.–(8) 4984
Eloot, K.–(8) 5496
El-Shall, M. S.–(8) 5063
Engdahl, G.–(8) 4689, 6476
Epstein, A. J.–(8) 6147
Ercole, A.–(8) 4987
Erickson, R. P.–(8) 4808
Eriksson, O.–(8) 4983, 5837
Erwin, J. K.–(8) 5687
Erwin, R. W.–(8) 4762, 5102
Escorcia-Aparicio, Ernesto J.–(8) 4532, 4964
Espeso, J. I.–(8) 6352
Étourneau, J.–(8) 6355
Ezekwenna, Peter C.–(8) 4587

F.-Calleja, J.–(8) 4936, 5217
Fagan, J. G.–(8) 6341
Fainstein, A.–(8) 6577
Fang, T. M.–(8) 5739
Fang, Ta-Ming–(8) 4759
Fang, W. W.–(8) 4790
Farrow, R. F. C.–(8) 5967, 6496
Fawcett, E.–(8) 6154
Fawcett, Eric–(8) 4802
Feder, R.–(8) 6426
Fedyunin, Y. N.–(8) 6642
Feiner, L. F.–(8) 5103
Fejer, M. M.–(8) 6186
Felcher, G.–(8) 4524
Felder, R. J.–(8) 5923, 5926
Feng, Y. C.–(8) 5345
Fernandez, J. Rodriguez–(8) 6364
Fernandez-Baca, J. A.–(8) 5398
Ferré, J.–(8) 5632
Fetisov, Y. K.–(8) 5721, 5730
Fidler, J.–(8) 5029, 6458
Figge, M.–(8) 4531
Filipkowski, M. E.–(8) 4525
Filoti, G.–(8) 5257
Fink, Anita–(8) 6084
Fiorillo, F.–(8) 4575
Fisch, Ronald–(8) 5088
Fisher, A. S.–(8) 5185
Fisher, Kevin D.–(8) 4502
Fishman, R. S.–(8) 4824
Fisk, Z.–(8) 6577
Florence, G.–(8) 6593
Flores, A. G.–(8) 5422, 6574
Flosdorff, A.–(8) 4641, 6054
Flynn, C. P.–(8) 4779
Fogarty, K. J.–(8) 6643
Folan, L. M.–(8) 5716
Foldeaki, M.–(8) 5995
Foner, S.–(8) 4740, 5071
Fontaine, A.–(8) 6497
Fontcuberta, J.–(8) 5182, 6596
Fontes, M. B.–(8) 5256
Fontijn, W. F. J.–(8) 5936
Foss, S.–(8) 6447
Foss, Sheryl–(8) 6447
Franklin, D. R.–(8) 5390
Fredkin, Donald R.–(8) 5755, 5762
Freeman, A. J.–(8) 4805, 5827, 5831, 6209, 6500
Freeman, M. R.–(8) 5898
Freibert, F.–(8) 4567, 4821, 5876
Freitag, Andrea E.–(8) 6303
Freitas, P. P.–(8) 6246, 6452
Friedman, Jonathan R.–(8) 6031
Friedmann, A.–(8) 5658, 5661
Fruchart, D.–(8) 4584, 4608, 5542
Fuerst, C. D.–(8) 4656, 5539, 5998
Fuest, A.–(8) 5582
Fujii, Toshitaka–(8) 5988
Fujimori, A.–(8) 5707, 5708
Fujimori, H.–(8) 4733, 5130
Fujita, E.–(8) 5351
Fujita, J.–(8) 4999
Fujiwara, H.–(8) 6286
Fujiwara, Hideo–(8) 4970
Fujiwara, Shuzo–(8) 4721
Fujiwara, Y.–(8) 6270
Fukutani, H.–(8) 5707, 5708
Fuller, C. J.–(8) 6405
Fullerton, Eric E.–(8) 4524, 6266
Fulmek, Paul L.–(8) 5761
Fumagalli, P.–(8) 5929, 6203
Furlani, E. P.–(8) 4692
Furubayashi, T.–(8) 6258
Fussell, Barry K.–(8) 5548

Futamoto, M.–(8) 5354, 5359

Gadetsky, S.–(8) 5667, 5687
Gadetsky, S. N.–(8) 5700
Gafney, H. D.–(8) 6025
Gago-Sandoval, P. A.–(8) 5590, 5605
Gair, S.–(8) 5554
Galéra, R. M.–(8) 6497
Gallagher, W. J.–(8) 4538, 4546, 4549
Galli, M.–(8) 6423
Gama, S.–(8) 5973
Gambino, R. J.–(8) 5253, 5929, 6025, 6285
Gambino, Richard J.–(8) 5776
Gammel, P. L.–(8) 6592
Gandit, P.–(8) 5823, 6370
Gandra, F. G.–(8) 5462
Gangopadhyay, S.–(8) 6286
Ganguly, R.–(8) 5260
Gao, J.–(8) 6470
Gao, Z.–(8) 5510
García, A.–(8) 6516, 6589
Garcia, F.–(8) 5220
García, J.–(8) 5175, 5178
Garcia, L. M.–(8) 6497
García, N.–(8) 6019, 6110
García-Mochales, P.–(8) 6019
García-Pablos, D.–(8) 6019, 6110
García Soldevilla, J.–(8) 6352
García Tello, P.–(8) 5479
Garifullin, I. A.–(8) 6298
Garif'yanov, N. N.–(8) 6298
Garshelis, I. J.–(8) 4756
Garwin, E. L.–(8) 6488
Gaspard, P.–(8) 5936
Gaulin, B. D.–(8) 4769, 5081, 6170, 6636
Gautier, F.–(8) 5834
Gavrin, A.–(8) 5306, 5309
Gayoso, M.–(8) 5955
Gehring, G. A.–(8) 5593
Gehring, P. M.–(8) 4762
Geiser, U.–(8) 6586
Geisler, H.–(8) 4765
Ghigna, P.–(8) 6624
Gider, S.–(8) 5324
Giles, R. C.–(8) 4685
Giljer, P.–(8) 5327
Gill, B. L.–(8) 5696
Gillies, M. F.–(8) 6452
Gingras, M. J. P.–(8) 6170, 6636
Giri, Anit K.–(8) 5479, 5955, 6611
Girt, Er.–(8) 4833
Girvin, S. M.–(8) 5096
Gjoka, M.–(8) 5539
Glavinas, E.–(8) 4695, 5652
Glenis, S.–(8) 5873
Glenn, Darin W.–(8) 6193
Gmelin, E.–(8) 5869, 5869, 6173
Godart, C.–(8) 5857, 6347, 6349
Goedkoop, J.–(8) 6497
Göktürk, H.–(8) 4857
Goldman, A. M.–(8) 4553
Gomez, R. D.–(8) 6063
Gomez, Romel D.–(8) 6441
Gómez Sal, J. C.–(8) 4815, 6352
Gong, G. Q.–(8) 4538, 6126
Gong, X. G.–(8) 5162
González, A. C.–(8) 5242
González, E.–(8) 6155
González, J.–(8) 5465, 5479, 6479, 6539
González, J. M.–(8) 5465, 5479, 5955, 6155, 6312, 6479, 6611
González-Calbet, J. M.–(8) 5182
Goodey, J. R.–(8) 4718
Goodman, K. W.–(8) 5626
Gorelik, S. S.–(8) 5500
Goremychkin, E. A.–(8) 6432
Görlitz, D.–(8) 4641, 6054
Gornakov, V. S.–(8) 5315, 6073
Gorría, P.–(8) 5146
Gortenmulder, T. J.–(8) 5221, 6358, 6361
Goryunov, Yu. V.–(8) 6298
Gotaas, J. A.–(8) 4746
Goto, T.–(8) 4647
Gouzerh, J.–(8) 5932
Govindaraju, M. R.–(8) 5453
Govorkov, S.–(8) 4518
Govorkov, S. A.–(8) 6051
Gradmann, U.–(8) 4984
Granados, X.–(8) 6596
Grandjean, F.–(8) 4584, 4587, 5945
Gray, S. J.–(8) 4987
Greedan, J. E.–(8) 6170, 6173, 6176, 6432, 6636
Greene, R. L.–(8) 4545, 4552, 4552, 5165, 5166, 5292
Greenough, R. D.–(8) 6219
Gregg, J.–(8) 4528
Gregg, J. F.–(8) 5593, 6247
Grigorenko, A. N.–(8) 6113
Grimes, Craig A.–(8) 4581, 5497
Grishin, A. M.–(8) 5860
Grünberg, P.–(8) 4782
Grundy, P. J.–(8) 4650, 4939, 6070
Gu, R. Y.–(8) 6255
Guenzburger, Diana–(8) 6429
Guilfoyle, S. J.–(8) 4939
Guillot, M.–(8) 4608, 5542, 5932, 5985
Guillot, Maurice–(8) 5979
Guimarães, A. P.–(8) 5468
Güntherodt, G.–(8) 6203
Güntherodt, H.-J.–(8) 5609
Gupta, A.–(8) 4538, 4546, 4549
Gupta, D.–(8) 5179
Gupta, H.–(8) 6045
Gupta, L. C.–(8) 5857, 6347, 6349
Gupta, R.–(8) 6079
Gupta, S.–(8) 5018, 5446, 5584
Gurney, B. A.–(8) 6295
Guruswamy, S.–(8) 4851, 6222
Gusev, S. A.–(8) 4625
Gutierrez, C. J.–(8) 4525, 5826, 6492
Gutiérrez, M. O.–(8) 4936
Guyot, M.–(8) 5472
Gyorgy, E. M.–(8) 5923, 5926

Hach, C.–(8) 6341
Hadjipanayis, G. C.–(8) 4590, 4616, 4827, 4837, 5106, 5152, 5302
Hafner, J.–(8) 4963, 5051
Hagiwara, M.–(8) 5245, 6167
Hajnal, J. V.–(8) 4685
Halada, Gary–(8) 5776
Hamacher, K.–(8) 4779, 4782
Hamaguchi, T.–(8) 5797
Hämäläinen, K.–(8) 6509
Hamdeh, H. H.–(8) 5431, 5435
Hammar, Philip R.–(8) 5392
Hanf, M. C.–(8) 4954
Hara, M.–(8) 5664
Harbison, J. P.–(8) 4967
Harding, C. J.–(8) 6150
Hardner, H. T.–(8) 4980
Harmon, B. N.–(8) 4799, 5409
Harp, G. R.–(8) 5967, 6496
Harris, K. D. M.–(8) 6150
Harris, V. G.–(8) 4561, 4890, 5345, 5431
Hart, A.–(8) 4915
Hasan, M. K.–(8) 5879
Hasegawa, Hideo–(8) 6376
Hasegawa, R.–(8) 6117
Hashi, S.–(8) 4574
Hashimoto, S.–(8) 5057
Hastings, J. B.–(8) 6509
Hatamura, Y.–(8) 5797
Hathaway, K. B.–(8) 6213
Hatwar, T. K.–(8) 5704
Hauschild, J.–(8) 4984
Hauser, Hans–(8) 5761
Hautot, Dimitri–(8) 4584
Havela, L.–(8) 6361, 6396, 6408
Hayano, S.–(8) 4699, 5214
Hayashi, K.–(8) 5907
Hayes, Alan–(8) 5776
He, L.–(8) 6489
Heagy, J. F.–(8) 5377
Heckens, Scott–(8) 6193
Heenan, R.–(8) 5146
Heffner, R. H.–(8) 4535
Hegde, H.–(8) 4614, 5961
Hehn, M.–(8) 4528, 5068
Heidmann, Juergen–(8) 6488
Heim, K. R.–(8) 5056
Heimel, J.–(8) 4922
Heinrich, B.–(8) 4518, 4954
Hellberg, C. S.–(8) 6414
Hellman, F.–(8) 5854, 5919
Hembree, G. G.–(8) 5056
Henk, J.–(8) 6426
Henning, P.–(8) 4567
Henry, L. L.–(8) 5811, 6129
Herbst, J. F.–(8) 5998
Hernandez, J. M.–(8) 6116
Hernàndez, J. M.–(8) 4686
Hernandez, Laura–(8) 5087
Hernandez, P.–(8) 5436
Hernando, A.–(8) 4815, 6539, 6549
Hicken, R. J.–(8) 4987
Hickey, B. J.–(8) 5119, 5816, 6250
Hiebl, K.–(8) 5241
Hikosaka, T.–(8) 5655
Hilfiker, James N.–(8) 6193
Hill, J. P.–(8) 4802
Hill, Peggy–(8) 5398
Hill-Cottingham, R. J.–(8) 4685
Hillebrands, B.–(8) 4531
Hillebrecht, F. U.–(8) 6508
Hines, W. A.–(8) 4596, 5530
Hirai, T.–(8) 4611
Hirayama, Y.–(8) 5359, 5664
Hiroki, Tomoyuki–(8) 5683
Hirota, Noriyuki–(8) 4721
Hjortstam, O.–(8) 4983, 5837
Ho, E. M.–(8) 6292
Ho, J. C.–(8) 5431, 5435
Höchst, Hartmut–(8) 6503
Hoines, L.–(8) 6151, 6234
Holden, A. P.–(8) 4650, 6070
Holdsworth, P. C. W.–(8) 4976
Holody, P.–(8) 5811
Homma, Takuro–(8) 4721
Honda, Naoki–(8) 5362, 5913
Honig, J. M.–(8) 5401
Hono, K.–(8) 5907
Hopkins, P. F.–(8) 6448
Hopster, H.–(8) 5619
Hori, T.–(8) 6633
Hori, Tomiei–(8) 5238, 5946
Horrocks, D. H.–(8) 4753
Horwitz, J. S.–(8) 6338
Hoshi, Y.–(8) 4945
Hosoe, Y.–(8) 5351, 5354
Hossain, S. A.–(8) 5817
Hossain, Z.–(8) 5857, 6349
Hou, C.–(8) 6286
How, H.–(8) 5739
How, Hoton–(8) 4759
Howard, J. K.–(8) 4762, 5330
Howe, D.–(8) 6342
Hsieh, Chien-Sheng–(8) 6522
Hsieh, W. T.–(8) 6568
Hsieh, Yung-Chieh–(8) 5700
Hsing, D. M.–(8) 4843
Hsu, Y. Y.–(8) 5863, 5866
Hu, Bo-Ping–(8) 5713
Hu, S. B.–(8) 5649
Hu, X.–(8) 5221, 6361
Hu, Xiao–(8) 5842
Hu, Y. M.–(8) 4790, 6276
Hu, Z.–(8) 4587, 5522, 5939, 5945, 6315, 6318
Huang, D. R.–(8) 5557, 5699, 6035
Huang, Der-Ray–(8) 5560
Huang, D-J.–(8) 6507
Huang, H. L.–(8) 6060
Huang, Huei Li–(8) 5415
Huang, J. C. A.–(8) 4790, 6276, 6282, 6533
Huang, M. Q.–(8) 5949, 6331
Huang, M.-Q.–(8) 5293
Huang, Ming-Zhu–(8) 4602, 5545
Huang, Q.–(8) 5857
Huang, W.–(8) 6196, 6199
Huang, Xiaohua–(8) 5742
Huang, Y. H.–(8) 5674
Huber, D. L.–(8) 6143
Huber, David–(8) 6503
Hubert, O.–(8) 4571
Hübner, W.–(8) 6177
Hug, E.–(8) 4571
Hug, Hans J.–(8) 5609
Humphrey, F. B.–(8) 6464
Hundley, M. F.–(8) 4535
Hung, John Y.–(8) 5548
Hurben, M. J.–(8) 5390
Hwang, H. Y.–(8) 4541
Hylton, T. L.–(8) 4762
Hyman, R. A.–(8) 5096

Iannarella, L.–(8) 5468
Ibarra, M. R.–(8) 4656, 4659, 5175, 5178, 6330
Ibsen, K. B.–(8) 4546
Ichihara, T.–(8) 5910
Ido, H.–(8) 4647, 5507, 6334
Ido, Hideaki–(8) 5224
Idzerda, Y. U.–(8) 4558, 5345, 5622, 6492, 6493
Igarashi, Masukazu–(8) 5576
Iglesias, I.–(8) 5217, 5472
Iguchi, Yasuo–(8) 5238
Iijima, Makoto–(8) 5602
Iio, K.–(8) 5707, 5708
Imura, Ryo–(8) 5576
Inaba, N.–(8) 5354
Inagaki, J.–(8) 5351
Inami, T.–(8) 4802
Indeck, R. S.–(8) 4695, 5652
Inglefield, H. E.–(8) 5845
Ings, J. B.–(8) 6341
Iñiguez, J.–(8) 5422, 5436, 6574
Inoue, A.–(8) 4836, 5149, 5472
Inoue, J.–(8) 4730
Inoue, Mitsuteru–(8) 5988
Inturi, V. R.–(8) 5904
Iqbal, Z.–(8) 6583
Irie, Y.–(8) 6231
Isamoto, Keiji–(8) 5988
Ise, Kazuyuki–(8) 5913
Iseki, Takayuki–(8) 4970
Ishii, Osamu–(8) 5483
Ishikawa, A.–(8) 5351
Ishiyama, K.–(8) 4574
Ishizaki, O.–(8) 4905
Isnard, O.–(8) 4584, 4608, 5542
Ito, H.–(8) 6273
Ito, T.–(8) 5507
Itoh, H.–(8) 4730

Itoh, K.–(8) 5452
Iwasaka, M.–(8) 4705, 4708
Iwasaka, Masakazu–(8) 4721
Iwasaki, H.–(8) 6399
Iwasaki, Shun-ichi–(8) 5362, 5913
Iwasaki, Y.–(8) 5057
Iwata, S.–(8) 6270

Jagger, J. E.–(8) 5992
Jain, V. K.–(8) 5260
Jakubovics, J. P.–(8) 6057
Jalics, S.–(8) 6045
James, W. J.–(8) 4587, 5522, 5939, 6315
Jamet, J. P.–(8) 5632, 5848
Jander, A.–(8) 4491, 5652
Japiassú, Gloria M.–(8) 6345
Jardim, R. F.–(8) 6564
Jarratt, J. D.–(8) 5606
Jaswal, S. S.–(8) 5942
Jayasekara, W. P.–(8) 5880
Jee, Chan-Soo–(8) 5403
Jeffers, F.–(8) 5658
Jellali, F.–(8) 6485
Jen, S. U.–(8) 6552
Jensen, J. H.–(8) 5199
Jewell, G. W.–(8) 6342
Jhon, Myung S.–(8) 5785, 5788
Jia, Kechang–(8) 4665, 6225
Jia, Q. X.–(8) 4535
Jiaand, Kechang–(8) 4668
Jiang, E. Y.–(8) 5440
Jiang, J. Samuel–(8) 5615
Jiang, Q.–(8) 5122
Jiles, D. C.–(8) 4749, 5453, 5493, 5510, 6045, 6219, 6470
Jimbo, M.–(8) 6237
Jin, Cai-Xia–(8) 5193
Jin, Q. Y.–(8) 4949
Jin, S.–(8) 5599
Jin, Zhi-qiang–(8) 5525
Jin Yang, Choong–(8) 5489
Jo, S.–(8) 5670
Johansson, B.–(8) 4983, 5837
Johnson, D.–(8) 5299
Johnson, P. D.–(8) 6507
Johnston, D. C.–(8) 5084
Jones, L.–(8) 6341
Jonker, B. T.–(8) 5125, 5195
Jönsson, B. J.–(8) 5063, 6583
Ju, H. L.–(8) 4552, 5165, 5166
Judy, J. H.–(8) 5277, 5327
Judy, Jack–(8) 4912
Judy, Jack H.–(8) 5782

Kabos, P.–(8) 5367
Kaczmarek, R.–(8) 6036
Kadin, A. M.–(8) 5179
Kaiser, H.–(8) 4775, 4779, 4782
Kakudate, Yozo–(8) 4721
Kakuno, K.–(8) 4653, 6542
Kalogirou, O.–(8) 5539
Kamada, O.–(8) 5976
Kamarád, J.–(8) 4656
Kambe, Takashi–(8) 5576
Kamenev, K.–(8) 5178
Kamiguchi, Y.–(8) 6399
Kamimura, T.–(8) 5707
Kaminski, D. A.–(8) 4749
Kamishima, K.–(8) 4647
Kaneko, T.–(8) 4611
Kanematsu, K.–(8) 5449, 5452
Kanematsu, Kazuo–(8) 5238
Kang, Soo-Choon–(8) 5785
Kao, C.-C.–(8) 5345, 6492, 6509
Kapitulnik, A.–(8) 6186
Kaplan, T. A.–(8) 6433
Kappler, J. P.–(8) 6497
Kapusta, Cz.–(8) 4599
Karis, Thomas E.–(8) 5788
Kariuki, B. M.–(8) 6150
Kasai, M.–(8) 5288
Katayama, T.–(8) 5708
Katsumata, K.–(8) 5245, 6167
Käufler, A.–(8) 4765
Kaul, S. N.–(8) 5146
Kawabe, H.–(8) 5707, 5708
Kawakami, R. K.–(8) 4532, 4964
Kawakita, Shinya–(8) 5339
Kawamura, Mitsutaka–(8) 4721
Kawana, Takahiro–(8) 4875
Kawawake, Y.–(8) 6231
Kawazoe, Yoshiyuki–(8) 5842
Kazmi, A. S.–(8) 4685
Keimer, B.–(8) 5022
Kelley, M. H.–(8) 5306
Kelly, D.–(8) 6253
Kemmler-Sack, S.–(8) 5257
Kemner, K. M.–(8) 5345, 5622, 6493
Kennedy, Robin J.–(8) 4570
Kennedy, S. J.–(8) 6161
Keren, A.–(8) 6636
Keszei, B.–(8) 5742
Keune, W.–(8) 5582
Khaliullin, G. G.–(8) 6298
Khapikov, A. F.–(8) 5315, 6073
Khater, M.–(8) 5826
Khizroev, S.–(8) 6586
Kida, A.–(8) 5583
Kief, M. T.–(8) 4766, 5008
Kiefl, R. F.–(8) 6636
Kikkawa, J. M.–(8) 5296, 6095
Kikuchi, Akira–(8) 5339
Kim, A. S.–(8) 4840, 5035
Kim, C.–(8) 5468
Kim, C. S.–(8) 5516
Kim, Chul Sung–(8) 5428, 5459, 5516
Kim, K. S.–(8) 5153, 5860
Kim, K. Y.–(8) 5153
Kim, M. J.–(8) 5696
Kim, Miyoung–(8) 5831
Kim, S. G.–(8) 5670
Kim, S. S.–(8) 5696
Kim, Sung Baek–(8) 5459
Kim, T. W.–(8) 5253
Kim, Won Tae–(8) 5476
Kim, Y. B.–(8) 5516
Kim, Y. K.–(8) 5446, 5584, 5596, 6386
Kinder, Lisa R.–(8) 4724
Kinoshita, T.–(8) 6508
Kioussis, Nicholas–(8) 4783, 6420
Kirby, R. D.–(8) 4786
Kirby, Roger D.–(8) 6206
Kirilyuk, A.–(8) 5632
Kirschner, J.–(8) 5618, 6426, 6504
Kisker, E.–(8) 6508
Kisker, H.–(8) 5143
Kiss, László F.–(8) 4811
Kitakami, O.–(8) 6074
Kitakami, Osamu–(8) 5250
Kitazawa, Koichi–(8) 4721
Klebanoff, L. E.–(8) 4796
Klein, Barry M.–(8) 4776
Klein, L.–(8) 6186
Kleinefeld, Th.–(8) 4531, 4922
Klicznik, A.–(8) 5609
Klik, I.–(8) 4919, 6533
Kneedler, E.–(8) 5125
Knobel, M.–(8) 5462
Kobayashi, H.–(8) 4999
Kobayashi, Kazuo–(8) 5602
Kobayashi, T.–(8) 5907
Kodama, N.–(8) 6467
Kodama, R. H.–(8) 5071
Koerkamp, M. Groot–(8) 5632, 6181
Koide, T.–(8) 5707, 5708
Koinkar, Vilas N.–(8) 5798
Kojima, A.–(8) 4836
Kojima, K.–(8) 6636
Kojima, Naomi–(8) 5602
Koknaeva, M.–(8) 4833
Kolb, E.–(8) 5270
Komatsu, K.–(8) 6542
Komiyama, K.–(8) 6237
Komoda, O.–(8) 4905
Komuro, Matahiro–(8) 5576
Kondo, Akio–(8) 5677
Kong, Linshu–(8) 5067, 5855, 6101
Konno, K.–(8) 6334
Koon, N. C.–(8) 4561, 4890
Koon, Norman C.–(8) 5841
Koopmans, B.–(8) 6181
Korenivski, V.–(8) 5923, 5926
Koroleva, L. I.–(8) 6617
Kos, A. B.–(8) 5820
Koshimoto, Yasuhiro–(8) 5483
Kottler, V.–(8) 4509
Kötzler, J.–(8) 4641, 6054
Kou, X. C.–(8) 6324
Koubouros, I.–(8) 5563
Kouvel, J. S.–(8) 5879
Kowalewski, M.–(8) 4954
Koziol, Z.–(8) 4662, 5992, 5995
Kozioł, Z.–(8) 4679
Krajewski, J. J.–(8) 5923
Kramer, M. J.–(8) 4847
Krasko, Genrich L.–(8) 4682
Kraus, P. A.–(8) 4553
Krause, T. W.–(8) 6042
Krauss, Peter R.–(8) 5066, 6101
Krebs, J. J.–(8) 4525, 5125, 5622, 6084, 6234
Krill, G.–(8) 6497
Krisch, M. H.–(8) 6509
Krishnan, Kannan M.–(8) 4848, 5169, 5321
Krishnan, R.–(8) 4936, 5472, 6246
Kroll, E. C.–(8) 6116
Kronmüller, H.–(8) 5143
Kryder, M. H.–(8) 4485, 4878, 4890, 5011, 5880
Ku, H. C.–(8) 5863, 5866, 6568
Kubo, K.–(8) 6433
Kuch, W.–(8) 5618, 6426, 6504
Kudrevatykh, N. V.–(8) 6330
Kume, Minoru–(8) 6402
Kunkel, H. P.–(8) 6561
Kuo, P. C.–(8) 6035
Kurbatova, Yu. N.–(8) 6132
Kurisu, H.–(8) 4884, 4896
Kuroda, K.–(8) 6451
Kuroki, Kazuhiko–(8) 6402
Kuwabara, M.–(8) 5564
Kuwahara, H.–(8) 5288
Kwon, S. J.–(8) 6299

Labarta, A.–(8) 5605
Lafdi, K.–(8) 6007
Laffargue, D.–(8) 6355
Lagarikov, A. N.–(8) 6532
Lai, C. C.–(8) 6568
Lai, Chih-Huang–(8) 6389
Laibowitz, R. B.–(8) 4549
Laidler, H.–(8) 6250
Lal, Brij B.–(8) 5336
Lam, T. T.–(8) 5645
Lam, Terence–(8) 4906
Lam, Terence T.–(8) 4909
Lambeth, D. N.–(8) 4496, 5011
Lambeth, David N.–(8) 4902, 5348
Lampel, G.–(8) 4734
Lang, P.–(8) 5129, 5638
Langman, R. A.–(8) 6134
Lascialfari, A.–(8) 6624
Lassailly, Y.–(8) 4734
Laughlin, D. E.–(8) 4496, 5345
Laughlin, David E.–(8) 4902, 5348, 6455
Lavers, J. D.–(8) 4671
Lebedev, Sergey V.–(8) 5982
Le Dang, K.–(8) 4554, 5099
Lederman, D.–(8) 5112
Lederman, M.–(8) 5303, 6067
Lee, B. H.–(8) 5482
Lee, C. S.–(8) 5649
Lee, Chan Young–(8) 5710
Lee, Choong Sub–(8) 5710
Lee, J.-G.–(8) 5752, 6051
Lee, J. S.–(8) 5459
Lee, Jaeyong–(8) 6120
Lee, K. C.–(8) 6568, 6571
Lee, K. G.–(8) 5696
Lee, Kong-Ju-Bock–(8) 6605
Lee, L. L.–(8) 4496
Lee, Li-Lien–(8) 4902
Lee, S.-H.–(8) 5023
Lee, S. K.–(8) 5670
Lee, Seung Wha–(8) 5428, 5516
Lee, T. D.–(8) 5357
Lee, W.-T.–(8) 4802
Lee, Y. H.–(8) 6276
Lee, Y. P.–(8) 5699
Lee, Young Jong–(8) 5516
Lee, Young-sook–(8) 5870
Lefmann, K.–(8) 5078, 5391
Le Gall, H.–(8) 5932
Leithe-Jasper, A.–(8) 5241
Leng, Q.–(8) 4766
Leslie-Pelecky, Diandra L.–(8) 5312
Letyuk, L. M.–(8) 5500
Leung, H. T.–(8) 6295
Leupold, H. A.–(8) 5551
Levashov, V. I.–(8) 5315, 6073
Levy, J.–(8) 6095
Levy, P. M.–(8) 6382
Lewis, L. H.–(8) 5513, 6470
Lewis, Laura Henderson–(8) 4848
Li, A. S. K.–(8) 4854
Li, D.–(8) 6618
Li, Dongqi–(8) 5838
Li, Fa-shen–(8) 5709
Li, Feiyue–(8) 4866, 4869
Li, Hong-Shuo–(8) 4622, 5713
Li, Lin–(8) 4578
Li, Q.–(8) 5165
Li, Qi–(8) 4552
Li, W.-H.–(8) 6568, 6571
Li, Yiqun–(8) 4998
Li, Youlin–(8) 5791
Li, Zisen–(8) 5188
Liang, Y. L.–(8) 4830, 5501, 6335
Liao, C. P.–(8) 5557
Liao, S. Y.–(8) 4790, 5599, 6282, 6533
Liechtenstein, A. I.–(8) 4805
Lin, C.–(8) 5440
Lin, C. H.–(8) 6035
Lin, C. L.–(8) 4812, 5403, 5873, 6405, 6608
Lin, C.-L.–(8) 5277
Lin, J. C.–(8) 5159
Lin, M. S.–(8) 5863
Lin, Y. F.–(8) 6568
Lind, D. M.–(8) 5102
Lind, David M.–(8) 5841
Liou, S. H.–(8) 5060, 5958, 6448
Liou, Y.–(8) 4790, 6282, 6533
Lipp, D.–(8) 5609
Lisyansky, A. A.–(8) 5091
Liu, B.–(8) 5649
Liu, C. S.–(8) 5432
Liu, F.–(8) 6028
Liu, Francis H.–(8) 5895
Liu, G. H.–(8) 4984
Liu, G. K.–(8) 6512

Liu, Guo–(8) 6176
Liu, J.–(8) 4753
Liu, Qingxia–(8) 4702
Liu, R. L.–(8) 4790
Liu, S. H.–(8) 4824
Liu, W.–(8) 5525
Liu, W. L.–(8) 6335
Liu, X.–(8) 5387
Liu, Y.–(8) 5060, 5333, 5958, 6507
Liu, Ying–(8) 5094
Liu, Z. J.–(8) 4678
Livne, Z.–(8) 5456
Lizzi, T.–(8) 4840
Lo, C. C. H.–(8) 6057
Lo, C. K.–(8) 4790, 6533
Lochner, E.–(8) 5102
Lochner, Eric–(8) 5841
Lodder, J. C.–(8) 6190, 6243
Lofland, S.–(8) 5991
Lofland, S. E.–(8) 5165, 5166
Lois, P.–(8) 4674
Loloee, R.–(8) 6129
Long, G. J.–(8) 6318
Long, Gary J.–(8) 4584, 4587, 5945
Loong, C.-K.–(8) 6512
Lopez de la Torre, M. A.–(8) 6364
López-Quintela, M. A.–(8) 5269
Lord, D. G.–(8) 4650, 6070
Lord, J. S.–(8) 4599
Lorenz, Bryen E.–(8) 6039
Lorenz, R.–(8) 4963, 5051
Lorenz, T.–(8) 4765
Loss, Daniel–(8) 6107
Lounasmaa, O. V.–(8) 5078
Loveless, M.–(8) 6222
Low, T. S.–(8) 4678, 5674
Lu, Feng–(8) 4759
Lu, Q. F.–(8) 6439
Lu, S. L.–(8) 5533
Lubitz, P.–(8) 6234, 6338
Lucas, C. A.–(8) 5169
Luce, T. A.–(8) 6177
Lukaszew, R. A.–(8) 4787
Luke, G. M.–(8) 6636
Lukina, L. N.–(8) 6617
Lumpp, Janet K.–(8) 5497
Lumsden, M. D.–(8) 5081
Luneau, D.–(8) 4698
Luo, C. P.–(8) 4899
Luo, H.–(8) 6318
Luo, Weili–(8) 6034
Luo, Y.–(8) 5645
Luo, Yansheng–(8) 4906, 4909
Luse, C. N.–(8) 4942
Lyberatos, A.–(8) 5703
Lynn, J. W.–(8) 5857, 6568

Ma, B. M.–(8) 4830, 5501, 6335
Ma, P.–(8) 5641
MacFarlane, W. A.–(8) 6636
Machado, F. L. A.–(8) 6546, 6555, 6558
Maciejewski, J.–(8) 6031
MacLaren, J. M.–(8) 5282, 5828, 6196, 6199
Madabhushi, R.–(8) 6063
Maeda, Atsushi–(8) 6402
Maekawa, S.–(8) 4730
Mahanti, S. D.–(8) 6433
Mahía, J.–(8) 5269
Maignan, A.–(8) 6173
Majetich, S. A.–(8) 5293
Majkrzak, C. F.–(8) 4762, 4782
Maki, K.–(8) 4857
Makino, A.–(8) 4836, 5472
Makovkin, A. V.–(8) 5721
Maletta, H.–(8) 5221
Malhotra, S. S.–(8) 5060, 5958, 6448
Malik, S. K.–(8) 6367
Mamin, H. J.–(8) 5644
Manago, Takashi–(8) 5126
Manalis, S.–(8) 6440
Mankey, G. J.–(8) 5626, 5635
Mann, S.–(8) 5324
Mansuripur, M.–(8) 5667, 5687, 5700
Mao, Ming–(8) 4769
Mao, Ming-xi–(8) 5709
Mao, O.–(8) 4605, 4619, 5536
Mao, Ou–(8) 5519
Maple, M. B.–(8) 4926, 6564
Mar, D. J.–(8) 5377
Marabelli, F.–(8) 6423
Maradudin, A. A.–(8) 5727
Maraner, A.–(8) 5406
Marasinghe, G. K.–(8) 4587, 5939
Marchon, B.–(8) 4508
Marezio, M.–(8) 4541
Marinero, E. E.–(8) 5680
Marini, S.–(8) 6621
Markin, P. E.–(8) 6330
Marks, R. F.–(8) 5967, 6496
Marmorino, J. L.–(8) 4644
Marquina, C.–(8) 4659, 5175, 5178, 6330
Martínez, B.–(8) 5182
Martinez, G.–(8) 5395
Martins, C. S.–(8) 6546
Martinson, L. S.–(8) 6164
Martynova, J.–(8) 6519
Marx, D.–(8) 5018
Massarotti, V.–(8) 6621
Masuda, S.–(8) 4653, 6542
Masumoto, T.–(8) 4836, 5130, 5149, 5472
Mathieu, Ch.–(8) 4531
Matsuda, T.–(8) 5075
Matsuda, Y.–(8) 5351
Matsuguma, I.–(8) 5318
Matsui, M.–(8) 5583
Matsumoto, Mitsunori–(8) 4881
Matsumoto, Morihiko–(8) 5486
Matsushita, N.–(8) 5247, 5910, 5970
Matsuura, M.–(8) 4884, 4896
Matsuyama, Hideo–(8) 6389
Matsuyama, K.–(8) 5318, 6643, 6646
Matveev, V. N.–(8) 5315, 6073
May, F.–(8) 4983
May, J.–(8) 6341
Mayergoyz, I. D.–(8) 5746, 6063, 6473, 6602
Mayergoyz, Isaak D.–(8) 6441
Mazumdar, Chandan–(8) 6347, 6349
McCall, S.–(8) 4567, 4821, 5876
McCallum, R. W.–(8) 4847, 5510
McCarter, M. K.–(8) 4851
McClelland, J. J.–(8) 6079
McEwen, K. A.–(8) 6364
McGuire, T. R.–(8) 4549
McHenry, M.–(8) 5949
McHenry, M. E.–(8) 5293
McIlroy, D. N.–(8) 5838
McKay, Susan R.–(8) 5087, 6146
McMichael, R. D.–(8) 5277, 5315, 5456, 5998, 6073
McNiff, E. J., Jr.–(8) 5071
Medeiros-Ribeiro, G.–(8) 5296
Medina, A. N.–(8) 5462
Meen, T. H.–(8) 6571
Mégy, R.–(8) 5270, 5632, 5848
Mehta, H.–(8) 5365
Meier, J.–(8) 6010
Meigs, G.–(8) 4558, 6492, 6493
Meinel, K.–(8) 6426
Melkebeek, J. A.–(8) 5496
Melo, L. G. C.–(8) 6546
Menard, D.–(8) 5136
Mendes, K. C.–(8) 6555
Mendoza, W. A.–(8) 6327
Meng, Q.–(8) 6190
Meng-Burany, X.–(8) 5152
Menon, Latika–(8) 6367
Menovsky, A.–(8) 6396
Menovsky, A. A.–(8) 6358
Mertig, I.–(8) 5276
Messner, W.–(8) 4485
Metin, S.–(8) 6295
Metz, A.–(8) 5078
Metzger, R.–(8) 6286
Metzger, Robert M.–(8) 4866, 4869
Meyer, P.–(8) 5632, 5848
Mezei, F.–(8) 6158
Michel, R.–(8) 5169
Michel, R. P.–(8) 4772, 4775
Michel, Steve–(8) 5826
Micklitz, H.–(8) 5256
Middleton, D. P.–(8) 4593, 5945, 6318
Mignot, J. M.–(8) 6396
Mihálik, M.–(8) 6396
Mihalisin, T.–(8) 4812, 5403, 5873, 6405, 6608
Miller, Joel S.–(8) 6147
Miller, L. L.–(8) 5084
Miller, M. M.–(8) 6234
Millot, F.–(8) 4554
Miloslavsky, Lena–(8) 5011
Milosvlasky, Lena–(8) 5895
Min, Byung G.–(8) 5788
Min, K.-I.–(8) 6228
Minor, M. K.–(8) 5005
Minvielle, Timothy J.–(8) 5116
Miotkowski, I.–(8) 6164, 6436
Mira, J.–(8) 5269
Miraglia, S.–(8) 4584, 4608, 5542
Mishra, S. R.–(8) 6318
Mishra, Sanjay R.–(8) 5945
Missell, F. P.–(8) 6312, 6546, 6555
Mitani, S.–(8) 4733, 5130
Mitchler, P. D.–(8) 5758
Mitsis, A.–(8) 5563
Miyajima, H.–(8) 4659, 5075
Miyajima, Hideki–(8) 5126, 6599
Miyajima, T.–(8) 5452
Miyamoto, Y.–(8) 6392
Miyashita, E.–(8) 5770
Miyata, Yoshimori–(8) 5486
Miyauchi, H.–(8) 5707, 5708
Miyazaki, T.–(8) 4977, 6262
Mochele, J. T.–(8) 6526
Modak, A. R.–(8) 5169
Modlin, Cory S.–(8) 4502
Mohri, K.–(8) 6532
Molins, E.–(8) 5182
Moloni, K.–(8) 6447
Momiji, H.–(8) 4905
Monachesi, P.–(8) 6423
Montenegro, F. C.–(8) 6555
Moodera, J. S.–(8) 6265
Moodera, Jagadeesh S.–(8) 4724
Moon, Ki-Seok–(8) 4991
Moon, R. M.–(8) 5022
Mora, J.–(8) 6596
Moran, Timothy J.–(8) 5109
Morchenko, A. T.–(8) 5500
Morel, R.–(8) 6289
Moreland, John–(8) 6448
Morellon, L.–(8) 4656
Mori, Toshinori–(8) 5483
Morimoto, K.–(8) 5040
Morin, B. G.–(8) 6147
Morisako, Akimitsu–(8) 4881
Moritani, Isao–(8) 5677
Moritomo, Y.–(8) 5288
Moschel, A.–(8) 4994
Moser, A.–(8) 5609
Moses, A. J.–(8) 4753
Moske, M.–(8) 4765
Moskowitz, Bruce M.–(8) 6064
Mountfield, K. R.–(8) 4787, 5011
Mryasov, O. N.–(8) 4805
Mühge, Th.–(8) 6298
Mulder, F. M.–(8) 4593
Müller, Gerhard–(8) 4629, 4632, 5227, 6630
Müller, K.-H.–(8) 5045
Muller, M. W.–(8) 4695, 5652
Mulloy, M.–(8) 5270
Muñoz, J. M.–(8) 5436, 6545
Muraoka, Hiroaki–(8) 5002
Murillo, N.–(8) 5465
Murthy, A. S.–(8) 4616, 4827, 5106, 5152, 5302
Myer, G. H.–(8) 6001
Myrtle, K.–(8) 4518, 4954

Na, J. G.–(8) 4893
Nagai, N.–(8) 5686
Nagarajan, R.–(8) 5857, 6347, 6349
Naik, R.–(8) 4787
Nakagawa, S.–(8) 5247, 5910, 5970, 6392
Nakagawa, Shigeki–(8) 5015, 5156
Nakagawa, Y.–(8) 6633
Nakagawa, Yasuaki–(8) 5946
Nakai, Junichi–(8) 5339
Nakajima, K.–(8) 4977
Nakajima, N.–(8) 5707, 5708
Nakajima, Tetsuo–(8) 5205
Nakamae, S. C.–(8) 6567
Nakamura, A.–(8) 5354
Nakamura, S.–(8) 6399
Nakamura, Y.–(8) 6642
Nakamura, Yoshihisa–(8) 5002, 6639, 6649
Nakano, K.–(8) 6439
Nakao, M.–(8) 5797
Nakatani, I.–(8) 5067, 6258
Nakaya, Y.–(8) 4699
Nakotte, H.–(8) 6361, 6408, 6411
Namjoshi, K. V.–(8) 4671
Nan Lin, I.–(8) 5432
Naoe, M.–(8) 4945, 5247, 5910, 5970, 6273, 6392
Naoe, Masahiko–(8) 4881, 5015, 5156
Narducci, A. A.–(8) 4718
Narita, N.–(8) 6167
Nash, J. M.–(8) 5367
Nashi, H.–(8) 5564
Nashima, O.–(8) 4647
Neely, M.–(8) 6602
Nelson, D. J.–(8) 4715
Neumeier, J. J.–(8) 4535
New, R. M. H.–(8) 5851
Ng, D. H. L.–(8) 4750, 4854, 6057
Nguyen, S. H.–(8) 4769
Nguyen, T.–(8) 5358
Nguyen, Tai D.–(8) 4848
Niarchos, D.–(8) 5539, 5563
Nicholson, D. M. C.–(8) 5282
Nickel, J. H.–(8) 4491
Nicolaides, D.–(8) 5091
Nicolaides, G. K.–(8) 5563
Niida, Hiroshi–(8) 5946
Nikitenko, V. I.–(8) 5315, 6073
Nikitin, P. I.–(8) 6113
Nikitin, V.–(8) 6095
Nikitov, S. A.–(8) 5365
Nikles, David E.–(8) 4860, 4863
Niraimathi, A. M.–(8) 5869, 5869, 6173
Nishimura, Naoki–(8) 5683
Nishinaga, T.–(8) 4957
Nishioka, K.–(8) 6286
Nishioka, Koichi–(8) 4970
Nixon, L.–(8) 6150

Nogués, J.–(8) 5112
Noh, T. H.–(8) 5153, 5459
Nolan, T. P.–(8) 5359
Noma, K.–(8) 5247, 5970
Nordman, C. A.–(8) 4553
Nordquist, K.–(8) 5889
Nordström, L.–(8) 5638
Nordström, Lars–(8) 4515
Norton, P. R.–(8) 4954, 5641
Nossov, A.–(8) 6370
Novak, M.–(8) 4698
Novo, J. M.–(8) 4815
Novotny, M. A.–(8) 6482
Novotny, Mark A.–(8) 5749
Nowakowski, D.–(8) 6143
Nozaki, Y.–(8) 5075
Nozaki, Yukio–(8) 6599
Nozières, Jean Pierre–(8) 6599
Numazawa, J.–(8) 5770
Nummila, K. K.–(8) 5078
Núñez-Regueiro, J. E.–(8) 5179

O'Barr, R.–(8) 5303, 6067
Obermyer, R. T.–(8) 5949, 6334
Obradors, X.–(8) 5182, 6596
O'Brien, W. L.–(8) 5623, 5629
O'Connor, Charles J.–(8) 5870, 6627
O'Connor, Teresa M.–(8) 5788
Odintsov, A. G.–(8) 6617
Ogale, S. B.–(8) 4545, 4552, 5292
O'Grady, K.–(8) 5590, 6034
Oh, Young Jei–(8) 5428
O'Handley, R. C.–(8) 5468, 5609, 5845
Ohashi, Masayoshi–(8) 5238
Ohinata, Y.–(8) 5655
Ohkubo, N.–(8) 5449, 5452
Ohmori, H.–(8) 5907
Ohnuki, S.–(8) 5686
Ohnuki, T.–(8) 4905
Ohnuma, S.–(8) 4733, 5130
Ohta, Masayuki–(8) 4721
Ohta, N.–(8) 4905, 5686
Okada, Takeshi–(8) 5683
Okamoto, Satoshi–(8) 5250
Oliver, S. A.–(8) 5431, 5435
Ono, T.–(8) 6382
Onodera, Hideya–(8) 5946
Onodera, Seiichi–(8) 4875
Oonk, M.–(8) 6129
Ortiz, C.–(8) 5321
Osborn, R.–(8) 6432
Oseroff, S. B.–(8) 5269, 6577
Osgood, R. M.–(8) 5851
Osgood, R. M., III–(8) 6189
O'Shea, M. J.–(8) 5299, 5435
Ostoréro, J.–(8) 5985
Ostrovskaya, N. V.–(8) 5730
O'Sullivan, J. A.–(8) 4695
Otani, Y.–(8) 4659, 5075
Otani, Yoshichika–(8) 5126, 6599
Oti, J. O.–(8) 5596, 6240, 6386
Ouchi, Kazuhiro–(8) 5362, 5913
Oudet, Xavier–(8) 5416
Ounadjela, K.–(8) 4528, 5068, 6247
Ouse, M.–(8) 6399

Padalia, B. D.–(8) 6347, 6349
Padovani, S.–(8) 5068
Paduan-Filho, A.–(8) 5236
Pakhomov, A. B.–(8) 6140
Palacio, F.–(8) 5236
Palme, W.–(8) 5384
Palstra, T. T. M.–(8) 4541
Pan, C. Y.–(8) 5162
Pan, J. L.–(8) 6035
Panagiotopoulos, I.–(8) 4616, 4827, 4837
Panchanathan, V.–(8) 4851
Panina, L. V.–(8) 6532
Pannetier, B.–(8) 5075
Pannetier, Bernard–(8) 6599
Pant, Bharat B.–(8) 6123
Pappas, C.–(8) 6158
Parakka, A. P.–(8) 6045
Paramonov, V. P.–(8) 6532
Parashikov, I.–(8) 5609
Pardavi-Horvath, M.–(8) 5742
Parekh, J. P.–(8) 5718
Park, C.-M.–(8) 6228
Park, J.-H.–(8) 4558, 6492, 6493
Park, J. K.–(8) 5357
Park, Jae Yun–(8) 5428
Park, K.–(8) 5195, 5357
Park, Ki-Ook–(8) 5785
Park, M. C.–(8) 4967
Park, S. J.–(8) 5879
Park, Seung Iel–(8) 5428
Park, Y.–(8) 4967
Parker, D. A.–(8) 4915
Parker, F. T.–(8) 5504
Parker, M. A.–(8) 4762, 5330
Parker, M. R.–(8) 5817, 6286
Parker, Martin R.–(8) 4970
Parkin, I. P.–(8) 6150
Parkin, S. S. P.–(8) 4980, 6078
Parra, R. E.–(8) 5242
Patterson, G. N.–(8) 6642
Patton, C. E.–(8) 5367, 5390
Patton, Steven T.–(8) 5802, 5916
Paul, D. I.–(8) 5609
Pavlovic, A. S.–(8) 5230
Pearson, J.–(8) 5838
Pease, R. F. W.–(8) 5851
Pechan, Michael J.–(8) 6266
Peck, Paul R.–(8) 5785
Peck, W. F., Jr.–(8) 5923
Pecora, L. M.–(8) 5377
Pedersen, J. S.–(8) 5146, 6173
Pekarek, T. M.–(8) 5401, 6164, 6436
Pelzl, J.–(8) 4929, 6266
Penfold, J.–(8) 6295
Peng, Liang-Ping–(8) 5718
Peng, Qingzhi–(8) 4916
Peredo, J. C.–(8) 6642
Pereira, L. G.–(8) 6555
Perera, P.–(8) 5299
Pérez Alcázar, G. A.–(8) 6155, 6611
Persiano, A. I. C.–(8) 5973
Peterman, D. W.–(8) 5378
Petford-Long, A. K.–(8) 6292
Petrenko, O. A.–(8) 6614
Petroff, P. M.–(8) 5296
Pflaum, J.–(8) 4929, 6266
Philips, D. A.–(8) 5496
Phillips, J. M.–(8) 5926
Phillips, Julia M.–(8) 5923
Piñol, S.–(8) 5182, 6596
Pinsard, L.–(8) 4554
Pinto, R. P.–(8) 6355
Pirkle, B. H.–(8) 5817
Pizzagalli, L.–(8) 5834
Pizzini, S.–(8) 6497
Platt, C. L.–(8) 5072
Pohm, A. V.–(8) 5889
Pokhil, Taras G.–(8) 6064
Pollard, R. J.–(8) 4939
Polushkin, N. I.–(8) 4625
Poon, Chin Y.–(8) 5799
Popkov, A. F.–(8) 5730
Popma, Th. J. A.–(8) 6190
Popović, Zoran S.–(8) 4555
Porter, D. G.–(8) 4695, 5652
Potenziani, E., II–(8) 5551
Pourarian, F.–(8) 5513, 6334
Powell, C. J.–(8) 5277
Prabhakar, A.–(8) 5374
Pratt, W. P., Jr.–(8) 5811, 6129
Prieur, J.–(8) 5270
Pringle, O. A.–(8) 4587, 5945, 6318
Prinz, G. A.–(8) 4525, 5387, 5622, 6084, 6234, 6492
Prokeš, K.–(8) 5221, 6358, 6361, 6396, 6408
Proksch, R.–(8) 6447
Proksch, Roger–(8) 6447
Psycharis, V.–(8) 5539
Pugh, V. J.–(8) 4644
Pulvirenti, P. P.–(8) 6219
Puri, R. K.–(8) 6515
Purwanto, A.–(8) 6408, 6411
Pustogowa, U.–(8) 6177
Putris, F. F.–(8) 5504

Qian, X. R.–(8) 4614, 5961
Qian, Y. H.–(8) 4949
Qian, You-Hua–(8) 5193
Qin, C-D.–(8) 4750, 4854, 6057
Qiu, Z. Q.–(8) 4532, 4964
Quichaud, G.–(8) 6485

Rachford, F. J.–(8) 5377
Radaelli, P. G.–(8) 4541
Rafailovich, M.–(8) 6025
Raju, N. P.–(8) 6170, 6173, 6176, 6636
Ramesh, A.–(8) 5453
Ramesh, R.–(8) 4545, 5292, 5935, 5991
Ramírez, R.–(8) 6479
Ramos, R. A.–(8) 6482
Rani, R.–(8) 5425
Ranjan, R.–(8) 5342
Rao, K. V.–(8) 5063, 5112, 5153, 5860, 6267, 6583
Raposo, V.–(8) 5422, 6574
Rasing, Th.–(8) 5632, 6181
Rasmussen, F. B.–(8) 5078
Rastelli, E.–(8) 5745, 5745
Rave, W.–(8) 6036
Ravet, M. F.–(8) 5068, 5848
Ravipati, Durga–(8) 5011
Rebizant, J.–(8) 6361
Redjdal, M.–(8) 6464
Reed, I. M.–(8) 6219
Regnault, L. P.–(8) 5099
Reich, D. H.–(8) 5391
Reich, Daniel H.–(8) 5392
Reiffers, M.–(8) 6352
Reimers, J. N.–(8) 6176
Renard, J. P.–(8) 4554, 5099, 5848
Renard, J.-P.–(8) 5270
Rengarajan, S.–(8) 5482
Repetto, M.–(8) 4575
Restorff, J. B.–(8) 6216
Revcolevschi, A.–(8) 4554, 5099, 5384, 5395
Rey, P.–(8) 4698
Rezende, S. M.–(8) 6309, 6546, 6555, 6558
Rhyne, J. J.–(8) 4779
Ribeiro, C. A.–(8) 5973
Richards, Howard L.–(8) 5749
Riedi, P. C.–(8) 4599, 5119, 6300
Rieke, Reuben D.–(8) 5312
Rigamonti, A.–(8) 6621, 6624
Rikvold, P. A.–(8) 6482
Rikvold, Per Arne–(8) 5749
Riley, C. D.–(8) 6342
Ripka, P.–(8) 5211
Ristau, R. A.–(8) 5330
Ritley, K. A.–(8) 4779
Ritter, C.–(8) 5869
Rivas, J.–(8) 4674, 5269, 5955
Rivas, M.–(8) 4936, 5217, 5472, 6545
Ro, M. D.–(8) 5696
Robertson, B. W.–(8) 5333
Robertson, J. L.–(8) 4524
Robinson, R. A.–(8) 6408, 6411
Röder, Heinrich–(8) 4632
Roderick, J. M.–(8) 5453
Roig, A.–(8) 5182
Rojdestvenski, I. V.–(8) 5724
Rojo, J. M.–(8) 4815
Rooney, P. W.–(8) 5854
Roschepkin, G. V.–(8) 6113
Rose, H. B.–(8) 6508
Rosenberg, M.–(8) 5257
Roshko, A.–(8) 5358, 6240
Roshko, R. M.–(8) 5758, 6618
Ross, C. A.–(8) 5342
Rossetti, G.–(8) 6624
Rotenberg, E.–(8) 5626
Roth, Ch.–(8) 6508
Rothberg, G. M.–(8) 4967
Rothman, J.–(8) 4976
Rottmayer, R.–(8) 5645
Rottmayer, Robert–(8) 4909, 5012, 5886
Rousseaux, F.–(8) 5068, 5848
Rudee, M. L.–(8) 5072
Rüdiger, U.–(8) 6203
Rudkowska, G.–(8) 5136
Rudkowski, P.–(8) 5136
Rueff, J. P.–(8) 6497
Rugar, D.–(8) 5644
Ruiz, X.–(8) 5439
Runge, K.–(8) 5075
Runge, Katharina–(8) 6599
Rupp, M.–(8) 4549
Russak, Michael A.–(8) 5336
Russek, S. E.–(8) 6240, 6386
Ryan, D. H.–(8) 6004, 6161

Saadi, M.–(8) 6485
Sabirianov, R. F.–(8) 5942
Sablik, M. J.–(8) 6134, 6525
Sá de Melo, C. A. R.–(8) 5412
Saeki, T.–(8) 5318
Sager, R. E.–(8) 4926
Saha, Shibaji–(8) 5233
Sahajwalla, V.–(8) 5149
Sahashi, M.–(8) 4611, 6399
Saito, K.–(8) 6399
Saito, Y.–(8) 4699, 5214
Sakakima, H.–(8) 6231
Sakuma, Akimasa–(8) 5570
Sakurada, S.–(8) 4611
Sakurai, M.–(8) 6270
Sakurai, T.–(8) 6074
Sal, J. C. Gómez–(8) 5146
Salamanca-Riba, L.–(8) 5195
Salamo, G.–(8) 6580
Salamo, G. J.–(8) 6593
Salashchenko, N. N.–(8) 4625
Salem-Sugui, S.–(8) 5462
Salomon, R. E.–(8) 6001
Samarasekara, P.–(8) 5425
Samarth, N.–(8) 6095
Samwer, K.–(8) 4765
Sánchez, D.–(8) 5256
Sanders, S. C.–(8) 5584, 6240
Sanjurjo, N. L.–(8) 5973
Sankar, S. G.–(8) 5949
Sanker, S. G.–(8) 6334
Santos, A. D.–(8) 5266, 6546
Sarachik, M. P.–(8) 6031
Sasada, I.–(8) 5490, 6077
Sasaki, S.–(8) 6167
Sato, K.–(8) 4896, 6439
Satomi, M.–(8) 6231
Satpathy, S.–(8) 4555
Schabes, M. E.–(8) 5342
Schaefer, D. M.–(8) 6234

Schaefer, H.-E.–(8) 5143
Schaf, J.–(8) 6154
Schäfer, M.–(8) 4782
Schäffer, Tilman E.–(8) 6447
Schalek, R.–(8) 5263
Schaper, L. W.–(8) 6593
Schatz, A.–(8) 5582
Scheidt, R.–(8) 4531
Scheinfein, M. R.–(8) 5056
Scherer, A.–(8) 5303
Schirmeisen, A.–(8) 5929, 6203
Schlottmann, P.–(8) 5419, 6414, 6417, 6605
Schlueter, J. A.–(8) 6586
Schmidlin, F.–(8) 4746
Schmidt, K. E.–(8) 5056
Schmidt, R.–(8) 5739
Schneider, C. M.–(8) 5618, 6426, 6504
Scholten, R. E.–(8) 6079
Schrefl, T.–(8) 5029, 6458
Schreiber, F.–(8) 4793, 4929, 6266
Schreyer, A.–(8) 4782
Schröder, Klaus–(8) 6522
Schroeder, P. A.–(8) 5811
Schuller, I.–(8) 6253
Schuller, Ivan K.–(8) 5109, 5112, 6266
Schulthess, T. C.–(8) 5282
Schultz, S.–(8) 5303, 6067
Schumann, F. O.–(8) 5635
Schwartz, J.–(8) 6567
Schweitzer, J. W.–(8) 6164
Scipioni, L.–(8) 4976
Scott, D. W.–(8) 4830, 5501, 6335
Scott, J. H.–(8) 5293
Scott, S.–(8) 6593
Sechovský, V.–(8) 5221, 6358, 6361, 6396, 6408
See, A. K.–(8) 4796
Seehra, M. S.–(8) 5185
Seehra, Mohindar S.–(8) 5230
Seffar, A.–(8) 5182
Selestino, R.–(8) 5826
Sellmyer, D. J.–(8) 4590, 4786, 4827, 4899, 5060, 5333, 5958
Semenov, V. G.–(8) 4625
Senda, Masakatsu–(8) 5483
Serena, P. A.–(8) 6019, 6110
Sereni, J. G.–(8) 6417
Sette, F.–(8) 6509
Seyedahmadian, M.–(8) 6001
Shaheen, S. A.–(8) 5425, 6327
Shan, Z. S.–(8) 4786, 4899, 5958
Shanabrook, B. V.–(8) 5125
Shand, P. M.–(8) 6164
Shapiro, A. J.–(8) 5315, 6073
Shapiro, A. L.–(8) 5854
Sharma, R. P.–(8) 4545, 4552
Shaw, K. A.–(8) 5102
Shaw, Kimberly A.–(8) 5841
Shen, Bao-Gen–(8) 5528, 5713
Shen, Bao-gen–(8) 5709
Shen, J. X.–(8) 4786, 5008
Shen, N. X.–(8) 5530
Sheng, L.–(8) 6255
Sheng, Q. G.–(8) 6420
Shepard, M.–(8) 4567, 4821, 5876
Shevchenko, N. B.–(8) 5152, 5302
Sheverev, V. A.–(8) 5716
Shi, Jing–(8) 5296
Shi, Zhu-Pei–(8) 4776
Shidara, T.–(8) 5707, 5708
Shieh, J. H.–(8) 5863, 5866
Shield, J. E.–(8) 4851
Shih, Tom I.-P.–(8) 5785
Shimada, K.–(8) 5707
Shimada, Y.–(8) 6074
Shimada, Yutaka–(8) 5250
Shimatsu, Takehito–(8) 5339
Shimazaki, K.–(8) 5686
Shimizu, Yutaka–(8) 5602
Shin, K. H.–(8) 5357, 6228
Shin, Sung-Chul–(8) 4991
Shin, T.–(8) 4967
Shinjo, T.–(8) 6382
Shiraishi, H.–(8) 6633
Shiraishi, Hiroshi–(8) 5238
Shirane, G.–(8) 4802
Shiroishi, Y.–(8) 5648
Shoji, H.–(8) 5564
Shoji, M.–(8) 5907
Shull, C. G.–(8) 5021
Shull, R. D.–(8) 6028
Sides, S. W.–(8) 6482
Sides, Scott W.–(8) 5749
Siegmann, Hans C.–(8) 6488
Siemensmeyer, K.–(8) 5078
Silver, Richard N.–(8) 4632
Silversten, John M.–(8) 5782
Simion, B. M.–(8) 5935, 5991
Simizu, S.–(8) 5949
Simmins, J. J.–(8) 6341
Simmons, R.–(8) 5671
Simon, Ch.–(8) 6173
Sin, Kyusik–(8) 5901
Sinclair, Robert–(8) 6393
Singer, B.–(8) 5102
Singer, Brian–(8) 5841
Singh, David J.–(8) 4515, 4818
Singleton, E. W.–(8) 4590, 4827
Sinha, S. K.–(8) 5857
Sinkovic, B.–(8) 4976
Sinnemann, Th.–(8) 5257
Sivertsen, J. M.–(8) 5277, 5327
Sivertsen, John–(8) 4912
Slavin, A. N.–(8) 5366, 5371, 5724
Smirnov-Rueda, R.–(8) 6479
Smit, P.–(8) 6519, 6526
Smith, Neil–(8) 6254
Smyth, J. F.–(8) 5898
Snowman, Daniel P.–(8) 5087
Snyder, J. E.–(8) 4890
Snyder, R. L.–(8) 6341
Sobolev, V. L.–(8) 5415, 6060
Soeda, M.–(8) 6047
Sohn, J. W.–(8) 5670
Sokoloff, J. B.–(8) 4564
Sokolov, J.–(8) 6025
Solé, R.–(8) 5439
Somasundaram, P.–(8) 5401
Sommer, R. L.–(8) 5139, 6117
Song, K.–(8) 6273
Song, Xing–(8) 4912
Sonier, J. E.–(8) 6636
Sooryakumar, R.–(8) 5387
Souche, Y.–(8) 5266, 6546
Sousa, J. B.–(8) 6246, 6355
Sowers, C. H.–(8) 4524
Spagna, S.–(8) 4926
Spanke, D.–(8) 6508
Speriosu, V. S.–(8) 6295
Spirlet, J. C.–(8) 6361
Spoddig, D.–(8) 4929, 6266
Srinivasan, G.–(8) 5185
Stafford, D. C.–(8) 5958
Stager, C. V.–(8) 6170, 6614
Stampe, P. A.–(8) 6561
Stamps, R.–(8) 4528
Stamps, R. L.–(8) 5387
Stancil, D. D.–(8) 5374
Stashkevich, A. A.–(8) 5371
Staudinger, R.–(8) 5367
Steiner, M.–(8) 5078
Stepanyuk, V. S.–(8) 5129
Sternlieb, B. J.–(8) 4802
Stiefel, B.–(8) 5609
Stiles, M. D.–(8) 4994, 5277, 5805
Stoeffler, D.–(8) 5834
Stolze, Joachim–(8) 4632, 5227
Stoyanov, Plamen–(8) 5841
Stoyonov, P.–(8) 5102
Ström, V.–(8) 5063, 5153, 6583
Ström, Valter–(8) 5860
Ström-Olsen, J. O.–(8) 4605, 4619, 4769, 5136, 5536
Su, Yen-Sheng–(8) 6433
Subbaraman, Kala–(8) 5368
Subramanian, M. A.–(8) 6173
Suemitsu, Katsumi–(8) 5156
Sugawara, Hiroharu–(8) 4721
Sugita, Y.–(8) 5648, 5664, 6451
Sugita, Yutaka–(8) 5576
Sugiyama, S.–(8) 5797
Sugiyama, Y.–(8) 5907
Suh, B. J.–(8) 5084
Suharyana, –(8) 5713
Sui, X.–(8) 4890
Sui, Y. C.–(8) 5525
Sui, Y. X.–(8) 4949
Sun, D. C.–(8) 5440
Sun, J. Z.–(8) 4538, 4546, 4549
Sun, Ji-jun–(8) 5709
Sun, Kunquan–(8) 5733
Sun, X. K.–(8) 5525, 6324
Sundaram, Ramesh–(8) 5916
Sunil, D.–(8) 6025
Suran, G.–(8) 5381
Suresh Babu, V.–(8) 5185, 5230
Suriono, Usman–(8) 5066
Suzuki, E.–(8) 4945
Suzuki, H.–(8) 6467
Suzuki, K.–(8) 5149, 6270
Suzuki, M.–(8) 5648
Suzuki, T.–(8) 4647, 5143, 5327, 5687, 6190
Suzuki, Takanobu–(8) 5224
Suzuki, Takao–(8) 5677
Suzuki, Y.–(8) 5708, 5923, 5926
Suzuya, K.–(8) 6512
Svoboda, P.–(8) 5221, 6361
Swainson, I. P.–(8) 6408, 6411
Swann, C. P.–(8) 5106
Swanson, R.–(8) 5658
Swartzendruber, L. J.–(8) 5315, 6073
Szpunar, J. A.–(8) 5202, 6042

Tagirov, L. R.–(8) 6298
Taguchi, T.–(8) 5655
Takahashi, H.–(8) 5564
Takahashi, Hiromasa–(8) 5576
Takahashi, Koyata–(8) 5677
Takahashi, M.–(8) 5700
Takahashi, Migaku–(8) 5339, 5564
Takahashi, Y.–(8) 6451
Takano, H.–(8) 5648
Takano, K.–(8) 5277, 5919
Takano, Ken-ichi–(8) 5002
Takano, Kentaro–(8) 4932
Takeda, Tsutomu–(8) 4875
Takei, Koji–(8) 5483
Takemura, Y.–(8) 4653, 6542
Takeshita, T.–(8) 5040
Takeuchi, A.–(8) 4836
Takeuchi, A. Y.–(8) 5220
Tako, K. M.–(8) 5767
Talyansky, V.–(8) 4545
Tamari, K.–(8) 4884, 4887
Tan, Minshen–(8) 5012
Tan, Swie-In–(8) 5012
Tanabe, S.–(8) 4999
Tanaka, Atsushi–(8) 5602
Tanaka, C. T.–(8) 6265
Tanaka, M.–(8) 4957, 4967
Tanaka, Satoshi–(8) 5156
Tanaka, Y.–(8) 5655
Tang, F. C.–(8) 4790
Tang, Jinke–(8) 5870
Tang, Li–(8) 5348
Tang, N.–(8) 6321
Tang, Y. Q.–(8) 6580, 6593
Taniguchi, K.–(8) 5318, 6646
Tanuma, Toshio–(8) 6402
Tao, Cuihong–(8) 6627
Tassi, A.–(8) 5745, 5745
Tayaoka, A.–(8) 6016
Tayaoka, E.–(8) 6016
Teh, C. T.–(8) 6060
Tehrani, S.–(8) 5889
Tejada, J.–(8) 4686, 5406, 5439, 6031, 6116, 6516, 6589
Templeton, T. L.–(8) 4635
ter Haar, L. W.–(8) 4715
Terris, B. D.–(8) 5644
Tesiero, James E.–(8) 6146
Teter, J. P.–(8) 6213, 6216, 6234
Tezuka, N.–(8) 6262
Theis-Bröhl, K.–(8) 4531, 4779
Theuss, H.–(8) 4990
Thevenot, J.–(8) 6420
Thibado, P. M.–(8) 5125
Thiel, R. C.–(8) 4593
Tholence, J. L.–(8) 4698
Thomas, G.–(8) 4846, 5935, 5991
Thomas, Gareth–(8) 4932
Thompson, C. V.–(8) 5845
Thompson, J. D.–(8) 4535
Thompson, S. M.–(8) 5593, 6247
Thomson, T.–(8) 5119, 6300
Tian, M. B.–(8) 5440
Tiberto, P.–(8) 4575
Tiefel, T. H.–(8) 5599
Tilak, A. S.–(8) 5551
Tischer, M.–(8) 4983
Tobin, J. G.–(8) 5626
Tognetti, Valerio–(8) 4638
Tokura, Y.–(8) 5288
Tomida, Toshiro–(8) 5443
Tomioka, Y.–(8) 5288
Tomiyama, F.–(8) 5648
Tomka, G. J.–(8) 4599
Toney, M. F.–(8) 5967
Tong, H.-C.–(8) 5645
Tong, Hua-Ching–(8) 4909, 5011, 5012, 5886, 5895
Tonner, B. P.–(8) 5623, 5629
Tonomura, A.–(8) 5075
Tonucci, R. J.–(8) 5303
Torgeson, D. R.–(8) 5084
Torikachvili, M. S.–(8) 6411
Torres, L.–(8) 5422, 5436, 6574
Totland, K.–(8) 4518
Tovar, M.–(8) 5269, 6577
Tran, L.–(8) 4491
Tran, M. Q.–(8) 5854
Tristan, L.–(8) 5826
Troper, Amós–(8) 6345
Trygg, J.–(8) 4983, 5837
Tsai, J. L.–(8) 5964
Tsamakis, D.–(8) 5563
Tsang, C.–(8) 6025
Tsifrinovich, V. I.–(8) 5716
Tsoukatos, A.–(8) 5018, 5446, 5584
Tsuda, H.–(8) 4708
Tsunashima, S.–(8) 6237, 6270
Tsunashima, Shigeru–(8) 5683
Tsutai, A.–(8) 4611
Tsutsumi, K.–(8) 6243
Tuan, H. S.–(8) 5718
Tun, Z.–(8) 4769, 6614
Tun, Zin–(8) 6176
Tuoriniemi, J. T.–(8) 5078
Turkki, T.–(8) 5063, 6583
Tyagi, S.–(8) 5166

Uchizawa, M.–(8) 4999
Uemura, Y. J.–(8) 6636
Ueno, S.–(8) 4705, 4708
Ueno, Shoogo–(8) 4711, 4721
Umehara, I.–(8) 6439

Vaia, Ruggero–(8) 4638
Vajda, Ferenc–(8) 5773
Valanju, A. P.–(8) 6536
Valenzuela, R.–(8) 6539, 6549
van der Heijden, P. A. A.–(8) 5103, 5936
van der Sluijs, A. J.–(8) 4734
van der Zaag, P. J.–(8) 5103, 5936
van de Straat, D. A.–(8) 4593
van de Veerdonk, R. J. M.–(8) 5936
Vandlik, J.–(8) 5742
van Dover, R. B.–(8) 5923, 5926
Van Drent, W. P.–(8) 6190
van Loosdrecht, P. H. M.–(8) 5395
van Schilfgaarde, M.–(8) 4799
Varga, L.–(8) 4995
Varga, Lajos K.–(8) 4811
Vas'ko, V. A.–(8) 4553
Vavra, W.–(8) 6084
Vazquez, M.–(8) 6549
Vázquez, M.–(8) 6539
Vázquez-Vázquez, C.–(8) 5269
Vega, A.–(8) 5834
Veillet, P.–(8) 4554, 5099, 5270, 5848
Vélu, E.–(8) 5270
Velu, E. M. T.–(8) 4496
Venkatesan, T.–(8) 4545, 4552, 4552, 5165, 5166, 5292, 5991
Venus, D.–(8) 4518, 6504
Veres, T.–(8) 6289
Verrucchi, Paola–(8) 4638
Viala, B.–(8) 5005
Victora, R. H.–(8) 6199
Viel, V.–(8) 6158
Vijayaraghavan, R.–(8) 6347, 6349
Virovets, T. V.–(8) 6617
Vitale, S.–(8) 5406
Vittoria, C.–(8) 5739
Vogel, J.–(8) 6497
Vugmeister, B. E.–(8) 6143
Vukajlović, Filip R.–(8) 4555
Vuorinen, R. T.–(8) 5078

Wakiyama, T.–(8) 5564
Waldfried, C.–(8) 5838
Wall, M. A.–(8) 4775
Wallace, W. E.–(8) 5949, 6331
Walmsley, N. S.–(8) 4915
Walser, R. M.–(8) 4933, 4948, 5482, 6306, 6536
Wan, H.–(8) 5504
Wang, C. T.–(8) 4772
Wang, D. S.–(8) 5827
Wang, Dingsheng–(8) 5831
Wang, Fang-Wei–(8) 5713
Wang, G.-C.–(8) 5122
Wang, Geng–(8) 5782
Wang, Guiqin–(8) 5473
Wang, J. Q.–(8) 6126
Wang, J. T.–(8) 4812, 6608
Wang, Jian-Qing–(8) 5587
Wang, Jie–(8) 5193
Wang, Jinghua–(8) 4665, 4668, 6225
Wang, Lien-Chang–(8) 5776
Wang, P. S.–(8) 4712
Wang, Q.–(8) 4929, 6266, 6300
Wang, R. C.–(8) 6593
Wang, S.–(8) 5880
Wang, Shan X.–(8) 5901, 6393
Wang, Shyh-Jier–(8) 5560
Wang, X. Q.–(8) 4812, 5873
Wang, Xindog–(8) 5827
Wang, Xindong–(8) 5831
Wang, Xue-Qin–(8) 5403
Wang, Xun–(8) 5193
Wang, Y.–(8) 4949
Wang, Y. D.–(8) 4949
Wang, Ya-Dong–(8) 5193
Wang, Yu–(8) 5193
Wang, Z.–(8) 6642
Wang, Z. D.–(8) 6255
Wang, Zhigang–(8) 5525, 6639, 6649
Warwick, A.–(8) 5626
Watanabe, K.–(8) 5797
Watanabe, N.–(8) 6077
Watson, M. L.–(8) 5590, 5593, 5605
Weerasooriya, S.–(8) 5674
Wei, D.–(8) 5658
Wei, Dan–(8) 5661
Weinberg, Harold–(8) 4711
Welch, D. O.–(8) 5513, 6470
Welch, David O.–(8) 4848
Welch, M. H.–(8) 4718
Weller, D.–(8) 4922, 4990, 5967
Weller, Dieter–(8) 6488
Wellock, K. P.–(8) 5816
Wendhausen, P. A. P.–(8) 5045
Werder, D. J.–(8) 5923
Werner, S. A.–(8) 4802
Wesseling, E.–(8) 5758
Westerholt, K.–(8) 6298
Westphal, C. H.–(8) 6564
White, R. L.–(8) 5851, 6189
White, R. M.–(8) 5113
White, Robert L.–(8) 5116, 6389
Whitman, L. J.–(8) 5125
Wierman, Kurt W.–(8) 6193, 6206
Wigen, P.–(8) 4528
Wigen, P. E.–(8) 5191, 5378
Wiggins, J.–(8) 5590, 5605
Wildberger, K.–(8) 5129
Willey, R. J.–(8) 5435
Williams, C. M.–(8) 4561
Williams, Damon–(8) 6627
Williams, Gwyn–(8) 6561
Williams, J. M.–(8) 6586
Willis, R. F.–(8) 5626, 5635
Wills, J. M.–(8) 4983, 5837
Wilmers, K.–(8) 5582
Wilson, Robert J.–(8) 5116
Win, W.–(8) 4933, 4948
Winand, J. M.–(8) 6361
Withanawasam, L.–(8) 4827, 4837
Wittborn, J.–(8) 5153
Woicik, J. C.–(8) 5345
Wolf, J. A.–(8) 5622
Wolf, J. K.–(8) 5658
Wolf, Jason–(8) 6331
Wolf, R. M.–(8) 5103, 5936
Wolff, P. A.–(8) 5196
Wong, Bunsen Y.–(8) 6455
Wong, H. K.–(8) 5188, 6279
Wong, K.–(8) 5324
Wongsam, M. A.–(8) 5767
Woollam, John A.–(8) 6193
Wu, Bingyao–(8) 5473
Wu, D. C.–(8) 5159
Wu, Guangheng–(8) 4665, 4668, 6225
Wu, J. M.–(8) 5432
Wu, K. T.–(8) 6285, 6341
Wu, M. D.–(8) 5557
Wu, R.–(8) 5827
Wu, Ruqian–(8) 4783, 6209, 6500
Wu, S. Y.–(8) 6568, 6571
Wu, S. Z.–(8) 5635
Wu, W. D.–(8) 6636
Wu, X. D.–(8) 4535
Wu, Xiaohua–(8) 5473
Wun-Fogle, M.–(8) 6216

Xiao, Gang–(8) 4538, 4546, 4549, 5587, 6126
Xiao, J. Q.–(8) 5306
Xiao, John Q.–(8) 5309
Xiao, Q. F.–(8) 5525
Xiao, Ying–(8) 6267
Xie, K.–(8) 5365
Xing, D. Y.–(8) 6255
Xing, Xinzhi–(8) 5883
Xiong, G. C.–(8) 4545, 4552, 4552, 5165, 5166
Xiong, Q.–(8) 6580, 6593
Xu, Dong–(8) 4998
Xu, J.–(8) 6507
Xu, Jun-Hao–(8) 6267
Xu, Weihua–(8) 5303
Xu, X. L.–(8) 6593
Xu, Y.–(8) 6013, 6137, 6140
Xu, You–(8) 5979
Xu, Zhenghe–(8) 4702
Xue, Y. Y.–(8) 6580

Yahisa, Y.–(8) 5351
Yajima, Y.–(8) 6451
Yakhmi, J. V.–(8) 5260
Yamada, I.–(8) 6167
Yamada, M.–(8) 5507
Yamada, T.–(8) 4653, 6542
Yamada, Y.–(8) 5583
Yamaguchi, M.–(8) 5952
Yamaguchi, Y.–(8) 5452
Yamaguchi, Yasuo–(8) 5238, 5946
Yamakawa, Kiyoshi–(8) 5913
Yamamoto, S.–(8) 4884, 4896
Yamamoto, T.–(8) 5354, 5490, 5907
Yamamoto, Takeshi–(8) 5988
Yamasaki, J.–(8) 6016, 6047
Yamashiro, Y.–(8) 4574
Yamauchi, T.–(8) 5490
Yan, X.–(8) 6013, 6022, 6137, 6140
Yan, Zheng–(8) 6200
Yanagida, Y.–(8) 4611
Yanase, Satoshi–(8) 5362
Yang, Bo–(8) 5755
Yang, C. L.–(8) 5866
Yang, D. P.–(8) 4596
Yang, H. D.–(8) 6571
Yang, H.-N.–(8) 5122
Yang, J.–(8) 4605, 4619, 5536, 5817
Yang, Jun–(8) 5519
Yang, Kun–(8) 5096
Yang, Q.–(8) 5811, 6129
Yang, W. T.–(8) 4790, 6282, 6533
Yang, Z. J.–(8) 5995
Yao, Y. D.–(8) 4790, 4919, 5533, 5599, 6282, 6341, 6533
Ye, M.–(8) 5378
Ye, Weichun–(8) 6048
Ye, Xiao-Guang–(8) 4906, 5886
Yelon, A.–(8) 5136
Yelon, W. B.–(8) 4587, 5522, 5939, 5945, 6315, 6318, 6367
Yewondwossen, M.–(8) 5992, 5995
Yi, J. Y.–(8) 5072
Ying, T. F.–(8) 5557
Yogi, T.–(8) 5358
Yokoi, Hiroyuki–(8) 4721
Yonamine, T.–(8) 5266
Yoneda, Y.–(8) 5770
Yonesu, A.–(8) 4574
Yoo, Yong Goo–(8) 5476
Yoon, Do Y.–(8) 5788
Yoshida, Hideki–(8) 4711
Yoshida, K.–(8) 5664
Yoshida, S.–(8) 4699
Yoshihiro, M.–(8) 5686
Yoshitani, T.–(8) 6392
Yoshizawa, Masami–(8) 5205
Yosida, T.–(8) 6167
You, Y. B.–(8) 5863, 5866
Young, I. R.–(8) 4685
Youssef, J. Ben–(8) 5381
Yu, C. C.–(8) 4750, 6057
Yu, Jinyue–(8) 6048
Yu, M.–(8) 5060
Yu, S. C.–(8) 5153
Yu, Seong Cho–(8) 5476
Yu, X. Y.–(8) 6270
Yu, Yongmin–(8) 4629
Yu. Galkin, V.–(8) 6154
Yuan, Samuel W.–(8) 5886
Yuasa, S.–(8) 4659
Yuen, T.–(8) 6001
Yun, E. J.–(8) 4933, 4948, 5482

Zabe, H.–(8) 6300
Zabel, H.–(8) 4782, 4793, 4929, 6266, 6298
Zamora, Ligia E.–(8) 6155, 6611
Zangwill, A.–(8) 4942, 4994
Zaspel, Craig E.–(8) 5368
Zazo, M.–(8) 5422, 5436, 6574
Zeidler, Th.–(8) 4531, 4782, 4793
Zeller, R.–(8) 5129, 5638
Zeltser, A. M.–(8) 6254
Zeng, X. T.–(8) 5188, 6279
Zeng, Xianglin–(8) 4998
Zhan, Wen-Shan–(8) 5713
Zhan, Wenshan–(8) 4665, 4668, 6225
Zhang, J.–(8) 5113
Zhang, Jian H.–(8) 6627
Zhang, Jianqiang–(8) 5473
Zhang, Jun-Xian–(8) 5528, 5709
Zhang, Kezhao–(8) 5762
Zhang, Q.–(8) 4561
Zhang, S.–(8) 6382
Zhang, S. Y.–(8) 6261
Zhang, Shu–(8) 5227, 6630
Zhang, Shufeng–(8) 4542
Zhang, X.–(8) 5406, 5522
Zhang, X.-G.–(8) 5282
Zhang, X. Q.–(8) 5312
Zhang, X. X.–(8) 4686, 5439, 5440, 6116, 6516, 6589
Zhang, Xijuan–(8) 5979
Zhang, Y. D.–(8) 4596, 5530
Zhang, Z. D.–(8) 5525, 6324
Zhao, B.–(8) 6022, 6137
Zhao, Dai–(8) 6503
Zhao, Jiwan–(8) 5473
Zhao, T.–(8) 6324
Zhao, Wei–(8) 5870
Zhao, X. G.–(8) 5525
Zhao, Xuegen–(8) 4665, 4668, 6225
Zhao, Z. G.–(8) 4626, 6321
Zharnikov, M.–(8) 5618, 6426, 6504
Zheng, Guobao–(8) 5742
Zheng, Qing-Qi–(8) 5162
Zheng, Y.–(8) 4590
Zheng, Y. X.–(8) 4949
Zheng, Yu-Xiang–(8) 5193
Zhong, Lieping–(8) 5831
Zhou, Li–(8) 4528
Zhou, S. M.–(8) 4949
Zhou, Shi-Ming–(8) 5193

Zhou, X. Z.–(8) 6561
Zhu, J.-G.–(8) 5645
Zhu, Jian-Gang–(8) 4906, 4909, 5886, 5892
Zhu, Jian-Xin–(8) 6255
Zhu, Nan-Chang–(8) 6393
Zhu, T.–(8) 5889
Zhu, Yimei–(8) 4848
Ziolo, R.–(8) 6031, 6116
Zoller, I.–(8) 6298
Zou, Liang-Jian–(8) 5162
Zuo, F.–(8) 6586
Zvyagin, A. A.–(8) 5419

AMERICAN INSTITUTE OF PHYSICS 500 Sunnyside Boulevard, Woodbury, NY 11797-2999

The American Institute of Physics (AIP) is a not-for-profit membership corporation chartered in New York State in 1931 for the purpose of promoting the advancement and diffusion of the knowledge of the science of physics and its application to human welfare. In order to achieve our purpose, we serve the sciences of physics and astronomy by serving the member societies, by serving individual scientists, and by serving students and the general public.

As leading scientific publishers, the American Institute of Physics and its Member Societies publish more than one-quarter of the world's research literature in all areas of physics including: general physics, applied physics, chemical physics, geophysics, plasmas and fluids, medical physics, nuclear and particle physics, astronomy, electronics, engineering, crystallograhy, instrument science, materials science, mathematics, acoustics, rheology, optics, and vacuum science. AIP publishes its own archival and translation journals, and provides publishing services to member and other organizations.

Member Societies

The American Physical Society
Judy Franz, Executive Officer
One Physics Ellipse
College Park, MD 20740-3844

Optical Society of America
David W. Hennage, Executive Director
2010 Massachusetts Avenue, N.W.
Washington, DC 20036

Acoustical Society of America
Charles Schmid, Executive Director
500 Sunnyside Blvd., Woodbury, NY 11797-2999

The Society of Rheology
Andrew M. Kraynik, Secretary
Department 1512
Sandia National Labs.
Albuquerque, NM 87185

American Association of Physics Teachers
Bernard V. Khoury, Executive Officer
One Physics Ellipse
College Park, MD 20740-3845

American Crystallographic Association
William L. Duax, Executive Officer
P.O. Box 96, Endicott Station
Buffalo, NY 14205-0096

American Astronomical Society
Peter B. Boyce, Executive Officer
1630 Connecticut Avenue, N.W.
Washington, DC 20009

American Association of Physicists in Medicine
Sal Trofi, Executive Director
One Physics Ellipse
College Park, MD 20740-3846

American Vacuum Society
William D. Westwood, Secretary
Bell-Northern Research, Ltd.
P.O. Box 3511, Station C
Ottawa, Ontario K1Y 4H7, Canada

American Geophysical Union
A. F. Spilhaus, Jr., Executive Director
1630 Connecticut Avenue, N.W.
Washington, DC 20009

Affiliated Societies

American Institute of Aeronautics and Astronautics, American Meteorological Society, American Nuclear Society, ASM International, Astronomical Society of the Pacific, Division of Physical Chemistry of ACS, Engineering Information, Inc., The Geological Society of America, Instrument Society of America, International Association of Mathematical Physicists, International Centre for Diffraction Data, Materials Research Society, Microscopy Society of America, Nuclear and Plasma Sciences Society of IEEE, Physics/Astronomy Section of the Council on Undergraduate Research, Physics Section of AAAS, Society for Applied Spectroscopy, SPIE—The International Society for Optical Engineering.

Corporate Associates: Approximately 175 leading corporations, by their membership, participate in and contribute to the support of AIP.

Publications

Physical Review A · Bernd Crasemann, *Editor,* Physics Dept., University of Oregon, Eugene, OR 97403
Physical Review B · P.D. Adams, *Editor,* The American Physical Society, 1 Research Rd., Box 1000, Ridge, NY 11961
Physical Review C · Sam Austin, *Editor,* Cyclotron Labs., Michigan State University, E. Lansing, MI 48824
Physical Review D · Lowell S. Brown and D.L. Nordstrom, *Editors,* APS, 1 Research Rd., Box 1000, Ridge, NY 11961
Physical Review E · Irwin Oppenheim, *Editor,* Dept. of Chemistry, Massachusetts Institute of Technology, Cambridge, MA 02139
Physical Review Abstracts · Reid Terwilliger, *Editor,* APS, One Physics Ellipse, College Park, MD 20740-3844
Physical Review Letters · J. Sandweiss, G. Basbas, S.G. Brown, and G.L. Wells, *Editors,* APS
APS News · Brian Schwartz, *Editor,* APS, One Physics Ellipse, College Park, MD 20740-3844
Bulletin of The American Physical Society · Brian Schwatz, *Editor,* APS, One Physics Ellipse, College Park, MD 20740-3844
Reviews of Modern Physics · David Pines, *Editor,* Loomis Lab. of Physics, 1110 W. Green St., Urbana, IL 61801
The Journal of the Acoustical Society of America · Daniel W. Martin, *Editor-in-Chief,* 7349 Clough Pike, Cincinnati, OH 45244
American Journal of Physics · Robert H. Romer, *Editor,* 222 Merrill Science Bldg., Box 2262, Amherst College, Amherst, MA 01002
The Astronomical Journal · Paul W. Hodge, *Editor*, Astronomy Dept.FM-20, University of Washington, Seattle, WA 98195
Publications of the Astronomical Society of the Pacific · Howard E. Bond, *Editor,* Space Telescope Science Institute, Baltimore, MD 21218
Bulletin of the American Astronomical Society · Peter B. Boyce, *Editor,* AAS
The Astrophysical Journal · Helmut A. Abt, *Managing Editor,* Kitt Peak National Observatory, Box 26732, Tucson, AZ 85726
The Journal of Chemical Physics · J.C. Light, *Editor,* James Franck Institute, The University of Chicago, Chicago, IL 60637
Journal of Mathematical Physics · Roger G. Newton, *Editor,* Indiana Univ., The Poplars, Rm. 324, Bloomington, IN 47405
Physics of Fluids · A. Acrivos, *Editor,* The Levich Institute, Steinman 202, CCNY, Convent Ave. at 140 St., New York, NY 10031
Physics of Plasmas · Ronald C. Davidson, *Editor,* Plasma Phys. Lab., Princeton Univ., P.O. Box 451, Princeton, NJ 08543
Journal of Applied Physics · Steven J. Rothman, *Editor,* Argonne Natl. Lab., Box 8296, Argonne, IL 60439-8296
Applied Physics Letters · Hartmut Wiedersich, *Editor,* Argonne Natl. Lab., Box 8296, Argonne, IL 60439-8296
Review of Scientific Instruments · Thomas H. Braid, *Editor,* Argonne Natl. Lab., Box 8293, Argonne, IL 60439-8293
Journal of Physical and Chemical Reference Data · Jean W. Gallagher, *Editor,* NIST, MS221/A3223, Gaithersburg, MD 20899
Physics Today · Gloria B. Lubkin, *Editor,* AIP, One Physics Ellipse, College Park, MD 20740-3843
Computers in Physics · Lewis Holmes, *Editor,* One Physics Ellipse, College Park, MD 20740-3843
Chaos · David K. Campbell, *Editor*, Dept. of Physics, University of Illinois–UC, Urbana, IL 61801
Journal of Vacuum Science and Technology A · Gerald Lucovsky, *Editor,* Dept. of Physics, N. Carolina State Univ., Raleigh, NC 27650
Journal of Vacuum Science and Technology B · Gary E. McGuire, *Editor,* MCNC, Research Triangle Park, NC 27709
Surface Science Spectra · C. E. Bryson, *Editor*, Surface/Interface, Inc., Mountain View CA 94041; Gary McGuire, *Editor*, MCNC, NC 27709
Medical Physics · J.S. Laughlin, *Editor,* Memorial Sloan-Kettering Cancer Center, 1275 York Ave., New York, NY 10021
Noise Control Engineering Journal · Alan H. Marsh, *Editor-in-Chief,* DyTec Engineering, Inc., 5092 Tasman Dr., Huntington Beach, CA 92649
Powder Diffraction · Deane K. Smith, *Editor-in-Chief,* Dept. of Geosci. and Mineralogy, Penn State Univ., University Park, PA 16802
AAPT Announcer · Bernard V. Khoury, *Editor,* AAPT, One Physics Ellipse, College Park, MD 20740-3845
The Physics Teacher · Clifford E. Swartz, *Editor,* Phys. Dept., State University of New York, Stony Brook, NY 11794
Journal of Rheology · Arthur B. Metzner, *Editor,* Dept. of Chemical Engineering, University of Delaware, Newark, DE 19716
Journal of the Optical Society of America A · Bahaa E. A. Saleh, *Editor*, 2010 Massachusetts Ave., N.W., Washington, DC 20036
Journal of the Optical Society of America B · Paul F. Liao, *Editor,* 2010 Massachusetts Ave., N.W., Washington, DC 20036
Applied Optics · William T. Rhodes, *Editor-in-Chief,* Dept. of Electr. & Computer Eng., Univ. of Colorado, Boulder, CO 80309-0425
Optics Letters · Peter W. E. Smith, *Editor,* Bellcore, 331 Newman Springs Rd., Red Bank, NJ 07701
Optics and Photonics News · Andrea Pendleton, *Editor,* 2010 Massachusetts Ave., N.W., Washington, DC 20036
Journal of Lightwave Technology · Donald B. Keck, *Editor,* Corning Glass Works, Sullivan Park FR29, Corning, NY 14830
The Journal of Undergraduate Research in Physics · R.E. Adelberger, *Editor,* Physics Dept., Guilford College, Greensboro, NC 27410

AIP Conference Proceedings

Acoustical Physics	JETP Letters	Physics of Atomic Nuclei	Semiconductors
Astronomy Reports	Low Temperature Physics	Physics of the Solid State	Journal of Optical Technology
Astronomy Letters	Optics and Spectroscopy	Plasma Physics Reports	Technical Physics
Crystallography Reports	Physics-Doklady	Physics of Particles and Nuclei	Technical Physics Letters
JETP			

Current Physics Index (CPI), quarterly and annual subject index with abstracts to all the above journals.
General Physics Advance Abstracts (GPAA), semimonthly advance abstracts of AIP-published physics literature.
Searchable Physics Information Notices (SPIN), monthly computer-readable tape of abstracts.
Current Physics Microform (CPM), monthly microfilm edition of all the above journals.
Current Physics Reprints (CPR), on-demand copies of any article in any of the above journals.
Physics Briefs (PB), semimonthly comprehensive index with abstracts to the world literature of physics.
PINET, an online physics information network.

Governing Board 1994–1995

Roland W. Schmitt, *Chair**
Reuben E. Alley
Benjamin Bederson
Roger A. Bell
Marc H. Brodsky *(ex officio)**
Robert L. Beyer*
Patricia E. Cladis
Charles Counselman, III
G. Brent Dalrymple*
Robert L. Dixon
William L. Duax
Judy R. Franz
Roderick M. Grant *(ex officio)**
Joseph E. Greene
David Hennage
David W. Hoffman*
Karen L. Johnston
Frank J. Kerr
Bernard V. Khoury*
Carl Kisslinger
Patricia K. Kuhl
Donald N. Langenberg
Tingye Li
Harry Lustig*
Christopher H. Marshall
Gregory B. McKenna
Duncan T. Moore
Norman F. Ness
C. Robert O'Dell
C. Kumar N. Patel
Burton Richter
Barrett H. Ripin
J. William Rogers, Jr.
Charles E. Schmid*
Benjamin Snavely
A. F. Spilhaus, Jr.
Hugo Steinfink
Richard Stern
Howard G. Voss*
Martin Walt
* executive committee

AIP Officers

Marc H. Brodsky, *Executive Director and CEO*
Roderick M. Grant, *Secretary*
Arthur T. Bent, *Treasurer and CFO*
Theresa C. Braun, *Director of Human Resources*
Darlene Walters, *Vice President, Publishing*
John S. Rigden, *Director of Physics Programs*

Publishing Services

James J. Donohue, *Director Publishing Services*
Edward P. Greeley, *Director Business Development and Society Services*
Douglas LaFrenier, *Director of Marketing*
Peggy Judd, *Director of Information Technology*
Maria Taylor, *Publisher AIP Press*
Carol Fleming, *Manager Publishing II Branch*
Doreene A. Berger, *Manager Journal Production I Division*
Maya Flikop, *Manager Translation Program Division*
Richard Kobel, *Manager Advertising Division*
John T. Scott, *Manager Editorial Operations Division*
Brian Schmitt, *Manager Circulation and Fulfillment Division*
Cheryl Taub, *Manager Composition I Division*
Denise Weiss, *Manager Books and Special Projects*
Janice Wilmot, *Manager Production II Division*

American Institute of Physics

A TRADITION IN PHYSICS PUBLISHING

AIP and Member Society Journals

Acoustical Physics
APS News
*Applied Physics Letters
Applied Physics Letters Online
Astronomical Journal
Astronomy Letters
Astronomy Reports
Bulletin of the American Astronomical Society
Bulletin of the APS
Chaos
Computers in Physics
Crystallography Reports
Current Physics Index
General Physics Advance Abstracts
*Journal of the Acoustical Society of America
*Journal of Applied Physics
*Journal of Chemical Physics
Journal of Experimental and Theoretical Physics
JETP Letters
*Journal of Mathematical Physics
Journal of Physical and Chemical Reference Data
Journal of Rheology
Low Temperature Physics
*Medical Physics
*Physical Review A: Atomic, Molecular and Optical Physics
*Physical Review B: Condensed Matter
*Physical Review C: Nuclear Physics
*Physical Review D: Particles and Fields
*Physical Review E: Statistical Physics, Plasmas, Fluids and Related Interdisciplinary Topics
Physical Review Abstracts
*Physical Review Index
*Physical Review Letters
Physics of Atomic Nuclei
*Physics of Fluids
*Physics of Plasmas
Physics of Particles and Nuclei
Physics of the Solid State
Physics–Doklady
*Physics Today
Plasma Physics Reports
*Powder Diffraction
*Review of Scientific Instruments
*Reviews of Modern Physics
Semiconductors
Surface Science Spectra
Technical Physics
Technical Physics Letters

*available on microfiche

Also Available:

Sample Copies
Sample copies are available to institutions considering a subscription.

Back Volumes
Back volumes are available in print, microfilm or microfiche.

Microform
Journals marked with an asterisk are available on microfilm and microfiche.

Special Discount Rates
Reduced rates are available for a variety of combination subscriptions. For details, contact AIP Circulation and Fulfillment.

Document Delivery
Obtain full-text copies of individual articles from core journals in physics – plus AIP and Member Society books and conference proceedings – through **Articles in Physics.** Documents are sent to you within 24 hours of your order via fax, mail or overnight express. For more information or to order call 1-800-480-PHYS or 415-259-5002. FAX: 415-259-5044. E-Mail: articles@aip.org

Online Access
Abstracts of journals published by AIP and Member Societies are available online in the SPIN database via the commercial service Dialog as well as on PINET, the AIP online information service. PINET also offers a current awareness database, Advance Abstracts, offering abstracts up to three months prior to their journal publication dates. Please call 516-576-2262 for additional information.

Book Program
AIP publishes a full line of monographs, proceedings, texts, and references. For further information in the U.S. and Canada contact William Phillips, Books Customer Service, at (516) 576-2411. Elsewhere, contact Susan Harrison, Oxford University Press, at +44 865-56767

Send orders and inquiries to:
American Institute of Physics
Circulation and Fulfillment
500 Sunnyside Boulevard
Woodbury, NY 11797-2999
Tel. (516) 576-2270
or (800) 344-6902
Fax (516) 576-9704
E-Mail: elecprod@pinet.aip.org

AMERICAN INSTITUTE of PHYSICS